

HANDBOOK OF RADIOACTIVITY ANALYSIS

FOURTH EDITION

VOLUME TWO

RADIOANALYTICAL APPLICATIONS

EDITED BY
MICHAEL F. L'ANNUNZIATA

Handbook of Radioactivity Analysis

Volume 2: Radioanalytical Applications

Fourth Edition

Edited by

Michael F. L'Annunziata

PERPUSTAKAAN PRIBADI AN-NUR SUNARYA

ELSEVIER

ACADEMIC PRESS
An imprint of Elsevier

Academic Press is an imprint of Elsevier
125 London Wall, London EC2Y 5AS, United Kingdom
525 B Street, Suite 1650, San Diego, CA 92101, United States
50 Hampshire Street, 5th Floor, Cambridge, MA 02139, United States
The Boulevard, Langford Lane, Kidlington, Oxford OX5 1GB, United Kingdom

Copyright © 2020 Elsevier Inc. All rights reserved.

No part of this publication may be reproduced or transmitted in any form or by any means, electronic or mechanical, including photocopying, recording, or any information storage and retrieval system, without permission in writing from the publisher. Details on how to seek permission, further information about the Publisher's permissions policies and our arrangements with organizations such as the Copyright Clearance Center and the Copyright Licensing Agency, can be found at our website: www.elsevier.com/permissions.

This book and the individual contributions contained in it are protected under copyright by the Publisher (other than as may be noted herein).

Notices
Knowledge and best practice in this field are constantly changing. As new research and experience broaden our understanding, changes in research methods, professional practices, or medical treatment may become necessary.

Practitioners and researchers must always rely on their own experience and knowledge in evaluating and using any information, methods, compounds, or experiments described herein. In using such information or methods they should be mindful of their own safety and the safety of others, including parties for whom they have a professional responsibility.

To the fullest extent of the law, neither the Publisher nor the authors, contributors, or editors, assume any liability for any injury and/or damage to persons or property as a matter of products liability, negligence or otherwise, or from any use or operation of any methods, products, instructions, or ideas contained in the material herein.

Library of Congress Cataloging-in-Publication Data
A catalog record for this book is available from the Library of Congress

British Library Cataloguing-in-Publication Data
A catalogue record for this book is available from the British Library

ISBN: 978-0-12-814395-7

For information on all Academic Press publications visit our website at https://www.elsevier.com/books-and-journals

Publisher: Susan Dennis
Acquisition Editor: Kathryn Eryilmaz
Editorial Project Manager: Hilary Carr
Production Project Manager: Prem Kumar Kaliamoorthi
Cover Designer: Matthew Limbert

Typeset by TNQ Technologies



Contributors

Nicole Barthe, Univ. Bordeaux, bioingénierie tissulaire, Bordeaux, France; INSERM, bioingénierie tissulaire, Bordeaux, France

Maria Betti, Directorate G - Nuclear Safety and Security, European Commission, DG Joint Research Centre, Karlsruhe, Germany; Formerly at the International Atomic Energy Agency, Environmental Laboratories, Monaco

Ana Cardona (In Memoriam), Institut Pasteur, Paris, France

Nicolas Carvou, Biospace Lab UK, Warwick, United Kingdom

Xiongxin Dai, China Institute for Radiation Protection, Taiyuan, Shanxi Province, China

Oleg B. Egorov, Medvio, LLC, West Richland, WA, United States

Konstantinos Eleftheriadis, Environmental Radioactivity Laboratory, Institute of Nuclear and Radiological Science & Technology, Energy & Safety, N.C.S.R. "Demokritos", Ag. Paraskevi, Attiki, Greece

Rudolf Engelbrecht, Radiochemistry, Seibersdorf Labor GmbH, Seibersdorf, Austria; Currently - Austrian Agency for Health and Food Security, GmbH, Vienna

Mats Eriksson, Swedish Radiation Safety Authority, Department of Radiation Protection, Stockholm, Sweden; Formerly at the International Atomic Energy Agency, Environmental Laboratories, Monaco

William Geist, Los Alamos National Laboratory, Safeguards Science Technology Group, Los Alamos, NM, United States

Željko Grahek, Laboratory for Radioecology, Ruđer Bošković Institute, Zagreb, Croatia

Jay W. Grate, Pacific Northwest National Laboratory, Richland, WA, United States

Agustín Grau Carles, Academia BIC, Madrid, Spain

Agustín Grau Malonda, CIEMAT, Madrid, Spain

Xiaolin Hou, Technical University of Denmark, Department of Environmental Engineering, Roskilde, Denmark; Lanzhou University, School of Nuclear Science and Technology, Lanzhou, China

Philip Hypes, Los Alamos National Laboratory, Hazardous Materials Management Group, Los Alamos, NM, United States

Alexandra Ioannidou, Aristotle University of Thessaloniki, Physics Department, Nuclear Physics Laboratory, Thessaloniki, Greece

Miroslav Ješkovský, Comenius University, Faculty of Mathematics, Physics and Informatics, Department of Nuclear Physics and Biophysics, Bratislava, Slovakia

Jakub Kaizer, Comenius University, Faculty of Mathematics, Physics and Informatics, Department of Nuclear Physics and Biophysics, Bratislava, Slovakia

Ivan Kontul', Comenius University, Faculty of Mathematics, Physics and Informatics, Department of Nuclear Physics and Biophysics, Bratislava, Slovakia

Michael J. Kristo, Lawrence Livermore National Laboratory, Livermore, CA, United States

Michael F. L'Annunziata, The Montague Group, Oceanside, CA, United States

Galina Lujanienė, SRI Center for Physical Sciences and Technology, Vilnius, Lithuania

Serge Maîtrejean, SMTJ Consulting, Paris, France

Monika Müllerová, Comenius University, Faculty of Mathematics, Physics and Informatics, Department of Nuclear Physics and Biophysics, Bratislava, Slovakia

Matthew J. O'Hara, Pacific Northwest National Laboratory, Richland, WA, United States

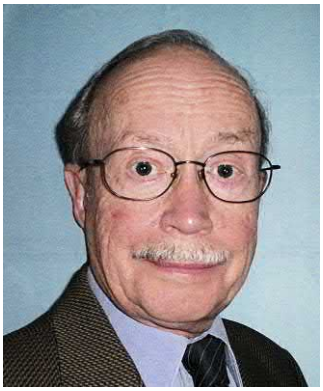
Pavel P. Povinec, Comenius University, Faculty of Mathematics, Physics and Informatics, Department of Nuclear Physics and Biophysics, Bratislava, Slovakia; Formerly at the International Atomic Energy Agency, Environmental Laboratories, Monaco

Peter Santi, Los Alamos National Laboratory, Safeguards Science Technology Group, Los Alamos, NM, United States

Jan Scholten, Institute of Geosciences, Kiel University, Kiel, Germany; Formerly at the International Atomic Energy Agency, Environmental Laboratories, Monaco

Nataša Todorović, University of Novi Sad, Faculty of Sciences, Department of Physics, Nuclear Physics Laboratory, Novi Sad, Serbia

About the Founding Editor



Michael F. L'Annunziata

Michael F. L'Annunziata, PhD, is the founding editor and coauthor of the *Handbook of Radioactivity Analysis*. He majored in chemistry with a BSc degree from St. Edward's University in 1965, and he was awarded MSc and PhD degrees from the University of Arizona, Tucson, in 1967 and 1970, respectively. His graduate thesis research in the 1960s, financed by the then US Atomic Energy Commission, dealt with the analysis of the radionuclides ^{89}Sr and ^{90}Sr and the remediation of soils contaminated with radiostrontium in the event of nuclear fallout, published as a thesis in 1967 (https://repository.arizona.edu/handle/10150/318640). After a short stint in the chemical industry (Amchem Products, Inc, Ambler, Pennsylvania) during 1970–71 as ^{14}C-tracer chemist, he joined the faculty at the Postgraduate College in Chapingo, Mexico, as a professor and thesis advisor during 1972–75, and during 1975–77, L'Annunziata was a senior research scientist at the Nuclear Center of the National Institute of Nuclear Research (ININ), Mexico, where he served also as a thesis research advisor to graduate students of chemistry of the Autonomous University of the State of Mexico in Toluca, Mexico, in the field of radionuclide analysis and applications. During 1977–91, he was a scientific officer in the Departments of Research and Isotopes and Technical Cooperation of the International Atomic Energy Agency (IAEA) in Vienna, Austria, where he served as IAEA Head of Fellowships and Training during 1987–91. From 1977 to 2007, he served as IAEA Expert in fact-finding, planning, and implementation assignments in peaceful applications of nuclear energy for development in more than 50 countries of the world in Asia, Africa, Europe, Latin America, and the Middle East. L'Annunziata was a member of the Board of Governors, International Science Programs at Uppsala University, between 1988 and 1991. His main research interests have been focused on the development of chemical and instrumental methods for the detection and measurement of radioactive nuclides as tracers in research. He was the first to postulate the soil microbial epimerization of myo-inositol to other inositol stereoisomers as a source of the stereoisomers of inositol phosphates in soils (PhD dissertation, 1970, https://dissexpress.proquest.com/dxweb/results.html?QryTxt=&By=L%27Annunziata&Title=&pubnum =) and in 1975 (*SSSA Journal* 39(2), 377–379) and first to demonstrate in 1977, with the use of the radioisotope carbon-14, the soil microbial epimerization of myo-inositol to chiro-inositol as a mechanism involved in the origin of the unique soil inositol phosphate stereoisomers (*SSSA Journal* 41(4), 733–736, https://dl.sciencesocieties.org/publications/sssaj/abstracts/41/4/SS0410040733). The first edition of the *Handbook of Radioactivity Analysis* was planned by L'Annunziata in 1995, and he edited and coauthored the subsequent editions, including the current fourth edition published by Elsevier in 2019. He has authored and coauthored 11 books since 1979 on radionuclide analysis and radiation physics among which his book entitled *Radioactivity: Introduction and History*, First Edition, published by Elsevier in 2007, was included on the Best Sellers List in Physics (*LibraryJournal Academic Newswire*) in 2008. His much expanded Second Edition entitled *Radioactivity: Introduction and History, From the Quantum to Quarks* (https://www.sciencedirect.com/book/9780444634894/radioactivity), published by Elsevier in 2016, was awarded an Honorary Mention in the 2017 PROSE AWARDS in the category of Chemistry and Physics.

Foreword

Radioactive sources play a significant role in promoting human development and health worldwide. Whether through its application to treat cancer, diagnose various diseases, develop new crop varieties, sterilize medical supplies, or provide clean energy, peaceful uses of radioactive sources are ubiquitous in our daily lives. These wide-ranging applications can only be implemented appropriately when radioactivity is measured precisely. Thus, the accurate measurement of nuclear radiation is indispensable for the peaceful applications of radioactive materials. For example, in fields such as nuclear medicine, whether for the treatment or diagnosis of disease, accurate measurements of radionuclides are essential. Dosimetric measurements are the cornerstone of safe and effective radiation therapy for the treatment of cancer whether for brachytherapy, proton beam therapy, or other sources of radiation therapy.

With more than 170 Member States in all continents of the world, the International Atomic Energy Agency (IAEA) serves as the global focal point for nuclear cooperation. The *Handbook of Radioactivity Analysis* will serve Member States as one of many tools available in the application of nuclear science and technology for peaceful purposes. The importance of this guidance is demonstrated by the wide range of areas in which the IAEA supports Member States to contribute to their well-being and development. Such examples include biological sciences research, insect pest control, health, fertilizer and water use efficiency, water resources and the environment including marine science and climate change, radiation technology, neutron diffraction, radiography and activation analysis, radiation processing in industry, radiation protection, nuclear power, nuclear safeguards, radiation preparedness and response, and research in the field of nuclear fusion, among others.

The *Handbook of Radioactivity Analysis* is now in its fourth edition since the successful first edition in 1998. Over the past two decades, this book has expanded in its scope from an initial 12 chapters to the current 22 chapters, encompassing the numerous modern applications and methods of radiation detection and measurement. The chapters in this book are written by experts from 16 countries around the world. This new edition will continue to serve as an important resource in our search to optimize radioactivity measurements both in research and in its applications, leading to the peaceful utilization of radioactive sources for health and development.

May Abdel-Wahab, MD, PhD, FACR
Director, Division of Human Health
Department of Nuclear Sciences and Applications
International Atomic Energy Agency, Vienna

Preface to the fourth edition

In 1996, I proposed to Academic Press the idea of a book that would provide readers with a reference source to state-of-the-art radiation detectors and methods of analysis of radionuclides and other sources of nuclear radiation. Thus, the first edition of this book was published in 1998 as a single volume with only 12 chapters, and the book has expanded in scope and depth over the past two decades with the current fourth edition and its 22 chapters in two volumes.

The numerous advances that have been made since the publication of the previous third edition warranted the partition of the *Handbook of Radioactivity Analysis* into two volumes. It was decided to separate the chapters into two categories, namely, Volume 1, *Radiation Physics and Detectors* and Volume 2, *Radioanalytical Applications*. The two volumes of this book were expanded greatly to provide material, which would serve as a valuable resource in teaching and a reference source to the researcher in his or her unique analytical requirements in the measurement of radioactive materials.

The first chapter in Volume 1, which was previously entitled *Radiation Physics and Radionuclide Decay*, was expanded to almost double in volume with a corresponding change in the chapter title to *The Atomic Nucleus, Nuclear Radiation, and the Interaction of Radiation with Matter*, which includes additional material helpful to supplement the academic curricula and aid in the decisions and calculations made by researchers in their measurement of nuclear radiation and radionuclide analysis. Current principles of operation of all classes of radiation detectors and their applications have been expanded and updated, including semiconductor detectors, gas ionization detectors, liquid and solid scintillation detectors, solid-state nuclear track detectors, Cherenkov detectors, calorimeters and bolometers, as well as advances in atom counting (i.e., mass spectrometry) for the measurement of radioactive and stable nuclides and radiation from other sources such as cosmic radiation, synchrotron radiation, and particle emissions from nuclear reactions.

In light of increased concern for radioactivity in the environment, a chapter was added on the *Analysis of Environmental Radionuclides* in Volume 2. Also, all chapters in Volume 2 have been expanded and updated with material required in the analysis of radionuclides and radiation in our land, air, and water resources, including the marine environment, as well as particle identification and measurement by Cherenkov counting, radiation counting statistics, radionuclide standardization, imaging techniques required in the applications of radionuclides in biological research and nuclear medicine, flow-cell analytical techniques, automation in radiochemical analysis together with analytical techniques required in the fields of nuclear safeguards and nuclear forensics.

Again, we have completed this book as an international effort by drawing upon the expertise of researchers and teachers from 16 countries of the world. Although coming from many branches of science, chapter authors all share one common objective, that being the most accurate measurement of radiation sources and radionuclides both natural and man-made, vital to all branches of science and human development. Readers interested in radiation physics, the applications of radionuclides and radiation sources, and how these have been vital to our well-being and development may refer to another text by the writer entitled "*Radioactivity: Introduction and History, From the Quantum to Quarks*" (ISBN: 978-0-444-63489-4), published in 2016 by Elsevier (https://www.elsevier.com/books/radioactivity/lannunziata/978-0-444-63489-4).

Women are the senior authors of three chapters in this new edition, which is evidence of the increasing role of women as leaders in this field of science. We may expect to see yet in the future an ever-increasing number of women, who will make great advances in this field of science following the pioneering examples of Marie Curie, Lise Meitner, Maria Goeppert-Mayer, Rosalind Franklin, Marietta Blau, and Chien-Shiung Wu, among others.

Mention of commercial products in this book does not imply recommendation or endorsement by the chapter authors or editor. Other or more suitable products may be available. Names of products are included for convenience or information purposes only.

I would like to thank the authors of each chapter, who have covered their fields of expertise with an unwavering commitment to meet the objectives of this book. Acknowledgment is extended to Kathryn Eryilmaz (nee Morrissey),

Aquisition Editor, at Elsevier in Cambridge for approaching me with the suggestion that we consider a fourth edition and for working with me during the planning stage of this book. Many thanks go to Hilary Carr, Elsevier Editorial Project Manager, for her constant support and advice throughout the writing and production of this book. I thank also Ashwathi P. Aravindakshan of Elsevier for her assistance in completing the legal requirements for the publication of this book. Appreciation is also extended to Prem Kumar Kaliamoorthi, Elsevier Production Project Manager, for his meticulous attention to every detail throughout the production process of this book. Thanks are also extended to Susan Dennis, Publisher of Elsevier Chemistry and Chemical Engineering Books, and Mona Zahir, Elsevier Editorial Project Manager, for their guidance and support during this project. Above all, I thank my wife Maria del Carmen (aka Reyna) for her understanding, encouragement, and unflagging patience.

Michael F. L'Annunziata, PhD

Acronyms, Abbreviations, and Symbols

A Mass number
A Ampere (1 A = 1 C/s), amplifier
a Year(s)
Å Angstrom (10^{-10} m = 0.1 nm)
AABW Antarctic Bottom Water
AAIW Antarctic Intermediate Water
AAS Atomic absorption spectrometry
AASI Advanced alpha-spectrometric simulation
ATTA Atom trap trace analysis
ABACC Brazilian–Argentine Agency for Accounting and Control of Nuclear Materials
ABEC aqueous biphasic extraction chromatography
AC Alternating current
ACC Antarctic Circumpolar Current
ACFM Actual cubic feet per minute (28.3 L/min.)
ADC Analog-to-digital converter
ADF Advanced digital filter
ADME Absorption, distribution, metabolism, and excretion
ADS Accelerator-driven subcritical reactor
AEC Automatic efficiency compensation, Atomic Energy Commission
AES Atomic emission spectrometry, Auger electron spectroscopy
AF Agulhas Front
AFM Atomic force microscope
AFS Atomic fluorescence spectrometry
α Alpha particle, internal conversion coefficient
∝ Proportional to
ag Attogram = 10^{-18} g
AGeV GeV per nucleon
AkeV keV per nucleon
A2LA American Association for Laboratory Accreditation
AM β-artemether, arithmetic mean
AMAD Activity median aerodynamic diameter
AMANDA Antarctic Muon and Neutrino Detector Array, South Pole
AMANDE Accelerator for Metrology and Neutron Applications in External Dosimetry, IRSN, France
AMAP Arctic Monitoring and Assessment Programme
AMeV MeV per nucleon
AMP Adenosine monophosphate, ammonium molybdophosphate, amplifier
amp. Amplifier
AMS Accelerator mass spectrometry
amu Atomic mass units
ANDA 7-Amino-1,3-naphthalenedisulfonic acid
ANFESH Ferric potassium hexacyanoferrate on a cellulose carrier
ANITA ANtarctic Impulsive Transient Antenna
ANL Argonne National Laboratory
ANN Artificial neural network
ANSI American National Standards Institute
ANSTO Australian Nuclear Science and Technology Organisation
ANTARES ANTArctic RESearch, Astronomy with a Neutrino Telescope and Abyss Environmental RESearch, Mediterranean Sea
ANZECC Australian and New Zealand Environment Conservation Council
APCI Atmospheric pressure chemical ionization
APD Avalanche photodiode
APDC Ammonium pyrrolidine dithiocarbamate
APE Alkyl phenol ethoxylate
APMP Asia–Pacific Metrology Program
APS Advanced Photon Source, Argonne National Laboratory
AQC Automatic quench compensation
AQCS Analytical Quality Control Services (of IAEA)
AQP(I) Asymmetric quench parameter of the isotope
ARC Agulhas Return Current
ARMCANZ Agriculture and Resource Management Council of Australia and New Zealand
AS Alpha spectrometry
ASTAR Alpha stopping power and range
ASTM American Society for Testing and Materials
atm Atmosphere (standard) = 1.01325×10^5 Pa
at % Atom percent
ATP Adenosine triphosphate
ATSDR Agency for Toxic Substances and Disease Registry
AUV Autonomous underwater vehicle
AWCC Active Well Coincidence Counter
AWE United Kingdom Atomic Weapons Establishment
β Particle relative phase velocity, beta particle
ββ Double-beta decay
β^- Negatron, negative beta particle
β^+ Positron, positive beta particle
b Barn = 10^{-28} m^2 = 10^{-24} cm^2
BAC *N,N′*-bisacrylylcystamine
bar 10^5 N/m^2 = 100×10^3 Pa
BBD 2,5-Di-(4-biphenylyl)-1,3,4-oxadiazole
BBO 2,5-Di(4-biphenylyl)oxazole
BBOT 2,5-Bis-2-(5-t-butyl-benzoxazolyl) thiophene
BCC Burst counting circuitry, Bragg curve counter
BDs Bubble detectors
BDE Bond dissociation energy
BE Binding energy
BEAGLE Blue Ocean Global Expedition
BEGe Broad-energy germanium detector

BGO Bismuth germanate ($Bi_4Ge_3O_{12}$)
BIPM Bureau international des poids et mesures, Sèvres, France
bis-MSB *p*-Bis-(*o*-methylstyryl)benzene
B_K *K*-shell electron binding energy
bkg, BKG Background
BNCT boron neutron capture therapy
BNL Brookhaven National Laboratory, Upton, New York
BOD Biological oxygen demand
BOMARC Boeing Michigan Aeronautical Research Center
BOREXINO BOron EXperiment, solar neutrino detector, Italy
Bq Becquerel = 1 dps
BQM Bqmeter (Consortium BQM, Czech Republic)
BR Branching ratio
BS Backscatter
BSA Bovine serum albumin
BSI The British Standards Institute
BSO Bismuth silicate ($Bi_4Si_3O_{12}$)
BSS Bonner sphere spectrometer, Board of Safety Standards
BT Bound tritium
BTP Bistriazinylpyridine
butyl-PBD 2-(4-t-Butylphenyl)-5-(4-biphenylyl)1,3,4-oxadiazole
BWR Boiling water reactor
c Speed of light in vacuum (2.9979×10^8 m/s)
C Coulomb (1 C = 1 A s)
°C Degrees Celsius
CAI Calcium–aluminum-rich inclusions
CaF_2(Eu) Europium-activated calcium fluoride
CALEX Calorimetry Exchange Program
CAM Continuous air monitoring
CAMAC Computer-automated measurement and control
CANDLES CAlcium fluoride for the study of Neutrinos and Dark matter by Low Energy Spectrometer
CANDU Canadian deuterium uranium reactor
CART Classification and regression tree algorithm
CAVE Counting lAboratory for enVironmental radionuclidEs, Monaco
CC Charged current (interaction), charge comparison, carbonate carbon
CCD Charge-coupled device
CCRI Consultative Committee for Ionizing Radiation
CD ROM Compact disc read-only memory
CDW Circumpolar Deep Water
CE Chemical etching, capillary electrophoresis
CEA Commissariat à l'Energie Atomique
CEFAS Centre for Environment, Fisheries and Aquaculture Science (UK)
CE-ICP-MS Capillary electrophoresis–inductively coupled plasma mass spectrometry
CELLAR Collaboration of European Low-level Underground Laboratories
CENTA Centre for Nuclear and Accelerator Technologies, Bratislava
CERN European Organization for Nuclear Research, Geneva
CET Compton efficiency tracing method
C_F Feedback capacitor
CF Calibration factor, correction factor
CFD Constant fraction discriminator
cfm Cubic feet per minute
CFN Cross-flow nebulizer
CGE Chamber Gram Estimator
Ch Channel
CHEREN2 Anisotropy detection model for Cherenkov counting efficiency
CHU Centre hospitalier universitaire
Ci Curie = 2.22×10^{12} dpm = 3.7×10^{10} dps = 37 GBq
CIAE China Institute of Atomic Energy
CICM Conventional integral counting method
CID Collision-induced dissociation
CIEMAT Centro de Investigaciones Energéticas, Medioambientales y Technológicas, Madrid
CIRIA Construction Industry Research and Information Association
cm Centimeter
cm/d Unit of flux from cm^3/cm^2 per day
CMB Cosmic microwave background
CMOS Complementary metal-oxide-semiconductor
CMPO Octyl(phenyl)-N,N-di-isobutylcarbamoylmethylphosphine oxide
CMX-4 Collaborative Materials Exercise (fourth by the ITWG)
C/N CIEMAT/NIST (efficiency tracing method)
CN Cellulose nitrate
CN* Unstable compound nucleus
CNC Condensation nuclei counter
CNET CIEMAT/NIST efficiency tracing
CNRS Centre National de la Recherche Scientifique, France
CNS Central nervous system
COG Center of gravity
COMPASS Community Pentascale Project for Accelerator Science and Simulation
COTS Commercial off-the-shelf (system)
cph, CPH Counts per hour
cpm, CPM Counts per minute, channel photomultiplier
cps, CPS Counts per second
CR-39 Polyallyldiglycol carbonate plastic SSNTD
CRESST Cryogenic Rare Event Search with Superconducting Thermometers
CRL Compound refractive lens
CRM Certified reference material
CS Calibration source
CSDA Continuous Slowing Down Approximation range
CSIC Instituto de Física Fundamental, Madrid
CsI(Na) Sodium-activated cesium iodide
CsI(Tl) Thallium-activated cesium iodide
CT Computerized tomography
CTBT Comprehensive Nuclear-Test-Ban Treaty
CTBTO Comprehensive Nuclear-Test-Ban Treaty Organization
CTD Conductivity/temperature/density detector
CTF Contrast transfer function
CTFE Chlorotrifluoroethylene
CTR Controlled thermonuclear reactor
cts Counts
CV Core valence
cv Column volume
CWOSL Continuous wave optically stimulated luminescence
CZT Cadmium zinc telluride (semiconductor detectors)
D Deuterium

d Days, deuteron, down quark
$\overline{\mathbf{d}}$ Antidown quark
2D Two-dimensional
DA Destructive analysis
Da Dalton (unified atomic mass unit, also abbreviated as u)
DAC Derived air concentration
DAP Diallyl phthalate
DASE Le Département analyse, surveillance, environnement, France
DATDA Diallyltartardiamide
DBD Double-beta decay
DC Direct current
DCC Digital coincidence counting
dc-GDMS Direct current−glow discharge mass spectrometry
DDCP Dibutyl-N,N-diethylcarbamylphosphonate
DDTC Diethyldithiocarbamate
DE Double escape
DEF Delayed ettringite formation
δ Delta rays
DEMO Demonstration Power Plant (fusion)
DESR Double external standard relation
DESY Deutsches Elektronen Synchrotron
Det. Detector
DF Decontamination factor
DF-ICP-MS Double focusing ICP-MS
DGA Diglycolamide
DIC Dissolved inorganic carbon
DIHEN Direct injection high-efficiency nebulizer
DIM Data interpretation module
dimethyl POPOP 1,4-Bis-2-(4-methyl-5-phenyloxazolyl)benzene
DiMF Decay in a magnetic field (method)
DIN Diisopropylnaphthalene
DIPE Diisopropyl ether
DIPEX Bis(2-ethylhexyl)methane-diphosphonic acid
DIRC Detector of internally reflected Cherenkov light
DJD Diffused junction detector
DLU Digital light units
DMCA Digital multichannel analyzer
DMF Digital microfluidics
DMG Dimethylglyoxime
DMM Direct matrices multiplication
DMSO Dimethyl sulfoxide
DNA Deoxyribonucleic acid
$\mathbf{D_2O}$ Heavy water
DOC Dissolved organic carbon
DOE US Department of Energy
DOELAP Department of Energy Laboratory Accreditation Program
DOM Digital optical module
DOP Dioctyl phthalate
DOT Digital overlay technique
dpm, DPM Disintegrations per minute
dps, DPS Disintegrations per second
DPSD Digital pulse shape discrimination
dpy, DPY Disintegrations per year
DQP Double quench parameter
DRAM Dynamic random access memory
DSA Defined solid angle
DSES Deep sea echo sounder
DSP Digital signal processing
DT Dead time
DTPA Diethylenetriamine pentaacetic acid
DTSA Desktop spectrum analyzer (software)
DU Depleted uranium
DWL Drinking water limit
DWPF Defense waste processing facility
$\boldsymbol{E}$ Counting efficiency, energy
$\boldsymbol{E_b}$ Binding energy
$\mathbf{e^+}$ Positron
$\mathbf{e^-}$ Electron, negatron
$\mathbf{e^-h^+}$ **or** $\mathbf{e-h}$ Electron−hole pair
EBq Exabecquerel (10^{18} Bq)
EC Electron capture, extraction chromatography, European Community, elemental carbon
ECD Effective cutoff diameter
ECDL Extended cavity diode laser
ECE Electrochemical etching
ECR Electron cyclotron resonance
ED Exponential decrease
EDS Energy dispersive spectrometer
EDTA Ethylenediamine tetraacetic acid
EDX Energy dispersive X-ray (spectrometer)
EDXRF Energy dispersive X-ray fluorescence
EESI-MS Extractive electrospray ionization tandem mass spectrometry
EeV Exaelectron volts (10^{18} eV)
$\mathbf{E_F}$ Fermi level
EF Enrichment factor
Eh Oxidation potential
EI Electron impact (e.g., in mass spectrometry)
EIA Enzyme immunoassay
EM Electromagnetic
EMA Extramural absorber
EMCCD Electron multiplier CCD
EML Environmental Measurement Laboratory, USA
EMPA Electron microprobe analysis
ENEA Italian National Agency for New Technologies, Energy and Sustainable Economic Development
ENSDF Evaluated Nuclear Structure Data File
EO Ethylene oxide
EPA US Environmental Protection Agency
EPCRA Emergency Planning and Community Right-to-Know Act
EPR Electron paramagnetic resonance
ERBSS Extended-range Bonner sphere spectrometer
erg Energy unit ($1\ \text{erg} = 6.2415 \times 10^{11}\ \text{eV} = 10^{-7}\ \text{J}$)
ES Elastic scattering, external standard
ESA European Space Agency, Paris; electrostatic analyzer
ESCR External standard channels ratio
ESI Electrospray ionization
ESIR WG Extended SIR Working Group
ESP External standard pulse
ESTAR Electron stopping power and range
esu Electrostatic unit
ET Efficiency tracing
ET-DPM Efficiency tracing disintegrations per minute (method)
ETH Eidgenössische Technische Hochschule, Zurich

ETV-ICP-MS Electrothermal vaporization−inductively coupled plasma mass spectrometry
E_{av} Average energy (beta particle)
E_{max} Maximum energy (beta particle), Compton electron energy maximum
E_{α} Alpha-particle energy
E_p Proton energy
E_{th} Threshold energy
EU European Union
EUChemS European Chemical Society
EURACHEM European organization for traceability of chemical measurements
EURADOS European Radiation Dosimetry Group
EURATOM European Atomic Energy Community
EUROMET European Collaboration in Measurement Standards
eV Electron volt $= 1.602176 \times 10^{-19}$ J $= 1.602176 \times 10^{-12}$ erg)
EXAFS X-ray absorption fine structure
°F Degrees Fahrenheit
FADC Fast analog digital converter
f_C Fraction of contemporary cabon
FDA US Food and Drug Administration
FDG Fluorodeoxyglucose
FDNPP Fukushima Dai-ichi Nuclear Power Plant, Japan
FDNPS Fukushima Dai-ichi Nuclear Power Station, Japan
FEP Full energy peak
FET Field effect transistor
FFF Field flow fractionation
fg Femtogram (10^{-15} g)
FGRM Flow-through gaseous radiochemical method
FI Flow injection
fm Fermi or femtometer (10^{-15} m)
f_M Fraction of modern carbon
fmol Femtomole (10^{-15} mol)
FNTD Fluorescent nuclear track detector
FOM Figure of merit
fov Field of view
***f*p** Fission products
FPGA Field programmable gate array
FSA Flow scintillation analysis
FS-DPM Full-spectrum disintegrations per minute (method)
FT Fission track
FTD Fission track dating
FT-ICR Fourier transform−ion cyclotron resonance
FTIR Fourier transform infrared spectroscopy
FWHM Full width at half-maximum
FWT Free water tritium
FWTM Full width at 10th maximum
g Gram, gluon
G # G-number (Grau's-number, quench-indicating parameter)
γ Gamma radiation
G-8 Group of Eight Countries (IAEA Member States)
GBq Gigabecquerels (10^9 Bq)
GC Gas chromatography
GC/MS Gas chromatography/mass spectrometry
GCR Galactic cosmic rays
GD Glow discharge
GDMS Glow discharge mass spectrometry
GEANT Geometry ANd Tracking Monte Carlo code
Ge(Li) Lithium-compensated germanium
GEM Gas electron multiplier
GEOSECS Geochemical Ocean Sections Programme
GEOTRACES International Study on Marine Biogeochemical Cycling of Trace Elements and their Isotopes
GERDA GERmanium Detector Array
GeV Gigaelectron volts (10^9 eV)
GHz Gigahertz (10^9 Hz)
GICNT Global Initiative to Combat Nuclear Terrorism
GIS Geographical Information System
GISP Greenland Ice Sheet Projects
GLOMARD Global Marine Radioactivity Database
GLP Good laboratory practice
GM Geiger−Müller
GM-APD Geiger-mode avalanche photodiode
GPa Gigapascal
GPC Gas proportional counting (counter)
GPD Geometric progression decrease
CPG Coplanar grid
GPS Global positioning system
GRB Gamma ray burst
GS-20 Glass scintillator
GSD Geometric standard deviation
GSI Gesellschaft für Schwerionenforschung mbH, Darmstadt, Germany
GSO:Ce Cerium-activated gadolinium orthosilicate (Gd_2SiO_5:Ce)
GUM Guide to the Expression of Uncertainty in Measurement
GW Groundwater, gate width
GW_e Gigawatt electrical (10^9 W_e)
Gy Gray (1 Gy $= 1$ J/kg $= 6.24 \times 10^{12}$ MeV/kg)
GZK Greisen-Zatsepin-Kuz'min process of *proton-photon* interactions
h Hours
h Plank's constant (6.626×10^{-34} J s), hours
$\hbar$ Plank's constant reduced ($h/2\pi$)
***H* #** Horrock's number (quench indicating parameter)
HBT 2-(2-Hydroxyphenyl)-benzothiazole
HDE Heat distribution error
HDEHP Bis(2-ethylhexyl)phosphoric acid
HDPE High-density polyethylene (moderator)
HEDPA 1-Hydroxyethane-1,1-diphosphonic acid
HEN High efficiency nebulizer
HEP High-energy particle
HEPES N-2-hydroxyethylpiperazine-N′-2-ethanesulfonic acid
HERA-B RICH Particle detector of the Hadron-Elektron-Ring-anlage, Hamburg, Germany
HERM High-energy radio monitor
HEU Highly enriched uranium
HEX-ICP-MS Hexapole collision cell ICP-MS
HEX-ICP-QMS Hexapole collision cell quadrupole mass spectrometry
3HF 3-Hydroxy flavone
hg Hectograms (10^2 g)
h-index Hirsh index
HIBA Hydroxy-i-butyric acid
HKG Housekeeping gene
HLNC High-level neutron coincidence counter
HLW High-level waste

HPB High-pressure Bridgman
HPGe High-purity germanium
HPIC High-performance ionic chromatography
HPLC High-performance liquid chromatography
HPMT Hybrid photomultiplier tube
HRAS High-resolution alpha spectrometry
HRGS High-resolution gamma spectrometry
HR-ICP-MS High-resolution inductively coupled plasma mass spectrometry
HT High tension
HV High voltage
HWHM Half width at half-maximum
HWZPR Heavy water zero power reactor
Hz Hertz (cycles per second)
$\mathbf{i_{in}}$ Current pulse
IAEA International Atomic Energy Agency, Vienna
IAEA-EL IAEA Marine Environment Laboratory, Monaco
IC Internal conversion, ion chromatography
ICC Ice condenser chamber
IC-ICP-MS Ion chromatography−inductively coupled plasma mass spectrometry
IC# Isotope center number
IceCube Neutrino Observatory, South Pole
IceTop Surface array of stations for IceCube
ICF Inertial confinement fusion
ICP Inductively coupled plasma
ICP-CC-QMS Quadrupole inductively coupled plasma mass spectrometry with hexapole collision cell
ICP-FT-ICR-MS Inductively coupled plasma Fourier transform ion cyclotron resonance mass spectrometry
ICP-MS Inductively coupled plasma mass spectrometry
ICP-OES Inductively coupled plasma optical emission spectrometer (spectra)
ICP-QMS Inductively coupled plasma quadrupole mass spectrometry
ICP-SFMS Double-focusing sector field inductively coupled plasma mass spectrometry
ICRP International Commission on Radiological Protection
ICRU International Commission on Radiation Units and Measurements
ID or i.d. Inner diameter, inner detector
IDA Isotope dilution analysis
IDMS Isotope dilution mass spectrometry
ID-TIMS Isotope dilution thermal ionization mass spectrometry
IE Ion exchange
IEC International Electrotechnical Commission, inertial electrostatic confinement
IECF Inertial electrostatic confinement fusion
IEEE Institute of Electrical and Electronics Engineers
IEF Isoelectric focusing gel electrophoresis
IFIN-HH Horia Hulubei National Institute of Physics and Nuclear Engineering, Romania
IGPC Internal gas proportional counting
IL-5 Interleukin-5
IMS International Monitoring System of the CTBT
in. Inch = 2.54 cm = 25.4 mm
INES International Nuclear and Radiological Event Scale
INFN Instituto Nazionale di Fisica Nucleare (Italy)
INGE International Noble Gas Experiment
INP Institute of Nuclear Physics, Tirana, Albania
IN2P3 Institut National de Physique Nucléaire et de Physique des Particules, France
INSERM Institut national de la santé et de la recherché médicale. France
I/O Input/output
IPA Instrument performance assessment, isopropyl alcohol
IPRI Laboratoire Primaire des Rayonnements Ionisants, France
IPT Intramolecular proton transfer
IR Infrared (spectroscopy)
IRA Institut Universitaire de Radiophysique, Lausanne, Switzerland
IRMM Institute for Reference Materials and Measurements, Geel
IRMS Isotope ratio mass spectrometry
IRSN Institute of Radiation Protection and Nuclear Safety, France
IS Internal standard
ISH *In situ* hybridization
ISO International Organization for Standardization
ISOCS In-Situ object calibration software
IS-SCR Internal standard and sample channels ratio
IT Isomeric or internal transition
ITER International Thermonuclear Experimental Reactor
ITU Institute for Transuranium Elements, Europe
ITWG Nuclear Forensics International Technical Working Group
IUPAC International Union of Pure and Applied Chemistry
IUPAP International Union of Pure and Applied Physics
J Joule = 1 N m = 1 kg m^2/s^2 = 1 W s
JAERI Japan Atomic Energy Research Institute
JET Joint European Torus reactor
JFET Junction field effect transistor
JCGM Joint Committee for Guidelines in Metrology
JINR Joint Institute for Nuclear Research, Dubna, Moscow Oblast
JRC Joint Research Centre (of European Commission)
$\boldsymbol{K}$ particle kinetic energy
$\boldsymbol{K^+}$, $\boldsymbol{K^-}$, $\boldsymbol{K^0}$ Kaons or K mesons
K Degrees Kelvin
ka Kiloannum (10^3 years)
KamLAND Kamioka Liquid Scintillator Anti-Neutrino Detector, Japan
KATRIN Karlsruhe TRItium Neutrino experiment
kBq Kilobecquerels (10^3 Bq)
KCFC Potassium cobalt ferrocyanide
kcps Kilocounts per second
KCRV Key comparison reference value
KEK The High Energy Accelerator Research Organization, Japan
keV Kiloelectron volts (10^3 eV)
kg Kilograms
kGy Kilogray
kHz Kilohertz
km.w.e km-water-equivalent
KNN k nearest neighbor algorithm
KRISS National Metrology Institute of Korea
KSTAR Korea Superconducting Tokamak Advanced Research fusion reactor
kt Kilotons
kV Kilovolts (10^3 V)
kW Kilowatts (10^3 W)
ky Kiloyears (10^3 y)

L, l Liters
LA Linear anode
LAAPD Large area avalanche photodiode
LAB Linear alkyl benzene, dodecylbenzene
LA-ICP-MS Laser ablation inductively coupled plasma mass spectrometry
LA-MC-ICP-MS Laser ablation multiple collector ICP-MS
λ Wavelength, decay constant, microliter (10^{-6} L), free parameter
λ_{nr} Nonrelativistic wavelength
λ_r Relativistic wavelength
LAMMA Laser microprobe mass analysis
LAN Local area network
LANL Los Alamos National Laboratory
LAr Liquid argon
LARA laser-assisted isotope ratio analysis
LAW Low-activity waste
LBD Ligand-binding domain
LBNL Lawrence Berkeley National Laboratory
LC Liquid chromatography
LCDW Lower circumpolar deep water
LCMS Liquid chromatography mass spectrometry
LD_{50} Median lethal dose
LED Light-emitting diode
LEGE Low-energy germanium detector
LENA Low-energy neutrino astrophysics detector
LET Linear energy transfer
LEU Low enriched uranium
LHCb RICH Large Hadron Collider beauty experiment detector at CERN
LHD Large Hadron Collider
LiI(Eu) Europium-activated lithium iodide
LIMS Laboratory Information Management System
LINAC or linac Linear accelerator
LIST Laser ion source trap
LL Lower level
LL-BSS Large ^{6}LiI(Eu) Bonner sphere spectrometer
LLC Liquid (mobile)−liquid (on solid phase) chromatography
LLCM Low-level count mode
LLD Lower limit of detection, lower level discriminator
LLE Liquid−liquid extraction
LLNL Lawrence Livermore National Laboratory
LLR Long-lived radionuclide
LMD Laser microdissection
LM-OSL Linear modulation optically stimulated luminescence
LN_2 Liquid nitrogen
LNE Laboratoire National de Métrologie et de E'ssais, France
LNGS Laboratori Nazionali del Gran Sasso, Italy
LNHB Laboratoire National Henri Becquerel, Saclay
LNMRI National Metrology Laboratory of Ionizing Radiation, Brazil
LOD Limit of detection
LOV lab-on-valve (system)
lp Line pairs
LPB Low-pressure Bridgman
LPI low-pressure cascade impactor
LPRI Laboratoire Primaire des Ionizants, Paris
LPS Lipopolysaccharide
LRAD Long-range alpha detector
LS Liquid scintillation, liquid scintillator, "linear-to-square" curve
LSA Liquid scintillation analysis (analyzer)
LSC Liquid scintillation counting (counter)
LSO Cerium-activated lutetium oxyorthosilicate ($Ce:Lu_2SiO_5$)
LSS Liquid scintillation spectrometer
LTC Live-time correction
LuAP Cerium-activated lutetium aluminum perovskite ($Ce:LuAlO_3$)
LY Light yield
LXe Liquid xenon
M Molar (solution concentration)
m Particle mass
m_0 Particle rest mass
m_r Speed-dependent particle mass
m Mass, meters, minutes
mA Milliampere (10^{-3} ampere)
Ma Megayear (10^{6} years)
mAbs Monoclonal antibodies
MACS Magnetically assisted chemical separations
MALDI Matrix-assisted laser desorption/ionization
MAPD Micropixel avalanche photodiode
MAPMT Multianode photomultiplier tube
MARG Microautoradiography
MARIS Marine information system
MARSSIM Multi-Agency Radiation Survey and Site Investigation Manual
MATLAB MATrix LABoratory (numerical computing and programming language)
mb Millibarn (10^{-3} b)
mBq Millibecquerels (10^{-3} Bq)
MBq Megabecquerels (10^{6} Bq)
mCi Millicurie (10^{-3} Ci) = 2.22×10^{9} dpm = 3.7×10^{7} dps = 37 MBq
MC Multiple ion counting
MCA Multichannel analyzer
MCF Moving curve fitting
MC-ICP-MS Multiple ion collector-ICP-MS
MCN Microconcentric nebulizer
MCNP Monte Carlo N-Particle code
MCNP-CP Monte Carlo N-Particle-Correlated Particle code
MCP Microchannel plate
MCP-PM Microchannel plate photomultiplier
MC-TIMS Multiple collector thermal ionization mass spectrometry
MD Molecular dynamics
MDA Minimal detectable activity
MDOA Methyldiooctylamine
METAS Federal Institute of Metrology, Berne-Wabern, Switzerland
METEPC Multielement tissue-equivalent proportional counter
MeV Megaelectron volts
MeVee Electron equivalent energy
MHSP Microhole and strip plate (imager)
MHz Megahertz (10^{6} Hz)
MIBK Methyl isobutyl ketone
MICAD Microchannel Array Detector
MICM Modified integral counting method
MICROMEGAS Micromesh gas detector
mg Milligram (10^{-3} g)
mGy Milligray

MIBK Methyl isobutyl ketone
min Minutes
mK MilliKelvin (10^{-3} K)
mL, ml Milliliter (10^{-3} L)
MLR Multiple linear regression
mM Millimolar (10^{-3} M)
mm Millimeter (10^{-3} m)
MM Magnetic monopoles
MMAD Mass median aerodynamic diameter
MMC Metallic magnetic calorimeter
mmol Millimole (10^{-3} mol)
MNP Magnetic nanoparticle
mol Mole (gram-molecular weight)
MΩ Megaohm (10^{6} Ω)
MOX Mixed oxide fuel
MP Multipurpose
M-P Mandel and Paule mean
MPa Megapascal (10^{6} Pa)
MPGD Micropattern gas detector
MPPC Multipixel photon counter
mrad Millirad (1 mrad = 10 μGy)
MRI Magnetic resonance imaging
mRNA Messenger RNA
MS Mass spectrometry
ms, msec Milliseconds (10^{-3} s)
MSAP Microscale sample automation platform
MSB Methylstyrylbenzene
MSC Microplate scintillation counting
MSD Mean standard deviation
MSE Multisite events
MSGC Microstrip gas counter
MSI Mass spectrometry imaging
MS/MS Tandem mass spectrometry
mSv Millisievert
MW Megawatt (10^{6} W)
Mt Megaton (10^{6} t)
MTO Magnetooptical trap
μ^+, μ^- Muons
μ Attenuation coefficient
μA Microampere (10^{-6} A)
μCi Microcurie (10^{-6} Ci) = 2.22×10^{6} dpm = 3.7×10^{4} dps = 37 kBq
μg Microgram (10^{-6} g)
μL Microliter (10^{-6} L)
μm Micrometer (10^{-6} m)
μPIC Micropixel gas chamber
μs, μsec Microseconds (10^{-6} s)
μ-XANES Microfocused X-ray absorption near edge structure
μ-XRF Microfocused X-ray fluorescence
MEK Methyl ethyl ketone
MW Megawatt (10^{6} W)
MWe Megawatt electrical
m.w.e. Meter water equivalent
MWPC Multiwire proportional chamber
MV Megavolts (10^{6} V)
MVC Multivariate calibration
N Newton = 1 kg m/s^2
N Neutron number
n Neutron
n Index of refraction
NA Avogadro's constant (6.022×10^{23}/mol)
nA Nanoampere (10^{-9} A)
NAA Neutron activation analysis
NAC *N*-acetylcystein
NADW North Atlantic Deep Water
NaI(Tl) Thallium-activated sodium iodide
NARC Neutrino Array Radio Calibration
NASA National Aeronautics and Space Administration, Washington, D.C.
NBL New Brunswick Laboratory of the US DOE
NBR Natural background rejection
NBS National Bureau of Standards (now NIST)
NC Neutral current (interaction)
NCD Neutral current detector
nCi Nanocurie (10^{-9} Ci)
NCM Normal count mode
NCRP National Council on Radiation Protection and Measurements
NDA Nondestructive analysis
NEA Nuclear Energy Agency of the OECD
$N_{e/h}$ Number of electron−hole pairs
NEMO Nautic Environment Marine Observatoire
NE-OBT Nonexchangeable organically bound tritium
NF-LA-ICP-MS Near-field laser ablation inductively coupled plasma mass spectrometry
ng Nanograms (10^{-9} g)
NHMRC National Health and Medical Research Council, Australia
NIDW North Indian Deep Water
NIM Nuclear instrument module
NIMH Nickel metal hydride
NIST National Institute of Standards and Technology, Gaithersburg
nm Nanometer (10^{-9} m)
NMI National Metrology Institute
NMM Neutron moisture meter
NMR Nuclear magnetic resonance
NNDC National Nuclear Data Center
NOI Nuclide of interest
NORM Naturally occurring radioactive materials
NP Nanoparticle
NPD 2-(1-Naphthyl)-5-phenyl-1,3,4-oxadiazole
NPE Nonyl phenol ethoxylate
NPL National Physical Laboratory, UK
NPO 2-(1-Naphthyl)-5-phenyloxazole
NPP Nuclear power plant
NRC United States Nuclear Regulatory Commission
ν Neutrino, photon frequency, particle velocity
$\overline{\nu}$ Antineutrino
$0\nu\beta\beta$ Neutrinoless double-beta decay
$2\nu\beta\beta$ Two-neutrino double-beta decay
nM Nanomolar (10^{-9} M)
nm Nanometer (10^{-9} m)
NMM Neutron moisture meter
NMR Nuclear magnetic resonance
NNDC National Nuclear Data Center, BNL, Upton, New York
NNFL National nuclear forensics library
NORM Naturally occurring radioactive material

NPT Nonproliferation Treaty
NRC Nuclear Regulatory Commission
ns, nsec Nanosecond (10^{-9} s)
NSTAR Neutron sandwich transmitter/activation-γ radiator
NT200 Neutrino telescope, Lake Baikal, Siberia
NTD-Ge Neutron transmutation-doped Ge
N-TIMS Negative ion thermal ionization mass spectrometry
NTP Normal temperature and pressure
NTS Nevada test site
NU Natural uranium
NUDAT Nuclear Database of the NNDC
NWT Nuclear weapons test
N/Z Neutron/proton ratio
OC Organic carbon
OD or o.d. Outer detector, outer diameter
OECD Organization for Economic Cooperation and Development
OES Optical emission spectrometry
OFHC Oxygen-free high thermal conductivity
OGE Optogalvanic effect
OHM National Office of Measurement, Budapest
OLLSC Online liquid scintillation counting
OM Optical module
OSL Optically stimulated luminescence
OTPC Optical time projection chamber
P Parity quantum number
p Particle momentum
p, p^+ Proton
Pa Pascal = 1 N/m^2 = 1 $kg/m \cdot s^2$
PAC Pulse amplitude comparison (comparator)
PADC Polyallyldiglycol carbonate
PAGE Polyacrylamide gel electrophoresis
PAN Polyacrylonitrile
PANDA Particles and nondestructive analysis
PAW Physics Analysis Workstation
PAZ Partial annealing zone
PBBO 2-(4′-Biphenylyl)-6-phenylbenzoxazole
PBD 2-Phenyl-5-(4-biphenylyl)-1,3,4-oxadiazole
PBO 2-(4-Biphenylyl)-5-phenyloxazole
PBq Petabecquerel (10^{15} Bq)
PBS Phosphate buffered saline
PC Proportional counter(ing), personal computer, paper chromatogram, polycarbonate
PCA Principal component analysis
PCB Polychlorinated biphenyl
pCi Picocurie (10^{-12} Ci)
PCR Principle component regression
PD Photodiode
PDA Pulse decay analysis
PDB Pee Dee Belemnite (standard)
PDD Pulse decay discriminator
PE Phosphate ester, polyethylene
PEC Power and event controller
PENELOPE PENetration and Energy Loss of Positrons and Electrons Monte Carlo code
PERALS Photon Electron Rejecting Alpha Liquid Scintillation
PET Positron emission tomography, polyethylene terephthalate
PETAC Pentaerythritol tetrakis allyl carbonate
PeV Petaelectron volts (10^{15} eV)
pF Picofarad (10^{-12} F)
PF Polar front
PFA Perfluoroalkoxy
PFZ Polar frontal zone
pg Picogram (10^{-12} g)
PGA Pulse gradient analysis
ph Photons
PHA Pulse height analysis
PHITS Particle and heavy ion transport code system
PHOSWICH PHOSphor sandWICH (detector)
π Pi constant = 3.14159
π^+, π^-, π^0 Pions or pi mesons
PI Polyimide, pressurized injection
PID Particle identification
PIM Parallel ionization multiplier
PIMS Positive-ion mass spectrometry
PIPS, PIPSi Passivated implanted planar silicon
PIXE Proton-induced X-ray emission
PKC Protein kinase C
PLC Proportional long counter
PLI Pulse length index
PLS Partial least squares
PLS-DA Partial least squares discriminant analysis
PLSR Partial least squares regression
PM Photomultiplier, particulate matter
PMM Power-moderated weighted mean
PMBP 1-Phenyl-3-methyl-4-benzoylpyrazolone-5
pMC Percent modern carbon
PMMA Polymethylmethacrylate
PMP 1-Phenyl-3-mesityl-2-pyrazoline
PMT Photomultiplier tube
PN Pneumatic nebulizers
PNNL Pacific Northwest National Laboratory
PNX Pacific Northwest eXtraction system
POM Polyoxymethylene
POPOP 1,4-Bis-2-(5-phenyloxazolyl)benzene
PPAC Parallel plate avalanche chamber
ppb Parts per billion
PPC P-type point contact
PPD 2,5-Diphenyl-1,3,4-oxadiazole
PPE Personal protective equipment
ppm Parts per million
ppmw Parts per million by weight
PPO 2,5-Diphenyloxazole
PS Plastic scintillator, polystyrene
ps Picosecond (10^{-12} s)
PSA Pulse shape analysis
PSD Pulse shape discrimination
PSf Plastic scintillator foils
psi 6.895×10^3 Pa = 68.95×10^{-3} bar = 51.715 torr
PSL Photostimulable light (or luminescence)
PSm Plastic scintillator microspheres
PSPC Position-sensitive proportional counter
PSr Plastic scintillator resins
PSUP Photomultiplier SUPport structure
P/T Peak-to-total ratio
PTB Physikalisch-Technische Bundesanstalt, Braunschweig
PTBT Partial Test-Ban Treaty

PTFE Polytetrafluoroethylene
P-TIMS Positive ion thermal ionization mass spectrometry
PTP *p*-Terphenyl
PUR Pileup rejector
PUREX Plutonium URanium EXtraction
PVC Polyvinyl chloride
PVD Physical vapor deposition
PVDF Polyvinyldifluoride
PVT Polyvinyl toluene
PWR Pressurized water reactor
PXE Phenyl-ortho-xylylethane
Q *Q* value of nuclear reactions
QA Quality assurance
QC Quality control
QC-CPM Quench-corrected count rate
QCD Quantum chromodynamics
QD Quadrupole
QDC Charge-to-digital converter
QE Quantum efficiency
QIP Quench-indicating parameter
QWBA Quantitative whole-body autoradiography
R Roentgen ($1R = 2.58 \times 10^{-4}$ C/kg)
RAC Radon activity concentration
rad Radiation-absorbed dose (1 rad = 10 mGy = 100 erg/g)
RAD Radon-in-air monitor
RAST Radioallergosorbent test
RBE Relative biological effectiveness
RDC Remote detector chamber
RDD Radiological dispersal device ("dirty bomb")
RE Recovery efficiency
REE Rare earth elements
REFIT Radialelectron fluence around ion tracks
REGe Reverse-electrode coaxial Ge detector
REL Restricted energy loss
rem Roentgen equivalent mammal (1 rem = 10 mSv)
RF Radiofrequency
$\mathbf{R_F}$ Feedback resister
RFQ Radiofrequency quadruple
RH Relative humidity
$\boldsymbol{\rho}$ Density (g cm^{-3}), neutron absorption cross section, resistivity
RIA Radioimmunoassay
RICE Radio Ice Cherenkov Experiment
RICH Ring imaging Cherenkov (counters/detectors)
RIMS Resonance ionization mass spectrometry
RIS Resonant ionization
RM Reference material
RMS Rosette multibottle samplers
RMT Radiometric technique
RNA Ribonucleic acid
Ro5 Ring of Five (European radionuclide monitoring labs)
ROI Region of interest (spectral)
ROSEBUD The Rare Objects Search with Bolometers UndergrounD collaboration
ROV Remotely operating vehicle
RPC Resistive plate chamber
RPH Relative pulse height
RSC Renewable separation column, relative sensitivity coefficient
RSD Relative standard deviation
RSF Relative sensitivity factor
RST Reverse spectral transform
s Seconds
SAF Subantarcticfront
SAH *S*-adenosyl-homocysteine
SalSa Salt sensor array
SAM Standard analysis method, *S*-adenosyl-methionine
SAMAD Surface area mean aerodynamic diameter
SAS Semiconductor α-spectrometry
SBD Surface barrier detector
SCA Single channel analyzer
SCC Software coincidence counting, squamous cell carcinoma
SCI Science Citation Index
SCR Sample channels ratio, solar cosmic rays
SCX Strong cation exchange
SD Standard deviation
SDCC Simplified digital charge comparison
SDD Silicon drift detector
SDP Silicon drift photodiode
SDT Shared dead time
SE Single escape, secondary electron
sec Seconds
SEC Size exclusion chromatography
SEGe Standard electrode coaxial Ge detector
SEM Scanning electron microscopy
SF Spontaneous fission
SFC Supercritical fluid extraction
SFD Scintillation fiber detector
SF-ICP-MS Sector field−inductively coupled plasma mass spectrometry
SFU Stacked filter unit
SGD Submarine groundwater discharge
SHE Superheavy elements
SHOTS Southern Hemisphere Oceans Tracer Studies
SHRIMP Sensitive high mass resolution ion microprobe
SI International System of Units, sequential injection, spray ionization
SIA Sequential injection analysis
SIE Spectral index of the external standard
$\boldsymbol{\sigma}$ Reaction cross section, thermal neutron cross section
Si(Li) Lithium-compensated silicon
SIMS Secondary ionization mass spectrometry
Si PIN Silicon p-i-n diode
SiPM Silicon photomultiplier
SIR International Reference System (Système Internationale de Référence)
SI-RSC Sequential injection renewable separation column
SIS Spectral index of the sample
SJD Silicon junction detector
SLAC Stanford Linear Accelerator Center
SLIM System for Laboratory Information Management
SLM Standard laboratory module
SLSD Scintillator-Lucite sandwich detector
SMAD Surface median aerodynamic diameter
SMDA Specific minimum detectable activity
S/N Signal-to-noise
SNAP Systems Nuclear Auxiliary Power
SNICS Source of Negative Ions by Cesium Sputtering

SNF Spent nuclear fuel
SNM Special nuclear material
SNMS Secondary neutral mass spectrometry
SNO Sudbury Neutrino Observatory, Canada
SNR Signal-to-noise ratio
SNS Spallation neutron source
SNTS Semipalatinsk nuclear test site, Eastern Kazakhstan
SOA Secondary organic aerosol
SOI Silicon-on-insulator
SOP Standard operating procedure
SPA Scintillation proximity assay
SPC Single photon counting
SPD Self-powered detector
SPE Single photon event, solid phase extraction, solid polymer electrolyte
SPECT Single photon emission computed tomography
SPME Solid phase microextraction
SQM Strange quark matter
SQP(E) Spectral quench parameter of the external standard
SQP(I) Spectral quench parameter of the isotope
SQS Self-quenched streamer
SQUID Superconducting quantum interference device
SR Superresolution, synchrotron radiation
sr Steradian
SRAM Static random access memory
SRM Standard reference material
SRS Savannah River Site
SSB Silicon surface barrier detector
SSDD Segmented silicon drift detector
SSE Single site events
SSM Standard service module, selective scintillating microsphere
SSNTD Solid-state nuclear track detector
ST Supersensitive
STD Shared dead time concept
STE Self-trapped excitation
STF Subtropical front
STM Scanning tunneling microscope
STNTD Solid-state nuclear track detection (detectors)
STP Standard temperature and pressure
STS Semipalatinsk test site
STUK Radiation and Nuclear Safety Authority, Finland
Sv Sievert (1 Sv = 1 Gy = 100 rem = 1 J/kg)
SVOC Semivolatile organic carbon
t Ton(s)
$t_{1/2}$, $T_{1/2}$ Half-life
T Particle kinetic energy
T Tritium, tesla = 1 V s/m^2
TAEK Turkish Atomic Energy Authority
TALSPEAK Trivalent Actinide–Lanthanide Separation by Phosphorus Extractants and Aqueous Komplexants process
TAR Tissue–air ratio
TAT Targeted alpha therapy
TBP Tributyl phosphate
TBq Terabecquerel (10^{12} Bq)
TC Total carbon
TCA Trichloroacetic acid
TCS True coincidence summing
TD Time discriminator
TDCR Triple-to-double coincidence ratio (method)
TDS Total dissolved solids
TEA Triethylamine
TEM Transmission electron microscopy
TENORM Technologically enhanced naturally occurring radioactive materials
TEPC Tissue-equivalent proportional counter
TES Transition edge sensor
TBAB Tetrabutylammonium bromide
TeV Teraelectron volts (10^{12} eV)
Tf Transfer factor (radionuclide)
TFTR Tokamak fusion test reactor
TFWT Tissue-free water tritium
THGEM Thick gas electron multiplier
THM Traveling heater method
tHM y^{-1} Metric tons of heavy metal per year
TI Transfer instrument
~ Approximately
TIMS Thermal ionization mass spectrometry
TINCLE Track-in-cleavage (technique)
TINT Track-in-track (technique)
TIOA Triisooctylamine
TL Thermoluminescence
TLA Trilaurylamine
TLC Thin-layer chromatography (chromatogram)
TLD Thermoluminescence dosimeter
TMA Trimethylamine
TMI Three Mile Island
TMOS Tetramethoxysilane
TMS Tetramethylsilane
TNOA Tri-*n*-octylamine
TNSA Target normal sheath acceleration
TNT Trinitrotoluene
TOA Top of the atmosphere, trioctyl amine
TOF Time-of-flight
TOP Time-of-propagation
TOPO Trioctylphosphine oxide
torr 133.3224 Pa
TP *p*-Terphenyl
TPPS Triphenylphosphine sulfide
TR Tritium sensitive
TRACOS Automatic system for nuclear track evaluations
TRE 12-O-Tetradecanoyl phorbol-13-acetate responsive element
TRI Toxic release inventory
TR-LSC Time-resolved liquid scintillation counting
TR-PDA Time-resolved pulse decay analysis
TRPO Trialkyl phosphine oxide
TSC Task sequence controller
TSCA Toxic Substance Control Act
TSEE Thermally stimulated exoelectron emission
tSIE Transformed spectral index of the external standard
tSIS Transformed spectral index of the sample
TSP Total suspended particle
TTA Tenoyl-tri-fluoro acetone
TTL Transistor–transistor logic
TU Tritium unit (0.119 Bq ^{3}H kg^{-1} H_2O or 7.14 DPM of ^{3}H L^{-1} H_2O or ratio of 1 atom ^{3}H:10^{18} atoms of ^{1}H)

u Atomic mass unit (1/12 mass of $^{12}C = 1.66054 \times 10^{-27}$ kg), up quark
$\bar{u}$ Antiup quark
u Particle speed
u_{nr} Nonrelativistic particle speed
u_r Relativistic particle speed
UCN Ultracold neutrons
UHE Ultrahigh energy
UL Upper level
ULB Ultralow background
ULD Upper level discriminator
ULEGE Ultralow-energy Ge
UNSCEAR UN Scientific Committee on the Effects of Nuclear Radiation
UOC Uranium ore concentrate
U.S.A.E.C. US Atomic Energy Commission (now NRC)
U.S. DOE US Department of Energy
USEPA US Environmental Protection Agency
USN Ultrasonic nebulizers
UV Ultraviolet
V Volts
V_0 Step voltage
VAX Digital Equipment Corporation trade name
VCCI Variable configuration cascade impactor
VHPLC Very-high-pressure liquid chromatography
VMEbus Versa Module Europa bus
VSiPMT Vacuum silicon photomultiplier tube
VUV Vacuum ultraviolet (spectral region)
VYNS Vinyl acetate and vinyl chloride copolymer
W Watt (1 W = 1 J/s)
w/w Weight/weight
WAK Wiederaufarbeitungsanlage (nucleal fuel reprocessing plant), Karlruhe
WBA Whole-body autoradiography
WBEC Weak base extraction chromatography
WCVB Waste concentration vapor body
WDS Wavelength dispersive spectrometer
WDX Wavelength dispersive X-ray (analyzer)
WHO World Health Organization
WIMP Weakly interacting massive particle
WIPP Waste Isolation Power Plant
WM Weighted mean
WMO World Meteorological Organization, Geneva
WNO World Nuclear Organization, London
WOCE World Ocean Circulation Experiment
WOMARS Worldwide Marine Radioactivity Studies
WRA Warfare radioactive agent
WSF Wavelength shifting fiber
WSOC Water-soluble organic carbon
wt% Weight percent
XAF X-ray absorption spectroscopy
XANES X-ray absorption near edge structure
XRD X-ray diffraction
XRF X-ray fluorescence
XtRA Extended range
y Years
YAG:Yb Yb-doped $Y_3Al_5O_{12}$
YAP:Ce Cerium-activated yttrium aluminum perovskite ($Ce:YAlO_3$)
YG Yttrium glass
YSi(Ce) Cerium-activated yttrium silicate
Z Atomic number
Z_2 Average atomic number
Z_{ef} **or** Z_{eff} Effective atomic number
ZCH Central Analytical Laboratory, Jülich
ZnS(Ag) Silver-activated zinc sulfide

Chapter 1

PERPUSTAKAAN PRIBADI AN-NUR SUNARYA

Environmental radioactivity monitoring

Rudolf Engelbrecht

Radiochemistry, Seibersdorf Labor GmbH, Seibersdorf, Austria; Currently - Austrian Agency for Health and Food Security, GmbH, Vienna

Chapter outline

I. Introduction: objective of environmental monitoring 1
II. Types of monitoring programs 2
A. Routine monitoring 2
B. Emergency preparedness 3
C. Emergency monitoring 3
III. Fundamentals of environmental monitoring 4
A. Design of environmental monitoring programs 4
B. Sampling strategies 7
C. Sample preparation 9
D. Measurement and quantification 10
E. Quality assurance/quality control 12
IV. Monitoring for internal exposure 14
A. Air 14
1. Aerosols 14
2. Online versus offline systems 14
3. Gaseous effluents 15
B. Soil, sediments, vegetation, and deposits 17
1. Laboratory based 17
2. In situ gamma spectroscopy 19
C. Water 20
1. Wastewater 23
2. Rain 23
3. Groundwater 23
4. Surface water 24
5. Drinking water 24
D. Foodstuff 24
1. Milk 24
2. Meat and fish 25
3. Vegetables, fruits, and cereals 26
4. Mixed diet 26
V. Monitoring for external exposure 26
A. Dose rate monitoring 26
B. Dose monitoring 27
VI. Mobile monitoring 27
A. Aerial measurements 27
B. Mobile laboratories 28
References 32
Further reading 40
Rudolf Engelbrecht 40

I. Introduction: objective of environmental monitoring

As recent history (e.g., IAEA, 2011; UNSCEAR, 2014; IAEA, 2015; IRSN, 2018) has shown to scientists and the public, transparent and comprehensible dose assessments, including estimation of doses as closely as possible to those actually received, are a fundamental basis of managing radiation protection. The most realistic assessment of doses is obtained by using measured activity concentrations in environmental media and measurements of external dose rates. Environmental monitoring provides data that permit the analysis and evaluation of radiation fields and radionuclide activity concentrations in environmental samples relevant to human exposure, primarily in air, drinking water, agricultural products, and natural foodstuffs, as well as in bioindicators that concentrate radionuclides and provide a measure of trends in activity levels.

Thus, environmental monitoring can be described as the exposition scenario–based systematic sampling and analysis of air, water, soil, and biota to assess environmental conditions. The objective of such monitoring is to obtain solid information that will serve as the basis for measures and political decisions. Environmental monitoring assessments can involve establishing baseline quality, uncovering environmental trends, identifying any variations, detecting new environmental issues, and determining the progress made to achieve environmental goals.

It is important to distinguish the specific aspects of environmental monitoring data obtained under normal

Handbook of Radioactivity Analysis: Volume 2. https://doi.org/10.1016/B978-0-12-814395-7.00001-5
Copyright © 2020 Elsevier Inc. All rights reserved.

operating conditions from those obtained under emergency conditions since the criteria for evaluation are completely different. Under normal operating conditions, data are often important for the statutory control of releases, but the levels set are to be related to human tissue doses. In case of a possible accidental release of radioactivity, the monitoring program aims at answering questions, such as Has an abnormal release occurred? Is there action to be taken? and Which remedial measures should be brought about? Thus, distinction can be made between the following different situations:

Routine monitoring—emergency preparedness—emergency monitoring.

For each of these situations, the type of monitoring program to be established is influenced by the source of radioactivity as well as the scale of the spatial and temporal boundaries of the environment to be monitored. In the end, the goal of monitoring the environment always is to obtain a profound set of data that will serve as a basis that enables authorities to implement measures for either preserving environmental values or preventing their deterioration.

II. Types of monitoring programs

A. Routine monitoring

Routine monitoring programs aim at providing information on the overall dose received by the population at large. The setup of the monitoring is the result of an optimization process in which the availability of measurement resources, the relative importance of different exposure pathways, and the levels of activity and dose in relation to the regulatory constraints are taken into consideration. Routine environmental radiation monitoring programs are designed specifically for each facility, taking into account site-specific factors, such as climate, site location, the design of the facility and its barriers, geological and geomorphological conditions, the off-site environment, and the population distribution (IAEA, 2004); these programs are conducted both on and outside the site giving rise to potential exposure of the public to radionuclides in the environment.

The life cycle of the routine programs for environmental monitoring comprises preoperational studies, performed to establish "baseline" environmental radiation levels and activity concentrations for the purpose of subsequently determining the impacts of the source, monitoring during the operational phase, and decommissioning or post-operation monitoring, performed as long as the facility remains a potential source of radionuclides that could be released to the environment. The complexity of the program depends on the identities, quantities, and chemical and physical forms of radionuclides that may be released and on the characteristics of the monitored environment. Once a monitoring program has been implemented, it should be reviewed periodically to ensure that it continually fulfills the objectives.

The purpose of routine environmental monitoring of airborne radioactivity is to monitor domestic and foreign facilities. Sampling of soils, sediments, or deposits serves as an indicator of long-term buildup of radioactivity in the environment. Measurement of ingredients in foodstuff and water is intended to complete the monitoring program for the migration of radionuclides in the food chain or to check the contamination of the public at large by ingestion. Monitoring locations for ground- and surface water, sediment, biota, and foodstuffs are related to the potential migration pathways determined by preoperational studies, and the frequencies of sampling and measurements are specified with a view to the timely detection of significant changes in the release rates and concentrations of radionuclides and the associated levels of human exposure in accordance with the monitoring objectives.

It has to be noted that radon monitoring, which forms the main exposure to radioactive sources to members of the public (UNSCEAR, 2000b), is not implemented in environmental monitoring programs but conducted in special radon survey programs (e.g., Friedmann et al., 2007).

Recent attention has been paid to radiation risk to the people and the environment caused by exposure to ionizing radiation originating from naturally occurring radioactive materials (NORMs). NORMs touch many aspects of life, starting with occupational risk, through some "contaminated" goods, leisure activities including spa visits and ending with a huge amount of bulk waste often dumped in our vicinity (Kathren, 1998; IAEA, 2003). Such alterations to the natural state result in an increment of radiation risk to the people as well as to nonhuman biota. Each particular type of NORM determines a unique scenario of exposure usually differing from those caused by the artificial radionuclides (Martin et al., 1997).

The measurements must be adequate to determine radiation levels and trends of environmental radioactivity at levels just detectable, the parameters needed for subsequent dose assessment, and compliance with national or international standards, constraints, or limits laid down for the protection of the population. These limits and constraints have values that are typically less than exposure due to natural background radiation. It is, thus, necessary to be able to identify the source and to circumscribe the extent of the radioactive material with reasonable accuracy.

The objectives of routine monitoring programs are to

- provide information to assess the adequacy of protection of the public,
- meet requirements of regulatory agencies,
- verify radionuclide containment and/or waste management practices,

- meet legal liability obligations, and
- provide public assurance.

B. Emergency preparedness

Environmental monitoring may be conducted continuously to serve as a detection system. Emergency preparedness monitoring is part of a strategy for data and information acquisition. The overall emergency strategy includes two different modes of information, namely, (1) acquisition, as there are physical measurements of relevant data on one hand and (2) modeling of situations as a tool for interpolation and extrapolation in time and space where measurement data are sparse on the other hand. It is usually more satisfactory to make provision for detecting an emergency at its source, but detection by environmental monitoring may be required in some situations, for example, near frontiers. In a nuclear accident, the prompt monitoring of a large area may be needed. For this reason, automatic measuring stations that will continuously measure the dose rate in the environment installed around major facilities are capable of early monitoring. Continuously operated off-site systems have the advantage that they can provide rapid indication, not only that a release to the environment has taken place but also of the direction in which the released material is moving. Off-site systems do have the disadvantage that the detectors need to be considerably more sensitive than if sited near to the possible point of release and also need to be extremely reliable if duplication is to be avoided.

All of these systems may include such devices as continuous air samplers capable of measuring concentrations of airborne particles, gaseous iodine, and any other radionuclides of particular concern or water samplers for continuously scanning the sky or bodies of water for radiation. If a facility may contain large amounts of tritium, some special device to measure tritium may well be installed. In each case, the readings being telemetered back to a control center.

Systems intended to detect airborne releases by the use of air samplers introduce complex techniques, if early warning is required, because of the presence of the natural decay products of radon and thoron. However, if time can be allowed for these to decay, a simple measurement of gross alpha- or gross beta-activity will indicate whether conditions are seriously abnormal, although it must always be remembered that gross activity results cannot be interpreted in terms of hazard to man. The intended use of the resultant information gives guidance to the choice of monitoring priorities of such networks.

The objectives of emergency preparedness monitoring are as follows:

- Detecting any release
- Predicting plume trajectory
- Early government and public information
- Planning of urgent population protection countermeasures
- Planning of agricultural countermeasures and food restrictions

C. Emergency monitoring

Under emergency conditions, environmental monitoring is the most informative source of data. The measurements of the radiation levels or the levels of radioactive contamination are required for rapid assessments of the situation to inform those responsible for controlling the emergency so that countermeasures can be put in hand as a matter of urgency. Monitoring in emergency situations is also a valuable and fundamental tool to verify the effectiveness of the actions taken, for example, evacuation, closing the areas, use of stable iodine tablets, or banning the consumption of foodstuffs or water from defined areas.

History has shown that the requirements for the emergency monitoring program and the nature of relevant data will evolve with time. The procedures used in emergency monitoring can conveniently be grouped into three phases, namely, detection, initial survey, and subsequent surveys.

In the initial emergency response following an accident, where information is required with as little delay as possible, rapid and relatively simple, albeit crude, analytical methods may be preferred. This usually means a lesser sensitivity and thus a greater risk for errors. However, in any emergency situation, it is important that the results can be obtained relatively quickly. Under most conditions, this would amount to the use of dose rate and survey instruments.

Nevertheless, it should be ensured that the types of instruments available are suitable for the measurement purposes. For example, if the released material consists of only tritium or plutonium, then the typical beta–gamma survey instruments are not of much use and appropriate special instruments and/or monitoring techniques should be used.

At the early stage of an accidental atmospheric release, external exposure includes the contribution of radiation from the plume. Thus, initial surveys in the release phase of the accident will be focused on measurements of cloud shine and on the sampling of radionuclides from the plume to assess doses from external exposure and inhalation. In the postrelease phase, external gamma dose rate measurements are attributable mainly to radiation from deposits on the ground. Close to the installation, these measurements may also include the contribution of radiation from the source.

The external dose rate measurements should be supplemented as soon as possible by nuclide-specific analysis of representative samples of mobile environmental media and biota through which radionuclides could migrate and

reach the human habitat and thereby enter the human body. These are atmospheric air, soil water and groundwater, surface water, sediments, biota, and foodstuffs. Groundwater should be monitored through monitoring wells located at a sufficient depth around and downstream of the facility. These measurements may be pursued over longer periods of time. However, the assessment of the impact of short-lived nuclides such as iodine and ruthenium isotopes will be possible only if measurements are performed within a few weeks after the accident.

Once a release has ceased and deposition levels have stabilized, nuclide-specific deposition densities of all gamma-emitting radionuclides can be acquired rapidly by the use of *in situ* gamma spectrometry. Nevertheless, laboratory analysis of a large number of samples of soil, plants, water, agricultural products, and natural foodstuffs will be necessary to supplement the data provided by the *in situ* measurements.

During such subsequent surveys, it also will be necessary to perform a large number of measurements in different media in view of an accurate a posteriori assessment of the radiological impact. Such an assessment fulfills the need for adequate information of the public and may serve also further scientific investigations.

The specific objectives of emergency radiation monitoring in the environment are to

- provide accurate and timely data on the levels, extent, and duration of radiation and environmental contamination with radionuclides,
- provide detail of the physical and chemical characteristics of the hazard,
- assist in preventing and controlling the spread of contamination,
- assist decision-makers on the implementation of urgent, intermediate-, and recovery-phase population protection countermeasures, agricultural countermeasures, and food restrictions
- provide information for the protection of emergency and recovery workers,
- provide information for the public on the degree of the hazard,
- provide information needed to identify any people for whom long-term medical screening is warranted,
- confirm the efficiency of protective actions.

III. Fundamentals of environmental monitoring

A. Design of environmental monitoring programs

Monitoring design provides answers to the following questions: What will be monitored? What are the parameters to be measured? How will these parameters be monitored? Where, when, and how frequently will the parameters be measured. A monitoring program will be as valuable and effective as the questions identified are specific and focused and can be used to guide the development of a monitoring plan.

To be consistent with the objectives and the design of any monitoring program, one has to consider types and characteristics of critical radionuclides, modes of their release to the environment, including mechanisms for the transfer of radionuclides through environmental media, dispersion and reconcentration mechanisms, and their seasonal variation, existing levels of radionuclides in the environment and their variability, and exposure pathways that make the major contributions to individual doses, leading to requirements in terms of sampling, sample treatment, measurement technique, and the lower limit of detection or minimal detectable activity (IAEA, 2005). Moreover, the nature of the environment, as the location of the facility in relation to population centers and their composition and densities, surface waters, oceans, geological, meteorological, hydrological, and other natural conditions, which might influence the dispersal of released radionuclides, has to be taken into account.

A key feature in designing environmental monitoring programs is the identification of potentially critical radionuclides, pathways, and groups or individuals potentially affected.

In the considerations of the limitation of dose to the general public from ionizing radiation, doses to individuals, to critical groups, and to the general population are distinguished. As early as 1965, the ICRP (1965) defined a critical group as that "whose exposure is homogeneous and typical of that of the most highly exposed individuals in the exposed population." In 2006, the ICRP introduced the new concept of a representative person, defining it as "an individual receiving a dose that is representative of the more highly exposed individuals in the population" (ICRP, 2006). The term "representative person" describes an individual with characteristics that reflect those of the group that receives the highest doses from a particular source, known as the representative person for the radionuclide in question, and replaces the "average member of the critical group" defined in previous publications of the ICRP. In any case, critical groups or the representative person may be in the vicinity of the installation or at some distant location. To assess the annual effective doses for both critical group and representative person, methods recommended by the International Atomic Energy Agency (IAEA, 1982; IAEA, 2001) can be used. A more conservative concept to assess doses to the public is given in US Regulatory Guide 1.109 and based on the individual of maximum dose (US NRC, 1977).

Routes from a source of radionuclides and/or radiation to a target individual or a population through media in the environment are defined in the exposure pathways.

There are two main categories of exposure pathway:

- External exposure from radionuclides present in the air or in material incorporated in, for example, soils or sediment, determined by direct measurements of external dose or by soil analysis.
- Internal exposure from the inhalation, ingestion, or immersion of radionuclides present in air or incorporated in water or foods, respectively. Immersion and inhalation are monitored by air sampling. Ingestion of radioactivity is monitored by means of food sampling, for example, milk, fish, and shellfish, or indicator organisms or materials.

Generally, a range of potential pathways that may be more complicated in reality need to be considered (Table 1.1). The relative importance of different exposure pathways will be dependent upon

- the magnitude of the discharge,
- the route of discharge and factors affecting it (e.g., stack height, meteorological conditions, etc.),
- the physical state or properties (e.g., emission type, energy, physical half-life, gas, liquid, or solid),
- the chemical characteristics (e.g., organic or inorganic form, oxidation state, speciation, etc.)
- the dosimetric importance of radionuclides,
- environmental characteristics (e.g., climate, type of biota, agricultural production, etc.); locations, ages, diets, and habits of the exposed individuals or population.

Under conditions of normal discharges and chronic (prolonged) exposure, the pathways are usually permanent and well defined. In case of emergency releases, the contributions via different pathways to the doses received by workers and the public may be different from the normal and transient. These differences should be considered when establishing the monitoring program. To protect the public and workers from deterministic health effects following major accidents, radiological criteria in emergencies may be different from those applied under conditions of normal discharges (e.g., additional monitoring data may be necessary).

Under normal operation conditions, that is, for routine environmental monitoring, those radionuclides are to be considered, which are limited in discharge permits or are significant components of a group limit (e.g., strontium-90 limited under any other beta/gamma-emitting radionuclide group limit). Other radionuclides may be required as a result of international obligations or backgrounds. Proven surrogate radionuclides may be used (e.g., where the radionuclide fingerprint is relatively stable). Since routine monitoring programs are designed to verify compliance with environmental standards at levels just detectable and which are for records only by low-level measurements, it is essential to be able to identify the source and to circumscribe the extent of the radioactive material with reasonable accuracy.

Preoperational assessments of the expected inventories of radionuclides during operation of a facility, the possible discharge pathways and the likely amounts that will be discharged to the environment, with due consideration of the

TABLE 1.1 Important exposure pathways to be considered in the monitoring program.

External exposure pathways	
Source of radiation → human	Direct exposure from a source
Source of radionuclides→ atmosphere or water body → human	Exposure due to the plume or water
Source of radionuclides → atmosphere or water body → human skin	Skin contact exposure
Source of radionuclides → atmosphere or water body → soil or sediment or building surface or vegetation → human	Exposure from deposited radionuclides on the ground, on the shores of rivers, lakes, or the sea; on walls, roofs, and floors; or on trees, bushes, and grass
Internal exposure pathways	
Source of radionuclides → atmosphere → human	Inhalation of radionuclides in the plume;
Source of radionuclides → water body → human	Ingestion of radionuclides in drinking water
Source of radionuclides → atmosphere or water body → (soil or sediment) → vegetation → meat, milk, eggs, vegetables, or marine food → human	Ingestion of radionuclides in food or beverages
Soil or sediment → human	Inhalation of resuspended radionuclides
Source of tritium → atmosphere → human	Absorption of tritium oxide through the skin

effluent treatment systems that will be installed, will help to define spatial and temporal boundaries and select types and numbers of samples and measurement methods. A preoperational program intended to establish baselines might also identify suitable indicator organisms or indicator materials for particular radionuclides. Indicators such as seaweeds, lichen, or suspended particulate matter are selected not because they represent a component of the human diet but because they concentrate radionuclides and provide a measure of trends in activity levels and hence may provide more sensitive information of environmental contamination.

Environmental monitoring during the decommissioning of a facility, such as uranium mines and mills, uranium enrichment plants, fuel fabrication facilities, nuclear reactors (IAEA, 1998, 1999; 2001, 2002a, 2002b), nuclear fuel reprocessing plants, and other radionuclide processing facilities, will be similar to that for the operational stage, modified to take account of changes in the source term, all materials exhibiting significant levels of activity (FAO, 1996) are removed as decommissioning proceeds. For both current and historical discharges, in-growth of daughters may need to be considered (e.g., ^{241}Am from ^{241}Pu).

The most important radionuclides to be assessed following a release of radionuclides from a uranium-fueled reactor to the environment are ^{134}Cs, ^{137}Cs(^{137m}Ba), ^{131}I, and other gamma emitters; the beta emitters ^{89}Sr, ^{90}Sr, and tritium; and the alpha emitters ^{238}Pu, $^{(239\ +\ 240)}$Pu, ^{241}Am, and ^{242}Cm. This group of radionuclides is most likely to be of concern due to internal exposure from inhalation and ingestion of food and water and to the contamination of environmental materials, which are part of the immediate pathways, leading to contamination of food (Table 1.2). Biological concentration in freshwater and marine systems can result in very rapid transfer and enrichment of specific radionuclides. Radionuclides that enter such systems can, in certain cases, be rapidly accumulated by plankton and algae, which serve as food for higher trophic levels; thus, the radionuclides become concentrated in organisms such as oysters, clams, shrimp, etc.

Radionuclides of particular concern in freshwater and marine food chains include ^{54}Mn, ^{55}Fe, ^{59}Fe, ^{60}Co, ^{65}Zn, ^{95}Zr, ^{95}Nb, ^{103}Ru, ^{106}Ru, ^{110m}Ag, ^{125}Sb, ^{131}I, ^{134}Cs, ^{137}Cs, ^{141}Ce, ^{144}Ce, and some of the transuranic elements.

Many other radionuclides would be present in debris from a nuclear accident; their potential contribution to human exposure depends on the type of accident and the circumstances at the time of the accident. Since there are several types of fuel, the spectra of radionuclides that would be present in accidental releases could be somewhat different.

The levels of radionuclides in the environment and food and their variability have been extensively compiled by the United Nations Scientific Committee on the Effects of Atomic Radiation (UNSCEAR, 2000b, 2000c). These reports contain information about the transfer of radionuclides between atmospheres, waters, soils, biota, and person and about human exposure to the various nuclides (UNSCEAR, 2000a, 2008).

What site or environment will be monitored, what will be measured, where will it be measured, and when and how frequently will it be measured are essential elements of a monitoring design. However, as the development of the monitoring design almost always requires clarification and prioritization, documenting the design, including rationale for decisions, is critical when the design is implemented and when the collected data are used for reporting to national policymakers, international forums, and the public.

Identification and assessment of the potentially critical radionuclides, pathways, and groups or individuals is a substantial prerequisite in designing environmental monitoring programs, directly affecting the nature and extent of the measurements. The selection of the major contributing radionuclides and their significant pathways to the predefined target population or individual direct the monitoring programs to the most important subjects. The following principles for the development of a practical monitoring program involve steps that are reasonably independent of local circumstances:

TABLE 1.2 Radionuclides of interest and related media in case of a nuclear accident.

Samples	Radionuclides
Air	^{131}I, ^{134}Cs, ^{137}Cs
Water	^{3}H, ^{89}Sr, ^{90}Sr, ^{131}I, ^{134}Cs, ^{137}Cs
Milk	^{89}Sr, ^{90}Sr, ^{131}I, ^{134}Cs, ^{137}Cs
Meat	^{134}Cs, ^{137}Cs
Other foods	^{89}Sr, ^{90}Sr, ^{134}Cs, ^{137}Cs
Vegetation	^{89}Sr, ^{90}Sr, ^{95}Zr, ^{95}Nb, ^{103}Ru, ^{106}Ru, ^{131}I, ^{134}Cs, ^{137}Cs, ^{144}Ce
Soil	^{89}Sr, ^{90}Sr, ^{134}Cs, ^{137}Cs, ^{238}Pu, $^{(239+240)}$Pu, ^{241}Am, ^{242}Cm

- Define the objective.
- Evaluate sources of direct radiation and radionuclides, especially the composition, concentrations, release rates, points of release, and physical and chemical forms of nuclides.
- Identify the pathways leading to exposure to man from source data by the use of analytical models for the possible pathways and by the use of experience gained at other sites and data on local meteorology, hydrology, and population distribution and diet.
- Select the significant pathways that may be critical in terms of their contributions to exposure and determine the critical population groups.
- Consider the available analytical methods to select the most effective combination of in situ measurements, sampling, chemical separation, and radionuclide analysis, that is, one that yields the required information with least effort.
- Determine the consequent measurement requirements to provide data for dose assessment for both normal and abnormal conditions.
- Allow for flexibility in the design as operational experience is accumulated and indicates that other types of measurements or measurement frequencies may be desirable as the pathways and the other program requirements become better defined.

B. Sampling strategies

The term sampling refers to strategies in selecting a subgroup from a larger group and then uses this subgroup as a basis for making inferences about the larger group. The sampling strategy designed and adopted must deliver the necessary confidence and power to allow the appropriate inferences to be drawn. To do that, a number of important factors should be considered, including the nature of the control measure, the contaminant concerned, the nature and location of the inputs, and statistical aspects of sampling and analysis. The resulting measurements made following the strategy should meet the requirements for emergency or regulatory management, or simply for compliance purposes. The theoretical sampling strategy provides, as a minimum, a plan of what and where to measure, how many sampling units to collect, the time frame over which sampling units should be collected, and the sampling frequency. The consultation of experienced statisticians during the sampling design process may be appropriate.

Generally, sampling strategies can be classified as either nonprobabilistic or probabilistic. Nonprobabilistic sampling is used when the sampling location of most interest is already known or on suspected sites with no need to sample elsewhere, that is, judgmental sampling by subjective selection of sampling locations. Probabilistic strategies, based on statistical considerations, on the other hand are common when it is possible to sample only a small percentage of the whole. This type of sampling involves a selection process in which each element in the population has an equal and independent chance of being selected. Five main methods include the following:

1. Judgmental (sample is taken on the judgment of the sampling person)
2. Simple random (arbitrary collection of samples, having the same probability of being included),
3. Stratified random (random sampling based on additional information)
4. Systematic random (random sampling within subdivided smaller areas of the original area)
5. Systematic grid (subdividing the area of concern and collecting samples from the intersections of the grid lines)

By using statistical methods, probabilistic sampling attempts to increase the probability that generalizations derived from the sample will be correct. Of the many types of sampling strategies described in the literature, all are useful in certain situations, but none is perfect. For example, a significant danger of using only probabilistic sampling techniques in field survey is that a major site may be overlooked, resulting in a skewed analysis and nonrepresentative result. In any kind of environmental monitoring program, the sample representativeness is an important issue. Representativeness in this context means that the sample should reflect the conditions in the environment from which it is taken. A representative sample may be defined as one being able to answer questions in terms of radiological information for which the analyses are performed. To put it in a more mathematical way, a representative sample parallels the key variables and characteristics under examination and allows the collected results to be generalized to a larger population of which it is a subset.

In general, nonprobability sampling is less likely to produce a set of specimens that is representative of the population than valid probabilistic sampling, but representativeness of environmental samples is difficult to demonstrate and usually considered justified by the procedure used to select the samples (Gilbert and Pulsipher, 2005). It is necessary to keep in mind that site-representative samples are not necessarily representative in a statistical sense. Accuracy and precision, which are quality requirements on the analysis process, are of not much worth if the samples are not representative to characterize site conditions.

The inherent variability of environmental samples necessitates careful design of sampling strategy. Since under monitoring conditions the reasons for the variability cannot be fully understood, a predefined sampling strategy should be used that is closely connected with an appropriate

statistical evaluation of the measured activities. In general, activity levels in terrestrial samples are subject to spatial and temporal variability caused by various factors such as inhomogeneous spatial distributions of the deposited radioactive material in soil, redistribution of radionuclides by wind or by water erosion, differences in soil conditions and agricultural practices, and the superposition of different exposure pathways such as foliar uptake and root uptake. Although this may not eliminate the uncertainty associated with activity levels in environmental samples, it may reduce the uncertainty and enable it to be quantified by statistical means.

In the case of normal discharges from licensed facilities, sampling locations should be selected close to points where the maximum exposure or deposition is expected, preferentially in the main wind direction for airborne discharges or downstream from the release point for aquatic discharges and at the site boundary for direct radiation from the source (Table 1.3).

Details of statistically based sampling designs, the process of identifying survey unit sizes, laying out systematic or random measurement grids, and methods for collecting samples are given in existing guidelines (e.g., NRC, 1998a; NRC, 1998b; NRC, 1992; CIRIA, 2000; BSI, 2001; MARSSIM, 2002; IAEA, 2005; USEPA, 2006; ICRUM, 2006), in international standards (e.g., ISO 18589-2, 2007), and in classic statistical sampling textbooks, including Cochran (1977), Thompson and Seber (1996), Thompson (2000), and Barnett (2002).

There are some considerations in sampling radionuclides beyond those shared with other types of environmental sampling. The type of radiation emitted by a radionuclide affects sample selection and eventual treatment, because relatively nonpenetrating radiation such as alpha particles must be measured in very small amounts of material, while gamma rays can be conveniently detected in bulk or unprocessed material.

A common problem in collecting and storing a sample of gas or liquid is loss of the radionuclide to the apparatus and container surfaces. Selection of relatively nonretentive materials and minimization of areas and collection and sample transition times are recommended. Information on the magnitude and rate of uptake by surfaces is widely scattered and qualitative, however, and no materials as appropriate to the entire spectrum of encountered radionuclides are known.

To minimize losses during sample collection and storage, containers of appropriate composition should be used. The liquid contents can be frozen, acidified, or otherwise modified, by adding a complexing agent or stable carrier. While it is important to avoid losses to container walls during storage, it is also important that the pretreatment will not induce a change in the distribution of the radionuclides between the liquid and particulate matter or induce volatility losses of radionuclides.

The sampling frequency will depend on the item to be measured and the variations with time in the activity concentration in the media. In routine monitoring, the temporal fluctuations are generally relatively low, so the frequency may consequently be low. The time intervals between measurements should reflect the half-lives of the radionuclides that are to be monitored. If the sampling time on a filter is long in comparison with the half-life of the radionuclide concerned, this radionuclide may not be detected and the purpose of the monitoring is missed.

Samples are either taken manually from the environment or accumulated in unattended devices and analyzed in the laboratory or possibly in the field. Some collection devices have detector and recording systems that measure sample emissions during collection. Depending on the time response, online and off-line sampling/measuring devices are distinguished. For continuous monitoring systems, sampling and counting times are identical, thus providing the information nearly real time. A reduction of sampling/counting time of online systems is tied to an expense of statistical error, which in turn would demand an increase in the alarm levels. Shortcomings of online sampling systems are in the limited possibilities of physical or radioanalytical sample preparations used to accumulate the radionuclides or for nuclide-specific techniques, thereby leading to lower limits of detection, which are higher compared with off-line sampling and measurement.

Nevertheless, determination of radionuclide concentrations in environmental materials collected and brought into a laboratory for analysis is the primary approach in environmental radioactivity measurement. Samples that yield

TABLE 1.3 Pathways and related samples to be taken.

Release	Pathway	Samples
Atmospheric	Inhalation	Air
	Ingestion	Foodstuff
	External	Soil, direct measurement of ambient dose equivalent
Liquid	Ingestion	Marine food
	External	Water, direct measurement of ambient dose equivalent

information most directly on radiation exposures of populations such as air, food, and water are of greatest interest in monitoring programs. In some circumstances, field measurements are sufficient, as there are a wide variety of in situ measurement techniques available, including box counters, portal monitors, in situ gamma spectroscopy systems, and direct measurements with handheld instruments. In situ surveys are able to determine the radiation field properties, identify radionuclides, and determine their approximate concentrations but characterized by limited numbers of measurements with relative long count times. Thus, they may be combined with sampling and laboratory analysis. Laboratory determinations usually yield better descriptions of the analyzed material, greater analytical accuracy, and the required sensitivity for radionuclides that do not emit penetrating radiation. On the other hand, sampling requires greater efforts, provides information less promptly, and requires additional interpretation for relating analytical results to the required environmental information.

The general principles that apply to all sampling activities include the following:

- The selection of types and location of in situ measurements or sample collections and analyses, as well as the sample size and collection frequency to identify the radionuclides of interest, is to be based on information sources and modes of transfer through the environment of radionuclides.
- The radionuclide concentration, the sensitivity of the radiation instruments, the capability of analytical methods, and the coordination of sampling and laboratory schedules define the numbers of samples.
- All necessary parts of the sample are to be collected, and the samples have to be adequately preserved, so that loss of radioactivity between the time of sampling and analysis is known or negligible.
- Sufficient background samples are needed to provide information on preexisting nuclides from those under consideration.
- Sufficient replicate samples should be collected to determine variability of concentrations.

C. Sample preparation

High-sensitivity environmental analyses share common technologies, methods, processes, and information needs regardless of whether they are being used under normal operation conditions or in emergency situations.

Generally, sample preparation may include, but is not limited to, removing extraneous material, homogenizing, splitting, drying, compositing, and final preparation of samples, to distinguish the desired radionuclides from others that interfere with the final measurement by producing a response in a detector, to increase the specific activity so that the radionuclides can be measured with improved sensitivity or accuracy, and to reduce self-absorption in the sample matrix for measurement of alpha and pure beta emitters and low-energy photons.

Sample preparation without recourse to special chemical separations is limited to total alpha-, beta-counting and gamma spectrometry, but the samples have to be brought in suitable form for measurement, which means a uniform distribution of the radioactive substances throughout the sample and the same sample size, thickness, and configuration within each group of samples. The question of homogeneity becomes even more important as the range of the radiation becomes shorter, since self-absorption and the sample detector geometry may vary in different parts of the sample. Calibration of these samples is usually performed with locally made standards having the same physical properties and known quantities of the appropriate radionuclides, in addition to traceable standards.

Any radiochemical analysis usually starts with obtaining a solution by the destruction of organic material in the sample. Materials that contain little organic matter can be dissolved directly, since the dissolution treatment with oxidizing acids will also remove the organic portion. Most samples, however, must be oxidized first by wet ashing (reaction with oxidizing agents in solution), dry ashing, with oxygen, or at room temperature with electrically excited oxygen. When samples are heated, care is to be taken to avoid loss of the desired constituents by volatilization and splatter. For example, samples to be analyzed for radioiodine cannot reliably be heated in the dry state but should be wet-ashed unless iodine is in one of its more highly oxidized states.

When igniting samples containing much organic matter, such as food, the temperature should be raised gradually over an extended period to avoid flame-burning and to minimize glow-burning. Losses of small particulates by spattering can occur under these conditions. A partial oxidation of biological samples with nitric acid, followed by ashing in a muffle furnace, allows a lower final temperature (400−450°C) and will oxidize some of the volatile elements to less volatile forms.

Destruction of organic matter does not complete the sample preparation process if chemical separations are to be performed and the inorganic ash must also be dissolved. Complete dissolution of the sample is not necessary if it can be shown that the desired nuclide is completely leached.

Incompletely oxidized samples (gray ash) will be acceptable for gamma spectroscopy and many subsequent dissolution procedures. Usually, the dissolution process of residues will oxidize small amounts of organic matter remaining after ashing, such as the gray ash. The samples may be entirely or almost entirely dissolved in nitric or hydrochloric acids, or in their mixtures. Substances not easily dissolved with acids must be fused with appropriate

fluxes to obtain a solution. The higher temperature increases the reaction rates but may vaporize some radionuclides. A combination of acids and fusion, such as that as much as possible of the sample, is first dissolved by mineral acids, including hydrofluoric acid, and the insoluble residue dissolved by fusion is often convenient.

Any dissolution procedure should also include steps to ensure that any added carrier or tracer is in the same chemical form as the nuclide being analyzed. Whatever method is used to measure the recovery of a chemical separation procedure, isotopic exchange or chemical and physical equivalency between the radionuclide in the sample and the added carrier or tracer is essential. Isotopic exchange such as converting multivalent elements to their highest or lowest oxidation states (e.g., hypochloride oxidation of iodine or ruthenium, sulfite reduction of plutonium), or complexing or dissolving radium and barium sulfates (diethylene triamine pentaactetic acid [DTPA] or sodium carbonate fusion), should be undertaken, as early as possible in the analysis, before any chemical or physical operations are performed that might result in loss of the desired nuclide. For many nuclides, dissolution in mineral acids is sufficient to effect isotopic exchange.

Attention must also be paid to the chemical and physical form, that is, the ionic or nonionic form and oxidation state, of the radionuclide aside from the isotopic exchange question, even when the carrier or tracer is not used. To put it in a simple way, the radionuclide must be brought into a form in which it undergoes the expected reactions in the separation process.

The fundamentals of the conventional radiochemical methods are precipitation, coprecipitation, ion exchange, and solvent extraction (ISO 18589-4, 2009; ISO 18589-5, 2009). A great variety of methods have been developed in the past, but the most valuable development of the past years has been the development of extraction chromatographic materials, such as Sr-specific crown ether-based material, Sr resin, or the transuranium element−specific extraction chromatographic materials, (UTEVA, TRU, TEVA resins), developed by Horwitz et al. (1991, 1992a, 1992b, 1993, 1995). These materials have become commercially available as the registered products of Eichrom Technologies, Inc. and TrisKem International SAS, and these have replaced conventional methods based on a series of precipitations.

In addition to procedures for the individual determination of the nuclides, a great variety of combined procedures for the simultaneous determination of actinides and radiostrontium isotopes in a variety of environmental substances based on different combinations of ion exchange separation and extraction chromatography or the even pure extraction chromatography have been developed (Moreno et al., 1997; La Rosa et al., 2001; Mellado et al., 2001; Maxwell, 2006, 2007; Maxwell and Culligan, 2009; Maxwell et al., 2010; Michel et al., 2008; Łokas et al., 2010; Spry et al., 2000; Lee et al., 2011; Wand et al., 2004; Berlioz et al., 2005; Thakkar, 2002; Tavcar and Benedik, 2005; Martin and Odell, 1998; Hrnececk et al., 2005; Srncik et al., 2008).

Typically combined procedures are starting with the separation of Pu and Th by anion exchange resins from concentrated HNO_3 solution from Sr and Am, which are collected together with other sample components in the effluent. Following preconcentration, Am can be separated using a TRU column. Additional purification from lanthanide impurities may be based on an anion exchange resin or the TEVA resin, whereas Sr is separated on a Sr resin column. Recently, three review papers about the analytical methodologies for the determination of plutonium as well as ^{241}Am and ^{90}Sr/^{90}Y have been published (Vajda and Kim, 2010a,b,c).

Attention must be paid to some important details. For example, the concentration of ^{239}Pu in surface or ocean water from fallout is of the order of 20 μBq/L, or about $5 \cdot 10^{-17}$ M, and this concentration is obtained with $2 \cdot 10^{7}$ atoms. In soil, a common plutonium concentration from fallout is about 2 mBq/g. This activity can be obtained from one plutonium oxide particle with a diameter of 0.1 μm. At the very low concentrations frequently encountered, contamination of the sample with extraneous radionuclides during processing must be avoided, and the blank value must be known and kept low and constant. In addition to a low blank, high radiochemical purity in the separation is also needed for good accuracy and sensitivity. Reagents must be carefully checked for radioactivity. For example, the environmental concentration of thorium is approximately 10^3 times that of the chemically similar plutonium; thus, decontamination from thorium by a factor of 10^5 or more is required for a satisfactory plutonium analysis.

These difficulties encountered as a result of very low concentrations can be avoided by adding macroquantities of inactive isotopes of the same element, or of similar elements if no stable isotope exists. This procedure, the use of carriers for radioactive tracers, is frequently used for measuring the chemical yield of a separation procedure. The chemical separations are greatly simplified since now the element can be expected to exhibit its normal behavior, and the analytical problem is no longer one in ultratrace chemistry.

D. Measurement and quantification

For a long time, the outstanding measurement method in environmental monitoring has been the determination of gross alpha- and gross beta activities applying gas-flow proportional counters after preparing a solid sample of known thickness and area. The sample can be the residue remaining after evaporation of a water sample, soil, sediment, ashed vegetation, or other solid material. Since the

samples generally contain an unknown radionuclide mixture, an arbitrary choice must be made in selecting a standard for calibration of the counting system and determining the conversion of sample counting rates to disintegration rates. The arbitrary but necessary choice of a standard nuclide introduces the largest uncertainty in the disintegration rates inferred from counting rates of thick samples, since correction factors are energy dependent, but by convention, the same alpha counting efficiency is assigned for all the alpha emissions and the same beta counting efficiency is assigned for all the beta emissions (ISO 18589-6, 2009).

Advances in gamma spectrometry, in alpha spectrometry and in liquid scintillation counting (LSC) and spectrometry for alpha and beta emitters, have obviated many of the reasons for measuring total activity, but low-cost gross measurements, preferably applying alpha/beta, separated LSC measurements (Sánchez-Cabeza, and Pujol, 1995; Zapata-García et al., 2009; Palomo et al., 2011; Schumacher et al., 2014) may still serve as a rapid and cost-effective screening procedure.

A very effective tool for measuring the concentration of radionuclides in soil, water, air filters, and swipes is presented by LSC. Samples or an aliquot may be placed directly into an LSC vial of cocktail and counted without further preparation or first processed by ashing, radiochemical, or solvent extraction, or pulverizing to place the sample in intimate contact with the LSC cocktail. Actions such as bleaching the sample may also be adequate to make the cocktail solution transparent to the wavelength of light it emits. Additionally, very-high-energy beta emitters (above 1.5 MeV) may be counted using liquid scintillation equipment without liquid scintillation cocktails by use of the Cerenkov light pulse emitted, as high-energy charged particles move through water or similar substances. The use of pulse shape discrimination has allowed increases in sensitivity by electronic discrimination against beta and gamma emitters. However, beta energy spectra are 10−100 times broader than gamma spectrum photopeaks so that quantitative determination of complex multienergy beta spectra is hardly possible.

Environmental samples containing gamma-emitting radionuclides can be measured by means of gamma spectroscopy. Although scintillation counters using a sodium iodide crystal with a thallium activator, NaI(Tl), have been a mainstay of gamma ray spectrometry since 1948, they are superseded by semiconductor-based assemblies with the detector of choice for most applications to be a high-resolution hyperpure germanium crystal (HPGe), whereas silicon detectors are used for gamma spectrometry at low energies. Germanium has the advantages with respect to silicon of a smaller bandgap (Ge: 0.665 eV vs. Si: 1.12 eV at 77 K) for better energy resolution and a higher Z (32 vs. 14) for better photoelectric absorption. The germanium detector is not as efficient as the NaI detector, but it is capable of distinguishing between very closely spaced energies. The energy resolution measured as the full width at half the peak maximum (FWHM) for typical coaxial germanium detectors is between 1.6 and 2.1 keV for 1.33 MeV gamma rays, depending on the size and quality of the detector. The peak-to-Compton ratio is generally 40−100, again depending on the size and quality of the detector.

Alpha spectrometry systems, typically, consist of the silicon diode surface barrier detector housed in a light-tight vacuum chamber, a bias supply, amplifier, analog-to-digital converter, multichannel analyzer, and computer. The bias is typically 25−100 V. The vacuum is typically less than 0.1 millitorr. Since the sample and detector are in a vacuum, most commonly encountered alpha energies will be detected with approximately the same efficiency, provided there is no self-absorption in the sample. The system is appropriate for all alphas except those from gaseous radionuclides. Samples have to be prepared by means of chemical separation. A known amount of a (diluted) standard solution (tracer) may be added before separation to determine the overall recovery of the sample from the chemical procedures and/or quantification by isotope dilution. Following conversion to a particulate having very little mass and collection on a special filter (microprecipitation), or collection from solution by electroplating onto a metal disk, the sample is then placed in the vacuum chamber at a fixed distance from the diode and analyzed. For environmental levels, counting times are in the order of 80,000 seconds or more, providing detection limits in the order of 1 mBq/g or below. Typical energy resolutions are in the range of 10−20 keV.

Alpha counting procedures are capable of sufficient sensitivity to determine levels for monitoring and dose assessment. However, the potential of long-term buildup of long-lived radionuclides indicates that more sensitive methods may be required to determine the routes and rates of movement through the environment. For these purposes, mass spectrometry provides a unique and valuable tool (Ross, 2008 and Becker, 2007, 2010).

For the determination of ^{239}Pu and ^{240}Pu, which can give direct information on the content of fissionable ^{239}Pu, mass spectrometric methods such as inductively coupled plasma mass spectrometry (ICP-MS) and accelerator mass spectrometry (AMS) are necessary (Povinec et al., 2001). ICP-MS has been widely applied for this purpose, although care must be taken to remove interferences like $^{238}UH^{+}$, which can influence the determination of ^{239}Pu (Hrnecek et al., 2002; Chiappini et al., 1996; Muramatsu et al., 1999, 2001). A partial review of how to overcome spectral overlaps in elemental ICP-MS was presented by Vanhaecke and Moens (2004).

For plutonium isotopes, the main advantage of AMS compared with conventional MS (TIMS, ICP-MS) is the

complete destruction of molecular isobars (e.g., $^{238}UH^{+}$ for ^{239}Pu) by stripping to high positive charge states in the terminal of the tandem accelerator (Oughton et al., 2001). Additionally, this method permits the determination of higher mass plutonium isotopes such as ^{242}Pu and ^{244}Pu in environmental samples (Fifield et al., 1996; Hrnecek et al., 2005).

Mass spectrometric methods have been reviewed for the determination of transuranium elements, for example, by Betti et al. (2006). Hou and Ross (2008) extensively compared radiometric and mass spectrometric methods for long-lived radionuclides. They concluded that mass spectrometric techniques, although susceptible to isobaric interference and the need of extensive equipment and infrastructure, are valuable rapid analytical methods for the determination of many long-lived radionuclides, including ^{99}Tc, ^{237}Np, and isotopes of uranium, thorium, and plutonium (Table 1.4).

E. Quality assurance/quality control

As the results of environmental monitoring are of fundamental importance not only to assess environmental conditions but also to support decision-making, policy development and prioritization of policies based on solid information, the application of quality assurance and quality control measures during the data collection process, data storage and access is a fundamental component of any effective environmental monitoring program to ensure quality and comparability of the analytical results. As a minimum, an adequate quality assurance program satisfies the general requirements established by the regulatory body. To minimize laboratory incidents, such as the mislabeling of samples or biased analyses, quality control and quality assurance concepts have been developed to assist the laboratory personnel to achieve a higher degree of transparency of procedures, minimize potential sources of error, standardize the handling of samples, instruments, and data, and in the end, decrease the rate of nonconformance results.

Particularly in the case of sensitive materials, this has been recognized as early as the 1950s in the nuclear industry, and concepts have been developed to assure traceability of materials, and of course, reliability of results. Many different branches of industry have adopted, refined, and further developed these concepts, because it has been realized that a formal quality control and quality assurance system helps achieve a stable level of high-quality output. It was only in the late 1980s that similar strategies became attractive to research laboratories and, in particular, EURACHEM and ISO started to set up guidelines and norms for the implementation of these measures (e.g., the ISO 9000 series). Finally, the idea of a formal accreditation of laboratories following quality guidelines was developed and now is widely accepted that—through the advent of international trade and exchange—an internationally agreed procedure for accreditation of analytical laboratories through national accreditation bodies is a proper means to enhance acceptance and legal recognition of analytical results worldwide. The global quality standard for analytical laboratories is the ISO/IEC 17025 (ISO, 2017). These standards set out specific management and technical requirements.

While management requirements are mainly related to the operation and effectiveness of the quality management system and more or less identical to ISO 9001 requirements, technical requirements focus on the qualification and competence of staff, testing methodology, infrastructure and equipment, and reporting of results.

The sampling, sample handling and preparation, analytical procedures, and other factors, which might have an influence on the result, have to be documented carefully, for example, as standard operating procedures (SOPs), to allow reevaluation of results if doubts about their reliability come up. SOPs detail the work processes that are conducted or followed within an organization and document the way activities are performed. The benefits of a valid SOP are reduced work effort combined with improved data comparability, credibility, and legal defensibility and promoted quality through consistent implementation of a process even if there are changes in personnel.

In addition, particular attention should be paid to the requirements on method validation, in terms of accuracy, repeatability and reproducibility, the use of calibration standards that are traceable to national or international standards, instrument calibration, and performance testing.

In providing robust and sound analytical results, it is inevitable to understand that every measurement will always be subject to a certain amount of uncertainty. Uncertainty is a measure giving the quality and accuracy not only of a sample analysis but of the measurement program.

Uncertainty in environmental monitoring results arises primarily from design errors, the nonrepresentativeness of samples and/or measurements, human errors, and measurement uncertainty. These uncertainties cannot be fully eliminated but can be reduced as far as possible.

Nonrepresentativeness occurs when the sampling or field measurement is unable to capture the complete extent of variability that exists for the radionuclide distribution in a survey unit. Since it is impossible in every situation to measure the residual radioactivity at every point in space and time, the results will be incomplete to some degree. It is also impossible to know with complete certainty the residual radioactivity at locations that were not measured, so the incomplete survey results give rise to uncertainty. The greater the natural or inherent variation in residual radioactivity, the greater the uncertainty associated with a decision based on the survey results. Representativeness in sampling and/or in field measurements can be optimized by

TABLE 1.4 Detection limits, separation, and counting times for radionuclides of interest in environmental media.

Nuclide	Method	Detection limit (mBq/Sample)	Preparation time	Count time	Reference
$^{239+240}$Pu, ^{238}Pu[a]	Alpha spectrometry	0.02	2–4 days	5 days	Varga et al. (2007)
^{241}Pu	LSC	11	2–3 days	5 hours	Liong Wee Kwong (2004)
^{224}Ra	Gamma spectrometry	70	-	1000 minutes	Parekh et al. (2003)
^{226}Ra	Gamma spectrometry	80	-	2400 minutes	Parekh et al. (2003)
	LSC	0.3–1.4	2h (+30 days ingrowth of ^{222}Rn)	6 hours	Sanchez-Cabeza and Pujol (1998)
	Alpha spectrometry	0.2–0.5	2–4 days	2 days	Purkl S and Eisenhauer (2003); Karamanis et al., 2006
^{228}Ra	Gamma spectrometry	110	-	2400 minutes	Parekh et al. (2003)
	LSC	0.1	1–2 days (+48 h ingrowth of ^{228}Ac)	60 minutes	Nour et al. (2004)
	LSC (Cerenkov counting)	0.3	1–2 days (+48 h ingrowth of ^{228}Ac)	100 minutes	L'Annunziata and coworkers (see Aleissa et al., 2008)
	Alpha spectrometry	0.2	2–4 days (+12 months ingrowth of ^{222}Rn)	3 days	Purkl and Eisenhauer (2003)
^{90}Sr/^{90}Y	LSC (Cerenkov)	10	1–2 days (+20days ingrowth of ^{90}Y)	3hours	Suomela et al. (1993)
	LSC	10	1–2 days (+20days ingrowth of ^{90}Y)	3hours	Popov et al. (2006)

[a]*Same detection limits are achievable for all other actinides.*

means of an appropriate sampling and measurement scheme as described above.

Whereas incorrect calibration may be detected and corrected at a later stage, errors in the treatment of the samples cannot readily be detected and corrected. Furthermore, the storage of samples allows the repetition of measurements on the samples that are obviously not correct. Regular training and exercises should be conducted for the staff to maintain the experience of personnel as an important precondition for high-quality work, especially under stress in emergencies.

Human errors may give rise to, for example, improper recording, loss of samples, incorrect labeling, cross-contamination during sample preparation, and contamination of measurement devices. Adequate training of personnel and quality assurance procedures should be used to reduce human errors, even in emergency conditions.

IV. Monitoring for internal exposure

A. Air

Monitoring of airborne radioactive material in either particulate or gaseous form in air is of particular importance to estimate radiation exposures from external radiation or inhaled radionuclides; it provides the first opportunity to identify the spectrum of radionuclides making up the contamination and transfer of the deposited radionuclides through the food chain. Except for radon, the noble gases are not of great concern for internal exposure but contribute to the external exposure (Mück and Henrich, 2001).

Since the natural radioactivity concentrations under normal conditions are significantly higher than the artificial activity concentrations, accumulation methods are required. If the concentration is needed, the volume of air is measured in terms of flow rate. When the radionuclide activity per total amount of the element is to be determined, a passive device, such as a bag of silica gel or zeolite suspended in air to collect tritiated water, may be satisfactory. Retention efficiency must be tested under operating conditions, and possible adverse effects on the collection efficiency by other gases at various concentrations should be tested. The chemical form of the radionuclide especially influences the collection efficiency. Data on atmospheric stability, wind speed, and wind direction under which the samples were collected should be noted.

1. Aerosols

Aerosol monitoring includes sampling and measuring units that collect dust by drawing air through a filter material. The filters coupled to air pumps are capable of accumulating particulates from a large volume of air onto a small surface; their radioactive content can be determined with good measuring efficiency. Electrostatic precipitators, cyclone collectors, and cascade impactors are in use to collect particles and classify them according to size.

Since the radionuclide concentrations are reported per unit volume of air (Bq/m^3), the air should be drawn through the filter at a known rate for a known period of time, preferably using an integrating flow meter to give the total volume. When high dust concentrations occur during sampling, it may not be possible to maintain a constant air flow through the filter. The collection efficiency may change during operation if too many solids accumulate.

Several types of filter material (glass fiber, paper, cellulose) are used for collecting aerosol materials. The type of filter is selected according to the needs for high collection efficiency, particle size selectivity, retention of gaseous iodine with the particles, and ease of radiochemical analysis. It may be desirable to change filter media for specific purposes or to use several filters in series.

Lozano et al. (2011) propose the use of quartz filters to collect alpha-emitting natural radionuclides.

Pure cellulose papers are useful for samples to be dissolved and analyzed radiochemically, but the analytical filter papers used to filter solutions are inefficient collectors for aerosols and clog easily. Of particular value for samples to be analyzed radiochemically are filters composed of polystyrene fibers. They are efficient and capable of sustaining high air flow rates without clogging, are readily destroyed in analysis by ignition at low temperatures ($\sim 300^{\circ}C$) or by wet ashing with oxidizing agents, are also soluble in many organic liquids, have the disadvantage of very low mechanical and tensile strength, and must be handled carefully. Fiberglass filters can function efficiently at high flow rates but require fluoride treatment for dissolution and generally contain some radionuclides, for example, ^{40}K, to complicate low activity analysis. Overviews of filter media, classification, performance data, collection efficiencies, and practical selection tables are available (e.g., Purchas and Sutherland, 2002; Ruzer and Harley, 2005; and Papastefanou, 2008).

2. Online versus offline systems

Aerosol filtration can be accomplished by either moving filter bands in online systems or offline with fixed filter sheets. Both solutions have their advantages and drawbacks, and obviously, they require different measuring arrangements and different data evaluation algorithms.

The concept of moving filter bands means that the adsorbing surface is (partially or totally) renewed from measurement to measurement. Thus, the sampled volume is relatively less than that of a fixed filter sheet with the same air rate ($\sim 25\ m^3$/hour compared with $100-1000\ m^3$/hour), and so does the accumulation of a suspected artificial radiocontamination as well. On the other hand, the amount

of accumulated natural radioactivity will also be less in this case. Radionuclides on air filters are dominated by the naturally occurring, short-lived particulate decay products of radon (1−20 Bq/m^3 in outdoor air) and will also include cosmogenic ^{7}Be.

The moving band concept has significant advantage over the fixed filter systems if the concentration of artificial radioactivity in the sampled air steeply increases. This step-function-like phenomenon can occur in local monitoring systems where the possible source of contamination is close to the sampling station. In regional systems, the activity concentration of artificial radionuclides may increase due to atmospheric dispersion of radioactivity emitted from a (probably) distant source. This dispersion process is governed by laws of long-distance diffusion so the increase cannot be as vivid as it is assumed for cases of local monitoring. Therefore, a slow buildup rate is expected so the "early warning" requires accumulation of radioactivity—this condition means the supremacy of fixed (or slowly moving) filter systems over those of fast filter increment. Moving filter facilities allow automatic operation up to 6 months and are particularly used in automatic monitoring networks. One automatic station design of the IMS (International Monitoring System) Radionuclide Network uses a small robot to cut the filter in pieces after the collection process, which are afterward stacked into a neat pile for gamma measurement. The cutting edge works well on glass fiber filter material but badly on organic ones (Medici et al., 2004).

Fixed filter devices only permit sampling periods of maximum 1 week and thus require considerable operational service. High sampling rates are achieved with high capacity blowers and large area filters. The filters are usually compressed to provide a standard counting geometry and are measured by gamma spectrometry. Most institutes perform correction from natural radioactivity by waiting 2−5 days before measuring the filter. Detection levels of a few μBq/m^3 can be obtained, for example, 10−30 μBq/m^3 for ^{140}Ba with an airflow of 1000 m^3/hour (Schulze et al., 2000). Subsequently the filters may be dry- or wet-ashed for radiochemical analysis of pure alpha or beta emitters (e.g., ^{239}Pu and ^{90}Sr) using alpha spectrometry or LSC, respectively.

Widely used measuring methods of online systems are as follows:

- Gross beta: That is, total beta radioactivity with correction for natural radioactivity (mostly influenced by radon daughters). The measuring instruments used are Geiger−Müller, gas flow proportional counter with different active surfaces, and plastic scintillators with ZnS coating, mostly in anticoincidence configuration. Depending on the methods used, the lower detection limits range between $5\cdot10^{-5}$ and 1 Bq/m^3. Distinction between natural and artificial radioactivity can be done very effectively by simultaneous coincidence counting of alpha decay and by assuming that there is no contribution of artificial alpha emitters. In this way, concentrations of artificial radioactivity down to 0.1 Bq/m^3 can be detected. One may also perform a second delayed beta-counting after, for example, 12 h (most short-lived daughters will then have decayed, except ^{212}Pb).
- Gross alpha: That is, total alpha minus natural alpha radioactivity. The measurement is done by gas flow proportional counters, with or without anticoincidence or passivated, ion-implanted planar silicon detectors (PIPS). Lower detection limits range between $1\cdot10^{-5}$ and $4\cdot10^{-2}$ Bq/m^3.
- Nuclide specific: To ensure optimum early warning, these instruments are designed to allow the simultaneous alpha−beta measurement and the nuclide-specific measurement. In the automatic mode, modern instruments are capable of reaching low detection limits by means of high-purity Ge detectors.

General aspects pertaining to online monitoring systems (IEC, 2002a, 2002b) and regarding both continuous and discontinuous sampling (ANSI, 1999; ISO-2889, 1975) of discharges to the atmosphere can be found in international standards.

3. Gaseous effluents

Effluents can be present in air in gaseous forms that are not collected on particulate filters. Thus, special cartridges of activated charcoals or zeolites, both of which also may be silver impregnated, are necessary for efficient collection. Flow rates through these cartridges are normally lower than those for normal aerosols. Drawback of these filters is that, depending on the concentration, they become saturated and have to be replaced. However, silver zeolite cartridges are very expensive, and charcoal cartridges are more commonly used.

Radioactive gases can be measured in many types of counters with suitable sample chamber or the gas being placed inside the detector and spectrometers, including coincident detection of different radiation types. To prepare a gas sample for counting, it should be separated from the air and purified. This process consists of separations by charcoal and molecular sieve columns and purification by drying and chemical reactions to remove the impurities (Cummings et al., 1971; Stevenson and Johns, 1971; Johns, 1973; Medici et al., 2004; Bowyer et al., 2002).

^{3}H and ^{14}C gas samples are usually not counted as gases, as ^{3}H is usually converted to water and ^{14}C gas samples are converted into benzene or similar liquid for counting in liquid scintillation counters. To use the liquid scintillation technique for radioactive gases, they must be soluble in the liquid scintillation medium.

a. Iodine measurement

Iodine in air can be bound to aerosols or in the gaseous state, each requiring special measuring techniques. Iodine sampling is carried out by means of "traditional" filter papers or charcoal drums. The filter paper captures the iodine attached to aerosols, the charcoal captures the gaseous iodine, and the combination of the two measures the total amount of iodine in air.

Filter sheets containing charcoal and iodine-specific impregnated material are available. The advantage of the latter is obvious: the filters can be replaced easily and automatically, and their measuring geometry provides much better counting efficiency.

As far as regional monitoring is concerned, the "expected" iodine radioisotopes are the relatively long-lived fission products ^{131}I, ^{132}I, and ^{133}I. All of them are beta and gamma emitters, so iodine filter sheets are coupled to the appropriate detectors described above. If further radiochemical processing of filter sheets is possible and required, the extremely long-lived ^{129}I can also be analyzed (Hou et al., 2009). ^{131}I concentrations in the order of hundreds of mBq/m^3 can be measured in 1 hour. In the case of an accident, the ratio of gaseous ^{131}I to ^{131}I attached to particulate matter can vary between 2 and 20.

b. Radon measurement

There are many different methods available for the measurement of radon and its short-lived decay products, active as well as passive, short term as well as continuous or time integrating monitors. Some of them are very sophisticated and promise an accuracy of the measurement in the order of a few percent. Many of those are very sensitive not only to radon but also to environmental parameters and therefore fail, for example, in a wet environment. Others are less accurate, but they give reliable information on radon under difficult conditions. Instruments are called active, when any kind of external or internal power supply is needed for operation. Instruments are passive, when no external power supply is necessary for operation.

For the detection of radon gas, only the instrument has to be designed in a way that the noble gas, separated by means of an aerosol filter from its decay products and other aerosols present in air, is permitted to enter the sensitive volume where the radon is allowed to decay for a defined period of time. Thus, the radon measurement is basically a radon and radon progeny measurement. In that case, all suitable detectors are applicable to detect charged particles and photons emitted from the decaying radon and its decay products. For reasons such as the selected alpha and / or beta particles and the insensitivity to photons, only ionization chambers, alpha spectrometers and scintillation methods (e.g. Lucas Cells) are used for the active measurement of radon gas.

Ionization chambers provide a theoretical sensitivity in the order of 10^{-14} A/becquerel at equilibrium. The detection limit is variable with the volume of the ionization chamber and the measuring time, which is in the order of 30 minutes to hours. Typically using a 1-L ionization chamber, one can detect about 5 Bq/m^3 with an uncertainty of 10%–20% (Pohl and Pohl-Rueling, 1976; Friedmann, 1983).

Lucas cells are containers coated inside with ZnS(Ag) and having a quartz window transparent to scintillation photons. The container is filled with radon containing air, and scintillation photons are measured after equilibrium with the short-lived radon progenies is reached. Since each alpha particle emitted from a decaying radon atom is followed by two others from the decaying radon progenies, the theoretical conversion factor is 3 pulses/becquerel. Practically, this factor is between 2 and 2.5 scintillations/becquerel.

For time-integrated measurements mainly passive instrumentation, such as adsorption on charcoal, diffusion chambers with and without filters, thermoluminescent detectors, or solid-state nuclear track detectors are used currently. Solid-state nuclear track detectors are made of materials such as cellulose nitrate (LR115), polycarbonate (Makrofol, Lexan), or allyldiglycol polycarbonate (CR39). The reading of these types of detectors is done after an (electro-)chemical etching process by optical devices, for example, as track density, changes in optical transparency, or by scintillation technique. As etching agent a solution of mainly potassium hydroxide or sodium hydroxide in different concentrations and varying ratios of ethanol are used, depending on the detector quality, the kind of etching process, and alpha energies to be detected.

Excellent reviews on solid-state nuclear track detectors are given by an OECD/NEA group of experts, published in OECD (1987), by Ilić and Durrani (2003), Guo et al. (2012), and in Chapter 3, Volume 1 of this book.

c. Noble gases other than radon

Krypton and xenon are inert noble gases and, therefore, usually one of the first radionuclides that can be emitted in processes that produce fission products. Due to their inert nature, krypton and xenon radioisotopes are unlikely to contribute significantly to internal exposure but are parts of the external exposure due to the plume after an accidental release to the air.

Furthermore, krypton and xenon do not have a major deposition rate from the atmosphere and therefore can travel long distances following a release and be detected with sufficiently sensitive instruments. In addition, the half-lives of some of their isotopes (^{85}Kr half-life: 10.8 years and ^{133}Xe half-life: 5.3 days) are nearly optimal for detection, because they are short enough that they do not build up in the atmosphere from decay of geological uranium or anthropogenic sources, yet they are long enough to

survive windborne travel distance from the source at detectable levels.

The major sources of ^{85}Kr are nuclear fuel reprocessing plants located in the northern hemisphere. Due to its long radioactive lifetime, ^{85}Kr has spread out all over the globe; typical background levels in the northern (southern) hemisphere are currently about 1.3 Bq m^{-3} of air. The yearly global release rate of ^{85}Kr to the atmosphere exceeds the removal rate by radioactive decay, resulting in a slow but continuous increase of atmospheric concentrations worldwide, which has been of some scientific concern (WMO, 1996). The well-known source term and its chemically inert properties make ^{85}Kr a useful tracer for studies of the regional and the global air circulation (Jacob et al., 1987; Zimmermann et al., 1989; WMO, 1996). Monitoring of ^{85}Kr may have some importance for nuclear safeguards (Kalinowski et al., 1998). Clandestine production of plutonium for nuclear weapons can be detected by the monitoring of ^{85}Kr in the air.

About 20 radioactive isotopes of xenon are formed in fission of heavy elements such as uranium or plutonium. Most of these isotopes decay within seconds, but a few have half-lives of several hours to several days and, thus, are detected in the environment near nuclear facilities such as medical isotope production facilities (Saey et al., 2010), near operating nuclear reactors, and also following nuclear explosions. This is one of the basic reasons why monitoring of radioactive noble gases in the atmosphere has been performed for decades. Radioxenon backgrounds range from well below 1 mBq m^{-3} in much of the southern hemisphere (Bowyer et al., 1997) to 1000 mBq/m^3 near medical isotope production facilities. However, most of the world has backgrounds in the range of 1−100 mBq/m^3. Radioactive xenon has four isotopes that are commonly detected by many groups and by the International Monitoring System (IMS) of the Comprehensive Nuclear-Test-Ban Treaty (Saey and De Geer, 2005). These isotopes are ^{131m}Xe ($t_{½} = 11.9$ d), ^{133}Xe ($t_{½} = 5.2$ d), ^{133m}Xe ($t_{½} = 2.2$ d), and ^{135}Xe ($t_{½} = 9.1$ h).

The basic techniques for measuring radioactive krypton or xenon isotopes in the atmosphere have been available for a number of years using a variety of methods (Ludwick, 1966; Schölch et al., 1966; Bernstrom and DeGeer, 1983; Kunz, 1989; Bowyer et al., 1996). Sensitive detection of krypton and xenon isotopes is commonly performed after separation of the gas from large volumes of air from the major interfering constituents of air, such as N_2, O_2, Ar, CO_2, H_2O, Rn, etc. by collecting the gas on adsorbents (e.g., through activated charcoal under reduced pressure at liquid nitrogen temperature) followed by the use of gas chromatography using CH_4 as a carrier gas to both further separate the xenon from radon and to insert the krypton or xenon gas into a favorable counting geometry. Several sources explain the state-of-the-art for this process in some detail (e.g., Stockburger et al., 1977; Ringbom et al., 2003).

Mainly, four automatic xenon measurement systems have been developed: the Automatic Radioanalyzer for Isotopic Xenon (ARIX), from the Khlopin Radium Institute (KRI), Russia; the Automated Radioxenon Sampler-Analyzer (ARSA), from the Pacific Northwest National Laboratory (PNNL), United States; the Swedish Automatic Unit for Noble Gas Acquisition (SAUNA), from Totalförsvarets Forskningsinstitut (FOI), Sweden; and the Système de Prélèvement d'Air Automatique en Ligne avec l'Analyse radioXénons atmosphériques (SPALAX) from Departement Analyse, Surveillance, Environnement du CEA (CEA/DASE), France. An overview of the system features can be found in Bowyer et al. (2002); Ringbom et al. (2003); and Fontaine et al. (2002).

B. Soil, sediments, vegetation, and deposits

Sampling of soils, deposits, and vegetation and subsequent measurement of radionuclide concentration is an appropriate method for evaluation of levels of ground contamination due to dry or wet deposition, the contribution to the evaluation of levels of total deposition per unit area on all surfaces, the prediction of dose rates, and time dependence of dose at the location, and with use of transfer coefficients, a rough estimate can be obtained for the future contamination of vegetables. Additionally, ground contamination may be a source of resuspension of radioactivity that may cause inhalation hazards and additional dispersion of radioactivity.

1. Laboratory based

a. Soil and sediments

Soil sample analysis is a common method of environmental monitoring. Sampling depths vary with the purpose of the study and the soil characteristics. The conventional sampling technique of soils is core sampling. Because the concentration of deposited radionuclides usually decreases rapidly with depth in undisturbed soil, one may have to sample as a function of depth, with both the collection area and the depth noted. For radionuclide availability studies, samples should be taken in crop areas with a coring tool to a depth of 5 cm or to the depth of the plow line.

Migration in the soil depends on the radionuclide and its chemical form and the soil type, but most artificial radionuclides are found in the upper 30 cm soil layer. Because of the possibility of large microscale variations of deposition, it is very important to take a sufficient amount of soil samples to obtain a reasonable estimate of the deposition of radioisotopes at a given site. The sample should also be

defined according to soil characteristics, agricultural status, and vegetation cover. The latter should be analyzed separately. Sampling tools vary, but any device that will cut a straight core will be satisfactory. Samples should be taken with coring tools of known diameter so that the ground area represented by the sample is accurately known. In general, about 10 cores (or a total surface area of at least 200 cm^2) are taken and composed to make a single sample.

Sediment is an indicator and accumulator of radionuclides that are insoluble and adsorbed on insoluble material in the aquatic system. Conventional collection is by a dredge dropped from a boat. The dredge mechanism is activated by contact with the benthos. For river sediments, it is of interest to describe the stream flow conditions that lead to benthal deposition and the movement of the sediment, as well as the characteristics of the sediment such as particle size distribution, soil type, ion-exchange capacity, and organic content. Collected samples are treated similarly to soil samples except that the accumulation from and interaction with the aquatic environment must be considered rather than deposition from air and uptake by grass.

Drying at low temperatures (50°C) to avoid the loss of radionuclides from the soil and hand mixing of soils or sediments prior to subsampling should be acceptable for gamma spectroscopy where a relatively large subsample is used (e.g., 150−500g). However, drying, grinding, and sieving prior to subsampling should be carried out where a small subsample (e.g., 5−10g) is to be taken for radiochemical analysis. Commercially available grinders, mills, pulverizers, mixers, and blenders are suitable. Hardened metals are best for the grinding surfaces, and it is not likely that radioactive contamination will be introduced into a sample with this equipment, except by cross-contamination from a high radioactive sample. To prevent this, thorough cleaning of equipment between samples is advisable. At this stage, a portion may be taken for gamma ray spectrometry.

If vegetation and organic debris are not discarded, the roots, mat, and vegetation should be cut into very fine particles so as to be distributed evenly; if they are to be discarded, these materials should be collected and weighed. Stones should be collected, weighed, and discarded. It can be assumed that the large rocks contain an insignificant fraction of the activity and are in effect voids in the sample. This has been shown experimentally for plutonium (Krey and Hardy, 1970). The mass of the discarded material should be taken into account, but not in calculating the specific activity of the soil. It provides, however, additional information to indicate the overall makeup of the growing area. In either case, the soil should be crushed, ground, or pulverized to a particle size predetermined by the analytical requirements. The need for preparing the material will also depend on the nature of the soil; for example, beach sand may not need grinding. In general, the soil should pass a mesh size of 2 mm. Activity in soil samples is reported on a dry weight basis in Bq/kg and on an area basis in Bq/m^2.

The question of complete dissolution versus leaching of soils is still being debated for certain analyses. Plutonium from worldwide fallout can be successfully leached with acids, if a plutonium tracer in the same chemical form is used to monitor the yield. Other forms of plutonium, such as those produced in a laboratory or fuel reprocessing plant by high temperature ignition, require digestion methods (e.g., high-pressure microwave, plasma, etc.) or repeated treatments with hydrofluoric and mineral acids for complete dissolution.

In typical radiochemical procedures to analyze for Pu, Am, and Sr in soils, 10 g of ashed material is taken for the analysis. If no stable strontium is present in the sample, 10 mg of strontium carrier and spikes of ^{243}Am and either ^{236}Pu or ^{242}Pu tracers are added. The selection of the amount of the spikes depends on the expected activity concentrations present in the sample, but typically 10−50 mBq of each are added. The use of HF will be recommended for sample dissolution to facilitate the total decomposition of the matrix, since ^{90}Sr might be contained in the lattice of the silicate material or in refractory oxides. The sequential treatment with mineral acids usually results in the dissolution of greater than 99% of the sample, and the resulting solution is filtered through a 0.2-μm polypropylene membrane filter. The leachate solution is used for the radiochemical separation of Pu from Am and Sr by anion exchange followed by the preconcentration of Am and Sr by coprecipitation with calcium oxalate. Am is separated from Sr by extraction chromatography using TRU resin. For further purification of the Am fraction (separation from rare earth elements), anion exchange chromatography is used. The final Sr separation and purification is performed by extraction chromatography using Sr resin (Vajda et al., 1992; Moreno et al., 1997). The measurement of the ^{90}Sr activity is performed by LSC using a low-energy window, which includes the entire ^{90}Sr spectrum plus some tailing from any ingrown ^{90}Y, and a high-energy window chosen above the ^{90}Sr maximum β-energy, which is used to measure ^{90}Y to correct the ^{90}Y tailing in the ^{90}Sr window. The recovery factor for ^{90}Sr (assuming a total isotopic exchange between the stable strontium isotopes and the measurand ^{90}Sr) is determined by gravimetry, and the calculation is based on a standardized strontium carrier solution. The quantification is performed by isotope dilution alpha spectrometry using ^{242}Pu or ^{236}Pu and ^{243}Am tracers.

b. Vegetation

Analysis of vegetation, such as grass and leaves, animal feeds, especially forage and field corn, provides important data for determining radionuclide concentrations in food

chains. Some materials have particular utility for identification: Spanish moss on trees being a natural filter for airborne particles, ground mosses, and lichens integrating radionuclide deposition over many years, and the leaves of perennial plants being useful for identifying nuclides collected in a particular growing season.

The vegetation cover from at least 1 m^2 of ground should be collected. The aim should be to obtain at least 0.5 kg. Smaller samples may be collected whenever the required radionuclide detection limit can be attained. Grass should be cut at the appropriate height (1−5 cm) to obtain an estimate of what a grazing animal would consume by simulating its grazing behavior. In drier climates or during sparse growing seasons, it may be necessary to sample nearer to the soil surface. Care must be taken to prevent the cut material from being contaminated with soil. It should be recognized that samples of vegetation cut this way will not represent exactly what the grazing animal consumes.

The vegetation may be analyzed in a fresh state, or if time permits and the loss of radioiodine is not of concern, it may be dried. Generally, grass is dried at temperatures not exceeding 105°C for 24 hours. The dried matter should be ground so that all particles pass through a 2-mm sieve. Samples must be weighed in a consistent manner so that the concentrations can be compared among samples. Activity on grass is reported on the basis of two weights (Bq/kg wet mass or Bq/kg dry mass) and area (Bq/m^2); hence, sample mass should be determined at collection and air-dried, oven-dried, or ashed. There is general agreement that vegetation requires complete dissolution.

If samples are collected to derive transfer coefficients or to represent certain exposure pathways, sample selection must be guided by factors such as growth patterns, wind direction frequencies, soil types, and farming practices. The amounts required for such analyses may refer to the entire sample, to the edible part, or to the part that collects or concentrates the radionuclides of interest. One should consider the pathway of radionuclides to the analyzed fractions, such as surface deposition, root uptake, and translocation from other parts of the plant.

c. Deposits

Dry and wet depositions of radionuclides are measured to follow the movement of radionuclides from air to terrestrial and aquatic media. In principle, a collector with an open surface ranging from 0.05 to 10 m^2 accumulates dust or precipitation for a specified time, and this material is analyzed for radionuclide content. The materials used for the collecting areas vary (stainless steel, plastic, polyester, PVC). To obtain concentration as well as deposition values, the amount of rainfall is measured after each collection. Typical sampling periods range from daily, over weekly to monthly. In normal circumstances, variations in time and space for the data from a number of sampling locations are gradual. For this reason, daily, weekly, or even monthly variations per sample location are not of radiological significance.

The container or collector surface should be washed to collect radionuclides that tend to adhere to surfaces or lined with a plastic sheet that is analyzed with the container contents. Water may be funneled through a filter or ion exchange system for collecting some radionuclides. Dry deposition is determined separately on material such as gummed paper or fibers that simulate grass. The same radionuclides are usually deposited in rain and collected with airborne particles, but relative amounts depend on the initial vertical distribution, particle sizes, and other characteristics.

Collectors intended to measure representative deposition should be placed so as to avoid effects by local factors, for example, air turbulence, shielding by buildings and vegetation, and sources of dust, fumes, and moisture.

2. In situ gamma spectroscopy

Introduced in the 1960s to determine natural background and weapons test fallout emitters in soil, the relevant gamma dose rate in the air above, and the relative contribution of the ^{238}U and ^{232}Th series and ^{40}K to the dose rate (Lowder et al., 1964a, 1964b; Beck, 1966; Beck et al., 1964), in situ (i.e., field) spectrometry soon appeared as a powerful tool to provide rapid and spatially representative estimates of environmental radioactivity. In essence, this technique consists of the collection of gamma spectra using a field-portable detector mounted on a tripod above the ground surface (typically 1 m) and subsequent elaboration of the full absorption peak areas multiplied by ad hoc coefficients calculated according to two fundamental assumptions:

- The source—in this case the soil—can be modeled as an infinite half-space (thus within the field of view of the detector, the ground surface should be relatively flat and free of any large obstacles, and the radionuclide activities are assumed to be uniform within this zone).
- The vertical distribution of radionuclides can be reasonably assumed to take account of attenuation by the soil matrix (typically uniform distribution for natural radionuclides and exponential distribution for artificial ones).

Under these conditions, it is possible to use a standard point source calibration performed in the laboratory (Beck, 1972; Beck et al., 1972; Cutshall and Larsen, 1986; Miller and Shebell, 1995). The calibration based on the relation of the absorption peak counting rate registered by the detector (N_f) to the exposure rate in air (I) above the ground, or the concentration or inventory of a particular nuclide (A) is

$$\frac{N_f}{I} = \frac{N_0}{\Phi} \cdot \frac{N_f}{N_0} \cdot \frac{\Phi}{I} \quad \text{or} \quad \frac{N_f}{A} = \frac{N_0}{\Phi} \cdot \frac{N_f}{N_0} \cdot \frac{\Phi}{A}$$

where

N/Φ is the counting rate from a particular spectrum absorption peak due to a unit primary photon flux density of energy E incident on the detector along the detector axis (normal to the detector face).
N_f/N_0 is the correction required to account for detector angular response,
Φ/I is the primary photon flux density with an energy E at the detector resulting from the decay of a particular radionuclide per unit exposure rate at the detector from all primary and scattered photons originating from this nuclide and any others present from its radioactive decay series.
Φ/A is the total photon flux density at the detector location per unit concentration or inventory of the nuclide.

The first two terms depend on the particular detector; Φ/I and Φ/A values depend only on the source composition and geometry and can be used for any spectrometer calibration. The factors are derived from γ-ray transport calculations. Tabulations of these data along with other pertinent information on the makeup of the environmental γ-radiation field can be found in Beck et al. (1972), Beck and de Planque (1968), and Beck (1972). A complete set of exposure rate values *(I/A)* close to 200 common fission and activation radionuclides at various exponential depth distributions in the soil can be found in Beck (1980).

With this calibration and the coefficients elaborated following Beck's method, the dose rate—produced by the unscattered and scattered fluence of gamma rays—can be estimated, and the radionuclide inventory calculated. Minimum detectable concentrations using a typical 25% relative efficiency p-type germanium detector and a 10-minute count time at typical background radiation levels for ^{60}Co, ^{137}Cs, ^{152}Eu, ^{226}Ra (based on measurement of progeny), and ^{228}Ac (to infer ^{232}Th) are all reported to be in the order of 1.8 Bq/kg (NRC, 1995).

The original method cannot be used for all kinds of source geometry, for example, indoors or urban outdoors, because it is not feasible to elaborate the buildup factors or produce calibration curves from which to derive the radionuclide activity concentrations in the source. Further limitations of the technique are mainly associated with the need of a priori assumptions about the distribution of nuclides in the soil, an important source of uncertainties of activity concentration estimates and dose rate evaluations, since dose rate is obtained as a sum of different radionuclide contributions to unscattered and scattered gamma flux at the detector.

Indoor and outdoor buildup factors and the estimate of the actual radionuclide distribution in soil have been obtained following two approaches: Monte Carlo simulation and the use of algorithms aimed to the direct elaboration of spectra. A parametric calibration was elaborated, based on the efficiency and geometric dimensions of the detector (Helfer and Miller, 1988). Another improvement was the introduction of a stripping method that subtracts partial absorption and the contribution from cosmic ray events from a collected spectrum. An important step for the diffusion of this technique was the publication of ICRU Report 53 (ICRU, 1994), which addressed the main aspects of in situ gamma spectroscopy.

Hence, since the pioneering work of Beck et al. (1972), the use of in situ gamma spectrometry measurements has become a well-established technique for documenting levels of environmental radioactivity in soils (e.g., Miller and Helfer, 1985; Helfer and Miller, 1988; Miller et al., 1994; Zombori et al., 1992; Lettner et al., 1996; Abelquist et al., 1996; Tyler et al., 1996), power reactor plumes (Gogolak, 1984), forests (Gering et al., 2002; Plamboeck et al., 2006), urban areas (Medeiros and Yoshimura, 2005; Clouvas et al., 2001, 2003; 2006; Svoukis and Tsertos, 2007), large areas (Cresswell et al., 2006; Tyler, 2004; Guillot, 2001; Hendriks et al., 2001), indoor gamma dose rate estimates (Miller, 1984; Miller and Beck, 1984; Clouvas et al., 1998, 2000), and building materials (Risica et al., 2001; Risica and Nuccetelli, 2001; Bochicchio et al., 2004).

C. Water

In addition to potential contamination with anthropogenic radionuclides, radium isotopes, ^{222}Rn, several short-lived daughter products of radon, and finally, two longer-lived decay products, ^{210}Pb and ^{210}Po, and to some extent uranium are of some concern in natural waters. Due to its low solubility, thorium is not generally considered to be a major environmental hazard. Radiological water quality guidelines have been developed regionally (ANZECC/ARMCANZ, 2000; NHMRC, 2004; USEPA, 2000; EU, 1998) and globally (WHO, 2008; WHO, 2011) for potable, livestock, watering irrigation, and recreational uses.

Sampling and preparation of water samples for analysis presents a number of problems not shared by other sample types and for which clearly defined answers are not available. The problems are caused principally by two situations: the samples are two-phase systems (i.e., the water contains some insoluble material) and the sometimes unpredictable behavior of many substances at very low concentration. The variable composition of natural waters adds to the problem.

Because a radioactive element of interest often is present in submicrogram quantities, a significant fraction may no longer exhibit their expected ionic behavior and be lost by adsorption on the surface of suspended particles or on

the surface of containers used in the examination. Even an ion as simple as cesium can be lost in trace amounts in glass containers by exchange with the potassium in the glass. Radionuclides at low activities may also exhibit many properties of colloids, and the term "radiocolloid" has been applied to such mixtures. For a discussion of radiocolloids, in general, see Crouthamel and Heinrich (1971), Olofsson et al. (1981, 1983), or Vilks and Bachinsk (1997). To reduce the effect of radiocolloid adsorption, an appropriate amount of the corresponding nonlabeled compounds (carrier) should be added to the system to lower the radiocolloid formation by the chemical dilution of the radioactivity (Keller, 1993).

To reduce the possibility of the loss of radionuclides on the walls, the sample is usually acidified. Most environmental water is close to neutral, and acidification to 0.1−0.5N is adequate. At this acidity, radioactive substances in particles in the sample can be leached (perhaps slowly) and appear in the solution, resulting in a considerable increase in the original soluble radioactivity. Also, iodine ions will slowly oxidize to iodine, and radioiodine in solution may be lost by volatilization if nitric acid is used. To prevent sorption of radionuclides on container walls between sampling and analysis, freezing may be a suitable method, but this is practical for small samples only, and the treatment of the insoluble portion still remains. If the sample has been stored before analysis, particularly at its natural acidity, it is advisable to transfer the sample to a second container with a solution—usually an acid—in which the sought-for activity is soluble. The wash solution can be added to the original solution or analyzed separately. The effectiveness of the washing procedure must be verified experimentally.

So, it would appear that the safest pretreatment procedure, if the suspended and dissolved fractions are desired separately, is to filter the water through membrane filter paper while collecting the sample in the field and acidify the sample immediately thereafter. The acid can be present in the receiving flask during filtration. In this way, the water is not in contact with the container walls until after acidification. If this procedure is impractical, the sample should be filtered as soon as possible after collection and the sample acidified immediately prior to filtration. Any inactive carriers or radioactive tracers used in the analyses should be added as soon as possible, preferably before acidification, filtration, or evaporation.

An efficient method for separating traces of actinide elements from solution introduced in the 1960s by Eakins and Gomm (1968) utilizes filtration through glass fiber paper at pH 5. Most actinides are absorbed almost completely on the glass fibers, indicating that silica in solution can adsorb many ions from solution.

A precaution observed in direct gamma spectrometry of water samples is the change in counting geometry that will occur if finely divided species become fixed on the container walls during counting. Such samples can be filtered, evaporated, or acidified, if the suspended material is soluble in dilute acid.

For gross activity measurements applying gas flow proportional counters, the water sample is dried by oven evaporation just below the boiling temperature or on a hot plate. The sample should be less than 3 mg cm^{-2} in thickness. The main error in this procedure is the loss of particles, which might become airborne during the drying process.

Although there are a number of international standards describing test methods for gross alpha and/or gross beta determination in water samples, for example, ISO 10704 "Water quality—Gross alpha and gross beta activity—Test method using thin source deposit" (ISO 10704, 2018); ISO 9696 "Water quality—Gross alpha activity—Test method using thick source" (ISO 9696, 2017); ISO 9697 "Water quality—Gross beta activity—Test method using thick source" (ISO 9697, 2018), the gross activity method is considered to be a screening procedure at best. For example, Oural et al. (1988) have shown that gross-alpha activity can underestimate actual activity because of partial volatilization of radon, short-lived radon daughters, and polonium during evaporation on the planchet. Until the short-lived radon daughters decay to a level supported by radium in the water, a time-dependent alpha activity results, which has little correspondence with actual water chemistry (Oural et al., 1987, 1989). Although nuclide-specific measurements are preferable in environmental monitoring, there are some attempts of gross counting applying LSC (Happel et al., 2004; Kleinschmidt, 2004; Wisser et al., 2006, Zapata-García et al., 2009), as it provides a rapid screening method with the ability to give at least hints of the radionuclide that has to be analyzed in the case of an unknown contamination.

Various methods have been described for the measurement of radium isotopes and ^{222}Rn. Besides gamma spectroscopy (e.g., ISO 13164-2, 2013; ISO 13165-3, 2016), liquid scintillation techniques are most common. The classical reference method for radon in water measurements has used a radon bubbler and the Lucas cell. Liquid scintillation techniques for ^{222}Rn in water, first described by Prichard and Gesell (1977), have the advantages of minimal sample preparation time, small sample sizes, and automatic sample changing, with achievable detection limits in the order of 0.37 Bq/L (Spaulding and Noakes, 1992), actually depending on the background, counting time, and acceptable degree of uncertainty. LSC instruments capable of alpha/beta discrimination are being used in the determination of radon and its daughters in ground water and drinking water since the 1990s (e.g., Schönhofer, 1989; Chalupnik and Lebecka, 1993; Irlweck and Wallner, 1993; Prichard et al., 1991) as well as

in surface water (Salonen, 1993). A standard method based on a two-phase extraction to determine ^{222}Rn in water samples is given in ISO 13164-4 (2015), the detection limit of which is 0.5 Bq/L at a measuring time of 1 hour and for a test sample of 10 mL.

Liquid−liquid extraction, ion exchange chromatography barium sulfate, and barium carbonate precipitation are the usual separation techniques used for radium. Specific extractants especially for use with alpha LSC, such as extractive scintillators (RADAEX) (McDowell and McDowell, 1994) or impregnated filter papers (Empore Radium Rad Disks) (Smith et al., 1997) for radium, have been developed. The extractive scintillator consists of an organic extractant solution, such as toluene, xylene, or mesitylene solution of a high-molecular-weight neocarboxylic acid together with the crown ether (dicyclohexano-21-crown-7), used in a mole ration 2:1 combined with a flour, PBBO, and naphthalene as energy transfer agent. This extractant separates radium from barium, strontium, and calcium by factors of 9.3, 12, and 58, respectively (McDowell and McDowell, 1994).

Analysis for ^{226}Ra may involve inferring the radium activity from a measurement of the ingrown daughter, ^{222}Rn (Parks and Tsuboi, 1978; Prichard et al., 1980; Cooper and Wilks, 1981; Horiuchi and Murakami, 1981; Nobrega et al., 1987; Chu and Khalique, 1990; Schönhofer et al., 1991), or applying pulse shape analysis to the determination of ^{226}Ra alpha particles (Cross and McBeth, 1976; Coombs, 1980; Noguchi et al., 1984; Burnett and Tai, 1992; Blackburn and Al-Masri, 1992; Saarinen and Suksi, 1992).

^{228}Ra determination may be based on counting ^{228}Ac (Petrow et al., 1964; Nour et al., 2004, L'Annunziata and coworkers (see Aleissa et al., 2008)) or the ^{228}Th alpha-emitting daughter, liquid scintillation beta−gamma coincidence spectrometry, and ^{220}Rn emanation (Orr, 1988), which is similar to ^{222}Rn emanation techniques used for ^{226}Ra. However, the latter approaches are limited by the slow ingrowth of the ^{228}Th ($T_{1/2} = 1.9$ years).

A time-saving method for the measurement of ^{226}Ra, ^{228}Ra, and ^{210}Pb in drinking water by applying Empore Radium Rad Disks and low-level liquid scintillation spectrometry has been developed by Schönhofer and Wallner (2001). Radium is concentrated by filtration of the sample through a membrane loaded with element-selective particles. The extracted nuclides are eluted with 0.25 M alkaline EDTA solution, which is then mixed with the LSC cocktail. Lead is coextracted, and therefore, ^{210}Pb interferes with ^{228}Ra to a certain extent. The collection efficiency for both lead and radium isotopes is about 100% (Schönhofer and Wallner, 2001; Wallner, 2002).

To determine low-level activity concentrations of ^{210}Po in water samples, large volume samples (>1 L) have to be provided. The samples have to be preconcentrated since direct evaporation (Katzlberger et al., 2001) of large volumes is very time-consuming and susceptible to losses of polonium (Oural et al., 1988).

Therefore, coprecipitation with iron hydroxide followed by a solvent extraction step with an extractant such as diisopropyl ether to remove Fe from the sample solution (Narita et al., 1989) or MnO_2 (Carvalho, 1997; Martin and Hancock, 2004) has commonly been used. Additional chemical purification using Sr resin (Vajda et al., 1997; Miura et al., 2000; Vrecek et al., 2004) or various solvent extractions prior to the final autodeposition of Po may be applied.

Besides gamma spectroscopy of evaporated water samples, analysis of ^{210}Pb in water samples can be based on autodeposition of the Pb-210 decay product Bi-210 on nickel according to the electrochemical series of metals. Due to its electrochemical characteristic, Po-210 is collected as well. The method consists of a chemical acid pulping, followed by a decay products buildup, the deposition and the measurement of the ^{210}Bi beta radiation. The deposition from HCl is more smoothly and quantitative to HNO_3 or H_2SO_4 (Figgis, 1961). In 1982, Richard J. Velten and Betty J. Jacobs developed a standard method for ^{210}Pb determination in drinking water (EPA, 1982) for LSC or low background end window counting. The method consists of a precipitation as chromate, purification from ^{210}Bi by selected dissolution of lead sulfide from a hydrochloric acid solution (1.5 N), and conversion of lead to the carbonate.

Activity concentrations in the range of less than 20 mBq−50 mBq/L can be achieved with measuring times between 3 and 12 hours with the standard method of ISO 13163, 2013 "Lead-210—Test method using liquid scintillation counting" (ISO 13163, 2013). The sample volume needed for this method is 0.5−1.5 L.

Tritium, produced during atmospheric thermonuclear tests, is used as a global transient tracer for studying dynamics in the hydrological cycle, recharge, renewal rate, flow velocity, and in conjunction with radiocarbon to determine groundwater age (Libby, 1953; Bergmann and Libby, 1957; Fontes, 1983; Günay, 2006; Lloyd, 1981; Sanchez-Cabeza and Pujol, 1999; Lehmann et al., 1993; Yurstsever, 1983; Wen et al., 2005, 2008; Borio et al., 2005).

Because natural levels of tritium are only marginally measurable by direct β-counting methods, the water samples are purified by distillation, followed by an isotopic enrichment procedure using electrolysis through direct current (Florkowski, 1963, 1992; Morgenstern et al., 1992). After the neutralization procedure by addition of $PbCl_2$, or CO_2, a new distillation is performed. Afterward, one aliquot of 8 mL is withdrawn to a scintillation vial with 12 mL of Ultima Gold LLT scintillation cocktail (PerkinElmer, Inc.) at a sample pH value ranging from 5 to 7.

Tritium (and its daughter ^{3}He) can also be measured using mass spectrometry, but other dissolved gases (H_2O, CO_2, O_2, N_2, etc.) must be removed first (Faure, 1986; Clark and Fritz, 1997).

Due to the specific characteristics of tritium (gas, relatively easily oxidized to HTO), combined with omnipotent presence of water vapor, the assay of low levels of tritium requires consideration of various types of contamination, the magnitude of which is depending strongly on specific procedures of sample handling, on the ambient tritium concentrations during sampling, storage and analysis, and the type of containers used to store the samples before the analysis. Sample contamination may originate from some types of watches with fluorescent tritium dials, tritium sources used in gas chromatography, targets used in neutron generators, or medical experiments where tritium is used as a tracer (Okada and Momoshima, 1993).

Tritium activity concentration is commonly reported in Tritium Units (TU). The TU is the ratio of tritium atoms to stable hydrogen-1 atoms or $[^{3}H]/[^{1}H]$, prior to weapons testing, and represents the number of tritium atoms per $1 \cdot 10^{18}$ hydrogen atoms. Hence, one TU is equivalent to 0.118 Bq kg^{-1} of water. With the electrolytic enrichment technique, detection limits in the order of 0.1−0.01 TU (11.8−1.18 mBq/kg) are achievable. If detection limits in the order of 10 Bq/kg (Bq/L) are to be achieved, distillation (probably multiple distillations) will suffice using low-level LSC instruments.

1. Wastewater

Wastewater often contains larger amounts of nonradioactive suspended and dissolved solids than water, and often, most of the radioactivity is in the solid phase. At the sampling of radioactive industrial wastes or similar materials, the high possibility of deposition of radioactivity on surfaces of glassware, plastic containers, and equipment, which may cause a loss of radioactivity and possible contamination of subsequent samples collected in inadequately cleansed containers, has to be considered.

Generally, the use of carriers in the analysis is ineffective without prior conversion of the solid phase to the soluble phase, since the radioelements may exhibit unusual chemical characteristics, because of the presence of complexing agents or the method of waste production. For example, tritium may be combined in an organic compound when used in the manufacture of luminous articles; radioiodine from hospitals may occur as complex organic compounds, compared with elemental and iodide forms found in fission products from the processing of spent nuclear fuels; uranium and thorium progeny often exist as inorganic complexes rather than oxides after processing in uranium mills; the ^{90}Sr titanate waste from a radioisotope heat source is quite insoluble compared with most other strontium wastes. Valuable information on the chemical composition of wastes, the behavior of radioelements, and the quantity of radioisotopes in use appears in the literature (e.g., Ghiloufi, 2009.)

2. Rain

The rainwater may be directly fed to a bottle or to an ion exchange column where the nuclides are fixed. Measurement of the activity in the collected rainwater and of the amount of rainfall allows the calculation of the average total deposition during the sampling period.

Contamination of rain water samples by airborne soil and surface dust can be minimized by locating the sampling stations on the roofs of buildings. Overhanging vegetation should be avoided. The most suitable size for the collector depends on the amount and frequency of precipitation in the area, as well as the frequency of collection. For areas receiving 5−25 cm precipitation per month, a collecting area of 0.1−0.2 m^2 is suggested. All materials in the collector must be transferred with great care to ensure that all the radioactive material is collected. The sides and bottom of the container should be scrubbed several times with a rubber spatula and rinsed with distilled water. If the containers are reused, care must be taken to avoid a buildup of contamination that will influence subsequent samples.

3. Groundwater

For most people, the source of water for domestic consumption and other uses is groundwater, often obtained from shallow, private wells, but more often obtained from public, community wells tapping the aquifer.

Besides possible contamination from effluent discharges, groundwater is prone to naturally occurring radionuclides. If valid judgments are to be made about the hazards and management of the radionuclides in ground water, it is necessary to understand the specific behavior of these radionuclides in the aquifer chemical systems, and that requires detailed knowledge of groundwater pH, reduction−oxidation potentials, with rock materials (Foss and Brooker, 1991). Chemical reactions, such as ion exchange, chemical complexing, and equilibration reactions with minerals and physical processes, such as alpha recoil (Osmond and Cowart, 1976; Osmand et al., 1983, 1984), can cause considerable departures from decay equilibrium within the uranium decay series.

Because of their greater mobility, uranium and ^{226}Ra are usually depleted relative to ^{230}Th on the surfaces of soil or rock particles (e.g., minerals and particulate organics). ^{238}U, ^{234}U,

and ^{226}Ra are, therefore, present in greater abundance in ground water than ^{230}Th. ^{222}Rn enters water by alpha recoil and/or leaching and migrates. ^{210}Po and ^{210}Pb also migrate to a lesser extent and are in disequilibrium to other isotopes in the U-238 series (Upchurch et al., 1991).

4. Surface water

Surface water comprises river, lake, or sea water and is one of the environmental compartments to which radioactive effluents from nuclear installations are authorized to be discharged. Radionuclides in surface waters can be found in the water phase or associated with suspended particles and can eventually become incorporated into sediments and living species. Natural radionuclides in river water include ^{3}H at levels of 0.02−0.1 Bq/L, ^{40}K (0.04−2 Bq/L), radium, radon, and their short-lived decay products (<0.4−2 Bq/L). The main fraction of ^{3}H in surface water, however, is due to human activities.

Some of the sampling methods are automatic and continuous and are designed to give an early warning in case of an accidental release. In all cases, additional information on the river flow rate is very important. Samples can be taken continuously (or daily) and are then bulked into monthly or quarterly analysis, or alternatively, spot samples are taken periodically and analyzed individually. The time and frequency of sampling is very important for rivers with large differences in seasonal hydrological variations.

Treatment of the water may consist of filtration, the filtered water and the suspended material being measured separately, ion exchange and subsequent washing of the ion exchange column, or evaporation (for direct measurement of the residue). Chemical separations are needed for ^{90}Sr, whereas ^{3}H is measured after multiple distillation or electrolytic enrichment. Usually, residual beta (total beta less ^{40}K activity) contamination is reported, although there is a clear tendency to perform nuclide-specific measurements by means of gamma spectrometry and LSC.

5. Drinking water

Drinking water is monitored because of its vital importance for human consumption, even though a severe radioactive contamination of this medium is rather improbable. Samples may be taken from ground or surface water supplies, from water distribution networks, mineral waters, etc. Spot samples are taken a few times a year and analyzed individually or samples are taken daily and bulked for monthly or quarterly analysis.

Sample treatment usually consists of sample evaporation for direct measurement of the concentrate or separation on ion exchange columns. More elaborate chemical separations are required for ^{90}Sr determination, whereas ^{3}H is generally measured following multiple distillation of the sample.

D. Foodstuff

Samples of food are of greatest interest because their analysis yields values of the radionuclide intake that contribute directly to dose. Foods that contribute 5% or more to the total diet intake should be collected for analyses. Food sampling should be undertaken first at the producer's and subsequently at the retail market. In general, food products should be prepared as for home use, bearing also in mind that like vegetation, all foodstuffs require complete dissolution. Analysis of individual foodstuffs can indicate whether and which countermeasures should be taken to reduce doses, whereas food sampling of mixed diets provides an estimation of total uptake. If, however, mixed diet samples are to be used, a separate mixed diet of baby foods should also be analyzed.

Following an emergency, it is important that specific food types are continued to be monitored, particularly foodstuffs coming from areas with high contamination and those accumulating radionuclides of interest, such as cesium or strontium.

1. Milk

Consumption of milk and dairy products has been shown to be one of the most important pathways for uptake of radionuclides from environment to man, as milk is likely to be contaminated by radioactive iodine and cesium within the first days after a release of volatile radionuclides. Milk can be collected from individual farms or from individual animals, raw milk at farms at processing centers, or bottled milk at the supermarket. It is, of course, essential to note the date of collection of the milk. At large processing centers, milk is pooled from several sources with different collection days at the local farms. The date of processing should therefore be taken as the reference date for sampling.

Liquid milk must be preserved for long-time storage. For periods of 1−2 weeks, milk is usually stored in a refrigerator near the freezing point. Storage at frozen-food temperatures (about −15°C) is suitable for longer periods. A preservative, such as formalin or sodium azide (3.5 mL of 5% aq. solution per liter), can be added to prevent souring if a longer period of storage is anticipated.

Before gamma spectrometric analysis, the milk samples are dried at low temperatures with stirring to avoid the formation of a protein skin on the surface, by adding milk in small quantities to the container in which evaporation occurs so only a small quantity is being heated at any one time, by coagulating the protein before evaporation, by heating the milk with rennin, or by freeze-drying. Chemical separation is applied for the determination of ^{90}Sr activity and separation of the water phase with subsequent distillation for the separation of ^{3}H.

In an emergency situation, the rapid analysis of ^{89}Sr and ^{90}Sr in milk is essential to protect humans from radiation exposure due to the intake of contaminated milk. Some methods using ion exchange resins have been attempted for rapid determination of radiostrontium in milk to avoid the usual process of drying, ashing, and acid leaching (Vaney et al., 1989; Baratta, 2000). Brun et al. (2003) summarized rapid methods of radiostrontium analysis in milk, compared several methods in terms of analysis time, and reported a procedure combining cation exchange resin, Sr-resin, oxalate, and $BaCrO_4$ precipitations to be appropriate for the analysis of ^{90}Sr within 48 hours (2002). However, it was difficult to apply this method to milk samples containing both ^{89}Sr and ^{90}Sr.

There have been some efforts to measure ^{89}Sr and ^{90}Sr simultaneously, such as using spectrum-unfolding methods (Hong et al., 2001), other full spectrum methods (Heilgeist, 2000), the three energy window approach (Eikenberg et al., 2005), and the constrained optimization function in three energy windows with MATLAB software (Chobola et al., 2006). All of these approaches tend to fail when the $^{89}Sr/^{90}Sr$ activity ratio is reasonably high, since small variations in the quenching level shifts the spectrum toward the low energy region, leading to significant counting errors in the ^{90}Sr energy region. Using two energy windows, Kim et al. (2009) reported relative bias due to spectrum shifting higher than 20%, when the $^{89}Sr/^{90}Sr$ activity ratio exceeded 10.

Cerenkov counting procedures for the determination of ^{89}Sr and ^{90}Sr have been reported by Melin and Suomela (1995), who applied an additional step to separate ^{90}Y after measuring ^{89}Sr, and Heckel and Vogl (2009). Both methods only have been demonstrated for low $^{89}Sr/^{90}Sr$ activity ratios, which would be exceeded likely in samples collected under emergency conditions.

Kim et al. (2010) introduced a combined counting method using Cerenkov and liquid scintillation where the sample was sequentially measured in Cerenkov and scintillation counting modes. ^{89}Sr and ^{90}Sr activities in milk samples of $^{89}Sr/^{90}Sr$ activity ratios as high as 35 could be measured within 1 day with less than 20% and 40% relative biases, respectively. A review paper on the analytical methodologies for the determination of radiostrontium isotopes has been published by Vajda and Kim (2010).

2. Meat and fish

Animals whose meat is consumed by the public can be collected at the normal time of slaughter. It is strongly recommended that rare wildlife (e.g., endangered species) should not be used in environmental sampling and measurement.

The animal usually is dissected to separate the edible portions of those tissues that are to a degree specific for radionuclides of interest. Unless the animal is very small, tissue from each animal is considered as a separate sample. Where the sample includes considerable water, it must be weighed at uniform water content. Because radionuclide concentrations in animal tissue tend to range widely, a sufficient number of animals must be collected to define the normal range of radionuclide concentrations.

Following an accidental release, meat becomes one of the main sources of radiocesium for humans. Contamination of meat is mainly the result of animal grazing, but contaminated drinking water might also be an important pathway, while inhalation is not likely to be a significant pathway to meat. Meat sampling should normally be done in such a way that the composite sample is representative of a large number of animals, although after heavy fallout, screening measurements of individual animals may be necessary.

Another pathway for the uptake of radiocesium by man following an accident constitutes contamination of fish, especially those from nutrient-deficient lakes. Obtaining a representative sample from an area containing many lakes may require some compromise since collection of samples from a large number of the lakes may be impracticable. Ocean fish will not take up as much radiocesium as freshwater fish, because of the dilution through the depth of the ocean and the effective dilution associated with the high potassium content in the water, but particulate-associated radionuclides can be enriched to high levels.

In a detailed program, fish are collected by species; in a less detailed program, fish typical of categories such as bottom feeders, insect eaters, and predators may be collected. Again, numerous replicate samples are desirable because of the usual difficulty in knowing whether a fish caught at a location had lived there for an extended period. Thus, the presence or absence of a radionuclide does not permit any definite conclusion concerning the presence of the radionuclide in water at that location. For some fish, more specific information concerning their location may be available; for example, dams, salinity gradients, and temperature gradients can be effective barriers in their movement. Besides their origin, fish are sorted per species and size (Saxen, 1990).

Shellfish such as clams or oysters, some species of macroalgae, and other filter feeders quickly take up the contaminants from the seawater and can also be used as biological indicators, having the advantage of being relatively stationary. The shells, meat, and, in some case, the fluid are analyzed separately. However, shellfish being filter feeders contain much sediment in the intestine. If this material is not also separated, the results can be seriously misleading.

The samples should be cleaned, and the edible portions should be retained for analyses. Masses are determined by subtracting the inedible portion from the total since loss of moisture from the edible portion during the time of preparation may amount to a sizable fraction of the mass. For fish, poultry, and meat samples, the bones are easily separated after heating for 1 hour at 150°C. The mass of the

sample must be referred to the mass of the genuine material after subtracting the mass of the bones. Subsequently, the samples are reduced to a homogeneous condition with an electric food-type blender. For direct measurements, 1 kg of fresh sample is generally sufficient.

When ashing foods, the temperature should be raised slowly until the upper limit of the temperature prior to ignition has been reached. It is important to recall that foods with high phosphorus content tend to ignite. When the upper limit has been reached, the temperature can be raised more rapidly to 450°C and samples can be ashed for about 16 hours. Temperatures higher than 450°C may result in losses of volatile radionuclides, for example, radiocesium. With proper adjustment, ignition can be avoided for all materials except those with large amounts of fat. Usually, 10−25 g of ashed samples is sufficient for analyses.

3. Vegetables, fruits, and cereals

Green leafy vegetables are very prone to external contamination during their growing season. In the early stages of fallout, green vegetables can be a very significant pathway for short-lived radionuclides. After harvesting, grain and rice are subjected to contamination only during storage, and only the outer layers would be contaminated. If fallout occurs during the growing season, radionuclides will be transported into the grain and rice through the plant growth process. It is relatively easy to select representative samples of grain and rice at harvest time. If the fallout occurs during the winter, grain will be contaminated only through root uptake in the next growing season.

In certain countries, as much as 50% of the dietary calcium may be derived from cereal grains, whereas fruits and vegetables may add another 25%. No special techniques are required for the sampling. Before analysis, however, samples should be treated in the same way as if being prepared for human consumption. Samples collected for an analysis should weigh approximately 500 g each.

4. Mixed diet

Radioactivity in mixed diet is measured to get "integral" information on the uptake of radionuclides by man via the food chain. For monitoring of mixed diets, it is more appropriate to provide the activity consumed per day per person (Bq d^{-1} p^{-1}) than expressing the radioactivity content of foodstuffs per unit weight. Samples are taken as ingredients or as complete meals, mostly at places where many meals are consumed (i.e., factory restaurants, schools). Treatment usually consists of mixing the sample prior to gamma spectroscopic measurement of ^{137}Cs and chemical separation to determine the ^{90}Sr activity. The most important natural radionuclide is ^{40}K (typically 100 Bq d^{-1} p^{-1}). Knowledge of the contamination of the individual ingredients together with the composition of the national diet can also lead to a representative figure of the mixed diet.

V. Monitoring for external exposure

The simplest and least expensive and thus most widespread method of radiological environmental monitoring of human exposure due to external sources of gamma radiation is the continuous and remote-controlled measurement of external gamma dose rate or gamma dose integrated over a certain time period. It is nonnuclide specific and provides information covering large areas but is not suitable for the distinction between artificial and natural radioactivity. The actual level of natural gamma dose rate is affected by numerous influences and conditions. Apart from regional variations, there are both slow and fast temporal variations due to the dependence of radon daughter concentrations in air and soil on meteorological parameters. All of them must be thoroughly determined and investigated before setting warning and alarm levels for the detection of artificial radioactivity. Nevertheless, alarm levels can be set at dose rates of the order of 100 nSv/hour above background.

A. Dose rate monitoring

Dose rate measurements in environmental monitoring are of specific importance since real-time information about the progression of a radioactive cloud is provided. To be able to cover the measuring range from natural radiation levels up to high dose rate levels encountered during accidental releases, two counters are usually built in a detector, one for low-range measurements and one for high-range measurements.

The most frequently used detectors are energy compensated, gas-filled counter tubes, mostly Geiger−Müller counters, ionization chambers and proportional counters, and scintillation detectors (e.g., NaI(Tl), plastic). Modern systems perform automatic background correction and are equipped with local electronics for data transfer and storage.

Depending on specific monitoring objectives, account may be taken of the occupations of different population groups in typical urban areas and their vicinity. For screening purposes, the dose rate is usually measured above undisturbed soil for large-scale radioactive contamination of the environment. When detailed monitoring of external radiation fields in inhabited areas is carried out, the dose rate should be measured in typical areas that are accessible to the public: in dwellings, public buildings, production areas, gardens, and recreation areas (beach, park, etc.).

For areas uniformly contaminated with radionuclides, the measurement data on dose rates are averaged across the monitored area, the background dose rate estimated and subtracted from the measurement data.

B. Dose monitoring

To obtain a cumulative dose measurement of the direct gamma radiation, integration dosimeters, such as film badges and thermoluminescence dosimeters (TLDs) are used, mostly on the perimeter fence of nuclear installations diameter and a number of concentric rings outside the site boundary of the facility placed in a moisture-resistant polyester pouch inside a polypropylene mesh cylindrical cartridge.

TLDs are commercially available that exhibit a linear dose response and are capable of accurately measuring the absorbed dose. The radiation-sensitive element of a TLD is a small quantity, typically less than 100 mg, of an inorganic crystal doped with metal impurities, which provide the crystal with the energy storage capacity as well as the luminescent properties, required to function as a thermoluminescent phosphor upon exposure to ionizing radiation. The most commonly used TLD phosphors are lithium fluoride (LiF), calcium fluoride (CaF), lithium borate ($Li_2B_4O_7$), calcium sulfate ($CaSO_4$), and aluminum oxide (Al_2O_3) activated with trace quantities of transition metal or rare earth metal ions.

A typically TL dosimeter has four thermoluminescent elements to measure radiation exposure, one of which uses an "open" window of 3 mg/cm^2 to minimize attenuation of beta radiation; the second incorporates a 160 mg/cm^2 plastic filter, the third and fourth are covered by an 850 mg/cm^2 lead filter (in addition to 160 mg/cm^2 of plastic) to attenuate low-energy photon radiation in a manner that is intended to compensate for the overresponse of calcium sulfate in this portion of energy spectrum. These values are in addition to the filtration imposed by the polyamide backing (11 mg/cm^2) on one face and the Teflon window (28 mg/cm^2) on the opposite face of each.

The TL response of the phosphor to ionizing radiation is indicated by measurement of the glow curve, which is the plot of the TL intensity versus temperature, measured as the phosphor is heated. Field dosimeters receive exposure both while in transit to and from the placement contractor and while in storage at the contractor's facility, as well as while they are at their monitoring locations. To determine the field exposure, it is necessary to estimate this additional exposure, which is designated transit exposure. Likely sources of transit exposure include shipments of medical and other radioisotopes in the mail, as well as natural terrestrial and cosmic radiation.

VI. Mobile monitoring

Aerial and vehicle-borne measurements are used for mapping of areas contaminated by nuclear fallout, direct sampling in the plume, natural sources concentrated in the environment by human activities, or locating of lost sources. Airborne and mobile gamma ray methods permit large-scale primary surveys for gamma-emitting radionuclides, since vast areas can be scanned very fast. Mobile laboratories allow on-site measurements that otherwise would have to be performed in a laboratory facility following a time-consuming transfer to the facility.

A. Aerial measurements

Helicopters or aeroplanes can be equipped for aerial mapping, which includes the following:

- Isodose and exposure contours calculated to a given height above ground
- Soil concentrations of specific radionuclides
- Total activity inventories of radionuclides of interest
- Gamma ray spectra

In general, there are several different flying parameters, such as speed of the aircraft, altitude, and line spacing depending on objectives of survey (Table 1.5). Depending on the situation and national authority requirements, a fixed-wing aircraft survey is usually performed at a height of about 200 m. Helicopter flying altitudes for a first survey are typically 90−120 m above ground depending on landscape (trees, buildings, power lines, etc.). Thus, the detector's field of view is in the range of 200−400 m^2.

TABLE 1.5 Possible flight patterns for helicopter surveys.

Name	Description	Applicability
Parallel Track Search	Parallel straight tracks with a length of some kilometers with a distance between the tracks of 300 m	Survey in flat or hilly landscape
Line Search	Flight along specified lines (e.g., roads, railway tracks, rivers) with parallel tracks with a distance of 300 m	Survey along traffic lines
Contour Search	Flight along geographic contour lines	Survey in deeply cut or mountainous terrain
Penetration Search	Flights from landmark to landmark on different tracks	Rapid detection of contaminated area borders

In the case of an accidental release to the air, it may prove very useful to carry out an aerial mapping at higher altitudes, in particular above the mixing boundary layer (e.g., 1500 m) for the three-dimensional circumscription of the cloud. After the passage of the plume, a rapid geographic mapping of the ground deposition can be carried out most easily and rapidly at low altitude.

A major requirement for both aircrafts is that the flying altitude should be kept as constant as possible. In structured terrain, the helicopters usually try to follow that structure. For helicopters, flying speed is typically between 60 and 150 km/hour in accordance with the characteristics of the helicopter, airplanes usually go faster (180−220 km/hour). Actual flight line spacing and altitudes depend on the activity and number of sources and the sensitivity of the monitoring system.

The systems are based on the measurement of the gamma flux density at the position of the detector, which may be specially developed gas-filled probes, single or banks of scintillation detectors (NaI(Tl), plastic) of large volumes, or even semiconductor detectors of the HPGe type. The readout may be simple count rates or calibrated to dose rate or means of gamma spectrometry. Measurements are made at least once every second, and the system live time is automatically logged and output with the data stream.

Ancillary equipment usually includes GPS navigation (real-time differential), radar altimeter, barometer, and thermometer. The radar altimeter, temperature, and pressure are used to correct gamma ray data for the height of the detector above the ground. Gamma rays are attenuated by air. The density of the air, which is, in turn, affected by the prevailing temperature and pressure, affects the degree of attenuation. Real-time differential GPS navigation is accurate to within about 5 m. The radar altimeter is accurate to about 2%. The GPS navigation equipment and radar altimeter record the instantaneous position and height of the aircraft every second. Temperature and pressure are also recorded every second.

In the case of a rather uniform ground contamination, the true exposure rate at a nominal height of 170 m is about one-tenth of that at 1 m above the contaminated ground surface, this factor being approximately independent of the initial gamma energy in the range of 0.4−1.5 MeV (Chamberlain et al., 1961). The increased count rate produced by a ground deposition of about 10 kBq/m^2 may, therefore, be of the same order of magnitude as the variations in count rate attributable to different geological formations. In addition, the recorded counts may vary significantly if the aircraft is not able to fly at a fixed altitude. Due to these reasons, estimates of the activity on ground are difficult. It is even more difficult for a point source than for a uniform contamination unless hovering above the source is possible. To be able to estimate the soil contamination due to individual radionuclides, the gamma spectrometer, the response of the detector as a function of the photon energy, and the angle of incidence (including possible shielding of the helicopter or fixed-wing aircraft itself) have to be known. Therefore, the spectrometer has to be calibrated for aerial measurements prior to any use.

The main corrections that must be applied to airborne gamma ray data are background correction, stripping correction, height correction, and sensitivity correction (reduction to elemental concentrations) (IAEA, 2003b). For each of these corrections, the approach taken to calibration is empirical. There are three main procedures for acquiring calibration data:

- high altitude background calibration flights, usually flown offshore in an area where there is low atmospheric radon, at a range of heights—typically 1.0, 1.5, 2.0, 2.5, 3.0, and 3.5 km above the water,
- ground calibrations over radioactive sources to determine empirically stripping ratios, and
- calibration flights over a calibration range to determine height attenuation coefficients and sensitivity coefficients (IAEA, 1991)

Airborne gamma ray spectrometers should be fully calibrated every 12 months (Grasty and Minty, 1995).

B. Mobile laboratories

A number of car-mounted detection systems for the detection and location of radioactive sources in large areas have been developed. Additionally, mobile laboratories have been equipped with all the equipment needed for in situ measurement of dose rates, and for the collection of air samples with aerosol filters and charcoal cartridges, and possibly of soil and biological samples, and for their immediate counting and spectrometric analysis. These instruments are basically similar to the corresponding handheld devices or laboratory instruments discussed so far or in following sections, respectively; they may, however, be powered by car batteries or mobile generators. For the sake of completeness, it should be mentioned that human body counters may be a very useful part of the mobile equipment.

Instrument manufacturers have designed systems specifically for carborne use or adaptable to a variety of platforms (vehicle, helicopter, or fixed wing) as listed in Table 1.6. Depending on the speed of the vehicle and strength of the source, the signal received by the detector at a distance is only for a short duration and may be very weak compared with natural background. For a fixed distance, the primary photon fluence due to a point source falls sharply as the detector moves along. The recently developed car-mounted systems use this falling for a crude localization of point sources. Concerning aerial measurements, the closer the flight line is to a pass directly over the

TABLE 1.6 Air- and vehicle-borne detection systems.

Product	NaI-SS	MDS	FHT 1376 MobiSys
Manufacturer Vendor	*ORTEC*	*Thermo Electron Corporation*	*Thermo Electron Corporation*
Primary use	Carborne	Airborne	Carborne
Purpose	Detection of radiation sources	Detection of radiation sources	Detection of radiation sources
Hardware	1 each 4″ × 4″× 16″ NaI(Tl) detector. • 2 each 25 mm diameter × 500 mm long ^{3}He tubes. Includes 4″ polyethylene (HDPE) moderator and to save weight, 0.5″-thick PE facing the operator. • 1 each ORTEC digiBASE electronics integrating both NaI and neutron pulse counting in a single device. • 1 each laptop computer with expansion slots for extra devices, e.g., wireless networking. • GPS with USB interface, mapping software	5 L volume scintillation detector; proportional detector; model FHT 752E, He-3 neutron detector (optional); six-channel GPS	5 L plastic scintillator, optional FH 40 GL-W survey meter, GPS
Detection capability	At 15 km/hour: ^{137}Cs 370 kBq (10 μCi) at 3 m,^{60}Co 629 kBq (17 μCi) at 6 m,^{252}Cf neutron 1.3 MBq (36 μCi) at 5 m	Scintillation detector: measurement range: 1 nSv/hour to 20 μSv/hour (0.1 μR/hour to mR/hour), energy threshold: 50 keV, sensitivity (^{137}Cs): 20,000 cps/μSv/hour, able to detect 2 μSv/hour (0.2 μR/hour) increase above background, at 120 km/hour in 100m height: 370 MBq (10 mCi); proportional detector: measurement range:10 nSv/hour to 1 Sv/hour (1μR/ to 10 R/hour), energy response: 36 keV to 1.3 MeV; neutron detector (optional): sensitivity: 10 cps/μS/hour for^{252}Cf	Sensitivity: Typical 20,000 cps/μSv per hour (^{137}Cs); Detection limits: Gross: approximately 2 nSv/hour equivalent count rate relative to background level (^{137}Cs); NBR: 20% artificial dose rate contribution to the current natural gamma background level typically
Display	Laptop	Laptop	Laptop
Readout	Waterfall plot, count rate versus time, count rate versus position, spectrum at a position	Not specified	Total gamma dose rate (1 nSV/hour to 20 μSv/hour measured by the NBR-detector), artificial gamma dose rate (NBR), raw data count rates for offline analysis; total gamma dose rate (100 nSv/hour to 100 mSv/hour) measured by the optional FH 40 GL-W survey meter
Power	12 V DC	12 V DC, 8 hours on supplied battery (detector package only)	12 V DC
Size (mm)	“Pelican type” containers	400 × 600 × 350	520 × 280 × 200 mm
Weight	50 kg	15.0 kg	14 kg
Operating temperature	Not specified	0 to 50°C	Not specified

Continued

TABLE 1.6 Air- and vehicle-borne detection systems.—cont'd

Product	NaI-SS	MDS	FHT 1376 MobiSys
Humidity	Waterproof housing and wiring	5%–95% noncondensing	
Ruggedness	Plastic housing	Zarges military grade Carry Case, NATO approved	
Special		All models also function with any standard probe from the FH40G series of digital survey meters. MAPTRACK software, included with the MDS, provides a real-time data feed into any standard version of ESRI 's ArcView/ArcGIS software (ArcView 3.3, ArcGIS versions 8 and 9)	Natural background rejection (NBR) and the advanced digital filter (ADF) technologies; implemented in German, English, and French. Other languages are available upon request

Product	Matrix MRDS	GR-660 carborne	GR-660 Airborne	Mobile microspec
Manufacturer Vendor	*Thermo Electron Corporation*	*SAIC*	*SAIC*	*Bubble Technology Industries*
Primary use	Fixed, mobile, or venue-driven	Carborne	Airborne	Carborne and airborne
Purpose	Detection of radiation sources	Detection and measurement of radiation sources	Detection and measurement of radiation sources	Detection and measurement of radiation sources
Hardware	NBR probe, neutron probe, no more specification given; GPS accurate up to 3 m	GPX-256: 4 L NaI 256 in^3 (maximum 2); SAIC Exploranium GR-320 (Resolution: 256 or 512 channel); optional: neutron detector	GPX-1024 NaI (16 L) minimum recommended; maximum 16; Exploranium radiation detection system GR-820 (Resolution: 256 or 512 channel)	Various sizes of NaI for gamma spectroscopy, Phoswich scintillator for beta, liquid scintillator and ^{3}He counter for neutrons, MCA
Detection capability	Capable of detecting and monitoring radiation sources ranging from 20 to 1500 KeV, sensitivity for internal probes not specified	Not specified	^{241}Am:15–40 kBq/m^2;^{137}Cs: 1–4 Bq/m^2;^{60}Co: 0.5–3 kBq/m^2	Not specified

Display	Laptop	Touch screen color display	LCD	Laptop
Readout	Not specified	Not specified	Not specified	Dose rate, cumulative dose, spectrum, mapping with on-board GPS
Power	Incorporating smart battery management technology, battery power up to 3 hours, vehicle AC power enabled	8–35 VDC, 85–260 VAC converter included	8–35 VDC, 85–260 VAC converter included	Built-in rechargeable NiMH (12h) or external 12–32 V power supply
Size (mm)	Not specified	793 × 216 × 177	444 × 533 × 508	Analyzer: 330 × 230 × 162
Weight	Not specified	33 kg	33 kg	Analyzer: 4.1 kg; Probe 1.5–4.0 kg
Operating temperature	Not specified	Not specified	Not specified	−20 to + 40°C
Humidity	Not specified	Not specified	Not specified	Not specified
Ruggedness	Complete vibration and shock tested	Not specified	Not specified	MIL810E; MIL461E
Special	Capacity to integrate an unlimited number of sensors of Thermo's full line of radiation probes through expansion modules; data uplink capabilities via WiFi technology 2.4 GHz, secure, binary communication, unaided signal distribution up to 1 mile wireless, aided signal unlimited area	Export program to convert to a wide selection of formats, including ASCII, Map Info and Arcview GIS software	Survey planner (airborne)	

source, the higher the rate of falling of fluence. Detectors mounted on a vehicle's roof increase the field of view (Killeen, 1979); nevertheless, the field of view of a carborne system is much closer to that of a portable rather than airborne system, and the speed of operation is much slower than that of an airborne system. Consequently, the resolution of the data along a carborne traverse is much greater than that of an airborne flight line.

However, the data are also much more susceptible to local variations such as soil composition, soil moisture content, surface water (e.g., puddles), transported versus in situ material, weathering, and outcrop exposure (IAEA, 2003a). In addition, buildings, trees, and topographic effects in even moderate terrain may have a significant effect on carborne data. Variations in the system background levels may be higher than for an airborne system, due to collection of dust, mud, etc., inside and outside the vehicle. Grasty and Cox (1997) showed that the efficiency of a carborne detector at locating nearby sources is highly dependent on the geometry of the detector, the shielding elements within the vehicle, and the spectrometer system. The shielding effect of the vehicle can be advantageous if sampling of the underlying road material is not desired. Lead shields can be utilized as well. Detection limits are determined by the detector volume and the velocity of the vehicle, which govern the signal-to-noise and the spatial wavelength resolution, respectively. System sensitivities can be determined by recording carborne data centered over a 15–20 m diameter area where the ground concentrations have been averaged from a grid of calibrated ground spectrometer measurements. A test line to monitor the system should be established in a stable area off-road (e.g., grass field) and "driven" on a daily basis. For determination of background count rates, Grasty and Cox (1997) suggest connecting the detector to a portable spectrometer and taking the measurements over a large body of water with a metal or fiberglass boat.

In the case of a nuclear emergency response, a more elaborate calibration scheme is required to account for the deposition and decay of anthropogenic radionuclides. Karlsson et al. (2000) compare ^{137}Cs measurements from nine carborne systems (11 detectors) acquired over a 200 km traverse and at four specific calibration sites, all during the same day. Even though each system was calibrated, the levels of ^{137}Cs, reported as equivalent surface activity, varied by a factor of 2. These differences were attributed mainly to different calibration procedures, but also possibly to geometry, shielding, or displacement of the systems.

Road-based measurements will typically follow an irregular network. Preparing grid images from such data can be difficult, but the minimum curvature algorithm (Briggs, 1974) is suitable if the gridding parameters are well chosen. The resultant images should be prepared with the road traverses superimposed so that the most reliable portions of the grid are easily determined. Profile presentation of the data, possibly incorporating manual contouring, may be more appropriate where the network is sparse.

References

Abelquist, E.W., Condra, R.D., Laudeman, M.J., 1996. Determination of uranium and thorium concentrations in high Z material samples using direct counting method of gamma spectroscopy. Radiat. Prot. Manage. 13, 42–49.

Aleissa, A.K., Almasoud, I.F., Islam, S.M., L'Annunziata, M.F., 2008. Radium-228 analysis of natural waters by Cherenkov counting. Appl. Radiat. Isot. 66 (12), 1954–1963.

American National Standards Institute, 1999. Sampling and Monitoring Releases of Airborne Radioactive Substances from the Stacks and Ducts of Nuclear Facilities. ANSI Standard N13.1-1999. ANSI, McLean, VA.

Australian and New Zealand Environmental and Conservation Council & Agricultural and Resource Management Council of Australia and New Zealand ANZECC/ARMCANZ, 2000. Australian and New Zealand Guidelines for Fresh and Marine Water Quality. National Water Quality Management Strategy Paper No. 4. Australian Government Publishing Service, Canberra. Australia.

Baratta, E.J., 2000. Strontium-89 and strontium-90 in milk. In: Horwitz, W. (Ed.), Official Methods of Analysis of AOAC International, seventeenth ed. AOAC International, Gaithersburg, Maryland, USA, pp. 3–6 (chapter 13).

Barnett, V.B., 2002. Sample Survey. Principles and Methods, third ed. Arnold, London. 173pp.

Beck, H.L., 1966. Environmental gamma radiation from deposited fission products, 1960 – 1964. Health Phys. 12, 313–322.

Beck, H.L., 1972. The physics of environmental gamma radiation fields. In: Adams, J.A.S., Lowder, W.M., Gesell, T.F. (Eds.), The Natural Radiation Environment II, pp. 101–134. CONF-720805-P1.

Beck, H.L., 1980. Exposure Rate Conversion Factors for Radionuclides Deposited on the Ground. USDOE Report EML-378.

Beck, H.L., de Planque, G., 1968. The Radiation Field in Air Due to Distributed Gamma-Ray Sources in the Ground. USAEC Report HASL-195.

Beck, H.L., Condo, W.J., Lowder, W.M., 1964. Spectrometric Techniques for Measuring Environmental Gamma Radiation. USAEC Report HASL-150.

Beck, H.L., De Campo, J.A., Gogolak, C.V., 1972. In Situ Ge(Li) and NaI(Tl) Gamma-Ray Spectrometry for the Measurement of Environmental Radiation. USAEC Report HASL-258.

Becker, J.S., 2007. Inorganic Mass Spectrometry: Principles and Applications. John Wiley and Sons, Chichester.

Becker, J.S., 2010. Determination of long-lived radionuclides in nuclear, environmental and clinical samples by ICP-MS and LA-ICP-MS. In: Gross, M.L., Caprioli, R.M. (Eds.), Encyclopedia of Mass Spectrometry, Elemental, Isotope Ratio Mass Spectrometry. Elsevier, New York, pp. 200–211.

Bergmann, F., Libby, W.F., 1957. Continental water balance, groundwater inventory and storage times, surface ocean mixing rates, and worldwide water circulation patterns from cosmic ray and bomb tritium. Geochim. Cosmochim. Acta 12, 277–296.

Berlioz, A.N., Sajenouk, A.D., Tryshyn, V.V., 2005. A technique for the determination of 90Sr, plutonium and americium in environmental samples. J. Radioan. Nucl. Chem. 263 (2), 307–310.

Bernstrom, B., DeGeer, L.-E., 1983. Mätning, Av Små Mängder Xenon-133 I Luft. FOA Rapport, C-20515-A1.

Betti, M., Heras, L.A., Tamborini, G., 2006. Mass spectrometric determination of transuranium elements. Appl. Spectrosc. Rev. 41 (5), 491–514.

Blackburn, R., Al-Masri, M.S., 1992. Determination of radium-226 in aqueous samples using liquid scintillation counting. Analyst 117 (12), 1949–1951. London.

Bochicchio, F., Nuccetelli, C., SETIL Working Group, 2004. A method to evaluate the contribution of building material to indoor gamma dose rate through outdoor measurements: preliminary results. Radiat. Prot. Dosim. 111, 413–416.

Borio, R.,A., Rongoni, A., Saetta, D.M.S., Desideri, D., Roselli, C., 2005. Radon and tritium measurements in drinking water in a region of central Italy (Umbria). J. Radioanal. Nucl. Chem. 266 (3), 397–403.

Bowyer, T.W., Abel, K.H., Hensley, W.K., Perkins, R.W., 1997. Ambient ^{133}Xe Levels in the Northeast United States. Journal of Environmental Radioactivity 37 (2), 143–153.

Bowyer, T.W., Schlosser, C., Abel, K.H., Auer, M., Hayes, J.C., et al., 2002. Detection and analysis of xenon isotopes for the comprehensive nuclear-test-ban treaty international monitoring system. J. Environ. Radioactiv. 59 (2), 139–151.

Bowyer, T.W., Abel, K.H., Hubbard, C.W., McKinnon, A.D., Perkins, R.W., Reeder, P.L., Thompson, R.C., Warner, R.A., 1996. Automatic radioxenon analyzer for CTBT monitoring, Rep. PNNL-11424. Pac. Northwest Natl. Lab, Richland, Wash.

Briggs, I.C., 1974. Machine contouring using minimum curvature. Geophysics 45 (5), 39–48.

British Standards Institute, 2001. Investigation of Potentially Contaminated Sites – Code of Practice. British Standard BS 10175:2001. British Standards Institute, London, 76 pp.

Brun, S., Kergadallan, Y., Boursier, B., Fremy, J., Janin, F., 2003. Methodology for determination of radiostrontium in milk: a review. Lait 83, 1–15.

Burnett, W.C., Tai, W.-C., 1992. Determination of radium in natural waters by alpha liquid scintillation. Anal. Chem. 64, 1691–1697.

Carvalho, F.P., 1997. Distribution, cycling and mean residence time of ^{226}Ra, ^{210}Pb and ^{210}Po in the Tagus estuary. Sci. Total Environ. 196, 151–161.

Chalupnik, S., Lebecka, J.M., 1993. Determination of ^{226}Ra, ^{228}Ra and ^{224}Ra in water and aqueous solutions by means of liquid scintillation counting. In: Noakes, J.E., Schoenhofer, F., Polach, H. (Eds.), Advances in Liquid Scintillation Spectrometry 1992, pp. 397–403. Radiocarbon.

Chamberlain, A.C., Garner, R.J., Williams, D., 1961. Environmental monitoring after accidential deposition of radioactivity. Reactor Sci. Technol. 14, 155.

Chiappini, R., Taillade, J.-M., Bré bion, S., 1996. Development of a high-sensitivity inductively coupled plasma mass spectrometer for actinide measurement in the femtogram range. J. Anal. Atom. Spectrom. 11, 497–503.

Chobola, R., Mell, P., Daroczi, L., Vincze, A., 2006. Rapid determination of radiostrontium isotopes in sample of NNP origin. J. Radioanal. Nucl. Chem. 267 (2), 297–304.

Chu, L., Khalique, A., 1990. Determination of ^{226}Ra in water by liquid scintillation counting. Trans. Am. Nucl. Soc. 61, 5–6.

Clark, I., Fritz, P., 1997. Environmental Isotopes in Hydrogeology. Lewis Publishers, Boca Raton.

Clouvas, A., Xanthos, S., Antonopoulos-Domis, M., 1998. Monte Carlo based method for conversion of in-situ gamma ray spectra obtained with a portable Ge detector to an incident photon flux energy distribution. Health Phys. 74, 216–230.

Clouvas, A., Xanthos, S., Antonopoulos-Domis, M., 2000. Derivation of indoor gamma dose rate from high resolution in situ gamma ray spectra. Health Phys. 79, 274–281.

Clouvas, A., Xanthos, S., Antonopoulos-Domis, M., 2001. Extended survey of indoor and outdoor terrestrial gamma radiation in Greek urban areas by in situ gamma spectrometry with a portable Ge detector. Radiat. Prot. Dosim. 94, 233–246.

Clouvas, A., Xanthos, S., Antonopoulos-Domis, M., 2003. A combination study of indoor radon and in situ gamma spectrometry measurements in Greek dwellings. Radiat. Prot. Dosim. 103, 363–366.

Clouvas, A., Xanthos, S., Antonopoulos-Domis, M., 2006. Simultaneous measurements of indoor radon, radon–thoron progeny and high-resolution gamma spectrometry in Greek dwellings. Radiat. Prot. Dosim. 118, 482–490.

Cochran, W.G., 1977. Sampling Techniques, third ed. Wiley and Sons, New York. 428pp.

Construction Industry Research and Information Association CIRIA, 2000. Best Practice Guidance for Site Characterisation. A Report from the SAFEGROUNDS Learning Network, CIRIA Publication W001.01 © CIRIA 2000. In: Managing Contaminated Land on Nuclear-Licensed and Defence Sites.

Coombs, E.G., 1980. High Resolution Alpha Spectroscopy by Liquid Scintillation Techniques. University of Maine at Orono (master's thesis).

Cooper, M.B., Wilks, M.J., 1981. Analytical Method for Radium (^{226}Ra) in Environmental Samples by the Use of Liquid Scintillation Counting. Report number ARLTR-040. Australian Radiation Lab, Melbourne.

Cresswell, A.J., Sanderson, D.C., White, D.C., 2006. ^{137}Cs measurement uncertainties and detection limits for airborne gamma spectrometry (AGS) data analysed using a spectral windows method. Appl. Radiat. Isot. 64, 247–253.

Cross, P., McBeth, G.W., 1976. Liquid scintillation alpha particle assay with energy and pulse shape discrimination. Health Phys. 30, 303–306.

Crouthamel, C.E., Heinrich, R.R., 1971. Radiochemical separations. Part I. In: Kolthoff, I.M., Elving, P.J. (Eds.), Treatise on Analytical Chemistry. John Wiley and Sons, New York, p. 5467.

Cummings, S.L., Shearin, R.L., Porter, C.R., 1971. A rapid method for determining ^{85}Kr in environmental samples. In: Rapid Methods for Measuring Radioactivity in the Environment. International Atomic Energy Agency, Vienna, p. 163.

Cutshall, N.H., Larsen, I.L., 1986. Calibration of a portable intrinsic Ge gamma-ray detector using point sources and testing for field applications. Health Phys. 51, 53–59.

Eakins, J.D., Gomm, P.J., 1968. The determination of gross alpha in urine by adsorption on glass fibre filter paper. Health Phys. 14, 461.

Eikenberg, J., Beer, H., Rüthi, M., Zumsteg, I., Vetter, A., 2005. Precise determination of 89Sr and 90Sr/90Y in various matrices: the LSC 3-window approach. In: Chalupnik, S., Schőnhofer, F., Noakes, J. (Eds.), LSC2005, Advances in Liquid Scintillation Spectrometry, Radiocarbon, pp. 237–249.

European Union, 1998. Drinking Water Directive. Council Directive 98/83/EC on the Quality of Water Intended for Human Consumption. European Commission.

Food and Agriculture Organization of the United Nations, International Atomic Energy Agency, Internatiational Labour Organisation, OECD Nuclear Energy Agency, Pan American Health Organization, World Health Organization, 1996. International Basic Safety Standards for Protection against Ionizing Radiation and for the Safety of Radiation Sources. Safety Series No. 115. IAEA, Vienna.

Faure, G., 1986. Principles of Isotope Geology, second ed. John Wiley and Sons, New York.

Fifield, L.K., Cresswell, R.G., di Tada, M.L., Ophel, T.R., Day, J.P., Clacher, A.P., King, S.J., Priest, N.D., 1996. Accelerator mass spectrometry of plutonium isotopes. Nucl. Instrum. Methods Phys. Res., Sect. B 117 (3), 295−303.

Figgis, P.E., 1961. The Radiochemistry of Polonium. NAS-NS 3037, U.S. Atomic Energy Commission.

Florkowski, T., 1963. Low-level Tritium Assay in Water Samples by Electrolytic Enrichment and Liquid-Scintillation Counting in the IAEA Laboratory. IAEA, No. 252.

Florkowski, T., 1992. Low-level Tritium Assay in Water Samples by Electrolytic Enrichment and Liquid-Scintillation Counting in the IAEA Laboratory. IAEA-SM-252/63. International Atomic Energy Agency, Vienna, Austria.

Fontaine, J.P., Blanchard, X., Pointurier, F., Taffary, T., 2002. Atmospheric xenon radioactive isotope monitoring. In: Proceedings from the International Conference on in Situ Nuclear Metrology as a Tool for Radioecology Conference, Fleurus, Belgium.

Fontes, J.C., 1983. Dating of Groundwater Guidebook on Nuclear Techniques. Technical Report Series No 91. IAEA, Vienna.

Foss, D.W., Brooker, H.R., 1991. Radiochemistry of Uranium-Series Isotopes in Groundwater, Departments of Geology and Physics. University of South Florida publication No 05-022-092.

Friedman, H., 1983. A portable radon meter. Rad. Prot. Dos. 4 (2), 119−121.

Friedmann, H., Atzmüller, C., Beck, C., Breitenhuber, L., Brunner, P., Fink, K., Fritsche, K., Gottsbachner, D., Hamernik, E., Hofmann, W., Hover, R., et al., 2007. Das österreichische nationale Radonprojekt (ÖNRAP), Projekt-Endbericht, Bundesministerium für Land- und Forstwirtschaft, Umwelt und Wasserwirtschaft. Bundesministerium für Gesundheit, Familie und Jugend.

Gering, F., Kiefer, P., Fesenko, S., Voigt, G., 2002. In situ gamma-ray spectrometry in forests: determination of kerma rate in air from ^{137}Cs. J. Environ. Radioact. 61, 75−89.

Ghiloufi, I., 2009. Study of ^{239}Pu, ^{144}Ce, and 90Sr behavior during radioactive waste treatment by thermal plasma technology. Plasma Chem. Plasma Process. 29 (4), 321−331.

Gilbert, R.O., Pulsipher, B.A., 2005. Role of sampling designs in obtaining representative data. Environ. Forensics 6, 27−33.

Gogolak, C.V., 1984. Rapid determinations of noble gas radionuclide concentrations in power reactor plumes. Health Phys. 46, 783−792.

Grasty, R.L., Cox, J.R., 1997. A car-borne gamma ray spectrometer system for natural radioactivity mapping and environmental monitoring. In: RESUME 95, Rapid Environmental Surveying Using Mobile Equipment, Report. Nordic Nuclear Safety Research Secretariat, pp. 71−90.

Grasty, R.L., Minty, B.R.S., 1995. A Guide to the Technical Specifications for Airborne Gamma−ray Surveys. Australian Geological Survey Organisation. Record 1995/60.

Guillot, L., 2001. Extraction of full absorption peaks in airborne gamma-spectrometry by filtering techniques coupled with a study of the derivatives. Comparison with the window method. *J. Environ. Radioact.* 53, 381−398.

Günay, G., 2006. Hydrology and hydrogeology of Sakaryabaşı Karstic springs, Çifteler, Turkey. Environ. Geol. 51, 229−240.

Guo, S.-L., Chen, B.-L., Durrani, S.A., 2012. Solid state nuclear track detectors. In: L'Annunziata, M.F. (Ed.), Handbook of Radioactivity Analysis, third ed. Elsevier, Amsterdam and Oxford, pp. 233−298.

Happel, S., Letessier, P., Ensinger, W., Eikenberg, J.H., Thakkar, A.H., Horwitz, E.P., 2004. Gross alpha determination in drinking water using a highly specific resin and LSC. Appl. Radiat. Isot. 61 (2−3), 339−344.

Heckel, A., Vogl, K., 2009. Rapid method for determination of the massic activitys of ^{89}Sr and ^{90}Sr. Appl. Radiat. Isot. 67, 794−796.

Heilgeist, M., 2000. Use of extraction chromatography, ion chromatography and liquid scintillation spectrometry for rapid determination of strontium-89 and strontium-90 in food in cases of increased release of radionuclides. Radioanal. Nucl. Chem. 245 (2), 249−254.

Helfer, I.K., Miller, K.M., 1988. Calibration factors for germanium detectors used for field spectrometry. Health Phys. 55, 15−29.

Hendriks, P.H., Limburg, J., de Meijer, R.J., 2001. Full-spectrum analysis of natural gamma-ray spectra. J. Environ. Radioact. 53, 365−380.

Hong, K.H., Cho, Y.H., Lee, M.H., Choi, G.S., Lee, C.W., 2001. Simultaneous measurement of 89Sr and 90Sr in aqueous samples by liquid scintilla counting using the spectrum unfolding method. J. Appl. Radiat. Isot. 54, 299−305.

Horiuchi, K., Murakami, Y., 1981. New determination of ^{226}Ra, ^{224}Ra, and ^{228}Ra in water. Extraction of radon and thoron and integral counting with a liquid scintillation counter. Nippon Kagaku Kaishi 1, 116−121.

Horwitz, E.P., Dietz, M.L., Fisher, D.E., 1991. SREX: a new process for the extraction and recovery of strontium from acidic nuclear waste streams. Solvent Extr. Ion Exch. 9 (1), 1−25.

Horwitz, E.P., Chiarizia, R., Dietz, M.L., 1992a. The application of novel extraction chromatographic materials to the characterization of radioactive waste solutions. J. Radioanal. Nucl. Chem. 161 (2), 575−583.

Horwitz, E.P., Dietz, M.L., Chiarizia, R., Diamond, H., Essling, A.M., Graczyk, D., 1992b. Separation and preconcentration of uranium from acidic media by extraction chromatography. Anal. Chim. Acta 266, 25−37.

Horwitz, E.P., Chiarizia, R., Dietz, M.L., Diamond, H., Nelson, D.M., 1993. Separation and Preconcentration of actinides from acidic media by extraction chromatography. Anal. Chim. Acta 284, 361−372.

Horwitz, E.P., Dietz, M.L., Chiarizia, R., Diamond, H., Maxwell III, S.L., Nelson, M.R., 1995. Separation and preconcentration of actinides by extraction chromatography using a supported liquid anion exchanger: application to the characterization of high-level nuclear waste solutions. Anal. Chim. Acta 310, 63−78.

Hou, X., Roos, P., 2008. Critical comparison of radiometric and mass spectrometric methods for the determination of radionuclides in environmental, biological and nuclear waste samples. Anal. Chim. Acta 608, 105−139.

Hou, X.L., Aldahan, A., Nielsen, S.P., Possnert, G., 2009. Time series of 129I and 127I speciation in precipitation from Denmark. Environ. Sci. Technol. 43 (17), 6522−6528.

Hrnececk, E., Steier, P., Wallner, A., 2005. Determination of plutonium in environmental samples by AMS and alpha spectrometry. Appl. Radiat. Isot. 63 (5−6), 633−638.

Hrnecek, E., Aldave de las Heras, L., Betti, M., 2002. Application of microprecipitation on membrane filters for Alpha Spectrometry, liquid

scintillation counting and mass spectrometric determination of plutonium isotopes. Radiochim. Acta 90 (9), 721−725.

International Commission on Radiation Units and Measurements, 2006. Sampling for Radionuclides in the Environment. ICRU Report 75. Journal of the ICRU 6(1). Oxford Univ. Press, Oxford, UK.

Ilić, R., Durrani, S.A., 2003. Solid state nuclear track detectors. In: L'Annunziata, M.F. (Ed.), Handbook of Radioactivity Analysis, second ed. Elsevier, Amsterdam and Oxford, pp. 179−237.

Institut de Radioprotection et de Sûreté Nucléaire, IRSN, 2018. Information Report. Detection in October 2017 of Ruthenium 106 in France and in Europe: Results of IRSN's Investigations.

International Atomic Energy Agency, 1982. Generic Models and Parameters for Assessing the Environmental Transfer of Radionuclides from Routine Releases: Exposure of Critical Groups. Safety Series 57, Vienna (1982).

International Atomic Energy Agency, 1991. Airborne Gamma Ray Spectrometer Surveying. Technical Reports Series, No. 323. IAEA, Vienna.

International Atomic Energy Agency, 1998. Radiological Characterization of Shut Down Nuclear Power Reactors for Decommissioning Purposes. Technical Reports Series No. 389. IAEA, Vienna.

International Atomic Energy Agency, 1999. Decommissioning of Nuclear Power Plants and Research Reactors. IAEA Safety Standards Series No. WS-G-2.1. IAEA, Vienna, 1999.

International Atomic Energy Agency, 2001. Generic Models for Use in Assessing the Impact of Discharges of Radioactive Substances to the Environment. Safety Reports Series No. 19. IAEA, Vienna.

International Atomic Energy Agency, 2002a. Management of Radioactive Waste from the Mining and Milling of Ores. IAEA Safety Standards Series No. WSG-1.2. IAEA, Vienna.

International Atomic Energy Agency, 2002b. Monitoring and Surveillance of Residues from the Mining and Milling of Uranium and Thorium. Safety Reports Series No. 27. IAEA, Vienna (2002).

International Atomic Energy Agency, 2003a. Extent of Environmental Contamination by Naturally Occurring Radioactive Material (NORM) and Technological Options for Mitigation. Technical Reports Series No. 4I9. IAEA, Vienna.

International Atomic Energy Agency, 2003b. Guidelines for Radioelement Mapping Using Gamma Ray Spectrometry Data. IAEA-TECDOC-1363. IAEA, Vienna.

International Atomic Energy Agency, 2004. Surveillance and Monitoring of Near Surface Disposal Facilities for Radioactive Waste. Safety Reports Series No. 35. IAEA, Vienna.

International Atomic Energy Agency, 2005. Environmental and Source Monitoring for Purposes of Radiation Protection. Safety Guide. IAEA Safety Standards Series No. RS G-1.8. IAEA, Vienna, 2005.

International Atomic Energy Agency, 2011. A International Fact Finding Expert Mission of the Fukushima Dai-Ichi NPP Accident Following the Great East Japan Earthquake and Tsunami (2011). http://www-pub.iaea.org/MTCD/meetings/PDFplus/2011/cn200/documentation/cn200_Final-FukushimaMission_Report.pdf.

International Atomic Energy Agency, 2015. The Fukushima Daiichi Accident. STI/PUB/1710. GC(59/14). IAEA, Vienna, 2015.

International Commission on Radiation Units and Measurements (ICRU), 1994. Gamma-ray Spectrometry in the Environment. ICRU Report 53. ICRU Publications, Bethesda, MD.

International Commission on Radiological Protection, 1965. Recommendations of the International Commission on Radiological Protection. ICRP Publication 9. Pergamon Press, London.

International Commission on Radiological Protection, 2006. Assessing Dose of the Representative Person for the Purpose of Radiation Protection of the Public and Optimisation of Radiological Protection: Broadening the Process. ICRP 101, Ann ICRP, 36 (3). Pergamon Press, London.

International Electrotechnical Commission, 2002a. Equipment for Continuous Monitoring of Radioactivity in Gaseous Effluents, Part 1: General Requirements. IEC 60761-1 Ed. 2.0. IEC, Geneva.

International Electrotechnical Commission, 2002b. Equipment for Continuous Monitoring of Radioactivity in Gaseous Effluents, Part 2: Specific Requirements for Radioactive Aerosol Monitors Including Transuranic Aerosols. IEC 60761-2 Ed. 2.0. IEC, Geneva.

Irlweck, K., Wallner, G., 1993. Determination of 226Ra in Lake Sediments by liquid scintillation counting of extractant ^{222}Rn. In: Noakes, J.E., Schoenhofer, F., Polach, H. (Eds.), Advances in Liquid Scintillation Spectrometry 1992, Radiocarbon, pp. 391−395.

International Organization for Standards ISO 10704, 2018. Water Quality − Gross Alpha and Gross Beta Activity − Test Method Using Thin Source Deposit. International Organization for Standards.

International Organization for Standards ISO 13163, 2013. Water Quality − Lead-210 − Test Method Using Liquid Scintillation Counting. International Organization for Standards.

International Organization for Standards ISO 13164-2, 2013. Water Quality − Radon-222 − Part 2: Test Method Using Gamma-Ray Spectrometry. International Organization for Standards.

International Organization for Standards ISO 13164-4, 2015. Water Quality − Radon-222 − Part 4: Test Method Using Two-phase Liquid Scintillation Counting. International Organization for Standards.

International Organization for Standards ISO 13165-3, 2016. Water Quality − Radium-226 − Part 3: Test Method Using Coprecipitation and Gamma-Spectrometry. International Organization for Standards.

International Organization for Standards ISO 18589-2, 2007. International Standard, Measurement of Radioactivity in the Environment. Soil. Part 2: Guidance for the Selection of the Sampling Strategy, Sampling and Pre-treatment of Samples. International Organization for Standards.

International Organization for Standards ISO 18589-4, 2009. International Standard, Measurement of Radioactivity in the Environment. Soil. Part 4. Measurement of Pu Isotopes by α-spectrometry. International Organization for Standards.

International Organization for Standards ISO 18589-5, 2009. International Standard, Measurement of Radioactivity in the Environment. Soil. Part5: Measurement of Strontium 90. International Organization for Standards.

International Organization for Standards ISO 18589-6, 2009. International Standard, Measurement of Radioactivity in the Environment. Soil. Part 6: Measurement of Gross Alpha and Gross Beta Activities. International Organization for Standards.

International Organization for Standards ISO 9696, 2017. Water Quality − Gross Alpha Activity − Test Method Using Thick Source. International Organization for Standards.

International Organization for Standards ISO 9697, 2018. Water Quality − Gross Beta Activity − Test Method Using Thick Source. International Organization for Standards.

International Organization for Standardization, ISO-2889, 1975. General Principles for Sampling Airborne Radioactive Materials. ISO, Geneva.

International Organization for Standards ISO/IEC 17025, 2017. General Requirements for the Competence of Testing and Calibration Laboratories. International Organization for Standards.

Jacob, D.J., Prather, M.J., Wofsy, S.C., McElroy, M.B., 1987. Atmospheric distribution of ^{85}Kr simulated with a general circulation model. J. Geophys. Res. 92 (D6), 6614–6626.

Johns, F.B., 1973. Portable apparatus and procedure fort he separation of krypton, xenon, and methane in air. In: Stanley, R., Moghissi, A.A. (Eds.), Noble Gases. US Environmental Protection Agency, Las Vegas, Nevada, p. 225. Report CONF-730915.

Kalinowski, M.B., Sartorius, H., Uhl, S., Weiss, W., 1998. Rückschließbarkeit auf Plutoniumabtrennung durch Auswertung von Messungen des atmosphärischen Krypton-85 in Wochenproben bei verschiedenen Abständen von der Wiederaufarbeitungsanlage Karlsruhe. Arbeitsbericht, IANUS 3/1998. TU Darmstadt, 30 Seiten.

Karamanis, D., Ioannides, K.G., Stamoulis, K.C., 2006. Determination of ^{226}Ra in aqueous solutions via sorption on thin films and α-spectrometry. Anal. Chim. Acta 573–574, 319–327.

Karlsson, S., Mellander, H., Lindgren, J., Finck, R., Lauritzen, B., 2000. RESUME 99, Rapid Environmental Surveying Using Mobile Equipment. Report from the NKS/BOK-1.2 Project Group Mobile Measurements and Measurement Strategies, NKS-15. Nordic Nuclear Safety Research Secretariat, 78 pp.

Kathren, R.L., 1998. NORM sources and their origins. Appl. Radiat. Isot. 49, 149–168.

Katzlberger, C., Wallner, G., Irlweck, K., 2001. Determination of ^{210}Pb, ^{210}Bi and ^{210}Po in natural drinking water. J. Radioanal. Nucl. Chem. 249, 191–196.

Keller, C., 1993. Grundlagen der Radiochemie, third ed. Otto Salle Verlag, Frankfurt am Main.

Kim, C.K., Al-Hamwi, A., Törvényi, A., Kis-Benedek, G., Sansone, U., 2009. Validation of rapid methods for the determination of radiostrontium in milk. Appl. Radiat. Isot. 67, 786–793.

Killeen, P.G., 1979. Gamma ray spectrometric methods in uranium exploration - Application and interpretation. In Geophysics and Geochemistry in the Search for Metallic Ores, edited by P.J. Hood, Geological Survey of Canada Economic Geology Report 31, pp 163-230.

Kim, C.K., Tarjan, S., Bokori, E., Molnar, Z., 2010. Improved rapid determination of 89Sr and90Sr in milk using Cerenkov and scintillation counting. In: Proceeding of International Conference on Advances in Liquid Scintillation Spectrometry. September 6-10, 2010, Paris, France.

Kleinschmidt, R.I., 2004. Gross alpha and beta activity analysis in water, a routine laboratory method using liquid scintillation analysis. Appl. Radiat. Isot. 61 (2–3), 333–338.

Krey, P.W., Hardy, E.P., 1970. Plutonium in Soil Around the Rocky Flats Plant. Report HASL-235. US Atomic Energy Commision, New York.

Kunz, C.O., 1989. ^{133}Xe: ambient air concentrations in upstate New York. Atmos. Environ. 238, 1827–1833.

La Rosa, J.J., Burnett, W., Lee, S.H., Levy, I., Gatsaud, J., Povinec, P.P., 2001. Separation of actinides, cesium and strontium from marine samples using extraction chromatography and sorbents. J. Radioanal. Nucl. Chem. 248 (3), 765–770.

Lee, M.H., Ahn, H.J., Park, J.H., Park, Y.J., Song, K., 2011. Rapid sequential determination of Pu, ^{90}Sr and ^{241}Am nuclides in environmental samples using an anion exchange and Sr-Spec resins. Appl. Radiat. Isot. 69 (2), 295–298.

Lehmann, B.E., Davis, S.N., Fabryka-Martin, J.T., 1993. Atmospheric and subsurface sources of stable and radioactive nuclides used for groundwater dating. Water Resour. Res. 29, 2027–2040.

Lettner, H., Andrási, A., Hubmer, A.K., Lovranich, E., Steger, F., Zombori, P., 1996. In situ gamma-spectrometry intercomparison exercise in Salzburg, Austria. Nucl. Instrum. Methods Phys. Res., Sect. A 369, 547–551.

Libby, W.F., 1953. The potential usefulness of natural tritium. Proc. Natl. Acad. Sci. 39, 245–247.

Liong Wee Kwong, L., Gastaud, J., La Rosa, J., Lee, S.H., Povinec, P.P., Wyse, E., 2004. Determination of ^{241}Pu in marine samples using coprecipitation with rare earth fluoride and liquid scintillation spectrometry. J. Radioanal. Nucl. Chem. 261 (2), 283–289.

Lloyd, J.W. (Ed.), 1981. Case-studies in Groundwater Resources Evaluation, first ed. Clarendon Press, Oxford, London, p. 113.

Lowder, W.M., Beck, H.L., Condo, W.J., 1964a. Spectrometric determination of dose rates from natural and fall-out gamma-radiation in the United States, 1962-63. Nature 202, 745.

Lowder, W.M., Condo, W.J., Beck, H.L., 1964b. Field Spectrometric Investigations of Environmental Radiation in the U.S.A. In: The Natural Radiation Environment. University of Chicago Press, Chicago, IL, pp. 597–616.

Lozano, R.L., Bolívar, J.P., San Miguel, E.G., García-Tenorio, R., Gázquez, M.J., 2011. An accurate method to measure alpha-emitting natural radionuclides in atmospheric filters: Application in two NORM industries. Nucl. Instr. Meth. Phys. Res. Sect. A (in press), Corrected Proof.

Ludwick, J.D., 1966. Xenon-133 as an atmospheric tracer. J. Geophys. Res. 71 (20), 4743–4748.

MARSSIM, 2002. Multi-Agency Radiation Survey and Site Investigation Manual (Revision 1). In: Nuclear Regulatory Commission NUREG-1575 Rev. 1. Environmental Protection Agency EPA 402-R-97-016 Rev. 1, Department of Energy DOE EH-0624 Rev. 1, August. http://www.epa.gov/radiation/marssim/obtain.html.

Martin, P., Hancock, G.J., 2004. Routine Analysis of Naturally Occurring Radionuclides in Environmental Samples by Alpha-Particle Spectrometry. Supervising Scientist Report 180. AGPS, Canberra. http://www.environment.gov.au/ssd/publications/ssr/180.html.

Martin, A., Mead, S., Wade, B.O., 1997. Materials Containing Natural Radionuclides in Enhanced Concentrations. Report No. EUR 17625 EN, Directorate General Environment, Nuclear Safety and Civil Protection. European Commission, Luxembourg.

Martin, J.P., Odell, K.J., 1998. The Development of Emergency Radioanalytical Techniques for the Determination of Radiostrontium and Transuranic Radioisotopes in Environmental Materials. Radioactivity and Radiochemistry 9 (3), 49.

Maxwell III., S.L., 2006. Rapid column extraction method for actinides and Sr-89/90 in water samples. J. Radioanal. Nucl. Chem. 267 (3), 537–543.

Maxwell III., S.L., 2007. Rapid Analysis of Emergency Urine and Water Samples. J. Radioanal. Nucl. Chem. 275 (3), 497–502.

Maxwell III., S.L., Culligan, B.K., 2009. New column separation method for emergency urine samples. J. Radioanal. Nucl. Chem. 279 (1), 105–111.

Maxwell III, S.L., Culligan, B.K., Noyes, G.W., 2010. Rapid separation of actinides and radiostrontium in vegetation samples. J. Radioanal. Nucl. Chem. 286 (1), p273–282.

McDowell, W.J., McDowell, B.L., 1994. Liquid Scintillation Alpha Spectrometry. CRC Press. Inc, Boca Raton, Florida.

Medeiros, F.H., Yoshimura, E.M., 2005. Influence of soil and buildings on outdoor gamma dose rates in Sao Paulo, Brazil. Health Phys. 88, 65–70.

Medici, F., Wernsperger, B., Valmari, T., 2004. Collection efficiency of particulate and xenon sampling in the international monitoring system of the comprehensive Nuclear Test-Ban Treaty. Appl. Radiat. Isot. 61 (2−3), 219−224.

Melin, J., Suomela, J., 1995. Rapid determination of ^{89}Sr and ^{90}Sr in food and environmental samples by Cerenkov counting. In: Rapid Instrumental and Separation Methods for Monitoring Radionuclides in Food and Environmental Samples, Final Report on an IAEA Co-ordinated Research Programme. International Atomic Energy Agency, Vienna, Austria. IAEA/AL/088.

Mellado, J., Llaurado, M., Rauret, G., 2001. Determination of Pu, Am, U, Th and Sr in marine sediment by extraction chromatography. Anal. Chim. Acta 443, 81−90.

Michel, H., Levent, D., Barci, V., Barci-Funel, G., Hurel, C., 2008. Soil and sediment sample analysis for the sequential determination of natural and anthropogenic radionuclides. Talanta 74 (5), 1527−1533.

Miller, K.M., 1984. A Spectral Stripping Method for a Ge Spectrometer Used for Indoor Gamma Exposure Rate Measurements. USDOE Report EML-419.

Miller, K.M., Beck, H.L., 1984. Indoor Gamma and Cosmic Ray Exposure Measurements Using a Ge Spectrometer and Pressurized Ionisation Chamber. Radiat. Prot. Dosim. 7, 185−189.

Miller, K.M., Helfer, I.K., 1985. In Situ Measurements of 137Cs Inventory in Natural Terrain. In: Environmental Radiation '85, Proceedings of the Eighteenth Midyear Topical Symposium of the Health Physics Society, 243-251 pp.

Miller, K.M., Shebell, P., 1995. In Situ Gamma-Ray Spectrometry - A Tutorial for Environmental Radiation Scientists. USDOE Report EML-557.

Miller, K.M., Shebell, P., Klemic, G.A., 1994. In Situ Gamma-Ray Spectrometry for the Measurement of Uranium in Surface Soils. Health Phys. 67, 140−150.

Miura, T., Kawabe, K., Kirita, H., 2000. Determination of ^{210}Po in reagent samples by alpha-ray spectrometry using extraction chromatographic resin. J. Radioanal. Nucl. Chem. 246, 327−330.

Moreno, J., Vajda, N., Danesi, P.R., Larosa, J.J., Zeiller, E., Sinojmeri, M., 1997. Combined Procedure for Determination of ^{90}Sr, ^{241}Am and Pu Radionuclides in Soil Samples. J. Radioanal. Nucl. Chem. 226 (1−2), 279−284.

Morgenstern, U., Hebert, D., Stolz, W., 1992. Electrolytic Tritium Enrichment of Natural Water Samples for Tritium Analysis. In: Noakes, J.E., Schönhofer, F., Polach, H.A. (Eds.), Liquid Scintillation Spectrometry, Proc. Of the Int. Conf. on Advances in LSC, LSC92", Vienna, Austria, Sept 14-18, 1992, Radiocarbon, Tucson 1993, pp. 355−360.

Mück, K., Henrich, E., 2001. Ascertaining and establishing the input parameters for prediction calculations with oecosys in case of emergency. In: Fachverband für Strahlenschutz (Ed.), Messen und Rechnen im Nuklearen Notfallschutz. TÜV Verlag, Köln.

Muramatsu, Y., Uchida, S., Tagami, K., Yoshida, S., Fujikawa, T., 1999. Determination of plutonium concentration and its isotopic ratio in environmental materials by ICP-MS after separation using ion-exchange and extraction chromatography. J. Anal. Atom. Spectrom. 14 (5), 859−865.

Muramatsu, Y., Yoshida, S., Tagami, K., Uchida, S., Ruhm, W., 2001. ICP-MS analysis of environmental plutonium. In: Kudo, A. (Ed.), Radioactivity in the Environment, Plutonium in the Environment—Edited Proceedings of the Second Invited International Symposium, vol. I. Elsevier, Amsterdam, pp. 63−77.

Narita, H., Harada, K., Burnett, W.C., 1989. Determination of ^{210}Pb, ^{210}Bi and ^{210}Po in natural waters and other materials by electrochemical separation. Talanta 36, 925−929.

National Health and Medical Research Council NHMRC, 2004. Australian Drinking Water Guidelines 6. National Water Quality Management Strategy. Australian Government Publishing Service, Canberra. Australia.

Nobrega, A.W., Sachett, I.A., Hespanol, E.C.B., 1987. Determination of ^{226}Ra by alpha spectrometry of liquid scintillation. Quin. Nova 10 (3), 175−179.

Noguchi, M., Satoh, K., Higuchi, H., 1984. Low level alpha activity measurements with pulse shape discrimination. Measurement system and the characteristics. Radioisotopes 33 (12), 835−840.

Nour, S., El-Sharkawy, A., Burnett, W.C., Horwitz, E.P., 2004. Radium-228 determination of natural waters via concentration on manganese dioxide and separation using diphonix ion exchange resin. Appl. Radiat. Isot. 61 (6), 1173−1178.

OECD, 1987. Organisation for Economic Co-operation and Development, 1987. In: Metrology and Monitoring of Radon, Thoron and Their Daughter Products. NEA Report of Experts, OECD Paris.

Okada, S., Momoshima, N., 1993. Overview of tritium: characteristics, sources and problem. Health Phys. 65, 595−609.

Olofsson, U., Allard, B., Andersson, K., Torstenfelt, B., 1981. Formation and Properties of Radiocolloids in Aqueous Solution - A Literature Survey. Department of Nuclear Chemistry, Chalmers University of Technology, Göteborg, Sweden.

Olofsson, U., Allard, B., Bengtsson, M., Torstenfelt, B., Andersson, K., 1983. Report SKBF-KBS-TR–83-08. Department of Nuclear Chemistry Chalmers University of Technology, Göteborg, Sweden, 33 pp.

Orr, J.C., 1988. Evaluation of counting methods for oceanic radium-228. J. Geophys. Res. 93 (C7), 8265−8278.

Osmond, J.K., Cowart, J.B., 1976. The theory and uses of natural uranium isotopic variations in hydrology. Atom. Energy Rev. 14, 621−679.

Osmond, J.K., Cowart, J.B., Ivanovich, M., 1983. Uranium isotopic disequilibrium in groundwater as an indicator of anomalies. J. Appl. Radiat. Isot. 34, 283−308.

Osmond, J.K., Cowart, J.B., Humphreys, C.L., Wagner, B.E., 1984. Radioelement Migration in Natural and Mined Phosphate Terrains. Fla. Inst. of Phosphate Res., Bartow, FL. Pub. No. 05-002-027, 131.

Oughton, D., Day, P., Fifield, K., 2001. Plutonium measurements using accelerator mass spectrometry: methodology and applications. In: Kudo, A. (Ed.), Radioactivity in the Environment, Plutonium in the Environment—Edited Proceedings of the Second Invited International Symposium, vol. I. Elsevier, Amsterdam, pp. 47−62.

Oural, C.R., Upchurch, S.B., Brooker, H.R., 1987. Radon progeny as sources of gross-alpha radioactivity anomalies. In: Natural Radiation and Technologically Enhanced Natural Radiation in Florida. Health Physics Society, pp. 79−91. Fla. Chap.

Oural, C.R., Upchurch, S.B., Brooker, H.R., 1988. Sampling interaquifer connector wells for polonium-210: Implications for gross-alpha analysis. In: Collins, A.G., Johnson, A.I. (Eds.), Ground-Water Contamination: Field Methods, Philadelphia, Amer. Sot. For Testing and Materials, pp. 290−303. Sp. Tech. Pub. 963.

Oural, C.R., Upchurch, S.B., Brooker, H.R., 1989. Radon progeny as sources of gross-alpha radioactivity anomalies. Health Phys. 55, 889−894.

Palomo, M., Villa, M., Casacuberta, N., Peñalver, A., Borrull, F., Aguilar, C., 2011. Evaluation of different parameters affecting the liquid scintillation spectrometry measurement of gross alpha and beta index in water samples. Appl. Radiat. Isot. 69 (9), 1274−128.

Papastefanou, C., 2008. Radioactive aerosols. In: Radioactivity in the Environment, vol. 12. Elsevier, Amsterdam and Oxford, pp. 1−171.

Parekh, P., Haines, D., Baari, A., Torres, M., 2003. Non-destructive determination of ^{224}Ra, ^{226}Ra and ^{228}Ra concentrations in drinking water by gamma spectroscopy. Health Phys. 85 (5), 613−620.

Parks, N.J., Tsuboi, K.K., 1978. Emulsion counting of radium and radon. Int. J. Appl. Radiat. Isot. 29 (2), 77−80.

Petrow, H.G., Cover, A., Schiessle, W., Parsons, E., 1964. Radiochemical determination of radium-228 and thorium-228 in biological and mineral samples. Anal. Chem. 36 (8), 1600−1603.

Plamboeck, A.H., Nylen, T., Agren, G., 2006. Comparative estimations of 137Cs distribution in a boreal forest in northern Sweden using a traditional sampling approach and a portable NaI detector. J. Environ. Radioactiv. 90, 100−109.

Pohl, E., Pohl-Rueling, J., 1976. Determination of environmental or occupational Rn-222 in air and water and Ra-226 in water with feasible and rapid methods of sampling and measurement. Health Phys. 31, 343−348.

Popov, L., Hou, X., Nielsen, S.P., Yu, Y., Djingova, R., Kuleff, I., 2006. Determination of radiostrontium in environmental samples using sodium hydroxide for separation of strontium from calcium. J. Radioanal. Nucl. Chem. 269, 161−173.

Povinec, P.P., La Rosa, J.J., Lee, S.H., Mulsow, S., Osvath, I., Wyse, E., 2001. Recent developments in radiometric and mass spectrometry methods for marine radioactivity measurements. J. Radioanal. Nucl. Chem. 248 (3), 713−718.

Prichard, H.M., Gesell, T.F., 1977. Rapid measurements of ^{222}Rn concentrations in water with a commercial liquid scintillation counter. Health Phys. 33, 577−581.

Prichard, H.M., Gesell, T.F., Meyer, C.R., 1980. Liquid scintillation analyses for Radium-226 and Radon-222 in potable waters. In: Peng, C., Horrocks, D.L., Alpen, E.L. (Eds.), Liquid Scintillation Counting Recent Applications and Development, vol. 1. Academic Press, London, pp. 347−355. Physical Aspects.

Prichard, H.M., Venso, E.A., Dodson, C.L., 1991. Liquid scintillation analysis of ^{222}Rn in water by alpha/beta discrimination. Radioact. Radiochem. 3 (10), 28−36.

Purchas, D.B., Sutherland, K., 2002. Handbook of Filter Media, second ed. Elsevier Advanced Technology, Oxford, UK. 572 pp.

Purkl, S., Eisenhauer, A., 2003. A rapid method for alpha-spectrometric analysis of radium isotopes in natural waters using ion-selective membrane technology. Appl. Radiat. Isot. 59 (4), 245−254.

Ringbom, A., Larson, T., Axelson, A., Elmgren, K., Johansson, C., 2003. C. SAUNA—A system for automatic sampling, processing, and analysis of radioactive xenon. Nucl. Instrum. Methods Phys. Res., Sect. A 508, 542−553.

Risica, S., Nuccetelli, C., 2001. Building materials as a source of population exposure to ionising radiation. Phys. Med. 17, 3−8.

Risica, S., Bolzan, C., Nuccetelli, C., 2001. Radioactivity in building materials: room model analysis and experimental methods. Sci. Total Environ. 272, 119−126.

Ross, P., 2008. Analysis of radionuclides using ICP-MS. In: Povinec, P.P. (Ed.), Radioactivity in the Environment, Analysis of Environmental Radionuclides, vol. 11. Elsevier, Amsterdam, pp. 295−330.

Ruzer, L.S., Harley, N.S. (Eds.), 2005. Aerosol Handbook. Measurement, Dosimetry, and Health Effects. CRC Press, Boca Raton, London, New York, Washington, D.C., 728 pp.

Saarinen, L., Suksi, J., 1992. Determination of uranium series radionuclides Pa-231 and Ra-226 using liquid scintillation counting (LSC). In: Report of the Nuclear Waste Commision of Finnish Power Companies.

Saey, P.R., De Geer, L.-E., 2005. Notes on radioxenon measurements for CTBT verification purposes. Appl. Radiat. Isot. 63 (5−6), 765−773.

Saey, P.R., Bowyer, T.W., Ringbom, A., 2010. Isotopic noble gas signatures released from medical isotope production facilities - Simulations and measurements. Appl. Radiat. Isot. 68 (9), 1846−1854.

Salonen, L., 1993. Measurement of low levels of ^{222}Rn in water with different commercial liquid scintillation counters and pulse-shape analysis. In: Noakes, J.E., Schoenhofer, F., Polach, H. (Eds.), Advances in Liquid Scintillation Spectrometry 1992, Radiocarbon, pp. 361−371.

Sánchez-Cabeza, J.A., Pujol, L., 1995. A rapid method for the simultaneous deteremination of gross alpha and beta activities in water samples using a low background liquid scintillation counter. Health Phys. 68 (5), 674−682.

Sanchez-Cabeza, J.A., Pujol, L.1, 1998. Simultaneous determination of radium and uranium activities in water samples using liquid scintillation counting. Analyst 123, 399−403.

Sanchez-Cabeza, J.A., Pujol, L.L., 1999. Study on the hydrodynamics of the Ebro River lower course using tritium as a radiotracer. Water Res. 33 (10), 2345−2356.

Saxen, R., 1990. Radioactivity of Surface Water and Freshwater Fish in Finland in 1987. STUK-A77.

Schoenhofer, F., Barnett, J.M., McKleevev, J., 1991. Determination of ^{222}Rn and ^{226}Ra in drinking water by low level scintillation counting − Surveys in Austria and Arizona. In: Ross, H., Noakes, J., Spaulding, J.D. (Eds.), Liquid Scintillation and Organic Scintillators. Lewis Publishers, pp. 537−545.

Schölch, J., Stich, W., Münnich, K.O., 1966. Measurement of radioactive xenon in the atmosphere. Tellus 18, 298−301.

Schönhofer, F., 1989. Determination of Radon-222 and Radium-226 in mineral water and drinking water − a Survey in Austria. Analyst 114, 1345−1347.

Schönhofer, F., Wallner, G., 2001. Very rapid determination of Ra-226, Ra-228, and Pb-210 by selective adsorption and liquid scintillation spectrometry. Radioact. Radiochem. 12 (2), 33−38.

Schulze, J., Auer, M., Werzi, R., 2000. Low level radioactivity measurement in support of the CTBTO. Appl. Radiat. Isot. 53 (1−2), 23−30.

Schumacher, B., Griggs, J., Askren, D., Litman, B., Shannon, B., Mehrhoff, M., Nelson, A., Schultz, M.K., 2014. Development of Rapid Radiochemical Method for Gross Alpha and Gross Beta Activity Concentration in Flowback and Produced Waters from Hydraulic Fracturing Operations. EPA/600/R-14/107. U.S. Environmental Protection Agency Office of Research and Development, Washington, DC, 20460. 2014.

Smith, L.L., Alvarado, J.S., Markun, F.J., 1997. An evaluation of radium-specific, solid-phase extraction membranes. Radioactivity and Radiochemistry 8 (1), 30−37.

Spaulding, J.D., Noakes, J.E., 1992. Determination of ^{222}Rn in drinking water using an alpha/beta liquid scintillation counter. In: Noakes, J.E., Schoenhofer, F., Polach, H. (Eds.), Advances in Liquid Scintillation Spectrometry 1992, Radiocarbon, pp. 373−381.

Spry, N., Parry, S., Jerome, S., 2000. The development of a sequential method for the determination of actinides and ^{90}Sr in power station effluent using extraction chromatography. Appl. Rad. Isot. 53 (1−2), 163−171.

Srncik, M., Hrnecek, E., Steier, P., Wallner, A., Wallner, G., Bossew, P., 2008. Vertical distribution of ^{238}Pu, $^{239(40)}$Pu, ^{241}Am, ^{90}Sr and ^{137}Cs in Austrian soil profiles. Radiochim. Acta 96 (9−12), 733−738.

Stevenson, D.L., Johns, F.B., 1971. Separation technique for the determination of ^{85}Kr in the environment. In: Rapid "Rapid Methods for Measuring Radioactivity in the Environment". International Atomic Energy Agency, Vienna, p. 157.

Stockburger, H., Sartorius, H., Sittkus, A., 1977. Messung der Krypton-85 und Xe-133-Aktivität der atmosphärischen Luft. Z. Naturforschung 32, 1249−1253.

Suomela, J., Wallberg, L., Melin, J., 1993. Methods for Determination of Strontium-90 in Food and Environmental Samples by Cherenkov Counting. Stockholm: SSI Report 96-111.

Svoukis, E., Tsertos, H., 2007. Indoor and outdoor in situ high-resolution gamma radiation measurements in urban areas of Cyprus. Radiat. Prot. Dosim. 123, 384−390.

Tavcar, P., Benedik, L., 2005. Determination of actinides and ^{90}Sr in spent ion exchange resins. Radiochim. Acta 93 (9), 623−635.

Thakkar, A., 2002. A rapid sequential separation of actinides using Eichrom's extraction chromatographic material. J. Radioan. Nucl. Chem. 252 (2), 215−218.

Thompson, S.K., 2000. Sampling. Wiley, New York, 341pp.

Thompson, S.K., Seber, G.A.F., 1996. Adaptive Sampling. Wiley, New York, 265pp.

Tyler, A.N., 2004. High accuracy in situ radiometric mapping. J. Environ. Radioactiv. 72, 195−202.

Tyler, A.N., Sanderson, D.C.W., Scott, E.M., 1996. Estimating and accounting for 137Cs source burial through in situ gamma spectrometry in salt marsh environments. J. Environ. Radioactiv. 33, 195−212.

United Nations Scientific Committee on the Effects of Atomic Radiation UNSCEAR, 2000a. Sources, Effects and Risks of Ionizing Radiation, Report to the General Assembly, with Scientific Annexes. In: Annex A., Dose Assessment Methodologies. New York, 63pp.

United Nations Scientific Committee on the Effects of Atomic Radiation UNSCEAR, 2000b. Sources, Effects and Risks of Ionizing Radiation, Report to the General Assembly, with Scientific Annexes. In: Annex B., Exposures from Natural Radiation Sources. New York, 74pp.

United Nations Scientific Committee on the Effects of Atomic Radiation UNSCEAR, 2000c. Sources, Effects and Risks of Ionizing Radiation, Report to the General Assembly, with Scientific Annexes. In: Annex C., Exposures to the Public from Man-Made Sources of Radiation. New York, 134pp.

United Nations Scientific Committee on the Effects of Atomic Radiation UNSCEAR, 2008. Sources, Effects and Risks of Ionizing Radiation, Report to the General Assembly, with Scientific Annexes. In: Report to the General Assembly, Scientific Annex B, vol. I. New York, 245pp.

United Nations Scientific Committee on the Effects of Atomic Radiation UNSCEAR, 2014. Sources, Effects and Risks of Ionizing Radiation (Report to the General Assembly). UNSCEAR 2013 Report. In: Scientific Annex A: Levels and Effects of Radiation Exposure Due to the Nuclear Accident after the 2011 Great East-Japan Earthquake and Tsunami, Scientific Committee on the Effects of Atomic Radiation (UNSCEAR), UN, New York (2014), vol. I.

United States Environmental Protection Agency USEPA, 1982. Determination of Lead-210 in Drinking Water. Method 909.0. In: Velden, R.J., Jacobs, B.J. (Eds.), Environmental Monitoring and Support Laboratory. United States Environmental Protection Agency, Cincinnati, Ohio, 45268.

Upchurch, Sam, Oural, C.R., Foss, D.W., Brooker, H.R., 1991. Radiochemistry of uranium-series isotopes in groundwater (chemical fate of uranium-daughter radionuclides in recharge wells. Central Florida phosphate district) (revised).

US Environmental Protection Agency, 2006. Guidance on Systematic Planning Using the Data Quality Objectives Process. QA/G-4. US EPA, Washington DC. EPA/240/B-06/001.

US Nuclear Regulatory Commission, 1977. Calculation of annual doses to man from routine from routine releases of reactor effluents for the purpose of evaluating compliance with 10CFR Part 50. Appendix I, Regulatory Guide 1, 109 Revision 1, 1 (1977).

U.S. Nuclear Regulatory Commission (NRC), 1998a. A Nonparametric Statistical Methodology for the Design and Analysis of Final Status Decommissioning Surveys (Revision 1). NUREG-1505 Rev. 1. Office of Nuclear Regulatory Research, Washington, DC.

U.S. Nuclear Regulatory Commission (NRC), 1998b. Minimum Detectable Concentrations with Typical Radiation Survey Instruments for Various Contaminants and Field Conditions. NUREG-1507. Office of Nuclear Regulatory Research, Washington, DC.

U.S. Nuclear Regulatory Commission (NRC), Oak Ridge Associated Universities, 1992. Manual for Conducting Radiological Surveys in Support of License Termination. Draft Report for Comment. NUREG/CR-5849. Washington, DC.

U.S. Nuclear Regulatory Commission (NRC), 1995. Proposed Methodologies for Measuring Low Levels of Residual Radioactivity for Decommissioning. NUREG-1506. Draft Report for Comment, Washington, DC.

United States Environmental Protection Agency USEPA, 2000. National Primary Drinking Water Regulations; Radionuclides. Final Rule vol. 9. In: Environmental Protection Agency 40 CFR Parts. United States of America, Washington, pp. 141−142, 2000.

Vajda, N., Kim, C.K., 2010. Determination of radiostrontium isotopes: A review of analytical methodology. Appl. Radiat. Isot. 68 (12), 2306−2326.

Vajda, N., Kim, C.K., 2010a. Determination of Pu isotopes by alpha spectrometry: a review of analytical methodology. J. Radioanal. Nucl. Chem. 283 (1), 203−223.

Vajda, N., Kim, C.K., 2010b. Determination of ^{241}Am by alpha spectrometry: a review of analytical methodology. J. Radioanal. Nucl. Chem. 284 (2), 341−366.

Vajda, N., Kim, C.K., 2010c. Determination of radiostrontium isotopes: a review of analytical methodology. App. Radiat. Isot. 68 (12), 2306−2326.

Vajda, N., Ghods-Esphanani, A., Cooper, E., Danesi, P.R., 1992. Determination of Radiostrontium in Soil Samples Using a Crown Ether. J. Radioanal. Nuc. Chem. 162 (2), 307−323.

Vajda, N., La Rosa, J., Zeisler, R., Danesi, P., Kis-Benedek, G., 1997. A novel technique for the simultaneous determination of ^{210}Pb and ^{210}Po using a Crown ether. J. Environ. Radioactiv. 37, 355−372.

Vaney, B., Friedli, C., Geering, J.J., Lerch, P., 1989. Rapid trace determination of radiostrontium in milk and drinking water. J. Radioanal. Nucl. Chem, Articles 134 (1), 87−95.

Vanhaecke, F., Moens, L., 2004. Overcoming spectral overlap in isotopic analysis via single- and multi-collector ICP−mass spectrometry. Anal. Bioanal. Chem. 378 (2), 232−240.

Varga, Z., Surányi, G., Vajda, N., Stefánka, Z., 2007. Improved sample preparation method for environmental plutonium analysis by ICP-SFMS and alpha-spectrometry. J. Radioanal. Nucl. Chem. 274 (1), 87−94.

Vilks, P., Bachinsk, D.B., 1997. Natural Colloids in Ground Water from Granite and Their Potential Impact on Radionuclide Transport. Report AECL-11635. Geochemistry Research Branch Whiteshell, Laboratories Pinawa. Manitoba ROE 1L0.

Vreček, P., Benedik, L., Pihlar, B., 2004. Determination of Pb-210 and Po-210 in sediment and soil leachates and in biological materials using a Sr-resin column and evaluation of column resin. Appl. Radiat. Isot. 60, 717−723.

Wallner, G., 2002. Determination of ^{228}Ra, ^{226}Ra, and ^{210}Pb in drinking water using liquid scintillation counting. In: Möbius, S., Noakes, J., Schönhofer, F. (Eds.), LSC 2001, Advances in Liquid Scintillation Spectrometry, Tucson: Radiocarbon, pp. 269−274.

Wand, J.-J., Chen, I.-J., Chiu, J.-H., 2004. Sequential isotopic determination of plutonium, thorium, americium, strontium and uranium in environmental and bioassay samples. Appl. Rad. Isot. 61 (2−3), 299−305.

Wen, X., Wu, Y., Su, J., Zhang, Y., Liu, F., 2005. Hydrochemical characteristics and salinity of groundwater in the Ejina basin, Northwestern China. Environ. Geol. 48, 665−675.

Wen, X.H., Wu, Y.Q., Wu, J., 2008. Hydrochemical characteristics of groundwater in Zhangye basin, Northwestern China. Environ. Geol. 55 (8), 1713−1724.

World Health Organisation (WHO), 2008. Guidelines for Drinking-Water Quality, Incorporating the First and Second Agenda, third ed. World Health Organisation, Geneva.

World Health Organisation (WHO), 2011. Guidelines for Drinking-Water Quality, Incorporating the First and Second Agenda, fourth ed. World Health Organisation, Geneva.

Wisser, S., Frenzel, E., Dittmer, M., 2006. Innovative procedure for the determination of gross-alpha gross-beta activities in drinking water. Appl. Radiat. Isot. 64 (3), 368−372.

World Meteorological Organisation (WMO), 1996. Environmental Pollution Monitoring and Research Programme Report Series No. 109. Report of an Expert Consultation on ^{85}Kr and ^{222}Rn: Measurements, Effects and Applications (Freiburg, Germany, 28−31 March 1995).

Report, Technical Series no 91. In: Yurstsever, Y. (Ed.), 1983. Guidebook on Nuclear Techniques in Hydrology. IAEA, Vienna.

Zapata-García, D., Llauradó, M., Rauret, G., 2009. Establishment of a method for the rapid measurement of gross alpha and gross beta activities in sea water. Appl. Radiat. Isot. 67 (5), 978−981.

Zimmermann, P.H., Feichter, J., Rath, H.K., Crutzen, P.J., Weiss, W., 1989. A global three-dimensional source-receptor model investigation using ^{85}Kr. Atmos. Environ. 23, 25−35.

Zombori, P., Nèmeth, I., Andrási, A., Lettner, H., 1992. In situ gamma-spectrometric measurement of the contamination in some selected settlements of Byelorussia (BSSR), Ukraine (UkrSSR) and the Russian Federation (RSFSR). J. Environ. Radioactiv. 17, 97−106.

Łokas, E., Mietelski, J.W., Kleszcz, K., Tomankiewicz, E., 2010. A sequential procedure for determining ^{238}Pu, $^{239+240}$Pu, ^{241}Am, ^{90}Sr, U and Th activities in soils and peats from Spitsbergen. Nukleonika 55 (2), 195−199.

Further reading

Brun, S., Bessac, S., Uridat, D., Boursier, B., 2000. Rapid method for determination of radiostrontium in milk. Radioanal. Nucl. Chem. 253 (2), 191−197.

Diaz Leon, J., Jaffe, D.A., Kaspar, J., Knecht, A., Miller, M.L., Robertson, R.G.H., Schubert, A.G., 2011. Arrival time and magnitude of airborne fission products from the Fukushima, Japan, reactor incident as measured in Seattle, WA, USA. J. Environ. Radioactiv. 102 (11), 1032−1038.

International Commission on Radiological Protection, 1985. Principles of Monitoring for the Radiation Protection of the Population. Publication 43, Ann ICRP, 15 (1). Pergamon Press, Oxford and New York.

Rudolf Engelbrecht



Rudolf Engelbrecht graduated in radioecology and radiochemistry at the Technical University of Vienna after which he joined the Austrian Research Center, Radio Protection Department. Since 2010, he has been the head of the Radiochemical Analytics Group of the Department of Radiation Safety and Applications of the Seibersdorf Labor GmbH, Austria. Since 2019, Rudolf has been with the Austrian Agency for Health and Food Security, GmbH in Vienna. His research activities can be summarized as radioanalytical methods as a prerequisite for risk assessments with some emphasis on the determination of committed effective dose. Methods comprise whole-body counting and excretion analysis as well as radiochemical analysis of environmental media. Most recent research focuses on the evaluation of exposure to technologically enhanced naturally occurring radioactive materials by alpha and gamma spectrometry.

Chapter 2

PERPUSTAKAAN PRIBADI AN-NUR SUNARYA

Environmental liquid scintillation analysis[1]

Xiaolin Hou[1,2] and Xiongxin Dai[3]

[1]Technical University of Denmark, Department of Environmental Engineering, Roskilde, Denmark; [2]Lanzhou University, School of Nuclear Science and Technology, Lanzhou, China; [3]China Institute for Radiation Protection, Taiyuan, Shanxi Province, China

Chapter outline

I. Introduction **42**
II. Low-level liquid scintillation counting theory **43**
A. Sources of background 43
B. Background reduction methods—instrument considerations 43
1. Enhanced passive/graded shielding 44
2. Active guard detectors 44
3. Pulse discrimination electronics 45
4. TR-LSC quasi-active detector guards 47
5. Counting region optimization 48
6. Process optimization 48
C. Background reduction methods—vial, vial holder, and cocktail considerations 49
1. Vials 49
2. Vial holders 49
3. Cocktail choice and optimization 50
D. Background reduction methods—environment 51
III. Alpha/beta discrimination **51**
A. Alpha/beta separation theory 51
B. Alpha/beta instrumentation 52
1. The PERALS spectrometer 53
2. Conventional LS spectrometers with pulse-shape discrimination 53
C. Cocktail and vial considerations 55
1. Cocktail choice 55
2. Vial choice 56
D. Alpha/beta calibration 56
1. Misclassification Calculations 57
2. Quenching and quench correction of percentage misclassification 57
IV. Triple-to-double coincidence ratio (TDCR) counting **58**
A. TDCR liquid scintillation counting 58
B. TDCR Cerenkov counting 59
V. Analysis of alpha-emitting transuranic nuclides **60**
A. Environmental occurrence and importance 60
B. Sample preparation and analysis 61
1. Alpha spectrometry 61
2. Mass spectrometry 61
3. Liquid scintillation counting (LSC) 61
VI. Analysis of beta-emitting radionuclides **62**
A. Tritium (^{3}H) 62
1. Environmental occurrence 62
2. Sample preparation and analysis 63
B. Radiocarbon (^{14}C) 66
1. Environmental occurrence 66
2. Sample preparation and analysis 67
3. Analysis of ^{14}C in fuels containing biogenic materials 70
C. Iron-55 (^{55}Fe) 73
1. Environmental occurrence 73
2. Sample preparation and analysis 73
D. Nickel-63 (^{63}Ni) 75
1. Environmental occurrence 75
2. Sample preparation and analysis 75
E. Strontium-89 and strontium-90/yttrium-90 (^{89}Sr and ^{90}Sr/^{90}Y) 77
1. Environmental occurrence 77
2. Sample preparation 77
3. LSC measurements 79
F. Technetium-99 (^{99}Tc) 81
1. Environmental occurrence 81
2. Sample preparation and analysis 82
G. Plutonium-241 (^{241}Pu) 84
1. Environmental occurrence 84
2. Sample preparation and analysis 84

1. Previous authors are LAINA SALONEN (retired) Radiation and Nuclear Safety Authority, FIN-00,881 Helsinki, Finland; LAURI KAIHOLA (retired), PerkinElmer, Inc., FIN-20,101 Turku, Finland; BRIAN CARTER, Ontario Power Generation Inc., Whitby, Ontario L1N 1E4, Canada; GORDON T. COOK, SUERC Radiocarbon Dating Laboratory, East Kilbride G75 0QF, Scotland, and CHARLES J. PASSO, JR., PerkinElmer, Inc.,Downers Grove, Illinois 60,515, USA.

Handbook of Radioactivity Analysis: Volume 2. https://doi.org/10.1016/B978-0-12-814395-7.00002-7
Copyright © 2020 Elsevier Inc. All rights reserved.

H. Other radionuclides (^{36}Cl, ^{41}Ca, ^{129}I) 85
1. Chloride-36 (^{36}Cl) 85
2. Iodine-129 (^{129}I) 87
3. Calcium-41 (^{41}Ca) 88
VII. Analysis of radionuclides from natural decay series 89
A. Uranium 89
1. Environmental occurrence and importance 89
2. Sample preparation and analysis 90
B. Gross alpha and beta measurements 91
C. Radon 95
1. Environmental occurrence and importance 95
2. Sample preparation and analysis 95
D. Radium 100
1. Environmental occurrence and importance 100
2. Sample preparation and measurement of ^{226}Ra, ^{228}Ra, ^{224}Ra, and ^{223}Ra 101
E. Lead-210 (^{210}Pb) [Bismuth-210 (^{210}Bi) and Polonium-210 (^{210}Po)] 104
1. Environmental occurrence and importance 104
2. Sample preparation and analysis 105
F. Thorium 107
1. Environmental occurrence and importance 107
2. Sample preparation and analysis 108
VIII. Spectrum deconvolution methods in environmental analysis 109
A. Spectrum deconvolution, unfolding, stripping, peak fitting 109
B. Approaches in LS beta spectrometry 109
C. Alpha spectrum unfolding 110
1. Energy resolution 110
2. High energy tailing 110
3. Software 111
D. Better energy resolution enables more complete separation 112
1. Cocktail and sample quench 112
2. Vial selection 112
3. Lower sample temperature 112
4. New detector designs 112
References 113
Xiaolin Hou 136
Xiongxin Dai 136

I. Introduction

Environmental liquid scintillation counting (LSC) is the measurement of both natural and anthropogenic radionuclides in the environment. In the vast majority of environmental applications, radionuclide concentrations are low and the contribution of instrument background to the precision of the measurement is significant. During the 1980s, a new generation of commercially manufactured liquid scintillation analyzers (LSAs) was introduced. These instruments were classified as "low level" because the background reduction features that were incorporated into them enabled the quantification of much lower radionuclide activities than were previously possible, i.e., the E^2/B (Figure of Merit (FOM)) factor is increased (where E = efficiency and B = background), and this results in an improvement in the minimum detectable activity (MDA). Well-documented examples of such improvements include (1) the extension of the effective age limit for radiocarbon dating from approximately 40,000 years to 55,000 and even up to 70,000 years (Polach et al., 1983; McCormac et al., 1993; Cook, 1995; Hogg, 2004; Hogg et al., 2007) and (2) the detection of approximately 1 Bq/L of ^{3}H in natural waters without electrolytic enrichment (Rank, 1993) and from 0.01 Bq/L down to 0.001 Bq/L with enrichment factors of 26 and 175, respectively (Morgenstern and Taylor, 2009).

In addition to the introduction of background reduction features, the incorporation of multichannel analyzers (MCAs) and microprocessor technology into modern LSAs has added spectrometric and sophisticated data handling capabilities that have made LSC a much more attractive analytical tool for environmental analyses. Because of these advances, low-level LSC is now commonly used for the following applications:

1. **Measurement of naturally occurring radionuclides, in many cases with respect to health issues**. Many are now routinely measured at natural environmental levels in a range of sample matrices including waters, sediments, soils, air, etc. These include isotopes of Ra, U and Th, ^{210}Pb, and ^{222}Rn (Möbius et al., 1993; Venso et al., 1993; Al-Masri and Blackburn, 1995; Pates et al., 1996a, 1996b; Tinker and Smith, 1996; Salonen and Hukkanen, 1997; Aupiais et al., 1998; Sato et al., 2000; Wallner, 2001; Salonen, 1993a, 1993b; 2009, 2010a; Fons-Castells et al., 2017; Mikalauskiene et al., 2018).
2. **Monitoring the environment for radionuclide releases associated with nuclear fuel cycle activities (fuel enrichment, fuel fabrication, power generation, and fuel reprocessing)**. This would mainly focus on beta-emitting radionuclides without significant gamma emissions, including ^{3}H, ^{14}C, ^{36}Cl, ^{55}Fe, ^{63}Ni, ^{89,90}Sr, ^{90}Y, ^{99}Tc, and ^{241}Pu, but could also include analysis of alpha-emitting radionuclides (Wilken and Joshi, 1991; Verrezen and Hurtgen, 1992; Ryan et al., 1993; Cook et al., 1995; Lee and Lee, 1999; Spry et al., 2000; Heilgeist, 2000; Tolmachyov et al., 2001). In addition, the analysis of effluent waters and other matrices for alpha activity is now widely reported (Cadieux et al., 1994; Dacheux and Aupiais, 1997; Mitchell et al., 2005). Some radionuclides in decommissioning of nuclear facilities can be measured by LSC,

i.e., ^{3}H, ^{14}C, ^{36}Cl, ^{41}Ca, ^{55}Fe, ^{63}Ni, ^{59}Ni, ^{90}Sr, ^{99}Tc, ^{129}I, ^{93}Zr, ^{93}Mo, and ^{241}Pu (Hou, 2005a, 2005b, 2007; Hou et al. 2005b, 2007; Vesely et al., 2008).

3. **Rapid methods developed for emergency preparedness and homeland security purposes**. The power of liquid scintillation spectrometry in the rapid collection of information in emergencies was demonstrated by Schönhofer and Weisz (1987) by the analysis of water samples collected from airplane wings at Vienna. The importance of LSC in rapid decision-making was pointed out by Schönhofer (1988). Numerous papers were published on rapid Sr/Y analyses by LSC of food and milk (Suomela et al., 1993; Günther et al., 2009; Kim et al., 2009; Kim, 2011 and references therein; Guerin et al., 2017a), air and water (Heckel and Vogl, 2009; Tayeb et al., 2015, 2016) and soil (Lee et al., 2011). Rusconi et al. (2004) discussed rapid analyses of drinking water for gross alpha and beta, ^{226}Ra, ^{234}U, ^{238}U, and ^{235}U. Eikenberg et al. (1996) measured gross alpha activity in urine. Piraner and Jones (2009) and Dai et al. (2013) applied LSC in urine analyses for radiological emergency preparedness. Portable instruments allow fast on-site detection of environmental radionuclides (Möbius, 2002).
4. **Studying the environmental processes**. This would mainly be carried out using radionuclides of natural origins and would include (1) ^{14}C dating (Thomson et al., 1995; Zaretskaia et al., 2001), (2) groundwater movement and dating using ^{3}H (Rank, 1993; Morgenstern and Taylor, 2009), and (3) marine sediment mixing, productivity, and particle flux studies using ^{234}Th (Pates et al., 1996b; Kersten et al., 1998; Nour et al., 2002; Anand et al., 2017) and ^{210}Pb/^{210}Bi/^{210}Po (Biggin et al., 2002).
5. **Analysis of ^{14}C content in air, plants, biofuel, biobased materials, and CO_2 emissions**. Conventional radiocarbon dating techniques with liquid scintillation spectrometry offer feasible analysis methods (Noakes et al., 2006; Dijs et al., 2006; Culp and Noakes, 2009, 2011; Yunoki and Saito, 2009; Norton, 2009; Norton and Woodruff, 2011; Idoeta et al., 2014; Graven, 2015; Keller et al., 2016; Niu et al., 2018).

The general theory of LSC is discussed in Chapter 6, Volume 1, while the focus of this chapter is confined to a discussion of the features that have enhanced the performance of LSAs and the application of these techniques to the measurement of environmentally significant radionuclides.

II. Low-level liquid scintillation counting theory

A. Sources of background

Instrument background is derived from many sources including natural radioactivity in the instrument's construction materials, e.g., the photomultiplier tubes (PMTs), natural radioactivity in the vial walls or cap, cosmic ray interactions with the vial walls and vial contents, and thermal ionizations in the PMTs, etc. These can be divided broadly into two categories termed quenchable and unquenchable background (Horrocks, 1985). Quenchable background comprises approximately one-third of the total, and it is primarily due to cosmic rays and other high-energy radiations that penetrate the lead shielding, the reflector, and the wall of the vial before interacting with the scintillation cocktail (Horrocks, 1985; van Cauter, 1986). In addition, radioactive contamination of the scintillation cocktail can add to the quenchable component. Quenchable background increases with increasing cocktail volume and is reduced by quenching agents (Horrocks, 1985). The pulse height spectrum extends beyond the ^{3}H and ^{14}C energy ranges, and the light pulses so produced are similar to those of true beta events.

Background events originating outside the cocktail are unaffected by quenching agents and thus are referred to as unquenchable (Horrocks, 1985). Unquenchable background events contribute approximately two-thirds of the total LSA background (van Cauter, 1986). The primary source is high-energy cosmic radiation and natural radioactivity in the vials, which interact with the vial and PMT glass surfaces to produce low-photon-yield Cerenkov events and fluorescence, which are primarily confined to the ^{3}H energy region. Unquenchable background can be distinguished electronically from valid scintillation events because the pulse pattern that results is characterized by a series (burst) of trailing low-photon-yield afterpulses that follow the initial prompt pulse (van Cauter, 1986). Typical pulse patterns due to quenchable and unquenchable events are illustrated in Fig. 2.1.

B. Background reduction methods—instrument considerations

Until the introduction of commercially manufactured low-level LSAs in the 1980s, almost all background reduction methods were attempted by the instrument users. They consisted mainly of modifications to existing instrumentation and included the following: increasing the amount of passive shielding, reducing the voltage applied to the PMTs, masking the PMTs or the vials to minimize PMT cross-talk, or using alternative low background materials for vials (mainly quartz or Teflon) or vial holder (e.g., Delrin) construction (Tamers, 1965; Calf and Polach, 1974; Noakes, 1977; Haas, 1979; Gupta and Polach, 1985). In addition, a number of experimental devices incorporating cosmic guard detectors were fabricated (Von Pietig and Scharpenseel, 1964; Alessio et al., 1976; Punning and Rajamäe, 1977; Iwakura et al., 1979; Jiang et al., 1983). However, it was not until background reduction features

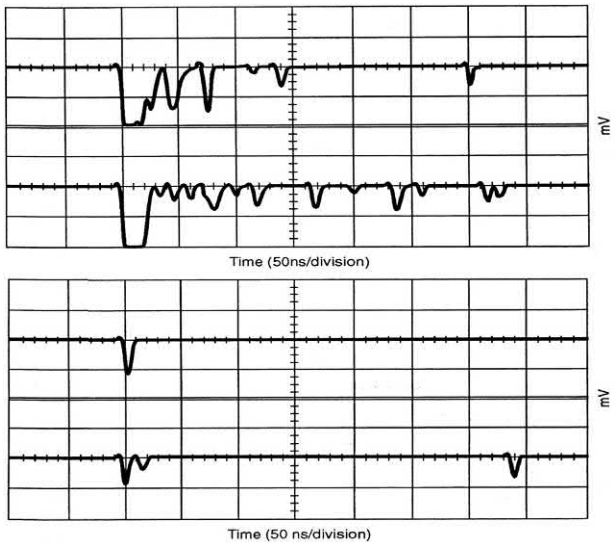


FIGURE 2.1 Typical photomultiplier tube (PMT) pulse shapes from (upper plot) unquenchable and (lower plot) quenchable events. The top halves of the upper plot and the lower plot are the pulses from the right-hand side PMT, and the bottom halves are the pulses from the left-hand side PMT (Passo and Roberts, 1996). *Reprinted by permission of* Radiocarbon*, University of Arizona, Tucson.*

were combined with modern microprocessor technology that the full potential of low-level LSA instrumentation was realized. Modern low-level instruments employ one or more of the following features to reduce background.

1. Enhanced passive/graded shielding

Some instruments employ large amounts of lead shielding. For example, the Wallac 1220 Quantulus has a shield of approximately 630 kg. This is composed primarily of low specific activity lead with graded cadmium and OFHC copper inner linings (Kojola et al., 1984). Also, the Beijing Nuclear Instrument Factory reported an LSA with a passive shield comprising a 7.5 cm thickness of lead and 4 cm of stainless steel, which has a total weight of 1500 kg (Guan and Xie, 1992). The Japanese Aloka LB-5 total weight with its lead shield is 900 kg. The low-level LSA manufactured by Simmax (China) also has a heavy lead shielding of 900 kg. These shields reduce the background from environmental gamma photons associated with building and instrument construction materials, as well as the "soft" cosmic muon component of background, and the graded cadmium and copper lining in the Quantulus shield absorbs secondary X-rays and thermal neutrons. However, passive shielding alone does not fully absorb high-energy gamma photons and the hard cosmic-ray component. Anticoincidence shielding (an active guard detector) or a quasi-active guard in combination with some type of pulse shape analysis are the most effective ways to reduce background (Kojola et al., 1984; Guan and Xie, 1992; Noakes and Valenta, 1996; Edler, 2017).

2. Active guard detectors

An active shield or guard detector consists of a volume of scintillating material (e.g., a plastic scintillator such as NE-110, a liquid scintillator, a large sodium iodide or a bismuth germanium oxide (BGO) crystal) and either one or two additional PMTs. This guard surrounds the detector assembly, and its PMTs are in anticoincidence with the sample PMTs (e.g., Kojola et al., 1984). Events detected only by the guard detector in the Quantulus can be saved as raw spectra for monitoring purposes. The sample events, which are simultaneously measured with the guard events, can be saved as a rejected sample event spectrum. At the same time, a net sample spectrum is also saved. Typically, the guard will reject much of the residual environmental gamma radiation, and more than 99% of the soft cosmic component and harder cosmic muon flux. This can reduce PMT cross-talk from Cerenkov light-induced pulses, which are primarily caused by the interaction of cosmic muons with the PMTs. Several types of active shields are employed in commercially available LSAs. For example, the Wallac 1414 Guardian employs an elastic plastic scintillator, the Wallac 1220 Quantulus uses a mineral oil–based liquid scintillator (Fig. 2.2), the single PMT counter ICELS (Theodórsson and Gudjónsson, 2009; Tudyka et al., 2010) uses a large sodium iodide crystal, the Aloka LB5 has a plastic shield, and the Quantulus GCT 6220 guard detector uses BGO crystal (Edler, 2017). These anti-Compton devices are true background event detectors. Quasi-active guard detectors are presented in Section 2.B.4.

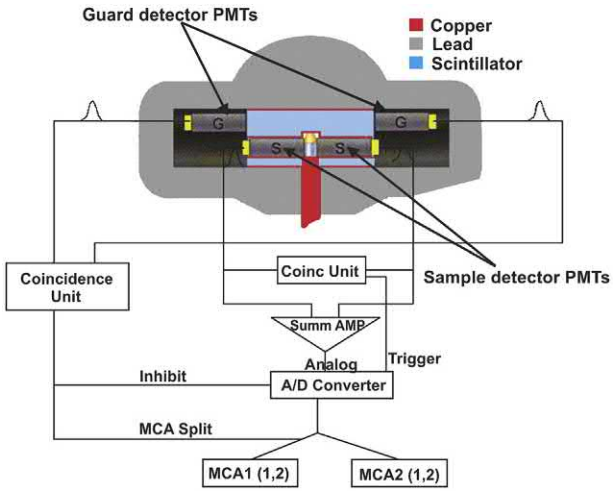


FIGURE 2.2 Schematic presentation of the active guard, passive shield, and detector chamber in the Wallac 1220 Quantulus. Original cadmium cylinder around the guard has now been replaced by copper. For the color version of the figure, the reader is referred to the online version of the book. *©1984–2019, PerkinElmer, Inc. All rights reserved. Printed with permission.*

3. Pulse discrimination electronics

a. Pulse shape analysis

A beta scintillation event is comprised of a fast (prompt) and a delayed component. The majority of the light (derived from excited singlet states) is within the prompt component (typically 2–8 ns in duration). The delayed component (produced largely by the annihilation of triplet states) may persist for several hundred nanoseconds. The relative amounts of light in the prompt and delayed components are dependent on the specific ionization induced by different types of particles. The pulse shape analyzer in the Quantulus is an analog device that integrates the tail of each pulse and compares this with the total pulse integral to produce an amplitude-independent parameter that relates to the pulse shape (Oikari et al., 1987). It is on this basis that PSA can be used for particle detection, which includes alpha–beta discrimination. Although the most effective use of PSA is for alpha counting, the technique has also been used for background discrimination (Kaihola, 1991). The background of glass vials is characterized by long scintillation light pulses or fluorescence due to the interaction of cosmic or other environmental radiation with the vial (much of the latter originates from the inherent radioactivity of the vial itself). PSA is used to separate these long scintillation events from the shorter scintillations of true beta events (Fig. 2.3). PSA values are adjustable within a finite range and the optimum value (in which E^2/B is maximized) can be determined automatically or empirically determined by the user. This optimum will be specific for vial type and chemistry. As in all pulse shape discrimination schemes, there is a finite probability of a slight decrease in counting efficiency due to the misclassification of events. Several of the leading LSA manufacturers, including Wallac, Hidex, and Beckman Coulter Instruments Inc. use some form of PSA that is capable of background reduction.

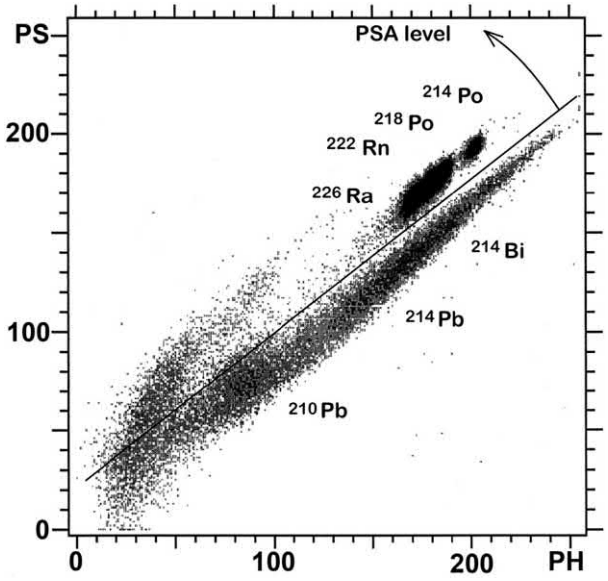


FIGURE 2.3 3D scatterplot of alpha and beta events from ^{226}Ra separated by the Wallac pulse shape analyzer (PSA), as recorded by an experimental LSC and displayed in pulse-height/pulse-shape coordinates (Kaihola et al., 1994). Slow fluorescence events from a glass vial form a streak above the beta background band in low channels. The spectra from a 1024 Ch MCA were saved in 256 Ch resolutions, and the event rate was originally illustrated by colors (Kaihola, unpublished).

b. Pulse amplitude comparison

This technique compares the ratio of the pulse amplitudes produced by the two PMTs (Soini, 1975). Photons produced in the cocktail from a radioactive decay event are evenly distributed, and the number impinging on each photocathode will be similar. Thus, the ratio of the sample pulse amplitudes will vary around a value of 1. Photons produced in the vial wall or in the PMTs will show greater variation, e.g., if scintillation is produced through the interaction of a cosmic muon with a PMT, the amplitude of the pulse observed by one PMT will differ from that observed by the other and the PAC ratio will deviate significantly from unity. Therefore, the pulse amplitude ratios will be less evenly distributed. Effectively, this is a PMT cross-talk reduction feature, and it is used in low-level LSA instruments manufactured by Wallac (Fig. 2.4). The PAC values are adjustable within a defined range and the optimum is empirically determined. Again, the use of PAC can lead to a small reduction in high-energy beta particle counting efficiency due to misclassification of events. PAC should not be applied for the measurement of low-energy beta-emitters and Cerenkov radiation as a small number of photons is generated per event, and a great disparity is observed in the number of detected photons at the PMTs.

c. Time-resolved liquid scintillation counting

This is another pulse shape discrimination technique, and it is used by the Packard Instrument Company (now PerkinElmer, Inc.) to reduce background count rates by discriminating the unquenchable component of background from true beta events and the quenchable background, on the basis of the number and energies of afterpulses that follow a prompt pulse event. Unquenchable background is the result of low photon yield Cerenkov events consisting of a prompt component followed by a delayed component comprising a burst of afterpulses (of single photoelectron magnitude) that can continue for as long as 5 microseconds (Dressler and Spitzer, 1967; Jerde et al., 1967; Roodbergen et al., 1972). The prompt pulses derived from true beta events will also be followed by afterpulses, which are caused by the collision of electrons with gas molecules inside the PMTs. The resulting ionized gas molecules take a significant time to migrate back to the photocathode where they produce secondary light

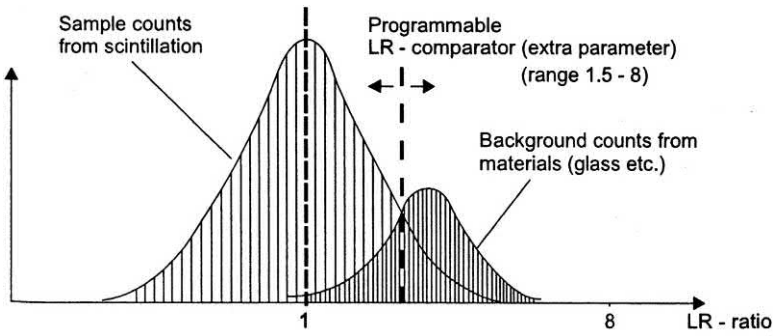


FIGURE 2.4 Schematic representation of the pulse amplitude comparator feature used by Wallac. *©1984−2011, PerkinElmer, Inc. All rights reserved. Printed with permission.*

pulses (afterpulses), and this can occur over a period of several microseconds, thereby emulating a background event. In addition, the higher the energy of the initial event, the greater will be the number of electrons liberated and the higher the probability of afterpulse production. Nevertheless, a greater number of afterpulses will usually result from an unquenchable background event than from a true scintillation event, for a given energy. Therefore, the solution is to incorporate a system that allows some afterpulses and in addition, this acceptance criterion is scaled with event energy. The acceptance criteria are stored in the form of a "burst look-up table" that correlates the acceptable number of afterpulses versus event energy. Valenta (1987) designed burst counting circuitry to discriminate unquenchable background events from true beta events on the basis of the number of burst afterpulses that follow the prompt pulse, relative to the amplitude of this prompt pulse. The total number of afterpulses is termed the pulse index, and this is used to produce three-dimensional information that is comprised of energy and time-resolved information (number of afterpulses) for each detected event. Fig. 2.5A demonstrates that a background sample produces a significant number of afterpulses or bursts at the low-energy end of the spectrum. In contrast, an unquenched ^{3}H sample generates few afterpulses and only at the high-energy end of the spectrum (Fig. 2.5B) while an air-quenched ^{3}H sample prepared in the laboratory (Fig. 2.5C) generates almost no afterpulses. Graded shielding is not required on these Tri-Carb LSAs because TR-LSC is effective at eliminating the background that is caused by the interaction of secondary X-rays with the counting chamber. In addition, background due to Cerenkov radiation and fluorescence, which is the result of the interaction of beta radiation from ^{40}K in the glass of the PMTs and counting vial, is also effectively eliminated.

Because true beta events are followed by afterpulses, there is a finite probability that valid events may be rejected, thus TR-LSC may reduce counting efficiency. In some applications, rejection of valid events is more probable, e.g., (1) in deoxygenated samples, (2) when using long fluorescence life-time (slow) scintillators that produce a significant delayed component, i.e., those cocktails that contain di-isopropyl naphthalene (DIN) and phenyl-ortho-xylylethane (PXE), and (3) with higher energy betaemitters (energies greater than or equal to ^{14}C) where the delayed component persists, even in the presence of oxygen. The

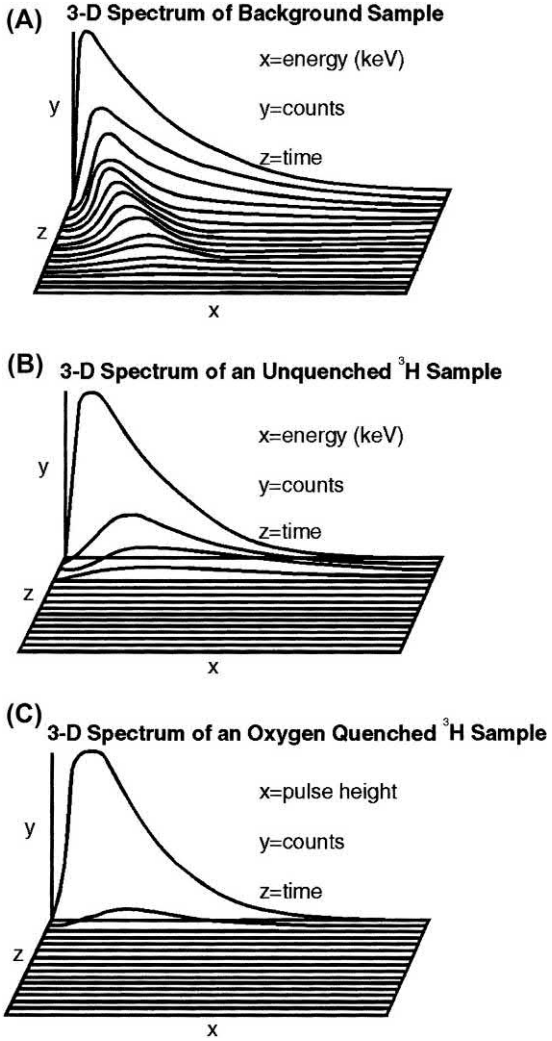


FIGURE 2.5 Three-dimensional plots of pulse height spectra in a Tri-Carb LSA for: (A) a background sample, (B) an unquenched ^{3}H sample, and (C) a laboratory prepared (quenched) ^{3}H sample. *©1994−2019, PerkinElmer, Inc. All rights reserved. Printed with permission.*

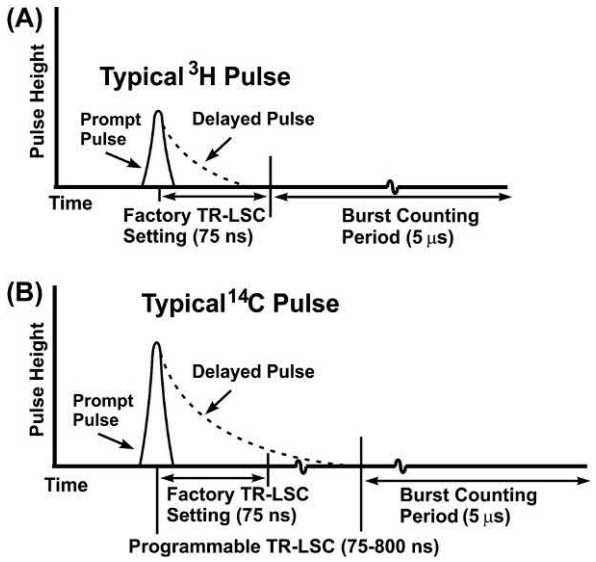


FIGURE 2.6 Schematic representations of (A) nonprogrammable TR-LSC and (B) programmable TR-LSC (Passo and Roberts, 1996). *Reprinted by permission of Radiocarbon, University of Arizona, Tucson.*

ability to optimize TR-LSC for all three of the above conditions was made possible by the introduction of programmable TR-LSC. TR-LSC has a preset delay of 75 ns between the onset of the prompt pulse and the commencement of afterpulse or burst counting. Programmable TR-LSC, on the other hand, provides the ability to adjust the delay between 75 and 800 ns (Passo and Kessler, 1993). Graphic representations of nonprogrammable and programmable TR-LSC are shown in Fig. 2.6.

4. TR-LSC quasi-active detector guards

a. Slow scintillating plastic

An additional feature to reduce background was incorporated into earlier Packard Tri-Carb XL models employing TR-LSC. This feature was in the form of a modified detector assembly that consisted of a long fluorescence lifetime scintillating plastic that surrounded the sample vial in the counting chamber (Valenta and Noakes, 1989). This plastic detector guard was optically coupled to the face of each PMT and was coated with a reflective material. It had very good optical transmission in the 400−500 nm range and the decay time of the slower component of the scintillating plastic was approximately 250 ns. When the slow fluor in the plastic (external to the sample) was excited by a high-energy gamma or muon event, which satisfied the instrument coincidence requirement, the phosphorescence of the slow fluor provided an extended burst of afterpulses that aided the background discrimination. Thus, the plastic acted as an active guard (but without dedicated PMTs). One factor that had to be stressed when using the plastic guard was that the emission spectrum of the cocktail should not significantly overlap the absorption spectrum of the guard. An appropriate secondary scintillator (e.g., POPOP, *bis*-MSB) was used to ensure that significant spectral overlap was avoided.

b. Bismuth germanate

A quasi-active detector guard, based on BGO ($Bi_4Ge_3O_{12}$), was developed by the Packard Instrument Company (Noakes and Valenta, 1996) and incorporated into the Tri-Carb 2770TR/SL, 3170TR/SL, 3110TR, 3180TR/SL models (Fig. 2.7) and the Quantulus GCT 6220 model (Edler, 2017). BGO is a nonhygroscopic scintillator that exhibits low afterglow, and its efficient gamma photon stopping power ($Z = 83$; density $= 7.13\ g\ cm^{-3}$) makes it an effective cosmic guard. BGO gamma detectors were first introduced commercially (circa 1979) for use in Computerized Tomography (CT) applications and, because of its high gamma cross-section, BGO has also been used in Positron Emission Tomography (PET), high-energy calorimetry, and medium-energy physics (Bicron Corporation, 1988). As a detector guard for LSA, BGO is used to discriminate against the gamma and muon components of cosmic background. Events that interact with BGO produce pulses, which are of much longer duration (at least a factor of 10) than beta and alpha pulses in the cocktail.

If an event interacts with the detector and satisfies the coincidence requirement, TR-LSC is then used to discriminate the longer cosmic background pulses from beta pulses. Similar to the slow scintillating plastic guard already discussed, the BGO guard completely surrounds the sample vial in the modified detector assembly. However, this detector assembly is not optimal for analysis of beta−gamma-emitting radionuclides where the gamma photons are coincident with the beta particle and sufficiently energetic to interact with the BGO guard as this increases the probability of misclassification of beta events as background. The same applies to high-energy beta particles from ^{90}Y, which can penetrate through the plastic vial into the guard resulting in a reduced ^{90}Y:^{90}Sr ratio in the lowest level counting modes.

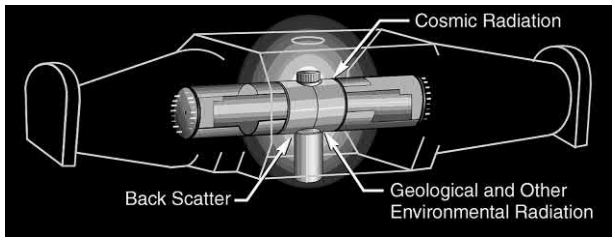


FIGURE 2.7 Schematic representation of the quasi active bismuth germanium oxide guard, passive shield, and detector chamber in the Packard 2770TR/SL. *©1994−2019, PerkinElmer, Inc. All rights reserved. Printed with permission.*

5. Counting region optimization

The detection limit of a measurement is determined by the signal-to-noise ratio. In LSC, the signal-to-noise ratio is expressed as the square of the detection efficiency divided by the background (E^2/B) and is termed the FOM. Counting region optimization is used to maximize the E^2/B and thereby improve the detection limit.

a. Region optimization procedures and requirements under constant quench conditions

A blank (background) and a standard sample containing the radionuclide of interest are required to optimize the counting region for that radionuclide. The requirements for proper region optimization include the following:

(1) The standard containing the radionuclide of interest should have sufficient known activity and must be in the same cocktail and quenched to the same degree as the unknown samples. Equivalent quench ensures that the region chosen gives the optimum E^2/B for the sample. Different quench levels will shift the counts in or out of the region and thus affect the counting efficiency in that region. The assumption is made that the unknown(s) will be quenched to the same degree. In reality, there will be slight differences in quench and, for this reason, once the optimum region is determined, quench correction should be applied to calculate the absolute activity. The quench curve should relate counting efficiency in the optimized region (for a series of known activity standards that are quenched to different degrees) to the quench indicating parameter (H-number, SQP(E), t-SIE, etc.). Production of this type of quench curve will account for the minor quench variations in the samples. Wallac 1400 LSC series employ a digital overlay technique (DOT) where chemically and color quenched reference spectra, stored in the memory of the counter, are fitted to the sample spectra. Rundt (1992) gives a comprehensive review of this technique.

(2) The blank should be quenched to the same degree as the standard and the unknown samples and prepared in the same way. Minor fluctuations in the degree of quenching will result in only small changes in the blank counts. Therefore, it is generally not necessary to construct a quench curve for the blank. Small changes in the blank spectrum will not adversely affect the optimum window determination.

By using a representative standard and an appropriate blank, a reasonable approximation to the optimum counting window can be determined for unknown samples near background levels. In some cases, it may be possible to use the unknown sample as the standard if the activity is several times the background. In this case, the count time should be long enough to minimize the error associated with the measurement. However, counting efficiency must still be determined. In many modern LSAs, region optimization can be performed automatically.

b. Region optimization under variable quench conditions

For samples that have highly variable quench, it may not be practical to maintain a fixed counting region and still maintain maximum counting sensitivity. A practical solution is to determine the equivalent, unquenched spectral endpoint by counting the least quenched sample in the batch of unknowns or by counting the least quenched standard of the quench set. Quench standards and samples are counted using this region setting with Automatic Quench Compensation (AQC is a Beckman patent), Automatic Efficiency Compensation (AEC is a derivative of AQC and is a Packard Feature), or an equivalent technique. AQC adjusts the upper limit of the counting region to the observed spectral endpoint of the quenched sample. By adjusting the region in this manner, background is reduced and high counting efficiency is maintained. For variably quenched samples, the use of AQC represents the best choice for maintaining high sensitivity, provided that the sample activity is sufficiently high to produce a good spectral endpoint. Accuracy of AQC and AEC will be reduced for a variable quench situation at very low count rates. The DOT technique employed by Wallac shifts from spectrum libraries to conventional fixed window counting, when total collected counts are less than 500 for the spectrum window.

6. Process optimization

The term “optimize” or “optimizing” is used in many areas to simply describe the process of determining the best or optimum windows (see Counting Region Optimization above) on an LSA, for a given sample geometry. While the counter is certainly an integral part of producing results, it is just that, a part. It is one step in a “process”, and it is this process which should always be considered for “optimization”. The process would include collection, storage, and preparation/extraction of the sample, the preparation for counting, and the actual sample counting. The goal of the optimization would be to attain the required results (precision, accuracy, and sensitivity) with the lowest cost per sample in terms of technician time, materials/equipment, and counter time. If the equipment is new, the counter performance must be determined prior to evaluating the process. The first step is to consider the process requirements:

1) What is the required lower limit of detection (LLD)?
2) Is waste production an important consideration?
3) Does the sampling process have restrictions (size, time, etc.)?
4) Is equipment time restricted?

5) Is sample preparation/extraction time limited?
6) Is sample storage limited?
7) Is cocktail/vial cost per sample important?

The second step is to define the current performance (LLD) of existing resources. Typical performance data for three counters are presented in Table 2.1. The third and final step is to consider all the factors from step 1 and employing the performance data from step 2, to arrive at the most efficient (optimum) procedure for the application. Given all of the process variables, this can become quite a challenge. By using a decision tree, such as the example in Fig. 2.8, the operation can be arranged into a fairly straightforward exercise. Counter setup and sample preparation can be widely varied and still meet the same sensitivity requirements. For example, assume that a laboratory currently uses the first counter from Table 2.1 (Counter A) and that the required LLD for the process is 3.7 Bq/L for ^{3}H. A new counter arrives (Counter C), and it must be integrated into the system. As shown, the performance of the new counter is significantly better and, if the same counting protocol is maintained, the samples will be "over counted". This additional performance can be exploited as shown in Table 2.2, to reduce either the required count time or sample volume.

C. Background reduction methods—vial, vial holder, and cocktail considerations

1. Vials

Any natural radioactivity in the walls or cap of the counting vial will obviously increase the background count rate and for this reason, glass vials with a low ^{40}K content are desirable. Plastic vials display lower background than glass, partly due to their lower radioactivity (especially much lower ^{40}K content) and also to their lower density, which results in a lower probability of particle/photon interactions with the vial walls. However, care must be exercised over the choice of scintillation cocktail when using plastic vials. Typically, cocktails based on diisopropylnaphthalene (DIN) and phenyl-ortho-xylylethane (PXE) will not attack the plastic vial, whereas cocktails containing solvents such as benzene, pseudocumene, and toluene can diffuse into the plastic wall. Low diffusion plastic vials that have a thin Teflon coating reduce solvent diffusion to some extent but do not completely eliminate it. Static charge may build up on plastic vials and this can lead to spurious high count rates (the typical static symptom). To prevent any buildup of static charge, it is suggested that vials with an antistatic coating should be used. The antistatic vials are slightly more expensive, but the costs associated with recounting samples usually more than offset any price difference. A built-in deionizer also removes static charge effectively. Vials manufactured from silica (Hogg et al., 1991; Hogg and Noakes, 1992; Wilson et al., 1996) and Teflon (Polach et al., 1983; Kalin and Long, 1989) are quite commonly used for radiocarbon dating and have been demonstrated to produce significant background reductions. Their main drawback is the comparatively high cost compared to low ^{40}K glass while a lack of uniformity of response has also been noted by Einarsson (1992) for silica vials. Additionally, great care must be taken in their cleaning between sample additions; however, under certain circumstances, e.g., where samples are very small or their ages are approaching the limit of detection, they can prove very beneficial. The buildup and removal of UV absorbing coating on glass vials from benzene has been investigated by Haas (1995). Copper–Teflon vials of 20-, 15-, 7-, and 3 mL sizes were originally designed for radiocarbon dating, as benzene permeation in solid Teflon is negligible. Copper caps provided additional shielding for external radiation, and this benefit was observed in standard liquid scintillation counters (Verrezen and Hurtgren, 2003). Gold-plated copper in caps and bases have been recently replaced by black polyoxymethylene (POM), as no advantage was gained in the Quantulus from this additional passive copper shielding.

2. Vial holders

Inert vial holders made from materials such as Delrin have been used to enable instruments such as the Quantulus to accept nonstandard-sized vials (particularly those made from silica) and indirectly, their use brings about background reductions (Hogg and Noakes, 1992; Kaihola et al., 1992). The slow scintillating plastic used as the material for construction of the quasi-active guard in the Packard Tri-Carb XL models was also used to produce vial holders that would accommodate 7-mL vials. The vial holders

TABLE 2.1 Instrument performance summary for ^{3}H analysis using 10 mL water and 10 mL scintillation cocktail.

Counter	Opt. window (keV)	Efficiency (%)	Bkgd (cpm)	Count time (min)	LLD (Bq/L)
A	0.0–3.5	21.82	2.08	200 (2 × 100)	3.7
B	0.0–5.5	20.03	1.53	200 (2 × 100)	3.4
C	0.0–4.0	23.71	0.95	200 (2 × 100)	2.3

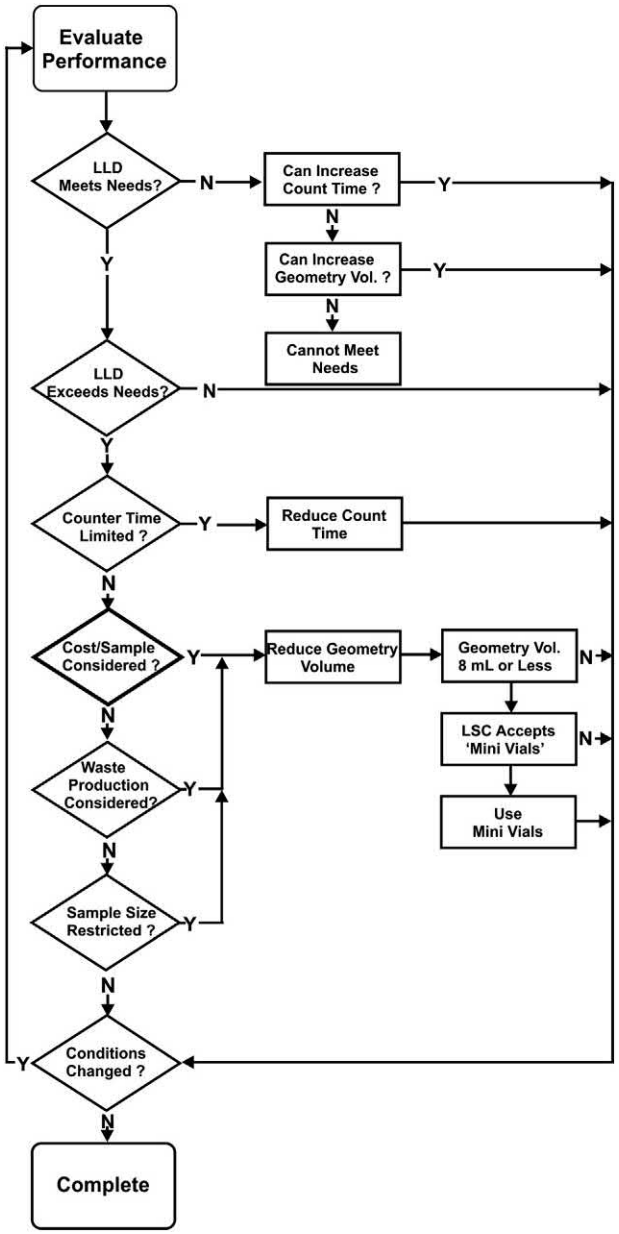


FIGURE 2.8 Process optimizing decision tree.

enhanced the background reduction even further when used in conjunction with the plastic guard; however, they were expensive and could be damaged by some solvents. They are very useful for applications such as radiocarbon dating where the total sample volume is often <7 mL. Where the sample size was not limited, the use of 20-mL vials (and therefore no vial holder) was preferable as the MDA from the smaller sample would be poorer. In addition, these vial holders are also used effectively in TR-LSC instruments that do not contain the plastic guard (Cook et al., 1989). Similarly, vial holders manufactured from BGO and designed to accommodate 7-mL vials were also used to provide additional background discrimination although, again they were expensive. These vial holders worked well in an instrument that had the BGO guard detector and electronics, but also performed quite well in other TR-LSC systems operating in the low-level count mode (Cook, 1995). Owing to their limited use and high cost, very few of these types of vial holder is now commercially available.

3. Cocktail choice and optimization

Overall, liquid scintillators should be prepared with reagents that are low in natural radioactivity. Ultima Gold LLT has been introduced by PerkinElmer with negligible ^{40}K content. When dealing with aqueous samples, the detection limit is also influenced by the loading capacity. The selected cocktail(s) should be evaluated to determine the sample to cocktail mixing ratio that will give the best performance. The cocktail should be tested at various sample loads through its rated capacity, while holding the total geometry constant. Each mixing ratio is tested using a background/standard pair to determine optimum windows and evaluate the LLD. In the example presented in Fig. 2.9, Ultima Gold LLT is evaluated from 10% to 60% sample loading, with a constant counting geometry of 20 mL.

The best performance for this example occurs at a 50% sample load (ratio = 1:1). Regardless of the total sample/cocktail volume, the best counting performance (LLD) will be achieved using an optimum 1:1 mixing ratio. The

TABLE 2.2 Example of optimizing to performance requirements for ^{3}H.

Counter	Sample vol. (mL)	Cocktail vol. (mL)	Efficiency (%)	Bkgd (cpm)	Count time (min)	LLD (Bq/L)
A	10	10	21.82	2.08	200 (2 × 100)	3.7
C[a]	3	3	24.11	0.41	400 (2 × 200)	3.7
C	10	10	23.71	0.95	90 (2 × 45)	3.7

[a] *8 mL vial.*

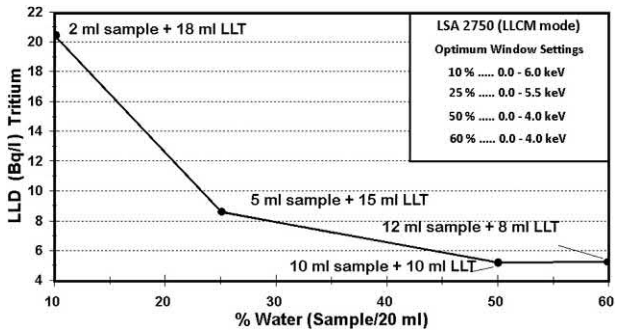


FIGURE 2.9 Example of cocktail performance evaluation for ^{3}H with the Tri-Carb 2750. *©1994–2019, PerkinElmer, Inc. All rights reserved. Printed with permission.*

detailed legend box in Fig. 2.9 outlines the optimum counting windows for each percent sample loading.

D. Background reduction methods—environment

To achieve optimum performance from an LSA, it is important to ensure that the instrument is stable. Lack of stability may be manifested by changes in efficiency, background, and the quench indicating parameter, etc. Stability is generally aided by placing the LSA in a stable counting environment, where temperature and humidity are controlled, the atmosphere is not corrosive, the power supply to the instruments is of good quality and direct access of sunlight to samples is prevented. As a general guide, samples should be allowed to stand for several hours (4–6) in the counter prior to counting, as this minimizes chemiluminescence and/or photoluminescence. The effects of chemiluminescence can also be reduced by the use of a chilling unit that cools the sample counting chamber.

Static is generated in the counter by the rubbing together of nonconducting materials in a dry environment, hence the requirement for controlling humidity. If the vial entering the counting chamber has a static charge, spurious photons will be generated as the charge dissipates. Static can be minimized by humidifying the counter or the counting room, by using antistatic vials and by employing the static controlling device, i.e., a deionizer, which is common to LSAs that have an automated sample changer. One should observe that the deionizer may not be fully effective when smaller vials are measured inside 20 mL-sized vented vial holders.

Temperature has played an important role in the operation of early liquid scintillation counters. The noise rates (singles rates) of early PMTs were much greater than today's and very dependent on operating temperature. For this reason, older instruments were refrigerated to reduce this noise level, and reductions in background count rates were significant beyond the effect of the coincidence circuitry. Refrigeration is not as critical for background reduction in modern instruments because of the introduction of lower-noise bialkali tubes and improvements in tube manufacturing. Today, refrigeration is often used for reasons other than cooling the PMTs. Temperature control may be necessary for special sample preparation (e.g., where a gel cocktail is required and gelling may be impaired within certain temperature ranges), in severe operating conditions to stabilize counting conditions, for minimizing chemiluminescence, or reducing static buildup.

As previously discussed, the contribution to background from high-energy radiation, which can penetrate passive shielding and interact with the vial walls and PMTs, etc., can be minimized by the use of active guard detectors and pulse shape analysis techniques. An alternative method for the reduction of high-energy radiation, which is particularly effective for instruments without the above features, is to choose a location that provides additional shielding against cosmic or environmental radiation. Examples of this include (1) Felsenkeller in Dresden (40 m overburden, 110 m water equivalent, Niese et al., 1998), (2) a specially designed counting laboratory at the University of Arizona that has 10 m of overburden (Kalin and Long, 1989), (3) a counting laboratory within the Warragamba Dam wall in Australia (Calf and Airey, 1982), (4) the IAEA Marine Environment Laboratory (Povinec et al., 2006), (5) the Gran Sasso laboratory under 3800 mwe (Plastino and Kaihola, 2004), and (6) Wallac's surface low-level laboratory (Kaihola et al., 1986). A review of underground laboratories was published by Niese (2008).

The Wallac surface low-level laboratory was constructed from low background materials and contained in a Faraday cage, where environmental gamma flux was 5% of the level observed outside. This leads to halving of ^{3}H background in the Quantulus (Kaihola et al., 1986). Mainly inherent PMT radioactivity is a reason preventing a lower reduction of sample background than expected from the level of environmental radioactivity.

III. Alpha/beta discrimination

A. Alpha/beta separation theory

The ability to measure the activity of alpha-emitting radionuclides by LSC has been recognized for many years. It has also been known that alpha- and beta-emitting radionuclides produce different pulse shapes at the PMT anode and may be separated on this basis (Buchtela et al., 1974; Thorngate et al., 1974; McKlveen and Johnson, 1975). Pulse shape discrimination techniques are well known and have been extensively applied to the rejection of gamma background in neutron spectrometry (Horrocks, 1970; Winyard et al., 1971) and to the isolation of fission events in LSC (Horrocks, 1963). These techniques are often referred to in the literature

by different instrument manufacturers as either pulse shape discrimination, pulse shape analysis, or pulse decay analysis. Different names arise because the techniques of pulse shape discrimination can vary, but all are based on electronic circuits that measure some aspect of pulse decay time.

Alpha/beta discrimination became commercially available in conventional LSAs since the late 1980s in the Quantulus. The 4π counting geometry of LSC yields approximately 100% counting efficiency for alpha-emitting radionuclides, which, coupled with the low alpha background count rates, provides an alternative to gross alpha/beta by gas flow proportional counting. For certain applications, alpha/beta LSC can also be a very useful alternative to conventional alpha spectrometry, which utilize passivated implanted planar silicon (PIPS) and silicon surface barrier (SSB) detectors; however, the much poorer resolution of LSC relative to semiconductor detectors can be a major disadvantage. This is because the relatively large amount of energy is required to produce a single photoelectron at the PMT photocathode.

To understand how the separation of alpha from beta events is accomplished, it is necessary to examine the processes at a molecular level. Alpha and beta events may be distinguished from one another in a liquid scintillator by examining the electronic pulses that are produced at the PMT anode of the detector. As described in the previous section, these pulses are made up of two components: the prompt and the delayed components, which occur in different proportions in alpha and beta pulses (Horrocks, 1974a). Fig. 2.10 demonstrates the difference in pulse shape between ^{36}Cl (beta-emitter) and ^{241}Am (alpha-emitter) in Insta-Gel cocktail (PerkinElmer, Inc.) containing 20% weight/volume naphthalene. These pulse shapes were measured at the PMT anode using a storage oscilloscope set on averaging mode to produce an average pulse shape. The photons incident on the cathode of the PMT originate from the radiative decay of excited singlet and triplet states of the fluor molecules in the cocktail. The prompt component arises from the fast, exponential decay of excited singlet states, while triplet states can produce photons only upon collision with another molecule in the triplet state, resulting in a longer lifetime of several hundred nanoseconds, thus producing the delayed component of the pulse (Brooks, 1979). The higher specific ionization of alpha particles causes a greater proportion of excited molecules to be in triplet states, and hence alpha pulses have a longer duration. The longer duration of alpha pulses is the basis of alpha/beta separation by pulse shape discrimination.

Most of the environmentally significant alpha-emitting radionuclides emit particles in the 4–8 MeV energy region, while the betas of interest typically have E_{max} values below 2.5 MeV. Separation of alpha from beta events is necessary, because the energy to light conversion yield

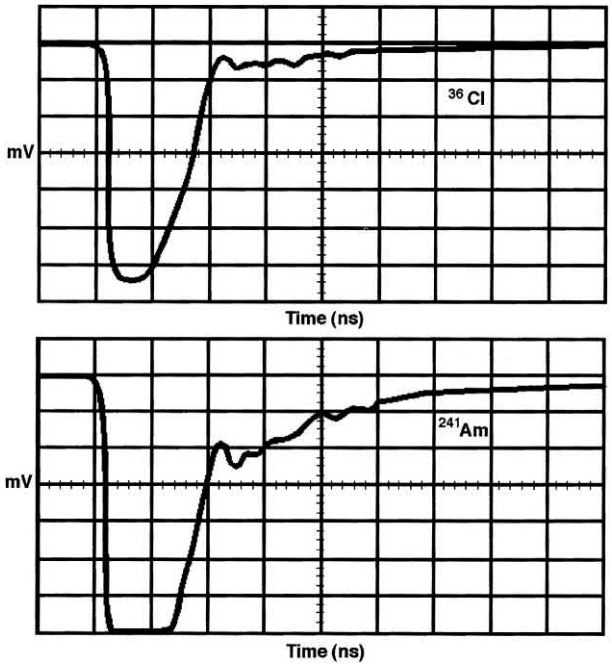


FIGURE 2.10 PMT pulse shapes for ^{36}Cl (beta) and ^{241}Am (alpha). *©1994–2019, PerkinElmer, Inc. All rights reserved. Printed with permission.*

from alpha particles is approximately a factor of 8–10 lower than from betas, with the result that alpha spectra are typically in the beta region. Fig. 2.11 illustrates the spectral overlap that is observed between ^{241}Am, which produces alpha particles in the region 5.4–5.5 MeV and ^{36}Cl, which has an E_{max} of 710 keV.

B. Alpha/beta instrumentation

Two types of LSC instruments can distinguish α from β events. These are the PERALS spectrometer (photon/electron-rejecting alpha liquid scintillation) and conventional LSAs with pulse-shape discrimination (PSD/PSA) electronics. Although both can simultaneously produce resolved α and β spectra, they are designed with different

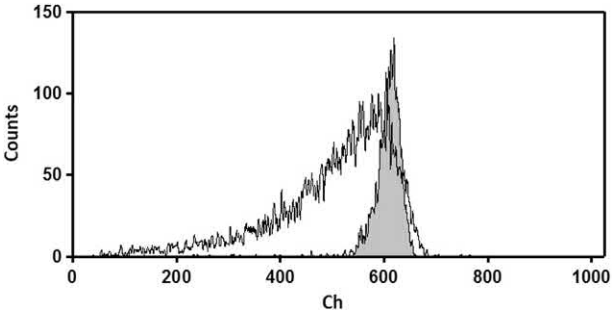


FIGURE 2.11 Logarithmic Quantulus Multi Channel Analyzer display for ^{36}Cl and ^{241}Am (gray) spectra.

purposes in mind and, hence, are generally best suited to different types of applications.

1. The PERALS spectrometer

This instrument was designed by the W. Jack McDowell, G. N. Case, and co-workers (McDowell and McDowell, 1994) as a method of α spectrometry in addition to conventional solid-state detection, and has its own characteristics, advantages, and disadvantages. Optics, sample preparation techniques and sample geometry are geared to producing the maximum α−α energy resolution by enhancing light output, as well as reducing interference from β and γ emissions. A cross section of the PERALS detector is illustrated in Fig. 2.12. As a result, the optics and geometry are not optimized for β spectrometry, and the lack of passive shielding and coincidence circuitry result in increased background in the β spectrum. McDowell and McDowell (1994) suggest that this instrument is really best suited for α measurements alone. A key element of the PERALS system is extractive scintillators, whereby an organophilic complexing agent, usually specific to a single element, is incorporated into the scintillation cocktail. This serves two purposes: (1) specific radionuclide extraction may be accomplished and (2) quenching caused by water, acid, or other sample impurities is minimized thereby maximizing light output which leads to improved energy resolution. A series of extractive scintillators for the analysis of a range of actinides and other naturally occurring radionuclides has been developed (McDowell and McDowell, 1994) and used successfully both with PERALS and other LSAs utilizing PSD. The authors also recommend purging all samples with nitrogen or an alternative oxygen-free gas to improve energy resolution even further by reducing oxygen quenching.

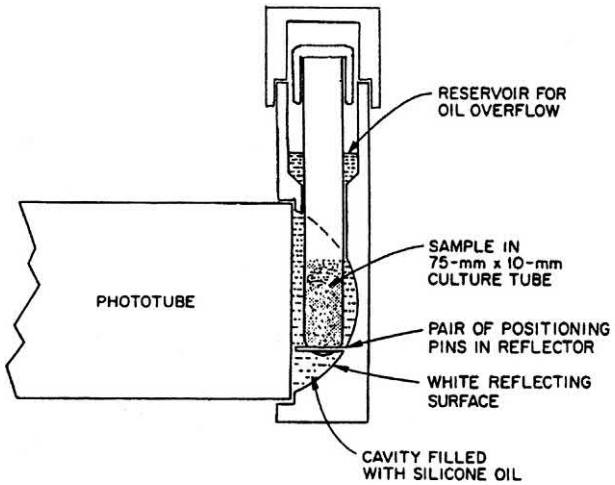


FIGURE 2.12 Cross-section of the PERALS© spectrometer (McDowell and McDowell, 1993). *Reprinted by permission of Radiocarbon, University of Arizona, Tucson.*

The advantages of this system are (i) high alpha-beta discrimination, producing > 99.9% rejection of β−γ events while maintaining a >99% counting efficiency for the α events, (ii) improved alpha resolution (200−300 keV FWHM) compared with a standard LS counter, and (iii) the observed backgrounds in the α spectra are typically lower than in a conventional counter. The sample vial is optically coupled to the PMT by silicone immersion fluid. This arrangement inhibits automatic sample changing.

2. Conventional LS spectrometers with pulse-shape discrimination

The major manufacturers of LSAs produce instruments capable of PSD for simultaneous determination of α and β activity. The α energy resolution that can be achieved by conventional LS spectrometers is 300 to >500 keV FWHM depending on sample quench level. The best reported resolution is 270 keV for the Quantulus at 5.5 MeV in an extracted sample (Yu-Fu et al., 1990). These conventional instruments have definite advantages for gross α−β analysis, for instance automatic sample changers are standard features, which are advantageous for routine analyses or for relatively short counting times. In some instances, the use of extractive scintillators is not practical or adds unnecessary complications to the sample preparation. For example, radon can be prepared for analysis by simply shaking a sample of water with a water-immiscible cocktail. However, the use of conventional LSAs does not preclude McDowell's methods. Finally, these instruments also allow the use of an α-emitting isotope as a yield tracer in the analysis of a β-emitting isotope and vice versa (e.g., Pates et al., 1996b).

As stated before, each manufacturer has its own method of PSD and these methods are referred to by different terminologies. This can be confusing, so we include here a discussion of various methods of PSD used with each instrument and explain the terms used.

a. Wallac Oy

Wallac Oy (now PerkinElmer, Inc.) has manufactured several α/β LSAs: Wallac 1219 Rackbeta SM, 1411, 1415, 1414 WinSpectral α/β and the Wallac 1414 Guardian DSA systems. These models have now been discontinued and only the Wallac 1220 Quantulus ultra low-level liquid scintillation spectrometer is still in production (Fig. 2.2). Wallac terms its version of PSD as pulse shape analysis (PSA), because all events, including discriminated events, can be saved as raw spectra. The pulse decay discriminator (PDD) settings are called PSA levels. Wallac's concept is similar to the one adopted by Brooks (1979), viz. PSA initiates the integration of the scintillation pulse tail charge after 50 ns from the leading edge and compares it with the total charge in the pulse (Oikari et al., 1987). The pulse length information is thus normalized to the pulse height to achieve

amplitude independence (*i.e.*, energy-independence). The optimum PSA level is a numeric parameter that is represented schematically by a line that separates the alpha from beta events. Events falling above the line are classified as α-events, and those below as β-events (Fig. 2.3). Both the 1414 Guardian and the 1220 Quantulus have active guard counters, in addition to other features that contribute to background reduction (See Section II for details).

b. Packard Instrument Co (Now PerkinElmer, Inc.).

The Tri-Carb 3100TR series of LSAs have an optional PSD feature called pulse decay analysis (PDA), with a TD called the pulse decay discriminator (PDD). PDA distinguishes between α and β events using the zero-crossing method of PSD, which is so named because each scintillation pulse is doubly differentiated and the time at which this new curve crosses the zero line is compared to the PDD value (Fig. 2.13). Pulses that cross in a shorter time are classified as β events and those that cross in a longer time are classified as α events. Again, this method should be amplitude-independent. These instruments can also reduce background by activation of the burst-counting circuitry (BCC) feature (see Section II for details). Time resolved pulse decay analysis (TR-PDA) is the combined use of TR-LSC background discrimination and pulse decay analysis. By applying TR-LSC to PDA, alpha events that are misclassified as beta are discriminated out by TR-LSC since the long delayed component of alpha pulses resemble background events. Thus, alpha events misclassified as betas will be eliminated from the beta MCA. In addition, the misclassification of beta events will also be reduced since the TR-PDA causes a shift to a higher optimum PDD value. At higher PDD values, fewer beta events can satisfy the time requirement for an alpha pulse and this reduces the beta spill into the alpha MCA. The net result of TR-PDA is a reduction in the misclassification of beta and alpha events. An added benefit of TR-PDA is that TR-LSC background discrimination allows simultaneous low-level beta counting, when suitable cocktails are selected to avoid excessive loss of alpha events in background reduction.

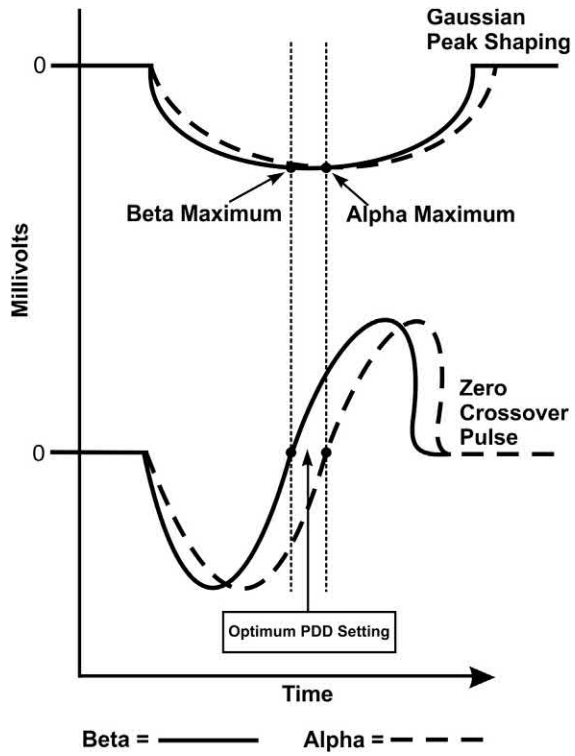


FIGURE 2.13 Schematic representation of the zero-crossing method of pulse shape discrimination used by Packard Instrument Co. *©1994–2019, PerkinElmer, Inc. All rights reserved. Printed with permission.*

c. Hidex Oy

A small, portable liquid scintillation counter and luminometer, Triathler was introduced by Hidex Oy in 1997, which allows measurement of several vial sizes in manual mode (Haaslahti et al., 2000). Low noise and radioactivity of a small single phototube reduces beta background to a moderate level with only a 10-mm thick lead shield and total weight of 9 kg. The counting window needs to be narrowed only for energy beta range to remove interfering PMT noise. Direct dpm counting method calibration curves are available for single label samples and quench monitoring with a ^{152}Eu external standard. An MCA is included with data acquisition firmware, and spectra are analyzed in Excel/Windows environment with an external computer. A pulse shape analyzer produces 3D spectra, and the selection of regions of interest can be made after measurements. Separation of alpha and beta events is done similarly to the Wallac PSA, which classifies the signal after 30 ns of pulse onset as the tail component of the pulse. Normalization of tail charge to the total charge of the pulse removes energy dependence of pulse length. This PSA level is called pulse length index (PLI).

This Instrument has been used for the analysis and control of environmental and man-made radionuclides, for instance on-site ^{222}Rn measurements in drinking water (Villalba et al., 2005). Several fast methods were presented for the analysis of environmental radionuclides using the Triathler, including ^{90}Sr by Li et al. (2009) and ^{226}Ra, ^{228}Ra, ^{224}Ra, ^{222}Rn, and ^{210}Pb by Möbius et al. (2006). Optimum results have been demonstrated with good α/β separation and consequently low background and the lowest LLD for ^{226}Ra down to 5 mBq/L in 1 hour counting time using 3M Rad Disk filtering in sample preparation.

The Triathler can also be equipped with an inbuilt NaI(Tl) crystal for detection of gamma radiation.

Another LSC model was introduced by Hidex Oy in 2008, which is a 3 PMT TDCR version, called Hidex 300 SL. The instrument total weight is 125 kg, of which the

lead shield comprises 90 kg. A robotic loading arm picks samples from a tray holding either 40 × 20 mL vials or 96 × 7 mL vials. Pulse shape analysis is a standard feature and a small external anticoincident guard detector reduces instrument background and thus allows greater sensitivity in monitoring environmental radionuclides. Substantial reduction of random PMT noise, sample luminescence signal and also glass vial Cerenkov background signal is achieved in triple PMT coincidence counting.

Swab and urine samples were tested with the 300 SL by Sas et al. (2010), Sas and Janda, (2017) with ^{90}Sr, ^{241}Am, and ^{239}Pu as model radionuclides. Dai et al. (2012a) developed a nasal swab method for quick screening of alpha and beta contaminations in the event of radiological/nuclear emergency. Murali et al. (2009) have presented alpha/beta discrimination for ^{90}Sr–^{90}Y/^{241}Am samples and Wisser et al. (2006) for gross alpha/gross beta samples. Wanke et al. (2012) compared the Hidex 300 SL system with a noncommercial instrument for metrological measurements. Deviations of the results between the instruments were found to be about +0.1% for ^{3}H, +0.22% for ^{55}Fe and only 0.02% for ^{109}Cd from the reference figure.

Krąpiec and Walanus (2011) ran an instrument without guard and external standard in triple coincidence mode for radiocarbon dating. Trailing edge of the pulse height spectrum corrected better for quenching correction in benzene than the TDCR method. For near-background samples the muon peak trailing edge performed better than that of the ^{14}C spectrum.

The 3 PMT TDCR LSAs, including the Hidex 300 SL, are described in detail in Chapter 6, Volume 1.

d. Beckman Coulter Inc.

The Beckman LS 6500 series include the optional capability for PSD, in which α and β scintillation pulses are distinguished by a ratio technique. The area of each pulse is found at times t_1 and t_2, corresponding to the prompt and delayed components respectively. The ratio of these areas is compared with the ratio of known α and β pulses, resulting in a TD called the R-value (Dodson, 1991). The R-values are plotted versus cpm response and the optimum TD setting is the R-value that provides the minimum spillover of alpha and beta events. Typically, this minimum is represented graphically as the minimum value between the alpha and beta R-value spectra. Beckman Coulter terminated LSC production in 2010.

C. Cocktail and vial considerations

1. Cocktail choice

a. Aqueous-accepting cocktails

Aqueous accepting cocktails are typically used in standard β-spectrometers and are quite suitable for gross alpha-beta measurements and where alpha/alpha resolution is not critical. They are infrequently used in the PERALS system. The reasons for this are as follows. The presence of surfactants and other additives in these cocktails (and, of course, the aqueous sample itself) causes a significant degree of quenching and therefore a reduction in light output. This in turn has an adverse effect on the degree of alpha-beta separation and alpha-alpha resolution. Thus, the degree of separation is always a trade-off against sample loading. In addition, standard cocktails for beta counting applications employing fast solvents such as xylene, pseudocumene, toluene, and alkylbenzenes do not result in pulse shapes to be sufficiently different for producing optimum separation of alpha from beta events. To overcome the poor separation, 20% naphthalene has been added to standard cocktails for alpha/beta separation applications (Oikari et al., 1987). Naphthalene improves alpha/beta separation by acting as an intermediate in the energy transfer process between the solvent and fluor (Brooks, 1979; McDowell and McDowell, 1994). This more energetically favorable route increases the production efficiency of excited fluor molecules. The production rate of fluor triplet states is especially enhanced, because energy transfer to triplet states relies on a physical approach and is affected by the concentration of both the fluors and the intermediate (naphthalene) in the cocktail. As more triplet states become occupied, the delayed component of the PMT anode pulse increases and has the effect of stretching the alpha pulses relative to the beta pulses. The ability of naphthalene to act as an intermediate in this way is the result of the extensive delocalization of its electrons. During the late 1980s and early 1990s, a range of cocktails based on the solvent di-isopropylnaphthalene (DIN) was introduced (Thomson, 1991). DIN has many advantages over the traditional cocktails including the fact that it is nontoxic, nonflammable, and biodegradable, and it is similar to naphthalene in its ability to stretch alpha pulses relative to betas and therefore to enhance alpha/beta separation. Cocktails based on DIN, PXE, or DIN together with a second "safe" solvent have now almost completely taken over from fast cocktails containing naphthalene. Furthermore, experiments to assess the suitability of (i) secondary fluors with a range of fluorescence lifetimes and (ii) some alternative scintillating cocktail solvents have failed to improve upon the alpha/beta separation efficacy provided by commercially available cocktail formulations (Pates et al., 1996c; Passo et al., 2002).

b. Extractive scintillators

Extractive scintillators are an elegant combination of two technologies (liquid scintillation and liquid-liquid extraction) in which an organophilic extractant is incorporated in an organic solvent in the presence of a fluor and naphthalene. Extractive scintillators enable extraction of the nuclide

TABLE 2.3 Properties of the commercially available extractive scintillators.

Extractive scintillator	Elements extracted	Applications
ALPHAEXα	Th, Pa, U, Np, Pu,	Any original matrix after conversion to:
	Am, Cm, Bk, Cf, Es,	1 M HNO_3 for Th, U(IV, VI); pH 2−3
	Fm, Md, No	1 M nitrate for others
URAEXα	Uranium selectivity	From 1 M sulfate at pH 2
THOREXα	Thorium and uranium	From 1 M sulfate at pH 2
POLEXα	Polonium selectively	From 7.5 M H_3PO_4, 0.01 M HCl
RADAEXα	Radium selectively	From 0.3 to 0.5 M $NaNO_3$ at pH 11-12
RADONSα	Radon selectively	Radon from water or aqueous solution
STRONEXα	Strontium selectively	From 0.3 to 1.0 M $NaNO_3$ at pH 9−11

of interest from an aqueous sample directly into the scintillator, and since virtually nothing except the radionuclide of interest is transferred, there is reduced quenching compared with that observed in aqueous-accepting cocktails. This results in improved separation of β−γ from α events and improved α−α resolution. There is also a reduction in the variations in quenching between samples, and this facilitates nuclide identification. Products for the extraction of uranium, thorium, plutonium, polonium, radium, and so on are all marketed by ETRAC Laboratories Inc., Knoxville and Oak Ridge, Tennessee (Table 2.3). A typical formulation for extraction of uranium would comprise 96.3 g of Adogen 364 (tertiary amine), 160 g of purified naphthalene, 4 g of the scintillator PBBO [2-(4′-biphenylyl-6-phenylbenzoxazole)] made up to 1 L with toluene (Bouwer et al., 1979). A comprehensive guide to the PERALS and extractive scintillators can be found in McDowell and McDowell (1994).

2. Vial choice

Experiments have shown that no significant improvements in the separation of alpha from beta events have been observed when using plastic vials, although peak resolution is improved. In addition, a progressive deterioration in separation with time (commencing within 48 hour of sample preparation) was observed when using plastic vials. This is due to the so-called plastic vial effect, i.e., the impregnation of cocktail into the vial wall, which then starts to scintillate producing longer pulses than the sample mixed with cocktail. Therefore, plain polyethylene vials should not be used for extractive cocktails. This effect is not seen in glass, Teflon-coated plastic, and Teflon vials. There was also no significant difference in pulse separation between 7 and 20 mL vials. Alpha spectra from glass vials are skewed to have a low-energy tail. This is caused by multiple internal reflections and subsequent losses of photons before light reaches the phototubes.

Alpha/beta separation with glass vials can be improved significantly by etching the outside wall of the vial (McKlveen and McDowell, 1984; Oikari et al., 1987). Careful optics design improves the light output and also improves spectrum resolution (Kossert et al., 2009; Nähle et al., 2009). Monte Carlo simulation of the light passage in LSC optics was done by Hurtado et al. (2009).

D. Alpha/beta calibration

To optimize alpha-beta separation performance, it is essential to determine the optimum TD setting at which there is equal and minimum spill of alpha pulses into the beta MCA and beta pulses into the alpha MCA. Fig. 2.14 illustrates the percent spillover or percent misclassification of ^{241}Am and ^{36}Cl samples in a Packard instrument. The determination of an optimum TD requires two standards, preferably, one of the pure alpha-emitter of interest and one of the pure beta-emitter of interest. For the most accurate results, the standards must be as nearly identical as possible to the unknown samples in their chemistry, volume, vial type, and so on. To achieve the optimum setting, each standard is counted individually at a range of TD settings. Some instruments perform this operation automatically while others perform it semiautomatically. It is possible to favor counting either alpha or beta events by adjusting the TD value appropriately to minimize interference from the other radionuclide (DeVol et al., 1996; Sanchez-Cabeza and Pujol, 1995; Pujol and Sanchez-Cabeza, 1997; Warwick and Croudace, 2002a, 2002b; Salonen, 2006).

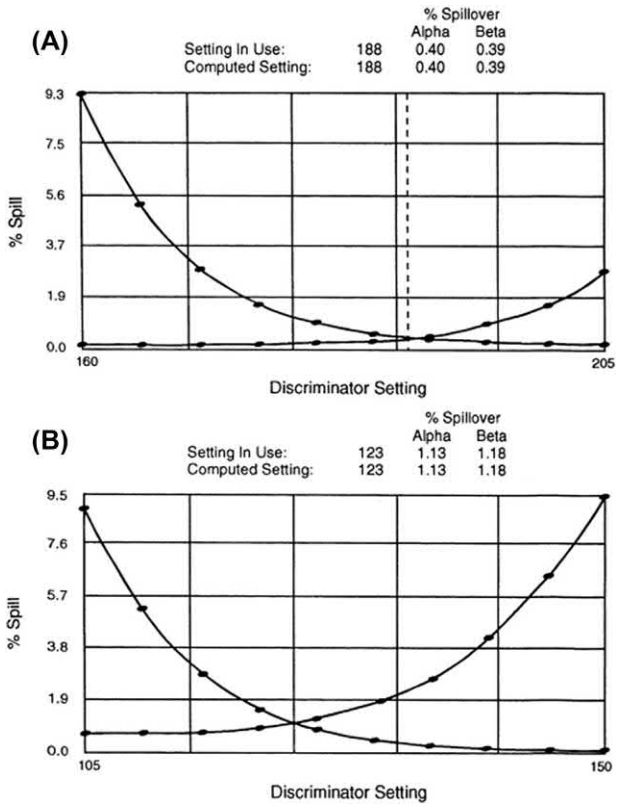


FIGURE 2.14 Percentage misclassification of ^{36}Cl and ^{241}Am in a Packard 2550TR/AB under (A) normal laboratory prepared levels of quenching and (B) artificially high levels of quenching. *©1994–2019, PerkinElmer, Inc. All rights reserved. Printed with permission.*

1. Misclassification Calculations

The calculation required to determine the actual cpm is essentially the same as that used in dual label studies and can be defined as follows:

X_α = alpha misclassification as beta
X_β = beta misclassification as alpha
A_T = true count rate due to alpha disintegrations
B_T = true count rate due to beta disintegrations
A_O = observed count rate in alpha MCA
B_O = observed count rate in beta MCA

Alpha into beta misclassification (X_α) is defined as the ratio of counts accumulated in the beta MCA to counts accumulated in both the alpha and beta MCAs as measured with the alpha standard.

$$X_\alpha = B_O/(A_O + B_O)$$

Similarly, beta into alpha misclassification (X_β) is defined as:

$$X_\beta = A_O/(A_O + B_O)$$

as measured with the beta standard.

It is important to understand that the count rate observed in each MCA is a function of both alpha and beta disintegrations because of the occurrence of some misclassification. This relationship can be defined as:

$$A_O = A_T - A_T X_\alpha + B_T X_\beta$$

$$B_O = B_T - B_T X_\beta + A_T X_\alpha$$

The first equation states that the observed count rate in the alpha MCA (A_O) is due mainly to counts from alpha disintegrations (A_T); however, this value will be reduced by the total number of alpha disintegrations counted in the beta MCA ($A_T X_\alpha$). Furthermore, beta counts falling into the alpha MCA must also be taken into account. This is accomplished by adding the $B_T X_\beta$ term. The calculation of the observed beta count rate (B_O) is the reverse of the calculation for the observed alpha count rate.

Solving for A_T and B_T and substitution of the A_T expression into the B_T expression and vice versa, we obtain the final equations for A_T and B_T:

$$A_T = \frac{A_O - A_O X_\beta - B_O X_\beta}{1 - X_\beta - X_\alpha}$$

and similarly

$$B_T = \frac{B_O - B_O X_\alpha - A_O X_\alpha}{1 - X_\alpha - X_\beta}$$

Example *of Misclassification calculation.* The calculation is further illustrated by counting mixtures of ^{36}Cl and ^{241}Am ranging from approximately 500 dpm of ^{36}Cl and 50,000 dpm of ^{241}Am to approximately 50,000 dpm of ^{36}Cl and 500 dpm of ^{241}Am in a total volume of 10 mL of cocktail (with appropriate background samples) at the optimum TD value.

The results were as follows:

Misclassification of alphas into the beta MCA (as a fraction) = 0.0071 = X_α
Misclassification of betas into the alpha MCA (as a fraction) = 0.0063 = X_β
Background in alpha-MCA = 0.69 cpm (0–2000 keV)
Background in beta-MCA = 39.6 cpm (0–2000 keV)

Table 2.4 lists the gross and background-corrected raw instrument data. Table 2.5 compares the actual alpha and beta activities in the vial with the calculated spill-corrected activities derived from the raw data.

2. Quenching and quench correction of percentage misclassification

In the PERALS system, all aspects of sample preparation (but principally the use of extractive scintillants) are geared toward minimizing quenching and maximizing the constancy of composition of samples. In standard LS counters,

TABLE 2.4 Gross and net (background corrected) raw data.

	Observed gross counts		Net counts (background subtracted)	
Sample no.	Beta-MCA	Alpha-MCA	Beta-MCA	Alpha-MCA
1	48,545	684	48,506	683
2	46,533	2731	46,494	2730
3	44,254	5313	44,215	5312
4	24,435	25,323	24,395	25,332
5	5208	46,131	5168	46,130
6	2833	47,160	2793	47,159
7	811	50,775	771	50,774

TABLE 2.5 Results of performing misclassification correction on the net count rates.

	Actual (vial) dpm		Spill corrected dpm	
Sample no.	^{36}Cl	^{241}Am	^{36}Cl	^{241}Am
1	48,684	449	48,811	378
2	46,694	2496	46,771	2453
3	44,187	5004	44,459	5068
4	24,315	24,847	24,369	25,348
5	4961	45,118	4869	46,429
6	2425	47,626	2472	47,481
7	507	49,595	411	51,135

when aqueous-accepting cocktails are employed, variations in quenching are much more likely and have to be accounted for in any calculations.

Fig. 2.14A and B represent misclassification plots determined in a Tri-Carb LSA instrument for the same activities of standards but under different quench conditions. Fig. 2.14A represents relatively unquenched conditions compared with Fig. 2.14B. Both the optimum TD value and the percentage misclassification of events change under these different conditions. It should be noted, however, that this effect will vary according to the isotopes being measured and may also vary, in a more limited fashion, from instrument to instrument. When the degree of quenching for a particular set of samples varies, there are two possible approaches. The first approach is to produce a single pair of alpha-beta standards that are similar in their quench-indicating parameter value to the least-quenched sample and then to progressively quench them and reoptimize the TD at each quench level. This produces a series of optimum TD values and percentage misclassifications for a range of quenching. The degree of sample quenching in each sample may then be measured by making a short count on each sample to determine the value of the quench-indicating parameter. Subsequently, the samples have to be counted at their individual optimum PDD conditions; however, this could conceivably require a separate counting protocol for each sample. The alternative approach is again to prepare a pair of standards that are equivalent in quenching to the least quenched samples, determine the optimum TD and then progressively quench the standards. However, in this approach, the misclassification is always determined at the original TD setting. This allows the construction of a plot of percentage misclassification versus quench-indicating parameter for a single TD setting. All samples may then be counted within a single protocol and a correction for misclassification as a function of quench is applied. This approach would be in addition to a quench curve that relates quenching to detection efficiency.

IV. Triple-to-double coincidence ratio (TDCR) counting

A. TDCR liquid scintillation counting

The TDCR method is an absolute standardization technique based on LSC developed for the determination of the activity of pure β-emitting and pure electron capture (EC) nuclides. The TDCR method requires a LSA equipped with three PMTs and two different coincident outputs, and the integration of theoretical calculation of counting efficiency is based on a physical and statistical model of the distribution of scintillation photons and their detection probability by the LSA. The principle of the TDCR method, the configuration about the TDCR detector system, the TDCR efficiency calculation technique as well as the applications of the TDCR method in radionuclide metrology have been described in detail in Chapter 6, Volume 1.

For the early applications, the TDCR method was exclusively employed in metrological laboratories for radionuclide standardization. Since the introduction of the first commercial TDCR LSA (Hidex 300 SL) by Hidex Oy in 2008, the TDCR method has been used more widely to radionuclide measurements in other applications such as environmental monitoring, radiological protection and biomedical studies.

As the nonlinearity of the scintillation response caused by the ionization-quenching phenomenon can be dealt with the TDCR method, the measured TDCR values have been used for quench correction. In TDCR LSC, triple and double coincidences are both measured. Since triple coincidences are more affected by chemical and color quench than double coincidences, a correlation between the quench level (or

counting efficiency) and the measured TDCR value can be established for quench correction. For pure beta-emitting radionuclides, the TDCR value usually approximates the overall counting efficiency. The TDCR efficiency calculation technique has been approved to be suitable for routine analysis of beta-emitting nuclides in samples with different quench levels (Simpson and Meyer, 1994).

For electron capture nuclides, such as ^{55}Fe, ^{41}Ca, and ^{139}Ce, there can be more than one counting efficiency corresponding to a given TDCR value, as the decay spectra are not continuous due to the contribution of two or more separated groups of scintillation energy from conversion electrons and gammas. Thus, the introduction of a new parameter into the algorithm of counting efficiency determination would be required to yield a single-valued efficiency versus TDCR curve (Broda, 2003).

Unlike external standard methods, TDCR is a universal method applicable for both chemical and color quenching, for aqueous and organic samples and for different cocktails and range of isotopes. In TDCR LSC, an external standard for monitoring quench level is not needed. The TDCR efficiency calculation technique enables the determination of pure beta-emitting and pure electron-capture nuclides in samples of various states of quench. Alternatively, quench correction can also be made with a curve fit option. Using a set of quench standard samples for the analyte nuclide, a standard quench curve of counting efficiency versus the TDCR value is first established, and the counting efficiency of an unknown sample can then be determined from the measured TDCR value of the sample. Once established, the TDCR quench curves are quite generic and do not need to be redone. In the Hidex 300SL LSA, a standard quench curve can be stored with the curve fit option, which can be automatically employed to determine the real counting efficiency based on the TDCR value of the sample.

The LSC instrument based on TDCR technique has been widely utilized for the determination of beta-emitters in a variety of environmental and biological samples for environmental monitoring, environmental tracing, radiocarbon dating, waste characterization and nuclear medicine etc. The TDCR method was demonstrated to be easy and sufficiently accurate for the determination of beta-emitting radionuclides in environmental and biological samples. The TDCR LSC has been used for the measurements of radionuclides including the following examples:

- ^{3}H, ^{210}Pb, ^{228}Ra, ^{99}Tc, ^{89}Sr, and ^{90}Sr in environmental water samples (Atkinson et al., 2014; Eikenberg et al., 2014; Guerin el al., 2017b; Dai and Kramer-Tremblay, 2014; Tayeb et al., 2016),
- ^{241}Pu, ^{90}Sr, and ^{63}Ni in radioactive waste and decommissioning samples (Taddei et al., 2013; Jaggi and Eikenberg, 2014; Priya et al., 2014), as well as
- ^{51}Cr, ^{90}Sr, and ^{32}P in various biological samples (Zoriy et al., 2016; Dai et al., 2013; Guerin el al., 2017a; Miura and Minai, 2017; Vernon et al., 2018).

Krąpiec and Walanus (2011) tested the Hidex 300SL for the determination of ^{14}C in radiocarbon dating. While the TDCR quench correction worked very well for determining the activity of ^{14}C in quench standards with high activity levels, it may not be preferred for the correction of benzene impurities in very low activity samples for radiocarbon dating. Thus, based on the observed position of the right slope of the ^{14}C or muons spectrum, a quench correction method was proposed and seemed to be more optimal for ^{14}C dating.

Using the Hidex TDCR LSA, several investigations have been carried out for the measurement of ^{55}Fe (an electron capture nuclide) in radioactive waste, irradiated steel, and urine samples (Taddei et al., 2013; Priya et al., 2014; Guerin and Dai, 2015). As an obvious discrepancy was observed between the measured TDCR value and the counting efficiency of ^{55}Fe, quench correction needed to be conducted by fitting with a quench calibration curve. The quench correction is particularly important for activity measurement of ^{55}Fe by LSC, because ferric ions in the sample could cause a strong color quenching and seriously reduce the counting efficiency. By obtaining a simple power function of counting efficiency versus the TDCR value with a set of quench standards, satisfactory results of quench correction for ^{55}Fe has been achieved (Guerin and Dai, 2015).

B. TDCR Cerenkov counting

The TDCR method can be used not only for activity measurement of typical beta-emitting isotopes by LSC but also for the determination of high-energy beta-emitting nuclides (e.g., ^{89}Sr, ^{90}Y, ^{32}P, ^{106}Rh, ^{204}Tl) by Cerenkov counting (Kossert, 2010).

In Cerenkov counting, fast electrons from beta decay moving in a dielectric and transparent medium (e.g., water) would produce Cerenkov photons, which can be directly detected using a LSC system with no use of scintillation media. The energy threshold of a radionuclide for Cerenkov light production in water is 263 keV. Although the efficiency of Cerenkov counting is usually lower in comparison with LSC, it has some significant advantages over LSC: (1) samples are counted directly without the need to add scintillation cocktail, which not only allows for a larger sample volume but also helps reduce time and cost on sample preparation and disposal problems; (2) the Cerenkov method can be used as a natural discrimination from low-energy beta- and alpha-emitting nuclides; (3) since Cerenkov photons are produced directly in sample solutions, no inhibition of the photon emission process due to fluorescence is involved; thus, Cerenkov counting is free of

chemical quenching. However, Cerenkov counting efficiency could be affected strongly by color quenching. Even very light color barely visible to the naked eye can produce a significant quench effect with a noticeable reduction in counting efficiency.

The color quench for Cerenkov counting is usually corrected by the internal standard method or quench curve method. The use of internal standards for color quench correction is applied by adding a known activity of the same radioisotope to the sample (after its counting) and recounting to determine the counting efficiency. Although this method is accurate, it is time consuming and cancels one of the main advantages of the Cerenkov method of keeping the original unadulterated sample. In most modern liquid scintillation systems, the quench correction for LSC is often performed by the quench curve method using external gamma-emitting radioisotopes such as ^{137}Cs, ^{226}Ra, ^{133}Ba, or ^{152}Eu. However, as a photon energy of >430 keV for the external source would be needed to produce Compton electrons above the threshold for the production of Cerenkov radiation (263 keV), those liquid scintillation counters containing ^{137}Cs and ^{133}Ba sources would not be applicable to quench correction in Cerenkov counting (Kamp and Blanchard, 1971; Takiue et al., 1996). Using a quench indicative parameter based on the integral area of the spectra measured with the external ^{152}Eu source of a Quantulus 1220 system, an ESAR (external source area ratio) method was proposed for color quench correction in Cerenkov counting (Tsroya et al., 2009, 2012). This method has been utilized for the determination of ^{90}Sr/^{90}Y activity in milk and urine samples (Tsroya et al., 2013a; 2013b).

In the TDCR technique, however, there is no need for constructing of quench correction curves using an external gamma source, because the effects of color quenching on Cerenkov efficiency can be automatically corrected based on the measured TDCR values. Unlike the conventional double coincidence counting techniques, the TDCR technique uses a triple coincidence counting method. For radionuclide standardization by Cerenkov counting with detection systems using two PMTs, Grau-Carles and Grau-Molonda (2006) have developed a free parameter model of light emission to compute Cerenkov counting efficiency. By adapting the Frank and Tamm theory for the production of Cerenkov photons, this free parameter model was extended for standardization with the TDCR detection systems (Kossert, 2010; Kossert et al., 2014). Based on the Monte Carlo code Geant4, Bobin et al. (2010) has also constructed a stochastic TDCR model to determine the Cerenkov efficiency using the experimental TDCR value. These TDCR Cerenkov models have been successfully tested for the activity standardizations of ^{90}Y, ^{89}Sr, and ^{68}Ge in nuclear medicine applications (Kossert et al., 2016; Thiam et al., 2017). The TDCR Cerenkov method would allow for calculation of the counting efficiency without an external or internal standard source.

Using a Hidex TDCR liquid scintillation counter, the TDCR Cerenkov method has been successfully used for quantitative determination of high-energy beta-emitters in environmental samples. An empirical correlation between the Cerenkov counting efficiency for ^{90}Y and the measured TDCR value was established for the correction of color quench effect on the determination of ^{90}Sr/^{90}Y in aqueous samples (Tayeb et al., 2014). The direct TDCR Cerenkov counting can serve as a rapid screening method for high-energy beta-emitting radionuclides in environmental water samples without any radiochemical separation procedure. For the measurements of ^{90}Sr−^{90}Y in groundwater samples collected in a contaminated riverbed, Olfert et al. (2014) compared the results by TDCR Cerenkov counting to those by LSC followed through radiochemical separation, and good agreements have been achieved. To date, the TDCR Cerenkov counting is still new to radioanalytical chemists, and only a few papers were published about its applications in environmental measurements (Olfert et al., 2014; Tayeb et al., 2015; Yang et al., 2017). In addition, Coha et al. (2016) studied the effects of measurement conditions on Cerenkov counting efficiency using three commercially available LSAs (including Triathler, Tri-Carb 3180, and Hidex 300 SL) with one-, two-, and three PMTs, and concluded that the TDCR Cerenkov counting would be well suited for routine quantitative determination of high energetic beta-emitting radionuclides in low-level environmental samples.

V. Analysis of alpha-emitting transuranic nuclides

A. Environmental occurrence and importance

The transuranium elements, neptunium (Np), plutonium (Pu), americium (Am), and curium (Cm), are products of nuclear weapons tests and nuclear fuel cycle operations particularly from reprocessing plants (Pimpl, 1992). With the exception of Pu and Am, which have been widely studied as part of global fallout following atmospheric weapons testing and nuclear accidents, the others are of environmental importance around fuel reprocessing and disposal sites (Hou and Roos, 2008; Qiao et al., 2009). The most common transuranium nuclides investigated in environmental studies are ^{238}Pu ($t_{1/2} = 87.74$ y), ^{239}Pu ($t_{1/2} = 2.41 \times 10^4$ y), ^{240}Pu ($t_{1/2} = 6563$ y), ^{241}Pu ($t_{1/2} = 14.4$ y) ^{241}Am ($t_{1/2} = 432.2$ y), and ^{244}Cm ($t_{1/2} = 18.1$ y). With the exception of ^{241}Pu, the other radionuclides are long-lived α-emitters and highly radiotoxic. ^{241}Am is a unique tracer in oceanographic and sedimentation studies, and its maximum concentration in the environment is estimated to be attained in the middle of the 21st

century (Hou and Roos, 2008) due to the decay of ^{241}Pu. The analysis of ^{241}Pu is discussed in other sections.

The differences in the plutonium isotopic ratios are used to trace the origin of the environmental contamination (Kershaw et al., 1995; Turner et al., 2003; Carbol et al., 2003; Ketterer et al., 2004; Kwong et al., 2004; Alamelu and Aggarwal, 2007; Hou and Roos, 2008; Varga et al., 2008; Zheng et al., 2013). For instance, the activity ratio of ^{238}Pu/$^{239+240}$Pu differs depending on whether the contaminations originate from releases from nuclear fuel reprocessing plants (0.25), nuclear tests (0.026), weapon grade uranium (0.014), or the Chernobyl accident (0.47). Owing to the high radiotoxicity of transuranium nuclides, the disposal of nuclear wastes is of particular concern, and strict restrictions govern the limits allowed for them in the environment. Environmental monitoring of transuranium nuclides around nuclear facilities is common and their determination in high-activity waste in nuclear fuel reprocessing cycles is important, as it will influence the method of final disposal (Prosser et al., 1994; Feng and He, 2009).

B. Sample preparation and analysis

Numerous methods have been applied to determine α-emitting transuranium nuclides in environmental and nuclear samples, which have been compiled and assessed in four comprehensive reviews by Hou and Roos (2008), Qiao et al. (2009), and Vajda and Kim (2010a, 2010b). These reviews deal with pre-treatments, pre-concentration, chemical separation, and various measurement methods, which are mostly tedious and challenging because of the complex environmental sample matrices and other radionuclides present. The chemical separation schemes are complicated, because the concentrations of transuranium nuclides are very low, their oxidation states have to be considered and they must be purified completely from other actinides in advance to avoid the interference of other radionuclides. The other actinides (such as U and Th) and fission products are usually present in much higher concentrations in most samples than those of transuranium nuclides. To achieve the best possible energy resolution by α-spectrometric analysis, the sample must be prepared as a thin-layer counting source. Likewise, their determination in high-activity waste is not trivial because of the low concentrations, the presence of β- and β/γ-emitting radionuclides and high salt concentrations.

1. Alpha spectrometry

The traditional methods for determining α-emitting transuranium nuclides in environmental samples are based on α-spectrometry. However, ^{239}Pu and ^{240}Pu isotopes cannot be distinguished by the standard α-spectrometers due to their similar α-particle energies; they exist as a sum peak in the α-spectrum. Likewise, due to their overlapping α-peaks, ^{244}Cm and ^{243}Cm isotopes are also indistinguishable by α-spectrometry. The typical radiochemical separation methods for transuranium elements are based on ion exchange, solvent extraction and extraction chromatography (EC). The EC techniques are commonly employed in the separation schemes partly owing to the availability of actinide-specific resins, TEVA, TRU, UTEVA, and DGA, which can be used with ion exchangers and Sr resin to the simultaneous determination of several actinides, Th, U, Pu, Am, Cm, and Np, and other radionuclides such as ^{226}Ra, ^{210}Pb, ^{137}Cs, and ^{90}Sr from a single sample (Alvarez and Navarro, 1996; Moreno et al., 1998; Pilviö et al., 1999; Pilviö and Bickel, 2000; La Rosa et al., 2001; Thakkar, 2001; Mellado et al., 2002; Wang et al., 2004; Tavčar and Benedik, 2005; Oh et al., 2009; Maxwell, 2006; Maxwell and Culligan, 2009b; Maxwell et al., 2014; Harrison et al., 2011; Luo et al., 2018). Sequential separation brings considerable savings in time needed for pre-concentration, pre-treatments, and the chemical separation, which is simpler and faster using EC than merely ion exchange (Dai and Kramer-Tremblay, 2011; 2014). Lee et al. (2011) developed a rather simple procedure for the determination of Pu, ^{90}Sr, and ^{241}Am in soil samples and obtained high chemical yields (71%−75%) for these nuclides in terrestrial soil samples. It was based on an anion exchange resin connected with a Sr-Spec column. ^{236}Pu, ^{242}Pu, ^{239}Np, and ^{243}Am (for Am and Cm) are the most commonly used yield tracers. The detection limits using α-spectrometry are of the order of 0.02−0.09 mBq for ^{238}Pu and ^{239,240}Pu and of 0.1−0.2 mBq for ^{241}Am with a few days of counting time (Hou and Roos, 2008; Qiao et al., 2009; Vajda and Kim, 2010a, 2010b; Dai and Kramer-Tremblay, 2014).

2. Mass spectrometry

Currently, long-lived transuranic radionuclides are often determined by mass spectrometric techniques, including ICP-MS (Chen et al., 2002a; Hou and Roos, 2008; Qiao et al., 2009; Vajda and Kim, 2010a, 2010b; Shi et al., 2011; Zheng et al., 2013), thermal ionization mass spectrometry (Callis and Abernathey, 1991; Cooper et al., 2000; Elliot et al., 2006; Shibahara et al., 2016) and accelerator mass spectrometry (Fifield et al., 1996; Child et al., 2008; Dai et al., 2012b, 2016). In this case, the isotopic ratio of ^{239}Pu and ^{240}Pu are also determined, but chemical separation prior to their detection by mass spectrometry is necessary. The detection limits for long-lived actinide isotopes with a half-life of $>10^4$ years by mass spectrometric techniques (especially AMS) are better than those obtained by α-spectrometry.

3. Liquid scintillation counting (LSC)

LSC using α/β discrimination has been used to measure transuranium nuclides in high-activity wastes (Yang, 1990;

Feng and He, 2009) and in bioassay samples (Yang et al., 1995; Eikenberg et al., 1999) following chemical separation by solvent extraction or extraction chromatography (EC). Yang (1990) used di-(2-ethylhexyl) phosphoric acid (HDEHP) and trialkyl phosphine oxide (TRPO) as extractants to separate Np, Pu, and Am from reactor waste samples. Yang et al. (1995) determined Pu in urine by extracting it with 30% TRPO in xylene from 1M HNO_3 solution where urine residue was dissolved following the removal of organic compounds. The chemical yields were between 80% and 95%. Feng and He (2009) proposed a new method for the determination of ^{237}Np, $^{238-240}$Pu, and ^{241}Am in high-active waste. It is based on combined α-spectrometric and LSC measurements and on the extraction of transuranic elements with TRPO and tenoyl-tri-fluor acetone (TTA). The source for the α-spectrometric measurement was prepared simply by evaporating the TRPO in xylene onto a stainless steel disk to determine the activity percentage of each α-emitter while their total activity was quantified by LSC using a sample prepared from the same solution. The activities of various transuranium nuclides were calculated using the results of these measurements. The complicated separations were then avoided and the advantage of the high counting efficiency by LSC was achieved. Moreover, only one step of extraction with TRPO is needed, if it is not necessary to know the relative amounts of ^{238}Pu, $^{239+240}$Pu, and ^{241}Am. Otherwise, another extraction step is needed to separate Pu from Am completely, because the α-peaks of ^{238}Pu (5.456 and 5.498 MeV) and ^{241}Am (5.443 and 5.486 MeV) overlap each other. This separation is performed using 0.5 mol/L TTA in xylene whereby the Pu (IV) is efficiently extracted into the organic phase while Am remains in the aqueous phase. The activity ratio of ^{238}Pu/$^{239+240}$Pu is obtained from the α-spectrometric measurement using a sample prepared from the organic phase as previously described. The extraction efficiencies with the TPRO and TTA extractants are nearly 100%. Eikenberg et al. (1999) used Actinide resin, with a trade name of DIPEX, for separating transuranium nuclides (Pu, Am, Cm) from urine. Their procedure was rather simple including partial oxidation of organic matter, sorption of the actinides on the resin, separation of the resin from the solution and stripping of the actinides from the resin with isopropanol. This was decomposed by oxidation with acids to have a transparent residue dissolved in 2 mL 0.5 M HCl, which was mixed with the LS cocktail. The chemical yields for various actinides, including U and Th isotopes and ^{233}Pa, were between 70% and 100%, whereas Ra (<5%) and Po (<3%) were purely adsorbed on the resin. One advantage of using LSC with α/β discrimination is that it eliminates any β-interferences that might have been co-extracted. Yang (1990) observed that α-activity can be quantitatively analyzed in the presence of a 10^5 excess of β-activity in high-activity waste. Detection limits depend on the sample volume used for the analysis and on the amount of beta interference that is present. Detection limits for Pu with the α/β LSC are of the order of 3−10 mBq/L for a 100−120 minute count time.

The PERALS LSC system in combination with extractive scintillators has been applied for the determination of a number of transuranium nuclides (Metzger et al., 1995; Dacheux and Aupiais, 1997, 1998; Aupiais, 1997; Aupiais et al., 1999). The detection limits are comparable to those achieved by ICP-MS or α-spectrometry.

VI. Analysis of beta-emitting radionuclides

LSC is the major technique for measurement of pure beta-emitting radionuclides, including the radionuclides that decay by electron capture. The most important radionuclides in view of environmental radioactivity, tracer application in various disciplines and nuclear waste management are ^{3}H, ^{14}C, ^{55}Fe, ^{63}Ni, ^{89}Sr, ^{90}Sr, ^{129}I, and ^{241}Pu. The updated analytical methods for these radionuclides using LSC are presented below.

A. Tritium (^{3}H)

1. Environmental occurrence

Tritium is a pure, low-energy beta-emitter ($E_{max} = 18.6$ keV) with a half-life of 12.32 years (Lucas and Unterweger, 2000). Tritium in the present environment has three major sources: (1) natural production in the upper atmosphere through cosmic ray reaction of nitrogen (^{14}N(n,^{3}H)^{12}C) and oxygen in the upper atmosphere (Hou, 2018); (2) residual activities from atmospheric nuclear weapons testing (Libby, 1963); and (3) on-going nuclear fuel cycle operations. Since the partial atmospheric nuclear test ban treaty in 1963, the worldwide levels of tritium in the environment have been decreasing at a rate approximately equal to its half-life (Okada and Momoshima, 1993). Generally, nuclear fuel cycle operations are of concern to the immediate locale only, with relatively minor contributions to more general environmental tritium levels. Regulated monitoring of specific sites and hydrological studies are the principal applications of environmental tritium analysis, and, of course, as the "background" levels decrease, there is a corresponding requirement for the measurement of lower and lower activities (Eyrolle et al., 2018).

Tritium activities in the field environmental tracer application are commonly described in terms of tritium units (TU), where 1 TU = 1 atom of tritium per 10^{18} atoms of hydrogen or 1 TU = 7.14 dpm/L of water = 0.119 Bq/L of water. The natural activities (without direct contamination from nuclear facilities) in precipitation vary from about

25 TU at high latitudes to about 4 TU in the equatorial zone (Geyh and Schleicher, 1990; Duliu et al., 2018).

2. Sample preparation and analysis

a. Sample handling

Samples taken for the purpose of tritium analysis should be sealed in airtight containers at the point of sampling (glass or high-density plastic is preferred), as the hydrogen from water or water-bearing samples is readily exchanged with atmospheric hydrogen in the form of water vapor. In the case of biological samples and some water-bearing biologically active samples (sludge and silt) that cannot be processed immediately, freezing is a good way to preserve the sample composition. Frozen samples should be thawed completely and the external areas of the container is dried prior to opening in order to minimize sample exposure to condensation of atmospheric water (onto the sample) or isotopic exchange with water vapor in the air. When samples are exposed, it should be assumed that contamination is a possibility, and steps to prevent or monitor this are required.

b. Sample preparation

The term "sample preparation" of this section refers to the processes required to render the separated sample of water form into a pure state (purified water or benzene), that is, ready to be mixed with the scintillation cocktail or fluor in preparation for LSC. Generally, three methods of preparation are employed for environmental tritium measurement of water. These are direct addition, electrolytic enrichment, and benzene synthesis, and the method of sample preparation depends on the type of analysis to be performed and tritium level in the samples. Biological and soil samples always require a tritium extraction/separation step regardless of the sample preparation method to be employed. Water samples require purification (distillation is the normal approach) prior to electrolytic enrichment and benzene synthesis analysis, but this step can be omitted with the direct addition method if the water is relative pure (no color and no high salt content). Tritium exists in biological samples as part of the water component (FWT, free water tritium) or as part of the organic structure (BT, bound tritium). The free water tritium is often separated from the sample by freeze drying and collecting the evaporated water. To analyze the bound tritium, the sample is dried (freeze drying or low-temperature oven drying at $\sim$60−80°C) and then combusted. The water of combustion is collected, purified as required, and analyzed by the direct addition method.

Direct Addition. Some water samples are relatively pure as received (*e.g.*, municipal drinking water) and can be counted without any purification steps. For routine operations this can be a significant consideration, because the purification step greatly increases the sample preparation time. Purification is recommended if (1) color is visible (includes cloudiness from suspended solids), (2) organics are present, (3) the sample history or source is unknown (may contain interfering chemicals causing high quench), and (4) high salt content (seawater and some ground water), which causes a high quench and much less sample size can be used. For a relatively pure water sample, it can be directly mixed with a scintillation cocktail and counted.

Electrolytic Enrichment. This procedure is based on the principle of selective isotopic enrichment using electrolysis. Because of the slightly higher binding energies, molecules of THO are not decomposed to form H_2 and O_2 as readily as H_2O or DHO (T = tritium, D = deuterium). Water samples are distilled, then made slightly alkaline (Stencel et al., 1995) by addition of Na_2O and placed in an electrolysis cell. A constant current (e.g., 10 A) is applied to the cell, and electrolytic decomposition of the water reduces the sample to about 1−5% of the initial volume. Isotopic fractionation, due to the higher binding energy, typically concentrates over 90% of the tritium in the remaining water. The concentrated sample is purified by distillation or vacuum distillation to remove the alkaline (NaOH) and counted after addition of scintillation cocktail. This procedure usually takes 5−10 days to complete depending on the size of cell/sample; therefore, multicell designs containing 20−40 cells are very common. During electrolysis, the temperature of the water sample in the cell needs to be cooled to a low temperature (2−4°C) to reduce the loss of water sample by evaporation. Modern electrolytical enrichment systems often include temperature control of samples ($\sim$2−4°C) and electronic regulation of the electrolysis process. Fig. 2.15 illustrates a schematic diagram of a cell for the electrolytical enrichment of tritium (Plastino et al., 2007). Each cell in the system must be characterized for isotopic separation performance, which is done by adding a known quantity of tritium to the cell to determine the "recovery of tritium". The recovery of tritium is related to the performance of each cell, but for the same quality, the performance of the cells should be similar. Fig. 2.16 shows a measured recovery of tritium in an electrolytical system with an initial volume of 500 mL and final remaining volume of 13−16 mL, a relative constant recovery of tritium was obtained regardless of the cells and volume of remaining water in 13−16 mL. However, it should be mentioned that if the volume of the remaining water is less than 13 mL, a significantly reduced recovery of tritium was observed. Therefore, the smallest volume of the remaining water has to be more than 13 mL for this system. The performance of the electrolytical enrichment system is often checked yearly, cells are spiked with a known activity of tritium water standard, and the recovery of tritium in each cell is checked against a known standard and the final remaining water volume. The enrichment factor (EF) is simply the recovery (RE) multiplied by the

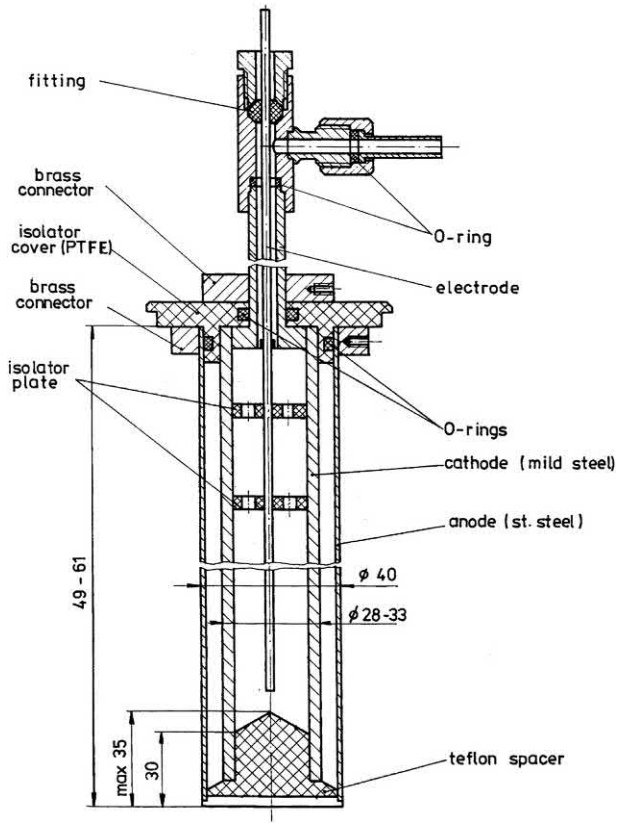


FIGURE 2.15 Electrolysis cell for enrichment of tritium in water.

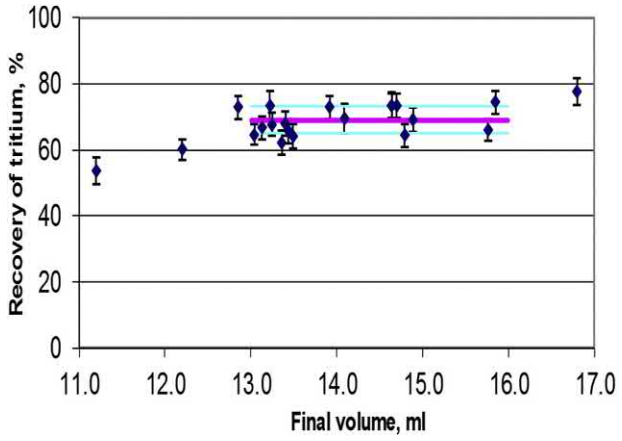


FIGURE 2.16 Recovery of tritium in electrolytical enrichment system with initial volume of 450 mL water.

initial weight (W_i) of sample divided by the final weight (W_f) of sample and is expressed as a numerical value (*e.g.*, enrichment factor = 15). The electrolysis cells are generally designed to handle 100−500 mL samples, with enrichment factors of 15 to >30.

$$EF = RE(W_i \div W_f)$$

For example, a 250-g water sample is enriched and 10 g of sample remains; the recovery is 91%. $EF = 0.91(250 \div 10) = 22.75$.

Benzene Synthesis. The third method of preparation is the synthesis of high-purity benzene from water samples (De Filippis and Noakes, 1991). Sample water is added to calcium carbide in an evacuated reaction vessel, to form acetylene (C_2H_2). The acetylene is then cyclotrimerized to high-purity benzene using a chromium or vanadium catalyst. For LSC of benzene, there is no requirement for the addition of a scintillation cocktail, as the fluors can be added in solid form directly to the counting vial. One sample per day per vacuum apparatus can be handled, with the production of 8−15 mL of high-purity benzene. Regardless of a larger volume of sample counted and less quenching of benzene compared to water, the method is only marginally more sensitive than direct addition because of no improvement in the hydrogen/tritium content in benzene (<8%) compared to H_2O (about 11%). Since the detection limit of tritium is not significantly improved, this method is generally not used. The method is included here only for completeness and will not be discussed further.

c. Tritium extraction/purification techniques

Low-level counting of tritium requires that water samples be reasonably pure and free from interfering substances. Given the wide variety of sample matrices that environmental monitoring programs may encounter, various cleanup/separation techniques are employed. If there is any doubt about the purity of a sample, it is always best to take proactive action, as repeating the analysis invariably costs more (manpower, equipment, and time) than the initial sample cleanup.

Filtration. Simple filtering of a "dirty" water sample often produces clear water by the removal of particles in suspension, which will cause physical quench during LSC measurement. This should be used only when the source of the sample is well known, such as a routinely sampled stream or well water, and there is little chance of the presence of interferences. This type of cleanup should be used only for samples containing suspended mud or silt. An alternative would be to allow the suspended material to settle down and then decant/suck the clear water sample for measurement. However, this action cannot remove the soluble interferences, such as salt and organic and colorful substance (e.g., humic substances), which need other purification action.

Distillation. Plain or vacuum distillation is useful for the purification of water samples that do not contain volatile materials but may have chemical contaminants that would render them unsuitable for analysis.

Ion Exchange. Mixed-bed ion exchange columns designed specifically for tritium analysis are commercially

available. A typical column (Eichrom Industries, Tritium Column) is composed of a prefilter and beds of anion, cation, and organic specific resins. It is designed to give results comparable to those of simple distillation. The column needs to be pre-conditioned with background water (tritium dead water) and then the sample is passed through for "cleanup". This type of column is a useful tool but should be used only with sample media that have been pretested and the cleanup performance verified. Simple water samples (groundwater, seawater, etc.) are likely candidates for this method. More complex samples, such as rainwater and lake water containing high organic substances, can become highly colored and require a more aggressive procedure.

Active Charcoal Adsorption. This is the method often applied to remove soluble organic substances before distillation or ion exchange purification, especially for a sample with a high content of organics, especially urine sample. Active charcoal powder in a ratio of 1:15−30 (by mass) to sample is mixed and allow to stand for 1−5 hours, the mixture is then filtered to remove the charcoal with adsorbed organics. The water is further distillated or treated with ion exchange chromatography for LSC measurement.

Freeze Drying. Freeze drying is the process whereby a sample is frozen and then exposed to high vacuum. The water contained in the sample goes from the solid phase directly to a vapor (sublimation), and if the vacuum is drawn through a cold trap, this vapor can be collected as pure water. Routine application of this process for the purposes of extracting pure water for tritium analysis is generally accomplished using custom glassware and cryogenic (liquid nitrogen, LN_2) cooling. The sample is first frozen to solid using a Dewar of LN_2; the Dewar is then moved to a collecting flask (cold trap) and a high vacuum applied. The ambient room temperature supplies sufficient heat to accelerate the sublimation process, which may take several hours (depending on the volume of water required). The water sample is collected in the cold trap (as deposited ice) and is simply melted and recovered for analysis.

Azeotropic Distillation. An azeotrope is a liquid mixture that has a constant boiling point and its vapor has the same composition as the liquid. Several compounds, such as toluene, benzene, and cyclohexane, form suitable azeotropes with water. These compounds have a cyclic structure, immiscible in water, so are resistant to exchange with external hydrogen. Cyclohexane is the preferred compound, as it is the least hazardous and provides a suitable level of performance in the extraction of water and measurement of tritium. The water azeotrope formed with cyclohexane (boiling point 80.7°C) contains 8.5% water, has a boiling point of 69.8°C. Azeotropic distillation (Moghissi et al., 1973) provides a simple method for extracting water from a wide variety of media (e.g., honey, milk, vegetation, soil, fish) for tritium analysis using LSC. Because these materials are largely composed of free water, an azeotropic distillation will generate, from a mixture of sample and cyclohexane, not necessarily azeotropic in proportion, an azeotropic vapor and, hence, distillate. The distillate separates into two layers with water in the bottom layer. Using suitable glassware, the distillate is collected and the water portion is taken for analysis.

Combustion: The organic bound tritium in biological samples and the strong binding of tritium within the crystal of grains of soil and sediment are often separated using combustion with oxygen flow and high temperature. In this case, tritium in organic substance is converted to water vapor and collected by condensing (Huang et al., 2014; Croudace et al., 2012). The firmly binding tritium in the crystal of soil and sediment grains and metals can be separated also by converting it into water vapor by combustion (Croudace et al., 2014; Warwick et al., 2010). The converted tritium in water vapor form is condensed and collected as liquid water, which is further purified with the methods presented above, and finally measured using LSC.

d. Background water

A tritium-free water needs to be used as blank (background water) to measure the background of the LSC. The quality of this water is the cornerstone of any program undertaking environmental tritium analysis, as it is used for subtraction of the measurement background. Deep wells and glacial aquifers are likely sources of tritium-free water due to their long period of isolation from atmospheric exposure. Identifying a suitable source of background water can be a challenging task, and communicating with laboratories with existing environmental tritium monitoring programs and hydrologist can save considerable effort and time in locating these sources. To evaluate the suitability of reference background water, it is simplest to use the electrolytic enrichment technique. A sample of the water is enriched by 15−30 times and analyzed by LSC, as a sample, using the original blank water as the background. This allows detection of any tritium present, at a much LLD (typically < 0.1 Bq/L). Suggestions on handling the background water supply are as follows: (1) obtain large batches (1−2 years supply), as it is more efficient and economical to validate, (2) store in airtight glass containers, and (3) implement procedures for handling, validation testing, and maintenance of testing and usage records.

e. Standards

Standards are used to measure the counting efficiency of tritium by the LS counter at different quench levels and volumes of water sample. A traceable tritium standard should be purchased in the form of HTO or other less quench compound. Aliquots are accurately dispensed/weighed and diluted to give solutions of known activity.

Common practice is to prepare stock solutions of high activity, which are then diluted to working standards. As a guideline, a small volume of the working standard solution (<1.0 mL) should contain sufficient activity to yield less than 0.1% counting error (at 1 sigma), when counted using the sample protocol. Keeping the tritium standard close to the guideline offers several advantages: (1) since a minimum of activity is used, potential cross contamination to samples is reduced; (2) some counters employ special background enhancing features that are sensitive to high count rates, and if the count rate of the standard exceeds the limit, inconsistent results can occur; (3) the lower the activity level employed, the more cost effective the use of the purchased tritium standard will be.

Suggestions for handling tritium standards are as follows: (1) store and prepare in airtight glass containers (i.e., dedicated volumetric flasks); (2) use stock and working solutions; (3) keep records of all certificates and preparation and testing of all stock and working solutions; and (4) dispense standards in a properly ventilated area, well away from any samples.

f. Quality control

The purpose of the quality control program is to demonstrate that the parameters involved in the production of results are within expected tolerances. The counting efficiency and background count rate are obtained for each batch of samples by including standards and background samples. These are satisfactory for demonstrating the equipment performance but do not validate the sample handling or preparation. Two other sample types are used to demonstrate that sample handling does not adulterate or contaminate the sample and that the preparation of samples for counting is acceptable:

(1) Process blank samples. Samples with low levels of tritium can easily be contaminated by external sources. A process blank sample is basically a sample of background water (tritium dead water) that is treated using the same processes as the sample. This sample is then counted along with the rest of the sample batch and compared with the regular background/blank to demonstrate the absence of contamination during the process. For example, if a batch of milk samples is freeze dried to extract water for tritium analysis, a process control sample would also be freeze dried and included in the sample batch.

(2) Quality control (QC) samples. The purpose of the QC sample is to introduce a sample with known activity into the handling process. Whenever a purification or extraction technique is performed, a QC sample is added to the batch and processed as a regular sample. Because the QC sample has known activity, this demonstrates the performance of the entire analytical and counting process. The QC sample is prepared by adding a measured amount of standard stock or working standard solution to a quantity of background water. The activity level required varies with the count conditions, but should be calculated to yield a 2 sigma counting error of the order of 10%. Charting the data from QC samples gives a historical baseline against which current results can be judged. This aids in detecting trends, poor sample preparation, and counting or counter problems.

g. Quality assurance

Quality assurance tests are independent tests performed to provide confidence in the analytical results, which is implemented by involving known and unknown (blind) samples from external agencies. A good example of this for tritium would be the Laboratory Intercomparison Program administered by some national and international organizations (e.g., the U.S. Environmental Protection Agency, and International Atomic Energy Agency). Water samples are distributed to the participating laboratories as "blind" samples for analysis. The analysis results are reported back to the organizer of the intercomparison, which are evaluated against the spiked value or average of the reported results. This serves as a check on the accuracy of the analysis process and gives insight into the performance of the laboratories. Intercomparisons with other laboratories using known and unknown samples are also useful when they can be arranged.

B. Radiocarbon (^{14}C)

1. Environmental occurrence

^{14}C has a half-life of 5730 years and decays by beta emission ($E_{max} = 156$ keV) to the stable nuclide ^{14}N. It is ubiquitous in our environment and also one of the most common radionuclides measured by LSC. Its occurrence in the environment is from three main sources: (1) natural production via the interaction of cosmically produced neutrons with atmospheric nitrogen in the upper atmosphere, (2) atmospheric nuclear weapons tests (principally during the 1950s and 1960s), and (3) discharges from facilities associated with the nuclear fuel cycle (principally nuclear power plants and fuel reprocessing plants). Additional minor sources include (1) discharges from facilities that synthesize radiolabeled compounds for biomedical, biological, and agricultural tracer studies; (2) discharges from hospitals, universities, research centers, and so on, of the labeled materials used in tracer studies; and (3) natural production by spallation reactions in surface rocks and soils.

The environmental applications of ^{14}C measurements can be divided into the following main categories:

1) Radiocarbon dating. The relatively constant natural production rate of ^{14}C in the upper atmosphere, its uniform uptake as $^{14}CO_2$ into living plant material, conversion to

plant carbohydrates, and subsequent transfer through the food chain are the basis of the radiocarbon dating technique. The end result of the food chain transfer is almost uniform labeling of all living organisms. ^{14}C dating is used in a wide range of scientific disciplines including archeology, geology, soil science, climate reconstruction, and oceanography, and LSC is a widely used measurement technique for ^{14}C dating (Thomson et al., 1995; Pessenda et al., 2001; Walker et al., 2001) besides the most sensitive accelerator mass spectrometry.

2) Environmental measurements. Typically, these measurements are performed on samples from the environment around facilities associated with the nuclear fuel cycle and facilities that produce labeled compounds. Although ^{14}C is not among the most abundant of the anthropogenic radionuclides that enter our environment as a result of nuclear fuel cycle activities, its long half-life, high environmental mobility, and ability to enter the food chain mean that it delivers one of the highest collective effective dose equivalents to the global population, hence the level of ^{14}C in the environment is critical for environmental monitoring of nuclear facilities (Buzinny et al., 1998; Gulliver et al., 2001; Isogai et al., 2002; UNSCEAR, 2008).
3) Food adulteration studies. Petroleum derivatives are occasionally used to adulterate natural food and drink products without the buyer's knowledge. Because petroleum-based products are sufficiently old, they contain no ^{14}C, and depletions in ^{14}C content are normally indicative of adulteration. Examples of this include the adulteration of wines, spirits, wine or cider vinegars, and other natural products (Schönhofer, 1989a, 1992).
4) Estimation of fossil fuel CO_2 emission. Carbon dioxide is the main greenhouse gas released to the atmosphere as a result of human activities. A 30% rise in CO_2 concentration has been observed since the start of the industrial revolution, which is mainly attributed to the increased use of fossil-based fuel for energy production and transportation. Since the ^{14}C in the fossil fuel is very low compared to biogenic materials, measurement of atmospheric ^{14}C levels and its distribution has been proposed for directly estimating the amount of fossil CO_2 releases, and has been widely applied in the past years (Keller et al., 2016; Turnbull et al., 2014; Niu et al., 2018; Graven, 2015).
5) Biogenic fuel composition measurement. For reducing the fossil CO_2 releases, one effort has been implemented by the addition of biogenic fuel (with present atmospheric ^{14}C) to the fossil fuel (with dead ^{14}C) in some levels. To monitor the level of biogenic fuel in the mixed fuel, ^{14}C in the fuel is measured using the LSC method.

2. Sample preparation and analysis

a. Sample preparation

Benzene synthesis. This is the preferred technique for radiocarbon dating because of its higher precision and sensitivity, although it is also used for environmental and food adulteration studies. Benzene synthesis involves the following steps: Carbon is first converted to CO_2 by combustion in a pure oxygen atmosphere for organic carbon samples or acid hydrolysis for inorganic carbon samples (e.g., shells and biogenic deep ocean sediments). The collected CO_2 is subsequently converted to lithium carbide by reaction with molten lithium, and on cooling, the addition of water causes the production of acetylene (Barker, 1953). The acetylene is then cyclotrimerized to benzene using a chromium- or vanadium-based catalyst (Noakes et al., 1963). Benzene is an ideal counting medium for the following reasons:

1) It is a clear aromatic solvent capable of dissolving sufficient fluor.
2) It has excellent energy transmission properties.
3) It has a high carbon content (92.3%).
4) It is relatively easy to synthesize.
5) It exhibits low quench.

In most instances, solid fluors would be added directly, rather than a scintillation cocktail. This minimizes volume additions and therefore any increase in quenchable background. The trend in the radiocarbon dating discipline has been to use only a primary fluor and to use it at relatively high concentrations (12−15 mg per gram of benzene) to facilitate weighing. This procedure would be common for researchers using instruments such as the Wallac 1220 Quantulus. This is now possible, because the wider wavelength response of modern PMTs has negated the requirement for a secondary fluor (wavelength shifter). A primary and a secondary fluor (*bis*-MSB) are recommended for users of Packard instruments with nonprogrammable TR-LSC. The recommended concentrations are 2.8 mg of *butyl*-PBD and 3.0 mg of *bis*-MSB per gram of sample benzene, and highly accurate techniques for dispensing such small weights are available (Cook et al., 1990a, 1990b; Anderson and Cook, 1991; Cook and Anderson, 1992). A primary fluor alone can be used with programmable TR-LSC provided the burst delay is increased beyond 75 ns. This method is mainly applied for the ^{14}C dating or the precise measurement of ^{14}C in low level or background level environmental samples. With the rapid development of accelerator mass spectrometry and its wide application, ^{14}C measurement for dating purpose is now mainly carried out by the AMS technique.

CO_2 Absorption. Direct absorption of CO_2 using quaternary amines is a widely used technique, particularly where the activities are enriched relative to natural

production. Carbo-Sorb E (PerkinElmer, Inc.) and Solusol (National Diagnostics) are examples of high-capacity carbon dioxide absorbers that are compatible with LSC cocktails. Direct absorption into inorganic bases is an alternative means of absorbing the CO_2 in which aqueous solutions of up to 1 M sodium hydroxide or methanolic solutions of 2 M sodium hydroxide have been used. However, these have three distinct disadvantages: they are strong quenching agents, they have low trapping capacities compared with the amines, and they produce severe chemiluminescence.

For CO_2 samples absorbed into base solutions, cocktails that can accept high-ionic-strength solutions are added. For low-precision measurements, the advantages of the absorption technique are that sample preparation is less time consuming than for benzene synthesis and the sample preparation apparatus is relatively simple. The major disadvantage of the CO_2 absorption technique is the relative small amount of carbon that can be absorbed. For example, 10 mL of Carbo-Sorb is approximately the maximum quantity that would be miscible with Permafluor E + scintillation cocktail in a 20 mL vial. This is capable of absorbing 58 mmol of CO_2, which is equivalent to 0.7 g of carbon. In comparison, it is possible to add approximately 19 g of carbon into a vial via benzene synthesis, although 3−7 g is more typical. Detailed information on the absorption technique has been reported (Qureshi et al., 1989; Canducci et al., 2013). This is the most often applied technique for the preparation of samples from nuclear facilities or surrounding environment, which have a relative high ^{14}C concentration. Thus, a small amount of sample (carbon) is sufficient for LSC measurement. Hou et al. (2005, 2007) have reported a method for the determination of ^{14}C in samples from nuclear decommissioning, such as graphite, concrete, and metals. ^{14}C was released from the sample matrix as CO_2 by oxidation combustion with O_2 flow at a temperature higher than 1000°C with Pt as catalyzer to convert all CO to CO_2. It was also confirmed that both organic and inorganic carbon in the sample can be completely converted to CO_2 in this condition. The released $^{14}CO_2$ was trapped using 8−12 mL of Carb-Sorb E solution filled into a column to ensure a high absorption efficiency. The trap solution was then mixed with Permafluor E+ scintillation cocktail for LSC measurement. The entire separation was implemented with a Sample Oxidizer (PerkinElmer Inc.), which makes the separation complete within 2 minutes. The major disadvantage of this method is the relatively small sample amount (0.2−1.0 g) that can be treated, which limits the analysis of large samples and the detection limit of the method. A tube furnace was also reported for separation of ^{14}C from solid samples using combustion. In this case, the sample amount can be increased to 20 g, which improves the detection limit (Hou, 2018). Fig. 2.17 illustrates the two systems for ^{14}C sample preparation. This method was also demonstrated to be applicable to other solid samples, such as soil, sediment, vegetations, tissues, exchange resin, filter, and plastic materials (Hou, 2018).

A method for the determination of ^{14}C in water samples was reported using evaporation and combustion for carbon separation and LSC for ^{14}C measurement (Hou, 2007). In environmental water samples, ^{14}C is present as both inorganic (carbonate) and organic associated form, evaporation with addition of stable carbonate as carrier is first used to concentrate ^{14}C and convert it to solid. The residue with concentrated ^{14}C was used for the analysis using the same procedure as other solid samples described above. In this way, the interfering radionuclides can be also removed, and only ^{14}C trapped in amine solution for LSC measurement.

Direct counting. On occasion, when adulteration of alcoholic drinks and biogenic fuel are studied, direct counting of the alcohol or fuel may be performed. Schönhofer (1989a) has demonstrated that direct counting of uncolored spirits with an ethanol concentration of about 40% v/v is feasible. A 1:1 ratio of spirit to cocktail (Quickszint 400 by Zinsser) was found to be suitable. For colored spirits and wine, distillation was required to concentrate and purify the ethanol. A 1:1 mixture of cocktail to 85%−90% ethanol was used.

For ^{14}C measurements in vinegar, acetic acid has been isolated by continuous extraction with di-isopropyl ether and subsequent distillation. Subsequently, 4 mL of concentrated acetic acid in 6 mL of Quickszint 400 cocktail were measured (Schönhofer, 1992).

b. Standards of ^{14}C

For ^{14}C dating purpose, the Primary Modern Reference Standard for radiocarbon measurements is wood from the AD 1890 tree ring (and therefore uncontaminated by fossil fuel CO_2 − Suess Effect), whose activity was measured in the 1950s and corrected for ^{14}C decay to the year of growth to determine the absolute activity. Radiocarbon ages are expressed in years B.P. (before present − where present is the year 1950). In practice, all laboratories use a Secondary Modern Reference Standard against which sample activities are determined. The secondary standard most commonly in use is Oxalic Acid SRM 4990C, which is distributed by the National Institute of Standards and Technology (Gaithersburg, USA). This reference material consists of a 1000-lb lot of oxalic acid prepared by fermentation of French beet molasses using *Aspergillus niger*; 0.7459 times the specific activity of this material (normalized to a $\delta^{13}C$ value of −25‰) is equal to the activity of the AD 1890 wood, which in turn equates to 226 Bq/kg of carbon.

For the measurement of ^{14}C in environmental and nuclear samples, ^{14}C standard solution is often applied. In this case, ^{14}C labeled organic compounds are the most

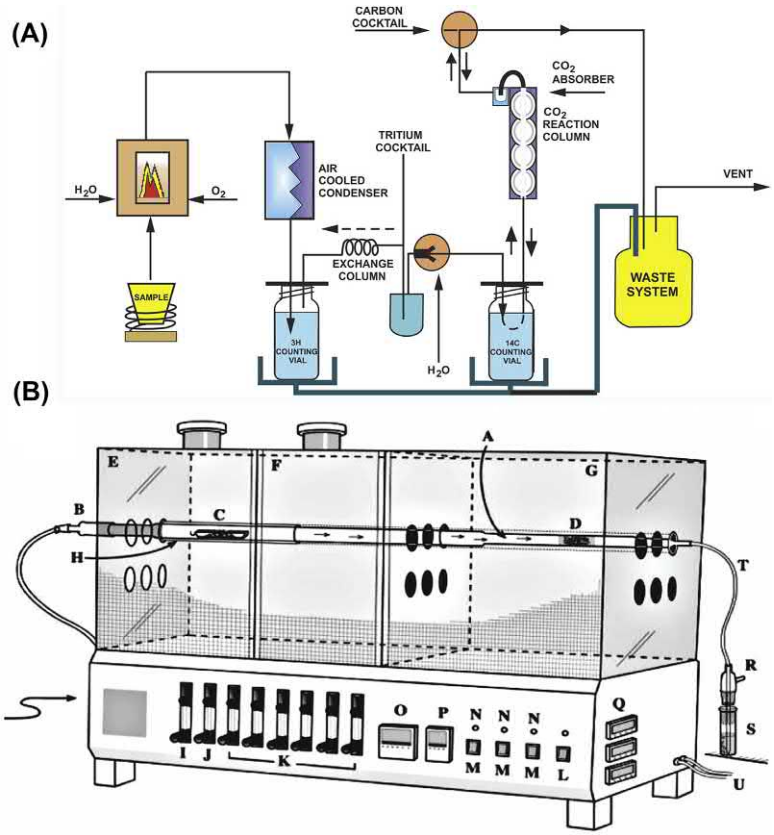


FIGURE 2.17 Diagram of two combustion systems for the separation of ^{14}C and tritium from solid samples.

commonly used form, such as NIST-4222d carbon-14-n-hexadecane standard solution provided by the National Institute of Standards and Technology. This standard solution can be directly mixed with scintillation cocktail for LSC measurement.

c. Quality assurance

There is an inevitable diversity of experimental approaches within radiocarbon dating facilities and in this situation, the issue of comparability of results among laboratories becomes paramount. Over the past 20 years, a number of international intercalibration programs have taken place (ISG, 1982; Scott et al., 1990, 2010; Rozanski et al., 1992; Gulliksen and Scott, 1995). These intercomparisons are of direct benefit to the participating laboratories as an independent check of laboratory performance and provide indirect benefit to the user communities. As a result of these studies, a range of natural samples (e.g., dendrochronologically dated wood, marine sediment, peat, barley, and so on) are available, albeit in limited quantities. These materials have known ages or consensus activities that cover the entire applied radiocarbon timescale. In addition, an annual intercomparison exercises have been organized by National Physical Laboratory, UK, for the determination of ^{14}C and other radionuclides in the spiked solutions and real samples from decommissioning of nuclear facilities.

d. Calculation of results and radiocarbon conventions

Most radiocarbon laboratories, in performing their calculations, use an activity value $A_{ON,}$ which is 74.59% of the measured net Oxalic Acid SRM 4990C activity (A_{OX}), normalized for ^{13}C fractionation according to:

$$A_{ON} = 0.7459A_{OX}\left[1 - \left\{2\left(25 + \delta^{13}C\right) / 1000\right\}\right]$$

(Measurements of $\delta^{13}C$ are made by stable isotope mass spectrometry and are relative to the VPDB (Vienna-Pee Dee Belemnite) standard. The PDB is a Cretaceous belemnite, *Belemnita americana*, from the PeeDee formation in South Carolina).

The term *percent modern* equates to the activity ratio $A_{SN}/A_{ON} \times 100\%$ where A_{SN} is the sample activity (A_S) normalized for sample fractionation to $-25‰$. However, the activity A_{ON} depends on the year of measurement (y) and has to be corrected for decay between 1950 and the year (y) of actual measurement. The *absolute international standard activity* is given by

$$A_{abs} = A_{ON}e^{\lambda(y-1950)}$$

where y is the year of oxalic acid measurement and $\lambda = 1/8267\ a^{-1}$ is based on the 5730 year half-life.

For geochemical and environmental ^{14}C studies, the term *absolute percent modern* (pM) is more commonly used. This is defined as:

$$pM = A_{SN}/A_{abs} \times 100\%$$

When one refers to 100% modern, this is effectively the specific activity that prevailed in 1890, prior to the onset of the Suess Effect; 100% modern is equivalent to 226 Bq/kg C.

For radiocarbon age calculations the equation is:

$$t = \frac{1}{\lambda} \ln \frac{A_{ON}}{A_{SN}}$$

where t = time (age), $\lambda = \ln 2/5568$ (where 5568 years is the Libby half-life of ^{14}C), A_{ON} is 74.59% of the measured net Oxalic Acid SRM 4990C activity (A_{OX}), normalized for ^{13}C fractionation, and A_{SN} is the sample activity (A_S) normalized for sample fractionation to $-25‰$.

A comprehensive discussion of the reporting of ^{14}C data is given in Stuiver and Polach (1977) and updated in Mook and van der Plicht (1999).

3. Analysis of ^{14}C in fuels containing biogenic materials

a. Carbon dioxide emissions and reduction measures

Carbon dioxide is the main greenhouse gas released to the atmosphere as a result of human activities. A 30% rise in CO_2 concentration has been observed since the start of the industrial revolution. Much of the increase came and will come from energy production, industrial emissions (Hämäläinen et al., 2007) and transportation using fossil-based fuels.

World-wide efforts are now pursued in order to slow down the predicted climate warming related to the rising carbon dioxide concentration in the atmosphere. Renewable energies are quickly developed and applied to reduce the utilization of fossil fuel. Among the renewable energies, biogenic energy is an important one. The raw biogenic materials can be converted to liquid fuel (biofuel), which can be added to the conventional fossil liquid fuel in some percentage. The European Parliament Directive, 2003/30/EC promotes the usage of biofuels or other renewable fuels for transport, and the Commission Green Paper 52000DC0769 sets the objective of a 20% substitution of conventional fuels by alternative fuels in the road transport sector by the year 2020. Pressures are mounting in US industry for increased utilization of biomass feedstocks and biotechnology in production (Currie et al., 2000). USDA Federal Biobased Products Preferred Procurement Program (FB4P) of 2002 encourages federal agencies to purchase products made of biobased materials instead of petroleum-based equivalents. The US Energy Policy Act of 2005 further refined the rules to identify and evaluate the bio-based products and issued tax credits for them. Its renewable fuels standard urges the doubling of the use of biorenewable ethanol and biodiesel (to annually $28 \times 10^6\ m^3$) by 2012. The Energy Independence and Security Act of 2007 raised the standard, to $140 \times 10^6\ m^3$ of annual renewable fuel use by 2022. Third party verification is required of a product's biobased content or mass of biobased carbon as a percent of the total organic carbon mass in the product in order to qualify for preferred procurement status and for tax credits.

b. Testing methods for product biocomponent verification

Bio-ethanol is the most common renewable component in gasoline, and it is chemically indistinguishable from synthetic ethanol. The only difference between the two is the isotopic composition of the carbon (Tamers, 2006). Synthetic ethanol comes from fossil raw materials with negligible amount of ^{14}C, and bio-ethanol is made of contemporary materials with environmental level of ^{14}C.

As discussed below, some methods have been reported for the evaluation of fossil CO_2 emission and the level of biogenic fuel applied for energy production:

1). ASTM D6866 Standard Method The ASTM International Radioisotope Standard Method D6866 contains three alternative radiocarbon dating methods to monitor the biobased carbon content in the sample, which may cover almost any type of solid, liquid, or gaseous products (ASTM D6866 - 11, 2011). The method applies to carbon dioxide emissions, waste fuels, biofuels, bioplastics, and other biopolymers.

Method A. The first ASTM Standard D6866 method is based on trapping CO_2 from a combusted sample into a Carbo-Sorb/methanol mixture. ULTIMA Gold is proposed as the scintillation cocktail to be used. The manufacturer of Carbo-Sorb E recommends trapping of up to 4.8 mmol CO_2 per mL, and Permafluor E+ as the cocktail, in a ratio of 1:1 or lower (Thomson and Burns, 1995).

Note that combustion of fuel cannot be done in an ordinary oxidizer due to the risk of explosion (Use a Parr oxygen combustion apparatus instead). The maximum total analytical uncertainty of 15% in the method is associated with sample preparation and actual counting.

Method B. The second method combines accelerator mass spectrometry (AMS) and isotope ratio mass spectrometry (IRMS) with an approach similar to the one used in routine radiocarbon dating. CO_2 is converted to graphite and the ratio of ^{14}C atoms relative to either the ^{12}C or ^{13}C atoms is measured (as opposed to measuring only decaying radiocarbon by radiometric counting). Uncertainties of

measurements in these two technologies are 1%−2% and 0.1%−0.5%, respectively.

Method C. Benzene synthesis is a conventional sample preparation method for ^{14}C dating by LSC, in which sample carbon is converted to benzene via CO_2, lithium carbide, and acetylene (Gupta and Polach, 1985). Primary (and secondary) fluors in solid form can be added directly to the benzene for sample counting in an LS spectrometer. Low background glass (low potassium glass) or Teflon vials are needed to minimize loss of benzene and reduce the background. As no liquid scintillation cocktail is added, the vial can contain the maximum amount of carbonaceous sample. Maximum total analytical uncertainty of 3% is associated with this method in ASTM D6866.

2). Tests according to the ASTM D6866 Standard Method Numerous radiocarbon laboratories have well established dating procedures suitable also for bio-materials testing. Some of them can already provide services related to this new application (Tamers, 2006).

Noakes et al. (2006) compared analytical methods for the certification of biobased products and found an inverse relationship between the analytical precision and the overall cost of the equipment and analysis. Methods A, B, and C allowed 0.2−1 g, 1 mg, and 2−10 g of carbon sample and yielded precisions of 8.80%, 0.88%, and 1.86%, respectively. Culp and Noakes (2009) pointed out that the inorganic carbon compounds, such as calcium carbonate, must be removed prior to the analysis of bio-based materials, and they discuss the removal methods. Norton and Devlin (2006) published results of a comparison study, where AMS and LSC laboratories using benzene synthesis had ± 3% (absolute) variation in results. Norton et al. (2007) reported that benzene synthesis and AMS yielded mean biobased content values that were within 1% content from one another. They interpreted the small difference as strong evidence that all of the carbon was converted to CO_2. Various sample matrices were successfully analyzed within ±3% of the real carbon content. Culp et al. (2011) used benzene synthesis in the analysis of biobased materials.

Oinonen et al. (2010) shortened the liquid sample combustion times to 10 minutes for AMS and analyzed gasoline and diesel fuel samples with better than ± 0.5% accuracy. Reddy et al. (2008) investigated diesel fuels and found that inaccurate blending may occur. Only one out of 10 retail samples met the specification in 2006, when analyzed by AMS with ±1% accuracy.

3). Other standard methods The ASTM D7026-04 provides a framework for collecting and handling samples for the determination of biobased content of materials by means of the carbon isotope method described in Test Methods D6866. ASTM D7459-08 describes sample collection for the speciation of biogenic and fossil-derived carbon dioxide emitted from stationary sources (ASTM D7459 - 08, 2008).

CEN 15747:2008, Solid recovered fuels-^{14}C-based methods for the determination of the biomass content, is only applicable to solid recovered fuels and is developed for the European Union Emission Trading Scheme. The analysis of the ^{14}C content can be applied both on the input (waste) and on the output (exhaust gases) from waste installation. Three methods are included in the technical standard, viz. CO_2 adsorption of up to 1 g carbon and subsequent LSC, gas proportional counting of CO_2 up to 1.4 g C in a 10 L counter at NTP, and AMS of 1 mg C. Special attention is given on the measurement of peat, which has a ^{14}C content well below that of other biobased material.

There is also a measurement standard for stationary combustion emission sources published in March 2011, ISO 13833, Stationary source emissions − determination of the ratio of biomass (biogenic) and fossil-derived carbon dioxide − radiocarbon sampling and determination. This standard combines the concepts of ASTM D6866 and D7459.

4). Direct analysis method, "Method D" Sample preparations in Methods A, B, and C do not pose limitations to sample matrices. However, Method A could not be directly used for oil samples, and Methods B and C are time consuming and more expensive. A more simple and direct method has also been applied in many labs for measuring the component of biogenic fractions in liquid fuel (Dijs et al., 2006; Idoeta et al., 2014; Kristof and Logar, 2013; Bronic et al., 2017; Stojkovic et al., 2017; Muir et al., 2015).

Method D: A wide range of liquid chemicals can be mixed directly with modern scintillation cocktails to make homogeneous and stable samples. Ethanol is a typical example, which has been measured in wines and liquors to detect falsifications by monitoring the ^{14}C content (Schönhofer, 1989a, 1992). This method can be also used to measure ^{14}C in fuel by extraction of ethanol in fuel or directly mixing fuel with scintillation cocktail.

Organic cocktails are also compatible with a wide range of gasoline/ethanol mixtures and diesel oil. The most often used commercial organic scintillation cocktails are Optifluor O, Ultima Gold F and OptiScint HiSafe, whereby ethanol, gasoline, and diesel fuels can be mixed with these cocktails in a suitable volume ratio. The best ratios of volume have been reported to be 14:6 diesel fuel mixing ratios and at 12.5:7.5 in pure ethanol samples. In addition, quench correction, range of channels in the LSC spectrum, and background (varies with vial type, sample type, ratio of sample to cocktail and measurement instrument) have to be considered for the ^{14}C measurement due to the low count

rates of ^{14}C in these types of samples. The spectrum was cut below Ch 150 with high bias setting, which totally eliminates all random noise and chemiluminescence. A stable sample count rate could therefore be achieved (Stojkovic et al., 2017).

Current-day bio-ethanol served as a reference sample and eliminated the need to correct for "bomb carbon." The method has good potential for determining the bio-ethanol content in commercial ethanol/gasoline blends. However, as the levels of pMC (percent modern carbon) of bio-ethanol from various locations are not the same, verification is needed for this variation. Fractionation corrections did not affect the final results, when reported to the nearest 1% of ethanol concentration. The LSC results can be accurate to within about 2% (absolute). It is likely that the accuracy can be improved by selecting a pipette designed for highly volatile, low viscosity liquids. The dependence of sample background on matrix effects should also be examined.

Norton (2009) tested fuel samples for ethanol from gas stations by mixing them with Permafluor E+ in a 1:1 volume ratio and counted them with quench correction. Norton and Woodruff (2011) mixed diesel fuels directly with a fluor and then analyzed samples in an LSC without further processing. Mean results from triplicate analyses were accurate within 0.4% in a 180 minutes counting time. Yunoki and Saito (2009) reported a two-step extraction of ethanol by water from the fuel mix for avoiding sample color. Water and ethanol was mixed with cocktail for LSC. In this method, fuel samples (100 g) containing 3% and 10% wt of bio-ethanol were mixed in glass vessels with 3 and 10 mL water and shaken. The water-ethanol phase was separated by centrifugation and then transferred to a scintillation vial, cocktail was added and ^{14}C was measured using LSC. An additional extraction was applied to the residual fuel and the process repeated to ensure all ethanol is extracted. A direct mix of 3 g fuel (gasoline or diesel) with cocktail for LSC counting of ^{14}C was also reported (Idoeta et al., 2014; Kristof and Logar, 2013; Bronic et al., 2017; Stojkovic et al., 2017; Muir et al., 2015). For the measurement of extracted ethanol, a standard/quench curve can be prepared using difference amounts (e.g., 0.5, 1, 2, 3, 4, 5, 7, and 10 g) of bio-ethanol spiked with a small volume of ($<$0.20 mL) unquenched ^{14}C standard and a certain volume of scintillation cocktail. A quench curve can be prepared using a similar method. Due to the strong color quench of diesel, special attention should be given and a small sample volume ($<$3 mL) is often applied for diesel samples. Background samples must be prepared with the same type and level of quench as the samples to be analyzed, as background count rate depends on sample quench. Much lower background of ^{14}C has been observed for oil compared to water, gasoline, and other samples (Stojkovic et al., 2017). A good fit between theoretical and experimental data was obtained for the two-step method, whereas a large discrepancy was found in the direct method applied for color quenched samples in the low concentration range.

5). Merits of the analysis methods Although Methods A, C, and "D" are less sensitive than AMS/IRMS in Method B, they have two distinct advantages:

1) Lower costs per evaluation and **2)** higher instrument availability worldwide. Sophisticated sample preparation methods are contained in Methods B and C.

The high cost of AMS instruments and sample backlogs at AMS facilities may not make Method B very attractive except for small sample sizes and when a high degree of precision is required (Noakes et al., 2006). LSC methods involve longer analysis time and lower precision, leading to a poorer detection limit compared to the AMS method, but make use of lower-priced equipment and offer a lower cost per analysis (Culp and Noakes 2009; Norton, 2009). The method of benzene preparation followed by LSC measurement also involves a more labor-intensive process, although the detection limit is much better than the Methods D and A.

Direct Method "D", which is not included in ASTM 6866, is clearly less time consuming, less expensive, adequate for practical biocomponent concentrations and a proven, conventional method. No chemical modification of the sample is required (Yunoki and Saito, 2009). No bomb effect correction is needed, when the reference sample is made of modern and known activity material (Norton, 2009; Norton and Woodruff, 2011). The direct method is also applicable for solid samples, if they can be dissolved in a suitable solvent or solubilized and further mixed with cocktail. The solvent should not be a strong quencher, and aromatic solvents are often compatible with scintillation cocktails.

c. Carbon dioxide and particulate analyses

CO_2 emission trading in Europe has been established and it is therefore important to distinguish between biogenic and fossil emissions. The standard methods ISO 13833, ASTM D6866 and D7459 apply in this work. Waste incineration has been widely applied to produce heat and energy, ^{14}C in the released CO_2 and source materials is applied to monitor the fossil CO_2 emission. AMS (Hämäläinen et al., 2007; Oinonen et al., 2010) and CO_2 absorption followed by LSC have been applied for this work (Staber et al., 2008; Silva et al., 2010). A comparison using ^{14}C monitor and the industry material classification methods for this purpose was conducted, and found to be comparable (Muir et al., 2015).

Air particulate analyses to identify their origin via the ^{14}C content has been conducted over a long time (Clayton et al., 1955; Lodge et al., 1960; Currie, 1978; Court et al., 1981, and reviewed by Currie et al. (2000). Recently, apportionment of biogenic and fossil particulates using the

AMS method has been intensively carried out (Gustafsson et al., 2009; Gilardoni et al., 2011; Heal et al., 2011; Szidat et al., 2009; Mouteva et al., 2017).

C. Iron-55 (^{55}Fe)

1. Environmental occurrence

^{55}Fe is produced by neutron activation reactions of two major stable iron isotopes: ^{54}Fe(n,γ)^{55}Fe and ^{56}Fe(n,2n)^{55}Fe. Since iron is the main component of construction materials in nuclear reactors, huge amounts of ^{55}Fe are produced in nuclear reactors and other nuclear facilities/devices with neutron production. ^{55}Fe enters into the environment mainly through the release of radioactive effluents of nuclear reactors, as well as atmospheric nuclear weapons tests in 1945−80. Nuclear accidents, nuclear reprocessing plants, and radiochemical and radiolabeling labs might also release some amount of ^{55}Fe to the environment.

^{59}Fe ($t_{½} = 44.5$ days) is produced through similar process by neutron activation of stable ^{58}Fe (0.28%). However, because of its relative short half-life and delayed discharges from the nuclear facilities, it is often not present in the environment. ^{59}Fe decays by emission of beta particles with high-energy gamma rays (1099.3 keV, 56.5% and 1292.6 keV, 43.2%). Thus, it can be easily measured by gamma spectrometry.

Determination of ^{55}Fe is often required for monitoring the radioactivity in the nuclear facilities and their discharges, as well as characterization and depository of nuclear wastes.

2. Sample preparation and analysis

^{55}Fe ($t_{1/2} = 2.7$ years) decays via electron capture to stable ^{55}Mn with the emission of Auger electrons and low-energy X-rays (5.89 keV, 16.9%). Measurement of ^{55}Fe can be carried out with an X-ray detector or gas flow proportional counter, but their counting efficiencies are very low (<1%). The most common and more sensitive technique is LSC. Due to the very low energy of the Auger electrons, ^{55}Fe has to be first separated from the sample matrix and then completely purified from other radionuclides prior to counting.

The separation of iron from the sample matrix (solution) is often carried out by hydroxide precipitation based on the formation of $Fe(OH)_3$ and $Fe(OH)_2$. However, for some special samples, the matrix component needs to be first removed. For instance, in an acid-dissolved lead sample, lead has to be removed by $PbSO_4$ precipitation to avoid the formation of a large amount of $Pb(OH)_2$ during the $Fe(OH)_3$ precipitation step. For aluminum samples, the bulk $Al(OH)_3$ in the $Fe(OH)_3$ precipitation step can be removed by adding more NaOH to > 0.2 M to convert $Al(OH)_3$ precipitate to soluble $NaAlO_2$ (Hou et al., 2005).

All transition metals can be coprecipitated with $Fe(OH)_3$ in alkali solution, among them the most important radionuclides are ^{60}Co, ^{63}Ni, ^{54}Mn, ^{152}Eu, and ^{154}Eu, and further chemical separation is needed to isolate iron from these interfering elements.

Chelating and anion exchange chromatography combined with solvent extraction have been used to separate iron from other nuclides (Konig et al., 1995; Warwick et al., 2001). The commonly used extraction reagents include ethyl acetate, isobutyl ketone, and isopropyl ether; particularly iron has a high partition coefficient in ethyl acetate (Warwick and Croudace, 2002). However, as solvent extraction is not very specific for iron, the decontamination of Fe from other metals is not satisfactory. To improve the separation efficiency of iron from other radionuclides, an extraction chromatography based on diisobutyl-ketone has been developed (Warwick and Croudace, 2002). A commercial solid phase extraction resin, the TRU resin, has also been applied to separate iron for the determination of ^{55}Fe (Dai and Kramer-Tremblay, 2014; Hou et al., 2015). One of the limitations of this resin is the low capacity of the small extraction chromatographic column (2 mL), which can only allow for the uploading of sample solutions with less than 2 mg iron. For sample with high iron content, such as soil, sediment and steel, anion exchange chromatography using strong basic anion resin (e.g., AG1x-4) has been confirmed to be a reliable method for the separation of iron from other interfering radionuclides with a high recovery (>95%) and a high decontamination factor ($>10^4$). This is mainly due to the high distribution coefficient of $FeCl_4^-$ on the anion resin in high concentration of HCl solution. Fig. 2.18 illustrates a separation procedure of iron from the most important interfering radionuclides using a strong anion exchange chromatography. In this way, ^{55}Fe can be completely separated from

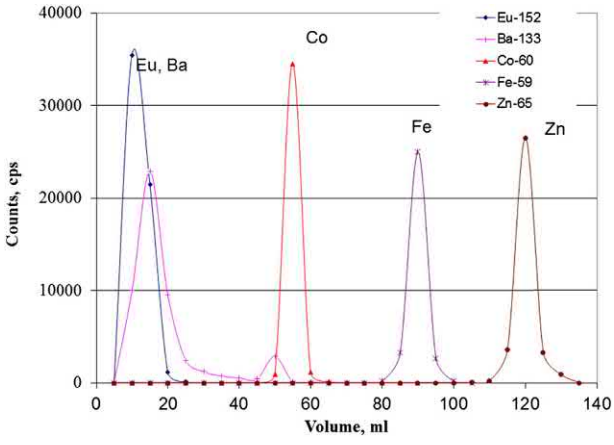


FIGURE 2.18 Separation of Eu, Ba, Co, Cu, Fe, and Zn by anion exchange chromatography (Bio-Rad AG1x-4, ϕ1 × 20 cm), 0−40mL: 9 mol/L HCl, 40−70mL:5 mol/L HCl, 70−105 mL: 0.5 mol/l HCl and 105−135: 0.05 mol/L HCl.

^{60}Co, ^{63}Ni, $^{152/154}$Eu, and ^{65}Zn. Other radionuclides, including all alkali and alkaline earth metals, could not form an anion complex with chloride and would also be removed. In combination with hydroxide precipitation, a chemical separation procedure has been applied for the separation of iron from different environmental and waste samples for ^{55}Fe determination. This method has also been used to investigate the distribution of ^{55}Fe in the environment surrounding a nuclear power plant (Gudelis et al., 2010). For samples with high iron content (>50 mg) and high ^{60}Co radioactivity, a repeated anion exchange chromatographic separation can effectively remove ^{60}Co with a high recovery of iron (Fig. 2.19).

A modified procedure using hydroxide precipitation followed by anion exchange chromatographic separation and LSC measurement has also been applied to the determination of ^{55}Fe in urine samples (Guerin and Dai, 2015). Due to a complicated matrix component in urine, the hydroxide precipitation step needs an adjustment of the concentration of NaOH to 2 M.

Ion chromatography using an HPLC system and a mixed cation/anion exchange column (CS-5, i.d. 9 mm, 25 cm length, Dionex, Idstein, Germany) has also been applied for the separation of ^{55}Fe for LSC measurement (Geckeis et al., 1997). This method is simple and fast, but the decontamination factor is not sufficient for the complete removal of ^{60}Co and other radioisotopes of transition metals; thus, it is not feasible for measuring ^{55}Fe in samples containing a high activity of ^{60}Co.

The distinct yellow color of Fe^{3+} can cause a very strong color quench and significantly reduce the counting efficiency of ^{55}Fe by LSC. Due to the very low energy (5–6 keV) of Auger electrons emitted by ^{55}Fe measured by LSC, the high color quench of iron solutions could reduce the counting efficiency to <10%, causing a high detection limit. A number of approaches have been adopted to reduce the color quenching of Fe, such as solvent extraction to transfer iron to an organic phase and reduction of Fe^{3+} to Fe^{2+} by ascorbic acid. It has not been possible to overcome the color quench of Fe completely. In addition, the Fe^{2+} is not very stable and can be oxidized to Fe^{3+} slowly in air, causing a gradually decreased counting efficiency. An effective method for removing the yellow color of Fe^{3+} using H_3PO_4 has been proposed (Warwick and Croudace, 2002; Hou et al., 2005). By this method, a colorless Fe^{3+} solution is obtained, and the counting efficiency is significantly improved to more than 40%. Since H_3PO_4 has a reduced quench effect and high compatibility with scintillation cocktail compared to other acids, the amount of Fe mixed with cocktail can thus be significantly increased. It

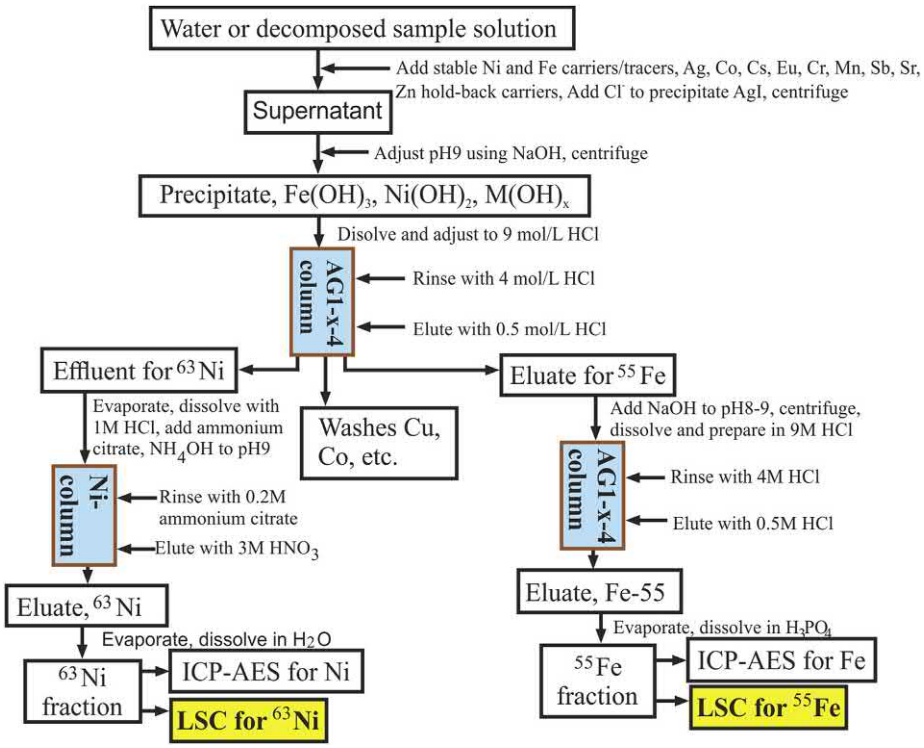


FIGURE 2.19 Analytical procedure for ^{55}Fe and ^{63}Ni in environmental and waste samples.

has been confirmed that for less than 10 mg Fe carrier, 40% counting efficiency is obtained, and for 200 mg Fe, the counting efficiency is 15% (Hou et al., 2005).

The counting efficiency of ^{55}Fe could also be affected by the addition of hydrochloric acid and phosphoric acid to the counting sample (Guerin and Dai, 2015). The counting efficiency as a function of the LSC cocktail/water ratio has been studied, and the results showed an obvious drop in counting efficiency from 62% for pure LS cocktail down to 30% for a 1:1 water/cocktail volume ratio using a Hidex 300 SL counter. An empirical formula of power function between the measured TDCR value and counting efficiency of ^{55}Fe was obtained, which can be used to correct the quench effect without a need to produce an external calibration curve.

D. Nickel-63 (^{63}Ni)

1. Environmental occurrence

^{63}Ni ($E_{max} = 67$ keV, $t_{1/2} = 101.2$ y) is a neutron activation product formed by neutron capture of stable nickel (^{62}Ni), released through corrosion of steel components, associated with the primary coolant system of nuclear power reactors. Another nickel isotope, ^{59}Ni ($t_{1/2} = 7.5 \times 10^4$ y) is similarly formed from stable ^{58}Ni. The initial activity ratio of ^{63}Ni/^{59}Ni is around 100 or more, and ^{59}Ni decays by electron capture with emission of X-rays. Given the low sensitivity of LSC to X-rays, ^{59}Ni has a very minor effect on the low-energy part of the beta spectrum of ^{63}Ni (Hou and Roos, 2008). Consequently, only ^{63}Ni is detected by LSC. ^{63}Ni in the environment originates from radioactive effluents from nuclear facilities and from nuclear weapons tests and accidents.

The principal requirement for the determination of ^{63}Ni is to characterize nuclear waste for decommissioning and radioactive waste disposal.

2. Sample preparation and analysis

Due to its low beta energy, the determination of ^{63}Ni requires chemical separation and purification of nickel from coexisting elements and radionuclides. Methods for determining ^{63}Ni have been reported for many sample matrices including liquid effluent, sludge, ion exchange resin, graphite, heavy concrete, steel, copper, lead, and aluminum from nuclear power plants and environmental samples like soil, sediment, sea water, fish, vegetation, and urine (Harvey and Sutton, 1970; Kojima and Furukawa, 1985; Holm et al., 1990; Lo et al., 1993; Kaye et al., 1994; Numajiri et al., 1994; Kramer, 1981; Russow and Dermietzel, 1990; Radwan et al., 1981; Skwarzec et al., 1994; Lee et al., 1997; Hou et al., 2005, 2015; Warwick and Croudace; 2006; Jordan et al., 2008; and Gudelis et al., 2010; Huang et al., 2017; Gautier et al., 2016). The most common sample matrices to be assayed are liquid effluents, waste from nuclear facilities, the coolant water from nuclear power plants, and environmental soil and sediment.

The sample matrix dictates whether any specific sample collection, preservation, pre-treatment, and pre-concentration processes are required. The pre-treatment of samples containing organic matter is started by wet or dry ashing after adding the carriers, and then continued by leaching the residue with concentrated HCl or HNO_3 to dissolve nickel and other elements. Stable nickel is added as carrier, and other elements as hold-back carriers, to determine chemical yield and to effectively separate nickel from other elements. Yield corrections have also been performed using ^{65}Ni as a tracer (Lee et al., 1997). Sample pre-concentration may be necessary to enable the analysis of low-activity environmental samples like seawater (Lo et al., 1993).

Many chemical separation methods for the ^{63}Ni assays take advantage of following processes:

1. Precipitation of $Fe(OH)_3$ with ammonia, coprecipitates many metals, while nickel remains in the supernatant.
2. Precipitation of nickel using an alcoholic solution of dimethylglyoxime (DMG) is highly selective for nickel in an alkaline medium and produces an insoluble Ni-DMG complex.
3. Anion exchange from HCl solution removes most of the activation products by adsorbing those as chloride complexes onto the column, while nickel passes through and is fully collected in the effluent and washing solutions.

Most of the separation methods for ^{63}Ni are performed using complicated, multistep procedures based on a combination of these processes and possibly completed with additional purification steps like solvent extraction, ion exchange and/or extraction chromatography (Kirby, 1961; Holm et al., 1990; Lo et al., 1993; Kaye et al., 1994; Skwarzec et al., 1994; Numajiri et al., 1994; Scheuerer et al., 1995; Lee et al., 1997; Dewberry et al., 1999; Hou et al., 2005; Warwick and Croudace; 2006; Jordan et al., 2008). Each separation step requires optimization and careful control of the conditions during processing to achieve consistent yields and desired purity of ^{63}Ni. Multistep separations are necessary for sample matrices like nuclear wastes, which include a great number of radionuclides with different chemical properties and with much higher concentrations than that of ^{63}Ni. Many methods referred here have been developed to be applicable to different types of sample matrices such as low- and high-active wastes from nuclear power plants and environmental samples (Kaye et al., 1994; Scheuerer et al., 1995; Lee et al., 1997; Hou et al., 2005; Warwick and Croudace, 2006; Jordan et al., 2008).

Williams et al. (1994) developed a method based on a series of separations using anion, cation exchange, and liquid extraction with tri-n-octylphosphine (TOPO) for the separation of ^{63}Ni from targets irradiated at the high flux

isotope reactor. This method was accomplished using simple fluid operations which are easily adapted for execution in hot cells. Based on the formation of specific complex/precipitation of Ni with DMG, three methods, i.e., Ni-DGA precipitation, Ni-DGA-solvent extraction, and DMG resin (Ni resin), have been applied in the separation of nickel from other radionuclides (Huang et al., 2017). Among other separation methods, extraction chromatography has become the most popular method applied in the ^{63}Ni separation. The extractive resins are based on dimethylglyoxime (DMG) which is coated onto a solid support such as Microethene (Testa et al., 1991) or coated onto an acrylic ester-based resin. This is known as Ni Resin, which is commercially available from Eichrom Industries and applicable with other separation techniques commonly used in assaying ^{63}Ni. Dewberry et al. (1999) used Ni Resin to determine ^{63}Ni in the presence of fission products and α- and β-emitting plutonium isotopes with activities up to 10^3 times the observed ^{63}Ni activity. Hou et al. (2005) developed a chemical separation procedure, which was started by hydroxide precipitation, continued with anion exchange and thereafter with the Ni Resin extraction chromatography. They used the method for determining ^{63}Ni and ^{55}Fe in nuclear waste samples including heavy concrete, aluminum, lead and graphite, and achieved high decontamination factors ($>10^5$) for all interfering radionuclides. Chemical yields were over 90% and the detection limit of 0.014 Bq for ^{63}Ni using a low-background LS spectrometer. This method has also been applied to environmental samples (Gudelis et al., 2010). Warwick and Croudace (2006) developed a method that was based on the same separation steps as those of Hou et al. (2005), but with the difference that the extraction chromatography separation using Ni resin was performed prior to the anion exchange. The residual ^{60}Co was removed during the anion exchange by adding Co-carrier prior to passing the ^{63}Ni solution through the anion exchange column. The same method was validated for separating ^{63}Ni and ^{55}Fe from reactor effluents, and the effect of ^{59}Ni on the ^{63}Ni beta spectrum was studied. It was reported that the separation characteristics and the detection limits for ^{63}Ni and ^{55}Fe were improved by applying extraction chromatography and that the chemical yields were over 90% in all cases, with no evidence of interference from activation products expected in reactor effluents. Also, it has been observed that ^{60}Co and ^{58}Co could not be sufficiently removed by using only Ni resin extraction chromatography, making the method unreliable and a correction has to be implemented to subtract the inference from ^{58}Co and ^{60}Co. Two sequential Ni resin chromatography separation steps can reduce the contribution of radioactive cobalt. Therefore, a separation step using anion exchange chromatography is necessary for samples with high radioactive cobalt isotopes (^{58}Co, ^{60}Co) (Hou et al., 2015). Fig. 2.19 illustrates a combined procedure for the separation of nickel and iron for the determination of ^{63}Ni and ^{55}Fe.

The sample preparation for measuring the ^{63}Ni activity by the LSC counter is quite simple. The eluate containing the sample fraction is collected from the chromatographic column at the end of separation procedure. The eluate is evaporated to near dryness and the residue is dissolved in a few milliliters of dilute HCl or HNO_3 which is placed in a LSC vial for counting. Attention has to be given when evaporating the Ni eluate to dryness, because nickel in the HNO_3 (3−12 M) eluate is present as $Ni(NO_3)_2$, which has a low boiling point (136.7°C) and can be easily lost during evaporation at high temperature (>137°C). Therefore, the eluate of Ni is often evaporated to near dryness (<0.5 mL) on a hotplate with low temperature (<120°C) in the end of the evaporation (<3 mL).

The counting efficiencies of the prepared sample of ^{63}Ni may vary from ~50% to ~80% depending on the sample composition. Quench corrections are applied in most cases. Many authors (Kramer, 1981; Russow and Dermietzel, 1990; Harvey and Sutton, 1970) have reported detection limits, which vary between 0.055 and 0.099 Bq/sample while others (Scheuerer et al., 1995; Hou et al., 2005; Warwick and Croudace, 2006; Jordan et al., 2008) have obtained significantly lower detection limits of 0.005−0.014 Bq/sample. The main reason for this difference is the higher background (20−25 cpm) of the older generation LSC counters compared to the low backgrounds (0.5−1.0 cpm) of modern instruments equipped with low-level count options. Modern instrumentation is equipped with background reduction features, as discussed in Section II.

Mellado et al. (2005) have evaluated the ability to rapidly determine individual radionuclide activities from the mixture of beta-emitters (^{55}Fe, ^{63}Ni, ^{99}Tc, ^{137}Cs, and ^{90}Sr/^{90}Y) present in radioactive wastes using multivariate calibration combined with limited chemical separations. The authors conclude that the combined data treatment procedure they applied was able to quantify all of the five tested radionuclides, in a single measurement. However, special care has to be taken with extremely quenched samples due to the increased uncertainty of the model with such samples. This technique could reduce the chemical separation steps required, which may simplify and reduce analysis costs, which is important in routine operations of nuclear reactors and in decommissioning.

Besides the radiometric techniques, ^{63}Ni can be also determined using accelerator mass spectrometry (AMS) (Wang et al., 2015). The comparison by Hou and Roos (2008) demonstrated that the detection limits (0.12−45 mBq) achieved by the AMS methods can be significantly lower than detection limits obtained by LSC. For both methods chemical separation is necessary. Nevertheless, the ^{63}Ni assays are mostly performed using

LSC, because of the accessibility of the LSC counters in radiochemical laboratories.

In summary, the current separation methods are suitable for assaying ^{63}Ni in nuclear waste and environmental samples. Very low ^{63}Ni activities in environmental samples can be analyzed using modern LSC spectrometers. The chemical yields have been over 90% for most sample matrices and the decontamination factors have been between 10^3 and 10^{11} for most of interfering radionuclides presenting in nuclear waste samples (Scheuerer et al., 1995; Hou et al., 2005; Warwick and Croudace; 2006).

E. Strontium-89 and strontium-90/yttrium-90 (^{89}Sr and ^{90}Sr/^{90}Y)

1. Environmental occurrence

^{90}Sr ($E_{max} = 546$ keV, $t_{1/2} = 28.8$ y) is a fission product and ^{89}Sr ($E_{max} = 1495$ keV, $t_{1/2} = 50.57$ d) is part of the mass 89 fission chain, so their main sources in the environment are atmospheric nuclear weapons testing, nuclear accidents, and discharges from nuclear facilities. Fallout from nuclear weapons testing is primarily responsible for the ^{90}Sr/^{90}Y concentrations found globally in the environment. ^{90}Sr is normally in equilibrium with its ^{90}Y daughter ($E_{max} = 2280$ keV and $t_{1/2} = 64.05$ hours) in the environment (Kossert and Schrader, 2004). ^{90}Sr is important for environmental monitoring because of its relatively high fission yield (5.7% for ^{235}U), its long physical and biological half-lives, and its transfer to food chains. It is highly toxic, because it accumulates in bone tissues which are exposed by high-energy betas of ^{90}Sr/^{90}Y. ^{89}Sr shares the same biological significance but is less hazardous. It has a much shorter physical half-life and thus will not have a long-term environmental impact. The term "radiostrontium" is used for two strontium isotopes of ^{90}Sr and ^{89}Sr. In nuclear explosions or reactor accidents, other short-lived strontium radioisotopes, e.g., ^{91}Sr ($t_{1/2} = 10$ hours), ^{92}Sr ($t_{1/2} = 3$ hours), and ^{91}Y ($t_{1/2} = 59$ d), are also released (Vajda and Kim, 2010c). Milk, meat, vegetation, water, soil, urine, and bone are the typical sample matrices that have been analyzed in environmental monitoring.

2. Sample preparation

The quantitative analysis of radiostrontium is based on four major considerations: sample pre-treatment, preconcentration, chemical separation, and beta counting (Vajda and Kim, 2010c). As strontium belongs to the alkaline earth elements, it mimics calcium in its behavior, but its amount is less abundant in most environmental samples. The assay of radiostrontium is difficult because three beta-emitting nuclides with overlapping beta spectra must be distinguished from each other and strontium must be separated from large amounts of calcium and from inactive and radioactive elements without significant losses. The pretreatments like drying, pre-concentration, ashing, digestion, and dissolution are tedious for many environmental samples, and furthermore, samples like soil, milk, and bone contain relatively large amounts of stable strontium, which is the most commonly used yield tracer for radiostrontium and requires additional Sr analysis for the yield corrections. Much of the emphasis on the assay of radiostrontium has been focused on the separation chemistry and the methods have developed over decades (Sunderman and Townley, 1960; L'Annunziata, 1967, 1971; Wilken and Joshi, 1991; Chen et al., 2002b; Vajda and Kim, 2010c). They are based on several principles: precipitation/coprecipitation, solvent extraction, ion chromatography or ion exchange, extraction chromatography, or combination of these techniques. In extraction chromatography, extractant is sorbed on an inert solid support material.

The oldest method for radiostrontium determination is based on precipitations and on using fumic nitric acid, it is hence referred to as classical or nitric acid method (Sunderman and Townley, 1960). In this method, strontium is separated from calcium and alkali metals by two successive nitric acid precipitations, from yttrium and fission products by the hydroxide precipitation and from barium, radium and lead by chromate precipitation. The strontium fraction is further purified by carbonate and nitrate precipitations. The strontium is finally precipitated as carbonate and measured with a low-background gas flow counter. The first counting result consists of the total strontium (^{89}Sr, ^{90}Sr) activity and of a small amount of ^{90}Y grown in the separated strontium sample. ^{90}Y is permitted to reach near secular equilibrium with ^{90}Sr. Thereafter, the strontium sample is dissolved and ^{90}Y is separated by precipitation as the hydroxide that is converted to the oxalate for the measurement of the ^{90}Y activity. The ^{90}Sr content is recalculated from the ^{90}Y activity and thereafter the ^{89}Sr content is calculated from the first counting of the sum activity of ^{89}Sr, ^{90}Sr, and ^{90}Y. This method is still used and some standard procedures are based on it (Wilken and Diehl, 1987; Bojanowski et al., 1990; IAEA, 1989; EPA, 1991; HASL and Chieco, 1997; ISO, 2010). The method is efficient but not selective for strontium. It nevertheless ensures the purification of the strontium and yttrium samples from the major interfering elements and radionuclides like alkali and alkaline earth metals, ^{91}Y, ^{140}Ba, ^{140}La, ^{226,228}Ra, ^{210}Pb, and fission products, because each precipitation can be repeated once or more if necessary. Consequently, the analysis of large samples and sample matrices with high mineral salt contents are also possible. Similar precipitations are often used for pre-concentration or they are combined with ion exchange or extraction chromatographic methods for removing or reducing other

element contents to lower level. Hence, the total column capacity will not be exceeded.

Currently, the most popular methods for radiostrontium analysis are based on the extraction chromatography using the Sr•Spec resin that was developed by Horwitz et al. (1991). In this resin, a crown ether [bis-4,4′(5′)-*tert*-butylcyclohexano-18-crown-6] in 1-octanol is grafted on an inert polymeric resin (Amberlite XAD-7 or Amberchrom CG-71 ms) and packed into a chromatographic column. Strontium is efficiently retained by the Sr•Spec resin from nitric acid solutions and that the resin is selective for strontium ions over calcium, magnesium, most other metals and fission products present in the synthetic nuclear waste solution. A procedure based on Sr resin was reported for the determination of ^{89}Sr and ^{90}Sr in urine (Dietz et al.,1991). It involved wet ashing, pre-concentration using calcium phosphate precipitation, dissolving the precipitate using HNO_3 and prepared in a 2M HNO_3−0.5M $Al(NO_3)_3$ solution and loading it onto the Sr Spec column. After rinsing the column with 8M HNO_3, strontium was eluted with 0.05M HNO_3 solution. Strontium was strongly adsorbed on the column, whereas most interfering elements, including yttrium, were removed with the feed and rinse solutions. Yields from the pre-concentration step and from column separation were reported to be around 95% ± 5% overall. Barium, lead, and tetravalent neptunium and plutonium are also retained by the column, and attention should be given to avoid these elements entering into the eluate of Sr. The Sr•Spec resin is commercially available, as well as pre-packed columns, from Eichrom Industries and TRISKEM. It is often referred as a Sr resin.

A very rapid bioassay method for emergency preparedness, based on direct separation of ^{90}Sr in acidified urine samples (to 8M HNO_3) using stacked TRU and Sr resin, was also developed with good decontamination factors of Ba, Pb, Pu, Th, and U (Dai et al., 2013). Today, there is a number of appropriate modifications from the Sr resin method for various matrices including a lot of experience and results on comparison and validation tests (Vajda et al., 1992; Altzitzoglou et al., 1998; Tait et al., 1997, 1998; Chu et al., 1998; Fliss et al., 1998; Scarpitta et al., 1999; Brun et al., 2002; Saxen, 2002; Günther et al., 2003; Grahek and Măcefat, 2005; Landstetter and Wallner, 2006; Eikenberg et al., 2006; Heckel and Vogl, 2009; Kim et al., 2009; Maxwell III and Culligan, 2009a; Maxwell et al., 2013, 2016; Surman et al., 2014; Olfert et al., 2014; Tayeb et al., 2016; Miura and Minai, 2017; Guerin et al., 2017a; Hou, 2017; Grahek et al., 2018). Some standard procedures are also based on using the Sr resin (ASTM D5811 - 08, 2008; ISO, 2009). In general, the separations using Sr resin are considered simple, rapid, economic, and safe. Moreover, the yields are mostly good (over 80%), the separation times are only some hours and the resin can be regenerated and reused. All these aspects are important in selecting a routine method for laboratories. The Sr resin can be combined with other extractive resins, such as TRU, TEVA, U/TEVA from Eichrom Industries or with ion exchangers to perform sequential separation of radiostrontium, actinides, thorium, ^{99}Tc or ^{55}Fe from a single sample aliquot (Alvarez and Navarro, 1996; Moreno et al., 1998; Altzitzoglou et al., 1998; Pilviö et al., 1999; Mellado et al., 2002; Wang et al., 2004; Harrison et al., 2011; Lee et al., 2002a; Grahek and Măcefat, 2004; Lee et al., 2011; Dai and Kramer-Tremblay, 2011, 2014).

The main advantages of these procedures are that only one pre-treatment is necessary, the whole sample can be used for analyses, if it is small or of low activity, and the amount of wastes will be decreased. Otherwise, a simple and rapid assay of radiostrontium in environmental water samples can be performed using the Empore Strontium Rad Disk from 3M Company, US (Scarpitta et al., 1999; Smith et al., 1996). In this method the pre-filtered water sample (1 L) is simply passed through the disk which had previously been conditioned with methanol and 2M HNO_3. Strontium is retained on the disk which can be used directly for counting of the radiostrontium activity with a gas proportional counter. The disk is selective for strontium and can retain up to 3 mg of Sr.

In addition to the Sr Spec resin provided by Triskem and Eichrom, other similar resins for the separation of strontium have been developed. AnaLigSr01 (or SuperLig 620) resin is prepared by covalently bonding of ligand, most likely a variation of an 18-crown-6 (18C6) structure on silica gel (Grahek et al., 2018). Another one was prepared by grafting two extractants, 4,40(50)-bis-t-butylcyclohexano-18-crown-6 and di(2-ethyl-hexyl) phosphoric acid onto Amber chrom CG-71 (Surman et al., 2014). These resins showed similar features in the separation of radiostrontium for the determination of ^{89}Sr and ^{90}Sr using LSC. However, they are not well commercialized and not easy to obtain. The most popular Sr resin is still the Sr Spec resin from Triskem and Eichrom.

To meet the requirement of emergency analysis, a number of rapid analytical methods have been reported for the determination of radiostronium. A rapid method applying the Sr Spec column was reported for the determination of radiostrontium in milk samples (Guerin et al., 2017a). In this method, after the addition of stable Sr as tracer and carrier, HCl and trichloroacetic acid were added to the sample to flocculate the suspended fat and proteins in milk. The sample was centrifuged and the strontium in the supernatant was precipitated as carbonate. Afterward, $SrCO_3$ was dissolved and prepared in 8M HNO_3 and purified using a Sr Spec column, the eluate of Sr in water was measured using LSC for ^{89}Sr and ^{90}Sr. For the determination of radiostronium in steel and iron samples, a procedure was reported by using SrF_2/CaF_2 precipitation for the separation of Sr from a large amount of iron, followed by the Sr Spec

column to purify strontium (Maxwell et al., 2017). It should be mentioned that the main limitation on the application of Sr Spec resin in the determination of radiostronium is its low capacity for Sr and the interferences of high calcium and salt content in a sample on the strontium separation. For a 1.5 g Sr Spec resin column, loading of no more than 5 mg Sr should be followed. For analysis of high Sr and Ca containing samples (e.g., bone ash), a large column or splitting sample into aliquots and loading to more Sr Spec columns is needed (Miura and Minai, 2017). For low-level environmental samples, large sample size is needed for the determination of ultra-low level ^{90}Sr, which often contains a large amount of stable Sr, Ca, Ba, other interferring elements and radionuclides, the simple extraction chromatography separation using Sr resin may not be suitable. Chen et al. (2002b) reported a simple method for the determination of ^{90}Sr in a large volume of seawater samples (45 L). In this method, strontium is first separated from seawater by coprecipitation of $CaCO_3$−$SrCO_3$ with the addition of stable strontium carrier of 0.3−0.5 g Sr and Na_2CO_3, the sample was heated to 90−95°C and kept for 2 hours. The precipitation is separated by settling overnight to remove the supernantant followed by centrifuging the remaining sludge. After dissolution of the $CaCO_3$−$SrCO_3$ using HCl, calcium is separated by hydroxide precipitation with the addition of NaOH to a final concentration of 0.5 M NaOH. In this condition, $Ca(OH)_2$ precipitate is formed, but strontium remains in the solution and separated from a large amount of calcium. Strontium in the supernatant is then separated as $SrCO_3$ precipitate by the addition of Na_2CO_3. The $SrCO_3$ precipitate is dissolved in HNO_3 solution and kept for 2−3 weeks for ingrowth of ^{90}Y with ^{90}Sr. To this solution, yttrium carrier is added, and then strontium is separated by adding H_2SO_4 to form $SrSO_4$ precipitate, and in this case, Ba and Ra remaining in the sample are also precipitated and removed from yttrium. ^{90}Y is then separated by adding oxalic acid to form yttrium oxalate precipitate, and ^{90}Sr in the precipitate is measured using low-background gas flow proportional counting. The main feature of this method is its capacity to handle high calcium samples. This method has also been applied to the analysis of milk, bone, and large size soil samples for ^{90}Sr (Popov et al., 2006).

In addition, solvent extraction and ion exchange chromatography are frequently used for separating radiostrontium from various environmental matrices (Vajda and Kim, 2010c). Tributyl phosphate (TBP) and bis-2-etytlhexylphosphoric acid (HDEHP) have been the most commonly used organic extractants to separate ^{90}Y from liquid samples, which is assumed to be in equilibrium with ^{90}Sr. Consequently, rapid assays of ^{90}Sr via its daughter nuclide are possible, e.g., in environmental water, liquid milk, or nuclear waste samples using Cerenkov counting or LSC (Martin, 1987; Suomela et al., 1993; Jabbar et al., 2009; ISO, 2010; Tayeb et al., 2015; Yang et al., 2017). The tedious pre-treatments of milk samples are as well avoided when strontium is first separated from fat and proteins using cation exchange resins and subsequently separated from interfering elements by other methods (Kim et al., 2009; Maxwell III and Culligan, 2009a).

Regardless of the separation method, the sample can be prepared for LSC or Cerenkov counting. At the end of the separation procedure, strontium is precipitated as the carbonate or the oxalate, then dissolved in dilute HCl or HNO_3 acid and mixed with the LS cocktail. The aqueous or organic eluates from the chromatographic columns can be used as such, or after processing further, for the sample preparation. They are mixed with the scintillation cocktail or measured directly by Cerenkov counting. Chemical yields of strontium and yttrium can be determined by gravimetric methods or atomic absorption spectrophotometry, flame photometry or using ^{85}Sr as a yield tracer.

3. LSC measurements

The simultaneous determination of ^{90}Sr and ^{89}Sr by LSC is possible using several approaches. The pure strontium sample can be measured merely by LSC after mixing with scintillation cocktail or directly by Cerenkov counting or by measuring the sample first by Cerenkov counting followed by adding scintillation cocktail for LSC. Because there are two unknowns, ^{90}Sr and ^{89}Sr, the strontium sample should be measured twice at various times during the ^{90}Y ingrowth or once in two counting windows. Thereafter ^{90}Sr and ^{89}Sr activities will be calculated from the two independent counts by two equations where the contribution of ^{90}Sr, ^{90}Y and ^{89}Sr on the counts in different counting windows are taken into account. These counts are corrected for efficiency and for the ^{90}Y ingrowth and the ^{89}Sr decay using the time, which has transpired from the separation of strontium from yttrium to the midpoint of the measurement. Because LS spectra of ^{90}Sr, ^{89}Sr, and ^{90}Y have different end-point energies, spectrum deconvolution or unfolding methods can be applied, and consequently only one measurement or one counting window is needed. For the same reason, the chemical separation of yttrium from strontium is unnecessary for the simultaneous assay of ^{90}Sr from ^{89}Sr unlike methods that utilize gas proportional counters. When ^{90}Y is separated, its activity is often measured by Cerenkov counting immediately after the separation. If only ^{90}Sr is to be determined, this measurement is sufficient, but in the occurrence of ^{89}Sr, the combined ^{89}Sr and ^{90}Sr activity should be measured in advance from the previously separated strontium sample.

a. Early LSC methods

Several methods of measuring radiostrontium have been reported (Uyesgi and Greenberg, 1965; Piltingsrud and Stencel, 1972; Randolph, 1975; Regan and Tyler, 1976;

Salonen, 1978; and Carmon, 1979). These are categorized as liquid scintillation and/or Cerenkov counting methods. Some early methods for the assay of ^{90}Sr and ^{89}Sr were based on Cerenkov counting immediately after the separation of strontium and yttrium and on the subsequent LSC after adding the scintillation cocktail and allowing some ingrowth of ^{90}Y (Randolph, 1975; Salonen, 1978). Other methods were based on two Cerenkov measurements (Regan and Tyler, 1976; Carmon, 1979). The measurements were usually performed in nonequilibrium conditions between ^{90}Sr and ^{90}Y and using optimized windows for both measurements. In the initial Cerenkov counting almost all counts are due to ^{89}Sr, because of the low beta-energy of ^{90}Sr (end point at 546 keV) resulting in a very low counting efficiency (less than 1.4%). Therefore, the ^{90}Sr counts are neglected in some methods in the calculations although these counts, as wells as those from ^{90}Y ingrowth, can easily been considered by determining the efficiencies of ^{90}Sr, ^{89}Sr and ^{90}Y separately in each counting window in LS and Cerenkov counting (Salonen, 1978). The inherent errors of the results will then be avoided especially when the first counting is more or less delayed. The uncertainties of the ^{90}Sr and ^{89}Sr concentrations depended mainly on the activity ratio of ^{90}Sr/^{89}Sr, on the degree of the ^{90}Y ingrowth and on the optimization of the energy windows (Randolph, 1975; Salonen, 1978; Carmon, 1979). No quench correction was required for routine samples prepared from well-purified strontium carbonate precipitate which was dissolved in dilute HCl and mixed with Insta-Gel (Randolph, 1975; Salonen, 1978). Constant quench conditions were obtained regardless of the sample composition variation in the range typical for routine analysis. Some early attempts at radiostrontium assay involved the suspension of the insoluble strontium precipitates into a suitable cocktail containing a gelling agent. One such method employed a suspension technique for the strontium carbonate containing ^{90}Sr, ^{90}Y, and ^{89}Sr and a spectrum unfolding computer program to determine the quantity of each of the three isotopes (Piltingsrud and Stencel, 1972). Another method involved dissolution of the ^{90}Sr carbonate into glacial acetic acid and adding of 2-ethylhexanoic acid to form strontium and yttrium 2-hexanoates which are then soluble in a toluene-based cocktail (Uyesgi and Greenberg, 1965).

b. Recent LSC methods

Current LS spectrometers can be applied in several ways to the simultaneous measurements of ^{89}Sr and ^{90}Sr. Some rapid assays are based on measuring the samples in the LS cocktail using the two- or three-window method (Amano and Yanase, 1990; Dietz et al., 1991; Tait and Wiechen, 1993; Fliss et al., 1998; Heilgeist, 2000; Günther et al., 2003; Eikenberg et al., 2006; Kim et al., 2009). Another method was based on using one open window for LS and Cerenkov counting and on employing a spectrum deconvolution method to calculate the ^{89}Sr and ^{90}Sr activities separately (Heckel and Vogl, 2009). Walter et al. (1993) performed a comparison study using three different methods to evaluate their applicability for low activity samples with high ^{89}Sr/^{90}Sr activity ratios, which usually occur in emergency situations. These methods were: 1) LS counting with two pulse height windows, 2) the combination of Cerenkov and LS counting with open windows, and 3) the combination of the Cerenkov and LS counting with two counting windows during LS counting. The methods were tested with variably quenched samples, at variable ^{89}Sr/^{90}Sr activity ratios and by applying automatic quench corrections. According to this study, the best method for the fresh fallout samples was the third method, which was accurate for the ^{89}Sr/^{90}Sr activity ratios from 0.2 up to 15. Reliable results were obtained using the second method, which is almost similar as referred to in the previous paragraph (Salonen, 1978). This approach simplifies quench corrections. Another alternative approach was recommended by Eikenberg et al. (2006), whereby the ingrown ^{90}Y would be separated from the Sr resin column and then measured by Cerenkov counting. In this method, strontium in the sample solution is first adsorbed onto the Sr Spec column, then waiting for 1−2 days to allow ingrowth of ^{90}Y on the column. The ingrown ^{90}Y is then eluted from the column using 8M HNO_3 and measured by Cerenkov counting. ^{89}Sr and ^{90}Sr are eluted afterward in the normal way using water or diluted HNO_3 (i.e., 0.05 M HNO_3) and measured by LS counting. In accord with all of these methods, the strontium sample can be measured immediately after separating strontium from yttrium. However, recounting at various times during the ^{90}Y ingrowth will confirm the results obtained, and also indicate whether interfering radionuclides have been eliminated during the chemical separation. The recounting also improves the separation of ^{89}Sr and ^{90}Sr when there is a large excess of ^{89}Sr. Fig. 2.20 illustrates the spectra of ^{89}Sr, ^{90}Sr, and ^{90}Y in the application where the measurement is based using two LSC windows (Kim et al., 2009).

The spectrum unfolding methods have been applied to radiostrontium determinations in aqueous solution (Hong et al., 2001; Lee et al., 2002b) and for the simultaneous separation of ^{90}Sr and ^{99}Tc (Lee et al.,2002a). This technique has been utilized successfully for the analysis of ^{90}Sr in bone samples in combination with the CIEMAT/NIST method for quench corrections (Altzitzoglou et al., 1998; Pilviö et al., 1999).

Using rapid separation methods, the total analysis time of radiostrontium in different sample matrices is 1−2 days or only some hours for samples such as water, aerosol, milk, and urine when the Sr resin is used for chemical separation (Heckel and Vogl, 2009; Kim et al., 2009; Maxwell III and Culligan, 2009a; Dai et al., 2013; Tayeb et al., 2016;

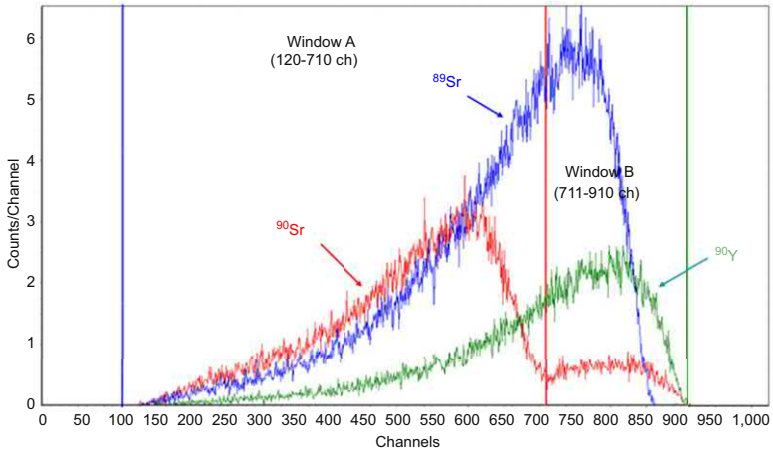


FIGURE 2.20 LSC spectra of ^{89}Sr, ^{90}Sr, and ^{90}Y (Kim et al., 2009). *Reprinted by permission of Elsevier © 2009.*

Guerin et al., 2017a). The detection limits by the current low-background LS spectrometers are typically less than 0.1 Bq (1−2 hours count time).

c. Cerenkov counting methods

Several attempts have been made to determine ^{89}Sr and ^{90}Sr simultaneously by Cerenkov counting (Randolph, 1975; Buchtela and Tschurlovits, 1975; Regan and Tyler, 1976; Carmon, 1979; Martin, 1987; Rucker, 1992; Chu et al., 1998; Vaca et al., 2001; Grahek and Măcefat, 2005; Günther et al., 2009). The determination is based on the fact that both ^{89}Sr and ^{90}Y can be detected by measurement of the Cerenkov radiation (photons) in colorless aqueous solutions with about 40% and 60% counting efficiency, respectively, while the counting efficiency of ^{90}Sr is less than 1.4% because of the low energy of its beta particles. The ^{89}Sr activity is determined almost exclusively from the freshly separated strontium sample when the first counting is performed immediately after the separation. Recounting is performed after some ingrowth of ^{90}Y from ^{90}Sr, and the calculation of the concentrations of ^{89}Sr and ^{90}Sr is possible from these two counts. Alternatively, ^{90}Y can be separated from the purified strontium sample after its ingrowth and counted separately (Carmon, 1979). When the ^{90}Sr activity alone is to be quantified, the calibrations and the calculations of the results are much simpler particularly after a complete ingrowth of ^{90}Y (Martin, 1987; Suomela et al., 1993; Friberg, 1997; Vaca et al., 2001; Torres et al., 2002; Wang et al., 2004; Jabbar et al., 2009; Harrison et al., 2011). In the methods mentioned previously, separation techniques like precipitation, ion exchange, solvent extraction, and extraction chromatography were used to isolate radiostrontium. In another method, the separation of ^{89}Sr and ^{90}Sr from water and milk samples was tested using a chelating resin, Chelite P (from Serva Company), and alginate spherules in batch form followed by the Cerenkov count (Günther et al., 2009). The milk samples were prepared without ashing and the results were obtained in 4 days by using 3 days for the ^{90}Y ingrowth. Because the Cerenkov counting is sensitive to color quenching, the effect of color quenching has been studied (Fujii and Takiue, 1988; Mosqueda et al., 2007), especially for samples in organic solutions (Suomela et al., 1993; Vaca et al., 2001). The Cerenkov counting techniques allow the use of ^{85}Sr as a yield tracer. The ^{85}Sr carrier decays via electron capture. It cannot produce Cerenkov radiation, and therefore, it is not detected by this counting. This makes radiostrontium assay simpler than determining the yield with a gravimetric method. For additional information on Cerenkov counting techniques, please refer to Chapter 6, Volume 2.

In summary, chemical separation of strontium has developed greatly, and the methods based on extraction chromatography have gained wide popularity. Rapid assays of radiostrontium are possible by combining such methods with low-background LS counting, which offer the ability to measure ^{89}Sr, ^{90}Sr, and ^{90}Y at very high counting efficiency immediately after the separation. The detection limits are less than 0.1 Bq with a 1−2 hours count time. A number of methods have been developed based on the extraction chromatography for emergency analysis, which requires analytical results in hours. Significant advances have also been made in analyzing radiostrontium simultaneously with other nuclides and in off-line or on-line monitoring models. These techniques are important in the future monitoring of nuclear wastes and in decommissioning of nuclear facilities.

F. Technetium-99 (^{99}Tc)

1. Environmental occurrence

^{99}Tc ($E_{max} = 293.5$ keV and $t_{1/2} = 2.11 \cdot 10^5$ y) is a pure beta-emitter which decays to stable ^{99}Ru (Laureano-Perez et al., 2010). It is a fission product of ^{235}U and ^{239}Pu and is mainly produced by thermal neutrons in nuclear reactors

with relatively high fission yields (6.1% from ^{235}U). Its presence in the environment is due to nuclear weapon tests and nuclear fuel cycle operations. The global inventory of ^{99}Tc from weapons testing is currently small. The main sources are nuclear reactors, although releases to the environment occur primarily from fuel reprocessing plants (Till, 1986). The principal reasons for the high level of interest in the analysis of ^{99}Tc in environmental samples are its very long half-life, high mobility and solubility as the pertechnetate ion (TcO_4^-) in oxidative conditions, and consequently its high transfer rate from soil to edible vegetation and from seawater to seaweeds. Under reducing conditions, it can be reduced to Tc^{4+} and strongly bound to sediments (Burke et al., 2010). ^{99}Tc is considered a long-term risk, because it is taken up readily by aquatic and terrestrial organisms (Degenkolb et al., 1994). Because Tc has no stable isotope, ^{99}Tc is the dominating isotope and used to study the behavior of this element in the environment. Studies have focused on marine and coastal environments owing to discharges from nuclear reprocessing plants (Ikäheimonen et al., 2002; Oliver et al., 2006; Begg et al., 2007; Keogh et al., 2007; Shi et al., 2012a, 2012b; 2013, 2016; Kolacinska et al., 2018; Barrera et al., 2016; Rodriguez et al., 2015; Jenkinson et al., 2014; Marshall et al., 2014). ^{99}Tc is one of the most significant components in the long-term storage and disposal of nuclear wastes (Zhang et al., 2010). In nuclear medicine, ^{99m}Tc ($t_{1/2} = 6$ hours) is used in high-activity amounts, which decay to ^{99}Tc, and becomes another source of ^{99}Tc in the environment.

2. Sample preparation and analysis

Chemical separation techniques including anion exchange, solvent extraction, selective precipitation, extraction chromatography, and even a combustion technique have been used to assay ^{99}Tc in various environmental samples, nuclear effluent and waste samples (Golchert and Sedlet, 1969; Holm et al., 1984; Cattarin et al., 1985; Silva et al., 1988; Jordan et al., 1995; Wigley et al., 1999; Tagami and Uchida, 1999; Gómez et al., 2001; Ikäheimonen et al., 2002; Lee et al., 2002a; Shi et al., 2012a, 2012b; 2013, 2016; Kolacinska et al., 2018; Guerin et al., 2017b, 2017c; Barrera et al., 2016; Rodriguez et al., 2015; Jenkinson et al., 2014; Marshall et al., 2014; Kabai et al., 2013). Because ^{99}Tc concentrations are generally very low, it is necessary to preconcentrate technetium from large sample sizes before the chemical separation. Direct evaporation of water samples is time consuming and not suitable for high salt containing samples (e.g., seawater); it also presents a risk in loss of Tc as the volatile heptoxide, if the temperature is increased sufficiently high. Loss of technetium might also occur during dry ashing of organic matter, unless some precautions are taken during evaporation or ashing (Wigley et al., 1999). Shi et al. (2012) investigated the stability of technetium in various chemical treatments including ashing of solid materials and evaporation of aqueous solution. It was reported that no significant loss of technetium was observed in ashing of seaweed under 800°C for less than 6 hours and under 500°C for soil and sediment samples. Evaporation of a solution to dryness in different concentrations of HNO_3 at less than 100°C does not cause obvious loss of technetium, while significant loss of technetium happens in HCl media, especially in high concentrations of HCl. However, if a small volume of solution (more than 0.5 mL) remained after evaporation, the loss of technetium can be highly reduced. Salt present in the solution can reduce the loss of technetium during evaporation.

^{99}Tc has no stable isotope to use as a carrier or for chemical yield monitoring. Although the analytical behavior of rhenium is quite similar to that of Tc, these elements can behave quite differently under certain conditions. Hence some precautions need to be taken if rhenium is used as a tracer (Anders, 1960; Mas et al., 2004). An advantage of using rhenium is that it is inexpensive and easier to handle than radioactive tracers (Gómez et al., 2001). ^{99m}Tc, obtained from a ^{99}Mo-^{99m}Tc generator has been used widely as a yield tracer in the radiochemical separation of ^{99}Tc for environmental samples, because it is readily available, and its emission of gamma rays (Hou and Roos, 2008). The disadvantage of the ^{99m}Tc tracer is that it may contain ^{99}Tc, ^{99}Mo, and ^{103}Ru as impurities, which may cause serious interference in the measurement of ^{99}Tc at low levels, requiring correction for each tracer solution used (Dowdall et al., 2004). Hou et al. (2007a) developed a simple method to produce the ^{99m}Tc tracer solution that is pure enough to be utilized in the analysis of low-level environmental samples. The ^{99m}Tc-^{99}Mo generator was first eluted using saline water (0.9% NaCl) for 3−5 times to remove the accumulated ^{99}Tc in the generator through decay of ^{99m}Tc and ^{99}Mo, the new ingrown ^{99m}Tc is then eluted after a suitable ingrowth time (1 minute−3 hours). The newly obtained ^{99m}Tc solution is then purified by passing it through an activated alumina cartridge to remove any ^{99}Mo and ^{103}Ru leaked from the column. The ^{99m}Tc activity is measured with a gamma spectrometer before preparing the sample for the LS counting. Thereafter, the sample is stored for a week to allow ^{99m}Tc to decay completely before measuring the ^{99}Tc activity by LSC. Another possibility for a yield tracer would be to use ^{95m}Tc (half-life = 61 d). ^{95m}Tc decays through electron capture with emission of gamma rays, and can be measured by counting the low-energy Auger electrons using LSC. Therefore, ^{99}Tc and ^{95m}Tc can be discriminated and measured by LS spectrum (Silva et al., 1988).

Chemical separation methods are mainly based on a combination of selective precipitations, ion exchange and solvent extraction using different extractants like DB18-C6

crown ether (dibenzo-18-crown-6), *tri-n*-octylamine (TnOA), and *tri-n*-butyl phosphate (TBP) (Holm et al., 1984; Wigley et al., 1999; Jordan et al., 1995). Separation of technetium using anion exchange chromatography is based on the very high affinity of TcO_4^- on the strong anion exchange resin in either diluted acid, alkaline, or neutral media. Chen et al. (1994) has reported a method for the determination of ^{99}Tc in seawater and other environment samples. ^{99}Tc is first pre-concentrated from a large volume of seawater samples (up to 200 L) using anion exchange chromatography. The filtered seawater is spiked with ^{99m}Tc tracer, and then loaded onto a big anion exchange column (2.5 cm in diameter and 40 cm in length, AG1x-4 resin, Cl^- form), after washing with diluted NaOH and diluted HNO_3 solution, ^{99}Tc is eluted from the column using 8−10 M HNO_3. The eluate is evaporated to a small volume (<10 mL), and treated with H_2O_2 and NaClO with heating to remove Ru. Afterward, the solution is converted to 1M H_2SO_4 medium, ^{99}Tc in the solution is further purified by solvent extraction using 5% triisooctylamine in xylene. The overall recovery of ^{99}Tc is more than 75% and the most interference can be completely removed to be able to measure background level ^{99}Tc in seawater samples (0.003mBq/L) using up to 500 L seawater.

Wigley et al. (1999) investigated all different steps of the analytical procedure including grinding, dry and wet ashing, dissolution, chemical separation, and measurement to find optimum conditions for separating ^{99}Tc from environmental samples. ^{95m}Tc was used as the chemical yield tracer. The first step of chemical separation was $Fe(OH)_3$ precipitation, which removed transition metals, actinides and lanthanides while Tc remained in the supernatant. The separation continued with an anion exchange chromatography in alkaline solution where Tc was retained in the column but alkali and alkaline earth ions and doubly charged transition metals passed through the column, and consequently interfering radionuclides such as ^{60}Co, ^{63}Ni, ^{90}Sr, and ^{137}Cs were removed. Tc was eluted from the column with concentrated HNO_3, which was then evaporated, and the residue was dissolved in 2 M H_2SO_4. The final purification of Tc from Ru, in H_2SO_4 solution, is accomplished by extraction using 5% tri-n-octylamine (TnOA) in xylene, the ^{106}Ru remains in aqueous phase. Recovery of the ^{99}Tc was determined immediately by gamma spectrometry measurement of ^{99m}Tc tracer and the sample left for 1 week to allow the ^{99m}Tc to decay completely. The extracted ^{99}Tc in TnOA-xylene was mixed with the scintillation cocktail and subsequently counted by LSC. Typical yields varied between 70 and 95%, and decontamination factors were between $10^3$and 10^6 for ^{137}Cs and ^{241}Am but only 3−5 for ^{106}Ru/^{106}Rh.

Jordan et al. (1995) obtained very high (10^5−10^8) decontamination factors for all important fission products, activation products and naturally occurring radionuclides, with chemical yields from 50% to 80%. The separation procedure is based on anion, cation exchange, and solvent extraction with TBP in H_2SO_4. Golchert and Sedlet (1969) reported a contamination factor of 1.3×10^4 for ^{106}Ru/^{106}Rh in environmental water samples. Their method was based on selective precipitations followed by solvent extraction using TnOA in xylene. They found that the Ru contamination factor was improved when it was removed initially by precipitation. This was accomplished by converting the Ru to a single species, Ru(VII), with NaOCl as oxidizer and then reducing it to the insoluble Ru(IV) oxide by the alcohol. The decontamination factor was improved by several hundred times and can be repeated if Ru activity is high. The overall chemical yield was 79.6%.

Selective extraction chromatographic methods using TEVA●Spec resin (Eichrom Industries, Darien, Illinois) and LSC or inductively coupled plasma mass spectrometry (ICP-MS) have become the most popular method for the determination of ^{99}Tc in environmental samples (Beals, 1992; Scarpitta, 1993; Gómez et al., 2001; Ikäheimonen et al., 2002; Lee et al., 2002a; Shi et al., 2012a, 2012b; Rodriguez et al., 2015; Jenkinson et al., 2014). Quantitative measurement of ^{99}Tc by LSC is viewed as a practical but also as the main approach, because of the more widespread accessibility of the LS counters, meanwhile it is also tolerant of isobaric ions (^{99}Ru and ^{98}Mo^{1}H) which is the major challenge in the ICP-MS measurement of ^{99}Tc (DOE, 1993; Hou and Roos, 2008). In environmental assays, the TEVA resin is used in combination with selective precipitations and anion exchange similarly to solvent extraction. The main purpose of the TEVA is to purify the Tc in the presence of Ru, which works very efficiently (Lee et al., 2002a). When the sample is loaded in a neutral solution or in 0.1M HNO_3 solution to a TEVA column, Tc is retained, while the Ru passes through the column. ^{99}Tc can be eluted with 4−8 M HNO_3 and an aliquot submitted for LSC. The overall yields by extraction methods are reported to be from 73% to 94%. Shi et al. (2012a) has reported a method for removing Ru from ^{99}Tc by pretreatment of the loading solution with 30% H_2O_2 in alkaline media, and found a significantly improvement in the removal of ruthenium in chromatographic separation using TEVA column. This might be attributed to the reduction of ruthenium in this process.

The LS counting efficiencies of ^{99}Tc are typically in the range of 70%−80% depending on sample composition and quenching. The backgrounds using low-background LS spectrometers are between 1.6 and 3.3 cpm, and the detection limits vary over a large range (0.16 mBq/L −1.7 Bq/kg) depending mainly on the count time and background level and sample size (Ikäheimonen et al., 2002; Jordan et al., 1995; Gómez et al., 2001; Wigley et al., 1999). The comparison study by Hou and Roos (2008) demonstrated that the detection limit by LSC is

approximately 17 mBq (2 hours count), which is about two orders of magnitude higher than those achieved by ICP-MS. Chemical separation is necessary for both methods.

Tarancon et al. (2017) have proposed the concept of combining the chromatographic separation with scintillation for the determination of radionuclides using LSC. In this method, a plastic scintillation resin is synthesized, in which the extraction reagent and scintillator are grafted on plastic beads. The plastic scintillation resin behaves as both extraction chromatographic resin and scintillator. The resin is prepared in a column, the sample solution is loaded to the column, the analyte radionuclide is adsorbed on the resin, and the matrix and interferring radionuclides are removed by rinsing. The scintillation resin with the analyte radionuclides in the column is directly measured by normal LSC. This research group has reported a method for the determination of ^{99}Tc in environmental and waste samples (Barrera et al., 2016). A specific plastic scintillation resin was synthesized by binding Aliquat 336 (trioctylmethylammonium chloride) as extractant to plastic scintillation microspheres. Here, the plastic scintillation microspheres (PSm) behaves like liquid scintillation cocktail but in a solid phase. PSm consists of a polymeric solvent and both primary and secondary scintillators, such as the classical PPO, POPOP, PTP, or bis-MSB. Fluor molecules remain encapsulated inside the PS solid. Fig. 2.21 illustrates a schematic diagram of the determination of ^{99}Tc using the plastic scintillation resin.

In summary, very low ^{99}Tc activities in environmental samples can be analyzed using several separation methods with current LS counters. The ^{99}Tc assay requires special attention to address the volatility of Tc and the separation difficulties encountered when trying to separate it from Ru, as well as from other elements depending on chemical conditions. Attention should also be paid to the ^{99m}Tc tracer, which may contain significant amounts of ^{99}Tc as an impurity.

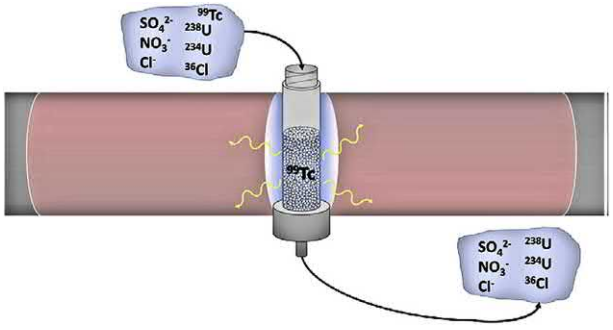


FIGURE 2.21 Schematic diagram of plastic scintillation for determination of ^{99}Tc. *Barrera et al. (2016); reprinted by permission of Elsevier © 2016.*

G. Plutonium-241 (^{241}Pu)

1. Environmental occurrence

Plutonium (Pu) was released to the environment from nuclear weapons tests and nuclear fuel cycle operations particularly from reprocessing plants (Pimpl, 1992; Hou and Roos, 2008; Qiao et al., 2009). There are four isotopes of plutonium present in the environment, namely, ^{238}Pu ($t_{1/2} = 87.74$ y), ^{239}Pu ($t_{1/2} = 2.41 \times 10^4$ y), ^{240}Pu ($t_{1/2} = 6563$ y), and ^{241}Pu ($t_{1/2} = 14.4$ y). Among all isotopes of plutonium, only ^{241}Pu is a beta-emitter with emission of low-energy β-particles ($E_{max} = 21$ keV); thus, it is less radiotoxic than other alpha-emitting plutonium isotopes. However, ^{241}Pu decays to α-emitting ^{241}Am, which is more radiotoxic than ^{241}Pu. The differences in the Pu isotopic ratios are used to trace the origin of the environmental contamination (Kershaw et al., 1995; Turner et al., 2003; Carbol et al., 2003; Ketterer et al., 2004; Kwong et al., 2004; Alamelu and Aggarwal, 2007; Hou and Roos, 2008; Varga et al., 2008, 2018; Alamalu and Aggarwal, 2016). For instance, the activity ratio of ^{241}Pu/$^{239+240}$Pu differs depending on whether the contaminations originate from releases of nuclear fuel reprocessing plants (25), nuclear tests (15), weapon grade uranium (3), or the Chernobyl accident of 1986 (Holm et al., 1992). Environmental monitoring of ^{241}Pu around nuclear facilities is needed, and its determination in high-activity waste in nuclear fuel reprocessing cycles is important, as it will influence the method of final disposal (Prosser et al., 1994; Feng and He, 2009). In fact, ^{241}Pu is the only significant beta-emitting transuranium nuclide in low-level radioactive waste from nuclear power plants (Martin, 1986). Liquid scintillation is the major method for its measurement, although mass spectrometry has also been widely applied for its determination (Oh et al., 2013; Jaggi et al., 2012; Alvardo et al., 2011; Dai et al., 2012b). ^{241}Am is the direct decay daughter of ^{241}Pu, therefore measurement of the ingrown ^{241}Am from ^{241}Pu using alpha spectrometry has also been used for the determination of ^{241}Pu. In addition, the decay of ^{241}Pu causes continuous formation of ^{241}Am, and the ^{241}Am concentration in the environment would gradually increase to a maximum concentration in the middle of the 21st century (Hou and Roos, 2008). ^{241}Am is a unique tracer in oceanographic and sedimentation studies.

2. Sample preparation and analysis

Many methods have been developed for the determination of plutonium in environmental and nuclear samples, as summerized in four comprehensive reviews by Hou and Roos (2008), Qiao et al. (2009), and Vajda and Kim (2010a; 2010b). The chemical separation schemes of ^{241}Pu are normally complicated, because the concentrations of ^{241}Pu are normally very low. Its oxidation states have to be considered during the

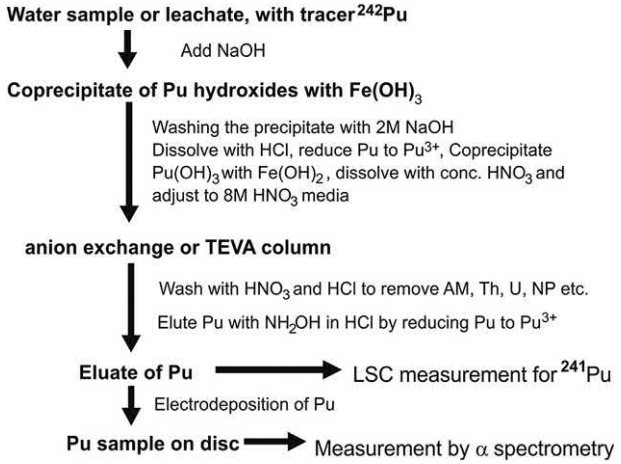


FIGURE 2.22 Diagram of chemical separation procedure for determination of plutonium isotopes.

separation, and plutonium has to be purified completely from other radionuclides in advance to avoid interference. Fig. 2.22 illustrates an often-applied analytical procedure for the determination of plutonium isotopes. In general, plutonium is first released from the solid sample matrix by acid leaching or alkaline fusion followed by acid dissolution. The released plutonium in the sample solution or in liquid samples (water sample) is then pre-concentrated by coprecipitation of hydroxide, fluoride, or phosphate. The precipitate is dissolved and plutonium is converted to Pu^{4+} valence state, which can be implemented by first reducing all plutonium to Pu^{3+} using strong reductant such as $KHSO_3$, and then oxidize Pu^{3+} to Pu^{4+} using $NaNO_2$, concentrated HNO_3 containing HNO_2 can be also used for this purpose. The prepared sample solution is loaded to an anion exchange column (e.g., AG 1x-4, or Dowex 1x-4) or TEVA extraction chromatographic column, followed by rinsing with HNO_3 to remove uranium and all transition elements, and finally HCl for Th removal. Plutonium absorbed on the column is then eluted by reducing it to Pu^{3+} using $NH_2.OH{-}HCl$ or using diluted HCl or diluted HF. The plutonium eluate is evaporated to dryness and dissolved in a small volume of diluted HCl for LSC measurement of ^{241}Pu.

^{241}Pu is a low-energy β-emitter, and LSC is the ideal measurement technique for determining its activity. While, other plutonium isotopes are alpha-emitters, and often measured using alpha spectrometry, especially ^{238}Pu which has to be measured by alpha spectrometry, because of the serious interference of ^{238}U for its measurement by mass spectrometry. Therefore, ^{241}Pu and other alpha-emitting plutonium isotopes are usually measured separately. This is often implemented that the separated plutonium is first electro-deposited on metal disc or micro-precipitated as NdF_3 coprecipitate on membrane filter and measured for alpha-emitting plutonium isotopes (^{238}Pu, ^{239,240}Pu and ^{242}Pu as chemical yield tracer) (Vajda and Kim, 2010a). Afterward, the Pu sample on the disk or filter paper is dissolved and measured using LSC for determining the ^{241}Pu activity. The initial α-spectroscopic measurement is required, if the measurement of all plutonium isotopes is necessary, and it provides the chemical yield for the ^{241}Pu analysis and reveals possible impurities in the purified Pu fraction. The Pu on stainless steel is dissolved in concentrated HNO_3 and then purified by solvent extraction or ion exchange, which is necessary if some interfering elements like Fe and Pt are present in the solution with Pu (Mietelski et al., 1999; Oh et al., 2009). They cause quenching which decrease the counting efficiency of ^{241}Pu and also increase misclassification (Condren et al., 1996; Kwong et al., 2004). The Pu coprecipitated with NdF_3 is prepared for LSC by placing the filter in the LS vial, dissolving Pu in a solution of H_3BO_3/HNO_3 and ethanol and adding the LS cocktail. The sample needs no quench corrections, because the membrane becomes translucent and the dissolver solution has no effect on the counting efficiency (Moreno et al., 1998; Kwong et al., 2004; Varga and Tarján, 2008). A constant counting efficiency of 37% could be applied for all samples (Moreno et al., 1998). The counting efficiency of ^{241}Pu was improved (48.8%) when it was separated with an extractive cocktail composed of HDEPH and scintillants in toluene (Yu-Fu et al., 1992). The application of the α/β discrimination feature in the LSC can reduce interferences and background in the low-energy β-region of the ^{241}Pu (Lee and Lee, 1999). A typical β-spectrum of ^{241}Pu with α-peak of other Pu-isotopes is shown in Fig. 2.23. The detection limits for ^{241}Pu are of the order of 30−100 mBq per sample based on a 100- to 600-minute count time (Pimpl, 1992; Moreno et al., 1998; Mietelski et al., 1999; Varga and Tarján, 2008). Paatero et al. (1994) reported a ^{241}Pu lower detection limit of 7 mBq for a lichen sample using the Quantulus and a 600-minute count time.

H. Other radionuclides (^{36}Cl, ^{41}Ca, ^{129}I)

The radionuclides discussed previously are the most important radionuclides in the environment in view of radiation protection and environmental monitoring. Meanwhile, many other anthropogenic radionuclides have also been released to the environment by human nuclear activity. Due to the long half-life and relative small amount of radioactivity compared to the above mentioned radionuclides, they are less important in the view of radiation risk, but they are more important in view of waste depository and are very useful for investigation of environmental processes. Among them, ^{36}Cl, ^{129}I, and ^{41}Ca are presented here.

1. Chloride-36 (^{36}Cl)

^{36}Cl is a long-lived ($t_{1/2} = 301$ ky) pure beta-emitter ($E_{max} = 709$ keV), formed by neutron activation reaction of stable chlorine ^{35}Cl(n,γ)^{36}Cl in a nuclear reactor. Less

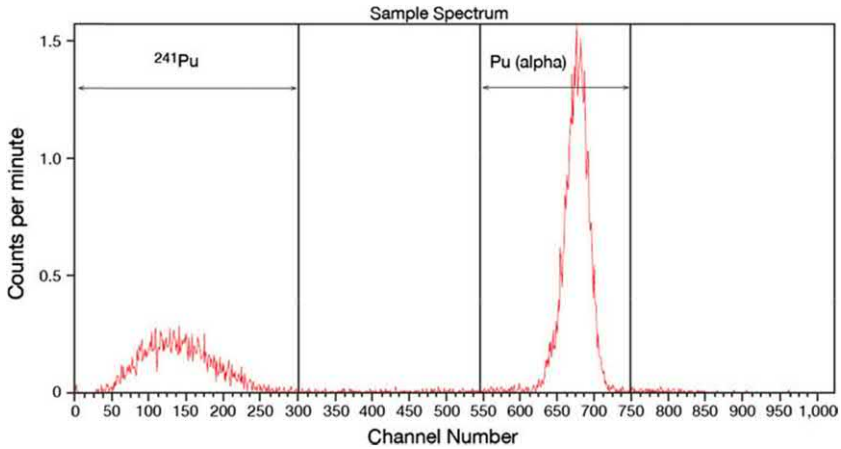


FIGURE 2.23 LSC spectra of a plutonium sample measured by the Quantulus LSC (Oh et al., 2013). *Reprinted by permission of Springer Nature © 2013.*

important sources are nuclear reactions induced by cosmic radiation in the atmosphere, water, and bedrock. Because of its low specific activity, ^{36}Cl is not considered a substantial danger to humans at present environmental levels. However, due to the high mobility of chlorine and its long half-live, ^{36}Cl is a useful tracer in interpreting environmental processes (Shaw et al., 2014; Muensterer et al., 2012; Fehn, 2012).

Many methods have been reported for the determination of ^{36}Cl in environmental and waste samples (Hammer-Rotzler et al., 2015; Hou et al., 2007b; Fréchou and Degros, 2005; Itoh et al., 2002a; Tolmachyov et al., 2001; Ashton et al., 1999; Szántó et al., 1998; Moir et al., 1995). For soil, concrete, and other solid materials, chlorine is separated from the sample in one of the following ways: vaporizing the chlorine to Cl_2 gas by subjecting the sample to high temperature or by boiling the sample in strong oxidizing acids. The released chlorine gas from the samples is captured in a NaOH solution. The sample can also be dissolved so that the chlorine remains in solution as chloride ions. In all three cases, a known amount of chlorine carrier, in the form of NaCl, for example, is added to the sample. Chlorine gas trapped in the NaOH solution is reduced with $NaNO_2$ to chloride, and the chloride is precipitated as silver chloride (AgCl) by adding $AgNO_3$ after acidifying the solution to a weakly acidic medium. Iodide precipitates along with the silver chloride, which means that the long-lived radionuclide ^{129}I, might also be present in the precipitate. Iodine can be removed by extracting the precipitate with NH_4OH, in which AgCl dissolves, but AgI does not. The AgI precipitate is discarded and the chloride in the NH_4OH solution is again precipitated by acidification to $pH < 2$. At the end of the analysis, the chemical yield of the separation is determined by measuring the amount of chlorine by ICP-MS or ion chromatography. Finally, ^{36}Cl in the purified AgCl precipitate is counted by LSC after dissolving the precipitate with ammonium and adding scintillation cocktail. Because of the relative high beta energy of ^{36}Cl, the counting efficiency of ^{36}Cl is normally higher than 85% depending on the quench level, and the need to be corrected using a quench curve or internal standard method. For nuclear waste samples, ^{36}Cl levels are sufficiently high to be measured by LSC. But for most environmental samples, especially samples with natural originated ^{36}Cl, the most sensitive method of accelerator mass spectrometry is needed, which can measure ^{36}Cl in the sample target with a $^{36}Cl/^{35}Cl$ atomic ratio of 10^{-15}.

Hou et al. (2007b) reported a method for the determination of ^{36}Cl in nuclear waste samples, including graphite, concrete, and metals. Fig. 2.24 illustrates an analytical procedure for the determination of ^{36}Cl in waste samples. In this method, the sample is first decomposed. A graphite sample is decomposed by acid digestion with a mixture of acid (H_2SO_4:HNO_3:$HClO_4$ = 15:4:1); metals such as lead, aluminum, and stainless steel are dissolved with 5M HNO_3, 5M H_2SO_4, and H_2SO_4−H_3PO_4, respectively. During the decomposition by heating, the solution is bubbled with nitrogen gas, and the released gas is trapped in three series if interconnected trapping solutions: one H_2O, and two with 0.4M NaOH. A concrete sample is decomposed by alkaline fusion by mixing the sample with NaOH−Na_2CO_3 and fused at 500°C for 3−4 hours, the fused cake is dissolved with H_2O, and the leachate is used for the determination of ^{36}Cl. Before sample decomposition, stable chloride as carrier and other stable element as hold back carriers are added. The decomposed sample solution is then transferred to a separation funnel. $NaHSO_3$ solution is added to convert all iodine to iodide, HNO_3 is then added to adjust $pH < 2$. After the addition of CCl_4, $NaNO_2$ solution is added to oxidize iodine to I_2, and chlorine is reduced to Cl^-, I_2 is then extracted to CCl_4 phase by shaking. $AgNO_3$ solution is added to the aqueous phase after extraction of iodine, and the solution is stirred to aggregate the AgCl precipitate. The

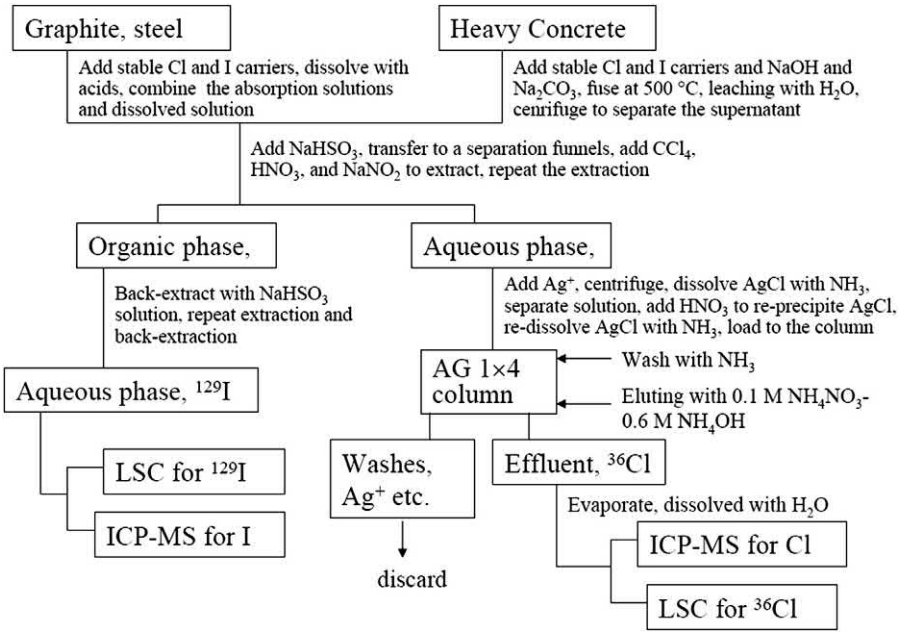


FIGURE 2.24 Analytical procedure for the determination of ^{36}Cl in nuclear waste samples (Hou et al., 2007a, 2007b).

AgCl precipitate is separated by centrifugation, and washed with 1 M HNO_3 to remove the interfering metal radionculides. The precipitate is dissolved with 25% NH_3, and HNO_3 is then added to the solution to pH < 2. The AgCl precipitate formed is separated by centrifugation and the supernatant (metal radionculides) is discarded. The AgCl precipitate is dissolved in 25% NH_3 solution, and the solution is loaded to an anion exchange column which is converted to OH^- form and conditioned with 25% NH_4OH. The column is washed with 25% NH_3 until there is no Ag^+ in the wash effluent. Chloride on the column is then eluted with 0.2 mol/L NH_4NO_3-0.6 mol/L NH_4OH. The eluate is evaporated to dryness on a hotplate. The residue is dissolved with 2 mL water, and transferred to an LSC vial. A small fraction of the solution (0.1 mL) is taken to measure stable chlorine by ICP-MS for chemical yield monitor. Scintillation cocktail (15 mL) is added to the remaining solution, and ^{36}Cl in the solution is measured by LSC. The decontamination factors for all interfering radionculides are higher than 10^6, and the recovery of Cl is higher than 90%. Since the final solution of ^{36}Cl is prepared in 2 mL of water, the quench level is very low and the counting efficiency is high (>98%). In addition, compared to the other methods of preparing the final ^{36}Cl sample in ammonium solution or suspending AgCl precipitate in scintillation cocktail, the measurement solution is stable and the measurement results are more precise and accurate.

2. Iodine-129 (^{129}I)

^{129}I decays by beta emission to the excited state of xenon isotope ^{129m}Xe with a beta-particle $E_{max} = 150$ keV. The decay of the excited state ^{129m}Xe takes place mostly by internal conversion with the emission of a low intensity (7.5%) of 39.6 keV gamma ray and some X-rays including 29.46 keV (20.4%) and 29.78 keV (37.7%). Therefore, ^{129}I can be measured by LSC and γ spectrometry, and LSC is more sensitive compared to γ spectrometry.

^{129}I is naturally present in the environment, generated in the atmosphere from xenon by nuclear reactions induced by cosmic radiation, and in the soil from uranium through spontaneous fission and fission due to thermal neutrons. The concentration of natural ^{129}I in the environment is so low that it is not usually expressed in terms of activity concentration, but in proportion to the only stable isotope of iodine, ^{127}I. Before the nuclear age, the $^{129}I/^{127}I$ atomic ratio was about 10^{-12} in the sea and somewhat higher in the terrestrial environment. Now, as a result of nuclear weapons tests, nuclear accidents, and emissions from nuclear facilities, the level of ^{129}I in the environment has risen, and the $^{129}I/^{127}I$ ratio has increased by several orders of magnitude, up to as much as 10^{-4} in the surrounding location of nuclear fuel reprocessing plants. The most extensive releases of ^{129}I to the environment occurred at the spent nuclear fuel reprocessing facilities at Sellafield (UK) and La Hague (France) since the early 1990s (Hou et al., 2009, 2001; 2002).

The very long half-life of ^{129}I (1.6×10^7 y) means that its specific activity is very low (6.5×10^6 Bq/g). Thus, radiometric methods including LSC are suitable only for samples in which the activity of the isotope is fairly high. Such samples are found in nuclear power plants and fuel reprocessing facilities, or environmental samples around

the reprocessing plants. Radiometric methods are not sensitive enough for measuring the very low activity concentrations of ^{129}I in the environment. More sensitive methods are neutron activation analysis and especially accelerator mass spectrometry (Hou et al., 1999).

When the activity is high enough, ^{129}I can be measured by LSC (Zulauf et al., 2010; Osman et al., 2016). In determining ^{129}I in the ion exchange resin used in the purification of the primary circuit of nuclear power plants, the iodine in the resin is eluted with NaOCl. In this case, iodide adsorbed on the exchange resin is oxidized to iodate, which has a low affinity to the resin, and it is eluted from the resin. Subsequently, KIO_3 is added to the solution as carrier, and the iodate is reduced to I_2 with hydroxylamine hydrochloride. The I_2 is then extracted into CCl_4 phase. Afterward, iodine is back extracted into water with $NaHSO_3$, which reduces I_2 to I^-. The iodide is then oxidized to I_2 with $NaNO_2$ in acidic medium, which is extracted with toluene. The iodine in the toluene is back extracted into aqueous solution with 0.01 M $NaHSO_3$. Scintillation cocktail is added to the aqueous solution and the activity of ^{129}I is measured by LSC. The detection limit of 0.6 Bq/L can be achieved (Puukko and Jaakkola, 1992).

For solid samples, such as soil, sediment, vegetation, and air particles, ^{129}I must be separated from the sample matrix and then purified for its measurement using LSC or other techniques. Based on its volatility, iodine is often separated from solid samples by combustion to release iodine in gaseous form (Muramatsu et al., 1995; Hou and Wang, 2016, 2018). The released iodine is trapped in NaOH solution, which is then used to separate iodine by extraction with CCl_4, as described above, for its measurement. In addition, alkali fusion can be also used to separate iodine from environmental samples, such as soil, sediment, air particles, vegetation, and animal tissues (Hou et al., 1999; Zhang et al., 2015). In this case, ^{125}I tracer is first added to the sample, NaOH is then mixed with the sample. After drying, the mixture is ashed/fused at 500−550°C for 3−4 hours. The ashed/fused sample is leached with hot water, and the leachate is separated from residue by filtration. Iodine in the leachate is finally separated by CCl_4 extraction, as described previously (Fig. 2.24) (Hou et al., 1999; Zhang et al., 2015). Fig. 2.24 illustrates a combined procedure for the determination of ^{129}I and ^{36}Cl in soil samples, in which alkaline fusion and acid digestion were applied for decomposition of samples and solvent extraction was applied for separation of ^{129}I from sample matrices and interference radionuclides. For the separation of iodine from water, milk, and urine samples, especially large volumes of seawater (30−50 L), an anion exchange chromatographic method has been reported by Hou et al. (2001, 2002). In this method, iodine in the water or other liquid samples is first reduced to iodide using $KHSO_3$ at pH < 2, the sample is loaded to an anion exchange column (AG1×-4, NO_3^- form), the adsorbed iodine is then eluted with 2 M $NaNO_3$ solution. The iodine in the eluate is separated by CCl_4 extraction. Iodine is finally obtained in a small volume of back extraction solution, which is used for LSC measurement or prepared in suitable target for neutron activation analysis or accelerator mass spectrometry measurement for ^{129}I.

3. Calcium-41 (^{41}Ca)

^{41}Ca, with a very long half-life (1.03×10^5 years), is mainly produced by neutron activation reaction of $^{40}Ca(n, \gamma)^{41}Ca$. It is also a naturally occurring radionuclide produced by the reaction of stable calcium (^{40}Ca) of the earth with neutrons from cosmic rays and fission of uranium (Fink et al., 1990). Human nuclear activities, including atmospheric nuclear weapons testing and operation of nuclear facilities have also released some ^{41}Ca to the environment. In the nuclear reactor, ^{41}Ca is mainly produced in the concrete shielding, because of its high calcium content and its exposure to the neutrons from the reactor. ^{41}Ca is an important radionuclide in the disposal of radioactive waste, because it can exist for a very long time with a high mobility in the environment and high bioavailability.

^{41}Ca decays to the ground state of ^{41}K by pure electron capture, emitting X-rays and Auger electrons of very low energy (0.3−3.6 keV), it can thus be measured by X-ray spectrometry and LSC. LSC is much more sensitive (Suárez et al., 2000; Itoh et al., 2002b; Hou, 2005a, 2005b; Warwick et al., 2009; Hampe et al., 2013), because of its low counting efficiency (<0.08%) by X-ray spectrometry and the low abundance of X-rays of ^{41}Ca (11.4% for 3.31 keV X-ray). Mass spectrometry techniques such as accelerator mass spectrometry (AMS) (Fink et al., 1990; Zerle et al., 1997) and resonance ionization mass spectrometry (RIMS) (Müller et al., 2000) are more sensitive techniques for its measurement and have also been used for its determination. A $^{41}Ca/^{40}Ca$ atomic ratio as low as 10^{-15} can be measured by AMS.

Due to the pure electron-capture decay of ^{41}Ca, chemical separation from the sample matrices and purification from all other radionuclides are necessary prior to the measurement of ^{41}Ca using LSC or other techniques. Suárez et al. (2000) reported a radiochemical separation procedure for the separation of calcium from other radionuclides, which is based on hydroxide precipitation of transition metals and chromate precipitation of Ba, Sr, and Ra with a chemical recovery of 40%. In this procedure, the separation of Ba, Sr, and Ra by chromate precipitation is very critical, because of very strict control of pH value. Ion exchange and extraction chromatography have also been used for the separation of calcium (Itoh et al., 2002b; Hampe et al., 2013). Anion exchange chromatography was used to remove all radionuclides presenting as anion in high concentration HCl media, and extraction chromatography

using TRU resin was applied to remove actinides and lanthanides. However, this procedure is not well suitable for the removal of alkaline earth radionuclides such as radioisotopes of strontium, radium and barium. A tertbutylmethylether/ethanol extraction step was proposed to extract calcium and to remove Sr, Ba, and Ra (Hampe et al., 2013). With all of these steps, a recovery of more than 65% and decontamination factor for most of interfering radionuclides are higher than 10^3. Hou (2005b) reported a simple and effective method for the determination of ^{41}Ca in ordinary and heavy concrete (containing more than 75% of $BaSO_4$) based on the relative low solubility production of $Ca(OH)_2$, compared to Sr, Ba, and Ra in NaOH solution. Calcium (mainly as calcium carbonate) is first leached using aqua regia, and the experiment shows that more than 95% of Ca can be leached out from the concrete sample in this step. There are three main steps for the separation of Ca from the interfering radionuclides, namely,

(1) Ca is first separated from the transition metals, such as Co, Eu, Fe, Ni, and tranuranics by precipitation at pH 9 using NaOH. In this step, the interfering radioisotopes of these elements are precipitated, while Ca remains in the solution with Sr, as well as Ba, Ra, Cs, etc.
(2) Ca and Sr in the supernatant are then precipitated as carbonates with Ba and Ra by adding Na_2CO_3 and separated from alkali metals and nonmetal elements.
(3) Ca is finally separated from Sr, Ba and Ra by precipitation of Ca as $Ca(OH)_2$ in 0.5 mol/L NaOH solution after dissolution of the carbonate precipitates. This is based on the low solubility of $Ca(OH)_2$ in high concentration of NaOH (higher than 0.5 mol/L) compared with Sr, Ba, and Ra. This step is repeated and the separated $Ca(OH)_2$ is dissolved with HCl for measurement using LSC after neutralizing to pH 6-8.

The chemical yield of ^{41}Ca of 80%−90% was obtained by the measurement of Ca before and after chemical separation using ICP-OES. The decontamination factor for the interfering radionuclides such as ^{60}Co, ^{152}Eu, ^{133}Ba, ^{85}Sr, ^{137}Cs, ^{55}Fe, and ^{63}Ni are higher than 10^5. The detection limit of the analytical method for ^{41}Ca is 0.020 Bq.

This method could not separate ^{45}Ca from ^{41}Ca. If both isotopes exist in the sample, interference of ^{45}Ca to the measurement of ^{41}Ca has to be corrected, which can be carried out by measurement of the contribution of ^{45}Ca to the counting window of ^{41}Ca in the lower channel. Due to the low energy of Auger electrons (0.3−3.6 keV) detected in the measurement of ^{41}Ca by LSC, the counting efficiency is relatively low (<25%), and highly influenced by quench. The separated calcium sample is normally prepared in a neutral solution of $CaCl_2$, and all other interfering elements (especially iron) have to be removed completely. The major quench effect is the amount of calcium in the samples. In addition, luminescence is also an interference for the measurement of ^{41}Ca, which has to be considered in the measurement of ^{41}Ca using LSC.

VII. Analysis of radionuclides from natural decay series

A. Uranium

1. Environmental occurrence and importance

Natural uranium has three isotopes ^{238}U ($t_{1/2} = 4.5 \cdot 10^9$ y), ^{235}U ($t_{1/2} = 7.0 \cdot 10^8$ y) and ^{234}U ($t_{1/2} = 2.5 \cdot 10^5$ y) which belong to two decay series. ^{238}U is the parent of the uranium series where ^{234}U belongs as a member, and ^{235}U is the parent of the actinium series. The atom abundances of ^{238}U, ^{235}U and ^{234}U are 99.2745%, 0.7200% and 0.0055%, respectively. ^{232}Th ($t_{1/2} = 1.4 \cdot 10^{10}$ y) starts the third natural decay series. The decay scheme of the uranium series is presented in Fig. 2.25. Uranium and thorium are widely distributed throughout the earth's crust, in surface and ground waters. The current worldwide average value of 33 Bq/kg for ^{238}U in soil is low, but the reported concentrations vary largely up to 1000 Bq/kg (UNSCEAR, 2008). Practically, almost all of the natural environmental radiation of terrestrial origin is due to radionuclides of the uranium and thorium series and to ^{40}K. The actinium series is of lesser importance due to its low abundance of natural uranium.

Because members of the natural series have different chemical and physical properties, they are separated from their parents and from each other in the course of normal geological processes, and the members of the series are rarely in radioactive equilibrium with each other. The disequilibrium ratios

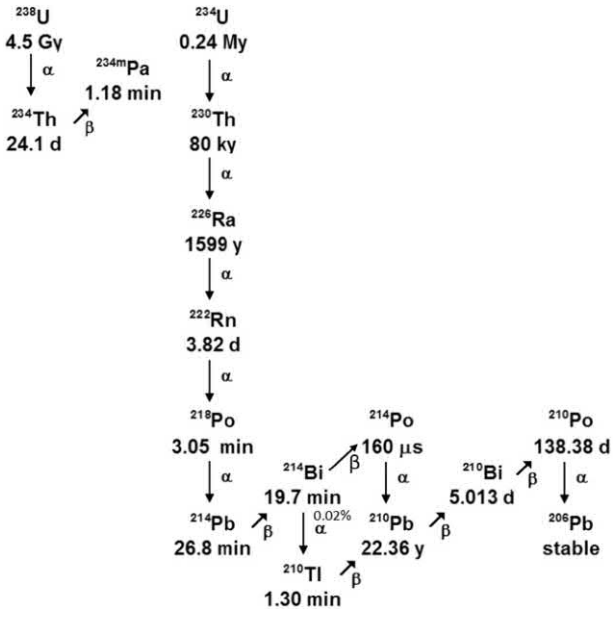


FIGURE 2.25 Decay scheme of uranium series (^{238}U).

between the members of uranium series are utilized widely in many studies in hydrology, age dating, marine chemistry, and exploration of uranium (Ivanovich et al., 1992). The disequilibrium state between ^{238}U and ^{234}U is rather common in nature, especially in waters. Depending on the origin of the water, the $^{234}U/^{238}U$ activity ratios can vary greatly; values ranging up to 30 have been reported in the groundwater. The main intake of uranium occurs through food. The contribution of drinking water is normally very low; but it can exceed the intake through food by several orders of magnitude, if uranium is present in drinking water sources (UNSCEAR, 2000, 2008). Uranium is retained in the body primarily in the skeleton. The major health effect from uranium is due to its chemical toxicity rather than to the radiotoxicity. Continuous uranium intakes may affect the human kidney, in particular, proximal tubular function (Zamora et al., 1998; Kurttio et al., 2002, 2006; Health Canada, 2010; WHO, 2011).

The limit of uranium in drinking water is set on the basis of its chemical toxicity. WHO has set a provisional guideline of 30 μg/L (WHO, 2011), and the limits in USA and Canada are 30 μg/L and 20 μg/L, respectively (EPA, 2009; Health Canada, 2010). The 30 μg/L natural uranium ($^{234}U/^{238}U$ activity ratio = 1) corresponds to 0.37 Bq/L of ^{238}U. Environmental monitoring of uranium and other natural radionuclides is of great concern due to the operation of nuclear fuel cycle installations and due to other industries where uranium containing minerals are processed (UNSCEAR, 2008).

2. Sample preparation and analysis

Today, the most common methods for uranium analysis are mass spectrometric, alpha-spectrometric, and LSC methods. Mass spectrometric methods are more than six orders of magnitude sensitive than the radiometric methods for ^{238}U and ^{232}Th due to their long half-lives, whereas their short-lived isotopes are best determined by radiometric methods (Hou and Roos, 2008). The sample preparation for the mass spectrometric analysis is often much easier and very small samples are needed for the analysis compared to the alpha spectrometric methods. Today, the multicollector systems both in TIMS and ICP-MS instruments have significantly contributed to making mass spectrometry a main tool for the high-precision assay of long-lived uranium and thorium isotopes (Bou-Rabee et al., 1995; Werner et al., 1997; Forte et al., 2001; Tagami and Uchida, 2004; Rathore, 2008; Andersen et al., 2009). The measurement time for one sample is only about 1 minute, and a great number of samples can be measured accurately in a short time. Also, ^{234}U can be determined using the MC-ICPMS and ICP-QMS instruments even though its isotopic abundance is extremely low ($^{234}U/^{238}U = 5.49 \cdot 10^{-5}$) compared to that of ^{238}U (Karpas et al., 2005). Alpha spectrometric methods have been used widely to determine uranium activities and $^{234}U/^{238}U$ activity ratios in environmental samples over several decades (Lieberman and Moghissi, 1968; Sill and Williams, 1969; Holm and Fukai, 1977; Singh and Wrenn, 1983; Anderson, 1984; Godoy et al., 1994; Hrnecec and Irlweck, 1995; Carter et al., 1999; Forte et al., 2001; Wang et al., 2004; Kovács et al., 2004; Bojanowski et al., 2005; Kozłowska et al., 2007; Wallner et al., 2008; Eikenberg et al., 2009; Jia et al., 2009; Kiliari and Pashalidis, 2010; Dircan and Sahin, 2016; Sonali et al., 2016; Jia, 2017; Kallithrakes-Kontos et al., 2018). The chemical separation methods are well established and the $^{234}U/^{238}U$ activity ratios are determined accurately, because the silicon surface-barrier or PIPS detectors provide a good resolution for α-particles from isotopes of uranium. These methods, however, assume that uranium is separated from the sample matrix as a pure fraction and that it is deposited on a metal disc as a thin layer to reduce self-absorption of alpha particles in the sample itself. Uranium can be separated either alone, or together with other actinides and radium, using several methods like precipitation, anion or cation exchange, liquid-liquid extraction or extraction chromatography or a combination of these. Uranium is finally electrodeposited onto a stainless-steel disk or it is coprecipitated as fluoride with CeF_3, LaF_3, or NdF_3, which is collected on a filter for the measurement with an alpha spectrometer. ^{232}U, ^{233}U, or ^{236}U is used as a yield tracer. The drawback of the method is that the alpha resolution will be impaired, if the uranium mass on the disk or the filter is too high. Hence, the uranium concentration should be assessed in advance to use the appropriate amount of sample and yield tracer for analysis. Because the sample size is limited, it usually means long counting times, probably several days.

Although ICP-MS and semiconductor alpha spectrometry are most common techniques for low-level uranium measurement, LS methods have been used to monitor for uranium in a variety of matrices including water, urine, phosphate containing materials, air, and fallout (Horrocks, 1974b; Miller, 1991; Prichard and Cox, 1991; Venso et al., 1993; Salonen, 1993a; Zelensky et al., 1993; Füeg et al., 1997; Sanchez-Cabeza and Pujol, 1998; Eikenberg et al., 1999; Forte et al., 2001; Bem and Wieczorkowski, 2002; Navarro et al., 2004; Aupiais, 2004a, 2004b; Antoniou et al., 2008). The LS methods are often used to screen uranium in drinking water for which purpose they are practical and cost-effective. The sample preparation is easy, and the LS spectrometers with α/β discrimination provide much information on the radionuclide composition in water as well. In some methods, water is concentrated directly in the LS vial by freeze-drying or evaporation, the residue is dissolved in dilute HCl, the cocktail is added and the sample is measured with LSC using α/β discrimination (Salonen, 1993a; Sanchez-Cabeza and Pujol, 1998; Zelensky et al., 1993). Uranium can also be extracted from a larger water sample. Prichard and Cox (1991) extracted it from a 1L water sample (acidified to pH 1.5 with HNO_3) into 20 mL of toluene containing the scintillants and bis(2-ethylhexyl)phosphoric acid (HDEHP) as an extractant and measured it with the PERALS spectrometer. Venso et al.

(1993) used the same extractant, HDEHP, but mixed it with a DIN-based cocktail. Bem and Wieczorkowski (2002) separated uranium and thorium from fallout samples by extracting them into 10 mL of 5% (w/w) tri-n-octylphosphine oxide (TOPO) in toluene from 10 mL of 3M HNO_3 where fallout residue had been dissolved by microwave digestion. The toluene was mixed with 10 mL of Ultima Gold LLT and measured with LSC using α/β discrimination. The only significant interfering radionuclide in the fallout samples was ^{210}Po which was removed by washing the toluene phase with 10 mL HNO_3.

Miller (1991) developed a rapid and economic method for the separation of uranium from urine. In this method, a 200 mL urine sample and an equal amount of concentrated HCl were mixed, the mixture was passed through an anion exchange column, impurities were first eluted from the column with HCl/HI acid mixture and thereafter uranium with 10 mL of 0.1M HCl. The destruction of the organic matter was not applied in this method, and therefore the analysis time was shortened. Eikenberg et al. (1999) developed a quite simple and fast procedure for the separation of actinides from urine. They used an extraction chromatography (Actinide Resin), which is based on the extractant with trade name DIPEX. Uranium and other actinides can be absorbed effectively on the resin and separated from the matrix. The separated actinides were evaporated and finally dissolved in 2 mL of 0.5 M HCl, then mixed with 12 mL of Ultima Gold AB and measured with a low-background LS spectrometer using α/β discrimination. The counting efficiency was 95%, the recoveries were between 90 and 100% and the detection limit was 1.5 mBq/L for a 0.5 L urine sample and for a 500 minutes counting time.

Antoniou et al. (2008) proposed an ion exchange method for the separation followed by LSC counting. Uranium was pre-concentrated from 1 L of ground water sample using a cation exchange resin, Chelex 100. The uranium was eluted from the resin with 30 mL of HNO_3 which was evaporated to incipient dryness. The residue was dissolved into 4 mL of 0.5M HCl and mixed with 16 mL of OptiPhase HiSafe three cocktail and measured with the Triathler. The detection limit was 30 mBq/L.

Leyba et al. (1995) tested an extractive scintillation cocktail, URAEX, to separate uranium from water and to measure the samples with the PERALS spectrometer. The results were comparable with those obtained by an alpha spectrometric method. The extraction efficiency for uranium decreased when nitrate and chloride concentrations were high and these samples have to be pre-treated. The whole separation time by this extraction method was short (30 minutes) compared to that by alpha spectrometry (6 hours). Extraction chromatography is becoming a popular technique for the separation of radionuclides. UTEVA resin has been widely used for the separation of uranium from various sample types. Uranium is first released from samples using acid dissolution or alkaline fusion followed by pre-concentration using coprecipitation with $Fe(OH)_3$, then prepared in 3M HNO_3 media, the sample solution is loaded to a UTEVA column. The uranium is strongly adsorbed on the column, all matrices and interfering radionuclides are removed by rinsing with 3M HNO_3 and 6M HCl, and the uranium is finally eluted from the UTEVA column with diluted HCl (0.02 M). After the eluate is reduced to a small volume, the solution can be mixed with scintillation cocktail for the LSC measurement of uranium (Qiao et al., 2015). Füeg et al. (1997) also used extractive chromatographic resin, UTEVA and extractive scintillation cocktails, URAEX, THOREX and RADEX, to separate ^{234}U, ^{238}U, Th isotopes and radium from soil samples and measured the samples with the PERALS spectrometer. U/Th-disequilibrium in soil was determined easily without using U- and Th-tracers. Aupiais (2004) developed a rapid and simple method to measure uranium in all types of water samples. Uranium separation was performed using an extractive scintillation cocktail, Alphaex, which contains HDEHP as extractant. The co-extraction of the interfering radionuclides such as ^{210}Po, Th-, and Pu-isotopes was prevented by complexing them with DTPA (final conc. 0.1M) and by adjusting the pH to 3.5 with 10M NH_3 before the extraction. The sample was measured with the PERALS spectrometer. However, some ^{210}Po was found to be extracted, because the yield with the ^{232}U tracer was over 100%. This was caused by ^{210}Po having an α-energy equal to that of ^{232}U. Hence, an additional step was included into the separation procedure for removing ^{210}Po using a silver powder. The separation time was 2 hours and the detection limit is 0.003 Bq/L for a 100 mL water sample and for a 4000 minutes count time. However, because of the low resolution of LSC to alpha-emitting radionuclides, the measured activity is the sum of total alpha activity or total activity of uranium when uranium was separated from other alpha-emitters.

In summary, the rapid LS methods are sensitive enough to determine the uranium concentration in drinking waters to achieve the regulations. The application of the α/β discrimination provides accurate results of uranium, and valuable information on additional radionuclides in water. The main disadvantage of the conventional LS counters is their poor resolution, which does not allow the determination of the concentration of individual uranium isotopes. Among them, the activity concentration of ^{234}U often exceeds that of ^{238}U in ground waters, and the radiation dose will be underestimated if only ^{238}U is determined and these isotopes are supposed to be in the equilibrium.

B. Gross alpha and beta measurements

Gross alpha and beta activity screening analyses are used for many purposes such as the monitoring of environmental and bioassay samples, low-level liquid effluents, workplace

surveys, characterization of low-level radioactive wastes and for assessing environmental contamination after accidental release (Salonen, 1993a; Sanchez-Cabeza and Pujol, 1995; Eikenberg et al., 1996; Cooper et al., 1998; Burnett et al., 2000; Warwick and Croudace, 2002a, 2002b; Verzilov et al., 2002; Kleinschmidt, 2004; Forte et al., 2006; Ruberu et al., 2008; Mizutani et al., 2009; Piraner and Jones, 2009; Zapata-García et al., 2009). Particularly drinking water supplies are screened by the gross alpha and beta analysis method, which is a highly useful control measure for the radiological characterization of water and as a factor in the decision as to whether further analyses by radionuclide-specific methods will be required. Urine samples from workers who potentially are exposed to radioactive contamination is also often screened by gross alpha and gross beta measurements to obtain an overview on internal exposure of radiation. The national and international regulations assume the radiological quality of drinking water to be controlled. The maximum contaminant level in public water supplies in the USA is 0.56 Bq/L (= 15 pCi/L) for gross alpha including radium but excluding uranium (EPA, 2009). The guideline activity concentrations of WHO (2011) are for gross alpha and gross beta to be 0.5 Bq/L and 1 Bq/L, respectively; whereas the European Union (1998) has set the screening values of 0.1 Bq/L for gross alpha and 1 Bq/L for gross beta. No further analyses are recommended under these screening levels, but if these levels are exceeded, radionuclides should be identified and their concentrations must be determined. Because the gross alpha and beta screening is a simple and rapid procedure, it often results in remarkable time and cost savings if the tedious radiochemical analyses are found unnecessary. The regular gross alpha and beta measurements are also a practical means for immediate detection of radioactive contamination in drinking water supplies, and it is possible that some radionuclides would remain unidentified if only radionuclide specific methods are applied. Some radionuclides which are in volatile compounds or in gaseous form are lost during the sample preparation. These are ^{3}H, ^{14}C, and radon which have to be determined by specific methods. These nuclides, as well as short-lived daughters of radon, are excluded from the gross alpha and gross beta screening analyses. In the normal situation, most important radionuclides to be screened by gross alpha and beta analyses in drinking water sources are the long-lived radionuclides, ^{234}U, ^{238}U, ^{226}Ra, ^{228}Ra and ^{210}Pb and ^{210}Po, from uranium and thorium decay series. The alpha and beta spectra of natural uranium, ^{226}Ra and ^{210}Pb in equilibrium with their short-lived daughters are illustrated in Fig. 2.26. ^{40}K occurs in variable amounts in all

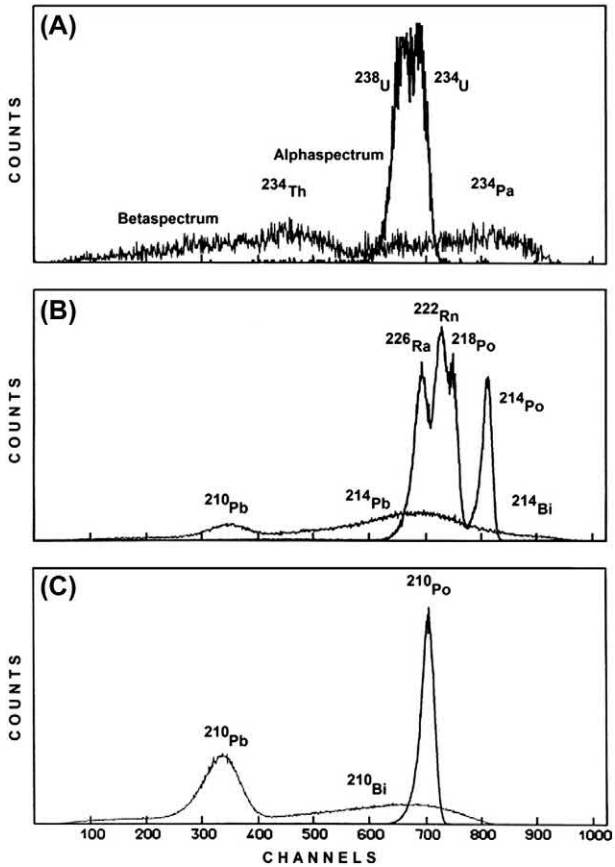


FIGURE 2.26 Alpha and beta spectra of (A) $^{234,238}U$ (natural uranium), (B) ^{226}Ra (in equilibrium with ^{222}Rn and its short-lived daughters), and (C) ^{210}Pb (in equilibrium with its daughters) from standard samples (Salonen, 1993a). *Reprinted by permission of Elsevier © 1993.*

natural waters, and its contribution to the gross beta counts can be significant. However, its determination is not important, because potassium is under homeostatic control in the body and its amount remains constant in healthy people. Gross alpha measurements are also used to screen transuranic elements in nuclear wastes and gross beta for fission products in reactor wastes and in accidental releases.

The methods commonly used for gross alpha and beta analysis in drinking water are based either on gas proportional counting (GPC) or on LSC techniques. Bonotto et al. (2009a) presented another method, which is based on a combination of a well-type NaI(Tl) scintillation detector and alpha spectrometry with surface barrier detectors. They tested the method and applied it successfully to the analyses of ground water samples. The conventional/standard method is based on GPC techniques. It involves the evaporation of a water sample to near dryness, quantitative transfer of the residue on a planchet and its subsequent counting (APHA/AWWA/WEF, 1998; ISO 9696, 2007; ISO 9697, 2008). Zikovsky (2002) used a faster sample preparation method whereby they precipitated alpha-emitters from ground water as sulfates (Ra) and hydroxides (Po, Th, and U) using Ba^{2+} and Fe^{2+} as carriers and obtained overall a yield higher than 80% for all nuclides and a better sensitivity than that obtained by the evaporation method. The disadvantages of the GPC method are: 1) sample preparation is tedious and labor-intensive, 2) there is a lack of high precision primarily owing to the inherent variability of the sample preparation technique and water composition, 3) sample size is strongly limited due to the total dissolved solids (TDS) which cause self-absorption of α-and β-particles, and 4) the counting efficiency is affected by TDS and the chemical composition of water (Ruberu et al., 2008; Martín Sánchez et al., 2009; Jobbágy et al., 2010). The small sample size combined with the relatively low counting efficiency of the GPC makes it difficult to attain low detection limits except by applying very long counting times. The reported detection limits of the GPC methods are 0.8 Bq/L for the gross alpha and 3 Bq/L for gross beta using a 22 hours counting time (Jobbágy et al., 2011), which could not meet the requirement of the regulation for screening of the gross alpha in drinking water (0.1−0.5 Bq/L).The LSC methods with α/β-discrimination avoids most of the difficulties typical of the GPC methods, although dissolved minerals or organics in water may cause variable quenching which must be considered in the calibrations (Sanchez-Cabeza and Pujol, 1995; Pates et al., 1996a; Pujol and Sanchez-Cabeza, 1997; Warwick and Croudace, 2002a, 2002b; Kleinschmidt, 2004; Ruberu et al., 2008; Zapata-García et al., 2009; Jobbágy et al., 2010). The LSC method involves the mixing of a water sample directly or after some concentration with the LS cocktail followed by LS counting using α/β-discrimination. If the sample is concentrated, the residue is dissolved into a few mL of dilute HCl, HNO_3, or H_3PO_4 prior to the addition of the LS cocktail. Water can be concentrated directly in the LS vials once or several times after successive evaporations using a freeze-dryer (Salonen, 1993a; Salonen and Hukkanen, 1997) or block heater (Kleinschmidt, 2004), or by the evaporation of the water sample in another vessel from which concentrated water or the residue is transferred to the LS vial (Sanchez-Cabeza and Pujol, 1995; Wisser et al., 2006; Forte et al., 2006; Ruberu et al., 2008; ASTM D7283-06, 2006; ISO 11704). Happel et al. (2004) used an extraction chromatographic resin to separate alpha-emitters from drinking water. The resin showed a strong affinity for actinides in tri-, tetra-, and hexavalent oxidation states and for Ra even in presence of large amounts of Ca. Radionuclide uptakes by the resin were greater than 80% even at very high Ca, K, Fe, carbonate, and sulfate contents. The sample preparation was fast, because it consists of the extraction of radionuclides from water to resin, the separation of the resin from water by filtration, the mixing of the dried resin with the scintillation cocktail followed by LS counting using α/β discrimination. The detection limits reported for the low-background LS spectrometers and the portable Triathler are between 0.01 and 0.08 Bq/L for gross alpha and 0.1−0.2 Bq/L for gross beta using 40−150 mL water samples and 3−8 hours counting times.

The calibrations of gross alpha and beta analyses include the optimization of the α/β discrimination performance and the determination of α- and β-counting efficiencies and spillovers in the selected α- and β-windows as presented previously in this chapter and elsewhere (ASTM D7283-06, 2006; ISO/DIS 11704). The α- and β-activities are calculated by the formulas where all these parameters are included. The results would be rather accurate for the real samples, if their composition and the quench levels agree to that of standard samples used for calibrations. This is not, however, the actual situation, and the calibrations become more complicated if variable quenching is corrected, because the optimum pulse decay (PD) setting (optimal PSA value), as well as efficiencies, backgrounds and spillovers, depend on quenching (Pates et al., 1996a, 1998; Bakir and Bem, 1996; DeVol et al., 1996, 2007; Pujol and Sanchez-Cabeza, 1997; Burnett et al., 2000; Bhade et al., 2010). Hence, each sample should be measured at its optimum PD setting, which is not a practical approach in routine measurements. The approaches to solve this problem are discussed previously in this chapter and elsewhere (Warwick and Croudace, 2002a, 2002b; Ruberu et al., 2008). Another drawback for performing precise calibrations is due to the fact that the optimum PD setting and alpha and beta spillovers depend on particle energies. The real samples may contain several α- and β-emitters with largely variable particle energies compared to those used for calibrations including the setting of the optimum PDD. The dependence of β-spillover on particle energy was recognized earlier than that of α-particles (Salonen, 2006;

DeVol et al., 2007). Salonen (2006) established the dependence of α-spillover on α-particle energy using ^{218}Po and ^{214}Po, which have a large difference in particle energies (1.69 MeV). DeVol et al. (2007) observed this effect using ^{241}Am and ^{239}Pu, which have particle energies differing only by 0.33 MeV. The optimum PDD setting is highly affected for higher-energy α- and β-emitters than for lower-energy emitters. The β-spillover increases with β-particle energy while α-spillover decreases with α-particle energy. With increasing quench, the higher energy β-particle produces a higher spillover compared to the lower-energy particles while the higher-energy α-particle produces a lower spillover compared to the low-energy particles at the same PSA level. In summary, the calibrations with appropriate quench corrections are necessary, although they would not provide accurate results for variably quenched samples with variable radionuclide composition. The calibrations would be simplest if the samples were unquenched and as similar as possible to the nuclides used for the PDD instrument calibration. It is preferable to perform the calibrations with α- and β-emitters with the energies equal to the averages of the nuclides expected to be in actual samples to be analyzed.

Fig. 2.27 illustrates the gross alpha and gross beta spectra of four ground water samples, which have been measured at the same PSA level set according to an unquenched sample. The measurements of these samples have been made 1 month after the sample preparation to establish the equilibrium between ^{222}Rn with its parent ^{226}Ra in order to enable the subtraction of the counts owing to ^{222}Rn and its short-lived daughter from the gross alpha and beta counts. The counts due to the β-emitting daughters (^{234}Th and ^{234}Pa) of ^{238}U are also subtracted after making appropriate ingrowth corrections. ^{234}U, ^{238}U, ^{226}Ra, ^{210}Pb, and ^{210}Po have been analyzed in these samples using radiochemical methods except ^{226}Ra that was determined directly from the gross alpha spectrum using the ^{214}Po peak (Salonen, 1993a). The increased quenching in the samples (Fig. 2.27) is indicated by the SQP(E) values, i.e., the magnitude of the SQP(E) decreases as quench increases). The spectra shifts to the left to different degrees and the alpha spillover increases on the smooth beta spectrum are visible in the region of ^{238}U which has lowest alpha energy. Thus, the difference between results obtained from gross alpha and radiochemical analyses is the greatest for the most quenched sample (Fig. 2.27B). The spillover corrections and setting of the PSA level at a lower value would improve the result of uranium-rich ground waters. The comparison of the spectra in Figs. 2.26 and 2.27 indicate quite clearly whether U, ^{226}Ra, and ^{210}Pb should be

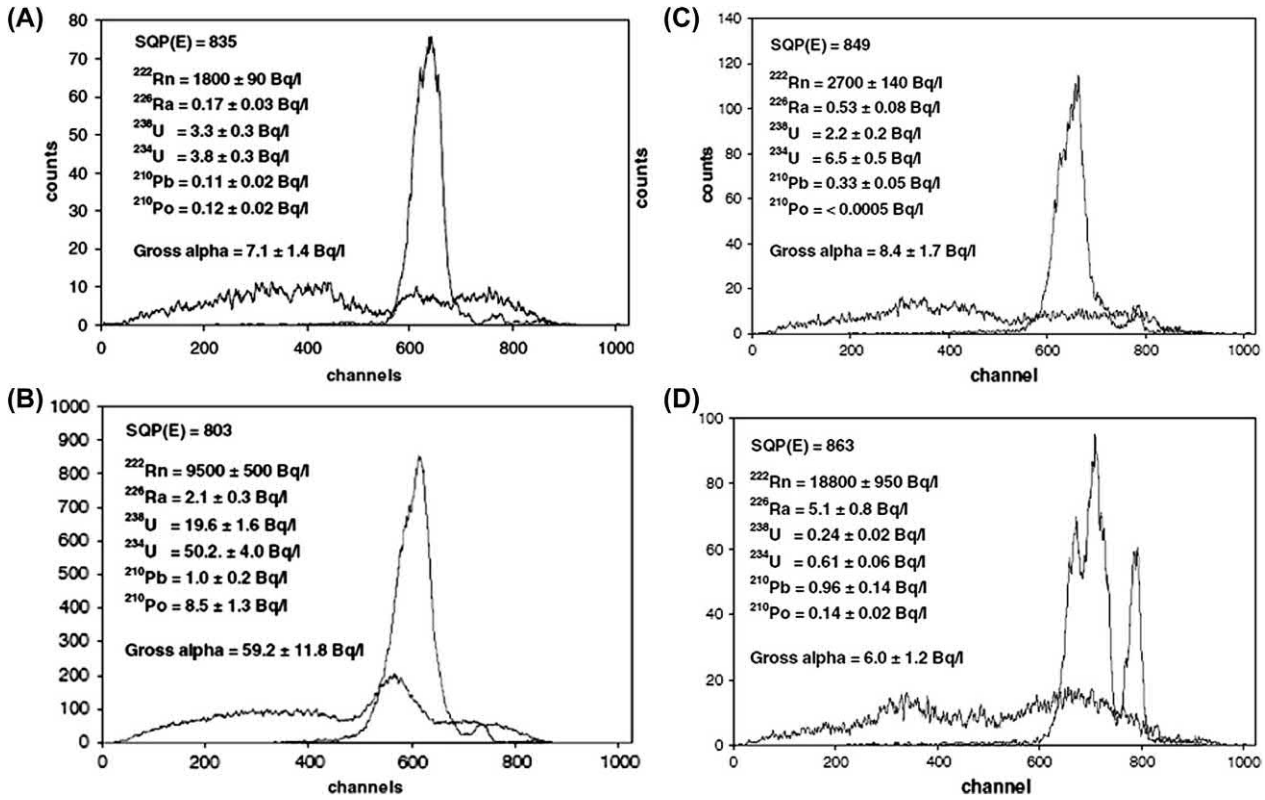


FIGURE 2.27 The gross alpha and beta spectra of the Quantulus from 4 drinking water samples originating from drilled wells (Salonen, 2006). *Reprinted by permission of* Radiocarbon, *University of Arizona, Tucson.*

analyzed by specific methods which is a big advantage compared to the GPC methods. ^{210}Po cannot be observed easily unless it exists almost alone in water.

In a similar manner, gross alpha and gross beta activities may be determined for a range of other environmental matrices. A filter sample is simply placed in the scintillation vial with the scintillation cocktail (Cooper et al., 1998). Urine samples have been prepared by mixing urine directly with the cocktail (Piraner and Jones, 2009) or after some processing which involve oxidation of organic substances with HNO_3, coprecipitation of actinides as phosphate, wet ashing using HNO_3 and H_2O_2, transfer of the nitrates to the chlorides, dissolution of the white residue in 0.2 M HCl followed by the addition of the cocktail (Eikenberg et al., 1996).

C. Radon

1. Environmental occurrence and importance

^{222}Rn ($t_{1/2} = 3.82$ d) is an inert radioactive gas and the immediate daughter product of ^{226}Ra in the uranium decay series (Fig. 2.25). ^{222}Rn is commonly known as radon. Other natural radon isotopes are ^{220}Rn ($t_{1/2} = 55.6$ seconds) and ^{219}Rn ($t_{1/2} = 3.96$ seconds), which are known as thoron and actinon, respectively. They arise in the decay series of ^{232}Th and ^{235}U, respectively. Uranium and thorium occur in all rocks and soils at varying concentrations. They produce ^{222}Rn and ^{220}Rn, which can diffuse from mineral grains into pore spaces and thereafter escape to air and dissolve in water. Because ^{220}Rn has a much shorter half-life than ^{222}Rn, it moves much shorter distances before decaying. Therefore, ^{220}Rn is of concern only where the concentration of ^{232}Th is high (UNSCEAR, 2006). Actinon (^{219}Rn) is not of significant concern for radiation exposure owing to its short half-life and to the low abundance of ^{235}U in natural uranium. Radon-222 is the most significant, and it is present in air and in ground and surface waters. Exposure to radon occurs by inhaling radon and by ingesting radon with water. The most important mechanism of exposure is the inhalation of radon and its short-lived decay products with indoor air. It accounts for the majority of the human exposure to radiation and presents the largest risk to human health from all natural sources of radiation by increasing the risk of lung cancer (UNSCEAR, 2006). The worldwide average annual dose from inhaled radon (1.26 mSv) is about half of the average dose from all natural sources of radiation (2.4 mSv) and about twice of the dose from all artificial sources (0.6 mSv) (UNSCEAR, 2008). Radon was first identified as a carcinogen by epidemiological studies of underground miners, and later by numerous epidemiological studies of the general population. An extensive overview on these studies is presented in the UNSCEAR 2006 report which summarizes all epidemiological studies performed in different countries and assesses lung cancer risks from occupational and residential radon exposures. It also summarizes the worldwide indoor radon concentrations based on national studies. The countrywide averages of radon indoor concentrations vary from 7 Bq m^{-3} to about 200 Bq m^{-3}, but much higher (up to 2745 Bq m^{-3}) values were observed at high-background areas. For single residences, indoor radon concentrations of 10,000−84,000 Bq m^{-3} have been reported from many countries. When radon-rich water is used as a household water, people are exposed both by radon ingested in water and by radon being released from tap water to indoor air during water use. Radon in drinking water also presents a risk of the development of internal organ cancers by radiation exposure of cells in the gastrointestinal tract and in other organs once radon is absorbed into the blood stream (NRC, 1999). In fact, the lung cancer risk from radon in drinking water is higher than that of stomach cancer, which is the most probable compared to other cancers. Usually radon from tap water is a smaller source in indoor air, because the major part of radon in indoor air arises from soil under the house and construction materials in some cases. Radon concentrations in surface waters are typically less than 4 Bq/L, while in ground waters the concentrations vary over a wide range up to 10,000 Bq/L or even higher.

As an inert gas, radon is an excellent tracer either alone or together with radium for studying geochemical, hydrogeological and oceanic processes like groundwater discharge rates, groundwater seepage, vertical turbulent mixing, gas exchange across the air-water interface, mixing processes between ground- and seawater and submarine groundwater discharges (Horiuchi et al., 1993; Cook et al., 2003, 2008; Purkl and Eisenhauer, 2004; Lamontagne et al., 2008; Murad et al., 2014). Radon is also a useful natural tracer in geophysical investigations, as in predicting earthquakes (King, 1985; Theodórsson, 1996; Yalım et al., 2007). In these studies, the radon concentration is determined in the field using an extraction method and a portable LS spectrometer or by bringing the sample into the laboratory for measurement with a low-background LS spectrometer.

2. Sample preparation and analysis

a. ^{222}Rn measurements in air

There exist numerous methods for monitoring radon and its daughters in air at homes and at workplaces. These include alpha track detection (filtered), unfiltered track detection, charcoal adsorption, liquid scintillation charcoal, continuous monitoring using an ionization chamber or scintillation cell, evacuated scintillation cell methods, electric ion chamber methods, grab radon methods, and several radon decay product measurement methods (WHO, 2009). The indoor radon concentrations both at homes and at workplaces are monitored most often using an integrated method with alpha track detectors, which consists of a small piece of special plastic or film

in a small container. Radon diffuses through a filter covering the holes inside the container, and the alpha particles of radon and its decay products strike the film and cause damage tracks. The tracks become visible by electrochemical etching and can be counted. Long exposure times (2–6 months) are necessary, because of less sensitivity of this method and the temporal and seasonal variation of indoor radon concentrations. Charcoal adsorption methods are appropriate mostly for screening because charcoal allows continual adsorption and desorption of radon, the method does not give a true integrated measurement over the exposure time. It gives radon concentration during the specific time, but does necessarily represent average concentration measured during longer periods of time. In this method, radon is adsorbed on activated charcoal granules packed in an airtight circular canister which is opened in the area to be sampled. Typical exposure times are between 2 and 7 days, thereafter the canister is closed and radon is determined via its daughters, ^{210}Pb and ^{210}Bi, by gamma spectrometry (George, 1984). The method is inexpensive and easy to use and therefore popular for screening at workplaces and mines. The liquid scintillation charcoal method is an attractive alternative to the gamma spectrometric method, because of its much higher sensitivity, simplicity and the ability to automate the counting of large numbers of samples. There are several modifications to this method for measuring radon in indoor air and radon emanation rates from soil (Prichard and Marlën, 1983; Buzinny, 1996; Schönhofer et al., 1995; Iimoto et al., 2008). In all of these methods, radon is adsorbed on activated charcoal in a small vial during a few days. Afterward, radon is extracted from the charcoal into toluene or into an LS cocktail to be measured. Radon emanation rates from soil can be determined in the laboratory or in situ (Wadach and Hess, 1985; Turtiainen, 2009). In the laboratory, a few grams of dried soil are weighed into a glass vial, soil is wetted with distilled water and an organic scintillation cocktail is added. The vial is closed tightly and stored for a month to attain the constant radon level emanated from soil before the measurement. Alternatively, radon can be trapped from the dried soil sample directly into the LS cocktail in a glass vial. This is performed in a tightly closed glass bottle where the soil is located at the bottom and the LS vial is hanging from a hook fixed into the stopper of the glass bottle (Turtiainen, 2009). The in-situ measurement is performed by hanging an open LS vial containing the cocktail inside a test hole or tube sunk into the soil (Horiuchi and Murakami, 1983).

b. ^{222}Rn measurements in water

Radon in water originates from the decay of ^{226}Ra, which is either dissolved in water or localized in rock or soil minerals in contact with water. Most of the radon in water originates from ^{226}Ra in minerals from where radon gas diffuses into pore spaces and dissolves in soil or ground water. Hence most of radon in water is unsupported and therefore its concentration in water is often orders of magnitude higher than that of ^{226}Ra dissolved in the same water. However, radon will not be transported far from its place of birth owing to its short half-life. Special attention should be paid to sample collection and its transport when undertaking radon measurements. Radon can easily escape from water during the sampling as well during the sample transport and storage, if the sampling vials are not gas-tight. Samples should also be collected into glass bottles or containers, because some radon will be lost by adsorption onto the surface of polyethylene bottles (Saito, 1983). The caps should be equipped with rubber or Teflon septum to prevent radon leakage from the bottle. Sampling instructions depend on the sampling situation and purpose. For drinking water samples appropriate sampling instructions are available, e.g., in the ASTM and ISO standards. The most widely used methods for determining radon in water are radon emanation, gamma counting and LSC, the last of which has become the most popular technique during the recent decade. These methods are based on the detection of radon gas and its short-lived α- and β-emitting daughters, the decay properties of which are shown in Table 2.6.

c. Emanation and gamma spectrometric methods

The earliest and still often used methods are those based on radon emanation (Lucas, 1957; EPA, 1987; Mathieu et al., 1988; Kitto et al., 1996; Belloni et al., 1995; Stringer and Burnett, 2004; Bonotto and Mello, 2006; de Oliveira Lucas et al., 2009). In these methods radon gas is transferred from water into an alpha scintillation cell called the Lucas cell, which is coated with solid scintillator, ZnS(Ag). The sample is usually collected into a glass bottle, transported to the laboratory where radon is stripped from water using a carrier gas (e.g., helium) and transferred into an evacuated Lucas cell. The stripping of radon from water (emanation) is performed using a special glass-ware bubbler, which is connected to the Lucas cell. Several improvements to the sampling bottle and radon emanation system design have been presented over the years, and the fragile glassware bubbler has been replaced with more practical radon degassing or vacuum extraction units for field sampling (Smethie and Schell, 1980; Mathieu et al., 1988; Kitto et al., 1996; Stringer and Burnett, 2004; de Oliveira Lucas et al., 2009). The emanation method requires extensive sample handling, but it is very specific and sensitive. Very low detection limits (0.04–1.0 mBq/L) have been achieved using improved sampling and bubbler devices and large (5–19 L) sample volumes (Mathieu et al., 1988; Kitto et al., 1996; Stringer and Burnett, 2004). The main advantage of the emanation method is its high sensitivity making it appropriate for determining very low radon activities. See also Chapter 9, Volume 1 for a description of the Lucas cell.

TABLE 2.6 Members of ^{226}Ra subseries and their most significant decay properties. Values obtained from NuDat (2016).

Radio-nuclide	Half-life	α-decay energy (MeV) and intensity (%)	β-decay energy (MeV) and intensity (%)	γ-emission energy (keV) and intensity (%)
^{226}Ra	1600 y	4.784(93.8), 4.601(6.2)	–	186.2 (3.64)
^{222}Rn	3.82 d	5.489 (99.9), 4.986 (0.1)	–	510 (0.076)
^{218}Po	3.10 minutes	6.002 (100)	–	–
^{214}Pb	27.1 minutes	–	0.667 (45.9), 0.724 (40.2), 1.019 (11.0)	351.9 (35.6), 295.2 (18.4), 242.0 (7.3)
^{214}Bi	19.9 minutes	–	3.270 (19.1),1.540 (17.6), 1.505 (17.0), 1.423 (8.1), 1.892 (7.4), 1.151 (4.4), 1.066 (5.6)	609.3 (45.5), 1764.5 (15.3), 1120.3 (14.9), 1238.1 (5.8), 2204.1 (4.9), 768.4 (4.9)
^{214}Po	163.6 μs	7.687 (100)	–	–

Gamma spectrometers equipped with NaI(Tl) or HPGe(Li) detectors are often used for measuring radon in water (Belloni et al., 1995; Al-Azmi et al., 2004; Bonotto and Mello, 2006; Talha et al., 2008). The determination is based on measuring the gamma photons of radon daughters, ^{214}Bi or ^{214}Pb, which are in equilibrium with the parent (Table 2.6). The water sample can be measured directly in gas-tight Marinelli beakers or radon is stripped with gas from a larger amount of water and then trapped into activated charcoal in a canister. The detection limits are quite high (1−9 Bq/L); however, the simplicity of sample preparation and the wide availability of gamma spectrometers renders it a potential alternative for measuring radon in water.

d. Liquid scintillation methods

The LS methods are based on the high solubility of radon in organic solvents such as toluene and xylene. Water samples can be prepared by introducing a small amount of water directly into the LS vial containing the cocktail either in the field or in the laboratory. If higher sensitivities are required, radon can be extracted from a larger water volume directly into the LS cocktail or into toluene to be mixed with the cocktail. The main advantages of the LS methods are their simple methodology, high sensitivity, and automatic sample counting.

Determination of the radon concentration in drinking water belongs to the routine analysis in environmental laboratories. The analysis is most often performed using the direct LS methods without any sample pre-concentration. The detection limits using the direct LS methods are mostly less than 1 Bq/L with a 20−60 minutes count, but lower (0.04−0.2 Bq/L) by applying longer count times and α/β discrimination (Prichard and Gesell, 1977; Schönhofer, 1989b; Spaulding and Noakes, 1993; Salonen, 1993b; Belloni et al., 1995; Gómez Escobar et al., 1996; Salonen and Hukkanen, 1997; Kozłowska et al., 1999; Maragheh et al., 2002; Cho et al., 2004; Galán López and Martín Sánchez, 2008). The detection limits by LS counting are low enough to meet the regulatory requirements as strict as in the USA where the limit is 11 Bq/L (EPA, 2009). The low detection limits are due to the high counting efficiency of radon and its daughters (^{218}Po, ^{214}Po) and to very low α backgrounds using α/β discrimination. The good efficiency is due to the fact that ^{222}Rn is measured when it is in equilibrium with its short-lived daughters (^{218}Po, ^{214}Pb, ^{214}Bi, and ^{214}Po), and consequently 3α- and 2β-particles are measured with nearly 100% efficiency in a wide-open counting window.

The most widely used direct method for ^{222}Rn in drinking water is the standard ASTM method (ASTM D5072_98, 1998). This method was originally developed by Prichard and Gesell (1977) and later modified by the U.S. EPA (Horton, 1983). The samples are prepared by injecting 10 mL of water with a syringe into a low potassium glass vial below an organic, water immiscible scintillation cocktail (10 mL). The vial is tightly capped and vigorously shaken for 1 minute. During the shaking, ^{222}Rn is extracted almost entirely from water into the cocktail, while other radionuclides, elements or minerals remain in the water. The samples are measured 3−4 hours later when the equilibrium between ^{222}Rn and its short-lived daughters has been established in the cocktail and ^{222}Rn has partitioned between the three phases: water, scintillation cocktail and air. The performance and reliability of this method has been demonstrated in numerous studies (Horton, 1983; Whittaker et al., 1987; Parsa and Horton, 1990; Vitz, 1991; Kinner et al., 1991; Kitto, 1994).

In another direct LS method, water is mixed with an emulsifying cocktail to have a homogeneous sample (Asikainen, 1981; Salonen, 1993b). In this method, the samples are prepared without using syringes or pipette fillers to avoid suction and ^{222}Rn release. The pipette tip is simply placed near to the bottom of the sampling bottle, from where water is allowed to enter the pipette up to the 10 mL level. Thereafter, the water is transferred onto the cocktail (12 mL) in a glass counting vial. The vial is tightly closed and vigorously shaken. Because this method involves direct mixing of water with cocktail, other radionuclides occurring in surface and ground waters are all observed and their effect on the results must be considered. The glass vials equipped with urea screw caps and Al foil liners have found to be radon gastight (Vitz, 1991; Salonen, 1993b; Kitto, 1994).

Salonen (2010a) compared two methods in the following two ways: (1) by preparing two phase and homogeneous samples similarly from the same ^{222}Rn-bearing ground water (35,000 Bq/L) according the method of homogeneous samples, and (2) by calibrating both methods with the ^{226}Ra standard solution according to their own calibration procedures (ASTM D5072_98, 1998; Salonen, 1993b). Three PerkinElmer organic cocktails: Betaplate Scint, Ultima Gold F and High Efficiency Mineral Oil Scintillator and one emulsifying cocktail, Ultima Gold XR (PerkinElmer, Inc.) were used. The measurements were implemented with the Wallac Quantulus using α/β discrimination to separately measure α- and β-emitting nuclides. The results from ^{222}Rn-bearing water samples were excellent. The results of ^{222}Rn in all parallel samples prepared in different cocktails were very consistent and remained very stable for 3 weeks during which the measurements were repeated (Salonen, 2009). The count rates of various two-phase samples were 3.6%−4.4% lower than those of the homogeneous samples, whereby the difference is due to the partition of ^{222}Rn into the water and air phases. All the results of the ^{226}Ra standard samples were not as good as expected on the basis of radon bearing water samples; the counting efficiencies of the two phase ^{226}Ra samples were partly too low and variable, the counts slowly decreased over time and 1-min shaking time was not sufficient to transfer radon to the organic phase although this

had been sufficient for the ^{222}Rn-bearing water samples. The ^{222}Rn-counting efficiencies derived from the homogeneous ^{226}Ra samples were equal and the samples remained very stable. An additional study was performed to examine whether ^{210}Pb, ^{210}Bi, and ^{210}Po, which were present in an old ^{226}Ra standard, could cause the instability of the two phase ^{226}Ra samples (Salonen, 2010b). It showed that these nuclides contributed to the instability and to the calibrations mostly through ^{210}Po, which had affinity to organic cocktails while ^{210}Pb and ^{210}Bi were hydrophilic and thus tended to remain in the water phase. The above studies demonstrated that the distribution of ^{222}Rn and its short-lived daughters between the two phases obviously depends on the existing chemical conditions such as the presence of acids and carriers in the ^{226}Ra standard solution, temperature, and vial material as assessed in the earlier studies (Vitz, 1991; Kinner et al., 1991; Kitto, 1994). Figs. 2.28 and 2.29 show the α- and β-spectra of ^{222}Rn-bearing water and ^{226}Ra samples prepared in Ultima Gold F and Ultima Gold XR. Fig. 2.28 indicates that no ^{226}Ra has been extracted into the organic cocktail, because the α-spectra of the two samples are quite identical while the α-peak broadening by ^{226}Ra and ^{210}Po is clearly visible for the homogeneous samples in Fig. 2.29. The effect of ^{226}Ra and other radionuclides can principally be eliminated by separately preparing the background sample for each water sample from the same water as the actual sample and by measuring it rapidly before the ingrowth of ^{222}Rn from ^{226}Ra (Salonen, 1993b). This involves a considerable amount of extra work. For most samples, the effect is insignificant because ^{222}Rn concentrations are often orders of magnitude higher than any of other radionuclides (Asikainen, 1981; Longtin, 1990; Salonen, 1994; Isam Salih et al., 2002; Vesterbacka et al., 2005).

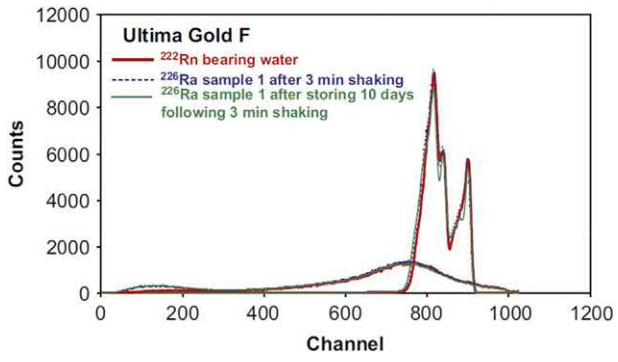


FIGURE 2.28 The α and β spectra of two-phase samples prepared from ^{222}Rn-bearing water and ^{226}Ra standard solution. The vertical scales of the ^{222}Rn and ^{226}Ra samples have been adjusted to correspond to the same ^{222}Rn activity. The two α spectra of the ^{226}Ra sample show that the counts decreased a little under both α peaks during the 10 days that the sample was stored and then measured without shaking. The ^{226}Ra standard has a low peak (chs 1−200) in the β spectra, which is due to the Cerenkov photons of ^{210}Bi accumulated with its parent (^{210}Pb) in the old ^{226}Ra standard. Similar Cerenkov peaks are not visible for ^{222}Rn-bearing water samples (Salonen, 2010a). *Reprinted by permission of Elsevier © 2010.*

The theoretical 500% counting efficiency of ^{222}Rn cannot be attained by LS counters such as the Quantulus or the Wallac Guardian due to their external guard counters and to the short-lived daughters of ^{222}Rn which occur in series with each other. Hence, the external guard counter observes the gamma photons of ^{214}Bi simultaneously with the α-particle of ^{214}Po in the detector (Salonen, 2006), and it eliminates about 19% of the β-counts of ^{214}Bi. ^{214}Po has a very short half-life (164 μs) and, therefore, part of its counts are lost because of the dead time (Salonen, 2006; Cassette et al., 2006), causing a decreased counting efficiency of ^{214}Po of 86% (Salonen, 1993b). The radon efficiencies ($3\alpha + 2\beta$) for the Ultima Gold XR and Ultima Gold F samples in fully open counting windows (1−1024 ch) were 446.0% and 429.5%, respectively, but higher, 480.8% and 465.2%, when the guard counter of the Quantulus was switched off (Salonen, 2009). According to these results, the overall counting efficiency of radon in Ultima Gold F cocktail is 3.7% lower than that in the Ultima Gold XR cocktail. This difference is a little smaller than that obtained with radon bearing water (4.2%). This is due to the interference of ^{210}Bi and ^{210}Po being present in an old ^{226}Ra standard solution. They increased the counting efficiency of radon in Ultima Gold F cocktail, because some ^{210}Po migrated from water to the cocktail and ^{210}Bi in water increased the counting efficiency of Cerenkov photon fraction (Salonen, 2010b). The best detection limits (0.02−0.05 Bq/L) were obtained by calculating the results from the counts in the α-window, which has a very low background (0.006−0.03 cpm). Because α- or β-spillovers depend on sample quench level, this should be considered in measuring variably quenched samples.

The comparison study (Salonen, 2010a) shows that the calibration is critical for obtaining accurate results. This assumption is supported by the observation that the counting coefficients of radon reported in the literature vary considerably although these could be assured quite easily using fully open counting windows for which the α+β efficiencies vary in rather narrow limits (450−490%) for different cocktails and sample volumes. Several intercomparison studies also demonstrate large variability between the results (Wiegand et al., 2000; Möbius and Salonen, 2002; Guiseppe et al., 2006; Vesterbacka et al., 2010). The validity of the calibrations can be checked with a ^{222}Rn standard, which does not contain ^{226}Ra at all (Hutchinson et al., 1986; Dean and Kolkowski, 2004; Havelka, 2009; Kitto et al., 2010). Such a ^{222}Rn standard is produced in a generator which consists of an encapsulated ^{226}Ra source placed in a small accumulation chamber filled with water and equipped with the connections for inlet and outlet waters. ^{222}Rn diffuses into the water through the polyethylene capsule where the ^{226}Ra standard solution is

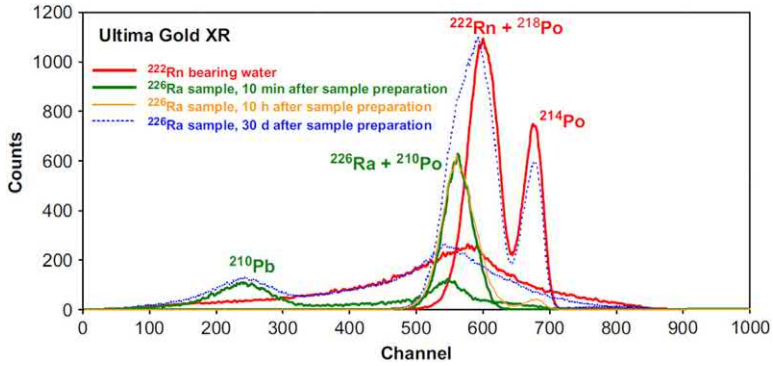


FIGURE 2.29 The α and β spectra of homogeneous samples prepared from ^{222}Rn-bearing water and ^{226}Ra standard solution. The vertical scales of these samples have been adjusted to correspond to the same ^{222}Rn activity. The spectra of the ^{226}Ra standard originate from the measurements performed at various times after sample preparation. The ^{214}Po peak is not visible in the α spectrum measured 10 minutes after sample preparation, while it is visible in the later (10 hours) spectrum as an indication of the rapid in-growth of ^{222}Rn and its daughters. The β spectrum reveals that a significant amount of ^{210}Pb had accumulated in the old ^{226}Ra standard (Salonen, 2010a). For the color version of this figure, the reader is referred to the online version of this book. *Reprinted by permission of Elsevier © 2010.*

enclosed. Yasuoka et al. (2005) have presented another alternative for the calibrations. It is based on a direct dpm method and on an internal counting.

e. Extraction of radon from a large water sample

Because ^{222}Rn concentrations in surface waters are generally very low, it has to be extracted from large water samples to ensure the sensitivity and precision of the analyses required in hydrological studies. This complicates the analysis, because the extraction efficiency must be determined and ^{222}Rn losses during the sample preparation must be assessed. The extraction of ^{222}Rn can be performed with toluene, toluene-based scintillation cocktail or other water-immiscible cocktail as extractant (Murakami and Horiuchi, 1979; Horiuchi et al., 1993; Bem et al., 1994; Hoehn and von Gunten, 1989; Purkl and Eisenhauer, 2004; Pates and Mullinger, 2007; Cook et al., 2008). ^{222}Rn is usually extracted from 0.5 to 1 L water sample with 20−40 mL of extractant. After shaking and allowing the layers to separate, a known proportion of the extractant is transferred into the scintillation vial for the measurement. The detection limits obtained by these methods are between 0.0015 and 0.02 Bq/L depending mainly on the count time and the sample volume. Pates and Mullinger (2007) studied thoroughly various factors which may have an effect on the extraction efficiency, ^{222}Rn losses, and the sensitivity and the accuracy of the measurement method. They used α/β-discrimination and obtained the detection limits of 0.020 and 0.015 Bq/L with the use of 20 mL of toluene and 30 mL of Ultima Gold F extractants, respectively, when the sample volume was 580 mL and the count time 60 minutes. They recommend only a single extraction, rather than two, and to use smaller sample volumes for practical reasons. The volume difference is partly compensated by using scintillation cocktail as extractant, because a greater proportion of it can be taken for the measurement. They concluded that the method is fast, simple, reproducible, and more sensitive than the ASTM method. Purkl and Eisenhauer (2004) extracted radon from 1 L of seawater with 22 mL of MaxiLight cocktail (Hidex, Finland) and measured the samples with a portable LS spectrometer, Triathler (Hidex, Finland), directly on board a research vessel. They re-extracted ^{222}Rn from the same water sample a month later when ^{222}Rn was in equilibrium with radium. The supported ^{222}Rn (equal to ^{226}Ra) was obtained from the latter extraction and the proportion of the unsupported ^{222}Rn from the difference of the two extractions. Submarine water samples could be analyzed directly using a two-phase sample (3.5 mL water and 3.5 mL organic cocktail) and α/β discrimination. The detection limit for this sample was 0.15 Bq/L using 3.5 hour count.

D. Radium

1. Environmental occurrence and importance

Radium has four naturally occurring isotopes, ^{226}Ra ($t_{1/2} = 1600$ y), which belongs to the ^{238}U decay series (Fig. 2.25), ^{228}Ra ($t_{1/2} = 5.75$ y), and ^{224}Ra ($t_{1/2} = 3.66$ d), which belong to the ^{232} Th day series (Fig. 2.31), and ^{223}Ra ($t_{1/2} = 11.43$ d), which belongs to the ^{235}U decay series. The term "radium" is commonly used in reference to ^{226}Ra. Radium is widespread in the environment. It is present in soil, minerals, foodstuffs, surface and ground waters, and many common materials. The worldwide average concentration of ^{226}Ra in soil is 32 Bq/kg (UNSCEAR, 2008). Radium is one of the most hazardous long-lived α-emitters in the environment, with respect to internal radiation exposure. As an alkaline earth element, radium is accumulated in the skeleton through a process similar to calcium. Food consumption is the main source of ^{226}Ra to

man. The contribution of water to total intake is usually small, if the drinking water supply originates from surface water (UNSCEAR, 2000). However, the radiation exposure through drinking water can be an important source, or even be extremely high, if the drinking water originates from ground water sources in contact with uranium rich minerals like granites or phosphates.

^{226}Ra concentrations over 40 Bq/L in drinking water has been reported (UNSCEAR, 2000). Due to the possible health hazard, regulations limit the maximum contaminant level in public water supplies for combined ^{226}Ra and ^{228}Ra to 0.19 Bq/L in the USA (EPA, 2009). The primary health concerns of radium have been directed to ^{226}Ra and ^{228}Ra and little attention has been given to the short-lived ^{224}Ra. The study of public water supplies in the USA has shown that ^{224}Ra can make a significant contribution to elevated measurements of gross α-activities (Parsa, 1998). ^{224}Ra has remained largely undetected in the past, due to its short half-life allowing the activity to decay during the delays in routine gross α-activity or radium measurements, which are not processed rapidly after sampling (EPA2009Parsa et al., 1999; Moon et al., 2003; EPA 2009). Earth, marine, and environmental scientists often determine ^{226}Ra, ^{228}Ra, ^{224}Ra, and ^{223}Ra in ground and surface waters, because these nuclides have proven useful as natural tracers to study geochemical processes, particularly in the marine environment (Burnett and Tai, 1992; Lamontagne et al., 2008). Radium assays are frequently carried out when environmental contamination around uranium mine and mills, phosphoric acid factories and coal mines is investigated (Moreno et al., 2000; Absi et al., 2004; Chalupnik et al., 2001; Vera Tomé et al., 2002a, 2002b; Carvalho et al., 2007). The ^{226}Ra concentrations in tissue, soil, sediment, and rock samples have also been determined by liquid scintillation methods (Gregory, 1972; Higuchi, 1981; Blackburn and Al-Masri, 1993; Juntunen et al., 2002).

2. Sample preparation and measurement of ^{226}Ra, ^{228}Ra, ^{224}Ra, and ^{223}Ra

There are a variety of methods for determining one or more radium isotopes in environmental samples using different chemical separation and measurement methods (Goldin, 1961; Horiuchi and Murakami, 1981; Sedlaček et al., 1980; Smith et al., 1988; Alvarado et al., 1995; Al-Masri and Blackburn, 1995; Baeza et al., 1998; Kim et al., 1999, 2017; Lawrie et al., 2000; Sato et al., 2000; Blanco et al., 2002; Aupiais, 2005; Purkl and Eisenhauer, 2003a; Bojanowski et al., 2005; Zoriy et al., 2005; Wallner et al., 2008; Dimova et al., 2007; Antovic and Svrkota, 2009; Tsai et al., 2010; Dinh et al., 2017; Fons-Castells et al., 2017).

The most common measurement methods are based on liquid scintillation, radon emanation, or alpha or gamma spectrometry. The chemical separation methods are mainly based on precipitation, cation exchange, extraction, adsorption, or a combination of these techniques. Several comparison studies have been made on the commonly used methods for the determination of ^{226}Ra and ^{228}Ra. Chałupnik et al. (2002) compared alpha spectrometric and LS spectrometric methods, Köhler et al. (2002) compared the radiometric methods; and Hou and Roos (2008) did the same but also included a mass spectrometric method in their comparison. Decaillon et al. (2004) validated a few chemical separation methods, and Vasile et al. (2010) performed a comparison using different chemical separation methods and measurement techniques for determining ^{226}Ra and ^{228}Ra in mineral waters.

a. Alpha and gamma spectrometric methods

Comparisons among the measurement methods for radium demonstrate that alpha spectrometry is the most sensitive radiometric method, because of its low background. To avoid impairing the resolution and chemical yield, radium must be separated carefully from the sample matrix and from other elements, including barium, and thereafter electrodeposited as a thin layer on a stainless steel disk or coprecipitated with $BaSO_4$ and/or $PbSO_4$ which is collected on a membrane filter (Hancock and Martin, 1991; Alvarado et al., 1995; Vargas et al., 1995; Crespo, 2000; Lawrie et al., 2000; Blanco et al., 2002; Chałupnik et al., 2002; Purkl and Eisenhauer, 2003b; Bojanowski et al., 2005; Dai et al., 2012a, 2012b, 2012c; Song et al., 2017). The high resolution of alpha spectroscopy for low mass samples permits the direct measurement of the concentrations of ^{226}Ra, ^{224}Ra, and ^{223}Ra, and analytical determinations of ^{226}Ra can be obtained in a much shorter time than by other methods based on the indirect determination through the ^{222}Rn daughter.

^{133}Ba (β/γ-emitter) is the most commonly used chemical yield tracer, but ^{225}Ra (via its α-emitting daughter ^{225}Ac) is also used (Hancock and Martin, 1991). ^{228}Ra can be measured directly from the same disk either by gamma spectrometry via the γ-emitting daughter, ^{228}Ac, after 2 days of ingrowth (Hughes et al., 2004) or by alpha spectrometry via its α-emitting grand-daughter, ^{228}Th, after 6−12 months of ingrowth (Eikenberg et al., 2001).

Radium is often separated using an efficient and simple method where radium isotopes are adsorbed on a MnO_2-coated polyamide disk or thin film which is measured directly with an alpha spectrometer (Surbeck, 1995, 2000; Eikenberg et al., 2001; Kovács et al., 2004; Karamanis et al., 2006).

The detection limits of ^{226}Ra and ^{228}Ra in environmental samples by alpha spectrometric methods are between 0.1 and 0.5 mBq and 0.2−0.3 mBq, respectively, and 0.1−1 Bq and 0.1−0.3 Bq, respectively, by gamma spectrometry (Hou and Roos, 2008; Eikenberg et al., 2001; Hughes et al., 2004; van Beek et al., 2010). Lower detection limits of 7.4−81 mBq by gamma spectrometry can be obtained when low-level gamma spectrometry is employed (shielded underground laboratory), and radium is separated

from the sample matrix or β−γ-coincidence techniques are used (Köhler et al., 2002).

The main advantage of the gamma spectrometric method is that ^{226}Ra, ^{228}Ra, and ^{224}Ra can be determined simultaneously using simple sample processing (Smith et al., 1997; Bonotto, 2004; Vasile et al., 2010).

b. Emanation methods

Emanation methods can be the best choice when low detection limits (0.02−0.002 Bq/L) are required (EPA, 2009; Sedlaček et al., 1980; Smith et al., 1988). Dimova et al. (2007) reported an automated analysis method for determining ^{223}Ra, ^{224}Ra, and ^{226}Ra in water samples, based on the pre-concentration of radium isotopes on MnO_2 Resin, followed by the emanation of their radon daughters (^{219}Rn, ^{220}Rn, ^{222}Rn) and analyses using a commercial radon-in-air analyzer.

The emanation method permits the determination of ^{226}Ra activity from the pre-concentrated sample after setting the sample aside for approximately 3 weeks and allowing radon ingrowth from ^{226}Ra. Sample analysis by the emanation method is simpler and the results can be obtained much faster than by alpha spectrometry.

c. Liquid scintillation counting methods

Low background LS spectrometry with α/β discrimination is the most popular technique for determining ^{226}Ra activity. This is due to the high counting efficiency, easy sample preparation and automatic sample counting. The typical detection limits are between 0.3 and 1.4 mBq for a 6 hour count time (Hou and Roos, 2008).

In practice, any measurement method for ^{222}Rn will also be relevant to ^{226}Ra (see Section C. Radon). There are many alternative methods for ^{226}Ra. In most of these methods ^{226}Ra is determined indirectly through ^{222}Rn and its short-lived daughters or together with them. In the latter case, a water sample containing ^{226}Ra is simply mixed with the cocktail either directly in the LS vial or after some pre-concentration, or ^{226}Ra can be separated chemically and mixed with the cocktail, followed by the measurement 3−4 weeks later when the equilibrium between ^{226}Ra and ^{222}Rn with its short-lived daughters is established (Schönhofer and Weitz, 1987; Salonen, 1993a; Chałupnik and Lebecka, 1993; Sanchez-Cabeza and Pujol, 1998). The counting efficiency of ^{226}Ra will then be high, close to 600%, in which case each of the 4α- and 2 β-particles (Table 2.6) are detected in fully open α- and β-windows with nearly 100% efficiency. In other methods using two-phase samples, the water containing ^{226}Ra is lying under the organic cocktail and ^{222}Rn produced by ^{226}Ra will transfer to the organic phase by shaking (Horiuchi and Murakami, 1981; Parsa and Horton, 1990) based on the high solubility of radon in organic solvent (scintillation cocktail). The counting efficiency of ^{226}Ra will now be near 500%, if full open windows are used. The pre-concentration is often performed using toluene, where ^{222}Rn is extracted from water into solvent and then mixed with the LS cocktail (Schönhofer, 1989b; Chalupnik et al., 1996; Bem et al., 1998; Möbius and Zeisberg, 2002; Forte et al., 2006; Desideri et al., 2007; Mosqueda et al., 2009; ISO/NP standard 13165-1). These methods are appropriate for monitoring ^{226}Ra in drinking and mineral waters, because the detection limits (5−60 mBq) attained by the low-background LS spectrometers and by the mobile Tri-athler are well below the detection limits set in the regulations.

The conventional method of separating ^{226}Ra from a sample matrix is the so-called barium sulfate method (Goldin, 1961; EPA, 2009). The method is still used for separating ^{226}Ra from water, and a number of new applications based on this separation have been reported after the low-background LS spectrometer with α/β separation became common in environmental laboratories (Suomela, 1993; Manjón et al., 1997; Bem et al., 1998; Kim et al., 2001; Chau et al., 2001; Wallner, 2002; Chałupnik et al., 2002; Repinc and Benedik, 2002; Villa et al., 2005; Kozłowska et al., 2007; Lasheen et al., 2007; Godoy et al., 2016). The analysis generally follows the basic steps. The Pb- and Ba-carriers are added into the water sample to coprecipitate radium with $BaSO_4$ and $PbSO_4$ at pH 1 with H_2SO_4. The precipitate is washed a few times with HNO_3 and then dissolved in alkaline EDTA. For further purification and separating radium from lead, radium is precipitated again as sulfate using an acetic acid solution at pH 4.5 and lead remains in solution. ^{210}Pb can be determined from this solution by precipitating it as the sulfate (Chałupnik and Lebecka, 1993; Kim et al., 2001; Chau et al., 2001; Wallner, 2002). Hence, this method enables the simultaneous analysis of ^{226}Ra, ^{228}Ra, and ^{210}Pb from the same water sample. The nitric acid wash and the re-precipitation of $RaSO_4$ in EDTA solution by adjusting to pH 4.5 to ensure high purification of radium from most interfering radionuclides, especially those belonging to natural series, ^{137}Cs and ^{90}Sr. The chemical yield can be determined gravimetrically or by using ^{133}Ba as a yield tracer. The Ra-$BaSO_4$ precipitates are prepared for the LS measurement by suspending fine crystal precipitates into a scintillation gel or by dissolving the precipitates in warm alkaline EDTA solution. $BaSO_4$ precipitate can be converted also to the more soluble $BaCO_3$, which is dissolved in HNO_3 and then mixed with the LS cocktail (Wallner, 2002; Repinc and Benedik, 2002). They also measured the samples shortly after the separation and calculated the ^{226}Ra concentration from its own alpha peak and thus obtained the results rapidly after the sampling. In that case, the ^{228}Ra activity can be calculated from the β-counts with the least amount of corrections owing to minor ingrowth of

^{214}Pb and ^{214}Bi. The detection limits reported for ^{226}Ra, ^{228}Ra and ^{210}Pb are 0.5−2 mBq, 4 mBq, and 2−5.2 mBq, respectively.

Selective extractants are also used for radium separation. One of these is the Empore Radium Rad Disk, which selectively extracts radium from water (Alvarado et al., 1995; Smith et al., 1997; Schönhofer and Wallner, 2001; Möbius et al., 2002; Decaillon et al., 2004; Wallner et al., 2008; Eikenberg et al., 2014). The Empore Radium Rad Disk exhibits a large capacity for radium, with recoveries ranging from 90 to 100% for the 1−3 L sample volumes. Water samples are acidified with HNO_3 to a 2M concentration and then passed through the disk. After washing the disk with 2M HNO_3, radium is eluted from the disk with 0.25M EDTA solution, which can be concentrated prior to mixing with the LS cocktail. Lead, strontium and barium are co-extracted with radium. High Ba concentrations reduce the Ra-recovery considerably, and the interfering ^{210}Pb should be separated from radium either before or after the elution (Smith et al., 1997; Möbius et al., 2002; Wallner et al., 2008). This method is not suitable for waters with a high content of salts (Decaillon et al., 2004). The detection limits reported for the Empore Radium Rad Disk extraction method vary between 1 and 2 mBq, 4−8 mBq and 2−6 mBq for ^{226}Ra, ^{228}Ra and ^{210}Pb, respectively.

Other possible extractants are sym-Di[4(5)-tert-butylbenzo]-16-crown-5-oxyacetic acid (DTBDB16C5-OAcH) (Chu and Lin, 2001), tricaprylmethylammonium chloride (Aliquat-336), triphenylphosphine sulfide (TPPS), or tri-n-octylphosphine (TOPO) dissolved in toluene with PPO and POPOP in order to obtain an extractive scintillation cocktail (Borai et al., 2008). A commercial extractive scintillation cocktail RADAEX is available, which was developed specifically for LSC measurement of radium (Case and McDowell, 1990), this cocktail has been successfully applied for the determination of radium in water (Aupiais et al., 1998; Gómez Escobar et al., 1999; Blanco Rodríguez et al., 2000; Möbius, 2002; Wallner, 2002; Aupiais, 2005). RADAEX can be combined also with other extractive scintillators to determine radium simultaneously with other nuclides. Blanco Rodríguez et al. (2000) presented a procedure where they applied RADAEX, URAEX, and THOREX for the sequential analysis of radium, uranium, and thorium. RADAEX also extracts lead that must be complexed before extraction in order to obtain a pure radium sample (Wallner, 2002).

The extraction of radium with RADAEX needs to be carried out in alkaline media (pH 10−12); however, large amount of metals in high salt content water will be precipitated in this condition. Therefore, this method cannot be directly applied for the analysis of high saline water samples. Aupiais (2005) presented an improvement on the RADAEX procedure for samples of high salinity, whereby α-hydroxyisobutyric acid (HIBA) solution is first added into the sample to form a complex with most of metals in the sample solution to prevent precipitation. However, HIBA could not prevent the extraction of uranium into the organic scintillation phase, causing a co-extraction of uranium into scintillation phase with radium. If uranium is assumed to be present, it should be removed by extraction with ALPAEX prior to the extraction of radium. The detection limits of ^{226}Ra using RADAEX vary between 19 and 26 mBq for the Quantulus LS spectrometer (Gómez Escobar et al., 1999; Blanco Rodríguez et al., 2000).

d. Determination of ^{228}Ra in natural waters

Nour et al. (2004) developed a rather simple procedure for separating ^{228}Ra from natural waters. This method is based on the indirect determination of ^{228}Ra through the ^{228}Ac daughter and on measuring its β-activity by LSC. The method includes a preconcentration step based on the coprecipitation of radium with MnO_2 and two extraction chromatographic column separations using Diphonix resin, which effectively retains actinides and lantanides while divalent cations like Ra and Ba pass through. In the first Diphonix column separation, U-, Th-isotopes and ^{90}Y as well as ^{228}Ac are retained in the column. Radium isotopes remain in the effluent and wash solutions, which are set aside for 30 hours to permit the ^{228}Ac ingrowth to attain secular equilibrium with ^{228}Ra. Thereafter ^{228}Ra and ^{228}Ac are separated from each other by the second Diphonix resin separation. The ^{228}Ac retained on the Diphonic column is eluted using 5 mL of 1 M HEDPA (1-hydroxyethane-1,1 diphosphonic acid) directly into a plastic LS vial and mixed with LS cocktail. The overall yield of this procedure is typically over 95% as determined by the ^{133}Ba-tracer, and the detection limit of 23.2 mBq/L was reported based on 1 L sample volume and 60 minutes counting time. L'Annunziata and coworkers (See Aleissa et al., 2008) used the same procedure with the only difference that the ^{228}Ac activity was measured by Cerenkov counting. The detection limit, for 1 L water volume and a 100 minutes count, was 53.8 mBq/L (3.24 dpm/L). Utilizing sodium salicylate as a wavelength shifter, at a concentration of 0.1 g/mL in the counting vial, yielded an increase in the Cerenkov counting efficiency of more than 3-fold for ^{228}Ac (38%). The increase in Cerenkov counting efficiency in this case was explained to be due to an increase in the refractive index produced by the high concentration of sodium salicylate. A recent study by Wang et al. (2018) showed that such a sharp increase in counting efficiency would be mainly attributed to the scintillation effect of the high concentration of sodium salicylate, with a small contribution to Cerenkov counting efficiency from the increase in the refractive index produced by sodium salicylate.

e. Preconcentration of radium isotopes from large water volumes

Preconcentration of radium isotopes from large water volumes (up to 1000 L) is often necessary when low-activity environmental waters are analyzed. Preconcentration methods are often based on the coprecipitation of radium with MnO_2 or on MnO_2-impregnated acrylic fiber followed by the dissolution of the radium for further purification by other methods (Michel et al., 1981; Baeza et al., 1998; La Rosa et al., 2001; Sidle et al., 2001; Saito et al., 2003; Nour et al., 2004; Aleissa et al., 2008; Lamontagne et al., 2008; van Beek et al., 2010; Bhangare et al., 2017; Schubert et al., 2018). A commercial MnO_2 resin (impregnated MnO_2 on a modified polyacrylonitrile (PAN) supporting material) is available from Triskem International (or Eichrom) for the separation of radium from water samples.

The investigation of the sorption characteristics of radium onto MnO_2 Resin with a goal to simplify the preconcentration of radium isotopes from natural waters shows that the MnO_2 Resin is appropriate for that purpose over a range of salinities. The sorption of Ra was especially favorable for low-salinity waters, like typical drinking waters, but it was highly dependent on pH with the most useful range from pH 4 to 8. At higher salinities, other alkaline earth elements (Mg, Ca, and Sr) compete with Ra for the free sorption sites in the MnO_2 Resin, and Ra is more effectively adsorbed onto MnO_2 Resin than Ba in seawater. This means that ^{133}Ba is not an appropriate yield tracer for saline waters (Moon et al., 2003).

f. Other methods

Sato et al. (2000) have used LSC combined with α/β coincidence for low-level measurements of radium. This method is based on the coincidence counting of the β-particle from ^{214}Bi and the α-particle from ^{214}Po (half-life = 164 μs). These paired pulses can be separated electronically from background events and single pulses from other radionuclides, giving significant reductions in background. Antovic and Svrkota (2009) used a γ-ray coincidence spectrometer with multidetector to determine ^{226}Ra in soil and sand samples and obtained a detection limit of 0.68 Bq/kg. A compact, single PMT LSC with automatic sample changer dedicated to analysis of the paired pulses has been developed by Gudjonsson and Theodorsson (2000). Low detection limits have been achieved using mass spectrometric methods following the preconcentration and chemical separation of radium from matrix (Zoriy et al., 2005; Tsai et al., 2010; Van Es et al., 2017; Lagace et al., 2017; Dalencourt et al., 2018).

In summary, the current LS instruments with sophisticated pulse shape analysis permit the determination of low concentrations of ^{226}Ra and ^{228}Ra in environmental samples using chemical separation and preconcentration methods. Regardless of that, for most methods that have been demonstrated to be accurate, the results for radium analysis are not necessarily satisfactory. Intercomparison studies have indicated that a substantial number of radium results are erroneous. In a world-wide intercomparison organized by the International Atomic Energy Agency (IAEA) the percentage of "not acceptable" results was 43% and 31% for two spiked water samples having the ^{226}Ra activity concentrations of 0.69 Bq/L and 1.93 Bq/L, respectively (IAEA/AQ/15, 2010). Another intercomparison exercise organized among 45 European laboratories also showed many discrepant results for radium isotopes in mineral waters (Wätjen et al., 2010). The results showed 19% of the results off by a factor of two or more, whereas the proportion of such results for uranium was only 6%. The participating laboratories of these two studies used very different methods for radium analyses, almost all of the methods described here.

An intercomparison also showed deviating results but with fewer outliers (Möbius and Salonen, 2002), and the best results were obtained using the $BaSO_4$ coprecipitation method and many of the deviating ^{226}Ra results had been determined using different extraction methods. It is obvious that chemical separation methods work for radium, as well as for uranium, with most of the problems involved in radium assays due to the presence of gaseous ^{222}Rn and its daughters which are chemically different elements, occurring in the same series. ^{222}Rn can be lost easily during the extraction, and its daughters can behave differently during the sample processing and measurement depending on the chemical conditions. Hence, attention should be paid to the various stages of analysis including an evaluation of the extraction and detection efficiencies, which are often assumed to be constant or close to 100%.

E. Lead-210 (^{210}Pb) [Bismuth-210 (^{210}Bi) and Polonium-210 (^{210}Po)]

1. Environmental occurrence and importance

^{210}Pb ($t_{1/2}$ = 22.2 y), ^{210}Bi ($t_{1/2}$ = 5.01 d) and ^{210}Po ($t_{1/2}$ = 138.4 d) constitute their own subseries in the ^{238}U decay series (Fig. 2.25). ^{210}Pb decays by emitting β particles (E_{max} = 63.5 keV), with γ emission (E_γ = 46.5 keV) and internal conversion to the β-emitting ^{210}Bi (E_{max} = 1161.5 keV) which decays to the α-emitting ^{210}Po (E_α = 5.3 MeV). The decay scheme of the ^{210}Pb subseries is shown in Fig. 2.30 (Laureano-Pérez et al., 2007). ^{210}Pb, ^{210}Bi, and ^{210}Po exist everywhere, in rock, soil, atmosphere, and natural waters, as a result of the ^{222}Rn decay and subsequent deposition. ^{210}Pb and ^{210}Po belong to the most toxic radionuclides, and 79% of the internal dose following ingestion of uranium and thorium series radionuclides is caused by ^{210}Pb and ^{210}Po (UNSCEAR, 2000).

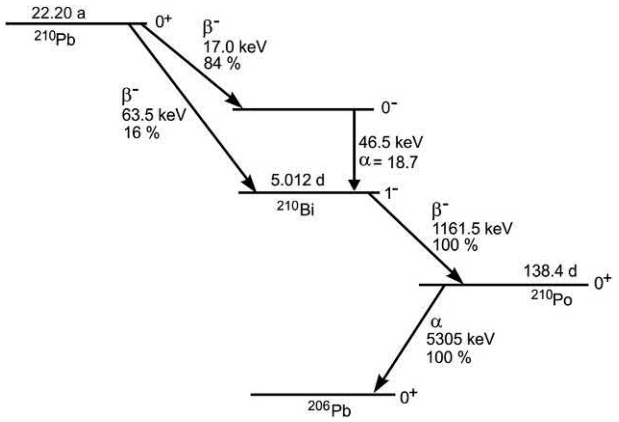


FIGURE 2.30 Decay scheme for the ^{210}Pb subseries (Laureano-Pérez et al., 2007). *Reprinted by permission of Elsevier © 2007.*

^{210}Pb accumulates in bone while ^{210}Po is distributed mainly to soft tissues. The main intake of ^{210}Pb and ^{210}Po is derived from the food, with the exception of smokers whose intake can significantly increase by inhalation because ^{210}Pb and ^{210}Po exist in tobacco (UNSCEAR, 2000). Although the origin of most of the ^{210}Po in the body is normally through ingestion of ^{210}Pb, some diets high in certain foodstuffs with enriched ^{210}Po are able to increase the normal intake of ^{210}Po considerably (NCRP, 1984; Matthews et al., 2007; Fowler, 2011; Persson and Holm, 2011). The ^{210}Po concentrations are high in seafood like fish, mollusks, and crabs, and high ^{210}Pb and ^{210}Po concentrations were found in reindeer and caribou meat (Hassona et al., 2008; Persson and Holm, 2011; Fowler, 2011; Carvalho, 2011). Drinking water usually constitutes a minor contribution to the normal intake of ^{210}Pb and ^{210}Po, but it can be significant for some population groups consuming ground water, particularly well or mineral waters of which very variable concentrations up to 21 Bq/L have been reported (UNSCEAR, 2000; Persson and Holm, 2011). The guideline value of WHO for ^{210}Pb and ^{210}Po in drinking water is 0.1 Bq/L (WHO, 2011). According to the recommendations of the European Commission (EURATOM, 2001), the maximum concentration of ^{210}Pb and ^{210}Po in drinking waters are 0.2 Bq/L and 0.1 Bq/L, respectively. Owing to the low permissible concentrations, much attention is paid to the analyses of ^{210}Pb and ^{210}Po in drinking waters.

^{210}Pb, ^{210}Bi and ^{210}Po have been widely used as tracers in studies on environmental processes (Peck and Smith, 2000; Papastefanou, 2006; Matthews et al., 2007; Zaborska et al., 2007; Persson and Holm, 2011; Baskaran, 2011; Fowler, 2011). All these elements are particle reactive species; this property has been used in the study of particle scavenging processes in aquatic and atmospheric environments. For example, ^{210}Pb is widely used to date sediments in seas, lakes and estuaries (Goldberg, 1963; Monna et al., 1996; Zaborska et al., 2007), to study bioturbation in slowly accumulating sediment systems, e.g., deep ocean sediments (Thomson et al., 1993) and accumulation rates in rapidly accumulating sediment systems, e.g., some peat profiles and lake sediments (MacKenzie et al., 1998). ^{226}Ra, ^{210}Pb, and ^{210}Po are used to estimate the rates at which reactive elements are removed from seawater by adsorption onto particles, to determine residence times of lead, other pollutants and materials in the oceans, and to assess redistribution of pollutants from the atmosphere in estuarine systems (Wu and Boyle, 1997; Zaborska et al., 2007; Matthews et al., 2007; Fowler, 2011; Mikalauskiene et al., 2018). ^{210}Po/^{210}Pb activity ratio measurements have been used to study biological productivity and boundary scavenging (Nozaki et al., 1976, 1997; 1998; Smith and Ellis, 1995). ^{222}Rn and its progenies, ^{210}Pb, ^{210}Bi, and ^{210}Po, are very useful tracers in quantifying several atmospheric processes such as circulation, mixing, stability, transport, and vertical movement of air masses, removal rate constants, and the residence time of aerosols, chemical behavior of analog species and washout ratios, and deposition velocities of aerosols (Peck and Smith, 2000; Papastefanou, 2006; Yamamoto et al., 2006; Baskaran, 2011; Persson and Holm, 2011).

2. Sample preparation and analysis

Traditional analysis methods of ^{210}Pb, ^{210}Bi, and ^{210}Po are based on three measurement techniques:

1) Direct counting by γ-spectrometry,
2) α-spectrometry,
3) β-counting using liquid scintillation (LS) or gas-proportional counters

The methods based on α and β counting require ^{210}Pb, ^{210}Bi, and ^{210}Po to be separated from the matrix and from other radionuclides. Because ^{210}Pb and ^{210}Po are found in disequilibrium in biological and most environmental samples, they have to be analyzed individually. Methods based on ICP-MS have also been investigated for the measurement of ^{210}Pb in water samples (Larivière et al., 2005). Owing to a very low mass concentration of ^{210}Pb in samples, it is necessary to pre-concentrate the sample and to separate ^{210}Pb from the matrix. The detection limit was about 90 mBq/L. The usability of the method is limited because of the stable lead, which cannot be removed from the sample by conventional methods and interferes in the measurement of ^{210}Pb.

a. Direct counting of ^{210}Pb by gamma spectrometry

The gamma spectrometric measurement of ^{210}Pb is implemented by counting the 46.5 keV gamma photon emissions of ^{210}Pb using an N-type HPGe gamma detector with a

beryllium or carbon epoxy thin window or planary HPGe detector. The difficulty in this method is the relative low counting efficiency of HPGe detectors combined with the low absolute intensity (4.25%) of 46.5 keV gamma photon. Consequently, the direct gamma spectrometric method requires the analysis of large sample sizes, long counting times, corrections for self-absorption and interferences from other γ- and X-rays (Cannizzaro et al., 1999; San Miguel et al., 2002; Ebaid and Khater, 2006; Lauria et al., 2006; Villa et al., 2007; Hou and Roos, 2008). The method is feasible but the measurement uncertainties is normally high (Cannizzaro et al., 1999; Zaborska et al., 2007). Samples commonly analyzed are peat, soils, and sediments (Thomson et al., 1993; MacKenzie et al., 1998; San Miguel et al., 2002; Lauria et al., 2006; Zaborska et al., 2007) and atmospheric aerosol particles which have been collected using high-volume air samplers (Cannizzaro et al., 1999; Papastefanou, 2006). The detection limit of this method for ^{210}Pb has been reported to be 440 mBq/sample for a 1000 minutes counting time (Ebaid and Khater, 2006). Grahek et al. (2006) developed a rapid procedure to separate ^{210}Pb and ^{90}Sr from sea and drinking water samples by chromatography using Sr resin and anion exchange resin, ^{210}Pb and ^{90}Sr were separated efficiently from large volumes of sample (10 L). The detection limit was 6 mBq/L for ^{210}Pb with the counting time of 100,000−200,000 seconds.

b. Measurement of ^{210}Pb and ^{210}Po by alpha spectrometry

The alpha spectrometric measurement of ^{210}Pb and ^{210}Po is a classical method for determining ^{210}Pb and ^{210}Po in various matrices. It is based on two spontaneous depositions of ^{210}Po onto a silver disc and on measuring the ^{210}Po activity with an alpha spectrometer (Flynn, 1968; Peck and Smith, 2000; Vesterbacka and Ikäheimonen, 2005; Ebaid and Khater, 2006; Matthews et al., 2007; Ruberu et al., 2007; Wallner et al., 2008; Benedik et al., 2009; Bonotto et al., 2009b; Jia et al., 2009; Hou and Roos, 2008; Henricsson et al., 2011; Carvalho, 2011; Idoeta et al., 2011). Following the first deposition of ^{210}Po, the sample solution is stored for several months to allow sufficient ingrowth of ^{210}Po from ^{210}Pb and then perform the second deposition of the newly generated ^{210}Po from ^{210}Pb. Besides silver, Ni and Cu are also used as spontaneous deposition materials. Environmental water samples are usually pre-concentrated either by evaporation or by coprecipitation with $Fe(OH)_3$ or MnO_2, and organic material is decomposed by wet digestion before dissolving the residue for the deposition. ^{208}Po or ^{209}Po are used as chemical yield tracers. The detection limits by this method are very low, down to 0.1−0.3 mBq, and the α-spectrometric methods are especially suited to the analysis of low-activity samples (Matthews et al., 2007). However, there are several potential problems associated with this method, not least of which is the length of time required for ^{210}Po ingrowth when ^{210}Pb is determined indirectly via its granddaughter, ^{210}Po. Some ^{210}Po compounds are volatile even at 100°C and can be lost during the evaporation and wet digestion (Vreček et al., 2004; Matthews et al., 2007; Henricsson et al., 2011). ^{210}Po can also be adsorbed onto the walls of the storage container during the storage between the two depositions (Vesterbacka and Ikäheimonen, 2005), all these issues have to be considered and well treated to obtain accurate results.

c. Measurement of ^{210}Pb, ^{210}Bi, and ^{210}Po by liquid scintillation counting

^{210}Pb is a beta-emitter, and can be measured by LSC. However, due to its low-energy beta particles (17.0 keV (84%) and 63.5 keV (16%)), it is often measured via its high beta-energy daughter, ^{210}Bi (1161.5 keV). The low-energy beta emission of ^{210}Pb is hardly detected by GPC, and it is sensitive to sample quenching in LSC (Lebecka et al., 1993; Kim et al., 2001; Villa et al., 2003, 2007; Blanco et al., 2004; Ebaid and Khater, 2006; Idoeta et al., 2011). The LS measurement is performed often after some ingrowth of ^{210}Bi, If the ^{210}Pb itself is measured, the interference from the ^{210}Bi low-energy tail into the ^{210}Pb counting window has to be considered (Lebecka et al., 1993; Kim et al., 2001; Blanco et al., 2004; Villa et al., 2007). Similarly using the GPC, it is unnecessary to wait for secular equilibrium between ^{210}Pb and ^{210}Bi, because the effect of ^{210}Pb on the ^{210}Bi counts is eliminated by covering the sample with a Mylar or aluminum foil (Ebaid and Khater, 2006; Ruberu et al., 2007; Jia et al., 2009).

The most common separation methods are: (i) precipitation of Pb as the sulfate, (ii) extraction chromatography, and (iii) solvent extraction. The separation of ^{210}Pb by coprecipitation as $Ba(Ra,Pb)SO_4$ is a traditional method by which radium isotopes and ^{210}Pb can be separated simultaneous from ground waters, soils and sediments (Lebecka et al., 1993; Chau et al., 2001; Kim et al., 2001; Blanco et al., 2004; Villa et al., 2007). After sample pretreatments, the chemical separation is started by adding stable Pb and Ba carriers as the yield tracers, followed by precipitation as the sulfate, the formed sulfate is then dissolved in alkaline EDTA. The separation of Pb from Ra is achieved by adjusting the pH to 4.2−4.5 of the EDTA solution of the sample with acetic acid. The Ra precipitates with $BaSO_4$, and the Pb remains in the solution. Afterward, the solution is further acidified to precipitate Pb as $PbSO_4$ and separate ^{210}Pb from the solution. The precipitate is washed with distilled water to remove other interfering radionuclides. The $^{210}PbSO_4$ can be prepared for LS counting by suspending it in a scintillation gel or dissolving it in

alkaline EDTA solution and then mixing with the LS cocktail. The sample is counted using LSC with α/β-discrimination, and the ^{210}Pb is determined from the spectrum of ^{210}Pb or the ingrown ^{210}Bi. ^{210}Pb can be also measured by Cerenkov counting of the ingrown ^{210}Bi after separation of ^{210}Pb (Al-Masri et al. 1997). The potential interferences from alpha and soft beta-emitters can be avoided in this method, but the counting efficiency of Cerenkov counting is comparatively low (20%). A 14%−16% counting efficiency of Cerenkov counting for ^{210}Bi was reported in the analysis of air filters (Dale et al. (2002). An increased Cerenkov counting efficiency form 17%−75% was achieved through the use of Triton X-100 and sodium salicylate as enhancers (Peck et al. 1998). Under these conditions, ^{210}Po caused some interference, which was not present in the absence of the enhancers. When Cerenkov counting was used for measurement of ^{210}Pb through ^{210}Bi, no scintillation cocktail is needed, the EDTA dissolution of $PbSO_4$ is directly applied for the measurement.

Extraction chromatography using Sr Spec resin have been applied to the separation of ^{210}Pb and ^{210}Po for their determination in various environmental and biological samples (Vajda et al. 1997; Vreček et al., 2004; Ruberu et al., 2007; Hassona et al., 2008; Sirelkhatim et al., 2008; Outola et al., 2008). This is based on the high adsorption of Pb and Po on this resin in dilute HCl solution, while ^{210}Bi does not. The sample is first decomposed and prepared in 2M HCl medium and loaded to a Sr Spec column, ^{210}Po and ^{210}Pb absorbed on the column were eluted from the column sequentially using 6M HNO_3 and 6M HCl, respectively. The HCl eluate was evaporated to dryness followed by converting lead from chloride to nitrate and by precipitating it as the oxalate for the yield determination. ^{210}Po was determined by alpha spectrometry using ^{208}Po as the yield tracer after spontaneous deposition on a metal disc. The separated ^{210}Pb was determined by LSC after dissolving PbC_2O_4 into 1 mL of 6M HNO_3 and mixing it with scintillation cocktail. In this method, ^{210}Po and ^{210}Pb were efficiently separated from other elements and interfering radionuclides (Vajda et al. 1997). Biggin et al. (2002) modified the Sr•Spec resin method for determining ^{210}Pb, ^{210}Bi and ^{210}Po in seawater using ^{212}Pb, ^{207}Bi, and ^{208}Po, respectively, as yield tracers. This method offers the opportunity to investigate the geochemical cycling of the ^{210}Pb/^{210}Bi/^{210}Po system in the marine environment and to use them as tracers of scavenging processes operating on time-scales ranging from a few days to tens of years.

Solvent extraction methods using a variety of extractants are also applied for the separation of ^{210}Po and ^{210}Pb in environmental samples (Véronneau et al., 2000; Matthews et al., 2007). POLEX is an extractive scintillation cocktail by which ^{210}Bi and ^{210}Po can be extracted into the cocktail from phosphoric acid solutions and subsequently measured by LSC using α/β discrimination (Monna et al., 1996; Wallner, 1997; Katzlberger et al., 2001; Aleissa et al., 2006; Landstetter and Katzlberger, 2006). ^{210}Pb, which remains in the aqueous phase, can be determined by two methods: (i) carrying out a second POLEX extraction on the same aqueous phase as the first one after allowing for ^{210}Bi ingrowth for 2 weeks, and (ii) taking a sample from the aqueous phase and mixing it with the cocktail for direct measurement of ^{210}Pb using LS measurement. Forte et al. (2009) recommended a toluene-based cocktail, which includes TOPO, naphthalene, and PBBO. Peck and Smith (2000) proposed a method using 0.2% DDTC (diethyldithiocarbamate) in chloroform to extract ^{210}Bi from rainwater samples, and Chen et al. (2001) used 5% TIOA (triisooctylamine) in xylene to extract ^{210}Po quantitatively from 10M HCl solution, while ^{210}Pb was not extracted.

F. Thorium

1. Environmental occurrence and importance

Thorium (Th) has three principal isotopes, ^{232}Th ($t_{1/2} = 1.41 \cdot 10^{10}$ y), ^{230}Th ($t_{1/2} = 7.54 \cdot 10^{4}$ y) and ^{228}Th ($t_{1/2} = 1.91$ y), all of which are alpha-emitters. ^{232}Th is the parent of the thorium series (Fig. 2.31) where ^{228}Th belongs as a member. ^{230}Th and the β-emitting ^{234}Th ($t_{1/2} = 24.1$ d), belong to the uranium series (Fig. 2.25). ^{234}Th is a very useful tracer in marine studies. Other natural Th isotopes are ^{231}Th ($t_{1/2} = 25.5$ hours) and ^{227}Th ($t_{1/2} = 18.7$ d) from the actinium series. Th is widely distributed over the earth's crust at different levels similarly as U. The worldwide average value of ^{232}Th in soil is about 45 Bq/kg, but the concentrations reported vary largely up to 360 Bq/kg (UNSCEAR, 2008). Th and U concentrations are high in igneous rocks of granite composition, some

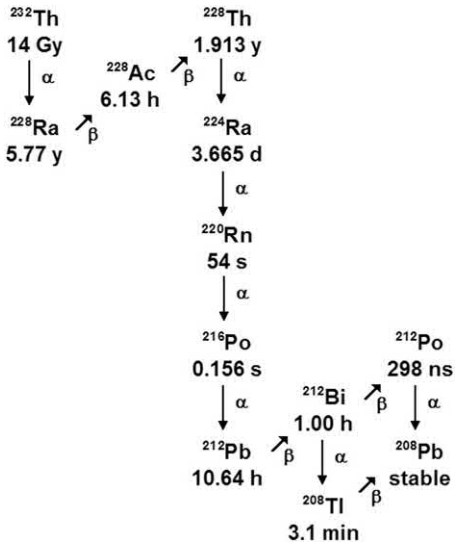


FIGURE 2.31 Decay scheme of thorium (^{232}Th).

shales and phosphate rocks, while high concentrations of Th are associated with minerals such as monazites and zirkons (UNSCEAR, 2000). In seawater, ^{232}Th concentration is very low, because Th has only one stable oxidation state, 4+, under all redox conditions in natural waters, and thorium ions (4+) are extremely particle reactive (Santschi et al., 2006). Consequently, Th is highly insoluble and of low environmental mobility in contrast to U, which occurs under oxidizing conditions in the 6+ oxidation state as the soluble uranyl ion (UO_2^{2+}, or carbonate complex). These contrasting geochemical behaviors have enabled any disequilibrium between the ^{234}Th/^{238}U daughter/parent pair to be used to study the temporal and spatial dynamics of particle and particle reactive species and other short-term processes occurring in the oceans (Geibert and Usbeck, 2004; Smith et al., 2004; Waples et al., 2006; Santschi et al., 2006; Buesseler et al., 2006; Anand et al. 2017, 2018). In the water column, the major applications for ^{234}Th/^{238}U disequilibrium have focused on either elucidating oceanic carbon fluxes or modeling reactive pollutant behaviors in coastal environments. In the sediment, this disequilibrium is typically used to study reworking processes (Martin and Sayles, 1987; Foster and Schimmield, 2002). Thorium is a radiotoxic element, but the exposure from thorium is generally very low, because of its less volatility and enrichment in foodstuff, accounting for only 0.8% of the internal dose from ingestion of natural series radionuclides (UNSCEAR, 2000). The main goal in the determination of thorium is environmental monitoring for mining, milling, and mineral processing industries and for occupational exposures of workers (Poole et al., 1995; Clulow et al., 1998; Chen et al., 2005; Saueia and Mazzilli, 2006; Carvalho et al., 2007; Arogunjo et al., 2009; Sartandel et al., 2009; Lipsztein et al., 2001; Al-Jundi et al., 2004; Ting et al., 1999; UNSCEAR, 2008).

2. Sample preparation and analysis

a. ^{232}Th, ^{230}Th, and ^{228}Th

The alpha-emitting thorium isotopes, ^{232}Th, ^{230}Th, and ^{228}Th, are determined mostly by α- and γ-spectrometry and mass spectrometric methods and rarely by LSC methods. For the long-lived ^{232}Th, the mass spectrometric methods (e.g., ICP-MS) are six orders of magnitude more sensitive than the α-spectrometric methods, while the short-lived ^{228}Th is preferably determined by α-spectrometry (Hou and Roos, 2008). Consequently, the mass spectrometric methods have become the main techniques for determining ^{232}Th and ^{230}Th in geochemical, environmental and bioassay studies (Clulow et al., 1998; Ting et al., 1999; Fujino et al., 2000; Unsworth et al., 2001; Lipsztein et al., 2001; Al-Jundi et al., 2004; Arogunjo et al., 2009; Harrison et al., 2011; Zoriy et al., 2010). For the α-spectrometric methods, Th is separated using ion exchange or extraction chromatography and thereafter electrodeposited onto a stainless-steel disk for α-counting (Poole et al., 1995; Clulow et al., 1998; Purkl and Eisenhauer, 2003a, 2003b; Wang et al., 2004; Hirose et al., 2004; Carvalho et al., 2007; Saueia and Mazzilli, 2006; Jia et al., 2009). Soil, sediment, and mineral samples are often determined by γ-spectrometric methods, which entail analysis based on measuring Th isotopes by their decay products in equilibrium with the parent nuclides. The measurements are performed using HPGe detectors (Vuković et al., 1996; Tzortzis and Tsertos, 2004; Shetty et al., 2006; Arogunjo et al., 2009; Sartandel et al., 2009). Wallner (1996) determined thorium in excretion samples of persons occupationally exposed to thorium, which was based on the combination of precipitation and extraction techniques and α-counting with the Quantulus. Fig. 2.32 illustrates the alpha spectra of ^{232}Th and ^{228}Th (in secular equilibrium) and the beta spectra of ^{234}Th and its daughter, ^{234m}Pa measured immediately after the thorium separation.

b. ^{234}Th

The radionuclide ^{234}Th ($t_{1/2} = 24.1$ d) is the immediate daughter of ^{238}U ($t_{1/2} = 4.47 \cdot 10^9$ y), emitting low-energy betas ($E_{max} = 199$ keV) with low-energy gamma photons at low probabilities (63.3 keV (4.8%) and 92.4–92.8 keV (5.6%)). Its daughter, ^{234}Pa ($t_{1/2} = 6.75$ hours), decays by the emission of a high-energy beta particle ($E_{max} = 2.29$ MeV), which can be used to determine the ^{234}Th activity of a sample. ^{234}Th activities in seawater are traditionally determined by gamma spectroscopy via the low probability gamma emissions, which consequently requires large sample volumes (>200 L) (Buesseler et al.,

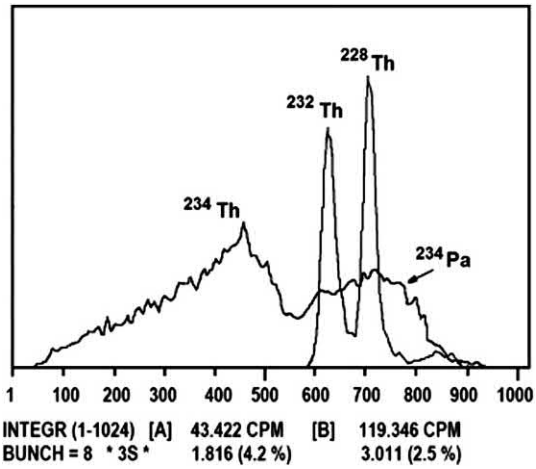


FIGURE 2.32 Spectra of a thorium sample measured immediately after the thorium extraction, containing 0.33 ± 0.02 Bq ^{232}Th (channel 580–675), 0.35 ± 0.02 Bq ^{228}Th (channel 675–760), ^{234}Th and ^{234}Pa in the β-spectrum between channel 550 and 900). Note that the two spectra have different energy scales (Wallner, 1996). *Reprinted by permission of Elsevier © 1996.*

1992, 2001; Schmidt and Reyss, 2000) and by the determination of the beta emissions from ^{234}Th and ^{234m}Pa by gas proportional counting (Coale and Bruland, 1987; Moran and Buesseler, 1993; Buesseler et al., 2001) or by liquid scintillation spectrometry (LSC) (Anderson et al., 1991; Pates et al., 1996b; Smith et al., 2004). The beta counting methods require sample volumes in the range of 2−100 L. The LSC method is briefly described below (Pates et al., 1996b). After the addition of Fe-carrier and the ^{230}Th yield tracer into a filtered seawater sample, thorium is coprecipitated with $Fe(OH)_3$ by addition of ammonium to pH 8−9, the coprecipitate is then dissolved in HCl. Following the removal of U and Fe from the HCl solution by anion exchange, Th is converted from chloride to nitrate, prepared in high concentration HNO_3 solution and further purified by anion exchange using a nitrate-form resin. After loading the sample solution and rinsing the column with HNO_3, thorium is finally eluted with diluted HCl, which is evaporated to prepare a sample for LS counting using α/β discrimination. A detection limit of 0.4 mBq/L for a 20 L sample and a counting time of 400 minutes has been achieved using this method. Preparation of the ^{230}Th yield tracer from uranite ore requires a complex procedure, the full details of which are given in Pates et al. (1996b). Smith et al. (2004) determined the chemical yield using a ^{229}Th tracer after electroplating the separated thorium onto a stainless-steel disk and counting it by α-spectrometry. Thereafter, thorium on the disc was removed using HNO_3, and the solution was evaporated to dryness. The residue was dissolved into 1 mL of 0.1 M HCl and transferred into an LS vial and mixed with 10 mL of Ultima Gold AB to achieve a good α/β discrimination with a low-background LS spectrometer. Nour et al. (2002) developed a similar method for the determination of ^{234}Th in sediments using ^{230}Th as yield tracer. An extraction chromatography using TEVA resin rather than ion exchange was used to separate and purify the thorium. ^{234}Th was measured via the ^{234m}Pa by Cerenkov counting with a counting efficiency of 27.6%. By adding LS cocktail and measurement by LSC using α/β discrimination, an efficiency of 156% was achieved, because both ^{234}Th and ^{234m}Pa are measured. An extensive review on the methodology for the ^{234}Th analysis in aquatic systems has been presented by Rutgers van der Loeff et al. (2006). It covers the sampling and analysis methods, recommendations on calibration procedures and production of standard reference materials.

VIII. Spectrum deconvolution methods in environmental analysis

A. Spectrum deconvolution, unfolding, stripping, peak fitting

Separation of multinuclide liquid scintillation spectra into components from individual radionuclides has been referred to, in the LSC literature, as spectrum deconvolution, unfolding, stripping and peak fitting. Deconvolution in this context is not the recovery of the pure spectrum from the composite one that has been blurred by the instrument (point or slit spread function in optical spectrometries, signal, image processing), but rather separation of merged emission peaks from each other. There are numerous factors in each sample that affect the LS spectrum and therefore removal of the instrument function automatically would be a formidable task.

Actually, isolation by mathematical deconvolution of instrument, temperature, vial, cocktail fluor and quench effects from composite spectra have not been applied in LSC at all. Usually the sum of squared differences of measured and model spectrum points is minimized and the best fit then found.

B. Approaches in LS beta spectrometry

Shapes and positions of liquid scintillation spectra depend on the sample matrix, as the sample itself mixed with scintillating cocktail is a part of the detector system. It is not an invariant light-emitting detector component, as NaI crystal in gamma spectrometers for instance. Quench is one reason for the difficulty in the development of automatic spectrum separation software for liquid scintillation spectrometry. Some tests in late 1980s at Wallac with MINUIT minimization software indicated that alpha spectrum shape is difficult to handle automatically. Later, a spectrum analysis software package, EASY View for Quantulus and 1400 series LSAs, included a nonautomatic, interactive spectrum stripping routine, where a set of quenched reference spectra are required to reduce multiple components from the beta and alpha spectra.

The latter instrument series analyzes up to three beta labels automatically using digital spectrum libraries. The method is called the Digital Overlay Technique (DOT) (Rundt, 1989, 1992; Kouru and Rundt, 1991). A library of six beta-emitters is stored in a reduced form as a function of chemical and color quench indices measured in conventional and safe cocktails and in plastic and glass vials leading to 4 combinations. The spectrum form is saved as recorded in up to 32 windows over the spectrum. A composite sample spectrum fit is achieved by taking up to three reference spectra at the measured quench index values and adjusting their activity ratios so that minimum error is achieved in the fit. The method contains background and chemiluminescence corrections and correction for the sample size. Sample quality count rate monitoring is also included (Wallac 1414 WinSpectral, 2001).

New radionuclide spectrum libraries can be created, and existing libraries fine-tuned to better fit the sample matrix (Kouru, 1991). The method can be applied to resolve ^{14}C and ^{35}S activities from a mixed sample.

Deterioration of PMT efficiency is automatically taken care of in the method, as the shift of the spectra means higher quench and spectrum libraries do have matching

spectra to correct for the PMT aging. The instrument versions, which have a pulse shape analyzer, can separate the alpha signal into its own spectrum.

Beta spectrum deconvolution is discussed in more detail in Chapter 6, Volume 1 and some references are given in the Sr section of this chapter.

C. Alpha spectrum unfolding

1. Energy resolution

Alpha spectra are monochromatic. Monochromatic emissions in LS beta spectra are seen only from conversion electrons, for instance in the ^{137}Cs spectrum.

The larger number of photons per decay is recorded, the smaller is the variation of their number, which relates to the observed width of the emission peak. Light yield is thus one factor affecting the energy resolution (Nähle et al., 2009). Poor alpha peak resolution in LSC, due to the modest number of detected photoelectrons by PMTs per decay event, poses a great difficulty.

If samples are not preconcentrated, water samples mixed with cocktail including most of the sample would usually give the best LLD. However, the alpha energy resolution deteriorates under quench close to 1 MeV FWHM and heavy peak overlay of multiple emissions makes it impossible to resolve them. In gross alpha counting, separation into components from different alpha-emitting radionuclides is not necessary.

Extractive cocktails could lead to low quench samples and thus much improved energy resolution. The PERALS alpha spectrometer is constructed to optimize light collection with optical coupling using immersion fluid between the PMT and sample tube and offers good resolution, which can be achieved in double PMT instruments only with equivalent sample and vial optimization.

Solutions to improve energy resolution are focusing on instrumentation and light yield from cocktails as has been done with the PERALS alpha spectrometer (McDowell, 1992) or the use of numerical methods to resolve poor resolution spectra.

Aupiais (2005) points out that the energy resolution is also a function of count rate. In the case of very low count rates, there is a strong probability for an α event to appear near the center of the related α peak because energy distribution follows a Poisson law. A practical consequence is a narrower peak at a lower count rate than that observed at higher count rate. If the full width at half maximum (FWHM) is fixed, an over-estimation of 30%–40% is observed.

2. High energy tailing

Aupiais and Dacheux (2000) have studied peak asymmetry in PERALS spectra produced with extractive cocktails and found that the main reason for the high-energy tail is internal conversion involving L and M shells. Peak asymmetry was studied for ^{210}Po, ^{214}Po, ^{218}Po, ^{228}Th, ^{230}Th, ^{232}Th, ^{232}U, ^{233}U, ^{234}U, ^{235}U, ^{238}U, ^{236}Pu, ^{238}Pu, ^{239}Pu, ^{242}Pu, ^{241}Am, ^{243}Am, and ^{244}Cm. The asymmetry is not observable with other LSCs, where water miscible cocktails are often used resulting in a poor energy resolution.

An electron is quickly ejected in internal conversion from the shell of the daughter nuclide, whose excited level has a life-time of less than a nanosecond. The instrument does not recognize these successive events as separate ones. The result is a sum of monoenergetic beta and alpha particle energies piling up as a separate peak on the higher energy side of the main alpha peak as illustrated in Fig. 2.33 (Aupiais, 2004a, 2004b; 2005). The distance of the conversion peak is enhanced, as about 8 times more light per electron is produced than per alpha-particle.

No asymmetry due to conversion electrons is present in major α emissions from ^{226}Ra, ^{224}Ra, ^{220}Rn, ^{222}Rn, ^{210}Po, ^{214}Po, and ^{218}Po, which are even-even nuclides (Aupiais, 2004b). Approximate 5% α emissions from for ^{224}Ra and ^{226}Ra produce internal conversion peaks at higher energies overlaying α peaks of their respective daughter nuclides and cannot be separated in LS spectra. The total contribution is about 2%.

All isolated alpha and internal conversion peaks (close to each other) are Gaussian in this analysis and have equal FWHM (Aupiais, 2005). The error due to the deconvolution is equal or within the statistical fluctuations and therefore neglected. Extra caution is necessary in the case of very low count rates, which require free adjustment of the peak width to avoid large errors.

Aupiais et al. (2003) enhanced the resolution obtained with a Tri-Carb liquid scintillation counter by reducing the

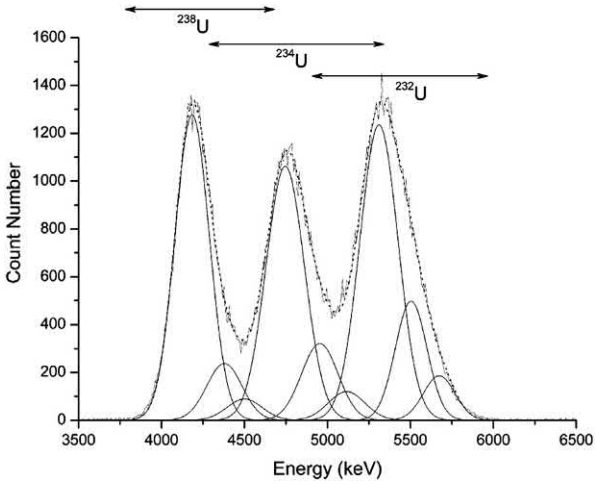


FIGURE 2.33 Energy spectrum of natural uranium doped with ^{232}U. Each isotope is fitted by three peaks – a main peak and two peaks of internal conversion (Aupiais, 2004a). *Reprinted by permission of Elsevier © 2004.*

optical path and by using extractive cocktails rather than water accepting cocktails for aqueous samples. The detection limits of the Tri-Carb were improved by 300%, but remained 40% lower than in PERALS. Tri-Carb energy resolution is improved by a factor of 2.

3. Software

Rusconi et al. (2004) and Forte et al. (2003) used aqueous samples and the Quantulus liquid scintillation counter to evaluate ^{238}U and ^{234}U content by applying spectral deconvolution with Canberra Genie 2k Interactive Peak Fit software. The ^{235}U contribution to total uranium was estimated to be lower than 2.5%, and it was neglected in the alpha spectra deconvolution. The method was compared with good results against two independent methods on some bottled water samples, viz. high-resolution alpha spectrometry on electrodeposited samples and ICP-MS (inductively coupled plasma mass spectrometry) on ^{238}U alone. Each sample was counted for 1000 minutes; the MDA for total uranium content was 0.4 mBq/L. Leyba et al. (1995) analyzed U isotope spectra from the PERALS spectrometer using three Gaussian functions in PeakFit software (Jandel Scientific Software, later acquired by Systat Software Inc.).

Bianchi et al. (2005) used Physics Analysis Workstation (PAW) from CERN in determining the ^{234}U/^{238}U ratio in environmental samples. Several free parameters are contained in the process: two activities, background spectrum shape, spectrum offset, peak width, and peak position of the first peak. The width and position of the second peak is based on a linear response, constant energy resolution and detection efficiency. The values of the fit parameters are obtained performing a Chi-squared minimization using MINUIT software from CERN. With ^{235}U contents greater than 0.26%, the average discrepancy with the reference values is 3.5% (with a maximum of 6.4%).

Nebelung and Baraniak (2007) examined ^{226}Ra and progeny, ^{233}U and ^{237}Np by liquid scintillation spectrometry using the Wallac 1414 WinSpectral Low-Level α/β LSA and low quenched aqueous samples. The detection limits are 0.02 Bq for α-emitting nuclides, and 0.09 Bq for β-emitting nuclides during 20 minutes of measurement.

^{226}Ra, ^{233}U and ^{237}Np can be determined in mutual activity ratios of 1:50 with a relative standard deviation of less than 4% for the major activity and 9% for the minor activity. If each nuclide is only present to 0.5 Bq, the spectrum of a 20 minutes counting time can also be exactly evaluated.

The authors used Origin Peak Fitting software (MicroCal Software Inc., now OriginLab Corporation) and asymmetric double sigmoidal function, a function that considers beside the peak center three peak widths. The errors were below 3%. The methods overestimate the first peak and gives 26% of total activity for ^{226}Ra instead of 25%.

Aupiais (2004a; 2004b) used Origin 7.0 peak fitting (OriginLab Corporation) software to resolve U spectra (Fig. 2.25).

Vera Tomé et al. (2002a) studied alpha peak shapes in extracted ^{226}Ra and progeny samples in High Efficiency Mineral Oil Scintillator using the Quantulus LSA and low-diffusion polyethylene (PE) vials. Peak shape was measured for radon and progeny in low diffusion PE and copper-teflon vials using mineral oil scintillator. Weak low-energy tailing was observed. This curve shape has been described by the mathematical functions formed by the convolution of a Gaussian with one or two left-handed exponential curves. The effect of sample shaking on peak asymmetry was tested. Less low-end asymmetry was observed with homogeneous samples. Also, a small shoulder on the high energy side of the peak disappeared. A Teflon-copper vial produces a peak shape closer to Gaussian than a plastic vial.

The best-fit curve can be calculated by using the nonlinear minimization method of Levenberg−Marquardt. The fit is independent on the logarithmic scale as the peaks lie in a very high-energy range. The same peak form was used by Verzilov et al. (2002) in the analysis of ^{234,238}U, ^{238,239,240}Pu, ^{241}Am and ^{244}Cm.

Stamoulis et al. (2010) analyzed ^{226}Ra and progeny, and ^{234}U and ^{238}U in preconcentrated water samples with the Tri-Carb 3170TR/SL LSA and Ultima Gold AB as scintillant. The alpha spectrum and the background were approximated with sums of exponential terms including the dependence of peak positions and half-widths on quench levels. Deconvolution of alpha spectra was carried out with Origin software. The detection limit was 8.2 mBq/kg for a 0.4 kg water sample for a 1000 minutes counting time, and the alpha detection efficiency was 97.4%.

RadSpectraDec software was developed by Ermakov et al. (2006) to analyze liquid waste, drill water, liquid leakages, potable water, etc. The deconvolution is a recursive minimization of the difference between a weighted multilabel model and experimental spectra. A premeasured spectrum library contains at least 10 model spectra for each radionuclide at different quench levels with CCl_4 as a chemical quench agent. Intermediate spectra are fitted to the required quenching parameters via an interpolation of two of the neighboring reference spectra. The developed approach can be applied to most scintillation cocktails and all modern LS counters with linear and logarithmic amplification, including the Tri-Carb, Quantulus, 1414 Guardian and Triathler. Export of the spectrum libraries to other LSCs is discussed by Ermakov et al. (2006).

The Tri-Carb 3100 LSA achieves an MDA of ~10−20 mBq for beta and 5 mBq for alpha-emitters in a 10 hours counting time. Its energy resolution is ~10% for alpha-emitters, and the PERALS spectrometer has 5% resolution at 150−300 keV.

Sixty alpha and beta labels are now in the spectrum library for the linear energy scale of the Tri-Carb 2550 TR/AB (Ermakov et al., 2006). For example, for the determination of natural decay chains, the following sets of convolved spectra were generated: ^{238}U, ^{234}Th+^{234m}Pa (in equilibrium), ^{232}Th, ^{228}Th, ^{210}Pb, ^{210}Bi, ^{210}Po, ^{235}U, ^{231}Th + ^{231}Pa(equ), ^{228}Ra + ^{228}Ac(equ), ^{234}U, ^{230}Th, ^{226}Ra, ^{226}Ra + ^{222}Rn + ^{218}Po + ^{214}Pb + ^{214}Bi + ^{214}Po (in equil.), ^{224}Ra + ^{220}Rn + ^{216}Po + ^{212}Pb + ^{212}Bi + ^{212}Po + ^{208}Tl (in equil.).

A rapid, 3 hours analysis of a technological sample (wash-out from the disk, "U-1", IRM, Zarechnyi) using the Tri-Carb 3170 TR/SL, ALPHAEX-extraction and Rad-SpectraDec software has been described by Ermakov et al. (2011).

Matzke (2002) investigated the propagation of uncertainties in several unfolding codes.

D. Better energy resolution enables more complete separation

1. Cocktail and sample quench

Resolution can be improved by reducing the aqueous sample to a cocktail mixing ratio which lowers the quench (i.e., increasing number of recorded photons per decay). The sample volume will be reduced in this case and lead to a higher LLD. Purge with oxygen-free, toluene-saturated (when toluene is compatible) argon (McDowell and McDowell, 1994). Extractive cocktails give the best energy resolutions.

The effect of quench is nicely demonstrated by Aupiais et al. (2003) by removing detergent from Ultima Gold AB in comparison with ALPHAEX extractive cocktail. Kossert et al. (2009) used mixtures of nonaqueous cocktails Ultima Gold F with water-miscible Ultima Gold AB, and the ratio 13 mL:2 mL gave the best resolution. Emulsifier in Ultima Gold AB, which does not produce light, was then adequate to accept 1 mL water.

Resolution of alpha spectra from solid samples is severely deteriorated by self-absorption.

2. Vial selection

Order of vial excellence in improving energy resolution: glass, plastic and Teflon vial. Glass vials show strong low-energy tailing due to the multiple reflections, which lead to loss of photons received by the PMTs.

Small vials, 16 mm in diameter and 5 mm in length have produced the best resolutions in PERALS spectrometer (Dacheux et al., 2000; Reboli et al., 2005). This choice does not apply to routine counters, which use 20 and 7 mL vials.

Etching, sandblasting and taping the outside surface of the glass vial improves energy resolution and so does a careful optics design (Verzilov et al., 2002; Kossert et al., 2009; Nähle et al., 2009). Bianchi et al. (2005) tested several vial types (made of glass, standard polyethylene, and high-density polyethylene) for energy resolution. The best results were obtained with teflon-coated, low-diffusion, high-density polyethylene vials from PerkinElmer, which exhibit a low background, high efficiency, good spectral resolution and slow solvent permeability.

3. Lower sample temperature

The counting efficiency is improved at a lower temperature of the sample and cocktail (Homma and Murase, 1987). This method is usually limited to stabilization of sample temperature to a few degrees below ambient using the instrument cooling unit, which also helps in reducing PMT dark current noise.

4. New detector designs

Cassette and Monnard (1999) show a hybrid PMT or HPMT which is composed of a planar silicon diode in a vacuum tube facing a photocathode. This detector is able to resolve multi-photoelectron peaks up to the 11th photoelectron in a scintillation spectrum and the peak resolution is approximately constant. A 15 keV photoelectron produces more than 4000 electron-hole pairs – relative standard deviation of the number of photoelectron pairs is 2%. Even a high gain PMT would reach only a 15% standard deviation.

Large area avalanche photodiodes have been tested (16 mm diameter) by Reboli et al. (2005). Energy resolutions are much improved in the higher energy range, 260 keV (3.9%) energy resolution for ^{216}Po versus PERALS′ 448 keV (6.6%) and ^{232}Th 200 keV (5.0%) versus PERALS′ 210 keV (5.3%). The improved resolution is not due to the higher quantum efficiency of photodiodes compared to PMTs, but to the uniformity of the spatial photo response. Reboli et al. (2005) suggest that even better results would be reached by using green scintillators with larger Stokes shift and blue-enhanced photodiodes.

According to Ivan et al. (2008), the HPMT is complex to operate. Solid-state photo detectors like avalanche photodiode arrays resolve single-photon events, but their actual dark counting rate prohibits their use in LS counters. Ivan et al. (2008) also tested channel photomultipliers (CPMs), which have low and stable dark counting rate and high gain allowing a good peak-to-valley ratio of the photoelectron peak. Contrary to the PMT, the pulse amplitude in a channel photomultiplier is not a function of the number of photons reaching the photocathode. This feature prohibits the use of channel photomultipliers for spectroscopy, which is a useful but not mandatory feature of an LS counter. They also do not reach the PMT performance with the current windows sizes of CPMs.

References

Absi, A., Villa, M., Moreno, H.P., Manjón, G., Periañez, R., 2004. Self-cleaning in an estuarine area formerly affected by ^{226}Ra anthropogenic enhancements. Sci. Total Environ. 329, 183–195.

Al-Azmi, D., Snopek, B., Sayed, A.M., Domanski, T., 2004. A simple bubbling system for measuring radon (^{222}Rn) gas concentrations in water samples based on the high solubility of radon in olive oil. J. Environ. Radioact. 71, 175–186.

Al-Jundi, J., Werner, E., Roth, P., Höllriegl, V., Wendler, I., Schramel, P., 2004. Thorium and uranium contents in human urine: influence of age and residential area. J. Environ. Radioact. 71, 61–70.

Al-Masri, M.S., Blackburn, R., 1995. Application of Cerenkov radiation for the assay of ^{226}Ra in natural water. Sci. Total Environ. 173/174, 53–59.

Al-Masri, M.S., Hamwi, A., Mikhlallaty, H., 1997. Radiochemical determination of ^{210}Pb in environmental water samples using Cerenkov counting. J. Radioanal. Nucl. Chem. 219, 73–75.

Alamelu, D., Aggarwal, S.K., 2007. Determination of ^{241}Pu/^{239}Pu atom ratio in pressurized heavy water reactors (PHWR)-Pu samples using liquid scintillation counting. J. Alloys Compd. 444–445, 652–655.

Aleissa, K.A., Islam, M.S., Alshammari, H., 2006. Measurement of ^{210}Po and ^{210}Pb in groundwater using an alpha liquid scintillation counter. In: Chałupnik, S., Schönhofer, F., Noakes, J. (Eds.), Advances in Liquid Scintillation Spectrometry, 2005. Radiocarbon Publishers, University of Arizona, Tucson, pp. 197–209.

Aleissa, K.A., Almasoud, F.I., Islam, M.S., L'Annunziata, M.F., 2008. Radium-228 analysis of natural waters by Cherenkov counting of Actinium-228. Appl. Radiat. Isot. 66, 1954–1963.

Alessio, M., Allegri, L., Bella, F., Improta, S., 1976. Study of background characteristics by means of high efficiency liquid scintillation counter. Nucl. Instrum. Methods Phys. Res. 137, 537–543.

Altzitzoglou, T., La Rosa, J.J., Nicholl, C., 1998. Measurement of ^{90}Sr in bone ash. Appl. Radiat. Isot. 49, 1313–1317.

Alvarado, J.S., Orlandini, K.A., Erickson, M.D., 1995. Rapid determination of radium isotopes by α spectrometry. J. Radional. Nucl. Chem. 194, 163–172.

Alvardo, J.A.C., Nedjadi, Y., Bochud, F., 2011. Determining the activity of Pu-241 by liquid scintillation counting. J. Radioanal. Nucl. Chem. 289, 375–379.

Alvarez, A., Navarro, N., 1996. Method for actinides and Sr-90 determination in urine samples. Appl. Radiat. Isot. 47, 869–873.

Amano, H., Yanase, N., 1990. Measurement of ^{90}Sr in environmental samples by cation-exchange and liquid scintillation counting. Talanta 37, 585–590.

Anand, S.S., Rengarajan, R., Sarma, V.V.S.S., Sudheer, A.K., Bhushan, R., Singh, S.K., 2017. Spatial variability of upper ocean POC export in the Bay of Bengal and the Indian Ocean determined using particle-reactive Th-234. J. Geophys. Res. Ocean. 122, 3753–3770.

Anand, S.S., Rengarajan, R., Sarma, V.V.S.S., 2018. ^{234}Th based carbon export flux along the Indian Geotraces G102 section in the Arabian Sea and the Indian Ocean. Global Bioerochem. C Cycles 32, 417–436.

Anders, E., 1960. The Radiochemistry of Technetium. Technical Report NAS-NS 3021. National Research Council.

Andersen, M.B., Erel, Y., Bourdon, B., 2009. Experimental evidence for ^{234}U-^{238}U fractionation during granite weathering with implications for ^{234}U/^{238}U in natural waters. Geochim. Cosmochim. Acta 73, 4124–4141.

Anderson, R.F., 1984. A method for determining the oxidation state of uranium in natural waters. Nucl. Instrum. Methods Phys. Res. 223, 213–217.

Anderson, R., Cook, G.T., MacKenzie, A.B., Harkness, D.D., 1991. The determination of ^{234}Th in water column studies by liquid scintillation counting. In: Ross, H., Noakes, J.E., Spaulding, J.D. (Eds.), Liquid Scintillation Counting and Organic Scintillators, 1989. Lewis Publishers, Michigan, pp. 461–470.

Antoniou, S., Tsiaili, A., Pashalidis, I., 2008. Alpha radiometry of uranium surface and groundwaters by liquid scintillation counting after separation of the radionuclide by cation exchange. Radiat. Meas. 43, 1294–1298.

Antovic, N., Svrkota, N., 2009. Measuring the radium-226 activity using a multidetector γ-ray coincidence spectrometer. J. Environ. Radioact. 100, 823–830.

APHA/AWWA/WEF, 1998. Standard Methods for the Examination of Water and Wastewater. American Public Health Association, American Water Works Association, Water Environmental Federation, twentieth ed. American Public Health Association, Washington, DC.

Arogunjo, A.M., Höllriegl, V., Giussani, A., Leopold, K., Gerstmann, U., Veronese, I., Oeh, U., 2009. Uranium and thorium in soils, mineral sands, water and food samples in a tin mining area in Nigeria with elevated activity. J. Environ. Radioact. 100, 232–240.

Ashton, L., Warwick, P., Giddings, D., 1999. The measurement of ^{36}Cl and ^{129}I in concrete wastes. Analyst 124 (4), 627–632.

Asikainen, M., 1981. State of disequilibrium between ^{238}U, ^{234}U, ^{226}Ra and ^{222}Rn in groundwater from bedrock. Geochim. Cosmochim. Acta 45, 201–206.

ASTM D5072 - 98, 1998. Standard Test Method for Radon in Drinking Water. ASTM International, West Conshohocken, PA. https://doi.org/10.1520/D5072-98. www.astm.org.

ASTM D7283 - 06, 2006. Standard Test Method for Alpha- and Beta-Activity in Water by Liquid Scintillation Counting. ASTM International, West Conshohocken, PA. https://doi.org/10.1520/D7283-06. www.astm.org.

ASTM D5811 - 08, 2008. Standard Test Method for Strontium-90 in Water. ASTM International, West Conshohocken, PA. https://doi.org/10.1520/D5811-08. www.astm.org.

ASTM D7459 - 08, 2008. Standard Practice for Collection of Integrated Samples for the Speciation of Biomass (Biogenic) and Fossil-Derived Carbon Dioxide Emitted from Stationary Emissions Sources. ASTM International, West Conshohocken, PA. https://doi.org/10.1520/D7459 − 08. www.astm.org.

ASTM D6866 - 11, 2011. Standard Test Methods for Determining the Biobased Content of Solid, Liquid, and Gaseous Samples Using Radiocarbon Analysis. ASTM International, West Conshohocken, PA. https://doi.org/10.1520/D6866-11. www.astm.org.

Atkinson, R., Eddy, T., Kuhne, W., Jannik, T., Brandl, A., 2014. Measurement of the tritium concentration in the fractionated distillate from environmental water samples. J. Environ. Radioact. 135, 113–119.

Aupiais, J., 1997. Alpha liquid scintillation measurement of plutonium in solution spiked by ^{236}Pu. J. Radioanal. Nucl. Chem. 218, 201–207.

Aupiais, J., 2004a. Rapid determination of uranium activity and concentration in water by alpha liquid scintillation with α/β discrimination. Anal. Chim. Acta 517, 221–228.

Aupiais, J., 2004b. Deconvolution of alpha liquid scintillation spectra for quantitative analysis of actinide elements in water samples. Radiochim. Acta 92, 125−132.

Aupiais, J., 2005. Radium measurement in water samples by α-liquid scintillation counting with α/β discrimination. Anal. Chim. Acta 532, 199−207.

Aupiais, J., Dacheux, N., 2000. Understanding the peak asymmetry in alpha liquid scintillation with α/β discrimination. Radiochim. Acta 88, 391−398.

Aupiais, J., Fayolle, C., Gilbert, P., Dacheux, N., 1998. Determination of Ra-226 in mineral drinking waters by alpha liquid scintillation with rejection of beta emitters. Anal. Chem. 70, 2353−2359.

Aupiais, J., Dacheux, N., Thomas, A.C., Matton, S., 1999. Study of neptunium measurement by alpha liquid scintillation with rejection of beta-gamma emitters. Anal. Chim. Acta 398, 205−218.

Aupiais, J., Aubert, C., Dacheux, N., 2003. Some rules to improve the energy resolution in alpha liquid scintillation with beta rejection. Radiochim. Acta 91, 63−69.

Baeza, A., del Río, L.M., Jiménez, A., 1998. Procedure for simultaneous determination of $^{223, 224, 226, 228}$Ra by alpha and gamma spectrometry. Radiochim. Acta 83, 53−60.

Bakir, Y., Bem, H., 1996. Application of pulse decay discrimination liquid scintillation counting for routine monitoring of radioactivity in drinking water. In: Cook, G.T., Harkness, D.D., MacKenzie, A.B., Miller, B.F., Scott, E.M. (Eds.), Liquid Scintillation Spectrometry, 1994. Radiocarbon Publishers, University of Arizona, Tucson, pp. 293−299.

Barker, H., 1953. Radiocarbon dating: large scale production of acetylene from organic material. Nature 172, 631−632.

Barrera, J., Tarancon, A., Bagan, H., Garcia, F., 2016. A new plastic scintillation resin for single-step separation, concentration and measurement of technetium-99. Anal. Chim. Acta. 936, 259−266.

Baskaran, M., 2011. ^{210}Po and ^{210}Pb as atmospheric tracers and global atmospheric ^{210}Pb fallout: a review. J. Environ. Radioact. 102, 500−513.

Beals, D., 1992. Measuring technetium-99 in aqueous samples by ICP-MS. In: Proceedings of the Third International Conference on Nuclear and Radiochemistry. Vienna, Austria.

Begg, J.D.C., Burke, I.T., Morris, K., 2007. The behaviour of technetium during microbial reduction in amended soils from Dounreay. UK. Sci. Total Environ. 373, 297−304.

Belloni, P., Cavaioli, M., Ingrao, G., Mancini, C., Notaro, N., Santaroni, P., Torri, G., Vasselli, R., 1995. Optimization and comparison of three different methods for the determination of ^{222}Rn in water. Sci. Total Environ. 173/174, 61−67.

Bem, H., Wieczorkowski, P., 2002. Determination of total alpha radioactivity of thorium and uranium radionuclides in fallout using alpha/beta LSC. In: Möbius, S., Noakes, J.E., Schönhofer, F. (Eds.), Advances in Liquid Scintillation Spectrometry, 2001. Radiocarbon Publishers, University of Arizona, Tucson, pp. 335−341.

Bem, H., Bakir, Y.Y.Y., Bou-Rabee, F., 1994. An improved method for low-level ^{222}Rn determination in environmental waters by liquid scintillation counting with pulse shape analysis. J. Radioanal. Nucl. Chem. Lett. 186, 119−127.

Bem, H., Bem, E.M., Majchrzak, I., 1998. Comparison of two methods for ^{226}Ra determination in mineral water. Nukleonika 43, 459−468.

Benedik, L., Vasile, M., Spasova, Y., Wätjen, U., 2009. Sequential determination of ^{210}Po and uranium radioisotopes in drinking water by alpha-particle spectrometry. Appl. Radiat. Isot. 67, 770−775.

Bhade, S.P.D., Reddy, P.J., Narayanan, A., Narayan, K.K., Babu, D.A.R., Sharma, D.N., 2010. Standardization of calibration procedures for quantification of gross alpha and gross beta activities using liquid scintillation counter. J. Radioanal. Nucl. Chem. 284, 367−375.

Bhangare, R.C., Sahs, S.K., Maity, S., Ajmal, P., Rathod, T.D., Tiwari, M., Pandit, G.G., 2017. Method for determination of radium in seawater using MnO_2 co-precipitation technique. J. Radioanal. Nucl. Chem. 313, 597−601.

Bianchi, D., Cortese, P., Dellacasa, G., Merlano, I., 2005. Determination of the isotopic ratio ^{234}U/^{238}U in liquid scintillation and environmental applications. Nucl. Instrum. Methods Phys. Res., Sect. A 553, 543−549.

Bicron Corporation, 1988. BGO (Bi4Ge3O12) Product Bulletin SC-103A. Newbury, Ohio.

Biggin, C.D., Cook, G.T., MacKenzie, A.B., Pates, J.M., 2002. Time-efficient method for the determination of ^{210}Pb, ^{210}Bi and ^{210}Po activities in seawater using liquid scintillation spectrometry. Anal. Chem. 74, 671−677.

Blanco, P., Lozano, J.C., Vera Tomé, F., 2002. On the use of ^{225}Ra as yield tracer and Ba(Ra)SO_4 microprecipitation in ^{226}Ra determination by α-spectrometry. Appl. Radiat. Isot. 57, 785−790.

Blanco, P., Lozano, J.C., Gómez Escobar, V., Vera Tomé, F., 2004. A simple method for ^{210}Pb determination in geological samples by liquid scintillation counting. Appl. Radiat. Isot. 60, 83−88.

Blanco Rodríguez, M.P., Vera Tomé, F., Lozano, J.C., Gómez Escobar, V., 2000. Sequential method for the determination of uranium, thorium and ^{226}Ra by liquid scintillation alpha spectrometry. Appl. Radiat. Isot. 52, 705−710.

Bobin, C., Thiam, C., Bouchard, J., Jaubert, F., 2010. Application of a stochastic TDCR model based on Geant4 for Cherenkov primary measurements. Appl. Radiat. Isot. 68, 2366−2371.

Bojanowski, R., Knapinska-Skiba, D., 1990. Determination of low-level ^{90}Sr in environmental materials: a novel approach to the classical method. J. Radioanal. Nucl. Chem. 138, 207−218.

Bojanowski, R., Radecki, Z., Burns, K., 2005. Determination of radium and uranium isotopes in natural waters by sorption of hydrous manganese dioxide followed by alpha spectrometry. J. Radioanal. Nucl. Chem. 264, 437−443.

Bonotto, D.M., 2004. Doses from ^{222}Rn, ^{226}Ra, and ^{228}Ra in groundwater from Guarani aquifer, south America. J. Environ. Radioact. 76, 319−335.

Bonotto, D.M., Mello, C.B., 2006. A combined method for evaluating radon and progeny in waters and its use at Guarani aquifer, São Paulo State, Brazil. J. Environ. Radioact. 86, 337−353.

Bonotto, D.M., Bueno, T.O., Tessari, B.W., Silva, A., 2009a. The natural radioactivity in water by gross alpha and beta measurements. Radiat. Meas. 44, 92−101.

Bonotto, D.M., Caprioglio, L., Bueno, T.O., Lazarindo, J.R., 2009b. Dissolved ^{210}Po and ^{210}Pb in Guarani aquifer groundwater, Brazil. Radiat. Meas. 44, 311−324.

Borai, E.H., Lasheen, Y.F., El-Sofany, E.A., Abdel-Rassoul, A.A., 2008. Separation and subsequent determination of low radioactivity levels of radium by extraction scintillation. J. Hazardous Mater. 156, 123−128.

Bou-Rabee, F., Bakir, Y., Bem, H., 1995. Contribution of uranium to gross alpha radioactivity in some environmental samples in Kuwait. Environ. Int. 21, 293−298.

Bouwer, E.J., McKlveen, J.W., McDowell, W.J., 1979. A solvent extraction-liquid scintillation method for assay of uranium and thorium in phosphate-containing material. Nucl. Technol. 42, 102−111.

Broda, R., 2003. A review of the triple-to-double coincidence ratio (TDCR) method for standardizing radionuclides. Appl. Radiat. Isot. 58 (5), 585–594.

Bronic, I.K., Barešic, J., Horvatincic, N., Sironic, A., 2017. Determination of biogenic component in liquid fuels by the 14C direct LSC method by using quenching properties of modern liquids for calibration. Radiat. Phys. Chem. 137, 248–253.

Brooks, F.D., 1979. Development of organic scintillators. Nucl. Instrum. Methods Phys. Res. 162, 477–505.

Brun, S., Bessac, S., Uridat, D., Boursier, B., 2002. Rapid method for determination of radiostrontium in milk. J. Radioanal. Nucl. Chem. 253, 191–197.

Buchtela, K., Tschurlovits, M., 1975. A new method for determination of Sr-89, Sr-90, and Y-90 in aqueous solution with the aid of liquid scintillation counting. Appl. Radiat. Isot. 26, 333–338.

Buchtela, K., Tschurlovits, M., Unfried, E., 1974. Eine Methode zur Unterschiedung von Alpha- und Beta-Strahlen in einem Flüssigszintillationsmessgerät. Int. J. Appl. Radiat. Isot. 25, 551–555.

Buesseler, K.O., Bacon, M.P., Cochran, J.K., Livingston, H.D., Casso, S.A., Hirschberg, D., Hartman, M.C., Fleer, A.P., 1992. Determination of thorium isotopes in seawater by non-destructive and radiochemical procedures. Deep-Sea Res. 39, 1103–1114.

Buesseler, K.O., Benitez-Nelson, C., Rutgers van der Loeff, M., Andrews, J., Ball, L., Crossin, G., Charette, M.A., 2001. An intercomparison of small- and large-volume techniques for thorium-234 in seawater. Mar. Chem. 74, 15–28.

Buesseler, K.O., Benitez-Nelson, C.R., Moran, S.B., Burd, A., Charette, M., Cochran, J.K., Coppola, L., Fisher, N.S., Fowler, S.W., Gardner, W.D., Guo, L.D., Gustafsson, Ö., Lamborg, C., Masque, P., Miquel, J.C., Passow, U., Santschi, P.H., Savoye, N., Stewart, G., Trull, T., 2006. An assessment of particulate organic carbon to thorium-234 ratios in the ocean and their impact on the application of ^{234}Th as a POC flux proxy. Mar. Chem. 100, 213–233.

Burke, I.T., Livens, F.R., Lloyd, J.R., Brown, A.P., Lawa, G.T.W., McBeth, J.M., Ellis, B.L., Lawson, R.S., Morris, K., 2010. The fate of technetium in reduced estuarine sediments: combining direct and indirect analyses. Appl. Geochem. 25, 233–241.

Burnett, W.C., Tai, W.-C., 1992. Determination of radium in natural waters by alpha liquid scintillation. Anal. Chem. 64, 1691–1697.

Burnett, W.C., Christoff, J., Stewart, B., Winters, T., Wilbur, P., 2000. Reliable gross alpha-/beta-particle analysis of environmental samples via liquid scintillation counting. Radioact. Radiochem. 11, 26–44.

Buzinny, M., 1996. A new approach to determining ^{222}Rn in air using liquid scintillation counting. In: Cook, G.T., Harkness, D.D., MacKenzie, A.B., Miller, B.F., Scott, E.M. (Eds.), Liquid Scintillation Spectrometry, 1994. Radiocarbon Publishers, University of Arizona, Tucson, pp. 137–140.

Buzinny, M., Likhtarev, I., Los, I., Talerko, N., Tsigankov, N., 1998. ^{14}C analysis of annual tree rings from the vicinity of the Chernobyl NPP. Radiocarbon 40, 373–379.

Cadieux, J.R., Clark, S., Fjeld, R.A., Reboul, S., Sowder, A., 1994. Measurement of actinides in environmental samples by photon-electron rejecting alpha liquid scintillation. Nucl. Instrum. Methods Phys. Res. Sect A 353, 534–538.

Calf, G.E., Airey, P.L., 1982. Liquid scintillation counting of C-14 in a heavily shielded site. In: Ambrose, W., Duerden, P. (Eds.), Archaeometry: An Australian Perspective. Australian National University Press, Canberra, Australia, pp. 351–356.

Calf, G.E., Polach, H.A., 1974. Teflon vials for liquid scintillation counting of carbon-14 samples. In: Stanley, P.E., Scoggins, B. (Eds.), Liquid Scintillation Counting: Recent Developments. Academic Press, New York, pp. 224–234.

Callis, E.L., Abernathey, R.M., 1991. High-precision isotopic analyses of uranium and plutonium by total sample volatilization and signal integration. Int J. Mass Spectro. Ion Proc. 93–105.

Canducci, C., Bartolomei, P., Magnani, G., Rizzo, A., Piccoli, A., Tositti, L., Esposito, M., 2013. Upgraded of the CO_2 direct absorption method for low-level ^{14}C liquid scintillation counting. Radiocarcon 55 (2–3), 260–267.

Cannizzaro, F., Greco, G., Raneli, M., Spitale, M.C., Tomarchio, E., 1999. Determination of ^{210}Po concentration in the air at ground-level by gamma-ray spectrometry. Appl. Radiat. Isot. 51, 239–245.

Carbol, P., Solatie, D., Erdmann, N., Nylén, T., Betti, M., 2003. Deposition and distribution of Chernobyl fallout fission products and actinides in a Russian soil profile. J. Environ. Radioact. 68, 27–46.

Carmon, B., 1979. The use of Cerenkov radiation for the assay of radiostrontium in aqueous solutions. Appl. Radiat. Isot. 30, 97–100.

Carter, H.E., Warwick, P., Cobb, J., Longworth, G., 1999. Determination of uranium and thorium in geological materials using extraction chromatography. Analyst 124, 271–274.

Carvalho, F.P., 2011. Polonium (^{210}Po) and lead (^{210}Pb) in marine organisms and their transfer in marine food chain. J. Environ. Radioact. 102, 462–472.

Carvalho, F.P., Oliveira, J.M., Lopes, I., Batista, A., 2007. Radionuclides from past uranium mining in rivers of Portugal. J. Environ. Radioact. 98, 298–314.

Case, G.N., McDowell, W.J., 1990. Separation of radium and its determination by photon-electron-rejecting alpha liquid scintillation (PERALS) spectrometry. Radioact. Radiochem. 1, 58–69.

Cassette, P., Monnard, E., 1999. A new liquid scintillation counter for the absolute activity measurement of radionuclides. Nucl. Instrum. Methods Phys. Res., Sect. A 422, 119–123.

Cassette, P., Sahagia, M., Grigorescu, L., Lépy, M.C., Picolo, J.L., 2006. Standardization of ^{222}Rn by LSC and comparison with α- and γ-spectrometry. Appl. Radiat. Isot. 64, 1465–1470.

Cattarin, S., Doretti, L., Mazzi, U., 1985. Determination of ^{99}Tc in urine by liquid scintillation counting to evaluate internal contamination. Health Phys. 11, 795–804.

Chałupnik, S., Lebecka, J.M., 1993. Determination of ^{226}Ra, ^{228}Ra and ^{224}Ra in water and aqueous solutions by liquid scintillation counting. In: Noakes, J.E., Schönhofer, F., Polach, H.A. (Eds.), Liquid Scintillation Spectrometry, 1992. Radiocarbon Publishers, University of Arizona, Tucson, pp. 397–403.

Chalupnik, S., Lebecka, J., Mielnikow, A., Michalik, B., 1996. Determining radium in water: comparison of methods. In: Cook, G.T., Harkness, D.D., MacKenzie, A.B., Miller, B.F., Scott, E.M. (Eds.), Liquid Scintillation Spectrometry, 1994, 103–109. Radiocarbon Publishers, University of Arizona, Tucson.

Chalupnik, S., Michalik, B., Wysocka, M., Skubacz, K., Mielnikow, A., 2001. Contamination of settling ponds and rivers as a result of discharge of radium-bearing waters from Polish coal mines. J. Environ. Radioact. 54, 85–98.

Chau, N.D., Chwiej, T., Chruściel, E., 2001. ^{226}Ra, ^{228}Ra and ^{210}Pb isotopes in some water samples of mines. J. Radioanal. Nucl. Chem. 250, 387–390.

Chałupnik, S., Mielnikow, A., Skubacz, K., 2002. Fast method of ^{226}Ra measurement by means of alpha spectroscopy and its comparison with liquid scintillation counting. In: Möbius, S., Noakes, J.E., Schönhofer, F. (Eds.), Advances in Liquid Scintillation Spectrometry, 2001. Radiocarbon Publishers, University of Arizona, Tucson, pp. 261–267.

Chen, Q.J., Dahlgaard, H., Nielsen, S.P., 1994. Determination of ^{99}Tc in seawater at ultra-low levels. Anal. Chim. Acta. 285, 177–180.

Chen, Q.J., Hou, X.L., Dahlgaard, H., Nielsen, S.P., Aarkrog, J., 2001. A rapid method for the separation of ^{210}Po and ^{210}Pb by TIOA extraction. J. Radioanal. Nucl. Chem. 249, 587–593.

Chen, Q., Dahlgaard, H., Nielsen, S.P., Aarkrog, A., 2002a. ^{242}Pu as tracer for simultaneous determination of ^{237}Np and ^{239,240}Pu in environmental samples. J. Radioanal. Nucl. Chem. 253, 451–458.

Chen, Q.J., Hou, X.L., Yu, Y.X., Dahlgaard, H., Nielsen, S.P., 2002b. Separation of Sr from Ca, Ba and Ra by means of $Ca(OH)_2$ and $Ba(Ra)Cl_2$ or $Ba(Ra)SO_4$ for the determination of radiostrontium. Anal. Chim. Acta 466, 109–116.

Chen, S.B., Zhu, Y.G., Hu, Q.H., 2005. Soil and plant transfer of ^{238}U, ^{226}Ra and ^{232}Th on a uranium mining-impacted soil from southeastern China. J. Environ. Radioact. 82, 223–236.

Child, D.P., Hotchkis, M.A., Williams, M., 2008. High sensitivity analysis of plutonium isotopes in environmental samples using accelerator mass spectrometry (AMS). J. Anal. Atom. Spectrom. 23, 765–768.

Cho, J.S., Ahn, J.K., Kim, H.-C., Lee, D.W., 2004. Radon concentrations in groundwater in Busan measured with a liquid scintillation counter method. J. Environ. Radioact. 75, 105–112.

Chu, T.-C., Lin, C.-C., 2001. The solvent extraction of radium using sym-Di[4(5)-tert-butylbenzo]-16-crown-5-oxyacetic acid. Appl. Radiat. Isot. 55, 609–616.

Chu, T.-C., Wang, J.-J., Lin, Y.-M., 1998. Radiostrontium analytical method using crown-ether compound and Cerenkov counting and its applications in environmental monitoring. Appl. Radiat. Isot. 49, 1671–1675.

Clayton, G.D., Arnold, J.R., Patty, F.A., 1955. Determination of sources of particulate atmospheric carbon. Science 122, 751–753.

Clulow, F.V., Davé, N.K., Lim, T.P., Avadhanula, R., 1998. Radionuclides (lead-210, polonium-210, thorium-230, and -232) and thorium and uranium in water, sediments, and fish from lakes near the city of Elliot Lake, Ontario, Canada. Environ. Pollut. 99, 199–213.

Coale, K.H., Bruland, K.W., 1987. Oceanic stratified euphotic zone as elucidated by ^{234}Th:^{238}U disequilibria. Limnol. Oceanogr. 32, 189–200.

Coha, I., Neufuss, S., Grahek, Ž., Němec, M., Nodilo, M., John, J., 2016. The effect of counting conditions on pure beta emitter determination by Cherenkov counting. J. Radioanal. Nucl. Chem. 310, 891–903.

Condren, O.M., León Vintro, L., Mitchell, P.I., Ryan, T.P., 1996. A new approach to quench correction when measuring ^{241}Pu in the presence of Pu-α by supported-disc liquid scintillation spectrometry. Appl. Radiat. Isot. 47, 875–878.

Cook, G.T., 1995. Enhanced low-level LSC performance for Carbon-14 dating using a bismuth germanate ($Bi_4Ge_3O_{12}$) quasi-active guard. Radioact. Radiochem. 6, 10–15.

Cook, G.T., Anderson, R., 1992. A radiocarbon dating protocol for use with Packard scintillation counters employing burst-counting circuitry. Radiocarbon 34, 381–388.

Cook, G.T., Harkness, D.D., Anderson, R., 1989. Performance of the Packard 2000CA/LL and 2250CA/XL liquid scintillation counters for ^{14}C dating. Radiocarbon 31, 352–358.

Cook, G.T., Naysmith, P., Anderson, R., Harkness, D.D., 1990a. Performance optimization of the Packard 2000 CA/LL liquid scintillation counter for ^{14}C dating. Nucl. Geophys. 4, 241–245.

Cook, G.T., Hold, A.G., Naysmith, P., Anderson, R., 1990b. Applicability of 'new technology' scintillation counters (Packard 2000 CA/LL and 2260 XL) for ^{14}C dating. Radiocarbon 32, 233–234.

Cook, P.G., Favreau, G., Dighton, J.C., Tickell, S., 2003. Determining natural groundwater influx into a tropical river using radon, chlorofluorocarbons and ionic environmental tracers. J. Hydrol. 277, 74–88.

Cook, P.G., Wood, C., White, T., Simmons, C.T., Fass, T., Brunner, P., 2008. Groundwater inflow to a shallow, poorly-mixed wetland estimated from a mass balance of radon. J. Hydrol. 354, 213–226.

Cooper, E.L., Cox, J.M., Workman, W.J., 1998. Analysis of Sr-90 and alpha-particle emitters on air filters and swipe samples using a liquid scintillation counter with alpha/beta discrimination. Radioact. Radiochem. 9, 25–40.

Cooper, L.W., Kelley, J.M., Bond, L.A., Orlandini, K.A., Grebmeier, J.M., 2000. Sources of the transuranic elements plutonium and neptunium in arctic marine sediments. Mar. Chem. 69, 253–276.

Court, J.D., Goldsack, R.J., Ferrari, L.M., Polach, H.A., 1981. The use of carbon isotopes in identifying urban air particulate sources. Clean Air 6–11.

Crespo, M.T., 2000. On the determination of ^{226}Ra in environmental and geological samples by γ-spectrometry using ^{225}Ra as yield tracer. Appl. Radiat. Isot. 53, 109–114.

Croudace, I.W., Warwick, P.E., Morris, J.E., 2012. Evidence for the preservation of technogenic tritium organic compounds in an estuarine sedimentary environment. Environ. Sci. Technol. 46 (1), 5704–5712.

Croudace, I.W., Warwick, P.E., Kim, D., 2014. Using thermal evolution profiles to infer tritium speciation in nuclear site metals: an aid to decommissioning. Anal. Chem. 86 (18), 9177–9185.

Culp, R., Noakes, J., 2009. Evaluation of biobased content ASTM Method 6866-06A: improvements revealed by liquid scintillation counting, accelerator mass spectrometry, and stable isotopes for products containing inorganic carbon. In: Eikenberg, J., Jäggi, M., Beer, H., Baehrle, H. (Eds.), Advances in Liquid Scintillation Spectrometry, 2008. Radiocarbon Publishers, University of Arizona, Tucson, pp. 269–278.

Culp, R.A., Noakes, J.E., Smith, D.R., Greenway, L., Smith, F.S., Markowicz, B.K., 2011. Bio-base product determination by ASTM method 6866-08 using liquid scintillation counting and benzene synthesis: Progress and performance in an expanding market. In: Cassette, P. (Ed.), Advances in Liquid Scintillation Spectrometry, 2010. Radiocarbon Publishers, University of Arizona, Tucson, pp. 23–34.

Currie, L.A., 1978. Environmental radiocarbon measurements. In: Grove, H.E. (Ed.), Proc. 1st Conf. Radiocarbon Dating with Accelerators. University of Rochester, Rochester, New York, pp. 372–390.

Currie, L., Klinedinst, D., Burch, R., Feltham, N., Dorsch, R., 2000. Authentication and dating of biomass components of industrial materials; links to sustainable technology. Nucl. Instrum. Methods Phys. Res., Sect. B 172, 281–287.

Dacheux, N., Aupiais, J., 1997. Determination of uranium, thorium, plutonium, americium and curium ultratraces by photon electron rejecting alpha liquid scintillation. Anal. Chem. 69, 2275–2282.

Dacheux, N., Aupiais, J., 1998. Determination of low concentrations of americium and curium by photon/electron rejecting alpha liquid scintillation. Anal. Chim. Acta 363, 279–294.

Dacheux, N., Aupiais, J., Courson, O., Aubert, C., 2000. Comparison and improvement of the determinations of actinide low activities using several liquid scintillation spectrometers. Anal. Chem. 72, 3150−3157.

Dai, X., Kramer-Tremblay, S., 2011. Sequential determination of actinide isotopes and radiostrontium in swipe samples. J. Radioanal. Nucl. Chem. 289, 461−466.

Dai, X., Kramer-Tremblay, S., 2014. Five-column chromatography separation for simultaneous determination of hard-to-detect radionuclides in water and swipe samples. Anal. Chem. 86, 5441−5447.

Dai, X., Liblong, A., Kramer-Tremblay, S., Priest, N., Li, C., 2012a. Optimisation of nasal swab analysis by liquid scintillation counting. J. Radiol. Prot. 32, 155−166.

Dai, X., Christl, M., Kramer-Tremblay, S., Synal, H., 2012b. Ultra-trace determination of plutonium in urine samples using a compact accelerator mass spectrometry system operating at 300 kV. J. Anal. Atom. Spectrom. 27, 126−130.

Dai, X., Kramer-Tremblay, S., Li, C., 2012c. Rapid determination of 226Ra in urine samples. Radiat. Prot. Dosim. 151, 30−35.

Dai, X., Cui, Y., Kramer-Tremblay, S., 2013. A rapid method for determining strontium-90 in urine samples. J. Radioanal. Nucl. Chem. 296, 363−368.

Dai, X., Christl, M., Kramer-Tremblay, S., Synal, H., 2016. Determination of atto- to femtogram levels of americium and curium isotopes in large-volume urine samples by compact accelerator mass spectrometry. Anal. Chem. 88, 2832−2837.

Dale, C.J., Dale, A.A., Warwick, P.E., Rowe, J.E., 2002. Rapid determination of ^{210}Po and ^{210}Pb (via ^{210}Bi) in air filters using alpha spectrometry and Cerenkov counting. In: Möbius, S., Noakes, J.E., Schönhofer, F. (Eds.), Advances in Liquid Scintillation Spectrometry, 2001. Radiocarbon Publishers, University of Arizona, Tucson, pp. 343−349.

Dalencourt, C., Michaud, A., Habibi, A., Leblanc, A., Lariviere, D., 2018. Rapid, versatile and sensitive method for the quantification of radium in environmental samples through cationic extraction and inductively coupled plasma mass spectrometry. J. Anal. Atom. Spectrom. 33, 1031−1040.

De Filippis, S., Noakes, J.E., 1991. Sample preparation of environmental samples using benzene synthesis followed by high-performance LSC. Trans. Am. Nucl. Soc. 64, 79−80.

de Oliveira Lucas, F., Chavés de Oliveira, I.J., Brenha Ribeiro, F., 2009. Development and calibration of a portable radon sampling system for groundwater ^{222}Rn activity concentration measurements. J. Environ. Radioact. 100, 875−883.

Dean, J.C.J., Kolkowski, P., 2004. The development of a ^{222}Rn standard solution dispenser at NPL. Appl. Radiat. Isot. 61, 95−100.

Decaillon, J.G., Bickel, M., Hill, C., Holmes, L., Altzitzoglou, T., 2004. Validation of methods for the determination of radium in waters and soil. Appl. Radiat. Isot. 61, 409−413.

Degenkolb, S.J., Neel, J.W., Papin, P.J., 1994. The effect of technetium-99 and environmental conditions on soybean physiology. J. Environ. Qual. 23, 1265−1271.

Desideri, D., Meli, M.A., Feduzi, L., Roselli, C., Rongoni, A., Saetta, D., 2007. ^{238}U, ^{234}U, ^{226}Ra, ^{210}Po concentrations of bottled mineral waters in Italy and their dose contribution. J. Environ. Radioact. 94, 86−97.

DeVol, T.A., Brown, D.D., Leyba, J.D., Fjeld, R.A., 1996. A comparison of four aqueous-miscible liquid scintillation cocktails with an alpha/beta discriminating Wallac 1415 liquid scintillation counter. Health Phys. 70, 41−46.

DeVol, T.A., Theisen, C.D., DiPrete, D.P., 2007. Effect of quench on alpha/beta pulse shape discrimination of liquid scintillation cocktails. Radiat. Safety J. 92, S105−S111.

Dewberry, R.A., Bibler, N.E., DiPrete, D.P., 1999. Measured ^{63}Ni contents in Savannah River Site high level waste and Defense Waste Processing Facility glass product by Ni-selective ion exchange purification and beta-decay counting. J. Radioanal. Nucl. Chem. 242, 81−89.

Dietz, M.L., Horwitz, E.P., Nelson, D.M., Wahlgren, N., 1991. An improved method for determining ^{89}Sr and ^{90}Sr in urine. Health Phys. 61, 871−877.

Dijs, I.J., van der Windt, E., Kaihola, L., van der Borg, K., 2006. Quantitative determination by ^{14}C analysis of the biological component in fuels. Radiocarbon 48, 315−323.

Dimova, N., Burnett, W.C., Horwitz, E.P., Lane-Smith, D., 2007. Automated measurement of ^{224}Ra and ^{226}Ra in water. Appl. Radiat. Isot. 65, 428−434.

Dinh, C.N., Rajchel, L., Van, H.D., Nowak, J., 2017. Ra-224 and the Ra-224/Ra-228 activity ratio in selected mineral waters from the Polish Carpathians. Geological Quart. 61, 771−778.

Dircan, A., Sahin, M., 2016. Comparison of acid leaching and fusion techniques to determine uranium in soil samples by alpha spectrometry. Appl. Radiat. Isot. 109, 189−192.

Directive 2003/30/EC of the European Parliament and of the Council of 8 May 2003 on the promotion of the use of biofuels or other renewable fuels for transport. Off. J. Eur. Union, 2003. L123/42.

Dodson, C., 1991. In: Alpha/Beta Discrimination on Liquid Scintillation Counters. Beckman Instruments Inc. Publication, Fullerton, California.

DOE, 1993. DOE/EM-0089T, Rev 1. In: DOE Methods for Evaluating Environmental and Waste Management Samples. National Technical Information Service, U.S. Department of Commerce, Springfield, Virginia.

Dowdall, M., Selnæs, Ø.G., Gwynn, J.P., Lind, B., 2004. On the use of ^{99}Mo/^{99m}Tc generators in the analysis of low levels of ^{99}Tc in environmental samples by radiochemical methods. Water Air Soil Pollut. 156, 287−297.

Dressler, K., Spitzer, L., 1967. Photomultiplier tube pulses induced by rays. Rev. Sci. Instrum. 38, 436−438.

Duliu, O.G., Varlam, C., Shnawaw, M.D., 2018. 18 years of continuous observation of tritium and atmospheric precipitations in Ramnicu Valcea (Romania): a time series analysis. J. Environ. Radioact. 190, 105−110.

Ebaid, Y.Y., Khater, A.E.M., 2006. Determination of ^{210}Pb in environmental samples. J. Radioanal. Nucl. Chem. 270, 609−616.

Edler, R.H., 2017. Measurement of 3H, gross α/β and 222Rn in drinking water using the new Quantulus GCT 6220. J. Radioanal. Nucl. Chem. 314, 695−699.

Eikenberg, J., Fiechtner, A., Rüthi, M., Zumsteg, I., 1996. A rapid screening method for determining gross alpha activity in urine using α/β LSC. In: Cook, G.T., Harkness, D.D., MacKenzie, A.B., Miller, B.F., Scott, E.M. (Eds.), Advances in Liquid Scintillation Spectrometry, 1994. Radiocarbon Publishers, University of Arizona, Tucson, pp. 283−292.

Eikenberg, J., Zumsteg, I., Rüthi, M., Bajo, S., Fern, M.J., Passo, C.J., 1999. Fast radiochemical screening of transuranium radionuclides in urine using actinide extractive resin and low-level α/β LSC. Radioact. Radiochem. 10, 19−30.

Eikenberg, J., Tricca, A., Vezzu, G., Bajo, S., Ruethi, M., Surbeck, H., 2001. Determination of ^{228}Ra, ^{226}Ra and ^{224}Ra in natural water via adsorption on MnO_2 - coated discs. J. Environ. Radioact. 54, 109−131.

Eikenberg, J., Beer, H., Rüthi, M., Zumsteg, I., Vetter, A., 2006. Precise determination of ^{89}Sr and ^{90}Sr/^{90}Y in various matrices: the LSC 3-window approach. In: Chałupnik, S., Schönhofer, F., Noakes, J. (Eds.), Advances in Liquid Scintillation Spectrometry, 2005. Radiocarbon Publishers, University of Arizona, Tucson, pp. 237−249.

Eikenberg, J., Jäggi, M., Beer, H., Rüthi, M., Zumsteg, 2009. Separation techniques for low-level determination of actinides in soil samples. Appl. Radiat. Isot. 67, 776−780.

Eikenberg, J., Beer, H., Jaggi, M., 2014. Determination of 210Pb and 226Ra/228Ra in continental water using HIDEX 300SL LS-spectrometer with TDCR efficiency tracing and optimized alpha-beta discrimination. Appl. Radiat. Isot. 93, 64−69.

Einarsson, S., 1992. Evaluation of a prototype low-level liquid scintillation multisample counter. Radiocarbon 34, 366−373.

Elliot, N.L., Bickel, G.A., Linauskas, S.H., Paterson, L.M., 2006. Determination of femtogram quantities of 239Pu and 240Pu in bioassay samples by thermal ionization mass spectrometry. J. Radioanal. Nucl. Chem. 267, 637−650.

EPA, 1987. Interim Protocols for Screening and Followup Radon and Radon Decay Product Measurements 520/1-86-014-1. U.S. Environmental Protection Agency, Washington, DC.

EPA, 1991. Method 3052, Sr-89 & Sr-90 in Water, Air Filter & Milk. EMSL-LV, Nuclear Radiation Assessment Division, Radioanalysis Branch, US Environmental Protection Agency. NRA 1.18.

EPA, 2009. 2009 Edition of the Drinking Water Standards and Health Advisories. EPA 822-R-09-011. Office of Water, U.S. Environmental Protection Agency, Washington, DC.

Ermakov, I.A., Malinovskiy, S.V., Kashirin, I.A., Tikhomirov, V.A., Sobolev, A.I., 2006. Rapid analysis of radionuclide composition (screening) of liquid samples via deconvolution of their LS spectra. In: Chałupnik, S., Schönhofer, F., Noakes, J. (Eds.), Advances in Liquid Scintillation Spectrometry, 2005. Radiocarbon Publishers, University of Arizona, Tucson, pp. 89−98.

Ermakov, A., Malinovskiy, S.V., Kashirin, I.A., Tikhomirov, V.A., Sobolev, A.I., 2011. Application of LSC-based techniques realized on Quantulus 1220 for rapid LWR assay of LWR resulting from nuclear transport facilities. In: LSC 2010, Advances in Liquid Scintillation Spectrometry (in press).

EURATOM 2001/928, 2001. Commission recommendation of 20 December 2001 on the protection of the public against exposure to radon in drinking water supplies. Off. J. Eur. Commun. L344/85. The Commission of the European Communities, Brussels.

European Union, 1998. Council Directive 98/83/EC of 3 November 1998 on the quality of water intended for human consumption. Off. J. Eur. Commun. L330/32. The Council of the European Union, Brussels.

Eyrolle, F., Ducros, L., Dizes, S.L., Beaugelin-Seiller, K., Charmasson, S., Boyer, P., Cossonnet, C., 2018. An updated review on tritium in the environment. J. Environ. Radioact. 181, 128−137.

Fehn, U., 2012. Tracing crustal fluids: application of natural I-129 and Cl-36. Annu. Rev. Earth Planet. Sci. 40, 45−67.

Feng, X.-G., He, Q.-G., 2009. Simultaneous determination of ^{237}Np, $^{238-240}$Pu and ^{241}Am in HNO_3 solution by combining extraction, liquid scintillation counting and α spectrometry. Nucl. Instrum. Methods Phys. Res. Sect. A 223, 165−171.

Fifield, L.K., Cresswell, R.G., Tada, M.D., et al., 1996. Accelerator mass spectrometry of plutonium isotopes. Nucl. Instrum. Meth., Sect. B 117, 295−303.

Fink, D., Klein, J., Middleton, R., 1990. Ca-41 −past, present and future. Nucl. Instrum. Methods Phys. Res. B52, 572.

Fliss, M., Botsch, W., Handl, J., Michel, R., Slavov, V.P., Borschtschenko, V.V., 1998. A fast method for the determination of strontium-89 and strontium-90 in environmental samples and its application to the analysis of strontium-90 in Ukrainian soils. Radiochim. Acta 83, 81−92.

Flynn, W.W., 1968. The determination of low levels of polonium-210 in environmental materials. Anal. Chim. Acta 43, 221−227.

Fons-Castells, J., Oliva, J., Tent-Petrus, J., Llaurado, M., 2017. Simultaneous determination of Ra-226, Ra-228 and Pb-210 in drinking water using 3M Empore (TM) RAD disk by LSC-PLS. Appl. Radiat. Isot. 124, 83−89.

Forte, M., Rusconi, R., Margini, C., Abbate, G., Maltese, S., Badalamenti, P., Bellinzona, S., 2001. Determination of uranium isotopes in food and environmental samples by different techniques: a comparison. Radiat. Prot. Dosim. 97, 325−328.

Forte, M., Rusconi, R., Di Caprio, E., Bellinzona, S., Sgorbati, G., 2003. Natural radionuclides measurements in Lombardia drinking water by liquid scintillation counting. In: Warwick, P. (Ed.), Environmental Chemical Analysis II. The Royal Society of Chemistry, Athenaeum Press Ltd., Gateshead, pp. 128−142.

Forte, M., Bertolo, A., D'Alberti, F., De Felice, P., Desideri, D., Esposito, M., Fresca Fantoni, R., Lorenzelli, R., Luciani, A., Magnoni, M., Marsili, F., Moretti, A., Queirazza, G., Risica, S., Rusconi, R., Sandri, S., Trevisi, R., Valentini Ganzerli, M.T., 2006. Standardized methods for measuring radionuclides in drinking water. J. Radioanal. Nucl. Chem. 269, 397−401.

Forte, M., Rusconi, R., Costantino, S., Cazzaniga, M.T., Sgorbati, G., 2009. Quick determination of ^{210}Pb in drinking and waste waters. In: Eikenberg, J., Jäggi, M., Beer, H., Baehrle, H. (Eds.), Advances in Liquid Scintillation Spectrometry, 2008, 305−312. Radiocarbon Publishers, University of Arizona, Tucson.

Fowler, S.W., 2011. ^{210}Po in the marine environment with emphasis on its behaviour within the biosphere. J. Environ. Radioact. 102, 448−461.

Fréchou, C., Degros, J.P., 2005. Measurement of ^{36}Cl in nuclear wastes and effluents: validation of a radiochemical protocol with an in-house reference sample. J. Radioanal. Nucl. Chem. 263 (2), 333−339.

Friberg, I., 1997. Development and application of a method for the determination of ^{90}Sr in environmental samples. J. Radioanal. Nucl. Chem. 226, 55−60.

Füeg, B., Tschachtli, T., Krähenbühl, U., 1997. Alpha liquid scintillation spectrometry used for the measurement of uranium/thorium-disequilibria in soil samples. Radiochim. Acta 78, 47−51.

Fujii, H., Takiue, M., 1988. Radioassay of dual-labeled samples by sequential Cherenkov counting and liquid scintillation efficiency tracing technique. Nucl. Instrum. Methods Phys. Res., Sect. A 273, 377−380.

Fujino, O., Umetani, S., Ueno, E., Shigeta, K., Matsuda, T., 2000. Determination of uranium and thorium in apatite minerals by inductively coupled plasma atomic emission spectrometry with solvent extraction separation into diisobutyl ketone. Anal. Chim. Acta 420, 65−71.

Galán-López, M., Martín-Sánchez, A., 2008. Present status of ^{222}Rn in groundwater in Extremadura. J. Environ. Radioact. 99, 1539−1543.

Gautier, C., Colin, C., Garcia, C., 2016. A comparative study using liquid scintillation counting to determine Ni-63 in low and intermediate level radioactive waste. J. Radioanal. Nucl. Chem. 308, 261−270.

Geckeis, H., Hentschel, D., Jensen, D., Gortzen, A., 1997. Determination of Fe-55 and 63Ni using semi-preparative ion chromatography, a feasibility study. Fresenius J. Anal. Chem. 357, 864–869.

Geibert, W., Usbeck, R., 2004. Adsorption of thorium and protactinium onto different particle types: experimental findings. Geochem. Cosmochim. Acta 68, 1489–1501.

George, A.C., 1984. Passive integrated measurement of indoor radon using activated carbon. Health Phys. 46, 867–872.

Geyh, M.A., Schleicher, H., 1990. Absolute Age Determination. Physical and Chemical Dating Methods and Their Application. Springer, Berlin, 514 pp.

Gilardoni, S., Vignati, E., Cavalli, F., Putaud, J.P., Larsen, B.R., Karl, M., Stenström, K., Genberg, J., Henne, S., Dentener, F., 2011. Better constraints on sources of carbonaceous aerosols using a combined ^{14}C – macro tracer analysis in a European rural background site. Atmos. Chem. Phys. Discuss. 11, 2503–2547.

Godoy, J.M., Lauria, D.C., Godoy, L.D.P., Cunha, R.P., 1994. Development of a sequential method for the determination of ^{238}U, ^{234}U, ^{232}Th, ^{230}Th, ^{228}Th, ^{228}Ra, ^{226}Ra, and ^{210}Pb in environmental samples. J. Radioanal. Nucl. Chem. 182, 165–169.

Godoy, J.M., Vianna, L.M., Godoy, M.L.D.P., Almeida, A.C., 2016. Determination of Ra-226 in produced water by liquid scintillation counting. J. Environ. Radioact. 160, 25–27.

Golchert, N.W., Sedlet, J., 1969. Radiochemical determination of technetium-99 in environmental water samples. Anal. Chem. 41, 669–671.

Goldberg, E.D., 1963. Geochronology with ^{210}Pb. In: Radioactive Dating. IAEA, Vienna, pp. 121–131.

Goldin, A.S., 1961. Determination of dissolved radium. Anal. Chem. 81, 406–409.

Gómez Escobar, V., Vera Tomé, F., Lozano, J.C., Martín Sánchez, A., 1996. Determination of ^{222}Rn and ^{226}Ra in aqueous samples using a low-level liquid scintillation counter. Appl. Radiat. Isot. 47, 861–867.

Gómez Escobar, V., Vera Tomé, F., Lozano, J.C., 1999. Extractive procedure for ^{226}Ra determination in aqueous samples by liquid scintillation counting. Radioact. Radiochem. 10, 17–21.

Gómez, M.B., Gutierrez, A.M., Camara, C., Gómez, V., 2001. Determination of ^{99}Tc in drinking waters by radiochemical techniques and inductively coupled plasma mass spectrometry (ICP-MS). Radioact. Radiochem. 12 (21–22), 27–35.

Grahek, Ž., Măcefat, M.R., 2004. Isolation of iron and strontium from liquid samples and determination of ^{55}Fe and $^{89,90}Sr$ in liquid radioactive waste. Anal. Chim. Acta 511, 339–348.

Grahek, Ž., Măcefat, M.R., 2005. Determination of radioactive strontium in seawater. Anal. Chim. Acta 534, 271–279.

Grahek, Ž., Mačefat, M.R., Lulić, S., 2006. Isolation of lead from water samples and determination of ^{210}Pb. Anal. Chim. Acta 560, 84–93.

Grahek, Z., Dulanska, S., Karanovic, G., Coha, I., Tucakovic, I., Nodilo, M., Matel, L., 2018. Comparison of different methodologies for the 90Sr determination in environmental samples. J. Environ. Radioact. 181, 18–31.

Grau-Carles, A., Grau-Malonda, A., 2006. CHEREN2. The Cherenkov counting efficiency by an anisotropy detection model. Comput. Phys. Commun. 174 (1), 30–34.

Graven, H.D., 2015. Impact of fossil fuel emissions on atmospheric radiocarbon and various applications of radiocarbon over this century. PNAS 112 (31), 9542–9545.

Gregory, L.P., 1972. A simplified separation of strontium, radium, and lead from environmental media by precipitation followed by fractional elution. Anal. Chem. 44, 2113–2115.

Guan, S., Xie, Y., 1992. Instrumentation and software for low-level liquid scintillation counting radiocarbon dating. Radiocarbon 34, 374–380.

Gudelis, A., Druteikiené, R., Luksiené, B., Gvozdaité, R., Nielsen, S.P., Hou, X., Mazeika, J., Petrosius, R., 2010. Assessing deposition levels of ^{55}Fe, ^{60}Co and ^{63}Ni in the Ignalina NPP environment. J. Environ. Radioact. 101, 464–467.

Gudjonsson, G.I., Theodorsson, P., 2000. A compact automatic low-level liquid scintillation system for radon-in water measurement by pulse pair counting. Appl. Radiat. Isot. 53, 377–380.

Guerin, N., Dai, X., 2015. Determination of 55Fe in urine by liquid scintillation counting. J. Radioanal. Nucl. Chem. 304, 1059–1069.

Guerin, N., Riopel, R., Rao, R., Kramer-Tremblay, S., Dai, X., 2017a. An improved method for the rapid determination of 90Sr in cow's milk. J. Environ. Radioact. 115–119.

Guerin, N., Gagne, A., Kramer-Tremblay, S., 2017b. A rapid method for the routine monitoring of 99 Tc by liquid scintillation counting. J. Radioanal. Nucl. Chem. 314, 2009–2017.

Guerin, N., Riopel, R., Kramer-Tremblay, S., de Sillva, N., Cornett, J., Dai, X.X., 2017c. Determination of Tc-99 in fresh water using TRU resin by ICP-MS. Anal. Chim. Acta. 988, 114–120.

Guiseppe, V.E., Stilwell, R., Hess, C.T., 2006. A laboratory intercomparison of radon in water measurements in Maine. Health Phys. 91, 354–360.

Gulliksen, S., Scott, E.M., 1995. TIRI report. Radiocarbon 37, 820–821.

Gulliver, P., Cook, G.T., MacKenzie, A.B., Naysmith, P., Anderson, R., 2001. Transport of Sellafield-derived ^{14}C from the Irish sea through the north channel. Radiocarbon 43, 869–877.

Günther, K., Preuße, W., Schmidt, S., Mehner, H.C., 2003. Application of modern radiochemical techniques to the determination of Sr-89/Sr-90 in environmental samples. Kerntechnik 68, 180–184.

Günther, K., Lange, S., Veit, M., 2009. A rapid method for determining ^{89}Sr and ^{90}Sr by Cerenkov counting. Appl. Radiat. Isot. 67, 781–785.

Gupta, S.K., Polach, H.A., 1985. Radiocarbon Dating Practices at ANU. Handbook. Radiocarbon Laboratory, Research School of Pacific Studies, Australian National University, Canberra, 176 pp.

Gustafsson, Ö., Kruså, M., Zencak, Z., Sheesley, R.J., Granat, L., Engström, E., Praveen, P.S., Rao, P.S.P., Leck, C., Rodhe, H., 2009. Brown clouds over South Asia: biomass or fossil fuel combustion? Science 323, 495–498.

Haas, H., 1979. Specific problems with liquid scintillation counting of small benzene volumes and background count rate estimations. In: Berger, R., Suess, H.E. (Eds.), Proceedings of the 9th International ^{14}C Conference. University of California Press, Berkeley, pp. 246–255.

Haas, H., 1995. Change of calibration parameters in frequently used vials in benzene scintillation counting. Radiocarbon 37, 737–742.

Haaslahti, J., Aalto, J., Oikari, T., 2000. A portable liquid scintillation counter for general LSC and high sensitivity alpha-counting applications. J. Radioanal. Nucl. Chem. 243, 377–381.

Hämäläinen, K.M., Jungner, H., Antson, O., Räsänen, J., Tormonen, K., Roine, J., 2007. Measurement of biocarbon in flue gases using ^{14}C. Radiocarbon 49, 325–330.

Hammer-Rotzler, B., Neuhausen, J., Vockenhuber, C., Boutellier, V., Wohlmuther, M., Tuerler, A., Schumann, D., 2015. Radiochemical determination of I-129 and Cl-36 in MEGAPIE, a proton irradiated lead-bismuth eutectic spallation target. Radiochim. Acta. 103, 745–758.

Hampe, D., Gleisberg, B., Akhmadaliev, S., Rugel, G., Merchel, S., 2013. Determination of Ca-41 with LSC and AMS: method development, modifications and applications. J. Radioanal. Nucl. Chem. 296, 617–624.

Hancock, G.J., Martin, P., 1991. Determination of radium in environmental samples by α particle spectrometry. Appl. Radiat. Isot. 42, 63–69.

Happel, S., Letessier, P., Ensinger, W., Eikenberg, J.H., Thakkar, A.H., Horwitz, E.P., 2004. Gross alpha determination in drinking water using a highly specific resin and LSC. Appl. Radiat. Isot. 61, 339–344.

Harrison, J.J., Zawadzki, A., Chisari, R., Wong, H.K.Y., 2011. Separation and measurement of thorium, plutonium, americium, uranium and strontium in environmental matrices. J. Environ. Radioact. 102, 896–900.

Harvey, B.R., Sutton, G.A., 1970. Liquid scintillation counting of nickel-63. Appl. Radiat. Isot. 21, 519–523.

HASL, 1997. Sr-01-RC, Sr-02-RC. In: Chieco, N.A. (Ed.), HASL-300, the Procedures Manual of the Environmental Measurements Laboratory, 28th edition, vol. II. US Department of Energy, New York.

Hassona, R.K., Sam, A.K., Osman, O.I., Sirelkhatim, D.A., La Rosa, J., 2008. Assessment of Committed Effective Dose due to consumption of Red Sea coral reef fishes collected from the local market (Sudan). Sci. Total Environ. 393, 214–218.

Havelka, M., 2009. Radon-in-water standard. Appl. Radiat. Isot. 67, 860–862.

Heal, M.R., Naysmith, P., Cook, G.T., Xu, S., Raventós Duran, T., Harrison, R.M., 2011. Application of ^{14}C analyses to source apportionment of carbonaceous $PM_{2.5}$ in the UK. Atmos. Environ. 45, 2341–2348.

Health Canada, 2010. Guidelines for Canadian drinking water quality. Summary table. In: Federal-Provincial-Territorial Committee on Drinking Water of the Federal-Provincial-Territorial Committee on Health and the Environment.

Heckel, A., Vogl, K., 2009. Rapid method for determination of the activity concentrations of ^{89}Sr and ^{90}Sr. Appl. Radiat. Isot. 67, 794–796.

Heilgeist, M., 2000. Use of extraction chromatography, ion chromatography and liquid scintillation spectrometry for rapid determination of strontium-89 and strontium-90 in food in cases of increased release of radionuclides. J. Radioanal. Nucl. Chem. 245, 249–254.

Henricsson, F., Ranebo, Y., Holm, E., Roos, P., 2011. Aspects on the analysis of ^{210}Po. J. Environ. Radioact. 102, 415–419.

Higuchi, H., 1981. Analytical methods for radium in environmental samples. Radioisotopes 30, 618–627.

Hirose, K., Honda, T., Yagishita, S., Igarashi, Y., Aoyama, M., 2004. Deposition behaviors of ^{210}Pb, ^{7}Be and thorium isotopes observed in Tsukuba and Nagasaki, Japan. Atmos. Environ. 38, 6601–6608.

Hoehn, E., von Gunten, H.R., 1989. Radon in groundwater: a tool to assess infiltration from surface waters to aquifers. Water Resour. Res. 25, 1795–1803.

Hogg, A.G., 2004. Towards achieving low background levels in routine dating by liquid scintillation spectrometry. Radiocarbon 46, 123–131.

Hogg, A., Noakes, J.E., 1992. Evaluation of high-purity synthetic silica vials in active and passive vial holders for liquid scintillation counting of benzene. Radiocarbon 34, 394–401.

Hogg, A., Polach, H., Robertson, S., Noakes, J.E., 1991. Application of high purity synthetic quartz vials to liquid scintillation low-level ^{14}C counting of benzene. In: Ross, H., Noakes, J.E., Spaulding, J.D. (Eds.), Liquid Scintillation Counting and Organic Scintillators, 1989. Lewis Publishers, Michigan, pp. 123–132.

Hogg, A.G., Fifield, L.K., Palmer, J.G., Turney, C.S.M., Galbraith, R., 2007. Robust radiocarbon dating of wood samples by high-sensitivity liquid scintillation spectroscopy in the 50–70 kyr age range. Radiocarbon 49, 379–391.

Holm, E., Fukai, R., 1977. Method for multi-element alpha-spectrometry of actinides and its application to environmental radioactivity studies. Talanta 24, 659–664.

Holm, E., Rioseco, J., Garcia-Leon, M., 1984. Determination of Tc-99 in environmental samples. Nucl. Instrum. Methods Phys. Res. 23, 204–207.

Holm, E., Oregioni, B., Vas, D., Petterson, H., Rioseco, J., Nilsson, U., 1990. Nickel-63: radiochemical separation and measurement with an on implanted silicon detector. J. Radioanal. Nucl.Chem. 138, 111–118.

Holm, E., Rioseco, J., Pettersson, H., 1992. Fallout of transuranium elements following the Chernobyl accident. J. Radioanal. Nucl. Chem. 156, 183–200.

Homma, Y., Murase, Y., 1987. Energy resolution of liquid scintillator for α-particles and internal conversion electrons at lower temperatures. J. Radioanal. Nucl. Chem. Lett. 119, 355–365.

Horiuchi, K., Murakami, Y., 1981. A new procedure for the determination of radium in water by extraction of radon and application of integral counting with a liquid scintillation counter. Appl. Radiat. Isot. 32, 291–294.

Horiuchi, K., Murakami, Y., 1983. A new method for the determination of radon in soil air by the "open vial" and integral counting with a liquid scintillation counter. J. Radioanal. Nucl. Chem. 80, 153–163.

Horiuchi, K., Ishii, T., Kobayashi, M., 1993. Liquid scintillation counting measurements of radon from seepage groundwater in Lake Biwa, Japan. In: Noakes, J.E., Schönhofer, F., Polach, H.A. (Eds.), Liquid Scintillation Spectrometry, 1992. Radiocarbon Publishers, University of Arizona, Tucson, pp. 383–390.

Horrocks, D., 1963. Interaction of fission fragments with organic scintillators. Rev. Sci. Instrum. 34, 1035–1040.

Horrocks, D., 1970. Pulse shape discrimination with organic scintillation solutions. Appl. Spectrosc. 24, 397–404.

Horrocks, D.L., 1974a. Applications of Liquid Scintillation Counting. Academic Press, London, 346 pp.

Horrocks, D.L., 1974b. Measurement of low levels of normal uranium in water and urine by liquid scintillation alpha counting. Nucl. Instrum. Methods Phys. Res. 117, 589–595.

Horrocks, D.L., 1985. Studies of background sources in liquid scintillation counting. Appl. Radiat. Isot. 36, 609–617.

Horton, T.R., 1983. Method and Result of EPA's Study of Radon in Drinking Water. US Environmental Protection Agency, Office of Radiation Programs, Washington DC. Report 520/5-83-027.

Horwitz, E.P., Dietz, M.L., Fisher, D., 1991. Separation and preconcentration of strontium from biological, environmental, and nuclear waste samples by extraction chromatography using a crown ether. Anal. Chem. 63, 522–525.

Hou, X.L., 2005a. Rapid analysis of ^{14}C and ^{3}H in graphite and concrete for decommissioning of nuclear reactor. Appl. Radiat. Isot 62, 871–882.

Hou, X.L., 2005b. Radiochemical determination of ^{41}Ca in reactor concrete for decommissioning. Radiochim. Acta 93, 611–617.

Hou, X.L., 2007. Radiochemical analysis of radionuclides difficult to measure or waste characterization in decommissioning of nuclear facilities. J. Radioanal. Nucl. Chem. 273, 43–48.

Hou, X.L., 2017. Determination of radionuclidic impurities in ^{99m}Tc eluate from $^{99m}Tc/^{99}Mo$ generator for quality control. J. Radioanal. Nucl. Chem. 314, 659–668.

Hou, X.L., 2018. Tritium and ^{14}C in the environment and nuclear facilities: sources and analytical methods. J. Nucl. Fuel Cycle Waste Technol. 16 (1), 11–39.

Hou, X.L., Roos, P., 2008. Critical comparison of radiometric and mass spectrometric methods for the determination of radionuclides in environmental, biological and nuclear waste samples. Anal. Chim. Acta 606, 105–139.

Hou, X.L., Wang, Y.Y., 2016. Determination of ultra-low level ^{129}I in vegetation using pyrolysis for iodine separation and accelerator mass spectrometry measurement. J. Anal. Atom. Spectrom. 31, 1298–1310.

Hou, X.L., Dahlgaard, H., Rietz, B., Jacobsen, U., Nielsen, S.P., Aarkrog, A., 1999. Determination of iodine-129 in seawater and some environmental materials by neutron activation analysis. Analyst 124, 1109–1114.

Hou, X.L., Dahlgaard, H., Nielsen, S.P., 2001. Chemical speciation analysis of ^{129}I in seawater and a priliminary investigation to use it as a tracer for geochemical cycle study of stable iodine. Mar. Chem. 74, 145–155.

Hou, X.L., Dahlgaard, H., Nielsen, S.P., 2002. Level and origin of iodine-129 in the Baltic sea. J. Environ. Radioact. 61, 331–343.

Hou, X.L., Østergaard, L.F., Nielsen, S.P., 2005. Determination of ^{63}Ni and ^{55}Fe in nuclear waste samples using radiochemical separation and liquid scintillation counting. Anal. Chim. Acta 535, 297–307.

Hou, X.L., Jensen, M., Nielsen, S.P., 2007a. Use of ^{99m}Tc from a commercial $^{99}Mo/^{99m}Tc$ generator as yield tracer for the determination of ^{99}Tc at low levels. Appl. Radiat. Isot. 65, 610–618.

Hou, X.L., Frøsig, L., Nielsen, S.P., 2007b. Determination of ^{36}Cl in nuclear waste from reactor decommissioning. Anal. Chem. 79, 3126–3134.

Hou, X.L., Hansen, V., Aldahan, A., Possnert, G., Lind, O.C., Lujaniene, G., 2009. Speciation of iodine-129 in the environment. Anal. Chim. Acta. 632, 181–196.

Hou, X.L., Togneri, L., Olsson, M., Englund, S., Gottfridsson, O., Forsstrom, M., Hirvonen, H., 2015. Standardization of Radioanalytical Methods for Determination of ^{63}Ni and ^{55}Fe in Waste and Environmental Samples. NKS-356. Nordic Nuclear Safety Research. http://www.nks.org/en/nks_reports/view_document.htm?id=111010213336225.

Hrnecec, E., Irlweck, K., 1995. Determination of uranium, thorium and radium from geological materials by microprecipitation and alpha-spectroscopy. Radiochim. Acta 68, 125–128.

Huang, Y.J., Fan, Z.B., Chen, C.F., Qin, H.J., Wu, L.S., Guo, G.Y., Yang, L.T., Shang-Guan, Z.H., 2014. Method validation and uncertainty evaluation of organic bound tritium analysis in environmental sample. J. Environ. Radioact. 134, 83–88.

Huang, F.Y.J., Su, T.Y., Tsai, T.L., Chao, J.H., 2017. Analysis of Ni-63 in radwastes by extraction chromatography and radiometric techniques. J. Radioanal. Nucl. Chem. 314, 879–886.

Hurtado, S., Villa, M., Manjon, G., Garcia-Tenorio, R., 2009. Monte Carlo simulation of a liquid scintillation counter using GEANT4 code. In: Eikenberg, J., Jäggi, M., Beer, H., Baehrle, H. (Eds.), Advances in Liquid Scintillation Spectrometry, 2008. Radiocarbon Publishers, University of Arizona, Tucson, pp. 155–159.

Hutchinson, J.M.R., Mullen, P.A., Collé, R., 1986. The NBS radon-water standard generator. Nucl. Instrum. Methods Phys. Res., Sect. A 247, 385–389.

IAEA, 1989. Measurement of Radionuclides in Food and the Environment. A Guidebook. Technical Report Series No. 295. IAEA, Vienna, 169 pp.

IAEA/AQ/15, 2010. Almera Proficiency Test Determination of Naturally Occurring Radionuclides in Phosphogypsum and Water. IAEA-CU-2008-04. International Atomic Energy Agency, IAEA, Vienna, Austria.

Idoeta, R., Herranz, M., Legarda, F., 2011. The disequilibrium between ^{210}Po and ^{210}Pb in raw and drinking waters. Appl. Radiat. Isot. 69, 196–200.

Idoeta, R., Pérez, E., Herranz, M., Legarda, F., 2014. Characteristic parameters in the measurement of ^{14}C of biobased diesel fuels by liquid scintillation. Appl. Radiat. Isot. 93, 110–113.

Iimoto, T., Akasaka, Y., Koike, Y., Kosako, T., 2008. Development of a technique for the measurement of the radon exhalation rate using an activated charcoal collector. J. Environ. Radioact. 99, 587–595.

Ikäheimonen, T.K., Vartti, V.P., Ilus, E., Mattila, J., 2002. Technetium-99 in *Fucus* and seawater samples in the Finnish coastal area of the Baltic Sea, 1999. J. Radioanal. Nucl. Chem. 252, 309–313.

Isam Salih, M.M., Pettersson, H.B.L., Lund, E., 2002. Uranium and thorium series radionuclides in drinking water from drilled wells: correlation to geology and bedrock radioactivity and dose estimation. Radiat. Prot. Dosim. 102, 249–258.

ISG, 1982. An inter-laboratory comparison of radiocarbon measurements in tree-rings. Nature 198, 619–623.

ISO 11704, 2010. Water Quality - Measurement of Gross Alpha and Beta Activity Concentration in Non-saline Water - Liquid Scintillation Counting Method. International Organization for Standardization, Geneva.

ISO, 2009. Measurement of Radioactivity in the Environment -Soil - Part: Measurement of Strontium 90. Standard 18589-5. International Organization for Standardization, Geneva.

ISO, 2010. Water Quality - Measurement of Strontium 90 and Strontium 89. Draft International Standard ISO/DIS 13160, International Organization for Standardization, Geneva.

ISO 9696, 2007. Water Quality - Measurement of Gross Alpha Activity in Non-saline Water - Thick Source Method. International Organization for Standardization, Geneva.

ISO 9697, 2008. Water Quality - Measurement of Gross Beta Activity in Non-saline Water - Thick Source Method. International Organization for Standardization, Geneva.

ISO/NP 13165-1, 2010. Water Quality – Measurement of Ra 226 Activity Concentration - Part 1: Liquid Scintillation Counting Method. International Organization for Standardization, Geneva.

Isogai, K., Cook, G.T., Anderson, R., 2002. Reconstructing the history of ^{14}C discharges from Sellafield: 1. Atmospheric discharges. J. Environ. Radioact. 59, 207–222.

Itoh, M., Watanabe, K., Hatakeyama, M., Tachibana, M., 2002a. Determination of ^{36}Cl in biological shield concrete using pyrohydrolysis and liquid scintillation counting. Analyst 127, 964–966.

Itoh, M., Watanabe, K., Hatakeyama, M., Tachibana, M., 2002b. Determination of ^{41}Ca in biological-shield concrete by low-energy X-ray spectrometry. Anal. Bioanal. Chem. 372, 532–538.

Ivan, C., Cassette, P., Sahagia, M., 2008. A new TDCR-LS counter using channel photomultiplier tubes. Appl. Radiat. Isot. 66, 1006–1011.

Ivanovich, M., Latham, A.G., Ku, T.L., 1992. Uranium-series disequilibrium applications in geochronology. In: Ivanovich, M., Harmon, R.S. (Eds.), Uranium-Series Disequilibrium: Applications to Earth, Marine, and Environmental Problems, second ed. Clarendon Press, Oxford, UK, pp. 62–94.

Iwakura, T., Kasida, Y., Inoue, Y., Tokunaga, N., 1979. A low-background liquid scintillation counter for measurement of low level tritium. In: Behavior of Tritium in the Environment. IAEA Proceedings Series. IAEA, Vienna, pp. 163–171.

Jabbar, T., Khan, K., Subhani, M.S., Akhter, P., 2009. Determination of ^{90}Sr in environment of district Swat, Pakistan. J. Radioanal. Nucl. Chem. ***279***, 377–384.

Jaggi, M., Eikenberg, J., 2014. Comparison of the TriCarb and Hidex 300 SL technique using measurements of 241Pu and 90Sr on various samples. Appl. Radiat. Isot. 93, 120–125.

Jenkinson, S.B., McCubbin, D., Kennedy, P.H.W., Dewar, A., Bonfield, R., Leonard, K.S., 2014. An estimate of the inventory of technetium-99 in the sub-tidal sediments of the Irish Sea. J. Environ. Radioact. 133. SI40–47.

Jerde, R.L., Paterson, L.E., Stein, W., 1967. Effect of high energy radiations on noise pulses from photomultiplier tubes. Rev. Sci. Instrum. 38, 1387–1395.

Jia, G.G., 2017. Sequential separation and determination of *uranium* and thorium isotopes in soil samples with Microthene-TOPO chromatographic column and alpha-spectrometry. J. Radioanal. Nucl. Chem. 311, 1007–1017.

Jia, G., Torri, G., Magro, L., 2009. Concentrations of ^{238}U, ^{234}U, ^{235}U, ^{232}Th, ^{230}Th, ^{228}Th, ^{226}Ra, ^{228}Ra, ^{224}Ra, ^{210}Po, ^{210}Pb and ^{212}Pb in drinking water in Italy: reconciling safety standards based on measurements of gross a and b. J. Environ. Radioact. 100, 941–949.

Jiang, H., Lu, S., Fu, S., Zhang, W., Zhang, T., Ye, Y., Li, M., Fu, P., Wang, S., Peng, C., Jiang, P., 1983. Model DYS low level liquid scintillation counter. In: McQuarrie, S.A., Ediss, C., Wiebe, L.I. (Eds.), Advances in Scintillation Counting. University of Alberta, Alberta Press, pp. 478–493.

Jobbágy, V., Wätjen, U., Meresova, J., 2010. Current status of gross alpha/beta activity analysis in water samples: a short overview of methods. J. Radioanal. Nucl. Chem. 286, 393–399.

Jobbágy, V., Kávási, N., Somlai, J., Dombovári, P., Gyöngyösi, C., Kovács, T., 2011. Gross alpha and beta activity concentrations in spring waters in Balaton Upland, Hungary. Radiat. Meas. 46, 159–163.

Jordan, D., Schupfner, R., Schüttelkopf, H., 1995. A new very sensitive LSC procedure for determination of Tc-99 in environmental samples. J. Radioanal. Nucl. Chem. 193, 113–117.

Jordan, N., Michel, H., Barci-Funel, G., Barci, V., 2008. Radiochemical produce and quantitative determination of the activation product ^{63}Ni in environmental soft water samples with high Ca and Mg phosphate concentration. J. Radioanal. Nucl. Chem. 275, 253–256.

Juntunen, P., Ruutu, A., Suksi, J., 2002. Determination of ^{226}Ra from rock samples using LSC. In: Möbius, S., Noakes, J.E., Schönhofer, F. (Eds.), Advances in Liquid Scintillation Spectrometry, 2001. Radiocarbon Publishers, University of Arizona, Tucson, pp. 299–302.

Kabai, E., Beyemann, M., Seeger, J., Savkin, B.T., Stanglmaier, S., Hiersche, L., 2013. Separation technique for the determination of Tc-99 in milk and dairy products in case of emergency. Appl. Radiat. Isot. 81, 36–41.

Kaihola, L., 1991. Liquid scintillation counting performance using glass vials in the Wallac 1220 Quantulus. In: Ross, H., Noakes, J.E., Spaulding, J.D. (Eds.), Liquid Scintillation Counting and Organic Scintillators, 1989. Lewis Publishers, Michigan, pp. 495–500.

Kaihola, L., Kojola, H., Kananen, R., 1986. Low level liquid scintillation counter performance in a low level surface laboratory. Nucl. Instrum. Methods. Phys. Res., Sect. B 17, 509–510.

Kaihola, L., Kojola, H., Heinonen, A., 1992. A minivial for small sample ^{14}C dating. Radiocarbon 34, 402–405.

Kaihola, L., Mäntynen, P., Nurmi, J., 1994. Method for use in liquid scintillation counting for detecting, recording and analyzing scintillation phenomena. US Patent 5 (357), 114.

Kalin, R.M., Long, A., 1989. Radiocarbon dating with the Quantulus in an underground counting laboratory: performance and background sources. Radiocarbon 31, 359–367.

Kallithrakes-Kontos, N.G., Xarchoulakos, D.C., Xarchoulakos, D.C., Boultadaki, P., Potiriadis, C., Kehagia, K., 2018. Selective membrane complexation and uranium isotopes analysis in tap water and seawater samples. Anal. Chem. 90, 4611–4615.

Karamanis, D., Ioannides, K.G., Stamoulis, K.C., 2006. Determination of ^{226}Ra in aqueous solutions via sorption on thin films and α-spectrometry. Anal. Chim. Acta 573–574, 319–327.

Karpas, Z., Lorber, A., Sela, H., Paz-Tal, O., Hagag, Y., Kurttio, P., Salonen, L., 2005. Determination of ^{234}U/^{238}U ratio: comparison of multi-collector ICPMS and ICP-QMS for water, hair and nails samples, and comparison with alpha-spectrometry for water samples. Radiat. Prot. Dosim. 118, 106–110.

Katzlberger, C., Wallner, G., Irlweck, K., 2001. Determination of ^{210}Pb, ^{210}Bi and ^{210}Po in natural drinking water. J. Radioanal. Nucl. Chem. 249, 191–196.

Kaye, J.H., Strebin, R.S., Nevissi, A.E., 1994. Measurement of ^{63}Ni in highly radioactive Hanford waste by liquid scintillation counting. J. Radioanal. Nucl. Chem. 180, 197–200.

Keller, E.D., Turnbull, J.C., Norris, M.W., 2016. Detecting long-term change in point source fossil CO^2 emissions with tree ring archives. Atom. Chem. Phys. https://doi.org/10.5194/acp-2015-919.

Keogh, S.M., Aldahan, A., Possnert, G., Finegan, P., León Vintró, L., Mitchell, P.I., 2007. Trends in the spatial and temporal distribution of ^{129}I and ^{99}Tc in coastal waters surrounding Ireland using *Fucus vesiculosus* as a bio-indicator. J. Environ. Radioact. 95, 23–38.

Kershaw, P.J., Woodhead, D.S., Lovell, M.B., Leonard, K.S., 1995. Plutonium from European reprocessing operations – its behaviour in the marine environment. Appl. Radiat. Isot. 46, 1121–1134.

Kersten, M., Thomsen, S., Priebsch, W., Garb-Schönberg, C.D., 1998. Scavenging and particle residence times determined from ^{234}Th/^{238}U disequilibria in the coastal waters of Mecklenburg Bay. Appl. Geochem. 13, 339–347.

Ketterer, M.E., Hafer, K.M., Mietelski, J.W., 2004. Resolving Chernobyl vs. global fallout contributions in soils from Poland using Plutonium atom ratios measured by inductively coupled plasma mass spectroscopy. J. Environ. Radioact. 73, 183–201.

Kiliari, T., Pashalidis, I., 2010. Simplified alpha-spectroscopic analysis of uranium in natural waters after its separation by cation-exchange. Radiat. Meas. 45, 966–968.

Kim, C.K., 2011. Improved rapid determination of ^{89}Sr and ^{90}Sr in milk using Cerenkov and liquid scintillation counting. In: Advances in Liquid Scintillation Spectrometry, 2010 (in print).

Kim, Y.-J., Kim, C.-K., Kim, C.-S., Yon, J.-Y., Rho, B.-H., 1999. Determination of ^{226}Ra in environmental samples using high-resolution inductively coupled plasma mass spectrometry. J. Radioanal. Chem. 240, 613–618.

Kim, Y.-J., Kim, C.-K., Lee, J.-I., 2001. Simultaneous determination of ^{226}Ra and ^{210}Pb in groundwater and soil samples by using the liquid scintillation counter – suspension gel method. Appl. Radiat. Isot. 54, 275–281.

Kim, C.K., Al-Hamwi, A., Törvényi, A., Kis-Benedek, G., Sansone, U., 2009. Validation of rapid methods for the determination of radio-strontium in milk. Appl. Radiat. Isot. 67, 786–793.

Kim, H., Jung, Y., Ji, Y.Y., Lim, J.M., Chung, K.H., Kang, M.J., 2017. Validation of a procedure for the analysis of Ra-226 in naturally occurring radioactive materials using a liquid scintillation counter. J. Environ. Radioact. 166, 188–194.

King, C.Y., 1985. Radon monitoring for earthquake prediction in China. Earthquake Pred. Res. 3, 47–68.

Kinner, N.E., Malley Jr., J.P., Clement, J.A., Quern, P.A., Schell, G.S., Lessard, C.E., 1991. Effects of sampling technique, storage, cocktails, sources of variation, and extraction on the liquid scintillation technique for radon in water. Environ. Sci. Technol. 25, 1165–1171.

Kirby, L.J., 1961. The Radiochemistry of Nickel. Technical Report NAS-NS 3051. National Academy of Sciences - National Research Council, Nuclear Science Series, Radiochemistry Techniques.

Kitto, M.E., 1994. Characteristics of liquid scintillation analysis of radon in water. J. Radioanal. Nucl. Chem. 185, 91–99.

Kitto, M.E., Kuhland, M.K., Dansereau, R.E., 1996. Direct comparison of three methods for the determination of radon in well water. Health Phys. 70, 358–362.

Kitto, M.E., Menia, T.A., Bari, A., Fielman, E.M., Haines, D.K., 2010. Development and intercomparison of a reusable radon-in-water standard. Radiat. Meas. 45, 231–233.

Kleinschmidt, R.I., 2004. Gross alpha and beta activity analysis in water - a routine laboratory method using liquid scintillation analysis. Appl. Radiat. Isot. 61, 333–338.

Köhler, M., Preuße, W., Gleisberg, B., Schäfer, I., Heinrich, T., Knobus, B., 2002. Comparison of methods for the analysis of ^{226}Ra in water samples. Appl. Radiat. Isot. 56, 387–392.

Kojima, S., Furukawa, M., 1985. Liquid scintillation counting of low activity ^{63}Ni. J. Radioanal. Nucl. Chem. Lett. 95, 323–330.

Kojola, H., Polach, H., Nurmi, J., Oikari, T., Soini, E., 1984. High resolution low-level liquid scintillation β-spectrometer. Appl. Radiat. Isot. 35, 949–952.

Kolacinska, K., Samczynski, Z., Dudek, J., Bojanowska-Czajka, A., Trojanowicz, M., 2018. A comparison study on the use of Dowex 1 and TEVA-resin in determination of Tc-99 in environmental and nuclear coolant samples in a SIA system with ICP-MS detection. Talanta 184, 527–536.

Konig, W., Schupfner, R., Schuttelkopf, H., 1995. A fast and very sensitive LSC procedure to determine Fe-55 in stell and concrete. J. Radioanal. Nucl. Chem. Articles 193 (1), 127–131.

Kossert, K., 2010. Activity standardization by means of a new TDCR-Čerenkov counting technique. Appl. Radiat. Isot. 68, 1116–1120.

Kossert, K., Schrader, H., 2004. Activity standardization by liquid scintillation counting and half-life measurements of ^{90}Y. Appl. Radiat. Isot. 60, 741–749.

Kossert, K., Ott, O., Nähle, O., 2009. Improved techniques for the activity standardization of ^{109}Cd by means of liquid scintillation spectrometry. In: Eikenberg, J., Jäggi, M., Beer, H., Baehrle, H. (Eds.), Advances in Liquid Scintillation Spectrometry, 2008. Radiocarbon Publishers, University of Arizona, Tucson, pp. 97–107.

Kossert, K., Carles, A.G., Nahle, O., 2014. Improved Čerenkov counting techniques based on a free parameter model. Appl. Radiat. Isot. 86, 7–12.

Kossert, K., Bokeloh, K., Ehlers, M., Nahle, O., Scheibe, O., Schwarz, U., Thieme, K., 2016. Comparison of (90)Y activity measurements in nuclear medicine in Germany. Appl. Radiat. Isot. 109, 247–249.

Kouru, H., 1991. A new quench curve fitting procedure: fine tuning of a spectrum library. In: Ross, H., Noakes, J.E., Spaulding, J.D. (Eds.), Liquid Scintillation Counting and Organic Scintillators. Lewis Publishers, Michigan, pp. 247–255.

Kouru, H., Rundt, K., 1991. Multilabel counting using digital overlay technique. In: Ross, H., Noakes, J.E., Spaulding, J.D. (Eds.), Liquid Scintillation Counting and Organic Scintillators. Lewis Publishers, Michigan, pp. 239–246.

Kovács, T., Bodrogi, E., Dombovári, P., Somlai, J., Németh, C., Capote, A., Tarján, S., 2004. ^{238}U,^{226}Ra, ^{210}Po concentrations of bottled mineral waters in Hungary and their committed effective dose. Radiat. Prot. Dosim. 108, 175–181.

Kozłowska, B., Hetman, A., Zipper, W., 1999. Determination of ^{222}Rn in natural water samples from health resorts in the Sudety mountains by the liquid scintillation technique. Appl. Radiat. Isot. 51, 475–480.

Kozłowska, B., Walencik, A., Dorda, J., Przylibski, T.A., 2007. Uranium, radium and ^{40}K isotopes in bottled mineral waters from Outer Carpathians, Poland. Radiat. Meas. 42, 1380–1386.

Kramer, G., 1981. Optimization of the analysis of nickel-63 in urine. In: Internal Report AECL-7248. Atomic Energy of Canada Ltd., Chalk River, Ontario.

Kristof, R., Logar, J.K., 2013. Direct LSC method for measurements of biofuels in fuel. Talanta 111, 183–188.

Krąpiec, M., Walanus, A., 2011. Application of the triple-photomultiplier liquid spectrometer Hidex 300 SL in radiocarbon dating. Radiocarbon 53, 543–550.

Kurttio, P., Auvinen, A., Salonen, L., Saha, H., Pekkanen, J., Mäkeläinen, I., Väisänen, S.B., Penttilä, I.M., Komulainen, H., 2002. Renal effects of uranium in drinking water. Environ. Health Perspect. 110, 337–342.

Kurttio, P., Harmoinen, A., Saha, H., Salonen, L., Karpas, Z., Komulainen, H., Auvinen, A., 2006. Kidney toxicity of ingested uranium from drinking water. Am. J. Kidney Dis. 47, 972–982.

Kwong, L.L.W., Gaustaud, J., La Rosa, J., Lee, S.H., Povinec, P.P., Wyse, E., 2004. Determination of ^{241}Pu in marine samples using co-precipitation with rare earth fluoride and liquid scintillation spectrometry. J. Radioanal. Nucl. Chem. 261, 283–289.

La Rosa, J.J., Burnett, W., Lee, S.H., Levy, I., Gastaud, J., Povinec, P.P., 2001. Separation of actinides, cesium and strontium from marine samples using extraction chromatography and sorbents. J. Radioanal. Nucl. Chem. 248, 765–770.

Lamontagne, S., Le Gal La Salle, C., Hancock, G.J., Webster, I.T., Craig, T., Simmons, C.T., Love, A.J., Julianne James-Smith, J., Smith, A.J., Kämpf, J., Fallowfield, H.J., 2008. Radium and radon radioisotopes in regional groundwater, intertidal groundwater, and seawater in the Adelaide Coastal Waters Study area: implications for the evaluation of submarine groundwater discharge. Mar. Chem. 109, 318–336.

Landstetter, C., Katzlberger, C., 2006. Rapid method for determining natural radionuclides in drinking water. In: Chałupnik, S., Schönhofer, F., Noakes, J. (Eds.), Advances in Liquid Scintillation Spectrometry, 2005. Radiocarbon Publishers, University of Arizona, Tucson, pp. 181–189.

Landstetter, C., Wallner, G., 2006. Determination of strontium-90 in deer bones by liquid scintillation spectrometry after separation on Sr-specific ion exchange columns. J. Environ. Radioact. 87, 315–324.

Larivière, D., Reiber, K.M., Evans, R.D., Cornett, R.J., 2005. Determination of ^{210}Pb at ultra-trace levels in water by ICP-MS. Anal. Chim. Acta 549, 188–196.

Lasheen, Y.F., Seliman, A.F., Abdel-Rassoul, A.A., 2007. Simultaneous measurement of ^{226}Ra and ^{228}Ra in natural water by liquid scintillation counting. J. Environ. Radioact. 95, 86–97.

Laureano-Pérez, L., Collé, R., Fitzgerald, R., Outola, I., Pibida, L., 2007. A liquid-scintillation-based primary standardization of ^{210}Pb. Appl. Radiat. Isot. 65, 1368–1380.

Laureano-Perez, L., Collé, R., Fitzgerald, R., Zimmerman, B.E., Cumberland, L., 2010. Investigation into the standardization of ^{99}Tc. Appl. Radiat. Isot. 68, 1489–1494.

Lauria, D.C., Carvalho, L.L., Conti, C.C., 2006. Comparison of different methods for ^{210}Pb determination in environmental samples. In: Chałupnik, S., Schönhofer, F., Noakes, J. (Eds.), Advances in Liquid Scintillation Spectrometry, 2005. Radiocarbon Publishers, University of Arizona, Tucson, pp. 211–216.

Lawrie, W.C., Desmond, J.A., Spence, D., Anderson, S., Edmondson, C., 2000. Determination of radium-226 in environmental and personal monitoring samples. Appl. Radiat. Isot. 53, 133–137.

Lebecka, J., Mielnikow, A., Chalupnik, S., Skubacz, K., 1993. Liquid scintillation counting of ^{210}Pb in grass and soil. In: Noakes, J.E., Schönhofer, F., Polach, H.A. (Eds.), Liquid Scintillation Spectrometry, 1992. Radiocarbon Publishers, University of Arizona, Tucson, pp. 455–459.

Lee, M.H., Lee, C.W., 1999. Determination of low level Pu-241 in environmental samples by liquid scintillation counting. Radiochim. Acta 84, 177–181.

Lee, C., Martin, J.E., Griffin, H.C., 1997. Optimization of ^{63}Ni measurement of in reactor waste samples using ^{65}Ni as a tracer. Appl. Radiat. Isot. 48, 639–642.

Lee, M.H., Chung, K.H., Lee, C.W., 2002a. Sequential radiochemical separation of ^{90}Sr and ^{99}Tc in aqueous samples and measurement by liquid scintillation counting. In: Möbius, S., Noakes, J.E., Schönhofer, F. (Eds.), Advances in Liquid Scintillation Spectrometry, 2001. Radiocarbon Publishers, University of Arizona, Tucson, pp. 397–403.

Lee, M.H., Chung, K.H., Choi, G.K., Lee, C.W., 2002b. Measurement of ^{90}Sr in aqueous samples using liquid scintillation counting with full spectrum DPM method. Appl. Radiat. Isot. 57, 257–263.

Lee, M.H., Ahn, H.J., Park, J.H., Park, Y.J., Song, K., 2011. Rapid sequential determination of Pu, ^{90}Sr and ^{241}Am nuclides in environmental samples using an anion exchange and Sr-Spec resins. Appl. Radiat. Isot. 69, 295–298.

Leyba, J.D., Vollmar, H.S., Fjeld, R.A., DeVol, T.A., Brown, D.D., Cadieux, J.R., 1995. Evaluation of a direct extraction/liquid scintillation counting technique for the measurement of uranium in water. J. Radioanal. Nucl. Chem. 194, 337–344.

Li, C., Sadi, B.B., Moodie, G., Daka, J.N., Lai, E.P.C., Kramer, G.H., 2009. Field deployable technique for ^{90}Sr emergency bioassay. Radiat. Prot. Dosim. 136, 82–86.

Libby, W.F., 1963. Moratorium tritium geophysics. J. Geophys. Res. 68, 4485–4494.

Lipsztein, J.L., Dias da Cunha, K.M., Azeredo, A.M.G., Julião, L., Santos, M., Melo, D.R., Simões Filho, F.F.L., 2001. Exposure of workers in mineral processing industries in Brazil. J. Environ. Radioact. 54, 189–199.

Lo, J.-M., Cheng, B.-J., Tseng, C.-L., Lee, J.-D., 1993. Preconcentration of ^{63}Ni in sea water for liquid scintillation counting. Anal. Chim. Acta. 281, 429–433.

Longtin, J., 1990. Occurrence of radionuclides in drinking water, a national survey. In: Cothern, C.R., Rebers, P.A. (Eds.), Radon, Radium and Uranium in Drinking Water, pp. 97–139. Chelsea.

Lucas, H.F., 1957. Improved low-level alpha-scintillation counter for radon. Rev. Sci. Instrum. 28, 680–683.

Lucas, L.L., Unterweger, M.P., 2000. Comprehensive review and critical evaluation of the half-life of tritium. J. Res. Nat. Inst. Stand. Technol. 105, 541–549.

Luo, M., Xing, S., Yang, Y., Song, L., Ma, Y., Wang, Y., Dai, X., Happel, S., 2018. Sequential analyses of actinides in large-size soil and sediment samples with total sample dissolution. J. Environ. Radioact. 187, 73–80.

L'Annunziata, M.F., 1967. The Chelation and Movement of ^{89}Sr-^{90}Sr(^{90}Y) in a Calcareous Soil (MSc thesis). University of Arizona, Tucson.

L'Annunziata, M.F., 1971. Birth of a unique parent-daughter relation: secular equilibrium. J. Chem. Educ. 48, 700–703.

MacKenzie, A.B., Logan, E.M., Cook, G.T., Pulford, I.D., 1998. A historical record of atmospheric depositional fluxes of contaminants in west-central Scotland derived from an ombrotrophic peat core. Sci. Total Environ. 222, 157–166.

Manjón, G., Vioque, I.A., Moreno, H.P., García-Tenorio, R., García-León, M., 1997. Determination of ^{226}Ra and ^{224}Ra in drinking waters by liquid scintillation counting. Appl. Radiat. Isot. 48, 535–540.

Maragheh, M.G., Husain, S.W., Asgharizadeh, Moosavi, F., Anbia, M., 2002. Determination of ^{222}Rn in Iranian mineral waters using liquid scintillation alpha-spectrometry. J. Radioanal. Nucl. Chem. 252, 349–351.

Marshall, T.A., Morris, K., Law, G.T.W., Mosselmans, J.F.W., Bots, P., Parry, S.A., Shaw, S., 2014. Incorporation and retention of 99-Tc(IV) in magnetite under high pH conditions. Environ. Sci. Technol. 48 (20), 11853–11862.

Martin, J.E., 1986. Determination of ^{241}Pu in low level radioactive wastes from reactors. Health Phys. 51, 621–631.

Martin, J.E., 1987. Measurement of ^{90}Sr in reactor wastes by Cerenkov counting of ^{90}Y. Appl. Radiat. Isot. 38, 953–957.

Martin, W.R., Sayles, F.L., 1987. Seasonal changes of particle and solute transport processes in nearshore sediments: ^{222}Rn/^{226}Ra and ^{234}Th/^{238}U disequilibrium at a site in Buzzards Bay, MA. Geochim. Cosmochim. Acta 51, 927–943.

Martín Sánchez, A., Sáenz García, G., Jurado Vargas, M., 2009. Study of self-absorption for the determination of gross alpha and beta activities in water and soil samples. Appl. Radiat. Isot. 67, 817–820.

Mas, J.L., Tagami, K., Shigeo Uchida, S., 2004. Method for the detection of Tc in seaweed samples coupling the use of Re as a chemical tracer and isotope dilution inductively coupled plasma mass spectrometry. Anal. Chim. Acta 509, 83–88.

Mathieu, G.G., Biscaye, P.E., Lupton, R.A., Hammond, D.E., 1988. System for measurement of ^{222}Rn at low levels in natural waters. Health Phys. 70, 989–992.

Matthews, K.M., Kim, C.-K., Martin, P., 2007. Determination of ^{210}Po in environmental materials: a review of analytical methodology. Appl. Radiat. Isot. 65, 267–279.

Matzke, M., 2002. Propagation of uncertainties in unfolding procedures. Nucl. Instrum. Methods Phys. Res., Sect. A 476, 230–241.

Maxwell III, S.L., Culligan, B.K., 2009a. Rapid method for determination of radiostrontium in emergency milk samples. J. Radioanal. Nucl. Chem. **279**, 757–760.

Maxwell, S., Culligan, B.K., Shaw, P.J., 2013. Rapid determination of radiostrontium in large soil samples. J. Radioanal. Nucl. Chem. 295, 965–971.

Maxwell, S.L., Culligan, B.K., Hutchison, J.B., Utsey, R.C., Mcalister, D.R., 2014. Rapid determination of actinides in seawater samples. J. Radioanal. Nucl. Chem. 300, 1175–1189.

Maxwell, S.L., Culligan, B., Hutchison, J.B., Utsey, R.C., Sudowe, R., McAlister, D.R., 2017. Rapid method to determination $^{89/90}$Sr in steel samples. J. Radioanal. Nucl. Chem. 314, 439–450.

McCormac, F.G., Kalin, R.M., Long, A., 1993. Radiocarbon dating beyond 50,000 years by liquid scintillation counting. In: Noakes, J.E., Schonhofer, F., Polach, H.A. (Eds.), Advances in Liquid Scintillation Spectrometry, 1992. Radiocarbon Publishers, University of Arizona, Tucson, pp. 125–133.

McDowell, W.J., 1992. Photon/electron-rejecting alpha liquid scintillation (PERALS®) spectrometry: a review. Radioact. Radiochem. 3, 26–44.

McDowell, W.J., McDowell, B.L., 1993. The growth of a radioanalytical method: alpha liquid scintillation spectrometry. In: Noakes, J.E., Schönhofer, F., Polach, H.A. (Eds.), Advances in Liquid Scintillation Spectrometry, 1992, 193–200. Radiocarbon Publishers, University of Arizona, Tucson.

McDowell, W.J., McDowell, B.L., 1994. Liquid Scintillation Alpha Spectrometry. CRC Press, Boca Raton, p. 184.

McKlveen, J.W., Johnson, W.R., 1975. Simultaneous alpha and beta particle assay using liquid scintillation counting with pulse shape discrimination. Health Phys. 28, 5–11.

McKlveen, J.W., McDowell, W.J., 1984. Liquid scintillation alpha spectrometry techniques. Nucl. Instrum. Methods Phys. Res. 223, 372–376.

Mellado, J., Llauradó, M., Rauret, G., 2002. Determination of actinides and strontium in fish samples by extraction chromatography. Anal. Chim. Acta 458, 367–374.

Mellado, J., Tarancón, A., García, J.F., Rauret, G., Warwick, P., 2005. Combination of chemical separation and data treatment for ^{55}Fe, ^{63}Ni, ^{99}Tc, ^{137}Cs and ^{90}Sr/^{90}Y activity determination in radioactive waste by liquid scintillation. Appl. Radiat. Isot. 63, 207–215.

Metzger, R.L., Jessop, B.H., McDowell, B.L., 1995. Bioanalysis of uranium, plutonium, and curium on breathing zone air samples by solvent extraction and PERALS spectroscopy. Radioact. Radiochem. 6, 46–56.

Michel, J., Moore, W.S., King, T., 1981. γ-ray spectrometry for determination of radium-228 and radium-226 in natural waters. Anal. Chem. 53, 1885–1889.

Mietelski, J.W., Dorda, J., Was, B., 1999. Pu-241 in samples of forest soil from Poland. Appl. Radiat. Isot. 51, 435–447.

Mikalauskiene, R., Maeika, J., Petroaius, R., Szwarczewski, P., 2018. Comparison of beta (LSC) and gamma (HPGe) spectrometric methods for lead-210 in chronological study. Geochronometria 45, 38–50.

Miller, T.J., 1991. Development of a rapid, economical and sensitive method for the routine determination of excreted uranium in urine. Anal. Lett. 24, 657–664.

Mitchell, P.I., León Vintró, L., Omarova, A., Burkitbayev, M., Jiménez Nápoles, H., Priest, N.D., 2005. Tritium in well waters, streams and atomic lakes in the east Kazakhstan oblast of the Semipalatinsk nuclear test site. J. Radiol. Prot. 25, 141–148.

Miura, T., Minai, Y., 2017. Radiometric analysis of ^{90}Sr in fish bone ash samples by liquid scintillation counting after separation by extraction chromatographic resin. J. Radioanal. Nucl. Chem. 313, 343–351.

Mizutani, T., Koarashi, J., Takeishi, M., 2009. Monitoring of low-level radioactive liquid effluent in Tokai reprocessing plant. J. Nucl. Sci. Technol. 46, 665–672.

Möbius, S., Kamolchote, P., Ramamonjisoa, T.-L., Yang, M., 1993. Rapid determination of Ra, Rn, Pb and Po in water using extractive liquid scintillation. In: Noakes, J.E., Schonhofer, F., Polach, H.A. (Eds.), Advances in Liquid Scintillation Spectrometry, 1992. Radiocarbon Publishers, University of Arizona, Tucson, pp. 413–416.

Möbius, S., 2002. Fast methods for field analysis of natural radionuclides - new approaches. In: Möbius, S., Noakes, J.E., Schönhofer, F. (Eds.), Advances in Liquid Scintillation Spectrometry, 2001. Radiocarbon Publishers, University of Arizona, Tucson, pp. 237–248.

Möbius, S., Salonen, L., 2002. Pilot intercomparison and workshop for radon and radium in water. In: Möbius, S., Noakes, J.E., Schönhofer, F. (Eds.), Advances in Liquid Scintillation Spectrometry, 2001. Radiocarbon Publishers, University of Arizona, Tucson, pp. 435–445.

Möbius, S., Zeisberg, H., 2002. Investigations on instrumental radium analysis by alpha/beta LS spectrometry. In: Möbius, S., Noakes, J.E., Schönhofer, F. (Eds.), Advances in Liquid Scintillation Spectrometry, 2001. Radiocarbon Publishers, University of Arizona, Tucson, pp. 275–282.

Möbius, S., Kamolchote, K., Rakotoarisoa, T., 2002. Extractive methods for fast radium analysis. In: Möbius, S., Noakes, J.E., Schönhofer, F. (Eds.), Advances in Liquid Scintillation Spectrometry, 2001. Radiocarbon Publishers, University of Arizona, Tucson, pp. 283–292.

Möbius, S., Rakotomanga, H., Lauria, D.C., Zafimanjato, L., 2006. Fast survey for key nuclides and group parameters in drinking water. In: Chałupnik, S., Schönhofer, F., Noakes, J. (Eds.), Advances in Liquid Scintillation Spectrometry, 2005. Radiocarbon Publishers, University of Arizona, Tucson, pp. 149–156.

Moghissi, A.A., Bretthauer, E.W., Compton, E.H., 1973. Separation of water from biological and environmental samples for tritium analysis. Anal. Chem. 45, 1565–1566.

Moir, D.L., Tarr, A.W., Ross, K.J., Delaney, H.G., 1995. Determination of ^{36}Cl and ^{12}C to ^{14}C ratios on spent moderator ion-exchange resins from BRUCE nuclear generating station A. J. Radioanal. Nucl. Chem. Lett. 200 (4), 365–373.

Monna, F., Mathieu, D., Marques Jr., A.N., Lancelot, J., Bernat, M., 1996. A comparison of PERALS® to alpha spectrometry and beta counting: a measure of the sedimentation rate in a coastal basin. Anal. Chim. Acta 330, 107–115.

Mook, W.G., van der Plicht, J., 1999. Reporting ^{14}C activities and concentrations. Radiocarbon 41, 227–239.

Moon, D.S., Burnett, W.C., Nour, S., Horwitz, P., Bond, A., 2003. Preconcentration of radium isotopes from natural waters using MnO_2 resin. Appl. Radiat. Isot. 59, 255–262.

Moran, S.B., Buesseler, K.O., 1993. Size-fractionated ^{234}Th in continental shelf waters of New England: implications for the role of colloids in oceanic trace metal scavenging. J. Marine Res. 51, 893–922.

Moreno, J., La Rosa, J.J., Danesi, P.R., Burns, K., Vajda, N., Sinojmeri, M., 1998. Determination of ^{241}Pu by LSC in combined procedure for Pu radionuclides, ^{241}Am and ^{90}Sr analysis in environmental samples. Radioact. Radiochem. 9, 35–44.

Moreno, H.P., Absi, A., Vioque, I., Manjón, G., García-Tenorio, R., 2000. Application of a liquid scintillation technique to the measurement of ^{226}Ra and ^{224}Ra in samples affected by non- nuclear industry waste. J. Radioanal. Nucl. Chem. 245, 309–315.

Morgenstern, U., Taylor, C.B., 2009. Ultra low-level tritium measurement using electrolytic enrichment and LSC. Isot. Environ. Health Stud. 45, 96–117.

Mosqueda, F., Villa, M., Vaca, F., Bolívar, J.P., 2007. Colour quenching corrections on the measurement of ^{90}Sr through Cerenkov counting. Anal. Chim. Acta 604, 184–190.

Mosqueda, F., Villa, M., Pates, J.M., Vaca, F., Borrego, E., 2009. Low-level measurement of ^{226}Ra via ^{222}Rn in natural water by LSC. In: Eikenberg, J., Jäggi, M., Beer, H., Baehrle, H. (Eds.), Advances in Liquid Scintillation Spectrometry, 2008, 145–154. Radiocarbon Publishers, University of Arizona, Tucson.

Mouteva, G.O., Randerson, J.T., Fahrni, S.M., Bush, S.E., Ehleringer, J.R., Xu, X.M., Santos, G.M., Kuprov, R., Schichtel, B.A., Czimczik, C., 2017. Using radiocarbon to constrain black and organic carbon aerosol sources in Salt Lake City. J. Geophys. Res. Atom. 122 (18), 9843–9857.

Muensterer, C., Fohlmeister, J., Christl, M., Schroeder-Ritzrau, A., Alfimov, V., Ivy-Ochs, S., Wackerbarth, A., Mangini, A., 2012. Cosmogenic Cl-36 in karst waters from Bunker Cave North Western Germany - a tool to derive local evapotranspiration? Geochim. Cosmochim. Acta 86, 138–149.

Muir, G.K.P., Hayward, S., Tripney, B.G., Cook, G.T., Naysmith, P., Herbert, B.M.J., Garnett, M.H., Wilkinson, M., 2015. Determination the biomass fraction of mixed waste fuels: a comparison of existing industry and ^{14}C-based methodologies. Waste Manage. 35, 293–300.

Müller, P., Blaum, K., Bushaw, B.A., Die, S., Geppert, C., Nähler, A., Nötershäuser, W., Trautmann, N., Wendt, K., 2000. Trace detection of 41Ca in nuclear reactor concrete by diode-laser based resonance ionization mass spectrometry. Radiochim. Acta 88, 487.

Murad, A., Alshamsi, D., Hou, X.L., Al Shidi, F., Al Kendi, R., Aldahan, A., 2014. Radioactivity in groundwater along the borders of Oman and UAE. J. Radioanal. Nucl. Chem. 299, 1653–1660.

Murakami, Y., Horiuchi, K., 1979. Simultaneous determination method of Radon-222 and Radon-220 by a toluene extraction-liquid scintillation counter. J. Radioanal. Nucl. Chem. 52, 275–283.

Murali, M.S., Kar, A., Kasyapa, K.R., Tomar, B.S., 2009. Alpha Beta Discrimination Using 300SL TDCR Liquid Scintillation Counter. Radiochemistry Division, Bhabha Atomic Research Centre, Trombay, Mumbai and Noki Technologies, Hyderabad.

Muramatsu, Y., Uchida, S., Sumiya, M., Ohmomo, Y., 1995. Iodine separation procedure for the determination of 129I and 127I in soil by neutron activation analysis. J. Radioanal. Nucl. Chem. Lett. 94, 329–338.

Nähle, O., Kossert, K., Brunzendorf, J., 2009. Study of light emission processes for the design of liquid scintillation counters. In: Eikenberg, J., Jäggi, M., Beer, H., Baehrle, H. (Eds.), Advances in Liquid Scintillation Spectrometry, 2008, 87–95. Radiocarbon Publishers, University of Arizona, Tucson.

Navarro, N., Rodriguez, L., Alvarez, A., Sancho, C., 2004. Rapid determination of alpha emitters using Actinide resin. Appl. Radiat. Isot. 61, 287–291.

NCRP, 1984. Exposures from the Uranium Series with Emphasis on Radon and its Daughters. National Council on Radiation Protection and Measurements. NCRP Report No. 77. Bethesda, MD.

Nebelung, C., Baraniak, L., 2007. Simultaneous determination of ^{226}Ra, ^{233}U and ^{237}Np by liquid scintillation spectrometry. Appl. Radiat. Isot. 65, 209–217.

Niese, S., 2008. Underground laboratories for low-level radioactivity measurements. In: Povinec, P.P. (Ed.), Radioactivity in the Environment, vol. 11. Elsevier Ltd., Amsterdam, pp. 209–239.

Niese, S., Köhler, M., Gleisberg, B., 1998. Low-level counting techniques in the underground laboratory "Felsenkeller" in Dresden. J. Radioanal. Nucl. Chem. 233, 167–172.

Niu, Z.C., Zhou, W.J., Feng, X., Feng, T., Wu, S.G., Cheng, P., Lu, X.F., Du, H., Xiong, X.H., Fu, Y.C., 2018. Atmospheric fossil fuel CO2 traced by CO2-14C and air quality index pollution observation in Beijing and Xiamem, China. Environ. Sci. Pollut. Res. 25 (17), 17109–17117.

Noakes, J.E., 1977. Considerations for achieving low level radioactivity measurements with liquid scintillation counters. In: Crook, M.A., Johnson, P. (Eds.), Liquid Scintillation Counting, vol. 4. Heyden, London, pp. 189–206.

Noakes, J.E., Valenta, R.J., 1996. The role of $Bi_4Ge_3O_{12}$ as an auxiliary scintillator for $\alpha/\beta/\gamma$ liquid scintillation counting and low level counting. In: Cook, G.T., Harkness, D.D., MacKenzie, A.B., Miller, B.F., Scott, E.M. (Eds.), Advances in Liquid Scintillation Spectrometry, 1994. Radiocarbon Publishers, University of Arizona, Tucson, pp. 283–292.

Noakes, J.E., Isbell, A.F., Stipp, J.J., Hood, D.W., 1963. Benzene synthesis by low temperature catalysis for radiocarbon dating. Geochim. Cosmochim. Acta 27, 797–804.

Noakes, J., Norton, G., Culp, R., Nigam, M., Dvoracek, D., 2006. A comparison of analytical methods for the certification of biobased products. In: Chałupnik, S., Schönhofer, F., Noakes, J. (Eds.), Advances in Liquid Scintillation Spectrometry, 2005. Radiocarbon Publishers, University of Arizona, Tucson, pp. 259–271.

Norton, G.A., 2009. Direct analysis of automotive fuels for bioethanol content using radiocarbon analysis. Radiocarbon 51, 995–1003.

Norton, G.A., Devlin, S.L., 2006. Determining the modern carbon content of biobased products using radiocarbon analysis. Bioresour. Technol. 97, 2084–2090.

Norton, G.A., Woodruff, M.X., 2011. Simplified radiocarbon analysis procedure for measuring the renewable diesel concentration in diesel fuel blends. J. Am. Oil Chem. Soc. https://doi.org/10.1007/s11746-011-1966-x. Publ. online 22 Nov 2011. (In Print).

Norton, G.A., Hood, D.G., Devlin, S.L., 2007. Accuracy of radioanalytical procedures used to determine the biobased content of manufactured products. Bioresour. Technol. 98, 1052–1056.

Nour, S., Burnett, W.C., Horwitz, E.P., 2002. ^{234}Th analysis of marine sediments via extraction chromatography and liquid scintillation counting. Appl. Radiat. Isot. 57, 235–241.

Nour, S., El-Sharkawy, A., Burnett, W.C., Horwitz, E.P., 2004. Radium-228 determination of natural waters via concentration on manganese dioxide and separation using Diphonix ion exchange resin. Appl. Radiat. Isot. 61, 1173–1178.

Nozaki, Y., Thomson, J., Turekian, K.K., 1976. The distribution of ^{210}Pb and ^{210}Po in the surface waters of the Pacific Ocean. Earth Planet. Sci. Lett. 32, 304–312.

Nozaki, Y., Zhang, J., Takeda, A., 1997. ^{210}Pb and ^{210}Po in the Equatorial Pacific and the Bering Sea: the effect of biological productivity and boundary scavenging. Deep-Sea Res. II 44, 2203–2220.

Nozaki, I., Dobashi, F., Kato, Y., Yamamoto, Y., 1998. Distribution of Ra isotopes and the ^{210}Pb and ^{210}Po balance in surface seawaters of the mid Northern Hemisphere. Deep-Sea Res. I 45, 1263–1284.

NRC, 1999. Evaluation of Guidelines for Exposures to Technologically Enhanced Naturally Occurring Radioactive Materials. National Research Council, National Academy Press, Washington D.C.

NuDat, 2016. Nuclear Structure & Decay Data, V. 2.7. Evaluated Nuclear Structure Data File (ENSDF). Database Version of 2016. National Nuclear Data Center, Brookhaven National Laboratory, NuDat2, U. S. A. https://www.nndc.bnl.gov/nudat2/chartNuc.jsp.

Numajiri, M., Oki, Y., Suzuki, T., Miura, T., Taira, M., Kanda, Y., Kondo, K., 1994. Estimation of nickel-63 in steel and copper activated at high-energy accelerator facilities. Appl. Radiat. Isot. 45, 509–514.

Oh, J.-S., Warwick, P.E., Croudace, I.W., 2009. Spatial distribution of ^{241}Am, ^{137}Cs, ^{238}Pu, ^{239,240}Pu and ^{241}Pu over 17 year periods in the Ravenglass saltmarsh, Cumbria, UK. Appl. Radiat. Isot. 67, 1484–1492.

Oh, J.S., Warwick, P.E., Croudace, I.W., Lee, S.H., 2013. Rapid measurement of ^{241}Pu activity at environment level using low-level liquid scintillation analysis. J. Radioanal. Nucl. Chem. 298, 353–359.

Oikari, T., Kojola, H., Nurmi, J., Kaihola, L., 1987. Simultaneous counting of low alpha and beta particle activities with liquid scintillation spectrometry and pulse shape analysis. Appl. Radiat. Isot. 38, 875–878.

Oinonen, M., Hakanpää-Laitinen, H., Hämäläinen, K., Kaskela, A., Jungner, H., 2010. Biofuel proportions in fuels by AMS radiocarbon method. Nucl. Instrum. Methods Phys. Res., Sect. B 268, 1117–1119.

Okada, S., Momoshima, N., 1993. Overview of tritium: characteristics, sources, and problems. Health Phys. 65, 595–609.

Olfert, J.M., Dai, X., Kramer-Tremblay, S., 2014. Rapid determination of 90Sr/90Y in water samples by liquid scintillation and Cherenkov counting. J. Radioanal. Nucl. Chem. 300, 263–267.

Oliver, L.R., Perkins, W.T., Mudge, S.M., 2006. Detection of technetium-99 in Ascophyllum nodosum from around the Welsh coast. Chemosphere 65, 2297–2303.

Osman, A.A.A., Bister, S., Riebe, B., Daraoui, A., Vockenhuber, C., Wacker, L., Walther, C., 2016. Radioecological investigation of H-3, C-14, and I-129 in natural waters from Fuhrberger Feld catchment, Northern Germany. J. Environ. Radioact. 165, 243–252.

Outola, I., Nour, S., Kurosaki, H., Inn, K., La Rosa, J., Lucas, L., Volkovitsky, P., Koepenick, K., 2008. Investigation of radioactivity in selected drinking water samples from Maryland. J. Radioanal. Nucl. Chem. 277, 155–159.

Paatero, J., Jaakkola, T., Reponen, A., 1994. Determination of ^{241}Pu deposition in Finland after the Chernobyl accident. Radiochim. Acta 64, 139–144.

Papastefanou, C., 2006. Residence time of tropospheric aerosols in association with radioactive nuclides. Appl. Radiat. Isot. 64, 93–100.

Parsa, B., 1998. Contribution of short-lived radionuclides to alpha particle radioactivity in drinking water and their impact on the safe drinking water act regulations. Radioact. Radiochem. 9, 41–50.

Parsa, B., Horton, T., 1990. Radon-222 in drinking water: an NJDEP-EERF collaborative study. Health Phys. 58, 209–212.

Parsa, B., Nemeth, W.K., Obed, R.N., 1999. The role of radon progenies in influencing gross alpha-particle determination in drinking water. Radioact. Radiochem. 11, 11–22.

Passo Jr., C.J., Kessler, M.J., 1993. Selectable delay before burst - a novel feature to enhance low-level counting performance. In: Noakes, J.E., Schönhofer, F., Polach, H.A. (Eds.), Advances in Liquid Scintillation Spectrometry, 1992, 51–57. Radiocarbon Publishers, University of Arizona, Tucson.

Passo Jr., C.J., Roberts, D.J., 1996. Expanded energy range for time-resolved liquid scintillation counting: an enhancement for programmable TR-LSC®. In: Cook, G.T., Harkness, D.D., MacKenzie, A.B., Miller, B.F., Scott, E.M. (Eds.), Liquid Scintillation Spectrometry, 1994. Radiocarbon Publishers, University of Arizona, Tucson, pp. 67–74.

Passo Jr., C.J., Cook, G.T., Thomson, J., 2002. The effects of substituted anthracenes and novel scintillating solvents in cocktail formulations for α/β separation in liquid scintillation spectrometry. In: Möbius, S., Noakes, J.E., Schönhofer, F. (Eds.), Advances in Liquid Scintillation Spectrometry, 2001. Radiocarbon Publishers, University of Arizona, Tucson, pp. 141–146.

Pates, J.M., Mullinger, N.J., 2007. Determination of ^{222}Rn in fresh water: development of a robust method of analysis by α/β separation liquid scintillation spectrometry. Appl. Radiat. Isot. 65, 92–103.

Pates, J.M., Cook, G.T., MacKenzie, A.B., 1996a. Alpha/beta separation liquid scintillation spectrometry: current trends. In: Cook, G.T., Harkness, D.D., MacKenzie, A.B., Miller, B.F., Scott, E.M. (Eds.), Advances in Liquid Scintillation Spectrometry, 1994. Radiocarbon Publishers, University of Arizona, Tucson, pp. 267–281.

Pates, J.M., Cook, G.T., MacKenzie, A.B., Anderson, R., Bury, S.J., 1996b. Determination of ^{234}Th in marine samples by liquid scintillation spectrometry. Anal. Chem. 68, 3783–3788.

Pates, J.M., Cook, G.T., MacKenzie, A.B., 1996c. The effect of cocktail fluors on pulse shapes and alpha/beta separation liquid scintillation spectrometry. In: Cook, G.T., Harkness, D.D., MacKenzie, A.B., Miller, B.F., Scott, E.M. (Eds.), Advances in Liquid Scintillation Spectrometry, 1994. Radiocarbon Publishers, University of Arizona, Tucson, pp. 317–326.

Pates, J.M., Cook, G.T., MacKenzie, A.B., Passo Jr., C.J., 1998. Implications of beta energy and quench level for alpha/beta liquid scintillation spectrometry calibration. Analyst 123, 2201–2207.

Peck, G.A., Smith, J.D., 2000. Determination of ^{210}Po and ^{210}Pb in rainwater using measurement of ^{210}Po and ^{210}Bi. Anal. Chim. Acta 422, 113–120.

Peck, G.A., Smith, J.D., Cooper, M.D., 1998. Enhanced counting efficiency of Cerenkov radiation from bismuth-210. J. Radioanal. Nucl. Chem. 238, 163–165.

Persson, B.R.R., Holm, E., 2011. Polonium-210 and lead-210 in the terrestrial environment: a historical review. J. Environ. Radioact. 102, 420–429.

Pessenda, L.C.R., Gouveia, S.E.M., Aravena, R., 2001. Radiocarbon dating of total soil organic matter and humin fraction and its comparison with ^{14}C ages of fossil charcoal. Radiocarbon 43, 595–601.

Piltingsrud, H.V., Stencel, J.R., 1972. Determination of ^{90}Y, ^{90}Sr, and ^{89}Sr in samples by use of liquid scintillation beta spectroscopy. Health Phys. 23, 121–122.

Pilviö, R., Bickel, M., 2000. Actinoid separations by extraction chromatography. Appl. Radiat. Isot. 53, 273–277.

Pilviö, R., La Rosa, J.J., Mouchel, P., Wordel, R., Bickel, M., Altzitzoglou, T., 1999. Measurement of low-level radioactivity in bone ash. J. Environ. Radioact. 43, 343–356.

Pimpl, M., 1992. Increasing the sensitivity of ^{241}Pu determination for emission and immission control of nuclear installations by aid of liquid scintillation counting. J. Radioanal. Nucl. Chem. 161, 429–436.

Piraner, O., Jones, R.L., 2009. Urine gross alpha/beta analysis by liquid scintillation counting for terrorism preparedness. In: Eikenberg, J., Jäggi, M., Beer, H., Baehrle, H. (Eds.), Advances in Liquid Scintillation Spectrometry, 2008. Radiocarbon Publishers, University of Arizona, Tucson, pp. 41–46.

Plastino, W., Chereji, I., Cuna, S., Kaihola, L., Felice, P.-D., Lupsa, N., Balas, G., Mirel, V., Berdea, P., Baciu, C., 2007. Tritium in water electrolytic enrichment and liquid scintillation counting. Radiat. Meas. 42, 68–73.

Polach, H., Gower, J., Kojola, H., Heinonen, A., 1983. An ideal vial and cocktail for low level scintillation counting. In: McQuarrie, S.A., Ediss, C., Weibe, L.I. (Eds.), Advances in Scintillation Counting. University of Alberta Press, Alberta, pp. 508–525.

Poole, A.J., Allington, D.J., Baxter, A.J., Young, A.K., 1995. The natural radioactivity of phosphate ore and associated waste products discharged into the eastern Irish Sea from a phosphoric acid production plant. Sci. Total Environ. 173/174, 137–149.

Popov, L., Hou, X., Nielsen, S.P., Yu, Y., Djingova, R., Kuleff, I., 2006. Determination of radiostrontium in environmental samples using sodium hydroxide for separation of strontium from calcium. J. Radioanal. Nucl. Chem. 269, 161–173.

Povinec, P.P., Comanducci, J.F., Levy-Palomo, I., Avaullee, F., 2006. IAEA-MEL's underground counting laboratory – the design and main characteristics. In: Povinec, P.P. (Ed.), Radioactivity in the Environment, vol. 8. Elsevier Ltd., Amsterdam, pp. 538–553.

Prichard, H.M., Cox, A., 1991. Liquid scintillation screening method for isotopic uranium in drinking water. In: Ross, H., Noakes, J.E., Spaulding, J.D. (Eds.), Liquid Scintillation Counting and Organic Scintillators. Lewis Publishers, Michigan, pp. 385–397.

Prichard, H.M., Gesell, T.F., 1977. Rapid measurements of radon-222 concentration in water with a commercial liquid scintillation counter. Health Phys. 33, 577–581.

Prichard, H.M., Marlën, K., 1983. Desorption of radon from activated carbon into a liquid scintillator. Anal. Chem. 55, 155–157.

Priya, S., Gopalakrishnan, R.K., Goswami, A., 2014. TDCR measurements of ^{3}H, ^{63}Ni and ^{55}Fe using Hidex 300SL LSC device. J. Radioanal. Nucl. Chem. 302 (1), 353–359.

Prosser, S.L., Popplewell, D.S., Lloyd, N.C., 1994. The radiological significance of ^{237}Np in the environment. J. Environ. Radioact. 23, 123–133.

Pujol, L., Sanchez-Cabeza, J.-A., 1997. Role of quenching on alpha/beta separation in liquid scintillation counting for several high capacity cocktails. Analyst 122, 383–385.

Punning, J.M., Rajamäe, R., 1977. Some possibilities for decreasing the background of liquid scintillation beta-ray counter. In: Povinec, P., Usacev, S. (Eds.), Low Radioactivity Measurements and Applications. Slovenske Pedagogicke Nakladatelstvo, Bratislava, pp. 169–171.

Purkl, S., Eisenhauer, A., 2003a. A rapid method for α–spectrometric analysis of radium isotopes in natural waters using ion-selective membrane technology. Appl. Radiat. Isot. 59, 245–254.

Purkl, S., Eisenhauer, A., 2003b. Solid-phase extraction using Empore™ Radium Rad Disks to separate radium from thorium. J. Radioanal. Nucl. Chem. 256, 473–480.

Purkl, S., Eisenhauer, A., 2004. Determination of radium isotopes and ^{222}Rn in a groundwater affected coastal area of the Baltic Sea and the underlying sub-sea floor aquifer. Mar. Chem. 87, 137–149.

Puukko, E., Jaakkola, T., 1992. Actinides and beta emitters in the process water and ion exchange resin samples from the Loviisa power plant. inis.iaea.org (https://inis.iaea.org/search/searchsinglerecord.aspx?recordsFor=SingleRecord&RN=24054662).

Qiao, J., Hou, X., Steier, P., Nielsen, S.P., Golser, R., 2015. Method for 236U determination in seawater using flow injection extraction chromatography and accelerator mass spectrometry. Anal. Chem. 87 (14), 7411–7417.

Qiao, J., Hou, X., Miró, M., Roos, P., 2009. Determination of plutonium isotopes in waters and environmental solids: a review. Anal. Chim. Acta 652, 66–84.

Qureshi, R.M., Aravena, R., Fritz, P., Drimmie, R.R., 1989. The CO_2 absorption method as an alternative to benzene synthesis method for ^{14}C dating. Appl. Geochem. 4, 625–633.

Radwan, M., Przybylska, A., Mykowska, E., Gibas, K., 1981. Measurement of nickel-63 low activity in samples of metals and alloys with the help of liquid scintillators. Appl. Radiat. Isot. 32, 97–99.

Randolph, R.B., 1975. Determination of strontium-90 and strontium-89 by Cerenkov and liquid scintillation counting. Appl. Radiat. Isot. 26, 9–16.

Rank, D., 1993. Environmental tritium in hydrology: present state (1992). In: Noakes, J.E., Schönhofer, F., Polach, H.A. (Eds.), Advances in Liquid Scintillation Spectrometry. Radiocarbon Publishers, University of Arizona, Tucson, pp. 327–334, 1992.

Rathore, D.P.S., 2008. Advances in technologies for the measurement of uranium in diverse matrices. Talanta 77, 9–20.

Reboli, A., Aupiais, J., Mialocq, J.C., 2005. Application of large area avalanche photodiodes for alpha liquid scintillation counting. Nucl. Instrum. Methods Phys. Res., Sect. A 550, 593–602.

Reddy, C.M., Demello, J.A., Carmichael, C.A., Peacock, E.E., Xu, L., Arey, J.S., 2008. Determination of biodiesel blending percentages using natural abundance radiocarbon analysis: testing the accuracy of retail biodiesel blends. Environ. Sci. Technol. 42, 2476–2482.

Regan, J.G.T., Tyler, J.F.C., 1976. The determination of Sr-90 and Sr-89 in water without separation of strontium from calcium. Analyst 101, 32–38.

Repinc, U., Benedik, L., 2002. Development of a method for the determination of ^{226}Ra by liquid scintillation counting. J. Radioanal. Nucl. Chem. 254, 181–185.

Rodriguez, R., Leal, L., Mianda, S., Ferrer, L., Avivar, J., Carcia, A., Cerda, V., 2015. Automation of Tc-99 extraction by LOV prior ICP-MS detection: application to environmental samples. Talanta 133. SI 88-93.

Roodbergen, S., Kroondijk, R., Verheul, H., 1972. Cerenkov radiation in photomultiplier windows and the resulting time shift in delayed coincidence time spectra. Nucl. Instrum. Methods Phys. Res. 105, 551–555.

Rozanski, K., Stichler, W., Gonfiantini, R., Scott, E.M., Beukens, R.P., Kromer, B., van der Plicht, J., 1992. The IAEA ^{14}C intercomparison exercise 1990. Radiocarbon 34, 506–559.

Ruberu, S.R., Liu, Y.G., Perera, S.K., 2007. Occurrence and distribution of ^{210}Pb and ^{210}Po in selected California groundwater wells. Health Phys. 92, 432–441.

Ruberu, S.R., Liu, Y.-L., Perera, S., 2008. An improved liquid scintillation counting method for the determination of gross alpha activity in groundwater wells. Health Phys. 95, 397–406.

Rucker, T.L., 1992. Calculational method for the resolution of ^{90}Sr and ^{89}Sr counts from Cerenkov and liquid scintillation counting. In:

Ross, H., Noakes, J.E., Spaulding, J.D. (Eds.), Liquid Scintillation Counting and Organic Scintillators. Lewis Publishers, Michigan, pp. 529–535.

Rundt, K., 1989. On the Determination and Compensation of Quench in Liquid Scintillation Counting (Ph.D. thesis). Department of Physical Chemistry, Åbo Akademi, Turku, Finland, 134 pp.

Rundt, K., 1992. Digital overlay technique in liquid-scintillation counting - a review. Radioact. Radiochem. 3, 14–25.

Rusconi, R., Azzellino, A., Bellinzona, S., Forte, M., Gallini, R., Sgorbati, G., 2004. Assessment of drinking water radioactivity content by liquid scintillation counting: set up of high sensitivity and emergency procedures. Anal. Bioanal. Chem. 379, 247–253.

Russow, R., Dermietzel, J., 1990. Determination of ^{63}Ni-activity in plant materials. Isotopenpraxis 26, 502–504.

Rutgers van der Loeff, M., Sarin, M.M., Baskaran, M., Benitez-Nelson, C., Buesseler, K.O., Charette, M., Dai, M., Gustafsson, Ö., Masque, P., Morris, P.J., Orlandini, K., Rodriquez y Buena, A., Savoye, N., Schmidt, S., Turnewitsch, R., Vöge, I., Waples, J.T., 2006. A review of present techniques and methodological advances in analyzing ^{234}Th in aquatic systems. Mar. Chem. 100, 190–212.

Ryan, T.P., Mitchell, P.I., Vives i Batlle, J., Sanchez-Cabeza, J.A., McGarry, A.T., Schell, W.R., 1993. Low-level 241Pu analysis by supported disk liquid scintillation counting. In: Noakes, J.E., Schönhofer, F., Polach, H.A. (Eds.), Advances in Liquid Scintillation Spectrometry. Radiocarbon Publishers, University of Arizona, Tucson, pp. 75–82, 1992.

Saito, M., 1983. Correction for loss of radon-222 in water sample caused by the use of a polyethylene bottle. Radioisotopes 32, 109–112.

Saito, T., Ohta, T., Koike, Y., Sato, J., 2003. A new analytical approach for ^{226}Ra and ^{228}Ra in environmental water. J. Radioanal. Nucl. Chem. 255, 535–538.

Salonen, L., 1978. Determination of Sr-90 and Sr-89 in environmental samples by liquid scintillation counting. In: Crook, M.A., Johnson, P. (Eds.), Liquid Scintillation Counting, vol. 5. Heyden and Son, London, pp. 17–31.

Salonen, L., 1993a. A rapid method for monitoring of uranium and radium in drinking water. Sci. Total Environ. 130/131, 23–35.

Salonen, L., 1993b. Measurement of low levels of ^{222}Rn in water with different commercial liquid scintillation counters and pulse-shape analysis. In: Noakes, J.E., Schönhofer, F., Polach, H.A. (Eds.), Liquid Scintillation Spectrometry, 1992. Radiocarbon Publishers, University of Arizona, Tucson, pp. 361–372.

Salonen, L., 1994. ^{238}U series radionuclides as a source of increased radioactivity in groundwater originating from Finnish bedrock. IHAS Publ. No. 222. In: Future Groundwater Resources at Risk, pp. 71–84.

Salonen, L., 2006. Alpha spillover depends on alpha energy: a new finding in alpha/beta liquid scintillation spectrometry. In: Chałupnik, S., Schönhofer, F., Noakes, J. (Eds.), Advances in Liquid Scintillation Spectrometry, 2005. Radiocarbon Publishers, University of Arizona, Tucson, pp. 135–148.

Salonen, L., 2009. Performance of two-phase and homogeneous sample compositions in measuring ^{222}Rn in drinking water. In: Eikenberg, J., Jäggi, M., Beer, H., Baehrle, H. (Eds.), Advances in Liquid Scintillation Spectrometry, 2008. Radiocarbon Publishers, University of Arizona, Tucson, pp. 133–144.

Salonen, L., 2010a. Comparison of two direct LS methods for measuring Rn in drinking water using α/β liquid scintillation spectrometry. Appl. Radiat. Isot. 68, 1970–1979.

Salonen, L., 2010b. Calibration of the direct LSC method for radon in drinking water: interference from ^{210}Pb and its progenies accumulated in ^{226}Ra standard solution. Appl. Radiat. Isot. 68, 131–138.

Salonen, L., Hukkanen, H., 1997. Advantages of low-back-ground liquid scintillation alpha spectrometry and pulse shape analysis in measuring ^{222}Rn, uranium and ^{226}Ra in groundwater samples. J. Radional. Nucl. Chem. 226, 67–74.

San Miguel, E.G., Pérez-Moreno, J.P., Bolívar, J.P., García-Tenorio, R., Martin, J.E., 2002. ^{210}Pb determination by gamma spectrometry in voluminal samples (cylindrical geometry). Nucl. Instr. Methods Phys. Res., Sect. A 493, 111–120.

Sanchez-Cabeza, J.A., Pujol, L., 1995. A rapid method for the simultaneous determination of gross alpha and beta activities in water samples using a low background liquid scintillation counter. Health Phys. 68, 674–681.

Sanchez-Cabeza, J.A., Pujol, L., 1998. Simultaneous determination of radium and uranium activities in natural water samples using liquid scintillation counting. Analyst 123, 399–403.

Santschi, P.H., Murray, J.W., Baskaran, M., Benitez-Nelson, C.R., Guo, L.D., Hung, C.-C., Lamborg, C., Moran, S.B., Passow, U., Roy-Barman, M., 2006. Thorium speciation in seawater. Mar. Chem. 100, 250–268.

Sartandel, S.J., Jha, S.K., Bara, S.V., Tripathi, R.M., Puranik, V.D., 2009. Spatial distribution of uranium and thorium in the surface soil around proposed uranium mining site at Lambapur and its vertical profile in the Nagarjuna Sagar Dam. J. Environ. Radioact. 100, 831–834.

Sas, D., Janda, J., 2017. Rapid determination of gross alpha/beta activity in urine with LSC. J. Radioanal. Nucl. Chem. 311 (1), 23–27.

Sas, D., Sládek, P., Janda, J., 2010. Measuring alpha and beta activity of filter and swab samples with LSC. J. Radioanal. Nucl. Chem. 286, 513–517.

Sato, K., Hashimoto, T., Noguchi, M., Nitta, W., Higuchi, H., Nishigawa, N., Sanada, T., 2000. A simple method for determination of ^{226}Ra in environmental samples by applying $\alpha-\beta$ coincidence liquid scintillation counting. J. Environ. Radioact. 48, 247–256.

Saueia, C.H.R., Mazzilli, B.P., 2006. Distribution of natural radionuclides in the production and use of phosphate fertilizers in Brazil. J. Environ. Radioact. 89, 229–239.

Saxen, R., 2002. Determination of Sr by extraction chromatography in the presence of ^{210}Pb in environmental samples. In: Möbius, S., Noakes, J.E., Schönhofer, F. (Eds.), Advances in Liquid Scintillation Spectrometry, 2001. Radiocarbon Publishers, University of Arizona, Tucson, pp. 389–395.

Scarpitta, S., 1993. Technetium-99 in water and vegetation by liquid scintillation analysis. In: 39th Annual Conference on Bioassay, Analytical, and Environmental Radiochemistry. Colorado Springs, Colorado.

Scarpitta, S., Odin-McCabe, J., Gaschott, R., Meier, A., Klug, E., 1999. Comparison of four ^{90}Sr groundwater analytical methods. Health Phys. 76, 644–656.

Scheuerer, C., Schupfner, R., Schüttelkopf, H., 1995. A very sensitive LSC procedure to determine Ni-63 in environmental samples, steel and concrete. J. Radioanal. Nucl. Chem. 193, 127–131.

Schmidt, S., Reyss, J.-L., 2000. Improvement in radiochemical and γ-counting procedures for the determination of ^{234}Th in seawater. Radiochim. Acta 88, 459.

Schönhofer, F., 1989a. Determination of ^{14}C in alcoholic beverages. Radiocarbon 31, 777–784.

Schönhofer, F., 1989b. Determination of radon-222 and radium-226 in mineral water and drinking water - a survey in Austria. Analyst 114, 1345–1347.

Schönhofer, F., 1992. ^{14}C in Austrian wine and vinegar. Radiocarbon 34, 768–771.

Schönhofer, F., 1998. The use of low-level liquid scintillation spectrometry for rapid measurement and decision making. Radioact. Radiochem. 9, 18–24.

Schönhofer, F., Weisz, J., 1987. Measurement by ultra low level liquid scintillation counting following the Chernobyl accident. J. Radioanal. Nucl. Chem. 115, 125–140.

Schönhofer, F., Pock, K., Friedmann, H., 1995. Radon surveys with charcoal and liquid scintillation counting. Field experience and comparison to other techniques. J. Radioanal. Nucl. Chem. 193, 337–346.

Schubert, M., Oberreich, M., Scholten, J., 2018. Preparation of MnO_2 coated fibers for gamma spectrometric measurement, A comparison of four practical approaches. J. Environ. Radioact. 189, 197–201.

Scott, E.M., Aitchison, T.C., Harkness, D.D., Cook, G.T., Baxter, M.S., 1990. An overview of all three stages of the international radiocarbon intercomparison. Radiocarbon 32, 309–319.

Scott, E.M., Cook, G.T., Naysmith, P., 2010. A report on phase 2 of the fifth international radiocarbon intercomparison (VIRI). Radiocarbon 52, 846–858.

Sedlaček, J., Ŝebesta, F., Beneŝ, P., 1980. Scintillation emanometric determination of radium-226 in waters using a new method of radium preconcentration. J. Radioanal. Chem. 59, 45–53.

Shaw, G.D., Conklin, M.H., Nimz, G.J., Liu, F.J., 2014. Groundwater and surface water flow to the Merced river, Yosemite valley, California: 36Cl and Cl- evidence. Water Resour. Res. 50, 1943–1959.

Shetty, P.K., Narayana, Y., Siddappa, K., 2006. Vertical profiles and enrichment pattern of natural radionuclides in monazite areas of coastal Kerala. J. Environ. Radioact. 86, 132–142.

Shi, K., Hou, X.L., Roos, P., Wu, W.S., 2011. Determination of Technetium-99 in environmental samples: a review. Anal. Chim. Acta 709, 1–20.

Shi, Y., Dai, X., Collins, R., Kramer-Tremblay, S., 2011. Rapid determination of uranium isotopes in urine by inductively coupled plasma-mass spectrometry. Health Phys. 101, 148–153.

Shi, K., Hou, X.L., Roos, P., Wu, W.S., 2012a. Stability of technetium and decontamination of Ru and Mo in determination of ^{99}Tc in environmental solid samples by ICP-MS. Anal. Chem. 84, 2009–2016.

Shi, K., Qiao, J.X., Roos, P., Wu, W.S., Hou, X.L., 2012b. Rapid determination of technetium-99 in large volume seawater samples using sequential injection extraction chromatographic separation and ICP-MS measurement. Anal. Chem. 84 (15), 6783–6789.

Shi, K., Hou, X.L., Roos, P., Nielsen, S.P., 2013. Seasonal variation of technetium-99 in Fucus vesiculosus and its application as an oceanographic tracer. Estuar. Coast. Shelf Sci. 127, 24–28.

Shi, K., Hou, X.L., Qiao, J.X., Sun, X.J., Roos, P., Wu, W.S., 2016. Analytical of technetium species and fractions in natural seaweed using biochemical separation and ICP-MS measurement. Anal. Chem. 88, 11931–11937.

Shibahara, Y., Kubota, T., Fujii, T., et al., 2016. Determination of isotopic ratios of plutonium and uranium in soil samples by thermal ionization mass spectrometry. J. Radioanal. Nucl. Chem. 307, 2281–2287.

Sidle, W.C., Shanklin, D., Lee, P.Y., Roose, D.L., 2001. ^{226}Ra and ^{228}Ra activities associated with agricultural drainage ponds and wetland ponds in the Kankakee Watershed, Illinois-Indiana, USA. J. Environ. Radioact. 55, 29–46.

Sill, C.W., Williams, R.L., 1969. Radiochemical determination of uranium and the transuranium elements in process solutions and environmental samples. Anal. Chem. 41, 1624–1632.

Silva, R.J., Evans, R., Rego, J.H., Buddemeier, R.W., 1988. Methods and results of Tc-99 analysis of Nevada test site ground waters. J. Radioanal. Nucl. Chem. 124, 397–405.

Silva, R., Novais, J.M., Martins-Dias, S., November 8-11, 2010. RDF biogenic content assessment and interfering materials. In: Proceedings Venice 2010, Third International Symposium on Energy from Biomass and Waste. Venice, Italy.

Simpson, B.R., Meyer, B.R., 1994. Direct activity measurement of pure beta-emitting radionuclides by the TDCR efficiency calculation technique. Nucl. Instrum. Methods Phys. Res. Sect. A 339, 14–20.

Sirelkhatim, D.A., Sam, A.K., Hassona, R.K., 2008. Distribution of ^{226}Ra–^{210}Pb–^{210}Po in marine biota and surface sediments of the Red Sea, Sudan. J. Environ. Radioact. 99, 1825–1828.

Skwarzec, B., Holm, E., Roos, P., Pempkowiak, J., 1994. ^{63}Ni in Baltic fish and sediments. Appl. Radiat. Isot. 45, 609–611.

Smethie Jr., W.M., Schell, W.R., 1980. Vacuum extraction of natural levels of radon from seawater. Mar. Chem. 8, 251–260.

Smith, J.N., Ellis, K.M., 1995. Radionuclide tracer profiles at the CESAR ice station and Canadian ice Island in the western arctic ocean. Deep-Sea Res. II 42, 1449–1470.

Smith, M.R., Lautensleger, A.W., Laul, J.C., 1988. A new method for the determination of radium-228, thorium-228, and radium-224 in groundwaters via thoron (radon-220). J. Radioanal. Nucl. Chem. 123, 107–119.

Smith, L.L., Orlandini, K.A., Alvarado, J.S., Hoffmann, K.M., Seely, D.C., Shannon, R.T., 1996. Application of Empore™ Strontium Rad Disks to the analysis of radiostrontium in environmental water samples. Radiochim. Acta 73, 165–170.

Smith, L.L., Alvarado, J.S., Markun, F.J., Hoffmann, K.M., Seely, D.C., Shannon, R.T., 1997. An evaluation of radium-specific, solid phase extraction membranes. Radioact. Radiochem. 8, 30–37.

Smith, K.J., León Vintró, L., Mitchell, P.I., Bally de Bois, P., Boust, D., 2004. Uranium–thorium disequilibrium in north-east Atlantic waters. J. Environ. Radioact. 74, 199–210.

Soini, E., 1975. Rejection of Optical Cross-Talk in Photomultiplier Tubes in Liquid Scintillation Counters. Wallac Report, Wallac Oy, Turku, Finland. 9 pp.

Sonali, P.D.B., Ajay, K., Priyanka, J.R., Rupali, K., Rajesh, V.K., Rajvir, S., Pradeepkumar, K.S., 2016. Comparison of radiometric and non-radiometric methods for uranium determination in groundwater of Punjab, India. J. Radioanal. Nucl. Chem. 307, 395–405.

Song, L., Yang, Y., Luo, M., Ma, Y., Dai, X., 2017. Rapid determination of radium-224/226 in seawater sample by alpha spectrometry. J. Radioanal. Nucl. Chem. 171, 169–175.

Spaulding, J.D., Noakes, J.E., 1993. Determination of ^{222}Rn in drinking water using an alpha/beta liquid scintillation counter. In: Noakes, J.E., Schönhofer, F., Polach, H.A. (Eds.), Liquid Scintillation Spectrometry, 1992. Radiocarbon Publishers, University of Arizona, Tucson, pp. 373–381.

Spry, N., Parry, S., Jerome, S., 2000. The development of a sequential method for the determination of actinides and Sr-90 in power station effluent using extraction chromatography. Appl. Radiat. Isot. 53, 163–171.

Staber, W., Flamme, S., Fellner, J., 2008. Methods for determining the biomass content of waste. Waste Manag. Res. 26, 78–87.

Stamoulis, K.C., Ioannides, K.G., Karamanis, D., 2010. Deconvolution of liquid scintillation alpha spectra of mixtures of uranium and radium isotopes. Anal. Chim. Acta 657, 108–115.

Stencel, J.R., Griesbach, O.A., Ascione, G., 1995. Practical aspects of environmental analysis for tritium using enrichment by electrolysis. Radioact. Radiochem. 6, 40–49.

Stojkovic, I., Nikolov, J., Tomic, M., Micic, R., Todorovic, N., 2017. Biogenic fraction determination in fuels – optimal parameters survey. Fuel 191, 330–338.

Stringer, C.E., Burnett, W.C., 2004. Sample bottle design improvements for radon emanation analysis of natural waters. Health Phys. 87, 642–646.

Stuiver, M., Polach, H.A., 1977. Reporting of ^{14}C data. Radiocarbon 19, 355–363.

Suárez, J.A., Rodriguez, M., Espartero, A.G., Piña, G., 2000. Radiochemical analysis of ^{41}Ca and ^{45}Ca. Appl. Radiat. Isot. 52, 407–412.

Sunderman, D.N., Townley, C.W., 1960. The Radiochemistry of Barium, Calcium and Strontium. Technical Report NAS-NS 3010. National Academy of Sciences - National Research Council, Nuclear Science Series, Radiochemistry Techniques.

Suomela, J., 1993. Method for Determination of Radium-226 in Water by Liquid Scintillation Counting. SSI-rapport 93-12. Statens strålskyddsinstitut, Stockholm.

Suomela, J., Wallberg, L., Melin, J., 1993. Methods for Determination of Strontium-90 in Food and Environmental Samples by Cerenkov Counting. SSI-rapport 93-11. Statens strålskyddsinstitut, Stockholm.

Surbeck, H., 1995. Determination of natural radionuclides in drinking water, a tentative protocol. Sci. Total Environ. 173/174, 91–99.

Surbeck, H., 2000. Alpha spectrometry sample preparation using selectively adsorbing thin films. Appl. Radiat. Isot. 53, 97–100.

Surman, J.J., Pates, J.M., Zhang, H., Happel, S., 2014. Development and characterization of a new Sr selective resin for the rapid determination of 90Sr in environmental water samples. Talanta 129, 623–628.

Szántó, Z., Hertelendi, E., Csongor, J., Gulyás, J., 1998. Determination of ^{36}Cl in Nuclear Waste. ATOMKI Annual Report (11), pp. 76–77.

Szidat, S., Ruff, M., Perron, N., Wacker, L., Synal, H.-A., Hallquist, M., Shannigrahi, A.S., Yttri, K.E., Dye, C., Simpson, D., 2009. Fossil and non-fossil sources of organic carbon (OC) and elemental carbon (EC) in Göteborg, Sweden. Atmos. Chem. Phys. 9, 1521–1535.

Taddei, M.H., Macacini, J.F., Vicente, R., Marumo, J.T., Sakata, S.K., Terremoto, L.A., 2013. A comparative study using liquid scintillation counting and X-ray spectrometry to determine ^{55}Fe in radioactive wastes. J. Radioanal. Nucl. Chem. 295 (3), 2267–2272.

Tagami, K., Uchida, S., 1999. Use of a combustion apparatus for low-level ^{99}Tc separations from soil samples. Radioact. Radiochem. 10, 30–34.

Tagami, K., Uchida, S., 2004. Use of TEVA resin for the determination of U isotopes in water samples by Q-ICP-MS. Appl. Radiat. Isot. 61, 255–259.

Tait, D., Wiechen, A., 1993. Use of liquid scintillation for fast determination of ^{89}Sr and ^{90}Sr in milk. Sci. Total Environ. 130/131, 447–457.

Tait, D., Haase, G., Wiechen, A., 1997. A fast method for the determination of ^{90}Sr in liquid milk by solid phase extraction with cryptand 222 on cation exchange resin. Kerntechnik 62, 96–98.

Tait, D., Haase, G., Wiechen, A., 1998. Solid phase extraction of strontium by cryptand 222 bound to Dowex 50W_8 for the determination of ^{90}Sr in liquid milk. Kieler Milchwirtschaftliche Forschungsberichte 50, 211–223.

Takiue, M., Natake, T., Fujii, H., Aburai, T., 1996. Accuracy of Cerenkov measurements using a liquid scintillation spectrometer. Appl. Radiat. Isot. 47, 123–126.

Talha, S.A., Lindsay, R., Newman, R.T., de Meijer, R.J., Maleka, P.P., Hlatshwayo, I.N., Mlwilo, N.A., Mohanty, A.K., 2008. γ-Ray spectrometry of radon in water and the role of radon to representatively sample aquifers. Appl. Radiat. Isot. 66, 1623–1626.

Tamers, M.A., 1965. Routine carbon-14 dating using liquid scintillation techniques. In: Chatters, R.M., Olson, E.A. (Eds.), Proceedings of the 6th Conference on Radiocarbon and Tritium Dating, pp. 53–67.

Tamers, M., June 2006. Distinguishing between 'bio-ethanol' and petroleum ethanol. Ethanol Prod. Mag. 106–109.

Tarancon, A., Bagan, H., Garcia, J.F., 2017. Plastic scintillators and related analytical procedures for radionuclide analysis. J. Radioanal. Nucl. Chem. 314, 555–572.

Tavčar, P., Benedik, L., 2005. Determination of actinides and ^{90}Sr in spent ion exchange resins. Radiochim. Acta 93, 623–625.

Tayeb, M., Dai, X., Corcoran, E.C., Kelly, D.G., 2014. Evaluation of interferences on measurements of 90Sr/90Y by TDCR Cherenkov counting technique. J. Radioanal. Nucl. Chem. 300, 409–414.

Tayeb, M., Dai, X., Corcoran, E.C., Kelly, D.G., 2015. Rapid determination of strontium-90 from yttrium-90 in seawater. J. Radioanal. Nucl. Chem. 304, 1043–1052.

Tayeb, M., Dai, X., Sdraulig, S., 2016. Rapid and simultaneous determination of strontium-90 and strontium-89 in seawater in emergency situations. J. Environ. Radioact. 153, 214–221.

Testa, C., Desideri, D., Meli, M.A., Roselli, C., 1991. Extraction chromatography in radioecology. Radioact. Radiochem. 2, 46–55.

Thakkar, A.H., 2001. Rapid sequential separation of actinides using Eichrom's extraction chromatographic material. J. Radioanal. Nucl. Chem. 248, 453–456.

Theodórsson, P., 1996. A new method for automatic measurement of low-level radon in water. Appl. Radiat. Isot. 47, 855–859.

Theodórsson, P., Gudjónsson, G.I., 2009. Ultra-stable single-phototube liquid scintillation system for radiocarbon dating. In: Eikenberg, J., Jäggi, M., Beer, H., Baehrle, H. (Eds.), Advances in Liquid Scintillation Spectrometry, 2008. Radiocarbon Publishers, University of Arizona, Tucson, pp. 253–260.

Thiam, C., Bobin, C., Bouchard, J., 2017. Adaptation of PTB's analytical modelling for TDCR–Cherenkov activity measurements at LNHB. J. Radioanal. Nucl. Chem. 314, 591–597.

Thomson, J., 1991. Di-isopropylnaphthalene - a new solvent for liquid scintillation counting. In: Ross, H., Noakes, J.E., Spaulding, J.D. (Eds.), Liquid Scintillation Counting and Organic Scintillators. Lewis Publishers, Michigan, pp. 19–34.

Thomson, J., Burns, D.A., 1995. Radio-carbon Dioxide ($^{14}CO_2$) Trapping and Counting. Application Note CS-001. PerkinElmer LAS (updated May 2005 by R. Edler).

Thomson, J., Colley, S., Anderson, R., Cook, G.T., MacKenzie, A.B., 1993. ^{210}Pb in the sediments and water column of the Northeast Atlantic from 47 to 59° N along 20° W. Earth Planet. Sci. Lett. 115, 75–87.

Thomson, J., Cook, G.T., Anderson, R., MacKenzie, A.B., Harkness, D.D., McCave, I.N., 1995. Radiocarbon age offsets in different-sized carbonate components of deep-sea sediments. Radiocarbon 37, 91–101.

Thorngate, J.H., McDowell, W.J., Christian, D.J., 1974. An application of pulse shape discrimination to liquid scintillation counting. Health Phys. 27, 123–126.

Till, J.E., 1986. Source terms for technetium-99 from nuclear fuel cycle facilities. In: Desmet, G., Myttenaere, C. (Eds.), Technetium in the Environment. Elsevier Applied Science Publishers, London, pp. 1–20.

Ting, B.G., Paschal, D.C., Jarrett, J.M., Pirkle, J.L., Jackson, R.J., Sampson, E.J., Miller, D.T., Claudill, S.P., 1999. Uranium and thorium in urine of United States residents: reference range concentrations. Exp. Res., Sect. A 81, 45–51.

Tinker, R.A., Smith, J.D., 1996. Simultaneous measurement of ^{226}Ra and ^{133}Ba using liquid scintillation counting with pulse shape discrimination. Anal. Chim. Acta 332, 291–297.

Tolmachyov, S., Ura, S., Momoshima, N., Yamamoto, M., Maeda, Y., 2001. Determination of Cl-36 by liquid scintillation counting from soil collected at the Semipalatinsk Nuclear Test Site. J. Radioanal. Nucl. Chem. 249, 541–545.

Torres, J.M., Tent, J., Llauradó, M., Rauret, G., 2002. A rapid method for ^{90}Sr determination in the presence of ^{137}Cs in environmental samples. J. Environ. Radioact. 59, 113–125.

Tsai, T.-L., Lin, C.-C., Wang, T.-Y., Wei, H.-J., Men, L.-C., 2010. Application of ICP-QMS for the determination of ultratrace-levels of ^{226}Ra in geothermal water and sediment samples. J. Radioanal. Nucl. Chem. 286, 145–154.

Tsroya, S., Pelled, O., German, U., Marco, R., Katorza, E., Alfassi, Z.B., 2009. Color quench correction for low level Cherenkov counting. Appl. Radiat. Isot. 67, 805–808.

Tsroya, S., Pelled, O., German, U., Katorza, E., Abraham, A., Alfassi, Z.B., 2012. A comparative study of color quenching correction methods for Cerenkov counting. Appl. Radiat. Isot. 70, 397–403.

Tsroya, S., Dolgin, B., German, U., Pelled, O., Alfassi, Z.B., 2013a. Fast determination of 90Sr/90Y activity in milk by Cherenkov counting. Appl. Radiat. Isot. 82, 332–339.

Tsroya, S., German, U., Pelled, O., Katorza, E., Alfassi, Z.B., 2013b. Determination of 90Sr–90Y activity in urine samples by using Cherenkov counting. Appl. Radiat. Isot. 73, 12–16.

Tudyka, K., Pazdur, A., Theodórsson, P., Michczynski, A., Pawlyta, J., 2010. The application of ICELS systems for radiocarbon dating. Radiocarbon 52, 1661–1666.

Turnbull, J.C., Keller, E.D., Baisden, T., Brailsford, G., Bromley, T., Norris, M., Zondervan, A., 2014. Atmos. Chem. Phys. 14 (10), 5001–5014.

Turner, M., Rudin, M., Cizdziel, J., Hodge, V., 2003. Excess plutonium in soil near Nevada Test Site, USA. Environ. Pollut. 125, 193–203.

Turtiainen, T., 2009. Measurement of radon emanation of drainage layer media by liquid scintillation counting. J. Radioanal. Nucl. Chem. 279, 325–331.

Tzortzis, M., Tsertos, H., 2004. Determination of thorium, uranium and potassium elemental concentrations in surface soils in Cyprus. J. Environ. Radioact. 77, 325–338.

UNSCEAR, 2000. Annex B: exposures from natural radiation sources. In: Sources and Effects of Ionizing Radiation. United Nations Scientific Committee on the Effects of Atomic Radiation UNSCEAR 2000 Report to the General Assembly, with Scientific Annexes, vol. I. SOURCES, United Nations, New York.

UNSCEAR, 2006. Annex E: sources-to-effects assessment for radon in homes and workplaces. In: Effects of Ionizing Radiation. United Nations Scientific Committee on the Effects of Atomic Radiation UNSCEAR 2008 Report to the General Assembly, vol. 2. United Nations, New York.

UNSCEAR, 2008. Sources and effects of ionizing radiation. In: Report to the General Assembly with Scientific Annexes Vol I. United Nations Scientific Committee on the Effects of Atomic Radiation, New York.

Unsworth, E.R., Cook, J.M., Hill, S.J., 2001. Determination of uranium and thorium in natural waters with a high matrix concentration using solid-phase extraction inductively coupled plasma mass spectrometry. Anal. Chim. Acta 442, 141–146.

US Energy Policy Act, 2005. Public Law 109–58.

Uyesgi, G.S., Greenberg, A.E., 1965. Simultaneous assay of Strontium-90 and Yttrium-90 by liquid scintillation spectrometry. Appl. Radiat. Isot. 16, 581–587.

Vaca, F., Manjón, G., Cuéllar, S., García-León, M., 2001. Factor of merit and minimum detectable activity for ^{90}Sr determination by gas-flow proportional counting or Cherenkov counting. Appl. Radiat. Isot. 55, 849–851.

Vajda, N., Kim, C.-K., 2010a. Determination of Pu isotopes by alpha spectrometry: a review of analytical methodology. J. Radioanal. Nucl. Chem. 283, 203–223.

Vajda, N., Kim, C.-K., 2010b. Determination of ^{241}Am isotope: a review of analytical methodology. J. Radioanal. Nucl. Chem. 284, 341–366.

Vajda, N., Kim, C.-K., 2010c. Determination of radiostrontium isotopes: a review of analytical methodology. Appl. Radiat. Isot. 68, 2306–2326.

Vajda, N., Ghods-Esphahani, A., Cooper, E., Danesi, P.R., 1992. Determination of radiostrontium in soil samples using crown ether. J. Radioanal. Nucl. Chem. 162, 307–323.

Vajda, N., La Rosa, J., Zeisler, R., Danesi, P., Kis Benedek, G., 1997. A novel technique for the simultaneous determination of ^{210}Pb and ^{210}Po using a crown ether. J. Environ. Radioact. 37, 355–372.

Valenta, R.J., 1987. Reduced Background Scintillation Counting. U.S. Patent No. 4,651,006.

Valenta, R.J., Noakes, J.E., 1989. Liquid Scintillation Measurement System with Active Guard Shield. U.S. Patent No. 4,833,326.

van Beek, P., Souhaut, M., Reyss, J.-L., 2010. Measuring the radium quartet (^{228}Ra, ^{226}Ra, ^{224}Ra, ^{223}Ra) in seawater samples using gamma spectrometry. J. Environ. Radioact. 101, 521–529.

van Cauter, S., 1986. Three dimensional spectrum analysis: a new approach to reduce background of liquid scintillation counters. In: Packard Instrument Company Application Bulletin 006. PerkinElmer Life and Analytical Sciences, Boston, pp. 1–8.

Van Es, E.M., Russell, B., Ivanov, P., Read, D., 2017. Development of a method for rapid analysis of Ra-226 in groundwater and discharge water samples by ICP-QQQ-MS. Appl. Radiat. Isot. 126, 31–34.

Varga, B., Tarján, S., 2008. Determination of ^{241}Pu in the environmental samples. Appl. Radiat. Isot. 66, 265–270.

Varga, B., Tarján, S., Vajda, N., 2008. Plutonium isotopes in the Hungarian environment. J. Environ. Radioact. 99, 641–648.

Varga, Z., Nicholl, A., Zsigrai, Z., Wallenius, M., Mayer, K., 2018. Methodology for the preparation and validation of plutonium age dating materials. Anal. Chem. 90, 4019–4024.

Vargas, M.J., Fernández de Soto, F., Mártin Sánchez, A., 1995. Energy resolution, yield and radon diffusion in the electrodeposition of radium. Nucl. Instrum. Methods Phys. Res., Sect. A 364, 349–353.

Vasile, M., Benedik, L., Altzitzoglou, T., Spasova, Y., Wätjen, U., González de Orduña, R., Hult, M., Beyermann, M., Mihalcea, I., 2010.

^{226}Ra and ^{228}Ra determination in mineral waters - comparison of methods. Appl. Radiat. Isot. 68, 1236−1239.

Venso, E.A., Prichard, H.M., Dodson, C.L., 1993. Measurement of isotopic uranium in Texas drinking water supplies by liquid scintillation with alpha-beta discrimination. In: Noakes, J.E., Schönhofer, F., Polach, H.A. (Eds.), Advances in Liquid Scintillation Spectrometry, 1992. Radiocarbon Publishers, University of Arizona, Tucson, pp. 425−430.

Vera Tomé, F., Gómez Escobar, V., Martín Sánchez, A., 2002a. Study of the peak shape in alpha spectra measured by liquid scintillation. Nucl. Instrum. Methods Phys. Res., Sect. A 85, 444−452.

Vera Tomé, F., Blanco Rodríquez, P., Lozano, J.C., 2002b. Distribution and mobilization of U, Th and ^{226}Ra in the plant-soil compartments of a mineralized uranium area in south-west Spain. J. Environ. Radioact. 59, 41−60.

Vernon, E.L., Smith, J.T., Jha, A.N., 2018. Relative comparison of tissue specific bioaccumulation and radiation dose estimation in marine and freshwater bivalve molluscs following exposure to phosphorus-32. J. Environ. Radioact. 192, 312−320.

Véronneau, C., Aupiais, J., Dacheux, N., 2000. Selective determination of polonium by photon electron rejecting alpha liquid scintillation (PERALS® System). Anal. Chim. Acta 415, 229−238.

Verrezen, F., Hurtgen, C., 1992. The measurement of Technetium-99 and Iodine-129 in waste water from pressurized nuclear-power reactors. Appl. Radiat. Isot. 43, 61−68.

Verrezen, F., Hurtgren, C., 2003. Low level liquid scintillation counting in a deep underground laboratory: backround reduction effects. In: Warwick, P. (Ed.), Environmental Chemical Analysis II. The Royal Society of Chemistry, Athenaeum Press Ltd., Gateshead, pp. 160−166.

Verzilov, Y., Curtius, H., Fachinger, J., 2002. Determination of alpha/beta radionuclides in concentrated salt brines from fuel leaching by liquid scintillation spectrometry using solvent extraction. In: Möbius, S., Noakes, J.E., Schönhofer, F. (Eds.), Advances in Liquid Scintillation Spectrometry, 2001. Radiocarbon Publishers, University of Arizona, Tucson, pp. 379−388.

Vesely, A., Trombitas, H., Lindauer, H., 2008. Determination of beta emitters in materials from research reactor decomissioning. In: Eikenberg, J., Jäggi, M., Beer, H., Baehrle, H. (Eds.), Advances in Liquid Scintillation Spectrometry, 2008. Radiocarbon Publishers, University of Arizona, Tucson, pp. 435−441.

Vesterbacka, P., Ikäheimonen, T.K., 2005. Optimization of ^{210}Pb determination via spontaneous deposition of ^{210}Po on a silver disk. Anal. Chim. Acta 545, 252−261.

Vesterbacka, P., Mäkeläinen, I., Arvela, H., 2005. Natural radioactivity in drinking water in private wells in Finland. Radiat. Prot. Dosim. 113, 223−232.

Vesterbacka, P., Pettersson, H., Hanste, U.M., Jakobson, E., Kolstad, T., Roos, P., Östergren, I., 2010. Intercomparison of Rn-222 determination from groundwater. Appl. Radiat. Isot. 68, 214−218.

Villa, M., Manjón, G., García-León, M., 2003. Study of colour quenching effects in the calibration of liquid scintillation counters: the case of ^{210}Pb. Nucl. Instr. Methods Phys. Res., Sect. A 496, 413−424.

Villa, M., Moreno, H.P., Manjón, G., 2005. Determination of ^{226}Ra and ^{224}Ra in sediments by liquid scintillation counting. Radiat. Meas. 39, 543−550.

Villa, M., Hurtado, S., Manjón, G., García-Tenorio, R., 2007. Calibration and measurement of ^{210}Pb using two independent techniques. Radiat. Meas. 42, 1552−1560.

Villalba, L., Colmenero Sujo, L., Montero Cabrera, M.E., Jiménez, A., Rentería Villalobos, M., Delgado Mendoza, C.J., Jurado Tenorio, L.A., Dávila Rangel, I., Herrera Peraza, E.F., 2005. Radon concentrations in ground and drinking water in the state of Chihuahua, Mexico. J. Environ. Radioact. 80, 139−151.

Vitz, E., 1991. Toward a standard method for determining waterborne radon. Health Phys. 60, 817−829.

Von Pietig, F., Scharpenseel, H.W., 1964. Alterbestimmung mit Flüssigkeits-Szintillations-Spektrometer, über die Wirksamkeit von Abschirmungsabnahmen. Atompraxis 7, 1−3.

Vreček, P., Benedik, L., Pihlar, B., 2004. Determination of ^{210}Pb and ^{210}Po in sediment and soil leachates and in biological materials using a Sr-resin column and evaluation of column reuse. Appl. Radiat. Isot. 60, 717−723.

Vuković, Ž., Mandić, M., Vuković, D., 1996. Natural radioactivity of ground waters and soil in the vicinity of the ash repository of the coal-fired power plant "Nikola Tesla" A − Obrenovac (Yugoslavia). J. Environ. Radioact. 33, 41−48.

Wadach, J.B., Hess, C.T., 1985. Radon-222 concentration measurements in soil using liquid scintillation and Track Etch. Health Phys. 48, 805−808.

Walker, M.J.C., Bryant, C., Coope, G.R., Harkness, D.D., Lowe, J.J., Scott, E.M., 2001. Towards a radiocarbon chronology of the late-glacial: sample selection strategies. Radiocarbon 43, 1007−1019.

Wallac 1414 WinSpectral, 2001. Digital Spectrum Analysis (DSA) Based Liquid Scintillation counter. Instrument Manual 1414-932-05. PerkinElmer, Turku, Finland.

Wallner, G., 1996. Thorium determination by liquid scintillation counting using an extractive cocktail. Environ. Int. 22, S101−S103.

Wallner, G., 1997. Simultaneous determination of ^{210}Pb and ^{212}Pb progenies by liquid scintillation counting. Appl. Radiat. Isot. 48, 511−514.

Wallner, G., 2002. Determination of ^{226}Ra, ^{228}Ra and ^{210}Pb in drinking water using liquid scintillation counting. In: Möbius, S., Noakes, J.E., Schönhofer, F. (Eds.), Advances in Liquid Scintillation Spectrometry, 2001. Radiocarbon Publishers, University of Arizona, Tucson, pp. 269−274.

Wallner, G., Wagner, R., Katzlberger, C., 2008. Natural radionuclides in Austrian mineral water and their sequential measurement by fast methods. J. Environ. Radioact. 99, 1090−1094.

Walter, K., Trautmann, N., Herrmann, G., 1993. Simultaneous determination of strontium-90 and strontium-89 by Cerenkov-radiation and liquid-scintillation counting: a re-evaluation for low-level counting. Radiochim. Acta 62, 207−212.

Wang, J.-J., Chen, I.-J., Chiu, J.-H., 2004. Sequential isotopic determination of plutonium, thorium, americium, strontium and uranium in environmental and bioassay samples. Appl. Radiat. Isot. 61, 299−305.

Wang, X.M., He, M., Ruan, X.D., Xu, Y.N., Shen, H.Z., Du, L., Xiao, C.J., Dong, K.X., Jiang, S., Yang, X.R., Lan, X.X., Wu, S.Y., Zhao, Q.Z., Cai, L., Pang, F.F., 2015. Measurement of ^{59}Ni and ^{63}Ni by accelerator mass spectrometry at CIAE. Nucl. Instrum. Method, Sect. B 361, 34−38.

Wang, Y.D., Yang, Y.G., Song, L.Y., Ma, Y., Luo, M.Y., Dai, X., 2018. Effects of sodium salicylate on the determination of Lead-210/Bismuth-210 by Cerenkov counting. Appl. Radiat. Isot. 139, 175−180.

Wanke, C., Kossert, K., Nahle, O., 2012. Investigations on TDCR measurements with the HIDEX 300 SL using a free parameter model. Appl. Radiat. Isot. 70 (9), 2176−2183.

Waples, J.T., Benitez-Nelson, C., Savoye, N., Rutgers van der Loeff, M., Baskaran, M., Gustafsson, Ö., 2006. An introduction to the application and future use of ^{234}Th in aquatic systems. Mar. Chem. 100, 166–189.

Warwick, P.E., Croudace, I.W., 2002a. Separation of Fe-55/59 from fission and activation products using a di isobutylketon based extraction chromatographic materials. In: Warwick, P. (Ed.), Proceedings of International Symposium on Environmental Radiochemical Analysis, Maidstone (GB), 18-20 Sep 2002. Royal Society of Chemistry, Cambridge.

Warwick, P.E., Croudace, I.W., 2002b. Measurement of gross alpha & beta activities in acid leachates using alpha-beta discriminating liquid scintillation counting. In: Möbius, S., Noakes, J.E., Schönhofer, F. (Eds.), Advances in Liquid Scintillation Spectrometry, 2001. Radiocarbon Publishers, University of Arizona, Tucson, pp. 75–82.

Warwick, P.E., Croudace, I.W., 2006. Isolation and quantification of ^{63}Ni and ^{55}Fe in reactor effluents using extraction chromatography and liquid scintillation analysis. Anal. Chim. Acta 567, 277–285.

Warwick, P.E., Cundy, A.B., Croudace, I.W., Bains, M.F.D., Dale, A.A.(, 2001. The uptake of iron-55 by marine sediment, macroalgae, and biota following discharge from a nuclear power station. Environ. Sci. Technol. 35, 2171–2177.

Warwick, P.E., Croudace, I.W., Hilegonds, D.J., 2009. Effective determination of the long-lived nuclide Ca-41 in nuclear reactor bioshield concretes: comparison of liquid scintillation counting and accelerator mass spectrometry. Anal. Chem. 81, 1901–1906.

Warwick, P.E., Kim, D., Croudace, I.W., 2010. Effective desorption of tritium diverse solid matrices and its application to routine analysis of decommissioning materials. Anal. Chim. Acta 676 (1–2), 93–102.

Wätjen, U., Benedik, L., Spasova, Y., Vasile, M., Altzitzoglou, T., Beyermann, M., 2010. EC comparison on the determination of ^{226}Ra,^{228}Ra, ^{234}U and ^{238}U in water among European monitoring laboratories. Appl. Radiat. Isot. 68, 1200–1206.

Werner, E., Roth, P., Wendler, I., Schramel, P., Hellmann, H., Kratzel, U., 1997. Feasibility of ICP-MS for the assessment of uranium excretion in urine. J. Radioanal. Nucl. Chem. 226, 201–203.

Whittaker, E.L., Akridge, J.D., Giovino, J., 1987. Two Test Procedures for Radon in Drinking Water: Interlaboratory Collaborative Study. US EPA Environmental Monitoring Systems Laboratory, Office of Research and Development, Las Vegas. EPA 600/2-87/082.

WHO, 2009. In: Zeeb, H., Shannoun, F. (Eds.), WHO Handbook on Indoor Radon - A Public Health Perspective. World Health Organization, Geneva, 95 pp.

WHO, 2011. Guidelines for Drinking-Water Quality, fourth ed. World Health Organization, Geneva. 541 pp.

Wiegand, J., Gellerman, R., Schott, B., 2000. Measuring radon and radium in water. Strahlenschutzpraxis 1, 54–57.

Wigley, F., Warwick, P.E., Croudace, I.W., Caborn, J., Sanchez, A.L., 1999. Optimised method for the routine determination of technetium-99 in environmental samples by liquid scintillation counting. Anal. Chim. Acta 380, 73–82.

Wilken, R.D., Diehl, R., 1987. Strontium-90 in environmental samples from Northern Germany before and after the Chernobyl accident. Radiochim. Acta 41, 157–162.

Wilken, R.D., Joshi, S.R., 1991. Rapid methods for determining ^{90}Sr, ^{89}Sr and ^{90}Y in environmental samples: a survey. Radioact. Radiochem. 2, 14–27.

Williams, D.F., ÓKelly, G.D., Knauer, J.P., 1994. Flowsheet for the recovery and purification of ^{63}Ni. Radiochim. Acta 64, 49–55.

Wilson, J.E., McCormac, F.G., Hogg, A.G., 1996. Small sample high-precision ^{14}C dating: characterization of vials and counter optimization. In: Cook, G.T., Harkness, D.D., MacKenzie, A.B., Miller, B.F., Scott, E.M. (Eds.), Advances in Liquid Scintillation Spectrometry, 1994. Radiocarbon Publishers, University of Arizona, Tucson, pp. 59–65.

Winyard, R., Lutkin, J.E., McBeth, G.W., 1971. Pulse shape discrimination in inorganic and organic scintillators. Nucl. Instrum. Methods Phys. Res. 95, 141–154.

Wisser, S., Frenzel, E., Dittmer, M., 2006. Innovative procedure for the determination of gross-alpha/gross-beta activities in drinking water. Appl. Radiat. Isot. 64, 368–372.

Wu, J., Boyle, E.A., 1997. Lead in the western North Atlantic Ocean: completed response to leaded gasoline phaseout. Geochim. Cosmochim. Acta 61, 3279–3283.

Yalım, H.A., Sandıkcıoglu, A., Ünal, R., Orhun, Ö., 2007. Measurements of radon concentrations in well waters near the Aksehir fault zone in Afyonkarahisar, Turkey. Radiat. Meas. 42, 505–508.

Yamamoto, M., Sakaguchi, A., Sasaki, K., Hirose, K., Igarashi, Y., Kim, C.K., 2006. Seasonal and spatial variation of atmospheric ^{210}Pb and ^{7}Be deposition: features of the Japan Sea side of Japan. J. Environ. Radioact. 86, 110–131.

Yang, D., 1990. Study on Determination of Np, Pu, and Am with Extraction-Liquid Scintillation Counting and its Application to Assay of Transuranium Elements in High-Level Waste (Ph.D. thesis). Tsinghua University, Beijing, Peoples Republic of China.

Yang, D.Z., Gou, Y.F., Zhu, Y.J., 1995. Study on liquid scintillation technique for bioassay of plutonium. J. Radioanal. Nucl. Chem. 194, 177–183.

Yang, Y., Song, L., Luo, M., Dai, X., Guo, X., 2017. A rapid method for determining 90Sr in leaching solution from cement solidification of low and intermediate level radioactive wastes. J. Radioanal. Nucl. Chem 314, 477–482.

Yasuoka, Y., Ishii, T., Sanada, T., Nitta, W., Ishimori, Y., Kataoka, Y., Kubo, T., Suda, H., Tokonami, S., Ishikawa, T., Shinogi, M., 2005. Measurement of radon concentration in water using direct dpm method of liquid scintillation counter. Int. Congr. Ser. 1276, 299–300.

Yu-Fu, Y., Salbu, B., Bjørnstad, H.E., Lien, H., 1990. Improvement for alpha-energy resolution in determination of low level plutonium by liquid scintillation counting. J. Radioanal. Nucl. Chem. Lett. 145, 345–353.

Yu-Fu, Y., Bjørnstad, H.E., Salbu, B., 1992. Determination of plutonium-239 + plutonium-240 and plutonium-241 in environmental samples using low-level liquid scintillation spectrometry. Analyst 117, 439–442.

Yunoki, S., Saito, M., 2009. A simple method to determine bioethanol content in gasoline using two-step extraction and liquid scintillation counting. Bioresour. Technol. 100, 6125–6128.

Zaborska, A., Carroll, J., Papucci, C., Pempkowiak, J., 2007. Intercomparison of alpha and gamma spectrometry techniques used in ^{210}Pb geochronology. J. Environ. Radioact. 93, 38–50.

Zamora, M.L., Tracy, B.L., Zielinski, J.M., Meyerhof, D.P., Moss, M.A., 1998. Chronic ingestion of uranium in drinking water: a study of kidney bioeffects in humans. Toxicol. Sci. 43, 68–77.

Zapata-García, D., Llauradó, M., Rauret, G., 2009. Establishment of a method for the rapid measurement of gross alpha and gross beta activities in sea water. Appl. Radiat. Isot. 67, 978–981.

Zaretskaia, N.E., Ponomareva, V.V., Sulerzhitsky, L.D., Zhilin, M.G., 2001. Radiocarbon studies of peat bogs: and investigation of South Kamchatka volcanoes and Upper Volga archaeological sites. Radiocarbon 43, 571–580.

Zelensky, A.V., Buzinny, M.G., Los', I.P., 1993. Measurements of ^{226}Ra, ^{222}Rn and uranium in Ukrainian groundwater using ultra low-level liquid scintillation counting. In: Noakes, J.E., Schönhofer, F., Polach, H.A. (Eds.), Liquid Scintillation Spectrometry, 1992. Radiocarbon Publishers, University of Arizona, Tucson, pp. 405–411.

Zerle, L., Faestermann, T., Knie, K., Korschinek, G., Nolte, E., 1997. The ^{41}Ca bomb pulse and atmospheric transport of radionuclides. J. Geophys. Res. 102 (D16), 19517.

Zhang, F., Parker, J.C., Brooks, S.C., Watson, D.B., Jardine, P.M., Gu, B., 2010. Prediction of uranium and technetium sorption during titration of contaminated acidic groundwater. J. Hazardous Mater. 178, 42–48.

Zhang, L.Y., Hou, X.L., Xu, S., 2015. Speciation analysis of 129I and 127I in aerosol using sequential extraction and mass spectrometry detection. Anal. Chem. 87 (13), 6937–6944.

Zheng, J., Tagami, K., Uchida, S., 2013. Release of plutonium isotopes into the environment from the Fukushima Daiichi Nuclear Power Plant accident: what is known and what needs to be known. Environ. Sci. Technol. 47, 9584–9595.

Zikovsky, L., 2002. Determination of alpha-radioactivity in ground water by precipitation of alpha-emitters with sulphates and hydroxides. J. Radioanal. Nucl. Chem. 251, 329–331.

Zoriy, M.V., Froning, M., Hill, P., 2016. Development and validation of a robust analytical method for the determination of ^{51}Cr in blood samples by liquid scintillation counting (LSC). J. Radioanal. Nucl. Chem. 310 (3), 1299–1302.

Zoriy, M.V., Varga, Z., Pickhardt, C., Ostapczuk, P., Hille, R., Halicz, L., Segal, I., Becker, J.S., 2005. Determination of ^{226}Ra at ultratrace level in mineral water samples by sector field inductively coupled plasma mass spectrometry. J. Environ. Monit. 7, 514–518.

Zoriy, P., Ostapczuk, P., Dederichs, H., Höbig, J., Lennartz, R., Zoriy, M., 2010. Biomonitoring of environmental pollution by thorium and uranium in selected regions of the Republic of Kazakhstan. J. Environ. Radioact. 101, 414–420.

Zulauf, A., Happel, S., Mokili, M.B., Bombard, A., Jungclas, H., 2010. Characterization of an extraction chromatographic resin for the separation and determination of Cl-36 and I-129. J. Radioanal. Nucl. Chem. 286, 539–546.

Xiaolin Hou



Xiaolin Hou is a Full Professor of the Technical University of Denmark (DTU) and Lanzhou University. His primary research interests include radioanalytical chemistry, characterization of decommissioning waste, speciation analysis of radionuclides and its application in environmental and geological sciences, environmental radioactivity and radioecology, measurement techniques of radionuclides including LSC, alpha and gamma spectrometry, ICP-MS, and AMS. Prof. Hou has led and actively participated in more than 30 research projects funded by EU, Nordic, Denmark, China, Norway, and Sweden. He is the author and coauthor of more than 220 papers in peer-reviewed scientific journals with an SCI total citation of more than 3200 times and *h*-index of 32. He has also published one monograph, written six chapters for books. He is now a nominated committee member of the Division of Nuclear and Radiochemistry of the EUChemS, associated editor of the *Journal of Environmental Radioactivity*, and editor board member of Scientific Reports, *Journal of Radioanalytical and Nuclear Chemistry*, and other three journals (e-mail: xiho@dtu.dk).

Xiongxin Dai



Xiongxin Dai earned his B.Sc. and M.Sc. degrees in Radiochemistry from Lanzhou University, China, and obtained a Ph.D. degree from the Institute of High Energy Physics, Chinese Academy of Sciences. He is presently a Principal Radiochemist and Director of the Nuclear and Radiation Frontier Technology Research Center at the China Institute for Radiation Protection. He worked as a postdoctoral fellow at the University of Vienna (Austria) and Oxford University (UK). He was also a senior research associate at Carleton University and Queen's University in Canada. Lately, he was the head of the Radiochemistry Section of Radiological Protection Research Branch at Chalk River Laboratories, Atomic Energy of Canada Limited. His research activities have included radioanalytical chemistry and related applications in the areas of radiological protection, environmental monitoring, environmental sciences, neutrino physics, geochemistry, etc. He has developed numerous radioanalytical methods for rapid and sensitive determination of difficult-to-detect radionuclides in various environmental and biological samples.

Chapter 3

PERPUSTAKAAN PRIBADI AN-NUR SUNARYA

Analysis of environmental radionuclides

Miroslav Ješkovský[1], Jakub Kaizer[1], Ivan Kontul'[1], Galina Lujanienė[2], Monika Müllerová[1] and Pavel P. Povinec[1]

[1]*Comenius University, Faculty of Mathematics, Physics and Informatics, Department of Nuclear Physics and Biophysics, Bratislava, Slovakia;*
[2]*SRI Center for Physical Sciences and Technology, Vilnius, Lithuania*

Chapter outline

I. Introduction **138**
II. Environmental radionuclides **138**
A. Primordial radionuclides 138
B. Radiogenic radionuclides 140
C. Cosmogenic radionuclides 143
D. Anthropogenic radionuclides 146
1. Nuclear weapons testing 146
2. Nuclear reactors 147
3. Nuclear fuel reprocessing plants 149
4. Nuclear accidents 149
5. Specific anthropogenic radionuclides 153
III. Radionuclide compartments **158**
A. Atmosphere 158
B. Hydrosphere 160
C. Biosphere 162
D. Pedosphere 163
IV. Analytical techniques **164**
A. Radiometric techniques 164
1. Alpha spectrometry 164
2. Beta counting 164
3. Gamma spectrometry 166
B. Low-energy inorganic mass spectrometry 167
1. Inductively coupled plasma mass spectrometry 167
2. Thermal ionization mass spectrometry 169
3. Resonance ionization mass spectrometry 169
4. Glow discharge mass spectrometry 170
5. Secondary ion mass spectrometry 170
6. ^{3}H-^{3}He ingrowth mass spectrometry 170
7. Positive-ion mass spectrometry 171
C. Accelerator mass spectrometry 171
1. Ion separation in accelerator mass spectrometry 171
2. Ion source 172
3. Injection system 173
4. Tandem accelerator 174
5. High-energy analyzer and ion detection 174
V. Radionuclide analyses **175**
A. Radioactive gases 175
1. Radiocarbon 175
2. Tritium 180
3. Argon, krypton, and xenon 183
4. Radon 187
B. Radionuclides on aerosols 189
1. Properties of aerosols 189
2. Sampling of aerosols 190
3. Examples of radionuclides on aerosols 191
C. Radionuclides in freshwater systems 199
1. Sampling of water 200
2. Examples of radionuclides in water systems 201
D. Radionuclides in soil 208
1. Preparation of soil samples for radionuclide analysis 208
2. Examples of radionuclides in soil 209
E. Radionuclides in biota 210
1. Radiocarbon and tritium 211
2. Radiocesium and radiostrontium 212
3. Radioiodine 213
F. Analysis of actinides 214
1. Sampling and pretreatment 215
2. Separation of actinides 216
3. Extraction chromatography 219
4. Multistage extraction chromatography column methods 221
5. Combined procedures for the determination of neptunium and other actinides 223
6. Source preparation 225
7. Examples of actinides in the environment 226
VI. International networks for monitoring of environmental radionuclides **233**
A. International monitoring system of CTBTO 233
B. European network "Ring of Five" 234
VII. Conclusions **234**
Acknowledgments **235**
References **235**
Miroslav Ješkovský **259**
Jakub Kaizer **259**
Ivan Kontul' **260**
Galina Lujanienė **260**
Monika Müllerová **260**
Pavel P. Povinec **261**

Handbook of Radioactivity Analysis: Volume 2. https://doi.org/10.1016/B978-0-12-814395-7.00003-9
Copyright © 2020 Elsevier Inc. All rights reserved.

I. Introduction

All nuclides that are nowadays present in the environment are either stable or unstable. The stability of any nucleus is determined by the number of neutrons and protons in its structure. A radioactive nuclide, or in short, radionuclide, is an unstable nuclide composed of the nucleus with the out of balance number of neutrons. Such nuclides have excess energy, which they sooner or later loose by decay processes, leading to the emission of gamma rays or subatomic particles, i.e., radiation. Depending on a particular radionuclide, it can either decay to a stable nuclide or another radioactive one, however, the ultimate fate of every radionuclide ever made is to become stable. If we do not count rare processes such as internal transition, a daughter nuclide is always a different element than its parent.

Although more than 100 years have passed since the discovery of radioactivity, many people still believe that radioactivity and exposure to radiation are problems, which emerged with the dawn of the nuclear era in the previous century, first of all due to nuclear weapon explosions and nuclear reactor accidents. Radionuclides are a natural part of the environment; they are continuously produced in the atmosphere, Earth's crust, or brought to our planet from the outer space, e.g., as a part of meteorites. From the place of their production, they can be distributed to other spheres of the environment by different transfer paths. It is not audacious to say that there is no material on Earth that does not contain any radionuclides. Furthermore, all living organisms, including humans take up millions of unstable nuclides by breathing, eating, and drinking every day without even noticing it, though amounts of inhaled/ingested radionuclides can significantly vary, as their concentration is dependent on location and time.

More than 340 nuclides were discovered on Earth, from which more than 90 nuclides are radioactive. Additionally, more than a 1000 nuclides have been synthesized in laboratories, although most of them are unstable. Elements with the atomic number greater than 83 do not form stable isotopes at all, which also applies to technetium ($Z = 43$).

Investigations of radionuclides in the environment have had a long tradition. Actually, we may say that papers published by Maria Curie after the discovery of radioactivity (e.g., on radium, polonium, etc.) were the first dealing with environmental radionuclides. Similarly, the first papers by George de Hevesy discussed environmental radionuclides, which later led to the discovery of natural radionuclides as tracers of environmental processes.

We shall cover in this chapter the analysis of radionuclides in the terrestrial environment as the marine environment is covered in Chapter 5, Volume 2.

II. Environmental radionuclides

All radioactive nuclides found in the environment can be divided into four main categories:

- Primordial—created during the formation of Earth
- Radiogenic—daughter radionuclides of primordial ones
- Cosmogenic—produced by interactions of cosmic ray particles with elements on Earth or in extraterrestrial materials
- Anthropogenic—produced during human nuclear activities

The first three groups could also be called as natural radionuclides, as they all were either formed during the nucleosynthesis (primordial radionuclides) and, because of their long half-lives, they can be still found in the environment or they have been permanently produced in the environment due to decay chains of primordial radionuclides (therefore, we call them radiogenic radionuclides), or they have been permanently produced on Earth by interactions of cosmic ray particles (cosmogenic radionuclides). Anthropogenic radionuclides form a special group produced from time to time by human activities, and not all of them can be found in the environment because of their short half-lives, production mechanisms, or ways of their possible releases to the environment.

An essential condition for the analysis of anything is to comprehensively understand the subject to be analyzed. In the following sections, we shall briefly characterize specificity and relevance of each group of radionuclides mentioned above. While focusing on the most important ones, we shall also describe basic properties, origin, abundance, and general distribution of selected environmental radionuclides, which are routinely analyzed by techniques discussed later in this chapter.

A. Primordial radionuclides

Primordial radionuclides were created about 4.5 billion years ago when the Sun and all planets of our solar system were formed. During the first stage of nucleosynthesis, which consisted of nuclear reactions initiated mainly by protons and alpha particles, the light stable and radioactive nuclides with mass numbers less than 60 were created. Heavier elements, i.e., those with mass numbers between 60 and 90, were primarily produced by capturing neutrons and subsequent emissions of beta particles. Neutron capture reactions also resulted in the formation of the heaviest nuclei ($Z \geq 92$), which could decay by emission of alpha particles or undergo nuclear fission because of high-repulsive Coulomb force. However, only

dozens of primordial radionuclides have survived until now, as most of them having half-lives much shorter than the time that passed since the nucleosynthesis simply decayed. These naturally occurring radionuclides either decay directly to stable nuclides or initiate decay chains (uranium, thorium, and actinium series). Summary of known primordial radionuclides with half-lives less than 1×10^{18} y is presented in Table 3.1. With the exception of ^{40}K, ^{87}Rb, uranium, and thorium, they are insignificant in terms of environmental concentrations and delivered radiation doses.

Due to the high abundance and ubiquity of potassium and due to the relatively high specific activity of ^{40}K (and a relatively short half-life of 1.25×10^9 y), its total activity in the Earth's crust and surface ocean substantially exceeds the cumulative activity of all other natural radionuclides (Table 3.1). The mean concentration of potassium in the lithosphere and surface seawater is roughly 2.09% and 3.99×10^2 mg L^{-1}, respectively, though its concentration in soils can vary substantially (UNSCEAR, 2000). ^{40}K is also present in living organisms with a content of about 0.2% of total potassium, which means that average humans, animals, and plants have approximately 60 Bq kg^{-1} of ^{40}K in their bodies (Yamagata, 1962). The biological half-life of ^{40}K, which is equal to the time of eliminating 50% of the radionuclide activity from the body, is about 30 days. From the chemical point of view, potassium is present in the environment almost exclusively in the form of monopositive cation (K^+), primarily because of its tendency to be easily oxidized. Primordial ^{40}K decays to stable ^{40}Ca while emitting beta particles with the maximum energy of 1.311 MeV or, with a much lower probability, to the excited state of the inert gas ^{40}Ar after capture of a K electron, followed by gamma ray emission with the energy of 1.461 MeV. The latter process is exploited in the K-Ar radiochronometric method, commonly used for dating in geochronology (Dalrymple and Lanphere, 1969; Turner et al., 1994; Schaeffer and Zähringer, 2012).

Natural rubidium consists of one stable, ^{85}Rb, and one radioactive primordial isotope, ^{87}Rb ($T_{1/2} = 4.97 \times 10^{10}$ y), which decays to ^{87}Sr purely by emission of beta particles with the maximum energy of 0.274 MeV. As rubidium is, same as potassium, part of the alkali metals group, they have similar physicochemical properties, leading to a fact that potassium is often replaced by rubidium in various chemical compounds. Moreover, both elements naturally accompany each other in different spheres of the environment. After ^{238}U, ^{232}Th and ^{187}Re, radioactive ^{87}Rb has the third highest specific activity among all primordial radionuclides, and this is the reason why its activity in the Earth's crust and surface seawaters is only one to two orders lower than the ^{40}K activity, even though potassium is much more abundant than rubidium in the respective compartments (Table 3.1). Total activity of ^{87}Rb in a human body (mass of 70 kg), in which it is assumed to behave comparable to potassium, is estimated to be roughly 300 Bq (Yamagata, 1962).

Two primordial uranium isotopes, ^{235}U ($T_{1/2} = 7.04 \times 10^8$ y) and ^{238}U ($T_{1/2} = 4.47 \times 10^9$ y) together with ^{232}Th ($T_{1/2} = 1.40 \times 10^{10}$ y), create three distinctive decay series (Figs. 3.1–3.3), comprising altogether 42 daughter radionuclides and 3 different stable isotopes of lead. The neptunium radioactive decay series is now extinct due to the short half-life (2.14×10^6 y) of the mother nuclide ^{237}Np, leaving only the very last nuclide, ^{209}Bi ($T_{1/2} = \sim 2 \times 10^{19}$ y), as a reminiscence of the existence of the series. The ^{235}U/^{238}U ratio in nature is considered to be stable, meaning that ^{235}U and ^{238}U make 0.72% and 99.27% of all naturally occurring uranium in the environment, respectively. The mean concentration of uranium in the lithosphere is 2.7 mg kg^{-1}. From about 200 of recognized uranium minerals, only several can be found in the form of ore, e.g., uraninite (UO_2), pitchblende (mixture of UO_2 and UO_3) or carnotite ($K_2(UO_2)_2(VO_4)_2 \cdot 3H_2O$). While the amount of uranium in terrestrial waters varies from less than 1 μg L^{-1} to a few mg L^{-1} (Lehto and Hou, 2011), it is quite homogenously distributed in the oceans ($\sim$3 μg L^{-1}). Because of this and the enormous volume of seawater present on Earth (some 1.3×10^9 km^3), oceans have been suggested as a potential future source of uranium for the nuclear industry (Kim et al., 2013; Kuo et al., 2015). Uranium can also undergo spontaneous fission, which leads to the production of fission productions of natural origin, such as ^{90}Sr or ^{99}Tc (Curtis et al., 1999; Tykva and Berg, 2004), though the probability for the process to occur is very low (5.5×10^{-5}% for ^{238}U).

Although an average thorium content in the bedrock (9.6 mg kg^{-1}) is about four times higher than that of uranium, their contribution to the natural radioactivity background is very similar due to much lower specific activity of ^{232}Th (Table 3.1), which represents approximately 99.9995% of the overall mass of thorium. Minerals containing exclusively thorium are very rare and are often found mixed with uranium. Monazite, in which thorium can comprise up to 12%, is considered as the main source of this element (Lehto and Hou, 2011). Unlike the case of uranium, the concentration of thorium in seawater is only $\sim$1 ng L^{-1}, which is roughly three orders of magnitude lower than the typical value for oxic groundwater bodies. In general, thorium is poorly soluble. In seawater, thorium is mostly in particulate form; therefore, it can be found in biological systems mostly in very low amounts. On top of that, removal of thorium from bones was observed to be

TABLE 3.1 Primordial radionuclides and their characteristics.

Nuclide	Half-life (years)	Decay mode	Relative abundance (%)	Specific activity (Bq g^{-1} of element)	Activity in Earth's crust (Bq kg^{-1})	Activity in surface seawater (Bq L^{-1})
^{40}K	1.25×10^{9}	β^-, EC	0.0117	3.10×10^{1}	6.47×10^{2}	1.24×10^{1}
^{50}V	2.0×10^{17}	EC (>93%)	0.250	3.31×10^{-6}	3.97×10^{-7}	8.27×10^{-12}
^{87}Rb	4.97×10^{10}	β^-	27.83	8.52×10^{2}	7.66×10^{1}	1.02×10^{-1}
^{113}Cd	8.04×1^{15}	β^-	12.23	1.78×10^{-3}	2.67×10^{-7}	1.96×10^{-10}
^{115}In	4.4×10^{14}	β^-	95.72	2.50×10^{-1}	6.26×10^{-5}	5.01×10^{-6}
^{123}Te	$>9.2 \times 10^{16}$	EC	0.89	1.04×10^{-5}		
^{138}La	1.06×10^{11}	β^-, EC	0.089	8.05×10^{-1}	3.14×10^{-2}	2.74×10^{-9}
^{144}Nd	2.1×10^{15}	α	23.80	1.04×10^{-2}	4.32×10^{-4}	2.92×10^{-11}
^{147}Sm	1.06×10^{11}	α	14.99	1.27×10^{2}	8.97×10^{-1}	5.73×10^{-8}
^{148}Sm	7.0×10^{15}	α	11.24	1.44×10^{-3}	1.01×10^{-5}	6.46×10^{-13}
^{149}Sm	$\sim 10^{16}$	α	13.82	1.23×10^{-3}	8.65×10^{-6}	5.52×10^{-13}
^{156}Dy	$>6.1 \times 10^{14}$	EC-EC	0.056	7.79×10^{-5}	4.05×10^{-7}	7.09×10^{-14}
^{174}Hf	2.0×10^{15}	α	0.16	6.08×10^{-5}	1.83×10^{-7}	4.26×10^{-13}
^{176}Lu	3.73×10^{10}	β^-, β^+, EC	2.59	5.22×10^{1}	4.18×10^{-2}	7.83×10^{-9}
^{180m}Ta	$>2.0 \times 10^{16}$	β^-, EC	0.012	4.41×10^{-7}	8.82×10^{-10}	8.82×10^{-16}
^{186}Os	2×10^{15}	α	1.59	5.66×10^{-4}		
^{187}Re	4.16×10^{10}	β^-	62.60	1.06×10^{3}	7.45×10^{-4}	4.26×10^{-6}
^{190}Pt	4.5×10^{11}	α	0.012	1.86×10^{-2}		
^{232}Th	1.40×10^{10}	α	100.0	4.07×10^{3}	3.91×10^{1}	4.07×10^{-6}
^{235}U	7.04×10^{8}	α	0.720	5.76×10^{2}	1.55	1.84×10^{-3}
^{238}U	4.47×10^{9}	α	99.27	1.24×10^{4}	3.34×10^{1}	3.96×10^{-2}

After Haynes (2017).

quite slow, leading to its accumulation with increasing age (Eisenbud and Gessel, 1997).

B. Radiogenic radionuclides

As already stated earlier, radiogenic radionuclides are part of three decay series, which all start with decay of primordial isotopes of uranium (^{235}U, ^{238}U) and thorium (^{232}Th). Interestingly, each series contains a radioactive isotope of radon, namely, actinon (^{219}Rn), thoron (^{220}Rn), and radon (^{222}Rn) and ends with a stable isotope of lead. Radiogenic radionuclides are produced by alpha- and beta transformations, though many of these radionuclides are also gamma emitters. Their half-lives cover a wide range, from several hundreds of microseconds (^{212}Po) to hundreds of thousands of years (^{234}U). More than 68% of the world annual average dose can be attributed to products of the radioactive natural decay series (UNSCEAR, 1988); however, only a few of them are really important from the radiological point of view.

In a closed system, activities of mother and daughter radionuclides of natural decay series, which are directly linked through subsequent decay, can reach equilibrium. The difference between the production from decay of its parent radionuclide and its respective decay into a next nuclide is equivalent to the activity of a progeny radionuclide. However, the ultimate condition for such a steady state to occur is that no radionuclides are delivered in or released from the system, which is rarely met in the environment (Ivanovich and Harmon, 1992; Ivanovich, 1994). If the half-life of the parent radionuclide (e.g., ^{210}Pb, $T_{1/2} = 22.6$ y) is substantially longer than the half-life of its daughter (^{210}Bi, $T_{1/2} = 5.01$ d), a so-called secular equilibrium can be achieved, which can be exploited for the

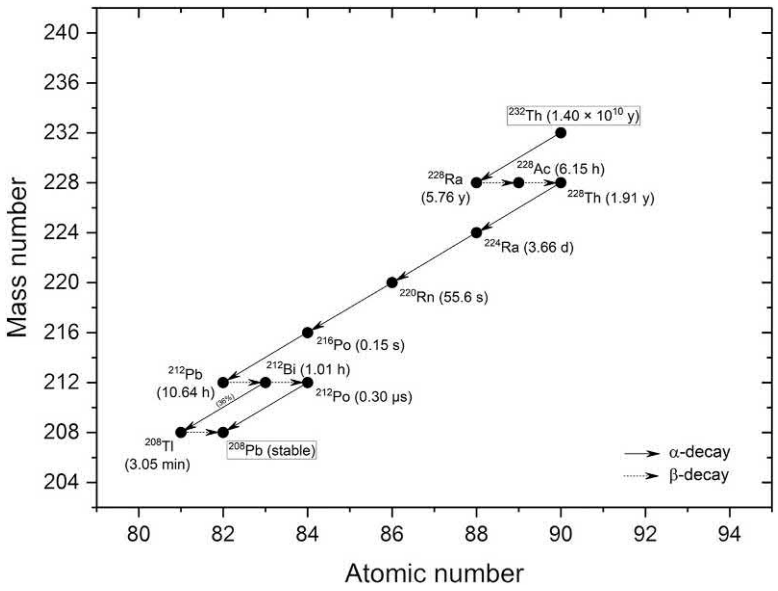


FIGURE 3.1 Thorium (^{232}Th) decay chain.

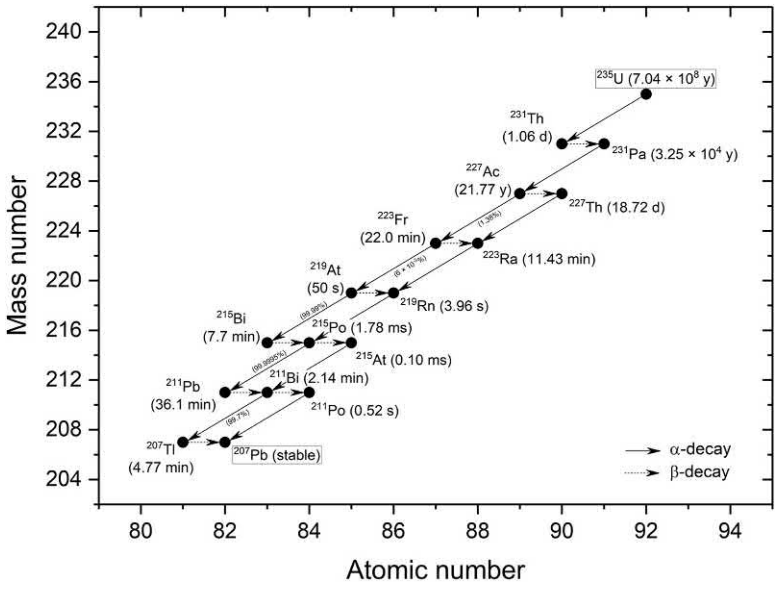


FIGURE 3.2 Uranium (^{235}U) decay chain.

determination of the activity of some hard-to-analyze radionuclides (Larivière and Guérin, 2010). Transient equilibrium is achievable when the half-lives of the mother and its daughter are quite comparable, e.g., in the case of ^{214}Bi ($T_{1/2} = 19.7$ minutes) and ^{210}Tl ($T_{1/2} = 1.30$ minutes), leading to a scenario in which both radionuclides would decay completely during their measurement. On the other hand, if the half-life of the parent radionuclide is shorter than that of the progeny, equilibrium cannot be accomplished under any circumstances.

The first crucial radiogenic radionuclide to discuss is ^{226}Ra ($T_{1/2} = 1.60 \times 10^3$ y), a decay product of long-lived ^{230}Th ($T_{1/2} = 7.56 \times 10^4$ y), which is part of the uranium decay series (Fig. 3.3), and while it is an almost pure alpha emitter, its contribution to the natural radiation exposure is insignificant, the opposite can be said for its beta- and gamma-emitting daughter nuclides. Various amounts of radium can be found in all types of rocks and soils, its mean lithospheric content is ~33 Bq kg^{-1} (Fukai and Yokoyama, 1982). Sandstones and limestones have generally by a factor of 2–3 lower activity concentration of ^{226}Ra than igneous rocks (Rankama and Sahama, 1950). Despite the earlier assumptions, it was shown that the content of ^{226}Ra in waters may be in near

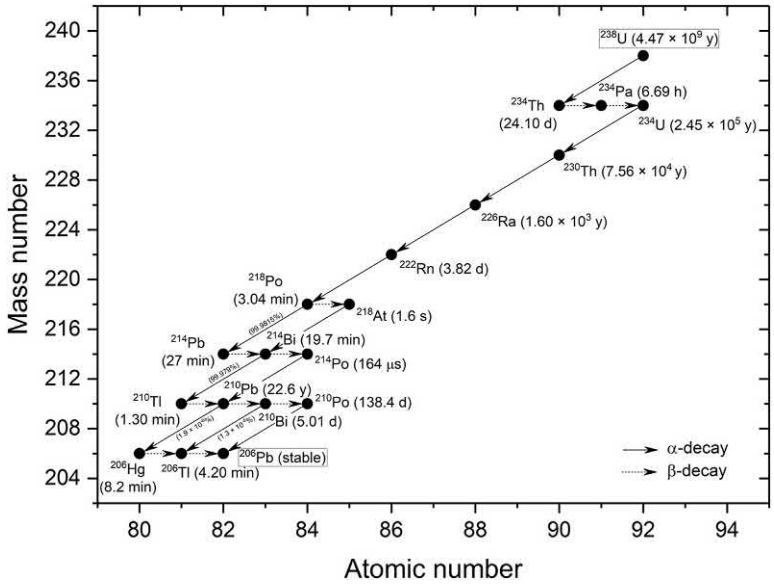


FIGURE 3.3 Uranium (^{238}U) decay chain.

equilibrium with ^{228}Ra ($T_{1/2} = 5.76$ y) originating from the thorium decay series. The mean surface water concentration of ^{226}Ra is much lower if compared to groundwater where it can be as high as around 900 Bq m^{-3} (Hess et al., 1985). The oceans contain even less radium (8.9×10^{-11} mg L^{-1} in average), which means that it is the third least abundant element determined in this particular reservoir. From the chemical point of view, radium is very close to calcium and barium; it is therefore transferred from soil and through the food chain in a similar way. However, due to the considerable variability of radium concentration in soil, its content in foods differs as well.

Even though there are three distinctive isotopes of radon produced in natural decay series, the most important one is ^{222}Rn ($T_{1/2} = 3.82$ d), which is a progeny of ^{226}Ra, discussed above. Radon decays by alpha particle emission, while also generating gamma rays with very low probability (<0.08%). Together with its mainly short-lived daughters (Fig. 3.3), radon's contribution to the world annual dose from background radiation is on the level of 1.2 mSv, representing roughly 50% of the overall dose (UNSCEAR, 1988). After smoking of tobacco products, radon has been recognized as the main source of lung cancer, responsible for tens of thousands of diseases worldwide (Tracy, 2010). Because of this, many countries have established national programs for the reduction of population exposure to radon. Such a nonnegligible effort usually requires conducting an extensive survey to determine radon levels at different places, e.g., at residential areas, like houses, schools, or kindergartens (Müllerová et al., 2016). As an example of results from this type of scrutiny, the mean indoor radon activity concentration of various buildings measured in Central European countries is depicted in Fig. 3.4.

Being a noble (inert) gas and having a relatively long half-life give radon some unique properties. First, it is extremely mobile and can be easily transported through the all spheres of the environment. After radon is generated by decay of solid radium in soil or rocks, it enters the porous system of the geologic body. While a part of the ^{222}Rn decays, the other fraction is either dissolved in water present in the capillary spaces or is released into the atmosphere together with soil gas. Radon can diffuse from soil gas to the air in the atmosphere, though this mechanism is much less relevant. Long-distant transport of radon is also

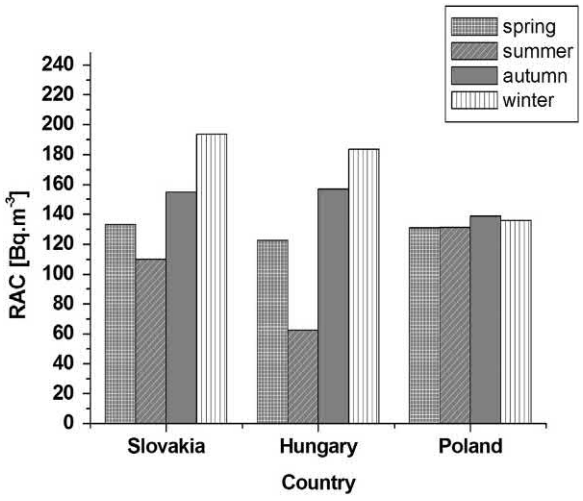


FIGURE 3.4 Mean indoor radon activity concentration (RAC) measured in various buildings in Slovakia, Hungary, and Poland for the whole year. *From Müllerová et al. (2016).* Printed with permission © Elsevier 2018.

possible due to convection or tectonic breaks in rocks. Groundwater content of ^{222}Rn, which depends on the intensity of emanation (release of gaseous decay products) and diffusion, can be quite high because of its good solubility in water, principally controlled by temperature and level of mineralization (Wilhem et al., 1977). It is important to note that spreading of radon through the environment leads to spreading of its more radiologically dangerous daughters as well.

Concentration of ^{222}Rn in the pedosphere, atmosphere, and waters is affected by several different factors. In soil, radon content typically ranges from 4 to 40 kBq m^{-3} (Eisenbud and Gessel, 1997), depending on the content of ^{226}Ra, emanation rate, porosity, and humidity and showing a positive asymptotic correlation with the increasing depth. Great variability, resulting in diurnal and seasonal variations, can be also observed in the case of outdoor radon whose average activity concentration is 3−18 Bq m^{-3} (Masarik, 2009), which is mostly influenced by geographic location, meteorological conditions, and rate of radon exhalation from the soil surface. Increased ^{222}Rn content in groundwater, where a wide spectrum of its activity concentration was found (1−1000 kBq m^{-3}; Hess et al., 1980), is dominantly connected with elevated levels of radium in rock.

Among other progenies of radon, ^{210}Pb with its fairly long half-life (22.6 y) is one of more interesting ones. It is produced via decays of six short-lived alpha and beta emitters, being the mother of ^{210}Po ($T_{1/2} = 138.4$ d). The average content of ^{210}Pb in the atmosphere, where it is readily attached to aerosols and can be transported over long distances before decaying, is about 5×10^{-4} Bq m^{-3} (UNSCEAR, 2000). Furthermore, airborne lead can be effectively washed out by processes of dry and wet deposition, consequently reaching soil, freshwater, and marine reservoirs. Typical rainwater concentration of ^{210}Pb ranges from 37 to 370 Bq m^{-3}, with the mean value of ∼74 Bq m^{-3} (Sýkora et al., 2017). Due to the tendency of toxic lead to accumulate in the human body, absorbed ^{210}Pb is eliminated only slowly, resulting in its deposition in bones (Demayo et al., 1982). Moreover, both ^{210}Pb and ^{210}Po are especially hazardous for tobacco smokers, where their rib content was observed to be by a factor of 2 higher than for nonsmokers (Holtzman and Ilcewicz, 1966).

C. Cosmogenic radionuclides

Cosmogenic radionuclides are continuously produced by interaction of energetic cosmic ray particles with atomic nuclei present in the stratosphere and on the Earth's surface or even beneath it (Lal and Peters, 1967; Gosse and Phillips, 2001). They also include radionuclides induced in situ on extraterrestrial material (meteorites, interstellar dust, moon, planets), which is then driven by the force of Earth's gravity. Cosmic ray particle fluxes consist of primary particles and secondary particles, generated by reactions of the primary ones with the atmospheric nuclei (Fig. 3.5). At ground altitude levels (<3 km), the flux of primary particles is almost negligible, and production of cosmogenic radionuclides is almost exclusively caused by secondary particles (Masarik, 2009). The composition of the cosmic radiation at the Earth's orbit vastly depends on its origin. While galactic cosmic rays (GCRs) are mostly created outside the boundaries of our solar system, solar cosmic rays (SCRs) are emitted from the Sun itself.

Typical GCR flux is composed of protons (∼87%), ^{4}He nuclei (∼12%), high-energy electrons (<1%), and some heavier nuclei with the atomic number between 4 and 26, although the occurrence of even heavier elements was also observed (Simpson, 1983). The average energy of highly penetrating cosmic ray particles is around tens GeV, with

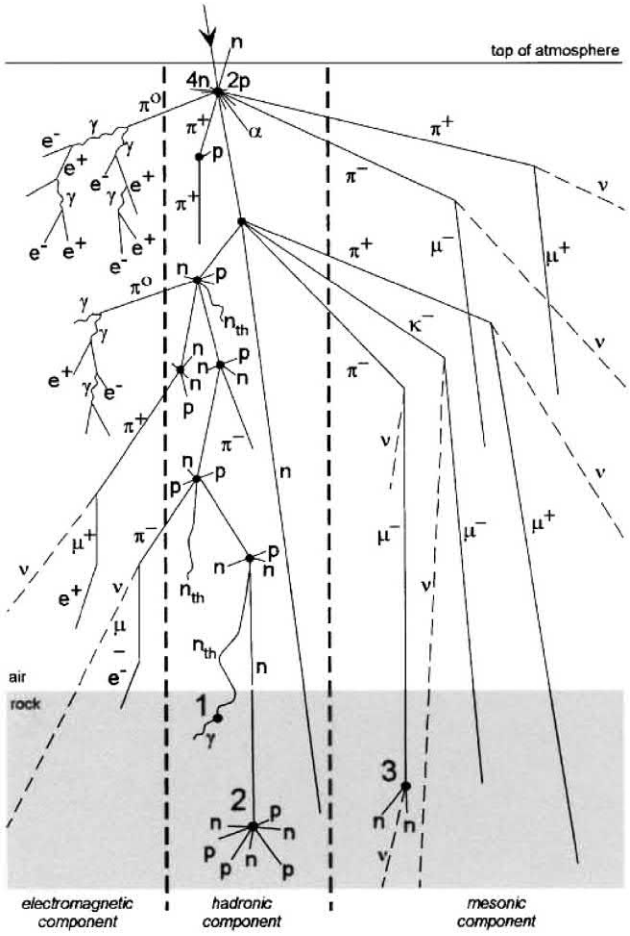


FIGURE 3.5 Production of secondary particles in the atmosphere and rock from cosmic ray extensive air shower. n, neutron; e, electron; p, proton; μ, muon; ν, neutrino; π, pion; γ, photon. Examples of in situ−produced cosmogenic radionuclides: (1) ^{35}Cl(n,γ)^{36}Cl; (2) ^{16}O(n,4p3n)^{10}Be; (3) ^{28}Si(n,p2n)^{26}Al. *From Gosse and Phillips (2001).* Printed with permission © Elsevier 2018.

the maximum energies of as much as 10^{11} GeV, though their spectral distribution is rather similar when compared with units of energy per nucleon. During the past several millions of years, the GCR flux intensity was constant within a factor of 2. On the contrary, the low-energy part of the GCR flux ($E < 1$ GeV nucleon^{-1}) varies significantly due to solar modulation, which is a result of interactions of approaching GCR particles with magnetic fields connected with the solar wind. The modulation becomes less effective with increasing energy of the particles.

In comparison with GCR, the SCR particles produced during solar particle events (e.g., solar eruptions) have substantially lower energy, i.e., on the level of 1−100 MeV. Because of this, they can interact with target nuclei only in the upper part of the atmosphere and at the northern or southern latitudes above 60 degrees where the shielding effect of the Earth's geomagnetic field is much weaker. The SCR particles are primarily composed of protons (~98%) and ^{4}He nuclei (~2%), whereas heavier nuclei or energetic electrons are not part of this type of extraterrestrial flux (Goswami et al., 1988). Strong temporal variations are observed in the case of the total SCR flux, with a mean value determined to be 75−100 nucleons cm^{-2} s^{-1} (Masarik, 2009). Overall, the long-term contribution of SCR to the production of cosmogenic radionuclides is quite small, with an exception when huge solar particle events happen, having a potential to locally enhance the generation of some radionuclides.

As indicated in the previous paragraph, primary and secondary particle fluxes depend on the latitude. The Earth's geomagnetic field and the atmosphere decrease the amount of incoming galactic or solar particles arriving at the surface of our planet. The efficiency of the magnetic fields to shield cosmic ray particles is a function of their energy, angle of incidence, and electric charge. If the particle energy is below the critical value, which is determined by angle of incidence and latitude, it is deflected by the geomagnetic field without reaching the surface. As a consequence, the production of cosmogenic radionuclides is more intensive around the magnetic poles and less intensive in the equatorial area (Lal and Peters, 1967; Masarik and Beer, 2009). Moreover, the altitudinal dependency of cosmic ray fluxes and subsequently the rate, at which radionuclides are produced, was observed as well. Secondary particles, generated by interaction of primary particles with atmospheric nuclei, have usually enough energy to propagate a hadronic cascade, resulting in the production of several generations of secondary particles. In this manner, the production intensity of induced cosmogenic radionuclides is maximal at the altitude of approximately 12−16 km, while steadily decreasing down to the sea level.

While there are tens of different cosmogenic radionuclides constantly produced, only part of them are truly interesting (Table 3.2). Their half-lives are of a wide range, from minutes (e.g., ^{34m}Cl) to more than 1 million years (^{10}Be). Cosmogenic radionuclides generated in the atmosphere act according to their physicochemical properties. In the gaseous form or as attached to aerosol, they are distributed by motion of air masses, and due to stratosphere−troposphere transport, they get to the lower parts of the atmosphere, and finally, they can be absorbed

TABLE 3.2 Characteristics of cosmogenic radionuclides.

Nuclide	Half-life	Decay mode	Production rate (10^{-3} atoms cm^{-2} s^{-1})[a]	Global inventory (PBq)[b]	Average concentration (10^{-3} Bq kg^{-1})[c]	
					Troposphere	Seawater
^{3}H	12.32 years	β^-	320	1300	1.2	7×10^{-1}
^{7}Be	53.28 days	EC	40	410	10	660
^{10}Be	1.39×10^{6} years	β^-	21	230		2×10^{-5}
^{14}C	5730 years	β^-	2050	12,000		5
^{22}Na	2.605 years	β^+	8.6×10^{-2}	0.44	1×10^{-3}	
^{26}Al	7.1×10^{5} years	β^+	1.4×10^{-1}	0.79		2×10^{-7}
^{32}Si	1.5×10^{2} years	β^-	1.6×10^{-1}	3.9		4×10^{-4}
^{32}P	14.28 days	β^-	8.1×10^{-1}	4.2	2.3×10^{-1}	
^{33}P	25.3 days	β^-	6.8×10^{-1}	3.5	1.3	
^{36}Cl	3.01×10^{5} years	β^-	2.1	5.6		1×10^{-2}

[a] *For ^{3}H, ^{7}Be, ^{10}Be, ^{14}C, and ^{36}Cl, from Masarik and Beer (2009); for the rest, from Lal and Peters (1967).*
[b] *From Lal and Peters (1967).*
[c] *From Eisenbud and Gessel (1997).*

by precipitation droplets and deposited on the Earth's surface. Therefore, the amount of precipitation can have significant influence on the concentration of these radionuclides at a particular site. On the other hand, some cosmogenic radionuclides have such short half-lives that they decay soon after their production; thus, they are irrelevant for scientific studies. The most salient cosmogenic radionuclides present in the environment are ^{3}H, ^{7}Be, and ^{14}C.

The heaviest naturally occurring isotope of hydrogen, tritium (^{3}H or T), is produced mainly in the lower parts of the stratosphere by the interaction of neutrons or protons with nitrogen and oxygen, i.e., dominantly in ^{14}N(n,T)^{12}C or ^{16}O(p,T)^{14}C reactions. Tritium is a pure beta emitter ($E_{max} = 18.6$ keV) with the relatively long half-life of 12.31 y, which enables its distribution through all spheres of the environment. Atmospheric tritium can be found in the form of gaseous water vapors (mostly as HTO or T_2O), molecular hydrogen (HT or T_2), and methane (e.g., CH_3T), all of which are easily incorporated into living organisms (Vichot et al., 2008). However, because tritiated methane is created in very low amounts and molecular hydrogen is rapidly oxidized into water, the only important form of ^{3}H in the atmosphere are water vapors (HTO), which participate in the hydrological cycle. As a part of water vapors, tritium is transferred onto the Earth's surface by precipitation and exchange between the atmospheric moisture and hydrosphere. Since diffusion characteristics of H_2O and HTO are almost the same, tritium is also found in groundwater. Activity concentration of tritium in waters is often expressed in tritium units (TU), where 1 TU is equivalent to the activity of 0.119 Bq L^{-1} or ^{3}H/^{1}H isotopic ratio of 10^{-18}. This roughly corresponds to the level of ^{3}H in large lakes and precipitation above oceans before the nuclear weapon testing era.

Generation of fairly short-lived ^{7}Be ($T_{1/2} = 53.28$ d) in the atmosphere is achieved by several spallation reactions on nitrogen and oxygen nuclei, e.g., ^{14}N(p,2α)^{7}Be, ^{14}N(n,^{8}Li)^{7}Be, or ^{16}O(n,^{10}Be)^{7}Be. Since these spallation reactions need high-energy incident particles, the majority (70%) of beryllium is created in the stratosphere by GCRs, whereas the rest in the troposphere by secondary particles or SCRs. After its production, ^{7}Be is converted to oxide or hydroxide form and adsorbed on aerosol in the accumulation mode, usually with the size of 0.04–2.0 μm and activity median aerodynamic diameter of 0.09 μm (Papastefanou and Ioannidou, 1995). Due to vertical mixing of stratospheric and tropospheric air masses, cosmogenic beryllium is transported to the lower parts of the atmosphere. Activity concentration of ^{7}Be near the surface shows typical seasonal variations with distinctive minima in winter and maxima in summer, for the most part caused by wet deposition (precipitation), vertical transport in the troposphere, seasonal shift of the tropopause, and horizontal movement of air masses. Furthermore, a strong correlation between the 11-year solar cycle and ^{7}Be concentration was also documented (Azahra et al., 2003). Radionuclide ^{7}Be decays via electron capture (EC) to ^{7}Li, emitting gamma rays ($E_\gamma = 477.6$ keV) with the 10.3% probability.

Radiocarbon ^{14}C ($T_{1/2} = 5730$ y) is by far the most studied cosmogenic radionuclide, which decays to stable nitrogen by emission of beta electrons ($E_{max} = 156$ keV). The most likely production route for radiocarbon is the interaction of neutrons with stratospheric nitrogen, that is ^{14}N(n,p)^{14}C. Other types of reactions, e.g., ^{16}O(n,^{3}He)^{14}C, ^{15}N(n,d)^{14}C, or ^{13}C(n,β)^{14}C, are also possible; however, their production rates are by at least three orders of magnitude lower (Schopper et al., 1967). The overall average production rate of natural ^{14}C in the atmosphere was calculated to be 2.05 atoms m^{-2} s^{-1} (Masarik and Beer, 2009), peaking at the geomagnetic pole areas. Due to rapid and thorough mixing of the atmospheric masses, radiocarbon concentration is very similar in all regions, regardless the latitude. Similarly to other cosmogenic radionuclides, the production of ^{14}C varies with the solar activity. Results of tree ring analyses clearly showed increased radiocarbon concentrations during the solar minima (Damon et al., 1989). Additionally, a correlation between ^{14}C content and 11-year solar cycle was observed in wines as well (Burchuladze et al., 1980).

Once produced, radiocarbon is quickly oxidized to $^{14}CO_2$, transported into the atmospheric boundary layer, hydrosphere, and, by photosynthesis, into the biosphere. As the long-term production of cosmogenic ^{14}C is practically steady, all living organisms contain about the same amount of ^{14}C (0.225 Bq g^{-1} C), which is exponentially depleted after their death, following the decay of radiocarbon, thus making it exploitable in radiocarbon dating (Libby, 1961). The ratio of cosmogenic radiocarbon to stable isotopes of carbon in the atmosphere is equal to

$$\frac{[^{14}CO_2]}{[^{12}CO_2] + [^{13}CO_2]} = 1 \times 10^{-12} \qquad (3.1)$$

where $[^{12}CO_2]$, $[^{13}CO_2]$ and $[^{14}CO_2]$ are equilibrium concentrations of the respective carbon dioxides present in the air. From the total global inventory of cosmogenic radiocarbon, the vast majority (~90%) is deposited in oceans, where its mean content is around 1.2×10^{9} atom L^{-1}. The rest of the radiocarbon is mainly distributed in the biosphere and atmosphere (Broecker and Peng, 1982).

The equilibrium concentration of radiocarbon in the environment, expressed by Eq. (3.1), was severely disturbed by different anthropogenic activities, whose effects were especially notable in the previous century. Massive combustion of fossil fuels, which started with the dawn of the industrial era, has been introducing large

amounts of ^{14}C-free carbon dioxide. As a result, the radiocarbon activity concentration in the atmosphere and consequently in the whole environment has been diluted. The observed Suess effect (Suess, 1955) has both impacts on a local/regional and on global scales. It is also one of the main reasons of seasonal variations of atmospheric radiocarbon. Opposite to the Suess effect, nuclear weapon testing and nuclear industry, whose influence is discussed in the next subchapter, have produced significant amounts of radiocarbon, overwhelming its activity from natural sources.

D. Anthropogenic radionuclides

Since the discovery of artificial radioactivity some 80 years ago, plentiful human activities have led to production of hundreds of different radionuclides of various half-lives, part of which has been eventually released to the environment. Therefore, anthropogenic radionuclides can be defined as all radionuclides that originate from anthropogenic sources. This not only includes artificially prepared radionuclides, which have not been detected in nature by present analytical techniques, but also those whose natural levels have been substantially increased as a consequence of intended human actions (e.g., nuclear weapon tests in the atmosphere, nuclear accidents) (Livingston and Povinec, 2000, 2002). The latter group mainly consists of long-lived radionuclides from uranium fission. Conveniently, anthropogenic radioactivity also includes so-called technologically enhanced naturally occurring radioactive materials (TENORMs), produced when dealing with naturally occurring radioactive materials (NORMs).

A lot of human activities can result in the modification of NORMs into TENORMs, which may lead to elevated concentrations of NORMs in by-products, end products, or even waste. Consumers and workers can be thus exposed to higher radiation doses. During extreme environmental situations, such as working in space or high-altitude flights, cosmic radiation can cause increased radiation exposure as well. Materials with increased concentration of natural radionuclides, namely uranium, thorium, and radium isotopes, and their respective progenies, are generally created due to change in environmental conditions, which result from the application of different processes. For example, groundwater extraction from aquifers may induce precipitation of salts containing increased amounts of ^{226}Ra, or sedimentation of NORMs can enhance their content of natural radionuclides. Similarly, NORM activities in slime and fines can be further increased by some fractionation processes (Paschoa and Steinhäusler, 2010). The issues of TENORMs are common in several types of industries, such as oil and gas industry, metal (uranium) and mineral mining, fertilizer and building material production, or water treatment.

Although many nuclear activities have caused the addition of anthropogenic radionuclides into the environment, only some of the activities have contributed in significant amounts. The largest contribution by far can be attributed to atmospheric nuclear weapon testing (mainly during the 1950s and early 1960s of the previous century), which resulted in production of huge amounts of radionuclides and their dispersion all over the globe due to air transport processes in the atmosphere. Continuous development in the field of nuclear energy has increased the number of nuclear reactors worldwide. Despite the fact that they can generate and possibly release a wide spectrum of radionuclides (fission products, transuranics, and activation products), the local impact of a normally operating nuclear power plant (NPP) on the environmental radioactivity level is barely measurable, which unfortunately does not apply in the case of nuclear accidents. While nuclear fuel reprocessing facilities represent another important source of anthropogenic radionuclides, the influence of various applications of radiation sources in industry, medicine, and science is negligible.

1. Nuclear weapons testing

Depending on which type of nuclear reaction occurs during their detonation, nuclear weapons can be classified into fission and fusion weapons, commonly referred as atomic and thermonuclear weapons. The former exploit uncontrolled chain fission of heavy nuclei (^{235}U, ^{239}Pu) into the lighter ones, the principle of the latter is based on fusion of light nuclei (deuterium, tritium, lithium), usually triggered by fission. Nuclear weapon explosion yield is generally expressed in equivalent mass of trinitrotoluene (TNT), i.e., the explosion of a 1 kt nuclear weapon would have the same destructive effect as if we would detonate 1 million of kilograms of TNT at once. The power of nuclear weapons seems even more enormous when one realizes that only tens grams of plutonium or uranium are needed to achieve the effect mentioned in the previous sentence.

Explosions of nuclear weapons are extremely fast processes. Almost all energy stored in nuclei to undergo fission or fusion is released within less than 1 μs and transformed into the form of blast (50%), thermal radiation (35%), and ionizing radiation (15%). While one-third of the ionizing radiation is emitted as gamma rays and neutrons in a few seconds after the explosion, the remaining part, representing 10% of the total released energy, can be attributed to the decay of induced radionuclides from the surrounding atmospheric or terrestrial material and fission products. At any given time t, the radioactivity in the location of nuclear weapon detonation A can be approximately calculated as

$$A = A_0 t^{-1.2} \tag{3.2}$$

where A_0 is the initial activity (Eisenbud and Gessel, 1997). Eq. (3.2) is a reasonable estimate for months after the explosion occurred ($t \leq 180$ d). It is worth to note that this calculation strongly depends on the yields of the radionuclides, generated during the nuclear burst.

More than 200 radionuclides of 35 elements are part of the initial fission product mixture, originated from a nuclear weapon detonation, though most of them are short-lived and decay soon after the explosion. The produced radioactive material comprises three distinctive fractions, depending on the explosive yield and height of the burst. The first group is primarily composed of large particles, which are highly radioactive and tend to fall out within several hours. Smaller particles dispersed in the troposphere usually contribute to fallout only after some time, as they behave in a similar way as aerosols, which are subject to specific laws of deposition. The last fraction of particles enter the stratosphere with the residence time of several years, meaning that they can be distributed all over the globe, and thus creating global radioactive fallout (Livingston and Povinec, 2002; Hirose and Povinec, 2015).

In the case of underground nuclear weapon tests, the contribution to global fallout is much smaller; however, gaseous products, such as ^{133}Xe and ^{85}Kr, can still vent through the ground, and eventually reach the atmosphere. The most salient long-lived global fallout radionuclides are summarized in Table 3.3.

The very first nuclear weapon was detonated on a desert of New Mexico in the United States in July 1945. Since then, more than 400 atmospheric tests were conducted by the United States, Soviet Union, United Kingdom, France, and China (Table 3.4). Additionally, hundreds of nuclear devices were detonated underground after 1963, when the United States, the United Kingdom, and Soviet Union signed a nuclear weapon test-ban agreement for atmospheric testing, though France, China, nor India did join the treaty and later conducted several detonations in the atmosphere. The number of underground tests vastly exceeded those made in open air, e.g., the United States alone made more than 800 tests in Nevada (Eisenbud and Gessel, 1997). With the exception of the abovementioned countries, Pakistan and North Korea declared to successfully test nuclear weapons. As the majority of the tests were performed in the Northern Hemisphere, radionuclides from global fallout were distributed mainly in the northern latitudes.

TABLE 3.3 Anthropogenic radionuclides in global fallout.

Radionuclide	Half-life (year)	Decay mode/energy (MeV)	Global fallout (PBq)[a]
^{3}H	12.31	β^-/0.0186 max	186×10^3
^{14}C	5730	β^-/0.156 max	213
^{85}Kr	10.73	β^-/0.067 max γ weak	185[c]
^{90}Sr	28.8	β^-/0.546 max	600
^{129}I	1.57×10^7	β^-/0.0150 max γ weak	0.4×10^{-3}
^{137}Cs	30.05	β^-/1.176 max γ/0.662	950
^{239}Pu	2.41×10^4	α/5.157 (70.8%) γ weak	12[b]
^{240}Pu	6560	α/5.168 (72.8%) γ weak	

[a] *From UNSCEAR (2008).*
[b] *From Hardy et al. (1973).*
[c] *From NCRP (1975).*

TABLE 3.4 Overall statistics of nuclear weapon testing in the atmosphere (UNSCEAR, 1982).

Country	Period	Number of tests	Estimated yield (Mt TNT)	
			Fission	Total
USA	1945–1962	193	72	139
USSR	1949–1962	142	111	358
France	1960–1974	45	11	12
China	1964–1980	22	13	21
United Kingdom	1952–1963	21	11	17
Total		423	218	547

2. Nuclear reactors

The main principle of the peaceful use of atomic energy in NPPs is controlled chain fission reaction of nuclei of specific elements, such as uranium, plutonium, and thorium (Fig. 3.6). The most common type of nuclear fuel contains enriched uranium, i.e., uranium oxide (U_3O_8) with the content of ^{235}U up to 3%–4%. It is produced in the form of ceramic pellets, which are sealed in resistant metal (e.g., zirconium alloy) tubes, bundled together into a nuclear fuel assembly. An assembly lasts usually for 3–4 years when it is necessary to replace it with the fresh one.

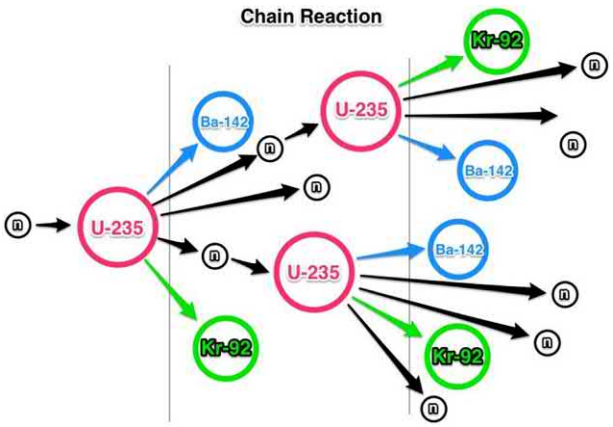


FIGURE 3.6 Fission chain reaction. For the color version of the figure, the reader is referred to the online version of the book. *From Costa et al. (2017).* Printed with permission © Elsevier 2018.

In the case of ^{235}U or ^{239}Pu, the fission yield is the highest when induced by thermal neutrons (<0.1 eV). Therefore, neutrons, which are generated as a result of fission and can have energies above 10 MeV, are needed to be slowed down. This is achieved with the use of a so-called moderator, present in-between the fuel assemblies or as a part of the nuclear fuel.

Moderation is based on elastic collisions of fission neutrons with nuclei of light elements, e.g., hydrogen, deuterium, or carbon. Light water, heavy water (D_2O), and graphite are nowadays the most frequently exploited moderators, depending on a reactor type. The criticality of the chain reaction is sustained by movement of controlled rods, composed of material able to absorb fission neutrons. The heat is generated by decay of fission products, their collision with nearby nuclei, and absorption of gamma rays, which is transferred from the reactor by a coolant. Numerous types of coolants have been developed, which can be in the form of gas (CO_2, N_2, He), liquids (H_2O, D_2O, hydrocarbons), or even molten salts (fluorides) and molten metals (Na, K, Hg) for advanced nuclear reactors (Breeze, 2016). The large majority (65%; IAEA, 2018) of world's NPPs are constituted by pressurized water reactors (PWRs), which use light water for both moderation and cooling.

Hundreds of radionuclides produced during normal operation of a nuclear reactor, which are mostly short-lived and decay within minutes or hours, comprise fission products (and their daughters), activation products, and transuranics. Because primary fission products have an excess of neutrons, they decay via consequent beta transmutations to stable nuclides, while often emitting gamma radiation. Tens of these decay chains occur simultaneously during operation, increasing the activity of fuel assemblies and determining the composition of the spent nuclear fuel (SNF). Plutonium ^{239}Pu is formed by parasitic capture of a neutron on ^{238}U, which is inherently present in the nuclear fuel based on (enriched or natural) uranium and has very low fission yield, followed by two subsequent beta decays of ^{239}U and ^{239}Np. Other heavier transuranics (e.g., ^{240}Pu, ^{241}Am, ^{242}Cm) are generated by additional neutron capture or beta decays. The average content of fission radionuclides and transuranics in a typical nuclear fuel assembly is given in Table 3.5.

The last group of radionuclides created in a running nuclear reactor is represented by activation products that are generated by nuclear reactions on stable nuclei of coolant, moderator, and construction materials of the reactor in (n,p), (n,α), (n,2n), or (n,γ) reactions. Unlike fission products, activation products are not part of decay chains and usually decay to stable daughters by a single beta emission. The variety of these radionuclides is affected by the presence of miscellaneous trace impurities in the structural components, which have a high cross section for neutron interactions. The most abundant activation product

TABLE 3.5 Content of selected radionuclides in a typical thermal reactor after two-thirds of the fuel campaign.

Radionuclide	Half-life	Specific fuel activity (MBq g^{-1})
^{3}H	12.31 years	1.1
^{14}C	5730 years	0.11
^{60}Co	5.27 years	111
^{85}Kr	10.73 years	222
^{90}Sr–^{90}Y	28.8 years –64.0 hours	1554
^{99}Mo–^{99}Tc	65.9 hours -2.11×10^5 years	34,410
^{132}Te	3.2 days	29,600
^{129}I	1.57×10^7 years	0.0011
^{131}I	8.0 days	20,350
^{133}Xe	5.3 days	40,700
^{134}Cs	2.07 years	3700
^{137}Cs	30.05 years	2331
^{141}Ce	32.5 days	33,670
^{239}Np	2.36 days	499,500
^{239}Pu	2.41×10^4 years	7.77
^{240}Pu	6560 years	15.5
^{241}Pu	14.33 years	2700
^{241}Am	432.6 years	2.37

After Clarke and MacDonald (1978).

is ^{60}Co ($T_{1/2} = 5.27$ y), created principally by the reaction ^{59}Co(n,γ)^{60}Co, and—to much lesser extent—in the reaction ^{60}Ni(n,p)^{60}Co, as well as captures of thermal neutrons on other isotopes of nickel, which is contained in the stainless steel, used for nuclear reactors. This strong gamma emitter can also be found in the coolant, in which it may be dispersed due to corrosion of construction materials. Other noticeable long-lived activation products are ^{3}H, ^{14}C, ^{55}Fe ($T_{1/2} = 2.74$ y), and ^{94}Nb ($T_{1/2} = 2.03 \times 10^{4}$ y), some of which are reviewed below.

If the nuclear reactor is operating under standard conditions, amounts of radioactive substances discharged into the environment are very low and may impact it only locally. Gaseous and liquids releases from NPPs contain direct fission products or radionuclides produced by activation. Even though the former should be hermetically sealed in the fuel assemblies, they may diffuse or leak into the coolant because of microscopic ruptures in the casing. Ubiquitous uranium on the surface of fuel rods or some other reactor elements may contribute to the unwanted presence of fission radionuclides as well. For PWRs, this means that the contamination can be spread through the whole primary loop; however, cleaning systems are used to remove these radionuclides for disposal, effectively reducing potential releases in the case of accident.

Since the successful launch of Fermi's reactor in Chicago in 1942, hundreds of nuclear reactors have been commissioned, either for commercial purposes of electricity generation, production of plutonium for nuclear weapons, and research or to power ships and submarines. Currently, there are 448 land-based nuclear power reactors in operation, with the cumulative installed electric capacity of about 390 GW_e, and with 59 new reactors under construction (IAEA, 2018). Approximately 25−30 t of highly radioactive SNF is produced per 1 GW_e (Macfarlane and Miller, 2007), meaning that some 11,000 t of SNF has been already created worldwide.

3. Nuclear fuel reprocessing plants

Commercial facilities for nuclear fuel reprocessing are nowadays the most significant prevailing sources of anthropogenic radionuclides (fission products of uranium and plutonium, activation products) in the global atmosphere. Reprocessing itself is conducted in several general steps. After removal of the fuel assembly from the nuclear reactor, it requires storage for months or more, so that its activity is lowered enough (by decay of short-lived radionuclides) that it can be transported to the facility and consequently reprocessed. First, the cladding of a fuel assembly, which acts as an ultimate barrier for radionuclide releases from nuclear fuel, is removed. By doing this, radionuclides (mainly isotopes of krypton, iodine, and tritium) in the gaseous form are released into the air. SNF is then divided into smaller parts and chemically dissolved. Residual uranium, plutonium, and other transuranics, together with fission products, are sequentially extracted with the use of radiochemical separation techniques and reagents. All worthless radionuclides end in the radioactive waste, which is further processed before being finally disposed.

Although low- and intermediate-level radioactive wastes are generated during reprocessing of SNF as well, high-level wastes, which may contain up to 99% of all fission products and transuranics, are much more problematic from the environmental point of view. Precise composition of these wastes depends on the reactor, from which the SNF was taken, and on the type of reprocessing. Besides radioactive substances (fission products, uranium, transuranics, activation products), they can also contain nonactive components, such as chemical reagents, corrosion products, or products of radiolysis.

Due to economic and technological constrains and potential environmental risk, there are only a small number of running nuclear fuel reprocessing plants. In Europe, the largest commercial facility is located in Sellafield (Great Britain) that is capable of reprocessing 2400 tHM y^{-1} (metric tons of heavy metal per year). The second plant is situated in La Hague (France), which is in operation since 1976 and has the capacity to process 1650 tHM y^{-1}. Additional plants are running in Mayak (Russia) and Kalpakkam (India), with the annual capacity of 400 tHM and 275 tHM of SNF, respectively. More facilities are in test periods, under construction, or planned in Japan and China (Hu et al., 2010). Atmospheric and liquid discharges from nuclear reprocessing plants in Europe are regularly monitored, especially the content of long-lived radionuclides (mainly ^{99}Tc, ^{129}I, ^{137}Cs, and plutonium isotopes).

4. Nuclear accidents

High requirements on the radiation safety of the NPP operation have been constantly increasing, mainly as a consequence of the accidents, which happened in the past. Despite the previous statement, NPP accidents have occurred again in recent times. Therefore, it is evident that further development and advancement in safety protocols and technologies will be necessary to avoid such catastrophic events and their outcomes, as in the case of the Chernobyl and Fukushima NPP accidents.

a. Three Mile Island (United States)

One of three most serious NPP accidents happened on March 28, 1979, at the Three Mile Island (TMI) site in the United States, when it was proven that even a relatively small mishap can cause severe consequences. Malfunction of a relief valve of a pressure vessel led to a series of unfortunate events (misjudgments of the reactor operator,

inappropriate manipulation with some devices and malfunction of others), which culminated in a loss-of-coolant accident and ultimately in melting of about 50% of the PWR reactor core. Large amounts of highly radioactive steam and water were released from the pressure vessel of the reactor into the containment. It was estimated that at maximum 480 PBq of radioactive gases (mostly ^{133}Xe) together with ~0.5 TBq of ^{131}I was vented to the atmosphere (Livingston and Povinec, 2000). The immediate determination of the environmental contamination was difficult, as the measuring range of the outer monitoring systems was surpassed.

Fortunately, the radiological impact of the TMI accident on the human population was insignificant. The highest doses, which were received by less than 300 people within ~3 km from the NPP, were estimated between 0.2 and 0.7 mSv (Gerusky, 1981). Such values would have a probability to cause one or two fatal cancer diseases for the whole exposed population (about 2 million of individuals in the distance of ~80 km). The exposure from ingestion or inhalation was much lower, and the highest dose from ^{131}I, which entered the body, was calculated to be around 0.05 mSv.

b. Chernobyl (Ukraine) nuclear power plant accident

The accident at the Chernobyl NPP in Ukraine (formerly Soviet Union), which occurred on April 25, 1986, was caused by several factors, though the main contribution can definitely be attributed to the human one. As a result of several thoughtless actions (extraction of manual control rods and violation of the rule about their minimal number, lowering the coolant inflow, disconnection of the automatic regulation for criticality adjustment, etc.) during the experimental test whether the reactor system would be able to continue operation in case the steam supply to turbines would be interrupted, the RBMK reactor reached the supercriticality state with the immediate evaporation of water coolant. The enormous pressure caused fuel channels to rupture. Hydrogen-oxygen mixture, produced from the exothermical reaction of the steam and zirconium, induced the second explosion. As a consequence, the graphite, which was used as moderator in the reactor, got ignited and the top of the reactor vessel was destroyed (Fig. 3.7). Radioactive emissions from the damaged reactor persisted for some 2 weeks after the accident. The damaged nuclear reactor was later enclosed in the concrete-iron sarcophagus (Fig. 3.8), which has recently been covered with a metallic cover (a dome, Fig. 3.9) to prevent further leakage of radionuclides to the environment.

The releases of radioactive substances to the atmosphere were indeed immense. For example, the ^{137}Cs aerosol activity in Bratislava (Slovakia, Central Europe) was increased by five orders of magnitude when in comparison



FIGURE 3.7 Chernobyl reactor after the accident. For the color version of the figure, the reader is referred to the online version of the book.



FIGURE 3.8 P. Povinec (in the middle) in front of the Chernobyl sarcophagus. For the color version of the figure, the reader is referred to the online version of the book.



FIGURE 3.9 Metallic cover (a dome) of the leaking Chernobyl sarcophagus. For the color version of the figure, the reader is referred to the online version of the book.

TABLE 3.6 Reactor core inventory of the Chernobyl nuclear power plant on April 26, 1986, and amounts of radionuclides released after the accident (OECD, 2002).

Radionuclide	$T_{1/2}$	Activity (PBq)	Total released activity (PBq)
^{90}Sr	28.8 years	200	10
^{131}I	8.0 days	3200	1760
^{133}Xe	5.3 days	6500	6500
^{137}Cs	30.05 years	280	85
^{239}Pu	2.41×10^4 years	0.85	0.03
^{240}Pu	6560 years	1.2	0.042

with the pre-Chernobyl data (Povinec et al., 1988). Radionuclides from the Chernobyl NPP accident could be detected all over the Northern Hemisphere. On the other hand, because the releases contaminated only the troposphere, no signal was detected in the Southern Hemisphere. It was estimated that the whole inventory of noble gases (radioisotopes of Xe and Kr) was emitted from the melted reactor core, together with 10%–20% of the inventory of tellurium, iodine, and cesium radioisotopes. The overall activity released to the air was estimated to be more than 12,000 PBq (Table 3.6).

To correctly evaluate the radiological effect of the Chernobyl NPP accident, it was necessary to consider the area of the affected land. Four separate areas were assessed: the NPP site and its near vicinity, the zone within 30 km from the site, the European part of the Soviet Union beyond the 30 km zone, and the European states outside of the Soviet Union. The mean whole-body dose for individuals from the 30 km zone was estimated to be 15 mSv. In-between 1986 and 1989, the population living in the Soviet Union beyond the 30 km zone was exposed to the dose of about 40 mSv. From more than 200 patients, who were professionally engaged in works during the accident and who were diagnosed to suffer acute radiation sickness, about 100 died. The obtained doses for the rest of Europe were relatively low (tens of μSv) and strongly dependent on the geographic location and rate of precipitation at the time of the accident (OECD, 2002).

The difficulties also arose for the land areas, contaminated by deposited radionuclides from the Chernobyl fallout, mainly ^{137}Cs, and in a minor way ^{90}Sr and plutonium isotopes (Fig. 3.10). The most affected countries were the Ukraine and Belarus, where the area of roughly 10,000 km^2 (mostly in Belarus) was contaminated with radiocesium at the level of more than 550 kBq m^{-2}, whereas for 3000 km^2, this value was greater than 1480 kBq m^{-2} (IAEA, 1996). A large part of the area

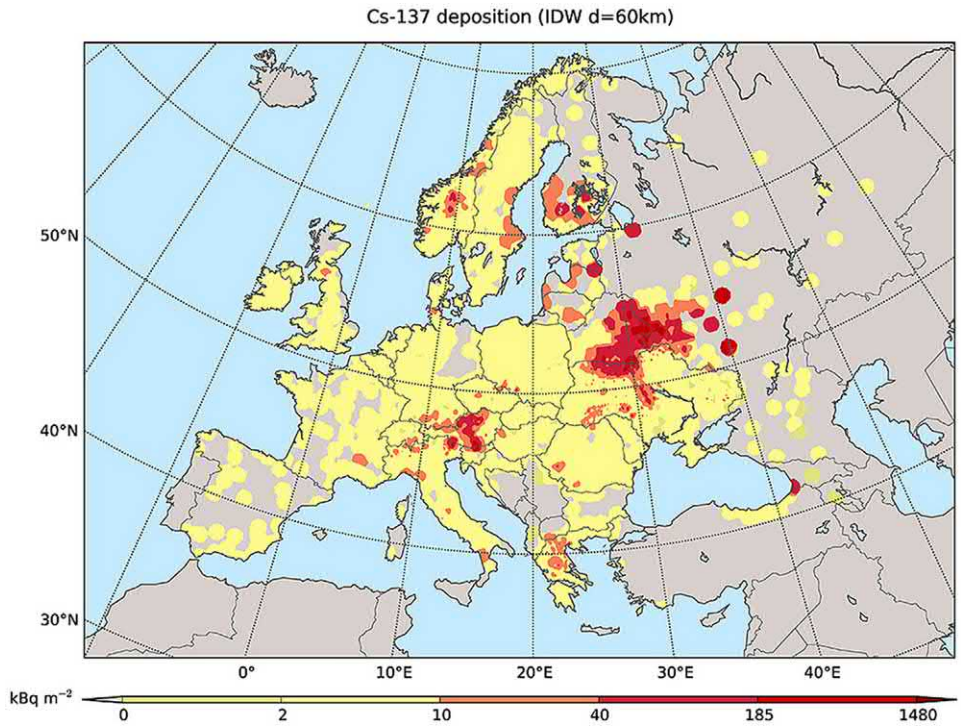


FIGURE 3.10 Total deposition of ^{137}Cs over Europe, irrespective to the source. Orange and red areas (>10 kBq m^{-2}) can be attributed to the Chernobyl nuclear power plant (NPP) accident origin. For the color version of the figure, the reader is referred to the online version of the book. *From Evangeliou et al. (2016).* Printed with permission © Elsevier 2018.

contaminated by radiocesium was used for agricultural purposes; thus, effective measures had to be implemented to lower the dose rate. This included adding potassium, liming soils, removal of livestock from affected pastures, decontamination in food production, and deep plowing.

c. Fukushima (Japan) nuclear power plant accident

On March 11, 2011, the Tōhoku earthquake (the magnitude of 9.0) with the epicenter located some 130 km offshore of the eastern coast of Japanese islands caused large tsunami waves, which among others struck the Fukushima Dai-ichi NPP, approximately 40 minutes after the most powerful tremor. The Fukushima NPP site was flooded with seawater, reaching the height of 15 m. Because the earthquake damaged transmission facilities, the NPP lost connection to electricity from the outer grid. On top of that, almost all backup power generators were completely destroyed, mainly because of the fact that they were situated below the sea level. Consequently, the cooling systems of the shutdown boiling water reactors (BWRs) in units 1−3 had to be connected to batteries; however, after a relatively short time, the batteries got depleted and the cooling systems were once again without power. Because the reactor cores continued to generate heat, which was critical to transfer, water was pumped into the reactor vessels. Several hours later, the first explosion occurred in unit 1, which was caused by accumulated hydrogen, created in the reaction of steam and zirconium. The situation in unit 2 was similar; however, the explosion at the top of the reactor building was averted by early measures. Unit 3 followed exactly the fate of unit 1, while part of the hydrogen generated here leaked even into unit 4, where another explosion occurred a bit later. The Fukushima accident thus represents the largest accident of NPP observed till now (Fig. 3.11), although total radionuclide releases were smaller when compared with the Chernobyl accident.

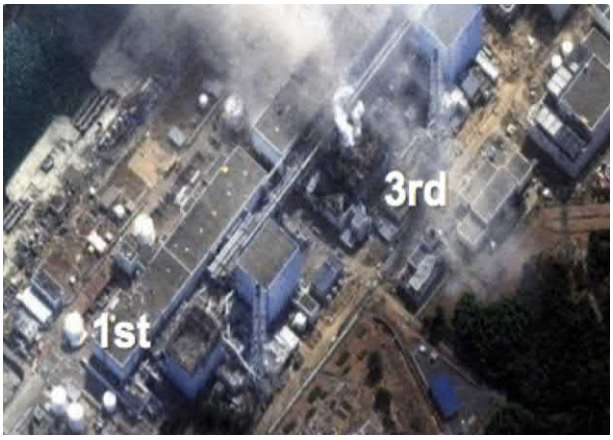


FIGURE 3.11 Damaged Fukushima nuclear power plant (NPP) after the reactor accidents. For the color version of the figure, the reader is referred to the online version of the book. *From Povinec et al. (2013a).*

As a result of the events described above, significant amounts of radioactive substances were released to the environment during the Fukushima NPP accident. The reactor core inventories contained a wide spectrum of radionuclides, though early monitoring was focused primarily on noble gases, ^{131}I, and radiocesium (^{137,134}Cs). First reasonable estimates showed that 160 PBq of ^{131}I and 15 PBq of ^{137}Cs were discharged to the atmosphere (Povinec et al., 2013a). Fig. 3.12 shows the estimated surface ^{137}Cs contamination in the Fukushima region. Atmospheric releases from the Fukushima NPP, recently reviewed by Hirose (2016), are given in Table 3.7.

Regarding the radiological effect of the Fukushima accident, received doses to NPP workers and population living in the vicinity of the site were low, except for a few cases. No individual suffering from acute radiation sickness was diagnosed. Six employees at the NPP were exposed to the dose greater than 250 mSv. Almost 200,000 people, who were screened until May 2011, showed no symptoms, which could be connected to radiation exposure (Povinec et al., 2013a).

The releases of radionuclides from the Fukushima NPP were detected all over the world (Masson et al., 2011; Nakano and Povinec, 2012; Povinec et al., 2012a,b,c, 2013a,b,c,d,e, 2017; Nakanishi and Tanoi, 2013; Povinec and Hirose, 2015; Hirose and Povinec, 2018). Determinations of activities of ^{131}I and radiocesium in atmospheric aerosol collected in Bratislava, which were conducted in the period shortly after the accident, suggested that at least three radioactive plumes arrived in Bratislava. Moreover, it was concluded that both horizontal and vertical transport caused negligible increases of activity concentrations in the ground-level air, and the impact on the atmosphere was by five orders of magnitude lower than in the case of the Chernobyl accident (Fig. 3.13; Povinec et al., 2012a). The influence on the radionuclide inventories of the oceans was studied as well (e.g., Povinec et al., 2013c; Aoyama et al., 2016; Povinec et al., 2017; Kaizer et al., 2018a), and this is covered partially in Chapter 5, Volume 2 of this book.

d. Other nuclear accidents

There were several other nuclear accidents, which caused regional or worldwide contamination of the environment by radionuclides, e.g., Windscale (former Sellafield) nuclear reprocessing facility in 1957 (UK), several accidents at the Mayak nuclear facility in the former Soviet Union (the largest one in 1957), a burn-up of US SNAP-19a satellite generator (containing ^{238}Pu) in the upper atmosphere of the Southern Hemisphere in 1964, accidents with US planes carrying plutonium bombs (in 1966 in Palomares, Spain, and in 1968 in Tula, Greenland), an accident at the Tokaimura (Japan) nuclear facility in 1997, and several

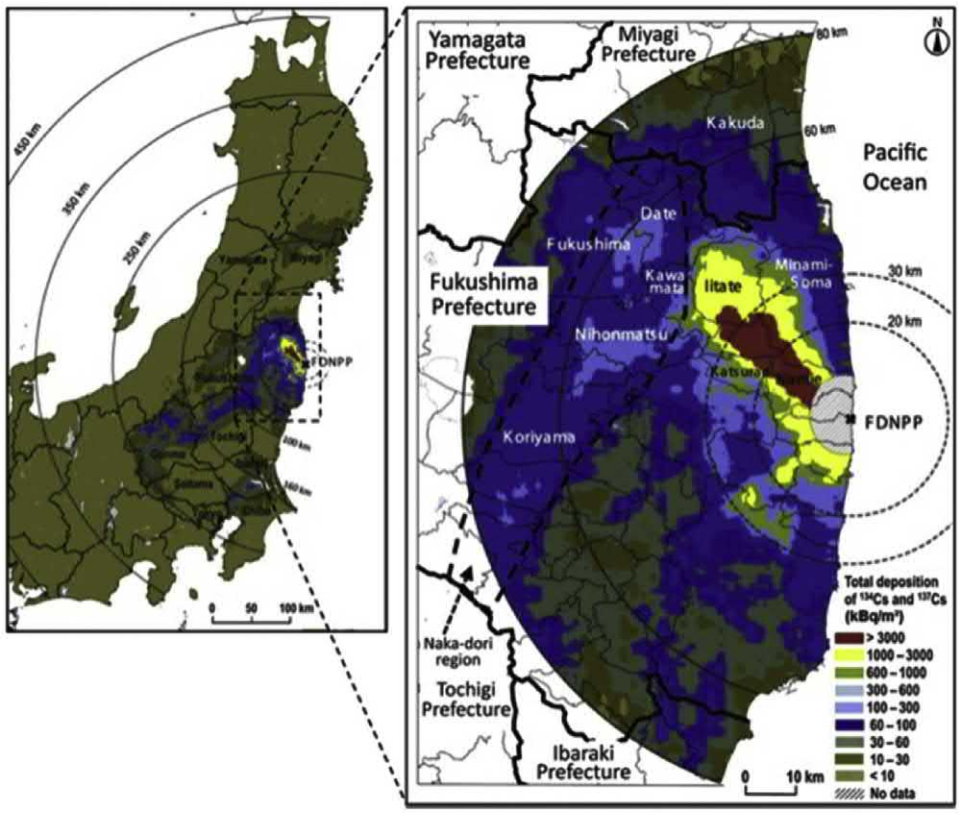


FIGURE 3.12 Surface contamination of ^{137}Cs around Fukushima nuclear power plant (NPP) (Hirose, 2016). For the color version of the figure, the reader is referred to the online version of the book. *Printed with permission © Elsevier 2018.*

TABLE 3.7 Estimations of atmospheric releases of gaseous and volatile radionuclides from the Fukushima NPP.

Radionuclide	$T_{1/2}$	Atmospheric releases (PBq)
^{85}Kr	10.73 years	44
^{133}Xe	5.3 days	11,400–20,000
^{131}I	8.0 days	65.2–380
^{134}Cs	2.07 years	11.8–18
^{137}Cs	30.05 years	6.1–35.9

After Hirose (2016).

small-scale accidents (Livingston and Povinec, 2002; Povinec, 2004).

5. Specific anthropogenic radionuclides

a. Tritium

The natural level of cosmogenic ^{3}H ($T_{1/2} = 12.31$ years) was severely disturbed by nuclear weapon testing and partially by operation of nuclear fuel reprocessing plants and nuclear reactors. While nuclear fuel reprocessing plants have released some 410 PBq of ^{3}H, the contribution from nuclear weapon testing was much more significant. Until the ratification of the test-ban treaty in 1963, around 186 EBq of anthropogenic tritium accumulated in the environment, from which 113 EBq was deposited in the oceans (IAEA, 2005). The main source of global fallout tritium was identified in explosions of thermonuclear weapons, where it was estimated that 1 Mt TNT could generate 0.26–1.8 EBq of ^{3}H, while for atomic weapons, the values are about two to three orders of magnitude lower.

In the case of light-water nuclear reactors, tritium is produced by ternary fission of uranium and activation of light nuclides, e.g., by the nuclear reaction ^{10}Be(n,2α)^{3}H. If the tritium yield for fission of ^{235}U by thermal neutrons is ~0.01%, then 555–740 TBq of ^{3}H per GW_e is annually produced in a light-water reactor by this route (IAEA, 1981). This amount is slightly increased by interactions of fission neutrons with impurities, such as ^{2}H, ^{3}He, ^{6,7}Li, ^{10,11}B, and ^{12}C, present in the construction material, coolant, and moderator of the reactor. According to Kahn et al. (1974), an earlier PWR could overall release tritium activity of 330 TBq GW_e y^{-1}; however, with the improvement of reactor design, as well as better maintenance and management of the reactor component systems,

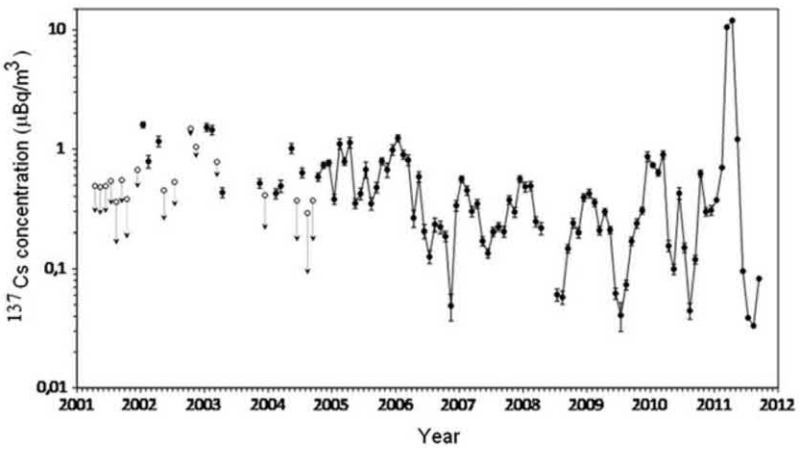


FIGURE 3.13 Time series of ^{137}Cs concentration in aerosols of Bratislava. The Fukushima signal is clearly distinguished. *Modified Povinec et al. (2012a).* Printed with permission © Elsevier 2018.

this value was reduced to around 30 TBq GW_e y^{-1} (IAEA, 2004). In general, PWRs generate and thus discharge more tritium than BWRs, but much less than heavy water reactors. When compared with the aforementioned sources, the impacts from nuclear reactor accidents have been almost negligible, influencing mostly only the local environment (e.g., Povinec et al., 2013a, 2013c; 2017; Kaizer et al., 2018a).

b. Carbon-14

The source terms for anthropogenic ^{14}C ($T_{1/2} = 5730$ years) are quite similar to those of tritium. During numerous explosions of nuclear weapons in the era of atmospheric testing, radiocarbon nuclei were produced by the same types of neutron interactions as the cosmogenic ones. One detonation could produce as much as 1.6 PBq per Mt TNT or more, leading to the estimation of ^{14}C global fallout inventory of 213 PBq (IAEA, 2005). Such huge amounts caused the increase of the atmospheric radiocarbon concentration in the Northern Hemisphere by 100% (Hua et al., 2013). As mixing between two hemispheres is limited and takes some time, the concentration in the Southern Hemisphere was elevated only by the factor of 1.7 (Grammer et al., 2015). Because of the natural carbon cycle, the change in the ^{14}C level was observable in other parts of the environment as well (Fig. 3.14).

Besides nuclear weapon explosions, radiocarbon is produced in nuclear reactors, and during nuclear fuel reprocessing, though on a much lower scale. Activation of nitrogen and the reactions $^{17}O(n,\alpha)^{14}C$ and $^{13}C(n,\gamma)^{14}C$ represent the main source of this nuclide in fuel, coolant, and moderator of the nuclear reactor. The last reaction is especially important for reactors using graphite as the moderator, like the one in the Chernobyl NPP. It was

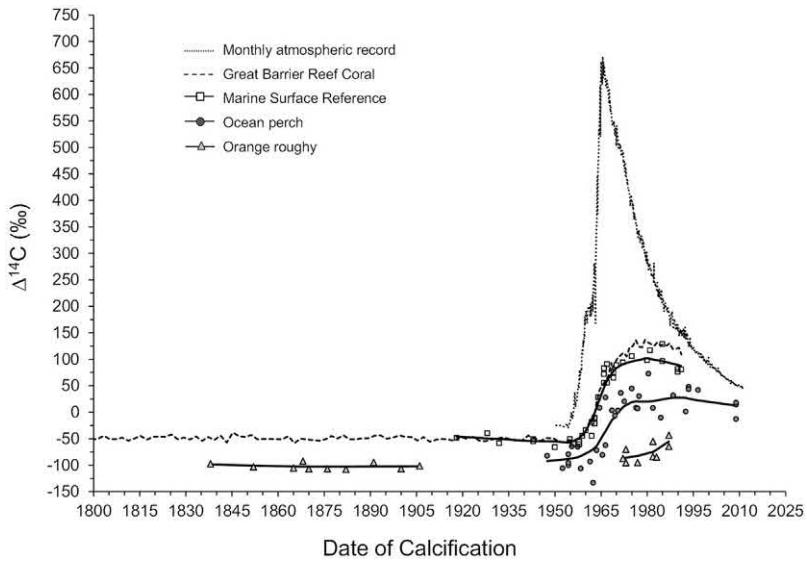


FIGURE 3.14 Time series of Δ^{14}C, representing excess/depletion of radiocarbon above its natural level (0.225 Bq g^{-1} C), in different reservoirs. *From Grammer et al. (2015).* Printed with permission © Elsevier 2018.

estimated that an average PWR can discharge to the air about 0.2 TBq y^{-1}, dominantly in the form of hydrocarbons (~85%), whereas airborne releases for heavy water reactors (mainly as CO_2) are expected to be on the level of 2–2.6 TBq y^{-1} (IAEA, 2004). For a reactor cooled by the mixture of carbon dioxide and nitrogen, amounts of ^{14}C discharges might be significant as well (Chudý and Povinec, 1982). The overall contribution of nuclear fuel reprocessing facilities to the radiocarbon inventory in the oceans was estimated to be 2 PBq (IAEA, 2005).

c. Strontium-90

The longest-lived isotope of strontium, ^{90}Sr ($T_{1/2} = 28.8$ y), decays by beta electron emission to another radionuclide, ^{90}Y ($T_{1/2} = 64$ hours), ingrowth of which is usually exploited for the determination of its mother. Radiostrontium (^{90}Sr and ^{89}Sr with $T_{1/2} = 56$ d) is highly radiotoxic, as it is intensively accumulated in human bones. This dangerous characteristic of ^{90}Sr was especially concerning at the end of the period of nuclear weapon testing when its deposition in the Northern Hemisphere was the highest and could reach up to 3 GBq km^{-2}. Due to the lower number of tests conducted and limited mixing of the hemispheres, the deposition of global fallout radiostrontium in the Southern Hemisphere was less than one-third that in the Northern Hemisphere (Eisenbud and Gessel, 1997). Local differences in deposition were also caused by the precipitation rate. In total, around 600 PBq of global fallout ^{90}Sr was spread all over the Earth's atmosphere, reaching the surface by 1970 (UNSCEAR, 2008).

Radiostrontium together with radiocesium are the main fission radionuclides in nuclear fuel that provide the majority of the activity of SNF in the first several hundred years. Since the construction barriers prevent ^{90}Sr to be released from the fuel matrix, it does not represent a radiation hazard in the final disposal of SNF. However, the barriers are removed during its reprocessing, resulting in transferring of radiostrontium into liquid wastes. About 7 PBq of ^{90}Sr has been introduced into the European seas as a consequence of authorized releases from the La Hague and Sellafield nuclear fuel reprocessing plants (IAEA, 2005). A similar amount was also accidentally discharged from the Chernobyl nuclear reactor (10 PBq; OECD, 2002) whose impact on the nearby water reservoir territory, which could be observable especially during winter months (Fig. 3.15). In the case of the Fukushima NPP, cumulative releases into the environment were much smaller and estimated to be around 2 PBq (Povinec et al., 2012b).

d. Technetium-99

With the atomic number of 43, technetium is surprisingly one of those elements that does not form stable isotopes.

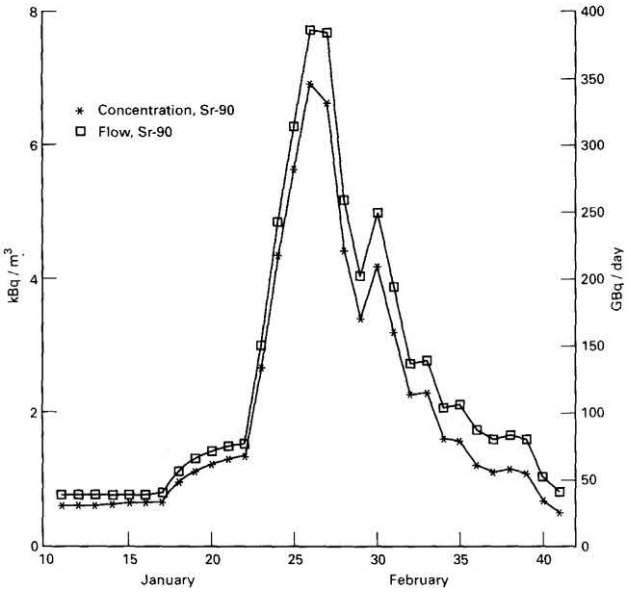


FIGURE 3.15 Temporal variations of the ^{90}Sr activity concentration in water (kBq m^{-3}), and radionuclide run-off (GBq day^{-1}) in January–February 1991 in the Pripyat River, near Chernobyl. *From Vakulovsky et al. (1994).* Printed with permission © Elsevier 2018.

For the long-lived beta emitter ^{99}Tc ($T_{1/2} = 2.1 \times 10^5$ years), this deficiency has caused nonnegligible problems in its determination by mass spectrometric techniques. Even though it can be produced naturally by fission of uranium or activation of Ru, Mo, and Nb isotopes in the Earth's crust, it was suggested that the amount of technetium (60 PBq) generated in this fashion has never entered other parts of the environment (Shi et al., 2012). Therefore, ^{99}Tc can be considered as strictly an anthropogenic nuclide, originating primarily from nuclear fuel reprocessing and nuclear weapon testing.

The largest producers of environmental ^{99}Tc are by far nuclear fuel reprocessing plants, which is well illustrated by the fact that the Sellafield facility has discharged liquid wastes containing roughly 1.7 PBq of this radionuclide into the sea (CEFAS, 2009). Global fallout inventory of technetium was calculated to be around 140 TBq (Aarkrog et al., 1986), whereas about 23.5 TBq was produced during underground nuclear weapon testing in Nevada (United States) and French Polynesia; however, most of this activity remained presumably beneath the surface of the testing sites (IAEA, 1998; Smith et al., 2003). A comparable amount was cumulatively generated in nuclear power reactors between 1971 and 2001, though it is expected that less than 10 GBq was unintentionally released into the environment during their operation (Shi et al., 2012). A small contribution (~1 TBq) could also be attributed to NPP accidents and applications of ^{99m}Tc in medicine (Aarkrog et al., 1988; Shi et al., 2012).

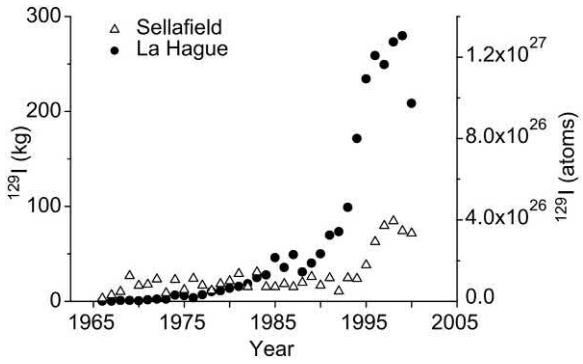


FIGURE 3.16 Annual liquid discharges of ^{129}I to the sea from the La Hague and Sellafield nuclear fuel reprocessing plants. *From Alfimov et al. (2004).* Printed with permission © Elsevier 2018.

e. Iodine-129

A relatively small natural inventory of beta decaying ^{129}I ($T_{1/2} = 1.57 \times 10^7$ y), generated by stratospheric interactions of cosmic rays with xenon, neutron reactions with tellurium, and spontaneous fission of uranium, is determined to be 650 GBq. Most of the activity has been deposited in the oceans, giving the prenuclear era isotopic ^{129}I/^{127}I ratio of 10^{-12} (Raisbeck and Yiou, 1999). Anthropogenic activities from nuclear weapon testing, accidents in NPP, and reprocessing facilities have increased this ratio up to 10^{-5}, while it was estimated that approximately 0.4 TBq of global fallout ^{129}I was transported into the oceans (IAEA, 2005). During the nuclear weapon testing period, around 370 GBq of long-lived iodine was deposited into the lithosphere (Eisenbud and Gessel, 1997).

Nuclear fuel reprocessing plants, namely the two in Europe, have produced more ^{129}I than natural production combined with all other anthropogenic sources. The annual liquid discharges from the La Hague and Sellafield plants, which have released altogether the ^{129}I activity of about 2.9 TBq into the atmosphere and 34.8 TBq into the sea (Hou et al., 2009a,b), are depicted in Fig. 3.16. The accidents in Chernobyl and Fukushima have also impacted the ^{129}I inventory, though the actual releases were calculated to be only 13 and 8.06 GBq, respectively (IAEA, 2003; Hou et al., 2013).

f. Cesium-137

Excluding a very rare probability of spontaneous fission of uranium, ^{137}Cs ($T_{1/2} = 30.05$ y) was produced and introduced into the environment exclusively by humans. Nuclear weapon testing, NPP accidents, and nuclear fuel reprocessing plants were identified as the prime sources of ^{137}Cs. Before its deposition, global fallout contained approximately 950 PBq of ^{137}Cs (UNSCEAR, 2008). Such immense activity, in fact the highest from all long-lived radionuclides, was generated due to very high fission yield for ^{137}Cs, induced by thermal neutrons (~6.3%). As can be seen in Fig. 3.17, where temporal changes in the ^{137}Cs deposition are shown, global fallout ^{137}Cs severely affected the Northern Hemisphere, whereas the Southern Hemisphere was barely contaminated. This can be explained by the fact that ^{137}Cs produced in the Northern Hemisphere was unable to reach southern parts of the atmosphere because of its quite short residence time, as opposed to, e.g., radiocarbon, in which case the difference between two spheres was less dramatic.

For the very same reason, mentioned in the case of nuclear weapons in the previous paragraph, nuclear fuel in the running nuclear reactor contains relatively large quantities of ^{137}Cs and ^{134}Cs ($T_{1/2} = 2.07$ years), which is also

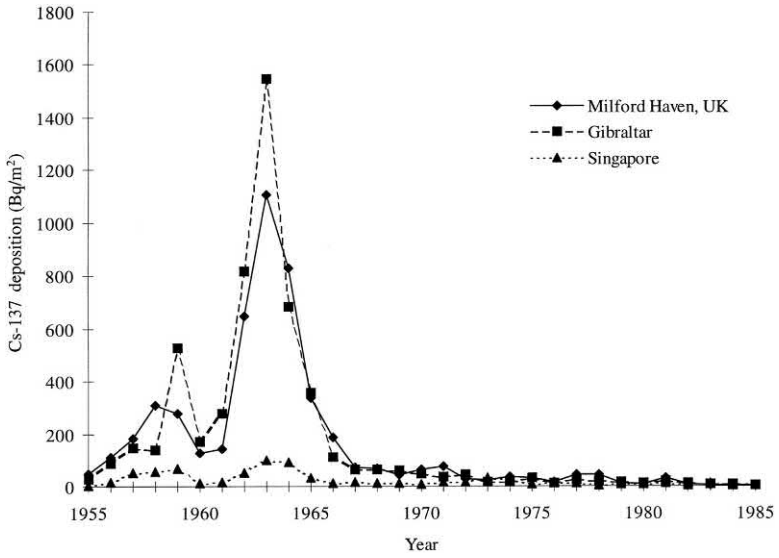


FIGURE 3.17 History of ^{137}Cs deposition for Milford Haven (UK), Gibraltar, and Singapore. *From Wright et al. (1999).* Printed with permission © Elsevier 2018.

produced by neutron capture on ^{133}Cs, the only stable isotope of cesium. The specific content of ^{137}Cs and ^{134}Cs in a fuel assembly of a typical thermal reactor after two-thirds of the fuel campaign was calculated to be roughly 2330 and 3700 MBq g^{-1}, respectively (Table 3.5) (Clarke and Macdonald, 1978). For a standard PWR, the concentration of ^{137}Cs of the primary was found to be by four orders of magnitude higher than the concentration of ^{90}Sr, which is caused by lower diffusivity of strontium isotopes (Eisenbud and Gessel, 1997). Nevertheless, releases of radiocesium from NPP are small in comparison with the global fallout inventory or accidental discharges, and it is hard to distinguish these releases from soil resuspension or burning of biomass effects (Sýkora et al., 2017; Ješkovský et al., 2018).

The ^{137}Cs/^{134}Cs activity ratio can be exploited to track origin of radioactive contamination as they both emit signature and reliably detectable gamma rays. For example, the ^{137}Cs/^{134}Cs activity ratio for liquid and airborne releases from the Fukushima accident was determined to be ~1, in agreement with the calculations of the core inventories for the damaged reactors (Povinec et al., 2013a). Because most of the atmospheric release from the Fukushima was deposited into the ocean, it has been recently estimated that the combined input of radiocesium to the North Pacific was in the range of 15–18 PBq (Aoyama et al., 2016), where it can potentially be used as a tracer for different oceanographic studies due to its unique properties (good solubility in seawater, long half-life, measurable on the mBq scale). According to the OECD (2002) report, the overall atmospheric discharges of ^{137}Cs from the Chernobyl NPP were much higher (85 PBq). On the other hand, nuclear fuel reprocessing facilities have produced in total some 40 PBq of radiocesium in their liquid effluents (IAEA, 2005).

g. Uranium-236

Potential of ^{236}U ($T_{1/2} = 2.3 \times 10^7$ years) for various environmental and geochemical studies was discovered only after the development of mass spectrometry techniques sensitive enough to determine its very low concentration in samples of interest. The most prevailing natural production routes of this uranium isotope are the thermal neutron capture ^{235}U(n,γ)^{236}U and reaction ^{238}U(n,3n)^{236}U. However, the total amount of naturally generated ^{236}U (0.07 GBq) is extremely low when compared with production from anthropogenic source terms (~10^3 GBq), mostly stored as a part of SNF. The ^{236}U/U ratio in uranium ores and deeper rock formations, undisturbed by human activities, was measured to be 10^{-11}–10^{-9} and 10^{-14}, respectively (Steier et al., 2008).

In the vicinity of nuclear fuel reprocessing plants, damaged nuclear reactors, or in the areas contaminated by depleted uranium, the ^{236}U/^{238}U isotopic ratio was found to be between 10^{-7} and 10^{-3}. The global fallout ^{236}U deposited on the Earth's surface was estimated to be around 2.2 GBq, comprised by directly generated ^{236}U during nuclear weapon explosions via the reactions mentioned above and by uranium originated from alpha decays of the deposited ^{240}Pu, produced also during the nuclear weapon testing. The latter production path resulted in the ^{236}U/^{238}U atomic ratio of (2.6–53) × 10^{-12} (Sakaguchi et al., 2009). Some examples of ^{236}U concentration measurements in the environment are shown in Fig. 3.18.

h. Plutonium isotopes

Other than negligible generation of ^{239}Pu ($T_{1/2} = 2.41 \times 10^4$ years) in uranium ores, where the mean atomic U/Pu ratio of 3.1×10^{12} was determined (Curtis et al., 1999), and its accumulation of around one tone in the natural Oklo uranium reactors in Gabon in Africa (Neu et al., 2010), all plutonium currently present in the environment originate from nuclear weapon testing and nuclear industry. Heavier plutonium isotopes are created by consequent neutron captures on ^{239}Pu, whose production route was discussed earlier in this chapter. Plutonium has high radiotoxicity, and with the exception of ^{241}Pu ($T_{1/2} = 14.33$ years), which decay by beta emission, all of its isotopes are alpha emitters.

Plutonium from global fallout has already been deposited onto the Earth's surface, where it has become part of soils, and into the ocean or terrestrial water sediments (Hirose and Povinec, 2015; Livingston et al., 2001). In total, about 15 PBq of plutonium was produced in the atmosphere as result of nuclear weapon testing, from which ^{239}Pu and ^{240}Pu ($T_{1/2} = 6560$ years) comprise 7.4 and 5.2 PBq, respectively (Lehto and Hou, 2011), corresponding to the ^{240}Pu/^{239}Pu isotopic ratio of ~0.18 (Lee et al., 2001). These activities vastly exceed the amounts released due to NPP accidents,

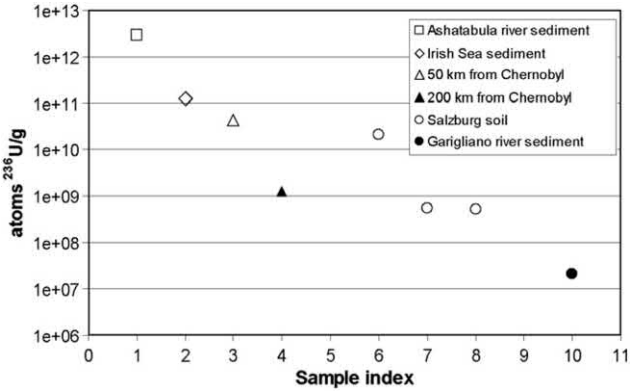


FIGURE 3.18 Concentration of ^{236}U in soil and sediment sample of various origins. *From Steier et al. (2008).* Printed with permission © Elsevier 2018.

accidental events with the aircrafts carrying nuclear weapons in the 1960s, and operation of nuclear fuel reprocessing plants at Sellafield and La Hague. Global fallout contained also other isotopes of plutonium (e.g., ^{238}Pu), their amounts were smaller but useful, as the ^{238}Pu/^{239,240}Pu activity ratio of 0.028 has been a good indicator of global fallout origin of plutonium when compared with other Pu source terms, generally showing higher ratios (Hirose and Povinec, 2015; Povinec et al., 2013a).

Although nuclear weapon testing in the open atmosphere was prohibited several decades ago, small amounts of anthropogenic plutonium have been still entering the environment as a consequence of dealing with uranium-based SNF. The ratio of plutonium isotopes in typical nuclear fuel changes with the duration of nuclear reactor operation. While the ^{240}Pu/^{239}Pu ratio reaches the value of around 0.16 after 1 year, it is increased to ~0.42 after two more years of nuclear reactor operation. After some 30 years, the ratio can be as high as 1.6, which is much higher than for weapon grade plutonium (WNA, 2018). Thus, analysis of the ^{240}Pu/^{239}Pu ratio could be used for identification of the source, from which plutonium was released into the environment.

TABLE 3.8 Concentrations of different constituents in particulate-free dry air near sea level.

Component	Volume (ppm)
N_2	780,840
O_2	209,480
Ar	9340
CO_2	350
Ne	18.2
CH_4	1.7
Kr	1.1
H_2	0.5
N_2O	0.3
CO	0.1
Xe	0.09
O_3	0.01–0.1
NO_2	0.02
NH_3	0.006
SO_2	0.002
Others	Less 0.0018

After Bailey et al. (2002).

III. Radionuclide compartments

A. Atmosphere

The atmosphere as the gaseous cover isolates Earth from space and represents the reservoir of the gases, needed by the life forms. It shields Earth from shortwave radiation and cosmic radiation and provides temperature balance from rapid heat exchange. Due to its small mass, great mobility, and chemical composition, it significantly differs from other spheres on Earth. The border of the Earth's magnetic field is considered as the upper border of the atmosphere, called magnetopause (the lowest altitude at 65,000 km), but usually for meteorological purposes, the stratopause (~50 km) is defined as the upper border. Compared with the Earth's radius (6378 km), the atmosphere is only a thin layer. There is about 50% of the atmosphere within 5 km above sea level and 90% within 12 km. The mass of the atmosphere is roughly 5.1×10^{18} kg, which is distributed over the 5.1×10^{14} m^2 of the Earth's surface, and represents pressure of about 10^4 kg m^{-2} at sea level (Bailey et al., 2002). The atmosphere usually contains water vapor, dust particles, and various gases (Table 3.8). However, concentrations of some trace constituents, like methane or carbon dioxide, have been increasing in last decades. The building block of the molecules is seldom replaced by radioactive nuclides such as ^{3}H, ^{14}C, and other. The concentrations of constituents may vary in different parts of the atmosphere. Table 3.8 does not include particulate matter (radius 10^{-7}–10^{-2} cm), which covers particles from molecular dimensions to large dust particles. Particulate matter in the atmosphere can be the result of human activities, impact of meteorites, volcanic activity, dust storms, forest fires, and ocean spray. The smallest particles, with radii of 0.1–1.0 μm, have a maximum concentration at about 18 km above the Earth's surface. Large particles can settle out of the atmosphere by gravitational settlement; furthermore, it is estimated that approximately 70% of the particles that enter the atmosphere are washed out back to surface as condensation nuclei of the water droplets that form rain clouds. Water droplets with radii from 1 to 50 μm are usually present in clouds; however, droplets with radii of 100 μm generally fall as a drizzle and larger droplets as rain.

The mixing characteristics of the atmosphere are influenced by its vertical temperature gradient. With increasing altitude, the properties of the atmosphere are changing rapidly; density and pressure are decreasing by exponential order. Similar behavior can be observed with temperature changes depending on day/night cycle, seasons, or as a result of vertical mixing of air masses. Exact changes of temperature and pressure with altitude can be described by an atmospheric model called the US Standard Atmosphere

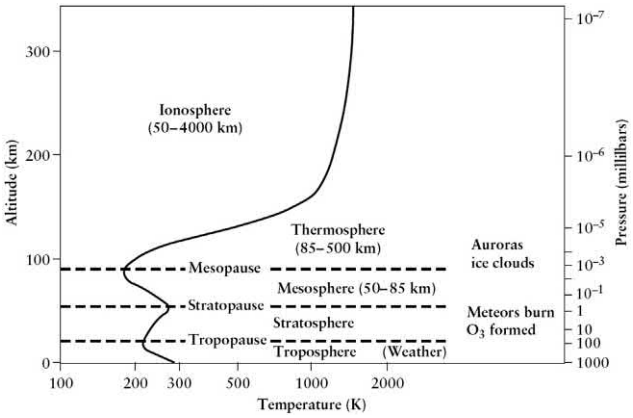


FIGURE 3.19 Temperature and pressure distribution in the atmosphere for different altitudes in US Standard Atmosphere model. *From Bailey et al. (2002).* Printed with permission © Elsevier 2018.

(Sissenwine et al., 1962). Several layers of atmosphere with different properties can be recognized from the model in Fig. 3.19. The closest layer to the Earth's surface is the troposphere with a height ranging from 8 km at polar latitudes to 18 km at the equator. Atmospheric water is mostly concentrated in the troposphere, and most of the physical processes forming weather occur in the troposphere. The temperature decrease with increasing altitude allows vertical mixing within the troposphere with vertical exchange of masses, momentum, and temperature, including water vapor transportation and dispersion of anthropogenic emissions. The boundary layer between the troposphere and the stratosphere is the tropopause. The height of the tropopause varies with latitude and with the season of the year, which is responsible for transport of air masses during spring and early summer from the stratosphere to the troposphere.

The stratosphere reaches up to 50 km with the maximum temperature of 0°C at its higher edge. Inversion conditions (the increase of the temperature with the altitude) are the reason for slow vertical mixing, and therefore, the pollution that reaches the stratosphere remains here even for several years.

In the range from 50 to 80 km, in the mesosphere, the temperature is again decreasing down to the lowest temperatures (−90°C) in the atmosphere. The course of temperature in the stratosphere and mesosphere is related with absorption of ultraviolet radiation by ozone. In higher altitudes (thermosphere), the temperature is rising. The velocity and mean free path of particles at high altitudes allow gases to escape to space.

To understand the global movements of the pollutants in the atmosphere, a simplified circulation in the atmosphere will be described. In general, there are two major reasons for circulation in the atmosphere. The first one is the difference in heating of the air masses by solar energy in equatorial and polar regions. In comparison with the atmosphere, the Earth's surface absorbs much more solar radiation, and by conduction, convection, and radiation from the ground, it heats the air in lower levels of atmosphere. The hot air is less dense and therefore tends to rise above it. In the equatorial region, the hot air rises to some height and flows toward the poles; however, in polar regions, the cold air travels near the surface toward the equator.

The second reason is the rotation of Earth; while the air near the equator rotates with the same velocity as Earth, the poles do not rotate and the air in these regions is static as well. The Coriolis effect describes the air movement between latitudes in which the speed of rotation is different, and this results in an unexpected component of wind speed with respect to the earth. A three-cell model describes the tree main prevailing wind directions in each hemisphere, as can be seen in Fig. 3.20. This model does not assume, however, the movement of the cells and the air exchange between them, but in comparison with Hadley's one-cell model (Hadley, 1735), it is a great improvement. Taking into consideration the global transport of air masses, the mean resident time of particulate matter in the lower atmosphere is between 3 and 22 days. When the aerosols reach the stratosphere, the mean resident time is 6 months to 5 years, and 5−10 years in the mesosphere.

Although radionuclides can be produced in the atmosphere, the pollutants are frequently released to the atmosphere from the surface. Once a gas, vapor, or aerosol has been introduced into the atmosphere, it is diluted by molecular and turbulent diffusion. While the diffusion coefficient for molecular diffusion is orders of magnitude lower than for turbulent, one can neglect it during the dilution

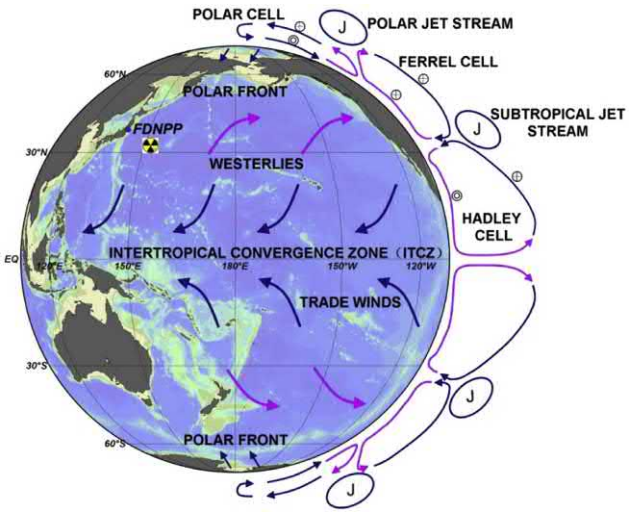


FIGURE 3.20 Three-cell model for motion of air masses around the globe. For the color version of the figure, the reader is referred to the online version of the book. *From Lin et al. (2015). Printed with permission © Elsevier 2018.*

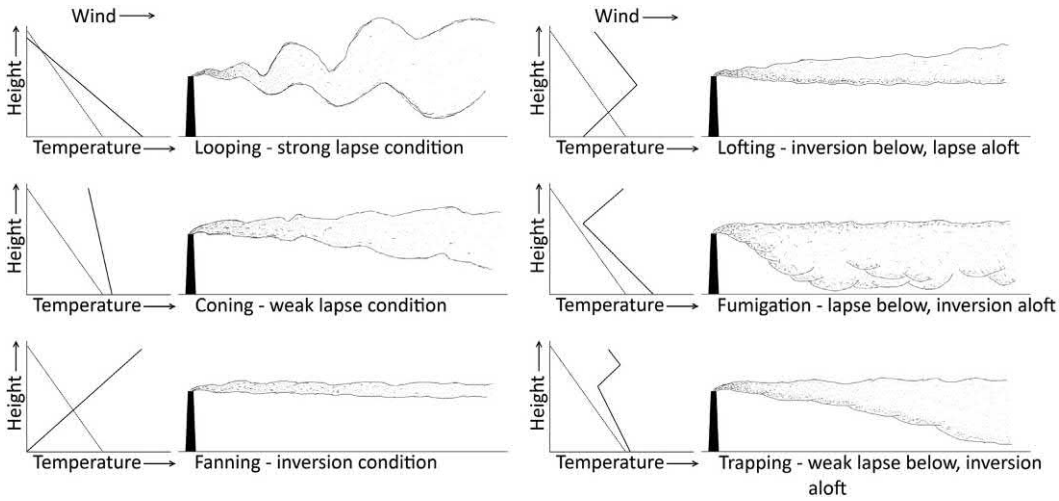


FIGURE 3.21 Stack-gas behavior of released pollutants under various stability conditions of atmosphere. Vertical stability is represented by temperature (black line) and dry adiabatic lapse rate (gray line).

processes (Eisenbud and Gessel, 1997). The vertical profile of the temperature greatly affects the stability of the atmosphere and therefore also the characteristics of dispersion, as can be seen in Fig. 3.21. When air temperature increases with altitude at some elevation, inversion conditions are formed. These temperature inversions trap rising air below effective stack height and result in accumulation of the pollutants.

B. Hydrosphere

The hydrosphere can be defined as the combined mass of all water present on Earth, either on its surface (oceans, river, lakes, glaciers) or under the ground (groundwater). Atmospheric moisture, mainly found in the form of vapor, snow, and rain, is also part of the hydrosphere. The overall mass of water in the hydrosphere is approximately 1.6×10^{21} kg. Only some 2.5% of the Earth's water is so-called freshwater, the rest is composed by seawater reservoirs. Water in the oceans covers about 71% of the planet's surface, whereas about 5% of the water mass is contained in the lithosphere. The largest reservoir of freshwater is incorporated in ice caps, glaciers, and permanent snow (68.7%), followed by groundwater (30.1%) (Gleick, 1996). Freshwater bodies support rather complex systems for living organisms. It has been estimated that about 12% of all animal species live in such ecosystems (Desonie, 2007). On top of that, millions of eukaryotic species can be found in the oceans (Mora et al., 2011).

Even though the total amount of water in respective reservoirs is more or less constant, water molecules are in permanent movement, which enables continuous exchange of water between the atmospheric, surface water, groundwater, and even living organisms. There are several transport processes of water (Fig. 3.22). Water is transferred to

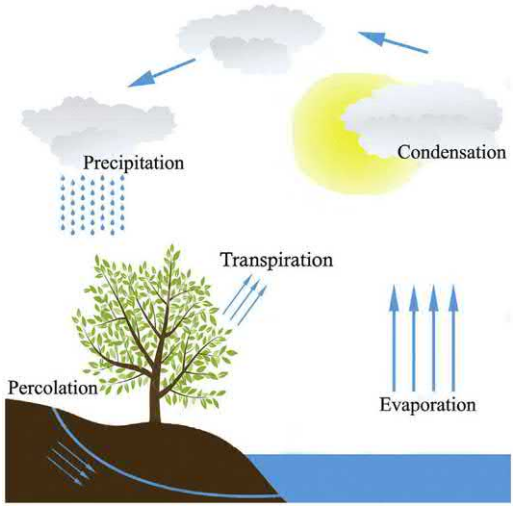


FIGURE 3.22 Schematic view of hydrological cycle. For the color version of the figure, the reader is referred to the online version of the book. *From Sadollah et al. (2015).* Printed with permission © Elsevier 2018.

the atmosphere from vegetation by transpiration, from surface of water bodies by evaporation, and from snow and ice by sublimation. In the air, if its temperature is lowered enough, it may be formed into clouds by condensation. Under the right conditions, water is transported back to the surface in the form of precipitates. Streams (rivers) assure flowing of liquid water from landscape areas to surface sources (lakes, ponds, seas), while part of it may be seeped into the ground by infiltration or may get even deeper where it can refill groundwater reservoirs (aquifers). The residence time of water in a particular reservoir depends on its type and may vary from days to hundreds of years (Table 3.9).

TABLE 3.9 Mean residence time of water in different reservoirs.

Reservoir	Mean residence time of water
Oceans	3100 years
Polar ice, glaciers	16,000 years
Groundwater	300 years
Freshwater lakes	1–100 years
Saline lakes	10–1000 years
Soil and subsoil moisture	280 days
Rivers	12–20 days
Atmospheric water vapor	9 days

After Wetzel (2001).

According to Lvovitch (1973), more water is evaporated from the surface of the oceans than is returned back by precipitation, while the opposite is true for continental areas where more water is transported onto lands than is transformed into vapors. Evaporation of oceans is the main source of continental water, which is unevenly distributed over the continents. For example, South America has the greatest total and groundwater runoff from all continents.

Recently, local fluctuations in the steady global water balance have been caused by anthropogenic activities, such as land clearing, exploitation of groundwater, and changes in drainage patterns. Before the end of the 21st century, the human-induced fraction of continental evaporation is expected to increase to about 50% by raising demand of water for agricultural and industrial uses. Therefore, freshwater will become a strategic material of the present century. This will further accelerate the rate of land freshwater turnover, which will be insufficient; thus large-scale desalinization of seawater will be necessary. Massive manipulations of surface waters at immense energy costs will eventually lead to changes of climate. As a result of huge modifications of large river systems, alterations of regional climate conditions have already been documented (Wetzel, 2001).

With the average depth of about 3700 m and the total volume of $\sim 1.35 \times 10^9$ km^3, oceans contain almost all Earth's water. While three-fourths of the oceans have a temperature in the range of 1–4°C, their overall average salinity and temperature is 3.47% and 3.51°C, respectively (Kennish, 2001). Because of wind action, a region with rapid mixing occurs near the surface of the oceans (the depth of 10–200 m). As a result of this mechanical mixing, the salinity, density, and temperature vertical gradients are fairly uniform. The surface and deeper water layers are generally separated by an intermediate zone, which can be as much as 1000 m deep and where density and salinity increases while temperature decreases with depth. Due to the fact that lighter (less dense) water overlies the heavier, vertical motions of water are restricted. Thus, the intermediate zone may limit exchange between the surface and deep layers, which can be important for the spreading of contaminants. The same might be said for surface currents that can transport large quantities of substances with the speed of tens kilometers per day.

Groundwater is an important source of water for agriculture, industry, and households, which might be reasoned by the fact that the world's volume of groundwater is by a factor of about 30 greater than the cumulative volume of water in lakes and rivers. Other aspect is that the quality of groundwater is usually better than the quality of water from surface sources. Groundwater only rarely occurs in underground pools or lakes but rather in saturated geological formations (aquifers), with the depth up to hundreds of meters. The amount of water potentially contained in the aquifer depends on porosity (percentage of pores) of its material where average porosities are between 30% and 40%, and for example, sediments have typical porosity of 10%–60% (Fetter, 2001). Permeability and the hydraulic gradient affecting the pressure determine the flow rate of the water in the geological formations. In general, groundwater is much less prone to contamination than surface water, because possible contaminating substances are often filtrated out during the infiltration. On the other hand, once the groundwater source gets contaminated, dissolved harmful substances are naturally removed from the source at a slow rate, about 4 cm d^{-1} (Desonie, 2007).

The atmosphere, soils, surface waters, and groundwater aquifers are connected via various transport pathways (Eisenbud and Gessel, 1997). Pollutants, which somehow occur in the deep underground aquifers, may reach surface waters and get distributed into the biosphere. Contaminants released to the atmosphere are deposited on surface waters or soils. From soils, polluting substances are removed by leaching into soil water or surface runoff. The fate of contaminants in the aquatic environment depends on several biological and physical processes. A suspended solid can be filtered by organisms, settle to bottom sediments, or become attached to plants. Dissolved contaminants can be adsorbed on inorganic and organic particulate matter or incorporated into the animals and plants. When the suspended solids settle at the bottom, they become part of the organic-rich substrate, useable by miscellaneous microorganisms. The sediments can act either as a sink for pollution or as a source when they are resuspended and redeposited at another place. If desorption occurs, the sediments may also act a secondary source.

Water has many unique properties connected with its molecular structure and unusual bonding, which makes it essential for life. A polar molecule of water forms in equilibrium an isosceles triangle, having a bond angle of 104.5° at oxygen and molecular electric dipole moment of

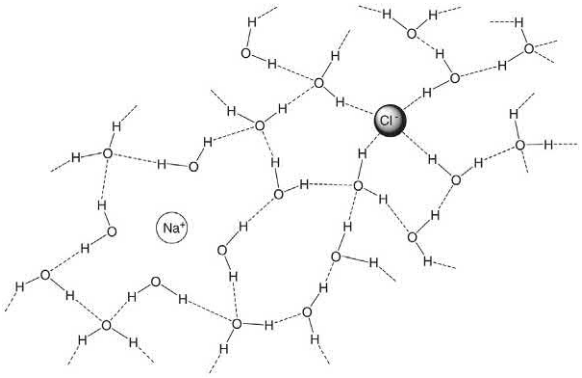


FIGURE 3.23 Illustration of hydrogen bonds in liquid water containing Na^+ and Cl^- ions. *From Maréchal (2007).* Printed with permission © Elsevier 2018.

1.85 D. The length of the O−H bond is 0.96×10^{-10} m. Probably the most characteristic feature of water is that it can create weak electrostatic interactions called hydrogen bonds between the oxygen atom of one molecule and hydrogen atoms of other molecules (Fig. 3.23). This means that each and every water molecule can be attracted by hydrogen bonds to four other ones. As a consequence of the existence of hydrogen bonds, water has many anomalous properties (e.g., unusually high melting and boiling point, highest density at 3.98°C, high specific heat capacity, lower density of the solid phase than the liquid phase, high viscosity and surface tension, etc.). Altogether, more than 70 water anomalies have been identified so far (Chaplin, 2018). A typical molecule of water in nature may be composed of three different oxygen ($^{16,17,18}O$) and hydrogen ($^{1,2,3}H$) isotopes, the molecule $^{1}H_2^{16}O$ being the most abundant. Because of its exceptional properties, water is the only substance naturally present in all phases. Another important feature of water is its relatively high capability to dissolve ions of inorganic and organic salts, which is crucial for continual transport of substances in the environment.

C. Biosphere

The biosphere is defined as a sum of all living organisms and their ecosystems on the planet. Another way of looking at the biosphere is as a layer of the planet where life forms live, evolve, and propagate. This definition allows one to define the boundaries of the biosphere where environmental conditions such as temperature, pressure, and chemical composition can no longer support any life forms. In the atmosphere, macroorganisms can be found in heights up to 11.2 km above sea level, as shown by a collision of an aircraft with a vulture at this altitude (Laybourne, 1974). However, microbial life forms can exist at even higher altitudes after being ejected high into the stratosphere during massive volcanic events. As an example, microorganisms were extracted and cultured from air at 41 km above sea level (Wainwright et al., 2003). In the oceans, both macroscopic and microscopic life forms are present even in the deepest parts of the Mariana Trench 10.9 km beneath the Pacific Ocean (Horikoshi, 2016). Single-cell and multicellular life has also been discovered in subsurface regions of Earth up to 3.6 km deep (Borgonie et al., 2011).

From a chemical point of view, living organisms in the biosphere are based on carbon−water chemistry, and carbon, oxygen, and hydrogen together with nitrogen and phosphorus are present in all organisms and make up more than 95% of living matter. In addition to these five elements, the most important biogenic elements are S, Na, K, Ca, Mg, and Cl, and they add up to 99% of living matter.

The biosphere permeates all of the environmental layers and closely interacts with them because they contain chemical elements and compounds necessary for life and procreation of living organisms—nutrients from the pedosphere, water from the hydrosphere, and gases from the atmosphere. These interactions together with reprocessing of organic material from dead organisms create material fluxes and cycles. This cyclic nature prevents depletion of material reservoirs essential to the biosphere. The most important cycles relating to the biosphere are water cycle and cycles of biogenic elements. These cycles are not independent; they are interconnected and often influence each other. Carbon, nitrogen, and sulfur (unlike other major biogenic elements) can take part in these interactions both in the form of gases and dissolved or undissolved in water (Smil, 2002). This makes them highly mobile, and their cycles are crucial for the biosphere. Other mineral biogenic elements can be transported only in water and are imported into the biosphere mainly by weathering processes from the lithosphere.

The water cycle (described in Section III.B) is essential for the biosphere as well, as water acts as a solvent, metabolite, and temperature buffer in the chemistry of living organisms and also as a living environment for many life forms. In terms of reservoir size, the biosphere is only a small part of the water cycle, but plant transpiration is a significant source of water input into the atmosphere.

Carbon is the most important biogenic element, and its cycle is therefore central to the entire biosphere. The carbon cycle consists of chemical and physical processes that exchange and accumulate carbon in different ecosystems, which represent carbon reservoirs. Major reservoirs of carbon are the atmosphere, terrestrial biosphere, oceans, and lithosphere. Atmospheric carbon is mainly in the form of CO_2, and it is biologically transported into the terrestrial biosphere by photosynthesis and becomes part of land organic matter. Autotrophic organisms store the assimilated carbon in their bodies, and heterotrophic organisms gain carbon by consuming other living organisms. A significant

part of the CO_2 converted to organic matter is emitted back into the atmosphere in the process of aerobic respiration and also by combustion of organic matter (either in wildfires or in the controlled burning of biomass).

Human civilization is also a part of the biosphere, and human activities can influence many of the aforementioned processes, including global water cycle and biogenic element cycling. A good example is the anthropogenic influence on the global carbon cycle. Human use of fossil fuels for energy generation added a new flux into the carbon cycle—removal of organic matter from sedimentary rocks and release of this fossil carbon into the atmosphere. Nitrogen and phosphorus cycles are heavily influenced by the production and use of synthetic fertilizers. The nuclear industry represents an input of radionuclides into the biosphere, some of which do not occur naturally in the environment. These anthropogenic interferences are usually faster than unperturbed processes in the biosphere and, therefore, it is hard to determine what the consequences of human activities in the biosphere will be on different time scales ranging from civilizational to geological.

The intensive cycling of materials within the biosphere itself and the interconnection of the biosphere with other environmental compartments is very important for environmental radioactivity studies, as these interactions determine which radionuclides migrate into the biosphere from other compartments and vice versa.

D. Pedosphere

The pedosphere is a layer of Earth formed mostly by soil, which originated from the lithosphere by rock erosion, actions of organisms, solar radiation, water, and air impacts, all during long geological times. The thickness of the soil layer is from a few cm to about 3 m. It is an interface between the lithosphere, atmosphere, hydrosphere, and biosphere. Soil comprises a multielement composition with some crucial elements such as carbon, oxygen, nitrogen, and phosphorus.

A fraction of organic carbon is stored in soil. Carbon from soil organic matter can be released as carbon dioxide by soil respiration (Raich and Schlesinger, 1992) or as a result of microbial decomposition. Exchange of carbon between the atmosphere and oceans is caused by a dynamic equilibrium of CO_2 dissolution in surface waters. Different solubilities in warmer water and colder water drive the so-called solubility pump that cycles carbon between surface and deep ocean waters. A similar biological pump is driven by photosynthesizing marine organisms (mainly phytoplankton) that fix carbon in their bodies, and after dying, they sink to the bottom of the ocean. Certain organisms can also combine calcium with carbonates dissolved in the water to create calcium carbonate in their shells. Carbon from these shells and dead phytoplankton is eventually sequestered in sediments on the ocean floor. Over geological time scales, these sediments create limestone and sedimentary rocks, and they become part of the lithosphere.

Although the lithosphere is the largest reservoir of carbon on Earth, its carbon is, however, relatively inert compared with other reservoirs, and therefore, it is cycled with the rest of the environment on very large time scales. Lithospheric carbon is bound in carbonate rocks and as organic matter in sedimentary rocks. Subduction of these carbon-containing rocks can produce carbon dioxide that is released into the atmosphere from volcanoes and volcanic vents.

Natural radioactivity in the Earth's environment depends primarily on geological and geographical conditions, appearing thus at different levels in soils of each region of the world (UNSCEAR, 2000). A number of natural radionuclides are observed as inherent soil contents, mainly ^{40}K and the isotopes of uranium and thorium with their daughter nuclides. With the use of nuclear technologies, anthropogenic radionuclides enter the soil environment as well, of which ^{137}Cs and ^{90}Sr are the most abundant ones. These radionuclides contribute to the radiation exposure, externally through gamma radiation and also internally through inhalation and the food chain.

Uranium and thorium isotopes are sources of radium isotopes (^{226}Ra, ^{228}Ra, ^{224}Ra), which are found in soil in trace concentrations. They are important sources of radon gas in the soil. The radon isotopes (^{222}Rn—uranium decay series, and ^{220}Rn—thorium decay series) are formed in soil by alpha decays of radium in the soil grains. After alpha decay of radium, radon atoms get kinetic energy as a consequence of their recoil. This energy is several times higher than the typical energy of a chemical bond, and therefore, radon atoms do not stay as a component of initial chemical structure, but they can migrate to the surface. The radon concentration in the soil air is thus created by radon atoms that reach the pores. The radon concentration in soil air varies depending on locality and time. It is mostly influenced by radium concentration in mother rock and by emanation processes, moisture, and permeability of soil layers. In common soils, the radon concentration decreases toward the surface very markedly, as radon is released into the outdoor atmosphere. In the long term, perspective ^{40}K, uranium and thorium isotopes, and their decay products, mainly radon, have been delivering the largest radiation doses to the public (EPA, 2007). In the soil air, the radon activity concentration reaches the value of several kBq m^{-3}, and it is not stable.

The interest in radon in the soil air is connected with a possibility of its use in the forecast of earthquake and volcanism (Igarashi et al., 1995; Weinlich et al., 2006), and also as a tracer of the transport of the other gases in the soil (CO_2, CH_4) (Dörr and Münnich, 1990).

IV. Analytical techniques

A. Radiometric techniques

Radioactive nuclides undergo radioactive decay and deexcite to the stable state with a characteristic half-life. The energy of the excited states can be released in several nuclear processes, i.e., by alpha decay, beta decay, EC, internal conversion, gamma ray emission, and spontaneous fission. By the detection of emitted particles and/or radiation, the radionuclides can be identified, and their activity concentration can be estimated. Several radiometric techniques have been developed, which meet the requirements for low-level analysis of radionuclides in the environment (e.g., Povinec, 2004, 2005, 2008a,b; Povinec et al., 2008).

1. Alpha spectrometry

During alpha decay, alpha particles with specific energy are emitted from the decaying radionuclide. Known radionuclides emit alpha particles in the energy range from 4 to 9 MeV. Alpha spectrometry uses a detector to record registered energy of the alpha particle in the form of a pulse height distribution. Several types of detectors, such as ionization chambers, proportional counters, and scintillation detectors, can be used for the determination of emitted alpha particle energy; however, semiconductor detectors are most frequently used. Statistical variations in interactions between alpha particle and the detector cause the emergence of energy broadening in the registered spectra. Ionization chambers have normally a high counting efficiency, but the energy resolution is very poor, unless equipped with a Frisch grid, which enables fast collection of the electrons by shielding the induction from the positive ions. Poor energy resolution of the proportional counters and liquid scintillation counters (about 20%) disadvantage the spectrometric use of these detectors, despite their 4π counting geometry. For some applications, solid scintillators such as CsI(Tl) and ZnS(Ag) are used as thin cover of the inner surface of the detector, i.e., Lucas cell. Because of the good counting efficiency and excellent energy resolution (0.5−1%), surface barrier and ion-implanted silicon semiconductor detectors are widely used in alpha spectrometry. Although the superior energy resolution, the small difference in the energy of alpha particles from a few radionuclides (^{239}Pu and ^{240}Pu, ^{214}Am and ^{238}Pu, ^{237}Np, ^{233}U, ^{234}U and ^{230}Th) makes the spectrometric separation of the peaks difficult.

Because of the significant energy losses of the alpha particles in the matter, measurements with solid detectors are carried out in a vacuum, to avoid energy losses in the air and additional energy straggling. The emitted alpha particles are registered within a thin surface layer of the detector, and the number of produced electron−hole pairs is proportional to the energy of the alpha particles. To avoid losses due to self-absorption and resulting reduction of counting efficiency and worsened energy resolution, the source containing the sample matrix should be as thin as possible. To remove the major matrix elements to minimize self-absorption and minor radionuclides with interfering energy of alpha particles, chemical separation is required. The thin layer of sample is prepared by electrodeposition on stainless steel disks; however, evaporation, coprecipitation, electrospraying, electrostatic precipitation, spontaneous deposition, molecular plating, and vacuum sublimation are also used (Lally and Glover, 1984). Sorption of some radionuclides on a thin manganese oxide film has been recently developed and used for alpha source preparation (Karamanis et al., 2007). To estimate the contribution of a technique to the sample counts, a procedure blank is often prepared. Concentrations of radionuclides in environmental samples are very low, and to obtain acceptable counting uncertainty, a long counting time is needed (i.e., 1−10 days for activities of about 10 mBq and below). For the absolute activity determination of an unknown radionuclide, a standard with known activity is determined in relation to the analyzed sample. A standard should be prepared from the same radionuclide to determine the detector efficiency, prepared, and measured under the same conditions. An alternative is to use an internal tracer, another isotope that is added to the sample during the radiochemical separation. The main advantage of alpha spectrometry is the relatively low cost of the equipment, a reasonable sensitivity because of the low background and the selectivity of alpha particles against other types of radiation (Povinec, 2004, 2010, 2011, 2013). The main disadvantages are the complicated chemical separations and long counting times (Miura et al., 1999). Radionuclides commonly determined by alpha spectrometry are listed in Table 3.10.

2. Beta counting

Radionuclides sensitive to beta decay are deexcited by emitting an electron (e^-) or a positron (e^+), together with an antineutrino or neutrino, respectively. Beta radiation does not have discrete energies because the two emitted particles (e^- and antineutrino or e^+ and neutrino) share the energy of the radioactive decay, and therefore, the resulting spectra is a continuous distribution of energies from 0 to maximum energy of the decay. The β^+-decaying radionuclides can be analyzed by gamma spectrometry of two emitted photons with energy of 511 keV, during the annihilation of the e^+. If an electron from an atomic shell is captured by the nucleus, the decay process called electron capture (EC) can be registered. The emission of the X-ray and/or Auger electrons follows EC, and therefore, the EC decaying radionuclides can be determined by X-ray spectrometry of emitted X-rays or by liquid scintillation counting (LSC) of the Auger electrons.

TABLE 3.10 Radionuclides commonly determined by alpha spectrometry (Hou and Roos, 2008).

Radionuclide	Half-life[a] (years)	Energy of main alpha particles (MeV) (abundance)	Detection limit[b] (ng)
^{226}Ra	1599	4.78 (94.5%), 4.60 (5.5%)	1.95×10^{-6}
^{229}Th	7.93 k	4.85 (56.2%), 4.90 (10.2%) 4.81 (9.3%), 5.05 (6.6%), 4.97(6.0%) 4.84 (5.0%), 4.98 (3.2%)	9.05×10^{-6}
^{230}Th	75.6 k	4.69 (76.3%), 4.62 (23.4%)	9.34×10^{-5}
^{232}Th	14 G	4.01 (78.2%), 3.95 (21.7%)	17.55
^{233}U	159 k	4.82 (84.4%), 4.78 (13.2%)	1.78×10^{-4}
^{234}U	245.3 k	4.77 (71.4%), 4.72 (28.4%)	3.09×10^{-4}
^{235}U	703 M	4.40 (55%), 4.37 (17.2%), 4.21 (5.7%) 4.60 (5.0%), 4.56 (4.2%)	0.89
^{236}U	23.42 M	4.49 (73.8%), 4.45 (25.9%)	2.97×10^{-2}
^{238}U	4.47 G	4.20 (79.0%), 4.15 (20.9%)	5.73
^{237}Np	2.14 M	4.79 (47.9%), 4.77 (33%), 4.64 (6.2%) 4.66 (3.3%)	2.74×10^{-3}
^{238}Pu	87.7	5.50 (70.9%), 5.46 (29.0%)	1.12×10^{-7}
^{239}Pu	24.1 k	5.16,873.3%), 5.14 (15.1%)	3.10×10^{-5}
^{240}Pu	6.56 k	5.17 (72.8%), 5.12 (27.1%)	8.48×10^{-6}
^{242}Pu	375 k	4.90 (77.5%), 4.86 (22.4%)	4.87×10^{-4}
^{244}Pu	81.2 M	4.59 (80.6%), 4.55 (19.4%)	0.11
^{241}Am	432.7	5.49 (84.6%), 5.44 (13.0%)	5.61×10^{-7}

[a]*Taken from Haynes (2017).*
[b]*The detection limit of alpha spectrometry was supposed to be 0.1 mBq.*
Printed with permission © Elsevier 2018.

The identification of the individual radionuclides from the spectrum of the beta particle is complicated, due to the continuous energy distribution in the spectrum of the emitted electrons in beta decay. Therefore, in practice, the identification of radioisotopes is based on the chemical separation of the radionuclide of interest, and low-level counting of beta emitters carried out by gas proportional counting (GPC) or LSC is used for the determination of activity. However, several radioisotopes can originate from one element (e.g., ^{89}Sr and ^{90}Sr), and despite the fact that some radioisotopes emit electrons with discrete energies (e.g., from internal transition and/or EC decay), the emitted electron cascade results in a complicated energy spectrum, which in parallel makes the accurate analysis of several beta decaying radioisotopes complicated.

During the LSC analysis, the radioactive sample solution is mixed with an organic liquid scintillator to form a homogeneous and colorless solution to minimize the self-absorption and maximize the counting efficiency. The activator molecules transform the released energy during the beta decay into excited states, and after their return to the ground state, photons are emitted. Photons are collected at the photocathode of the photomultiplier tube and converted to electrons, which are multiplied by the dynodes to form a pulse of several millivolts. The procedure of sample preparation for the LSC is relatively simple, together with using internal or external standards. LSC can be used also for isotopes decaying with the emission of conversion electrons or via EC (e.g., ^{41}Ca and ^{55}Fe). However, the counting efficiency for these decay modes is rather low (<30%), due to the low energy of the Auger electrons (<20 keV) (Hou and Roos, 2008; Povinec and Sanchez-Cabeza, 2006).

For the GPC, two approaches are used; in the first one, the sample is converted to the gaseous form and it is used as the filling for the detector. This method can be used for ^{3}H and ^{14}C, whereas methane is used as the filling gas. The second approach is similar to alpha spectrometry, where a thin sample is prepared and usually a Geiger–Muller (GM) detector with thin window is used for the counting of beta decays.

For the analysis of environmental samples, a low-level GPC is required. This can be achieved by passive (thick lead shield) and active shielding of the counter using an

anticoincidence mode with a detector surrounding the counter to suppress the counts coming from the natural background. A background count rate of 0.1 counts per minute (CPM) and the detection limit less than 1.5 mBq for ^{99}Tc and ^{90}Sr was reported for a commercial low-level GM counter produced at the Risø National Laboratory, Denmark (Hou et al., 2007). By using a multiwire proportional counter, Povinec (1978) achieved a background of 5 cpm with active anticoincidence shielding.

In comparison with the GPC, the background for the LSC is higher. With the use of the commercial QuantulusTM Ultra low-level LSC developed by Wallac (presently produced by Perkin–Elmer, United States), the background for the ^{3}H and ^{99}Tc window is about 0.5 and 1.5 cpm, respectively (Hou and Roos, 2008). Radionuclides commonly determined by beta spectrometry are listed in Table 3.11.

3. Gamma spectrometry

If the nucleus is in an excited state, i.e., as a consequence of alpha or beta decay, it can deexcite to the ground state by emitting gamma radiation with characteristic energy. Those emitted gamma rays can be registered by the spectrometer, and the source radionuclide can be identified and counted. Several or only one gamma ray can be emitted during the deexcitation process, and even more than one decay process may be observed. Gamma spectrometers are then designed to follow the decay modes of investigated radionuclides (Zvara et al., 1994).

Several types of detectors can be used for the registration and measurement of gamma rays, such as scintillation detectors (NaI, CsF, and ZnS), gas-filled detectors, and semiconductor detectors (based on Si, Ge, CdTe, and GaAs crystals). It is required that information about the deposited energy of the gamma ray in the detector can be recorded by the energy spectrum. The development of the high-purity germanium detectors (HPGe) in the 1980s was a great step in the maintenance of the detector, and the recent development of large-volume Ge crystals favors the use of germanium detectors by many laboratories. Small silicon (e.g., Si(Li) or silicon-drifted detectors [SDDs]) or planar germanium (low-energy germanium [LEGe]) detectors are

TABLE 3.11 Radionuclides commonly determined by beta spectrometry with detection limits for liquid scintillation counting (LSC) and gas proportional counting (GPC) (Hou and Roos, 2008).

Radionuclide	Half-life (years)	Decay	E_{max} (keV) (abundance)	Detection limit LSC (ng)	Detection limit GPC (ng)
^{3}H	12.31	β^-	18.6	2.50×10^{-8}	
^{14}C	5730	β^-	156.5	7.41×10^{-5}	
^{36}Cl	301,000	β^-	708.6	8.10×10^{-3}	2.33×10^{-3}
^{41}Ca	99,000	EC		3.41×10^{-3}	
^{55}Fe	2.75	EC		1.28×10^{-7}	
^{63}Ni	99	β^-	66.9	6.78×10^{-6}	3.39×10^{-6}
^{79}Se	330,000	β^-	151.1	0.072	0.038
^{89}Sr	0.1386	β^-	1459.1	1.47×10^{-8}	2.62×10^{-9}
^{90}Sr	28.9	β^-	546	2.66×10^{-6}	5.64×10^{-7}
^{99}Tc	213,000	β^-	293.7	0.021	5.62×10^{-3}
^{129}I	17×10^{6}	β^-	154.2	1.88	
^{135}Cs	2.3×10^{6}	β^-	269.3	0.313	0.0835
^{210}Pb	22.6	β^-	17.0 (84%) 63.5 (16%)	8.40×10^{-6}	3.78×10^{-6}
^{228}Ra	5.76	β^-	39.4 (50%) 25.7 (20%) 12.8 (30%)	1.41×10^{-6}	
^{234}Th	0.066	β^-	199.1 (70.3%) 106.5 (26.8%)	1.55×10^{-8}	
^{241}Pu	14.33	β^-	20.8	5.59×10^{-6}	

Printed with permission © Elsevier 2018.

routinely used for the measurement of low-energy gamma (<100 keV) and X-rays, with an energy resolution of about 130 eV for the 5.0 keV line of ^{55}Fe. Recently, BEGe (broad-energy germanium) detectors have become popular, offering higher detection efficiency for medium-energy gamma rays.

To sustain the counting efficiency, a thin window (usually from low Z material such as beryllium, carbon composite, or Si_3N_4) is required for good transition of gamma and X-rays to the crystal. Larger Ge detectors are better suited for gamma rays with higher energies (>30 keV), usually with an energy resolution of about 2 keV for the 1332 keV line of ^{60}Co. Due to the low absorption of gamma rays in the materials, radionuclides that emit high-energy gamma rays can be measured without any treatment or preparation. Therefore, radionuclides such as ^{60}Co, ^{65}Zn, ^{54}Mn, ^{94}Nb, ^{106}Ru, ^{133}Ba, ^{134}Cs, ^{137}Cs, ^{144}Ce, ^{152}Eu, ^{154}Eu, and ^{241}Am are routinely measured in environmental samples by gamma spectrometry.

To identify radionuclides in the spectrum, precise energy calibration is needed, constructed from energies of known standards. If the activity concentration is determined in the sample, efficiency calibration is required either from a standard with similar geometry and composition or by Monte Carlo simulations (Povinec et al., 2008; Povinec, 2012; Kováčik et al., 2013). A disadvantage of gamma spectrometry is normally a high background induced by cosmic ray interactions, radioactive contamination of construction materials of the detector, and surrounding environment. Therefore, shielding is necessary to achieve an acceptable detection limit. For the low-background gamma spectrometer on the surface, radioactive clean materials are needed for the construction of detectors and background shielding, whereas additional suppression of cosmic ray muons by anticosmic shielding is required for better sensitivity (Povinec et al., 2004, 2005; 2006; Sýkora et al., 2008). If a lower detection limit has to be reached, the detector efficiency needs to be increased and the detector background needs to be suppressed. To suppress the cosmic ray component of the detector background, it is useful to locate it deep underground (several thousand meters of water equivalent) (Laubenstein et al., 2004; Niese, 2008).

More information on low-level alpha- and beta counting using radiometric techniques (including underground detection systems) can be found in Chapter 5, Volume 2.

B. Low-energy inorganic mass spectrometry

Unlike in the case of radiometric methods, which are used to detect characteristic radiations emitted by the decay of radionuclides to determine their quality and/or quantity, inorganic mass spectrometry techniques are based on the direct measurements of atoms (ions) of radionuclides. Mass spectrometry is especially useful for the analysis of long-lived radionuclides because the longer the half-life, the lower is the radioactivity of the radionuclide and the more sensitive mass spectrometry techniques are in comparison with radiometry. Plentiful applications in various fields of radionuclide analysis, such as the determination of natural radionuclides in high-purity materials, environmental monitoring, characterization of nuclear materials, radiobioassay measurements, radioactive waste control, geochronology and geochemistry, and even health and food control, have proven how important the development of inorganic mass spectrometry has been. The mass spectrometry methods allow multielemental determinations of radionuclide concentrations at ultratrace levels (Becker, 2012).

Although there are several low-energy mass spectrometry methods available, basic principles are practically the same for all of them. Typical modern instrumentation for mass spectrometry is composed of three essential components. First, ions are produced, accelerated, and focused in an ion source, which is the signature part of every mass spectrometry technique. After the ion source, ions in the beam are separated according to their respective mass-to-charge ratios in the region called the analyzer. As the last step, the separated ion beams are measured by a collector, either sequentially (single collector) or simultaneously (multicollector). The detection of ions itself in the collector is most commonly achieved by a Faraday cup or electron multiplier.

Here, we shall briefly discuss conventionally exploited low-energy inorganic mass spectrometry techniques, namely inductively coupled plasma mass spectrometry (ICP-MS), secondary ion mass spectrometry (SIMS), resonance ionization mass spectrometry (RIMS), glow discharge mass spectrometry (GDMS), positive-ion mass spectrometry (PIMS), and ^{3}He ingrowth spectrometry for tritium analysis.

1. Inductively coupled plasma mass spectrometry

A possibility to combine the ICP source with a quadrupole mass analyzer was introduced in the 1980s (Houk et al., 1980). Since then, ICP-MS has been developed into the most successful and frequently used inorganic mass spectrometry technique for the determination of isotopic ratios in the trace and ultratrace concentration range. ICP-MS offers a few advantages over other analytical techniques. Current systems are capable of measuring many samples with high precision and accuracy in a relatively short time. Furthermore, the general design of the ICP source allows ionizing of the sample—the nebulized solution or laser-ablated material—directly under atmospheric pressure. This enables an easy coupling of ICP-MS with different separation techniques, such as liquid chromatography, gas

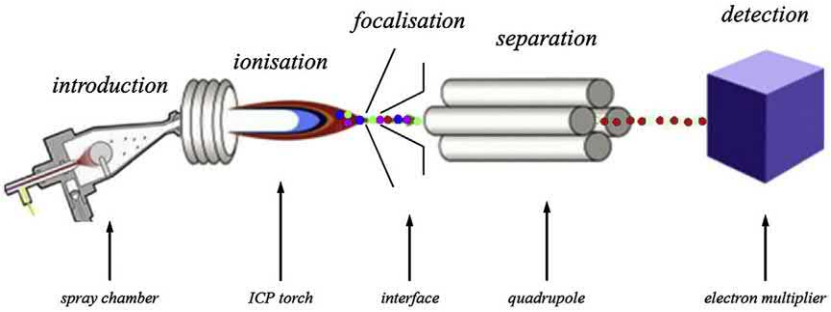


FIGURE 3.24 Simplified scheme of generic inductively coupled plasma mass spectrometry (ICP-MS) system. For the color version of the figure, the reader is referred to the online version of the book. *From Aceto (2016).* Printed with permission © Elsevier 2018.

chromatography, capillary electrophoresis, solid-phase microextraction, and others (Becker, 2012).

The generic scheme of the ICP-MS system and basic steps of any ICP-MS measurement are shown in Fig. 3.24. In the spray chamber, small droplets of the aerosol, produced from an aqueous sample by the nebulization process, are passed further into the plasma torch. There, chemical compounds are decomposed and ionized into atomic ions in argon plasma at the temperature of 6000−8000 K, with the typical efficiency better than 90% (Hou and Roos, 2008). The positively charged ions are focused by ion optics and extracted into the mass spectrometer through a sample and skimmer cones (interface). Well-designed ion optics can produce good detection limits, stable signal in sample matrices, and low background. Separation of ions based on mass-to-charge ratio is usually conducted by a quadrupole time-of-flight (TOF) analyzer or combination of electrostatic and magnetic sectors, where a double-focusing sector-field analyzer is generally considered to be superior to the quadrupole. In the end, the ions emerging from the mass analyzer are counted by a detector (electron multiplier or Faraday cup).

As in every mass spectrometry technique, ICP-MS is limited by the fact that the signal from ions of interest (e.g., $^{99}Tc^{+}$) can be disturbed by various interfering ions, such as polyatomic ions ($^{98}Mo^{1}H^{+}$), single isobaric ions ($^{99}Ru^{+}$), or single atomic ions causing tailing ($^{98}Mo^{+}$ or $^{100}Mo^{+}$). Some interference can be eliminated by increasing the resolution; however, others are more problematic and require the use of more advanced approaches, such as the exploitation of radiochemistry separation methods for sample preparation (Lehto and Hou, 2011), using more than one collector (Wieser and Schwieters, 2005), implementing dynamic collision/reaction cells to the system (Becker, 2012), coupling ICP-MS with a Fourier transform ion cyclotron resonance system (Barshick et al., 2000), or using the Orbitrap mass spectrometer (Koppenaal et al., 2011). Additionally, laser ablation, special sample introduction systems, electrothermal vaporization or hydride formation, or using cold plasma can also help to solve interference problems and matrix effect in ICP-MS measurements (Becker, 2012; Povinec et al., 2001).

After some necessary development, dynamic collision/reaction cells in ICP-MS have become more and more popular, especially for quadrupole systems (Tanner et al., 2002; Roos, 2008). In principle, collision/reaction gas (e.g., H_2, He, CO_2, NH_3, CH_4) presented in a cell reacts and collides with various ion molecules. As a consequence, polyatomic interfering ions are converted to noninterfering species, whereas the analyte can be transformed into another type of ion. Moreover, interfering isobars can also be removed due to different reaction rates of the analyte and isobar with the reaction gas. A typical collision cell, operating in the radio frequency (RF) mode, is positioned before the mass analyzer. A good example of the application of collision/reaction cells in ICP-MS are measurements of ^{129}I ($T_{1/2} = 1.57 \times 10^{7}$ years), which has a serious interferent ^{129}Xe present in the Ar carrier gas. In a hexapole cell, $^{129}Xe^{+}$ ions can react with the mixture of O_2 and He, transfer their charge to the gases, and get removed as neutral atoms before the mass analyzer. The polyatomic ions $^{127}I^{1}H^{2+}$ are also eliminated, which significantly improves the detection limit up to 0.4 pg g^{-1} (Becker, 2012; Lehto and Hou, 2011; Wyse et al., 2001). Other long-lived radionuclides (e.g., ^{93}Mo, ^{99}Tc, ^{107}Pd, ^{126}Sn, ^{151}Sm, ^{236}U, and ^{239}Pu) determined by quadrupole ICP-MS with a hexapole collision/reaction cell have the limits of detection in the range of 0.03 and 0.3 pg mL^{-1} (Becker, 2002).

Several parameters (abundance of interferents, background signal, measured element, sensitivity of the instrument) determine the detection limit for an ICP-MS measurement of radionuclides, which typically varies between 1 fg mL^{-1} and 10 ng mL^{-1}. Precision for isotopic ratio measurements by double-focusing sector-field ICP-MS can be as high as 0.02%, which is possible to improve by using a multiions collector device instead of a single collector by a factor of about 10, while it is a bit lower (0.1−0.5%) in the case of conventional quadrupole ICP-MS (Lehto and Hou, 2011). As isobaric interferences and background are generally higher for low-to-intermediate mass radionuclides, the limit of detection of ICP-MS is substantially better for high-mass radionuclides. Therefore, besides aforementioned radionuclides and some others (e.g., ^{79}Se, ^{90}Sr, ^{93}Zr, ^{135}Cs, ^{210}Pb, ^{226}Ra), isotopes of

actinides are most common radionuclides analyzed by ICP-MS (Nisi et al., 2009).

2. Thermal ionization mass spectrometry

Thermal ionization—ionization of atoms after contact with a very hot surface—has been known for several decades (first time observed in 1906); however, thermal ionization mass spectrometry (TIMS) has been profitably used since the 1980s. In TIMS, usually a small volume of liquid sample is evaporated and afterward ionized by resistive heating using a filament surface. Materials with high melting point and high purity, such as rhenium, tantalum, tungsten, and platinum are used as filament materials. Positive ions or molecules are generally used in TIMS; however, negative ions can be used, e.g., for boron, because of higher sensitivity of BO_2^- compared with $Na_2BO_2^+$, $Rb_2BO_2^+$, or $Cs_2BO_2^+$ (Klö;tzli, 1992). To eliminate the suppressive effects of ion formation by impurity elements in the solution, a pure chemical form is required for analyzed elements (Aggarwal, 2016), which results in time-consuming chemical preparation. Sample of about 0.5−1 μL aqueous solution with 1M HNO_3 is dried on the filament, and a particular ion is generated. To enhance the ionization yield of the measured element, ionization enhancers such as silica gel or H_3PO_4 and additives such as graphite and H_4SiO_4 can be used with the sample solution. After production, ions are accelerated to low energies, separated according to their mass, and registered usually in a multi-Faraday cup detection system.

With the development of fully automated systems for TIMS, the precision of isotopic ratio measurements is better than 0.01%, and by using normalization corrections for the isotope fractionation, the precision of 0.001% can be achieved (Hou and Roos, 2008). In comparison with other mass spectrometry techniques, the main limiting factors for the accuracy of TIMS in isotopic ratios measurements are the mass fractionation effects; however, by internal calibration and by using isotopic standard reference materials (e.g., from NIST—National Institute of Standards and Technology or IRMM—Institute of Reference Materials and Measurements) with known isotopic ratios, those effects could be minimized. The isotope dilution method, when a known amount of the precalibrated spike of long-lived isotopic solution of the same element, whose concentration needs to be determined, is added to the solution or solid, is frequently used. Since the determination of the studied isotope by isotope dilution mass spectrometry depends on the collected charge of the isotope−amount ratio, the data are not affected by incomplete recovery in chemical treatment.

The determination of ratios for radiogenic elements in geology, as well as tracer studies, is the primary application of TIMS. In geology, the determination of an age of a closed system could be measured by the ratio of the growth of daughter isotopes from radioactive decay and is referred as geochronology. TIMS is successfully used for dating of different matrixes by the determination of U-Pb (Crowley et al., 2015; Frechen et al., 2007; Waas et al., 2011; Zhong et al., 2017), Rb-Sr (de Meyer et al., 2014; Kanjanapayont et al., 2012; Li et al., 2008; Nebel and Mezger, 2008), and Nb-Sm (Guo et al., 2016; Henjes-Kunst et al., 2014). It is also used in cosmological studies for the analysis of different isotopes in extraterrestrial objects (Bermingham et al., 2018, 2016; Bonnand et al., 2016). Uranium isotopes can be precisely and accurately measured by TIMS in environmental monitoring (Taylor et al., 1998) and in nuclear forensic analysis (Bürger et al., 2007; Kraiem et al., 2011; Radulović et al., 2018; Rim et al., 2017). TIMS can be also used in environmental studies for the determination of plutonium isotopes (Lee et al., 2018; Xing et al., 2018).

3. Resonance ionization mass spectrometry

In resonance ionization, photons of precisely tuned lasers are used for excitation and ionization of valence electrons in the neutral atoms. RIMS combines the resonance laser ionization and mass spectrometry techniques. Before resonance ionization, only a neutral gas from sample material had to be produced by techniques such as laser evaporation, thermal evaporation by ion sputtering techniques, whereas the formation of ions had to be avoided or separated from produced gas. Sample material from a heated W or Re filament is usually thermally vaporized, and one or more lasers with chosen wavelength, according to the ionization scheme, are used for the ionization of only atoms of the element of interest. For resonant ionization, two or more precisely tuned lasers are used for excitation of the electron in ground state to intermediate excited states of hyperfine structure and excite the electron until it leaves the ionized atom. Whereas each element has a unique electron configuration, resonance ionization provides nearly complete isobaric suppression. High ionization efficiency, high transmission mass spectrometers, and low background ion detection enable a detection limit in the 10^{-15} to 10^{-18} g range and sensitivity better than 10^{13}, achieved by a combination of isotope selectivity of mass spectrometers and isobar selectivity in the laser resonant ionization (Hou and Roos, 2008). Although the basic principles of the resonant ionization were known for many years, described by Zandee and Bernstein (1979) and later Hurst and Payne (1988), the full utilization of the technique was achieved after the mid-1990s, when high enough power density lasers were developed. Due to its excellent sensitivity, resonant ionization is widely used in studies of nuclear structures (Fedosseev et al., 2012; Lassen et al., 2006). At present, there are no commercial RIMS instruments in the market; therefore, only several laboratories have developed the

technique for routine trace analysis. RIMS isotope analysis and the determination of many long-lived radioisotopes of interest such as ^{41}Ca (Bushaw et al., 2001), ^{90}Sr (Bushaw and W. Nortershauser, 2000), ^{135}Cs (Pibida et al., 2004), ^{236}U (Bushaw et al., 2007), and plutonium isotopes (Bürger et al., 2006; Raeder et al., 2012) have been developed and can be used for the analysis of environmental, biological, nuclear forensics, and technical samples (Erdmann et al., 2008; Wendt and Trautmann, 2005).

4. Glow discharge mass spectrometry

GDMS involves the sputtering of usually a solid sample (liquid as a dried solution) by Ar^+ ions produced in gas glow discharge. Typically, from 10 to 100 Pa of Ar is used to produce sufficient ions, which are accelerated toward the sample on the cathode surface, with energies from hundreds to thousands eV. Due to charge-up effects on the sample, the analysis of nonconducting materials is difficult by GDMS. Therefore, several techniques, such as mixing with high-purity metal powder or the use of a secondary cathode, have been applied during the analysis of electrically insulating samples. Neutral atoms sputtered from the sample are ionized in the glow discharge plasma, by Penning and/or electron impact ionization or charge exchange processes; the positively charged ions are extracted from the ion source to the spectrometer. The method was established as a powerful and efficient analytical tool for determination of trace elements analysis and depth profiling in bulk materials or thin films (Di Sabatino, 2014). With the microfabricated glow discharge plasma in the ion source, pixel mapping of the solid samples allows a relative fast determination of the surface distribution of the studied element (Gamez and Finch, 2018; Tian et al., 2016) and a 3D distribution by using depth profiling for each pixel. By using pulsed glow discharge in combination with gated TOF spectrometer, even spectra produced by different ionization mechanisms can be collected (Pereiro et al., 2011).

Although sputtering and ionization occurs at a different location in different times of the instrument, matrix effects are minimized and calibration with quantification of the device is much simplified. Since the sample preparation for GDMS analysis is very simple and samples can be directly analyzed, the risk of contamination is low. GDMS is used for the determination of trace elements in bulk solid samples, but it was also successfully applied for the fast analysis (without chemical separation, like for ICP-MS and TIMS) of uranium (Ganeev et al., 2017) and plutonium isotopes (Betti and Aldave de las Heras, 2004). However, the application of GDMS in the determination of radionuclides is limited due to its low sensitivity and limited accessibility (Hou and Roos, 2008).

5. Secondary ion mass spectrometry

In SIMS, the primary-focused ion beam of sufficiently high ion energy (up to 40 keV) is used to sputter the surface of the sample material. This is rather similar to GDMS, but the production of the primary beam is different. Depending on the analyzed element and required information, a primary ion beam made of, e.g., Ga^+, Cs^+, O_2^+, or O^-, can be chosen for high sputtering and ionization yield. Sputtered secondary particles, like clusters, neutrals, and about 1−5% sputtered ions, are after production and ionization in the ion source analyzed by mass spectrometry techniques. During the sputtering, molecular ion formation is often observed, and large matrix effects make the quantification of analytical results very difficult; nevertheless, by using a standard reference material, a precision of 0.002% can be reached (Hou and Roos, 2008). The main use of SIMS is in surface mapping and depth profiling of elements and isotopic ratios on solid samples with submicrometer resolution (Guerquin-Kern et al., 2005). Therefore, SIMS can be combined with a high-resolution spectrometric technique, such as TOF or accelerator mass spectrometry (AMS), to obtain unique information about surface distribution. It is often used for the identification and characterization of elements and isotopes in biological tissues (Shao et al., 2018a), small particles in aerosols (Huang et al., 2017), and liquid and solid samples. "Hot" particle identification and spatial distribution of radionuclides in nuclear materials can be determined with the SIMS technique by nuclear safeguards (Ranebo et al., 2007; Tamborini and Betti, 2000; Veniaminov, 2000).

6. ^{3}H-^{3}He ingrowth mass spectrometry

Due to its very low natural abundance ($^3H/^1H = \sim 10^{-18}$), direct analysis of tritium at trace levels by mass spectrometry techniques is still a challenge. To overcome this problem, ^{3}H-^{3}He ingrowth spectrometry has been developed, which is based on the determination of ^{3}He—produced by the decay of tritium—and back calculation of ^{3}H activity (Clarke et al., 1976). Currently, it is the most sensitive method for $^3H/^1H$ isotope ratios that can be measured down to 10^{-20}, which corresponds to the tritium activity of 0.01 TU or 1.19×10^{-3} Bq L^{-1}. The technique is mostly exploited for the analysis of seawater where the concentration of ^{3}H is beyond the measuring capabilities of radiometric methods; however, other types of water samples may be analyzed as well. To avoid possible contamination, the water sample is usually distilled prior its analysis. After that, the sample is transferred and hermetically sealed in a stainless steel container, where it is degassed by a vacuum pump. As tritium decays, the concentration of ^{3}He is slowly increased until the sufficient number of helium atoms is reached, which may take some

6 months. Before the measurement, the tritiogenic helium fraction is separated, purified, and isotopically diluted with a high-purity ^{4}He spike. The actual determination of ^{3}He/^{4}He can be conducted by a 90 degrees sector-field noble gas spectrometer (Palcsu et al., 2010; Papp et al., 2012).

7. Positive-ion mass spectrometry

Despite its overall versatility, AMS has some disadvantages, connected mainly with the need to use sputter negative ions sources (as discussed later). PIMS, recently developed and successfully tested by Freeman et al. (2015), might have the potential to overcome these limitations. The method is based on the opposite principle of the convenient tandem AMS, i.e., positive ion beam produced in the ion source (e.g., RF plasma source or electron cyclotron resonance ion source) is converted to the negative one with the use of a stripper channel, completely omitting acceleration. In radiocarbon measurements, the 140−280 keV carbon ion beams and N_2 or isobutane gases used for stripping showed enough efficiency to reproduce the >50,000 years radiocarbon age range of AMS. The mass separation of interfering ions (N^+, N^{2+}, CH^+, CH^{2+}, etc.) was performed by combining electrostatic analyzers (ESAs) with 90 degrees double-focusing magnets. PIMS could theoretically be more efficient and much faster than AMS, enabling high-precision analyses in seconds or even in real time. Besides radiocarbon, first results from the development of ^{26}Al-PIMS have been published as well (Shanks and Freeman, 2015).

C. Accelerator mass spectrometry

In mass spectrometry, the ions are formed from the sample, accelerated to energy E (ranging in keV) and afterward separated according to their mass. However, when studying some rare radioisotopes, the molecular interference becomes a problem; therefore, several methods were developed to suppress the formation and to separate the unwanted mimic molecules and ions. By accelerating the ions into higher energies (ranging in MeV), the ambiguities with identification of atomic and molecular ions with the same mass can be almost removed. This technique (called AMS) is able to measure isotopic ratios for specific elements to a level of 10^{-15} per ion. It was first used by Alvarez and Cornog (1939) for the detection of ^{3}He with the 88-inch Berkeley cyclotron, but the true potential of the technique was revealed by Muller (1977), where the method for the detection of ^{14}C and ^{10}Be by particle accelerator was described. Shortly afterward, AMS methods for other long-lived radionuclides were developed, including ^{10}Be (Raisbeck et al., 1978), ^{26}Al (Raisbeck et al., 1979), ^{36}Cl (Elmore et al., 1979), ^{41}Ca (Raisbeck and Yiou, 1979), and ^{129}I (Elmore et al., 1980).

Nowadays, AMS has evolved into an ultrasensitive technique for isotope analysis with a wide range of applications described in many articles and conference proceedings from 1978 up to 2017 (Gove, 1978; Gove et al., 1987; Henning et al., 1981; Wölfli et al., 1984; Yiou and Raisbeck, 1990; Fifield et al., 1994; Jull et al., 1997; Kutschera et al., 2000; Nakamura et al., 2004; Knezovich et al., 2007; Calcagnile et al., 2010; Zondervan et al., 2013; Braucher and Bourlès, 2015). The AMS became the most sensitive analytical technique for the analysis of radionuclides in the environment (Povinec, 2018a,b; Povinec et al., 2018ab). Long-lived radionuclides commonly measured by AMS are listed in Table 3.12.

1. Ion separation in accelerator mass spectrometry

Similar to conventional (low-energy) mass spectrometry, AMS does not directly measure the concentration in the

TABLE 3.12 Long-lived radionuclides commonly measured by accelerator mass spectrometry.

Radionuclide	^{10}Be	^{14}C	^{26}Al	^{36}Cl	^{41}Ca	^{129}I
Half-life (years)	1.51 M	5.73 k	720 k	301 k	103 k	15.7 M
Stable isotopes	^{9}Be	^{12,13}C	^{27}Al	^{35,37}Cl	$^{40\text{-}42,43,44}$Ca	^{127}I
Stable isobars	^{10}B	^{14}N*	^{26}Mg*	^{36}Ar*, ^{36}S	^{41}K	^{129}Xe*
Chemical form	BeO	C	Al_2O_3	AgCl	CaH_2/CaF_2	AgI
Sample size (mg)	0.5	0.01−1	2	1	10	2
Sensitivity (atom ratio)	2×10^{-15}	1×10^{-15}	2×10^{-15}	1×10^{-15}	5×10^{-15}	4×10^{-14}

*Does not form negative ions.
After Tuniz et al. (1998).

sample quantitatively but uses a stable nuclide, usually from the same element, as a reference. The result is therefore a ratio of trace to reference ions, called also the isotopic ratio. Before the ions are registered, they have to be produced from sample material and properly separated by using different trajectories in electric and magnetic fields. Often, the ions should be well focused for elimination of the suppressed background. By combination of the electric, magnetic, and radiofrequency fields, the chosen mass is filtered out from the produced ion beam. In ESA, a potential difference ΔU is applied between cylindrical or spherical electrodes at a distance d, whereas the ion beam follows a circular trajectory with a radius r_0. When an ion with charge q and energy E enters the ESA, the trajectory can be described by the equation:

$$\frac{E}{q} = \frac{\Delta U r_0}{2d} \tag{3.3}$$

Therefore, the ESA acts as a filter for the ions with the same E/q; and for ions with the small relative energy deviation, spatial separation at image position can be written as

$$\Delta x = r_0 \frac{\Delta E}{E} \tag{3.4}$$

Furthermore, the magnetic field separates the ions according to their momentum over charge. According to the Lorentz force, for the movement of the ion in the homogenic magnetic field perpendicular to the ion trajectory, the following equation can be written as

$$\frac{p}{q} = \frac{\sqrt{2ME}}{q} = Br_0 \tag{3.5}$$

where p is the momentum of the ion, M is the ion mass, B is the magnetic field strength, and r_0 is, in this case, the nominal beam radius of the magnet. Spatial separation of the ions with a small relative energy or mass deviation can be written as

$$\Delta x = 2r_0 \left(\frac{\Delta E}{E} + \frac{\Delta M}{M} \right) \tag{3.6}$$

By a combination of electric and magnetic fields, a velocity filter or Wien filter can be used. Uniform magnetic and electric fields at right angles and perpendicular to the incident beam can cancel the forces affecting the chosen ion and results in a straight nominal trajectory. Placing the electrostatic deflector plates with a distance d and a potential difference ΔU inside of a magnet with the field strength B, only the neutral or ion with velocity v will pass the filter

$$v = \sqrt{\frac{2E}{M}} = \frac{\Delta U}{Bd} \tag{3.7}$$

If the image is at a distance s from the center of the Wien filter with length l, the spatial separation can be obtained:

$$\Delta x = \frac{lsq\Delta U}{4Ed} \left(\frac{\Delta M}{M} - \frac{\Delta E}{E} \right) \tag{3.8}$$

Even by using the selectors or filters, different unwanted particles may reach the detector, which influence the detection limit of the spectrometer. This includes atomic and molecular isobars, ions with the same M/q and E/q as the chosen ion, ions with the incorrect mass, energy, or charge that mimic the path of the ions of interest in filters and selectors. Most of these limitations are drastically reduced by using the accelerator in the mass spectrometry system. A typical AMS facility consists of an ion source, injector (low energy separation), ion accelerator, analyzer (high-energy separation), and detection system for separated ions (Fig. 3.25).

2. Ion source

If the tandem accelerator is used for the AMS measurement, negative ions have to be produced from the sample material. Since noble gases do not form negative ions and intensive negative ions of some other elements (e.g., N, Mg, Mn, Zn, Cd, and Hg) are unstable to reach the terminal of the tandem accelerator, the AMS measurements of all elements are restricted. Due to a low ion current, the molecular ions such as hydrides or oxides are preferred for many elements (e.g., Be, Ca, Sr, Ba, U, Pu, etc.). For radionuclides, such as ^{14}C, ^{26}Al, and ^{129}I, the ion source is an important first step in isobar separation because of the instability of ^{14}N, ^{26}Mg, and ^{129}Xe negative ions. The choice of used ion depends on its production from sample material, negative ion yield, and suitable chemistry of preparation. For other types of accelerators such as Van de Graaff, cyclotron, or LINAC, a positive ion source is required.

In AMS applications, a Cs—sputter source (Middleton, 1983) is successfully used because of its relative stability, and because it can provide various ion beams with sufficient intensity. Several (up to 200 positions) samples of few milligrams (or less) are generally pressed into the metal holder and can be installed into the ion source. In the source, the Cs is evaporated from its reservoir, thermally ionized by hot surface, and the produced Cs^+ ions are accelerated and focused on the sample material, where these are used for sputtering of the sample ions (Fig. 3.26). Condensed Cs on the surface of the sample material provides additional enhancement of the negative ion yield (Nadeau et al., 1987). Negative ions produced by sputtering from the sample material are afterward preaccelerated to keV energies to undergo energy and mass separation and to reach the tandem accelerator.

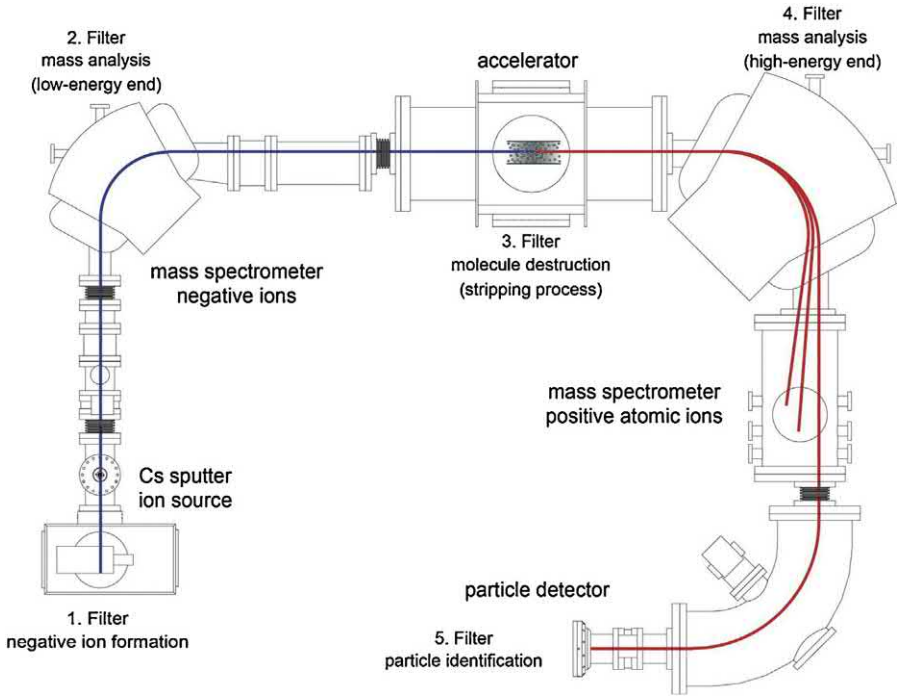


FIGURE 3.25 Scheme of small accelerator mass spectrometry (AMS) system used in ETH. For the color version of the figure, the reader is referred to the online version of the book. *From Synal (2013).* Printed with permission © Elsevier 2018.

If the samples in the ion source are close to each other, a small fraction of sputtered ions or vaporized atoms can be transferred from one sample to another or to nearby electrodes and insulators. By measuring the other sample, these transferred atoms could bias the results and are called "cross-contamination" or "memory effect." The microprobe ion source was developed by scanning the surface of the sample with focused Cs^+ beam. Secondary produced ions are afterward analyzed by AMS, and the surface profile of the studied radionuclide can be constructed (Döbeli et al., 1994; Freeman, 1993; Grabowski et al., 2007). Ion optics of the Cs^+ and extracted ions is crucial to reach the lowest detection limits. The Source of Negative Ions by Cesium Sputtering (SNICS) ion source for solid samples of the Centre for Nuclear and Accelerator Technologies (CENTA) laboratory at Comenius University, Bratislava, is shown in Fig. 3.27.

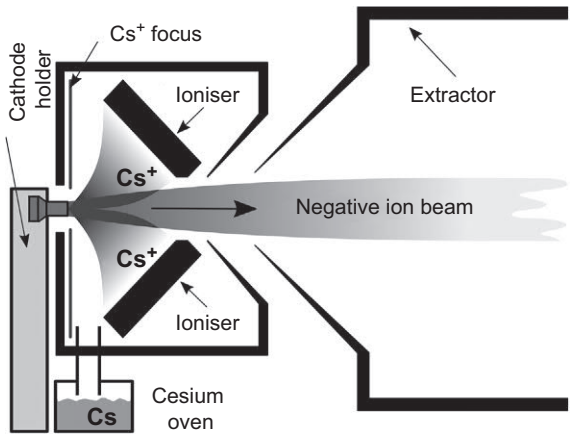


FIGURE 3.26 Schematic view of the SNICS (Source of Negative Ions by Cesium Sputtering) ion source.

3. Injection system

The injector system includes the beam transport with beam analysis before entering the accelerator. This includes the



FIGURE 3.27 The SNICS ion source for solid samples of the CENTA laboratory. For the color version of the figure, the reader is referred to the online version of the book. CENTA, Centre for Nuclear and Accelerator Technologies; SNICS, Source of Negative Ions by Cesium Sputtering.

ESA and injecting magnet for the proper energy and mass separation of the ions produced in the ion source. As we mentioned before, the result of the AMS measurement is an isotopic ratio; therefore, the measurement of two masses is needed. In general, there are two ways for measuring the reference and the trace isotope. The first method is simultaneous injection, which uses usually two magnets (*analyzer* and *recombinator*) to inject two analyzed beams into the accelerator. Mass separation is done at the first magnet (*analyzer*), whereas the second magnet recombines the beams into one. While the simultaneous beams of the isotopes pass together through the ion beam elements, they experience all the fluctuations in the system together. However, the intensity of the trace element current is orders of magnitude lower than the current of the reference isotope injected simultaneously into the accelerator, and this can enlarge the background by charge-changing reactions in the stripper tube.

The second method uses sequential injection, where only one isotope is measured at a certain time and the other is measured in the sequence after. This requires periodical changes of the injection setup. Since the magnet design requires time in the order of several seconds for switching the mass of measured isotopes, rather than a magnetic field, the energy of the ions is adjusted. By applying a switched voltage to an insulated magnet box, the ions can be accelerated or decelerated in the order of microseconds. Fast-switched steerers are applied before and after the magnet for correction of unavoidable differences in the trajectories. Disadvantages of this method are that the variations of source current and ion transmission through the accelerator shorter than the rate of injection, cannot be observed, and that the trace isotope is counted only for a short time. Also, large variations in beam intensity can cause a problem for the accelerator and power supplies of the beam guiding elements. The injector comprises also focusing and beam shaping elements, together with beam intensity and position monitoring. For better suppression of isobaric ions, the laser photo detachment can be used in the injection part for AMS measurements (Berkovits et al., 1990; Forstner et al., 2008). Fig. 3.28 shows the injection part of the CENTA laboratory with the injection electromagnet.



FIGURE 3.28 The injection part of the CENTA laboratory with injection electromagnet. For the color version of the figure, the reader is referred to the online version of the book. CENTA, Centre for Nuclear and Accelerator Technologies.

4. Tandem accelerator

In the AMS system, tandem electrostatic accelerators are widely used, where the positive charged electrode, called the terminal, is used for acceleration of negative ions in the first step. When the beam is passing through the terminal, the ions undergo a so-called stripping process, where in charge exchange reactions with gas or foil, they will lose several electrons. Positive ions are again accelerated in second step, and the total energy of the ion after acceleration is given by

$$E = \left((V_{in} + V_T) \frac{M_{out}}{M_{in}} + qV_T \right) e \tag{3.9}$$

where $V_{in}e$ is energy of the injected ions (e is the electron charge), V_T is the terminal voltage, M_{in} and M_{out} are masses of the ions entering and leaving the accelerator (in case they are not equal), and q is the charge state of the positive ion. The choice of terminal voltage depends on the accelerator and radionuclide to be analyzed. Better identification can be achieved by higher charge states with higher energies, especially for stable isobar separation.

From 1977, where nuclear physics laboratories adopted their large tandems (6−15 MV terminal voltage) to AMS, more dedicated instruments were developed based mostly on 3 MV tandems, and recently, even compact AMS systems, with a terminal voltage down to 200 kV, were successfully used for the determination of standard AMS nuclides such as ^{10}Be, ^{14}C, ^{26}Al, and ^{129}I (Synal, 2013). Fig. 3.29 shows the Pelletron tandem accelerator (nominal voltage 3 MV) of the CENTA laboratory.

5. High-energy analyzer and ion detection

Before the trace isotope is counted in the detector, the separation and identification is needed. The apparent identification of an isotope requires the determination of its charge and nuclear mass. The most common approach combines two different types of analyzers, namely, magnetic to select an ion with required ME/q^2 and electrostatic for the proper E/q selection. Many different approaches were developed in AMS for isobar separation in the last



FIGURE 3.29 The Pelletron tandem accelerator (nominal voltage 3 MV) of the CENTA laboratory. For the color version of the figure, the reader is referred to the online version of the book. CENTA, Centre for Nuclear and Accelerator Technologies.



FIGURE 3.30 Bratislava group at the high energy part of the CENTA tandem accelerator (from the left: Ivan Kontul', Ján Pánik, Pavel Povinec, Jakub Kaizer, and Miroslav Ješkovský). For the color version of the figure, the reader is referred to the online version of the book. CENTA, Centre for Nuclear and Accelerator Technologies.

decades incorporating additional stripping stages followed by another energy and mass separation, gas-filled magnet, etc. (Miltenberger et al., 2017).

After the trace isotopes are filtered by high-energy separation, ions are registered as events in the ion detector. Identification of the ions in the detector is based on total ion energy, residual energy, rate of energy loss, velocity, range, and angle of registered ion. Solid-state detectors (e.g. surface barrier Si or Si diode detectors) are widely used because they are easy to handle, but they are vulnerable to radiation damage and their energy resolution is lower compared to other ion detectors. Ionization chambers have better energy resolution for heavy ions and for isobar discrimination, and chambers with multiple anodes can provide information about energy losses. Time-of-flight (TOF) systems have the highest mass resolution; however, energy and angular spread with no distinction against isobaric ions are main disadvantages. The high energy part of the CENTA laboratory is shown in Fig. 3.30.

V. Radionuclide analyses

A. Radioactive gases

Both naturally occurring and anthropogenically produced radionuclides can be present in the environment in gaseous form. Radioactive gases are of great interest from the radioecological point of view because of their high mobility in the environment and their contribution to both internal and external radiation doses. However, they have also been very useful as tracers of transport and mixing processes in the atmosphere and exchange processes between the environmental compartments (e.g., stratosphere–troposphere, northern–southern atmosphere, atmosphere–ocean, atmosphere–biosphere, atmosphere–pedosphere, etc.).

We will focus on sampling, sample preparation, and analysis of radioactive noble gases (radioisotopes of argon, krypton, xenon, and radon) and gases containing radiocarbon (CO_2, CO, and hydrocarbons) and tritium (water vapor, hydrogen gas, and hydrocarbons). These gases are sampled mainly from the atmosphere, but they are also present in soil air or dissolved in groundwater and oceans. A low abundance of these gases together with their low isotopic ratios results in the need for the collection of relatively large volume samples to obtain enough radioactive gas for analysis. This generates requirements not only for the characteristics of sampling process but also for sample preparation procedures and measurement methods. In general, sampling of gases from the atmosphere is based on pumping air through a medium that separates the gas of interest from the rest of the pumped sample by physical or chemical absorption. Prior to interaction with the separating medium, the sampled air is usually pumped through a filter to prevent any particulate matter from entering the gas handling part of the sampling apparatus. Sample preparation procedures aim to further separate the gas of interest from other gases and its purification for analysis. Both radiometric and mass spectrometry methods have been used to analyze concentrations of studied gaseous radionuclides.

1. Radiocarbon

Radiocarbon ($T_{1/2} = 5730$ y) is a part of the carbon cycle together with stable carbon isotopes; in the course of this cycle, radiocarbon can be found in several gaseous forms—CO_2, CO, CH_4, and other volatile hydrocarbons. Analysis of radiocarbon content in these gases can be used in environmental sciences and geosciences, e.g., in studies concerning fossil carbon emissions from industrial activities (Povinec et al., 2012c), and also to monitor ^{14}C releases from nuclear industry (Povinec et al., 2008).

Carbon dioxide is the most widely studied gas containing ^{14}C, and robust methodologies for its sampling have been developed over the years (Povinec et al., 1968). The sample air is pumped via an aerosol filter, and the CO_2 is captured and separated from the rest of the air. There are several methods for CO_2 capture—chemisorption in a hydroxide solution, cryogenic capture, and adsorption in molecular sieves and zeolites. Cryogenic capture is based on the freezing of gaseous CO_2 into dry ice at liquid nitrogen temperatures (−196°C). Such a sampling method requires a cryogenic system capable of maintaining these low temperatures. This method is rarely used for long-term sampling because of the relative complexity of such cryogenic systems and also because of its low selectivity. Other gases from the air will be partially condensed at liquid nitrogen temperatures, if the pressure inside the sampling system is not kept lower than the atmospheric pressure. However, liquid nitrogen is widely used for cryogenic transport of carbon dioxide in vacuum sample preparation lines for CO_2 samples obtained by other sampling methods. CO_2 can be separated from the sampled air in molecular sieves and zeolite materials (e.g., 13X molecular sieve). These materials have relatively high specificity and capture efficiency. After the sampling, they are placed inside a glass vacuum system, and the collected CO_2 is desorbed by heating the adsorbent. The desorption process needs to be optimized to avoid fractionation (change in isotopic ratios) and memory effects (contamination of subsequent samples) caused by incomplete desorption of CO_2 (Palonen and Oinonen, 2013). Water is usually adsorbed and desorbed together with CO_2 and needs to be separated after the desorption by a desiccant or by condensation/freezing. Molecular sieves and zeolites can be reused after desorption and thorough regeneration.

When using a hydroxide solution (most commonly NaOH) for a continuous sampling, the air is bubbled through this solution, and the chemical reaction between CO_2 and hydroxide creates carbonate (Na_2CO_3 when NaOH is used) that remains dissolved in the solution. Alternatively, a short-term sample can be taken in the field by exposing the hydroxide solution to air in a vessel with high surface area. The amount and concentration of hydroxide depend on the sampling flow rate, sampling period, and required sample size. After sampling, carbon in the form of carbon dioxide needs to be liberated from the exposed hydroxide solution. This can be achieved chemically by reacting the dissolved carbonates with barium chloride. The result of this reaction is barium carbonate, which is not soluble in water, and it precipitates from the solution. After sedimentation, it has to be separated from the solution and dried. Hydrolysis of the resulting barium carbonate with a concentrated acid in a glass vacuum line yields the sample CO_2 (Povinec et al., 2015). The same can be achieved by adding the acid directly into the exposed hydroxide solution (Svetlik et al., 2006). Carbonates in the solution react with the added acid, and CO_2 is released.

In addition to CO_2, other gaseous radiocarbon species can be sampled and analyzed—carbon monoxide and volatile hydrocarbons (C_nH_m). These analyses are usually done as a part of NPP monitoring studies, where ^{14}C is one of the most important radionuclides released into the environment during routine operation of NPPs. The aim of these studies is to determine the speciation of radiocarbon in gaseous releases. Differential samplers are used for simultaneous sampling of gases containing ^{14}C (Hertelendi et al., 1989). A diagram of such a sampler is shown in Fig. 3.31. First, CO_2 needs to be removed from the air by methods mentioned previously, and the CO_2-free air is pumped through a material that causes oxidation of CO to CO_2 (e.g., Hopcalite catalyst—mixture of manganese and copper oxides). CO_2 produced from CO is absorbed, and it can be analyzed separately. The air then passes through a heated palladium (or platinum–palladium) catalyst where methane and higher hydrocarbons are converted to CO_2.

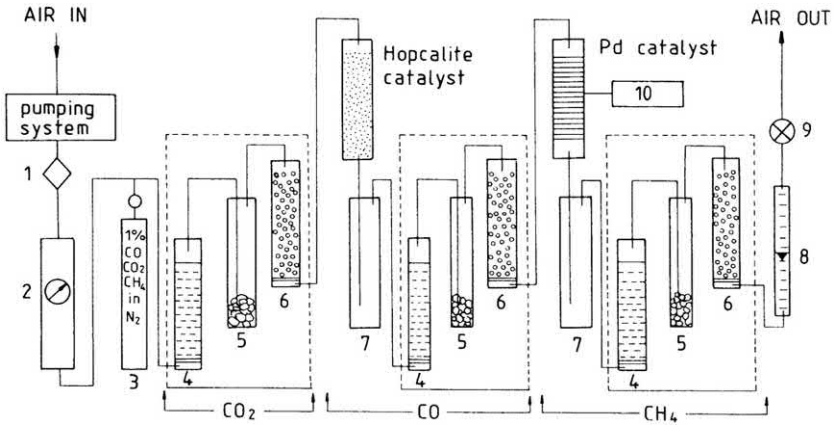


FIGURE 3.31 Schematic of a sampling system designed for separation of CO_2, CO and C_nH_m hydrocarbons from the sampled air. 1—aerosol filter, 2—gas meter, 3—carrier gas, 4—3M NaOH solution, 5—drop catcher, 6—drying columns, 7—buffer flask, 8—flow rate meter, 9—regulating valve, 10—regulated heater. *From Hertelendi et al. (1989).* Printed with permission © The American Journal of Science.

The resulting CO_2 is absorbed and represents another separate sample. The CO contribution to radiocarbon releases is usually negligible, and only CO_2 and C_nH_m are routinely sampled and analyzed. A different approach to CO_2 and C_nH_m sampling is using two parallel sampling systems, one only with CO_2 capture and the second with heated palladium−platinum catalyst followed by CO_2 absorption (Molnar et al., 2007). The sample from the first system represents CO_2 alone, and the second system represents sum of CO_2 and C_nH_m hydrocarbons.

Grab sampling of air for the purpose of radiocarbon analysis is also possible. If small samples are sufficient for analysis, evacuated vessels are opened to the air at the sampling location and sealed subsequently for transport into the laboratory (Graven et al., 2007). If larger samples are required, air is pumped with a compressor into empty pressure vessels (Tecl and Svetlik, 2009).

a. Gas proportional counting of ^{14}C

GPC is a measurement method that relies on the detection of electrons emitted from ^{14}C during its nuclear decay. Because the energy of these particles is very low (maximum energy of 156 keV), internal counters are necessary for these measurements. The radiocarbon sample needs to be a part of the counting gas itself. Several carbonaceous gases can be used as counting gas—carbon dioxide, methane, acetylene, and ethane. Use of CO_2 as counting gas is advantageous in the sense that in addition to release of the absorbed CO_2 sample, there is no further chemical sample treatment required. The disadvantage of CO_2 is that the electron drift velocity in carbon dioxide is relatively low, and therefore, it is very sensitive to electronegative impurities in the gas, e.g., oxygen (Povinec, 1992). Even small amounts of oxygen (ppm levels) can reduce the counting efficiency due to capture of drifting electrons by oxygen. Before using the CO_2 sample as filling for the gas proportional counter, it needs to be rigorously cleaned from these impurities. Purification methods include passing the CO_2 through an activated charcoal bed, heated elemental copper granules (removes oxygen), and heated silver wool (removes sulfur and halogens). Several cycles of purification may be necessary to achieve the required gas purity.

Hydrocarbon gases are much less sensitive to impurities and offer a good alternative as counting gases. However, additional sample preparation steps are necessary to transform the sample from carbon dioxide to hydrocarbon form. Methane is produced by cyclic hydrogenation of CO_2 in hydrogen gas catalyzed by ruthenium. Production of acetylene is done by reacting CO_2 with molten lithium metal and adding water to the resulting lithium carbide. Acetylene can be further used to prepare ethane by hydrogenation in the presence of palladium catalyst. The advantage of acetylene and ethane is that these molecules contain two carbon atoms, and therefore, twice the amount of carbon can be placed into the gas proportional counter of the same volume compared with methane or CO_2. These hydrocarbon-producing reactions have to be performed with highest possible efficiency to prevent any isotopic fractionation in the samples. The prepared gases also need to be purified from any unreacted reagents and impurities introduced during sample preparation. The additional preparation steps (chemical reaction as well as purification procedures) increase the risk of contamination by extraneous radiocarbon or ^{14}C-free carbon (from chemical reagents and catalysts). During sample preparation of gases for GPC, radon ^{222}Rn from radium impurities in catalysts, reagents, and purification mediums can be introduced into the sample (Horvatinčić et al., 1995). Its decay would increase count rate in the detector. While there are some methods for radon removal, it is much simpler to use the short half-life of radon (3.8 days) to remove its influence. The prepared samples are usually stored for 4−5 weeks before measurement to ensure that both radon and its daughter radionuclides decay to undetectable levels.

There are many variations of GPC detectors with different building materials, active shielding methods, anode and cathode geometries, etc. The sensitive volume of gas proportional counters is in the range of several tens of milliliters to several liters (Otlet et al., 1986). Fig. 3.32 shows an example of a large-volume gas proportional detector with sensitive volume of 4.6 L. Most of GPC systems were developed for relatively large environmental samples where it is usually possible to obtain large amounts of sample material. The advantage of large-volume GPC detectors is higher count rate and shorter counting time. But there are also many small-volume GPC systems for applications where sample size is limited. The low count rates require a much longer measurement time, and these systems have to be designed with very stable counting characteristics for long-time periods.

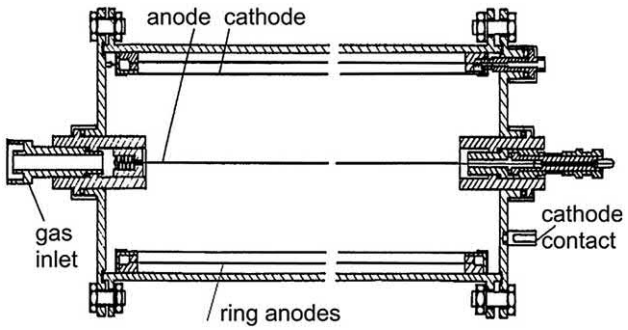


FIGURE 3.32 Schematic diagram of a multiwire gas proportional counter. The inner detector registers beta electrons from the sample, and the ring counter surrounding it is used as active shielding for background suppression. *From Povinec (1978).* Printed with permission © Elsevier 2018.

The background count rate of GPC detectors is lowered by placing them underground and surrounding them in shielding materials (old lead, electrolytic copper, iron, neutron-absorbing materials, etc.). This passive shielding is not enough to decrease the background to necessary levels, and active shielding is required. Guard counters (usually scintillation detectors or gas proportional counters) can be placed around the GPC detector inside the shielding, and the counts from them are used to veto nonsample counts by anticoincidence electronics. The guard counter can also be a part of the GPC detector's construction. The GPC detector can be made from two counters with the same cylindrical cathode—one cylindrical counter where the sample counts will be detected and the other one surrounding it and acting as active shielding (Povinec, 1978). The gas proportional counter in Fig. 3.32 uses this configuration.

In addition to GPC measurement of the sample itself, a standard reference material needs to be measured together with background samples. Standard reference materials are combusted in oxygen to produce CO_2, which is processed by the same methods as the analyzed samples. ^{14}C-free fossil gases are used as background. These measurements are evaluated according to ^{14}C data conventions (Stuiver and Polach, 1977). The further development of GPC detectors has diminished considerably with the advent of AMS, especially due to the introduction of affordable compact AMS systems specifically designed for ^{14}C measurements (Synal, 2013).

b. Liquid scintillation counting of ^{14}C

LSC is widely used for ^{14}C analysis because LSC systems often offer higher sample throughput compared with gas proportional counters. The basis of LSC measurement methods for ^{14}C analysis of gases is the conversion of the sample CO_2 into a suitable organic compound that can be used as solvent for the scintillation cocktail. The preferred solvent for use in LSC of radiocarbon is benzene, as its properties are compatible with its use as solvent for scintillation cocktails and its carbon content is higher than 90%. The sample CO_2 is reacted with molten lithium metal to produce lithium carbide. Addition of water converts the carbide into acetylene gas, which is then catalytically trimerized to benzene (Tamers, 1975). Yields of these chemical reactions need to be monitored, and consistent routine procedures need to be established and followed to exclude any fractionation or sample cross-contamination. Samples are stored for several weeks before their measurement to allow the radon and its daughters to decay below detectable levels. A modification of benzene recovery temperature from the catalyst can lead to removal of radon from the final benzene sample and can obviate the need for this waiting time (Hood et al., 1989). Modern LSC machines equipped with pulse shape discrimination systems can evaluate the radon contamination by identifying counts from radon progeny and calculating a correction factor for the measured ^{14}C activity (Theodórsson, 2005).

In certain applications, the sample hydroxide solution or other CO_2-absorbing chemical compounds (e.g., Carbosorb) can be mixed directly with certain liquid scintillation cocktails (Horvatinčić et al., 2004). This offers a quick and relatively simple method for LSC measurement of radiocarbon, but due to relatively low absorbing capacity of these chemicals, the carbon density of such samples is much smaller than benzene samples. This leads to lower precision and longer counting times.

Direct LSC measurement of $BaCO_3$ precipitate is also possible. The CO_2 is sampled by absorption in NaOH solution, and $BaCO_3$ precipitated from the sample solution can be added to certain scintillation cocktails and measured directly without hydrolysis and benzene synthesis. This method is used mainly in monitoring of gaseous radiocarbon releases in the vicinity of NPPs (Vokal and Kobal, 1997).

c. Accelerator mass spectrometry of ^{14}C

A general description of the AMS systems has been covered in Section IV.C; here, we shall focus only on the applications of AMS for ^{14}C analysis. The most important difference between AMS and decay counting methods is the required sample size. While GPC and LSC require samples with grams of carbon for routine measurement, optimal sample size for AMS analysis is milligrams of carbon, and with recent developments in ion source technology and sample preparation procedures, even samples with several tens of micrograms of carbon are available for AMS measurement. In addition, sample throughput of AMS can be much higher than that of decay counting methods.

Most AMS systems use solid graphite targets as sample matrix for ion beam generation. The sample CO_2 therefore needs to be converted into graphite form by catalytic reduction. Several methods for graphitization exist, each employing a different approach to reduction of carbon dioxide gas into graphite on an iron powder acting as catalyst (e.g., Liong Wee Kwong et al., 2004b; Povinec et al., 2015b). Other iron group metals can be used as well, but the majority of AMS laboratories use iron powder for this purpose. Hydrogen reduction method uses hydrogen gas as reducing agent (Němec et al., 2010a). The sample CO_2 and hydrogen gas are closed in a reactor volume with iron powder, which is heated to temperatures above 500°C. The chemical reaction $CO_2 + 2\ H_2 \rightarrow C + 2\ H_2O$ yields graphite and water. The produced water could interfere with the reaction and needs to be trapped in a part of the reactor either cryogenically or by a desiccant material

(e.g., magnesium perchlorate). The pressure of gases inside the reactor decreases due to deposition of graphite on the heated iron catalyst. This pressure decrease can be monitored by a pressure transducer, and the reaction yield can be calculated based on these data. The zinc method does not use any gases other than the sample CO_2, similarly as it has been used for CH_4 synthesis in GPC (Povinec, 1972). The sample is loaded into the reactor with separately placed zinc and iron powders heated externally by electric ovens. CO_2 is reduced to CO on the surface of hot zinc, and the reaction $2CO \rightarrow CO_2 + C$ produces graphite and carbon dioxide, which is again reduced on hot zinc (Slota et al., 1987). These methods can be relatively labor intensive, and to accommodate the high sample throughput of some AMS laboratories, sealed tube graphitization methods were developed. In these methods, the sample CO_2 is cryogenically transported into a glass test tube with the required reagents, and the tube is subsequently flame sealed and placed into a muffle furnace or an electrical heater. One of these methods uses iron powder as catalyst and substrate for graphite formation placed in a smaller tube inside the larger sealed tube and titanium hydride and zinc as reagents (Xu et al., 2007). In temperatures around 500°C, hydrogen is released from titanium hydride and the sample CO_2 is reduced to CO on hot zinc and in hot hydrogen. CO then reacts with hydrogen and is deposited as graphite on iron powder. Zinc also reacts with the water produced in this reaction and generates hydrogen. There is also a sealed tube method that uses zinc as the sole reduction agent without the use of titanium hydride as a source of hydrogen (Orsovszki and Rinyu, 2015). The graphitization process is very sensitive to impurities in the sample CO_2, especially sulfur and halogens, which can act as catalytic poisons for the graphitization reaction. CO_2 needs to be purified prior to reduction to graphite. Gas purification in heated copper and silver wool columns is routinely used. The graphite deposited on iron powder is removed from the reactor or graphitization tube and is pressed into metal cathodes suitable for the ion source.

Graphitization is a possible source of sample contamination with extraneous carbon. Because routine AMS samples are very small (around 1 mg of carbon), even relatively small contamination introduced in the sample preparation process can be significant and these procedures need to be rigorously studied and tested in regard to possible contamination sources. The contamination sources forming this background are the reactor materials, residual gas in the gas handling line, and chemical reagents. Blank samples from ^{14}C-free materials are also subjected to the same preparation procedures as samples and radiocarbon standards to determine background levels necessary for background corrections. In general, the ^{14}C background levels increase with decreasing sample size (Brown and Southon, 1997). Every measurement batch must have several standards and blanks for stable isotope and background corrections (Rom et al., 1997).

For very small samples (<50 μg of carbon), the graphitization process can be challenging due to lower yields and higher blank values. In recent years, gas ion sources utilizing CO_2 gas for ion beam generation have been developed and successfully applied for AMS analysis of small samples (Bronk Ramsey et al., 2004; Povinec et al., 2009a). The sample CO_2 is injected directly into cesium ion source in helium flow which produces negative ions that are necessary for tandem AMS systems. These gas ion sources generally produce low negative ion currents and in conjunction with a small sample size result in lower precision of ^{14}C results.

Fig. 3.33 shows the layout of a typical AMS system based on a tandem accelerator. The graphite target is sputtered, and negative ions are formed and extracted into the beam line. The ions are separated by mass in the injection magnet, and masses 12, 13, and 14 are sequentially injected into the accelerator. In the high voltage terminal in stripping medium (gas or foil), positive ions are formed and further accelerated into the high energy part of the system. The molecular ions with same mass as carbon ions are dissociated in this step. Following the acceleration, the ions are separated by their charge and energy in an ESA. The charge state for further analysis is chosen depending on charge state yields dependent on terminal voltage and stripping characteristics. Charge state 3+ is generally used in most systems with terminal voltage in megavolt range. A magnetic analyzer is used to separate $^{14}C^{3+}$ ions and direct them into an end detector. The masses 12 and 13 for the stable carbon isotopes are measured in Faraday cups. The $^{14}C^{3+}$ ions are counted in an energy-sensitive ionization detector, usually a semiconductor detector or gas ionization chamber.

Several compact AMS systems have been developed in recent years for ^{14}C-dedicated AMS (Synal, 2013). They are equipped with smaller accelerators with lower voltage and therefore have to use lower charge states. Modifications to the stripping process and accelerator construction enable efficient dissociation of interfering molecular isobars even at these charge states. The modern AMS systems could also avoid preparation of solid graphite targets, as a gas ion source containing the CO_2 sample can be used for ^{14}C measurements. A very recent promising development in ^{14}C mass spectrometry is the PIMS (for details, see Section IV.B).

Two sources have changed ^{14}C levels in the atmosphere: nuclear bomb tests and to a lesser degree also the nuclear industry. Radiocarbon was released in large quantities during atmospheric weapon tests during the 1950s and early 1960s, as well as during two major NPP accidents in Chernobyl (1986) and in Fukushima (2011). However, there is another anthropogenic effect caused by the fossil

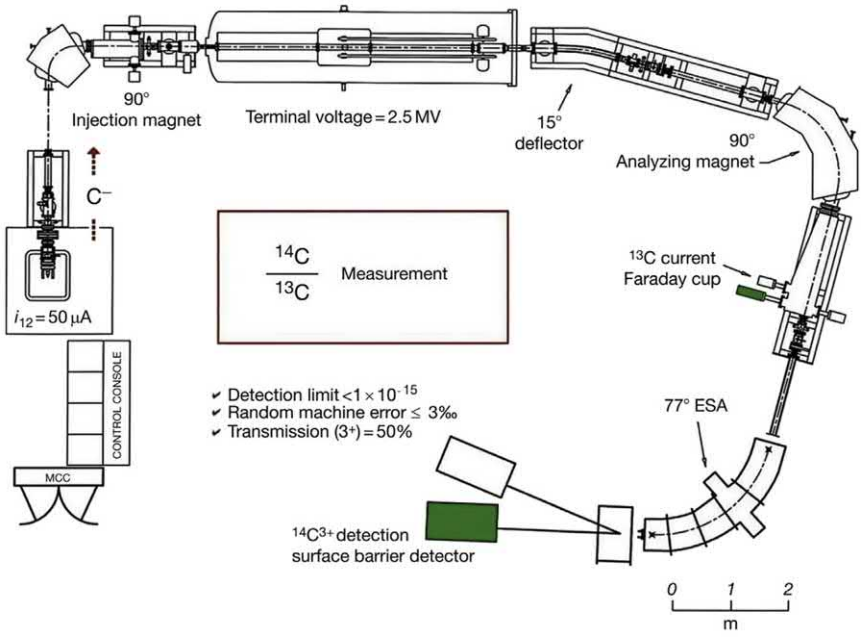


FIGURE 3.33 Example of a radiocarbon accelerator mass spectrometry (AMS) system (University of Arizona, Tucson, United States) and its component parts. *From Jull (2013).* Printed with permission © Elsevier 2018.

fuel combustion, which influences the ^{14}C concentration in the atmosphere (Levin et al., 1980; Levin and Kroner, 2004; Segl et al., 1983). This effect is well seen through the $^{14}CO_2$ season variations.

Radiocarbon results are presented as $\Delta^{14}C$ values, which were calculated relative to the NIST (National Institute of Standards and Technology, Gaithersburg, United States) ^{14}C oxalic acid standard, and corrected for the isotopic fractionation using the formula (Stuiver and Polach, 1977)

$$\Delta^{14}C = \delta^{14}C - \left(2\delta^{13}C + 50\right)\left(1 + \frac{\delta^{14}C}{1000}\right)\left(‰\right), \tag{3.10}$$

where

$$\delta^{14}C = \left(\frac{A}{A_S} - 1\right)1000 \quad \left(‰\right). \tag{3.11}$$

A represents the activity of a sample, A_s is the corrected activity of the NIST standard, and

$$\delta^{13}C = \left(\frac{\frac{^{13}C}{^{12}C}}{\left(\frac{^{13}C}{^{12}C}\right)_s} - 1\right)1000 \tag{3.12}$$

where $(^{13}C/^{12}C)_s$ is the isotopic ratio of the PDB standard. The uncertainty was estimated as a partial derivation of the above $\Delta^{14}C$ expression, which was mainly composed of statistical Poisson uncertainty of decay counting (~5‰ at 1 σ level); contributions from systematic sources (e.g., sample collection and preparation, gas pressure in the counter, barometric effect, and background) were estimated (on the basis of repeated analyses of the NIST ^{14}C oxalic acid standard, background, and cross-check samples) to be below 2‰.

As an example, we present in Fig. 3.34 results of measurement of atmospheric $^{14}CO_2$ activity in the vicinity of the Jaslovské Bohunice NPP and in Bratislava, which represents a heavily urbanized and industrialized area in Slovakia (about 60 km from Jaslovské Bohunice) (Povinec et al., 1968, 1986a,b, 2009b). These results show increased radiocarbon levels due to releases from the NPP and also extremely low levels caused by the dilution of radiocarbon in the atmosphere by ^{14}C-free fossil fuel emissions.

2. Tritium

Tritium ($T_{1/2}$ = 12.32 y) is sampled from the environment in these gaseous forms—tritiated water vapor (HTO, including DTO and T_2O), tritiated hydrogen gas (HT, including DT and T_2), and tritium-containing volatile hydrocarbons (often referred to as CH_3T). Measurement of tritiated gases has been carried out mainly in studies focusing on releases from reprocessing plants and NPPs (Connan et al., 2017; Zhang et al., 2018).

In air samplers for tritium analysis, the air is pumped into the sampling system through an aerosol filter, and the water vapor is collected as the first step. Molecular sieves, zeolites, and silica gel are widely used for this purpose. The amount and type of molecular sieve material depends on the sample size and its humidity. The hydrogen gas sample

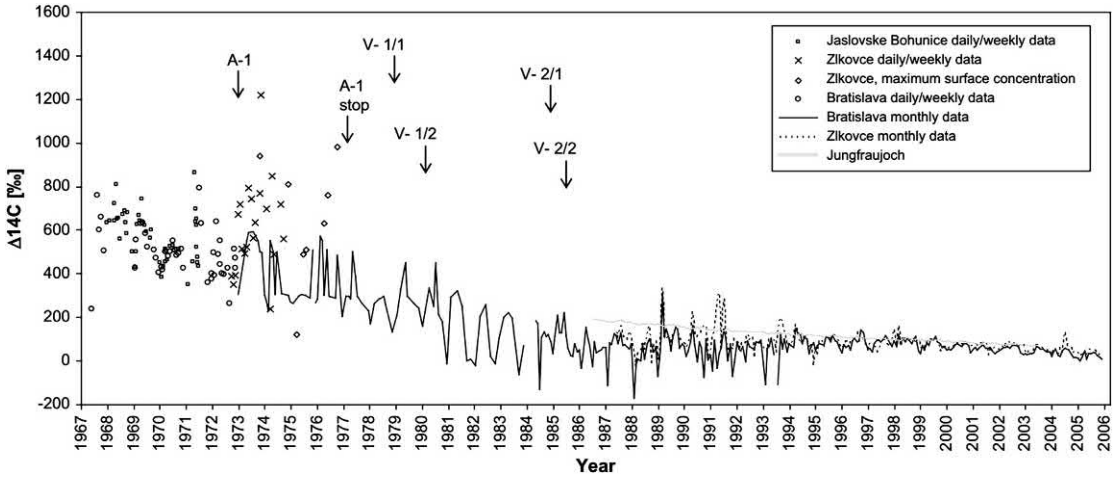


FIGURE 3.34 Radiocarbon in atmospheric CO_2 at the Bohunice NPP and Bratislava sampling station in Slovakia. $\Delta^{14}C$ is defined as relative enrichment or depletion of ^{14}C in the sample compared with international oxalic acid standard. Jungfraujoch data set (a thin gray line, Levin and Kromer, 2004) represents clean air background without any local fossil carbon sources or anthropogenic ^{14}C source. *From Povinec et al., (2009b).* Printed with permission © Elsevier 2018.

is collected next by converting the hydrogen to water by oxidation catalyzed by palladium or platinum at temperatures ranging from room temperature to 100°C. The resulting water is trapped in the same way as the atmospheric water vapor in the first step. The hydrocarbon sample is collected in the form of water after conversion of hydrocarbons to water by palladium catalyst at elevated temperatures (~300°C). The samples are then desorbed from the sorbents and condensed to liquid water. Fig. 3.35 shows an example of tritium sampler with HTO, HT, and hydrocarbon separation.

a. Gas proportional counting of ^3H

Similarly, as in the case of radiocarbon, the beta particles emitted by tritium during its nuclear decay have a low energy (maximum energy is 18.6 keV), and they need to be measured in internal counters. The tritium sample has to be used as a component of the counting gas. Methane is an ideal gas for this purpose; it can be labeled by radiocarbon and tritium (Povinec, 1980). Simultaneous measurement of both ^{14}C and ^3H is also possible by GPC (Povinec, 1975; Mace et al., 2017). Methane is synthesized from hydrogen and carbon dioxide in the presence of a heated ruthenium catalyst. To produce hydrogen from water, zinc powder is placed into the reactor volume together with sample water. Heating of the zinc powder and water causes a chemical reaction between zinc and water producing zinc oxide and hydrogen gas. Hydrogen reacts with CO_2, and methane is produced. Alternatively, reaction of sample water with heated aluminum carbide can be used for methane synthesis.

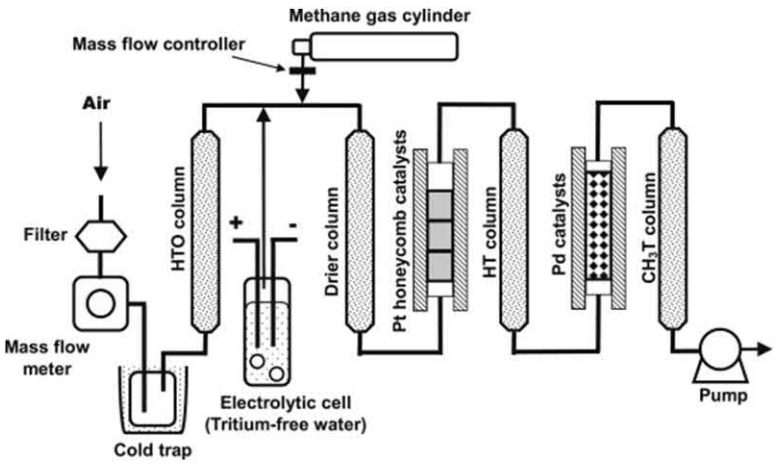


FIGURE 3.35 Tritium sampling system with HTO, HT, and hydrocarbon differentiation. *From Akata et al. (2011).* Printed with permission © Elsevier 2018.

In general, similar types of GPC detectors are used for tritium analysis as for radiocarbon measurement (see previous section). The same advantages and limitations apply for ^{3}H measurement as well. The GPC method of tritium measurement is still used in some laboratories, but because it requires additional and relatively complex sample preparation procedures, most laboratories use LSC for routine measurement of tritium samples.

The method of simultaneous ^{3}H and ^{14}C counting by GPC has been a trigger for development of the method for simultaneous activity and background measurement (Povinec, 1981).

b. Liquid scintillation counting of ^{3}H

LSC is by far the most used method for measurement of tritiated gases and sampled in the form of water, and water can be then mixed with a scintillation cocktail and measured by liquid scintillation. The sample preparation is based on removal of other radionuclides from the sample and its purification from any compounds that could react with the scintillation cocktail or act as a quenching agent during the measurement. Both of these goals can be achieved by distillation of the sample. The majority of radionuclides that could interfere with tritium detection has much higher boiling point than water and will be separated from the sample during the distillation process (Lehto and Hou, 2011). Impurities from the water are also removed in the course of distillation. The purity of the water can be determined by measurement of its conductivity, and the distillation step can be repeated several times to achieve the required water purity. Benzene synthesis as was described in previous section about radiocarbon can also be used to incorporate the sample hydrogen into solvent for the scintillation cocktail.

Current natural ^{3}H levels are usually too low for direct measurement with good precision, and tritium enrichment is necessary for these samples. The most widespread method is electrolytic enrichment. Sample water is loaded into an electrolytic cell with an anode and cathode. H^{+} ions are drawn to the cathode, and there, they produce hydrogen gas. OH^{-} ions move toward the anode where they produce oxygen gas and H^{+} ions. That means the water molecules gradually dissociate. The probability of dissociation of a water molecule containing tritium is lower than the probability for water molecule without tritium. Therefore, the gradual dissociation of the sample enriches it in tritium. The required enrichment level and sample size depends on the characteristics and detection limits of the LSC system, but in general, ^{3}H enrichment by a factor 10–50 can be achieved (Lehto and Hou, 2011). The electrolytic enrichment is done in batches, and in every batch, a number of samples with known ^{3}H activity and tritium-free samples (old water) are enriched together with the unknown samples. This way, the recovery efficiency of the enrichment process and any ^{3}H contamination can be determined and taken into account during data evaluation. The enriched sample is distilled again to purify it, and then, it can be added into a suitable scintillation cocktail for direct measurement by LSC.

The precision of the results depends on counting time and characteristics of the LSC system used. There are many LSC systems commercially available, and their counting characteristics are the dominant factor influencing the measurements. Background of the LSC detection system itself and quality and radiopurity of the scintillation vials are also contributing factors (Liong Wee Kwong et al., 2001).

c. ^{3}H-^{3}He ingrowth mass spectrometry

For samples with low tritium content, mass spectrometry of ^{3}He (decay product of tritium) can be used to determine the tritium activity. This measurement technique is called the ^{3}He ingrowth method (see also Section IV.B), and it is used mainly for water samples, but the gaseous forms of tritium are sampled in the form of water, and if the volume of the sampled air is large enough, this method can in principle be used for these measurements as well. The sample water needs to be degassed first to remove any helium already present in the sample, and the sample is then sealed and stored. Over the course of the storage, tritium decays and produces ^{3}He in the sample. The length of the storage period (from several weeks to months) depends on the presumed tritium levels, sample size, and detection limits of the mass spectrometer (Jean-Baptiste et al., 1992; Palcsu et al., 2010). After the storage period, the ingrown helium is released, purified, and measured in a noble gas mass spectrometer. The results of the mass spectrometric measurements together with the duration of the ingrowth period are then used in the calculation of tritium levels in the sample.

d. Accelerator mass spectrometry of ^{3}H

Previous methods described require relatively large samples, but the AMS allows tritium analysis of small samples in the region of milligrams. The samples in the form of water need to be converted into solid form suitable for cesium ion sources used in AMS systems. The optimal sample preparation appears to be synthesis of titanium hydrides. The sample is loaded into a glass tube with zinc powder or granules at the bottom and titanium powder in a smaller tube. Water is cryogenically frozen inside the tube, and when reasonable vacuum is achieved, the glass tube is flame sealed and placed into a muffle furnace at 400–550°C (Chiarappa-Zucca et al., 2002; Pánik et al., 2017). The water vapor will react with zinc to produce hydrogen gas, which in turn reacts with titanium yielding

titanium hydrides. Titanium hydrides can be then pressed into cathodes and placed into an AMS ion source. The measurement of ^{3}H using AMS follows the same principles as described in the previous section dealing with ^{14}C. Because of very low $^{3}H/^{1}H$ isotopic ratios in the environment and background problems (of the order of 10^{-18}), the AMS technique has not been applied in environmental studies. The ^{3}H AMS analysis has been used mainly for biomedical applications and biogenic tritium studies (Love et al., 2002; Roberts et al., 1994).

As a typical example of ^{3}H measurements in the atmosphere, we present in Fig. 3.36 a Chernobyl ^{3}H record measured in Bratislava.

3. Argon, krypton, and xenon

Radioactive isotopes of these noble gases are used for dating in hydrogeology (Collon et al., 2004b), monitoring of NPP and reprocessing plants (Cimbák et al., 1986; Igarashi et al., 2000), and also global monitoring of nuclear weapon tests (Wernsperger and Schlosser, 2004), recently organized in the framework of the CTBTO (for details, see Section VI.A). Most important radionuclides from this group with their respective half-lives are shown in Table 3.13. ^{39}Ar and ^{81}Kr are long-lived radionuclides, and their production in nuclear fission is negligible. On the other hand, ^{37}Ar, ^{131m}Xe, ^{133}Xe, ^{133m}Xe, and ^{135}Xe are short-lived and are efficiently produced in nuclear fission, and they act as indicators of nuclear weapon tests.

Generally, relatively large volumes of air were required, ranging from 1000 L (Cimbák et al., 1986) to more than 10,000 L (Nitta et al., 2014; Yokochi et al., 2013) for sampling of noble gases in the atmosphere and subsequent analysis by GPC. However, the newly developed measurement techniques allow krypton and xenon analysis of air volumes in range 1−50 L possible (Tu et al., 2014). Sampling by continuous air flow is done in laboratories where continuous monitoring of radioactive noble gases in the atmosphere is the purpose of these measurements (Cimbák and Povinec, 1985; Igarashi et al., 2000). In the field, grab sampling is used—samples are collected by an air compressor unit and stored in pressure vessels for transport to the laboratory where the separation of noble gases takes place. Other radioactive gases can be separated from these grab samples in addition to noble gases prior to their extraction from the sample (Tecl and Svetlik, 2009). In some cases (sampling in difficult terrain, remote areas, etc.), transport of large quantities of bulk gas in pressure vessels is impractical, and preconcentration of noble gases is necessary (Yokochi et al., 2013).

TABLE 3.13 Most important radioisotopes of noble gases (NuDat, 2018).

Nuclide	Half-life
^{37}Ar	35.04 days
^{39}Ar	269 years
^{81}Kr	2.29×10^{5} years
^{85}Kr	10.74 years
^{131m}Xe	11.84 days
^{133}Xe	5.24 days
^{133m}Xe	2.2 days
^{135}Xe	9.14 hours

For noble gases, the most widely used adsorption medium is granulated activated charcoal at low temperatures. These low temperatures are achieved either by placing the column with activated charcoal into Dewar vessel filled with liquid nitrogen or by cryogenic air chillers (Bowyer et al., 1997, 1999). Lower pressure is maintained in these adsorption columns to prevent condensation of oxygen and nitrogen at liquid nitrogen temperatures. High water vapor content in the sampled air can negatively influence adsorption on activated charcoal, as water vapor can block some of the capillaries in the charcoal and effectively decrease its active surface area (Scarpitta and Harley, 1990). Therefore, when sampling gases with high humidity, water vapor traps have to be placed before the activated charcoal bed. These can be in the form of glass or metal vessels cooled to lower temperatures to promote water condensation and freezing or packed with water-absorbing material such as silica gel or molecular sieves. In recent years, alternative materials to activated charcoal have been studied for use in noble gas sampling, and some polycarbonate materials (e.g., Makrolon, Makrofol, and their equivalents) show good absorption abilities for radon and other noble gases (Mitev et al., 2018; Möre and Hubbard, 1997). However, further studies of their properties in regard to noble gas sampling are required before

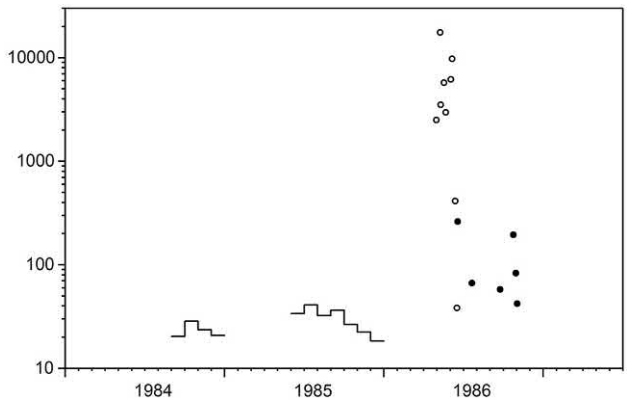


FIGURE 3.36 Tritium in the Bratislava air (*open dots*) and rain (*full dots*) after the Chernobyl accident.

they are widely used in these measurements (Pressyanov et al., 2004).

Some of the radioactive noble gases (e.g., ^{81}Kr, ^{85}Kr, and ^{39}Ar) can be used for radioisotope dating of groundwater, and they need to be extracted from water. Low solubility of noble gases in water means that large water samples are required. As an example, 1 liter of ocean water contains on average about 0.5 mL of argon and 0.1 μL of krypton (Collon et al., 2004b). Due to this fact, noble gases are most commonly extracted in the field by degassing. There are two types of degassing systems—vacuum cylinder extraction and membrane extraction. In vacuum cylinder extraction systems (Collon et al., 2000; Sturchio et al., 2004), sampled water is pumped from the studied reservoir and sprayed into an evacuated cylindrical container. According to Henry's law, the gases dissolved in water will be transferred to the gas phase to achieve solubility equilibrium, and the released gases can be compressed into pressure vessels for transport to the laboratory. A second approach to extraction is using hydrophobic semipermeable membranes (Yokochi, 2016). In these systems, water is pumped around a cylindrical hydrophobic membrane that prevents liquid water to penetrate inside, but allows gases to permeate through its pores into the volume enclosed by the membrane. Gases from this volume are then pumped into storage vessels for transport.

The basis of sample preparation procedures for the analysis of radioactive noble gases is the separation of the noble gas from other gases present in the bulk sampled gas and removal of any impurities that could influence the measurement characteristics. For grab samples, adsorption of noble gases on an activated carbon bed must be done prior to these procedures. The pressure vessel is connected to a gas handling line at the laboratory, and its contents are ventilated into the line with cooled activated carbon bed. In this step, water vapor and carbon dioxide are removed from the bulk gas. Water is either cryogenically trapped or absorbed in some hygroscopic material (silica gel, molecular sieve, zeolites, etc.). Carbon dioxide can be removed by a soda lime column, molecular sieve, or similar materials with high CO_2 affinity. In continuous flow sampling systems, these molecules are also removed from the pumped air before noble gas adsorption.

In the first step of sample preparation, any incondensable gases in the volume with cooled activated charcoal can be removed by evacuating this volume while increasing the activated carbon temperature (but not heating it to more than room temperature). Pumping can also remove any condensed gases like oxygen from the charcoal. Alternatively, the charcoal column is allowed to warm to room temperature, and most of these gases can be pumped out, whereas noble gases are retained in the activated charcoal (Igarashi et al., 2000). Pumping can lead to some sample loss, so flushing with helium is also a possible way to remove these additional gases. Small amounts of oxygen can be removed by oxidation of copper in a column heated to 600°C (Purtschert et al., 2013). The noble gases can be further purified by cascade desorption at different temperatures, repeated desorption, and resorption in another activated carbon column and cryogenic distillation. Especially in radiometric analysis of xenon isotopes, the presence of radon in the final purified sample can interfere with the radiometric measurement of noble gases because decays of radon progeny can significantly affect signals from radioxenon. This is particularly important for radioxenon measurements of subsurface air, which has usually much higher radon concentration than surface air. The adsorption coefficient of radon in activated charcoal is several times higher than that of xenon, and thus, the addition of a small activated charcoal bed to the sample purification process can effectively remove radon interference from the sample (Zhou et al., 2013b).

Further purification is done by means of gas chromatography. Noble gases are desorbed by heating the adsorbent and transported in a carrier gas through a gas chromatography column. The gases eluted from the column are monitored by a thermal conductivity detector. The detector can distinguish noble gases from other gases (mainly O_2 and N_2) and allows discarding them, hence purifying the noble gases. This process can be repeated, if necessary, to achieve the required gas purity. Most widely used carrier gases are helium, methane, and nitrogen (Bowyer et al., 1999; Igarashi et al., 2000; Yokochi, 2016). To be able to calculate the specific activity of noble gases in the sampled air, the amount of recovered noble gas needs to be determined. This information can be obtained during gas chromatography by calculating the area under the peak corresponding to the studied noble gas in the response of the thermal conductivity detector with a standard calibration curve (Zhou et al., 2013a).

a. Gas proportional counting of radioactive noble gases

GPC is best suited for radionuclides with short and medium half-lives—^{37}Ar, ^{39}Ar, ^{85}Kr, and radioxenon isotopes. ^{39}Ar and ^{85}K decay by emission of beta particles; therefore, GPC is the most widely used method, but other detectors such as GM counters (Nitta et al., 2014) or scintillation crystals can also be applied (Wilhelmová et al., 1986). A large number of possible gas proportional counter configurations and sizes and filling pressures have been employed in these analyses. The counter characteristics are determined by size of the air sample, final sample volume, required precision, and other factors. The amount of separated noble gases is not large enough to fill GPC detectors; the sample is added to a suitable counting gas. Methane or P10 counting gas (10% methane + 90% argon) to fulfill this role in most GPC detectors for noble gas measurement. ^{37}Ar decays by

EC, and its detection by GPC is based on the detection of X-rays or Auger electrons that accompany this decay (Aalseth et al., 2011).

The long-lived ^{81}Kr was first detected by GPC (Loosli and Oeschger, 1969), but its long half-life and low isotopic abundance make the GPC method too inefficient for its practical use for air or water samples (typically about 0.5 mL of krypton gas can be extracted from 500 L of air or 16,000 L of water). The increased ^{85}Kr activity in modern krypton also makes it impossible to detect ^{81}Kr by decay counting methods in air samples.

b. Gamma spectrometry of radioactive noble gases

Radioxenon isotopes are measured by high-resolution gamma spectrometry using high-purity germanium (HPGe) detectors or beta−gamma coincidence using scintillation detectors. These methods allow the simultaneous measurement of all four radioxenon isotopes (Table 3.13). This makes it possible to calculate their activity ratios, and that provides the possibility of source identification in nuclear weapon tests monitoring. When using high-resolution gamma spectrometry, the extracted xenon sample is placed into a gas cell, which is adjacent to the crystal of the detector. The gamma rays from the decay of radioxenon isotopes are detected in the spectrometer and the individual radioxenon isotopes, and their activity can be determined. Most systems use one HPGe detectors for the measurement (Fontaine et al., 2004; Zhou et al., 2013a), but to increase the full energy peak efficiency, two HPGe detectors can be placed onto the sample gas cell (Xie et al., 2014). A typical gamma spectrum of ^{131m}Xe and ^{133}Xe is shown in Fig. 3.37. Peaks from gamma rays emitted by radon progeny ^{212}Pb and ^{214}Pb are also visible in the spectrum, but their activity is lower than ^{133}Xe activity. This has been achieved by a very efficient radon removal step in the sample preparation methodology (Zhou et al., 2013b).

BEGe detectors offer energy resolution comparable with HPGe detectors, but they have a higher detection efficiency for X-rays and low-energy gamma rays. BEGe detectors have been utilized therefore for detection of both gamma rays and X-rays emitted by radioxenon to improve the detection limits (Le Petit et al., 2006).

Systems utilizing beta−gamma coincidence detection for radioxenon measurement use the gas cell with the sample for the detection of emitted beta particles and a scintillation crystal surrounding this cell for the detection of gamma rays. An example of such system is shown in Fig. 3.38. The walls of the gas cell are manufactured from a plastic scintillator material, and the attached photomultipliers detect the beta particles. The sample xenon may diffuse into these materials and cause a memory effect, but a suitable coating for the cell walls can minimize this effect (Bläckberg et al., 2011).

Low-level decay counting requires background reduction, which is achieved by both passive and active shielding. The passive shielding is in the form of radiopure shielding materials (lead, copper, iron, neutron-absorbing materials, etc.). Active shielding is realized by guard counters (gas proportional counter, scintillation detectors, etc.).

c. Accelerator mass spectrometry of radioactive noble gases

AMS is routinely used for the analysis of long-lived cosmogenic radionuclides by employing a tandem accelerator. However, this method cannot be used for noble gases because it relies on the production of negative ions, and these gases do not easily form stable or metastable negative ions. With certain modifications, AMS with

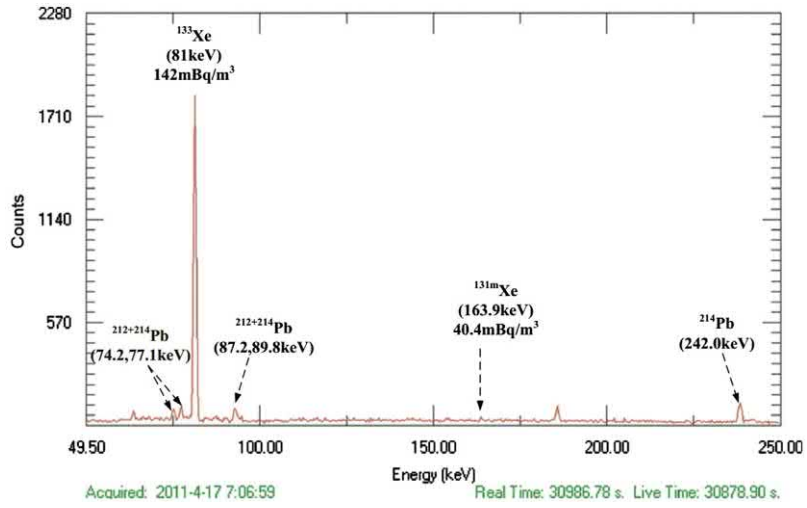


FIGURE 3.37 Gamma spectrum of a xenon sample containing ^{131m}Xe and ^{133}Xe. Peaks from radon progeny ^{212}Pb and ^{214}Pb are also visible, but their activity is very low due to efficient radon removal in sample preparation process. *From Zhou et al. (2013a).* Printed with permission © *Elsevier 2018.*

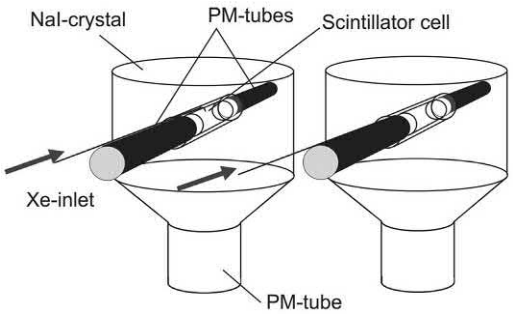


FIGURE 3.38 A schematic diagram of beta–gamma coincidence detection system for radioxenon measurements. *From Ringbom et al. (2003).* Printed with permission © *Elsevier 2018.*

positive ions was used for analysis of two long-lived noble gas radionuclides—^{39}Ar and ^{81}Kr. In both cases, an ECR (electron cyclotron resonance) ion source was used to produce positive ions from Ar and Kr gas samples. For ^{81}Kr analysis, the full stripping method was used to separate ^{81}Kr from its main isobaric background ^{81}Br (the source of bromine at these levels is not known). For efficient full stripping to the $^{81}Kr^{36+}$ charge state in a beryllium foil, ions produced in the ECR had to be accelerated in a superconducting cyclotron to 3.6 GeV and only then could these ions be separated in a mass spectrometer and identified in ΔE-E detector (Collon et al., 1997). Full stripping cannot be used for ^{39}Ar (with ^{39}K as its main isobaric background) because it only works in cases when the proton number of the measured isotope is higher than the proton number of the interfering isobar. Therefore, AMS with a gas-filled magnet was used for this separation. Positive ^{39}Ar ions accelerated by linear accelerator to 232 MeV entered the gas-filled magnetic analyzer, where their trajectories were bent due to the presence of the magnetic field, and their different interaction with gas in the analyzer made it possible to separate ^{39}Ar and ^{39}K (Collon et al., 2004a). These measurements show the possibility of using AMS for ^{39}Ar and ^{81}Kr, but the technical complexity of these methods prevents them from being used routinely at the current stage of development.

d. Atom trap–trace analysis

Atom trap–trace analysis (ATTA) is an atom-counting system developed for analysis of krypton isotopes ^{81}Kr and ^{85}Kr (Chen et al., 1999). The schematic of an ATTA system is shown in Fig. 3.39. A separated krypton gas sample is fed into the ATTA system through a discharge zone, where a part of the krypton atoms is excited by the discharge to metastable level $5s[3/2]_2$. An atomic beam of thermal krypton atoms is transversely cooled and focused prior to entering a Zeeman slower. In this part of the apparatus, the atomic beam is cooled down and subsequently injected into a magnetooptical trap (MTO). It consists of a spatially variable quadrupole magnetic field and focused laser beams. Laser beams with a wavelength of 811 nm repeatedly excite the $5s[3/2]_2$–$5p[5/2]_3$ cycling transition, thereby trapping the $5s[3/2]_2$ atoms in the magnetic field of the MTO. The trapping laser beam induces fluorescence emission from the trapped atoms. When frequency of this laser matches very precisely the resonance frequency for this transition, small isotopic shifts in the atomic transition frequency between isotopes make it possible to distinguish individual isotopes and trap them atom by atom. The photons from fluorescence emission of the chosen isotope are detected by a photodiode detector or a CCD camera. In addition to the measurement of the number of ^{81}Kr and ^{85}Kr atoms, the capture rate of stable isotope ^{83}Kr with known isotopic abundance needs to be determined to evaluate the ^{81}Kr/Kr and ^{85}Kr/Kr ratios. They are required for calculations of the ^{81,85}Kr specific activity in the measured sample. The ATTA method can also be used for the analysis of ^{39}Ar (Welte et al., 2010). The amount of sample required for ATTA analysis is much smaller than for other analytical methods. ATTA can measure ^{81}Kr and ^{85}Kr in samples as small as 1 L of air and ^{39}Ar in 0.1 L of air (Lu et al., 2014; Tu et al., 2014).

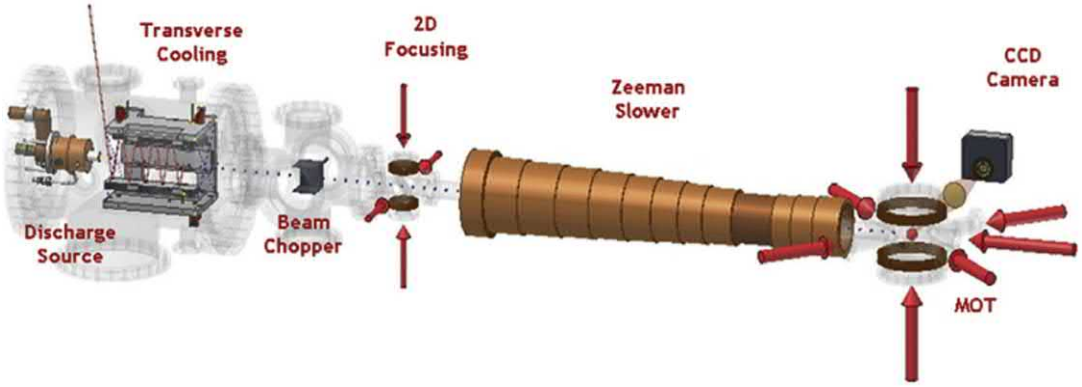


FIGURE 3.39 Schematic of ATTA-3 system at Argonne National Laboratory. *From Jiang et al. (2012).* Printed with permission © *Elsevier 2018.*

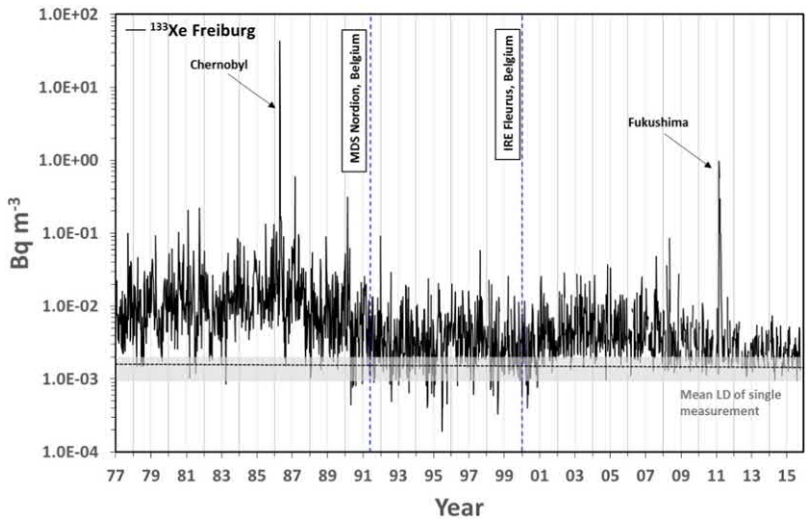


FIGURE 3.40 ^{133}Xe activity concentration in air sampled in Freiburg, Germany. *From Schlosser et al. (2017).* Printed with permission © *Elsevier 2018.*

As a typical example of measurements of radioactive noble gases in the atmosphere, Fig. 3.40 illustrates results of ^{133}Xe measurements in Freiburg (Germany) covering the period of 1977−2015. Distinct peaks from ^{133}Xe released during the Chernobyl and Fukushima nuclear accidents are clearly visible in the data. The ^{133}X activity concentration slowly decreases due to improvements in nuclear reprocessing and medical isotope production technologies (Schlosser et al., 2017).

4. Radon

Radon concentration in the air has been measured by many different types of detectors, for example, by scintillation detectors (Lucas cells), ionization chambers (suitable for continual monitoring), electret detectors, track detectors, and thermoluminescent detectors for integral measurements. Each detector has its advantages and disadvantages. Radon in the air has been measured either by directly passing the air through the detector or indirectly by the absorption of the air on a suitable medium, e.g., an activated charcoal. Radon from larger volumes of the air can be collected by cooling of the charcoal column. Radon is then transferred from the charcoal column to the scintillation chamber (Beláň et al., 1992). There are also available commercially produced instruments (e.g., AlphaGUARD, RAD-7), which have detection sensitivities good enough to perform many radon investigations in the environment.

As an example, we present a large-volume (4.5 L) cylindrical scintillation chamber used for radon monitoring of the ground-level air in Bratislava (Beláň et al., 1992). The air is sucked through the scintillation chamber (located 1.5 m above the land) with a flow rate of 0.5 L min^{-1}. At the entrance of the chamber, a filter removing aerosols and radon progeny was installed (Figs. 3.41 and 3.42). A 10 L delay volume was incorporated in the intake line to ensure that the air entering the chamber will no longer contain thoron (^{220}Rn) with a half-life of 56 s. Subsequently, radon activity concentrations belonging to 2−h intervals were calculated using the Ward and Borak (1991) method. To achieve favorable geometrical conditions for the efficient

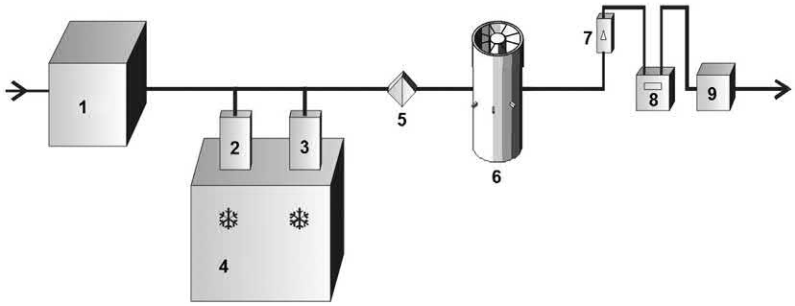


FIGURE 3.41 Air supply line for the large-volume scintillation chamber: 1−10 L delay volume, 2—water trap (−30°C), 3—column filled with granulated silica gel, 4—cooler, 5—aerosol filter, 6—large-volume scintillation chamber, 7—flow rate meter, 8—gas-meter, 9—pump. *From Beláň et al. (1992).*

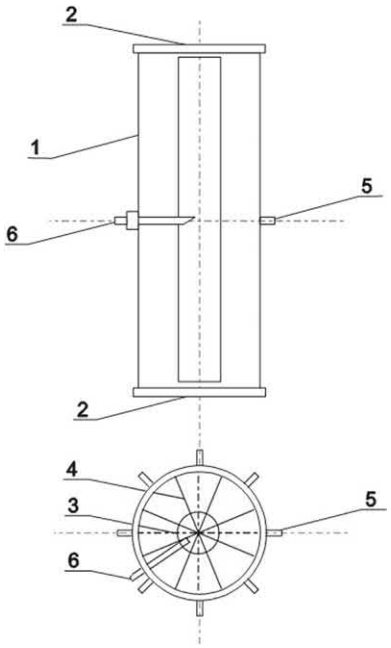


FIGURE 3.42 The large-volume scintillation chamber: 1—chamber tube, 2—glass windows, 3—central sector, 4—compartments, 5—gas inlets, 6—gas outlet. *From Beláň et al. (1992).*

detection of radon, the inner space of the chamber is divided into nine sectors (Fig. 3.41). The detector has a response time (time to half-peak magnitude) of 30 minutes, and a lower limit of detection of 1.7 Bq m^{-3} with uncertainty of 30% (Bulko et al., 2018).

As an example of the long-term monitoring of radon levels in the atmosphere, we present in Fig. 3.43 the average monthly radon activity concentrations for the years 1991−2005 measured in the Bratislava ground air. Spring minima and maxima occurring in various months of the second half of the year can be seen in the annual ^{222}Rn courses for all the years. However, the individual years differ from each other quite considerably. Fig. 3.44 shows the mean daily courses of ^{222}Rn activity concentration for individual months in the Bratislava air from 1991 to 2006. The monthly mean diurnal waves of the ^{222}Rn activity concentration are also shown. The average daily courses of ^{222}Rn activity concentrations have a form of waves with a maximum in the morning and minimum in the afternoon. These variations are directly connected with variations of the solar radiation flux during a day. Nocturnal accumulation of radon typically occurs in shallow mixing layers caused by temperature inversions. When the sun rises in the morning and heats the ground, which in turn warms the surface layer of the atmosphere, the temperature inversion is destroyed, and remixing of radon takes place in increasingly higher layers, with a consequent decrease in radon concentration near the ground. Minimum radon concentrations are normally reached in the late afternoon, corresponding to the maximum depth of the mixing layer. The composite seasonal cycle of outdoor radon is illustrated in detail in Fig. 3.45 with minima in April and maxima in January (Bulko et al., 2018), which reflect seasonal bias in the stability of the lower atmosphere, with more frequent, prolonged inversion periods during autumn and winter months as compared with summer.

A comparison of ^{222}Rn and ^{210}Pb (a daughter product) records in the Bratislava air is presented in Fig. 3.46. Generally, the ^{210}Pb activity concentrations (measured on aerosols) follow the radon ones as expected. This documents again that the ^{222}Rn activity concentrations are influenced mainly by radon exhalation rates from the ground and by turbulent diffusion in the atmosphere.

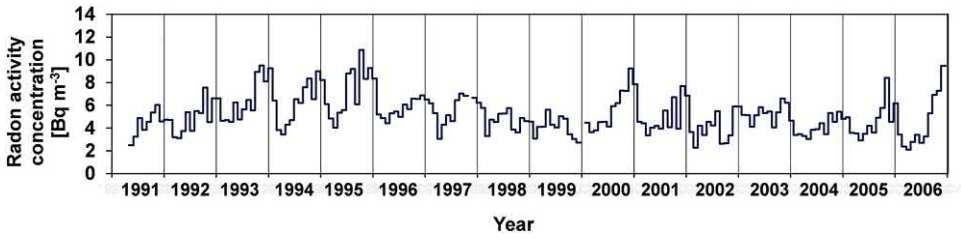


FIGURE 3.43 Monthly mean values of ^{222}Rn activity concentration in the surface layer of the atmosphere in Bratislava.

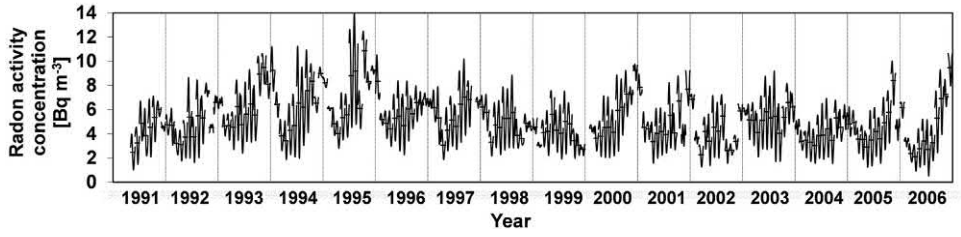


FIGURE 3.44 The mean daily courses of ^{222}Rn activity concentration for individual months in the Bratislava atmosphere.

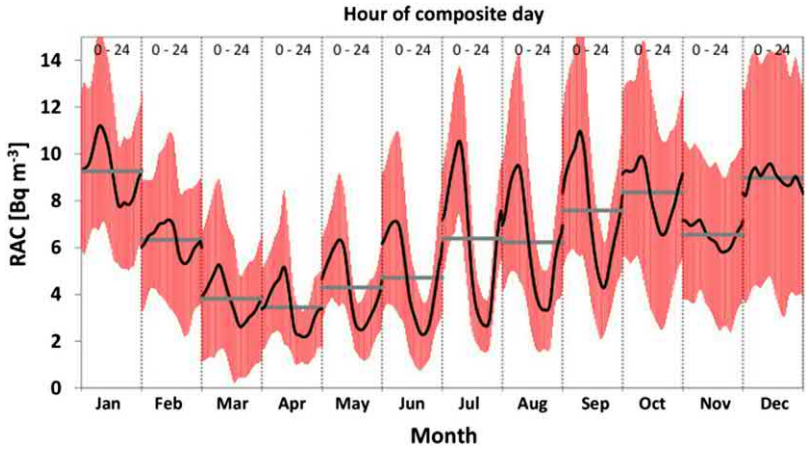


FIGURE 3.45 Example of seasonal cycle of outdoor radon in Bratislava in 1994 (gray horizontal lines delineate average monthly values of RAC, red color represents standard deviations of the data). *From Bulko et al. (2018).* Printed with permission © *Elsevier 2018.*

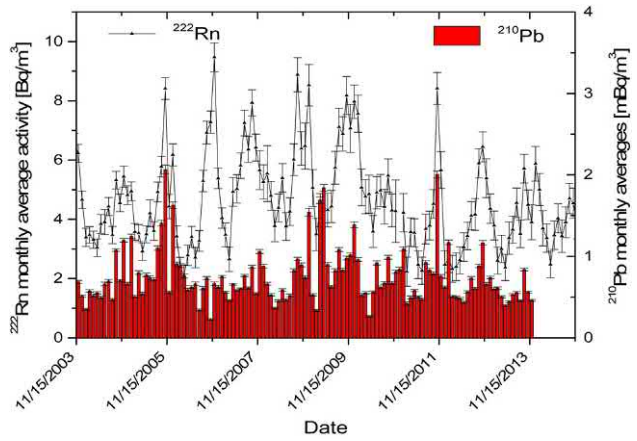


FIGURE 3.46 Comparison of ^{222}Rn and ^{210}Pb activity records in the Bratislava air. *From Sýkora et al. (2017).* Printed with permission © *Elsevier 2018.*

B. Radionuclides on aerosols

1. Properties of aerosols

An aerosol can be defined as an in-air particle, which is so small that their gravity fall is much smaller compared with in-air velocities. Aerosol particles can be divided into

- **(i)** Dust—solid particles abraded from surfaces and dispersed into air
- **(ii)** Smokes or fumes—solid or liquid particles condensed from the vapor phase
- **(iii)** Mist—droplets of water with other matter in solution or suspension

Dust is formed during the breakdown of solid material and is characterized by irregular and flaky shape. Fume is formed during the condensation of vapor as very small primary particles with spherical or crystalline shape. The formation of an aerosol from a pure radioactive substance is unusual (Chamberlain, 1967). Usually, radioactive substances are adsorbed on, attached to, or incorporated in the particles of other matter. In the atmosphere, some radioactivity is in gaseous form, but much of it is presented as aerosol particles. The main natural sources of aerosols are sea salt particles emitted from the oceans by evaporated sea spray, mineral dust from soils and rocks, volcanic dust, biogenic particles (e.g., pollen), and the reaction products of atmospheric gases as a result of heat and the influence of sunlight. Aerosols of anthropogenic origin include emissions during domestic heating using coal or wood, from industrial plants, from transportation, from agricultural activities, or from large forest fires. Radioactive aerosols often carry electric charge as a result of attached ions produced by cosmic rays and other ionizing radiation. The small particles also serve as nuclei for the condensation of water and other vapors. Therefore, size distribution of aerosol particles consists of several modes:

- **(i)** Aitken nuclei (<0.1 μm)
- **(ii)** Accumulation mode (0.1 μm < and <2.0 μm)
- **(iii)** Coarse mode (>10.0 μm)

Several main categories of aerosol particles can be classified by their physical characteristics. This is important for the characterization of aerosol health effects. An inhalable fraction contains the largest particles, which can enter the nose or mouth under average conditions. Inhalable particles that can reach the thorax are known as the thoracic fraction. These particles are also called coarse particulate matter (PM) and are composed of solid particles or liquid droplets with an average diameter greater than 2.5 μm and less than 10 μm (called also PM-10).

Particles that can reach the alveolar region of the lungs are known as the respirable fraction, but do not necessarily deposit there. These particles are usually in an accumulation mode, and there is a strong tendency for them to stay in suspension in air. They are called fine particulate matter and usually referred to as PM-2.5 (average diameter is less than 2.5 μm).

2. Sampling of aerosols

Depending the needs for radiometric measurements, aerosol radioactivity monitoring can be done by continuous and integral sampling. Both solutions require different arrangements of the sampling devices and have their advantages and disadvantages. Continuous online systems are frequently used for local monitoring, where the possible source of radioactive contamination is located (i.e., surroundings of NPPs), and therefore, information is needed as fast as possible about increased radioactivity levels. Aerosols are usually sampled by collecting on different kinds of filters by passing the sampled air through the filter. For the online sampling, the concept of the moving band is used, where aerosols are collected on filter in shape of a band, which is moving by at constant velocity, while aerosols are deposited in a dedicated part of the band. This step-like deposition represents the time development of the radioactive aerosols with time resolution of about several minutes. By moving the band, much less aerosols are collected in comparison with fixed filters, even though a comparable pumping system is used, and therefore, the detection limit is much higher for online systems. More detailed information about online monitoring systems can be found in documents from the International Electrotechnical Commission (IEC, 2002a; IEC, 2002b).

For regional monitoring, where the radioactivity from a distant source is much diluted due to the atmospheric dispersion processes, the fixed filters are preferred over those of fast response. Expected slow buildup rates of radioactivity on the filters require much larger samples to reach better detection limits. High-capacity pumping and large-area filters result in a high sampling rate, which together with relative long exposure times allow the achievement of detection levels of a few mBq m^{-3} (Schulze et al., 2000).

The task of aerosol sampling is to get a representative sample of particles from the air into the measuring device. Pumping of the ambient air through the filtration system by the vacuum pump at the end of the system is frequently used. Collection of aerosols from the atmosphere by using the filtration is relative straightforward; however, several conditions need to be followed. Since the radionuclide concentrations are reported per unit volume of air (Bq m^{-3}), usually an integrating flow meter is used to give a total volume of sampled air per known period of time. All the particles from a known volume of air have to be collected, without loss, breaking up particles or losing particles by evaporation or gaining them by condensation. Flow rate in the inlet of the sample device has to be the same as the flow rate in the device, to ensure representativeness of the sample. When the sampling velocity is equal to the velocity inside the device, it is called isokinetic sampling; otherwise, discrimination can occur for smaller or larger particles. If the velocity of the sample airstream is larger than the velocity of the airstream in the device, then the larger particles cannot make the abrupt change and are discriminated in the sample, i.e., the smaller particles are collected more efficiently, and vice versa (Macášek, 2008). Attention has to be paid to a correction for a sampled volume of air because the flow meters are usually calibrated in standard conditions (101 kPa atmospheric pressure and 20°C ambient temperature), and by using volume measured at different conditions can lead to 5% difference in activity concentration. The real volume V_R can be calculated as

$$V_R = V_M \frac{\rho_{20} p_0 T}{\rho_0 p T_0} \tag{3.13}$$

where V_M is the measured air volume, $\tilde{n}_{20}$ is the air density corresponding to standard conditions (1.205 kg/m^3), p_0 is the atmospheric pressure at 0°C (101,325 Pa), T is air temperature during the sampling in K, $\tilde{n}_0$ is air density at 0°C (1.293 kg/m^3), p is atmospheric pressure during the sampling in Pa, and T_0 is temperature of 0°C (273.15 K). During the evaluation of especially short-lived radionuclides, the corrections for decay during the sampling t_1, between sampling and measurement t_2, and during the measurement t_3 have to be applied as follows:

$$A_{corr} = A_{meas} \frac{t_1 ln2}{T_{1/2}\left(1 - 2^{-t_1/T_{1/2}}\right)} 2^{t_2/T_{1/2}} \frac{t_3 ln2}{T_{1/2}\left(1 - 2^{-t_3/T_{1/2}}\right)} \tag{3.14}$$

where $T_{1/2}$ is the half-life of the measured radionuclide.

The most commonly used device for aerosol sampling is a high-volume sampler. An air turbine is used to pull an air sample of about 2000 m^3 or more through a filter sheet. For specific purposes, proper filter media may be desirable. According to desired needs, such as high collection efficiency, particle size selectivity, low-flow resistance, high mechanical strength, low-background activity, temperature stability, retention of gaseous fraction, and ease of radiochemical analysis, the proper filter type should be selected. If complete particle size spectra are of interest, the multichannel (parallel) or multistage (series) arrangement of filters is used. The size of particles passed through several filters can be calculated from the hydrodynamic parameters of sampling (Maher and Laird, 1985). Depending on the monitored radionuclide, the filter after collection is prepared for analysis by, e.g., pressing to standard shape, burning, dissolving in organic solvents, or washing by oxidizing agents.

When particle size classification is needed, electrostatic precipitators, cyclone collectors, and cascade impactors can be used for sampling. For the impactors or impingers, the particles are collected on a selected surface, as the airstream is sharply deflected. As the sampled air flows into the first cascade of jets in the impactor, large particles with

significant momentum strike the collecting surface and remain trapped on this stage. Smaller particles with less momentum are diverted away from the collecting surface by the diverted airstream and continue to the next stage. As the air proceeds further into the impactor, smaller and smaller jets are used to force the air to higher velocities, and when smaller particles receive sufficient kinetic energy, they stay trapped on the collecting surface of the size-depending stage. By coating the collection surface with a thin layer of grease or adhesive, the tendency to stick the particles on the collecting surface can be increased. After collection, the impactor is carefully disassembled with each stage containing different sizes of collected aerosols. The sorted collected material provides information about particle size distribution, and when it is used for activity measurements, size distribution of radionuclide carrying particles can be obtained.

For the collection of condense water vapors or liquid aerosols, a condensation or dehumidifier sampling device can be used. A liquid nitrogen or refrigeration unit is used to cool the condensation surface where the liquid sample is collected for further analysis.

3. Examples of radionuclides on aerosols

a. Tritium

The main forms of tritium in the atmosphere are water vapor (HTO), as well as tritiated hydrogen (HT), tritiated methane, and other organic gases. It is also present in the form of tritiated aerosol particles; however, this form of aerosols is poorly documented. Usually, it corresponds to artificially produced tritiated molecules arising from resuspensions of labeled soil particles, bioaerosols composed of bacteria, aerosols emitted from terrestrial biomass, or aerosols produced by industrial operations handling tritium (Eyrolle et al., 2018). It is expected that tritium retention in plasma facing materials such as tungsten is a major concern for future fusion reactors.

b. ^{7}Be

One of the most abundant cosmogenic radionuclides in the atmosphere is ^{7}Be with a production rate of about 400 atoms $m^{-2}s^{-1}$ (Masarik and Beer, 2009). It decays by EC to ^{7}Li with 10.3% probability of emission of the 477.6 keV gamma ray, and therefore, it can be relatively easily determined by gamma spectrometric techniques. However, AMS can be used as well for the determination of ^{7}Be and with several orders of magnitude better sensitivity compared with gamma counting (Hidy et al., 2018; Raisbeck and Yiou, 1988).

^{7}Be is produced mainly in the stratosphere (about 70%); however, about 30% is produced also in troposphere (Masarik and Beer, 1999). A steep vertical concentration gradient between the upper and lower troposphere was observed as a result of relatively high production rates of ^{7}Be in the upper troposphere in combination with its transport from the lower stratosphere to the upper troposphere (Feely et al., 1989).

The residence time of ^{7}Be was estimated to be of 25–30 days in the troposphere and ~1 year in stratosphere (Raisbeck et al., 1981). Further details about particles size distributions carrying ^{7}Be can be found in Chapter 4, Volume 2. There are different concentrations of ^{7}Be depending on altitude and latitude as illustrated in Fig. 3.47. The dominant modulation of GCRs, which are mainly responsible for production of cosmogenic nuclides, is solar activity. Several authors reported a variation of ^{7}Be concentrations depending on the 11-year solar cycle (Ďurana et al., 1996; Cannizzaro et al., 2004; Steinmann et al., 2013), which can be seen in Fig. 3.48. Variations in the production of the ^{7}Be are not the only reason for variations of the activity concentrations in the ground-level atmosphere. Meteorological factors are also responsible, such as exchange of air masses between stratosphere and troposphere, vertical transport of air masses, horizontal transport of air masses from higher to lower latitude, and scavenging by precipitations (Feely et al., 1989). ^{7}Be is therefore widely used as a tracer for atmospheric dynamics and transport processes. The Be concentrations during the year show seasonal changes with high values in spring–summer and low values in autumn–winter months. The amplitude of the seasonal pattern also varies at the same latitude from year to year. Sýkora et al. (2017) reported a weekly trend of ^{7}Be in ground level atmosphere of Bratislava in Fig. 3.49. Elevated ^{7}Be concentrations during the warm season appear to be a result of the vertical transport of air masses during this season. Furthermore, in mid-latitudes (above 40°N), during the summer months, the tropopause is higher than in winter (Gerasopoulos et al., 2001). In winter, the atmosphere is more stable, and the tropopause is lower than in summer; therefore, ^{7}Be values in surface air are lower. During the spring period, stratosphere to troposphere exchange processes are enhanced, which result in a significant increase of the ^{7}Be concentration. Gerasopoulos et al. (2001) studied the changes of the ^{7}Be concentration at high altitudes due to meteorological conditions. They have found positive correlation between tropopause height and ^{7}Be concentration at the three Alpine stations, as well as negative correlation between ^{7}Be values and the relative humidity. The negative correlation with humidity can be related to wet scavenging; however, Steinmann et al. (2013) reported for ^{7}Be concentrations similar variations as for precipitations. They explained this unexpected correlation by additional ^{7}Be input during the summer due to the stratospheric contribution, which compensates wet deposition of ^{7}Be in this time.

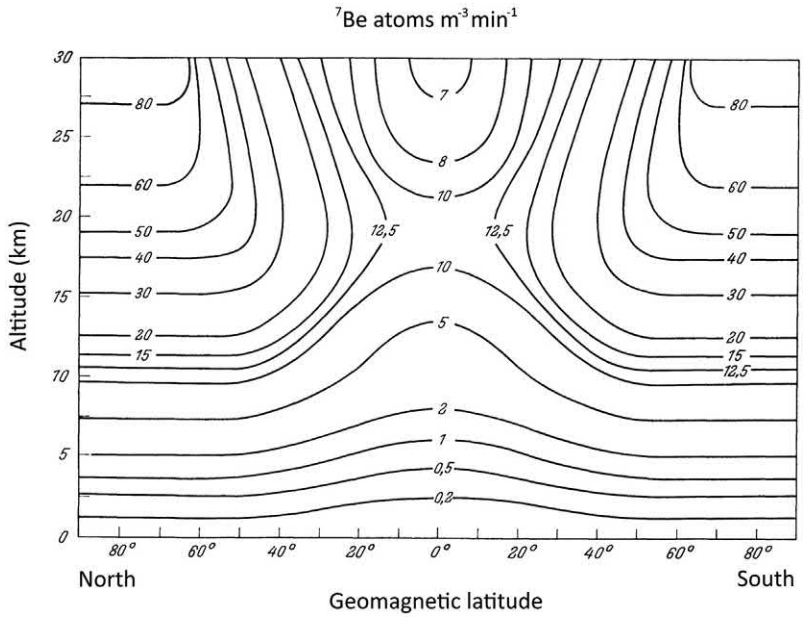


FIGURE 3.47 Production rate of ^{7}Be in atmosphere (at standard temperature and pressure) over different latitudes. *From Lal and Peters (1967).* Printed with permission © Springer 2018.

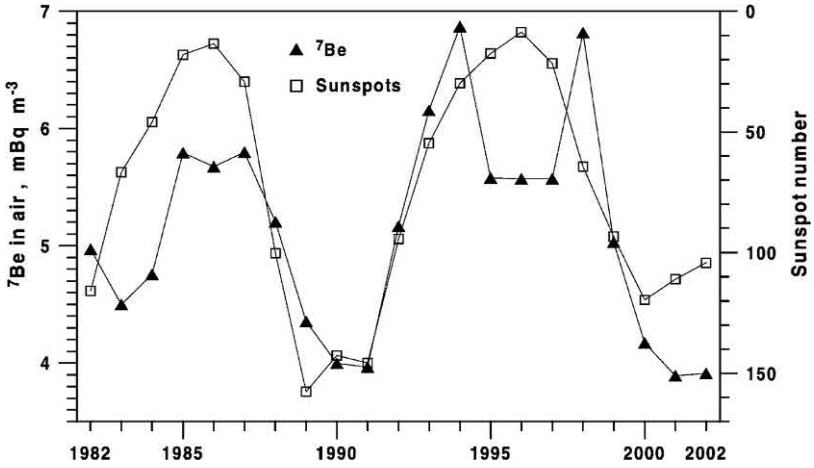


FIGURE 3.48 Annual averages of ^{7}Be concentrations in negative correlation (scales in opposite direction) with sun activity (represented by sunspot number). *From Cannizzaro et el. (2004).* Printed with permission © *Elsevier 2018.*

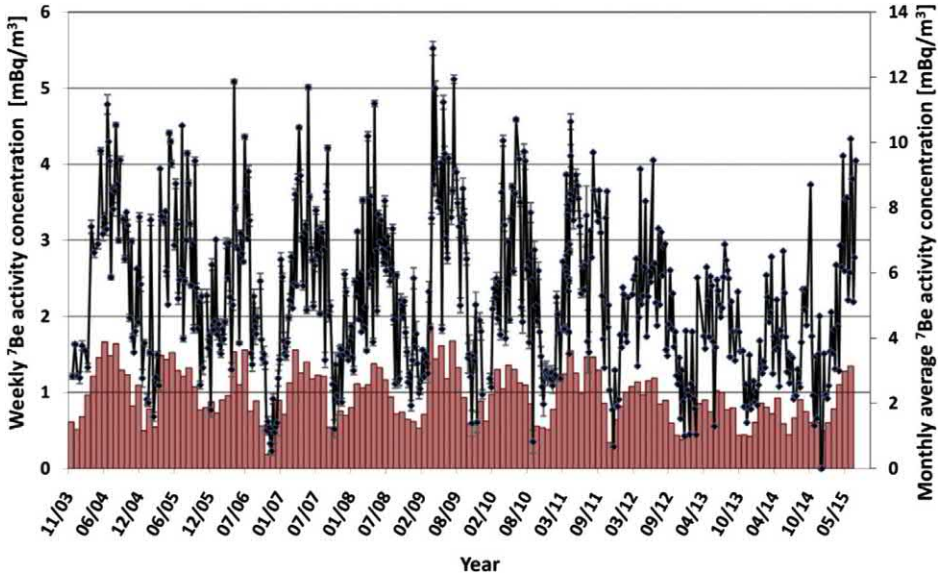


FIGURE 3.49 Seasonal variations of ^{7}Be in ground-level atmosphere of Bratislava. *From Sýkora et al. (2017).* Printed with permission © *Elsevier 2018.*

c. ^{10}Be

^{10}Be is another beryllium isotope, which is produced in the atmosphere by cosmic rays. Compared with ^{7}Be, it is a long-lived radioisotope with half-life of 1.5×10^{6} years, and the production pattern in the atmosphere is more or less similar to ^{7}Be; however, the dynamics of ^{10}Be in atmosphere is more complicated. It undergoes beta decay to ^{10}B, but due to its very long half-life, the AMS technique is successfully used for the determination of ^{10}Be in various samples. Freshly produced ^{10}Be is normally of interest, which becomes part of aerosols in the accumulation mode, and this is known as "atmospheric ^{10}Be." However, ^{10}Be produced in the Earth's surface layers and deposited aerosol particles with ^{10}Be on the surface can enter the atmosphere in the form of dust as well, and this is known as "terrestrial ^{10}Be." It is complicated to separate these two fractions of aerosols; therefore, the sampling location can be chosen to minimize the terrestrial fraction (high altitude, arctic, and Antarctic region), or a correction for this fraction can be applied, when the abundance of terrestrial ^{10}Be in aerosol is known or measured. The same chemistry of ^{10}Be as ^{7}Be predestined the accumulation in the same aerosol mode.

Since sample preparation for AMS requires the destruction of the sample, nondestructive analysis, like gamma spectrometry, is performed before the AMS ^{10}Be measurement. The main isobar, responsible for background in AMS measurement of ^{10}Be, is ^{10}B, and therefore, the main objective of chemical preparation is to minimize boron content in the sample. Depending on the filter used for aerosol collection and further analysis of additional radionuclides (such as ^{26}Al and ^{36}Cl), the sample is spiked with a known amount of ^{9}Be as a carrier and leached with HNO_3 and/or HCl solution. To separate the beryllium from boron, iron, and aluminum, cation exchange process (e.g., DOWEX 50W x 8 resin) and/or solvent extraction (e.g., ethylene diamine tetraacetic acid [EDTA] for Al content reduction) can be used. After purification, $Be(OH)_2$ is precipitated by diluted ammonia and transformed to BeO, which is used as sample material in the ion source, by heating to 800–950°C. For better electric and thermal conductivity, the sample powder is mixed with pure Nb or Ag. During the AMS measurement, $^{10}Be^{16}O^{-}$ ion is produced in the ion source, and $^{10}Be^{3+}$ ion is accelerated and separated for the ^{10}Be/^{9}Be determination. For normalization during the measurement, NIST SRM 4325 standard (^{10}Be/^{9}Be $= 2.68 \times 10^{-11}$) can be used. Generally, the statistical and instrumental error of the measurement is below 5%, and the background ^{10}Be/^{9}Be in the order of 10^{-15} can be achieved (Tuniz et al., 1998).

Together with ^{7}Be, ^{10}Be is used as a tracer of stratospheric circulation and stratosphere–troposphere exchange processes. Yamagata et al. (2010) showed that the concentration of ^{10}Be and ^{7}Be in the troposphere is not decreased by the precipitation, without a cyclonic pressure drop. Beryllium isotopes penetrate into the upper troposphere in spring season and mix uniformly; therefore, the ^{10}Be/^{7}Be ratio is a sensitive tracer of stratospheric air. Jordan et al. (2003) described that ^{10}Be/^{7}Be ratios can provide valuable information about various mechanisms of stratospheric-to-troposphere exchange, including changing seasonal structure of the stratosphere, tropopause folding, and the effect of synoptic systems. They observed seasonality in the ^{10}Be/^{7}Be ratios as a result of downwelling of air with elevated ratios from higher stratosphere in the spring and summer (for midlatitudes) and from the ^{7}Be decay during descent in the winter polar vortex (for high latitudes).

^{10}Be carrying aerosols can be stored also in natural reservoirs, such as sediments and ice (glacier and continental glacier) (Smith et al., 2000). Due to its long half-life, it can serve as a probe to past atmospheres by using deep profile of such a reservoir. The past solar activity was successfully reconstructed by using ^{10}Be in the ice core from Dome Fuji, as can be seen in Fig. 3.50 by comparison with ^{14}C in tree rings record. Within the Greenland Ice Sheet Projects (GISP1 and 2), several ice cores were drilled in Greenland, and different characteristics and radionuclides, including ^{10}Be, were measured between 3288 and 40,055 years BP (Finkel and Nishiizumi, 1997). Beer et al. (1990) used the distribution of ^{10}Be in 300 m ice cores for the determination of past 11-year solar cycles.

d. ^{14}C

Carbon is one of the main components of atmospheric aerosols. Total carbon (TC) in carbonaceous aerosols

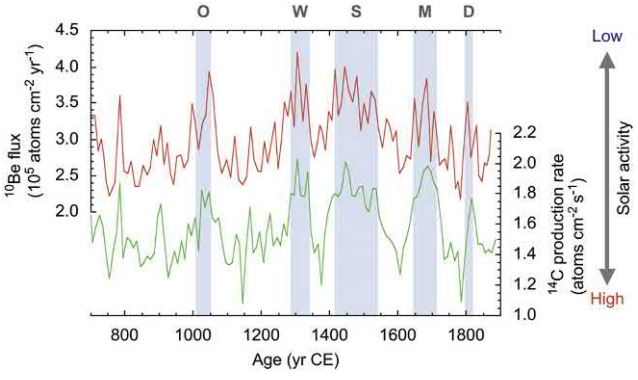


FIGURE 3.50 The comparison of ^{10}Be and ^{14}C record of the ^{10}Be flux of the Dome Fuji ice core and the ^{14}C production rate for 700–1900 years CE. The five-point averaged δ^{18}O values were used for the estimation of the snow accumulation rate for calculating the ^{10}Be flux (O: Oort (1010–1050 years); W: Wolf (1280–1340 years); S: Spörer (1420–1540 years); M: Maunder (1645–1715 years); D: Dalton (1795–1820 years)). From Horiuchi et al. (2008). *Printed with permission* © Elsevier 2018.

consists of elemental (EC) and organic (OC) carbon. There is also a small fraction of carbonate carbon (CC), but it is often neglected except for a few particular situations such as erosion, sand storms, and building constructions, which are reported in the literature (Cuccia et al., 2011; Querol et al., 2009; Yubero et al., 2011). EC is produced mainly by the incomplete combustion of fossil and biomass fuels, and it is the most refractory carbon fraction with high efficiency of solar light absorption. OC is carbon accommodated in organic matter, which is composed of thousands of chemical constituents, which makes a complete characterization difficult.

Carbon aerosols can be directly released into the atmosphere as primary particles from anthropogenic and biogenic sources. Major anthropogenic emissions to the atmosphere result from fossil fuel combustion and biomass burning. Biogenic aerosols mainly include pollen, plant debris, fungal spores, and bacteria as primary particles; however, it can be generated also from a gaseous precursor as secondary organic aerosol (SOA) (Jacobson et al., 2000; Schell et al., 2001). Sources of SOA are important regarding biogenic versus anthropogenic precursors and its contribution to primary OC (Kavouras and Stephnou, 2002). ^{14}C determinations offer a unique possibility for source identification of carbonaceous aerosol particles, such as apportionment of fossil/nonfossil sources (Currie, 2000). This isotopic method permits a direct distinction of contemporary and fossil carbon in ambient aerosols because fossil materials are so old, which ^{14}C has already decayed. In atmospheric studies, $^{14}C/^{12}C$ ratios are often given as fractions of contemporary carbon, f_C (Currie et al., 1989). This parameter includes a correction of the fraction of modern carbon (f_M) for the residual ^{14}C from nuclear bomb excess, and Levin et al. (2003) suggest that biogenic aerosol originates from fresh organic material.

^{14}C is a beta decaying radionuclide that can be determined by LSC and GPC; however, for atmospheric studies, the mass of the collected aerosol is in order of mg, and therefore, the AMS technique is widely used. Most of the filters contain fossil or modern carbon, which can significantly influence results. Quartz fiber filters are successfully used for sampling of carbonaceous aerosol; however, semivolatile organic carbon (SVOC) can adsorb on the quartz surface. Szidat et al. (2004) estimated that SVOC contributes $8 \pm 5\%$ to total OC and therefore can be neglected. After collection, aerosols are combusted to CO_2 in a vacuum apparatus and separated to EC and OC fractions according to thermal separation. It has been noted also that water-soluble organic carbon (WSOC) can undergo pyrolysis (Yu et al., 2002) and the inorganic compounds produced can catalyze precombustion (Wang et al., 2010); therefore, WSOC is frequently removed (Szidat et al., 2009; Zencak et al., 2007). Separation of the OC fraction is usually performed by sample precombustion at about 340°C in oxygen atmosphere for several minutes (about 10 minutes are usually sufficient) to avoid EC contamination (Zhang et al., 2010). After cryogenic separation of the CO_2 produced from OC, the residual sample is combusted at about 650°C for EC determination. To separate the different carbon fractions, the approach proposed by Szidat et al. (2006) can be used (Fig. 3.51). For the AMS measurement, CO_2 can be directly used in the ion source; otherwise, graphite is produced and sputtered for C^- ion beam creation (for details, see Section V.A).

Bernardoni et al. (2013) analyzed emissions of fossil fuel in Milan (Italy) during the winter time. OC was dominated by modern carbon contributions (63%), and EC was of fossil fuel origin (84%). In TC emission, modern nonfossil sources (55%) prevailed on fossil fuel contribution (45%). Szidat et al. (2004) observed the same trend in the urban background area in Zürich (Switzerland), where biogenic OC dominated the composition of total OC and TC concentrations, whereas anthropogenic OC strongly correlates with EC. They attributed the result to the formation of SOA, which was indicated also by correlation with other meteorological factors, such as maximum temperature, ozone maxima, and biogenic isoprene concentrations. Chen et al. (2015) used ^{14}C and $\delta^{13}C$ in EC as a tracer of dust source regions in Beijing (China).

By aerosol sampling methods, natural archives (ice and sediments) can be used for the analysis of OC and EC concentrations in the past. For ice sampling, it is suitable to use a drilling technique without organic solution. After separation of the core to time-related sections, the ice is slowly melted to reduce stress and crack formation. Aerosols are separated from the melted sample by filtration with a quartz fiber filter. The next step in the preparation is the same as for the aerosols collected from the atmosphere. Jenk et al. (2006) reported a long-term record (covering the period 1650–1940) of water-insoluble OC and EC

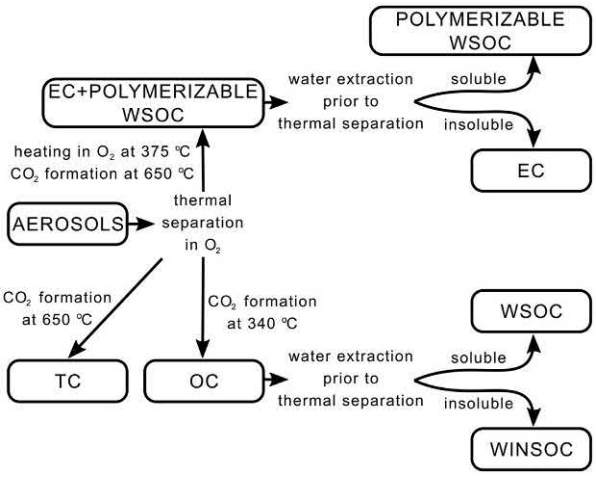


FIGURE 3.51 Principal steps for separation of different carbon fractions.

fractions based on ice core samples from the Fiescherhorn glacier in Switzerland. They published that a concentration of OC in 1940 was a factor of 3 higher than the biogenic background level in 1850 (24 ± 7 μg kg^{-1} of ice) and the anthropogenic input of EC (in 1940) to be 50 ± 9 μg kg^{-1} of ice.

As ice cores, sediments can be used for anthropogenic identification of carbonaceous aerosols as well; however, the separation of each fraction is more complicated, and therefore, many studies quantify only bulk characteristics. The general strategy in the separation of total OC from sediment includes the removal of carbon bound in carbonate fraction from soils and minerals by diluted HCl (2%), homogenization, drying, and combustion of the sample in oxygen atmosphere at 850−900°C. Guo et al. (2004) used the CTO375 method for the determination of EC in Siberian Arctic coastal sediments and confirmed the preservation of terrestrial organic matter from the west to the east Arctic coast, which is in agreement with the distribution pattern of permafrost zone.

e. ^{22}Na

^{22}Na is a cosmogenic radionuclide with a half-life of 2.602 years. It is produced by spallation reaction with argon, primary in the atmosphere. As other cosmogenic radionuclides, it is relatively fast oxidized and becomes part of the atmospheric aerosol. ^{22}Na has a similar behavior in the atmosphere as ^{7}Be; however, its production rate is only about 8.6×10^{-3} atoms m^{-2} s^{-1} (Lal and Peters, 1967). It is a β^+ decaying radionuclide with emission of gamma photons with energy of 1275 keV and, therefore, can be determined by gamma spectrometry. Due to its very low concentration in the atmosphere (below 0.5 μBq m^{-3}), the determination of ^{22}Na is problematic, and high-volume aerosol samplers are needed (in the order of 100,000 m^3), which use rather big filters (e.g., ASS 500 using Petryanov filtering cloth with dimensions of 0.57×0.45 m). For better detection efficiency, the large filters are usually compressed to smaller discs. With this sampling method and by using a HPGe detector with 25% efficiency situated in a low-level background shield with anticosmic veto, a detection limit of 0.1 μBq m^{-3} (1 week of measurement) for ^{22}Na can be achieved (Błażej and Mietelski, 2014).

Information about the ^{22}Na concentration can be used for studies of atmospheric processes, such as vertical turbulent movement, stratosphere-to-troposphere transport, and washout from the atmosphere. Hoffman et al. (2017) published a multiyear worldwide database and data set of ^{22}Na concentrations from 54 monitoring sites. Steinmann et al. (2013) observed the same increase in ^{22}Na activity as ^{7}Be in ground level air in Switzerland during March and May caused by stratosphere-to-troposphere exchange.

f. ^{26}Al

In addition to ^{10}Be, ^{26}Al is another long-lived cosmogenic radionuclide with a half-life of 0.708×10^6 years, which has been rarely applied to climate and atmospheric studies. It can be produced in the atmosphere with a production rate of 1.4 atoms m^{-2} s^{-1} by spallation of argon (known as atmospheric ^{26}Al), and it is further produced in the terrestrial environment by spallation of silicon (known as terrestrial ^{26}Al). Another source of ^{26}Al is material of extraterrestrial origin, such as interplanetary dust or meteorites (known as extraterrestrial ^{26}Al).

^{26}Al is β^+ decaying to stable ^{26}Mg with the emission of characteristic 1808.7 keV (99.7% probability) and 1129.7 keV (2.5% probability) gamma photons. Therefore, it can be determined relatively well by gamma spectrometry; however, the detection limit for ^{26}Al is in the order of 0.4 mBq g^{-1} (Povinec et al., 2009c) for a surface laboratory and in the order of 0.05 mBq g^{-1} by using a coincidence technique in an underground laboratory (Arnold et al., 2002). This is far above the ^{26}Al activity concentration in the atmosphere, that is, in the order of pBq g^{-1}, and therefore, AMS must be used for analysis (Middleton and Klein, 1987).

^{10}Be and ^{26}Al behave in many respects similarly, and therefore, the procedure for sample preparation of ^{26}Al is the same as for ^{10}Be, with the exception of the last chemical step before Al precipitation. After leaching the filter with collected aerosols in HCl, aerosols are separated by filtration and Al is extracted by ion exchange, precipitated as hydroxide and after washing with double-distilled water converted into oxide during the heating at 700−900°C. The main isobar affecting the detection limit of ^{26}Al AMS measurement is ^{26}Mg. Because Mg does not form stable negative ions, and by using $^{26}Al^-$ as injection ions, even tandems with relative low terminal voltage (Raisbeck et al., 1987 successfully used 1.9 MV) can be used for the acceleration of 3^+ charge state to achieve reasonable sensitivity. It is known that Al_2O_3 does not yield high-intensity Al^- beams; therefore, large tandems (with a terminal voltage above 6 MV) with AlO^- as injection ion are used, where better separation by using 7^+ charge state can be obtained and therefore higher sensitivity can be reached (^{26}Al/^{27}Al in the order of 10^{-16}).

The production rate of ^{26}Al in the atmosphere is about 300 times lower than that of ^{10}Be and 6 times higher in surface rocks; therefore, the ^{26}Al/^{10}Be ratio can be used to study the terrestrial and extraterrestrial contribution to atmospheric ^{26}Al and ^{10}Be. Auer et al. (2009) determined ^{26}Al/^{10}Be ratios in aerosol samples from both hemispheres to be constant and equal to 1.89×10^{-3}. This ratio has not differed from the ratio measured in Antarctic surface fin. These measurements indicate a minor influence of in situ

produced and resuspended to atmospheric ^{26}Al as well as no significant impact of the stratosphere-to-troposphere exchange. The constant $^{26}Al/^{10}Be$ ratio in Antarctic fin and atmospheric aerosol predisposes the suitability of use of the ratio as chronometer of old archives, such as glacier ice.

g. ^{131}I

Iodine-131 is a short-lived isotope of iodine, which exists in the atmosphere in several forms, as particle-associated iodine (particulate iodine), inorganic gaseous iodine (I_2, HI, HOI), and organic gaseous iodine (CHI_3, CH_2I_2, $CH_3CH_2CH_2I$, etc.) (Yoshida and Muramatsu, 1995). Iodide, iodate, and organic iodine are soluble species of iodine that exist in the aerosol form (Hou et al., 2009a). Molecular iodine (I_2), which may be released, i.e., from seaweed, could be converted to active I and react with O_3 to form IO, which leads to the production of new particles. Because of its bioavailability, especially concentrated in thyroids, isotopes of iodine are important for health and in radiological studies. They are highly mobile in the environment and follow usual transfer processes in the atmosphere. After deposition, iodine can be taken up by plants and enter the food chain.

^{131}I is a fission product of uranium and plutonium, which can be released to the atmosphere during a NPP accident or from a radionuclide production facility. It has been used for medical purposes, mainly for the treatment of thyroid diseases. It decays with a half-life of 8.02 days by β^- decay to ^{131}Xe, accompanied by the emission of gamma rays with energy 364.5 keV (81.7%), 637 keV (7.2%), and 284.3 keV (6.1%). Therefore, ^{131}I can be determined relatively easily by gamma spectrometry, and it is monitored around nuclear facilities. A higher concentration of ^{131}I was registered after the accidents in Chernobyl (Fig. 3.52) and Fukushima by many laboratories.

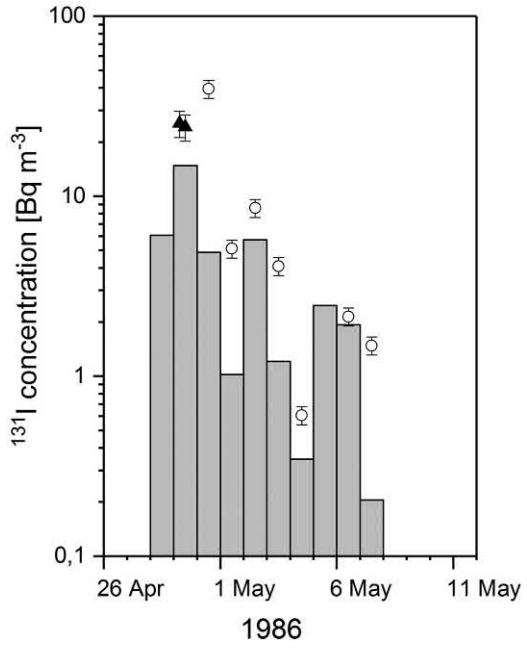


FIGURE 3.52 ^{131}I in the Bratislava air after the Chernobyl accident. *After Povinec et al. (1988).*

h. ^{129}I

The longest-lived isotope of iodine is ^{129}I ($T_{1/2} = 15.7 \times 10^6$ years), which decays by emitting beta particles ($E_{max} = 154.4$ keV), gamma rays (e.g., 39.6 keV) as well as X-rays. Although it can be measured by gamma, X-ray spectrometry, and LSC beta counting, neutron activation analysis, ICP-MS, and AMS are common techniques used for the registration and determination of ^{129}I. After collection, iodine in aerosols can be sequentially extracted in different forms using deionized water and sodium hydroxide solution (for the water-soluble and organic fractions), followed by alkaline ashing and water leaching (for the insoluble fraction) (Zhang et al., 2015b). Iodide and iodate can be further separated using anion exchange techniques (for more detailed description of sample preparation and measurement techniques, see Section V.C). It is produced naturally by reactions of cosmic rays with Xe and by fission of uranium. The main contribution to the environment is, however, from human nuclear activities, where discharges from nuclear reprocessing plants dominate. Zhang et al. (2015a) concluded that the main source of ^{129}I in the aerosols in Denmark is the reemission of marine discharged ^{129}I in the surface water near the European nuclear reprocessing plants.

^{129}I was demonstrated to be a useful geochemical tracer in the marine environment and in the atmosphere, since the identification of natural ^{127}I sources is difficult, and it can be used as a proxy for the reconstruction of the ^{131}I concentration during nuclear accidents. Wershofen and Aumann (1989) studied the chemical forms of iodine released from the WAK nuclear fuel reprocessing plant in Germany. They found that the dominant release of ^{129}I is in gaseous organic iodine species (in 1987, it was 66%−34%, relative decreasing of specie with increasing distance); however, the particulate contribution was relatively low (in 1987, it was 1.7%−9.7%, relative increasing of specie with increasing distance). Similar results were observed in Lithuania and Japan for the speciation of iodine during the Chernobyl accident, where 60%−80% was identified in organic gaseous form, 10% in the inorganic gaseous component, and less than 35% in aerosol form (Nedveckaite and Filistowicz, 1993; Noguchi and Murata, 1988). The high fraction of organic form of ^{129}I and consequently also ^{131}I may be associated with conversion of speciation during long-distance transport (Hou et al., 2009a). A major form of ^{129}I as $^{129}I_2$ released from the damaged nuclear reactor during the Fukushima accident might be in Tsukuba

aerosols attributed to a large fraction of inorganic ^{129}I. This agrees with the finding that most of the ^{129}I in the seawater is in the form of iodide, whereas the iodate form contains most of the ^{127}I (Hou et al., 2013). However, a large fraction of ^{129}I in organic-bound iodine might be associated with the $^{129}I_2$ released from Fukushima reactors, which has a high reactivity with the organic particles from vegetation and therefore can be I_2 in the atmosphere converted to organic associated iodine (Xu et al., 2015).

i. ^{137}Cs

^{137}Cs is a relatively long-lived radionuclide produced anthropogenically by nuclear activities without a natural contribution. It is beta decaying to ^{137}Ba and ^{137m}Ba, which can deexcite by emission of 661.7 keV gammas with 0.851 probability to the ground state, which is the most common way to analyze ^{137}Cs in the environment. To reach the lowest detection limit, HPGe detectors with high efficiency are widely used for the determination of ^{137}Cs, and a large volume of air must be filtered. Quartz fiber filters are frequently used for sampling, but if the determination of other radionuclides does not involve chemistry, cellulose and nucleopore filters can be used as well. For a sample collected from about 50,000 m^3 of air and with the use of a HPGe detector with 70% relative efficiency situated in a low-level background shield, a detection limit of 0.05 μBq m^{-3} (for 1 week measurement) can be achieved for a surface laboratory (Povinec et al., 2012a). Because of its high abundance and accumulation in human tissue, ^{137}Cs has been important from the point of view of delivering radiation doses to the public. Cesium has similar physical and chemical properties as potassium and rubidium, and because of its solubility in water, it is frequently found in the aquatic environment and can easily enter biological organisms. After its release into the atmosphere, ^{137}Cs is rapidly associated with aerosol particles, or it can become part of aerosols during their formation, e.g., during biomass burning and formation of dust particles, or after graphite fires and fuel melting (e.g., as during the Chernobyl accident). ^{137}Cs in the terrestrial environment exists mainly in vegetation and soil, where it was deposited by dry and wet deposition usually in the past. The highest ^{137}Cs levels in the atmosphere were registered in 1963 after the atmospheric nuclear weapon tests carried out in 1961−62 at Novaya Zemlya, which together with previous tests resulted in a global contamination of the environment (global fallout) (Povinec et al., 2013a). In Europe, the atmospheric ^{137}Cs levels were strongly influenced by the Chernobyl (Ukraine) accident in 1986, during the reactor core burning. In 2011, during the accident in Fukushima (Japan), the NPP Dai-ichi released to the atmosphere a significant amount of ^{137}Cs, which was registered above natural background almost all around the world (Masson et al., 2011; Povinec et al., 2013a,b,c; Povinec and Hirose, 2015).

^{134}Cs is another radioactive isotope of cesium, which is produced artificially by nuclear fission. It decays by beta decay to ^{134}Ba with a half-life of 2.06 years and the emission of several gammas, among which the most intensive are the 604.7 keV (with 97.6% probability of emission) and 795.9 keV (85.5%) lines. Therefore, it can be measured directly with ^{137}Cs by gamma spectrometry. Due to its relative short half-life, compared with ^{137}Cs, it can be used as an indicator of a "fresh" release from NPPs, reprocessing plants, or release during an accident. Kobayashi et al. (2015) estimated the $^{134}Cs/^{137}Cs$ ratio after the Fukushima accident, corrected to March 11, 2011, due to their different radioactive decay, to be 1.06 ± 0.04. Most of the ^{137}Cs presently found in the ground-level atmosphere comes from resuspension of this deposited cesium in soil and from biomass burning. The local resuspension of ^{137}Cs is influenced by factors such as wind velocity, intensity and frequency of rainfall, type and structure of soil, and moisture content of the soil (Kulan, 2006); therefore, seasonal variations can be observed (Ješkovský et al., 2018) as can be seen in Fig. 3.53. Although the ^{137}Cs levels in the Bratislava are increased by about five orders of magnitude, the ^{7}Be activity concentrations were still higher, as can be seen from a comparison presented in Fig. 3.54.

^{137}Cs on atmospheric aerosols has also been used to qualitatively and quantitatively identify natural atmospheric events, such as long-range dust transport (Igarashi et al., 2005, 2011; Pham et al., 2017; Sýkora et al., 2017) or biomass burning (Bourcier et al., 2010). Resuspension of soil particles (Lee et al., 2002; Kulan, 2006; Pham et al., 2011; Povinec et al., 2012a,b,c; Sýkora et al., 2012) and biomass burning (Bourcier et al., 2010; Masson et al., 2009; Stoulos et al., 2014) represent at present the major sources of ^{137}Cs variations in the atmosphere, in contradiction to past variations, which were due to transport of bomb produced ^{137}Cs from the stratosphere to the troposphere. Most of the events with higher ^{137}Cs concentrations were observed during winter, which could be due to the biomass burning with higher concentrations of Chernobyl-derived ^{137}Cs involved in wood (Ješkovský et al., 2018).

j. ^{40}K

Potassium-40 enters the air via resuspension from the surface soil. The main source of ^{40}K in the air is its transport by wind from the soil. High correlation between the average ^{137}Cs and ^{40}K activity concentrations has been found (Sýkora et al., 2017), confirming similar origin (a resuspension from soil) and behavior of these radionuclides in the atmosphere. The concentrations of ^{137}Cs and ^{40}K in the ground-level air are characterized by seasonal variation with winter maxima and summer minima. The increased atmospheric ^{137}Cs and ^{40}K levels observed during the autumn−winter season may be mainly due to surface soil resuspension, biomass burning, radionuclide transport by

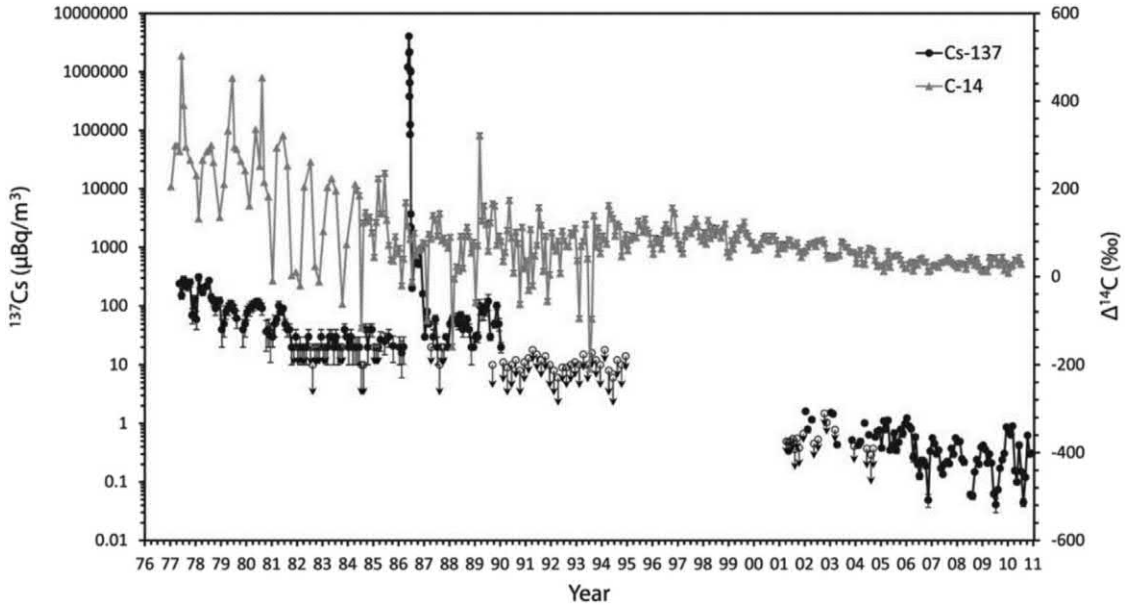


FIGURE 3.53 Atmospheric levels of ^{137}Cs and ^{14}C in Bratislava before and after the Chernobyl accident (Povinec et al., 2012a,b,c). *Printed with permission* © Elsevier 2018.

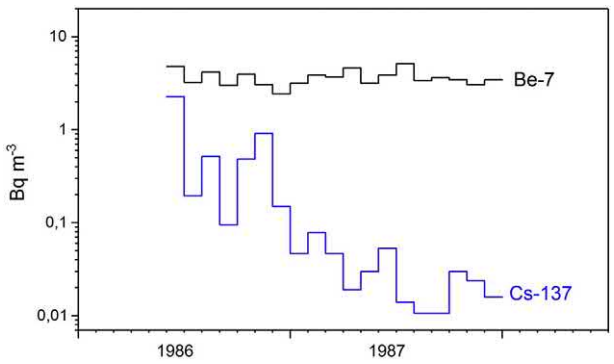


FIGURE 3.54 Comparison of ^{7}Be and ^{137}Cs activity concentrations in the Bratislava air during the Chernobyl accident.

winds, and specific meteorological conditions during winter with temperature gradient inversions. The ^{137}Cs/^{40}K activity ratio for the surface air (0.07) is close to the value observed in soil (0.05), which indicate a predominance of soil resuspension processes on the atmospheric concentrations of these radionuclides during the winter season (Sýkora et al., 2012). ^{40}K has been found as the best tracer to study a resuspension of radionuclides from soil, including its comparison with possible resuspension of ^{137}Cs from surface soil.

k. Radon and its daughters

Uranium and thorium primordial isotopes in the soil and rocks decay following their decay chains. The radionuclides radon (^{222}Rn) and thoron (^{220}Rn) of the uranium and thorium decay chains are noble gases formed by decay of ^{226}Ra and ^{224}Ra, respectively. These gases can emanate from the soil grains to the air-filled pores and are transported through the pores of the material by molecular diffusion or by convection until they enter the atmosphere. The exhalation rate of radon and thoron depends on several factors, such as the soil type, and ^{222}Ra and ^{224}Ra concentrations in the soil; however, at a given location, it can be considered roughly constant. They are released to the atmosphere, where they are, together with their daughters, distributed by turbulent air mixing. The difference in the half-life of ^{222}Rn (3.8 d) and ^{220}Rn (55 seconds) is important for the release from the ground and the distribution in the atmosphere above the ground. Radon daughters can be divided into "short-lived" radionuclides ^{210}Po (3.05 minutes), ^{214}Pb (26.8 minutes), ^{214}Bi (19.7 minutes), and ^{214}Po (164 µs) with half-lives below 30 minutes, and "long-lived" radionuclides ^{210}Pb (22.3 years), ^{210}Bi (5.01 days), and ^{210}Po (138.4 days). All thoron daughter products can be considered as "short-lived"; however, the most important radionuclide is ^{212}Pb (10.6 hours).

These daughters are often electrically charged and become attached to aerosol particles in the atmosphere with high mobility. After the radon radioactive decay, the freshly produced radionuclides react very fast (<1 seconds) with air vapors and trace gases, whereas small particles, called clusters, with diameters from 0.5 to 5 nm are formed. In addition to the cluster formation, decay products can attach to the existing aerosol in the atmosphere within 1−100 seconds, which results in the formation of radioactive aerosols with radon and thoron decay products. The

removal of these radionuclides from the atmosphere occurs by radioactive decay or by atmospheric processes, such as dry deposition, rainout, or washout. The size distribution of the decay products formed aerosols is an important parameter for the estimation of radiation dose by inhalation because the deposition of aerosol particles in the human lung depends primarily on particle size.

Besides the impact on the human health, radon with the daughters can be used as a tracer of atmospheric transport and identification of air masses derived from continental areas. Short-lived daughters of radon can be continuously monitored by an alpha detector, registering ^{214}Po on aerosols collected by pumping the air through a measured particle filter (Stanys et al., 1998). The measured signal is a representation of all precursors (^{212}Po, ^{214}Pb, and ^{214}Bi) attached to aerosols. Thoron can be monitored only in the lower atmosphere because of its short half-life, but at larger distances, the longer-lived decay product ^{212}Pb can be used. The activity of the ^{212}Pb can be determined by alpha measurements of the decay products (^{212}Bi and ^{212}Po).

From "long-lived" daughters of radon, ^{210}Bi and ^{210}Po can be registered by beta counting after chemical separation from several days of collected aerosols (Zhang and Luo, 1983; Carvalho, 1995; Jia et al., 2001; Sethy et al., 2015; Jia, 2018). ^{210} Pb decays by β^- decay; it can be, however, determined by γ-spectrometry with registering of the 46.5 keV gammas. This is a low-energy gamma, and therefore, a Ge detector with a low Z window (made of Be or C) must be used for getting sufficient detector efficiency.

Although the half-life of ^{210}Pb is 22.26 years, the residence time of ^{210}Pb in the lower troposphere is about 1–2 weeks (Papastefanou, 2006). This means that aerosols scavenging by precipitations and gravitational settling on the Earth's surface are responsible for the removal of ^{210}Pb from the atmosphere. Concentrations of ^{210}Pb in the atmosphere are influenced by mineral content of local soil, continentality of the region, precipitations, and anthropogenic factors. Since ^{210}Pb in continental air originates from the Earth's surface, its concentrations decrease with increasing altitude and distance from the shore. The seasonal variations of ^{210}Pb were observed by several authors with higher concentrations in late autumn and winter, and minimum in summer (Vecchi et al., 2005). The maximum ^{210}Pb can be attributed to frequent inversion conditions in surface layers and the resulting buildup of radon and its daughters. In winter months, this process can be hindered by low emanation of radon from the frozen and/or snow-covered soil (Hötzl and Winkler, 1987). Lower activity concentrations of ^{210}Pb in summer months can be related to a higher intensity of vertical mixing within the troposphere in this season and by higher precipitation removing the aerosols, which may result in a decrease of activity. Due to different origins, ^{210}Pb is usually compared with ^{7}Be activities, which allows quantification of the stratospheric influence in the surface level. The annual cycles of ^{10}Be, ^{7}Be, and ^{210}Pb were recorded at coastal Antarctica for 25 years and can be seen in Fig. 3.55. The ^{7}Be/^{210}Pb ratio helps assess the amount and timing of other stratospheric species to surface levels of atmosphere. ^{210}Pb is also released during industrial activity such as coal mining and burning, melting of ores in steelworks, and use of agricultural fertilizers.

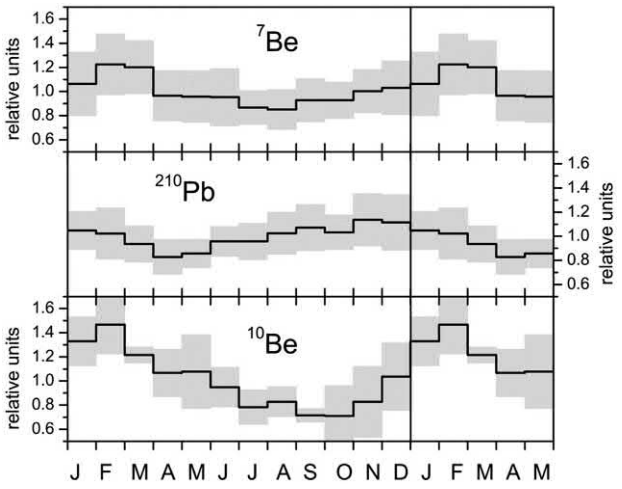


FIGURE 3.55 Seasonal cycles of mean monthly values for ^{7}Be, ^{10}Be, and ^{210}Pb at Neumayer station (Antarctica) (Elsässer et al., 2011). *Printed with permission © John Wiley & Sons A/S.*

C. Radionuclides in freshwater systems

The selection of the best suited sampling equipment and related supplies mainly depends on the chemical form of the target radionuclide and what kind of water is going to be sampled. Regardless of the type, water samples are generally processed right after their collection to avoid potential irreversible physicochemical changes of radionuclide species (Macášek, 2008). If this is not the case, water samples should be stored in hermetically sealed containers to prevent volatile radionuclides from being evaporated. To reduce adsorption of radionuclides onto the walls of the container, suitable amounts of carriers may be added, together with HNO_3 or HCl to lower their pH value to some 1–3. However, for some radionuclides, e.g., radiocarbon or radioiodine, this step cannot be applied, as it could result in their partial or even complete loss. Water samples are often prefiltrated through a filter paper, and if finer filtration is required, the standard 0.45 μm membrane filters can be used as well. Filters are made of various inert materials (fluorocarbon or polyethersulfone polymers, cellulose, polycarbonate) so that they do not bias the analysis of radionuclides of interest. In this part, we shall focus only on terrestrial water samples, as seawater samples are comprehensively discussed in Chapter 5, Volume 2.

1. Sampling of water

a. Precipitation

Precipitation is typically sampled integrally on a weekly/monthly basis or discretely (separately). Polyethylene or fluorocarbon polymer reagent bottles and stainless steel pot collectors can be exploited for collection of rainwater and snow. In the case of radionuclides prone to evaporation, it is reasonable to use a funnel type collector. Wet deposition is clearly accompanied by dry deposition, though collection of the latter can be simply avoided by covering of the sampling container with a plastic film or sheet, removable during precipitation. A protective net that prevents different debris from mixing with the sample is normally installed over the top of the container. An upgrade of a funnel collector with an ion exchange column enables one to preconcentrate more than 90% of the most important radionuclides that are extracted on the column as the precipitate passes through it (Lehto and Hou, 2011).

b. Groundwater

Groundwater samples can be collected from monitoring wells by suction lift and positive displacement pumps that are preferably selected because they do not generate a vacuum, which is also true for submersible pumps. A bailer or similar thief-type sampler and pumps installed in supply wells are used to sample groundwater as well. For the collection of groundwater under natural gradient conditions, specifically designed multilayer samplers have been developed (Margaritz et al., 1989). Sampling at remote sites from ephemeral, urban storm drains, and small streams is sometimes conducted with automatic pumping samplers that have fixed-depth intake (Macášek, 2008). In some cases, it is important to isolate borehole inflows from their underlying or overlying strata during the sampling to prevent mixing of waters (Povinec et al., 2010, 2013d).

c. Surface and depth water profiles

Surface water samples from lakes and rivers can be collected with a polyethylene bottle, barrel, or bucket ($<$20 L) or by a submersible pump if larger volumes are needed ($>$20 L). In special cases, a screen can also be used. The sampling container is usually washed with the sampled water, which is then discarded. Cross-contamination of the samples can be easily avoided by discarding first several liters of the water. A surface water sampling device installed on a ship enables continuous sampling, which is especially useful if a greater number of samples are taken. Such a device is also equipped with various sensors for the determination of the physicochemical parameters (e.g., temperature, salinity, Eh, pH, dissolved oxygen concentration) of the water (Lehto and Hou, 2011). It is important to note that there might be a difference between surface samples collected by containers and those collected by screens due to the surface microlayer, generally enriched in heavy metal, organic, and bacterial species (Macášek, 2008).

If one is interested in the vertical distribution of radionuclides, it is necessary to sample the water core. Sampling of the depth profile in a shallow lake or river can be conducted by a single submersible pump. The precise depth of sampling is determined by the length of the sampling cable/tube. To keep it straight so that the depth measurement is accurate, some kind of heavy weight is normally attached to it. For sampling of deeper water bodies, a Nansen or later developed Niskin bottle equipped with different sensors can be used, as they are commonly exploited in the seawater sampling (see Chapter 5, Volume 2). Circular frame rosette systems, which can mount up to 36 bottles, are available for large-scale simultaneous sampling (Lehto and Hou, 2011).

d. Sediment pore water

In general, pore water can be extracted either in the laboratory after coring the sediment or in situ using one of many available sampling devices. Although the former method is straightforward and easy to conduct, it has some disadvantages, i.e., it may alter the composition of the sample due to transport, redox variations, temperature and pressure changes, and solid−solution interactions during extraction and storage (Lehto and Hou, 2011). Thus, special systems for in situ extraction of the pore water have been developed in a way that they usually ensure that no further manipulation with the water is needed after the sampling. Despite the fact that the in situ water extraction method can significantly lower the risk of composition changes in the sample, the procedure is more complex and reliably useable only to the depth of several meters.

e. Ice cores

Different types of drilling systems, which can be used even at high elevation and work at relatively fast rate (e.g., 1.65 m h^{-1}; Iizuka et al., 2016) producing ice cores as long as tens to thousands of meters, have been developed for sampling of ice. After drilling, the surface of the ice sample can be washed with warm deionized water to remove external impurities. For further separation of atmospheric and in situ−produced radionuclides, the ice must be melted, either spontaneously or with the use of a heating device, such as microwave oven. Depending on the radionuclide(s) of interest, filtration may be applied, and the pH of the obtained water should be adjusted accordingly.

2. Examples of radionuclides in water systems

a. Tritium

Tritium is one of those rare radionuclides whose concentration in waters is effectively measurable by both radiometric and mass spectrometry techniques. For a sample with the ^{3}H activity concentration above $\sim$1 Bq L^{-1}, tritium is easily determined by LSC, after the sample is mixed with appropriate scintillation cocktail. However, as a low-energy beta emitter, tritium is sensitive to quenching effects and the presence of interfering radionuclides. Thus, the water sample is distilled (usually at pH > 9) prior to the LSC measurement to remove possible sources of interferents (Lehto and Hou, 2011). GPC was also used for tritium determination in earlier days (Povinec et al., 1972); however, nowadays mostly LSC is used, except in the cases when small samples should be analyzed (e.g., a direct analysis of methane).

In principle, conventional radiometric methods, namely LSC, can be used for samples with the tritium activity concentration beyond their limit of detection, if ^{3}H in the water is first enriched by electrolysis. The process is based on electric decomposition of water molecules into gaseous oxygen and hydrogen, which are then released from the sample. As dissociation of tritiated water (HTO) is slightly less probable than normal water (H_2O), the concentration of tritium is increased with the decreasing volume of the sample. For example, a sample with the original volume of 0.1−0.5 L is concentrated into the 3−10 mL volume, whereas tritium is enriched by a factor of 10−50, resulting in an improvement of the detection limit for LSC to the level of 0.1−0.02 Bq L^{-1} (Lehto and Hou, 2011). A standard of known tritium activity, usually prepared from water without ^{3}H, must be processed and measured the same way as the sample in order to determine the enrichment factor of electrolysis.

The most sensitive method for tritium analysis in water is definitely ^{3}H-^{3}He ingrowth mass spectrometry, which can measure the $^{3}H/^{1}H$ isotopic ratio down to 10^{-20} (Clarke et al., 1976; Palcsu et al., 2010; Papp et al., 2012). This exceptional technique, which utilizes the determination of stable ^{3}He produced by the decay of tritium to back-calculate the original ^{3}H activity in the sample, has already been discussed (Sections IV.B and V.A). AMS may also be used for the determination of tritium; however, its detection limit is by five to seven orders of magnitude lower if compared with ^{3}He ingrowth mass spectrometry (Roberts et al., 2000). AMS is thus potentially exploitable mainly for waters with a relatively high activity of tritium (e.g., liquid discharges from nuclear installations) or ^{3}H-labeled samples in various biological experiments (Dingley et al., 1998; Love et al., 2004; Brown et al., 2005). Of course, nontrivial sample preparation is necessary for tritium AMS as well. First, water is let to react with elemental zinc powder at the elevated temperature to produce hydrogen, which is then absorbed on pure Ti to obtain titanium hydride, an excellent material for sputtering in the ion source of AMS. Both reactions run at the elevated temperature (450−550°C), which can be conducted in a single sealed quartz tube (Chiarappa-Zucca et al., 2002; Pánik et al., 2017).

Controlled liquid discharges from NPPs containing large activities of tritium can significantly affect the reservoir into which they are released. On the other hand, increased concentrations enable an easier tracing of tritium in various fractions of living organisms, such as plants, which are grown in the reservoir or in its vicinity. Long-term monitoring of surface water of the Mohelno reservoir in Czechia, where both inlet and outlet of the cooling water for the Dukovany NPP are located, showed fluctuating activity concentrations of ^{3}H up to 700 Bq L^{-1} (Fig. 3.56; Svetlik et al., 2014). As a consequence of discharging, high activities were also found in various plant species, which were sampled in the Mohelno reservoir or its adjacent parts. The mean activity concentration of nonexchangeable organically bound tritium (NE-OBT) and tissue-free water tritium (TFWT) fractions was determined to be roughly 24 Bq kg^{-1} and 35 Bq L^{-1}, respectively (Simek et al., 2017). The more distant from the outlet, lower activity of NE-OBT and TFWT was measured in plants from the reservoir (Kořínková et al., 2016). Experimental results like these may be used to study metabolic pathways and kinetics of the release of different ^{3}H chemical forms.

b. Radiocarbon

Radiocarbon can be found in water in the form of dissolved inorganic carbon (DIC) and dissolved organic carbon (DOC), partially as particulate matter as well. The fraction that passes through a filter contains dissolved carbon. The procedures applied for further sample processing depend on the selected method for analysis of ^{14}C content. In the case of AMS, where only low amounts of samples are necessary, DIC is usually extracted and cleaned from water vapor and other impurities in a dedicated vacuum line (Bard et al., 1989; Molnár et al., 2013; Kaizer et al., 2016a; Povinec et al., 2016). After addition of acid to reduce CO_2 solubility, high-purity inert gas (He or N_2) is bubbled through the water sample, or the sample can also be heated to obtain the same result (Molnár et al., 2013). This way, released CO_2 is passed through a system of water traps, until it is frozen in final trap(s) with liquid nitrogen. Extraction of organic carbon can be achieved by combustion, or potassium perchlorate and oxygen reactions, supported by ultraviolet light (Purdy et al., 1992; McNichol et al., 1994). The carbon dioxide sample, thus obtained, is either converted to graphite, as was discussed in the previous section, or directly introduced into the ion source of the AMS.

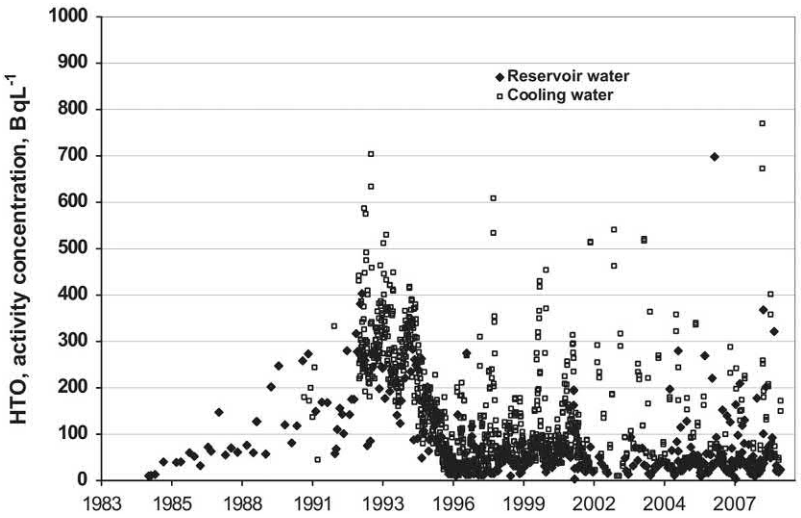


FIGURE 3.56 Time series of the tritium activity concentration (Bq L^{-1}) in the Dukovany NPP's cooling water and in the Mohelno reservoir. *From Svetlik et al. (2014).* Printed with permission © *Elsevier 2018.*

For radiometric analytical methods, the initial volume of samples is generally much higher than for AMS. While the DIC is typically extracted in the form of $BaCO_3$ precipitate, which is produced by reaction with a Ba^{2+} solution, organic forms of dissolved carbon can be converted to CO_2 by wet oxidation at elevated temperatures. For LSC, carbonates can be directly mixed with the scintillation cocktail (Svetlik et al., 2017) or they can be converted to benzene (C_6H_6), which is a better scintillation solvent. Another advantage of benzene is that its synthesis, which is based on trimerization of acetylene generated from the sample CO_2, results in an almost quantitative transfer of sample carbon to solvent carbon (Polach, 1987). In the case of GPC, carbonates are acidified, e.g., by H_3PO_4, to back-release carbon oxide that is used to produce methane (Povinec, 1972), as was described earlier for gas samples.

Radiocarbon together with stable isotopes has been frequently exploited to study the origin and dynamics of groundwater and to better understand its formation, age, infiltration areas, and vulnerability to contamination. For example, investigations of the spatial distribution of ^{14}C and $\delta^{13}C$ of the mineral and thermal waters in Slovakia showed quite large isotopic variability. The corrected radiocarbon apparent ages of the studied groundwater samples were determined to be between 7000 and 32,000 years, suggesting that the waters recharged mainly during the early Holocene, Würm 3, and Würm 2−3 periods (Povinec et al., 2010). The consequent research of the largest Central Europe underground water source, Žitný Island of southwestern Slovakia, showed that the majority of groundwater samples are of recent origin (Fig. 3.57). The results of the study also indicated that a confined aquifer was formed in the eastern part of the island, and the Danube River system is the main source of groundwater at Žitný Island (Povinec et al., 2013d).

Monitoring of anthropogenic radiocarbon in waters is also important. To assess its radiological impact, ^{14}C concentration in the effluents from NPPs or other nuclear installations has to be first evaluated. In the case of two Czech pressurized water reactor (PWR) NPPs, Temelín and Dukovany, the mean activity concentration values for the sum of all chemical forms of ^{14}C in the liquid effluents in the year 2015 were conservatively determined to be around 1.6 and 0.1 Bq L^{-1}, respectively. In the same year, the cumulative discharge of radiocarbon was 738 GBq for the Dukovany NPP and 584 GBq for the Temelín NPP, whereas the volume of 2.7×10^4 m^3 and 3.1×10^4 m^3 was overall released in the liquid form from the latter and the former, respectively. This would mean the instantaneous ^{14}C releases into the water streams would be about 0.007% and 0.0004% of the total quantity of the radiocarbon discharged into the environment for Temelín and Dukovany NPPs, respectively (Svetlik et al., 2017). Interestingly, the determined ^{14}C releases are much lower when compared with the values for other PWR-type NPPs reported elsewhere (Kunz, 1985; Magnusson et al., 2008).

c. Chlorine-36

As a long-lived radionuclide, ^{36}Cl is commonly exploited in dating of groundwater or as a tracer in environmental processes, in which its concentration is so low that it can be determined only by AMS. Radiometric methods, i.e., LSC, could be useable for waters originating from nuclear waste processing, though such applications are quite off the scientific interest. The detection limit for AMS is around 1 nBq or the $^{36}Cl/^{35}Cl$ isotopic ratio of 10^{-15} (Synal et al., 1994). The main challenge in the AMS determination of ^{36}Cl is the stable ^{36}S isobar with the relative abundance of 0.02%. A detector can have a count rate 100 times greater

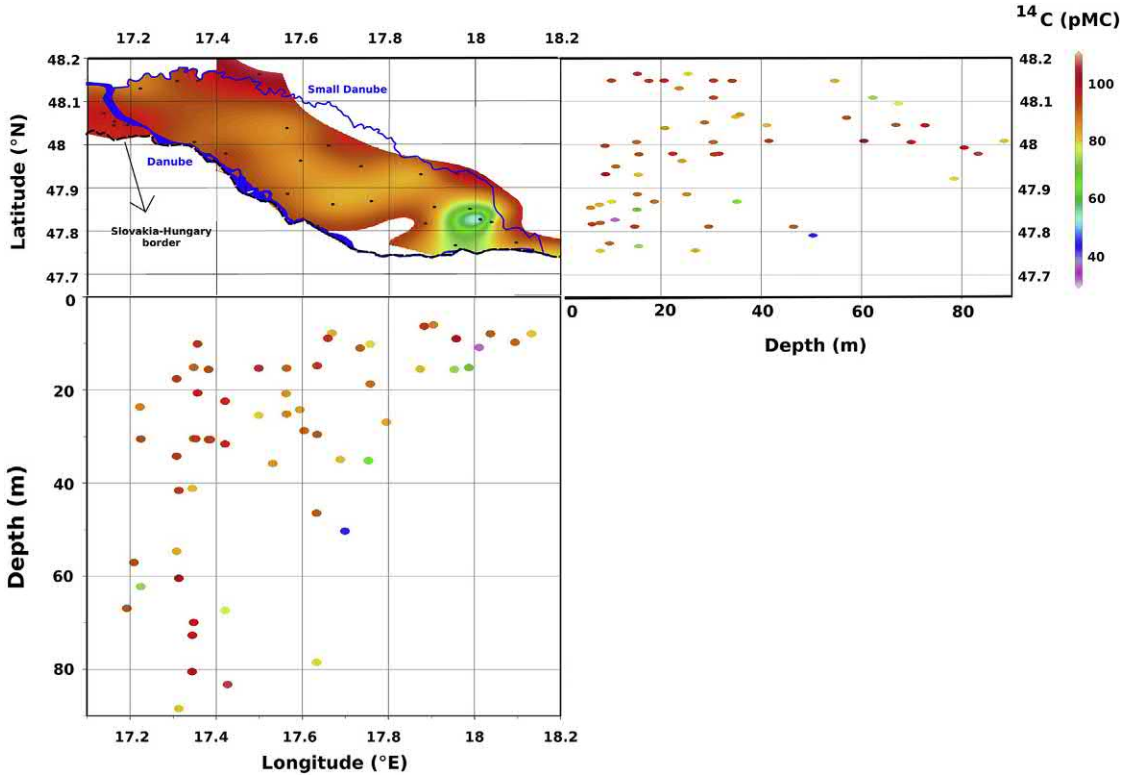


FIGURE 3.57 Latitudinal and longitudinal spatial and vertical distribution of radiocarbon (pMC) in groundwater of Žitný ostrov (100% pMC = 0.236 Bq g^{-1} C). *From Povinec et al. (2013d).* Printed with permission © Cambridge University Press.

than that from a sample with the $^{36}Cl/^{35}Cl$ ratio of 10^{-12} if nanograms of sulfur are present in the ion source target (Tuniz et al., 1998). To reduce the background from ^{36}S, one can use novel techniques to improve the measuring system for isobar suppression (Wilcken et al., 2010; Martschini et al., 2013) and try to remove sulfur as much as possible during the chemical separation of ^{36}Cl from the sample.

Separation of chlorine from the sample in the form of Cl^- ions is fairly simple. By adding stable chloride carrier and a small excess of Ag^+ ions to the acidified sample (pH = 1−2), water-insoluble silver chloride is formed, which is the preferred AMS target material. Because there is no suitable tracer, the chemical yield of ^{36}Cl separation is controlled gravimetrically, though the precipitation is usually close to being quantitative. However, silver sulfate salts are readily formed as well. This problem can be solved by dissolving the precipitate in pure NH_3(aq) and adding saturated barium nitrate solution. The precipitate of formed $BaSO_4$ is discarded, and AgCl is reprecipitated if the solution is again acidified (Fig. 3.58; Tosaki et al., 2007). Moreover, sulfur can also be effectively removed by methods based on ion exchange column chromatography (Nakata and Hasegawa, 2011).

With the development and increasing availability of AMS, dating of water reservoirs using ^{36}Cl has become much more feasible, though its reliability might be questionable in some cases. Although an overall good correlation was found between dating with the use of ^{81}Kr and ^{36}Cl for 1-million-year-old Saharan groundwater, two results from this study showed significantly higher (lower) $^{36}Cl/Cl$ ratio. It was suggested that these discrepancies might have been caused by the subsurface input of nucleogenic ^{36}Cl, or chlorine having lower $^{36}Cl/Cl$ ratio, which demonstrate that ^{36}Cl dating may be susceptible to additions of Cl along a flow path (Sturchio et al., 2004). Furthermore, results from dating of the Vostok snow indicated that ^{36}Cl data in central Antarctic regions, where accumulation of ice is rather low, are most likely unreliable due to various postdeposition processes affecting the gaseous form of chlorine (Delmas et al., 2004). On the contrary, the ^{36}Cl bomb pulse was successfully used for dating of modern groundwater (Tosaki et al., 2007).

d. Technetium-99

The determination of beta-emitting ^{99}Tc can be conducted by LSC or GPC in the activity range of 1−100 mBq, after its separation from water and purification, whose chemical yield is trackable with the use of short-lived gamma-emitting ^{99m}Tc ($T_{1/2}$ = 6.01 hours), or one of the stable isotopes of rhenium, the closest element to technetium (Lehto and Hou, 2011). Mass spectrometric methods, such

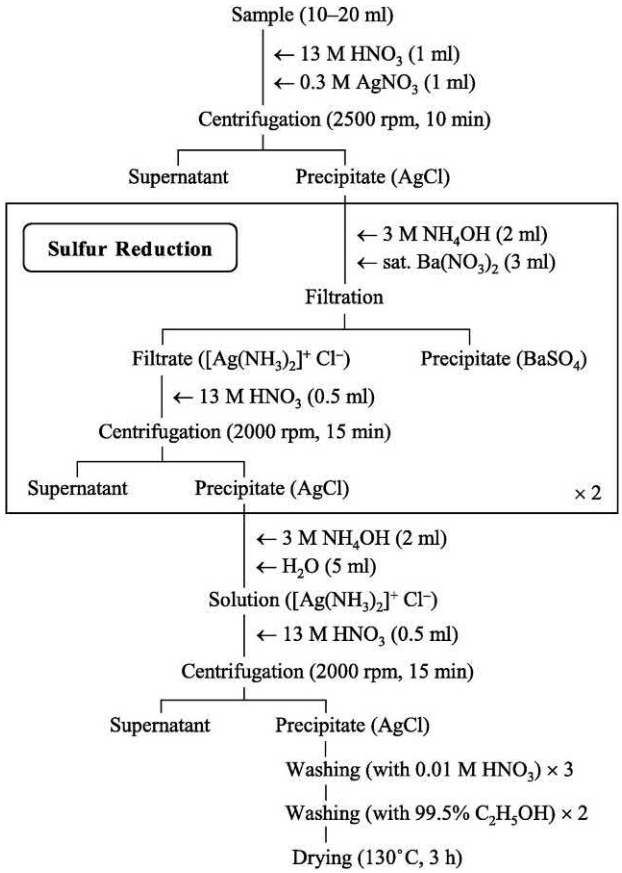


FIGURE 3.58 Schematic diagram of sample preparation for accelerometer mass spectrometry (AMS) determination of ^{36}Cl concentration in water. *From Tosaki et al. (2007).* Printed with permission © *Elsevier 2018.*

as ICP-MS RIMS, TIMS, and AMS can be also used to measure ^{99}Tc in water, reaching the detection limit up to 1−10 μBq in a sample (Hou and Roos, 2008). The most common form of technetium present in oxic water is the quite soluble and mobile pertechnetate ion that only sparingly creates complexes and that can be reduced to Tc(IV). For large-volume samples (50−200 L), the preconcentration of ^{99}Tc by anion exchange column chromatography or iron hydroxide precipitation is usually the first step in its radiochemical separation. Further separation from interferents can be achieved by solvent extraction, ion exchange, and extraction chromatography.

For the extraction of ^{99}Tc from matrix elements, chromatographic methods are generally exploited more than solvent extraction. As both anion exchange and extraction chromatography have some specific disadvantages, their combination results in better removal of matrix and interfering components (Shi et al., 2012). An example analytical procedure for the determination of low-level ^{99}Tc by ICP-MS based on a two-step chromatographic separation from large-volume water samples is shown in Fig. 3.59. After the acidified sample is heated at 90°C sufficiently long to decompose organics, saturated NaOH solution is added to remove actinides and transition metals by precipitation. Neutralized supernatant is then loaded on the first column filled with anion exchange resin (Bio-Rad AG1-X4). Dilute nitric acid is used to wash out most of the cations, while retained ^{99}Tc is eluted by 10 M HNO_3. Following evaporation of the eluate to near dryness, technetium is separated from Mo and Ru on an Eichrom UTEVA resin column in a similar way than in the case of the anion exchanger (Keith-Roach et al., 2002). If AMS is employed for ^{99}Tc determination instead of ICP-MS, the HNO_3 eluate is mixed with aluminum containing Re or Nb, evaporated to dryness, and baked at 400−450°C to obtain metal oxides, which are used as sputtering material (Wacker et al., 2004). The potential of technetium fluoride for sputtering in AMS has been recently studied as well (Zhao and Litherland, 2010).

Assessment of fission-produced ^{99}Tc might be important for the evaluation of the impact of nuclear installations, such as facilities for the production of nuclear weapon material or reprocessing plants, which have discharged radioactive liquid wastes into freshwater ecosystems. One of such facilities was the Savannah River Site in the United States, where a monitoring study showed slightly higher activity concentrations of ^{99}Tc (0.02−0.04 Bq L^{-1}) in several freshwater samples. Groundwater migration from beneath old seepage basins, used for the disposal of wastewater-containing radionuclides from the site, was identified as the reason for elevated values (Beals and Hayes, 1995). Another example is the Russian Mayak reprocessing plant, where the ^{99}Tc activity concentration up to 2.15 Bq L^{-1} was determined for one of the freshwater samples (Skipperud et al., 2007).

e. Iodine-129

Depending on its activity concentration, ^{129}I in water can be measured by radiometric methods (gamma- and X-ray spectrometer, LSC), neutron activation analysis (NAA), ICP-MS, or AMS. While radiometric methods and ICP-MS can be normally used to determine higher activities of ^{129}I (e.g., in spent fuels), NAA and AMS are capable of measuring of low-level water samples, reaching the detection limit of 1 μBq and 1 nBq, respectively (Povinec et al., 2000; Hou and Roos, 2008). NAA of ^{129}I is based on the reaction (n,γ), yielding short-lived ^{130}I ($T_{1/2}$ = 12.3 hours), which decays to a stable isotope of xenon, while emitting high-energy gamma rays. Except for direct measurements of mid-to-high-level waters by radiometric methods or ICP-MS, radiochemical separation of iodine is mandatory for its determination. If no carrier is added to the sample before separation, NAA can be used also for the determination of stable ^{127}I and consequently the $^{129}I/^{127}I$ isotopic ratio (Hou et al., 1999, 2009a).

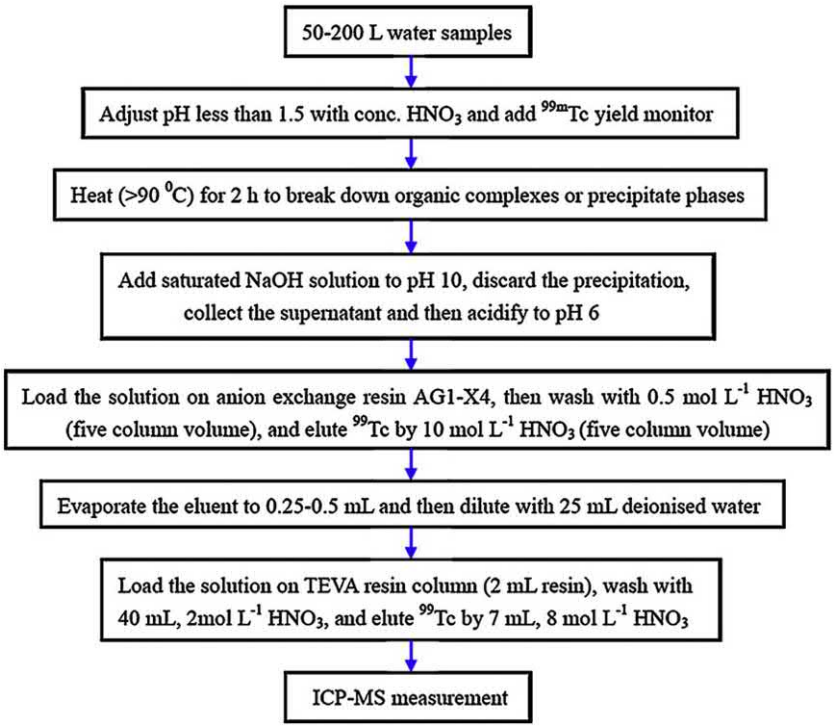


FIGURE 3.59 Diagram of radiochemical procedure for measurement of ^{99}Tc in water samples, combining anion exchange and extraction chromatography. *From Shi et al. (2012).* Printed with permission © *Elsevier 2018.*

Procedures applied for the separation of iodine from natural waters are usually the same, regardless of the analytical technique. Iodine is present in natural waters in the inorganic (as iodide and iodate) and organic form. Radiochemical separation of total inorganic ^{129}I can be conducted by two principle methods: solvent extraction and ion exchange chromatography (Lehto and Hou, 2011; Povinec et al., 2015a). In the case of the former, which is based on the solubility difference of iodine in immiscible aqueous and organic phases, stable iodine carrier (e.g., Woodward Iodine with the ^{129}I/^{127}I ratio of 10^{-13}) is first added to the filtered acidified (pH ~ 2) sample. Then, all iodate is converted to iodide by a reducing agent, such as $NaHSO_3$, and consequently, iodide is oxidized to elemental iodine (I_2) by $NaNO_2$ that can be easily extracted by some organic solvents ($CHCl_3$ or CCl_4). After separation of two phases, iodine in the form of I^- is back-extracted to a fresh portion of deionized (distilled) water. The preparation of the final target depends on the selected analytical method (Hou et al., 2009a). For example, iodine is typically precipitated as AgI, which is mixed with high-purity silver powder after being cleaned and dried, and then pressed into a target holder for AMS measurement (Povinec et al., 2000, 2015a).

Ion exchange chromatography exploits a very high affinity of iodide ions to bind to the exchanger, which is part of a resin, generally packed in a column. If only total inorganic iodine in water is to be determined, the first steps (acidification, carrier addition, conversion to I^-) are identical to those mentioned above (Povinec et al., 2015). After loading the sample on the column with the anion exchange resin in the nitrate form, ions of interfering elements (e.g., Cl^-) are washed out by the 0.1−0.2 M HNO_3 or $NaNO_3$ solution, and strongly bound iodide is eluted with 0.5−2 M HNO_3 or $NaNO_3$ (Hou et al., 2009a; Kaizer et al., 2016a,b). Another option is to convert iodide to iodate, which has a very low affinity to the exchanger, and thus is easily eluted from the column (Lehto et al., 2012). The chemical yield of ^{129}I separation for both described procedures can be determined gravimetrically from the mass of the final target (e.g., AgI for AMS), or by the addition of gamma ray−emitting ^{125}I ($T_{1/2} = 59.4$ days) tracer to the sample before the separation.

The distribution of ^{129}I species, which influences its biological uptake and mobility, is analyzed to assess consequences of radioactive contamination in the environment (Salbu, 2007). The combination of solvent extraction and anion exchange chromatography is often used for the separation of different iodine species from waters (Hou et al., 2009a; Lehto et al., 2012). An example flowchart of such combination is depicted in Fig. 3.60. While subsequent anion exchange chromatography steps are necessary to completely separate the organic fraction, inorganic iodide is preconcentrated on the first column, eluted, and processed by solvent extraction. Similarly, the iodate fraction is eluted from the second chromatographic column and converted to

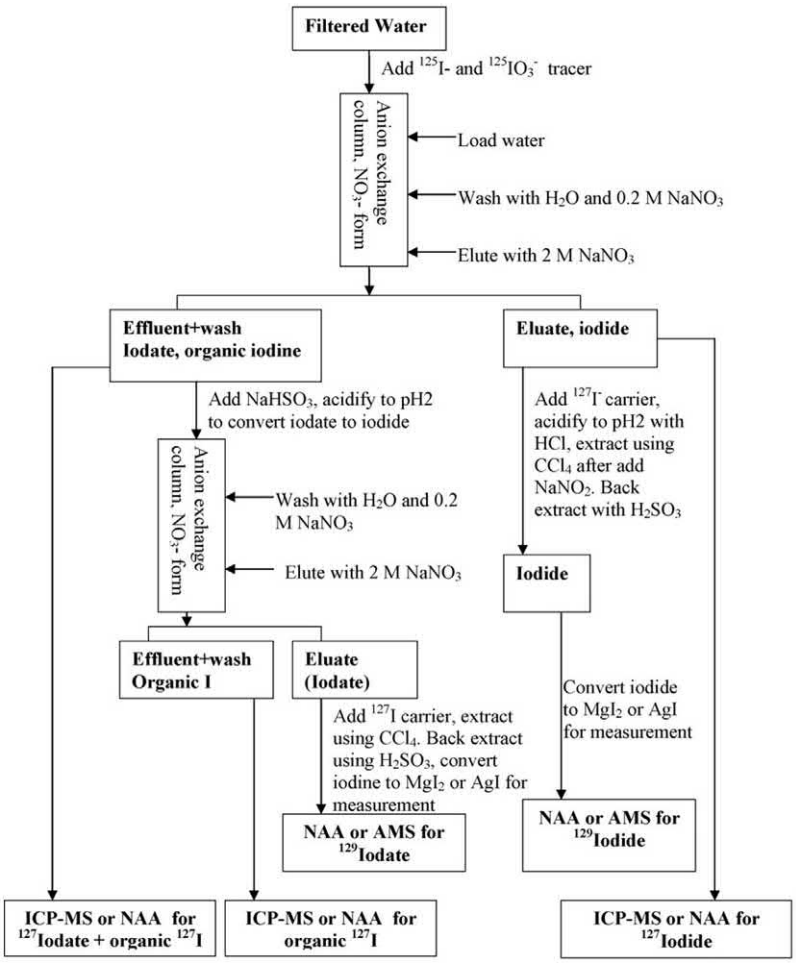


FIGURE 3.60 Diagram of analytical procedure for speciation analysis of iodine in water. *From Hou et al. (2009a).* Printed with permission © *Elsevier 2018.*

the target. The chemical yield of the method is above average (~75%; Hou et al., 2001); however, it is unusable for the determination of organic ^{129}I. Heating of the water sample in hydroxide and ethanol mixture before the separation, which should decompose organic materials and convert released organic iodine into the inorganic form, has been suggested as a possible solution (Schwehr et al., 2005).

Isotopes of iodine, ^{129}I and ^{127}I, and their speciation in natural waters have been studied frequently to evaluate the contribution of various anthropogenic sources of ^{129}I and their transfer between the atmosphere and hydrosphere compartments. In the Scandinavian countries, the $^{129}I/^{127}I$ ratio and the concentration of ^{129}I in rain waters in the range of $(13.9-46.9) \times 10^{-8}$ and $(0.04-29.8) \times 10^{9}$ at L^{-1}, respectively, were observed, which was by at least one order of magnitude lower than in the sea. Similar but less varying values were determined for lakes as well. The iodide form was found to be dominant in the ^{129}I speciation in precipitation (Aldahan et al., 2009; Hou et al., 2009b; Lehto et al., 2012). The annual wet deposition of total inorganic ^{129}I in Finland was calculated to be around 5.4×10^{-4} Bq m^{-2}, which was by about three orders of magnitude lower than the ^{90}Sr deposition at that time (Paatero et al., 2010; Lehto et al., 2012). Reemission from seas, which are affected by discharges from La Hague and Sellafield reprocessing plants, and consequent precipitation over the land are regarded as the main source of increased concentrations of ^{129}I in the terrestrial waters in current-day Europe (Hou et al., 2009a,b; Lehto et al., 2012; Michel et al., 2012).

f. Radiocesium

Similar to other alkali metals, cesium is readily dissolved in water in the form of hydrated Cs^+—only a small portion (<1%) is attached to the particulate matter. Due to the fact that both ^{134}Cs and ^{137}Cs emit high-energy gamma radiation, their activities can be quite easily determined by gamma spectrometry (see Section IV.A), where aerosol samples have been discussed. In the case of low-level samples, where direct measurements by gamma

spectrometry are not possible, radiocesium can be preconcentrated from water samples by cation exchange resin, evaporation, or precipitation with the use of highly selective reagents, such as ammonium phosphomolybdate (AMP) or transition metal hexacyanoferrates. Adsorption on cation exchange resin is suitable for terrestrial water, as its capacity is usually sufficient to extract all cations from several tens of liters. Although the precipitation method is widely exploited for pretreatment of seawater (Roos et al., 1994), it is in principle useable for freshwater as well. Copper hexacyanoferrate complex is slightly advantageous over AMP, as it tends to adsorb less of interfering ^{40}K, and unlike precipitation by AMP, which requires acidification of the sample to pH 1.5−2.0, copper hexacyanoferrate works in the natural pH range.

The limit of detection for the determination of radiocesium in water by gamma spectrometry is typically 50 mBq for a 50 mL sample (Hou and Roos, 2008); however, this value is strongly dependent on the detection efficiency, background of the detector, detector setup, and time of measurement. Thus, the limit of detection can be further enhanced by changing the stated parameters. One of the options is to use a Marinelli beaker, which fits well around the HPGe or scintillation detector (Ahmed et al., 2009). This improves the detection efficiency and consequently the detection limit for low-level environmental water samples (Lavi et al., 1997). Another possibility is to use a HPGe spectrometer with anticosmic/antiCompton shielding or to operate the spectrometer in a shallow or deep underground laboratory (Povinec et al., 2004, 2005, 2008, 2011; Aoyama et al., 2011, 2016), which can improve detection limits at least by an order of magnitude.

Capabilities to monitor radiocesium in the environment have proved to be very important, especially after the NPP accidents in Chernobyl and Fukushima. In the case of the Fukushima accident, the origin of radioactivity in wet deposition could be identified by the ^{137}Cs/^{134}Cs activity ratio of around 1, which could be measured by not only gamma spectrometry but also ICP-MS (Ohno and Muramatsu, 2014). The Fukushima signal was detected in rainwater samples all over the globe, as summarized by Lee et al. (2013). In Western Europe (France), radiocesium activity in rainwater peaked at the level of ∼10 mBq L^{-1}, approximately 3 weeks after the accident (Masson et al., 2015), which is similar to the Central Europe data for total (wet plus dry) deposition reported by Povinec et al. (2012a), who also documented a decrease of the ^{137}Cs activity with the increasing precipitation rate, as opposed to cosmogenic ^{7}Be (Fig. 3.61).

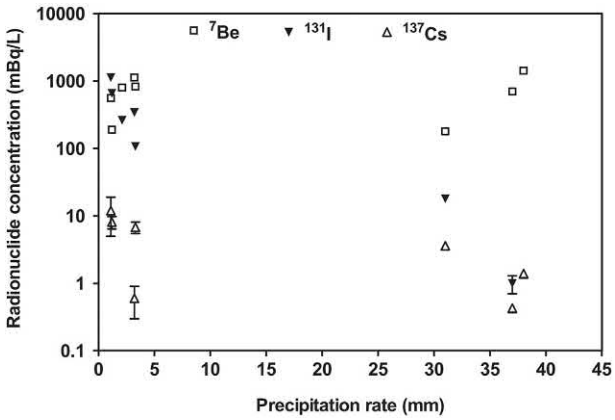


FIGURE 3.61 Correlation between concentration of ^{7}Be, ^{131}I, and ^{137}Cs and precipitation rate, determined in Bratislava after the Fukushima accident. *From Povinec et al. (2012a).* Printed with permission © *Elsevier 2018.*

g. Radon

Radon (mostly ^{222}Rn) can be simply determined by gamma spectrometry of its daughter nuclides or by LSC, if its concentration in water is high enough. Another possibility is to use in situ underwater gamma spectrometry (Povinec et al., 1996), which can also provide monitoring time series of its concentration in water (for details, see Chapter 5, Volume 2). If the concentration is too low to be measured directly, radon must be preconcentrated. This can be accomplished by bubbling nonactive carrier gas (e.g., helium) through the sample and collecting the gas fraction into a cooled activated carbon cartridge for later analysis, or directly into an evacuated measuring cell. Radon determination is most frequently conducted by the cell of the Lucas type that utilizes zinc sulfide (ZnS) painted (sprayed) on the inside walls as a scintillator (Lucas, 1957). Silica gel and cotton wool can be placed into a tube, which connects the Lucas cell and sampling bottle, to prevent water droplets produced during the bubbling to be introduced into the cell. When the radioactive equilibrium between radon and its progenies is established, which takes some 4 hours, radon activity is counted and its concentration in the original water sample is back-calculated. Using the described method, the detection limit of 1 Bq L^{-1} for radon in water is reachable (Blahušiak et al., 2017). Another option for radon measurement is to use a flow-through scintillation flask instead of collection cell (Ward and Borak, 1991).

Monitoring of radon concentration in groundwater sources is important for assessment of radiological risk from radon exposure, especially at places like thermal spas. Additionally, estimating the correlation between the meteorological parameters and radon concentration may help to correctly determine the radon risk. For example, the mean radon activity concentration (RAC) in fountain water at different thermal spas in Slovakia was found to be 62.3 Bq L^{-1}, corresponding to the annual dose due to ingestion of ^{222}Rn for adults of 13.1 μSv, which is by a factor of about

12 lower than the dose due to inhalation of radon, determined for the very same places (Blahušiak et al., 2017). The results from another investigation suggest that rainfall may significantly influence the content of radon in borehole water. In fact, each increase of RAC in borehole water analyzed in this study was preceded by heavy rainfall. On top of that, radon water content was in a positive correlation with the state of the water in the borehole. It is also interesting to point out that the observed decrease of RAC in the October–March period was much slower than anticipated, probably due to the horizontal movement of water (Fig. 3.62) (Smetanová et al., 2010).

D. Radionuclides in soil

1. Preparation of soil samples for radionuclide analysis

Soil samples are usually collected according to IAEA guidelines from a 1 m^2 area up to depth of 10 cm. After the sampling process, soil samples are dried at 105°C during 24 hours to remove any available moisture. Stones and plant roots are removed from the soils before soil is crushed and prepared for gamma spectrometry and the determination of main physical and chemical soil characteristics.

The soil samples are then homogenized, weighed, and hermetically sealed in the plastic containers, for example, Marinelli beakers, for 30 days. This is the time required for reaching the radioactive equilibrium between radon and its decay products, required for proper gamma spectrometry analysis. The radon decay products are then identified usually using a high-purity germanium (HPGe) detector. Gamma spectrometry is a sensitive method of analysis that can yield analytical data for several different nuclides in a single sample analysis. HPGe detectors should be shielded in suitable lead/iron/copper shields to achieve a low background (e.g., Sýkora et al., 2008). The concentrations of radionuclides are then calculated from peak areas of registered gamma rays after appropriate efficiency and energy calibration. The ^{226}Ra concentration is usually calculated from the peaks of ^{214}Bi and ^{214}Pb with energies of 609 and 352 keV, respectively. The ^{232}Th concentration is usually calculated from the peaks of ^{208}Tl (583 and 860 keV). The ^{40}K concentration is determined from the peak area of registered gamma rays with the energy of 1460 keV, and the ^{137}Cs concentration is calculated from the peak with the energy of 662 keV. Nondestructive gamma spectrometry measurements are possible, however, only for radionuclides emitting gamma rays. Other radionuclides emitting alpha rays or beta rays require chemical separations, similar to those described in Sections IV.A, B, C and V.B, C, E.

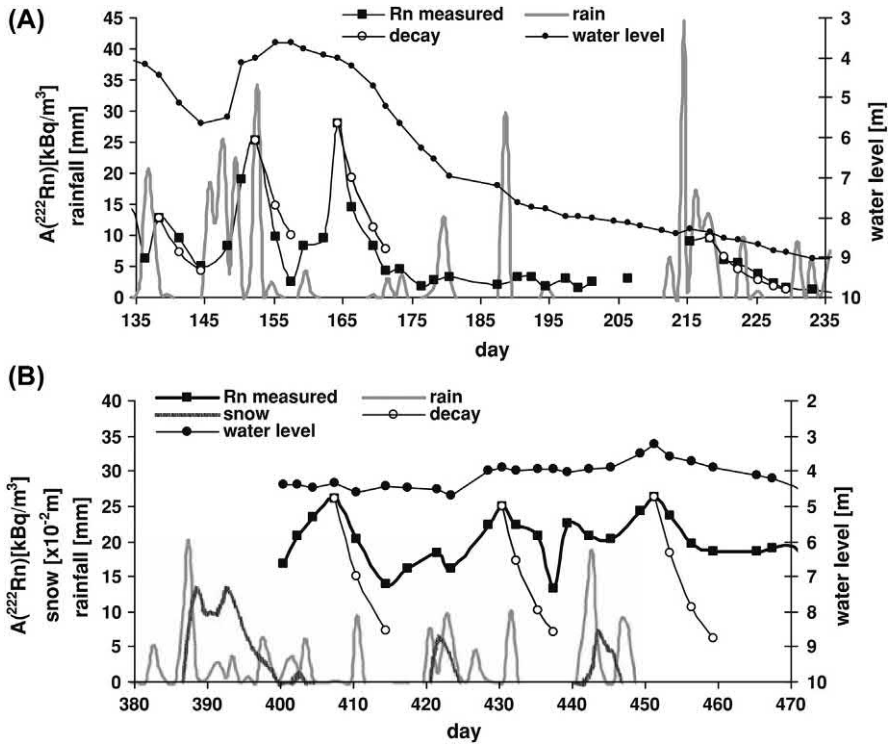


FIGURE 3.62 Time series of radon activity concentration (RAC) in borehole water and its decay, rainfall (snow), and water level in (A) summer and (B) winter at the Modra-Piesok observatory (Smetanová et al., 2010). *Printed with permission © Springer 2018.*

2. Examples of radionuclides in soil

We shall focus in this section only on two radionuclides, one is representing a radiogenic radionuclide (^{222}Rn), and the second one is representing anthropogenic radioactivity of soil (^{137}Cs). The other interesting radionuclides from the natural sources would be ^{40}K and U and Th and their decay products. From the anthropogenic radionuclides, it would be mainly ^{90}Sr.

a. Radon

The radon (usually ^{222}Rn) concentration in soil can be measured by grab sampling or continuously with a suitable monitor. Soil air is sucked into the scintillation cell (e.g., Lucas cell) through a collection rod from a depth of 0.8 m. For continual monitoring of ^{222}Rn in the soil, air is sucked from the depth of 0.8 m, dried in the refrigerator (at −30°C), and then is allowed to enter the Lucas cell (Müllerová et al., 2014). The flow rate and route length before detector are chosen in such way that no thoron (^{220}Rn) reaches the detector. Aerosols with radon decay products are captured on filter, so only ^{222}Rn enters the detector. The ^{222}Rn concentration has been calculated according to the method published by Ward and Borak (1991). The monitor allows the measurement of radon activity concentration in the soil air at the level of about 10 kBq m^{-3} with a relative uncertainty of 1.5% for a 1-h-long measuring interval. This precision is also sufficient for the study of daily radon variations in the soil air.

The character of the annual course of the radon activity concentration in the soil air depends mainly on the soil type and on the temperature variations of the outdoor atmosphere during a year and on the precipitations and the soil moisture. The typical annual course of the radon activity concentration in the soil air show courses with summer minimum and winter maximum. During hot and dry summer, an increase of ventilation at the surface is observed, which can cause a decrease of the radon activity concentration in the soil. From Fig. 3.63, it can be seen that typical annual courses of radon activity concentration occur in the soil air with summer minima and winter maxima (Müllerová et al., 2014). The typical annual courses can be modified not only by precipitation (at the end of April and in May 2006) but also by mild winters. Because of low quantity of snow precipitation and because of the higher temperature of the outdoor atmosphere, increases of the radon activity concentration in autumn months or maximum in winter months in 2006 were not observed. With the use of these annual courses of the radon concentration, there is the possibility of observing an anticorrelation between the radon concentration in the soil and atmospheric temperature. For years when precipitation is high, no correlation between the course of the radon activity concentration in the soil air and temperature of the outdoor atmosphere is observed (Müllerová et al., 2008). The influence of precipitation is strongest in the lower (0.4 m) than deeper (0.8 m) layers of the soil. It was also found that the time lag between precipitation and increased radon activity concentration was dependent on the depth at which radon was measured (Müllerová et al., 2014). Characteristic annual courses of radon activity concentration in the soil air (with summer minima and winter maxima) can be disturbed also by mild winters.

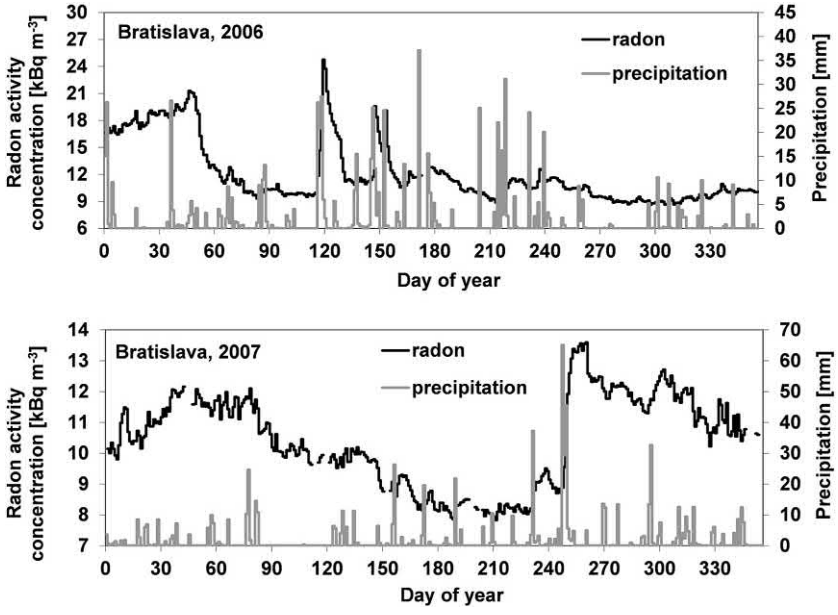


FIGURE 3.63 Average daily values of the radon activity concentration in the soil air and of precipitation in Bratislava in 2006 and 2007 (Müllerová et al., 2014).

Daily variations of the radon concentration in the soil air could be considered as short-term changes from the point of view of the half-life of radon. The analysis of the data confirms that regular daily changes of radon concentration in the soil air are connected with daily changes of atmospheric pressure. An increase of atmospheric pressure leads to a decrease of the radon concentration in the near-surface layer of the soil air and vice versa. In common soils, the radon concentration decreases toward the surface very markedly, as radon is released into the outdoor atmosphere on the surface. This process is called exhalation. Numerical values of the measurements of ^{222}Rn exhalation from the soil have applications in meteorology, determining the equivalent mixing height, testing of pollutant transport models in the atmosphere, engineering geology, as well as in other fields. The radon exhalation rate is influenced by a lot of varying factors like physical and chemical characteristics of the soil, soil structure, ^{226}Ra content, emanation coefficient, permeability, soil humidity, variations of meteorological parameters (temperature, pressure, precipitation), and others. Numerous authors compared the values of radon exhalation rate with meteorological parameters (Dueñas et al., 1997; Koarashi et al., 2000; Mazur and Kozak, 2014; Ferry et al., 2001; Prasad et al., 2012; Müllerová et al., 2018), radium content in the soil (Sahoo et al., 2010; Lawrence et al., 2009), or their dependence on grain size (Immé et al., 2014). The influence of rainfall has also been discussed in several works. In other works, Dueñas et al. (1997), Ferry et al. (2001), and Müllerová et al. (2018) observed that increased soil humidity as a consequence of rainfall caused a decrease in radon exhalation rate. Others (Lawrence et al., 2009; Faheem and Matiullah, 2008) found that initially radon exhalation rate increased with the increase in water content, but as the water content increased even more, it started to decrease. However, the results are unequivocal and differ for various types of soil as well as for climate regions.

b. ^{137}Cs

The main reservoirs of the anthropogenic ^{137}Cs in the present day are soil and vegetation, which took the ^{137}Cs from the soil, where it was deposited in the past, mainly due to global fallout and the Chernobyl and Fukushima NPP accidents. During the nuclear weapon tests, ^{137}Cs was mixed in the stratosphere and deposited on the terrestrial surface as global fallout, reflecting atmospheric circulation and its latitude dependence. In contrast, ^{137}Cs atmospheric deposition after nuclear accidents displayed heterogeneously mostly locally or regionally, mostly depending on the weather conditions that prevailed shortly after the emissions (Chartin et al., 2013; Korsakissok et al., 2013). ^{137}Cs released from all sources has primarily been deposited on the Earth's surface by dry and wet deposition. The concentration of ^{137}Cs in the soil depends on factors such as wind velocity, intensity and frequency of rainfall, type and structure of soil, and moisture content of the soil (Kulan, 2006). The major way of ^{137}Cs deposition is wet fallout; it is therefore strongly dependent on the precipitation. ^{137}Cs may then migrate in soil depth at a rate depending on processes controlling this transfer and on soil characteristics. The migration of ^{137}Cs in soils is governed by a combination of different physicochemical factors, for example, the type of soil, soil chemistry, organic carbon content, biological activity, climatic conditions, the pH, and organic matter content (Kirchner et al., 2009; Valcke and Cremers, 1994; Staunton et al., 2002). The most important determining factor, however, is the qualitative and quantitative clay content of the soil.

The penetration of ^{137}Cs into soil is a very slow process (Krstić et al., 2004; Szabó et al., 2012). The geochemical analysis supports the idea that the ^{137}Cs gets adsorbed by the clay minerals illite and kaolinite during the migration process. The concentration of ^{137}Cs in undisturbed soil profiles decreases with depth. ^{137}Cs is characterized by a strong affinity for fine soil particles, and this is therefore widely used to quantify soil erosion, but it is also employed to quantify the relative contribution of sources delivering sediment to rivers (Ben Slimane et al., 2013). However, its ability to trace vertical transfers of solid matter in soils was much less investigated. Although the soil formation occurs over much longer periods, individual pedological processes may be characterized by temporal variations with a succession of active and inactive periods throughout the entire story of soil development. The use of ^{137}Cs as a tracer provides therefore a relevant tool to understand and quantify those variations during the last 50 years (Jagercikova et al., 2015). The concentration of ^{137}Cs is significantly higher in undisturbed soils compared with agricultural soils (Mesrar et al., 2017). Forest soils are the richest in ^{137}Cs; fallow and cropland soils contain less of this radionuclide. The content of ^{137}Cs in soils decreased as the soil reaction increased; however, it was increasing with higher organic carbon content (Królak et al., 2008).

E. Radionuclides in biota

Biota samples represent a very wide spectrum of sample types from biosphere, including animal tissues and remains, vegetation samples, plant remains, biomedical samples, and foodstuffs. The measurement of miscellaneous radionuclides in these samples is used in radiation monitoring, radiometric dating, environmental studies, and geosciences. Because the biosphere is intimately connected to other radionuclide compartments, a whole range of radionuclides from these compartments can be present in biota samples as well. There are a large number of radionuclides present in the biosphere; this section focuses on some of the most

frequently analyzed radionuclides in biota samples—^{14}C, ^{3}H, $^{134,137}Cs$, ^{90}Sr, and ^{131}I.

1. Radiocarbon and tritium

a. Carbon-14

Carbon-14 as the radioisotope of the main biogenic element can be present in all organic molecules. Vegetation samples are one of the most studied sample types in terms of radiocarbon levels because they are linked with radiocarbon in the atmosphere via photosynthesis. Annual growth rings of trees in particular are very useful samples for ^{14}C analysis; they can be used as a record of past radiocarbon levels in the biosphere. The radiocarbon tree ring record has been dendrochronologically extended as far as 14,000 years into the past (Hua et al., 2009). Measurements of past ^{14}C levels are used for calibration purposes in radiocarbon dating (Reimer et al., 2013) and for studies of solar cycles (Miyahara et al., 2008; Povinec et al., 1983) and solar or extrasolar phenomena (Jull et al., 2018). Tree ring samples have also been used to retrospectively study radiocarbon activity influenced by excess ^{14}C around a radioactive waste disposal facility (Janovics et al., 2016), in the vicinity of NPPs (Ežerinskis et al., 2018; Janovics et al., 2013; Ješkovský et al., 2015) and ^{14}C levels influenced by fossil CO_2 sources in urbanized and industrialized areas (Kontul' et al., 2017; Rakowski et al., 2008). Fig. 3.64 shows results from ^{14}C measurement in annual growth rings in the vicinity of a PWR-type NPP in Slovakia. Comparison of tree ring and atmospheric CO_2 measurements shows that an excess ^{14}C released into the atmosphere outside the vegetation season of the tree is not recorded in growth rings. Other plant materials have been used to determine the impact of NPPs on the surrounding biosphere (Svetlik et al., 2012).

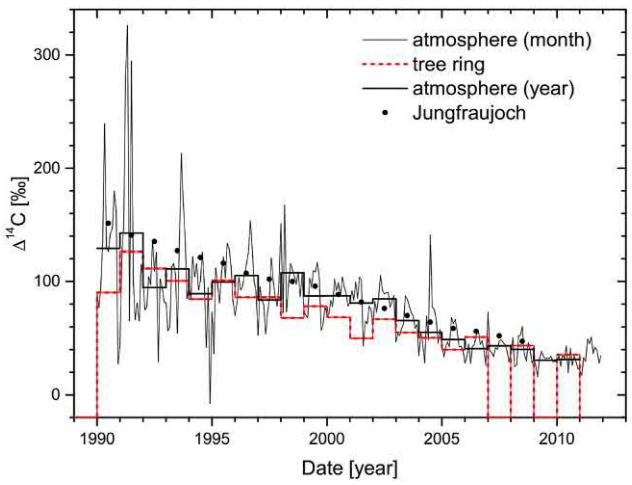


FIGURE 3.64 Tree ring and atmospheric radiocarbon data from Žlkovce sampling station in the vicinity of Bohunice nuclear power plant (NPP) in Slovakia. *From Ješkovský et al. (2015).* Printed with permission © *Elsevier 2018.*

Biota samples are very diverse, and therefore, it is hard to generalize any sampling methods for radiocarbon analysis. In cases where no specialized sampling procedures are necessary, the general rule of sampling needs to be followed—the sample should be representative of the studied attribute or process. For example, when vegetation is sampled, it should be considered what biomass accumulation period is represented by different parts of the plant. Sampling methods also depend on the required sample size given by the measurement method used. AMS requires samples with milligrams of carbon or less, whereas radiometric methods (GPC and LSC) require samples larger by several orders of magnitude (grams of carbon). Tree ring sampling illustrates this point very well—when GPC and LSC were the dominant ^{14}C measurement methods, whole tree sections had to be sampled to reach the required sample size and in the case of AMS a core from an increment borer provides enough material for analysis.

Sample preparation procedures aim to remove any contamination from the samples and extract a suitable material or chemical fraction for subsequent combustion. For plant and animal remains, specific carbonaceous compounds are chosen, which best represent the sample material (cellulose from wood, collagen from bones and teeth, etc.). While bulk wood samples can yield good results, measurement of cellulose extracted from these samples is considered more reliable because once cellulose is formed during plant growth, it is not mobile and is confined to material from the given growing season. Widely used cellulose extraction methods are based on removal of lignin by bleaching agents (Němec et al., 2010b). Most organic materials contain a mixture of organic compounds, and if radiocarbon levels in individual compounds are of interest, compound-specific radiocarbon analysis is applied. For ^{14}C analysis of all biota samples, the sample carbon needs to be converted into CO_2 by combustion or chemical oxidation. Large biota samples for radiometric measurements are combusted in a stream of pure oxygen (Kaizer et al., 2018b). Smaller samples for AMS analysis are usually combusted in a closed volume. The oxygen necessary for oxidation of carbon into CO_2 can be provided in the form of oxygen gas or solid materials CuO and MnO_2. Combustion with CuO or MnO_2 permits this process in flame-sealed glass tubes placed into a muffle furnace, which considerably increases sample throughput. The produced CO_2 is then released and collected by cracking the glass tubes in vacuum. Recently, a sealed tube method for organic materials combining combustion and graphitization into a one-step procedure has been developed.

When the samples are in the form of CO_2, the subsequent sample preparation methods and measurement

techniques are the same as described in the section dealing with radiocarbon in gases (Section V.A).

b. Tritium

Hydrogen is an inseparable component of a living organism, and the concentration of its radioactive isotope ^{3}H is of great interest in health and nuclear safety studies as well as environmental and biomedical sciences. Two chemical forms of tritium are present in biota samples—tritiated water absorbed in the sample material and organic-bound tritium. Tritium is widely used as a tracer for labeled molecules in biomedical research and the measurement of ^{3}H in organic matter can be used to determine the impact of nuclear installations on organisms living in their surrounding area (Krištof et al., 2017). Tree rings represent a well-defined record of past tritium levels similar to ^{14}C, and they have been successfully used to reconstruct past ^{3}H levels around tritium labeling facilities and nuclear weapon test sites (Love et al., 2004), NPPs, and reprocessing plants (Fuma and Inoue, 1995). Tree ring data set in Fig. 3.65 represents organic-bound tritium concentration in biosphere of Japan during the period of numerous nuclear weapon tests and subsequent years. The decrease of tritium levels after the test ban treaty in Tokai has been perturbed due to releases from nuclear facilities operating close to this site.

Tritiated free water and organic-bound tritium can be extracted and processed separately. The sample is dried in an apparatus with a water trap for the evaporated free water. Azeotropic distillation is an alternative method of free water extraction (Vagner et al., 2014). The dried sample is combusted in oxygen or oxidized in plasma. CO_2 and H_2O are produced during this process, and the water is recovered and used to represent the activity of organic-bound tritium in the sample. In analysis of tritium-labeled molecules or detailed studies of ^{3}H activity in different compounds of the sample, complex chemical procedures to isolate the individual compounds may be necessary prior to combustion/oxidation.

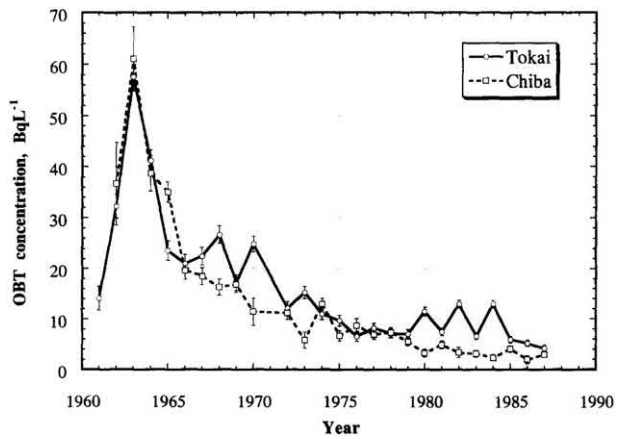


FIGURE 3.65 Concentration of organic-bound tritium (OBT) in tree rings from Tokai village (close to a nuclear power plant and nuclear reprocessing plant) and Chiba city. OBT concentration is decay corrected to the growth year of the ring and is expressed as tritium activity Bq/L of combustion water. *From Fuma and Inoue (1995).* Printed with permission *© Elsevier 2018.*

The subsequent sample preparation procedures for the separated water and ^{3}H measurement methods are the same as described in previous sections dealing with tritium in other sample types (Sections V.A and V.C). For tissue samples measured by LPC, a solubilization sample preparation method is often used—corrosive, and oxidative compounds (e.g., perchloric acid, sodium hypochlorite, hydrogen peroxide, and other commercial solubilizers) are added into the sample. The sample material is digested into compounds soluble in appropriate scintillation cocktails. Choice of solubilizer and solubilization protocol must be chosen according to type of sample tissue so that the scintillation mix is stable, colorless, and with minimal quenching.

2. Radiocesium and radiostrontium

a. Radiocesium

Radiocesium isotopes (^{134}Cs, ^{135}Cs, ^{137}Cs) belong to the most important fission and neutron activation products released into the environment, and their levels in the biosphere are frequently measured to assess doses originating from these radionuclides and to study their migration between and within different radionuclide compartments. Analysis of these radioisotopes in plant and animal tissues has been used in connection with the impact of global nuclear tests fallout and Chernobyl and Fukushima nuclear accidents (Falandysz et al., 2015; Mahara et al., 2015; Strandberg, 1994). The measurement of $^{134}Cs/^{137}Cs$ ratio can be used for biospheric radiocesium source apportionment (Chino et al., 2016).

Both ^{134}Cs and ^{137}Cs are gamma emitters, and their activity in biota samples is measured mainly by gamma spectrometry. After representative biota samples are taken, they are homogenized and dried. In most cases (especially when dealing with samples with enhanced radiocesium activity), no further sample preparation is necessary before gamma spectrometric measurement. Samples have to be placed in a container or pressed into shape appropriate for the detection system geometry. ^{134}Cs and ^{137}Cs are then identified by their gamma lines (^{134}Cs—604 keV and 795 KeV, ^{137}Cs—662 keV). Samples with very low radiocesium content need to be concentrated prior to measurement. Radiocesium enrichment of biota samples is done by heating the samples to several hundreds of degrees (ashing). Ashing removes most of the organic sample matrix, considerably decreasing sample size and enriching the sample in cesium. The ashing temperature should not be higher than 450°C to prevent volatilization of cesium (Koh et al., 1999). In principle, radiocesium can be leached and

extracted from samples by precipitation with ammonium phosphomolybdate or potassium cobalt hexacyanoferrate (Lehto and Hou, 2011).

Because of its long half-life (2.3×10^6 years) and emitted soft beta radiation ($E_{max} = 269$ keV), cesium-135 is radiologically not very important; however, it has been of interest as a tracer of environmental processes. Its analysis in the environment is a challenge; recently, however, there have been new developments in the ICP-MS and AMS sectors.

b. Radiostrontium

Radiostrontium isotopes (^{89}Sr, ^{90}Sr) are fission products, which can be released into the environment from various nuclear installations. Since strontium has similar chemical properties as calcium, it is retained in bones (Froidevaux et al., 2010) and therefore needs to be monitored in a range of environmental samples, including biota samples. Milk, meat, and other foodstuffs are often analyzed mainly for its ^{90}Sr content (as ^{89}Sr has a much shorter half-life, 50.57 days) in regard to radiation doses received by ingestion (Rantavaara, 2008). Measurements of ^{90}Sr in human bones and teeth can also help in reconstruction of ^{90}Sr fallout from nuclear weapon tests and Chernobyl accidents (Stamoulis et al., 1999). ^{90}Sr is also of interest in radionuclide transfer studies (Outola et al., 2009; Semioshkina et al., 2007).

Strontium needs to be chemically separated from the sample matrix, and two ^{90}Sr separation methods most widely used are coprecipitation and extraction chromatography. They are both designed to separate strontium from the sample; in particular, they focus on the separation of strontium from chemically very similar calcium. The simplest coprecipitation method uses sample mixed with fuming nitric acid to precipitate strontium, whereas calcium remains in solution. This precipitation step needs to be repeated several times before all calcium is extracted, and other elements can be removed by coprecipitation (Shao et al., 2018b). The main disadvantage of this method is the danger of working with fuming nitric acid. Extraction chromatography on the other hand uses resin with high strontium affinity for its separation from interfering elements (Grahek et al., 2018). Prior to strontium separation, the sample may need to be ashed or dissolved; it depends on the method and specific separation protocol used.

^{90}Sr is a pure beta emitter ($E_{max} = 0.54$ MeV), and it decays into ^{90}Y, which is beta emitter as well ($E_{max} = 2.27$ MeV). The measurement methods are based on the detection of the emitted beta particles by GPC or LSC. When a gas detector is used, the strontium precipitate from the chemical separation is filtered and dried and placed onto the detector window. In the case of the LSC method, the dried precipitate is dissolved and mixed with a suitable scintillation cocktail. ^{90}Sr can be measured immediately after the chemical separation by beta spectrometry. In this rapid method, the beta spectrum of ^{90}Sr decay is measured and evaluated before ingrowth of its daughter nuclide ^{90}Y. Another approach is to store the samples for several weeks to wait for ingrowth of ^{90}Y (secular equilibrium of ^{90}Sr and ^{90}Y is reached after 2 weeks) and then measure the combined beta spectrum of ^{90}Sr and ^{90}Y. There is also a possibility to measure and evaluate beta spectrum of ^{90}Y alone; however, it requires chemical separation of Y from Sr in the sample after ^{90}Y ingrowth.

Cherenkov counting can also be used for ^{90}Sr (^{90}Y) determination. The chemically separated strontium precipitate is dissolved in aqueous HNO_3 solution and after ^{90}Y ingrowth placed in a vial into LSC detection system (no scintillation cocktail is added). The emitted beta particles have a high enough energy to produce Cherenkov radiation in aqueous solutions, and the LSC system detects these light signals and ^{90}Sr activity in the sample can be determined based on the measured spectra.

In addition to radiometric methods, ICP-MS has been shown to be applicable for ^{90}Sr analysis. Several problems complicate the use of this measurement technique for ^{90}Sr (interference from ^{90}Zr and polyatomic isobars, peak tailing from ^{88}Sr) resulting in higher detection limits compared with radiometric methods. New technical and methodological improvements for ^{90}Sr ICP-MS measurements are being developed (Russell et al., 2017). At this stage, this method offers considerably higher sample throughput compared with radiometric methods at the expense of higher detection limits and is used mainly for samples heavily contaminated with ^{90}Sr.

3. Radioiodine

a. Iodine-131

Fission product ^{131}I ($T_{1/2} = 8.02$ days) is a very important radionuclide in view of radiation protection because it can be released from various nuclear installations and its volatility makes it highly mobile in the environment. Because of its relatively high bioavailability, it readily enters the biosphere and propagates through the food chain. Milk and milk products in particular are analyzed for ^{131}I activity. Studies focused on ^{131}I activity in milk have been performed following the Chernobyl and Fukushima accidents (Martin et al., 1988; Perrot et al., 2012). Fig. 3.66 shows the activity of ^{131}I in cow milk from Slovakia following the Chernobyl accident in 1986. Transport of iodine from feed to milk has been studied in several controlled feeding experiments (Howard et al., 1993; Vandecasteele et al., 2000).

^{131}I can be measured by beta or gamma counting. Counting of 364.5 keV gamma rays by HPGe or NaI(Tl) detectors and LSC are widely used for ^{131}I analysis. In

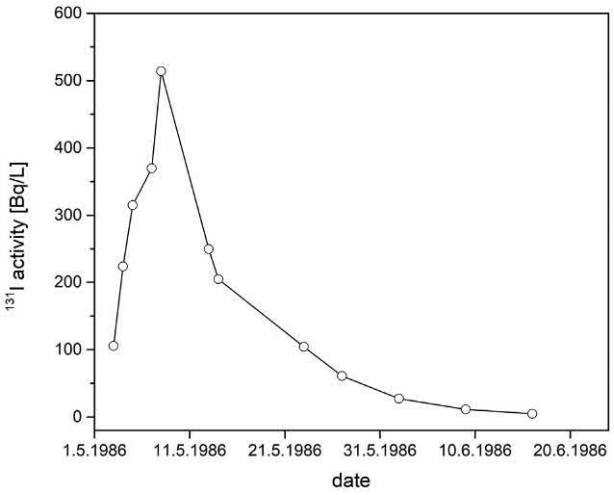


FIGURE 3.66 Iodine-131 activity in cow milk in Slovakia following the Chernobyl accident in 1986.

principle, samples containing ^{131}I may be measured directly without any pretreatment (gamma spectrometry), but usually some sample volume reduction and preconcentration are necessary. Evaporation, ashing, and chemical digestion can be employed to this effect. The LSC measurement requires a suitable form of the preconcentrated sample to facilitate its uniform mixture with liquid scintillator. Iodine separation methods detailed in Section V.C dealing with water samples can be used for ^{131}I extraction as well.

b. Iodine-129

Iodine-129, because of its very long half-life (15.7×10^6 y) and soft beta radiation ($E_{max} = 154.4$ keV), is radiologically not very important; however, it can be used for reassessment of radiation doses, which were delivered by ^{131}I. It has also been used as a useful environmental tracer. ^{129}I in environmental samples has been analyzed mostly by AMS or ICP-MS.

F. Analysis of actinides

Environmental radioactivity is usually associated with the presence of NORMs in the Earth's crust. The most important alpha emitters representing the group of NORM radionuclides are ^{238}U and ^{232}Th, as well as their decay series. Besides the NORM, there are a number of artificial radionuclides released into the environment during the nuclear explosion and as a result of nuclear accidents, among them alpha-emitting actinides.

Naturally occurring radionuclides are present in the Earth's crust, in raw materials and minerals. Although human activities related to the natural resources, involving minerals and raw materials, produce large amounts of waste, they cannot cause significantly greater exposure levels in comparison with normal background levels and usually are not of concern for radiation protection. Nevertheless, industrial activities that exploit these resources can result in enhanced exposures required to be controlled by regulations. The main regulatory attention has been focused on industries working on the mining and processing of uranium ore due to a direct consequence of the radioactivity in the ore and as a part of the nuclear fuel cycle. However, activity levels of thorium and uranium at the industrially exploited rare earth deposits exceed average worldwide reported values for soil up to 30 and 200, respectively (IAEA, 2011). Natural and artificial radionuclides found in the environment, as well as their inclusion in terrestrial and aquatic food chains, could have adverse health effects due to their transfer to humans via ingestion of food or inhalation of particulate matter.

Radiological protection in response to growing concerns about environmental pollution and public exposure resulting from the use of nuclear energy and commercial activities related to natural resources requires the development of reliable radioanalytical methods and standard reference materials (Calmet, 2014; Maringer et al., 2017). In addition, sensitive methods are needed for the applications of natural and anthropogenic radionuclides as tracers to study environmental processes (e.g., Chamizo et al., 2015; Povinec et al., 2004, 2016).

Alpha spectrometry is one of one of the most widely used techniques for the isotopic composition measurement of actinides (such as thorium, uranium, neptunium, plutonium, americium, curium, polonium, and radium) in the environmental samples. In recent years, however, there has been growing interest in low- and high-energy mass spectrometry methods, as already discussed in Sections IV.B and IV.C. Critical comparisons of radiometric and mass spectrometric techniques for the quantitative determination of alpha-emitting radionuclides in environmental, biological, and nuclear waste samples were provided in many publications during the last decade (Gascó et al., 2002; Hou and Roos, 2008; Ayranov et al., 2009; Aggarwal, 2016; Van Es et al., 2017). Among the advantages of the mass spectrometric techniques—fast analyses, improved data quality for ^{238}U/^{235}U ratios, measurements of ^{239}Pu and ^{240}Pu isotopes separately, and improved sensitivity for long-lived nuclides are usually mentioned. The main problems such as isobaric interferences, polyatomic interferences, peak tailing, isotopic fractionation, beam instability, and matrix effects have been indicated as well. The main advantages of alpha spectrometry are high sensitivity, reliability, application of alpha-emitting internal standards, and low sensitivity of alpha detectors to beta and gamma radiation and removal of competing radionuclides during radiochemical procedures (Levy et al., 2011). In some environmental radionuclide studies, it is advantageous to analyze actinides by LSC, e.g., in the case of ^{241}Pu (Liong Wee Kwong et al., 2004a).

1. Sampling and pretreatment

Depending on the objective of the radionuclide analysis, the appropriate measurement and processing technique could involve various steps, adjusted to meet particular requirements: sampling, preservation, pretreatment, separation, source preparation, measurement, and evaluation. Samples should be collected using the appropriate equipment, and several procedures have already been described, e.g., Csuros (1994), Koide and Bruland (1975), Martin and Hancock (1992). Usually, there are no requirements for field preparation and preservation of soil and sediment samples for actinide analyses. Although in some sampling protocols during shipping and storage, it is recommended to keep soil samples at 4°C; however, this is not normally applied for the radiochemical analysis. Water samples are generally acidified after collection. Generally, soil, sediment and biota samples are usually dried at 80−110°C for 12−48 hours and then ashed at 450−800°C for 12−48 hours to destroy organic matter. If samples contain nonashed carbon particles, it is recommended to moisten the residue with concentrated nitric acid, fume it off to dryness, and ash the sample again (e.g., Pimpl and Higgy, 2001). Other samples can have specific requirements for the field sample preparation and preservation, such as filtering and acidification of water samples as well as freezing samples at −20°C to reduce biological activity or chemical preservations of radionuclides or media.

Radioanalytical separation must ensure the separation of matrix elements abundant in environmental samples and remove alpha-emitting radionuclides, interfering with the peaks in the spectrum. In addition, sample preparation should provide a thin source for the best spectral resolution. Radioanalytical procedures involve preconcentration, the chemical separation of analytes (e.g., precipitation, coprecipitation, distillation, ion exchange, solvent extraction, and extraction chromatography), and the source preparation for measurements.

Decomposition of solid samples can be achieved by means of different methods (dry or wet ashing, dissolution in various acid combinations or fusion techniques) providing complete or partial access to analytes (Bock, 1979). In the analyses of actinides, samples are usually ashed at 450−550°C for 16 hours. The application of higher temperatures is not recommended because of the formation of refractory particles. However, a decrease in ^{239,240}Pu activity concentrations in soil was observed when the ashing temperature exceeded 450°C. It was found that ashing of soil samples at temperatures of 600°C for 4°h resulted in losses of about 40% of ^{239,240}Pu activities (Wang et al., 2015). The formation of refractory materials, such as plagioclase-like silicate insoluble in nitric acid, was confirmed by the XRD analysis of soil samples. Volatile radionuclide ashing requires much lower temperatures, e.g., to avoid losses. Samples for polonium analysis cannot be heated at a temperature higher than 150°C but can be digested by wet ashing using HCl and HNO_3, including aqua regia (Martin and Hancock, 1992; Vaaramaa et al., 2010). However, the Po losses at 70−80°C during wet ashing of ∼30% for open glass beakers, ∼ 20% for Kjeldahl flasks, and ∼17% for the microwave digestion were reported by Henricsson et al. (2011).

Complete or nearly complete dissolution of the solid matrix can be achieved by the application of concentrated or fuming nitric acid, aqua regia, sulfuric acid, or mixtures of concentrated nitric acid with perchloric acid or hydrofluoric acid. Pu and Am from environmental samples were leached with concentrated nitric acid and 30% hydrogen peroxide after ashing at 450°C for 8°h, and the microwave digestion treatment using HF was applied for residue (Sekine et al., 1987), while Hamato (1982) applied nitric acid and hydrogen peroxide after soil ashing at 550°C for Am determination. A choice of the dissolution procedure can affect results and usually requires additional studies. Although 8 mol L^{-1} HNO_3 is most commonly used in the actinide sample preparation, the application of HF acid is important for extraction of Pu isotopes from samples containing "hot" particles. The leaching ability of different reagents toward Pu isotopes in the Chernobyl soil indicated that the amount of extracted Pu could vary by a factor of 10 in samples containing "hot" particles depending on the method (Lujaniene et al., 2002, 2009). Three methods—leaching with 0.1 mol L^{-1} HNO_3 or 8 mol L^{-1} HNO_3 and decomposition with $HF + HNO_3 + HClO_4$—were compared to check the optimal condition for measuring the global fallout ^{236}U in the Hiroshima soil samples. The concentration estimated from the 0.1 mol L^{-1} HNO_3 leaching was obviously lower as compared with 8 mol L^{-1} HNO_3 leaching and complete decomposition. The amount of ^{236}U extracted with 8 mol L^{-1} HNO_3 and $HF + HNO_3 + HClO_4$ decomposition was similar; thus, leaching with 8 mol L^{-1} HNO_3 was recommended for the soil sample preparation (Sakaguchi et al., 2012). Pimpl and Scuettelkopf (1986) applied two-stage leaching of 8 mol L^{-1} HNO_3/0.9 mol L^{-1} HF and 5 mol L^{-1} HNO_3/1 mol L^{-1} $Al(NO_3)_3$ to dissolve refractory material (PuO_2) from 100 g of soil ash or up to 20 g of other samples, after the addition of ^{236}Pu as an internal standard for the chemical yield estimation. Nevertheless, Benedik and Trdin (2017) showed a discrepancy in activity concentrations of ^{237}Np obtained using different decomposition procedures.

The leaching and decomposition can be accelerated by applying high-pressure and microwave techniques (Amoli et al., 2007; Khattab, 2016). Yoshida et al. (2007) developed a microwave decomposition system to prepare samples for measuring ^{240}Pu/^{239}Pu atom ratios by high-resolution ICP-MS. Concentrations of ^{239,240}Pu in soil samples after the microwave decomposition were found to

be higher than those after the nitric acid extraction and the $^{240}Pu/^{239}Pu$ ratio lower by 1%. Soil and sediment samples for U measurements by alpha spectrometry were ashed at 550°C and digested with concentrated acids (HNO_3:HCl:HF—5:5:3 mL, respectively) in closed PTFE-vessels using a Mars 5 (CEM, USA) microwave system (Popov, 2013).

A fusion technique is appropriate for sample decomposition in the presence of refractory particles as well as for geological samples, and it may include the application of hydroxides, peroxides, fluorides, pyrosulfates, carbonates, or borates (Bock, 1979; Dean, 1995; Warwick et al., 2001; Galindo et al., 2007; Huang et al., 2007). Among advantages of the fusion method are the disuse of highly toxic reagents (e.g., HF), more complete dissolution of refractory material, simplicity, and reproducibility (Huang et al., 2007). Complete soil sample dissolutions can be achieved using the potassium fluoride–pyrosulfate fusion technique for actinide determination (Smith et al., 1992). Although the fusion technique is one of the convenient methods for digestion of soil samples, it is not suitable for all radionuclides.

2. Separation of actinides

A special case we shall deal with is ^{236}U, which has been recently frequently used in terrestrial and marine tracer studies thanks to the development of AMS measurement techniques. Solvent extraction but more often anion exchange and extraction chromatography are utilized for the separation of uranium from low-level water matrices and its consequent purification. The procedures are based on the fact that metallic elements in HCl and HNO_3 media adsorb differently to anion exchange or extraction chromatography resins, i.e., while uranium can, in principle, form both nitrate and chloride complexes, it is adsorbable on various resins; this is not true for most elements occurring in their typical valence states (Faris and Buchanan, 1964; Kraus and Nelson, 1955). A single column filled with Eichrom UTEVA or DOWEX resin can be used for the separation of uranium from possible interferents; however, the second column may be applied to ensure their complete removal (Quinto et al., 2009; Eigl et al., 2013). In short, uranium from water is preconcentrated on $Fe(OH)_2$ precipitate, and then it is leached in HNO_3 solution, which is loaded on the column with the preconditioned resin. The elution of uranium retained on UTEVA and DOWEX can be achieved by 0.01 M HCl and 7.2 M HNO_3, respectively. After evaporation of the eluate to dryness, fuming of the residue with, e.g., H_2O_2 and dilution in a small amount of HCl or HNO_3, uranium is once again coprecipitated on ferric hydroxide. The precipitate is separated, dried, and calcinated to finalize the target material for AMS.

Due to the low specific activity and abundance of ^{236}U, the only possibility to determine ^{236}U in environmental water samples is by AMS, which enables the measurement of the $^{236}U/^{238}U$ isotopic ratios down to 10^{-15} using high-energy filters while reaching the detection limit of 10^4 atoms (Tuniz et al., 1998). ICP-MS and TIMS could be also used; however, their sensitivity is by some six orders of magnitude lower (Steier et al., 2008; Sakaguchi et al., 2009). Conventionally, a solid target for AMS measurements of ^{236}U is prepared in the form of uranium oxide coprecipitated on ferric oxide. A more novel approach has been developed, which exploits UF_4 as the target material (Wang et al., 2013). Although the preparation of the latter is more complex, similar or even higher ionization yields have been reported for uranium fluoride (Povinec et al., 2015b). Uranium, together with other actinides, is typically scavenged from freshwater, which was beforehand spiked with a known amount of ^{233}U ($T_{1/2} = 1.59 \times 10^5$ years), by ferric hydroxide precipitate.

Liquid–liquid extraction, ion exchange chromatography, and extraction chromatography as well as precipitation and/or coprecipitation were generally applied for the separation of actinides from various matrixes. Liquid–liquid extraction procedures received a wide application for the actinide separation and purification from environmental samples. Tributyl phosphate (TBP), methyl-i-butyl ketone (MIBK), bis-2-ethylhexyl-phosphoric acid (HDEHP), dibutyl-N,N-diethylcarbamoylphosphonate (DDCP), thenoyl-tri-fluoroacetone (TTA), tri-n-octylamine (TNOA), phenyl-3-methyl-4-benzoyl-5-pyrazolone (PMBP), t-octylphosphine oxide (TOPO), and carbamoylmethyl-phosphine oxide (CMPO) in a mixture with carbamoylmethyl-phosphine oxide (CMPO) used for extraction chromatography are mostly used in analytical procedures for the determination of actinides.

HDEHP is a common extractant used in Am, Cm, Pu, and Th separations. HDEHP has been used for the separation of Am together with Cm and the lanthanides. Bernabee et al. (1980) extracted Am and trivalent lanthanides from 72% $HClO_4$ by 15% HDEHP in n-heptane. Then, 99.8% of Am was back-extracted with 4 mol L^{-1} HNO_3, whereas Pu(IV) remained in the organic phase. Holm et al. (1979) extracted Am(III) and Th(IV) from 0.01 to 0.001 mol L^{-1} HNO_3 and back-extracted Am(III) and rare earth elements with 4 mol L^{-1} HCl. Murray and Statham (1976) applied 9 mol L^{-1} HC1 for the back extraction. It was found that iron extracted with Am and high manganese concentrations resulted in reduced recoveries. The techniques were optimized by the separation of plutonium isotopes using anion exchange as well as by the removal of iron using solvent extraction and manganese elimination by cation exchange (Livens and Singleton, 1989).

HDEHP was studied for the separation of neptunium, plutonium, americium, and curium in the presence of large amounts of uranium. U(VI), Np(VI), Pu(IV), Pu(VI), Am(III), and Cm(III) were extracted with 1 mol L^{-1} HDEHP in kerosene from 0.1 mol L^{-1} HNO_3. Am and Cm were back-extracted in 5 mol L^{-1} HNO_3. Then, Np was back-extracted with 1 mol L^{-1} $HNO_3/NH_2OH{\cdot}HNO_3$ followed by the back extraction of Pu(III) with 3 mol L^{-1} $HCl/TiCl_3$ (Ramebäck and Skillberg, 1998).

In the separation of Am from soil samples, Am (III) and lanthanides were extracted into the DDCP from 12 mol L^{-1} nitric acid and then back-extracted into 2 mol L^{-1} nitric acid (Ballestra and Fukai, 1983). TTA was used to purify americium. Am(III) along with lanthanides was extracted into 0.5 mol L^{-1} TTA in xylene at pH 4.0 and back-extracted into 1 mol L^{-1} nitric acid. A reduction in Am recovery during extraction was observed when pH values were lower than 3 (to about 70% at pH 3 and 35% at pH 2.5). The recovery was improved by the use of 0.1 mol L^{-1} TTA in isobutanol (Sekine et al., 1987).

Hursthouse et al. (1991, 1992) used TTA to extract Np(IV), after oxidation state adjustment using $NH_2OH{\cdot}HCl$, in soil and sediment sample preparation for ICP-MS, alpha spectrometry, and NAA. High decontamination factors (DFs) and recovery of 56% were reported for Pu separation from marine sediment samples prior to measurements of ^{239}Pu, ^{240}Pu, ^{241}Pu, and ^{242}Pu by sector-field inductively coupled mass spectrometry (SF-ICP-MS). An extraction with 0.5 mol L^{-1} TTA in xylene was used to separate Pu isotopes from uranium, americium, and curium, followed by purification using anion exchangers (Donard et al., 2007).

TTA was also widely applied in combination with anion exchange for ^{237}Np determinations in soil and sediments by alpha spectrometry, ICP-MS, and NAA. Neptunium is usually extracted from 1 mol L^{-1} solutions into 0.5 mol L^{-1} TTA in toluene or xylene after Np(VI) and Np(V) oxidation state adjustment to Np(IV) (Hursthouse et al., 1991, 1992). The similar analytical method was applied to separate ^{237}Np from environmental water samples after iron-oxy-hydroxide coprecipitation in the presence of sulfite. Residue was redissolved in 9 mol L^{-1} HCl and loaded onto the anion exchange column. Np oxidation state adjustment was performed with $NH_2OH{\cdot}HCl$. Np was eluted from the column with 5 mol L^{-1} HCl, extracted with TTA/xylene, and back-extracted from the organic phase with 8 mol L^{-1} HNO_3. The chemical yield of the separation procedure was estimated by the gamma counting rates before and after Np extraction, using ^{239}Np as a tracer. An internal standard—^{242}Pu was added to the samples prepared for AMS measurements (Keith-Roach et al., 2001).

Lindahl et al. (2004) applied TTA extraction in combination with the ion exchange anion column (BioRad AG1 1-x4, analytical grade 100−200 mesh chloride form) for Np separation from Swedish lichen (*Cladonia stellaris*). Samples in 9 mol L^{-1} HCl were passed through an ion exchange anion column. Np(IV) was eluted with 4 mol L^{-1} HCl, evaporated and dissolved in 1 mol L^{-1} HCl. Aqueous ferrous(II) chloride solution was used to reduce Np(V) to Np(IV). The Np(IV) was extracted into 0.5 mol L^{-1} TTA in xylene and back-extracted with 9 mol L^{-1} HCl. Then, samples were passed through a final ion exchange anion column. The chemical yield was monitored by measuring the activity of ^{239}Np (Ec = 104 and 107 keV) with a high-purity germanium (HPGe) detector. ^{242}Pu was used as an internal standard for the high-resolution inductively coupled plasma mass spectrometry (HR-ICP-MS) measurements.

Microthene-710 (microporous polyethylene, 50−100 mesh) and the KL-I-IDEHP resin (50% di(2-ethyl-hexyl) phosphoric acid, 60−100 mesh) were used for plutonium and americium determination in lichen and moss as indicators of atmospheric radioactivity. Pu was separated from HCl solutions by a Microthene-TNOA column, while for americium, separation and purification with a KL-HDEHP column and PMBP-TOPO extraction were applied (Jia et al., 1997).

In the sequential separation method for Pu, ^{241}Am, and ^{90}Sr determination in soil samples developed by Jia et al. (1998), Pu was separated by a Microthene-TNOA column, whereas ^{90}Y (for ^{90}Sr determination) was separated from Am using an HDEHP column. Then, Am was finally purified on another HDEHP column and MBP/TOPO extraction prior to preparation of alpha sources. The DFs of Pu and Am from ^{210}Po and of ^{90}Y from ^{210}Bi were $> 10^5$, 10^6, and 10^4, respectively. The reported detection limits were 1.2 mBq kg^{-1} for Pu and 1.7 mBq kg^{-1} for Am. Pimpl and Scuettelkopf (1986) applied TOPO/cyclohexane for Pu extraction from large soil samples and air filters (up to 100 g). Coprecipitation with LaF_3 and anion exchange with Dowex 1x2, 50−100 mech followed by the TOPO/cyclohexane extraction was used for the final purification. The TOPO/cyclohexane extraction followed by the subsequent TEVA, TRU-TEVA separation of Pu, Am, and Cm from the soil, and aerosol samples was reported (Pimpl and Higgy, 2001; Ayranov et al., 2005; Lujaniene and Sapolaite, 2005; Lujaniene, 2013).

Diglycolamides (DGAs), such as *N*,*N*,*N*′,*N*′-tetraoctyl diglycolamide (TODGA) and *N*,*N*,*N*′,*N*′-tetradecyl-diglycolamide (TDDGA), were applied for the determination of actinides in environmental samples due to high distribution coefficients for actinides and lanthanides in the strong acid range (>3 mol L^{-1} HNO_3) (Sasaki and Choppin, 1996).

a. Coprecipitation

Coprecipitation techniques are well established and are in regular use in environmental radionuclide sample preparation for measurements. Coprecipitation is an important part of chemical separation, purification, and source preparation for alpha counting. Coprecipitation has been widely used for the preconcentration and elimination of matrix elements from both liquid samples and extracts following leaching or complete dissolution of solid samples as well as for the separation of interfering radionuclides and the improvement of the DF of analytes. The coprecipitation behavior of radionuclides is discussed in detail in following reviews and textbooks:

i. fluorides such as NdF_3, LaF_3, CeF_3, CaF_2 (Rao and Cooper, 1995; Lindahl et al., 2004; Maxwell and Culligan, 2006; Varga et al., 2007a,b; Vajda et al., 2009a,b; Maxwell et al., 2010a; Maxwell et al., 2011a; Wang et al., 2017b; Luo et al., 2018),
ii. ferric and ferrous hydroxides—$Fe(OH)_2$ and/or $Fe(OH)_3$ (Keith-Roach et al., 2001; Chen et al., 2002; Giardina et al., 2006; Qiao et al., 2010; Lemons et al., 2018),
iii. phosphates—$CaHPO_4$, $Ca_3(PO_4)_2$ (Kimura, 1990; Thakkar, 2001; Hölgye, 2007; Maxwell 2006, 2008a; Maxwell et al. 2010a, 2011b; Maxwell and Culligan, 2009a, 2011a),
iv. oxalates (CaC_2O_4) (Salminen et al., 2009; Kenna, 2009),

which are the most commonly used carriers for the actinide coprecipitation and the matrix element removal during chemical separation from water, soil, sediments, and biological samples.

Although coprecipitation with MnO_2 was mainly used for high salinity (seawater, high-salinity spring water) samples, MnO_2-impregnated cellulose, and MnO_2-coated discs were also applied for Ra preconcentration from continental river, ground, and tap water samples (Eikenberg et al., 2004; Bojanowski et al., 2005; Sharabi et al., 2010; Rodríguez et al., 2016).

Preconcentration and separation of ^{226}Ra (also used for ^{238}U determination) from the matrix elements of various samples (water, soil, and biological samples) were performed using $PbSO_4$ (Sill, 1987a; Kehagia et al., 2007), $Pb(NO_3)_2$ (Lozano et al., 2010), and $BaSO_4$ (Bojanowski et al., 2002; Rodríguez et al., 2016; Straub et al., 2018). Coprecipitation of Ra with $Ba(Ra)SO_4$ based on the method developed by Sill (1987b) was also commonly used for Ra source preparation (e.g., Medley et al., 2015). According to recent studies, the matrix effect should be taken into account, which could significantly reduce the recovery of Ra during the preconcentration using $BaSO_4$, MnO_4, and RadDisc techniques (Nelson et al., 2014). Suarez-Navarro et al. (2017) successfully applied [Ba + Fe] coprecipitation techniques for the determination of U, Pu, Th, and Po in water samples.

b. Ion exchange

Ion exchange resins are frequently used for the separation and preconcentration of radionuclides from environmental samples due to their low cost and broad application ranges. Among the most commonly used cation exchangers, there are strongly acidic sulfonated resins containing $-SO_3^-$ groups and less acidic phosphorylated and carboxylated resins. The affinity of the cations for exchange sites increases with the increasing charge and decreasing hydrated ion radius. Anion exchangers contain amines as functional groups. Strongly basic anion exchangers with substituted quaternary amines are capable of retaining tetra- and hexavalent actinides from concentrated nitric and hydrochloric acid solutions.

c. Cation exchange

Cation exchange resins have been used to preconcentrate actinides from groundwater (Fjeld et al., 2005). Cation exchange chromatography (Bio-Rad AG 50WX8 or Dowex 50WX8 resins) is frequently used for Ra preconcentration and separation from the matrix elements, e.g., Ca and Mg (Saito et al., 2003; Larivière et al., 2005; Al-Mukren et al., 2015; Dulanská et al., 2018). Samples can be loaded on the resin in dilute HCl and HNO_3 and Ra stripped with 4–9 mol L^{-1} HCl or 4–5 mol L^{-1} HNO_3. Separation of Ra from Ba is a crucial interference in mass spectrometry, and the source preparation for alpha spectrometry can be achieved in combination of cation exchange with complexing agents, e.g., EDTA, which was recently replaced by the application of strontium-specific resin (Volpe et al., 1991; Larivičre et al., 2007; Copia et al., 2015; Zhang et al., 2015; Dalencourt et al., 2018).

Cation exchange chromatography was applied to separate Am from the lanthanides on the column with the temperature-controlled jacketed (87°C) using hydroxy-isobutyric acid (α-HIBA) and aminopolyacetic acids (e.g., EDTA and DTPA) as eluents (Choppin and Silva (1956). Cation exchange chromatography with gradient elution using 0.16–0.4 mol L^{-1} α-HIBA allowing the separation of Am and Cm from lanthanides when large environmental samples of 100–200 g were analyzed (Ageyev et al., 2005).

The separation of Am from lanthanides on anion exchangers is based on Am(III) adsorption from methanol–nitric acid systems: 0.5 mol L^{-1} HNO3–95% MeOH (Guseva et al., 1976), 1 mol L^{-1} HNO_3–93% MeOH (Holm et al., 1979; Livens and Singleton, 1989; Hamato, 1982), 1 mol L^{-1} HNO_3–90% MeOH (Holm and Fukai, 1976; Bains and Warwick, 1993). Methanol–HNO_3 and HCl systems with 0.5–1.0 mol L^{-1} HNO_3 and 90%–96% methanol for load and stripping with HCl (Livens and

Singleton, 1989) or HNO_3 (Bains and Warwick, 1993) were applied for environmental sample analyses.

Trivalent actinides were separated from lanthanides using concentrated (>8 mol L^{-1}) NH_4SCN solution as eluent (Surls and Choppin, 1957), whereas the best separation was achieved with 1−2 mol L^{-1} NH_4SCN solution containing 50%−70% methanol, ethanol, or propanol (Guseva and Tikhomirova, 1974). This procedure was applied for the final purification of the Am fraction from the interfering components in large environmental samples (Holm et al., 1979). One mol L^{-1} HNO_3/93% methanol solution containing Am and lanthanides was loaded on an anion exchange resin column; lanthanides were removed with dilute HCl/NH_4SCN/methanol followed by Am and Cm stripping using 1.5 mol L^{-1} HCl/80% methanol. In a similar procedure for final Am purification from 50 g of soil, Hamato (1982) used 1 mol L^{-1} HNO_3/93% methanol, 0.1 mol L^{-1} HCl/0.5 mol L^{-1} NH_4SCN/80% methanol, and 1.5 mol L^{-1}HCl/86% methanol solutions as load, wash, and strip solutions, respectively. Am separation from lanthanides (based on these procedures) has been applied for various environmental matrixes (e.g., IAEA, 2014).

Anion exchange chromatography was widely applied for the separation and purification of plutonium isotopes from environmental matrixes (LaRosa et al., 2005; Jakopic et al., 2007). Pu can be loaded on an anion resin in tetravalent oxidation state in 8 mol L^{-1} HNO_3 and matrix elements, and Am and U are removed by washing with 8 mol L^{-1} HNO_3. The possible interferences, primarily Th, can be eluted with 9 mol L^{-1} HCl and then Pu(III) stripped by freshly prepared 9 mol L^{-1} HCl solution containing 0.1 mol L^{-1} NH_4I as a reducing agent (IAEA, 2014). On anion exchange resins, Pu can also be separated from HCl solutions. Pu(IV) is loaded on the column in 9 mol L^{-1} HCl, and after washing, Pu is stripped using a reducing agent e.g., 0.36 mol L^{-1} HCl/0.01 mol L^{-1} HF (Lee et al., 2008).

Neptunium can be separated from complex environmental matrixes by anion exchange chromatography from nitric and hydrochloric acid solutions. The separation of Np from Pu is achieved when Np and Pu are reduced to tetravalent and trivalent states, respectively. Nitrate complexes of Np(IV) and Th(IV) are adsorbed from 8 mol L^{-1} HNO_3 on the anion exchange resin (Germian and Pinte, 1990). Another most common analytical method involves adsorption of anionic nitrate complexes of Np(IV), Pu(IV), and Th(IV) from 8 mol L^{-1} HNO_3 on the anion exchange resin and their sequential separation. The reduction/oxidation cycle using hydrazine sulfate (reduction step) and $NaNO_2/H_2O_2$ (oxidation step) was applied. Thorium was eluted with 9−10 mol L^{-1} HCl, plutonium elution was performed with a mixture of 9−10 mol L^{-1} HCl + NH_4I (or HI), and finally, neptunium was stripped with 4.5 mol L^{-1} HCl + HF or 1−4 mol L^{-1} HCl (Michel et al., 1999; LaRosa et al., 2005; Benedik and Trdin, 2017). Pu and Np can be stripped in the same fraction when both radionuclides are measured together (Qiao et al., 2011).

3. Extraction chromatography

Despite the wide application and certain advantages of the conventional anion exchange techniques, they suffer from the lack of selectivity in comparison with liquid−liquid extraction analytical methods. However, the main disadvantage of the solvent extraction is the large amount of organic waste generated during the separation procedure. Extraction chromatography (EXC) resins were developed over the past 30 years to overcome these problems and to improve selectivity, to provide higher separation efficiency, and to reduce the amount of hazardous waste produced during the separation. In addition, newly developed methods with folding resins in a multistage column ensure rapid sequential analyses. The use of vacuum boxes and small-sized resin facilities is important for time saving and is critical for emergency response methods.

New developed EC materials for the separation of actinides with well-defined physical and chemical properties, distribution coefficients, and extraction kinetics have become commercially available from EiChrom Co. and Triskem SAS. The EC materials or so-called solid-state extraction chromatography were applied for the environmental radioactivity needs by developing analytical separation procedures for environmental samples.

a. TEVA resins

The TEVA resin composed of quaternary amine-based (Aliquat 336) liquid anion exchanger supported on the inert material of Amberchrom CG-71 ms was developed by Horwitz et al. (1995) for the separation of tetravalent actinides. The TEVA resin has been widely applied for Pu and Np analysis due to its high capacity factors (k′) for Pu(IV) 3×10^4 and Np(IV) 4×10^3 in 6 mol L^{-1} HNO_3 as compared with k′ for Th and U(VI) in HNO_3 solutions and comparatively low selectivity for U and Th in concentrated HCl solutions.

TEVA resin was applied for the separation of Pu from environmental samples (1−5 g) after a CaF_2 coprecipitation (Varga et al., 2007a). The oxidation state of Pu(IV) was adjusted by $NaNO_2$. The sample was loaded in 3 mol L^{-1} HNO_3 followed by rinsing with 3 mol L^{-1} HNO_3 and 6 mol L^{-1} HNO_3, and then, Pu was stripped with 0.1 mol L^{-1} HNO_3/0.1 mol L^{-1} HF. The reported Pu recovery was 72%−93%, and the DF for U, Th, and Am was $\sim 10^5$.

Pu separation (Pu recovery > 60 and DF for U > 100) for AMS measurements from environmental samples with TEVA was used by Chamizo et al. (2008). Pu(IV) was loaded on the column in 3 mol L^{-1} HNO_3/$Al(NO_3)_3$,

followed by washing with 6 mol L^{-1} HCl and stripping with 0.5 mol L^{-1} HCl. TEVA resins were also used for Pu separation from environmental samples (soil and sediments) for plutonium measurements by mass spectrometry including the atom ratio determination (e.g., Momoshima et al., 1997). A simple, express online analytical method for Pu separation from soil and sediment samples and measurement by quadrupole ICP-MS was developed by Epov et al. (2007). Flow injection chromatography using TEVA resin was optimized to preconcentrate and separate Pu from the sample matrix elements, including ^{238}U. L-Ascorbic acid was found to be most suitable for the Pu oxidation state adjustment to Pu(IV) prior to EC.

Anton et al. (2006) used TEVA for the separation of Np from soil contaminated with weapons grade Pu. After acid leaching with HNO_3/HF, Pu was separated using anion exchange chromatography, whereas TEVA was used for the separation of Np from U and Th. $NaNO_2$ was used for the oxidation state adjustment. Np was stripped from the column with 0.02 mol L^{-1} HNO_3/0.02 mol L^{-1} HF. Np and Pu recoveries were 68%−89% and 53%−89%, respectively.

Pu and Np were separated from river sediments and measured by ICP-MS or SF-ICP-MS. The adjustment of the oxidation state was performed with hydroxylamine hydrochloride or $FeSO_4$+$NaNO_2$ followed by separation using TEVA with high recoveries for Pu 90% and Np 70% (Kenna, 2002, 2009).

A rapid method for the determination of ^{237}Np and Pu isotopes in large soil samples (up to 200 g) has been developed by Maxwell et al. (2011a). They applied acid leaching with 15 mol L^{-1} HNO_3, Fe/Ti hydroxide precipitation, and an LaF_3 matrix removal step followed by a rapid column separation process with TEVA resin resulted in the high chemical recoveries (88% for Pu), effective removal of interferences, and reduced analytical time.

TEVA resin was applied for the separation of Am(III) from lanthanides, which was performed by loading the sample in 2 mol L^{-1} NH_4SCN−0.1 mol L^{-1} formic acid solution followed by the elution of lanthanides with 1 mol L^{-1} NH_4SCN−0.1 mol L^{-1} HCOOH, and Am and Cm were eluted with 0.25−2 mol L^{-1} HCl (Horwitz et al., 1995).

b. UTEVA resins

UTEVA resin composed of dipentylpentylphosphonate−impregnated Amberlite XAD-7 EC was developed by Horwitz et al. (1992) to separate U and tetravalent actinides. The estimated k′ capacity factors for Pu(IV), Np(IV), U(VI), and Th(IV) in 8 M HNO_3 are 10^3, 4×10^2, 4×10^2, and 2×10^2, respectively. UTEVA is not often used as a single column for the separation of actinides; however, a single UTEVA column can be applied for the separation of thorium and uranium (Pilvio and Bickel, 2000). High recoveries of >90% and DFs of >2000 for U in Pu and Np fractions were reported for a single UTEVA column procedure developed for the determination of uranium, neptunium, plutonium, and americium in synthetic mixtures (Morgenstern et al., 2002). The oxidation state adjustment was performed with 0.3% H_2O_2 in 6 mol L^{-1} HNO_3; then, samples loaded on UTEVA column were followed by washing of the column with 6 mol L^{-1} HNO/0.3% H_2O_2. Pu was stripped from the column with 2 mol L^{-1} HNO_3, containing ascorbic acid and hydroxyl ammonium nitrate, Np with 2 mol L^{-1} HNO_3/0.1 mol L^{-1} oxalic acid, and finally, Np was eluted with ammonium bioxalate, $(NH_4)_2C_2O_4$.

A single UTEVA column coupled online to an ICP-MS detector was applied for the separation and detection of U, Th, and Np in environmental samples. Mohr's salt and $NaNO_2$ were used to convert the Pu and Np oxidation state to the (IV) and to retain tetra- and hexavalent actinides on UTEVA in 3 mol L^{-1} HNO_3. 0.1 mol L^{-1} oxalic acid was used as eluent (Perna et al., 2001). UTEVA was used in an ion chromatograph directly connected to ICP-MS for express (within 60 minutes) analyses of environmental samples of 1 g (Ohtsuka et al., 2006).

The separation of Pu, Np, Th, and U from environmental samples using a single UTEVA column and two-stage UTEVA EC was used for alpha spectrometry source preparations with the reported recoveries of 69%−92% for Pu as well as 65%−82% and 66%−93% for Pu and Np, respectively (Vajda et al., 2003; Osvath et al., 2009, 2010). A single UTEVA column was also applied for Pu and U separation and Pu measured by alpha spectrometry, while U was measured using TIMS (Croudace et al., 1998).

c. TRU resins

TRU resin composed of a tri-n-butyl phosphate (TBP) solution of the bifunctional organophosphorous extractant octyl(phenyl)-*N*,*N*-di(iso-butyl)-carbamoyl-methyl-phosphine oxide (CMPO) adsorbed on Amberlite XAD-7 was developed to separate all transuranium elements except the tetra- and hexavalent species (Horwitz et al., 1993). High capacity factors were found for Pu(IV), Np(IV), Th, and U(VI), in HNO_3 ($k' \sim 10^3$−10^5), while for Am the k′ is ~100.

In sequential separation of actinides using a single TRU column recommended by Horwitz et al. (1993), the sample was loaded onto a column in 2 mol L^{-1} HNO_3 after Pu reduction to Pu(III). The first Am was eluted with 4 mol L^{-1}HCl, followed by Pu stripping with 4 mol L^{-1} HCl/0.1 mol L^{-1} hydroquinone, and finally, Th, Np, and U were eluted with 1.5 mol L^{-1} HCl, 1 mol L^{-1} HCl/0.03 mol L^{-1} oxalic acid, and 0.1 mol L^{-1} ammonium bioxalate, respectively.

Am, Pu, and U were frequently separated from air filter and water samples. The sample was loaded in 8 mol L^{-1} $HNO_3/NaNO_2$. Am was eluted with 0.025 mol L^{-1} HNO_3, and Pu and U together with bioxalate. According to recommendations, due to possible cross-contamination, firstly, Pu should be separated using anion exchange chromatography, and the TRU resin used only for Am purification. This procedure was followed by many laboratories later, including the IAEA Laboratories at Seibersdorf and Monaco (Moreno et al., 1997, 1998; IAEA, 2014; LaRosa et al., 1989, 2001; 2005; Povinec, 2004; Lee et al., 2005; Levy et al., 2011).

Truscott et al. (2001) developed the online solid phase extraction method for the determination of ^{232}Th, ^{237}Np, ^{238}U, ^{239}Pu, ^{240}Pu, ^{241}Am, and ^{243}Am in environmental samples with a column containing TRU-SpecTM resin coupled with SF-ICP-MS. Sequential separation of Pu and U was achieved by on-column reduction of Pu with titanium(III) chloride, and Am and Pu were eluted with a solution of 0.006 mol L^{-1} titanium(III) chloride in 4 mol L^{-1} HCl, and then the other analytes were eluted with 0.1 mol L^{-1} ammonium hydrogen oxalate. Absolute detection limits were 0.7, 0.85, 0.6, and 0.65 fg for ^{237}Np, ^{239}Pu, ^{241}Am, and ^{243}Am, respectively.

Vajda et al. (2009b) slightly modified the TRU EC procedure of Horwitz et al. (1993) and applied it for the rapid determination of Am, Pu, Th, and U in small environmental samples (1 g) by alpha spectrometry. The procedure evolved $LiBO_2$ fusion and CaF_2 coprecipitation, Pu oxidation state adjustment to Pu(IV) using $NaNO_2$. The sample was loaded in 2 mol L^{-1} HNO_3. Am was eluted with 4 mol L^{-1} HCl, and Pu was stripped after on-column reduction with 4 mol L^{-1} HCl/0.1 mol L^{-1} $TiCl_3$. High recoveries were reported for both Am (96%) and Pu (85%).

4. Multistage extraction chromatography column methods

The most frequently used multistage techniques for actinide separation from environmental samples are based on the tandem column set of UTEVA-TRU (Thakkar, 2001). This method involved preconcentration of actinides with calcium phosphate (pH = 9), dissolution in 3 mol L^{-1} HNO_3/1 mol L^{-1} $Al(NO_3)_3$, and Pu oxidation state adjustment to Pu(III) with ferrous sulfamate and ascorbic acid. The tandem columns of the UTEVA (first) and the TRU (second) were used for the separation. The columns were separated after the sample loading and washing. Th and Np were subsequently eluted with 5 mol L^{-1} HCl/0.05 mol L^{-1} oxalic acid, respectively. On the TRU column, Pu was oxidized to Pu(IV) with 2 mol L^{-1} HNO_3/0.1 mol L^{-1} $NaNO_2$ and stripped with 4 mol L^{-1} HCl, and then Am was eluted with 0.1 mol L^{-1} ammonium bioxalate. This method with high recoveries (>80% for Pu, > 72% for Am, and >79% for U) and with comparatively high DF > 10^4 for U in the Pu fraction was slightly modified and applied in different standard procedures for the determination of actinides in biological and environmental samples (e.g., Jakopic et al., 2007; Varga et al., 2007a, 2007b).

A simple automated separation system was developed using UTEVA, TRU, and Sr resins for the determination of uranium, thorium, plutonium, americium, and strontium in water and urine samples by alpha spectroscopy, ICP-QMS, and multi-low-level counter (Zoriy et al., 2010). The method provides the rapid (from 60 to 100 minutes) and accurate separation of the elements with recoveries from 68% to 98%.

a. DIPEX resins

DIPEX (ACTINIDE) resin is a diphosphonic acid extractant supported on an inert polymeric substrate (Horwitz et al., 1997). The resin has high affinity for actinides from dilute acid solutions ($k' \sim 10^7$ for Pu(IV) and Np(IV), while $\sim 10^8$ for Am). In addition to the high affinity for actinides in the tri-, tetra-, and hexavalent oxidation states, the DIPEX resin has excellent selectivity for Am(III) over Al(III) or Fe(III) in comparison with the DIPHONIX chelating ion exchange resin. The resin can be used to preconcentrate actinides from bulk samples or complex matrices followed by the stripping of actinides from the resin together with the extractant using alcohol or wet oxidation. Actinides from soil solutions and large volume water samples were preconcentrated by DIPEX resin (Burnett et al., 1997). The extractant was removed from the resin by isopropanol, sodium hydroxide fusion was applied to oxidize the DIPEX, and actinides were precipitated using calcium phosphate. Actinides were separated on a UTEVA-TRU tandem column setup with variable recoveries (31%−1% for Pu, 22%−99% for Am, and 60%−85% for U). High Pu recoveries (>80%) were reported by Qu et al. (1998) after Pu and Am preconcentration from human tissue by the DIPEX resin, followed by the separation of Pu using anion exchange chromatography.

b. DIPHONIX resins

DIPHONIX resin (Chiarizia et al., 1997; Horwitz et al., 1997) is the chelating ion exchange resin containing the geminally substituted diphosphonic acid groups chemically bound to a styrenic-based polymer matrix. The DIPHONIX capacity factors for the actinide retention from dilute acids are close to those of its analog the DIPEX resin. The DIPHONIX resin received limited application due to problems with the removal of actinides, which can be eluted with strong complexing agents (e.g., HEDPA (1-hydroxyethylidene diphosphonic acid). Kim et al. (2000) oxidized HEDPA by ozonation or by Fenton's reagent to remove actinides from the DIPHONIX after

preconcentration. Although large loss of uranium was found, high recoveries (~85%) for Am, Pu, and U and high selectivity for Am, Pu, and U separation from large soil and sediment samples were claimed. Maxwell and Nichols (2000) applied a microwave digestion technique to remove actinides from the DIPHONIX resin. Actinides were separated using TEVA-UTEVA-TRU columns from large soil samples with high selectivity, consistent tracer recoveries, and minimal waste. High recoveries (70%−78%) for Am and inconstant (37%−93%) for Pu were reported for actinide stripped from DIPHONIX resin with 6 mol L^{-1} HNO_3 and 4 mol L^{-1} HCl/0.015 mol L^{-1} $TiCl_3$, respectively.

c. DGA resins

DGA resins (Horwitz et al., 2005) consists of *N*,*N*,*N*′,*N*′-tetra-octyldiglycolamide sorbed onto Amberchrom CG-71 resin (DGA Resin, Normal) or *N*,*N*,*N*′,*N*′-tetrakis-2-ethylhexyldiglycolamide (DGA resin, branched). DGA can strongly retain Am ($k' > 10^4$ in concentrated > 1 mol L^{-1} HNO_3 solutions) and Pu(IV) ($k' > 10^3$ in 0.1−10 mol L^{-1} HNO_3). DGA resin can be used for the separation and purification of americium and curium from various complicated environmental matrices, such as soil and water.

Recently, a single DGA column method was developed to separate Am and Pu from soil and sediments (10 g) for alpha spectrometry and AMS measurements. Samples were digested with 16 mol L^{-1} HNO_3 at 110°C for 24 hours. Sodium nitrite was applied for oxidation state adjustment, and the load solution was 8 mol L^{-1} HNO_3/0.05 mol L^{-1} $NaNO_2$. The column was subsequently rinsed with 8, 3, and 0.1 mol L^{-1} HNO_3, then Am was eluted with 0.1 mol L^{-1} HCl, and finally, Pu was stripped with 0.1 mol L^{-1} HCl/0.02 mol L^{-1} $TiCl_3$. NdF_3 coprecipitation was used for alpha spectrometry source preparation and adapted as the source for AMS. A simple chemical separation method in combination with the solid phase extraction (SPE) vacuum manifold resulted in a separation turnover of a total of 60 samples a day. The reported recoveries were 95 ± 10−99 ± 6 for Am and 97 ± 5−98 ± 6 for Pu. This method enabled the reduction of the amount of waste solutions generated during the procedure, as well as the time and costs required to separate these analytes. The method was validated using standard reference materials IAEA-384 and IAEA-385 obtained from the International Atomic Energy Agency (Kazi et al., 2014).

A rapid method using stacked TEVA-TRU-DGA cartridges for the determination of actinides in large soil samples (up to 200 g) by alpha spectrometry was reported by Maxwell and Culligan (2006) and Maxwell (2008a). The technique involves NaOH fusion followed by actinide preconcentration with $Ce(OH)_3$, coprecipitation with CeF_3, and dissolution in 8 mol L^{-1} HNO_3. Th and Pu(IV) ware separated on TEVA, whereas Am/Cm separated with the TRU-DGA multistage column. Americium eluted from TRU with 4 mol L^{-1} HCl was transferred to the DGA column and stripped from DGA with diluted 0.25 mol L^{-1} HCl solution. Recoveries for the whole procedure were 76%−98% for Am and 61%−92% for Pu. A similar technique was applied for the analysis of water (up to 1 L) samples (Maxwell, 2006).

A rapid method for the separation and preconcentration of actinides in urine samples was developed for measurements of longer-lived actinides (^{239}Pu, ^{242}Pu, ^{237}Np, ^{243}Am, ^{234}U, ^{235}U, and ^{238}U) by ICP-MS and short-lived actinides (^{236}Pu, ^{238}Pu, ^{239}Pu, ^{241}Am, ^{243}Am, and ^{244}Cm) by alpha spectrometry (Maxwell and Jones, 2009). The stacked TEVA-TRU-DGA resin columns and vacuum box technology were used to ensure rapid separations. From large urine aliquots (100 mL), actinides were preconcentrated with calcium phosphate. The final load solution contained 3 mol L^{-1} HNO_3/1 mol L^{-1} $Al(NO_3)_3$. The reduction/oxidation cycle using sulfamic acid and ascorbic acid to reduce Pu to Pu(III), ferric nitrate to facilitate ^{237}Np (if separation was desired) reduction to Np(IV), and sodium nitrite to oxidize Pu to Pu(IV) was applied. Pu/Np and Th were separated on TEVA, and Pu/Np was stripped with 0.25 mol L^{-1} HCl−0.005 mol L^{-1} HF−0.0001 mol L^{-1} $TiCl_3$. Am/Cm was eluted from TRU resin onto DGA resin with 4 mol L^{-1} HCl. The TRU resin cartridges were removed, and the DGA resin was rinsed with 1 mol L^{-1} HNO_3 and 0.1 mol L^{-1} HNO_3 to remove any residual uranium. Am and Cm were eluted using 0.25 mol L^{-1} HCl. The application of DGA allows Am/Cm elution with 0.25 mol L^{-1} HCl, which is more suitable for ICP-MS measurements, and can provide additional decontamination from U. The simplicity, speed (24 samples in <3 h), and high recoveries (>90%) of this method make it attractive for radiological emergency response. A multidimensional (MD) separation method using TEVA/DGA EC for the analysis of actinides in environmental samples was developed and tested for alpha spectrometry and ICP-MS. To remove interferences and enable proper identification and quantification, actinides (Th, U, Np, Pu, and Am) were separated after oxidation state adjustment firstly in 9 M HCl, and secondly in 3 M HNO_3. High separation selectivity and recoveries (98, 100, 94, 98, and 99 ± 2% for Th, U, Np, Pu, and Am, respectively, were achieved. Reusability of the resins was found to be ≤ 9. The separation technique was tested on reference material (CRM-IAEA-384). Data obtained of actinide measurements by alpha spectrometry and ICP-MS agreed well with absolute relative bias of 1.9%−23% (Guérin and Dai, 2013).

A rapid simplified method for the determination of Pu and Np in water samples using a stacked column set of TEVA and DGA resins was developed by Maxwell et al. (2011a). Pu(IV) and Np(IV) were retained on a TEVA

column, and then Pu was reduced to Pu(III) and transferred to a DGA column together with U. From the DGA, U was eluted with 0.1 mol L^{-1} HNO_3 and Pu(III) was stripped with 0.02 mol L^{-1} HCl/0.005 mol L^{-1} HF/0.0005 mol L^{-1} $TiCl_3$. ^{239}Pu, ^{242}Pu, and ^{237}Np were measured by ICP-MS, whereas ^{236}Pu, ^{238}Pu, and ^{239}Pu were counted by alpha spectrometry. High recoveries and DFs for U (from Np—10^4 and Pu—10^5) were reported. The TEVA and DGA resin column method was also applied for the separation Pu, Np, and Am from 10 to 20 g completely dissolved soil samples using sodium hydroxide fusion (Maxwell et al., 2015). The method has allowed the reduction of sample time processing and enabled lower detection limits for plutonium, neptunium, and americium in environmental soil samples.

Stacked TEVA, TRU, and DGA resin cartridge separation techniques followed by accelerated furnace heating, a rapid sodium hydroxide fusion method, and a lanthanum fluoride matrix removal step were widely applied for rapid actinide analyses in environmental, food, and bioassay matrices using alpha and/or mass spectrometry (Maxwell et al., 2011b, 2012, 2013, 2014). Chemical separation using TRU, DGA-N, and DGA-B EC resins was also employed to remove interfering elements, including Bi, Hf, Hg, Pb, Pt, Pu, and Tl in the complex environmental samples prior to ^{241}Am measurements by mass spectrometry (Wang et al., 2017).

5. Combined procedures for the determination of neptunium and other actinides

The separation of radionuclides from complex environmental matrices usually requires a combination of methods to ensure sufficient decontamination or separation of several elements from a single sample. There are a huge number of combined procedures, many of which have been discussed above as examples of particular techniques and in various reviews dedicated to a certain radionuclide. Various combinations of ever developed techniques have been used for the separations, if they produced a positive result: solvent extraction and anion exchange chromatography or EC, two-, three-stage columns were frequently used for actinide separation. However, newly developed highly selective materials allow the efficient separation of actinides from 10 g soil using a single DGA column (e.g., Kazi et al., 2014). Nevertheless, combined procedures are still in range, due to various reasons, involving newly developed techniques and conventional methods.

The TEVA-UTEVA-TRU column set was applied for the separation of actinides by Horwitz et al. (1995). Later, various modifications of this method or new developments were applied for the analysis of radionuclides in environmental and biological samples (e.g., Mathew et al., 1981; Smith et al., 1995; Moody et al., 1998; Pilvio and Bickel, 1998; Maxwell and Culligan, 2006; Maxwell, 2006; Lee et al., 2007; Maxwell, 2008b; Maxwell and Faison, 2008, Maxwell et al., 2010a,b,c; 2011c; La Rosa et al., 2010; Qiao et al., 2014 etc).

Recently developed combined methods, most frequently based on DGA resin due to its high affinity for actinides (as mentioned above), are cost-effective, extremely selective, fast (to meet emergency response requirements) and produce sources suitable for measurements using alpha and mass spectrometry.

A new and rapid separation method for ^{234,235,236,238}U, ^{230,232}Th, ^{239,240}Pu, ^{237}Np, ^{241}Am, and ^{90}Sr using TEVA-DGA columns was reported by Habibi et al. (2015). After Pu and Np oxidation state adjustment to Pu(IV) and Np(IV), samples were loaded on TEVA-DGA in 3 mol L^{-1}. Th(IV), Pu(IV), and Np(IV) were retained on the TEVA resin, whereas Am(III), U(VI), and Sr(II) on the DGA one. The matrix elements were removed by washings with 3 mol L^{-1} HNO_3. Columns were separated, the following fractions were obtained: (1) Th, Np, and Pu were eluted with 2.5 m mol L^{-1} HEDPA as the fraction from TEVA, (2) U and Sr were stripped from the DGA column with 0.1 mol L^{-1} HNO_3, (3) Am, Y, and Zr (naturally present in the sample) were eluted from the DGA using 2.5 m mol L^{-1} HEDPA. The three fractions can be measured immediately after their collection due to compatibility with ICP-MS. The overall yields exceeded 80% for all radionuclides. The radiochemical separation time (including counting time) required < 7 hours for eight river water samples analyses.

The extraction behavior of interfering elements on TEVA resin; decontamination of U using TEVA, UTEVA, and DGA resins; and the effect of coprecipitation on Pu detection using ICP-MS were studied by Wang et al. (2017a) with the aim of developing a new chemical separation method for rapid Pu determination in soil and sediment samples. The developed method involved: HNO_3 leaching; CaF_2/LaF_3 coprecipitation to remove matrix elements and U; the TEVA + UTEVA + DGA procedure for the removal of U, Pb, Bi, Tl, Hg, Hf, Pt, and Dy; and ICP-MS measurements. The method was tested for $^{239+240}$Pu activity as well as for ^{240}Pu/^{239}Pu and ^{241}Pu/^{239}Pu isotopic ratio measurements by analyzing soil, freshwater sediment, and ocean sediment standard reference materials. These studies resulted in stable and high Pu recoveries (90%−97% for soil; 92%−98% for sediment) and high DF of U (1.6×10^7) and the short analytical time of 12 hours. In addition, the lowest detection limits yet reported in the literature estimated for ^{241}Pu on the basis of a 1 g soil sample of 0.56 μBq g^{-1} (0.24 fg g^{-1}) for ^{239}Pu, 1.2 μBq g^{-1} (0.14 fg g^{-1}) for ^{240}Pu, and 0.34 mBq g^{-1} (0.09 fg g^{-1}) were achieved.

Stacked columns of AGMP-1M-DGA resins were used to simultaneously separate Pu and Am/Cm from a complex

matrix of large-size soil and sediment samples (20 g) with total sample dissolution using lithium metaborate fusion (Luo et al., 2018). Matrix elements were successfully removed using hydroxide and CeF_3 coprecipitation. The oxidation state was adjusted with $NaNO_2$, then the sample was loaded onto AGMP-1M-DGA columns, and the columns were rinsed with 8 mol L^{-1} HNO_3 and disconnected. From the AGMP-1M column, Th was eluted with 12 mol L^{-1} HCl followed by Pu stripping with 0.2 mol L^{-1} HNO_3+0.05 mol L^{-1} HF and Pu coprecipitated with HTiO. The precipitate was dissolved in 1 mL of concentrated HNO_3, and after oxidation state adjustment with $NaNO_2$, the sample was loaded onto a preconditioned 0.1g TEVA column. The column was rinsed with 12 mol L^{-1} HCl and 8 mol L^{-1} HNO_3. Finally, Pu was eluted with 0.1 mol L^{-1} HCl+0.05 mol L^{-1} HF. An aliquot of 1 mL of the Pu eluate was used for analysis of ^{239}Pu and ^{240}Pu by ICP-MS and the rest—for the counting by alpha spectrometry. From the DGA resin, after rinsing with 11 mol L^{-1} HCOOH to remove the residual HNO_3 and $NaNO_2$, Am and Cm were eluted together with a prepared solution (20 mL of 0.05 mol L^{-1} HCOOH, 10 mL of 12 mol L^{-1} NH_4SCN, and 0.5 mL of 4 mol L^{-1} HCOOH). The solution was loaded onto on anion AGMP-1 M resin column and preconditioned with 2 mol L^{-1} NH_4SCN+0.5 mol L^{-1} HCOOH. The column was rinsed with 1.5 mol L^{-1} NH_4SCN+0.5 mol L^{-1} HCOOH to remove lanthanides, and Am/Cm was then eluted with 0.25 mol L^{-1} HCl. Then, an additional purification was performed using coprecipitation with HTiO, and TEVA and DGA columns (filled with 0.1 g of resin). Am/Cm was eluted from the DGA resin with 0.05 mol L^{-1} HCl. The solution was used for alpha counting source preparation by CeF_3 microprecipitation. The reported average chemical recoveries were 84 ± 10% for Pu and 91 ± 7% for Am. The estimated time required for analysis of a batch of 12 samples, including coprecipitation and separation, was typically 2.5 days.

An analytical method for simultaneous determination of Cs and Pu isotopes in river suspended particles of small sample size (1−2 g) was developed to monitor the transport and fate of ^{135}Cs and ^{137}Cs as well as ^{239}Pu and ^{240}Pu in the land−ocean system (Cao et al., 2016). Cs and Pu were sequentially preconcentrated using ammonium molybdophosphate and ferric hydroxide coprecipitation, respectively. Two-stage anion exchange (using AG 1x8-AG MP-1) chromatography was applied for Pu chemical separation and purification for Pu separation and purification (Bu et al., 2013). Pu was eluted from AG MP-1 with concentrated HBr. The sample was evaporated, heated to destroy HBr traces, and redissolved in 4% HNO_3 in the preparation for measurements, and finally, Cs and Pu isotopes were measured by ICP-MS/MS and SF-ICP-MS, respectively. The developed method allowed the removal of the interfering elements of U ($^{238}U^1H^+$ and $^{238}U^2H^+$ for ^{239}Pu and ^{240}Pu, respectively) and Ba ($^{135}Ba^+$ and $^{137}Ba^+$ for ^{135}Cs and ^{137}Cs, respectively) with DFs of $1-8 \times 10^6$ and 1×10^4, respectively. Soil reference materials were used to test the method. The detected ^{135}Cs/^{137}Cs and ^{240}Pu/^{239}Pu atom ratios and ^{239,240}Pu activities were a good agreement with the certified/information values. In addition, the developed method was employed for the determination of Cs and Pu in the suspended particles in land and water samples collected from Fukushima Prefecture after the FDNPP accident. The ^{135}Cs/^{137}Cs atom ratios (0.329−0.391) and ^{137}Cs activities (23.4−152 Bq g^{-1}) indicated that the contamination of the suspended particulate matter was mostly derived from the FDNPP accident, whereas ^{240}Pu/^{239}Pu atom ratios (0.182−0.208) were of global fallout origin. Cs isotopes were separated using AGMP-1M −AG 50Wx8 resin columns. Mo, Sb, and Sn were retained on the AGMP-1M anion exchange column, whereas Cs was adsorbed on AG 50Wx8 cation exchange column. The AG 50Wx8 column was rinsed with 1 mol L^{-1} NH_4OH, and H_2O and Cs were eluted with 1.5 mol L^{-1} HCl, whereas Ba remained on the AG 50Wx8 resin.

A rapid method for ultratrace Pu detection in urine sample with high ^{238}U decontamination factor ($DF = 3.8 \times 10^6$) was reported (Ni et al., 2018). The technique involves acid digestion, coprecipitation with CaF_2/LaF_3, EC separation (based on the method by Wang et al., 2017b), and SF-ICP-MS measurements. The separation of Pu was performed using TEVA-UTEVA-DGA resin cartridges. TEVA-UTEVA-DGA resins were preconditioned with 3 mol L^{-1} HNO_3. The sample was loaded onto the TEVA resin followed by rinses with 3 mol L^{-1} HNO_3 to remove Ca, Fe, and rare earth elements, 1 mol L^{-1} HNO_3 to remove U, Pb, Tl, and Pt, and 9 mol L^{-1} HCl to remove Th, Bi, and Hf. The TEVA (1) was connected to UTEVA (2) and DGA (3) cartridges, and 3 mol L^{-1} HNO_3−0.1 mol L^{-1} ascorbic acid−0.02 mol L^{-1} Fe^{2+} was used to elute Pu from TEVA resin onto DGA resin by reducing it from Pu(IV) to Pu(III). From the DGA resin, U was eluted with 0.1M HNO_3, and finally, Pu was stripped with 0.5M HCl−0.1M $NH_2OH{\cdot}HCl$. The final eluent was evaporated and redissolved in 0.7 mL of 4% ultrapure HNO_3 with 0.02 ng mL^{-1} Rh as internal standard in preparation for SF-ICP-MS measurement.

The ^{242}Pu recovery was stable for 20 and 100 mL urine bioassays with an average value of 72.7 ± 5.5%. The reported detection limits for ^{239}Pu, ^{240}Pu, and ^{241}Pu were 0.016, 0.016, and 0.019 fg mL^{-1} for 20 mL as well as 0.003, 0.002, and 0.003 fg mL^{-1} for 100-mL urine samples, respectively. The time required for completing procedures for 20- and 100-mL urine bioassays were 9.5 and 11 hours, respectively, and 1 day for analysis of 10 samples. The developed technique can become a promising tool

for rapid response to radiological emergencies and rapid screening of unexpected occupational exposures due to low detection limits and high sample throughput.

A new sequential separation method was developed for the determination of Po and Pu, Am, and U in drinking water samples for emergency response or routine water analyses (Benedik et al., 2009; Fernández et al., 2012; Lemons et al., 2018). TEVA chromatography was for the first time applied to polonium and plutonium separation. This method involves a rapid Fe^{3+} coprecipitation to remove matrix interferences, Pu oxidation state adjustment to Pu(IV), and an incubation (~1 hours at 50–60°C) for Po(II) to turn to Po(IV). The Po and Pu were separated on a TEVA column, whereas Am and U separation was performed on a TRU column. Microprecipitation of Po with copper sulfide (CuS) and micro-coprecipitation of actinides using neodymium fluoride (NdF_3) were applied for source preparation for alpha spectrometry measurements (Lemons et al., 2018).

6. Source preparation

Proper source preparation is an important part of sample processing, as it can improve DFs for the entire procedure and provide accurate measurements. There are three known methods for the preparation of a source for alpha spectrometry: evaporation, microcompound, and electrodeposition. Coprecipitation using a microcrystalline precipitate and electrodeposition methods are most often used to obtain a source for alpha spectrometry (ASTM standards D3084-05).

Micro-coprecipitation of actinides on rare earth fluorides (Nd, Ce, or La), often with NdF_3, followed by filtration on a smooth surface membrane filter of fine pore size (0.1–0.2 μm), yields a good-quality alpha source (ASTM Test Method C1163, Sill, 1987a,b; Hindman, 1983). The membrane filter preconditioning can improve peak resolution. The preparation of sources for alpha spectrometry involves NdF_3 coprecipitation, the filter pretreatment with CeF_3, or NdF_3 substrate solution and filtration through a 0.1-μm membrane filter. CeF_3 microprecipitation for the preparation of Am/Cm sources for alpha spectrometry is described by Dai, X. (2011). The most frequently used method for Ra source preparation is coprecipitation with $BaSO_4$ (Sill, 1987a,b).

During the electrodeposition procedure, actinides are electrochemically plated from an electrolyte solution onto a cathode planchet of polished metal (usually stainless steel). The anode is typically Pt wire or gauze, often rotating to mix the solution; alternatively, sufficient agitation can be provided by gas formed at the anode. Electrodeposition is usually carried out at a constant current density (0.5–1 A cm^{-2}) and low voltage (<10 V) for ~2 h. A standard procedure for electroplating actinide ammonium sulfate solutions was published in 2000 and reapproved in 2010 (ASTM C1284-00). A variety of electrolytes (sulfate, oxalate, acetate buffers, etc.) and electrodeposition cells (depending on the size of cathode) have been used. Deposition recoveries are usually in the range from 90% to 99% depending on the method.

Recently developed setups for the electrodeposition involve disposable electrodeposition cells made from scintillation vials, an ultrasonic bath, and a rotating Pt anode based on the methods by Talvitie (1972), Hallstadius (1984), and Tomé and Sanchez (1991).

Optimization of electrodeposition procedures for the preparation of ^{238}U sources for high-resolution alpha particle spectrometry indicated that the best energy resolution was achieved with sources produced in saturated NH_4NO_3, on polished stainless steel discs using a spirally wound platinum anode (Jobbágy et al., 2012). The best sources were in a diameter of ~20 mm with a maximum surface density of 26 μg cm^{-2}.

The optimized copper sulfide (CuS) microprecipitation (0.05 mg of Cu^{2+} in 10 mL of 1 M HCl) was applied to prepare thin-layer polonium (Po) sources for alpha spectrometry counting (Guérin and Dai, 2013). It was reported that the procedure is simple as well as faster, cheaper, and more convenient in comparison with the traditional spontaneous plating on metallic discs, and the obtained yields were comparable (80%–90%). The effects of Cu^{2+}, Ag^{+}, Fe^{3+}, Fe^{2+}, Pb^{2+}, and Ni^{2+} on the yield and the resolution of the alpha peaks were estimated.

We may conclude at the end of this section that significant efforts have been made to assess the feasibility of detection techniques (e.g., alpha spectrometry and mass spectrometry), to compare and evaluate or/and reestimate the accuracy of conventional techniques, e.g., anion exchange and extraction chromatography as well as electrodeposition and coprecipitation for sample preparation (Oh et al., 2014; Krmpotić et al., 2018; Vasile et al., 2018).

A special attention has been paid to complete sample dissolution and to development methods for the separation of radionuclides from complex environmental samples as well as to estimate analyte losses at the all stages of sample preparation: digestion, separation, source preparation, and measurement (Epov et al., 2005a,b; Henricsson et al., 2011; Maxwell et al., 2011a,b,c; Wang et al., 2017b).

Recent studies have shown that ICP-MS can provide a relatively fast and accurate determination of long-lived actinides in environmental samples (see also Section IV.B). New developments in the online detection system showed obvious advantages and led to a high sample throughput in comparison with other radiometric and mass spectrometric techniques. Progress in the analytical separation, careful selection of eluents compatible with the mass spectrometric approach, and the use of highly selective EC materials, such as DGA, TEVA, and UTEVA allow a significant reduction in problems associated with

interferences and matrix effects (Ito et al., 2011; Habibi et al., 2015; Wang et al., 2017a; Ni et al., 2018). Measurements of isotope ratios (e.g., $^{239}Pu/^{240}Pu$ and $^{236}U/^{238}U$) by ICP-MS to estimate the source of radionuclides in the environment are the most promising for future applications (Yang et al., 2017); however, a combination of alpha and mass spectrometric techniques is useful in determining plutonium isotope ratios, including $^{238}Pu/^{239}Pu$ (Esaka et al., 2017).

Progress in recent developments of new AMS methods to measure actinides in environmental samples (see also Section IV.C) benefits the future application of this sensitive analytical technique at ultratrace levels required for environmental studies (Quinto et al., 2009; Christl et al., 2014; Kazi et al., 2014; Cornett et al., 2015; Schneider et al., 2017). The development of new automatic systems with the use of new advanced materials and technologies in combination with improved analytical methods (e.g., a single DGA column) will provide lower detection limits, increase the analytical throughput of environmental samples, and reduce the cost of analysis (e.g., Qiao et al., 2011; Yang et al., 2016).

Recently developed radioanalytical procedures can provide sources of equally high quality, both for alpha and mass spectrometric measurements. Nevertheless, in the case of inadequate quality of a source, the nondestructive alpha spectrometry method allows for additional purification of the sample. Despite the fact that general trends indicate a rapid improvement of mass spectrometric techniques, alpha spectrometry will remain in demand as a simple, cost-efficient, and highly selective technique for a long time.

New methods based on modern materials, such as the dibenzo-18-crown-6 ether (DB-18CE-6)-functionalized silica (SiO_2) disk for the rapid analysis of ^{226}Ra by alpha spectrometry and a phosphate–sulfate bifunctional polymer layer surface-grafted membrane, suitable for the alpha spectrometric measurements due to high affinity for Pu(IV), are rather promising for the future monitoring and rapid response to radiological emergencies (S. Paul et al., 2015; Mohamud et al., 2017).

7. Examples of actinides in the environment

a. Uranium-236 in terrestrial waters

Uranium-236 is the most commonly applied isotope of uranium in environmental trace studies, both in the terrestrial and in the marine environments. Latest developments in AMS and radiochemical separation techniques have enabled the reliable determination of ^{236}U concentrations even in relatively small water samples (1.5–2 L), supporting the potential of this radionuclide to be a very good tracer of hydrological processes. If we look at the results of recent measurements of ^{236}U and natural uranium in terrestrial waters, we can see that the $^{236}U/^{238}U$ ratios are higher for rivers (rivulets) than for seas and oceans (Table 3.14). Such a difference may be attributed to the surface runoff of global fallout ^{236}U deposited on land, which is accumulated in rivers, but diluted in oceans by large amounts of natural uranium. The values of the $^{236}U/^{238}U$ isotopic ratio above 10^{-9} indicate that the samples were clearly affected by anthropogenic nuclear activities, expect the sample from Gastein whose ratio was determined to be by a factor of about 10 times lower than for high-grade ore (Steier et al., 2008). Very high concentrations of ^{236}U found in Irish Sea is due to the contribution of the Sellafield reprocessing plant (Eigl et al., 2013, 2016).

b. Transuranics on atmospheric aerosols

Measurements of transuranics in aerosol samples started after nuclear weapon tests when large amounts of anthropogenic radionuclides were released into the atmosphere, which led to global fallout with impact on the total environment. The burn-up of the SNAP 9A satellite in the

TABLE 3.14 Concentration of ^{236}U and $^{236}U/^{238}U$ isotope ratios in various water samples.

Sample	Sample type	$^{236}U/^{238}U$	^{236}U (mBq L^{-1})	^{236}U (atom L^{-1})
Rio Negro	River	2.73×10^{-8}	4.9×10^{-6}	5.2×10^{6}
Danube	River	1.08×10^{-8}	2.3×10^{-5}	2.5×10^{7}
Salzburg	Rivulet	$(2.1–11.4) \times 10^{-8}$	$(0.8–3.5) \times 10^{-4}$	$(0.8–3.7) \times 10^{8}$
	Well water	2.1×10^{-8}	1.1×10^{-4}	1.2×10^{8}
Gastein	Well water	$(6.2–7.0) \times 10^{-12}$	–	–
Black sea	Seawater	3.63×10^{-9}	2.8×10^{-5}	3.0×10^{7}
Irish sea	Seawater	2.04×10^{-6}	1.3×10^{-2}	1.4×10^{10}
Hawaii	Seawater	5.74×10^{-9}	3.5×10^{-5}	3.8×10^{7}

After Steier et al. (2008); Srncik et al., 2010; Eigl et al. (2013).

atmosphere had a global impact as well, as it caused a several-fold increase in the $^{238}Pu/^{239,240}Pu$ activity ratio in 1964. Contributions of other sources, e.g., from the Chernobyl and Fukushima accidents, had only local/regional or continental impacts, similarly, as well as accidents of US warplanes in Greenland and Spain carrying Pu (UNSCEAR, 1982; Vintró et al., 2000).

Temporal variations of $^{239,240}Pu$ concentrations in stratospheric and surface air of the Northern Hemisphere have recently been summarized by Hirose and Povinec (2015). The highest Pu activity concentrations were detected in the upper stratosphere at 20–40 km height in 1963 (Fig. 3.67), following the former Soviet Union large-scale atmospheric nuclear weapon tests in Novaya Zemlya in 1961 and 1962. An increase in stratospheric $^{239,240}Pu$ activities (Fig. 3.67B) was also observed after the Chinese nuclear tests (6.5 Mt in October 14, 1970, 2.5 Mt in June 27, 1973, and 4 Mt in November 17, 1976) in the 1970s (UNSCEAR, 2000). It is believed that fine aerosol particles carrying radionuclides could remain in the stratosphere until the 2000s. To support this hypothesis, Alvarado et al. (2014) measured the increase in Pu activity concentrations in the troposphere, observed during the Eyjafjallajökull eruption in Iceland in 2010, which was explained by the scavenging effect of volcanic ash particles on stratospheric aerosol carrying Pu isotopes and their increased transport into the troposphere. After careful analyses of long-term experimental data, including measurements during volcanic eruptions, published by different laboratories, Hirose and Povinec (2015) showed that the activities of stratospheric plutonium exponentially decreased with an apparent residence time of 1.5 ± 0.5 years. Authors concluded that the surface plutonium until the early 1980s was controlled by the stratospheric inputs, while global dust events and biomass burning were responsible for wide variations in the lower stratospheric and upper tropospheric activity concentrations and ratios of Pu isotopes in the 2000s. The mean tropospheric residence time of 71 days was estimated for plutonium-bearing aerosol particles after atmospheric nuclear weapon tests, consistent with other researches (Holloway and Hayes, 1982; Warneke et al., 2002).

Activity concentrations of ^{238}Pu, $^{239,240}Pu$, and ^{241}Pu in aerosol samples collected at Sodakylä, Finland (67°22′N, 26° 39′E) in 1963 were $<0.1-3.6 \pm 0.5$ μBq m^{-3}, $0.4 \pm 0.1-95 \pm 3$ μBq m^{-3}, and $<16-1730 \pm 70$ μBq m^{-3}, respectively. Clear seasonal variation with the highest activities found in spring and summer was explained by the springtime-enhanced transport of plutonium-bearing aerosol particles from the stratosphere to the troposphere. The reported $^{238}Pu/^{239,240}Pu$ activity ratios (from 0.014 ± 0.003 to 0.32 ± 0.11) were characteristic of the global fallout from nuclear weapon testing (Salminen and Paatero, 2009).

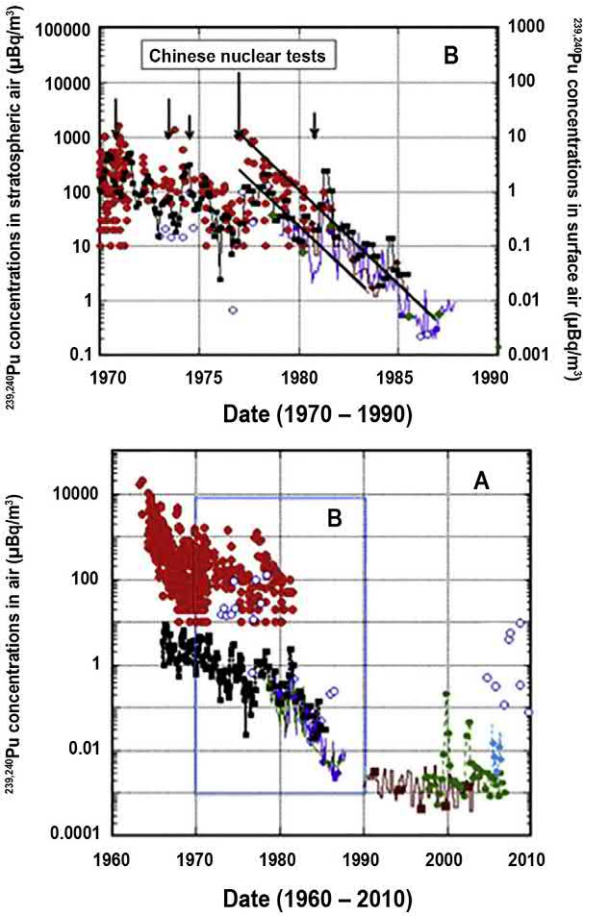


FIGURE 3.67 Temporal variations of $^{239,240}Pu$ concentrations in stratospheric and surface air of the Northern Hemisphere (after Hirose and Povinec, 2015). Closed red circles: the upper stratosphere, 20–40 km height (Leifer and Juzdan, 1986; EML, 1999); open blue circles: the lower stratosphere, 10.1–14.2 km height (Alvarado et al., 2014); closed black squares: the surface air, New York (EML, 1999); brown closed rhombic: the surface air Beaverton Oregon (EML, 1999); green closed rhombic: the surface air, Milford Haven (Playford et al., 1993); purple squares: the surface air, Tsukuba (Hirose and Sugimura, 1984, 1990); brown closed squares: the surface air (Wershofen and Arnold, 2005); green closed circles: the surface air, Prague (Hölgye, 2008); blue closed rhombic: the surface air, Vilnius (Lujaniene et al., 2006, 2012a). For the color version of the figure, the reader is referred to the online version of the book. *Licensed under a Creative Commons Attribution 4.0 International License.*

The $^{240}Pu/^{239}Pu$ atom ratio in air filters collected at Sodankylä in 1963 (later measured using SF-ICP-MS) ranged typically from 0.15 ± 0.01 to 0.30 ± 0.06, indicating that global fallout was the main Pu source (Salminen-Paatero et al., 2012). Transport of aerosol particles from the Novaya Zemlya test site as a possible source of Pu pollution was identified by a set of three-dimensional air mass back-trajectories ending at Sodankylä during 1963 calculated using the trajectory model Hybrid Single-Particle Lagrangian Integrated Trajectory (HYSPLIT).

Plutonium and uranium concentrations and atom ratios in archived air filters collected at ground level at nine stations in Norway during 1957−58 and 1961−62 (measured using AMS) showed large variations of ^{236}U (0.17−23 nBq m^{-3}) and $^{239,\ 240}$Pu (1.3−782 μBq m^{-3}). The ^{240}Pu/^{239}Pu (0.0517−0.237) and ^{236}U/^{239}Pu (0.0188−0.7) atom ratios indicated tropospheric fallout from the Semipalatinsk or Novaya Zemlya test sites (Wendel et al., 2013).

Alteration in data on activity concentrations and ratios obtained by different researches can be attributed to sampling location, season, and duration as well as to the efficiency of used filters for submicron particles (typical for stratospheric aerosols), the losses of which can significantly alter Pu isotopic ratios and result in incorrect estimation of the contamination source (Valmari et al., 2002; Hirose and Povinec, 2015).

The main source of the ^{238}Pu in the stratosphere was derived from the burn-up of the SNAP-9A satellite over the South Pacific Ocean in 1964, as the nuclear test-derived ^{238}Pu constituted only about 2% of the stratospheric inventory of ^{238}Pu in 1966 (Krey, 1968). It was reported that about 24% over the northern hemisphere and about 76% of the SNAP-9A-derived ^{238}Pu was deposited over the southern hemisphere during the period from 1965 to 1986 with a residence time of 1.2 years (Thakur et al., 2017) or with apparent stratospheric residence time of 1.7 ± 0.4 years (Hirose and Povinec, 2015). Higher activities of ^{238}Pu detected in the lower stratosphere during the 2000s resulted not from the SNAP-9A burn-up accident or the atmospheric nuclear weapon tests, but from other unknown sources. The ^{238}Pu activity concentrations in surface air in 1990−2007 measured by Kierepko et al. (2016) in Krakow (Poland) ranged from 0 to 2.1 μBq m^{-3} (average value of 0.00024 μBq m^{-3}) and in Bialystok (Poland) varied from 0.059 to 87.1 μBq m^{-3} (average value of 0.002 μBq m^{-3}). Low activities of ^{238}Pu in surface air were also found in Prague (Hölgye, 2008) and in Braunschweig (Wershofen and Arnold, 2005). However, unusually high ^{238}Pu concentrations were detected in air samples in Paris in 1988, in samples collected at Astana (51.2°N, 71.4°E, Kazakhstan, about 600 km west from Semipalatinsk) in 2001, at Mayak and other Siberian regions (Martin and Thomas, 1988; Oughton et al., 2001; Salminen et al., 2004).

The southern hemisphere was less polluted by radionuclides since 90% of the nuclear weapon tests were conducted in the northern hemisphere. The southern hemisphere data from the French monitoring Program at Mururoa Island (1986−1991) in the South Pacific and from the Environmental Measurement Laboratory (EML) database (1965−1985) were summarized by Thakur et al. (2017). The EML is now the National Urban Security Technology Laboratory.

After the Chernobyl accident, an increase in the ^{239,240}Pu activity concentrations in the surface air was detected at many European monitoring stations (Sinkko et al., 1987; Rosner et al., 1990. Irlweck et al., 1993; Manić-Kudra et al., 1995) with the highest activities up to 140 μBq m^{-3} found at Dukovany, located about 200 km southeast of Prague (Hölgye and Filgas, 1987). High activities of actinides (up to 10,000 μBq m^{-3} for Pu) detected in aerosol samples in Vilnius were attributed to the short distance (∼480 km) from the damaged reactor and transport of "hot" particles (on large-diameter aerosols) of different activities and composition (Lujaniene et al., 2009). A large number of "hot" particles (up to 10,000 particles per m^3), including ^{233}U, ^{234}U, ^{235}U, ^{238}Pu, ^{239}Pu, ^{240}Pu, ^{241}Pu, ^{242}Cm, and ^{244}Cm, were found in air filters exposed on April 28−29 and on April 30, 1986 (Lujanas et al., 1994). Measurements of ^{238}Pu/^{239,240}Pu activity (0.44−0.50) and ^{240}Pu/^{239}Pu atom (0.41−0.42) ratios confirmed that Pu in "hot" particles was derived from the Chernobyl accident. In spite of the fact that "hot" particles of 0.5−150 μm in diameter were mainly deposited within the 30-km restriction zone (Sandals et al., 1993), they were detected in the former USSR and many European countries (Lujanas et al., 1994; Pöllänen et al., 1997, 2002; Gerstmann et al., 2004; Salminen-Paatero et al., 2012).

Measurements of ^{240}Pu/^{239}Pu atom ratio (0.13 ± 0.01−0.53 ± 0.03) in aerosol, lichen, peat, grass, and hot particle samples collected in Finland immediately after the Chernobyl accident in 1986 showed the global fallout from nuclear weapon testing and deposition from the Chernobyl accident as the main Pu sources (Salminen-Paatero et al., 2012). The contribution of the Chernobyl-derived ^{239}Pu in aerosol, grass, and two hot particle samples was estimated to be 90%, 100%, 75%, and 100%, respectively.

Activity concentrations of ^{239,240}Pu in surface atmosphere at Milford Haven, Neuherberg, and Braunschweig in 1986−2003 were <2.5−9.5, 0.53−8.1, and 0.39−4.5 nBq m^{-3}, respectively (Playford et al., 1993; Pan and Stevenson, 1996; Wershofen, and Arnold, 2005), whereas higher activities from 0.53 to 217 nBq m^{-3} were found in Prague during the period from 1997 to 2006 (Hölgye, 2008). A decrease of the Chernobyl-derived radionuclides in the atmosphere was observed about 1 year after the accident, and variations in the airborne activity concentrations were linked to the resuspension, dust storms, and biomass burning events (Lujaniene et al., 1999, 2009).

b. Transuranics in soil

Transuranics in soil varied widely depending on the distance from the Chernobyl and on the meteorological conditions at different locations during the accident and passage of the Chernobyl plume. The observed contamination levels presented in several publications

(e.g., De Cort et al., 1998) provide useful information on the behavior of radionuclides of global fallout and after the Chernobyl accident in soil. Great efforts have been made to study the migration behavior of Pu, Am, and Np in soil after nuclear explosions and the Chernobyl accident (e.g., Livens and Baxter, 1988; Pavlotskaya et al., 1991, 1994, 1995; Bunzl et al., 1994; 1995; Lujaniene et al., 2002; Carbol et al., 2003). The effect of soil mineralogical and granulometric compositions, content of organic matter (including humic and fulvic acids), and speciation of radionuclides on the migration rate and bioavailability were studied in laboratory as well as in field experiments.

The sequential extraction procedure was used to study bonding of ^{239,240}Pu and ^{241}Am (derived from the global fallout) with various soil components in six successive layers of an undisturbed grassland soil. It was found that >57% of the studied radionuclides were mostly associated with the soil organic matter. The activity of actinides 30−40 years after their deposition in readily exchangeable fractions was <1% for Pu and on average by a factor of 7 higher for Am, and almost identical migration rates were found for both radionuclides (Bunzl et al., 1990, 1992, 1995).

The migration rates of the Chernobyl-derived ^{137}Cs and ^{239,240}Pu originated mainly from the atmospheric nuclear tests studied at three sites in undisturbed grassland soils in the Czech Republic. A compartment model was applied to calculate the migration rates of ^{239,240}Pu and ^{137}Cs. The migration rate studied in convection transport increased with depth for both radionuclides. The estimated migration rates of ^{239,240}Pu and ^{137}Cs, using the diffusion transport model, varied from 0.65 to 0.94 and from 0.18 to 0.99 cm year^{-1}, respectively (Hölgye and Malý, 2000).

The interaction of Am and Pu with organic matter in a gley soil from the west Cumbria (UK), with massic activities in its surface horizon of 5−10 kBq kg^{-1} for ^{239,240}Pu and comparable ^{241}Am levels, was investigated by Livens and Singleton (1991). Humic and fulvic acids were isolated by conventional alkali extraction and then studied by gel filtration, treatment with organic solvents, and differential flocculation procedures. Actinides were found to be bound mainly with clay-humite fractions. Am should be more mobile due to its greater association with fulvic acids. Higher ^{241}Am mobility as compared with Pu isotopes in the Chernobyl soil was reported by Lujaniene et al. (2002). Higher Chernobyl-derived ^{241}Am mobility was confirmed by measurements of ^{241}Am/^{239,240}Pu ratios in water and sediments in Finish lakes (Lehto, 2009; Lusa et al., 2009). In addition, authors reported higher ^{241}Am uptake by fish in comparison with Pu isotopes.

Complicated behavior of ^{137}Cs, ^{90}Sr, ^{241}Am, and ^{239,240}Pu radionuclides was reported from two radioactive fallout plumes at the Semipalatinsk test site. The studied radionuclides were mainly found in the soil fraction of 500−1000 μm, with enrichment factors ranging from 1.2 to 3.8, at the plume generated by the surface nuclear test, whereas radionuclides were associated with the soil fraction of 250−500 μm (enrichment factors 1.1 − 5.1) in samples from the plume where surface nuclear tests were not conducted (Kabdyrakova et al., 2018).

Transfer factors (Tfs) for ^{137}Cs, ^{90}Sr, ^{241}Am, and ^{239,240}Pu radionuclides obtained for the spots with different contamination type at the Semipalatinsk test site showed wide variations. The highest Tfs were characteristic of radioactive stream flows and warfare radioactive agent (WRA) test zones. The transfer factors decreased in the following order: ^{90}Sr > ^{137}Cs > ^{239,240}Pu > ^{241}Am; in addition, the ^{90}Sr Tf was higher by a factor of 8 in comparison with the ^{137}Cs Tf and by a factor of 16 as compared with the ^{239,240}Pu Tf, while the ^{239,240}Pu Tf exceeded the ^{241}Am Tf by a factor of 3. As an exception, the Tf of studied radionuclides decreased in the sequence: ^{90}Sr > ^{239,240}Pu > ^{137}Cs in the WRA test area (Larionova et al., 2018).

^{239,240}Pu and ^{137}Cs association with soil particles of different sizes was also studied in soil samples from the natural environment collected at two locations in China. The highest activities of ^{137}Cs and Pu isotopes were found in the fraction of < 2 μm. An increase in ^{239,240}Pu/^{137}Cs activity ratios in coarse soil fractions showed a lower transport potential for Pu isotopes as compared with the ^{137}Cs, indicating suitability of Pu isotopes for application as soil erosion tracers (Xu et al., 2017).

Recently, Pu isotopes were applied to estimated soil erosion rates in different regions (Meusburger et al., 2018; Portes et al., 2018).

Speciation of radionuclides (including redox speciations) in environmental samples was intensively studied to explain behavior as well as to predict migration and bioavailability (e.g., Moulin and Moulin, 2001; Choppin, 2007; Geckeis and Rabung, 2008; Kenna, 2009). Special interest was focused on the effect of microorganisms on the migration and speciation of radionuclides related to the prediction of radionuclide migration around the radioactive waste repositories and remediation of the contaminated sites (e.g., Shuklaet al., 2017).

Vegetation, litter, and soil drill core samples were collected in the contaminated area at Fukushima in 2013 and 2015 to study the origin of ^{240}Pu/^{239}Pu and ^{236}U/^{238}U ratios using AMS. ^{240}Pu/^{239}Pu ratios indicated the global fallout as the main source in the samples, whereas the Fukushima-derived reactor plutonium was identified unambiguously in some vegetation and litter samples. This assumption is confirmed by the detection of ^{236}U. The strong localization indicated that the small quantities of Pu isotopes were most likely released in the form of particulate matter (Schneider et al., 2017). The release of Pu isotopes into the environment during the Fukushima accident was also reported in several studies (Zheng et al., 2012;

Schneider et al., 2013; Yamamoto et al., 2012, 2014; Xu et al., 2016; Imanaka et al., 2012; Tanaka et al., 2014; Steinhauser et al., 2015) and ^{236}U (Sakaguchi et al., 2014; Shinonaga et al., 2014; Yang et al., 2016).

c. Pu isotope ratios

Progress in analytical and instrumental techniques for long-lived radionuclides, such as the development of new selective materials for radioanalytical separation, AMS (ICP-MS) as well as the need of the fingerprinting and contamination sources estimation, resulted in a growing interest in the estimation and reevaluation characteristic atom and activity ratios of radionuclides in environmental samples. Wide variations of Pu atom ratios derived from different sources were demonstrated, e.g., by Taylor et al. (2001), Warneke et al. (2002), Ketterer et al. (2004) and others as shown in Fig. 3.68.

Further achievements in this field have enabled the application of Pu as a new tool to study environmental processes such as the transport of Saharan dust in Europe (Pham et al., 2005 Povinec et al., 2008), North America dust sources (Arimoto et al., 2005), transport of dust from China deserts in Asia (Choi et al., 2006; Igarashi et al., 2009), and other environmental processes in Europe and worldwide (Lee et al., 2002; Chamizo et al., 2010; Hirose et al., 2010).

Large variations of the Pu isotope ratios observed during nuclear weapon tests were attributed to different Pu atom ratios, which resulted from the low- and high-yield tests and mixing rates in the stratosphere and troposphere, as indicated by $^{240}Pu/^{239}Pu$ atom ratios in daily aerosol samples collected in Finland in 1963 (Salminen-Paatero et al., 2012). Measurements of $^{240}Pu/^{239}Pu$ ratios in polar ice sheets as well as in archived samples of grass, roe deer antlers, and corals showed that differences in these ratios for premoratorium and postmoratorium periods offer possibility of using these ratios as a geochronological tool for marine, glacial, lake, and soil studies (Fig. 3.69).

The $^{240}Pu/^{239}Pu$ atom ratios estimated at the contaminated sites are important for source identification, e.g., for the Semipalatinsk NWT site ($^{240}Pu/^{239}Pu = 0.044$), for the Nuclear Complex Mayak ($^{240}Pu/^{239}Pu = 0.028$), and for the Siberian Chemical Complex Tomsk-7 ($^{240}Pu/^{239}Pu = 0.049 - 0.051$) (Yamamoto et al., 1996; Beasley et al., 1998; Gauthier-Lafaye et al., 2008; Stille et al., 2008).

The atom ratios of Pu isotopes and of ^{237}Np measured in archived soil samples collected in the 1970s from 54 locations around the world were reported for the Northern hemisphere to be $^{240}Pu/^{239}Pu = 0.180 \pm 0.014$, $^{241}Pu/^{239}Pu = 0.00194 \pm 0.00028$, $^{242}Pu/^{239}Pu = 0.0039 - \pm 0.0007$, and $^{237}Np/^{239}Pu = 0.48 \pm 0.07$ and for the Southern hemisphere to be $^{240}Pu/^{239}Pu = 0.185 \pm 0.047$, $^{241}Pu/^{239}Pu = 0.0020 \pm 0.0009$, $^{242}Pu/^{239}Pu = 0.0048 - \pm 0.0021$, and $^{237}Np/^{239}Pu = 0.34 \pm 0.03$ (Kelley et al., 1999).

Studies of the $^{240}Pu/^{239}Pu$ atom ratio variability in Australian soil showed ranges from 0.045 to 0.197, with average values of 0.139 ± 0.017, 0.111 ± 0.052 and 0.160 ± 0.027 in the $10-20^{o}S$, $20-30^{o}S$, and $30-40^{o}S$ latitudes, respectively. It was found that the $^{240}Pu/^{239}Pu$ atom ratio of 0.069 estimated for Central Australia corresponds to local fallout from the nuclear weapon tests carried out by the United Kingdom in Australia (Maralinga: 0.113 and Montebello: 0.045), whereas the average ratios

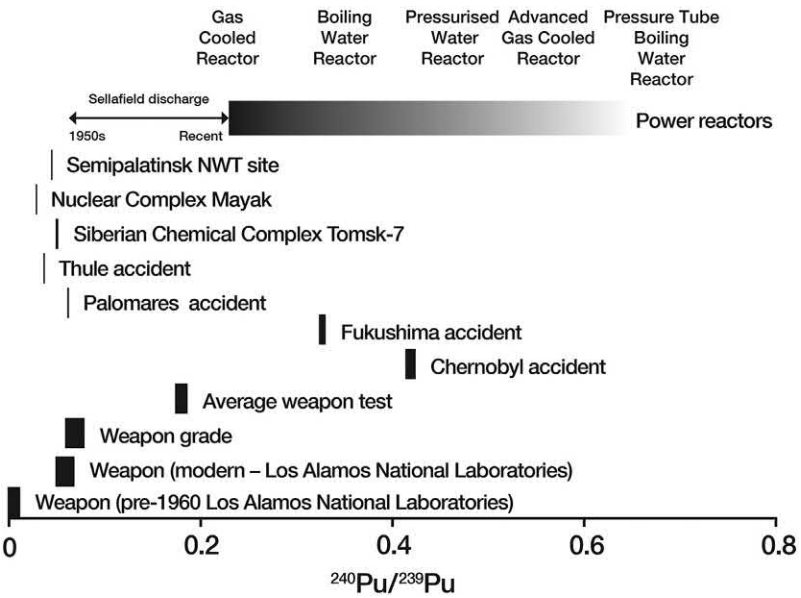


FIGURE 3.68 $^{240}Pu/^{239}Pu$ atom ratios from different nuclear sources. *Updated from Taylor et al. (2001).*

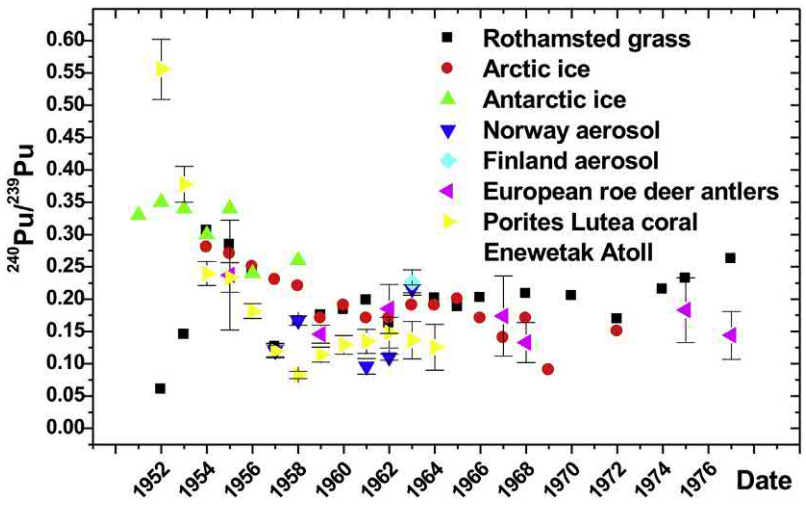


FIGURE 3.69 $^{240}Pu/^{239}Pu$ atom ratios in the Arctic and Antarctic ice sheets (average values, data from Koide et al., 1985), as well as in archived samples of grass, aerosol, roe deer antlers, and corals (data from Warneke et al., 2002; Salminen-Paatero et al., 2012 (average value); Wendel et al., 2013 (average values); and Froehlich et al., 2016, 2017). For the color version of the figure, the reader is referred to the online version of the book.

for the 20−30°S and 30−40°S bands are mainly characteristic for global fallout with average values of 0.139 and 0.177, respectively. The slightest deviation of 6% from the typical value of the $^{240}Pu/^{239}Pu$ ratio for the southern hemisphere (0.171) was found for soil samples collected at the 30−40°S latitude band (Lal et al., 2017).

The characteristic Pu isotopes atom ($^{240}Pu/^{239}Pu$) and activity ($^{238}Pu/^{239}Pu$) ratios in soil and sediments after the B-52 aircraft accident with Pu bombs were estimated as follows: for the Thule (Greenland) samples $^{240}Pu/^{239}Pu = 0.033 \pm 0.003$ and $^{238}Pu/^{239}Pu = 0.0150 \pm 0.0017$, while for the Palomares (Spain) samples, the ratios were higher, $^{240}Pu/^{239}Pu = 0.056 \pm 0.003$ and $^{238}Pu/^{239}Pu = 0.0275 \pm 0.0012$ (Mitchell et al., 1997). The differences in atom and activity Pu ratios for the Thule and Palomares samples were attributed to conditions (e.g., reactor types, operating history, integrated neutron flux, etc.) under which the plutonium was originally produced.

High $^{238}Pu/^{239,240}Pu$ activity ratios (0.014−0.5) and $^{240}Pu/^{239}Pu$ atom ratios (0.10−0.44) were measured in aerosol samples collected in April−May 1986 after the Chernobyl accident at Braunschweig (Germany, Arnold and Wershofen, 2000; Wershofen et al., 2001), in Krakow and Bialystok (Poland, Kierepko et al., 2016), Prague (Czech Republic, Holgye, 2008), Nurmijarvi (Finland, Salminen-Paatero et al., 2012), and Vilnius (Lithuania, Lujaniene et al., 2012a). In Tsukuba (Japan, Hirose and Sugimura, 1990), the $^{238}Pu/^{239,240}Pu$ activity ratio during the period from May 3 to June 1, 1986, ranged from 0.08 to 0.33 with an average value of 0.19 (Fig. 3.70). In spite of the sharp decrease of Pu activity concentrations during 1986, higher $^{238}Pu/^{239,240}Pu$ activity ratios were still found in the atmosphere even 20 years after the Chernobyl accident, which were attributed to the transport of Pu isotopes with aerosol and hot particles released during the Chernobyl accident, as well as to resuspension of the Chernobyl-derived plutonium from soil.

The Chernobyl-derived $^{240}Pu/^{239}Pu$ atom ratios in the troposphere have been studied worldwide, including speciation and particle size distributions of aerosol and soil samples inside the restricted Chernobyl zone. Large variations in the $^{240}Pu/^{239}Pu$ atom ratios outside of the Chernobyl zone, from about 0.05 to 0.5, have been observed (Fig. 3.71). Dust storms (resuspension from soil) and, to a lesser extent, biomass burning were responsible for redistribution of the Chernobyl-derived plutonium in the troposphere. An exponential decrease in the $^{240}Pu/^{239}Pu$ atom ratios from 0.30 to 0.19 was observed during 1995−2003 (Lujaniene et al., 2009), which was attributed to a decrease in the amount of the Chernobyl-derived Pu in the atmosphere due to its deposition and mixing with global fallout Pu. The residence time of the Chernobyl-derived Pu in the atmosphere for this period was found to be 1.6 ± 0.4 y. This value is not consistent with the mean tropospheric residence time of plutonium-bearing aerosols (71 d), observed after atmospheric nuclear weapon tests (Holloway and Hayes, 1982). The difference may reflect the Pu behavior in the atmospheric and terrestrial environments, including the resuspension and transport of Pu from the contaminated regions.

The frequency distribution of the $^{240}Pu/^{239}Pu$ atom ratio in aerosol samples collected during 1995−2006 shows a lognormal bimodal distribution (Lujaniene et al., 2012b). The first mode with median value of 0.195 (0.155 − 0.215) corresponds to the global fallout ratio of 0.17−0.19 characteristic for the northern hemisphere (Kelley et al., 1999). The second mode with median value of 0.253

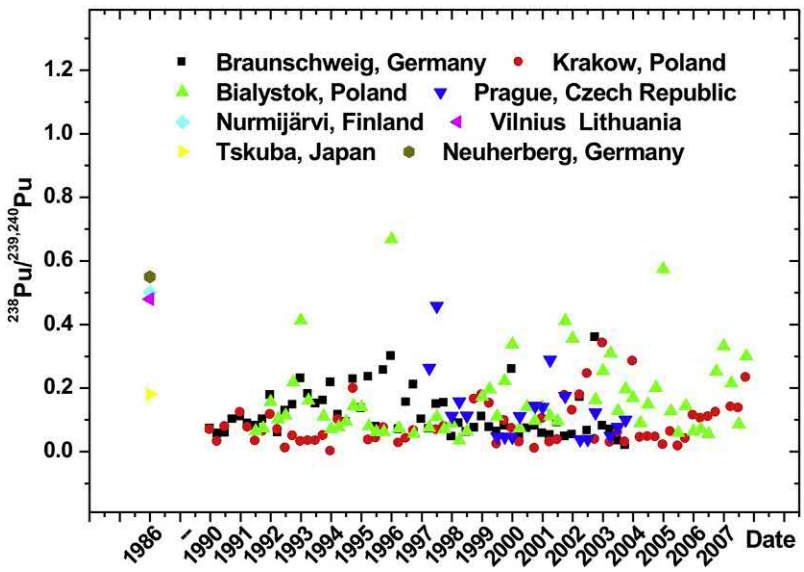


FIGURE 3.70 $^{238}Pu/^{239,240}Pu$ activity ratios in aerosol samples collected after the Chernobyl accident in Japan (Hirose and Sugimura, 1990), Germany (Rosner et al., 1990; Wershofen and Arnold, 2005), Czech Republic (Hölgye, 2008), Lithuania (Lujaniene et al., 2009), Finland (Salminen-Paatero et al., 2012), and Poland (Kierepko et al., 2016). For the color version of the figure, the reader is referred to the online version of the book.

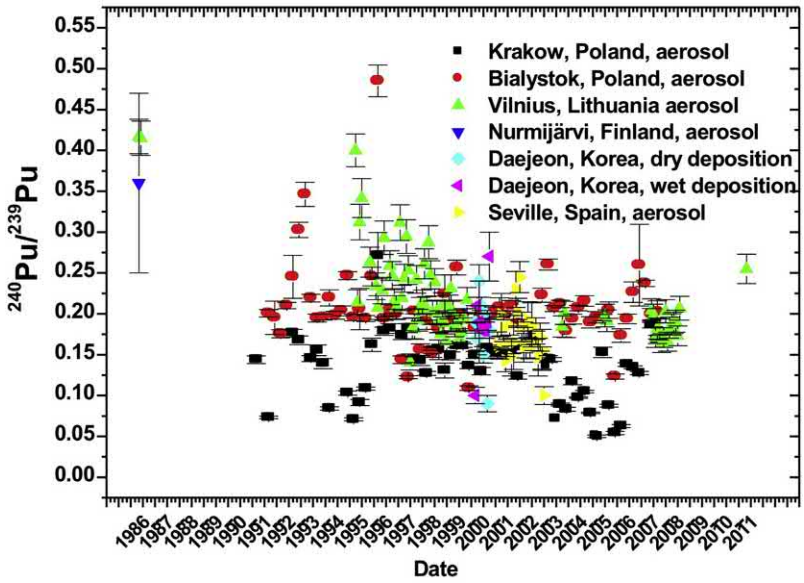


FIGURE 3.71 $^{240}Pu/^{239}Pu$ atom ratios in atmospheric samples collected after the Chernobyl accident in Poland (Kierepko et al., 2016), Lithuania (Lujaniene et al., 2009, 2012b), Finland (Salminen-Paatero et al., 2012), South Korea (Hirose et al., 2004), and Spain (Chamizo et al., 2010). For the color version of the figure, the reader is referred to the online version of the book.

(0.225 − 0.285) could be attributed to the nuclear reactor Pu with characteristic $^{240}Pu/^{239}Pu$ atom ratio of 0.23−0.67 (Warneke et al., 2002).

On the other hand, the characteristic Fukushima-derived Pu activity ratios—$^{238}Pu/^{239,240}Pu$ (1.2), $^{241}Pu/^{239,240}Pu$ (102), and $^{240}Pu/^{239}Pu$ atom ratio of 0.30−0.33—were measured in upper soil layers, in litter, and in black dust samples (Zheng et al., 2012, 2013; Sakaguchi et al., 2014; Yamamoto et al., 2014). The bimodal frequency distribution of $^{240}Pu/^{239}Pu$ atom ratios was found in soil samples after the Fukushima accident with the first peak close to the global fallout value and the second peak at 0.245−0.312 with different contributions of the Fukushima-derived Pu (Yang et al., 2017).

Because of low-release rates of Pu during the Fukushima accident, and long-range transport from Japan to Europe, the observed activity concentrations were below detection limits. Successful Pu measurements were mostly carried out only in soil samples collected in Japan, and in river or coastal sediments. A statistically significant increase in the $^{240}Pu/^{239}Pu$ atom ratio of 0.244 ± 0.018 (Fig. 3.71) was found in large-volume aerosol samples collected during March 23−April 15, 2011 in Vilnius (Lithuania), which could be attributed to the Fukushima

accident (Lujaniene et al., 2012a). However, similar increases in the $^{240}Pu/^{239}Pu$ atom ratios were observed in Europe during pre-Fukushima time as well, which were probably associated with Pu resuspension from soil or biomass burning.

VI. International networks for monitoring of environmental radionuclides

A. International monitoring system of CTBTO

The Comprehensive Nuclear-Test-Ban Treaty (CTBT) was opened for signature in 1996. When the Treaty entered into force, it banned atmospheric, underwater, and underground nuclear explosions. The International Monitoring System (IMS) is being set up with the aim of detecting violations of the CTBT. It is a global system utilizing the most modern technology available, which besides seismic, hydroacoustic, and infrasound stations also includes radionuclide monitoring stations for monitoring of radioactive aerosols and of radioactive noble gases. It should be able to detect any nuclear explosion conducted in the underground, underwater, or atmosphere. The IMS consists of 321 monitoring stations to monitor the planet for any sign of a nuclear weapon test, and presently, about 90% of monitoring stations have already been installed (www.CTBTO.org).

The monitoring network includes 80 radionuclide monitoring stations carrying out a continuous worldwide observation of aerosol samples of radionuclides. The network is supported by 16 radionuclide laboratories hosting expertise in environmental monitoring, providing independent additional analysis of IMS samples, assisting in data evaluation and identification of measured radionuclides. The laboratories also analyze samples collected and measured at monitoring stations to provide quality control of a station's air sample measurements. The radionuclide stations are capable of detecting radioactive debris from atmospheric explosions or vented by underground or underwater nuclear explosions. The 80 radionuclide stations operate in four world regions: Europe and Eurasia, Mediterranean and Africa, Asia and Oceania, and America. Each region is supported by four radionuclide laboratories. It should be stressed that the modern radionuclide technology is the only one that can unambiguously confirm an explosion connected with a nuclear weapon test.

Half of all radionuclide stations is equipped with technology capable of monitoring of radioactive noble gases. This technology is crucial for the detection of nuclear explosions carried out underground or underwater when aerosol releases may be delayed or not detectable at all. From radioactive noble gases, the best candidates for tracing nuclear explosions are radioisotopes of xenon, namely ^{133}Xe ($T_{1/2} = 5.2$ d) and ^{135}Xe ($T_{1/2} =$ 9.1 hours) and two isomers, ^{131m}Xe ($T_{1/2} = 11.8$ d) and ^{133m}Xe ($T_{1/2} = 2.2$ d) due to their suitable half-lives and decay modes with emissions of beta rays and/or gamma rays. The argon and krypton radioisotopes, e.g., ^{85}Kr ($T_{1/2} =$ 10.7 y), because of their excessively long half-lives, decay modes, and large releases from nuclear and pharmaceutical industry are not first-class nuclear test tracers.

Xenon radioisotopes together with ^{85}Kr have been measured in the atmosphere from 1970s, mostly applied cryogenic separation and gas counting techniques (Kunz and Paperiello, 1976; Stockburger et al., 1977; Cimbák and Povinec, 1985; Cimbák et al., 1986; Igarashi et al., 2000, 2005). IMS radionuclide monitoring stations should be capable, however, to monitor radioxenon concentrations in the atmosphere continuously; therefore, continuous air sampling and measurements should be carried out (Schulze et al., 2000; Bowyer et al., 2002; Saey and De Geer, 2005; Plastino et al., 2010) (see also Section V.A.3). Usually, HPGe gamma spectrometers or beta−gamma coincidence spectrometers based on plastic and NaI(Tl) scintillation detectors have been used, which enable the calculation of activity ratios of xenon radioisotopes in collected air samples. Typical detection limits are below 1 mBq m^{-3}. Complementary to radionuclide aerosol monitoring, the International Noble Gas Experiment (INGE) was established in 1999 to test the measuring of radioactive noble gases released by nuclear explosions (Auer et al., 2004, 2010).

However, even with the development of sophisticated radioxenon monitoring systems, an unambiguous detection of nuclear explosions is a very difficult task because of variations of xenon radioisotopes in the atmosphere connected with different release rate scenarios (nuclear fuel reprocessing facilities, nuclear reactors, radiopharmaceutical industry), meteorological conditions, etc. Therefore, a proper understanding of background and atmospheric variations of radioactive xenon isotopes in the atmosphere is crucial for assessing undeclared nuclear activities (Schulze et al., 2000; Schöppner and Plastino, 2014; Saey, 2007, 2009; Postelt, 2014). Atmospheric transport modeling in support of CTBT verification, especially analysis of backward trajectories, has become therefore as important as direct experimental monitoring of radioxenon levels in the atmosphere (De Geer et al., 1996; Wotawa et al., 2003; Stocki et al., 2005; Stohl et al., 2005; Becker et al., 2007; De Meutter et al., 2016; Bianchi et al., 2018; Longo et al., 2018).

The accident at the Fukushima NPP on March 2011, which originated due to a devastating tsunami damaging the NPP's infrastructure, was a good cross-check for performance of adjacent IMS radionuclide stations operating in East Asia, as well as for modeling groups assessing the radioxenon release-rate scenarios and modeling atmospheric radionuclide transport. Reported experimental

TABLE 3.15 List of underground nuclear weapon test carried out by North Korea.

Date	Oct 9, 2006	May 25, 2009	Feb 12, 2013	Jan 6, 2016	Sept 9,2016	Sept 3, 2017
Yield (eq. kt TNT)	0.6–2	2–5.4	6–16	7–16	15–25	70–280

activities at the IMS radionuclide stations as well as atmospheric modeling results, estimation of radioxenon release rates, and tracing atmospheric processes contributed to the assessment of the Fukushima impact on the regional and global scales (Stohl et al., 2012; Povinec et al., 2013a; Eslinger et al., 2014).

Presently, the IMS has mostly been focusing on assessment of signals from nuclear weapon tests carried out by North Korea. Altogether six tests were declared between 2006 and 2017 (Table 3.15). The last one with a yield of 70–280 TNT (eq.) was declared to be a hydrogen bomb but may only be a boosted fission bomb (Saey et al., 2007; Ringbom et al., 2009, 2014; De Meutter et al., 2017, 2018). The situation is complicated by the fact that only 6–8 weeks after the test, increased levels of some of the xenon radioisotopes were observed in a few radionuclide monitoring stations.

A good example is the third test carried out in 2013 when suspicious detections of ^{131m}Xe and ^{133}Xe were made by one IMS station in Japan and one in Russia (Ringbom et al., 2009; De Meutter et al., 2018). The experimental signal was attributed to a nuclear explosion, mainly based on their unusual occurrence compared with the station's record (Ringbom et al., 2014). An inverse atmospheric transport and dispersion modeling showed that the nuclear test could be the source of radioxenon; however, a second source in East Asia should be considered also as a civilian background source (De Meutter et al., 2018). Bayesian methods to find source parameters have also confirmed the nuclear test as a radioxenon source (Eslinger and Schrom, 2016).

Another example could be the nuclear test carried out in 2016 when elevated ^{133}Xe concentrations were measured by the IMS radionuclide stations (De Meutter et al., 2017). However, the lack of presence of other radioxenon isotopes could indicate a civilian source or at least a contribution from this source.

Gathered experience with assessment of North Korean nuclear weapon tests clearly shows that further developments, both on experimental and on modeling sides, will be required. Continuous and simultaneous measurements of all four xenon radioisotopes will be a must, especially in critical regions where nuclear tests could be expected (Kalinowski et al., 2010; Topin et al., 2015). Together with atmospheric transport and dispersion modeling, this will provide a powerful tool for assessing undeclared nuclear weapon tests, although radioxenon contributions from regional civilian sources remain a great challenge, especially if their locations are not well known (Achim et al., 2016; Eslinger et al., 2016).

B. European network "Ring of Five"

Ring of Five (Ro5) is an unformal group of European laboratories exchanging data on atmospheric radioactivity, which triggered studies in several countries, evaluating obtained results and writing joint publications. Originally, only five countries were included in this network; however, presently almost all European countries have been engaged in the Ro5 activities. Large-scale investigations started with measuring and evaluation of the Fukushima accident impact on the European countries (Masson et al., 2011).

In January–February 2017, traces of particulate ^{131}I were detected by about 30 monitoring stations in the European atmosphere with concentrations ranging from 0.1 to 10 μBq m^{-3} (except at one location in Russia with mBq m^{-3}). Inverse modeling indicated that a combination of multiple sources was responsible for the elevated ^{131}I levels, namely a radiopharmaceutical production unit in Western Russia and medical uses of ^{131}I in Europe (Masson et al., 2018a,b).

More recently, in October 2017 and several months afterward, more than 30 European laboratories reported the presence of ^{106}Ru in the atmosphere with concentrations from about 10 μBq m^{-3} to more than 100 mBq m^{-3} (Masson et al., 2018b). The ^{106}Ru was also detected in rain samples as well as in grass. The widespread detection at such considerable levels suggested a source term that would meet or exceed the criteria of an accident at level 4–5 of the International Nuclear Event Scale (INES). The data evaluation and computer modeling suggested that the release could originate in Russia, in the Southern Urals region (Russia).

VII. Conclusions

We have covered in this chapter the analysis of radionuclides in the terrestrial environment, as the marine environment has been covered in Chapter 5, Volume 2. We have seen that great progress has been made both in radioanalytical aspects and in environmental radioactivity studies either for radioecological purposes or in applications of radionuclides as tracers of processes in the atmosphere–hydrosphere–pedosphere–biosphere ecosystems.

Great developments have been made in radioanalytical technologies when, from simple gas counting systems, we moved to very sophisticated accelerator-based technologies not only decreasing required sample size from kilograms to milligrams but also improving the sensitivities by five to six orders of magnitude. Large-volume Ge detectors (frequently operating deep underground) have been the most important breakthrough for the analysis of short- and medium-lived radionuclides in the radiometrics sector, whereas ICP-MS and AMS revolutionized the analytical technologies for long-lived radionuclides.

Radionuclides of very different origin found in the terrestrial environment, from the primordial ones (^{40}K, ^{235}U, ^{238}U, ^{232}Th) to radiogenic (radium isotopes, ^{222}Rn, ^{210}Po, ^{210}Pb, etc.), cosmogenic (^{3}H, ^{7}Be, ^{10}Be, ^{14}C, ^{22}Na, etc.), and finally anthropogenic radionuclides (^{3}H, ^{14}C, ^{90}Sr, ^{137}Cs, ^{236}U, transuranics, etc.) have been investigated for assessment of the impacts of the nuclear industries on the total environment (including humans), as well as for a better understanding of their transport between environmental compartments and resulting variations in their concentrations.

We have not finished yet our work on the development of new radioanalytical technologies with the aim to further increase detection sensitivities, which would open doors for new environmental studies using radionuclides as valuable tracers, including climate change investigations, and specifically, a clear identification of natural and anthropogenic impacts on climate, which represent one of the most important challenges for the future environmental radioactivity research.

Acknowledgments

The authors are indebted to their institutional colleagues for cooperation in the development of radioanalytical methods and their applications in environmental radioactivity studies. Special thanks go also to our foreign colleagues, namely P.K. Aggarwal, R. Golser, K. Hirose, Y. Igarashi, K.G.W. Inn, A.J.T. Jull, W.E. Kieser, O. Masson, S.-H. Lee, M. Molnár, U. Morgenstern, N. Ogrinc, L. Palcsu, M.K. Pham, W. Plastino, P. Steier, I. Svetlik, and F. Terrasi for long-term fruitful collaboration in environmental radioactivity studies. The Bratislava group acknowledges support provided by the EU Research and Development Operational Program funded by the ERDF (projects 26240120012, 26240120026 and 26240220004), by the International Atomic Energy Agency (projects SLR 0/008, SLR 0/009, SLR 1001 and RER 7008), by the Slovak Research and Development Agency (Projects APVV 15-0576 and APVV-0516-10), and by the VEGA Scientific Granting Agency of Slovakia (Projects 1/0891/17 and 1/0783/14).

References

Aalseth, C.E., Day, A.R., Haas, D.A., Hoppe, E.W., Hyronimus, B.J., Keillor, M.E., Mace, E.K., Orrell, J.L., Seifert, A., Woods, V.T., 2011. Measurement of ^{37}Ar to support technology for on-site inspection under the comprehensive nuclear-test-BanTreaty. Nucl. Instrum. Methods Phys. Res. A 652, 58–61.

Aarkrog, A., et al., 1986. Timer trend of ^{99}Tc in seaweed from Greenland waters. In: Desmet, G., Myttenaeare, C. (Eds.), Technetium in the Environment. Elsevier, London, pp. 69–78.

Aarkrog, A., Carlsson, L., Chen, Q.J., Dahlgaard, H., Holm, E., Huynh-Ngoc, L., Jensen, L.H., Nielsen, S.P., Nies, H., 1988. Origin of technetium-99 and its use as a marine tracer. Nature 335, 338–340.

Aceto, M., 2016. The use of ICP-ms in food traceability. In: Espiñeira, M., Santaclara, F.J. (Eds.), Advances in Food Traceability Techniques and Technologies. Woodhead Publishing, Amsterdam, pp. 137–164.

Achim, P., et al., 2016. Characterization of Xe-133 global atmospheric background: implications for the international monitoring system of the comprehensive nuclear-test-ban treaty. J. Geophys. Res. Atmosph. 121, 4951–4966.

Ageyev, V.A., Odintsov, O.O., Sajeniouk, A.D., 2005. Routine radiochemical method for the determination of ^{90}Sr, ^{238}Pu, $^{239+240}$Pu, ^{241}Am and ^{244}Cm in environmental samples. J. Radioanal. Nucl. Chem. 264, 337–342.

Aggarwal, S.K., 2016. Thermal ionisation mass spectrometry (TIMS) in nuclear science and technology – a review. Anal. Methods 8, 942–957.

Ahmed, A.S., Capello, K., Chiang, A., Cardenas-Mendez, E., Kramer, G.H., 2009. Optimization of geometric parameters for Marinelli beaker to maximize the detection efficiency of an HPGe detector. Nucl. Instrum. Methods Phys. Res. A. 610, 718–723.

Akata, N., Kakiuchi, H., Shima, N., Iyogi, T., Momoshima, N., Hisamatsu, S., 2011. Tritium concentrations in the atmospheric environment at Rokkasho, Japan before the final testing of the spent nuclear fuel reprocessing plant. J. Environ. Radioact. 102, 837–842.

Aldahan, A., Persson, S., Possnert, G., Hou, X.L., 2009. Distribution of ^{127}I and ^{129}I in precipitation at high European latitudes. Geophys. Res. Lett. 36, L11805.

Alfimov, V., Aldahan, A., Possnert, G., Winsor, P., 2004. Anthropogenic iodine-129 in seawater along a transect from the Norwegian coastal current to the North Pole. Mar. Pollut. Bull. 49, 1097–1104.

Al-Mukren, A.-J.H., Ebaid, Y.Y., El-Sharkawy, A., Al-Ghamdi, H., 2015. Determination of radium in water by gamma spectrometry using commercial cation exchange resins: comparison and validation. Rom. J. Phys. 60, 257–265.

Alvarado, J.A.C., Steinmann, P., Estier, S., Bochud, F., Haldimann, M., Froidevaux, P., 2014. Anthropogenic radionuclides in atmospheric air over Switzerland during the last few decades. Nat. Commun. 5, 3030.

Alvarez, L.W., Cornog, R., 1939. Helium and hydrogen of mass 3. Phys. Rev. 56, 613.

Amoli, H.S., Barker, J., Flowers, A., 2007. Closed vessels microwave digestion method for uranium analysis of soils using alpha-spectroscopy. J. Radioanal. Nucl. Chem. 273, 281–284.

Anton, M.P., Espinosa, A., Aragon, A., 2006. Radiochemical determination of ^{237}Np in soil samples contaminated with weapon grade plutonium. Czech. J. Phys. 56, D241–D246.

Aoyama, M., Fukasawa, M., Hirose, K., Hamajima, Y., Kawano, T., Povinec, P.P., Sanchez-Cabeza, J.A., 2011. Cross equator transport of ^{137}Cs from North Pacific Ocean to South Pacific Ocean (BEAGLE2003 cruises). Prog. Oceanogr. 89, 7–16.

Aoyama, M., Kajino, M., Tanaka, T.Y., Sekiyama, T.T., Tsumune, D., Tsubono, T., Hamajima, Y., Inomata, Y., Gamo, T., 2016. ^{134}Cs and ^{137}Cs in the north Pacific Ocean derived from the March 2011 TEPCO

Fukushima Dai-ichi nuclear power plant accident, Japan. Part two: estimation of ^{134}Cs and ^{137}Cs inventories in the North Pacific Ocean. J. Oceanogr. 72, 67–76.

Arimoto, R., Webb, J.L., Conley, M., 2005. Radioactive contamination of atmospheric dust over southeastern New Mexico. Atmos. Environ. 39, 4745–4754.

Arnold, D., Wershofen, H., 2000. Plutonium isotopes in ground-level air in Northern Germany since 1990. J. Radioanal. Nucl. Chem. 243, 409–413.

Arnold, D., Neumaier, S., Sima, O., 2002. Deep underground gamma spectrometric measurement of ^{26}Al in meteorite samples. Appl. Radiat. Isot. 56, 405–408.

Auer, M., et al., 2004. Intercomparison experiments of systems for the measurement of xenon radionuclides in the atmosphere. Appl. Radiat. Isot. 60, 863–877.

Auer, M., Kumberg, T., Sartorius, H., Wernsperger, B., Schlosser, C., 2010. Ten years of development of equipment for measurement of atmospheric radioactive xenon for the verification of the CTBT. Pure Appl. Geophys. 167, 471–486.

Auer, M., Wagenbach, D., Wild, E.M., Wallner, A., Priller, A., Miller, H., Schlosser, C., Kutschera, W., 2009. Cosmogenic ^{26}Al in the atmosphere and the prospect of a ^{26}Al/^{10}Be chronometer to date old ice. Earth Planet. Sci. Lett. 287, 453–462.

Ayranov, M., Krähenbühl, U., Röllin, S., Burger, M., 2009. Sensitivity of DF-ICP-MS, PERALS and alpha-spectrometry for the determination of actinides: a comparison. J. Radioanal. Nucl. Chem. 279, 475–480.

Ayranov, M., Krähenbühl, U., Sahli, H., Röllin, S., Burger, M., 2005. Radiochemical separation of actinides from environmental samples for determination with DF–ICP–MS and alpha spectrometry. Radiochim. Acta 93, 249–257.

Azahra, M., Camacho-García, A., González-Gómez, C., López-Peñalver, J.J., El Bardouni, T., 2003. Seasonal ^{7}Be concentrations in near-surface air of Granada (Spain) in the period 1993-2001. Appl. Radiat. Isot. 59, 159–164.

Bailey, R.A., Clark, H.M., Ferris, J.P., Krause, S., Strong, R.L., 2002. Chemistry of the Environment. Academic Press, San Diego.

Bains, M.E.D., Warwick, P.E., 1993. The separation of actinides from lanthanides by anion exchange in methanol/hydrogen chloride medium, and its application to routine separation. Sci. Total Environ. 130/131, 437–445.

Ballestra, S., Fukai, R., 1983. An improved radiochemical procedure for low level measurements of americium in environmental matrices. Talanta 30, 45–48.

Bard, E., Arnold, M., Toggweiler, J.R., Maurice, P., Duplessy, J.-C., 1989. Bomb ^{14}C in the Indian Ocean measured by accelerator mass spectrometry: oceanographic implications. Radiocarbon 31, 510–522.

Barshick, C.M., Duckworth, D.C., Smith, D.H., 2000. Inorganic Mass Spectrometry. Marcel Dekker, New York.

Beals, D.M., Hayes, D.W., 1995. Technetium-99, iodine-129 and tritium in the waters of the Savannah River site. Sci. Total Environ. 173/174, 101–115.

Beasley, T.M., Kelley, J.M., Orlandini, K.A., Bond, L.A., Aarkrog, A., Trapeznikov, A.P., Pozolotina, V.N., 1998. Isotopic Pu, U and Np signatures in soils from Semipalatinsk-21, Kazakh Republic and the southern Urals, Russia. J. Environ. Radioact. 39, 215–230.

Becker, A., et al., 2007. Global backtracking of anthropogenic radionuclides by means of a receptor-oriented ensemble dispersion modeling system in support of Nuclear-Test-Ban Treaty verification. Atmos. Environ. 41, 4520–4534.

Becker, J.S., 2002. State of the art and progress in precise and accurate isotope ratio measurements by ICP-MS and LA-ICP-MS. J. Anal. At. Spectrom. 17, 1172–1185.

Becker, J.S., 2012. Inorganic mass spectrometry of radionuclides. In: L'Annunziata, M.F. (Ed.), Handbook of Radioactivity Analysis, third ed. Academic Press, Oxford, pp. 833–870.

Beer, J., et al., 1990. Use of ^{10}Be in polar ice to trace the 11-year cycle of solar activity. Nature 347, 164–166.

Beláň, T., Böhm, R., Ďurana, L., Grguľa, M., Holý, K., Levaiová, D., Povinec, P., Richtariková, M., Šivo, A., 1992. Investigation of radionuclide variations in the Bratislava air. In: Povinec, P.P. (Ed.), Rare Nuclear Processes. World Scientific, Singapore, pp. 345–366.

Ben Slimane, A., Raclot, D., Evrard, O., Sanaa, M., Lefèvre, I., Ahmadi, M., Tounsi, M., Rumpel, C., Ben Mammou, A., Le Bissonnais, Y., 2013. Fingerprinting sediment sources in the outlet reservoir of a hilly cultivated catchment of Tunisia. J. Soils. Sediments. 13, 801–815.

Benedik, L., Trdin, M., 2017. Determination of low level Np-237 by various techniques. Appl. Radiat. Isot. 126, 208–213.

Benedik, L., Vasile, M., Spasova, Y., Wätjen, U., 2009. Sequential determination of ^{210}Po and uranium radioisotopes in drinking water by alpha-particle spectrometry. Appl. Radiat. Isot. 67, 770–775.

Berkovits, D., Boaretto, E., Hollos, G., Kutschera, W., Naaman, R., Paul, M., Vager, Z., 1990. Study of laser interaction with negative ions. Nucl. Instrum. Methods Phys. Res. B 52, 378–383.

Bermingham, K.R., Gussone, N., Mezger, K., Krause, J., 2018. Origins of mass-dependent and mass-independent Ca isotope variations in meteoritic components and meteorites. Geochim. Cosmochim. Acta 226, 206–223.

Bermingham, K.R., Mezger, K., Scherer, E.E., Horan, M.F., Carlson, R.W., Upadhyay, D., Magna, T., Pack, A., 2016. Barium isotope abundances in meteorites and their implications for early Solar System evolution. Geochim. Cosmochim. Acta 175, 282–298.

Bernabee, R.P., Percival, D.E., Hindman, F.D., 1980. Liquid extraction separation and determination of Pu and. Am. Anal. Chem. 52 (14), 2351–2353.

Bernardoni, V., et al., 2013. Radiocarbon analysis on organic and elemental carbon in aerosol samples and source apportionment at an urban site in Northern Italy. J. Aerosol Sci. 56, 88–99.

Betti, M., Aldave de las Heras, L., 2004. Glow discharge spectrometry for the characterization of nuclear and radioactively contaminated environmental samples. Spectrochim. Acta Part B At. Spectrosc. 59, 1359–1376.

Bianchi, S., Longo, A., Plastino, W., Povinec, P.P., 2018. Evaluation of ^{7}Be and ^{133}Xe atmospheric radioactivity time series measured at four CTBTO radionuclide stations. Appl. Radiat. Isot. 132, 24–28.

Bläckberg, L., et al., 2011. Investigations of surface coatings to reduce memory effect in plastic scintillator detectors used for radioxenon detection. Nucl. Instrum. Methods Phys. Res. A 656, 84–91.

Blahušiak, P., Holý, K., Müllerová, M., Smetanová, I., 2017. Radon concentrations in selected thermal waters in Slovakia. Radiat. Prot. Dosim. 177, 186–189.

Błażej, S., Mietelski, J.W., 2014. Cosmogenic ^{22}Na, ^{7}Be and terrestrial ^{137}Cs, ^{40}K radionuclides in ground level air samples collected weekly in Kraków (Poland) over years 2003–2006. J. Radioanal. Nucl. Chem. 300, 747–756.

Bock, R., 1979. A handbook of decomposition methods in analytical chemistry. Internat. Textbook Comp., London.

Bojanomski, R., Radecki, Z., Piekoś, R., 2002. Rapid determination of ^{226}Ra and uranium isotopes in solid samples by fusion with lithium metaborate and alpha spectrometry. Sci. World J. 2, 1891−1905.

Bojanowski, R., Radecki, Z., Burns, K., 2005. Determination of radium and uranium isotopes in natural waters by sorption on hydrous manganese dioxide followed by alpha-spectrometry. J. Radioanal. Nucl. Chem. 264, 437−443.

Bonnand, P., Williams, H.M., Parkinson, I.J., Wood, B.J., Halliday, A.N., 2016. Stable chromium isotopic composition of meteorites and metal−silicate experiments: implications for fractionation during core formation. Earth Planet. Sci. Lett. 435, 14−21.

Borgonie, G., García-Moyano, A., Litthauer, D., Bert, W., Bester, A., Van Heerden, E., Möller, C., Erasmus, M., Onstott, T.C., 2011. Nematoda from the terrestrial deep subsurface of South Africa. Nature 474, 79−82.

Bourcier, L., Sellegri, K., Masson, O., Zangrando, R., Barbante, C., Gambaro, A., Pichon, J.-M., Boulon, J., Laj, P., 2010. Experimental evidence of biomass burning as a source of atmospheric ^{137}Cs, puy de Dôme (1465 m a.s.l.), France. Atmos. Environ 44, 2280−2286.

Bowyer, T.W., Abel, K.H., Hensley, W.K., Panisko, M.E., Perkins, R.W., 1997. Ambient Xe-133 levels in the Northeast US. J. Environ. Rad. 37, 143−153.

Bowyer, T.W., Abel, K.H., Hubbard, C.W., Panisko, M.E., Reeder, P.L., Thompson, R.C., Warner, R.A., 1999. Field testing of collection and measurement of radioxenon for the comprehensive test ban treaty. J. Radioanal. Nucl. Chem. 240, 109−122.

Bowyer, T.W., et al., 2002. Detection and analysis of xenon isotopes for the Comprehensive Nuclear-Test- Ban Treaty international monitoring system. J. Environ. Rad. 59, 139−151.

Braucher, R., Bourlès, D. (Eds.), 2015. Proceedings of the thirteenth international conference on accelerator mass spectrometry. Nucl. Instrum. Methods Phys. Res. B, 361, pp. 1−706.

Breeze, P., 2016. Nuclear power. Academic Press, Amsterdam.

Broecker, W.S., Peng, T.-H., 1982. Tracers in the Sea. Lamont-Doherty Geological Observatory, Palisades.

Bronk Ramsey, C., Ditchfield, P., Humm, M., 2004. Using a gas ion source for radiocarbon AMS and GC-AMS. Radiocarbon 46, 25−32.

Brown, K., Dingley, K.H., Turteltaub, K.W., 2005. Accelerator mass spectrometry for biomedical research. Methods Enzymol 402, 423−443.

Brown, T.A., Southon, J.R., 1997. Corrections for contamination background in AMS ^{14}C measurements. Nucl. Instrum. Methods Phys. Res. B 123, 208−213.

Bu, K., Cizdziel, J.V., Dasher, D., 2013. Plutonium Concentration and ^{240}Pu/^{239}Pu atom ratio in biota collected from Amchitka Island, Alaska: recent measurements using ICP−SFMS. J. Environ. Radioact. 124, 29−36.

Bulko, M., Holý, K., Müllerová, M., 2018. On the relation between outdoor ^{222}Rn and atmospheric stability determined by a modified Turner method. J. Environ. Radioact. 189, 79−92.

Bunzl, K., Kracke, W., 1990. Simultaneous determination of ^{238}Pu,$^{239+240}$Pu,^{241}Pu,^{241}Am,^{242}Cm,^{244}Cm, ^{89}Sr, and ^{90}Sr in vegetation samples, and application to Chernobyl-fallout contaminated grass. J. Radioanal. Nucl. Chem. Art. 138, 83−91.

Bunzl, K., Kracke, W., Schimmack, W., 1992. Vertical migration of plutonium-239 + -240, americium-241 and caesium-137 fallout in a forest soil under spruce. Analyst 117, 469−474.

Bunzl, K., Förster, H., Kracke, W., Schimmack, W., 1994. Residence times of fallout 239+240Pu, 238Pu, 241Am and 137Cs in the upper horizons of an undisturbed grassland soil. J Environ. Radiact. 22 (1), 11−27.

Bunzl, K., Flessa, H., Kracke, W., Schimmack, W., 1995. Association of fallout 239+240Pu and 241Am with various soil components in successive layers of a grassland soil. Environ. Sci. Technol. 29, 2513−2518.

Burchuladze, A.A., Pagava, S.V., Povinec, P., Togonidze, G.I., Usačev, S., 1980. Radiocarbon variations with the 11-year solar cycle during the last century. Nature 287, 320−322.

Bürger, S., Buda, R.A., Geckeis, H., Huber, G., Kratz, J.V., Kunz, P., von Gostomski, C.L., Passler, G., Remmert, A., Trautmann, N., 2006. Isotope selective ultratrace analysis of plutonium by resonance ionisation mass spectrometry. In: Povinec, P.P., Sanchez-Cabeza, J.A. (Eds.), Radionuclides in the Environment. Elsevier, Amsterdam, pp. 581−591.

Bürger, S., Riciputi, L.R., Turgeon, S., Bostick, D., McBay, E., Lavelle, M., 2007. A high efficiency cavity ion source using TIMS for nuclear forensic analysis. J. Alloys Compd. 444−445, 660−662.

Burnett, W.C., Corbett, D.R., Schultz, M., Horwitz, E.P., Chiarizia, R., Dietz, M., Thakkar, A., Fern, M., 1997. Preconcentration of actinide elements from soil and large volume of water samples using extraction chromatography. J. Radioanal. Nucl. Chem. 226, 121−127.

Bushaw, B.A., Nörtershäuser, W., 2000. Resonance ionization spectroscopy of stable strontium isotopes and ^{90}Sr via $5s^2\ {}^1S_0 \rightarrow 5s5p\ {}^1P_1 \rightarrow 5s5d\ {}^1D_2 \rightarrow 5s11f\ {}^1F_3 \rightarrow Sr^+$. Spectrochim. Acta B 55, 1679−1692.

Bushaw, B.A., Nörtershäuser, W., Müller, P., Wendt, K., 2001. Diode-laser-based resonance ionization mass spectrometry of the long-lived radionuclide ^{41}Ca with $<10^{-12}$ sensitivity. J. Radioanal. Nucl. Chem. 247, 351−356.

Bushaw, B.A., Raeder, S., Ziegler, S.L., Wendt, K., 2007. Triple-resonance autoionization of uranium optimized for diode laser excitation. Spectrochim. Acta B 62, 485−491.

Calcagnile, L., D'Onofrio, A., Fedi, M., Mandò, P.A., Quarta, G., Terrasi, F., Tuniz, C. (Eds.), 2010. Proceedings of the eleventh international conference on accelerator mass spectrometry. Nucl. Instrum. Methods Phys. Res. B, 268, pp. 693−1360.

Calmet, D., 2014. ISO standards on test methods for radioactivity monitoring of food and the environment radiation. Emergency Medicine 3, 7−20.

Cannizzaro, F., Greco, G., Raneli, M., Spitale, M.C., Tomarchio, E., 2004. Concentration measurements of ^{7}Be at ground level air at Palermo, Italy - comparison with solar activity over a period of 21 years. J. Environ. Radioact. 72, 259−271.

Cao, L., Zheng, J., Tsukada, H., Pan, S., Wang, Z., Tagami, K., Uchida, S., 2016. Simultaneous determination of radiocesium (^{135}Cs, ^{137}Cs) and plutonium (^{239}Pu, ^{240}Pu) isotopes in river suspended particles by ICP-MS/MS and SF-ICP-MS. Talanta 159, 55−63.

Carbol, P., Solatie, D., Erdmann, N., Nylén, T., Betti, M., 2003. Deposition and distribution of Chernobyl fallout fission products and actinides in a Russian soil profile. J. Environ. Radioact. 68, 27−46.

Carvalho, F.P., 1995. Origins and concentrations of ^{222}Rn, ^{210}Pb, ^{210}Bi and ^{210}Po in the surface air at Lisbon, Portugal, at the Atlantic edge of the European continental landmass. Atmos. Environ. 29, 1809−1819.

CEFAS, Centre for Environment, Fisheries and Aquaculture Science, 2009. Radioactivity in food and the environment. RIFE-15.

Chamberlain, A.C., 1967. Radioactive aerosols and vapours. Contemp. Phys. 8, 561–581.

Chamizo, E., Jiminez-Ramos, M.C., Wacker, L., Vioque, I., Calleja, A., Garcia-Leon, M., Garcia-Tenorio, R., 2008. Isolation of Pu isotopes from environmental samples using ion chromatography for accelerator mass spectrometry and alpha spectrometry. Anal. Chim. Acta 606, 239–245.

Chamizo, E., García-León, M., Enamorado, S.M., Jiménez-Ramos, M.C., Wacker, L., 2010. Measurement of plutonium isotopes, ^{239}Pu and ^{240}Pu, in air-filter samples from Seville (2001-2002). Atmos. Environ. 44, 1851–1858.

Chamizo, E., López-Lora, M., Villa, M., Casacuberta, N., López-Gutiérrez, J.M., Pham, M.K., 2015. Analysis of ^{236}U and plutonium isotopes, ^{239,240}Pu, on the 1 MV AMS system at the Centro Nacional de Aceleradores, as a potential tool in oceanography. Nucl. Instrum. Methods Phys. Res. B 361, 535–540.

Chaplin, M., 2018. Anomalous properties of water. Water structure and science. Available on-line: http://www1.lsbu.ac.uk/water/water_anomalies.html.

Chartin, C., Evrard, O., Onda, Y., Patin, J., Lefévre, I., Ottlé, C., Ayrault, S., Lepage, H., Bonté, P., 2013. Tracking the early dispersion of contaminated sediment along rivers draining the Fukushima radioactive pollution plume. Anthropocene 1, 23–34.

Chartin, C., Evrard, O., Onda, Y., Patin, J., Lefévre, I., Ottlé, C., Ayrault, S., Lepage, H., Bonté, P., 2013. Tracking the early dispersion of contaminated sediment along rivers draining the Fukushima radioactive pollution plume. Anthropocene 1, 23–34.

Chen, B., Jie, D., Shi, M., Gao, P., Shen, Z., Uchida, M., Zhou, L., Liu, K., Hu, K., Kitagawa, H., 2015. Characteristics of ^{14}C and ^{13}C of carbonate aerosols in dust storm events in China. Atmos. Res. 164–165, 297–303.

Chen, C.Y., Li, Y.M., Bailey, K., O'Connor, T.P., Young, L., Lu, Z.T., 1999. Ultrasensitive isotope trace analyses with a magneto-optical trap. Science 286, 1139–1141.

Chen, Q., Dahlgaard, H., Nielsen, S.P., Aarkrog, A., 2002. ^{242}Pu as a tracer for simultaneous determination of ^{237}Np and ^{239,240}Pu in environmental samples. J. Radioanal. Nucl.Chem. 253, 451–458.

Chiarappa-Zucca, M.L., Dingley, K.H., Roberts, M.L., Velsko, C.A., Love, A.H., 2002. Sample preparation for quantitation of tritium by accelerator mass spectrometry. Anal. Chem. 74, 6285–6290.

Chiarizia, R., Horwitz, E.P., Alexandratos, S.D., Gula, M.J., 1997. Diphonix® resin: a review of its properties and applications. Sep. Sci. Technol. 32, 1–35.

Chino, M., Terada, H., Nagai, H., Katata, G., Mikami, S., Torii, T., Saito, K., Nishizawa, Y., 2016. Utilization of ^{134}Cs/^{137}Cs in the environment to identify the reactor units that caused atmospheric releases during the Fukushima Daiichi accident. Sci. Rep. 6, 31376.

Choppin, G.R., Silva, R.J., 1956. Separation of the lanthanides by ion exchange with a-hydroxi-isobutyric acid. J. Radioanal. Nucl. Chem. 3, 153–154.

Choi, M.S., Lee, D.S., Choi, J.C., Cha, H.J., Yi, H.I., 2006. ^{239,240}Pu concentration and isotope ratio (^{240}Pu/^{239}Pu) in aerosols during high dust (Yellow Sand) period, Korea. Sci. Total Environ. 370, 262–270.

Choppin, G.R., 2007. Actinide speciation in the environment. J. Radioanal. Nucl. Chem. 273, 695–703.

Christl, M., Dai, X., Lachner, J., Tremblay, S.K., Synal, H.A., 2014. Low energy AMS of americium and curium. Nucl. Instrum. Method Phys Res B 331, 225–232.

Chudý, M., Povinec, P., 1982. Radiocarbon production in CO_2 coolant of nuclear reactor. Acta Phys. Univ. Comen. 22, 127–131.

Cimbák, Š., Čechová, A., Grgula, M., Povinec, P., Šivo, A., 1986. Anthropogenic radionuclides ^{3}H, ^{14}C, ^{85}Kr, and ^{133}Xe in the atmosphere around nuclear power reactors. Nucl. Instrum. Methods Phys. Res. B 17, 560–563.

Cimbák, Š., Povinec, P., 1985. ^{85}Kr atmospheric concentration in Bratislava from 1980 to 1983. Environ. Int. 11, 65–69.

Clarke, R.H., Macdonald, H.F., 1978. Radioactive releases from nuclear installations. Prog. Nucl. Energy 2, 77–152.

Clarke, W.B., Jenkins, W.J., Top, Z., 1976. Determination of tritium by mass spectrometric measurement of ^{3}He. Int. J. Appl. Radiat. Isot. 27, 515–522.

Collon, P., Antaya, T., Davids, B., Fauerbach, M., Harkewicz, R., Hellstrom, M., 1997. Measurement of ^{81}Kr in the atmosphere. Nucl. Instrum. Methods Phys. Res. 123, 122–127.

Collon, P., et al., 2000. ^{81}Kr in the Great Artesian Basin, Australia: a new method for dating very old groundwater. Earth Planet. Sci. Lett. 182, 103–113.

Collon, P., et al., 2004a. Development of an AMS method to study oceanic circulation characteristics using cosmogenic ^{39}Ar. Nucl. Instrum. Methods Phys. Res. B 223–224, 428–434.

Collon, P., Kutschera, W., Lu, Z.-T., 2004b. Tracing noble gas radionuclides in the environment. Annu. Rev. Nucl. Part. Sci. 54, 39–67.

Connan, O., Hébert, D., Solier, L., Maro, D., Pellerin, G., Voiseux, C., Lamotte, M., Laguionie, P., 2017. Atmospheric tritium concentrations under influence of AREVA NC La Hague reprocessing plant (France) and background levels. J. Environ. Radioact. 177, 184–193.

Copia, L., Nisi, S., Plastino, W., Ciarletti, M., Povinec, P.P., 2015. Low-level ^{226}Ra determination in groundwater by SF-ICP-MS: optimization of separation and pre-concentration methods. J. Anal. Sci. Technol. 6, 22.

Cornett, R.J., Kazi, Z.H., Zhao, X.-L., Chartrand, M.G., Charles, R.J., Kieser, W.E., 2015. Actinide measurements by AMS using fluoride matrices. Nucl. Instrum. Methods Phys. Res. B 361, 317–321.

Costa, D.A., Cournoyer, M.E., Merhege, J.F., Garcia, V.E., Sandoval, A.N., 2017. A primer on criticality safety. J. Chem. Heal. Saf. 24, 7–13.

Croudace, I., Warwick, P., Taylor, R., Dee, S., 1998. Rapid procedure for plutonium and uranium determination in soils using a borate fusion followed by ion-exchange and extraction chromatography. Anal. Chim. Acta. 371, 217–225.

Crowley, Q.G., Key, R., Noble, S.R., 2015. High-precision U-Pb dating of complex zircon from the Lewisian Gneiss Complex of Scotland using an incremental CA-ID-TIMS approach. Gondwana Res 27, 1381–1391.

Csuros, M., 1994. Environmental Sampling and Analysis for Technicians. Lewis Publishers, Boca Raton.

Cuccia, E., Piazzalunga, A., Bernardoni, V., Brambilla, L., Fermo, P., Massabò, D., Molteni, U., Prati, P., Valli, G., Vecchi, R., 2011. Carbonate measurements in PM10 near the marble quarries of Carrara (Italy) by infrared spectroscopy (FT-IR) and source apportionment by positive matrix factorization (PMF). Atmos. Environ. 45, 6481–6487.

Currie, L.A., 2000. Evolution and multidisciplinary frontiers of ^{14}C aerosol science. Radiocarbon 42, 115–126.

Currie, L.A., Stafford, T.W., Sheffield, A.E., Klouda, G.A., Wise, S.A., Fletcher, R.A., Donahue, D.J., Jull, A.J.T., Linick, T.W., 1989. Microchemical and molecular dating. Radiocarbon 31, 448–463.

Curtis, D., Fabryka-Martin, J., Dixon, P., Cramer, J., 1999. Geochim. Cosmochim. Acta 63 (2), 275.

Dai, X., 2011. Isotopic uranium analysis in urine samples by alpha spectrometry. J. Radioanal. Nucl. Chem. 289, 595−600.

Dalencourt, C., Michaud, A., Habibi, A., Leblanc, A., Larivière, D., 2018. Rapid, versatile and sensitive method for the quantification of radium in environmental samples through cationic extraction and inductively coupled plasma mass spectrometry. J. Anal. At. Spectrom. 33, 1031−1040.

Dalrymple, B., Lanphere, M.A., 1969. Potassium-Argon Dating: Principles, Techniques, and Applications to Geochronology. Freeman, New York.

Damon, P.E., Cheng, S., Linick, T.W., 1989. Fine and hyperfine structure in the spectrum of secular variations of atmospheric ^{14}C. Radiocarbon 31, 704−718.

De Geer, L.E., 1996. Atmospheric radionuclide monitoring: a Swedish perspective. In: Huseby, E.S., Dainty, A.M. (Eds.), Monitoring a Comprehensive Nuclear-Test-Ban Treaty. Kluwer Acad., Dordrecht, pp. 157−177.

De Meutter, P., Camps, J., Delcloo, A., Deconninck, B., Termonia, P., 2016. On the capability to model the background and its uncertainty of CTBT-relevant radioxenon isotopes in Europe by using ensemble dispersion modelling. J. Environ. Rad. 165, 180−190.

De Meutter, P., Camps, J., Delcloo, A., Termonia, P., 2017. Assessment of the announced North Korean nuclear test using long-range atmospheric transport and dispersion modelling. Sci. Rep. 7, 8762. https://doi.org/10.1038/s41598-017-07113-y.

De Meutter, P., Camps, J., Delcloo, A., Teronia, P., 2018. Source localisation and its uncertainty quantification after the third DPRK nuclear test. Sci. Rep. 8, 10155. https://doi.org/10.1038/s41598-018-28403-z.

de Meyer, C.M.C., Baumgartner, L.P., Beard, B.L., Johnson, C.M., 2014. Rb−Sr ages from phengite inclusions in garnets from high pressure rocks of the Swiss Western Alps. Earth Planet. Sci. Lett. 395, 205−216.

Dean, J.A., 1995. Analytical Chemistry Handbook. McGraw-Hill, New York.

De Cort, M., Dubois, G., Fridman, Sh.D., Germenchuk, M.G., Izrael, Yu.A., Janssens, A., Jones, A.R., Kelly, G.N., Kvasnikova, E.V., Matveenko, I.I., Nazarov, I.M., Pokumeiko, Yu.M., Sitak, V.A., Stukin, E.D., Tabachny, L.Ya., Taturov, S.Yu., Avdyushin, S.I., 1998. Atlas of Caesium Deposition on Europe after the Chernobyl Accident. European Commission report EUR16737, Luxembourg.

Delmas, R.J., Beer, J., Synal, H.-A., Muscheler, R., Petit, J.-R., Pourchet, M., 2004. Bomb-test ^{36}Cl measurements in Vostok snow (Antarctica) and the use of ^{36}Cl as a dating tool for deep ice cores. Tellus B 56, 492−498.

Dubois, G., Fridman, Sh.D., Germenchuk, M.G., Izrael, Yu.A., Janssens, A., Jones, A.R., Kelly, G.N., Kvasnikova, E.V., Matveenko, I.I., Nazarov, I.M., Pokumeiko, Yu.M., Sitak, V.A., Stukin, E.D., Tabachny, L.Ya., Taturov, S.Yu., Avdyushin, S.I., Delmas, R.J., Beer, J., Synal, H.-A., Muscheler, R., Petit, J.-R., Pourchet, M., 2004. Bomb-test 36Cl measurements in Vostok snow (Antarctica) and the use of 36Cl as a dating tool for deep ice cores. Tellus B 56, 492−498.

Demayo, A., Taylor, M.C., Taylor, K.W., Hodson, P.V., Hammond, P.B., 1982. Toxic effects of lead and lead compounds on human health, aquatic life, wildlife plants, and livestock. CRC Crit. Rev. Environ. Control 12, 257−305.

Desonie, D., 2007. Hydrosphere: Freshwater Systems and Pollution. Chelsea House Publishers, New York.

Di Sabatino, M., 2014. Detection limits for glow discharge mass spectrometry (GDMS) analyses of impurities in solar cell silicon. Measurement 50, 135−140.

Dingley, K.H., Roberts, M.L., Velsko, C.A., Turteltaub, K.W., 1998. Attomole detection of ^{3}H in biological samples using accelerator mass spectrometry: application in low-dose, dual-isotope tracer studies in conjunction with ^{14}C accelerator mass spectrometry. Chem. Res. Toxicol. 11, 1217−1222.

Döbeli, M., Nebiker, P.W., Suter, M., Synal, H.A., Vetterli, D., 1994. Accelerator SIMS for trace element detection. Nucl. Instrum. Methods Phys. Res. B 85, 770−774.

Donard, O.F.X., Bruneau, F., Moldovan, M., Garraud, H., Epov, V.N., Boust, D., 2007. Multi-isotopic determination of Pu (^{239}Pu, ^{240}Pu, ^{241}Pu and ^{242}Pu) in marine sediments using sector field inductively coupled plasma mass spectrometry. Anal. Chim. Acta 587, 170−179.

Dörr, H., Münnich, K.O., 1990. ^{222}Rn flux and soil air concentration profiles in West-Germany. Soil ^{222}Rn as tracer for gas transport in the unsaturated soil zone. Tellus B 42, 20−28.

Dueñas, C., Fernández, M.C., Carretero, J., Liger, E., Pérez, M., 1997. Release of ^{222}Rn from some soils. Ann. Geophys. 15, 124−133.

Dulanská, S., Štofaníková, M., Mátel, L., Novák, I., Šauša, O., Maťko, I., Zvachová, S., 2018. Preparation and characterization of MnO2- SiO2 composite resin for ^{226}Ra pre-concentration in water samples. Appl. Rad. Isot. 140, 96−101.

Durana, L., Chudy, M., Masarik, J., 1996. Investigation of ^{7}Be in the Bratislava atmosphere. J. Radioanal. Nucl. Chem. 207, 345−356.

Eigl, R., Srncik, M., Steier, P., Wallner, G., 2013. ^{236}U/^{238}U and ^{240}Pu/^{239}Pu isotopic ratios in small (2 L) sea and river water samples. J. Environ. Radioact. 116, 54−58.

Eigl, R., Steier, P., Winkler, S.R., Sakata, K., Sakaguchi, A., 2016. First study on ^{236}U in the Northeast Pacific Ocean using a new target preparation procedure for AMS measurements. J. Environ. Radioact. 162−163, 244−250.

Eikenberg, J., Bajo, S., Beer, H., Hitz, J., Ruethi, M., Zumsteg, I., Letessier, P., 2004. Fast methods for determination of anthropogenic actinides and U/Th- series isotopes in aqueous samples. Appl. Radiat. Isot. 61, 101−106.

Eisenbud, M., Gessel, T., 1997. Environmental Radioactivity from Natural, Industrial & Military Sources. Academic Press, New York.

EML, Environmental Measurements Laboratory, 1999. EML Databases and Sample Archives. Available on-line: http://www.wipp.energy.gov/NAMP/EMLLegacy/databases.htm.

Elmore, D., Fulton, B.R., Clover, M.R., Marsden, J.R., Gove, H.E., Naylor, H., Purser, K.H., Kilius, L.R., Beukens, R.P., Litherland, A.E., 1979. Analysis of ^{36}Cl in environmental water samples using an electrostatic accelerator. Nature 277, 22−25.

Elmore, D., et al., 1980. Determination of ^{129}I using tandem accelerator mass spectrometry. Nature 286, 138−140.

Elsässer, C., Wagenbach, D., Weller, R., Auer, M., Wallner, A., Christl, M., 2011. Continuous 25-yr aerosol records at coastal Antarctica. Tellus B Chem. Phys. Meteorol. 63, 920−934.

EPA, Environmental Protection Agency, 2007. Ionizing radiation Fact book. Office of Radiation and Indoor Air. EPA-402-F-06-061.

Epov, V.N., Benkhedda, K., Evans, R.D., 2005a. Determination of Pu isotopes in vegetation using a new on-line FI-ICP-DRC-MS protocol after microwave digestion. J. Anal. At. Spectrom. 20, 990–992.

Epov, V.N., Benkhedda, K., Cornett, R.J., Evans, R.D., 2005b. Rapid determination of plutonium in urine using flow injection on-line preconcentration and inductively coupled plasma mass spectrometry. J. Anal. At. Spectrom. 20, 424–430.

Epov, V.N., Douglas Evans, R., Zheng, J., Donard, O.F.X., Yamada, M., 2007. Rapid fingerprinting of ^{239}Pu and ^{240}Pu in environmental samples with high U levels using on-line ion chromatography coupled with high-sensitivity quadrupole ICP-MS detection. J. Anal. At. Spectrom. 22, 1131–1137.

Erdmann, N., Passler, G., Trautmann, N., Wendt, K., 2008. Resonance ionization mass spectrometry for trace analysis of long-lived radionuclides. In: Povinec, P.P. (Ed.), Analysis of Environmental Radionuclides. Elsevier, Amsterdam, pp. 331–354.

Esaka, F., Yasuda, K., Suzuki, D., Miyamoto, Y., Magara, M., 2017. Analysis of plutonium isotope ratios including ^{238}Pu/^{239}Pu in individual U–Pu mixed oxide particles by means of a combination of alpha spectrometryand ICP-MS. Talanta 165, 122–127.

Eslinger, P.W., Schrom, B.T., 2016. Multi-detection events, probability density functions, and reduced location area. J. Radioanal. Nucl. Chem. 307 (3), 1599–1605.

Eslinger, P.W., et al., 2014. Source term estimation of radioxenon released from the Fukushima Dai-ichi nuclear reactors using measured air concentrations and atmospheric transport modeling. J. Environ. Rad. 127, 127–132.

Eslinger, et al., 2016. International challenge to predict the impact of radioxenon releases from medical isotope production on a comprehensive nuclear test ban treaty sampling station. J. Environ. Radioact. 157, 41–51.

Evangeliou, N., Hamburger, T., Talerko, N., Zibtsev, S., Bondar, Y., Stohl, A., Balkanski, Y., Mousseau, T.A., Møller, A.P., 2016. Reconstructing the Chernobyl Nuclear Power Plant (CNPP) accident 30 years after. A unique database of air concentration and deposition measurements over Europe. Environ. Pollut. 216, 408–418.

Eyrolle, F., Ducros, L., Le Dizès, S., Beaugelin-Seiller, K., Charmasson, S., Boyer, P., Cossonnet, C., 2018. An updated review on tritium in the environment. J. Environ. Radioact. 181, 128–137.

Ežerinskis, Ž., Šapolaitė, J., Pabedinskas, A., Juodis, L., Garbaras, A., Maceika, E., Druteikienė, R., Lukauskas, D., Remeikis, V., 2018. Annual variations of ^{14}C concentration in the tree rings in the vicinity of Ignalina Nuclear Power Plant. Radiocarbon. https://doi.org/10.1017/RDC.2018.44 (in press).

Faheem, M., Matiullah, 2008. Radon exhalation and its dependence on moisture content from samples of soil and building materials. Radiat. Meas. 43, 1458–1462.

Falandysz, J., Zalewska, T., Krasińska, G., Apanel, A., Wang, Y., Pankavec, S., 2015. Evaluation of the radioactive contamination in fungi genus Boletus in the region of Europe and Yunnan Province in China. Appl. Microbiol. Biotechnol. 99, 8217–8224.

Faris, J.P., Buchanan, R.F., 1964. Anion exchange characteristics on the elements in nitric acid medium. Anal. Chem. 36, 1157–1158.

Fedosseev, V.N., Kudryavtsev, Y., Mishin, V.I., 2012. Resonance laser ionization of atoms for nuclear physics. Phys. Scr. 85, 058104.

Feely, H.W., Larsen, R.J., Sanderson, C.G., 1989. Factors that cause seasonal variations in Beryllium-7 concentrations in surface air. J. Environ. Radioact. 9, 223–249.

Fernández, P.L., Gómez, J., Ródenas, C., 2012. Evaluation of uncertainty and detection limits in ^{210}Pb and ^{210}Po measurement in water by alpha spectrometry using ^{210}Po spontaneous deposition onto a silver disk. Appl. Radiat. Isot. 70, 758–764.

Ferry, C., Beneito, A., Richon, P., Robe, M.C., 2001. An automatic device for measuring the effect of meteorological factors on Rn-222 flux from soils in the long term. Radiat. Prot. Dosim. 93, 271–274.

Fetter, C.W., 2001. Applied Hydrogeology. Prentice Hall, Upper Saddle River.

Fifield, L.K., Fink, D., Sie, S., Tuniz, C. (Eds.), 1994. Proceedings of the 6th international conference on accelerator mass spectrometry. Nucl. Instrum. Methods Phys. Res. B, 92, pp. 1–524.

Finkel, R.C., Nishiizumi, K., 1997. Beryllium-10 concentrations in the Greenland Ice Sheet Project 2 ice core from 3-40 ka. J. Geophys. Res. Ocean. 102, 26699–26706.

Fjeld, R.A., DeVol, T.A., Leyba, J.D., Paulenova, A., 2005. Measurement of radionuclides using ion chromatography and on-line radiation detection. J. Radioanal. Nucl. Chem. 263, 635–640.

Fontaine, J.-P., Pointurier, F., Blanchard, X., Taffary, T., 2004. Atmospheric xenon radioactive isotope monitoring. J. Environ. Radioact. 72, 129–135.

Forstner, O., Andersson, P., Diehl, C., Golser, R., Hanstorp, D., Kutschera, W., Lindahl, A., Priller, A., Steier, P., Wallner, A., 2008. Isobar suppression in AMS using laser photodetachment. Nucl. Instrum. Methods Phys. Res. B 266, 4565–4568.

Frechen, M., Sierralta, M., Oezen, D., Urban, B., 2007. Uranium-series dating of peat from central and Northern Europe. In: Sirocko, F., Litt, T., Claussen, M. (Eds.), The Climate of Past Interglacials. Springer, Heidelberg, pp. 92–118.

Freeman, S.P.H.T., 1993. Imaging SIMS with an accelerator (and biomedical applications). Nucl. Instrum. Methods Phys. Res. B 79, 627–630.

Freeman, S.P.H.T., Shanks, R.P., Donzel, X., Gaubert, G., 2015. Radiocarbon positive-ion mass spectrometry. Nucl. Instrum. Methods Phys. Res. B 361, 229–232. https://doi.org/10.1016/j.nimb.2015.04.034.

Froehlich, M.B., Steier, P., Wallner, G., Fifield, L.K., 2016. European roe deer antlers as an environmental archive for fallout ^{236}U and ^{239}Pu. J. Environ. Radioact. 151, 587–592.

Froehlich, M.B., Tims, S.G., Fallon, S.J., Wallner, A., Fifield, L.K., 2017. Nuclear weapons produced ^{236}U, ^{239}Pu and ^{240}Pu archived in a Porites Lutea coral from Enewetak Atoll. J. Environ. Radioact. 178–179, 349–353.

Froidevaux, P., Bochud, F., Haldimann, M., 2010. Retention half times in the skeleton of plutonium and ^{90}Sr from above-ground nuclear tests: a retrospective study of the Swiss population. Chemosphere 80, 519–524.

Fukai, R., Yokoyama, Y., 1982. Natural radionuclides in the environment. In: Hutzinger, O. (Ed.), Handbook of Environmental Chemistry. Springer, Berlin, pp. 47–60.

Fuma, S., Inoue, Y., 1995. Simplified and sensitive analysis of organically bound tritium in tree rings to retrospect environmental tritium levels. Appl. Radiat. Isot. 46, 991–997.

Galindo, C., Mougin, L., Nourreddine, A., 2007. An improved radiochemical separation of uranium and thorium in environmental samples involving peroxide fusion. Appl. Radiat. Isot. 65, 9–16.

Gamez, G., Finch, K., 2018. Recent advances in surface elemental mapping via glow discharge atomic spectrometry. Spectrochim. Acta B 148, 129–136.

Ganeev, et al., 2017. Direct isotope analysis of Chernobyl microparticles using time-of-flight mass spectrometry with pulsed glow discharge. Microchem. J. 132, 286–292.

Gascó, C., Antón, M.P., Delfanti, R., Gonzalez, A.M., Meral, J., Papucci, C., 2002. Variation of the activity concentrations and fluxes of natural (^{210}Po, ^{210}Pb) and anthropogenic (^{239,240}Pu, ^{137}Cs) dionuclides in the Strait of Gibraltar (Spain). J. Environ. Radioact. 62, 241–262.

Gauthier-Lafaye, F., Pourcelot, L., Eikenberg, J., Beer, H., Le Roux, G., Rhikvanov, L.P., Geckeis, H., Rabung, T., 2008. Actinide geochemistry: from the molecular level to the real system. J. Contaminant Hydrology 102, 187–195.

Geckeis, H., Rabung, T., 2008. Actinide geochemistry: from the molecular level to the real system. J. Contam. Hydrol. 102, 187–195.

Gerasopoulos, E., et al., 2001. A climatology of ^{7}Be at four high-altitude stations at the Alps and the Northern Apennines. Atmos. Environ 35, 6347–6360.

Germian, P., Pinte, G., 1990. Neptunium-237 in the marine environment, determination in animal and plant species in the English Channel: biological indicators and trophic relationships. J. Radioanal. Nucl. Chem. Art. 138, 49–61.

Gerstmann, U.C., Rosner, G., Schramel, P., 2004. Bioavailability of $^{239+240}$Pu and ^{137}Cs in aerosol and deposited dusts: a comparative study by fractional extraction. Radiation and Environmental Biophysics 43, 111–117.

Gerusky, T.M., 1981. Three mile island: assessment of radiation exposure and environmental contamination. NY Ann. Sci. 365, 54–62.

Giardina, I., Andreocci, L., Bazzarri, S., Mancini, L., Battisti, P., 2006. A comparison of different radiochemical methods applicable for the determination of plutonium isotopes in urine via alpha spectrometry. Czech. J. Phys. 56, D265–D270.

Gleick, P.H., 1996. Water resources. In: Schneider, S.H. (Ed.), Encyclopedia of Climate and Weather. Oxford University Press, New York, pp. 817–823.

Gosse, J.C., Phillips, F.M., 2001. Terrestrial in situ cosmogenic nuclides: theory and application. Quat. Sci. Rev. 20, 1475–1560.

Goswami, J.N., McGuire, R.E., Reedy, R.C., Lal, D., Jha, R.J., 1988. Solar flare protons and alpha particles during the last three solar cycles. J. Geophys. Res. 93, 7195–7205.

Gove, H.E. (Ed.), 1978. Proceedings of the First Conference on Radiocarbon Dating with Accelerators. University of Rochester, New York.

Gove, H.E., Litherland, A.E., Elmore, D. (Eds.), 1987. Proceedings of the 4th international Symposium on accelerator mass spectrometry. Nucl. Instrum. Methods Phys. Res. B29, pp. 1–455.

Grabowski, K.S., Knies, D.L., Cetina, C., 2007. Trace element AMS at NRL: initial use of a modified SIMS ion source. Nucl. Instrum. Methods Phys. Res. B 259, 27–30.

Grahek, Ž., Dulanská, S., Karanović, G., Coha, I., Tucaković, I., Nodilo, M., Mátel, Ľ., 2018. Comparison of different methodologies for the ^{90}Sr determination in environmental samples. J. Environ. Radioact. 181, 18–31.

Grammer, G.L., Fallon, S.J., Izzo, C., Wood, R., Gillanders, B.M., 2015. Investigating bomb radiocarbon transport in the southern Pacific Ocean with otolith radiocarbon. Earth Planet. Sci. Lett. 424, 59–68.

Graven, H.D., Guilderson, T.P., Keeling, R.F., 2007. Methods for high-precision ^{14}C AMS measurement of atmospheric CO_2 at LLNL. Radiocarbon 49, 349–356.

Guérin, N., Dai, X., 2013. Rapid preparation of polonium counting sources for alpha spectrometry using copper sulfide microprecipitation. Anal. Chem. 85, 6524–6529.

Guerquin-Kern, J.-L., Wu, T.-D., Quintana, C., Croisy, A., 2005. Progress in analytical imaging of the cell by dynamic secondary ion mass spectrometry (SIMS microscopy). Biochim. Biophys. Acta - Gen. Subj. 1724, 228–238.

Guo, L., Semiletov, I., Gustafsson, Ö., Ingri, J., Andersson, P., Dudarev, O., White, D., 2004. Characterization of Siberian Arctic coastal sediments: implications for terrestrial organic carbon export. Global Biogeochem. Cycles 18, GB1036.

Guo, Z., Li, J., Xu, X., Song, Z., Dong, X., Tian, J., Yang, Y., She, H., Xiang, A., Kang, Y., 2016. Sm-Nd dating and REE Composition of scheelite for the Honghuaerji scheelite deposit, Inner Mongolia, Northeast China. Lithos 261, 307–321.

Guseva, L.I., Lebedev, I.A., Myasoedov, B.F., Tikhomirova, G.S., 1976. Isolation of transplutonium elements on ionites in aqueous/alcohol media. In: Spitsyn, V.I., Katz, J.J. (Eds.), Proceedings of the Moscow Symposium on the Chemistry of Transuranium Elements. Pergamon, Oxford, pp. 55–59.

Guseva, L.I., Tikhomirova, G.S., 1974. Isolation of transplutonium elements on anionites by means nitric acid and ammonium thiocyanate. Sov. Radiochem. 16, 153–156.

Habibi, A., Boulet, B., Gleizes, M., Larivière, D., Cote, G., 2015. Rapid determination of actinides and ^{90}Sr in river water. Anal. Chim. Acta. 88, 3109–3116.

Hadley, G., 1735. Concerning the cause of the general trade-winds. Philos. Trans. 39, 58–62.

Hallstadius, L.A., 1984. Method for the electrodeposition of actinides. Nucl. Instrum. Methods Phys. Res. 223, 266–267.

Hamato, A., 1982. An anion exchange method for the determination of ^{241}Am and plutonium in environmental and biological samples. J. Radioanal. Nucl. Chem. 75, 265–273.

Hardy, E.P., Krey, P.W., Volchok, H.L., 1973. Global inventory and distribution of fallout plutonium. Nature 241, 444–445.

Haynes, W.M. (Ed.), 2017. CRC Handbook of Chemistry and Physics. CRC Press, Boca Raton.

Henjes-Kunst, F., Prochaska, W., Niedermayr, A., Sullivan, N., Baxter, E., 2014. Sm–Nd dating of hydrothermal carbonate formation: an example from the Breitenau magnesite deposit (Styria, Austria). Chem. Geol. 387, 184–201.

Henning, W., Kutschera, W., Paul, M., Smither, R.K., Yntema, J.L. (Eds.), 1981. Proceedings of the 2nd Symposium on Accelerator Mass Spectroscopy. Argonne National Laboratory, Chicago.

Henricsson, F., Ranebo, Y., Holm, E., Roos, P., 2011. Aspects on the analysis of ^{210}Po. J. Environ. Radioact. 102, 415–419.

Hertelendi, E., Uchrin, G., Ormai, P., 1989. ^{14}C release in various chemical forms with gaseous effluents from the Paks nuclear power plant. Radiocarbon 31, 754–761.

Hess, C.T., Michel, J., Horton, T.R., Prichard, H.M., Coniglio, W.A., 1985. The occurrence of radioactivity in public water supplies in the United States. Health Phys 48, 553–586.

Hess, C.T., Casparius, R.E., Norton, S.A., Brutsaert, W.F., 1980. Investigation of natural levels of radon-222 in groundwater in Maine for assessment of related health effects. In: Gesell, T.S., Lowder, W.M. (Eds.), The Natural Radiation Environment III. NTIS, Springfield, pp. 529–546.

Hidy, A.J., Brown, T.A., Tumey, S.J., Zimmerman, S.R.H., Gharibyan, N., Frank, M., Bench, G., 2018. A new ^{7}Be AMS capability established at CAMS and the potential for large datasets. Nucl. Instrum. Methods Phys. Res. B 414, 126−132.

Hindman, F.D., 1983. Neodymium fluoride mounting for alpha spectrometry determination of uranium, plutonium and americium. Analyt. Chem. 55, 2460−2461.

Hirose, K., 2016. Fukushima Daiichi nuclear power plant accident: atmospheric and oceanic impacts over the five years. J. Environ. Radioact. 157, 113−130.

Hirose, K., Sugimura, Y., 1984. Plutonium in the surface air in Japan. Health Phys 46, 1281−1285.

Hirose, K., Sugimura, Y., 1990. Plutonium isotopes in the surface air in Japan: effect of Chernobyl accident. J. Radioanal. Nucl. Chem. Art. 138, 127−138.

Hirose, K., Kim, C.K., Kim, C.S., Chang, B.W., Igarashi, Y., Aoyama, M., 2004. Wet and dry deposition patterns of plutonium in Daejeon, Korea. Sci. Total Environ. 332, 243−252.

Hirose, K., Igarashi, Y., Aoyama, M., Inomata, Y., 2010. Depositional behaviors of plutonium and thorium isotopes at Tsukuba and Mt. Haruna in Japan indicate the sources of atmospheric dust. J. Environ. Radioact. 101, 106−112.

Hirose, K., Povinec, P.P., 2015. Sources of plutonium in the atmosphere and stratosphere - troposphere mixing. Sci. Rep. 5, 15707.

Hirose, K., Povinec, P.P., 2018. Long-term variations of ^{90}Sr and ^{137}Cs in surface and deep waters of the Sea of Japan: characteristics, behavior and the Fukushima impact. Sci. Rep. (in print).

Hoffman, I., Lewis, B., Chan, P., Ungar, K., 2017. Analysis of ^{22}Na using a spectral summation technique on high-volume aerosol samples. J. Environ. Radioact. 169−170, 151−158.

Hölgye, Z., 2007. Coprecipitation of polonium with bismuth phosphate. J. Radioanal. Nucl. Chem. 274, 647−649.

Hölgye, Z., 2008. Plutonium isotopes in surface air of Prague in 1986 − 2006. J. Environ. Radioact. 99, 1653−1655.

Hölgye, Z., Filgas, R., 1987. Determination of ^{239,240}Pu in surface air in several localities in Czechoslovakia in 1986 in connection with the Chernobyl radiation accident. J. Radioanal. Nucl. Chem. 119, 21−28.

Hölgye, Z., Malý, M., 2000. Sources, vertical distribution, and migration rates of ^{239,240}Pu, ^{238}Pu, and ^{137}Cs in grassland soil in three localities of central Bohemia. J. Environ Radioact. 47, 135−147.

Holloway, R.W., Hayes, D., 1982. Mean residence time of plutonium in the troposphere. Environ. Sci. Technol. 16, 127−129.

Holm, E., Fukai, R., 1976. Determination of americium and curium by ion-exchange in nitric acid-methanol for environmental analysis. Talanta 23, 853−855.

Holm, E., Ballestra, S., Fukai, R., 1979. A method for ion exchange separation of low levels of americium in environmental materials. Talanta 26, 791−794.

Holtzman, R.B., Ilcewicz, F.H., 1966. Lead-210 and polonium-210 in tissues of cigarette smokers. Science 153, 1259−1260.

Hood, D., et al., 1989. Radon elimination during benzene preparation for radiocarbon dating by liquid scintillation spectrometry. Radiocarbon 31, 254−259.

Horikoshi, K., 2016. Extremophiles: Where It All Began. Springer, Tokyo.

Horiuchi, K., Uchida, T., Sakamoto, Y., Ohta, A., Matsuzaki, H., Shibata, Y., Motoyama, H., 2008. Ice core record of ^{10}Be over the past millennium from Dome Fuji, Antarctica: a new proxy record of past solar activity and a powerful tool for stratigraphic dating. Quat. Geochronol. 3, 253−261.

Horvatinčić, N., Barešić, J., Krajcar Bronić, I., Obelić, B., 2004. Measurement of low ^{14}C activities in a liquid scintillation counter in the Zagreb radiocarbon laboratory. Radiocarbon 46, 105−116.

Horvatinčić, N., Obelić, B., Krajcar Bronić, I., Srdoč, D., Bistrović, R., 1995. Sources of radon contamination in ^{14}C dating. Radiocarbon 37, 749−757.

Horwitz, E.P., Dietz, M., Chiarizia, R., Dietz, M.L., Diamond, H., 1993. Separation and preconcentration of actinides from acidic media by extraction chromatography. Anal. Chim. Acta 281, 361−372.

Horwitz, E.P., Dietz, M., Chiarizia, R., Diamond, H., Maxwell, S.L., Nelson, M.R., 1995. Separation and preconcentration of actinides by extraction chromatography using a supported liquid anion exchanger: application to the characterization of high-level nuclear waste solutions. Anal. Chim. Acta 310, 63−78.

Horwitz, E.P., Dietz, M.L., Chiarizia, R., Diamond, H., Essling, A.M., Graczyk, D., 1992. Separation and preconcentration of uranium from acidic media by extraction chromatography. Anal. Chim. Acta 266, 25−37.

Horwitz, E.P., Chiarizia, R., Dietz, M.L., 1997. DIPEX: a new extraction chromatographic material for the separation and preconcentration of actinides from aqueous solution. React. Funct. Polym. 33, 25−36.

Horwitz, E.P., McAlister, D.R., Bond, A.H., Barrans Jr., R.E., 2005. Novel extraction chromatographic resins based on tetraalkyldiglycolamides: characterization and potential applications. Solvent Extr. Ion Exch. 23, 319−344.

Hötzl, H., Winkler, R., 1987. Activity concentrations of ^{226}Ra, ^{228}Ra, ^{210}Pb, ^{40}K and ^{7}Be and their temporal variations in surface air. J. Environ. Radioact. 5, 445−458.

Hou, X., Aldahan, A., Nielsen, S.P., Possnert, G., 2009b. Time series of ^{129}I and ^{127}I speciation in precipitation from Denmark. Environ. Sci. Technol. 43, 6522−6528.

Hou, X., Dahlgaard, H., Nielsen, S.P., 2001. Chemical speciation analysis of ^{129}I in seawater and a preliminary investigation to use it as a tracer for geochemical cycle study of stable iodine. Mar. Chem. 74, 145−155.

Hou, X., Dahlgaard, H., Rietz, B., Jacobsen, U., Nielsen, S.P., Aarkrog, A., 1999. Determination of 129I in seawater and some environmental materials by neutron activation analysis. Analyst 124, 1109−1114.

Hou, X., Hansen, V., Aldahan, A., Possnert, G., Lind, O.C., Lujaniene, G., 2009a. A review on speciation of iodine-129 in the environmental and biological samples. Anal. Chim. Acta 632, 181−196.

Hou, X., Jensen, M., Nielsen, S.P., 2007. Use of ^{99m}Tc from a commercial ^{99}Mo/^{99m}Tc generator as yield tracer for the determination of ^{99}Tc at low levels. Appl. Radiat. Isot. 65, 610−618.

Hou, X., Povinec, P.P., Zhang, L., Shi, K., Biddulph, D., Chang, C.-C., Fan, Y., Golser, R., Hou, Y., Ješkovský, M., Jull, A.J.T., Liu, Q., Luo, M., Steier, P., Zhou, W., 2013. Iodine-129 in seawater offshore fukushima: distribution, inorganic speciation, sources, and budget. Environ. Sci. Technol. 47, 3091−3098.

Hou, X., Roos, P., 2008. Critical comparison of radiometric and mass spectrometric methods for the determination of radionuclides in environmental, biological and nuclear waste samples. Anal. Chim. Acta 608, 105−139.

Houk, R.S., Fassel, V.A., Flesch, G.D., Svec, H.J., Gray, A.L., Taylor, C.E., 1980. Inductively coupled argon plasma as an ion source

for mass spectrometric determination of trace elements. Anal. Chem. 52, 2283–2289.

Howard, B.J., Beresford, N.A., Mayes, R.W., Lamb, C.S., 1993. Transfer of ^{131}I to sheep milk from vegetation contaminated by chernobyl fallout. J. Environ. Radioact. 19, 155–161.

Hu, Q.H., Weng, J.Q., Wang, J.S., 2010. Sources of anthropogenic radionuclides in the environment: a review. J. Environ. Radioact. 101, 426–437.

Hua, Q., Barbetti, M., Fink, D., Kaiser, K.F., Friedrich, M., Kromer, B., Levchenko, V.A., Zoppi, U., Smith, A.M., Bertuch, F., 2009. Atmospheric ^{14}C variations derived from tree rings during the early Younger Dryas. Quat. Sci. Rev. 28, 2982–2990.

Hua, Q., Barbetti, M., Rakowski, A.Z., 2013. Atmospheric radiocarbon for the period 1950–2010. Radiocarbon 55, 2059–2072.

Huang, S., Sholkovitz, E.R., Conte, M.H., 2007. Application of high-temperature fusion for analysis of major and trace elements in marine sediment trap samples. Limnol. Oceanogr. 5, 13–22.

Huang, D., Hua, X., Xiu, G.-L., Zheng, Y.-J., Yu, X.-Y., Long, Y.-T., 2017. Secondary ion mass spectrometry: the application in the analysis of atmospheric particulate matter. Anal. Chim. Acta. 989, 1–14.

Hurst, G.S., Payne, M.G., 1988. Elemental analysis using resonance ionization spectroscopy. Spectrochim. Acta B 43, 715–726.

Hursthouse, A.S., Baxter, M.S., Livens, F.R., Duncan, H.J., 1991. Transfer of Sellafield-derived ^{237}Np to and within the terrestrial environment. J. Environ. Radioact. 14, 147–174.

Hursthouse, A.S., Baxter, M.S., Mckay, K., Livens, F.R., 1992. Evaluation of methods for the assay of neptunium and other long-lived actinides in environmental matrices. J. Radioanal. Nucl. Chem. 157, 281–294.

IAEA, International Atomic Energy Agency, 1998. Technical Report. The Radiological Situation at the Atolls of Mururoa and Fangataufa: Inventory of Radionuclides Underground at the Atolls, vol. 3. IAEA, Vienna.

IAEA, International Atomic Energy Agency, 2011. IAEA Reports Series. Radiation Protection and Norm Residue Management in the Production of Rare Earths from Thorium Containing Minerals, vol. 68. IAEA, Vienna.

IAEA, International Atomic Energy Agency, 2014. A Combined Procedure for Determination of Plutonium Isotopes, ^{241}Am and ^{90}Sr in Environmental Samples. IAEA, Vienna.

IAEA, International Atomic Energy Agency, 2003. Chernobyl's Legacy: Health, Environmental and Socio-Economic Impacts. IAEA, Vienna.

IAEA, International Atomic Energy Agency, 2005. Worldwide marine radioactivity studies (WOMARS): Radionuclide levels in oceans and sea. IAEA-TECDOC-1429. IAEA, Vienna.

IAEA, International Atomic Energy Agency, 2018. Nuclear Power Reactors in the World. IAEA, Vienna.

IAEA, International Atomic Energy Agency, 1981. Handling of Tritium Bearing Wastes. Technical Reports Series No. 203. IAEA, Vienna.

IAEA, International Atomic Energy Agency, 1996. One decade after Chernobyl: Summing up the consequences of the accident. IAEA, Vienna.

IAEA, International Atomic Energy Agency, 2004. Management of Waste Containing Tritium and Carbon-14. Technical Report Series No. 421. IAEA, Vienna.

Igarashi, G., Saeki, S., Takahata, N., Sumikawa, K., Tasaka, S., Sasaki, Y., Takahashi, M., Sano, Y., 1995a. Ground-water radon anomaly before the Kobe earthquake in Japan. Science 269, 60–61.

Igarashi, G., et al., 1995b. Ground-water radon anomaly before the Kobe earthquake in Japan. Science, New Series 269 (5220).

Igarashi, Y., Aoyama, M., Hirose, K., Povinec, P., Yabuku, S., 2005. What anthropogenic radionuclides (^{90}Sr and ^{137}Cs) in atmospheric deposition, surface soils and aeolian dusts suggest for dust transport over Japan. Water, air. & Soil Pollution 5, 51–69.

Igarashi, Y., Fujiwara, H., Jugder, D., 2011. Change of the Asian dust source region deduced from the composition of anthropogenic radionuclides in surface soil in Mongolia. Atmos. Chem. Phys. 11, 7069–7080.

Igarashi, Y., Sartorius, H., Miyao, T., Weiss, W., Fushimi, K., Aoyama, M., Hirose, K., Inoue, H.Y., 2000. ^{85}Kr and ^{133}Xe monitoring at MRI, Tsukuba and its importance. J. Environ. Radioact. 48, 191–202.

Igarashi, Y., Inomata, Y., Aoyama, M., Hirose, K., Takahashi, H., Shinoda, Y., Sugimoto, N., Shimizu, A., Chiba, M., 2009. Possible change in Asian dust source suggested by atmospheric anthropogenic radionuclides during the 2000s. Atmos. Environ. 43, 2971–2980.

Iizuka, Y., Matoba, S., Yamsaki, T., Oyabu, I., Kadota, M., Aoki, T., 2016. Glaciological and meteorological observations at the SEDome site, southeastern Greenland Ice Sheet. Bull. Glaciol. Res. 34, 1–10.

Imanaka, T., Endo, S., Sugai, M., Ozawa, S., Shizuma, K., Yamamoto, M., 2012. Early radiation survey of Iitate Village, which was heavily contaminated by the Fukushima Daiichi accident, conducted on 28 and 29 march 2011. Health Phys 102, 680–686.

Immé, G., Catalano, R., Mangano, G., Morelli, D., 2014. Radon exhalation measurements for environmental and geophysics study. Radiat. Phys. Chem. 95, 349–351.

International Electrotechnical Commission, 2002a. Equipment for Continuous Monitoring of Radioactivity in Gaseous Effluents, Part 1: General Requirements. IEC 60761-1 Ed. 2.0. IEC, Geneva.

International Electrotechnical Commission, 2002b. Equipment for Continuous Monitoring of Radioactivity in Gaseous Effluents, Part 2: Specific Requirements for Radioactive Aerosol Monitors Including Transuranic Aerosols. IEC 60761-2 Ed. 2.0. IEC, Geneva.

Irlweck, K., Khademi, B., Henrich, E., Kronraff, R., 1993. 239,240, ^{238}Pu, ^{90}Sr, ^{103}Ru and ^{137}Cs concentrations in surface air in Austria due to dispersion of Chernobyl releases over Europe. J. Environ. Radioact. 20, 133–148.

Ito, K., Hasebe, N., Hasebe, A., Arai, S., 2011. The matrix effect on ^{238}U and ^{232}Th measurements using pressed powder pellets by LA-ICP-MS. Geochem. J. 45, 375–385.

Ivanovich, M., Harmon, R.S., 1992. Uranium Series Disequilibrium: Applications to Earth, Marine and Environmental Sciences'. Clarendon Press, Oxford.

Ivanovich, M., 1994. Uranium series disequilibrium: concepts and applications. Radiochim. Acta 64, 81–94.

Jobbágy, V., Van Ammel, R., Marouli, M., 2012. Electrode Position Source Preparation for ^{238}U Alpha Source: Parameter Settings. European Commission Joint Research Centre Institute for Reference Materials and Measurements, p. 11. Report for EMRP Metro Fission project. Report EUR 25353 EN.

Jacobson, M.C., Hansson, H.-C.C., Noone, K.J., Charlson, R.J., 2000. Organic atmospheric aerosols: review and state of the science. Rev. Geophys. 38, 267–294.

Jagercikova, M., Cornu, S., Le Bas, C., Evrard, O., 2015. Vertical distributions of ^{137}Cs in soils: a meta-analysis. J. Soils Sediments 15, 81–95.

Jakopic, R., Tavcar, P., Benedik, L., 2007. Sequential determination of Pu and Am radio isotopes in environmental samples; a comparison of two separation procedures. Appl. Radiat. Isot. 65, 504−511.

Janovics, R., Kelemen, D.I., Kern, Z., Kapitány, S., Veres, M., Jull, A.J.T., Molnár, M., 2016. Radiocarbon signal of a low and intermediate level radioactive waste disposal facility in nearby trees. J. Environ. Radioact. 153, 10−14.

Janovics, R., Kern, Z., Güttler, D., Wacker, L., Barnabás, I., Molnár, M., 2013. Radiocarbon impact on a nearby tree of a light-water VVER-type nuclear power plant, Paks, Hungary. Radiocarbon 55, 826−832.

Jean-Baptiste, P., Mantisi, F., Dapoigny, A., Stievenard, M., 1992. Design and performance of a mass spectrometric facility for measuring helium isotopes in natural waters and for low-level tritium determination by the ^{3}He ingrowth method. Int. J. Radiat. Appl. Instrumentation. A 43, 881−891.

Jenk, T.M., Szidat, S., Schwikowski, M., Gäggeler, H.W., Brütsch, S., Wacker, L., Synal, H.-A., Saurer, M., 2006. Radiocarbon analysis in an Alpine ice core: record of anthropogenic and biogenic contributions to carbonaceous aerosols in the past (1650-1940). Atmos. Chem. Phys. 6, 5381−5390.

Ješkovský, M., Lištjak, M., Sýkora, I., Slávik, O., Povinec, P.P., 2018. Anthropogenic ^{137}Cs on atmospheric aerosols in Bratislava and around nuclear power plants in Slovakia. J. Environ. Radioact. 184−185, 77−82.

Ješkovský, M., Povinec, P.P., Steier, P., Šivo, A., Richtáriková, M., Golser, R., 2015. Retrospective study of ^{14}C concentration in the vicinity of NPP Jaslovské Bohunice using tree rings and the AMS technique. Nucl. Instrum. Methods Phys. Res. B 361, 129−132.

Jia, G., 2018. Simultaneous determination of 210Po and 210Pb in solid samples: a new method for 210Pb determination. Appl. Radiat. Isot. 137, 12−17.

Jia, G., Desideri, D., Guerra, F., Meli, M.A., Testa, C., 1997. Determination of plutonium and americium in moss and lichen samples. J. Radioanal. Nucl. Chem. 220, 15−19.

Jia, G., Testa, C., Desideri, D., Guerra, F., Roselli, C., 1998. Sequential separation and determination of plutonium, americium-241 and strontium-90 in soils and sediments. J. Radioanal. Nucl. Chem. 230, 21−27.

Jia, G., Belli, M., Blasi, M., Marchetti, A., Rosamilia, S., Sansone, U., 2001. Determination of ^{210}Pb and ^{210}Po in mineral and biological samples. J. Radioanal. Nucl. Chem. 247, 491−499.

Jiang, W., et al., 2012. An atom counter for measuring ^{81}Kr and ^{85}Kr in environmental samples. Geochim. Cosmochim. Acta 91, 1−6.

Jordan, C.E., Dibb, J.E., Finkel, R.C., 2003. ^{10}Be/^{7}Be tracer of atmospheric transport and stratosphere-troposphere exchange. J. Geophys. Res. 108, 4234.

Jull, A.J.T., 2013. AMS radiocarbon dating. In: Elias, S.A., Mock, C.J. (Eds.), Encyclopedia of Quaternary Science. Elsevier, Amsterndam, pp. 316−323.

Jull, A.J.T., Beck, J.W., Burr, G.S., (Eds.), 1997. Proceedings of the 7th international conference on accelerator mass spectrometry. Nucl. Instrum. Methods Phys. Res. B 123, 1−612.

Jull, A.J.T., et al., 2018. More rapid ^{14}C excursions in the tree-ring record: a record of different kind of solar activity at about 800 BC? Radiocarbon. https://doi.org/10.1017/RDC.2018.53 (in press).

Kabdyrakova, A.M., Lukashenko, S.N., Mendubaev, A.T., Kunduzbayeva, A.Y., Panitskiy, A.V., Larionova, N.V., 2018. Distribution of artificial radionuclides in particle-size fractions of soil on fallout plumes of nuclear explosions. J. Environ. Radioact. 186, 45−53.

Kahn, B., Blanchard, R.L., Brinck, W.L., Kriecer, H.L., Kolde, H.E., Averett, W.J., Gold, S., Martin, A., Gels, G.L., 1974. Radiological Surveillance Study a t the Haddam Neck PWR Nuclear Power Station. Report No. EPA-520/374-007. US. Environmental Protection Agency, Washington.

Kaizer, J., Aoyama, M., Kumamoto, Y., Molnár, M., Palcsu, L., Povinec, P.P., 2018a. Tritium and radiocarbon in the western North Pacific waters: post-Fukushima situation. J. Environ. Radioact. 184−185, 83−94.

Kaizer, J., Ješkovský, M., Povinec, P.P., Šivo, A., 2016a. Advancement in the ^{14}C and ^{129}I sample processing and target preparation for accelerator mass spectrometry at CENTA. In: Ioannidou, A., Povinec, P.P. (Eds.), Proc. Of the ENVIRA 2015 Conf: New Challenges with New Analytical Technologies. Aristotle University of Thessaloniki, Thessaloniki, pp. 15−21.

Kaizer, J., Ješkovský, M., Qiao, J., Zhang, L., Hou, X., Povinec, P.P., 2016b. Chromatographic separation methods for preparation of iodine-129 and plutonium targets in AMS measurements. Acta Phys. Univ. Comenianae LIII 101−109.

Kaizer, J., Obuch, J., Kontul', I., Šivo, A., Richtáriková, M., Čech, P., Povinec, P.P., 2018b. Methods of radiocarbon determination in wine and bone samples by gas proportional counting technique. Radiocarbon 60, 1139−1149. https://doi.org/10.1017/RDC.2018.20.

Kalinowski, M.B., et al., 2010. Discrimination of nuclear explosions against civilian sources based on atmospheric xenon isotopic activity ratios. Pure and Applied Geophysics 167, 517−539.

Kanjanapayont, P., Klötzli, U., Thöni, M., Grasemann, B., Edwards, M.A., 2012. Rb−Sr, Sm−Nd, and U−Pb geochronology of the rocks within the Khlong Marui shear zone, southern Thailand. J. Asian Earth Sci. 56, 263−275.

Karamanis, D., Stamoulis, K., Ioannides, K.G., 2007. Natural radionuclides and heavy metals in bottled water in Greece. Desalination 213, 90−97.

Kavouras, I.G., Stephnou, E.G., 2002. Particle size distribution of organic primary and secondary aerosol constituents in urban, background marine, and forest atmosphere. J. Geophys. Res. 107, 4069.

Kazi, Z.H., Cornett, J.R., Zhao, X., Kieser, L., 2014. Americium and plutonium separation by extraction chromatography for determination by accelerator mass spectrometry. Anal. Chim. Acta 829, 75−80.

Kehagia, K., Potiriadis, C., Bratakos, S., Koukouliou, V., Drikos, G., 2007. Determination of ^{226}Ra in urine samples by alpha spectrometry. Radiat. Prot. Dosim. 127, 293−296.

Keith-Roach, M.J., Turup, S., Oughton, D.H., Dahlgaard, H.H., 2002. Comparison of two ICP-MS set-ups for measuring ^{99}Tc in large volume water samples. Analyst 127, 70−75.

Keith-Roach, M.J., Day, J.P., Fifield, L.K., Livens, F.R., 2001. Measurementof ^{237}Np in environmental water samples by accelerator mass spectrometry. Analyst 126, 58−61.

Kelley, J.M., Bond, L.A., Beasley, T.M., 1999. Global distribution of Pu isotopes and Np-237. Sci. Total Environ. 238, 483−500.

Kenna, T.C., 2002. Determination of plutonium isotopes and neptunium-237 in environmental samples by inductively coupled plasma mass

spectrometry with total sample dissolution. J. Anal. At. Spectrom 17, 1471–1479.

Kenna, T.C., 2009. Using sequential extraction technique to assess the partitioning of plutonium and neptunium-237 from multiple sources in sediments from the Ob River (Siberia). J. Environ. Radioact 100, 547–557.

Kennish, J.M., 2001. Practical Handbook of Marine Science. CRC Press, New York.

Ketterer, M.E., Hafer, K.M., Mietelski, J.W., 2004. Resolving Chernobyl vs. global fallout contributions in soils from Poland using Plutonium atom ratios measured by inductively coupled plasma mass spectrometry. J. Environ. Radioact. 73, 183–201.

Khattab, M., 2016. Determination of uranium concentrations and $^{234}U/^{238}U$ activity ratio in some granitic rock samples by alpha spectrometry: application of a radiochemical procedure. Radiat. Prot. Environ. 39, 122–127.

Kierepko, R., Mietelski, J.W., Ustrnul, Z., Anczkiewicz, R., Wershofen, H., Holgye, Z., Kapała, J., Isajenko, K., 2016. Plutonium isotopes in the atmosphere of Central Europe: isotopic composition and time evolution vs. circulation factors. Sci. Total. Environ. 569–570, 937–947.

Kim, K.G., Burnett, W.C., Horwitz, E.P., 2000. Efficient preconcentration and separation of actinide elements from large soil and sediments samples. Anal. Chem. 72, 4882–4887.

Kim, J., Tsouris, C., Mayes, R.T., Oyola, Y., Saito, T., Janke, C.J., Dai, S., Schneider, E., Sachde, D., 2013. Recovery of uranium from seawater: a review of current status and future research needs. Sep. Sci. Technol. 48, 367–387.

Kimura, T., 1990. Simultaneous determination of neptunium, plutonium, americium and curium using coprecipitation with bismuth phosphate. J. Radioanal. Nucl. Chem. 139, 297–305.

Kirchner, G., Strebl, F., Bossew, P., Ehlken, S., Gerzabek, M.H., 2009. Vertical migration of radionuclides in undisturbed grassland soils. J. Environ. Radioact. 100 (9), 716–720.

Klötzli, U.S., 1992. Negative thermal ionisation mass spectrometry: a new approach to boron isotope geochemistry. Chem. Geol. Isot. Geosci. Sect. 101, 111–122.

Knezovich, J., Brown, T., Buchholz, B., Finkel, R., Guilderson, T., Kashgarian, M., Nimz, G., Ognibene, T., Tumey, S., Vogel, J. (Eds.), 2007. Proceedings of the tenth international conference on accelerator mass spectrometry. Nucl. Instrum. Methods Phys. Res. B, vol. 259, pp. 1–816.

Koarashi, J., Amano, H., Andoh, M., Iida, T., 2000. Estimation of ^{222}Rn flux from ground surface based on the variation analysis of ^{222}Rn concentration in a closed chamber. Radiat. Prot. Dosim. 87, 121–131.

Kobayashi, S., Shinomiya, T., Kitamura, H., Ishikawa, T., Imaseki, H., Oikawa, M., Kodaira, S., Miyaushiro, N., Takashima, Y., Uchihori, Y., 2015. Radioactive contamination mapping of north-eastern and eastern Japan by a car-borne survey system, Radi-Probe. J. Environ. Radioact. 139, 281–293.

Koh, S., Aoki, T., Katayama, Y., Takada, J., 1999. Losses of elements in plant samples under the dry ashing process. J. Radioanal. Nucl. Chem. 239, 591–594.

Koide, M., Bruland, K.W., 1975. The electrodeposition and determination or radium by isotopic dilution in sea water and sediments simultaneously with other natural radionuclides. Anal. Chim. Acta 75, 1–19.

Koide, M., Bertine, K.K., Chow, T.J., Goldberg, E.D., 1985. The $^{240}Pu/^{239}Pu$ ratio, a potential geochronometer. Earth Planet. Sci. Lett. 72, 1–8.

Kontul', I., Ješkovský, M., Kaizer, J., Šivo, A., Richtáriková, M., Povinec, P.P., Čech, P., Steier, P., Golser, R., 2017. Radiocarbon concentration in tree-ring samples collected in the south-west Slovakia (1974–2013). Appl. Radiat. Isot. 126, 58–60.

Koppenaal, D., Barinaga, C.J., Carado, A.J., Liezers, M., 2011. Development and use of Orbital Trapping Techniques for Elemental Analysis. Pittcon, New York.

Korsakissok, I., Mathieu, A., Didier, D., 2013. Atmospheric dispersion and ground deposition induced by the Fukushima Nuclear Power Plant accident: a local-scale simulation and sensitivity study. Atm. Environ. 70, 267–279.

Korsakissok, I., Mathieu, A., Didier, D., 2013. Atmospheric dispersion and ground deposition induced by the Fukushima Nuclear Power Plant accident: A local-scale simulation and sensitivity study. Atmos. Environ. 70, 267–279.

Kořínková, T., Svetlik, I., Fejgl, M., Povinec, P.P., Simek, P., Tomaskova, L., 2016. Occurrence of organically bound tritium in the Mohelno lake system. J. Radioanal. Nucl. Chem. 307, 2295–2299.

Kováčik, A., Sýkora, I., Povinec, P.P., 2013. Monte Carlo and experimental efficiency calibrationof gamma-spectrometers for non-destructive analysis of large volume samples of irregular shapes. J. Radioanal. Nucl. Chem. 298, 665–672.

Kraiem, M., Richter, S., Kühn, H., Aregbe, Y., 2011. Development of an improved method to perform single particle analysis by TIMS for nuclear safeguards. Anal. Chim. Acta 688, 1–7.

Kraus, K.A., Nelson, F. (Eds.), 1955. Proc. Intern. Conf. On the Peaceful Uses of Atomic Energy. United Nations, New York.

Krey, P.W., 1968. Atmospheric burnup of a plutonium-238 generator. Science 156, 769–771.

Krištof, R., Košenina, S., Zorko, B., Logar, J.K., 2017. Tritium in organic matter around Krško nuclear power plant. J. Radioanal. Nucl. Chem. 314, 675–679.

Krmpotića, M., Rožmarića, M., Benedik, L., 2018. Investigation of key factors in preparation of alpha sources by Electrodeposition. Appl. Radiat. Isot. 136, 37–44.

Królak, E., Krupa, B., Sarnowska, K., Karwowska, J., 2008. Isotopes: cesium-137 and potassium-40 in soils of the Powiat of Garwolin (Prosince of Mazowsze). J. Elementol. 13, 81–90.

Krstić, D., Nikezić, D., Stevanović, N., Jelić, M., 2004. Vertical profile of ^{137}Cs in soil. Appl. Radiat. Isot. 61, 1487–1492.

Kulan, A., 2006. Seasonal ^{7}Be and ^{137}Cs activities in surface air before and after the Chernobyl event. J. Environ. Radioact. 90, 140–150.

Kunz, C., 1985. Carbon-14 discharge at three light-water reactors. Health Phys 49, 25–35.

Kunz, C.O., Paperiello, C.J., 1976. Xenon-133: ambient activity from nuclear power stations. Science 192, 1235–1237.

Kuo, L.J., Janke, C.J., Wood, J.R., Strivens, J.E., Das, S., Oyola, Y., Mayes, R.T., Gill, G.A., 2015. Characterization and testing of amidoxime-based adsorbent materials to extract uranium from natural seawater. Ind. Eng. Chem. Res. 55, 4285–4293.

Kutschera, W., Golser, R., Priller, A., Strohmaier, B. (Eds.), 2000. 8th international conference on accelerator mass spectrometry. Nucl. Instrum. Methods Phys. Res. B 172, pp. 1–978.

Lal, D., Peters, B., 1967. Cosmic ray produced radioactivity on earth. In: Flugg, S. (Ed.), Handbook of Physics. Springer, Berlin, pp. 551–612.

Lal, R., Fifield, L.K., Tims, S.G., Wasson, R.J., 2017. ^{239}Pu fallout across continental Australia: implications on ^{239}Pu use as a soil tracer. J. Environ. Radioact. 178–179, 394–403.

Lally, A.E., Glover, K.M., 1984. Source preparation in alpha spectrometry. Nucl. Instrum. Methods Phys. Res. 223, 259–265.

Larionova, N.V., Lukashenko, S.N., Kabdyrakova, A.M., Kunduzbayeva, A.Y., Panitskiy, A.V., Ivanova, A.R., 2018. Transfer of radionuclides to plants of natural ecosystems at the Semipalatinsk Test Site. J. Environ. Radioact. 186, 63–70.

Larivière, D., Brownell, D.K., Epov, V.N., Cornett, R.J., Evans, R.D., 2007. Determination of ^{226}Ra in sediments by ICP-MS: a comparative study of three sample preparation approaches. J. Radioanal. Nucl. Chem. 273 (2), 337–344.

Larivière, D., Epov, V.N., Reiber, K.M., Cornett, R.J., Evans, R.D., 2005. Micro-extraction procedures for the determination of Ra226 in well waters by SF-ICP-MS. Anal. Chim. Acta 528, 175–182.

Larivière, D., Guérin, N., 2010. Natural radioactivity. In: Atwood, D.A. (Ed.), Radionuclides in the Environment. Wiley, New York, pp. 1–18.

La Rosa, J.J., Burnett, W., Lee, S.H., Levy, I., Gastaud, J., Povinec, P.P., 1989. Separation of actinides, cesium and strontium from marine samples using extraction chromatography and sorbents. IAEA Technical Report Series, TRS-295. IAEA, Vienna.

La Rosa, J.J., Burnett, W.C., Lee, S.H., Levy, I., Gastaud, J., Povinec, P.P., 2001. Separation of actinides, cesium and strontium from marine samples using extraction chromatography and sorbents. J. Radioanal. Nucl. Chem. 248, 765–770.

La Rosa, J.J., Gastaud, J., Lagan, L., Lee, S.H., Levy-Polomo, I., Povinec, P.P., Wyse, E., 2005. Recent developments in analysis of transuranics (Np, Pu, Am) in seawater. J. Radioanal. Nucl. Chem. 263, 427–436.

La Rosa, J.J., Mietelski, J.W., Wyse, E., 2010. Pilot measurements of 237Np in forest litter from Poland. J. Radioanal. Nucl. Chem. 283, 385–387.

Lassen, J., Bricault, P., Dombsky, M., Lavoie, J.P., Geppert, C., Wendt, K., 2006. Resonant ionization laser ion source project at TRIUMF. Hyperfine Interact 162, 69–75.

Laubenstein, M., et al., 2004. Underground measurements of radioactivity. Appl. Radiat. Isot. 61, 167–172.

Lavi, N., Alfassi, Z.B., Drndarski, N., 1997. Calibration of Marinelli vessels for measurement of radioactive environmental samples. Nucl. Instrum. Methods Phys. Res. A 385, 376–380.

Lawrence, C.E., Akber, R.A., Bollhöfer, A., Martin, P., 2009. Radon-222 exhalation from open ground on and around a uranium mine in the wet-dry tropics. J. Environ. Radioact. 100, 1–8.

Laybourne, R.C., 1974. Collision between a vulture and an aircraft at an altitude of 37,000 feet. Wilson Bull 86, 461–462.

Le Petit, G., Jutier, C., Gross, P., Greiner, V., 2006. Low-level activity measurement of ^{131}Xe^{m}, ^{133}Xe^{m}, ^{135}Xe and ^{133}Xe in atmospheric air samples using high-resolution dual X–γ spectrometry. Appl. Radiat. Isot. 64, 1307–1312.

Lee, S.H., Pham, M.K., Povinec, P.P., 2002. Radionuclide variations in the air over Monaco. J. Radioanal. Nucl. Chem. 254, 445–453.

Lee, S.H., LaRosa, J.J., Gautaud, J., Povinec, P.P., 2005. The development of sequential separation methods for the analysis of actinides in sediments and biological materials using anion-exchange resins and extraction chromato-graphy. J. Radioanal. Nucl. Chem 263, 419–425.

Lee, M.H., Jung, E.C., Kim, W.H., Jee, K.Y., 2007. Sequential separation of the actinides in environmental and radioactive waste samples. J. Alloys Compd. 444–445, 544–549.

Lee, S.H., Povinec, P.P., Wyse, E., Hotchkis, M.A.C., 2008. Ultra-low-level determination of ^{236}U in IAEA marine reference materials by ICPMS and AMS. Appl. Radiat. Isot. 66, 823–828.

Lee, C.-G., Park, J., Lim, S.H., 2018. Accurate determination of minor isotope ratios in individual plutonium–uranium mixed particles by thermal ionization mass spectrometry. Nucl. Eng. Technol. 50, 140–144.

Lee, M.H., Kim, J.Y., Kim, W.H., Yung, E.C., Jee, K.Y., 2008. Investigation of the oxidation states of plutonium isotopes in a hydrochloric acid solution. Appl. Radiat. Isot. 66, 1975–1979.

Lee, S.H., Gastaud, J., La Rosa, J.J., Kwong, L.L.W., Povinec, P.P., Wyse, E., Fifield, L.K., Hausladen, P.A., Di Tada, L.M., Santos, G.M., 2001. Analysis of plutonium isotopes in marine samples by radiometric, ICP-MS and AMS techniques. J. Radioanal. Nucl. Chem. 248, 757–764.

Lee, S.H., Heo, D.H., Kang, H.B., Oh, P.J., Lee, J.M., Park, T.S., Lee, K.B., Oh, J.S., Suh, J.K., 2013. Distribution of ^{131}I, ^{134}CS, ^{137}Cs and ^{239,240}Pu concentrations in Korean rainwater after the Fukushima nuclear power plant accident. J. Radioanal. Nucl. Chem. 296, 727–731.

Lehto, J., 2009. Americium in the finish environment. Boreal Environment Research 14, 427–437.

Lehto, J., Hou, X., 2011. Chemistry and Analysis of Radionuclides: Laboratory Techniques and Methodology. Wiley, New York.

Lehto, J., Räty, T., Hou, X., Paatero, J., Aldahan, A., Possnert, G., Flinkman, J., Kankaanpää, H., 2012. Speciation of ^{129}I in sea, lake and rain waters. Sci. Total Environ. 419, 60–67.

Leifer, R., Juzdan, Z.R., 1986. The High Altitude Sampling Program: Radioactivity in the Stratosphere. US Department of Energy, New York. Final Report EML-458.

Lemons, B., Khaing, H., Ward, A., Thakur, P., 2018. A rapid method for the sequential separation of polonium, plutonium, americium and uranium in drinking water. Appl. Radiat. Isot. 136, 10–17.

Livens, F.R., Baxter, M.S., 1988. Chemical associations of artificial radionuclides in Cumbrian soils. J. Environ. Radioact. 7, 75–86.

Levin, I., Münnich, K.O., Weiss, W., 1980. Radiocarbon 22, 379–391.

Levin, I., Kromer, B., 2004. The tropospheric $^{14}CO_2$ level in mid-latitudes of the northern hemisphere (1959-2003). Radiocarbon 46, 1261–1272.

Levin, I., Kromer, B., Schmidt, M., Sartorius, H., 2003. A novel approach for independent budgeting of fossil fuel CO_2 over Europe by $^{14}CO_2$ observations. Geophys. Res. Lett. 30, 2194.

Levy, I., et al., 2011. Marine anthropogenic radiotracers in the Southern Hemisphere: new sampling and analytical strategies. Prog. Oceanogr. 89, 120–133.

Li, Q.-L., Chen, F., Yang, J.-H., Fan, H.-R., 2008. Single grain pyrite Rb–Sr dating of the Linglong gold deposit, eastern China. Ore Geol. Rev. 34, 263–270.

Libby, W.F., 1961. Radiocarbon dating. Science 133, 621–629.

Lin, W., Chen, L., Yu, W., Ma, H., Zeng, Z., Lin, J., Zeng, S., 2015. Radioactivity impacts of the fukushima nuclear accident on the atmosphere. Atmos. Environ. 102, 311–322.

Lindahl, P., Roos, P., Eriksson, M., Holm, E., 2004. Distribution of Np and Pu in Swedish lichen samples (cladonia stellaris) contaminated by atmospheric fallout. J. Environ. Radioact. 73, 73–85.

Liong Wee Kwong, L., La Rosa, J.J., Lee, S.-H., Povinec, P.P., 2001. Liquid scintillation spectrometry of beta-emitters in marine samples. J. Radioanal. Nucl. Chem. 248, 751–755.

Liong Wee Kwong, L., Gastaud, J., La Rosa, J., Lee, S.H., Povinec, P.P., Wyse, E., 2004a. Determination of ^{241}Pu in marine samples using co-precipitation with rare earth fluoride and liquid scintillation spectrometry. J. Radioanal. Nucl. Chem. 261, 283−289.

Liong Wee Kwong, L., Povinec, P.P., Jull, A.J.T., 2004b. Preparation of graphite targets from small marine samples for AMS radiocarbon measurements. Radiocarbon 46, 133−139.

Livens, F.R., Singleton, D.L., 1989. Evaluation of methods for the radiometric determination of americium-241 in environmental samples. Analyst 114, 1097−1101.

Livens, F.R., Singleton, D.L., 1991. Plutonium and americium in soil organic matter. J. Environ. Radioact. 13, 323−339.

Livingston, H.D., Povinec, P.P., 2000. Anthropogenic marine radioactivity. Ocean Coast. Manag. 43, 689−712.

Livingston, H.D., Povinec, P.P., Ito, T., Togawa, O., 2001. The behaviour of plutonium in the Pacific Ocean. In: Kudo, A. (Ed.), Plutonium in the Environment. Elsevier, Amsterdam, pp. 267−291.

Livingston, H.D., Povinec, P.P., 2002. A millennium perspective on the contribution of global fallout radionuclides to ocean science. Health Phys 82, 656−668.

Longo, A., Bianchi, S., Plastino, W., 2018. Xenon and radon time series analysis: a new methodological approach for characterising the local scale effects at CTBT radionuclide network. Appl. Radiat. Isot. 139, 209−216.

Loosli, H.H., Oeschger, H., 1969. ^{37}Ar and ^{81}Kr in the atmosphere. Earth Planet. Sci. Lett. 7, 67−71.

Love, A.H., Hunt, J.R., Roberts, M.L., Southon, J.R., Chiarappa-Zucca, M.L., Dingley, K.H., 2002. Use of tritium accelerator mass spectrometry for tree ring analysis. Environ. Sci. Technol. 36, 2848−2852.

Love, A.H., Hunt, J.R., Vogel, J.S., Knezovich, J.P., 2004. Improving tritium exposure reconstructions using accelerator mass spectrometry. Anal. Bioanal. Chem. 379, 198−203.

Lozano, J.C., Tomé, F.V., Rodríguez, P.B., Prieto, C., 2010. A sequential method for the determination of ^{210}Pb, ^{226}Ra, and uranium and thorium radioisotopes by LSC and alpha-spectrometry. Appl. Radiat. Isot. 68, 828−831.

Lu, Z.T., et al., 2014. Tracer applications of noble gas radionuclides in the geosciences. Earth-Science Rev. 138, 196−214.

Lucas, H.F., 1957. Improved low-level alpha-scintillation counter for radon. Rev. Sci. Instrum. 28, 680−683.

Lujanas, V., Mastauskas, A., Lujaniene, G., Spirkauskaite, N., 1994. Development of radiation in Lithuania. J. Environ. Radioact. 23, 249−263.

Lujaniene, G., 2013. Determination of Pu, Am and Cm in environmental samples. In: Proceedings of the International Symposium on Isotopes in Hydrology, Marine Ecosystems, and Climate Change Studies: Monaco, March 27-April 1, 2011, vol. 2. IAEA, Vienna, pp. 411−418.

Lujaniene, G., Lujanas, V., Jankunaite, D., Ogorodnikov, B.I., Mastauskas, A., Ladygiene, R., 1999. Speciation of radionuclides of the Chernobyl origin in aerosol and soil samples. Czech. J. Phys. 49, 107−112.

Lujaniene, G., Plukis, A., Kimtys, E., Remeikis, V., Jankunaite, D., Ogorodnikov, B.I., 2002. Study of ^{137}Cs, ^{90}Sr, ^{239,240}Pu, ^{238}Pu and ^{241}Am behavior in the Chernobyl soil. J. Radioanal. Nucl. Chem. 251, 59−68.

Lujaniene, G., Sapolaite, J., 2005. Determination of cesium, americium and plutonium isotopes in the environmental samples. In: Ilus, E. (Ed.), Proc. Of the Nordic Nuclear Safety Research NKS-140 Seminar, Tartu, 24-25 October, 2005. NKS, Roskilde, pp. 113−115.

Lujaniene, G., Sapolaite, J., Remeikis, V., Lujanas, V., Jermolajev, A., 2006. Cesium, americium and plutonium isotopes in ground level air of Vilnius. Czech. J. Phys. Suppl. D. 56, D55−D66.

Lujaniene, G., Aninkevicius, V., Lujanas, V., 2009. Artificial radionuclides in the atmosphere over Lithuania. J. Environ. Radioact. 100, 108−119.

Lujaniene, G., Valiulis, D., Bycenkiene, S., Sakalys, J., Povinec, P.P., 2012a. Plutonium isotopes and ^{241}Am in the atmosphere of Lithuania: a comparison of different source terms. Atmos. Environ. 61, 419−427.

Lujaniene, G., Bycenkiene, S., Povinec, P.P., Gera, M., 2012b. Radionuclides from the Fukushima accident in the air over Lithuania: measurement and modeling approaches. J. Environ. Radioact. 114, 71−80.

Luo, M., Xinga, S., Yang, Y., Song, L., Ma, Y., Wanga, Y., Dai, X., Happel, S., 2018. Sequential analyses of actinides in large-size soil and sediment samples with total sample dissolution. J. Environ. Radioact. 187, 73−80.

Lusa, M., Lehto, J., Leskinen, A., Jaakkola, T., 2009. ^{137}Cs, ^{239,240}Pu and ^{241}Am in bottom sediments and surface water of Lake Päijänne, Finland. J. Environ. Radioact. 100, 468−476.

Lvovitch, M.I., 1973. The global water balance. Trans. Amer. Geophys. Union 54, 28−42.

Macášek, F., 2008. Sampling techniques. In: Povinec, P.P. (Ed.), Analysis of Environmental Radionuclides. Elsevier, Amsterdam, pp. 17−47.

Mace, E., et al., 2017. Simultaneous measurement of tritium and radiocarbon by ultra-low-background proportional counting. Appl. Radiat. Isot. 126, 171−174.

Macfarlane, A.M., Miller, M., 2007. Nuclear energy and uranium resources. Elements 3, 185−192.

Magnusson, A., Aronsson, P.O., Lundgren, K., Stenstrom, K., 2008. Characterization of ^{14}C in Swedish light water reactors. Health Phys 95, S110−S121.

Mahara, Y., Ohta, T., Ogawa, H., Kumata, A., 2015. Atmospheric direct uptake and long-term fate of radiocesium in trees after the fukushima nuclear accident. Sci. Rep. 4, 7121.

Maher, E.F., Laird, N.M., 1985. EM algorithm reconstruction of particle size distributions from diffusion battery data. J. Aerosol Sci. 16, 557−570.

Manić-Kudra, S., Paligorić, D., Novković, D., Smiljanić, R., Milošević, Z., Subotić, K., 1995. Plutonium isotopes in the surface air at Vin_ca-Belgrade site in May 1986. J. Radioanal. Nucl. Chem. 199, 27−34.

Maréchal, Y., 2007. The Hydrogen Bond and the Water Molecule. Elsevier, Amsterdam.

Margaritz, M., Wells, M., Amiel, A.J., Ronen, D., 1989. Application of a multi-layer sampler based on the dialysis cell technique for the study of trace metals in ground water. Appl. Geochem. 4, 617−624.

Maringer, F.J., et al., 2017. Advancements in NORM metrology − results and impact of the European joint research project MetroNORM. Appl. Radiat. Isotop. 126, 273−278.

Martin, P., Hancock, G.J., 1992. Routine analysis of naturally occurring radionuclides in environmental samples by alpha-particle spectrometry, Research report 7, Supervising Scientist for the Alligator Rivers

Region. AGPS, Canberra, p. 111. ISSN 0810-9966, v ISBN 0 644 25667 2.

Martin, C.J., Heaton, B., Robb, J.D., 1988. Studies of ^{131}I, ^{137}Cs and ^{103}Ru in milk, meat and vegetables in North East Scotland following the Chernobyl accident. J. Environ. Radioact. 6, 247–259.

Martin, J.M., Thomas, A.J., 1988. Anomalous concentrations of atmospheric plutonium-238 over Paris. J. Environ. Radioact. 7, 1–16.

Martschini, M., et al., 2013. AMS of ^{36}Cl with the VERA 3 MV tandem accelerator. Nucl. Instrum. Methods Phys. Res. B 294, 115–120.

Masarik, J., 2009. Origin and distribution of radionuclides in the continental environment. In: Froehlich, K. (Ed.), Environmental Radionuclides: Tracers and Timers of Terrestrial Processes. Elsevier, Amsterdam, pp. 1–26.

Masarik, J., Beer, J., 1999. Simulation of particle fluxes and cosmogenic nuclide production in the Earth's atmosphere. J. Geophys. Res. Atmos. 104, 12099–12111.

Masarik, J., Beer, J., 2009. An updated simulation of particle fluxes and cosmogenic nuclide production in the Earth's atmosphere. J. Geophys. Res. 114, D11103.

Masson, O., Piga, D., Le Roux, G., Mary, J., de Vismes, A., Gurriaran, R., Renaud, P., Saey, L., Paulat, P., 2009. Recent trends and explanation for airborne ^{137}Cs activity level increases in France. Radioprotection 44, 327–332.

Masson, O., et al., 2011. Tracking of airborne radionuclides from the damaged fukushima Dai-ichi nuclear reactors by European networks. Environ. Sci. Technol. 45, 7670–7677.

Masson, O., de Vismes Ott, A., Bourcier, L., Paulat, P., Ribeiro, M., Pichon, J.M., Sellegri, K., Gurriaran, R., 2015. Change of radioactive cesium (^{137}Cs and^{134}Cs) content in cloud water at an elevated site in France, before and after the Fukushima nuclear accident: comparison with radioactivity in rainwater and in aerosol particles. Atmos. Res. 151, 45–51.

Masson, O., et al., 2018a. Potential source apportionment and meteorological conditions involved in airborne 131I detections in January/February 2017 in Europe. Environ. Sci. Technol. 52, 8488–8500.

Masson, O., et al., 2018b. European Monitoring of Airborne Traces of Radioactive Ruthenium from an Undeclared Major Nuclear Release in Fall 2017 (in preparation).

Mathew, E., Matkar, V.M., Pillai, K.C., 1981. Determination of Pu, Am and Cm in environmental materials. J. Radioanal. Chem. 62, 267.

Maxwell, S.L., 2008a. Rapid method for determination of plutonium, americium and curium in large soil samples. J. Radioanal. Nucl. Chem. 275, 395–402.

Maxwell, S.L., 2008b. Rapid analysis of emergency urine and waters samples. J. Radioanal. Nucl. Chem. 275, 497–502.

Maxwell, S.L., 2006. Rapid extraction method for actinides and $^{89/90}$Sr in water samples. J. Radioanal. Nucl. Chem. 267, 537–543.

Maxwell, S.L., Culligan, B.K., 2006. Rapid column extraction method for actinides in soil. J. Radioanal. Chem 270, 699–704.

Maxwell, S.L., Culligan, B.K., 2009. Rapid separation method for emergency water and urine. J. Radioanal. Nucl. Chem. 279, 901–907.

Maxwell, S.L., Faison, D.M., 2008. Rapid column extraction method for actinides and strontium in fish and other animal tissue samples. J. Radioanal. Nucl. Chem. 275, 605–612.

Maxwell, S.L., Jones, V.D., 2009. Rapid determination of actinide in urine by inductively coupled plasma mass spectrometry and alpha spectrometry: a hybrid approach. Talanta 80, 143–150.

Maxwell, S.L., Nichols, S.T., 2000. Actinide recovery method for large soil samples. Radioact. Radiochem. 11, 46–54.

Maxwell, S.L., Culligan, B.K., Noyes, G.W., 2010a. Rapid separation of actinides and radiostrontium in vegetation samples. J. Radioanal. Nucl. Chem. 286, 273–282.

Maxwell, S.L., Culligan, B.K., Jones, V.D., Nichols, S.T., Bernard, M.A., Noyes, G.W., 2010b. Determination of ^{237}Np and Pu isotopes in large soil samples by inductively couples plasma mass spectrometry. Anal. Chim. Acta 682, 130–136.

Maxwell, S.L., Culligan, B.K., Noyes, G.W., 2010c. Rapid separation method for actinides in emergency airfilter samples. Appl. Radiat. Isot 68, 2125–2131.

Maxwell, S.L., Culligan, B.K., Jones, V.D., Nichols, S.T., Bernard, M.A., Noyes, G.W., 2011a. Rapid determination of ^{237}Np and Pu isotopes in water by inductively coupled plasma mass spectrometry and alpha spectrometry. J. Radioanal. Nucl. Chem. 287, 223–230.

Maxwell, S.L., Culligan, B.K., Noyes, G.W., 2011b. Determination of ^{237}Np and Pu isotopes in large soil samples. Appl. Radiat. Isot 69, 917–923.

Maxwell, S.L., Culligan, B.K., Jones, V.D., Nichols, S.T., Noyes, G.W., Bernard, M.A., 2011c. Rapid determination of ^{237}Np and plutonium isotopes in urine by inductively coupled plasma mass spectrometry and alpha spectrometry. Health Phys 101, 180–186.

Maxwell, S.L., Culligan, B.K., Kelsey-Wall, A., Shaw, P.J., 2012. Rapid determination of actinides in emergency food samples. J. Radioanal. Nucl. Chem. 292 (1), 339–347.

Maxwell, S.L., Culligan, B.K., Hutchison, J.B., 2013. Rapid fusion method for determination of plutonium isotopes in large rice samples. J. Radioanal. Nucl. Chem. 298 (2), 1367–1374.

Maxwell, S.L., Culligan, B.K., Hutchison, J.B., Utsey, R.C., McAlister, D.R., 2014. Rapid determination of actinides in seawater samples. J. Radioanal. Nucl. Chem. 300 (3), 1175–1189.

Maxwell, S.L., Culligan, B., Hutchison, J.B., McAlister, D.R., 2015. Rapid fusion method for the determination of Pu, Np, and Am in large soil samples. J. Radioanal. Nucl. Chem. 305, 599–608.

Mazur, J., Kozak, K., 2014. Complementary system for long term measurements of radon exhalation rate from soil. Rev. Sci. Instrum. 85, 022104.

McNichol, A.P., Osborne, E.A., Gagnon, A.R., Fry, B., Jones, G.A., 1994. TIC, TOC, DIC, DOC, PIC, POC - unique aspects in the preparation of oceanographic samples for ^{14}C-AMS. Nucl. Insttruments Methods Phys. Res. B 92, 162–165.

Medley, P., Martin, P., Bollhöfera, A., Parryc, D., 2015. ^{228}Ra and ^{226}Ra measurement on a $BaSO_4$ co-precipitation source. Appl. Rad. Isot. 95, 200–207.

Mesrar, H., Sadiki, A., Faleh, A., Quijano, L., Gaspar, L., Navas, A., 2017. Vertical and lateral distribution of fallout ^{137}Cs and soil properties along representative toposequences of central Rif, Morocco. J. Environ. Radioact. 169–170, 27–39.

Meusburger, K., Porto, P., Mabit, L., La Spada, C., Arata, L., Alewell, C., 2018. Excess Lead-210 and Plutonium-239+240: two suitable radiogenic soil erosion tracers for mountain grassland sites. Environ Res 160, 195–202.

Mitchell, P.I., Vintro, L.L., Dahlgaard, H., Sanchez-Cabez, J.A., 1997. Perturbation in the ^{240}Pu/^{239}Pu global fallout ratio in local sediments following the nuclear accidents at Thule (Greenland) and Palomares (Spain). Sci. Total. Environ. 202, 147–153.

Michel, H., Barci-Funel, G., Dalmasso, J., Ardisson, G., 1999. One step ion exchange process for the radiochemical separation of americium,

plutonium and neptunium in sediments. J. Radioan. Nucl. Chem. 240, 467–470.

Michel, R., et al., 2012. Iodine-129 and iodine-127 in European seawaters and in precipitation from Northern Germany. Sci. Total Environ 419, 151–169.

Middleton, R., 1983. A versatile high intensity negative ion source. Nucl. Instrum. Methods Phys. Res. 214, 139–150.

Middleton, R., Klein, J., 1987. ^{26}Al: measurement and applications [and discussion]. Philos. Trans. R. Soc. A Math. Phys. Eng. Sci. 323, 121–143.

Miltenberger, K.U., Müller, A.M., Suter, M., Synal, H.A., Vockenhuber, C., 2017. Accelerator mass spectrometry of ^{26}Al at 6 MV using AlO− ions and a gas-filled magnet. Nucl. Instrum. Methods Phys. Res. B 406, 272–277.

Mitev, K., Cassette, P., Tartès, I., Georgiev, S., Dimitrova, I., Pressyanov, D., 2018. Diffusion lengths and partition coefficients of ^{131m}Xe and ^{85}Kr in Makrofol N and Makrofol DE polycarbonates. Appl. Radiat. Isot. 134, 269–274.

Miura, T., Hayano, K., Nakayama, K., 1999. Determination of ^{210}Pb and ^{210}Po in environmental samples by alpha ray spectrometry using an extraction chromatographic resin. Anal. Sci. 15, 23–28.

Miyahara, H., Nagaya, K., Masuda, K., Muraki, Y., Kitagawa, H., Nakamura, T., 2008. Transition of solar cycle length in association with the occurrence of grand solar minima indicated by radiocarbon content in tree-rings. Quat. Geochronol. 3, 208–212.

Mohamuda, H., van Esa, E.M., Sainsbury, T., Ivanov, P., Russell, B., Regan, P.H., Warda, N.I., 2017. Progress towards the development of a rapid analytical approach for separation of ^{226}Ra using dibenzo-18-crown-6 ether functionalised silica (SiO_2) disks. Rad. Phys. Chem. 140, 57–60.

Molnar, M., Bujtas, T., Svingor, É., Futo, I., Svetlik, I., 2007. Monitoring of atmospheric excess ^{14}C around Paks nuclear power plant, Hungary. Radiocarbon 49, 1031–1043.

Molnár, M., Hajdas, I., Janovics, R., Rinyu, L., Synal, H.A., Veres, M., Wacker, L., 2013. C-14 analysis of groundwater down to the millilitre level. Nucl. Instrum. Methods. Phys. Res. B 294, 573–576.

Momoshima, N., Kakiuchi, H., Maeda, Y., Hirai, E., Ono, T., 1997. Identification of the contamination source of plutonium in environmental samples with isotopic ratios determined by inductively coupled plasma mass spectrometry and alpha-spectrometry. J. Radioanal. Nucl. Chem. 221, 213–217.

Moody, C.A., Glover, S.E., Stuit, D.B., Filby, R.H., 1998. Preconcentration and separation of thorium, uranium, plutonium and americium in human soft tissues by extraction chromatography. J. Radioanal. Nucl. Chem. 234, 183–187.

Mora, C., Tittensor, D.P., Adl, S., Simpson, A.G.B., Worm, B., 2011. How many species are there on earth and in the ocean? PLoS Biol 9, e1001127.

Möre, H., Hubbard, L.M., 1997. ^{222}Rn absorption in plastic holders for alpha track detectors: a source of error. Radiat. Prot. Dosim. 74, 85–91.

Moreno, J., Vajda, N., Danesi, P.R., LaRosa, J.J., Zeiller, E., Sinojmeri, M., 1997. Combined procedure for determination of ^{90}Sr, ^{241}Am and Pu radionuclides in soil samples. J. Radioanal. Nucl. Chem. 226, 279–284.

Moreno, J., LaRosa, J.J., Danesi, P.R., Burns, K., Vajda, N., Sinojmeri, M., 1998. Determination of ^{241}Pu by LSC in combined procedure for Pu radionuclides, ^{241}Am and ^{90}Sr analysis in environmental samples. Radiact. Radiochem. 9, 35.

Morgenstern, A., Apostolidis, C., Carlos-Marquez, R., Mayer, K., Molinet, R., 2002. Single-column extraction chromatographic separation of U, Pu, Np and. Am. Radiochim. Acta 90, 81–85.

Moulin, V., Moulin, C., 2001. Radionuclide speciation in the environment. Radiochim. Acta 89, 773–778.

Muller, R.A., 1977. Radioisotope dating with a cyclotron. Science 196, 489–494.

Müllerová, M., Holý, K., Polášková, A., Holá, O., 2008. Seasonal variations of ^{222}Rn in soil air. In: Industrial Toxicology 08. Slovak University of Technology, Bratislava, pp. 150–156.

Müllerová, M., Holý, K., Bulko, M., 2014. Daily and seasonal variations in radon activity concentration in the soil air. Radiat. Prot. Dosim. 160, 222–225.

Müllerová, M., Holý, K., Bulko, M., 2018. Study of radon exhalation from the soil. J. Radioanal. Nucl. Chem. 315, 237–241.

Müllerová, M., et al., 2016. Indoor radon survey in Visegrad countries. Appl. Radiat. Isot. 110, 124–128.

Murray, C.N., Statham, G., 1976. Application of a solvent extraction procedure using Di-2-ethyl Hexyl Phosphoric acid (HDEHP) for the separation of some transuranic elements in environmental samples. Deut. Hydrograph. Zeitschr. 29, 69–75.

Nadeau, M.J., Kieser, W.E., Beukens, R.P., Litherland, A.E., 1987. Quantum mechanical effects on sputter source isotope fractionation. Nucl. Instrum. Methods Phys. Res. B 29, 83–86.

NCRP, National Council on Radiation Protection and Measurements, 1975. Krypton-85 in the atmosphere – Significance and control technology. Report 44 (Bethesda, Maryland).

Nakamura, T., Kobayashi, K., Matsuzaki, H., Murayama, M., Nagashima, Y., Oda, H., Shibata, Y., Tanaka, Y., Furukawa, M. (Eds.), 2004. Proceedings of the ninth international conference on accelerator mass spectrometry. Nucl. Instrum. Methods Phys. Res. B, 223-224, pp. 1–878.

Nakanishi, T.M., Tanoi, K. (Eds.), 2013. Agricultural Implications of the Fukushima Nuclear Accident. Springer, New York.

Nakano, M., Povinec, P.P., 2012. Long-term simulations of the ^{137}Cs dispersion from the Fukushima accident in the world ocean. J. Environ. Radioact. 111, 109–115.

Nakata, K., Hasegawa, T., 2011. Improvement of pre-treatment method for ^{36}Cl/Cl measurement of Cl in natural groundwater by AMS. Nucl. Instrum. Methods Phys. Res. B 269, 300–307.

Nebel, O., Mezger, K., 2008. Timing of thermal stabilization of the Zimbabwe Craton deduced from high-precision Rb–Sr chronology, Great Dyke. Precambrian Res 164, 227–232.

Nedveckaite, T., Filistowicz, W., 1993. Determination of gaseous and particulate ^{129}I in atmospheric air by neutron activation analysis. J. Radioanal. Nucl. Chem. Art. 174, 43–47.

Nelson, A.W., May, D., Knight, A.W., Eitrheim, E.S., Mehrhoff, M., Shannon, R., Litman, R., Schultz, M.K., 2014. Matrix complications in the determination of radium levels in hydraulic fracturing flowback water from Marcellus Shale. Environ. Sci. Technol. Lett. 1, 204–208.

Němec, M., Wacker, L., Gäggeler, H., 2010a. Optimization of the graphitization process at AGE-1. Radiocarbon 52, 1380–1393.

Němec, M., Wacker, L., Hajdas, I., Gäggeler, H., 2010b. Alternative methods for cellulose preparation for AMS measurement. Radiocarbon 52, 1358–1370.

Neu, M.P., Goff, G.S., Runde, W., 2010. Plutonium. In: Atwood, D.A. (Ed.), Radionuclides in the Environment. Wiley, New York, pp. 289–314.

Ni, Y., Zheng, J., Guo, Q., Men, W., Tagami, K., Uchida, S., 2018. Rapid determination of ultra-trace plutonium isotopes (^{239}Pu, ^{240}Pu and ^{241}Pu) in small-volume human urine bioassay using sector-field inductively coupled plasma mass spectrometry. Anal. Chim. Acta 1000, 85–92.

Niese, S., 2008. Underground laboratories for low-level radioactivity measurements. Radioact. Environ. 11, 209–239.

Nisi, S., et al., 2009. Comparison of inductively coupled mass spectrometry and ultra-low-level gamma-ray spectroscopy for ultra-low background material selection. Appl. Radiat. Isot. 67, 828–832.

Nitta, W., Sanada, T., Isogai, K., Schlosser, C., 2014. Atmospheric ^{85} Kr and ^{133} Xe activity concentrations at locations across Japan following the fukushima Dai-ichi nuclear power plant accident. J. Nucl. Sci. Technol. 51, 712–719.

Noguchi, H., Murata, M., 1988. Physicochemical speciation of airborne ^{131}I in Japan from Chernobyl. J. Environ. Radioact. 7, 65–74.

NuDat, 2018. Nuclear structure & decay data, v 2.7. Evaluated Nuclear Structure Data File (ENSDF). National Nuclear Data Center. Brookhaven National Laboratory, USA.

OECD, Organisation for Economic Co-operation and Development, 2002. Chernobyl: Assessment of Radiological and Health Impacts: 2002 Update of Chernobyl: Ten Years On. OECD, Paris.

Oh, J.-S., Warwick, P.E., Croudace, I.W., Lee, S.-H., 2014. Evaluation of three electrodeposition procedures for uranium, plutonium and americium. Appl. Radiat. Isot. 87, 233–237.

Ohno, T., Muramatsu, Y., 2014. Determination of radioactive cesium isotope ratios by triple quadrupole ICP-MS and its application to rainwater following the Fukushima Daiichi Nuclear Power Plant accident. J. Anal. At. Spectrom. 29, 347–351.

Ohtsuka, Y., Takaku, Y., Nishimura, K., Kimura, J., Hisamatsu, S., Inaba, J., 2006. Rapid method for the analysis of plutonium isotopes in a soil sample within 60 min. Anal. Sci. 22, 309–311.

Orsovszki, G., Rinyu, L., 2015. Flame-sealed tube graphitization using zinc as the sole reduction agent: precision improvement of Environ-MICADAS ^{14}C measurements on graphite targets. Radiocarbon 57, 979–990.

Osváth, S., Vajda, N., Molnár, Z., 2009. Development of a complex method for the determination of actinoides. J. Radioanal. Nucl. Chem. 281, 461–465.

Osváth, S., Vajda, N., Molnár, Z., Széles, É., Stefánka, Z., 2010. Determination of ^{237}Np, ^{93}Zr and other long-lived radionuclides in medium and low level radioactive waste samples. J. Radioanal. Nucl. Chem. 286, 675–680. https://doi.org/10.1007/s10967-010-0738-7.

Otlet, R.L., Huxtable, G., Sanderson, D.C.W., 1986. The development of practical systems for ^{14}C measurement in small samples using miniature counters. Radiocarbon 28, 603–614.

Oughton, D., Day, P., Fifield, K., 2001. Plutonium measurements using accelerator mass spectrometry: methodology and application. Radioactivity Environ 1, 47–62.

Outola, I., Saxén, R.L., Heinävaara, S., 2009. Transfer of ^{90}Sr into fish in Finnish lakes. J. Environ. Radioact. 100, 657–664.

Paatero, J., Saxén, R., Buyukay, M., Outola, I., 2010. Overview of strontium-89,90 deposition measurements in Finland 1963–2005. J. Environ. Radioact. 101, 309–316.

Palcsu, L., Major, Z., Köllo, Z., Papp, L., 2010. Using an ultrapure ^{4}He spike in tritium measurements of environmental water samples by the 3He-ingrowth method. Rapid Commun. Mass Spectrom. 24, 698–704.

Palonen, V., Oinonen, M., 2013. Molecular sieves in $^{14}CO_2$ sampling and handling. Radiocarbon 55, 416–420.

Pan, V., Stevenson, K.A., 1996. Temporal variation analysis of plutonium baseline concentration in surface air from selected sites in continental US. J. Environ. Radioact. 32, 239–257.

Pánik, J., Ješkovský, M., Kaizer, J., Kontul', I., Zeman, J., Povinec, P.P., 2017. Preparations for AMS analysis of hydrogen isotopes at the CENTA laboratory. In: Lujaniené, G., Povinec, P.P. (Eds.), Proc. Of the ENVIRA 2017 Conf.: Radionuclides as Tracers of Environmental Processes. SRI, Vilnius, pp. 22–23.

Papastefanou, C., 2006. Residence time of tropospheric aerosols in association with radioactive nuclides. Appl. Radiat. Isot. 64, 93–100.

Papastefanou, C., Ioannidou, A., 1995. Aerodynamic size association of ^{7}Be in ambient aerosol. J. Environ. Radioact. 26, 273–282.

Papp, L., Palcsu, L., Major, Z., Rinyu, L., Tóth, I., 2012. A mass spectrometric line for tritium analysis of water and noble gas measurements from different water amounts in the range of microlitres and millilitres. Isotopes Environ. Health Stud. 48, 494–511.

Paschoa, A.S., Steinhausler, F. (Eds.), 2010. Technologically Enhanced Natural Radiation. Elsevier, Oxford.

Paul, S., Pandey, A.K., Shah, R.V., Aggarwal, S.K., 2015. Chemically selective polymer substrate based direct isotope dilution alpha spectrometry of Pu. Anal. Chim. Acta 878, 54–62.

Pavlotskaya, F.I., Kazinskaya, I.Y., Korobova, E.M., Myasoedov, B.F., Emelyanov, V.V., 1991. Migration of Chernobyl plutonium in soils. J. Radioanal. Nucl. Chem . 147 (1), 159–164.

Pavlotskaya, F.I., Goryachenkova, T.A., Yeme_lyanov, V.V., Kazinskaya, I.Y., Barsukova, K.V., Myasoyedov, B.F., 1994. Modes of occurrence of plutonium in hot particles. Geochem. Int 31, 62–69.

Pavlotskaya, F.I., Kazinskaya, I.Y., Goryachenkova, T.A., Barsukova, K.V., Yemel'yanov, V.V., Myasoyedov, B.F., 1995. Plutonium content in soils of some nonchernozem regions affected by the Chernobyl accident. Eur. Soil Sci. 7 (6), 33–39.

Pereiro, R., Solà-Vázquez, A., Lobo, L., Pisonero, J., Bordel, N., Costa, J.M., Sanz-Medel, A., 2011. Present and future of glow discharge — time of flight mass spectrometry in analytical chemistry. Spectrochim. Acta B 66, 399–412.

Perna, L., Betti, M., Barrero Moreno, J.M., Fuoco, R., 2001. Investigation on the use of UTEVA as a stationary phase for chromatography separation of actinides on-line to inductively coupled mass spectrometry. J. Anal. At. Spectrom 16, 26–31.

Perrot, F., Hubert, P., Marquet, C., Pravikoff, M.S., Bourquin, P., Chiron, H., Guernion, P.-Y., Nachab, A., 2012. Evidence of ^{131}I and ^{134,137}Cs activities in Bordeaux, France due to the Fukushima nuclear accident. J. Environ. Radioact. 114, 61–65.

Pham, M.K., La Rosa, J.J., Lee, S.-H., Oregioni, B., Povinec, P.P., 2005. Deposition of Saharan dust in Monaco rain 2001–2002: radionuclides and elemental composition. Phys. Scripta 71, 14–17.

Pham, M.K., Betti, M., Nies, H., Povinec, P.P., 2011. Temporal changes of ^{7}Be, ^{137}Cs and ^{210}Pb activity concentrations in surface air at Monaco and their correlation with meteorological parameters. J. Environ. Radioact. 102, 1045–1054.

Pham, M.K., Chamizo, E., Mas Balbuena, J.L., Miquel, J.C., Martín, J., Osvath, I., Povinec, P.P., 2017. Impact of Saharan dust events on

radionuclide levels in Monaco air and in the water column of the northwest Mediterranean Sea. J. Environ. Radioact. 166, 2−9.

Pibida, L., McMahon, C.A., Bushaw, B.A., 2004. Laser resonance ionization mass spectrometry measurements of cesium in nuclear burn-up and sediment samples. Appl. Radiat. Isot. 60, 567−570.

Pilvio, R., Bickel, M., 2000. Actinoid separations by extraction chromatography. Appl. Radiat. Isot 53, 273−277.

Pilvio, R., Bickel, M., 1998. Separation of actinides from a bone ash matrix with extraction chromatography. J. Alloys Compd. 271−273, 49−53.

Pimpl, M., Scuettelkopf, H., 1986. The measurement of Pu in Environmental samples and in Gaseous and liquid effluents of nuclear installations. Report SLU-REC-61.l. Swedish University of Agricultural Sciences, Uppsala, pp. 53−62.

Pimpl, M., Higgy, R.H., 2001. Improvement of Am and Cm determination in soil samples. J. Radioanal. Nucl. Chem. 248, 537−541.

Plastino, W., Plenteda, R., Azzari, G., Becker, A., Saey, P.R.J., Wotawa, G., 2010. Radioxenon time series and meteorological pattern analysis for CTBT event categorisation. Pure Appl. Geophys. 167, 559−573.

Playford, K., Toole, J., Adsley, I., 1993. Radioactive fallout in air and rain: results to the end of 1991. Report DOE/RAS/93.003, AEA-EE-0498. Department of the Environment, London.

Polach, H.A., 1987. Evaluation and status of liquid scintillation counting for radiocarbon dating. Radiocarbon 29, 1−11.

Pöllänen, R., 2002. Nuclear fuel particles in the environment—characteristics, atmospheric transport and skin doses. University of Helsinki, Department of Physical Sciences, Faculty of Science, ISBN 951-712-529-1. Academic Dissertation, May 2002.

Pöllänen, R., Valkama, I., Toivonen, H., 1997. Transport of radioactive particles from the Chernobyl accident. Atmos. Environ. 31 (21), 3575−3590.

Popov, L., 2013. Novel method for determination of uranium isotopes in environmental samples by liquid−liquid extraction with triisooctylamine in sulfuric and hydrochloric acid media. J. Radioanal. Nucl. Chem. 298, 555−562.

Portes, R., Dahms, D., Brandová, D., Raab, G., Christl, M., Kühn, P., Ketterer, M., Egli, M., 2018. Evolution of soil erosion rates in alpine soils of the Central Rocky Mountains using fallout Pu and $\delta^{13}C$. Earth Planet. Sci. Lett. 496, 257−269.

Postelt, F., 2014. Potential of spectrum categorisation concepts using radionuclide ratios for comprehensive nuclear-test-ban treaty verification. Pure Appl. Geophys. 171, 593−697.

Povinec, P., 1972. Preparation of methane gas for proportional ^{3}H and ^{14}C counters. Radiochem. Radioanal. Letters 9, 127−135.

Povinec, P., 1975. The analysis of ^{3}H and ^{14}C labelled compounds in the form of doubly labelled methane. Int. J. Appl. Radiat. Isot. 26, 465−469.

Povinec, P., 1978. Multiwire proportional counters for low-level ^{14}C and ^{3}H measurements. Nucl. Instrum. Methods 156, 441−446.

Povinec, P., 1980. Simultaneous ^{3}H and ^{14}C counting by a CH_4 filled proportional counter. Nucl. Instrum. Methods 177, 465.

Povinec, P., 1981. Simultaneous activity and background measurement by the same detector. Int. J. Appl. Rad. Isotopes 32, 729.

Povinec, P., 1992. ^{14}C gas counting: is there still a future? Radiocarbon 34, 406−413.

Povinec, P.P., 2004. Developments in analytical technologies for marine radioactivity studies. In: Livingston, H.D. (Ed.), Marine Radioactivity. Elsevier, Amsterdam, pp. 237−294.

Povinec, P.P., 2005. Ultra-sensitive radionuclide spectrometry: radiometrics and mass spectrometry synergy. J. Radioanal. Nucl. Chem. 263, 413−417.

Povinec, P.P. (Ed.), 2008a. Analysis of Environmental Radionuclides. Elsevier, Amsterdam.

Povinec, P.P., 2008b. Low-level gamma-ray spectrometry for environmental samples. J. Radioanal. Nucl. Chem. 276, 771−777.

Povinec, P.P., 2010. Trends in radiometrics and mass spectrometry technologies: synergy in environmental analyses. J. Radioanal. Nucl. Chem. 286, 401−407.

Povinec, P.P., 2011. New analytical technologies for new science. J. Anal. Sci. Technol. 2, A15−A21.

Povinec, P.P., 2012. New gamma-spectrometry technologies for environmental sciences. J. Anal. Sci. Technol. 3, 42−71.

Povinec, P.P., 2013. Recent developments in radioanalytical technologies for environmental investigation. J. Radioanal. Nucl. Chem. 295, 537−544.

Povinec, P.P., 2018a. Analysis of radionuclides at ultra-low levels: a comparison of low and high- energy mass spectrometry with gamma-spectrometry for radiopurity measurements. Appl. Radiat. Isot. 126, 26−30.

Povinec, P.P., 2018b. New ultra-sensitive radioanalytical technologies for new science. J. Radioanal. Nucl. Chem. 316, 893−931.

Povinec, P., Saro, S., Chudy, M., Seliga, M., 1968. The rapid method of carbon-14 counting in atmospheric carbon dioxide. Intern. J. Appl. Rad. Isotopes 19, 877−881.

Povinec, P., Chudý, M., Šeliga, M., Šáró, Š., Szarka, J., 1972. Tritium analysis with an ethane-filled proportional counter. J. Radioanal. Chem. 12, 513−518.

Povinec, P., Burchuladze, A.A., Pagava, S.V., 1983. Short-term variations in radiocarbon concentration with the 11-year solar cycle. Radiocarbon 25, 259−266.

Povinec, P., Šivo, A., Chudy, M., 1986a. Seasonal variations of anthropogenic radio- carbon in the atmosphere. Nucl. Instrum. Methods Phys. Res. B 17, 556−559.

Povinec, P., Chudy, M., Šivo, A., 1986b. Anthropogenic radiocarbon: past, present and future. Radiocarbon 28, 668−672.

Povinec, P., Chudý, M., Sýkora, I., Szarka, J., Pikna, M., Holý, K., 1988. Aerosol radioactivity monitoring in Bratislava following the Chernobyl accident. J. Radioanal. Nucl. Chem. Lett. 126, 467−478.

Povinec, P.P., Osvath, I., Baxter, M.S., 1996. Underwater gammaspectrometry with HPGe and NaI(Tl) detectors. Appl. Radiat. Isot. 47, 1127−1133.

Povinec, P.P., Oregioni, B., Jull, A.J.T., Kieser, W.E., Zhao, X.-L., 2000. AMS measurements of ^{14}C and ^{129}I in seawater around radioactive waste dump sites. Nucl. Instrum. Methods Phys. Res. B 172, 672−678.

Povinec, P.P., La Rosa, J.J., Lee, S.-H., Mulsow, S., Osvath, I., Wyse, E., 2001. Recent developments in radiometric and mass spectrometric methods for marine radioactivity measurements. J. Radioanal. Nucl. Chem. 248 (3), 713−718.

Povinec, P.P., Comanducci, J.F., Levy-Palomo, I., 2004. IAEA-MEL's underground counting laboratory in Monaco − background characteristics of HPGe detectors with anti-cosmic shielding. Appl. Radiat. Isot. 61, 85−93.

Povinec, P.P., Comanducci, J.F., Levy-Palomo, I., 2005. IAEA-MEL's underground counting laboratory (CAVE) for the analysis of radionuclides in the environment at very low-levels. J. Radioanal. Nucl. Chem. 263, 441−445.

Povinec, P.P., Comanducci, J.-F., Levy-Palomo, I., Avaullee, F., 2006. IAEA-MEL's underground counting laboratory - the design and main characteristics. Radioact. Environ. 8, 538–553.

Povinec, P.P., Sanchez-Cabeza (Eds.), 2006. Radionuclides in the Environment. Elsevier, Amsterdam.

Povinec, P.P., Šivo, A., Šimon, J., Holý, K., Chudý, M., Richtáriková, M., Morávek, J., 2008. Impact of the Bohunice nuclear power plant on atmospheric radiocarbon. Appl. Radiat. Isot. 66, 1686–1690.

Povinec, P.P., Litherland, A.E., von Reden, K.F., 2009a. Developments in radiocarbon technologies: from the Libby counter to compound specific AMS analyses. Radiocarbon 51, 45–78.

Povinec, P.P., Chudý, M., Šivo, A., Šimon, J., Holý, K., Richtáriková, M., 2009b. Forty years of atmospheric radiocarbon monitoring around Bohunice nuclear power plant, Slovakia. J. Environ. Radioact. 100, 125–130.

Povinec, P.P., Sýkora, I., Porubčan, V., Ješkovský, M., 2009c. Analysis of 26Al in meteorite samples by coincidence gamma-ray spectrometry. J. Radioanal. Nucl. Chem. 282, 805–808.

Povinec, P.P., Franko, O., Šivo, A., Richtáriková, M., Breier, R., Aggarwal, P.K., Araguás-Araguás, L., 2010. Spatial radiocarbon and stable carbon isotope variability of mineral and thermal waters in Slovakia. Radiocarbon 52, 1056–1067.

Povinec, P.P., Aoyama, M., Fukasawa, M., Hirose, K., Komura, K., Sanchez-Cabeza, J.-A., Gastaud, J., Ješkovský, M., Levy, I., Sýkora, I., 2011. ^{137}Cs water profiles in the South Indian Ocean – an evidence for accumulation of pollutants in the subtropical gyre. Prog. Oceanogr. 89, 17–30.

Povinec, P.P., Sýkora, I., Holý, K., Gera, M., Kováčik, A., Brest'áková, L., 2012a. Aerosol radioactivity record in Bratislava/Slovakia following the Fukushima accident - a comparison with global fallout and the Chernobyl accident. J. Environ. Radioact. 114, 81–88.

Povinec, P.P., Hirose, K., Aoyama, M., 2012b. Radiostrontium in the western North Pacific: characteristics, behavior, and the fukushima impact. Environ. Sci. Technol. 46, 10356–10363.

Povinec, P.P., Holý, K., Chudý, M., Šivo, A., Sýkora, I., Ješkovský, M., Richtáriková, M., 2012c. Long-term variations of ^{14}C and ^{137}Cs in the Bratislava air – implications of different atmospheric transport processes. J. Environ. Radioact. 108, 33–40.

Povinec, P.P., Hirose, K., Aoyama, M., 2013a. Fukushima Accident: Radioactivity Impact on the Environment. Elsevier, New York.

Povinec, P.P., Gera, M., Holý, K., Hirose, K., Lujanienė, G., Nakano, M., Plastino, W., Sýkora, I., Bartok, J., Gažák, M., 2013b. Dispersion of Fukushima radionuclides in the global atmosphere and the ocean. Appl. Radiat. Isot. 81, 383–392.

Povinec, P.P., et al., 2013c. Cesium, iodine and tritium in NW Pacific waters-a comparison of the Fukushima impact with global fallout. Biogeosciences 10, 5481–5496.

Povinec, P.P., Ženišová, Z., Šivo, A., Ogrinc, N., Richtáriková, M., Breier, R., 2013d. Radiocarbon and stable isotopes as groundwater tracers in the Danube River basin of SW Slovakia. Radiocarbon 55, 1017–1028.

Povinec, P.P., Šivo, A., Ješkovský, M., Svetlik, I., Richtáriková, M., Kaizer, J., 2015. Radiocarbon in the atmosphere of the Žlkovce monitoring station of the Bohunice NPP: 25 Years of continuous monthly measurements. Radiocarbon 57, 355–362.

Povinec, P.P., Sýkora, I., Gera, M., Holý, K., Brest'áková, L., Kováčik, A., 2013e. Fukushima-derived radionuclides in ground-level air of Central Europe: a comparison with simulated forward and backward trajectories. J. Radioanal. Nucl. Chem. 295, 1171–1176.

Povinec, P.P., Hirose, K., 2015. Fukushima radionuclides in the NW Pacific, and assessment of doses for Japanese and world population from ingestion of seafood. Sci. Rep. 5, 9016.

Povinec, P.P., et al., 2015a. Development of the accelerator mass spectrometry technology at the Comenius University in Bratislava. Nucl. Instrum. Methods Phys. Res. B 361, 87–94.

Povinec, P.P., et al., 2015b. A new IBA-AMS laboratory at the Comenius University in Bratislava (Slovakia). Nucl. Instrum. Methods Phys. Res. B 342, 321–326.

Povinec, P.P., Masarik, J., Ješkovský, M., Breier, R., Kaizer, J., Pánik, J., Richtáriková, M., Staníček, J., Šivo, A., Zeman, J., 2016. Recent results from the AMS/IBA laboratory at the Comenius University in Bratislava: preparation of targets and optimization of ion sources. J. Radioanal. Nucl. Chem. 307, 2101–2108.

Povinec, P.P., Liong Wee Kwong, L., Kaizer, J., Molnár, M., Nies, H., Palcsu, L., Papp, L., Pham, M.K., Jean-Baptiste, P., 2017. Impact of the Fukushima accident on tritium, radiocarbon and radiocesium levels in seawater of the western North Pacific Ocean: a comparison with pre-Fukushima situation. J. Environ. Radioact. 166, 56–66.

Povinec, P.P., et al., 2018. ^{U}ltra-sensitive radioanalytical technologies for underground physics experiments. J. Radioanal. Nucl. Chem. https://doi.org/10.1007/s10967-018-6105-9 (in print).

Prasad, G., Ishikawa, T., Hosoda, M., Sorimachi, A., Sahoo, S.K., Kavasi, N., Tokonami, S., Sugino, M., Uchida, S., 2012. Seasonal and diurnal variations of radon/thoron exhalation rate in Kanto-loam area in Japan. J. Radioanal. Nucl. Chem. 292, 1385–1390.

Pressyanov, D.S., Mitev, K.K., Stefanov, V.H., 2004. Measurement of ^{85}Kr and ^{133}Xe in air by absorption in Makrofol. Nucl. Instrum. Methods Phys. Res. A 527, 657–659.

Purdy, C.B., Burr, G.S., Rubin, M., Helz, G.R., Mignerey, A.C., 1992. Dissolved organic and inorganic C-14 concentrations and âges for coastal-plain aquifers in southern Maryland. Radiocarbon 34, 654–663.

Purtschert, R., Yokochi, R., Sturchio, N.C., 2013. Krypton-81 dating of old groundwater. In: Isotopes Methods for Dating Old Groundwater. IAEA, Vienna, pp. 91–124.

Qiao, J., Hou, X., Roos, P., Miro, M., 2010. Rapid and simultaneous determination of neptunium and plutonium isotopes in environmental samples by extraction chromatography using sequential injection analysis and ICP–MS. J. At. Anal. Spectr. 25, 1769–1779.

Qiao, J., Hou, X., Roos, P., Miro, M., 2011. High-throughput sequential injection method for simultaneous determination of plutonium and neptunium in environmental solids using macroporous anion-exchange chromatography, followed by inductively coupled plasma mass spectrometric detection. Anal. Chem. 83, 373–381.

Qiao, J., Xu, Y., Hou, X., Miró, M., 2014. Comparison of sample preparation methods for reliable plutonium and neptunium urinalysis using automatic extraction chromatography. Talanta 128, 75–82.

Qu, H., Stuit, D., Glover, S.E., Love, S.F., Filby, R.H., 1998. Preconcentration of plutonium and americium using the Actinide-CUTM Resin for human tissue analysis. J. Radioanal. Nucl. Chem. 234, 175–181.

Querol, X., et al., 2009. African dust contributions to mean ambient PM10 mass-levels across the Mediterranean Basin. Atmos. Environ. 43, 4266–4277.

Quinto, F., Steier, P., Wallner, G., Wallner, A., Srncik, M., Bichler, M., Kutschera, W., Terrasi, F., Petraglia, A., Sabbarese, C., 2009. The first use of ^{236}U in the general environment and near a shutdown nuclear power plant. Appl. Radiat. Isot. 67, 1775−1780.

Radulović, V., Kolšek, A., Fauré, A.-L., Pottin, A.-C., Pointurier, F., Snoj, L., 2018. Qualification of heavy water based irradiation device in the JSI TRIGA reactor for irradiations of FT-TIMS samples for nuclear safeguards. Nucl. Instrum. Methods Phys. Res. A 885, 139−144.

Raeder, S., Hakimi, A., Stöbener, N., Trautmann, N., Wendt, K., 2012. Detection of plutonium isotopes at lowest quantities using in-source resonance ionization mass spectrometry. Anal. Bioanal. Chem. 404, 2163−2172.

Raich, J.W., Schlesinger, W.H., 1992. The global carbon dioxide flux in soil respiration and its relationship to vegetation and climate. Tellus B 44, 81−99.

Raisbeck, G.M., Yiou, F., 1999. ^{129}I in the oceans: origins and applications. Sci. Total Environ 237−238, 31−41.

Raisbeck, G.M., Yiou, F., 1979. Possible use of ^{41}Ca for radioactive dating. Nature 277, 42−44.

Raisbeck, G.M., Yiou, F., 1988. Measurement of ^{7}Be by accelerator mass spectrometry. Earth Planet. Sci. Lett. 89, 103−108.

Raisbeck, G.M., Yiou, F., Bourlès, D., Lestringuez, J., Deboffle, D., 1987. Measurements of ^{10}Be and ^{26}Al with a tandetron AMS facility. Nucl. Instrum. Methods Phys. Res. B 29, 22−26.

Raisbeck, G.M., Yiou, F., Fruneau, M., Loiseaux, J.M., 1978. Beryllium-10 mass spectrometry with a cyclotron. Science 202, 215−217.

Raisbeck, G.M., Yiou, F., Fruneau, M., Loiseaux, J.M., Lieuvin, M., Ravel, J.C., 1981. Cosmogenic ^{10}Be/^{7}Be as a probe of atmospheric transport processes. Geophys. Res. Lett. 8, 1015−1018.

Raisbeck, G.M., Yiou, F., Stephan, C., 1979. ^{26}Al measurement with a cyclotron. J. Phys. Lett. 40, 241−244.

Rakowski, A.Z., Nakamura, T., Pazdur, A., 2008. Variations of anthropogenic CO_2 in urban area deduced by radiocarbon concentration in modern tree rings. J. Environ. Radioact. 99, 1558−1565.

Ramebäck, H., Skillberg, M., 1998. Separation of neptunium, plutonium, americium and curium from uranium with di-(2-ethylhexyl)-phosphoric acid (HDEHP) for radiometric and ICP-MS analysis. J. Radioanal. Nucl. Chem. 235, 229−233.

Ranebo, Y., Eriksson, M., Tamborini, G., Niagolova, N., Bildstein, O., Betti, M., 2007. The Use of SIMS and SEM for the characterization of individual particles with a matrix originating from a nuclear weapon. Microsc. Microanal. 13, 179−190.

Rankama, K., Sahama, T.G., 1950. Geochemistry. University of Chicago Press, Chicago.

Rantavaara, A., 2008. Ingestion doses in Finland due to ^{90}Sr, ^{134}Cs, and ^{137}Cs from nuclear weapons testing and the Chernobyl accident. Appl. Radiat. Isot. 66, 1768−1774.

Rao, R.R., Cooper, E.L., 1995. Separation of low levels of actinides by selective oxidation/reduction and co-precipitation with neodymium fluoride. J. Radioanal. Nucl. Chem. 197, 133−148.

Reimer, P.J., et al., 2013. IntCal13 and Marine13 radiocarbon age calibration curves 0−50,000 Years cal BP. Radiocarbon 55, 1869−1887.

Rim, J.H., et al., 2017. Determination of origin and intended use of plutonium metal using nuclear forensic techniques. Forensic Sci. Int. 273, e1−e9.

Ringbom, A., Larson, T., Axelsson, A., Elmgren, K., Johansson, C., 2003. SAUNA—a system for automatic sampling, processing, and analysis of radioactive xenon. Nucl. Instrum. Methods Phys. Res. A 508, 542−553.

Ringbom, A., et al., 2009. Measurements of radioxenon in ground level air in South Korea following the claimed nuclear test in North Korea on October 9, 2006. J. Radioanal. Nucl. Chem. 282, 773−779.

Ringbom, A., et al., 2014. Radioxenon detections in the CTBT international monitoring system likely related to the announced nuclear test in North Korea on February 12, 2013. J. Environ. Radioact. 128, 47−63.

Roberts, M.L., Hamm, R.W., Dingley, K.H., Chiarappa-Zucca, M.L., Love, A.H., 2000. A compact tritium AMS system. Nucl. Instrum. Methods Phys. Res. B 172, 262−267.

Roberts, M.L., Velsko, C., Turteltaub, K.W., 1994. Tritium AMS for biomedical applications. Nucl. Instrum. Methods Phys. Res. B 92, 459−462.

Rodríguez, R., Borràs, A., Leal, L., Cerdà, V., Ferrer, L., 2016. MSFIA-LOV system for ^{226}Ra isolation and pre-concentration from water samples previous radiometric detection. Anal. Chim. Acta 911, 75−81.

Rom, W., Golser, R., Kutschera, W., Priller, A., Steier, P., Wild, E., 1997. Systematic investigations of ^{14}C measurements at the Vienna environmental research accelerator. Radiocarbon 40, 255−263.

Roos, P., Holm, E., Persson, R.B.R., 1994. Comparison of AMP precipitate method and impregnated $Cu_2[Fe(CN)_6]$ filters for the determination of radiocesium concentrations in natural waters. Nucl. Instrum. Methods Phys. Res. A 339, 282−286.

Roos, P., 2008. Analysis of radionuclides using ICP-MS. In: Povinec, P.P. (Ed.), Analysis of Environmental Radionuclides. Elsevier, Amsterdam, pp. 295−330.

Rosner, G., Hötzl, H., Winkler, R., 1990. Simultaneous radiochemical determination of plutonium, strontium, uranium, and iron nuclides and application to atmospheric deposition and aerosol samples. Fresenius' J. Anal. Chem. 338, 606−609.

Russell, B., García-Miranda, M., Ivanov, P., 2017. Development of an optimised method for analysis of ^{90}Sr in decommissioning wastes by triple quadrupole inductively coupled plasma mass spectrometry. Appl. Radiat. Isot. 126, 35−39.

Sadollah, A., Eskandar, H., Bahreininejad, A., Kim, J.H., 2015. Water cycle algorithm with evaporation rate for solving constrained and unconstrained optimization problems. Appl. Soft Comput. 30, 58−71.

Saey, P.R.J., 2007. Ultra-low-level measurements of argon, krypton and radioxenon for treaty verification purposes. ESARDA Bull 36, 42−55.

Saey, P.R.J., 2009. The influence of radiopharmaceutical isotope production on the global radioxenon background. J. Environ. Rad. 100, 296−406.

Saey, P.R.J., De Geer, L.E., 2005. Notes on radioxenon measurements for CTBT verification purposes. Appl. Radiat. Isot. 63, 765−773.

Saey, P.R., et al., 2007. A long distance measurement of radioxenon in Yellowknife, Canada, in late October 2006. Geophysical Research Letters 34, L20802. https://doi.org/10.1029/2007GL030611.

Sahoo, B.K., Mayya, Y.S., Sapra, B.K., Gaware, J.J., Banerjee, K.S., Kushwaha, H.S., 2010. Radon exhalation studies in an Indian uranium tailings pile. Radiat. Meas. 45, 237−241.

Saito, T., Ohta, T., Koike, Y., Sato, J., 2003. A new analytical approach for ^{226}Ra and ^{228}Ra in environmental waters. J. Radioanal. Nucl. Chem. 255, 535−538.

Sakaguchi, A., Kawai, K., Steier, P., Quinto, F., Mino, K., Tomita, J., Hoshi, M., Whitehead, N., Yamamoto, M., 2009. First results on ^{236}U levels in global fallout. Sci. Total Environ. 407, 4238−4242.

Sakaguchi, A., Kadokura, A., Steier, P., Takahashi, Y., Shizuma, K., Hoshi, M., Nakakuki, T., Yamamoto, M., 2012. Uranium-236 as a new oceanic tracer: a first depth profile in the Japan Sea and comparison with caesium-137. Earth Planet. Sci. Lett. 333−334, 165−170.

Sakaguchi, A., Steier, P., Takahashi, Y., Yamamoto, M., 2014. Isotopic compositions of U-236 and Pu isotopes in "black substances" collected from roadsides in Fukushima Prefecture: fallout from the fukushima Dai-ichi nuclear power plant accident. Environ. Sci. Technol. 48, 3691−3697.

Salbu, B., 2007. Speciation of radionuclides e analytical challenges within environmental impact and risk assessments. J. Environ. Radioact. 96, 47−53.

Salminen, S., Outola, I., Jaakkola, T., Pulli, S., Zilliacus, R., Lehto, J., 2004. Method for determining plutonium in air filters in detection of nuclear activities. Radiochim. Acta. 92, 467−473.

Salminen, S., Paatero, J., Roos, P., Helariutta, K., 2009. ^{237}Np in peat and lichen in Finland. J. Radioanal. Nucl. Chem. 281, 405−413.

Salminen, S., Paatero, J., 2009. Concentrations of ^{238}Pu, ^{239,240}Pu and ^{241}Pu in the surface air in Finnish Lapland in 1963. Boreal Environ. Res. 14, 827−836.

Salminen-Paatero, S., Nygren, U., Paatero, J., 2012. ^{240}Pu/^{239}Pu mass ratio in environmental samples in Finland. J. Environ. Radioact. 113, 163−170.

Sandals, F.J., Segal, M.G., Viktorova, N., 1993. Hot particles from Chernobyl: a review. J. Environ. Radioact. 18, 5−22.

Sasaki, Y., Choppin, G.R., 1996. Solvent extraction of Eu, Th, U, Np and Am with N,N'-dimethyl-N,N'-dihexyl-3-oxapentanediamide and its analogous compounds. Anal. Sci. 12, 225−230.

Scarpitta, S.C., Harley, N.H., 1990. Adsorption and desorption of noble gases on activated charcoal: II. ^{222}Rn studies in a monolayer and packed bed. Health Phys 59, 393−404.

Schaeffer, O.A., Zähringer, J., 2012. Potassium Argon Dating. Springer, New York.

Schell, B., Ackermann, I.J., Hass, H., Binkowski, F.S., Ebel, A., 2001. Modeling the formation of secondary organic aerosol within a comprehensive air quality model system. J. Geophys. Res. Atmos. 106, 28275−28293.

Schlosser, C., Bollhöfer, A., Schmid, S., Krais, R., Bieringer, J., Konrad, M., 2017. Analysis of radioxenon and Krypton-85 at the BfS noble gas laboratory. Appl. Radiat. Isot. 126, 16−19.

Schneider, S., Walther, C., Bister, S., Schauer, V., Christl, M., Synal, H.-A., Shozugawa, K., Steinhauser, G., 2013. Plutonium release from Fukushima Daiichi fosters the need for more detailed investigations. Sci. Rep. 3, 2988.

Schneider, S., Bister, S., Christl, M., Hori, M., Shozugawa, K., Hans-Arno Synal, H.-A., Steinhauser, G., Walther, C., 2017. Radionuclide pollution inside the Fukushima Daiichi exclusion zone, part 2: forensic search for the "Forgotten" contaminants Uranium-236 and plutonium. Appl. Geochem. 85, 194−200.

Schopper, E., Lohrmann, E., Mauck, G., 1967. Nukleonen in der Atmosphäre. In: Flügge, S. (Ed.), Handbuch der Physik, vol. XLVI/2. Springer, Berlin, pp. 373−550.

Schoeppner, M., Plastino, W., 2014. Determination of the global coverage of the IMS xenon-133 component for the detection of nuclear explosions. Sci. Glob. Secur. 22, 209−234.

Schulze, J., Auer, M., Werzi, R., 2000. Low level radioactivity measurement in support of the CTBTO. Appl. Radiat. Isot. 53, 23−30.

Schwehr, K.A., Santschi, P.H., Elmore, D., 2005. The dissolved organic iodine species of the isotopic ratio of ^{129}I/^{127}I: a novel tool for tracing terrestrial organic carbon in the estuarine surface waters of Galveston Bay. Texas. Limnol. Oceanogr. Meth. 3, 326−337.

Segl, M., Levin, I., Schoch-Fischer, H., Münnich, M., Kromer, B., Tschiersch, J., Otto, K., 1983. Atmospheric ^{14}C variations. Radiocarbon 25, 583−592.

Sekine, K., Imai, T., Kasai, A., 1987. Liquid—liquid extraction separation and sequential determination of plutonium and americium in environmental samples by alpha-spectrometry. Talanta 34, 567−570.

Semioshkina, N., Proehl, G., Savinkov, A., Voigt, G., 2007. The transfer of ^{137}Cs and ^{90}Sr from feed to rabbits. J. Environ. Radioact. 98, 166−176.

Sethy, N.K., Sutar, A.K., Rath, P., Jha, V.N., Ravi, P.M., Tripathi, R.M., 2015. A review of radio chemical analysis and estimation of ^{210}Po in soil matrices. J. Radiat. Res. Appl. Sci. 8, 590−596.

Shanks, R.P., Freeman, S.P.H.T., 2015. 160 keV ^{26}Al-AMS with a single-stage accelerator mass spectrometer. Nucl. Instrum. Methods Phys. Res. B 361, 307−310.

Shao, C.-F., Zhao, Y., Wu, K., Jia, F.-F., Luo, Q., Liu, Z., Wang, F.-Y., 2018a. Correlated secondary ion mass spectrometry-laser scanning Confocal microscopy imaging for single cell-principles and applications. Chinese J. Anal. Chem. 46, 1005−1016.

Shao, Y., Yang, G., Tazoe, H., Ma, L., Yamada, M., Xu, D., 2018b. A review of measurement methodologies and their applications to environmental ^{90}Sr. J. Environ. Radioact. 192, 321−333.

Sharabi, G., Lazar, B., Kolodny, Y., Teplyakov, N., Halicz, L., 2010. High precision determination of ^{228}Ra and ^{228}Ra/^{226}Ra isotope ratio in natural waters by MC-ICPMS. Int. J. Mass Spectrom. 294, 112−115.

Shi, K., Hou, X., Roos, P., Wu, W., 2012. Determination of technetium-99 in environmental samples: a review. Anal. Chim. Acta 709, 1−20.

Shinonaga, T., Steier, P., Lagos, M., Ohkura, T., 2014. Airborne plutonium and non-natural uranium from the fukushima DNPP found at 120 km distance a few Days after reactor hydrogen explosions. Environ. Sci. Technol. 48, 3808−3814.

Shukla, A., Parmar, P., Saraf, M., 2017. Radiation, radionuclides and bacteria: an in-perspective review. J. Environ. Radioact. 180, 27−35.

Sill, C.W., 1987a. Precipitation of actinides as fluorides or hydroxides for high-resolution alpha spectrometry. Nucl. Chem. Waste Manag. 7, 201−216.

Sill, C.W., 1987b. Determination of radium-226 in ores, nuclear wastes and environmental samples by high-resolution alpha spectrometry. Nucl. Chem. Waste Manag. 7, 239−256.

Simek, P., Korínková, T., Svetlik, I., Povinec, P.P., Fejgl, M., Malátová, I., Tomaskova, L., Stepan, V., 2017. The valley system of the Jihlava river and Mohelno reservoir with enhanced tritium activities. J. Environ. Radioact. 166, 83−90.

Simpson, J.A., 1983. Elemental and isotopic composition of the galactic cosmic rays. Ann. Rev. Nucl. Part. Sci. 33, 321−381.

Sinkko, K., Aatonen, H., Mustonen, R., Taipale, T.K., Juutilainen, J., 1987. Airborne Radioactivity in Finland After the Chernobyl Accident in 1986. STUK-A56. Finnish Centre fo Radiation and Nuclear Safety, Helsinki.

Sissenwine, N., Dubin, M., Wexler, H., 1962. The U.S. Standard atmosphere, 1962. J. Geophys. Res. 67, 3627−3630.

Skipperud, L., Oughton, D.H., Rosten, L.S., Wharton, M.J., Day, J.P., 2007. Determination of technetium-99 using electrothermal vaporization inductively coupled plasma-mass spectrometry (ETV-ICP-MS) and NH_4OH as chemical modifier. J. Environ. Radioact. 98, 251−263.

Slota, P.J., Jull, A.J.T., Linick, T.W., Toolin, L.J., 1987. Preparation of small samples for ^{14}C accelerator targets by catalytic reduction of CO. Radiocarbon 29, 303–306.

Smetanová, I., Holý, K., Müllerová, M., Polášková, A., 2010. The effect of meteorological parameters on radon concentration in borehole air and water. J. Radioanal. Nucl. Chem. 283, 101–109.

Smil, V., 2002. The Earth's Biosphere: Evolution, Dynamics, and Change. The MIT Press, Boston.

Smith, A.M., Fink, D., Child, D., Levchenko, V.A., Morgan, V.I., Curran, M., Etheridge, D.M., Elliott, G., 2000. ^{7}Be and ^{10}Be concentrations in recent firn and ice at Law Dome, Antarctica. Nucl. Instrum. Methods Phys. Res. B 172, 847–855.

Smith, D.K., Finnegan, D.L., Bowen, S.M., 2003. An inventory of long-lived radio- nuclides residual from underground nuclear testing at the Nevada test site, 1951–1992. J. Environ. Radioact. 67, 35–51.

Smith, L.L., Crain, J.S., Yaeger, J.S., Horwitz, E.P., Diamond, H., Chiarizia, R., 1995. Improved separation method for determining actinides in soil samples. J. Radioanal. Nucl. Chem. 194, 151–156.

Smith, L.L., Markun, F., Ten Kate, T., 1992. Comparison of acid leachate and fusion methods to determine plutonium and americium in environmental samples. Analyt. Chem. Lab., Argonne Natl. Lab. Argonne Report ANL/ACL 92/2, 13.

Srncik, M., Steier, P., Wallner, G., 2010. Determination of the isotopic ratio $^{236}U/^{238}U$ in Austrian water samples. Nucl. Instrum. Methods Phys. Res. B 268, 1146–1149.

Stamoulis, K.C., Assimakopoulos, P.A., Ioannides, K.G., Johnson, E., Soucacos, P.N., 1999. Strontium-90 concentration measurements in human bones and teeth in Greece. Sci. Total Environ. 229, 165–182.

Stanys, T., Holy, K., Petruf, P., 1998. Alpha spectrometric method for determination of radon and thoron daughter activity. Acta Phys. Univ. Comenianae XXXIX, 97–109.

Staunton, S., Dumat, C., Zsolnay, A., 2002. Possible role of organic matter in radiocaesium adsoprtion in soils. J. Environ. Radioact. 58 (2–3), 163–173.

Steier, P., et al., 2008. Natural and anthropogenic ^{236}U in environmental samples. Nucl. Instrum. Methods Phys. Res. B 266, 2246–2250.

Steinhauser, G., et al., 2015. Post-accident sporadic releases of airborne radionuclides from the fukushima Daiichi nuclear power plant site. Environ. Sci. Technol. 49, 14028–14035.

Steinmann, P., Zeller, M., Beuret, P., Ferreri, G., Estier, S., 2013. Cosmogenic ^{7}Be and ^{22}Na in ground level air in Switzerland (1994–2011). J. Environ. Radioact. 124, 68–73.

Stockburger, H., Sartorius, H., Sittkus, A., 1977. Messung der Kr-85- und Xe-133-Aktivität der atmosphärischenLuft. Z. Naturforsch. 32a, 1249–1253.

Stille, P., Renaud, P., Mezhibor, A., 2008. Radioisotope contaminations from releases of the Tomsk-Seversk nuclear facility (Siberia, Russia). J. Environ. Radioact. 99, 680–693.

Stocki, T.J., et al., 2005. Automated radioxenon monitoring for the comprehensive nuclear Test-Ban Treaty in two distinctive locations: Ottawa and Tahiti. J. Environ. Radioact. 80, 305–326.

Stohl, A., Forster, C., Frank, A., Seibert, P., Wotawa, G., 2005. Technical note: the Lagrangian particle dispersion model FLEXPART version 6.2. Atmos. Chem. Phys. 5, 2461–2474.

Stohl, A., Seibert, P., Wotawa, G., Arnold, D., Burkhart, J.F., Eckhardt, S., Tapia, C., Vargas, A., Yasunari, T.J., 2012. Xenon-133 and caesium-137 releases into the atmosphere from the Fukushima Dai-ichi nuclear power plant: determination of the source term, atmospheric dispersion, and deposition. Atmos. Chem. Phys. 12, 2313–2343.

Stoulos, S., Ioannidou, A., Vagena, E., Koseoglou, P., Manolopoulou, M., 2014. Post-Chernobyl ^{137}Cs in the atmosphere of Thessaloniki: a consequence of the financial crisis in Greece. J. Environ. Radioact. 128, 68–74.

Strandberg, M., 1994. Radiocesium in a Danish pine forest ecosystem. Sci. Total Environ. 157, 125–132.

Straub, M., Pittet, P.-A., Amzalag, G., Bochud, F., Baechler, S., Froidevaux, P., 2018. Determination of ^{226} Ra at low levels in environmental, urine, and human bone samples and ^{223}Ra in bone biopsy using alpha-spectrometry and metrological traceability to $^{229}Th/^{225}Ra$ or ^{226}Ra. Analytica Chimica Acta. https://doi.org/10.1016/j.aca.2018.05.007 (in press).

Stuiver, M., Polach, H.A., 1977. Discussion: reporting of ^{14}C data. Radiocarbon 19, 355–363.

Sturchio, et al., 2004. One million year old groundwater in the Sahara revealed by krypton-81 and chlorine-36. Geophys. Res. Lett. 31, 1–4.

Suarez-Navarro, J.A., Pujol, L., Suarez-Navarro, M.J., 2017. Determination of specific alpha-emitting radionuclides (uranium, plutonium, thorium and polonium) in water using [Ba+Fe]-coprecipitation method. Appl. Radiat. Isot. 130, 162–171.

Suess, H.E., 1955. Radiocarbon concentration in modern wood. Science 122, 415–417.

Surls, J.P., Choppin, G.R., 1957. Ion exchange study of thiocyanate complexes of actinides and lanthanides. J. Radioanal. Nucl. Chem. 4, 62–73.

Svetlik, I., Fejgl, M., Malátová, I., Tomaskova, L., 2014. Enhanced activities of organically bound tritium in biota samples. Appl. Radiat. Isot. 93, 82–86.

Svetlik, I., Fejgl, M., Povinec, P.P., Kořínková, T., Tomášková, L., Pospíchal, J., Kurfiřt, M., Striegler, R., Kaufmanová, M., 2017. Determination of chemical forms of ^{14}C in liquid discharges from nuclear power plants. J. Environ. Radioact. 177, 256–260.

Svetlik, I., Fejgl, M., Turek, K., Michalek, V., Tomaskova, L., 2012. ^{14}C studies in the vicinity of the Czech NPPs. J. Radioanal. Nucl. Chem. 292, 689–695.

Svetlik, I., Tomaskova, L., Molnar, M., Svingor, E., Futo, I., Pinter, T., Rulik, P., Michalek, V., 2006. Monitoring of atmospheric $^{14}CO_2$ in central European countries. Czech. J. Phys. 56, 291–297.

Sýkora, I., Ješkovský, M., Janik, R., Holý, K., Chudý, M., Povinec, P.P., 2008. Low-level single and coincidence gamma-ray spectrometry. J. Radioanal. Nucl. Chem. 276, 779–787.

Sýkora, I., Povinec, P.P., Bresťáková, L., Florek, M., Holý, K., Masarik, J., 2012. Resuspension processes control variations of ^{137}Cs activity concentrations in the ground-level air. J. Radioanal. Nucl. Chem. 293, 595–599.

Sýkora, I., Holý, K., Ješkovský, M., Müllerová, M., Bulko, M., Povinec, P.P., 2017. Long-term variations of radionuclides in the Bratislava air. J. Environ. Radioact. 166, 27–35.

Synal, H.-A., 2013. Developments in accelerator mass spectrometry. Int. J. Mass Spectrom. 349–350, 192–202.

Synal, H.-A., Beer, J., Bonani, G., Lukasczyk, C., Suter, M., 1994. ^{36}Cl measurements at the Zürich AMS facility. Nucl. Instrum. Methods Phys. Res. B 92, 79–84.

Szabó, K.Z., Udvardi, B., Horváth, Á., Bakacsi, Z., Pásztor, L., Szabó, J., Laczkó, L., Szabó, C., 2012. Cesium-137 concentration of soils in pest county, Hungary. J. Environ. Radioact. 110, 38–45.

Szidat, S., et al., 2004. Radiocarbon (^{14}C)-deduced biogenic and anthropogenic contributions to organic carbon (OC) of urban aerosols from Zürich, Switzerland. Atmos. Environ. 38, 4035−4044.

Szidat, S., Jenk, T.M., Synal, H.-A., Kalberer, M., Wacker, L., Hajdas, I., Kasper-Giebl, A., Baltensperger, U., 2006. Contributions of fossil fuel, biomass-burning, and biogenic emissions to carbonaceous aerosols in Zurich as traced by ^{14}C. J. Geophys. Res. 111, D07206.

Szidat, S., Ruff, M., Perron, N., Wacker, L., Synal, H.-A., Hallquist, M., Shannigrahi, A.S., Yttri, K.E., Dye, C., Simpson, D., 2009. Fossil and non-fossil sources of organic carbon (OC) and elemental carbon (EC) in Göteborg, Sweden. Atmos. Chem. Phys. 9, 1521−1535.

Talvitie, N.A., 1972. Electrodeposition of actinides for alpha spectrometric determination. Anal. Chem. 44, 280−283.

Tamborini, G., Betti, M., 2000. Characterisation of radioactive particles by SIMS. Microchim. Acta 132, 411−417.

Tamers, M.A., 1975. Chemical yield optimization of the benzene synthesis for radiocarbon dating. Int. J. Appl. Radiat. Isot. 26, 676−682.

Tanaka, K., Shimada, A., Hoshi, A., Yasuda, M., Ozawa, M., Kameo, Y., 2014. Radiochemical analysis of rubble and trees collected from fukushima Daiichi nuclear power station. J. Nucl. Sci. Technol. 51, 1032−1043.

Tanner, S.D., Baranov, V.I., Bandura, D.R., 2002. Reaction cells and collision cells for ICP-MS: a tutorial review. Spectrochim. Acta B 57, 1361−1452.

Taylor, R.N., Croudace, I.W., Warwick, P.E., Dee, S.J., 1998. Precise and rapid determination of ^{238}U/^{235}U and uranium concentration in soil samples using thermal ionisation mass spectrometry. Chem. Geol. 144, 73−80.

Taylor, R.N., Warneke, T., Milton, J.A., Croudace, I.W., Warwick, P.E., Robert, W., Nesbitt, R.W., 2001. Plutonium isotope ratio analysis at femtogram to nanogram levels by multicollector ICP-MS. J. Anal. At. Spectrom. 16, 279−284.

Tecl, J., Svetlik, I., 2009. Determination of gaseous radionuclide forms in the stack air of nuclear power plants. Appl. Radiat. Isot. 67, 950−952.

Thakkar, A., 2001. Rapid sequential separation of actinides using Eichrom's extraction chromatographic material. J. Radioanal. Nucl. Chem. 248, 453−456.

Thakur, P., Khaing, H., Salminen-Paatero, S., 2017. Plutonium in the atmosphere: a global perspective. J. Environ. Radioact. 175−176, 39−51.

Theodórsson, P., 2005. Simultaneously measuring ^{14}C and radon in benzene dating samples. Radiocarbon 47, 231−234.

Tian, C.-Y., Ding, X.-L., Yin, J.-W., Duan, Y.-X., 2016. Preliminary study of microfabricated glow discharge plasma for mass spectrometry imaging. Chinese J. Anal. Chem. 44, 8−12.

Tomé, F.V., Sanchez, A.M., 1991. Optimizing the parameters affecting the yield and energy resolution in the electrodeposition of uranium. Appl. Radiat. Isot. 42 (2), 135−140.

Topin, S., et al., 2015. Spalax new generation: new process design for a more efficient xenon production system for the CTBT noble gas network. J. Environ. Radioact. 149, 43−50.

Tosaki, Y., et al., 2007. Application of ^{36}Cl as a dating tool for modern groundwater. Nucl. Instrum. Methods Phys. Res. B 259, 479−485.

Tracy, B.L., 2010. Radon. In: Atwood, D.A. (Ed.), Radionuclides in the Environment. Wiley, New York, pp. 191−206.

Truscott, J.B., Jones, P., Fairman, B.E., Evans, E.H., 2001. Determination of actinides elements at femtogram per gram levels environmental samples by on-line solid phase extraction and sector-field-inductively coupled plasma mass spectrometry. Anal. Chim. Acta 433, 245−253.

Tu, L.-Y., Yang, G.-M., Cheng, C.-F., Liu, G.-L., Zhang, X.-Y., Hu, S., 2014. Analysis of Kr-85 and Kr-81 in a few liters of air. Anal. Chem. 86, 4002−4007.

Tuniz, C., Bird, J.R., Fink, D., Herzog, G.F., 1998. Accelerator Mass Spectrometry: Ultrasensitive Analysis of Global Science. CRC Press, Boca Raton.

Turner, S., Regelous, M., Kelley, S., Hawkesworth, C., Mantovani, M., 1994. Magmatism and continental break-up in the South Atlantic: high precision ^{40}Ar-^{39}Ar geochronology. Earth Planet. Sci. Lett. 121, 333−348.

Tykva, R., Berg, D. (Eds.), 2004. Man-Made and Natural Radioactivity in Environmental Pollution and Radiochronology. Springer, Dordrecht.

UNSCEAR, United Nations Scientific Committee on the Effects of Atomic Radiation, 1982. Ionizing Radiation: Sources and Biological Effects (United Nations, New York).

UNSCEAR, United Nations Scientific Committee on the Effects of Atomic Radiation, 1988. Sources, Effects and Risks of Ionizing Radiation. (United Nations, New York).

UNSCEAR, United Nation Scientific Committee on the Effects of Atomic Radiation, 2000. Sources and Effects of Ionizing Radiation (United Nations, New York).

UNSCEAR, United Nations Scientific Committee on the Effects of Atomic Radiation, 2008. Sources and Effects of Ionizing Radiation (United Nations, New York).

Vagner, I., Varlam, C., Faurescu, I., Faurescu, D., 2014. Organically bound tritium level in vegetation at ICIT tritium removal facility. J. Radioanal. Nucl. Chem. 303, 2559−2563.

Vajda, N., Molnár, Z., Kabai, E., Osvath, S., 2003. Simultaneous determination of long-lived radionuclides in environmental samples. In: Birsen, N., Kadyrzhanov, K.K. (Eds.), Environmental Protection against Radioactive Pollution. Springer, Dordrecht, pp. 133−146.

Vajda, N., Torvenyi, A., Kis-Benedek, Kim, C.K., 2009a. Development of extraction chromatographic separation procedures for the simultaneous determination of actinides. Radiochim. Acta 97, 9−16.

Vajda, N., Torvenyi, A., Kis-Benedek, G., Kim, C.K., Bene, B., Macsik, Zs., 2009b. Rapid method for the determination of actinides in soil and sediment samples by alpha spectrometry. Radiochim. Acta. 97, 395−401.

Vakulovsky, S.M., Nikitin, A.I., Chumichev, V.B., Katrich, I.Y., Voitsekhovich, O.A., Medinets, V.I., Pisarev, V.V., Bovkum, L.A., Khersonsky, E.S., 1994. Cesium-137 and strontium-90 contamination of water bodies in the areas affected by releases from the chernobyl nuclear power plant accident: an overview. J. Environ. Radioact. 23, 103−122.

Valcke, E., Cremers, A., 1994. Sorption-desorption dynamics of radiocaesium in organic mater soils. Sci. Tot. Environ. 157, 275−283.

Valmari, T., Tarvainen, M., Lehtinen, J., Rosenberg, R., Honkamaa, T., Ossintsev, A., Lehtimäki, M., Taipale, A., Ylätalo, S., Zilliacus, R., 2002. Aerosol Sampling Methods for Wide Area Environmental Sampling (WAES). STUK-YTO-TR 183 Report. STUK, Helsinki.

Van Es, E.M., Russell, B.C., Ivanov, P., Read, D., 2017. Development of a method for rapid analysis of Ra-226 in groundwater and discharge water samples by ICP-QQQ-MS. Appl. Radiat. Isot. 126, 31−34.

Vandecasteele, C.M., Van Hees, M., Hardeman, F., Voigt, G., Howard, B.J., 2000. The true absorption of ^{131}I, and its transfer to milk in cows given different stable iodine diets. J. Environ. Radioact. 47, 301−317.

Vaaramaa, K., Aro, L., Solatie, D., Lehto, J., 2010. Distribution of ^{210}Pb and ^{210}Po in boreal forest soil. Sci. Total Environ. 408 (24), 6155–6171.

Varga, Z., Surányi, G., Vajda, N., Stefánka, Z., 2007a. Determination of plutonium in environmental samples by inductively coupled plasma sector field mass spectrometry and alpha spectrometry. Microchem. J. 85, 39–45.

Varga, Z., Suranyi, G., Vajda, N., Stefanka, Z., 2007b. Improved sample preparation method for environmental plutonium analysis by ICP-SFMS and alpha-spectrometry. J. Radioanal. Nucl. Chem. 274, 87–94.

Vasile, M., Jacobs, K., Bruggeman, M., Van Hoecke, K., Dobney, A., Verrezen, F., 2018. On the sequential separation and quantification of 237 Np, 241 Am, thorium, plutonium, and uranium isotopes in environmental and urine samples. Appl. Radiat. Isot. 134, 455–460.

Vecchi, R., Marcazzan, G., Valli, G., 2005. Seasonal variation of ^{210}Pb activity concentration in outdoor air of Milan (Italy). J. Environ. Radioact. 82, 251–266.

Veniaminov, N.N., 2000. Secondary ion mass spectrometry in studies of occupational dust particles from plants with nuclear fuel cycle. J. Anal. Chem. 55, 263–269.

Vichot, L., Boyer, C., Boissieux, T., Losset, Y., Pierrat, D., 2008. Organically bound tritium (OBT) for various plants in the vicinity of continuous atmospheric tritium release. J. Environ. Radioact. 99, 1636–1643.

Vintró, L., Smith, K.J., Lucey, J.A., Mitchell, P.I., 2000. The environmental impact of the Sellafield discharges. In: SCOPE-RADSITE Workshop Proceedings, Brussels, 4–6, p. 27.

Vokal, B., Kobal, I., 1997. Radiocarbon releases at the Krško nuclear power plant. Radiocarbon 39, 285–292.

Volpe, A.M., Olivares, J.A., Murrelli, M.T., 1991. Determination of radium isotope ratios and abundances in geological samples by thermal ionization mass spectrometry. Anal. Chem. 63, 913–916.

Waas, D., Kleinmann, A., Lepper, J., 2011. Uranium-series dating of fen peat horizons from pit Nachtigall in northern Germany. Quat. Int. 241, 111–124.

Wacker, L., Fifield, L.K., Tims, S.G., 2004. Developments in AMS of ^{99}Tc. Nucl. Instrum. Methods Phys. Res. B 223–224, 185–189.

Wainwright, M., Wickramasinghe, N.C., Narlikar, J.V., Rajaratnam, P., 2003. Microorganisms cultured from stratospheric air samples obtained at 41 km. FEMS Microbiol. Lett. 218, 161–165.

Wang, Z., Yang, G., Zheng, J., Cao, L., Yu, H., Zhu, Y., Tagami, K., Uchida, S., 2015. Effect of ashing temperature on accurate determination of plutonium in soil samples. Anal Chem 87, 5511–5515.

Wang, Z., Zheng, J., Tagami, K., Uchida, S., 2017a. Extraction behaviors of interfering elements on TRU and DGA resins for ^{241}Am determination by mass spectrometry. J. Radioanal. Nucl. Chem. 312, 151–160.

Wang, Z., Zheng, J., Ni, Y., Men, W., Tagami, K., Uchida, S., 2017b. High-performance method for determination of Pu isotopes in soil and sediment samples by sector field-inductively coupled plasma mass spectrometry. Anal. Chem. 89, 2221–2226.

Wang, X., Dong, K., He, M., Wu, S., Shan Jiang, S., 2013. Study of UF^- extraction in accelerator mass spectrometry measurement of ^{236}U. Nucl. Technol. 182, 235–241.

Wang, Y., Chung, A., Paulson, S.E., 2010. The effect of metal salts on quantification of elemental and organic carbon in diesel exhaust particles using thermal-optical evolved gas analysis. Atmos. Chem. Phys. 10, 11447–11457.

Ward, D.C., Borak, T.B., 1991. Determination of time varying ^{222}Rn concentrations using flow-through scintillation flasks. Health Phys 61, 799–807.

Warneke, T., Croudace, I.W., Warwick, P.E., Taylor, R.N., 2002. A new ground-level fallout record of uranium and plutonium isotopes for northern temperate latitudes. Earth Planet. Sci. Lett. 203, 1047–1057.

Warwick, P.E., Croudace, I.W., Oh, J.-S., 2001. Radiochemical determination of ^{241}Am and Pu(α) in environmental materials. Anal. Chem. 73, 3410–3416.

Weinlich, F.H., Faber, E., Boušková, A., Horálek, J., Teschner, M., Poggenburg, J., 2006. Seismically induced variations in Mariánské Lázně fault gas composition in the NW Bohemian swarm quake region, Czech Republic — a continuous gas monitoring. Tectonophysics 421, 89–110.

Welte, J., Ritterbusch, F., Steinke, I., Henrich, M., Aeschbach-Hertig, W., Oberthaler, M.K., 2010. Towards the realization of atom trap trace analysis for ^{39}Ar. New J. Phys. 12.

Wendel, C.C., Fifield, L.K., Oughton, D.H., Lind, O.C., Skipperud, L., Bartnicki, J., Tims, S.G., Høibraten, S., Salbu, B., 2013. Long-range tropospheric transport of uranium and plutonium weapons fallout from Semipalatinsk nuclear test site to Norway. Environ. Int. 59, 92–102.

Wendt, K., Trautmann, N., 2005. Recent developments in isotope ratio measurements by resonance ionization mass spectrometry. Int. J. Mass Spectrom. 242, 161–168.

Wernsperger, B., Schlosser, C., 2004. Noble gas monitoring within the international monitoring system of the comprehensive nuclear test-ban treaty. Radiat. Phys. Chem. 71, 775–779.

Wershofen, H., Aumann, D.C., 1989. Iodine-129 in the environment of a nuclear fuel reprocessing plant: VII. Concentrations and chemical forms of ^{129}I and ^{127}I in the atmosphere. J. Environ. Radioact. 10, 141–156.

Wershofen, H., Arnold, D., 2005. Radionuclides in Ground-Level Air in Braunschweig – Report of the PTB Trace Survey Station From 1998 to 2003. Radioaktivität PTB-Ra-45. Physikalische - Technische Bundesanstalt, Braunschweig.

Wershofen, H., Arnold, D., Steinkopff, T., 2001. Measurement of plutonium isotopes in ground-level air in Northern-Germany - history and recent results. Nukleonika 46, 155–159.

Wetzel, R.G., 2001. Limnology: Lake and River Ecosystems. Academic Press, San Diego.

Wieser, E.M., Schwieters, J.B., 2005. The development of multiple collector mass spectrometry for isotope ratio measurements. Int. J. Mass Spectrom. 242, 97–115.

Wilcken, K.M., Freeman, S.P.H.T., Dougans, A., Xu, S., Loger, R., Schnabel, C., 2010. Improved ^{36}Cl AMS at 5 MV. Nucl. Instrum. Methods Phys. Res. B 268, 748–751.

Wilhelm, E., Battino, R., Wilcock, R.J., 1977. Low-pressure solubility of gases in liquid water. Chem. Rev. 77, 219–262.

Wilhelmová, L., Dvořák, Z., Tomášek, M., Štukheil, K., 1986. Application of the CaF_2(Eu) scintillator to ^{85}Kr monitoring in atmospheric air samples. Int. J. Appl. Radiat. Isot. 37, 429–432.

WNA, World Nuclear Association, 2018. Plutonium. Plutonium in the Reactor Core. Avalaible on-line: http://www.worldnuclear.org/information-library/nuclear-fuel-cycle/fuel-recycling/plutonium.aspx.

Wölfli, W., Polach, H.A., Andersen, H.H. (Eds.), 1984. Proceedings of the 3rd international Symposium on accelerator mass spectrometry. Methods Phys. Res. B, 5, pp. 1–448.

Wotawa, G., et al., 2003. Atmospheric transport modelling in support of CTBT verification: overview and basic concepts. Atmos. Environ. 37, 2529–2537.

Wright, S.M., Howard, B.J., Strand, P., Nylén, T., Sickel, M.A.K., 1999. Prediction of ^{137}Cs deposition from atmospheric nuclear weapons tests within the Arctic. Environ. Pollut. 104, 131–143.

Wyse, E., Lee, S.-H., La Rosa, J.J., Povinec, P.P., de Mora, S.J., 2001. ICP-sector field mass spectrometry analysis of plutonium isotopes: recognizing and resolving potential interferences. J. Anal. Atom. Spectrom. 16, 1107–1111.

Xie, F., He, X., Jiang, W., Zhang, X., Shi, Q., Wu, S., Liu, L., Zhang, C., Chen, L., 2014. Development of a radioxenon measurement system and its application in monitoring Fukushima nuclear accident. Radiat. Phys. Chem. 97, 85–89.

Xing, S., Zhang, W., Qiao, J., Hou, X., 2018. Determination of ultra-low level plutonium isotopes (^{239}Pu, ^{240}Pu) in environmental samples with high uranium. Talanta 187, 357–364.

Xu, C., Zhang, S., Sugiyama, Y., Ohte, N., Ho, Y.-F., Fujitake, N., Kaplan, D.I., Yeager, C.M., Schwehr, K., Santschi, P.H., 2016. Role of natural organic matter on iodine and Pu-239,240 distribution and mobility in environmental samples from the northwestern Fukushima Prefecture, Japan. J. Environ. Radioact. 153, 156–166.

Xu, S., Zhang, L., Freeman, S.P.H.T., Hou, X., Shibata, Y., Sanderson, D., Cresswell, A., Doi, T., Tanaka, A., 2015. Speciation of radiocesium and radioiodine in aerosols from Tsukuba after the Fukushima nuclear accident. Environ. Sci. Technol. 49, 1017–1024.

Xu, X., Trumbore, S.E., Zheng, S., Southon, J.R., McDuffee, K.E., Luttgen, M., Liu, J.C., 2007. Modifying a sealed tube zinc reduction method for preparation of AMS graphite targets: reducing background and attaining high precision. Nucl. Instrum. Methods Phys. Res. B 259, 320–329.

Xu, Y., Pan, S., Wu, M., Zhang, K., Hao, Y., 2017. Association of Plutonium isotopes with natural soil particles of different size and comparison with ^{137}Cs. Sci. Total Environ. 581–582, 541–549.

Yamagata, N., 1962. The concentration of common cesium and rubidium in human body. J. Rad. Res. 3, 9–30.

Yamagata, T., Sugihara, S., Morinaga, I., Matsuzaki, H., Nagai, H., 2010. Short term variations of ^{7}Be, ^{10}Be concentrations in atmospheric boundary layer. Nucl. Instrum. Methods Phys. Res. B 268, 1135–1138.

Yamamoto, M., Tsukatani, T., Katayama, Y., 1996a. Residual radioactivity in the soil of the Semipalatinsk-21 nuclear test site in the former USSR. Health Phys 71, 142–148.

Yamamoto, M., Tsumura, A., Katayama, Y., Tsukatani, T., 1996b. Plutonium isotopic composition in soil from the former Semipalatinsk nuclear test site. Radiochim. Acta 72, 209–215.

Yamamoto, M., Takada, T., Nagao, S., Koike, T., Shimada, K., Hoshi, M., Zhumadilov, K., Shima, T., Fukuoka, M., Imanaka, T., Endo, S., Sakaguchi, A., Kimura, S., 2012. An early survey of the radioactive contamination of soil due to the Fukushima Dai-ichi Nuclear Power Plant accident, with emphasis on plutonium analysis. Geochem. J. 46, 341–353.

Yamamoto, M., Sakaguchi, A., Ochiai, S., Takada, T., Hamataka, K., Murakami, T., Nagao, S., 2014. Isotopic Pu, Am and Cm signatures in environmental samples contaminated by the fukushima Dai-ichi nuclear power plant accident. J. Environ. Radioact. 132, 31–46.

Yang, G., Tazoe, H., Yamada, M., 2016. Determination of ^{236}U in environmental samples by single extraction chromatography coupled to triple-quadrupole inductively coupled plasma-mass spectrometry. Anal. Chim. Acta 944, 44–50.

Yang, G., Tazoe, H., Hayano, K., Okayama, K., Yamada, M., 2017. Isotopic compositions of ^{236}U, ^{239}Pu, and ^{240}Pu in soil contaminated by the fukushima Daiichi nuclear power plant accident. Sci. Rep. 7, 13619. https://doi.org/10.1038/s41598-017-13998-6 1.

Yiou, F., Raisbeck, G. (Eds.), 1990. Proceedings of the 5th international conference on accelerator mass spectrometry. Nucl. Instrum. Methods Phys. Res. B, 52, pp. 211–630.

Yokochi, R., 2016. Recent developments on field gas extraction and sample preparation methods for radiokrypton dating of groundwater. J. Hydrol. 540, 368–378.

Yokochi, R., Sturchio, N.C., Purtschert, R., Jiang, W., Lu, Z.T., Mueller, P., Yang, G.M., Kennedy, B.M., Kharaka, Y., 2013. Noble gas radionuclides in Yellowstone geothermal gas emissions: a reconnaissance. Chem. Geol. 339, 42–51.

Yoshida, S., Muramatsu, Y., Yamazaki, S., Bannai, T., 2007. Distribution of nuclear bomb Pu in Nishiyama area, Nagasaki, estimated by accurate and precise determination of ^{240}Pu/^{239}Pu ratio in soils. J. Environ. Radioact. 9, 85–93.

Yoshida, S., Muramatsu, Y., 1995. Determination of organic, inorganic and particulate iodine in the coastal atmosphere of Japan. J. Radioanal. Nucl. Chem. Art. 196, 295–302.

Yu, J.Z., Xu, J., Yang, H., 2002. Charring characteristics of atmospheric organic particulate matter in thermal analysis. Environ. Sci. Technol. 36, 754–761.

Yubero, E., Carratalá, A., Crespo, J., Nicolás, J., Santacatalina, M., Nava, S., Lucarelli, F., Chiari, M., 2011. PM10 source apportionment in the surroundings of the San Vicente del Raspeig cement plant complex in southeastern Spain. Environ. Sci. Pollut. Res. 18, 64–74.

Zandee, L., Bernstein, R.B., 1979. Laser ionization mass spectrometry: extensive fragmentation via resonance-enhanced multiphoton ionization of a molecular benzene beam. J. Chem. Phys. 70, 2574–2575.

Zencak, Z., Elmquist, M., Gustafsson, Ö., 2007. Quantification and radiocarbon source apportionment of black carbon in atmospheric aerosols using the CTO-375 method. Atmos. Environ. 41, 7895–7906.

Zhang, T., Bain, D., Hammack, R., Vidic, R.D., 2015. Analysis of radium-226 in high salinity wastewater from unconventional gas extraction by inductively coupled plasma-mass spectrometry. Environ. Sci. Technol. 49, 2969–2976.

Zhang, L.Y., Hou, X., Xu, S., 2015a. Speciation analysis of ^{129}I and ^{127}I in aerosols using sequential extraction and mass spectrometry detection. Anal. Chem. 87, 6937–6944.

Zhang, L.Y., Hou, X.L., Xu, S., 2015b. Speciation of ^{127}I and ^{129}I in atmospheric aerosols at Risø, Denmark: insight into sources of iodine isotopes and their species transformations. Atmos. Chem. Phys. Discuss. 15, 25139–25173.

Zhang, Q., Liu, T., Yang, L., Meng, D., Song, D., 2018. Monitoring and management of tritium from the nuclear power plant effluent. IOP Conf. Ser. Earth Environ. Sci. 108, 042057.

Zhang, Y.L., Liu, D., Shen, C.D., Ding, P., Zhang, G., 2010. Development of a preparation system for the radiocarbon analysis of organic carbon in carbonaceous aerosols in China. Nucl. Instrum. Methods Phys. Res. B 268, 2831–2834.

Zhang, C., Luo, D., 1983. Measurement of mixed radon and thoron daughter concentrations in air. Nucl. Instrum. Methods 215, 481–488.
Zhao, X.L., Litherland, A.E., 2010. Studies of anions from sputtering II: ^{99}Tc and ^{99}Ru. Nucl. Instrum. Methods Phys. Res. B 268, 812–815.
Zheng, J., Tagami, K., Uchida, S., 2013. Release of plutonium isotopes into the environment from the fukushima Daiichi nuclear power plant accident: what is known and what needs to Be known. Environ. Sci. Technol. 47, 9584–9595.
Zheng, J., Tagami, K., Watanabe, Y., Uchida, S., Aono, T., Ishii, N., Yoshida, S., Kubota, Y., Fuma, S., Ihara, S., 2012. Isotopic evidence of plutonium release into the environment from the Fukushima DNPP accident. Sci. Rep. 2, 304.
Zhong, Y.-T., Mundil, R., Xu, Y.-G., Wang, G.-Q., Zhang, Z.-F., Ma, J.-L., 2017. Development of CA-ID-TIMS zircon U–Pb dating technique at Guangzhou Institute of Geochemistry, Chinese Academy of Sciences. Solid Earth Sci 2, 55–61.
Zhou, C., Zhou, G., Feng, S., Jin, Y., Zhao, X., Cheng, Z., Huang, X., Xu, H., Zhou, X., 2013a. Atmospheric radioxenon isotope monitoring in Beijing after the Fukushima nuclear power plant accident. Appl. Radiat. Isot. 72, 123–127.
Zhou, C., et al., 2013b. The determination of trace amounts of natural ^{133}Xe in gas under high radon activity concentration levels. J. Environ. Radioact. 122, 9–15.
Zondervan, A., Prior, C., Bruhn, F., Sparks, R. (Eds.), 2013. Proceedings of the Twelfth International Conference on Accelerator Mass Spectrometry. Nucl. Instrum. Methods Phys. Res. B, 294, pp. 1–714.
Zoriy, P., Flucht, R., Burrow, M., OMtapczuk, P.A., Lennartz, R., Zoriy, M., 2010. Development of a relatively cheap and simple automated separation system for a routine separation procedure based on extraction chromatography. J. Radioanal. Nucl. Chem. 286, 211–216.
Zvara, I., Povinec, P., Sykora, I., 1994. Determination of very low levels of radioactivity. Pure Appl. Chem. 66, 2537–2586.

Miroslav Ješkovský



Dr. Miroslav Ješkovský finished his PhD studies at the Comenius University in Bratislava (Slovakia) in 2009. Afterward, he continued his research as an Assistant Professor at the Faculty of Mathematics, Physics, and Informatics of the Comenius University. The main objectives of his research have been focused on natural and anthropogenic radionuclides in the environment. He used gamma spectrometry methods for the identification and quantification of radionuclides in various environmental samples and contributed to the development of a low-background HPGe spectrometer used in the Department of Nuclear Physics and Biophysics. After establishment of the new CENTA facility in Bratislava, Miroslav Ješkovský concentrated his work on the development and utilization of accelerator techniques such as accelerator mass spectrometry (AMS) and ion beam analysis (e.g., PIXE, PIGE, RBS, etc.) for the determination of stable and long-lived radioisotopes in the environment. In recent years, he has been participating in the development of radiometric and mass spectrometry methods for radiopurity measurements with detection limits down to nBq g^{-1} for underground physics experiments searching for rare nuclear processes and decays.

Jakub Kaizer



Dr. Jakub Kaizer finished his PhD in environmental physics at the Comenius University in Bratislava in 2015, and in the same year, he joined the research staff of the Department of Nuclear Physics and Biophysics of the Faculty of Mathematics, Physics, and Informatics of the Comenius University. He has been contributing to the ongoing development of the Centre for Nuclear and Accelerator Technologies (CENTA) since 2013, the scientific program of which is devoted to radiocarbon dating, studies of long-lived radionuclides in the environment, and ion beam analyses. In his research, he is mainly focused on low-level radioactivity environmental studies (e.g., impact of the Fukushima accident), development of accelerator mass spectrometry and ion beam techniques, and radiopurity measurements of various materials used in the large-scale physics experiment, such as the SuperNEMO experiment. He has (co)authored 17 papers in peer-reviewed scientific journals.

Ivan Kontul′



Dr. Ivan Kontul' received his PhD in environmental physics at the Comenius University in Bratislava (Slovakia) in 2019. His research is focused on the development of analytical methods for the analysis of cosmogenic radionuclides (mainly radiocarbon, ^{14}C) using radiometric and accelerator mass spectrometry, as well as on their applications in radiocarbon dating and environmental radioactivity studies. He also takes part in regular monitoring of radiocarbon activity of atmospheric carbon dioxide in heavily industrialized and urbanized regions as well as in the areas in the vicinity of nuclear power plants, including transfer of radionuclides to biota (e.g., in tree rings).

Galina Lujanienė



Dr. Galina Lujanienė received her PhD at the Vilnius University (Lithuania) in 1993. She then worked as a permanent research scientist at the Institute of Physics, as well as a visiting scientist in several European institutes. She has 30 years' experience in environmental radioactivity investigations—assessment of consequences of the Chernobyl and Fukushima accidents, monitoring of radionuclides in the environment, estimation of radionuclide sources in the environment (forest fires, dust storms, hot particles, aerosols, and suspended particles in the atmosphere, fresh- and seawater, and sediments), studies related to the radionuclide migration in soil and clay minerals, speciation of radionuclides and development of new radioanalytical and radiochemistry methods. Galina Lujanienė was involved as a leading scientist in more than 10 international and national projects. Since 2010, she has been the head of Radiochemical Laboratory at the SRI Centre for Physical Sciences and Technology in Vilnius. Currently, her research focuses on applications of radionuclides in traces studies and development of methods for removing radionuclides from contaminated liquid matrices. She was a principal supervisor of six PhD students. Galina has published more than 100 scientific papers in recognized journals and delivered many invited lectures at international conferences.

Monika Müllerová



Dr. Monika Müllerová received her PhD from the Comenius University in Bratislava (Slovakia) in 2009. She has been working as a scientific researcher at the Faculty of Mathematics, Physics, and Informatics of the Comenius University. Her research interests have focused on the monitoring of radionuclides in the environment, specifically on the study of radon behavior in the environment, as well as on the development of detectors for environmental radioactivity monitoring. In recent years, she has focused her research mainly on radon in houses, workplaces, and kindergartens, and on the calculation of effective radiation doses to the public from radon.

Pavel P. Povinec



Prof. RNDr. Pavel Povinec, DrSc., obtained his PhD degree in Physics from the Comenius University in Bratislava in 1974. He worked at the Department of Nuclear Physics of the Faculty of Mathematics and Physics of the Comenius University as an assistant professor, associated professor (1978), and professor of Physics (1984), also as the head of the Department (1981−1992), focusing on developments of radiometric methods for the analysis of radionuclides at very low levels with wide applications in nuclear (rare nuclear decays), environmental (radionuclides as tracers, radiocarbon dating), and space physics (radionuclides in lunar samples and meteorites). From 1993 to 2005, he worked at the IAEA's Marine Environment Laboratories in Monaco as the head of the Radiometrics Laboratory responsible for the development of radiometric (including underground laboratory) and mass spectrometry methods (ICP-MS, AMS) for marine radioactivity studies. Pavel Povinec has led several international projects on assessment of dumping of radioactive wastes, on impacts of nuclear weapon test sites, on worldwide marine radioactivity studies (WOMARS), on submarine groundwater discharge studies, on the development of global marine radioactivity databases (GLOMARD/MARIS), etc. After his return to the Comenius University, he established at the Faculty of Mathematics, Physics, and Informatics a Centre for Nuclear and Accelerator Technologies (CENTA) focusing on the development of IBA and AMS methods and their wide applications in nuclear, material, environmental, and biomedical sciences. He supervised 26 PhD students, published more than 20 books and book chapters and more than 700 referred papers with more than 13,000 citations, organized more than 20 international conferences, and delivered more than 50 invited talks.

Chapter 4

PERPUSTAKAAN PRIBADI AN-NUR SUNARYA

Radioactive aerosol analysis*

Konstantinos Eleftheriadis[1] **and Alexandra Ioannidou**[2]

[1]Environmental Radioactivity Laboratory, Institute of Nuclear and Radiological Science & Technology, Energy & Safety, N.C.S.R. "Demokritos", Ag. Paraskevi, Attiki, Greece; [2]Aristotle University of Thessaloniki, Physics Department, Nuclear Physics Laboratory, Thessaloniki, Greece

Chapter outline

I. Introduction **263**
A. What is a radioactive aerosol? 263
B. Radioactive aerosol formation 264
II. Radioactive aerosol sampling and measurement **265**
A. Aerodynamic particle sizing 265
1. Aitken nuclei mode particles 266
2. Accumulation mode particles 267
3. Coarse-particle mode particles 267
B. Instrumentation 267
1. High-volume air samplers 269
2. Aerosol cascade impactors 269
III. Radioactive aerosols in ambient air **283**
A. Radon and thoron decay product aerosols 283
B. Radioactive aerosols associated with the cosmic ray–produced radionuclides 286
C. Radioactive aerosols in the workplace environment 289
1. Mine aerosols 289
D. Radioactive aerosols associated with the operation of high-energy particle accelerators 290
E. Fission product radionuclide aerosols 291
1. Nuclear bomb tests 292
2. The comprehensive Test Ban Treaty 293
3. Chernobyl accident 293
4. Fukushima accident 297
IV. Residence time of radioactive aerosols **301**
A. Residence time of tropospheric aerosol particles associated with the cosmic ray–produced radionuclides 302
B. Residence time of tropospheric aerosol particles associated with the radon decay product radionuclides 304
C. Residence time of tropospheric aerosol particles associated with the fission product radionuclides 307
References **307**
Further reading **312**
Konstantinos Eleftheriadis **313**
Alexandra Ioannidou **313**

I. Introduction

A. What is a radioactive aerosol?

An aerosol, in general, is the system of liquid or solid particles suspended in a gas medium. In the atmosphere, the gas medium is air, and the system is the atmospheric aerosol. It is often that aerosol particles contain natural or anthropogenic radionuclides. In that case and in terms of their composition and activity, the term radioactive aerosol applies. The size of aerosol particles ranges from a few nanometers (10^{-9} m) to several hundreds of micrometers (10^{-6} m). Various names, such as Aitken nuclei, smoke, fume, or haze (for the smaller particles) and dusts, mists, fogs, or ashes (for larger ones), have been used in the nomenclature of atmospheric aerosols.

All aerosol particles are formed by chemical reactions of precursor species, condensation of gases or vapors or by mechanical processes. They may be transformed by coagulation or condensation of semivolatile species, and their concentration in air may change during aerosol transport, mixing with a different aerosol and dilution. They may be removed from the atmosphere and settle on surfaces, which act as a sink. The residence time of aerosol particles in the atmosphere varies from some days near the earth's surface in the troposphere to a year or more in the stratosphere.

Atmospheric aerosol transport and interaction with surfaces is mainly governed by the particle mechanical properties, condensation or evaporation of species as well

* Author of this chapter in the previous edition was Constantin Papastefanou.

Handbook of Radioactivity Analysis: Volume 2. https://doi.org/10.1016/B978-0-12-814395-7.00004-0
Copyright © 2020 Elsevier Inc. All rights reserved.

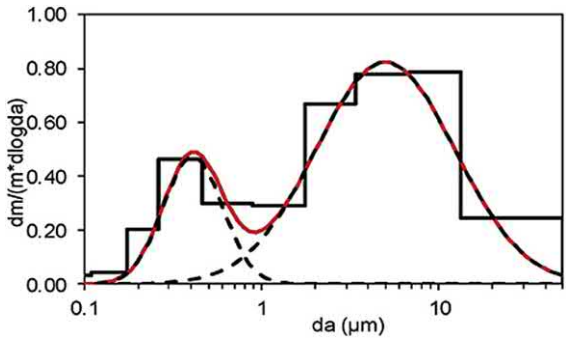


FIGURE 4.1 Average mass size distribution of ambient aerosols in terms of aerodynamic diameter during Sahara dust events measured by Berner impactors. The mass distribution was normalized by total mass concentration. The *red line* displays the inverted size distribution assuming a sum of lognormal modes. The *black broken line* displays these two modes (coarse and fine). For the color version of the figure, the reader is referred to the electronic version of this book. *From Vasilatou et al. (2017).*

as their electrical charge. All these properties are strongly dependent on their size.

The definition of fine and coarse particles as smaller and larger than 1 μm diameter, respectively, originated from the fact that the most frequent atmospheric aerosol size distribution is bimodal, i.e., one mode occurs below 1 μm diameter, and the other above 1 μm diameter (Whitby, 1975; NRC, 1979). Fig. 4.1 shows that more coarse particles are observed during Sahara dust events due to the dominance of mineral dust even within an urban area (Athens, Greece). In atmospheric aerosol particle-size distributions, fine particles result from nucleation processes involving natural and anthropogenic gaseous precursors, primary anthropogenic emissions (usually combustion) and condensation and coagulation of the former, whereas coarse particles are produced by mechanical processes. Some particles serve as nuclei, cloud condensation nuclei, and ice nuclei depending on their hygroscopic properties and meteorological conditions. Small and large ions carry electrical charges. Small ions are clusters of atoms or molecules carrying a charge. Their stability depends on their charge. Larger ions are merely aerosol particles that carry one or more electric charges. Large particles of 0.1−1.0 μm in diameter and giant particles of above 10.0 μm diameter are terms also applied in characterizing the atmospheric aerosol particles.

Aerosol particles are considered those solid or liquid particles with sizes between 1 nm and 100 μm. The size of an atom is of the order of 10^{-10} m or 10^{-4} μm or 0.1 nm (the Bohr radius $r_1 = 0.5292 \times 10^{-10}$ m), while the size of an atomic nucleus is of the order of 10^{-14} m or 10^{-8} μm or 10^{-5} nm. An aerosol particle having a diameter of some nanometers (or 10^{-2} μm) is a hundred times or more, larger than an atom, and thus consists of few atoms, clusters of atoms, or molecules.

Primary particles, such as road dust, sea salt spray from oceans, and cement dust, do not change form after emission, whereas a substantial fraction of mass of the secondary particles, such as photochemically produced sulfates and photochemical smog, is formed by in situ chemical reactions involving gases.

Monitoring and particular aerosol characterization studies have led to a revolution in both our knowledge and our understanding of atmospheric aerosols. Atmospheric sciences, particle technology, industrial hygiene, and health effects studies of pollutants are different fields in that way.

B. Radioactive aerosol formation

When a radioactive nuclide decays, electrons are stripped from the parent atom by its recoil, and decay products are formed as positive ions. These ions can attract liquid and even solid material, thus forming clusters of atoms or particles in the submicron region ranging from 0.001 to 0.01 μm. Air is permanently ionized by radiation from natural radioactivity of air and by cosmic radiation, which consists mostly of positively charged particles, 85% protons, 10% alpha particles, and, in smaller percentage, stripped nuclei of heavier elements being positively charged, such as Fe, Co, and Ni. Production of an ion pair requires 35.6 eV, if ionization is by alpha particles and 32.5 eV, if ionization is by fast electrons. In the free atmosphere, the rate of production of small ions is in balance with the rate of neutralization by recombination and the rate of attachment to condensation nuclei. Condensation nuclei are mostly the Aitken nuclei, which are submicrometer particles in the range of 0.005−0.01 μm.

In air containing water vapor, the positive ions are mostly hydrated protons, p^+ or H^+ $(H_2O)_n$, where n may be any number between 1 and 8. Negative ions are probably mostly hydrated O^- or OH^-. The formation of clusters of water molecules around ions is very rapid, but the clusters do not grow beyond about 0.001 μm (1 nm) diameter and remain as small ions until they become attached to condensation nuclei. They then become large ions. Large ions themselves can be classified into two size ranges. The nuclei mode (Aitken nuclei) centered on 0.01 μm (10 nm) is distinct from the accumulation mode, centered on 0.1 μm (100 nm). The number of particles in the nuclei mode is greater than the number in the accumulation mode, but their total surface area is less, and it is surface area, which determines the probability of attachment of small ions to particles with diameter of order of 0.1 μm (100 nm) or less (Papastefanou and Bondietti, 1987; Gini et al., 2013). Thus, the large ions are mostly in the accumulation mode. The distinction between small and large ions is well established in atmospheric electricity. The existence of intermediate ions in the size range of 0.001−0.010 μm (1−10 nm) has

been confirmed. If sulfate or nitrate vapors are present in air, their molecules would be dissolved in the water clusters, and these will then grow into the intermediate ion range.

A possible mechanism for formation of radiolytic nuclei is radiolysis of water, leading to formation of H_2O_2, which then oxidizes traces of SO_2 to give H_2SO_4. Addition of O_3 to the air can also increase nuclei production, whereas addition of NO, a well-known radical scavenger, can inhibit it.

The radionuclide ions in the atmosphere exist in two forms: (1) as "unattached clusters" with a diffusion equivalent diameter size ranging from 0.5 to 5 nm and (2) as "aerosol-attached clusters" with particle diameters varying between 5 and 3000 nm. Reported values of the diffusion coefficients in the literature range from 0.01 to 0.1 cm^2/s (Raabe, 1968; Porstendörfer and Mercer, 1979). Most of the previous studies on the diffusion coefficient did not consider the importance of the electrical charge of the radionuclide ions and the air humidity. Neutralization of radionuclide ions depends on their concentrations and on the humidity in air.

Dankelman et al. (2001) determined the neutralization rates of ^{218}Po ions in air by electron transfer process in "normal" environmental outdoor and indoor air with natural trace gases and found that it is small and can be neglected under "normal humidity" (RH: 30−95%) and radionuclide concentrations.

Radioactive aerosols emit charged particles and, thus, themselves become charged (Barrett et al., 2009). A common case is the beta-emitting aerosols, such as the radioactive fission products, that could be released into the atmosphere in certain conceivable (although extremely unlikely) accidents in nuclear reactors (Chernobyl reactor accident, April 26, 1986). The emitted beta particles will cause ionization in the atmosphere, and these ions can subsequently attach to the aerosol. Due to the highly ionized environment, the net mean charge on the aerosol is small, although it may be sufficient to affect coagulation (Clement et al., 1995). However, Clement and Harisson (1992, 2000) have noted that, in the environment, charging effects can be important.

Vivas et al. (2008) developed a low-level radioactive charger based on ^{241}Am (0.24 μCi). The performance of the weak radioactive ^{241}Am ionizer was assessed experimentally and by means of a numerical model based on Fuchs theory. The results showed that the ^{241}Am ionizer charges to steady-state aerosol particles less than 250 nm at number concentrations up to 106/cm^3 at a maximum flow rate of 2.51/min. These conditions correspond to values of the particle to ion concentration ratio less than unity and a residence time of 5 seconds. For particle to ion concentrations above unity, the model predicts that the time to steady state increases strongly with both particle size and aerosol particle concentration. Aerosol particle charging can be controlled and brought to an equilibrium charge distribution when exposed to an excess of an ionized air stream by means of a radioactive source. The charge distribution of what is defined a Boltzmann equilibrium has been empirically calculated by Wiedensohler (1988).

II. Radioactive aerosol sampling and measurement

A. Aerodynamic particle sizing

Very early, Aitken (1923) showed that most particles in the atmosphere were smaller than 0.1 μm diameter and that their concentration varied from some hundreds per cm^3 over the ocean to millions per cm^3 in urban areas. Junge (1955, 1963, 1972) measured the atmospheric aerosol number size distribution and concentration in urban and nonurban areas as functions of altitudes and site. He established the standard form for plotting size distribution data: log of dN/dD_p versus log D_p, where N is the number and D_p is the particle diameter. He observed that this plot was a straight line that could be described by the equation: $dN/dDp = AD_p^{-k}$, where A and k were constants. He also noted that in the range from 0.1 to 10.0 μm particle diameter, k was approximately equal to 4.0. This distribution mode was widely known as "Junge distribution" or "the power law distribution."

Friedlander (1961) later showed that by balancing the aerosol source and removal rates, a portion of the resultant theoretical number distribution steady state could be fitted reasonably well by Junge distribution. Clark and Whitby (1967), by fitting the Junge distribution to 52 atmospheric distributions, found that the constant A was equal to 0.4 multiplied by the aerosol volume concentration ($\mu m^3/cm^3$). This agrees with the value predicted by Friedlander.

Whitby et al. (1972, 1975) found that, although the number size distribution established by Junge was not a good model, the surface and mass or volume-size distribution was normally bimodal, with one mode being approximately 0.3 μm diameter and the other ranging from 5.0 to 15.0 μm diameter.

In Fig. 4.2 (Seinfeld and Pandis, 2016), the normalized frequency plots of number, surface, and volume or mass distributions are presented. Note the bimodal distribution of mass. Each weighting shows features of the distribution not shown by the other plots. In Fig. 4.2, the apparent area under the curves is proportional to the number, surface area, and volume or mass in a given size range. Most particles, i.e., the number distribution, are <0.01 μm diameter. The number of particles decreases sharply with increasing size. The volume or mass distribution is bimodal: one mode is approximately 0.7 μm diameter, and the other is approximately 7.0 μm diameter. The mass of

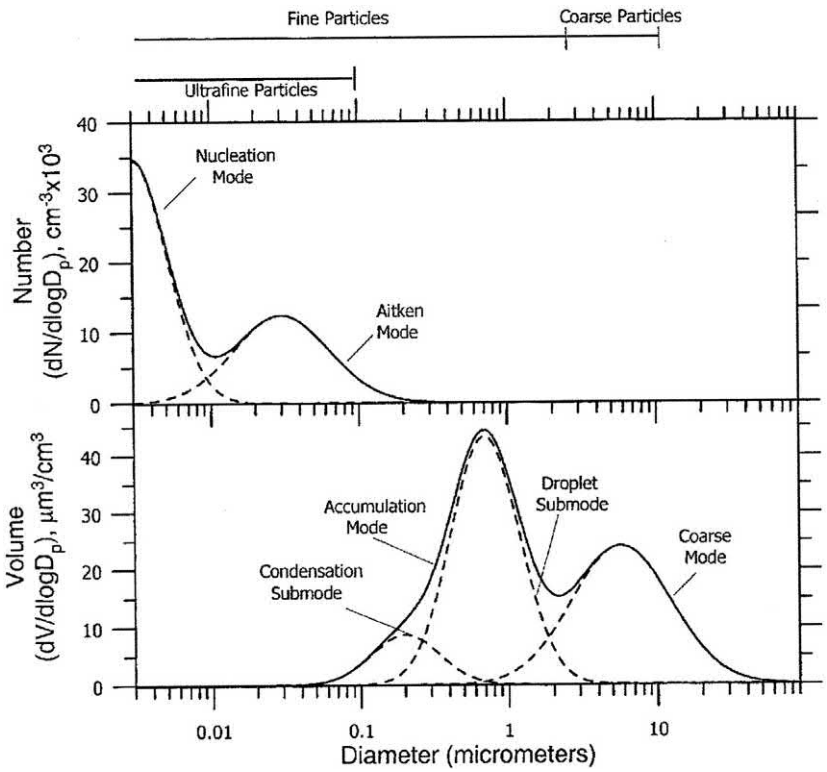


FIGURE 4.2 Typical number and volume distributions of atmospheric particles with the different modes. *From Seinfeld and Pandis (2016); reprinted with permission from John Wiley and Sons © 2016.*

fine particles of size smaller than 2.0 μm is almost equal to the mass of coarse particles with size larger than 2.0 μm.

Atmospheric aerosol size distributions consist basically of three separate modes:

1. Aitken nuclei mode for smaller than 0.1 μm diameter particles, i.e., 0.015 μm
2. Accumulation mode for smaller than 2.0 μm but larger than 0.1 μm diameter particles, i.e., 0.3 μm
3. Coarse mode for larger than 2.0 μm diameter particles, i.e., 10.0 μm

Depending on their source, there may be from one to three distinct maxima as peaks in the surface and volume or mass distributions. *The activity size distribution of radionuclide-associated aerosol particles is surface distribution* (Gini et al., 2013, 2016).

Washout by rain greatly reduces the Aitken nuclei mode and coarse-particle mode but has little effect on the accumulation mode in the trimodal size distribution (Whitby, 1975). The origin of each mode of atmospheric aerosol size distribution can be associated with various aerosol formation mechanisms, such as Brownian motion of particles smaller than 0.1 μm in diameter, which causes the particles to diffuse and by collisions to coagulate to larger sizes. Coagulation generates multimodal distributions and affects the shape and the chemical composition of particles. The aerodynamic size distribution of radionuclide-associated aerosol particles is, as mentioned above, a surface distribution, and so it is trimodal, the first mode being the so-called Aitken nuclei mode, the second the accumulation mode, and the third the coarse-particle mode. Analytically, these modes can be summarized as follows.

1. Aitken nuclei mode particles

The nuclei or Aitken nuclei mode accounts for most of the Aitken nuclei count and originates primarily from the condensation and coagulation of highly supersaturated vapors. There is evidence that a prominent nuclei mode in the size distribution indicates the presence of substantial amounts of fresh aerosol. Many particles in the nuclei mode raise the Aitken nuclei. Usually, they do not greatly increase the aerosol mass concentration because the nuclei mode rarely accounts for more than a few percent of the total mass.

Whitby et al. (1975) found that the nuclei mode might contain over 25 mg/m^3 of aerosol. Whitby et al. (1976) also observed distributions in which the nuclei mode contained more volume than the accumulation mode. Because particles may serve as nuclei for the condensation of water vapor, condensation is an important growth mechanism for submicrometer aerosol particles. Examples are fogs and hazes formed when the humidity exceeds 60%.

2. Accumulation mode particles

The twin mechanisms of coagulation and heterogeneous nucleation (condensation of one material to another) tend to accumulate the submicrometer aerosol particle mass in this mode (Whitby and Cantrell, 1976; Willeke and Whitby, 1975). Because of the sharp decrease in the particles, larger than 0.3 μm in diameter, little mass is transferred from the accumulation mode to the coarse-particle-size range. Sedimentation and impaction tend to increase the relative concentration of the smallest mechanically produced particles and then accumulate in this mode. Salt from sea spray is typically present as particles in the 1−5 μm size range, outside the normal accumulation mode.

The radionuclide-associated aerosols (radioactive aerosols) peak in the accumulation mode, as this mode is the main one in terms of surface area distribution (Papastefanou and Bondietti, 1987; NRC, 1979) (Fig. 4.2).

3. Coarse-particle mode particles

In the coarse-particle mode, practically all aerosol particles at a relative humidity (RH) below 100% originate from mechanical processes. Most of the particles originate from condensation processes occurring in the atmosphere. Coarse particles are produced from natural and/or man-made (anthropogenic) mechanical processes. The origin, behavior, and removal processes of fine particles are almost entirely independent of the coarse particles.

The multimodal nature of the size mass distribution is supported by evidence from the size distributions of chemical elements, radionuclides, or compounds in aerosols. These are emitted as smokes or fumes and exist mostly in the fine particle size range. These aerosols eventually coagulate and become mixed throughout the accumulation mode. In the accumulation mode, the geometric mean size is nearly equal to the mass or volume geometric mean size. Elements in the soil, e.g., silicon, are mostly in the coarse-particle-size range. Elements, such as sulfur, which are produced by condensation processes from anthropogenic sources, are principally in the fine particle-size range. The size distribution of elements in the soil is similar to the mass distribution of the coarse-particle mode.

B. Instrumentation

The great diversity of application, the size range of atmospheric aerosol particles, the physical and chemical concentration variations, and the variety of measurement principles available imply many different combinations of application and measurement methods and procedures. It is impossible to obtain particle size information on the entire five-decade size range of 0.001−100 μm. Therefore, one expects to apply different instrumental techniques, measuring different size parameters, for submicrometer versus supermicrometer-sized aerosols. The methods applied for atmospheric aerosol sampling include filters and cascade impactors, which collect the aerosol particles onto a surface. The collected sample must therefore be evaluated for size and composition. Because accumulation mode aerosols (fine aerosol particles) contain a substantial fraction of liquid material at normal temperatures and humidity, these fine aerosol particles must be sized in situ without precipitation. In some extreme cases, such as the case of Los Angeles smog, the liquid content may be as high as 75% or 80% of the total mass (Ho et al., 1974).

Many aerosol measuring techniques (methods), such as the condensation nuclei counter (CNC), and filter collectors, integrate some response function of the instrument with the particle-size distribution. In the particle-counting method, the response is essentially equal to the integral of the number distribution weighting. By weighing the filter, the integrating measurement is the integral of the mass weighting of the distribution. Cascade impactors, such as Lundgren impactors, designed with inlet cutoffs well above those used for atmospheric aerosol sampling, showed that particles up to several hundreds of micrometers in diameter were present in the atmosphere under certain conditions (Lundgren, 1973). Most mass sampling methods, including the high-volume sampler (Stevens et al., 1976), truncate the distribution, thereby giving concentrations less than those actually existing.

Due to the simplicity of construction and use and the relative sharp cutoff characteristics, cascade impactors have been widely used for the size classification and size-classified chemical analysis of aerosols. Table 4.1 lists the most important integrating sampling methods with their main characteristics. Table 4.2 gives the most important differential, size-resolving methods used by aerosol cascade impactors to sample and measure atmospheric aerosol particles. The part of the particle-size distribution and the modes that dominate the sensitivity of the methods are indicated. The upper and lower size limits are nominal values for the most commonly used methods. Cost, complexity, operational requirements, calibration problems, and the demands of the particular evaluation to be used also affect the choice of methods. For example, chemical analysis usually requires that a sample be collected and then taken to the evaluation device. This normally requires a collection-type method, such as the high-volume filter collectors. Simplicity during sampling may mandate the use of a particular collection method despite its disadvantages. The rapid development of modern electronics and inexpensive acquisition systems has led to in situ, automatic, and complex monitoring techniques. Collection methods are being replaced with both physical and chemical analyses in situ, automatic methods, and digital electronic devices.

TABLE 4.1 Major integral sampling and measurement methods used for measuring atmospheric aerosols.

Method or instrument	Effective size limit (μm)		Lower concentration limit	Measurement principle
	Lower	Upper		
Hi-vol filter and other filters—measures all of the nonvolatile mass in accumulation mode and most of that in the coarse-particle mode depending on sampling efficiency.	None	25	2 $\mu g/m^3$	Filter weighing
Integrating nephelometer—essentially responsive to the in situ mass in the accumulation mode only.	0.15	2	1% of air scattering (about 1 $\mu g/m^3$)	Light scattering
Condensation or Aitken nuclei counter (ANC)—for combustion-dominated aerosols, measures the nuclei mode; for aged aerosols, measures number in accumulation mode.	0.0035	0.05–0.2	1 cm^3	Condensation—high supersaturation
Electrostatic charger—with diffusion charging upper limit is about 2 μm; senses both nuclei and accumulation modes.	0.007–0.02	2–25	1 $\mu g/m^3$	Charging and precipitation
Cloud condensation nuclei counter (CNC)—lower size limit depends on supersaturation and design; measures part of nuclei mode and most of accumulation mode.	0.01	1	100 cm^3	Condensation – low supersaturation
Ice nuclei counter (INC)—measures only those few particles capable of causing supercooled water drops to freeze; responsive to part of the accumulation mode sizes and most of the coarse-particle mode sizes.	None	Unknown	10^{-5}/L	Ice nucleation
Quartz crystal—electrostatic version measures nuclei and accumulation modes and part of coarse-particle mode; impaction version measures two-thirds of accumulation mode and most of the coarse-particle mode.	0.01 electrostatic; 0.3 impactor	10; 20	1 $\mu g/m^3$	Frequency charge of crystal
β attenuation—performance dependent on counting period, collection surface mass.	None (on filter)	20	2–5 $\mu g/m^3$	*β* attenuation
Contact electrification—useful only for high concentrations; sensitivity varies over 50/1 range for different materials.	10	1000	100 $\mu g/m^3$	Impact and charge measurement
Dust fall—relation to concentration is very dependent on location, wind velocity, and collector design.	5	None	None	Settling and weighing
Acoustic counter—has been used primarily to count ice crystals as a sensor on ice nuclei counter.	5	100	1/L	Acoustic pulse from particle transit

From Papastefanou (2008). Printed with permission from Elsevier Copyright (2008).

TABLE 4.2 Major size-resolving methods used for measuring atmospheric aerosols.

Method or instrument	Effective size limit (μm)		Maximum number of size intervals practical	Lower concentration limit (μm)	Measurement principle
	Lower	Upper			
Cascade impactors—measures one-half to two-thirds of accumulation mode, all of coarse-particle mode; particle bounce is a serious problem in some applications.	0 (filter) 0.3 (last stage)	30	8	1 μg/m^3/stage	Inertial impaction
Dichotomous virtual impactors—one filter collects fine particles and one collects coarse particles; no bounce problem.	0 (filter) 2 (for cut on 2nd filter)	30	2	1 μg/m^3/stage	Virtual impaction
Crystal microbalance impactor—measures one-half of nuclei mode, all of accumulation mode and coarse-particle mode; subject to particle bounce on dry aerosols.	0 (filter) 0.06 (last stage)	30	10	0.02 μg/stage 1 μg/m^3/stage	Impaction, quartz crystal sensing
Spiral centrifuge—measures one-half of nuclei mode, all of accumulation mode, and part of coarse-particle mode; sensitivity depends on method of evaluation; mass determination is difficult.	0.06	10	20	10 μg/m^3	Centrifuge onto filter
Optical particle counters—single counter useful for only one decade of size; requires calibration; sensitive to shape and refractive index.	0.3 (commercial) 0.1 (research)	3 −100	>200 passible 20 useful	1 particle/L	Light scattering from single particles
Electric mobility—can measure nuclei and accumulation modes; can resolve σ_g of 1.4 without correction and 1.25 σ_g with correction.	0.006	1	15	1 μg/m^3	Diffusion charging and electric mobility measurement

From Papastefanou (2008). Printed with permission from Elsevier Copyright (2008).

1. High-volume air samplers

A high-volume sampler or a total suspended particulate (TSP) high-volume air sampler is used for the collection of TSP matter in ambient air with no preference to size selection. It is used to determine the concentration of TSPs, or it can be used to determine the identity of the particulates. It does not use a particle separator, which results in the collection of all ambient particulates.

The TSP high-volume air sampler collects particulates at a flow rate between 40 and 60 ft^3/min over a constant sampling period. The vacuum motors pull ambient air onto an 8 × 10 inch (1 inch = 2.54 cm) filter media (glass fiber, paper, quartz fiber filters) (Fig. 4.3). The filters are weighed pre- and postsample, and the weight is used to determine the TSP matter.

A TSP high-volume sampler can be composed of an anodized aluminum outdoor shelter with a gabled roof assembly. The sampler can also include a timing device to turn the instrument on and off, a filter holder to hold the filter media in place, a vacuum motor, a device to control the flow, a pressure recorder to record the flow rate, and an elapsed time indicator to count the sample time (Fig. 4.4).

2. Aerosol cascade impactors

Cascade impactors are instruments, which have been extensively used for sampling and separating airborne particles for determining the aerodynamic size classification of aerosol particles. There are three kinds of cascade impactors: inertial impactors, virtual impactors, and particle trap impactors. These are made by aluminum, 316 stainless steel, and titanium.

Inertial impactors have been used extensively to measure aerosol size distribution and to collect samples for further chemical analysis. It consists of an acceleration nozzle and a flat plate. In inertial impactors, particles larger than the cutoff diameter of the impactor will impact on the collection plate, whereas particles smaller than the cutoff diameter will follow the streamlines and not collected on the plate. Many researchers have investigated inertial impactors to collect and separate aerosol particles and found

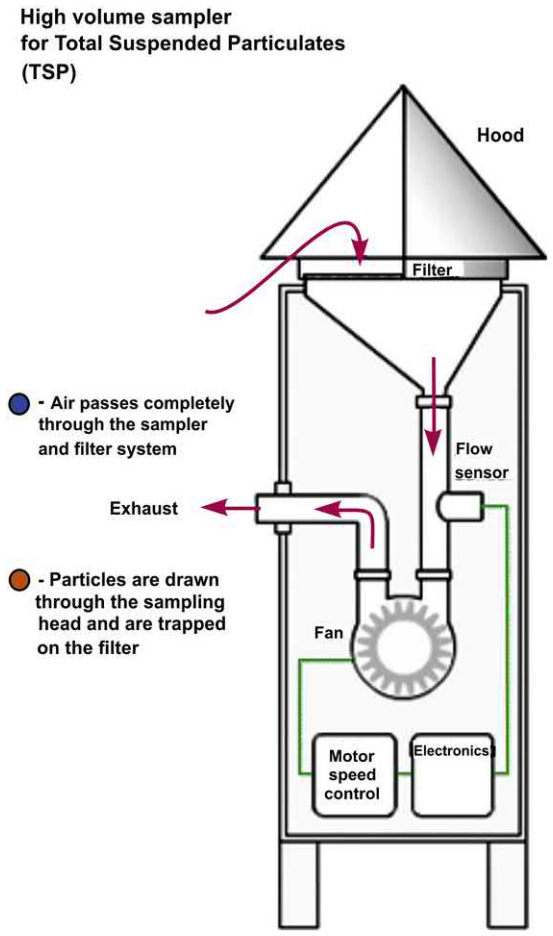


FIGURE 4.3 A description of the workings of a total suspended particulate high-volume air sampler. For the color version of the figure, the reader is referred to the electronic version of this book. *TISCH Environmental web site, https://tisch-env.com/high-volume-air-sampler/TSP. Printed with permission from TISCH Environmental © 1999.*



FIGURE 4.4 Total suspended particulate high-volume air sampler. For the color version of the figure, the reader is referred to the electronic version of this book. *TISCH Environmental web site, https://tisch-env.com/high-volume-air-sampler/TSP. Printed with permission from TISCH Environmental © 1999.*

inherent problems, which were particle bounce and reentrainment (Dzubay and Rickel, 1978; Markowski, 1984; Marple, 1970; Marple and Liu, 1974).

Virtual impactors have been designed to eliminate problems of bounce and reentrainment and to allow the collection of larger particles (Chen et al., 1986; Marple and Chein, 1980). In a virtual impactor, the intake air is typically divided into two air streams: the major and the minor flow. The major flow carries most of the fine particles smaller than the cutoff diameter, and the minor flow carries all the coarse particles above the cutoff diameter with a small fraction of the fine particles. Various studies on virtual impactors have been carried out for particle collection and concentration since the late 1980s. Meyer and Lee (1994) used a virtual impactor as a means for concentrating metal aerosol suspended in the air to enhance the performance of an inductively coupled plasma analyzer. Kim et al. (2000) designed and tested multinozzle virtual impactors for high-volume particle collection. Virtual impactors, however, have an inherent problem that a small fraction of the fine particles is collected with large particles.

A particle trap impactor (cup impactor) has been designed by Biswas and Flagan (1988), who intended to collect particles in the trap rather than to sample aerosol particles. Tsai and Cheng (1995) investigated the effect of solid-particle loading on the collection efficiency of an impactor with different impaction surface designs. The particle-trap impactor was applied to a sampling inlet with a cutoff diameter of 10 or 2.5 μm (Kim et al., 1998, 2003). Major advantages of the particle-trap impactors are their freedom from particle bounce-off and the problem of overload. The designs of particle trap impactors are based on those of inertial impactors and virtual impactors. The particle trap impactors are similar to inertial impactors in that they use inertial force and do not have a minor flow rate. Also, the particle-trap impactors are somewhat similar

to virtual impactors in that they have virtual space to collect the particles.

Even though inertial and virtual impactors have been widely used for aerosol collection and separation, particle-trap impactors have not been used extensively. Further studies on particle-trap impactors are needed. In addition, most of particle-trap impactors employ the design of inertial impactors for their design parameters, though actually the design of particle-trap impactors is different from that of inertial impactors. Therefore, there still remains the necessity for the study on the accurate design parameters of the particle-trap impactors.

The earliest and most fundamental work in inertial impactor theory was conducted in the early 1950s by Ranz and Wong (1952). In this work, they showed that the collection of a particle by an obstacle is a function of what is defined as the inertial impaction parameter:

$$K = \frac{C\rho_p U D_p^2}{18\mu D_c} \tag{4.1}$$

where U is the relative velocity, ρ_p is the particle density, D_p is the particle diameter, μ is the gas viscosity, D_c is the diameter of the round jet, and C is the Cunningham slip correction factor.

Data from inertial cascade impactors are normally presented as 50% effective cutoff diameters (ECDs). For the Andersen cascade impactors, containing round jets, and flat collection surfaces, the 50% ECD would yield a value of 0.14 for the inertial impaction parameter K. The Cunningham slip correction factor is equal to

$$C = 1 + 0.16x10^{-4}/Dp$$

for normal temperatures and pressures. This factor corrects for the fact that as particle diameters approach the mean free path length of the gas molecules, they tend to "slip" between gas molecules more easily and are therefore more easily able to cross the bulk flow streamlines. The collection efficiency is therefore slightly greater than that would be predicted by inertial impaction theory for particle diameters of the order of 1 or 2 μm. The overlapping of particle size between stages, which is naturally inherent in all cascade impaction devices, is minimized in Andersen's samplers by design. Ranz and Wong (1952) noted that as a particle passes through a jet, its nearness to the axis of the jet is one of the factors that determines whether or not the particle will reach the impaction surface. In contrast to competitive samplers, which have larger rectangular jets in each stage, the Andersen sampler has 400 small, round jets. Travel of the particle is thus confined near the axis of the jets. The average distance of the particles from the axis of the jets is very much less than in other cascade impactors. Ranz and Wong (1952) also observed that round jets have sharper cutoffs than rectangular jets. The Andersen sampler, therefore, on a theoretical basis, should have a sharper cutoff.

Another inherent advantage of the Andersen air samplers is that single circular orifice and multiple rectangular orifice impactors by design must operate with high orifice velocities. This results in more turbulent flow, greater reentrainment, and a skewing of the size distribution toward the lower end, i.e., the indicated size distribution being smaller than it really is.

The basic configuration shown in Fig. 4.5 (Mercer et al., 1970; Andersen, 1976; Marple and Willeke, 1979; Raabe, 1979) is simple. A jet of aerosol from a nozzle is directed at an impaction surface: the high inertia; large particles cross the air streamlines and strike the impaction plate, whereas the smaller particles with less inertia are not collected but remain airborne and pass onto a second nozzle-impactor plate arrangement. The second nozzle is of a smaller diameter than the first nozzle, which increases the velocity and inertia of all the remaining aerosol particles. The larger of the previously uncollected particles thus have sufficient inertia to be collected by the second stage. This process continues as the aerosol stream enters successive stages of the cascade impactor. The final element of a cascade

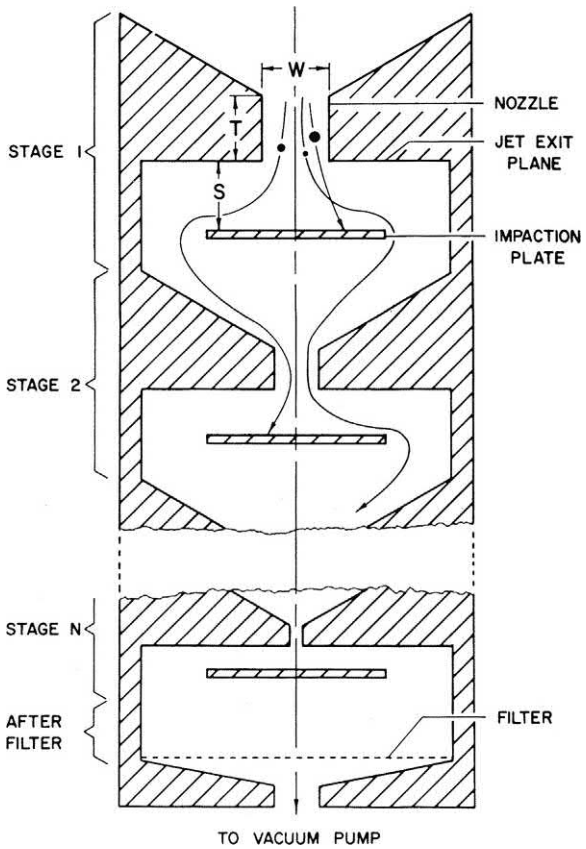


FIGURE 4.5 A schematic of an aerosol cascade impactor with trajectories shown for aerosol particles of two different sizes. *From Papastefanou (2008). Printed with permission from Elsevier Copyright (2008).*

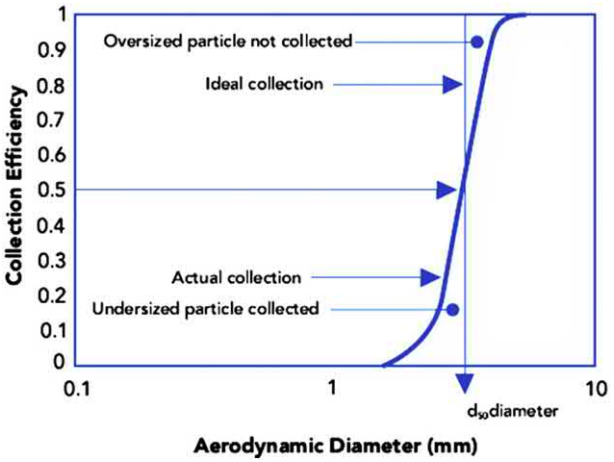


FIGURE 4.6 Efficiency curve for a typical impactor. For the color version of the figure, the reader is referred to the online version of the book. *From Copley Scientific Brochure (2019). Printed with permission from Copley Scientific 2019*

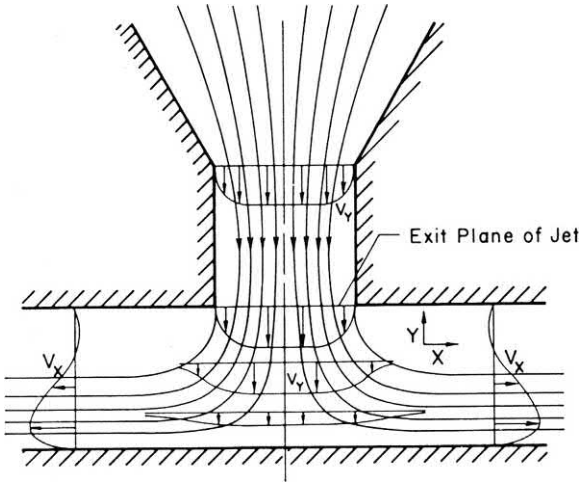


FIGURE 4.7 Flow fields in a rectangular impactor ($S/W = 1$, $T/W = 1$, $Re = 3000$). *From Papastefanou (2008). Printed with permission from Elsevier © 2008.*

impactor is usually a filter, which collects all particles too small to be collected by the last impaction stage. The nozzles of each stage can be of any shape but are normally rectangular or round. The nozzles of each stage of the Andersen cascade impactors are round. Many cascade impactors have several nozzles of an identical size at a given stage with the aerosol jets from the nozzles impinging upon a common impaction surface.

The most important characteristic of an impactor stage is the collection efficiency curve, which gives the fraction of particles of a given size collected from the incident aerosol stream as a function of particle size. Ideally, an impactor would collect all particles larger than a certain size and none of the smaller ones, which would correspond to the sharp ideal cutoff illustrated in Fig. 4.6. The efficiency curve of a typical real impactor, also shown in Fig. 4.6, spans over a range of particle sizes but still has a good sharpness of cut. It has been shown (Marple and Liu, 1975) that ideal impactor behavior can be obtained, if the following two requirements are met:

1. In the region between the jet exit plane and the impaction plate, the Y-component of fluid velocity is a function of Y only (Y is parallel to the center line of the nozzle, Fig. 4.7).
2. The Y-component of the velocity of the particles as the jet exit plane is uniform across the jet.

These two requirements are reduced to only the first requirement, if the velocity of the particles is equal to the fluid velocity at the exit plane of the jet. Such requirements are nearly met in a real impactor, as can be seen by the velocity profiles in Fig. 4.7 for a rectangular impactor. It can be seen that the velocity component perpendicular to the jet exit plane, Vy, is independent of X over a major portion of the jet, where X is the distance from the jet center line. However, this criterion is not met in the boundary layer near the wall. Particles passing through this region are the cause for the nonideal cutoff characteristics at the larger efficiencies of the real impactor performance curve shown in Fig. 4.6. A schematic diagram of Andersen cascade impactor stages is shown in Fig. 4.8 (Marple and Willeke, 1979). This figure shows how impaction occurs at the orifice–collector interfaces. The use of an impactor with a single circular orifice for each jet provides a convenient method for determining the aerodynamic size distribution of an easily assayed aerosol such as of radioactive material (Raabe, 1979). Submicrometer aerosols, or condensation nuclei, in the diameter are most readily measured for number concentration and size distribution by diffusion batteries and CNCs (Sinclair et al., 1979).

The impaction characteristics of the cascade impactors are governed by the fluid's velocity flow field, which in turn is specified by the Navier-Stokes equations. A solution of the Navier-Stokes equations (Marple et al., 1974) reveals that the velocity flow field is a function of the physical configuration of the impactor and the Reynolds number, *Re*, of the flow passing through the nozzle. The Reynolds number is dimensionless and, based on the hydraulic diameter of the nozzle, is defined as

$$R_e = \frac{\rho V_0 W}{\mu} \tag{4.2}$$

For round cascade impactors, and

$$R_e = \frac{\rho V_0 2W}{\mu} \tag{4.3}$$

for rectangular cascade impactors, where r is the fluid density, in g/cm^3, V_0 is the mean velocity at the nozzle throat,

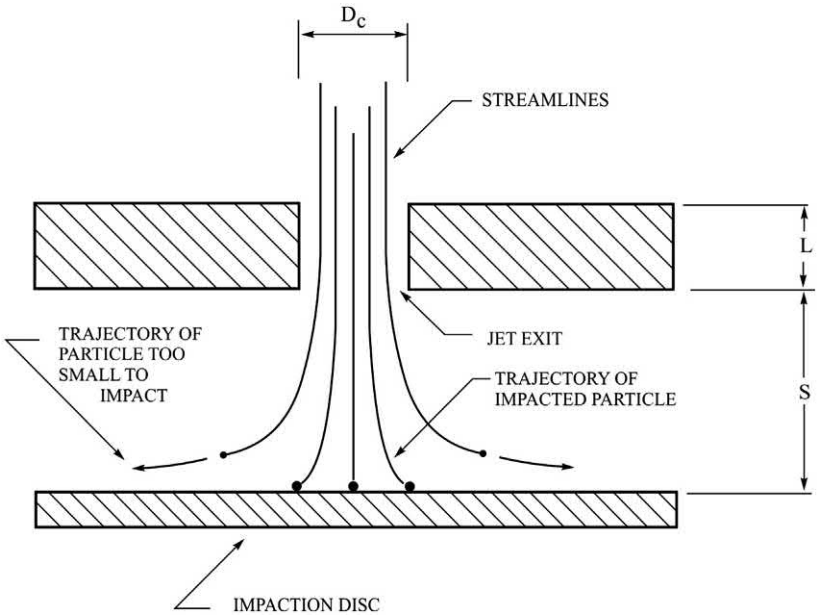


FIGURE 4.8 A schematic diagram of an aerosol cascade impactor stage. *From Tisch Environmental, Inc. (1999). Printed with permission from Tisch Environmental © 1999.*

in cm/s, W is the nozzle diameter or width, in cm, and μ is the fluid viscosity, in poise (g/cm s). Furthermore, the trajectory of the aerosol particles in the flow field, which determines whether or not the particles are collected, is found by solving the particles' equation of motion (Marple and Liu, 1974), the solution of which is a function of the particles' Stokes number and of the parameters that characterize the flow field. The Stokes number is defined as the ratio of the aerodynamic particle stopping distance to the radius, or half-width, of the impactor throat

$$Stk = \frac{\rho_p C V_0 D_p^2 \Big/ 18\mu}{W/2} \tag{4.4}$$

where ρ_p is the particle density, in g/cm^3, C is the Cunningham slip correction factor, and Dp is the particle diameter, in cm. The square root of the Stokes number, $(Stk)^{1/2}$, is a dimensionless particle size.

The collection efficiency of a cascade impactor is, therefore, a function of the Stokes number, the Reynolds number, and the physical configuration of the impactor. It has been found that the physical configuration for either a round or rectangular nozzle can be sufficiently specified by the value of nozzle's diameter or width, W, the nozzle-to-plate distance, S, and the nozzle throat length, T (Marple, 1970). Since the Stokes number and the Reynolds number are dimensionless, it is convenient to express the physical dimensions in dimensionless form by expressing all dimensions in units of the jet width, such as S/W and T/W.

The inertial cascade impactors are multistage cascade impactors. The Mercer-style cascade impactor is a seven-stage cascade impactor operating at low flow rate, e.g., 50−150 cm^3/min (Mercer et al., 1970; Raabe, 1979). Other inertial impactors are the Andersen cascade impactors, such as the 1 ACFM (actual cubic feet per minute) eight-stage cascade impactor operating at a flow rate of 28 L/min, which is described in the next paragraphs (Andersen, 1976), the Lundgren-type eight-stage cascade impactor operating at a flow rate of 1 L/min, with the samples at stages collected on Teflon, and the final stage being quartz (Lundgren, 1967; Marley et al., 2000), and the Berner-type nine-stage low-pressure cascade impactor (LPI) with a nominal volumetric flow rate of 28.9 L/min (1 ACFM), with the samples at stages collected on aluminum foil (Berner and Lurzer, 1980; Winkler et al., 1998). In this category also is classified the dichotomous sampler, which is used for air pollution studies and utilizes a virtual impactor with two emerging aerosol flows to separate the coarse and fine fractions of atmospheric aerosol particles and operates at 1 m^3/h (16 L/min) (Hinds, 1999).

The aerosols are collected on impaction substrates stamped from Teflon, aluminum foils, polycarbonate membranes from all stages of the cascade impactors of any type, and the smallest fraction on the backup glass fiber filter. After the end of collection, the collecting substrates are carefully removed from the impactor and are reweighed for evaluation of the size distribution, i.e., mass or volume distribution of the particles. Then, the substrates are folded and compressed to provide suitable geometry for measurement of the activity of radionuclides associated with aerosol particles with a high-resolution and high-efficiency low-background gamma ray spectrometric system linked

with a high-purity Ge detector for the determination of the activity size distribution of the radioactive aerosols.

Aerosol particulates in the atmosphere could be measured also by a standard gravimetric technique described by Qadir and Zaidi (2006).

Singh et al. (2010) developed a variable configuration cascade impactor (VCCI) comprised of seven normal-pressure and four low-pressure stages for aerosol size distribution measurements. In configuration 1, it operates as a low-pressure impactor with a sampling flow rate of 10 L/min and classifies the particles from 0.1 to 21 μm in 11 size classes. In configuration 2, it operates as a normal-pressure impactor, with a sampling flow rate of 45 L/min and classifies the particles from 0.53 to 10 μm in seven size classes.

a. Description

The Andersen 1 ACFM ambient aerosol sampler (Andersen, 1976) comprises the following:

Eight aluminum stages are held together by three spring clamps and gasketed with O-ring seals (Fig. 4.9). Each impactor stage contains multiple precision-drilled orifices. When air is drawn through the aerosol sampler, multiple jets of air in each stage direct any airborne particles toward the surface of the collection plate for that stage. The size of jets is constant for each stage but is smaller in each succeeding stage. Whether a particle is impacted on any stage depends on its aerodynamic dimension. The range of particle sizes collected on each stage depends on the jet velocity of the stage and the cutoff of the previous stage. Any particle not collected on the first stage follows the air stream around the edge of the plate to the next stage, where it is either impacted or passed onto the succeeding stage, and so on until the jet velocity is sufficient for impaction.

Stages 0–6 have integral air inlet sections that contain 400 orifices. Stage 7 contains 201 orifices. The inlet sections are approximately 3.125″ (inches) in diameter. The orifices are progressively smaller from top to bottom stages, ranging from 0.0625″ diameter in stage 0 to 0.0100″ diameter in stage 7. Each stage has a removable stainless steel or glass (3.25″ diameter) collection plate. The exhaust section of each stage is approximately 0.75″ larger in diameter than the collection plate, allowing unimpacted particles to go around the plate and into the next stage (Fig. 4.10).

A constant air sample flow of 1 ACFM aerosol cascade impactor, that is 28.316 L/min, is provided by a continuous duty vacuum pump. Flow rate is controlled by an adjustable valve on the pump, and periodic calibration is needed. Flow rate adjustments are also needed. The aerosol cascade impactor is supplied with a built-in backup filter, which will

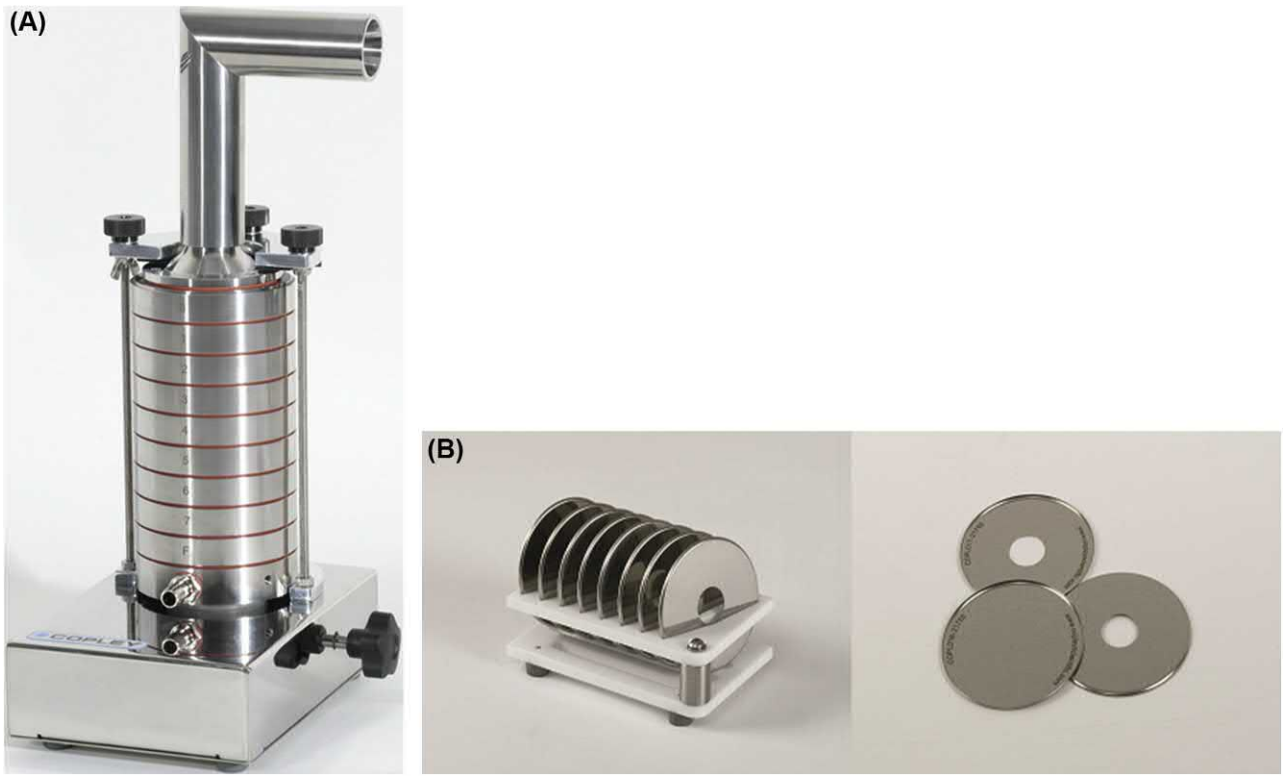


FIGURE 4.9 (A) Eight-stage nonviable Andersen cascade impactor (ACI) and (B) ACI collection plates. For the color version of the figure, the reader is referred to the online version of the book. *(B) From Copley Scientific. Printed with permission from Copley Scientific.*

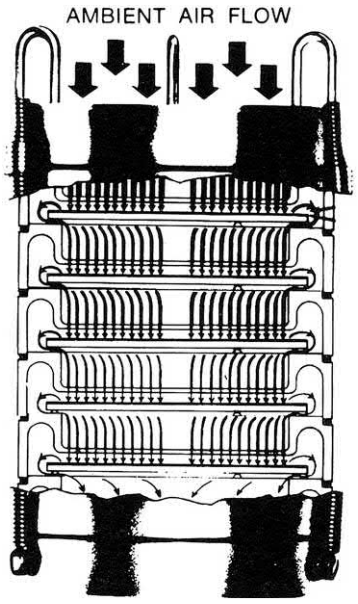


FIGURE 4.10 A schematic cross section view of the nonviable impactor stages. Progressively smaller orifices increase the orifice velocity in eight successive stages causing impaction of smaller aerosol particles onto the collection disks of each succeeding stage. *From Tisch Environmental, Inc. (1999). Printed with permission from TISCH Environmental Copyright 1999.*

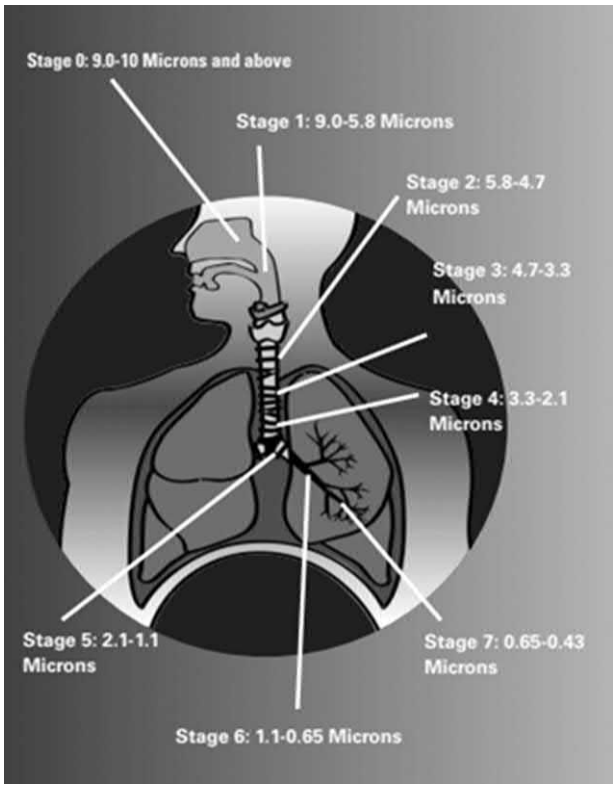


FIGURE 4.11 The 1 ACFM (actual cubic feet per minute) cascade impactor has been designed on the basis of the workings of the human respiratory system. *ThermoFisher Brochure. Printed with permission from ThermoFisher.*

accommodate an 81-μm filter disk. Normally, a binderless glass fiber filter medium is used because of its high collection efficiency for submicrometer aerosol particles. The 1 ACFM cascade impactor has been designed on the basis of the workings of the human respiratory system (Fig. 4.11)

The following are the ECDs for each stage of 1 ACFM cascade impactor (Table 4.3).

The Andersen LPI (Andersen, 1984) is really an adaptor assembly, which is used with stages 0−7 of an Andersen 1 ACFM ambient aerosol cascade impactor to extend the range of particle classification below 0.4 μm. Standard aerosol cascade impactors are normally used to classify particles down to approximately 0.4 μm aerodynamic diameter. However, many aerosols such as cigarette smoke and diesel exhaust are predominantly sub-0.4 μm in diameter. The 50% effective cutpoint of an impactor is given by

$$D_{p50} = \left(\frac{9\mu STK_{50}D_j}{\rho_p C V_j}\right)^{1\frac{1}{2}} \tag{4.5}$$

where μ is the gas viscosity, in poise (g/cm s); STK_{50} is the Stokes number (dimensionless); D_j is the jet diameter, in cm; ρ_p is the particle density, in g/cm^3; C is the Cunningham slip correction factor; and V_j is the jet velocity, in cm/s. For any given geometry, the gas viscosity, Stokes number, and particle density are fixed.

Therefore, to get a smaller cutpoint, the diameter of the jet can be reduced to increase the velocity through the jet or increase the Cunningham slip correction factor. Reducing the jet diameter to less than 0.0254 cm is difficult because the jet to collection surface spacing should be less than 10 jet diameters. Increasing the jet velocity causes unacceptable levels of particle bouncing. That leaves the Cunningham slip correction factor as the best variable.

The Cunningham slip correction factor is a measure of how easily a particle can slip in between gas molecules when crossing the bulk flow streams to reach the impaction surface. Reducing the gas pressure will increase the Cunningham slip correction factor. The Andersen LPI represents the state of the art for the particle sizing devices.

The low-pressure configuration includes eight atmospheric pressure stages and five low-pressure stages. The complete assembly consists of the following:

1. Brass hose barb connector for gas outlet
2. Base plate with three hold-down bolts
3. Stage LF—low-pressure filter stage
4. Stages L5, L4, L3, L2, and L1—low-pressure impactor stages

TABLE 4.3 Effective cutoff diameters (ECDs, in μm) of 1 ACFM (actual cubic feet per minute) Andersen-type cascade impactor stages.

Stage	ECD (μm)	Size range (μm)	Number of orifices
0	11.0	11.0 and above	400
1	7.0	7.0–11.0	400
2	4.7	4.7–7.0	400
3	3.3	3.3–4.7	400
4	2.1	2.1–3.3	400
5	1.1	1.1–2.1	400
6	0.7	0.7–1.1	400
7	0.4	0.4–0.7	201
F	0	0–0.4	Filter holder

5. Critical orifice stage with brass pressure tap and three hold-down springs for atmospheric-pressure stages
6. Three nuts and washers for tightening down low-pressure section to seal
7. Stages 0, 1, 2, 3, 4, 5, 6, 7—atmospheric-pressure stages
8. Inlet cone
9. Seven solid stainless steel collection plates
10. Seven stainless steel collection plates with open centers
11. Collection substrates, solid
12. Collection substrates with open centers
13. Vacuum pump
14. Pressure-measuring device (manometer)

The following are the ECDs for each stage of LPI (Table 4.4).

Ideally the pressure tap downstream of the critical orifice should be connected to a precision absolute pressure gauge, so the absolute pressure can be measured directly. Alternately, the pressure tap can be connected to a 16″-0-16″ U-tube mercury manometer and used in conjunction with a mercury barometer to determine the absolute pressure downstream of the critical orifice.

The pump should be switched on to initiate aerosol sampling. The "bleed valve" is then quickly adjusted to obtain an absolute pressure at the pressure tap of 114 mm Hg (0.15 ATM or 4.4″ Hg). Other absolute pressures can be used, but the cutpoints of the low-pressure stages will have to be recalculated. At least 400 mm Hg (16″ Hg) pressure drop should be maintained across the critical orifice to maintain the critical airflow rate of 3 L/min. This means that the critical airflow can be maintained at elevations where the atmospheric pressure is greater than approximately 525 mm Hg.

TABLE 4.4 Effective cutoff diameters (ECDs, in μm) of the Andersen-type low-pressure cascade impactor stages.

Stage	ECD (μm)
0	35.0
1	21.7
2	15.7
3	10.5
4	6.6
5	3.3
6	2.0
7	1.4
L1	0.90
L2	0.52
L3	0.23
L4	0.11
L5	0.08
LF	0

The sampling time should be selected so as to collect at least 1 mg of particulate per stage and not over 10 mg per stage. The lower limit is based on weighing accuracy, and the upper limit is based on preventing overloading. As a rule of thumb, the aerosol sampling time using the LPI will be approximately a multiple of 10 times the sampling time using the standard 1 ACFM aerosol cascade impactor since the airflow rate is approximately 1/10. To minimize the aerosol sampling time, collection substrates should be used

to minimize tare weights, and extra care should be taken with all weight measurements to minimize weighing errors.

b. Assembly

The complete assembly of an Andersen 1 ACFM aerosol cascade impactor consists of an inlet cone, nine stages, eight collection plates, and a backup filter. The stages are numbered 0, 1, 2, 3, 4, 5, 6, 7, and F. Stage 0 is an orifice stage only. Stage F contains the collection plate for stage 7 and the backup filter. Each stage contains an O-ring (neoprene-standard, Teflon-optional) for sealing. In addition, there is a large diameter O-ring inside stage F, which holds the backup filter in place.

The impactor assembly begins by placing stage F on the base plate stage, which is bolted to the base plate. A preweighted glass fiber backup filter is inserted into stage F and the large diameter O-ring placed into position around the periphery of the filter. Next, a preweighted collection plate 7 is placed onto stage F, so that the plate rests on the three raised, notched metal seats to prevent plate movement. There is no differentiation between top and bottom for the glass plates. The stainless steel plates should be placed with the curved lip down, so that a raised, smooth surface is exposed for particle impingement. This is followed by stage 7, collection plate 6, stage 6, and so on until cone is positioned last.

It should be noted that there are three metal pins extending from the base of each orifice stage. These pins hold the collection plates in place, so that the aerosol sampler can be used in any sampling orientation. In addition, special collection substrates are used other than the glass and stainless steel plates because of lighter tare weight and/or specific analytical requirements. These collection materials consist of glass fiber, cellulose aluminum foil, vinyl metricel, and other materials, which must be placed into the inverted stainless steel collection plate. The substrate surface must be leveled with the top of the curved stainless steel lip to maintain jet to collection surface spacing. In this orientation, the aerosol sampler should be used in an upright position at all times. After the aerosol sampler has been assembled, the outlet nipple on the base stage is connected to the pump intake port with the rubber tubing supplied with the aerosol sampler.

In the assembly of an Andersen low-pressure aerosol cascade impactor, the pump should be checked to be certain that it is operating properly and is capable of pulling 3 L/min at 27″ Hg pressure drop. The pump is designed for these conditions; however, continuous operation at pressure drops greater than 28″ Hg can burn out the pump motor.

All collection substrates should be preconditioned, if necessary, and greased. The substrates for the low-pressure stages should always be greased if at all possible. Good results have been reported at temperatures up to 200°C (392°F) (Lundgren and Balfour, 1980). This high-viscosity spray may be applied directly onto the collection disks (aluminum foil) by passing the spray over the foils two or three times with the spray can held at arms length from the substrate. The greased foils should then be preconditioned in an oven at approximately 100°C (212°F) for approximately 1 hour to drive off any volatiles in the grease. The substrates should then be desiccated and weighed to obtain the tare weight of the greased foil. Once the substrate and backup filter tare weights have been documented, the sampler is ready to be assembled for operation.

High-volume slotted cascade impactor The High-volume cascade impactors attached to any high-volume air sampler fractionate suspended particulates into as many as six different size fractions. The slotted impactor design separates particulates from larger than 7.2 μm to less than 0.49 μm while operating at a flow rate of 40 cfm. The cascade design of this impactor collects particles on small lightweight substrates that are analyzed for respirable particulate matter. There are several models available with 1, 4, 5, and 6 impactor stages allowing for ultimate flexibility. Their cutoff diameters according to their flow rate are given in Table 4.5.

The mechanism is the following: suspended particulates enter through the high-volume cascade impactor through the first set of parallel slots on the first stage. Particulates that are too large to travel to the next stage are impacted on the collection substrate, and the smaller particles remain in the air stream and travel to the next stage. The slots on each stage are the same width, but as the particulates continue through, the slots become successively smaller (Fig. 4.12) and most of the particulates will eventually become impacted on one of the collection substrates (e.g., slotted glass fiber-, quartz fiber-, and aluminum fiber substrates). After the last stage, the smallest particles will be collected on the backup filter, which will be weighed for particle size distribution.

TABLE 4.5 Size fractions of a high-volume slotted cascade impactor (TISCH Environmental website).

Stage no.	40 cfm	20 cfm
1	7.2 μm	10.2 μm
2	3.0 μm	4.2 μm
3	1.5 μm	2.1 μm
4	0.95 μm	1.4 μm
5	0.49 μm	0.73 μm
6	—	0.41 μm
High-volume filter	0	0



FIGURE 4.12 High-volume slotted cascade impactor. *From Tisch Environmental, Inc. (1999). Printed with permission from TISCH Environmental Copyright 1999.*

c. Aerosol sampling—sampling artifacts

The problem of sampling aerosols from the ambient atmosphere has been considered from a theoretical point of view by Liu and Pui (1981). Following a review of the various aerosol samplers and inlets used in ambient aerosol sampling, the factors contributing to high sampling efficiency for large particles and the major mechanisms for particle loss in sampling inlets are impaction on external surfaces, and impaction, turbulent deposition, and sedimentation on internal surfaces. Therefore, an efficient inlet is one for which these losses are minimized.

When the aerosol sampler is ready to sample, the vacuum pump is turned on and a sample stream of 1 ACFM (one cubic foot per minute) air will flow through the aerosol sampler. Fig. 4.10 in fact shows how impaction occurs at the orifice-collector interfaces. Normally, there is no variation in flow rate throughout the sampling period since a constant pressure drop is maintained (no filtration occurs except at the backup filter, resulting in minimal pressure changes).

The particle-size range collected at each stage of the eight stages depends on the orifice velocity of the specific stage, the distance between the orifices and the collection surface, and the collection characteristics of the preceding stage. The combination of a constant flow rate and successively smaller diameter orifices increases the velocity of sampled air, as it cascades through the aerosol sampler, resulting in the impaction of progressively smaller particles in succeeding stages. At 1 ACFM aerosol cascade impactor, the particle fractionation ranges from 11.0 to 0.4 μm diameter according to a similar fractionation within the human respiratory system. Particles too small to be impacted on the last collection plate are collected in the backup filter, which is an optional, integral part of the aerosol sampler. Normal aerosol sampling periods vary from a few minutes to several hours, depending on the sensitivity of the analytical procedure. Ten mg of particulate matter on any one stage represents an approximate upper limit because of reentrainment problems. Overloading the aerosol sampler can be detected easily by visual inspection and is rarely encountered in industrial hygiene applications. Whenever oversampling occurs, rather than having well-defined, discrete piles of particulates, trails of particles can be seen leading from the sample deposits toward the periphery of the plate. This type of aerosol sample should be discarded.

After the aerosol sampling has been completed, the aerosol sampler is disassembled. The collection plates and backup filter are removed and replaced with fresh, preconditioned, preweighted collection media. After conditioning, the collection media can be weighed for net particulate accumulations, or the particulate matter can be analyzed radiologically or chemically for the various components of interest. Since airborne particulates have hygroscopic characteristics, all collection media used in the aerosol cascade impactor should be preconditioned prior to weighing, both before and after a sampling cycle, in a desiccator. Filter weighing should be made to an accuracy of $\pm$ 0.02 mg and a precision of $\pm$ 0.01 mg. It should be kept in mind that whenever an aerosol sample has been collected, the particle sizing has already been completed. To determine the nature of the radioactivity or mass size distribution, the required radiological and gravimetric and/or chemical analyses is performed.

d. Filter collection media

The analytical requirements determine the type of collection surface used. Normally, the stainless steel and glass plates are not used as the collection surfaces for gravimetric determinations because of the high tare weight-to-sample weight ratio. Glass fiber filters are normally used for these analyses because of their light weight and nonhygroscopic properties. However, other types of collection media are required for most radiological and chemical determinations because of the high and variable trace metal background levels in glass fiber. Stainless steel plates are used in many applications where the collected aerosol sample is washed off for subsequent radiological and chemical analyses. Glass plates are used rarely and only when there is a need to look at the collected aerosol particles optically. It is impossible to correlate aerodynamic dimensions with physical size because of the unknown particle density and shape characteristics. In addition, the aerosol particles might have scattered on impaction, which will not affect the aerodynamic sizing but would affect any optical sizing significantly.

For the radiological analysis, the plates of all stages and the glass fiber filter are measured by a high-purity, high-resolution, and high-efficiency Ge detector by the method of gamma spectrometry, and the measurement time is reduced in the mean time of the aerosol sampling, that is,

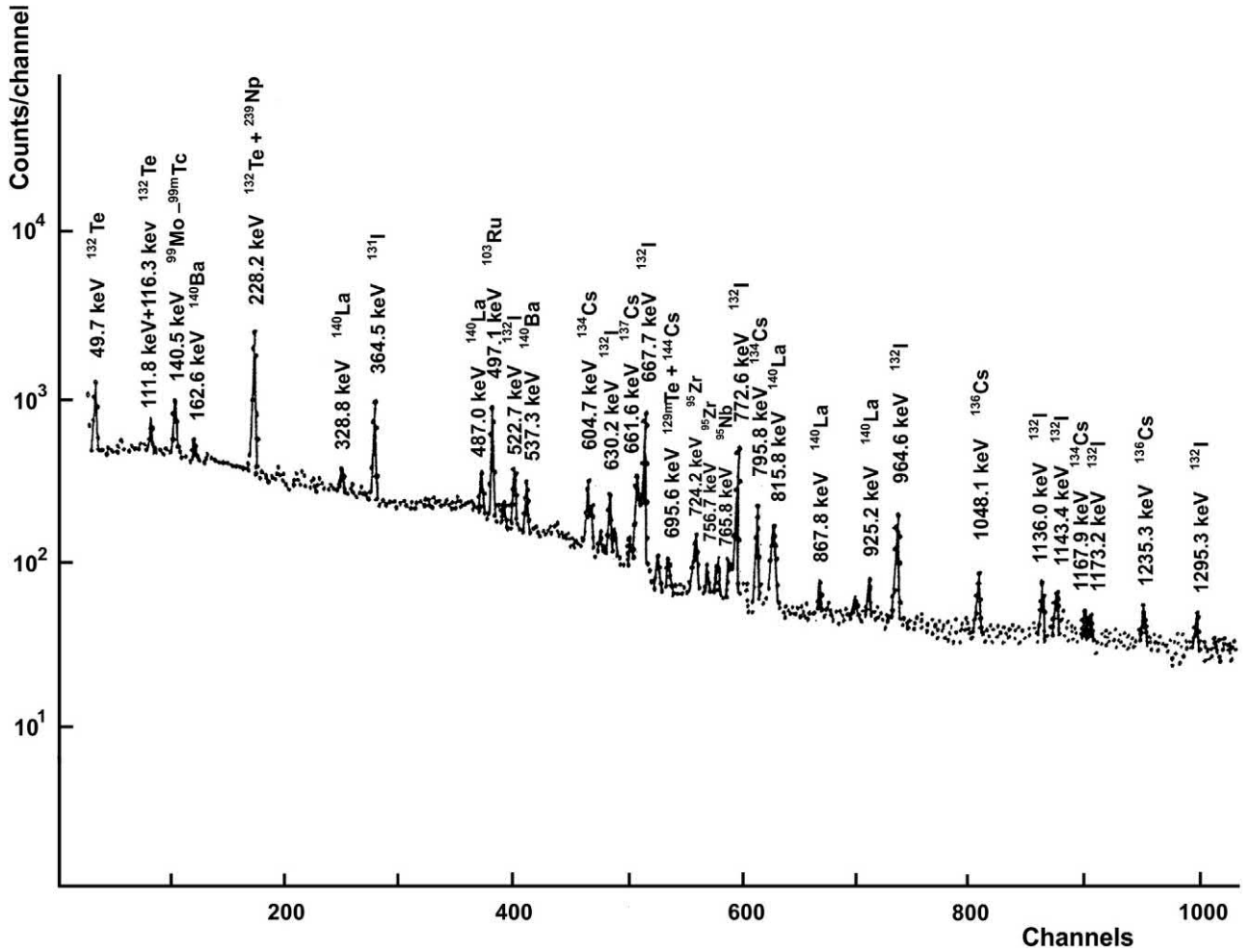


FIGURE 4.13 A typical γ-ray spectrum of the backup filter of an aerosol sampling measurement at Thessaloniki, Greece, obtained after the Chernobyl reactor accident (April 26, 1986). Printed with permission from Elsevier © 2012.

between the start time and the end time of the measurement, and a little earlier than the half-time. In Fig. 4.13, a typical gamma ray spectrum of the backup filter of an aerosol sampling measurement is presented and shows so many γ-photon peaks due to fission product radionuclides and neutron activation of various materials from the fallout due to the Chernobyl reactor accident (April 26, 1986).

By using the collected data of radioactivity of the plates and the backup filter, the activity size distribution of the radionuclides versus the aerodynamic particle diameter, D_p, is obtained; a typical plot for ^{7}Be is presented in Fig. 4.14. Finally, the activity median aerodynamic diameter (AMAD) is estimated for each radionuclide and the geometric standard deviation (σ_g).

e. Data interpretation

The steps that need to be made in any aerosol sampling are as follows:

1. Determination of the radioactive content of *i*th radionuclide in Bq of each plate of the stages and/or the change in weight in g for each stage in the aerosol cascade impactor, including the backup filter.
2. Add up all the amounts to obtain the total radioactivity in Bq and/or of the changes in weight (mass) to obtain the total particulate weight collected.
3. The amount collected on each stage to be divided by the total volume in m^3 collected to determine the percentage of the total Bq/m^3 collected in each size fraction (Table 4.5).
4. The particle density should be considered as 1.0 g/cm^3, the density of water, so that the particle sizes can be reported as equivalent aerodynamic diameters.
5. Selection of the lower size (smallest number) for each size range. This number represents the ECD for each stage. This ECD can also be obtained from Fig. 4.15.
6. Plotting the results on a log-probability graph with the ECD as the ordinate and the cumulative percent less

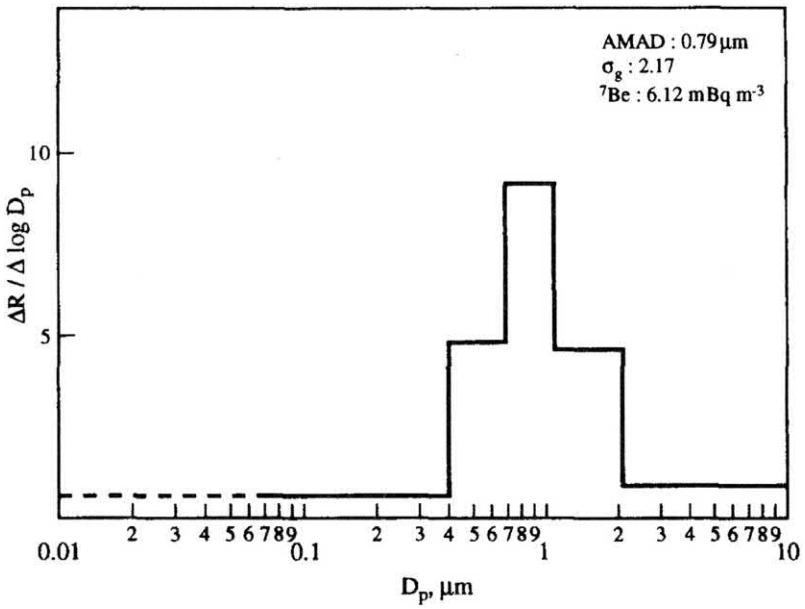


FIGURE 4.14 Aerodynamic size distribution of ^{7}Be ambient aerosols obtained in Thessaloniki, Greece (September 21, 1992). *AMAD*, activity median aerodynamic diameter. *From Papastefanou and Ioannidou (1995). Printed with permission from Elsevier © 1995.*

than the size range by weight as the abscissa (Fig. 4.16), or use a specific calculating program

7. Assuming a lognormal particle-size distribution, the particle-size geometric standard deviation, σ_g is given by

$$\sigma_g = \left(\frac{84.13\%\ \text{diameter}}{50\%\ \text{diameter}}\right) = \left(\frac{50\%\ \text{diameter}}{15.87\%\ \text{diameter}}\right) \quad (4.6)$$

Whenever these two geometric standard deviations are not equal (such as represented in a bimodal distribution), then the size distribution is not represented by a straight line (not really lognormal). A better method of presenting σ_g is

$$\sigma_g = \left(\frac{84.13\%\ \text{diameter}}{15.87\%\ \text{diameter}}\right)^{1/2} \quad (4.7)$$

Typically, the particle-size distribution is "lognormal." The spread of the particle-size distribution is characterized by the geometric standard deviation. The AMAD value of aerosol particles gives the diameter of aerosol particles, where above and below this diameter exists the 50% of the activity of radioactive nuclide. Generally, the particle-size information should be presented in graphical form rather than merely reporting the mass median aerodynamic diameter (MMAD) and σ_g. By plotting Fig. 4.16 Aerodynamic size distribution of ^{7}Be ambient aerosols obtained in Thessaloniki, Greece (September 21, 1992). From Papastefanou (2008)8, the ECD and cumulative percent on a log-probability graph and the particle concentration for any size range can be determined. Correspondingly, the AMAD and the corresponding σ_g are also determined.

8. From Table 4.6 and Fig. 4.16, it can be seen that approximately 98.2% of this aerosol sample is respirable (below 7.00 µm), and that the MMAD is 1.8 µm and σ_g is 1.94 µm for an aerosol sampling labeled as I, which is unimodal distribution, while for another aerosol sampling labeled as II, which is bimodal distribution, the MMAD is 2.1 µm and the σ_g is 6.09. The same procedure is followed for the determination of the AMAD, and the corresponding σ_g, in any aerosol sampling.

f. Calibration

Since the size fraction for each stage is determined by the orifice velocities, it is important that the aerosol sampler be operated at 1 ACFM airflow rate. For this reason, the unit should be periodically recalibrated, and whenever nonstandard temperatures and pressures are encountered, calibration should be performed at the aerosol sampling conditions. Rubber tubing of smaller diameter or length different from that supplied with the aerosol cascade impactor must not be used unless the airflow rate is readjusted.

The pump, which is used, is equipped with an adjustable valve. The lock nut must be tightened always on the adjustment valve after the airflow rate has been set. To adjust the airflow, the screw must be turned in to increase the airflow and out to decrease the airflow. The pump-impactor assembly is calibrated before use of the 1 ACFM airflow rate at ambient temperature and pressure

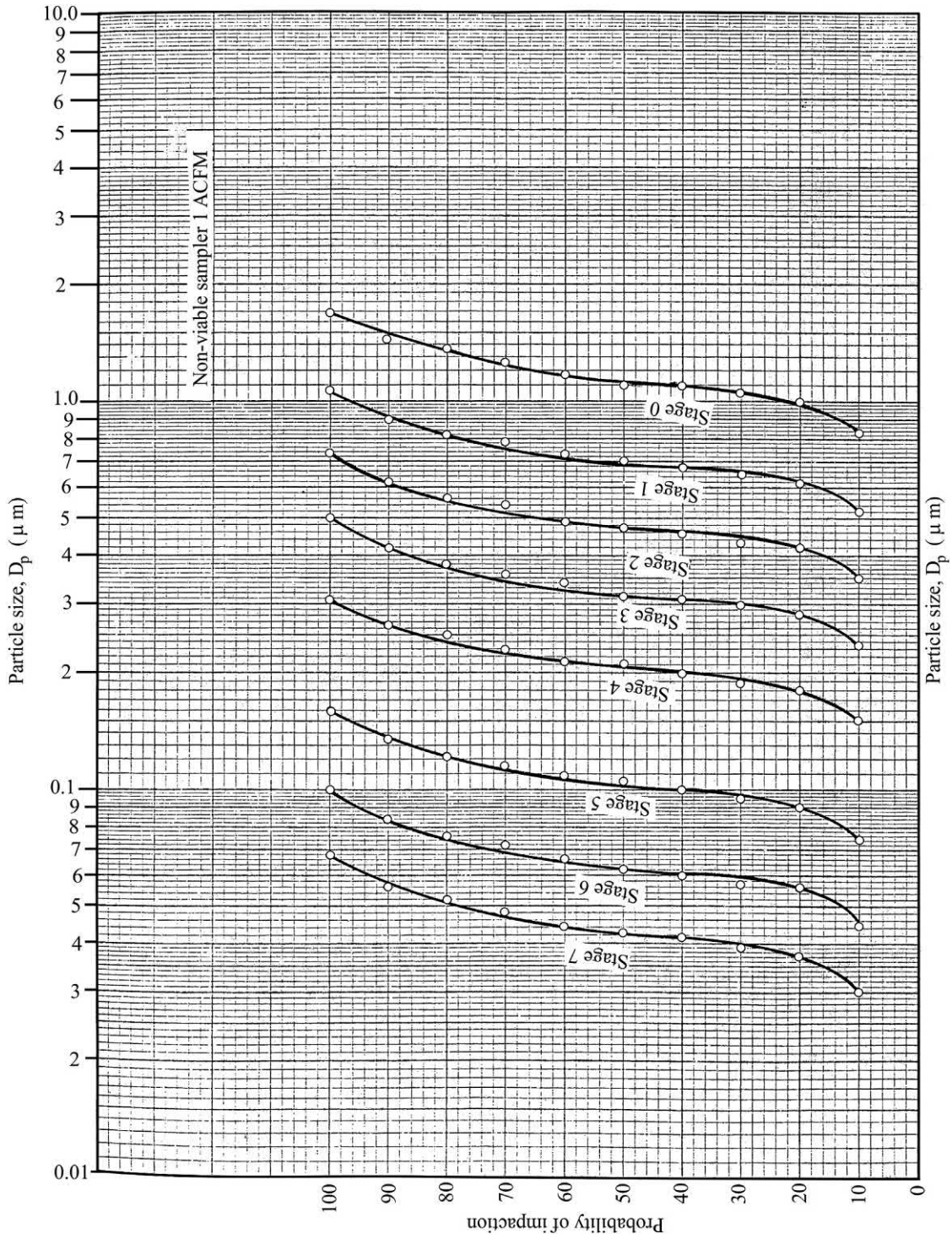


FIGURE 4.15 Probability of aerosol particle impaction at eight stages of a nonviable Andersen-type 1 ACFM (actual cubic feet per minute) cascade impactor versus particle diameter, *Dp*. Printed with permission from Elsevier.

levels. In order to recalibrate at any sampling environment, the following procedure must be conducted:

A calibrated dry gas meter must be placed upstream from the aerosol sampler. A short 100 interior diameter hose with approximately a ¼" wall must be attached to the inlet nozzle (cone) of the aerosol cascade impactor and the other end to the outlet of a dry gas meter. The pump valve must be adjusted until pulling 1 ACFM airflow rate over a

Particle size distribution data

Particle size, D_p (μm)	Percent in size range I	Percent in size range II	Cumulative % less than size range I	Cumulative % less than size range II
≥11.0	0.6	9	99.4	91
7.0 - 11.0	1.2	8	98.2	83
4.7 - 7.0	5.8	11	92.4	72
3.3 - 4.7	13.7	15	78.7	57
2.1 - 3.3	33.3	7	45.4	50
1.1 - 2.1	30.4	5	15.0	45
0.7 - 1.1	7.0	3	8.0	42
0.4 - 0.7	5.8	10	2.2	32
0 - 0.4 <4	2.2	32	0	0

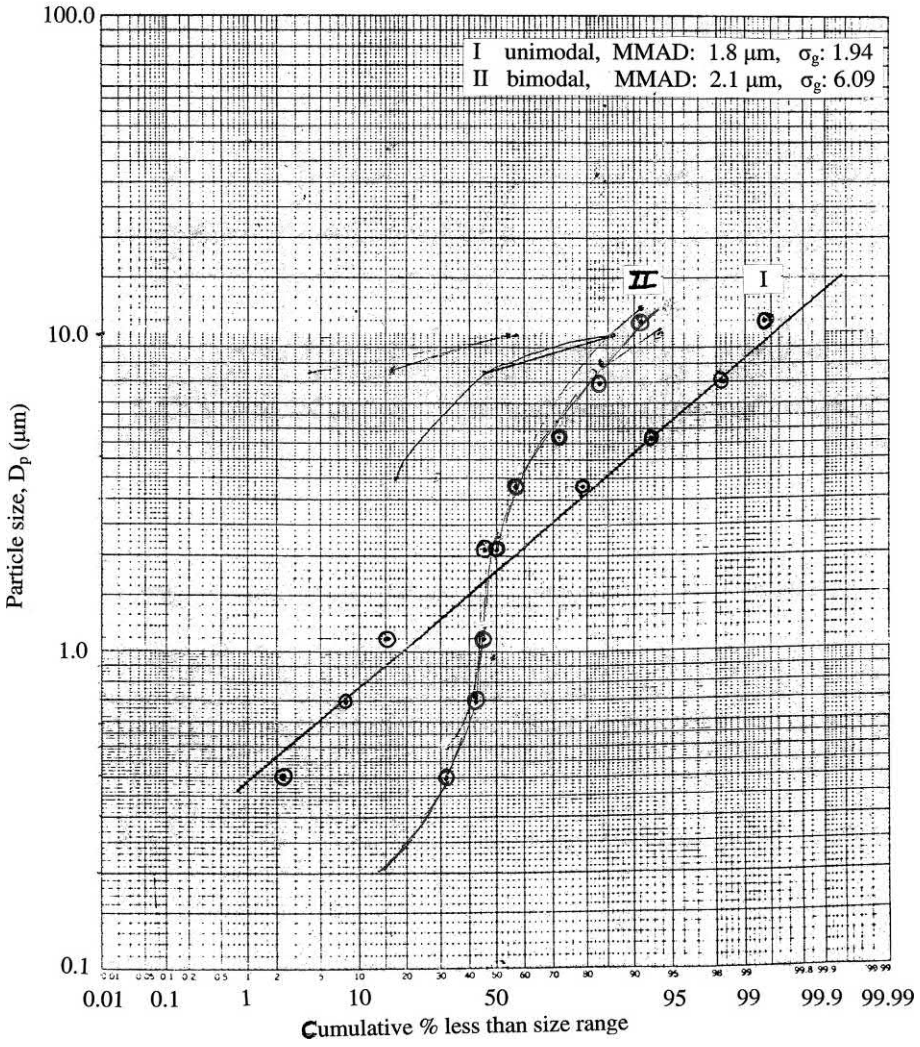


FIGURE 4.16 Graph on log-probability paper of cumulative % less than the size range by weight versus particle size (μm). Printed with permission from Elsevier.

3 minutes test time period as determined by an accurate stop watch. After maintaining 1 ACFM airflow rate for 3 minutes, the lock nut must be tightened on the adjustment valve.

Because of the 1.4 ACFM free airflow rating of the motor and pump, up to 50 feet of tubing can be used between the aerosol sampler and pump while still maintaining 1 ACFM airflow rate through the sampler. The pump and motor are guaranteed by the manufacturer and should not be disassembled for any reason. The pump and motor require no lubrication. The airflow rate of the 12 V DC pump will vary with voltage. One ACFM airflow rate can be drawn through the aerosol cascade impactor, provided the voltage of the pump is maintained near 12 V.

TABLE 4.6 Aerosol sampling data collected by 1 ACFM Andersen-type cascade impactor.

Stage	Tare (g)[a]	Final (g)	Net (mg)	% In size range	Cumulative % less than size range	Size range (μm)	ECD (μm)
0	1.000	1.0009	0.09	0.6	99.4	11.0 and above	11.0
1	1.000	1.0017	0.17	1.2	98.2	7.0–11.0	7.0
2	1.000	1.0082	0.82	5.8	92.4	4.7–7.0	4.7
3	1.000	1.0194	1.94	13.7	78.7	3.3–4.7	3.3
4	1.000	1.0472	4.72	33.3	45.4	2.1–3.3	2.1
5	1.000	1.0431	4.31	30.4	15.0	1.1–2.1	1.1
6	1.000	1.0100	1.00	7.0	8.0	0.7–1.1	0.7
7	1.000	1.0082	0.82	5.8	2.2	0.4–0.7	0.4
Backup filter	1.000	1.0031	0.31	2.2	0	0–0.4	0
			14.18				

ACFM, actual cubic feet per minute; *ECD,* effective cutoff diameters.
[a]*Note: Collection substrates will seldom weight exactly the same.*

III. Radioactive aerosols in ambient air

A. Radon and thoron decay product aerosols

Radon (^{222}Rn) and thoron (^{220}Rn) are gases that formed as decay products of uranium and thorium in the uranium and thorium series in soil and rocks. They are emitted from the ground into the atmosphere, where they decay and form decay products, radioisotopes of polonium (Z = 84), bismuth (Z = 83), and lead (Z = 82), which either remain airborne until they decay or are deposited by rain and by diffusion to the ground. The decay of ^{222}Rn (radon) and ^{220}Rn (thoron) in the atmosphere produces low-vapor-pressure decay products, which coagulate with other freshly produced nuclei or condense on existing accumulation mode aerosols. These radioisotopes include ^{218}Po ($T_{1/2}$ = 3.05 minutes), ^{214}Pb ($T_{1/2}$ = 26.8 minutes), and ^{212}Pb ($T_{1/2}$ = 10.64 hours). A long-lived radioisotope in the ^{222}Rn decay chain, ^{210}Pb ($T_{1/2}$ = 22.3 y), is produced about an hour after attachment of ^{218}Po.

There is considerable information about radon decay product aerosols in ambient air (outdoors) and even in residences (indoors) (Mercer and Stowe, 1971; Kruger and Andrews, 1976; Porstendörfer and Mercer, 1978, 1979, 1980; Kruger and Nöthling, 1979; Porstendörfer et al., 1979; George and Breslin, 1980; Becker et al., 1984; George et al., 1984; Bondietti et al., 1987; Papastefanou and Bondietti, 1987; Porstendörfer, 1994; Grundel and Porstendörfer, 2004; Papastefanou, 2009a; Dlugosz et al., 2010).

The concentrations of radon (^{222}Rn) in ambient air are about 10 and 40 Bq/m^3 in indoor air, whereas the concentrations of thoron (^{220}Rn) in outdoor air are about 10 Bq/m^3 and approximately the same indoors (UNSCEAR, 1993, 2000). The concentrations of the radon (^{222}Rn) decay products in outdoor air are 19.05 Bq/m^3 for ^{218}Po, 3.88 Bq/m^3 for ^{214}Pb, 5.26 Bq/m^3 for ^{214}Bi, 0.5 mBq/m^3 for ^{210}Pb, and 0.050 mBq/m^3 for ^{210}Po, whereas the concentrations of thoron (^{220}Rn) decay products in outdoor air are 0.055 Bq/m^3 for ^{212}Pb and 0.575 Bq/m^3 for ^{212}Bi (UNSCEAR, 2000).

Study of the behavior of ^{222}Rn and ^{220}Rn decay products in air is important for assessing the natural background radiation exposures received by general populations through the inhalation route (Mishra et al., 2009). Among the several aspects of decay product behavior, deposition on surfaces is of special significance because of its prominent role in activity removal by plate out and consequent occurrence of decay product disequilibrium with the precursor gases. Due to their high diffusivities and ability to stick to surfaces, the freshly formed decay products soon attach to existing aerosol particles, thereby giving rise to a continuous activity size distribution. This distribution is broadly classified into two modes, namely, the fine fraction (2 nm diameter) and the coarse fraction (100 nm diameter). The activity size distribution, brought about by the attachment process, is governed by the concentration and distribution of atmospheric aerosols. The application of standard Jacobi (1972) model applies to dynamics of radon decay product aerosols.

Alpha decay carries away positive charge, and electrons are stripped from the precursor atom by its recoil. Therefore, the decay products are formed as positive

ions. Air is ionized by radiation from the naturally occurring radionuclides in the air and on the ground and by cosmic rays. Production of one ion pair requires 32.5 eV of ionization caused by fast electrons and 35.6 eV if by alpha particles. The total energy dissipated in air per decay of ^{222}Rn depends on the equilibrium ratio of radon decay products.

In the free atmosphere, the rate of production of small ions is in balance with the rate of neutralization by recombination and the rate of attachment to condensation nuclei. Condensation nuclei, otherwise called Aitken nuclei, are submicrometer particles mainly produced by combustion processes. In air containing water vapor, positive ions are mostly hydrated protons, H^+ $(H_2O)n$, where n may be any number between 1 and 8. Negative ions are mostly hydrated O^- or OH^-. The formation of clusters of water molecules around ions is very rapid, but in unpolluted air, the clusters do not grow beyond 1 nm diameter and remain as small ions until they become attached to condensation nuclei. They then become large ions.

Large ions themselves can be classified in two size ranges, the nuclei mode centered on 0.01 μm which is distinct from the accumulation mode and those centered on 0.1 μm (Whitby, 1978). In urban air, the number of particles in the nuclei mode is greater than the number of particles in surface area, which determines the probability of attachment of small ions to particles with diameters of the order of 0.1 μm or less. Thus, the large ions are mostly in the accumulation mode. The distinction between small and large ions is well established in atmospheric electricity. The existence of intermediate ions is in the size range 0.001−0.01 μm. If sulfates and nitrates are formed photochemically in air, molecules of acid will dissolve in the water clusters, and these will then grow into the intermediate ion range (Raes, 1985).

Reaction products can be created in air by radiolytic as well as photolytic processes. The radiolytic nuclei are initially uncharged, indicating that ions are not required for their formation. A possible mechanism for formation of radiolytic nuclei is radiolysis of water vapor, leading to formation of H_2O_2, which then oxidizes traces of SO_2 to give H_2SO_4. Increased formation of radiolytic nuclei occurs in air when SO_2 is added. Addition of O_3 to the air also increases nucleus production, whereas addition of NO, a well-known radical scavenger, inhibits it.

The radon decay product aerosols in the atmosphere are generated in two steps. After the formation from the radon isotope (^{222}Rn), the freshly generated decay product radionuclides react very fast (<1 seconds) with trace gases and air vapors, and become small particles, called clusters or unattached radionuclides with diameters ranging from 0.5 to 500 nm (Fig. 4.17A and B) (Porstendorfer, 1994; Porstendorfer et al., 2005). Besides the cluster formation, these radionuclides attach to the existing aerosol particles in the atmosphere within 1−100 seconds, forming the radon decay product aerosols (radioactive aerosols).

About 46% of the 46 low-pressure impactor measurements made over a 10-month period showed a radioactivity peak in the 0.11- to 0.23-μm region, whereas 39% showed a peak in the 0.23- to 0.52-μm region. The remaining 15% of the measurements resulted in activity size distributions, where ^{214}Pb and ^{212}Pb activities were highest in different size ranges in the same spectrum. On the average, about 76% of the ^{214}Pb activity and 67% of the ^{212}Pb activity were found to be associated with aerosol particles in the 0.08- to 1.4-μm size range. The activity associated with aerosol particles smaller than 0.08 μm can also be substantial. Lead-214 is generally enriched in the accumulation mode aerosol, particularly between 0.11 and 0.52 μm, where most of the surface area and mass occurs, whereas the Aitken nuclei fraction (below 0.08 μm) contained a higher percentage of ^{212}Pb activity compared with ^{214}Pb activity in 69.6% of the measurements (Bondietti et al., 1987; Papastefanou and Bondietti, 1987).

The radon decay products become associated with atmospheric aerosol particles by condensation or coagulation processes that are surface area related. The activity size distribution of ^{214}Pb aerosols showed a small shift to larger particle sizes relative to ^{212}Pb aerosols. The shift of ^{214}Pb to a slightly higher size distribution compared with ^{212}Pb was also found using 1 ACFM and high-volume cascade impactors. The higher flow rates of these impactors, as well as the ability to measure high-volume activity by gamma ray spectrometry, made us confident that this shift was real and not a data analysis artifact. The larger median size of ^{214}Pb aerosols was attributed to a-recoil depletion of smaller aerosol particles following the decay of the aerosol-associated ^{218}Po. Subsequent ^{214}Pb condensation on all particles effectively enriches larger-sized aerosols. Pb-212 does not undergo this recoil-driven redistribution. Even considering recoil following ^{214}Po α-decay, the average ^{210}Pb-labeled aerosol grows by a factor of 2 during its atmospheric lifetime. Early morning and afternoon measurements indicated that similar size associations of ^{214}Pb occur, despite humidity differences and the potential for fresh particle production in the afternoon.

The longer half-life of ^{212}Pb (10.64 hours) compared with ^{214}Pb (26.8 minutes) might favor the presence of larger aerosol associations of ^{212}Pb, if coagulation rates are fast relative to radioactive decay rates, although cascade impactor measurements may not be sensitive enough to record this effect. Instead, the measurements indicated that the shorter-lived chain (^{218}Po, ^{214}Pb, etc.) was more often associated with larger aerosol particle sizes than the longer-lived chain (^{216}Po, ^{212}Pb, etc.).

The ^{214}Pb shift might be explained by the fact that a significant fraction of the 3.05-min ^{218}Po atoms, precursor of ^{214}Pb, should themselves attach to an existing aerosol

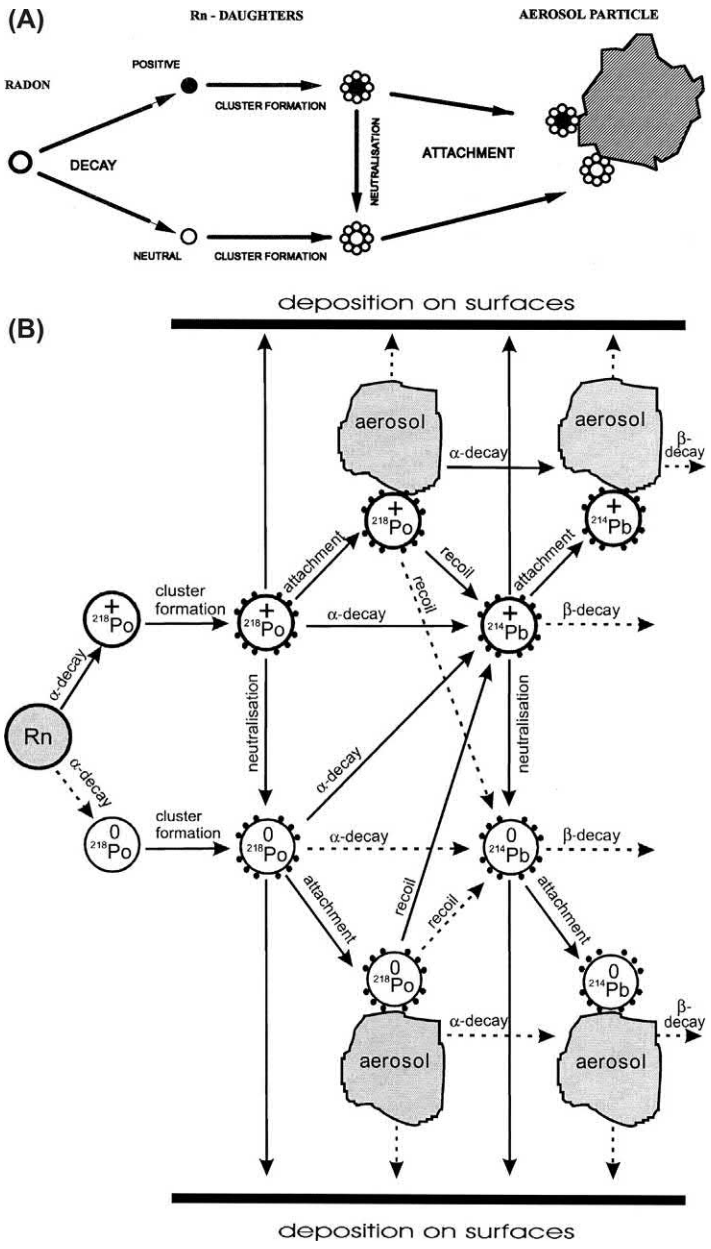


FIGURE 4.17 (A) Basic processes of radon decay product behavior in air defining "unattached" and "aerosol-attached" particle activities. (B) Processes of ^{218}Po and ^{214}Pb in air. *(A) From Porstendörfer (1994). Printed with permission from Elsevier Copyright (1994). (B) From Porstendörfer et al. (2005). Printed with permission from Oxford University Press Copyright (2005).*

particle or coagulate with other nuclei during their lifetime, as their mean attachment half-lives are of the order of a minute or less. When this attached ^{218}Po α-decays, the recoiling ^{214}Pb atom can escape the aerosol particles. Complete recoil loss would occur if the particle diameter, D_p, of the aerosol were smaller than the range of the recoiling nucleus. In water, this recoil range is 0.13 μm and should be somewhat less in the atmospheric aerosols that have a density closer to 1.5 g/cm^3. By contrast, very little of the 0.146 ms-^{216}Po would attach before decaying to ^{212}Pb, because of its short life relative to attachment times. A considerable fraction of the ^{214}Pb should undergo recoil detachment, particularly from aerosol particles with diameters smaller than 0.1 μm (diameter approximating the recoil range). The probability of loss would decrease with increasing particle radius. If the recondensing ^{214}Pb behaves like the original ^{214}Po, the net effect would be a shift of ^{214}Pb to a larger particle-size distribution.

Since the subsequent β-decays of ^{212}Pb and ^{214}Pb + ^{214}Bi do not result in significant recoil, the α-measurement

of ^{214}Po- and the ^{212}Pb-decay products is in reality tracing the aerosol size distribution of a ^{220}Rn-decay product atom (^{212}Pb), which has condensed only once and a ^{222}Rn-decay product atom (^{214}Pb) that has probably condensed more than once. This stability of the Pb isotopes is the basis for the generic reference to ^{212}Pb and ^{214}Pb size distributions.

The AMADs of ^{214}Pb aerosols determined with the low-pressure impactor data varied from 0.10 to 0.37 μm (average 0.16 μm) and for ^{212}Pb aerosols from 0.07 to 0.25 μm (average 0.12 μm). For the ^{210}Pb aerosols, the AMADs varied from 0.28 to 0.49 μm (average 0.37 μm). ^{210}Pb is produced by α-decay of ^{214}Po, the event used to quantify ^{214}Pb distributions on the LPIs. While the relationship between the aerodynamic sizes of ^{214}Pb and ^{210}Pb is complicated, because of the large differences in their atmospheric lifetimes, ^{210}Pb has always found to be associated with larger aerosols than ^{214}Pb. So, the AMADs of radon decay product aerosols are in the accumulation mode between 0.11 and 0.52 μm.

B. Radioactive aerosols associated with the cosmic ray–produced radionuclides

Relatively short-lived radionuclides with half-life about a few days, of cosmogenic origin, such as ^{7}Be ($T_{1/2} = 53.3$ d), ^{32}P (14.3 d), ^{33}P (25.3 d), and ^{35}S (87.4 d), occur permanently in the atmosphere. There is another category of long-lived radionuclides with half-life larger than a year, such as ^{3}H ($T_{1/2} = 12.5$ y), ^{10}Be (1.5×10^{6} y), ^{14}C (5730 y), ^{22}Na (2.6 y), ^{26}Al (7.3×10^{5} y), ^{32}Si (280 y), ^{36}Cl (3.01×10^{5} y), ^{39}Ar (269 y), and ^{81}Kr (2.1×10^{5} y), also occurring in the atmosphere. All the above-mentioned radionuclides are formed continuously by the interaction of cosmic ray particles with matter (atmosphere). Most of them are formed by spallation processes of light atmospheric nuclei, such as nitrogen ($Z = 7$), oxygen ($Z = 8$), and even carbon ($Z = 6$) or heavier atmospheric nuclei, such as sodium ($Z = 11$), phosphorus ($Z = 15$), sulfur ($Z = 16$), potassium ($Z = 19$), and calcium ($Z = 20$) (NCRP, 1987), when they absorb protons and even neutrons of cosmic origin. The production of ^{24}Na and ^{38}Cl by neutron activation of stable isotopes ^{23}Na and ^{37}Cl, respectively, is an exception.

Of the above radionuclides, ^{7}Be has a high isotope production rate in the atmosphere (8.1×10^{-2} atoms/cm^2 s), and as it is a gamma emitter (477.6 keV gammas, 11% yield), it can easily be detected and measured in the atmospheric air, in precipitation, and in vegetation as well. Its average concentrations in the tropospheric air are about 12.5 mBq/m^3 (UNSCEAR, 2000) and 700 Bq/m^3 in rainwater (UNSCEAR, 1982). Sodium-22 is also a positron and gamma emitter (511 keV gammas, annihilation peak), but its production rate in the atmosphere is too small (8.6×10^{-5} atoms/cm^2 s), and its concentration in the tropospheric air is 0.0021 mBq/m^3 (UNSCEAR, 2000). All the other referred radionuclides are mostly beta emitters with low production rates in the atmosphere and very low concentrations in the troposphere.

Beryllium-7 is a relatively short-lived ($T_{1/2} = 53.3$ d, $\tau = 1/\lambda = 77$ d) naturally occurring radionuclide of cosmogenic origin, which is formed by spallation processes of light atmospheric nuclei, such as carbon ($Z = 6$), nitrogen ($Z = 7$), and oxygen ($Z = 8$), when they absorb protons and even neutrons of the primary component of cosmic radiation (Bruninx, 1961, 1964; Rindi and Charalambous, 1967; Silberberg and Tsao, 1973; Ioannidou and Papastefanou, 1994; Papastefanou, 2009b), according to the following reactions:

$$^{12}_{6}\mathrm{C} + \mathrm{p} \rightarrow {}^{7}_{4}\mathrm{Be} + {}^{6}_{3}\mathrm{Li} \qquad {}^{12}_{6}\mathrm{C} + \mathrm{n} \rightarrow {}^{7}_{4}\mathrm{Be} + {}^{6}_{2}\mathrm{He}$$

$$^{14}_{7}\mathrm{N} + \mathrm{p} \rightarrow {}^{7}_{4}\mathrm{Be} + 2{}^{4}_{2}\mathrm{He} \qquad {}^{14}_{7}\mathrm{N} + \mathrm{n} \rightarrow {}^{7}_{4}\mathrm{Be} + {}^{8}_{3}\mathrm{Li}$$

$$^{16}_{8}\mathrm{O} + \mathrm{p} \rightarrow {}^{7}_{4}\mathrm{Be} + {}^{10}_{5}\mathrm{B} \qquad {}^{16}_{8}\mathrm{O} + \mathrm{n} \rightarrow {}^{7}_{4}\mathrm{Be} + {}^{10}_{4}\mathrm{Be}$$

$$^{16}_{8}\mathrm{O} + \mathrm{p} \rightarrow {}^{7}_{4}\mathrm{Be} + {}^{7}_{3}\mathrm{Li} + {}^{3}_{2}\mathrm{He}$$

$$^{16}_{8}\mathrm{O} + \mathrm{n} \rightarrow {}^{7}_{4}\mathrm{Be} + {}^{6}_{2}\mathrm{He} + {}^{4}_{2}\mathrm{He}.$$

Once ^{7}Be is formed in the troposphere, it rapidly associates primarily with submicron-sized aerosol particles (Bondietti et al., 1987). Beryllium-7 in these fine aerosols may subsequently enter the marine as well as the terrestrial environment and vegetation via wet or dry depositional events. Following deposition, ^{7}Be will tend to associate with particulate material (particle-reactive element).

Beryllium-7 has come to be recognized as a potential tool in studying environmental processes, such as aerosol transit and residence times in the troposphere (Martell, 1970), aerosol deposition velocities (Young and Silker, 1980), and aerosol trapping by above ground vegetation (Bondietti et al., 1984).

Beryllium-7 as well as other natural radionuclides like $^{212+210}$Pb, ^{22}Na, ^{35}S, and $^{32+33}$P participate in the formation and growth of the accumulation mode aerosols (0.07–2 μm diameter), which is a major reservoir of pollutants in the atmosphere. Following its production by gas-phase nuclear transformation, this isotope condenses on the aerosol population, growing by condensation of nonradioactive species (e.g., H_2SO_4 or organics), and the fate of ^{7}Be will become the fate of the carrier aerosols (Bondietti et al., 1988). On the behavior of ^{7}Be with atmospheric aerosols, it was concluded from early aerosol studies that considerable coagulation occurred during migration from the stratosphere and upper troposphere to ground level (Lockhart et al., 1965b; Gaziev et al., 1966).

Atmospheric aerosol size distribution appeared to follow a trimodal distribution expected for condensation-derived aerosols. This trimodal distribution of atmospheric aerosols showed the following mode ranges: the Aitken nuclei mode ranges from 0.003 to 0.07 μm (average 0.015 μm); the accumulation mode ranges from 0.07 to 2 μm (average 0.3 μm); and the coarse mode ranges from 2 to 36 μm (average larger than 10 μm) (NRC, 1979).

Young et al. (1975) reported that ^{7}Be is attached primarily to submicron-sized particles in the atmosphere. A histogram of the activity size distribution of ^{7}Be versus aerodynamic diameter (D_p) is represented in Fig. 4.18A. This distribution was selected by Papastefanou and Ioannidou (1995) from 11 atmospheric aerosol sampling measurements made over an almost 2-year period at Thessaloniki, Greece (40 degrees38′N, 22 degrees58′E) by using Andersen 1 ACFM cascade impactors at a flow rate of 1.7 m^3/h (28.3 L/min or 1 ft^3/min).

According to their observations, about 88% of ^{7}Be was found to be present as particles smaller than 1.1 μm in diameter, and less than 1% was found to be present as particles larger than 7 μm in diameter. This means that ^{7}Be aerosols are accumulation mode aerosols. This is also evident from the plot of Fig. 4.18A. The reported AMAD values varied from 0.76 to 1.18 μm (average 0.90 μm), and σ_g varied from 1.86 to 2.77 (average 2.24). The AMAD and (σ_g) calculations were made by plotting the cumulative distributions on log-normal probability graph. They also showed that 60% of the ^{7}Be activity was associated with particles with diameter smaller than 1.1 μm. Similar results are reported by Ioannidou (2012).

Beryllium-7 aerosol measurements carried out by Papastefanou and Ioannidou (1995) at sea level in a coastal area, at a hilly area, 250 m height, and on the top of a mountain, 1000 m height, showed that the ^{7}Be activity size distribution dominated a smaller size range of aerosol particles with an AMAD of 0.68 μm ($\sigma_g = 2.18$) at a height of 250 m and an AMAD of 0.68 μm ($\sigma_g = 2.24$) at a height of 1000 m, showing a dependency on height. In marine environments at sea level, the ^{7}Be activity size distribution dominated a higher size range of aerosol particles with an AMAD of 0.82 μm ($\sigma_g = 1.88$).

Bondietti et al. (1987) in 13 measurements in an almost 1-year period (June 1985−March 1986) at Oak Ridge, Tennessee, with temperate latitude (35 degrees58′N, 84 degrees30′W) and wet climate showed that the AMAD varied from 0.29 to 0.50 μm (average 0.35 μm) and that the fraction of ^{7}Be-associated aerosols above 1.4 μm was usually between 5% and 10%, i.e., analytically, 4.5% was found in the 1.4−2.1 μm size range, 1.1% in the 2.1−4.2 μm size range, and only 0.2% in sizes greater than 4.2 μm. They also concluded that cosmogenic radionuclides, such as ^{7}Be and ^{35}S, were associated with smaller aerosols and in respect of the longer-lived radionuclides, such as ^{210}Pb, a decay product of ^{222}Rn of terrestrial origin, which were associated with larger aerosols.

Röbig et al. (1980) reported that the distribution of the long-lived radionuclide ^{7}Be was shifted to large particle sizes due to large residence times of ^{7}Be in the atmosphere. An equivalent aerodynamic diameter of about 0.65 μm for ^{7}Be might have resulted from the plot of the activity size distribution of the ambient air obtained by a high-volume cascade impactor (flow rate 68 m^3/h) at Gottingen, Germany (51°32′N, 9°55′E). Shifts to large particle sizes were also observed when the RH increased during rainfalls. Much later, Grundel and Porstendorfer (2004) observed

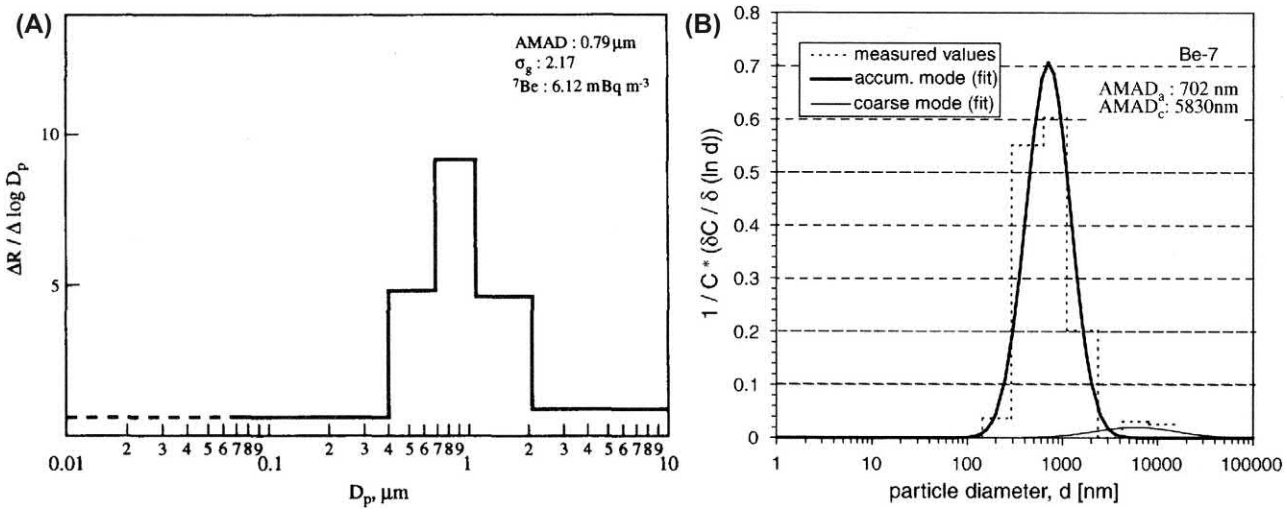


FIGURE 4.18 (A) Aerodynamic size distribution of ^{7}Be ambient aerosols. (B) Relative activity size distribution of ^{7}Be in outdoor air. *(A) From Papastefanou and Ioannidou (1995); reprinted with Permission from Elsevier Copyright (1995). (B) From Grundel and Porstendörfer (2004). Printed with permission from Elsevier Copyright (2004).*

that the results of the ^{7}Be measurements for a period of 4 weeks, carried out in outdoor air of a suburb area of the town of Göttingen, showed no activity fraction in the nucleation (Aitken nuclei) mode, but a small amount of the activity (5%) in the coarse mode size range (Fig. 4.18B). The accumulation mode of ^{7}Beaerosols with an activity fraction of 95% has an AMAD value of 702 nm.

Winkler et al. (1998) in 46 measurements in a period of $1^{1/3}$ years (December 1994−March 1996) at Munich-Neuherberg, Germany (48°13′N, 11°36′E) showed that the AMAD of ^{7}Be aerosols ranged from 0.44 to 0.74 μm (average 0.57 μm) and that seasonal effects during the period of high ^{7}Be air concentrations, i.e., in the summer period, when relatively low values of the AMAD (0.45−0.52 μm) have been observed. They also concluded that the AMADs, ranged between the MMADs, and the surface median aerodynamic diameters, SMADs, of the ambient aerosols, indicating that this radionuclide is involved in the transformation process of the tropospheric aerosols after formation in the stratosphere and upper troposphere.

Yu and Lee (2002) in 14 measurements at Hong Kong (22°18′N, 114°10′E) for a 3½ month's period (November 26, 2001−March 8, 2002) found that the AMAD of ^{7}Be-aerosols varied from 0.33 to 1.15 μm (average 0.67 μm). They concluded that the AMADs of ^{7}Be aerosols are anticorrelated to ^{7}Be concentrations in air and are correlated to RH and the mean cloud cover, whereas temperature does not affect the AMADs of ^{7}Be aerosols.

Apart from these, Lujaniene et al. (2001) reported larger ^{7}Be AMAD values varied from 1.12 to 2.06 μm (average 1.45 μm) in a northern latitude at Vilnius, Lithuania (54°41′N, 25°19′E). The investigated data rather indicate that the AMAD of ^{7}Be aerosols increases with increasing latitudes (latitudinal effect). As cosmic radiation increases with latitude, the number of ^{7}Be atoms and ions formed increases also with latitude, and so, there are more ^{7}Be atoms and ions available to form small aerosol particles in the nucleation (Aitken nuclei) mode, which then grow or become attached directly to the existing large particles in the accumulation and in the coarse-particle modes by increasing the AMAD of ^{7}Be aerosols.

Cho et al. (2007) reported that the mass size distribution of ^{7}Be aerosols in ambient air showed a bimodal distribution with a higher peak around 0.49 μm and a smaller peak between 3 and 7.2 μm. The AMAD decreased with increasing ambient ^{7}Be concentrations. The mean residence times by using a mean growth rate of 0.004 mm/h were estimated to be 2.5−6.4 days. The AMAD of the ^{7}Be aerosols has an increasing tendency with higher RH and increases with an increasing temperature, but the temperature dependency of AMAD should be explained with geological and meteorological conditions.

In the activity size distribution of ambient aerosols, ^{7}Be is shifted to large particle sizes in the presence of pollutants. Removal of small aerosol particles in the submicron size range of the activity size distribution, either by scavenging or by deposition of particles on any surface, may result in a depletion of small particles in the activity size distribution. Subsequent ^{7}Be condensation on all aerosols effectively enriches large particles in the activity size distribution. The radioactive aerosol is only generated by attachment, and there is no nucleation in contrast to the sulfate aerosol (nucleation + attachment) (Hopke, 1991). Freshly produced ^{7}Be should attach to an existing aerosol or coagulate with other nuclei during its lifetime, as mean attachment half-lives are of the order of a minute or less (Porstendörfer and Mercer, 1980).

Papastefanou and Ioannidou (1996) reported that sites where the AMAD of ^{7}Be aerosol was varied between 0.62 and 0.74 μm were located on lines with direction of wind blown (local wind). These streamlines of air masses are transferring pollutants from an industrial zone to the urban air and the marine environment over the sea surface. In the area influenced from the industrial zone, the AMAD of ^{7}Be aerosol was varied between 0.82 and 1.00 μm, which is higher than that observed out of the industrial zone.

Ioannidou (2011) measured the activity size distribution of ^{7}Be aerosols in association with trace metals in the urban environment and showed that the AMAD, ranged from 0.58 to 1.22 μm (averaging 0.80 μm), indicating post-condensation growth either in the upper atmosphere or after mixing in the boundary layer. It was shown that more than 80% of the ^{7}Be activity was associated with particles smaller than 1.3 μm. The AMAD values were anti-correlated with ^{7}Be activities, whereas they were correlated with RH, with high confidence ($R = 0.2$, $P < .00,813$). The composition of the associated particles was basically Ca, Si, and S. Among the heavy metals determined, Fe was the most abundant, followed by Cu. Minor amounts of Pb, Cr, and Ni were presented in coarse size ranges of the aerosol particles. The amount of Fe increased with decreasing particle size, displaying positive correlation with AMAD of ^{7}Be in the case of strong winds from NW direction and indicating the transport of polluted air from the industrial area of the city of Thessaloniki, Northern Greece (40°N).

Finally, Ioannidou et al. (2019) found that greatest ^{7}Be AMAD values observed at the most polluted areas, despite the season of the year, whereas lower AMAD observed in nonpolluted environments (of mountain Monte Rosa and lake Maggiore).

The activity size distribution of ^{7}Be aerosols depends probably on the location of formation. Most of ^{7}Be atoms and the ^{7}Be aerosols are generated in the upper region of the atmosphere, where other aerosol conditions exist than in the lower atmosphere.

Studies in Arctic environment have been conducted by Ioannidou and Paatero (2014) and Paatero et al. (2017). More specifically AMAD values of ^{7}Be aerosol were

determined by 12 measurements with a high volume cascade impactor in subarctic northern Finland. The ^{7}Be AMAD values ranged between 0.54 and 1.05 μm (average 0.83 μm), whereas a residence time of about 8 days applied to aerosols of 0.83 μm diameter, representing the residence of aerosol particles in arctic environment. The observed positive correlation between AMAD values and RH% explained by the fact that condensation during high relative humidity conditions becomes more intense, resulting in increased particle sizes of atmospheric aerosols. Greater aerosol particle sizes indicate a higher wet scavenging rate of aerosols, and as a result, lower activity concentration of ^{7}Be in the atmosphere, explaining the anticorrelation between the AMAD values and activity concentrations of ^{7}Be. But the aforementioned associated with possibly higher scavenging rates of aerosols does not necessarily alone explain the anticorrelation between the AMAD and the ^{7}Be activities. The air mass origin associated with synoptic scale weather phenomena may contribute to that too. The Flextra model was used to assess the transport pattern and to explain the deviation in radionuclide activity concentrations and AMAD values observed in the site of investigation.

In subarctic northern Finland, the activity size distribution of ^{210}Pb has been studied also in ambient aerosols, which were determined from high-volume cascade impactor samples collected. Most of the ^{210}Pb activity was incorporated in accumulation mode aerosol particles. The AMAD values of ^{210}Pb aerosol particles ranged from 0.53 to 0.98 μm, while the 38%–61% of ^{210}Pb activity was found to be associated with aerosol particles smaller than 0.69 μm. A slight descending tendency of ^{210}Pb activity median aerodynamic diameter was observed as a function of increasing ^{210}Pb activity concentration. This is related to the continental origin of airborne ^{210}Pb on one hand and various aerosol particle growth processes on the other hand. Also, a clear tendency toward a higher ^{7}Be/^{210}Pb activity ratio as a function of increasing aerosol particle diameter was observed. This, in turn, reflects the different origin of ^{210}Pb, exhalation of ^{222}Rn into the air, and ^{7}Be, formation via cosmic ray–induced spallation reactions in the upper troposphere and the stratosphere.

C. Radioactive aerosols in the workplace environment

The model of the respiratory tract produced by the International Commission on Radiological Protection (ICRP66, 1994) recommends default AMADs of 5 μm for occupational exposure and 1 μm for exposure of members of the public.

The distributions of measured AMADs for all workplaces and for different industries were well fitted by single lognormal functions characterized by their median and geometric standard deviation. Median values of AMAD for all workplaces, for the nuclear power industry and for fuel handling facilities, were 4–5 μm (Dorrian and Bailey, 1996). The median value for uranium mills was 7.3 μm. Doses for standard workers for a 5–11 μm AMAD are similar to those at 4 μm. For ^{234}U, doses for a 5 μm AMAD are at least 80% of those for a 7.3 μm AMAD. Therefore, the 5 μm default recommended by the International Commission on Radiological Protection (ICRP) provides realistic dose estimates for workers (Dorrian and Bailey, 1996).

The AMADs (in μm) and geometric standard deviations (σ_g), noted as GSDs, of the activity size distributions for aerosols collected in different work environments are given in Table 4.7.

1. Mine aerosols

Aerosols from mine sources have particle-size distributions that are determined by both the mining method and the source of the aerosol (Cantrell et al., 1987). A size distribution summarizing the physical characteristics of mine aerosols is shown in Fig. 4.19 (Willeke and Baron, 1993). The shape of the aerosol size distribution is influenced by the different sources contributing to the aerosol. This figure displays some of these sources and the physical mechanisms, such as condensation and coagulation that transfer aerosol mass from one size to another. It should be noted that these mechanisms and the general shape of the distribution are not unique to mine aerosols.

There are three distinct aerosol size ranges identifiable by features in measured mine aerosol size distributions:

1. The smallest of these from 0.001 to 0.08 μm is the Aitken nuclei range, which contains primary aerosols from combustion sources, such as diesel engines and secondary aerosols or chain aggregates formed by coagulation of primary aerosols.
2. The next size range from 0.08 to approximately 1.0 μm is termed the accumulation range. It contains emissions in this size range plus aerosols accumulated by mass transfer through coagulation and condensation processes from the Aitken nuclei range.
3. The last range from 1.0 to approximately 40 μm is termed the coarse-particle range. Aerosols within this size fraction generally result from mechanical processes such as rock fracture and bulk material handling. Mineral dust aerosol reentrained by mine haulage vehicles during the load-haul-dump cycle is an example of an in-mine emission that will contribute aerosols to this size range.

For convenience, the Aitken nuclei and the accumulation ranges are combined in a single fine-particle range. A division is usually made between this range and the coarse-

TABLE 4.7 Activity median aerodynamic diameters (AMADs, in μm) and geometric standard deviations (σ_g), noted as GSDs, of the activity size distributions for aerosols collected in different work environments.

		Coarse mode			Accumulation mode		
Work environment	Nuclide	Fraction (%)	AMAD (μm)	GSD	Fraction (%)	AMAD (μm)	GSD
Sandblasting	^{60}Co	100	3.4	2.3	–	–	–
	^{131}I	100	2.9	2.4	–	–	–
	^{137}Cs	100	3.0	2.3	–	–	–
	^{140}Ba	100	3.1	2.3	–	–	–
	^{140}La	100	3.1	2.3	–	–	–
	^{141}Ce	100	3.1	2.4	–	–	–
Thermal arc cutting	^{60}Co	97	3.2	1.9	3	–	–
	^{54}Mn	97	3.1	1.9	3	–	–
	^{134}Cs	51	3.2	1.9	49	0.29	2.2
	^{137}Cs	50	3.2	1.9	50	0.28	2.2
Grinding	^{51}Cr	100	4.1	2.0	–	–	–
	^{54}Mn	100	4.2	2.0	–	–	–
	^{58}Co	100	3.9	1.9	–	–	–
	^{59}Fe	100	4.2	2.0	–	–	–
	^{60}Co	100	3.7	2.0	–	–	–
Noble gas progeny (off-gas sump room)	^{88}Rb	–	–	–	100	0.41	1.8
	^{138}Cs	4	7.8	2.4	96	0.43	1.9
Noble gas progeny (SJAE room)	Gross beta	4	6.2	1.7	96	0.44	1.9

From Papastefanou (2008). Printed with permission from Elsevier Copyright (2008).

particle range at 1.0 μm. This distinction is possible because sources of aerosols in the two ranges are usually different, and the coarse-particle range contains very little mass transferred from the accumulation range by coagulation. In each of the ranges mentioned, the size distribution of mine aerosols can exhibit a maximum or mode, which takes its name from the size range in which it occurs. Hence, the maximum in the accumulation range is termed the accumulation mode.

Radioactive isotopes, such as ^{238}U, ^{218}Po, ^{214}Pb-^{214}Bi, and ^{210}Pb-^{210}Po, characterized the mine aerosols.

D. Radioactive aerosols associated with the operation of high-energy particle accelerators

Particle accelerators and their surroundings are locations of residual radioactivity production that is induced by the interaction of high-energy particles with matter. In high-energy accelerators, nonradioactive aerosols are abundantly generated during machine operation. Radioactive atoms, which are produced through various nuclear reactions in the air of accelerator tunnels, attach to nonradioactive aerosols and form radioactive aerosols. These aerosol particles might be inhaled by workers who enter the tunnel just after the beam stop. Their particle size is very important information for estimation of internal exposure doses.

During accelerator operation, radioactive nuclides are produced by the interaction between the primary and secondary particles ($E \geq 30$ MeV) from the machine and the atmospheric air in the accelerator halls. Spallation reactions in solid machine parts can also lead to the formation of radioactive nuclides. If the air is confined in the accelerator hall, there will be no release of radioactive nuclides into the outside zones during operation of the machine. When the machine is stopped, an unexpected concentration of radioactive nuclides in the air may be present.

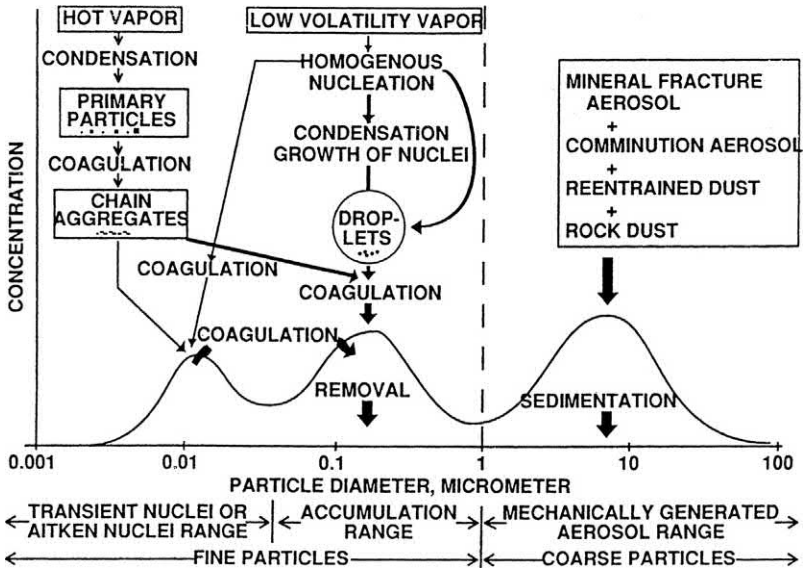


FIGURE 4.19 Idealization of an atmospheric surface area distribution showing the principle modes, sources of mass, and the processes involved in mass transfer and removal. *From Whitby (1978). Printed with permission from Elsevier Copyright (1978).*

Radioactive dust is produced from activated machine parts by normal erosion or mechanical wear. Dust in the accelerator halls is also activated when it is in suspension in the air or when it is deposited on the machine components. The principal radioisotopes found in dust are those produced from the constituents of the machine parts. Radioactive aerosols are produced from activated air in the accelerator hall (Charalambous and Rindi, 1967).

Thus far, little is known of the size distribution and the mechanisms of aerosol formation. Radioactive atoms are formed with high kinetic energy and/or charges and can interact with their surroundings as hot atoms. Subsequent reactions with ambient nonradioactive aerosols are considered to result in the formation of radioactive aerosols. It seems likely that the ^{7}Be aerosols are formed by the attachment of ^{7}Be to nonradioactive aerosols.

Oki et al. (2000) employed a screen-type diffusion battery for the aerosol size analysis. And they placed an aluminum chamber in the EP2 beam line of the 12-GeV proton synchrotron at the High Energy Accelerator Research Organization (KEK). They reported that the AMAD of ^{7}Be and ^{24}Na aerosol was between 0.01 and 0.04 μm and was always larger than the MMAD of the nonradioactive aerosols. The size for radioactive aerosols was much smaller than ordinary atmospheric aerosols.

Kondo et al. (1984) found that the particle size distributions of radioactive nuclides formed in accelerator beamline tunnels and measured by using a diffusion battery is lognormal had a geometric mean radius of about 28 nm. They used a parallel plate diffusion battery and a (CNC) for collecting aerosols at the KEK 12-GeV proton synchrotron in the National Laboratory for High Energy Physics at Tsukumba-gun, Ibaraki-ken, Japan (35°42′N, 139°46′E). They examined the aerosol size distribution of ^{7}Be produced by the spallation reaction of nitrogen, N, and/or oxygen, O, atoms in air in an integrated high-energy hadron flux around the sampling inlet about 5×10^{6} particles/cm^{2} s for particles with $E \geq 30$ MeV, which decreased with increasing energy. The mean geometric radius was $\sigma_g = 0.027 \pm 0.005$ μm and for the geometric standard deviation $\log \sigma_g = 0.36 \pm 0.02$ or $\sigma_g = 2.3$. They observed that naturally occurring radioactive aerosols of radon and/or thoron decay products also have a similar size distribution, but their mean geometric radii were slightly greater than the obtained values for the ^{7}Be aerosols. They also reported that the size distribution of radioactive aerosols of fission product radionuclides due to atomic bomb tests differs in the stratosphere and troposphere depending on the characteristics of ambient nonradioactive aerosols. For the nonradioactive aerosols, the size distribution was of a lognormal shape with a mean geometric radius $\sigma_g = 0.01$ μm and for the geometric standard deviation $\log \sigma_g = 0.3$ or $\sigma_g = 2.3$, whereas the aerosol concentration was $1.5 - 4.3 \times 10^{5}$/cm^{3}.

E. Fission product radionuclide aerosols

Following an accident at a nuclear power station, great amounts of radioactive aerosols are emitted into the troposphere because airborne fission product radionuclides interact with the environment and a carrier is responsible for their long-range transport and the atmospheric diffusion. Radioactive isotopes, such as ^{103}Ru, ^{131}I, ^{132}Te, and ^{137}Cs, characterized these aerosols. The particle size of a

fission product aerosol and the distribution of fission products between particulate and vapor phases depend on the mechanism of release to the atmosphere.

In a nuclear explosion, some physicochemical fractionation of radionuclides may occur, particularly if the explosion is near the ground. Everything in the vicinity is vaporized by the heat of the explosion, but within less than a minute, the fireball cools to a temperature in the range 1000−2000°C, and refractory materials, such as metal oxides and silicates, condense to form aerosol particles (Glasstone and Dolan, 1977). Refractory fission products and plutonium are incorporated into these aerosol particles. Less refractory fission products condense later onto the surfaces of the aerosol particles. Those with gaseous precursors, e.g., ^{90}Sr and ^{137}Cs, condense, as they are formed by the decay of their parent nuclides. The refractory fission products are distributed between particles according to their mass or volume (diameter cubed). The more volatile fission products and those with volatile parents are distributed according to a power of d_p between d_p and d_p^2. Per unit mass, there is then more activity in the smaller particles. The particle size depends on the volumetric concentration of condensing material and decreases as the fireball expands. The earlier a fission product condenses, the larger the particles in which it is incorporated, and the quicker it is lost by fallout to the ground.

At distances of about 100 km from ground zero of the explosion site, the aerosol particle size of fallout ranges from a few μm to a few 100 μm. Fission products with volatile precursors are enhanced by about a factor of 2 compared with refractory fission products. The greater the fractionation, the smaller the particles (Hicks, 1982).

The fireballs created in an explosion at high altitude are very large, but no ground-based material is incorporated. So, the condensation aerosol particles are very small, with 90% of the activity in particles less than 0.3 μm in diameter (Drevinsky and Pecci, 1965). Coagulation takes place with the natural stratospheric aerosol, which is thus labeled with fission products. In the troposphere, there is further coagulation, and near ground most activity is in the 0.3−1 μm size range (Lockhart et al., 1965a). Any fractionation of fission products in the explosions is evened out by the process of coagulation, and there is no evidence of fractionation in particles sampled near ground.

1. Nuclear bomb tests

The first nuclear test was carried out by the United States in July 1945, followed by the Soviet Union in 1949, the United Kingdom in 1952, France in 1960, and China in 1964 (CTBTO web site). At that time, there were no measurements regarding the radioactive aerosol size distribution. At the beginning, there were just total dose rate reports.

Prior to 1950, only limited consideration was given to the health impacts of worldwide dispersion of radioactivity from nuclear testing. Public protests in the 1950s and concerns about the radionuclide ^{90}Sr and its effect on mother's milk and babies' teeth were instrumental in the conclusion of the Partial Test Ban Treaty (PTBT) in 1963. The PTBT banned nuclear testing in the atmosphere, outer space, and under water, but not underground, and was signed by the United States, the Soviet Union, and the United Kingdom. However, France and China did not sign and conducted atmospheric tests until 1974 and 1980, respectively.

Although underground testing mitigated the problem of radiation doses from short-lived radionuclides such as ^{131}I, large amounts of plutonium, ^{129}I, and ^{135}Cs were released underground. In addition, exposure occurred beyond the test site if radioactive gases leaked or were vented.

The United States conducted 1032 nuclear tests between 1945 and 1992: mainly at the Nevada Test Site (NTS) and at various other sites. Between 1951 and 1958, around 100 nuclear weapons tests were conducted in the atmosphere at the NTS. The average yield for the atmospheric tests was 8.6 kilotons (kt). The fallout from the tests contained radionuclides and gases, which were transported thousands of miles away from the NTS by winds. As a result, people living in the United States during these years were exposed to varying levels of radiation.

Between 1946 and 1958, the United States carried out 67 nuclear weapons tests at Bikini and Enewetak atolls in the Marshall Islands in the Pacific Ocean. Following the detonation of the 15 Mt Castle Bravo test on March 1, 1954—the most powerful nuclear device ever detonated by the United States—the fallout caused contamination over an area of more than 11,000 square km, spreading traces of radioactive material as far as Australia, India, Japan, the United States, and parts of Europe. The fallout consisted of coral rock, soil, and other debris sucked up in the fireball and made intensively radioactive by the nuclear reaction.

Between 1949 and 1989, 456 atomic and thermonuclear devices were exploded at the Semipalatinsk Test Site (STS) in Russia under conditions of tight confidentiality. Explosions were conducted on the surface and in the atmosphere. Five of the surface tests were unsuccessful and resulted in the dispersion of plutonium into the environment, with the first test on August 29, 1949, unexpectedly contaminating villages to the northeast of the STS.

The approximate cumulative explosive yield of the tests conducted before 1963, when the Soviet Union signed the PTBT, was 6.4 Mt. More than 300 test explosions were conducted underground after 1961. Between October 1961 and October 1989, 224 tests were conducted there. The last test took place on February 12, 1989, and resulted in a leakage of large amounts of the radioactive noble gases xenon and krypton.

The United Kingdom conducted 12 atmospheric tests between 1952 and 1957 on Australian territory. From 1957 to 1958, nine atmospheric tests followed over Christmas Island (Kiritimati) and Malden Island in the central Pacific Ocean, some of which were considerably more powerful than the bombs dropped on Hiroshima and Nagasaki. The remaining 24 UK nuclear tests were conducted jointly with the United States at the NTS. A major nuclear test was detonated at Emu Field in the South Australian desert on October 15, 1953, sending a radioactive cloud known as the "Black Mist" over a 250 km^2 area.

France was the fourth nation to join the "Nuclear Club" when it successfully detonated a large nuclear device in Algeria in 1960. Over the next 5 years, France conducted 17 nuclear weapons tests at two locations in Algeria: 4 were atmospheric tests and 13 were detonated underground. The total amount of ^{239}Pu dispersed as a result of the 45 announced French atmospheric tests, including the 4 in Algeria, would be about 6750 Ci, assuming 150 Ci per test. On this basis, the amount of ^{137}Cs and ^{90}Sr dispersed into the atmosphere would have been 1.7 million curies and 1.1 million curies, respectively. About one half of the cesium and strontium remains in the atmosphere, on the ground, and in water bodies. French testing in the Pacific was the source of almost all the atmospheric fission product contamination, due to the much larger number of tests and the far greater yields of the French tests there than in Algeria.

After its first test on October 16, 1964, China exploded 45 nuclear bombs at the Lop Nor site, approximately 265 km southeast of Urumqi in the Xinjiang region in western China. The 23 atmospheric and 22 underground tests ranged in yield from about 1 kt to about 4 Mt. The total amount of ^{239}Pu released to the atmosphere as a result of the 23 atmospheric nuclear tests is estimated at 3300 Ci, approximately 48 kg in weight. One millionth of a gram of ^{239}Pu can cause cancer if inhaled. A further 2 million curies of ^{137}Cs and 1.3 million curies of ^{90}Sr were released into the atmosphere.

2. The comprehensive Test Ban Treaty

The Comprehensive Test Ban Treaty (CTBT) bans all nuclear explosions on earth whether for military or for peaceful purposes. The basic obligations of the Treaty are to prohibit States Parties from carrying out any nuclear explosion. It also prohibits any encouragement of or participation in the carrying out of any nuclear explosion. The technology that provides the means to identify and prove a possible violation of the Treaty is the radionuclide technology, which is of crucial importance to the entire verification effort. The 80-station "radionuclide monitoring" network enables a continuous worldwide observation of aerosol samples of radionuclides. The network is supported by 16 radionuclide laboratories hosting expertise in environmental monitoring and providing independent additional analysis of International Monitoring System (IMS) samples.

A radionuclide particulate monitoring station contains an air sampler, detection equipment, computers, and a communication setup. At the air sampler, air is forced through a filter, which retains more than 85% of all particles that reach it. Filters are replaced daily. The used filter is first cooled for a period of 24 hours and then measured for another 24 hours in the detection device at the monitoring station. The result is a gamma-ray spectrum, which is sent to the International Data Center for further analysis.

On an experimental basis, half of all radionuclide stations (i.e., 40) are equipped with the noble gas monitoring technology to test the measuring of radionuclide noble gases released by nuclear explosions. Radioactive noble gas isotopes—in particular xenon isotopes—are among the fission products generated in a nuclear explosion. Due to their property of being inert, these xenon isotopes will not attach to debris or dust to form larger particles. They remain in their gaseous state, and some of them will seep through layers of rock and sediment until they escape into the air. Exposed to prevailing winds, they are dispersed in the atmosphere and may, after a certain period of time, be detected thousands of kilometers away from the explosion site.

Ideal radionuclide monitoring sites are windy, exposed places where the passing air really hits the air sampler used to collect particulates transported by the wind. The objective of the CTBTO's radionuclide monitoring network is to detect this residual radiation in the form of radioactive particles or noble gas, even if only in miniscule amounts.

All systems in the International Noble Gas Experiment (INGE) project work in a similar way. Air is pumped into a charcoal-containing purification device where the noble gas xenon is isolated. Contaminants of different kinds, such as dust, water vapor, and other chemical elements, are eliminated. The resulting air contains higher concentrations of xenon, in its both stable and unstable (i.e., radioactive) form. The radioactivity of the isolated and concentrated xenon is measured, and the resulting spectrum is sent to the data center in Vienna for further analysis.

3. Chernobyl accident

After the Chernobyl accident, large and highly radioactive particles were found in at least 15 European countries (Pöllänen et al., 1997). Small particles are usually composed of volatile species, such as iodine and cesium, whereas most large particles, often referred to as "hot particles," have compositions similar to those of nuclear fuel.

According to Pöllänen et al. (1997), particles > 20 μm in aerodynamic diameter were transported hundreds of

kilometers from the plant, and they were sufficiently active (>100 kBq) to cause acute health hazards. Most particles found at a large distance (>500 km) from the plant were <1 μm in diameter although coarse particles up to tens of micrometers were also found. Near the plant, particles up to hundreds of micrometers in diameter were found (Cuddihy et al., 1989; Salbu et al., 1994; Krivokhatsky et al., 1991, as cited in Pöllänen et al., 1997). Radioactive materials from Chernobyl were transported throughout Europe during the 10-day release period. After April 26, the proportion of large particles in the release plume was much smaller than during the initial stages of the accident. Particles >20 μm in aerodynamic diameter, however, were found in Hungary, Romania, Bulgaria, and Greece. Trajectory analyses show that these countries were affected during the later periods of the accident (Fig. 4.20).

Mala et al. (2013) reported for the Czech Republic the activity size distribution of man-made radionuclides after the Chernobyl accident. These radionuclides fell into two categories: refractory radionuclides (^{140}Ba, ^{140}La ^{141}Ce, ^{144}Ce, ^{95}Zr, and ^{95}Nb) and volatile radionuclides (^{134}Cs, ^{137}Cs, ^{103}Ru, ^{106}Ru, ^{131}I, and ^{132}Te). The AMAD of the refractory radionuclides was approximately three times higher than the AMAD of the volatile radionuclides; nevertheless, the size distributions for volatile radionuclides having a mean AMAD value of 0.51 μm.

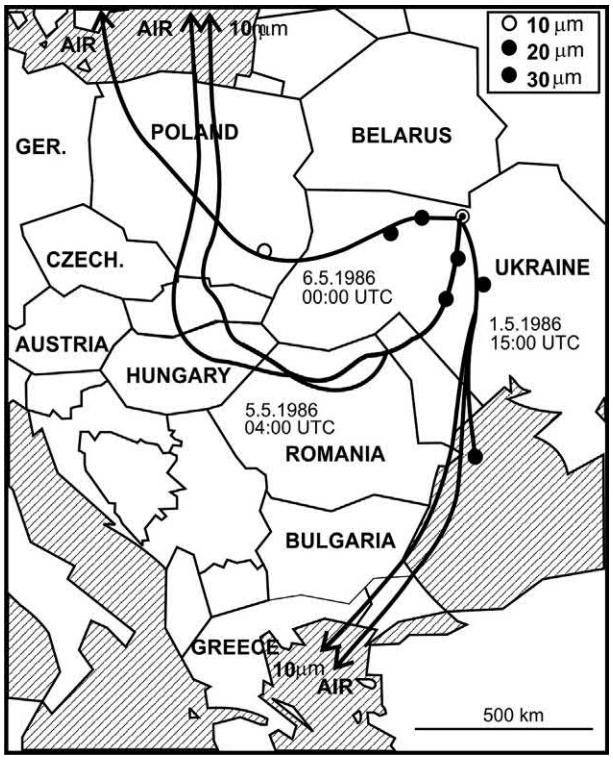


FIGURE 4.20 Route of air parcels and particles with aerodynamic diameters between 10 and 30 μm originating from Chernobyl on May 1 at 15:00 hours, May 5 at 06:00 hours, and May 6, 1986, at 00:00 hours UTC. Release height is 700 m. The trajectories for a particle 10 μm in diameter do not necessarily hit the ground due to large-scale vertical flows. The trajectories for particles 20 and 30 μm in aerodynamic diameter are terminated. *From Pöllänen et al. (1997). Printed with permission from Elsevier Copyright (1997).*

Jost et al. (1986) sampled aerosols with an Andersen impactor in Spiez, Switzerland (46°41′N, 7°39′E), from April 30 to May 13, 1986, and in Zurich, Switzerland (47°23′N, 8°32′E), from May 2 to 8, 1986, with a Berner impactor, soon after the accident. In the Spiez region, ^{131}I had a rather different activity size distribution from other fission product radionuclides, such as ^{103}Ru and ^{137}Cs. Most ^{131}I was found in the size fraction on the backup filter (<0.47 μm), whereas ^{103}Ru and ^{137}Cs showed a pronounced maximum at 0.93 μm (geometric mean diameter). In Zurich, a similar activity size distribution is shown with the maximum for ^{131}I at 0.35 μm and at 0.71 μm for ^{103}Ru, ^{132}Te, and ^{137}Cs. Different activity size distributions between the two regions were due to the different cutoff diameters of the aerosol sampling devices. The activity size distributions for ^{103}Ru, ^{132}Te, and ^{137}Cs are very similar to the concentration patterns of prominent ions, such as NH_4^-or SO_4^{2-} and NO_3^-, as determined by ion chromatography.

As iodine (^{131}I) was mainly (about 80%) present in the gas or vapor phase, the adsorption of gaseous species onto aerosol particles was strongly surface correlated (Papastefanou and Bondietti, 1987). These surface distributions for environmental aerosols usually peak at size fractions with particle diameters ≤0.4 μm (Seinfeld, 1986; Whitby et al., 1972). Therefore, it is concluded that the activity size distribution observed for ^{131}I does not reflect the primary particles released at Chernobyl but rather the surface distribution of the aerosols at the sampling sites. By contrast, ^{103}Ru, ^{131}Te, and ^{137}Cs were presumably ejected as particles or attached very early to aerosol particles and grew by coagulation with other particles during transport. It is therefore reasonable that their activity size distribution resembles that of the main inorganic ions (sulfate, nitrate, and ammonium), which may be transported also over long distances.

Bondietti and Brantley (1986) evaluated the aerodynamic sizes of the aerosol-associated fission product radionuclides from the Chernobyl accident in four aerosol samplings made during the period from May 7 to June 13, 1986, at Oak Ridge, Tennessee (35°58′N, 84°17′W), using Sierra high-volume cascade impactors and low-background intrinsic Ge coaxial and well-type detectors. The Chernobyl activity was shown to be mostly submicrometer in size, and the particle size increased significantly over the measurement period. They also observed that only a small fraction of the aerosol-associated ^{131}I was soluble in $CHCl_3$, whereas both ^{103}Ru and $^{134-137}$Cs were less soluble than natural radionuclides, indicating some association with

aerosols produced by the accident. They measured the aerosol-associated ^{131}I and its chemical composition by one cascade impactor operated from May 7 to 16, 1986 with a charcoal-impregnated final filter instead of the normal glass-fiber filter. Based on the ^{131}I activity size distributions on both charcoal-equipped and normal cascade impactors, they estimated that 40% of the airborne ^{131}I was aerosol-associated and that very little gas-to-aerosol transformation of ^{131}I occurred during its transit at long distances. The <0.41 μm aerosol ^{131}I fraction consisted of about 20% I_2, or I^- (or other $CHCl_3$-soluble species). No IO_3^- was detected. The 0.41–0.73 μm size fractions showed similar $CHCl_3$-soluble species.

Table 4.8 lists the activity mean aerodynamic diameter, AMAD, in μm, of fission product radionuclide aerosols of Chernobyl origin together with the ^7Be-associated aerosols of cosmogenic origin at Oak Ridge, Tennessee (35°58′N, 84°17′W). The particle sizes increased considerably during the measurement period. By contrast, cosmogenic ^7Be, which is initially associated with very small aerosol particles, was continually being added to the aerosol population. In the first two measurements, 2% of the fission product radionuclide aerosol particles were found to be larger than 2.1 μm, strongly suggesting the absence of any significant mechanical suspension of reactor material into the free troposphere. The behavior and sizes of the fission product radionuclides are consistent with the long-range transport of isotopes released by volatilization, which condensed on or with ambient or accident-produced aerosols. Zircon-95 or other rare-earth fission product radionuclides were not found in the aerosol samples. About 27% of the $^{134-137}Cs$ and 46% of the $^{103-106}Ru$ were not rapidly dissolved in cold 2 M HCl. This behavior was very different from what was observed for natural ^7Be, ^{210}Pb, or ^{212}Pb, which become associated with natural aerosols by surface condensation and are quite soluble. That poor solubility may indicate that some of the aerosol-associated fission product radionuclides were incorporated into reactor-derived materials, which condensed in the hot plume leaving the reactor core.

In contrast to the findings of Bondietti and Brantley (1986), Jost et al. (1986) found no increase of the AMAD, during the measurement period. They believed that this increase might not reflect the original release at Chernobyl but was due to transport effects. Apart from this, the size distribution in the fallout of nuclear weapons tests (Lockhart et al., 1965b), in contrast to the activity size distribution found in the stratosphere, is shifted toward smaller particles (Persson and Sisefsky, 1971).

Lujaniene et al. (1997) reported that the AMAD, of the soluble aerosols of ^{137}Cs of Chernobyl origin, varied in the range of 0.10–0.86 μm at Vilnius, Lithuania (54°41′N, 25°19′E), and the size of cesium radioisotopes stuck to insoluble aerosol particles in all the samples was similar (about 1 μm).

Kauppinen et al. (1986) also sampled ambient radioactive aerosols of Chernobyl origin at Helsinki, Finland (60°10′N, 24°58′E), during May 7–14, 1986, for the evaluation of the activity size distribution. They used 11-stage multijet compressible flow low-pressure Berner impactors (modified HAUKE 25/0.015 LPI) covering 0.03–0.16 μm aerodynamic diameter size range, AMAD. A Liu-type aerosol inlet was connected to the LPI inlet to minimize the effect of wind on the aspiration efficiency. Polycarbonate films of 10-μm thickness were used as impaction substrates. To prevent coarse-particle bounce, the films on the stages collecting particles greater than 1 μm were greased thinly with a uniform layer of Apiezon L-grease. The amount of grease on the film was 30–300 μg. The mass of collected particles was determined by weighing substrate films carefully before and after sampling with a microbalance. Before gravimetric analysis, the films were exposed to an ion stream generated by a polonium α-active source, to reduce the effect of electrical charge on the weighing results. Before the radioactivity analysis, the films (donut shaped, in the middle of which are the particle deposition spots) were cut into four equal pieces and laid above each other, to achieve better γ-counting geometry. As a result, the samples could be approximated with diskette geometry. The amount of radioactive isotopes in

TABLE 4.8 Activity median aerodynamic diameters (in μm) of chernobyl fission product radionuclide and cosmogenic ^7Be-aerosols measured at Oak Ridge, Tennessee (36°N).

Date	^{131}I	^{137}Cs	^{134}Cs	^{103}Ru	^{106}Ru	^{140}Ba	^7Be
May 7–16	0.37	0.40	0.40	0.37	ND	ND	0.38
May 20–23	0.32	0.48	0.43	0.44	0.44	0.45	0.39
May 30–June 3	ND	0.67	0.66	0.60	ND	ND	0.48
June 6–13	ND	0.72	0.71	0.62	ND	ND	0.36

ND, not detected or measured with >25% uncertainty.

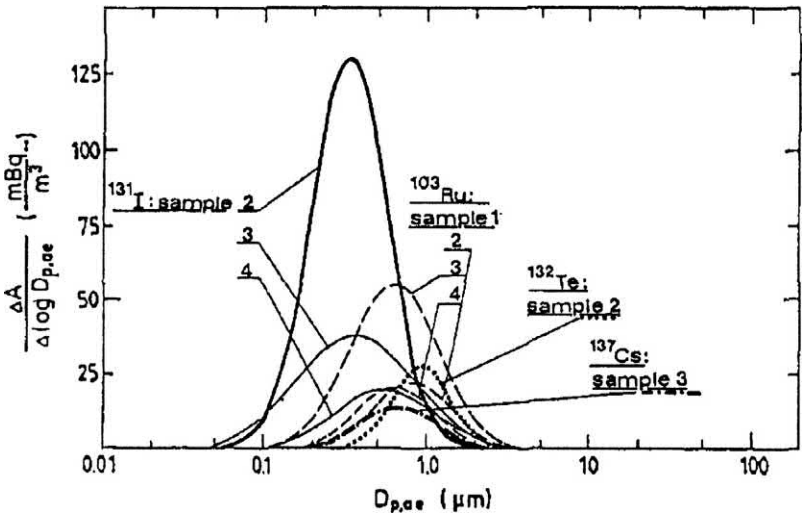


FIGURE 4.21 Activity size distribution curves of Helsinki, Finland, atmospheric aerosols. *From Papastefanou (2008). Printed with permission from Elsevier copyright (2008).*

the aerosol samples was determined by measuring their γ-spectra with a cylindrical Ge(Li) detector. During the measurements, the crystal was ventilated with aged pressurized air to reduce the iodine background.

In Fig. 4.21, the lognormal fits of ^{103}Ru, ^{131}I, ^{132}Te, and ^{137}Cs activity size distributions of four samples of Helsinki atmospheric aerosols are shown. All the activity size distributions are unimodal. The modal parameters, such as AMAD, σ_g, and the modal concentration for the accumulation mode mass and surface area size distributions (calculated from mass size distribution assuming unit density spherical particles) and for the activity size distributions, are given in Table 4.9. Iodine-131 activity size distributions differ clearly from the activity size distributions of ^{103}Ru, ^{132}Te, and ^{137}Cs. The AMAD of ^{131}I was smaller than that of ^{103}Ru, ^{132}Te, and ^{137}Cs. In two samples (samples 2 and 3), the AMAD was almost equal to the surface area mean aerodynamic diameter (SAMAD) of the accumulation mode, and in one sample (sample 4), the AMAD was equal to the MMAD, of the accumulation mode. The AMAD of ^{131}I seems to grow, whereas the AMAD of ^{103}Ru decreases, as the aerosol particles age.

Another case of radioactive aerosols associated with fission product radionuclides is that formed in the environment of nuclear power plants. Environments in the nuclear power plants are quite complex. Vaporization, condensation, fragmentation, and gas-to-particle conversion are all evolved in reactor vessels and containments.

TABLE 4.9 Geometric mean aerodynamic diameter* (DG_{ae}, in μm), geometric standard deviation (σ_g), noted as SG, and modal concentrations (*C*, in mBq/m^3) for the activity size distributions and for the accumulation mode mass and surface area sire distributions of chernobyl fission product radionuclide aerosols measured at Helsinki, Finland (60°N).

	Sample 2			Sample 3			Sample 4		
	DG_{ae}, μm	SG	*C*, mBq/m^3	DG_{ae}, μm	SG	*C*, mBq/m^3	DG_{ae}, μm	SG	*C*, mBq/m^3
Mass	0.42	1.7	20[a]	0.44	1.8	15[a]	0.57	1.9	25[a]
Surface area	0.32	1.7	321[b]	0.31	1.8	251[b]	0.38	1.9	318[b]
^{103}Ru	0.83	1.8	14	0.63	1.9	46	0.65	1.7	12
^{131}I	0.33	1.7	98	0.36	2.3	39	0.57	2.0	17
^{132}Te	0.93	~1.5	13						
^{137}Cs				0.63	1.8	9			

[a]*Accumulation mode mass concentration, μg/m^3.*
[b]*Accumulation mode surface area concentration, μm^2/cm^3.*
From Papastefanou (2008). Printed with permission from Elsevier Copyright (2008).

Practices such as sandblasting, grinding, and thermal arc cutting further complicate the situation of aerosol production and dispersion. These aerosols, however, may be grouped into several categories, e.g., the coarse mode and the accumulation mode. Coarse-mode particles with a diameter greater than about 1 μm are generally created by mechanical processes such as fragmentation. Finer particles, with a diameter <1 μm, are mostly derived from processes such as combustion and gas-to-particle conversion.

Analyses of such radioactive aerosols were performed by Yu et al. (1993) at the Chin-Shan Nuclear Power Plant, NPP, in Taiwan, consisting of a 636-MWe boiling water reactor that has been in operation since 1977. They used Andersen ambient cascade impactors (1 ACFM normal cascade impactors at an airflow rate of 28.3 L/min) with a preseparator to discriminate large particles with an aerodynamic diameter greater than 10 μm. For the segregation of smaller size aerosol particles in the accumulation mode, they applied a low-pressure adaptor to the Andersen cascade impactor. At an airflow rate of 3 L/min, the effective cutoff aerodynamic diameter of sampled aerosols by the Andersen LPI was between 0.08 and 35 μm. Fission products, including ^{131}I, ^{140}Ba, and ^{140}La, and the activation product, ^{60}Co, were the main radionuclides of the aerosols generated by sandblasting the steam turbine components. Long-lived activation products, ^{60}Co, ^{54}Mn, and ^{134}Cs, and the fission product, ^{137}Cs, constituted the major radionuclides in aerosols produced by the thermal-arc-cutting process on the waste concentration vapor body. Grinding activities on the heat-exchanger pipes produced aerosols containing mostly activated radionuclides, such as ^{60}Co and ^{54}Mn. Aerosols produced at the off-gas sump room contained mainly short-lived noble gas decay products, such as ^{88}Rb, ^{138}Cs, and ^{139}Ba.

A plot of the activity size distribution, which is a bimodal lognormal distribution for ^{137}Cs-bearing aerosols, is shown in Fig. 4.22. The AMAD of the accumulation mode is 0.29 μm and σ_g is 2.2, whereas the AMAD of the coarse mode is 3.2 μm and σ_g is 1.9. Cesium-137 could be produced directly from fission or as decay product of ^{137}Xe gaseous fission product radionuclide. The direct ^{137}Cs (fission product radionuclide) gives rise to aerosols in the coarse mode, whereas the coagulation of ^{137}Xe decay product (^{137}Cs) gives rise to aerosols in the accumulation mode. A plot of the activity size distribution for some major radionuclides associated with aerosols is shown in Fig. 4.23.

4. Fukushima accident

An earthquake of magnitude 9.0 occurred on March 11, 2011, on the Pacific Ocean side of northern Honshu, Japan, followed by a tsunami that struck the east coast of the Tohoku region and caused a serious nuclear accident at the Fukushima Daiichi Nuclear Power Plant. Emission of radioactive nuclides into the atmosphere started on March 12. The accidental releases from the Fukushima Daiichi NPP resulted in an increase in levels of artificial radioactivity in parts of the Japanese terrestrial environment and the marine environment to the east of Japan. The majority of the atmospheric releases occurred during the period from March 12 to 23, 2011 (Terada et al., 2012).

It is clear that a wide range of radionuclides are known to have been released to the atmosphere during the accident at the Fukushima Daiichi NPP (Table 4.10). Most have been detected by radiological measurements of environmental media. The fission noble gases ^{85}Kr and ^{133}Xe were released during the early phase of the accident. Nearly the entire inventories of these gases were released as a result of venting, explosions, and other events in Units 1, 2, and 3.

Very low levels of semi- and low-volatile elements were released. In particular, low-volatile gamma-emitting fission products, including isotopes of ruthenium, ^{140}Ba/^{140}La, and cerium, have not been detected at significant levels in the area around the Fukushima Daiichi NPP. During the accident, the release was mainly due to core overheating and fuel melting, without the presence of air; less volatile elements were therefore not released. Similarly, only very low levels of isotopes of strontium and the actinides, including plutonium, were released owing to the nature of the accident. This contrasts with the releases from the Chernobyl NPP, where there was an explosion at an operating reactor releasing fragments containing these less volatile elements.

Variations in the emission rates, in the physical and chemical properties of individual elements released from each of the three damaged reactors and in the changing meteorological conditions during this period, resulted in complex and heterogeneous dispersion of the radioactive material (Table 4.11). The spatial variation of deposition densities on land was further complicated by the influence of precipitation, topography, and land cover.

Following the events at the Fukushima Daiichi NPP in March 2011, the monitoring of radionuclides in the environment was increased throughout the Northern Hemisphere. The network of the CTBTO monitoring stations detected enhanced levels of isotopes of xenon, iodine, and cesium in the air. Some additional radionuclides—isotopes of tellurium, ^{140}Ba/^{140}La, ^{90}Mo/^{99m}Tc, ^{110m}Ag, and ^{111}Ag—were also detected in air samples collected across the United States and Europe. However, these measured activity concentrations were considerably (more than a thousand times) lower than the activity concentrations

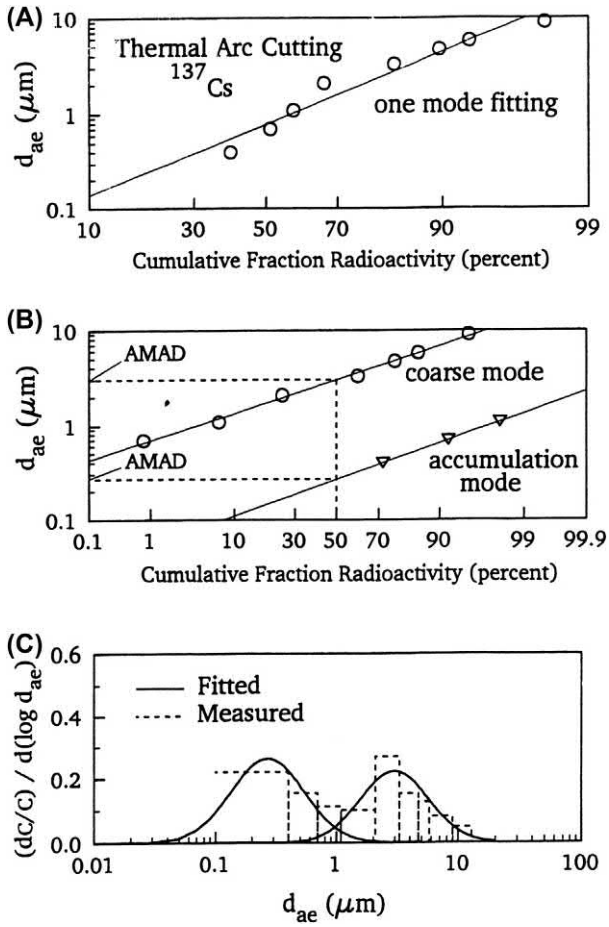


FIGURE 4.22 Activity size distribution of ^{137}Cs-bearing aerosols collected during the thermal-arc-cutting process, shown in terms of the following: (A) cumulative distribution with one mode fitting, (B) cumulative distribution with two modes fitting, and (C) differential distribution with two modes fitting solid curves are the fitting result using a lognormal function. *From Papastefanou (2008). Printed with permission from Elsevier Copyright (2008).*

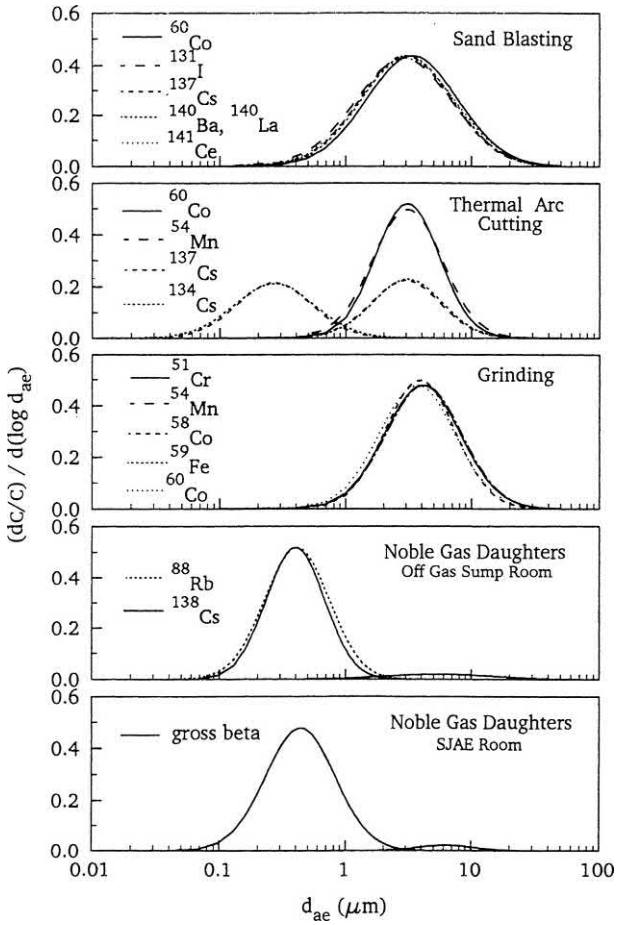


FIGURE 4.23 Fitting results of the differential activity size distribution of radioactive aerosols collected during different practices and in various environments. *From Papastefanou (2008). Printed with permission from Elsevier Copyright (2008).*

observed in Japan. Radionuclides from the releases from the Fukushima Daiichi NPP were detected in most of the countries in the Northern Hemisphere, but, as expected, there was little activity detected in the southern hemisphere, owing to the low exchange of air masses across the equator (Thakur et al., 2013).

The contaminated air masses were transported across the Pacific toward the North American continent (Bowyer et al., 2011), toward Europe (Kritidis et al., 2012; Masson et al., 2011, 2013) and Central Asia, despite dispersion and washout along the trip. Radionuclides such as ^{131}I, ^{134}Cs, and ^{137}Cs were detected in different locations throughout Europe. The first European detection from Fukushima

TABLE 4.10 Summary of release estimates for the more significant radionuclides to the environment form the Fukushima Daiichi Nuclear Power Station (IAEA, 2015).

Radionuclide	Inventory in units 1 to 3 at reactor shutdown (PBq)	Release to the atmosphere (PBq)	Release to the ocean (PBq)	
			Direct	Indirect
^{131}I	6000	100–500	About 10–20	60–100
^{137}Cs	700	6–20	3–6	5–8

TABLE 4.11 Estimated atmospheric releases of key radionuclides (PBq) (IAEA, 2015).

Nuclide	All estimates	Early estimates excluded[a]
^{131}I	90–700	100–400
^{137}Cs	7–50	7–20
^{133}Xe	500–15,000	6000–12,000

[a]*Estimated releases excluding those made in March–April 2011.*

fallout occurred between March 19 and March 20 in Iceland, between March 19 and March 21 in the northern part of Scandinavia, and between March 23 and 24 for most of the other European countries. Increasing levels were generally noticed during March 28 to March 30 in central Europe, whereas a second peak was also detected between April 3 and April 5 (Masson et al., 2011).

The observed air activity concentrations in Europe after the Fukushima accident are three to four orders of magnitude lower than activity levels encountered in Eastern Europe after the Chernobyl accident in April 1986 (Kritidis et al., 2012). In Europe, ^{134}Cs had not been measured in the atmosphere since the middle of the 1990s due to its fairly short half-life of 2.06 years, whereas ^{137}Cs was still measurable before the Fukushima accident at trace levels below 1 mBq/m^3 (Arctic Monitoring and Assessment Programme (AMAP), 2010; Masson et al., 2013). However, in soil samples, ^{137}Cs remaining from Chernobyl fallout accident and global fallout from past nuclear weapon tests is still detected.

There are numerous publications reporting the levels of contamination in various places all over the world; however, there are only few publications dealing with the size distribution of radioactive nuclides following the Fukushima accident.

There are some data on the size distribution of radioactive aerosols collected more than 1 month after the accident (Doi et al., 2013; Kaneyasu et al., 2012). Miyamoto et al. (2014) started collecting the radioactive aerosols 6 and 59 days after the accident with a low-volume cascade impactor at the JAEA-Tokai located 114 km south of the Fukushima Daiichi Nuclear Power Station. This may be the earliest size-fractionated sampling at a short distance from the site on record. Their first sampling was of 14.7 days and started on March 17, whereas the second one of 3.8 days started on May 9, 2011. They used an LPI (eight-stage with a backup filter, Tokyo Dylec, AN-200) with flow rate of 28.3 L/min, and the total sampling volume was 599 m^3 for the first sampling and 154 m^3 for the second one. The impactor was placed in a container house to avoid contamination of radioactivity in the environment. The cutoff value diameters were 11, 7.0, 4.7, 3.3, 2.1, 1.1, 0.65, and 0.43 μm. Wrapping film made of polyethylene and nylon of 14 μm in thickness was used as impaction substrates, and a glass-fiber filter (8.0 cm in diameter, T60A20, PALLFLEX Products, Co.) was used for collecting particles of <0.43 μm. For a typical aerosol of 0.3 μm in diameter, the filter collection efficiency is 96.40%.

The size distributions of ^{134}Cs, ^{136}Cs, ^{137}Cs, ^{129m}Te, ^{140}Ba, and ^{131}I in the first collection (March 2011) are presented in Fig. 4.24. The distributions of ^{134}Cs and ^{137}Cs in the second collection (May 2011) are also shown in the same figure. The AMADs of the three Cs nuclides in the first collection were the same, 1.5–1.6 μm, and there was a small peak at ~6 μm. In the second collection, the AMADs of ^{134}Cs and ^{137}Cs split into three peaks, at < 0.5 μm, 0.94 μm, and 7.8 μm. The change of diameter implies that the emission process or transportation mechanism of radioactive Cs may have changed between March and May. The AMAD of ^{131}I was 0.45 μm, and there was also a broad peak at 4 μm.

Doi et al. (2013) reported that the AMADs of ^{131}I, ^{134}Cs, and ^{137}Cs from dust samples collected at the beginning of April 2011 were 0.7 μm, 1.8 μm, and 1.5 μm, respectively. The diameter of ^{134}Cs and ^{137}Cs in their samples collected in the middle of April 2011 was 1.0 μm. Kaneyasu et al. (2012) reported the AMADs of ^{134}Cs and ^{137}Cs in dust samples collected in May 2011 were 0.54 and 0.53 μm, respectively. As noted by Kaneyasu et al. (2012), the carrier phase of radioactive Cs for the 0.5-μm size may consist of aerosols, including sulfates, whereas those for the 5- to 10-μm sizes may consist of soil particles and sea salts. Radioactive iodine including ^{131}I may be released as a gas phase and transported with fine particles of <0.5 μm in diameter, including sulfate aerosols and carbonaceous.

Masson et al. (2013) reported the size distribution of radioactive aerosol particles in many European countries (France, Austria, the Czech Republic, Poland, Germany, and Greece) immediately after the Fukushima accident. The AMAD ranged between 0.25 and 0.71 μm for ^{137}Cs, from 0.17 to 0.69 μm for ^{134}Cs, and from 0.30 to 0.53 μm for ^{131}I, thus, in the "accumulation mode" of the ambient aerosol (0.1–1 μm). The AMAD values did not show large differences from place to place compared with what was observed concerning bulk airborne levels registered on the European scale. They observed that when air masses arrived in Europe, AMADs for ^{131}I were about half those for cesium isotopes. Higher AMAD for cesium probably results from higher AMAD observed at the early stage of the accident in Japan. Lower AMAD for ^{131}I can be explained by the adsorption of gaseous iodine on particles of all sizes met during transport, especially for small particles. Additionally, weathering conditions (rain)

encountered during transport and in Europe in March and April contributed to the equilibrium of the gaseous to total ^{131}I ratio. AMAD slightly increased with time for ^{131}I, whereas a clear decreasing trend was observed with the AMADs for ^{137}Cs and ^{134}Cs. On average, the associated geometric standard deviation (GSD) appeared to be higher for iodine than for cesium isotopes. These statements also bear out a gaseous ^{131}I transfer on ambient particles of a broad size range during transport. Highest weighted activity levels were found on the 0.49−0.95 μm and on the 0.18−0.36 μm size ranges in France and in Poland, respectively. The contribution from resuspension of old deposited ^{137}Cs was assessed for the coarse particle fractions only for the first sampling week.

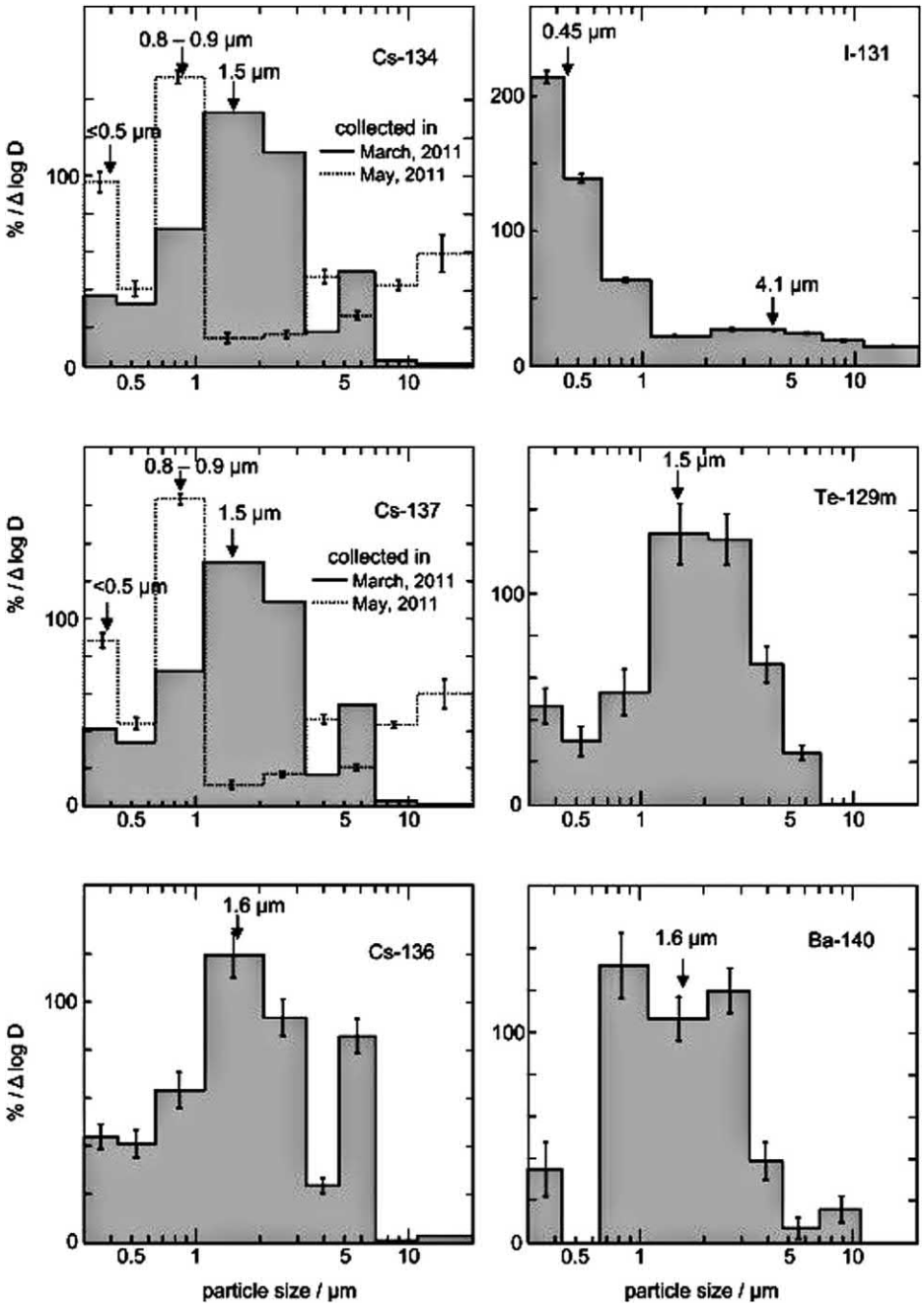


FIGURE 4.24 Activity size distribution of radionuclides. The solid lines show the distributions of the sample collected in the period of March 17−April 1, 2011, and the dotted lines show those collected in the period of May 9−13, 2011. The activity median aerodynamic diameter is also shown in each distribution. *From Miyamoto et al. (2014). Printed with permission from Elsevier Copyright (2014).*

Malá et al. (2013) reported for the Czech Republic the activity size distribution of man-made radionuclides ^{131}I, ^{134}Cs, ^{137}Cs, and natural ^{7}Be in five sets of samplings, after the Fukushima accident. All distributions were unimodal. The arithmetic means of the AMADs and GSDs of ^{131}I, ^{134}Cs, and ^{137}Cs from all sets of samplings were 0.43 μm and 3.6, respectively. The mean ^{7}Be AMAD value was 0.41 μm, and the mean GSD value was 3.0.

IV. Residence time of radioactive aerosols

The residence time of atmospheric aerosol particles in the lower atmosphere, assuming that the air in the troposphere is considered as a well-mixed reservoir (closed system), is a function of various removal processes, the most important being

1 dry deposition by impaction, diffusion, and sedimentation, and
2 wet deposition by rain drops (precipitation scavenging)

as a result of processes occurring both within and below the rain cloud. There could be variations in the removal rates at different continental locations of the globe (Lehmann and Sittkus, 1959), over the oceans (Koch et al., 1996), and at high altitudes of the atmosphere (Martell, 1970; Moore et al., 1973) due to changes in meteorological conditions. There is also a dependence of the tropospheric aerosol residence time on the latitude (Ehhalt, 1973; Balkanski et al., 1993; Koch et al., 1996).

The residence time of atmospheric aerosol particles can be estimated by means of radioactive nuclides as tracers, which become attached to aerosol particles and are removed with them as they are scavenged by precipitation or undergo dry fallout (Warneck, 1988). Several methods have been used for estimating the mean residence time of atmospheric aerosol particles. These include measurements of the activities and ratios of

(i) cosmic ray−produced radionuclides, such as ^{7}Be ($T_{1/2} = 53.3$ d) (Shapiro and Forbes-Resha, 1976; Winkler et al., 1998; Yu and Lee, 2002),
(ii) radioactive decay products of radon, ^{222}Rn, and thoron, ^{210}Rn, which emanate from continental surfaces into the atmosphere, such as ^{210}Pb ($T_{1/2} = 22.3$ y), ^{210}Bi ($T_{1/2} = 5.01$ d), and ^{210}Po ($T_{1/2} = 138.38$ d) (Francis et al., 1970; Poet et al., 1972; Lambert et al., 1982, 1983; Marley et al., 2000; Baskaran and Shaw, 2001), and
(iii) fission product radionuclides from man-made explosions from nuclear weapons testing or reactor accidents at nuclear facilities, such as ^{89}Sr ($T_{1/2} = 50.5$ d), ^{90}Sr ($T_{1/2} = 28.8$ y), and ^{140}Ba ($T_{1/2} = 12.79$ d) (Kuroda, 1982).

However, there is disagreement between the derived values of the residence times due to various processes, including the fact that they refer to different portions of the atmosphere, e.g., cosmic ray−produced radioisotopes refer to upper troposphere or lower stratosphere, such as ^{7}Be, and radon decay products, such as ^{210}Pb, ^{210}Bi, and ^{210}Po that refer to lower troposphere, and also due to the existence of different sources for some radioisotopes, such as ^{210}Po.

The collection of atmospheric aerosol particles is carried out with high-volume jet air samplers, type TFIA-2 of Staplex having glass-fiber filters type TFAGF 810 of Staplex, highly retentive for particulate material, 20.32 × 25.40 cm (8″ × 10″) in dimensions and 99.28% collection efficiency for submicron particles as small as 0.3 μm and over. The airflow rate of these samplers is regulated from 1.7 m^3/min (60 cfm) to 1.92 m^3/min (68 cfm) (average 1.84 m^3 $min^{=1}$ or 65 cfm). The length of each collection period is 24 hours. The size fractionation of atmospheric aerosol particles is carried out with aerosol cascade impactors, type Andersen 2000, as follows: (i) The 1-ACFM design is operated at an airflow rate of 28 L/min (1 ft^3/min). Its stages have ECD of 0.4, 0.7, 1.1, 2.1, 3.3, 4.7, 7.0, and 11.0 μm. (ii) The low-pressure modification, which alters the impactor's operation by increasing the resolution in the submicron region, involves a regulated airflow rate of 3 L/min, five low-pressure stages (114 mm Hg, which is the absolute pressure downstream of the critical orifice) for the submicron region, and eight atmospheric pressure stages for separating aerosol particles above 1.4 μm. The ECDs of the low-pressure stages are 0.08, 0.11, 0.23, 0.52, and 0.90 μm, whereas for the upper stages, they are 1.4, 2.0, 3.3, 6.6, 10.5, 15.7, 21.7, and 35.0 μm (iii) The high-volume cascade impactors have a regulated airflow rate either of about 0.57 m^3/min (20 cfm) or of 1.13 m^3/min (40 cfm), and the ECDs are 0.41, 0.73, 1.4, 2.1, 4.2, and 10.2 μm for the 20 cfm configuration or 0.49, 0.95, 1.5, 3.0, and 7.2 μm for the 40 cfm configuration at the standard temperature and pressure atmospheric conditions (25.0 and 760 mm Hg). The stainless steel plates supplied by the manufacturer are used for collection of the aerosol particles. Either polycarbonate or glass-fiber backup filters are used to collect all particles below the 0.08-μm collection plate for the LPIs, below the 0.4-μm collection plate for the 1 ACFM impactors, and below the 0.41-μm or 0.49-μm collection plate for the high-volume cascade impactors.

The length of each collection period varies from 1 to 24 hours for ^{7}Be, and ^{210}Pb, ^{210}Bi, and ^{210}Po, depending on impactor type and objective. The activity of ^{7}Be-associated aerosol particles is measured through its gamma-ray peak of 477.6 keV using a high-resolution (e.g., 1.9 keV at

1.33 MeV of ^{60}Co), high-efficiency (e.g., 42%), low-background HPGe detector. The uncertainty of the gamma-counting system for ^{7}Be measurements must be better than 8.5%. The activity of ^{210}Pb- and ^{210}Bi-associated aerosol particles is measured by a low-background phoswich scintillation detector system having a background of about 2 cpm and efficiency usually higher than 40% for counting beta radiation. This system is consisted of a thin CaF_2(Eu) primary crystal with a decay time of 0.23 ms. The samples are counted long enough to obtain a statistical accuracy better than 5%. It must be noted that ^{210}Pb and ^{210}Bi are chemically separated and measured for their activities. A detailed description of the analytical method and technique is established and analytically presented by Jaworowski (1963). The activity of lead-210 might also be measured by a surface barrier Ge detector through its gamma peak of 46.5 keV. The activity size distribution and the AMAD of the aerosol particles are determined upon the measurement of the activities of the aerosol-associated radioactive nuclides.

The activity aerodynamic size distribution of a sample of ^{7}Be atmospheric aerosol obtained by 1 ACFM cascade impactor is shown in Fig. 4.14 (Papastefanou and Ioannidou, 1995). The activity aerodynamic size distribution of a sample of ^{210}Pb-atmospheric aerosol obtained by a high-volume cascade impactor is shown in Fig. 4.25 (Bondietti et al., 1987).

A. Residence time of tropospheric aerosol particles associated with the cosmic ray–produced radionuclides

A method for estimating the residence time of tropospheric aerosol particles associated with the cosmic ray–produced radionuclides, such as ^{7}Be, is based on the aerosol particle growth rate, that is, the change of particle diameter with respect to time, which was estimated to be 0.004–0.005 μm/h (McMurry and Wilson, 1982), and the difference between the AMAD, of a radionuclide, e.g., ^{7}Be and the size of Aitken nuclei in the size distribution of aerosol particles, which is 0.015 μm (NRC, 1979). The AMAD of all radionuclides is in the accumulation mode of the size distribution of atmospheric aerosol particles, which ranges between 0.1 and 2.0 μm (NRC, 1979; Papastefanou and Bondietti, 1987).

Table 4.12 shows data for the AMAD, of atmospheric aerosol particles associated with ^{7}Be and ^{210}Pb atoms. Regarding the ^{7}Be-aerosols, the AMAD values varied from 0.33 to 1.18 μm (Bondietti and Brantley, 1986; Papastefanou and Ioannidou, 1995; Reineking and Porstendörfer, 1995; Winkler et al., 1998; Yu and Lee, 2002; Porstendörfer and Grundel, 2003; Papastefganou, 2009b), whereas for the ^{210}Pb aerosols, the AMAD values varied from 0.28 to 0.77 μm (Sanak et al., 1981; Reineking and Porstendörfer, 1995; Winkler et al., 1998;

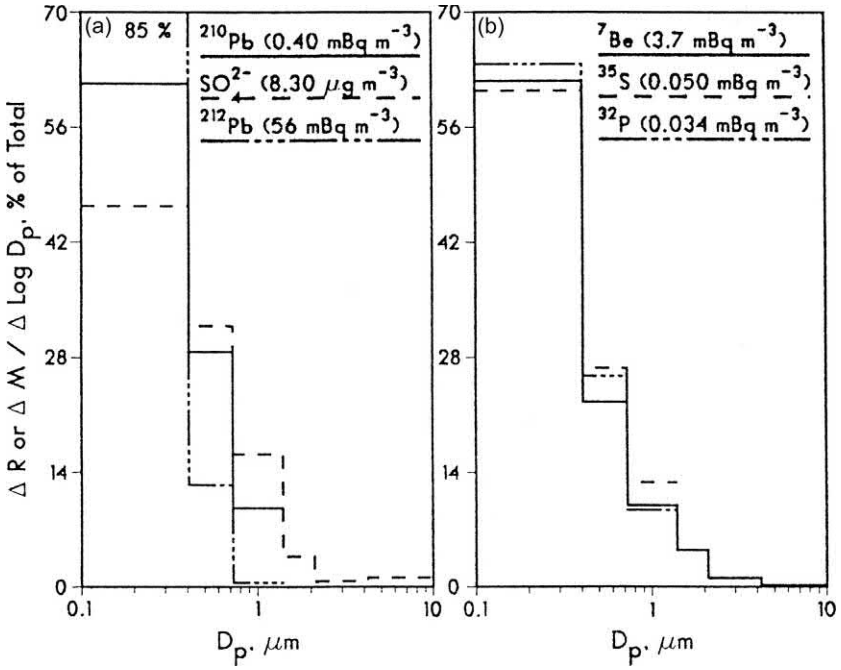


FIGURE 4.25 Aerodynamic size (Dp) distributions of radionuclides (*R*) and SO_4^- (M) derived from a 7-day aerosol sampling carried out using two high-volume cascade impactors. ^{212}Pb, ^{35}S, ^{32}P, and ^{210}Pb were only measured on three stages, < 1.4 μm. Lower D_p limits are arbitrary. *From Papastefanou (2008). Printed with permission from Elsevier Copyright (2008).*

TABLE 4.12 Activity median aerodynamic diameters (in μm) of ^{7}Be- and^{210}Pb-atmospheric aerosols.

^{7}Be	^{210}Pb	References
0.76–1.18 (avg. 0.90)	–	This work
–	0.60, 0.61 0.63, 0.77 (avg. 0.60)	Sanak et al. (1981)
0.36, 0.38, 0.39, 0.48	–	Bondietti and Brantley. (1986)
0.65–1.09 (avg. 0.77)	0.56	Reineking and Porstendő;rfer (1995)
0.44–0.74 (avg. 0.57)	0.28–0.74 (avg. 0.53)	Winkler et al. (1998)
0.33–1.15 (avg. 0.67)	–	Yu and lee (2002)
0.70	0.55	Porstendő;rfer and Grundel (2003)

From Papastefanou (2008). Printed with permission from Elsevier Copyright (2008).

Porstendörfer and Grundel, 2003). The residence time, τ_R, is described by a formula (Papastefanou and Ioannidou, 1995; Papastefganou, 2009b):

$$\tau_R = \mathrm{AMAD}_{\mathrm{mean}} - \frac{\mathrm{Size}_{\mathrm{Aitken\ nuclei}}}{\mathrm{Mean\ particle\ growth\ rate}} \qquad (4.8)$$

The residence time of atmospheric aerosol particles associated with ^{210}Pb, a decay product of soil emanated radon-222, could be determined, because ^{7}Be and ^{210}Pb have a common association with atmospheric aerosol particles (Dibb and Jaffrezo, 1993).

Residence times of tropospheric aerosols derived from ^{7}Be and ^{210}Pb concentrations in air are presented in Table 4.12. Papastefanou and Ioannidou (1995) estimated residence times for ^{7}Be aerosols varying between 7.4 and 8.9 days (average 8.0 days) with corresponding AMAD values of aerosol particles associated with ^{7}Be varying from 0.76 to 1.18 μm (average 0.90 μm) (Table 4.12) for 12 measurements of aerosol samplings carried out during a 1½-year period, thus included all seasons, at Thessaloniki region (48°38′N, 22°58′E), Northern Greece, with dry (precipitation-free) climate at temperate latitude.

Winkler et al. (1998) estimated residence times 5–6 days for ^{7}Be aerosols and 4–5 days for ^{210}Pb aerosols, in 46 measurements of aerosol samplings carried out during a 1¼-year period in ground level air at a semirural area at Neuherberg, Germany (48°13′N,11°36′E), 490 m above sea level.

Shapiro and Forbes-Resha (1976) much earlier estimated a mean tropospheric aerosol residence time for ^{7}Be-bearing aerosols of 35.4 days, significantly higher, i.e., more than four times higher, at Fullerton, California (33°52′N, 117°55′W), also at midlatitude for an almost 2-year period with relatively light precipitation.

Yu and Lee (2002) more recently estimated mean residence times for ^{7}Be-associated aerosols ranging from 2.6 to 4.8 days based on 14 measurements of aerosol samplings carried out during a 4-month period (November–March), 20 m above ground at Hong Kong (22°18′N, 114°10′E), including winter and spring measurements.

Balkanski et al. (1993) following a global three-dimensional model, which uses meteorological parameters, such as precipitation scavenging, computed residence times for ^{210}Pb aerosols in the tropospheric column of about 5 days at southern midlatitudes up to 80°S and 10–15 days in the tropics (30°S-30°N). Values at northern midlatitudes up to 80°N varied from about 5 days in winter to about 10 days in summer. The residence time of ^{210}Pb produced in the lowest 0.5 km of atmosphere is on the average four times shorter than that of ^{210}Pb produced in the upper atmosphere. They found that the tropospheric residence time is a function of latitude according to the following equation (Ehhalt, 1973):

$$\tau_R = C/\Phi \qquad (4.9)$$

where C is the tropospheric column of a radionuclide extending from the surface up to the model layer just below the tropopause, and Φ is the total depositional flux out of the column at a given latitude.

Koch et al. (1996) following a three-dimensional chemical tracer model as Balkanski et al. (1993) calculated tropospheric aerosol residence times of 9 days for ^{210}Pb aerosols at different latitudes from 80°S to 80°N. The respective residence times of ^{7}Be aerosols were 21 days reflecting the high-altitude versus low-altitude source regions of these two tracers. They also found that the tropospheric residence time is a function of latitude (Balkanski et al., 1993) according to Eq. (4.10).

The data of Table 4.13 admit residence times of tropospheric aerosols in the range 2.6–35.4 days, crowding these into two groups of values 2.6–15 days (average 8.8 days) and 21–35.4 days (average 28.2 days). The lower values are applicable only to the boundary layer near the earth's

TABLE 4.13 Residence times of tropospheric aerosols derived from ^{7}Be and ^{210}Pb activities in air (days).

Investigation	Coordinates	Period	^{7}Be	^{210}Pb	References
Thessaloniki, Greece	40°38′N, 22°58′E	November 21, 1991–June 22, 1993	7.4–8.9 (avg. 8.0)	–	This wok
Neuherberg, Germany	48°13′N, 11°36′E	December 22, 1994–March 21, 1996	5–6	4.5	Winkler et al. (1998)
Fullerton, California	33°52′ 117°55′W	September 1973–July 1975	35.4	–	Shapiro and Forbes-Resha (1976)
Hong Kong	22°18′N, 114°10′E	November 26, 2001–March 08, 2002	2.6–11.6	–	Yu and Lee (2002)
Northern hemisphere	30°N–80°N	Computed by modeling	–	5–10	Balkanski et al. (1993)
Tropics	30°S–30°N	Computed by modeling	–	10–15	Balkanski et al. (1993)
Southern hemisphere	30°S–80°S	Computed by modelling	–	5	Balkanski et al. (1993)
South to north	80°S–80°N	Calculated by modeling	21	9	Koch et al. (1996)

From Papastefanou (2008). Printed with the permission from Elsevier Copyright (2008).

surface, and the higher values are appropriate to the troposphere as a whole (Junge, 1963). Martell and Moore (1974) came to the opposite conclusion, namely, that the high values are due to the contribution of stratospheric aerosols, whereas the lower values represent the true tropospheric residence time essentially independent of altitude.

B. Residence time of tropospheric aerosol particles associated with the radon decay product radionuclides

A method for estimating the residence time of tropospheric aerosol particles associated with radon decay product radionuclides is based on the radioactivity of a pair of genetically related radioisotopes, such as ^{210}Pb, ^{210}Bi or ^{210}Pb, ^{210}Po according to the sequential disintegrations in the beta decay scheme, as

$$^{210}\mathrm{Pb} \xrightarrow{\beta^-,\ 22.3\ \mathrm{y}} {}^{210}\mathrm{Bi} \xrightarrow{\beta^-,\ 5.01\ \mathrm{d}} {}^{210}\mathrm{Po} \xrightarrow{\alpha,\ 138.38\ \mathrm{d}} {}^{206}\mathrm{Pb}\ (\mathrm{stable})$$

The residence time, τ_R, is described be the formulas (Papastefanou, 2009a)

$$\tau_R = {}^{1}/_{\lambda_{\mathrm{Bi}}} \cdot \frac{\lambda_{\mathrm{Bi}} N_{\mathrm{Bi}}/\lambda_{\mathrm{Pb}} N_{\mathrm{Pb}}}{1 - (\lambda_{\mathrm{Bi}} N_{\mathrm{Bi}}/\lambda_{\mathrm{Pb}} N_{\mathrm{Pb}})} \tag{4.10}$$

where $\lambda_{\mathrm{Bi}} \cdot N_{\mathrm{Bi}}$ is the activity of ^{210}Bi, $\lambda_{\mathrm{Pb}} \cdot N_{\mathrm{Pb}}$ is the activity of ^{210}Pb in air, and $\lambda_{\mathrm{Bi}} = 0.138\ \mathrm{d}^{-1}$ is the decay constant of ^{210}Bi. Eq. (4.10) is derived from the equation of the production and removal of radionuclides assuming steady-state equilibrium:

$$\frac{dN_{\mathrm{Bi}}}{dt} = \lambda_{\mathrm{Pb}} N_{\mathrm{Pb}} - (\lambda_{\mathrm{Bi}} + \lambda_{\mathrm{R}}) N_{\mathrm{Bi}} = 0 \tag{4.11}$$

where $\lambda_{\mathrm{R}} = 1/\tau_{\mathrm{R}}$ is the first-order rate constant for removal of aerosols from the atmosphere by all processes, that is, the inverse of residence time, τ_R. The ratio of the activities $\lambda_{\mathrm{Bi}} \cdot N_{\mathrm{Bi}}/\lambda_{\mathrm{Pb}} \cdot N_{\mathrm{Pb}}$ in Eq. (4.10) varied from 0.42 to 0.85 (Moore et al., 1972).

If the activity of ^{210}Po, $\lambda_{\mathrm{Po}} \cdot N_{\mathrm{Po}}$ is considered and $\lambda_{\mathrm{Po}} = 5.0\ 10^{-3}\ \mathrm{d}^{-1}$ is the decay constant of ^{210}Po, then the activity ratio of ^{210}Po and ^{210}Pb is given by the equation (Papastefanou, 2009a)

$$\frac{\lambda_{\mathrm{Po}} \cdot N_{\mathrm{Po}}}{\lambda_{\mathrm{Pb}} \cdot N_{\mathrm{Pb}}} = \frac{\tau_R^2}{(\tau_R + 1/\lambda_{\mathrm{Bi}}) \cdot (\tau_R + 1/\lambda_{\mathrm{Po}})} \tag{4.12}$$

from which the residence time, τ_R, is determined as

$$\tau_R = \frac{-b + (b^2 - 4ac)^{1/2}}{2a} \tag{4.13}$$

where

$$\begin{aligned} a &= \lambda_{\mathrm{Pb}} \cdot N_{\mathrm{Pb}} - \lambda_{\mathrm{Po}} \cdot N_{\mathrm{Po}} \\ b &= -\lambda_{\mathrm{Po}} \cdot N_{\mathrm{Po}} (1/\lambda_{\mathrm{Bi}} + 1/\lambda_{\mathrm{Po}}) \\ c &= -\lambda_{\mathrm{Po}} \cdot N_{\mathrm{Po}} \cdot \frac{1}{\lambda_{\mathrm{Bi}} \cdot \lambda_{\mathrm{Po}}} \end{aligned} \tag{4.14}$$

$$\lambda_{\mathrm{Bi}} = 0.138\ \mathrm{d}^{-1} \text{ and } \lambda_{\mathrm{Po}} = 5 \times 10^{-3}\ \mathrm{d}^{-1}$$

The ratio of the activity $\lambda_{\mathrm{Po}} \cdot N_{\mathrm{Po}}/\lambda_{\mathrm{Pb}} \cdot N_{\mathrm{Pb}}$ in Eq. (4.12) varied between 0.054 and 0.092 (Moore et al., 1972).

The residence time, τ_R, can also be determined through the ratio of activities of radon, ^{222}Rn, $\lambda_{\mathrm{Rn}} \cdot N_{\mathrm{Rn}}$ and ^{210}Pb, $\lambda_{\mathrm{Pb}} \cdot N_{\mathrm{Pb}}$ in air according to the sequential equation disintegrations in the alpha and beta decay scheme as:

$$^{222}\mathrm{Rb} \xrightarrow{\alpha,\ 3.824\ \mathrm{d}} {}^{218}\mathrm{Po} \xrightarrow{\alpha,\ 3.05\ \mathrm{m}} {}^{214}\mathrm{Pb} \xrightarrow{\beta^-,\ 26.8\ \mathrm{m}} {}^{214}\mathrm{Bi}$$

$$\xrightarrow{\beta^-,\ 19.7\mathrm{m}} {}^{214}\mathrm{Po} \xrightarrow{\alpha,\ 163\ \mu\mathrm{s}} {}^{210}\mathrm{Pb} \xrightarrow{\beta^-,\ 22.3\ \mathrm{y}}$$

and Eq. (4.11) by the formula (Papastefanou, 2009a)

$$\tau_R = \frac{1}{\lambda_{\mathrm{Pb}}} \cdot \frac{1}{\frac{\lambda_{\mathrm{Rn}} \cdot N_{\mathrm{Rn}}}{\lambda_{\mathrm{Pb}} \cdot N_{\mathrm{Pb}}} - 1} = \frac{1}{\lambda_{\mathrm{Pb}}} \cdot \frac{\lambda_{\mathrm{Pb}} \cdot N_{\mathrm{Pb}}}{\lambda_{\mathrm{Rn}} \cdot N_{\mathrm{Rn}}} \tag{4.15}$$

where $\lambda_{\mathrm{Pb}} = 8.5 \times 10^{-5}\ \mathrm{d}^{-1}$ is the decay constant of ^{210}Pb and $\frac{\lambda_{Rn} \cdot N_{Rn}}{\lambda_{Pb} \cdot N_{Pb}} \gg 1$.

The ratio of the activities $\lambda_{\mathrm{Rn}} \cdot N_{\mathrm{Rn}} / \lambda_{\mathrm{Pb}} \cdot N_{\mathrm{Pb}}$ in Eq. (4.15) varied from 282 to 7700 (Moore et al., 1972).

Residence times of tropospheric aerosols derived from ^{210}Bi/^{210}Pb, ^{210}Po/^{210}Pb, and ^{222}Rn/^{210}Pb activity ratios in air are presented in Table 4.14.

Papastefanou and Bondietti (1991) estimated tropospheric aerosol residence times ranging from 4.8 to 15.3 days (average 8.2 days) based on the ^{210}Bi/^{210}Pb activity ratios for 21 measurements of aerosol samplings carried out during an annual period at Oak Ridge, Tennessee (35°58′ N, 84°17′ W), at temperate latitude with high precipitation (wet climate).

Poet et al. (1972) estimated tropospheric aerosol residence times ranging from 1.59 to 13 days (average 5.4 days) when based on the ^{210}Bi/^{210}Pb activity ratios and from 11 to 77 days (average 24 days) when based on the ^{210}Po/^{210}Pb activity ratios for 20 measurements of aerosol samplings carried out in surface air during a 4½-year period at Boulder, Colorado (40°01′N, 105°17′W). They concluded that a mean tropospheric residence time of about 4 days could be applied for aerosol particles in the lower troposphere and about a week for aerosol particles in precipitation. They also found that the mean aerosol residence time increases with altitude within the troposphere by a factor of less than 3 (Moore et al., 1973).

Francis et al. (1970) estimated a mean atmospheric residence time for ^{210}Pb of 9.6 days ± 20% based on the ^{210}Po/^{210}Pb activity ratios from the dust of filtrate (larger than 0.22 μm in diameter) collected during a 3-month period (May−August) at Madison, Wisconsin (43°05′N, 89°22′W).

Marley et al. (2000) estimated residence times for seven aerosol samples collected at Argonne, Illinois (41.7°N, 88.0°W) during a 2-year period, three aerosol samples collected at Phoenix, Arizona, one sample collected at Socorro, New Mexico, and five samples collected at Mexico City, Mexico. Based on the ^{210}Bi/^{210}Pb activity ratios, they resulted in residence times of 6−67 days, whereas the ^{210}Po/^{210}Pb activity ratios suggested residence times of 33−66 days for the aerosols below 2 μm in size.

Much earlier, Fry and Menon (1962) in 12 measurements carried out during a 7-month period (spring and summer) at Fayetteville, Arkansas (36°03′N, 78°54′W), indicated apparent aerosol residence times ranging from 2.4 to 25.6 days (average 8.5 days), based on the ^{210}Bi/^{210}Pb activity ratios in Arkansas rains. Gavini et al. (1974) also estimated residence times varied from 3 to 240 days (average 29 days) from ^{210}Bi/^{210}Pb activity ratios and from 2 to 320 days (average 40 days) from ^{210}Po/^{210}Pb activity ratios in Arkansas rains.

Baskaran and Shaw (2001) based on ^{210}Po/^{210}Pb activity ratios estimated residence times of arctic haze aerosols, from the upper atmosphere to the arctic atmosphere varied between 12 and 32 days from two measurements carried out during an 1½-year period (winter) at Poker Flat (65.1°N, I47.5°W) and between 0 and 39 days from eight measurements carried out during a 2-month period (winter) at Eagle (69.5°N, 141.2°W) in Alaska.

Very early, Lehmann and Sittkus (1959) estimated aerosol residence times of 20 days from ^{210}Po/^{210}Pb activity ratios in air at Freiburg, Germany (47°59′N, 7°51′E), whereas Peirson et al. (1966) estimated aerosol residence times of 40 days from ^{210}Po/^{210}Pb activity ratios in air at Milford Haven, Wales (51°40′N, 5°02′E).

Lambert et al. (1982) estimated aerosol residence times varied from 8.8 to 10.5 days based on the ^{210}Bi/^{210}Pb activity ratios in air, whereas later in another work, they estimated aerosol residence times varied from 7 to 9 days (average 8.58 days) based on the ^{210}Bi/^{210}Pb activity ratios in air, near the Paris area during a 6-year period (Lambert et al., 1983)

Gäggeler et al. (1995) during a 1-year period carried out measurements on the activities of ^{214}Pb, ^{210}Pb, and ^{212}Pb in air at high altitude in Jungfraujoch, Switzerland (46°32′N, 07°59′E) as high as 3450 m with an epiphaniometer. They estimated aerosol residence times varied between 1 and 12 days (average 6 days) from the ^{214}Pb/^{210}Pb activity ratios.

Rangarajan (1992), based on the ^{210}Bi/^{210}Pb activity ratios in air, estimated a mean residence time of the natural radioactive aerosols in the planetary boundary layer at Bombay, India (18°58′N, 72°50′E) around 8 days from 43 measurements carried out during the long dry period, October to May.

The data of Table 4.14 display residence times of lower values, as low as 1.59 days, and higher values, as high as 320 days. Mostly, the lower τ_R values were determined from the ^{210}Bi/^{210}Pb activity ratios and higher τ_R values from the ^{210}Po/^{210}Pb activity ratios. Low τ_R values were also determined from the ^{222}Rn/^{210}Pb activity ratios.

Poet et al. (1972) concluded that longer apparent residence time values for τ_R based on the ^{210}Po/^{210}Pb activity ratios than for τ_R based on the ^{210}Bi/^{210}Pb activity ratios. The difference may be explained by the presence of a mixture of aerosols of various apparent ages, of which older aerosols (those of greater age) contribute most of ^{210}Po. On

TABLE 4.14 Residence times of tropospheric aerosols derived from $^{210}Bi/^{210}Pb$, $^{210}Po/^{210}Pb$, $^{222}Rn/^{210}Pb$, $^{89}Sr/^{90}Sr$, and $^{140}Ba/^{90}Sr$ activity ratios in air (days).

Investigation	Coordinates	Period	$^{210}Bi/^{210}Pb$	$^{210}Po/^{210}Pb$	$^{222}Rn/^{210}Pb$	References
Oak Ridge, Tennessee	35°58′N, 84°17′W	October 15, 1984–September 16, 1985	4.8–15.3 (avg. 8.2)	–	–	This work
Boulder, Colorado	40°01′N, 105°17′W	September 05, 1967–January 02, 1972	1.59–1.30 (avg. 5.4)	11–77	2.2–3.4	Poet et al. (1972), Moore et al. (1972, 1973)
Argonne, Illinois	41.7°N, 88.0°W	June 1996–August 1996	6–67	33–66	–	Marley et al. (2000)
Madison, Wisconsin	43°51′N, 89° 22′W	June 01, 1966–August 16, 1966	–	9.6	–	Francis et al. (1970)
Fayetteville, Arkansas	35°03′N, 78°54′W	February 02, 1961–August 23, 1961	2.4–25.6 (avg. 8.5)	–	–	Fry and Menon (1962)
Fayetteville, Arkansas	35°03′N, 78°54′W	April 09, 1973–April 18, 1974	3–240 (avg. 20)	2–320 (avg. 40)	–	Gavini et al. (1974)
Poker Flat, Alaska	65.1°N, 147.5°W	January 08, 1996–February 26, 1996	–	11.9–32	–	Baskaran and Shaw (2001)
Eagle, Alaska	69.5°N, 141.2°W	January 10, 1996–March 15, 1996	–	0–38.9	–	Baskaran and Shaw (2001)
Jungfraujoch, Switzerland	46°32′N, 07°59′E	January 1991–December 1991	–	1–12 (avg. 6)	–	Gaggeler et al. (1995)
Freiburg, Germany	47°59′N, 7°51′E	–	–	20	–	Lehmann and Sittkus (1959)
Gif-sur-Yvette, France	48°52′N, 2°20′E	1978–83	8.8–10.5 7–9	–	6.5 6.77	Lambert et al. (1982, 1983)
Milford Haven, Wales	51°40′N, 5°02′W	–	–	40	–	Peirson et al. (1966)
Bombay, India	18°58′N, 72°50′E	October 1987–May 1988	8	–	–	Rangarajan (1992)
El-Minia, Egypt	28°N, 30°45′E	January 1999–December1999	4.3–12.87 (avg. 9.83)	–	–	Ahmed et al. (2000)

From Papastefanou (2008). Printed with the Permission from Elsevier Copyright (2008).

the other hand, the solid products of radon-222 decay, that is ^{210}Pb, ^{210}Bi, and ^{210}Po, might arise from sources other than radioactive decay within the atmosphere. Poet et al. (1972) showed that up to 85% of ^{210}Po in the atmosphere is of terrestrial origin, and the vertical profile of ^{210}Po was found to differ appreciably from that expected from the decay of ^{222}Rn.

Lambert et al. (1979) indicated that volcanic gases are very rich in long-lived radon decay products, especially in ^{210}Po relative to ^{210}Pb. Soil particles are the most likely contributors, since a part of the tropospheric aerosols originates at the earth's surface. Coal burning and forest fires presumably are additional sources of radionuclides.

Dlugosz et al. (2010) calculated aerosol residence times from the ^{210}Po/^{210}Pb ratio ranging from 7 to 120 days in the urban air of Lodz, Poland.

C. Residence time of tropospheric aerosol particles associated with the fission product radionuclides

Apart from the activity ratios of the radon-222 decay product radionuclides, the residence time of tropospheric aerosols could be derived from the activity ratios of the fission product radionuclides released into the atmosphere during the explosions from nuclear weapons testing or nuclear reactor accidents, such as ^{89}Sr/^{90}Sr and ^{140}Ba/^{90}Sr. These isotopic ratios were considered as nuclear clocks. The applicability of the radioisotope ratios depends on the steady-state conditions held at the time and place of measurements and the kind of the sample whether they are surface air or precipitation (rain or snow) for the radioisotope activity determination.

Kuroda (1982) following the 22nd, 23rd, and 24th Chinese Weapons Tests at Lop Nor Desert (40°N, 90°E) of September 17, 1977, March 13, 1978, and December 14, 1978, respectively, calculated mean residence times of ^{90}Sr based on the ^{89}Sr/^{90}Sr and ^{140}Ba/^{90}Sr activity ratios in atmospheric precipitation in the corresponding period at Fayetteville, Arkansas (35°03′N, 78°54′W), where the nuclear debris passed over there for the second time, ranging from 5 to 12 days and 6 to 11 days. The difference in the mean residence times may be attributable to the difference in the average particle-size distributions of th`e debris, which passed over Fayetteville, Arkansas, for the first and second time. It is likely that large fallout particles were removed from the atmosphere more rapidly than smaller particles, and hence the nuclear debris that arrived at Fayetteville for the second time consisted of finer particles than that arrived earlier, and hence the mean residence time for the former was longer than for the latter.

Kristiansen et al. (2012) using a unique high-precision global measurement data set collected over several months after the accident at the Fukushima Dai-ichi nuclear power plant in March 2011 estimated the removal times of radioactive nuclides from the atmosphere. The noble gas ^{133}Xe released during the accident served as a passive tracer of air mass transport for determining the removal times of ^{137}Cs and ^{131}I via the decrease in the measured ratios ^{137}Cs/^{133}Xe and ^{131}I/^{133}Xe over time. After correction for radioactive decay, the ^{137}Cs/^{133}Xe ratios reflect the removal of aerosols by wet and dry deposition, whereas the ^{137}Cs/^{133}Xe ratios are also influenced by aerosol production from gaseous ^{131}I. The estimated removal times for ^{137}Cs were 10.0−13.9 days and for ^{131}I were 17.1−24.2 days, respectively, during April and May 2011. The removal time of ^{131}I is longer due to the aerosol production from gaseous ^{131}I; thus the removal time for ^{137}Cs serves as a better estimate for aerosol lifetime. The removal time of ^{131}I is of interest for semivolatile species.

The values of mean residence times based on the ^{210}Bi/^{210}Pb activity ratios, 2−78 days, and ^{210}Po/^{210}Pb activity ratios, 9−243 days (Table 4.14), are much greater than the values of the residence times obtained from the fission product radionuclide activity ratios. The differences are real and are attributable to the fact that, while the fresh fission product radionuclides were injected by the Chinese 22nd, 23rd, and 24th tests almost exclusively into the troposphere, the radon decay product radionuclides found in rain are mixtures of two different components: tropospheric and stratospheric. The radon decay products in the lower stratosphere are descending rapidly during the winter and mixing with the tropospheric component, whereas such a mixing process is occurring less frequently in summer and fall periods (Kuroda et al., 1978).

It is interesting to speculate on the following sequence of events: suppose that a large quantity of nuclear debris was injected into the stratosphere during the fall period. A large concentration of fission product radionuclides with an apparent "age" of several months will be located in the lower stratosphere during the early spring months of the following year. Now, suppose that these fission product radionuclides were brought down by a violent storm, which penetrated the tropopause (Dingle, 1965). If a mixture of radon decay product radionuclides, whose apparent "age" was also several months (Burton and Stewart, 1960), was located in the lower stratosphere together with the fission product radionuclides, approximately concordant residence times should be obtained from the ^{89}Sr/^{90}Sr and ^{210}Po/^{210}Pb activity ratios in rainwater at the ground level.

References

Ahmed, A.A., Mohammed, A., Ali, A.A., El-Hussein, A., Barakat, A., 2000. A study on aerosol residence time in El-Minia, Egypt. J. Aerosol Sci. 31 (S1), 470−471.

Aitken, J., 1923. In: Knott, C.G. (Ed.), Collected Scientific Papers of John Aitken. L.L.D., F.R.S. Cambridge University Press, London, p. 591.

Andersen, A.A., 1976. 1-ACFM Ambient Particles Sizing Samplers. Andersen Inc., Atlanta, GA, p. 21.

Andersen, A.A., 1984. Low-Pressure Impactor. Technical Manual. Andersen Samplers, Inc., Atlanta, GA, p. 29.

Balkanski, P.J., Jacob, D.J., Gardner, G.M., Graustein, W.C., Turekian, K.K., 1993. Transport and residence times of tropospheric aerosols inferred from a global three-dimensional simulation of Pb. J. Geophys. Res. 98 (D11), 20573–20586. https://doi.org/10.1029/93JD02456.

Barrett, J.C., Clement, C.F., Virdee, A.B.S., 2009. The removal of radioactive aerosols by electric fields. J. Aerosol Sci. 40, 185–192.

Baskaran, M., Shaw, G.E., 2001. Residence time of arctic haze aerosols using the concentrations and activity ratios of ^{210}Po, ^{210}Pb and ^{7}Be. J. Aerosol Sci. 32, 443–452.

Becker, K.H., Reineking, A., Scheibel, H.G., Porstendörfer, J., 1984. Radon daughter activity size distributions. Radiat. Prot. Dosim. 7, 147–150.

Berner, A., Lurzer, C., 1980. Mass distributions of traffic aerosols at Vienna. J. Phys. Chem. 84, 2079–2083.

Biswas, P., Flagan, R.C., 1988. The particle trap impactor. J. Aerosol Sci. 19, 113–121.

Bolsunovsky, A., Dementyev, D., 2011. Evidence of the radioactive fallout in the center of Asia (Russia) following the Fukushima nuclear accident. J. Environ. Radioact 102 (11), 1062–1064.

Bondietti, E.A., Brantley, J.N., 1986. Characteristics of Chernobyl radioactivity in Tennessee. Nature 322, 313–314.

Bondietti, E.A., Brantley, J.N., Rangarajan, C., 1988. Size distributions and growth of natural and Chernobyl-derived submicron aerosols in Tennessee. J. Environ. Radioact. 6, 99–120.

Bondietti, E.A., Hoffmann, F.O., Larsen, L.L., 1984. Air-to-vegetation transfer rates of natural submicron aerosols. J. Environ. Radioact. 1, 5–27.

Bondietti, E.A., Papastefanou, C., Rangarajan, C., 1987. Aerodynamic size associations of natural radioactivity with ambient aerosols. In: Radon and its Decay Products: Occurrence, Properties, and Health Effects. American Chemical Society, Washington, D.C., pp. 377–397. ACS Symposium Series No. 331.

Bowyer, T.W., Biegalski, S.R., Cooper, M., Eslinger, P.W., Haas, D., Hayes, J.C., Miley, H.S., Strom, D.J., Woods, V., 2011. Elevated radioxenon detected remotely following the Fukushima nuclear accident. J. Environ. Radioact. 102 (7), 681–687.

Bruninx, E., 1961. High-energy Nuclear Reaction Cross-Sections. I. CERN Report 61e1, Geneva, Switzerland.

Bruninx, E., 1964. High-energy Nuclear Reaction Cross-Sections. III. CERN Report 64e17, Geneva, Switzerland.

Burton, W.M., Stewart, N.G., 1960. Use of long-lived natural radioactivity as an atmospheric tracer. Nature 186, 584–589.

Cantrell, B.K., Zeller, H.W., Williams, K.L., Cocalis, J., 1987. Monitoring and Measurement of In-Mine Aerosol: Diesel Emissions, vol. 9141. Bu Mines IC, Washington, DC, pp. 18–40.

Charalambous, S., Rindi, A., 1967. Aerosol and dust radioactivity in the halls of high-energy accelerators. Nucl. Instrum. Meth. 56, 125–135.

Chen, B.T., Yeh, H.C., Cheng, Y.S., 1986. Performance of a modified virtual impactor. Aerosol Sci. Technol. 5, 369–376.

Cho, Y.H., Lee, W., Chung, K.H., Choi, G.S., Lee, C.W., 2007. Seasonal variation and activity size distribution of 7Be in ambient air. J. Radioanal. Nucl. Chem. 274 (3), 531–538.

Clark, W.E., Whitby, K.T., 1967. Concentration and size distribution measurements of atmospheric aerosols and a test of the theory of self-preserving size distributions. J. Atmos. Sci. 24, 677–687.

Clement, C.F., Harisson, R.G., 1992. The charging of radioactive aerosols. J. Aerosol Sci. 23, 481–504.

Clement, C.F., Harisson, R.G., 2000. Enhanced localised charging of radioactive aerosols. J. Aerosol Sci. 31, 363–378.

Clement, C.F., Clement, R.A., Harisson, R.G., 1995. Charge distributions and coagulation of radioactive aerosols. J. Aerosol Sci. 26, 1207–1225.

Copley Scientific Brochure, 2019. https://www.copleyscientific.com/files/ww/brochures/Inhaler%20Testing%20Brochure%202019_Low%20%20Res.pdf.

Cuddihy, R.G., Finch, G.L., Newton, G.J., Hahn, F.F., Mewhinney, J.A., Rothenberg, S.J., Powers, D.A., 1989. Characteristics of radioactive particles released from the Chernobyl nuclear reactor. Environ. Sci. Technol. 23, 89–95.

Dankelman, V., Reineking, A., Porstendörfer, J., 2001. Determination of neutralisation rates of 218Po ions in air. Radiat. Prot. Dosim. 94, 353–357.

Dibb, J.E., Jaffrezo, J.-L., 1993. Beryllium-7 and Lead-210 in aerosol and snow in the dye 3 gas, aerosol and snow sampling program. Atmos. Environ. 27A, 2751–2760.

Dingle, A.N., 1965. Stratospheric trapping by intense convective storms: implication for public health in the United States. Science 148, 227–229.

Dlugosz, M., Grabowski, P., Bem, H., 2010. ^{210}Pb and ^{210}Po radionuclides in the urban air of Lodz, Poland. J. Radioanal. Nucl. Chem. 283, 719–725.

Doi, T., Masumoto, K., Toyoda, A., Tanaka, A., Shibata, Y., Hirose, K., 2013. Anthropogenic radionuclides in the atmosphere observed at Tsukuba: characteristics of the radionuclides derived from Fukushima. J. Environ. Radioact. 122, 55–62.

Dorrian, M.D., Bailey, M.R., 1996. Particle size distribution of radioactive aerosol measured in the workplace and the environment. J. Aerosol Sci. 27 (Suppl. I), S439–S440.

Drevinsky, P.J., Pecci, J., 1965. Size and vertical distributions of stratospheric radioactive aerosols. In: Klement Jr., A.W. (Ed.), Radioactive Fallout from Nuclear Weapons Tests. U.S. Department of Commerce, Springfield, VA. CONF 765.

Dzubay, T.G., Rickel, D.G., 1978. In: Russel, P.A., Hutchings, A.E. (Eds.), Electron Microscopy and X-Ray Application. Ann Arbor Science, Ann Arbor, Michigan, pp. 3–209.

Ehhalt, D.H., 1973. Turnover times of 137Cs and HTO in the troposphere and removal rates of natural particles and water vapor. J. Geophys. Res. 78, 7076–7086.

Francis, C.W., Chesters, G., Haskin, L.A., 1970. Determination of ^{210}Pb mean residence time in the atmosphere. Environ. Sci. Technol. 4 (7), 586–589.

Friedlander, S.K., 1961. Theoretical considerations for the particle size spectrum of the stratospheric aerosol. Am. Meteor. Soc. J. Meteor. 18, 753–759.

Fry, L.M., Menon, K.K., 1962. Determination of the tropospheric residence time of lead-210. Science 137, 994–995.

Gaggeler, H.W., Jost, D.T., Baltensperger, U., Schwikowski, M., 1995. Radon and thoron decay product and ^{210}Pb measurements at Jungfraujoch, Switzerland. Atmos. Environ. 29 (5), 607–616.

Gavini, K.B., Beck, J.N., Kuroda, P.K., 1974. Mean residence times of the longlived radon daughters in the atmosphere. J. Geophys. Res. 79, 4447–4452.

Gaziev, Y.I., Malakhov, S.G., Nazarov, L.E., Silantiev, A.N., 1966. The size distribution of radioactive particles from nuclear weapons tests and their transport in the atmosphere. Tellus 18, 474–485.

George, A.C., Breslin, A.J., 1980. The distribution of ambient radon and radon daughters in residential buildings in the New Jersey and New

York area. In: Natural Radiation Environment III, vol. 2. National Technical Information Service, Springfield, VA, pp. 1272−1292. CONF-780422.

George, A.C., Knutson, E.O., Sinclair, D., Wilkening, M.H., Andrews, L., 1984. Measurement of radon daughter aerosols in Socorro, New Mexico. Aerosol Sci. Technol. 3, 277−281.

Gini, M.I., Helmis, C.G., Eleftheriadis, K., 2013. Cascade Epiphaniometer: an instrument for aerosol "Fuchs" surface area size distribution measurements. J. Aerosol Sci. 63, 87−102.

Gini, M.I., Helmis, C., Melas, A.D., Papanastasiou, D., Orfanopoulos, G., Giannakopoulos, K.P., Drossinos, Y., Eleftheriadis, K., 2016. Characterization of carbon fractal-like aggregates by size distribution measurements and theoretical calculations. Aerosol Sci. Technol. 50 (2), 133−147.

Glasstone, S., Dolan, P.J., 1977. The Effect of Nuclear Weapons. U.S.Department of Defense, Springfield, VA.

Grundel, M., Porstendörfer, J., 2004. Differences between the activity size distributions of the different natural radionuclide aerosols in outdoor air. Atmos. Environ. 38, 3723−3728.

Hicks, H.G., 1982. Calculation of the concentration of any radionuclide deposited on the ground by offsite fallout from a nuclear detonation. Health Phys. 46, 585−610.

Hinds, W.C., 1999. Aerosol Technology. Properties, Behaviour, and Measurement of Airborne Particles. John Wiley & Sons, Inc., New York.

Ho, W., Hidy, G.M., Govan, R.M., 1974. Microwave measurements of the liquid. In: Lodge, J.P., Chen, T.L. (Eds.), Water Content of Atmospheric Aerosols. American Industrial Hygiene Association, Akron, Ohio, pp. 103−126. J. Appl. Meteorol. 9, 828-829.

Hopke, P.K., 1991. The initial atmospheric behaviour of radon decay products. In: Kay, J.K., Keller, G.E., Miller, J.F. (Eds.), Indoor Air Pollution. Lewis Publishers, Chelsea, U.K, pp. 141−169.

IAEA, 2015. The Fukushima Daiichi Accident - Radiological Consequences Technical, vol. 4/5.

ICRP Publication 66, 1994. Ann. ICRP 24 (1−3).

Ioannidou, A., Papastefanou, C., 1994. Atmospheric beryllium-7 concentrations and sun spots. Nucl. Geophys. 8 (6), 539−543.

Ioannidou, A., 2011. Activity size distribution of ^{7}Be in association with trace metals in the urban area of the city of Thessaloniki, Greece. Atmos. Environ. 45 (6), 1286−1290.

Ioannidou, A., 2012. ^{7}Be aerosols and their deposition on the sea: a possible method to estimate trace metals deposition on the sea. J. Environ. Radioact. 108, 29−32.

Ioannidou, A., Paatero, J., 2014. Activity size distribution and residence time of ^{7}Be aerosols in the Arctic atmosphere. Atmos. Environ. 88, 99−106.

Ioannidou, A., Eleftheriadis, K., Gini, M., Gini, L., Manenti, S., Groppi, F., 2019. Activity size distribution of radioactive nuclide 7Be at different locations and under different meteorological conditions. Atmos. Environ. 212, 272−280.

Jacobi, W., 1972. Activity and potential a-energy of 222Rn and 220Rn daughters in different air atmospheres. Health Phys. 22, 441−450.

Jaworowski, Z., 1963. The determination of lead-210 and bismuth-210 in biological materials. Nukleonika 8 (5), 333−340.

Jost, D.T., Gaggeler, H.W., Baltensperger, U., Zinder, B., Haller, P., 1986. Chernobyl fallout in size-fractionated aerosol. Nature 324, 22−23.

Junge, C.E., 1955. The size distribution and aging of natural aerosols as determined from electric and optical data on the atmosphere. Am. Meteor. Soc. J. Meteor. 12, 13−25.

Junge, C.E., 1963. Air Chemistry and Radioactivity. Academic Press, New York, p. 382.

Junge, C.E., 1972. Our knowledge of the physico-chemistry of aerosols in the undisturbed marine environment. J. Geophys. Res. 77, 5183−5200.

Kaneyasu, N., Ohashi, H., Suzuki, F., Okuda, T., Ikemori, F., 2012. Sulfate aerosol as a potential transport medium of radiocesium from the Fukushima nuclear accident. Environ. Sci. Technol. 46, 5720−5726.

Kauppinen, E.I., Hillamo, R.E., Aaltonen, S.H., Sinkko, K.T.S., 1986. Radioactivity size distributions of ambient aerosols in Helsinki, Finland, during May 1986 after the Chernobyl accident: preliminary report. Environ. Sci. Technol. 20, 1257−1259.

Kim, D.S., Hong, S.B., Kim, H.T., Lee, J.H., Lee, K.W., 2003. Design and performance evaluation of low-volume $PM_{2.5}$ inlet for analyzing chemical composition. Part. Part. Syst. Char. 20, 130−134.

Kim, D.S., Kim, M.C., Lee, K.W., 2000. Design and performance evaluation of multi-nozzle impactors for concentrating particles. Part. Part. Syst. Char. 17, 244−250.

Kim, H.T., Kim, Y.J., Lee, K.W., 1998. New PM_{10} inlet design and evaluation. Aerosol Sci. Technol. 29, 350−354.

Koch, D.M., Jacob, D.J., Graustein, W.C., 1996. Vertical transport of tropospheric aerosols as indicated by 7Be and ^{210}Pb in a chemical tracer model. J. Geophys. Res. 101 (D13), 18651−18666.

Kondo, K., Muramatsu, H., Kanda, Y., Takahara, S., 1984. Particle size distribution of 7Be-aerosols formed in high energy accelerator tunnels. J. Appl. Radiat. Isot. 35, 939−944.

Kristiansen, N.I., Stohl1, A., Wotawa, G., 2012. Atmospheric removal times of the aerosol-bound radionuclides ^{137}Cs and ^{131}I measured after the Fukushima Dai-ichi nuclear accident − a constraint for air quality and climate models. Atmos. Chem. Phys. 12, 10759−10769.

Kritidis, P., Florou, H., Eleftheriadis, K., Evangeliou, N., Gini, M., Sotiropoulou, M., Diapouli, E., Vratolis, S., 2012. Radioactive pollution in Athens, Greece due to the Fukushima nuclear accident. J. Environ. Radioact. 114, 100−104.

Krivokhatsky, A.S., Dubasov, Y.V., Smirnova, E.A., Skovorodkin, N.V., Savonenkov, V.G., Alexandrov, B.M., Lebedev, E.L., 1991. Actinides in the near release from the chenobyl NPP accident. J. Radioanal. Nucl. Chem. 147, 141−151.

Kruger, J., Andrews, M., 1976. Measurement of the attachment coefficient of radon-220 decay products to monodispersed aerosols. J. Aerosol Sci. 7, 21−36.

Kruger, J., Nothling, J.F., 1979. A comparison of the attachment of the decay products of radon-220 and radon-222 to monodispersed aerosols. J. Aerosol Sci. 10, 571−579.

Kuroda, P.K., 1982. Use of radioactive isotopes as atmospheric tracers. In: Labrecht, R.M., Morcos, N. (Eds.), Applications of Nuclear and Radiochemistry. Pergamon Press, New York, pp. 457−481.

Kuroda, P.K., Daniel, P.Y., Nevissi, A., Beck, J.N., Meason, J.L., 1978. Atmospheric residence times of strontium-90 and lead-210. J. Radioanal. Nucl. Chem. 43, 443−450.

Lambert, G., Buisson, A., Sanak, J., Ardouin, B., 1979. Modification of the atmospheric polonium-210 to lead-210 ratio by volcanic emissions. J. Geophys. Res. 84 (C11), 6980−6986.

Lambert, G., Polian, G., Sanak, J., Ardouin, B., Buisson, A., Jegou, A., Leroulley, J.C., 1982. Cycle du radon et de ses descendants: application a 1'etude des exchanges troposphere-stratosphere. Ann. Geophys. 38, 497–531.

Lambert, G., Sanak, J., Polian, G., 1983. Mean residence time of submicrometer aerosols in the global troposphere. In: Pruppacher, H.R., Semonin, R.G., Slinn, W.G.N. (Eds.), Precipitation Scavenging, Dry Deposition and Resuspension. Elsevier, New York, pp. 1353–1359.

Lehmann, L., Sittkus, A., 1959. Bestimmung von Aerosolverweilzeiten aus den RaD und RaF-Gehalt der atmospharischen Luft und des Niederschlages. Naturwissenschaft 46, 9–10.

Liu, B.Y.H., Pui, D.Y.H., 1981. Aerosol sampling inlets and inhalable particles. Atmos. Environ. 15, 589–600.

Lockhart, L.B., Patterson, R.L., Saunders, A.W., 1965a. Distribution of airborne activity with particle size. In: Klement Jr., A.W. (Ed.), Radioactive Fallout from Nuclear Weapons Tests. U.S. Department of Commerce, Springfield, VA. CONF 765.

Lockhart Jr., L.B., Patterson Jr., R.L., Saunders Jr., A.W., 1965b. The size distribution of radioactive atmospheric aerosols. J. Geophys. Res. 7, 6033–6041.

Lujaniene, G., Ogorodnikov, A., Budyka, A.K., 2001. Size distribution and chemical associations of cosmogenic and artificial radionuclides in ambient aerosols. J. Aerosol Sci. 32 (S1), 535–536.

Lujaniene, G., Ogorodnikov, B.I., Budyka, A.K., Skitovich, V.I., Lujanas, V., 1997. An investigation of changes in radionuclide carrier properties. J. Environ. Radioact. 35 (1), 71–90.

Lundgren, D.A., 1967. An aerosol sampler for determination of particle concentration of size and time. J. Air Pollut. Control Assoc. 17, 225.

Lundgren, D.A., 1973. Mass Distribution of Large Atmospheric Particles (Ph.D. thesis). University of Minnesota, Minneapolis, Minnesota, p. 161.

Lundgren, D.A., Balfour, W.D., 1980. Use and Limitations of In-Stack Impactors. EPA Report 600/2-80-048, February 1980.

Malá, H., Rulík, P., Becková, V., Mihalík, J., Slezáková, M., 2013. Particle size distribution of radioactive aerosols after the Fukushima and the Chernobyl accidents. J. Environ. Radioact. 126, 92–98.

Markowski, G.R., 1984. Reducing blow off in cascade impactor measurement. Aerosol Sci. Technol. 3, 431–439.

Marley, N.A., Gaffney, O.S., Drayton, P.J., Cunningham, M.M., Orlandini, K.A., Paode, R., 2000. Measurement of ^{210}Pb, ^{210}Po and ^{210}Bi in size-fractionated atmospheric aerosols: an estimate of fine-aerosol residence times. Aerosol Sci. Technol. 32, 569–583.

Marple, V.A., 1970. A Fundamental Study of Inertial Impactors (Ph.D. dissertation). University of Minnesota, Particle Technology Laboratory, Minneapolis, MN. Publication No. 44.

Marple, V.A., Chein, C.M., 1980. Virtual impactors: a theoretical study. Environ. Sci. Technol. 14, 976–984.

Marple, V.A., Liu, B.Y., 1974. Characteristics of laminar jet impactors. Environ. Sci. Technol. 8, 648–654.

Marple, V.A., Liu, B.Y.H., 1975. On fluid flow and aerosol impaction in inertial impactors. J. Colloid Interface Sci. 53, 31–34.

Marple, V.A., Liu, B.Y.H., Whitby, K.T., 1974. On the flow fields of inertial impactors. ASME J. Fluids Eng. 96, 394–403.

Marple, V.A., Willeke, K., 1979. Aerosol impactors. In: Aerosol Measurement. University Presses of Florida, Gainesville, FL D.A, pp. 90–107.

Martell, E.A., 1970. Transport patterns and residence times for atmospheric trace constituents vs. altitude. In: Radionuclides in the Environment, vol. 93. American Chemical Society, Washington, D.C, pp. 138–157. Adv. Chem. Ser.

Martell, E.A., Moore, H.E., 1974. Tropospheric aerosol residence times: a critical review. J. Rech. Atmos. 8, 903–910.

Masson, O., et al., 2011. Tracking of airborne radionuclides from the damaged Fukushima Dai-Ichi nuclear reactors by European networks. Environ. Sci. Technol. 45 (18), 7670–7677.

Masson, O., Ringer, W., Malá, H., Rulik, P., Dlugosz-Lisiecka, M., Eleftheriadis, K., Meisenberg, O., De Vismes-Ott, A., Gensdarmes, F., 2013. Size distributions of airborne radionuclides from the Fukushima nuclear accident at several places in Europe. Environ. Sci. Technol. 47 (19), 10995–11003.

McMurry, P.H., Wilson, J.C., 1982. Growth laws for the formation of secondary ambient aerosols: implications for chemical conversion mechanisms. Atmos. Environ. 16, 121–134.

Mercer, T.T., Tillery, M.I., Newton, G.J., 1970. A multi-stage, low flow rate cascade impactor. J. Aerosol Sci. 1 (1), 9–15.

Mercer, T.T., Stowe, W.A., 1971. Radioactive aerosols produced by radon in room air. In: Inhaled Particles III, vol. II. Unwin Brothers Limited. The Gresham Press, Surrey, England, pp. 839–851.

Meyer, G.A., Lee, K.W., 1994. Real time determination of metal hazardous air pollutants in flue gas emissions. Process Control Qual. 6, 187–192.

Mishra, R., Mayya, Y.S., Kushwaha, H.S., 2009. Measurement of ^{222}Rn/^{220}Rn progeny deposition velocities on surfaces and comparison with theoretical models. J. Aerosol Sci. 40, 1–15.

Miyamoto, Y., Yasuda, K., Magara, M., 2014. Size distribution of radioactive particles collected at Tokai, Japan 6 days after the nuclear accident. J. Environ. Radioact. 132, 1–7.

Moore, H.E., Poet, S.E., Martell, E.A., 1972. Tropospheric aerosol residence times indicated by radon and radon-daughter concentrations. In: Adams, J.A.S., Lowder, W.M., Gessel, T.F. (Eds.), Natural Radiation Environment II. Technical Information Center/U.S. Department of Energy, Washington D.C., pp. 775–786. CONF-720805-P2.

Moore, H.E., Poet, S.E., Martell, E.A., 1973. ^{222}Rn, ^{210}Pb, ^{210}Bi and ^{210}Po profiles and aerosol residence times versus altitudes. J. Geophys. Res. 78 (30), 7065–7075.

NCRP, 1987. National Council on Radiation Protection and Measurements. Exposure of the Population in the United States and Canada from Natural Background Radiation. Report No. 94.

NRC, 1979. Airborne Particles. National Research Council. University Park Press, Baltimore.

Oki, Y., Kanda, Y., Kondo, K., Endo, A., May 2000. Particle size of radioactive aerosols generated during machine operation in high-energy proton accelerators. In: IRPA-10: 10. International Congress of the International Radiation Protection Association; Hiroshima (Japan); 14-19 May 2000, vol. 1. Japan Health Physics Society, Tokyo (Japan). ; [6 pp.].

Paatero, J., Ioannidou, A., Ikonen, J., Lehto, J., 2017. Aerosol particle size distribution of atmospheric lead-210 in northern Finland. J. Environ. Radioact. 172, 10–14.

Papastefanou, C., 2008. Radioactive aerosols. In: Radioactivity in the Environment, vol. 12. Elsevier, Amsterdam and Oxford, pp. 1–171.

Papastefanou, C., 2009a. Radon decay product aerosols in ambient air. Aerosol Air Qual. Res. 9, 385–393.

Papastefanou, C., 2009b. Beryllium-7 aerosols in ambient air. Aerosol Air Qual. Res. 9, 187–197.

Papastefanou, C., Bondietti, E.A., 1987. Aerodynamic size associations of ^{212}Pb and ^{214}Pb in ambient aerosols. Health Phys. 53, 461–472.

Papastefanou, C., Bondietti, E.A., 1991. Mean residence times of atmospheric aerosols in the boundary layer as determined from ^{210}Bi/^{210}Pb activity ratios. J. Aerosol Sci. 22 (7), 927–931.

Papastefanou, C., Ioannidou, A., 1995. Aerodynamic size association of ^{7}Be in ambient aerosols. J. Environ. Radioact. 26, 273–282.

Papastefanou, C., Ioannidou, A., 1996. Influence of air pollutants in the ^{7}Be size distribution of atmospheric aerosols. Aerosol Sci. Technol. 24, 102–106.

Peirson, D.H., Cambray, R.S., Spicer, G.S., 1966. Lead-210 and polonium-210 in the atmosphere. Tellus 18, 427–433.

Persson, G., Sisefsky, J., 1971. Health Phys. 21, 421–442 (as cited in Jost et al., 1986).

Poet, S.E., Moore, H.E., Martell, E.A., 1972. Lead-210, bismuth-210 and polonium-210 in the atmosphere: accurate ratio measurement and application to aerosol residence time determination. J. Geophys. Res. 77 (33), 6515–6527.

Pöllänen, R., Valkama, I., Toivonnen, H., 1997. Transport of radioactive particle from the Chernobyl accident. Atmos. Environ. 31 (21), 3575–3590.

Porstendörfer, J., 1994. Properties and behaviour of radon and thoron and their decay products in the air. J. Aerosol Sci. 25, 219–263.

Porstendörfer, J., Grundel, M., 2003. Comparison of the activity size distribution of the radionuclide aerosols in outdoor air. In: Dresden Symposium on Radiation Protection, 2003 Protection. March 3e7, 2003, Dresden, Germany. Book of Abstracts. Dresden University of Technology, Dresden (Germany), p. 24.

Porstendörfer, J., Mercer, T.T., 1978. Influence of nuclei concentration and humidity upon the attachment rate of atoms in the atmosphere. Atmos. Environ. 12, 2223–2228.

Porstendörfer, J., Mercer, T.T., 1979. Influence of electric charge and humidity upon the diffusion coefficient of radon decay products. Health Phys. 37, 191–199.

Porstendörfer, C., Mercer, T., 1980. Diffusion coefficient of radon decay products and their attachment rate to the atmospheric aerosol. In: Gesell, Thomas, F., Wayne, M. (Eds.), Natural Radiation Environment III, vol. 1. National Technical Information Service, Springfield, VA, pp. 281–293. Lowder. CONF 780422.

Porstendörfer, J., Pagelkopf, P., Grundel, M., 2005. Fraction of the positive ^{218}Po and ^{214}Pb clusters in indoor air. Radiat. Prot. Dosim. 113 (3), 342–351.

Porstendörfer, J., Röbig, G., Ahmed, A., 1979. Experimental determination of the attachment coefficients of atoms and ions on monodispersed aerosols. J. Aerosol Sci. 10, 21–28.

Qadir, M.A., Zaidi, J.H., 2006. Characteristics of the aerosol particulates in the atmosphere in an urban environment at Faisalabad, Pakistan. J. Radioanal. Nucl. Chem. 267, 545–550.

Raabe, O.G., 1968. Measurement of the diffusion coefficient of radium. Nature 217, 1143–1145.

Raabe, O.G., 1979. Design and use of the Mercer-style impactor for characterization of aerosol aerodynamic size distributions. In: Aerosol Measurement. University Presses of Florida, Gainesville, FL, pp. 135–140.

Raes, F., 1985. Description of the properties of unattached ^{218}Po and ^{212}Pb particles by means of comparison of the classical theory of cluster formation. Health Phys. 49, 1177–1187.

Rangarajan, C., 1992. A study of the mean residence time of the natural radioactive aerosols in the planetary boundary layer. J. Environ. Radioact. 15, 193–206.

Ranz, W.E., Wong, J.B., 1952. Jet impactors for determining the particle size distribution of aerosols. Arch. Ind. Hyg. Occup. Med. 5, 464–477.

Reineking, A., Portendorfer, J., 1995. Time variations of size distribution of aerosol-attached activities of ^{212}Pb, ^{210}Pb and ^{7}Be in the outdoor atmosphere. In: Natural Radiation Environment VI, 5e9 June, 1995, Montreal, Canada. Book of Abstracts. Clarkson University, Potsdam, NY, p. 199.

Rindi, A., Charalambous, S., 1967. Airborne radioactivity produced at high energy accelerators. Nucl. Instrum. Meth. 47, 227–232.

Röbig, G., Becker, K.H., Hessin, A., Porstendörfer, J., Scheibel, H.G., 1980. A cascade impactor calibration for measurement of activity size distributions in the atmosphere. In: Proceedings of 8th Conference in Aerosol Science. Georg-August-University, Göttingen, Germany, pp. 96–102.

Salbu, B., Krekling, T., Oughton, D.H., Ostby, G., Kashparov, V.A., Brand, T.L., Day, J.P., 1994. Hot particles in accidental releases from Chernobyl and Windscale nuclear installations. Analyst 119, 125–130.

Sanak, J., Gaudry, A., Lambert, G., 1981. Size distribution of ^{210}Pb aerosols over oceans. Geophys. Res. Lett. 8 (10), 1067–1069.

Seinfeld, J.H., 1986. Atmospheric Chemistry and Physics of Air Pollution. Wiley, New York.

Seinfeld, J.H., Pandis, S.N., 2016. Atmospheric Chemistry and Physics: From Air Pollution to Climate Change. John Wiley and Sons, Inc, p. 342.

Shapiro, M.H., Forbes-Resha, J.L., 1976. Mean residence time of ^{7}Be-bearing aerosols in the troposphere. J. Geophys. Res. 81 (15), 2647–2649.

Silberberg, R., Tsao, C.H., 1973. Cross Sections of Proton-Nucleus Interactions at High Energies. Report NRL 7593. Naval Research Laboratory, Washington, D.C.

Sinclair, D., Countess, R.J., Liu, B.Y.H., Pui, D.Y.H., 1979. Automatic analysis of submicron aerosols. In: Aerosol Measurement. University of Florida Press, Gainesville, FL, pp. 544–563.

Singh, S., Sapra, B.K., Khan, A., Kothalkar, P.K., Mayya, Y.S., 2010. Development of a variable configuration cascade impactor for aerosol size distribution measurements. Atmos. Environ. 44, 795–802.

Stevens, R.K., McFarland, A.R., Wedding, J.J., 1976. Comparison of the virtual dichotomous sampler with the high-volume sampler. In: Proceedings of the 171st Meeting of the American Chemical Society, Division of Environmental Chemistry, New York, NY April 4-9, 1976, vol. 16 (1), pp. 84–85. Paper No. 25.

Terada, H., Katata, G., Chino, M., Nagai, H., 2012. Atmospheric discharge and dispersion of radionuclides during the Fukushima Dai-ichi nuclear power plant accident, Part II: verification of the source term and analysis of regional-scale atmospheric dispersion. J. Environ. Radioact. 112, 141–154.

Thakur, P., Ballard, S., Nelson, R., 2013. An overview of Fukushima radionuclides measured in the northern hemisphere. Sci. Total Environ. 458–460, 577–613.

TISCH Environmental TSP High Volume Air Sampler. https://tisch-env.com/high-volume-air-sampler/TSP.

Tisch Environmental, Inc. Model 20-800 Ambient Cascade Impactor (Non-viable) Operations Manual Serial Number S/N 012 June 1999.

Tsai, C.J., Cheng, Y.H., 1995. Solid particle collection characteristics on impaction surfaces of different designs. Aerosol Sci. Technol. 23, 96–106.

UNSCEAR, 1982. United Nations Scientific Committee on the Effects of Atomic Radiation. Ionizing Radiation: Sources and Biological Effects. United Nations, New York.

UNSCEAR, 1993. United Nations Scientific Committee of the Effects of Ionizing Radiation. Sources and Effects of Ionizing Radiation. United Nations, New York.

UNSCEAR, 2000. United Nations Scientific Committee on the Effects of Ionizing Radiation. Sources and Effects of Ionizing Radiation. United Nations, New York.

Vasilatou, V., Manousakas, M., Gini, M., Diapouli, E., Scoullos, M., Eleftheriadis, K., 2017. Long term flux of Saharan dust to the Aegean sea around the Attica region, Greece. Front. Mar. Sci. 4, 42. https://doi.org/10.3389/fmars.2017.00042.

Vivas, M.M., Hontanon, E., Schmidt-Ott, A., 2008. Design and evaluation of a low-level (0.24 mCi) radioactive aerosol charger based on ^{241}Am. J. Aerosol Sci. 39, 191–210.

Warneck, P., 1988. Chemistry of the Natural Atmosphere. Academic Press, Inc., San Diego (U.S.A.), pp. 360–373.

Whitby, K.T., Husar, R.B., Liu, B.Y.H., 1972. The aerosol size distribution of Los Angeles smog. J. Colloid Interface Sci. 39, 177–204.

Whitby, K.T., 1975. Modelling of Atmospheric Aerosol Particle Size Distributions. A Progress Report on EPA Research Grant No. R800971. Sampling and Analysis of Atmospheric Aerosols. Particle Technology Laboratory Report No.253. Environmental Division, Mechanical Engineering Department, University of Minnesota.

Whitby, K.T., Clark, W.E., Marple, V.A., Sverdrup, G.M., Sem, G.J., Willeke, K., Liu, B.Y.H., Pui, D.Y.H., 1975. Characterization of California aerosols- 1. Size distribution of freeway aerosol. Atmos. Environ. 9, 463–482.

Whitby, K.T., Cantrell, B.K., 1976. Atmospheric aerosols- characteristics and measurements. In: International Conference on Environmental Sensing and Assessment. Las Vegas, Nevada, September 14-17, 1975. Institute of Electrical and Electronics Engineers, New York.

Whitby, K.T., Kittelson, D.B., Cantrell, B.K., Barsic, N.J., Dolan, D.F., Tervestad, L.D., Nieken, D.J., Wolf, J.L., Wood, J.R., 1976. Aerosol size distributions and concentrations measured during the general motor proving grounds sulphate study. In: The General Motors/ Environmental Protection Agency Sulphate Dispersion Experiment. Rep. EP A-600/3-76-035. Environmental Protection, Research Triangle Park, NC, pp. 29–80.

Whitby, K.T., 1978. The physical characteristics of sulphur aerosols. Atmos. Environ. 12, 135–159.

Wiedensohler, 1988. An approximation of the bipolar charge distribution for particles in the submicron size range. J. Aerosol Sci. 19, 387–389.

Willeke, K., Whitby, K., 1975. Atmospheric aerosols: size distribution interpretation. J. Air Pollut. Control Assoc. 25, 529–534.

Willeke, K., Baron, P.A., 1993. Aerosol Measurement: Principles, Techniques, and Applications. Van Nostrand Reinhold, New York.

Winkler, R., Dietl, F., Franck, G., Tschierch, J., 1998. Temporal variation of ^{7}Be and ^{210}Pb size distribution in ambient aerosol. Atmos. Environ. 32 (6), 983–991.

Young, J.A., Tanner, T.M., Thomas, C.W., Wogman, A., Petersen, M.R., 1975. Concentrations and rates of removal of contaminants from the atmosphere in a downwind of st. Louis. Pacific Northwest laboratory annual report for 1974 to the USAEC division of Biomedical and environmental research. Atmos. Sci. (Part 3) 70–76.

Young, J.A., Silker, W.B., 1980. Aerosol deposition velocity on the Pacific and Atlantic oceans, calculated from 7Be measurements. Earth Planet. Sci. Lett. 50, 92–104.

Yu, C.C., Tung, C.J., Hung, I.F., Tseng, C.L., 1993. Analyses of radioactive aerosols to support accurate internal dose assessments at Chin-Shan nuclear power plant. Health Phys. 65, 147–155.

Yu, K.N., Lee, L.Y.L., 2002. Measurements of atmospheric ^{7}Be properties using high-efficiency gamma spectroscopy. Appl. Radiat. Isot. 57, 941–946.

Further reading

Andersson, K.J., Fogh, C.L., Byrne, M.A., Roed, J., Goddard, A.J., Hotchkiss, S.A., 2002. Radiation dose implications of airborne contaminant deposition to humans. Health Phys. 82 (2), 226–232.

Brightwell, J., Carter, R.F., 1977. Comparative measurements of the short term lung clearance and translocation of PuO_2 and mixed Na_2O & PuO_2 aerosols in mice. In: Walton, W.H. (Ed.), Inhaled Particles IV. Pergamon, Oxford, pp. 285–301. Part 1.

Cahill, T.A., Eldred, R.A., Feeney, P.J., Beveridge, P.J., Wilkinson, L.K., 1990. Trans. AWMA 213–222.

Carter, R.F., Stewart, K., 1971. On the oxide formed by the combustion of plutonium and uranium. In: Walton, W.H. (Ed.), Inhaled Particles III, vol. 2. Pergamon, Oxford, pp. 819–838.

Cheng, Y.S., Guilmette, R.A., Zhou, Y., Gao, J., LaBone, T., Whicker, J.J., Hoover, M.D., 2004. Characterization of plutonium aerosol collected during an accident. Health Phys. 87, 596–605.

Elder, J.C., Conzales, M., Ettinger, H.J., 1974. Plutonium aerosol size characteristics. Health Phys. 27, 45–53.

Fifield, L.K., 2008. Accelerator mass spectrometry of long-lived heavy radionuclides. Radioact. Environ. 11, 263–293.

Hall, D.J., Waters, R.A., 1986. An improved, readily available dustfall gauge. Atmos. Environ. 20, 219–222.

Hall, D.J., Upton, S.L., 1988. A wind tunnel study of the particle collection efficiency of an inverted Frisbee used as a dust deposition gauge. Atmos. Environ. 22 (7), 1383–1394.

Holgye, Z., Schlesingerova, E., 2010. Further results in search for transuranic elements in effluents discharged to air from nuclear power plants. J. Radioanal. Nucl. Chem. 286, 341–345.

Hounam, R.F., Sherwood, R.J., 1965. The cascade centripeter: a device for determining the concentration and size distribution of aerosols. Am. Industr. Hyg. J. 26, 122–131.

Kondo, K., 2006. Radioactive airborne species formed in the air in high energy accelerator tunnels. J. Nucl. Radiochem. Sci. 7 (1), R31–R36.

Kutkov, V., 2000. Results of in vivo monitoring of the witnesses of the chernobyl accident. Radiat. Prot. Dosim. 89 (3), 193–197.

Lal, D., Suess, H.E., 1968. The radioactivity of the atmosphere and the hydrosphere. Annu. Rev. Nucl. Sci. 18, 407–434.

Larivière, D., Brownell, D., Epov, V., Cornett, R., Evans, R., 2007. Determination of ^{226}Ra in sediments by ICPMS: a comparative study of three sample preparation approaches. J. Radioanal. Nucl. Chem. 273, 337–344.

Lee, M.H., Lee, C.W., 1999. Determination of Cs-137, Sr-90 and fallout Pu in the volcanic soil of Korea. J. Radioanal. Nucl. Chem. 239, 471–476. https://doi.org/10.1007/bf02349053.

Mann, J.R., Kirchner, R.A., 1967. Evaluation of lung burdens following acute inhalation exposure to highly insoluble PuO2. Health Phys. 13, 877–882.

Mitchell, R.I., Pilcher, J.M., 1959. Improved cascade impactor for measuring aerosol particle sizes. Ind. Eng. Chem. 51 (9), 1039–1042.

Moss, W.D., Hyatt, E.C., Schulte, H.F., 1961. Particle size studies on plutonium aerosols. Health Phys. 5, 212–218.

Muramatsu, Y., Hamilton, T., Uchida, S., Tagami, K., Yoshida, S., Robison, W., 2001. Measurement of ^{240}Pu/^{239}Pu isotopic ratios in soils from the Marshall Islands using ICP-MS. Sci. Total Environ. 278 (1–3), 151–159.

Paatero, J., Hatakka, I., Mattsson, R., Lehtinen, I., 1994. A comprehensive station for monitoring atmospheric radioactivity. Radiat. Prot. Dosim. 54, 33–39.

Papastefanou, C., 2006. Residence time of tropospheric aerosols in association with radioactive nuclides. Appl. Radiat. Isot. 64, 93–100.

Papastefanou, C., Ioannidou, A., 1997. Beryllium-7 aerosols in ambient air. Environ. Int. 22 (Suppl. 1), S125–S130.

Ralph, M.O., Barrett, C.F., 1984. A Wind Tunnel Study of the Efficiency of Three Deposit Gauges. LR 499(AP). Warren Spring Laboratory.

Reshetin, V.P., 2005. Estimation of radioactivity levels associated with a ^{90}Sr dirty bomb event. Atmos. Environ. 39 (25), 4471–4477.

Varga, Z., Suranyi, G., Vajda, N., Stefanka, Z., 2007. Determination of plutonium and americium in environmental samples by inductively coupled plasma sector field spectrometry and alpha spectrometry. Microchem. J. 85, 39–45.

Wedding, J.B., McFarland, A.R., Cermak, J.E., 1977. Large particle collection characteristics of ambient aerosol samplers. Environ. Sci. Technol. 11, 387–390.

Konstantinos Eleftheriadis



Dr. Konstantinos Eleftheriadis is a **Director of Research at NCSR Demokritos**, Head of the Aerosol Group and the Environmental Radioactivity Laboratory at the Institute of Nuclear & Radiological Sciences & Technology, Energy & Safety. He has research expertise on Physicochemical aerosol characterization and nuclear analytical techniques with respect to climatic active aerosol species, nano-particle metrology, development of novel sampling and measurement techniques for aerosol particles, exposure of humans to aerosol contaminants, such as, heavy metals and radioactive pollutants, and retrieval of emission source impact, source apportionment and receptor modeling. Primary Investigator for Demokritos in several European Framework Programs (EU FP) and DG-ENV programmes, IAEA Regional projects & other National programmes. Dr. Konstantinos Eleftheriadis has established infrastructure, including the Athens GAW/ACTRIS Demokritos station, the Mt. Helmos Free Troposphere Aerosol and GHG station and the QA/QC physical aerosol properties lab facility. He has served as National Counterpart for Greece in Regional IAEA programmes. He has supervised 12 PhD thesis and 10 MSc project thesis; and has more than 150 publications in peer reviewed journals. Invited reviewer and evaluator for project proposals by a) EURAMET European Metrology Research, and the Czech Academy of Sciences Grant program. Dr. Konstantinos Eleftheriadis has carried out three expert missions for the IAEA in the Environment Program for Africa and the Middle East, and he is a Member of the National Emergency Action Plan "Xenokratis" and Founding Member and President of the Hellenic Association for Aerosol Research.

Alexandra Ioannidou



Alexandra Ioannidou is a professor at Aristotle University of Thessaloniki, Physics Department, Nuclear Physics Laboratory. She has research expertise on radiation physics and isotopes, radiation protection and environmental radioactivity—radioecology, environmental radioactivity from the Chernobyl and Fukushima accidents and effects of radioactive pollutants by their dispersion, contamination and decontamination, as well as on radioactive aerosols and their behavior in various environments, including the Arctic. Alexandra Ioannidou has steady interaction with the international scientific community through joint research projects, publications in international journals, conferences, meetings, and working in institutes abroad. Alexandra Ioannidou has supervised numerous thesis works by students for the PhD, MSc, and BSc degrees. She has more than 100 publications in peer-reviewed international journals and conferences, and she is a reviewer in more than 20 international scientific journals.

Chapter 5

PERPUSTAKAAN PRIBADI AN-NUR SUNARYA

Marine radioactivity analysis

Pavel P. Povinec[1,5], Mats Eriksson[2,5], Jan Scholten[3,5] and Maria Betti[4,5]

[1]Comenius University, Faculty of Mathematics, Physics and Informatics, Department of Nuclear Physics and Biophysics, Bratislava, Slovakia; [2]Swedish Radiation Safety Authority, Department of Radiation Protection, Stockholm, Sweden; [3]Institute of Geosciences, Kiel University, Kiel, Germany; [4]Directorate G - Nuclear Safety and Security, European Commission, DG Joint Research Centre, Karlsruhe, Germany; [5]Formerly at the International Atomic Energy Agency, Environmental Laboratories, Monaco

Chapter outline

I. Introduction 316
II. Sampling techniques 317
A. Seawater sampling 317
B. Sediment sampling 318
C. Biota sampling 319
D. Sampling of particulate matter 320
III. Underwater gamma-ray spectrometry 321
A. Towed detector systems 323
B. Stationary detector systems 323
C. Applications of underwater gamma-ray spectrometry 324
1. Mururoa and Fangataufa lagoons 324
2. Novaya Zemlya bays 325
3. Mapping of coastal sediments in the Irish Sea 325
4. Monitoring of ^{137}Cs in Irish Seawaters 326
5. Submarine groundwater discharge studies 326
IV. Analysis of natural radionuclides 328
A. Thorium, protactinium, and uranium isotopes 329
1. Sampling of seawater 329
2. Sampling of particulate matter and sediments 329
3. Dissolving of particulate matter and sediments 329
4. Ion-exchange separation 330
5. Electrodeposition of Th, U, and Pa 331
B. Thorium-234 331
1. Sediments 331
2. Seawater 331
C. Polonium-210 and Lead-210 332
1. Seawater 332
2. Digestion of filters and sediments 333
3. Plating of ^{210}Po 333
D. Radium isotopes 334
1. Measurement of ^{223}Ra and ^{224}Ra 334
2. Measurement of ^{228}Ra and ^{226}Ra 334
E. Radon-222 335
F. Beryllium-7 335
V. Analysis of anthropogenic radionuclides 335
A. Preparation of samples for radionuclide analysis 335
B. Shipboard chemistry for seawater samples 336
1. Transuranics 336
2. Cesium 336
3. Strontium 337
C. Laboratory chemistry for seawater samples 337
1. Transuranics 337
2. Cesium 338
3. Strontium 339
D. Laboratory chemistry for sediment and biota samples 339
VI. Activity measurement techniques 340
A. Radiometric methods 340
1. Low-level alpha-spectrometry 340
2. Low-level beta-spectrometry 340
3. Low-level gamma-spectrometry 341
4. Underground laboratories 342
B. Mass spectrometry methods 344
1. ^{3}He in-growth spectrometry for ^{3}H analysis 345
2. Inductively coupled plasma mass spectrometry 345
3. Thermal ionization mass spectrometry 346
4. Resonance ionization mass spectrometry 346
5. Accelerator mass spectrometry 347
6. Laser-based ^{14}C spectroscopy 349
7. Positive-ion mass spectrometry 350
8. Comparison of detection limits 350
VII. Analysis of radioactive particles 350
A. Radioactive particle studies 350
1. Safeguards applications 351
2. Radiological impact studies 351
3. Geo-chemical behavior studies of radionuclides 352
B. Protocols for studying radioactive particles 352
1. Nondestructive analysis 354
2. Semi-destructive analysis of particles 358
3. Destructive analysis on particles 359
VIII. Management of data quality 359
A. Laboratory Information Management system 359
B. Intercomparison exercises 360
C. Reference materials 362
IX. Marine radioactivity databases 362

Handbook of Radioactivity Analysis: Volume 2. https://doi.org/10.1016/B978-0-12-814395-7.00005-2
Copyright © 2020 Elsevier Inc. All rights reserved.

X. Examples of marine radioactivity studies 365
A. Worldwide marine radioactivity studies 365
1. The ^{137}Cs time series in the Atlantic Ocean 365
2. The ^{137}Cs time series in the Pacific Ocean 369
3. The ^{137}Cs time series in the Indian Ocean 369
4. Radionuclide tracing of water masses in the South Indian Ocean 370
B. Southern Hemisphere Ocean Tracer Studies 372
C. Marine radioactivity impact of the Fukushima accident 375
XI. Conclusions 375
Acknowledgments 377
References 377
Pavel P. Povinec 391
Mats Eriksson 391
Jan Scholten 392
Maria Betti 392

I. Introduction

Analyses of radionuclides in the marine environment and their applications in studying oceanographic processes have a long history. The first studies started in the late 1950s with investigations of ^{226}Ra in seawater (Koczy, 1958). Later, many other natural radionuclides (mainly U and Th isotopes and their decay products) found applications in marine sciences. After the introduction of anthropogenic radionuclides to the marine environment from atmospheric nuclear tests (e.g., ^{3}H, ^{14}C, ^{90}Sr, ^{137}Cs, Pu isotopes and others), it was recognized that these radionuclides represent powerful tools as tracers, which can be used effectively for the investigation of transport of water masses in oceans, in studying processes in the water column and in sediment, and mechanisms for the transfer of radionuclides to the marine biota (Broecker and Peng, 1982; IAEA, 1999, 2006; Livingston and Povinec, 2002; Povinec, 2004; Povinec and Sanchez-Cabeza, 2006; Povinec et al., 2013a). Another group of radionuclides utilized in marine studies is represented by the cosmogenic radionuclides (^{7}Be, ^{10}Be, ^{26}Al, ^{32}Si, ^{37}Ar, ^{39}Ar, ^{81}Kr, and others), produced by interaction of cosmic rays with atmospheric atoms (Lal, 1999).

Traditionally, marine radionuclide studies have always been limited by the techniques available for sampling (starting with a few hundred liters of seawater), as well as methods available for the analysis of radionuclides in the marine environment. The water sampling has developed from the reversing simple Nansen bottles into the present multibottle Rosette systems coupled with CTD detectors for measuring conductivity (C), temperature (T), and depth (D), combining thus water sampling and CTD measurements in one cast for the total water column. Robotic systems based on remotely operating vehicles and autonomous underwater vehicles, and other sophisticated sampling techniques, which use satellite views of sea areas for the optimization of sampling, are the examples of the present state-of-the-art technologies in marine sampling (Povinec and Sanchez-Cabeza, 2006; Povinec, 2008a, 2013; Povinec et al., 2013a).

Marine radionuclide activity measurements started with simple radiochemical separation methods and Geiger–Müller counters for activity measurements, which were later developed into the age of robotic radiochemical separation and purification technologies, sophisticated detectors working online with powerful computers (sometimes with satellite data transmission from continuous underwater radionuclide monitors), and coupled gas chromatography (GC) and mass spectrometry (MS) systems (Povinec et al., 2009).

An important breakthrough in marine radionuclide technologies was a change in the philosophy of radionuclide analysis. We shifted from the concept of waiting for radionuclide decays and subsequent counting of decay products (what has big disadvantages in the case of long-lived radionuclides), to the direct counting of radioactive atoms as if they would be stable, using highly sensitive mass spectrometers, working either with low-energy ions (e.g., thermal ionization mass spectrometry (TIMS), inductively coupled plasma mass spectrometry (ICPMS), resonance ionization mass spectrometry (RIMS)) or ions accelerated to levels of up to hundreds of MeV in accelerator mass spectrometry (AMS) (Povinec, 2004, 2008a, 2011, 2013).

This move from simple radioanalytical techniques to the present sophisticated state-of-the-art technologies has also been accompanied by a considerable change in the philosophy of oceanic studies (Livingston and Povinec, 2002; Povinec, 2004, 2011, 2013). It has been recognized that the world ocean cannot be investigated anymore in small institutional projects, typical of the time period from the 1960s to the 1970s, but large-scale global oceanic investigations carried out by international communities are necessary for a complex study of oceanic processes. Several such projects using radionuclides as tracers were carried out in the past, which contributed significantly to oceanic science, examples of which are the following:

- Geochemical Ocean Sections Program (GEOSECS)—a first global project on the distribution of ^{3}H, ^{14}C, ^{137}Cs, Pu isotopes in the world ocean;
- World Ocean Circulation Experiment (WOCE)—the largest worldwide project carried out till now with applications of radionuclides (^{3}H and ^{14}C);
- Worldwide Marine Radioactivity Studies (WOMARS)—the project carried out by the International Atomic

Energy Agency (IAEA) in cooperation with many marine and analytical laboratories, having the largest coverage of the world ocean with anthropogenic radionuclides (^{3}H, ^{14}C, ^{90}Sr, ^{129}I, ^{137}Cs, ^{241}Am, Pu isotopes) in the water column and sediment;
- Southern Hemisphere Oceans Tracer Studies (SHOTS)—a round-the-globe transect at 20 degrees S (^{3}H, ^{14}C, ^{90}Sr, ^{137}Cs, ^{241}Am, Pu isotopes) carried out by the Meteorological Research Institute (Tsukuba, Japan) and IAEA in collaboration with several marine and analytical laboratories; and
- GEOTRACES (www.geotraces.org)—the largest international worldwide project carried out at present on global marine biogeochemical cycles of trace elements and their isotopes.

In marine radioactivity studies, we have to deal with conflicting phenomena while planning and executing the sampling expeditions and the laboratory analyses. A sample size versus analysis determines the minimum size of samples required to accomplish the expected results with available laboratory techniques for radionuclide analyses. As the levels of anthropogenic radionuclides in the marine environment have been decreasing for the last 50 y after their main injection to the marine environment (Livingston and Povinec, 2002; Povinec, 2004; Povinec et al., 2013a; Hirose and Povinec, 2015), we have been forced to develop very highly sensitive radioanalytical technologies for minimizing the size of marine samples, especially seawater. On the other hand, with the increasing price of ship time we have been forced to minimize the sample size (and thus the sampling time). For example, seawater volumes usually sampled by the typical Rosette systems are 10−20 L, which is challenging for radiometric techniques (RMTs) (typical water volumes for ^{137}Cs and ^{239,240}Pu analysis in the water column are 200 and 400 L, respectively) currently in competition with mass spectrometry methods such as AMS and ICPMS (Povinec, 2005, 2010, 2011, 2013).

We shall review sampling, radiochemical, and measuring techniques for analysis of radionuclides in the marine environment with emphasis on recent developments in the field. In several cases, we shall illustrate the state of the art of the radioanalytical techniques together with recent developments and results obtained in the International Atomic Energy Agency's Environment Laboratories (IAEA-EL) in Monaco.

II. Sampling techniques

Generally, four types of samples—water, sediment, biota, and particulate matter—are used for the investigation of radionuclides in the marine environment. Therefore, we shall deal with each group of samples separately. A sampling strategy should be designed well in advance of real sampling in the marine environment (Scott and Dixon, 2008; Macášek, 2008).

A. Seawater sampling

The sensitivity of analytical methods often demands the analysis of large samples (e.g., hundreds of liters of seawater) in order to obtain meaningful results, especially in the case of radiometric methods (e.g., alpha-, beta-, and gamma-ray spectrometry). Therefore, a reduction in the volume of water sampled would be a great advantage, as this would be reflected also in the reduction in the time needed for sampling. This has important implications on financial budgets of cruises, as the ship time is very expensive (around 50 k€ per day for open ocean sampling). Therefore, more sensitive methods of radionuclide analysis than those offered by traditional RMTs are needed. As will be discussed later, if AMS, ICPMS, or TIMS are used, only small-volume samples are needed for the analysis of several long-lived radionuclides in the water column. For example, ^{14}C or ^{129}I analysis by AMS requires only 0.5 L of water. The ^{239}Pu or ^{240}Pu analysis by AMS or TIMS requires only around 10 L of water. For other radionuclides analyzed by γ-ray spectrometry (e.g., ^{137}Cs) or β-ray spectrometry (e.g., ^{90}Sr), measurements in low-background underground laboratories would seem to be the solution for decreasing sample volumes to about 10 L (Aoyama and Hirose, 2008; Povinec et al., 2008a, 2013a).

Two kinds of water samples are collected during oceanographic cruises. Small-volume samples, e.g., separate samples each of 0.5 L, are required for ^{3}H analysis (by a light isotope mass spectrometer, which analyzes the decay product of ^{3}H (i.e., ^{3}He) and for ^{129}I and ^{14}C analyses by AMS (^{14}C sample is usually poisoned with mercury chloride to prevent any biological activity). These samples are filtered only (by a 0.45-μm membrane filter) on board the ship, and then carefully bottled to prevent any exchange of air with water. All the preparation chemistry is then carried out in the home laboratory.

Water sampling for traditional radionuclide analysis by RMTs requires collection of large-volume samples (100−500 L). This is very laborious and time consuming, especially if water has to be raised onto the ship deck from several kilometer depths (Povinec et al., 2003a). The operation with large-volume (around 100 L, 200 L, 500 L) samplers (e.g., of the Gerard−Ewing type) usually made from glass fiber reinforced plastic (Fig. 5.1) is very difficult and time consuming. After collection, the water is filtered (0.45 μm) and transferred by a pump to precipitation tanks for pretreatment.

The need for accurate and timely radiochemical measurements is the driving force behind the search for rapid methods with high selectivity, excellent purification



FIGURE 5.1 Large-volume seawater samplers of Gerard Ewing type (270 L), and deployment of the sampler. For the color version of the figure, the reader is referred to the online version of the book.



FIGURE 5.2 Rosette/CTD multibottle seawater sampling system. For the color version of the figure, the reader is referred to the online version of the book.

factors, and good chemical recoveries. Large-volume samples are too large to be transported to the laboratory; therefore, preconcentration should be carried out on shipboard. Consequently, the most important development in seawater sampling has been the introduction of the CTD/Rosette multibottle samplers (CTD/RMS) illustrated in Fig. 5.2. They have been employed for the collection of both small- and medium-volume samples by using one bottle per depth layer, or several bottles at the same depth. The volume and number of Niskin bottles used in a CTD/RMS sampler vary from type to type. Further advantages of the CTD/RMS sampler are online monitoring of oceanographic parameters, e.g., pressure, temperature, conductivity/salinity, dissolved oxygen, and sound velocity. Twenty-four sets of CTD data can be collected every second. The CTD/RMS system is submerged during operation at a vertical speed of 1−1.5 m/s, and the CTD data are monitored in real time in a dry laboratory on shipboard. The data obtained during downcast are usually used as the CTD profile data; seawater samples are collected during the upcast. In general, two casts, one shallow (up to about 1000 m) and one deep, are enough for deepwater sampling. In this way, the whole water column can be sampled more accurately and with only two casts (Povinec et al., 2004a, 2004b, 2004c).

B. Sediment sampling

Box corers or multiple corers, illustrated in Fig. 5.3, are usually used for sediment sampling down to a sediment depth of around 60 cm, although shallow samples can be obtained by hand sampling (Lee et al., 2017). Both types of corers have their advantages and disadvantages. Box corers allow subsampling of cores by the insertion of a plastic tube into the recovered sediment. They are easier to control and show relatively large undisturbed sediment surfaces. Simple grab corers (Fig. 5.3) have been used only for bulk surface sediment sampling, when radionuclide distribution with depth is not required for the study. A pinger fixed around 50 m above the corer is used for reading the relative distance of the box core from the seafloor, which is registered by an echo-sounder on the shipboard. The last 50−60 m from the bottom are recorded by a deep-sea echo sounder (DSES), and the winch cable is slowly lowered until the corer hits the bottom. The changes in cable tension are continuously recorded on an X−Y chart recorder. After successful retrieval of a box core, plastic tubes may be used to subcore sediments by slow penetration into the collected sediment (Fig. 5.3). Special care must be taken not to compress the sediment column by modifying the force while maintaining equal sediment surface levels inside and outside the wall of the plastic tube. When sediments are too cohesive, a vacuum pump should be used to ease the core liner into the sediment. The tubes containing sediment are capped on the top and plugged at the bottom with a plastic stopper with silicone O-rings to make the plugging water tight. After X-ray investigations for studying micro- and macrosediment structures (which can also be done later in the home laboratory on an extra collected tube), the tubes are sliced



FIGURE 5.3 Preparation of the box corer (left), multicorer (center), and a simple grab corer (right) for the bottom sediment sampling, and subsectioning of the box core. For the color version of the figure, the reader is referred to the online version of the book.

into predetermined sections (usually 0.5−1 cm thick) in the wet laboratory on the shipboard. Each sediment section is placed in a preweighted plastic container and kept at 4°C until the appropriate conditions for wet weighing are encountered. The samples are freeze-dried in the home laboratory and weighed again, thus determining the total sediment weight. This information is used to determine water content, bulk density, porosity, and the mass depth of the sediment column sampled, which are the sediment parameters needed for the correct interpretation of radionuclide results. The sediment remaining in the box after subsampling, usually from 0 to 5 cm, is squeezed to obtain pore water. The pore water is then filtered through a 0.45-μm filter and stored at 4°C in small bottles for subsequent analyses in the home laboratory.

A Kullenberg corer (Fig. 5.4) was used for the sampling of sediment columns a few meters in length (Povinec et al., 1999). As surface layers of sediment are usually compressed during sampling, this type of corer, which acts as a gravity corer, is not suitable for sampling surface sediment layers.

C. Biota sampling

Plankton invertebrates are collected using plankton nets generally of four different mesh sizes (1000, 500, 250, and 100 μm) with a ring aperture of around 1 m and a length of a few meters (Fig. 5.5). The nets are towed horizontally or rarely vertically. When towing horizontally at a depth of 10−20 m, it is possible to use nets with different meshes simultaneously (except for 100 μm nets which are very fragile and with which special precautions must be taken). The ship's speed is maintained at about 1 knot to avoid damaging both the nets and the animals collected. The sampling period is usually a few hours. The total volume of water, which passes through the nets, is estimated by a fixed current meter centered at the opening of one of the plankton nets. Upon retrieval of the net from the water, the collected animals are placed in labeled plastic containers and studied. Finally, they are frozen in plastic bags and cooled in a box cooler containing dry ice during transportation to the home laboratory.



FIGURE 5.4 Deployment of the Kullenberg corer in the Mururoa lagoon (left), radiation contamination checks of the sediment core in the plastic tube (center), and two sections of the sediment core (right). For the color version of the figure, the reader is referred to the online version of the book.

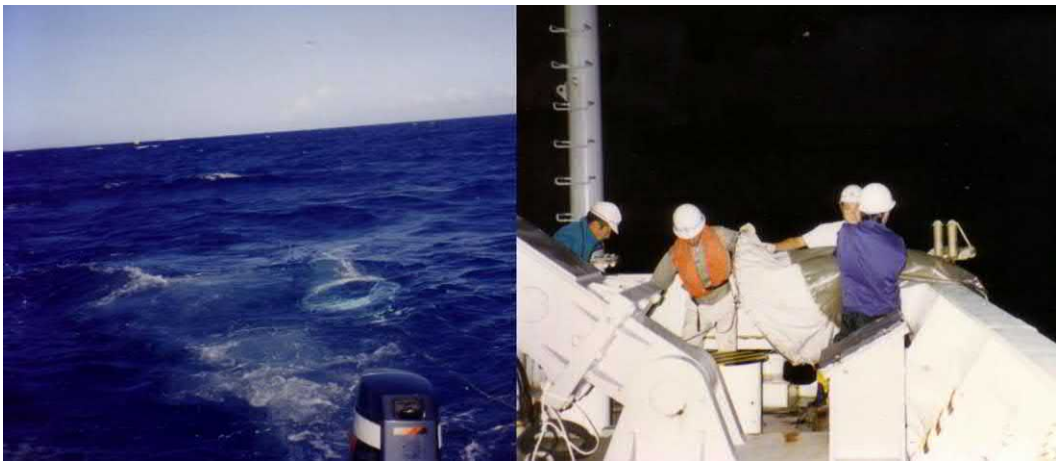


FIGURE 5.5 Plankton sampling with a net in the Mururoa lagoon (left) and recuperation of the net after plankton sampling (right). For the color version of the figure, the reader is referred to the online version of the book.

Samples of fresh algae are usually collected on plastic foils moored in the water column (Fig. 5.6). Fish, shellfish, and seaweeds are collected in a traditional way.

D. Sampling of particulate matter

A sediment trap consists of an upward-facing funnel that directs sinking particulate organic and inorganic material toward a mechanism for their collection and preservation (Fig. 5.7). The traps may be arranged as free floating or moored systems remaining in the water column for periods of months, thus enabling seasonal and annual changes in particle fluxes to be recorded. These studies have broadened our knowledge of ocean particulate dynamics and their links with the ocean carbon cycle (Fowler et al., 2000). Traps are often moored at a specific depth in the water column (usually below the mixed layer) in a particular location, but some are so-called Lagrangian traps that drift with the surrounding ocean currents (though they may remain at a fixed depth). The most important development



FIGURE 5.6 Recuperation of a plastic foil with algae after its exposition in the Mururoa lagoon. For the color version of the figure, the reader is referred to the online version of the book.

in the sediment trap sampling technique is the microprocessor-controlled sampling using sediment traps with sampling bottles changed according to pre-programmed time intervals, thus enabling the development of a continuous time series over a number of years. A formaldehyde solution in the bottles prevents the deterioration of sampled particulate matter throughout the sampling period.

III. Underwater gamma-ray spectrometry

A complimentary detection method to a traditional sampling and laboratory analysis is a direct, in situ analysis of radionuclides, e.g., in the air, soil, water, or sediment. We shall focus in this chapter only on underwater γ-ray spectrometry and applications in the aquatic environments. Such a novel approach can have several advantages, as complicated and laborious sampling, preconcentration and separation techniques, and long-term measurements are not necessary. On the other hand, mapping of γ-emitters in large surface areas is possible, which otherwise would require long-term sampling and measurement periods (Noakes et al., 1999; Jones, 2001; Osvath et al., 1999a; Osvath and Povinec, 2001; Povinec et al., 2001a). Further advantages include the screening of sunken or dumped radioactive objects (Osvath et al., 1999b), a continuous analysis of radionuclides in water replacing a sporadic short-term sampling and analysis, a real-time reporting of data, observation of temporal changes, and the development of a time series of data collected (Soukissian et al., 1999; Wedekind et al., 2000; Povinec, 2004; Van Put et al., 2004; Osvath et al., 2005; Povinec et al., 2006a, 2006b; 2008a, 2008b, 2008c; Tsabaris et al., 2012).

The systems most commonly used for the underwater γ-ray spectrometry are based on NaI(Tl) or BGO (bismuth germanate) detectors. The advantages of NaI(Tl)-based systems are firstly related to the high detection efficiency of NaI(Tl) crystals at much lower cost than equivalent HPGe crystals. Moreover, NaI(Tl)-based systems can be built sufficiently robust and are adequate for long-term underwater deployment. In addition, polycrystalline NaI(Tl) materials can be obtained with identical optical characteristics and far better thermal and mechanical strength than single crystals, thus further improving the shock resistance and thermal stability of the system. The drawbacks of NaI(Tl)-based systems are the high power consumption required for the operation of the photomultiplier tube and a relatively poor energy resolution of the detector (with peaks tens of times wider than those in spectra recorded with HPGe detectors). HPGe-based systems on the other hand have the advantage of good energy resolution and hence excellent radionuclide identification capability (Povinec et al., 1996, 2008a; Osvath et al., 1999a, 1999b). An HPGe (20% relative efficiency) underwater γ-ray spectrometer utilizes liquid propane cooling (Povinec et al., 1996). Because of the special cooling required for the working regime (the detector after its exposition in water should be cooled again down to the liquid propane temperature), the detector could operate underwater only for about 10 hours. The system was tested in the Irish Sea (Povinec et al., 1996), and the resultant spectra represent the first set of high-resolution seawater/seabed γ-ray spectra ever recorded in situ. Fig. 5.8 illustrates, as an example, a γ-spectrum obtained with the underwater HPGe detector in the Stepovoy Bay of the Novaya Zemlya island (the Kara Sea) where dumping of radioactive wastes was carried out in the past (Povinec et al., 1997; Osvath et al., 1999b).

Electrically cooled HPGe γ-ray detectors using Stirling cycle refrigerators have also been developed. The size of such a detector assembly is small and its power consumption is only ∼1 W (Kobayashi et al., 1998). Other available types of detectors, such as CsI crystals (pure or doped with Tl or Na), fluorides (e.g., CsF and BaF_2), or semiconductor detectors which do not require external cooling (e.g., CdTe, CdZnTe, HgI_2, and GaAs), have not become competitive

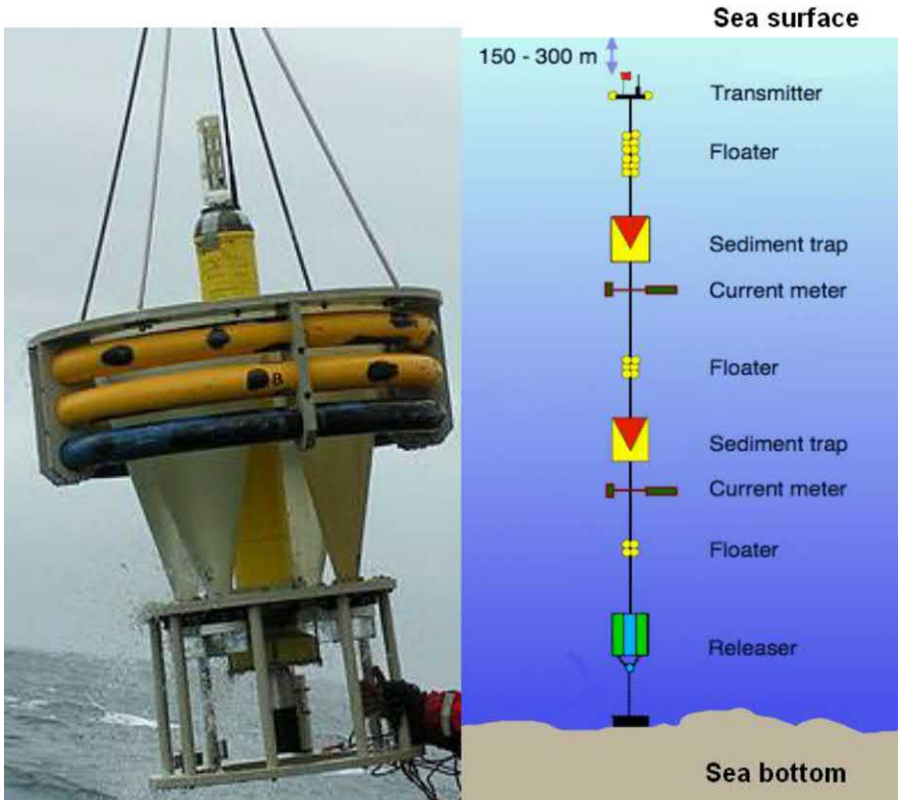


FIGURE 5.7 Recuperation of a sediment trap for the sampling of sinking particulate organic and inorganic material in the ocean (left), and mooring system for deployment of sediment traps (right). For the color version of the figure, the reader is referred to the online version of the book.

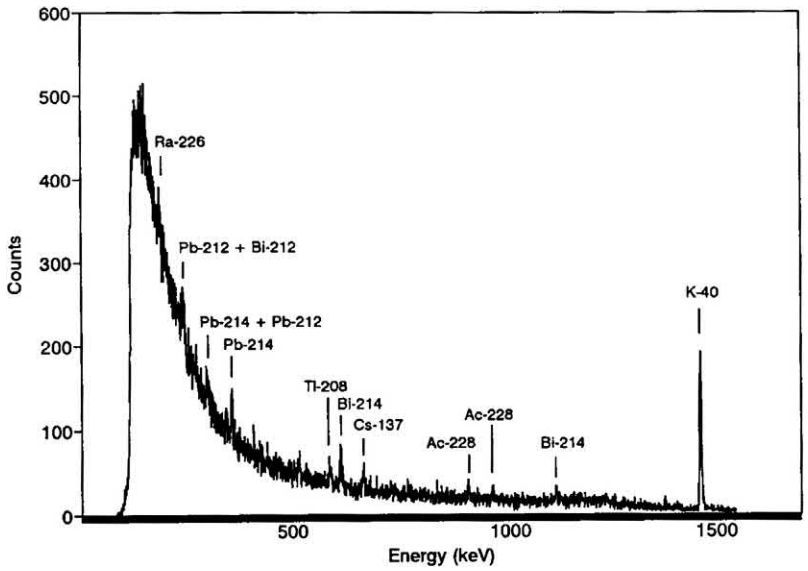


FIGURE 5.8 The γ-spectrum obtained with the underwater HPGe detector in the Stepovoy Bay of the Novaya Zemlya island (the Kara Sea) where dumping of radioactive wastes was carried out in the past. *Modified after Osvath et al. (1999a). Printed with permission © Elsevier 1999.*

with NaI(Tl) and HPGe detectors mainly because of their lower efficiency for the detection of γ-rays in the energy interval 30−3000 keV. Higher-energy *β-ray* emitters, such as ^{90}Sr, could be monitored in water either via Cherenkov radiation and/or via bremsstrahlung (Chernayev et al., 1999).

A. Towed detector systems

We shall describe, as an example, an in situ γ-spectrometric system consisting of a NaI(Tl) probe operating with a shipboard computer, a power supply, and data acquisition electronics (Osvath and Povinec, 2001). A stainless steel tubular probe casing houses a 152 × 51 mm NaI(Tl) ruggedized crystal; a high gain photomultiplier tube; pressure, temperature, and seabed roughness sensors; and electronic circuit boards, which provide power to the sensors and process the signals (Fig. 5.9). Data are transferred from the probe to the logging computer every second and can be sequentially stored. A generated 300-channel spectrum covers the energy range from 100 to 3000 keV. The logging program on the computer allows the monitoring of the spectrum recording and of the total count rate, bottom ruggedness, pressure, and temperature. The energy calibration of the γ-ray spectrometer was carried out using ^{137}Cs and ^{60}Co radioactive sources. The energy resolution for 662 keV (^{137}Cs) γ-rays was 6.5%. The efficiency calibration was done using a ^{137}Cs source dispersed in a polyethylene tank 1 m in diameter and 1 m high, filled with freshwater. The tank was later filled with seawater with natural concentration of ^{40}K (1462 keV), ^{226}Ra, and ^{222}Rn and its daughter products. Background measurements were carried out with the detector immersed in the tank filled with freshwater without any additional tracers (Povinec et al., 2006a, 2006b).

Another example of the state-of-the-art technology is a mobile underwater γ-spectrometer developed by the Japan Atomic Energy Research Institute (JAERI, 2005). The ROV-based system is equipped with γ-detectors (NaI(Tl) and HPGe), CTD, water and sediment sampling devices, cameras, etc., as illustrated in Fig. 5.10. The system has been used for seawater monitoring and sea-bottom prospection in coastal waters of Japan (JAERI, 2005).

B. Stationary detector systems

The NEMO (Nautic Environment Marine Observatory), a stationary underwater monitoring system, based on a NaI(Tl) detector (Fig. 5.11), is another type of in situ γ-ray spectrometer (Osvath et al., 2005). It records γ-ray spectra in water together with a suite of environmental parameters including seawater temperature, conductivity, current speed, and its direction. These data may be transmitted via a satellite link to a base station. The monitor's capabilities can be further expanded by adding sensors for meteorological (wind speed and direction, air temperature, and pressure) and oceanographic measurements (wave height, direction and period, water temperature and salinity profiles, light attenuation, chlorophyll-A, and hydrocarbon content measurements). The water current speed and its direction are measured with a three-axis ultrasonic transducer, with ranges of 0−300 cm/s and 0−360 degrees and uncertainties of 3% and 2%, respectively. The temperature sensor has an operational range of −5°C to +45°C with an uncertainty of 0.1°C. Salinity is determined from conductivity measurements performed with an electrodeless induction type cell. The sensors are suspended 4 m underwater on a structure attached to a floating buoy.

The NaI(Tl) detector, 76 mm in diameter and 76 mm in length, made of ruggedized crystal, has a 7% resolution for

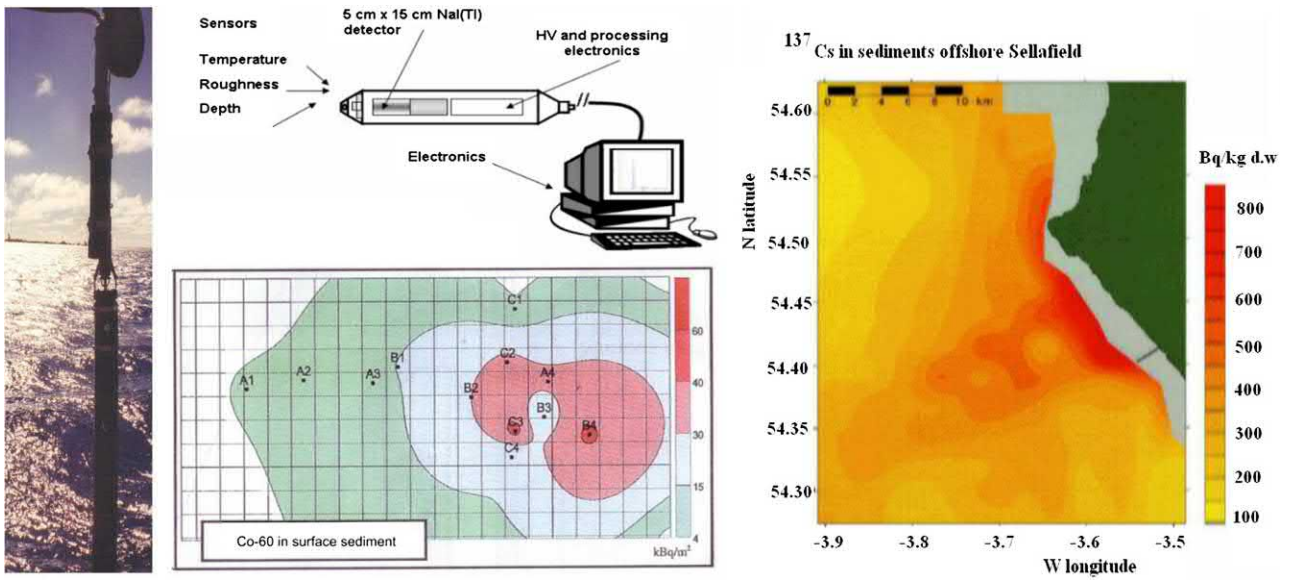


FIGURE 5.9 Underwater γ-ray spectrometer (top); its deployment in the Mururoa lagoon with a camera (left); ^{60}Co in Fangataufa lagoon sediments (bottom); and ^{137}Cs in sediments offshore Sellafield (right). For the color version of the figure, the reader is referred to the online version of the book.

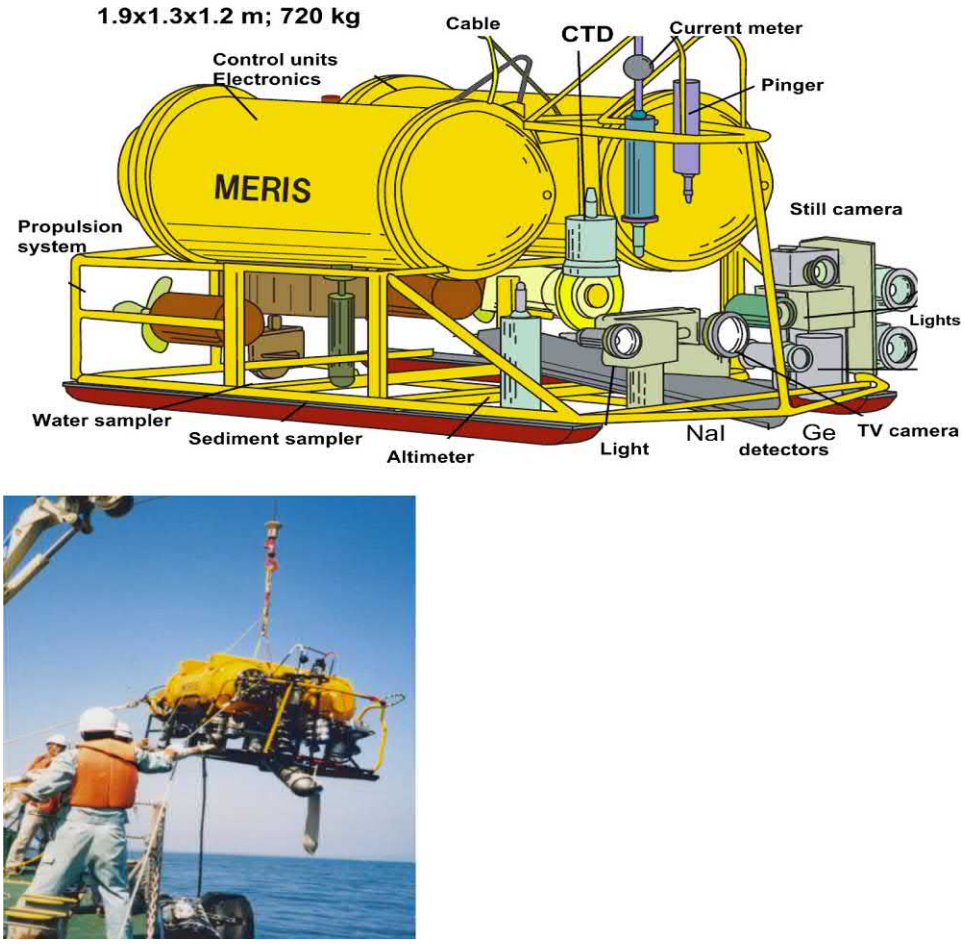


FIGURE 5.10 Remotely operating vehicle—based system for prospection of the sea developed by the Japan Atomic Energy Research Institute. For the color version of the figure, the reader is referred to the online version of the book. *From JAERI (2005); printed with permission of the Japan Atomic Energy Agency. Printed with permission © 2005 Japan Atomic Energy Agency.*

662-keV γ-rays (^{137}Cs). The calibration of the NaI(Tl) detector was carried out in a tank filled with seawater spiked with ^{137}Cs. The efficiency was estimated to be 2.1×10^{-4} s^{-1}/(Bq/m^3) under the ^{137}Cs photopeak. The limit of detection for ^{137}Cs in water is 19 Bq/m^3 for a 24-h spectrum integration time or 4 Bq/m^3 for a 30-day integration time. The buoy is equipped with signal processing electronics, including a microcomputer and a marine transceiver, as well as with a set of batteries. An integrated GPS receiver continuously records the buoy position. The instruments and batteries are maintained in a nitrogen atmosphere in an air- and water-tight container. The NEMO's autonomy is supported by a set of solar panels installed on the instrument container. The satellite antenna and visual signal devices are mounted on the top deck, about 4 m above water level. The NEMO observatory was deployed in the Irish Sea with satellite data transmission to the IAEA-EL, Monaco (Osvath et al., 2005; Povinec et al., 2008a).

C. Applications of underwater gamma-ray spectrometry

1. Mururoa and Fangataufa lagoons

A survey of Mururoa and Fangataufa lagoons in the French Polynesia (the South Pacific Ocean) was carried out with the aim to assess their radioactive contamination (water, sediment, and biota) after nuclear weapons testing (Povinec et al., 1999). ^{60}Co and ^{137}Cs were the main γ-ray emitters present in lagoon sediment. The in situ sediment measurements were used to guide the sediment sampling campaign in the most contaminated areas of the lagoons where surface tests of nuclear weapons had taken place. A distribution of ^{60}Co in the Fangataufa lagoon sediment (Fig. 5.9) showed activities up to 60 kBq m^{-2}. A good correlation ($R^2 = 0.8$) found between ^{60}Co and ^{239,240}Pu concentrations (^{239,240}Pu is the radionuclide of the main interest in lagoon sediments) enabled the estimation of ^{239,240}Pu inventories on the basis of ^{60}Co mapping and

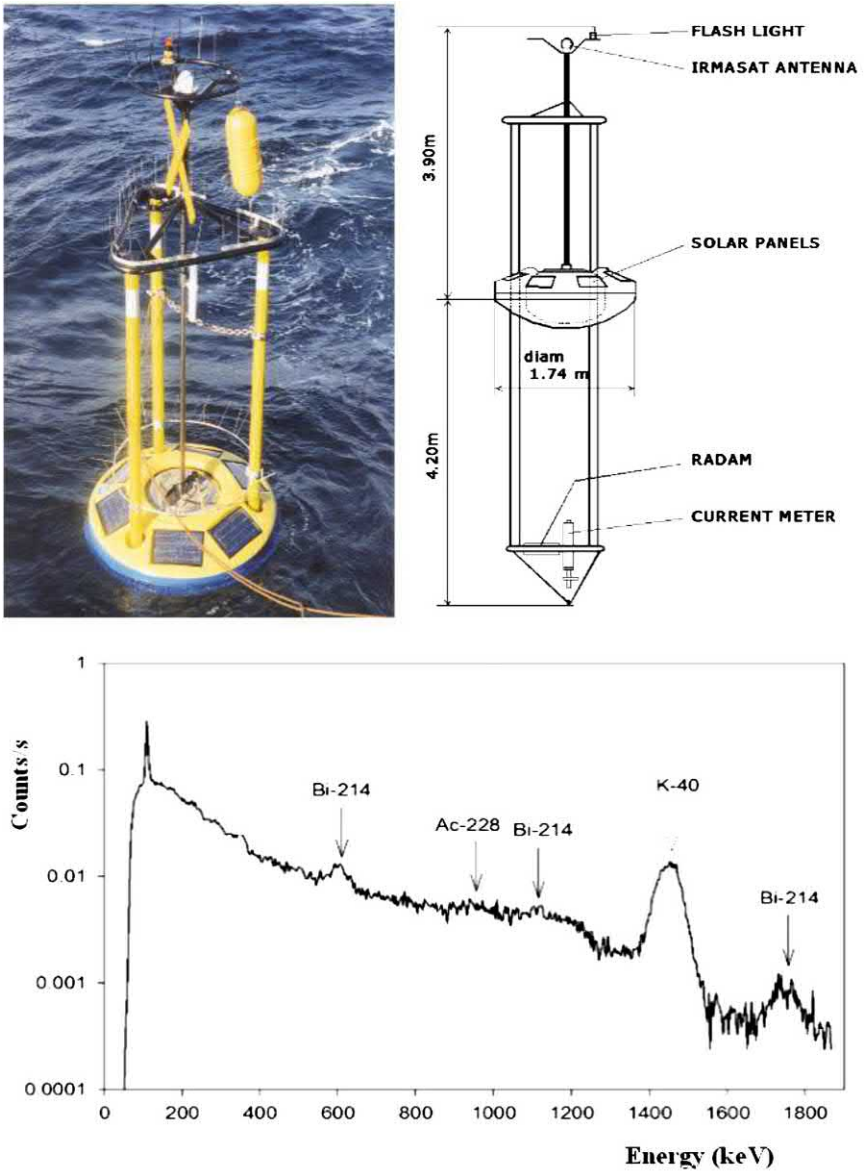


FIGURE 5.11 The NEMO (Nautic Environment Marine Observatory), a stationary underwater monitoring system, based on a NaI(Tl) detector (top), and a γ-spectrum of seawater (bottom) measured in the Irish Sea during a heavy rain when the ^{137}Cs peak (662 keV) was masked by the ^{214}Bi peak (609 keV) as a result of washout of radon decay products from the air. *Modified after Osvath et al. (2005). Printed with permission, Springer Science + Business Media Copyright, 2005.*

laboratory analysis of ^{239,240}Pu in sediments (Osvath et al., 1999a; Povinec et al., 1999).

2. Novaya Zemlya bays

Novaya Zemlya bays in the Kara Sea were visited with the aim to assess radioactive contamination of water and sediment after the dumping of radioactive wastes (Povinec et al., 1997). Fig. 5.8 shows a γ-spectrum measured with the underwater HPGe detector with propane cryogenic cooling at one of the stations in Stepovoy Bay. The far superior resolution of the HPGe detector has enabled observation of a low ^{137}Cs concentrations, which were not visible in the NaI(Tl) γ-spectrum. The ^{137}Cs sediment contamination close to dumped radioactive containers was up to 10 kBq/kg dry weight (Osvath et al., 1999b).

3. Mapping of coastal sediments in the Irish Sea

Seabed γ-mapping of radionuclides (mainly ^{137}Cs) was carried out in the Irish Sea close to the Sellafield nuclear reprocessing facility. Fig. 5.9 shows the distribution of ^{137}Cs in surface sediments close to the outlet of liquid

discharges from the Sellafield reprocessing facility. The measured ^{137}Cs levels in the sediment were up to 1 kBq/kg dry weight. They were lower by 40%–70% than the results obtained 10 years ago, documenting that a remobilization of ^{137}Cs in sediment of the Irish Sea has been effective (Osvath and Povinec, 2001; Osvath et al., 2001).

4. Monitoring of ^{137}Cs in Irish Seawaters

In situ stationary γ-monitoring of radionuclides in seawater in the NW Irish Sea with satellite data transmission to IAEA-EL, Monaco, was carried out using the NEMO system with the objective of searching for resuspension of ^{137}Cs from sediment and studying possible changes in its concentration in surface water associated with releases from the Sellafield reprocessing facility. The second aim was to search for changes in circulation patterns of the western Irish Sea gyre during the summer months. The obtained results indicate that at the time scale of months, no significant changes were detectable in ^{137}Cs concentration in seawater. Fluctuations of ^{137}Cs levels over shorter time scales were within the range of uncertainty (Osvath et al., 2005). Fig. 5.11 shows a γ-ray spectrum of water (at 4-m water depth) taken with the NEMO observatory in the Irish Sea during a heavy rain when the ^{137}Cs peak (662 keV) was completely masked by the ^{214}Bi peak (609 keV) as a result of washout of radon decay products from the air. The dominant peak in the spectrum is due to ^{40}K.

5. Submarine groundwater discharge studies

The in situ, fully automatic γ-spectrometers for continuous monitoring of radionuclides in the aquatic environment were also applied to the monitoring of natural radionuclides such as ^{40}K, ^{228}Ra, and radon decay products, which are commonly used as tracers for studying marine and coastal processes. A frequently studied coastal process is submarine groundwater discharge (SGD) because of its potential importance in the management of freshwater resources in coastal areas (Burnett et al., 2006; Povinec et al., 2006a, 2006b, 2008a, 2008b, 2008c, 2012). New technologies developed in recent years have been used to carry out temporal and spatial monitoring of SGD via the analysis of radon and its decay products emitting γ-rays. Radon is a conservative tracer in groundwater–seawater systems, and because its concentration in groundwater is much higher than in seawater, it is an ideal tracer for studying groundwater–seawater interactions (Burnett et al., 2006). ^{222}Rn is a decay product of ^{226}Ra (half-life 1600 y) in the ^{238}U natural decay chain, and due to its short half-life (3.82 d), it is a suitable tracer for studying dynamic systems that are usually found in coastal regions. ^{222}Rn daughters are short-lived radionuclides such as ^{214}Pb and ^{214}Bi, which undergo alpha- and beta-decays to medium-lived ^{210}Pb (22.2 y) and ^{210}Po (138 d), and finally to the stable ^{206}Pb. In the ^{232}Th natural decay chain, there is another radon isotope, ^{220}Rn (also called thoron), with a shorter half-life (55.6 s). ^{220}Rn is a decay product of ^{224}Ra (half-life 3.66 d) which further decays to several short-lived daughter products, including ^{208}Tl (half-life 183 s), and finally to stable ^{208}Pb.

As short-lived daughter products of both radon isotopes, ^{222}Rn and ^{220}Rn, emit γ-rays, in situ γ-spectrometry would be a suitable nondestructive technique of their analysis in seawater, replacing time-consuming analysis of ^{222}Rn in the marine environment (Povinec et al., 2006b, 2006c). In situ γ-spectrometry has the advantage that it also can analyze simultaneously other radionuclides, e.g., ^{40}K, ^{228}Ra (via its daughter ^{228}Ac), ^{234}Th–^{234}Pa, and others. The best-visible γ-lines in the γ-ray spectrum of seawater are due to ^{214}Bi (609, 1120, and 1765 keV) for ^{222}Rn daughters, and due to ^{212}Pb (239 keV) and ^{208}Tl (583 and 2615 keV) for ^{220}Rn decay products. Fig. 5.12 compares γ-spectra of groundwater and seawater measured by the NaI(Tl) detector presented in Fig. 5.9. The main differences between groundwater and seawater are well visible—groundwater shows higher concentrations of ^{222}Rn decay products and absence of ^{40}K.

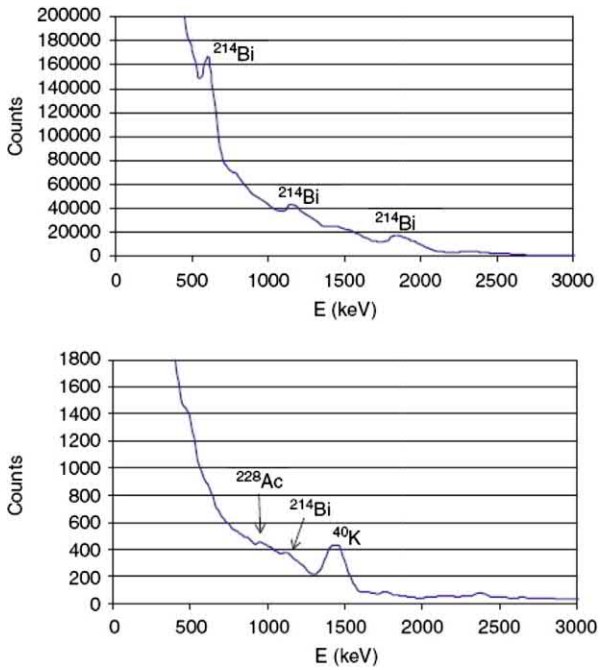


FIGURE 5.12 A comparison of γ-spectra of groundwater (top) and seawater (bottom) measured by the NaI(Tl) detector (Fig. 5.9) in the Donnalucata intercomparison. The main difference is the higher concentrations of ^{222}Rn decay products and absence of ^{40}K in groundwater. *Modified after Povinec et al. (2006c). Printed with permission © Elsevier 2006.*

a. Sicily/Italy SGD site

Time series data of ^{222}Rn in seawater, salinity, and tide were recorded with the small NaI(Tl) submersible detector (Fig. 5.9) at a site close to the coast in the southeastern Sicily (near Donnalucata town). Results presented in Fig. 5.13 document that, after the maximum tide, the ^{222}Rn activity concentration of seawater was at a minimum (down to 2.3 kBq/m^3), and after the minimum tide, the ^{222}Rn activity concentration was at maximum (up to 4.8 kBq/m^3) with a delay of about 1 hour. A shift of approximately 2 hours was observed between the maximum tide and the salinity maximum. It is interesting to see that even small changes in the water level, observed, e.g., during March 21 and 22, made corresponding changes in ^{222}Rn activity concentrations (Povinec et al., 2006a, 2006b).

b. Brazil SGD site

Continuous underwater γ-spectrometry measurements were carried out in several bays along the Ubatuba coast (Povinec et al., 2008b, 2008c, 2008d). The ^{222}Rn activity concentration in seawater during time-series measurements varied between 1.0 and 5.2 kBq/m^3, while the tide varied between 4.4 and 5.6 m, and generally, the salinity record followed the tide record. The calculated SGD fluxes from radon measurements showed similar patterns with time as the ^{222}Rn concentrations (Fig. 5.13). The SGD fluxes obtained from ^{222}Rn measurements varied between 8 and 35 cm/d (the unit is cm^3/cm^2 per day), with an average value of 21 ± 10 cm/d, and they were in reasonable agreement with those obtained from seepage measurements (Povinec et al., 2008b). The spatial ^{222}Rn activity concentrations observed at eight stations varied between 50 and 200 Bq/m^3 (Povinec et al., 2008c). Fortunately, due to elevated concentrations of ^{232}Th in the region, it was possible to measure for the first time nondestructively ^{228}Ra in seawater (via its daughter gamma-ray emitter ^{228}Ac) as well as ^{220}Rn (via its daughter product ^{208}Tl). ^{228}Ra and ^{220}Rn activity concentrations measured in Flamengo and Picinguaba bays varied between 1.6 and 3.3 Bq/m^3. They

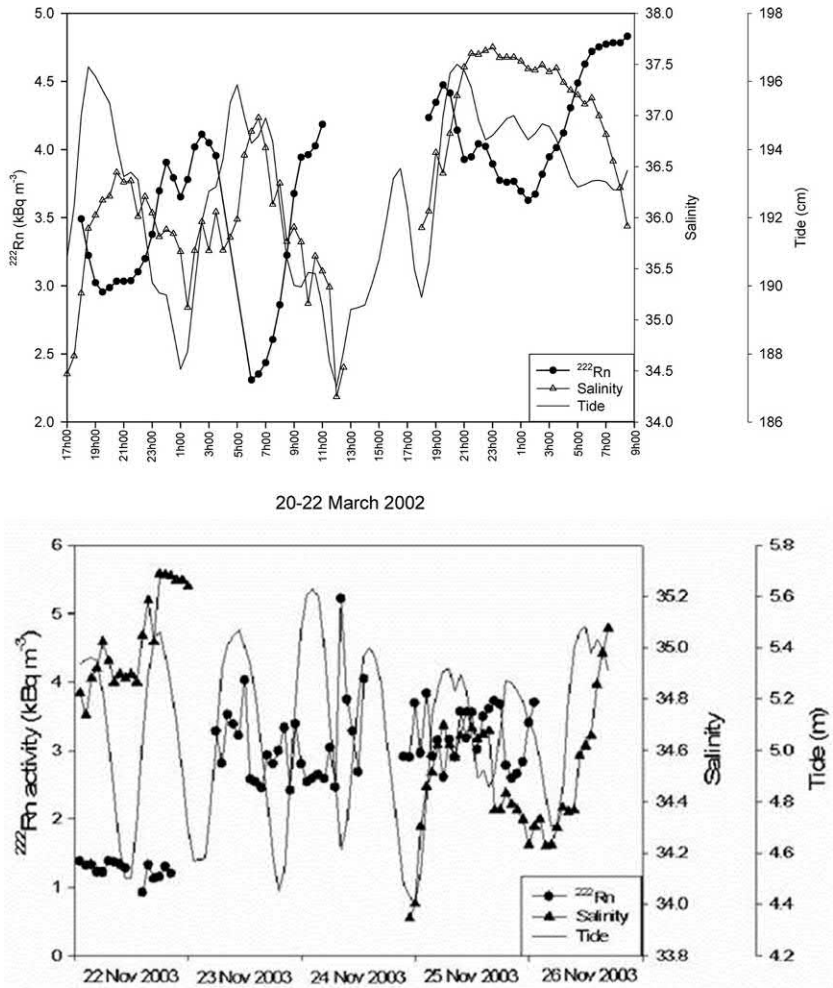


FIGURE 5.13 Time series of ^{222}Rn (^{214}Bi) concentrations in seawater offshore Donnalucata, Sicily/Italy (top), and Ubatuba, Brazil (bottom), versus salinity and tide. *Modified after Povinec et al. (2006b, 2008c). Printed with permission © Elsevier 2006, 2008.*

were following the ^{222}Rn concentrations measured at the same stations (Povinec et al., 2008c).

IV. Analysis of natural radionuclides

The natural radioactive thorium–uranium decay series (Fig. 5.14) provides a natural clock for several transport and reaction processes in the marine environment. Relatively soluble radionuclides (e.g., U, Ra, and Ac) besides insoluble radionuclides (e.g., Th, Pa, and Pb) cause daughter/parent disequilibria in certain compartments of the marine environment, which can be utilized to derive times scales of oceanic processes (Cochran and Krishnaswami, 2008). We can distinguish between radionuclides which are highly particle reactive in seawater and which are produced by the decay of soluble parent radionuclides, e.g., Th/U, Pa/U, and Pb/Ra (Rutgers van der Loeff and Moore, 1999). Such radionuclides are particularly useful for various studies of the marine environment including:

- Estimation of particle fluxes in the water column (^{234}Th/^{238}U and ^{210}Po/^{210}Pb) (Coale and Bruland, 1985; Eppley, 1989; Nozaki et al., 1991; Rutgers van der Loeff et al., 2006).
- Determination of sediment accumulation rates (^{230}Th/^{234}U, ^{210}Pb) (Allen et al., 1993; Appleby, 2013; Bacon, 1984; Baskaran and Naidu, 1995; Scholten et al., 1994).
- High-precision age dating of corals for the reconstruction of past climate changes (^{230}Th/^{234}U, ^{231}Pa/^{235}U) (Edwards et al., 2003; Stirling and Andersen, 2009; van Calsteren and Thomas, 2006).
- Determination of water mass circulation in the geological past (^{231}Pa/^{230}Th) (Hayes et al., 2015; Moran et al., 2002; Vogler et al., 1998; Yu et al., 1996).
- Calibration of sediment trapping efficiency (^{234}Th/^{234}U, ^{230}Th) (Buesseler, 1991; Buesseler et al., 2006; Scholten et al., 2001).
- Quantification of particle flux caused by resuspension of sediments (^{234}Th/^{238}U) (Bacon and Rutgers van der Loeff, 1989; Rutgers van der Loeff et al., 2002).

Soluble daughter radionuclides such as ^{228}Ra, ^{226}Ra, ^{224}Ra, ^{223}Ra, and ^{227}Ac which are produced by the decay of insoluble parents as well as ^{222}Rn and the cosmogenic ^{7}Be are particularly useful for studies of water mass mixing, upwelling, as well as the determination of eddy diffusion coefficients (Berelson et al., 1982; Burnett and Dulaiova, 2003; Geibert et al., 2002; Kadko, 2009, 2017; Ku and Luo, 2008; Moore, 2000).

We will describe the techniques most frequently used to analyze the radionuclides in marine studies, i.e., thorium isotopes, ^{231}Pa, uranium isotopes, radium isotopes, ^{210}Pb, ^{210}Po, ^{222}Rn, and ^{7}Be. In general, the type of analytical technique applied to the measurement of these radioisotopes will depend on the available instrumentation (e.g., mass spectrometry and/or radiometric methods) and the environment studied. We will describe here the most common procedures but will also give references to alternative methods where deemed appropriate. For latest developments in sampling protocols and analytical techniques, the reader is referred to the program "International Study on Marine Biogeochemical Cycling of Trace Elements and their Isotopes (GEOTRACES)" (www.geotraces.org).

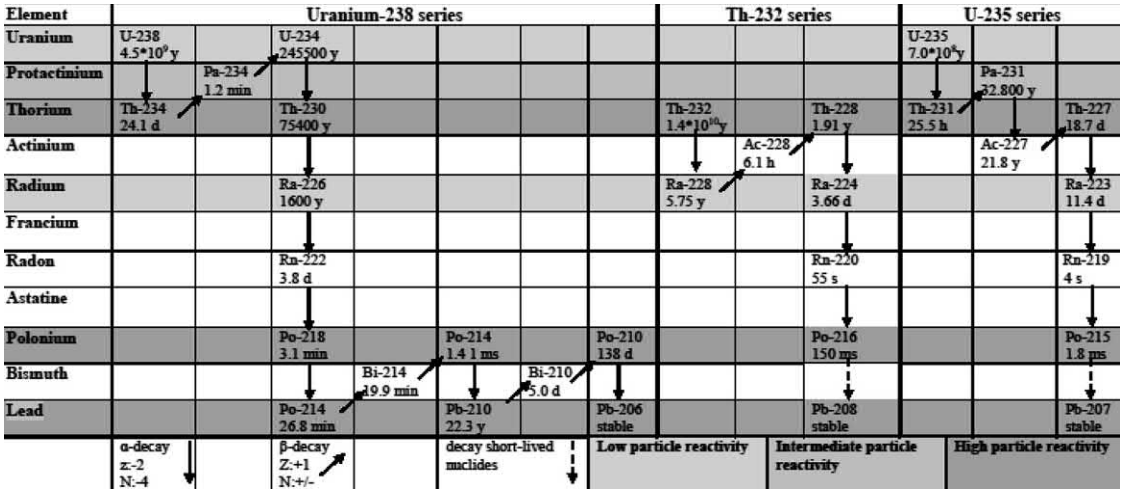


FIGURE 5.14 The uranium–thorium decay series with half-lives of the radioisotopes.

A. Thorium, protactinium, and uranium isotopes

1. Sampling of seawater

Due to the low concentrations of ^{230}Th and ^{231}Pa in seawater (~0.1−50 fg/L), previous investigations used in situ filtration pumps (McLane, Challenger) to determine these radioisotopes by means of α-spectrometry (Rutgers van der Loeff and Moore, 1999). The pumps are equipped with particle filters and in-line MnO_2 impregnated cartridges which adsorb the dissolved radionuclides. This technique permits the determination of particulate and dissolved matter from the same volume of water. However, due to advances in analytical measurement techniques, the preferred method for the determination of ^{230}Th and ^{231}Pa in seawater is now mass spectrometry (TIMS, ICPMS, multi-collector ICPMS (MC-ICPMS)) (Anderson et al., 2012). This technique combines smaller sample sizes with much higher precision of the measurements. About 2−5 L (for ^{230}Th) and 10−20 L (for ^{231}Pa) of seawater (filtered or unfiltered) are filled in acid-clean bottles or cubi-containers. After collection, the samples are acidified with concentrated HCl to pH ≤ 2. Further processing of the samples at sea has the advantage of avoiding transport of large water volumes but requires a determination of the exact sample volumes and the possibility for handling of radioactive yield tracers on ships. As tracers, ^{229}Th ($T_{½}$ = 1700 y; note that the tracer solution should have a ^{229}Th/^{230}Th ~ >1 × 10^4) and ^{233}Pa ($T_{½}$ = 27 days) are used. The ^{233}Pa tracer solution is obtained by milking ^{237}Np (Shen et al., 2003) or by neutron activation of ^{232}Th (Bourdon et al., 1999). After adding appropriate amounts of spikes, the sample is stored for ~24 hours to allow for chemical equilibration. Further preconcentration can be achieved by adsorption of Th and Pa on Fe-hydroxides, Mg-hydroxides, or Mn-hydroxides. For Fe-precipitation, 0.05 mL $FeCl_3$ (50 mg Fe/mL; cleaned by extraction in isopropyl) per liter is added and, after allowing for equilibration (~24 hours), ammonium is added to increase the pH ~7−8. The Fe-precipitates are allowed to settle, and the supernatant is siphoned off. For preconcentration using Mg-hydroxides, NH_4OH (ultraclean) is added until white precipitates form, which are allowed to settle, and the supernatant is siphoned off (Scholten et al., 2008). In order to reduce the amount of precipitates, HNO_3 is carefully added. Samples have to be shaken after each acid addition, and after centrifugation, the supernatant is siphoned off. For preconcentration using Mn-hydroxides, a few drops of ultraclean concentrated ammonium hydroxide are added together with 0.75 mg/L $KMnO_4$ and 2 mg/L $MnCl_2$ (Rutgers van der Loeff et al., 2006). After 24 hours, the MnO_2 precipitates are filtered on 1-μm filters.

Due to a high concentration of uranium (~3 ng/L = ~2.4 dpm/L) only ~10 mL of seawater is needed for mass spectrometric measurements of uranium. If α-spectrometry is the method of choice, about 2 L of seawater are required. The first preconcentration step is via Fe-hydroxide precipitation, as described above. As the yield tracer, a double ^{233}U−^{236}U spike for mass spectrometric measurements or a single ^{236}U (^{232}U for α-spectrometry) spike may be used.

2. Sampling of particulate matter and sediments

Determination of ^{230}Th and ^{231}Pa on suspended particulate matter using MC-ICPMS requires seawater volumes of about 10−20 L for ^{230}Th and 100−200 L for ^{231}Pa. Such volumes from deep waters can be obtained using in situ filtration pumps equipped with membrane/polycarbonate filters (0.4 μm or 1 μm pore size).

The relatively high ^{230}Th, ^{231}Pa, and uranium concentrations in sediments allow their determination using conventional α-spectrometry. The amount of sediment needed normally varies between 0.05 and 0.25 g depending on the origin and composition of the sediments.

3. Dissolving of particulate matter and sediments

The determination of ^{230}Th, ^{231}Pa, and uranium in suspended particles and in sediments requires digesting of the sample matrix in the presence of ^{229}Th, ^{233}Pa, and uranium yield tracers. The ^{233}Pa contains trace amounts of ^{232}Th which may bias thorium measurements, especially when, e.g., suspended particles with low thorium concentrations are analyzed. For such samples, it is recommended that the spikes be added after dissolving the particle filter and separating the solution (gravimetrically) into a thorium fraction (~10% of the total solution) and into a protactinium fraction (Scholten et al., 2008).

Particles on membrane and/or polycarbonate filters can be dissolved in a microwave oven in a mixture of 2 mL conc. HF and 4−6 mL conc. HNO_3 (Negre et al., 2009). Thereafter, the solution is evaporated down to near dryness on a hot plate and taken up in conc. HNO_3 (note that working with HF in open vessels requires special fume hoods, i.e., with water rinsing of the outlet channels). This step is repeated twice in order to remove any fluorides. Thereafter, the sample is dissolved in 2 M HCl and 1 μL $FeCl_3$ (50 mg Fe/mL; cleaned by extraction in isopropyl alcohol) is added followed by precipitation of Fe-hydroxides by adding appropriate amounts of conc. NH_3. This step removes alkali and alkali earth metals. The precipitates are centrifuged down, and the supernatant is

siphoned off. The precipitate is washed three times with Milli-Q water. If no microwave is available, filters can be leached following the procedure described by (Landing and Lewis, 1991): The filters are placed for 4 hours in a Teflon beaker on a hot plate in a mixture containing 1 mL conc. HF and ~20 mL "aqua regia" (mixture of conc. HNO_3 and conc. HCl). The filters are then removed from the solution and rinsed with 6 M HCl. The solution is evaporated down to near dryness on a hot plate. The sample is taken up in a few mL of conc. HNO_3 and is evaporated down to near dryness; this step is repeated twice. Finally, the sample is taken up in diluted HCl, and 1 μL $FeCl_3$ is added followed by Fe-hydroxide precipitation caused by adjusting the pH to 7–8 using conc. NH_3. The precipitates are centrifuged down and washed three times with Milli-Q water.

Total dissolution of marine sediments is best achieved by using a microwave (Gupta and Bertrand, 1995; Kuss, 1992; Negre et al., 2009). About 50–200 mg of homogenized freeze-dried sediment is placed in the Teflon beakers of the microwave, and appropriate amounts of ^{229}Th, ^{233}Pa, and ^{236}U spikes are added. Then a mixture of 10 mL conc. HNO_3, 4 mL conc. HCl, and 6 mL of conc. HF is added. It is advisable to wait for carbonate dissolution before processing the samples in the microwave to avoid overpressure. Thereafter the solution is evaporated to near dryness. Negre et al. (2009) report a better chemical recovery for protactinium, if an additional step with 9 mL of reverse aqua regia (6 mL HNO_3 + 3 mL HCl) is added. The solution is evaporated down to near dryness and taken up in 6 mL conc. HNO_3. This step is repeated twice. A further step to remove alkaline and alkaline earth metals by Fe-hydroxide precipitation (as described above) may facilitate subsequent ion-exchange procedures.

The dissolution of sediments may also be achieved by conventional digestion techniques using open vessels or Teflon bombs applying hot-plate heating with a mixture of HNO_3/HF (3 mL/2 mL) followed by evaporation to near dryness. Thereafter a few mL of conc. $HClO_4$ are added and fumed at ~190°C. Complete dissolution may be hampered due to the presence of minerals such as zircon and barite which are difficult to dissolve; the above procedure may have to be applied multiple times. In a final step, the sample is taken up in diluted HCl; ~1 μL $FeCl_3$ is added followed by the addition of NH_3 to precipitate Fe-hydroxides which are centrifuged. The precipitate is further washed and centrifuged with Milli-Q water three times.

4. Ion-exchange separation

Both mass spectrometry and α-spectrometry measurements of thorium, protactinium, and uranium require further purification in order to remove interferences in masses and in the α-energy spectrum. These purifications are achieved by chromatographic resins which can extract certain elements from solutions. The most commonly used resins are the anion-exchange resins (e.g., Bio-Rad AG1-X8, Dowex AG1-X8; Eichrom 1-X8; see e.g., Anderson and Fleer, 1982; Auro et al., 2012; Edwards et al., 1986/87; Rutgers van der Loeff and Moore, 1999), UTEVA resin (Kretschmer et al., 2010; Rodriguez y Baena et al., 2006) and TRUE resin (Bourdon et al., 1999; Goldstein and Stirling, 2003; Luo et al., 1997).

The anion-exchange resin AG1-X8 (e.g., from Bio-Rad, Eichrome), which is most commonly used for α-spectrometric measurements of thorium, protactinium, and uranium in sediments, require several column separations (Anderson and Fleer, 1982). First, the column (depending on the size of the sample up to 13 cm long and of a diameter up to 13 mm) is conditioned with 9 M HCl. The sample is dissolved in 9 M HCl and poured over the column, washed three times the column volume (cv) with 9 M HCl. This step elutes all the Th (as well as alkali and earth alkali elements). Thereafter the column is rinsed 3× cv with 9 M HCl + 0.13 M HF to remove Pa, and in the final step U together with Fe is eluted with 3 cv 0.1 M HNO_3. The three fractions are evaporated to near dryness (forming of precipitates should be avoided), and 8 M HNO_3 is added. The Th and U fractions are poured over separate AG1-X8 columns conditioned with 8 M HNO_3. The columns are rinsed with 3 cv 8 M HNO_3 to remove Ca (Th fraction) and Fe (U fraction). Th and U are eluted with 3 cv 9 M HCl and 3 cv 0.1 M HNO_3, respectively. After evaporating to dryness, a tiny yellow or brown spot should remain. Large reddish or white material will result in poor electroplating. The Pa fraction is evaporated down to near dryness in the presence of 8 M HNO_3 at least twice to remove all fluoride. The Pa fraction is dissolved in 9 M HCl and poured over AG1-X8 column conditioned with 9 M HCl, and Pa is eluted with 3 cv 9 M HCl + 0.13 M HF. This last step removes any remaining thorium and uranium. After evaporating down three times in the presence of 8 M HNO_3, the Pa sample is ready for electroplating. Recently, poor Th recovery and an increase in procedure blanks were reported for Th seawater analyses when using Bio-Rad columns filled with AG1-X8 resin (Auro et al., 2012). These authors modify the method for Th and Pa seawater analyses described above by using Eichrom anion exchange resin (100–200 μm mesh) and Eichrom Environmental Express columns together with higher acid concentrations.

In extraction chromatography using TRUE resin (Goldstein and Stirling, 2003; Luo et al., 1997), about 2–10 mL (depending on sample sizes) of TRU resin is conditioned with 6 cv 0.01 M HCl and 4 cv 10 M HCl. The sample is dissolved in 10 M HCl, and an equal volume of 10 M HCl plus saturated H_3BO_3 (to complex HF) is added. The sample is loaded on the column and washed with 1× cv 9 M HCl (note that the elution contains the radium

fraction). Thorium is eluted by adding 1 cv of 4 M HCl and then 10 cv of 1.2 M HCl. Uranium and protactinium are washed from the column by adding 10 cv 0.1 M HCl +0.05 M HF. In a further AG1-8X column conditioned with 9 M HCl, Pa is separated from U and remaining Th. Other authors use slightly different acid concentrations for the Th, Pa, and U separations (e.g., Bourdon et al., 1999; Luo et al., 1997).

In extraction chromatography using UTEVA, the sample is loaded in 4 M HNO_3 on a column conditioned with 4 M HNO_3. In order to increase the recovery of Th, it is recommended that chemical analogs such as Ti^{4+} and Zr^{4+} (~1 mg) be added when conditioning the UTEVA columns (Rodriguez y Baena et al., 2006). This is especially important for samples with little matrix such as seawater samples. Di- and trivalent ions (e.g., Mn, Fe, Ca, Pb, Bi, Ra and Ac) are washed from the column by 3 cv 4 M HNO_3, whereas hexavalent U and tetravalent Th ions are not (Horwitz et al., 1993). Th is eluted with 3 cv 6 M HCl, U, and Pa by 3 cv of 0.02 M HCl + 0.02 M HF. Pa is further purified using AG1-8X column as described above.

5. Electrodeposition of Th, U, and Pa

We describe here the procedure of Rutgers van der Loeff and Moore (1999) which is based on a previously published paper of Krishnaswami and Sarin (1976). This method is suitable for electroplating of Th, U, and Pa. The sample in a beaker is taken up in 1 mL 0.01 M HNO_3 and transferred into an electroplating Teflon cell equipped with cleaned silver or stainless steel disks on its base. The beaker is rinsed twice with 1 mL NH_4Cl buffer (pH = 2) followed by a 1 mL rinse of saturated ammonium oxalate. A transfer pipette may be used to remove the solution quantitatively from the beaker. The plating cell is placed on a magnetic stirrer in the fume hood and connected to the power supply, which should be current-limited at 0.8 A. Agitating the solution in the Teflon cell prevent blocking of the electrode surface by bubbles. After about 20–30 minutes the resistance will increase so that the power supply will increase up to 6 V. After about 50–60 minutes when the current drops to ~0.2 A, plating can be terminated by adding 1–2 mL of conc. NH_3. The plating cell is disconnected from the power supply and the disk is washed with Milli-Q and ethanol.

A Th platting may also be performed by NdF_3 precipitation (Rodriguez y Baena et al., 2006). To the Th fraction (in 9 M HCl) 100 µL of 1 mg Nd^{3+}/mL (as $NdCl_3$ in 1 M HCl) and 5 mL of concentrated HF is added and mixed. Th is co-precipitated with the NdF_3. The solution is allowed to stand for 0.5–2 hours, and then the NdF_3(Th) suspension is filtered through a polypropylene membrane filter (0.1 µm porosity, 25 mm diameter). The precipitate is washed three times with 2 mL of diluted (ca. 4%) HF followed by two washes with 1.5–2 mL of 80% ethanol solution. The NdF_3(Th)-loaded filter is allowed to dry for at least 15 minutes.

The activity of the sample can be calculated as

$$A = A_{Tracer} \cdot \frac{counts_A}{counts_{Tracer}} \cdot \frac{1}{weight} \quad (5.1)$$

where A (in Bq/g) is the activity of isotope of interest, A_{Tracer} is the activity of the yield tracer, $counts_A$ are the counts/s of the isotope of interest determined via α-spectrometry, $counts_{Tracer}$ are the counts/s of the yield tracer determined via α-spectrometry, and weight is the amount of sample (in g) used for the analyses.

B. Thorium-234

1. Sediments

The determination of ^{234}Th in sediments can be done using γ-spectrometry of about 100 g of dried and grounded sediment which is filled in the appropriate geometry. Better detection limits are achieved if ^{234}Th is measured by β-counting (Turnewitsch et al., 2000). About 10 g of dry sediment is leached for about 4–5 hours in 100 mL of near boiling 6 M HCl in the presence of a yield tracer. Thereafter the particles are centrifuged off (DeMaster et al., 1991). Further purification is achieved by Fe-hydroxide precipitation followed by chemical purification as described in Section IV.A.4.

2. Seawater

The technique for sampling of ^{234}Th in the water column depends on the environment and the objective of the study. A detailed discussion on the various methods and their methodological protocols can be found in Cochran and Masque (2003), Rutgers van der Loeff and Moore (1999), and Rodriguez y Baena et al. (2006). A decision chart which assists in finding the appropriate method was published by Rutgers van der Loeff et al. (2006). The two main sampling techniques are large-volume sampling using in situ filtration pumps and small-volume sampling.

Large-volume sampling is conducted using *in situ* filtration pumps equipped with particle filters and two in-line MnO_2 impregnated cartridges. Measurements of particulate ^{234}Th can be performed directly by β-counting or γ-spectrometry (Buesseler et al., 1992), or by dissolving the particulate filter followed by chemical separation for thorium as described above. The cartridges containing the dissolved ^{234}Th can be prepared for γ-spectrometry measurements either by ashing in a muffle furnace (Buesseler et al., 1992) or melting/crushing (Buesseler et al., 1995), and putting them into a standard geometry. Care should be taken for precise calibration of β- and γ-detectors for the different sample sizes and geometries of particulate filters (Rutgers van der Loeff et al., 2006). Alternatively,

cartridges may also be leached in acid (>3N HCl) solutions in a recirculating system followed by chemical purification as further outlined below Rutgers van der Loeff and Moore (1999). The activity of ^{234}Th is then calculated as

$$Th_{Activity} = \frac{A}{1 - \frac{B}{A}} \tag{5.2}$$

where A and B are the activities of the first and second cartridges, respectively (Livingston and Cochran, 1987).

Calculation of ^{234}Th activities using Eq. (5.2) requires the extraction efficiencies of cartridges A and B to be the same. Various field studies observed, however, extracting efficiencies ranging from 65% to ~100% (Rutgers van der Loeff et al., 2006 and references therein). Applying constant extraction efficiency may cause both random and systematic errors in calculated ^{234}Th activities that are highest when the extraction efficiency is lowest.

If high precision and accuracy are required, a small-volume sampling (2–20 L) is the method of choice for ^{234}Th determination. From a volume of seawater, ^{234}Th may be preconcentrated using Fe-hydroxide precipitation in the presence of a ^{230}Th yield tracer (Rutgers van der Loeff and Moore, 1999). As U is coprecipitated with Fe-hydroxides, rapid chemical chromatographic separation is required in order to minimize the in-growth correction for ^{234}Th from the decay of ^{238}U. A further complication arises from the fact that the amount of U coprecipitated with Fe-hydroxides must be precisely known to perform the in-growth correction (Smith et al., 2004). Therefore, a ^{236}U yield tracer must be added prior to the preconcentration with Fe-hydroxides, and after chemical purification uranium is measured via α-spectrometry or MC-ICPMS.

The ^{234}Th protocol using MnO_2 as the preconcentration step for ^{234}Th avoids the complication of ^{234}Th in-growth correction as the amount of U which coprecipitates with MnO_2 is negligible. The MnO_2 precipitates from large sample (~20 L) can be measured directly by β-counting and no yield tracer is necessary, as the recovery for ^{234}Th is considered as nearly quantitative (Rutgers van der Loeff et al., 2006). Most recent studies use sample volumes of 2–5 L due to ease in sample collection, processing, and low overall analytical blank. This procedure needs only ~10% of the reagents used for the 20 L MnO_2 precipitation method (Buesseler et al., 2001). Due to the difficulty to maintain reproducibility especially when many samples are processed, it is recommended to use yield tracers. Pike et al. (2005) and Rodriguez y Baena et al. (2006) developed a two-spike method in which the first spike ^{230}Th accounts for losses during MnO_2 precipitation, and the second spike (^{229}Th or ^{228}Th) for the loss of ^{230}Th during the chemical separation process. After β-counting for ^{234}Th, the filters are dissolved in the presence of the appropriate yield tracers followed by chemical purification. Depending on the availability of instrumentation, the tracers are measured by α-spectrometry and/or MC-ICPMS. A comparison of the one- and two-spike methods is shown in Fig. 5.15.

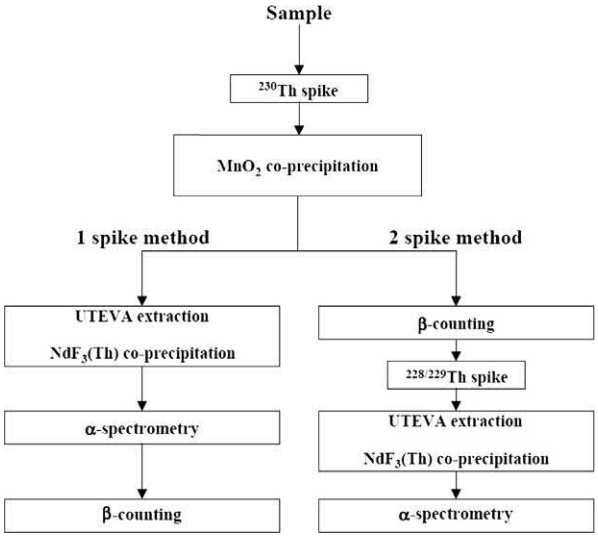


FIGURE 5.15 Flowchart of ^{234}Th measurement procedures using one and two spikes. *From Rodriguez y Baena et al. (2006). Printed with permission from Elsevier © 2006.*

The ^{234}Th activity at the time of sampling ($^{234}Th_{to}$) in Bq is calculated using the following equation, which combines data on the ^{234}Th net count rate, chemical recovery of the MnO_2 co-precipitation, efficiency of the β-detectors, and in-growth from ^{238}U activity in the sample:

$$^{234}Th_{to} = \frac{^{234}Th_{net}}{^{234}Th_{yielded}} \cdot (\beta - \text{efficiency})^{-1} \cdot \left(e^{-\lambda t}\right)^{-1} \cdot {}^{238}U \cdot \left(1 - \left(e^{-\lambda t}\right)\right) \tag{5.3}$$

where $^{234}Th_{net}$ is the net ^{234}Th count rate in cps at the time of MnO_2/FeOOH coprecipitation as determined by β-counting, $^{234}Th_{yield}$ is the recovery of ^{234}Th as determined by α-spectrometry of ^{228}Th (or ^{230}Th), (β-efficiency) is the efficiency of the β-counting, λ is the decay constant of ^{234}Th, t is the time between sampling and MnO_2/FeOOH precipitation, and ^{238}U is the activity of ^{238}U in Bq at the time of sampling.

C. Polonium-210 and Lead-210

1. Seawater

In seawater, ^{210}Po ($T_{½} = 138$ days) and ^{210}Pb ($T_{½} = 22.3$ y) are normally in radioactive disequilibrium. In order to measure both isotopes by means of α-spectrometry, two analytical steps are required (Baskaran and Swarzenski, 2007; Masqué et al., 2002; Rigaud et al., 2013; Rutgers van der Loeff and Moore, 1999). In a first step, the so-called *in situ* ^{210}Po is measured. In a second step, after

storing the sample for a minimum of ~½ year, the ^{210}Po is determined which was produced by the decay of ^{210}Pb. Thus, this measurement provides the data on ^{210}Pb. In seawater, the measurements of ^{210}Po and ^{210}Pb are usually done in the same sample (Fleer and Bacon, 1984). An approximately 20–50 L sample of water is filtered through a 0.45-μm membrane/nuclepore filter (or 0.7 μm GFF). For the determination of particulate ^{210}Po/^{210}Pb in the open ocean, at least 30 L are necessary. The filtrate is collected in 20 L containers, and the weight is determined. The filtrate is acidified to pH < 2 using conc. HCl, and 10 mg of stable Pb plus the ^{209}Po yield tracer are added. Depending on the preconcentration method, 100 mg Fe or 20 mL of saturated $KMnO_4$ solution are added, homogenized, and stored overnight for isotope equilibration.

For Fe-precipitation, the filtrate is neutralized with NH_4OH solution to pH 8–8.5 and the precipitate is allowed to settle overnight. Thereafter, the clear solution is siphoned off with a water jet pump and the precipitates are transferred to 250 mL Nalgene bottles for transport to the home lab. Here the precipitate is centrifuged down and then washed three times with Milli-Q water and centrifuged again.

For Mn-precipitation, NaOH is dissolved in Milli-Q water and added to the sample while stirring; the pH is ~9. Then 20 mL of 0.5 M $MnCl_2$ are added so that MnO_2 gets precipitated. After a few minutes the pH is controlled and adjusted to pH 8, if necessary. The solution is stirred for 5 minutes, and the precipitate is allowed to settle. The supernatant is siphoned off with a water jet pump. For the transport to the home lab, the precipitate is stored in 500 mL bottles. Here the precipitates are centrifuged and washed three times.

2. Digestion of filters and sediments

A microwave digestion is the most convenient way for dissolving filters and sediments (50–500 mg). A preweighted ^{209}Po spike (~1–5 dpm), stable Pb (~10 mg), 5 mL conc. HNO_3, 2 mL conc. HCl, 3 mL HF 40%, and 10 mL Milli-Q water are added to the sample in the microwave reactor. After the total dissolution of the sample, 1.1 g of H_3BO_3 is added followed by further heating in the microwave. The solution is quantitatively transferred to 50 mL Teflon beakers, evaporated to almost dryness, and 2 mL of concentrated HCl are added. This last step is repeated three times in order to assure complete removal of HNO_3 traces. The sample is then diluted to an appropriate volume of 0.5/0.6 M HCl, and it is ready for Po electroplating. Note that ^{210}Po and ^{210}Pb in sediments are usually in equilibrium. Thus, the addition of stable Pb is not required and only one plating step is performed (as described below).

3. Plating of ^{210}Po

We describe here the technique used at the IAEA Environment Laboratories in Monaco (I), and the one described by Rutgers van de Loeff and Moore (1999) (II).

a. Technique I

The precipitate is dissolved in 0.5 M HCl. It may be necessary to add a few drops of conc. HCl to completely dissolve the precipitate. Then the solution is transferred quantitatively into 30 mL HDPE Nalgene bottles and some ascorbic acid powder is added until yellow color disappears. This step should complex Fe which otherwise would prohibit the spontaneous electroplating of Po. High amounts of ascorbic acid may be necessary (i.e., 1 mol $C_6H_8O_6$ per 2 mol Fe(III) or ~150 mg $C_6H_8O_6$ per 100 mg Fe(III)). A silver disk followed by a support disk (a stainless steel disk) is placed on the mouth of the Nalgene bottle, and closed with the plastic cap after having made a hole in the center of the cap. The bottle is turned upside down and, after making a little hole into the Nalgene bottle to allow excess pressure to escape, it is set on a hot plate at a temperature of 70–80°C for 5 hours plating. Afterward the silver disk is removed, and the remaining solution is poured in a 50-mL Teflon beaker. A piece of silver foil/scrap about 2 × 2 cm in size is placed into the Teflon beaker for about 24 hours in order to remove any Po traces which eventually may have remained in the solution. Thereafter, the silver foil is removed. A 5-mL aliquot from the solution is obtained for further Pb-recovery check using atomic adsorption or ICP-MS. The solution is spiked again with ^{209}Po and stored for at least 6 months to allow for the in-growth of ^{210}Po from ^{210}Pb. Thereafter Po is replated again from the solution after the addition of 1 mL of the ascorbic acid solution.

b. Technique II

The precipitate is dissolved in 0.5 M HCl, transferred quantitatively into 50 mL Teflon beakers and a magnetic stirring ball is added. Ascorbic acid powder is added until the yellow color disappears. In order to prevent adding too much ascorbic acid, it is recommended to wait after each addition since the solution of the powder and complexation of Fe is slow. A silver disk (which is covered on one side with plastic) is placed using plastic tweezers on the bottom of the beaker. The hot plate is set to a temperature of 80–90°C (a temperature probe in a Teflon beaker filled with water may be used as a temperature control) and slowly stirred. The plating proceeds for 4 hours. Note: Regularly check the color; if the solution is yellow, more ascorbic acid has to be added. If the color remains, there is probably an excess of ascorbic acid being broken down. If the silver disk gets a dark coating, the plating should be

terminated. After 4 hours the disk is removed with plastic tweezers, it is rinsed with 2 mol/L HCl, then with Milli-Q, and then with ethanol. The solution is stored at least for one night with scrap silver so that any remaining Po is removed. Thereafter about 3 mL of conc. HNO_3 is added, and the solution is evaporated to dryness. The beaker is rinsed with 2 M HCl, evaporated again, and taken up in ~0.5 M HCl for storage for a minimum of half a year to allow ingrowths of ^{210}Po from ^{210}Pb. Thereafter an appropriate amount of ^{209}Po is added (the spike should have twice the expected activity of ^{210}Po) and then Po is electroplated as described above. The plating solution is diluted to 500 mL, and stable Pb is measured by means of flame atomic adsorption.

The activities of ^{210}Po and ^{210}Pb are calculated using the following equations (García-Orellana and García-León, 2002):

$$^{210}\mathrm{Po} = \frac{P_1 - {}^{210}\mathrm{Pb}\cdot\gamma(t_1 - t_0)}{e^{-\lambda_{\mathrm{Po}}(t_1 - t_0)}} \tag{5.4}$$

$$^{210}\mathrm{Pb} = \left(\frac{\left(P_2 - P_1\cdot e^{-\lambda_{\mathrm{Po}}(t_2 - t_1)}\right)}{\gamma(t_2 - t_1)}\right)\cdot e^{-\lambda_{\mathrm{Pb}}(t_1 - t_0)} \tag{5.5}$$

where P_1 and P_2 are the activities measured at time t_1 and t_2, respectively, λ_{Po} and λ_{Pb} are the decay constants of ^{210}Po and ^{210}Pb, respectively, and $\gamma(t_2{-}t_1) = {}^{210}\mathrm{Po}_{(t)}/{}^{210}\mathrm{Pb}(t_0)$ is the function given by Batman's equation for the three related radionuclides (^{210}Po, ^{210}Bi, and ^{210}Pb) assuming that at time t_0 there is a certain activity of the parent nuclide ^{210}Pb and none of the daughters are present. A more complex calculation of ^{210}Po and ^{210}Pb activities including uncertainties is presented in Rigaud et al. (2013).

D. Radium isotopes

The sampling and measurement techniques for radium isotopes, i.e., ^{223}Ra ($T_{½} = 11.4$ days), ^{224}Ra ($T_{½} = 3.7$ days), ^{228}Ra ($T_{½} = 5.75$ y), ^{226}Ra ($T_{½} = 1600$ y) in seawater, depend on the objective of the investigation, the isotopes of interest, and the availability of analytical instrumentation (Charette et al., 2012). In most cases, large-sample volumes >20 L are required so that applications of preconcentration procedures are necessary (Henderson et al., 2013). Radium can be extracted from seawater by $BaSO_4$ precipitation (Li et al., 1980; Rutgers van der Loeff and Moore, 1999). A barium chloride solution is added slowly to 30–60 L of seawater while stirring the sample for 1–2 hours. The precipitate is allowed to settle, and the supernatant is siphoned off. The precipitate is dried and weighed to determine the recovery using the $BaSO_4$:$BaCl_3$ mass ratio of 1.883. Another radium preconcentration method uses Empore Rad Disks in the presence of a ^{225}Ra (= ^{229}Th) yield tracer (Purkl and Eisenhauer, 2003b). The most convenient method to extract radium from large seawater volumes is by passing the water through a column containing MnO_2-coated fiber (Mn-fiber) (Moore et al., 1985). For the preparation of Mn-fiber, see Rutgers van der Loeff and Moore (1999). This extraction method removes radium nearly quantitatively (97 ± 3%), if the water flow rate is < 1 L/min (Moore, 2007). The Mn-fiber can be used for the determination of all radium isotopes.

1. Measurement of ^{223}Ra and ^{224}Ra

Although the measurements of ^{223}Ra and ^{224}Ra are possible by means of α-spectrometry (Hancock and Martin, 1991; Purkl and Eisenhauer, 2003a), this method is not frequently applied due to lengthy chemical procedures. The method of choice for the analysis of the short-lived radium isotopes ^{223}Ra and ^{224}Ra is the delayed coincidence technique of Moore and Arnold (1996). The Mn-fiber is placed in a closed-loop circulation system, and a helium stream sweeps off the ^{219}Rn and ^{220}Rn produced by the decay of ^{223}Ra and ^{224}Ra, respectively. Radon circulates in a Lukas cell where α-particles from the decay of Rn and daughters are recorded. For more details on the measurement technique, see Garcia-Solsona et al. (2008), Moore (2008), Scholten et al. (2010) and Moore and Cai (2013). Kim et al. (2001) describe a method in which ^{224}Ra on the Mn-fiber is measured using a commercially available radon-in-air monitor (RAD 7, Durridge) to count ^{220}Rn released from the Mn-fiber. Other methods use ultralow-level γ-spectrometry for ^{223}Ra and ^{224}Ra determination after having ashed or leached the Mn-fiber (Elsinger et al., 1982; Van Beek et al., 2010).

2. Measurement of ^{228}Ra and ^{226}Ra

The first determinations of ^{226}Ra in seawater were performed by measuring the daughter ^{222}Rn, which was extracted from 20 L of seawater and measured in scintillation cells (Key et al., 1979b; Mathieu et al., 1988) (see Section E). Other studies use a delayed coincidence counting technique (as described above), radon-in-air monitors (see Section E) and liquid scintillation counting for ^{226}Ra determinations (Peterson et al., 2009; Purkl and Eisenhauer, 2004; Sanchez-Cabeza et al., 2010; Waska et al., 2008). Recent advances in mass spectrometry (MC-ICPMS and TIMS) allow the determination of ^{226}Ra in sample volumes < 0.5 L (Bourquin et al., 2011; Foster et al., 2004; Hsieh and Henderson, 2011; Sharabi et al., 2010). For high-activity estuarine or coastal samples, γ-spectrometry offers an easy method of measuring ^{226}Ra and ^{228}Ra via ^{214}Bi and ^{214}Pb (^{226}Ra daughters) and ^{228}Ac (^{228}Ra daughter) as described by Reyss et al. (1995) and Schmidt and Reyss (1996). The Mn-fibers can be prepared for γ-measurements by ashing the fibers at 820°C for 16 hours and placing the ash in a sealed vial (Charette et al., 2001). The vial is stored for 3–4 weeks to allow

^{222}Rn and daughters to equilibrate with ^{226}Ra. Alternatively, the Mn-fiber can be leached in a Soxhlet extraction apparatus (Rutgers van der Loeff and Moore, 1999) or leached in a beaker in a mixture of hot hydroxylamine hydrochloride and 20% HCl. After the fiber is bleached and washed three times with 20% HCl, the solution is filtrated and 10 mL of saturated $BaCl_2$ is added. Then, while steering and heating to near boiling, 25 mL 7 M H_2SO_4 is added slowly. The precipitate is allowed to settle down and the supernatant is siphoned off. The precipitate is washed with Milli-Q water and placed in a gamma counting vial (note that due to the high density of $BaSO_4$, the emanation of ^{222}Rn is <2% (Michel et al., 1981; Scholten et al., 2013). Compressing the Mn-fiber after mixing with an adhesive (e.g., powdered sugar) is a less laborious method for the preparation of Mn-fibers for gamma measurements (Schubert et al., 2018).

Due to low ^{228}Ra content in the open ocean and due to the relatively high detection limits of γ-spectrometry, a determination of ^{228}Ra via ^{228}Th in-growth may be necessary. Following the procedure described in Moore et al. (1985) and Rutgers van der Loeff and Moore (1999), the Ba(Ra)SO_4 precipitated is converted to Ba(Ra)CO_3 by fusing it with a mixture of K_2CO_3 and Na_2CO_3. In order to remove any traces of thorium, a few μL of $FeCl_2$ solution is added and thorium is precipitated with the Fe-hydroxides after adjusting the pH to 7−8 using concentrated NH_3. Then Ba and Ra are coprecipitated with K_2CO_3 solution, and the precipitate is stored for 5−20 months to allow ^{228}Th to partially equilibrate. The Ba(Ra)CO_3 precipitate is dissolved in HCl, followed by the addition of Fe and ^{230}Th yield tracer. Thorium is concentrated by Fe-hydroxide precipitation, and the remaining supernatant containing ^{226}Ra is quantitatively recovered and measured as described above. The Fe-hydroxide precipitate is dissolved in 9 M HCl followed by chromatographic purification and electroplating as already described. The ^{228}Th/^{230}Th activity ratio is determined by α-spectrometry, and ^{228}Th is calculated from the activity of the spike. The initial ^{228}Ra activity of the sample is calculated by multiplying the measured ^{228}Th activity by the reciprocal of the fraction of ^{228}Th/^{228}Ra equilibrium. The result is decay-corrected for the time elapsed from sample collection to the initial purification and precipitation of Ba(Ra)CO_3.

E. Radon-222

^{222}Rn concentration in seawater are usually low (~1mBq/L), thus large (>20 L) seawater volumes are required for ^{222}Rn determinations. ^{222}Rn can be measured using alpha spectrometry (Key et al., 1979a; Mathieu et al., 1988; Schlosser et al., 1984): It is extracted from a water sample with a carrier gas (nitrogen, helium) which is bubbled through the water sample. The gas flows over a stainless steel trap cooled with liquid nitrogen or a charcoal-filled trap cooled with dry ice where ^{222}Rn adsorbs. After the water sample is completely degassed the traps are heated and ^{222}Rn is transferred to evacuated scintillation cells ("Lukas cell"). The sample is stored for about 1−2 hours to allow ingrowth of ^{222}Rn daughters (^{218}Po, ^{214}Po). For the calculation of the ^{222}Rn activity a decay correction from the time of sampling, the efficiency of the counter, the background of the detector and well as the blank (note that glass containers may be a source of ^{222}Rn) must be taken into account.

For spatial mapping of ^{222}Rn concentrations in coastal waters, radon-in-air monitors (e.g., RAD-7 (Durridge); AlphaGuard (Saphymo)) are appropriate methods (Burnett and Dulaiova, 2003; Burnett et al., 2001). Seawater is constantly pumped through an air−water exchanger (RAD-Aqua (Durridge) or MiniModule (Membrana)) that strips ^{222}Rn from the water to a closed air loop connected to a radon-in-air monitor (Schmidt et al., 2008). The radon-in-air concentration is converted to the final ^{222}Rn-in-water concentration using the water/air partitioning coefficient which is calculated based on the salinity and the temperature of the sampled seawater (Schubert et al., 2012).

F. Beryllium-7

Due to low particle reactivity, ^{7}Be is present in seawater predominantly in the dissolved phase. The short half-life ($T_{1/2} = 53.3$d) and the low concentrations in seawater require large water volumes for ^{7}Be determinations. About ~100−700 L of seawater is pumped into barrels and a stable Be-9 yield tracer (500 ml of a 1000ppm Be atomic adsorption standard solution) is added (Kadko, 2009). The water is pumped (10 L/min) over iron-impregnated acrylic fibers (Krishnaswami et al., 1972) which adsorb beryllium. An aliquot of the effluent that passes the fiber is taken for Be-9 determinations by atomic adsorption or ICPMS. From the Be-9 concentration measured, the Be extraction efficiency is determined. The fibers are dried and ashed; the ash is then pressed in pellets which are placed on a low-level germanium detector where ^{7}Be is detected by the gamma peak at 478 keV.

V. Analysis of anthropogenic radionuclides

A. Preparation of samples for radionuclide analysis

As sampling of marine materials such as seawater, sediment, and biological material including sediment trap samples is difficult and expensive, it is desirable to analyze as many radionuclides as possible on a minimum single sample aliquot. Numerous methods have been published

for the determination of anthropogenic radionuclides in marine samples, including precipitation methods, use of ion-exchange resins, extraction chromatography, liquid–liquid solvent extraction, etc. (La Rosa et al., 2001, 2005; Lee et al., 2001, 2005a; 2010; Povinec, 2004; Levy et al., 2011). Radionuclide separation using liquid–liquid solvent extractions is time consuming and generates substantial volumes of organic wastes. One of the most popular methods, a separation using ion-exchange resins, is effective for large samples and reasonable in cost relative to extraction chromatography resins such as TEVA, UTEVA, and TRU (Eichrom Industries). However, the process requires the use of many chemicals, it is time consuming and produces large amounts of chemical wastes. Extraction chromatography reduces the number of chemicals needed, as well as the processing time. Nevertheless, large samples still need preconcentration techniques such as coprecipitation to reduce the amount of matrix before extraction chromatography can be applied. On the basis of the advantages of anion-exchange resins and extraction chromatography methods, sequential separation procedures were developed by the IAEA-EL for the analysis of radionuclides in marine samples.

The preparation chemistry for three of the most frequently analyzed radionuclides (^{90}Sr, ^{137}Cs, and Pu isotopes) will be described in detail using the methods adopted at the IAEA-EL in order to demonstrate the present state-of-the-art techniques (La Rosa et al., 2001, 2005; Lee et al., 2001, 2005a; Povinec, 2004; Levy et al., 2011).

B. Shipboard chemistry for seawater samples

1. Transuranics

Transuranics, cesium and strontium, are usually preconcentrated on the shipboard in precipitation tanks (Fig. 5.16) in three steps. Samples of about 400 L of filtered (0.45 μm cutoff) seawater are transferred into precipitation tanks and acidified by 250 mL of concentrated HCl followed by the addition of tracers (e.g., ^{85}Sr, ^{134}Cs, ^{242}Pu, and ^{243}Am) and carriers (Fig. 5.17). Then 125 mL of saturated $KMnO_4$ is added and mixed by bubbling air for 15 minutes. This is followed by the addition of 250 mL of 0.5 M $MnCl_2$ and subsequently 150 g of NaOH is added to adjust the pH to 6–7. Finally, 2–3 mL of H_2O_2 is added to transform the $Mn(OH)_2$ to MnO_2 ($Mn(OH)_2 + H_2O_2 \geq MnO_2 + 2H_2O$), which is then stirred for 30 minutes. The sample is then left to stand for 4–5 hours to enable the separation of the precipitate from the sample solution. The supernatant is then transferred to a different plastic tank for preconcentration of cesium with ammonium molybdophosphate (AMP). The precipitate is transferred to a plastic container for further separation and determination of transuranics in the home laboratory.



FIGURE 5.16 Precipitation tanks (400 L) for seawater on the shipboard. For the color version of the figure, the reader is referred to the online version of the book.

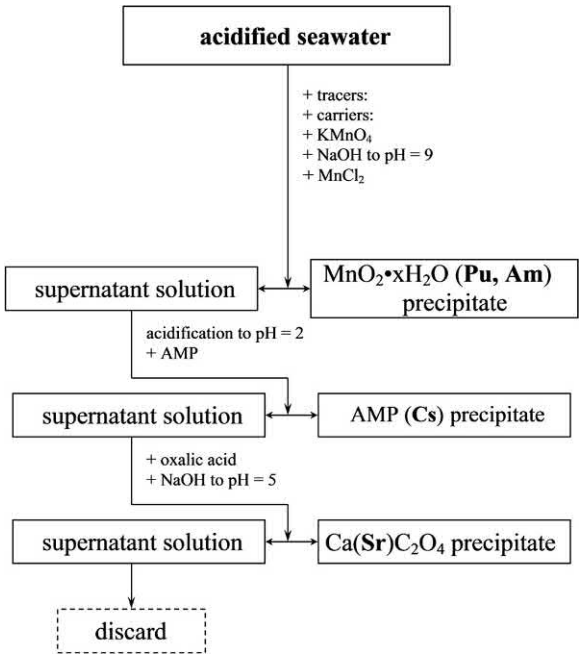


FIGURE 5.17 Preconcentration procedures for transuranics, ^{137}Cs and ^{90}Sr, carried out on the shipboard. *Modified after Povinec (2004). Printed with permission © Elsevier 2005.*

2. Cesium

The supernate from the previous step is acidified (pH 1.5–2.0) with 350 mL of concentrated HCl, and mixed by bubbling air for 15 minutes. Two mL of H_2O_2 is then added to dissolve traces of MnO_2 solids. Then 30 g of AMP, slurred in 100 mL of demineralized water, is added, and the sample bubbled for 30 minutes, and left to stand for 4–5 hours to allow the precipitate to settle. The solution is then transferred to another plastic tank to separate strontium by oxalate coprecipitation. The AMP precipitate is

transferred to a plastic container for further separation and determination of cesium in the home laboratory.

3. Strontium

Oxalic acid (500 g), dissolved in 1 L of boiling demineralized water, is added to the supernate, which is stirred by bubbling air for 15 minutes. 400 g of NaOH is then added to adjust the pH to 6−7, resulting in white oxalate precipitate. The sample is stirred for 30 minutes and left to stand for 4−5 hours to allow the precipitate to settle. The supernate sample is then discarded and the oxalate precipitate collected and stored for further separation and determination of strontium in the home laboratory.

C. Laboratory chemistry for seawater samples

1. Transuranics

Manganese dioxide containing Pu and Am isotopes obtained from shipboard preconcentration is prepared from the suspension in the home laboratory (after checking pH of the liquid) using a combination of settling, decantation/siphoning of the supernatant liquid, and centrifugation. The procedure is described in Fig. 5.18. Further separation of Pu and Am from the iron matrix is carried out by the separation of Pu (IV) using an anion-exchange resin column from 8 M HNO_3 followed by the recovery of Am from the column eluate. An alternative method has been developed by Burnett et al. (1997) using the Eichrom UTEVA + TRU double column. The flowchart for the method as adapted for mass spectrometry measurements of small-volume water samples (<20 L) is shown in Fig. 5.19 (Lee et al., 2001, 2005a; La Rosa et al., 2001, 2005; Levy et al., 2011). With the traditional method, the typical chemical recoveries of Pu and Am from several hundred liters of seawater are in the range of 40−60% and 60−80%, respectively. The resulting α-ray spectra of Pu and Am electrodeposited sources show good radiochemical purity and well-resolved peaks. With the extraction chromatography double-column method, the Am and Pu sources have

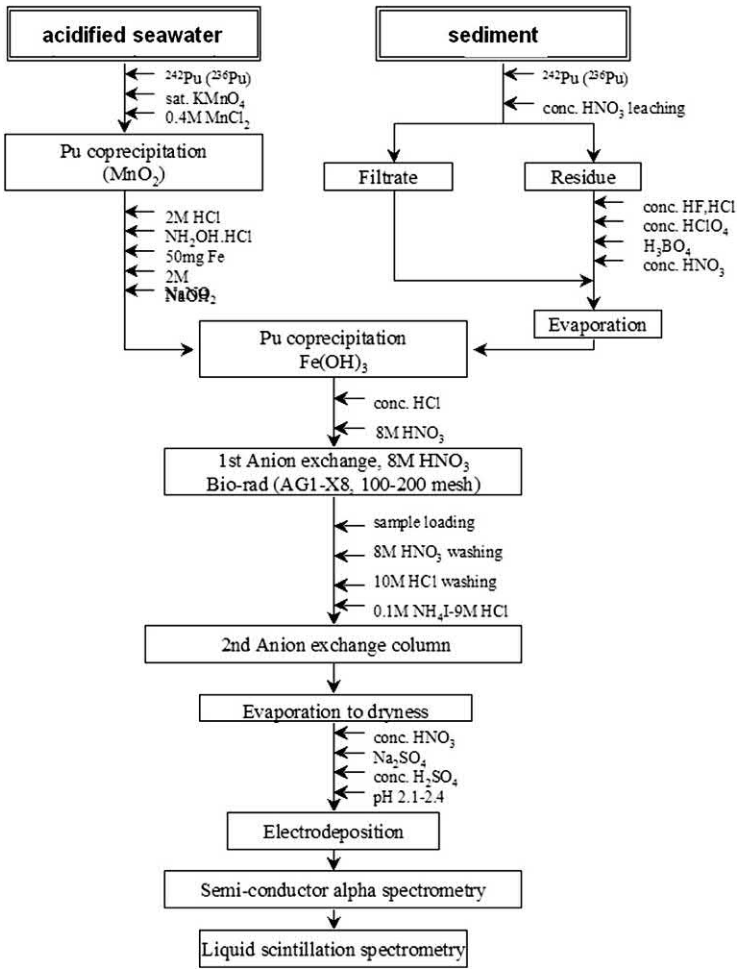


FIGURE 5.18 Plutonium separation from seawater and sediment samples. *Modified after Povinec (2004). Printed with permission © Elsevier 2004.*

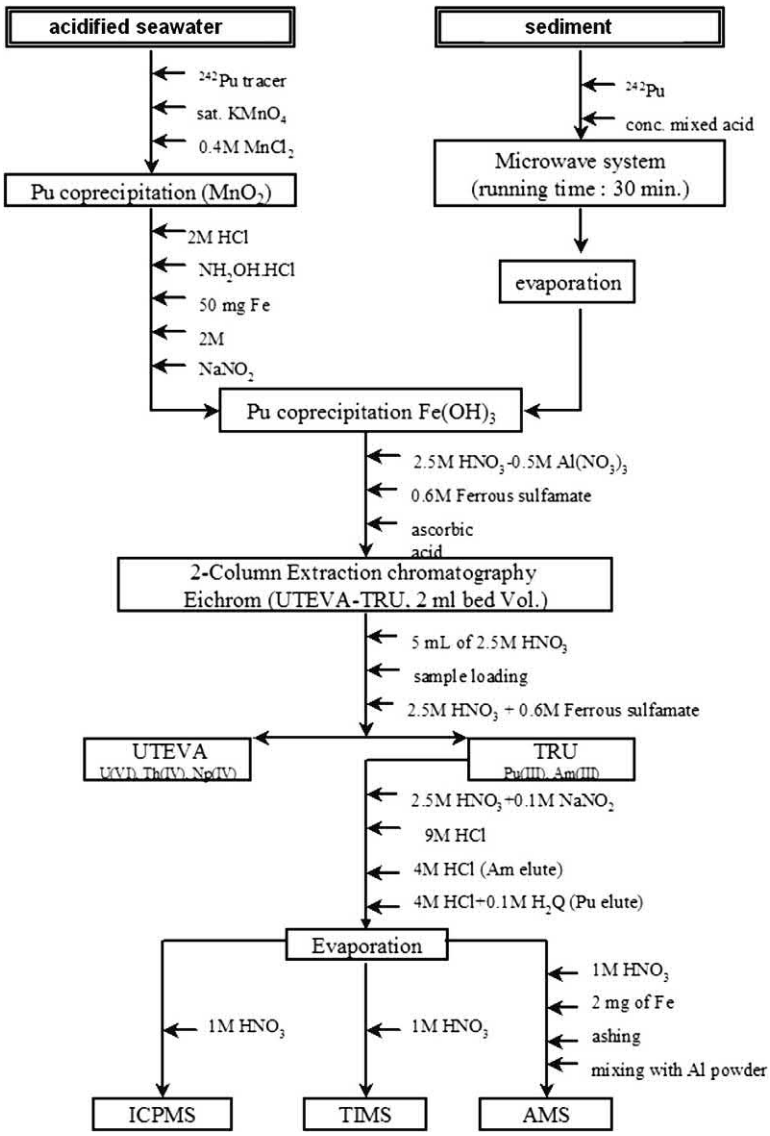


FIGURE 5.19 Plutonium separation for mass spectrometry analysis. *Modified after Povinec (2004). Printed with permission © Elsevier 2004.*

high chemical recoveries (~90% in each case), and the excellent-quality α-spectra shows no visible foreign peaks. In large-volume seawater samples, it is expected that additional purification of the Pu and Am fractions from the TRU column would be necessary; however, small working volumes permit easy and fast chemical operations with less time spent on evaporation steps. In particular, Pu and Am may be retained together on the same TRU column (unlike the traditional method). Small-volume water samples suitable for ICP-MS or AMS measurements of Pu isotopes show very good results. In Am separation and purification, sources produced by both methods show good chemical recoveries, purity, and spectral resolution. In the reprocessing of Am electrodeposition onto disks, one cycle of TEVA + TRU columns gives excellent decontamination from Po with very little loss of Am.

2. Cesium

The AMP suspension (10–20 L) is allowed to settle, and the supernatant solution is decanted or siphoned away. The remaining suspension is centrifuged, and the remaining AMP solid is washed with water and acidified to pH 2. The flowchart for cesium procedures is given in Fig. 5.20. A

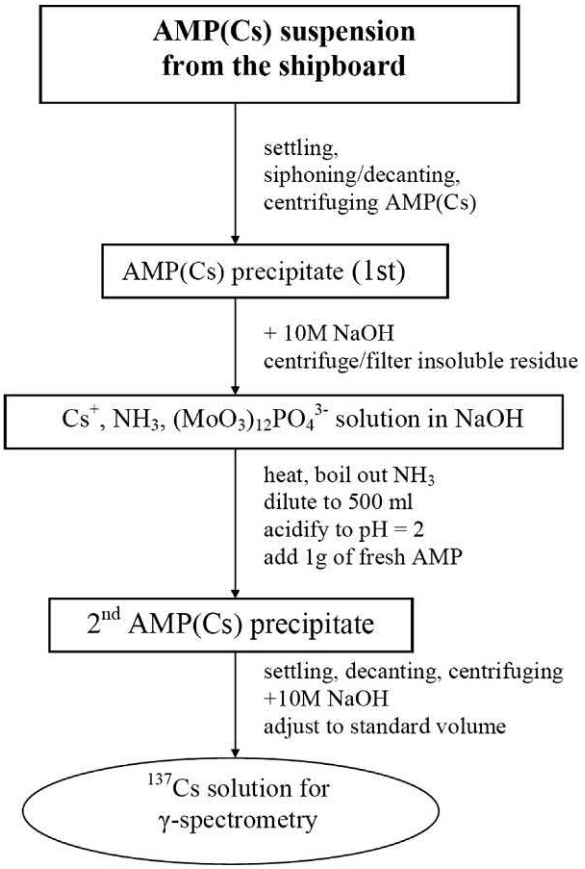


FIGURE 5.20 Cesium separation for γ-spectrometry measurements. *Modified after Povinec (2004). Printed with permission © Elsevier 2004.*

comparison of two sorbents for the collection of cesium (ferric-potassium hexacyanoferrate on a cellulose carrier—ANFEZH, and potassium cobalt ferrocyanide—KCFC) with the AMP was made (La Rosa et al., 2001). It shows that AMP and KCFC quantitatively collect Cs tracer in 20 minutes, whereas ANFEZH does so more slowly and incompletely after 180 minutes. Experimentally derived Cs capacities of the sorbents show that AMP has the highest capacity for Cs sorption and ANFEZH the lowest.

3. Strontium

The strontium chemical separation and purification procedure is illustrated in Fig. 5.21. The calcium oxalate suspension is transferred to a large beaker and allowed to settle. The supernatant solution is siphoned off, and the precipitate washed several times with water to remove the seawater. It is then dried and ashed at 600°C to convert the oxalate to carbonate. After separation, ^{90}Sr is measured by liquid scintillation spectrometry (LSS) (chemical recovery 67%, ^{90}Sr counting efficiency 92%, and background 1.2/min (Liong Wee Kwong et al. (2001)) or by milking ^{90}Y from the purified strontium fraction followed by ^{90}Y counting in a gas flow β-counter or by LSS. Typical

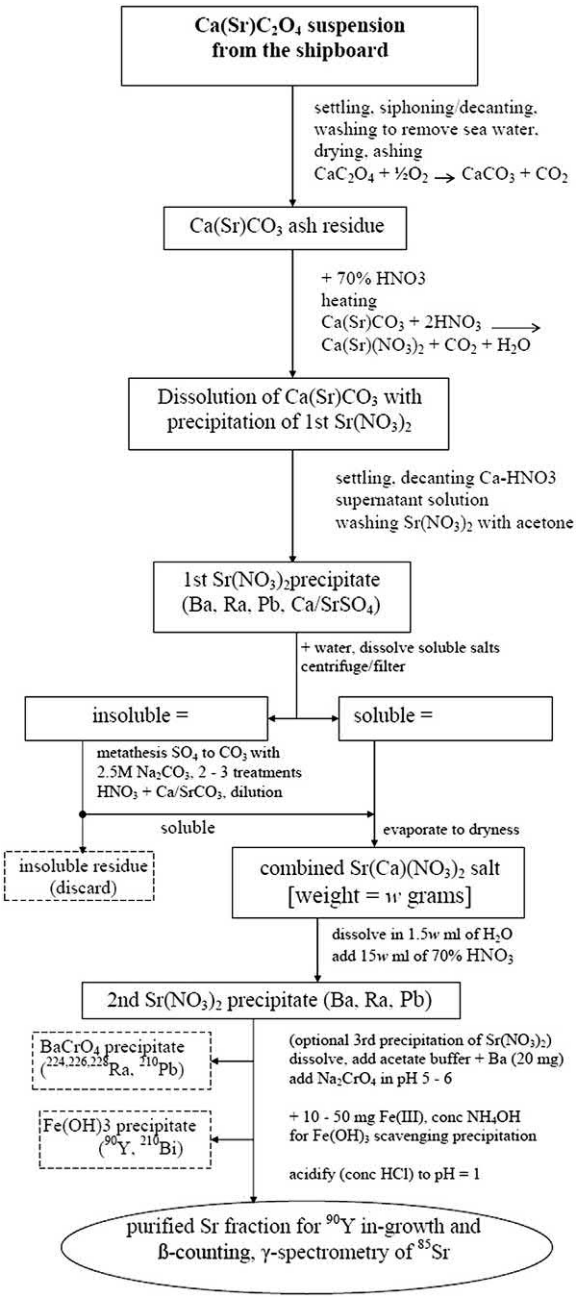


FIGURE 5.21 Strontium separation for β-counting. *Modified after Povinec (2004). Printed with permission © Elsevier 2004.*

parameters are 50% Sr chemical recovery, 90% Y chemical recovery, 48% ^{90}Y counting efficiency, 0.1/min for the gas counter-background, and the detection limit of 3 mBq.

D. Laboratory chemistry for sediment and biota samples

A suitable quantity of a dry, ground solid sample is weighed into a porcelain crucible and ignited at 550°C in an electric furnace to avoid production of refractory

plutonium compounds (e.g., PuO_2) which could be formed at higher temperatures. All or part of the remaining ash is transferred to a PTFE beaker and slurred with 2 M HNO_3. Known amounts (typically 10–20 mBq) of radiochemical yield determinants (e.g., ^{242}Pu and ^{243}Am) are added to the suspension, which is heated for several hours to preclude possible vigorous reactions and evaporated to a conveniently small volume. Either an acid leaching method (8 M HNO_3) or an aggressive dissolution method (using concentrated HNO_3, HCl, and HF) is used for the extraction of actinides from the samples. Especially, the acid leaching method for anthropogenic radionuclides (e.g., Pu, Am, Cs, and Sr) have been widely adopted by a number of laboratories to accommodate large sample sizes. Alternatively, the dissolution method using a combination of HNO_3, HCl, and HF, or a high-temperature, molten salt fusion method can replace the acid leaching method. However, these total dissolution methods can be more time consuming, costly (in terms of amounts of reagents and equipment such as Pt crucibles), and hazardous. Both methods were applied on sea sediments and biological materials, focusing on the global fallout radionuclides, and no remarkable differences were found between the acid leaching (8 M HNO_3) and total dissolution method using the combination of HNO_3, HCl, and HF. This suggests that the leaching method is generally acceptable to analyze the anthropogenic radionuclides in marine samples.

Further, the sediment and biota samples could be treated in a similar way as seawater samples for the separation of radionuclides by anion-exchange resin, or separation and purification by extraction chromatography (e.g., TRU, TEVA, and UTEVA resins). Anion exchange has proved to be a strong tool to treat large-volume samples, and extraction chromatography shows an excellent selectivity and reduction of the amounts of acids. The best results have been obtained by the application of the combined procedure using anion-exchange resin and extraction chromatography. The combined method allows the treatment of large sample sizes and provides excellent selectivity, high chemical recoveries, and reduction of the amounts of acids. A disadvantage of the extraction chromatography method is an increase in price per analysis of one sample (Lee et al., 2001, 2005a; Povinec, 2004). The prepared samples can be then measured either by radiometric (α-spectrometry, β-spectrometry) or by mass spectrometry methods (ICP-MS, AMS, etc.).

VI. Activity measurement techniques

A. Radiometric methods

1. Low-level alpha-spectrometry

Semiconductor α-spectrometry (SAS) has been widely used for the analysis of α-emitters (mainly actinides) in marine samples (e.g., Bowen et al., 1980; Livingston et al., 2001). Other techniques, such as ionization chambers and track detectors, have not been used in the analysis of marine samples, mainly because of poorer energy resolution. Therefore, the most important developments in SAS have been in the radiochemistry sector, as previously discussed. However, one development we would like to mention here, as the major disadvantage of high-resolution SAS compared to mass spectrometry techniques, is the difficulty in resolving ^{239}Pu and ^{240}Pu peaks. Large surface ($\sim$10 mm in diameter) silicon detectors frequently used in SAS cannot resolve this duplet. However, by using high-resolution silicon detectors and special deconvolution software, this problem can be solved (Leon Vintro et al., 1996). The disadvantage here is that due to the smaller detector surface, sensitivity is lower and only samples with relatively higher concentrations of α-emitters can be analyzed. This is one of the reasons why mass spectrometry techniques are more and more widely used for the analysis of Pu and Am isotopes in the marine environment (Baxter, 1993; Buesseler, 1997; Kelley et al., 1999; Fifield, 2008; Hou and Ross, 2008; Povinec et al., 2008a).

2. Low-level beta-spectrometry

Several anthropogenic radionuclides (e.g., ^{3}H, ^{85}Kr, ^{90}Sr, and ^{241}Pu) are found in the marine environment, which are still analyzed by β-counting or β-spectrometry, mainly because their half-lives are too short to be analyzed by mass spectrometers. For some *β-ray* emitters, such as ^{14}C and ^{129}I, which were previously analyzed by β-spectrometry, AMS is at present the most widely used technique. Other radionuclides, such as ^{99}Tc, are still analyzed by β-spectrometry, although ICP-MS (and AMS) have been successfully applied as well, and in the future, mass spectrometry techniques will prevail for these radionuclides (Hou and Ross, 2008). The most important breakthrough in β-spectrometry was the introduction of low background LSS, which are now mainly used for the analysis of short-lived *β-ray* emitters in the marine environment (Povinec et al., 2008a). The advantage of low-level LSS over low-level gas counting is the higher detection efficiency of LSS and its capability as a β-spectrometer, registering only those β-electrons with energies inside the *β-ray* spectrum, and not all β-electrons registered by e.g., Geiger–Müller counters. We shall illustrate the possibilities of LSS techniques using a few examples—^{3}H (maximum energy of β-electrons 18.6 keV; $T_{1/2} = 12.3$ y) and ^{241}Pu (maximum energy of β-electrons 20.8 keV; $T_{1/2} = 14.4$ y). ^{3}H analysis by LSS without enrichment has a detection limit of about 2 TU (1 tritium unit (TU) is the ratio of 1 atom of ^{3}H to 10^{18} atoms of ^{1}H). Operation of the LSS underground can improve the detection limit by about a factor of two (Povinec et al., 2008a). Electrolytic enrichment can further

lower the detection limit to 0.02 TU (Taylor, 1977; Groening et al., 2009; Morgenstern and Taylor, 2009), which is similar to the value obtained by ^{3}He in-growth mass spectrometry (Clarke et al., 1976). For ^{3}H analysis of surface waters contaminated by radioactive discharges, simple LSS is the best solution. The Quantulus liquid scintillation spectrometer (formerly produced by Wallac Oy and now by PerkinElmer, Inc.), which benefits from the low background achieved with the use of an anti-coincidence shielding of the counting vial, can reach a background of 0.4/min, detection efficiency of 20%, and detection limit of ~1 TU (10 mL distilled water sample is directly mixed with 10 mL of the scintillation cocktail) (Liong Wee Kwong et al., 2001). Similar counting parameters are obtained with the Packard LSS (now produced by PerkinElmer, Inc.), which uses the pulse shape discrimination method for decreasing the spectrometer's background. Recently, an electrolysis apparatus utilizing solid polymer electrolyte has been developed (which greatly simplifies the enrichment procedure), and with LSS ^{3}H concentrations in water down to 0.02 TU can be measured (Saito et al., 2000).

Another good example of the advantageous use of LSS is in the analysis of ^{241}Pu. As it is a pure β-emitter, it cannot be analyzed simultaneously with other plutonium isotopes using α-spectrometry. However, the disk with electrodeposited Pu after α-spectrometry measurement can be placed in a polyethylene vial containing a liquid scintillator (e.g., Insta-Gel cocktail produced by PerkinElmer). Using the pulse shape analysis method, α-rays can be separated from *β-rays* registered by LSS (see Chapter 6, Volume 1 and Chapter 2, Volume 2 of this book). Typical counting parameters are 5 mL of cocktail, 12% efficiency, 0.3 min^{-1} background, and detection limit of 0.03 Bq (Liong Wee Kwong et al., 2004a). Although ^{241}Pu has the highest activity concentrations in environmental samples compared to other Pu isotopes, the direct counting is not sufficiently sensitive for many applications. Therefore, the more preferable method is leaching plutonium from the stainless steel disk after α-spectrometry (or to separate a portion of Pu sample before its electrodeposition on the disk), and dissolving the sample in the counting vial, enabling 4π geometry measurements, thus increasing the detection efficiency by a factor of two (Liong Wee Kwong et al., 2004a).

3. Low-level gamma-spectrometry

The most important development in the radiometrics sector was the utilization of large-efficiency HPGe detectors in underground laboratories (Povinec et al., 2004a, 2008a, 2010; Aoyama and Hirose, 2008; Levy et al., 2011). Low-level γ-spectrometry with HPGe detectors is an effective tool in the study of marine radioactivity, which exhibits the following advantages:

- an excellent energy resolution that permits the analysis of various radionuclides in composite samples selectively and very often nondestructively (e.g., in sediments);
- the high efficiency of recently produced HPGe detectors (up to 200% relative to a 76 mm diameter × 76 mm NaI(Tl) crystal).

Although the most effective way of increasing the sensitivity of a spectrometer is to increase its counting efficiency and the amount of analyzed sample, frequently the only possible way is to decrease its background (Michel, 2001). The background components in a typical low-level HPGe detector, not situated deep underground, are cosmic radiation (cosmic muons, neutrons, and material activation), environmental radioactivity, radioactivity of construction materials, radioactivity of the detector, radon, and its progenies (Heusser, 1995). For present day, carefully designed low-level HPGe γ-spectrometers, operating not deep underground, the dominating background component is cosmic rays, mainly cosmic muons (Heusser, 1995; Vojtyla and Povinec, 2000, 2006; Povinec et al., 2008a; Breier and Povinec, 2009, 2010). However, in the majority of marine applications, a simple γ-spectrometer with an HPGe detector of about 100% efficiency (especially if the sample size permits the use of a well detector) is the usual choice (Aoyama and Hirose, 2008).

In single HPGe spectrometers, there is no protection against cosmic ray muons; therefore, a spectrometer with an anticosmic shielding will provide a better sensitivity. The anti-Compton spectrometer is a powerful technique for reducing the detector's background because it combines both the anticosmic and the anti-Compton suppression of background (Cooper and Perkins, 1972; Debertin and Helmer, 1998; Reidel et al., 2000) in which the scattered photons escaping from the principal detector volume can be detected by a sufficiently large NaI(Tl) or BGO crystal surrounding the detector. The simplest anti-Compton spectrometer can be made using a Ge detector and an NaI(Tl) crystal with a well. Using a Ge detector in a large NaI(Tl) crystal (about 30 cm diameter × 30 cm), the Compton suppression factor should reach values above 10 (for $E\gamma \leq 1.5$ MeV), and thereby decreasing detection limits more than threefold (Zvara et al., 1994). Usually, a well-designed anti-Compton spectrometer can be used simultaneously as a coincidence and anti-Compton spectrometer. Although the detection efficiency is reduced in coincidence spectrometers, a considerable decrease in background (by about two orders of magnitude) makes these spectrometers superior for very low-level γ-spectrometry (Sýkora et al., 2008). The most sophisticated spectrometric system is, however, the multidimensional γ-spectrometer (Cooper and Perkins, 1971b; Povinec, 1981) in which signals from the analyzing detectors create

three-dimensional spectra (volumetric peaks) which can contain both coincidence and noncoincidence peaks. Analyzing electronics, if two HPGe detectors are used, require 8000 × 8000 channels, which, with present state-of-the-art computer electronics, is not difficult. The background can be reduced more than two orders of magnitude.

4. Underground laboratories

In low-level γ-spectrometry, muon-induced background becomes dominant for large-volume HPGe detectors, as the most prominent peaks observed (i.e., the annihilation peak and neutron activation peaks) are due to cosmic ray interactions (Povinec et al., 2008a; Povinec, 2012). Monte Carlo simulations of background spectra of detectors are possible to carry out prior to the construction of a low-level spectrometry system and thus predict its characteristics and parameters (Vojtyla and Povinec, 2000; Povinec et al., 2008a). The simulation tools based on the GEANT code, developed by CERN, proved to be capable of modeling background characteristics of detectors and thus enable the optimization of the design of low-level γ-spectrometric installations. Computing power is no longer a problem, as desktop computers of sufficient speed and power are available. Therefore, the influence of various parameters on the detector background can be studied well in advance, and the cosmic muon−induced background can be estimated before a low-level detector system is constructed. Simulations of the characteristics of HPGe detectors placed inside a lead shield without and with anti-Compton shielding in surface or shallow underground laboratories revealed useful trends in design of such systems. Given the detector setup, its background spectra induced by cosmic ray muons can be scaled down by a factor corresponding to the shielding depth (Breier and Povinec, 2009, 2010; Breier et al., 2016, 2017, 2018).

Simulations with various shields showed that the background depends mainly on the thickness, dimensions, and lining of the shield (Vojtyla and Povinec, 2000, 2006). The shape of the shield (cylindrical or rectangular) has almost no effect on the background provided that the inner dimensions are similar. The best results were obtained for the smallest shields with the low-Z materials in the lining. The background characteristics most affected are the maximum of the background continuum with a count rate of 450 d^{-1} keV^{-1} in a shield lined with 1 cm of copper compared to the count rate of 190 d^{-1} keV^{-1} in a lead-only shield. The use of shields with removable linings is recommended for applications where lead X-rays do not have a disturbing effect. It is inadvisable to build an unnecessarily large shield. In a medium-size shield, the integral background count rate (0−1500 keV) is expected to reach count rates of about 85 $minute^{-1}$, and the count rate in the annihilation peak is estimated to be about 4400 d^{-1} keV^{-1}, whereas the maximum count rate in the background continuum should be approximately 210 d^{-1} keV^{-1} (at sea level). A well-type detector intended for the counting of small samples inside the well should be placed into a tight shield without lining. In this case, the integral background count rate can be as low as 50 $minute^{-1}$, the count rate in the annihilation peak can be reduced to 900 d^{-1} keV^{-1}, and the maximum counting rate in the background continuum can be minimized to only about 100 d^{-1} keV^{-1}. Simulations at 20 m.w.e. (meters of water equivalent) underground showed that the features simulated background spectra remain unchanged, except that all the count rates scaled down by a factor of about 3 (Breier and Povinec, 2010).

The nucleonic component of cosmic rays (mainly neutrons) is attenuated at 10 m.w.e. by three orders of magnitude; however, the muonic component remains at this shielding layer without notable reduction (by a factor of 2 only; Povinec et al., 2008a). To decrease the muonic component by a factor of 10, shielding over 50 m.w.e. is needed. At 1000 hg/cm^2 depth, the reduction in muon flux can be as high as 10^6 (Povinec et al., 2008a). Therefore, muon-induced background can be lowered significantly either by operating the detector deep underground or by using an anticosmic detector located above the HPGe crystal which operates as a veto detector. The use of anticosmic shielding is advantageous also in shallow underground laboratories operating at depths only down to several hundred meters of water equivalent (Povinec et al., 2008a).

Backgrounds of HPGe detectors in CELLAR (Collaboration of European Low-level Underground Laboratories) laboratories (Laubenstein et al., 2004) are compared in Fig. 5.22. Although the IAEA-EL laboratory in Monaco is

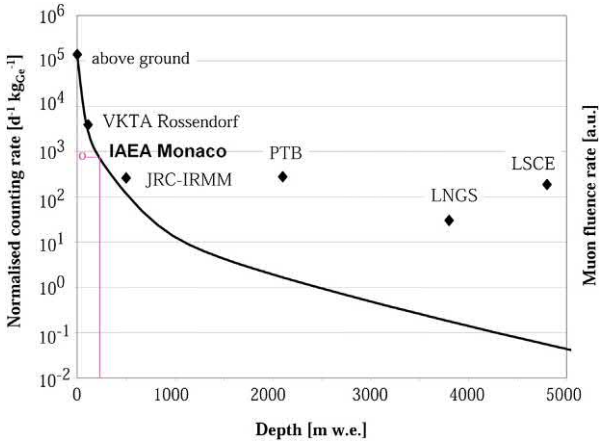


FIGURE 5.22 A comparison of backgrounds of HPGe detectors operating in CELLAR underground laboratories. The background of the HPGe detector with anticosmic shielding operating in the IAEA Monaco laboratory (35 m w.e.) is similar to that operating at 250 m w.e. *Modified after Laubenstein et al. (2004). Printed with permission © Elsevier 2006.*

operating at 35 m.w.e. only, thanks to the anticosmic veto shielding, its background is comparable with laboratories operating at depths of around 250 m.w.e. The CAVE (**C**ounting l**A**boratory for en**V**ironmental radionuclid**E**s) laboratory in Monaco (Povinec, 2004; Povinec et al., 2004a, 2005a, 2006d,e) is equipped with a common lead shield housing four large-volume HPGe detectors (Fig. 5.23). An anticosmic veto shielding was made of plastic scintillation detectors surrounding the lead shield which protect the HPGe detectors against cosmic radiation. Such a novel design, supported by Monte Carlo simulations, when several HPGe detectors are shielded against cosmic rays by a common guard detection system, has been used for the first time in low-level γ-spectrometry. The CAVE also houses an anti-Compton γ-spectrometer, comprising an n-type HPGe detector and NaI(Tl) anticoincidence shielding placed in a lead shield, and a liquid scintillation β-spectrometer. The HPGe detectors, housed in the common lead shield surrounded by the anticosmic guard, are the following (Povinec et al., 2008e; Levy et al., 2011):

a. 100% relative efficiency coaxial detector (CANBERRA) with cryostat made of electrolytic copper with carbon window;
b. 150% relative efficiency well-type detector (CANBERRA) with cryostat made of electrolytic copper (well dimensions: 32.5 mm diameter, depth 73 mm); well walls made of thin copper;
c. 170% relative efficiency coaxial detector (EURISYS) with cryostat and window made of pure aluminum;
d. 200% relative efficiency well-type detector (CANBERRA) with cryostat made of electrolytic copper (well dimensions—25 mm diameter, 60 mm depth); well walls made of thin copper.



FIGURE 5.23 The CAVE (Counting lAboratory for enVironmental radionuclidEs) laboratory in the IAEA-EL, Monaco, houses four large-volume HPGe detectors placed in a common lead shield protected against cosmic rays with anticosmic veto shielding made of plastic scintillators. *Modified after Povinec et al. (2008a). Copyright Institute of Physics. Slovak Academy of Sciences. All rights reserved.*

ORTEC modular electronics have been used for signal processing and data acquisition. During all measurements, radon is expelled from the detector chambers by the evaporation of nitrogen from the detector's Dewar containers, thus keeping background during measurements stable. It should be stressed that this detection system is used only for the analysis of low-activity samples. The measured background of HPGe detectors with anticosmic veto shielding is compared by Povinec et al. (2008e). As the volumes of the detectors differ significantly, it is necessary to compare their background characteristics per kg of Ge. The total detector background per kg of Ge in the energy window 40−2000 keV decreases with increasing detector volume, i.e., from 290 h^{-1} kg^{-1} Ge for the 100% efficiency detector to 205 h^{-1} kg^{-1} Ge for the 200% efficiency detector. However, the background with the anticosmic veto shielding does not follow this rule, but clearly shows a larger contribution of radioactive contamination of the detector materials to its background. The lowest total background with the anticosmic veto shielding was obtained for the 150% efficiency detector (27 h^{-1} kg^{-1} Ge), the highest for the 170% efficiency detector (59 h^{-1} kg^{-1} Ge). The 170% efficiency detector has the cryostat made of "pure" aluminum; however, this has been clearly contaminated by U and Th (and their decay products), as well as by ^{40}K. Generally, aluminum is, from the point of view of radioactive contamination, not a suitable construction material.

It is important that construction materials be carefully tested by the manufacturing companies for the presence of radionuclides before the detector construction, especially for the detector's cryostat and its window (Laubenstein, 2017). Monte Carlo simulations of background characteristics of HPGe detectors operating in Gran Sasso (Breier et al., 2017) and Modane (Breier et al., 2018) showed that measured background was due to radioactive contamination of construction parts of the detectors and surroundings by two and three orders of magnitude higher than the predicted cosmic ray contribution. Therefore radiopurity of construction materials is playing a dominant role in obtaining low background, not only for applications in marine radioactivity studies, but generally for rare nuclear physics investigations (Povinec, 2017, 2018a,b; Palušová et al., 2018; Povinec et al., 2018).

However, it has also been a surprise that three detectors with copper cryostats, ordered as low background detectors for an underground laboratory from the same company (CANBERRA), had very different background characteristics.

The background γ-ray spectra of HPGe detectors operating in the Monaco laboratory are shown in Fig. 5.24. The highest background reduction with the anticosmic veto shielding was obtained for the 150% efficiency detector (factor 9) and the lowest for the 170% efficiency detector

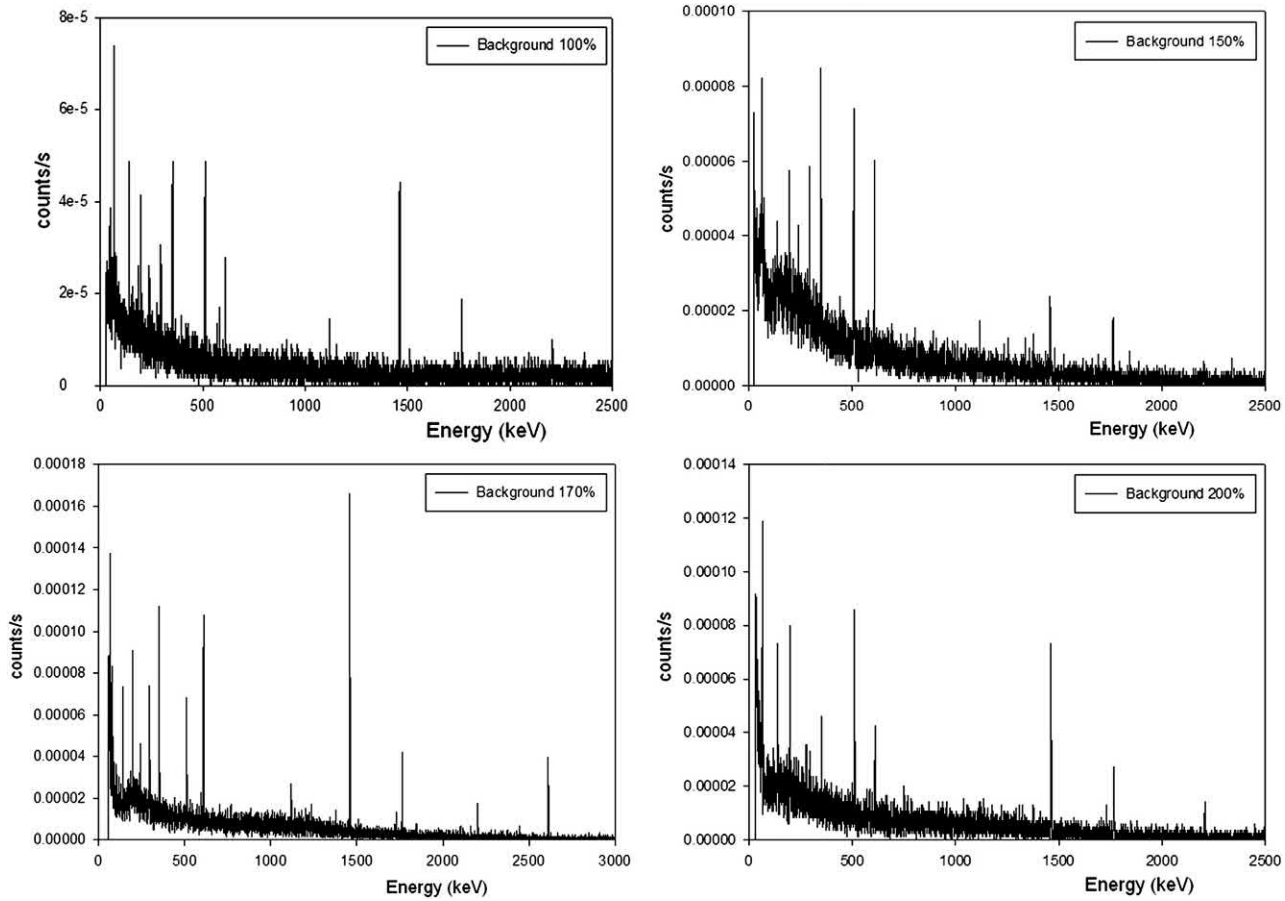


FIGURE 5.24 Background γ-spectra of HPGe detectors operating in the CAVE laboratory (35 m w.e.) with 12.5 cm lead shield and anticosmic veto shielding. *Modified from Levy et al. (2011). Printed with permission © Elsevier 2011.*

(factor 4). The 100% and 200% efficiency detectors have the reduction factors within these limits (factors 7 and 6, respectively). The important finding is that the annihilation peak at 511 keV is still dominant in all background spectra. This peak is produced by annihilation of electrons and positrons in the shield and in the detector, which are products of the interaction of secondary cosmic rays with materials surrounding the detector. The second important finding is a large background continuum, which has a maximum at around 200 keV. This background continuum is produced by the interactions of cosmic muons with the lead shield, as previously discussed. Both observations indicate that it would be advantageous to operate the detectors in a deeper underground laboratory.

The underground counting laboratory with anticosmic shielding of detectors effectively decreases the background of large-volume HPGe detectors, especially when operating in anticosmic, anti-Compton, or coincidence modes. The anticosmic shielding has proved to be a valuable investment, as the background of HPGe detectors operating at shallow depths is comparable with underground laboratories operating at moderate depths of about 250 m.w.e.

The new underground technology with anticosmic shielding enabled the analysis of ^{137}Cs in small-volume (around 10 L) seawater samples from the Atlantic and Indian oceans, what was not possible earlier. It has been possible to decrease the sample volume by about a factor of 10, which greatly reduces sampling time, and the same seawater volumes could be used for γ-spectrometry as well as for mass spectrometry measurements (Povinec, 2004; Povinec et al., 2008a; Levy et al., 2011).

B. Mass spectrometry methods

Several mass spectrometric techniques have been successfully applied in the past for the analysis of isotopes in the marine environment. These techniques have entailed the use of traditional isotope mass spectrometers (White and Wood, 1988), like those used for the analysis of light isotopes such as ^{2}H, ^{3}He, ^{4}He, ^{13}C, ^{15}N, and ^{18}O. The traditional isotopic technique has not been successful in the analysis of radioactive isotopes in marine samples, mainly because of problems with high background. ^{3}He, which is a decay product of ^{3}H, has been successfully analyzed for the

determination of very low concentrations of tritium. ICP-MS and TIMS have been used for the analysis of several long-lived radionuclides, along with RIMS (Michel, 2001; Povinec, 2004; Ross, 2008; Erdmann et al., 2008; Povinec et al., 2008a). AMS has increased the number of radionuclides from ^{14}C to transuranics, and because the background of the system is significantly reduced by accelerating analyzed ions up to several tens of MeV (Kutschera et al., 2000), AMS has become the most sensitive technique at present for the analysis of long-lived radionuclides in the environment (Kutschera, 2005, 2010; Jull et al., 2008; Fifield, 2008; Povinec et al., 2008a).

1. ^{3}He in-growth spectrometry for ^{3}H analysis

The ^{3}H decay product, ^{3}He, is very rare, so its analysis is most suitable for measuring ^{3}H concentrations down to 0.01 TU (Clarke et al., 1976; Palcsu et al., 2010). At present, this is the most sensitive method of isotopic analysis as isotopic ratios of $^{3}H/^{1}H$ can be measured down to 10^{-20}, which represents the lowest isotopic ratio analyzed in the environment. The only disadvantage of the ^{3}He method is the long waiting period (about 6 months) for in-growth of ^{3}He in a water sample hermetically sealed in a glass flask. On the other hand, if appropriate sampling techniques and containers are used for water sampling, it is possible to analyze ^{3}He and ^{4}He gases in the water column simultaneously. The helium isotopes can give additional information on the water age ($^{3}H-^{3}He$ method) and on circulation of water masses in the ocean (^{4}He). If a given water parcel in the sea is not subject to mixing with water of different ages, the relation between its ^{3}He content becomes the time (age) elapsed since the last contact with the atmosphere (Schlosser et al., 1999).

2. Inductively coupled plasma mass spectrometry

With the introduction of the present state-of-the-art high-resolution ICP-MS machines, this technique has been dominating in the analysis of long-lived radionuclides in the marine environment (Sturup et al., 1998; Chiappini et al., 1999; Wyse et al., 2001; Ross, 2008; Hou and Ross, 2008). The principal advantages of ICP-MS are its capacity to determine long-lived radioisotopes of metallic elements down to fg levels, to analyze aqueous samples directly and rapidly (in a few minutes), to keep a low cost per analysis, and to analyze small samples. However, ICP-MS is not free of matrix and isotopic effects, and the formation of chlorides and oxides requires extra careful purification procedures, e.g., extraction chromatography. A steady increase over the past decade in radioanalytical applications using ICP-MS has resulted in a decrease in both the price of instruments and detection limits. New-generation sector field instruments with double-focusing and even multicollector systems have improved sensitivity (by about an order of magnitude) and precision over traditional quadrupole machines (Wyse et al., 2001; Ross, 2008; Hou and Ross, 2008; Povinec et al., 2008a; Nisi et al., 2009). ICP-MS has been used in both higher-resolution and lower-resolution modes. The higher-resolution mode has the advantage of addressing polyatomic interferences, although it cannot solve all the problems with isobaric interferences, which may be caused by incomplete separation chemistry. On the other hand, maximum sensitivity can be reached in the lower-resolution mode. Thus, a combination of the two modes appears to be the best compromise for reaching maximum sensitivity and controlling interferences. The higher count rates under lower-resolution mode give better analytical peaks with lower uncertainties and optimal data quality. Analytes with a relatively strong probability of polyatomic interferences (e.g., ^{238}U which produces a hydride peak that would interfere with ^{239}Pu) should always be scanned. Even so, there are problems with the relatively poor abundance sensitivity of sector field ICP-MS in the measurement of isotopes with one mass below an abundance peak (e.g., ^{237}Np in the presence of high ^{238}U) and two mass units below (e.g., ^{230}Th in the presence of ^{232}Th or ^{236}U in the presence of high ^{238}U content). Even when sample matrices are reasonably clean, and care has been taken to minimize oxides during tuning, measurements made near the detection limit are sensitive to overestimation due to polyatomic interferences. The use of chromatographic resins (Lee et al., 2001, 2005a, 2008, 2009a) has been found to be a suitable technique for processing small volumes, removing possible interferences by additional cleaning, as well as for cleaning leached plutonium samples electrodeposited on stainless steel disks, previously analyzed by SAS.

Production and certification of reference materials have also gained from the introduction of ICP-MS, as this has been used as an effective method for the certification of concentrations of Th, U, and Pu isotopes in various reference materials—seawater, sediment, and biota (Lee et al., 2001, 2005a, 2005b; 2008, 2009a; Inn et al., 2001; Pham et al., 2006a, 2006b; 2008, 2010a; 2010b, 2011; Povinec et al., 2007).

Although molecular, isobaric, and isotopic interferences remain crucial for successful operation of ICP-MS, this technique has a large potential for automation by direct coupling with the new generation of chromatography instruments. ICP-MS has been widely applied, e.g., on the analysis of long-lived radioisotopes of actinides in seawater, sediment, and biota, such as Th, U, Np, and Pu isotopes (Chiappini et al., 1999; La Rosa et al., 2001, 2005; Lee et al., 2001, 2005a; 2008, 2009a; Ross, 2008; Hou and Ross, 2008). Long-lived fission radionuclides, such as ^{99}Tc and ^{129}I, have been studied in seawater and seaweeds (Hou et al., 2009). Usually solution neutralization has been

applied for liquid samples with detection limits below pg. The ETV (electrothermal vaporization) technique has also been used for determining U and Pu isotopes in seawater and ^{129}I in seaweeds (Hou and Ross, 2008).

3. Thermal ionization mass spectrometry

Until the introduction of ICP-MS, TIMS was the most widely used technique for ultralow analysis of long-lived radionuclides (especially actinides) in the marine environment. TIMS has proved to be a highly sophisticated analytical method providing the most precise isotope ratio determinations with precision down to a few ppm (White and Wood, 1988). With TIMS, positive ions are produced in the spectrometer's ion source by evaporating a sample from a heated metal surface. Source filaments are usually chosen from metals with relatively high work functions, high melting points, and the necessary purity and mechanical properties (e.g., platinum, rhenium, tantalum, or tungsten). After heavy separation chemistry, samples are loaded as highly purified solutions onto the filament or by electrodeposition. By adding a known quantity of yield tracer to the sample, isotope dilution analysis is used to measure concentrations below the fg scale (Inkret et al., 1998). Interferences from isobars and mass discrimination between isotopes of a given element need to be carefully evaluated and excluded by chemical purification and control of ionization conditions. Nevertheless, the problem of interferences with TIMS is not as great as in ICP-MS. This problem has been solved when using the total sample evaporation method, as the sample is completely evaporated from the filament. The final results are given in averaged isotopic mean values when measurement has been completed and no measurable amount of sample is left on the filament. Thus, the limiting factor of TIMS in environmental analysis is very often the purity of the sample, as improvements and innovations in mass spectrometer hardware have augmented analytical precision. The new state-of-the-art TIMS machines with multicollector arrays have considerably improved operation in multidynamic mode, producing a sensitivity of around 10^5 atoms for ^{239}Pu, which is comparable to AMS. When using measurement techniques with the extreme sensitivity of TIMS at levels below 10^{-15} g per sample, it is very important to minimize the effects of airborne dust particles, reagents, glassware, etc. which can all contribute significantly to the sample blank and, as a result, to analytical detection limits which are actually defined by the contamination of the blank sample. For this reason, successful TIMS requires more careful sampling, very clean chemical processing, and a higher level of instrumental expertise than any other method. The main advantage of TIMS is its high sensitivity for actinides (more than an order of magnitude higher than for SAS), as well as the possibility of measuring ^{240}Pu/^{239}Pu ratios in low-level samples and identifying the origin of plutonium in marine samples (Buesseler and Scholkovitz, 1987; Lewis et al., 2001). A wide range of ^{240}Pu/^{239}Pu atom ratios have been found in the marine environment: from 0.05 in Mururoa lagoon sediment, through global fallout ratio (0.186) to discharges of plutonium from reprocessing plants (e.g., 0.24 for Irish seawater or 0.20 for Irish Sea sediment) (Kershaw et al., 1999), to 0.30 in Bikini lagoon sediment (Muramatsu et al., 2001). It has been found (Buesseler, 1997) that plutonium delivered as stratospheric fallout appears to be relatively soluble and has a longer residence time in seawater than plutonium from close-in fallout, which is more rapidly removed from the water column to deep-ocean sediments. Highly sensitive TIMS has been used for size-fractionated plutonium isotope studies in the coastal environment (Dai et al., 2001).

4. Resonance ionization mass spectrometry

RIMS is based on highly efficient and selective ionization of elements by tunable lasers and subsequent analysis of ions by a mass spectrometer (Baxter, 1993; Wendt et al., 2000; Becker, 2007). It has been found to be a powerful technique with the main advantages in almost complete isotopic suppression, high ionization efficiency, low background, and high isotopic selectivity, resulting in an overall sensitivity of detection limits down to the fg scale (Erdmann et al., 2008). As only atoms of the desired element (or isotope) are excited and ionized by laser, undesired ions in the mass spectrometer can be suppressed to a significant extent. Therefore, of the various applications of RIMS, ultralow-level determination of long-lived radionuclides in the environment has been the most widely acknowledged (Erdmann et al., 2008). As ICP-MS is very often limited by molecular effects which very often create isobaric interferences (as occasionally occurs with TIMS as well), RIMS together with AMS is currently the most selective technique with minimum interferences for the analysis of long-lived radionuclides in the marine environment at very low levels. However, compared to the more widely used ICP-MS or TIMS, RIMS is yet a very complicated technique requiring a lot of skill and strong technical support. It would seem that RIMS will remain an alternative technique to AMS whenever AMS cannot be used effectively because of insufficient or no production of negative ions (e.g., in the case of ^{81}Kr), strong isobaric interferences or other sources of background. RIMS has been applied successfully in the analysis of several long-lived radionuclides in the environment such as, ^{81}Kr, ^{90}Sr, and ^{99}Tc (Kramer et al., 1986; Wendt et al., 2000) with a detection limit for ^{239}Pu down to 10^6 atoms (Erdmann et al., 2008). Especially, ultratrace isotope detection of noble gases (^{39}Ar and ^{81}Kr) are still a challenging task which has recently been addressed also by AMS, as well as by optical spectroscopy using a magneto-

optical trap and collinear laser photon burst spectroscopy (Kutschera et al., 2000; Bailey et al., 2000). Although the application of RIMS in environmental radionuclide studies has been very limited, its great potential could be in speciation studies, especially when it is coupled to chromatographic systems. As an alternate mass spectrometry technique, it may also play an important role in certification of reference materials.

5. Accelerator mass spectrometry

The first successful attempts to analyze isotopes using accelerated ions were made by Alvarez and Cornog (1939); however, the technique was forgotten for almost 40 y. Attempts were made to use cyclotrons (Muller, 1977, 1978), as well as tandem accelerators (Bennett et al., 1978; Nelson et al., 1977) for acceleration of ions, but the problems with current stability in cyclotrons led latter to the widespread of tandem accelerators in AMS.

The real breakthrough was the development of dedicated tandem accelerators for AMS, firstly for ^{14}C and then for other radionuclides as well, such as ^{10}Be, ^{26}Al, and ^{129}I (Donahue et al., 1990; Kilius et al., 1987; Tuniz et al., 1998). The AMS consists of three main parts—the ion source, the accelerator, and the mass spectrometer illustrated in Fig. 5.25 (see also Chapter 8 Volume 1 of this book). As in tandem accelerators, only negative ions can be used for acceleration, therefore AMS technique can only be applied for those elements (the great majority) forming negative ions. For elements which only form positive ions (e.g., noble gases), cyclotrons can be used, e.g., for the analysis of ^{39}Ar and ^{81}Kr (Kutschera et al., 2000). Very promising AMS systems use a combination of AMS and IBA (Ion Beam Analysis) for better identification of elements of interest in the samples (e.g., Povinec et al., 2015a,b,c, 2016b). The AMS technologies have been extensively reviewed by Kutschera et al. (2000, 2005), Fifield (2000, 2008), Becker (2007), Jull et al. (2008), and Povinec et al. (2008a), including their applications for analysis, e.g., ^{3}H, ^{14}C, ^{10}Be, ^{26}Al, ^{32}Si, ^{39}Ar, ^{99}Tc, ^{129}I, U, Pu isotopes in environmental studies (Kutschera et al., 2005, 2016; McHargue et al., 2000; Kobayashi et al., 2000; Lawson et al., 2000). Some other long-lived radionuclides have been successfully analyzed by AMS (or are under development) with possible applications in marine sciences, including ^{32}Si (Treacy et al., 2000), ^{36}Cl (Hatori et al., 2000; Jacobsen et al., 2000), ^{53}Mn (Knie et al., 2000), ^{135}Cs (Zhao et al., 1999), and ^{237}Np (Fifield, 2000).

The most important development in the AMS sector has been the small "desktop" AMS systems with 0.2 MV accelerator voltage (Suter et al., 2000; Skog, 2007; Synal et al., 2007), which eliminated the need for pressure tanks. This interesting design has been a new competitor to larger AMS machines for ^{14}C analysis, having important impact on environmental and archeological research. In general, however, as the operating terminal voltage used for AMS decreases, the technical engineering difficulties increase, as below 200 kV stripping efficiencies are too low. These small AMS machines have also considerable potential for applications to the analysis of ^{10}Be, ^{129}I, and actinides (Synal et al., 2007; Fifield et al., 2008; Suter et al., 2010).

a. Examples of radionuclide analyses with AMS

Tritium ($T_{1/2} = 12.23$ y): The AMS prototypes (Roberts et al., 2000), based on a radio frequency quadruple linac, can measure $^{3}H/^{1}H$ ratios down to 10^{-13} only (and with further improvement probably down to 10^{-15}) in milligram-sized samples, which makes its application possible only in biological research dealing with ^{3}H-labeled compounds. Another possibility, of course, would be to analyze ^{3}He (the daughter product of ^{3}H decay as it was done originally by Alvarez and Cornog, 1939) in the same way as in isotope mass spectrometry, but this would require the use of an ion source with positive ions.

Carbon-14 ($T_{1/2} = 5730$ y): This is the most frequently analyzed radionuclide by AMS (Povinec et al., 2009). Fig. 5.25 shows how great developments have been done during the last 50 years in measuring environmental radiocarbon (Povinec et al., 2009). Radiocarbon has been analyzed by AMS in seawater samples as a worldwide tracer of water mass movement in the WOCE (World Ocean Circulation Experiment) program (Key, 1996; Key et al., 2002, 2004; McNichol et al., 2000) as well as in several other works (e.g., Key et al., 1996, 2002; Povinec et al., 2000, 2004a, 2004b, 2004c; 2010; Aramaki et al., 2001; Bhushan et al., 2003; Kumamoto et al., 2011). It has also been used for the investigation of sediment dynamics (Somayajulu et al., 1999), dating of deep-sea sediments (Brown et al., 2000), as well as in studies of ^{14}C in marine biota (Yoneda et al., 2000) and in corals, also in connection with the El Nino phenomenon (Guilderson and Schrag, 1998; Key et al., 2004; Kilbourne et al., 2010).

A typical schema of the ^{14}C line used for the preparation of graphite samples is shown in Fig. 5.26 (the line is used at the Comenius University of Bratislava, Povinec et al., 2015a)). Usually only dissolved inorganic carbon is extracted from the water sample by acidification of the water sample to pH 3, and the carbon dioxide released in a flow of high-purity oxygen (or nitrogen) is collected in traps cooled with liquid nitrogen (in other applications dissolved organic carbon can be extracted from larger samples using a different technique). After purification, the CO_2 is converted to graphite over, e.g., an Fe catalyst (Liong Wee Kwong et al., 2004b; Jeskovsky et al., 2015; Kontuľ et al., 2017; Kaizer et al., 2018a). The graphite

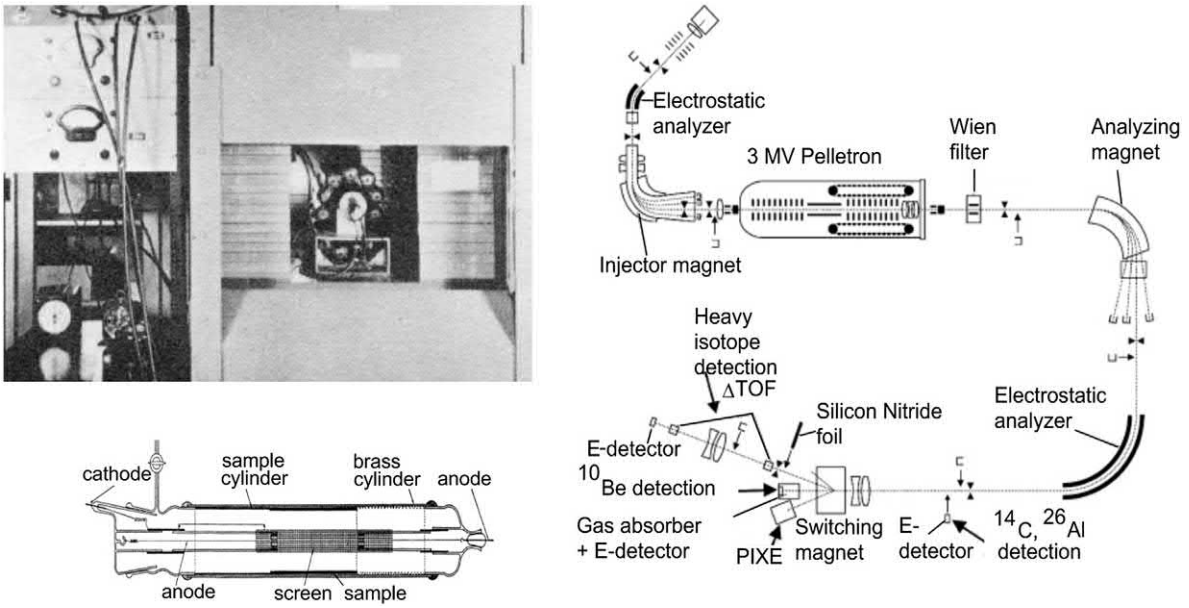


FIGURE 5.25 From a simple solid cathode gas counter developed for radiocarbon dating by Libby (1955) to an AMS system (VERA Laboratory at Vienna University; Kutschera, 2005) and from Povinec et al. (2009); Copyright 2009 Arizona Board of Regents on behalf of the University of Arizona. AMS, accelerator mass spectrometry.

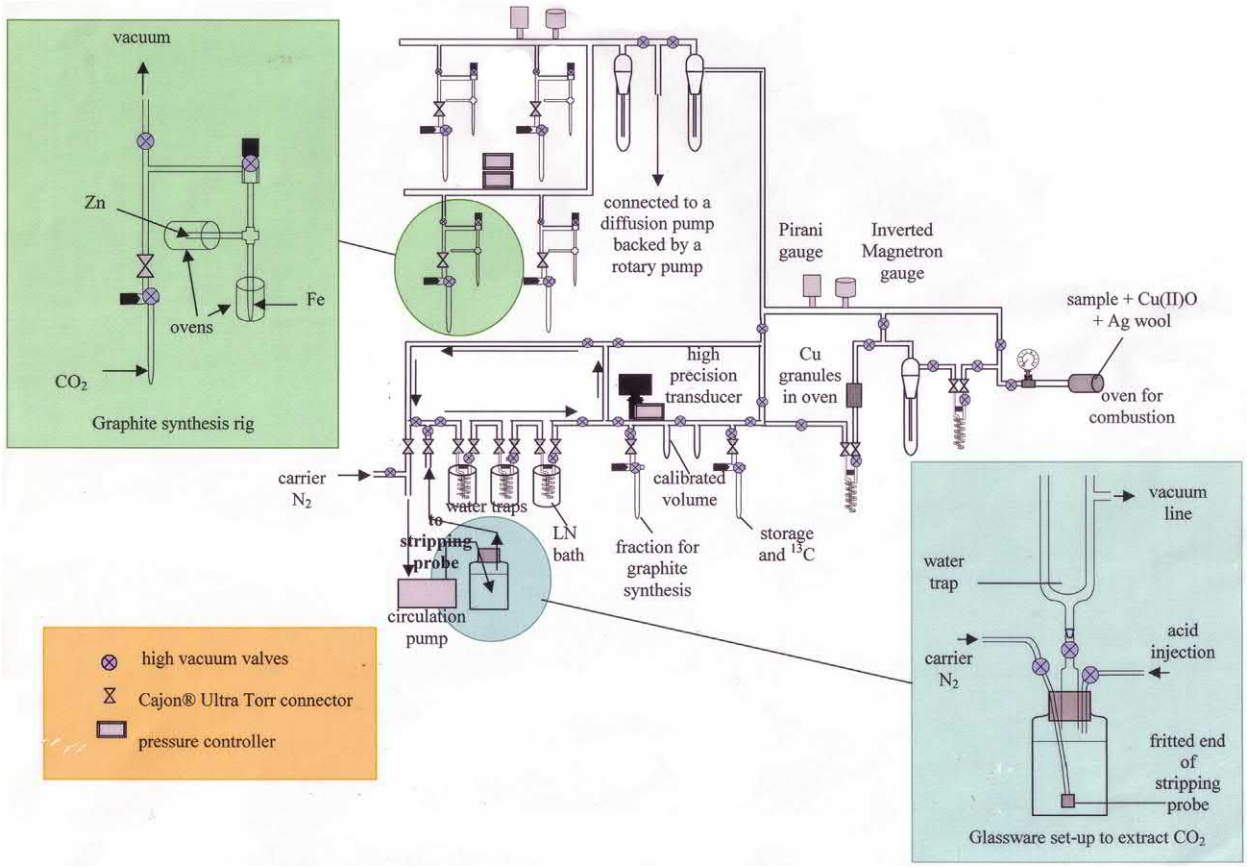


FIGURE 5.26 A schema of a ^{14}C line used at the Comenius University of Bratislava for the preparation of graphite targets for AMS. AMS, accelerator mass spectrometry.

sample is inserted in a sample holder and fixed in the carousel of the ion source. Carbon ions liberated from the graphite sample are accelerated to energies of a few MeV/nucleon and further analyzed by magnetic and electrostatic spectrometers. The precision of AMS measurements is typically below ±5‰.

Technetium-99 ($T_{1/2} = 2.13 \times 10^5$ y): It has been widely distributed in the marine environment through global fallout and releases from nuclear reprocessing plants. It was determined in the past by RMTs as well by TIMS, ICPMS, and RIMS and applied in oceanic water studies (Beasley and Lorz, 1986; Kershaw et al., 1999; Bergquist et al., 2000; Hou and Ross, 2008).

Iodine-129 ($T_{1/2} = 15.7 \times 10^6$ y): It has been widely used as an oceanic tracer to study water transport (Beasley and Lorz, 1986; Raisbeck and Yiou, 1999; Fehn and Snyder, 2000; Povinec et al., 2000, 2010, 2011, 2013b; Hou et al., 2013). Half-liter seawater samples collected and stored without additives are treated in the laboratory following the schema given in Fig. 5.27. A NaI carrier (10 mg) is added to the sample, and after several preparation steps, the AgI sample produced is used as a target for AMS analysis. The results of ^{129}I analysis in seawater samples can be expressed either as activity concentrations (Bq/m^3), as a concentration (^{129}I atoms/L), or as an ^{129}I/^{127}I ratio (Povinec et al., 2000; Santschi and Schwehr, 2004). AMS measurements should be normalized with respect to a reference material. No background subtraction is necessary as the AMS background is very low. Nonetheless, subtraction of a blank sample, processed in a similar way to the real samples, is usually necessary (Povinec et al., 2010).

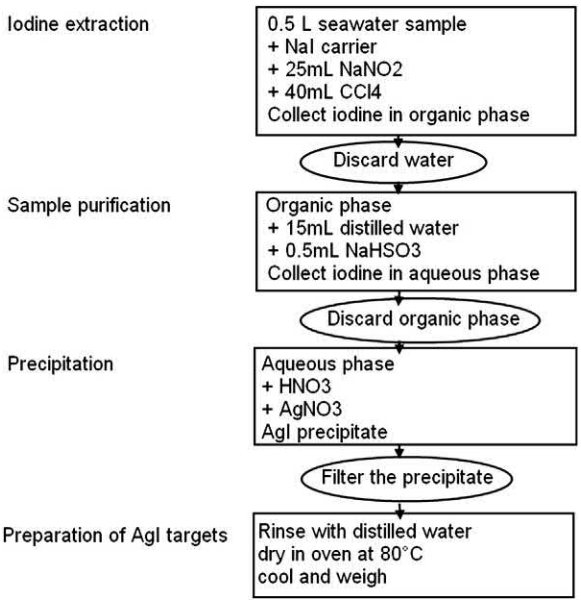


FIGURE 5.27 Flowchart for the preparation of AgI targets for ^{129}I analysis in seawater by AMS. AMS, accelerator mass spectrometry. *Modified after Povinec et al. (2000). Reprinted with permission © Elsevier 2000.*

Uranium isotopes: In the uranium isotopic sector, the most interesting development was the AMS ability to analyze ^{236}U in environmental samples (Hotchkis et al., 2000; Berkovits et al., 2000). This isotope has been a challenge for AMS, as it is embedded in a matrix of ^{235}U and ^{238}U which are potentially sources of background (Lee et al., 2008). The principal applications could be in the area of safeguards, as the ^{236}U/^{238}U ratio clearly shows the reactor origin of uranium. Recently, the ^{236}U/^{238}U ratio has been used as an indicator of the use of depleted uranium in military munitions (Danesi et al., 2003). Because of the long half-life of ^{236}U, it has also been used as oceanographic tracer (e.g., Sakaguchi et al., 2012; Castrilejjo et al., 2017).

Plutonium isotopes: AMS has also been used for the analysis of Pu isotopes (^{239}Pu, ^{240}Pu, and ^{242}Pu) in marine samples (e.g., Oughton et al., 2001; Lee et al., 2001, 2008, 2009a; Povinec, 2004, 2005, 2008, 2010; Lujanienė et al., 2015, 2016, 2017). The samples were prepared either by leaching electrodeposited plutonium from stainless steel disks previously analyzed by SAS or by direct preparation of small-volume samples using Eichrom resins (Fig. 5.19). In the final stage of sample preparation for AMS, the plutonium is dispersed in an iron oxide matrix, adjusted to the atom ratios of ^{242}Pu/Fe from 10^{-10} to 10^{-9}, evaporated to dryness, and baked at 550°C to obtain Fe_2O_3. The resulting sample is then mixed with Al powder (in the proportion of 4:1 by weight), which acts as an electrical and thermal conductor. Finally, the sample is pressed into the sample holders, fixed in the carousel, and analyzed by AMS. The activities of Pu isotopes in a sample are calculated on the basis of the isotopic dilution technique using either ^{236}Pu (if ^{242}Pu is to be analyzed) or ^{242}Pu as tracers. In general, a good agreement was found in Pu analysis using the different techniques. The ICP-MS results were very often slightly higher (up to 10%) than the SAS results (for combined ^{239,240}Pu data) and the AMS results (Povinec et al., 2008a, 2010; Lee et al., 2009a). These discrepancies may have been caused by experimental errors contributing to the total uncertainty. It has often been seen with ICP-MS analyses of Pu isotopes that some matrix or interference effects (such as a contribution of ^{238}U, polyatomic chlorides and oxides, and different forms of hydrates) could contribute to the final results. However, for the ^{240}Pu/^{239}Pu atom ratios, AMS and ICP-MS results were in very good agreement. The relative precision of ^{239,240}Pu results obtained to date by SAS, AMS, and ICP-MS was around 5% (Povinec et al., 2010).

6. Laser-based ^{14}C spectroscopy

The recent development in the mass spectrometry technologies is represented by a laser ^{14}C spectroscopy

(Murnick et al., 2007, 2008). The system is based on the specificity of narrow laser resonances coupled with the sensitivity provided by standing waves in an optical cavity, and detection via impedance variations. The technique combines the optogalvanic effect with laser-assisted isotope ratio analysis, which is a technique based on the existence of large isotope shifts in molecular spectra. The analyzer uses a unique resonance between a specific molecular transition in the molecule $^{14}CO_2$ and the narrow-band output of a laser based on the same molecular transition. The laser spectroscopy has been extended from its current use for the precision analysis of $^{13}CO_2$ to analysis of $^{14}CO_2$. Calibration experiments with a 15-W CO_2 laser demonstrated detection limits for the $^{14}C/^{12}C$ ratio near 10^{-15}. The laser ^{14}C spectroscopy represents an alternative ^{14}C measurement technique, suitable for routine laboratory use. Possible applications may include biomedical and pharmacological studies using radiocarbon as a tracer at global fallout concentrations, thus enabling direct therapeutic tests of drug metabolism on people. It is expected that the method can also be applied for the detection of other trace radionuclides.

7. Positive-ion mass spectrometry

It has been recognized from the beginning of the AMS era that an advantage of the tandem accelerator–based AMS using negative ions for acceleration (e.g., isobaric suppression of ^{14}N vs. ^{14}C as ^{14}N does not form negative ions) may be a disadvantage when using sputter ion sources with solid targets instead of plasma ion sources (RF plasma source or Electron Cyclotron Resonance (ECR) ion source), which are more efficient and capable of greater current outputs. Although with the introduction of a direct ^{14}C analysis using CO_2 gas ion sources simplified the sample preparation, however, the output currents have been very low requiring thus long counting times.

The most important recent development in ^{14}C mass spectrometry analysis has been therefore an introduction of the positive-ion mass spectrometry (PIMS), a new approach in "desktop" ^{14}C systems that would compete with single-stage AMS systems (Wilcken et al., 2010; Freeman et al., 2015; NEC, 2018). The PIMS uses an ECR ion source to produce carbon beams directly from CO_2. The positive carbon beams are accelerated from the ion source to a differentially pumped charge exchange gas cell. Interfering nitrogen and hydrocarbon molecules are then eliminated during the charge exchange process. The ECR source is intrinsically capable of very large ion beam production, it is self-cleaning, and has no memory effects. The PIMS should be therefore more efficient and much faster than AMS. First results indicate that a ^{14}C age limit of about 50,000 years is feasible (Freeman et al., 2015).

TABLE 5.1 Detection limits (in Bq).

Method	^{14}C	^{129}I	^{236}U	^{240}U
Radiometrics	10^{-4}	10^{-2}	10^{-3}	10^{-5}[a]
ICP-MS	–	10^{-3}	5×10^{-8}	5×10^{-6}
TIMS	–	10^{-8}	10^{-10}	5×10^{-7}
RIMS	–	–	–	10^{-6}
AMS	10^{-7}	10^{-10}	10^{-10}	2×10^{-7}

[a] *For $^{239,240}Pu$.*

Moreover, the PIMS may not be restricted to ^{14}C measurements only. Modifying the ECR ion source to accept solid samples, it has been demonstrated that large aluminum positive ion beams could be produced with a plasma ion source as well (Shanks and Freeman, 2015).

8. Comparison of detection limits

A comparison of detection limits for a number of long-lived radionuclides measured by the radiometrics, ICP-MS, TIMS, and AMS, is given in Table 5.1. It can be seen that the most sensitive technique is AMS, which gives the lowest detection limits (three to eight orders of magnitude lower than those obtained by the radiometric methods).

Further development and more frequent use of mass spectrometry techniques (TIMS, ICP-MS, AMS, and RIMS) for ultralow-level analysis of long-lived radionuclides are expected. The AMS will be used more widely as "desktop" machines operating at 250–500 kV voltages. Accelerators working with positive ions (e.g., for ^{39}Ar and ^{81}Kr analysis) will be further developed and applied in marine studies. Direct coupling of ICP-MS (liquid sources) and AMS (gas sources) with the new generation of chromatographs (e.g., GC/MS-AMS systems) will be further developed and applied in marine studies. Other long-lived radionuclides analyzed with mass spectrometry methods, such as ^{135}Cs, ^{237}Np, and others, will enlarge the group of radionuclides used in oceanic tracer studies.

VII. Analysis of radioactive particles

A. Radioactive particle studies

Radioactive substances and their concentrations are usually assumed to be homogeneously distributed within the sample, and also to some degree in the environment. Sample protocols have been developed with geo-statistical methods in order to gain a representative sample for further analysis and, from the sample results, the activity concentrations are calculated, and extrapolations of the concentrations are made to the area where the samples were taken. However,

in some cases these protocols cannot be used due to a heterogeneous radioactive contamination pattern. This is especially true where the radioactivity is bound to discrete particles leading to a very heterogeneous activity distribution. Usually this is the case when the contamination is due to explosions or fire of nuclear material. In such events, the material is pulverized and the particle-size distribution of the debris is so-called log-normal; the effect of such contamination can be seen in the hypothetical example given in Fig. 5.28. A log-normal size distribution also means that the activity/mass distribution of the particles is log-normal, and a consequence of such distributions is that relatively few particles bear the main activity/mass released in the event (Eriksson, 2002). This fact makes them very important to be considered in radiological studies. The IAEA has defined radioactive particles as: "aggregation of radioactive atoms that give rise to an inhomogeneous distribution of radionuclides significantly different from that of the matrix background" (IAEA, 2011). A recent interest of such particles, also sometimes called "hot particles," can be seen in the number of PhD thesis and publications published since the end of 1990s. However, a lack of research in the field is clear, in order to get a full understanding of the environmental behaviors of such particles (Salbu et al., 2018). The number of recent published articles is still small compared to more classical radiological studies. One explanation of this may be that particle studies can be more difficult to conduct as many advanced microanalytical techniques usually are required, not normally present in laboratories conducting a radiological program. It can also be difficult to interpret and extrapolate results gained from particles, as usually they are site specific and similar particles cannot be found elsewhere in the environment.

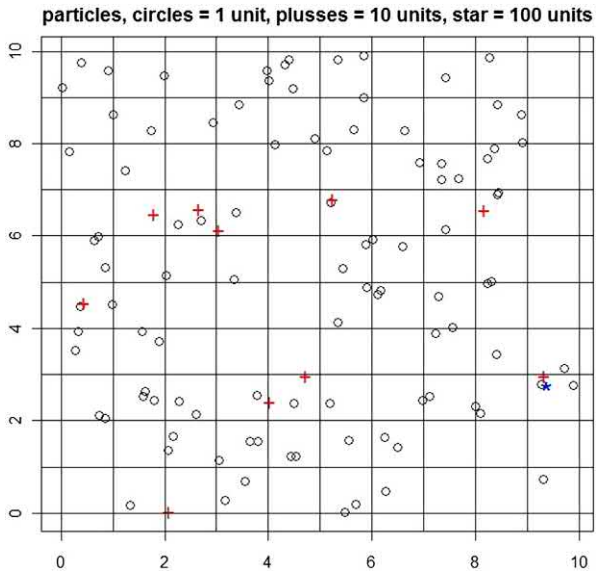


FIGURE 5.28 Hypothetical example of a spatial heterogeneous contamination with the activity associated to particles belonging to a log-normal size distribution. It can be observed that about 30% of the squares (that may represent a typical sample size) have no particles, and only about 10% of the cells have the expected average value of 3 units per cell; thus, the inventory in the particles contaminated area has a higher probability to be underestimated and much care must be taken to design an adequate sampling strategy in order to gain a correct inventory. For the color version of the figure, the reader is referred to the online version of the book.

Radioactive particles are mainly studied in three different areas for their radiochemical, chemical, and physical characterization, namely, (1) nuclear safeguard work, (2) radiological studies, and also to some extent (3) geo-chemical behavior studies. In this chapter, the analytical methods developed for particle analysis will be highlighted; however, it will rather be an overview than a review on the subject. For more extensive information on the specific techniques, that will be mentioned, the reader should refer to text books. It will be shown that in the three areas named above, many of the analytical techniques applied in the particle studies are complementary and are necessary for a proper characterization of the particles. It is important to note that the more conventional methods routinely used for homogeneous samples may produce erroneous results if they are carelessly applied to radioactive particles.

1. Safeguards applications

As a result of the increased demands for nuclear inspections in relation to the nonproliferation treaty (NPT) following the discovery of the Iraq nuclear program in 1991, it was realized that there is a need to improve the method used for detecting nuclear activities (Doyle, 2008). One of these improvements that was adopted in the IAEA safeguards program was the so-called "environmental monitoring" for the analysis of isotopic fingerprints of nuclear material. In the "environmental monitoring" method, samples are taken inside and in the vicinity of nuclear facilities (Donohue, 1998, 2002; Axelsson et al., 2009). In these samples, the nuclear and isotopic fingerprints are determined in order to reveal uranium isotopic enrichment, fuel fabrication, or reactor operation. Typically, these samples are collected with a piece of cloth that swipes surfaces and collects microscopic-sized particles. These particles are then later analyzed either as single particles or as a bulk sample (the whole piece of cloth containing many particles) for the nuclear and isotopic fingerprint.

2. Radiological impact studies

In radiological impact studies, radioactive (hot) particles have gotten into focus in the last 15 years or so. The interest has mainly increased as more advanced analytical techniques have become available resulting in a deeper understanding of the particles, in combination with the findings

of several studies, which have shown that in some cases the radioactive particles are extremely important to consider. It has been shown that in accidents and incidents releasing nuclear material after fire and/or explosions, most of the released nuclear material is associated with few large-sized radioactive particles (Eriksson, 2002; Shevchenko, 2004; Kaltofen and Gundersen, 2017). This is the effect of a so-called log-normal size distribution, where the few large-sized objects carry most of the released mass/activity. In sites contaminated in this way, the radioactivity distribution is extremely heterogeneous, making representative sampling very difficult. One should keep this in mind, as most radiological sampling strategies are based on the assumption that the radioactivity is homogenously distributed in an area or within the subsamples from the area. As radionuclide inventory estimates are essential in determining the source terms, one must take these few large-sized particles into account; however, usually one has a "needle in a haystack problem." Fig. 5.28 illustrates this problematic situation. Several studies have focused on these particles, examples are given later, to reveal the source term of the accident. It has also been shown that the radioactive particles must be taken into account in radiation dosimetry estimates (e.g., Jaeschke and Bradshaw, 2015). In the case of respiratory-available particles (aerodynamic diameters less than 10 μm), which are attached to the skin, highly localized absorbed equivalent doses can be achieved. This may result in biological and medical consequences for the exposed person. In radiological studies with a focus on the radioactivity uptake and transfer in food webs, it is important to note the difference between particle-associated radioactivity compared to the normally assumed homogenously distributed activity. Most of the experiments conducted to measure transfer factors and Kd's use a different chemical form (ionic tracer solution added to the system) from particles where the radioactive elements are in a solid phase. It is very important to take into account a chemical speciation in such investigations. Several studies have now been conducted on solid-state speciation of radionuclides attached to particles.

3. Geo-chemical behavior studies of radionuclides

The third thematic area where particles are important is in geo-chemical behavior studies of radionuclides. As mentioned above, the chemical speciation of the radioactive elements will determine their solubility and mobility in the ecosystem. In order to fully assess the long-term consequences of a radioactive contaminated area involving particles, like nuclear accident sites as well as in nuclear fuel facilities and uranium mine tailings, it is essential to perform speciation studies. These studies involve both laboratory and field conditions and include sequential extraction experiments, physical speciation using synchrotron radiation-based techniques, and dissolution/leaching studies in selected solutions. It has been shown that radiological assessments based on the assumption of homogenous activity distribution (average bulk mass or surface activity) will be biased in the case of contamination of radioactivity bound to particles. The dissolution/weathering of some type of radioactive particles will increase over time. Further, it was shown that weathering rates will depend on the particle composition, structural changes occurring during the release scenario (e.g., transformation from UO_2 to U_3O_8), and on local chemical conditions and transformation processes occurring after deposition (e.g., pH, redox conditions, and bioerosion) (Kashparov et al., 2004).

In the following section, an overview of the most common techniques applied to radioactive particle studies is presented. A schematic view summarizing these techniques is presented in Fig. 5.29. It is not possible to give in this chapter an extensive review of all applied techniques with all references. More detailed information can be found in PhD theses (Eriksson, 2002; Pöllänen, 2002; Jernström, 2006; Lind, 2006; Ranebo, 2009; Gostic, 2010; IAEA, 2011) and in the NATO Science for Peace and Security Series (Oughton and Kashparov, 2009).

B. Protocols for studying radioactive particles

There has been a lack of standard analytical techniques and protocols on the collection, isolation, and further analysis of radioactive particles. In addition, no certified reference materials exist for the validation of their analysis, even though potential material has been produced (Erdmann et al., 2000; Ranebo et al., 2010a). In 2000, the IAEA initiated a coordinated research project with the aim to fill these gaps and to develop standardized methodologies. The

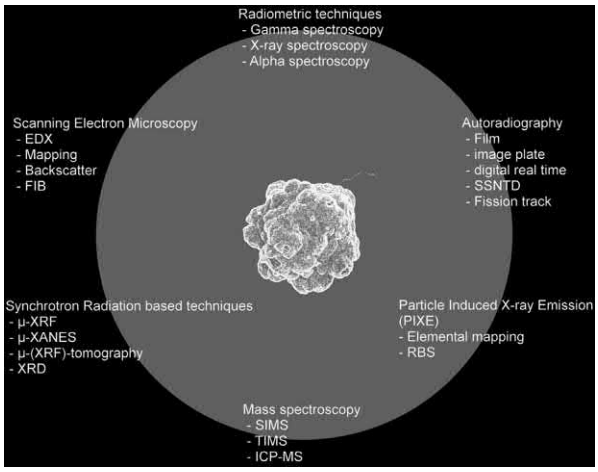


FIGURE 5.29 The most common radioanalytical techniques applied in studies of radioactive particles.

participants of this project produced a useful IAEA publication summarizing all the activities (IAEA, 2011).

The protocol for studying radioactive particles highly depends on the application and on which questions the analyses are assumed to answer. However, commonly to all applications are that the studies start with the nondestructive analysis (e.g., radiometric measurements) followed by the semidestructive analysis (e.g., SIMS) and finally with the destructive particle analysis (e.g., particle dissolution and ICP-MS).

Before any analysis can be performed, the particles must be identified and separated from the bulk sample (e.g., sediment, soil, and wipe sample). The preferable technique to use in this process depends highly on the radioactive particle decay mode and its activity.

For particles consisting of high-activity gamma-emitting radionuclides, a so-called sample splitting technique using a gamma spectrometer can be used. This is an effective separation method in the case of a large sample, as after about 20 splittings only a few grains remain, if the starting bulk mass sample is of about 150 g (Eriksson et al., 2005a). In the case of a search for actinide particles, this separation method can be enough in order to identify the particle with a simple loupe. Actinide particles with a size above 100 μm can be seen with a loupe magnifying, e.g., eight times, and usually these particles can be distinguished from the bulk SiO_2 particles. In the loupe, the actinide particles have a dark greenish color and the SiO_2 particles have a lighter brown-yellow color. Potential particles may exist which could be separated with a pipette and a drop of distilled water. The drop is placed on the top of the actinide particle and then everything (water drop + particle) is sucked up into the pipette again. The particle in the pipette can then be placed on a detector for verification and then further placed on a sample support. An alternative to this is to place the remaining particles on a new support where they are fixed, e.g., on double adhesive carbon tape of a graphite planchet fixed with isopropanol alcohol. The particles can then be identified on the support either in a SEM/EDX system or with autoradiography techniques (Fig. 5.30). Another effective technique for the identification of actinide particles from a large bulk sample is the use of high-resolution X-ray computed tomography (CT) instrumentation (Gostic, 2010). This technique was used to identify and separate high-radioactive particles from the contaminated soil in the BOMARC missile site in New Jersey, USA. The high-resolution X-ray CT was used to identify potential particles in soil cores, assuming that actinide particles have a much higher density than the bulk soil. From the CT images, the depths in the cores were determined, and the core slices with the particles were checked with a NaI(Tl)γ-detector.

The above-mentioned techniques cannot be used in the case of radioactive particles containing alpha- and beta-decaying elements of a low activity (<0.1 Bq). In the case of such particles, autoradiography technique is the alternative. However, if the particles consist of fissile material, also the fission track techniques can be used. Several different autoradiography techniques exist which work differently. The solid-state nuclear track detection (SSNTD) technique has been widely used for identifying radioactive particles (e.g., Jernström, 2006). A detailed description of SSNTD can be found in this book, Chapter 3, Volume 1 (see also Ilić and Durrani, 2003). The SSNTD technique is based on the principle that ionizing particles emitted in the nuclear disintegrations process, which hit a detector, form microscopic tracks in the detector material. The detectors can be of various materials, such as plastic, mineral, or glass. After the exposure, the detectors must be treated by etching them with alkaline solution to enlarge the tracks so that they can be visible with an optical microscope. A commonly used detector is the cellulose nitrate films, which are sensitive in the detection of alpha and heavy ion rays. The radioactive particles are recognized from where tracks have formed clusters, star-shaped patterns, on the film. Image plates are also commonly used techniques which are based on the principle that the ionizing radiation emitted by the radioactive particle interacts with the plate, and deposits its energy, which is "stored" in the detector. This information (the absorbed radiation dose) is, after exposure, read out by using laser light to achieve a de-excitation process of the trapped electrons, and the fluorescence signal is proportional to the energy deposited in the detector. Real-time digital autoradiography techniques also exist. They have the advantage because they are fast and do not require any posttreatment (e.g., etching or readout) as an image is given directly on

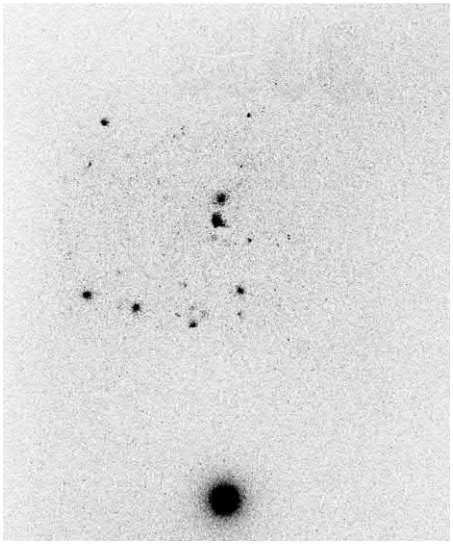


FIGURE 5.30 An autoradiograph of a sediment sample containing radioactive particles emitting alpha-, beta-, and X-rays from the decay of Pu-, U-isotopes. *The film is a tritium image plate from Fuji.*

the computer screen. These techniques are described in detail elsewhere (Eriksson et al., 2002; Zeissler, 1997; Ljunggren, 2003) and in Chapter 9, Volume 2 of this book.

1. Nondestructive analysis

After the particles have been separated from the bulk matrix, depending on the aim of the studies, they are usually subjected to multiple analyses. In order to achieve as much information as possible, the first set of analysis would be the so-called nondestructive analysis, i.e., gamma-ray, X-ray, and direct alpha-spectrometry and charge particle and X-ray-based scanning techniques such as scanning electron microscopy and X-ray fluorescence (XRF) for surface analysis and elemental distribution mapping (Betti et al., 2008). Some systems have an integrated approach making several nondestructive analyses simultaneously such as the system known as PANDA (particles and nondestructive analysis) (Turunen et al., 2009). The PANDA has detectors for gamma ray, X-ray, and alpha ray detection, to determine the radionuclide activities and ratios besides determining the particles location on the sample support simultaneously.

a. Gamma ray, X-ray, and alpha spectrometry on particles

Radioactive particles can contain both actinide elements and short-lived fission and/or activation radionuclides. In the latter, the main bulk material of the particle is usually a nuclear fission material (i.e., nuclear fuel or bomb fragments) containing uranium and/or plutonium. This signifies that the photon energy range is from the X-ray energy range (10−25 keV for the characteristic *L* X-rays of, e.g., U and Pu) to the MeV region for radionuclides such as ^{137}Cs and ^{60}Co. An alternative to using two different detectors, such as an X-ray detector (e.g., Si(Li)) and an HPGe detector, one can use a broad energy germanium (BEGe) detector to detect photons in this large energy range with a high efficiency. The energy resolution of the BEGe is not as good as an X-ray detector; however, it has a high detection efficiency to detect photons in the range of ∼10 keV to a few MeV.

The activity determination of particles containing radionuclides emitting high-energy gamma rays is fairly straightforward (Pöllänen et al., 1999). The particles can be considered as a point source, and for photons with energy higher than a few hundred keV, the self-attenuation in the particles is not a problem and the efficiency calibration is easily achieved. In the low-energy region, it is much more problematic as self-attenuation in the particles can be high leading to difficulties in obtaining a good efficiency calibration. The L X-rays, emitted following the ejection of a conversion electron in the internal conversion disintegration process, of the ^{238,239,240}Pu and ^{241}Am occurring in the radioactive particles, have been measured in several studies, as illustrated in the left spectra in Fig. 5.31. From these measurements, the activities and the isotopic and radionuclide ratios have been determined (Jernström et al., 2006; Komura et al., 1984; Eriksson et al., 2005a; Mitchell et al., 1997). The efficiency calibration has been carried out generally by determining the ^{241}Am efficiency from a point source and assuming a neglectable self-absorption in this source. It is theoretically possible to determine the Pu isotopic ratios using this technique by solving a linear equation system (Eriksson et al., 2005a). However, in practice this is very difficult, especially for particles with low activity (less than few Bq). In order to solve the linear

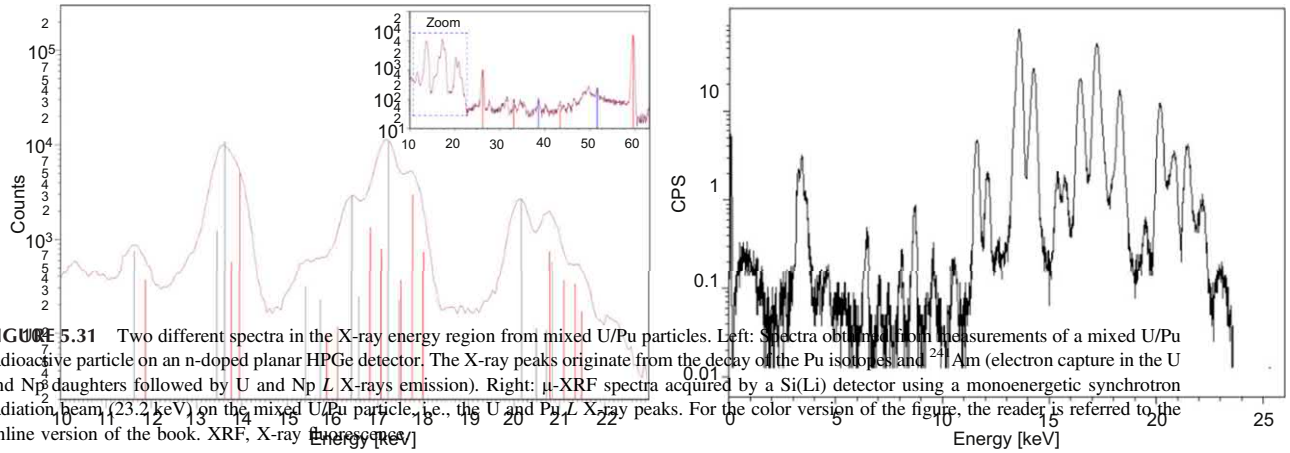


FIGURE 5.31 Two different spectra in the X-ray energy region from mixed U/Pu particles. Left: Spectra obtained from measurements of a mixed U/Pu radioactive particle on an n-doped planar HPGe detector. The X-ray peaks originate from the decay of the Pu isotopes and ^{241}Am (electron capture in the U and Np daughters followed by U and Np *L* X-rays emission). Right: μ-XRF spectra acquired by a Si(Li) detector using a monoenergetic synchrotron radiation beam (23.2 keV) on the mixed U/Pu particle, i.e., the U and Pu *L* X-ray peaks. For the color version of the figure, the reader is referred to the online version of the book. XRF, X-ray fluorescence.

equation system and obtain results with low uncertainty (or acceptable uncertainties), long acquisition times would be required for the measurements in a system with very low background, as the muon continuum and multiple scattering from other gamma rays will be pronounced in the X-ray region of the full gamma-ray spectra. In addition, the differences in the emission probabilities for the different Pu isotopes are small and the data for these emissions have relative large uncertainties. The abovementioned problems often result in nonexisting solutions to the linear equation systems, i.e., negative activity for one or more nuclides. However, if the particle is simultaneously measured with an alpha and a gamma spectrometer, such as the PANDA system, and the spectra are acquired in an event mode (also called list mode or time-stamp mode), one can simplify the spectra by only acquiring the events that are associated with α-rays originating from the ^{239,240}Pu decay (Peräjärvi et al., 2011). By this gating, X-ray spectra can be constructed exclusively from the two radionuclides, without any multiple scattering photon background or any continuum from cosmic muons. For radioactive particles containing higher activity (>100 Bq of ^{239,240}Pu), the isotopic ratios can be determined directly from the gamma ray lines associated with the ^{239}Pu and ^{240}Pu decays (Jernström et al., 2006; Gostic, 2010).

A Finnish research group at the Radiation and Nuclear Safety Authority (STUK) has been working extensively on high-resolution direct alpha-spectrometry on radioactive particles. They have produced software, an advanced alpha-spectrometric simulation (AASI), for simulating energy spectra in alpha-spectrometry (Siiskonen and Pöllänen, 2004). In AASI, the geometrical detection efficiency and energy loss of the alpha rays in the source and in the material between the source and detector can be simulated. In addition, it is possible to specify characteristics of the radioactive particles and of the alpha detector, which are taken into account in the simulations. Several radioactive particle applications have been demonstrated using this program as well as activity ratios and density estimates for the particles (Ranebo et al., 2010b).

b. Scanning electron microscopy coupled with X-ray detectors

In radioactive particle studies, the nondestructive scanning electron microscopy (SEM) technique is essential. With the use of SEM, multiple information is gained. In the case of many particles on a sample support (e.g., a safeguard sample), particle-size distribution can be determined. In addition, SEM provides information on morphology, the surface, and subsurface structure, and identifies and localizes high-density (high-atomic number) particles. The SEM images are also used as guiding "maps" when the particles should be relocated for analysis by another technique, e.g., in the XRF and SIMS experiments described below (Fig. 5.32). Compared to the conventional optical microscope, an SEM offers advantages including high magnification, large depth of focus (providing a sharp high-resolution image on a large part of the particle, size range for radioactive particles from sub-micrometers up to millimeters), high-resolution and elemental surface composition when coupled with an X-ray detector system.

The principle of SEM imaging is summarized as follows: The sample or specimen surface is irradiated with a scanned (rastered) electron beam emitted from a filament (electron gun). The impinging electrons undergo scattering interactions with the surface and subsurface atoms, either by elastic or by inelastic interactions. Each interaction will result in one or more electrons (secondary electrons) leaving the interaction point. The secondary electrons can in turn undergo scattering interactions in the sample, leading to many events throughout a volume determined by the electron beam energy and the cross section for each element in the irradiated point.

The two different electron scattering processes are used in SEM for imaging. The backscatter (BS) imaging utilizes the elastic scattered electrons (more than 90° from the

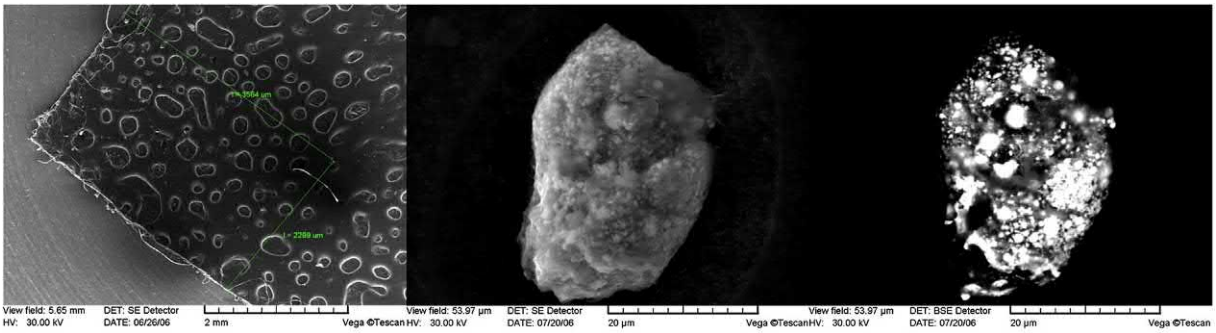


FIGURE 5.32 SEM images of a radioactive particle originating from the Thule accident on its sample support. Left: guiding map of the particle position on the sample support to relocate particle in other systems. Middle: Secondary electron (SE) image providing the dimensions and morphology. Right: Backscatter (BS) image showing the regions with the high Z element uranium and plutonium.

impinging beam direction, called backscattered electrons) that are reemitted away from the surface toward a PIPS detector. The elastic scattering cross section for backscattered electrons increases with the atomic number (Z). This is used in the BS imaging to distinguish, e.g., uranium particles from bulk soil particles mostly consisting of SiO_2, as illustrated in Fig. 5.32 (Ranebo et al., 2007). In the inelastic scattering, the impinging electron energy is delivered to the sample atoms and may result in excitations/ionizations from which secondary electrons are emitted. Most of the secondary electrons will be absorbed in the sample and therefore do not escape the sample surface or reach the detector. The secondary electrons generated at a shallow depth in the sample will be able to reach the detector. As a consequence of this, they are very sensitive to the sample topography and are used for high-magnification SEM images (Fig. 5.32) in the so-called secondary electron (SE) mode. In the inelastic scattering interactions, some of the atoms in the excited state will radiate a characteristic X-ray or Auger electrons. As the X-ray is characteristic for each element, elemental information of the specimen is gained. Two types of X-ray detector systems are used generally and coupled to the SEM, namely, energy-dispersive X-ray (EDX) or wavelength-dispersive X-ray (WDX) analyzers. In order to perform quantitative elemental analysis from the X-ray spectra, several interaction cross sections must be known in combination with liner attenuation coefficients for the sample material as well as the energy spectra of the impinging energy beam (Garratt-Reed and Bell, 2003). In theory, the radioactive particle X-ray spectra are compared with a set of standards in order to estimate the elemental composition. Some EDX/WDX systems have good analytical programs to process the spectra and evaluate the elemental composition. However, very few include the option to analyze the actinide elements. The National Institute of Standards and Technology (NIST) provides free software (Desktop Spectrum Analyzer, DTSA) with some options for the analysis of SEM-generated X-ray spectra including the actinide elements (Newbury and Myklebust, 2005; NIST, 2011).

c. Microbeam X-ray fluorescence techniques applied to particles

In this section, an overview of the nondestructive XRF techniques applied to radioactive particle studies will be given. We will focus on the applications rather than the theories behind the techniques. Common to these techniques is that they have very little to do with radioactivity, as these are atomic-sensitive techniques that give information on elements and the chemical environment of the atoms rather than the decay processes in the nucleus. It is justified to discuss these techniques in this book, as many studies related to radioactive particles apply these techniques as a part of the particle characterization and for information on the source term description. The most utilized technique in this sense is the synchrotron radiation-based micro-X-ray fluorescence (μ-XRF). This technique has been shown to be a powerful tool for obtaining elemental compositions and their distribution in radioactive particles (Lind et al., 2005; Lind, 2006; Eriksson et al., 2005a). The use of X-ray tube-based μ-XRF systems (Wegrzynek et al., 2005) has been applied as well to the particle-induced X-ray emission with nuclear microprobe technique (μ-PIXE) for the study of radioactive (Jiménez-Ramos et al., 2012). The abovementioned techniques are applied commonly to studies on particles containing a bulk mass of uranium and/or plutonium. The detection limits of the techniques do not allow the mapping of short-lived radionuclides at the amounts at which they are present in the particles. The shortest-lived radionuclide that has been mapped by this technique, to the authors knowledge, is the ^{241}Am (432 y) in particles originating from the BOMARC accident in 1960 (Gostic, 2010).

d. Synchrotron radiation–based XRF

The intensity of the characteristic X-rays is proportional to the elemental concentration in the particle as well as the excitation beam intensity. The use of synchrotron radiation (SR) as a source for the excitation beam has several advantages compared to the use of, e.g., an X-ray tube. First, a tunable monochromatic beam with a high and known photon flux is used, simplifying the elemental characteristic X-ray intensity calculation to concentrations. Second, the beam can be focused and scanned over different areas enabling two-dimensional (2D) and three-dimensional (3D) elemental mapping of the particles. In addition, the density fluctuation in the particles can be determined from the X-ray transmission measurements of the SR-beam. With recent developments in X-ray optics, improved spatial resolution in the images has been achieved. The earlier focusing devices were of capillary type, and the SR-beam could be focused from 1 mm size down to a focus spot of around 20 μm in diameter. With the use of so-called compound refractive lenses (CRLs), a focus of less than 1 μm can be achieved (Simon et al., 2006). This makes the CRL optics superior to the capillary optics in the study of radioactive particles, as typically the size range of the particles is from 1 up to $\sim$500 μm. Early studies of SR μ-XRF using capillary optics made erroneous conclusions of the homogeneity of the U/Pu distribution in radioactive particles (Eriksson et al., 2005a). The reason for this was that the μ-XRF focus on the particle was more or less in the same order as the particles, making the analysis more like an average bulk elemental analysis. When the particles were analyzed with a tenfold smaller focus using CRL, heterogeneities could be observed in the U/Pu distribution.

However, the μ-XRF elemental maps are still a 2D projection of a 3D object, meaning that information is smeared out in the SR-beam direction. A full understanding of the 3D elemental distribution cannot be gained from the 2D scans. In order to gain the full-volume elemental distribution in particles, the SR μ-XRF experimental setup was modified by assembling an X-ray lens in front of the X-ray detector, forming a so-called confocal μ-XRF setup. Confocal μ-XRF enables 3D scans and gains the elemental distributions within the studied sample. Another great advantage of the confocal μ-XRF setup is that "low"-density volumes can be analyzed within the radioactive particle. This is important if it is expected that the particles have been leached and started to dissolve the surface rime of the particle, as it then probably has a lower density than the inner core. In classical μ-XRF, this is not possible to study, as the fully exited volume of the primary beam impinging on the particle is analyzed. If heterogeneities exist in the density/concentrations of the different elements in this exited volume, most of the fluorescence photons will come from the areas with highest density/concentration of the element biasing the elemental ratio evaluation. The difference between the approaches has been demonstrated by comparing U/Pu mass ratios derived from the summed confocal μ-XRF spectra (bulk information) measured in the full-particle volume with the measured mean U/Pu mass ratio derived in all confocal measured volumes (Jimenez-Ramos et al., 2010). In the calculated mean elemental ratio in the confocal μ-XRF scan, volumes with low density/concentration have equal weight in affecting the mean ratio as volumes with high density/concentration. The ratio in the high-density volumes can be considered as representative for the bulk of the particles. If one expects that leaching/corrosion processes have been affecting the particles leading to depletion and lower density (concentration) of elements on the surface, the confocal μ-XRF technique is ideal for the analysis of such surfaces, where classical μ-XRF would fail. By this important analysis, an understanding can be developed on the geo-chemical behavior that these particles have in the environment.

High-resolution μ-tomography (absorption μ-CT) has been demonstrated on radioactive particles showing internal structures as well as density distributions in the submicrometer scale (Salbu et al., 2001). Combined X-ray absorption and fluorescence microtomography have been used to obtain the 3D elemental distribution in radioactive particles (Wegrzynek et al., 2005; Eriksson et al., 2005a). The combined technique first reconstructs the absorption tomogram and uses this for the photon attenuation correction of the characteristic X-ray elements in the particle. The reconstruction is based on the radon transform referred to as the filtered back-projection. An example of the combined X-ray absorption and fluorescence microtomography is shown in Fig. 5.33.

e. X-ray absorption spectroscopy

The binding energies of atomic core electrons are dependent on the oxidation state of the atom as well as the surrounding chemical environment (chemical binding to neighbor atoms). The chemical form of the radionuclides will determine the leach ability and solubility in the environment of the elements bound to the particle. The oxidation state can also be used to predict the formation of the particle, as demonstrated for radioactive particles discharged from the Chernobyl accident in 1986 (Salbu et al., 2001, 2005). Oxidation states can be studied with the use of a highly chromatized, tunable monoenergetic synchrotron radiation light in X-ray absorption spectroscopy (XAF) studies. In radioactive particle studies, the microfocused X-ray absorption near edge structure (μ-XANES) has been used for the determination of U and Pu oxidation state distributions in particles. One example of uranium L_{III} μ-XANES can be seen in Fig. 5.34. Confocal μ-XANES (Bielewski et al., 2009) as well as tomographic XANES

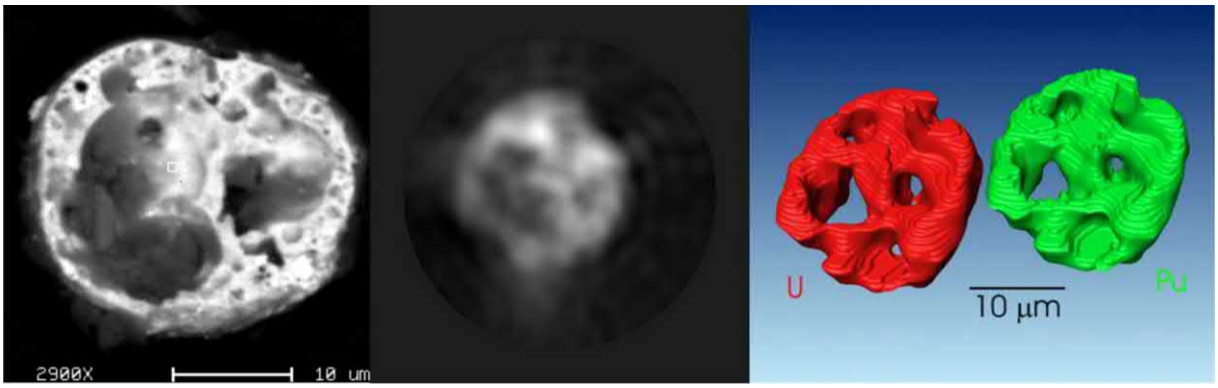


FIGURE 5.33 SEM image of a mixed U/Pu particle originating from Thule (left); a tomographic reconstruction of the density distribution in one section of the particle (middle); and the full 3D reconstruction of both U and Pu in the particle derived by combined SR X-ray absorption and fluorescence microtomography (right). For the color version of the figure, the reader is referred to the online version of the book.

(Lechelle et al., 2004) have been used to get the 3D information of the oxidation states (electron-binding energies) in the particles. Usually oxidation-state standards are measured and used to "translate" binding energies to the oxidation state distributions in the particle. It should be mentioned that the high X-ray dose given to the particles during the measurements may be of a problem. For example, one type of Pu oxidation state standard crystal (Pu(+4)-oxylate) shows a rapid reduction in the oxidation state from Pu+4 to Pu+3 (Eriksson et al., 2005b). This finding shows an effect that may occur also in radioactive particles under study, and this effect has not been considered in the solid-state oxidation state determinations by μ-XANES analysis of actinide particles.

Synchrotron radiation–based micro-X-ray diffraction (μ-XRD) can be used as a complement to the XAF determination of the chemical species of the elements present in particles (Salbu et al., 2004; Lind et al., 2009).

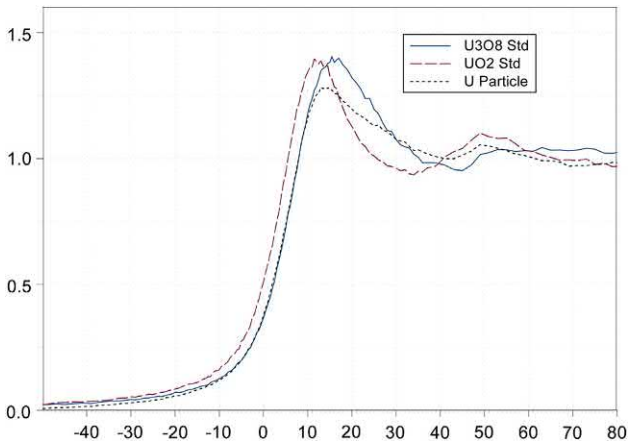


FIGURE 5.34 Uranium L_{III} μ-XANES on a radioactive particle and two spectra from particles with known uranium molecular formula (UO_2 and U_3O_8) used as oxidation state standards.

2. Semi-destructive analysis of particles

Secondary ion mass spectrometry (SIMS) has successfully been applied to the characterization of radioactive particles and the nuclear fingerprint. One of the advantages, compared to the ICP-MS, is that the particle does not need to be dissolved and no radiochemical separation is required that could bias the fingerprint signals. This is especially important when the uranium isotopic ratios are to be determined. As an example, a radioactive particle with the size of ~50 μm originating from the Thule accident typically contains 10–100 ng of the uranium isotopes. As natural uranium is present almost everywhere in our environment and laboratories, cross-contamination is a potential risk and may bias the ICP-MS results (Eriksson et al., 2008). SIMS can be operated in several different modes and provide information of the most superficial layers of the particles as well as deeper layers when conducting depth profiling. Besides serving as a mass analyzer, it is also an ion microscope, providing mass images of the sample. In the SIMS analysis, a primary ion beam is focused onto the sample surface, sputtering the surface atoms that generate secondary ions from the target area, which are then accelerated into a mass analyzer (Vickerman, 1989, see also Chapter 8, Volume 1 of this book). The production of secondary ions has different efficiency for different elements which also depends on the matrix. As the mass spectra contain masses (isotopes) from different elements of the particle, important corrections must be made to correctly interpret the elemental isotopic composition (Ranebo et al., 2007, 2009; Simons, 1986).

Fig. 5.35 illustrates, as an example, an SEM image of a radioactive particle with a crater on the top, produced by

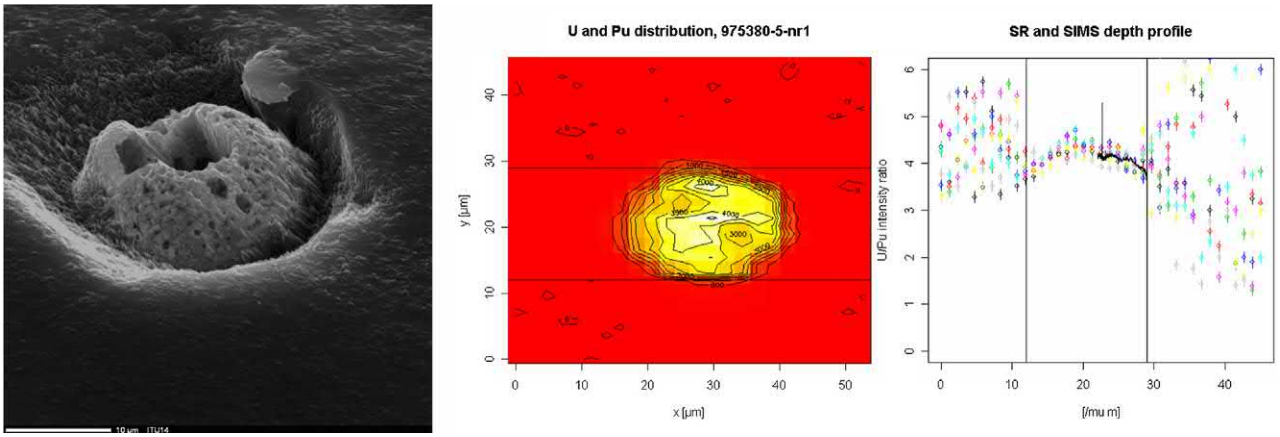


FIGURE 5.35 SEM image of a radioactive particle with a crater on the top produced by SIMS in the depth profile analysis (left); confocal SR m-XRF derived Pu and U distributions in one section of the particle (middle); the SR-derived U/Pu ratio line scans and superimposed the total SIMS-derived U/Pu mass ratio (black line) (right). For the color version of the figure, the reader is referred to the online version of the book. SIMS, secondary ion mass spectrometry; SR, synchrotron radiation; XRF, X-ray fluorescence.

SIMS during the depth profile analysis. Confocal SR m-XRF derived Pu and U distributions in one section of the particle, together with the SR-derived U/Pu ratio line scans, and the total SIMS-derived U/Pu mass ratio.

3. Destructive analysis on particles

In order to analyze the nuclear fingerprint with, e.g., ICP-MS or high-resolution alpha-spectrometry for the determination of isotopic ratios, the radioactive particles must first be totally dissolved, and a radiochemical separation of the dissolved particle should be conducted. Radiochemical separations are described elsewhere in this book; however, some specific notes concerning actinide particles should be mentioned.

Dissolution of (U, Pu)O_2 hot particles is notoriously difficult requiring mineral acids (Keller, 1971; Eriksson, 2002). It is very important to check that complete dissolution of the particles had occurred in the dissolution process. This can be done by comparing the ^{241}Am gamma activity, measured by, e.g., an HPGe detector on the whole particle, with the activity of ^{241}Am determined after dissolution and chemical separation with, e.g., alpha spectrometry.

Two efficient (U, Pu)O_2 particle dissolution methods have been described (Eriksson et al., 2008), where the full-particle matrix was dissolved. In this method, the particles were dissolved in a small amount of a mixed solution of hydrofluoric and nitric acids (ratio 1:3) in high-pressure Teflon cells. The closed Teflon cells were then placed on a hot plate, which maintained that the mixture was under pressure for 24 hours. The solution was then evaporated to dryness. In addition, the use of microwave digestion using a mixture with 7 mL of HF, 7 mL of HNO_3, and 1.5 mL of HCl was proved to be effective in totally dissolving the particles. The microwave Teflon cell was heated for 20 minutes at a maximum pressure of 250 psi (17.2 bar) and a maximum temperature of 200°C. In order to break the Pu-fluoride complexes formed in the dissolution process, 25 mL of saturated boric acid was added, and the mixture was heated for another 20 minutes in the microwave oven. The solutions from both dissolution methods with the totally dissolved particles were evaporated to dryness, and 0.3 mL of HNO_3 was added and evaporated to dryness, which was repeated three times. This was done to ensure that all the Pu-fluoride complexes were destroyed, which would cause problems in the ICP-MS measurements.

In addition, one of the challenges of working with hot particles is the determination of the U isotopic composition, as these particles typically contain a 10th of ng of uranium, and these amounts are typically equivalent to procedure blank values of U found in normal laboratories; thus, the radiochemistry must be conducted under ultrapure conditions, preferably in clean laboratories in order to not bias the U isotopic signature of the particles.

VIII. Management of data quality

The production of good-quality data is an important prerequisite for any environmental investigations if meaningful results should be obtained. Quality assurance (QA) as a system of activities and actions (Garfield, 1992) has two main components:

1. Quality assessment—a mechanism to verify that the system is operating within acceptable limits;
2. Quality control (QC)—a mechanism to control data quality (errors).

The objectives of the QA program include maintaining a continuous assessment and control of data quality, identifying proper analytical methods, providing permanent records of the performance of instruments, standardizing analytical procedures, ensuring sample integrity, improving sample recording, and identifying training needs. The common aim of all these objectives is to provide high-quality data. The QA functions include the development (or selection) of proper methods of sampling, sample preservation, sample pretreatment, sample analysis and methods for evaluation and reporting of results. Furthermore, they include intralaboratory and interlaboratory methods of validation and evaluation, establishing quality control guidelines and maintaining quality control sample programs. A laboratory without a proper QA program cannot operate successfully. This is especially important when the laboratory produces series of data that are of interest in regional or worldwide programs (Povinec et al., 2005b).

A QA program (including good laboratory practices) should be described in one of the most important laboratory documents—the QA manual. It should contain QA policy and objectives, staff responsibilities, description of sampling/analytical methods, field measurements, sample handling protocols, data reduction, data evaluation (including uncertainty budget, e.g., Dovlete and Povinec, 1999), description of materials and standards used, QA procedures, results of interlaboratory comparisons, and the recording database. The QA manual should be regularly updated with any new developments in the laboratory.

A. Laboratory Information Management system

Accurate and precise determinations of radionuclide concentrations in marine samples are important aspects of the assessment of the marine environment and the use of radionuclides in studies of oceanographic processes. Data credibility is becoming essential in regional and worldwide programs to which laboratories with different practices contribute, especially if the resulting data are input into regional and global radionuclide databases.

In order to deal with an increasing number of incoming samples and/or to follow more closely their life cycle

within an analytical laboratory, a computerized system is generally used to increase track ability and to support good laboratory practice (Nakagawa, 1994). Additional reasons for the development of the Laboratory Information Management System (LIMS) rest in sharing methods, results, and reports (including sample history) within the laboratory members in a very flexible way. The impacts of LIMS implementation may be expected in the altering and improving of working habits of individual laboratory members, and in changes of laboratory management practices. The main objectives of the LIMS may be summarized in three points:

- Improved laboratory management with workload monitoring, resource allocation, and computerized instrumental control;
- Improved data management with easy retrieval and security of data, improved data accuracy, improved data consistency, and improved track ability;
- Increased laboratory throughput with improved performance, efficiency, and capabilities.

The System for Laboratory Information Management (SLIM) which is used at the IAEA-EL Monaco is a computerized system designed to suit the sample processing and analytical operations specific to a marine environment laboratory running a wide range of projects involving the measurement of radioactive and nonradioactive contaminants and tracers and global-scale support to analytical quality (Bartocci et al., 2006). The system is custom-tailored to the laboratory needs, but it is flexible enough to be adaptable for use in other environmental analytical labs.

The design of the SLIM database structure was the first step of the system development. While no changes are needed foreseeably in the developed backbone structure, the database implementation can evolve with software, hardware, and communication-related options, one key area being that of analytical instrument—computer interface. The structure of the SLIM database can be divided into three distinct parts:

1. Collection of information—a database where information is organized in tables allowing fast and easy retrieval.
2. Sample tracking—to report the status of samples (progress reporting), and their history. This allows a systematic traceability and controls the flow of the operational steps.
3. Reporting of results—the data reporting and validation of results.

Different programs and protocols can be used depending on needs, which provide an enhancement of data accuracy and consistency.

B. Intercomparison exercises

The International Atomic Energy Agency's Environment Laboratories in Monaco have been assisting marine laboratories in quality assurance and control for over 40 years (Parr et al., 1998; Povinec et al., 1999; Povinec and Pham, 2001; Pham et al., 2006a; Sanchez-Cabeza et al., 2008). This has been done through the IAEA's Analytical Quality Control Services (AQCS) by organizing intercomparison exercises and proficiency tests for the analysis of radionuclides in the marine environment, by establishing QA programs in the participating laboratories, by providing examples of QA manuals, and by QA training and QA missions. Both worldwide and regional intercomparison exercises are the most important part of a laboratory's QA program. These exercises have helped considerably laboratories in their assessment of their performance, supplied them with reference materials and enabled them to gather information on their performance. Although there has been remarkable growth both in the number of participating laboratories (from 40 to more than 150) and in the quality of data, the performance of all participating laboratories in these exercises is not yet satisfactory.

We shall illustrate recent developments in the performance of laboratories in four intercomparison exercises organized by the IAEA-EL, namely IAEA-385 (Irish Sea sediment), IAEA-414 (Irish Sea and North Sea fish flesh), IAEA-437 (mussel sample from the Mediterranean Sea), and IAEA-443 (seawater from the Irish Sea), by comparing the results obtained for the analysis of ^{239,240}Pu (Fig. 5.36). This radionuclide belongs to the group of radionuclides where improvements in analytical performance have been made recently, thanks to the introduction of ICP-MS and AMS techniques. It can be seen that generally a good agreement has been reached among the laboratories using different radioanalytical techniques (except for the IAEA-414 where several laboratories reported outliers).

Following the ISO (1997) recommendations for the assessment of laboratory performance, Z-score methodology has been introduced in the evaluation of intercomparison results, namely

$$Z = (x_i - x_a)/s_b \tag{5.6}$$

where x_i is the robust mean of the reported values of massic activity in the sample, x_a is the assigned value (a mean value of accepted results), and s_b is the target standard deviation (Cofino and Wells, 1994). The performance of a laboratory is considered acceptable if the difference between the robust mean of the laboratory and the assigned value (in s_b units) is less than or equal to two. The analysis is regarded as being out of control when $|Z| > 3$. The Z-score evaluation represents a simple method which gives

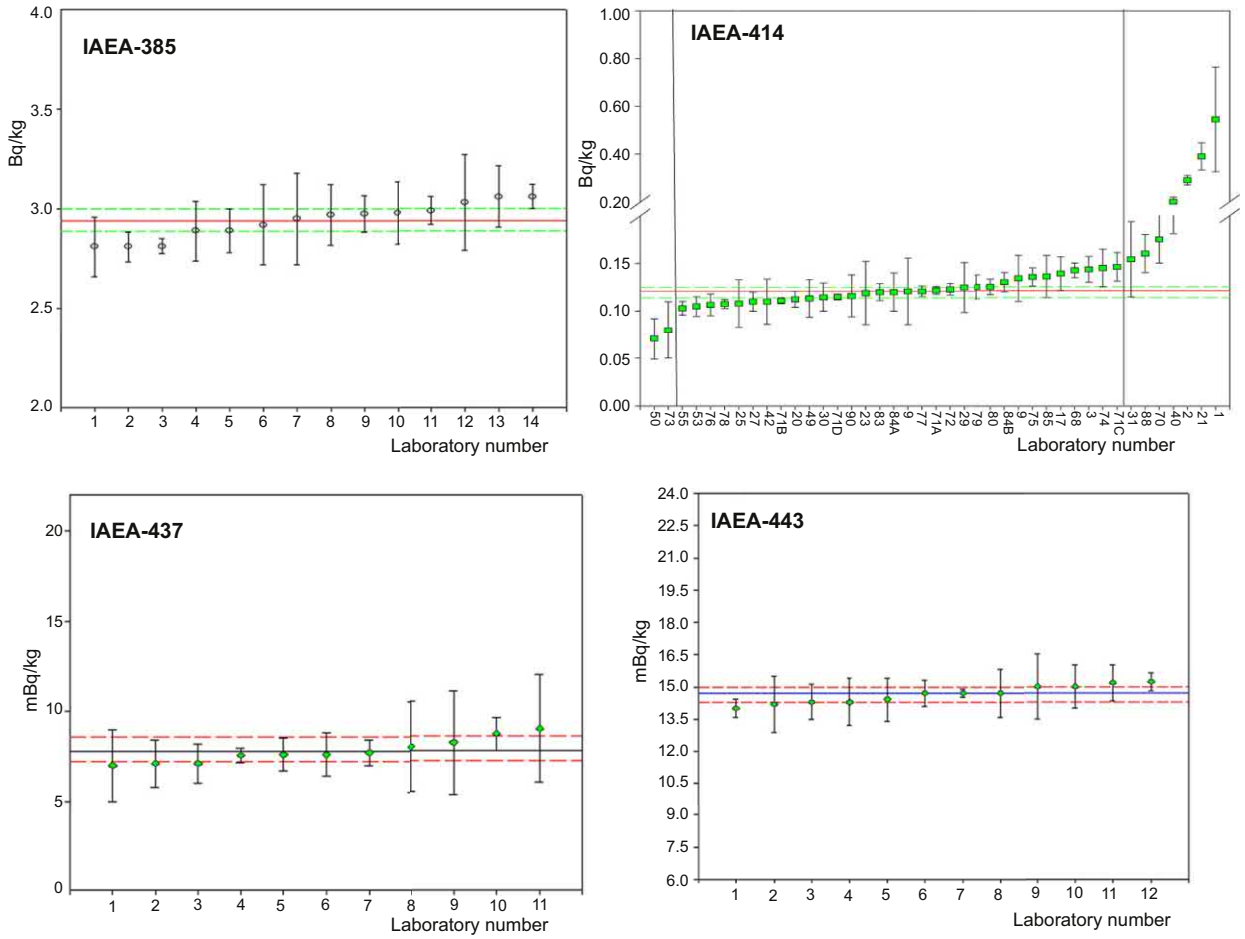


FIGURE 5.36 Results of $^{239+240}$Pu analysis in intercomparison exercises recently organized by the IAEA-EL. The full horizontal lines represent the medians, the broken lines represent the confidence intervals (95% level), and the results on the sides of the vertical lines are outliers.

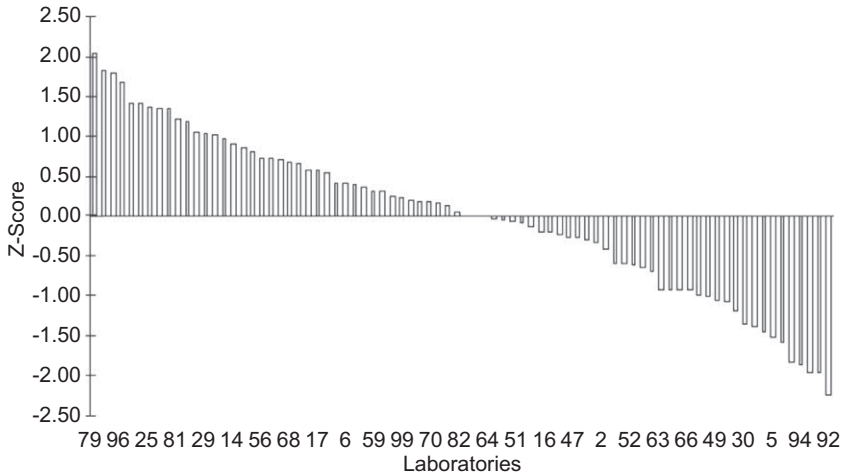


FIGURE 5.37 Z-score analysis of ^{137}Cs data reported for the reference material IAEA-385 (Irish Sea sediment). *Modified after Pham et al. (2008). Reprinted with permission © Elsevier 2008.*

participating laboratories a normalized performance score for bias. As an example, Fig. 5.37 illustrates a Z-score distribution for ^{137}Cs in the reference material IAEA-385 (Irish Sea sediment). The performance of laboratories in this instance was very good.

C. Reference materials

Reference materials (RMs) represent samples of well-established properties used for the assessment of analytical methods. More rigorous materials—certified reference materials (CRMs) or standard reference materials (SRMs), issued by the National Institute of Standards and Technology—NIST, USA (Inn et al., 2001; Outola et al., 2006), have property values certified by technically valid procedures (at least with two independent methods) traceable to SI units (ISO, 1996, 1997). RMs and CRMs have great impact on the development of methods of known accuracy. They represent important benchmarks in QA, identifying weaknesses in methodologies, detecting training needs, upgrading the quality of laboratories' performances, and assessing the validity of analytical methods. The reference methods can only be accepted on the basis of interlaboratory tests performed on selected CRMs. The CRMs should be available for the different environmental matrices, e.g., water, sediment, and biota, as well as for technical materials (Povinec et al., 2016a). The required long-term availability of CRMs (over 10 y) necessitates their long-term stability and the collection and preparation of large-volume samples (over 100 kg). The relative precision of all reported data should be better than 5%. This would require highly homogenized samples thoroughly tested for any inhomogeneities of major elements. The principal analyses should be accompanied by supporting characterization, e.g., for multielemental composition, mineralogy, particle-size distribution, and radionuclide speciation studies. At least two independent analytical methods should be used for reporting certified values. This may not be a major problem in the case of radionuclides, where different methods are available (e.g., RMT, ICP-MS, TIMS, and AMS). In this respect, neutron activation analysis techniques play an important role as really undependable methods for radionuclide analyses. The specific needs for the production of CRMs for mass spectrometric methods (e.g., AMS, ICP-MS, and TIMS), where usually small samples with very low radionuclide concentrations are necessary and which require special treatment, should be addressed. Table 5.2 lists RMs for the analysis of anthropogenic and natural radionuclides in marine sediments, seawater, and biota, which are either available or under production.

TABLE 5.2 Reference materials for radionuclides in the marine environment produced by the IAEA-EL.

Code	Origin matrix	Reference
IAEA-381	Irish Sea seawater	Povinec et al. (2002)
IAEA-384	Fangataufa lagoon sediment	Povinec et al. (2007)
IAEA-395	Irish Sea sediment	Pham et al. (2008)
IAEA-418	Mediterranean Sea seawater	Pham et al. (2010b)
IAEA-414	Irish Sea and North Sea fish flesh	Pham et al. (2006b)
IAEA-437	Mediterranean Sea mussel	Pham et al. (2010a)
IAEA-443	Irish Sea seawater	Pham et al. (2011)
IAEA-410	Bikini atoll sediment	Pham et al. (2016)
IAEA-412	Pacific ocean sediment	Pham et al. (2016)
IAEA-415	Atlantic ocean fish flesh	In preparation
IAEA-438	Baltic Sea fish flesh	In preparation
IAEA-442	North Sea fish flesh	In preparation
IAEA-446	Baltic Sea seaweed	Pham et al. (2014)

IX. Marine radioactivity databases

The IAEA's Environment Laboratories in Monaco have been developing in its Radiometrics Laboratory a database called Marine Information System (MARIS) (Povinec et al., 2006f). The input database for the MARIS has been the Global Marine Radioactivity Database (GLOMARD) on the distribution of radionuclides in the marine environment (Povinec et al., 2004b). The block scheme of the database is shown in Fig. 5.38.

The IAEA's Marine Information System is a relational database, which is based on the GIS (Geographical Information System), covering the distribution of radioactive and stable isotopes, and in the near future also other tracers (organic compounds and tracer metals) in the marine environment, as well as supporting oceanographic parameters such as seawater temperature, salinity, and sea bathymetry (www.maris.iaea.org).

The main objective of MARIS is to provide information on radioactive contamination of the marine environment by grouping and storing available data on the most important radionuclides in the world oceans and seas (in the open sea as well as in coastal zones), specifically in seawater, particulate matter, biota, and sediment (Povinec et al., 2004b,

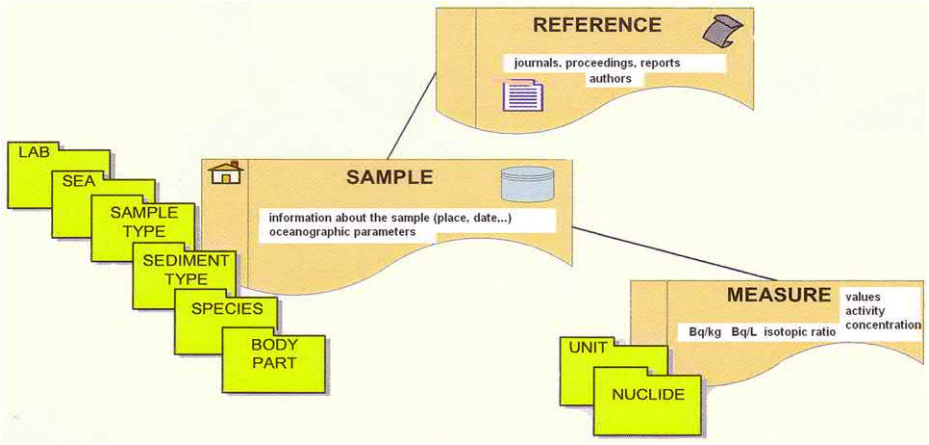


FIGURE 5.38 Organization of the MARIS database. For the color version of this figure, the reader is referred to the electronic version of this book.

2005b). Quantification of the sources of radionuclides in the world's oceans and seas, computer modeling of the dispersion of radionuclides, and radiological assessment studies require that marine laboratories should be provided with information on the past and present levels of radionuclides in the marine environment. The IAEA has been acting as a clearing house for information on radioactive contaminants in the marine environment. It provides data on marine radionuclide levels to laboratories for future assessment studies and the evaluation of trends in the contamination of the marine environment. The collection, synthesis, and interpretation of data on marine radioactivity in the world ocean have been carried out with the following objectives:

1. to provide immediate and up-to-date information on radionuclide levels and inventories in the seas and oceans;
2. to provide a snapshot of radionuclide levels at any time in any location;
3. to investigate changes with time in radionuclide levels and inventories;
4. to provide data for validation of computer models on the dispersion of radionuclides in the marine environment;
5. to provide bases for assessments of radiation doses to local, regional, and global human populations and to marine biota;
6. to identify gaps in available information.

The data provided by MARIS have been used as the international reference source on radionuclide contamination of the marine environment so that any further contributions from nuclear industry, radioactive waste disposal sites, nuclear weapons test sites, and possible nuclear accidents can be identified.

The second main objective of MARIS is to provide information on the distribution of radioactive isotopes (and

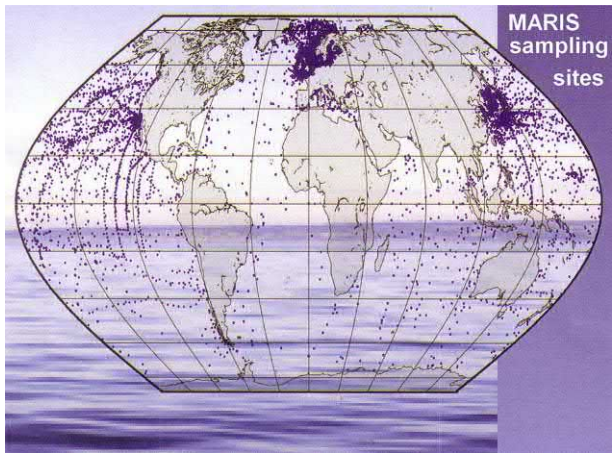


FIGURE 5.39 Sampling sites included in the MARIS database. For the color version of the figure, the reader is referred to the online version of the book.

in future also stable isotopes, tracer metals, and organic compounds) in the world oceans and seas, which could be used as tracers for the investigation of marine processes. This part of the database will grow substantially in the near future, so that data on all important oceanic tracers will be available to laboratories for oceanographic investigations. Fig. 5.39 shows that the MARIS is covering all oceanic basins. The data stored in MARIS could be used for water and sediment dynamics studies, investigation of processes in the water column, seawater–sediment interactions, seawater–groundwater interactions, etc., as well as validation of models used in climate change studies. Data on supporting oceanographic parameters such as seawater temperature, salinity, and sea bathymetry are mainly available to laboratories from Internet sources.

Fig. 5.40 shows, as an example, the distribution of ^{137}Cs in surface waters in the North European Seas, as extracted from the MARIS database. The figure documents the impact of ^{137}Cs discharges from the Sellafield and La

Hague reprocessing facilities, as well as the impact of the Chernobyl accident on surface waters of the North European Seas (Kershaw et al., 1999; Livingston and Povinec, 2000). Global fallout radionuclides and those discharged from nuclear reprocessing plants at Sellafield and La Hague, which have been transported to the Arctic Ocean and adjacent seas, represent a substantial new tracer signal in the Arctic following on the heels of the global fallout. The distinctive time and composition signatures of these two signals are of great value in studies on the circulation and ventilation of the deep waters.

A similar extraction from the MARIS database is presented in Fig. 5.41 for the distribution of ^{137}Cs in surface waters of the northwest Pacific Ocean (Povinec et al., 2003a), information which has been crucial for studying the impact of the Fukushima accident on waters of the North Pacific Ocean.

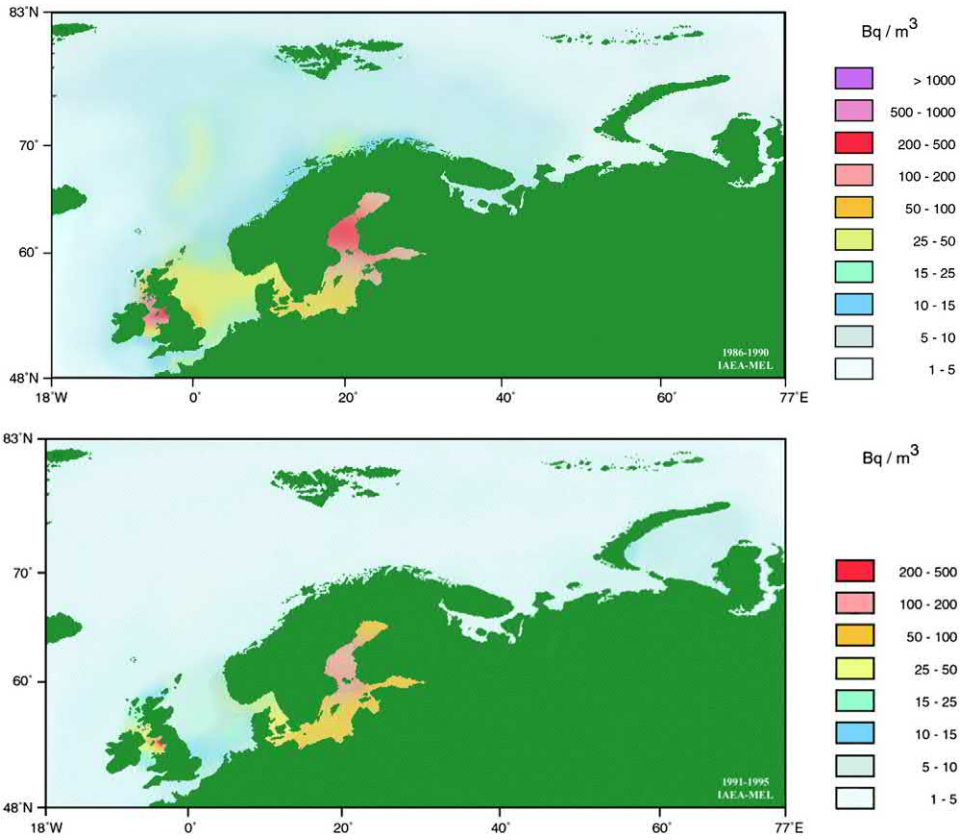


FIGURE 5.40 Distribution of ^{137}Cs in surface waters of the North European Seas after releases from the Sellafield and La Hague reprocessing facility, and after the Chernobyl accident, as extracted from the MARIS database. *Modified after Povinec et al. (2003a). For the color version of the figure, the reader is referred to the online version of the book.*

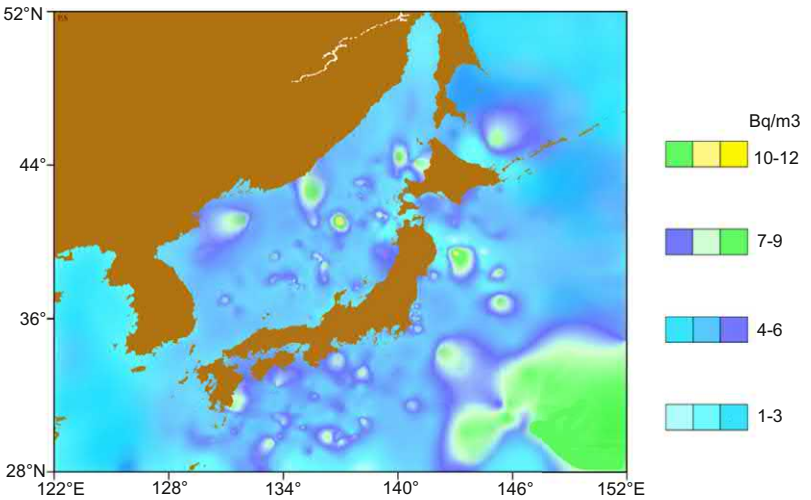


FIGURE 5.41 Distribution of ^{137}Cs in surface waters of the northwest Pacific Ocean as extracted from the MARIS database. For the color version of the figure, the reader is referred to the online version of the book.

The Meteorological Research Institute in Tsukuba (Japan) developed a HAM database which contains data on the distribution of ^{137}Cs in seawater of the world ocean (Aoyama and Hirose, 2004). The database has been used for the investigations of a time series of this radionuclide in surface waters, as well as for water profile studies (Aoyama et al., 2006, 2011; Inomata et al., 2009).

X. Examples of marine radioactivity studies

A. Worldwide marine radioactivity studies

We shall illustrate applications of radionuclides as tracers of oceanic processes on results obtained in the framework of the IAEA international project Worldwide Marine Radioactivity Studies (WOMARS) carried out between 1996 and 2002 in collaboration with several marine and analytical laboratories (Povinec et al., 2005b; IAEA, 2005). Some of the WOMARS results were published in the special issue of *Deep-Sea Research* II, **50**, 17–21, 2003 (Povinec et al., 2003a, 2003b; 2003c, 2003d; Bhushan et al., 2003; Ito et al., 2003; Lee et al., 2003a, 2003b; Moon et al., 2003; Mulsow et al., 2003).

The aim of the WOMARS project was to identify major sources of anthropogenic radionuclides in the world's oceans, to develop the knowledge of the distribution of key radionuclides in the water column and in sediment, and to study the development with time of radionuclide concentrations in water and sediment (Livingston et al., 2001; Povinec et al., 2003a, 2005b; IAEA, 2005). Three anthropogenic radionuclides, ^{90}Sr, ^{137}Cs, and ^{239,240}Pu, were chosen as the most important and radiologically typical of each class of marine radioactivity (beta, gamma, and alpha emitters). They are the most abundant anthropogenic radionuclides present in the marine environment and could lead to the highest radiation doses to humans and marine biota (Aarkrog et al., 1997). The WOMARS results confirmed that the dominant source of anthropogenic radionuclides in the marine environment is global fallout. The total ^{137}Cs input from global fallout was estimated to be 311 PBq for the Pacific Ocean, 201 PBq for the Atlantic Ocean, 84 PBq for the Indian Ocean, and 7.4 PBq for the Arctic Ocean. For comparison, about 40 PBq of ^{137}Cs was released to the marine environment from Sellafield and La Hague reprocessing plants. The Chernobyl accident contributed about 16 PBq of ^{137}Cs into seas, mainly the Baltic and Black Seas (Povinec et al., 2005b; IAEA, 2005).

For studying the distribution of radionuclides and their time series, the world ocean was divided into latitudinal belts/boxes, for which average radionuclide concentrations were estimated. In addition, where available, time trends in radionuclide concentrations in surface waters were studied and mean effective residence times/half-lives of radionuclides in these areas, as well as in the world ocean were estimated.

The Atlantic and Arctic Oceans, together with their marginal seas, were divided into boxes 18–30. The main boxes include the Arctic (18–20), the north (25,28), and the south (29,30) Atlantic Ocean. The rest has been reserved for the marginal seas (IAEA, 2005). The Pacific Ocean with marginal seas was divided into latitudinal boxes 1–13 (Fig. 5.42) on the basis of known ocean current systems, the location of nuclear test sites, the availability of recent data, and the probability of a relatively uniform distribution of radionuclides. Twelve boxes have been delineated in the Pacific Ocean and one box has been attributed to the Southern Ocean. The Sea of Japan has been given a separate box because of its oceanographic specificity and importance in marine radioactivity studies. Box 1 (north of 40 degrees N) is the subarctic Pacific Ocean, where the largest fallout rates of ^{137}Cs and ^{90}Sr over the Pacific Ocean were observed in the 1960s (Aoyama et al., 2001a, 2001b, 2006). Boxes 2 and 3 (25°–40 degrees N) are upstream and downstream of the Kuroshio Extension, respectively, where the water masses of the Kuroshio and Oyashio Currents mix (this box will contain most of radionuclides released to the sea after the Fukusfima accident). Boxes 4 and 5 (5–25 degrees N) are downstream and upstream of the North Equatorial Current, a typical oligotrophic ocean current corresponding to the subtropical gyre (Box 5 also includes the California Current). These boxes include the Pacific Proving Grounds nuclear weapons tests sites (Bikini, Enewetak, Johnston Atolls, and others), especially important for plutonium. The subtropical region of the northwestern Pacific was affected by local fallout as opposed to the subtropical region of the northeastern Pacific. Boxes 6 and 7 (5 degrees S–5° N) are downstream and upstream of the South Equatorial Current, respectively. The boundary between Boxes 4, 5 and 6, 7 is approximately at the Equatorial Counter-Current. Box 7 includes the Equatorial upwelling region. Boxes 8 and 9 (5°–25 degrees S) are downstream and upstream of the South Equatorial Current, respectively. The boundary between boxes 6, 7 and 8, 9 approximately corresponds to the South Equatorial Counter-Current. Box 9 includes the French nuclear weapons test sites (Mururoa and Fangataufa). Box 10 (25 degrees–40 degrees S) corresponds to the Tasman Sea. Box 11 (25 degrees–40 degrees S) is the midlatitude region of the South Pacific. Boxes 12 (40 degrees–60 degrees S) and 13 (below 60 degrees S) include the Southern Ocean and the Antarctic Circumpolar Current.

The Indian Ocean was divided into three boxes—box 15 covers the north and central part, box 16 includes the Indian Ocean Subtropical gyre, and box 17 covers the South Indian Ocean.

1. The ^{137}Cs time series in the Atlantic Ocean

Data used for the calculation of effective half-lives of ^{137}Cs in some of the boxes of the Atlantic Ocean are shown in Fig. 5.43. ^{90}Sr and ^{137}Cs showed similar effective half-lives of 16 ± 4 and 19 ± 4 y, respectively, for the North

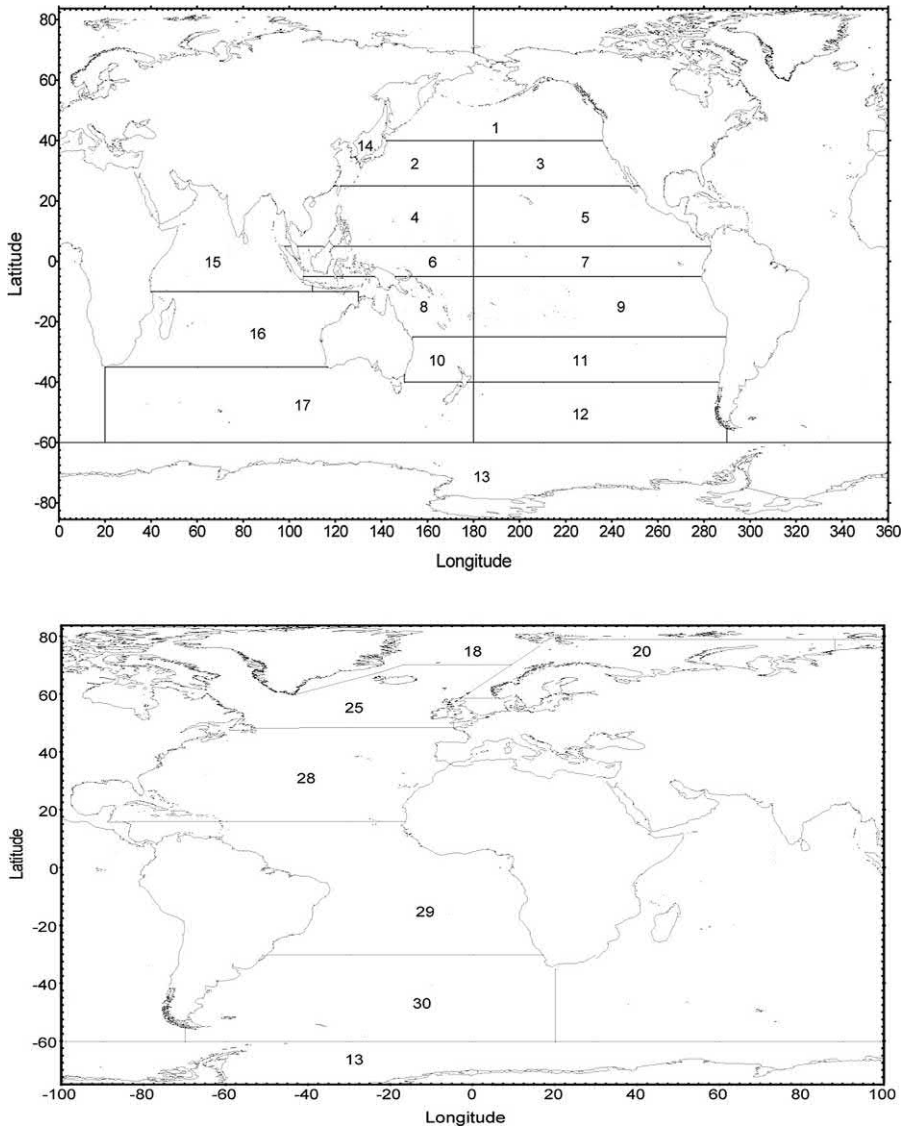


FIGURE 5.42 Latitudinal belts in the Pacific, Indian, and Atlantic Oceans. *Modified after Povinec et al. (2005b).*

Atlantic, 24 ± 2 and 24 ± 6 y for the central Atlantic, and 17 ± 9 and 20 ± 6 y for the South Atlantic Ocean. The average of all Atlantic data is 22 ± 2 and 20 ± 3 y, for ^{90}Sr and ^{137}Cs, respectively. The ^{239,240}Pu data gave an average value for all the Atlantic Ocean of 9 ± 1 y.

A specific situation is in the Irish Sea (box 23) where the discharges from the reprocessing plant at Sellafield dominated the radionuclide source term. The maximum discharge of ^{137}Cs and other β-emitting nuclides from the Sellafield reprocessing facility occurred in 1975 (5.2 PBq). Afterward, the discharges have been decreasing down to the TBq levels (UNSCEAR, 2000). As the distribution of ^{90}Sr, ^{137}Cs, and ^{239,240}Pu in the Irish Sea has been controlled by discharges, effective half-lives were not calculated (Fig. 5.43). The North Sea (Box 22) has been receiving contamination from the reprocessing plants at Sellafield and Cap de la Hague by the prevailing residual currents from the Irish Sea and the English Channel. Consequently, the concentrations of ^{137}Cs, ^{90}Sr, and other radionuclides follow with delay the temporal trends of the discharges.

Due to significantly decreasing discharges in recent years, the concentrations of ^{137}Cs, ^{90}Sr, and transuranics are presently only slightly above the global fallout levels for North Atlantic surface water. Remobilization of ^{137}Cs from highly contaminated sediment in the Irish Sea is now the dominant source also for water contamination of the North Sea.

The accident at Chernobyl deposited large quantities of radionuclides over the northern part of the Baltic Sea (Box 21). The levels of ^{137}Cs in the Baltic Sea were

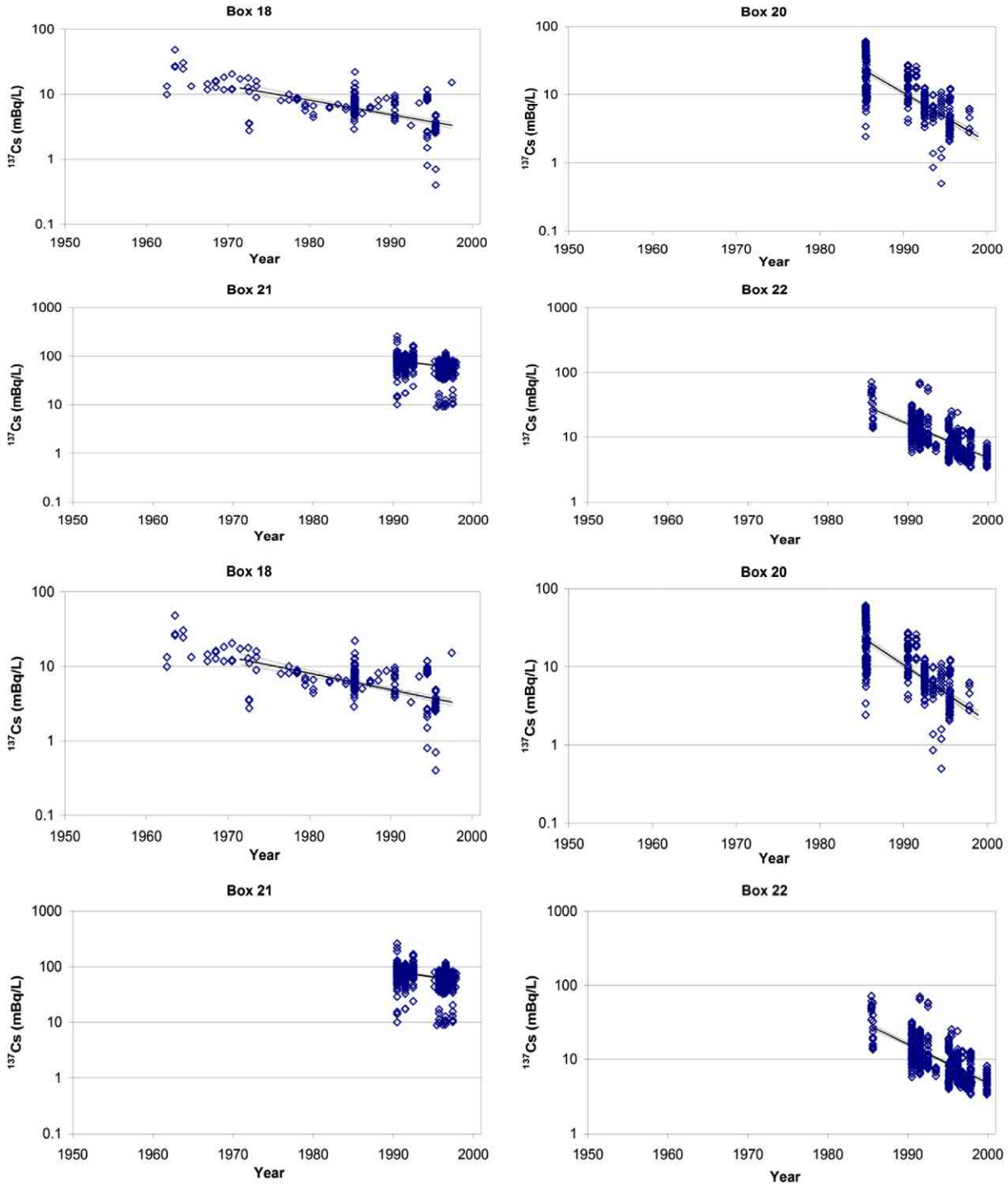


FIGURE 5.43 The ^{137}Cs surface water time series in some of the boxes of the Atlantic Ocean.

dominated by this fallout from 1986 onward. Before 1986, ^{137}Cs was due to global fallout and the inflow of North Seawater through the Danish Straits. The ^{137}Cs surface water time series are given in Fig. 5.43. The calculated effective half-lives for ^{90}Sr, ^{137}Cs, and ^{239,240}Pu in the Baltic Sea are 12 ± 2, 14 ± 2, and 5 ± 1 y, respectively.

Combining all available data for ^{90}Sr, ^{137}Cs, and ^{239,240}Pu in the Atlantic Ocean, the effective half-lives could be calculated (keeping in mind that they could have been affected by releases from reprocessing plants and the Chernobyl accident). The effective half-lives for ^{90}Sr, ^{137}Cs, and ^{239,240}Pu are 22 ± 2, 20 ± 3, and 9 ± 1 y, respectively.

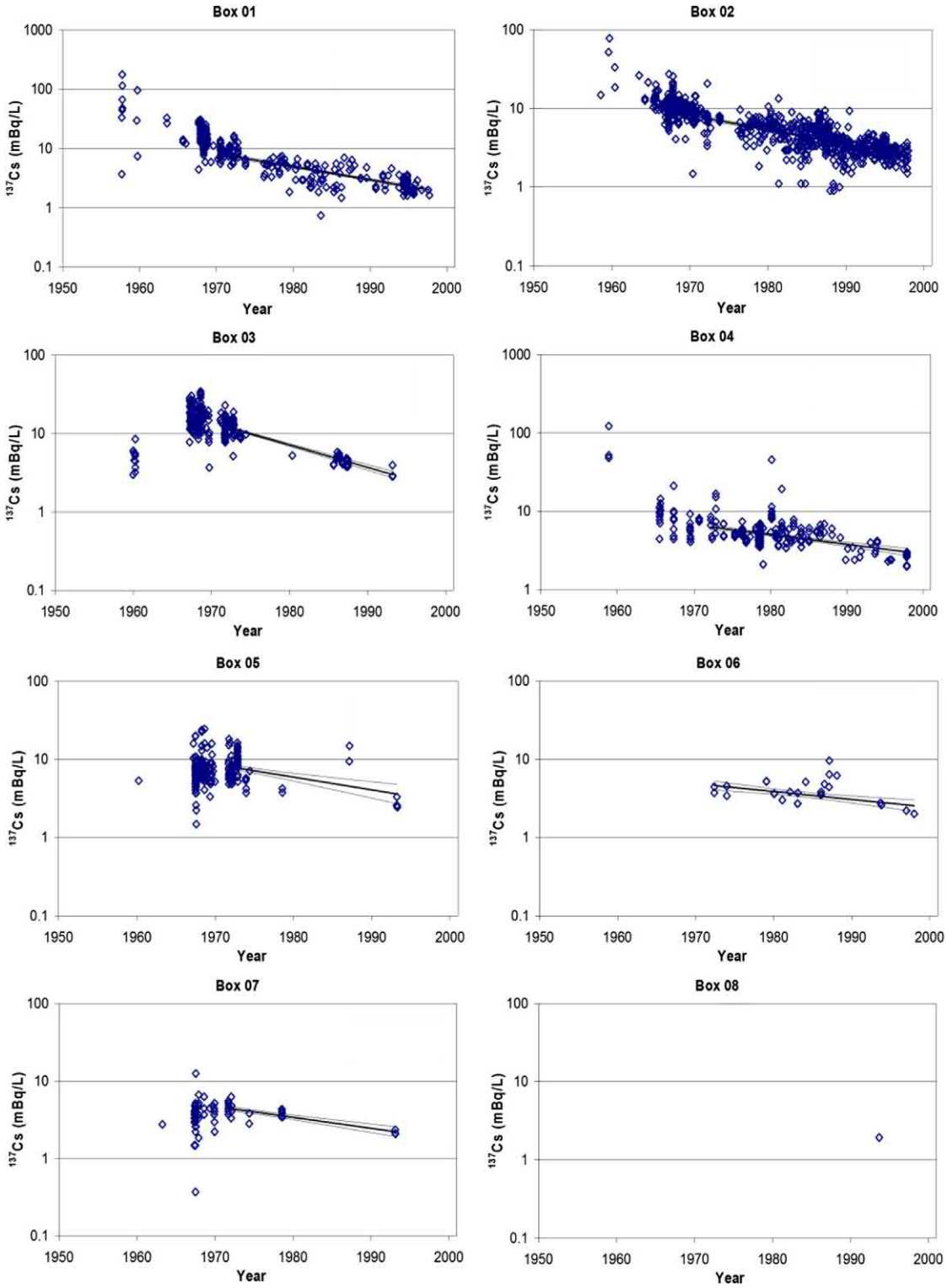


FIGURE 5.44 The ^{137}Cs surface water time series in some of the boxes of the Pacific Ocean.

2. The ^{137}Cs time series in the Pacific Ocean

The surface water ^{137}Cs time series for some selected boxes in the Pacific Ocean are presented in Fig. 5.44. The effective half-life of ^{137}Cs in surface water in each box ranged from 11 to about 30 y. The shortest effective half-life of ^{137}Cs is observed in the midlatitude of the eastern North Pacific (Box 3). The longest effective half-life of ^{137}Cs is found in the Equatorial Pacific (Boxes 6 and 7) and in the eastern subtropical South Pacific (Box 9).

The effective half-life of ^{90}Sr in surface water in each box ranged from 10 to 21 y. The shortest effective half-life of ^{90}Sr is observed in the eastern North Pacific (Box 3). The longest effective half-life of ^{90}Sr occurs in the Equatorial Pacific (Boxes 6 and 7), which is the same area as for ^{137}Cs. The effective half-life of ^{90}Sr seems to be a little less than that of ^{137}Cs; however, the data are not precise enough to confirm this.

The effective half-life of ^{239,240}Pu in surface water in each box ranged from 5 to about 15 y. The shortest effective half-life of ^{239,240}Pu is observed in the midlatitude region of the northeastern Pacific (Box 3), similarly as for ^{137}Cs. These findings suggest that the midlatitude region of the northeastern Pacific is a sink of anthropogenic radionuclides. The surface water mass in the midlatitude region of the northeastern Pacific is penetrated under the surface layer of the subtropical gyre. The longest effective half-life of ^{239,240}Pu is found in the eastern Equatorial Pacific (Box 7), as is the case for ^{137}Cs and ^{90}Sr. At present, the eastern Equatorial Pacific seems to behave as a source of anthropogenic radionuclides. The effective half-life of ^{239,240}Pu is generally shorter than that of ^{137}Cs in each box. Plutonium is a particle-reactive radionuclide as opposed to ^{137}Cs and ^{90}Sr, i.e., plutonium reacts with biogenic particles in surface water, sinks with attached particles, and is remobilized as a result of the biological decomposition of particles in deeper water (Baxter et al., 1995; Hirose et al., 2003).

In South Pacific surface water, the effective half-lives of the radionuclides investigated appear to be longer than in the North Pacific. When corrected for radioactive decay, surface ^{137}Cs in the South Pacific (except for Box 11) has gradually increased over the past three decades. This may suggest that ^{137}Cs in the North Pacific is transported to the South Pacific because the major input of ^{137}Cs due to global and local fallout occurred in the North Pacific.

When the ^{137}Cs data for the North, Equatorial, and South Pacific are grouped, the corresponding mean effective half-lives are 13 ± 1 (North), 22 ± 1 (South), and 23 ± 3 y (Equatorial Pacific). All Pacific data together give an effective half-life of ^{137}Cs of 14 ± 1 y. The corresponding ^{90}Sr and ^{239,240}Pu effective half-lives for the whole Pacific Ocean are 13 ± 1 and 7 ± 1 y, respectively (Table 5.3).

3. The ^{137}Cs time series in the Indian Ocean

Surface water ^{137}Cs concentration time series for Boxes 15–17 of the Indian Ocean is presented in Fig. 5.45. The estimated effective half-lives of ^{90}Sr, ^{137}Cs, and ^{239,240}Pu in surface water for different latitudinal boxes are given in Table 5.3. ^{90}Sr data were very sparse so any estimation of effective half-lives was not possible. ^{137}Cs data enabled to calculate the effective half-life which is 20 ± 2 y for the

TABLE 5.3 Mean effective half-lives of ^{90}Sr, ^{137}Cs, and ^{239,240}Pu in surface water.

		Mean effective half-life ± 1σ[a](y)		
Area	**Boxes**	**^{90}Sr**	**^{137}Cs**	**^{239,240}Pu**
North Atlantic	25 + 28	16 ± 4	19 ± 4	9 ± 0.6
Central Atlantic	29	24 ± 2	24 ± 5	10 ± 3
South Atlantic	30	17 ± 9	20 ± 6	11 ± 5
All Atlantic	25–30	22 ± 2	20 ± 3	9 ± 1
North Pacific	1–5	12 ± 1	13 ± 1	7 ± 1
Equatorial Pacific	6 + 7	21 ± 2	23 ± 3	10 ± 2
South Pacific	8–12	18 ± 1	22 ± 1	12 ± 4
All Pacific	1–12	13 ± 1	14 ± 1	7 ± 11
North Indian	15		20 ± 2	21 ± 8
South Indian	16 + 17		22 ± 4	9 ± 1
All Indian	15–17		21 ± 2	9 ± 1
All oceans	1–30	19 ± 3	20 ± 2	9 ± 1

[a]*Error weighted averaged values.*

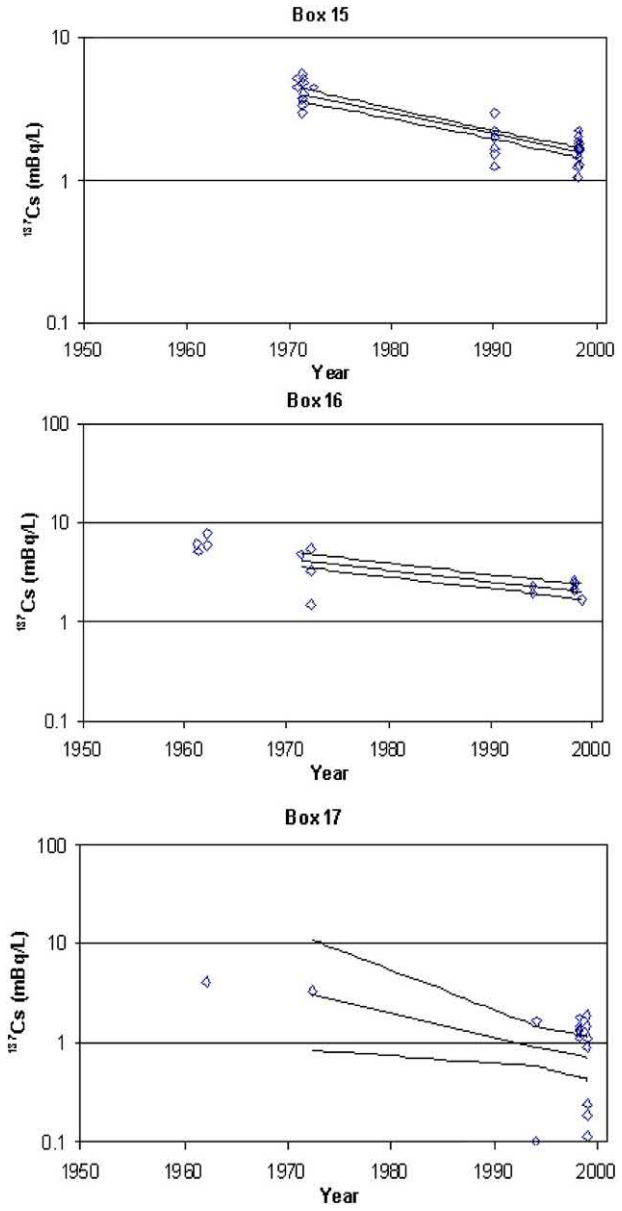


FIGURE 5.45 The ^{137}Cs surface water time series in some of the boxes of the Indian Ocean.

North and 22 ± 4 y for the South Indian Ocean. The average value for the all Indian Ocean is 21 ± 2 y. The uncertainty in ^{239,240}Pu data was too high, except for Box 17 which gave an effective half-life of 9 ± 1 y.

Data for all oceans (Table 5.3) gave the mean effective half-lives for ^{90}Sr and ^{137}Cs as 19 ± 3 and 20 ± 2 y, respectively. As expected, the half-life is similar for both radionuclides; therefore, one can accept a mean value of 19 ± 2 y. The ^{239,240}Pu effective half-life in surface water is 9 ± 1 y. The corresponding residence times of ^{90}Sr (^{137}Cs) and ^{239,240}Pu in surface water are 27 ± 2 and 13 ± 1 y, respectively. The differences between the effective residence times/half-lives of ^{90}Sr and ^{137}Cs are, within uncertainties, the same. Longer residence times can be seen in both the central Pacific and the central Atlantic Oceans.

The results obtained in the framework of the WOMARS project provided the most complete data set available on levels of anthropogenic radionuclides in the marine environment. The results have been used as the international reference source on the average levels of anthropogenic radionuclides in the marine environment, so that any further contributions from nuclear reprocessing plants (Povinec et al., 2003c), radioactive waste dumping sites (Sjöblom et al., 1999; Povinec et al., 2001a, 2001b), nuclear bomb test sites (Povinec et al., 1999), and nuclear accidents (Povinec et al., 2003c) can be identified.

4. Radionuclide tracing of water masses in the South Indian Ocean

The South Indian Ocean plays a key role in the exchange of water masses between the Equator and Antarctica (Ganachaud and Wunsch, 2000), and between the Southern Hemisphere basins (Ridgway and Dunn, 2007), important for a better understanding of global oceanic processes and the climate (Broecker, 1991; Key et al., 2004). South of the 40 degrees S, the wind-driven Antarctic Circumpolar Current (ACC), going around Antarctica, transports cold waters from the Atlantic Sector of the Southern Ocean via the South Indian Ocean to the South Pacific Ocean. The banded structure of the ACC in the South Indian Ocean consists of several narrow jets associated with sharp hydrographic fronts due to the presence of the Crozet and Kerguelen Plateaus (Tomczak and Godfrey, 1994). From the north of the Crozet Islands to the downstream area, there exists a very strong triple frontal zone where the Agulhas Front (AF), Subtropical Front (STF), and Subantarctic Front (SAF) converge into a narrow band of 100–200 km wide, with sharp across-front changes in temperature, salinity, and oxygen content (Park et al., 2002). Strong ocean currents formed in this area characterize the South Indian Ocean as the most dynamic region of the World Ocean (Rahmstorf, 2006). The dominant current system affecting the circulation in the Crozet Basin is the AF, characterized by warm and saline subtropical waters carried by the Agulhas Return Current (ARC). Extending eastward into the basin, up to 60 degrees E, the AF recirculates to the north, as a part of the southern limb of the anticyclonic Indian Ocean Subtropical gyre (Park et al., 2002). The STF forms a boundary between the subtropical surface water and cooler, fresher subantarctic surface water (Pollard et al., 2002). It represents the northernmost frontal jet that passes through Drake Passage and is generally regarded as circumpolar in extent. The SAF is located at the northern boundary of the Polar Frontal Zone (PFZ), a transition region between the SAF and the Polar Front (PF).

The distribution of radionuclide tracers in the South Indian Ocean is therefore expected to be controlled by the banded structure of the fronts. It has therefore been a great challenge to collect water samples in such a complex and dynamic region, and to use isotopic tracers (^{3}H, ^{14}C, ^{129}I, and stable ^{2}H and ^{18}O) to investigate the movement of water masses in the frontal zones (Lee et al., 2009a, 2009b; Povinec et al., 2011a, 2011b).

Ocean observations and water sampling (1999) was carried out as a part of the ANTArctic RESearch (ANTARES) IV cruise (Park et al., 2002; Coppola et al., 2004, 2006; Lee et al., 2009b) in the offshore of the northwest of Kerguelen Islands and east of Crozet Islands between 32 degrees−48 degrees S and 51 degrees−70 degrees E. The observed ^{3}H, ^{14}C, and ^{129}I water profiles (Fig. 5.46) show typical features—the concentrations were highest at the surface (or subsurface at 100−200 m), then were gradually decreasing with depth, and relatively invariable with depth in deep and bottom waters. ^{3}H concentrations were below detection limit (0.02 TU) between 1000 and 2500 m at Sts. 7 and 3; however, levels comparable to surface were observed at bottom waters at both stations. In contrast to this, St. 8 shows threefold higher ^{3}H levels for the surface waters. The ^{14}C profile also shows a downward transport of bomb-produced ^{14}C to the depth of about 2000 m. The ^{3}H, ^{14}C, and ^{129}I data clearly show the presence of different water masses in the Crozet Basin. The ^{3}H concentrations largely decrease below the 1000 m water depth at which CDW (Circumpolar Deep Water) appears, formed by the deepwater circulation and ventilation south of 40 degrees S (You, 2000). The depletion of ^{3}H in the CDW in the STF and SAF fronts may be related to the intrusion of North Atlantic Deep Water (NADW) especially to LCDW (lower CDW), characterized by salinity maximum (Park et al., 1993). NADW injects its water into the CDW in the South Atlantic by mixing and entrainment, and then flows into the southwest Indian Ocean, south of Africa between 35 degrees S and 40 degrees S. Considering very low ^{3}H concentrations (5−24 mTU) observed in the South Atlantic bottom water (Jenkins et al., 1983), which is predominantly affected by the NADW, and taking into account the replenishment of the CDW by lateral transport of the NADW from the South Atlantic to the South Indian Ocean on a time scale of 4−10 y, the contribution of the NADW to the CDW may explain the observed ^{3}H minima. Except for the AF, STF, and SAF, which control radionuclide distribution in surface and subsurface waters, several other water masses can be identified in the basin (Fig. 5.47). The intermediate waters, represented by AAIW (Antarctic Intermediate Water), eliminate the differences observed in the surface layer. The same is true for the deep and bottom waters. Higher ^{129}I levels observed between 1500 and 2500 m water depths are probably due to the presence of NIDW (North Indian Deep Water). The lowest ^{129}I levels found at 1000−2000 m water depth may be due to intrusion of NADW carrying low

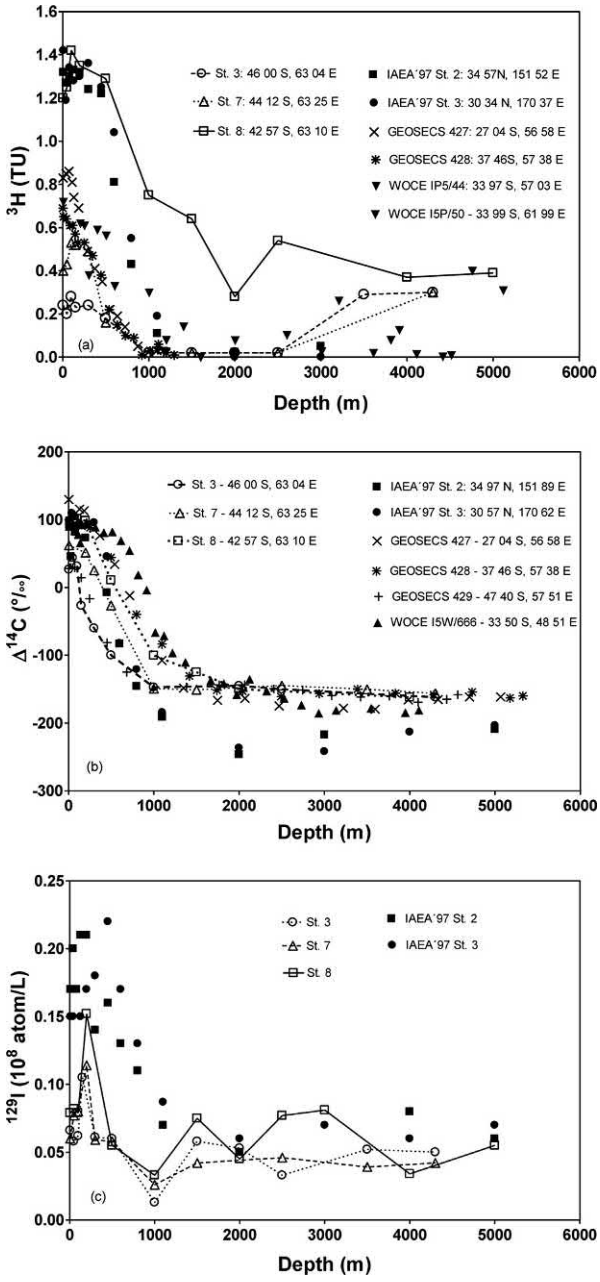


FIGURE 5.46 The ^{3}H, ^{14}C, and ^{129}I water profiles in the South Indian Ocean compared with nearest GEOSECS (Östlund and Brescher, 1982; Stuiver and Östlund, 1983) and WOCE (www.eWOCE.org) stations. ^{3}H, ^{14}C, and ^{129}I obtained for the N. Pacific (IAEA′97 cruise, Povinec et al., 2003a, 2010) are also shown.

radionuclide concentrations. Low, but measurable ^{129}I levels were found at bottom waters which could be attributed to AABW (Antarctic Bottom Water).

The spatial distribution of ^{3}H in the South Indian Ocean (Fig. 5.48) suggests that the highest levels were observed in the main stream of the subtropical gyre. It is evident that the gyre flow is strongest at 40−43 degrees S, west of 65 degrees E, where highest ^{3}H levels were observed. This is a

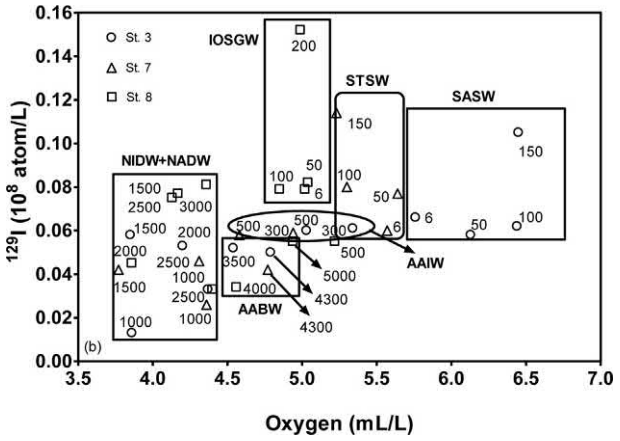


FIGURE 5.47 The dependence of ^{129}I concentration in seawater on the dissolved oxygen. Different water masses could be identified: IOSGW—Indian Ocean Subtropical Gyre Water, STSW—Subtropical Surface Water, SASW—Subantarctic Surface Water, AAIW—Antarctic Intermediate Water, NADW—North Atlantic Deep Water; NIDW—North Indian Deep Water, AABW—Antarctic Bottom Water. Water depths in meters are also shown. *Modified after Povinec et al. (2011a).*

clear influence of the gyre on the downstream radionuclide transport from its western boundary associated with the Agulhas Retroflection (Povinec, 2010b). The atmospheric deposition of global fallout tritium in the Southern Hemisphere was highest during the late sixties in the latitude belt 40−50 degrees S (Weiss and Roether, 1980). However, ^{3}H water profiles across the basin, combined with WOCE data south of 34 degrees S (decay-corrected to 1999), show higher surface and subsurface ^{3}H levels at 20 degrees S and 40 degrees S latitude belts. This indicates an accumulation of tritium within the subtropical gyre on a time scale of several decades. The gyre acts as a reservoir, maintaining higher radionuclide concentrations in the region. Simultaneously, higher tritium levels can be seen in the transect around 40 degrees S and 60 degrees E, at water depths below 3000 m, which should be due the advection of AABW.

The ^{14}C distribution map with the combined WOCE and ANTARES data for the South Indian Ocean is also presented in Fig. 5.48. We can see high ^{14}C concentrations observed along the subtropical gyre (20−40 degrees S) at the top 500 m, and a sharp decrease south of 40 degrees S, as observed in the ^{3}H data as well.^{14}C water profile data clearly show a penetration of bomb ^{14}C around 40 degrees S (transect at 60 degrees E) down to almost 5000 m (we could see this for tritium as well), which documents that the South Indian Ocean is an important sink of anthropogenic carbon. The high phytoplankton biomass in the studied region was found to be fueled by the natural iron inputs from shallow topography close to islands (Pollard et al., 2009).

We may conclude that the radionuclide variations with latitude observed in the South Indian Ocean are not due to the latitudinal atmospheric deposition patterns of global fallout, but due to the redistribution of radionuclides by ocean currents and mixing, and due to spatial constraints given by different water masses present in the region. The South Indian Ocean appears to have been acting on a time scale of several decades as a reservoir of contaminants transported from the Northern Indian and Pacific Oceans. The observed distribution of isotopic tracers reflects the complex dynamics and advection of different water masses, which makes this basin one of the most interesting oceanographic places in the world ocean.

B. Southern Hemisphere Ocean Tracer Studies

As an example of recent studies on the distribution of radionuclides in the world ocean, we shall discuss results obtained in the framework of the Southern Hemisphere Ocean Tracer Studies (SHOTS). The project was carried out during 2002−10 by the international collaboration comprising laboratories from the IAEA (Environment Laboratories, Monaco), Japan (Meteorological Research Institute, Tsukuba; Japan Agency for Marine-Earth Science and Technology, Yokosuka; Sophia University, Tokyo; University of Kanazawa), Slovakia (Comenius University of Bratislava), and South Korea (Korea Institute of Nuclear Safety). Several analytical laboratories participated in the project as well. The results of this study were recently published as a special issue of the journal *Progress in Oceanography* (Aoyama et al., 2011; Gastaud et al., 2011; Hirose et al., 2011; Kumamoto et al., 2011; Povinec et al., 2011a, 2011b; Sanchez-Cabeza et al., 2011; Tsumune et al., 2011; Levy et al., 2011).

It has been recognized that global fallout ^{137}Cs may be used for tracing exchange of seawater between the ocean basins because higher deposition regions of global fallout radionuclides have been found in the western part of midlatitudes in the North Pacific Ocean (Aoyama et al., 2006; Inomata et al., 2009). In the framework of the SHOTS project, water profile samples were collected during the round-the-globe BEAGLE2003 (Blue Ocean Global Expedition). The samples were analyzed for ^{137}Cs, ^{3}H, ^{90}Sr, and Pu isotopes, as well as for other tracers (e.g., nutrients).

As an example of low-level γ-spectrometry applications in marine sciences, we shall present high-density ^{137}Cs profiles in the water column of the world ocean. These are the first high-density ^{137}Cs profiles obtained till now for the main oceanic basins. It has been possible to get such profiles, thanks to analysis of ^{137}Cs in underground laboratories, which were able to achieve the required sensitivity for 10-fold smaller volumes of water samples. With the sampling of small (10 L) water samples, it was possible to use Rosette/CTD systems, which was not possible before, as large-volume samplers (>100 L) were required. The sampling of water column at large volumes resulted in long sampling times, which had strong financial limitations, as the ship time became too expensive.

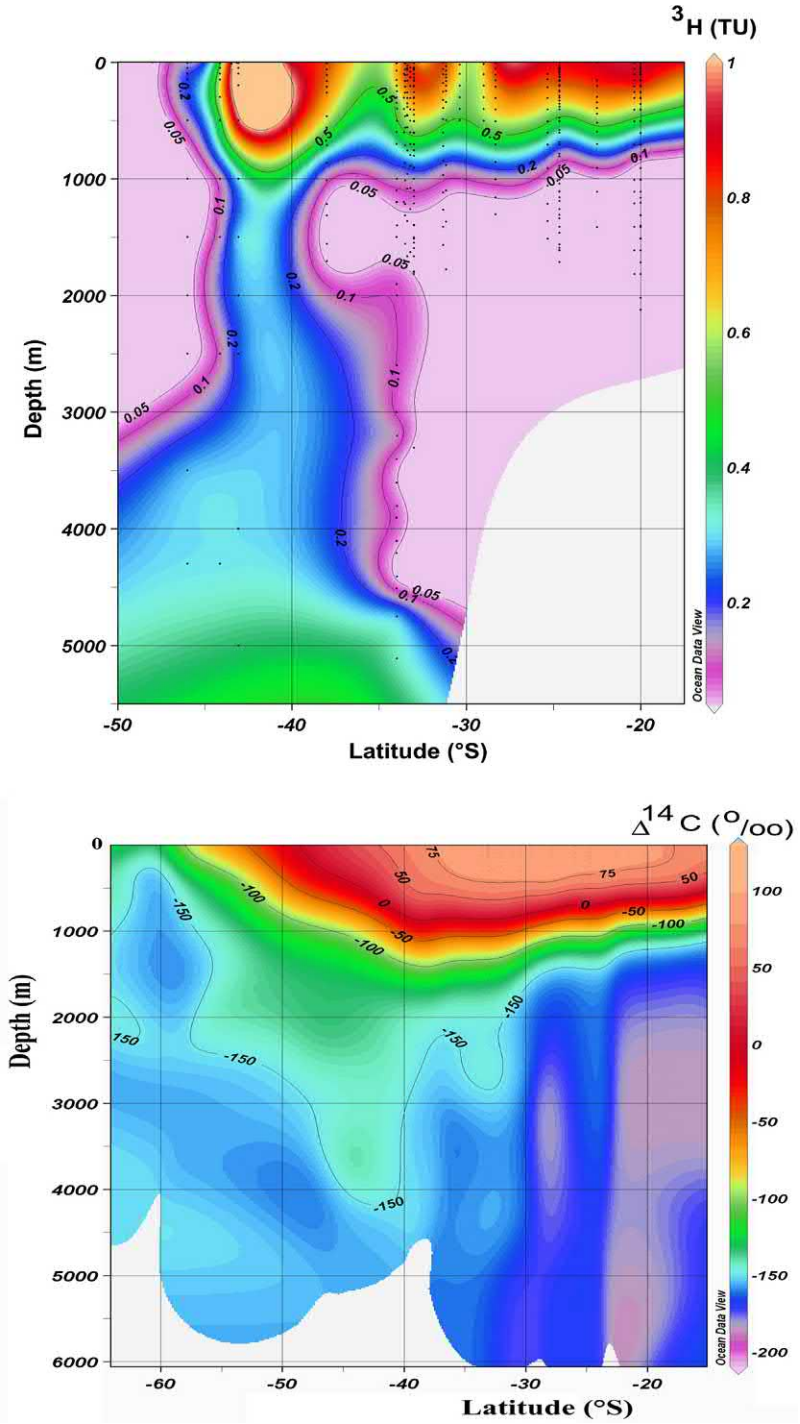


FIGURE 5.48 Spatial distribution of ^{3}H and ^{14}C in waters of the South Indian Ocean (ANTARES data were combined with nearest WOCE stations (www.eWOCE.org)). Higher ^{3}H concentrations were observed at the main stream of the Indian Ocean Subtropical Gyre at ~40 degrees S (as well as at ~20 degrees S, as indicated by the WOCE data). Downward tritium and radiocarbon transport around 40 degrees S (at 60 degrees E) can be seen as well. For the color version of the figure, the reader is referred to the online version of the book. *Modified after Povinec et al. (2011a).*

The ^{137}Cs transect along the 20 degrees S latitude in the Atlantic, Indian, and Pacific Oceans is shown in Fig. 5.49 (Sanchez-Cabeza et al., 2011; Povinec et al., 2011a, 2011b; Aoyama et al., 2011). The main feature presented in this figure is a transport of global fallout ^{137}Cs from the northwestern Pacific Ocean to the South via the Equator, and its accumulation in the Tasman Sea (Hirose et al., 2007, 2009; 2011; Aoyama et al., 2011). The ^{137}Cs labeled

waters are transported via the Indonesian Seas to the Indian Ocean, where they are again accumulating in the subtropical gyre operating at 20 degrees and 40 degrees S. Finally, the ^{137}Cs is transported by the Agulhas current system to the South Atlantic Ocean, where it became a part of the South Atlantic circulation.

We shall discuss in more detail the circulation processes in the Indian Ocean. Fig. 5.49 shows a presence of two cores of higher ^{137}Cs concentrations at 100 degrees E and 60 degrees E in the water column depth between 100 and 200 m. The subsurface maximum of ^{137}Cs concentration measured near 100 degrees E (2.1 mBq/L) is the highest level observed in southern hemisphere seawater, which is of the same level as the maximum ^{137}Cs concentration observed in North Pacific surface water (Povinec et al., 2003a). It is impossible to construct the observed ^{137}Cs cores only from a direct input of global fallout ^{137}Cs onto the Indian Ocean. Therefore, the ^{137}Cs cores must be due to an input of the North Pacific ^{137}Cs throughout the Indonesian seas into the cyclonic eddy of the Indian Ocean Subtropical gyre. By a factor of three increase of ^{137}Cs inventories then would be expected from global fallout in the South Indian Ocean along the 20 degrees S latitude (up to 1240 Bq/m^2), which are comparable with ^{137}Cs inventories in the northwestern Pacific, confirming an input of the North Pacific ^{137}Cs into the South Indian Ocean subtropical gyre. The estimated residence time of ^{137}Cs in surface waters of the subtropical Indian Ocean (~30 y) is twofold higher than for the North Pacific Ocean, documenting an accumulation of cesium in the Indian Ocean subtropics. All these findings suggest that the South Indian Ocean subtropical gyre is a significant reservoir of anthropogenic pollutants that have been transported from the North Pacific Ocean to the south on a time scale of several decades, which has important implications for the protection of the marine environment.

Fig. 5.49 also shows ^{3}H profiles in the world ocean obtained in the framework of the WOCE project (www.eWOCE.org). We can see that the ^{3}H profiles obtained 10 years earlier for the Indian Ocean have similar features, i.e., the existence of two ^{3}H maxima for subsurface waters at 100 degrees and 60 degrees E. The ^{137}Cs and ^{3}H sections

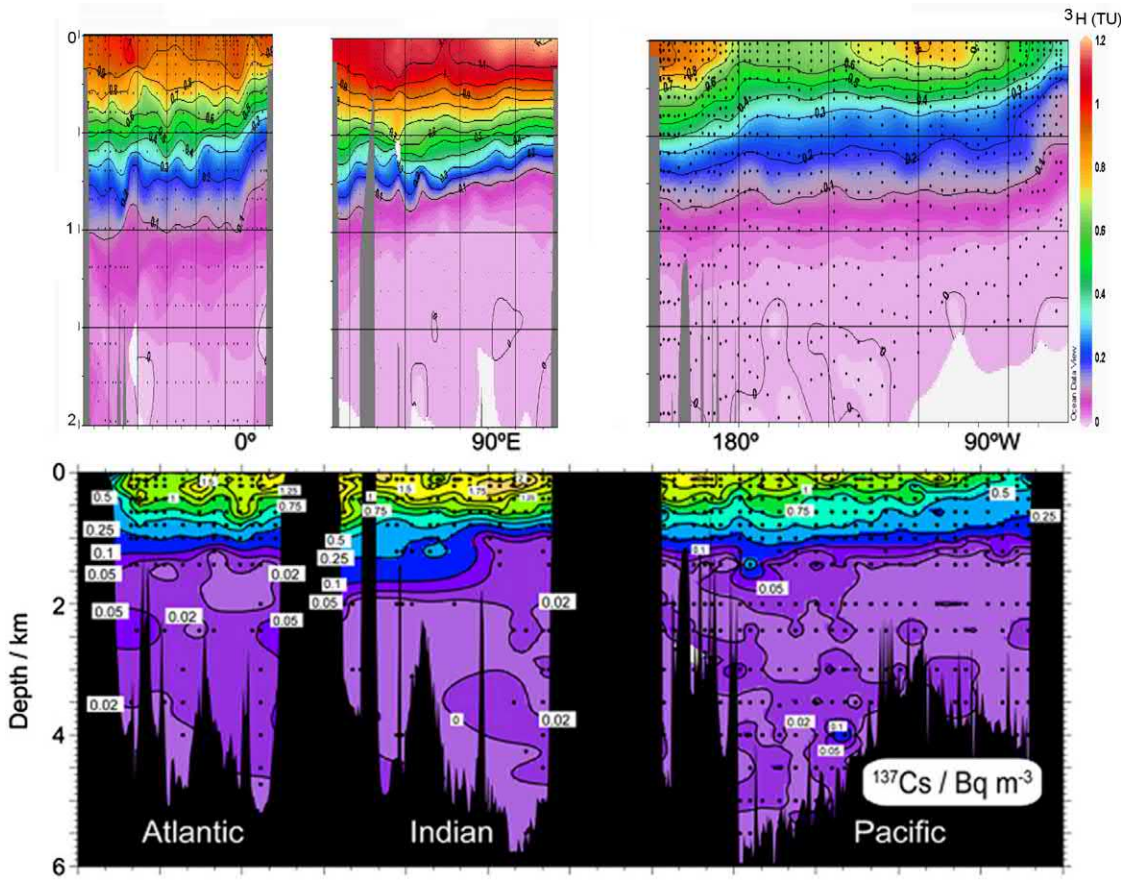


FIGURE 5.49 Tritium (WOCE data, www.eWOCE.org) and ^{137}Cs (SHOTS data after Aoyama et al., 2011; Povinec et al., 2011b; and Sanchez-Cabeza et al., 2011) profiles in the world ocean waters along 20 degrees S. For the color version of the figure, the reader is referred to the online version of the book.

provide valuable information on differences in the spreading of water masses between the main oceanic basins, and from the surface into the interior of the world ocean on a time scale of about 10 y.

C. Marine radioactivity impact of the Fukushima accident

The high tsunami, which followed after the strong earthquake of magnitude 9 on March 11, 2011, damaged the Fukushima Dai-ichi Nuclear Power Plant (NPP) in Japan, resulting in large radionuclide releases. Three nuclear reactors which were in operation during the earthquake could not cool down because of loss of electricity. The total atmospheric releases of ^{131}I and ^{134}Cs + ^{137}Cs were estimated to be around 153 PBq and 15−20 PBq, respectively. The discharged radionuclides also included ^{3}H, ^{14}C, ^{90}Sr, ^{132}Te, ^{132}I, ^{136}Cs, etc., as well as radioactive noble gases (^{133}Xe, ^{135}Xe) (Povinec et al., 2012a, 2012b, 2013a; Aoyama et al., 2013, 2016; IAEA, 2015; Hirose, 2016). As the prevailing wind direction in Japan was from the west to the east, the radioactive plume was mainly transported over the Pacific Ocean to America, and then over the Atlantic Ocean to Europe (Masson et al., 2011; Povinec et al., 2013a, b, c).

The nuclear accident at the Fukushima Dai-ichi NPP increased ^{137}Cs concentrations in coastal seawater in March 2011 up to 68 kBq/L, eight orders of magnitude above the global fallout background (Povinec et al., 2013a; Povinec and Hirose, 2015). This increase was due to direct liquid releases of ^{137}Cs contaminated fresh and later also seawater to coastal waters, which was estimated to be around 4 PBq (Tsumune et al., 2012; Povinec et al., 2013a; Aoyama et al., 2016). The ^{131}I/^{137}Cs activity ratio in surface seawater offshore Fukushima indicated that most of the radiocesium observed in coastal waters was the result of a direct discharge to the ocean (Hou et al., 2013). Due to the transport of water masses from the Japanese coast to the open western North Pacific by the coastal currents (Nakano and Povinec, 2012; Tsumune et al., 2012), the high ^{137}Cs concentrations observed in 2011 in coastal seawater decreased rapidly with apparent half-life of about 1 year (Povinec and Hirose, 2015). The typical ^{137}Cs activity concentrations in coastal waters in 2011−12 were from a few mBq/L to a few Bq/L (Aoyama et al., 2013; Buesseler et al., 2012; Povinec et al., 2013a, 2017; Kumamoto et al., 2013).

From a radiological point of view, ^{137}Cs has been considered to be the most important anthropogenic radionuclide in the marine environment because of its large releases, relatively long half-life, and its relative high bioavailability. It represents the anthropogenic radionuclide without a natural contribution, which was released in large quantities after atmospheric nuclear weapons tests, as well from the Chernobyl nuclear reactor accident, and after authorized releases from nuclear reprocessing facilities to coastal waters (Livingston and Povinec, 2000, 2002). When comparing the Fukushima atmospheric radionuclide releases with the Chernobyl ones, we see that they were lower for ^{131}I and ^{137}Cs by about a factor of 12 and 7, respectively. The Fukushima accident was classified on the INES (International Nuclear and Radiological Event Scale) scale at the maximum level of 7 (IAEA, 2011), similarly as the Chernobyl accident. The largest radioactivity (around 950 PBq) released to the atmosphere till now was, however, from atmospheric tests of nuclear weapons.

The ^{137}Cs due to its large releases to the marine environment with subsequent impact on marine biota, as well as due to its accumulation in human tissues has been recognized as the most important radionuclide for delivering radiation doses to the public from the consumption of food (Aarkrog et al., 1997; Livingston and Povinec, 2000; Povinec and Hirose, 2015). Fukushima-derived radiation doses estimated for the Japanese population from consumption of seafood were estimated to be (0.6 ± 0.4) mSv/y. The individual effective dose commitment from consumption of radioactive-contaminated fish caught in the open Pacific Ocean was estimated to be (0.07 ± 0.05) mSv/y. These doses are comparable or much lower than doses delivered from the consumption of natural ^{210}Po in fish and in shellfish (0.7 mSv/y), and they are below the worldwide accepted limit of 1 mSv/y (Povinec and Hirose, 2015). More detail information on the environmental radioactivity impact of the Fukushima accident can be found in books (Povinec et al., 2013a; Nakanishi and Tanoi, 2013).

As there has not been serious radiological consequences from the Fukushima-derived radionuclides in the marine environment, recent investigations have been focusing on using Fukushima radionuclides as tracers in oceanographic studies, namely on investigations of oceanic currents, transport of water masses and investigation of processes in the water column (Nakano and Povinec, 2012; Povinec and Hirose, 2012; Povinec et al., 2013c, 2017; Kumamoto et al., 2013, 2014; 2015; Aoyama et al., 2013, 2016; Inomata et al., 2017; Hirose and Povinec, 2018; Kaizer et al., 2018b).

XI. Conclusions

There have been several important innovations in sampling, shipboard measurements, and laboratory analysis of radionuclides in the marine environment. Innovations in the RMTs included applications of high-efficiency HPGe detectors used both in the laboratory and on shipboard. Stationary underwater γ-ray monitors based on NaI(Tl) detectors with satellite data transmission, and towing systems based on NaI(Tl) and HPGe detectors have been used for the monitoring of radionuclides in seawater and on the seabed.

SAS remains a powerful technique for the analysis of α-emitters because of the simplicity of measurement, reasonable resolution, and sensitivity for radionuclides with shorter half-lives. Low-activity samples, however, require

long counting times, and the separation of ^{239}Pu and ^{240}Pu is difficult, and at very low levels impossible because of very low counting rates.

The most important achievements for laboratory analysis of γ-emitters in the marine samples have been the development of high-efficiency HPGe detectors operating in underground laboratories, sometimes with anticosmic shielding. For example, thanks to decreasing the water volume required for analysis by about a factor of 10 (to about 10 L), it has been possible to carry out investigations on the spatial distribution of ^{137}Cs in the water column of the world oceans.

In the mass spectrometry sector, a new state-of-the-art TIMS, operating in multidynamic mode with a multicollector detection system, achieved better precision and accuracy in isotopic ratio and isotope concentration measurements. The TIMS is now the most sensitive low-energy mass spectrometry technique, relatively free of interferences, widely used for mass spectrometry of long-lived actinides. The ICP-MS has proved to be powerful tool for the analysis of long-lived radionuclides because of its high sensitivity, rapid analysis, multi-isotopic composition capability, and the low cost per analysis. Nevertheless, there could be problems with molecular, isobaric, and isotopic interferences even if careful purification procedures are used. The RIMS with its sensitivity similar to ICP-MS is still not a "desktop" technique that would permit widespread use; however, it is important as a complementary technique, almost free of interferences, e.g., for the certification of reference materials.

The most exciting breakthrough in the analysis of long-lived radionuclides in the marine environment has been made in the AMS sector. The AMS systems operate at the highest sensitivities with minimum sample size, and small matrix and interference effects. However, AMS operations are complex, and experienced operators are needed, which means this method is costly. However, small AMS systems have been developed recently which are of comparable size to sophisticated ICPMS and TIMS.

Natural radionuclides such as ^{210}Pb, ^{210}Po, radium, uranium and thorium isotopes, and others, have been used widely as natural tracers of water and sediment dynamics, particle association, transport, and fate. For example, indirect measurements of particulate organic carbon fluxes using ^{234}Th/^{238}U disequilibria in the water column contributed to a better understanding of environmental change. Another example is ^{210}Pb dating of sediments which has provided temporal information necessary for the interpretation of the depositional history of nonradioactive contamination in coastal sediments. The radiotracers have improved our knowledge of the transfer of radionuclides and critical elements, such as toxic metals, to marine organisms. This has been especially important for a better understanding and assessment of the impact of both radioactive and nonradioactive contamination in coastal areas. The main target areas are those which have been impacted by land-based sources of contamination, and they have been used extensively for marine food resources.

Analysis and applications of anthropogenic radionuclides in the marine environment have also been mastered. These contributed to better understanding of water circulation between the oceanic basins, and processes in the water column and in sediment. Anthropogenic radionuclides from global fallout (such as ^{3}H, ^{14}C, ^{90}Sr, ^{137}Cs, ^{241}Am, Pu isotopes, and others), Chernobyl and Fukushima accidents (Povinec et al., 2013a; Hirose and Povinec, 2015) have been due to their unique time-marker labeling of seawater, marine organisms, and sediments widely used as oceanic tracers. They will further contribute to the wide growth of knowledge of the physical, chemical, biological, and sedimentary processes, which occur in the oceans. Given the relevance of the marine processes to studies of the linkages between oceans and climate, the anthropogenic radionuclides in oceans will be exploited as useful tracer tools for many decades to come.

Great innovations have been made in the analysis of radionuclides on particles, where several new techniques have been successfully applied including SIMS, AMS, scanning electron microscopy coupled with X-ray detectors, microbeam XRF analysis, synchrotron radiation-based XRF, and other techniques. The new technologies enabled us to proceed from bulk sample analyses to single microparticles analyses, and they will be widely applied in speciation studies of radionuclides associated with colloid and particles for a better understanding of processes in the water column, water−sediment interactions, and biological uptake of radionuclides.

However, there is still room for new exciting developments. As examples we could mention PIMS and laser-based analytical technique for ^{14}C analysis, which represent alternative techniques to AMS. Ultra-trace isotope detection of noble gases (^{39}Ar and ^{81}Kr) is still a challenging task, which has recently been addressed by a magneto-optical trap and collinear laser photon burst spectroscopy. Laser microprobe mass analysis (LAMMA), Fourier transform-ion cyclotron resonance (FT-ICR) method, and atom trap trace analysis (ATTA) are the new technologies, which could improve detection limits by several orders of magnitude. New trends in ultralow-level technologies may be expected with further developments of new mass spectrometry methods, probably based on ion traps technologies. The single atom-counting technologies thus will become available for a wide range of applications in various branches of the sciences. A further transfer in philosophy of analyses from bulk sample analyses to compound-specific isotope analyses with online coupling of analytical instruments will continue. Results obtained with coupling of GC/MS with AMS are very encouraging, and they will surely bring new applications in science (Povinec et al., 2009).

These new developments will further enhance applications of radionuclides as tracers in marine studies. Thanks to new isotopic tracers, better detection limits, and smaller samples, new exciting investigations are expected to be carried out, which will further improve our knowledge of oceanic processes. They will also contribute to a better understanding toward protecting the marine environment, elucidating the impact of the climate change on the world ocean.

Acknowledgments

The authors express their appreciation to colleagues from the IAEA-EL (J.-F. Comanducci, I. Levy, L. Liong Wee Kwong, H. Nies, B. Oregioni, I. Osvath, M.K. Pham, and others) and the Comenius University (R. Breier, M. Ješkovský, J. Kaizer, I. Kontuľ, J. Staníček, I. Sýkora, A. Šivo, and others) for cooperation in the development and applications of radiometric and mass spectrometry methods for the analysis of radionuclides in the marine environment. The collaboration with M. Aoyama (Fukushima University), W.C. Burnett (State University of Florida), K. Fifield (Australian National University), R. Golser (University of Vienna), Y. Hamajima (University of Kanazawa), K. Hirose (Sophia University in Tokyo), G.H. Hong (KIOST, Republic of Korea), M. Hotchkis (ANSTO, Australia), Y. Igarashi (MRI, Japan), Y. Ikeuchi (JCAC, Japan), T. Ito (JAERI, Japan), A.J.T. Jull (University of Arizona), W.E. Kieser (University of Toronto), Y. Kumamoto (JAMSTEC, Japan), M. Laubenstein (LNGS, Italy), S.-H. Lee (KRISS, Republic of Korea), G. Lujanienė (SCI, Lithuania), M. Molnár (ATOMKI, Hungary), U. Morgenstern (Institute of Geological and Nuclear Sciences, New Zealand), M. Nakano (JAERI, Japan), J. de Oliveira (IPEN, Brazil), L. Palcsu (ATOMKI, Hungary), S. Shima (JMS, Mutsu), P. Steier (University of Vienna), I. Svetlik (Inst. Nucl. Phys., Czech Republic), M. Taniguchi (RIHN, Kyoto), F. Terrasi (second University of Naples), O. Togawa (JAERI, Japan), and Z. Top (University of Miami) is highly acknowledged. The senior author acknowledges support provided by the EU Research and Development Operational Program funded by the ERDF (projects 26240120012, 26240120026, and 26240220004), by the International Atomic Energy Agency (projects SLR 0/008, SLR 0/009, SLR1001, and RER 7008), by the Slovak Research and Development Agency (Projects APVV 15-0576 and APVV-0516-10), and by the VEGA Scientific Granting Agency of Slovakia (Projects 1/0891/17 and 1/0783/14). The International Atomic Energy Agency is grateful for the support provided to its Environment Laboratories by the Government of the Principality of Monaco.

References

Aarkrog, A., Baxter, M.S., Bettencourt, A.O., Bojanowski, R., Bologa, A., Charmasson, S., Cunha, I., Delfanti, R., Duran, E., Holm, E., Jeffree, R., Livingston, H.D., Mahapanyawong, S., Nies, H., Osvath, I., Pingyu, L., Povinec, P.P., Sanchez, A., Smith, J.N., Swift, D.A., 1997. Comparison of doses from ^{137}Cs and ^{210}Po in marine food: a major international study. J. Environ. Radioact. 34, 69−90.

Allen, J.R., Rae, J.E., Longworth, G., Hasler, S.E., Ivanovich, I., 1993. A comparison of the ^{210}Pb dating technique with three other independent dating methods in an oxide estuarine salt-marsh sequence. Estuaries 16, 670−677.

Alvarez, L.W., Cornog, R., 1939. Helium and hydrogen of mass 3. Phys. Rev. 56, 613.

Anderson, R.F., Fleer, A.P., 1982. Determination of natural actinides and plutonium in marine particulate material. Anal. Chem. 54, 1142−1147.

Anderson, R.F., Fleisher, M.Q., Robinson, L.F., Edwards, R.L., Hoff, J., Moran, S.B., Rutgers van der Loeff, M.M., Thomas, A.L., Roy-Barman, M., François, R., 2012. GEOTRACES intercalibration of ^{230}Th, ^{232}Th, ^{231}Pa, and prospects for ^{10}Be. Limnol. Oceanogr. Methods 10, 179−213.

Aoyama, M., Hirose, K., Miyao, T., Igarashi, Y., Povinec, P.P., 2001a. ^{137}Cs activity in surface water in the western North Pacific. J. Radioanal. Nucl. Chem. 248, 789−793.

Aoyama, M., Hirose, K., Miyao, T., Igarashi, Y., Povinec, P.P., 2001b. Temporal variation of ^{137}Cs inventory in the western North Pacific. J. Radioanal. Nucl. Chem. 248, 785−787.

Aoyama, M., Hirose, K., 2004. Artificial radionuclide database in the Pacific Ocean: HAM database. Sci. World J. 4, 200−215.

Aoyama, M., Hirose, K., Igarashi, Y., 2006. Re-construction and up-dating our understanding on the global weapons tests ^{137}Cs fallout. J. Environ. Monitor. 8, 431−438.

Aoyama, M., Hirose, K., 2008. Radiometric determination of anthropogenic radionuclides in seawater. In: Povinec, P.P. (Ed.), Analysis of Environmental Radionuclides. Elsevier, Amsterdam, pp. 137−162.

Aoyama, M., Fukasawa, M., Hirose, K., Hamajima, Y., Kawano, T., Povinec, P.P., Sanchez-Cabeza, J.A., 2011. Cross equator transport of ^{137}Cs from North Pacific Ocean to south Pacific Ocean (BEAGLE2003 cruises). Prog. Oceanogr. 89, 7−16.

Aoyama, M., Tsumune, D., Hamajima, Y., 2013. Distribution of ^{137}Cs and ^{134}Cs in The North Pacific Ocean: impacts of the TEPCO Fukushima-Daiichi NPP accident. J. Radioanal. Nucl. Chem. 296, 535−539.

Aoyama, M., et al., 2016. ^{134}Cs and ^{137}Cs in The north Pacific Ocean derived from the March 2011 TEPCO Fukushima Dai-ichi nuclear power plant accident, Japan. Part one: surface pathway and vertical distributions. J. Oceanogr. 72, 53−65.

Appleby, P., 2013. ^{210}Pb dating: thirty-five years on. J. Paleolimnol. 49, 697−702.

Aramaki, T., Mizushima, T., Kuji, T., Povinec, P.P., Togawa, O., 2001. Distribution of radiocarbon in the southwestern North Pacific. Radiocarbon 43, 857−867.

Auro, M.E., Robinson, L.F., Burke, A., Bradtmiller, L.I., Fleisher, M.Q., Anderson, R.F., 2012. Improvements to 232-thorium, 230-thorium, and 231-protactinium analysis in seawater arising from GEOTRACES intercalibration. Limnol. Oceanogr. Methods 10, 464−474.

Axelsson, A., Fischer, D.M., Penkin, M.V., 2009. Use of data from environmental sampling for IAEA safeguards. Case study: uranium with near-natural ^{235}U abundance. J. Radioanal. Nucl. Chem. https://doi.org/10.1007/s10967-009-0149-9.

Bacon, M.P., 1984. Glacial to interglacial changes in carbonate and clay sedimentation in the Atlantic Ocean estimated from ^{230}Th measurements. Isot. Geosci. 2, 97−111.

Bacon, M.P., Rutgers van der Loeff, M.M., 1989. Removal of thorium-234 by scavenging in the bottom nepheloid layer of the ocean: earth Planet. Sci. Lett. 92, 157−164.

Bailey, K., Chen, C.Y., Du, X., Li, Y.M., Lu, Z.-T., O'Connor, T.P., Young, L., 2000. ATTA − A new method of ultrasensitive isotope trace analysis. Nucl. Instrum. Methods Phys. Res. B 172, 224−227.

Bartocci, J., Ramadan, H., Osvath, I., Povinec, P.P., 2006. Development of a laboratory management system at IAEA-MEL. In: Isotopes in Environmental Studies. Aquatic Forum 2004. IAEA, Vienna, pp. 617−618.

Baskaran, M., Naidu, A.S., 1995. ^{210}Pb-derived chronology and the fluxes of ^{210}Pb and ^{137}Cs isotopes into continental shelf sediments, east

Chukchi Sea, Alaskan Arctic. Geochim. Cosmochim. Acta 59, 4435–4448.

Baskaran, M., Swarzenski, P.W., 2007. Seasonal variations on the residence times and partitioning of short-lived radionuclides (^{234}Th, ^{7}Be and ^{210}Pb) and depositional fluxes of ^{7}Be and ^{210}Pb in Tampa Bay, Florida. Mar. Chem. 104, 27–42.

Baxter, M.S., 1993. Resonance ionization mass spectrometry. In: IAEA-TECDOC-683 Development and Evaluation of Alternative Radioanalytical Methods, Including Mass Spectrometry for Marine Materials. IAEA, Vienna, pp. 53–64.

Baxter, M.S., Fowler, S.W., Povinec, P.P., 1995. Observations of plutonium in the oceans. Appl. Radiat. Isot. 46, 1213–1223.

Beasley, T.M., Lorz, H.V., 1986. A review of the biological and geochemical behaviour of technetium in the marine environment. J. Environ. Radioact. 3, 1–22.

Becker, J.S., 2007. Inorganic Mass Spectrometry: Principles and Applications. John Wiley and Sons, Chichester.

Bennett, C.L., Beukens, R.P., Clover, M.R., Gove, H.E., Liebert, R.B., Litherland, A.E., Purser, K.H., Sondheim, W.E., 1978. Radiocarbon dating with electrostatic accelerators: dating of milligram samples. Science 201, 345–347.

Berelson, W.M., Hammond, D.E., Fuller, C., 1982. Radon-222 as a tracer for mixing in the water column and benthic exchange in the southern California borderland. Earth Planet. Sci. Lett. 61, 41–54.

Bergquist, B.A., Marchetti, A.A., Martinelli, R.E., McAninch, J.E., Nimz, G.J., Proctor, I.D., Southon, J.R., Vogel, J.S., 2000. Technetium measurements by accelerator mass spectrometry at LLNL. Nucl. Instrum. Methods Phys. Res., Sect. B 172, 328–332.

Berkovits, D., Feldstein, H., Ghelberg, S., Hershkowitz, A., Navon, E., Paul, M., 2000. Nucl. Instr. Meth. B172, 372–376.

Betti, M., Eriksson, M., Jernström, J., Tamborini, G., 2008. Environmental radioactive particles: a new challenge for modern analytical instrumental techniques in support of radioecology. In: Povinec, P.P. (Ed.), Analysis of Environmental Radionuclides. Elsevier, Amsterdam, pp. 355–370.

Bhushan, R., Dutta, K., Mulsow, S., Povinec, P.P., Somayajulu, B.L.K., 2003. Distribution of natural and man-made radionuclides during the reoccupation of GEOSECS stations 413 and 416 in the Arabian Sea: temporal changes. Deep-Sea Res. II 50, 2777–2784.

Bielewski, M., Eriksson, M., Himbert, J., Betti, M., Belloni, F., Falkenberg, G., 2009. Fast method of XANES data collection suitable for oxidation state mapping. J. Radioanal. Nucl. Chem. 282, 355–359.

Bourdon, B., Joron, J.-L., Allègre, C.J., 1999. A method for ^{231}Pa analysis by thermal ionization mass spectrometry in silicate rocks. Chem. Geol. 157, 147–151.

Bourquin, M., van Beek, P., Reyss, J.L., Riotte, J., Freydier, R., 2011. Determination of ^{226}Ra concentrations in seawater and suspended particles (NW Pacific) using MC-ICP-MS. Mar. Chem. 126, 132–138.

Bowen, V.T., Noshkin, V.E., Livingston, H.D., Volchok, H.L., 1980. Fallout radionuclides in the Pacific Ocean; vertical and horizontal distributions, largely from GEOSECS stations. Earth Planet. Sci. Lett. 49, 411–434.

Breier, R., Povinec, P.P., 2009. Monte Carlo simulation of background characteristics of low-level gamma-spectrometers. J. Radioanal. Nucl. Chem. 282, 799–804.

Breier, R., Povinec, P.P., 2010. Simulation of background characteristics of low-level gamma-ray spectrometers using Monte Carlo method. Appl. Radiat. Isot. 68, 1231–1235.

Breier, R., Hamajima, Y., Povinec, P.P., 2016. Simulations of background characteristics of HPGe detectors operating underground using the Monte Carlo method. J. Radioanal. Nucl. Chem. 307, 1957–1960.

Breier, R., Laubenstein, M., Povinec, P.P., 2017. Monte Carlo simulation of background characteristics of a HPGe detector operating underground in the Gran Sasso National Laboratory. Appl. Radiat. Isot. 126, 188–190.

Breier, R., Brudanin, V.B., Loaiza, P., Piquemal, F., Povinec, P.P., Rukhadze, E., Rukhadze, V., Štekl, I., 2018. Environmental radionuclides as contaminants of HPGe gamma-ray spectrometers: Monte Carlo simulations for Modane underground laboratory. J. Environ. Radioact. 190–191, 134–140.

Broecker, W.S., Peng, W.H., 1982. Tracers in the Sea. Eldigo Press, New York, p. 690.

Broecker, W.S., 1991. The great ocean conveyor. Oceanography 4, 79–89.

Brown, L., Cook, G.T., Mackenzie, A.B., Naysmith, P., Anderson, R., Thomson, J., Nixon, S., 2000. Characterisation of differential mixing of foraminifera and bulk carbonate in NE Atlantic sediments. Nucl. Instrum. Methods Phys. Res., Sect. B 172, 490–494.

Buesseler, K.O., 1991. Do upper-ocean sediment traps provide an accurate record of particle flux? Nature 353, 420–423.

Buesseler, K.O., 1997. The isotopic signature of fallout plutonium in the North Pacific. J. Environ. Radioact. 36, 69–83.

Buesseler, K.O., Scholkovitz, E.R., 1987. The geochemistry of fallout plutonium in the North Atlantic: I. A pore water study in shelf, slope and deep-sea sediments. Geochim. Cosmochim. Acta 51, 2605.

Buesseler, K.O., Cochran, K.J., Bacon, M.P., Livingston, H.D., Casso, S.A., Hirschberg, D., Hartman, M.C., Fleer, A.P., 1992. Determination of thorium isotopes in seawater by nondestructive and radiochemical procedures. Deep-Sea Res. 39, 1103–1114.

Buesseler, K.O., Andrews, J.A., Hartman, M.C., Belastock, R., Chai, F., 1995. Regional estimates of the export flux of particulate organic carbon derived from thorium-234 during the JGOFS EqPac program. Deep Sea Res. II 42, 777–791.

Buesseler, K.O., Benitez- Nelson, C., Rutgers van der Loeff, M., Andrews, J., Ball, L., Crossin, G., Charette, M.A., 2001. An intercomparison of small-and large-volume techniques for thorium-234 in seawater. Mar. Chem. 74, 15–28.

Buesseler, K.O., Benitez-Nelson, C.R., Moran, S.B., Burd, A., Charette, M., Cochran, J.K., Coppola, L., Fisher, N.S., Fowler, S.W., Gardner, W.D., Guo, L.D., Gustafsson, O., Lamborg, C., Masque, P., Miquel, J.C., Passow, U., Santschi, P.H., Savoye, N., Stewart, G., Trull, T., 2006. An assessment of particulate organic carbon to thorium-234 ratios in the ocean and their impact on the application of ^{234}Th as a POC flux proxy. Mar. Chem. 100, 213.

Buesseler, K.O., Jayne, S.R., Fisher, N.S., Rypina, I.I., Baumann, H., Baumann, Z., Breier, C.F., Douglass, E.M., George, J., Macdonald, A.M., Miyamoto, H., Nishikawa, J., Pike, S.M., Yoshida, S., 2012. Fukushima-derived radionuclides in the ocean and biota off Japan. Proc. Natl. Acad. Sci. 109, 5984–5988.

Burnett, W.C., Dulaiova, H., 2003. Estimating the dynamics of groundwater input into the coastal zone via continuous radon-222 measurements. J. Environ. Radioact. 69, 21–35.

Burnett, W.C., Corbet, D.R., Schultz, M., Horwitz, E.P., Chiarizia, R., Dietz, M., Thakkar, A., Fern, M., 1997. Preconcentration of actinides elements from soils and large volume water samples using extraction chromatography. J. Radioanal. Nucl. Chem. 226, 121–127.

Burnett, W.C., Kim, G., Lane-Smith, D., 2001. A continuous monitor for assessment of ^{222}Rn in the coastal ocean. J. Radioanal. Nucl. Chem. 249, 167–172.

Burnett, W.C., Aggarwal, P.K., Aureli, A., Bokuniewicz, H., Cable, J.E., Charette, M.A., Kontar, E., Krupa, S., Kulkarni, K.M., Loveless, A., Moore, W.S., Oberdorfer, J.A., Oliveira, J., Ozyurt, N., Povinec, P.P., Privitera, A.M.G., Rajar, R., Ramessur, R.T., Scholten, J., Stieglitz, T., Taniguchi, M., Turner, J.V., 2006. Quantifying submarine groundwater discharge in the coastal zone via multiple methods. Sci. Total Environ. 367, 498–543.

Castrillejo, M., Casacuberta, N., Christl, M., Garcia-Orellana, J., Vockenhuber, C., Synal, H.-A., Pere Masqué, P., 2017. Anthropogenic ^{236}U and ^{129}I in the Mediterranean Sea: first comprehensive distribution and constrain of their sources. Sci. Total Environ. 593–594, 745–759.

Charette, M.A., Buesseler, K.O., Andrews, J.E., 2001. Utility of radium isotopes for evaluating the input and transport of groundwater-derived nitrogen to a Cape Cod estuary. Limnol. Oceanogr. 46, 465–470.

Charette, M.A., Dulaiova, H., Gonneea, M.E., Henderson, P.B., Moore, W.S., Scholten, J.C., Pham, K.M., 2012. GEOTRACES radium isotopes interlaboratory comparison experiment. Limnol. Oceanogr. Methods 10, 451–463.

Chernayev, A.M., Gapanov, I.A., Lapushkina, L.V., 1999. Development of an underwater Cherenkov detector to reveal sources of technogenic radionuclides. IAEA-SM-354/93P, Vienna, pp. 417–419. In: Proceedings of the International Symposium on Marine Pollution, IAEA-TECDOC-1094, Vienna, pp. 417–419.

Chiappini, R., Pointurier, F., Millies-Lacroix, J.-C., Lepetit, G., Hemet, P., 1999. ^{240}Pu/^{239}Pu isotopic ratios and $^{239+240}$Pu total measurements in surface and deep waters around Mururoa and Fangataufa atolls compared with Rangiroa atoll (French Polynesia). Sci. Total Environ. 237/238, 269–276.

Clarke, W.B., Jenkins, W.J., Top′, Z., 1976. Determination of tritium by mass-spectrometric measurements of ^{3}He. Int. J. Appl. Radiat. Isot. 27, 512–522.

Coale, K.H., Bruland, K.W., 1985. ^{234}Th:^{238}U disequilibria within the California current. Limnol. Oceanogr. 30, 22–33.

Cochran, J.K., Krishnaswami, S., 2008. U-Th series nuclides in aquatic systems. In: Baxter, M.S. (Ed.), Radioact. Environ, vol. 13, p. 440.

Cochran, J.K., Masque, P., 2003. Short-lived U/Th series radionuclides in the ocean: tracers for scavenging rates, export fluxes and particle dynamics. Rev. Miner. Geochem. 52, 461–492.

Cofino, W.P., Wells, D.E., 1994. Design and evaluation of the QUASIMEME inter-laboratory performance studies: a test case for robust statistics. Mar. Pollut. Bull. 29, 149–158.

Cooper, J.A., Perkins, R.W., 1971. An anticoincidence-shielded dual Ge(Li) gamma-ray spectrometer for low-level environmental radionuclide analysis and gamma-gamma coincidence studies. Nucl. Instrum. Methods 94, 29–38.

Cooper, J.A., Perkins, R.W., 1972. A versatile Ge(Li)-NaI(Tl) coincidence-anticoincidence gamma-ray spectrometer for environmental and biological problems. Nucl. Instrum. Methods 99, 125–146.

Coppola, L., Roy-Barman, M., Mulsow, S., Povinec, P.P., Jeandel, C., 2004. Low particulate organic carbon export in the frontal zone of the Southern Ocean (Indian Sector) revealed by ^{234}Th. Deep-Sea Res. I 52, 51–68.

Coppola, L., Roy-Barman, M., Mulsow, S., Povinec, P.P., Jeandel, C., 2006. Thorium isotopes as traces of particles dynamics and deep-water circulation in the Indian sector of the Southern Ocean (ANTARES IV). Mar. Chem. 100, 299–313.

Dai, M.H., Buesseler, K.O., Kelley, J.M., Andrews, J.E., Pike, S., Wacker, J.F., 2001. Size-fractionated plutonium isotopes in a coastal environment. J. Environ. Radioact. 53, 9–25.

Danesi, P.R., Markowicz, A., Chinea-Cano, E., Burkart, W., Salbu, B., Donohue, D., Ruedenuer, F., Hedberg, M., Vogt, S., Zaharadnik, P., Ciurapinski, A., 2003. Depleted uranium particles in selected Kosovo samples. J. Environ. Radioact. 64, 143–154.

Debertin, K., Helmer, R.G., 1998. Gamma and X-Ray Spectrometry with Semiconductor Detectors. Elsevier, Amsterdam.

DeMaster, D.J., Brewster, D.C., McKee, B.A., Nittrouer, C.A., 1991. Rates of particle scavenging, sediment reworking, and longitudinal ripple formation at the HEBBLE site based on measurements of ^{234}Th and ^{210}Pb. Mar. Geol. 99, 423–444.

Donahue, D.J., Jull, A.J.T., Linick, T.W., Toolin, L.J., 1990. Radiocarbon measurements at the University of Arizona AMS facility. Nucl. Instrum. Methods Phys. Res., Sect. B 52, 224–228.

Donohue, D.L., 1998. Strengthening IAEA safeguards through environmental sampling and analysis. J. Alloys Comp. 271–273, 11–18.

Donohue, D.L., 2002. Strengthened nuclear safeguards. Anal. Chem. 74, 28A–35A.

Dovlete, C., Povinec, P.P., 1999. Quantification of uncertainty in gamma-spectrometry – a Monte Carlo approach. Acta Phys. Univ. Comenianae XL 43–55.

Doyle, J.E. (Ed.), 2008. Nuclear Safeguards, Security, and Nonproliferation: Achieving Security with Technology and Policy. Elsevier, Burlington.

Edwards, R.L., Chen, J.H., Wasserburg, G.J., 1986. ^{238}U-^{234}U-^{230}Th-^{232}Th systematics and the precise measurements of time over the past 50,000 years. Earth Planet. Sci. Lett. 81, 175–192.

Edwards, R.L., Gallup, C.D., Cheng, H., 2003. Uranium-series dating of marine and lacustrine carbonates. Rev. Miner. Geochem. 52, 363–405.

Elsinger, R.J., King, P.T., Moore, W.S., 1982. Radium-224 in natural waters measured by [gamma]-ray spectrometry. Anal. Chim. Acta 144, 277–281.

Eppley, R.W., 1989. New production: history, methods, problems. In: Berger, W.H., Smetacek, V.S., Wefer, G. (Eds.), Productivity of the Oceans: Present and Past. John Wiley, New York, pp. 85–97.

Erdmann, N., Betti, M., Stetzer, O., Tamborini, G., Kratz, J.V., Trautmann, N., van Geel, J., 2000. Production of monodisperse uranium oxide particles and their characterization by scanning electron microscopy and secondary ion mass spectrometry. Spectrochim. Acta Part B Atom. Spectrosc. 55, 1565–1575.

Erdmann, N., Passler, G., Trautmann, N., Wendt, K., 2008. Resonance ionization mass spectrometry for trace analysis of long-lived radionuclides. In: Povinec, P.P. (Ed.), Analysis of Environmental Radionuclides. Elsevier, Amsterdam, pp. 331–354.

Eriksson, M., 2002. On Weapons Plutonium in the Arctic Environment (Thule, Greenland) (PhD thesis). Risø-R-1321 Risø National Laboratory, Roskilde, Denmark.

Eriksson, M., Ljunggren, K., Hindorf, C., 2002. Plutonium hot particle separation techniques using real-time digital image systems. Nucl. Instrum. Methods Phys. Res., Sect. A 488, 375–380.

Eriksson, M., Osán, J., Jernström, J., Wegrzynek, D., Simon, R., Chinea-Cano, E., Markowicz, A., Bamford, S., Tamborini, G., Török, S., Falkenberg, G., Alsecz, A., Dahlgaard, H., Wobrauschek, P., Streli, C., Zoeger, N., Betti, M., 2005a. Source term identification of environmental radioactive Pu/U particles by their characterization with non-destructive spectrochemical analytical techniques. Spectrochim. Acta Part B Atom. Spectrosc. 60, 455–469.

Eriksson, M., Betti, M., Himbert, J., Tamborini, G., Falkenberg, G., 2005b. Rapid change of Pu oxidation state in Pu-oxalate crystals by 19 keV photons. In: Hamburger Synchrotronstrahlungslabor (HASYLAB) am Deutschen Elektronen-Synchrotron (DESY) in der Helmholtz-Gemeinschaft HGF. DESY Annual Report DESY, Hamburg.

Eriksson, M., Lindahl, P., Roos, P., Dahlgaard, H., Holm, E., 2008. U, Pu, and Am nuclear signatures of the Thule hydrogen bomb debris. Environ. Sci. Technol. 42, 4717–4722.

Fehn, U.m, Snyder, G., 2000. ^{129}I in the Southern Hemisphere: global redistribution of an anthropogenic isotope. Nucl. Instrum. Methods Phys. Res., Sect. B 172, 366–371.

Fifield, L.K., 2000. Advances in accelerator mass spectrometry. Nucl. Instrum. Methods Phys. Res., Sect. B 172, 134–143.

Fifield, L.K., 2008. Accelerator mass spectrometry of longlived heavy radionuclides. In: Povinec, P.P. (Ed.), Analysis of Environmental Radionuclides. Elsevier, Amsterdam, pp. 263–294.

Fleer, A.P., Bacon, M.P., 1984. Determination of Pb-210 and Po-210 in seawater and marine particulate matter. Nucl. Instrum. Meth. Phys. Res. 223, 243–249.

Foster, D.A., Staubwasser, M., Henderson, G.M., 2004. ^{226}Ra and Ba concentrations in the Ross Sea measured with multicollector ICP mass spectrometry. Mar. Chem. 87, 59–71.

Fowler, S.W., Noshkin, V.E., La Rosa, J., Gastaud, J., 2000. Temporal variations in plutonium and americium inventories and their relation to vertical transport in the northwestern Mediterranean Sea. Limnol. Oceanogr. 45, 446–458.

Freeman, S.P.H.T., Shanks, R.P., Donzel, X., Gaubert, G., 2015. Radiocarbon positive-ion mass spectrometry. Nucl. Instrum. Methods Phys. Res. B 361, 229–232.

Ganachaud, A., Wunsch, C., 2000. Improved estimates of global ocean circulation, heat transport a mixing from hydrographic data. Nature 408, 453–457.

García-Orellana, I., García-León, M., 2002. An easy method to determine ^{210}Po and ^{210}Pb by alpha spectrometry in marine environmental samples. Appl. Radiat. Isot. 56, 633–636.

Garcia-Solsona, E., Garcia-Orellana, J., Masqué, P., Dulaiova, H., 2008. Uncertainties associated with ^{223}Ra and ^{224}Ra measurements in water via a delayed coincidence counter (RaDeCC). Mar. Chem. 109, 198–219.

Garfield, F.M., 1992. Quality Assurance Principles for Analytical Laboratories. AOAC Int., New York.

Garratt-Reed, A.J., Bell, D.C., 2003. Energy Dispersive X-Ray Analysis in the Electron Microscope. In: Microscopy Handbooks, vol. 49. BIOS Scientific Publishers Limited, Oxford.

Gastaud, J., Povinec, P.P., Aoyama, M., Hirose, K., Sanchez-Cabeza, J.A., Levy, I., Roos, P., Rezzoug, S., 2011. Transport and scavenging of Pu in surface waters of the southern Hemisphere Oceans. Prog. Oceanogr. 89, 92–100.

Geibert, W., Rutgers van der Loeff, M.M., Hanfland, C., Dauelsberg, H.-J., 2002. Actinium-227 as a deep-sea tracer: sources, distribution and applications. Earth Planet. Sci. Lett. 198, 147–165.

Goldstein, S.J., Stirling, C.H., 2003. Techniques for measuring uranium-series nuclides: 1992–2002. In: Bourdon, B., Henderson, G.M., Lundstrom, C.C., Turner, S.P. (Eds.), Uranium-Series Geochemistry, Reviews in Mineralogy and Geochemistry, vol. 52, pp. 23–57.

Gostic, R.C., 2010. Characterization of Plutonium Particles Originating from the BOMARC Accident -1960. PhD Thesis, UNLV Theses/Dissertations/Professional Papers/Capstones. Paper 313. http://digitalcommons.library.unlv.edu/thesesdissertations/313.

Groening, M., Auer, R., Brummer, D., Jaklitsch, M., Sambandam, C., Tanweer, A., Tatzber, H., 2009. Increasing the performance of tritium analysis by electrolytic enrichment. Isot. Environ. Health Stud. 45, 118–125.

Guilderson, T.P., Schrag, D.P., 1998. Abrupt shift in subsurface temperatures in the tropical Pacific associated with changes in El Nino. Science 281, 240–243.

Gupta, J.G.S., Bertrand, N.B., 1995. Direct ICP-MS determination of trace and ultratrace elements in geological materials after decomposition in a microwave oven. I. Quantitation of Y, Th, U and the lanthanides. Talanta 42, 1595–1607.

Hancock, G.J., Martin, P., 1991. Determination of Ra in environmental samples by alpha-particle spectrometry. Appl. Radiat. Isot. 42, 63–69.

Hatori, S., Nawata, H., Ohseki, M., Matsuzaki, H., Misawa, T., Kobayashi, K., 2000. Gas-filled magnet at MALT — Measurement of ^{36}Cl. Nucl. Instrum. Methods Phys. Res. B 172, 211–217.

Hayes, C.T., Anderson, R.F., Fleisher, M.Q., Huang, K.-F., Robinson, L.F., Lu, Y., Cheng, H., Edwards, R.L., Moran, S.B., 2015. ^{230}Th and ^{231}Pa on geotraces GA03, the U.S. geotraces North Atlantic transect, and implications for modern and paleoceanographic chemical fluxes. Deep Sea Res. Part II Top. Stud. Oceanogr. 116, 29–41.

Henderson, P., Morris, P., Moore, W., Charette, M., 2013. Methodological advances for measuring low-level radium isotopes in seawater. J. Radioanal. Nucl. Chem. 296, 357–362.

Heusser, G., 1995. Low-radioactivity background techniques. Ann. Rev. Nucl. Part. Sci. 45, 543–590.

Hirose, K., Aoyama, M., Povinec, P.P., 2003. Concentration of particulate plutonium in surface and deep-water samples collected during the IAEA'97 expedition. Deep-Sea Res. Part II Top. Stud. Oceanogr. 50, 2639–2647.

Hirose, K., 2016. Fukushima Daiichi nuclear power plant accident: atmospheric and oceanic impacts over the five years. J. Environ. Radioact. 157, 1–18.

Hirose, K., Aoyama, M., Fukasawa, M., Kim, C.S., Komura, K., Povinec, P.P., Sanchez-Cabeza, J.A., 2007. Plutonium and ^{137}Cs in surface water of the south Pacific Ocean. Sci. Total Environ. 381, 243–255.

Hirose, K., Aoyama, M., Povinec, P.P., 2009. ^{239,240}Pu/^{137}Cs ratios in the water column of the North Pacific: a proxy of biogeochemical processes. J. Environ. Radioact. 100, 258–262.

Hirose, K., Kim, C.S., Yim, S.A., Aoyama, M., Fukasawa, M., Komura, K., Povinec, P.P., Sanchez-Cabeza, J.A., 2011. Vertical profiles of plutonium in the central South Pacific. Prog. Oceanogr. 89, 101–107.

Hirose, K., Povinec, P.P., 2015. Sources of plutonium in the atmosphere and stratosphere-troposphere mixing. Sci. Rep. 5, 15707. https://doi.org/10.1038/srep15707.

Hirose, K., Povinec, P.P., 2018. Long-term variations of ^{90}Sr and ^{137}Cs in surface and deep waters of the Sea of Japan: characteristics, behavior and the Fukushima impact. Sci. Rep. (in print).

Horwitz, E.P., Chiarizia, R., Dietz, M.L., Diamond, H., Nelson, D.M., 1993. Separation and preconcentration of actinides from acidic media by extraction chromatography. Anal. Chim. Acta 281, 361–372.

Hotchkis, M.A.C., Child, D., Fink, D., Jacobsen, G.E., Lee, P.J., Mino, N., Smith, A.M., Tuniz, C., 2000. Measurement of ^{236}U in environmental media. Nucl. Instrum. Methods Phys. Res. B 172, 659–665.

Hou, X., Hansen, V., Aldahan, A., Possnert, G., Lind, O.C., Lujaniené, G., 2009. A review on speciation of ^{129}I in environmental and biological samples. Anal. Chim. Acta 632, 181–196.

Hou, X., Roos, P., 2008. Critical comparison of radiometric and mass spectrometric methods for the determination of radionuclides in environmental, biological and nuclear waste samples. Anal. Chim. Acta 608, 105–139.

Hou, X.L., Povinec, P.P., Zhang, L.Y., Biddulph, D., Chang, C.-C., Fan, Y.K., Golser, R., Jeskovsky, M., Jull, A.J.T., Liu, Q., Shi, K.L., Steier, P., Zhou, W.J., 2013. Iodine-129 in seawater offshore Fukushima: distribution, speciation, sources, and budget. Environ. Sci. Technol. 47, 3091–3098.

Hsieh, Y.-T., Henderson, G.M., 2011. Precise measurement of ^{228}Ra/^{226}Ra ratios and Ra concentrations in seawater samples by multi-collector ICP mass spectrometry. J. Anal. Atom. Spectrom. 26, 1338–1346.

IAEA, International Atomic Energy Agency, 1999. Marine Pollution. IAEA, Vienna, p. 694, p. 694.

IAEA, International Atomic Energy Agency, 2005. Worldwide Marine Radioactivity Studies (WOMARS). IAEA-TECDOC-1429. IAEA, Vienna, p. 187.

IAEA, International Atomic Energy Agency, 2006. Isotopes in Environmental Studies. Aquatic Forum 2004. IAEA, Vienna, p. 710.

IAEA International Atomic Energy Agency, 2011. Radioactive Particles in the Environment: Sources, Particle Characterization and Analytical Techniques. IAEA TECDOC-1163. IAEA, Vienna.

IAEA, International Atomic Energy Agency, 2015. The Fukushima Daiichi Accident. IAEA, Vienna.

Ilić, R., Durrani, S.A., 2003. Solid state nuclear track detectors. In: L'Annunziata, M.F. (Ed.), Handbook of Radioactivity Analysis, second ed. Elsevier, Amsterdam, pp. 179–237.

Inkret, W.C., Efurd, D.W., Miller, G., Rokop, D.J., Benjamin, T.M., 1998. Applications of thermal ionization mass spectrometry to the detection of 239Pu and 240Pu intakes. Int. J. Mass Spectrom. 178, 113–120.

Inn, K.G.W., McCurdy, D., Bell III, T., Loesch, R., Morton, J.S., Povinec, P., Burns, K., Henry, R., Barss, N.M., 2001. Standard, intercomparisons and performance evaluations for low-level and environmental radionuclide mass spectrometry and atom counting. J. Radioanal. Nucl. Chem. 249 (1), 109–113.

Inomata, Y., Aoyama, M., Hirose, K., 2009. Analysis of 50-y record of surface ^{137}Cs concentrations in the global ocean using the HAM-global database. J. Environ. Monitor. 11, 116–125.

Inomata, Y., et al., 2017. Rapid recirculation of FNPP1 derived radiocesium suggesting new pathway of subtropical mode water in the western North Pacific to the Sea of Japan. Ocean Sci. Discuss. https://doi.org/10.5194/os-2017-90.

ISO, International Organization for Standardization, 1996. Quality System Guidelines for the Production of Reference Materials. Guide 34. ISO/IEC, Geneva.

ISO, International Organization for Standardization, 1997. Proficiency Testing and Interlaboratory Comparisons. Guide 43 1. ISO/IEC, Geneva.

Ito, T., Povinec, P.P., Togawa, O., Hirose, K., 2003. Temporal and spatial variations of anthropogenic radionuclides in Japan Sea waters. Deep-Sea Res. II 50, 2701–2711.

Jacobsen, G.E., Hotchkis, M.A.C., Fink, D., Child, D.P., Tuniz, C., Sacchi, E., Levins, D.M., Povinec, P.P., Mulsow, S., 2000. AMS measurement of ^{129}I, ^{36}Cl and ^{14}C in underground waters from Mururoa and Fangataufa atolls. Nucl. Instrum. Methods Phys. Res. B 172, 666–671.

Jaeschke, L., Bradshaw, S., 2015. Retention of radioactive particles and associated effects in the filter-feeding marine mollusc *Mytilus edulis*. Sci. Total Environ. 502, 1–7.

JAERI, Japan Atomic Energy Research Institute, 2005. JAERI Research Report 2005-028. JAERI, Tokai-mura, p. 121.

Jenkins, W.J., Lott, D.E., Pratt, M.W., Boudreau, R.D., 1983. Anthropogenic tritium in South Atlantic bottom water. Nature 305, 45–46.

Jernström, J., 2006. Development of Analytical Techniques for Studies on Dispersion of Actinides in the Environment and Characterization of Environmental Particles (Ph.D. thesis). Helsinki University, Finland.

Jernström, J., Eriksson, M., Simon, R., Tamborini, G., Bildstein, O., Carlos Marquez, R., Kehl, S.R., Hamilton, T.F., Ranebo, Y., Betti, M., 2006. Characterization and source term assessments of radioactive particles from Marshall Islands using non-destructive analytical techniques. Spectrochim. Acta B 61, 971–979.

Jeskovsky, M., Povinec, P.P., Steier, P., Sivo, A., Richtarikova, M., Golser, R., 2015. Retrospective study of ^{14}C concentration in the vicinity of NPP Jaslovske Bohunice using tree rings and the AMS technique. Nucl. Instrum. Methods Phys. Res. B 361, 129–132.

Jimenez-Ramos, M.-C., Eriksson, M., García-López, J., Ranebo, Y., García-Tenorio, R., Betti, M., Holm, E., 2010. A comparison of two micro-beam X-ray emission techniques for actinide elemental distribution in microscopic particles originating from the hydrogen bombs involved in the Palomares (Spain) and Thule (Greenland) accidents. Spectrochim. Acta B 65, 823–829.

Jiménez-Ramos, M.C., García-López, J., Eriksson, M., Jernström, J., García-Tenorio, R., 2012. PIXE analysis of U and Pu from hot particles: K-lines vs L-lines. Nucl. Instrum. Methods Phys. Res., B 273, 118–121.

Jones, D.G., 2001. Development and application of offshore gamma-rayspectrometrymeasurements: A review. J. Environ. Radioact. 53, 313–333.

Jull, A.J.T., Burr, G.S., Beck, J.W., Hodgins, G.W.L., Biddulph, D.L., McHargue, L.R., Lange, T.E., 2008. Accelerator mass spectrometry of long-lived light radionuclides. In: Povinec, P.P. (Ed.), Analysis of Environmental Radionuclides. Elsevier, Amsterdam, pp. 241–262.

Kadko, D., 2009. Rapid oxygen utilization in the ocean twilight zone assessed with the cosmogenic isotope ^{7}Be. Glob. Biogeochem. Cycles 23.

Kadko, D., 2017. Upwelling and primary production during the U.S. GEOTRACES east Pacific zonal transect. Glob. Biogeochem. Cycles 31, 218–232.

Kaizer, J., buch, J., Kontul, I., Sivo, A., Richtarikova, M., Cech, P., Povinec, P.P., 2018a. Methods of radiocarbon determination in wine and bone samples by gas proportional counting technique. Radiocarbon. https://doi.org/10.1017/RDC.2018.20.

Kaizer, J., Aoyama, M., Kumamoto, Y., Molnár, M., Palcsu, L., Povinec, P.P., 2018b. Tritium and radiocarbon in the western North Pacific waters: post-Fukushima situation. J. Environ. Radioact. 184–185, 83–94.

Kaltofen, Gundersen, 2017. Radioactively-hot particles detected in dusts and soils from Northern Japan by combination of gamma spectrometry, autoradiography, and SEM/EDS analysis and implications in radiation risk assessment. Sci. Total Environ. 607/608, 1065–1072.

Kashparov, V.A., Ahamdach, N., Zvarich, S.I., Yoschenko, V.I., Maloshtan, I.M., Dewiere, L., 2004. Kinetics of dissolution of Chernobyl fuel particles in soil in natural conditions. J. Environ. Radioact. 72 (3), 335–353.

Kelley, J.M., Bond, L.A., Beasley, T.M., 1999. Global distribution of Pu isotopes and ^{237}Np. Sci. Total Environ. 237/238, 483–500.

Keller, C., 1971. The Chemistry of the Transuranic Elements. Verlag Chemie GmbH, Weinheim, pp. 380–392.

Kershaw, P.J., McCubbin, D., Leonard, K.S., 1999. Continuing contamination of north Atlantic and Arctic waters by Sellafield radionuclides. Sci. Total Environ. 237/238, 119–132.

Key, R.M., 1996. WOCE Pacific Ocean radiocarbon program. Radiocarbon 38, 415–423.

Key, R.M., Brewer, R.L., Stockwell, J.H., Guinasso, N.L.J., Schink, D.R., 1979. Some improved techniques for measuring radon and radium in marine sediments and in seawater. Mar. Chem. 7, 251–264.

Key, R.M., Guinasso, N.L.J., Schink, D.R., 1979b. Emanation of radon-222 from marine sediments. Mar. Chem. 7, 221–250.

Key, R., Quay, P., Jones, G., McNichol, A., von Reden, K., Schneider, R., 1996. WOCE AMS radiocarbon .1. Pacific Ocean results (P6, P16 and P17). Radiocarbon 38, 425–518.

Key, R., Quay, P., Schlosser, P., McNichol, A., von Reden, K., Schneider, R., Elder, K., Stuiver, M., Ostlund, H., 2002. WOCE radiocarbon IV: Pacific Ocean results; P10, P13N, P14C, P18, P19 & S4P. Radiocarbon 44, 239–392.

Key, R.M., Kozyr, A., Sabine, C.L., Lee, K., Wanninkhof, R., Bullister, J.L., Feely, R.A., Millero, F.J., Mordy, C., Peng, T.-H., 2004. A global ocean carbon climatology: results from global data analysis project (GLODAP). Glob. Biogeochem. Cycles 18 (4), GB4031. https://doi.org/10.1029/2004GB002247.

Kilbourne, K.H., Quinn, T.M., Webb, R., Guilderson, T., Nyberg, J., Winter, A., 2010. Coral windows onto seasonal climate variability in the northern Caribbean since 1479. Geochem. Geophys. Geosyst. 11 (10) art. no. Q10006.

Kilius, L.R., Rucklidge, J.C., Litherland, A.E., 1987. Accelerator mass spectrometry of ^{129}I at IsoTrace. Nucl. Instrum. Methods B 29, 72–76.

Kim, G., Burnett, W.C., Dulaiova, H., Swarzenski, P.W., Moore, W.S., 2001. Measurement of ^{224}Ra and ^{226}Ra activities in natural waters using a radon-in-air monitor. Environ. Sci. Technol. 35, 4680–4683.

Knie, K., Faestermann, T., Korschinek, G., Rugel, G., Ruhm, W., Wallner, C., 2000. High-sensitivity AMS for heavy nuclides at the Munich Tandem accelerator. Nucl. Instrum. Methods Phys. Res. B 172, 717–720.

Kobayashi, T., Nagai, H., Kobayashi, K., 2000. Concentration profiles of ^{10}Be in large manganese crusts. Nucl. Instrum. Methods Phys. Res., B 172, 579–582.

Kobayashi, Y., Takahashi, R., Shima, S., Katagiri, M., Takahashi, K., 1998. Development of a submersible Ge gamma-ray detector system. In: Int. Symp. on Marine Pollution. IAEA, Vienna, pp. 530–531.

Koczy, F.F., 1958. Natural radium as a tracer in the ocean. In: Proceedings of the 2nd International Conference of Peaceful Uses of Atomic Energy. Geneva, vol. 18, pp. 351–357.

Komura, K., Sakanoue, M., Yamamoto, M., 1984. Determination of ^{240}Pu/^{239}Pu ratio in environmental samples based on the measurements of Lx/α-ray activity ratio. Helth Phys. 46, 1213–1219.

Kontuľ, I., Jeeškovsky, M., Kaizer, J., Šivo, A., Richtarikova, M., Povinec, P.P., Čech, P., Steier, P., Golser, R., 2017. Radiocarbon concentration in tree-ring samples collected in the south-west Slovakia (1974–2013). Appl. Radiat. Isot. 126, 58–60.

Kramer, S.D., Hurst, G.S., Chen, C.H., Payne, M.G., Allman, S.L., Philips, R.C., Lehmann, B.E., Oescher, H., Loosli, H.H., Willis, R.D., Thonnard, N., 1986. Analysis of ^{81}Kr in groundwater using laser resonance ionization spectroscopy. Nucl. Instrum. Methods Phys. Res. B 17, 395–401.

Kretschmer, S., Geibert, W., Rutgers van der Loeff, M.M., Mollenhauer, G., 2010. Grain size effects on $^{230}Th_{xs}$ inventories in opal-rich and carbonate-rich marine sediments. Earth Planet. Sci. Lett. 294, 131–142.

Krishnaswami, S., Lal, D., Somayajulu, B.L.K., Dixon, F.S., Stonecipher, S.A., Craig, H., 1972. Silicon, radium, thorium, and lead in seawater: in-situ extraction by synthetic fibre. Earth Planet. Sci. Lett. 16, 84–90.

Krishnaswami, S., Sarin, M.M., 1976. The simultaneous determination of Th, Pu, Ra isotopes, ^{210}Pb, ^{55}Fe, ^{32}Si and ^{14}C in marine suspended phases. Anal. Chim. Acta 83, 143–156.

Ku, T.-L., Luo, S., 2008. Ocean circulation/mixing studies with decay-series isotopes. In: Krishnaswami, S., Cochran, J.K. (Eds.), Radioactivity in the Environment, vol. 13, pp. 307–344.

Kumamoto, Y., Murata, A., Watanabe, S., Fukasawa, M., 2011. Temporal and spatial variations in bomb-produced radiocarbon along BEAGLE2003 lines – revisits of WHP P06, A10, and IO3/I04 in the Southern Hemisphere Oceans. Prog. Oceanogr. 89, 49–60.

Kumamoto, Y., et al., 2013. Fukushima-derived radiocesium in the northwestern Pacific Ocean. Appl. Radiat. Isot. 81, 335–339.

Kumamoto, Y., Aoyama, M., Hamajima, Y., Aono, T., Kouketsu, S., Murata, A., Kawano, T., 2014. Southward spreading of the Fukushima-derived radiocesium across the Kuroshio extension in the north Pacific. Sci. Rep. 4, 4276.

Kumamoto, Y., Aoyama, M., Hamajima, Y., Murata, A., Kawano, T., 2015. Impact of Fukushima-derived radiocesium in the western North Pacific Ocean about ten months after the Fukushima Dai-ichi nuclear power plant accident. J. Environ. Radioact. 140, 114–122.

Kuss, H.M., 1992. Applications of microwave digestion technique for elemental analyses. Fresenius J. Anal. Chem. 343, 788–793.

Kutschera, W., 2005. Progress in isotope analysis at ultra-trace level by AMS. Int. J. Mass Spectrom. 242, 145–160.

Kutschera, W., 2010. AMS and climate change. Nucl. Instrum. Methods Phys. Res. B 268, 693–700.

Accelerator mass spectrometry. Proceedings of the 8th international conference on accelerator mass spectrometry. In: Kutschera, W., Golser, R., Priller, A., Strohmeier, B. (Eds.), Nucl. Instrum. Methods B 172, 997.

Kutschera, W., 2016. Accelerator mass spectrometry: State of the art and perspectives. Adv. Phys. X1, 570–579.

Lal, D., 1999. An overview of five decades of studies in cosmic ray produced nuclides in oceans. Sci. Total Environ. 237/238, 3–13.

Landing, W.M., Lewis, B.L., 1991. Collection, processing, and analysis of marine particulate and colloidal material for transition metals. In: Urd, D.C., Spencer, D.W. (Eds.), Marine Particles: Analysis and Characterization, vol. 63. Geophysical Monographs, pp. 263–272.

La Rosa, J.J., Burnett, W., Lee, S.-H., Levy, I., Gastaud, J., Povinec, P.P., 2001. Separation of actinides, cesium and strontium from marine samples using extraction chromatography and sorbents. J. Radioanal. Nucl. Chem. 248 (3), 765–770.

La Rosa, J., Gastaud, J., Lagan, L., Lee, S.H., Levy-Palomo, I., Povinec, P.P., Wyse, E., 2005. Recent developments in the analysis of transuranics (Np, Pu, Am) in seawater. J. Radioanal. Nucl. Chem. 263, 427–436.

Laubenstein, M., 2017. Screening of materials with high purity germanium detectors at the Laboratori Nazionali del Gran Sasso. Int. J. Mod. Phys. A 32, 1743002.

Laubenstein, M., Hult, M., Gasparro, J., Arnold, D., Neumaier, S., Heusser, G., Köhler, M., Theodórsson, P., 2004. Underground measurements of radioactivity. Appl. Radiat. Isot. 61, 167–172.

Lawson, E.M., Elliott, G., Fallon, J., Fink, D., Hotchkis, M.A.C., Hua, Q., Jacobsen, G.E., Lee, P., Smith, A.M., Tuniz, C., Zoppi, U., 2000. AMS at ANTARES – the first 10 years. Nucl. Instrum. Methods Phys. Res. B 172, 95–99.

Lechelle, J., Bleuet, P., Martin, P., Girard, E., Bruguier, F., Martinez, M.A., Somogyi, A., Simionovici, A., Ripert, M., Valdivieso, F., Goeuriot, P., 2004. Micro-XANES and X-ray microtomography study of oxidation state, morphology, and chemistry evolution during nuclear fuel sintering. IEEE Trans. Nucl. Sci. 51, 1657–1661.

Lee, S.-H., Gastaud, J., La Rosa, J.J., Liong Wee Kwong, L., Povinec, P.P., Wyse, E., Fifield, L.K., Hausladen, P.A., De Tada, L.M., Santos, G.M., 2001. Analysis of plutonium isotopes in marine samples by radiometric, ICP-MS and AMS techniques. J. Radioanal. Nucl. Chem. 248 (3), 757–764.

Lee, S.-H., Gastaud, J., Povinec, P.P., Hong, G.H., Kim, S.H., Chung, C.S., Lee, K.W., Pettersson, H.B.L., 2003a. Distribution of plutonium and americium in the marginal seas of the northwest Pacific Ocean. Deep-Sea Res. II 50, 2727–2750.

Lee, S.H., La Rosa, J.J., Levy-Palomo, I., Oregioni, B., Pham, M.K., Povinec, P.P., Wyse, E., 2003b. Recent inputs and budgets of ^{90}Sr, ^{137}Cs, ^{239},^{240}Pu and ^{241}Am in the northwest Mediterranean Sea. Deep-Sea Res. II 50, 2817–2834.

Lee, S.-H., La Rosa, J., Gastaud, J., Povinec, P.P., 2005a. The development of sequential separation methods for the analysis of actinides in sediments and biological materials using anion-exchange resins and extraction chromatography. J. Radioanal. Nucl. Chem. 263, 419–425.

Lee, S.-H., Povinec, P.P., Wyse, E., Pham, M.K., Hong, G.-H., Chung, C.S., Kim, S.-H., Lee, H.J., 2005b. Distribution and inventories of ^{90}Sr, ^{137}Cs, ^{241}Am and Pu isotopes in sediments of the northwest Pacific Ocean. Mar. Geol. 216, 249–263.

Lee, S.H., Povinec, P.P., Wyse, E., Hotchkis, M.A.C., 2008. Ultra-low-level determination of ^{236}U in IAEA marine reference materials by ICPMS and AMS. Appl. Radiat. Isot. 66, 823–828.

Lee, S.H., Povinec, P.P., Gastaud, J., La Rosa, J.J., Wyse, E., Fifield, L.K., 2009a. Determination of plutonium isotopes in seawater samples by Semiconductor Alpha Spectrometry, ICP-MS and AMS techniques. J. Radioanal. Nucl. Chem. 282, 831–835.

Lee, S.-H., Povinec, P.P., Gastaud, J., Oregioni, B., Coppola, L., Jeandel, C., 2009b. Radionuclides as tracers of water fronts in the South Indian Ocean - ANTARES IV results. J. Oceanogr. 65, 397–406.

Lee, S.H., Povinec, P.P., Chisholm, J.R.M., Levy, I., Miquel, J.-C., Oh, J.-S., 2017. Distribution of natural and anthropogenic radionuclides in northwest Mediterranean coastal sediments. J. Environ. Radioact. 172, 145–159.

Leon Vintro, L., Mitchell, P.I., Condren, O.M., Moran, M., Battle, V.I.,J., Sanchez-Cabeza, J.A., 1996. Determination of the ^{240}Pu/^{239}Pu atom ratio in low activity environmental samples by alpha spectrometry and spectral deconvolution. Nucl. Instrum. Methods Phys. Res. A 369, 597–602.

Levy, I., Povinec, P.P., Aoyama, M., Hirose, K., Sanchez-Cabeza, J.A., Comanducci, J.-F., Gastaud, (.), J., Yim, S.A., 2011. Marine anthropogenic radiotracers in the Southern Hemisphere: new sampling and analytical strategies. Prog. Oceanogr. 89, 120–133.

Lewis, D., Miller, G., Duffy, C.J., Efurd, D.W., Inkret, W.C., Wagner, S.E., 2001. Los Alamos National Laboratory thermal ionisation mass spectrometry results from intercomparison study of inductively coupled plasma mass spectrometry, thermal ionization mass spectrometry, and fission track analysis of μBq quantities of ^{239}Pu in synthetic urine (LA-UR-001698). J. Radioanal. Nucl. Chem. 249, 115–120.

Li, Y.-H., Feely, H.W., Toggweiler, J.R., 1980. ^{228}Ra and ^{228}Th concentrations in GEOSECS Atlantic surface waters. Deep-Sea Res. 27, 545–555.

Libby, W.F., 1955. Radiocarbon Dating. University of Chicago Press, Chicago, p. 175.

Lind, O.C., 2006. Characterisation of Radioactive Particles in the Environment Using Advanced Techniques (Ph.D. thesis). Norwegian University of Life Sciences, Aas, Norway.

Lind, O.C., Salbu, B., Janssens, K., Proost, K., Dahlgaard, H., 2005. Characterization of uranium and plutonium containing particles originating from the nuclear weapons accident in Thule, Greenland, 1968. J. Environ. Radioact. 81, 21–32.

Lind, O.C., Salbu, B., Skipperud, L., Janssens, K., Jaroszewicz, J., De Nolf, W., 2009. Solid state speciation and potential bioavailability of depleted uranium particles from Kosovo and Kuwait. J. Environ. Radioact. 100, 301–307.

Liong Wee Kwong, L., La Rosa, J.&J., Lee, S.-H., Povinec, P.P., 2001. Liquid scintillation spectrometry of beta-emitters in marine samples. J. Radioanal. Nucl. Chem. 248 (3), 751–755.

Liong Wee Kwong, L., Gastaud, J., La Rosa, J., Lee, S.H., Povinec, P.P., Wyse, E., 2004a. Determination of ^{241}Pu in marine samples using co-precipitation with rare earth fluoride and liquid scintillation spectrometry. J. Radioanal. Nucl. Chem. 261, 283–289.

Liong Wee Kwong, L., Povinec, P.P., Jull, A.J.T., 2004b. Preparation of graphite targets from small marine samples for AMS radiocarbon measurements. Radiocarbon 46, 133–139.

Livingston, H., Cochran, J., 1987. Determination of transuranic and thorium isotopes in ocean water: in solution and in filterable particles. J. Radioanal. Nucl. Chem. 115, 299–308.

Livingston, H.D., Povinec, P.P., 2000. Anthropogenic marine radioactivity. Ocean Coast Manag. 43, 689–712.

Livingston, H.D., Povinec, P.P., Ito, T., Togawa, O., 2001. The behaviour of plutonium in the Pacific Ocean. In: Kudo, A. (Ed.), Plutonium in the Environment. Elsevier, Amsterdam, pp. 267–291.

Livingston, H.D., Povinec, P.P., 2002. A millennium perspective on the contribution of global fallout radionuclides to ocean science. Health Phys. 82, 656–668.

Ljunggren, K., 2003. Beta Camera: Development and Applications (PhD Thesis). LUJI-RADFYS-AVH-6/2003 Lund University, Sweden.

Lujaniene, G., Mažeika, J., Li, H.-C., Petrošius, R., Barisevičiute, R., Jokšas, K., Remeikaite-Nikiene, N., Malejevas, V., Garnaga, G., Stankevičius, A., Kulakauskaite, I., Povinec, P.P., 2015. Δ14C and δ13C variations in organic fractions of Baltic Sea sediment. Radiocarbon 57, 481–492.

Lujanienė, G., Mažeika, J., Li, H.C., Petrošius, R., Barisevičiūtė, R., Joksas, K.J., Remeikaitė-Nikienė, N., Malejevas, V., Garnaga, G., Stankevičius, A., Povinec, P.P., 2016. Δ14C and δ 13C as tracers of organic carbon in Baltic Sea sediments collected in coastal waters off Lithuania and in the Gotland Deep. J. Radioanal. Nucl. Chem. 307, 2231–2237.

Lujaniene, G., Povinec, P.P., Li, H.-C., Barisevičiūtė, R., Remeikaitė-Nikienė, N., Malejevas, V., Garnaga-Budrė, G., Terrassi, F., Pánik, J., Kaizer, J., Šemčuk, S., Jokšas, K., Tracevičienė, D., Stankevičius, A., 2017. Carbon and Pu isotopes in Baltic Sea sediments. Appl. Radiat. Isot. 126, 49–53.

Luo, X., Rehkämper, M., Lee, D.-C., Halliday, A.N., 1997. High precision $^{230}Th/^{232}Th$ and $^{234}U/^{238}U$ measurements using energy filtered ICP magnetic sector multiple collector mass spectrometry. Int. J. Mass Spectrom. Ion Process. 171, 105–117.

Macášek, F., 2008. Sampling techniques. In: Povinec, P.P. (Ed.), Analysis of Environmental Radionuclides. Elsevier, Amsterdam, pp. 17–48.

Masqué, P., Sanchez-Cabeza, J.A., Bruach, J.M., Palacios, E., Canals, M., 2002. Balance and residence times of ^{210}Pb and ^{210}Po in surface waters of the northwestern Mediterranean Sea. Cont. Shelf Res. 22, 2127–2146.

Masson, O., Baeza, A., Bieringer, J., Brudecki, K., Bucci, S., Cappai, M., Carvalho, F.P., Connan, O., Cosma, C., Dalheimer, A., Didier, D., Depuydt, G., De Geer, L.E., De Vismes, A., Gini, L., Groppi, F., Gudnason, K., Gurriaran, R., Hainz, D., Halldorsson, O., Hammond, D., Hanley, O., Holey, K., Homoki, Z., Ioannidou, A., Isajenko, K., Jankovic, M., Katzlberger, C., Kettunen, M., Kierepko, R., Kontro, R., Kwakman, P.J.M., Lecomte, M., Leon Vintro, L., Leppänen, A.-P., Lind, B., Lujaniene, G., Mc Ginnity, P., Mahon, C.M., Mala, H., Manenti, S., Manolopoulou, M., Mattila, A., Mauring, A., Mietelski, J.W., Møller, B., Nielsen, S.P., Nikolic, J., Overwater, R.M.W., Palsson, S.E., Papastefanou, C., Penev, I., Pham, M.K., Povinec, P.P., Ramebäck, H., Reis, M.C., Ringer, W., Rodriguez, A., Rulik, P., Saey, P.R.J., Samsonov, V., Schlosser, C., Sgorbati, G., Silobritiene, B.V., Söderström, C., Sogni, R., Solier, L., Sonck, M., Steinhauser, G., Steinkopff, T., Steinmann, P., Stoulos, S., Sykora, I., Todorovic, D., Tooloutalaie, N., Tositti, L., Tschiersch, J., Ugron, A., Vagena, E., Vargas, A., Wershofen, H., Zhukova, O., 2011. Tracking of airborne radionuclides from the damaged Fukushima Dai-Ichi nuclear reactors by European networks. Environ. Sci. Technol. 45, 7670–7677.

Mathieu, G.G., Biscayne, P.E., Lupton, R.A., Hammond, D.E., 1988. System for measurement of ^{222}Rn at low levels in natural waters. Health Phys. 55, 989–992.

McHargue, L.R., Donahue, D., Damon, P.E., Sonett, C.P., Biddulph, D., Burr, G., 2000. Geomagnetic modulation of the late Pleistocene cosmic-ray flux as determined by ^{10}Be from Blake Outer Ridge marine sediments. Nucl. Instrum. Methods Phys. Res. B 172, 555–561.

McNichol, A.P., Schneider, R.J., von Reden, K.F., Gagnon, A.R., Elder, K.L., Key, R.M., Quay, P.D., 2000. Ten years after - the WOCE AMS radiocarbon program. Nucl. Instrum. Methods Phys. Res. B 172, 479–484.

Michel, R., 2001. Environmental radioactivity measuring methods. In: Brechignac, F., Hoeard, B.J. (Eds.), Radioactive Pollutants. EDP Sciences, Les Ulis, pp. 27–62.

Michel, J., Moore, W.S., King, P.T., 1981. Gamma-ray spectrometry for determination of radium-228 and radium-226 in natural waters. Anal. Chem. 53, 1885–1889.

Mitchell, P.I., Leon Vintro, L., Dahlgaard, H., Gasco, C., Sanchez-Cabeza, J.A., 1997. Perturbation in the Pu-240/Pu-239 global fallout ratio in local sediments following the nuclear accidents at Thule (Greenland) and Palomares (Spain). Sci. Total Environ. 202, 147–153.

Moon, D.-S., Hong, G.H., Kim, Y.I., Baskaran, M., Chung, C.S., Kim, S.H., Lee, H.Y., Lee, S.H., Povinec, P.P., 2003. Accumulation of anthropogenic and natural radionuclides in bottom sediments of the Northwest Pacific Ocean. Deep-Sea Res. II 50, 2649–2673.

Moore, W.S., 2000. Determining coastal mixing rates using radium isotopes. Cont. Shelf Res. 20, 1993–2007.

Moore, W.S., 2007. Seasonal distribution and flux of radium isotopes on the southeastern U.S. continental shelf. J. Geophys. Res. 112, C10013.

Moore, W.S., 2008. Fifteen years experience in measuring ^{224}Ra and ^{223}Ra by delayed-coincidence counting. Mar. Chem. 109, 188.

Moore, W.S., Arnold, R., 1996. Measurement of ^{223}Ra and ^{224}Ra in coastal waters using a delayed coincidence counter. J. Geophys. Res. 101, 1321–1329.

Moore, W.S., Cai, P., 2013. Calibration of RaDeCC systems for ^{223}Ra measurements. Mar. Chem. 156, 130–137.

Moore, W.S., Key, R.M., Sarmiento, J.L., 1985. Techniques for precise mapping of ^{226}Ra and ^{228}Ra in the ocean. J. Geophys. Res. 90, 6983–6994.

Moran, S.B., Shen, C.-C., Edmonds, H.N., Weinstein, S.E., Smith, J.N., Edwards, R.L., 2002. Dissolved and particulate ^{231}Pa and ^{230}Th in the Atlantic Ocean: constraints on intermediate/deep water age, boundary scavenging, and $^{231}Pa/^{230}Th$ fractionation. Earth Planet. Sci. Lett. 203, 999–1014.

Morgenstern, U., Taylor, C.B., 2009. Ultra Low-level tritium measurement using electrolytic enrichment and LSC. Isot. Environ. Health Stud. 45, 96–117.

Muller, R.A., 1977. Radiocarbon dating with a cyclotron. Science 196, 489.

Muller, R.A., 1978. Radioisotope dating with the LBL 88" cyclotron. In: Gove, H.E. (Ed.), Proceedings of the First Conference on Radiocarbon Dating with Accelerators. University of Rochester, Rochesterhttp. homepage.univie.ac.at/walter.kutschera/AMS/AMS-1.pdf.

Mulsow, S., Povinec, P.P., Somayajulu, B.L.K., Oregioni, B., Liong Wee Kwong, L., Gastaud, J., Top, Z., Morgenstern, U., 2003. Temporal (^{3}H) and spatial variations of ^{90}Sr, $^{239,240}Pu$ and ^{241}Am in the Arabian sea: GEOSECS stations revisited. Deep-Sea Res. II 50, 2761–2775.

Muramatsu, Y., Hamilton, T., Uchida, S., Tagami, K., Yoshida, S., Robison, W., 2001. Measurement of $^{240}Pu/^{239}Pu$ isotopic ratios in soils from the Marshall Islands using ICP-MS. Sci. Total Environ. 278, 151–159.

Murnick, D.E., Dogru, O., Ilkmen, E., 2007. Laser based ^{14}C counting, an alternative to AMS in biological studies. Nucl. Instrum. Methods Phys. Res. B 259, 786–789.

Murnick, D.E., Dogru, O., Ilkmen, E., 2008. Intracavity optogalvanic spectroscopy, a new ultra-sensitive analytical technique for ^{14}C analysis. Anal. Chem. 80, 4820–4824.

Nakagawa, A.S., 1994. LIMS: Implementation and Management. The Royal Society of Chemistry, London.

Nakanishi, T.M., Tanoi, K. (Eds.), 2013. Agricultural Implications of the Fukushima Nuclear Accident. Springer, New York.

Nakano, M., Povinec, P.P., 2012. Long-term simulations of the ^{137}Cs dispersion from the Fukushima accident in the world ocean. J. Environ. Radioact. 111, 109–115.

NEC, National Electrostatic Corp, 2018. PIMS Update. NEC Newsletter.

Negre, C., Thomas, A.L., Mas, J.L., Garcia-Orellana, J., Henderson, G.M., Masque, P., Zahn, R., 2009. Separation and Measurement of Pa, Th, and U isotopes in marine sediments by microwave-assisted digestion

and multiple collector inductively coupled plasma mass spectrometry. Anal. Chem. 81, 1914−1919.

Nelson, D.E., Korteling, R.G., Stott, W.R., 1977. Carbon-14: direct detection at natural concentrations. Science 198, 507−508.

Newbury, D.E., Myklebust, R.L., 2005. Simulation of electron-excited X-ray spectra with NIST-DIH desktop spectrum analyzer (DTSA). Surf. Interface Anal. 37, 1045−1053.

Nisi, S., et al., 2009. Comparison of inductively coupled mass spectrometry and ultra-low-level gamma-ray spectroscopy for ultra-low background material selection. Appl. Radiat. Isot. 67, 828−832.

NIST, National Institute for Standardization and Technology, 2011. In: Fiori, C., Swyt-Thomas, C., Myklebust, B. (Eds.), Desktop Spectrum Analyzer (DTSA). Internet home page. http://www.cstl.nist.gov/div837/Division/outputs/DTSA/oldDTSA.htm.

Noakes, J.E., Noakes, S.E., Dvoracek, D.K., Culp, R.A., Bush, B., 1999. Rapid coastal survey of anthropogenic radionuclides, metals, and organic compounds in surficial marine sediments. Sci. Total Environ. 237/238, 449−458.

Nozaki, Y., Tsubota, H., Kasemsupaya, V., Yashima, M., Ikuta, N., 1991. Residence times of surface water and particle-reactive ^{210}Pb and ^{210}Po in the East China and Yellow Seas. Geochim. Cosmochim. Acta 55, 1265−1272.

Östlund, H.G., Brescher, R., 1982. Tritium Laboratory Data. Report No. 2. University of Miami, Miami, USA.

Osvath, I., Povinec, P.P., Baxter, M.S., 1999a. Kara Sea radioactivity assessment. Sci. Total Environ. 237−238, 167−179.

Osvath, I., Povinec, P.P., Huynh-Ngoc, L., Comanducci, J.-F., 1999b. Underwater gamma-surveys of Mururoa and Fangataufa lagoons. Sci. Total Environ. 237/238, 277−286.

Osvath, I., Povinec, P.P., 2001. Seabed γ-ray spectrometry: applications at IAEA-MEL. J. Environ. Radioact. 53, 335−349.

Osvath, I., Povinec, P.P., Baxter, M.S., Huynh-Ngoc, L., 2001. Mapping of the distribution of ^{137}Cs in Irish Sea sediments. J. Radioanal. Nucl. Chem. 248, 735−739.

Osvath, I., Povinec, P.P., Livingston, H.D., Ryan, T.P., Mulsow, S., Commanducci, J.-F., 2005. Monitoring of radioactivity in NW Irish Sea water using a stationary underwater gamma-ray spectrometer with satellite data transmission. J. Radioanal. Nucl. Chem. 263, 437−440.

Oughton, D., Day, P., Fifield, K., 2001. Plutonium measurement using accelerator mass spectrometry: methodology and applications. In: Kudo, A. (Ed.), Plutonium in the Environment. Elsevier, Amsterdam, pp. 47−62.

Radioactive particles in the environment. In: Oughton, D., Kashparov (Eds.), 2009. NATO Science for Peace and Security Series C: Environmental Security. Springer, Dordrecht.

Outola, I., Filliben, J., Inn, K.G.W., La Rosa, J., McMahon, C.A., Peck, G.A., Twining, J., Sanchez-Cabeza, J.A., 2006. Characterization of the NIST seaweed standard reference material. Appl. Radiat. Isot. 64, 1242−1247.

Palcsu, L., Major, Z., Köllo, Z., Papp, L., 2010. Using an ultrapure ^{4}He spike in tritium measurements of environmental water samples by the ^{3}He-ingrowth method. Rapid Commun. Mass Spectrom. 24, 698−704.

Palušová, V., Breier, R., Piquemal, F., Povinec, P.P., 2018. Monte Carlo simulation of environmental background sources of a HPGe detector operating in Modane underground laboratory. J. Radioanal. Nucl. Chem. (in print).

Park, Y.-H., Gambéroni, L., Charriaud, E., 1993. Frontal structure, water masses and circulation in the Crozet Basin. J. Geophys. Res. 98, 12,361−12,385.

Park, Y.-H., Pollard, R.T., Read, J.F., Leboucher, V., 2002. A quasi-synoptic view of the frontal circulation in the Crozet Basin during the Antares-4 cruise. Deep-Sea Res. II 49, 1823−1842.

Parr, R.M., Fajgelj, A., Dekner, R., Vera Ruiz, H., Carvalho, F.P., Povinec, P.P., 1998. Analytical quality assurance programmes to meet the present and future needs of developing countries. J. Anal. Chem. 360, 287−290.

Peräjärvi, K., Ihantola, S., Pöllänen, R., Toivonen, H., Turunen, J., 2011. Determination of ^{235}U, ^{239}Pu, ^{240}Pu, and ^{241}Am in a nuclear bomb particle using a position-sensitive α-γ coincidence technique. Environ. Sci. Technol. 45, 1528−1533.

Peterson, R.N., Burnett, W.C., Dimova, N., Santos, I.R., 2009. Comparison of measurement methods for radium-226 on manganese-fiber. Limnol. Oceanogr. Methods 7, 196−205.

Pham, M.K., Gastaud, J., La Rosa, J., Lee, S.-H., Levy-Palomo, I., Oregioni, B., Povinec, P.P., 2006a. Recent IAEA reference materials and intercomparison exercises for radionuclides in the marine environment. Radioact. Environ. 8, 617−628.

Pham, M.K., Sanchez-Cabeza, J.A., Povinec, P.P., Arnold, D., Benmansour, M., Bojanowski, R., Carvalho, F.P., Wyse, E., 2006b. Certified reference material for radionuclides in fish flesh sample IAEA-414 (mixed fish from the Irish Sea and North Sea). Appl. Radiat. Isot. 64, 1253−1259.

Pham, M.K., Sanchez-Cabeza, J.A., Povinec, P.P., Andor, K., Arnold, D., Benmansour, M., Bikit, I., Wyse, E., 2008. A new Certified Reference Material for radionuclides in Irish sea sediment (IAEA-385). Appl. Radiat. Isot. 66, 1711−1717.

Pham, M.K., Betti, M., Povinec, P.P., Benmansour, M., Bojanowski, R., Bouisset, P., Calvo, E.C., Varga, Z., 2010a. A new reference material for radionuclides in the mussel sample from the Mediterranean Sea (IAEA-437). J. Radioanal. Nucl. Chem. 283, 851−859.

Pham, M.K., Betti, M., Povinec, P.P., Alfimov, V., Biddulph, D., Gastaud, J., Kieser, W.E., Suzuki, T., 2010b. Certified reference material IAEA-418: 129I in Mediterranean Sea water. J. Radioanal. Nucl. Chem. 286, 121−127.

Pham, M.K., Betti, M., Povinec, P.P., Benmansour, M., Bünger, V., Drefvelin, J., Engeler, C., Zheng, J., 2011. A Certified Reference Material for Radionuclides in the Water Sample from Irish Sea (IAEA-443).

Pham, M.K., Benmansour, M., Carvalho, F.P., Chamizo, E., Degering, D., Engeler, C., Gasco, C., Gwynn, J.P., Harms, A.V., Hrnecek, E., Ibanez, F.L., Ilchmann, C., Ikaheimonen, T., Kanisch, G., Kloster, M., Llaurado, M., Mauring, A., MØller, B., Morimoto, T., Nielsen, S.P., Nies, H., Norrlid, L.D.R., Pettersson, H.B.L., Povinec, P.P., Rieth, U., Samuelsson, C., Schikowski, J., Êilobritiene, B.V., Smedley, P.A., Suplinska, M., Vartti, V.-P., Vasileva, E., Wong, J., Zalewska, T., Zhou, W., 2014. Certified reference material IAEA-446 for radionuclides in Baltic Sea seaweed. Appl. Radiat. Isot. 87, 468−474.

Pham, M.K., van Beek, P., Carvalho, F.P., Chamizo, E., Degering, D., Engeler, C., Gasco, C., Gurriaran, R., Hanley, O., Harms, A.V., Herrmann, J., Hult, M., Ikeuchi, Y., Ilchmann, C., Kanisch, G., Kis-Benedek, G., Kloster, M., Laubenstein, M., Llaurado, M., Mas, J.L., Nakano, M., Nielsen, S.P., Osvath, I., Povinec, P.P., Rieth, U., Schikowski, J., Smedley, P.A., Suplinska, M., Sykora, I., Tarjan, S., Varga, B., Vasileva, E., Zalewska, T., Zhou, W., 2016. Certified

reference materials for radionuclides in Bikini Atoll sediment (IAEA-410) and Pacific Ocean sediment (IAEA-412). Appl. Radiat. Isot. 109, 101–104.

Pike, S.M., Buesseler, K.O., Andrews, J., Savoye, N., 2005. Quantification of ^{234}Th recovery in small volume sea water samples by Inductively Coupled Mass Spectrometry. J. Radioanal. Nucl. Chem. 263, 355–360.

Pollard, R.T., Lucas, M.I., Read, J.F., 2002. Physical controls on biological zonation in the Southern Ocean. Deep-Sea Res. II 49, 3289–3305.

Pollard, R.T., et al., 2009. Southern Ocean deep-water carbon export enhanced by natural iron fertilization. Nature 457, 577–589.

Pöllänen, R., Ikäheimonen, T., Klemola, S., Juhanoja, J., 1999. Identification and analysis of a radioactive particle in a marine sediment sample. J. Environ. Radioact. 45, 149–160.

Pöllänen, R., 2002. Nuclear fuel particles in the environment - characteristics, atmospheric transport and skin doses. J. Radioanal. Nucl. Chem. 288, 603–611.

Povinec, P.P., 1981. Dual-parameter gamma-ray spectrometer for low-level counting. Isotopenpraxis 18, 92–97.

Povinec, P.P., 2004. Developments in analytical technologies for marine radioactivity studies. In: Livingston, H.D. (Ed.), Marine Radioactivity. Elsevier, Amsterdam, pp. 237–294.

Povinec, P.P., 2005. Ultra-sensitive radionuclide spectrometry: radiometrics and mass spectrometry synergy. J. Radioanal. Nucl. Chem. 263, 413–417.

Radioactivity in the environment series, 11. In: Povinec, P.P. (Ed.), 2008a. Analysis of Environmental Radionuclides. Elsevier, Amsterdam, p. 532.

Povinec, P.P., 2008b. Low-level gamma-ray spectrometry for environmental samples. J. Radioanal. Nucl. Chem. 276, 771–777.

Povinec, P.P., 2010a. Trends in radiometrics and mass spectrometry technologies: synergy in environmental analyses. J. Radioanal. Nucl. Chem. 286, 401–407.

Povinec, P.P., 2010b. Indian ocean. In: Encyclopedia of Inorganic Chemistry. Radionuclides in the Environment. Wiley, New York, 2010.

Povinec, P.P., 2011. New analytical technologies for new science. J. Anal. Sci. Technol. 2, A15–A21.

Povinec, P.P., 2012. New gamma-spectrometry technologies for environmental sciences. J. Anal. Sci. Technol. 3, 42–71.

Povinec, P.P., 2013. Recent developments in radioanalytical technologies for environmental investigation. J. Radioanal. Nucl. Chem. 295, 537–544.

Povinec, P.P., 2017. Background constrains of the SuperNEMO experiment for neutrinoless double beta-decay searches. Nucl. Instrum. Methods Phys. Res. A 845, 398–403.

Povinec, P.P., 2018a. Analysis of radionuclides at ultra-low levels: a comparison of low and high- energy mass spectrometry with gamma-spectrometry for radiopurity measurements. Appl. Radiat. Isot. 126, 26–30.

Povinec, P.P., 2018b. New ultra-sensitive radioanalytical technologies for new science. J. Radioanal. Nucl. Chem. https://doi.org/10.1007/s10967-018-5787-3.

Povinec, P.P., Osvath, I., Baxter, M.S., 1996. Underwater gamma-spectrometry with HPGe and NaI(Tl) detectors. Appl. Radiat. Isot. 47, 1127–1133.

Povinec, P.P., Osvath, I., Baxter, M.S., Harms, I., Huynh-Ngoc, L., Liong Wee Kwong, L., Pettersson, H.B.L., 1997. IAEA-MEL's contribution to the investigation of Kara Sea radioactivity and radiological assessment. Mar. Pollut. Bull. 35, 235–241.

Povinec, P.P., Woodhead, D., Blowers, P., Bonfield Cooper, M., Chen, Q.J., Dahlgaard, H., Dovlete, C., Fox, V., Froehlich, K., Gastaud, J., Gröning, M., Hamilton, T., Ikeuchi, Y., Kanisch, G., Krüger, A., Liong Wee Kwong, L., Matthews, M., Morgenstern, U., Mulsow, S., Pettersson, H.B.L., Smedley, P., Taylor, B., Taylor, C., Tinker, R., 1999. Marine radioactivity assessment of Mururoa and Fangataufa atolls. Sci. Total Environ. 237/238, 249–267.

Povinec, P.P., Oregioni, B., Jull, A.J.T., Kieser, W.E., Zhao, X.-L., 2000. AMS measurements of ^{14}C and ^{129}I in seawater around radioactive waste dump sites. Nucl. Instrum. Methods Phys. Res., Sect. B 172, 672–678.

Povinec, P.P., La Rosa, J.J., Lee, S.-H., Mulsow, S., Osvath, I., Wyse, E., 2001a. Recent developments in radiometric and mass spectrometric methods for marine radioactivity measurements. J. Radioanal. Nucl. Chem. 248 (3), 713–718.

Povinec, P.P., Jull, A.J.T., Burr, G.S., 2001b. Radiocarbon in seawater at radioactive waste dumping sites in the Northeast Atlantic and Northwest Pacific. Radiocarbon 43, 879–886.

Povinec, P.P., Pham, M.K., 2001. IAEA reference materials for quality assurance of marine radioactivity measurements. J. Radioanal. Nucl. Chem. 248, 211–216.

Povinec, P.P., Badie, C., Baeza, A., Barci-Funel, G., Bergan, T.D., Bojanowski, R., Burnett, W., Eikenberg, J., , L.K., Gastaud, J., Goroncy, I., Herrmann, J., Hotchkis, M.A.C., Ikaheimonen, T.K., Jakobson, E., Kalimbadjan, J., La Rosa, J.J., Lee, S.-H., Liong Wee Kwong, L., Lueng, W.M., Nielsen, S.P., Noureddine, A., Pham, M.K., Rohou, J.-N., Sanchez-Cabeza, J.A., Suomela, J., Suplinska, M., Wyse, E., 2002. Certified reference material for radionuclides in seawater IAEA-381 (Irish Sea water). J. Radioanal. Nucl. Chem. 251, 369–374.

Povinec, P.P., Livingston, H.D., Shima, S., Aoyama, M., Gastaud, J., Goroncy, I., Hirose, K., Huyhn-Ngoc, L., Ikeuchi, Y., Ito, T., La Rosa, J., Liong Wee Kwong, L., Lee, S.-H., Moriya, H., Mulsow, S., Oregioni, B., Pettersson, H., Togawa, O., 2003a. IAEA'97 expedition to the NW Pacific Ocean – results of oceanographic and radionuclide investigations of the water column. Deep-Sea Res. II 50, 2607–2638.

Povinec, P.P., Delfanti, R., Gastaud, J., La Rosa, J., Morgenstern, U., Oregioni, B., Pham, M.K., Salvi, S., Top, Z., 2003b. Anthropogenic radionuclides in the Indian Ocean surface waters – the Indian Ocean transect 1998. Deep-Sea Res. II 50, 2751–2760.

Povinec, P.P., Bailly Du Bois, P., Kershaw, P.J., Nies, H., Scotto, P., 2003c. Temporal and spatial trends in the distribution of ^{137}Cs in surface waters of Northern European Seas - a record of 40 years of investigations. Deep-Sea Res. Part II: Topical Stud. Oceanogr. 50, 2785–2801.

Povinec, P.P., Froehlich, K., Gastaud, J., Oregioni, B., Pagava, S.V., Pham, M.K., Rusetski, V., 2003d. Distribution of ^{90}Sr, ^{137}Cs and ^{239,240}Pu in Caspian sea water and biota. Deep-Sea Res. Part II: Topical Stud. Oceanogr. 50, 2835–2846.

Povinec, P.P., Comanducci, J.F., Levy-Palomo, I., 2004a. IAEA-MEL's underground counting laboratory in Monaco – background characteristics of HPGe detectors with anti-cosmic shielding. Appl. Rad. Isotopes 61, 85–93.

Povinec, P.P., Hirose, K., Honda, T., Ito, T., Scott, E.M., Togawa, O., 2004b. Spatial distribution of ^{3}H, ^{90}Sr, ^{137}Cs and ^{239,240}Pu in surface waters of the Pacific and Indian Oceans – GLOMARD database. J. Environ. Radioact. 76, 113–137.

Povinec, P.P., Aramaki, T., Burr, G.S., Jull, A.J.T., Liong Wee Kwong, L., Togawa, O., 2004c. Radiocarbon in the water column of the south-western North Pacific ocean − 24 years after GEOSECS. Radiocarbon 46, 583−594.

Povinec, P.P., Comanducci, J.F., Levy-Palomo, I., 2005a. IAEA-MEL's underground counting laboratory (CAVE) for the analysis of radionuclides in the environment at very low-levels. J. Radioanal. Nucl. Chem. 263, 441−445.

Povinec, P.P., Aarkrog, A., Buesseler, K.O., Delfanti, R., Hirose, K., Hong, G.-H., Ito, T., Livingston, H.D., Nies, H., Noshkin, V.E., Shima, S., Togawa, O., 2005b. ^{90}Sr, ^{137}Cs and ^{239,240}Pu concentration surface water timeseries in the Pacific and Indian Oceans. WOMARS results. J. Environ. Radioact. 81, 63−87.

Povinec, P.P., et al., 2006a. The marine information system (MARIS). In: Isotopes in Environmental Studies. IAEA, Vienna, pp. 68−69.

Povinec, P.P., Sanchez-Cabeza, 2006. Radionuclides in the Environment. Elsevier, Amsterdam, p. 646.

Povinec, P.P., Aggarwal, P.K., Aureli, A., Burnett, W.C., Kontar, E.A., Kulkarni, K.M., Moore, W.S., Schiavo, M.A., 2006b. Characterisation of submarine groundwater discharge offshore south-eastern Sicily. J. Environ. Radioact. 89, 81−101.

Povinec, P.P., Comanducci, J.F., Levy-Palomo, I., Oregioni, B., 2006c. Monitoring of submarine groundwater discharge along the Donnalucata coast in the south-eastern Sicily using underwater gamma-ray spectrometry. Cont. Shelf Res. 26, 874−884.

Povinec, P.P., Levy-Palomo, I., Comanducci, J.-F., de Oliveira, J., Oregioni, B., Privitera, A.M.G., 2006d. Submarine groundwater discharge investigations in Sicilian and Brazilian coastal waters using an underwater gamma-ray spectrometer. Radioact. Environ. 8, 373−381.

Povinec, P.P., Comanducci, J.-F., Levy-Palomo, I., Avaullee, F., 2006e. IAEA-MEL's underground counting laboratory - the design and main characteristics. Radioact. Environ. 8, 538−553.

Povinec, P.P., Scotto, P., Osvath, I., Ramadan, H., 2006f. The marine information system (MARIS). In: Aquatic Forum 2004 Isotopes in Environmental Studies. IAEA, Vienna, pp. 68−69.

Povinec, P.P., Pham, M.K., Sanchez-Cabeza, J.A., Barci-Funel, G., Bojanowski, R., Boshkova, T., Burnett, W.C., Wyse, E., 2007. Reference material for radionuclides in sediment IAEA-384 (Fangataufa Lagoon sediment). J. Radioanal. Nucl. Chem. 273, 383−393.

Povinec, P.P., Betti, M., Jull, A.J.T., Vojtyla, P., 2008a. New isotope technologies for environmental physics. Acta Phys. Slovaca 58, 1−154.

Povinec, P.P., Bokuniewicz, H., Burnett, W.C., Cable, J., Charette, M., Comanducci, J.-F., Kontar, E.A., Taniguchi, M., 2008b. Isotope tracing of submarine groundwater discharge offshore Ubatuba. Results of the IAEA-UNESCO SGD project. Brazil J. Environ. Radioact. 99, 1596−1610.

Povinec, P.P., de Oliveira, J., Braga, E.S., Comanducci, J.-F., Gastaud, J., Groening, M., Levy-Palomo, I., Top, Z., 2008c. Isotopic, trace element and nutrient characterization of coastal waters from Ubatuba inner shelf area, south-eastern Brazil. Estuarine. Coastal Shelf Sci. 76, 522−542.

Povinec, P.P., Osvath, I., Comanducci, J.-F., 2008d. Underwater gamma-ray spectrometry. Radioact. Environ. 11, 449−479.

Povinec, P.P., Vojtyla, P., Comanducci, J.-F., 2008e. Monte Carlo simulation of background characteristics of gamma-ray spectrometers-a comparison with experiment. Radioact. Environ. 11, 163−208.

Povinec, P.P., Litherland, A.E., von Reden, K.F., 2009. Developments in radiocarbon technologies: from the Libby counter to compound specific AMS analyses. Radiocarbon 51, 45−78.

Povinec, P.P., Lee, S.-H., Liong Wee Kwong, L., Oregioni, B., Groening, M., Jull, A.J.T., Kieser, W.E., Morgenstern, U., Top, Z., 2010. Tritium, radiocarbon, ^{90}Sr and ^{129}I in the Pacific and Indian oceans. Nucl. Instrum. Methods Phys. Res., Sect. B 268, 1214−1218.

Povinec, P.P., Breier, R., Coppola, L., Groening, M., Jeandel, C., Jull, A.J.T., Kieser, W.E., Top, Z., 2011a. Tracing of water masses using a multi isotope approach in the southern Indian Ocean. Earth Planet. Sci. Lett. 302, 14−26.

Povinec, P.P., Aoyama, M., Fukusawa, M., Hirose, K., Komura, K., Sanchez-Cabeza, J.A., Gastaud, J., Ješkovský, M., Levy, I., Sýkora, I., 2011b. ^{137}Cs water profiles in the South Indian Ocean - an evidence for accumulation of pollutants in the subtropical gyre. Prog. Oceanogr. 89, 17−30.

Povinec, P.P., Hirose, K., 2012. Radionuclides as tracers of ocean currents. In: Encyclopedia of Sustainability Science and Technology. Springer, New York.

Povinec, P.P., Burnett, W.C., Beck, A., Bokuniewicz, H., Charette, M., Gonneea, M.E., Groening, M., Ishitobi, T., Kontar, E., Liong Wee Kwong, L., Marie, D.E.P., Moore, W.S., Oberdorfer, J.A., Peterson, R., Ramessur, R., Rapaglia, J., Stieglitz, T., Top, Z., 2012a. Isotopic, geophysical and biogeochemical investigation of submarine groundwater discharge: IAEA-UNESCO intercomparison exercise at Mauritius Island. J. Environ. Radioact. 104, 24−45.

Povinec, P.P., Hirose, K., Aoyama, M., 2012b. Radiostrontium in the western North Pacific: characteristics, behavior and the Fukushima impact. Environ. Sci. Technol. 46, 10356−10363.

Povinec, P.P., Hirose, K., Aoyama, M., 2013a. Fukushima Accident: Radioactivity Impact on the Environment. Elsevier, New York, p. 382.

Povinec, P.P., Aoyama, M., Biddulph, D., Breier, R., Buesseler, K., Chang, C.C., Golser, R., Hou, X.L., Jeskovsky, M., Jull, A.J.T., Kaizer, J., Nakano, M., Nies, H., Palcsu, L., Papp, L., Pham, M.K., Steier, P., Zhang, L.Y., 2013b. Cesium, iodine and tritium in NW Pacific waters - a comparison of the Fukushima impact with global fallout. Biogeosciences 10, 5481−5496.

Povinec, P.P., Gera, M., Hirose, K., Lujaniene, G., Nakano, M., Plastino, W., 2013c. Dispersion of Fukushima radionuclides in the global atmosphere and the ocean. Appl. Radiat. Isot. 81, 383−392.

Povinec, P.P., Hirose, K., 2015. Fukushima radionuclides in the NW Pacific, and assessment of doses for Japanese and world population from ingestion of seafood. Sci. Rep. 5, 9016. https://doi.org/10.1038/srep09016.

Povinec, P.P., Masarik, J., Kus, P., Holy, K., Jeskovsky, M., Breier, R., Stanicek, J., Sivo, A., Richtarikova, M., Kovacik, A., Szarka, J., Steier, P., Priller, A., 2015a. A new IBA-AMS laboratory at the Comenius University in Bratislava (Slovakia). Nucl. Instrum. Methods Phys. Res. B 342, 321−326.

Povinec, P.P., Masarik, J., Jeskovsky, M., Kaizer, J., Sivo, A., Breier, R., Panik, J., Stanicek, J., Richtarikova, M., Zahoran, M., Zeman, J., 2015b. Development of the accelerator mass spectrometry technology at the Comenius University in Bratislava. Nucl. Instrum. Methods Phys. Res. B 361, 87−94.

Povinec, P.P., et al., 2015c. Joint Bratislava−Prague studies of radiocarbon and uranium in the environment using accelerator mass spectrometry and radiometric methods. J. Radioanal. Nucl. Chem. 304, 67−73.

Povinec, P.P., Pham, M.K., Busto, J., Cerna, C., Degering, D., Hamajima, Y., Holy, K., Hult, M., Jeskovsky, M., Koehler, M., Kováčik, A., Laubenstein, M., Loaiza, P., Mamedov, F., Marquet, C.,

Mott, J., Mullerova, M., Perrot, F., Piquemal, F., Reyss, J.-L., Saakyan, R., Simgen, H., Soule, B., Staníček, J., Sýkora, I., Štekl, I., 2016a. Reference material for natural radionuclides in glass designed for underground experiments. J. Radioanal. Nucl. Chem. 307, 619–626.

Povinec, P.P., Masarik, J., Ješkovský, M., Breier, R., Kaizer, J., Pánik, J., Richtáriková, M., Staníček, J., Šivo, A., Zeman, J., 2016b. Recent results from the AMS/IBA laboratory at the Comenius University in Bratislava. J. Radioanal. Nucl. Chem. 307, 2101–2108.

Povinec, P.P., Liong Wee Kwong, L., Kaizer, J., Molnar, M., Nies, H., Palcsu, L., Papp, L., Pham, M.K., Jean-Baptiste, P., 2017. Impact of the Fukushima accident on tritium, radiocarbon and radiocesium levels in seawater of the western North Pacific Ocean: a comparison with pre-Fukushima situation. J. Environ. Radioact. 166, 56–66.

Povinec, P.P., Benedik, L., Breier, R., Jeskovsky, M., Kaizer, J., Kamenik, J., Kucera, J., Loaiza, P., Nisi, S., Palusova, V., Piquemal, F., 2018. Ultra-sensitive radioanalytical technologies for underground physics experiments. J. Radioanal. Nucl. Chem. (in print).

Purkl, S., Eisenhauer, A., 2003a. A rapid method for alpha-spectrometric analysis of radium isotopes in natural waters using ion-selective membrane technology. Appl. Radiat. Isot. 59, 245–254.

Purkl, S., Eisenhauer, A., 2003b. Solid-phase extraction using EmporeTM Radium Rad Disks to separate radium from thorium. J. Radioanal. Nucl. Chem. 256, 473–480.

Purkl, S., Eisenhauer, A., 2004. Determination of radium isotopes and ^{222}Rn in a groundwater affected coastal area of the Baltic Sea and the underlying sub-sea floor aquifer. Mar. Chem. 87, 137–149.

Rahmstorf, S., 2006. Thermohaline Ocean Circulation. In: Elias, S.A. (Ed.), Encyclopedia of Quaternary Sciences. Elsevier, Amsterdam.

Raisbeck, G.M., Yiou, F., 1999. I-129 in the ocean: origins and applications. Sci. Total Environ. 237/238, 31–41.

Ranebo, Y., Eriksson, M., Tamborini, G., Niagolova, N., Bildstein, O., Betti, M., 2007. The use of SIMS and SEM for the characterization of individual particles with a matrix originating from a nuclear weapon. Microsc. Microanal. 13, 179–190.

Ranebo, Y., Hedberg, P.M.L., Whitehouse, M.J., Ingeneri, K., Littmann, S., 2009. Improved isotopic SIMS measurements of uranium particles for nuclear safeguard purposes. J. Anal. Atom. Spectrom. 24, 277–287.

Ranebo, Y., 2009. Physical Characterization of Actinide Particles - A Study on Novel Techniques for Radiological and Nuclear Safeguard Investigations (Ph.D thesis). Lund University, Sweden.

Ranebo, Y., Niagolova, N., Erdmann, N., Eriksson, M., Tamborini, G., Betti, M., 2010a. Production and characterization of monodisperse plutonium, uranium, and mixed uranium–plutonium particles for nuclear safeguard applications. Anal. Chem. 82, 4055–4062.

Ranebo, Y., Pöllänen, R., Eriksson, M., Siiskonen, T., Niagolova, N., 2010b. Characterization of radioactive particles using non-destructive alpha spectrometry. Appl. Radiat. Isot. 68 (9), 1754–1759.

Reidel, T., Hentig, R.V., Feilitzsch, F.V., 2000. Anticompton spectrometer element studies. Appl. Radiat. Isot. 53, 231–236.

Reyss, J.L., Schmidt, S., Legeleux, F., Bonté, P., 1995. Large, low background well-type detectors for measurements of environmental radioactivity. Nucl. Instrum. Methods Phys. Res., Sect. A 357, 391–397.

Ridgway, K.R., Dunn, J.R., 2007. Observational evidence for a Southern Hemisphere oceanic supergyre. Geophys. Res. Lett. 34, L13612. https://doi.org/10.1029/2007GL030392.

Rigaud, S., Puigcorbé, V., Cámara-Mor, P., Casacuberta, N., Roca-Martí, M., Garcia-Orellana, J., Benitez-Nelson, C.R., Masqué, P., Church, T., 2013. A methods assessment and recommendations for improving calculations and reducing uncertainties in the determination of ^{210}Po and ^{210}Pb activities in seawater. Limnol. Oceanogr. Methods 11, 561–571.

Roberts, M.L., Hamm, R.W., Dingley, K.H., Chiarappa-Zucca, M.L., Love, A.H., 2000. A compact tritium AMS system. Nucl. Instrum. Methods Phys. Res., Sect. B 172, 262–267.

Rodriguez y Baena, A.M., Miquel, J.C., Masque, P., Povinec, P.P., La Rosa, J., 2006. A single vs. double spike approach to improve the accuracy of ^{234}Th measurements in small-volume seawater samples. Mar. Chem. 100, 269–281.

Ross, P., 2008. Analysis of radionuclides using ICPNS. In: Povinec, P.P. (Ed.), Analysis of Environmental Radionuclides. Elsevier, Amsterdam, pp. 295–330.

Rutgers van der Loeff, M., Sarin, M.M., Baskaran, M., Benitez-Nelson, C., Buesseler, K.O., Charette, M., Dai, M., Gustafsson, Ö., Masque, P., Morris, P.J., Orlandini, K., Rodriguez y Baena, A., Savoye, N., Schmidt, S., Turnewitsch, R., Vöge, I., Waples, J.T., 2006. A review of present techniques and methodological advances in analyzing ^{234}Th in aquatic systems. Mar. Chem. 100, 190–212.

Rutgers van der Loeff, M.M., Meyer, R., Rudels, B., Rachor, E., 2002. Resuspension and particle transport in the benthic nepheloid layer in and near Fram Strait in relation to faunal abundances and ^{234}Th depletion. Deep-Sea Res. I 49, 1941–1958.

Rutgers van der Loeff, M.M., Moore, W.S., 1999. Determination of natural radioactive tracers. In: Grasshoff, K., Kremling, K., Ehrhardt, M. (Eds.), Methods of Seawater Analysis. WILEY-VCH, Weinheim, pp. 365–397.

Saito, M., Iwamoto, S., Sumino, T., 2000. Tritium concentration in Aquatic Environment determined by SPE tritium enrichment apparatus. In: Inaba, J., Hisamatsu, S., Ohtouka, Y. (Eds.), Proceedings: Distribution and Speciation of Radionuclides in the Environment. IES Press, Rokkasho.

Sakaguchi, A., Kadokura, A., Steier, P., Takahashi, Y., Shizuma, K., Goshi, M., Nakakuki, T., Yamamoto, M., 2012. Uranium-236 as a new oceanic tracer: a first depth profile in the Japan/East Sea and comparison with caesium-137. Earth Planet. Sci. Lett. 333–334, 165–170.

Salbu, B., Krekling, T., Lind, O.C., Oughton, D.H., Drakopoulos, M., Simionovic, A., Snigireva, I., Snigirev, A., Weitkamp, T., Adams, F., Janssens, K., Kashparov, V.A., 2001. High energy X-ray microscopy for characterisation of fuel particles. Nucl. Instrum. Methods Phys. Res., Sect. A 467–468, 1249–1252.

Salbu, B., Lind, O.C., Skipperud, L., 2004. Radionuclide speciation and its relevance in environmental impact assessments. J. Environ. Radioact. 74, 233–242.

Salbu, B., Janssens, K., Lind, O.C., Proost, K., Gijsels, L., Danesi, P.R., 2005. Oxidation states of uranium in depleted uranium particles from Kuwait. J. Environ. Radioact. 78, 125–135.

Salbu, et al., 2018. Challenges associated with the behaviour of radioactive particles in the environment. J. Environ. Radioact. 186, 101–115.

Sanchez-Cabeza, J.A., Pham, M.K., Povinec, P.P., 2008. IAEA programme on the quality of marine radioactivity data. J. Environ. Radioact. 99, 1680–1686.

Sanchez-Cabeza, J.-A., Liong Wee Kwong, L., Betti, M., 2010. Method to determine ^{226}Ra in small sediment samples by ultralow background liquid scintillation. Anal. Chem. 82, 6847−6853.

Sanchez-Cabeza, J.A., Levy, I., Gastaud, J., Eriksson, M., Osvath, I., Aoyama, M., Povinec, P.P., Komura, K., 2011. Transport of North Pacific ^{137}Cs labeled waters to the South-eastern Atlantic Ocean. Prog. Oceanogr. 89, 31−37.

Santschi, P.H., Schwehr, K.A., 2004. ^{129}I/^{127}I as a new environmental tracer or geochronometer for biogeochemical or hydrodynamic processes in the hydrosphere and geosphere: the central role of organo-iodine. Sci. Total Environ. 321, 257−271.

Schlosser, P., Bayer, R., Boenisch, G., Cooper, L.W., Ekwurzel, B., Jenkins, W.J., Khatiwala, S., Pfirman, S., Smethie, W.M., 1999. Pathways and residence times of dissolved pollutants in the ocean derived from transient tracers and stable isotopes. Sci. Total Environ. 237/238, 15−30.

Schlosser, P., Rhein, M., Roether, W., Kromer, B., 1984. High-precision measurement of oceanic ^{226}Ra. Mar. Chem. 15, 203−216.

Schmidt, A., Schlueter, M., Melles, M., Schubert, M., 2008. Continuous and discrete on-site detection of radon-222 in ground- and surface waters by means of an extraction module. Appl. Radiat. Isot. 66, 1939−1944.

Schmidt, S., Reyss, J.-L., 1996. Radium as internal tracer of Mediterranean outflow water. J. Geophys. Res. 101, 3589−3596.

Scholten, J., Botz, R., Paetsch, H., Stoffers, P., Weinelt, M., 1994. High resolution uranium-series dating of Norwegian-Greenland Sea sediments: ^{230}Th vs. ^{18}O. Mar. Geol. 121, 77−85.

Scholten, J.C., Fietzke, F., Vogler, S., Rutgers van der Loeff, M., Mangini, A., Koeve, W., Waniek, J., Stoffers, P., Antia, A., Kuss, J., 2001. Trapping efficiencies of sediment traps from the deep eastern North Atlantic: the ^{230}Th calibration. Deep Sea Res. II 48, 2383−2408.

Scholten, J.C., Fietzke, J., Mangini, A., Garbe-Schönberg, C.D., Eisenhauer, A., Schneider, R., Stoffers, P., 2008. Advection and scavenging: effects on ^{230}Th and ^{231}Pa distribution off southwest-Africa. Earth Planet. Sci. Lett. 271, 159−169.

Scholten, J.C., Osvath, I., Pham, M.K., 2013. ^{226}Ra measurements through gamma spectrometric counting of radon progenies: how significant is the loss of radon? Mar. Chem. 156, 146−152.

Scholten, J.C., Pham, M.K., Blinova, O., Charette, M.A., Dulaiova, H., Eriksson, M., 2010. Preparation of Mn-fiber standards for the efficiency calibration of the delayed coincidence counting system (RaDeCC). Mar. Chem. 121, 206−214.

Schubert, M., Oberreich, M., Scholten, J., 2018. Preparation of MnO_2 coated fibers for gamma spectrometric measurements - a comparison of four practical approaches. J. Environ. Radioact. 189, 197−201.

Schubert, M., Paschke, A., Lieberman, E., Burnett, W.C., 2012. Air-water partitioning of ^{222}Rn and its dependence on water temperature and salinity. Environ. Sci. Technol. 46, 3905−3911.

Scott, E.M., Dixon, P.M., 2008. Statistical sampling design for radionuclides. In: Povinec, P.P. (Ed.), Analysis of Environmental Radionuclides. Elsevier, Amsterdam, pp. 3−16.

Shanks, R.P., Freeman, S.P.H.T., 2015. 160keV ^{26}Al-AMS with a single-stage accelerator mass spectrometer. Nucl. Instrum. Methods Phys. Res. B 361, 307−310.

Sharabi, G., Lazar, B., Kolodny, Y., Teplyakov, N., Halicz, L., 2010. High precision determination of ^{228}Ra and ^{228}Ra/^{226}Ra isotope ratio in natural waters by MC-ICPMS. Int. J. Mass Spectrom. 294, 112−115.

Shen, C.-C., Cheng, H., Edwards, R.L., Moran, S.B., Edmonds, H.N., Hoff, J.A., Thomas, R.B., 2003. Measurement of attogram quantities of ^{231}Pa in dissolved and particulate fractions of seawater by isotope dilution thermal ionization mass spectroscopy. Anal. Chem. 75, 1075−1079.

Shevchenko, S.V., 2004. On the uncertainty in activity measurements for samples containing "hot particles". Appl. Radiat. Isot. 61, 1303−1306.

Siiskonen, T., Pöllänen, R., 2004. Simulation of alpha particle spectra from aerosol samples. Appl. Radiat. Isot. 60, 947−953.

Simon, R., Nazmov, V., Reznikova, E., Mohr, J., Saile, V., 2006. Hard X-ray imaging and microscopy with lithographic CRL developed at ANKA synchrotron radiation facility. Proc. 8th Int. Conf. X-ray Microscopy IPAP Conf. Ser. 7, 115−116.

Simons, D.S., 1986. Single particle standards for isotopic measurements of uranium by secondary ion mass spectrometry. J. Trace Microprobe Tech. 4, 185−195.

Sjöblom, K.-L., Salo, A., Michael Bewers, J., Cooper, J., Dyer, R.S., Lynn, N.M., Mount, M.E., Woodhead, D., 1999. International Arctic seas assessment project. Sci. Total Environ. 237−238, 153−166.

Skog, G., 2007. The single stage AMS machine at Lund University: Status report. Nuclear Instruments and Methods in Physics Research B259, 1−6.

Smith, K.J., León Vintró, L., Mitchell, P.I., Bally de Bois, P., Boust, D., 2004. Uranium-thorium disequilibrium in north-east Atlantic waters. J. Environ. Radioact. 74, 199−210.

Somayajulu, B.L.K., Bhushan, R., Sarkar, A., Burr, G.S., Jull, A.J.T., 1999. Sediment deposition rates on the continental margins of the eastern Arabian Sea using ^{210}Pb, ^{137}Cs and ^{14}C. Sci. Total Environ. 237/238, 429−439.

Soukissian, T.H., Chronis, G.T., Nittis, K., 1999. POSEIDON: operational marine monitoring system for Greek seas. Sea Technol. 40, 31−37.

Stirling, C.H., Andersen, M.B., 2009. Uranium-series dating of fossil coral reefs: extending the sea-level record beyond the last glacial cycle. Earth Planet. Sci. Lett. 284, 269−283.

Stuiver, M., Ostlund, H.G., 1983. GEOSECS Indian ocean and mediterranean radiocarbon. Radiocarbon 25, 1−29.

Sturup, S., Dahlgaard, H., Nielsen, S.C., 1998. High resolution inductively coupled plasma mass spectrometry for the trace determination of plutonium isotopes and isotope ratios in environmental samples. J. Anal. Atom. Spectrom. 13, 1321−1326.

Suter, M., Jacob, S.W.A., Synal, H.A., 2000. Tandem AMS at sub-MeV energies − status and prospects. Nucl. Instrum. Methods Phys. Res., Sect. B 172, 144−151.

Suter, M., Müller, A.M., Alfimov, V., Christl, M., Schulze-König, T., Kubik, P.W., Synal, H.-A., Vockenhuber, C., Wacker, L., 2010. Are compact ams facilities a competitive alternative to larger tandem accelerators? Radiocarbon 52, 319−330.

Sýkora, I., Jesškovskyý, M., Janik, R., Holyý, K., Chudý, M., Povinec, P.P., 2008. Low-level single and coincidence gamma-ray spectrometry. J. Radioanal. Nucl. Chem. 276, 779−787.

Synal, H.-A., Stacker, M., Suter, M., 2007. MICADAS: a new compact radiocarbon AMS system. Nucl. Instrum. Methods Phys. Res. B 259, 7−13.

Taylor, C.B., 1977. Tritium enrichment of environmental waters by electrolysis: development of cathodes exhibiting high isotopic separation and precise measurement of tritium enrichment factors. In: Povinec, P., Usačev, S. (Eds.), Low-radioactivity Measurements and Applications. SPN, Bratislava, pp. 131−140.

Tomczak, M., Godfrey, J.S., 1994. Regional Oceanography: An Introduction. Pergamon Press, New York, p. 422.

Treacy Jr., D.J., Knies, D.L., Grabowski, K.S., Hubler, G.K., DeTurck, T.M., Mignerey, A.C., 2000. Determination of ^{32}Si by AMS at the US Naval research laboratory. Nucl. Instrum. Methods Phys. Res., Sect. B 172, 321−327.

Tsabaris, C., Patiris, D.L., Karageorgis, A.P., Eleftheriou, G., Papadopoulos, V.P., Georgopoulos, D., Papathanassiou, E., Povinec, P.P., 2012. In-situ radionuclide characterization of a submarine groundwater discharge site at Kalogria Bay, Stoupa, Greece. J. Environ. Radioact. 108, 50−59.

Tsumune, D., Aoyama, M., Hirose, K., Bryan, F.O., Lindsay, K., Danabasoglu, G., 2011. Transport of ^{137}Cs in the Southern Hemisphere in an ocean general circulation model. Prog. Oceanogr. 89, 38−48.

Tsumune, D., et al., 2012. Distribution of oceanic ^{137}Cs from the Fukushima Daiichi Nuclear Power Plant simulated numerically by a regional ocean model. J. Environ. Radioact. 111, 100−108.

Tuniz, C., Bird, J.R., Fink, D., Herzog, G.F., 1998. Accelerator Mass Spectrometry: Ultrasensitive Analysis for Global Science. CRC Press, Boca Raton, p. 371.

Turnewitsch, R., Witte, U., Graf, G., 2000. Bioturbation in the abyssal Arabian Sea: influence of fauna and food supply. Deep-Sea Res. II 47, 2877−2911.

Turunen, J., Peräjärvi, K., Pöllänen, R., Toivonen, H., 2009. PANDA—a novel instrument for non-destructive sample analysis. Nucl. Instrum. Methods Phys. Res., Sect. A 613, 177−183.

UNSCEAR, United Nations Scientific Committee on the Effects of Atomic Radiation, 2000. Sources and Effects of Ionizing Radiation. United Nations, New York.

Van Beek, P., Souhaut, M., Reyss, J.L., 2010. Measuring the radium quartet (^{228}Ra, ^{226}Ra, ^{224}Ra, ^{223}Ra) in seawater samples using gamma spectrometry. J. Environ. Radioact. 101, 521−529.

Van Calsteren, P., Thomas, L., 2006. Uranium-series dating applications in natural environmental science. Earth Sci. Rev. 75, 155.

Van Put, P., Debauche, A., De Lellis, C., Adam, V., 2004. Performance level of an autonomous system of continuous monitoring of radioactivity in seawater. J. Environ. Radioact. 72, 177−186.

Vickerman, J.C., 1989. The SIMS phenomenon − the experimental parameters. In: Vickerman, J.C., Brown, A., Reed, N.M. (Eds.), Secondary Ion Mass Spectrometry − Principles and Applications. Oxford University Press, Oxford, U.S., New York.

Vogler, S., Scholten, J., Rutgers van der Loeff, M.M., Mangini, A., 1998. ^{230}Th in the eastern North Atlantic: the importance of water mass ventilation in the balance of ^{230}Th. Earth Planet. Sci. Lett. 156, 61−74.

Vojtyla, P., Povinec, P.P., 2000. A Monte Carlo simulation of background characteristics of low-level HPGe detectors. Appl. Radiat. Isot. 53, 185−190.

Vojtyla, P., Povinec, P.P., 2006. Monte Carlo simulation of the muon-induced background of an anti-Compton gamma-ray spectrometer placed in a surface and underground laboratory. Radioact. Environ. 8, 529−537.

Waska, H., Kim, S., Kim, G., Peterson, R.N., Burnett, W.C., 2008. An efficient and simple method for measuring ^{226}Ra using the scintillation cell in a delayed coincidence counting system (RaDeCC). J. Environ. Radioact. 99, 1859−1865.

Wedekind, Ch., Schilling, G., Grüttmüller, M., Becker, K., 2000. Marineenvironmental radioactivity monitoring by "in-situ" radiation detection. Kerntechnik 65, 190−194.

Wegrzynek, D., Markowicz, A., Bamford, S., Chinea-Cano, E., Bogovac, M., 2005. Micro-beam X-ray fluorescence and absorption imaging techniques at the IAEA Laboratories. Nucl. Instrum. Methods Phys. Res., Sect. B 231, 176−182.

Weiss, W., Roether, W., 1980. The rates of tritium input to the world oceans. Earth Planet. Sci. Lett. 49, 435−436.

Wendt, K., Trautmann, N., Bushaw, B.A., 2000. Resonant laser ionization mass spectrometry: an alternative to AMS? Nucl. Instrum. Methods Phys. Res., Sect. B 172, 162−169.

White, F.A., Wood, G.M., 1988. Mass Spectrometry − Applications in Science and Engineering. Wiley-Interscience, New York.

Wilcken, K.M., Freeman, S.P.H.T., Xu, S., Dougans, A., 2010. Attempted positive ion radiocarbon AMS. Nucl. Instrum. Methods Phys. Res. B 268, 712−714.

Wyse, E., Lee, S.-H., La Rosa, J.J., Povinec, P.P., de Mora, S.J., 2001. ICP-sector field mass spectrometry analysis of plutonium isotopes: recognizing and resolving potential interferences. J. Anal. Atom. Spectrom. 16, 1107−1111.

Yoneda, M., Kitagawa, H., Van Der Plicht, J., Uchida, M., Tanaka, A., Uehiro, T., Shibata, Y., Ohno, T., 2000. Pre-bomb marine reservoir ages in the western north Pacific. Nucl. Instrum. Methods Phys. Res., Sect. B 172, 377−381. Preliminary result on Kyoto University collection.

You, Y., 2000. Implications of the deep circulation and ventilation of the Indian ocean on the renewal mechanism of North Atlantic deep water. J. Geophys. Res. 105, 23895−23926.

Yu, E.-F., Francois, R., Bacon, M.P., 1996. Similar rates of modern and last-glacial ocean thermohaline circulation inferred from radiochemical data. Nature 379, 689−694.

Zeissler, C.J., 1997. Comparison of semiconductor pixel array, phosphor plate, and track-etch detectors for alpha autoradiography. Nucl. Instrum. Methods Phys. Res., Sect. A 392, 249.

Zhao, X.-L., Kieser, W.E., Litherland, A.E., Smith, J.N., Fowler, S.W., Miquel, J.-C., 1999. The AMS analysis of ^{129}I and ^{135}Cs: Oceanographic tracing and pollution source identification. IAEA-SM354/105. IAEA, Vienna, pp. 243−248.

Zvara, I., Povinec, P., Sykora, I., 1994. Determination of very low levels of radioactivity. Pure Appl. Chem. 66, 2537−2586.

Pavel P. Povinec



Prof. RNDr. **Pavel Povinec**, DrSc, obtained his PhD degree in physics from the Comenius University in Bratislava in 1974. He worked at the Department of Nuclear Physics of the Faculty of Mathematics and Physics of the Comenius University as Associated Professor (1978) and Professor of physics (1984), also as Head of the Department (1981−92), focusing on developments of radiometric methods for analysis of radionuclides at very low levels with wide applications in nuclear (rare nuclear decays), environmental (radionuclides as tracers, radiocarbon dating), and space (radionuclides in lunar samples and meteorites) physics. From 1993 to 2005, he worked at the IAEA's Marine Environment Laboratories in Monaco as Head of the Radiometrics Laboratory responsible for the development of radiometric (including underground laboratory) and mass spectrometry methods (ICP-MS, AMS) for marine radioactivity studies. He has led several international projects on assessment of dumping of radioactive wastes, on impacts of nuclear weapons test sites, on worldwide marine radioactivity studies (WOMARS), on submarine groundwater discharge studies, on the development of global marine radioactivity databases (GLOMARD/MARIS), etc. After his return to the Comenius University, he established at the Faculty of Mathematics, Physics and Informatics the Centre for Nuclear and Accelerator Technologies (CENTA) focusing on the development of IBA and AMS methods and their wide applications in nuclear, material, environmental, and biomedical sciences. He supervised 26 PhD students, published over 20 books and book chapters and over 700 referred papers with over 13,000 citations, organized over 20 international conferences, and delivered over 50 invited talks.

Mats Eriksson



Associate Professor **Mats Eriksson** received his PhD in radiation physics from the Lund University (Sweden) in 2002 and became a docent in radiation physics at Linköping University in 2011. He has worked at Risoe National Laboratory in Roskilde, Denmark (1998−2003), at the Institute for Transuranic Elements, EC-JRC, in Karlsruhe, Germany (2003−05), at the IAEA's Environmental Laboratories in Monaco (2005−12), and presently he chairs his time between the Linköping University and the Swedish Radiation Safety Authority (SSM) in Stockholm. His research interests have been on environmental radioactivity and radioanalytical methods, specifically on investigations of contaminated marine environment after accidents involving nuclear weapons, as well as on radioactive particles to study the behavior of actinides in natural conditions. A wide range of analytical techniques has been applied in these studies, including traditional radiometric methods (gamma- and alpha-spectrometry), mass spectrometric techniques (ICP-MS, AMS, SIMS) and synchrotron light-based techniques (μ-XRF, μ-XANES) with the aim to study physical and chemical properties of the contamination.

Jan Scholten



Dr. **Jan Christoph Scholten** received his PhD from the University of Heidelberg (Germany) in 1988. From 2005 to 2011, he worked at the IAEA's Environment Laboratory in Monaco, and he is now a senior research scientist at the Institute of Geosciences, Kiel University (Germany). His research interests focus on the application of natural radionuclides in marine process studies. For age dating of carbonate-poor sediments from high latitudes, he applied the thorium-230 excess method. Later, he concentrated his work on the distribution and behavior of thorium and protactinium in seawater of the Arctic, North Atlantic, and Southeast Atlantic Oceans, and in the Arabian Sea. The application of thorium-230 to calibrate the particle flux intercepted by sediment traps was one of his most recognized studies. In recent years, he has focused his research on submarine groundwater discharge and how radium isotopes and radon can be used for the detection and quantification of this process in different coastal settings.

Maria Betti



Dr. **Maria Betti** obtained her PhD in chemistry from the University of Pisa in 1984 with a specialization in environmental, instrumental and radiochemistry. From 1985 to 1991, she served at the Italian National Research Council and at the Department of Chemistry and Industrial Chemistry of the University of Pisa, where she has continued to lecture until 2012. She has research experience at different research laboratories in Europe and in the United States. As of March 1, 1991, she joined the European Commission as Head of the Analytical Chemistry Sector at the Institute for Transuranium Elements (DG Joint Research Centre, JRC) in Karlsruhe. In March 2008, she was appointed as Director of the IAEA Marine Environment Laboratories in Monaco, as seconded in the interest of the service from the European Commission. As of October 1, 2012, she rejoined the EC as Director of the Institute for Environment and Sustainability (IES) at the DG JRC, located in Ispra. As of April 16, 2015, she is Director of the EC Joint Research Centre, former Institute for Transuranium Elements, and since July 2016 Directorate G for Nuclear Safety and Security and Director of the JRC Karlsruhe site owning responsibility of the nuclear license of the site. Maria Betti is author of about 200 peer-reviewed publications in international journals with high impact of factors in the field of analytical chemistry, radiochemistry, environmental and instrumental chemistry, and nuclear safeguards. In 2012, she was the international winner of the "Prix Monte-Carlo Femme de l'Année" for the establishment after the RIO+20 summit of the International Centre on Ocean Acidification at the IAEA office in the Principality of Monaco. From 2004 to 2008, she chaired the JRC Women and Science Network. In November 2016, Maria Betti has been honored with the magnificent distinction by the Ordre de Saint Charles (Principality of Monaco).

Chapter 6

PERPUSTAKAAN PRIBADI AN-NUR SUNARYA

Cherenkov counting

Michael F. L'Annunziata[1], Željko Grahek[2] and Nataša Todorović[3]

[1]*The Montague Group, Oceanside, CA, United States;* [2]*Laboratory for Radioecology, Ruđer Bošković Institute, Zagreb, Croatia;* [3]*University of Novi Sad, Faculty of Sciences, Department of Physics, Nuclear Physics Laboratory, Novi Sad, Serbia*

Chapter outline

I. Introduction 394
II. Discovery of Cherenkov radiation 396
III. Theory and properties of Cherenkov radiation 396
A. Interpretation by Il'ja M. Frank and Igor Y. Tamm 397
B. Quantum mechanical interpretation 399
C. Threshold condition 401
D. Threshold energies 402
E. Photon spatial asymmetry 404
F. Photon spectrum and radiation intensity 407
G. Cherenkov photon emissions and counter geometry 410
IV. Quenching and quench correction 410
A. Internal standardization 411
B. Sample channels ratio 411
C. Sample spectrum quench indicating parameters 413
1. Counting region 413
2. Quench correction 413
D. External standard quench correction 415
V. Cherenkov counting parameters 418
A. Sample volume 418
B. Counting vials 420
C. Wavelength shifters 426
D. Ionic liquids 429
E. Refractive index 429
F. Sample physical state 431
VI. Cherenkov counting in the dry state 431
VII. Radionuclide analysis with silica aerogels 434
VIII. Cherenkov counting in microplate format 437
A. Sample-to-sample cross-talk 437
B. Sample volume effects 438
C. Quench correction 438
IX. Multiple radionuclide analysis 439
A. Sequential Cherenkov and liquid scintillation analysis 439
1. Sequential Cherenkov counting and efficiency tracing 440
2. $^{89}Sr + {}^{90}Sr(^{90}Y)$ analysis by Cherenkov counting with subsequent LSA 441
B. Cherenkov analysis with wavelength shifters 444
X. Radionuclide standardization 445
A. Cherenkov counting efficiency—detection probability function, CHEREN 446
B. Anisotropy detection model—CHEREN2 448
C. TDCR Cherenkov counting 450
1. Anisotropy detection model 450
2. Stochastic GEANT4 model in Cherenkov counting 453
D. Standardization of ^{210}Pb 455
E. Routine TDCR activity analysis 456
XI. Gamma ray detection and discrimination 457
XII. Particle identification 460
A. Threshold and differential Cherenkov counters 461
B. Mirror- or lens-focused RICH counters 464
C. Proximity-focusing RICH counters 466
D. Time-of-propagation Cherenkov counters 471
E. Time-of-flight Cherenkov counters 472
XIII. Neutrino detection and measurement 476
A. Large light-water Cherenkov detectors 476
B. Large D_2O neutrino target 477
C. Neutrino telescopes in lake and ocean floors 478
D. Neutrino astronomy in Artic ice 482
E. Radio Cherenkov counting 483
XIV. Applications in radionuclide analysis 485
A. Phosphorus-32 485
B. Strontium-89 and Strontium-90 (Yttrium-90) 491
1. Cherenkov counting of ^{89}Sr with $^{90}Sr(^{90}Y)$ 491
2. Sequential Cherenkov counting and liquid scintillation analysis 495
C. Strontium-90(yttrium-90) exclusive of strontium-89 498
1. Chemical separation and Cherenkov counting of ^{90}Y 498
2. Chemical separation and Cherenkov counting of ^{90}Sr with ^{90}Y ingrowth 500
D. Yttrium-90 502
E. Other applications 502
XV. Advantages and disadvantages in radionuclide analysis 508
XVI. Recommendations in radionuclide analysis 509
References 509
Further reading 528
Michael F. L'Annunziata 529
Željko Grahek 529
Nataša Todorović 530

Handbook of Radioactivity Analysis: Volume 2. https://doi.org/10.1016/B978-0-12-814395-7.00006-4
Copyright © 2020 Elsevier Inc. All rights reserved.

I. Introduction

Photons of visible radiation are produced when a charged particle travels through a transparent medium at a speed greater than the speed of light in that medium. The medium may be any liquid or solid provided it is transparent. These photons are referred to as Cherenkov radiation in honor of the Russian physicist Pavel A. Čerenkov for his basic research and discovery of the properties of this unique radiation (see Čerenkov, 1934a, 1937d). The process, that gives rise to Cherenkov photons, is referred to as the Cherenkov effect. In the scientific literature, four variations of the contemporary spelling or naming of Čerenkov radiation can be found, namely, (1) *Čerenkov radiation* after the Russian, which is the spelling used by Pavel Čerenkov in most of his original papers (Čerenkov, 1934a,b, 1936, 1937a–d, 1938a–c); (2) *Vavilov–Čerenkov radiation*, in honor also of Sergei Ivanovich Vavilov (1891–1951), who was the doctoral research advisor to Pavel Čerenkov during the pioneering discoveries of Cerenkov radiation; (3) *Cherenkov radiation*, which provides the English pronunciation from the Russian Č. This is also the spelling used by Cherenkov (1986) in his last publication; and it is the spelling adopted by the Nobel Foundation (http://nobelprize.org/index.html); and (4) *Cerenkov radiation*, which is the anglicized version. All four versions of the spelling are found in the current scientific literature. Throughout this chapter, the writer will adopt the spelling *Cherenkov*, for the following reasons: (1) it conforms with that used by Pavel Cherenkov in his last paper (Cherenkov, 1986) entitled "At the Threshold of Discovery", that appeared in the journal *Nuclear Instruments and Methods in Physics Research*, (2) it is the spelling adopted by *Chemical Abstracts*, (3) it is the spelling adopted by the Nobel Foundation, and (4) it is the spelling adopted most often by authors of papers in the journal *Nuclear Instruments and Methods in Physics Research*.

The Cherenkov effect and the resulting radiation produced by a charged particle traveling in a transparent medium at a velocity exceeding the speed of light in that medium were predicted theoretically as early as 1888 by Heaviside (1888, 1889, 1892, 1899, 1912a,b), but long forgotten until the radiation was discovered finally by Cherenkov (see Čerenkov, 1934a,b) and interpreted by Frank and Tamm (1937). Heaviside's early prediction was based on a traveling point charge; as the electron was discovered by J.J. Thompson years later in 1897. Govorkov (2005) reviewed the historical significance of Heaviside's prediction, namely, that Heaviside first predicted theoretically that a point charge (*e.g.*, electron) would produce a conical wavefront if it were to travel at a speed greater than the speed of light in a medium. Heaviside's prediction was before Einstein's theory of relativity, which holds that matter cannot travel faster than light in a vacuum; however, matter can travel faster than light in a medium. In the time of Heaviside, even outer space was not considered to be a vacuum but to consist of an "ether", and therefore, according to Heaviside, the conical wavefront would be produced in the "ether" as well as any other medium, provided the point charge travels at a speed exceeding that of light in that medium. In the words of Govorkov (2005),

> *"A genius, Heaviside was half a century in advance of his time in his calculations and predictions, but unfortunately he was not understood by his contemporaries. His works were forgotten, and scientists had to start from the beginning, this time from experiment"* [i.e., *the experiments and discovery by Cherenkov (see Čerenkov, 1934a,b, 1936, 1937a–d, 1938a–c)*].

The German physicist, Sommerfeld (1904), also predicted a radiation wavefront that would be produced by an electron traveling at a speed exceeding the speed of light in a medium. Sommerfeld's prediction was with no apparent knowledge of the previous theories of Heaviside. Electrons, as well as other charged particles, with sufficient energy can indeed travel faster than light in media where light travels at speeds less than its speed in a vacuum. The speed of light in a transparent medium is defined by the index of refraction, n, of the medium where $n = c/v$ and c is the velocity of light in a vacuum and v the velocity of light in the medium. Heaviside (1912a) had even calculated the geometry and angle of emission of the electromagnetic wavefront relative to the axis of travel of the charged particle. Also, Afanasiev et al. (1999) explain that the early theoretical predictions of Heaviside, namely, that a conical radiation wavefront would arise when the point charge velocity exceeds the light velocity in a medium, had been forgotten by the scientific community until 1974 when they were revived by Tyapkin (1974) and Kaiser (1974).

Cherenkov radiation was observed by Marie Curie in 1910. She observed in a dark room a pale blue light from concentrated radium solutions as related in a biography by her daughter Curie (1941). The radiation was researched by Lucien Mallet (1926, 1928, 1929). He found that the light would be emitted by a variety of transparent bodies when exposed to radioactive sources; however, the unique origin and anisotropic properties of the radiation were yet to be discovered. It was not until the extensive work of Cherenkov (see Čerenkov, 1934–38) and the theoretical interpretations of Frank and Tamm (1937), who shared the 1958 Nobel Prize in Physics with Cherenkov, was the origin and properties of Cherenkov radiation finally understood. Comprehensive treatments on the theory, properties, and history of Cherenkov radiation are available from Frank (1960), Jelley (1958, 1961), Ritson (1961) and in a book by the writer (L'Annunziata, 2016). A concise overview will be provided in this chapter.

Cherenkov radiation consists of a continuous spectrum of wavelengths extending from the ultraviolet region into the visible part of the spectrum peaking at about 420 nm (see Kulcsar et al., 1982; Claus et al., 1987). Only a negligible amount of photon emissions is found in the infrared or microwave regions.

Cherenkov photon emission is the result of local polarization along the path of travel of the charged particle with the emission of electromagnetic radiation when the polarized molecules return to their original states (Gruhn and Ogle, 1980). This has been described by Marshall (1952) as the electromagnetic "shock" wave that is analogous to the acoustical shock wave or sonic boom created by supersonic aircraft. The Cherenkov radiation is propagated as a conical wave front, that is, the radiation is emitted as a cone in the direction of particle travel, as illustrated in Fig. 6.1. The figure illustrates the effect of a high-energy proton traveling through a transparent medium at a speed greater than the speed of light in the medium; and similar effects are produced by other high-energy charged particles, such as electrons and beta-particles when their energy is sufficient to provide them with speeds exceeding that of light in transparent media.

Cherenkov radiation, when produced at significant levels, can be employed for the efficient measurement of radioactivity. This was first demonstrated by Belcher (1953), who used a liquid-nitrogen cooled single photomultiplier to measure Cherenkov radiation intensity in terms of count rates per mCi of various radionuclides in aqueous solution. However, it was not until dual photomultiplier liquid scintillation analyzers became available commercially and in widespread use in the early 1960s, did practical research into Cherenkov counting for the measurement of radioactivity begin. Although the production of Cherenkov radiation does not involve the scintillation phenomenon, a conventional liquid scintillation counter can detect and count Cherenkov photons emitted from a given sample in a standard counting vial. Certain radionuclides may be counted in water or other suitable transparent medium without the use of scintillation fluor or any other chemical reagents. They may even be counted in the dry state, albeit at a diminished counting efficiency, where the glass or plastic vial wall containing the sample acts as the transparent medium for the production of Cherenkov photons.

Cherenkov counting of radionuclides in an aqueous medium (*i.e.*, without scintillation cocktail) leaves the sample in an unadulterated state that maintains the sample suitable for any other chemical tests deemed necessary in a given research study. This technique is popular for the assay of relatively high-energy β-particle-emitting nuclides. The threshold β-particle energy for the production of Cherenkov radiation is discussed subsequently in this chapter. The ease of sample preparation, low cost (no need for fluors and fluor solvents), and the automated counting available with a liquid scintillation analyzer are among the principal reasons for the widespread use of this counting method. The Cherenkov effect is also an important tool in nuclear particle physics including the detection, measurement, and discrimination of muons, pions, kaons, and protons, among others. Even neutrinos, which carry no charge and cannot produce the Cherenkov effect, are detected indirectly by the Cherenkov effect produced through neutrino-electron elastic scattering (ES) interactions, and charged current (CC) and neutral current (NC) reactions with detector nuclei. The principles of the Cherenkov effect and its application to the detection and measurement of radionuclides and nuclear particles will be discussed in this chapter.

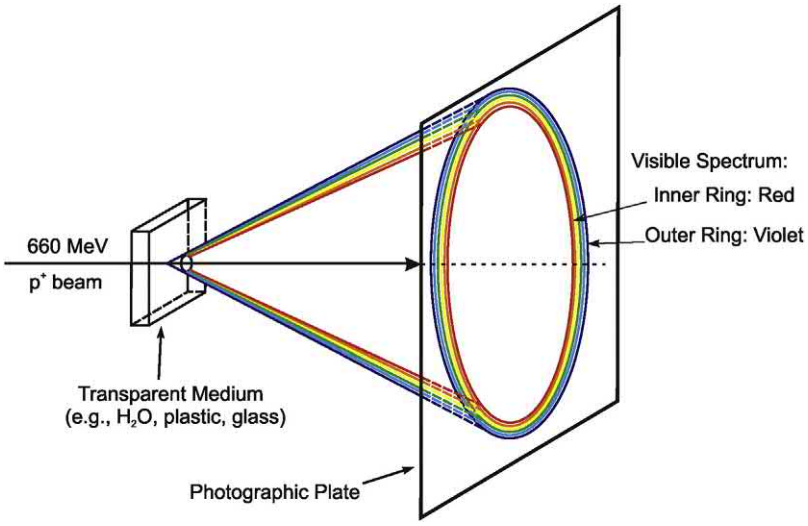


FIGURE 6.1 Diagram of the Cherenkov radiation cone and an experimental arrangement for obtaining photographs of the cone section in the plane of a photographic plate placed perpendicular to the path of high-speed (660 MeV) protons in an accelerator beam. Color of the cone and ring, which is observable in electronic format was added by the writer according to the depiction provided by Govorkov (2005). *From Cherenkov's Nobel Lecture (1958), printed with permission © 1958 The Nobel Foundation.*

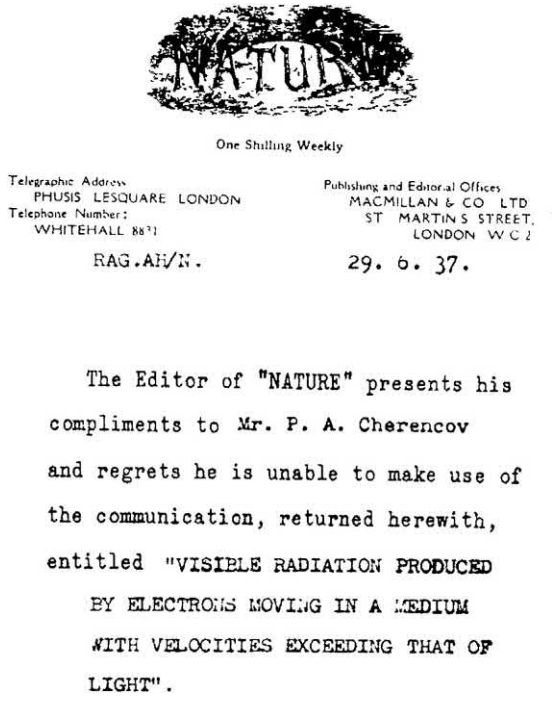
II. Discovery of Cherenkov radiation

In 1933 Sergei I. Vavilov was Head of the USSR State Optical Institute and Head of the Academy of Science Physics Department in Leningrad (now Saint Petersburg, Russia) and since 1934 was named the P.N. Lebedev Institute of Physics of the Russian Academy of Sciences. He organized teams of young scientists to carry out research in neutron physics and luminescence. Sergei Vavilov was then one of the world's leading scientists in the field of luminescence. At that time, Vavilov believed the glow of blue light emitted by highly radioactive solutions was due to luminescence. Vavilov had a doctoral student whose name was Pavel Alekseyevich Cherenkov. For his doctoral research, Vavilov proposed that Pavel Cherenkov work on the topic of "*The luminescence of uranyl salt solutions under the influence of hard gamma radiation*". High-energy gamma radiation would induce the production of a weak blue light from solutions of uranium salts, and it was thought, that this might be due to the occurrence of luminescence. Vavilov and Cherenkov started the research to investigate what they thought was luminescence. Sophisticated photomultiplier detectors were not available in 1933; however, Vavilov had developed a visual method of measuring low light intensities very close to the thresholds of human vision. To observe and measure the intensities of this weak light, Cherenkov had to adapt his eyes by remaining in a dark room for an hour or more before taking any measurements.

Cherenkov found that the weak light was emitted not only from the uranium salt in sulfuric acid solution when irradiated with strong gamma rays, but that there was a background glow from the solvent itself, that is, when sulfuric acid solution without the uranium solute was irradiated with the hard gamma-rays. Bolotovski et al. (2004) give an account that Vavilov asked Cherenkov to investigate other solvents that were highly purified to see if these also emitted light when irradiated. Cherenkov determined that 16 different pure solvents produced about the same intensity of blue light when these were irradiated with the hard gamma radiation. Various attempts to quench the effect were unsuccessful, which provided evidence that the phenomenon was not fluorescence. What was occurring was obvious to them at this point. This was not fluorescence, but that the light emission was a new phenomenon of origin yet unknown to mankind. They had discovered a new radiation, which they reported in two papers back-to-back in the 1934 Proceedings of the USSR Academy of Sciences (Čerenkov, 1934a,b; Vavilov, 1934). In his paper, Vavilov (1934) provided a preliminary theory on the origin of the radiation. He proposed that Compton electrons produced by the hard gamma radiation would yield a type of Bremsstrahlung radiation. He was correct in the conclusion that the mysterious light was being produced by the Compton electrons; however, the mysterious light was not the result of Bremsstrahlung. It was yet of unknown origin. It would not be until a few years later (1935–38) with more research by Čerenkov (1936, 1937a–d, 1938a–c) and theoretical calculations by Frank and Tamm (1937), would it be understood finally that the new radiation was produced by charged particles when these particles had sufficient energy to travel at a speed in excess of the speed of light in the transparent medium. The new radiation soon became known as "Vavilov–Cherenkov radiation". Pavel Cherenkov, Il'ja Frank, and Igor Tamm shared the Nobel Prize in Physics in 1958 "for the discovery and interpretation of the Cherenkov Effect". Sergei Vavilov would have shared in the prize had he not passed away several years before. Very interesting accounts of the life and works of Pavel Cherenkov are provided in papers by Govorkov (2005), Belousov (2006), and by his daughter Cherenkova (2008). A very detailed treatment of the life and pioneering experiments of Pavel A. Cherenkov and the works of Il'ja M. Frank and Igor Y. Tamm is provided in a previous book by the writer (L'Annunziata, 2016).

III. Theory and properties of Cherenkov radiation

Some of the unique properties of the radiation discovered by Čerenkov (1936, 1937a–d, 1938a–c) were (1) the radiation was produced by charged particles, (2) the intensity of the radiation was a function of the particle energy and the properties of the solution (*i.e.*, its index of refraction), (3) the light was polarized and the emission of the light was asymmetric, that is, it was emitted only in the direction of travel of the charged particles, (4) the radiation was emitted at specific angles to the direction of travel of the charged particles and the angle of emission was a function of the particle velocity (*i.e.*, particle energy) and the index of refraction of the medium. Frank and Tamm (1937) analyzed Cherenkov's findings and concluded, as described subsequently, that this phenomenon could only occur if the charged particle traveled in the transparent medium at a speed in excess of the speed of light in that medium. Cherenkov wrote up his findings in a paper submitted to the journal *Nature*, which was rejected by the journal in a letter dated 19 June 1937, illustrated in Fig. 6.2, as there was an atmosphere of distrust among some of the scientific community concerning this new theory. After consulting with Vavilov on the rejection by *Nature*, Cherenkov transferred the paper without any changes to a new envelope addressed to *Physical Review* published by the American Physical Society; and the paper was published in the next issue of *Physical Review* (see Čerenkov, 1937d).



NATURE

One Shilling Weekly

Telegraphic Address:
PHUSIS LESQUARE LONDON
Telephone Number:
WHITEHALL 8831

Publishing and Editorial Offices
MACMILLAN & CO LTD
ST MARTIN'S STREET,
LONDON W C 2

RAG.AH/N. 29. 6. 37.

The Editor of "NATURE" presents his compliments to Mr. P. A. Cherencov and regrets he is unable to make use of the communication, returned herewith, entitled "VISIBLE RADIATION PRODUCED BY ELECTRONS MOVING IN A MEDIUM WITH VELOCITIES EXCEEDING THAT OF LIGHT".

FIGURE 6.2 Letter to Pavel Cherenkov from the editors of the journal *Nature* rejecting his historic findings for publication. *From Cherenkov (1986), reprinted with permission from Elsevier © 1986.*

A. Interpretation by Il'ja M. Frank and Igor Y. Tamm

Once it was understood that Vavilov and Cherenkov had discovered a new and previously unknown phenomenon, Il'ja Frank and Igor Tamm of the Theoretical Physics Division of the P.N. Lebedev Institute of Physics in Moscow took notice and went to work on the interpretation of this new phenomenon. Their findings were published in a joint paper entitled "*Coherent Visible Radiation of Fast Electrons Passing through Matter*" (Frank and Tamm, 1937). They explained the Cherenkov effect is caused by a charged particle traveling in a medium at a speed in excess of the speed of light in that medium. It was known from Einstein's theory of relativity that matter could not travel in excess of the speed of light in a vacuum ($c = 2.99 \times 10^8$ m/s); however, in a gas, liquid, or solid medium, the velocity of light will be less than its velocity in a vacuum and, an elementary charged particle with sufficient energy could travel in such media at speeds exceeding that of light. The charged particle in passing through the electron clouds of a medium would create an electromagnetic shock wave analogous to that of a "sonic boom" created by a jet airplane or projectile traveling in the atmosphere at a speed exceeding that of sound. In the words of Frank and Tamm (1937):

> *We shall consider an electron moving with constant velocity v along [an] axis through a medium characterized by its index of refraction n. The field of the electron may be considered as the result of superposition of spherical waves of retarded potential, which are being continually emitted by the moving electron and are propagated with the velocity* (c/n) *[See Fig. 6.3]. It is easy to see that all these consecutive waves emitted will be in phase along the directions making the angle* θ *with the axis of motion [of the particle], if only v, n, and* θ *do satisfy the condition*

$$\cos\theta = \frac{1}{\beta n} \tag{6.1}$$

> *where* $\beta = v/c$. *Thus there will be a radiation emitted in the direction* θ, *whereas the interference of waves will prevent radiation in any other direction.*

The term β of Eq. (6.1) is the relative phase velocity of the charged particle, that is, the velocity of the particle, v, divided by the speed of light in a vacuum, c. Frank and Tamm (1937) demonstrated that the above condition described by Eq. (6.1) can be fulfilled only if

$$\beta n > 1 \tag{6.2}$$

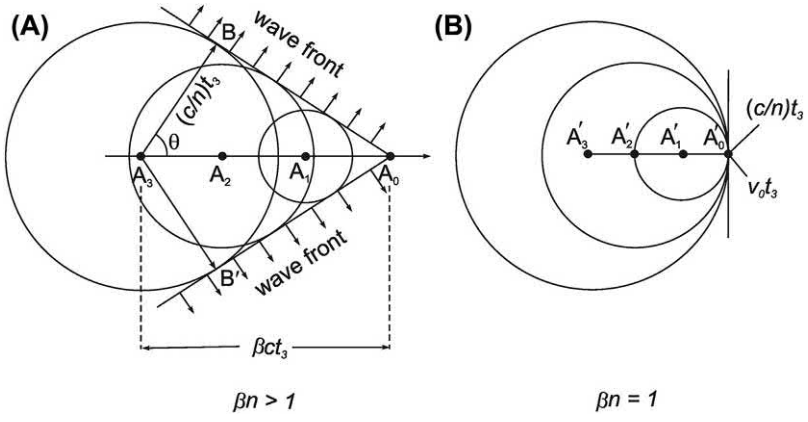


FIGURE 6.3 A Huygens construction of the spherical waves of retarded potential produced by a charged particle traveling along an axis in a refractive medium from points A_3 to A_0 at two velocities, namely (A) $\beta n > 1$ and (B) $\beta n = 1$. *Adapted from Nobel Lecture of Il'ja Frank (1958). Printed with permission © 1958 The Nobel Foundation.*

that is, the product of the relative phase velocity of the particle (β) and the index of refraction of the medium (n), must be greater than unity.

In his Nobel Lecture, Frank (1958) derived Eq. (6.1) from the distance of travel of the spherical wave front relative to the distance traveled by the electron as seen in Fig. 6.3. In the words of Frank (1958) in his Nobel Lecture with the writer's words in brackets:

> *We have to consider each point of the particle trajectory as a source of waves. In this case, the wave phase is determined by the instant of passage of the particle through a given point. Let us assume that at moment* $t = -t_3$ *the emitter was at point* A_3*, at moment* $t = -t_2$ *at point* A_2*, at moment* $t = -t_1$ *at* A_1*, and, finally, at the moment of observation* $t = 0$ *at* A_0 *[see Fig. 6.3].*
>
> *The velocity of the waves is equal to the phase velocity of light* c/n *… The surfaces of the rays are simply spheres whose radii for points* A_3*,* A_2*,* A_1*, and* A_0 *are* $(c/n)t_3$*,* $(c/n)t_2$*,* $(c/n)t_1$*, and 0, respectively [see Fig. 6.3A]. The envelope of these spheres evidently represents a cone of circular cross-section with the apex at* A_0*. Its generatrices in the plane of the drawing are* A_0B *and* A_0B'*.*
>
> *According to the Huygens' principle, the directions of the rays are defined by the radius vectors drawn from some center of the waves to the point of tangency with the envelope. For example, [in Fig. 6.3] it is* A_3B *and* A_3B' *coinciding with the generatrices of the wave normal cone.*
>
> *From Fig. 6.3 it is not difficult to determine the magnitude of the threshold velocity. When the velocity diminishes, the distances between points* A *decrease. The threshold case arises when point* A*, occupies the position* A_0' *on the surface of the sphere [This case is depicted separately in Fig. 6.3B.) At lower velocities, one of the spheres lies completely within the other and they do not have a common envelope. In the threshold case* $[\beta n = 1]$*, they have only a common point of tangency,* A_0'*. Thus, evidently* $(c/n)t_3 = v_0t_3$*, i.e.,* $v_0 = c/n$*. The cone of wave normals is compressed in the direction of velocity v, and the wave cone transforms into a plane perpendicular to the axis of motion at point* A_0' *[Fig. 6.3B].*

From Fig, 6.3a the equation defining the angle θ as a function of the particle phase velocity β and index of refraction n, that is, $\cos\theta = 1/\beta n$, is derived from the distances of travel of the wavefront with respect to that traveled by the charged particle. The velocity v of travel of the wavefront in a particular medium is a function of the index of refraction n of the medium, since by definition $n = c/v$. The distance traveled by the wavefront from A_3 to B of Fig. 6.3A is the product of velocity and time t or $A_3B = vt_3$, and the distance traveled by the charged particle in the same time span from A_3 to A_0 is the product of the particle velocity in the medium v_p and time t_3 or $A_3A_0 = v_pt_3$, which may be written as $A_3A_0 = (v_p/c)ct_3$. Since the particle phase velocity β is defined as v_p/c, the distance A_3A_0 traveled by the charged particle becomes $A_3A_0 = \beta ct_3$. The angle of emission θ of the Cherenkov radiation with respect to the direction of travel of the charged particle is defined as

$$\cos\theta = \frac{A_3B}{A_3A_0} = \frac{(c/n)t_3}{\beta ct_3} = \frac{1}{\beta n} \tag{6.3}$$

Thus, the Cherenkov photons are anisotropic, that is, the photons are not emitted in all directions; rather, the photons are conical, *i.e.*, they are emitted as a cone at an angle θ. The angle of emission is a function of the phase velocity (β) of the particle and the index of refraction (n) of the medium within which the particle is traveling. If the particle is assigned a maximum velocity, where β approaches unity, there will be a maximum angle of emission θ of the Cherenkov photons, and the angle would be a function of the index of refraction of the medium or

$$\cos\theta_{\max} = \frac{1}{n} \quad \text{when} \quad \beta = 1 \tag{6.4}$$

For example, if an electron traveling in water is assigned a maximum velocity, where $\beta = 1$, and the index of refraction of water $n = 1.333$ at the sodium line (589.0 nm) at 20°C (Haynes, 2011), the maximum angle of emission of Cherenkov photons in water would be calculated according to Eq. (6.4) as

$$\theta_{\max} = \cos^{-1}\frac{1}{1.333} = 41.4^0 \tag{6.5}$$

Frank and Tamm (1937) calculated the total energy, W, radiated by an electron via the Cherenkov effect through a cylindrical region of medium of length, l, where the axis of the cylinder coincided with the line of motion of the electron. Under the assumption that β is constant over a short length, dl, of the electron track, they derived the equation

$$W = \frac{e^2\, l}{c^2}\int_{\beta n>1}\omega d\omega\left(1 - \frac{1}{\beta^2 n^2}\right) \tag{6.6}$$

where ω is the frequency of the Cherenkov radiation. The lower limit of the integral, $\beta n > 1$, is the threshold condition for the production of Cherenkov photons in any medium. Frank and Tamm (1937) established the equation to be valid provided that l should be large in comparison with the wave length λ of the Cherenkov radiation emitted. Čerenkov (1938c) took Eq. (6.6) of Frank and Tamm and evaluated the energy, W, radiated by an electron taking under consideration that the magnitude of β will vary greatly over the entire path length of the electron. Čerenkov stated (1938c) the following:

> *In reality, the motion of an electron in the medium involves a considerable change in velocity and, accordingly, magnitude* β *will vary greatly in different sections of the path of the electron. Hence on the assumption that a but*

relatively small region of the spectrum is examined, within which β may be considered as constant, formula 6.6 with reference to the true motion of the electron should be written as follows:

$$W = \frac{e^2}{c^2}\int \omega d\omega \int_{\beta n>1}\left(1-\frac{1}{\beta^2 n^2}\right)dl \tag{6.7}$$

where β depends on l.

Frank and Tamm (1937) thus calculated the rate of radiated energy per path length of travel, *dW/dl*, to be of the order of only several kilovolts per centimeter. Thus, the electron energy loss via the emission of Cherenkov radiation would be a negligible quantity of energy in comparison to the energy lost by the electron by other mechanisms, such as ionization. Čerenkov (1938c) confirmed this through calculations and experimentation and concluded that the radiation expended by β-particles from Ra(B + C) (*i.e.*, ^{214}Pb + ^{214}Bi) via the emission of Cherenkov radiation amounts to a value of the order of only 0.1% of the total energy of the β-particles.

From Eq. (6.6) Frank and Tamm (1937) deduced the following equation for the number of photons, *N*, emitted by an electron within the limits of a given spectral region confined by the wavelengths λ_1 and λ_2 for a constant β, that is, for a short length of the electron track where the phase velocity of the electron remains relatively constant to be

$$N = 2\pi\alpha\left(\frac{1}{\lambda_1}-\frac{1}{\lambda_2}\right)\left(1-\frac{1}{\beta^2 n^2}\right) \tag{6.8}$$

where α is the fine structure constant ($\alpha \approx 1/137$). From Eq. (6.8), Frank and Tamm (1937) calculated that a 500 keV electron, which would correspond to $\beta^2 = 0.75$, traveling in water, where $n = 1.33$, would produce approximately 10 photons per 0.1 cm within the visible region between $\lambda_1 = 4000$ Å and $\lambda_2 = 6000$ Å as follows:

$$N = 2(3.14)(1/137)\left(\frac{1}{4\times10^{-5}\text{cm}}-\frac{1}{6\times10^{-5}\text{cm}}\right)\left(1-\frac{1}{(0.75)(1.33)^2}\right) \tag{6.9}$$

$$= 101 \text{ photons/cm} = 10 \text{ photons/0.1 cm}.$$

The above approximation by Frank and Tamm was confirmed with more precise calculations by Belcher (1953), who calculated the integral number of Cherenkov photons produced by an electron as a function of its varying phase velocity over the entire effective range of travel of the electron in water ($n = 1.33$) and Perspex plastic medium ($n = 1.50$). The effective range of travel of the electron is that of its highest energy or highest phase velocity ($\beta = \beta_{max}$) to a lower energy as a result of reduced velocity in the medium corresponding to the threshold phase velocity or $\beta = 1/n$ at which point Cherenkov photons are not produced. The calculations of Belcher are treated in more detail further on in this chapter.

B. Quantum mechanical interpretation

The theory of Cherenkov radiation explained by Frank and Tamm is based on classical electrodynamics, and successfully explains the main characteristics of radiation in terms of its spectral properties (i.e., its coherence and anisotropy). However, Cherenkov radiation is attributed to the radiation produced by a uniformly moving charged particle in a medium, and consequently it appears that the theory allows for a violation of the laws of conservation (Kobzev, 2010, 2014). Intuitively, we know that any violation is not possible. However, within the framework of classical electrodynamics, it could appear as such. Therefore, for a rigorous treatment of the Cherenkov phenomenon, it is necessary to reach for the tools of quantum theory, although some controversy cannot be avoided (Ginzburg, 1977; Skobel'tsyn 1977). Such a rigorous treatment delves deep into quantum electrodynamics (Jauch and Watson, 1948a, 1948b, 1949; Feynman, 1950; Ivanov et al., 2016). Through the following basic principles of the quantum approach, an explanation of the Cherenkov effect is provided (Supek, 1990; Ginzburg, 1996, 2005; Afanasiev et al., 2006; Wang, 2015). In the quantum mechanical approach, the motion of a "free charged particle (electron)" can be expressed by that of a plane wave $\boldsymbol{u}$:

$$u = e^{-i\mathrm{kr}} \tag{6.10}$$

where $\boldsymbol{u}$ is characterized by wave vector $\mathbf{k}$ and position $\mathbf{r}$. Formally, on the basis of the matrix elements for a charged particle (electron) transition from state $\mathbf{k}$ to state $\mathbf{k}'$, we can write

$$\int e^{-i\mathrm{qr}} u_{\mathrm{k}} u_{\mathrm{k}'} d\tau \tag{6.11}$$

where $\boldsymbol{d\tau}$ is the space increment and $\mathbf{q}$ is the photon wave vector. This is equivalent to the following equation:

$$\int e^{i(-\mathrm{k}+\mathrm{q}+\mathrm{k}')\mathrm{r}} d\tau \tag{6.12}$$

from which it can be concluded that the electron emits photons through the conservation of the total wave vectors or momentum $\mathbf{k} = \mathbf{q} + \mathbf{k}'$. The conservation of momentum imposes that the matrix element should be different from zero and that the electron will produce photons without constant motion. This conclusion is incorrect, because in the matrix elements, the Dirac function for the transition probability $\boldsymbol{\delta(E_0 - E_1)}$ should be taken into account, due to the law of the conservation of energy (Jauch and Watson, 1948; 1948a; Feynman, 1950; Supek, 1990). The Dirac function $\boldsymbol{\delta(E - E' - \hbar\omega)}$ is different from zero only in

the case when energy conservation is fulfilled, where $\boldsymbol{E_0}$ is the initial energy of an electron, and $\boldsymbol{E_1} = \boldsymbol{E'} + \hbar\boldsymbol{\omega}$ is the sum of the energies of the electron $\boldsymbol{E'}$ and photon $\hbar\boldsymbol{\omega}$ (Supek, 1990). The energy $\boldsymbol{E}$ of a relativistic particle (i.e., electron) is written as

$$E = c\sqrt{m_0^2c^2 + p^2}, \tag{6.13}$$

an expression of Eq. (1.373) derived in Chapter 1, Volume 1, namely,

$$E^2 = \left(m_0c^2\right)^2 + (pc)^2 \tag{6.14}$$

which is the relativistic energy−momentum relation where m_0 is the particle rest mass (i.e., intrinsic mass), p is the particle momentum, and c is the speed of light in a vacuum (see Eqs. (1.371) to (1.373) of Chapter 1, Volume 1, Section XI.A. "Dual Nature Wave and Particle"). The change in particle energy can be obtained by differentiation of Eq. (6.13) $\boldsymbol{dE/dp}$

$$\frac{dE}{dp} = \frac{2cp}{2\sqrt{m^2c^2 + p^2}} \tag{6.15}$$

By changing of $\boldsymbol{dE}$ and dp with ΔE and Δp gives

$$\Delta E = \frac{cp\Delta p}{\sqrt{m^2c^2 + p^2}} \tag{6.16}$$

The energy of a photon (ε) is the product of the speed of light and its momentum Π, as derived in Chapter 1, Volume 1 (see Eq. 1.375)

$$\varepsilon = c\Pi \tag{6.17}$$

The photon momentum should be equal to the change in electron momentum (ε) or

$$\varepsilon = c\Delta p \tag{6.18}$$

The division of Eqs. (6.16) and (6.18) provides a comparison of the energy and momentum changes of the electron and photon, or

$$\frac{\Delta E}{\varepsilon} = \frac{p}{\sqrt{m^2c^2 + p^2}} < 1 \tag{6.19}$$

As the relation $\Delta E/\varepsilon < 1$, the relation $\Delta E = \varepsilon$ cannot be fulfilled without the addition of energy to the electron, if the photon carries off part of the momentum. On the contrary, if the electron loses energy to photon energy, then it should disperse part of the momentum. The conservation law for the electron and photon momentum is written, according to the previously described Eq. (6.16), as

$$\Delta p = \frac{\sqrt{p^2 + m^2c^2}}{cp}\Delta E \tag{6.20}$$

and

$$\Pi = \frac{\Delta E}{c} \tag{6.21}$$

Dividing Eqs. (6.20) and (6.21) provides a comparison of the particle and photon momentum as

$$\frac{\Delta p}{\Pi} = \frac{\sqrt{p^2 + m_0^2c^2}}{p} > 1 \tag{6.22}$$

Thus, the spontaneous electron production of photons is possible only in the case of electron retardation in other particles or when the particle velocity $v > c/n$ (Supek, 1990), where n is the refractive index of the medium through which the particle travels. In other words, when the speed of the electron is greater than the speed of light in a medium, Cherenkov radiation will occur. In this fashion, on the basis of the quantum mechanical approach, Ginzburg (1940, 1996, 2005) developed the theory of Cherenkov radiation. He used Eq. (6.13) to express the particle energy as

$$E_{0,1} = c\sqrt{m^2c^2 + p_{0,1}^2} \tag{6.23}$$

and its momentum as

$$p_{0,1} = \frac{m_0v_{0,1}}{\sqrt{1 - \left(v_{0,1}^2/c^2\right)}} \tag{6.24}$$

where the term $m_0\Big/\sqrt{1 - (v^2/c^2)}$ is the expression for the relativistic mass of a particle as derived in Chapter 1, Volume 1, Section VII.E. "Energy and Mass in Relativity" (see also Eqs. (6.32) and (6.34) further on in this chapter). The terms $E_{0,1}$ and $p_{0,1}$ are the energy and momentum of a charged particle of rest mass m_0 before (0) and after (1), the emission of a photon of energy $\hbar\boldsymbol{\omega}$, and momentum $\hbar\mathbf{k} = (\hbar\boldsymbol{\omega}/\boldsymbol{c})$ $(\mathbf{k}/\mathrm{k})$, where $k = \omega/c$. Eqs. (6.22) and (6.23) have no solution with $\boldsymbol{\omega} > 0$ at $v < c$, whereby radiation is impossible. Let us assume that a charged particle with rest mass m_0 and momentum p_0 is moving in a medium with refractive index n. After propagation, it emits a photon with momentum p_1. The radiated photon is emitted at an angle θ_0 with the direction of propagation governed by the conservation of momentum, which requires (Wang, 2015)

$$p^2 = p_0^2 + p_1^2 - 2p_0p_1\cos\theta_0 \tag{6.25}$$

The energy conservation relation and solution for $\cos\theta_0$ gives (Ginzburg, 1996, 2005)

$$\cos\theta_0 = \frac{c}{n(\omega)v_0}\left[1 + \frac{\hbar\omega(n^2 - 1)}{2m_0c^2}\sqrt{1 - (v_0^2/c^2)}\right] \tag{6.26}$$

In the case when

$$\frac{\hbar\omega}{m_0c^2} << 1 \tag{6.27}$$

Eq. (6.24) becomes

$$\cos\theta = \frac{1}{\beta n(\omega)} \tag{6.28}$$

where β is the relative phase velocity of the particle, that is, the velocity of the particle in a medium divided by the speed of light in a vacuum (v/c) and n is the index of refraction of the medium. Eq. (6.26) is the threshold condition for the production of Cherenkov photons in a transparent medium of refractive index n, where n is a function of wavelength $\omega = 2\pi c/\lambda$. This is natural because condition (6.26) becomes classical in the case when $\mathrm{h} \to 0$. This means that the classical limit corresponds to the neglect of recoil (a change in the particle momentum p_0) due to "photon emission in a medium" with momentum $\hbar\mathbf{k}$, as noted by Ginzburg (1996). According to Ginzburg (1996), the conservation laws may be formulated in the classical domain under the condition that the relationship between the emitted electromagnetic energy and radiation momentum be taken into account. An explanation of the Cherenkov radiation mechanism in the context of energy and momentum conservation laws is not trivial and sometimes provokes controversy, which can be seen from the recent papers of Kobzev (Kobzev, 2010, 2014) and also from the discussions of Ginzburg and Skobel'tsyn (Ginzburg, 1977; Skobel'tsyn 1977).

Kobzev stipulates that "the Vavilov-Cherenkov radiation microscopic mechanism does not contradict with the basic laws" (see Kobzev, 2010, 2014). The radiation arises from the interaction of the moving charge with bound charges that are spaced fairly far away from its trajectory. The Cherenkov radiation mechanism bears a slowing down character, but it differs fundamentally from bremsstrahlung, primarily because the Vavilov–Cherenkov radiation onset results from a two-stage process. First, the moving particle polarizes the medium; and then, the already polarized atoms radiate coherently, provided that the particle velocity exceeds the phase speed of light in the medium (as illustrated in Fig. 6.4). If the particle velocity is less than the phase speed of light in the medium, the polarized atoms return energy to the outgoing particle. In this case, "radiation is not observed" (Kobzev, 2010).

Even nowadays we encounter the misconception that Cherenkov radiation is in some way associated with ionization. In terms of energy loss, the ionization process dominates over Cherenkov radiation, but a very small part of ionization energy appears as light, so that Cherenkov radiation in the optical part of the spectrum is dominant. Some substances, such as scintillators, will produce light from the ionization process. However, this cannot be seen as Cherenkov radiation. Namely, light emitted in association with the ionization process will appear at a time, after the original ionizing event, determined by the specific lifetimes of the atomic energy states responsible for the emission. For this light, coherence between the wavelets from the different portions of the track, the characteristic cone, and the velocity threshold do not exist. As a consequence, such light is emitted isotropically. This is in contrast to Cherenkov radiation, which is characterized by threshold, coherence, and anisotropic properties. On the other hand, a consideration of the energy exchange between the particle and a single individual atom involved in the Cherenkov process shows a very small energy transfer. Jelley (1961) showed that the energy exchange is only 8×10^{-13} eV for blue light. This is far below the energy required for excitation as well as ionization.

C. Threshold condition

As discussed in the previous section, the threshold condition for the production of Cherenkov radiation in a transparent medium is given by

$$\beta n = 1 \tag{6.29}$$

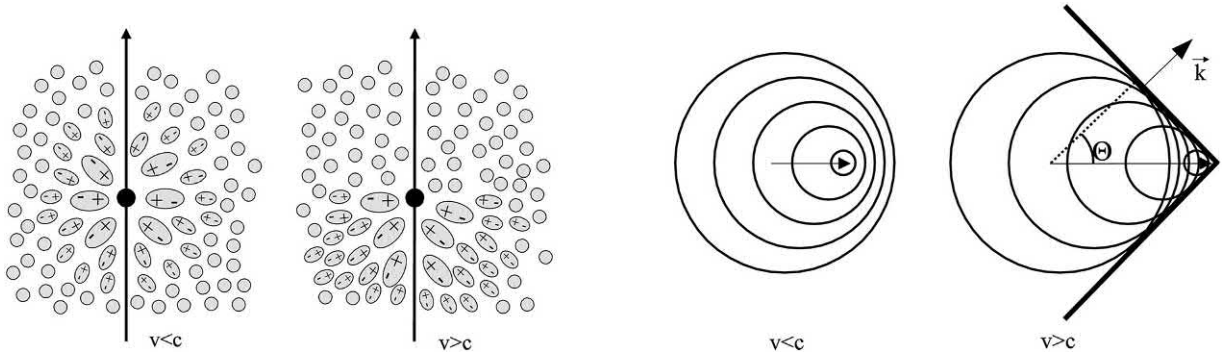


FIGURE 6.4 Left: Illustration of the polarization of the medium induced by the crossing of a relativistic particle. Right: Construction of Cherenkov wavefront. *From de Naurois and Mazin (2015), reprinted with permission © 2015 Elsevier Masson SAS. All rights reserved.*

where β is the relative phase velocity of the particle, that is, the velocity of the particle divided by the speed of light in a vacuum, and n is the refractive index of the medium (*i.e.*, the ratio of the velocity of light in a vacuum to its velocity in the medium). Only charged particles that possess

$$\beta > 1/\mathrm{n} \tag{6.30}$$

produce Cherenkov photons in transparent media (Frank and Tamm, 1937). The value of β of the charged particle is dependent on its kinetic energy, which is obtained from the equation describing the total energy of the particle. As described in Chapter 1 of Volume 1 of this book (see Eqs. 1.269 to 1.271 of Chapter 1, Volume 1), the total energy (E_{tot}) of a particle is the sum of its kinetic (E_K) and rest energies (m_0c^2) or

$$E_{tot} = E_K + m_0c^2 = \gamma m_0c^2 \tag{6.31}$$

and

$$E_K = \gamma m_0c^2 - m_0c^2 \tag{6.32}$$

where

$$\gamma = \frac{1}{\sqrt{1-(u^2/c^2)}} \text{ and } u^2/c^2 = \beta^2 \tag{6.33}$$

u is the particle speed and $u < c$. (The particle speed is often represented with the symbol v or u.) If m_0 is the particle rest mass, then the particle relativistic mass, m_r, which is the speed-dependent mass of the particle, would be defined as

$$m_r = \frac{m_0}{\sqrt{1-(u^2/c^2)}} = \frac{m_0}{\sqrt{1-\beta^2}} \tag{6.34}$$

Thus, for a particle traveling at relativistic speed, Eq. (6.32) can be expressed as

$$E_K = m_0c^2\left[\frac{1}{(1-\beta^2)^{1/2}} - 1\right] \tag{6.35}$$

where m_0 is the particle rest mass in grams, c is the velocity of light in a vacuum (equal to 2.99×10^{10} cm/s), and E_K is the kinetic energy in erg (where 1.602×10^{-12} ergs = 1 eV). Eq. (6.35) can be solved for β to give the expression for the phase velocity of the particle as a function of its energy or

$$\beta = \left[1 - \left(\frac{1}{(E_K/m_0c^2)+1}\right)^2\right]^{1/2} \tag{6.36}$$

The value of the rest energy for an electron is $m_0c^2 = (9.11 \times 10^{-28}\ \mathrm{g})\ (2.99 \times 10^{10}\ \mathrm{cm/s})^2 = 8.14 \times 10^{-7}$ ergs. The energy in ergs may be converted to electron volts as follows: $(8.14 \times 10^{-7}\ \mathrm{ergs})/(1.602 \times 10^{-12}\ \mathrm{ergs/eV}) = 511$ keV. Substituting the value of 511 keV for m_0c^2 in Eq. (6.36) and solving for β gives

$$\beta = \left[1 - \left(\frac{1}{(E_K/511\ \mathrm{keV})+1}\right)^2\right]^{1/2} \tag{6.37}$$

Thus, the value of β, where electrons or beta particles are concerned, is dependent upon the electron or beta-particle energy, E_K, in keV according to Eq. (6.37).

D. Threshold energies

As noted above, the particle phase velocity, β, is a critical factor in the production of Cherenkov photons in a medium of given index of refraction, n, that is, Cherenkov radiation will occur only when $\beta > 1/n$. Consequently the particle energy, upon which the particle phase velocity is dependent, is a critical factor. Thus, a minimum or threshold energy of the particle must be reached when traveling in a medium of given index of refraction before Cherenkov photons will be produced. If we apply the threshold value of β for the production of Cherenkov photons from Eq. (6.29), *i.e.*, $\beta = 1/n$, to Eq. (6.37), we will obtain the threshold energy that electrons or beta-particles must possess for the production of Cherenkov radiation as a function of the index of refraction of the medium as

$$E_{\mathrm{th}} = 511\ \mathrm{keV}\left[\left(1 - \frac{1}{n^2}\right)^{-1/2} - 1\right] \tag{6.38}$$

When water is the transparent medium, where $n = 1.333$ (at 20°C at the sodium line, *i.e.*, 589.0 nm), the threshold energy for the production of Cherenkov photons by electrons or beta-particles is calculated according to Eq. (6.38) to be 262 keV (or 0.262 MeV) as follows:

$$E_{\mathrm{th}} = 511\ \mathrm{keV}\left[\left(1 - \frac{1}{n^2}\right)^{-1/2} - 1\right]$$

$$= 511\ \mathrm{keV}\left[\frac{1}{\sqrt{1 - \frac{1}{(1.333)^2}}} - 1\right]$$

$$= 262\ \mathrm{keV}$$

Thus, only electrons or beta-particles that possess energy in excess of 262 keV or 0.262 MeV produce Cherenkov photons in water.

We can write Eq. (6.38) in general terms for the calculation of the threshold energy of charged particles of any mass as follows

$$E_{\mathrm{th}} = m_0c^2\left[\left(1 - \frac{1}{n^2}\right)^{-1/2} - 1\right] \tag{6.39}$$

where m_0 is the particle rest mass and c is the velocity of light in a vacuum (2.99×10^{10} cm/s).

As described in Eq. (6.39), the threshold energy for the Cherenkov effect (*i.e.*, Cherenkov photon production) will vary according to the particle rest mass and index of refraction of the medium. The energy required for the production of Cherenkov photons, E_{th}, increases with particle mass, and it will be lower for media of higher index of refraction. For example, according to Eq. (6.39), electrons or beta-particles traveling through polyethylene plastic of refractive index $n = 1.52$, will have the following calculated threshold energy of 167 keV or 0.167 MeV, which is considerably lower than the threshold energy of 262 keV or 0.262 MeV for the production of Cherenkov photons in water:

$$E_{th} = m_0c^2\left[\left(1-\frac{1}{n^2}\right)^{-1/2}-1\right]$$

$$= \left(9.10938\times10^{-28}g\right)\left(2.99792\times10^{10}\text{cm/sec}\right)^2$$

$$\left[\frac{1}{\sqrt{1-\frac{1}{(1.52)^2}}}-1\right]$$

$$= 8.18707\times10^{-7}\text{ergs}\left[\frac{1}{\sqrt{0.5671745}}-1\right]$$

$$= \left(\frac{8.18707\times10^{-7}\text{ergs}}{1.602\times10^{-12}\text{ergs/eV}}\right)\left[\frac{1}{0.753109}-1\right]$$

$$= \left(0.5110\times10^{6}\text{eV}\right)(0.3278)$$

$$= 0.167\text{ MeV or }167\text{ keV}$$

Thus, the use of plastic, which has a higher index of refraction than water, as a counting medium through which β particles must travel, will reduce the threshold energy for the production of Cherenkov photons and increase the detection efficiency of radionuclides measured by Cherenkov counting (L'Annunziata and Passo, 2002).

Table 6.1 lists the calculated threshold energies of particles of differing mass in media of differing index of refraction calculated according to Eq. (6.39). A medium within which Cherenkov photons are produced is referred to as a *Cherenkov Radiator*.

Data in Table 6.1 illustrate that the threshold energy for a particular particle decreases in media of increasing index of refraction. Also, the threshold energy required for the production of Cherenkov photons in any particular medium increases proportionally with the mass of the particle. Thus, by the selection of a medium of given index of refraction, it is possible to discriminate between particles of different energies or mass, which is discussed further on in this chapter. Beta-emitting radionuclides of high E_{max} (e.g., ^{90}Y with $E_{max} = 2280$ keV) can be analyzed efficiently with a Cherenkov radiator of low index of refraction (e.g., aerogel with n = 1.05 listed in Table 6.1), which has a high beta-particle or electron threshold energy thereby discriminating against background radiation from low-energy beta-particles and Compton electrons resulting from gamma-radiation background. The application of aerogel Cherenkov radiators for the detection of high-energy beta-emitting radionuclides is discussed further on in this chapter. Fig. 6.5 provides an excellent illustration of the relation between Cherenkov threshold energy for beta-particles or electrons and index of refraction of the Cherenkov radiator with data points calculated according to Eq. (6.38) or (6.39) (Yoo et al., 2013). The highest threshold energy (~1160 keV) illustrated in the graph of Fig. 6.5 is

TABLE 6.1 Particle threshold energies in MeV for the production of Cherenkov photons in media (Cherenkov radiators) of different index of refraction.

Medium	Index of refraction (*n*)	Particle threshold energy in MeV[a]		
		Electron[b]	Muon[c]	Proton[d]
Air	1.00027712[e]	21.2	4380.9	38925.9
Silica aerogel[f]	1.05	1.16	240.7	2139.0
Water	1.33	0.262	54.1	480.7
Glass[g]	1.47	0.186	38.5	341.9
Plastic[h]	1.52	0.167	34.6	307.6
Ceramic[i]	2.1	0.070	14.5	128.7
Diamond	2.4[e]	0.051	10.6	93.9

[a] *Calculated according to Eq. (6.39). The index of refraction (n) is wavelength dependent; and the value will vary slightly according to the wavelength chosen. The wavelength often used is that of the sodium D line at 589 nm.*
[b] *Energy equivalent mass of electron (m_0c^2) = 0.511 MeV.*
[c] *Energy equivalent mass of muon (m_0c^2) = 105.6 MeV.*
[d] *Energy equivalent mass of proton (m_0c^2) = 938.3 MeV.*
[e] *Index of refraction of air measured at the sodium D line at STP.*
[f] *Silica aerogel index of refraction (n) will vary according to mode of manufacture. The value of n = 1.05 is taken from experiments of Brajnik et al. (1994, 1995) and Pestotnik et al. (2002).*
[g] *Borosilicate glass tested for electrons or beta-particles by L'Annunziata and Passo (2002).*
[h] *Polyethylene plastic tested for electrons or beta-particles by L'Annunziata and Passo (2002).*
[i] *Commercial ceramic tested for electrons and beta-particles by Takiue et al. (2004) and Minowa et al. (2009).*
From L'Annunziata (2016); reprinted with permission from Elsevier © 2016.

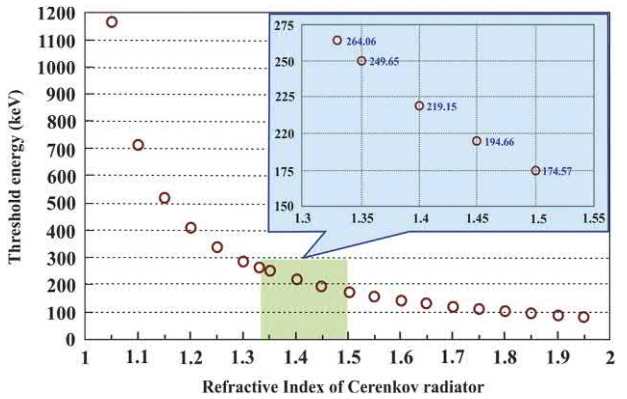


FIGURE 6.5 Cerenkov threshold energy for electrons as a function of refractive index of the Cerenkov radiator. *From Yoo et al. (2013), reprinted with permission from Elsevier © 2013.*

that of an aerogel radiator with index of refraction n = ~ 1.05. The expanded section of the graph provides data points determined experimentally by Yoo et al. (2013) with liquid radiators of differing index of refraction. Yoo et al. (2013) report the development of a fiber optic Cherenkov radiation sensor that is coupled to the Cherenkov radiator for the detection and measurement of beta-particles.

E. Photon spatial asymmetry

An important property of Cherenkov radiation is its asymmetry, that is, the directional emission of the Cherenkov photons. Cherenkov radiation is not emitted in all directions. When Čerenkov (1936) discovered the asymmetric properties of this radiation, he knew he had discovered a type of radiation yet unknown. Frank and Tamm (1937) explained the spatial asymmetry of the radiation as a result of the charged particle traveling in a medium at a velocity exceeding the velocity of light in the medium. Frank and Tamm (1937) theorized that when the phase velocity of the charged particle, β, exceeded the reciprocal of the index of refraction, n, of the medium, that is, $\beta > 1/n$, Cherenkov photons are emitted as a cone at an angle, θ, to the direction of the charged particle as depicted in Figs. 6.1, 6.6 and 6.7. According to the theory of Frank and Tamm (1937), the angle, θ, of photon emission would be defined by the relationship

$$\cos\theta = \frac{1}{\beta n} \tag{6.40}$$

which was derived earlier in this chapter.

Čerenkov (1937b) tested the theory of Frank and Tamm (1937) using gamma rays directed at a vessel of water to create high-energy electrons in the water via the Compton effect. He then measured the angles of emission of the photons relative to the direction of the incident gamma radiation. Cherenkov found a broad range of photon emission angles in water with a maximum around 30 degrees. The

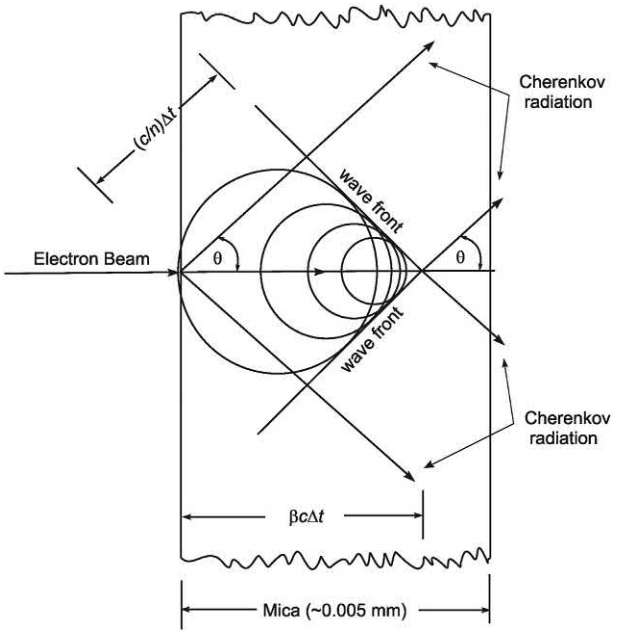


FIGURE 6.6 A thin section of mica used by Collins and Reiling (1938) and Wyckoff and Henderson (1943) as the transparent medium for the production of Cherenkov photons by a beam of high-energy electrons of uniform energy. The thin section of Cherenkov radiator would assure minimal loss of electron energy in traversing the mica. *From L'Annunziata (2016); reprinted with permission from Elsevier © 2016.*

maximum angle of emission would depend on the phase velocity of the Compton electron, β, and thus on the energy of the electron. Although Cherenkov definitely was able to demonstrate the spatial asymmetry of the newly discovered photons, the Compton electrons unfortunately are not unidirectional and can display wide angles of deflection relative to the direction of the gamma rays that created them. Consequently, Cherenkov's results were not precise enough to demonstrate irrefutably Frank and Tamm's theory that cos $\theta = 1/\beta n$. It was not until monoenergetic electrons were used by researchers, such as Collins and Reiling (1938) and Wyckoff and Henderson (1943), could the angle of photon emission, θ, be accurately measured. They directed electrons of uniform energy into thin sections of transparent media such as mica, glass, cellophane, and water. A thin section of Cherenkov radiator assured insignificant loss of electron energy in traversing the medium.

According to the theory of Frank and Tamm (1937) the angle, θ, illustrated in Fig. 6.6, is defined by the equation

$$\cos\theta = \frac{\text{distance of travel of radiation front in the medium}}{\text{distance of travel of charged particle in the medium}} \tag{6.41}$$

or

$$\cos\theta = \frac{(\text{speed of light in the medium})(\Delta t)}{(\text{speed of particle in the medium})(\Delta t)} \tag{6.42}$$

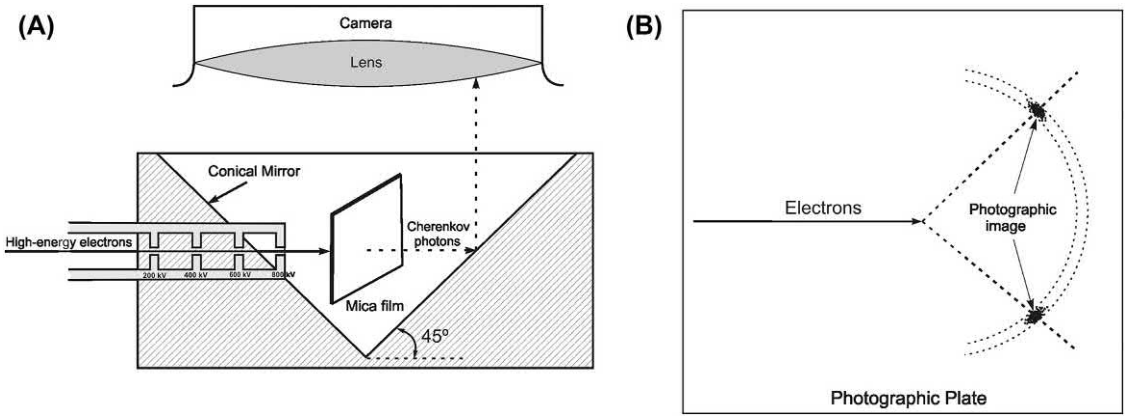


FIGURE 6.7 Basic experimental arrangement used by Collins and Reiling (1938) and Wyckoff and Henderson (1943) to demonstrate the relation cos $\theta = 1/\beta n$. In (A) an electron gun provides electrons of uniform energy by accelerating electrons across potentials varying from 200 to 800 kV. Wyckoff and Henderson (1943) produced electrons with energies over the range of 240−815 keV and Collins and Reiling (1938) accelerated electrons up to 2000 keV. The electrons in (A) traverse the mica film and produce cones of Cherenkov radiation. The Cherenkov photons are produced only in the direction of the electrons, and the photons are reflected off the conical mirror toward the camera. The photographic plate in (B) provides two spots produced by the Cherenkov radiation cone reflected in two dimensions from which the angle θ can be calculated. *From L'Annunziata (2016); reprinted with permission from Elsevier © 2016.*

where Δt is a time interval. Using the notation provided in Figs. 6.3 and 6.6, we can then write

$$\cos\theta = \frac{(c/n)t}{\beta ct} \tag{6.43}$$

The term $(c/n)t$ represents the distance of travel of the radiation wavefront measured by the product of the velocity of the light in the medium (c/n) and time (t), while the term βct measures the distance of particle travel according to $\beta ct = (v/c)ct = vt$ where v is the velocity of the particle in the medium, c the speed of light in a vacuum, and t is time. From Eq. (6.43) we obtain the expression

$$\cos\theta = \frac{1}{\beta n} \tag{6.44}$$

when $\beta = 1/n$, which is the threshold condition for the production of Cherenkov photons (Eq. 6.44), the charged particle possesses a threshold energy where Cherenkov radiation is yet to be produced, that is, cos $\theta = 1$ and $\theta = 0$. When $\beta > 1/n$, the charged particle possesses sufficient energy and velocity to produce Cherenkov photons, which are emitted in the exact forward direction of the charged particle at an angle θ, as defined according to Eq. (6.44).

As the particle energy, E, of Eq. (6.36) increases to relativistic speeds, the value of β approaches unity and cos θ approaches $1/n$ of Eq. (6.44). Thus, the maximum angle of emission of a Cherenkov photon produced by a charged particle in any transparent medium would occur when the charged particle possesses a high energy to the point where the value of β of Eq. (6.36) approaches unity or

$$\cos\theta = \frac{1}{n}, \text{ when } \beta \text{ approaches } 1 \tag{6.45}$$

If we consider the case of mica as the transparent medium with index of refraction $n = 1.59$, such as that tested by Collins and Reiling (1938) and Wyckoff and Henderson (1943), the maximum possible angle of emission of Cherenkov photons in the mica are calculated to be

$$\cos\theta = \frac{1}{1.59} = 0.6289$$

and $\theta = 51.0$ degrees.

According to the theory of Frank and Tamm (1937), Cherenkov photons are emitted at more acute angles for charged particles just above their threshold energy and cannot exceed an emission angle of 51.0 degrees in mica, even for the most energetic particles.

Collins and Reiling (1938) and Wyckoff and Henderson (1943) tested the theory of Frank and Tamm by shooting electrons of various energies at mica, and they measured accurately the angles of emission of the Cherenkov photons as a function of electron energy. They could then compare the experimentally obtained emission angles, θ, with those calculated according to the relation cos $\theta = 1/\beta n$. The key component of their experimental arrangement, illustrated in Fig. 6.7, included a conical mirror to reflect the Cherenkov photons such as that designed by Čerenkov (1937b) in his initial experiments with Compton electrons.

The theoretical angles of emission (θ) of Cherenkov photons produced by electrons in mica with an index of refraction, $n = 1.59$, are plotted in Fig. 6.8. According to the Frank and Tamm theory (1937), where cos $\theta = 1/\beta n$, the theoretical angles of emission will vary from zero at the threshold electron energy to the highest emission angle for the relativistic electrons of highest energy where β approaches 1, its highest possible value. Collins and Reiling

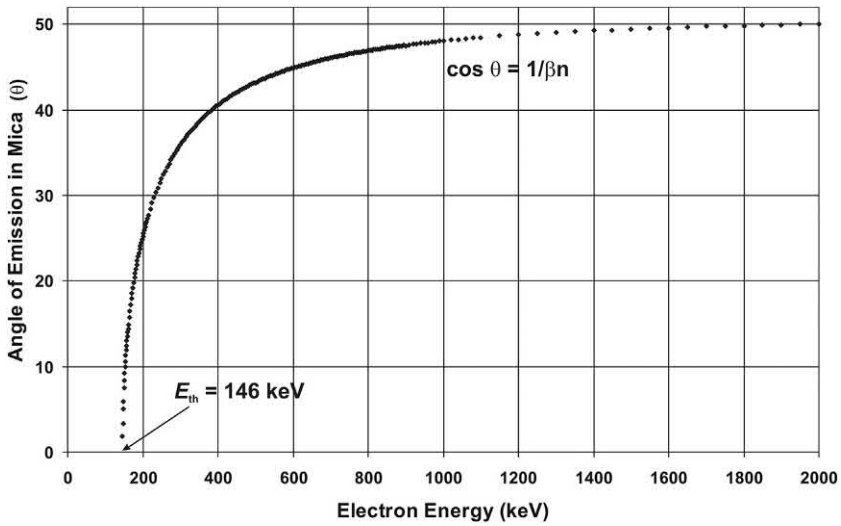


FIGURE 6.8 Cherenkov photon emission angles (θ) in mica of index of refraction, $n = 1.59$, as a function of electron energy calculated according to $\cos\theta = 1/\beta n$. The threshold energy E_{th} of electrons (146 keV) for the production of Cherenkov photons in the mica was calculated according to Eq. (6.39). *From L'Annunziata (2016); reprinted with permission from Elsevier © 2016.*

(1938) and Wyckoff and Henderson (1943) found the experimentally measured angles of emission to agree very closely to the theoretical values over the electron energy range of 240−1900 keV within about 1 degree. In addition to mica, thin films of other transparent media of different index of refraction including thin films of glass and cellophane, were tested by Wyckoff and Henderson (1943), and the measured and theoretically calculated values of θ agreed to within 1 degree. The slight discrepancy between the measured and calculated values was considered due to slight unavoidable bending or imperfections of the thin films used.

We can conclude from the above that, for a particle of given mass and charge, the angle of emission of the Cherenkov photons will depend on the particle phase velocity (β), which is a function of its energy as well as the index of refraction of the medium. The maximum angle of emission of Cherenkov photons will, of course, differ for media of different index of refraction. In the fields of particle and nuclear physics the Cherenkov effect has been exploited for the identification of particles based on their mass and velocity, which in any given medium of known index of refraction, will govern the angle of emission of the Cherenkov photons. The concepts of particle identification by measurement of Cherenkov emissions is discussed further on in this chapter and reviewed in detail by Križan (2017, 2013, 2009, 2007, 2001), Nappi (2011), Iijima (2010). Ullaland (2003), Joram (2002) and Va'vra (2000).

Later in life, approximately 20 years after his historic research on the visible spectrum of the newly discovered radiation, Cherenkov commented on the spatial distribution and the visible spectrum of the radiation in his Nobel Lecture (with writer's comments in brackets) given on December 11, 1958, as follows:

> *If we consider the picture [of the radiation] not in the [2-dimensional] plane but spatially, then the radiation must spread out along the surface of a cone whose axis forms the path of an electrically charged particle while the surface line forms with this axis the angle [θ].*
>
> *If we place [a] photographic plate perpendicular to the beam of high-speed particles [See Fig. 6.1], we shall obtain, in addition to an image of the track of the beam, also a photograph of the radiation in the form of a ring.*
>
> *… we have in our considerations assumed some fixed frequency. In reality, however, the radiation spectrum is continuous. Since the medium exhibits dispersion, i.e., the refractive index is dependent on the frequency, this means that the light of different wavelengths is propagated at angles which, even with strictly constant velocity of the particles, differ somewhat from one another.*
>
> *Thus, the radiation is broken up as in spectral analysis. The radiation cone will consequently show a definite intensity, and in the case of a medium with normal dispersion the spectral red will lie in the inner part of the cone while the violet is on the outside. That this is actually so was shown by a photograph showing part of the ring with a color plate.*

An example of a typical image of the Cherenkov radiation in the form of a ring surrounding a central image of a beam of high-speed particles obtained with modern silicon photomultipliers, rather than photographic film described above by Cherenkov, is illustrated in Fig. 6.9 The ring

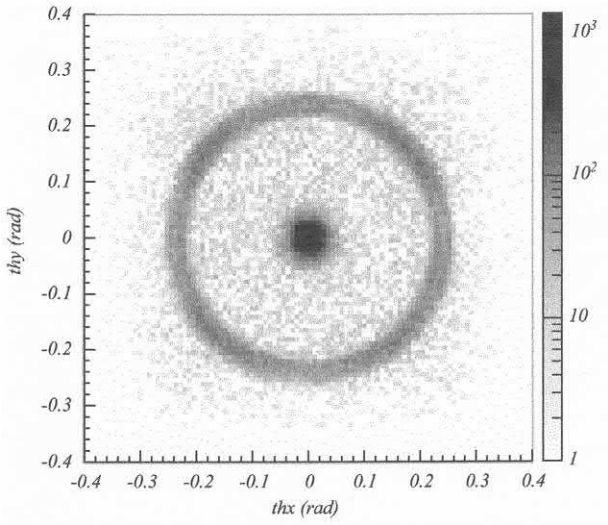


FIGURE 6.9 The distribution of hits in the Cherenkov angle space [*i.e.*, θ in y coordinates (*thy*) against θ in x coordinates (*thx*) imaged with silicon photomultipliers with noise distributions subtracted and without the use of light guides. *From Dolenec et al. (2011), reprinted with permission from Elsevier © 2011.*

image of Cherenkov photons was produced by a 120 GeV/c pion interaction with an aerogel radiator; and the Cherenkov photons emitted were detected by silicon photomultipliers described further on in this chapter. The dark image at the very center of the ring is due to the high-speed particle beam.

F. Photon spectrum and radiation intensity

Cherenkov radiation consists of a continuous spectrum of wavelengths extending from the near ultraviolet region into the visible part of the spectrum peaking at about 420 nm (Kulcsar et al., 1982; Claus et al., 1987). Only a negligible amount of photon emissions is found in the infrared or microwave regions. In Cherenkov's early work, he found the Cherenkov cone of radiation to comprise the visible spectrum (see Fig. 6.1). He observed specifically that the outer ring of the radiation cone was violet and its inner ring was red. Jelley (1958) explains that a medium is always dispersive, and consequently the radiation is restricted to those frequency bands for which $n(\omega) > 1/\beta$, where $n(\omega)$ is the index of refraction at a particular frequency band. Jelley adds that the absorption bands in media, that are transparent at visible wavelengths, limit the radiation to the near ultraviolet and longer wavelengths.

In their classic interpretation of the Cherenkov effect, Frank and Tamm (1937) calculated the total energy, W, radiated by an electron via the Cherenkov effect, through a cylindrical region of medium of length, l, where the axis of the cylinder coincided with the line of motion of the electron. Under the assumption that β is constant over a short length, dl, of the electron track, they derived the equation

$$W = \frac{e^2 l}{c^2} \int_{\beta n > 1} \omega d\omega \left(1 - \frac{1}{\beta^2 n^2}\right) \tag{6.46}$$

where ω is the frequency of the Cherenkov radiation. The lower limit of the integral, $\beta n > 1$, is the threshold condition for the production of Cherenkov photons in any medium. Frank and Tamm (1937) established the equation to be valid provided that l should be large in comparison with the wave length λ of the Cherenkov radiation emitted. Čerenkov (1938c) took Eq. (6.46) of Frank and Tamm and evaluated the energy, W, radiated by an electron taking into consideration that the magnitude of the electron velocity, *i.e.*, the magnitude of β, will vary greatly over the entire path length of travel of the electron. Čerenkov (1938c) thus expressed Eq. (6.46) with β as a variable depending on its length of travel l or:

$$W = \frac{e^2}{c^2} \int \omega d\omega \int_{\beta n > 1} \left(1 - \frac{1}{\beta^2 n^2}\right) dl \tag{6.47}$$

Frank and Tamm (1937) calculated the rate of radiated energy per path length of travel, dW/dl, to be of the order of only several kilovolts per centimeter. Thus, it was found that the electron energy loss via the emission of Cherenkov radiation would be a negligible quantity of energy in comparison to the energy lost by the electron by other mechanisms, such as ionization (This was discussed by Jelley, 1961 as mentioned in III. B.). Čerenkov (1938c) confirmed this through calculations and experimentation and concluded that the radiation expended by β-particles from Ra(B + C), *i.e.*, ^{214}Pb + ^{214}Bi, via the emission of Cherenkov radiation amounts to a value of the order of only 0.1% of the total energy of the particles.

From Eq. (6.46) Frank and Tamm (1937) deduced the equation for the Cherenkov photon radiation intensity, *i.e.*, the number of photons emitted by an electron per path length of travel, as follows:

$$dN = 2\pi\alpha \left(\frac{1}{\lambda_1} - \frac{1}{\lambda_2}\right) \left(1 - \frac{1}{\beta^2 n^2}\right) dl \tag{6.48}$$

where dN is the number of photons emitted in path length dl within the spectral region defined by the wavelengths λ_1 and λ_2, α is the fine structure constant ∼ 1/137, and β and n are the particle phase velocity and the index of refraction of the medium, respectively. From Eq. (6.48), Belcher (1953) assumed the index of refraction to be constant over the spectral range studied and expressed the total

number, N_E, of photons radiated along the track of a particle of initial energy E and brought to rest within the medium as

$$N_E = 2\pi\alpha\left(\frac{1}{\lambda_1}-\frac{1}{\lambda_2}\right)\int_{\beta=\beta_{max}}^{\beta=1/n}\left(1-\frac{1}{\beta^2 n^2}\right)dl \qquad (6.49)$$

where β_{max} is the maximum phase velocity, *i.e.*, the initial phase velocity of the particle, and $1/n$ is the limiting phase velocity of the particle, *i.e.*, the velocity at which Cherenkov photons cease to be produced. Belcher (1953) reduced Eq. (6.49) to read

$$N_E = A\int_{\beta=\beta_{max}}^{\beta=1/n}\left(1-\frac{1}{\beta^2 n^2}\right)dl \qquad (6.50)$$

where $A = 2\pi\alpha[(1/\lambda_1 - 1/\lambda_2)]$. For the spectral range of $\lambda_1 = 3000$ to $\lambda_2 = 7000$ Å, the value of A is calculated to be

$$\begin{aligned} A &= 2\pi\alpha\left(\frac{1}{\lambda_1}-\frac{1}{\lambda_2}\right) \\ &= 2(3.14)(0.007297)\left(\frac{1}{3\times10^{-5}\text{cm}}-\frac{1}{7\times10^{-5}\text{cm}}\right) \\ &= 874\ \text{cm}^{-1} \end{aligned} \qquad (6.51)$$

Over the defined spectral range, Eq. (6.50) is reduced to

$$N_E = 874\int_{\beta=\beta_{max}}^{\beta=1/n}\left(1-\frac{1}{\beta^2 n^2}\right)dl \qquad (6.52)$$

Belcher (1953) evaluated the integral defined by Eq. (6.52) by firstly determining the range–energy function for an electron in water ($n = 1.33$ and $\rho = 1.00$ g/cm^3) and Perspex plastic ($n = 1.50$ and $\rho = 1.18$ g/cm^3). He plotted the values of $\left(1-1/\beta^2 n^2\right)$ against the range of electrons in water and Perspex plastic. He then evaluated Eq. (6.52) by graphical integration to obtain the expected values of N_E as a function of electron energy in water or Perspex plastic, which is illustrated in Fig. 6.10. As can be seen in Fig. 6.10, photons are not produced by electrons below 0.175 MeV in the Perspex plastic or 0.260 MeV in water, which are the respective threshold energies for the Cherenkov Effect in these two materials.

Frank and Tamm (1937) made an approximate calculation that a 500 keV electron, which would correspond to $\beta^2 = 0.75$, traveling in water, where $n = 1.33$, would produce approximately 10 photons per 0.1 cm within the visible region between $\lambda_1 = 4000$ Å and $\lambda_2 = 6000$ Å according to Eq. (6.48), i.e.,

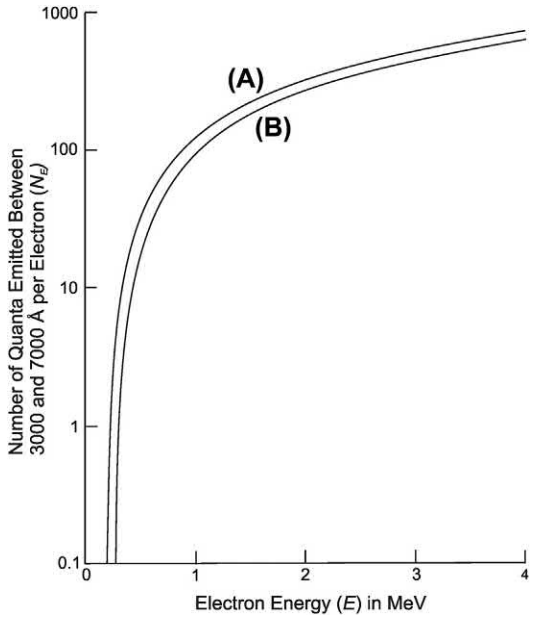


FIGURE 6.10 A plot of the number of Cherenkov photons in the spectral range of 3000–7000 Å produced by an electron in (A) Perspex plastic ($n = 1.50$) and (B) water ($n = 1.33$) over its entire range of travel as a function of electron energy. *From Belcher (1953), reprinted with permission ©1953 The Royal Society.*

$$\begin{aligned} \frac{dN}{dl} &= 2\pi\alpha\left(\frac{1}{\lambda_1}-\frac{1}{\lambda_2}\right)\left(1-\frac{1}{\beta^2 n^2}\right) \\ &= 2(3.14)\left(\frac{1}{137}\right)\left(\frac{1}{4\times10^{-5}\text{cm}}-\frac{1}{6\times10^{-5}\text{cm}}\right) \\ &\quad\left(1-\frac{1}{(0.75)(1.33)^2}\right) \\ &= 94.1\ \text{photons/cm} \approx 10\ \text{photons/0.1 cm} \end{aligned}$$

Their approximation came very close to the above more precise calculations of Belcher (1953), which indicate that a 0.500 MeV electron would produce approximately 20 photons in water (Fig. 6.10). With a range of 0.2 cm in water, the rate of photons production by a 0.5 MeV electron would be 10 photons per 0.1 cm.

The above calculations for the number of photons emitted as a function of a single electron of known energy in a transparent medium are more complex when dealing with β-particles. This is so, because β-particles are emitted from radionuclides with a broad spectrum of energies between 0 and E_{max}. In such a case, Belcher (1953) noted that

it is necessary to combine the function N_E of Eq. (6.49) or (6.50) with the energy distribution function of the electrons released within the medium. He therefore elaborated that, if p_E is the probability of release of an electron possessing energy between the limits E and $(E + dE)$, then the average total intensity I of Cherenkov photon emission per electron is given by the following:

$$I = \int_0^{E_{\max}} p_E N_E dE. \tag{6.53}$$

The property of photon intensity is of particular relevance in studies on the measurement of Cherenkov radiation for particle identification and radionuclide analysis, a subject to be dealt with further on in this chapter. The photon intensity is also expressed in terms of the number of Cherenkov photons created per unit photon energy. As noted by Križan (2001) for particles above the threshold $\beta = 1/n$, that is $\beta > 1/n$, the number of Cherenkov photons emitted per unit photon energy in a medium of particle path length L is

$$\frac{dN}{dE} = L\frac{\alpha}{\hbar c}\sin^2\theta \tag{6.54}$$

where α is the fine structure constant (1/137), $\hbar$ is Planck's constant divided by 2π (*i.e.*, $h/2\pi = 6.582 \times 10^{-16}$ eV·s, c is the speed of light in a vacuum or 2.998×10^{10} cm/s, and θ is, as previously defined, the angle of emission of the Cherenkov photons relative to the direction of travel of the charged particle. Taking the values of the aforementioned constants, the term $\alpha/\hbar c$ of Eq. (6.54) becomes 370 eV^{-1} cm^{-1}. From Eq. (6.54), Križan (2001) calculated, that in 1 cm of water, a particle track where $\beta = 1$ (ultrarelativistic or most energetic particle possible) emits $N = 320$ photons in the spectral range of visible light ($\Delta E \approx 2$ eV). Since a high-energy electron (*e.g.*, 1000 GeV) does not lose significant energy in 1 cm of water, otherwise the angle of emission would diminish as the electron loses energy and its velocity reduces, the above number of 320 photons is calculated as follows:

Since the angle of emission θ of the Cherenkov photons for a particle of given energy and velocity is defined by

$$\cos\theta = \frac{1}{\beta n} \tag{6.55}$$

and, because the charged particle at ultrarelativistic speeds approaches the speed of light in a vacuum or β approaches 1, we can write

$$\cos\theta = \frac{1}{n} \tag{6.56}$$

If water is the medium

$$\cos\theta = \frac{1}{1.333} = 0.75018 \tag{6.57}$$

and then

$$\cos^{-1}0.75018 = 41.4^{\circ} \tag{6.58}$$

Thus, the number of photons emitted (ΔN) over the energy range of the visible spectrum ($\Delta E \approx 2$ eV) in the particle path length of 1 cm in water is calculated according to Eq. (6.54) as

$$\begin{aligned}\Delta N &= L\frac{\alpha}{\hbar c}\sin^2\theta\Delta E \\ &= (1\text{ cm})\left(370\text{ eV}^{-1}\text{cm}^{-1}\right)\left(\sin^2 41.4^{\circ}\right)(2\text{ eV}) \\ &= 320\text{ photons}\end{aligned}$$

In the instrumental detection of Cherenkov photons there is an efficiency factor, which defines the efficiency of an instrument to detect the photons. With an average instrumental detection efficiency of $\varepsilon = 0.1$ over the spectral interval in the example given above, only $N = 32$ photons would be measured. The detection efficiency for Cherenkov photons should not be confused with the term counting efficiency of each particle that interacts with the medium, which is employed in radionuclide analysis, as it will be seen in this chapter that Cherenkov counting efficiencies can be >70% or >0.70.

The number of photons emitted per path length of electron travel in the wavelength interval between λ_1 and λ_2 is calculated by Sowerby (1971) according to

$$\frac{dN}{dl} = 2\pi\alpha z^2\left(\frac{1}{\lambda_1} - \frac{1}{\lambda_2}\right)\sin^2\theta \tag{6.59}$$

where α is the fine structure constant ($e^2/\hbar c = 1/137$), z is the particle charge ($z = 1$ for electrons or beta particles), and the refractive index of the medium and particle velocity appear in the $\sin^2\theta$ term. Over the visible range of wavelengths from $\lambda_1 = 400$ to $\lambda_2 = 700$ nm, Eq. (6.59) becomes

$$\begin{aligned}\frac{dN}{dl} &= 2(3.14)(.007297)(1)^2 \\ &\quad\left(\frac{1}{4\times10^{-5}\text{cm}} - \frac{1}{7\times10^{-5}\text{cm}}\right)\sin^2\theta \\ &= 490\sin^2\theta\text{ cm}^{-1}\end{aligned} \tag{6.60}$$

Sundaresan (2001) also estimated the number of photons N per path length L to be

$$N/L = 490\sin^2\theta\text{ cm}^{-1}, \tag{6.61}$$

The emission angle θ would diminish as the particle loses energy and velocity. It can be considered constant over particle path lengths where the particle does not undergo significant energy loss.

G. Cherenkov photon emissions and counter geometry

The Cherenkov effect is the result of a physical disturbance caused by the high-energy charged particle along its path of travel resulting in a directional anisotropic emission of light. Therefore, there is no chemical fluorescence nor the relatively long excitation decay times associated with fluorescence.

Conventional liquid scintillation counters equipped with photomultiplier tubes (PMTs) are most often used to count the individual beta-particle emissions by detecting the Cherenkov photons produced by a beta particle that may be emitted from samples containing β-particle-emitting radionuclides in solution within transparent liquid media or deposited onto the surface of other types of media such as glass or plastic. The directional emission of Cherenkov photons is a disadvantage when conventional liquid scintillation spectrometers are used for counting Cherenkov photons. The photocathodes of most liquid scintillation counters consist of two PMTs positioned at 180 degrees relative to each other. This is not an optimum arrangement for the detection of Cherenkov photons; however, reflector material on the surface of the counting chamber walls facilitates the detection of the Cherenkov photons, which otherwise would not reach the PMTs in coincidence. Thus, when conventional liquid scintillation counters are employed for Cherenkov counting, the counting efficiencies are inferior to the theoretical maximum efficiencies.

Extensive treatments of the origin and interpretation of Cherenkov radiation are given by Marshall (1952), Belcher (1953), Cherenkov (1958), Jelley (1958, 1961), Gruhn and Ogle (1980), and Kulcsar et al. (1982), and in a book by the writer (L'Annunziata, 2016), and a comprehensive theoretical and practical treatment of Cherenkov radiation and its application to radionuclide standardization is available in a book by Grau Carles and Grau Malonda (1996a).

IV. Quenching and quench correction

The first demonstration of the potential of counting Cherenkov photons to measure the activity of radionuclides was reported by Belcher (1953), a former colleague of the writer at the International Atomic Energy Agency. He used a single photomultiplier cooled with liquid nitrogen to reduce background due to thermal noise and measured Cherenkov radiation intensity in terms of count rates per mCi of various radionuclides in aqueous solution. With the subsequent development of low-background dual PMT counters, the technique of counting Cherenkov photons has become a very useful tool in the measurement of radionuclide activities. One of the great advantages of Cherenkov counting is the potential radioactivity analysis of the sample in its original state (i.e., aqueous solution or other suitable solvent) without the need to add any reagents. The principle interference is color quenching, which can occur when sample color reduces the Cherenkov photon intensity emitted by a sample to be measured.

Chemical quenching in Cherenkov counting is nonexistent because Cherenkov photons arise from a physical formation of a wavefront in the medium in contrast to chemical fluorescence, which occurs in the liquid scintillation phenomenon. However, color quenching can be very significant in Cherenkov counting, greater than that which may occur in standard liquid scintillation counting techniques, as reported by Elrick and Parker (1968), because Cherenkov photon intensities are weaker and cover a wider spectrum of wavelengths than those produced in scintillation. The counting efficiency in Cherenkov radioassay is determined by one of the quench correction techniques subsequently discussed. The most common quench correction method is based on various mathematical indicators called quench indicating parameters (QIPs), as reported by Tsroya et al. (2012). In practice, Cherenkov counting usually involves quench correction based on indexes used in LSC systems. The QIPs fall into two categories: those based on calculations of parameters from the spectrum of the sample containing the radioactive material, and those based on parameters calculated from the spectra obtained with an external source. In the first category, the conventional methods are based on using the relationship between the pulse height distribution shift and counting efficiency. The parameters used are the sample channels ratio (SCR) and spectral index of the sample (SIS). In studies by Mosqueda et al. (2007) and Vaca et al. (1998), the SCR correction method was used. Takiue et al. (1996) employed the SIS method too, but they mentioned the potential advantage of the external standard method, which they could not use because of the low gamma energy of their external source. A disadvantage of the methods based on the measured samples is that they depend on the activity of the sample and cannot be applied to low-activity samples because of the high statistical uncertainty. There is no such problem when an external radiation source is used. Therefore, most common quench correction methods in liquid scintillation counting use external γ-ray sources. These methods include the external source channel ratio (ESCR), the sample quench parameter of the external standard (SQP(E)), and the transformed spectral index of the external standard (tSIE). The ESCR method is similar to the SCR method, using the ratio between the two channel ranges of the outer source spectrum. Kamp and Blanchard (1971) applied the ESCR method to the external ^{226}Ra—^{241}Am source spectrum for quench correction in Cherenkov counting. Other researchers, e.g., Nascimento (1977) and Elrick and Parker (1968), used an additional high-energy gamma source in the system that could

produce a Cherenkov effect in the sample. In a study by Tarancón et al. (2002a), the SIS, tSIE, and SCR indexes were compared in measurements of the activity of a $^{90}Sr/^{90}Y$ source by means of the Cherenkov counting, LSC, and plastic scintillation techniques.

A. Internal standardization

This method is described in Chapter 6, Volume 1. It is highly accurate, if performed properly. The main disadvantage of this quench correction technique is that it is time consuming, as it requires the counting of each sample before and after the addition of standard.

B. Sample channels ratio

This method is described in Chapter 6, Volume 1 and in previous texts by the writer (L'Annunziata, 1979; 1984a; 1987). The SCR technique was a most popular method of monitoring for quench with the older-generation liquid scintillation counters equipped with a single channel analyzer for data storage and pulse height gain control. Contemporary liquid scintillation analyzers are equipped with a multichannel analyzer (MCA), which permit the facile measurement of a sample spectrum QIP such as SIS or SQP(I) described in Chapter 6, Volume 1. Nevertheless, the SCR technique is accurate and is still used by researchers. The SCR technique is particularly applicable to Cherenkov counting color quench correction when the counter is not equipped with an external standard that emits gamma rays with sufficient energy to produce the Cherenkov effect in sample counting vials. Some examples of the application of the SCR technique to the Cherenkov counting analysis of particular radionuclides will be cited here.

A good example of the SCR technique applied to color quench correction in the Cherenkov counting of ^{32}P and ^{36}Cl can be taken from the work of Fujii and Takiue (1988a). To establish the SCR, the pulse height discriminators of a given counting window (*e.g.*, Channel A) are selected generally to encompass all pulse events, and the discriminator settings for another counting window (*e.g.*, Channel B) are selected to encompass only a part of the pulse height spectrum for the least quenched sample as illustrated in Fig. 6.11. When quench occurs, the ratio of counts in Channel B (Fig. 6.11) to counts in Channel A (B:A) will change as pulse heights shift from right to left (higher to lower magnitude) along the pulse height spectrum. After testing various widths for Channel B, the optimum width of Channel B is selected as that which gives the most linear plot over the greatest range of detection efficiency. Therefore, counting a series of quenched standards containing variable color quench levels similar to those described in Table 6.2 will produce a SCR quench correction curve of percent counting efficiency versus SCR. Examples of SCR color quench correction curves for ^{32}P and ^{36}Cl are illustrated in Fig. 6.12, as reported by Fujii and Takiue (1988a) from counting channels illustrated in Fig. 6.11. The counting efficiency for the SCR quench correction curve is calculated from the count rate of the

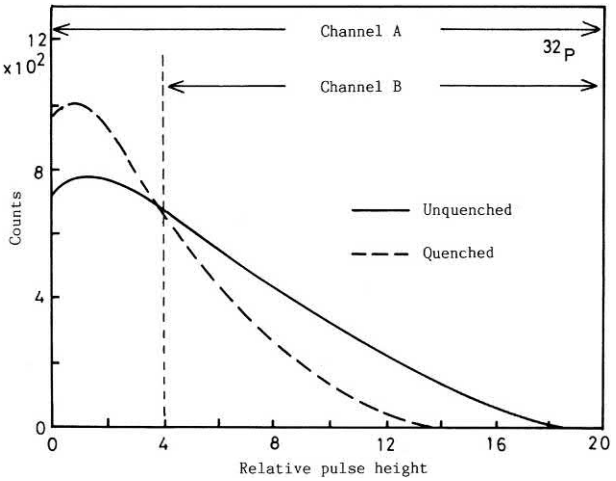


FIGURE 6.11 ^{32}P Cherenkov pulse height distribution and channel settings for the sample channels ratio (SCR) method. The pulse height distribution shifts toward low pulse height with color quenching. *From Fujii and Takiue (1988a), reprinted with permission from Elsevier ©1988.*

TABLE 6.2 Constituents of ^{32}P nonquenched (vial 1) and quenched (vials 2 to 10) standards in water for the preparation of a Cherenkov counting quench correction curve.[a]

	Vial constituents (mL)		
Vial number	H_2O	Quenching agent (0.01% CrO_3)[b]	Standard [^{32}P] phosphate
1	14.0 mL	0.0 mL	1.0 mL
2	13.5	0.5	1.0
3	13.0	1.0	1.0
4	12.0	2.0	1.0
5	11.0	3.0	1.0
6	10.0	4.0	1.0
7	9.0	5.0	1.0
8	8.0	6.0	1.0
9	6.0	8.0	1.0
10	4.0	10.0	1.0

[a] *From L'Annunziata (1987), reprinted with permission from Elsevier © 1987.*
[b] *The CrO_3 concentration in the standards varies over the range of 0%–0.0066%, producing a yellow color of increasing intensity.*

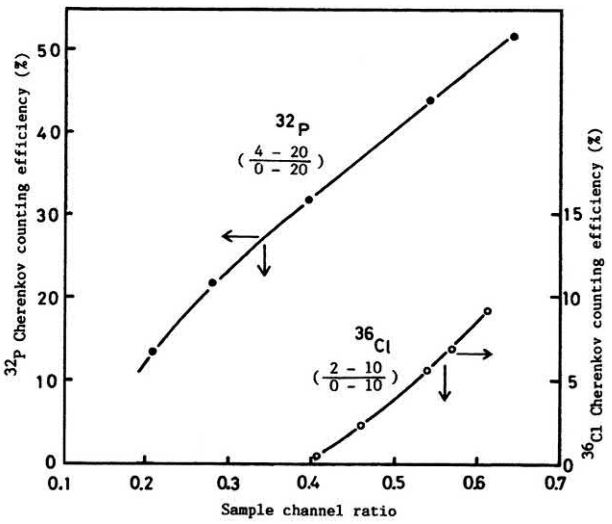


FIGURE 6.12 Color quench correction curves for the sample channels ratio method in the Cherenkov measurement of ^{32}P and ^{36}Cl. *From Fujii and Takiue (1988a), reprinted with permission from Elsevier ©1988.*

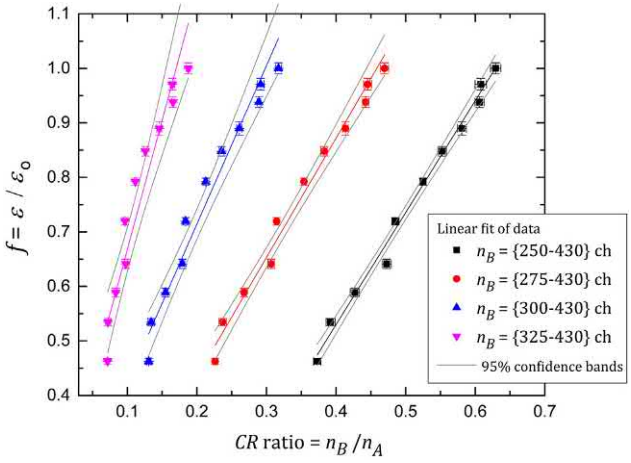


FIGURE 6.13 Calibration correction—SCR method. *From Todorović et al. (2017), reprinted with permission from Elsevier ©2017.*

wide-open Channel (A) The SCR value of an unknown sample will give the percent counting efficiency from the quench correction curve. The activity of the sample in DPM is then obtained by dividing the count rate from Channel A (the wide-open counting region) by the decimal value of the percent counting efficiency.

There is no set rule for the establishment of window widths in the SCR quench correction method. It is only important, that the wider or most open counting window or channel provide an acceptable or optimum detection efficiency for the radionuclide of interest; and the more narrow window yields an SCR color quench correction curve that yields the most accurate monitor of color quench in the experimental samples. With this in mind, Mosqueda et al. (2006, 2007) carried out statistical analyses to determine the optimum channel widths for the establishment of SCR color quench correction curves for the low-level Cherenkov counting of ^{90}Sr/^{90}Y. The objective of such optimization is to attain optimum lower limits of detection.

In order to determine the relationship between color factor (f) and CR, Todorović et al. (2017) prepared a set of 10 standards of the same ^{90}Sr/^{90}Y activity which was added to a growing concentration of colored attenuation (yellow dye). As the range of the B window should be started from the channel with the highest count rate, four different windows were selected and the CR factor determined. The results of the measurements indicate that the color factor (f) value increases as the channel ratio factor (CR) approaches the reference value (for which f = 1). According to certain published data, the dependence f(CR), over a wide range from 0.2 to 1, obeys a second order polynomial fit (Vaca et al., 1998; Mosqueda et al., 2007), although the results obtained in the examined range very well describe a linear fit, as shown in Fig. 6.13, and as reported in Todorović et al. (2017).

The SCR technique has been applied to color quench correction in the Cherenkov counting of several radionuclides. Stubbs and Jackson (1967) prepared a series of color-quenched standards in liquid scintillation counting vials each containing ^{32}P of the same activity (1.85 kBq) and increasing amounts of Scarlet R or Naphthol Yellow S dye as color quencher. The quantity of dye per vial ranged from 0.01 to 3.00 mg. The SCR technique has been employed successfully for counting efficiency determinations in the Cherenkov counting of ^{42}K in biological samples by Moir (1971) and of ^{34m}Cl, ^{36}Cl, and ^{38}Cl, as well as ^{32}P by Wiebe et al. (1980), who used a 1% solution of potassium dichromate in water as the color quenching agent for the preparation of standard quench correction curves.

The SCR technique was also used for the determinations of ^{36}Cl and ^{32}P in tissue solubilizer solutions (see Bem et al., 1983). The SCR technique for the color quench correction in the Cherenkov counting of ^{90}Y was reported by Torres et al. (1996) in the environmental analysis of ^{90}Sr. The writer has employed the SCR quench correction technique successfully for the assay of ^{32}P in water using 0.01% CrO_3 as a quenching agent (L'Annunziata, 1984a, 1987). Increasing amounts of CrO_3 solution, which is yellow in color, are added to a series of liquid scintillation vials, each containing the same activity of ^{32}P standard (*e.g.*, 3.7 kBq/mL) as described in Table 6.2. Water is added to bring the quenched standards to a uniform and optimum volume. Also 0.01% aqueous $K_2Cr_2O_7$, which is yellow in color, serves as a good quenching agent for the preparation of quenched standards (L'Annunziata, 1987).

Although a yellow color is used in the above procedure, Stubbs and Jackson (1967) and Bem et al. (1980) report identical SCR quench correction curves when either a yellow or a red dye is employed as the quenching agent. The SCR technique for quench correction has been employed successfully by Frič and Palovčíková (1975) and Karamanos et al. (1975) for the assay of ^{32}P and ^{210}Pb, Carmon and Dyer (1987) for the Cherenkov assay of ^{106}Ru, Takiue et al. (1993, 1996) for the Cherenkov measurements of ^{36}Cl, ^{32}P, and ^{90}Sr(^{90}Y), and Vaca et al. (1998) and Tarancón et al. (2002a) for the Cherenkov efficiency calibration of ^{90}Y colored samples. For low-activity samples, Tarancón et al. (2002a) found the SCR technique and the sample spectrum quench indicating parameter (SIS) suitable for color quench correction in the Cherenkov counting of ^{90}Sr/^{90}Y at low level in water samples with relative errors of <5%. They consider the SCR method the better option of the two quench correction techniques for color quench correction in ^{90}Sr/^{90}Y measurements, as the SCR method was found to be less dependent on the sample activity level. This was due to the fact that the SIS quench indicating parameter is dependent on the measurement of the total spectrum, which includes the background spectrum; whereas, the windows used for the SCR technique in the low-level measurement of ^{90}Sr/^{90}Y can be chosen to minimize the contribution of the background spectrum.

C. Sample spectrum quench indicating parameters

Modern liquid scintillation analyzers are equipped with a MCA, which permits the measurement of a sample spectrum quench-indicating parameter (QIP) such as SIS or SQP(I) described in Chapter 6, Volume 1. The use of a sample spectrum quench-indicating parameter to correct for color quench in Cherenkov counting offers several advantages over the previously described SCR quench correction technique, among which are the following: (1) the time consuming procedure of testing several channel region settings to produce the most linear SCR quench correction curve is avoided, (2) error arising from different count rates in two counting regions required to produce a SCR are avoided, and (3) computer automation in the measurement of the sample spectrum and the QIP associated with the sample spectrum results in ease of preparation and error reduction in generating the plot of the quench correction curve and in the automated reading of the quench correction curves to determine counting efficiencies of unknown samples. The accuracy of the determination of the sample spectrum QIP [*i.e.*, SIS or SQP(I)] is sample count-rate dependent; and for low-level counting a sample must be counted for sufficient time to attain a well-defined sample pulse height spectrum from which the instrument will measure the sample spectrum QIP.

The use of a sample spectrum QIP requires first a determination of an optimum counting region, which is described subsequently.

1. Counting region

The counting region must first be defined by observing the pulse height spectrum of the Cherenkov photons with the computer monitor display from the MCA of the liquid scintillation analyzer. A colorless sample of the radionuclide of interest is placed into a plastic liquid scintillation vial; and the sample pulse height spectrum is observed as illustrated in Fig. 6.14. Plastic counting vials are recommended, instead of glass, for highest Cherenkov photon detection efficiency and lower backgrounds (see Section V.B of this chapter). A colorless sample is selected, as this would represent the least quenched sample achievable. The pulse heights originating from Cherenkov radiation in water do not generally exceed the equivalent of ~50 keV for pulse height spectra calibrated on an energy scale. This may differ for other instruments that do not use such a scale; however, the limits of the pulse height spectra can be determined easily on the computer monitor output from the MCA. For the example illustrated in Fig. 6.14, the counting region can be defined by setting the lower level (LL) discriminators and upper level (UL) discriminators at 0–30 keV, respectively.

2. Quench correction

Although there is no chemical quench in Cherenkov counting, color quench correction is necessary if samples are colored even to a slight extent. In many applications of

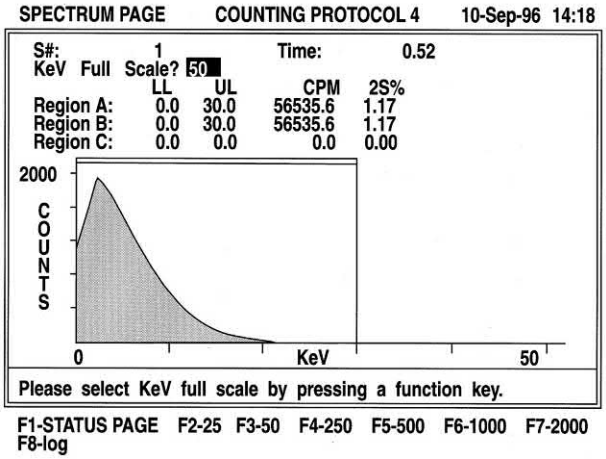


FIGURE 6.14 Pulse height spectrum produced by Cherenkov photons from a sample of ^{32}P in water as seen on the computer monitor of a PerkinElmer Tri-Carb 2300 TR liquid scintillation analyzer. A counting region of 0–30 keV was selected to encompass all pulse heights originating from the ^{32}P radionuclides in the sample. *From L'Annunziata (1997), © 1997–2019 PerkinElmer, Inc. Printed with permission.*

biology, biochemistry, environmental monitoring, and agricultural research, among other fields, the radionuclide of interest [*e.g.*, ^{32}P, ^{89}Sr, $^{90}Sr/^{90}Y$] must be analyzed in animal or plant tissue. The tissue may be ashed in a muffle furnace to destroy the organic matter and to put the radionuclide in soluble form. Then the ash may be dissolved in dilute acid. This may leave the sample colorless or at times with only a slight yellow color. Other applications may find the radionuclide already in solution; and it may be desirable not to alter the sample chemically so that the sample may be counted directly. This would permit other studies to be carried out on unadulterated samples. If samples are colored to any extent and decolorization is not performed, a color quench correction curve will be needed.

A color quench correction curve is prepared from a series of color-quenched standards of the nuclide of interest, such as described in the previous Section IV.B of this chapter. The quenched standards can be prepared by adding varying amounts of aqueous coloring agent, such as 0.01% CrO_3 or 0.01% $K_2Cr_2O_7$, to a series of scintillation counting vials as formulated in Table 6.2. A known activity of the radionuclide of interest is added to each vial and the sample volumes are brought up the optimum volume or the volume to be used for the experimental samples. It is important to keep in mind that the volume of the quenched standards, the type of counting vials used (*e.g.*, plastic or glass), and the counting region selected for the quench correction curve should be the same as those used for the analysis of unknown samples.

The quench standards are counted in the optimum region, such as the region of 0–30 keV illustrated in Fig. 6.14; and the count rates (CPM) and QIP of each of the color-quenched standards are recorded. From the count rates and the known disintegration rates of each standard, the counting efficiency of each color-quenched standard is calculated as follows:

$$E_{std} = \frac{CPM_{std}}{DPM_{std}}, \tag{6.62}$$

where E_{std} is the counting efficiency of the quenched standard, CPM_{std} is the count rate of the standard obtained in the previously defined counting region, and DPM_{std} is the known disintegration rate of the quenched standard. Each calculated value of E_{std} is plotted against the pulse height spectrum QIP (*e.g.*, SIS, or SQP(I)) as illustrated in Fig. 6.15. The quench correction curve illustrated in Fig. 6.15 is a plot of the counting efficiency versus the SIS for the radionuclide ^{86}Rb. It was prepared from seven quenched standards in seven counting vials containing a known and exact activity of ^{86}Rb and increasing concentrations of CrO_3 over the range of 0%–0.005% as reported by L'Annunziata and coworkers (see Noor et al., 1996). This CrO_3 concentration range fits within the range of CrO_3 concentrations of the standards described in Table 6.2.

The SIS is derived from the mean pulse height of the spectrum. The magnitude of the SIS provides a measure of the photon intensities escaping the counting vials. This serves as an excellent QIP for Cherenkov counting. Via multichannel analysis, the liquid scintillation analyzer measures the SIS for each quench standard and calculates the counting efficiency of each standard according to Eq. (6.62). The quench correction curve is stored in the memory of the LSA computer; and it is used for the automatic determination of counting efficiencies of all unknown experimental samples from the value of the SIS of each sample. Therefore, in practice, when an experimental

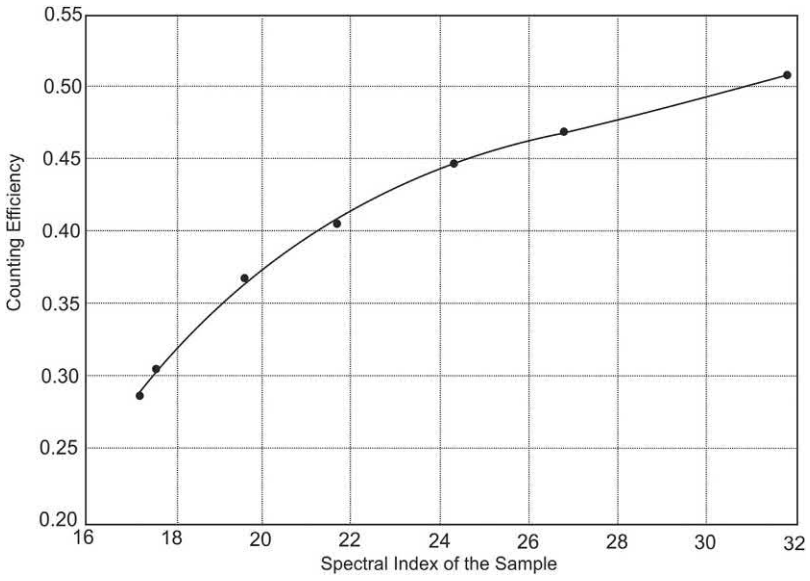


FIGURE 6.15 Color quench correction curve for the Cherenkov counting efficiency determination of ^{86}Rb in water using the Spectral Index of the Sample (SIS) as the quench-indicating parameter. Polyethylene plastic vials were used and the volumes of standards were 15 mL. *From L'Annunziata and coworkers (see Noor et al., 1996), reprinted with permission from Elsevier © 1996.*

sample of unknown activity is counted, its count rate (CPM) is measured in the specified counting region and the SIS of the sample is determined by the LSA. The instrument computer program will take the value of the SIS and extract the sample counting efficiency from the stored color quench correction curve of counting efficiency versus SIS. The instrument will then calculate and print out the activity of the experimental sample according to the equation

$$DPM_S = \frac{CPM_S}{E} \tag{6.63}$$

where DPM_S is the activity in disintegrations per minute of the radionuclide sample, CPM_S is the Cherenkov photon count rate of the radionuclide sample in the counting region selected (*e.g.*, 0−30 keV of Fig. 6.13), and E is the Cherenkov photon counting efficiency of the radionuclide sample obtained from the quench correction curve.

The SIS quench indicating parameter was used successfully by Blasiyh Nuño and Korob (2007) for the preparation of color quench correction curves in the Cherenkov counting of ^{234m}Pa and ^{231}Th with optimum detection efficiencies of 63% and 1.6%, respectively. Similar detection efficiencies and SIS values for ^{234m}Pa were measured by Alamelu and Aggarwal (2009). Quantitative activity recoveries are obtained when using SIS as the QIP as tested by the writer for ^{32}P sample activities (L'Annunziata, 1997). The sample spectrum quench indicating parameter was utilized successfully by Torres et al. (1996) for color quench correction in the Cherenkov counting of ^{90}Y for the analysis of ^{90}Sr in environmental samples.

When the Cherenkov photon count rates are low, as in the measurement of environmental samples, error can occur in the measurement of the SIS because at low activity levels a long counting time is required to measure the sample spectrum quench indicating parameter. Samples should be counted for sufficient time to reach a % 2 sigma (% 2S) of 0.5% standard deviation of the count rate in order to get a good measurement of the sample spectrum upon which the value of the QIP depends. Consequently, when count rates are low, caution should be taken when using the sample spectrum QIP as described previously in Section IV.B. Alternatively, an external standard QIP may be used with certain instruments that are equipped with external standards emitting gamma-radiation of sufficient energy to produce significant Cherenkov photons in the sample vials from Compton electrons. This is described in the following Section IV.D.

D. External standard quench correction

Ross (1980), Smith (1981) and Takiue et al. (1996) reported that the use of external standards is not always applicable to quench correction in Cherenkov counting, because the external standards commonly supplied with some liquid scintillation counters produce Compton electrons from γ-ray interactions, which are too far below the threshold energy for the production of Cherenkov radiation in sample counting vials. However, commercial liquid scintillation analyzers of LKB Rack Beta Instruments are equipped with an ^{226}Ra external standard, which emits considerable quantities of high-energy gamma radiation from daughter nuclides in its decay chain, can produce appreciable numbers of Compton electrons with energies above the Cherenkov threshold of 262 keV in water. A quench-indicating parameter based on the ^{226}Ra external standard, known as the G-number (G #), was patented by Grau Carles and Grau Malonda (1992) to permit the liquid scintillation quench correction of samples under extreme levels of quench where Cherenkov counting in liquid scintillation analysis would predominate. The writer envisages that the G # could be applied also to color quench correction when the Cherenkov Effect is the only source of photons. The G # is described in Section V.C.6 of Chapter 6, Volume 1 and by Grau Carles et al. (1993a).

A more recent study of external standard color quench correction in low-level Cherenkov counting of ^{90}Sr/^{90}Y was made by Tsroya et al. (2009). They demonstrated the use of the ^{152}Eu external standard that is equipped with the PerkinElmer Quantulus low-level LSC, for Cherenkov counting color quench correction. The ^{152}Eu external standard decays by EC in 72.1% of the decays to ^{152}Sm and by negatron (β^-) emission in the remaining 27.9% of the nuclear decays to ^{152}Gd, and only a trace 0.02% of the nuclides decay by positron (β^+) emission (see NuDat 2.7, 2018) and Appendix A. The nuclear decay of the ^{152}Eu external standard is followed with abundant γ-ray emissions of energy capable of producing Cherenkov photons in water. The relevant γ-ray lines with their energies in MeV and their intensities in % are the following: 1.41 MeV (22%), 1.13 (13%), 1.09 (12%), 0.965 (15%), and 0.779 (14%). The threshold Compton electron energy for the production of Cherenkov photons in water is 0.262 MeV or 262 keV as calculated previously by Eq. (6.38); and the threshold γ-ray energy for the production of Compton electrons of 0.262 MeV in water is 0.421 MeV as determined in Section XI of this chapter. All of the γ-ray energy lines from ^{152}Eu decay are well above the gamma threshold energy. Tsroya et al. (2009) demonstrate that the ^{152}Eu external standard yields excellent Cherenkov photon pulse height spectra with a simple 10-min counting time; and the area under the pulse height spectra is a function of the color quench in the sample. Fig. 6.16 illustrates six pulse height spectra produced by aqueous samples quenched with increasing amounts of $K_2Cr_2O_7$ quenching agent, which produces a yellow color. The pulse height spectra move from right to left or from higher to lower pulse height as a function of sample color quench; and the total area under

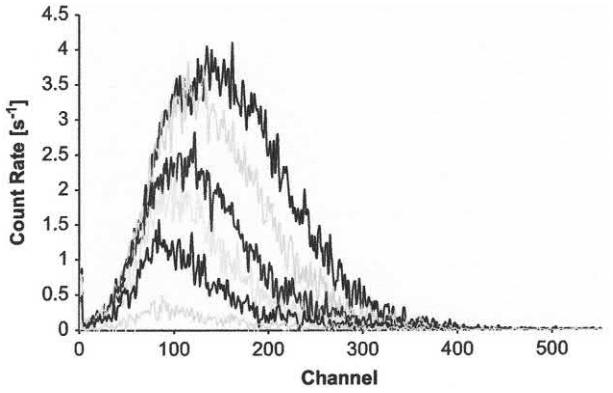


FIGURE 6.16 Cherenkov pulse height spectra obtained with the ^{152}Eu external source of a PerkinElmer Quantulus 1220 LSC for different $K_2Cr_2O_7$ concentrations in the range of 6.67−4050 mg/L. *From Tsroya et al. (2009), reprinted with permission from Elsevier © 2009.*

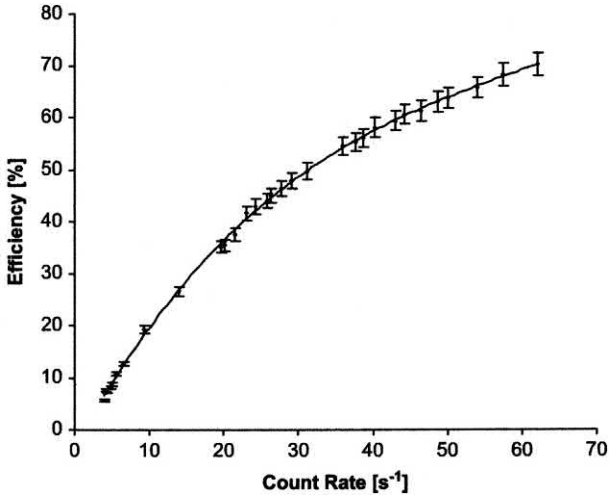


FIGURE 6.17 Quench correction curve for the Cherenkov counting of ^{90}Sr/^{90}Y based on an ^{152}Eu external source. The statistical uncertainty of the count rate was in the range of 0.5%−1.5% and is not shown in the figure. *From Tsroya et al. (2009), reprinted with permission from Elsevier © 2009.*

the pulse height spectra or the external standard counts also diminishes with quench as illustrated in Fig. 6.16.

Tsroya et al. (2009) prepared color-quenched standards for Cherenkov counting with a series of counting vials containing 35.5 Bq of ^{90}Sr/^{90}Y standard in secular equilibrium and increasing amounts of $K_2Cr_2O_7$ color quenching agent in the range of 6.67−4050 mg/L in 20 mL of water in polyethylene plastic vials. The quenching agent yields increasing intensities of yellow color with concentration. The quench correction curve was obtained by counting each vial of the series of quenched standards for a period of 10 minutes with and without exposure to the ^{152}Eu external source of the Quantulus LSC and plotting the detection efficiency versus the external source count rate, as illustrated in Fig. 6.17.

The importance of the application of the external ^{152}Eu standard to the determination of color quench is the potential for accurate external-standard quench correction in low-level Cherenkov counting. Tsroya et al. (2009) calculated the ^{90}Y minimum detectable activities (MDAs) to range from 5.74 to 63.0 mBq/mL over the range of detection efficiencies of 68.5% for clear unquenched samples to 5.35% for highly color-quench samples with corresponding backgrounds of 0.018 s^{-1} to 0.0084 s^{-1} and 10 minutes. counting times.

Tsroya et al. (2012) also compared the performances of color quenching corrections in the SCR and External Standard Area Ratio (ESAR) methods by using various conventional parameters (SIS, tSIE, SQP(E)). The Quantulus 1220 (Wallac Oy, Finland) and measurements of activities of ^{90}Sr/^{90}Y in aqueous solutions were used for the experiments. In the SCR method, the shift in the pulse-height spectrum due to color quenching is measured by the ratio of the counts in two different windows: window B, which corresponds to the high-energy region of the spectrum, and window A, which usually includes the whole spectrum. The ESAR method, initially proposed by Tsroya et al. (2009), consists of two stages. In the first stage, the pulse height spectra with and without the external ^{152}Eu source are stored, and by subtraction the net spectrum of the external source is obtained. The area of this net spectrum is used as an indicator to determine the quench correction factor. In the second stage, the sample is counted for a preset time chosen to achieve the desired statistical accuracy. The activity is calculated from the spectrum obtained in the second stage using the quench correction factor obtained in the first stage. For this purpose, the ratio of the counts in Channel B to the counts in Channel A as a function of the quencher concentration $K_2Cr_2O_7$ was calculated for different settings of Window B, while Window A was left constant to include the whole spectrum. Five ranges were tested for Window (B). It was shown that the most sensitive ranges in Window B are Channels 100−1024, and the greatest change in sensitivity is observed in $K_2Cr_2O_7$ concentrations up to 100−150 mg/L. The measurements with the ^{90}Sr/^{90}Y solution for the SCR method for the same window give the highest sensitivity change in Channels 150−250. The ESCR and SCR dependence on quencher concentration can be seen in Figs. 6.18 and 6.19.

In order to determine the optimal setting for Window B, a polynomial function was found to fit the data of each graph, and its derivative was calculated. The derivative was used for the estimation of the optimal window range for the measurement of low-level activities. A comparison of the performances of the different correction methods was made by using the measured spectra and a calculation of the QIP values. The performance of the method at different

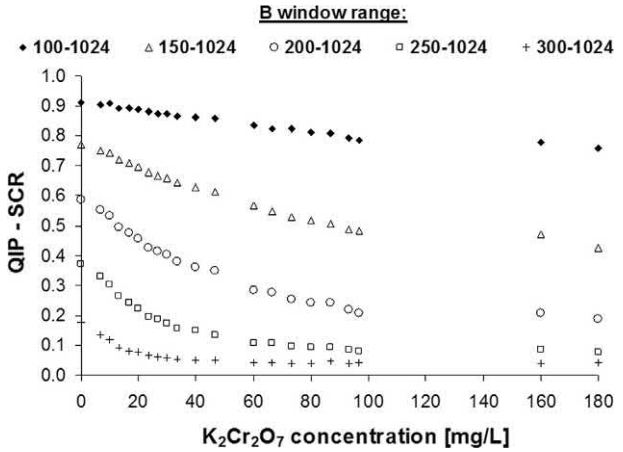


FIGURE 6.18 QIP values for the $^{90}Sr/^{90}Y$ aqueous solution (SCR) at different Window B settings. *From Tsroya et al. (2012); reprinted with permission from Elsevier © 2012.*

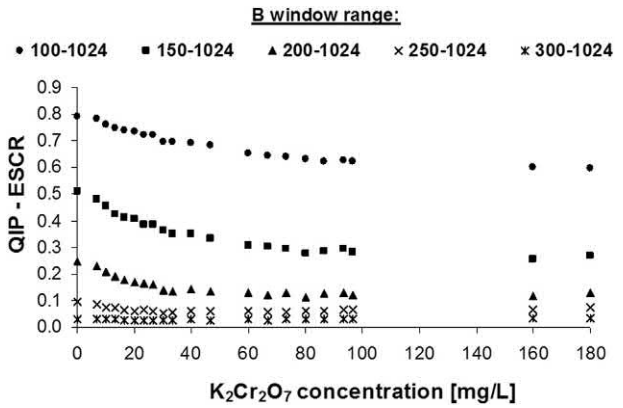


FIGURE 6.19 QIP values for the outer ^{152}Eu source (ESCR) at different Window B settings. *From Tsroya et al. (2012), reprinted with permission from Elsevier © 2012.*

quencher concentrations was normalized to the unquenched value of the specific indicator. It was shown that only the proposed External Source Area Ratio (ESAR) method is adequate for practical use in the whole range of the quencher concentrations, because the QIP value changes monotonously with a high sensitivity to the concentration. The application of the statistical uncertainties to the analysis of each method showed that for the low quencher concentration and the external source, the relative standard deviations of the different methods are similar, ranging from 1.18% to 1.99%. This increases with increases in the concentrations. The smallest increase in the relative standard deviation is for the SIS method (by a factor of 2.19), while the largest (by a factor of 4.62) is for the SQP(E) method. The change for the ESAR method is by a factor of 2.58. However a test of the performance of the ESAR and other methods by means of a comparison of the calibration curves of each method (one for QIP vs. efficiency was constructed) showed the advantages of the ESAR method. The calibration curves were used to quantitatively determine ^{90}Sr concentrations in spiked samples. QIPs were calculated for each spectrum using each of the quench correction methods, and the activity was evaluated using the corresponding calibration curve (polynomial fit). For low quencher concentrations, all methods (except SQP(E)) ensure an accurate determination with small standard deviations. With increases in quencher concentration up to 900 mg/L, a reasonably accurate determination remains for all the methods but with much higher relative standard deviations except for the ESAR method. Further increases in quencher concentration result in a deterioration of the accuracy for all methods, except ESAR, to the limits of eligibility. The ESAR method, even at a high quencher concentration, gives an acceptable result with a deviation of about 8% from the target value.

The ESAR method described here is preferable for low levels; and it is the most sensitive correction method as it works over a very wide range of quenching degrees. Tsroya et al. (2013a, 2013b) exploited these characteristics for the development of the methodology for ^{90}Sr determination in highly quenched samples like urine and milk. For ^{90}Sr determination in urine samples, an efficiency calibration curve specific for urine was prepared for a wide range of quenching levels. The influence of the color fading effect on the quench level due to changes in urine color over time was examined. As shown in Fig. 6.20, ESAR rises over time, so the correction is performed for delayed counting.

The ESAR color quench correction method provides an accuracy of results within a range of ±11.5%. Before counting, the separation method for potassium removal was employed due to the possible contribution of ^{40}K in the Cherenkov measurement. A similar approach was used in

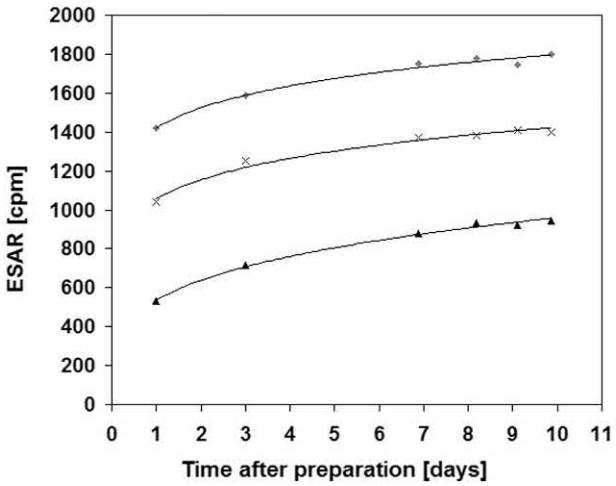


FIGURE 6.20 Dependence of the color quench parameter (ESAR) on the time elapsed after preparation for three samples with different quench levels. *From Tsroya et al. (2013a); reprinted with permission from Elsevier © 2013.*

the method developed for ^{90}Sr determination in different kinds of milk samples (Tsroya et al., 2013b).

Low-level Cherenkov counting of ^{228}Ac for ^{228}Ra analysis in natural water samples with the Quantulus 1220 LSC is reported by L'Annunziata and coworkers (see Aleissa et al., 2008). They report a calculated MDA of 3.24 dpm/L with a Cherenkov photon detection efficiency of 10.9% for ^{228}Ac and a Cherenkov background count rate of 0.317 cpm.

In contrast to conventional Cherenkov counting, in the Triple to Double Coincidence Ratio (TDCR) technique, external calibration is not needed because the effects of color quenching on the Cherenkov efficiency can be automatically corrected based on the measured TDCR values (Kossert, 2010). However, Tayeb et al. (2014) examined the effect of color quenching on ^{90}Y TDCR efficiency. Yellow and brown colorants were chosen because the absorption spectra extended from 350 to 500 nm for yellow and 350−600 nm for brown. These fall in the spectral response range of the TDCR instrument PMTs (commercially available Hidex 300 SL, Electron Tubes 9102 KA PMTs, sensitivity range 290−630 nm, peaking at 370 nm). As illustrated in Fig. 6.21, the ^{90}Y counting efficiency gradually decreased as the light absorption of the colorant increased; and the TDCR correction for the effects of geometry and quenching can yield a difference between the measured and expected activities within 7.5%.

The TDCR technique was primarily developed for radionuclide standardization, as described in Section IX.C of Chapter 6, Volume 1, and the reader can find the principle of the methodology there. The principle of TDCR Cherenkov counting in radionuclide standardization and in the routine analysis of radionuclide activity is discussed further on in this chapter.

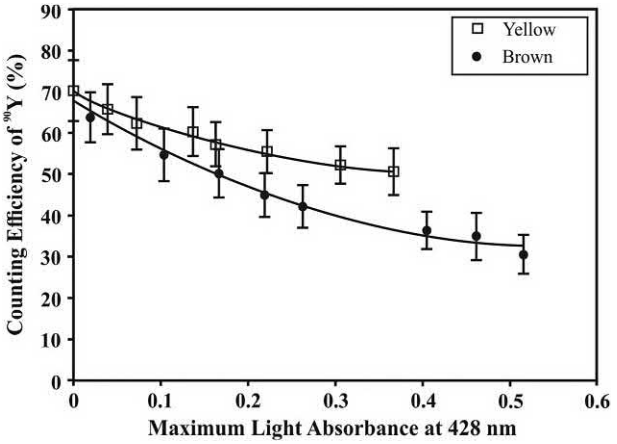


FIGURE 6.21 Effect of color quenching, depicted as counting efficiency of ^{90}Y (15 mL deionized water counted in 20-mL plastic vials), as a function of maximum light absorption by the dye. Error bars indicate combined statistical and systematic uncertainties in counting efficiency at 1 sigma. *From Tayeb et al. (2014), reprinted by permission from Springer Nature © 2014.*

V. Cherenkov counting parameters

The detection efficiencies in Cherenkov counting may be optimized by controlling several counting parameters in addition to the optimum counting region settings previously described. These parameters, which are easily controlled, are discussed subsequently.

A. Sample volume

The detection efficiency of Cherenkov photons can be dependent significantly on the sample volume. The optimum volume may differ from one instrument to another and even from one nuclide to another measured with the same instrument as well as the type of vial used (*e.g.*, glass or plastic). For example, Clausen (1968) reported an optimum volume of 10−11 mL for the Cherenkov counting of ^{32}P with the liquid scintillation counter used. This volume dependence was also tested by Wiebe et al. (1980) for the Cherenkov counting of ^{34m}Cl, ^{36}Cl, ^{38}Cl, and ^{32}P and, for the same instrument, the volume dependence was greatest for ^{38}Cl. The volume in this case also affects the pulse-height spectral shape. This effect was explained by Wiebe et al. (1980) on the basis of the extended range (up to 2.5 cm in water) of the high-energy beta particles emitted from ^{38}Cl ($E_{max} = 4.91$ MeV), which would, for the larger volumes (>4 mL), give rise to more pulses at greater pulse heights. The extended range in water provided by the larger sample volumes also results in an increase in the number of photons produced owing to the longer particle path length of travel. This consequently results in an increase in the probability of producing a detectable pulse. Several other works may be cited where volume effects on the Cherenkov counting efficiency of various nuclides were studied including the following: ^{214}Bi and ^{214}Pb by Al-Masri and Blackburn (1995a); ^{119m}Cd by Ramesh and Subramanian (1997); ^{32}P by L'Annunziata (1997), BenZikri (2000), and L'Annunziata and Passo (2002); ^{86}Rb by L'Annunziata and coworkers (see Noor et al., 1996); and ^{90}Y by Coursey et al. (1993) and L'Annunziata and Passo (2002); and ^{90}Y(^{90}Sr) by Tayeb et al. (2014); and ^{89}Sr, ^{90}Y(^{90}Sr) by Grahek et al. (2012) and Coha et al. (2016).

Volume effects are clearly discernible between different vial types, such as glass and plastic vials, as illustrated in Fig. 6.22. The figure also illustrates that the effect of volume on counting efficiency is more significant in glass then plastic vials. This was also observed in studies by Vaca et al. (1998) and L'Annunziata and Passo (2002) comparing plastic and glass vials in the Cherenkov counting of ^{90}Y. The effects of vial type are discussed in the next section of this chapter. It is important, therefore, that each

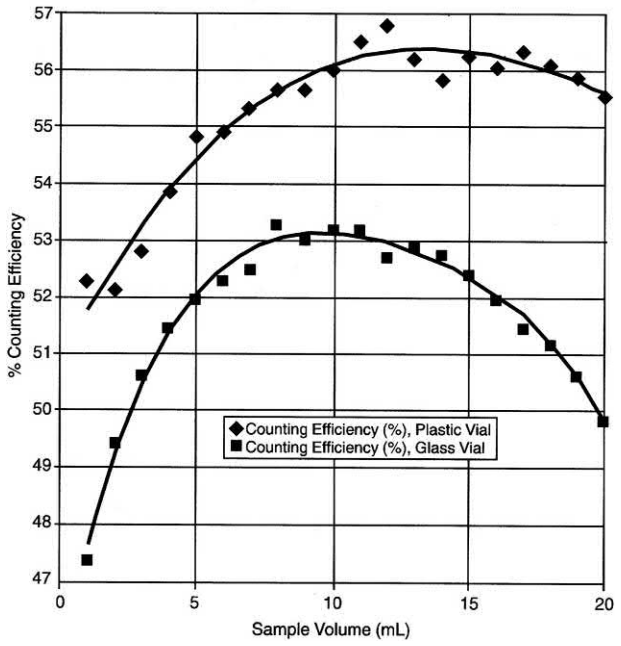


FIGURE 6.22 Effect of sample volume on the Cherenkov counting efficiency of ^{32}P in water with polyethylene plastic and glass counting vials measured with a PerkinElmer Tri-Carb 2300 TR liquid scintillation analyzer. *From L'Annunziata and Passo (2002), reprinted with permission from Elsevier © 2002.*

instrument, vial type, and radionuclide to be analyzed by Cherenkov counting be tested for sample volume effects. These tests can be performed as follows:

1. Place a small volume (e.g., 1.0 mL) of a known activity (DPM) of the aqueous solution of the radionuclide of interest into a 20-mL capacity counting vial.
2. Determine the count rate (CPM) of the sample in the appropriate counting region that encompasses the entire Cherenkov photon pulse height spectrum (e.g., 0–30 keV), and calculate the percent counting efficiency $(\%E)$ according to the equation

$$\%E = \frac{CPM}{DPM}(100) \tag{6.64}$$

3. Add an additional 1.0 mL of pure water to the sample in the counting vial to increase the total volume to 2.0 mL.
4. Recount the sample in the same counting region and calculate again the new counting efficiency according to Eq. (6.64).
5. Repeat steps 3 and 4 until a total sample volume of 20 mL is reached.
6. The $\%E$ versus sample volume is then plotted.

As illustrated in Fig. 6.22, sample volume can have a significant effect on sample count rate and detection efficiency. The effect of sample volume on counting efficiency is greater in glass counting vials, higher counting efficiencies are observed with plastic vials, and only very small changes in counting efficiency ($\sim$1%) occurred in polyethylene plastic vials when sample volumes varied from 9 to 20 mL for the particular vials, radionuclide, and instrument used for these tests. The effect of sample volume on detection efficiency is due to the directional characteristics of Cherenkov radiation. Because Cherenkov photons are emitted at specific angles to the direction of travel of the β particle, changes in volume can affect the angles of deflection by the reflector material in the surrounding counting chamber walls *vis-à-vis* the face of the PMTs. However, plastic counting vials disperse the radiation, reducing its directional properties, whereby the effect of sample volume on detection efficiency is further reduced. Also plastic generally has a higher index of refraction than glass, which would lower the threshold energy for the production of Cherenkov photons by beta particles traveling through the vial walls. The advantages of plastic counting vials in Cherenkov counting are explained further in the following Section V.B of this chapter.

Obviously, if reproducible counting efficiencies are to be maintained, it is necessary that the optimum counting volume be determined experimentally for the particular instrument, vial type, and nuclide employed and that this volume be used for every sample. This can be confirmed with results from literature. Grahek at al. (2012) showed that the detection efficiency of ^{89}Sr and ^{90}Y(^{90}Sr) on the Tri-Carb 2770 TR/SL counter in low-level count mode (LLCM) is higher in plastic than in a glass vial, rises with volume up to 10 mL, and becomes constant from 10 to 16 mL for both types of vial. Coha et al. (2016) examined the influence of the volume of different media on ^{89}Sr and ^{90}Y detection efficiency in low potassium borosilicate glass vials with three different types of instrument with one, two and three PMTs: the Triathler, Tri-Carb 3180 TR/SL and Hidex 300 SL. They showed that the detection efficiency of ^{89}Sr increases with the sample volume to a maximum in the volume interval between 8 and 14 mL, and then slightly decreases depending on the device and type of media used. For ^{90}Y(^{90}Sr), the detection efficiency is constant for volumes above 8 mL when measured with the Tri-Carb, but again slightly decreases with the Hidex 300 SL and Triathler above 14 mL, as illustrated in Fig. 6.23.

Tayeb et al. (2016) examined the influences of volume and counting vial type and size on the Cherenkov counting efficiency of ^{90}Y for the Hidex 300 SL counter. The effects were evaluated using various volumes of 0.1 M HCl. They showed that the counting efficiency of ^{90}Y was in the range of 69%–73% for plastic vials and 59%–64% for glass vials. No observable differences occurred in the counting efficiencies of either plastic vials or glass vials when sample volumes changed, as shown in Fig. 6.24. The

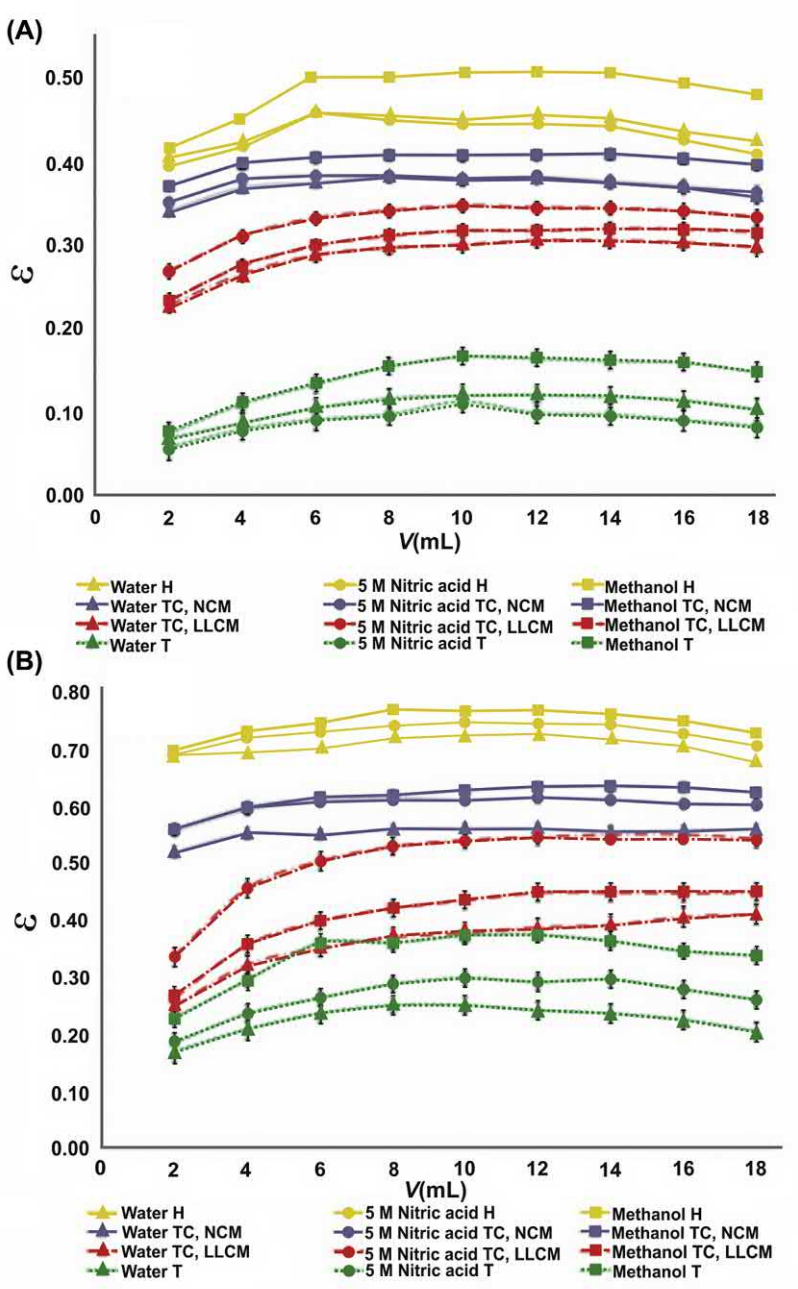


FIGURE 6.23 Dependence of Cherenkov detection efficiency of (A) ^{89}Sr (A *200 Bq) and (B) ^{90}Sr/^{90}Y (A*60 Bq) on volume of different solvents in glass vials. Hidex 300 SL (H), Tri-Carb (TC) in LLCM and NCM and Triathler (T) were used. Counting time was 20 minutes. *From Coha et al. (2016), reprinted by permission from Springer Nature © 2016.*

average counting efficiencies of the glass vials were lower than in the plastic vials by 8% and 10% for each of the 7 and 20-mL vials, respectively.

B. Counting vials

Plastic counting vials produce higher Cherenkov counting efficiencies than glass vials. Because a significant fraction of Cherenkov radiation is emitted in the ultraviolet region, one might assume that the improved detection efficiency in plastic vials is due to the transmission of the UV radiation by the plastic; however, the UV radiation could be absorbed by the glass face of the PMT. Increased Cherenkov detection efficiency provided by plastic counting vials is considered to be due in part to the dispersive or scattering effects of the plastic on the directional (anisotropic)

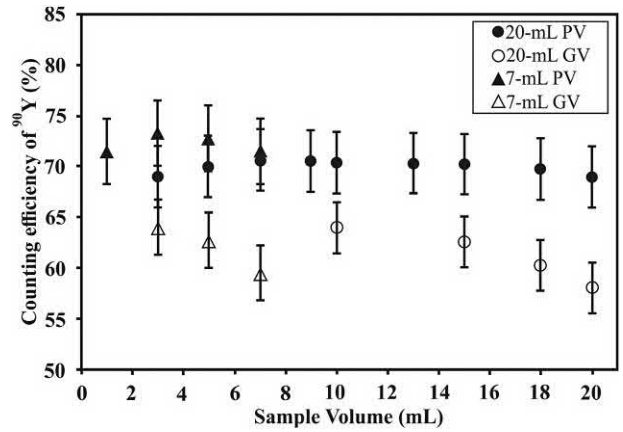


FIGURE 6.24 Counting efficiency of ^{90}Y counted in plastic (PV) and glass vials (GV) as a function of sample volume. Error bars indicate combined statistical and systematic uncertainties in counting efficiency at 1 sigma. *From Tayeb et al. (2014); reprinted by permission from Springer Nature © 2014.*

Cherenkov photons according to Kellogg (1983) and Grau Carles and Grau Malonda (1996a). As described by Takiue et al. (1996), the use of plastic vials changes the directional nature of Cherenkov photons to an isotropic emission, which increases the photon capture efficiency of the PMTs. The pulse height spectra resulting from Cherenkov photons transmitted by plastic and glass counting vials containing ^{86}Rb in water were compared by L'Annunziata and coworkers (see Noor et al. 1996). The photons emitted from the plastic vials were of higher number and pulse height than those emitted by glass vials. The optimum Cherenkov counting efficiency of 53% for ^{86}Rb was obtained with polyethylene plastic vials compared to a 43% counting efficiency when glass vials were used. A similar affect was observed by L'Annunziata and coworkers (see Aleissa et al., 2008) in the Cherenkov counting of ^{228}Ac. The pulse height spectrum from Cherenkov photons produced by aqueous solutions of ^{228}Ac in plastic vials was larger than that produced in glass vials as illustrated in Fig. 6.25 where the optimum detection efficiency of 10.9% was obtained when polyethylene plastic vials were used and 6.6% with glass vials.

Another factor for the improved Cherenkov counting efficiencies obtained with plastic vials over glass vials was demonstrated by L'Annunziata and Passo (2002) with dry samples of ^{90}Y to be due to the higher index of refraction of polyethylene plastics ($n = 1.50-1.54$) compared to that of borosilicate glass ($n = 1.468-1.487$). The higher index of refraction of the plastic yields a lower beta-particle threshold energy for the production of Cherenkov photons when beta particles pass through the walls of the counting vial. The threshold energies for the production of Cherenkov photons in polyethylene plastic and borosilicate glass are calculated according to Eq. (6.38) to be 167 and 183 keV, respectively.

Ross (1980) and Kellogg (1983) reported that polyethylene vials give significantly higher counting efficiencies and lower backgrounds than glass vials. Furthermore, polystyrene vials can offer an improved counting efficiency, which may be due to a weak scintillation effect in the polystyrene. Mietelski et al. (2006) measured slightly increased Cherenkov counting efficiencies for ^{90}Sr/^{90}Y when pieces of polystyrene were immersed into the aqueous solutions prior to counting. In addition to improved counting efficiency, plastic counting vials produce lower backgrounds than glass vials as demonstrated in the Cherenkov counting of ^{90}Y by Passo and Cook (1994), Vaca et al. (1998), and L'Annunziata and Passo (2002), Cherenkov counting of ^{32}P by L'Annunziata (1997), and Cherenkov counting of ^{188}Re by Kushita and Du (1998). Therefore, plastic counting vials provide higher Cherenkov counting figures of merit (FOMs). The term figure of merit is used to optimize sample counting conditions. It is calculated as

$$FOM = \frac{E^2}{B}, \tag{6.65}$$

where E is the counting efficiency expressed as a percent and B is the background count rate in counts per minute

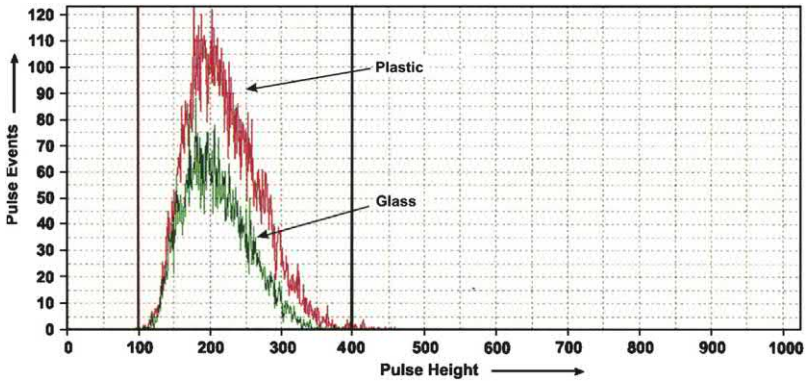


FIGURE 6.25 The Cherenkov photon pulse height spectra produced by beta-particle emissions from ^{228}Ac in aqueous solutions in polyethylene plastic (upper curve) and borosilicate glass vials (lower curve) in a PerkinElmer Quantulus 1220 LSC. *From L'Annunziata and coworkers, see Aleissa et al. (2008), reprinted with permission from Elsevier © 2008.*

TABLE 6.3 ^{32}P Cherenkov counting performance.[a]

Vial type	Count Mode	Counting efficiency (%)	Background[b] (CPM)	Figure of merit (E^2/B)
Plastic[c]	NCM[d]	56.7	16.6	193.7
Glass	NCM	50.2	29.1	86.6

[a]*From L'Annunziata (1997). Printed with permission © 1997–2010 PerkinElmer, Inc.*
[b]*Background measurements were made with triplicate samples of pure water in the counting region of 0–30 keV (LL–UL) and counted for 200 minutes each with a % 2 sigma (%2S) standard deviation of 3.0% with a PerkinElmer Tri-Carb 2300 TR liquid scintillation analyzer.*
[c]*Polyethylene plastic.*
[d]*NCM represents normal count mode where high-sensitivity count mode for low-level counting is not activated.*

TABLE 6.4 ^{90}Sr(^{90}Y) Cherenkov counting performance in a wide-open counting region of 0–30 keV and in an optimized counting region providing optimized FOMs.[a]

Vial type	Count mode	% Efficiency	Background (CPM)	Figure of merit (E^2/B)
0–30 keV window				
Plastic	NCM	71.7	15.8	325
Plastic	LLCM	67.2	11.1	407
Glass	NCM	62.7	24.0	164
Glass	LLCM	53.8	8.0	362
Optimized window				
Plastic	NCM	68.8	13.1	361
Plastic	LLCM	65.6	9.7	444
Glass	NCM	61.5	21.2	178
Glass	LLCM	49.8	6.6	376

[a]*From Passo and Cook (1994). Printed with permission © 1994–2010 PerkinElmer. Inc.*

(CPM). By increasing counting efficiency and/or reducing background, we improve the FOM and the sensitivity of the instrument to measure the radioactivity of the sample. The counting efficiencies, backgrounds, and calculated FOMs for polyethylene plastic and low-potassium glass vials in the Cherenkov counting of ^{32}P in water are listed in Table 6.3, and similar data for the Cherenkov counting of ^{90}Sr(^{90}Y) in water are provided in Table 6.4. The FOM of the Cherenkov counting of ^{32}P is more than doubled on shifting from glass to polyethylene plastic counting vials, and the FOM for the Cherenkov counting of ^{90}Sr(^{90}Y) is improved by almost threefold when shifting glass vials in normal count mode (NCM) to polyethylene plastic vials in LLCM. This is the case for either a wide-open Cherenkov photon counting region of 0–30 keV according to data provided in Table 6.4 or an optimized counting region (*i.e.*, a narrower counting region providing optimized FOMs), as demonstrated by data in Table 6.4. The LLCM listed in Table 6.4 refers to a patented pulse discrimination (TR-LSC) method of reducing background Chapter 6, Volume 1.

In the context of sensitivity enhancement, Grahek et al. (2012) extensively investigated the influence of vial type and media on the background fluctuation and detection efficiency of ^{89}Sr and ^{90}Y(^{90}Sr). They tested the performance of the TriCarb 2770 TR/SL and 3180 TR/SL in a fully open-counting region (0–2000 keV) and LLCM with the aim of maximizing sensitivity in real counting conditions. The background fluctuation was examined by measuring empty and media-filled (nitric acid, water, ethanol, methanol) glass and plastic vials. The measurement was performed by counting each vial for 100 minutes 10 times in controlled conditions, where the temperature and humidity in the counting room were 18–24°C and 35%–55%, respectively. The reported average background level for the different media is about 25% higher for glass vials in relation to plastic vials for both empty and filled vials. An examination of the influence of vials and media (water, nitric acid, methanol, ethanol) on ^{89}Sr and ^{90}Y(^{90}Sr) detection efficiency confirmed that efficiency in plastic vials is higher than in glass vials for both isotopes in all examined media. However, a decrease in the detection efficiency of both isotopes with an increase in the concentration of nitric acid in plastic vials was observed, while in glass vials efficiency slightly increased. The authors attributed these facts to the reaction of HNO_3 at higher concentrations with the plastic vial walls. They assumed that the reaction reduces vial transparency and causes the absorption of photons in the wall, reducing detection efficiency. All results are summarized in Tables 6.5–6.7.

In thorough studies made on the accuracy and reliability of Cherenkov counting, Takiue et al. (1993, 1996) demonstrates a further advantage of plastic over glass counting vials. They used methyl red and bromocresol green as color quenching agents to study the accuracy of quench correction curves based on the SCR or SIS as quench-indicating parameter for the Cherenkov counting of ^{90}Sr(^{90}Y), ^{32}P, and ^{36}Cl in glass and plastic vials for both turbid and clear samples. Turbid samples were prepared by adding small amounts of milk to the aqueous counting medium. The quench correction curves for turbid and clear solutions of the radionuclides were different in glass vials, where the turbid solutions provided higher counting efficiencies as

TABLE 6.5 Cherenkov counting efficiencies of ^{89}Sr and $^{90}Y(^{90}Sr)$—TriCarb instruments.

	Glass vial		Plastic vial	
2770 TR/SL	**ε(^{89}Sr)**	**ε(^{90}Y(^{90}Sr))**	**ε(^{89}Sr)**	**ε(^{90}Y(^{90}Sr))**
1M HNO_3	0.2710 ± 0.0041	0.4508 ± 0.0090	0.3106 ± 0.0046	0.5038 ± 0.0100
3M HNO_3	0.2801 ± 0.0042	0.4661 ± 0.0093	0.3097 ± 0.0046	0.5020 ± 0.0100
5M HNO_3	0.2844 ± 0.0042	0.4738 ± 0.0095	0.2993 ± 0.0045	0.5150 ± 0.0103
8M HNO_3	0.2933 ± 0.0044	0.4831 ± 0.0097	0.2895 ± 0.0043	0.4778 ± 0.0095
H_20	0.2228 ± 0.0033	0.3564 ± 0.0071	0.2539 ± 0.0038	0.3501 ± 0.0070
CH_3OH	0.2343 ± 0.0035	0.3575 ± 0.0071	0.2825 ± 0.0042	0.3227 ± 0.0064
C_2H_5OH	0.1734 ± 0.0026	0.3424 ± 0.0068	0.2746 ± 0.0041	0.3384 ± 0.0068
3180 TR/SL				
1M HNO_3	–	–	0.3346 ± 0.0043	0.5338 ± 0.0100
3M HNO_3	–	–	0.3397 ± 0.0043	0.5430 ± 0.0100
5M HNO_3	–	–	0.3433 ± 0.0044	0.5545 ± 0.0103

From Grahek et al. (2012); reprinted by permission from Springer Nature © 2012.

TABLE 6.6 Level of background radiation for glass and plastic vials and different type of counting media.

	Glass vial			Plastic vial		
	2 mL	**5 mL**	**15 mL**	**2 mL**	**5 mL**	**15 mL**
	b ± s (cpm)[a]	**b ± s (cpm)**	**b ± s (cpm)**	**b ± s (cpm)**	**b ± s (cpm)**	**b ± s (cpm)**
HNO_3 range	2.28 ± 0.25	2.37 ± 0.23	2.95 ± 0.20	1.57 ± 0.12	1.82 ± 0.20	2.21 ± 0.12
	2.11–2.73	2.05–2.65	2.70–3.25	1.37–1.69	1.51–1.91	2.06–2.37
H_2O range	2.10 ± 0.28	2.19 ± 0.18	2.71 ± 0.32	1.46 ± 0.13	1.65 ± 0.17	1.81 ± 0.20
	1.79–2.32	2.04–2.41	2.37–3.18	1.31–1.67	1.44–1.89	1.68–2.13
CH_3OH range	2.01 ± 0.22	2.28 ± 0.21	2.64 ± 0.24	1.69 ± 0.16	1.76 ± 0.13	1.88 ± 0.24
	1.82–2.29	2.09–2.37	2.30–2.87	1.54–1.95	1.61–1.93	1.72–2.3
C_2H_5OH range	2.09 ± 0.29	2.36 ± 0.13	2.80 ± 0.14	1.60 ± 0.09	1.62 ± 0.08	1.69 ± 0.08
	1.68–2.35	2.20–2.57	2.72–2.92	1.50–1.70	1.51–1.70	1.60–1.75
Empty vial range		2.28 ± 0.34			1.82 ± 0.19	
		1.60–2.73			1.30–2.03	

[a] *b ± s is the average ± standard deviation counts per minute (10 counting, 100 minutes).*
From Grahek et al., 2012; reprinted by permission from Springer Nature © 2012.

illustrated in Fig. 6.26. This is probably a result of the dispersion of the directional Cherenkov radiation by the turbidity. However, Takiue et al. (1996) demonstrate that plastic vials give identical quench correction curves for either turbid or clear solutions. All values of percent counting efficiency and quench-indicating parameter fall directly on the same quench correction curve for both turbid and clear solution when plastic counting vials are used, as illustrated in Fig. 6.26.

Cherenkov counting with aqueous samples in plastic vials offers an added advantage because samples may be stored in these vials indefinitely. Relatively short-lived nuclides (*e.g.*, ^{32}P, $t_{½} = 14.3$ days) can be stored as aqueous solutions in the plastic vials until they decay to

TABLE 6.7 Figure of merit (FOM) for TriCarb 2770 TR/SL.

	Plastic vial	Glass vial		Plastic vial	Glass vial	
		FOM[a] ^{90}Sr	P/G	FOM ^{89}Sr		P/G
1M HNO_3	1148	688	1.67	436	249	1.75
H_20	554	469	1.18	356	183	1.94
CH_3OH	554	484	1.14	424	208	2.03
C_2H_5OH	677	418	1.62	446	107	4.16

[a] $FOM = E^2(\%)/A_b(cpm)$.
From Grahek et al. (2012); reprinted by permission from Springer Nature © 2012.

background levels, permitting sample disposal as simple water (see Kellogg, 1983).

Milanović and Grahek (2015) reported for Tri-Carb measurements, that the Cherenkov detection efficiency for ^{89}Sr and ^{90}Y increased when a small plastic vial is inserted in the outer 20 mL vial (holder) and filled with liquid. This corresponds with Kellogg's (1983) enhancement of detection efficiencies when using a combination of 5 mL polyethylene inserted in glass 20 mL vials. Coha et al. (2016) extended their examination to different types of instrument, with one, two and three PMTs: the Triathler, Tri-Carb 3180 TR/SL, and Hidex 300 SL. For determining detection efficiency, the procedure shown in Fig. 6.27 was followed.

A series of aqueous solutions containing radionuclides (^{36}Cl, ^{89}Sr, ^{32}P, and ^{90}Sr/^{90}Y) were prepared and counted on the Hidex 300 SL and Tri-Carb 3180 TR/SL. After efficiency determinations, the outer vials were filled with water and the samples were recounted. The results, summarized in Table 6.8, demonstrate that the detection efficiencies did not significantly change for the Hidex 300 SL but did increase for the Tri-Carb 3180 TR/SL. To explain this phenomenon, the authors took into consideration four main factors: geometrical changes, the penetration of high-energy β-particles into the water in the volume of the outer vial, the absorption and scattering of the Cherenkov photons, and the efficiency limits imposed by the construction of the detection systems.

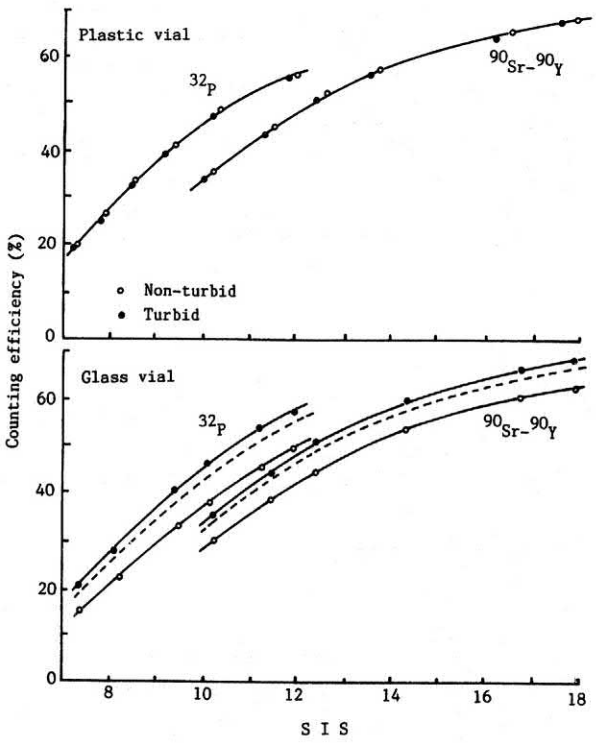


FIGURE 6.26 Color quench correction curves for the Cherenkov measurement of ^{32}P and ^{90}Sr(^{90}Y) for clear and turbid samples in plastic and glass vials using SIS as the quench-indicating parameter. *From Takiue et al. (1996), reprinted with permission from Elsevier © 1996.*

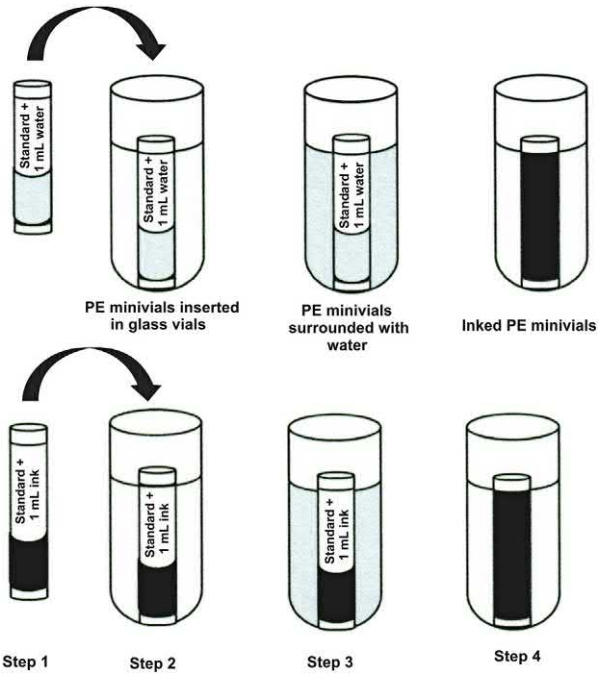


FIGURE 6.27 Scheme of the experimental setup. *From Coha et al. (2016), reprinted by permission from Springer Nature © 2016.*

TABLE 6.8 Cherenkov counting efficiencies for standard radionuclide solutions in 1 mL of a water or an ink on Hidex 300 SL and Tri-Carb (LLCM and NCM).

	Hidex 300 SL		Tri-Carb 3180 TR/SL			
			LLCM		NCM	
Standard	ε (%)	$\varepsilon_{\text{surrounded with water}}$ (%)	ε (%)	$\varepsilon_{\text{surrounded with water}}$ (%)	ε (%)	$\varepsilon_{\text{surrounded with water}}$ (%)
1 mL water solution						
^{36}Cl	14.24 ± 1.51	13.71 ± 1.55	7.74 ± 1.71	8.29 ± 1.90	8.74 ± 2.12	9.16 ± 1.89
^{89}Sr	50.09 ± 1.45	50.44 ± 1.51	30.13 ± 1.60	32.47 ± 1.70	41.97 ± 1.66	43.27 ± 1.53
^{32}P	57.00 ± 1.46	57.29 ± 1.42	–	–	–	–
*^{90}Sr/^{90}Y	70.41 ± 1.30	70.11 ± 1.35	39.13 ± 1.47	50.21 ± 1.51	63.70 ± 1.53	69.45 ± 1.28
1 mL inked solution						
^{36}Cl	1.89 ± 2.32[b]	2.36 ± 2.23	0. 32 ± 3.55	0. 56 ± 3.35	0. 49 ± 3.05	0.58 ± 3. 45
^{89}Sr	10.01 ± 1.73	12.95 ± 1.79	1.94 ± 3.14	3.69 ± 2.87	4.77 ± 2.42	4.86 ± 2.42
^{32}P	15.12 ± 1.65	17.62 ± 1.75	–	–	–	–
[a]^{90}Sr/^{90}Y	22.39 ± 1.57	27.26 ± 1.82	4.80 ± 2.15	12.63 ± 2.38	13.75 ± 2.01	19.47 ± 1.58

The activities of the samples were 100 Bq.
[a]*In equilibrium.*
[b]*1.89 ± 2.32 signifies that efficiency is 0.0189 ± 0.0004.*
From Coha et al. (2016); reprinted by permission from Springer Nature © 2016.

The authors reported that the detection efficiency for the Hidex 300 is energy dependent, so that for low energies, charged particles cannot penetrate into the surrounding water, i.e., the Cherenkov photons are absorbed and scattered in the water and the overall efficiency is lower compared to a situation when only air is present, while high-energy charged particles penetrate into the surrounding water where they cause additional Cherenkov emissions. As a fraction of such particles is energy dependent and increase from ^{89}Sr to ^{90}Sr/^{90}Y, this process can compensate losses of the primary Cherenkov photons in the surrounding water and results with almost constant detection efficiency. They also assumed that the three PMTs of the Hidex with refiection paint encompass fully the cylindrical geometry of the vial. For Tri-Carb measurements, it is assumed that not all of the photons from the inner vial are detected by the two PMTs; and that a significant fraction of Cherenkov photons are generated in the wall of the inner vial, where most of the β-radiation is absorbed. They assumed that the light scattering in the surrounding water results in more isotropic radiation, which can be more efficiently detected due to the principle of Tri-Carb time-resolved technology. This correlated with the large efficiency increase for counting in LLCM. To additionally test these hypotheses, a set of experiments with labeled ink solutions, a blackened inner vial, and outer ink solution was carried out. The sample of black ink spiked with the radioactive standard was used as the sample in the inner vial. The authors reported that the efficiencies are remarkably high on the Hidex 300 SL (except for lower-energy ^{36}Cl), whereas on the Tri-Carb the efficiency for ^{90}Y is 14% and only 5% in LLCM (see Table 6.8). They assumed that the Cherenkov light was totally absorbed by the ink and that the measured efficiency represents a fraction of the Cherenkov photons originating from interactions in the walls of the inner and outer vials. Therefore, in the following experiment, the outer walls of the mini-vials were blackened with black paint. In this case, the Hidex 300 SL and Tri-Carb still detected some events of ^{90}Y. In such cases, and whether water or ink was present as the sample in the inner vial, the Cherenkov detection efficiency of ^{90}Y was 10% for the Hidex 300 SL and 8% for the Tri-Carb. This was attributed to the production of Cherenkov photons by the passing of high-energy electrons through the walls of the mini-vials. It was shown that mini-vials surrounded with ink solution result in negligible detection

efficiencies. However, when they were surrounded by water, the detection efficiencies increased. The greatest increase (about 2.5 times) was observed for ^{90}Y in LLCM on the Tri-Carb. The authors stated that the test with ink indicates the possibility of using Cherenkov counting for activity determination in highly quenched samples and that two radionuclides may be discriminated in a mixture by deliberately changing color quench (Coha et al., 2016).

Todorović et al. (2017) investigated the influence of the type of scintillation vial on the Cherenkov background of the Quantulus 1220. The variations in background in the polyethylene plastic vials, high-performance glass vials and low ^{40}K glass vials for the 20 mL volume distilled water samples are presented in Table 6.9.

The background measured with the glass vial is higher than that obtained with the plastic vial by almost one order of magnitude (Table 6.9) because of the presence of natural ^{40}K and U isotopes in the glass, which makes it unadvisable for low-level counting. In addition, due to the effects of the dispersion or scattering of anisotropic (oriented) photons in plastic, their distribution becomes isotropic, causing increases in the counting efficiency. Polyethylene also has a higher refractive index (n = 1.5−1.54) than borosilicate glass (n = 1.468−1.487), which decreases the energy threshold for Cherenkov radiation production from 183 to 167 keV. As a consequence of the above results, polyethylene plastic vials were selected for the current analysis. A sample volume of 20 mL was chosen for routine analysis in order to minimize the color effects and maximize the volume useful for the sample solution.

From the data and examples described above, it is clear that polyethylene plastic vials give the highest Cherenkov counting efficiencies and most accurate results when compared with glass counting vials. Glass vials can give higher counting efficiencies if wavelength shifters are used, as discussed in the following.

TABLE 6.9 Optimal type of scintillation vial selection (for channel 130−430).

Vial type	Efficiency E [%]	Background B [cpm]	$FOM = \frac{E^2}{B}$
Polyethylene vial	45.86(9)	0.48	4383
High-performance glass vial	32.45(19)	1.26	836
Low ^{40}K glass vial	32.24(14)	0.84	1237

Adapted from Todorović et al. (2017).

C. Wavelength shifters

The ultraviolet component of Cherenkov radiation, which may pass plastic vials, can be absorbed partially by the glass of the PMT. Certain compounds, such as the sodium and potassium salts of 7-amino-1,3-naphthalenedisulphonic acid (ANDA) in 100 mg/L concentration, are successfully employed as wavelength shifters by absorbing the ultraviolet photons and reemitting them isotropically in the visible region, as demonstrated by Parker and Elrick (1966, 1970) and Elrick and Parker (1968). Wavelength shifters, as defined by Dai et al. (2008) are generally fluorescent organic chemicals containing polyaromatic hydrocarbons or heterocycles in their molecular structure, which absorb photons and reemit them at longer wavelengths. Also, the directional character of Cherenkov photons and the ultimate emission of their shorter wavelengths are reduced by the emission of the radiation in all directions at longer wavelengths more efficiently detected by PMTs.

Lauchli (1969, 1971) reported that weak beta-particle emitters such as ^{36}Cl require 5 mM ANDA, and strong beta-particle emitters, such as ^{86}Rb and ^{40}K, require 2.5 mM ANDA for optimum counting efficiencies. ANDA was demonstrated to be useful for the routine counting of ^{36}Cl, ^{40}K, and ^{86}Rb in plant materials, providing counting efficiencies of 13%, 79%, and 61%, respectively, for samples containing 1 g of digested plant tissue, and 23%, 93%, and 70%, respectively, for samples not containing plant tissue. Only a small increase in Cherenkov counting efficiency of ^{188}Re from 53% to 55% in glass vials with the addition of 100 mg/L of ANDA was demonstrated by Kushita and Du (1998); however, the counting efficiency slightly dropped from 58% to 54% with the addition of ANDA wavelength shifter in plastic vials. This effect is unusual and unexplained. The writer can only note that ^{188}Re emits higher-energy beta particles [*i.e.*, three beta transitions of 2120 keV (79% intensity), 1970 keV (20% intensity), and ∼1900 keV (1% intensity)] than all other radionuclides studied with wavelength shifters, and possibly a greater fraction of the Cherenkov photons are created in the visible rather then the ultraviolet.

In most cases, significant increases in Cherenkov counting efficiencies are achievable with wavelength shifters, which could be advantageous if the sample is not needed for further studies or chemical analysis, for which the wavelength shifter may act as a contaminant. ANDA may also be employed as a wavelength shifter in the Cherenkov counting of ^{59}Fe as reported by Kannan (1975).

Frič and Finocchiaro (1975) found anthranilic acid and quinine to be effective as wavelength shifters for the Cherenkov counting of ^{32}P. Concentrations of 10^{-3} M anthranilic acid and 2×10^{-3} M quinine increased the counting efficiency of ^{32}P from 47.2% to 58.4% and from 47.2% to 54%, respectively. Bezaguet et al. (1979) reported

an increase in the light output by a factor of about 3.8 when ANDA is employed as a wavelength shifter at a concentration of 10 mg/L.

Many chemical compounds have been tested for their wavelength shifting properties. Some are sensitive to pH, salt concentration, and storage in the sample solution for periods of several hours, a few days, or weeks. van Ginkel (1980) tested the stability and wavelength-shifting properties of several organic compounds, and some of their properties are listed in Table 6.10. The pH sensitivity of wavelength shifters has been studied in detail by Kellogg (1983); and it was demonstrated that the use of wavelength shifters is not appropriate when the sample pH can vary to a significant degree. Sample pH can affect the fluorescent properties of the wavelength-shifting molecule and consequently cause the counting efficiency to vary.

Also Ross (1971), Paredes et al. (1980), and Bem et al. (1983) indicated that care should be exercised when wavelength shifters are used, because some shifters show chemical decomposition over several hours. This can lead to color quenching and a reduction in counting efficiency. The tremendous increase in detection efficiency of ^{32}P from 55.5% in pure water to 85% in a high concentration of sodium salicylate (1 g/mL), as seen in Table 6.10, is reportedly due to an increase in the index of refraction, which would lower the threshold energy for the production of Cherenkov photons by beta particles in water. Sodium salicylate was tested by L'Annunziata and coworkers (see Aleissa et al., 2008) and found to increase the Cherenkov photon detection efficiency of ^{228}Ac from 10.9% to 38% for the analysis of ^{226}Ra after adding 1.4 g of sodium salicylate to each polyethylene counting vial containing 14.0 mL of ^{228}Ac in aqueous solution after the isolation of the ^{228}Ac off of a Diphomix ion exchange column. Sodium salicylate should be tested for each application because, as noted in Table 6.10, it is highly susceptible to pH and ionic strength. It can exhibit color under certain conditions. Peck et al. (1998) reported an enhancement of ^{210}Bi detection efficiency in the presence of Triton X-100 and sodium salicylate of 97%. In order to enhance the Cherenkov efficiency of ^{90}Sr, Reddy et al. (2017) compared the effect of glycerol and sodium salicylate as wavelength shifters on ^{90}Sr detection efficiency by means of Cherenkov measurement. They showed that the Cherenkov detection efficiency of ^{90}Sr depends on the concentration of the wavelength shifters, and was enhanced 3.8–7.5 times with the addition of sodium salicylate, while the addition of glycerol doubled the detection efficiency, as illustrated in Table 6.11.

Wang et al. (2018) also used sodium salicylate to enhance the detection efficiency of Cherenkov photons. In this study, authors found that the addition of sodium salicylate could significantly increase the counting efficiencies of ^{210}Pb/^{210}Bi in aqueous samples. Meanwhile, a sharp increase of the counting efficiency for the alphas from ^{210}Po was also observed with the addition of high concentration of sodium salicylate, implying that scintillation light photons are produced. At low concentration (<0.5 mg g^{-1}) of sodium salicylate, only a small increase in Cherenkov counting efficiency for ^{210}Bi by the wavelength-shifting effect could be observed. Meanwhile, the Cherenkov counting efficiency for ^{210}Bi at high concentration (>1 mg g^{-1}) of sodium salicylate would significantly increase due to the scintillation effect.

TABLE 6.10 Effect of different wavelength shifters, dissolved in distilled water, on the counting of Cherenkov radiation from ^{32}P, using polyethylene counting vials, vial constituents of 10 mL, an amplifier gain of 30%, and discriminator settings of 20–1000.[a]

Compound	Concentration used (g/L)	Counting efficiency (%)
Water in glass vial		51.0
Water in quartz vial		53.0
Water in polyethylene vial		55.5
β-Methylumbelliferone[b]	0.2	67.0
Esculin[b]	0.4	73.0
Quinine sulfate[c]	1.0	68.4
Quinine[c]	1.0	66.2
	10.0	76.0
	25.0	77.0
Thymine	0.5	65.9
Alloxazin	0.1	55.1
Pyrimidine-HCl	5.0	56.4
Quinolinic acid	0.5	53.3
Sodium dihydrobenzoate	1.0	66.3
Pentobarbitol	1.0	57.3
Phenobarbitol	1.0	57.0
Lumichrome	0.001	57.2
Sodium salicylate[d]	0.5	66.8
	1.0[e]	68.0
	100[e]	76.0
	1000[e]	85.0

[a] *From van Ginkel (1980) reprinted with permission from Elsevier © 1980.*
[b] *Stable in the pH range 3–11.*
[c] *Can only be used at pH 0–3.*
[d] *Highly sensitive to pH change and salt concentration.*
[e] *Refractive index is increased.*

TABLE 6.11 Effect of wavelength shifters on Cherenkov counting efficiency of ^{90}Sr.

Sodium salicylate (g)	Count rate before addition (a)	Count rate after addition (b)	Effect of wavelength shifter(b/a)	Glycerol (g)	Count rate before addition (a)	Count rate after addition (b)	Effect of wavelength shifter (b/a)
0.1022	16.2	61.6	3.8	0.5	15.6	18.5	1.2
0.2011	16.8	80.6	4.8	1.5	15.4	17.2	1.1
0.3011	16.5	95.7	5.8	2.5	16	22.4	1.4
0.4011	16.3	122	7.5	3.5	15.5	23.6	1.5
0.5011	16.9	101.7	6.0	5.5	16.3	25.3	1.6
0.6011	16.4	101.7	6.2	6.0	16.2	28.5	1.8
0.7011	17.5	103.3	5.9	6.5	15.3	29.9	2
0.8811	4.91	30.3	6.1	7.5	15.9	29.8	1.9

From Reddy et al. (2017); reprinted by permission from Springer Nature © 2017.

PPO has excellent wavelength shifting properties in Cherenkov counting. However, it cannot be incorporated directly into water. Takiue et al. (1984) devised a method for introducing PPO into water in the form of a micelle by first preparing a PPO−ethanol solution. A 2-mL sample of PPO−ethanol is added to 13 mL of aqueous solution of ^{32}P for Cherenkov counting. The counting efficiency for ^{32}P was 68.4% (optimum), which was 1.6 times as high as that measured with conventional Cherenkov counting (42.3%). The optimum concentration of PPO in the counting vial was reported to be 0.02 g/L. Although the use of such a wavelength shifter can significantly increase the counting efficiency, it must be kept in mind that the detection process is no longer a purely physical one, and thus, chemical quenching becomes possible. Takiue et al. (1996) increased the Cherenkov counting efficiency of ^{32}P in water from 50% to 65% using 4-methylumbelliferone as a wavelength shifter while demonstrating that turbid and clear samples of ^{32}P in glass scintillation vials give the same quench correction curve when wavelength shifter is used.

A disadvantage of wavelength shifters in certain circumstances can be that the counting sample may be rendered useless for subsequent chemical tests or analyses, because the wavelength shifter may act as a contaminant and interfere in these analyses. In the biosciences Cherenkov counting of ^{32}P can be advantageous when the sample is left in an unadulterated form in aqueous solution whereby the ^{32}P can be analyzed and the sample used for subsequent biological or chemical tests.

Some aromatic wavelength shifters and solvents of high refractive index act as scintillants and, for this reason, Cherenkov counting with these compounds as solvents is at times referred to as Cherenkov−scintillation counting. An example is methyl salicylate, which has a high refractive index ($n = 1.5369$); and according to Eq. (6.38), the calculated beta-particle energy threshold for Cherenkov production is reduced from 262 keV in water ($n = 1.333$) to 162 keV in methyl salycylate ($n = 1.5369$).

Wiebe et al. (1978) reported counting efficiencies of 50.3% and 14.4% for ^{18}F and ^{14}C in methyl salicylate in the coincidence counting mode. Higher counting efficiencies were obtained in the singles counting mode. This mode of counting is discussed later in this chapter. The SCR method was employed to determine counting efficiencies, and the standard curves (%E vs. SCR) were prepared using chlorobenzene or dimethyl sulphoxide as a quenching agent. In the case of ^{18}F measurement, the methyl salicylate acts as an efficient Cherenkov−scintillation medium, because both Cherenkov and scintillation phenomena occur. Positrons are emitted from ^{18}F ($E_{max} = 636$ keV), well over the beta-particle threshold energy for Cherenkov production. However, the beta particles emitted from ^{14}C ($E_{max} = 155$ keV) do not reach the threshold energy for Cherenkov production in methyl salicylate, and consequently this solvent only serves as an inefficient scintillation flour for ^{14}C.

To keep the advantages of using a wavelength shifter while still counting under pure Cherenkov conditions free of chemical quenching, Ross (1976) and Takiue and Ishikawa (1978) fabricated a counting vial containing two chambers, which separate the sample from the wavelength-shifting solution (see also L'Annunziata, 1984a, 1987). The vial consists of an outer chamber used to contain the wavelength-shifting solution, and an inner chamber of approximately 10-mL volume contains the radionuclide and solvent (*e.g.*, water). The wavelength-shifting solution is sealed permanently in the outer chamber by an all-glass seal. The entire inner vial is made of quartz so that the ultraviolet radiation can pass the inner chamber wall before reaching the solution of wavelength shifter. The vials are reusable, and to prevent contamination the sample can be

contained in a polyethylene bag placed within the inner chamber. Ross (1976) reported an increase in counting efficiency of ^{89}Sr by a factor of 1.88 when dimethyl-POPOP is used in the wavelength-shifting chamber as compared to pure water. Greater improvements in counting efficiency would be expected for lower energy beta-particle emitters such as ^{36}Cl. The main disadvantage of this technique is that the volume of sample that may be conveniently counted is reduced by a factor of two. This method of Cherenkov counting has not had many recent applications.

Another approach to the application of wavelength shifters external to the sample solution is the application of a thin film or coat of wavelength shifter onto the faces of the PMTs devised by Grande and Moss (1983). Pure quartz and plastic vials are transparent to the ultraviolet fraction of Cherenkov photons. However, this ultraviolet radiation can be absorbed in part by the glass faces of the PMTs. This absorption is obviated by the application of a coating of wavelength shifter to the glass PMT face. The coating designed by Grande and Moss (1983) consists of 5.7% p-terphenyl and 3.1% bis-MSB in a polyethyl methacrylate matrix. The transparent coating has an average quantum efficiency of 91% in the wavelength range of 200−400 nm.

Dai et al. (2008) tested several water-soluble wavelength shifting compounds including coumarin derivatives to increase the Cherenkov photon detection efficiency for the Sudbury Neutrino Observatory (SNO) heavy water Cherenkov detector. They found the water soluble carbostyril 124 and Alexa Fluor 350 increased the detection efficiency of Cherenkov photons. A concentration of only 15.4 ppm of carbostyril 124 resulted in an increase in the net gain of 4.4 ± 0.5. The wavelength shifters tested were pH-insensitive with strong absorbency below 350 nm and high reemission between 350 and 500 nm wavelength. These wavelength shifting compounds show potential for the Cherenkov counting of radionuclides; but they have not been tested yet for this purpose.

D. Ionic liquids

Ionic liquids (ILs) are organic salts with melting points near room temperature, with 100°C as the agreed arbitrary upper limit (Weingärtner, 2008). The ionic nature of these liquids gives them distinctive physicochemical properties compared with traditional organic solvents, which are mostly toxic, volatile, and flammable, while the chemical characteristics of either cation and/or anion give ILs a tunable solvation power (Welton, 1999; Isik et al., 2014). A moderate thermal stability, low flammability, and good conductivity are some of the remarkable features that justify their nascent application, e.g., in nuclear technology (Sun et al., 2012). Mirenda et al. (2018) proposed the use of a novel fluorescent IL, 1-butyl-3-methylimidazolium 8-hydroxypyrene-1,3,6-trisulfonate (BMIMHPTS), to act as a wavelength shifter of the Cherenkov photons generated from 1-butyl-3-methylimidazolium chloride (BMIMCl). They found that ^{18}F and ^{32}P efficiencies increase up to 124% and 14%, respectively, compared with the values obtained with pure BMIMCl. With this improvement, IL mixtures become a good alternative, when using the TDCR−Cherenkov technique, in standardizing radionuclides with electron emission energies close to the threshold energy in water (~260 keV). As an advantage compared to other solvents, they concluded that an IL mixture can be reused, in the case of short-lived radionuclides, by simply removing all the water content in a vacuum oven.

E. Refractive index

From Eqs. (6.38) and (6.39), it is evident that the energy threshold for the production of Cherenkov radiation by electrons (beta particles) is a function of the refractive index. An increase in the refractive index of the medium should lower the energy threshold for the production of Cherenkov photons and increase the detection efficiency for a beta-particle emitting radionuclides. The detection efficiency should increase to some extent for all beta-emitting nuclides with an E_{max} above the threshold energy in pure water, because the beta-particle energies constitute a broad spectrum between zero and E_{max}.

Ross (1969) found that the Cherenkov Effect and detection efficiencies are significantly increased only for radionuclides that have a low beta-particle E_{max}, as illustrated in Table 6.12. This may be explained by the fact that a smaller fraction of the total beta-particle energy spectra of high-energy beta particle-emitting nuclides is below 262 keV.

Wiebe and Ediss (1976) reported very high Cherenkov counting efficiencies for ^{36}Cl ($E_{max} = 714$ keV) using a high-refractive index methyl salicylate ($n = 1.5369$) as the counting medium. Counting efficiencies of 82.4% and 91.6% were reported, depending on the counter employed. The high counting efficiencies were reported to be due not only to the increased refractive index (thus lowered Cherenkov threshold energy) but also to the wavelength-shifting and scintillation properties of this solvent, as discussed in the previous Section V.C of this chapter.

The high refractive indexes of concentrated solutions of sodium salicylate in water (100−1000 g/L) provided significant increases in counting efficiency of ^{32}P (see Table 6.10). Likewise, as discussed in the previous Section V.C of this chapter, sodium salicylate increased the Cherenkov photon detection efficiency of ^{228}Ac from 10.9% to 38% for the analysis of ^{226}Ra after adding 1.4 g of sodium salicylate to each polyethylene counting vial containing 14.0 mL of ^{228}Ac in aqueous solution (Aleissa et al., 2008).

Wang et al. (2018) conducted experiments to test the effect of the refractive index on the Cherenkov counting

TABLE 6.12 Cherenkov response as a function of solvent refractive index.[a]

Nuclide	E_{max} (MeV)	Detection efficiency (%)			
		n = 1.3220[b]	n = 1.4026[c]	n = 1.4353[d]	n = 1.4644[e]
^{99}Tc	0.295	0.01	–	–	1.02
^{204}Tl	0.765	16.1	19.6	21.4	23.2
^{32}P	1.710	50.2	50.9	51.3	51.6

[a] *From Ross (1969) reprinted with permission © 1969 American Chemical Society.*
[b] *Water.*
[c] *53 wt% glycerol.*
[d] *75 wt% glycerol.*
[e] *95 wt% glycerol.*

TABLE 6.13 Refractive index of the NaCl and sodium salicylate (SS) solutions with different concentrations and the counting efficiencies of ^{210}Bi using the ^{210}Pb standard solution.[a]

Salt concentration (mg g^{-1})	Refractive index			Counting efficiency (%)		
	SS	NaCl	NaCl + 10 mg g^{-1}SS	SS	NaCl	NaCl + 10 mg g^{-1}SS
0.0	1.3333	1.3333	1.3354	15.5 ± 0.3	15.5 ± 0.3	51.4 ± 08
10.0	1.3354	1.3350	1.3373	51.4 ± 0.8	15.6 ± 03	52.5 ± 0.8
47.0	1.3435	1.3417	1.3440	104.2 ± 1.4	15.4 ± 0.3	45.1 ± 0.7
89.0	1.3526	1.3490	1.3511	115.0 ± 1.5	16.1 ± 0.3	41.8 ± 0.7
163.0	1.3695	1.620	1.3644	122.9 ± 1.6	17.1 ± 0.3	36.0 ± 0.6

[a] *From Wang et al. (2018) reprinted with permission from Elsevier ©2018.*

efficiency of ^{210}Bi. However, the increase in the counting efficiency of ^{210}Bi by adding sodium salicylate could have been attributed either to the wavelength shifting effect or the change of refractive index. In order to check the sole effect of the refractive index, with no interference from wavelength shifter on Cherenkov efficiency, sodium chloride (NaCl) solutions were also prepared for comparison. As shown in Table 6.13, the changes in the refractive indices for the NaCl solutions were very close to those for the sodium salicylate solutions at the same concentrations of the added salt. For the NaCl samples, a very small increase in counting efficiency was observed with increasing NaCl concentrations (i.e., refractive index), which was very different from the sharp increase noted for the sodium salicylate samples as illustrated in Fig. 6.28.

Wang et al. (2018) also found that after adding 10 mg g^{-1} of sodium salicylate to the NaCl samples, the counting efficiencies dramatically increased but the refractive indices increased only a little. This demonstrated that the significant increase in the counting efficiency with the addition of sodium salicylate was not due to the change of the refractive index. For the NaCl + 10 mg g^{-1} sodium salicylate (SS) samples, the counting efficiency decreased

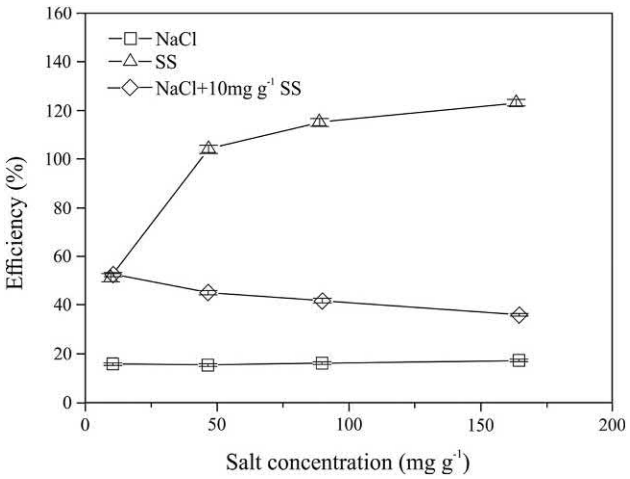


FIGURE 6.28 The counting efficiency of ^{210}Bi (using ^{210}Pb standard) as a function of salt concentration (refractive index). *From Wang et al. (2018), reprinted with permission from Elsevier © 2018.*

with an increase in NaCl concentration (see Fig. 6.28), possibly due to chemical quenching caused by chloride ions acting as chemical scavengers for the excitation state of the sodium salicylate molecules, which was reported by

van Ginkel (1980). The results imply that, with the addition of 10 mg g^{-1} or more of sodium salicylate, the detection of scintillation light rather than Cherenkov photons may have contributed to a significant portion of the counting efficiency, since the Cherenkov counting would not have been affected by chemical quenching. These results demonstrate that a small increase in the refractive index with the addition of sodium salicylate (from 1.3333 with no SS to 1.3695 with 163 mg g-1 of SS added) would contribute a negligibly small amount to the dramatic increase of the counting efficiency (from 15.5% to 122.9%, Table 6.13).

A unique approach is the use of very high index of refraction ($n = 2.1$) transparent ceramic plates to measure Cherenkov photons produced by the low-energy beta emitting radionuclides ^{14}C ($E_{max} = 155$ keV) and ^{45}Ca ($E_{max} = 258$ keV) reported by Takiue et al. (2004) and Minowa et al. (2009). Initial studies were carried out by Takiue et al. (2004), who deposited ~0.02 mL of ^{14}C or ^{45}Ca solution onto thin transparent polyester film and dried at room temperature. The deposited radionuclide was covered with another layer of polyester film to avoid contamination; and the radionuclide in the polyester film sandwich was placed between two very fine transparent high-refractive-index ($n = 2.1$) ceramic plates having dimensions of 25 × 10 mm and 0.4 mm thickness. The polyester film prevented contamination of the high refractive index ($n = 2.1$) ceramic plates permitting their repetitive use. The sandwich of ceramic plates containing the radionuclide of interest (*i.e.*, ^{14}C or ^{45}Ca) was mounted vertically in a 20-mL glass liquid scintillation counting vial and counted in a PerkinElmer Tri-Carb 2750 TR LSC. These initial tests yielded Cherenkov photon detection efficiencies of 1.5% and 2.3% for ^{14}C and ^{45}Ca, respectively. This was the first report of the detection and counting of Cherenkov photons from the low-energy beta particles emitted by ^{14}C or ^{45}Ca. The very high index of refraction of the ceramic plates ($n = 2.1$) lowers the threshold energy for the production of Cherenkov photons by beta particles, according to Eqs. (6.38) and (6.39) described previously, from 262 keV (when water is the medium, $n = 1.333$) to 70 keV (when the ceramic plate is the medium, $n = 2.1$). Further studies by Minowa et al. (2009) were carried out with an improved translucent ceramic, LUMICERA, developed by the Murata Manufacturing Co., Ltd., Kyoto, Japan. In this case the Cherenkov counting of ^{14}C was performed in a microplate format with a PerkinElmer MicroBeta plate counter. Minowa et al. (2009) applied and dried carbon-14 between two sheets of polyethylene film as described above and sandwiched the film between two sheets of the LUMICERA ceramic plates placed onto a filter plate cassette for counting with the PerkinElmer MicroBeta plate counter, as illustrated in Fig. 6.29. They report a Cherenkov photon counting efficiency of 5.0 ± 0.5 for ^{14}C. This report demonstrates an improvement in the

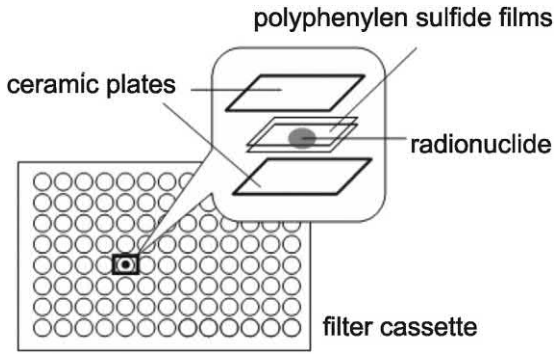


FIGURE 6.29 Arrangement for the Cherenkov counting of ^{14}C in a microplate format with high-refractive-index ceramic plates. *From Minowa et al. (2009). Printed with permission from Radiocarbon, University of Arizona © 2009 Arizona Board of Regents on behalf of the University of Arizona.*

Cherenkov counting of weak beta emitters, such as ^{14}C, and the potential of using a microplate format for the Cherenkov counting of weak beta emitters, such as ^{14}C ($E_{max} = 155$ keV), ^{35}S ($E_{max} = 167$ keV, and ^{45}Ca ($E_{max} = 257$ keV).

Mirenda et al. (2018) concluded that the relatively high refractive index of BMIMCl makes it very convenient for this kind of measurement. BMIMCl/BMIMHPTS mixtures were prepared with the addition of weighted amounts of both ILs. The density of all solutions was 1.07 g/mL. The samples were heated at 60°C in a water bath, and mixed for a day with magnetic stirring to ensure complete homogenization. Afterward, the mixtures were cooled to room temperature. All measurements were performed at the thermostatic condition of 20°C. The refractive indices of the IL mixtures were measured at 589.3 nm in a thermostatized Abbemat 300 automatic refractometer (Anton Paar). The values obtained for BMIMCl with and without BMIMHPTS were n = 1.509(1).

F. Sample physical state

The measurement of radionuclides by the production and counting of Cherenkov photons is not restricted to liquid samples, as discussed previously in Section V.E, where the counting of dried ^{14}C and ^{45}C on ceramic plates was discussed. Also, Cherenkov radiation may be counted with dry and solid samples in plastic or glass counting vials. This is discussed in the following Section VI of this chapter.

VI. Cherenkov counting in the dry state

The Cherenkov counting of ^{14}C and ^{45}Ca in the dry state on high-refractive-index ceramic plates was discussed previously in Section V.E. The Cherenkov counting of radionuclides in the dry state can, under certain circumstances, be more advantageous such as in the analysis of

biochemicals on filter material, electrophoresis gels, thin-layer chromatograms, and paper swipes taken for radioactivity monitoring. In some circumstances, particularly with high-energy beta emitters, such as ^{90}Y, the Cherenkov counting in the dry state can yield FOMs comparable to Cherenkov counting in aqueous solution.

The first report of the Cherenkov counting of a radionuclide in the dry state was provided by Hülsen and Prenzel (1968), who analyzed the activity of ^{32}P tracer nuclide in green algae by counting the Cherenkov photons. The dry algal matter was collected on glass fiber filter and deposited into glass or plastic counting vials. They reported a counting efficiency of 13% for ^{32}P in the dry state in glass vials and a twofold increase in counting efficiency when plastic vials were used. More modern instrumentation can yield higher counting efficiencies. Berger (1984) reported a 25% counting efficiency of Cherenkov radiation from ^{32}P in the dry state compared to a 56% counting efficiency with the nuclide in aqueous solution. The method of Berger (1984) involved measuring ^{32}P on dry glass filters placed flat on the bottom of air-filled glass scintillation vials. He demonstrated the analysis of dry samples of ^{32}P in recombinant DNA procedures where enzyme-catalyzed reactions were carried out in volumes of 10 μL or less. In this case, the ^{32}P samples were deposited onto glass fiber filters, dried under heat lamps, and then inserted into glass counting vials yielding a counting efficiency of $25 \pm 1\%$ using a conventional LSA. The Cherenkov radiation is produced in the glass wall of the scintillation vial. The air in the vial makes no detectable contribution to the production of Cherenkov radiation, as air has a very low index of refraction (see Table 6.1).

Bunnenberg et al. (1987) describe the Cherenkov counting of radionuclides on aerosol filters in the dry state. The filters of 50-mm diameter are sealed in polyethylene foil to avoid contamination and loss of activity. The filters are rolled and inserted into the borehole of solid Plexiglas with the shape of a normal 20-mL scintillation vial. The Cherenkov photon emissions are measured with a conventional liquid scintillation analyzer. Cherenkov counting efficiencies of 44.2% and 65.8% were reported for the measurement ^{89}Sr and ^{90}Sr(^{90}Y) in the Plexiglas vials.

Counting efficiencies of 10% and 14% are reported for the Cherenkov counting of ^{32}P in the dry state in the sample wells of 24-well and 96-well OptiPlates, which are white microplates used with a microplate scintillation and luminescence counter (see Anonymous, 1996). Counting efficiencies are increased with the addition of water to the sample in the microplate wells; however, the possibility of analyzing ^{32}P samples in the dry state without any additive, even water, is a good option to have available.

There are numerous examples of the Cherenkov counting of ^{32}P in the dry state and a few will be cited including the following: dried Whatman filters, millipore filters, nitrocellulose filters, and Nytran membrane filters (Jeske et al., 2015; Sharifulin, 2015; Hunter et al., 2014; Mori et al., 2012; Shehata et al., 2012; Schuster et al., 2010; Arutyunova et al., 2003; Tan et al., 2003; Drobnies et al., 2002), 96-well glass fiber filtration plates (Luo et al., 2018), glutathione sepharose resin beads (Rajyaguru et al., 2012), lyophilized 5′-nucleotide monophosphates (Lehmann and Bass, 1999), precipitated covalent histone−DNA complexes (Angelov et al., 2000), dried samples on Whatman phosphocellulose paper and filter discs (Golub et al., 2011; Kisseljova et al., 2010; Schmöle et al., 2010; Torres-Marquez et al., 2010; Lynn Bostrom et al., 2009; Kuznetsov et al., 2004; Luciani et al., 2000), dried polyacrylamide gels (Masłyk et al., 2018; Grundt et al., 2017; Xu et al., 2015; Yip et al., 2014; Janeczko et al., 2012; Bastin-Coyette et al., 2011; Beauchesne et al., 2009, 2010; Frączyk et al., 2010; Sunil et al., 2007; Gallo et al., 2006; Bélanger et al., 2002; Gittens et al., 2002), and dried DE-81 and P81 ion exchange paper and filters associated with kinase polymerase activity studies (Ampofo et al., 2010; Meng et al., 2010; Alto et al., 2006; Ivanov et al., 2006; Moore et al., 2002).

Although ^{32}P samples on filter discs and other materials can be counted in the dry state in conventional counting vials, it should be noted that this would be recommended only when it is necessary to keep the samples in the dried state or it is necessary to control the counting geometry (*e.g.*, samples that will not dissolve off the filter discs). If, however, the material on the filter discs is water soluble and adding water to the counting vial to the optimum Cherenkov counting volume would assure removal of the ^{32}P-labelled molecules into the aqueous medium, the Cherenkov detection efficiencies would be increased considerably. This is due to the fact that an optimum counting volume of water in the counting vial would serve as a medium for the production of Cherenkov photons in addition to the walls of the counting vial.

A linear logarithmic relationship between Cherenkov counting efficiencies and average energies of the emitted beta particles and internal conversion electrons was demonstrated by Morita-Murase et al. (2000). For this study they used standards of ^{32}P, ^{36}Cl, ^{60}Co, and ^{137}Cs in the dry state, and the counting efficiencies reported for the particular dry sample geometries were $38.8 \pm 0.1\%$, $5.2 \pm 0.03\%$, $0.69 \pm 0.02\%$, and $4.98 \pm 0.13\%$, respectively. Based on these results and the correlation that exists between Cherenkov counting efficiency and logarithm of the γ-ray energy, they estimated that the Cherenkov counting efficiencies of ^{214}Pb and ^{214}Bi due to γ-rays would be $0.003 \pm 0.0006\%$ and $0.09 \pm 0.003\%$, respectively.

Much attention is focused on the production and applications of ^{90}Y in the form of radiopharmaceuticals for medical research and cancer treatment (*e.g.*, Bobin et al.,

2017; Drude et al., 2017; Goel et al., 2017; Kossert et al., 2016; Wright et al., 2016; Lee et al., 2015; Satterlee et al., 2015; Volotskova et al., 2014; Burdick et al., 2011; MacKie et al., 2011; Nardelli et al., 2011; Nicolas et al., 2011; Sato, 2011; Šrank et al., 2010; Xiques Castillo et al., 2009, 2010) as well as the concern for ^{90}Sr(^{90}Y) in the environment and Cherenkov counting methods for the analysis of ^{89}Sr + ^{90}Sr/^{90}Y (*e.g.*, Uesugi et al., 2018; Herranz et al., 2017; Pan et al., 2017; Holmgren et al., 2014, 2016; Tayeb et al., 2016; Zhou et al., 2016; Grahek and Rožmarić-Mačefat, 2005, 2006, 2013; St-Amant et al., 2011; Groska et al., 2012; Vesely et al., 2011; Vajda and Kim, 2010; Maxwell and Culligan, 2009a,b,c; O'Hara et al., 2009; Tsroya et al., 2009, 2012, 2013a,b). Cherenkov counting has proven to be among the most facile and inexpensive method of analysis for ^{90}Y in aqueous solutions at relatively high detection efficiencies of 39%−68% (Coursey et al., 1993). The Cherenkov counting of ^{90}Y in the dry state was proposed as a practical alternative and tested by L'Annunziata and Passo (2002). The Cherenkov counting of dry samples can exhibit the deleterious effect of self-absorption; and thus would be recommended only when necessary such as the radionuclide sample adhered to a filter disc or smear, which cannot be released into soluble form. The detection efficiency for ^{90}Y in the dry state in polyethylene plastic vials was slightly higher than that obtained for ^{90}Y in 20-mL of water in glass vials (Table 6.14). Also, the Cherenkov counting backgrounds are lower in the plastic vials than those obtained with glass counting vials. The counting efficiencies of ^{90}Y in Table 6.14 were measured with standards of ^{90}Sr(^{90}Y) in secular equilibrium; and the ^{90}Sr contribution to the Cherenkov counting efficiencies can be ignored since the maximum Cherenkov counting efficiency for ^{90}Sr is only ~ 1% as reported by Rucker (1991), Chang et al. (1996), and Cook et al. (1998).

Higher Cherenkov counting efficiencies are obtained with plastic counting vials over glass vials as explained in Section V.B of this chapter, and this remains regardless of whether or not the samples are counted in the dry state or in solution. The higher index of refraction of polyethylene plastic ($n = 1.50-1.54$) over borosilicate glass ($n = 1.468-1.487$) yields a lower beta-particle threshold energy (167 keV) for the production of Cherenkov photons in plastic as compared to the energy threshold in glass (183 keV). In the dry state, air is the only medium in addition to the vial walls for the production of Cherenkov photons. Air has a low index of refraction ($n = 1.00027712$) at the Sodium D line at STP (Haynes, 2011). According to Eqs. (6.38) and (6.39), electrons would have to exceed the threshold energy of 2.12×10^4 keV or 0.0212 GeV for the production of Cherenkov photons in air. Consequently, no Cherenkov photons are produced by beta particles in air, and only the counting vial walls are the source of Cherenkov photons from sample beta-particle emissions when the samples are in the dry state. Gases as media for the production of Cherenkov photons are limited to the measurement of high-energy particles in the upper MeV and GeV regions, as noted in Table 6.1 earlier in this chapter. Iodice et al. (1998) calculated the threshold energy for the production of Cherenkov photons by electrons or positrons in CO_2 at STP ($n = 1.00041$) to be 0.017 GeV.

When counting radionuclide samples in the dry state, it is expected that increasing the wall thickness of the plastic would increase the Cherenkov counting efficiency (L'Annunziata and Passo, 2002). Increasing the path length of travel of the beta particles in the plastic should increase the number of Cherenkov photons according to Eq. (6.54) or, according to Sundaresan (2001), over the visible range of Cherenkov wavelengths (400−700 nm) the number of Cherenkov photons produced per path length of travel can be approximated according to Eq. (6.61) described previously in this chapter. The Cherenkov counting efficiencies for ^{90}Y in the dry state in polyethylene plastic vials listed in Table 6.14 were produced in vials of 1-mm thickness. Thicker-walled (2 mm) plastic counting vials are available

TABLE 6.14 Cherenkov counting of ^{90}Sr(^{90}Y) in the dry state and in water.[a]

		^{90}Y counting efficiency (%)		Background (cpm)		FOM[c]	
Medium	Volume[b] (mL)	Glass[d]	Plastic[e]	Glass[d]	Plastic[e]	Glass[d]	Plastic[e]
Air[f]	20	51.3	66.9	22.2	20.4	119	219
Water	20	66.2	73.4	21.4	16.1	205	334

[a] *From L'Annunziata and Passo (2002) reprinted with permission from Elsevier © 2002.*
[b] *Volume of the medium (air volume for dry samples or water volume).*
[c] *Figure of merit calculated as the percent counting efficiency squared divided by the background count rate (CPM),* i.e. E^2/B.
[d] *Borosilicate glass vials.*
[e] *Polyethylene plastic vials (1-mm thickness).*
[f] *The medium for air-dried samples. Samples are air-dried at the bottom of the counting vials.*

commercially (MaxiVial, PerkinElmer, Inc). The counting efficiencies listed in Table 6.14 for air-dried samples leave the samples at the bottom of the counting vial. Because of the counting geometry effects described previously in Section V.A for samples of low volume vis-à-vis the PMT centers, increased Cherenkov counting efficiencies are expected if the dried samples (*e.g.*, dried aqueous samples, filter or swipe material) are elevated on a 1-cm-thick polyethylene plastic disk of a suitable diameter placed on the bottom of the counting vial. The elevated sample should reduce the geometry effect as well as increase the amount of plastic medium in the vial to enhance the production of Cherenkov photons.

Caution is recommended when counting samples in the dry state because of self-absorption that will occur to varying degrees depending on the sample thickness and density. Self-absorption, that is, the absorption of beta-particle radiation by the sample, can reduce significantly the detection efficiency. If the sample thickness is such that self-absorption may occur at any appreciable extent or be suspect, an internal radionuclide standard could be used to determine the degree to which self-absorption occurs. Such an internal standard is first applied to a dissolved sample, which is then dried before counting. The effect of the amount of dry residue on the Cherenkov counting efficiency of the standard can be measured by varying the amounts of residue that would occur after sample drying. If, on the other hand, Cherenkov counting is carried out on dry filter material or smear material placed within counting vials, the effect of the filter material on self-absorption can be tested by adding radionuclide standard solution to the filter material. The filter material is then dried and counted. Cherenkov detection efficiencies for standards counted with and without the presence of filter material will provide a quantitative measure of self-absorption.

VII. Radionuclide analysis with silica aerogels

One of the principle advantages of analyzing radionuclides by counting Cherenkov photons is that no interference will arise from radionuclides in the sample with decay emissions below the threshold energy of the detector medium for the production of Cherenkov photons. Thus, when water is the detector medium ($E_{th} = 262$ keV), there is no interference from radionuclides such as ^{3}H ($E_{max} = 18.6$ keV), ^{14}C ($E_{max} = 156$ keV), and ^{35}S ($E_{max} = 167$ keV). However, interfering radionuclides, such as ^{60}Co ($E_{max} = 315$ keV), ^{89}Sr ($E_{max} = 1490$ keV), and ^{137}Cs (two beta branches: $E_{max} = 514$ keV at 94% intensity and $E_{max} = 1180$ keV at 6% intensity), which have beta-spectral maximal energies above the Cherenkov threshold energy of 262 keV for water, are present in samples sometimes encountered in the environment particularly where fission-product contamination is of concern. For the Cherenkov analysis of $^{90}Sr(^{90}Y)$ in the environment, Brajnik et al. (1994, 1995) and Pestotnik et al. (2002, 2008) demonstrated the discrimination against the interfering radionuclides by the use of low-refractive index silica aerogel counting medium.

Silica aerogel is a highly porous and transparent solid material. Aerogels are described by Fricke and Tillotson (1997) as transparent, highly porous, open cell, low density foams. A silica aerogel has an index of refraction that varies according to its density, which can be controlled during its manufacture over the range of $n = 1.005$ to 1.26. Some reviews on the production, properties, and applications of silica aerogels are given by Sashkina et al. (2018), Smirnova and Gurikov (2018), Vareda et al. (2018), Deng et al. (2017), Duan et al. (2016), Tabata et al. (2016, 2015, 2012, 2010), Adachi et al. (2011, 2008, 1995), Barnaykov et al. (2011), Rivas Murillo et al. (2010). An excellent history of silica aerogel discovery and production together with aerogel characteristics and applications are related by Fricke and Tillotson (1997). The first aerogels were produced by the pioneer Steven S. Kistler (1931, 1932) during the time that he was teaching at the College of the Pacific in Stockton, California, which is described in historical accounts by Ayers (2000) and Hunt and Ayers (2011). Kistler reasoned that gels consisted of a suspension of independent solid and liquid phases whereby, if the liquid phase were removed from the gel quickly in a nondisturbing manner, the solid phase would remain behind as a porous material with the same shape as the original gel suspension. Modern silica aerogels were later produced by Nicolaon and Teichner (1968), who devised the use of organosilanes for the preparation of aerogels, which has developed into the modern sol-gel method.

The production of silica aerogels is described in works cited in the previous paragraph and in a patent held by Matsushita Electric Works, Ltd. (1992). In brief, silica aerogels are produced firstly with the formation of silica alcogel $\{SiO_2\}_n$ by the polycondensation of orthosilicic acid, $nSi(OH)_4$, formed via the hydrolysis of tetramethoxysilane (TMOS), $Si(OCH_3)_4$, in methanol solution in the presence of ammonia as catalyst according to the following:

$$n\mathrm{Si(OCH_3)_4} + 4n\mathrm{H_2O} \xrightarrow{\mathrm{NH_3}} n\mathrm{Si(OH)_4} + 4n\mathrm{CH_3OH} \quad (6.66)$$

$$n\mathrm{Si(OH)_4} \longrightarrow \{\mathrm{SiO_2}\}_n + 2n\mathrm{H_2O} \quad (6.67)$$

The concentrations of ammonia and solvent (*e.g.*, ethanol) used in the polymerization are varied to adjust to the desired density and refractive index of the final product. For example, silica aerogel refractive indices are reported to range from 1.0275 to 1.0324 for aerogel densities that vary from 0.0985 to 0.1140 g/cm^3 (Ishino et al., 2001); and an

aerogel with a refractive index below 1.005 has been developed with the very low density of 0.02 g/cm^3 (Tabata et al., 2010). The final product of silica aerogel is obtained by drying at a supercritical point to remove the ethanol solvent and transform the alcogel into silica aerogel without creating cracks in the porous substance or volume shrinkage. Aerogels exhibit a crushing strength of about 10 kg/cm^2 and are prepared in various sizes to accommodate particular instrumental configurations (*e.g.*, 10−30 cm in diameter and 2−5 cm thickness) for radionuclide analysis or studies of relativistic particles in high energy physics. The development of aerogel detectors with light guides containing wavelength shifter between the aerogel and phototubes to increase light collection has been studied by Barnykov et al. (1998). Also, silica aerogels have been prepared doped with fluors to increase the efficiency of detection of Cherenkov photons (Bockhorst et al., 1995). Silica aerogels are available commercially from several producers in North America, Europe, and Asia; and the names of the commercial suppliers are listed by Smirnova and Gurikov (2018).

Brajnik et al. (1994, 1995) and Pestotnik et al. (2002) selected a silica aerogel with an index of refraction of $n = 1.055$, which would yield a threshold energy of 1092 keV (1.09 MeV) according to Eqs. (6.38) and (6.39), to create a detector system for the analysis of ^{90}Sr/^{90}Y in the environment via the exclusive Cherenkov counting of the daughter ^{90}Y ($E_{max} = 2280$ keV). Other beta-emitting radionuclides such as ^{137}Cs, ^{60}Co, and ^{89}Sr, which are normally encountered in the environment would not cause any significant interference, as their beta-energy spectral end points (E_{max}) are well under the aerogel Cherenkov threshold energy with the exception of ^{89}Sr. In the case of ^{89}Sr, only a small fraction of its beta particles extend beyond 1092 keV, and covering the aerogel detector entrance and sides with aluminum foil further discriminated against any interference of this nature while, at the same time, improve the light collection efficiency. They placed a multiwire proportional chamber (MWPC) between the radionuclide source and silica aerogel detector. The beta source is placed directly on the MWPC, and in coincidence mode the background count rates were reported to be as low as 2 counts per hour or 0.033 CPM yielding detection limits as low as 0.1 Bq for ^{90}Sr(^{90}Y).

Further advances were made by Pestotnik et al. (2008) in the development of Cherenkov detector for ^{90}Sr. They obtained an aerogel with greater transparency for Cherenkov photons in the wavelength of highest photomultiplier sensitivity and with a lower index of refraction, $n = 1.047$, with 40 mm transmission length at $\lambda = 400$ nm. At the index of refraction, $n = 1.047$, the threshold energy for the production of Cherenkov photons by a beta particle is 1213 keV or 1.21 MeV, which further discriminates against ^{89}Sr beta particles. The aerogel Cherenkov detector for measuring ^{90}Sr is illustrated in Fig. 6.30. It consists of an aerogel Cherenkov radiator measuring $5 \times 5 \times 5$ cm coupled to a multiwire proportional counter (MWPC) and two Hamamatsu multianode photomultipliers. The aerogel radiator is covered with an aluminized mylar foil to increase light yield to the photomultipliers. All radiations escaping from a sample (*e.g.*, beta and gamma) pass through the MWPC before entering the aerogel Cherenkov radiator. A charged particle, such as a beta particle, will create ionization in the MWPC and thus register the event as a positive hit to trigger data acquisition. A gamma ray passing through the MWPC could thereby be rejected, thus reducing background. A scintillation detector illustrated above the apparatus in Fig. 6.30 was used to detect and veto background cosmic-ray particles.

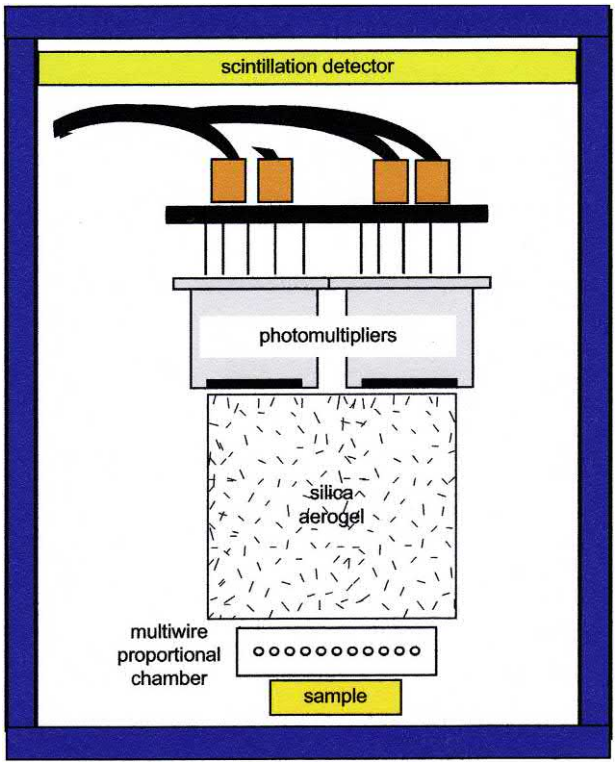


FIGURE 6.30 Silica aerogel Cherenkov detector for measuring ^{90}Sr activity. *From Pestotnik et al. (2008), reprinted with permission from Elsevier © 2008.*

Pestotnik et al. (2008) calibrated the detector with four radionuclide sources, namely, ^{137}Cs, ^{32}P, ^{90}Sr/^{90}Y, and ^{42}K. Radionuclide relative detection efficiencies were measured by dividing the number of Cherenkov photon events with the number of events registered by the MWPC. The efficiencies of the sources tested were plotted against their beta-particle energy maxima (E_{max}), which is illustrated in Fig. 6.31. The detection efficiencies are a function of the beta spectra end-point energies of the radionuclide source. The relative detection efficiency for ^{90}Sr/^{90}Y was 0.024, which is more than a twofold improvement over the

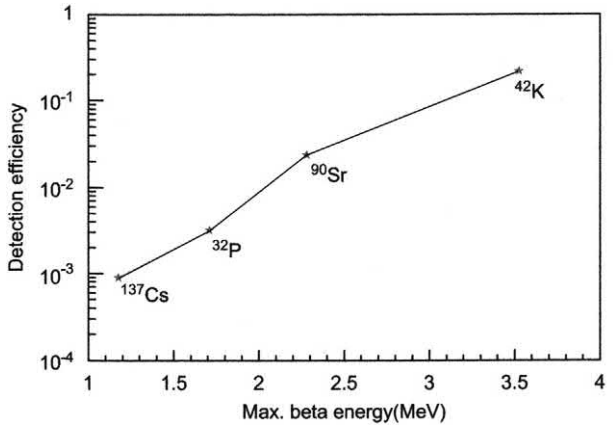


FIGURE 6.31 Cherenkov photon detection efficiency of the aerogel Cherenkov counter defined as count rate divided by appropriate activity as a function of beta spectrum end-point energy. *From Pestotnik et al. (2008), reprinted with permission from Elsevier © 2008.*

earlier detector developed by Pestotnik et al. (2002). The activity of ^{90}Sr is easily determined from the ^{90}Y activity, as both radionuclides would have the same activity if in secular equilibrium at the time of analysis, or by calculation, from the time interval that the ^{90}Y was separated from its ^{90}Sr parent. The low backgrounds achieved demonstrate the potential of this silica aerogel Cherenkov detector design as a radiation monitor for ^{90}Sr/^{90}Y in the environment.

A further development is an aerogel Cherenkov counter for the monitoring of fission products in the environment derived from the work of Ito et al. (2016a,b, 2014) and Ijima et al. (2014, 2013). This work arose as a consequence of the Fukushima nuclear accident from the need to monitor ^{90}Sr/^{90}Y in the environment in the presence of beta-emissions from ^{137}Cs and ^{40}K. They utilized a Cherenkov silica aerogel radiator with a refractive index of 1.034, which has a beta-particle threshold energy capable of detecting beta-particles from the ^{90}Sr daughter ^{90}Y ($E_{max} = 2280$ keV) within a background of beta-particles of ^{137}Cs ($E_{max} = 1180$ keV, 6% and 0.514 keV, 94%) and ^{40}K ($E_{max} = 1325$ keV) as well as discriminate from gamma-ray background radiation. The detector is most sensitive to beta radiation from ^{90}Sr/^{90}Y with a reduced sensitivity to radiation from other sources.

The basic design of the detector, described by Ito et al. (2016a), is illustrated in Fig. 6.32. The trigger component consists of scintillating fibers with fiber ends connected to PMTs (not illustrated). The trigger will register incoming beta-particles and cosmic-ray muons. The aerogel Cherenkov counter consists of silica aerogel of 30 mm thickness with an index or refraction $n = 1.034$, which has a threshold energy of 1498 keV for the production of Cherenkov photons by beta-particles as calculated according to Eq. (6.38) or 6.39. This threshold energy is sufficient to discriminate the ^{90}Y beta particles ($E_{max} = 2280$ keV) from the ^{137}Cs and ^{40}K beta-particle emissions that possess energies below the 1498 keV threshold. The Cherenkov photons produced in the aerogel are detected by means of a light guide consisting of wavelength shifting fibers (WLSFs), which absorb the Cherenkov photons and reemit them shifted to a longer wavelength. The WLSFs are of two types consisting of a purple to blueshift and a blue to greenshift. PMTs (not illustrated in Fig. 6.32) provide a readout of the Cherenkov photon emissions over a photosensitive area of 300 cm^2. The veto component, consisting of a plastic scintillator measuring 400 × 200 × 5 mm coupled to a PMT (not illustrated), provides signals to suppress background events due to cosmic-ray muons. A 10 mm block of aluminum set between the aerogel

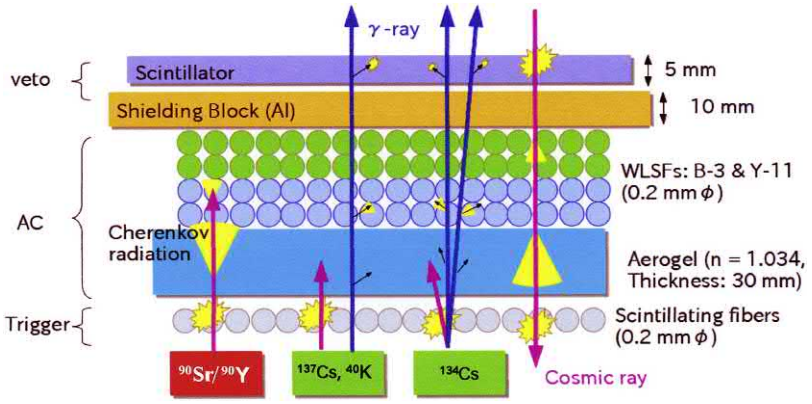


FIGURE 6.32 A sketch of the structure of the real-time ^{90}Sr counter comprising the trigger counter (Trigger) consisting of scintillating fibers, the aerogel Cherenkov (AC) counter with wavelength-shifting fibers (WLSFs), and the veto counter (veto) for the suppression of cosmic-ray background radiation. The magenta, blue, and back arrows represent the charged beta-particle, gamma ray, and knocked-out electron (e.g., Compton electron), respectively. The yellow cone shapes and spreading shapes denote Cherenkov radiation and scintillation emissions, respectively. Color is visible in the electronic version of the book. *From Ito et al. (2016a,b). Identification of 90Sr/40K based on Cherenkov detector for recovery from the Fukushima nuclear accident. JPS Conf. Proc. 11, 07002, https://doi.org/10.7566/JPSCp.11.07002, © The Author(s).*

Cherenkov (AC) counter and veto scintillation detector will block all beta particles while permitting the detection of gamma rays from the isotopes of ^{137,134}Cs and ^{40}K, as illustrated in Fig. 6.32. Ito et al. (2016a) calculated the detection limits for ^{90}Sr to be 52 ± 8 Bq/kg in seafood and 1.7 ± 0.3 Bq/kg in seawater with this real-time ^{90}Sr counter having an effective area of 300 × 100 mm.

A similar detector design was developed by Ito et al. (2018) for the measurement of ^{214}Bi by the counting of Cherenkov photons produced in silica aerogel. The detector would enable the real-time study of ^{214}Bi, which is one of the radon progenies, which may remain airborne contributing to the increasing number of lung cancer cases worldwide as the elderly population increases. An aerogel radiator with a refractive index $n = 1.041$ was utilized, which has a threshold energy of 1328 keV for beta particles calculated according to Eq. (6.38) or 6.39. Bismuth-214 emits beta-particles with maximum energy of 3270 keV. Thus, a large number of the beta-particle emissions from ^{214}Bi possess energies above 1328 keV capable of producing Cherenkov photons in the aerogel while discriminating against background radiation from radionuclides emitting beta-particles with a lower energy maximum. Ito et al. (2018) demonstrate that the ^{214}Bi beta-particle events in the detector are recorded when they are registered in both the scintillating fibers and aerogel radiator, but not the veto counter. Cosmic-ray muons will register events in all of the three detectors, namely, the veto counter, Cherenkov radiator and scintillation fibers.

VIII. Cherenkov counting in microplate format

The measurement of radionuclides by liquid scintillation in a microplate format is described in detail in Chapter 6, Volume 1 (Liquid Scintillation Analysis: Principles and Practice) and Chapter 9 (Solid Scintillation Analysis) of Volume 1. These sections describe the design and operation of multiple detector systems for the simultaneous analysis of up to 12 samples in a 24-, 96-, or 384-sample well microplate. In addition to the simultaneous analyses of samples by liquid and solid scintillation in a microplate format as described in Chapters 6 and 9 of Volume 1, a microplate scintillation and luminescence counter can be used to analyze Cherenkov radiation from high-energy β particle-emitting radionuclides, such as ^{32}P and ^{86}Rb.

The sample wells of microplates have a considerably smaller sample capacity than liquid scintillation counting vials. Consequently, the Cherenkov counting efficiencies and sample count rates achievable are lower with samples in the microplate format. Nevertheless, the high sample throughput available with microplate counters with a 12-phototube assembly allowing the simultaneous counting of up to 12 samples (see Chapters 6 and 9 of Volume 1) make Cherenkov counting of samples in the microplate format an attractive option.

The radionuclide ^{32}P with an $E_{max} = 1710$ keV and ^{86}Rb, which decays by two beta branches with an $E_{max} = 1770$ keV at 88% intensity and $E_{max} = 680$ keV at the remaining 22% intensity, yield suitable Cherenkov counting efficiencies in the limited sample volumes of 1.5 mL and 350 μL for the 24-well and 96-well microplates, respectively. The high sample throughput and inexpensive sample analysis possible with Cherenkov counting make the microplate format of Cherenkov counting very appealing. Most applications are in the biosciences and some examples may be obtained from the following works: Cherenkov counting of ^{32}P in a microplate format (Latz et al., 2013; Strandin et al., 2011; Talbot et al., 2010; Dherbecourt et al., 2006; Roof et al., 2006; Cutshall et al., 2005; Laroche-Joubert et al., 2003, 2002; Deschênes and Doucet 2000) and Cherenkov counting of ^{86}Rb in a microplate format (Talka et al., 2015, 2013; Töpfer et al., 2008; Bogdanova et al., 2005; Kuo et al., 2005; Castle et al., 2003; Brek Eaton et al., 2003; Völkel et al., 2001; Berenbrink et al., 2000).

Some detector and sample properties should be considered to optimize Cherenkov counting of samples in microplates. These are described subsequently.

A. Sample-to-sample cross-talk

In the case of the microplate counter design, where up to 12 PMTs are automatically situated above or on top of as many as 12 sample wells in close proximity there exists the possibility of sample-to-sample cross-talk. This can occur when the β-particle energy is of sufficient magnitude to be able to travel from one sample well to an adjacent well and cause interference by creating Cherenkov photons in the well of a neighboring sample.

Sample-to-sample cross-talk can be determined by adding a radioactivity spike (*e.g.*, ^{32}P in water) to one sample well and only pure water to the surrounding eight sample wells of the microplate. The percent cross-talk can then be calculated by determining the count rates above background in the wells containing only water as a percentage of the radioactivity detected by the PMT above the sample well containing the ^{32}P spike.

The percent cross-talk and percent detection efficiencies in the Cherenkov counting of ^{32}P were tested with the PerkinElmer TopCount microplate counter, which utilizes up to 12 adjacent PMTs above 12 adjacent microplate sample wells. These are listed in Table 6.15 together with background measurements for samples in 24- and 96-well OptiPlates as well as the 96-well UniFilter and 96-well FlexiFilter microplates. The filter microplates are

TABLE 6.15 Cherenkov counting performance in 96- and 24-well OptiPlate microplates and 96-well UniFilter and FlexiFilter microplates with a PerkinElmer TopCount scintillation and luminescence counter.[a]

Microplate type	Cross-talk (%)	Counting efficiency (%)	Background (CPM)
96-well OptiPlate (200 µL sample)	0.4	25	20
24-well OptiPlate (1.0 mL sample)	0.3	25	93
UniFilter-96 GF/B (wet, 20 µL)	1.0	24	38
FlexiFilter nylon (wet, 20 µL)	2.0	25	38

[a]*From Anonymous (1996) reprinted with permission from PerkinElmer, Inc. Printed with permission © 1996–2010 PerkinElmer, http://www.perkinelmer.com/lab-solutions/resources/docs/APP_TopCountCerenkovCountingPerfMicroplt.pdf, accessed April 4, 2018.*

described in Chapters 6 and 9 of Volume 1. The percent cross-talk values for Cherenkov counting, listed in Table 6.15, are low in all cases and generally negligible for the 200 µL and 1.0 mL samples in the 96- and 24-well OptiPlates. The detection efficiencies of 25% are about one-half the efficiencies attainable with Cherenkov counting using the conventional liquid scintillation analyzer. However, the high sample throughput for unattended counting offered by microplate counting is the trade-off, which might be preferred. For example, up to 40 microplates can be stacked in a TopCount microplate counter allowing for the unattended analysis of up to 3840 samples when a 96-well microplate is used (i.e., 96-wells × 40 plates).

B. Sample volume effects

The effects of sample volume on the Cherenkov counting efficiency of ^{32}P in 96- and 24-well microplates are provided in Table 6.16. The volume effects are significant for the relatively small sample volumes tested in the 96-well microplates, which can have a total capacity of 350 μL per sample well. For the larger sample sizes of 500−1500 μL of the 24-well microplates, there is no significant effect of sample volume on the Cherenkov detection efficiency.

The larger volumes of water in the 24-well microplate provide a greater probability for a larger number of high-energy β particles to have a longer path of travel in the aqueous medium for the production of Cherenkov photons. Samples of very small aqueous volume will have less detector medium (i.e., water) for Cherenkov photon production. A significant number of beta particles near the sample surface can escape into the air or microplate wall without producing any significant Cherenkov effect. The larger sample sizes of the 24-well microplate provide, for the most part, higher counting efficiencies than smaller samples of the 96-well plates.

Cherenkov counting of ^{32}P in samples in the dry state in 96- and 24-well OptiPlates is also possible, albeit at a lower detection efficiency (see Table 6.16).

TABLE 6.16 Cherenkov counting performance versus volume of aqueous sample of ^{32}P in 96-well and 24-well OptiPlate microplates with a PerkinElmer TopCount scintillation and luminescence counter.[a]

96-Well OptiPlate		24-Well OptiPlate	
Sample size (µL)	Counting efficiency (%)	Sample size (µL)	Counting efficiency (%)
Dry	10	Dry	14
10	12	500	22
25	14	1000	22
50	15	1500	23
100	18	–	–
300	26	–	–

[a]*From Anonymous (1996). Printed with permission from PerkinElmer, Inc. © 1996–2010, http://www.perkinelmer.com/lab-solutions/resources/docs/APP_TopCountCerenkovCountingPerfMicroplt.pdf.*

C. Quench correction

As previously discussed, there is no chemical quench in Cherenkov counting. However, color in the sample will absorb Cherenkov photons, reduce pulse heights, and consequently reduce counting efficiency. Therefore, when samples are colored, it is important to determine the degree of quench in each sample well of the microplate sample holder and determine the counting efficiency of each sample. From the counting efficiency, the sample activities in disintegrations per minute can be determined.

Because up to 12 samples can be counted simultaneously in a microplate scintillation counter and high sample throughput is generally a requirement with this type of counter and sample format, the most automated method of measuring sample quench and counting efficiency is to utilize a sample spectrum quench-indicating parameter (QIP), such as SIS, as previously described in Section IV.C.2 of this chapter.

The MicroBeta and TopCount microplate scintillation counters utilize the Spectrum Quench Parameter of the Isotope (SQP(I)) and the transformed Spectral Index of the Sample (tSIS) as a sample spectrum QIP. The tSIS is similar to the SIS used with the conventional liquid scintillation analyzers. These QIPs are described in detail in Chapter 6 of Volume 1. The SQP(I) and tSIS measure the magnitudes and other characteristics of the sample pulse height spectrum to provide a parameter to measure the degree of quench in the sample. Color quench in Cherenkov counting reduces Cherenkov photon intensities emitted by a sample and consequently reduces the sample pulse height spectrum according to the degree of quench. For example, the tSIS is a unitless number that reflects the magnitude of the pulse height spectrum; that is, as the quench level of a sample increases, the magnitude of the sample pulse height spectrum diminishes together with the value of the tSIS. The scintillation and luminescence counter can measure automatically the value of the QIP for each sample directly from the Cherenkov pulse height spectrum of the sample. It is necessary, therefore, only to establish a quench correction curve of percent counting efficiency versus the QIP from a set of color quench standards of the nuclide under study (e.g., ^{32}P, ^{86}Rb or other high-energy beta emitter) in water. From such a curve stored in the memory of the instrument computer, the microplate counter can determine automatically the Cherenkov counting efficiency of each sample in each well from the QIP value of each sample. It is important to keep in mind that the color quench correction curve is good only for a particular radionuclide, instrument, and microplate format and type of microplate. The procedures to follow for the preparation of quenched standards and the preparation of a quench correction curve for the Cherenkov counting in microplate sample format is available from the instrument supplier and from PerkinElmer by Anonymous (1993, http://www.perkinelmer.co.jp/Portals/0/resource/products_ls/ls_cocktails/pdf/tca-015.pdf), which is adaptable to any microplate scintillation counter.

From the sample count rate (CPM), the microplate analyzer automatically calculates the counting efficiency of each quenched standard using the DPM value of the radionuclide standard and the simple relation %E = CPM/DPM. The analyzer will also determine automatically the values of QIP from the pulse height spectra of each color-quenched standard in each sample well, and the quench correction curve of percent counting efficiency versus QIP (e.g., SQP(I) or tSIS) will be plotted automatically and stored in the memory of the analyzer computer. An example of a typical color quench correction curve is illustrated in Fig. 6.33. The DPM of ^{32}P of subsequent unknown experimental samples can be determined automatically by the analyzer by measuring the count rate (CPM) and the QIP of each sample. From the QIP value of a given sample and the color quench correction curve, the instrument will determine the counting efficiency of the sample. It will use the decimal value of the percent counting efficiency and the count rate of the sample to calculate the disintegration rate (DPM) of the sample.

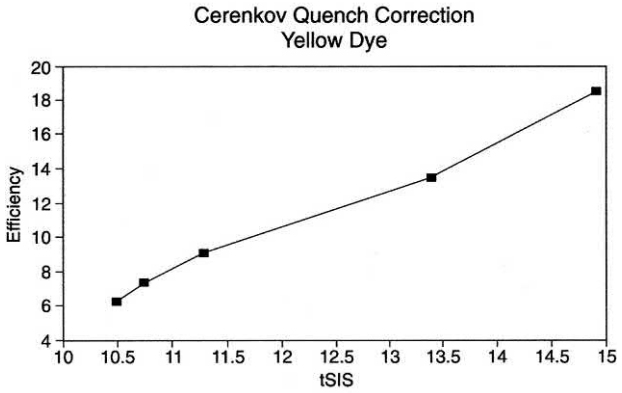


FIGURE 6.33 Example of a typical color quench correction curve for the Cherenkov counting of ^{32}P with a microplate scintillation and fluorescence counter (e.g., MicroBeta or TopCount). *From Anonymous (1996), ©1996–2018 PerkinElmer, Inc. Printed with permission, http://www.perkinelmer.com/lab-solutions/resources/docs/APP_TopCountCerenkovCountingPerfMicroplt.pdf.*

IX. Multiple radionuclide analysis

A. Sequential Cherenkov and liquid scintillation analysis

The conventional measurement of dual β particle-emitting radionuclides in the same sample by liquid scintillation analysis requires three or four quench correction curves for the determination of the same number of counting efficiencies depending on the method used, for example, exclusion and inclusion dual-region analysis, as described in Chapter 6, Volume 1. The methods can be considered tedious sometimes for the inexperienced in these techniques, particularly when preset optimum counting regions have not been established and set by the instrument manufacturer. When radionuclide mixtures consisting of two radionuclides, one of which emits beta particles with an energy maximum exceeding the threshold energy for the Cherenkov Effect in water ($E_{max} > 262$ keV) and the other radionuclide with an energy maximum < 262 keV and no interfering gamma-radiation of energy > 422 keV (threshold energy for the Cherenkov effect via Compton electrons), the activities of the two radionuclides may be resolved by a combination of Cherenkov counting followed by liquid scintillation counting (LSC).

1. Sequential Cherenkov counting and efficiency tracing

In this approach to dual radionuclide analysis, Cherenkov counting is used to obtain the activity of one of two radionuclides in a mixture; and the subsequent liquid scintillation counting (LSC) by efficiency tracing provides the total activity of the two nuclides. By difference, the activities of each radionuclide may be found. Fujii and Takiue (1988a,b) developed a simplified method of analyzing mixtures of dual radionuclides, which has a single requirement, namely that one of the radionuclides of the dual mixture emit β particles with an $E_{max} > 262$ keV in sufficient number to be measurable by Cherenkov counting in aqueous solution. The method of Fujii and Takiue (1988a,b) involves sequential Cherenkov and LSA counting; and it was developed for both dual β emitters and dual $\alpha-\beta$ emitters as mixtures. The method is described subsequently.

Examples of nuclide pairs that meet the above β-particle energy criterion are $^{32}P-^{14}C$, $^{32}P-^{35}S$, $^{32}P-^{45}Ca$, $^{32}P-^{33}P$, $^{36}Cl-^{35}S$, and $^{36}Cl-^{45}Ca$, among others. Some of these nuclide pairs proved to be useful tools in the elucidation of reaction mechanisms and pathways in studies of biosynthesis, as reviewed by L'Annunziata (1984b). The method involves first counting the Cherenkov photons of an aqueous solution of a nuclide pair to determine the activity or DPM of the high-energy radionuclide of the pair (*e.g.*, ^{32}P or ^{36}Cl of the above examples). Scintillation cocktail is then added to the aqueous solution of the nuclide pair, and the total activity (*e.g.*, DPM) of the sample is determined by the efficiency tracing (ET-DPM) method. The activity of the low-energy β emitter of the dual-radionuclide mixture is determined by difference between the total DPM of the sample and the DPM of the higher energy β emitter measured by Cherenkov counting.

The ET-DPM method, that is used here, is described in Section V.F.3 Chapter 6, Volume 1. It should not be confused with the CIEMAT/NIST efficiency tracing, which is a primary standardization technique also described in Chapter 6, Volume 1. The ET-DPM method was first described by Takiue and Ishikawa (1978), developed further by Ishikawa et al. (1984), Fujii and Takiue (1988a,b), and demonstrated for practical activity measurements by L'Annunziata and coworkers (see Noor et al., 1996) and Takiue et al. (2004). The following is an outline of the procedure based on the method developed by Fujii and Takiue (1988a):

1. An aqueous sample containing the dual-radionuclide mixture is counted in a 20-mL polyethylene plastic liquid scintillation counting vial in a counting region, which will receive the pulse events from Cherenkov photons. A typical counting region is 0–30 keV for LL and UL discriminator settings for pulse heights calibrated on an energy scale. The recommended volume of the solution to be counted is 5 mL. The volume should be constant for all samples, and this volume should be the same as the color quenched standards used to determine the Cherenkov color quench correction curve.

   Note 1: As described in Section V.B of this chapter, polyethylene plastic vials give higher counting efficiencies than glass vials, and the effect of sample volume on Cherenkov counting efficiency is reduced with the polyethylene plastic vials. Therefore, plastic vials are recommended over glass vials.

   Note 2: The sample volume of 5 mL is selected because the Cherenkov counting efficiency can be reduced markedly at volumes of less than 5 mL depending on the instrument (see Fig. 6.22), and room must remain in the vial to add scintillation fluor cocktail at a later step in the procedure. It is important to keep the aqueous sample at a constant volume (e.g., 5 mL), because sample volume will affect Cherenkov counting efficiency. If the sample volume is less than 5 mL add water to the counting vial to bring the volume up to 5 mL before analysis by Cherenkov counting.
2. Use a color quench correction curve to determine the Cherenkov counting efficiency of the sample and to convert the count rate (CPM) to disintegration rate (DPM) of the higher energy β emitter of the dual-nuclide mixture. See Section IV of this chapter on methods of color quench correction.

   Note: Chemical quench does not occur in Cherenkov counting. Even if samples are colorless, it is convenient to use a color quench correction curve for Cherenkov counting, because most modern liquid scintillation analyzers are programmed to provide automatic DPM calculations of experimental samples via a quench correction curve. Also, the use of an established color quench correction curve in Cherenkov counting will eliminate a possible source of error in counting efficiency determinations, as the writer has experienced that even a very slight color can produce significant quench in Cherenkov counting.
3. Add 10 mL of a liquid scintillation fluor cocktail to the aqueous sample in the scintillation vial after Step 2 is complete.

   Note: A fluor cocktail should be selected that will mix homogeneously with the 5 mL of aqueous sample. See Chapter 7, Volume 1 for information on the selection of fluor cocktails. Some examples of suitable fluor cocktails are Ultima Gold XR and Insta-Gel, which have high water holding capacities; the latter fluor cocktail forms a homogeneous gel at high water loads.

4. Determine the total DPM of the sample using the Efficiency Tracing with ^{14}C DPM method (ET-DPM). This method is simple and it is described in detail in Section V.F.3 of Chapter 6, Volume 1. The method will give the total DPM of the sample automatically without any need for a quench correction curve. The total DPM of the sample, therefore, represents the sum of the activities of the two radionuclides in the mixture.
5. Subtract the activity (DPM) of the higher-energy radionuclide determined by Cherenkov counting of the sample in Step 2 from the total sample DPM determined in Step 4 to yield the activity in DPM of the lower-energy β emitter of the dual radionuclide mixture.

This method can also be applied to the analysis of dual mixtures of alpha- and beta-emitting radionuclides as demonstrated by Fujii and Takiue (1988b). Alpha emitters will not give rise to Cherenkov photons because the threshold energy for the production of Cherenkov radiation by α particles in water medium is >1000 MeV or $>10^6$ keV as explained by Fujii and Takiue (1988b), and as calculated according to Eq. (6.39) discussed earlier in this chapter. Many radionuclides that decay by the emission of α particles also emit γ rays. However, γ radiation from α-emitting radionuclides would interfere with this method when the γ radiation possesses an energy >0.422 MeV to produce Compton electrons >0.262 MeV of energy sufficient to produce Cherenkov photons. Consequently, the above method of analysis of dual-radionuclide mixtures is applicable to α- and β-emitting radionuclide pairs when the β emitter of the pair has β-particle emissions of sufficient number in excess of 262 keV energy to produce measurable Cherenkov radiation, and the α-emitter does not have accompanying gamma emissions of energy in excess of 0.422 MeV. The method was demonstrated by Fujii and Takiue (1988b) with the ^{32}P–^{241}Am radionuclide pair. Quantitative activity determinations of the two radionuclides are obtained according to the procedure just described. When the mixture is first counted in water, the Cherenkov radiation is measured from the ^{32}P to provide the DPM of that radionuclide only. Adding liquid scintillation fluor cocktail to the aqueous mixture and subsequent analysis by the ET-DPM method provides the total DPM of the $^{32}P + {}^{241}Am$ mixture. Subtraction of the ^{32}P DPM obtained by Cherenkov counting from the total DPM of the mixture provides the activity of the ^{241}Am. The theory and practice of ET-DPM for β emitters as single nuclides or mixtures is described in detail in Section V.F.3 of Chapter 6, Volume 1. The application of the method to mixtures of α and β emitters was demonstrated by Fujii and Takiue (1988b), and an example of efficiency tracing curves for a ^{32}P–^{241}Am mixture is given in Fig. 6.34. As illustrated in the Figure, the curves are extrapolated to 100% counting efficiency where CPM = DPM irrespective of quench

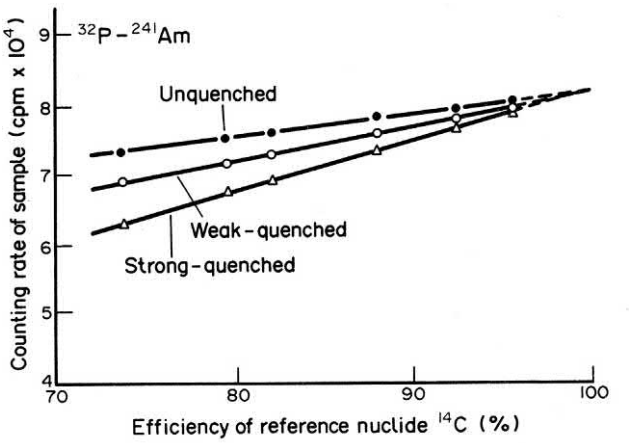


FIGURE 6.34 Efficiency tracing curves of a ^{32}P–^{241}Am mixture at three levels of quench. Each extrapolated value up to 100% counting efficiency provides the total activity of the sample to be measured. *From Fujii and Takiue (1988b), reprinted with permission from Elsevier © 1988.*

level. See Section V.F.3 of Chapter 6, Volume 1 for detailed information on this technique. The method should be applicable to many dual mixtures of α and β emitters when the β emitters can be measured by Cherenkov counting.

The sequential Cherenkov and LSA method was successfully employ by Morel and Fardeau (1989) for the analysis of ^{32}P–^{33}P in studies of phosphate fertilizer use efficiency. The writer and coworkers (see Noor et al., 1996) have applied the sequential Cherenkov counting and LSA analysis by ET-DPM method to analyze the triple-radionuclide mixture of ^{86}Rb–^{35}S–^{33}P. The total DPM of the mixture was determined by the ET-DPM method and the activity of ^{86}Rb of the triple-radionuclide mixture was determined by Cherenkov counting in water with 100% recoveries for several activity proportions of the triple-radionuclide mixture, as illustrated in Table 6.17. The difference of the two measurements provided the activities of the $^{35}S+{}^{33}P$ mixture. The activities of the ^{35}S and ^{33}P are determined by liquid scintillation analysis of the dual mixture after the ^{86}Rb decays to a negligible level according to its half-life ($t_{1/2}= 18.8$ days).

2. $^{89}Sr + {}^{90}Sr(^{90}Y)$ analysis by Cherenkov counting with subsequent LSA

Another example of a nuclide pair, which receives much interest and which can be analyzed by sequential Cherenkov and liquid scintillation counting, is freshly isolated ^{89}Sr–^{90}Sr (Walter et al., 1993; Poletiko et al., 1994; Clark, 1995; Martin and Odell, 1998; Heckel and Vogl, 2009; Kim et al., 2009a,b; Tovedal et al., 2009; Vajda and Kim, 2010; Groska et al., 2012; Grahek et al., 2012; Olfert et al., 2014; Dai and Kramer-Trembly, 2014; Tayeb et al., 2016; Holmgren Rondahl and Ramebäck, 2018). This method of

TABLE 6.17 Percent recoveries of calculated activities of five composite mixtures or $^{86}Rb–^{35}S–^{33}P$ determined by efficiency tracing DPM (ET-DPM) technique and the component activities of ^{86}Rb determined by Cherenkov counting and combined $^{35}S + ^{33}P$ obtained by difference.[a]

Sample DPM[b] ^{86}Rb:^{35}S:^{33}P	Total DPM (Actual)	Total DPM (ET)	Total DPM Recovery (%)	^{86}Rb DPM (Cherenkov)	^{86}Rb DPM Recovery (%)	$^{35}S–^{33}P$ DPM (Difference)	$^{35}S+^{33}P$ DPM Recovery (%)
4326:7294:7194	18,814	18,671	99.2	4387	101.4	14,284	98.6
2146:3620:3424	9190	9185	99.9	2199	101.2	6986	99.2
1042:1794:1550	4386	4408	100.5	1070	102.7	3338	99.8
3113:5510:4620	13,243	13,237	100.0	3171	101.9	10,666	99.4
432.3:742.6:646.1	1821	1819	99.9	445.5	103.1	1373.5	98.9

[a]*From L'Annunziata and coworkers (Noor et al., 1996) reprinted with permission from Elsevier © 1996.*
[b]*in hundreds.*

approach to the analysis of $^{89}Sr + ^{90}Sr(^{90}Y)$, requires firstly the radiochemical separation of $^{89}Sr + ^{90}Sr$ in a strontium fraction separate from all other chemical elements or radionuclides of the sample. The separation of strontium, by chemical fractionation of strontium or by ion exchange separation with a Sr-specific resin, yields $^{89}Sr + ^{90}Sr$, which is analyzed immediately by Cherenkov counting. If the freshly separated $^{89}Sr + ^{90}Sr$ is counting immediately for a relatively short counting time, ingrowth of ^{90}Y daughter can be neglected (Kim et al., 2009a,b). After 1 hour of preparation of freshly isolated $^{89}Sr + ^{90}Sr$, the ingrowth of ^{90}Y daughter with ^{90}Sr parent is only 1.06% of the maximum ^{90}Y activity of secular equilibrium (L'Annunziata, 1971), which is calculated according to Eq. (1.574) provided in Section XVII.C of Chapter 1, Volume 1. Cherenkov counting of the freshly isolated $^{89}Sr + ^{90}Sr$ provides the activity of the ^{89}Sr ($E_{max} = 1490$ keV). The contribution of ^{90}Sr ($E_{max} = 546$ keV) to the Cherenkov effect is very low and ignored. Its Cherenkov photon detection efficiency is only ~1%.

Once the ^{89}Sr activity is determined by Cherenkov counting of the freshly isolated $^{89}Sr + ^{90}Sr$, liquid scintillation cocktail is added to the counting vial; and the radiation from the $^{89}Sr + ^{90}Sr(^{90}Y)$ is then detected by liquid scintillation counting. The time of radiochemical separation of the strontium (*i.e.*, time of isolation of $^{89}Sr + ^{90}Sr$) must be recorded, as it is necessary to calculate the contribution of ^{90}Y to the count rate arising from the ingrowth of ^{90}Y from the time of separation of ^{90}Sr to the time of counting (see Section VIII.A.2.b of Chapter 6, Volume 1.). Kim et al. (2009a,b) recommends the subtraction of the ^{89}Sr activity determined by Cherenkov counting from the total activity $^{89,90}Sr$. The ^{89}Sr activity, measured by Cherenkov counting, may be imputed into Eq. (6.47) of Chapter 6, Volume 1. for the calculation of the ^{90}Sr activity. Heckel and Vogl (2009) describe the radiochemical elution of strontium on a column of Sr resin with 7 mL of 0.05M HNO_3 followed by the immediate Cherenkov counting of the dilute nitric acid eluate for the measurement of ^{89}Sr activity. The method is illustrated in Fig. 6.35. Cherenkov counting is followed by the X-ray fluorescence analysis of the elemental strontium in the eluate to measure the chemical yield. Liquid scintillation cocktail is then added to the vial to measure the radiation emissions of $^{89}Sr + ^{90}Sr(^{90}Y)$. They used a spectral deconvolution method to calculate the activities due to ^{89}Sr and ^{90}Sr. The spectral technique of dual LSA counting regions described by Kim et al. (2009a,b) may also be used (see Section VIII.A.2.b of Chapter 6, Volume 1.).

The detection procedures are summarized by Holmgren-Rondahl and Ramebäck (2018), as illustrated in Fig. 6.36. Holmgren-Rondahl and Ramebäck (2018) tested the method of spectrum deconvolution and the method of spectrum subtraction in combination with Cherenkov measurements to reach the optimal conditions for the determination of unknown activity ratios of $^{89}Sr/^{90}Sr$ in radiological emergency situations. The determination methodology is shown in Fig. 6.35. After separating the strontium in the Sr column with 8M HNO_3, there follows: (A) determination of ^{89}Sr by means of Cherenkov counting; (B) ^{90}Y separation from ^{90}Sr on Sr resin column with 8M HNO_3 and Cherenkov counting of the ^{90}Y and the subsequent addition of an Optiphase HiSafe 3 cocktail in a fraction of strontium, and measuring $^{89,90}Sr$ using the subtraction method, (C) adding the scintillation cocktail Optiphase HiSafe 3 to the Sr fraction and measuring $^{89,90}Sr$ using spectrum deconvolution. Sample aliquots prior to cocktail addition were taken for yield determinations in

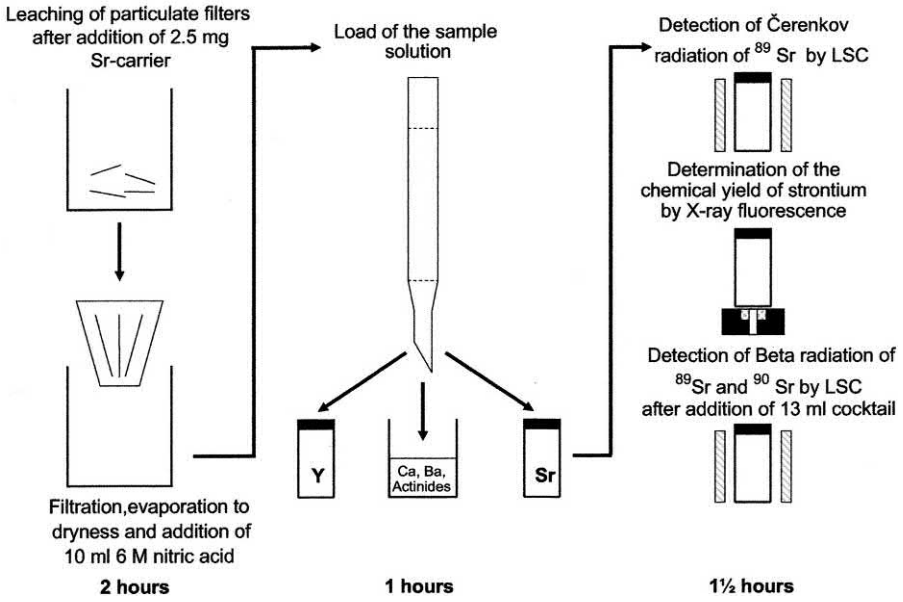


FIGURE 6.35 Radiochemical separation of strontium on a column of Sr resin. The Sr is eluted with a final volume of 7 mL of 0.05 M HNO_3 into a liquid scintillation counting vial. The vial is analyzed immediately thereafter by Cherenkov counting for ^{89}Sr, followed by X-ray fluorescence analysis for total strontium to determine the chemical yield, and finally liquid scintillation cocktail is added for the liquid scintillation counting of $^{89}Sr + {}^{90}Sr(^{90}Y)$. *From Heckel and Vogl (2009f), reprinted with permission from Elsevier © 2009.*

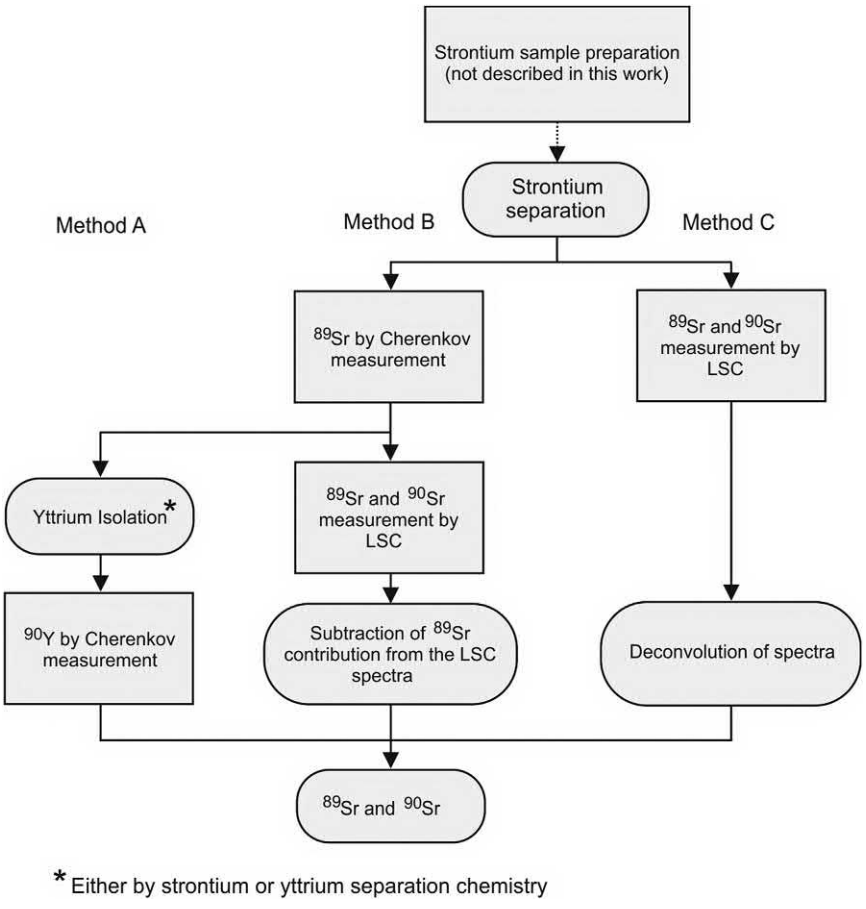


FIGURE 6.36 A schematic representation of the methods used in this work, a second chemical separation (Method A, left), spectrum subtraction (Method B, middle) and spectrum deconvolution (Method C, right). *Original figure courtesy of S. Holmgren-Rondahl, Swedish Defense Research Agency, Sweden, from Holmgren-Rondahl and Ramebäck (2018), reprinted with permission from Elsevier©2018.*

inductively coupled plasma–optical emission spectrometry (ICP-OES). The analysis time and uncertainty measurement for each particular method was calculated. The method of spectrum subtraction and deconvolution results in a high measurement uncertainty for ^{90}Sr, especially in the case of large ^{89}Sr/^{90}Sr activity ratios, implying that the obtained results are in fact below the detection limit for ^{90}Sr. The method of Cherenkov measurement of ^{89}Sr immediately after strontium separation and ^{90}Y after the second separation from strontium gave the lowest measurement uncertainty for the entire range of different activity ratios. Therefore, it can be concluded that this method has an advantage over the others, regardless of the time horizon, due to the separation of yttrium.

A similar approach was used earlier Groska et al. (2012). They described the radiochemical separation of strontium and yttrium in columns of Sr and DGA resin followed by the immediate Cherenkov counting of both fractions. Cherenkov counting is followed by the atomic absorption spectrometric determination of the elemental strontium and yttrium in the eluate to measure the chemical yield. A ProSafe HC scintillation cocktail is used to measure the activities of ^{89}Sr + ^{90}Sr(^{90}Y) in the strontium fraction. It is measured three times: immediately after Sr separation by Cherenkov technique, right after the Sr eluate is mixed with a scintillation cocktail, and 2 weeks later.

The yttrium fraction is measured immediately after elution by Cherenkov counting. The activities of ^{89}Sr and ^{90}Sr are calculated by a combination of LSC and Cherenkov measurement in both yttrium and strontium fractions. Groska et al. (2012) in the same paper also described a method for the determination of ^{89,90}Sr in liquid radioactive waste in which ^{91}Y is present. ^{91}Y as a pure beta emitter with $E_{\beta max} = 1.55$ MeV produces Cherenkov photons and interferes with ^{90}Y during Cherenkov counting.

Therefore, the radiochemical separation of strontium from yttrium in Sr resin and radiation measurement of ^{89}Sr + ^{90}Sr(^{90}Y) by liquid scintillation counting is used for quantification of ^{89}Sr and ^{90}Sr. The individual determination of ^{90}Y and ^{91}Y is also possible by means of a combination of Cherenkov and LSC counting, as described by Zhu et al. (1990).

Tayeb et al. (2016) used a similar separation method, but improved radiochemical separation by using double stacked Sr-resin cartridges which enable minimal loss of Sr and improve chemical yield by at least 25%. Strontium and yttrium were eluted from the Sr and DGA column with 8 mL of deionized water and 9 mL of 0.05M HCl respectively, followed by the immediate Cherenkov counting of the strontium fraction for ^{89}Sr activity determination. The method is illustrated in Fig. 6.79 in section XIV B of this chapter. After Cherenkov counting, an aliquot of the sample is withdrawn for chemical yield determination by means of ICP-MS. An Ultima gold AB scintillation cocktail is then added to both the Y and Sr fractions to measure the activities of ^{89}Sr + ^{90}Sr(^{90}Y) and ^{90}Y. The activities of ^{89}Sr and ^{90}Sr are calculated according to the methodology described in the IAEA report (IAEA, 2013).

B. Cherenkov analysis with wavelength shifters

Dual-radionuclide analysis by Cherenkov counting by the same conventional methods (*e.g.*, dual-region counting) used in liquid scintillation analysis is not practical, because of the high degree of overlap of the pulse height spectra of Cherenkov photons of the β emitting radionuclides. To overcome this difficulty and still make dual-radionuclide analysis possible by Cherenkov counting, Fujii and Takiue (1988c) developed a method that utilizes only one counting region while measuring the changes in the pulse height distributions and counting efficiencies of the two radionuclides in the mixture before and after the addition of wavelength shifter.

As described in Section V.C of this chapter, the addition of wavelength shifter to a sample containing β emitters, which produce Cherenkov radiation in a medium such as water, changes both the emission wavelength and the directional anisotropic nature of the Cherenkov photons into isotropic emissions. Hence, these effects of wavelength shifters improve the photon capture potential of the Cherenkov radiation by the PMTs, which increases the Cherenkov counting efficiencies of the two radionuclides in a mixture. In general, the effect of wavelength shifter on counting efficiency is greater for lower-energy β emitters (*e.g.*, ^{36}Cl) than for higher-energy β emitters (*e.g.*, ^{32}P). The effects of wavelength shifter on the Cherenkov pulse height spectra produced by ^{32}P and ^{36}Cl are illustrated in Fig. 6.37. If the effects of wavelength shifter on the counting efficiencies are significantly different, the method of Fujii and Takiue (1988c) may be applied to the DPM measurements of dual radionuclides in a mixture by Cherenkov counting. The method is based on the following simple conditions and equations:

A sample containing a mixture of two β-emitting radionuclides, whereby both radionuclides produce Cherenkov radiation in a nonscintillating medium (*e.g.*, water), will give different count rates n_A and n_B when counted without and with wavelength shifter, respectively according to the equations

$$n_A = D_1 e_{1A} + D_2 e_{2A}, \tag{6.68}$$

and

$$n_B = D_1 e_{1B} + D_2 e_{2B}, \tag{6.69}$$

where D_1 and D_2 are the activities (*e.g.*, DPM) of the two radionuclides, and e_{1A}, e_{1B}, e_{2A}, and e_{2B} are the counting efficiencies of the two radionuclides in the counting conditions without and with the wavelength shifter, respectively.

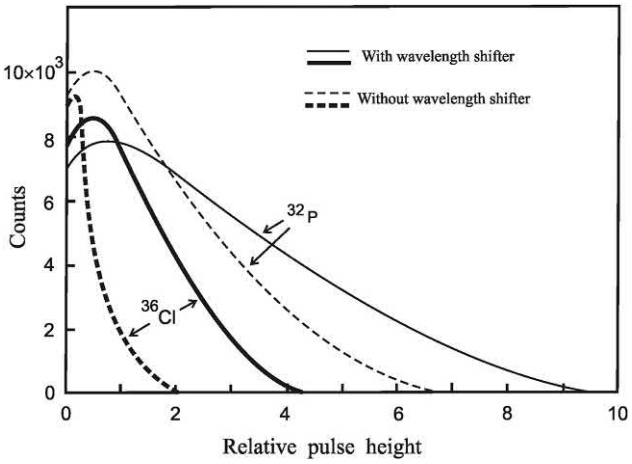


FIGURE 6.37 Pulse height distributions in ^{32}P and ^{36}Cl Cherenkov measurements without and with wavelength shifter (PPO: 0.03 g/L). The samples have the same activity. *From Fujii and Takiue (1988c), reprinted with permission from Elsevier © 1988.*

Eqs. (6.68) and (6.69) are solved simultaneously for the two unknown values D_1 and D_2 to give

$$D_1 = \frac{n_A e_{2B} - n_B e_{2A}}{e_{1A} e_{2B} - e_{1B} e_{2A}}, \tag{6.70}$$

$$D_2 = \frac{n_A e_{1B} - n_B e_{1A}}{e_{1B} e_{2A} - e_{1A} e_{2B}}. \tag{6.71}$$

We can see the similarities of the above Eqs. (6.68) to (6.71) with Eqs. (6.38) and (6.39) of Chapter 6, Volume 1. The equations defining count rates and disintegration rates for radionuclides producing Cherenkov radiation are derived from data produced in one counting region only, whereas, the similar equations described in Chapter 6, Volume 1 are derived from data originating from two different counting regions.

Eqs. (6.70) and (6.71) are solved for the disintegration rates of the two radionuclides by determining the count rates from the sample and counting efficiencies of the radionuclides without and with the introduction of wavelength shifter. An outline of the procedure used by Fujii and Takiue is as follows:

1. Only one counting region is used. This can be defined by setting the LL and UL discriminators to encompass the entire Cherenkov pulse height spectrum in its highest pulse height distribution possible, that is, when wavelength shifter is present.
2. After defining the counting region, 10 mL of the sample in a water medium is counted in a scintillation counting vial without wavelength shifter to yield the count rate n_A.
3. Wavelength shifter is introduced into the sample by adding 2 mL of one of the following solutions: 0.03 g/L PPO in ethanol or 0.2 g/L of 4-methyl-umbelliferone. The sample is counted again to yield the count rate n_B.
4. Counting efficiencies are determined by taking two other 10-mL aliquots of the unknown sample, adding 0.1 mL of reference standards of the two radionuclides of the mixture, and counting before and after the addition of wavelength shifter. The internal standardization technique is described in Section V.A of Chapter 6, Volume 1.

Fujii and Takiue (1988c) demonstrate quantitative recoveries with this technique for the ^{32}P–^{36}Cl and ^{86}Rb–^{36}Cl radionuclide mixtures.

Other radionuclide mixtures could be analyzed by this method provided that the ratios e_{1A}/e_{1B} and e_{2A}/e_{2B} of increase of the Cherenkov counting efficiencies are significantly different from each other because Eqs. (6.68) and (6.69) cannot be solved when e_{1A}/e_{1B} is equal to e_{2A}/e_{2B}. According to Fujii and Takiue (1988c), the magnitude of the increase of Cherenkov counting efficiency with the addition of wavelength shifter for lower-energy β emitters is larger than that for higher-energy β-emitters (Ross, 1976; Takiue et al., 1984). For example, in the case of the ^{36}Cl and ^{32}P mixture, Fujii and Takiue (1988c) report that the increase of Cherenkov counting efficiency (27%) for ^{36}Cl with PPO wavelength shifter is 2.9 times as high as the counting efficiency (9.5%) without wavelength shifter. This was larger than the increase, by the order of magnitude of 1.2, for the ^{32}P Cherenkov counting efficiencies after the addition of wavelength shifter.

X. Radionuclide standardization

The concepts of radionuclide standardization by liquid scintillation, that is, the determination of the absolute activity of samples, upon which the activity of other samples is traceable, are described in detail in Chapter 6 of Volume 1 and Chapter 7 of Volume 2. Radionuclide standardization is not used generally to determine sample activities in the routine measurement of radionuclides in applied research or radionuclides in the environment; rather, radionuclide standardization is a technique required to determine the absolute activity of a sample often to less than 1% uncertainty as a primary standard upon which the activities of other standards may be traced.

Liquid scintillation analysis (LSA) is often used for the standardization of radionuclides because of the higher detection efficiencies achieved in LSA compared to Cherenkov counting. However, under certain circumstances, as explained by Grau Carles and Grau Malonda (1995) and Grau Malonda and Grau Carles (1998a,b), Cherenkov counting can be advantageous in the calibration of certain radionuclides where the detection of low-energy electrons by LSA can complicate the elaboration of the standardization model. In the case of Cherenkov counting, the Cherenkov energy threshold (262 keV in pure water) serves

as a discriminator for low-energy electrons, that is, only electrons of energy above the Cherenkov threshold energy (*i.e.*, $E > 262$ keV) in water are detected and only these electron energy distributions are included in the calculation of the detection efficiency. The concepts and techniques that have been applied to the standardization of radionuclides by Cherenkov counting are included in this section.

A. Cherenkov counting efficiency—detection probability function, CHEREN

The first development of a Cherenkov counting technique, which may be applied universally to the standardization of all radionuclides that emit radiations (beta or gamma) producing the Cherenkov effect, was reported by Grau Carles and Grau Malonda (1995, 1998). The objective of this work was to develop a method for the computation of the Cherenkov counting efficiency, which should correct for previously unexplained discrepancies in the predicted and experimental values. The differences in experimental counting efficiencies between ^{36}Cl and ^{204}Tl serve as an example of such a discrepancy, where the counting efficiency of ^{36}Cl ($E_{\max} = 710$ keV) is 70% greater than the counting efficiency of ^{204}Tl ($E_{\max} = 763$ keV). Although the maximum energy of the β emissions of ^{36}Cl is less than that of ^{204}Tl, the experimental counting efficiency of ^{36}Cl is extraordinarily much greater than that of ^{204}Tl.

New concepts were introduced by Grau Carles and Grau Malonda (1995) to explain unusual Cherenkov counting efficiencies such as those presented in the above example of ^{36}Cl and ^{204}Tl.

These concepts are (1) intrinsic Cherenkov counting efficiency, ε_k, which is the ratio between counted pulses and emitted particles over the Cherenkov energy threshold, and (2) Cherenkov yield, r_k, which is the ratio between emitted particles over the Cherenkov energy threshold and the total number of emitted particles. These terms, to be further defined subsequently, were used to explain the unusual behavior of ^{36}Cl and ^{204}Tl by showing that the intrinsic Cherenkov counting efficiencies of the two radionuclides were similar (10%), whereas the Cherenkov yields of the two differ significantly, namely 65% for ^{36}Cl and 40% for ^{204}Tl.

The method requires prior calibration with two standards, namely ^{36}Cl and ^{32}P, upon which the counting efficiency of any other radionuclide with β emissions or Compton electron energies greater than the Cherenkov threshold energy may be determined. Grau Carles and Grau Malonda (1995) used the new concepts of intrinsic Cherenkov counting efficiency and Cherenkov yield to define the Cherenkov counting efficiency ε_c according to the equation

$$\varepsilon_c = r_k \varepsilon_k, \tag{6.72}$$

where r_k is the Cherenkov yield (*i.e.*, the ratio of the emitted particles over the Cherenkov threshold energy to the total number of emitted particles) and ε_k is the intrinsic counting efficiency (*i.e.*, the ratio of the counted pulses to the emitted particles over the Cherenkov threshold energy), that is,

$$\begin{aligned}\varepsilon_c = r_k \varepsilon_k &= \frac{\text{emitted particles} > E_{th}}{\text{total \# of emitted particles}} \\ &\times \frac{\text{counted pulses}}{\text{emitted particles} > E_{th}} \\ &= \frac{\text{counted pulses}}{\text{total \# of emitted particles}}\end{aligned}$$

where E_{th} is the Cherenkov threshold energy. The Cherenkov yield was obtained by Grau Carles and Grau Malonda (1995) from the β-particle distributions as follows:

$$r_k = \frac{\int_{W_k}^{W_m} N(W)dW}{\int_1^{W_m} N(W)dW}, \tag{6.73}$$

where W_k and W_m are the Cherenkov threshold energy and the maximum β-particle or end-point energy, respectively, and $N(W)$ is the β-particle energy distribution.

The intrinsic Cherenkov efficiency is achieved by counting pulses arising from Cherenkov photon events and relating the number of counted pulses with the detection probability $f(W)$ according to the equation

$$\varepsilon_k = \int_{W_k}^{W_m} N(W) f(W) dW. \tag{6.74}$$

Eq. (6.74) can be used to calculate the counting efficiency of any β emitter, with a known $\beta-$particle energy distribution $N(W)$ over the Cherenkov threshold energy, once the function $f(W)$ is known. The Cherenkov counting efficiency for pure β-particle emitters, which is the ratio of detected to emitted particles is then defined by Grau Carles and Grau Malonda (1998) as

$$\varepsilon_C = \int_{W_k}^{W_m} N(W) f(W) dW \Big/ \int_1^{W_m} N(W) dW \tag{6.75}$$

The end-point energy or energy maximum, W_m, and the Cherenkov threshold energy W_k, are expressed in units of rest mass, that is,

$$W = 1 + \frac{E[\text{keV}]}{511} \tag{6.76}$$

and E is the β-particle energy in keV and 511 is the energy equivalence of the beta-particle rest mass in keV. They defined the emission probability $N(W)$ for a β-particle in the energy range between $W + dW$ as

$$N(W) = C(W)(W-1)^{1/2}(W_m - W)^2 \times WF(Z,W)dW \tag{6.77}$$

where the functions $F(Z,W)$ and $C(W)$ are the electron density ratio (or Fermi function) and the shape factor function of the beta transition, respectively; and Z is the atomic number of the daughter nuclide. The beta spectrum shape factor is an important component of the Cherenkov counting efficiency calculations.

According to the solution of Grau Carles and Grau Malonda (1995, 1998), the function $f(W)$ is zero for energies below the threshold energy, W_k, and unity for electrons (β particles) that have sufficient energy for total detection, that is, the detection probability is nearly 1 for electrons of $E > 1$ MeV or 1000 keV in water. In the regions intermediate to these limits, the detection probability increases exponentially according to the following:

$$\begin{aligned} f(W) &= a(W - W_k)^n, && W_k \le W < W_u \\ f(W) &= 1, && W \ge W_u \end{aligned} \tag{6.78}$$

where W_u is the minimum energy that corresponds to the total detection and a and n are parameters defined by least squares fitting using the radionuclides ^{36}Cl and ^{32}P as standards. When all of the β particles are partially detected $W_m < W_u$, the minimum condition is defined as

$$\min \sum_{i=1}^{\nu} \left[\varepsilon_{k_i} - a \int_{W_k}^{W_m} N_i(W)(W - W_k)^n \, dW \right]^2 \tag{6.79}$$

where ν is the total number of radionuclides involved in the fitting. When $W_m > W_u$ the minimum condition is defined as

$$\min \sum_{i=1}^{\nu} \left[\varepsilon_{k_i} - a \int_{W_k}^{W_u} N_i(W)(W - W_k)^n dW - \int_{W_u}^{W_m} N_i(W) dW \right]^2. \tag{6.80}$$

Both of the above conditions are used to characterize the parameter n and obtain the values of a and W_u by least-squares fitting.

Using ^{36}Cl and ^{32}P as standards, Grau Carles and Grau Malonda applied Eqs. (6.78)–(6.80) to obtain the detection probability function $f(W)$ for the particular liquid scintillation spectrometer they used as follows:

$$f(W) = 0.5424(W - 1.5004)^{1.60}$$

$$1.5005 \le W < 2.9662$$

$$f(W) = 1, W \ge 2.9662$$

The value of 1.5004 for W_k was calculated in light of the fact that the ^{36}Cl and ^{32}P standards were counted in 15 mL of 1M HCl instead of pure water. The index of refraction of 1M HCl reduces the Cherenkov threshold energy to 255.7 keV. Therefore, W_k is calculated as

$$W_k = \frac{255.7\text{keV}}{511\ \text{keV}} + 1 = 1.5004$$

The importance of this technique is that the above detection probability function, once determined, can then be used to calculate the counting efficiency of any other radionuclide that emits β particles or γ rays that produce Compton electrons, over the Cherenkov threshold energy of 255.7 keV in 15 mL of 1M HCl with the particular liquid scintillation spectrometer used. If the solution type (i.e., counting medium), solution volume, vial type, or instrument is changed, the detection probability function is refitted.

Grau Carles and Grau Malonda (1995) reported good agreement between experimental and computed counting efficiencies, as illustrated in Table 6.18. The counting efficiencies of ^{36}Cl and ^{32}P of Table 6.18 show no discrepancy between experimental and calculated values because these two nuclides are used as the standards. The nuclides ^{60}Co and ^{137}Cs deserve attention because both are β and γ emitters.

In the case of ^{60}Co, the β-particle emissions make a negligible contribution to the production of Cherenkov photons; however, its two γ-ray emissions of 1.33 and 1.17 MeV produce Compton electrons of sufficient energy to yield Cherenkov radiation. Therefore, the Cherenkov counting efficiency calculation for ^{60}Co is calculated according to

$$\varepsilon = \varepsilon(\gamma_1) + \varepsilon(\gamma_2) - \varepsilon(\gamma_1)\varepsilon(\gamma_2), \tag{6.81}$$

TABLE 6.18 Experimental and computed Cherenkov counting efficiencies.[a]

Nuclide	Efficiency experimental	Efficiency computed	Discrepancy (%)
^{36}Cl	0.0666	0.0666	0.0
^{204}Tl	0.0402	0.0404	0.6
^{89}Sr	0.374	0.377	0.9
^{32}P	0.468	0.468	0.0
^{90}Sr + ^{90}Y	0.620	0.631	1.8
^{60}Co	0.0561	0.0556	0.7
^{137}Cs	0.0493	0.0475	3.7

[a] *From Grau Carles and Grau Malonda (1995) reprinted with permission from Elsevier © 1995.*

where $\varepsilon(\gamma_1)$ and $\varepsilon(\gamma_2)$ are the counting efficiencies for the Compton electrons produced by each of the two γ rays, and the product of the two efficiencies considers the simultaneous Compton interaction of the two γ rays of ^{60}Co.

The application of this method to the standardization of ^{137}Cs is more complicated, because this nuclide decays by two β branches with emissions over the Cherenkov threshold energy. It reaches secular equilibrium with its daughter nuclide ^{137m}Ba, which undergoes a 662-keV γ-ray decay transition that results in 89% abundance of 662-keV γ-ray emissions and 11% abundance of internal conversion electrons, a fraction of which are above the Cherenkov threshold energy.

The above method was successfully used by Navarro et al. (1997) to determine the counting efficiency and activity of ^{234}Th by Cherenkov counting to within 1.5% uncertainty. The computer program, CHEREN, which includes the beta spectrum shape factor as an important component, for the calculation of the Cherenkov counting efficiency is described by Grau Carles and Grau Malonda (1998) together with the calculated Cherenkov counting efficiencies of 39 radionuclides. The influence of the β-spectrum shape factor on the calculated results was demonstrated in this and other works (Grau Carles, 1995; Grau Carles and Grau Malonda, 1995; 1996b; Grau Malonda and Grau Carles, 2002).

B. Anisotropy detection model—CHEREN2

In an effort yet to reduce further the uncertainty in radionuclide standardization by Cherenkov counting, Grau Malonda and Grau Carles (1998a,b) introduced a new model based on two parameters that depend on the measurement conditions and on the equipment, but not on the nature of the radionuclide. The anisotropic character of Cherenkov radiation reduces the experimental counting efficiency and complicates its theoretical computation. According to the new model, the directional character of Cherenkov radiation and the amount of energy that Cherenkov light must transfer to create one photoelectron at the photocathode are defined as two new free parameters (see Section IX, Chapter 6, Volume 1 for the definition of free parameter). This model offers the advantage of calculating the Cherenkov counting efficiency regardless of the refractive index or acid concentration of the medium as well as it allows the inclusion of physical effects of the counting medium such as the effect of liquid density on the electron range or deceleration and the effects of light absorption bands in the near ultraviolet on the Cherenkov radiation.

As explained by Grau Malonda and Grau Carles (1998a,b), the calculation of the counting efficiency of an electron of energy E requires the evaluation of the total number of photons k emitted in the wavelength interval (λ_1, λ_2) per unit path length of electron travel according to Frank and Tamm (1937) described by the equation

$$\frac{dk}{dx} = 2\pi\alpha\left(\frac{1}{\lambda_1}-\frac{1}{\lambda_2}\right)\left(1-\frac{1}{\beta^2 n^2}\right) \tag{6.82}$$

where α is the fine structure constant, n and β are the index of refraction of the medium and electron relative phase velocity previously described in Eqs. (6.29) and (6.30) of this chapter; and the wavelength interval includes those Cherenkov radiation frequencies to which the photocathode of the PMT is sensitive. Because Cherenkov light is emitted as a cone, a given Cherenkov event is mainly oriented toward one of the two photomultipliers of a 2-PMT LSA (e.g., photomultiplier (A), while the other photomultiplier (B) receives light from the same Cherenkov event that is reflected or diffused by the reflective walls of the counting chamber. Grau Malonda and Grau Carles (1998a,b) define the free parameter α as the anisotropy coefficient, which gives the rate of Cherenkov photons directed toward photomultiplier A, and β as the rate of photons directed toward photomultiplier B where

$$\alpha+\beta = 1 \tag{6.83}$$

When $\alpha = 1$ and $\beta = 0$, the anisotropic properties of the LSA is displayed at a maximum when only photomultiplier A detects the Cherenkov photons originating from a given beta-particle emission and no event is recorder by the LSA in coincidence counting. The minimum value for α is 0.5, corresponding to the maximum value for β. The number of Cherenkov photons traveling directly toward photomultipliers A and B are defined as $k\alpha$ and $k(1-\alpha)$, respectively. If s and w represent the transmission probabilities and photocathode quantum efficiencies, respectively, the number of photons generated at the photocathodes of photomultipliers A and B are written as $ksw\alpha$ and $ksw(1-\alpha)$, respectively. With these variables defined and taking the free parameter q as the product of the probabilities s and w under the assumption that the generation of photoelectrons at the PMT photocathode follows the Poisson law, Grau Malonda and Grau Carles (1998a,b) derived the Cherenkov counting efficiency ε_B of pure β emitters as

$$\varepsilon_B = \int_{E_k}^{E_0} N(E)\{1-\exp[-qk(E)\alpha]\}\{1-\exp[-qk(E)(1-\alpha)]\}dE \tag{6.84}$$

where $N(E)$ is the β-particle energy distribution, α and q are two free parameters defined previously, and E_k and E_0 are the Cherenkov threshold and maximum β-particle energies, respectively, and the function $N(E)$ was normalized according to the following:

$$\int_0^{E_0} N(E)dE = 1 \tag{6.85}$$

For radionuclides that decay by internal conversion the counting efficiency calculation defined by Eq. (6.84) was modified by Grau Malonda and Grau Carles (1998a,b) to account for nine possible electron conversion possibilities. Also, for radionuclides that decay by pure gamma-ray emission, the counting efficiency calculation was expressed to account for Compton electrons with energies above the Cherenkov threshold of the counting medium, as well as to include the gamma-photon escape probability. When both gamma-ray emission and internal conversion processes occur in radionuclide decay, the counting efficiency calculation was expressed as a sum according to both decay probabilities.

The robustness of the calculations for Cherenkov counting efficiency was demonstrated by Grau Malonda and Grau Carles (1998a,b) for several radionuclides in a variety of media and sample volumes, in glass or plastic vials, and with two liquid scintillation analyzers (PerkinElmer 2500 TR and LKB Rack Beta); and they obtained very close discrepancies between experimental and computed counted efficiencies. The free parameters α and q were evaluated for the various sample media and vial types. The value of the anisotropy coefficient α remained a constant value of 0.790 while the parameter q increased for plastic vials and took on the values of 0.181 and 0.179 for HCl and water media, respectively. It was found that the free parameter α was independent of the sample medium, volume, vial material or scintillation spectrometer; whereas, the free parameter q depended substantially on the volume of medium, vial material, and slightly on the nature of the solvent or medium. The following serve as examples of computed counting efficiencies expressed as a decimal (i.e., 100% = 1.0) reported by Grau Malonda and Grau Carles (1998b) with the discrepancy between the computed and experimental counting efficiencies expressed as a percent: ^{36}Cl, 0.0913 (−0.88%); ^{204}Tl, 0.0526 (−1.94%); ^{89}Sr, 0.428 (0.92%); ^{32}P, 0.522 (−1.36%); ^{90}Sr, 0.673 (1.17%), ^{210}Bi, 0.1310 (−0.61%); ^{234m}Pa, 0.542 (0.73%); ^{137}Cs + ^{137m}Ba, 0.0722 (0.41%); and ^{40}K, 0.394 (0.76%).

The anisotropy detection model was developed further by Grau Carles and Grau Malonda (2006) with the publication of the computer program CHEREN2 for the determination of Cherenkov counting efficiencies in radionuclide standardizations. The anisotropy detection model is based on the principle that the generation of photoelectrons at the PMT photocathode obeys the Poisson law; and it makes use of two free parameters for the calculation of the Cherenkov counting efficiency, namely, the anisotropy coefficient α, which gives the rate of Cherenkov photons that are emitted directly toward one of the two photomultipliers, and the coefficient q, which is defined as the average energy that the Cherenkov light must possess to create one photoelectron at the PMT photocathode.

Under the assumption that the generation of photoelectrons at the PMT photocathode follows the Poisson law, Grau Carles and Grau Malonda (1996a, 2006) and Grau Malonda and Grau Carles (1998a,b) describe the counting efficiency ε for one electron of kinetic energy E as

$$\varepsilon(E) = \left(1 - e^{-qk\alpha}\right)\left(1 - e^{-qk(1-\alpha)}\right) \tag{6.86}$$

where α and q are the free parameters defined in the previous paragraph, and k is the number of Cherenkov photons generated by the electron. They then generalize Eq. (6.84) for the Fermi β-particle distributions $N(E)$ to define the computed Cherenkov counting efficiency, $\varepsilon_C^{\text{th}}$, for a pure β-particle emitting nuclide in a transparent medium of refractive index n as

$$\varepsilon_C^{\text{th}} = \int_{E_k}^{E_m} N(E)\varepsilon(E)dE \Big/ \int_0^{E_m} N(E)dE \tag{6.87}$$

and for $\beta-\gamma$-ray emitters, for which the γ-ray contribution to the Cherenkov counting efficiency is small (<2%) the following expression is applied

$$\varepsilon_C^{\text{th}} = \sum_{i=1}^{M} p_i \frac{\int_{E_k}^{E_{m_i}} N_i(E)\varepsilon(E)dE}{\int_0^{E_{m_i}} N_i(E)dE} \tag{6.88}$$

where M is the number of β-decay branches, which have transition energies above the β-particle threshold energy, and p_i is the probability of the decay transition. The threshold energy is computed in CHEREN2 (Grau Carles and Grau Malonda, 2006) from the refractive index, n, of the counting medium according to

$$E_k = \frac{m_0c^2}{\left(1 - 1/n^2\right)^{1/2}} - m_0c^2 \tag{6.89}$$

described previously in this chapter (see Eq. 6.39). For the case of the electron or β-particle, Eq. (6.89) is expressed as described previously in this chapter by Eq. (6.38) or

$$E_{\text{th}} = 511 \text{ keV}\left[\left(1 - \frac{1}{n^2}\right)^{-1/2} - 1\right] \tag{6.90}$$

CHEREN2 includes, as previously discussed, the calculation of the counting efficiency of an electron of energy E, which requires the evaluation of the total number of photons k emitted in the wavelength interval (λ_1 to λ_2) per unit path length of electron travel according to Frank and Tamm theory (1937) described by the equation

$$\frac{dk}{dx} = 2\pi\alpha\left(\frac{1}{\lambda_1} - \frac{1}{\lambda_2}\right)\left(1 - \frac{1}{\beta^2 n^2}\right) \tag{6.91}$$

where $\beta^2 = (W^2 - 1)/W^2$ and $W = E/m_0c^2 + 1$. Grau Carles and Grau Malonda (2006) include into the above equation an energy-to-range relationship in order to integrate the number of photons k emitted along the particle pathway

x, because this number will vary as the particle loses energy along its path of travel. The range of the electron in centimeters is calculated according to the following empirical formula of Flammersfield (1946) described by Paul and Steinwedel (1955).

$$x = 0.11\left(\sqrt{1 + 22.4E^2} - 1\right)/\rho \qquad (6.92)$$

where ρ is the density of the counting medium and E is the kinetic energy of the β-particle in MeV. See Eq. (1.253) of Chapter 1, Volume 1 where this empirical formula is discussed. The numerator of the equation yields the range of the β-particle in units of g/cm^2; and inclusion of the density in the denominator yields the range in units of cm. More precise ranges and graphs are available from the online computer program ESTAR "Electron Stopping Power and Range" available from the National Institute of Standards and Technology (NIST) at https://physics.nist.gov/PhysRefData/Star/Text/method.html (accessed on August 8, 2018).

In the search for the values of the two free parameters α and q in CHEREN2, a constant value of 0.790 for the anisotropy coefficient α is assumed, as this was demonstrated previously to be the case (Grau Malonda and Grau Carles, 1998a,b). The parameter q is then determined in CHEREN2 by making the difference between the computed and the measured counting efficiencies a minimum for two radionuclide standards ^{36}Cl and ^{32}P. These two radionuclide standards were selected by Grau Carles and Grau Malonda (2006) for three reasons, namely, (i) the radionuclide half-lives are sufficiently long, (ii) the maximum-point energy is below 1 MeV in the case of ^{36}Cl ($E_{max} = 0.714$ MeV) and it is over 1 MeV for ^{32}P ($E_{max} = 1.710$ MeV), which allows for the determination of an average value of q yielding the best results, because the Fermi distributions of the two radionuclides cover a wide range of energies, and (iii) the shape factor functions of ^{36}Cl and ^{32}P are well known. The best value for the parameter q is computed in CHEREN2 that simultaneously agrees with the measured counting efficiencies for ^{36}Cl and ^{32}P by defining the parameters q_1 and q_2 according to the two minimization processes

$$\min_{q_1}\left\{\left|\frac{\varepsilon_C^{th}(^{36}\mathrm{Cl}) - \varepsilon_C^{exp}(^{36}\mathrm{Cl})}{\varepsilon_C^{exp}(^{36}\mathrm{Cl})}\right|\right\} \quad \text{and} \quad \min_{q_2}\left\{\left|\frac{\varepsilon_C^{th}(^{32}\mathrm{P}) - \varepsilon_C^{exp}(^{32}\mathrm{P})}{\varepsilon_C^{exp}(^{32}\mathrm{P})}\right|\right\} \qquad (6.93)$$

where ε_C^{th} and ε_C^{exp} are the computed and experimental Cherenkov counting efficiencies. The optimum values for the coefficient q is calculated in CHEREN2 as the average $(q_1 + q_2)/2$. Grau Carles and Grau Malonda (2006) tested CHEREN2 for the Cherenkov counting efficiency determinations of 39 radionuclides with beta emissions over the Cherenkov threshold energy of 255.96 keV in a counting medium of 1M HCl ($n = 1.341$), the vast majority of which were determined with discrepancies of $<1\%$.

Grau Carles and Grau Malonda (2006) note that counting efficiency calculations are strongly dependent on the shape factor function of radionuclide β-particle transitions. Consequently much effort has been placed on the accurate measurement of β-spectra shape factor functions (Grau Carles, 1995, 2005; Grau Carles and Grau Malonda, 1996b; Grau Carles and Kossert, 2006; 2007; Grau Carles et al., 2008).

The computer program CHEREN2 designed by Grau Carles and Grau Malonda (2006) described in the previous paragraphs was utilized by Kossert (2010) of the Physikalisch-Technische Bundesanstalt (PTB) and Kossert et al. (2014) to facilitate the calculation of the radionuclide beta emission spectra and to account for the variations of the beta spectra shape factor functions $C(W)$ in the measurement of Cherenkov counting efficiencies for the standardization of radionuclides with analyzers equipped with three PMTs and utilization of the triple-to-double channels ratio (TDCR) technique. This PTB model was adapted by Thiam et al. (2017) at the Laboratoire National Henri Becquerel taking into account the physical properties of the specific TDCR measurements. The utilization of analyzers equipped with three PMTs for the standardization of radionuclides by the TDCR method is described subsequently in this chapter.

C. TDCR Cherenkov counting

The Triple to Double Coincidence Ratio (TDCR) efficiency calculation technique is applied to the primary standardization of radionuclides by liquid scintillation, as described in detail in Section IX.C of Chapter 6, Volume 1 and by Cherenkov counting as described subsequently in this section. The reader is invited to peruse that material, as these principles will not be reiterated here.

1. Anisotropy detection model

The anisotropy detection model of Grau Malonda and Grau Carles (1998a,b) and Grau Carles and Grau Malonda (2006) described in the previous Section B was developed for the Cherenkov counting standardization of radionuclides with spectrometers containing two PMTs commonly encountered throughout the world. Kossert (2010) and Kossert et al. (2011a, 2014) and Thiam et al. (2017) describe the same model applied to the standardization of radionuclides with spectrometers, which utilize three PMTs and the triple-to-double coincidence ratio (TDCR) efficiency calculation technique.

In this approach, Kossert (2010) applies a new formula for the determination of the anisotropy coefficient α, and

the free parameter q, which is derived from the ratio of triple to double coincidences. As described previously by Eq. (6.91), the anisotropy model applied to the TDCR Cherenkov counting technique includes in the calculation of the counting efficiency of an electron of energy E, the evaluation of the total number of photons k emitted in the wavelength interval (λ_1 to λ_2) per unit path length of electron travel according to the equation of Frank and Tamm (1937) written as

$$\frac{dk}{dx} = 2\pi\alpha\left(\frac{1}{\lambda_1} - \frac{1}{\lambda_2}\right)\left(1 - \frac{1}{\beta^2 n^2}\right) \tag{6.94}$$

The empirical equation of Flammersfield (1946) described by Paul and Steinwedel (1955),

$$x = 0.11\left(\sqrt{1 + 22.4E^2} - 1\right)/\rho \tag{6.95}$$

described previously, is applied for the range in centimeters of the electron (*i.e.*, β-particle) as a function of electron energy in MeV and density ρ of the counting medium. Kossert (2010) obtained $k(E)$ by the numerical integration

$$k(E) = \int_{\text{th}}^{E} \frac{dk}{dx}\frac{1}{\rho dE/dx}dE \tag{6.96}$$

where dk/dx is computed according to Eq. (6.94) where the limits "th" refer to the Cherenkov threshold energy and E the maximum or end-point β-particle energy; and the electron stopping powers dE/dx are obtained from linear interpolation of values provided by the ESTAR database of the National Institute of Standards and Technology (ESTAR, 2018, https://physics.nist.gov/PhysRefData/Star/Text/ESTAR.html). Kossert plotted the solution to $k(E)$ for 1M HCl, which was used as the solvent for the radionuclide standardization. The Cherenkov photon production as a function of initial electron energy is illustrated in Fig. 6.38.

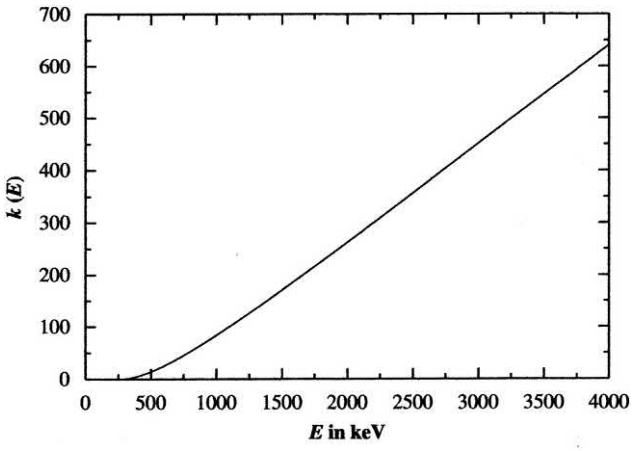


FIGURE 6.38 Number of Cherenkov photons created, $k(E)$, in 1 M mol/L HCl as a function of the initial electron energy. *From Kossert (2010), reprinted with permission from Elsevier © 2010.*

Eqs. (6.84) and (6.85) of Grau Carles and Grau Malonda (1996a,b, 2006) and Grau Malonda and Grau Carles (1998a,b), described previously in this chapter, are combined to give the following expression of the Cherenkov counting efficiency for a spectrometer detection system with two photomultipliers:

$$\varepsilon_2 = \int_{E_{\text{th}}}^{E} N(E)\left(1 - e^{-qk(E)\alpha}\right)\left(1 - e^{-qk(E)(1-\alpha)}\right)dE \tag{6.97}$$

where, as described previously, the coefficient q is a free parameter and α is the anisotropy coefficient.

For measurements with three photomultipliers, Kossert (2010) expresses the Cherenkov counting efficiency for triple coincidences as

$$\varepsilon_T = \int_{E_{\text{th}}}^{E} N(E)\left(1 - e^{-qk(E)\alpha_1}\right)\left(1 - e^{-qk(E)\alpha_2}\right) \times \left(1 - e^{-qk(E)\alpha_3}\right)dE \tag{6.98}$$

where the anisotropy is defined by only one parameter defining the coefficients $\alpha_1 = \alpha$, $\alpha_2 = 3/2(1-\alpha)\alpha$, and $\alpha_3 = 1 - 3/2(1-\alpha)\alpha - \alpha$. Likewise, the Cherenkov counting efficiency for the logical sum of double coincidences was expressed as

$$\varepsilon_D = \int_{E_{\text{th}}}^{E} N(E)\left[\begin{array}{l}\left(1 - e^{-qk(E)\alpha_1}\right)\left(1 - e^{-qk(E)\alpha_2}\right) + \left(1 - e^{-qk(E)\alpha_1}\right)\left(1 - e^{-qk(E)\alpha_3}\right) \\ +\left(1 - e^{-qk(E)\alpha_2}\right)\left(1 - e^{-qk(E)\alpha_3}\right) - 2\left(1 - e^{-qk(E)\alpha_1}\right)\left(1 - e^{-qk(E)\alpha_2}\right) \\ \left(1 - e^{-qk(E)\alpha_3}\right)\end{array}\right]dE \tag{6.99}$$

The Cherenkov radiation is emitted as a cone at a given angle between zero and 41.4 degrees in water dependent on the β-particle energy. Thus, Kossert (2010) considered a solid angle, Ω, of the Cherenkov cone, as a measure of the anisotropy of the Cherenkov photons, and utilized the following semi-empirical formula for the energy-dependent anisotropy coefficient:

$$\alpha(E) = x\left(\frac{2}{3} - \frac{1}{3}\frac{\Omega}{4\pi}\right) = x\left(\frac{1}{2} + \frac{1}{6\beta n}\right) \tag{6.100}$$

where x is the only variable defining the anisotropy; and the value of $x = 0.655$ was used. Kossert utilized the computer program CHEREN2 of Grau Carles and Grau Malonda (2006), which facilitates the calculation of the radionuclide beta spectra and allows for adjusting the beta-spectra shape functions.

This new TDCR Cherenkov counting technique was tested for the activity measurements of the following radionuclides with uncertainties in % reported by Kossert (2010): ^{32}P (0.42%), ^{89}Sr (0.62%), ^{90}Y (0.43%), ^{106}Rh (0.58%), and ^{204}Tl (2.6%). Further work on the TDCR Cherenkov counting technique were reported by Kossert et al. (2011a), which was carried out in light of the fact that initial tests on the standardization of ^{36}Cl revealed high discrepancies with results obtained with liquid scintillation counting. They discovered, that in the case of ^{36}Cl, there was the need to refine the ^{36}Cl shape-factor function in light of beta-spectrum determinations made by Grau Carles (2005) and Rotzinger et al. (2008). Kossert et al. (2011a) derived a new shape-factor function based on the spectral measurements of Rotzinger et al. (2008), which yielded an improved Cherenkov TDCR measurement of ^{36}Cl with a discrepancy of only 0.16% between the calculated and experimental measurement. This also provides confirmation of the beta-spectrum measurements of Rotzinger et al. (2008) for ^{36}Cl.

Kossert (2010) and Kossert et al. (2011a) point out numerous advantages of this technique, particularly in view of the first commercial TDCR liquid scintillation counter (Hidex 300 SL) available from Hidex (Hidex, Oy, Finland). Also, numerous TDCR systems have been constructed worldwide as described in Section IX.C of Chapter 6, Volume 1. Kossert et al. (2011a) reported the first tests indicating that the TDCR standardization method can also be applied with the new Hidex-TDCR counter. The successful application of the commercially available Hidex-TDCR counter to radionuclide standardization by Cherenkov counting is reported by others including Wanke et al. (2012) and Kossert et al. (2014). The Hidex 300 SL TDCR counter commercially available for radionuclide standardization is a modified Hedex 300 SL version of the standard Hidex 300 SL counter referred to as the METRO version. This version provides the coincidences between any pair of the three PMTs. Kossert et al. (2014) compared the Hidex 300 SL (METRO version) with the well-known German home-made TDCR counter of the Physikalisch-Technische Bundesanstalt (PTB) and reported deviations between the experimental and calculated Cherenkov counting efficiencies for ^{90}Y, ^{89}Sr and ^{32}P to be well below 1% for the Hidex 300 SL; and for ^{90}Y the mean relative deviation was less than 0.1%.

Improvements to the free parameter model in the Cherenkov counting standardization technique was introduced by Kossert et al. (2014). These improvements comprise the inclusion of (i) the dependence of the refractive index of water on the wavelength as the threshold energy for the production of Cherenkov photons is wavelength dependent, (ii) the wavelength dependence of the PMT response, and (iii) an account of the potential asymmetry of efficiencies in a detector system with three PMTs. Thus, Kossert et al. (2014) assigned three free parameters to each individual PMT and compared the computed Cherenkov efficiencies for a triple-to-double coincidence ratio (TDCR) system to experimental data for ^{32}P, ^{89}Sr and ^{90}Y. The differences between the calculated and experimental efficiencies were well under 1%.

Mirenda et al. (2014) used a high refractive index 1-butyl-3-methyllimidazolium chloride (BMIMCl) IL (ionic liquid) to standardize an ^{18}F solution. With an index of refraction of $n = 1.54$, the threshold energy for the production of Cherenkov photons is lowered to $\sim$164 keV from $\sim$262 keV for water. Fluorine-18 emits positrons with an E_{max} of 634 keV. The reduction in the threshold energy with the high refractive index IL ($n = 1.54$) made it possible to increase the Cherenkov counting efficiency (ε_D) for the logical sum of double coincidences from $\sim$2% obtained in 1M aqueous solution of HCl ($n = 1.34$) to $\sim$ 7% (Mirenda et al., 2014). They standardized an ^{18}F sample by the TDCR liquid scintillation with ^{18}F in Ultima Gold AB scintillation cocktail and by the TDCR Cherenkov counting method with the ^{18}F in BMIMCl IL. Both methods yielded ^{18}F activities of 67.70 $\pm$ 0.45 Bq/mg and 68.89 $\pm$ 1.62 Bq/mg for the TDCR liquid scintillation and TDCR Cherenkov counting methods.

To improve on the TDCR Cherenkov counting standardization of ^{18}F in the high refractive ionic liquid (BMIMCl), Mirenda et al. (2018) by adding a wavelength shifting highly fluorescent IL, 1-butyl-3-methyllimidazolium-8-hydroxypyrene-1,3,6-trisulfonate (BMIMHPTS) for the Cherenkov counting medium. The BMIMHPTS shifts the emission wavelength of the Cherenkov photons to a wavelength more sensitive to the PMTs. Mirenda et al. (2018) demonstrate that the addition of wavelength shifting BMIMHPTS to the high refractive index BMIMCl IL increased the efficiencies for the logical sum of double coincidences (ε_D) by 124% and 14% for ^{18}F and ^{32}P, respectively. They demonstrate that the addition of BMIMHPTS wavelength shifter breaks the anisotropy of the Cherenkov emission; and the error between the experimental and theoretical efficiencies, for example in ^{32}P, is reduced from 0.64% to 0.27% with one parameter $\alpha = 0.42$ used to describe anisotropic emission of the Cherenkov emission.

Among the advantages of this Cherenkov counting technique are the measurement of ^{90}Y and ^{32}P as standards required for nuclear medicine and the biological sciences, respectively, and the measurement of isotopes of Sr (i.e., ^{89}Sr and ^{90}Sr) and ^{210}Pb useful as standards for applications

in studies of these isotopes in the environment. Also, the method can be used to obtain useful information on the beta spectra of radionuclides in light of the high sensitivity of the method to shape-factor functions.

2. Stochastic GEANT4 model in Cherenkov counting

Bobin et al. (2010) developed a stochastic modeling approach, based on the Monte Carlo code GEANT4, to the TDCR standardization of radionuclides by Cherenkov counting as an alternative to the standard TDCR liquid scintillation technique. The objective of the model was to simulate the various optical processes that occur in the counting chamber as a result of the Cherenkov Effect, which leads to the production of photoelectrons in the three PMTs. They validated the model with measurements of ^{90}Y activity from sources previously standardized by the conventional TDCR liquid scintillation technique.

The GEANT4 simulation toolkit and its applications are described by Agostinelli et al. (2003) and Allison et al. (2006); and recent developments described by Allison et al. (2016), which include refinements to the GEANT4 code. These refinements include a linear decrease in the mean number of Cherenkov photons generated as the radiating particle slows down and a calculation of the reflectivity of optical photons from a metal surface. With GEANT4, Bobin et al. (2010) calculated the coincidences between the photomultipliers by simulating the optical processes that occur inside the TDCR counting chamber as a result of the Cherenkov photons created within the sample solution, sample vial wall, and windows of the three photomultipliers to the ultimate production of photoelectrons at the photocathodes of the three PMTs. Bobin et al. (2010) also confirmed the findings of Thiam et al. (2010) that Cherenkov photons are produced within the windows of the photomultipliers as a consequence of Compton scattering; and that such effects should be included in TDCR efficiency calculations. Thiam et al. (2011) further demonstrated the simulation code GEANT4 as an alternative to the standard model with the standardization of ^{11}C with a relative combined standard uncertainty of 0.85%. which is a radionuclide of short half-life (e.g., ^{11}C, $t_{½} = 20.37$ minutes) and low Cherenkov detection efficiency ($\sim$20%, $E_{max} = 960$ keV). Thiam et al. (2011) emphasize that the GEANT4 code provides an excellent alternative to the standard model; and that the implementation of a stochastic calculation of coincidences between PMTs requires a simulation of the propagation of optical photons from their creation in the optical chamber of the counter to the production of photoelectrons in the PMTs. Also they note that the Cherenkov TDCR measurements for short-lived radionuclides can be a good alternation to liquid scintillation standardization methods, because the measurements are made directly with the radionuclide in aqueous solution where chemical and ionization quenching are nonexistent. Lourenço et al. (2015) demonstrated the use of the GEANT4 code for the standardization of ^{90}Y-labeled resin microspheres used for selective internal radiation therapy (SIRT) for the treatment of liver cancer. Activity concentrations of ^{90}Y were measured with a relative combined standard uncertainty of 0.44%. As an alternative to the classical approach for standardization, Lourenço et al. (2015) point out that the Monte Carlo code GEANT4 toolkit provides all that is needed for the simulation of the transport of the ionizing radiation and the resulting Cherenkov or scintillation photons depending on the method used (Cherenkov counting or LSA). They note that the propagation of each Cherenkov photon produced along the track of the charged particle is simulated with respect to refraction and reflection processes occurring at the interfaces of the components of the optical cavity of the counting chamber. Also, they note that in the GEANT4 modeling, the PMT defocusing is simulated by a second binomial trial using a focusing parameter, which is applied in a similar manner as the free parameter in the analytical model used in liquid scintillation.

a. Production of Cherenkov photons in PMT windows

In the liquid scintillation analysis of γ- and β-γ-emitting radionuclides the response of the liquid scintillation analyzer to the gamma-ray photons is considered a result of cocktail excitation due to Compton electron interactions. Thiam et al. (2010) and Bobin et al. (2010) carried out experimentations and calculations with GEANT4 to demonstrate, that beta- or gamma interactions in the fused-silica windows of the PMTs can produce significant Cherenkov photons; and, that such effects should be included in counting efficiency calculations.

Thiam et al. (2010) placed solid γ-emitting sources of ^{54}Mn (836 keV), ^{137}Cs (662 keV), and ^{60}Co (1173 keV) of known activity within the counting chamber in lieu of a counting vial, as illustrated in Fig. 6.39. For each γ-emitting source they obtained significant responses for double and triple coincidences. They concluded that a strong correlation between the counting of double coincidences and the TDCR ratio indicated that Compton diffusion in the windows of the PMTs leads to the emission of Cherenkov photons. Thiam et al. (2010) point out that the fused silica windows of the PMTs have a refractive index $n = 1.47$ at 400 nm, which would attribute to the windows a Cherenkov threshold energy of 186 keV for electrons, as calculated according to Eq. (6.38) described earlier in this chapter.

Simulation based on the Monte Carlo GEANT4 provided confirmation of the Cherenkov Effect in the PMT windows. Thiam et al. (2010) calculated the double

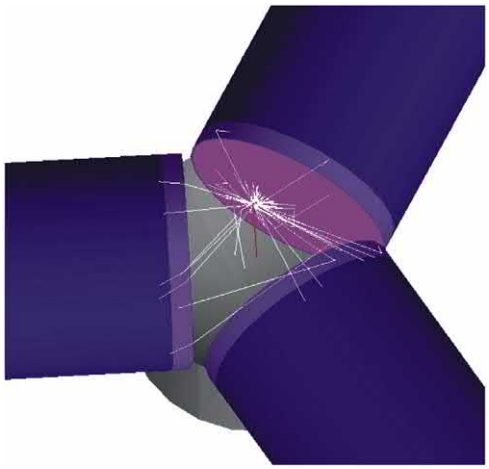


FIGURE 6.39 Tracking of the Cherenkov photons created by Compton diffusion in a photomultiplier window. It illustrates the illumination of the other photomultiplier windows leading to double or triple coincidences. For the color version of this figure the reader is referred to the online version of this book. *From Thiam et al. (2010), reprinted with permission from Elsevier © 2010.*

coincidences from the simulated Cherenkov photons refracted at the interface between the fused silica window of a PMT and its photocathode. The experimental and calculated double coincidence efficiencies are provided in Table 6.19. The calculation of the double coincidences included various physical processes such as the creation and propagation of the Cherenkov photons, and refraction and reflections in the optical cavity of the counter. Table 6.19 illustrates also the increase in double coincidence efficiencies proportional with the γ-energies obtained by experiment were confirmed in the simulation. This effect was explained as due to the creation of anisotropic Cherenkov photons along the trajectory of the Compton electrons arising from Compton diffusion in the photomultiplier windows. Cherenkov photons illuminate all photomultipliers leading to double and triple coincidence counting.

TABLE 6.19 Experimental and Calculated Double Coincidence Efficiencies for Different γ-energies.[a]

γ-ray emission	Experimental double coincidence efficiency (%)	Calculated double coincidence efficiency (%)
662 keV (Cs-137)	0.66 (5)	0.56 (7)
835 keV (Mn-54)	1.00 (4)	1.1 (1)
1173 and 1332 keV (Co-60)	4.5 (1)	3.6 (2)

[a]*Values in parenthesis represent % uncertainties.*
From Thiam et al. (2010). Reprinted with permission from Elsevier © 2010.

Thiam et al. (2010) conclude that detection efficiency measurements based on the TDCR and CIEMAT/NIST methods of primary radioactivity measurements by liquid scintillation should include the existence of Cherenkov photon generation in the photomultiplier windows. Bobin et al. (2010) provided additional evidence for the production of Cherenkov photons in the fused silica PMT windows by high-energy (>1 MeV) β-particles, that can reach the PMT windows from the counting vial. This is discussed in the following section.

b. Standardization of Yttrium-90

Radionuclide standardization by liquid scintillation requires the determination of a free parameter (see Section IX of Chapter 6, Volume 1). Standardization by Cherenkov counting, as described above by the Anisotropy Model, requires the use of a second parameter, α, the anisotropy coefficient, which characterizes the directional properties of Cherenkov photons. Rather than use an additional free parameter, Bobin et al. (2010) applied the TDCR method to Cherenkov counting using stochastic modeling based on the Monte Carlo code GEANT4. The model was used to calculate the coincidences between the photomultipliers by simulating the various optical processes of the Cherenkov photons emitted by a radionuclide in aqueous solution from a counting vial in a TDCR counter. The stochastic method of the TDCR Cherenkov method was validated with the activity determination of ^{90}Y.

Various tools in GEANT4 were selected by Bobin et al. (2010) and Lourenço et al. (2015) to simulate different physical processes that occur in the optical chamber (illustrated in Fig. 6.40) of the TDCR counter including properties of Cherenkov emission in transparent media (aqueous solution, borosilicate glass vial walls, and fused silica photomultiplier windows), Cherenkov threshold, anisotropic emission, and continuous spectral distributions of the Cherenkov photons. The simulation of electrons and Bremsstrahlung-generated photons were also included. Polyethylene plastic vials were expected to yield better detection efficiencies; however, Bobin et al. (2010) considered it more practical to carry out the initial modeling tests with borosilicate glass vials, which have more defined optical properties (e.g., refractive index and optical transmission).

Bobin et al. (2010) and Lourenço et al. (2015) took into consideration the creation of Cherenkov photons in the wall of the counting vial and fused silica photomultiplier window; although most of the Cherenkov photons arise from the counting solution. When the β-particle energy is sufficient, it can reach the photomultiplier window creating Cherenkov photons in the fused silica of the PMT window.

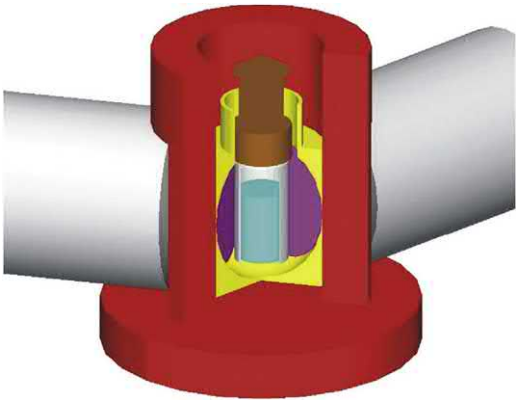


FIGURE 6.40 GEANT4 modeling of the TDCR counter including the counting vial for Cherenkov primary measurements. The counting vial is hung inside the optical chamber using a blackened element. A reflecting Teflon cavity (63 mm diameter) is modeled using a "dielectric-metal boundary with a lambertian-type reflectivity of 95%. For the color version of this figure, the reader is referred to the online version of the book. *From Bobin et al. (2010), reprinted with permission of Elsevier © 2010.*

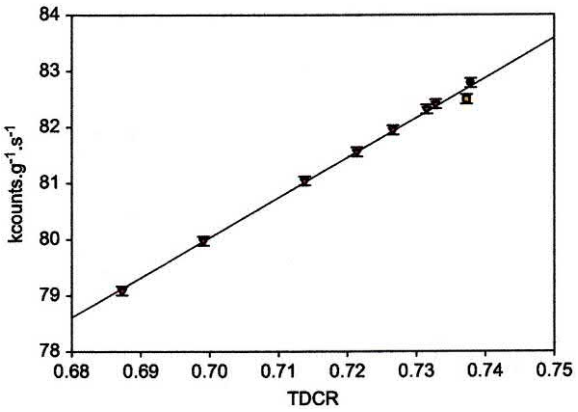


FIGURE 6.41 Counting rates per mass (logical sum of double coincidences) plotted according to the experimental TDCR value in the case of three different ^{90}Y sources. Photomultiplier defocusing was applied to one of these samples (triangular plots). *From Bobin et al. (2010), reprinted with permission of Elsevier © 2010.*

Cherenkov photons can also arise from the PMT window as a consequence of Compton scattering from high-energy Bremsstrahlung radiation from the decelerating β-particle. Bobin et al. (2010) found the effect of Bremsstrahlung to be less significant; however, they determined that as much as $\sim 0.25\%$ of the measured radionuclide activity concentration is due to Cherenkov photons produced outside of the counting solution and vial, *i.e.*, in the PMT windows. To confirm this, they used a black cover around the counting vial to absorb the Cherenkov photons arising from the counting solution and vial wall; and the ^{90}Y detection efficiency to double coincidences amounted to $\sim 1.3\%$. Bobin et al. (2010) tested the modeling, based on GEANT4, using the same procedure applied in the case of TDCR liquid scintillation measurements. For that purpose, systematic trends were checked for activity concentrations determined according to different TDCR values obtained by defocusing the photomultipliers. An example of count rates of the logical sum of double coincidences for three ^{90}Y sources according to various TDCR values are illustrated in Fig. 6.41. The count rates for one of these sources are plotted according to various TDCR values obtained by defocusing the photomultipliers. The stochastic calculations included a simulation of the photomultiplier defocusing to alter the detection efficiency. As explained by Bobin et al. (2010), the calculation of double and triple coincidences is based on a second binomial trial applied to the photoelectrons produced at each PMT bialkali photocathode. With this objective, they used a focusing parameter as the probability of a photoelectron to reach the first dynode. This focusing parameter would be comparable to the free parameter used in the liquid scintillation method described in Chapter 6 of Volume 1. For each experimental TDCR value, the detection efficiency to double coincidences between photomultipliers is calculated by adjusting the focusing parameter.

Maximum ^{90}Y detection efficiencies (double coincidences) of 70% were reported with some variability depending on the shape factors used for the β-spectrum calculation. A homemade code based on the work of Grau Malonda (1999) and Wilkinson (1970) was used to test the simulation sensitivity to the calculated ^{90}Y β-spectrum according to three shape factors. Activity determinations by this stochastic Cherenkov TDCR method agreed with ^{90}Y standardized by the TDCR liquid scintillation method with a relative combined standard uncertainty of 0.37%

Bobin et al. (2010) conclude that Cherenkov counting may be used as an alternative to liquid scintillation, as samples are less sensitive to the time required by liquid scintillation for the chemical stability of samples; and Thiam et al. (2011) report favorable tests for the standardization of the short-lived ^{11}C, which is commonly used in radiopharmaceuticals. Also they conclude, that in the case of γ-emitters, consideration should be given to the emission of Cherenkov photons as a result of Compton scattering in PMT windows in order to avoid biases that can be encountered in the standardization of radionuclides, such as ^{54}Mn (Thiam et al., 2010 and Bobin et al. (2010).

D. Standardization of ^{210}Pb

The first primary standardization of ^{210}Pb by Cherenkov counting was reported by Arinc et al. (2011). This work is quite unique in its approach as it involves a combination of Cherenkov counting of the daughter nuclide ^{210}Bi in combination with the CIEMAT/NIST liquid scintillation efficiency tracing technique. The decay chain of ^{210}Pb, illustrated in Fig. 6.42, is favorable to its standardization by

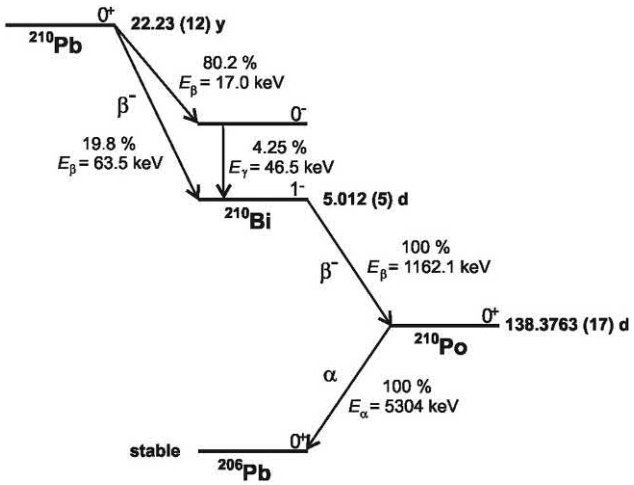


FIGURE 6.42 Simplified decay chain of ^{210}Pb. *From Arinc et al. (2011), reprinted with permission from Elsevier © 2011.*

Cherenkov counting. Only its ^{210}Bi daughter nuclide decays by high-energy β-emission sufficient to produce the Cherenkov Effect. Neither the weak β-particles from the decay from ^{210}Pb, the weak γ-emissions from the decay of ^{210}Bi, nor the α-emissions from the decay of ^{210}Po can interfere with the Cherenkov counting of the ^{210}Bi daughter nuclide in the primary standardization of the ^{210}Pb.

A solution of ^{210} Pb at or near secular equilibrium was standardized by Arinc et al. (2011) by the following basic steps: (1) The ^{210}Po is removed from the ^{210}Pb/^{210}Bi on a column of Sr Spec resin. (2) The ^{210}Pb and ^{210}Bi are separated on a second column of Sr Spec resin. (3) Aliquots of ^{210}Bi are taken and prepared in Ultima Gold liquid scintillation cocktail in counting vials for standardization by the CIEMAT/NIST efficiency tracing technique with ^{3}H (see Chapter 6, Volume 1). (4) Aliquots of ^{210}Bi and ^{210}Pb are taken and placed into separate plastic counting vials with inactive carrier in 2 mol/dm^3 HNO_3 for Cherenkov counting. (5) The Cherenkov count rates of the separated ^{210}Bi and ^{210}Pb samples prepared in the previous step were measured repeatedly and alternately with samples of standardized ^{210}Bi as a function of time for 33 days. (6) The ingrowth and decay of ^{210}Bi in the ^{210}Pb solution; and a least-squares fit to the decay curve of ^{210}Bi was used to determine the activity concentration of ^{210}Pb and ^{210}Bi at the time of separation. General ingrowth and decay calculations relevant to secular equilibrium are provided in an earlier paper by the writer (L'Annunziata, 1971) and described in detail in Chapter 1, Volume 1. The precise calculations used in the case of the secular equilibrium between ^{210}Pb(^{210}Bi) are given by Arinc et al. (2011).

The alternate counting of standardized ^{210}Bi with the separated ^{210}Pb and ^{210}Bi was carried out by Arinc et al. (2011) to determine the Cherenkov counting efficiency as a function of time. An average Cherenkov counting efficiency for the ^{210}Bi was found to be 0.1406 ± 0.0002. The CIEMAT/NIST standardization of the ^{210}Bi required correction for ingrowth of ^{210}Po. Also, for the standardization of ^{210}Bi, the beta shape factor was taken from Grau Carles and Grau Malonda (1996b) and a *kB* value of 0.0075 MeV was used for the standardization. The theoretical counting efficiency of the ^{210}Bi for the CIEMAT/NIST standardization was computed using a National Physics Laboratory beta code based on the EFFY code of García Toraño and Grau Malonda (1985). The ^{210}Pb standardization by Cherenkov counting was reported by Arinc et al. (2011) to have a combined relative standard uncertainty of 0.66%.

E. Routine TDCR activity analysis

The application of the Hidex 300 SL TDCR counter to the routine Cherenkov counting for the activity analysis of radionuclides emitting beta-particles with sufficient energy to produce the Cherenkov effect, such as ^{36}Cl, ^{89}Sr, ^{32}P and ^{90}Sr/^{90}Y, has been demonstrated by Yang et al. (2017), Amano et al. (2016), Coha et al. (2016), Jäggi and Eikenberg (2014), Olfert et al. (2014) and Tayeb et al. (2014). The Cherenkov detection efficiencies of three commercially available liquid scintillation analyzers equipped with differing numbers of PMTs, namely the Hidex 300 SL (3 PMTs), the Tri-Carb 3180 (2 PMTs), and the Triathler (1 PMT), were compared by Coha et al. (2016). With standards of ^{36}Cl, ^{32}P, ^{89}Sr and ^{90}Y, Coha et al. (2016) conclude that the best Cherenkov counting efficiencies are obtained with the Hidex 300 SL (see Fig. 6.43) and when methanol is used as a solvent; and the low-level versions of the Tri-Carb and Hidex 300 SL are comparable in Cherenkov detection efficiency. The lower counting efficiency of a low-level counting mode (LLCM), such as the Tri-Carb LLCM illustrated in Fig. 6.43 is expected, because instrument settings are adjusted to count low-levels of activity with greatly reduced background at a cost of detection efficiency yielding higher FOMs. The Triathler, produced by Hidex, Oy, Finland) is a small and robust portable instrument equipped with only 1 PMT. As reported by Coha et al. (2016), the Triathler instrument is suitable for monitoring of surface contamination via wipe tests from one laboratory to another; and it can be taken into the field for emergency response applications for rapid on site environmental radiation monitoring.

The application of Cherenkov counting in the routine analysis of radionuclide activity is discussed in more detail further on in this chapter.

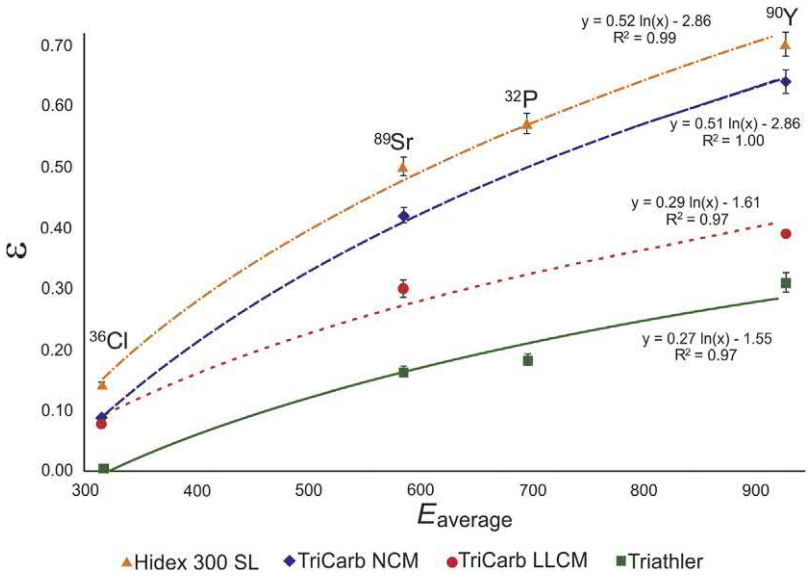


FIGURE 6.43 Cherenkov counting efficiency of radionuclides (A ~ 100 Bq) as a function of their $E_{\beta\text{-average}}$. Samples were counted for 20 minutes. *From Coha et al. (2016), reprinted with permission from Springer Nature © 2016.*

XI. Gamma ray detection and discrimination

Gamma radiation can produce Cherenkov photons indirectly through gamma-ray photon−electron interactions as the gamma radiation travels through a transparent medium. The number of photons emitted by a Cherenkov detector is generally only approximately 1% of the number emitted by a good scintillator for the same gamma-ray energy loss (Sowerby, 1971). Although the Cherenkov detection efficiencies of gamma radiation are relatively low, unique applications of the Cherenkov Effect for the analysis and discrimination of gamma radiation exist, and the effect plays an important role as a source of background in various methods of radioactivity analysis. One should always be aware of the potential for gamma radiation to produce Cherenkov photons.

An auspicious outcome of the production of Cherenkov photons by gamma radiation is the potential to discriminate against gamma radiation that is of insufficient energy to produce the Cherenkov effect. Gamma rays that penetrate a transparent medium will produce Cherenkov photons via Compton interactions (see Fig. 6.44) provided the gamma-ray photons are of sufficient energy to produce Compton electrons with energies above the threshold energy for the production of Cherenkov photons in that medium. Deleterious background radiation produced by Compton scattering can be reduced with the proper selection of a detector consisting of a Cherenkov radiator with a threshold energy below which Cherenkov photons will not be produced.

The transfer of gamma-ray photon energy (E_γ) to an atomic electron via a Compton interaction produces a Compton electron with energy, E_e, within the range

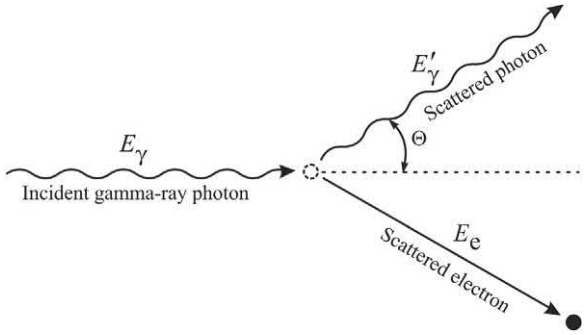


FIGURE 6.44 A Compton interaction whereby an incident gamma-ray photon (E_γ) collides with an atomic electron. Gamma-ray photon energy is transferred to the electron, which is ejected from the atom. The gamma-ray photon is scattered (E'_γ) at an angle (Θ) to the incident photon trajectory. *From L'Annunziata (2016); reprinted with permission from Elsevier 2016.*

between near zero and a maximum. Near zero energy would be transferred to an atomic electron when the gamma-ray photon only glances off the atomic electron; and the maximum energy would be transferred when the gamma-ray photon makes a head-on collision with the atomic electron and the angle of scatter (Θ) is 180 degrees to the incident photon trajectory. The magnitude of the scattered electron energy (E_e) may be expressed by the equation

$$E_e = E_\gamma - E'_\gamma - \phi \tag{6.101}$$

where E_γ and E'_γ are the incident and scattered photon energies, respectively; and ϕ is the electron binding energy. The electron binding energy can be neglected, as it is negligible compared to the incident and scattered photon

energies. Thus, the scattered electron energy (E_e) can be expressed as

$$E_e = E_\gamma - E'_\gamma \tag{6.102}$$

The expression for the scattered photon energy (E'_γ) is a function of the incident photon energy (E_γ), the angle of photon scatter (Θ) and the rest mass of the electron ($m_0c^2 = 0.511$ MeV); and it is written as

$$E'_\gamma = \frac{E_\gamma}{1 + (E_\gamma/0.511)(1 - \cos\Theta)} \tag{6.103}$$

An excellent derivation of Eq. (6.103) is provided by Lilley (2001). When there is a maximum incident photon energy transfer to the atomic electron, there is a head-on collision of the photon with the atomic electron; and the photon is backscattered where $\Theta = 180$ degrees. Thus, under circumstances where there is maximum photon energy transfer to an atomic electron with $\Theta = 180$ degrees, the scattered photon energy is written as

$$E'_\gamma = \frac{E_\gamma}{1 + (2E_\gamma/0.511)} \tag{6.104}$$

And the maximum scattered electron energy is written as

$$E_e = E_\gamma - \frac{E_\gamma}{1 + (2E_\gamma/0.511)} \tag{6.105}$$

where E_γ is the gamma-ray photon energy in MeV and the term $E_\gamma - \left[E_\gamma \big/ \left(1 + \left(2E_\gamma \big/ 0.511\right)\right)\right]$ defines the scattered photon energy at 180 degrees Compton scatter as previously defined in Chapter 1, Volume 1.

To produce Cherenkov photons, the Compton electron must possess energy in excess of the Cherenkov threshold energy, E_{th}, defined by Eq. (6.38) or (6.39) derived previously in this chapter, that is

$$E_{th} = 511 \text{ keV}\left[\left(1 - \frac{1}{n^2}\right)^{-1/2} - 1\right] \tag{6.106}$$

For example, the threshold energy E_{th} for electrons in water, at an index of refraction $n = 1.333$ (at 20°C and at the sodium line, *i.e.*, 589.0 nm), according to Eq. (6.106) is calculated to be 262 keV. (The reader may find small differences in the calculated threshold energy in the literature depending on the index of refraction, which is wavelength specific). A Compton electron must possess, therefore, energy in excess of 262 keV to produce Cherenkov photons in water. In this case, however, the gamma-ray photon must possess an energy in excess of 421 keV calculated according to the inverse of Eq. (6.105) above or

$$E_\gamma = E_e + \frac{E_\gamma}{1 + (2E_\gamma/0.511)} \tag{6.107}$$

where E_e is the maximum Compton electron energy. Thus, from the above Eq. (6.107), the equation for the threshold gamma-ray photon energy for the production of Cherenkov photons from Compton electrons in any transparent medium can be written as

$$(E_\gamma)_{th} = (E_e)_{th} + \frac{(E_\gamma)_{th}}{1 + \left(2(E_\gamma)_{th}/0.511\right)} \tag{6.108}$$

where $(E_\gamma)_{th}$ is the threshold gamma-ray photon energy for the production of Cherenkov photons from Compton electrons and $(E_e)_{th}$ is the threshold electron energy for the production of Cherenkov photons in a transparent medium. For example, if we take the scattered electron energy E_e to be 0.262 MeV, which is the threshold electron energy, $(E_e)_{th}$, for Cherenkov photon production in water, we can calculate the threshold gamma-ray energy for the production of Cherenkov photons in water as

$$\begin{aligned}(E_\gamma)_{th} &= 0.262 \text{ MeV} + \frac{(E_\gamma)_{th}}{1 + \left(2(E_\gamma)_{th}/0.511\right)} \\ &= 0.421 \text{ MeV}\end{aligned} \tag{6.109}$$

Threshold gamma-ray photon energies will vary according to the index of refraction of the medium, and these are provided graphically in Fig. 6.45 for gamma radiation and electrons or beta particles.

Although Cherenkov detection efficiencies for gamma-ray Compton electrons are low, the phenomenon is applied to both detect and discriminate against gamma radiation of energy below the threshold energy for the production of Cherenkov photons. For example, threshold detectors of the proper index of refraction can be selected to provide the following advantages over other low-energy detectors to discriminate against Compton scatter background radiation. A variety of media, which vary significantly in refractive index, can be selected to discriminate against gamma radiation of specific energy. For example, silica aerogels of low refractive index ($n = 1.026$) can be used to discriminate against gamma rays of relatively higher energy (2.0 MeV) while a transparent medium of high refractive index such as flint glass ($n = 1.72$) can serve to discriminate against relatively low-energy gamma radiation (0.25 MeV). Fig. 6.45 illustrates the potential for gamma-ray Compton electron and beta-particle or electron energy discrimination according to refractive index of the detector medium.

Sowerby (1971) points out that Cherenkov detectors provide the following advantages over other detectors for low-energy gamma radiation:

- **(i)** Cherenkov detectors are insensitive to gamma rays of energy less than the Cherenkov threshold energy for the gamma-ray Compton electrons,
- **(ii)** The threshold energy can be set by the refractive index of the transparent medium, and
- **(iii)** The Cherenkov radiator provides instantaneous light emission unlike scintillation light from a phosphor,

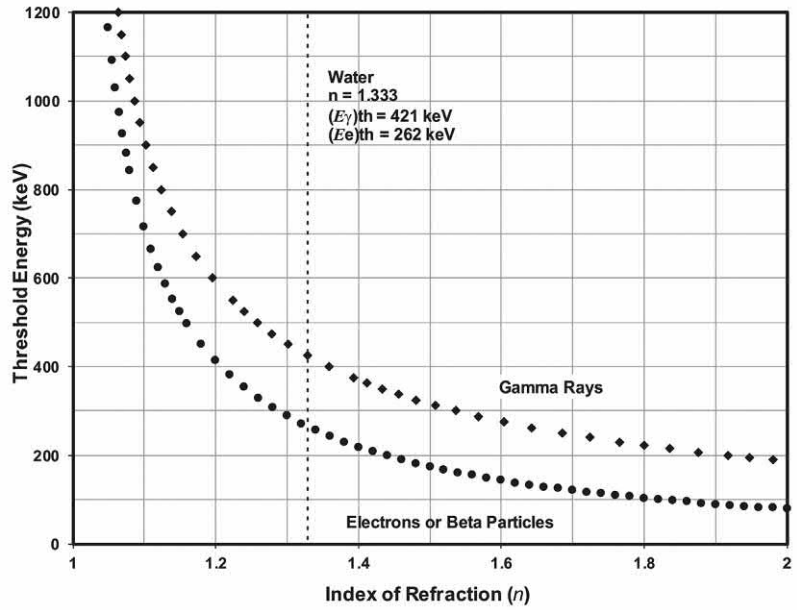


FIGURE 6.45 Threshold energies for the production of Cherenkov radiation as a function of index of refraction of the detector medium for gamma rays and electrons or beta particles. The threshold energies for electrons or beta particles are calculated according to Eq. (6.106), and the gamma-ray photon threshold energies are calculated according to Eq. (6.108) as the gamma rays that yield Compton electrons of the threshold energy via 180 degrees Compton scatter. The vertical broken line at n = 1.33 identifies the index of refraction of water, which crosses at the threshold energy of 262 keV for electrons or beta-particles and 421 keV for Gamma-ray-created Compton electrons. *From L'Annunziata (2016), reprinted with permission from Elsevier © 2016.*

which has a characteristic decay time. Therefore, Cherenkov detectors can provide most accurate timing information.

Rose and Erickson (2015) have calibrated Cherenkov detectors constructed of quartz ($n = 1.4585$ at 588 nm) for the interrogation scanning of cargo containers with monoenergetic photons. They note that scintillator detectors have a decay time measured in microseconds; whereas Cherenkov photon emissions are nearly instantaneous and with fast pulse processing equipment the Cherenkov photons can be measured in picoseconds. They confirm that quartz has unique properties advantageous as a Cherenkov radiator for photon imaging from gamma-ray Compton electrons, which are the following: (i) quartz has a higher density than most materials used as a Cherenkov radiator, such as water or acrylic, permitting the use of smaller detectors to match photon interaction probability, (ii) Quartz is not hydrophilic like many solid scintillation detectors; and it is resistant to thermal expansion in a wide range of operating temperatures (0−40°C), (iii) Due to the available high purity of quartz, it has a high internal reflectivity allowing more Cherenkov photons to reach the PMT, (iv) The quartz can be easily light-proofed; and it is resistant to neutron activation and weather conditions. The index of refraction of quartz (n = 1.4585) provides a 0.191 MeV beta particle or electron threshold energy for the production of Cherenkov photons calculated according to Eq. (6.106) and a gamma-ray Compton electron Cherenkov threshold of 0.336 MeV calculated according to Eq. (6.108). The two threshold energies are illustrated with the vertical broken line for quartz in Fig. 6.46. The calculated gamma-ray Compton electron Cherenkov threshold of 0.336 MeV guarantees that no Compton electron arising from a gamma-ray photon under 0.336 MeV will be detected. Moreover, the calculated gamma-ray Compton electron threshold energies represent the maximum Compton electron energies that arise from head-on collisions of gamma-ray

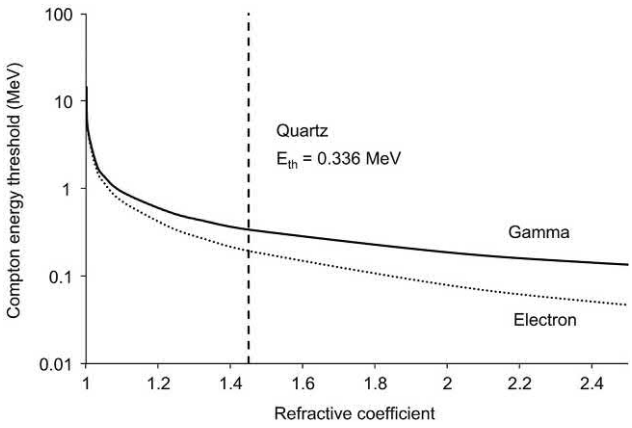


FIGURE 6.46 Compton energy threshold energies on a logarithmic scale (solid Gamma line) are plotted against the refractive index (coefficient). The dotted line is the curve for the beta-particle or electron threshold energies for the production of Cherenkov photons in a transparent medium. The vertical broken line is that of quartz with a refractive index of 1.4585. The line crosses at it Compton energy threshold at 0.336 MeV for the production of Cherenkov photons by gamma-ray Compton interactions and its electron or beta-particle energy threshold of 0.191 MeV for the production of Cherenkov photons in a transparent medium. *Figure from Rose and Erickson (2015); reprinted with permission from Elsevier © 2015.*

photons with atomic electrons. An auspicious outcome is that these interactions are rare, as noted by Rose and Erickson (2015), particularly at lower energies; and in the case of quartz, signal generation from these Compton electrons are low until approximately 0.55 MeV gamma-rays enter the detector, which is referred to as the effective threshold. Thus, in the case of quartz, a large portion of the background radiation is below the effective threshold of 0.55 MeV, which does not produce any signal in the detector.

Rose and Erickson (2015) demonstrate that Cherenkov detectors can be calibrated with gamma-ray energy sources; however, with much lower resolution than that available with scintillation detectors. Cherenkov detectors do not provide the photopeak resolutions available with solid scintillation detectors. By coupling a quartz Cherenkov radiator to a PMT, Rose and Erickson (2015) demonstrated that certain characteristics of the Cherenkov Compton emission spectra, such as tail slopes, inflection points, and shoulder of the emission spectra can be used to assign maximum energy deposition, most probable Compton electron energy corresponding to the energy of the incident gamma-ray photon, and average energy deposition in the Cherenkov detector. Fig. 6.47 illustrates one example of the Cherenkov emission spectra produced by several gamma-ray sources of increasing gamma-ray energy from 662 to 4440 keV. The peaks and shoulders of the spectra illustrated provide information on the average energy transferred to the Compton electron during Compton scattering in the Cherenkov detector. For example, Rose and Erickson (2015) point out that the peak or shoulder at 2.7 MeV in the PuBe spectrum is the average energy transferred to a Compton electron in the 4.4 MeV scattering event. Average energies transferred to a Compton electron by the Co-60 and Th-232 can also be derived from the shoulders of their respective spectra. However, for the lower energy gamma source of Cs-137, the average energy from Compton scattering cannot be derived.

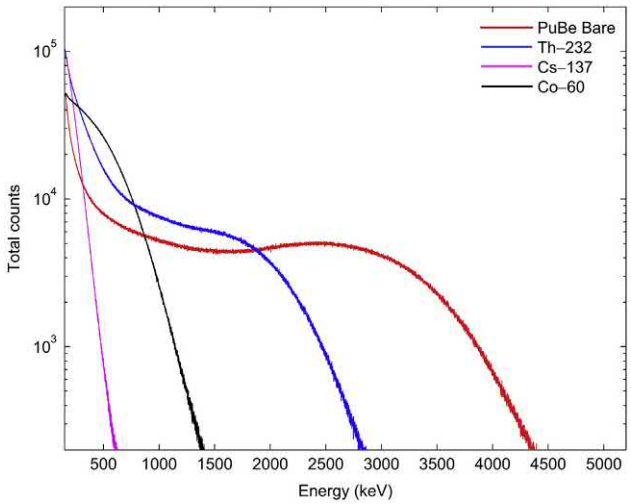


FIGURE 6.47 Calibrated spectral response of a 2-inch (5.08 cm) long quartz Cherenkov detector to gamma-ray sources. The spectra from left to right with photon energy in parenthesis are from Cs-137 (662 keV), Co-60 (1173 and 1332 keV), Th-232 (1614 keV maximum) and PuBe (4400 keV). The color coding of the spectra is visible in the electronic version of the figure. *From Rose and Erickson (2015); reprinted with permission from Elsevier © 2015.*

Another application of gamma-ray detection is the Cherenkov verification technique used in nuclear safeguards to verify the authenticity of irradiated nuclear fuel, which is one of the important tasks performed by the International Atomic Energy Agency (IAEA). The IAEA nuclear safeguards program audits the national declarations of fuel inventories to insure no illicit diversion of nuclear material has occurred. High levels of gamma radiation are emitted by fission products in irradiated nuclear fuel. The irradiated fuel stored under water will produce Cherenkov light as a result of Compton scattering in the water surrounding the fuel. A Digital Cherenkov Viewing Device (DCVD) containing a UV-transmitting lens coupled to a UV-sensitive charge-coupled device (CCD) and image monitor enables the real-time imaging of the UV light portion of the Cherenkov radiation in the presence of normal room lighting (Attas et al., 1990, 1992; 1997; Kuribara, 1994; Kuribara and Nemoto, 1994; Lindsey et al., 1999; IAEA, 2003; Chen et al., 2007; Håkansson and Jonter, 2007; Molander, 2008; Zendel, 2008; Chen et al., 2010; Grape et al., 2010; Branger et al., 2014). The presence of fission products and the nature of their distribution, as indicated by the Cherenkov glow, are used as evidence of fuel verification. As noted by Rossa and Peerani (2013), over 80% of the material currently placed under nuclear safeguards is in the form of spent fuel assemblies. The main goal of nuclear safeguards inspections is to verify that no nuclear material has been diverted to other purposes; and the Digital Cherenkov Viewing Device is used to detect the gross and partial defect from the assembly by viewing the Cherenkov light emitted from Compton electrons and beta-particles emitted from nuclear fuel assemblies stored in water pools (Branger et al., 2014). Gross defect is the replacement of an entire fuel assembly with a dummy made of other material such as natural uranium, while partial defect relates to the removal of fuel pins inside the fuel assembly (Rossa and Peerani, 2013).

XII. Particle identification

Cherenkov counters are applied in particle physics research for the determination of particle mass (m) and velocity (β) for particle identification (PID). Cherenkov detectors of various designs are applied to the discrimination and identification of high-energy particles, among which are threshold and differential Cherenkov counters,

ring-imaging Cherenkov (RICH) detectors, as well as Cherenkov counters that utilize time of propagation (TOP) and time of flight (TOF) measurements. Extensive reviews on the applications of Cherenkov detectors to particle identification are available in the journal literature including Križan (2017, 2013, 2009, 2007), Harnew (2014), Lippmann (2012), Engelfried (2011), Nappi (2011), Iijima (2010), Websdale (2008), Ullaland (2003) and Va'vra (2003). A concise overview of the principles and techniques applied to the application of the Cherenkov effect to particle identification will be given here. For more comprehensive coverage of the instrumentation and techniques, the reader may peruse the extensive review articles cited above.

A. Threshold and differential Cherenkov counters

As defined by Denisov and Stoyanova (2006), *threshold Cherenkov counters* are those than can detect all particles with velocities $\beta > 1/n$, where β is the relative phase velocity of the particle (i.e., v/c or velocity of the particle divided by the speed of light in a vacuum) and n is the refractive index of the detector medium. Lippmann (2012) describes the threshold counter as one which will measure the intensity of the Cherenkov photons to measure particles with velocities exceeding β, and classifies the *differential counter* as one which will focus only Cherenkov photons of a certain emission angle onto a detector and thus detect particles in a narrow interval of velocities, such as described by Abbon et al. (2015) and Lurkin et al. (2017). Also, Križan (2017) defines a threshold counter as one that will discriminate between particles that are below the Cherenkov threshold from those that are above threshold, as only those particles above the Cherenkov threshold will produce Cherenkov photons. The Cherenkov emission angle (θ) is, as described previously by Eq. (6.1), a function of the particle phase velocity and refractive index of the detector medium, or $\cos\theta = 1/\beta n$. A third type of counter described further on in this chapter is the *imaging Cherenkov detector*, which is defined by Lippmann (2012) as the detector that makes maximum use of the available information (Cherenkov angle and number of photons produced) and divided into two main categories, namely, RICH (Ring Imaging Cherenkov) and DIRC (Detection of Internally Reflected Cherenkov light) devices. The DIRC devices include Time-of-Propagation (TOP) Cherenkov counters described further on in this chapter.

Threshold Cherenkov counters consist of Cherenkov detectors of differing refractive index, which may be utilized to discriminate particles of different mass based on the differing Cherenkov threshold energies that the detectors possess for the particles. For example, if we consider a beam of two types of particles of different mass (m), such as pions ($\pi^{\pm}$, $m = 139.6$ MeV/c^2) and kaons ($K^{\pm}$, $m = 493.7$ MeV/c^2), a Cherenkov detector may be selected of a given refractive index (n) such that the particle of higher mass does not produce Cherenkov radiation, as described by Montgomery (2013). This would be the case, if the threshold condition for the production of Cherenkov radiation is not met by the particle of higher mass, that is, $\beta < 1/n$. Sundaresan (2001) describes another example of the application of two Cherenkov detectors of different refractive index, namely silica aerogel ($n = 1.01-1.03$) and pentane ($n = 1.357$) whereby particles of lower mass, such as 10 GeV kaons ($m = 493.7$ MeV/c^2) produce Cherenkov photons in the two Cherenkov detector media, whereas particles of higher mass such as protons ($m = 939.3$ MeV/c^2) produce Cherenkov photons only in the silica aerogel. Siudak et al. (2008) describe the use of a threshold Cherenkov detector of silica aerogel with refractive index $n = 1.05$, which exhibits a very high detection efficiency for pions with momenta $\geq$900 MeV/c. Thus, to detect K^+ particles a huge background of scattered pions could be suppressed using the aerogel Cherenkov detectors. Only the pions would produce Cherenkov photons; the kaons were below the threshold velocity. Adachi et al. (1995) describe a threshold Cherenkov counter for the identification of $\pi^{\pm}$ and $K^{\pm}$ in a particle beam. Silica aerogel with refractive index of 1.0127 with 14-cm thickness was used as the detector and PMTs for the measurement of Cherenkov photons. The threshold momentum for the detection of $\pi^{\pm}$ and $K^{\pm}$ was determined to be 0.863 GeV/c and 3.05 GeV/c, respectively.

Two threshold Cherenkov detectors operated in tandem are described by Asaturyan et al. (2005) for the identification of $\pi/K/p$ particles. Two different aerogel materials were used with index of refraction $n = 1.030$ and 1.015, respectively. The threshold momenta P_{th} in units of GeV/c for muons, pions, kaons, and protons in the two types of aeorogels detector materials are provided in Table 6.20.

The threshold momentum over which a particle of mass, m, will exceed the phase velocity of light in the medium and produce Cherenkov photons, is a function of the

TABLE 6.20 Threshold momenta (P_{th} in GeV/c) for particles in two aerogel threshold detectors of refractive index n.

Type of particle	P_{th} in $n = 1.030$	P_{th} in $n = 1.015$
μ	0.428	0.608
π	0.565	0.803
K	2.000	2.840
P	3.802	5.379

From Asaturyan et al. (2005), reprinted with permission from Elsevier © 2005.

particle mass and refractive index of the medium, n, as described by Asaturyan et al. (2005), according to the expression

$$P_{th}C = \frac{mc^2}{\sqrt{n^2-1}} \tag{6.110}$$

where P_{th} is the threshold momentum for the production of Cherenkov radiation, m is the particle mass, c is the speed of light in a vacuum, and n is the index of refraction of the medium.

Eq. (6.110) is derived from the equation for the total energy (E_{tot}) of a particle described previously (Eq. 1.269) in Section X.E.2 of Chapter 1, Volume 1, namely, the total energy (E_{tot}) of a particle is the sum of its kinetic (K) and rest energies (mc^2) or

$$E_{tot} = K + mc^2 = \gamma mc^2 \tag{6.111}$$

where

$$\gamma = \frac{1}{\sqrt{1-(v^2/c^2)}} = \frac{1}{\sqrt{1-\beta^2}} \tag{6.112}$$

as described previously in Eq. (1.271) of Chapter 1, Volume 1. Thus, Eq. (6.111) can then be expressed as

$$\left(mc^2\right)_{tot} = \frac{mc^2}{\sqrt{1-\beta^2}} \tag{6.113}$$

As the threshold condition of the production of Cherenkov photons is

$$\beta_{th} = 1/n \tag{6.114}$$

we can substitute $1/n$ for β in Eq. (6.113) to give

$$\left(mc^2\right)_{tot} = \frac{mc^2}{\sqrt{1-(1/n)^2}}, \tag{6.115}$$

where

$$\gamma_{th} = \frac{1}{\sqrt{1-(1/n)^2}} = \frac{n}{\sqrt{n^2-1}} \tag{6.116}$$

and Eq. (6.115) can be transposed to

$$\left(mc^2\right)_{tot} = \frac{(mc^2)n}{\sqrt{n^2-1}} \tag{6.117}$$

If the particle phase velocity at the Cherenkov threshold is

$$\beta_{th} = (v/c)_{th} = 1/n \tag{6.118}$$

and we multiply each side of Eq. (6.117) by β_{th} to give the following:

$$\beta_{th}\left(mc^2\right) = \frac{\beta(mc^2)n}{\sqrt{n^2-1}} \tag{6.119}$$

and

$$(v/c)_{th}\left(mc^2\right) = \frac{(1/n)(mc^2)n}{\sqrt{n^2-1}} \tag{6.120}$$

and

$$(mv)_{th}c = \frac{mc^2}{\sqrt{n^2-1}} \tag{6.121}$$

and

$$P_{th}c = \frac{mc^2}{\sqrt{n^2-1}} \tag{6.122}$$

which is the final equation used to calculate the threshold particle momentum for the production of Cherenkov radiation in a medium of refractive index n. For example, the threshold momentum, P_{th}, of the muon for the production of Cherenkov photons in aerogel of refractive index, $n = 1.030$, would be calculated as follows:

The energy equivalence of the muon mass, $m_\mu c^2 = 105.658$ MeV, is obtained from tables of physical constants (NIST, 2018) or calculated according to Eqs. (1.8) to (1.11) described in Chapter 1 of Volume 1; and the threshold momentum calculated as

$$\begin{aligned} P_{\text{th}}c &= \frac{m_\mu c^2}{\sqrt{n^2-1}} \\ &= \frac{105.658\ \text{MeV}}{\sqrt{(1.030)^2-1}} \\ &= 428.14\ \text{MeV} \\ P_{\text{th}} &= 0.428\ \text{GeV}/c \end{aligned} \tag{6.123}$$

which is equivalent to the value quoted in Table 6.20. An aerogel detector with refractive index $n = 1.015$ will yield a minimum momentum for the Cherenkov Effect of 0.608 GeV/c calculated according to Eq. (6.122).

The difference in count rates from Cherenkov photons produced in the two detectors yield the relative numbers of the heavier and lighter particles. This is illustrated by Fig. 6.48, which is a plot of the number of photoelectrons (N_{pe}) collected by PMT photon detectors as a function of particle momentum (P) in GeV/c. From the figure it can be seen that the $n = 1.030$ aerogel will permit good pion/proton discrimination up to 4 GeV/c, while the $n = 1.015$ aerogel material can be used for pion/kaon discrimination

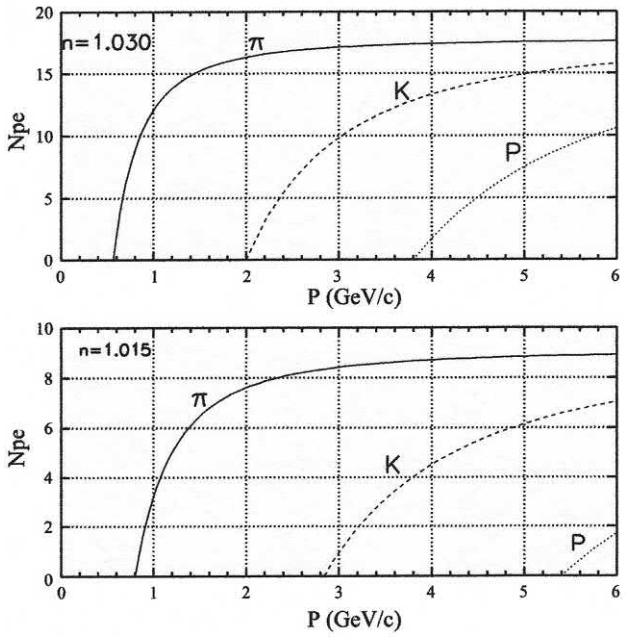


FIGURE 6.48 Particle separation using aerogel Cherenkov detectors with an index of refraction $n = 1.030$ (top) and $n = 1.015$ (bottom). Electrons (positrons) are above threshold over essentially the full momentum range. *From Asaturyan et al. (2005), reprinted with permission from Elsevier © 2005.*

in the momentum range of 1−3 GeV/c, and for pion/proton separation up to 6 GeV/c (Asaturyan et al., 2005).

As described previously in this chapter by Eq. (6.48), the number of Cherenkov photons emitted per path length of travel in the wavelength range of λ_1 and λ_2 is a function of the particle velocity β and the refractive index n of the medium or Cherenkov radiator, that is,

$$\frac{dN}{dl} = 2\pi\alpha Z^2\left(\frac{1}{\lambda_1}-\frac{1}{\lambda_2}\right)\left(1-\frac{1}{\beta^2 n^2}\right) \tag{6.124}$$

where α is the fine structure constant (1/137) and Z is the charge on the particle. In most cases, $Z = 1$; and this term is often omitted from the equation. As described by Asaturyan et al. (2005) and Denisov and Stoyanova (2006), Eq. (6.124) reduces to the expression for the number of Cherenkov photons produced by a particle of charge ($Z = 1$) per particle path length (L) of travel in the wavelength region between λ_1 and λ_2 to the following:

$$N = 2\pi\alpha L\left(\frac{1}{\lambda_1}-\frac{1}{\lambda_2}\right)\sin^2\theta \tag{6.125}$$

where θ is given by the well-known expression $\cos\theta = 1/\beta n$.

All Cherenkov photons are not detected by the photodetectors; and thus, the reflectivity M of the diffuse light box and the aerial fraction ε of coverage by the photodetectors must be included, as described by Carlson (1986), Poelz (1986) and Asaturyan et al. (2005) to give the expression for the average number of photons hitting the photomultiplier tubes, N_e, as

$$N_e = 2\pi\alpha L\left(\frac{1}{\lambda_1}-\frac{1}{\lambda_2}\right)\left(1-\frac{1}{\beta^2 n^2}\right)\frac{\varepsilon}{1-M(1-\varepsilon)} \tag{6.126}$$

From Eqs. (6.125) and (6.126), the number of Cherenkov photons detected is usually expressed as

$$N_e = N_0 L\sin^2\theta \tag{6.127}$$

where N_0 is the "figure-of-merit" or "quality factor", characterized by Engelfried (2011) and Lippmann (2012), Križan (2013), Beckford et al. (2014), as the figure depends on the quality and wavelength interval of the photon detection system including the efficiency of light transmission, collection and detection. Typical values of N_0 are between 50 and 100 cm^{-1} (Križan, 2013).

A gaseous carbon dioxide Cherenkov threshold detector has been designed for the measurement of 16.75 MeV gamma rays that accompany deuterium−tritium fusion (Mack et al., 2003, 2006; Caldwell et al., 2003; Kim et al., 2009a,b). The deuterium−tritium fusion reaction is discussed in Chapter 1, Volume 1, and in an earlier book (L'Annunziata, 2016). The fusion reaction generally results in the release of 17.58 MeV energy with the emission of a 14 MeV neutron and 3.5 MeV alpha particle. Alternatively, 16.75 MeV gamma rays may accompany the deuterium−tritium fusion with a branching ratio of the order of 10^{-5} γ/14 MeV neutron (Herrmann et al., 2016). Although the gamma-ray emission is less abundant, the observed high-energy gamma-ray signal in the Cherenkov detector is proportional to the observed 14 MeV fusion neutron yield and independent of neutron-induced gamma rays (Mack et al., 2003, 2006). The Cherenkov detection energy threshold is set by the pressure of the CO_2 gas; which detects the high-energy Compton electrons.

A Cherenkov detector arrangement reported by Perrino et al. (2001) provides an example of two Cherenkov detectors operated in tandem together with time-of-flight (TOF) measurements to discriminate between pions (π^+), positrons (e^+), and protons (p^+). The experimental setup consisted of a CO_2 gas detector ($n = 1.00041$) providing excellent detection for positrons, and a silica aerogel detector with a refractive index $n = 1.025$ providing (π, p) discrimination in the 1−4 GeV/c range with Cherenkov thresholds of 0.62 and 4.2 GeV/c for pions and protons, respectively. Pions and protons at 1 and 2 GeV/c are below the Cherenkov threshold in the CO_2 gas. Complementary data provided by time-of-flight measurements between two BC408 scintillation detectors separated at a 23 m distance along the particle beam enabled the tagging of protons. TOF measurements are determined by signals between detectors permitting the determination of the speed of a

particle, and with its total energy signal, the mass of the ion can be identified (Lilley, 2001).

Dual Cherenkov threshold detectors with aerogel radiators having two different refractive indices, $n = 1.015$ and 1.008 were designed by Allkofer et al. (2007, 2008) to operate in tandem to discriminate between kaons and protons in the momentum range of 4−8 GeV/c. Diffuse reflector foils coated with wavelength shifter increased the Cherenkov light yield by 50%. To discriminate between pions and kaons in the same 4−8 GeV/c momentum range, Horikawa et al. (2008) designed a threshold Cherenkov detector using perfluorobutane (C_4F_{10}) gas radiator, which has a refractive index $n = 1.00137$ at the 300 nm wavelength. In the C_4F_{10} gas, kaons are well below the threshold for the Cherenkov effect in the entire 4−8 GeV/c momentum range. Sokolov et al. (2009) designed an aerogel threshold Cherenkov detector with a thin Fresnel lens between the aerogel radiator and photomultiplier. The Fresnel lens focalizes the Cherenkov light onto a relatively small diameter photomultiplier reducing costs incurred in the use of one or more large diameter PMTs.

B. Mirror- or lens-focused RICH counters

The Ring Imaging Cherenkov (RICH) detector is designed principally for particle identification, as it can provide information on the velocity, β, and the charge of the particle, z; and complementary information provided by rigidity measurements using a magnetic tracker can provide the identity of the particle according to its mass (Pinto da Cunha et al., 2000). The possibility of precisely measuring the dimensions of a Cherenkov ring image together with instrumental design proposals and calculations for the determination of particle velocities of electrons, muons, pions, kaons, and protons may be attributed to Roberts (1960a,b). In one of his very detailed papers, Roberts (1960b) states the following:

> *A new type of Čerenkov radiation detector is proposed, in which the light emitted by a single particle traversing a radiator is imaged, by means of a lens or mirror focused at infinity, on the cathode of an image intensifier tube. The image is a ring, whose diameter measures accurately the Čerenkov cone angle, and thus the particle velocity. In addition, the coordinates of the center of the circular image accurately indicate the orientation of the particle trajectory …*

Some early designs of RICH detectors included the use of optical lenses to focus the Cherenkov photons as a ring image onto a photon-imaging plane, as described by Giese et al. (1970). Much of the pioneering work on RICH detectors was carried out by Thomas Ypsilantis and Jaques Sequinot (see Sequinot and Ypsilantis, 1977), and thorough treatments on the theory of RICH counters are available from Sequinot and Ypsilantis (1994) and Ypsilantis and Sequinot (1994). Several detector geometries and designs are reviewed by Križan (2017, 2013, 2007), Lippmann (2012), Engelfried (2011), Iijima (2010), Kerzel (2010), Ullaland (2003) and Glässel (1999).

The classic spherical-mirrored RICH detector, reviewed by Sequinot and Ypsilantis (1977) was designed to accept particles that originate from any 4π direction; and this classical RICH geometry is illustrated in Fig. 6.49. The illustration shows a particle trajectory passing through a Cherenkov radiator of refractive index n enclosed in a spherical mirror. The Cherenkov photon detector has a concentric spherical surface of smaller radius. The space between the outer surface of the photon detector and inner spherical mirror is filled with a transparent medium of a given refractive index [e.g., gas, C_4F_{10} ($n = 1.0015$), liquid, C_6F_{14} ($n = 1.276$), crystalline NaF ($n = 1.33$), or silica aerogel ($n = 1.01-1.02$)] to serve as the Cherenkov radiator (Pinto da Cunha et al., 2000). The Cherenkov radiator is chosen according to the mass and momenta of the particles to be identified, as the emission of Cherenkov radiation at an angle θ (or θ_c of Fig. 6.49) must satisfy the threshold condition $\beta > 1/n$. At the moment the particle penetrates the Cherenkov radiator, the Cherenkov radiation is emitted at an angle θ_c according to the particle velocity, β, and the refractive index (n) of the Cherenkov radiator as

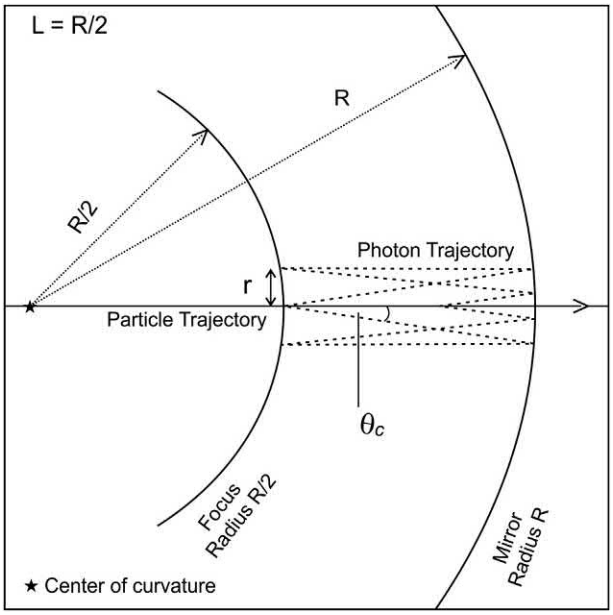


FIGURE 6.49 Working principle of a classical RICH detector. A spherical mirror surrounds a spherical photon detector. Cherenkov photon trajectories are drawn (dashed lines) in the small angle approximation surrounding the particle trajectory, which depict the emitted conical Cherenkov light and cone image (ring) reflected onto the detector surface. The radius of the light cone image is labeled r. *From Engelfried (2011), reprinted with permission from Elsevier © 2011.*

defined by Eq. (6.1) previously in this chapter, that is, cos $\theta_c = 1/\beta n$. The radiator dimensions used by Pinto da Cunha et al. (2000) were 2 cm thickness and 50 cm radius. The Cherenkov photons are reflected off the inner surface of the outer spherical mirror as a ring of light onto the conical detector surface. The ring has a radius, r, which is measured to determine the particle velocity or particle mass, if its momentum is measured. An imaging detector is used to provide an image of the ring of Cherenkov light and its coordinates relative to the vertex.

As described by Engelfried (2011), the Cherenkov photons emitted under the angle θ_c are focused (in a small angle approximation) by the spherical mirror of radius R onto a focal sphere of radius $R/2$, whereby the focal length $f = R/2$, upon which the photons form a ring of radius r (see Fig. 6.49) defined by the equation

$$r = f \tan\theta_c = \frac{R}{2}\tan\theta_c \tag{6.128}$$

The number of photons detected is defined by Eq. (6.127) described previously.

Numerous RICH detectors have been designed with mirrors to reflect and focus the Cherenkov photons onto a suitable plane of photon detectors as well as lenses to enhance images of Cherenkov rings with the objective of measuring the radius r. An example of one of several RICH detectors now in use is the COMPASS RICH-1 detector described by Agarwala et al. (2018), Abbon et al. (2010, 2011, 2015) and illustrated in Fig. 6.50. COMPASS is the acronym for Community Pentascale Project for Accelerator Science and Simulation. As illustrated in Fig. 6.50 (upper side view), an incoming nuclear particle enters the COMPASS RICH-1 detector, which is filled with gaseous C_4F_{10} radiator ($n = 1.00140$ at 150 nm). Cherenkov photons are produced along the particle path; and the ring image is condensed and reflected off a 21 m^2 wall of 116 spherical mirror elements toward a photon detector. Photon detectors are illustrated in both the upper and lower halves of the RICH detector to accommodate incoming particles either above or below a hadron beam. Ring imaging is provided by multi-anode PMTs with pixel size of $\sim 4.2 \times 4.2$ mm^2 coupled to individual telescopes of fused silica lenses and a concentrator lens to enlarge the effective active area of the photon detectors. Examples of ring images provided by multianode photomultiplier detectors are illustrated in Figs. 6.51 and 6.54. Many other RICH detector designs are used worldwide, including the HERA-B RICH detector (particle detector of the Hadron-Elektron-Ringanlage, Hamburg, Germany) reviewed by Križan (2017, 2013), Lippmann (2012), Starič (2005), Ariño et al. (2004), Gorišek (2004) and Korpar (2003), and the LHCb RICH detector (Large Hadron Collider beauty experiment at CERN) reviewed by He (2017), Papanestis and D'Ambrosio (2017), Cardinale (2016), Papanestis (2014), Kim et al. (2011), Mulheim (2011), Forty (2010) and Kerzel (2010).

For a Cherenkov radiator of given refractive index n, the radius r in the small angle approximation is a function of the particle mass m and momentum p according to the following (Engelfried, 2011):

$$r = f\sqrt{2 - \frac{2}{n}\sqrt{1 + \frac{m^2c^2}{p^2}}} \tag{6.129}$$

Thus, if the particle momentum p is known or measured (e.g., in a magnetic spectrometer, Engelfried, 2011), the particle mass m can be calculated from the radius r of the Cherenkov cone or ring; and conversely, if the particle mass is known, the particle velocity β or momentum p can be calculated. Also, as described by Lippmann (2012), with the knowledge of the Cherenkov angle θ and particle momentum p, the determination of the particle mass m is possible according to the following derivation:

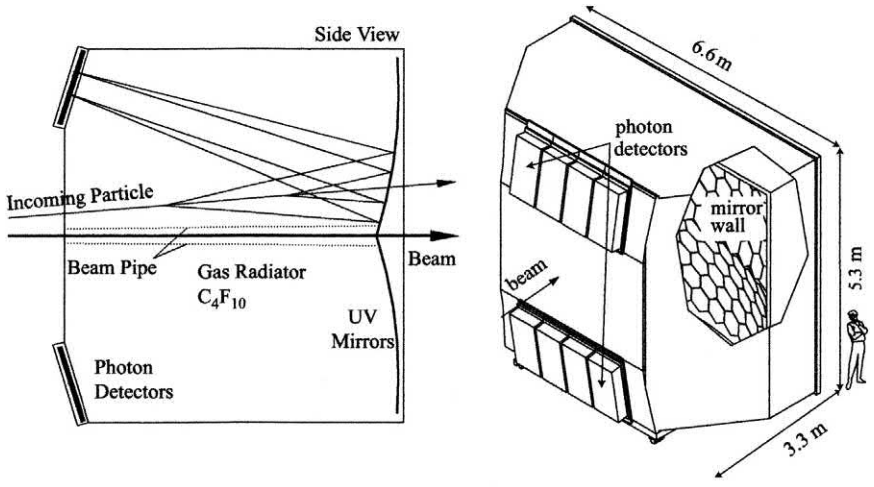


FIGURE 6.50 A scheme of the principle and an artist's view of the COMPASS RICH-1 detector. The side view (left) illustrates Cherenkov photons produced by an incoming particle inside the C_4F_{10} gas-filled detector and the focusing of the photons by mirrors onto the photon detectors for ring imaging. An exterior view (right) shows the locations of the photon detectors in the upper and lower halves of the detector and an inside view of a multifaceted photon focusing mirror wall. A sketch of a human figure is illustrated to the right to provide an idea of the magnitude of the detector. *From Abbon et al. (2011), reprinted with permission from Elsevier © 2011.*

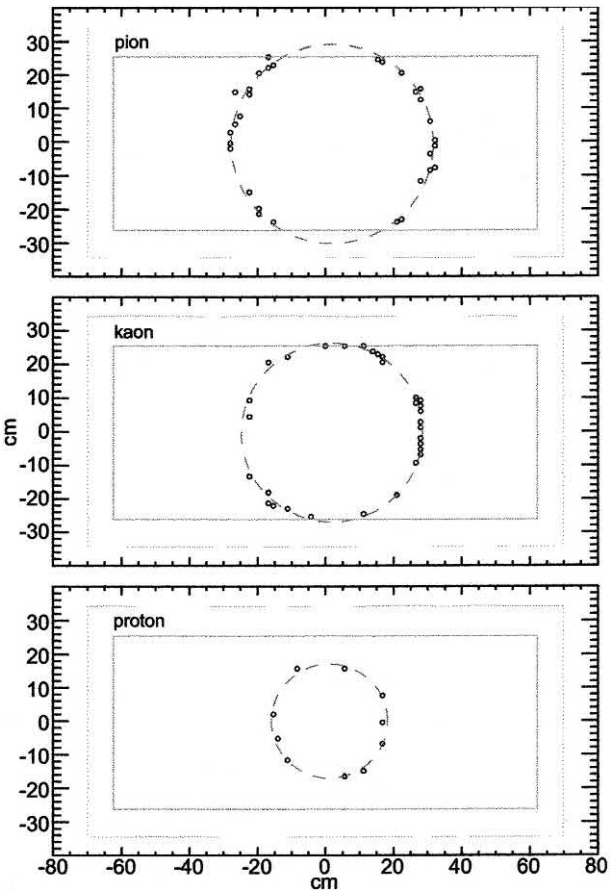


FIGURE 6.51 Sample event displays at 40 GeV/*c* pion (top), kaon (middle), and proton (bottom) rings in the RICH counter. Small circles indicate Cherenkov-photon hit PMTs. The dashed circles show the rings reconstructed from the PMT hits. *From Graf et al. (2010), reprinted with permission from Elsevier © 2010.*

Since the angle of Cherenkov photon emission θ is a function of the particle velocity and radiator refractive index n or

$$\cos\theta = \frac{1}{\beta n} \tag{6.130}$$

and the particle phase velocity β is a function of its mass and momentum according to

$$\beta = \frac{1}{\sqrt{\left(\frac{mc}{p}\right)^2 + 1}}, \tag{6.131}$$

the two Eqs. (6.130) and (6.131) can be combined to give an equation for the particle mass m as a function of its momentum and the angle of emission of the Cherenkov photons, that is,

$$m = \frac{p}{c}\sqrt{n^2\cos^2\theta - 1} \tag{6.132}$$

For a given particle momentum p and given refractive index n of the Cherenkov radiator, it can be stated that, the smaller the mass of the particle, the greater will be the Cherenkov angle θ and the greater will be the radius r of the Cherenkov ring. This is illustrated by the Cherenkov ring images for pion, kaon, and proton particles at 40 GeV/*c* momentum in Fig. 6.51, which was obtained by Graf et al. (2010) with a RICH counter filled with CO_2 gas just above atmospheric pressure as the Cherenkov radiator. The CO_2 gas has a refractive index $n = 1.00045$ at the 300 nm wavelength, which gave threshold momenta of $P = 4.5$ GeV/*c* for pions, 17 GeV/*c* for kaons, and 31 GeV/*c* for protons.

Various radiator materials of differing index of refraction (n) are selected for RICH detectors in order to discriminate between particles of differing mass and momentum. For example, Kerzel (2010) and Lippmann (2012) describe the use of three radiator substances of differing refractive index to discriminate between particles in various ranges of momentum as illustrated in Fig. 6.52. These are silica aerogel ($n = 1.03$), which is used to detect and discriminate particles in the momentum range up to $\sim$ 10 GeV/*c*, and C_4F_{10} ($n = 1.0014$) for the momentum range of $10 \leq P \leq 40$ GeV/*c*, and CF_4 ($n = 1.0005$) for particles in the range of $16 \leq P \leq 100$ GeV/*c*.

C. Proximity-focusing RICH counters

The proximity-focusing RICH detectors do not utilize mirrors or lenses to focus the Cherenkov ring image; rather the image is focused by proximity. As noted by Websdale (2008), proximity-focusing effectively means no focusing. Various proximity focusing RICH detectors are described by Šantelj et al. (2017), Torassa (2016) and Križan (2013). An example of a proximity-focusing RICH detector, used to discriminate kaons from pions with particle momentum up to 2.4 GeV/*c*, is that described by Mammoliti et al. (2011). The detector utilizes 1.5-cm-thick liquid Freon (C_6F_{14}) as the radiator and a CsI photoconverter separated by a distance of only 10 cm for Cherenkov ring imaging, illustrated in Fig. 6.53. A charged particle that exceeds its Cherenkov threshold energy in the liquid Freon ($n = 1.28$ at 180 nm wavelength) emits Cherenkov photons in the Freon in the form of a cone at an angle θ to the particle trajectory. The Cherenkov photons pass through a proximity gap filled with CH_4 at STP; and the photons are then converted into photoelectrons by a 300 nm thick CsI film deposited onto electrode pad planes of a multiwire proportional chamber (MWPC) providing a two-dimensional localization of the Cherenkov photon hits (Garibaldi et al., 2003; Cusanno et al., 2004; Iodice et al., 2005; Lippmann, 2012). An average of 12.4 photoelectrons per ring is collected with a gain of $\sim 5 \times 10^4$, which

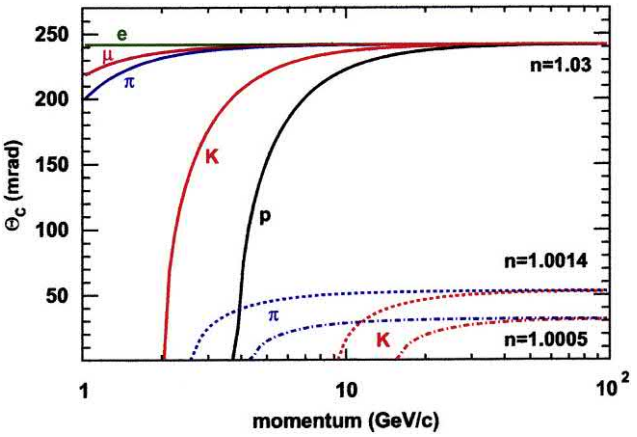


FIGURE 6.52 Cherenkov angles as a function of momentum for different particle species and for three different values of refractive index n corresponding to three radiator materials used in the LHCb RICH setup. *Lippmann (2012), reprinted with permission from Elsevier © 2012.*

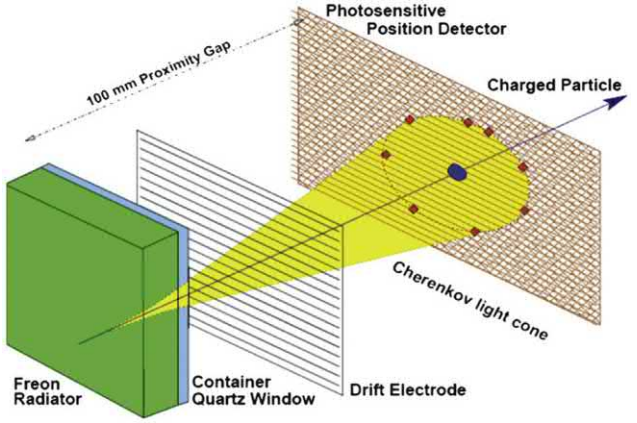


FIGURE 6.53 Artist's view of a proximity-focusing RICH counter. *From Mammoliti et al. (2011); reprinted with permission from Elsevier © 2011.*

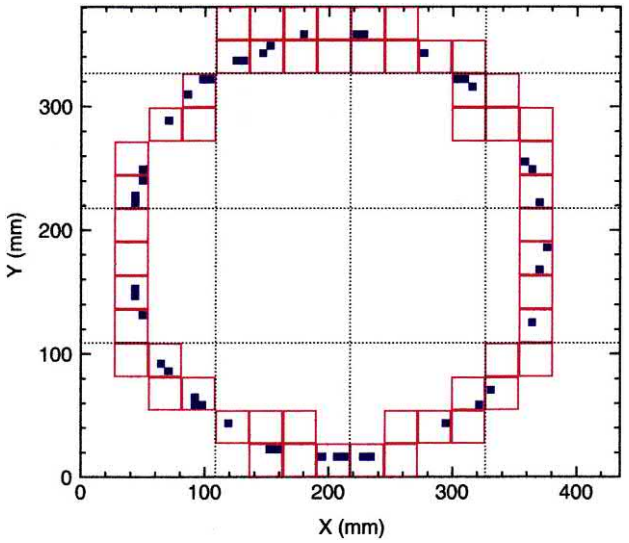


FIGURE 6.54 Cherenkov ring image. Each darkened square represents a hit. Each solid hollowed box corresponds to a multianode photomultiplier tube. *From Artuso et al. (2006), reprinted with permission from Elsevier © 2006.*

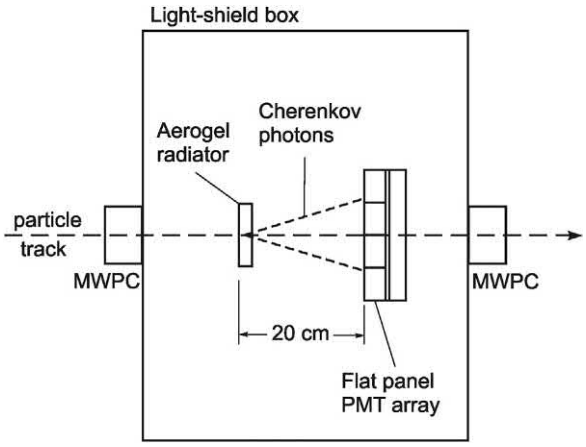


FIGURE 6.55 Experimental arrangement of a proximity-focusing RICH detector with an array of flat-panel position-sensitive PMTs. *From Matsumoto et al. (2004), reprinted with permission from Elsevier © 2004.*

provides the signal location for construction of the ring image (Mammoliti et al., 2011).

Among the methods used to record Cherenkov ring images is the utilization of a flat panel of numerous multianode PMTs. An example may be taken from the work of Artuso et al. (2006), which is illustrated in Fig. 6.54. Cherenkov photon hits onto individual PMTs produce the 2-dimension signal localization of the Cherenkov photons, which are reconstructed into the ring image. A schematic diagram of a typical proximity-focusing RICH counter is that described by Pestotnik et al. (2017, 2004), Torassa (2016), Korpar et al. (2005), and Križan et al. (2005) and Matsumoto et al. (2004), which is illustrated in Fig. 6.55. This RICH detector employs two $5 \times 5\,\text{cm}^2$ multiwire proportional chambers (MWPCs) to provide precise measurement of the particle track. The MWPCs are constructed of 20 μm diameter, gold-plated tungsten anode wires with 2-mm pitch equipped with 90% AR + 10% CH_4 gas flow providing a position read-out by delay lines on the x- and y-cathode strips. MWPCs are gas ionization detectors, developed by Nobel Laureate Georges Charpak and coworkers (Charpak et al., 1968, 1970; Charpak, 1969, 1970; Charpak and Sauli, 1978, 1979), contain an array or grid of uniformly spaced anode wires sandwiched between two other grids of uniformly spaced cathode wires. The two outer cathode planes are oriented at right angles to one another, and the sandwich of these grids is contained in a chamber of proportional counting gas such as an Ar + CH_4 gas mixture. Output signals provide the x- and y-coordinates of the ionizing particles entering the grid. See

L'Annunziata (1987) and Chapter 2 of Volume 1 for additional references and information on MWPCs.

As illustrated in Fig. 6.55, after passing through the first MWPC, the high-energy particles continue on to penetrate a silica aerogel Cherenkov radiator (10−25 mm thick). The refractive index ($n = 1.05$) of the aerogel provide discrimination of pions and kaons in the momenta range of 0.5−4 GeV/c. The Cherenkov photons produced in the aerogel are detected by an array of flat-panel multianode PMTs. The multichannel PMTs are connected to an analog memory board providing a readout of the PMT signals. The position sensitivity of the readout yields a Cherenkov angle resolution per photon of 10 mrad (Matsumoto et al., 2004).

The ARICH (Aerogel Ring Imaging CHerenkov) counter is a proximity-focusing RICH counter with a unique design for high-resolution Cherenkov ring imaging and particle identification. It is under development for installation in the Belle II spectrometer for the next generation B meson physics experiment with the SuperKEKB asymmetric e^+e^- collider (Super B-factory) at the High Energy Accelerator Research organization in Tsukuba, Ibaraki, Japan (Šantelj et al., 2017). An image of the location of the proximity-focusing ARICH detector within the Belle II structure is illustrated in Fig. 6.56. An introduction to the objectives of the B-factory at the KEK is provided by the writer in a previous book (L'Annunziata, 2016); and several detailed reviews on the development and principle of the ARICH detector are provided by Hataya et al. (2017), Inami (2017), Pestotnik et al. (2017), Šantelj et al. (2017), Yusa et al. (2017), and Nishida et al. (2014).

The ARICH detector is used to identify a charged particle from the angle of emission of the Cherenkov photons

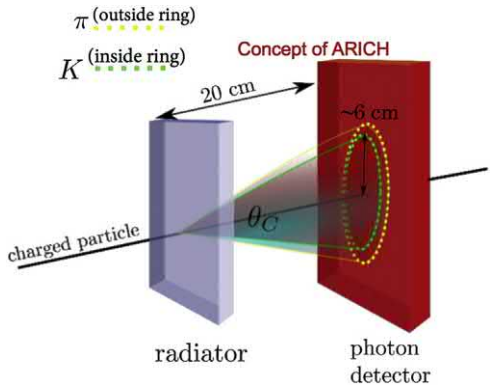


FIGURE 6.57 The concept of the ARICH. Color is visible in the electronic version of the book. *From Torassa (2016), reprinted with permission from Elsevier © 2016.*

emitted from the aerogel Cherenkov radiator, as illustrated in Fig. 6.57. A charged particle traveling through the aerogel radiator produces Cherenkov photons at an angle θ_C to the particle trajectory. Heavier particles produce Cherenkov photons in the aerogel radiator at more acute angles of emission and the resultant images of the Cherenkov rings registered by the photon detector have a smaller radius than rings produced by the lighter particles. Illustrated are two rings of ~6 cm in radius; and the inner Cherenkov ring (shorter radius) is illustrated produced by the heavier particle; and the outer ring is produced by the lighter particle. The heavier particle (e.g., kaon) will produce Cherenkov photons at a smaller angle of emission (θ_C) than the lighter particle (e.g., pion), as illustrated in Fig. 6.57.

As there is no focusing lens in the ARICH detector, the distance between the aerogel radiator and photon detector is

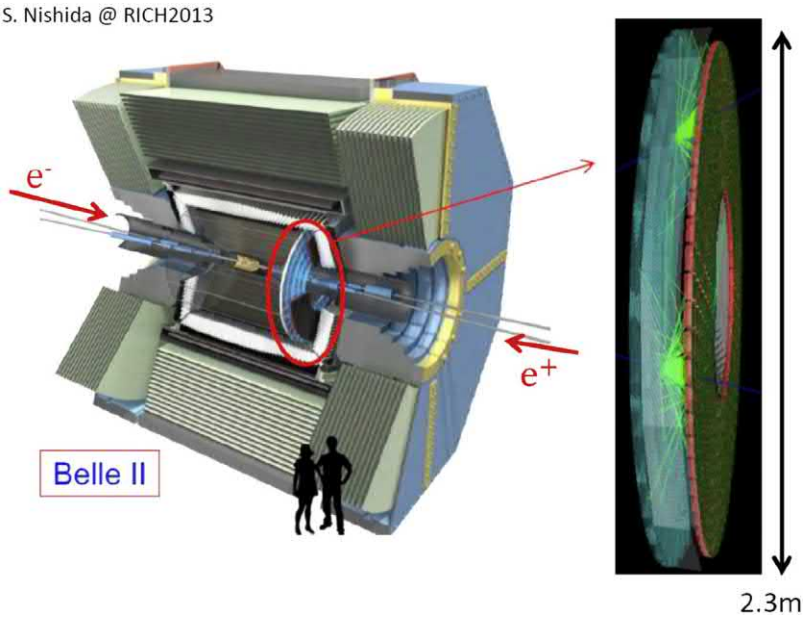


FIGURE 6.56 Left: Image of the ARICH proximity-focusing ring imaging Cherenkov detector within the Belle II structure. Two human figures are illustrated to provide a perspective of the magnitude of the Belle II structure. Right: An image and diameter of the ARICH. *From Inami (2017), reprinted with permission from Elsevier © 2017.*

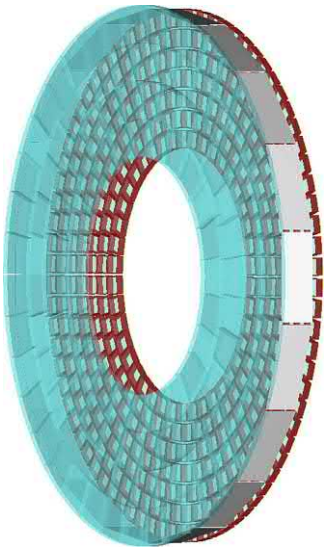


FIGURE 6.58 The basic geometry configuration of the proximity-focusing ARICH detector. From left to right are illustrated the aerogel radiator (blue), planar reflective mirrors, and photon detector (brown), Color is visible in the electronic version of the Figure. *From Šantelj et al. (2017), reprinted with permission from Elsevier © 2017.*

only 20 cm from the front surface of the aerogel to the photo detector. The ARICH detector is consequently relatively thin compared to its diameter, as illustrated in Fig. 6.58. The figure illustrates from left to right, the aerogel radiator, planar mirrors, and the photon detector consisting of an array of Hybrid Avalanche Photo Detectors (HAPDs). The numerous squares constituting the photon detector, illustrated in Fig. 6.58, are 420 HAPDs covering an area of 3.5 m^2; and the planar mirrors positioned at the outermost edge of the detector redirect photons produced from charged particles that pass near the edge that would otherwise be lost (Nishida et al., 2014). The aerogel radiator is made up of two layers of aerogel tiles with an approximate size of 18 × 18 × 2 cm with two layers of 124 tiles constituting the entire aerogel radiator area (Šantelj et al., 2017). Of the two layers of aerogel tiles, the first layer through which the particle will travel first has an index of refraction ($n_1 = 1.045$) slightly less than that of the second layer ($n_2 = 1.055$) through which the particle will travel before exiting the aerogel radiator. This arrangement yields an overlap of two Cherenkov rings produced by the two layers of aerogel resulting in an improvement in Cherenkov angle resolution, as illustrated and described further on in this chapter (see Fig. 6.61). The principle of the HAPD operation in the imaging of the Cherenkov photon rings is described by Šantelj et al. (2017).

Križan (2001) provides another excellent example of the use of position-sensitive PMTs to produce high-resolution images of Cherenkov rings. They used 2300 position-sensitive PMTs with a 2.8 m long C_4F_{10} gas radiator ($n = 1.00135$) yielding an average number of 32 Cherenkov photons per ring produced by 50 GeV/c kaons or pions and about twice that number of photons per ring when produced by overlapping e^+e^- pairs. Cherenkov photon resolutions of approx. 1 mrad provided discrimination of kaons and pions of momentum as high as 50 Gev/c. Examples of Cherenkov rings imaged by the signal outputs of position-sensitive PMTs were illustrated previously in Figs. 6.51 and 6.54.

A disadvantage of using conventional multianode PMTs for the imaging of Cherenkov photon rings is their sensitivity to high magnetic fields. Alternatives to multianode PMTs include silicon photomultipliers and hybrid photon detectors of the proximity focusing type (e.g., CsI deposited onto a cathode pad plane) for ring imaging in magnetic fields of 1.5T (Harnew, 2014; Križan, 2013; Lippmann, 2012; Pestotnik et al., 2011, 2007; Korpar et al., 2010, 2008; Dolenec et al., 2011). Silicon photomultipliers are semiconductor photosensitive devices consisting of an avalanche photodiode (APD) matrix on a silicon substrate and operating in the Geiger mode (Dolgoshein et al., 2006; Renker, 2006). The silicon photomultipliers are capable of measuring single photon events in a proximity-focusing RICH counter. They have the advantages of a low operating voltage, small dimensions, and photodetection efficiency higher than PMTs while, at the same time, insensitive to high magnetic fields; however, their main disadvantage is their relatively high dark noise count rate (Dolenec et al., 2011). To increase the detection efficiency of the silicon photomultipliers, light guides and light concentrates have been employed, and an example of a highly resolved silicon photomultiplier Cherenkov ring image produced by pion interaction with an aerogel radiator is illustrated in Fig. 6.59. The individual dots on the ring are individual photon hits.

A linear relation between Cherenkov angle θ_c and particle momentum is described by Križan (2001) to be

$$\theta_C^2 = \frac{\theta_0^2 - m^2}{p^2} \tag{6.133}$$

where $\theta_0^2 = 2(n-1)$, m is the particle mass and p is the particle momentum. The relation between the variables θ_c^2 and $1/p^2$ as defined by Eq. (6.133) is linear and thus the plot of θ_c^2 against $1/p^2$ for a particle of given mass would be a straight line. Fig. 6.60 illustrates the linear relationship between θ_c^2 and $1/p^2$ for particles of different mass, namely, protons ($m = 938.27$ MeV/c^2), kaons ($m = 493.67$ MeV/c^2), pions ($m = 139.57$ MeV/c^2) and electrons ($m = 0.511$ MeV/c^2). In Fig. 6.60, the measured ring Cherenkov angle is plotted as a function of the particle momentum, where the Cherenkov thresholds in gaseous C_4F_{10} radiator for pions, kaons, and protons are given in the figure caption. Abbon et al. (2011) points out with Fig. 6.60, that in the small

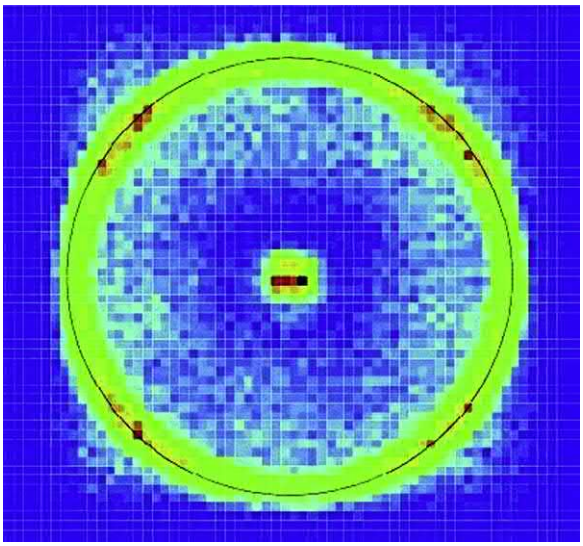


FIGURE 6.59 Cherenkov ring for hits within a 5 ns time window as recorded by an array of silicon photomultipliers described by Korpar et al. (2010) in a pion test beam *From Križan (2013), reprinted with permission from Elsevier © 2013.*

angle approximation, the relationship between the two variables θ^2 and $1/p^2$ is linear with a slope proportional to the squared mass of the corresponding particle; and the bands start at the Cherenkov threshold and have a common intercept corresponding to the maximum Cherenkov angle. Thus, measurement of the Cherenkov angle of emission in radians (rad) can be used to determine the velocity of a particle from its momentum or identify the particle from its known momentum.

A main issue in the performance of proximity focusing RICH counters is the optimization of the Cherenkov angle resolution per particle track, which is measured as

$$\sigma_{\text{track}} = \sigma_\theta / \sqrt{N_{\text{pe}}} \tag{6.134}$$

where σ_{track} is the resolution measured in mrad, σ_θ is the single photon resolution, and N_{pe} is the number of photoelectrons collected by the photon detector. Researchers have found that the proper association of nonhomogeneous Cherenkov radiators can improve the Cherenkov angle resolution per track as well as increase the number of photoelectrons collected by the photon detectors, N_{pe}, by 50% without deteriorating the angular resolution σ_θ (Pestotnik et al., 2017; Torassa, 2016; Nishida et al., 2014; Križan, 2013, 2009, 2007; Lippmann, 2012; Adachi et al., 2011, 2007; Websdale, 2008; Iijima et al., 2005; Korpar et al., 2005). As described by Križan (2009), the number of detected Cherenkov photons increases with the length of the Cherenkov radiator; however, in a proximity focusing RICH counter, the single photon resolution degrades with increased radiator length, because of the uncertainty in the point of photon emission. This is illustrated in Fig. 6.61A where it is seen that, for a homogeneous radiator of refractive index n and given length, the Cherenkov ring image resolution is a function of the radiator length. Križan (2009) indicates that for a given geometry, the optimal radiator thickness is approximately 20 mm. The limitation of resolution and radiator thickness can be overcome to a certain extent by use of a nonhomogeneous radiator, which is a radiator consisting of two or possibly three layers of aerogel of differing refractive index adjoined back-to-back, as illustrated in Fig. 6.61B and C. Such an arrangement can be made only with aerogel radiator, as silica aerogels can be fabricated over a range of refractive indices ($n = 1.005$ to 1.26), as described previously in Section VII of this chapter. As described by Križan (2009), with the appropriate selection of refractive indices of consecutive aerogel radiator layers, it is possible to achieve overlapping of the corresponding Cherenkov rings on the photon detector (see Fig. 6.61). This is a type of focusing of the Cherenkov photons by reducing the spread of the photons due to the uncertainty of the point of emission from the radiator, which may encompass any point in the radiator along the particle track, from the point of entrance of the particle to its point of exit. To achieve Cherenkov ring image focusing in this manner, the refractive indices must gradually increase from the upstream to the downstream layer. This is

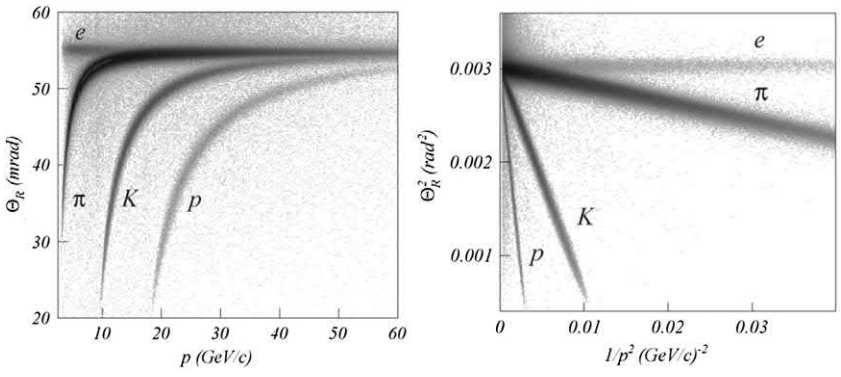


FIGURE 6.60 The measured ring Cherenkov angle θ_R versus the particle momentum p (left) with Cherenkov thresholds at ~ 2.5, 9, and 17 GeV/c for pions, kaons, and protons, respectively, and θ_R^2 versus $1/p^2$ (right) in a C_4F_{10} gaseous radiator. *From Abbon et al. (2011), reprinted with permission from Elsevier © 2011.*

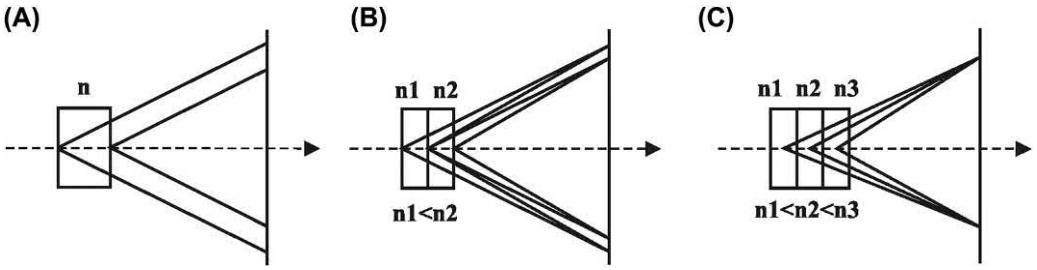


FIGURE 6.61 Effects of nonhomogeneous aerogel Cherenkov radiators (*e.g.*, dual and triple radiator combinations) that may improve ring-image resolution: (A) single radiator of refractive index n, (B) focusing dual radiator having indices of refraction $n1$ and $n2$ where $n1 < n2$ and the radiator of highest refractive index is downstream with the direction of particle and photons, and (C) focusing multiple radiator combination with the indices of refraction gradually increasing from $n1$ to $n3$ of the aerogel layers from upstream to downstream. *From Iijima et al. (2005), reprinted with permission from Elsevier © 2005.*

the technique used in the construction of the ARICH detector described previously where two aerogel radiator tiles are placed back-to-back each of only 2 centimeters thickness and with indices of refraction $n1 = 1.045$ and $n2 = 1.055$. (Šantelj et al., 2017). If the sequence of refractive indices of the layers is reversed, i.e., $n1 > n2$, from upstream to downstream, dual rings would be observed (Iijima et al., 2005; Korpar et al., 2005.

D. Time-of-propagation Cherenkov counters

A time-of-propagation (TOP) Cherenkov counter is a DIRC (Detector of Internally Reflected Cherenkov light) counter used for particle identification. The TOP counter provides a measurement of the time-of-propagation (TOP) of Cherenkov photons in a narrow (2 cm thick) quartz bar; and various designs are described by Harnew (2014), Inami (2014, 2011, 2008), Križan (2013), Matsuoka (2013), Lippmann (2012), Nishimura (2011), Starič (2011), Nishimura et al. (2010), Enari et al. (2002), Akatsu et al. (2000) and Ohshima (2000). The basic structure of the Time-of-Propagation Cherenkov counter is illustrated in Fig. 6.62. The TOP detector consists of a quartz Cherenkov radiator bar with the general approximate dimensions: 20 mm-thickness, 60 mm-width, 3150 mm-length). The time-of-propagation counter utilizes the principle of total internal reflection of Cherenkov photons produced in the quartz radiator; and it measures the position and precise arrival time of propagated photons at the radiator ends (Inami, 2014, 2011; Matsuoka, 2013). A focusing mirror is located at the back end of the bar (mirror not identified in Fig. 6.62) for focusing the Cherenkov photons. The mirror is flat at the backward end to reflect the Cherenkov light toward the forward end where the photon detector is located. The Cherenkov photons are focused horizontally onto the photon detector plane, and the time-of-propagation is measured by the photon detector. The method is based on the following principles: (1) the Cherenkov photon emission angle (θ_c), illustrated in Fig. 6.63, is a function of the particle velocity (β) according to the relation $\cos\theta_c = 1/\beta n$ where n is the refractive index of the Cherenkov radiator, (2) the time-of-propagation (TOP) of photons in a light guide with internal-total-reflection characteristics can be calculated as a function of the photon emission angle, and (3) a correlation between time-of-propagation and photon emission angle would provide information on particle identification. Notice from the example provided in Fig. 6.63, the Cherenkov photon emission angle created by the pion (π) is less acute than that created by the kaon (K) and the time-of-propagation of the Cherenkov photons derived from the pion is shorter than derived by the kaon.

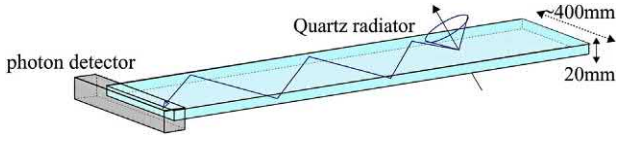


FIGURE 6.62 Schematic overview of the TOP counter. The path of a particle emitted from interaction point of the negatron-positron collider is illustrated by an arrow penetrating the quartz bar from below and producing Cherenkov photons when passing through the quartz radiator bar. The emitted Cherenkov photons are propagated inside the quartz radiator and detected by the photon detector at the bar end. The TOP counter measures the propagation time. *From Inami (2014), reprinted with permission from Elsevier © 2014.*

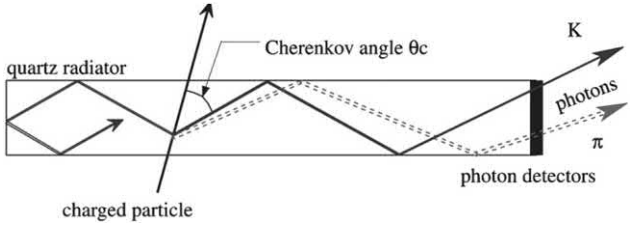


FIGURE 6.63 A side view schematic of the time-of-propagation (TOP) concept. The path length difference of Cherenkov photons emitted from a pion and a kaon within the radiator bar together with the difference in time-of-flight from the interaction point (i.e., particle origin) to the Cherenkov quartz radiator results in a difference in the Cherenkov photon arrival time at the photodetector. *From Nishimura et al. (2010), Nishimura (2011) and Iijima (2011), reprinted with permission from Elsevier © 2010.*

As noted by Inami (2011), time-of-propagation differences of 200 ps or more are found for normal incident 2 GeV/c K^+ and π^+, the time resolution for single photon detection needs about 40 ps. An additional property, that is utilized, is the time-of-flight (TOF) from the interaction point, which is the point of collision between the accelerated particles (e.g., e^+e^-) to the counter. The interaction point of the e^+e^- collider can be 1 meter away from the quartz bar. The distance from the interaction point affects the difference in the Cherenkov photons' arrival time at the photon detector additively in most cases (Inami, 2011), thereby improving the discrimination of particles (e.g. $\pi^{\pm}$ and $K^{\pm}$). Inami (2014) reports the application of the TOP counter mainly for the separation of $\pi^{\pm}$ and $K^{\pm}$ for the upgrade to the SuperKEKB/Belle II experiment at The High Energy Accelerator Research Organization (KEK) at Tsukuba, Ibaraki, Japan. In the Belle II experiment, the typical difference in the Cherenkov photon arrival times for photons produced by the $K^{\pm}$ and $\pi^{\pm}$ ranges between 150 and 200 ps; and measured with a time resolution of $\sigma \sim 40$ ps for each photon (Inami, 2014).

E. Time-of-flight Cherenkov counters

For a beam of particles of known momentum, a measurement of the time-of-flight (TOF) between a start and stop counter (*e.g.*, Cherenkov detectors) separated by several meters yields the mass of the particle (Va'vra et al., 2009; Ronzhin et al., 2010), a property key to particle identification. Numerous reviews on various designs of time-of-flight Cherenkov counters are found in the literature and current designs are reviewed by Gys et al. (2017), Harnew et al. (2016), Dey et al. (2015), Alici and ALICE Collaboration (2014), van Dijk et al. (2014), Križan (2013) and Lippmann (2012). Only the basic principles and some illustrative examples of time-of-flight Cherenkov measurements are made for particle identification.

An excellent example of the application of TOF Cherenkov counters is the utilization of proximity-focusing RICH detectors in conjunction with TOF measurements to supplement data for particle identification.

The relativistic momentum of the particle is expressed as

$$p = \gamma m v \tag{6.135}$$

where

$$\gamma = \frac{1}{\sqrt{1-\beta^2}} \tag{6.136}$$

is the relativistic Lorentz transformation factor (Airapetian et al., 2005; Lippmann, 2012), as described previously by Eq. (1.271) in Chapter 1, Volume 1, m is the particle mass, v is the particle velocity, and β is the relativistic phase velocity of the particle, that is, the velocity of the particle divided by the speed of light in a vacuum (v/c). From Eq. (6.136), Lippmann (2012) expresses the mass of the particle in terms of its momentum and phase velocity as

$$m = \frac{p}{c\beta\gamma} \tag{6.137}$$

as $\beta = v/c$; where the particle momentum may be determined by its curvature in a magnetic field and the particle velocity may be determined by time of flight and Cherenkov radiation measurements. From Eqs. (6.136) and (6.137), we can write the expression

$$\frac{mc}{p} = \frac{\sqrt{1-\beta^2}}{\beta} \tag{6.138}$$

which can be transformed to express the particle velocity β in terms if its mass m and momentum p as

$$\beta = \frac{1}{\sqrt{\left(\frac{mc}{p}\right)^2 + 1}} \tag{6.139}$$

The particle velocity β, as described by Lippmann (2012) is determined by time-of-flight (TOF) measurements of the particle flight time t over a given distance L along the particle trajectory; and β would then be expressed as

$$\beta = \frac{v}{c} = \frac{L}{tc} \tag{6.140}$$

Eqs. (6.139) and (6.140) may be used to write an equation for the particle mass m from measurements of L, t, and p, as described by Lippmann (2012) as

$$m = \frac{p}{c}\sqrt{\frac{c^2t^2}{L^2} - 1} \tag{6.141}$$

Thus, for particles of known momentum, Cherenkov detectors separated by the distance L, which can provide the start and stop signals for the measurement of t, can provide the data necessary to calculate the particle mass. In turn, Eq. (6.141) may be transposed to express the time t for a particle of mass m and momentum p to travel the distance L as

$$t = \frac{L}{c}\sqrt{1 + \left(\frac{mc}{p}\right)^2} \tag{6.142}$$

Lippmann (2012) points out that, if two particles with masses m_A and m_B carry the same momentum, their flight time difference can be calculated as

$$|t_A - t_B| = \frac{L}{c}\left|\sqrt{1 + \left(\frac{m_Ac}{p}\right)^2} - \sqrt{1 + \left(\frac{m_Bc}{p}\right)^2}\right| \tag{6.143}$$

Accurate measurements of the start and stop signals are provided by two radiation detectors. One detector is located upstream from the particle beam or trajectory and the second detector to provide the stop signal or end of the measured particle trajectory. Cherenkov photons, produced in the window of a PMT of a proximity-focusing RICH counter, have been used conveniently to provide the stop signal for TOF measurements (Iijima, 2010; Iijima et al., 2008; Križan, 2007, 2009; Adachi et al., 2007; Korpar et al., 2007). As illustrated in Fig. 6.64, Cherenkov photons, produced by a nuclear particle in the window of a microchannel plate PMT, are used to provide a stop signal for the measurement of time of flight, while the Cherenkov photons produced by the particle in passing through the aerogel detector yield ring imaging data. Thus, time-of-flight measurements supplement other particle identification methods, such as RICH counting.

An example of an arrangement where the concept of proximity-focusing RICH and TOF measurements are combined in the same detector is taken from the work of Iijima et al. (2008). The concept is illustrated in Fig. 6.65. The start signal for the measurement of time of flight of kaons and pions, illustrated in Fig. 6.65, is the interaction point (IP) and the stop signal is the signal registered by Cherenkov photons produced in the window of the PMT (referred to as a "Window Hit" in Fig. 6.65. The distance of particle travel L for the calculation of time of flight t and particle mass according to Eqs. (6.141) to (6.143) is measured in the experimental arrangement illustrated in Fig. 6.65 as $L = 1.8\text{ m} + 0.2\text{ m}$. Cherenkov photons produced by the particle passing through the aerogel detector are detected by the PMTs to yield ring image data; and the detection of a Cherenkov photon is referred to as a "Ring Hit" in Fig. 6.65. In addition to ring image, additional time-of-flight (TOF) information of the particle is obtained by

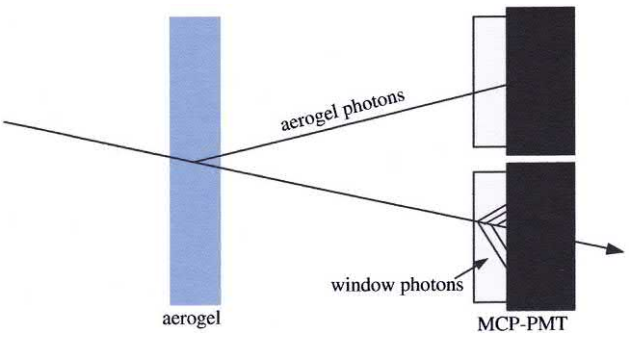


FIGURE 6.64 Schematic view of a combined proximity focusing RICH and TOF counter. Cherenkov photons produced by the charged particle in passing through the window of the microchannel plate photomultiplier tube (MCP-PMT) provide the stop signal for time of flight measurements. Cherenkov photons produced by the particle as it passes through the aerogel detector are detected by another MCP-PMT for ring imaging data. *From Križan (2009), reprinted with permission from Elsevier © 2009.*

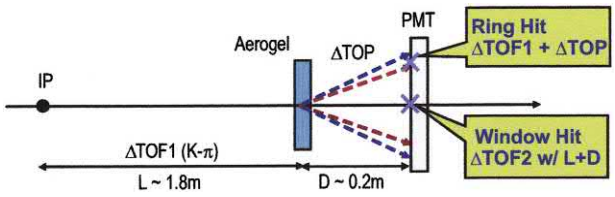


FIGURE 6.65 Concept of a RICH counter with TOF capability. *From Iijima et al. (2008), reprinted with permission of Elsevier © 2008.*

measuring TOF from the IP point to the aerogel detector (ΔTOF1 of Fig. 6.65) plus the time of propagation (TOP) of the Cherenkov photon from the aerogel radiator to the PMT (ΔTOP of Fig. 6.65). Iijima et al. (2008) measured TOF differences for 2 and 4 GeV/c kaons and pions to be 147 and 37 ps, respectively, for the "Ring Hits" and 184 and 47 ps for the "Window Hits". Such TOF measurements permit the identification of particles having momenta below the Cherenkov threshold (*i.e.*, when no Cherenkov photons are produced) in the aerogel radiator of refractive index $n = 1.03-1.05$, which is $\approx$ 1.5 GeV/c for kaons and $\approx$3 GeV/c for protons (Iijima et al., 2008).

The microchannel plate PMT photodetector is a very fast device with a reported time resolution per single photon to be $\sim$50 ps (Iijima et al., 2008). The power of TOF measurements to separate particles ($n_{\sigma_{TOF}}$) is a function of the TOF difference between the two particles ($t_A - t_B$) and the resolution of the TOF measurement (σ_{TOF}) or

$$n_{\sigma_{TOF}} = \frac{|t_A - t_B|}{\sigma_{TOF}} \tag{6.144}$$

With particle momentum $p >> mc$, Lippmann (2012) points out that the approximation

$$\sqrt{1 + (mc/p)^2} \approx 1 + (mc)^2/2p^2 \tag{6.145}$$

And from Eqs. (6.143)–(6.145), the separation power becomes

$$n_{\sigma_{TOF}} = \frac{|t_A - t_B|}{\sigma_{TOF}} = \frac{Lc}{2p^2\sigma_{TOF}}\left|m_A^2 - m_B^2\right| \tag{6.146}$$

For a given length (L) of measured particle trajectory of 3.5 m, the separation power of particles as a function of particle momentum and time resolution is illustrated in Fig. 6.66. Lippmann (2012) demonstrates from the separation power curves of Fig. 6.66, that assuming a time resolution in the range of 100–60 ps and requiring a separation power of $n_{\sigma_{TOF}} = 3$, the upper limits for the momentum are in the range of 2.1 GeV/c to 2.7 GeV/c for K/π separation and 3.5 GeV/c to 4.5 GeV/c for K/p separation.

Under development is a unique time-of-flight Cherenkov detector consisting of a panel of quartz plates (1 cm in width) as the Cherenkov radiators equipped with microchannel plate photomultipliers, described by Gys

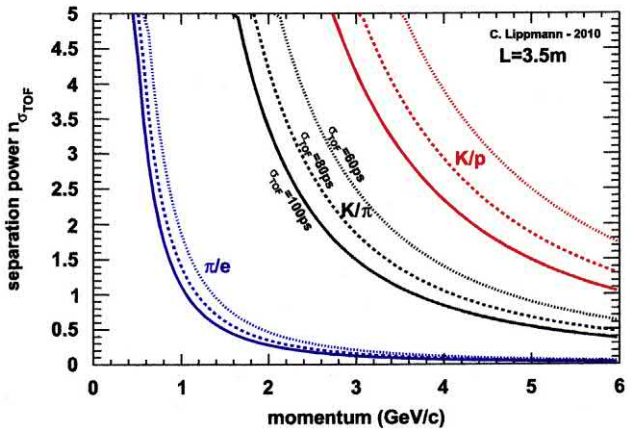


FIGURE 6.66 Particle separation with TOF measurements in three different system time resolutions ($\sigma_{TOF} = 60$, 80 and 100 ps) and for a track length $L = 3.5$ m. Infinitely good precisions on momentum and track length are assumed. Color is visible in the electronic version of the book. *From Lippmann (2012), reprinted with permission from Elsevier © 2012.*

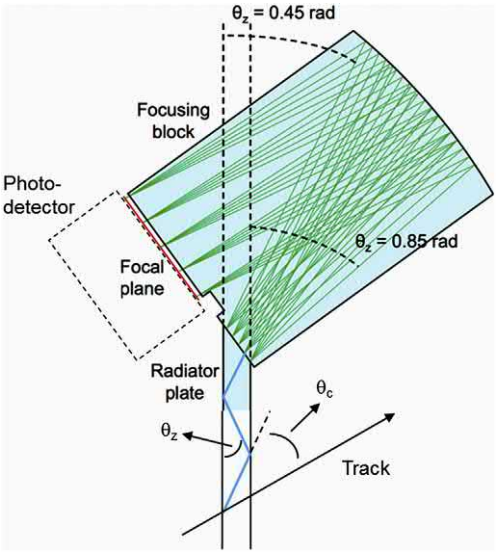


FIGURE 6.67 Schematic principle of the TORCH detector. A particle created at an interaction point of an accelerator beam at a distance of 10 m arrives at the 1-cm-thick quartz bar and passes through the bar creating Cherenkov photons. Some of the photons are reflected internally and focused onto microchannel plate photon detectors for determination of their arrival time. *Gys et al. (2017), reprinted with permission from Elsevier from © 2017.*

et al. (2017), Harnew et al. (2016), van Dijk et al. (2014), Križan (2013) and Charles and Forty (2011). The detector, known as TORCH (Timing Of internally Reflected Cherenkov photons) was designed to detect and discriminate particles following the interaction of colliding proton beams at the CERN Large Hadron Collider beauty experiment (LHCb). The detector is placed 12 m downstream of the interaction point. The detector has a specific design, which provides the Cherenkov angle (θ_C) and TOF measurements for the identification of particles of momentum up to 10 GeV/c.

The TORCH counter utilizes quartz plates of 1 cm thickness as the Cherenkov radiator. A charged particle (e.g., K/π) originating at the interaction point at distance of 10 m travels through the 1 cm quartz plate producing Cherenkov photons in the process. Some of the Cherenkov photons are trapped within the quartz plate by total internal reflection, as illustrated previously in Figs. 6.62 and 6.63. The internally trapped Cherenkov photons created in the 1-cm-thick plate is focused on to microchannel plate (MCP) photon detectors, as illustrated in Fig. 6.67, for measurement of their time of arrival. As described by Harnew et al. (2016), Cherenkov photons produced in the 1-cm thick quartz travel to the periphery of the detector by total internal reflection and their angles and arrival times are measured with the microchannel plate PMTs. The technique makes use of the measurement of the Cherenkov angle θ_c and the arrival time of the photon at the periphery of the quartz radiator bar.

Charles and Forty (2011) describe the calculations involved in the identification of kaons and muons with the TORCH. Only an abbreviated summary will be provided here; and a more detailed treatment may be obtained from Charles and Forty (2011) among other works cited previously. At the LHCb experiment, particles in the momentum range from 2 to 100 GeV/c can be identified by four methods, outlined by Charles and Forty (2011), which are summarized as follows.

(i) The first of these methods is the use of RICH detectors, independent of the TORCH detector described here. The principles of the RICH detectors were described previously in this chapter.

(ii) The second method of particle identification is by Cherenkov time-of-flight (TOF) measurement from the time that the particle is emitted from its origin, namely, the point of interaction, to its arrival at the Cherenkov detector at a distance of 12 m. Charles and Forty (2011) note that if a particle of mass m and momentum p is detected at position x and time t after travel from its origin, then the time of flight would be expressed as

$$t = \frac{x}{c}\sqrt{1+\left(\frac{m}{p}\right)^2} \approx \frac{x}{c}\left[1+\frac{1}{2}\left(\frac{m}{p}\right)^2\right] \tag{6.147}$$

and the difference in arrival times of kaons and pions would be a function of the mass difference of the two particles or

$$t_K - t_\pi = \frac{x}{c}\frac{1}{2p^2}\left[m_K^2 - m_\pi^2\right] \tag{6.148}$$

A fast response time provided by the Cherenkov detector is important for kaon identification in the

momentum range of 2−10 GeV/c. For a particle path length of 10 m, Charles and Forty (2011) calculate that a per-track time resolution of 12.5 ps and a per-photon time resolution less than 90 ps would be required.

(iii) The third method for charged particle identification, described by Charles and Forty (2011) is by the measurement of the time of propagation (TOP) or τ_γ of the Cherenkov photons over a path length d_γ. A charged particle traveling from the interaction point to the thin (10 mm) plane of the optically dense quartz detector will pass through the quartz producing Cherenkov photons emitted at an angle (θ_C) dependent on the phase velocity (β) of the particle and index of refraction (n) of the quartz radiator, where the threshold condition is

$$\cos\theta_C = \frac{1}{\beta n} \tag{6.149}$$

The Cherenkov photons propagate at the group velocity c/n_g and

$$n_g = c\frac{t_\gamma}{d_\gamma} \tag{6.150}$$

Charles and Forty (2011) point out that the relationship between n and n_g is a nonlinear function depending on the medium according to

$$n_g = n - \lambda\frac{dn}{d\lambda} \tag{6.151}$$

After solving for n from n_g, the particle phase velocity (β) and mass (m) are calculated according to

$$\beta = \frac{1}{n\cos\theta_C} \tag{6.152}$$

and

$$m = p\sqrt{n^2\cos^2\theta_C - 1} \tag{6.153}$$

(iv) A fourth approach combines the methods of particle time of flight and Cherenkov photon time of propagation described above with the utilization of the TORCH detector. A charged particle passes through the thin (10 mm) plane of quartz and the Cherenkov photons propagate via internal reflection to the periphery of the quartz radiator bar. Charles and Forty (2011) note that the arrival time of a Cherenkov photon at the edge of the plane is the sum of the time of flight of the particle track to the point of Cherenkov photon emission in the quartz, t, and the time of propagation of the Cherenkov photon in the medium (i.e., quartz), t_γ, which is calculated according to

$$t + t_\gamma = \frac{x}{c}\sqrt{1 + \left(\frac{m}{p}\right)^2} + \frac{d_\gamma n_g}{c} \tag{6.154}$$

and n_g is determined from

$$n = \frac{1}{\beta\cos\theta_C} = \frac{\sqrt{m^2 + p^2}}{p\cos\theta_C} \tag{6.155}$$

Harnew et al. (2016) underscore that the technique relies on the measurement of the Cherenkov angle θ_C and the arrival time of the Cherenkov photon at the periphery of the quartz radiator bar. The vertical dimension of the quartz detector plane is a direct measure of the angle of the Cherenkov photon path with the vertical axis (θ_Z), as described by van Dijk et al. (2014); and this track information with the photon hit provides an accurate measure of the photon path length (see Fig. 6.68). The focusing block at the edge of the detector plane can accept θ_Z values between 0.45 and 0.85 rad. The TORCH detector consists of 18 thin (10 mm) quartz modules each measuring 250 × 66 cm with their individual focusing block and photodetectors arranged in a fashion to completely surround the beam pipe of the large hadron collider up to ~ 30 m^2 time-of-flight Cherenkov detector. More detailed schematics are available from Harnew et al. (2016).

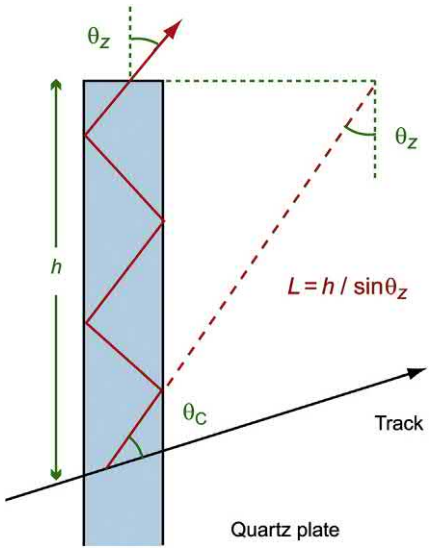


FIGURE 6.68 A particle track passing through the 10-mm-thick quartz detector creating Cherenkov photons at an angle θ_C with definition of the angle θ_Z and calculation of the distance (L) of photon propagation along the photodetector plane. *From Charles and Forty (2011), reprinted with permission from Elsevier © 2011.*

XIII. Neutrino detection and measurement

Cherenkov detectors, which utilize very large volumes of transparent material, such as water, heavy water, and ice have been designed to detect neutrinos from various sources such as solar neutrinos, atmospheric neutrinos of the cosmic ray showers, geo-neutrinos, artificially produced neutrinos arising from nuclear reactors and accelerators, and ultra−high energy (UHE) astrophysical neutrinos. Since neutrinos do not carry charge, they do not produce the Cherenkov effect. The Cherenkov photons, that are detected, are those produced by charged particles resulting from neutrino interactions such as the elastic scattering (ES) of electrons in the detector medium or via charged current (CC) or neutral current (NC) interactions of neutrinos with neutrons or protons of atomic nuclei. These neutrino interactions and the Cherenkov effect that they produce are described in detail in Chapter 1, Volume 1. Even ultra−high energy (UHE) astrophysical neutrino interactions with atomic nuclei can produce particles yielding Cherenkov radio waves, which are detected with antennas.

Very large volumes of water or ice, both naturally or artificially contained, are used as the transparent medium for the detection of Cherenkov photons produced by neutrino interactions. These detectors are designed to detect and measure neutrinos, and even discriminate between neutrinos of specific flavor, from various sources such as solar neutrinos, atmospheric neutrinos of the cosmic-ray showers, geo-neutrinos, and artificially produced neutrinos arising from nuclear reactors and accelerators.

Only a brief review of some of the methods used for the Cherenkov detection of neutrinos will be given here. More detailed information is available from the references cited and in a previous book by the writer (L'Annunziata, 2016).

A. Large light-water Cherenkov detectors

The world's largest ring-imaging water Cherenkov detector is the Super-Kamiokande detector, which is located in the Mozumi mine near the village of Higashi−Mozumi, Gifu, Japan. The detector cavity lies under the peak of Mt. Ikenoyama of 1000 m of rock or 2700 m-water-equivalent (m.w.e.) providing a shield against cosmic ray muons of energy < 1.3 TeV (Fukuda et al., 2003). The detector consists of a 50 kiloton stainless-steel water tank, 39 m in diameter and 42 m tall, illustrated in Fig. 6.69. The inner detector (ID) contains 11,129 inward-facing hemispherical PMTs each of 50 cm in diameter. Optically isolated from the inner detector are 1885 outward-facing hemispherical PMTs each of 20 cm diameter, which constitute part of the outer detector (OD). As described by Fukuda et al. (2003) neutrino interactions are identified via the Cherenkov light emitted by the charged particles that are produced in the ID. Events due to charged particles originating from events external to the inner detector are identified by the OD PMTs. The size, shape, and orientation of the Cherenkov light pattern produced by signals collected by the PMTs on the ID walls are used to identify the event as single-ring arising from electrons, single-ring arising from muons, or multiring events.

A brief history of the detector is given by Nishino et al. (2009); and current and future research are discussed by Li (2017), Kajita et al. (2016) and Nakahata (2015). The Super-Kamiokande detector has been in operation since 1996. The detector has yielded data leading to notable contributions in studies of neutrino flavor mixings and their masses (Ashie et al., 2005; Wendell, 2013; Okumura, 2015; Kajita et al., 2016), measurements of atmospheric and solar neutrinos and artificial accelerator-based neutrinos (Hosaka et al., 2006; Smy, 2013; Carminati, 2015; Renshaw, 2015;

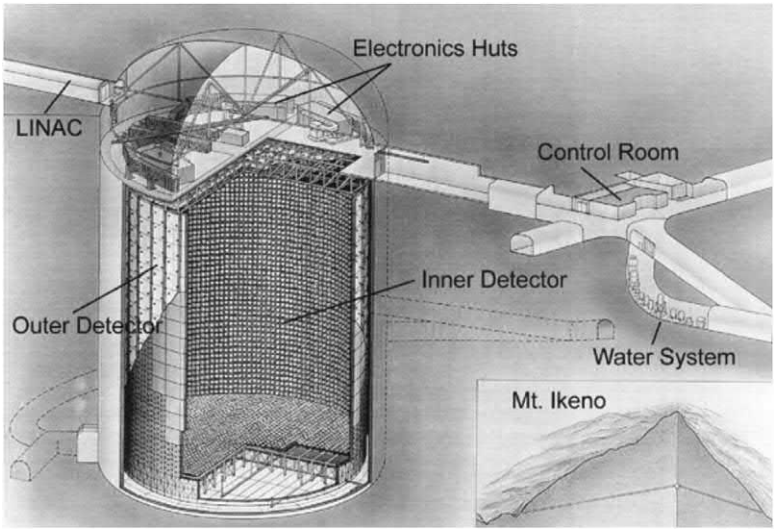


FIGURE 6.69 A sketch of the Super-Kamiokande Cherenkov detector under Mt. Ikenoyama, Japan. *From Fukuda et al. (2003) and Nishino et al. (2009), reprinted with permission from Elsevier © 2003.*

Abe et al., 2016; Desai and Liu, 2016; Sekiya, 2016; Li, 2017), and cosmic neutrinos from supernova explosions (Ikeda et al., 2007; Zhang, 2015; Himmel and Scholberg, 2016).

The Nobel Prize in Physics 2015 was awarded in one part to Takaaki Kajita of the University of Tokyo, Kashiwa, Japan for his work with the Super-Kamiokande Collaboration and in another part to Arthur B. McDonald of Queens University, Kingston, Canada for his work with the Sudbury Neutrino Observatory (SNO) Collaboration, which resulted in the words of the Nobel Committee "the discovery of neutrino oscillations, which shows that neutrinos have mass." The SNO detector is described in the next section of this chapter. From the detection and analysis of neutrinos they were able to demonstrate that neutrinos can oscillate from one flavor to another; and this would be possible only if neutrinos have mass. The Super-Kamiokande detected atmospheric neutrinos. The muon neutrinos (ν_μ) that arrived at the Super-Kamiokande detector from the atmosphere above were more numerous than the muon neutrinos that traveled through the globe and collided with the detector from below. This demonstrated that the muon neutrinos that traveled longer (i.e., through the earth) had more time to change into a neutrino of another flavor (e.g., ν_e or ν_τ). In addition, the SNO measured the solar electron neutrino (ν_e) intensity, as only electron neutrinos are produced by the Sun. Neutrinos of all three flavors (i.e., ν_e, ν_μ, and ν_τ) could also be detected by the deuterium in the SNO. As described by the Nobel Committee, the electron neutrinos were smaller in number than expected whereas the combined number of the three neutrino flavors corresponded to expectations, which indicated that the electron neutrinos had changed into a neutrino of another flavor (Rose, 2015).

The Super-Kamiokande (Super-K) is a 50 kton water detector. In the planning stage is the construction of the Hyper-Kamiokande (Hyper-K) as the next generation water detector (Li, 2017), which will consist of two identical tanks each with 520 kton of total volume and 380 kton of fiducial volume. The Hyper-K will have a fiducial volume 16 times greater than the current Super-K; and it will be equipped with 99,000 newly developed 50-cm PMTs for the inner detector and 25,000 20-cm PMTs for the outer detector with improved quantum efficiency. This will provide an instrument with greater potential for measuring atmospheric neutrinos, supernova burst neutrinos, geoneutrinos and in the search for proton decay (Nakahata, 2015; Hadley, 2016; Li, 2017).

B. Large D_2O neutrino target

A large Cherenkov detector, which utilized 1 kton of heavy water (D_2O) as the medium for the detection of solar and atmospheric neutrinos, is The Sudbury Neutrino Observatory (SNO). The SNO started collecting data in 1999. It is located at a depth of 2092 m (5890 ± 200 m.w.e) in the Vale-INCO Creighton Mine, outside Sudbury, Canada. The detector, illustrated in Fig. 6.70, consists of a 12 m diameter acrylic vessel containing D_2O target surrounded by 7 tons of H_2O shielding. The acrylic vessel housing the D_2O is surrounded by a 17.8 m diameter geodesic sphere (PSUP) illustrated in Fig. 6.70, holding 9456 inward-looking and 91 outward-looking 20 cm PMTs equipped with light concentrators to provide an effective coverage of ~54%. The volume of H_2O outside the geodesic support structure served as a cosmic-ray veto system and as a shield against natural radioactivity of the surrounding rock and construction materials (Boudjemline et al., 2010).

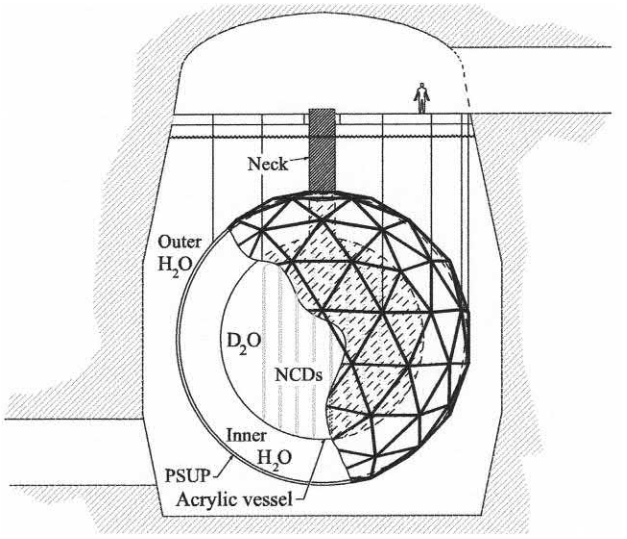


FIGURE 6.70 Layout of the SNO Cherenkov detector. The D_2O (1000 tons) was contained within an acrylic vessel. This volume could be accessed via the neck. The Neutral Current Detectors (NCDs), illustrated as vertical lines in the acrylic vessel housing the D_2O, were employed in the third phase of the experiment. The acrylic vessel was surrounded by water for shielding the radioactivity from the rock (outer H_2O) and photomultiplier tubes (inner H_2O). The photomultiplier SUPport Structure (PSUP) held the photomultiplier tubes and light concentrators. *From Boudjemline et al. (2010), reprinted with permission from Elsevier © 2010.*

The SNO detector was designed to measure the flux of neutrinos produced by ^8B decays in the Sun and to measure neutrino oscillations (Barros, 2013). As described in the previous section of this chapter, one-half of the Nobel Prize in Physics 2015 was awarded to Arthur B. McDonald of Queens University, Kingston, Canada for his work with the Sudbury Neutrino Observatory (SNO) Collaboration for the discovery of neutrino oscillation, which provides evidence that neutrinos have mass (Rose, 2015).

The current D_2O neutrino target of SNO will be replaced with a liquid scintillator in the search for neutrinoless double beta decay; and it will be renamed as SNO+,

as discussed in Chapter 6, Volume 1. The methods of neutrino detection used by SNO will be discussed here in light of the unique neutrino detection properties of heavy water.

The physics of neutrino detection in SNO are described in detail by Graham (2003), Formaggio (2009), Prior (2009), Hallin (2010) and Barros (2013). See also Chapter 1, Volume 1 of this book for an introduction to neutrino interactions with matter. A brief summary of neutrino detection in SNO will be provided here. The deuterium of the D_2O in SNO distinguishes it as a unique detector for solar neutrinos over H_2O detectors, because deuterium can be used to observe all three neutrino flavors, namely, the electron, muon, and tau neutrinos (ν_e, ν_μ, ν_τ). As described by Prior (2009), Barros (2013), and Bellerive et al. (2016), the SNO could measure the flux of ^{8}B neutrinos originating from the solar proton−proton chain via the following three distinct reactions, which are described in more detail in Chapter 1, Volume 1:

1. The charged-current reaction (CC):

$$\nu_e + d \rightarrow p + p + e^- \tag{6.156}$$

where the electron energy is well correlated with the energy of the electron neutrino. The electron neutrino ν_e is the only neutrino flavor that is able to convert the deuterium into two protons and a negatron.

2. The neutral-current reaction (NC):

$$\nu_x + d \rightarrow p + n + \nu_x \tag{6.157}$$

in which all of the neutrino flavors participate ($x = e$, μ, or τ) equally, provides a measurement of the total neutrino flux over the energy threshold of 2.2. MeV.

3. The elastic scattering (ES) reaction:

$$\nu_x + e^- \rightarrow \nu_x + e^- \tag{6.158}$$

is sensitive to all neutrino flavors, but with a reduced sensitivity to ν_μ and ν_τ. From this reaction and the anisotropic property of the Cherenkov radiation, the directional information of the neutrino can be determined. The Cherenkov light from the electron is measured for the detection of the ES and CC reactions; and the signal for the NC reaction is provided by the capture of a neutron by a nucleus.

Prior (2009) and Hallin (2010) describe the three techniques used to detect the neutrons from the NC reaction. The neutrons captured on the deuterium nucleus create a 6.26 MeV gamma ray. The gamma rays could be distinguished from the electrons by quantifying the isotropy of the Cherenkov light. Gamma rays undergo Compton scatter and consequently they create more isotropic hit patterns then electrons. A significant difference in the CC and NC flux measured was the first direct evidence for neutrino flavor transformation (Prior, 2009). In a second phase of the work, 2000 kg of NaCl was dissolved into the D_2O to enhance the neutron capture cross-section. Neutron capture on the ^{35}Cl nucleus results in a cascade of gamma-ray emissions at an 8.6 MeV threshold, which allows for a better separation of neutron capture events from other Cherenkov events. In a subsequent third phase, the NaCl was removed from the D_2O and ^{3}He counters were incorporated into the SNO detector (identified as Neutral Current Detectors, NCDs, in Fig. 6.70). The ^{3}He detectors increased the neutron capture cross-section. Another important application of the heavy-water Cherenkov detector is the detection and measurement of the high-energy muons that are created by cosmic-ray showers and atmospheric neutrino interactions. Atmospheric neutrinos are created from the decay of charged mesons (Formaggio, 2009), which are created by the interaction of primary cosmic rays with the Earth's atmosphere, as described in Chapter 1, Volume 1 and by the writer in a previous book (L'Annunziata, 2016). As described by Formaggio (2009) and Katz (2009), the atmospheric neutrino interactions are detected through the high-energy muons created via the charged-current reaction

$$\nu_\mu(\overline{\nu}_\mu) + N \rightarrow \mu^-(\mu^+) + X \tag{6.159}$$

with nuclei N of materials that surround the detector, and the overhead muons are created predominately in the Earth's upper atmosphere. Neutrino measurements from SNO are reported by Aharmim et al. (2005, 2007, 2008), Formaggio (2009), Barros (2013), and Bellerive et al. (2016).

C. Neutrino telescopes in lake and ocean floors

While the previously discussed Super-Kamiokande and SNO Cherenkov detectors for the measurement of neutrinos are very large man-made detectors, there are now in operation and in the planning, much larger detectors up to a km^3 in volume. These are based on the utilization of very huge natural bodies of water or ice as underwater detectors of neutrinos referred to as neutrino telescopes, which are reviewed by Katz (2009) Montaruli (2009a), Zornoza (2014) and Kappes (2016). Modern neutrino telescopes are derived from the original idea proposed by Markov and Zheleznykh (1961) of using a large body of water (or ice) as a detector of charged leptons (particularly muons, See Eq. 6.159) arising from charged-current (CC)

neutrino interactions with water nuclei. In their original paper Markov and Zheleznykh (1961) wrote

> *It is noteworthy that not only μ-mesons (from the reactions involving neutrinos) produced in the detector itself, but also the μ-mesons from the adjoining layers of the ground ('the cushion') are detected in the experiment … Owing to a long path of μ-mesons in the substance, the set up may collect μ-mesons from a stratum equivalent to a 500 m layer of water (the path of a μ-meson of energy 10^{11} eV) … A small neutrino interaction cross-section makes it possible to perform experiments deep underground and thus isolate the reactions (with the production of μ-mesons …) from the neutrinos coming from the lower hemisphere, i.e. passing through the earth. This experimental arrangement can in principle exclude the cosmic-ray background. All known particles with the exception of neutrinos are absorbed by scores of kilometres of the substance and thus are entirely screened by the planet … In underground experiments the relatively small background makes it possible to use large detector 'masses', which compensates to a certain degree for the weakness of high energy neutrino fluxes.*

The objective of neutrino astronomy, that is, the detection and measurement of neutrinos to observe astronomical objects and processes that are inaccessible to optical telescopes is expressed by Montaruli (2009a,b), who explains

> *… examples can be found in astronomy and history that show that whenever new instruments are pointed to the sky unexpected discoveries are possible. So the discovery of some astrophysical neutrino source not yet seen with other messengers … is possible. Neutrinos are good messengers due to their weakly interacting properties and due to the fact that, being neutral, they allow us to point back to their sources.*

Neutrino telescopes, as defined by Montaruli (2009a) are a three-dimensional array of photomultipliers (PMTs) to detect the Cherenkov light produced by charged particles with velocity in the radiator (water or ice) larger than that of light. The spacing between strings holding the Cherenkov photon sensors (PMTs) are governed by the properties of the radiator (water or ice) and the energy region of interest. Measurements of charged particles resulting from neutrino interactions with energies above 10 PeV require very large detector volumes with cubic-kilometer dimensions.

There are currently several large-scale neutrino telescopes in operation, which utilize Cherenkov photon detection and measurement, including, the BAIKAL Neutrino Telescope project in Lake Baikal in Siberia (Aynutdinov et al., 2011; Avrorin et al., 2013, 2014, 2016), ANTARES (Astronomy with a Neutrino Telescope and Abyss Environmental RESearch) in the Mediterranean Sea (Carr, 2008; Ageron et al., 2011; Aguilar et al., 2011; Brunner, 2011; Costantini, 2011; Margiotta, 2015; Spurio, 2015, 2017; De Bonis, 2016), and IceCube/AMANDA (Antarctic Muon and Neutrino Detector Array) at the South Pole (Achterberg et al., 2006; Berghaus, 2009; Montaruli, 2009b; Abbasi et al., 2010, 2011; Hultqvist, 2011; Neronov and Semikoz, 2016; Toscano and IceCube Collaboration, 2017), and the KM3NeT, which is a multi-km^3 detector in the Mediterranean Sea (Zornoza, (2014; Sapienza, 2015; Hofestädt, 2016; Margiotta, 2016). Reviews of underwater, underice, and underground measurements of neutrinos is available from Zornoza, 2014), Sapienza (2015), Hofestädt (2016), Margiotta (2016).

The BAIKAL neutrino telescope in Lake Baikal is described by Avrorin et al. (2011, 2014) and consists of an array of 10,385 PMTs enclosed in a transparent pressure sphere. Each of these constitutes an optical module (OM). The OMs are suspended in the lake on vertical cables forming a string of detectors. The telescope is configured in an arrangement of 27 clusters of strings, which are connected to the shore with individual electro-optical cables. Each of the 27 clusters is composed of eight 705 m long strings of OMs; and seven strings are arranged uniformly around a central string. Each string is comprised of 48 OMs spaced along the string by 15 m at water depths of 600−1300 m below the lake surface (see Fig. 6.71). Central strings of neighboring clusters are separated by 300 m; and the clusters are spaced over an area of 2 km^2 (Avrorin et al., 2014). The units are kept vertical in the lake bottom by buoys (Katz, 2009). The vertical units of OMs anchored on the lake bottom are distributed to cover a 2 km^2 circular area providing a 20 Mton Cherenkov H_2O detector. The detector is designed to record Cherenkov photons produced by high-energy muons resulting from charged-current reactions of high-energy neutrinos with nuclei.

The ANTARES neutrino telescope is a deep-sea neutrino telescope located at a depth of 2475 m in the Mediterranean Sea, 42 km from La Seyne sur-Mer in the South of France (Ageron et al., 2011; Costantini, 2011; Spurio, 2015; Margiotta, 2015; De Bonis, 2016). The detectors consist of 12 lines of 480 m length equipped with optical modules (OMs) anchored to the sea bed and kept vertical in the sea with buoys (see Fig. 6.72). Each line is equipped with 885 OMs. Each OM contains a 25 cm PMT housed in a 43 cm glass sphere directed at a 45 degree angle toward the sea bed. The space between the windows of the PMTs and their protective glass spheres are filled with a gel to provide their optical connection. The lines of detectors (OMs) are distributed at distances of 14.5 m from each other. As described by Aguilar et al. (2011), the main objective of ANTARES is to search for high-energy neutrinos of astrophysical origin. This is achieved by the detection of Cherenkov photons induced by the passage of relativistic particles (*e.g.*, muons) resulting from neutrino interactions in the material (sea water) surrounding the

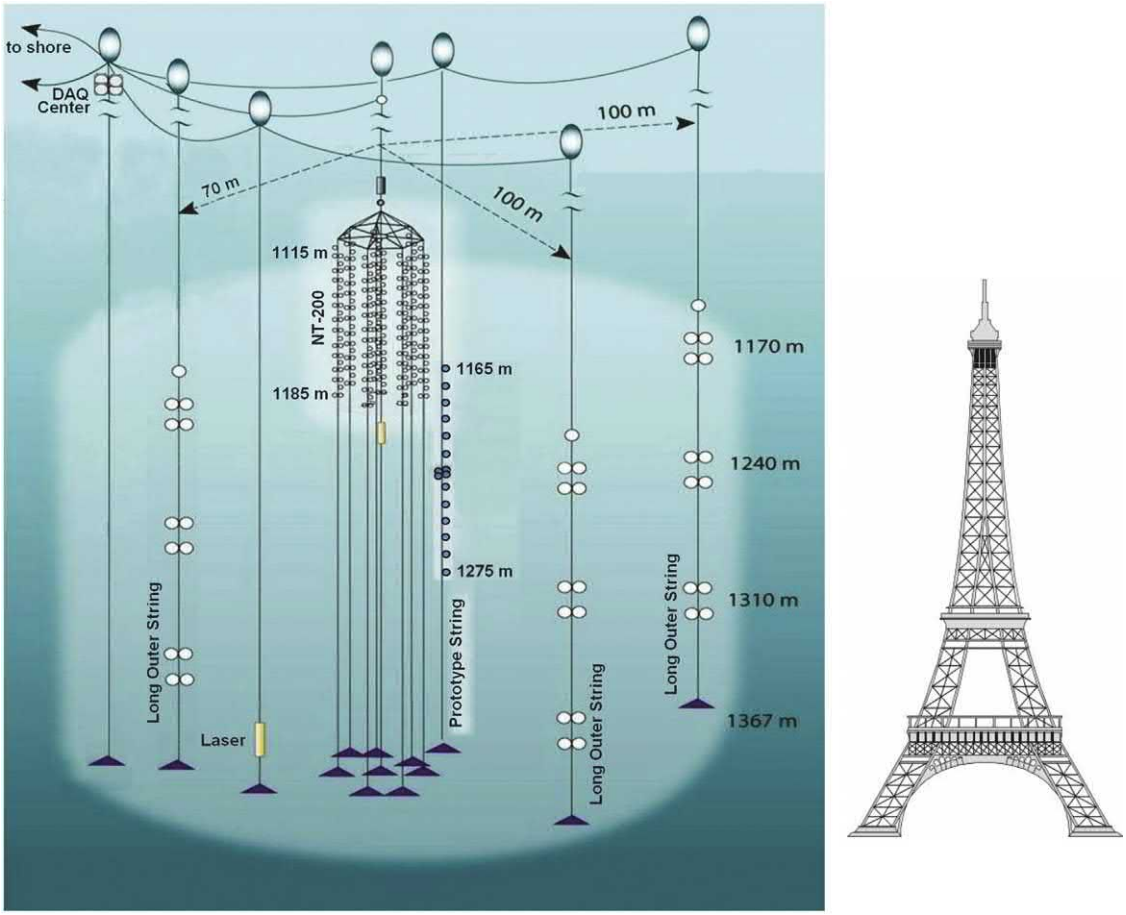


FIGURE 6.71 The BAIKAL Neutrino Telescope. A cluster of strings (one of 27 clusters encompassing 2 km^2 of lake waters) supported by buoys reach the Baikal lake floor to a depth of 1367 m. Optical modules containing PMTs for the detection of Cherenkov photons are attached to the strings (white circles). An image of the Eiffel Tower was included by the writer for a perspective of the magnitude of the detector. *Figure from Avrorin et al. (2011), reprinted with permission from Elsevier © 2011.*

detector including earth under the sea bed (see Fig. 6.73). The three-dimensional grid of PMTs or OMs is used to measure the arrival time and position of the Cherenkov photons, and their track reconstruction requires the knowledge of the relativistic arrival times of the Cherenkov photons at the PMTs (Aguilar et al., 2011; Costantini, 2011). The direction of the muon (created by a CC neutrino reaction with a nucleus; see Eq. 6.159) is reconstructed using the fact that it emits Cherenkov photons at a well-defined angle and does not suffer from multiple scattering at high energies. Thus, a simplified detector geometry is used composed of straight vertical lines and a simplified fit, which considers only direct Cherenkov photons within a narrow time window (Brunner, 2011).

The KM3NeT Neutrino Telescope is a deep-sea detector that is currently under construction at a depth between 2 and 5 km in the Mediterranean Sea; and reviews on the design, implementation and objectives of the detector are provided by Hernández-Rey (2014), Sapienza (2015), Hofestädt (2016), and Margiotta (2016). The following is a brief description of the neutrino detector design and objectives from the excellent review by Hernández-Rey (2014).

The placement of the neutrino telescope deep below the sea serves as a shield against the background of the cosmic-ray showers produced in the earth's atmosphere; and the darkness at the deep ocean water serves as an excellent medium for the detection of Cherenkov radiation produced by a charged particle, such as a muon, resulting from a high-energy neutrino CC reaction with an atomic nucleus in the sea floor or in the waters surrounding the detectors. Hernández-Rey (2014) notes that an array of photo sensors at sufficient depth in the sea can record the Cherenkov light induced by upcoming muon tracts that can originate exclusively from neutrinos that have traversed the earth and reacted with an atomic nucleus in the vicinity of the telescope array (see Fig. 6.74). High-energy neutrinos will produce high-energy muons via the CC interactions, which can travel several kilometers providing an effective detector volume for the neutrino telescope to detect and measure the

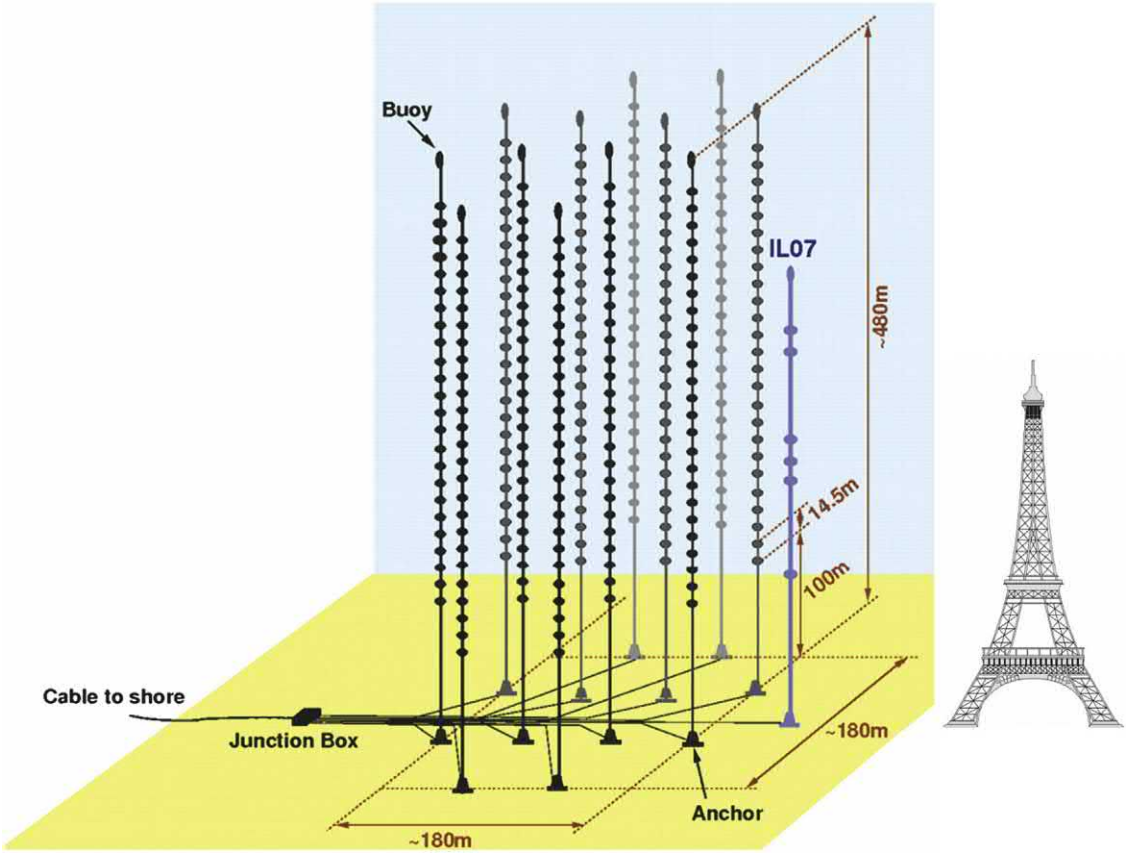


FIGURE 6.72 Schematic view of the ANTARES detector. A figure of the Eiffel Tower is inserted by the writer to give a perspective of the magnitude of the detector. *From Ageron et al. (2011), reprinted with permission from Elsevier © 2011.*

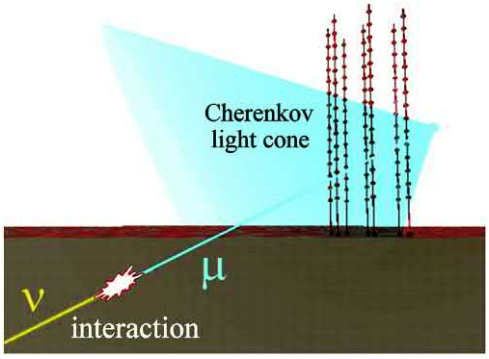


FIGURE 6.73 Principle of detection of high-energy muon neutrinos in an underwater neutrino telescope. The incoming neutrino that traversed the earth interacts with the material around the detector to create a muon. The muon produces Cherenkov light in the sea water which is then detected by a matrix of light sensors. The original spectrum of light emitted from the muon is attenuated in the water such that the dominant wavelength range detected is between 350 and 500 nm. *From Ageron et al. (2011), reprinted with permission from Elsevier © 2011.*

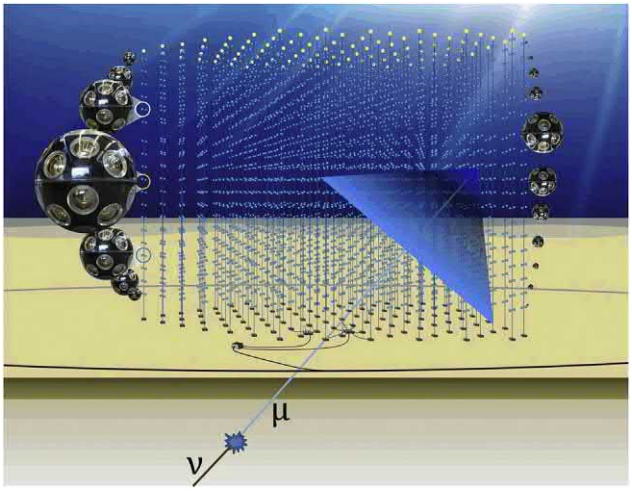


FIGURE 6.74 Artist view of a KM3NeT neutrino telescope with its array of spherical optical modules installed on long strings. The neutrino detection principle is illustrated whereby a high-energy neutrino produces a high-energy muon via a charged current reaction and the detection of the Cherenkov photons produced by the muon along its track. A Cherenkov cone is illustrated along the muon track in view of the optical modules of the neutrino telescope. On the left of the figure are enlarged illustrations of the circular optical modules each containing 31 three-inch (7.6 cm) PMTs housed in a 17-inch (43.2 cm) diameter pressure-resistant sphere. *From Margiotta (2016), reprinted with permission from Elsevier © 2016.*

resultant Cherenkov radiation. The measurement of Cherenkov photons from high-energy neutrino-to-muon interactions can yield the direction of travel of the neutrino, as the angle between the muon and its parent neutrino is low at high energies. Also, Hernández-Rey (2014) underscores that the neutrino energy, E, can be estimated within a factor of 2−3 by means of the measurement of the energy deposited in the detector by the corresponding muon track; and the showers of the cosmic radiation can provide yet better energy resolution of the order of 0.1−0.2 in log E scale.

When completed, the KM3NeT neutrino telescope will contain more than 12,000 optical modules containing PMTs installed on long strings referred to as detector units. The detector will be deployed at three sites, namely, three sites located near Toulon, France (40 km offshore and seabed at 2500 m), Capo Passero (80 km offshore and seabed at 3500 m) and Pylos, Greece (20 km offshore and seabed between 2500 and 5000 m). The optical modules are spherical in shape with a 17-inch diameter containing 31 PMTs together with the electronics for the PMT signal measurements of the Cherenkov photons and the transmission of data to shore.

Hernández-Rey (2014) notes that the main objective of the KM3NeT neutrino telescope is the measurement of astrophysical sources of neutrinos, which should provide information on the origin of cosmic rays. The primary target is Galactic sources and the primary channel for measurement is the CC interaction of the muon neutrino, as described previously; however, other neutrino sources and channels will also be targets.

D. Neutrino astronomy in Artic ice

The IceCube Neutrino Observatory is located at the South Pole. The observatory is composed of 86 instrumented strings, each holding 60 digital optical modules (DOMs) separated along each string by a distance of 17 m, which provide a total of 5160 photomultipliers. The strings supporting the DOMs are inserted into vertical drill-holes deep within the clear polar ice at depths between 1.5 and 2.5 km (Zornoza, 2014). An artist's depiction of the IceCube neutrino observatory is provided in Fig. 6.75. The drill holes are made with a special hot-water drilling technique whereby the water in the hole containing the instrumented strings of DOMs refreezes. Each DOM contains a 25 cm PMT in a glass pressure housing facing downward. The 86 strings of DOMs are separated by a distance of 125 m and distributed uniformly to provide a Cherenkov detector with PMTs extending throughout an effective volume of approximately 1 km^3 of clear ice. Toscano (2017) underscores that the one cubic kilometer of highly transparent glacial Antarctic ice provides the requirements for the detection of the faint Cherenkov photon emissions from the

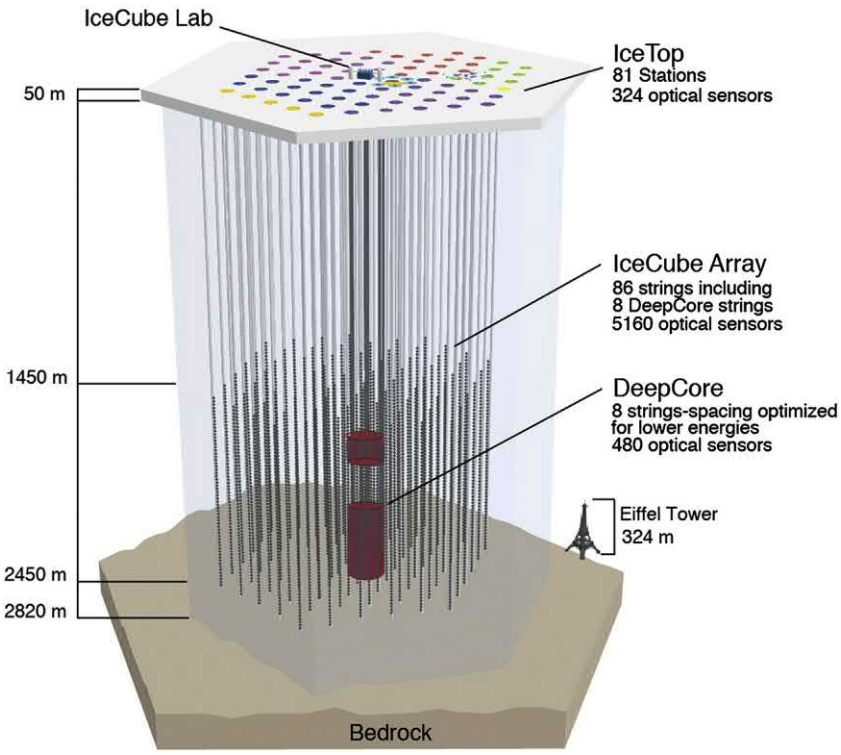


FIGURE 6.75 Artist cross-section of the IceCube detector, showing the IceTop array at the surface of the ice and the IceCube array roughly 2.5 km below. The DeepCore strings are shown in the shaded region at the middle of the IceCube detector. An image of the Eiffel Tower is provided in the lower right-hand portion of the figure to provide a perspective of the detector dimensions. *From Aartsen et al. (2016), reprinted with permission from Elsevier © 2016.*

secondary charged particles produced in neutrino interactions with the ice or the bedrock below at energies above 100 GeV. Also, a more densely instrumented DeepCore subarray (see Fig. 6.75), installed at the bottom center of IceCube, with an interstring spacing of 60 m and inter-DOM spacing of 7 m, provides a lower detection energy threshold of 10 GeV for neutrino oscillation research.

The ICECube neutrino observatory contains an additional component, called IceTop, which is a surface array of stations established for the Cherenkov detection of cosmic-ray air showers. Each IceTop station is located above each instrumented string (depicted as circular spots around the IceCube Lab in Fig. 6.75); and it consists of two tanks of clear ice monitored by two DOMs running at two different gains to achieve a dynamic detection range (Hultqvist, 2011).

The construction of IceCube was completed in 2011. Prior to its completion, measurements were carried out with a limited number of instrumented strings under the project name of AMANDA (Abbasi et al., 2010, 2011). As described by Abbasi et al. (2010), the strings of DOMs distributed in the deep ice core detect secondary muons via the CC interaction $\nu_\mu + N \rightarrow \mu + X$ (see Eq. 6.159). The muons are detected by the Cherenkov Effect, when they travel faster than the speed of light in ice, *i.e.*, $0.8c$, where c is the speed of light in a vacuum. Tamburro (2014) points out that at the altitude of IceTop, secondary cosmic-ray particles are sampled near the cosmic-ray shower maximum, which allows the precise measurement of the energy spectrum of primary cosmic rays with an energy resolution of 10% above 10^{16} eV. He also notes that events seen in coincidence by both IceTop and the deep detector (see Fig. 6.76) give clear insights into the nuclear composition of cosmic rays for energies that span PeV (10^{15} eV) to EeV (10^{18} eV). At muon energies above 1 TeV, additional Cherenkov light is detected, which arises from particles produced in the muon interactions, such as bremsstrahlung, pair production, and photonuclear reactions. The amount of Cherenkov light detected by the DOMs rises with the muon energy, which reflects also the energy of the parent neutrino. Thus, the detected light intensity can be used to determine the primary neutrino energy spectrum (Abbasi et al., 2010).

Toscano (2017) provides a summary of results from IceCube and its future expansion. Among these developments, which fall within the main goal of IceCube being the detection of astrophysical neutrinos, was the discovery in 2013 of a high-energy diffuse flux of neutrino events with energy ranging from the tens of TeV up to a few PeV of cosmic origin. This represents the first observation of astrophysical neutrinos; and the challenges presented with the current limited IceCube event sample underscores the need to overcome these challenges with a larger experimental detector volume. In this light, Toscano (2017) reports that there are plans to expand IceCube from its current 1 km^3 detector volume up to 10 km^3, dubbed IceCube-Gen2, which would include a radio Cherenkov array for ultra-high energy neutrino detection.

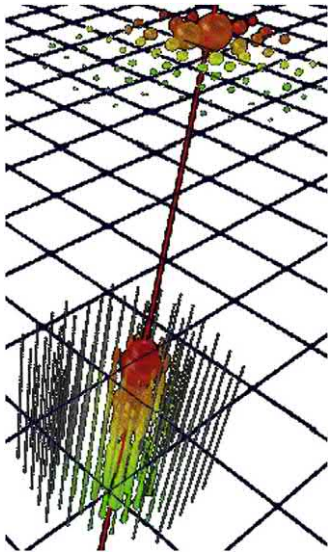


FIGURE 6.76 Cosmic ray coincident event recorded by IceCube. Triggered DOMs are indicated with colored spheres whose volume is proportional to the registered signal. Signal times are indicated with colors from red to green, red being the earliest. This event is reconstructed with an energy of 3×10^{17} eV and a zenith angle of 11.5 degrees. *For the color version of the figure, the reader is referred to the online version of the book. From Tamburro (2014), reprinted with permission from Elsevier © 2014.*

Reviews on the neutrino measurements obtained by IceCube are provided by Hussain (2014), Taboada (2014), Tamburro (2014), Neronov and Semikoz (2016), Toscano (2017), Tosi (2017), Xu (2017), and Aartsen et al. (2016, 2018).

E. Radio Cherenkov counting

There is an ongoing search for ultra-high energy (UHE) neutrinos with energies above 10^{18} eV to beyond the decade of 10^{20} eV and to find answers to their astrophysical origin. Varner (2010) underscores that protons of such high energy cannot travel far through the cosmic microwave background (CMB) without interacting, which would mean that such UHE neutrinos should be produced nearby; although there is no evidence for nearby point sources. The origin and properties of the cosmic microwave background are reviewed by the writer in a previous text (L'Annunziata, 2016). The loss or degradation of the UHE proton flux is due to the interaction of protons exceeding $\sim 4 \times 10^{19}$ eV with the cosmic microwave background photons forming a Δ^+ resonance (Gerhardt et al., 2010; Varner, 2010). The Δ^+ decay results in a chain of decays leading to ultra-high energy (UHE) neutrinos according to the GZK process; and these UHE neutrinos are also called GZK neutrinos. The GZK process is derived from the findings of Greisen (1966)

and Zatsepin and Kuz'min (1966) where UHE protons would interact with CMB photons according to the process:

$$p + \gamma \rightarrow \Delta^{+} \rightarrow n + \pi^{+} \tag{6.160}$$

where the subsequent π^{+} decay leads to a flux of UHE neutrinos according to

$$\pi^{+} \rightarrow \mu^{+} + \nu_{\mu} \tag{6.161}$$

$$\mu^{+} \rightarrow e^{+} + \nu_{e} + \overline{\nu}_{\mu} \tag{6.162}$$

UHE neutrinos, which interact in matter, produce a shower of particles. The particle shower produces ultimately a radio pulse of short duration ($\sim$1 ns) via a process known as the Askaryan Effect (Askaryan, 1962, 1965). As described by Gerhardt et al. (2010), Varner (2010) and Kravchenko (2012), the Askaryan Effect is the resultant radio emission due to the production of an excess of negative charge following the UHE neutrino interactions in matter. The particle shower that follows the interaction of a UHE neutrino with matter progresses with the Compton scattering of electrons and the annihilation of positrons resulting in a relativistic net negative charge excess of the order of magnitude of 20%–30% of the total number of charged particles in the shower. The charged particles are relativistic, and in a transparent medium such as ice or salt, they will emit Cherenkov radiation. Gerhardt et al. (2010) elucidate, that long wavelengths compared to the lateral spread of the shower add coherently; and the Cherenkov radiation is proportional to the square of the charge excess, *i.e.*, the intensity is a function of the square of the neutrino energy. In ice, the coherence yields radio waves with frequencies up to a few GHz.

Numerous detector designs have been implemented to measure the coherent Cherenkov emission at radio frequencies resulting from UHE neutrino interactions in massive transparent media. A thorough review of the numerous methods of detection of radio Cherenkov emissions is provided by Schröder (2017), and only a few examples will be described briefly here. One of these, is RICE (Radio Ice Cherenkov Experiment), described by Kravchenko (2012). The RICE experiment was installed in the South Pole with radio dipole antennas submerged deep within the ice in a 3D grid. The experiment included sensor arrays co-deployed with the IceCube experiment described previously in Part D of this section. The extension of the project was named NARC for Neutrino Array Radio Calibration. The dipole antennas are tuned to 200–500 MHz bandwidth in ice at a depth of 100–300 m below the ice surface. The RICE hardware has been modified for its implementation for the detection of radio Cherenkov emissions in boreholes of the IceCube experiment described preciously.

An illustrative example of radio Cherenkov measurements is the design of the ANITA (ANtarctic Impulsive Transient Antenna) experiment, which makes use of the entire Antarctic ice sheet as the neutrino target volume, is described by Varner (2010). The ANITA concept is illustrated in Fig. 6.77. A balloon capable of maintaining a 30- to 40-day flight with a large antenna payload at an altitude of $\sim$37 km above the Antarctic ice sheet records events in the 200–1200 MHz frequency range. At the altitude of $\sim$37 km, Allison et al., 2017 notes that the ANITA can monitor an extremely large volume of Antarctic ice equivalent to $\sim 1.6 \times 10^{6}$ km^{3}.

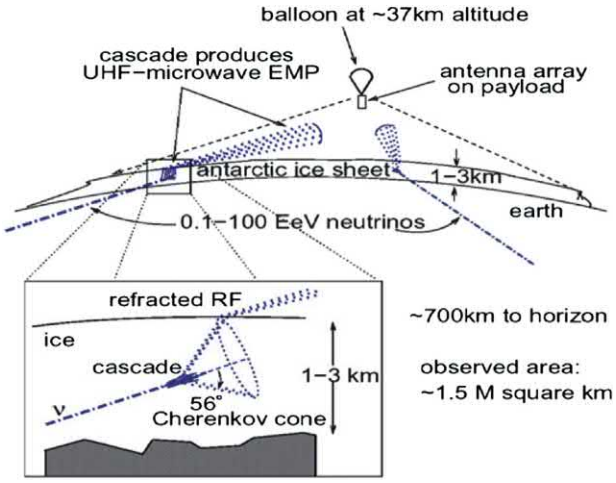


FIGURE 6.77 The ANITA concept: Antarctic ice sheet as detector and observation from a long duration balloon payload. The insert in the lower part of the figure illustrates a UHE neutrino interaction in the ice resulting in the emission of radio waves as a Cherenkov cone within a 3 km depth of the ice sheet and the refracted radiofrequency as it escapes the ice. The upper figure illustrates two conical emissions from the Antarctic ice sheet from 2 UHE (0.1–100 EeV) neutrino interactions and the antenna-equipped balloon above. *From Varner (2010) and Jones (2014), reprinted with permission from Elsevier © 2010–14.*

The ANITA balloon payload is equipped with up to 48 horn antennas, for the measurement of radio emissions at high frequencies of 200–1200 MHz. Schröder (2017) reports that at this frequency range detection is expected only for showers with favorable geometry: The Cherenkov cone of the shower must hit the antenna, which limits the detection to (i) near-horizontal air showers and (ii) neutrino-induced cascades in the overflown ice. ANITA has measured dozens of cosmic-ray air showers of energies of $\sim 10^{19}$ eV (Schoorlemmer et al., 2016; Hoover et al., 2010). For most of these high-energy air showers ANITA measured the radio signal after it was reflected off the ice rather than measure the radio signal directly (Alvarez-Muñiz et al., 2015).

An experimental design similar to ANITA is TAROGE (Taiwan Astroparticle Radiowave Observatory for Geosynchrotron Emissions) described by Chen et al. (2015) and Schröder (2017). The TAROGE experimental design is similar to that of ANITA with the exception that the radio

Cherenkov emissions are detected by an antenna receiver on a mountain top instead of a high-altitude balloon. The TAROGE receiver is designed to detect the Cherenkov radio emissions from UHE cosmic-ray showers either directly in the atmosphere or reflected off the ocean floor as well as those produced by CC interactions of neutrinos in the ocean floor.

Numerous radio Cherenkov detection designs are described in a very comprehensive review by Schröder (2017); and the reader is invited to peruse this work. Among these are the ARA (Askaryan Radio Array) described by Allison et al. (2017), which include antennas on the ice surface near the IceTop array illustrated earlier in this chapter. ARIANNA (Antarctic Ross Ice Shelf Antenna Neutrino Array) on the ross Ice Shelf at the Antarctic coast (Barwick et al., 2017), and TREND (Tianshan Radio Experiment for Neutrino Detection) in the Xianjiang Province, China, which is a radio-quiet zone permitting the design of a self-triggering detection of cosmic-ray showers. There are several other radio Cherenkov detector arrangements reviewed by Schröder (2017).

A unique detector arrangement is the Salt Sensor Array (SalSA) described by Connolly (2012). SalSa entails the deployment of an antenna array into one of many naturally occurring salt formations called diapirs that are found throughout the world. These consist of ~10 km deep salt beds originating from 100 to 200 million year old dried sea salt. As described by Connolly (2012), these salt beds have purities of ~95% and exhibit long attenuation lengths in the radio microwave frequency range. The volumes of these salt formations extend into the 10's-of-km^3, which can provide an excellent target material for UHE neutrinos. Arrays of antenna inserted vertically deep within the salt deposits can capture the radio Cherenkov signal created by particle cascades from UHE neutrino interactions in the salt. However, Schröder (2017) points out that due to the larger attenuation length of radio waves in ice, and because of the large available ice volumes at Antarctica and on Greenland, ice seems to be the medium of choice for future large-scale detectors of several 10 or 100 km^3.

Other methods, such as the Lunar Cherenkov technique described by Bray et al. (2012, 2015), McFadden et al. (2012), Mevius et al. (2012), and Schröder (2017), are aimed at detecting a nanosecond pulse of Cherenkov emissions, which are produced during UHE cosmic ray and neutrino interactions in the Moon's regolith. Earth-based radio telescopes would detect the coherent Cerenkov radiation emitted when the UHE neutrinos interact in the outer layers of the Moon. The maximum intensity of the coherent Cherenkov emission is reached at a frequency of about 3 GHz, where the radiation is concentrated in a narrow cone around the Cherenkov angle. Bray et al. (2012) describe the Parkes radio telescope, which is a single dish of 64 m diameter and 20 cm multi-beam receiver. They describe the technique used for aiming of the telescope whereby a radio pulse from a lunar Cherenkov event is expected to come from the limb of the Moon with radial polarization.

XIV. Applications in radionuclide analysis

The application of Cherenkov counting to the activity analysis of radionuclides is popular in those cases where the Cherenkov counting efficiency of the radionuclide of interest is adequate to meet particular detection limits required. Table 6.21 provides approximate Cherenkov counting efficiencies of radionuclides listed according to the E_{max} of the β particles emitted by each radionuclide. The E_{max} is listed, as the Cherenkov detection efficiency of radionuclides is a function of the beta-particle threshold energy (E_{th}) and the refractive index (n) of the medium calculated according to Eq. (6.39). For example, if water is the medium ($n = 1.333$), the Cherenkov counting efficiency would be a function of the number of β particles of $E > 262$ keV relative to the total number of β particles emitted by the radionuclide. Cherenkov counting is popular, when counting efficiencies are adequate, because of the ease of sample preparation and low expense incurred in the preparation and disposal of samples. Because water is generally the medium of counting, and fluor scintillation cocktail is not used, samples are often left in an unadulterated state suitable for subsequent tests such as chemical analysis, spectrometric analysis, chromatographic tests, or even chemical compound extraction and isolation. Some references to the application of Cherenkov counting to the analysis of specific radionuclides not already cited in this chapter are provided in the following paragraphs.

A. Phosphorus-32

Cherenkov counting of ^{32}P in aqueous extracts has become very popular, particularly because of the easy and inexpensive sample preparation techniques involved as well as the relatively high counting efficiencies obtained (L'Annunziata, 1997; L'Annunziata and Passo, 2002). As chemical quenching does not exist in pure Cherenkov counting, sample preparation techniques may be employed with little concern for the type of reagents used, and sample color may be bleached by chemicals with no quenching effect.

Cherenkov counting of ^{32}P in the dry state applied to research in the biological and physical sciences was reviewed previously in Section VI of this chapter. The popularity of Cherenkov counting of ^{32}P in aqueous media is more popular, due to obvious reasons including improved detection efficiency, as illustrated by numerous reports in the chemical, biological, and agricultural research

TABLE 6.21 Beta-energy transition maxima and Cherenkov counting efficiencies of radionuclides listed in order of increasing mass number.

Nuclide	E_{max} (keV)[a]	Counting efficiency[b] (%)	References
^{14}C	155 (100%)	1.5[c]	Takiue et al. (2004)
		5.0[c]	Minowa et al. (2009)
^{16}N	10,419 (28%)	%E[d]	Verzilov et al. (2006)
	4289 (66.2%)		
	3302 (4.8%)		
	1547 (1.0%)		
^{18}F	635 (97%)	50%[e]	Wiebe et al. (1978), Spinelli et al. (2011)
^{24}Na	1390 (100%)	41.9	Grau Carles and Grau Malonda (2006)
^{32}P	1710 (100%)	57	Takiue et al. (1993)
^{34m}Cl	2488 (29%)	57	Wiebe et al. (1980)
	1311 (26%)		
	500 (1%)		
^{36}Cl	710 (98%)	6.6	Grau Carles and Grau Malonda (1995)
^{38}Cl	4913 (57.6%)	66	Wiebe et al. (1980)
	2770 (11.1%)		
	1111 (31.3%)		
^{40}K	1310 (89%)	55	Pullen (1986)
^{42}K	3560 (81.3%)	75	Buchtela and Tschurlovits (1975)
	1970 (18.4%)		
^{43}K	1810 (1.3%)	13.1	Grau Carles and Grau Malonda (2006)
	1240 (3.5%)		
	825 (87%)		
	465 (8%)		
^{45}Ca	258 (100%)	2.3[c]	Takiue et al. (2004)
^{47}Ca	1980 (16.1%)	15.4	Grau Carles and Grau Malonda (2006)
	684 (83.9%)		
^{59}Fe	475 (51.2%)	5.8[f]	Scarpitta and Fisenne (1996)
	273 (48.5%)		
^{60}Co	1490 (0.1%)	5.6	Grau Carles and Grau Malonda (1995)
	670 (0.2%)		
	315 (99.7%)		
^{76}As	2970 (50%)	70.3	Grau Carles and Grau Malonda (2006)
	2410 (31%)		
	1780 (7%)		
	1180 (3%)		
	540 (3%)		
	320 (3%)		

Continued

TABLE 6.21 Beta-energy transition maxima and Cherenkov counting efficiencies of radionuclides listed in order of increasing mass number.—cont'd

Nuclide	E_{max} (keV)[a]	Counting efficiency[b] (%)	References
^{86}Rb	1770 (91.5%)	53	L'Annunziata and coworkers (see Noor et al. (1996))
	680 (8.5%)		
^{89}Sr	1490 (100%)	42	Rucker (1991); Chang et al. (1996)
^{90}Sr	546 (100%)	1	Rucker (1991); Chang et al. (1996)
^{90}Y	2280 (100%)	72	L'Annunziata and Passo (2002), Van Hemert et al.(2006)
^{91}Y	1540 (100%)	47.4	Grau Carles and Grau Malonda (2006)
^{99}Mo	1210 (84%)	24.2	Grau Carles and Grau Malonda (2006)
	840 (2%)		
	450 (14%)		
^{99}Tc	292 (100%)	1[f]	Scarpitta and Fisenne (1996)
^{106}Rh	3540 (78.6%)	62	Carmon and Dyer (1987)
	3029 (8.1%)		
	2413 (0.6%		
	2407 (10%)		
	1979 (1.8%)		
^{111}Ag	1040 (92%)	18.6	Grau Carles and Grau Malonda (2006)
	790 (1.1%)		
	695 (6.0%)		
	425 (0.9%)		
^{113m}Cd	585 (99.9%)	1	Kossert et al. (2011b)
^{115m}Cd	1620 (97%)	35	Bem et al. (1978);
	680 (3%)		Ramesh and Subramanian (1997)
^{118}Re	2120 (79%)	53	Kushita and Du (1998)
	1970 (20%)		
	<1900 (1%)		
^{122}Sb	1980 (26%)	41.5	Grau Carles and Grau Malonda (2006)
	1410 (67%)		
	723 (4%)		
^{124}Sb	2329 (21%)	20.8	Grau Carles and Grau Malonda (2006)
	1600 (7%)		
	966 (9%)		
	610 (49%)		
	240 (14%)		
^{129}Te	1450 (70%)	38.1	Grau Carles and Grau Malonda (2006)
	989 (15%)		
	690 (4%)		
	290 (11%)		
^{129m}Te	1600 (36%)	14.8	Grau Carles and Grau Malonda (2006)

Continued

TABLE 6.21 Beta-energy transition maxima and Cherenkov counting efficiencies of radionuclides listed in order of increasing mass number.—cont'd

Nuclide	E_{max} (keV)[a]	Counting efficiency[b] (%)	References
^{131m}Te	2417 (2.8%)	2.9	Grau Carles and Grau Malonda (2006)
	771 (1.9%)		
	529 (1%)		
	518 (12%)		
	492 (2%)		
	437 (27%)		
	416 (4%)		
^{131}Te	2085 (59.3%)	52.7	Grau Carles and Grau Malonda (2006)
	1633 (21.6%)		
	1358 (1.2%)		
	1137 (2.6%)		
	1088 (10%)		
	808 (1.3%)		
^{134}Cs	658 (70%)	2.4	Rao et al. (2000a,b)
	415 (3%)		
	89 (27%)		
^{137}Cs	1170 (8%)	5.5	Torres et al. (2002)
	510 (92%)		
^{133}I	1400 (94%)	26.0	Grau Carles and Grau Malonda (2006)
	500 (6%)		
^{139}Cs	4213 (85%)	80.2	Grau Carles and Grau Malonda (2006)
	2930 (6.2%)		
	2102 (0.8%)		
	1863 (1.2%)		
^{139}Ba	2317 (70.0%)	80.2	Grau Carles and Grau Malonda (2006)
	2151 (29.7%)		
	896 (0.3%)		
^{140}Ba	1020 (24%)	12.2	Grau Carles and Grau Malonda (2006)
	1006 (38%)		
	887 (4.4%)		
	582 (9.3%)		
	469 (23.8%)		
^{140}La	2160 (8%)	37.9	Grau Carles and Grau Malonda (2006)
	1680 (18%)		
	1370 (46%)		
	1150 (19%)		
	857 (4%)		
	510 (5%)		

Continued

TABLE 6.21 Beta-energy transition maxima and Cherenkov counting efficiencies of radionuclides listed in order of increasing mass number.—cont'd

Nuclide	E_{max} (keV)[a]	Counting efficiency[b] (%)	References
^{143}Ce	1400 (17%)	24.9	Grau Carles and Grau Malonda (2006)
	1130 (40%		
	740 (5%)		
	500 (12%)		
	220 (6%)		
^{143}Pr	932 (100%)	13.9	Grau Carles and Grau Malonda (2006)
^{144}Pr	3000 (97.8%)	77.7	Grau Carles and Grau Malonda (2006)
	2300 (1.2%)		
	807 (1%)		
^{147}Nd	810 (83%)	6.7	Grau Carles and Grau Malonda (2006)
	490 (0.3%)		
	410 (0.7%)		
	369 (15%)		
	215 (1%)		
^{156}Eu	2460 (32%)	18.7	Grau Carles and Grau Malonda (2006)
	1215 (11%)		
	495 (34%)		
	300 (23%)		
^{170}Tm	968 (76%)	15.2	Grau Carles and Grau Malonda (2006)
	884 (24%)		
^{186}Re	1069 (71%)	16.9	Grau Carles and Grau Malonda (2006)
	932 (22%)		
^{188}Re	2120 (79%)	58	Kushita and Du (1998)
	1970 (20%)		
	1900 (1%)		
^{194}Ir	2234 (85.4%)	59.9	Grau Carles and Grau Malonda (2006)
	1905 (9.3%)		
	1612 (1.3%)		
	1311 (0.3%)		
	967 (2%)		
	755 (0.6%)		
^{198}Au	1372 (0.02%)	14.0	Grau Carles and Grau Malonda (2006)
	961 (99%)		
	285 (0.98%)		
^{204}Tl	763 (97.4%)	6.4	Grau Carles and Grau Malonda (2006)
^{206}Tl	1530 (100%)	39.7	Grau Carles and Grau Malonda (2006)

Continued

TABLE 6.21 Beta-energy transition maxima and Cherenkov counting efficiencies of radionuclides listed in order of increasing mass number.—cont'd

Nuclide	E_{max} (keV)[a]	Counting efficiency[b] (%)	References
^{210}Bi	1162 (100%)	14.0	Arinc et al. (2011),Salonen (2010), Hurtado et al. (2003), Dale et al. (2002)
^{210}Pb/^{210}Bi	(see ^{210}Bi, this table)		
^{228}Ac	2180 (10.1%)	10.0	L'Annunziata and coworkers (see Aleissa et al. (2008))
	1850 (9.6%)		
	1700 (6.7%)		
	1110 (53%)		
	640 (7.6%)		
	450 (13%)		
^{228}Th	580 (from ^{212}Pb)[g]	53	Al-Masri and Blackburn (1994)
	1790 (from ^{208}Tl)[g]		
	2250 (from ^{212}Bi)[g]		
^{234m}Pa	2269 (97.6%)	60.5	Grau Carles and Grau Malonda (1996a,b, 2000)
	1459 (1%)		Grau Malonda and Grau Carles (2000)
	1224 (1%)		Alamelu and Agarwal (2009)
^{234}Th	From ^{234m}Pa[g]	60	Navarro et al. (1997); Nour et al. (2002)
	(see ^{234m}Pa, this table)		Blasiyh Nuño and Korob (2007)
^{238}U	(from ^{234m}Pa)[g]	62	Blackburn and Al-Masri (1994)
^{226}Ra/^{222}Rn	1505 (from ^{214}Bi, 16%)[g]	77	Blackburn and Al-Masri (1993)
	1540 (from ^{214}Bi, 16%)[g]		Al-Masri and Blackburn (1995a,b, 1999)
	3270 (from ^{214}Bi, 24%)[g]		
	1030 (from ^{214}Pb, 6%)[g]		
	650 (from ^{214}Pb, 41%)[g]		
	590 (from ^{214}Pb, 52%)[g]		
^{214}Bi/^{214}Pb	(see ^{226}Ra, this table)		

[a] *Where more than one β-decay transition occurs for a given radionuclide, the % intensity of each transition is provided in parenthesis.*
[b] *Counting efficiencies will vary from instrument to instrument and vial type (e.g., glass or plastic). Also, measurements made with older less efficient photomultiplier tubes provided lower counting efficiencies than can be expected from contemporary more efficiency phototubes. No attempt is made in this table to categorize the counting efficiencies according to the aforementioned governing factors that will affect slightly the counting efficiency values reported. The counting efficiencies listed are intended to provide a general idea of their orders of magnitude relative to the energies and intensities of the β-particle emissions. The counting efficiencies are values reported of nuclides in water without wavelength shifter unless otherwise noted.*
[c] *Measured with a high refractive index transparent ceramic.*
[d] *Nitrogen-16 is a high-energy beta-emitter (E_{max} = 10.4 MeV) and short-lived (half-life = 7.13 s). A Cherenkov detection efficiency is not available; however, the nuclide is detected by on-line Cherenkov counting to monitor D–T fusion following activation of ^{16}O by 14 MeV fusion neutrons via the ^{16}O(n,p)^{16}N reaction (Verzilov et al., 2006).*
[e] *A combination of Cherenkov and scintillation counting in high refractive index methyl salicylate (n = 1.5369).*
[f] *Measured in 10 mL aqueous 25 mM 7-amino-1,3-naphthalene disulfonic acid (ANSA) wavelength shifter.*
[g] *Daughter nuclide.*

sciences including those of Asokan et al. (2004), Baxter et al. (2002), Beauchesne et al. (2010), Bem et al. (1980), BenZikri (2000), Chow (1980), Court et al. (2004), Das (2007), Fardeau (1984), Frič and Palovčíková (1975), Kim et al. (2001), Anil Kumar et al. (2009), L'Annunziata (1997), L'Annunziata and Passo (2002), Lefebvre and Glass (1981), Lewis et al. (2007), Lickly et al. (1988), Louvandini et al. (2008), MacDonald and Storey (2005), Martin et al. (2011), Morel and Fardeau (1989), Murányi et al. (2005), Nunthawarasilp et al. (2007), Østby and Krøkje (2002), Peluso et al. (2005), Rowinska et al. (1975, 1987), Rubio et al. (2004), Schneider and Seifert (2010), Sheeba and Asha (2009), Singh et al. (2005), Smith et al. (1972), Srivastava and D'Souza (2007), Sunil et al. (2007), Szemraj et al. (2005), Tuffen et al. (2002), Tuininga et al. (2002), Uz et al. (2002), Warshawsky et al. (2002), Wells et al. (2001), Wiebe et al. (1971), Wu et al. (2005), and Xu et al. (2007), among many others. Glass (1978) described a very simple and rapid sample preparation technique where ^{32}P- or ^{86}Rb-labelled plant material is ashed directly in glass liquid scintillation vials. An aqueous solution of 2.5 mM ANDA wavelength shifter can be added before counting to increase counting efficiencies. The addition of wavelength shifter is not necessary. Wahid et al. (1985) described a nitric-perchloric acid wet digestion procedure for the preparation of ^{32}P in plant material for Cherenkov counting. However, the writer prefers to ash the plant material at 500°C for 1 hour in a muffle furnace, because perchloric acid digestions are hazardous and tedious. The plant ash is dissolved with 2 mL of concentrated HNO_3 and transferred directly into a scintillation counting vial for Cherenkov counting. Subsequent to ashing and Cherenkov counting the analysis of total phosphorus by colorimetry via a phosphomolybdate blue complex is possible (L'Annunziata, unpublished work). Chemical analysis can be conveniently performed on samples before or after Cherenkov counting as no organic scintillation cocktails are added, which would interfere with chemical analyses. An example may be taken from the work of Palmer (1969) and Schneider (1971). These investigators determined the amounts of total phosphorus in biological samples by means of colorimetry using the phosphomolybdate blue complex method. The intensity of the blue color is proportional to the concentration of phosphorus in the sample according to Beer's law. After total phosphorus analysis, the activity of ^{32}P in the sample is determined by bleaching or decolorizing the blue complex at a high pH followed by Cherenkov counting of the colorless solution. However, the writer of this chapter prefers to carry out the Cherenkov counting of the samples before the colorimetric analysis of total phosphorus, because (1) the relative short half-life of ^{32}P ($t_{1/2}$ = 14.3 days) often warrants counting the samples without too much delay when sample activities are at their highest, and (2) bleaching of the samples to remove the blue color of the phosphomolybdate complex is not required when Cherenkov counting precedes colorimetry.

B. Strontium-89 and Strontium-90 (Yttrium-90)

The radionuclide ^{90}Sr ($t_{½}$ = 28.8 y) reaches secular equilibrium with its daughter ^{90}Y ($t_{½}$ = 64.06 hours). The ^{90}Sr is traditionally assayed in biological and radio-toxicological samples by separation and removal of strontium from other radionuclides in the sample; and this is followed by the radioassay of the parent–daughter nuclide ^{90}Sr/^{90}Y after a period of time to allow for the ingrowth of the ^{90}Y with its parent ^{90}Sr (L'Annunziata, 1971, see also a treatment of secular equilibrium between ^{90}Sr/^{90}Y in Chapters 1 and 6 of Volume 1). Alternatively, the daughter nuclide ^{90}Y may be extracted from the sample when it is at or near secular equilibrium with its parent ^{90}Sr. The ^{90}Y may then be measured; and the activity at the time of separation from its parent calculated. The analysis of ^{90}Sr(^{90}Y) may include also the analysis of the shorter-lived radionuclide ^{89}Sr ($t_{½}$ = 50.5 d) as discussed in Chapters 6 of Volume 1, because the two radioisotopes of strontium can be encountered in the same sample as fission products (L'Annunziata and Fuller, 1968).

The first reports on the application of Cherenkov counting to the analysis of ^{89}Sr and ^{90}Sr(^{90}Y) were by Buchtela and Tschurlovits (1975) from the Atominstitut in Vienna, Austria and Randolph (1975) from the US Atomic Energy Commission, Health Services Laboratory in Idaho Falls. Both papers were printed in the same journal volume. Since these pioneering papers, Cherenkov counting has become a popular method for the analysis of ^{89}Sr and ^{90}Sr(^{90}Y). Contemporary procedures may be divided into two groups, those that include the analysis of samples containing mixtures of combined ^{89}Sr–^{90}Sr(^{90}Y) and the more simplified case of samples containing only the parent/daughter radionuclides ^{90}Sr(^{90}Y). These two cases are described in this section with examples of contemporary methods.

1. Cherenkov counting of ^{89}Sr with ^{90}Sr(^{90}Y)

The Cherenkov counting of samples containing ^{89}Sr with ^{90}Sr(^{90}Y) is appealing, because both ^{89}Sr and ^{90}Y produce significant Cherenkov radiation. See Table 6.21 where ^{89}Sr and ^{90}Y are listed with Cherenkov counting efficiencies in water of ~40% and ~70%, respectively. Walter et al. (1993) demonstrated the simultaneous analysis of ^{89}Sr, ^{90}Sr(^{90}Y) by Cherenkov counting. The low Cherenkov counting efficiency of ~1% for ^{90}Sr in water facilitates the determination of ^{89}Sr in a freshly isolated ^{89}Sr–^{90}Sr mixture, that is, a ^{89}Sr–^{90}Sr mixture from which the ^{90}Y daughter is removed fresh by ion exchange, chemical precipitation, or other methods. After the chemical separation

of strontium from yttrium, Cherenkov counting of the sample is carried out at two different times and dates (t_1 and t_2). The first counting, t_1, is carried out directly after the chemical separation of strontium from yttrium, because the count rate will be derived mainly from the ^{89}Sr in the sample due to the very low ^{90}Sr Cherenkov detection efficiency (~1%). The Cherenkov photon count rate is determined again at time t_2, which is performed 3–5 days or more after the chemical separation of strontium. The period of time from t_1 and t_2 provides sufficient time for the significant ingrowth of ^{90}Y.

Banavali et al. (1992) used carbonate precipitation and extraction chromatography to isolate the radioactive strontium, which is analyzed by Cherenkov counting yielding primarily ^{89}Sr activity. After a few days to permit ingrowth of ^{90}Y, the sample is recounted by Cherenkov counting to permit the activity determination of ^{90}Y. The ^{90}Sr in the sample is calculated by the amount of ^{90}Y ingrowth from the time of radiostrontium isolation. See Chapter 1 for calculations of ingrowth of daughter nuclide with parent after the separation of radionuclides in secular equilibrium. The contribution of ^{90}Sr activity to the Cherenkov count rate of freshly prepared mixtures of ^{89}Sr–^{90}Sr cannot be ignored when the ^{90}Sr activity is higher than that of ^{89}Sr.

Chang et al. (1996) report a method utilizing Cherenkov counting and activity calculations for the analysis of mixtures of ^{89}Sr and ^{90}Sr(^{90}Y); and this method was utilized by Popov et al. (2006) to include accurate measurements of the chemical yields of strontium. The date and time of the chemical separation of strontium and yttrium are recorded as t_0. Following the chemical separation of strontium from yttrium (See Fig. 6.79), the activity of ^{89}Sr + ^{90}Sr is measured by Cherenkov counting at time t_1, for which the date and specific time is recorded. After a period of 3–5 days, the sample is counted again at time t_2, for which the date and time is also recorded. Strontium-85, which is added as a tracer to the sample before the chemical cleanup or separation of the strontium from yttrium, is analyzed by gamma-spectrometry, to determine the chemical yield of strontium.

A freshly prepared sample following chemical cleanup or isolation of stable and radioactive strontium from other elements (*i.e.*, yttrium was removed and discarded) is counted in a 15 mL aqueous solution contained in a plastic counting vial. The sample is counted in a region of 0–40 keV or other suitable counting window, which is sufficient to encompass all pulse heights produced by Cherenkov radiation. The 0–40 keV counting window is only an example where pulse height spectra are plotted on a scale calibrated to keV energy. The channel numbers illustrated in Fig. 6.78 are equivalent to approximately 0–50 keV, when the channel numbers are calibrated against beta-particle energies in keV as illustrated.

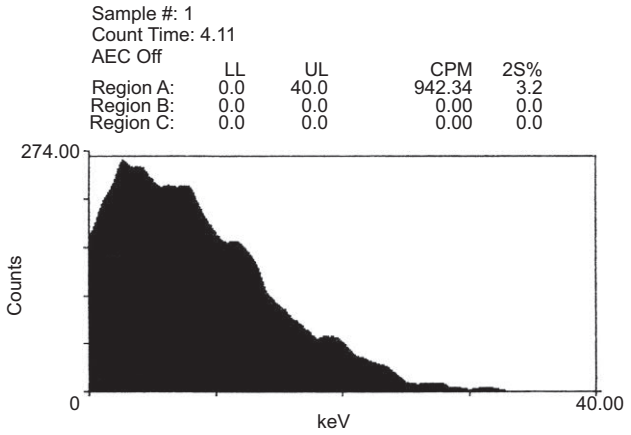


FIGURE 6.78 Cherenkov pulse height spectrum of ^{90}Sr(^{90}Y) in 10 mL H_2O in a plastic counting vial using a Packard 2750TR/LL liquid scintillation analyzer and a counting region of 0–40 keV. The sample contains 1300 DPM each of ^{90}Sr and ^{90}Y in secular equilibrium. Approximately 1% of the Cherenkov photons originate from ^{90}Sr; 71% arise from ^{90}Y. *From L'Annunziata (1997), unpublished work of the writer.*

The purified strontium samples are counted for sufficient time to provide a two sigma counting error of <2%, and the count rate, time, and date and time of ^{90}Y separation are recorded. The sample is allowed to sit for 3–5 days to permit significant ingrowth of ^{90}Y with ^{90}Sr, and the sample is then recounted in the same vial. The count rate and time of the second counting are recorded. The two count rates are used in Eqs. (6.163) to (6.167) to determine the activities of ^{89}Sr and ^{90}Sr. The equations used are found according to the derivations of Chang et al. (1996) and modified by Popov et al. (2006) as follows:

When a sample containing ^{89}Sr and ^{90}Sr is purified by separation from the ^{90}Y daughter, at time t_0, the total activity of the purified strontium is the sum of the two activities or

$$A_{t_0} = A_{^{90}Sr} + A_{^{89}Sr} \tag{6.163}$$

When the sample is counted for the first time t_1, there will have occurred during the interim of t_1-t_0 some ingrowth of ^{90}Y, and the ^{89}Sr decays slightly ($t_{1/2}$ = 50.5 days) while the ^{90}Sr will not undergo any significant decay ($t_{1/2}$ = 28.8 years). Therefore, at time t_1, when the first count rate is determined, the total activity in the sample is expressed as

$$\begin{aligned} A_{t_1} &= A_{^{90}Sr}\left[e^{-\lambda_1(t_1-t_0)}\right] + A_{^{90}Y} + A_{^{89}Sr}\left[e^{-\lambda_3(t_1-t_0)}\right] \\ &= A_{^{90}Sr}\left[e^{-\lambda_1}(t_1-t_0)\right] + A_{^{90}Sr}\left[1-e^{-\lambda_2(t_1-t_0)}\right] \\ &\quad + A_{^{89}Sr}\left[e^{-\lambda_3(t_1-t_0)}\right] \end{aligned} \tag{6.164}$$

where $A_{^{90}Sr}$, $A_{^{90}Y}$, $A_{^{89}Sr}$, λ_1, λ_2,and λ_3 are the activities in DPM and the decay constants for ^{90}Sr, ^{90}Y, and ^{89}Sr, respectively. At the time of the second counting, t_2, there

will be additional ingrowth of ^{90}Y and decay of ^{89}Sr in accord with the time difference from the time of counting and time of separation of strontium from yttrium, t_2-t_0, which is expressed as:

$$A_{t_2} = A_{^{90}Sr}\left[e^{-\lambda_1(t_2-t_0)}\right] + A_{^{90}Sr}\left[1-e^{-\lambda_2(t_2-t_0)}\right] + A_{^{89}Sr}\left[e^{-\lambda_3(t_2-t_0)}\right] \quad (6.165)$$

At time t_1, the Cherenkov count rate (CPM) C_{t_1} of the sample is expressed as

$$C_{t_1} = E_{^{90}\mathrm{Sr}}A_{^{90}\mathrm{Sr}}\left[e^{-\lambda_1(t_1-t_0)}\right] + E_{^{90}\mathrm{Y}}A_{^{90}\mathrm{Sr}}\left[1-e^{-\lambda_2(t_1-t_0)}\right] + E_{^{89}\mathrm{Sr}}A_{^{89}\mathrm{Sr}}\left[e^{-\lambda_3(t_1-t_0)}\right] + C_b \quad (6.166)$$

where $E_{^{90}Sr}$, $E_{^{90}Y}$, and $E_{^{89}Sr}$ are the counting efficiencies (CPM/DPM) of each nuclide and C_b is the background count rate.

At time t_2, the Cherenkov count rate C_{t_2} is expressed as

$$C_{t_2} = E_{^{90}\mathrm{Sr}}A_{^{90}\mathrm{Sr}}\left[e^{-\lambda_1(t_2-t_0)}\right] + E_{^{90}\mathrm{Y}}A_{^{90}\mathrm{Sr}}\left[1-e^{-\lambda_2(t_2-t_0)}\right] + E_{^{89}\mathrm{Sr}}A_{^{89}\mathrm{Sr}}\left[e^{-\lambda_3(t_2-t_0)}\right] + C_b \quad (6.167)$$

When the chemical yield of strontium, η_{Sr}, and sample volume or weight, V, are included, as reported by Popov et al. (2006), Eqs. (6.166) and (6.167) are solved to give the activities of ^{89}Sr and ^{90}Sr by the following equations

$$A_{^{89}Sr} = \frac{\dfrac{C_{t_1}-C_b}{\eta_{\mathrm{Sr}}\cdot V} - A_{^{90}\mathrm{Sr}}\cdot E_{^{90}\mathrm{Sr}}\cdot e^{-\lambda_1\cdot\Delta t_1} - A_{^{90}\mathrm{Sr}}\cdot E_{^{90}\mathrm{Y}} + A_{^{90}\mathrm{Sr}}\cdot E_{^{90}\mathrm{Y}}\cdot e^{-\lambda_2\cdot\Delta t_1}}{E_{^{89}\mathrm{Sr}}\cdot e^{-\lambda_3\cdot\Delta t_1}} \quad (6.168)$$

$$A_{^{90}Sr} = \frac{e^{-\lambda_3\cdot\Delta t_1}\cdot(C_{t_2}-C_b) - e^{-\lambda_3\cdot\Delta t_2}\cdot(C_{t_1}-C_b)}{\eta_{\mathrm{Sr}}\cdot V\{E_{^{90}\mathrm{Sr}}[e^{-\lambda_1\cdot\Delta t_2}\cdot e^{-\lambda_3\cdot\Delta t_1} - e^{-\lambda_1\cdot\Delta t_1}\cdot e^{-\lambda_3\cdot\Delta t_2}] + E_{^{90}\mathrm{Y}}[e^{-\lambda_3\cdot\Delta t_1}\cdot(1-e^{-\lambda_2\cdot\Delta t_2}) - e^{-\lambda_3\cdot\Delta t_2}\cdot(1-e^{-\lambda_2\cdot\Delta t_1})]\}} \quad (6.169)$$

where $\Delta t_1 = t_1 - t_0$ and $\Delta t_2 = t_2 - t_0$, and the chemical yield η_{Sr} is measured in % and expressed in the above equations as a decimal (e.g., 70% yield = 0.70) and the sample volume or weight V may be expressed in units of dm^3 or kg.

When ^{89}Sr is absent from the sample Chang et al. (1996) and Popov et al. (2006) show that Eq. (6.169) for the activity (DPM) of ^{90}Sr is simplified to

$$A_{^{90}Sr} = \frac{C_{t_2}-C_{t_1}}{\eta_{\mathrm{Sr}}\cdot V\cdot E_{^{90}\mathrm{Y}}[e^{-\lambda_2\cdot\Delta t_1} - e^{-\lambda_2\cdot\Delta t_2}]} \quad (6.170)$$

This method involves only the Cherenkov counting of the sample at two time intervals following the separation of radiostrontium from the radioyttrium daughter. For several standard mixtures of ^{89}Sr–^{90}Sr(^{90}Y) tested by Chang et al. (1996) a mean error of only 2.5% was reported for calculated ^{89}Sr and ^{90}Sr mixtures. Popov et al. (2006) provide also the calculations for the minimal detectable activities.

Chu et al. (1998) demonstrated the analysis of ^{89}Sr–^{90}Sr(^{90}Y) by separating the strontium from yttrium on a column of crown-ether Eichrom Sr resin (Horwitz et al., 1991, 1992; Vajda et al., 1992). The ^{90}Y and ^{89}Sr + ^{90}Sr fractions are separated and eluted from an 8-mm dia. × 40-mm long column of Eichrom Sr resin, and the two fractions are analyzed by Cherenkov counting. The ^{90}Sr activity is derived from the calculated activity of ^{90}Y, as the ^{90}S and ^{90}Y were in secular equilibrium, that is, their activities were equal prior to chemical separation. A similar analytical approach was taken by Grahek et al. (1999). A column of Eichrom Sr Spec resin was also used by Grahek and Rožmarić Mačefat (2004, 2005) to isolate strontium in liquid radioactive waste and seawater followed by successive Cherenkov counting for the determination of ^{89,90}Sr. Lazare et al. (2009) separated ^{90}Sr from other elements including yttrium by high pressure ion chromatography followed by liquid scintillation analysis; and they point to the potential of applying Cherenkov counting when ^{89}Sr is found to occur in significant levels of activity. Günther et al. (2009) isolated strontium by elution from a Chelite P chelating resin followed by Cherenkov counting immediately after isolation of strontium and after 3 days to allow for ^{90}Y ingrowth. St-Amant et al. (2011) extracted strontium using high-performance ion chromatography (HPIC) followed by Cherenkov counting immediately after the strontium purification for the quantification of ^{89}Sr followed by a second Cherenkov counting of the same sample after 10–14 days to quantify the ^{90}Sr activity based on ^{90}Y ingrowth.

Regardless of the detection method, the determination of ^{89,90}Sr requires the chemical isolation of pure strontium prior to detection and quantification. The selection of detection method, such as measurement with proportional counters, LSC with a cocktail, Cherenkov counting or a combination of LSC and Cherenkov counting, determines to what extent the isolated strontium should be purified, as

well as the conditioned methods of chemical isolation. In addition to the chemical isolation procedure, the method of detection also depends on the type of sample and the level of ^{89}Sr and ^{90}Sr activity. Consequently, there is no single methodology for isolation, but the simplest and most efficient is chosen. However, this does not mean that it is not demanding or complex. The detection and quantification of ^{89,90}Sr with proportional counters and LSC generally requires the removal of all interfering elements, both radioactive and stable. The presence of radioactive but also other stable isotopes prevents accurate quantification due to the appearance of self-adsorption with a proportional counter and due to chemical and color quenching with LSC. The advantage of Cherenkov counting is that it is not sensitive to the presence of stable isotopes and other elements (except in the case of intense coloration), which in certain circumstances permits larger quantities of strontium. It also allows for a so-called rapid determination. This takes several days, while the classic mode of determination requires almost 3 weeks. Therefore, Cherenkov counting in combination with strontium isolation procedures recently have largely relied on extraction with chromatographic separation using highly selective resins (Sr resin, Analig01Sr and Superlig620. The Analig01Sr and/or Superlig 620 is prepared by covalently bonding of ligand, most likely a variation of an 18-crown-6 (18C6) structure on silica gel (Zhang et al., 1997); and it presents the possibility of creating a methodology for the determination in very different samples. A typical example of the complexity of determination in the presence of active and stable isotopes is the determination of ^{89,90}Sr in seawater. Seawater contains 8 mg/L strontium. Consequently, sometimes it takes a couple of dozen liters of water for analysis (determination of very low activity), meaning that the fraction of strontium can contain up to several hundred milligrams of Sr. In this case, ^{89}Sr detection is hampered and the chemical isolation results in a reduction in the chemical yield of strontium. However, in Cherenkov counting the amount of stable strontium or residue of calcium does not affect the accuracy of the quantification (Grahek and Rožmarić Mačefat, 2005; Reddy et al., 2017). In developing the method of determination in seawater, Tayeb et al. (2016) encountered the problem of a reduction in the chemical yield in much smaller sample amounts. For this reason, separation was performed by using double-stacked Sr-resin cartridges illustrated in Fig. 6.79, which provided a minimal loss of Sr and improved the chemical yield by at least 25%. Strontium and yttrium were eluted from the Sr and DGA resin column with 8 mL of deionized water and 9 mL of 0.05 M HCl. This was followed by the immediate Cherenkov counting of the strontium fraction for ^{89}Sr activity determination, while ^{90}Sr was determined through ^{90}Y detection. This method has already been described in Section IX.A. and illustrated in Fig. 6.79.

The synergy between the various separation techniques and Cherenkov counting in the determination of ^{89,90}Sr in the presence of a series of radioactive isotopes can be seen in the development of an ^{89,90}Sr determination method as impurities in the production of ^{99}Tc radiopharmaceuticals, as demonstrated by Hou (2017). Technetium-99m is the principal radioisotope used in medical diagnostics and is mainly provided through a ^{99}Mo/^{99m}Tc generator. ^{99}Mo used for nuclear medical purposes is produced by the irradiation of enriched ^{235}U in a nuclear reactor and contains fission and activation products. Fig. 6.80 shows the methodology for determining low-activity ^{89,90}Sr in ^{99}Tc. After separating the radionuclide array in the anionic column, ^{89,90}Sr was isolated in the Sr columns. Cherenkov counting was applied twice to measure ^{89}Sr and ^{90}Sr. The first measurement was performed immediately after the Sr−resin column separation. The measured counts were mainly derived from the beta particle of ^{89}Sr. The ^{90}Sr in the separated strontium fraction was measured 7−10 days after the separation through Cherenkov counting of the ^{90}Y grown from the ^{90}Sr. It was shown that the contribution of

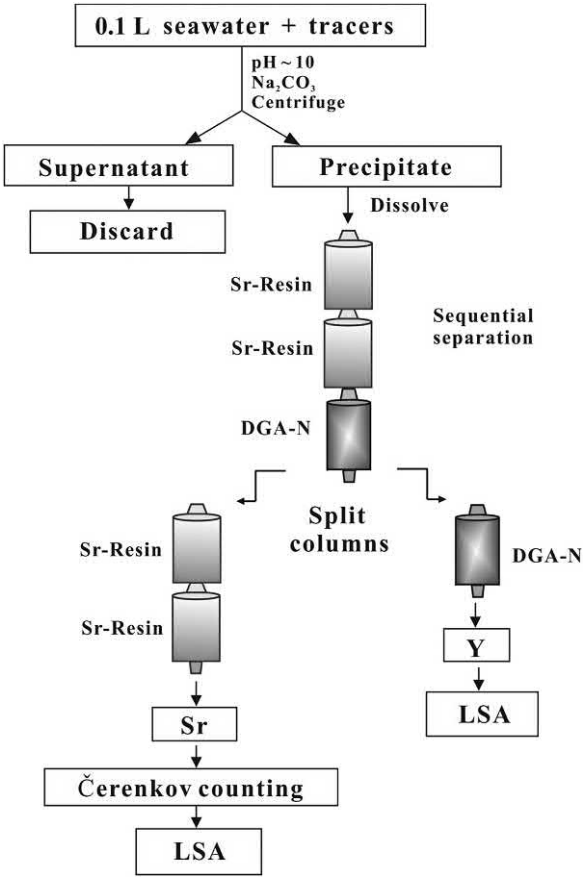


FIGURE 6.79 Flow chart of coprecipitation of 0.1 L seawater. The ^{90}Y (identified as Y in the figure may be analyzed most readily by Čerenkov counting in lieu of liquid scintillation analysis (LSA)). *From Tayeb et al. (2016), reprinted with permission from Elsevier © 2016.*

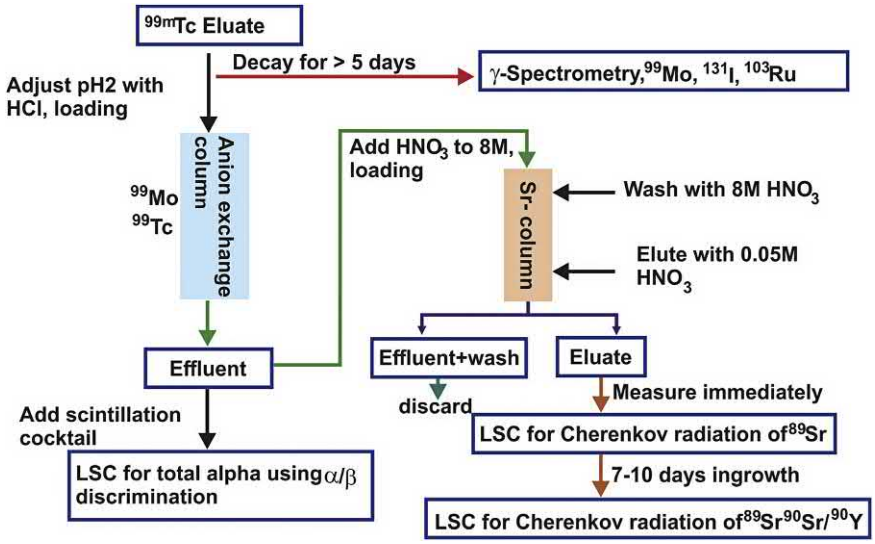


FIGURE 6.80 Schematic diagram of the sequential separation procedure for the determination of impurity radionuclides in ^{99m}Tc eluate. *Original Figure courteously of Dr X. Hou, Technical University of Denmark, from Hou (2017), reprinted with permission from Springer Nature© 2017.*

^{90}Sr (through ^{90}Y) had to be corrected if the ^{89}Sr measurement was performed more than 2 hours after separation.

Milanović and Grahek (2015) developed a method for determining ^{89,90}Sr in drinking water which includes the quantitative capture of ^{89,90}Sr in the SuperLig 620 column from a large volume of water samples and their on-column detection via Cherenkov counting. The SuperLig 620 column acts as a specific strontium separator and a sensor for Cherenkov counting. The method enables the determination of ^{89}Sr and ^{90}Sr above 30 mBq L^{-1} with good accuracy within 64 hours.

The described methods are applicable to the determination of ^{89}Sr and ^{90}Sr in a limited ratio of activity, which is usually not greater than 10, as demonstrated by Tovedal et al. (2008, 2009) and Grahek et al. (2012). When the ratio of activity is higher, the quantification of lower activity isotopes is not reliable or even impossible. However, the additional separation of yttrium and the determination of ^{90}Sr by means of ^{90}Y decay solves this problem. Tovedal et al. (2009), Holmgren et al. (2014), and Holmgren-Rondahl and Ramebäck (2018) demonstrated that the combination of Sr and Y separation in Sr resin and Cherenkov counting can reliably determine both isotopes in a ratio greater than 100:1. In the first step, strontium is separated and measured immediately after separation to determine ^{89}Sr. After a few days, the yttrium is separated from the fraction and ^{90}Sr is determined by ^{90}Y Cherenkov counting (see Fig. 6.36 in paragraph IX.A). The authors proposed this method for the analysis of fresh fallout after a nuclear explosion when the ratio between ^{89}Sr and ^{90}Sr can be 170:1.

Other strontium and yttrium isotopes, ^{91}Sr, ^{92}Sr, ^{91}Y, ^{92}Y, and ^{93}Y, produce Cherenkov radiation due to their sufficiently high beta energy, and as a consequence they interfere when determining ^{89}Sr and ^{90}Sr. Therefore, Tovedal et al. (2009) and Holmgren et al. (2014, 2016) developed a ^{89,90}Sr determination methodology that relies on double separation and a time lag to decay the isotopes ^{91}Sr ($t_{1/2}$ = 9.63 hours) and ^{92}Sr ($t_{1/2}$= 2.71 hours). However, the isotope ^{91}Sr decays to ^{91}Y with a half-life of 58.5d ($E_{\beta max}$ = 1.54 MeV) and may disturb ^{90}Sr determination through ^{90}Y decay. Zhu et al. (1990) determined ^{90}Sr and ^{91}Y in grass samples after the Chernobyl accident by extracting the yttrium from the sample and using Cherenkov counting in the selection of the ^{90}Y counting window to determine ^{90}Sr and then LSC with graphic separation to determine ^{91}Y. Grahek et al. (2012) investigated the possibility of the simultaneous determination of ^{89}Sr and ^{90}Sr in the presence of a third isotope that produces Cherenkov radiation. Changes in overall activity over time were observed and the activity of each isotope was calculated as a three-equation system with three unknowns of activity of individual isotopes in three counting time intervals. It has generally been shown that such a method of determination does not produce adequate results, but it is also shown that under certain conditions ^{91}Y can be determined. From the decay of ^{90}Y activity during its first half-life, the activity of ^{90}Y is calculated, while the activity of ^{91}Y is calculated from the difference in total activity and the activity of ^{90}Y. In experiments, ^{89}Sr was used instead of ^{91}Y due to its similar half-life and close beta energies.

2. Sequential Cherenkov counting and liquid scintillation analysis

Other methods used for the analysis of ^{89}Sr–^{90}Sr(^{90}Y) mixtures involve the sequential counting of the Cherenkov

radiation followed by liquid scintillation counting, which was first introduced by the pioneering work of Buchtela and Tschurlovits (1975) and Randolph (1975).

a. Sequential analysis without wavelength shifter

Rucker (1991) describes a sequential Cherenkov radiation and liquid scintillation analysis procedure for the analysis of ^{89}Sr–^{90}Sr(^{90}Y). The method involves purification of the sample, which includes removal of yttrium from the sample by hydroxide scavenging followed by strontium precipitation as a carbonate. The strontium carbonate is washed, dried, and weighed to calculate the percent chemical recovery of standardized strontium carrier. The precipitate is dissolved in 5 mL of 0.3 M HCl, and the aqueous solution is analyzed by Cherenkov counting without the use of any wavelength shifter to improve Cherenkov counting efficiencies, which provides a count rate primarily from the ^{89}Sr in the sample. After Cherenkov counting, scintillation fluor cocktail is added to the sample to provide a liquid scintillation count rate in one wide counting region not confined to spectral resolutions for the measurement of ^{89}Sr and ^{90}Sr. The two count rate determinations, the first Cherenkov counting and the second liquid scintillation counting, used optimized discriminator settings for the counting regions. Count ratios in each region for Cherenkov and LSC are used to correct for the fraction of the Cherenkov counts due to ^{90}Sr and the fraction of both counts (Cherenkov and LSC) due to the early ingrowth of ^{90}Y.

The following equations, derived by Rucker (1991), are provided to illustrate the basis of the method leading to the working equations:

The Cherenkov count rates, which are the first ones determined for a sample, originate primarily from ^{89}Sr (*e.g.*, Cherenkov counting efficiency 40%), with only a very small contribution from ^{90}Sr (1% counting efficiency) and the early ingrowth of ^{90}Y described by the equation

$$C_1 = {}^{89}\text{Sr cpm}_c + {}^{90}\text{Sr cpm}_c + {}^{90}\text{Y cpm}_c \qquad (6.171)$$

where C_1 is the net (background subtracted) Cherenkov count rate and cpm_c represents the Cherenkov counts per minute obtained from each nuclide. The liquid scintillation count rate comes primarily from the ^{89}Sr and ^{90}Sr of the sample with only a small contribution from the early ingrowth of ^{90}Y. The net count rate from liquid scintillation analysis, C_2, is therefore described by the following equation:

$$C_2 = {}^{89}\text{Sr cpm}_l + {}^{90}\text{Sr cpm}_l + {}^{90}\text{Y cpm}_l \qquad (6.172)$$

where cpm_l is the liquid scintillation count rate from each nuclide. Rucker (1991) then defines the count rates due to the early ingrowth of ^{90}Y, in Cherenkov counting and LSC, in terms of the ^{90}Sr count rates when the elapsed times are known from the time of chemical separation of ^{90}Y to the time of Cherenkov counting and the time of liquid scintillation counting as follows:

$$C_1 = {}^{89}\text{Sr cpm}_c + ({}^{90}\text{Sr cpm}_c)(A_1) \qquad (6.173)$$

and

$$C_2 = {}^{89}\text{Sr cpm}_l + ({}^{90}\text{Sr cpm}_l)(A_2) \qquad (6.174)$$

where

$$A_1 = 1 + (D_1)\left(1 - e^{-\lambda t_c}\right) \qquad (6.175)$$

and

$$A_2 = 1 + (D_2)\left(1 - e^{-\lambda t_l}\right) \qquad (6.176)$$

where $D_1$is the ratio of the Cherenkov counting efficiency of ^{90}Y to the Cherenkov counting efficiency of ^{90}Sr (*i.e.*, $\varepsilon^C_{^{90}\text{Y}}/\varepsilon^C_{^{90}\text{Sr}}$), t_c is the time from chemical separation of strontium from yttrium to Cherenkov counting, D_2 is the ratio of the liquid scintillation counting efficiency of ^{90}Y to the liquid scintillation counting efficiency of ^{90}Sr (*i.e.*, $\varepsilon^l_{^{90}\text{Y}}/\varepsilon^l_{^{90}\text{Sr}}$), t_l is the time from chemical separation of strontium from yttrium to liquid scintillation counting, and λ is the ^{90}Y decay constant.

The Cherenkov count rates and liquid scintillation count rates of each nuclide are demonstrated by Rucker (1991) to be related to their ratio of counting efficiencies by the two counting methods as follows:

$${}^{89}\text{Sr cpm}_c = ({}^{89}\text{Sr cpm}_l)(B_1) \qquad (6.177)$$

and

$${}^{90}\text{Sr cpm}_c = ({}^{90}\text{Sr cpm}_l)(B_2) \qquad (6.178)$$

where B_1 is the ratio of the ^{89}Sr Cherenkov counting efficiency to ^{89}Sr liquid scintillation counting efficiency (*i.e.*, $\varepsilon^C_{^{89}\text{Sr}}/\varepsilon^l_{^{89}\text{Sr}}$) and B_2 is the ratio of the ^{90}Sr Cherenkov counting efficiency to ^{90}Sr liquid scintillation counting efficiency (*i.e.*, $\varepsilon^C_{^{90}\text{Sr}}/\varepsilon^l_{^{90}\text{Sr}}$). Eqs. (6.177) and (6.178) are then incorporated into Eq. (6.173) to give

$$C_1 = ({}^{89}\text{Sr cpm}_l)(B_1) + ({}^{90}\text{Sr cpm}_l)(B_2)(A_1) \qquad (6.179)$$

The ratios of the counting efficiencies are determined experimentally by counting standards of known activity. The use of standard quench correction curves of counting efficiency versus a QIP should also be feasible. It is important to keep in mind, however, that an accurate determination of the counting efficiency of ^{90}Sr is best carried out with a freshly prepared sample, which has undergone only negligible ingrowth of daughter ^{90}Y from the time of chemical separation of parent and daughter to the time of determination of the counting efficiency of ^{90}Sr.

Rucker (1991) solved simultaneously Eqs. (6.174) and (6.179) to give

$$^{90}\text{Sr cpm}_l = \frac{[(B_1)(C_2) - C_1]}{[(B_1)(A_2) - (B_2)(A_1)]} \tag{6.180}$$

and

$$^{89}\text{Sr cpm}_l = C_2 - (A_2)(^{90}\text{Sr cpm}_l) \tag{6.181}$$

The count rates of ^{89}Sr and ^{90}Sr obtained from Eqs. (6.180) and (6.181) can then be converted to activities (DPM) by dividing by their respective liquid scintillation counting efficiencies. Using the activity conversion of Rucker (1991), the sample disintegration rates can be expressed in terms of activity units per sample volume by including the sample volume, strontium recovery rate from the chemical separation, and a conversion factor to activity units as follows:

$$^{90}\text{Sr in pCi/L} = \frac{(^{90}\text{Sr cpm}_l)}{\left[\left(\varepsilon^l_{^{90}\text{Sr}}\right)(V)(R)(2.22\ \text{DPM/pCi})\right]} \tag{6.182}$$

and

$$^{89}\text{Sr in pCi/L} = \frac{(^{89}\text{Sr cpm}_l)}{\left[\left(\varepsilon^l_{^{89}\text{Sr}}\right)(V)(R)(2.22\ \text{DPM/pCi})\right]} \tag{6.183}$$

where $\varepsilon^l_{^{90}\text{Sr}}$ and $\varepsilon^l_{^{89}\text{Sr}}$ are the liquid scintillation counting efficiencies of ^{90}Sr and ^{89}Sr, respectively, V is the sample volume in liters (L), R is the chemical recovery in decimal percent, and 2.22 DPM/pCi is the conversion factor from sample DPM to pCi.

Quantitative recoveries are reported by Rucker (1991) using various mixtures of ^{89}Sr and ^{90}Sr standards. Obviously, the analysis of ^{90}Sr activity represents also the activity of its daughter nuclide ^{90}Y, which reaches secular equilibrium as ^{90}Sr(^{90}Y) after approximately 18 days (L'Annunziata, 1971). Groska et al. (2012) used this principle to test the methods of determination of radiostrontium in milk and water samples as well as radioactive waste. Analytical methods using selective Sr resin for Sr separation and DGA resin for Y separation with liquid scintillation spectrometry and Cherenkov counting were used for ^{89,90}Sr determination. Relations for activity calculation in different counting combinations according to the recommended procedure of the IAEA for the determination of ^{89}Sr and ^{90}Sr in milk samples in emergency situations (IAEA, 2013) were used. The calculation techniques are compared in terms of the trueness and accuracy of the results and the limit of detection. Uncertainties and detection limits were calculated using the spreadsheet method. Holmgren-Rondahl and Ramebäck (2018) used a similar approach, with respect to uncertainty measurements when determining ^{90}Sr in the presence of huge ^{89}Sr activity.

b. Sequential analysis with wavelength shifter

Walter et al. (1993) describe the activity analysis of mixtures of ^{89}Sr and ^{90}Sr(^{90}Y) using Cherenkov counting with wavelength shifter followed by liquid scintillation analysis. A wavelength shifter was used during Cherenkov counting to increase the Cherenkov counting efficiencies of ^{89}Sr and ^{90}Sr.

As in the previous method, the ^{89}Sr and ^{90}Sr of the sample are separated from ^{90}Y by chemical means. The γ-ray emitters ^{85}Sr and ^{88}Y are used as tracers to measure the chemical yields in the separation procedures, because they do not cause interference in Cherenkov or liquid scintillation counting with the exception of count rate measurements of low activity samples.

Once purified, the radiostrontium samples are counted for Cherenkov radiation in 6 mL of aqueous solution in a counting region that accepts all pulse events arising from Cherenkov photons. The aqueous solution used for Cherenkov counting was doped with a 4.0 g/L concentration of the sodium salt of 1-naphthylamine-4-sulfonic acid as wavelength shifter. Walter et al. (1993) report increases in Cherenkov counting efficiency with the wavelength shifter by a factor of 1.55 for ^{89}Sr and 3.2 for ^{90}Sr compared to detection efficiencies without a shifter. Cherenkov counting efficiencies reported with wavelength shifter are ^{90}Sr 6.3%, ^{89}Sr 64%, ^{90}Y 81%, ^{85}Sr 0.3%, and ^{88}Y 0.2%. The latter two nuclides are used as tracers to determine the yields of the chemical separation of Sr and Y, respectively, from the sample.

After the Cherenkov counting of the samples, 10 mL of liquid scintillation fluor cocktail are added to the 6 mL of aqueous solution in each sample counting vial. The liquid scintillation assay was carried out without counting region limitations, and quench correction was determined with calibration curves of counting efficiency versus an external standard quench-indicating parameter. However, in the previous step of Cherenkov counting, an external standard QIP cannot be used in most cases as described previously in this chapter.

After completion of the two count rate determinations on the same sample, Walter et al. (1993) used the following equations to convert the count rates to ^{89}Sr and ^{90}Sr disintegration rates:

$$D_{89} = \frac{1}{f_\varepsilon}\left[R_C\varepsilon^L_{90} - R_L\varepsilon^C_{90}\right] \tag{6.184}$$

$$D_{90} = \frac{1}{f_\varepsilon}\left[R_L\varepsilon^C_{89} - R_C\varepsilon^L_{89}\right] \tag{6.185}$$

with

$$f_\varepsilon = \varepsilon_{90}^L \varepsilon_{89}^C - \varepsilon_{89}^L \varepsilon_{90}^C \tag{6.186}$$

where D_{89} and D_{90} are the disintegration rates (DPM) of ^{89}Sr and ^{90}Sr, R_C and R_L are the net count rates (CPM) corrected for background for the Cherenkov counting and liquid scintillation counting of a sample, respectively, ε_{89}^C and ε_{90}^C are the Cherenkov counting efficiencies for ^{89}Sr and ^{90}Sr, respectively, and ε_{89}^L and ε_{90}^L are the liquid scintillation counting efficiencies of ^{89}Sr and ^{90}Sr, respectively.

A sequential Cherenkov counting followed by dual-region liquid scintillation analysis technique described by Walter et al. (1993), permits the assay of ^{89}Sr and ^{90}Sr even after significant ingrowth of ^{90}Y up to 6.6 half-lives of ^{90}Y with average deviations of only 6.6% from the true values.

C. Strontium-90(yttrium-90) exclusive of strontium-89

The Cherenkov analysis of ^{90}Sr(^{90}Y) in the absence of ^{89}Sr may involve one of following methods of approach: (1) the chemical separation of the yttrium from other elements in the sample, when the parent-daughter nuclides ^{90}Sr/^{90}Y are in equilibrium, followed by the Cherenkov counting of ^{90}Y in aqueous media or (2) The separation of strontium from other elements in the sample followed by the Cherenkov counting of ^{90}Sr including the ingrowth of its daughter nuclide ^{90}Y. These methods will be discussed subsequently in this section.

1. Chemical separation and Cherenkov counting of ^{90}Y

The chemical separation of yttrium from other elements of the sample after secular equilibrium of the ^{90}Sr(^{90}Y) is reached, followed by the counting of the separated ^{90}Y activity, and the calculation of the ^{90}Y activity at the time of its separation from strontium was the traditional method of analysis of ^{90}Sr(^{90}Y) in secular equilibrium (L'Annunziata, 1971). Once the ^{90}Y is separated from ^{90}Sr, it will decay by its half-life of 64.06 hours. The activity of ^{90}Y at the time of chemical separation from its parent is used to determine the activity of ^{90}Sr. The time of chemical separation and the time of Cherenkov counting of the isolated ^{90}Y are recorded. The ^{90}Y decay that occurs during that period is calculated to arrive at the ^{90}Y activity at the time of chemical separation from its parent ^{90}Sr, when the parent and daughter nuclides were in secular equilibrium, that is, when the activities or DPM values of the two radionuclides were equal as discussed in Chapter 1, Volume 1.

Several examples of the application of the above technique to the analysis of ^{90}Sr are available from the literature including works by Bjornstad et al. (1992), Breban et al. (2004), Dewberry et al. (2000), Ghods et al. (1994), Jabbar et al. (2009), Laissaoui et al. (2002), Llauradó et al. (2001), Martin (1987), Mosqueda et al. (2006), Poletiko et al. (1994), Popov et al. (2009), Rao et al. (2000a,b), Shabana et al. (1996), Shawky and El-Tahawy (1999), Scarpitta et al. (1999), Suomela et al. (1993), Torres et al. (1999, 2002), and Vaca et al. (1999, 2001a,b). Some researchers elect to separate the ^{90}Sr(^{90}Y) by chemical precipitation of ^{90}Y followed by Cherenkov counting of ^{90}Y (Shawky and El-Tahawy, 1999; Jabbar et al., 2009). Several researchers have adopted the method based on that of Bjornstad et al. (1992) and Suomela et al. (1993), which involves the separation of ^{90}Sr and ^{90}Y by chemical extraction of ^{90}Y with 5%−10% HDEHP (di-2-ethyl-hexyl-phosphoric acid) in toluene (Laissaoui et al., 2002; Llauradó et al., 2001; Mosqueda et al., 2006; Torres et al., 1999, 2002; Vaca et al., 1999, 2001a,b). The ^{90}Y in the organic phase is then back-extracted with 3M HNO_3, precipitated as $Y(OH)_3$, and then redissolved in aqueous solution for Cherenkov counting of ^{90}Y. A brief description of the method used is provided below. Detailed procedures are available from the original papers.

The Swedish Radiation Protection Institute has issued a detailed procedure for the Cherenkov analysis of ^{90}Sr in food and environmental samples authored by Suomela et al. (1993). The procedure entails the following basic steps (1) ashing of the organic samples at 610°C, (2) dissolution of the ash in dilute acid, (3) the addition of yttrium carrier (10 mg of stable Y^{3+}) to facilitate extraction and chemical separation of yttrium, (4) extraction with HDEHP in toluene at low pH to remove ^{90}Y (The Sr−Y separate at this stage of the procedure. The time of the extraction is noted, because the separated ^{90}Y can be observed to decay at its half-life of 64.06 hours. The Y collects in the organic phase, and the Sr remains in the aqueous phase). (5) back-extraction of the organic phase with 3M HNO_3 to transfer the Y into the aqueous phase, (6) precipitation of yttrium from the aqueous phase as yttrium hydroxide at high pH, (7) dissolution of the yttrium hydroxide in 1 mL of conc. HNO_3, (8) dilution of the dissolved yttrium hydroxide with 14 mL of distilled water, (9) transfer of the solution to a 20-mL plastic scintillation counting vial, and finally (10) counting of the ^{90}Y in a counting region set to receive pulse events arising from Cherenkov photons. The ^{90}Sr of the sample is calculated according to the equation:

$$A_{90_{Sr}} = \frac{(R - R_0)e^{\lambda \Delta t}}{(E)(f)} \tag{6.187}$$

where $A_{^{90}Sr}$ is the activity of ^{90}Sr in becquerels or disintegrations per second (DPS), R is the gross ^{90}Y Cherenkov count rate of the sample in counts per second, R_0 is the background Cherenkov count rate, that is, count rate of a

blank counting vial in counts per second, λ is the decay constant of ^{90}Y in units of hours^{-1},

$$\lambda = 0.693/t_{1/2} = 0.693/64.06 \text{ hours} = 0.0108 \text{ h}^{-1} \quad (6.188)$$

Δt is the time interval in hours between the chemical separation of ^{90}Y and the time of counting, E is the decimal equivalent of the percent Cherenkov counting efficiency of ^{90}Y, and f is the chemical yield of the extracted yttrium.

Tayeb et al. (2015) developed a rapid method for the indirect determination of ^{90}Sr from its progeny ^{90}Y in seawater. The method consists of yttrium coprecipitation with hydrous titanium oxide (HTiO), yttrium separation in DGA-N and TDCR Cherenkov counting for ^{90}Y determination. LSA was used for quantifying yttrium recovery both through ^{90}Y and ^{90}Sr activity. The activity of ^{90}Y is calculated where Cherenkov counting efficiency was calculated as $\varepsilon_{Ch} = 0.9(\text{TDCR})^{0.75}$. The coprecipitation technique removed the excessive dominant salts of the seawater and enabled the sequential measurement of ^{90}Y. The mean chemical recovery was 88 ± 7%. The minimum detectable concentrations of ^{90}Y measured by Cherenkov counting and LSA techniques were 0.11 and 0.18 Bq L^{-1} respectively for 1 L of seawater, and 1 hour of counting time on a Hidex liquid scintillation counter. Sample preparation time was estimated to be 4 hours for a set of 10 samples.

Similarly, Yang et al. (2017) used TDCR Cherenkov counting and ^{90}Y separation from a sample matrix and interfering radionuclides through two coprecipitation steps, with hydrous titanium oxide followed by yttrium fluoride (YF_3) precipitation, to develop a rapid method for the determination of ^{90}Sr in a leaching solution for cement solidification. The performance of the method was examined using spiked samples with various activities of ^{90}Sr. The separation of Sr and Y during the coprecipitation steps was checked by X-ray fluorescence analysis by determining the Sr and Y contents in dissolved HTiO and YF_3 precipitates. Yttrium recovery was determined by UV-VIS spectrometry measuring yttrium chlorophosphonazo III complex absorbance at 673 nm in the presence of oxalic acid and Na_2EDTA. The results of ^{90}Sr determination showed a 10% deviation. The attained MDA was about 0.3 Bq L^{-1} for the 0.2 L sample and 86 ± 8% mean recovery within 1.5 hour counting time on a Hidex 300 SL counter.

Amano et al. (2016) also used TDCR Cherenkov counting after the isolation of ^{90}Y by coprecipitation with iron hydroxide and oxalic acid. The dissolved oxalate precipitate was loaded on the DGA resin, and the ^{90}Y eluate was analyzed by Cherenkov counting with a Hidex 300 SL/SLL TDCR. The MDA for this method is about 14 mBq/kg-wet. The supposed 1 kg-wet sample is treated and the chemical yield is 100%. ^{90}Sr(^{90}Y) concentration activities were determined in plant samples collected near the Fukushima Daiichi Nuclear Power Plants.

If samples are color quenched, the Cherenkov counting efficiency of ^{90}Y can be determined with a color quench correction curve of percent counting efficiency versus a sample spectrum quench indicating parameter as described by Poletiko et al. (1994) or by the SCR method employed by Vaca et al. (1998), Tarancón et al. (2002a,b), Mosqueda et al. (2007) and Todorović et al. (2017) and also expounded upon in detail in Section IV of this chapter. The Cherenkov counting efficiencies of ^{90}Y may be determined with a standard of ^{90}Sr(^{90}Y) in secular equilibrium. As described previously in this section the optimum Cherenkov counting efficiency of ^{90}Y in water is ~70%, while that of ^{90}Sr is only ~1% (see Fig. 6.78). Therefore, the use of standards of ^{90}Sr(^{90}Y) in secular equilibrium for the preparation of ^{90}Y Cherenkov color quench correction curves is convenient, as very little contribution (~1%) to the total Cherenkov count rate is made by Cherenkov photons from ^{90}Sr. Sample spectrum quench indicating parameters can be difficult to measure accurately with low activity samples. In such cases, Tarancón et al. (2002a,b) recommends the SCR method of color quench correction, as it is less dependent on the sample count rate than a sample spectrum quench indicating parameters. In most cases, the internal standard method described in Section IV of this chapter is the most reliable, as the measurement of internal standards is independent of sample activity. If wavelength shifters are used to increase Cherenkov counting efficiencies, quenching may occur as a result of the addition of wavelength shifter (Vesely et al., 2011). An alternative method for the measurement of color quench is the use of an external standard ^{152}Eu, equipped with the Quantulus 1220 analyzers, which was demonstrated by Tsroya et al. (2009, 2012, 2013a,b) as illustrated by Figs. 6.17–6.20 in Section IV.D of this chapter.

The chemical yield of yttrium is included in Eq. (6.187), as the chemical extraction of yttrium from the sample will not be complete. The method used by Suomela et al. (1993) is practical because it involves chemical titration of the sample taken from the counting vial after Cherenkov counting is completed to determine the chemical yield. The aqueous sample of yttrium is transferred from the counting vial to an Erlenmeyer flask and diluted with water to permit titration with xylenol orange indicator with 0.1M Titriplex III to a yellow color. The mL of titrant required to reach the endpoint are recorded as T_{sample}. The procedure is repeated with a standard by titrating the same volume of yttrium carrier as had been added to the sample during the chemical separation and extraction procedure for yttrium. The mL of titrant required for the standard is recorded as T_{standard}. The chemical yield f of Eq. (6.187) is calculated as

$f = T_{\text{sample}}/T_{\text{standard}}$. The yttrium chemical yield after Cherenkov counting can also be determined by atomic absorption spectrometry (AAS), ICP-OES or MS and by UV-ViS spectrophotometry, as described previously in this paragraph (Yang et al., 2017). For determination by AAS or ICP-MS/OES, an aliquot from the yttrium fraction should be taken and transferred to a flask, diluted and measured with an available instrument. The yield is usually calculated as a ratio between the determined and initial concentrations.

2. Chemical separation and Cherenkov counting of ^{90}Sr with ^{90}Y ingrowth

An alternative method of ^{90}Sr analysis is to measure the ingrowth of ^{90}Y with its parent ^{90}Sr by Cherenkov counting after the chemical separation of strontium from other elements in the sample. An advantage of this approach to ^{90}Sr analysis is that secular equilibrium between the parent–daughter nuclides ^{90}Sr(^{90}Y) need not be achieved at the time of chemical separation. It is necessary only to record the date and time of chemical separation of strontium, as this is the time that the strontium is free of its daughter nuclide ^{90}Y and daughter ingrowth begins. The chemical separation and isolation of strontium may be carried out by chemical precipitation methods (Scarpitta et al., 1999; Rao et al., 2000a,b) or by isolation of strontium on a column of Sr-specific (*e.g.*, Sr-Spec resin, Eichrom, Darien, IL, USA) ion exchange resins (Grahek et al., 2006; Harrison et al., 2011; Taylor et al., 2007; Tovedal et al., 2008; Wang et al., 2004; Wood et al., 2008). Desirable limits of detection for low activity samples will depend on the counting time and level of ingrowth of ^{90}Y. These variables were analyzed in detail by Tovedal et al. (2008), who give the general equation for the calculated ^{90}Sr activity at the time of its chemical separation as

$$A_{\text{Sr}}^{0} = \frac{R_{\text{Y}} - R_b}{\psi U(1 - e^{-\lambda_{\text{Y}} t})} \tag{6.189}$$

where R_{Y} in the count rate of ^{90}Y in CPS, R_b is background count rate in CPS, Ψ is the Cherenkov counting efficiency, U is the strontium chemical yield, λ_{Y} is the decay constant of ^{90}Y (see Eq. 6.188) and t is the time between the chemical separation of the strontium and the time of counting. Secular equilibrium is discussed in detail in Chapter 1, Volume 1, where a derivation is provided for the basic equation expressed in Eq. (6.189). The reader may compare Eq. (6.189) with those derived in Chapter 1, Volume 1.

The analysis of ^{90}Sr is usually time-consuming due to time needed to await for ^{90}Y ingrowth. There are some situations, as noted in Holmgren et al. (2016), when an acceleration of the measurement method is desirable: situations requiring rapid results in order to make urgent decisions and to maximize the throughput of samples in a limited available time span. Holmgren et al. (2016) developed a mathematical model in order to minimize the total analysis time, with the focus on the measurement of ^{90}Y during ingrowth after an initial chemical separation of ^{90}Sr and without the presence of any other yttrium/strontium isotopes. The model defines a case where the continuous ingrowth of ^{90}Y exists when determining ^{90}Sr. The model provides a tool which can be used to estimate the initial time of ingrowth, as well as individual measurement times for each consecutive sample with different detection limits and instrument backgrounds. Using the definition of the detection limit and the fact that for a given counting time the detection limit is constant and that the MDA varies depending on the instrument background, detection efficiency, sample volume, chemical yield, etc., the minimal detectable activity of ^{90}Y was expressed as follows:

$$\text{MDA}\ (^{90}\text{Y}) = \frac{1}{\Psi \cdot U \cdot V_s} \cdot \left[\left(\frac{k^2 + 2k\sqrt{2} \cdot \sqrt{R_b \cdot t_{m,n}}}{1 - e^{-\lambda_Y \cdot t_{m,n}}} \right) \cdot \lambda_Y \right] \tag{6.190}$$

where Ψ represents the counting efficiency ^{90}Y in cps/Bq, λ_Y is the decay constant of ^{90}Y, R_b is the instrument background count rate, $t_{m,n}$ is the measurement time of the sample n, U is the chemical yield of the strontium, and V_S is the sample volume in liters. When describing the MDA for ^{90}Sr, the following equation applies:

$$\text{MDA}(^{90}\text{Sr}) = \text{MDA}(^{90}\text{Y}) \cdot \frac{e^{\lambda_Y \cdot t_{cool,n}}}{1 - e^{-\lambda_Y \cdot t_{i,n}}} \tag{6.191}$$

The ingrowth time for the sample n is given by $t_{i,n}$, and $t_{cool,n}$ is the time of decay for ^{90}Y. In order to account for the ingrowth during measurement, an approximation for decay during acquisition is used. As long as the measurement time ($t_{m,n}$) is less than 0.2t½ (^{90}Y), the resulting underestimation of the ^{90}Sr activity is lower than 1% (Tovedal et al., 2008). The approximation substitutes $t_{i,n}$ with the expression $t_{i,n} + 0.5t_{m,n}$, giving the equation:

$$\text{MDA}(^{90}\text{Sr}) = \frac{\left[\frac{k^2 + 2k\sqrt{2} \cdot \sqrt{R_b t_{m,n}}}{(1 - e^{-\lambda_Y t_{m,n}})} \cdot \lambda_Y \right]}{\Psi \cdot U \cdot V_s \left[1 - e^{\lambda_Y (t_{i,n} + 0.5 t_{m,n})} \right]} \tag{6.192}$$

The ingrowth time for sample n is equal to the total analysis time ($t_{i,n} = t_{i,n\text{-}1} + t_{m,n\text{-}1} = t_{tot,n\text{-}1}$), the ingrowth time plus measurement time, for sample n-1. The results for a series of samples were obtained by solving Eq. (6.192) with regard to $t_{m,n}$ after allowing an initial ingrowth time for sample 1 (t_i,1), and then iterating the equation for all the samples in the series. The results obtained were compared with results from the standard method, obtained in a similar way and with results calculated according to a previous optimization carried out by Tovedal et al. (2008), as illustrated in Fig. 6.81.

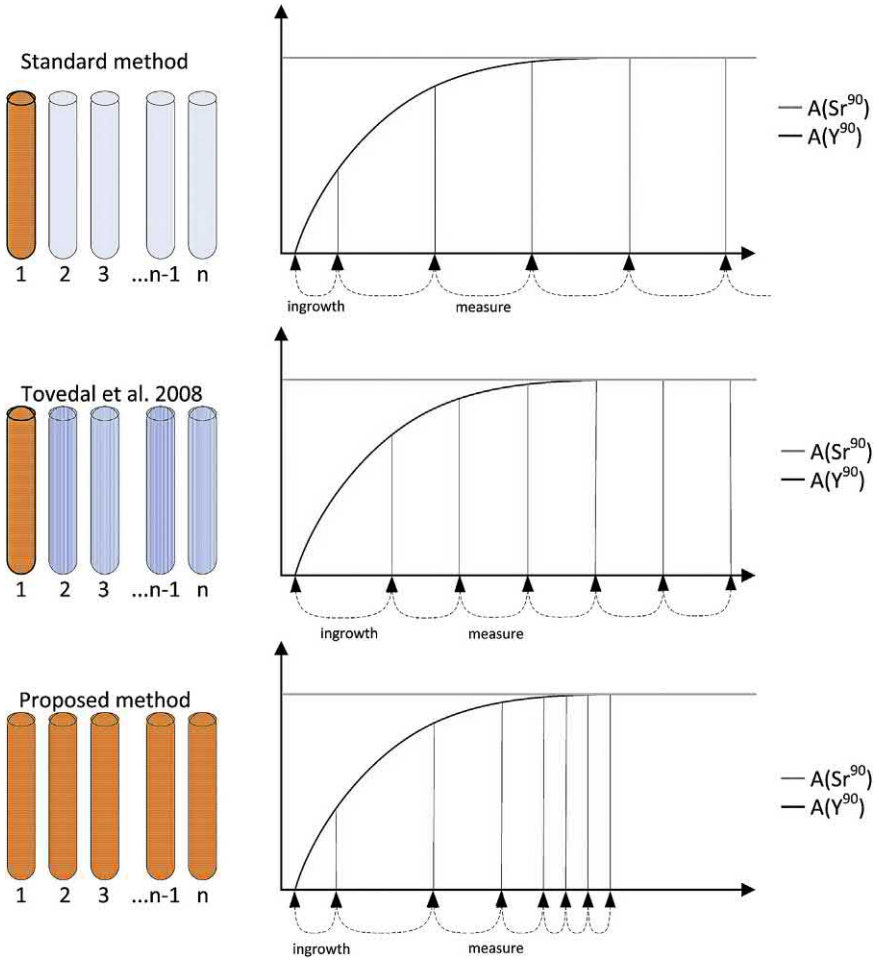


FIGURE 6.81 An illustration of the different methods. The blue (vertical lines) sample tubes represent the samples in a measurement series that were considered when determining the MDA. The orange-brown (horizontal lines) sample tubes represent the number of samples, and their individual time of ingrowth, in a measurement series when determining the MDA. The Figure also shows how the total analysis time (i.e., the time for ingrowth and measurements) is affected by the different methods. (For interpretation of the references to color in this Figure legend, the reader is referred to the electronic version of the book.) *From Holmgren et al. (2016), reprinted with permission from Elsevier © 2016.*

By using the fixed MDA and iterating the measurement time for each consecutive sample, the total analysis time will be less, as illustrated in Fig. 6.82. It was found that by optimization, the total analysis time for 10 samples can be decreased greatly from 21 to 6.5 hours when assuming an MDA of 1 Bq/L and with a background count rate of approximately 0.8 cpm.

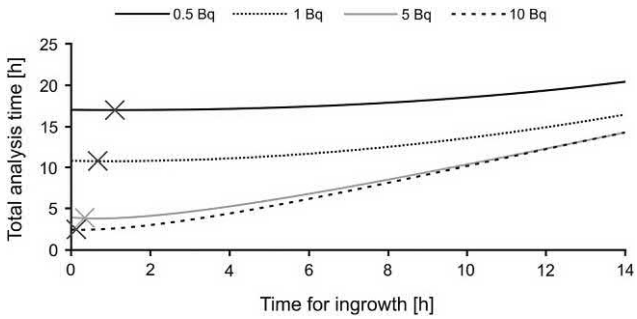


FIGURE 6.82 Change in total analysis time, for 10 samples, with varying time for ingrowth. Minima for the different MDA (Bq/L) are marked in the figure. *From Holmgren et al. (2016), reprinted with permission from Elsevier © 2016.*

Holmgren-Rondahl et al. (2017) also used the same methodology for the determination of ^{90}Sr when its daughter ^{90}Y is measured during its decay after chemical separation. It was found that the measurement times increased for each subsequent sample, since there is a longer decay time before measurement. Compared to the previous approach, the gain in total analysis time is not so significant, especially in the case when low background instruments are analyzed.

Recent works by Qiao et al. (2017), Grahek et al. (2018), and Shao et al. (2018) perform a method comparison for the determination of ^{90}Sr in different kinds of samples to identify the advantages and pitfalls in different methods. The methods differ in sample pretreatment and chemical separation, as well as the detection step, where an LSA, Cherenkov counting and proportional counter were compared. The detection limit, MDA, accuracy/precision, analytical time and robustness of the method were assessed. By comparison of every step in the method, it is shown that the Cherenkov measurement has the advantage in terms of the analytical time taken. A comparison of other parameters

shows that there is no significant difference between Cherenkov counting and other detection methods, i.e., that the advantage or disadvantage depends on the choice of method of sample preparation and chemical separation. The accuracy of determination and MDA depends on the efficiency of the detection and chemical yield, which depends on the type of sample, sample pretreatment and the chemical separation procedure. There are a number of options for combining the sample pretreatment and chemical separation procedure so that Cherenkov counting can be part of virtually any combination of these procedures. The literature thus describes a number of methods using Cherenkov counting for the quantitative determination of ^{89,90}Sr. Cherenkov detection efficiency, as one of the key parameters for accurate and reliable quantitative determination, depends on the type of available instrument. Therefore, Table 6.22 gives an overview of selected determination methods with a brief description of the separation method, the strontium isotopes that are determined by the indication of the method of determination (yttrium ingrowth or decay), the type of sample to which the method is applied, the type of instrument used for Cherenkov measurement, and the detection efficiency for each isotope for that instrument. The data was taken from the references given in the last column.

D. Yttrium-90

The analysis of ^{90}Y is noted here, because of the increased attention the nuclide is receiving in terms of its medical applications in the pure form, that is, extracted or "milked" in pure form without contamination from its parent ^{90}Sr. Goffredo et al. (2011), Šrank et al. (2010), and Dietz and Horwitz (1992), among others, underscore the therapeutic applications of ^{90}Y including the radiolabeling of antibodies for tumor therapy and the production of radiolabeled particles for the treatment of liver malignancies, among others. Although the liquid scintillation counting efficiency of ^{90}Y is 100% with the exception of samples under unusually high quench conditions, Cherenkov counting is often the method of choice for the routine analysis of this nuclide, because of the high Cherenkov counting efficiencies achieved and low cost of analysis. Cherenkov counting efficiencies of ^{90}Y reach up to ~70% in pure water and >80% with wavelength shifter under optimum conditions (see Jurkin and Wierczinski, 2008; L'Annunziata and Passo, 2002; Passo and Cook, 1994; Van Hemert et al., 2006; Walter et al., 1993; Xiques Castillio et al., 2009).

E. Other applications

In addition to the previously cited popular applications of Cherenkov counting to the analysis of ^{32}P, ^{89}Sr, ^{90}Sr/^{90}Y, and isolated ^{90}Y, numerous other, less common analytical applications are reported in the literature. Some of these are cited next.

The very first detection and measurement of ^{14}C and ^{45}Ca by Cherenkov photon counting was reported by Takiue et al. (2004) and improvements to the technique were reported by Minowa et al. (2009). The radionuclide ^{14}C and ^{45}Ca emit relatively low-energy beta particles with energy maxima (E_{max}) of 155 and 258 keV, respectively. While these energies are below the Cherenkov threshold energy of 262 keV in water medium, Takiue et al. (2004) and Minowa et al. (2009) used a high refractive index ceramic medium, which lowered the threshold energy for the production of Cherenkov photons to 70 keV. A Cherenkov photon detection efficiency of 5.0% for ^{14}C was reported by Minowa et al. (2009) with an improved ceramic Cherenkov radiator. While the detection efficiency is relatively low, it is more than adequate for the detection and measurement of ^{14}C at facilities where radionuclide sources and labeled compounds are prepared or synthesized.

A new technique, referred to as Cherenkov luminescence imaging, has appeared in the scientific literature. This method is under development in the biological and medical sciences for the in vitro and in vivo imaging of high-energy negatron emitters (*e.g.*, ^{32}P and ^{131}I) and positron emitters (*e.g.*, ^{18}F, ^{64}Cu, ^{89}Zr, and ^{124}I), among other beta emitters. Robertson et al. (2009) reported studies utilizing optical imaging of Cherenkov radiation from ^{18}F for in vivo imaging. Further reports have demonstrated the use of commercial optical instrumentation equipped with charge-coupled detectors (CCDs) for the measurement of Cherenkov radiation produced by high-energy negatron and positron emitters as a potentially new technique for in vivo radionuclide imaging (Ruggiero et al., 2010; Spinelli et al., 2010, 2011; Boschi et al., 2011; Lucignani, 2011).

Numerous radionuclides are listed in Table 6.21 together with their reported Cherenkov photon detection efficiencies and corresponding literature citations. In addition to these, the following deserve mention:

Bem et al. (1978) described the Cherenkov counting of ^{115m}Cd in blood and animal tissue with counting efficiencies of approximately 35%. Rengan and Sun (2004) also used Cherenkov counting of ^{115m}Cd to measure the sorption characteristics of chelating resins.

For studies involving the removal of ^{106}Ru from nuclear waste solutions, Carmon and Dyer (1987) report the Cherenkov counting of this radionuclide in aqueous solution in the presence of weak β emitters. The optimum Cherenkov counting efficiency of ~62% was reported. Fujii et al. (2002) describe the design of a large volume (1L) Cherenkov counting system to monitor high-energy β emitters, namely ^{89}Sr, ^{90}Y, and ^{32}P, in liquid waste with detection limits of 0.003−0.007 and 0.001−0.003 Bq/mL for 5 and 20 minutes measurements, respectively. The

TABLE 6.22 List of selected methods for the analysis of radiostrontium/radioyttrium by Cherenkov counting or a combination of LSA and Cherenkov counting.

Method outline	Isotope	Instrument	Sample	Cherenkov efficiency	References
Cherenkov counting of ^{89}Sr, ^{90}Sr, and ^{90}Y in aqueous solution	^{89}Sr, ^{90}Y	Tri-Carb Model 3380	Aqueous	$\varepsilon(^{90}Y) = 0.65^{p}$ $\varepsilon(^{89}Sr) = 0.50^{p}$	Buchtela and Tschurlovits (1975)
Sr separated from Y by hydroxide precipitation, Sr precipitated as carbonate, Cherenkov counting ^{89}Sr, $^{90}Sr(^{90}Y)$, LSA recounting (Insta gel)	^{89}Sr, $^{90}Sr(^{90}Y)$	Beckman LS 200	ns	$\varepsilon(^{90}Y) = 0.28^{g}$ $\varepsilon(^{89}Sr) = 0.41^{g}$	Randolph (1975)
Isolation of Sr, Ca without mutual separation, ^{89}Sr, ^{90}Sr Cerenkov counting in presence of Ca (HCl solution)	^{89}Sr, ^{90}Y, $^{90}Sr(^{90}Y)$	Tri-Carb (ns)	Natural water, liquid effluent from NPP	$\varepsilon(^{90}Y) = 0.565-0.603^{p}$ $\varepsilon(^{89}Sr) = 0.358-0.384^{p}$ $\varepsilon(^{90}Sr) = 0.007-0.017^{p}$	Regan and Tyler (1976)
Sr,Y separation (ref 1,2 in Carmon, 1979), Cerenkov measurement of ^{89}Sr and ^{90}Y without interference from ^{90}Sr (aqueous solution)	^{89}Sr, ^{90}Y	Tri-Carb Model 3390	Aqueous solution	$\varepsilon(^{90}Y) = 0.46^{p}$, 0.34^{g} $\varepsilon(^{89}Sr) = 0.26^{p}$,$0.18^{g}$ $\varepsilon(^{90}Sr - ^{90}Y) = 0.46^{p}$, 0.34^{g} $\varepsilon(^{90}Sr) = 0.006^{p}$, 0.003^{g}	Carmon (1979)
Extraction of Y with HDEHP [di(2-ethylhexyl)phosphoric acid], Cerenkov counting (aqueous solution)	^{90}Y	Tri-Carb Model 3390	Urine	$\varepsilon(^{90}Y) = 0.43^{p}$	Carmon and German (1982)
Extraction of Sr, Y with DBP (dibutylphosphate), stripping of ^{90}Y with 1 M $HN0_3$, Cerenkov counting	^{90}Y	ns	Water (lake, drinking)	nr	Batarekh and Teherani (1986)
TBP (tri-n-butylphosphate) extraction of Y from sample after sample pretreatment, Cherenkov counting	^{90}Y	Beckman LS 6800	Reactor waste (liquids, resins, smears)	$\varepsilon(^{90}Y) = 0.34^{ns}$	Martin (1987)
TBP (tributylphosphate) extraction of Y from ashed sample, Cherenkov counting and LSA	^{91}Y, ^{90}Y	ns	Grass	$\varepsilon(^{90}Y) = 0.25^{p}$	Zhu et al. (1990)
Extraction of Y with DBP, TBP HDEHP [di(2-ethylhexyl)phosphoric acid], purification of Y by stripping and extraction processes. Cherenkov counting	^{90}Y	Tri-Carb 2250A	Biological samples	$\varepsilon(^{90}Y) = 0.21^{g}$	Ghods et al. (1994)
Dionex ion chromatographic system, separation of ^{90}Y, Cherenkov counting for recovery determination in water spiked with $^{90}Sr(^{90}Y)$	^{90}Y	LKB Wallac 1215 Rackbeta	Water, urine	$\varepsilon(^{90}Y) = 0.432^{c}$	Cobb et al. (1994)
Y,Sr separation by different method, Cherenkov counting (in HCl)	^{89}Sr, ^{90}Y, $^{90}Sr(^{90}Y)$	Tri-Carb CA2200	Radioactive waste	$\varepsilon(^{90}Y) = 0.68^{p}$ $\varepsilon(^{90}Sr - ^{90}Y) = 0.683^{p}$ $\varepsilon(^{89}Sr) = 0.42^{p}$ $\varepsilon(^{90}Sr) = 0.003^{p}$	Chang et al. (1996)

Continued

TABLE 6.22 List of selected methods for the analysis of radiostrontium/radioyttrium by Cherenkov counting or a combination of LSA and Cherenkov counting.—cont'd

Method outline	Isotope	Instrument	Sample	Cherenkov efficiency	References
Citric acid addition, Y extraction with 10% HDEHP in toluene, Cherenkov counting (HNO_3)	^{90}Y	Tri-Carb 2000 CA/LL	Soil, water, milk, biological samples	ε (^{90}Y) = 0.62^{ns}	Torres et al. (1996)
TBP (tributylphosphate) extraction of Y, Th removal with 5% TOPO (tri-noctyl phosphine oxide) in toluene, Cherenkov counting	^{90}Y	Tri-Carb 1905 AB/LA	Soil, sediment, IAEA-367	$\varepsilon(^{90}Y) = 0.662^{p}$	Tinker et al. (1997)
Soil leaching, Y extraction with 1M HDEHP dissolved in Nysolvin 75A an aliphatic kerosene, Cherenkov counting in organic phase	^{90}Y	LKB Wallace Rackbeta 1219	Soil	$\varepsilon(^{90}Y) = 0.648^{p}$ leaching 0.697^{p} pure organic phase	Friberg (1997)
Sr separation on Sr resin (bis-4,4′(5′)[(t-butyl)cyclohexano]-l8-crown-6 adsorbed onto inert polymer support), Cherenkov counting (aqueous)	^{89}Sr, $^{90}Sr(^{90}Y)$	Tri-Carb 2560 TR/XL	Soil, milk, vegetation	$\varepsilon(^{90}Y) = 0.35^{ns}$ $\varepsilon(^{89}Sr) = 0.28^{ns}$ $\varepsilon(^{90}Sr) = 0.0059^{ns}$	Chu et al. (1998)
Clay leaching, Y extraction with 1M HDEHP, Cherenkov counting in organic phase	^{90}Y	LKB Wallace Rackbeta 1219	Bentonite clay	$\varepsilon(^{90}Y) = 0.75^{g}$	Ramebäck and Skålberg (1999)
Sr separation on Sr resin column (5M HNO_3), Cherenkov counting (HNO_3)	$^{90}Sr(^{90}Y)$	Tri-Carb 2770 TR/SL	Water, soil	$\varepsilon = {}^{90}Sr(^{90}Y) = 0.54^{p}$ (HNO_3) $\varepsilon = {}^{90}Sr(^{90}Y) = 0.35^{p}$ (H_2O)	Grahek et al. (1999)
Leaching, evaporate residue, $SrCO_3$ precipitation, dissolve in 8M HNO_3, Cherenkov counting in presence of interfering isotope	$^{90}Sr(^{90}Y)$	Tri-Carb 1550	Water, soil, sediment	$\varepsilon(^{90}Y) = 0.50^{g}$ $\varepsilon(^{89}Sr) = 0.27^{g}$ $\varepsilon(^{90}Sr) = 0.02^{g}$	Rao et al. (2000a,b)
Y extraction with 5% HDEHP in toluene, Cherenkov counting in 2M HNO_3	^{90}Y	Quantulus 1220	IAEA soil-6, IAEA- 375	$\varepsilon(^{90}Y) = 0.60^{p}$	Laissaoui et al. (2002)
Sr separation on Sr resin, Cherenkov counting (5M HNO_3)	^{89}Sr, $^{90}Sr(^{90}Y)$	Tri-Carb 2770 TR/SL	Liquid waste	$\varepsilon(^{89}Sr) = 0.3525^{p}$ $\varepsilon(^{90}Sr - {}^{90}Y) = 0.5566^{p}$	Grahek and Rožmarić Mačefat (2004)
Sr,Y separation by different methods, Cherenkov counting	$^{90}Sr(^{90}Y)$, ^{90}Y	LKB Wallac Guardian	Biological samples, water, soil, etc	$\varepsilon(^{90}Y) = 0.55^{ns}$	Popov et al. (2006)
TBP (tributylphosphate) extraction of Y, Cherenkov counting (2M HNO_3)	^{90}Y	Quantulus 1220	Wheat, soil	$\varepsilon(^{90}Sr - {}^{90}Y) = 0.70^{p}$, 0.585^{p} (narrow window)	Gerstmann and Tschöpp (2006)
Direct Cherenkov measurement	$^{90}Sr(^{90}Y)$	Quantulus 1220	Water, milk	ε=(^{90}Sr–^{90}Y) = 0.489^{p} water	Stamoulis et al. (2007)
Sr separation on Sr resin column, Cherenkov counting (0.05M HNO_3)	$^{90}Sr(^{90}Y)$	Quantulus 1220	Milk	$\varepsilon(^{90}Y) = 0.65^{p}$	Tovedal et a.l (2008)

Sr preconcentration and separation from interfering radionuclide on Superlig 620 column, Y elution with ammonium citate, Cherenkov counting of ^{90}Y, of line and on line detection (fully automated procedure)	^{90}Y	Tri-Carb 3100 TR/SL	Water	$\varepsilon(^{90}Sr - ^{90}Y) = 0.531^{ns}$	O'Hara et al. (2009)
Sr separation on Sr resin column, Y separation on Ln resin column (HDEHP on inert support), Y separation by HDEHP, Cherenkov counting (HNO_3)	^{89}Sr, ^{90}Y	Quantulus 1220	BWR coolant water	nr	Tovedal et al. (2009, 2009a), Holmgren et al., 2014.
Sr separation by combination of chelating resin and alaginate, $BaCl_2$ elution and Cherenkov counting	^{89}Sr, $^{90}Sr(^{90}Y)$	Tri-Carb 3170 TR/SL	Water, milk	$\varepsilon(^{90}Y) = 0.39^{g}$ $\varepsilon(^{89}Sr) = 0.24^{g}$	Günther et al. (2009)
Sr separation on Sr resin column, Cherenkov counting 0.05M HNO_3	$^{90}Sr(^{90}Y)$	Tri-Carb (ns)	Environmental samples (water soil, seaweed)	nr	Harrison et al. (2011)
Sr separation on Sr resin column, Y separation on DGA (N,N,N′,N′-tetra-n-octyldiglycolamide on inert support Cherenkov counting (HCl)	$^{90}Sr(^{90}Y)$	Quantulus 1220	Milk, water, liquid radioactive waste	$\varepsilon(^{90}Y) = 0.642^{ns}$ $\varepsilon(^{89}Sr) = 0.40^{ns}$	Groska et al. (2012), IAEA (2013)
Y extraction with 20% HDEHP in toluene, Cherenkov counting in diluted HNO_3	^{90}Y	Quantulus 1220	Soil, IAEA 375	$\varepsilon(^{90}Sr–^{90}Y) = 0.732^{p}$	Karacan (2011)
Sr solid phase extraction AnaLig®Sr01, Sr Na_4EDTA elution, Cherenkov counting$^{90}Sr(^{90}Y)$ Na_4EDTA solution	$^{90}Sr(^{90}Y)$	Tri-Carb 2900 TR	IAEA 375, radioactive waste	$\varepsilon(^{90}Y) = 0.50–0.60^{p}$	Dulánská et al. (2011, 2012)
Sr solid-phase extraction AnaLig®Sr01, Sr RAD disc, 3M Empore disc, Na_4EDTA elution, extraction chromatographic on Sr resin column by using HNO_3, Cherenkov counting$^{90}Sr(^{90}Y)$ Na_4EDTA solution	$^{90}Sr(^{90}Y)$	Tri-Carb 2900 TR	Underground water	$\varepsilon(^{90}Y) = 0.50–0.60^{p}$	Ometáková et al. (2011)
Sr solid phase extraction AnaLig®Sr01, Sr RAD disc, Na_4EDTA elution, extraction chromatographic on Sr resin column by using HNO_3, Cherenkov counting	$^{90}Sr(^{90}Y)$	Tri-Carb 2900 TR	Liquid samples, proficiency test, urine	nr	Drábová et al. (2012, 2014), Dulanská et al. (2013)
Direct Cherenkov counting$^{90}Sr(^{90}Y)$	$^{90}Sr(^{90}Y)$	Quantulus 1220	Urine, milk	ε ($^{90}Sr–^{90}Y$) = 0.677 water	Tsroya et al. (2013a, 2013b)
Sr separation on Sr resin column ($HCl + HNO_3$), Cherenkov counting, (HCl)	^{89}Sr, $^{90}Sr(^{90}Y)$	Tri-Carb 3180 TR/SL	Liquid radioactive waste	$\varepsilon(^{90}Y) = 0.415^{p}$ $\varepsilon(^{89}Sr) = 0.289^{p}$ 25% lower than in HNO_3	Grahek et al. (2013)
Five column separation of different isotopes Sr separation on Sr resin column, Cherenkov counting	^{89}Sr, $^{90}Sr(^{90}Y)$	Hidex 300 SL	Water, swipe	nr	Dai and Kramer-Trembly (2014)

Continued

TABLE 6.22 List of selected methods for the analysis of radiostrontium/radioyttrium by Cherenkov counting or a combination of LSA and Cherenkov counting.—cont'd

Method outline	Isotope	Instrument	Sample	Cherenkov efficiency	References
Titanium dioxide coprecipitation (HTiO), Y separation on DGA resin (N,N,N′,N′-tetra-n-octyldiglycolamide on inert support), Cherenkov counting (HNO_3)	^{90}Y	Hidex 300 SL	Seawater	$\varepsilon = 0.9(TDCR)^{0.75}$, $\varepsilon(^{90}Y) = 0.72^{p}$	Tayeb et al. (2014, 2015)
Y separation on DGA-N Cherenkov counting 0.05 HCl	^{90}Y	Hidex 300 SL	Water	$\varepsilon = 0.9(TDCR)^{0.75p}$	Olfert et al. (2014)
Sr separation on Sr resin column, Cherenkov counting 0.05M HNO_3	$^{90}Sr(^{90}Y)$	Tri-Carb 2700	Leaf, bark	nr	Kubota et al. (2015)
Concentration with cation exchanger, Sr separation on Sr resin column (8M HNO_3), Cherenkov counting 0.05M HNO_3 (automated separation)	^{89}Sr, $^{90}Sr(^{90}Y)$	Quantulus 1220	Milk	$\varepsilon(^{90}Y) = 0.635^{g}$ $\varepsilon(^{89}Sr) = 0.415^{g}$ $\varepsilon(^{90}Sr) = 0.017^{g}$	Chung et al. (2015)
Sr separation on Sr resin column (8M HNO_3), Cherenkov counting in 0.5M HNO_3 (automated separation)	$^{90}Sr(^{90}Y)$	Quantulus 1220	Seawater	nr	Kim et al. (2015)
Sr capture on SuperLig 620 column (molecular recognition), Sr Cherenkov counting on column surrounded with 5M HNO_3 in 20 mL plastic vial (automated separation)	^{89}Sr, $^{90}Sr(^{90}Y)$	Tri-Carb 3180 TR/SL	Water, liquid waste	$\varepsilon(^{90}Sr{-}^{90}Y) = 0.4428^{g}$ $\varepsilon(^{89}Sr) = 0.3041^{g}$ $\varepsilon(^{90}Sr{-}^{90}Y) = 0.5537^{p}$ $\varepsilon(^{89}Sr) = 0.3344^{p}$	Milanović and Grahek (2015)
Y extraction with 10% HDEHP in toluene, Cherenkov counting in diluted HNO_3	^{90}Y	Quantulus 1220	Bilberry	$\varepsilon(^{90}Y) = 0.73^{p}$	Aslan et al. (2015)
Y separation on DGA resin (N,N,N′,N′-tetra-n-octyldiglycolamide), Cherenkov counting in 1M HNO_3	^{90}Y	Hidex 300 SL/SLL	Edible plant samples	$\varepsilon(^{90}Y) = 0.57^{ns}$	Amano et al. (2016)
Carbonate precipitation, Sr separation by using double-stacked Sr-resin cartridges, Y separation on DGA resin, Cherenkov counting of strontium	^{89}Sr, $^{90}Sr(^{90}Y)$	Hidex 300 SL	Seawater	$\varepsilon(^{90}Y) = 0.69^{p}$ $\varepsilon(^{89}Sr) = 0.\ 452^{p}$ $\varepsilon(^{90}Sr) = 0.043^{p}$ (window 20–350)	Tayeb et al. (2016)
Sr separation on Sr resin column, Cherenkov counting (HNO_3)	$^{90}Sr(^{90}Y)$	Quantulus 1220	Soil	nr	Qiao et al. (2017)
Y separation on DGA resin and TRU resin ((octylphenyl-N,N-di-isobutyl carbamoylmethyl phosphine oxide in tri-n-butyl phosphate, CMPO/TBP), Cherenkov counting 1M HNO_3	^{90}Y	Quantulus 1220	Food (meat, cheese, ice cream, lasagna etc)	$\varepsilon(^{90}Y) = 0.47{-}0.54^{p}$	Pan et al. (2017)

Sr separation from ^{99m}Tc eluate, anion exchange and Sr resin (8M HNO_3), Cherenkov counting in 0.05M HNO_3	^{89}Sr, ^{90}Sr(^{90}Y)	Quantulus 1220	^{99m}Tc eluate for medical application	$\varepsilon(^{90}Y) = 0.58^{g}$ $\varepsilon(^{89}Sr) = 0.345^{g}$ (window 20–450)	Hou (2017)
Sr carbonate precipitation, separation on Sr resin column (8M HNO_3), Cherenkov counting in 0.1 M HNO_3	^{90}Sr(^{90}Y)	Quantulus 1220	Liquid	$\varepsilon(^{90}Y) = 0.66^{p}$	Kim et al. (2017)
Sr, Y extraction with 10% HDEHP in toluene, Cherenkov counting in organic and aqueous phase	^{90}Sr(^{90}Y), ^{90}Y	Quantulus 1220	Water	$\varepsilon(^{90}Sr–^{90}Y) = 0.907^{p}$	Reddy et al. (2017)
Sr solid phase extraction AnaLig®Sr01, Na_4EDTA elution, Cherenkov counting Sr in Na_4EDTA solution	^{90}Sr(^{90}Y)	Tri-Carb 3100 TR	Bone ash	$\varepsilon(^{90}Y) = 0.56^{p}$	Dulanská et al. (2017)
Y coprecipitation with titanium hydroxide (HTiO) and YF_3, ^{90}Y Cherenkov counting	^{90}Y	Hidex 300 SL	Solid radioactive waste	$\varepsilon = 0.9(TDCR)^{0.75}$ $\varepsilon(^{90}Y) = 0.72^{ns}$	Yang et al. (2017)
Direct measurement	^{90}Sr(^{90}Y)	Quantulus 1220	Water	$\varepsilon(^{90}Sr–^{90}Y) = 0.4586^{p}$ $\varepsilon(^{90}Sr–^{90}Y) = 0.3224^{g}$ (window 20–350)	Todorović et al. (2017)
Ca,Sr phosphate precipitation, separation on Sr resin column (8M HNO_3), Cherenkov counting (0.05 M HNO_3)	^{89}Sr, ^{90}Sr(^{90}Y)	Quantulus 1220	Urine, water	nr	Ridone et al. (2017)
Sr,Y separation different method (Sr resin, mixed solvent anion exchange, Sr resin in combination of mixed solvent anion exchange, Chernkov counting (3–5M HNO_3)	^{89}Sr, ^{90}Sr(^{90}Y)	Tri-Carb3180 TR/SL	Liquid waste, water, vegetation, soil, bone ash	$\varepsilon(^{90}Sr–^{90}Y) = 0.555^{p}$, $\varepsilon(^{89}Sr) = 0.345^{p}$	Grahek et al. (2012) Grahek et al. (2018)
Sr separation on Sr resin column 8M HNO_3, ^{90}Y separation from ^{89,90} Sron Sr resin Cherenkov counting (HNO_3)	^{89}Sr,^{90}Y	Quantulus 1220	Aqueous model samples	$\varepsilon\ (^{90}Y) = 0.586$, $\varepsilon(^{89}Sr) = 0.389$ $\varepsilon(^{90}Sr) = 4.34 \cdot 10^{-4}$	Holmgren-Rondahl and Ramebäck (2018)

^{89}Sr, ^{90}Sr(^{90}Y)–^{89}Sr determination, ^{90}Sr-determination through ^{90}Y ingrowth.
^{89}Sr, (^{90}Y)–^{89}Sr determination, ^{90}Sr determination through ^{90}Y decay.
^{90}Sr(^{90}Y)–^{90}Sr determination through ^{90}Y ingrowth.
^{90}Y–yttrium isolation, ^{90}Sr determination through ^{90}Y decay.
$\varepsilon(^{90}Y)$–Cherenkov counting efficiency for ^{90}Y.
$\varepsilon\ (^{90}Sr–^{90}Y)$–Cherenkov counting efficiency for ^{90}Y–^{90}Sr in equilibrium.
nr–not reported.
ns–not specified.
p – efficiency in plastic vials (polyethylene and/or Teflon coated, see detail in reference).
g – efficiency in glass vials (normal or low potassium, see detail in reference).

Cherenkov counting of ^{90}Sr in radioactive waste can be complicated by the presences of ^{137}Cs among other radionuclides that emit high energy beta or gamma radiation. Consequently radionuclide cleanup for the extraction of ^{90}Sr on specific ion exchange resins may be needed (Torres et al., 2002), as described earlier in this chapter. Alternatively, Chitra et al. (2011) utilized gamma spectrometry for the analysis of the ^{137}Cs and Cherenkov counting for the measurement of ^{90}Sr.

^{228}Th and ^{234}Th can be analyzed via Cherenkov counting of their β-emitting daughters. Al-Masri and Blackburn (1994) and Nour et al. (2002) demonstrate the analysis of these nuclides when in secular equilibrium with their daughters. The ^{234m}Pa daughter nuclide of ^{234}Th yields a Cherenkov counting efficiency of up to 62% and the ^{212}Bi, ^{212}Pb, and ^{208}Tl daughter nuclides of ^{228}Th can be detected with a reported Cherenkov counting efficiency of up to 53%. The Cherenkov analysis of ^{234}Th can be used for the determination of uranium when ^{234}Th is in secular equilibrium with its parent ^{238}U (see Blackburn and Al-Masri, 1994; Al-Masri and Blackburn, 1994; Bower et al., 1994; Alamelu and Aggarwal, 2009; Gulin et al., 2013).

^{210}Pb has been applied to studies of container adsorption of Pb(II) by Pacer (1990); and Cherenkov counting utilized for the measurement of ^{210}Pb in air filters (Dale et al. (2002) and in lead shields (Hurtado et al., 2003) and. The analysis of ^{210}Pb by Cherenkov counting is possible only through the detection of the Cherenkov photons produced by the daughter nuclide ^{210}Bi, which reaches secular equilibrium with its parent nuclide. The Cherenkov counting efficiency of ^{210}Pb(^{210}Bi) without wavelength shifter is reported to range between 14% and 18% (Arinc et al., 2011; Salonen, 2010; Dale et al., 2002; Hurtado et al., 2003; Blais and Marshall, 1988).

Peck et al. (1998) described the measurement of ^{210}Bi by Cherenkov counting in a commercial liquid scintillation counter. The counting efficiency in water was 0.17 counts per second per Becquerel (17%). When the enhancers Triton X-100 (15% v/v) and sodium salicylate (1% m/v) are added to the solution the counting efficiency for ^{210}Bi increases from 17% to 75%. The ^{210}Po daughter of ^{210}Bi causes interference of 0.85 counts per second per Becquerel in the presence of the enhancers but not in water. When ^{210}Bi and ^{210}Po were present in secular equilibrium the total counting efficiency was 160%. When ^{210}Bi and ^{210}Po are not in secular equilibrium the ^{210}Po can be removed immediately before counting by plating onto silver foil. The use of the enhancers gives a substantial increase in counting efficiency compared to counting in water. Compared with solutions used in liquid scintillation counting, the enhancer solution is inexpensive and can be disposed of without environmental hazard.

Blackburn and Al-Masri (1993) and Al-Masri and Blackburn (1995a,b) demonstrated the analysis of ^{222}Rn and ^{226}Ra via the Cherenkov counting of their β-emitting daughters ^{214}Bi and ^{214}Pb with a Cherenkov counting efficiency of 77%. These techniques were subsequently applied to the analysis of ^{222}Rn in surface waters (Al-Masri and Blackburn, 1999).

The Cherenkov counting efficiency of ^{36}Cl is low. An optimum counting efficiency of only 6.6% can be expected due to the low E_{max} of its β particles (see Table 6.21). Nevertheless, Holst et al. (2000) elected to analyze ^{36}Cl tracer nuclide in biological studies by Cherenkov counting because analysis could be carried out without liquid scintillation cocktail, which would render the sample useless for further studies.

L'Annunziata and coworkers (see Aleissa et al., 2008) describe the first assay of isolated ^{228}Ac by Cherenkov counting and its application to the measurement of ^{228}Ra in natural waters. The activities of ^{228}Ra, determined from the Cherenkov counting of ^{228}Ac, are calculated back to the time of ^{228}Ac separation from ^{228}Ra in secular equilibrium. Optimum Cherenkov detection efficiencies of ^{228}Ac in aqueous solution contained in polyethylene plastic counting vials was reported to be in the range of 10.7%−10.9%.

Buchtela and Tschurlovits (1975) reported a Cherenkov counting efficiency of ~75% for ^{42}K in water. It has very limited use as a tracer nuclide, because of its relative short half-life of 12.36 hours. The isotope ^{40}K can be analyzed also in water with a Cherenkov detection efficiency of 55% as reported by Pullen (1986), and the Cherenkov counting technique has been applied by Rao et al. (2000a,b) to the analysis of ^{40}K in natural water samples. Because of the lack of a suitable radiotracer for K and the close chemistry of the Rb and K elements, it is at times possible to use ^{86}Rb as a tracer for potassium. L'Annunziata and coworkers (see Noor et al. 1996) and Tuininga et al. (2002), report the use of ^{86}Rb as a radiotracer with a Cherenkov counting efficiency of up to 55% in water.

XV. Advantages and disadvantages in radionuclide analysis

It is obvious that Cherenkov counting cannot compete with liquid scintillation counting as far as highest possible counting efficiency is concerned. In addition, Cherenkov counting in aqueous media cannot be used for the analysis of very low-energy beta-particle emitters. However, if very high counting efficiencies are not necessary, Cherenkov counting of relatively high-energy beta-particle emitters has the following advantages over liquid scintillation counting:

1. Samples may be counted directly in aqueous solution or in organic solvents

2. No floors, fluor cocktails, or other compounds need be added, and thus the samples to be analyzed remain unadulterated and suitable for subsequent studies or analysis.
3. A larger volume of sample may be counted in a 20-mL counting vial since fluor solution is not needed.
4. Chemical quenching is nonexistent. Solutes may change the refractive index of the medium and consequently the beta-particle energy threshold for Cherenkov production, but chemical quench per se does not occur.
5. Time and expense are saved in sample preparation. The use of expensive organic fluors or fluor cocktails, which are customarily used in liquid scintillation analysis, is avoided.
6. There is no interference from other radionuclides that cannot produce Cherenkov photons in aqueous media (e.g., ^{3}H, ^{14}C, ^{125}I) and other nuclides that do not emit beta-particles of energy equal to or in excess of the threshold energy for the production of Cherenkov photons in aqueous media ($E_{th} = 262$ keV) or radionuclides that do not yield Compton electrons of sufficient energy to create Cherenkov photons.
7. There are no chemical fluor disposal problems associated with Cherenkov counting.

XVI. Recommendations in radionuclide analysis

The following recommendations can be made to facilitate the Cherenkov analysis of radionuclides and optimize Cherenkov counting performance:

1. Always use plastic vials for Cherenkov counting unless a wavelength shifter is used. Plastic vials provide higher Cherenkov counting efficiencies and lower background than glass vials (i.e., higher FOMs). In addition, they are less expensive than glass and unbreakable.
2. Unless samples are totally colorless or have a constant quench level, prepare a color quench correction curve based on the color of the experimental samples. A color quench correction curve is preferred at all times, because even slight amounts of color could cause significant quench and loss of counting efficiency. Also, most contemporary liquid scintillation analyzers can use the sample spectrum quench-indicating parameter and a quench correction curve stored in the instrument computer for automatic conversion of Cherenkov count rate to activity, which facilitates automation and high sample throughput.
3. For samples of low Cherenkov count rates, such as in the counting of environmental samples, the liquid scintillation analyzer will require long counting times to determine a sample spectrum quench-indicating parameter [*e.g.*, SIS or SQP(I)]; error can still occur. In such cases, an internal standard method or an external standard, such as ^{152}Eu, described by Tsroya et al. (2009) and discussed in Section IV.D of this chapter, may be used to determine the Cherenkov counting efficiency.
4. Maintain the samples for counting at a constant volume in counting vials unless it can be verified through testing that there are no significant volume effects on counting efficiency over a certain range of volume changes.
5. All samples should be counted for a period of time sufficient to achieve a % 2 sigma (% 2S) error of 1% or lower to ensure accurate count determinations and good measurements of the sample spectrum quench indicating parameter.

References

Aartsen, M.G., et al., 2016. Neutrino oscillation studies with IceCube-DeepCore. Nucl. Phys. B 908, 161–177.

Aartsen, M.G., et al., 2018. Astrophysical neutrinos and cosmic rays observed by IceCube. Adv. Space Res. 62, 2902–2930.

Abbasi, R., Abdou, Y., Abu-Zayyad, T., Adams, J., Aguilar, J.A., Ahlers, M., Andeen, K., Auffenberg, J., Bai, X., Baker, M., et al., 2010. The energy spectrum of atmospheric neutrinos between 2 and 200 TeV with the AMANDA-II detector. Astropart. Phys. 34, 48–58.

Abbasi, R., Abdou, Y., Abu-Zayyad, T., Actis, O., Adams, J., et al., 2011. Search for neutrino-induced cascades with five years of AMANDA data. Astropart. Phys. 34, 420–430.

Abbon, P., Alexeev, M., Angerer, H., Birsa, R., Bordalo, P., et al., 2010. Design and construction of the fast photon detection system for COMPASS RICH-1. Nucl Instrum. Methods Phys. Res., Sect. A 616, 21–37.

Abbon, P., Alexeev, M., Angerer, H., Baum, G., Birsa, R., et al., 2011. Particle identification with COMPASS RICH-1. Nucl Instrum. Methods Phys. Res., Sect. A 631, 26–39.

Abbon, P., Adolph, C., Akhunzyanov, R., Alexandrov, Y., Alexeev, M.G., 2015. The COMPASS setup for physics with hadron beams. Nucl Instrum. Methods Phys. Res., Sect. A 779, 69–115.

Abe, K., Haga, Y., Hayato, Y., Ikeda, M., Iyogi, K., et al., 2016. Real-time supernova neutrino burst monitor at Super-Kamiokande. Astropart. Phys. 81, 39–48.

Achterberg, A., Ackermann, M., Adams, J., Ahrens, J., Andeen, K., Atlee, D.W., Baccus, J., Bahcall, J.N., Bai, X., Baret, B., et al., 2006. First year performance of the IceCube neutrino telescope. Astropart. Phys. 26, 155–173.

Adachi, I., Sumiyoshi, T., Hayashi, K., Iida, N., Enomoto, R., Tsukada, K., Suda, R., Matsumoto, S., Natori, K., Yokoyama, M., Yokogawa, H., 1995. Study of a threshold Cherenkov counter based on silica aerogels with low refractive indices. Nucl Instrum. Methods Phys. Res., Sect. A 355, 390–398.

Adachi, I., Fujita, K., Fukushima, T., Gorišek, A., Hayashi, D., Iijima, T., Ikado, T., Ishikawa, T., Kawai, H., Korpar, S., Kozakai, Y., Križan, P., et al., 2007. A study of proximity focusing RICH with aerogel radiator. Nucl Instrum. Methods Phys. Res., Sect. A 580, 1042–1045.

Adachi, I., Ishii, Y., Kawai, H., Kuratani, A., Tabata, M., 2008. Study of a silica aerogel for a Cherenkov radiator. Nucl Instrum. Methods Phys. Res., Sect. A 595, 180–182.

Adachi, I., Tabata, M., Kawai, H., Sumiyoshi, T., 2011. Study of transparent silica aerogel with high refractive index. Nucl Instrum. Methods Phys. Res., Sect. A 639, 222–224.

Afanasiev, G.N., Kartavenko, V.G., Stepanovsky, Y.P., 1999. On Tamm's problem in the Vavilov-Cherenkov radiation theory. J. Phys. D: Appl. Phys. 32, 2029–2043.

Afanasiev, G.N., Lyubchenko, M.V., Stepanovsky, Y.P., 2006. Fine structure of the Vavilov–Cherenkov radiation. Proc. R. Soc. A 462, 689–699.

Agarwala, J., Alexeev, M., Azevedo, C.D.R., Birsa, R., Bradamante, F., et al., 2018. Novel MPGD based detectors of single photons in COMPASS RICH-1. Nucl Instrum. Methods Phys. Res., Sect. A. https://doi.org/10.1016/j.nima.2017.11.011 (in press).

Ageron, M., et al., 2011. ANTARES: the first undersea neutrino telescope. Nucl Instrum. Methods Phys. Res., Sect. A 656, 11–38.

Agostinelli, S., Allison, J., Amako, K., Apostolakis, J., Araujo, H., Arce, P., Asai, M., Axen, D., Banerjee, S., Barrand, G., et al., 2003. Geant4 – a simulation toolkit. Nucl Instrum. Methods Phys. Res., Sect. A 506, 250–303.

Aguilar, J.A., Al Samarai, I., Albert, A., André, M., Anghinolfi, M., Anton, G., Anvar, S., Ardid, M., Assis Jesus, A.C., Astraatmadja, T., et al., 2011. Time calibration of the ANTARES neutrino telescope. Astropart. Phys. 34, 539–549.

Aharmim, B., for the SNO Collaboration, et al., 2005. Electron energy spectra, fluxes, and day-night asymmetries of 8B solar neutrinos from measurements with NaCl dissolved in the heavy-water detector at the Sudbury Neutrino Observatory. Phys. Rev. C 72, 055502.

Aharmim, B., for the SNO Collaboration, et al., 2007. Determination of the νe and total 8B solar neutrino fluxes using the Sudbury Neutrino Observatory Phase I data set. Phys. Rev. C 75, 045502.

Aharmim, B., for the SNO Collaboration, et al., 2008. Independent measurement of the total active 8B solar neutrino flux using an array of 3He proportional counters at the Sudbury neutrino observatory. Phys. Rev. Lett. 101, 111301.

Airapetian, A., Akopov, N., Amarian, M., Avakian, H., Avetissian, A., Avetisyan, E., Filippone, B.W., Kaiser, R., Zohrabian, H., 2005. The time-of-flight technique for the HERMES experiment. Nucl Instrum. Methods Phys. Res., Sect. A 540, 305–310.

Akatsu, M., Aoki, M., Fujimoto, K., Higashino, Y., Hirose, M., Inami, K., Ishikawa, A., Matsumoto, T., Misono, K., Nagai, I., Ohshima, T., Sugi, A., Sugiyama, A., Suzuki, S., Tomoto, M., Okuno, H., 2000. Time-of-propagation Cherenkov counter for particle identification. Nucl Instrum. Methods Phys. Res., Sect. A 440, 124–135.

Alamelu, D., Aggarwal, S.K., 2009. Determination of $^{235}U/^{238}U$ atom ratio in uranium samples using liquid scintillation counting. Talanta 77, 991–994.

Aleissa, K.A., Almasoud, F.I., Islam, M.S., L'Annunziata, M.F., 2008. Radium-228 analysis of natural waters by Cherenkov counting of actinium-228. Appl. Radiat. Isot. 66, 1954–1963.

Alici, A., ALICE Collaboration, 2014. Particle identification with the ALICE time-of-flight detector at the LHC. Nucl Instrum. Methods Phys. Res., Sect. A 766, 288–291.

Allison, J., Amako, K., Apostolakis, J., Araujo, H., Dubois, P.A., Asai, M., et al., 2006. Geant4 developments and applications. IEEE Trans. Nucl. Sci. 53, 270–278.

Allison, J., Amako, K., Apostolakis, J., Arce, P., Asai, M., Bagli, E., Bagulya, A., et al., 2016. Recent developments in GEANT4. Nucl. Insrtrum. Methods Phys. Res., Sect. A 835, 186–225.

Allison, P., et al., 2017. Constraints on the ultra-high-energy neutrino flux from Gamma-Ray bursts from a prototype station of the Askaryan radio array. Astropart. Phys. 88, 7–16.

Allkofer, Y., Amsler, C., Horikawa, S., Johnson, I., Regenfus, C., Rochet, J., 2007. A novel aerogel Cherenkov detector for Dirac-II. Nucl. Insrtrum. Methods Phys. Res., Sect. A 582, 497–508.

Allkofer, Y., Amsler, C., Horikawa, S., Regenfus, C., Rochet, J., 2008. A new aerogel Cherenkov detector for Dirac-II. Nucl. Insrtrum. Methods Phys. Res., Sect. A 595, 84–87.

Al-Masri, M.S., Blackburn, R., 1994. Simultaneous determination of ^{234}Th and ^{228}Th in environmental samples using Cerenkov counting. Radiochim. Acta 65, 133–136.

Al-Masri, M.S., Blackburn, R., 1995a. Application of Cerenkov radiation for the assay of ^{226}Ra in natural water. Sci. Total Environ. 173/174, 53–59.

Al-Masri, M.S., Blackburn, R., 1995b. Radiochemical determination of ^{226}Ra using Cerenkov counting. J. Radioanal. Nucl. Chem., Articles 195, 339–344.

Al-Masri, M.S., Blackburn, R., 1999. Radon-222 and related activities in surface waters of the English Lake District. Appl. Radiat. Isot. 50, 1137–1143.

Alto, N.M., Shao, F., Lazar, C.S., Brost, R.L., Chua, G., Mattoo, S., McMahon, S.A., Ghosh, P., Highes, T.R., Boone, C., Dixon, J.E., 2006. Identification of a bacterial type III effector family with G protein mimicry functions. Cell 124, 133–145.

Alvarez-Muñiz, J., Carvalho Jr., W.R., García-Fernández, D., Schoorlemmer, H., Zas, E., 2015. Simulations of reflected radio signals from cosmic ray induced air showers. Astropart. Phys. 66, 31–38.

Amano, H., Sakamoto, H., Shiga, N., Suzuki, K., 2016. Method for rapid screening analysis of Sr-90 in edible plant samples collected near Fukushima, Japan. Appl. Radiat. Isot. 112, 131–135.

Ampofo, E., Kietzmann, T., Zimmer, A., Jakupovic, M., Montenarh, M., Götz, C., 2010. Phosphorylation of the von Hippel–Lindau protein VHL by protein kinase CK2 reduces its protein stability and affects p53 and HIF-1α mediated transcription. Int. J. Biochem. Cell Biol. 42, 1729–1735.

Angelov, D., Charra, M., Seve, M., Côte, J., Saadi, K., Dimitrov, S., 2000. Differential remodeling of the HIV-1 nucleosome upon transcription activators and SWI/SNF complex binding. J. Molec. Biol. 302 (2), 315–326.

Anil Kumar, R., Vasu, K., Velayudhan, K.T., Ramachandran, V., Suseela Bhai, R., Unnikrishnan, G., 2009. Translocation and distribution of 32P labelled potassium phosphonate in black pepper *Piper nigrum* L. Crop Protect 28, 878–881.

Anonymous, 1996. Cerenkov Counting Performance on the TopCount™ Microplate Scintillation and Luminescence Counter. TopCount Topics, TCA-024. PerkinElmer, Inc., Waltham, MA, USA, p. 4. http://www.perkinelmer.com/lab-solutions/resources/docs/APP_TopCountCerenkovCountingPerfMicroplt.pdf.

Arinc, A., Johansson, L.C., Gilligan, C.R.D., Pearce, A.K., 2011. Standardisation of ^{210}Pb by Čerenkov counting. Appl. Radiat. Isot. 69, 768–772.

Ariño, I., Bastos, J., Broemmelsiek, D., Carvalho, J., Chmeissani, M., Conde, P., Davila, J., Dujmić, D., Eckmann, R., Garrido, L., et al., 2004. The HERA-B ring imaging Cherenkov counter. Nucl. Instrum. Methods Phys. Res., Sect. A 516, 445–461.

Artuso, M., Boulahouache, C., Blusk, S., Butt, J., Dorjkhaidav, O., Menaa, N., Mountain, R., Muramatsu, H., Nandakumar, R., Randrianarivony, K., Sia, R., Skwarnicki, T., Stone, S., Wang, J.C.,

Zhang, K., 2006. Performance of a C4F8O gas radiator ring imaging Cherenkov detector using multi-anode photomultiplier tubes. Nucl. Instrum. Methods Phys. Res., Sect. A 558, 373–387.

Arutyunova, E.I., Danshina, P.V., Domnina, L.V., Pleten, A.P., Muronetz, V.I., 2003. Oxidation of glyceraldehyde-3-phosphate dehydrogenase enhances its binding to nucleic acids. Biochem. Biophys. Res. Commun. 307, 547–552.

Asaturyan, R., Ent, R., Fenker, H., Gaskell, D., Huber, G.M., Jones, M., Mack, D., Mkrtchyan, H., Metzger, B., Novikoff, N., Tadevosyan, V., Vulcan, W., Wood, S., 2005. The aerogel threshold Cherenkov detector for the high momentum spectrometer in Hall C at Jefferson. Lab. Nucl. Instrum. Methods Phys. Res., Sect. A 548, 364–374.

Ashie, Y., et al. Super-Kamiokande Collaboration, 2005. Measurement of atmospheric neutrino oscillation parameters by Super-Kamiokande I. Phys. Rev D 71 (11), 112005.

Askaryan, G.A., 1962. Excess negative charge of an electron-photon shower and its coherent radio emission. Sov. Phys. JETP 14 (2), 441–443.

Askaryan, G.A., 1965. Coherent radio emission from cosmic showers in air and dense media. Sov. Phys. JETP 21 (3), 658.

Aslan, N., Yücel, U., Kahraman, G., Kurt, A., Yeltepe, E., Özvatan, S., Kaya, N., Gündoğdu, G., Mert, H., 2015. Determination of ^{90}Sr via Cherenkov counting and modified Eichrom methods in bilberry matrix in the context of BIPM supplementary comparison. J. Radioanal. Nucl. Chem. 303, 2019–2026.

Asokan, K.P., Sebastian, J., Jayachandran, N., Unny, V.K.P., 2004. Facile preparation of potassium ^{32}P-phosphonate. J. Radioanal. Nucl. Chem. 262 (3), 767–769.

Attas, E.M., Chen, J.D., Young, G.J., 1990. A Cherenkov viewing device for used-fuel verification. Nucl. Instrum. Methods Phys. Res., Sect. A 299, 88–93.

Attas, E.M., Chen, J.D., Young, G.J., 1992. An ultraviolet imager for nuclear safeguards inspectors. In: Proceedings of the International Meeting on Electron Tubes and Image Intensifiers, San Jose, CA, Feb. 10-12, 1992. Proc SPIE, vol. 1655, pp. 50–57.

Attas, E.M., Burton, G.R., Dennis Chen, J., Young, G.J., Hildingsson, L., Trepte, O., 1997. A nuclear fuel verification system using digital imaging of Cherenkov light. Nucl. Instrum. Methods Phys. Res., Sect. A 384, 522–530.

Avrorin, A., et al., 2011. The Baikal neutrino experiment. Nucl. Instrum. Methods Phys. Res., Sect. A 626–627, 513–518.

Avrorin, A.V., et al., 2013. Current status of the BAIKAL-GVD project. Nucl. Instrum. Methods Phys. Res., Sect. A 725, 23–26.

Avrorin, A.D., et al., 2014. The prototyping/early construction phase of the BAIKAL-GVD project. Nucl. Instrum. Methods Phys. Res., Sect. A 742, 82–88.

Avrorin, A.D., et al., 2016. Status of the early construction phase of Baikal-GVD. Nucl. Part. Phys. Proc. 273–275, 314–320.

Ayers, M., 2000. The Pioneer: Samule Kistler. Microstructured Materials Group. Environmental Energy Technology Division, E. O. Lawrence Berkeley National Laboratory, University of California, U. S. Department of Energy. http://eetd.lbl.gov/ecs/aerogels/kistler-early.html.

Aynutdinov, V., Avrorin, A., Balkanov, V., Belolaptikov, I., Bogorodsky, D., Budnev, N., Danilchenko, I., Domogatsky, G., Doroshenko, A., Dyachok, A., et al., 2011. The Baikal neutrino project: present and perspective. Nucl. Instrum. Methods Phys. Res., Sect. A 628, 115–119.

Banavali, A.D., Moreno, E.M., McCurdy, 1992. Strontium-89, strontium-90 analysis by Eichrom column chemistry and Cerenkov counting. Abstract. In: Proc. 38th Annual Conf. On Bioassay, Analytical and Environmental Radiochem. Santa Fe, New Mexico.

Barnykov, M.Y., Buzykaev, A.R., Danilyuk, A.F., Ganzhur, S.F., Goldberg, I.I., Kolachev, G.M., Kononov, S.A., Kravchenko, E.A., Mikerov, V.I., Muraviova, T.M., Minakov, G.D., Onuchin, A.P., Sidorov, A.V., Tayursky, V.A., 1998. Development of aerogel Cherenkov counters with wavelength shifters and phototubes. Nucl. Instrum. Methods Phys. Res., Sect. A 419, 584–589.

Barnaykov, A.Y., Barnaykov, M.Y., Beloborodov, K.I., Bobrovnikov, V.S., Buzykaev, A.R., Golubev, V.B., Gulevich, B.V., Danilyuk, A.F., Kononov, S.A., Kravchenko, E.A., Martin, K.A., Onuchin, A.P., Porosev, V.V., Serednyakov, S.I., 2011. Status of aerogel production in Novosibirsk. Nucl Instrum. Methods Phys Res., Sect. A 639, 225–226.

Barros, N., on behalf of the SNO Collaboration, 2013. Final results from SNO. Nucl. Phys. B Proc. Suppl. 237–238, 107–110.

Barwick, S.W., et al., 2017. Radio detection of air showers with the ARIANNA experiment on the Ross Ice Shelf. Astropart. Phys. 90, 50–68.

Bastin-Coyette, L., Cardoen, S., Cmal, C., de Viron, E., Arts, A., Amsailale, R., Van Den Neste, E., Bontemps, F., 2011. Nucleoside analogs induce proteasomal down-regulation of p21 in chronic lymphocytic leukemia cell lines. Biochem. Pharmacol. 81, 586–593.

Batarekh, M.K., Teherani, D.H., 1986. Determination of ^{90}Sr in various kinds of water after Chernobyl accident in Austria. J. Radioanal. Nucl. Chem. Lett. 108 (3), 133–138, 1986.

Baxter, J.W., Pickett, S.T.A., Dighton, J., Carreiro, M.M., 2002. Nitrogen and phosphorus availability in oak forest stands exposed to contrasting anthropogenic impacts. Soil Biol. Biochem. 34, 623–633.

Beauchesne, É., Desjardins, P., Hazell, A.S., Butterworth, R.F., 2009. Altered expression of tight junction proteins and matrix metalloproteinases in thiamine-deficient mouse brain. Neurochem. Int. 55, 275–281.

Beauchesne, É., Desjardins, P., Butterworth, R.F., Hazell, A.S., 2010. Up-regulation of caveolin-1 and blood–brain barrier breakdown are attenuated by N-acetylcysteine in thiamine deficiency. Neurochem. Int. 57, 830–837.

Beckford, B., De la Puente, A., Fujii, Y., Hashimoto, O., Kaneta, M., et al., 2014. Performance study of wavelength shifting acrylic plastic for Cherenkov light detection. Nucl. Instrum. Methods Phys. Res., Sect. A 735, 78–82.

Bélanger, M., Desjardins, P., Chatauret, N., Butterworth, R.F., 2002. Loss of expression of glial fibrillary acidic protein in acute hyperammonemia. Neurochem. Int. 41, 155–160.

Belcher, E.H., 1953. The luminescence of irradiated transparent media and the Čerenkov effect. I. The luminescence of aqueous solutions of radioactive isotopes. Proc. Royal Soc. A216, 90–102.

Bellerive, A., Klein, J.R., McDonald, A.B., Noble, A.J., Poon, A.W.P., for the SNO Collaboration, 2016. The Sudbury neutrino observatory. Nucl. Phys. B 908, 30–51.

Belousov, A.S., 2006. Cherenkov radiation and Cherenkov detectors in the Cherenkov laboratory. Radiat. Phys. Chem. 75, 837–844.

Bem, E.M., Bem, H., Reimschussel, W., 1978. The use of Cherenkov radiation in the measurement of cadmium-115m in blood and other tissues. Bull. Environm. Contam. Toxicol. 19, 677–683.

Bem, E.M., Bem, H., Reimschuessel, W., 1980. Determination of phosphorus-32 and calcium-45 in biological samples by Čerenkov and liquid scintillation counting. Int. J. Appl. Radiat. Isot. 31, 371–374.

Bem, E.M., Bem, H., Reimschussel, W., 1983. Direct determination of phosphorus-32 or chlorine-36 in tissue solubilizer solutions by Cherenkov scintillation counting. J. Radioanal. Chem. 79, 69–76.

BenZikri, A., 2000. Cerenkov counting. Health Phys 79 (5), S70–S71.

Berenbrink, M., Völkel, S., Heisler, N., Nikinmaa, M., 2000. O_2-dependent K^+ fluxes in trout red blood cells: the nature of O_2 sensing revealed by the O_2 affinity, cooperativity and pH dependence of transport. J. Physiol. **526**1, 69–80.

Berger, S.L., 1984. The use of Cherenkov radiation for monitoring reactions performed in minute volumes: examples from recombinant DNA technology. Anal. Biochem. 136, 515–519.

Berghaus, P., for the IceCube Collaboration, 2009. Muons in IceCube. Nucl. Phys. B Proc. Suppl. 196, 261–266.

Bezaguet, A., Geles, C., Reucroft, S., Marini, G., Martellotti, G., 1979. Experience with di-potassium-2-amino-6,8-naphthalene-disulphonic acid as a wavelength shifter in a water Cherenkov detector. Nucl. Instrum. Meth. 158, 303–306.

Bjornstad, H.R., Lien, H.N., Yu-Fu, Y., Salbu, B., 1992. Determination of ^{90}Sr in environmental and biological materials with combined HDEHP solvent extraction – low liquid scintillation counting technique. J. Radioanal. Nucl. Chem., Articles 156 (1), 165–173.

Blackburn, R., Al-Masri, M.S., 1993. Determination of radon-222 and radium-226 in water samples by Cerenkov counting. Analyst 118, 873–876.

Blackburn, R., Al-Masri, M.S., 1994. Determination of uranium by liquid scintillation and Cerenkov counting. Analyst 119, 465–468.

Blais, J.S., Marshall, W.D., 1988. Determination of lead-210 in admixture with bismuth-210 and polonium-210 in quenched samples by liquid scintillation counting. Anal. Chem. 60, 1851–1855.

Blasiyh Nuño, G.A., Korob, R.O., 2007. Influence of ^{231}Th in the activity determination of ^{234}Th by Cerenkov counting. Appl. Radiat. Isot. 65, 539–544.

Bobin, C., Thiam, C., Bouchard, J., Jaubert, F., 2010. Application of a stochastic TDCR model based on GEANT4 for Cherenkov primary measurements. Appl. Radiat. Isot. 68, 2366–2371.

Bobin, C., Thiam, C., Chauvenet, B., 2017. A radionuclide calibrator based on Cherenkov counting for activity measurements of high-energy pure β-emitters. Appl. Radiat. Isot. 119, 60–65.

Bockhorst, M., Heinloth, K., Pajonk, G.M., Begag, R., Elaloui, E., 1995. Fluorescent dye doped aerogels for the enhancement of Cherenkov light detection. J. Non–Cryst. Solids 186, 388–394.

Bogdanova, A., Grenacher, B., Nikinmaa, M., Gassmann, M., 2005. Hypoxic responses of Na^+/K^+ ATPase in trout hepatocytes. J. Exp. Biol. 208, 1793–1801.

Bolotovski, B.M., Vavilov, Y.N., Schmeleva, A.P., November 12, 2004. Sergei Vavilov: Luminary of Russian Physics. Cern Courier. Institute of Physics, London.

Boschi, F., Calderan, L., D'Ambrosio, D., Marengo, M., Fenzi, A., Calandrino, R., Sbarbati, A., Spinelli, A.E., 2011. In vivo ^{18}F-FDG tumour uptake measurements in small animals using Cerenkov radiation. Eur. J. Nucl. Med. Mol. Imag. 38 (1), 120–127.

Boudjemline, K., Cai, B., Cleveland, B.T., Evans, H.C., Ewan, G.T., Farine, J., Ford, R.J., Guillian, E., Hallin, A.L., Hallman, E.D., et al., 2010. The calibration of the Sudbury Neutrino Observatory using uniformly distributed radioactive sources. Nucl. Instrum. Methods Phys. Res., Sect. A 620, 171–181.

Bower, K., Angel, A., Gibson, R., Robinson, T., Knobeloch, D., Smith, B., 1994. Alpha-beta discrimination liquid scintillation counting for uranium and its daughters. J. Radioanal. Nucl. Chem. 97–107. Articles 181.

Brajnik, D., Korpar, S., Medin, G., Starič, M., Stanovnik, A., 1994. Measurement of ^{90}Sr activity with Cherenkov radiation in a silica aerogel. Nucl. Instrum. Methods Phys. Res., Sect A 353, 217–221.

Brajnik, D., Medin, G., Stanovnik, A., Starič, M., 1995. Determination of high energy β-emitters with a Ge spectrometer or Cherenkov radiation in an aerogel. Sci. Total Environ. 173/174, 225–230.

Branger, E., et al., 2014. Image Analysis as a Tool for Improved Use of the Digital Cherenkov Viewing Device for Inspection of Irradiated PWR Fuel Assemblies. Uppsala University. Technical Report. http://uu.diva-portal.org/smash/record.jsf?pid=diva2%3A766776&dswid=6609.

Bray, J.D., Ekers, R.D., Roberts, P., Reynolds, J.E., James, C.W., Phillips, C.J., McFadden, R.A., Protheroe, R.J., Aartsen, M., Alvarez-Muñiz, J., 2012. Status and strategies of current LUNASKA lunar Cherenkov observations with the Parkes radio telescope. Nucl. Instrum. Methods Phys. Res., Sect A 662, s95–s98.

Bray, J.D., Ekers, R.D., Roberts, P., Reynolds, J.E., James, C.W., Phillips, C.J., Protheroe, R.J., McFadden, R.A., Aartsen, M., 2015. A lunar radio experiment with the Parkes radio telescope for the LUNASKA project. Astropart. Phys. 65, 22–39.

Breban, D.C., Paunescu, N., Moreno-Bermudez, J., Margineanu, R., 2004. Activity concentrations of selected artificial and natural radionuclides in water and sediment samples from the North Western Black Sea, 1999. J. Radioanal. Nucl. Chem. 260 (3), 503–508.

Brek Eaton, J., Peng, J.-H., Schroeder, K.M., George, A.A., Fryer, J.D., Krishnan, C., Buhlman, L., Kuo, Y.-P., Steinlein, O., Lukas, R.J., 2003. Characterization of human α4β2-nicotinic acetylcholine receptors stably and heterologously expressed in native nicotonic receptor-null SH-EP1 human epithelial cells. Mol. Pharmacol. 64, 1283–1294.

Brunner, J., for the ANTARES Collaboration, 2011. The ANTARES neutrino telescope—status and first results. Nucl. Instrum. Methods Phys. Res., Sect A 626–627, S19–S24.

Buchtela, K., Tschurlovits, M., 1975. A new method for determination of ^{89}Sr, ^{90}Sr and ^{90}Y in aqueous solution with the aid of liquid scintillation counting. Int. J. Appl. Radiat. Isot. 26, 333–338.

Bunnenberg, C., Kraul, K., Kühn, W., 1987. Analysis of beta-nuclides by Cherenkov-spectrometry. Nucl. Instrum. Methods Phys. Res., Sect. A 255, 346–350.

Burdick, M.J., Neumann, D., Pohlman, B., Reddy, C.A., Tendulkar, R.D., Macklis, R., 2011. External beam radiotherapy followed by ^{90}Y inritumomab tiuxetan in relapsed or refractory bulky follicular lymphoma. Int. J. Radiat. Oncol. Biol. Phys. 79 (4), 1124–1130.

Caldwell, S.E., Berggren, R.R., Davis, B.A., Evans, S.C., Faulkner Jr., J.R., Garcia, J.A., Griffith, R.L., Lash, D.K., Lerche, R.A., Mack, J.M., Morgan, G.L., Moy, K.J., Oertel, J.A., Sturges, R.E., Young, C.S., 2003. Observation of d–t gamma rays. Rev. Scient. Instrum. 74 (3), 1837–1841.

Cardinale, R., On behalf of the LHCb RICH Coillaboration, 2016. The upgraded LHCb RICH detector: Status and perspectives. Nucl. Instrum. Methods Phys. Res., Sect. A 824, 9–11.

Carlson, P., 1986. Aerogel Cherenkov counters: construction principles and applications. Nucl. Instrum. Methods Phys. Res., Sect. A 248, 110–117.

Carminati, G., for the Super-Kamiokande Collaboration, 2015. The new wide-band solar neutrino trigger for Super-Kamiokande. Phys. Proc. 61, 666–672.

Carmon, B., 1979. The use of Cerenkov radiation for the assay of radiostrontium in aqueous solutions. Int. J. Appl. Radiat. Isot. 30, 97–100.

Carmon, B., German, U., 1982. Radioassay of low ^{90}Sr activities by early counting of the Cerenkov Radiation induced by the ingrowing daughter nuclide ^{90}Y. Health Phys 42 (4), 529–530.

Carmon, B., Dyer, A., 1987. Čerenkov spectroscopic assay of fission isotopes. II. Čerenkov counting of ^{106}Ru on UV-colour-quenched solutions containing other β-emitters. J. Radioanal. Nucl. Chem., Articles 109, 229–236.

Carr, J., 2008. Data from the ANTARES neutrino telescope. Nucl. Instrum. Methods Phys. Res., Sect. A 588, 80–85.

Castle, N.A., London, D.O., Creech, C., Fajloun, Z., Stocker, J.W., Sabatier, J.-M., 2003. Maurotoxin: a potent inhibitor of intermediate conductance Ca^{2+}-activated potassium channels. Mol. Pharmacol. 63, 409–418.

Chang, T.-M., Chen, S.-C., King, J.-Y., Wang, S.-J., 1996. Rapid and accurate determination of $^{89/90}$Sr in radioactive samples by Cerenkov counting. J. Radioanal. Nucl. Chem., Articles 204, 339–347.

Charles, M.J., Forty, R., 2011. TORCH: time of flight identification with Cherenkov radiation. Nucl. Instrum. Methods Phys. Res., Sect. A 639, 173–176.

Charpak, G., 1969. Particle detection by gas discharges. J. Phys. Paris Colloq. 2, 86–96.

Charpak, G., 1970. Evolution of the automatic spark chambers. An. Rev. Nucl. Sci. 20, 195–254.

Charpak, G., Sauli, F., 1978. The multistep avalanche chamber: a new high-rate, high-accuracy gaseous detector. Phys. Letts. 78B, 523–528.

Charpak, G., Sauli, F., 1979. Multiwire proportional chambers and drift chambers. Nucl. Instrum. Methods 162, 405–428.

Charpak, G., Bouchlier, R., Bressani, T., Favier, J., Zupancic, C., 1968. The use of multiwire proportional counters to select and localize charged particles. Nucl. Instrum. Methods 62, 262–268.

Charpak, G., Rahm, D., Steiner, M., 1970. Some developments in the operation of multiwire proportional chambers. Nucl. Instrrum. Methods 80, 14–34.

Čerenkov, P.A., 1934a. Visible light from clear liquids under the action of gamma radiation. C.R. Dokl. Akad. Nauk, SSSR 2 (8), 451–454.

Čerenkov, P.A., 1934b. Sichtbares Leichten von Reinen Flüssigkeiten unter der Einwirkung von γ-Strahlen. C.R. Dokl. Akad. Nauk, SSSR 2 (8), 455–457.

Čerenkov, P.A., 1936. Die Wirkung eines Magnetfeldes auf das durch Gamma-Strahlen Hervorgerfene sichtbare Leuchten der Flüssigkeiten. Dokl. Akad. Nauk, SSSR 3 (9), 413–416.

Čerenkov, P.A., 1937a. Sichtbares Leuchten der Reinen Flüssigkeiten unter der Einwirkung von Harten β-Strahlen. Dokl. Akad. Nauk, SSSR 14 (3), 101–105.

Čerenkov, P.A., 1937b. Winkelverteilung der Intensität des Leuchtens, das durch ã-Strahlen in Reinen Flüssigkeiten Hervorgerufen wird. Dokl. Akad. Nauk, SSSR 14 (3), 105–107.

Čerenkov, P.A., 1937c. Visible radiation of pure liquids under the action of fast electrons. Byull. Akad. Nauk, SSSR 4–5, 455–492.

Čerenkov, P.A., 1937d. Visible radiation produced by electrons moving in a medium with velocities exceeding that of light. Phys. Rev. 52, 378–379.

Čerenkov, P.A., 1938a. Spatial distribution of visible radiation produced by fast electrons. Dokl. Akad. Nauk, SSSR 21 (7), 319–321.

Čerenkov, P.A., 1938b. The spectrum of visible radiation produced by fast electrons. Dokl. Akad. Nauk, SSSR 20 (9), 651–655.

Čerenkov, P.A., 1938c. Absolute output of radiation caused by electrons moving within a medium with super-light velocity. Dokl. Akad. Nauk, SSSR 21 (8), 116–121.

Chen, C.C., et al., 2015. Taiwan astroparticle radiowave observatory for geo-synchrotron emissions TAROGE. Proc. of Science PoS ICRC2015 663.

Chen, J.D., et al., 2010. Detection of partial defects using a digital Cerenkov viewing device. In: Proceedings of IAEA Symposium on International Safeguards: Preparing for FutureVerification Challenges.

Chen, J.D., Gerwing, R., Keeffe, R., Larsson, M., Jansson, K., Hildingsson, I., Lindberg, B., Sundkvist, E., Meijer, U., Thorsell, M., Ohlsson, M., 2007. Long-cooled spent fuel verification using a digital Cherenkov viewing device. International Atomic Energy. Report IAEA-SM-367/14/07.

Cherenkov, P.A., 1958. Nobel Lecture: radiation of particles moving at a velocity exceeding that of light, and some of the possibilities for their use in experimental physics. Stockholm, December 11, 1958. In: Nobel Lectures, Physics, 1942-62." 1964. Nobel Foundation Staff. Elsevier Publishing, Amsterdam.

Cherenkov, P.A., 1986. At the threshold of discovery. Nucl. Instrum. Methods Phys. Res., Sect. A 248, 1–4.

Cherenkova, E.P., 2008. The discovery of the Cherenkov radiation. Nucl. Instrum. Methods Phys. Res., Sect. A 595, 8–11.

Chitra, S., Viswanathan, S., Rao, S.V.S., Sinha, P.K., 2011. Uptake of cesium and strontium by crystalline silicotitanates from radioactive wastes. J. Radioanal. Nucl. Chem. 287 (3), 955–960.

Chow, N.P., 1980. Improved Čerenkov counting of ^{32}Phosphorus. In: Peng, C.T., Horrocks, D.L., Alpen, E.L. (Eds.), Liquid Scintillation Counting, Recent Applications and Development, vol. 1. Academic Press, New York and London, pp. 387–388.

Chu, T.-C., Wang, J.-J., Lin, Y.-M., 1998. Radiostrontium analytical method using crown-ether compound and Cerenkov counting and its applications in environmental monitoring. Appl. Radiat. Isot. 49 (12), 1671–1675.

Chung, K.H., Kim, H., Lim, J.M., Ji, Y.Y., Choi, G.S., 2015. Rapid determination of radiostrontium in milk using automated radionuclides separator and liquid scintillation counter. J. Radioanal. Nucl. Chem. 304, 293–300.

Clark, S.B., 1995. Separation and determination of radiostrontium in calcium carbonate matrices of biological origin. J. Radioanal. Nucl. Chem. 194, 297–302.

Claus, R., Seidel, S., Sulak, L., Bionta, R.M., Blewitt, G., et al. numerous authors, 1987. A waveshifter light collector for a water Cherenkov detector. Nucl. Instrum, Methods Phys. Res., Sect. A 261, 540–542.

Clausen, T., 1968. Measurement of phosphorus-32 activity in a liquid scintillation counter without the use of scintillator. Anal. Biochem. 22, 70–73.

Coha, I., Neufuss, S., Grahek, Ž., Nemec, M., Nodilo, M., John, J., 2016. The effect of counting conditions on pure beta emitter determination by Cherenkov counting. J. Radioanal. Nucl. Chem. 310, 891–903.

Collins, G.B., Reiling, V.G., 1938. Čerenkov radiation. Phys. Rev. 54, 499–503.

Connolly, A., 2012. Review of underground salt attenuation measurements for SalSA. Nucl. Instrum, Methods Phys. Res., Sect. A 662, S196–S197.

Cook, G.T., Passo Jr., Carter, B.D., 1998. Environmental liquid scintillation analysis. In: L'Annunziata, M.F. (Ed.), Handbook of Radioactivity Analysis, first ed. Academic Press, San Diego, pp. 331–386.

Costantini, H., 2011. The ANTARES deep-sea neutrino telescope: operation and calibration. Nucl. Instrum, Methods Phys. Res., Sect. A 639, 26–29.

Coursey, B.M., Calhoun, J.M., Cessna, J.T., 1993. Radioassays of yttrium-90 used in nuclear medicine. Nucl. Med. Biol. 20 (5), 693–700.

Court, N.W., Kuo, I., Quigley, O., Bogoyevitch, M.A., 2004. Phosphorylation of the mitochondrial protein Sab by stress-activated protein kinase 3. Biochem. Biophys. Res. Commun. 319, 130–137.

Cobb, J., Warwick, P., Carpenter, R.C., Morrison, R.T., 1994. Determination of strontium-90 in water and urine samples using ion chromatography. Analyst 119, 1759–1764.

Cusanno, F., Garibaldi, F., Cisbani, E., Colilli, S., De Cataldo, G., De Leo, R., Giuliani, F., Gricia, M., Lagamba, L., Lucentini, M., Reitz, B., Santavenere, F., Urciuoli, G.M., 2004. A RICH detector for strangeness physics in Hall A at Jefferson. Lab. Nucl. Instrum. Methods Phys. Res., Sect. A 525, 163–167.

Curie, E., 1941. Madam Curie. Heinemann, London.

Cutshall, N.S., O'Day, C., Prezhdo, M., 2005. Rhodamine derivatives as inhibitors of JSP-1. Bioorg. Med. Chem. Lett. 15, 3374–3379.

Dai, X., Kramer-Tremblay, S., 2014. Five-column chromatography separation for simultaneous determination of hard-to-detect radionuclides in water and swipe samples. Anal. Chem. 86, 5441–5447.

Dai, X., Rollin, E., Bellerive, A., Hargrove, C., Sinclair, D., Mifflin, C., Zhang, F., 2008. Wavelength shifters for water Cherenkov detectors. Nucl. Instrum. Methods Phys. Res., Sect. A 589, 290–295.

Dale, C.J., Dale, A.A., Warwick, P.E., Rowe, J.E., 2002. Rapid determination of ^{210}Po and ^{210}Pb via ^{210}Bi in air filters using alpha spectrometry and Cerenkov counting. In: Möbius, S., Noakes, J., Schönhofer, F. (Eds.), "LSC 2001, Advances inLiquid Scintillation Spectometry, Radiocarbon. University of Arizona, Tucson, pp. 343–349.

Das, H.A., 2007. Measurement of diffusion coefficients by radioanalysis. J. Radioanal. Nucl. Chem. 273 (3), 753–757.

De Bonis, G., 2016. Recent results of the ANTARES neutrino telescope. Nucl. Part. Phys. Proc. 273–275, 419–424.

de Naurois, M., Mazin, D., 2015. Détecteurs au sol en astronomie gamma de très haute énergie. Comp. Rend. Phys. 16, 610–627.

Deng, Y., et al., 2017. The relationship between the silica wet-gels relative optical transmittance at 500 nm and structural features of silica aerogels. Ceramics Int 43, 10668–10672.

Denisov, S.P., Stoyanova, D.A., 2006. Cherenkov counters in experiments at IHEP accelerator. Radiat. Phys. Chem. 75, 856–861.

Desai, S., Liu, D.W., 2016. A search for evidence of solar rotation in Super-Kamiokande solar neutrino dataset. Astropart. Phys. 82, 86–92.

Deschênes, G., Doucet, A., 2000. Collecting duct Na^+/K^+-ATPase activity is correlated with urinary sodium excretion in rat nephrotic syndromes. J. Am. Soc. Nephrol. 11, 604–615.

Dewberry, R.A., Leyba, J.D., Boyce, W.T., 2000. Observation and measurement of ^{79}Se in Savannah River Site high level waste tank fission product waste. J. Radioanal. Nucl. Chem. **245**3, 491–500.

Dey, B., Borsato, M., Arnaud, N., Leith, D.W.G.S., Nishimura, K., et al., 2015. Design and performance of the focusing DIRC detector. Nucl. Instrum. Methods Phys. Res., Sect. A 775, 112–131.

Dherbecourt, O., Cheval, L., Bloch-Faure, M., Meneton, P., Doucet, A., 2006. Molecular identification of Sch28080-sensitive K-ATPase activities in the mouse kidney. Pflügers Archiv. Eir. J. Physiol. **451** (6), 769–775.

Dietz, M.L., Horwitz, E.P., 1992. Improved chemistry for the production of yttrium-90 for medical applications. Appl. Radiat. Isot. 43, 1093–1101.

Dolenec, R., Chagani, H., Korpar, S., Križan, P., Pestotnik, R., Stanovnik, A., 2011. Tests of a silicon photomultiplier module for detection of Cherenkov photons. Nucl. Instrum. Methods Phys. Res., Sect. A 628, 398–402.

Dolgoshein, B., Balagura, V., Buzhan, P., Danilov, M., Filatov, L., Garutti, E., Groll, M., Ilyin, A., Kantserov, V., Kaplin, V., et al., 2006. Status report on silicon photomultiplier development and its applications. Nucl. Instrum. Methods Phys. Res., Sect. A 563, 368–376.

Drábová, V., Strišovská, J., Dvorská, L., Kuruc, J., 2012. Validation of ^{90}Sr separation method using molecular recognition product AnaLig® Sr01 gel and extraction chromatography Sr® resin. J. Radioanal. Nucl. Chem. 2012 292, 1141–1145.

Drábová, V., Dulanská, S., Galanda, D., Remenec, B., Strisŏvska, J., 2014. Determination of ^{90}Sr in radioactive concentrate from nuclear power plant Mochovce. J. Radioanal. Nucl. Chem. 299, 1661–1664.

Drobnies, A.E., Davies, S.M.A., Kraayenhof, R., Epand, R.F., Epand, R.M., Cornell, R.B., 2002. CTP:phosphocholine cytidylyltransferase and protein kinase C recognize different physical features of membranes: differential responses to an oxidized phosphatidylcholine. Biochim. Biophys. Acta 1564, 82–90.

Drude, N., Tienken, L., Mottaghy, F.M., 2017. Theranostic and nanotheranostic probes in nuclear medicine. Methods 130, 14–22.

Duan, Y., Jana, S.C., Lama, B., Espe, M.P., 2016. Hydrophobic silica aerogels by silylation. J. Non-cryst. Solids. 437, 26–33.

Dulanská, S., Remenec, B., Mátel, Galanda, D., Molnar, A., 2011. Preconcentration and determination of ^{90}Sr in radioactive wastes using solid phase extraction techniques. J. Radioanal. Nucl. Chem. 288, 705–708.

Dulanská, S., Remenec, B., Mátel, L., Durkot, E., 2012. Rapid determination of ^{239,240}Pu, ^{238}Pu, ^{241}Am and ^{90}Sr in radioactive waste using combined SPE sorbents AnaLig®Pu02, AnaLig®Sr01 and TRU®Resin. J. Radioanal. Nucl. Chem. 293, 81–85.

Dulanská, S., Remenec, B., Bilohuštin, J., Labaška, M., Galanda, D., 2013. Rapid determination of ^{90}Sr in urine samples using AnaLig®Sr01. J Radioanal. Nucl. Chem. 295, 2189–2192.

Dulanská, S., Remenec, B., Mátel, L., Darázŏva, L., Galanda, D., 2017. Determination of ^{90}Sr in bone samples using molecular recognition technology product AnaLig®Sr-01. J. Radioanal. Nucl. Chem. 311, 29–33.

Enari, Y., et al., 2002. Progress report on Time-Of-Propagation counter—a new type of ring imaging Cherenkov detector. Nucl. Instrum. Methods Phys. Res., Sect. A 494, 430–435.

Engelfried, J., 2011. Cherenkov light imaging—Fundamentals and recent developments. Nucl. Instrum. Methods Phys. Res., Sect. A 639, 1–6.

Elrick, R.H., Parker, R.P., 1968. The use of Cerenkov radiation in the measurement of β-emitting radionuclides. Int. J. Appl. Radiat. Isot. 19, 263–271.

ESTAR, 2018. "Stopping Power and Range Tables for Electrons" NIST. National Institute of Standards and Technology, Gaithersburg, Maryland, USA. https://physics.nist.gov/PhysRefData/Star/Text/ESTAR.html.

Fardeau, J.C., 1984. Results of direct measures of the utilization coefficient in fertilizers by isotopic labelling with ^{32}P, ^{15}N and ^{40}K. Fert. Agric. 86, 23–30.

Feynman, R.P., 1950. Mathematical formulation of the quantum theory of electromagnetic interaction. Physical Review 80, 440–457.

Flammersfield, A., 1946. Eine Beziehung zwischer Energie und Reichweite für Beta-Strahlen kleiner und mittler Energie. Naturwissenschaften 33, 280–281.

Formaggio, J.A., for the SNO Collaboration, 2009. Measurement of atmospheric neutrinos at the Sudbury neutrino observatory. Nucl. Phys. A 827, 498c–500c.

Forty, R., 2010. The RICH system of LHCb. Nucl. Instrum. Methods Phys. Res., Sect. A 623, 294–296.

Frączyk, T., Kubiński, K., Masłyk, M., Cieśla, J., Hellman, U., Shugar, D., Rode, W., 2010. Phosphorylation of thymidylate synthase from various sources by human protein kinase CK2 and its catalytic subunits. Bioorg. Chem. 38, 124–131.

Frank, I.M., 1958. Optics of light sources moving in refractive media. Nobel lecture. December 11, 1958. In: Nobel foundation staff (Ed.), Nobel lectures in Physics, 1942-1962. Elsevier Publishing, Amsterdam.

Frank, I.M., 1960. Optics of light sources moving in refractive media. Science 131, 702–712.

Frank, I.M., Tamm, I.G., 1937. Coherent visible radiation of fast electrons passing through matter. Dokl. Akad. Nauk, SSSR 14, 109.

Friberg, I., 1997. Development and application of a method for the determination of ^{90}Sr in environmental samples. J. Radioanal. Nucl. Chem. 226, 55–60.

Frič, F., Finocchiaro, V., 1975. Cherenkov counting efficiency increase of phosphorus-32 using anthranilic acid or quinine as a wavelength shifter. Radiochem. Radioanal. Lett. 21, 205–210.

Frič, F., Palovčíková, V., 1975. Automatic liquid scintillation counting of ^{32}P in plant extracts by measuring the Cerenkov radiation in aqueous solutions. Int. J. Appl. Radiat. Isot. 26, 305–311.

Fricke, J., Tillotson, T., 1997. Aerogels: production, characterization, and applications. Thin Solid Films 297, 212–223.

Fujii, H., Takiue, M., 1988a. Radioassay of dual-labeled samples by sequential Cherenkov counting and liquid scintillation efficiency tracing technique. Nucl. Instrum. Methods Phys. Res., Sect. A 273, 377–380.

Fujii, H., Takiue, M., 1988b. Radioassay of alpha- and beta-emitters by sequential Cherenkov and liquid scintillation countings. Int. J. Radiat. Appl. Instrum., Part A. Appl. Radiat. Isot. 39, 327–330.

Fujii, H., Takiue, M., 1988c. Radioassay of dual-labeled samples with a Cherenkov counting technique. Nucl. Instrum. Methods Phys. Res., Sect. A 265, 558–560.

Fujii, H., Matsuno, K., Takiue, M., 2002. Construction of a liquid waste monitor using the Cerenkov technique for nuclear medicine. In: Proceedings of the LSC 2001 Conference", Karlsruhe, Germany, May 7-11, 2001. 425-428, Radiocarbon, Tucson.

Fukuda, S., Fukuda, Y., Hayakawa, T., Ichihara, E., Ishitsuka, M., Itow, Y., Kajita, T., Kameda, J., Kaneyuki, K., Kasuga, S., et al., 2003. The Super-Kamiokande detector. Nucl. Instrum. Methods Phys. Res., Sect. A 501, 418–462.

Gallo, R.M., Bryant, I., Fry, R., Williams, E.E., Riese II, D.J., 2006. Phosphorylation of ErbB4 on Tyr1056 is critical for inhibition of colony formation by prostate tumor cell lines. Biochem. Biophys. Res. Commun. 349, 372–382.

García Toraño, E., Grau Malonda, A., 1985. EFFY2, A new program to compute the counting efficiency of beta particles in liquid scintillators. Comput. Phys. Commun. 36, 307–312.

Garibaldi, F., Cisbani, E., Colilli, S., Cusanno, F., Frullani, S., Fratoni, R., Giuliani, F., Gricia, M., Iodice, M., et al., 2003. A proximity focusing RICH detector for kaon physics at Jefferson lab Hall A. Nucl. Instrum. Methods Phys. Res., Sect. A 502, 117–122.

Gerhardt, L., Klein, S., Stezelberger, T., Barwick, S., Dookayka, K., Hanson, J., Nichol, R., 2010. A prototype station for ARIANNA: a detector for cosmic neutrinos. Nucl. Instrum. Methods Phys. Res., Sect. A 624, 85–91.

Gerstmann, U.C., Tschöpp, V., 2006. Determination of ^{90}Sr/^{90}Y in wheat grains, soil, and deposition samples by TBP extraction and Cherenkov Counting. Radiocarbon 40, 197–204.

Ghods, A., Hussain, M., Mirna, A., 1994. Rapid determination of ^{90}Sr in foodstuffs and environmental material. Radiochim. Acta 65, 271–274.

Giese, R., Gildemeister, O., Paul, W., Schuster, G., 1970. A high resolution Cherenkov chamber. Nucl. Instrum. Methods 88, 83–92.

Ginzburg, V.L., 1940. Quantum theory of the light radiation from the electron moving uniformly in medium. Zh. Eksp. Theor. Fiz. 10, 589–600.

Ginzburg, V.L., 1977. Remarks on D. V. Skobel'tsyn's paper, "Paradoxes of the quantum theory of the Vavilov-Cerenkov and Doppler effects. Sov. Phys. Usp. 20, 546.

Ginzburg, V.L., 1996. Radiation by uniformly moving sources Vavilov - Cherenkov effect, transition radiation, and other phenomena. Sov. Phys. Usp. 39, 973–983.

Ginzburg, V.L., 2005. About Science, Myself and Others. CRC Press, pp. 72–73.

Gittens, J.R., Schuler, M.A., Strid, Å., 2002. Identification of a novel nuclear factor-binding site in the Pisum sativum sad gene promoters. Biochim. Biophys. Acta 1574, 231–244.

Glass, A.D.M., 1978. An improved method of sample preparation for the radioassay of β-particle emitters by Čerenkov counting. Int. J. Appl. Radiat. Isot. 29, 75–76.

Glässel, P., 1999. The limits of the ring image Cherenkov technique. Nucl. Instrum. Methods Phys. Res., Sect. A 433, 17–23.

Goel, S., England, C.G., Chen, F., Cai, W., 2017. Positron emission tomography and nanotechnology: a dynamic duo for cancer theranostics. Adv. Drug. Deliv. Rev. 113, 157–176.

Goffredo, V., Paradiso, A., Ranieri, G., Gadaleta, C.D., 2011. Yttrium-90 90Y in the principal radionuclide therapies: an efficacy correlation between peptide receptor radionuclide therapy, radioimmunotherapy and transarterial radioembolization therapy. Ten years of experience 1999–2009. Crit. Rev. Oncol./Hematol. 80, 393–410.

Ghods, A., Hussain, M., Mirna, A., 1994. Rapid determination of ^{90}Sr in foodstuffs and environmental material. Radiochimica Acta 65, 271–274.

Golub, A.G., Bdzhola, V.G., Briukhovetska, N.V., Balanda, A.O., Kukharenko, O.P., Kotey, I.M., Ostrynska, O.V., Yarmoluk, S.M., 2011. Synthesis and biological evaluation of substituted thien[2,3-d] pyrimidin-4-ylthiocarboxylic acids as inhibitors of human protein kinase CK2. Eur. J. Med. Chem. 46, 870–876.

Gorišek, A., 2004. Particle identification performance of the HERA-B RICH. Nucl. Instrum. Methods Phys. Res., Sect A 518, 590–592.

Govorkov, B.B., 2005. Cherenkov detectors in Cherenkov's laboratory. Nucl. Instrum. Methods Phys. Res., Sect A 553, 9–17.

Graf, N., Lebedev, A., Abrams, R.J., Akgun, U., Aydin, G., Baker, W., Barnes Jr., P.D., Bergfeld, T., Beverly, L., Bujak, A., Carey, D., et al., 2010. Charged kaon mass measurement using the Cherenkov effect. Nucl. Instrum. Methods Phys. Res., Sect. A 615, 27–32.

Graham, K., for the SNO Collaboration, 2003. Solar neutrino results from SNO and implications for neutrino oscillations. Nucl. Phys. A 721, 556c–559c.

Grahek, Ž., Rožmarić Mačefat, M., 2004. Isolation of iron and strontium from liquid samples and determination of ^{55}Fe and ^{89,90}Sr in liquid radioactive waste. Anal Chim. Acta 511, 339–348.

Grahek, Ž., Rožmarić Mačefat, M., 2005. Determination of radioactive strontium in seawater. Anal. Chim. Acta 534, 271–279.

Grahek, Ž., Zečević, N., Lulić, S., 1999. Possibility of rapid determination of low-level ^{90}Sr activity by combination of extraction chromatography separation and Cherenkov counting. Anal Chim. Acta 399, 237–247.

Grahek, Ž., Košutić, K., Rožmarić-Mačefat, M., 2006. Strontium isolation from natural samples with Sr resin and subsequent determination of ^{90}Sr. J. Radioanal. Nucl. Chem. **268**2, 179–190.

Grahek, Ž., Karanović, G., Nodilo, M., 2012. Rapid determination of ^{89,90}Sr in wide range of activity concentration by combination of yttrium, strontium separation and Cherenkov counting. J. Radioanal. Nucl. Chem. 292, 555–569.

Grahek, Ž., Milanović, I., Nodilo, M., Rožmarić, M., 2013. Sequential separation of Fe and Sr from liquid samples by using Sr resin and rapid determination of ^{55}Fe and ^{89,90}Sr. Appl. Radiat. Isot. 81, 42–48.

Grahek, Ž., Dulanská, S., Karanović, G., Coha, I., Tucaković, I., Nodilo, M., Mátel, I., 2018. Comparison of different methodologies for the ^{90}Sr determination in environmental samples. J. Environ. Radioact. 181, 18–31.

Grande, M., Moss, G.R., 1983. An optimized thin film wavelength shifting coating for Cherenkov detection. Nucl. Instrum. Meth. 215, 539–548.

Grape, S., Jacobsson Svard, S., Lindberg, B., Hjalmarsson, A., 2010. Modeling Cherenkov light from irradiated nuclear fuel assemblies using GEANT. In: IAEA Symposium on International Safeguards "Preparing for Future Verification Challenges". 1-5 November 2010, Vienna.

Grau Carles, A., 1995. New methods for the determination of β-spectra shapefactor coefficients. Appl. Radiat. Isot. 46 (2), 125–128.

Grau Carles, A., 2005. Beta shapefactor determinations by the cutoff energy yield method. Nucl. Instrum. Methods Phys. Res., Sect A 551, 312–322.

Grau Carles, A., Grau Malonda, A., December 29, 1992. Precise System for the Determination of the Quench Parameter of Radioactive Samples in Liquid Phase. Registry of Industrial Property, Madrid, Spain. Patent P. 9202639.

Grau Carles, A., Grau Malonda, A., 1995. Radionuclide standardization by Cherenkov counting. Appl. Radiat. Isot. 46, 799–803.

Grau Carles, A., Grau Malonda, A., 1996a. Aplicación de la Radiación Cherenkov a la Metrología de Radionucleidos. Editorial CIEMAT, Madrid, p. 140.

Grau Carles, A., Grau Malonda, A., 1996b. Precision measurement of the RaE shape factor. Nucl. Phys. A 596, 83–90.

Grau Carles, A., Grau Malonda, A., 1998. CHEREN, the Cherenkov counting efficiency. Comp. Phys. Commun. 111, 258–264.

Grau Carles, A., Grau Malonda, A., 2006. CHEREN2, the Cherenkov counting efficiency by an anisotropy detection model. Comp. Phys. Commun. 174, 30–34.

Grau Carles, A., Kossert, K., 2006. New advances in the determination of the ^{87}Rb shape factor function. Nucl. Phys. A 767, 248–258.

Grau Carles, A., Kossert, K., 2007. Measurement of the shape-factor functions of the long-lived radionuclides ^{87}Rb, ^{40}K and ^{10}Be. Nucl. Instrum. Methods Phys. Res., Sect. A 572, 760–767.

Grau Carles, A., Grau Malonda, A., Rodríguez Barquero, L., 1993a. Cherenkov radiation effects on counting efficiency in extremely quenched liquid scintillation samples. Nucl. Instrum. Methods Phys. Res., Sect. A 334, 471–476.

Grau Carles, A., Kossert, K., Grau Malonda, A., 2008. Determination of the shape factor of ^{90}Sr by means of the cutoff energy yield method. Appl. Rdaiat. Isot. 66, 1021–1025.

Grau Malonda, A., 1999. Ree Parameter Models in Liquid Scintillation Counting. In: F. Editorial CIEMAT, Madrid, ISBN 84-7834-350-4, p. 416.

Grau Malonda, A., Grau Carles, A., 1998a. The anisotropy coefficient in Cerenkov counting. In: Proc. ICRM 1997. National Institute of Standards and Technology, Gaithersburg, MD.

Grau Malonda, A., Grau Carles, A., 1998b. The anisotropy coefficient in Cerenkov counting. Appl. Radiat. Isot. 49 (9–11), 1049–1053.

Grau Malonda, A., Grau Carles, A., 2000. Standardization of electron-capture radionuclides by liquid scintillation counting. Appl. Radiat. Isot. 52, 657–662.

Grau Malonda, A., Grau Carles, A., 2002. Half-life determination of ^{40}K by LSC. Appl. Rdaiat. Isot. 56, 153–156.

Greisen, K., 1966. End to the cosmic-ray spectrum? Phys. Rev. Lett. 1617, 748–750.

Groska, J., Molnár, Z., Bokori, E., Vajda, N., 2012. Simultaneous determination of ^{89}Sr and ^{90}Sr: comparison of methods and calculation techniques. J. Radioanal. Nucl. Chem. 295, 2189–2192.

Gruhn, C.R., Ogle, W., 1980. In: Peng, C.-T., Horrocks, D.L., Alpen, E.L. (Eds.), Liquid Scintillation Counting, Recent Applications and Development, vol. 1. Academic Press, New York and London, pp. 357–374.

Grundt, K., Thiede, B., Østvold, A.C., 2017. Identification of kinases phosphorylating 13 sites in the nuclear, DNA-binding protein NUCKS. Biochim. Biophys. Acta 1865, 359–369.

Gulin, S.B., Gorelov, Y.S., Sidorov, I.G., Proskurnin, V.Y., 2013. Disk mini-adsorbers with radial flow for determination of ^{234}Th concentration in seawater. J. Radioanal. Nucl. Chem. 295, 855–860.

Günther, K., Lange, S., Veit, M., 2009. A rapid method for determining ^{89}Sr and ^{90}Sr by Cerenkov counting. Appl. Rdaiat. Isot. 67, 781–785.

Gys, T., Brook, N., Castillo García, L., Cussans, D., Föhl, K., Forty, R., et al., 2017. The TORCH detector R & D: status and perspectives. Nucl. Instrum. Methods Phys. Res., Sect. A 876, 156–159.

Hadley, D.R., On behalf of the Hyper-K Collaboration, 2016. The Hyper-K experiment: present and R&D for the next decade. Nucl. Instrum. Methods Phys. Res., Sect. A 824, 630–634.

Håkansson, A., Jonter, T., 2007. An Introduction to Nuclear Non-proliferation and Safeguards. Swedish Nuclear Power Inspectorate, p. 140. SKI Report 2004:44, ISSN: 1104-1374.

Hallin, A.L., 2010. Neutrino physics from SNO. Prog. Part. Nucl. Phys. 64, 199–201.

Harnew, N., 2014. Alternative particle identification techniques to Cherenkov detectors. Nucl. Instrum. Methods Phys. Res., Sect. A 766, 274–282.

Harnew, N., Brook, N., Castillo García, L., Cussans, D., Föhl, K., et al., 2016. The TORCH time-of-flight detector. Nucl. Instrum. Methods Phys. Res., Sect. A 824, 106–110.

Harrison, J.J., Zawadzki, A., Chisari, R., Wong, H.K.Y., 2011. Separation and measurement of thorium, plutonium, americium, uranium and strontium in environmental matrices. J. Environ. Radioact. 102, 896–900.

Hataya, K., Adachi, I., Dolenec, R., Iori, S., Iwata, S., et al., 2017. Development of the ARICH monitor system for the Belle II experiment. Nucl. Instrum. Methods Phys. Res., Sect. A 876, 176−180.

Haynes, W.M., 2011. CRC Handbook of Chemistry and Physics, 92nd ed. CRC Press, Boca Raton, FL.

He, J., 2017. Real-time calibration and alignment of the LHCb RICH detectors. Nucl. Instrum. Methods Phys. Res., Sect. A 876, 13−16.

Heaviside, O., 1888. The electromagnetic effects of a moving charge. The Electrician 22, 147−148.

Heaviside, O., 1889. On the electromagnetic effects due to the motion of electricity through a dielectric. Phil. Mag. 27, 324−339.

Haeviside, O., 1892. Electrical Papers, vol. II. Macmillan & Co., London, pp. 494−497.

Heaviside, O., 1899. Note on the motion of a charged body at a speed equal to or greater than that of light. pp. 533-536. In: Electromagnetic Theory, vol. 2. The Electrician Printing and Publishing Co, London, p. 592. Reprinted in 2001 by Elibron Classics, Adamant Media Corp., Boston.

Heaviside, O., 1912a. Theory of the steady rectilinear motion of a point-charge or 'electron' through the ether when u < v and when u > v. pp. 25-28. In: Electromagnetic Theory, vol. 3. The Electrician Printing and Publishing Co., London, p. 556. Reprinted in 2001 by Elibron Classics, Adamant Media Corp., Boston.

Heaviside, O., 1912b. The steady rectilinear motion in its own line of a terminated electrified line when u > v, and interpretation of the impure conical wave following an electron. pp. 30-33. In: Electromagnetic Theory, vol. 3. The Electrician Printing and Publishing Co., London, p. 556. Reprinted in 2001 by Elibron Classics, Adamant Media Corp., Boston.

Heckel, A., Vogl, K., 2009. Rapid method for determination of the activity concentrations of ^{89}Sr and ^{90}Sr. Appl. Rdaiat. Isot. 67, 794−796.

Hernández-Rey, J.J., The KM3NeT Collaboration, 2014. The KM3NeT neutrino telescope: status and prospects. Nucl. Instrum. Methods Phys. Res., Sect. A 742, 77−81.

Herranz, M., Idoeta, R., Rozas, S., Legarda, F., 2017. Analysis of the use of the IAEA rapid method of ^{89}Sr and ^{90}Sr in milk for environmental monitoring. J. Environ. Radioact. 177, 48−57.

Herrmann, H.W., Hoffman, N., Wilson, D.C., Stoeffl, W., Dauffy, L., Kim, Y.H., McEvoy, A., Young, C.S., Mack, J.M., Himmel, A., Scholberg, K., 2016. Supernova neutrino detection. Nucl. Part. Phys. Proc. 273−275, 1897−1901.

Himmel, A., Scholberg, K., 2016. Supernova neutrino detection. Nucl. Part. Phys. Pros. 273−275, 1897−1901.

Hofestädt, J., for the KM3NeT Collaboration, 2016. ORCA: measuring the neutrino mass hierarchy with an underwater Cherenkov DetectorNucl. Part. Phys. Proc., 273−275, 2669−2671.

Holmgren, S., Tovedal, A., Jonsson, S., Nygren, U., Ramebäck, H., 2014. Handling interferences in ^{89}Sr and ^{90}Sr measurements of reactor coolant water: a method based on strontium separation chemistry. Appl. Radiat. Isot. 90, 94−101.

Holmgren, S., Tovedal, A., Björnham, O., Ramebäck, H., 2016. Time optimization of ^{90}Sr measurements: sequential measurement of multiple samples during ingrowth of ^{90}Y. Appl. Radiat. Isot. 110, 150−154.

Holmgren-Rondahl, S., Ramebäck, H., 2018. Evaluation of different methods for measuring ^{89}Sr and ^{90}Sr: measurement uncertainty for the different methods as a function of the activity ratio. Appl. Radiat. Isot. 140, 87−95.

Holmgren-Rondahl, S., Tovedal, A., Björnham, O., Ramebäck, H., 2017. Time optimization of ^{90}Sr determinations: sequential measurement of multiple samples during decay of ^{90}Y. J. Radioanal. Nucl. Chem. 311, 1143−1148.

Holst, P.B., Christophersen, C., Engvild, K.C., 2000. In vivo incorporation of radioactive ^{36}Cl, a method for monitoring chloro compounds in biological material. J. Chromatogr. A 903, 267−270.

Hoover, S., et al., 2010. Observation of ultrahigh-energy cosmic rays with the ANITA Balloon-Borne radio interferometer. Phys. Rev. Lett. 105, 151101.

Horikawa, S., Allkofer, Y., Amsler, C., Brekhovskikh, V., Kuptsov, A., Pentia, M., Zhabitsky, M., 2008. The C_4F_{10} Cherenkov detector for Dirac-II. Nucl. Instrum. Methods Phys. Res., Sect. A 595, 212−215.

Horwitz, E.P., Fisher, D., Dietz, M.L., 1991. Separation and preconcentration of strontium from biological, environmental and nuclear waste samples by extraction chromatography using crown ether. Anal. Chem. 63, 522−525.

Horwitz, E.P., Chiarizia, R., Dietz, M.L., 1992. A novel and strontium-selective extraction chromatographic resin. Solvent Extract. Ion Exchange 102, 313−336.

Hosaka, J., Super-kamiokande collaboration, et al., 2006. Solar neutrino measurements in super-Kamiokande-I. Phys. Rev. D 7311, 112001.

Hou, X., 2017. Determination of radionuclidic impurities in ^{99m}Tc eluate from ^{99}Mo/^{99m}Tc generator for quality control. J. Radioanal. Nucl. Chem. 314 (2), 659−668.

Hülsen, W., Prenzel, U., 1968. "Dry" counting of ^{32}P in liquid scintillation counters. Anal. Biochem. 26, 483−484.

Hultqvist, K., 2011. IceCube: physics, status, and future. Nucl. Instrum. Methods Phys. Res., Sect. A 626−627, S6−S12.

Hunt, A., Ayers, M., 2011. History of Silica Aerogels. Microstructured Materials Group, Environmental Energy Technology Division, E. O. Lawrence Berkeley National Laboratory, University of California, U. S. Department of Energy. http://eetd.lbl.gov/ecs/aerogels/sa-home.html.

Hunter, R.W., et al., 2014. Mechanism of action of compound-13: an α1-selective small molecule activator of AMPK. Chem. Biol. 21, 866−879.

Hurtado, S., García-Tenorio, R., García-León, M., 2003. 210Pb determination in lead shields for low-level γ-spectrometry applying two independent radiometric techniques. Nucl. Instrum. Methods Phys. Res., Sect. A 497, 381−388.

Hussain, S., for the IceCube collaboration, 2014. Measurements of the cosmic ray spectrum and average mass with IceCube. Adv. Space Res. 53, 1470−1475.

IAEA, 2003. Safeguards Techniques and Equipment". International Nuclear Verification Series. International Atomic Energy Agency, Vienna, ISBN 92-0-109403-5, p. 82.

IAEA, 2013. Analytical Quality in Nuclear Applications Series No. 27, Rapid Simultaneous Determination of ^{89}Sr and ^{90}Sr in Milk: A Procedure Using Cerenkov and Scintillation Counting. International atomic energy agency, Viena, pp. 9−10. ISSN 2074−7659.

Ijima, S., Ito, H., Kumogoshi, D., Satoshi, K., Kawai, H., Tabata, M., et al., 2013. Development of realtime 90Sr counter. In: IEEE Nuclear Science Symposium and Medical Imaging Conference 2013 NPO1-169. https://doi.org/10.1109/NSSMIC.2013.6829625.

Ijima, S., Han, S., Ito, H., Kawai, H., Kodama, S., Kumogoshi, D., 2014. Development of realtime ^{90}Sr counter used in low rate radioactive. In: Nuclear Science Symposium and Medical Imaging Conference NSS/MIC, 2014 IEEE. https://doi.org/10.1109/NSSMIC.2014.7431090.

Iijima, T., 2010. Recent topics of particle identification and photo-detection. Nucl. Instrum. Methods Phys. Res., Sect. A 623 (1), 48–56.

Iijima, T., 2011. Status and perspectives of vacuum-based photon detectors. Nucl. Instrum. Methods Phys. Res. A 639, 137–143.

Iijima, T., Korpar, S., Adachi, I., Fratina, S., Fukushima, T., Gorišek, A., Kawai, H., Konishi, H., Kozakai, Y., Križan, P., et al., 2005. A novel type of proximity focusing RICH counter with multiple refractive index aerogel radiator. Nucl. Instrum. Methods Phys. Res., Sect. A 548, 383–390.

Iijima, T., Adachi, I., Dolenec, R., Petelin, A., Fujita, K., Gorišek, A., Hara, K., Hayashi, D., Ikado, T., Kawai, H., Korpar, S., Kozakai, Y., Križan, P., et al., 2008. Studies of a proximity focusing RICH with aerogel radiator for future Belle upgrade. Nucl. Instrum. Methods Phys. Res., Sect. A 595, 92–95.

Ikeda, M., Takeda, A., Fukuda, Y., Vagins, M.R., Abe, K., Iida, T., Ishihara, K., Kameda, J., Koshio, Y., Minamino, A., et al., 2007. Search for supernova neutrino bursts at super-Kamiokande. Astrophys. J. 669 (1), 519–524.

Inami, K., 2008. Development of a TOP counter for the Super B factory. Nucl. Instrum. Methods Phys. Res., Sect. A 595, 96–99.

Inami, K., 2011. TOP counter prototype R&D. Nucl. Instrum. Methods Phys. Res., Sect. A In Press.

Inami, K., Belle II PID group, 2014. TOP counter for particle identification at the Belle II experiment. Nucl. Instrum. Methods Phys. Res., Sect. A 766, 5–8.

Inami, K., 2017. Cherenkov light imaging in particle and nuclear physics experiments. Nucl. Instrum. Methods Phys. Res., Sect. A 876, 278–281.

Iodice, M., Cisbani, E., Colilli, S., Crateri, R., Frullani, S., Garibaldi, F., Giuliani, F., Gricia, M., Lucentini, M., Mostarda, A., Pierangeli, L., Santavenere, F., Urciuoli, G.M., De Leo, R., Lagamba, L., Leone, A., Perrino, R., Kerhoas, S., Lugol, I.C., Mazaev, B., Vernin, P., Zaccarian, A., 1998. The CO_2 gas Cherenkov detectors for the Jefferson Lab Hall-A spectrometers. Nucl. Instrum. Methods Phys. Res., Sect. A 411, 223–237.

Iodice, M., Cisbani, E., Colilli, S., Cusanno, F., Frullani, S., Fratoni, R., Garibaldi, F., Gricia, M., Lucentini, M., Pierangeli, L., Santavenere, F., Urciuoli, G.M., et al., 2005. Performance and results of the RICH detector for kaon physics in Hall A at Jefferson. Lab. Nucl. Instrum. Methods Phys. Res., Sect. A 553, 231–236.

Ishikawa, H., Takiue, M., Aburai, T., 1984. Radioassay bu an efficiency tracing technique using a liquid scintillation counter. Appl. Radiat. Isot. 35, 463–466.

Ishino, M., Chiba, J., En'yo, H., Funahashi, H., Ichikawa, A., et al., 2001. Mass production of hydrophobic silica aerogel and readout optics of Cherenkov light. Nucl. Instrum. Methods Phys. Res., Sect. A 457, 581–587.

Isik, M., Sardon, H., Mecerreyes, D., 2014. Ionic liquids and cellulose: dissolution, chemical modification and preparation of new cellulosic materials. Int. J. Mol. Sci. 15, 11922–11940.

Ito, H., Iijima, S., Han, S., Kawai, H., Kodama, S., Kumogoshi, D., et al., 2014. Development of real time ^{90}Sr counter applying Cherenkov light detection. In: Technology and Instrumentation in Particle Physics 2014, Amsterdam. http://pos.sissa.it/.

Ito, H., Han, S., Kobayashi, A., Kaneko, N., Kawai, H., Tabata, M., 2016a. Identification of ^{90}Sr/^{40}K based on Cherenkov detector for recovery from the Fukushima nuclear accident. In: Proc. Int. Symp. On Radiat. Detectors and Their Uses. JPS Conf. Proc., vol. 11, p. 07002.

Ito, H., Kobayashi, A., Kawai, H., Kodama, S., Mizuno, T., Tabata, M., 2016b. Identification of ^{90}Sr and ^{40}K based on Cherenkov radiation at lower background suppressed cosmic rays. In: Nuclear Science Symposium, Medical Imaging Conf. And Room-Temperature Semiconductor Detector Workshop NSS/MIC/RTSD,. https://doi.org/10.1109/NSSMIC.2016.8069700.

Ito, H., Emoto, Y., Fujihara, K., Kawai, H., Kimura, S., Kodama, S., Mizuno, T., 2018. Study and search for main reason of lung cancers based on Cherenkov radiation in environmental radiation. EPJ Web Conf. 170, 09006. https://doi.org/10.1051/epjconf/201817009006.

Ivanov, A.V., Korovina, A.N., Tunitskaya, V.L., Kostyuk, D.A., Rechinsky, V.O., Kukhanova, M.K., Kochetkov, S.N., 2006. Development of the system ensuring a high-level expression of hepatitis C virus nonstructural NS5B and NS5A proteins. Protein Expr. Purif. 48, 14–23.

Ivanov, I.P., Serbo, V.G., Zaytsev, V.A., 2016. Quantum calculation of the Vavilov-Cherenkov radiation by twisted electrons. Phyical Review A 93, 05382511.

Jabbar, T., Khan, K., Subhani, M.S., Akhter, P., 2009. Determination of ^{90}Sr in environment of district Swat, Pakistan. J. Radioanal. Nucl. Chem. **279**2, 377–384.

Jäggi, M., Eikenberg, J., 2014. Comparison of the TriCarb and Hidex 300 SL technique using measurements of ^{241}Pu and ^{90}Sr on various samples. Appl. Radiat. Isot. 93, 120–125.

Janeczko, M., et al., 2012. CK2a and CK2a0 subunits differ in their sensitivity to 4,5,6,7-tetrabromo- and 4,5,6,7-tetraiodo-1H-benzimidazole derivatives. Eur. J. Med. Chem. 47, 345–350.

Jauch, J.M., Watson, K.M., 1948a. Phenomenological Qunatum Electrodinamics. Physical Review 74, 950–957.

Jauch, J.M., Watson, K.M., 1948b. Part II. Interaction of the field with charges. Physical Review 74, 1485–1493.

Jauch, J.M., Watson, K.M., 1949. Part III. Dispersion. Physical Review 75, 1249–1261.

Jelley, J.V., 1958. Cerenkov Radiation and its Applications. Pergamon Press, New York.

Jelley, J.V., 1961. Cerenkov radiation: its origin, properties and applications. Contemp. Phys 3, 45–57.

Jeske, M., et al., 2015. The crystal structure of the Drosophila germline inducer Oskar identifies two domains with distinct vasa helicase- and RNA-binding activities. Cell Rep. 12, 587–598.

Jones, W.V., 2014. Evolution of scientific ballooning and its impact on astrophysics research. Adv. Space Res. 53, 1405–1414.

Joram, C., 2002. The evolution of the Cherenkov imaging technique in high energy physics. Nucl. Phys. B Proc. Suppl 109B, 153–161.

Jurkin, D., Wierczinski, B., 2008. Analysis of the kinetic stability if yttrium chelates by free-ion selective radiotracer extraction. J. Radioanal. Nucl. Chem. 277 (1), 91–96.

Kaiser, T.R., 1974. Heaviside radiation. Nature 274, 400–401, 8 Feb. 1974.

Kajita, T., Kearns, E., Shiozawa, M., 2016. Establishing atmospheric neutrino oscillations with Super-Kamiokande. Nucl. Phys. B. 908, 14–29.

Kamp, A.J., Blanchard, F.A., 1971. Quench correction in Cerenkov counting: channels ratio and external source channels ratio methods. Anal. Biochem. 44, 369–380.

Kannan, S., 1975. Measurement of ^{59}Fe in plant materials using Cerenkov radiation. Int. J. Appl. Radiat. Isot. 26, 557–558.

Kappes, A., IceCube Collaboration, 2016. Exploring the universe with very high energy neutrinos. Nucl. Part. Phys. Proc. 273–275, 125–134.

Karamanos, R.E., Bettany, J.R., Rennie, D.A., 1975. Lead-210 assay in soil and plant material using Cerenkov radiation. Can. J. Soil Sci. 55, 407–413.

Karacan, F., 2011. The simple radiochemical determination of ^{90}Sr in environmental solid samples by solvent extraction. J. Radioanal. Nucl. Chem. 288, 685–691.

Katz, U.F., 2009. Underwater neutrino telescopes. Nucl. Phys. B. Proc. Suppl. 188, 245–251.

Kellogg, T.F., 1983. The effect of sample composition and vial type on Cerenkov counting in a liquid scintillation counter. Anal. Biochem. 134, 137–143.

Kerzel, U., 2010. The LHCb RICH detectors. Nucl. Instrum. Methods Phys. Res., Sect. A 617, 283–286.

Kim, G., Burnett, W.C., Dillon, K.S., 2001. A pre-concentration technique for determination of ^{32}P in natural waters. J. Radioanal. Nucl. Chem. 249 (2), 381–384.

Kim, C.K., Al-Hamwi, A., Törvényi, A., Kis-Benedek, G., Sansone, U., 2009a. Validation of rapid methods for the determination of radiostrontium in milk. Appl. Rdaiat. Isot. 67, 786–793.

Kim, Y., Herrmann, H.W., Langenbrunner, J.R., Young, C.S., Evans, S.C., Sedillo, T.J., McEvoy, A.M., Stoeffl, W., Horsfield, C., Rubery, M., 2009b. Abstracts ICOPS 2009. In: IEEE International Conference on Plasma Science, 1-5 June 2009. Plasma Science, ISBN 978-1-4244-2617-1.

Kim, G.Y., On behalf of the LHCb RICH collaboration, 2011. The RICH detectors for the upgraded LHCb experiment. Nucl. Instrum. Methods Phys. Res., Sect. A 639, 278–281.

Kim, H., Chung, K.H., Jung, Y., Jang, M.A., Kang, M.J., Choi, G.S., 2015. A rapid and efficient automated method for the sequential separation of plutonium and radiostrontium in seawater. J. Radioanal. Nucl. Chem. 304, 321–327.

Kim, H., Lim, J.M., Chung, K.H., Lee, W., 2017. Analytical method for the determination of gross beta, ^{90}Sr, ^{226}Ra and Pu isotopes in environmental samples. J. Radioanal. Nucl. Chem. 312, 523–529.

Kisseljova, K., Kuznetsov, A., Baudy-Floc'h, M., Järv, J., 2010. Aza-β^3-amino acid containing peptidomimetics as cAMP-dependent protein kinase substrates. Bioorg. Chem. 38, 229–233.

Kistler, S.S., 1931. Coherent expanded aerogels and jellies. Nature 127, 741.

Kistler, S.S., 1932. Coherent expanded-aerogels. J. Phys. Chem. **36**1, 52–64.

Kobzev, A.P., 2010. The mechanism of Vavilov–Cherenkov radiation. Physics of Particles and Nuclei 41, 452–470.

Kobzev, A.P., 2014. On the radiation mechanism of a uniformly moving charge. Physics of Particles and Nuclei 48, 628–653.

Korpar, S., 2003. HERA-brich. Nucl. Instrum. Methods Phys. Res., Sect. A 503, 41–45.

Korpar, S., Adachi, I., Fratina, S., Fukushima, T., Gorišek, A., Iijima, T., Kawai, H., Konishi, H., Kozakai, Y., Križan, P., Matsumoto, T., et al., 2005. RICH with multiple aerogel layers of different refractive index. Nucl. Instrum. Methods Phys. Res., Sect. A 553, 64–69.

Korpar, S., Adachi, I., Fujita, K., Fukushima, T., Gorišek, A., Hayashi, D., Iijima, T., Ikado, T., Ishikawa, T., Kawai, H., Kozakai, Y., Križan, P., et al., 2007. Proximity focusing RICH with TOF capabilities. Nucl. Instrum. Methods Phys. Res., Sect. A 572, 432–433.

Korpar, S., Dolenec, R., Hara, K., Iijima, T., Križan, P., Mazuka, Y., Pestotnik, R., Stanovnik, A., Yamaoka, M., 2008. Silicon photomultiplier as a detector of Cherenkov photons. Nucl. Instrum. Methods Phys. Res., Sect. A 595, 161–164.

Korpar, S., Chagani, H., Dolenec, R., Križan, P., Pestotnik, R., Stanovnik, A., 2010. A module of silicon photo-multipliers for detection of Cherenkov radiation. Nucl. Instrum. Methods Phys. Res., Sect. A 613, 195–199.

Kossert, K., 2010. Activity standardization by means of a new TDCR–Čerenkov counting technique. Appl. Radiat. Isot. 68, 1116–1120.

Kossert, K., Nähle, O., Grau Carles, A., 2011a. Čerenkov counting and liquid scintillation counting of ^{36}Cl. In: LSC 2010, Advances in Liquid Scintillation Spectrometry. Radiocarbon. University of Arizona, Tucson.

Kossert, K., Nähle, O., Warwick, P.E., Wershofen, H., Croudace, I.W., 2011b. Activity determination and nuclear decay data of 113mCd. Appl. Radiat. Isot. 69, 500–505.

Kossert, K., Grau Carles, A., Nähle, O.J., 2014. Improved Čerenkov counting techniques based on a free parameter model. Appl. Radiat. Isot. 86, 7–12.

Kossert, K., et al., 2016. Comparison of ^{90}Y activity measurements in nuclear medicine in Germany. Appl. Radiat. Isot. 109, 247–249.

Kravchenko, I., 2012. Recent results from the RICE experiment at the South Pole. Nucl. Instrum. Methods Phys. Res., Sect. A 662, S42–S45.

Križan, P., 2001. Recent progress in Čherenkov counters. IEEE Trans. Nucl. Sci. **48**4, 941–949.

Križan, P., 2007. Detectors for particle identification. Nucl. Instrum. Methods Phys. Res., Sect. A 581, 57–64.

Križan, P., 2009. Recent progress in particle identification methods. Nucl. Instrum. Methods Phys. Res., Sect. A 598, 130–137.

Križan, P., 2013. Overview of particle identification techniques. Nucl. Instrum. Methods Phys. Res., Sect. A 706, 48–54.

Križan, P., 2017. RICH detectors: analysis methods and their impact on physics. Nucl. Instrum. Methods Phys. Res., Sect. A 876, 272–277.

Križan, P., Adachi, I., Fratina, S., Fukushima, S., Gorišek, A., Iijima, T., Kawai, H., Konishi, H., Korpar, S., Kozakai, Y., Matsumoto, T., et al., 2005. Proximity focusing RICH with flat panel PMT as photon detector and aerogel as radiator. Nucl. Instrum. Methods Phys. Res., Sect. A 553, 58–63.

Križan, P., Adachi, I., Bertović, I., Fujita, K., Fukushima, T., Gorišek, A., Hayashi, D., Iijima, T., Ikado, K., Iwabuchi, M., Kawai, H., Korpar, S., et al., 2007. Proximity focusing RICH with TOF capabilities. Nucl. Phys. B Proc. Suppl. 172, 227–230.

Kulcsar, F., Teherani, D., Altmann, H., 1982. Study of the spectrum of Cherenkov light. J. Radioanal. Chem. 68, 161–168.

Kubota, T., Shibahara, Y., Fukutani, S., Fujii, T., Ohta, T., Kowatari, M., Mizuno, S., Takamiya, K., Yamana, H., 2015. Cherenkov counting of ^{90}Sr and ^{90}Y in bark and leaf samples collected around Fukushima Daiichi Nuclear Power Plant. J. Radioanal. Nucl. Chem. 303, 39–46.

Kuo, Y.-P., Xu, L., Brek Eaton, J., Zhao, L., Wu, J., Lukas, R.J., 2005. Roles of nicotinic acetylcholine receptor subunit large cytoplasmic loop sequences in receptor expression and function. J. Pharmac. Exp. Therapeut. 314 (1), 455–466.

Kuribara, M., 1994. Spent fuel burnup estimation by Cerenkov glow intensity measurement. IEEE Trans. Nucl. Sci. 41 (5), 1736–1739.

Kuribara, M., Nemoto, K., 1994. Development of new UV – I.I. Cerenkov viewing device. IEEE Trans. Nucl. Sci. 41 (1), 331–335.

Kushita, K.N., Du, J., 1998. Radioactivity measurement of ^{188}Re by Cherenkov counting. Appl. Radiat. Isot. 49 (9–11), 1069–1072.

Kuznetsov, A., Uri, A., Raidaru, G., Järv, J., 2004. Kinetic analysis of inhibition of cAMP-dependent protein kinase catalytic subunit by the peptide–nucleoside conjugate AdeAhxArg$_6$. Bioorg. Chem. 32, 527–535.

L'Annunziata, M.F., 1971. Birth of a unique parent-daughter relation: secular equilibrium. An experiment in radioisotope techniques. J. Chem. Educ. 48, 700–703.

L'Annunziata, M.F., 1979. Radiotracers in Agricultural Chemistry. Academic Press, New York and London.

L'Annunziata, M.F., 1984a. The detection and measurement of radionuclides. In: L'Annunziata, M.F., Legg, J.O. (Eds.), Isotopes and Radiation in Agricultural Sciences, vol. 1. Academic Press, New York and London, pp. 142–231.

L'Annunziata, M.F., 1984b. Agricultural biochemistry: reaction mechanisms and pathways in biosynthesis. In: L'Annunziata, M.F., Legg, J.O. (Eds.), Isotopes and Radiation in Agricultural Sciences, vol. 2. Academic Press, New York and London, pp. 106–182.

L'Annunziata, M.F., 1987. Radionuclide Tracers, Their Detection and Measurement. Academic Press, New York and London, p. 505.

L'Annunziata, M.F., 1997. Cerenkov Counting of 32P - Instrument Performance Data. PerkinElmer, Inc., Waltham. MA, USA, p. 6. Counter Intel. Tri-Carb LSC Application Note, 002. http://las.perkinelmer.com/Content/applicationnotes/app_tricarbcerenkovcntingp32.pdf.

L'Annunziata, M.F., 2016. Radioactivity: Introduction and History, from the Quantum to Quarks. Elsevier, Amsterdam and Boston, p. 902.

L'Annunziata, M.F., Fuller, W.H., 1968. The chelation and movement of ^{89}Sr-^{90}Sr^{90}Y in a calcareous soil. Soil Sci 105, 311–319.

L'Annunziata, M.F., Passo Jr., C.J., 2002. Cherenkov counting of yttrium-90 in the dry state; correlations with phosphorus-32 Cherenkov counting data. Appl. Radiat. Isot. 56, 907–916.

Laissaoui, A., Mulsow, S., Benmansour, M., La Rosa, J.J., IbnMajah, M., 2002. A sensitive method based of HDEHP extraction and LSS for the determination of ^{90}Sr in solid samples. J. Radioanal. Nucl. Chem. 253 (2), 335–337.

Laroche-Joubert, N., Marsy, S., Michelet, S., Imbert-Teboul, M., Doucet, A., 2002. Protein kinase A-independent activation of ERK and H,K-ATPase by cAMP in native kidney cells. J. Biol. Chem. **277** 21, 18598–18604.

Laroche-Joubert, N., Marsy, S., Luriau, S., Imbert-Teboul, M., Doucet, A., 2003. Mechanism of activation of ERK and H–K–ATPase by isoproterenol in rat cortical collecting duct. Renal Physiol 284 (5), F948–F954.

Latz, A., Mehlmer, N., Zapf, S., Mueller, T.D., Wurzinger, B., Pfister, B., Csaszar, E., Hedrich, R., Teige, M., Becke, D., 2013. Salt stress triggers phosphorylation of the Arabidopsis vacuolar K^+ channel TPK1 by calcium-dependent protein kinases CDPKs. Molec. Plant 6 4, 1274–1289.

Lazare, L., Crestey, C., Bleistein, C., 2009. Measurement of ^{90}Sr in primary coolant of pressurized water reactor. J. Radioanal. Nucl. Chem. 279 (2), 633–638.

Läuchli, A., 1969. Radioassay for β-emitters in biological materials using Cerenkov radiation. Int. J. Appl. Radiat. Isot. 20, 265–270.

Läuchli, A., 1971. Application of Cerenkov counting to ion transport studies in plants. In: Horrocks, D.L., Peng, C.-T. (Eds.), Organic Scintillators and Liquid Scintillation Counting. Academic Press, New York and London, pp. 771–782.

Lee, D.S., Im, H.-J., Lee, Y.-S., 2015. Radionanomedicine: widened perspectives of molecular theragnosis. Nanomed.: Nanotech, Biol., Med. 11, 795–810.

Lefebvre, D.D., Glass, A.D.M., 1981. A rapid method for the separation of mixed ^{32}P- and ^{86}Rb-labelled plant extracts by anion-exchange chromatography. Int. J. Appl. Radiat. Isot. 32, 116–117.

Lehmann, K.A., Bass, B.L., 1999. The importance of internal loops within RNA substrates of ADAR1. J. Molec. Biol. **291**1, 1–13.

Lewis, A.M., Masgrau, R., Vasudevan, S.R., Yamasaki, M., O'Neill, J.S., Garnham, C., James, K., Macdonald, A., Ziegler, M., Galione, A., Churchill, G.C., 2007. Refinement of a radioreceptor binding assay for nicotinic acid adenine dinucleotide phosphate. Anal. Biochem. 371, 26–36.

Li, Z., on behalf of the Super-Kamiokande and Hyper-Kamiokande collaborations, 2017. Atmospheric neutrinos and proton decay in Super-Kamiokande and Hyper-Kamiokande. Nucl. Part. Phys. Proc. 287–288, 147–150.

Lickly, T.D., Quinn, T., Blanchard, F.A., Murphy, P.G., 1988. Determination of migration of phosphorus-based additives from food packaging material into food-simulating solvents by neutron activation/Cerenkov counting. Appl. Radiat. Isot. 39, 465–470.

Lilley, J.S., 2001. Nuclear Physics. John Wiley & Sons, Ltd., New York, p. 393.

Lindsey, C.S., Lindblad, T., Waldemark, K., Hildingsson, L., 1999. Nuclear fuel assembly assessment project and image categorization. In: Proceedings of the Ninth Workshop on Virtual Intelligence, Dynamic Neural Networks. Royal Institute of Technology, KTH, Stockholm, Sweden, June 22-26, 1998. Proc. SPIE, vol. 3728, pp. 491–499.

Lippmann, C., 2012. Particle identification. Nucl. Instrum. Mehtods Phys. Res., Sect. A 666, 148–172.

Llauradó, M., Torres, J.M., Tent, J., Sahuquillo, A., Muntao, H., Rauret, G., 2001. Preparation of a soil reference material for the determination of radionuclides. Anal. Chim. Acta 445, 99–106.

Lourenço, V., Bobin, C., Chisté, V., Lacour, D., Rigoulay, F., Tapner, M., Thiam, C., Ferreux, L., 2015. Primary standardization of SIR-Spheres based on the dissolution of the ^{90}Y-labeled resin microspheres. Appl. Radiat. Isot. 97, 170–176.

Louvandini, H., Vitti, D.M.S.S., Abdalla, A.L., McManus, C.M., 2008. Phosphorus kinetics in growing hair sheep. Small Rumin. Res. 76, 183–189.

Luciani, M.G., Hutchins, J.R.A., Zheleva, D., Hupp, T.R., 2000. The C-terminal regulatory domain of p53 contains a functional docking site for cyclin A. J. Molec. Biol. 300 (3), 503–518.

Lucignani, G., 2011. Čerenkov radioactive optical imaging: a promising new strategy. Eur. J. Nucl. Med. Mol. Imag. 383, 592–595.

Luo, Z., Rosenberg, A.J., Liu, H., Han, J., Tu, Z., 2018. Syntheses and in vitro evaluation of new S1PR1 compounds and initial evaluation of a lead F-18 radiotracer in rodents. Eur. J. Med. Chem. 150, 796–808. https://doi.org/10.1016/j.ejmech.2018.03.035.

Lurkin, N., On behalf of the NA62 Collaboration, 2017. The kaon identification system in the NA62 experiment at the CERN SPS. Nucl. Instrum. Mehtods Phys. Res., Sect. A 845, 443–446.

Lynn Bostrom, S., Dore, J., Griffith, L.C., 2009. CaMKII uses GTP as a phosphate donor for both substrate and autophosphorylation. Biochem. Biophys. Res. Commun. 390, 1154–1159.

MacDonald, J.A., Storey, K.B., 2005. Mitogen-activated protein kinases and selected downstream targets display organ-specific responses in the hibernating ground squirrel. Int. J. Biochem. Cell Biol. 37, 679–691.

Mack, J.M., Berggren, R.R., Caldwell, S.E., Evans, S.C., Faulkner Jr., J.R., Lerche, R.A., Oertel, J.A., Young, C.S., 2003. Observation of high-energy deuterium–tritium fusion gamma rays using gas Cherenkov detectors. Nucl. Instrum. Mehtods Phys. Res., Sect. A 513, 566–572.

Mack, J.M., Berggren, R.R., Caldwell, S.E., Christensen, C.R., Evans, S.C., Faulkner Jr., J.R., Griffith, R.L., Hale, G.M., King, R.S., Lash, D.K., Lerche, R.A., Oertel, J.A., Pacheco, D.M., Young, C.S., 2006. Remarks

on detecting high-energy deuterium−tritium fusion gamma rays using a gas Cherenkov detector. Radiat. Phys. Chem. 75, 551−556.

MacKie, S., de Silva, S., Aslan, P., Ladd, L., Houang, M., Cade, D., Delprado, W., 2011. Super selective radio embolization of the porcine kidney with ^{90}Yttrium resin microspheres: a feasibility, safety and dose ranging study. J. Urology 185, 285−290.

Mallet, L., 1926. Luminescence of water and organic substances subjected to gamma radiation. Compt. Rend. Acad. Sci. Paris 183, 274−275.

Mallet, L., 1928. Spectral study of the luminescence of water and carbon disulfide under gamma radiation. Compt. Rend. Acad. Sci. Paris 187, 222−223.

Mallet, L., 1929. The ultra-violet radiation of substances subjected to γ-rays. Compt. Rend. Acad. Sci. Paris 188, 445−447.

Mammoliti, F., Bellini, V., Cisbani, E., Cusanno, F., Garibaldi, F., Giusa, A., de Jager, K., Russo, G., Sperduto, M.L., Sutera, C.M., Urciuoli, G.M., 2011. A RICH detector for hadron identification at JLab. Appl. Radiat. Isot. 69 (8), 1118−1120.

Margiotta, A., on behalf of the ANTARES Collaboration, 2015. The ANTARES neutrino telescope: recent results with 5-years data. Nucl. Part. Phys. Proc. 265−266, 258−260.

Margiotta, A., on behalf of the KM3NeT Collaboration, 2016. Perspectives of the KM3NeT project. Nucl. Part. Phys. Proc. 279−281, 182−189.

Markov, M.A., Zheleznykh, I.M., 1961. On high energy neutrino physics in cosmic rays. Nucl. Phys. 273, 385−394.

Marshall, J., 1952. Particle counting by Cerenkov radiation. Phys. Rev. 86, 685−693.

Martin, F., Barends, S., Jaeger, S., Schaeffer, L., Prongidi-Fix, L., Eriani, G., 2011. Cap-Assisted internal Initiation of translation of histone H4. Molec. Cell 41, 197−209.

Martin, J.E., 1987. Measurement of ^{90}Sr in reactor wastes by Cerenkov counting of ^{90}Y. Appl. Radiat. Isot. 38, 953−957.

Martin, J.P., Odell, K.J., 1998. The development of emergency radio-analytical techniques for the determination of radiostrontium and transuranic radioisotopes in environmental materials. Radioact. Radiochem. 93, 49−60.

Masłyk, M., et al., 2018. A representative of arylcyanomethylenequinone oximes effectively inhibits growth and formation of hyphae in Candida albicans and influences the activity of protein kinases in vitro. Saudi Pharmac. J. 26, 244−252.

Matsumoto, T., Korpar, S., Adachi, I., Fratina, S., Iijima, T., Ishibashi, R., Kawai, H., Križan, P., Ogawa, S., Pestotnik, R., Saitoh, S., Seki, T., Sumiyoshi, T., Suzuki, K., Tabata, T., Uchida, Y., Unno, Y., 2004. Studies of proximity focusing RICH with an aerogel radiator using flat-panel multi-anode PMTs Hamamatsu H8500. Nucl. Instrum. Methods Phys. Res., Sect. A 521, 367−377.

Matsuoka, K., Belle II PID Group, 2013. Design and performance study of the TOP counter. Nucl. Instrum. Methods Phys. Res., Sect. A 732, 357−360.

Maxwell III, S.L., Culligan, B.K., 2009a. New column separation method for emergency urine samples. J. Radioanal. Nucl. Chem. 279 (1), 105−111.

Maxwell III, S.L., Culligan, B.K., 2009b. Rapid method for determination of radiostrontium in emergency milk samples. J. Radioanal. Nucl. Chem. 279 (3), 757−760.

Maxwell III, S.L., Culligan, B.K., 2009c. Rapid separation method for emergency water and urine samples. J. Radioanal. Nucl. Chem. 279 (3), 901−907.

McFadden, R., Ekers, R., Roberts, P., 2012. A new method to calibrate ionospheric pulse dispersion for UHE cosmic ray and neutrino detection using the Lunar Cherenkov technique. Nucl. Instrum. Methods Phys. Res., Sect. A 662, S234−S237.

Meng, R., Götz, C., Montenarh, M., 2010. The role of protein kinase CK2 in the regulation of the insulin production of pancreatic islets. Biochem. Biophys. Res. Commun. 401, 203−206.

Mevius, M., Buitink, S., Falcke, H., Hörandel, J., James, C.W., McFadden, R., Scholten, O., Singh, K., Stappers, B., ter Veen, S., 2012. Detecting ultra high energy neutrinos with LOFAR. Nucl. Instrum. Methods Phys. Res., Sect. A 662, S26−S28.

Mietelski, J.W., Gaca, P., Bielec, J., 2006. Optimization of counting conditions for Cerenkov radiation by LSC. pp. 13-17. In: Chałupnik, S., Schönhofer, F., Noakes, J. (Eds.), "LSC 2005, Advances in Liquid Scintillation Spectrometry, Radiocarbon. University of Arizona, Tucson.

Milanović, I., Grahek, Ž., 2015. Semi-automated procedure for the determination of ^{89,90}Sr in environmental samples by Cherenkov counting. J. Radioanal. Nucl. Chem. 303, 1453−1457.

Minowa, H., Yoshizawa, Y., Takiue, M., 2009. Cherenkov counting of carbon-14 using a translucent ceramic with high refractive index. In: Eikenberg, J., Beer, H., Baehrie, H. (Eds.), "LSC 2008, Advances in Liquid Scintillation Spectrometry, Radiocarbon. University of Arizona, Tucson, pp. 119−123.

Mirenda, M., Rodrigues, D., Arenillas, P., Gutkowski, K., 2014. Ionic liquids as solvents for liquid scintillation technology. Čerenkov counting with1-Butyl-3-Methylimidazolium Chloride. Radiat. Phys. Chem. 98, 98−102.

Mirenda, M., Rodrigues, D., Ferreyra, C., Arenillas, P., Sarmiento, G.P., Krimer, N., Japas, M.L., 2018. Ionic liquids as solvents for Čerenkov counting and the effect of a wavelength shifter. Appl. Radiat. Isot. 134, 275−279.

Moir, A.T.B., 1971. Channels ratio quench correction using Čerenkov radiation for the assay of ^{42}K in biological samples. Int. J. Appl. Radiat. Isot. 22, 213−216.

Molander, M., 2008. Quantitative Image Analysis of Cherenkov Light from Nuclear Fuel Assemblies. Uppsala University, p. 41. UPTEC F08 047, ISSN: 1401-5757.

Montaruli, T., 2009a. Review on neutrino telescopes. Nucl. Phys. B Proc. Suppl. 190, 101−108.

Montaruli, T., 2009b. Neutrino astronomy in the ice. Nucl. Phys. B Proc. Suppl. 188, 239−244.

Montgomery, R.A., 2013. A ring imaging Cherenkov detector for CLAS12. Nucl. Instrum. Methods Phys. Res., Sect. A 732, 366−370.

Moore, F., Asbóth, G., López Bernal, A., 2002. Thromboxane receptor signaling in human myometrial cells. Prostaglandins Lipid Mediators 67, 31−47.

Morel, C., Fardeau, J.C., 1989. The uptake by crops of fresh and residual phosphatic fertilizers by simultaneous measurements with ^{32}P and ^{33}P. Appl. Radiat. Isot. 40, 273−278.

Mori, Y., Nakamura, Y., Ohuchi, S., 2012. Inhibitory RNA aptamer against SP6 RNA polymerase. Biochem. Biophys. Res. Commun. 420, 440−443.

Morita-Murase, Y., Murakami, I., Homma, Y., 2000. Cherenkov counting efficiencies for β^--emitters in dry state in glass vials. Chem Lett 10, 1158−1159.

Mosqueda, F., Vaca, F., Villa, M., Manjón, G., 2006. Optimization of the channel ratio method for color quenching correction for measurement of ^{90}Sr via Cerenkov counting. In: Chałupnik, S., Schönhofer, F., Noakes, J. (Eds.), "LSC 2005, Advances in Liquid Scintillation Spectrometry, Radiocarbon. University of Arizona, Tucson, pp. 19−29.

Mosqueda, F., Villa, M., Vaca, F., Bolivar, J.P., 2007. Colour quenching corrections on the measurement of ^{90}Sr through Cerenkov counting. Anal. Chim. Acta 604, 184−190.

Murányi, A., Derkach, D., Erdődi, F., Kiss, A., Ito, M., Hartshorne, D.J., 2005. Phosphorylation of Thr695 and Thr850 on the myosin phosphatase target subunit: Inhibitory effects and occurrence in A7r5 cells. FEBS Lett. 579, 6611–6615.

Nakahata, M., 2015. Future prospects of super-Kamiokande and hyper-Kamiokande. Phys. Proc. 61, 568–575.

Nappi, E., 2011. Advances in charged particle identification techniques. Nucl. Instrum. Methods Phys. Res., Sect. A 628, 1–8.

Nardelli, A., Castaldi, E., Ortosecco, G., Speranza, A., Storto, G., Pace, L., Salvatore, M., 2011. Enhancement of reaction conditions for the radiolabelling of DOTA-peptides with high activities of yttrium-90. Appl. Radiat. Isot. 69, 52–55.

Nascimento, V.F., 1977. Fitting a ^{60}Co external source to a liquid scintillation system for the estimation of the ^{32}P Cerenkov effect detection efficiency. Appl. Radiat. Isot 28, 789–790.

Navarro, N., Grau Carles, A., Alvarez, A., Salvador, S., Gomez, V., 1997. Standardization of ^{234}Th by Cerenkov counting. Appl. Radiat. Isot. 48, 949–952.

Neronov, A., Semikoz, D., 2016. Evidence the Galactic contribution to the IceCube astrophysical neutrino flux. Astropart. Phys. 75, 60–63.

Nicolaon, G.A., Teichner, S.J., 1968. New preparation process for silica xerogels and aerogels, and their textural properties. Bull. Soc. Chim. France 19685, 1900–1906. U.S. Patent No. 3,672,833 1972.

Nicolas, G., Giovacchini, G., Müller-Brand, J., Forrer, F., 2011. Targeted radiotherapy with radiolabeled somatostatin analogs. Endocrin. Metab. Clin. N. Am. 40, 187–204.

Nishida, S., Adachi, I., Hamada, N., Hara, K., Iijima, T., 2014. Aerogel RICH for the Belle II forward PID. Nucl. Instrum. Methods Phys. Res., Sect. A 766, 28–31.

Nishimura, K., 2011. The time of propagation counter for Belle II. Nucl. Instrum. Methods Phys. Res., Sect. A 639, 177–180.

Nishimura, K., Browder, T., Hoedlmoser, H., Jacobson, B., Kennedy, J., Rosen, M., Ruckman, L., Varner, G., Wong, A., Yen, W., 2010. An imaging time-of-propagation system for charged particle identification at a super B factory. Nucl. Instrum. Methods Phys. Res., Sect. A 623, 297–299.

Nishino, H., Awai, K., Hayato, Y., Nakayama, S., Okumura, K., Shiozawa, M., Takeda, A., Ishikawa, K., Minegishi, A., Arai, Y., 2009. High-speed charge-to-time converter ASIC for the Super-Kamiokande detector. Nucl. Instrum. Methods Phys. Res., Sect. A 610, 710–717.

NIST, 2018. The NIST Reference on Constants, Units, and Uncertainty. National Institute of Standards and Technology, Physical Measurement Laboratory, Gaithersburg, MD, USA. http://physics.nist.gov/cuu/Constants/.

Noor, A., Zakir, M., Rasyid, B., Maming, L'Annunziata, M.F., 1996. Cerenkov and liquid scintillation analysis of the triple label ^{86}Rb–^{35}S–^{33}P. Appl. Radiat. Isot. 47, 659–668.

Nour, S., Burnett, W.C., Horwitz, E.P., 2002. ^{234}Th analysis of marine sediments via extraction chromatography and liquid scintillation counting. Appl. Radiat. Isot. 57, 235–241.

NuDat 2.7, 2018. National Nuclear Data Center, Brookhaven National Laboratory, Upton, NY, USA. http://www.nndc.bnl.gov/nudat2/reCenter.jsp?z=33&n=41.

Nunthawarasilp, P., Petmitr, S., Chavalitshewinkoon-Petmitr, P., 2007. Partial purification and characterization of DNA polymerase β-like enzyme from Plasmodium falciparum. Molec. Biochem. Parisitol. 154, 141–147.

O'Hara, M.J., Burge, S.R., Grate, J.W., 2009. Automated radioanalytical system for the determination of ^{90}Sr in environmental water samples by ^{90}Y Cherenkov radiation counting. Anal. Chem. 81, 1228–1237.

Ohshima, T., 2000. Test result of time-of-propagation Cherenkov counter. Nucl. Instrum. Methods Phys. Res., Sect. A 453, 331–335.

Okumura, K., 2015. Atmospheric neutrino oscillation and mass hierarchy determination in Super-Kamiokande. Phys. Proc. 61, 619–626.

Olfert, J.M., Dai, X., Kramer-Tremblay, S., 2014. Rapid determination of ^{90}Sr/^{90}Y in water samples by liquid scintillation and Cherenkov counting. J. Radioanal. Nucl. Chem. 300, 263–267.

Ometáková, J., Dulanská, S., Mátel, L., Remenec, B., 2011. A comparison of classical ^{90}Sr separation methods with selective separation using molecular recognition technology products AnaLig SR-01® gel, 3M Empore™ Strontium Rad Disk and extraction chromatography Sr®Resin. J. Radioanal. Nucl. Chem. 290, 319–323.

Østby, L., Krøkje, Å., 2002. Cytochrome P450 CYP1A induction and DNA adducts in a rat hepatoma cell line Fao, exposed to environmentally relevant concentrations of organic compounds, singly and in combinations. Environ. Toxicol. Pharmacol. 12, 15–26.

Pacer, R.A., 1990. Effect of container adsorption on the ^{210}Pb/^{210}Bi secular equilibrium relationship in spiked aqueous solutions. J. Radioanal. Nucl. Chem., Articles 139, 255–262.

Palmer, F.B.S.C., 1969. Measurement of phosphorus-32 following colorimetric phosphorus determination. Anal. Biochem. 31, 493–501.

Pan, J., Emanuele, K., Maher, E., Lin, Z., Healey, S., Regan, P., 2017. Analysis of radioactive strontium-90 in food by Čerenkov liquid scintillation counting. Appl. Radiat. Isot. 126, 214–218.

Papanestis, A., on behalf of the LHCb RICH collaboration, 2014. The LHCb RICH system; detector description and operation. Nucl. Instrum. Methods Phys. Res., Sect. A 766, 14–18.

Papanestis, A., D'Ambrosio, C., on behalf of the LHCb RICH collaboration, 2017. Performance of the LHCb RICH detectors during the LHC Run II. Nucl. Instrum. Methods Phys. Res., Sect. A 876, 221–224.

Paredes, C.H., Landolt, R.R., Kessler, W.V., Shoemaker, R.L., 1980. A comparison of proportional and Cherenkov counting for sulfur tablet neutron dosimeters. Health Phys 39, 564–566.

Parker, R.P., Elrick, R.H., 1966. The assay of β-emitting radioisotopes using Cerenkov counting. Int. J. Appl. Radiat. Isot. 17, 361–362.

Parker, R.P., Elrick, R.H., 1970. Cerenkov counting as a means of assaying β-emitting radionuclides. In: Bransome Jr., E.D. (Ed.), The Current Status of Liquid Scintillation Counting. Grune and Stratton, New York and London, pp. 110–122.

Passo Jr., C.J., Cook, G.T., 1994. Handbook of Environmental Liquid Scintillation Spectrometry. PerkinElmer Life and Analytical Sciences, Boston.

Paul, W., Steinwedel, H., 1955. Interactions of electrons with matter. In: Siegbahn, K. (Ed.), Beta- and Gamma-Ray Spectroscopy. North Holland, Amsterdam.

Peck, G.A., Smith, J.D., Cooper, M.B., 1998. Enhanced counting efficiency of Cerenkov radiation from bismuth-210. J. Radioanal. Nucl. Chem. 238 (1- 2), 163–165.

Peluso, M., Hainaut, P., Airoldi, L., Autrup, H., Dunning, A., Garte, S., Gormally, E., Malaveille, C., Matullo, G., Munnia, A., Riboli, E., Vineis, P., investigators, E.P.I.C., 2005. Methodology of laboratory measurements in prospective studies on gene–environment interactions: the experience of GenAir. Mutation Res 574, 92–104.

Perrino, R., Lagamba, L., Cisbani, E., Colilli, S., Crateri, R., LeLeo, R., Frullani, S., Garibaldi, F., Giuliani, F., Gricia, M., Iodice, M., Iommi, R., Leone, A., Lucentini, M., Mostarda, A., Nappi, E., Pierangeli, L., Santavenere, F., Urciuoli, G.M., 2001. Performances of the aerogel threshold Cherenkov counter for the Jefferson lab Hall A spectrometers in the 1-4 GeV/c momentum range. Nucl. Instrum. Methods Phys. Res., Sect. A 457, 571–580.

Pestotnik, R., Križan, P., Korpar, S., Bračko, M., Starič, M., Stanovnik, A., 2002. Investigation of ^{90}Sr detection with Cherenkov radiation in silica aerogels. In: Proceedings of IEEE Symposium on Nuclear Science and Medical Imaging Including Nuclear Power Systems." , Nov. 4-9, 2001, San Diego, IEEE, Piscataway, NJ.

Pestotnik, R., Adachi, I., Fratina, S., Iijima, T., Ishibashi, R., Kawai, H., Korpar, S., Križan, P., Ogava, S., Matsumoto, T., et al., 2004. Proximity focusing RICH with flat panel PMT Hamamatsu H8500 as photon detector and aerogel radiator. Nucl. Instrum. Methods Phys. Res., Sect. A 525, 158–162.

Pestotnik, R., Dolenec, R., Korpar, S., Križan, P., Petelin, A., 2007. Silicon photomultiplier as a position sensitive detector of Cherenkov photons. Nucl. Instrum. Methods Phys. Res., Sect. A 581, 457–460.

Pestotnik, R., Korpar, S., Križan, P., Dolenec, R., 2008. Cherenkov detector of ^{90}Sr based on aerogel as radiator. Nucl. Instrum. Methods Phys. Res., Sect. A 595, 278–280.

Pestotnik, R., Dolenec, R., Korpar, S., Križan, P., Stanovnik, A., 2011. Module of silicon photomultipliers as a detector of individual Cherenkov photons. Nucl. Instrum. Methods Phys. Res., Sect. A 639, 99–102.

Pestotnik, R., Adachi, I., Dolenec, R., Hataya, K., Iori, S., 2017. The aerogel ring imaging Cherenkov system at the Belle II spectrometer. Nucl. Instrum. Methods Phys. Res., Sect. A 876, 265–268.

Pinto da Cunha, J., Neves, F., Lopes, M.I., 2000. On the reconstruction of Cherenkov rings from aerogel radiators. Nucl. Instrum. Methods Phys. Res., Sect. A 452, 401–421.

Poelz, G., 1986. Aerogel Cherenkov counters at DESY. Nucl. Instrum. Methods Phys. Res., Sect. A 248, 118–129.

Poletiko, C., Lemercier, R., Leiba, B., Llug, P., 1994. Measurement of strontium-90 by the Cerenkov counting technique. J. Radioanal. Nucl. Chem., Articles 178, 131–141.

Popov, L., Hou, X., Nielsen, S.P., Yu, Y., Djingova, R., Kuleff, I., 2006. Determination of radiostrontium in environmental samples using sodium hydroxide for separation of strontium from calcium. J. Radioanal. Nucl. Chem. 269 (1), 161–173.

Popov, L., Mihailova, G., Hristova, I., Dimitrova, P., Tzibranski, R., Avramov, V., Naidenov, I., Stoenelova, B., 2009. Separation of strontium from calcium by the use of sodium hydroxide and its application for the determination of ling-term background activity concentrations of ^{90}Sr in 100 km area around Kozloduy Nuclear Power Plant Bulgaria. J. Radioanal. Nucl. Chem. 279 (1), 49–64.

Prior, G., On behalf of the SNO collaboration, 2009. Results from the Sudbury neutrino observatory phase III. Nucl. Phys. B Proc. Suppl. 188, 96–100.

Pullen, B.P., 1986. Cerenkov counting of ^{40}K in KCl using a liquid scintillation spectrometer. J. Chem. Educ. 63, 971.

Qiao, J., Salminen-Paatero, S., Holmgren Rondahl, S., Bourgeaux-Goget, M., Roos, P., Lagerkvist, P., Sträberg, E., Ramebäck, H., 2017. Inter-laboratory exercise with an aim to compare methods for ^{90}Sr and ^{239,240}Pu determination in environmental soil samples. J Radioanal. Nucl. Chem. 314, 813–826.

Rajyaguru, P., She, M., Parker, R., 2012. Scd6 targets eIF4G to repress translation: RGG motif proteins as a class of eIF4G-binding proteins. Molec. Cell 45, 244–254.

Ramebäck, H., Skålberg, M., 1999. A separation procedure for the analysis of ^{90}Sr, ^{154}Eu, and the actinides ^{237}Np, ^{239}Pu, ^{241}Am and ^{244}Cm. J Radioanal. Nucl. Chem. 240 (2), 661–663.

Ramesh, A., Subramanian, M.S., 1997. Trace determination if tellurium using liquid scintillation and Cerenkov counting. Analyst 122, 1605–1610.

Randolph, R., 1975. Determination of strontium-90 and strontium-89 by Cerenkov and liquid-scintillation counting. Int. J. Appl. Radiat. Isot. 26, 9–16.

Rao, D.D., Mehendarge, S.T., Chandramouli, S., Hegde, A.G., Mishra, U.C., 2000a. Application of Cherenkov radiation counting for determination of ^{90}Sr in environmental samples. J. Environ. Radioact. 48, 49–57.

Rao, D.D., Sudheendran, V., Baburajan, A., Chandramouli, S., Hegde, A.G., Mishra, U.C., 2000b. Measurement of high energy gross beta and ^{40}K by Cerenkov counting in liquid scintillation analyzer. J. Radioanal. Nucl. Chem. 243 (3), 651–655.

Reddy, P.J., Pulhani, V., Dhole, S.D., Dahiwale, S.S., Bhade, S.P.D., Anilkumar, S., Singh, R., 2017. Development of rapid solvent extraction based radioanalytical technique for estimation of ^{90}Sr in the presence of natural and anthropogenic radionuclides. J. Radioanal. Nucl. Chem. 314, 359–370.

Regan, J.G.T., Tyler, J.F.C., 1976. The determination of ^{90}Sr and ^{89}Sr in water without separation of strontium from calcium. Analyst 101, 32–38.

Rengan, K., Sun, B.-C., 2004. Sorption of ZnII and CdII by chelating resins: comparison of three resins. J. Radioanal. Nucl. Chem. 262 (1), 175–182.

Renker, D., 2006. Geiger-mode avalanche photodiodes, history, properties and problems. Nucl. Instrum. Methods Phys. Res., Sect. A 567, 48–56.

Renshaw, A., for the Super-Kamiokande Collaboration, 2015. Solar neutrino results from Super-Kamiokande. Phys. Proc. 61, 345–354.

Ridone, S., Arginelli, D., Botta, M.C., 2017. Determination of ^{90}Sr in urine samples and ^{89}Sr/^{90}Sr in water samples by chemical separation and Cherenkov counting with LSC system. J. Radioanal. Nucl. Chem. 314, 789–795.

Ritson, D.M., 1961. Techniques of High Energy Physics. Interscience, New York.

Rivas Murillo, J.S., Bachlechner, M.E., Campo, F.A., Barbero, E.J., 2010. Structure and mechanical properties of silica aerogels and xerogels modeled by molecular dynamics simulation. J. Non-cryst. Solids 356, 1325–1331.

Roberts, A., 1960a. Čerenkov detector accurately measuring velocity and direction over a wide range. Rev. Scient. Instrum. 31, 579–580.

Roberts, A., 1960b. A new type of Čerenkov detector for the accurate measurement of particle velocity and direction. Nucl. Instrum. Methods 9, 55–66.

Robertson, R., Germanos, M.S., Li, C., Mitchell, G.S., Cherry, S.R., Silva, M.D., 2009. Optical imaging of Cerenkov light generation from positron-emitting radiotracers. Phys. Med. Biol. 54, N355.

Ronzhin, A., Albrow, M.G., Demarteau, M., Los, S., Malik, S., Pronko, A., Ramberg, E., Zatserklyaniy, A., 2010. Development of a 10 ps level time of flight system in the Fermilab test beam facility. Nucl. Instrum. Methods Phys. Res., Sect. A 623, 931–941.

Roof, R.A., Jin, Y., Roman, D.L., Sunahara, R.K., Ishii, M., Mosberg, H.I., Neubig, R.R., 2006. Mechanism of action and

structural requirements of constrained peptide inhibitors of RGS proteins. Che, Biol. Drug Des. 67, 266–274.

Rose, J., 2015. The Chameleons of Space. The Royal Swedish Academy of Sciences, p. 6. https://www.nobelprize.org/nobel_prizes/physics/laureates/2015/popular-physicsprize2015.pdf.

Rose Jr., P.,B., Erickson, A.S., 2015. Calibration of Cherenkov detectors for monoenergetic photon imaging in active interrogation applications. Nucl. Instrum. Methods Phys. Res., Sect. A 799, 99–104.

Ross, H.H., 1969. Measurement of β-emitting nuclides using Cherenkov radiation. Anal. Chem. 41, 1260–1265.

Ross, H.H., 1971. Performance parameters of selected waveshifting compounds for Cerenkov counting. In: Horrocks, D.L., Peng, C.-T. (Eds.), Organic Scintillators and Liquid Scintillation Counting. Academic Press, New York and London, pp. 757–769.

Ross, H.H., 1976. Theory and application of Cherenkov counting. In: Noujaim, A.A., Ediss, C., Wiebe, L.I. (Eds.), Liquid Scintillation Science and Technology. Academic Press, New York and London, pp. 79–91.

Ross, H.H., 1980. Recent applications of Cherenkov radiation. In: Peng, C.-T., Horrocks, D.L., Alpen, E.L. (Eds.), Liquid Scintillation Counting, Recent Applications and Development, vol. I. Academic Press, New York and London, pp. 375–385.

Rossa, A.L., Perrani, P., 2013. Development of a model for the approximation of the neutron and photon flux in a BWR spent fuel assembly. Ann. Nucl. Energy 57, 256–262.

Rotzinger, H., Linck, M., Burck, A., Rodrigues, M., Loidl, M., Leblanc, E., Fleischmann, L., Fleischmann, A., Enss, C., 2008. Beta spectrometry with magnetic calorimeters. J. Low Temp. Phys. 151 (3–4), 1087–1093.

Rowinska, L., Jaskolska, H., Radwan, M., 1975. Determination of phosphorus-32 activity using Cherenkov radiation. Isotopenpraxis 11, 223–225.

Rowinska, L., Walis, L., Panczyk, E., Dalecki, W., Kusowski, M., 1987. Application of Cherenkov radiation to study some technical processes. Nukleonika 32, 111–130.

Rubio, I., Pusch, R., Wetzker, R., 2004. Quantification of absolute Ras-GDP/GTP levels by HPLC separation of Ras-bound [32P]-labelled nucleotides. J. Biochem. Biophys. Methods 58, 111–117.

Rucker, T.L., 1991. Calculational method for the resolution of ^{90}Sr and ^{89}Sr counts from Cerenkov and liquid scintillation counting. In: Ross, H., Noakes, J.E., Spaulding, J.D. (Eds.), Liquid Scintillation Counting and Organic Scintillators. Lewis Publishers, Chelsea, MI, pp. 529–535.

Ruggiero, A., Holland, J.P., Lewis, J.S., Grimm, J., 2010. Cerenkov luminescence imaging of medical isotopes. J. Nucl. Med. 51, 1123–1130.

Salonen, L., 2010. Calibration of the direct LSC method for radon in drinking water: interference from 210Pb and its progenies accumulated in 226Ra standard solution. Appl. Radiat. Isot. 68, 131–138.

Šantelj, L., Adachi, R., Dolenec, K., Hataya, S., Iori, S., et al., 2017. Recent developments in software for the Belle II aerogel RICH. Nucl. Instrum. Methods Phys. Res., Sect. A 876, 104–107.

Sapienza, P., on behalf of the KM3NeT collaboration, 2015. High energy neutrino astronomy and neutrino mass hierarchy with KM3NeT: status and perspectives. Nucl. Part. Phys. Proc. 265–266, 221–226.

Sashkina, K.A., et al., 2018. Zeolite/silica aerogel composite monoliths and microspheres. Micropor. Mesopor. Materials. 263, 106–112.

Sato, K.T., 2011. Yttrium-90 radioembolization for the treatment of primary and metastatic liver tumors. Semin. Roentgenol. **46** 2, 159–165.

Satterlee, A.B., Yuan, H., Huang, L., 2015. A radio-theranostic nanoparticle with high specific drug loading for cancer therapy and imaging. J. Controlled Release 217, 170–182.

Scarpitta, S.C., Fisenne, I.M., 1996. Cerenkov counting as a compliment to liquid scintillation counting. Appl. Radiat. Isot. 47, 795–800.

Scarpitta, S., Odin-McCabe, J., Gaschott, R., Meier, A., Klug, E., 1999. Comparison of four ^{90}Sr groundwater analytical methods. Health Phys 76 (6), 644–656.

Schmöle, A.-C., Brennführer, A., Karapetyan, G., Jaster, R., Pews-Davtyan, A., Hübner, R., Ortinau, S., Beller, M., Rolfs, A., Frech, M.J., 2010. Novel indolylmaleimide acts as GSK-3β inhibitor in human neural progenitor cells. Bioorg. Med. Chem. 18, 6785–6795.

Schneider, E.H., Seifert, R., 2010. Sf9 cells: a versatile model system to investigate the pharmacological properties of G protein-coupled receptors. Pharmacol Therapeut 128, 387–418.

Schneider, P.B., 1971. Determination of specific activity of ^{32}P-labeled compounds using Cherenkov counting. J. Nucl. Med. 12, 14–16.

Schoorlemmer, H., Belov, K., Romero-Wolf, A., García-Fernández, D., Bugaev, V., et al., 2016. Energy and flux measurements of ultra-high energy cosmic rays observed during the first ANITA flight. Astropart. Phys. 77, 32–43.

Schröder, F.G., 2017. Radio detection of cosmic-ray air showers and high-energy neutrinos. Prog. Part. Nucl. Phys. 93, 1–68.

Schuster, J., Fröjmark, A.-S., Nilsson, P., Badhai, J., Virtanen, A., Dahl, N., 2010. Ribosomal protein S19 binds to its own mRNA with reduced affinity in Diamond-Blackfan anemia. Blood Cells Mol. Dis. 45, 23-18.

Sekiya, H., 2016. Solar neutrinos in super-Kamiokande. Nucl. Part. Phys. Proc. 273–275, 1749–1752.

Sequinot, J., Ypsilantis, T., 1977. Photo-ionization and Cherenkov ring imaging. Nucl. Instrum. Methods 142, 377–391.

Sequinot, J., Ypsilantis, T., 1994. A historical survey of ring imaging Cherenkov counters. Nucl. Instrum. Methods Phys. Res., Sect. A 343, 1–29.

Shabana, E.I., Al-Hussan, K.A., Al-Jaseem, Q.K., 1996. Adaptation of a radioanalytical method for strontium-90 to different kinds of environmental samples and its application for the investigation of some samples in the Riyadh region. J. Radioanal. Nucl. Chem., Letters 212, 229–240.

Shao, Y., Yang, G., Tazoe, H., Maa, L., Yamada, M., Xu, D., 2018. A review of measurement methodologies and their applications to environmental ^{90}Sr. Journal of Environmental Radioactivity 192, 321–333.

Sharifulin, D.E., 2015. Molecular contacts of ribose-phosphate backbone of mRNA with human ribosome. Biochim. Biophys. Acta **184**9, 930–939.

Shawky, S., El-Tahawy, M., 1999. Distribution pattern of ^{90}Sr and ^{137}Cs in the Nile Delta and the adjacent regions after Chernobyl accident. Appl. Radiat. Isot. 50, 435–443.

Sheeba, M.S., Asha, V.V., 2009. Cardiospermum halicacabum ethanol extract inhibits LPS induced COX-2, TNF-α and iNOS expression, which is mediated by NF-κB regulation, in RAW264.7 cells. J. Ethnopharmacol. 124, 39–44.

Shehata, S.N., et al., 2012. Analysis of substrate specificity and cyclin Y binding of PCTAIRE-1 kinase. Cell. Signall. 24, 2085–2094.

Siudak, R., Budzanowski, A., Chatterjee, A., Clement, H., Dorochkevitsch, E., Ernst, J., Hawranek, P., Hinterberger, F., Jahn, R., Jarczyk, L., et al., 2008. A threshold Cherenkov detector for K^+/π^+ separation using silica aerogel. Nucl Instrum. Methods Phys. Res., Sect. A 596, 311–316.

Singh, D., Kumar, A., Raghu Ram, E.V.S., Habib, S., 2005. Multiple replication origins within the inverted repeat region of the Plasmodium falciparum apicoplast genome are differentially activated. Molec. Biochem. Parasitol. 139, 99–106.

Skobel'tsyn, D.V., 1977. Paradoxes of the quantum theory of the Vavilov-Cerenkov and Doppler effects. Sov. Phys. Usp. 20, 528–545.

Smirnova, I., Gurikov, P., 2018. Aerogel production: current status, research directions, and future opportunities. J. Supercrit. Fluids 134, 228–233.

Smith, B.S.W., 1981. The contribution of the counting vial to variable quench in Cerenkov counting. Int. J. Appl. Radiat. Isot. 32, 760–762.

Smith, R.D., Anderson, J.J.B., Ristic, M.M., Huxsoll, D.L., 1972. The use of Cerenkov radiation in ^{32}P-labeled platelet survival studies. Int. J. Appl. Radiat. Isot. 23, 513–517.

Smy, M., for the Super-Kamiokande Collaboration, 2013. Super-Kamiokande's solar ν results. Nucl. Phys. B Proc. Suppl. 235–236, 49–54.

Sokolov, O., Paic, G., Alfaro, R., 2009. Aerogel detector with a Fresnel lens focalization. Nucl. Instrum. Methods Phys. Res., Sect. A 601, 276–281.

Sommerfeld, A., 1904. Zur Elektronentheorie. II. Grundlage für eine allgemeine Dynamik des Elektrons. Königliche gesellschaft der Wissenschaften zu Göttingen. Mathematischphysikalische Klass. Nachrichten 363–439.

Sowerby, B.D., 1971. Čerenkov detectors for low-energy gamma rays. Nucl Instrum. Methods Phys. Res. 97, 145–149.

Spinelli, A.E., D'Ambrosio, D., Calderan, L., Marengo, M., Sbarbati, A., Boschi, F., 2010. Cerenkov radiation allows in vivo optical imaging of positron emitting radiotracers. Phys. Med. Biol. 55, 483.

Spinelli, A.E., Boschi, F., D'Ambrosio, D., Calderan, L., Marengo, M., Fenzi, A., Menegazzi, M., Sbarbati, A., Del Vecchio, A., Calandrino, R., 2011. Cherenkov radiation imaging of beta emitters: in vitro and in vivo results. Nucl Instrum. Methods Phys. Res., Sect. A 648, S310–S312.

Spurio, M., on behalf of the ANTARES Collaboration, 2015. Results from the ANTARES neutrino telescope with six years of data. Phys. Proc. 61, 450–458.

Spurio, M., on behalf of the ANTARES Collaboration, 2017. Results from the ANTARES neutrino telescope. Nucl. Part. Phys. Proc. 291–293, 175–182.

Šrank, J., Melichar, F., Filyanin, A.T., Tomeš, M., Beran, M., 2010. Preparation of $^{90}YCl_3$ radiopharmaceutical precursor for nuclear medicine using technology of centrifugal extractors. Appl. Radiat. Isot. 68, 2163–2168.

Srivastava, M., D'Souza, S.F., 2007. Assessment of agronomic efficacy of phosphatic fertilizers for cotton crop in vertisol using ^{32}P radiotracer technique. J. Radioanal. Nucl. Chem. 274 (2), 397–401.

St-Amant, N., Whyte, J.C., Rousseau, M.-E., Lariviere, D., Kurt Ungar, R., Johnson, S., 2011. Radiostrontium and radium analysis in low-level environmental samples following a multi-stage semi-automated chromatographic sequential separation. Appl. Radiat. Isot. 69, 8–17.

Stamoulis, K.C., Ioannides, K.G., Karamanis, D.T., Patiris, D.C., 2007. Rapid screening of ^{90}Sr activity in water and milk samples using Cherenkov radiation. J Environ. Radioact. 93, 144–156.

Starič, M., for the HERA-B RICH group, 2005. HERA-B RICH: performance and physics impact. Nucl Instrum. Methods Phys. Res., Sect. A 553, 210–214.

Starič, M., 2011. Pattern recognition for the time-of-propagation counter. Nucl Instrum. Methods Phys. Res., Sect. A 639, 252–255.

Strandin, T., et al., 2011. The cytoplasmic tail of hantavirus Gn glycoprotein interacts with RNA. Virology 418, 12–20.

Stubbs, R.D., Jackson, A., 1967. Channels ratio colour quenching correction in Čerenkov counting. Int. J. Appl. Radiat. Isot. 18, 857–858.

Sun, X., Luo, H., Dai, S., 2012. Ionic liquids-based extraction: a promising strategy for the advanced nuclear fuel cycle. Chem. Rev. 112, 2100–2128.

Sundaresan, M.K., 2001. Handbook of Particle Physics. CRC Press LLC, Boca Raton, FL, p. 446.

Sunil, V.R., Patel, K.J., Nilsen-Hamilton, M., Heck, D.E., Laskin, J.D., Laskin, D.L., 2007. Acute endotoxemia is associated with upregulation of lipocalin 24p3/Lcn2 in lung and liver. Exp. Mol. Pathol. 83, 177–187.

Suomela, J., Wallberg, L., Melin, J., 1993. Methods for Determination of Strontium-90 in Food and Environmental Samples by Cerenkov Counting. SSI-Report 93-11, ISSN 0282-4433. Swedish Radiation Protection Institute, 171 16 Stockholm.

Supek, I., 1990. Theoretical Physics and Matter Structure, Part II (in Croatian). Školska knjiga, pp. 702–704.

Szemraj, J., Sobolewska, B., Gulczynska, E., Wilczynski, J., Zylinska, L., 2005. Magnesium sulfate effect on erythrocyte membranes of asphyxiated newborns. Clin. Biochem. 38, 457–464.

Tabata, M., Adachi, I., Ishii, Y., Kawai, H., Sumiyoshi, T., Yokogawa, H., 2010. Development of transparent silica aerogel over a wide range of densities. Nucl. Instrum. Methods Phys. Res., Sect A 623, 339–341.

Tabata, M., Adachi, I., Kawai, H., Kubo, M., Sato, T., 2012. Recent progress in silica aerogel Cherenkov radiator. Phys. Proc. 37, 642–649.

Tabata, M., et al., 2015. Fabrication of silica aerogel with $n = 1.08$ for e^+/μ^+ separation in a threshold Cherenkov counter of the J-PARC TREK/E36 experiment. Nucl. Instrum. Methods Phys. Res., Sect A 795, 206–212.

Tabata, M., et al., 2016. Large-area silica aerogel for use as Cherenkov radiators with high refractive index, developed by supercritical carbon dioxide drying. J Supercrit. Fluids 110, 183–192.

Taboada, I., IceCube collaboration, 2014. Neutrino astrophysics with IceCube. Nucl. Instrum. Methods Phys. Res., Sect A 742, 71–76.

Takiue, M., Ishikawa, H., 1978. Improvement of Cherenkov counting method. Radioisotopes 27, 123–127.

Takiue, M., Fujii, H., Ishikawa, H., 1984. PPO-Ethanol system as wavelength shifter for the Cherenkov counting technique using a liquid scintillation counter. Nucl. Instrum. Methods Phys. Res., Sect A 227, 571–575.

Takiue, M., Fujii, H., Aburai, T., 1993. Reliability of activity determined by Cerenkov measurements in a liquid scintillation counter. In: Noakes, J.E., Schönhofer, F., Polach, H.A. (Eds.), Liquid Scintillation Spectrometry 1992, Radiocarbon, pp. 69–73.

Takiue, M., Natake, T., Fujii, H., Aburai, T., 1996. Accuracy of Cerenkov measurements using a liquid scintillation spectrometer. Appl. Radiat. Isot. 47, 123–126.

Takiue, M., Yoshizawa, Y., Fujii, H., 2004. Cerenkov counting of low-energy beta-emitters using a new ceramic with high refractive index. Appl. Radiat. Isot. 61, 1335–1337.

Talbot, J.N., Roman, D.L., Clark, M.J., Roof, R.A., Tesmer, J.J.G., Neubig, R.R., Traynor, J.R., 2010. Differential modulation of mu-

opioid receptor signaling to adenylyl cyclase by RGS proteins 4 or 8 and 7 in permeabilised C6 cells is Gα subtype dependent. J. Neurochem. **112** (4), 1026−1034.

Talka, R., et al., 2013. Nicotine−morphine interactions at α4β2, α7 and α3* nicotinic acetylcholine receptors. Eur. J. Pharmacol. 701, 57−64.

Talka, R., Salminen, O., Tuominen, R.K., 2015. Methadone is a non-competitive antagonist at the α4β2 and α3* nicotinic acetylcholine receptors and an agonist at the α7 nicotinic acetylcholine receptor. Basic & Clinical Pharmacol. & Toxicol. 116, 321−328.

Tamburro, A., IceCube Collaboration, 2014. Cosmic ray spectrum, composition, and anisotropy measured with IceCube. Nucl. Instrum. Methods Phys. Res., Sect A 742, 35−41.

Tamm, I., 1939. Radiation emitted by uniformly moving electrons. J. Phys. 1, 439−454.

Tan, E., Zu, X.L., Yeoh, G.C., Besant, P.G., Attwood, P.V., 2003. Detection of histidine kinases via a filter-based assay and reverse-phase thin-layer chromatographic phosphoamino acid analysis. Anal. Biochem. 323, 122−126.

Tarancón, A., Alonso, E., García, J.F., Rauret, G., 2002a. Comparative study of quenching correction procedures for ^{90}Sr/^{90}Y determination by Cerenkov, liquid scintillation and plastic scintillation techniques. Anal. Chim. Acta 471, 135−143.

Tarancón, A., García, J.F., Rauret, G., 2002b. Mixed waste reduction in radioactivity determination by using plastic scintillators. Anal. Chim. Acta 463, 125−134.

Tayeb, M., Dai, X., Corcoran, E.C., Kelly, D.G., 2014. Evaluation of interferences on measurements of ^{90}Sr/^{90}Y by TDCR Cherenkov counting technique. J. Radioanal. Nucl. Chem. 300, 409−414.

Tayeb, M., Dai, X., Corcoran, E.C., Kelly, D.G., 2015. Rapid determination of ^{90}Sr from ^{90}Y in seawater. J. Radioanal. Nucl. Chem. 304, 1043−1052.

Tayeb, M., Dai, X., Sdraulig, S., 2016. Rapid and simultaneous determination of Strontium-89 and Strontium-90 in seawater. J. Environ. Radioact. 153, 214−221.

Taylor, V.F., Evans, R.D., Cornett, R.J., 2007. Rapid dissolution of large environmental samples for the determination of fission products. J. Radioanal. Nucl. Chem. 274 (3), 545−553.

Thiam, C., Bobin, C., Bouchard, J., 2010. Simulation of Cherenkov photons emitted in photomultiplier windows by Compton diffusion using the Monte Carlo code GEANT4. Appl. Radiat. Isot. 68, 1515−1518.

Thiam, C., Bobin, C., Bouchard, J., 2011. Radiopharmaceutical ^{11}C activity measurements by means of the TDCR Cerenkov method based on a GEANT4 stochastic modeling. In: LSC2010, Advances inLiquid Scintillation Spectrometry. Proceedings of the 2010 International Conference onLiquid Scintillation Spectrometry, Paris, France, 6-10 September 2010 Philippe Cassette. Radiocarbon. The University of Arizona, Tucson, AZ, USA, pp. 341−348, 978-0-9638314-7.

Thiam, C., Bobin, C., Bouchard, J., 2017. Adaptation of PTB's analytical modelling for TDCR−Cherenkov activity measurements at LNHB. J. Radioanal. Nucl. Chem. 314 (2), 591−597.

Tinker, R.A., Smith, J.D., Cooper, M.B., 1997. Determination of strontium-90 in environmental samples containing thorium. Analyst 122, 1313−1317.

Töpfer, M., Burbiel, C.E., Müller, C.E., Knittel, J., Verspohl, E.J., 2008. Modulation of insulin release by adenosine A, receptor agonists and antagonists in INS-1 cells: the possible contribution of $^{86}Rb^{+}$ efflux and $^{45}Ca^{2+}$ uptake. Cell Biochem. Funct. **26**8, 833−843.

Todorović, N., Stojković, I., Nikolov, J., Tenjović, B., 2017. ^{90}Sr determination in water samples using Cerenkov radiation. J. Environ. Radioact. 169−170, 197−202.

Torassa, E., on behalf of the Belle II PID Group, 2016. Particle identification with the TOP and ARICH detectors at Belle II. Nucl. Instrum. Methods Phys. Res., Sect A 824, 152−155.

Torres, J.M., García, J.F., Llauradó, M., Rauret, G., 1996. Rapid determination of strontium-90 in environmental samples by single Cerenkov counting using two different colour quench curves. Analyst 121, 1737−1742.

Torres, J.M., Llauradó, M., Rauret, G., 1999. Microwave-assisted pretreatment of environmental samples for the determination of ^{90}Sr. Anal. Chim. Acta 379, 135−142.

Torres, J.M., Tent, J., Llauradó, M., Rauret, G., 2002. A rapid method for ^{90}Sr determination in the presence of ^{137}Cs in environmental samples. J. Environ. Radioact. 59, 113−125.

Torres-Marquez, E., Sinnett-Smith, J., Guha, S., Kui, R., Waldron, R.T., Rey, O., Rozengurt, E., 2010. CID755673 enhances mitogenic signaling by phorbol esters, bombesin and EGF through a protein kinase D-independent pathway. Biochem. Biophys. Res. Commun. 391, 63−68.

Toscano, D., IceCube Collaboration, 2017. Neutrino astronomy at the South Pole: latest results from the IceCube neutrino observatory and its future development. Nucl. Instrum. Methods Phys. Res., Sect A 876, 72−75.

Tosi, D., on behalf of the IceCube Collaboration, 2017. Astrophysical neutrinos: IceCube highlights. Nucl. Part. Phys. Proc. 291−293, 167−174.

Tovedal, A., Nygren, U., Ramebäck, H., 2008. Determination of ^{90}Sr in preparedness: optimization of total analysis time for multiple samples. J. Radioanal. Nucl. Chem. **276**2, 357−362.

Tovedal, A., Nygren, U., Ramebäck, H., 2009. Methodology for determination of ^{89}Sr and ^{90}Sr in radiological emergency: I. Scenario dependent evaluation of potentially interfering radionuclides. J. Radioanal. Nucl. Chem. 282, 455−459.

Tovedal, A., Nygren, U., Lagerkvist, P., Vesterlund, A., Ramebäck, H., 2009a. Methodology for determination of ^{89}Sr and ^{90}Sr in radiological emergency: II. Method development and evaluation. J. Radioanal. Nucl. Chem. 282, 461−466.

Tsroya, S., Pelled, O., German, U., Marco, R., Katorza, E., Alfassi, Z.B., 2009. Color quench correction for low level Cherenkov counting. Appl. Radiat. Isot. 67, 805−808.

Tsroya, S., Pelled, O., German, U., Katorza, E., Abraham, A., Alfassi, Z.B., 2012. A comparative study of color quenching correction methods for Cerenkov counting. Appl. Radiat. Isot. 70, 397−403.

Tsroya, S., German, U., Pelled, O., Katorza, E., Alfassi, Z.B., 2013a. Determination of ^{90}Sr-^{90}Y activity in urine samples by using Cerenkov counting. Appl. Radiat. Isot. 73, 12−16.

Tsroya, S., Dolgin, B., German, U., Pelled, O., Alfassi, Z.B., 2013b. Fast determination of ^{90}Sr/^{90}Y activity in milk by Cherenkov counting. Appl. Radiat. Isot. 82, 332−339.

Tuininga, A.R., Dighton, J., Gray, D.M., 2002. Burning, watering, litter quality and time effects on N, P, and K uptake by pitch pine Pinus rigida seedlings in a greenhouse study. Soil Biol. Biochem. 34, 865−873.

Tuffen, F., Eason, W.R., Scullion, J., 2002. The effect of earthworms and arbuscular mycorrhizal fungi on growth of and ^{32}P transfer between Allium porrum plants. Soil Biol. Biochem. 34, 1027−1036.

Tyapkin, A.A., 1974. The first theoretical prediction of the radiation discovered by Vavilov and Čerenkov. Sov. Phys. Uspekhi 17, 288.

Uesugi, M., Watanabe, R., Sakai, H., Yokoyama, A., 2018. Rapid method for determination of ^{90}Sr in seawater by liquid scintillation counting with an extractive scintillator. Talanta 178, 339−347.

Ullaland, O., 2003. Update in particle identification. Nucl. Phys. B Proc. Suppl. 125, 90−99.

Uz, T., Qu, T., Sugaya, K., Manev, H., 2002. Neuronal expression of arylalkylamine N-acetyltransferase AANAT mRNA in the rat brain. Neurosci. Res. 42, 309−316.

Vaca, F., Manjón, G., García-León, M., 1998. Efficiency calibration of a liquid scintillation counter for ^{90}Y Cherenkov counting. Nucl. Instrum. Methods Phys. Res., Sect. A 406, 267−275.

Vaca, F., Manjón, G., García-León, M., 1999. ^{90}Sr in an alkaline pulp mill located in the south of Spain. J. Environ. Radioact. 46, 327−344.

Vaca, F., Manjón, G., García-León, M., 2001a. The presence of some artificial and natural radionuclides in a Eucalyptus forest in the south of Spain. J. Environ. Radioact. 56, 309−325.

Vaca, F., Manjón, G., Cuéllar, S., García-León, M., 2001b. Factor of merit and minimum detectable activity for ^{90}Sr determinations by gas-flow proportional counting or Cherenkov counting. Appl. Radiat. Isot. 55, 849−851.

Vajda, N., Kim, C.-K., 2010. Determination of radiostrontium isotopes: a review of analytical methodology. Appl. Radiat. Isot. 68, 2306−2326.

Vajda, N., Ghods, E.A., Cooper, E., Danesi, P.R., 1992. Determination of Radiostrontium in soil samples using a crown ether. J. Radioanal. Nucl. Chem., Articles 162 (2), 307−323.

van Dijk, M.W.U., Brook, N.H., Castillo García, L., Cowie, E.N., Cussans, D., 2014. TORCH − a Cherenkov based time-of-flight detector. Nucl. Instrum. Methods Phys. Res., Sect. A 766, 118−122.

van Ginkel, G., 1980. An investigation of various wavelength-shifting compounds for improving counting efficiency when ^{32}P-Čerenkov radiation is measured in aqueous samples. Int. J. Appl. Radiat. Isot. 31, 307−312.

Van Hemert, F.J., Sloof, G.W., Schimmel, K.J.M., Vervenne, W.L., Van Eck-Smit, B.L.F., Busemann-Sokole, E., 2006. Radiopharmaceutical management of ^{90}Y/^{111}In labeled antibodies: shielding and quantification during preparation and administration. Ann. Nucl. Med. **20**8, 575−581.

Vareda, J.P., et al., 2018. Effect of different types of surfactants on the microstructure of methyltrimethoxysilane-derived silica aerogels: a combined experimental and computational approach. J. Colloid Interface Sci. 512, 64−76.

Varner, G.S., 2010. Radio detection of ultra high energy neutrinos. Nucl. Instrum. Methods Phys. Res., Sect. A 623, 413−415.

Vavilov, S.I., 1934. О возможных причинах синеГо үсвечения жидкостей. C.R. Dokl. Akad. Nauk, SSSR 2, 457−459.

Va'vra, J., 2000. Particle identification methods in high-energy physics. Nucl. Instrum. Methods Phys. Res., Sect. A 453, 262−278.

Va'vra, J., 2003. Novel photon detectors for RICH applications. Nucl. Instrum. Methods Phys. Res., Sect. A 502, 172−182.

Va'vra, J., Leith, D.W.G.S., Ratcliff, B., Ramberg, E., Albrow, M., Ronzhin, A., Ertley, C., Natoli, T., May, E., Byrum, K., 2009. Beam test of a Time-of-Flight detector prototype. Nucl. Instrum. Methods Phys. Res., Sect. A 606, 404−410.

Verzilov, Y., Nishitani, T., Ochiai, K., Kutsukake, C., Abe, Y., 2006. Development of a new fusion power monitor based on activation of flowing water. Fusion Eng. Design 81, 1477−1483.

Vesely, A., Trombitas, H., Lindauer, H., 2011. Use of Cerenkov counting for the determination of ^{90}Sr in a radwaste treatment facility. In: LSC 2010, Advances in Liquid Scintillation Spectrometry. Radiocarbon. University of Arizona, Tucson.

Völkel, S., Berenbrink, M., Heisler, N., Nikinmaa, M., 2001. Effects of sulfide on K^+ flux pathways in red blood cells of crucian carp and rainbow trout. Fish Physiol. Biochem. 243, 213−223.

Volotskova, O., Sun, C., Pratx, G., Xing, L., 2014. Cherenkov radiation energy transfer CRET as novel strategy for tumor imaging and delineation. Int. J. Radiat. Oncol. 901 (Suppl. l), S791.

Wahid, P.A., Kamalam, N.V., Sankar, S.J., 1985. Determination of phosphorus-32 in wet-digested plant leaves by Cerenkov counting. Int. J. Appl. Radiat. Isot. 36, 323−324.

Walter, K., Trautmann, N., Herrmann, G., 1993. Simultaneous determination of strontium-90 and strontium-89 by Cerenkov-radiation and liquid-scintillation counting: a re-evaluation for low-level counting. Radiochim. Acta 62, 207−212.

Wang, J.J., Chen, I.J., Chiu, J.H., 2004. Sequential isotopic determination of plutonium, thorium, americium, strontium and uranium in environmental and bioassay samples. Appl. Radiat. Isot. 61, 299−305.

Wang, Z.Y., 2015. Extension to de Broglie formula of quantum mechanics. International Letters of Chemistry, Physics and Astronomy 50, 50−60.

Wang, Y., Yang, Y., Song, L., Ma, Y., Luo, M., Dai, X., 2018. Effects of sodium salicylate on the determination of Lead-210/Bismuth-210 by Cerenkov counting. Appl. Radiat. Isot 139, 175−180.

Wanke, C., Kossert, K., Nähle, O.J., 2012. Investigations on TDCR measurements with the HIDEX 300 SL using a free parameter model. Appl. Radiat. Isot. 70, 2176−2183.

Warshawsky, D., Dowty, H.V., LaDow, K., Succop, P., Talaska, G., 2002. Reduction of a 7,12-dimethylbenz[a]anthracene DNA adduct in rat mammary tissue in vivo when pretreated with tamoxifen. Toxicol. Lett. 132, 71−79.

Websdale, D.M., 2008. Review of Cherenkov imaging devices in particle and nuclear physics experiments. Nucl. Instrum. Methods Phys. Res., Sect. A 595, 12−18.

Weingärtner, H., 2008. Understanding ionic liquids at the molecular level: facts, problems, and controversies. Angew. Chem. Int. Ed. Engl. 47, 654−670.

Wells, J.M., Thomas, J., Boddy, L., 2001. Soil water potential shifts: developmental responses and dependence on phosphorus translocation by the saprotrophic, cord-forming basidiomycete Phanerochaete velutina. Mycol. Res. **105**7, 859−867.

Welton, T., 1999. Room-temperature ionic liquids. solvents for synthesis and catalysis. Chem. Rev. 99, 2071−2084.

Wendell, R., for the Super-Kamiokande collaboration, 2013. Super-Kamiokande atmospheric neutrino oscillation analysis. Nucl. Phys. B Proc. Suppl. 237−238, 163−165.

Wiebe, L.I., Ediss, C., 1976. Methyl salicylate as a medium for radioassay of chlorine-36 using a liquid scintillation spectrometer. In: Noujaim, A.A., Ediss, C., Wiebe, L.I. (Eds.), Liquid Scintillation Science and Technology. Academic Press, New York and London, pp. 93−102.

Wiebe, L.I., Helus, F., Maier-Borst, W., 1978. Čerenkov counting and Čerenkov-scintillation counting with high refractive index organic ligands using a liquid scintillation counter. Int. J. Appl. Radiat. Isot. 29, 391−394.

Wiebe, L.I., McQuarrie, S.A., Ediss, C., Maier-Borst, W., Helus, F., 1980. Liquid scintillation counting of radionuclides emitting high-energy beta radiation. J. Radioanal. Chem. 60, 385–394.

Wiebe, L.I., Noujaim, A.A., Ediss, C., 1971. Some aspects of the measurement of ^{32}P Cerenkov radiation in water by a liquid scintillation spectrometer. Int. J. Appl. Radiat. Isot. 22, 463–467.

Wilkinson, D.H., 1970. The evaluation of finite nuclear size effects in allowed β-decay. Nucl. Phys. A 158, 476–486.

Wood, M.D., Marshall, W.A., Beresford, N.A., Jones, S.R., Howard, B.J., Copplestone, D., Leah, R.T., 2008. Application of the ERICA integrated approach to the Drigg coastal sand dunes. J. Environ. Radioact. 99, 1484–1495.

Wright, C.L., Pan, Q., Knopp, M.V., Tweedle, M.F., 2016. Advancing theranostics with tumor-targeting peptides for precision otolaryngology. World J. Otorhinonaryngology-Head Neck Surg. 2, 98–108.

Wu, M., Sherwin, T., Brown, W.L., Stockley, P.G., 2005. Delivery of antisense oligonucleotides to leukemia cells by RNA bacteriophage capsids. Nanomed. Nanotechnol. Biol. Med. 1, 67–76.

Wyckoff, H.O., Henderson, J.E., 1943. The spatial asymmetry of Cerenkov radiation as a function of electron energy. Phys. Rev. 641 (2), 1–6.

Xiques Castillo, A., Isaac-Olivé, K., Casanova González, E., Beckford, D., Leyva Montaña, R., Montero Álvarez, A., Olivé Álvarez, E., 2009. An adapted purification procedure to improve the quality of ^{90}Y for clinical use. Radiochim. Acta 97, 739–746.

Xiques Castillo, A., Pérez-Malo, M., Isaac-Olivé, K., Mukhallalati, H., Casanova González, E., Torres Berdeguez, M., Cornejo Díaz, N., 2010. Production of large quantities of ^{90}Y by ion-exchange chromatography using an organic resin and a chelating agent. Nucl. Med. Biol. 37, 935–942.

Xu, D., for the IceCube Collaboration, 2017. Exploring the universe with neutrinos: recent results from IceCube. Nucl. Part. Phys. Proc. 287–288, 139–142.

Xu, P., et al., 2015. Gene expression levels of Casein kinase 1 CK1 isoforms are correlated to adiponectin levels in adipose tissue of morbid obese patients and site-specific phosphorylation mediated by CK1 influences multimerization of adiponectin. Molec. Cell. Endrocrin. 406, 87–101.

Xu, Y., Toh, K.L., Jones, C.R., Shin, J.-Y., Fu, Y.-H., Ptáček, L.J., 2007. Modeling of a human circadian mutation yields insights into clock regulation by PER2. Cell 128, 59–70.

Yang, Y., Song, L., Luo, M., Dai, X., Guo, X., 2017. A rapid method for determining ^{90}Sr in leaching solution from cement solidification of low and intermediate level radioactive wastes. J. Radioanal. Nucl. Chem. 314 (1), 477–482.

Yip, Y.Y., et al., 2014. Differences in c-Jun N-terminal kinase recognition and phosphorylation of closely related stathmin-family members. Biochem. Biophys. Res. Commun. 446, 248–254.

Yoo, W.J., Han, K.-T., Shin, S.,H., Seo, J.K., Jeon, D., Lee, B., 2013. Development of a Cerenkov radiation sensor to detect low-energy beta-particles. Appl. Radiat. Isot. 81, 196–200.

Ypsilantis, T., Sequinot, J., 1994. Theory of ring imaging Cherenkov counters. Nucl. Instrum. Methods Phys. Res., Sect. A 343, 30–51.

Yusa, Y., Adachi, I., Dolenec, R., Hayata, K., Iori, D., et al., 2017. Test of the HAPD light sensor for the Belle II aerogel RICH. Nucl. Instrum. Methods Phys. Res., Sect. A 876, 149–152.

Zatsepin, G.T., Kuz'min, V.A., 1966. Upper Limit of the spectrum of cosmic rays. JETP Lett 4, 78–80.

Zendel, M., 2008. IAEA safeguards equipment. Int. J. Nucl. Ener. Sci. Techn. **4**1, 72–80.

Zhang, X.X., Bradshaw, J.S., Izatt, R.M., 1997. Enantiomeric recognition of amine compounds by chiral macrocyclic receptors. Chem. Rev. 97, 3313–3362.

Zhang, Y., for Super-Kamiokande Collaboration, 2015. Search for supernova relic neutrinos with 2.2 MeV gamma tagging at Super-Kamiokande-IV. Phys. Proc. 61, 384–391.

Zhou, L., Rao, R., Corcoran, E., Kelly, D., 2016. Distribution of radionuclides between atmosphere and ash during combustion of contaminated vegetation. J. Environ. Radioact. 165, 159–167.

Zhu, S., Ghods, A., Veselsky, J., Schelenz, R., 1990. Interference of ^{91}Y with the rapid determination of ^{90}Sr originating from the Chernobyl fallout debris. Radiochimica Acta 51, 195–198.

Zornoza, J.D., 2014. Results and prospects of deep under-ground, underwater and under-ice experiments. Nucl. Instrum. Methods Phys. Res., Sect. A 742, 130–138.

Further reading

Al-Masri, M.S., 1996. Cerenkov counting technique. J. Radioanal. Nucl. Chem., Articles 207, 205–213.

Anonymous, 1993. Quench and Quench Correction. TopCount Topics, TCA-015. PerkinElmer, Inc., Waltham, MA, USA, p. 8. http://www.perkinelmer.co.jp/Portals/0/resource/products_ls/ls_cocktails/pdf/tca-015.pdf.

Aynutdinov, V., Balkanov, V., Belolaptikov, I., Bezrukov, L., Borschov, D., Budnev, N., Chensky, A., Danilchenko, I., Davidov, Y., Domogatsky, G., et al., 2006. Search for a diffuse flux of high-energy extraterrestrial neutrinos with the NT200 neutrino telescope. Astropart. Phys. 25 (2), 140–150.

Bolotovskii, B.M., 2009. Vavilov-Cherenkov radiation: its discovery and application. Phys.-Usp. 52, 1099–1110.

Grichine, V.M., 2001. On irreducible fluctuations of Cherenkov radiation. Nucl. Instrum. Methods Phys. Res., Sect. A 463, 418–423.

Horsfield, C.J., Rubery, M., Miller, E.K., Ali, Z.A., 2010. Diagnosing inertial confinement fusion gamma ray physics. Rev. Sci. Instrum. **81** 10, 10D333.

Ivan, C., Cassette, P., Sahagia, M., 2008. A new TDCR-LS counter using channel photomultiplier tubes. Appl. Radiat. Isot. 66, 1006–1011.

Kellogg, T.F., 1982. Triton-X-100 acts as a scintillant when used as a wavelength shifter in Čerenkov counting systems. Int. J. Appl. Radiat. Isot. 33, 165–170.

Križan, P., Korpar, S., Iijima, T., 2006. Study of a nonhomogeneous aerogel radiator in a proximity focusing RICH detector. Nucl. Instrum. Methods Phys. Res., Sect. A 565, 457–462.

Lide, D.R., 1997. Handbook of Chemistry and Physics, 77th ed. CRC Press, Boca Raton.

Matsushita Electric Works, Ltd, 1992. Japanese Patent Early Publication KOKAI No. 1992-198238.

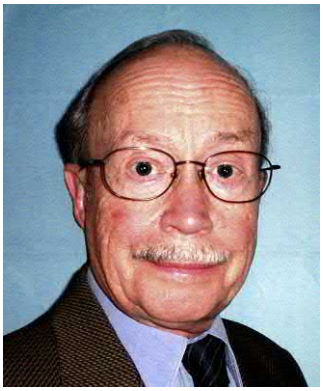
Muheim, F., On behalf of the LHCb RICH collaboration 2011. The ring imaging Cherenkov detectors of the LHCb experiment. Nucl. Instrum. Methods Phys. Res., Sect. A 639, 11-14.

Neamtan, S.M., 1953. The Cerenkov effect and the dielectric constant. Physical Review 92, 1362–1367.

Spinelli, A.E., Ferdeghini, M., Cavedon, C., Zivelonghi, E., Calandrino, R., Fenzi, A., Sbarbati, A., Boschid, F., 2013. First human Cerenkography. J. Biomed. Optics 18, 020502-1-3.

Yamato, A., 1982. An anion exchange method for the determination of ^{241}Am and plutonium in environmental and biological samples. J. Radio. Nucl. Chem. 75, 265–273.

Michael F. L'Annunziata



Michael F. L'Annunziata, Ph.D. is the Founding Editor and co-author of the Handbook of Radioactivity Analysis now in its Fourth Edition. His graduate thesis research at the University of Arizona, Tucson, AZ, USA in the 1960s, financed by the then U.S. Atomic Energy Commission, dealt with the analysis of ^{89}Sr and ^{90}Sr in the event of nuclear fallout. During 1970–71, he worked in the chemical industry (Amchem Products, Inc., Ambler, PA, USA) as ^{14}C-tracer chemist. Michael was then appointed Professor at the Postgraduate College, Chapingo, Mexico (1972–75) and Senior Research Scientist and graduate thesis advisor at the Nuclear Center of the National Institute of Nuclear Research (ININ), Mexico City during (1975–77). Michael served as Scientific Officer in the Department of Research and Isotopes and Department of Technical Co-operation of the International Atomic Energy Agency (IAEA) in Vienna, Austria during 1977–91 and Head of IAEA Fellowships and Training during 1987–91. Michael F. L'Annunziata was first to postulate the soil microbial epimerization of myo-inositol to other inositol stereoisomers as the chemical pathway and origin of the various inositol phosphate stereoisomers in soils (Ph.D. dissertation, 1970, https://dissexpress.proquest.com/dxweb/results.html?QryTxt=&By=L%27Annunziata&Title=&pubnum =) and in 1975 (*SSSA Journal* 39(2), 377–9), and first to demonstrate in 1977, with the use of the radioisotope carbon-14, the soil microbial epimerization of myo-inositol to chiro-inositol as a mechanism involved in the origin of the unique soil inositol phosphate stereoisomers (*SSSA Journal* 41(4), 733–6, https://dl.sciencesocieties.org/publications/sssaj/abstracts/41/4/SS0410040733). From 1977 to 2007, he served as IAEA Expert in peaceful applications of nuclear energy in over 50 countries of the world in Europe, Asia, Africa, Latin America and the Middle East. His book entitled "Radioactivity: Introduction and History", First Edition, published by Elsevier, was on the Best Sellers List in Physics (*LibraryJournal Academic Newswire* in 2008); and his much expanded Second Edition entitled "Radioactivity: Introduction and History, From the Quantum to Quarks" published by Elsevier in 2016 (https://www.sciencedirect.com/book/9780444634894/radioactivity) was awarded an Honorary Mention in the 2017 PROSE AWARDS in the category of Chemistry & Physics.

Željko Grahek



Željko Grahek earned his undergraduate B.Sc. in chemical technology 1987 and PhD degree in analytical chemistry 1997 from the Faculty of Chemical Engineering and Technology, University of Zagreb. His research interest is focused on the development of novel separation and detection techniques for the determination of alpha and beta emitters in complex samples, optimization and automation of radionuclide determination methods, the application of Cherenkov counting in the development of rapid methods for pure beta-emitter determinations, as well as the study of radionuclide behavior in the environment. He is the

author of more than 40 papers in international scientific journals and conference proceedings. His current position is Senior Research Associate at the Ruđer Bošković Institute in Zagreb and Head of the Radioecology Laboratory in the Division of Marine and Environmental Research.

Nataša Todorović



Dr. Nataša Todorović is Full Professor of Nuclear Physics in the Department of Physics, University of Novi Sad, Serbia. Her main research fields are related to low level alpha, beta and gamma spectroscopy with applications in different research fields. She is working on the development and implementation of fast and precise LSC methods including gross alpha/beta, radon, $^{90}Sr/^{90}Y$, ^{3}H, and ^{14}C determinations. Nataša Todorović is the author of 62 papers in Current Content journals, author of two books, co-author of six contributions in books, and more than 60 contributions in other journals, books or conference proceedings. She is Coordinator of one National Project and one Bilateral Project. Nataša Todorović participated in International Projects COST Action TU1301 "NORM4Building", and is currently part of EURAMET EMPIR project MetroRADON – Metrology for Radon Monitoring (EMPIR 16ENV10), IPA projects and CEEPUS Action "Education, Training and Research in Radioecology".

Chapter 7

PERPUSTAKAAN PRIBADI AN-NUR SUNARYA

Radionuclide standardization

Agustín Grau Malonda[1] **and Agustín Grau Carles**[2]
[1]*CIEMAT, Madrid, Spain;* [2]*Academia BIC, Madrid, Spain*

Chapter outline

I. Introduction **532**
II. Absolute direct methods **532**
A. Beta–gamma coincidences 532
1. Principles of the method 533
2. Radionuclide standardization methods based on beta–gamma coincidence 535
3. Applications of the beta–gamma coincidence method in radionuclide standardization. Differentiation by type of beta counter 538
4. Applications of the beta–gamma coincidence method. Standardization of radionuclides and determination of nuclear constants 543
5. Application of the tracer method 544
6. Applications of a two-dimensional method of extrapolation 544
7. Beta–gamma coincidences. Generation of extrapolation curves 544
8. Digital systems for beta–gamma coincidence 544
B. Beta–gamma anticoincidences 544
1. Anticoincidence method with nonextending dead time 545
2. Live-timed anticoincidence counting with extending dead-time corrections 546
3. Applications of the method of anticoincidence Beta−gamma Radionuclide standardization 546
C. Beta–gamma correlations 547
1. Introduction 547
2. Theoretical description of the beta−gamma correlations method 548
3. Applications of the Beta−gamma correlations method to radionuclide standardization 549
D. Gamma–gamma coincidences 549
1. Introduction to the sum peak method 549
2. Theoretical description of the sum peak method 550
3. Dead time and pileup corrections 551
4. Applications of the sum peak method 552
III. Solid angle primary methods **555**
A. 4π proportional counting 556
B. 2π proportional counting 556
C. $4\pi\gamma$ counting 556
D. 4π windowless sandwich detectors 556
E. $4\pi\beta\gamma + 4\pi$ sum counting 557
F. Defined solid angle 557
G. Internal gas counting 559
1. Theoretical description of internal gas counting 560
2. Some experimental aspects of internal gas counting 560
3. Applications of internal gas counting to radionuclide standardization 560
H. Liquid scintillation counting 563
1. Importance of the beta spectrum in the standardization of Co-60 570
I. Calorimetric detectors 574
1. Classic calorimetry 574
2. Cryogenic calorimeter 577
IV. Relative methods **578**
A. Calibration methods based on gamma ray spectrometry 578
1. Description of the general method 578
2. Heath method 580
3. Semi-empirical methods 581
4. Monte Carlo technique 582
B. Measurement of high activity. Ionization chambers 584
1. Calibration of ionization chamber radionuclides 585
2. Applications of ionization chambers 586
3. Considerations on the calculation of ionization chamber efficiency 588
V. Reference systems **590**
A. The SIR of gammas 590
1. Measurement of short half-life gamma emitters 592
B. The SIR of betas 592
VI. Preparation of radioactive samples **595**
A. Introduction 595
B. Sample preparation for radionuclide metrology 596
1. Supports for extended samples 596
2. Dilutions in aqueous solutions 596
3. Drops deposit in the sample holder 597
4. Determination of mass 597
5. Methods for verifying and improving the quality of the source 597
References **600**
Agustín Grau Malonda **624**
Agustín Grau Carles **624**

Handbook of Radioactivity Analysis: Volume 2. https://doi.org/10.1016/B978-0-12-814395-7.00007-6
Copyright © 2020 Elsevier Inc. All rights reserved.

I. Introduction

The activity of a radionuclide can be determined by applying different measurement procedures. The application of all these procedures depends on different parameters, particularly radionuclide decay. However, the determination of activity is often difficult due to various circumstances connected with radioactivity. The measure is not direct in the sense that an instrument cannot be applied to obtain activity directly as the weight of an object can be measured on scales or the length of a rod can be measured with a meter. Radioactive emission is a random process and, therefore, what an instrument measures is radiation emission and the activity of a radioactive sample is the average value of radioactive emission per unit of time. Furthermore, radiation measurement is indirect, so we have to consider the interaction of radiation with matter.

Finally, radioactivity measures are very sensitive but not very accurate, so that a measurement with an uncertainty of less than 1% is considered to be extremely accurate.

In this chapter we consider primary methods of radioactivity measurement (Debertin, 1996; Quinn, 1997; Pommé, 2007) and relative methods. The primary methods are based on the measurement of counts and time. Sometimes we use other complementary measurements such as corrections: geometric or other standardized radionuclides. But these measures are never comparative measures of activity. A borderline case is the tracer method in its two aspects: (CIEMAT/NIST method) based on the additional measure of the activity of a standard (^{3}H or ^{54}Mn) serving as a "sensor" for the scintillator quality of the scintillator−sample mixture and the effectiveness of the measuring geometry and the photomultiplier.

Relative methods can be comparative or interpolated. In comparative methods, a problem sample is compared with a standard sample of the same radionuclide calibrated by a primary method. In the relative method, by interpolation we obtain a calibration curve using standardized samples and obtain the activity of the sample by interpolation of a parameter linked to the activity of the sample. For example, in gamma spectrometry we use the area of the full energy peaks as a parameter, so the interpolation parameter is the energy of the emitted photons. In this chapter we will only consider the relative method by interpolation.

In Section II we study calibration methods based on the coincidence or anticoincidence of two radiations: coincidence, anticoincidence, and correlation in beta−gamma, and gamma−gamma, X−gamma and X−X coincidence, using high resolution semiconductor detectors.

Section III is devoted to primary methods based on the solid angle with which the detector sees the sample. We consider 2π and 4π solid angles, mainly in the standardization of alpha emitters, but also we consider beta and gamma emitters of low energy. Detection systems in the case of 2π solid angle are proportional counters (PCs) and in the 4πcase may be PCs, liquid scintillation counters, gas detectors or calorimeters. Defined solid angle (DSA) (below 2π) methods used in the standardization of alpha emitters are the methods with least uncertainty when they are applied properly.

In Section IV we study methods based on gamma spectrometry, for its wide application, and ionization chambers, for their ability to measure relatively high activity and high stability and reproducibility. If adequate models are developed, measures with both procedures can become primary.

Section V is devoted to the International Reference System known as SIR, on two fronts: the SIR of gammas, fully established and providing exceptional service in maintaining traceability to the international level, and the SIR of betas that started with pure beta emitters and now has been extended to nuclides decaying by electron capture.

Finally, in Section VI, we discuss the different methods of preparing quantitatively radioactive samples. We describe the procedures for preparing ultrathin films on which to deposit the radioactive solutions and methods for depositing quantitatively drops of radioactive material and methods for verifying and improving the quality of the radioactive sources.

II. Absolute direct methods

A. Beta−gamma coincidences

The $4\pi\beta-\gamma$ coincidence techniques are, among the methods of primary standardization, those that allow activity values of a sample to be obtained with lower uncertainty. The first descriptive work of such measures are due to Steyn and Haasbroek (1958), Campion (1959), Gandy (1961, 1962, 1963), Houtermans and Miguel (1962), Williams and Campion (1963), Brinkman (1961), Baerg et al. (1964), Baerg (1966), Williams and Birdseye (1966) and Grigorescu (1973), and Funck et al. (1983). These studies define the principles of the method and the required corrections.

The equations developed for this technique include both the effects of detectors and the parameters of complex radionuclide decay schemes. As counting efficiencies are not known in complex cases, correction terms are introduced for estimation purposes. The application of correction equations enables us not only to determine the sample's activity but also to obtain beta branch intensity values in decay schemes.

1. Principles of the method

a. Radionuclides with simple decay schemes

In its ideal form, the beta–gamma coincidence method only applies to the standardization of radionuclides with simple decay schemes. In this case, beta emission is followed by coincident nonconverted gamma emission. It is assumed that beta detectors only respond to beta radiation and gamma detectors to gamma radiation. In addition, the coincidence only records the simultaneous pulse emission of both detectors. For a point source with activity n_0 and detection efficiencies ε_β and ε_γ:

$$n_\beta = n_0\varepsilon_\beta \tag{7.1}$$

$$n_\gamma = n_0\varepsilon_\gamma \tag{7.2}$$

$$n_c = n_0\varepsilon_\beta\varepsilon_\gamma \tag{7.3}$$

where, n_β, n_γ, and n_c are the counting rates of beta, gamma, and coincidence channels, respectively.

When the source is extended, in which case the detection efficiencies may vary from one point to another, the total activity of the source N_0 and the counting rates, N_β, N_γ, and $N_c$are related by the expressions:

$$N_\beta = N_0\overline{\varepsilon}_\beta \tag{7.4}$$

$$N_\gamma = N_0\overline{\varepsilon}_\gamma \tag{7.5}$$

$$N_c = N_0\overline{\varepsilon_\beta\varepsilon_\gamma} \tag{7.6}$$

where $\overline{\varepsilon}_\beta$ and $\overline{\varepsilon}_\gamma$ are the average values of the basic efficiencies. If we integrate over the surface of the sample, the values obtained coincide with the counting efficiencies ε_β and ε_γ for the total sample. However, as was shown by Putman (1950), the mean value of the product $\overline{\varepsilon_\beta\varepsilon_\gamma}$ coincides with the product of the total efficiency when at least one of the detectors has the same efficiency on all points of the sample. This condition is satisfied by the gamma detectors. In the case of beta detectors based on a PC, this condition is not fulfilled. But it is true when the beta detector is a liquid scintillator. Henceforth, we will consider that the condition is met by both scintillation and PCs. Then

$$N_\beta = N_0\varepsilon_\beta \tag{7.7}$$

$$N_\gamma = N_0\varepsilon_\gamma \tag{7.8}$$

$$N_c = N_0\varepsilon_\beta\varepsilon_\gamma \tag{7.9}$$

verifying that

$$N_0 = \frac{N_\beta N_\gamma}{N_c} \tag{7.10}$$

These are the fundamental equations of beta–gamma coincidence in the ideal case. In practice, beta detectors are sensitive to gamma radiation and the above equations require correction. Furthermore, a gamma transition may have internal conversion. Thus, another correction to consider is the existence of conversion electrons.

Beta detectors sensitive to gamma radiation In most cases, beta detectors are sensitive to gamma radiation, so the above equations need to include the detection efficiency for the gamma radiation, denoted as $\varepsilon_{\beta\gamma}$. To detect a gamma photon as a beta count, the gamma photon cannot coincide with a beta particle. As the probability of not detecting a beta particle is $(1-\varepsilon_\beta)$, multiplying by $\varepsilon_{\beta\gamma}$ we obtain the probability of counting a gamma photon in the beta counter. Therefore, the above equations become the following:

$$N_\beta = N_0[\varepsilon_\beta + (1-\varepsilon_\beta)\varepsilon_{\beta\gamma}] \tag{7.11}$$

$$N_\gamma = N_0\varepsilon_\gamma \tag{7.12}$$

$$N_c = N_0\varepsilon_\beta\varepsilon_\gamma \tag{7.13}$$

and the equation to calculate the sample's activity is:

$$\frac{N_\beta N_\gamma}{N_c} = N_0\left[1 + \frac{(1-\varepsilon_\beta)}{\varepsilon_\beta}\varepsilon_{\beta\gamma}\right] \tag{7.14}$$

In the ideal case, N_0 was obtained directly from the measured quantities: N_β, N_γ, and N_c. But we now also need to know the efficiencies: ε_β and $\varepsilon_{\beta\gamma}$. To solve this equation we must relate ε_β and $\varepsilon_{\beta\gamma}$ with the measured count rates: N_β, N_γ, and N_c. The usual method is to take different values for these quantities, ε_β and $\varepsilon_{\beta\gamma}$ and extrapolate to obtain activity N_0. The general aspects of the activity calculation will be considered later when we discuss the general case of radionuclide standardization.

Converted gamma transitions Internal conversion of gamma transitions contributes to the beta channel with a count rate n_{ec} when the coincident beta particle is not detected. Therefore:

$$n_{ec} = N_0(1-\varepsilon_\beta)\varepsilon_{ce}\frac{\alpha}{1+\alpha} \tag{7.15}$$

where ε_{ce} is the probability of detecting the conversion electrons in the beta channel and α is the total internal conversion coefficient. In many cases, when the energy is relatively high, converted electrons are detected with 100% efficiency. When the energy of the converted electrons is low, detection of X-rays and Auger electrons can compensate for the low energy of converted electrons and high counting efficiencies are obtained. In this case $\alpha\varepsilon_{ec}$ should be replaced by:

$$\sum_i \alpha_i\left[\varepsilon_i + (1-\varepsilon_i)\varepsilon(X,A)_i\right] \tag{7.16}$$

where α_i is the internal conversion coefficient of the i-shell, ε_i is the beta detector efficiency for conversion electrons of

the i-shell, and $\varepsilon(X,A)$ is the probability of detecting at least one X-ray or Auger electron in the beta counter following conversion electron emission from the i-shell.

As internal conversion electron transitions compete with gamma photon emissions, converted electrons can reduce gamma−photon counts. The counting rates for the detection of gamma photons and for the coincidence channel are, respectively:

$$N_\gamma = N_0 \frac{\varepsilon_\gamma}{1+\alpha} \tag{7.17}$$

$$N_c = N_0 \frac{\varepsilon_\beta \varepsilon_\gamma}{1+\alpha} \tag{7.18}$$

where ε_γ is the intrinsic efficiency for gamma−ray detection. It is assumed that X-rays, arising from internal conversion, are excluded from detection in the gamma channel by appropriate energy discrimination.

Beta counter sensitivity to gamma radiation A gamma ray detected by the beta counter will only be counted if the respective beta particle is not detected. Thus:

$$n_{\beta\,\gamma} = N_0(1-\varepsilon_\beta)\frac{\varepsilon_{\beta\,\gamma}}{1+\alpha} \tag{7.19}$$

where $\varepsilon_{\beta\,\gamma}$ is the intrinsic efficiency of the beta counter for gamma photons. On the other hand, accidental coincidences occur due to the presence of gamma−ray cascades and Compton scattering. The probability of such coincidences, which we denote as ε_c, increases the number of coincidences in:

$$n_c = N_0(1-\varepsilon_\beta)\varepsilon_c \tag{7.20}$$

The value of ε_c is reduced significantly if the gamma channel is discriminated.

Gamma detector sensitivity to beta radiation The interaction of beta particles in the gamma detector is not probable and easily avoided in PCs by inserting absorbent material between the sample and the gamma detector. When liquid scintillation counters are used, the walls of the vial prevent beta particles from reaching the gamma detector. When beta particle energy is high, Bremsstrahlung occurs and interacts with the gamma radiation detector. Campion (1959) studied this problem and concluded that errors due to this process are practically negligible and disappear when beta detector efficiency approaches 100%. On the other hand, the problem can be entirely avoided by appropriate adjustment of the γ-detector threshold.

Beta−gamma angular correlation The angular correlation factor for beta−gamma coincidences was studied by Campion (1959), concluding that the correlation is expected in the case of forbidden beta transitions. The asymmetry factor was energy dependent and decreasing with beta energy. However, the correlation effect is small and cancels when the beta detector efficiency is equal to unity.

General expressions for single beta−gamma transitions The general equations for a decay scheme involving a single $\beta-\gamma$ transition are:

$$N_\beta = N_0\left[\varepsilon_\beta + (1-\varepsilon_\beta)\left(\frac{\alpha\varepsilon_{ce} + \varepsilon_{\beta\,\gamma}}{1+\alpha}\right)\right] \tag{7.21}$$

$$N_\gamma = N_0 \frac{\varepsilon_\gamma}{1+\alpha} \tag{7.22}$$

$$N_c = N_0\left[\frac{\varepsilon_\beta \varepsilon_\gamma}{1+\alpha} + (1-\varepsilon_\beta)\varepsilon_c\right] \tag{7.23}$$

where ε_{ec} is the efficiency for the internal conversion electrons.

b. Radionuclides with complex decay schemes

When the decay scheme has several beta and gamma branches, the equations for beta, gamma, and coincidence counting rates are more complicated (Baerg, 1973; Smith, 1978, 1987; Smith and Stuart, 1975). When the decay scheme has n branches with intensity a_i and at least one of the branches has one or more associated gamma transitions:

$$N_\beta = N_0 \sum_i a_i\left[\varepsilon_{\beta_i} + \left(1-\varepsilon_{\beta_i}\right)\left(\frac{\alpha\varepsilon_{ce} + \varepsilon_{\beta\gamma}}{1+\alpha}\right)_i\right] \tag{7.24}$$

$$N_\gamma = N_0 \sum_i a_i \varepsilon_{\gamma i} \tag{7.25}$$

$$N_c = N_0 \sum_i a_i\left[\varepsilon_{\beta i}\varepsilon_{\gamma i} + \left(1-\varepsilon_{\beta_i}\right)\varepsilon_{ci}\right] \tag{7.26}$$

where the summations extended over the n branches. The subscript i refers to the i-beta branch. a_i is the fractional branching ratio, ε_{β_i} is the β-detection efficiency of the i-beta branch, α is the total internal conversion coefficient associated with this β-branch, $(\varepsilon_{ce})_i$ is the β-detector efficiency for these internal conversion electrons associated with the i-branch, and ε_{ci} is the efficiency of the detector for i-rays associated with branch i, and $\varepsilon_{\gamma i} = \left(\frac{\varepsilon_\gamma}{1+\alpha}\right)_i$ is the efficiency of the γ-detector for γ-rays associated with branch i.

If we define C_i as the ratio of beta inefficiencies (Grigorescu, 1973):

$$C_i = \frac{1-\varepsilon_{\beta i}}{1-\varepsilon_{\beta s}} \tag{7.27}$$

where $\varepsilon_{\beta i}$ is the beta efficiency of the i-beta branch and $\varepsilon_{\beta S}$is the β-detector efficiency for any one arbitrarily selected β-group.

From Eqs. (7.24)–(7.26) we have:

$$\frac{N_\beta N_\gamma}{N_c} = N_0\left[1+(1-K)\left(\frac{1-N_c/N_\gamma}{N_c/N_\gamma}\right)\right] \tag{7.28}$$

or

$$N_\beta = N_0[1+k(1-N_c/N_\gamma)] \tag{7.29}$$

with

$$K = \frac{\sum a_i C_i\left\{1-[(\alpha\varepsilon_{ce}+\varepsilon_{\beta\gamma})/(1+\alpha)]_i\right\}}{\sum a_i\varepsilon_{\gamma i}C_i(1-\varepsilon_{ci}/\varepsilon_{\gamma i})}\sum a_i\varepsilon_{\gamma i} \tag{7.30}$$

In general, the graph of the function (7.28) is linear provided C_i changes just slightly with N_c/N_γ.

The best fit of the graph corresponds to:

$$\frac{\varepsilon_{\gamma 1}(1-\varepsilon_{c1}/\varepsilon_{\gamma 1})}{\left(1-\dfrac{\alpha\varepsilon_{ce}+\varepsilon_{\beta\gamma}}{1+\alpha}\right)_1} = \ldots = \frac{\varepsilon_{\gamma i}(1-\varepsilon_{ci}/\varepsilon_{\gamma i})}{\left(1-\dfrac{\alpha\varepsilon_{ce}+\varepsilon_{\beta\gamma}}{1+\alpha}\right)_i}$$

$$\ldots = \frac{\varepsilon_{\gamma s}(1-\varepsilon_{cs}/\varepsilon_{\gamma s})}{\left(1-\dfrac{\alpha\varepsilon_{ce}+\varepsilon_{\beta\gamma}}{1+\alpha}\right)_s} = E \tag{7.31}$$

where E is constant for a given setting (for good counting statistics E should be as large as possible).

In this case K is independent of C_i and reduced to:

$$K = \sum a_i\frac{\left(1-\dfrac{\alpha\varepsilon_{ce}+\varepsilon_{\beta\gamma}}{1+\alpha}\right)_i}{1-\varepsilon_{ci}/\varepsilon_{\gamma i}}$$

$$= \sum a_i\left[1-\left(\frac{\alpha\varepsilon_{ce}+\varepsilon_{\beta\gamma}}{1+\alpha}\right)_i+\frac{\varepsilon_{ci}}{E}\right]$$

$$= 1-\sum a_i\left[\left(\frac{\alpha\varepsilon_{ce}+\varepsilon_{\beta\gamma}}{1+\alpha}\right)_i-\frac{\varepsilon_{ci}}{E}\right] \tag{7.32}$$

In this equation, K represents the correction of gamma sensitivity for the beta detector. In practice, we can use less restrictive conditions:

$$\varepsilon'_{\gamma 1} = \ldots = \varepsilon'_{\gamma i} = \ldots = \varepsilon'_{\gamma s} \tag{7.33}$$

where

$$\varepsilon'_{\gamma i} = \varepsilon_{\gamma i}(1+\alpha)_i \tag{7.34}$$

Let us consider some nuclides as examples:

^{198}Au has the efficiencies ε_{412} and ε_{676} for the gamma rays of 412 and 676 keV, respectively. Condition (7.33) becomes:

$$\varepsilon_{412} = \varepsilon_{412}+\varepsilon_{676}(1-\varepsilon_{412})$$

To ensure compliance with this equality, the second term of the equation must be negligible compared to the first. This is achieved by setting a very narrow window in the 412 keV peak. The ε_{676} efficiency thus becomes negligible and also the term $\varepsilon_{676}(1-\varepsilon_{412})$.

For ^{131}I we have:

$$\varepsilon_{365} = \varepsilon_{637} = \varepsilon_{732} = 0.54\varepsilon_{503}$$

The last term of the equality is negligible because the abundance of 503 keV gammas is very small. In this case a discrimination level of 330 keV is sufficient to ensure compliance with equality.

Eq. (7.28) enables us to obtain the sample's activity from the count rates without recourse to data from the decay scheme. The procedure is a primary standardization method for the radionuclides for which the equation may be applicable. We simply determine the constant K for a given detection system and each radionuclide, by appropriate variation of the N_c/N_γ parameter.

2. Radionuclide standardization methods based on beta–gamma coincidence

a. Bidimensional extrapolation

Smith and Stuart (1975) developed a new coincidence technique applying two-dimensional extrapolation. They showed that, for some radionuclides, the beta count rate could be expressed as a function of at least two observed beta efficiencies, and that the absolute rate of disintegration could be obtained by simultaneous extrapolation to 100% for two or more dimensions. This reduces the systematic uncertainties in the efficiency extrapolation, as the shape of the extrapolation function is unknown, the extrapolation should coincide. In the two-dimensional case, for example, the two extrapolations must agree at the same point. They applied their procedure to the absolute standardization of ^{57}Co and ^{134}Cs.

b. Tracer method

The efficiency tracing technique was proposed by Campion et al. (1960). The experimental procedures are well established and the sources of uncertainties in the experiment were discussed by Williams and Goodier (1967). By applying this method, the accuracy of the measurement of specific activity for low-energy beta emitters is greatly improved. However, the type B uncertainty introduced by the extrapolation cannot be avoided. The final uncertainty of the specific activity of the low-energy pure beta emitter is still of the order of 1%–4% (Barnes et al., 1971; Baerg and Bowes, 1960; Merritt et al., 1960; Steyn, 1973; Lowenthal and Wyllie, 1973).

The tracer technique can be described as follows: we prepare a series of samples containing the nuclide emitting

only beta particles (pure beta emitter) with a suitable beta–gamma emitter (tracer). A varying amount of carrier is added to the samples so that they present variable surface density. We measure beta detection efficiency ε_β relative to the tracer in a $4\pi\beta - \gamma$coincidence system. After this measurement, the tracer is left to decay. Then we count the samples in the same detector to determine the count rate due to the pure beta emitter, the half-life of which is much longer. This count rate is drawn against the measured efficiency of the tracer. The line obtained is extrapolated to 100% efficiency to determine pure beta emitter activity. In general, all corrections that involve the factor $(1-\varepsilon_\beta)$ can be neglected, both in the counting rate $4\pi\beta$ and in the efficiency determination, as they only add a linear term and these magnitudes are zero for 100% efficiency. As the beta–gamma nuclide is only required for a measure of efficiency and then disintegrates, its activity does not need to be known.

When a long half-life tracer is used, we need to know the activity of the tracer in each sample. Therefore, the contribution of the tracer to the total beta count rate of each sample is determined from the efficiency and amount of activity added. This is then subtracted to obtain the pure beta emitter activity. Alternatively, the total beta count rate of each source drawn against the efficiency of the tracer can be extrapolated to 100% efficiency to obtain the sum of the decay rates (activities) of both nuclides. These decay rates are subtracted from the total decay rate to obtain the activity of the pure beta emitter.

c. Dead time and resolving time corrections

Numerous studies have been published concerning corrections for dead time and resolution time in the past. The most prominent are, in chronological order, Campion (1959), Gandy (1961, 1962), Bryant (1963), and Grigorescu (1973). Other less precise equations are due to Brinkman (1961) and Haywood (1961). These equations correspond to the expression:

$$N_c = PC + C_i$$

where N_c is the net counting rate of coincidences, C is the true coincidence rate in the coincidences channel, C_i is the accidental coincidence rate, and P is the probability of both beta and gamma channels being free in an arbitrary time. In the equations, in addition to the beta, gamma, and coincidence counting rates, N_β, N_γ, and N_c, the dead time θ is introduced in all three channels, together with the resolving time τ. Grigorescu (1973) provides tables of C_i, P, and N_c showing the Campion, Gandy, Bryant, and Grigorescu equations.

Dead time We will describe two models of dead time in the behavior of counting systems: nonparalyzable dead time and paralyzable dead time. In nonparalyzable models, the system responds to the arrival of an event with the creation of a fixed dead time during which the system does not respond to the arrival of new events and, furthermore, counts the pulse generated by the dead time.

In paralyzable systems, the system responds to the arrival of an event with a dead time during which the arrival of another event will lengthen the initial dead time but not result in counting the new event which is lost. So it will only count the initial event.

Nonparalyzable dead time If we designate the rate of incident events (or rate of interactions) as n, the rate of counted events as m and the dead time as τ, in the case of nonparalyzable systems, the relation between these three magnitudes is obtained from the number of lost events. The rate of lost events is on the one hand equal to $n - m$. On the other hand, if we take into account that the total dead time per unit of time is $m\tau$, then the number of counts lost per unit of time is $nm\tau$. So:

$$n - m = nm\tau$$

and

$$n = \frac{m}{1 - m\tau}$$

This expression has been applied in Example 8.13, Chapter 8 of this book.

In the case of a nonparalyzable model, successive events between intervals must be considered.

The Poisson distribution treats all intervals as independent. If the average rate of events per unit of time is n, the probability of not counting any event in a time interval t, during which nt events are generated, is on average:

$$P_0 = \frac{(nt)^0}{0!}e^{-nt} = e^{-nt}$$

The probability of an event occurring in time $dt$is simply ndt. The combined probability that no event occurs during time t and an event in time $t + dt$ is $ne^{-nt}dt$. Therefore, the probability dP_t of the duration of a particular interval being between t and $t + dt$ is:

$$dP_t = ne^{-nt}dt$$

If we have a large number N of intervals, the number of intervals greater than t_1 but less than t_2 is:

$$P = \int_{t_1}^{t_2} ne^{-nt}dt = e^{-nt_1} - e^{-nt_2}$$

If we want to obtain the number of intervals greater than that of τ, we will integrate between $t_1 = \tau$ and $t_2 = \infty$. The result is:

$$P = e^{-n\tau}$$

The rate of occurrence of such intervals is obtained by multiplying by n. Therefore, in a paralyzable model:

$$m = ne^{-n\tau}$$

This expression has a maximum in:

$$\frac{dm}{dn} = e^{-n\tau} - n\tau e^{-n\tau} = 0$$

This happens when

$$m = \frac{1}{\tau}\, e^{-1} = \frac{1}{\tau e}$$

Suppose that a nonparalyzable counter has counted a maximum of 50,000 accounts per second: the dead time will be:

$$\tau = \frac{1}{50000 \times e} = 7.36 \times 10^{-6} s = 7.36 \mu s$$

We will emphasize that when $n << 1/\tau$ (small dead time)

Nonparalyzable model $m = \frac{n}{1+n\tau} \approx n(1 - n\tau)$

Paralyzable model $m = e^{-n\tau} \approx n(1 - n\tau)$

d. Efficiency variation

Both in coincidence and anticoincidence techniques, we have to use a method called efficiency variation or extrapolation. This requires having different values of the beta count rate for different values of N_c/N_γin order to carry out the extrapolation of that relationship to the value of 1. This has been carried out with one of the following five methods:

1. Self-absorption variation
2. Foil-absorption variation
3. Threshold level variation
4. Wet extrapolation
5. Ink-jet printing (Sato et al., 2008)

The self-absorption method was the first to be used. It consists of incorporating increasing amounts of inactive carrier to increase self-absorption and thus decrease the detection efficiency of beta particles.

The method of interposing foils is possibly the most common. Beta efficiency is changed by using absorbers on one or both sides of the source. The absorbers are made of collodion film coated with a thin gold layer ($\approx$20 $\mu g cm^{-2}$) or aluminized MYLAR of different thickness.

Threshold level variation is especially useful since it is nondestructive and avoids other sources of error (e.g., sampling and foiling) that may obscure the results. Other advantages arise with electron capture and internal conversion processes. Threshold level variation is applied in the case of PCs operating at higher than atmospheric pressure, while the foil-absorption method is used with PCs working at atmospheric pressure.

Wet extrapolation was proposed by Zajic (1987). It uses absorption change during the drying of water droplets added to the surface of the source. A wet source is inserted into the PC and measured, while detection efficiency in the PC increases as the water evaporates. This method enables a smooth decrease of source self-absorption and can be reproduced using the same source. Sochorova et al. (2008) applied this procedure to the standardization of ^{54}Mn, ^{139}Ce, ^{88}Y, and ^{57}Co.

Sato et al. (2008) varied the counting efficiency of the sources by adding aqueous black pigment ink (Epson ICBK24), which is electrically conductive. The ink is sprayed on the sources with an ink-jet printer (Mastermind MMP-13100BT, the OEM product "DTG digital, the KIOSK" is available outside of Japan, http://www.dtgdigital.com). This printer has a flat motorized table and the printing position and pattern can be computer controlled. Adobe illustrator and a Macintosh computer were used for drawing a figure (filled rectangle) over the source. Ink was sprayed twice on the source with 40% color density scale with black-pigment ink; the sources were again measured by $4\pi\beta-\gamma$ coincidence. Overpainting of a single source can be repeated several times to obtain varying thicknesses of ink, so several data points can be obtained from one source to develop the $4\pi\beta-\gamma$ efficiency curve.

e. Biparametric extrapolation

Smith and Stuart (1975) presented an extension of the $4\pi\beta-\gamma$ coincidence technique. They showed that, for some radionuclides, the beta count rate could be expressed as a function of at least two observed β-efficiencies, and that the absolute disintegration rate could be obtained by simultaneous extrapolation to 100% efficiency in two or more dimensions. As examples of this generalization of the extrapolation technique, they described measurements of two nuclides, ^{57}Co measured with a PC as the β detector and ^{134}Cs, measured with a liquid scintillator, as the β detector.

Koskinas et al. (2002), Fig. 7.1, determined the activity of a solution of ^{152}Eu by a biparametric extrapolation curve obtained from two selected γ-windows. ^{152}Eu decays 27% by β^-emission and 73% by electron capture and β^+ emission. Both branches are followed by γ-ray emission. Measurements were carried out in a 4πPC–HPGe detection system. The efficiencies were changed by external absorbers. Calibration was performed by selecting two γ-ray windows: 334 keV following β^- decay and 1408 keV following the electron capture and β^+ processes.

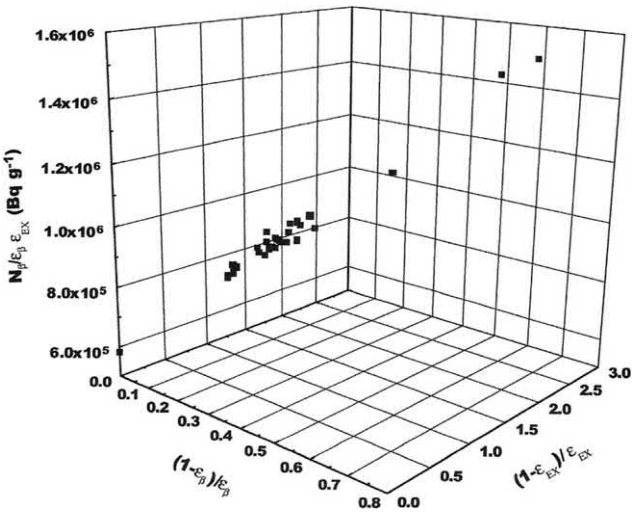


FIGURE 7.1 The biparametric extrapolation curve. *From Koskinass et al. (2002), reprinted with permission of Elsevier Science © 2002.*

The disintegration rate N_0 was determined by changing the efficiency value, using external absorbers over and below the radioactive source made of conducting collodion films previously coated with a 40 μgcm^{-2} gold layer. Activity was determined by simultaneous extrapolation to zero of inefficiency parameters. $\left(1-N_{ci}/N_{\gamma i}\right)/\left(N_{ci}/N_{\gamma i}\right)$

Chylinski and Radoszewski (1992) used a two-parametric method with coincidence and anticoincidence $4\pi(LS)-\gamma$ counting to standardize ^{22}Na. The electronic circuit contained a two-stage coincidence system. The first-stage coincidence unit formed the β-counting channel. Two scintillation counters with NaI(Tl) crystals working in sum mode formed the γ-counting channel. The second-stage coincidence and anticoincidence units were connected to the output of these two counting channels. The extrapolation curves as a function of the ratio $(1-\varepsilon_\beta)/\varepsilon_\beta$ were obtained by changing the high voltage on the photomultipliers.

Chylinski (1992) presents a new version of the tracer technique for measuring EC nuclides. Both the coincidence and anticoincidence methods were used simultaneously in the experiment. He presents the results of ^{134}Cs and ^{55}Fe activity measurements when traced by ^{139}Ce and ^{54}Mn. In this new version of the tracer technique, dependence on the amount of pure beta emitter relative to the tracer amount in the source is eliminated.

Chylinski and Radoszewski (1996) presented the basic relationships, as well as experimental results, for a generalized tracer method, with a multiparameter coincidence and anticoincidence system, for absolute activity measurements of pure beta-emitters. A liquid scintillation counter, with two photomultipliers working in coincidence, was used for beta particle detection and two NaI(Tl) crystals for gamma-ray detection.

A double extrapolation procedure was applied: first, extrapolation as a function of tracer counting efficiency and second, extrapolation as a function of emitter to tracer concentration ratio in the mixed radioactive solution. The second extrapolation procedure minimizes the count uncertainty involved in the first procedure.

The experimental results were illustrated by ^{63}Ni and ^{147}Pm activity measurements with the same tracer: ^{60}Co. The uncertainties obtained were within a 1% limit for a 0.99 confidence level.

Chylinski et al. (2000) measured 12 radionuclides: ^{133}Ba, ^{90}Sr, ^{99}Mo, ^{85}Sr, ^{65}Zn, ^{139}Ce, ^{192}Ir, ^{60}Co, ^{241}Am, ^{152}Eu, ^{169}Yb. They used a multidetection scintillation head for $4\pi(LS)-\gamma$ coincidence and anticoincidence with double-parametric registration.

Chylinski et al. (2002) applied a multimethod of radionuclide standardization with a "triangular scheme" of disintegration. The system is based on the multiparametric coincidence and anticoincidence methods. They presented considerations and experimental data of ^{51}Cr-activity measurement using the above methods.

3. Applications of the beta–gamma coincidence method in radionuclide standardization. Differentiation by type of beta counter

Radionuclide standardization procedures have improved significantly in the last 10 years. International comparisons and the SIR system have effectively contributed to this improvement. In the case of beta–gamma coincidence, uncertainties have been reduced and the number of radionuclides that can be measured by the beta–gamma coincidence method has increased. Below is a list of the most important studies on the subject published in the last decade.

a. Beta–gamma coincidence with proportional counter

^{18}F. Primary activity standardizations were performed on solutions of ^{18}F, using $4\pi\beta-\gamma$ coincidence counting by means of a PC, with efficiency variation achieved by the use of absorbers, and liquid scintillation counting (LSC) according to the CIEMAT/NIST method. A β^+-emission probability of 96.86% was used for both methods (Schrader et al., 2007). Combined relative standard uncertainty (k = 1) (Square root of the sum of quadratic components) was 0.40% and 0.30%, respectively. Sahagia et al. (2014a,b) apply the $4\pi\beta-\gamma$ coincidence method, using positron annihilation quanta and extrapolation of efficiency. Uncertainty was 0.58%.

^{22}Na. Nähle et al. (2008) apply two procedures based on variation of detector source distance. Zero distance extrapolation enables us to obtain the efficiency of the sum

peak and therefore the activity of the sample. Dias et al. (2010) use a PC coupled to a single or pair of NaI(Tl) scintillation crystals. They use Monte Carlo codes to calculate the extrapolation curve of coincidences.

^{31}Si. Koskinas and Dias (1993) measured the gamma-ray probability per decay of Si-31. A $4\pi\beta-\gamma$ coincidence method and the efficiency tracing technique were applied using ^{24}Na as the tracer. A calibrated HPGe spectrometer was used to count the gamma rays.

^{42}K. Simoes et al. (2001) measured the gamma-ray emission probabilities per decay of ^{42}K transitions. The activity of samples was measured in a $4\pi\beta$(PC)$-\gamma$ coincidence system and the gamma-ray measurements were performed in an HPGe spectrometer. The intensity of the 1524 keV gamma ray obtained was (0.1813 ± 0.0014).

^{54}Mn. Havelka et al. (2006) determined the activity of ^{54}Mn and ^{65}Zn by $4\pi\beta$(PC)$-\gamma$ coincidence counting with efficiency variation performed by altering the self-absorption in the sources and by the computer discrimination method. Sochorová et al. (2008) used a wet extrapolation method (absorption change during the drying of a water droplet onto the source surface) to standardize electron capture radionuclides (^{54}Mn, ^{139}Ce, ^{88}Y, ^{57}Co). Havelka (2012) improve the optimal setting of coincidence parameters for EC-β^+ radionuclides. A new procedure based on the coincidence to total PC ratio, a multigamma window combined with subwindows fractions and a source test for PC detection efficiency were introduced.

^{56}Co, ^{57}Co. Havelka and Sochorova (2008) presented a system of digital coincidences for the calibration of these radionuclides. The system consists of a PC and an HPGe detector for the gamma channel (Havelka et al., 2002, 2004, 2006). The Software Coincidence Counting (SCC) uses the conventional method of altering the sample's self-absorption and the computer discriminator method. It also used a conventional PC and two NaI(Tl) detectors. The extrapolation method uses the sample's self-absorption for the efficiency variation by adding extra mass to the sample. The differences between the coincidence results from the conventional method and SCC do not exceed 0.4% and 0.1% for ^{56}Co and ^{57}Co, respectively, which are smaller than the respective uncertainties. Koskinas et al. (2010) standardized ^{57}Co with two $4\pi\beta$(PC)$-\gamma$ coincidence systems. The first coupled the PC to a pair of NaI(Tl) detectors, the second used a HPGe detector.

^{59}Fe. Koskinas et al. (2016) standardized ^{59}Fe using a $4\pi\beta$(PC)$-\gamma$ coincidence system. The experimental setup consisted of a thin window gas flow PC coupled to a NaI(Tl) scintillator and a HPGe detector. The beta efficiency was changed using Collodion films and aluminum foils as external absorbers. Zhang et al. (2016) standardize ^{59}Fe and ^{60}Co using $4\pi\beta$(PC)$-\gamma$ (NaI(Tl)) digital coincidence counting (DCC) and efficiency extrapolation.

^{60}Co. Havelka et al. (2004) described a new procedure to obtain the resolving time and the accidental coincidence corrections. In this procedure a true coincidence resolving time rate is calculated from the records of time and amplitude data of individual pulses. Kawada et al. (2012) present a simple and versatile data acquisition system for software coincidence and pulse-height discrimination in $4\pi\beta-\gamma$ coincidence experiments. They apply this system to ^{60}Co, ^{134}Cs, and ^{152}Eu. Zhang et al. (2016) developed DCC with two NaI(Tl) gamma detectors and a $4\pi\beta$ PC. Kossert et al. (2018) measured the activity of ^{60}Co using four methods: $4\pi\beta-\gamma$ coincidence counting and LSC. The agreement between the different methods shows that the atomic exchange effect and screening corrections in the beta spectrum calculation are correct for a good agreement between liquid scintillation measurements.

^{72}Ga. It is an interesting nuclide because of its high gamma energy. It emits intense gamma rays at 630, 834, 2202, 2491, and 2508 keV. These energies fill the range from 1369 to 2754 keV, of interest in gamma-ray spectrometry. The drawback is that this nuclide has a short half-life of 14.10 hours, which makes it of local interest (Koskinas et al., 2006b).

^{99m}Tc. Sahagia (2006) calibrated this radionuclide using the 4π(PC)$-\beta$ coincidence method. She used three different procedures, all based on beta−gamma coincidences. The first is based on the coincidence between the conversion electrons (119.5−142.6) keV and X-rays. The second used the coincidence between the conversion electrons of 2.13 keV, measured by the PC, and the gamma rays of 140.5 keV. In the third procedure, she counted the whole spectrum of radiations detected in the PC and the γ-rays. The latter was described by Goodier and Williams (1966) and then by Ayres and Hirshfield (1982) with an uncertainty of 0.95%. They measured the total spectrum in the PC, obtaining general and specific equations for ^{99m}Tc. The conclusions from comparing the three procedures are as follows. The first is highly efficient, as it involves short-range extrapolation. The disadvantage of this method is the high Compton background under the X-ray peak. The second method has the advantage of a low slope of extrapolation. The third is simple and has a high count rate, but a greater extrapolation interval, with a steep slope.

^{134}Cs. García-Toraño et al. (2002a) calibrated this radionuclide through three methods: liquid scintillation, $4\pi\beta-\gamma$, and $4\pi\gamma$. They applied the CIEMAT/NIST LSC method. For coincidence measurements, they used a conventional system with two gamma windows: from 550 to 650 keV and from 750 to 850 keV. The main difference with the Grigorescu (1973) approach is that it suggests a narrower window for the 605 keV photon or the use of a discrimination level of more than 700 keV. In the approach established in this chapter the following relationship is approximately fulfilled:

$$\varepsilon_{800} = 0.13\varepsilon_{1365} + 0.87\varepsilon_{800} = 0.42\varepsilon_{1038} + 0.12\varepsilon_{1168}$$

For $4\pi\gamma$ calibration, they used a NaI(Tl) well crystal; and the Monte Carlo method was applied using the PENELOPE program (Salvat et al., 2006). The results obtained with the three methods were consistent within 0.65%.

Kawada et al. (2012) constructed a powerful and versatile bidimensional data acquisition system and carried out $4\pi\beta(\text{PC})-4\pi\gamma$ measurements of ^{60}Co, ^{134}Cs, and ^{152}Eu as examples.

To vary the mass, Sochorová and Auerbach (2014) use the wet efficiency extrapolation method to standardize the ^{134}Cs. The most significant item on the list of uncertainties is the uncertainty of extrapolation. Preparation of samples with lower self-absorption will be the subject of further research.

^{152}Eu. This radionuclide was calibrated by Grigorescu et al. (2002) and Park et al. (2002) in the context of an international comparison organized by the BIPM. ^{152}Eu is a gamma-ray emitter that is important in radionuclide metrology for the calibration of gamma spectrometers in both energy and efficiency. The solution was prepared in ampoules by the PTB. Solutions were measured at the BIPM in the SIR ionization chambers and then sent to participating laboratories. The work was carried out in the IFIN-HH Radionuclide Metrology Laboratory, where the solution was calibrated using an extrapolation method in conjunction with beta efficiency by applying the foil absorption procedure to modify the beta efficiency of the samples. They used a measurement system consisting of a PC $4\pi\beta$ and a crystal of NaI(Tl). There was no more than 0.5% impurity in the samples. They used a gamma window from 180 to 1500 keV. Dead time was 10 μs. The uncertainty obtained was 0.24% and was mainly due to the component of the extrapolation procedure.

Koskinas et al. (2002) calibrated the ^{152}Eu solution applying the $4\pi\beta-\gamma$ coincidence technique. They used a P-10 gas-filled PC operating at 0.1 MPa, coupled with an HPGe gamma detector. They used two discrimination windows for the gamma channel, one linked to the beta (344 keV) and the other to electron capture events (1408 keV), to determine the efficiencies for beta particles, X-rays, and Auger electrons in the proportional counter. The activity of the samples was determined using two-parameter extrapolation (Cox and Isham, 1977; Smith, 1987) obtained for the two windows.

Johansson et al. (2003b) apply six direct methods for the standardization of ^{152}Eu: two methods using the same equipment are $4\pi\beta(\text{PC})-\gamma$ coincidence counting and $4\pi\beta(\text{PC})-\gamma$ sum counting. The equipment was a pressurized PC (Ar-CH_4) for counting electrons and low energy photons and a 15 × 15 cm NaI(Tl) well crystal for counting gamma rays.

Havelka and Sochorová (2010) standardize ^{152}Eu and ^{152}Sb using a new SCC system. They demonstrate the advantages of the software coincidence system in setting and checking the optimal counting parameters. Havelka (2012) improves the SCC system for the standardization of EC-β^+ radionuclides.

Dias et al. (2013) developed a Monte Carlo simulation code ESQUEMA to be used as a benchmark for radionuclide standardization. ^{152}Eu was standardized by $4\pi\beta(\text{PC})-\gamma$ coincidence system and compared to Monte Carlo simulation.

^{182}Ta. Koskinas et al. (2008) applied the $4\pi\beta-\gamma$ method and extrapolation technique for the calibration of ^{182}Ta. They used a PC and a 76 mm × 76 mm NaI(Tl) detector. Beta efficiency was varied with collodion films previously coated with 20 μg/cm^2 of gold, and aluminum foil was applied to both sides of the sample. To obtain the coincidence events, two windows were used for the gamma channel, the first from 40 to 300 keV and the second from 1000 to 1300 keV.

^{241}Am. A very interesting application (Koskinas et al., 2006a) is the calibration of a solution of ^{241}Amusing a $4\pi\alpha-\gamma$ coincidence system. The PC, which detects the alpha particles, has P-10 gas, operates at 0.1 MPa, and has an aluminum window of 0.1 mm on the external wall to minimize gamma ray attenuation. Two extrapolation techniques (foil absorbers and threshold level variation) are applied to determine activity. Alpha efficiency variation is performed using two methods: the first uses external absorber collodion films coated with 20 μg cm^{-2} of gold, and the second uses electronic discrimination, changing the threshold of the alpha spectrum. The results of the two methods are comparable: 295.31 ± 1.06 and 296.44 ± 1.07 kBq g^{-1} and consistent within experimental uncertainty (Table 7.1).

b. Beta−gamma coincidence with a liquid scintillation counter (4π(LS)ex-γ)

^{139}Ce, ^{125}I, ^{192}Ir, ^{65}Zn. The beta−gamma coincidence technique $4\pi(\text{LS})\text{ex}-\gamma$, based on a beta liquid scintillation detector, has been successfully applied to the standardization of these radionuclides by Van Wyngaardt and Simpson (2006a). The four radionuclides were measured by the liquid scintillation extrapolation method. The last three radionuclides (^{125}I, ^{192}Ir, and ^{65}Zn) were part of a BIPM intercomparison. These four EC nuclides were standardized using variations of the coincidence extrapolation technique. The advantages of using liquid scintillation in the 4π channel are: absence of self-absorption (allowing measurement of Auger electrons with relatively high efficiency), relatively simple sample preparation, and highly reproducible sample geometry. This last advantage generated good reproducibility of the counting efficiency of

TABLE 7.1 Radionuclides standardized by coincidences $4\pi\beta(PC)-\gamma$ and references.

Radionuclides	References
^{18}F	Schrader et al. (2007) Sahagia et al. (2014a,b) Fitzgerald et al. (2014)
^{22}Na	Nähle et al. (2008)
^{31}Si	Koskinas and Dias (1993)
^{35}S	Koskinas et al. (2014b)
^{42}K	Simöes et al. (2001)
^{54}Mn	Havelka et al. (2006) Sochorová et al. (2008). Havelka (2012)
^{56}Co	Havelka and Sochorová (2008)
^{57}Co	Havelka and Sochorová (2008) Sochorová et al. (2008) Koskinas et al. (2010) Havelka (2012)
^{58}Co	Havelka and Sochorová (2008) Havelka (2012)
^{59}Fe	Miyahara and Watanabe (1984) Zhang et al. (2016) Koskinas et al. (2016)
^{60}Co	Miyahara et al. (1992) Havelka et al. (2004) Kawada et al. (2012) Havelka (2012) Zhang et al. (2016) Kossert et al. (2018)
^{64}Cu	Kawada (1986) Wanke et al. (2010) Havelka (2012) Havelka and Sochorová (2014) Yamazaki et al. (2018)
^{65}Zn	Havelka et al. (2006) Kossert et al. (2006b) Havelka (2012)
^{67}Cu	Sahagia et al. (2018)
^{67}Ga	Dias et al. (2014)
^{68}Ga	Koskinas et al. (2014a,b)
^{72}Ga	Koskinas et al. (2006b)
^{88}Y	Sochorová et al. (2008) Park et al. (2002)
^{99}Mo	Ayres and Hirsfeld (1982)
^{99}Tc	Dias et al. (2013) Sahagia et al. (2014a,b)
^{99m}Tc	Goodier and Williams (1966) Ayres and Hirsfeld (1982) Sahagia (2006)
^{110m}Ag	Garcia Toraño et al. (2000)
^{111}Ag	Collins et al. (2014)
^{111}In	Rezende et al. (2012) Matos et al. (2014)
^{123}I	Rezende et al. (2012) Dias et al. (2013)
^{124}I	Sahagia et al. (2016)
^{124}Sb	Iwahara et al. (2009a) Chauvenet et al. (2010) Havelka and Sochorová (2010) Havelka (2012)
^{126}I	Fonseca (1997)
^{128}I	Miyahara et al. (1994)
^{129}I	Altzitzoglou and Rozkov (2016)
^{133}Ba	Nedjady et al. (2012)
^{134}Cs	Miyahara and Watanabe (1984) Miyahara et al. (1992) Garcia toraño et al. (2002a) Kawada et al. (2012) Sochorová and Auerbach (2014)
^{137}Cs	Sochorová and Auerbach (2014)
^{139}Cs	Sochorová et al. (2008)
^{151}Sm	Altzitzoglou and Rozkov (2016)
^{152}Eu	Grigorescu et al. (2002) Park et al. (2002) Koskinas et al. (2002) Johansson et al. (2003b) Havelka and Sochorová (2010) Kawada et al. (2012) Havelka (2012) Dias et al. (2013)
^{165}Dy	Miyahara and Katoh (2004)
^{166m}Ho	Nedjadi et al. (2008) Nedjadi et al. (2012) Altzitzoglou and Rozkov (2016)
^{167}Ga	Nähle (2018)
^{169}Yb	Iwahara et al. (2000) Delgado et al. (2001)
^{177}Lu	Dias et al. (2010) Rezende et al. (2012) Kossert et al. (2012) Dias et al. (2013) Dryák et al. (2016)
^{182}Ta	Koskinas et al. (2008)
^{186}Re	Schönfeld et al. (1994b) Miyahara et al. (2000)
^{188}Re	Miyahara et al. (2000)
^{192}Ir	Fonseca et al. (2001)
^{198}Au	Dias et al. (2013)
^{241}Am	Koskinas et al. (2006a)
$^{141}Ce/^{141}Pr$	Schönfeld et al. (1992)
$^{68}(Ge+Ga)$	Grigorescu et al. (2004)

Continued

X-rays and Auger electrons, and consistent results between the counted samples. This technique was applied previously to ^{201}Tl (Simpson and Meyer, 1994b). In the case of ^{139}Ce, the counting system consisted of two photomultipliers in coincidence, which detected the light produced by the scintillator sample, and a crystal of NaI(Tl) to detect gamma rays.

The expression used to calibrate the radioactive sample is obtained as described below. First, the count rate, $N_S = N_0[f + (1-f)PP_S + (1-f)(1-P)\varepsilon_{AX}]$, from the liquid scintillation coincidence system is given by:

$$N_S = N_0[f + (1-f)PP_S + (1-f)(1-P)\varepsilon_{AX}] \quad (7.35)$$

where N_0 is the activity of the sample, f is the emission probability for the converted electrons, ε_{AX} is the detection efficiency of the emissions subsequent to EC (X-rays and Auger electrons), P is the probability that the gamma rays interact with the scintillator solution, and P_S is the detection probability of Compton electrons together with the particles emitted in the electron capture process giving a sum pulse. The conversion electrons are detected with 100% efficiency.

The gamma counting rate given by the NaI(Tl) detector is:

$$N_\gamma = N_0[(1-f)(1-P)\varepsilon_\gamma] \quad (7.36)$$

where ε_γ is the detection efficiency of events in the full-energy peak. The coincidence rate is:

$$N_C = N_0[(1-f)(1-P)\varepsilon_{AX}\varepsilon_\gamma] \quad (7.37)$$

from Eqs. (7.36) and (7.37) we have:

$$\frac{N_C}{N_\gamma} = \varepsilon_{AX} \quad (7.38)$$

Eq. (7.35) can be expressed as:

$$\frac{N_S N_\gamma}{N_C} = N_0(1-f)(1-P) + N_0[f + (1-f)PP_S]\frac{N_\gamma}{N_C} \quad (7.39)$$

When $N_\gamma/N_C \to 1$ and $P_S \to 1$, Eq. (7.39) becomes:

$$\frac{N_S N_\gamma}{N_C} \to N_0 \quad (7.40)$$

When N_γ/N_C is varied, we expect that P_S changes due to the low energy of the Compton electron spectrum. If the variation of P_S is linear, so will be the variation with respect to N_γ/N_C. Fig. 7.2 shows the extrapolation curves for three gamma windows. The points designated as Photopeak correspond to a window that covers the full-energy peak for gamma rays of 166 keV. The points designated as (K X-ray peak to end of photopeak) correspond to a window that extends from the X-ray peak to the full energy absorption peak. Finally, the points marked as "Iodine escape peak and photopeak" correspond to a window that includes the escape peak and the full energy absorption peak. The lines fitting the data sets were obtained with a third-order polynomial, with the second-order coefficient equal to zero.

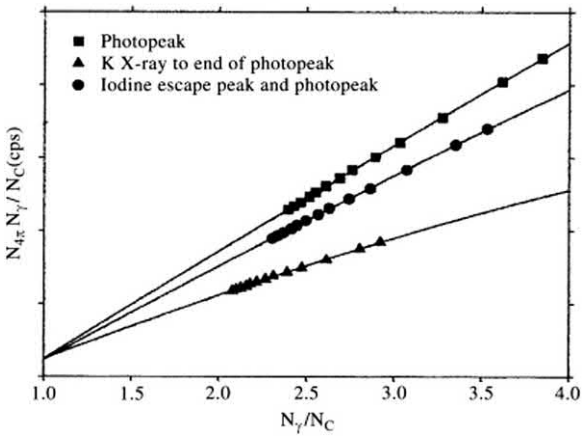


FIGURE 7.2 Extrapolation curves for three gamma windows. *From Van Wyngaardt and Simpson (2006a,b), reprinted with permission from Elsevier Science © 2006.*

Standardization of ^{192}Ir is more problematic because of the complexity of the spectrum; a method similar to that of ^{139}Ce has been used.

^{65}Zn can be standardized with the coincidence data without extrapolation (Simpson and Morris, 2004a). However, the extrapolation gives excellent results.

^{125}I is calibrated by applying the extrapolation technique using the equations of Simpson and Meyer (1989) (Table 7.2).

^{60}Co. Dias et al. (2008) have developed a $4\pi\beta-\gamma$ coincidence detector using plastic scintillators for beta detection in 4π geometry. The gamma detector used was a NaI(Tl) crystal. The new system improved the efficiency of the old PC, which was 60%, and obtained an efficiency of 77% for the new beta detector based on plastic scintillators.

c. beta–gamma coincidence with plastic scintillation sheets

A $4\pi\beta(PS)-4\pi\gamma$ coincidence counting with plastic scintillation was described by Nedjadi et al. (2010). This technique is very useful for standardizing the activity of short-lived radionuclides used in nuclear medicine. The technique is less cumbersome than the usual $4\pi(PC)-\gamma$. The Swiss National Metrological Institute (IRA-METAS) has set up this new coincidence system. They standardize ^{18}F. A similar system was already used to standardize ^{18}F by Yamada et al. (2008). In this technique, the beta detector is composed of two thin plastic scintillators sandwiching the source, coupled to a photomultiplier tube. The beta detector with the source is inserted into a large well type NaI(Tl) scintillator detector for γ-ray detection. Table 7.3

TABLE 7.2 Radionuclides standardized by coincidences $4\pi\beta(\text{LS})-\gamma$ and references.

Radionuclides	References
^{14}C (tracer ^{60}Co)	Bobin et al. (2016)
^{18}F	Evgeny et al. (2016) Fitzgerald et al. (2014) Capogni et al. (2016)
^{22}Na	Evgeny et al. (2016)
^{51}Cr	Bobin et al. (2012)
^{54}Mn	Bobin et al. (2016)
^{56}Mn	Evgeny et al. (2016)
^{57}Co	Van Rooy et al. (2018) Ziemek et al. (2018)
^{59}Fe	Bobin et al. (2016) Van Rooy et al. (2016)
^{60}Co	Hwang et al. (2006) Johansson and Sephton (2010) Lee et al. (2011) Kulkarni et al. (2013) Evgeny et al. (2016) Kossert et al. (2018) Collins et al. (2018)
^{68}Ge/^{68}Ge	Van Wyngaardt et al. (2018)
^{99}Tc	Bobin et al. (2018)
^{99m}Tc	Van Rooy et al. (2018)
^{111}Ag	Collins et al. (2014)
^{111}In	Dziel et al. (2016)
^{131}Cs	Kulkarni et al. (2016)
^{131}I	Kulkarni et al. (2016)
^{134}Cs	Hwang et al. (2006) Da Silva et al. (2018b)
^{153}Sm	Dziel et al. (2014)
^{177}Lu	Simpson et al. (2012).

TABLE 7.3 Radionuclides standardized by coincidences $4\pi\beta(\text{PS})-4\pi\gamma$ (Plastic Scintillation Sheets) and references.

Radionuclides	References
^{18}F	Yamada et al. (2008) Nedjadi et al. (2010) Duran et al. (2018)
^{41}Ar	Xie et al. (2015)
^{59}Fe	Yamada et al. (2016)
^{60}Co	Dias et al. (2008) Kawada et al. (2004) Kawada et al. (2012) Unno et al. (2018)
^{99}Mo	Yamada et al. (2010)
^{99m}Tc	Yamada et al. (2010)
^{133}Ba	Nedjadi et al. (2012) Duran et al. (2018)
^{134}Cs	Kawada et al. (2004) Kawada et al. (2012) Nedjadi et al. (2012) Kawada et al. (2014) Yunoki et al. (2016) Unno et al. (2018)
^{152}Eu	Kawada et al. (2012) Yamada et al. (2006)
^{154}Eu	Yamada et al. (2006)
^{166m}Ho	Nedjadi et al. (2012) Duran et al. (2018)

shows the main radionuclides standardized with this procedure and the references.

4. Applications of the beta–gamma coincidence method. Standardization of radionuclides and determination of nuclear constants

^{65}Zn. In 2006, an exercise called International EUROMET action 721, was organized in order to obtain more reliable decay data in the decay of ^{65}Zn (Bé, 2006; Bé et al., 2010). Nine laboratories participated by sending their activity measurement results and the intensity [50.22 (11)%] of the 1115 keV gamma ray. Except for two participants, who individually used an ionization chamber method and LSC, all the laboratories measured the activity by means of the $4\pi\beta-\gamma$ coincidence method. In the context of this project, we should highlight the contribution of Kossert et al. (2006a,b). The result of the activity measurement was combined with gamma spectroscopy measurements to investigate photon emission probabilities. The half-life of ^{65}Zn was measured, with improved accuracy, by a 4π ionization chamber, which was also used to measure secondary activity. In addition, a new secondary calibration procedure using LSC was tested. In general, the combined relative uncertainty was found to be 0.2% and 0.4% for $4\pi\beta-\gamma$ coincidence counting and LSC, respectively. The activity measured by LSC proved to be only 0.05% lower than that obtained by the coincidence method. The results obtained with the ionization chamber were even better and the relative standard deviation was estimated at 0.3%. These results confirm the excellent long-term stability of the ionization chamber.

5. Application of the tracer method

^{35}S, ^{63}Ni, and **^{185}W.** Yan et al. (2002) measured the activity of these pure beta-emitting radionuclides using ^{60}Co and ^{134}Cs as tracers. The uncertainties of the final results for the three pure beta emitters were 0.5% at the 99.7% confidence level. Beta theory was applied to calculate Fermi relations between the beta spectra of the five radionuclides. The authors reinvestigate the influence of spectral shapes and the value of the maximum energy of the nuclide tracers in the activity of pure beta emitter samples. They also investigate the type B uncertainty introduced by the upper limit of the region of adjustment (for radionuclides with low counting efficiency), by the power of the polynomial fit (for the tracer ^{60}Co), the lower limit for the region of adjustment (due to self-absorption), and by the gate setting for gamma rays (when ^{134}Cs is used as a tracer).

^{89}Sr. Razdolescu et al. (2002) calibrated ^{89}Sr using two methods. The first was the TDCR technique, using a liquid scintillation system. The second was the efficiency tracing technique using ^{60}Co as a tracer and a $4\pi\beta-\gamma$ coincidence system. The activity of the samples was determined by a general curve extrapolation procedure using data from various sources. The results obtained with both methods agreed within their combined uncertainties. Csete et al. (2002) calibrated a solution of ^{89}Sr at the National Office of Measurement (OHM) using two different methods. The first was the conventional $4\pi\beta$ method of counting with two gas flow PCs operating with methane gas (Szörenyi and Vágvölgyi, 1984). The second method of measurement was $4\pi\beta-\gamma$ using ^{22}Na as a tracer. The beta efficiency for each of these techniques was 100%. The agreement between the results of the methods was 0.5%.

6. Applications of a two-dimensional method of extrapolation

^{166m}Ho, ^{58}Co, and **^{88}Y.** Yuan et al. (2002) applied the $4\pi\beta-\gamma$ coincidence method to the standardization of these radionuclides. In the case of nuclides ^{88}Y and ^{166m}Ho, three gamma windows were established to study systematic error caused by the use of different gamma ray windows. To eliminate the effect of the large difference in the efficiencies of the counter between electron capture events and positron decay, a two-dimensional extrapolation method was applied in the case of ^{58}Co. The results of the measurements of the three radionuclides have been used to link to the SIR of the BIPM through two APMP (Asia–Pacific Metrology Program) regional comparisons.

7. Beta–gamma coincidences. Generation of extrapolation curves

^{54}Mn. Sato et al. (2008) used a novel technique to vary the efficiency of radioactive counting samples to be measured in a $4\pi\beta-\gamma$ system by varying the beta efficiency as follows. They covered the radioactive sample with varying amounts of an electrically conductive pigment used in inkjet printers. This method can be used to prepare samples needed to generate multiple extrapolation curves.

8. Digital systems for beta–gamma coincidence

For years, the traditional method of data collection for counting with the $4\pi\beta-\gamma$ coincidence technique used analog electronics. Modules used have been single-channel analyzers, linear gates, units of dead time and delay, time-amplitude converters, and multichannel analyzers. The high cost of the acquisition and maintenance of these systems has led to the search for more robust and flexible counting systems. The National Physical Laboratory (NPL) and the Australian Nuclear Science and Technology Organization (ANSTO) collaborated in the development of a digital coincidence system (DCC) to be used in $4\pi\beta-\gamma$ systems (Keightley and Watt, 2002). This chapter presents a system overview and a good analysis of its advantages. Details of these coincidence systems were published previously (Buckman et al., 1998; Butcher et al., 2000), followed by a comprehensive review by Keightley and Park (2007).

^{152}Eu and **^{88}Y**. Park et al. (2002) measured the activities of these radionuclides by the DCC technique and compared the results with those obtained with traditional coincidence techniques. ^{152}Eu activity was determined by extrapolation of the efficiency functions obtained with three gamma gates. The result obtained with the DCC system showed good agreement, to within a 2%, with the result obtained with the traditional method. The uncertainty for DCC was 0.19% and 0.21% for the conventional method. ^{88}Y activity was obtained by the DCC method and the reliability of the results was tested within the inter-Asia Pacific Metrology Program (APMP).

B. Beta–gamma anticoincidences

In anticoincidence counting techniques, only gamma events not coincident with beta events are counted. The coincidence rate is obtained as the difference between total and noncoincidence counting rates. This method has certain advantages for removing instrumental effects, particularly in the case of nuclides with excited gamma states. There are two methods for measuring anticoincidence: the first is based on nonextending dead time and the second measures live time with extending dead time circuits. The anticoincidence system based on nonextending dead time was the first to be employed. However, the one based on live time is now the most commonly used, and involves the simplest electronics (Tables 7.4 and 7.5).

TABLE 7.4 Radionuclides standardized by anticoincidences $4\pi\beta(\text{PC})-\gamma$ and references.

Radionuclides	References
^{60}Co	Kawada et al. (1970) Lu and Wang (2003)
^{67}Ga	Santry et al. (1987)
^{134}Cs	Kawada et al. (1970) Lu and Wang (2003)
^{170}Tm	Chylinski et al. (1972)
^{166m}Ho	Lu and Wang (2003)
^{110m}Ag – ^{110}Ag	Kawada et al. (1970)

TABLE 7.5 Radionuclides standardized by anticoincidences $4\pi\beta(\text{LS})-\gamma$ and references.

Radionuclides	References
^{18}F	Fitzgerald et al. (2014)
^{51}Cr	Da Silva et al. (2008b)
^{55}Fe	Da Silva et al. (2008b)
^{60}Co	Fitzgerald Schultz (2008)
^{64}Cu	Bergeron and Fitzgerald (2018)
^{67}Ga	Da Silva et al. (2008b)
$^{68}(Ga+Ge)$	Da Silva et al. (2018a)
^{99}Tc	Lucas (1998)
^{99m}Tc	Fitzgerald (2016)
^{106}Ru/Rh	Da Silva et al. (2017)
^{124}Sb	Da Silva et al. (2008a)
^{124}I	Fitzgerald (2016)
^{129}I	Fitzgerald (2016)
^{131}I	Da Silva et al. (2008a)
^{134}Cs	Da Silva et al. (2018a,b)
^{210}Pb	Fitzgerald Schultz (2008)
^{241}Am	Da Silva et al. (2008a)

1. Anticoincidence method with nonextending dead time

This method was introduced by Bryant (1962, 1967) and only requires correction for dead time and background, avoiding correction for accidental coincidences. In the case of coincident beta–gamma radiation, only gamma signals that precede or follow the signals in the beta channel in minimum time T are accepted as anticoincidence gamma events. This is achieved by delaying the gamma signal by a fixed time T and closing an anticoincidence gate on the gamma channel for a fixed time $2T$ after each beta signal. By choosing an appropriate T, we assure that we never count accidental anticoincidences.

According to Bryant (1962), the expression for the rate of disintegrations N_0 is given, in the case of correlated beta–gamma anticoincidences, with the expression:

$$N_0 = \frac{\left(\frac{N_\beta}{1-N_\beta T_\beta} - B_\beta\right)\left(\frac{N_\gamma}{1-N_\gamma T_\gamma} - B_\gamma\right)}{\frac{N_\gamma}{1-N_\gamma T_\gamma} - \frac{N_{\gamma A}}{1-N_\beta(T_\beta+2T)} - (B_\gamma - B_{\gamma A})} \quad (7.41)$$

where N_β and N_γ are the count rates in the beta and gamma channel, respectively; $N_{\gamma A}$ is the count rate of the gamma anticoincidences, T_β and T_γ are the beta and gamma dead time, and $2T$ is the time that the gate has to remain closed. B_β, B_γ, and $B_{\gamma A}$ are the background rates of the beta, gamma, and anticoincidence channels, respectively.

The anticoincidence method has advantages in the case of delayed gamma emission (Bryant, 1967), as in isomeric states with a short half-life. In this case, the anticoincidence gate has to remain closed for a time τ in addition to the time $2T$, as mentioned earlier. In this instance no signal from the daughter nuclide, in the counting channel (channel B), can pass through the gate to be accepted as an anticoincidence, unless at least one time T before and after at least one signal in the time $T+\tau$ on the parent radiation channel (channel A). If $T+\tau$ is equal to m half-lives of the state that produces the delayed radiation, the probability that a coincidence was recorded as an anticoincidence is 2^{-m}. Choosing m properly, the ratio of incorrectly recorded anticoincidence signals can be as small as desired.

The anticoincidence rate can be corrected for dead time, if we know the proportion of time that the gate is open and the time that the channel counting the daughter nuclide radiation is active. The anticoincidence rate corrected for dead time (not for background) is:

$$N_{CA} = \frac{N_R(1+N_A T_A)}{\exp[-N_A(2T+\tau)] - N_R T_B(1+N_A T_A)} \quad (7.42)$$

where N_R is the anticoincidence rate not corrected for dead time, N_A is the count rate in the channel counting parent radiation corrected by dead time, T_A is the dead time in the channel counting parent radiation, T_B is the dead time of the channel counting daughter radiation, $2T+\tau$ is the time, after the end of a period of dead time, in the parent radiation channel, during which the anticoincidence gate remains closed.

The probability of the anticoincidence gate being open is the product of the probability that channel A is alive and has been alive for at least one time period of $2T+\tau$. These probabilities are, respectively, $1/(1+N_A T_A)$ and $\exp[-N_A(2T+\tau)]$.

De Carlos and Granados (1973) introduced the Shared Dead Time (SDT) concept and method, and the principle on which the instrumentation is based. The basic idea of the SDT concept is to prevent the situation in which one channel is open while the other is blocked. They impose on both channels the same occupation time intervals by simultaneous blockade. The overlapping process disappears and the three dead times of the three channels have a unique dead time, at the expense of a greater loss of counts.

2. Live-timed anticoincidence counting with extending dead-time corrections

Anticoincidence counting using live-timed extending dead-time corrections (Baerg et al., 1976) removes all corrections due to instrumental effects. The method consists of first delaying the gamma signal with respect to the beta signal for an amount greater than any beta−gamma jitter and possible delay of beta pulses; then combining the beta and gamma logic signals so that one logical pulse triggers the extending dead time generator circuit. The extending dead time, τ, is adjustable and must have a value greater than the beta−gamma "jitter" and the delay (for example, $\tau \geq 2\,\mu s$). The output pulses of this circuit are applied as gate signals for simultaneously closing a channel with a live time clock and beta and gamma channels. A small delay (≈ 5 ns) in the gate allows the beta and gamma pulses that initiated the extending dead time to reach their counting channel and be recorded before the gates close.

This system ensures that only the gamma events not correlated with the events of the beta channel are counted in the gamma channel. This is a consequence of the extending nature of dead time; no other pulse (beta or gamma) can be detected in the time interval τ that precedes the observed pulse. It can also be shown that any beta event correlated with a gamma event can be registered because the gamma signal ensures that the channel will already be blocked by a signal on the gate initiated by a correlated beta event.

The live time clock, controlled by the gate triggered by the same impulses that control the beta and gamma channel count, cumulatively measures the time intervals of the combined $\beta-\gamma$ series. The counts accumulated in each channel are divided by the accumulated live time results in the correct count rate for the respective channel. The anticoincidence technique does not require corrections for the effects of resolving time or by dead time or by the $\beta-\gamma$ jitter effects. It only requires knowledge of the background rate and application of the corrections for isomeric state decay.

3. Applications of the method of anticoincidence Beta−gamma Radionuclide standardization

a. Applications of nonextending anticoincidence dead time

^{170}Tm. Chylinski et al. (1972) described the electronics and presented the measurement method using a $4\pi\beta-\gamma$ anticoincidence system that enables the absolute measurement of radioactive solutions. The systematic error is less than 0.1%, showing that the system works in an efficient and stable way. Comparing the results of measuring the radioactive concentration of a solution of ^{170}Tmusing the anticoincidence and coincidence methods shows the advantages of the presented method. The difference between the results of the two methods is 0.4%.

^{60}Co, ^{110m}Ag − ^{110}Ag, ^{134}Cs. Kawada et al. (1970) used a $4\pi\beta-\gamma$ system with a Ge(Li) detector and an anticoincidence system for measuring radionuclides with complex decay schemes without resorting to corrections for the decay scheme. They used the full gamma spectrum in both the gamma and anticoincidence channel. They applied the method to the standardization of ^{60}Co, ^{134}Cs, and ^{110m}Ag − ^{110}Ag, and compared the results with those obtained by other methods. The use of anticoincidence instead of the coincidence procedure has advantages in $4\pi\beta-\gamma$ systems with particular reference to accuracy and precision.

b. Applications of live-timed anticoincidence counting with extending dead time

^{241}Am, ^{124}Sb, and **^{131}I.** Da Silva et al. (2008a) described a coincidence and anticoincidence system that is composed of a cell for LSC, instead of a PC detector, and a 3" × 3" NaI(Tl) crystal. Live time measurements with an extended dead time device in the anticoincidence system were used to eliminate dead time corrections. ^{241}Am, ^{124}Sb, and ^{131}I were measured to test the system. Extrapolation curves were obtained by electronic discrimination in the liquid scintillation detector. The results are consistent with those obtained with a high pressure PC.

^{60}Co and **^{210}Pb.** Fitzgerald and Schultz (2008) use a photomultiplier tube to detect the scintillations of the liquid scintillator and a well-type NaI(Tl) crystal for gamma emission. The beta efficiency was varied by a discriminator. Three windows are used for the gamma channel: G1 for the Compton region, G2 for the full-energy peak, and G3 for the sum peak. The live time and the sum dead time were 100 μs. The containers were hemispheres containing 4 mL of HiSafe-3 LS-cocktail for ^{60}Co and 4 mL of PCS LS scintillation cocktail for ^{210}Pb.

^{60}Co, ^{137}Cs, and **^{166m}Ho.** Lu and Wang (2003) describe a system in which gamma radiation is measured with an HPGe detector and the β-counter is a PC. The Combined Standard Uncertainties for each of the aforementioned radionuclides were 0.24%, 0.33%, and 0.44%, respectively. Compared with the coincidence system, the ^{60}Co and ^{137}Cs results were satisfactory. For ^{166m}Ho, results from other methods have greater uncertainty due to the complexity of the nuclide's decay scheme. However, the anticoincidence technique has some shortcomings. First, the anticoincidence system is linked to the decay scheme, which introduces some uncertainties due to the lack of precision of the decay scheme data. Moreover, the anticoincidence channel uncertainty may be higher due to the low count rate.

^{51}Cr, ^{55}Fe, and **^{67}Ga.** Da Silva et al. (2008b) calibrated these radionuclides by anticoincidence counting using a live time clock with extending dead time. The chapter discusses the difficulties of the method and the uncertainties of the measurement results. Finally, they compare these results with those obtained using other methods of measurement. **^{67}Ga.** Santry et al. (1987) applied the live time technique with anticoincidence for the absolute standardization of ^{67}Ga. In contrast to the coincidence method, no dead time corrections, resolving time or effects due to e$-\gamma$-time jitter, are required in this case. This was achieved by extending the system dead time by several times the longest half-life. It was only necessary to apply background and decay corrections.

^{210}Pb. Laureano-Perez et al. (2007) standardized ^{210}Pb in solution by applying the CIEMAT/NIST method, using tritium as a tracer. As a confirmatory method they used high-resolution gamma spectrometry (HPGe), and $2\pi\alpha$ spectrometry with a Si barrier detector to determine the activity of ^{210}Po. From this activity they determined the activity of ^{210}Pb. They assumed that the sample of ^{210}Pb was in equilibrium. This procedure had been applied previously by Lucas (1998).

^{99}Tc. Lucas (1998) obtained the activity concentration of ^{99}Tc by applying an anticoincidence system with live time to a $4\pi\beta$(LS)$-\gamma$ counter. He used ^{60}Co as a tracer. He also applied the CIEMAT/NIST LSC method. In this case, he examined the influence of the shape factor of the second forbidden nonunique beta transition. Three gamma channels were used in the anticoincidence technique and the SD of the obtained activity ranged from 0.35% to 0.39%, according to the channel used.

^{134}Cs. Da Silva et al. (2018b) standardized ^{134}Cs applying three methods: $4\pi\beta-\gamma$ live-timed anticoincidence counting, $4\pi\beta-\gamma$ coincidence counting, and CIEMAT/NIST liquid scintillation methods. The standardization was made in order to reduce the uncertainty in ^{134}Cs. The agreement between the results of the three methods was excellent.

^{68}(Ge + Ga) and ^{18}F. Da Silva et al. (2018a) standardize ^{68}(Ge + Ga) using three methods: $4\pi\beta-\gamma$ live-timed anticoincidence counting, $4\pi\beta-\gamma$ coincidence counting, and the TDCR method. The results obtained were consistent. The difference between the calibration factors of ^{68}(Ge + Ga) and ^{18}F was lower than 0.3%, demonstrating that ^{68}(Ge + Ga) can be used as a substitute for ^{18}F in quality control tests in radiation measurement equipment used in nuclear medicine.

^{106}Ru/Rh. Da Silva et al. (2017) standardized ^{106}Ru/Rh. The high β produced by the decay of ^{106}Ru to ^{106}Pd is used in radiotherapy for treating eye cancer. ^{106}Ru can be standardized directly by coincidence or anticoincidence counting; however, as it is in equilibrium with ^{106}Rh, the activity of ^{106}Ru can be obtained by the activity of ^{106}Rh. The results of both procedures were quite satisfactory.

C. Beta–gamma correlations

1. Introduction

In a pioneer paper, Friedlander (1964), following Goldansky and Podgoretsky (1955), proposed applying correlation techniques to radionuclide standardization. The author suggested that the correlation method had two major advantages over the conventional $4\pi\beta-\gamma$ method: the application of small corrections to the count rate for the elimination of accidental coincidences, and statistical accuracy that was independent from the total number of observed coincidences. Williams and Sara (1968) examined these potential benefits in the case of absolute measurements using the $4\pi\beta-\gamma$ technique to perform the calibrations with the maximum precision. To this end, they directly compared the two methods. These authors found that correction of the total count rate is higher with the correlation method than the traditional method. Their conclusions were that the correlation method used to observe coincident events shows no advantage over the traditional method. The statistical accuracy is at most equal to the traditional method and dependence on the count rate is higher. Later, Lewis et al. (1973) applied the correlation method to radionuclide standardization in which there is a long half-life level. This is an excellent study; and they applied it to the standardization of ^{75}Se, ^{67}Ga, and ^{85}Sr, as well as the detection and estimation of "after pulses" in LSC.

The measurement of activity using correlation techniques can be applied to radionuclides with delayed states without detailed knowledge of the decay scheme and, therefore, is superior to the conventional coincidence method. In the case of coincidences without delay, the conventional method is better than correlation except when the exact form of the covariance by dead time is known. When this occurs, the correlation method has advantages

over conventional counting since no corrections are required for resolving time. Müller (1975) also gave a good theoretical explanation of the correlation in $4\pi\beta-\gamma$ counters.

We consider two situations: one of which uses two detectors to obtain the correlation. Such is the case when applied to ^{85}Sr. In the other case, only one detector is used for the correlation. Hence, the radionuclide has a typical decay scheme. The first excited level is a prompt gamma emission. The second excited level has a measurable half-life with highly converted delayed gamma emission. ^{67}Ga and ^{75}Se are good examples.

2. Theoretical description of the beta–gamma correlations method

The basic idea of correlation counting is to determine the counting rate of genetically correlated event pairs by statistical analysis of the events without coincidence, and therefore, without the problems related to timing effects. The method is based on the fact that radioactivity is a process described by Poisson statistics. The distribution of the number of events occurring in a well-defined time interval of length T is accumulated with a large number of successive measurements.

In general, the method involves determining the number of events n_i, occurring in an interval T, for a number of intervals N and calculating the moments of the distribution of the number of events per interval.

For example, the average number of events per interval is:

$$m = \frac{\sum_i n_i}{N} \tag{7.43}$$

and the second moment about the mean (i.e., the variance) is:

$$V = \frac{\sum_i n_i^2}{N} - \frac{\left(\sum_i n_i\right)^2}{N^2} \tag{7.44}$$

If events are radioactive decays, detected by a counter with zero dead time, the events follow the Poisson distribution and then, for a sufficiently large N, the average number of events per interval $\overline{n}$ can be obtained from m and V. In this simple case, the variance does not provide additional information, as the expected value is:

$$E[V] = m \tag{7.45}$$

but in more complex cases, the correlation method has considerable advantages. We will discuss two situations in which the correlation method gives good results (Lewis et al., 1973).

Situation 1. When the intermediate state has a significant half-life, covariance depends on the decay constant λ and T (length of the intervals, not to be confused with the half-life). The number of parent–daughter pairs c_i recorded in the i interval, ignoring the effects of dead time, are distributed according to a Poisson distribution and the covariance estimate is the mean value c of c_i.

$$c = N_0 T \varepsilon_p \varepsilon_d \left(1 - \frac{1 - e^{-\lambda T}}{\lambda T}\right) = N_0 T \varepsilon_p \varepsilon_d f(\lambda, t) \tag{7.46}$$

When $\lambda T \to \infty$, parent and daughter are simultaneous, and $f(\lambda, T) \to 1$. For small λT, we have $f(\lambda, T) \approx \lambda T/2$, which is reasonable.

In deriving the covariance modified by dead time, we have to deduce the probability of losing a parent event correlated with the loss of the respective correlated daughter. In this case, the probability should be modified and written as $g(\lambda, \tau_p, \tau_d) c_i (c_i - 1) \Theta_c$, where

$$g(\lambda, \tau_p, \tau_d) = 1 - \exp[-\lambda(\tau' - \tau_c)] \frac{1 - \exp(-2\lambda\tau_c)}{2\lambda\tau_c} \tag{7.47}$$

and τ' is the longer of τ_p and τ_d

Expectation values are given by:

$$X' \approx X[1 - (2p\Theta_p + 2d\Theta_d - c\Theta_c g(\lambda, \tau_p, \tau_d))] \tag{7.48}$$

which again is sufficiently accurate for dead time losses of a few percent.

Situation 2. When we have a nuclide whose decay scheme shows an excited long-term state that is preceded by an excited state that decays instantly and parent and daughter events are indistinguishable, both radiations are detected in the same detector. One example is a beta decay followed by an internal converted γ-transition. If we measure $n_i = p_i + d_i$ (parent + daughter), the quantity n_i does not follow a Poisson distribution. Setting $p_i = x_i + c_i$ and $d_i + y_i + c_i$, where x_i and y_i are uncorrelated events, we have:

$$E(V) = n + 2c \tag{7.49}$$

here

$$c = N_0 T \varepsilon_p \varepsilon_d \left[\left(1 - \frac{\tau}{T}\right) - \frac{1 - \exp[-\lambda(T - \tau)]}{\lambda T}\right] \exp(-\lambda t) \tag{7.50}$$

and substituting

$$f(\lambda, T, \tau) = \left[\left(1 - \frac{\tau}{T}\right) - \frac{1 - \exp[-\lambda(T - \tau)]}{\lambda T}\right] \exp(-\lambda t) \tag{7.51}$$

we have

$$c = N_0 T \varepsilon_P \varepsilon_d f(\lambda, T, \tau) \tag{7.52}$$

as a fraction of the daughter events is lost in the dead time of the parent. The MSD is deduced by substituting $n_i = n + \delta x_i + \delta y_i + 2\delta c_i$ in Eqs. (7.44) and (7.45). When $N \gg 1$, we have:

$$\sigma_V^2 \approx \frac{2V^2 + V + 12c}{N} \tag{7.53}$$

The mean count and the variance can be obtained from the same data and the magnitude $2c$(equal to $V - n$) can be extracted directly with an MSD of $(4c + 2V^2)/N$.

The expression for a_i, being $a_i\Theta$ the probability of losing one event of $n_i$due to rate effects, must be modified as follows:

$$a_i = n_i(n_i - 1) - 2c_i - h(\lambda, \tau)(n_i - c_i - 1)q_i - h^*(\lambda, \tau)q_i c_i \tag{7.54}$$

The term $2c_i$ takes into account the fact that the components of any pair cannot annihilate each other. Factors $h(\lambda, \tau)\Theta$ and $h^*(\lambda, \tau)\Theta$ represent the probability that if a parent whose daughter was lost originally in its dead time is lost, the daughter may now be recorded outside the dead time in which its parent is lost. In the i^{th} interval there are q_i of these parent events and:

$$h(\lambda.\tau) = \frac{\varepsilon_d[1 - \exp(-h\lambda t) - \lambda\tau \exp(-\lambda\tau)]}{\lambda\tau(1 - \exp(-\lambda\tau))} \tag{7.55}$$

And

$$h^*(\lambda\tau) = \frac{\varepsilon_d \exp(-\lambda\tau)[1 - \exp(-\lambda\tau)]^2}{2\lambda\tau} \tag{7.56}$$

The mean count observed for small dead time losses is:

$$n' \approx n - n^2\Theta(1 - \delta_1) \tag{7.57}$$

$$n' \approx n - n^2\Theta + h(\lambda, \tau)(n - c)q\Theta + h^*(\lambda, \tau)qc\Theta \tag{7.58}$$

This expression can be an approximation of

$$n' = n\left(1 + \frac{n\Theta}{1 + \delta_1}\right)^{-1} \tag{7.59}$$

which is exact for $\delta = 0$.

The expected value of the observed variance, for small dead time losses, is:

$$V' = V - 3V\Theta(n - h(\lambda, \tau)q) - 2c\Theta(n + h(\lambda, \tau)q) - 5qc\Theta[h(\lambda, \tau) - h^*(\lambda\tau)] \tag{7.60}$$

3. Applications of the Beta–gamma correlations method to radionuclide standardization

^{75}Se. Smith and Woods (1994) standardized a solution containing ^{75}Se. They measured the radionuclide's activity simultaneously by coincidence and by correlation, as part of the international comparison organized by the BIPM in 1992. The correlation measurement provided an explicit correction to take into account the isomeric state of the daughter (^{75}As) and enable a direct measurement of the half-life of the isomeric level (16.23 ± 0.33 ms). The half-life was obtained by measuring the fraction of correlated pairs (c/n) as a function of the time $T$of the correlation range. Three similar sources were measured in the same conditions in the range of 1–150 ms. It is shown that (c/n) must be proportional to $f(\lambda_m, T, \tau)$, for constant conditions. A least squares nonlinear fitting was applied to the function

$$\frac{c}{n} = Bf(\lambda_m, T, \tau) \tag{7.61}$$

where B and λ_m are unknown parameters, and gave $\chi^2 = 1.01$with the half-life of 16.23±0.33 ms. Data points were weighted according to their variances.

Janssen (1990) presented a data acquisition system based on a VMEbus. This system was developed to determine the activity of radioactive samples using the correlation count method. The paper provides a detailed description of the components of the data acquisition system and the method's principles. By way of example, Janssen describes the measurement of a sample of ^{75}Se using a pressurized PC and a NaI(Tl) detector working in coincidence. He describes the system's operation. The correlation method has been used to experimentally determine the fraction of pairs of genetically correlated events in the PC.

Hwang et al. (1996) presented a data acquisition system to carry out experiments for correlation counting. All beta–gamma signals are recorded simultaneously in a static random access memory (SRAM). The coincidence resolving time and the multiple gamma gates are selected by a computer program and the efficiency functions are obtained by computer discrimination. The method applies well to the activity determination of radionuclides with intermediate levels with relatively long half-lives.

They applied the procedure to ^{75}Se. The fraction of delayed events was studied through a system with a pressurized PC and a NaI(Tl) detector. The measurement time of each sample was 9000 s, which was sufficient not only to achieve the efficiencies of electron capture detection, but also to obtain the variation of efficiency curves for the fraction of pairs of correlated events in the PC. These fractions were obtained by sequentially extracting the data in 2×10^5 intervals of 45 minutes duration for each level of discrimination assigned to the pulse amplitude spectrum from the PC. The results were compared with others obtained previously.

D. Gamma–gamma coincidences

1. Introduction to the sum peak method

Radiation coincidence has been used for the primary standardization of radionuclides. In all cases, a pair of detectors

is used to record the interaction of two coincident radiations: $\beta-\gamma$, $\gamma-\gamma$, $X-(X,\gamma)$, etc. and the detector counts are used to determine the activity of the sample using coincidence or anticoincidence counting.

The sum peak method is based on the same coincidence principles but requires a single X- or gamma ray detector and its associated electronics. In this method, activity is determined from the gamma spectrum using the count rates of the full-energy single peaks, the sum peak due to the coincidence of two gamma rays, and the total counting rate of the spectrum.

The advantage of the sum peak method lies in the simplicity of both the technique and the detector system. The sum peak method requires a gamma detector and the electronics chain for spectrometry, while the coincidence method requires two detectors with their time modules. The sum peak method has another advantage when compared with the relative measurement technique used in gamma spectrometry. The measure requires an accurate calibration curve (counting efficiency vs. energy) for a given source-detector geometry. Therefore, it is influenced by the experimental conditions regarding source-detector geometry, photon energy, and sample activity.

The sum peak method was initially developed by Brinkman and Aten (1963, 1965) and Brinkman et al. (1963a,b, 1965). They measured nuclides ^{60}Co, ^{46}Sc, ^{22}Naand ^{18}F with a NaI(Tl) well detector, correcting for the effect of the angular correlation between the two coincident gamma cascade photons. ^{60}Co and ^{46}Scare nuclides that decay by β^-emission and two coincident gamma photons. They canceled the angular correlation by placing the source on the detector surface. They also obtained 2π geometry. For ^{22}Na, a $\beta^+-\gamma$, the radioactive source was placed on the surface detector well, thus obtaining the sample's activity without measuring the angular correlation between annihilation photons and gamma ray emission. They also measured the sample inside the well and determined the effect of the angular correlation of annihilation radiation and gamma rays.

From the ^{22}Na spectrum they obtained the count rates of annihilation peaks, gamma peaks and sum peak, and the detection efficiency of annihilation radiation and gamma rays. They determined the count rates in the peaks of annihilation gamma and sum spectrum and the result was then used to correct the angular correlation of ^{18}F, a pure positron emitter. Accuracy was between 2% and 5%.

Another sum peak method, using NaI(Tl) crystals, was developed by Zajic (1986). The detection system comprised two NaI(Tl) crystals and the respective temporal electronics. In this case both coincidence and anticoincidence were used. The summation method with two detectors was first used by Hutchinson et al. (1973). However, Zajic improved the method's accuracy by correcting for dead time, pulse pileup and random coincidences. ^{88}Y and^{207}Bi were measured in 4π geometry and therefore do not require correction for angular correlation. The estimated total uncertainties were 1.4% and 2.4% for ^{88}Y and ^{207}Bi, respectively.

The application of Ge detectors for the sum peak method was carried out by Martin and Taylor (1992) to standardize ^{125}I. They took dead time and pileup into consideration but failed to correct for angular correlation. The measure was carried out by diluting several samples with different dilution activity. The activity concentration of the initial solution was obtained by extrapolation of the samples with different concentrations to zero mass. The resulting uncertainty was under 2%.

Asano et al. (1996) measured ^{60}Cowith a Ge detector applying a theoretical correction for angular correlation. The radioactive source was placed 8.7 cm away from the detector surface. Angular correlation correction was performed applying a Monte Carlo simulation using the correlation functions of the gamma ray cascade. As the angular correlation correction increases with source detector distance, in this case the correction was 9%. They did not mention corrections for dead time, pileup pulse, and accidental coincidences. The uncertainty achieved was estimated at around 1%.

Kim et al. (2003) conducted a detailed study of the sum peak method and applied it to ^{60}Co, using sources with activities between 25 and 350 kBq. The radiation detector used was an HPGe crystal and the samples were placed at distances ranging from 0.5 to 8 cm. The high count rate generated problems due to increased dead time, pulse pileup, and accidental coincidences in the sum peak. A greater distance between the source and detector reduces these problems. However, a greater distance between the source and the detector implies a significant decrease in count rate at the peak sum. Therefore, the angular correlation and the corrections associated with the high count rates are inevitable problems in this type of measurement. Correction for the angular correlation was carried out applying a Monte Carlo simulation. Pulse pileup was corrected by extrapolation varying amplifier time.

2. Theoretical description of the sum peak method

We only consider the case of two coincident photons, both with 100% decay. Other more complex cases such as emission of less than 100% or positron emission can be found in the references cited above.

If we denote sample activity as N_0, and N_1 and N_2 are the counting rates in the full-energy gamma peaks, expressed in the same units of time as activity, we have:

$$N_1 = N_0\varepsilon_1^p\left[1-\varepsilon_2^t\overline{W}(0)\right]L_p \tag{7.62}$$

$$N_2 = N_0\varepsilon_1^p\left[1-\varepsilon_1^t\overline{W}(0)\right]L_p \tag{7.63}$$

where ε_1^p and ε_2^p are the efficiencies of the full-energy peak, and ε_1^t and ε_2^t are the total efficiencies. Subscripts 1, 2 denote the corresponding gamma ray. On the other hand, $\overline{W}(0)$ and L_p are the correction factors for angular correlation and pileup pulses, respectively. The count rate at the sum peak due to the coincidence of the two photons is denoted by N_{12} and the total counting rate by N_t. Therefore:

$$N_{12} = n_0\varepsilon_1^p\varepsilon_2^p\overline{W}(0)L_p + G \tag{7.64}$$

$$N_t = \left[\varepsilon_1^t + \varepsilon_2^t - \varepsilon_1^t\varepsilon_2^t\overline{W}(0)\right] \tag{7.65}$$

where G is the correction factor for pileup pulses. In the last equation, it is assumed that the total loss of counts by pulse pileup is negligible. Strictly speaking, the definition of $\overline{W}(0)$ in the above equations is slightly different. We should distinguish between factor ε^p for the full-energy peaks for the partial absorption factorε^t. Usually they have the same value for any combination of the two detectors for gamma rays, as was shown by Kim et al. (2002). From the above equations, it follows that the activity of the sample is given by:

$$N_0 = \left[\frac{N_1N_2}{(N_{12}-G)L_p} + N_t\right]\overline{W}(0) \tag{7.66}$$

The probability of counting coincident gamma ray cascade depends on detection efficiency, detection geometry, and the angular correlation $\overline{W}(\theta)$ of cascade gamma rays. Rose (1953) and Camp and Van Lehn (1969) calculated angular correlation $\overline{W}(\theta)$ to estimate the effect of finite angular resolution on coincidence counting with finite size detectors.

In the case of a single HPGe detector, without a collimator, $\theta = 0$ and $\beta^{\max}$ (the maximum incidence angle of the gamma-ray) cover the detector face. In the case of ^{60}Co, Kim et al. (2002) estimated $\overline{W}(0)$ and found that the effective angular correlation factor ranged from 1 to 1.1, when the distance between the source and the detector is from 0 to 5 cm. For distances from 5 to 25 cm, the angular correlation factor remained constant and equal to 1.1. The main radionuclides standardized by the sum peak method are shown in Table 7.6.

TABLE 7.6 Radionuclides standardized by sum-peak method and references.

Radionuclides	References
^{22}Na	Iwahara et al. (2007) De Oliveira et al. (2012) Ogata et al. (2015) Ogata et al. (2016)
^{57}Co	Shi et al. (2005) Iwahara et al. (2009a,b) Novcovic et al. (2012) Ababneh and Eyadeh (2015)
^{60}Co	Brikman et al. (1963a,b) Sutherland and Buchanan (1967) Oderkerk and Brinkman (1990) Kawano and Ebihara (1990) Vidmar et al. (2009) Suvaila et al. (2013) Marsoem et al. (2014) Ababneh and Eyadeh (2015) Ogata et al. (2015) Ogata et al. (2016) Kajimoto et al. (2015) El-Khatib et al. (2017) Aso et al. (2018) Nemes et al. (2018)
^{65}Zn	Oliveira et al. (2012)
^{88}Y	Kajimoto et al. (2015) Korun et al. (2016)
^{125}I	Harper et al. (1963) Eldridge and Crowether (1964) Horrocks and Klein (1975) Eddiss and Abrams (1981) Dias and Koskinas (1995) De Felice and Mytebery (1995) Wang et al. (2001) Da Silva et al. (2006) Capogni et al. (2006) Grau Carles and Grau Malonda (2011) Marsoem et al. (2014)
^{133}Ba	Arnold and Sima (2006) Novcovic et al. (2007b) Vidmar et al. (2014) Ababneh and Eyadeh (2015) Vidmar et al. (2016) El-Khatib et al. (2017)
^{134}Cs	Ogata et al. (2016) Shizuma et al. (2016) Ogata et al. (2018)
^{152}Eu	Vidmar et al. (2014) El-Khatib et al. (2017) Ferreira Filho et al. (2018)

3. Dead time and pileup corrections

The random nature of the temporal emission of gamma radiation and the finite processing time of the pulses produced give rise to two important phenomena in gamma radiation detection: dead time and pulse pileup. In the processing of pulses generated by gamma radiation, the detector system is insensitive to the reception of new gamma rays for a finite time called dead time. Dead time produces a loss of pulses from the incident gamma rays and therefore affects the total counts to be recorded by the spectrometer. Moreover, consecutive gamma ray pulses can pile up due to finite resolution time. This pileup can distort

the gamma spectrum in a region and increase or decrease the number of counts of a peak.

Dead time is usually corrected by an ADC working in a live time mode. Piled-up pulse losses are described by effective dead time τ_P (Debertin and Helmer, 1988) defined as the time interval between two consecutive pulses that cause the loss of a count in the gamma peak. Consideration of pileup requires a definition of the effective resolution time of coincidence τ_R (Knoll, 1989) as the time interval between two consecutive pulses that produce a gain in the peak sum counts. Therefore, the correction factors due to these effects are:

$$L_P = 1 - \tau_P N \tag{7.67}$$

and

$$G = 2\tau_R N_1 N_2 \tag{7.68}$$

where N_1 and $N_2$are defined in (7.62) and (7.63) and N is the detector count rate. It is assumed that all nonregistered counts that were below the lower level or above the upper level discriminators can be neglected. Pulse width and magnitudes τ_P and τ_R are closely related. The pulse formed by (CR)−(RC)^2 in the amplifier is expressed analytically by the following equation:

$$V(t) = \frac{1}{2}\left(\frac{t}{\tau}\right)\exp\left(-\frac{t}{\tau}\right) \tag{7.69}$$

where $V(t)$ is the pulse height, in time t, and τ is the time constant RC from circuit (CR)−(RC)^2. The preamplifier output signal is assumed to be a step function and pole-zero cancellation was complete. Parameters τ_P and τ_R depend on τ and the pileup can be reduced by decreasing τ. The activity measured for τ without correction for pileup is

$$N(\tau) = \left[\frac{N_1(\tau)N_2(\tau)}{N_{12}(\tau)} + T(\tau)\right]W(0) \tag{7.70}$$

where $N_1(\tau)$, $N_2(\tau)$, and $T(\tau)$ are measured with the time constant τ. In this expression $N_0(\tau)$ is similar to N_0, but does not include pileup corrections. Both are the same when the time constant is zero, i.e., $N_0 = N_0(0)$. The value of $N_0(0)$ is obtained in practice by obtaining $N_0(\tau)$ for different values of τ and extrapolating to $\tau = 0$.

4. Applications of the sum peak method

^{125}I. The sum peak method was applied by Harper et al. (1963) and Eldridge and Crowther (1964) to calibrate ^{125}I. This radionuclide decays by electron capture to the state of 35 keV of ^{125m}Te, which in turn decays to the ground state by gamma emission or electron conversion. The emission of conversion electrons and the subsequent atomic rearrangement produces K X-ray emission of 27.4 and 31 keV. The spectrum has two peaks, the first of which corresponds to 2K X-rays, but the proximity of their energies does not permit their resolution. The second peak is the sum peak and corresponds to coincidence of gamma and K X-rays. Given the low energy photons, the Compton effect is negligible in the case of NaI(Tl) detectors. The activity is given by:

$$N_0 = \frac{P_1 P_2}{(P_1 + P_2)^2}\frac{(A_\mathrm{I} + 2A_\mathrm{II})^2}{A_\mathrm{II}} \tag{7.71}$$

where P_1 is the probability per decay of K X-ray emission in electron capture. ($P_1 = P_K\omega_K$), and P_2 is the sum of the probabilities for the 35 keV gamma ray and the K X-ray emitted in internal conversion ($P_2 = (1+\alpha_K\omega_K)/(1+\alpha_T)$). A_I and A_II are the areas of the first and second peaks of the spectrum expressed as counts per second.

Horrocks and Klein (1975) analyzed the decay scheme of ^{125}I and calculated the emission probabilities of each of the various decay pathways. They deduced an equation for calculating the decay rate by the coincidence method from the probability of disintegration. While the Eldridge and Crowther (1964) equation is accurate in 1% with this method, the authors argue that we can calculate the activity of any radionuclide by measuring the single and sum peaks.

Eddiss and Abrams (1981) established a technique for determining the activity of ^{125}I using a multisample gamma counter. They extended the method and deduced an equation to calculate the uncertainty of the measured activities. The validity of the equation was tested and they found that it was satisfactory. They described a technique for selecting appropriate counting conditions.

Dias and Koskinas (1995) described a new method for correcting accidental coincidences (summing pileup) when determining the activity of ^{125}I by applying the Eldridge and Crowther equation (1964). The results were compared with those obtained with the X−(X,γ) coincidence method. The corrections were estimated using a Monte Carlo code. Other predictions were made for other detection efficiencies and electronic shaping times. They used two 3" ×3" NaI(Tl) crystals.

Two of the seven calibration techniques employed for standardization of ^{125}I by Pommé et al. (2005a,b) were based on the sum peak method with a single detector, applying the Eldridge and Crowther equation (1964). The measurements were performed with two detectors sensitive to photons from 35 keV gamma rays and X-rays of 27.4 and 31 keV, but insensitive to other radiations (electrons and low-energy X-rays). NaI(Tl) and CsI(Tl) detectors were applied with good resolution to separate the peaks with only a small overlap. The 6"× 6" NaI(Tl) detector with a well had a total efficiency of 75.7%. The uncertainty of the measurement with the NaI(Tl) detector was 0.3% (1 σ). The CsI(Tl) detector was a 4π counting sandwich spectrometer and consisted of two CsI(T1) crystals, 55 mm in

diameter and 25 mm high (Denecke, 1994). To stop the electrons emitted in the process of atomic deexcitation, a spherical cavity between the two is covered with 0.12-mm-thick absorbent polyethylene. The low-energy radiation was removed with a low-energy discriminator, set at around 14 keV.

De Felice and Mytebery (1995) describe an intercomparison for measuring the absolute activity of ^{125}I by the sum peak method by the Primary Standard Laboratories for Ionizing Radiation of Italy (ENEA) and (INP) in Albania. Radioactive sources were prepared by ENEA from a solution of ^{125}I. The sources were measured at ENEA and INP. The results were perfectly consistent. The deviation of the ENEA and INP results was 0.5% with a total uncertainty of both results of 0.3% (1 σ). The paper describes the instrumentation and experimental procedures used in this comparison by both these institutions.

Capogni et al. (2006) applied the sum peak method (Eldridge and Crowther, 1964) for the absolute measurement of ^{125}I activity. They experimentally determined the dependence of the count rate corrections for the random sum of counts and the effects of dead time for different count rates in various experimental conditions. They used two NaI(Tl) crystals of different volumes. The crystal was connected to a system for recording pulses with different characteristics, with a live time correction circuit with or without rejection of pile-up pulses (with or without pile-up rejection live time correction circuits) (PUR/LTC). They proposed a theoretical model to explain the different behavior found experimentally. They show that the dependence of the count rate will be drastically reduced by use of PUR/LTC.

With the introduction of germanium detectors, peaks can be obtained with a better resolution. Thus the first peak of the spectrum of ^{125}I obtained with a NaI(Tl) crystal comprises three peaks: two X-ray K_α (27.38 keV) and K_β (30.97 keV), and gamma emission (35.5 keV). For well detectors we obtain peaks in the spectrum of given energies. When using a flat crystal, however, we also obtain the escape peaks for the X-ray energy of 17.5 and 21.1 keV. Therefore, in the case of a germanium detector plane the number of peaks in the spectrum is five in the first peak of the NaI(Tl). The second peak obtained with a NaI(Tl) crystal is broken down into five peaks, in the case of a well crystal, corresponding to coincidences $K_\alpha + K_\alpha$: (54.76 keV), $K_\alpha + K_\beta$ (58.35 keV), $K_\beta + K_\beta$ (61.9 keV), $K_\alpha + \gamma$ (62.87 keV), and $K_\beta + \gamma$ (66.5 keV). The peaks of 61.9 and 62.87 keV are difficult to separate. In the case of a flat crystal we obtain the coincidences of X-rays of ^{125}Te with the escape of X-rays of germanium, i.e., escape peaks corresponding to $K_\alpha + K_\alpha +$ escape Ge (44.9 keV) and $K_\alpha + K_\beta +$ escape Ge (48.5 keV). A spectrum of ^{125}I obtained with a plane Ge detector can be seen in Da Silva et al. (2006), and a spectrum of the same radionuclide obtained with a well crystal is presented in the study by Wang et al. (2001). In this study, the equation to compute the activity of a sample from the peaks of the spectrum without having to resort to nuclear or atomic constants is obtained.

Da Silva et al. (2006) standardized ^{125}I with a germanium plane detector. The equation used to determine the activity of the sample was the same as that estimated by Brinkman et al. (1977) for ^{123}I:

$$N_0 = T + \frac{N_\gamma N_X}{N_{X\gamma}} - \frac{N_{XX} N_\gamma^2}{N_{X\gamma}^2} \tag{7.72}$$

where $N_X =$ Single X, $N_{XX} =$ coincidence XX, $N_{X\gamma} =$ coincidence X-γ

Da Silva et al. (2006) applied the sum peak method to standardize ^{125}I. ^{54}Mn and ^{125}I were standardized in the intercomparison organized by the BIPM, while the ^{203}Hg was part of the traceability of the National Laboratory for Ionizing Radiation Metrology (LNMRI)/Brazil. The activity of ^{125}I was obtained applying the Eldridge and Crowther (1964) equation and Brinkman et al. (1977) equation to spectra obtained using a germanium detector. As the expression of Brinkman does not use atomic data, uncertainties obtained with this method are inferior to those obtained with the Eldridge and Crowther equation (1964). Radioactive sources were placed on the surface of the 3″ × 3″ NaI(Tl) and germanium detectors, and into the well of the 5″ × 5″ NaI(Tl) well crystal. All samples were measured once at 10^4 s each, so that counting statistical uncertainty was less than 0.1%. They obtained five spectra of each sample and the calculation was performed using the MAESTRO program (2002) incorporated into a multichannel analyzer.

Wang et al. (2001) obtain the following equation for well Ge detector:

$$N_0 = T + \frac{N_\gamma N_{\alpha\beta}}{N_{\beta\gamma}(N_{\alpha\alpha} + N_{\alpha\beta})}\left[N_\alpha + N_\beta - N_\gamma\left(\frac{N_{\alpha\beta}}{2N_{\beta\gamma}} + \frac{N_6}{N_{\beta\gamma}} - \frac{2N_{\alpha\alpha}}{N_{\alpha\beta}}\right)\right] \tag{7.73}$$

where N_α, N_β, and N_γ are the counting rates at the single peaks. $N_{\alpha\alpha}$, $N_{\alpha\beta}$, $N_{\alpha\gamma}$, $N_{\beta\beta}$, and $N_{\beta\gamma}$ are the sum picks and $N_6 = N_{\beta\beta} + N_{\alpha\gamma}$. The energy of $E_{\alpha\alpha} = 62.0$ keV and $E_{\alpha\gamma} = 62.8$ keV, consequently the two peaks overlap.

The equations of Eldridge and Crowther (1964), Brinkmann et al. (1977), and Wang et al. (2001) can be deduced from a general procedure described in the paper by Grau Carles and Grau Malonda (2011). Given the generality of the method, the resulting new possibilities, and the fact that new research can be done, we will describe this

method and its consequences in some detail. This paper also analyzes the Eldridge and Crowther (1964) equation and concludes that counting efficiencies are average efficiencies taking both the full-energy peak and the Compton contribution into account which is not negligible for Ge detectors.

The method is based on the following set of equations, valid for an ^{125}I spectrum obtained with a Ge-well detector. The basic equations are the following.

If N_0 designates the activity of a ^{125}I sample, and N_α, N_β and N_γ the counting rates at the single peaks we have the following expression:

$$N_\alpha = N_0[P_{1\alpha}\varepsilon_\alpha(1-t_1)+P_{2\alpha}\varepsilon_\alpha(1-t_2)] \tag{7.74}$$

where $P_{1\alpha}$ and $P_{2\alpha}$ are the probabilities for the K_α X-ray in EC and IC emission, respectively; ε_α is the photoelectric detection efficiency of K_α X-ray, and t_1 and t_2 are the total emission detection efficiencies for EC and IC plus gamma, respectively. This equation is obvious if we recall that $N_0P_{1\alpha}\varepsilon_\alpha$ is the number of K_α X-photons detected by the detector. These photons do not all go to the N_α peak. Those coincident with other radiations such as $K_\alpha X$ and $K_\beta X$, from IC, more gamma photons emitted in the gamma decay go to the $N_{\alpha\alpha}$, $N_{\alpha\beta}$, and $N_{\alpha\gamma}$ peaks, respectively. On the other hand, neither do the X-rays that have not interacted by the photoelectric effect go to the N_α peak. Hence, the term $(1-t_2)$ takes into account the probability of noncoincidence. Similarly, $K_\alpha X$ photons emitted in IC are $N_0P_{2\alpha}\varepsilon_\alpha$ and those that coincide in their interaction with the $K_\alpha X$ photons emitted in the EC do not go to N_α peak. Hence, the term $(1-t_1)$ takes into account the probability of noncoincidence. For the N_β peak we have:

$$N_\beta = N_0[P_{1\beta}\varepsilon_\beta(1-t_1)+P_{2\beta}\varepsilon_\beta(1-t_2)] \tag{7.75}$$

where $P_{1\beta}$ and $P_{2\beta}$ are the K_β X-ray emission probabilities due to EC and IC, respectively, and ε_β is the efficiency of photoelectric detection of K_β X-rays. On the other hand, we have:

$$N_\gamma = N_0P_\gamma\varepsilon_\gamma(1t_1) \tag{7.76}$$

where P_γ and ε_γ are the gamma emission probabilities and photoelectric detection efficiency, respectively.

For the sum-peaks $N_{\alpha\alpha}$, $N_{\alpha\beta}$, $N_{\alpha\gamma}$, $N_{\beta\beta}$, and $N_{\beta\gamma}$ we have:

$$N_{\alpha\alpha} = N_0P_{1\alpha}P_{2\alpha}\varepsilon_\alpha^2 \tag{7.77}$$

$$N_{\alpha\beta} = N_0(P_{1\alpha}P_{2\beta}+P_{1\beta}P_{2\alpha})\varepsilon_\alpha\varepsilon_\beta \tag{7.78}$$

$$N_{\alpha\gamma} = N_0P_{1\alpha}P_\gamma\varepsilon_\gamma \tag{7.79}$$

$$N_{\beta\beta} = N_0P_{1\beta}P_{2\beta}\varepsilon_\beta^2 \tag{7.80}$$

$$N_{\beta\gamma} = N_0P_{1\beta}P_\gamma\varepsilon_\beta\varepsilon_\gamma \tag{7.81}$$

The total count rate of the total spectrum is:

$$T = N_0(t_1+t_2-t_1t_2) = N_0[1-(1-t_1)(1-t_2)] \tag{7.82}$$

and

$$t_1 = N_0P_{1\alpha}t_{1\alpha}+N_0P_{1\beta}t_{1\beta} \tag{7.83}$$

and

$$t_2 = N_0P_{2\alpha}t_{2\alpha}+N_0P_{2\beta}t_{2\beta} \tag{7.84}$$

To these equations we must add the equation of symmetry:

$$P_{1\alpha}P_{2\beta} = P_{1\beta}P_{2\alpha} \tag{7.85}$$

This equation enables the writing of Eq. (7.78) in two ways:

$$N_{\alpha\beta} = 2N_0P_{1\alpha}P_{2\beta}\varepsilon_\alpha\varepsilon_\beta \tag{7.86}$$

and

$$N_{\alpha\beta} = 2N_0P_{1\beta}P_{2\alpha}\varepsilon_\alpha\varepsilon_\beta \tag{7.87}$$

These equations are the same as those of Wang et al. (2001). The important point to keep in mind is that Eqs. (7.74) and (7.75) are not independent, as shown in the Appendix of Grau Carles and Grau Malonda (2011). The fact that they are not independent indicates that instead of Eqs. (7.74) and (7.75), any linear combination of both can be used, that is:

$$N_\alpha + \lambda N_\beta$$

Where λ can take any rational value. In Grau Carles and Grau Malonda (2011) we have taken four par values, which are: $\lambda = 0$ (only Eq. 7.74 is taken for N_α), $\lambda = 1$ (the sum $N_\alpha + N_\beta$ is taken), $\lambda = -1$ (the difference $N_\alpha - N_\beta$is taken), and $1/\lambda = 0$ (only Eq. 7.75 is taken). We have deduced 24 valid equations to calculate the activity of ^{125}I. In the paper, the discrepancies between the activities of each equation and the result of Wang et al. (2001) are shown, as are the standard deviations of the activity of each equation. Six of these typical deviations are lower than that of Wang et al. (2001). For example, the equation for $\lambda = 0$:

$$N_0 = T + \frac{N_\alpha N_\gamma N_{\alpha\beta}}{2N_{\alpha\alpha}N_{\beta\gamma}} - \frac{N_\gamma^2 N_{\alpha\beta}^2}{4N_{\alpha\alpha}N_{\beta\gamma}^2} \tag{7.88}$$

The first question that arises is how to obtain an equation that minimizes the standard deviation. It must take into account that the calculations are based on the experimental values published by Wang et al. (2001). Other experimental values could make other equations most accurate.

Ferreira Filho et al. (2018) standardized ^{152}Eu, a radionuclide with a complex decay scheme using a method similar to that proposed by Grau Carles and Grau Malonda (2011).

^{57}Co. Iwahara et al. (2009b) applied the sum peak method with a germanium detector for the calibration of

^{57}Co. The main features of the ^{57}Co.decay scheme are that it decays by electron capture, followed by gamma rays of three different energies; and it has a level with a half-life of 98 seconds. The equation used to compute the activity of a sample is very similar to the classic equation:

$$N_0 = T + \frac{N_X N_1}{N_{X1}} \tag{7.89}$$

where N_X is the count rate of the peak of 6.39 and 6.40 keV X-rays, N_1 is the counting rate of 14.41 keV gamma-ray, and N_{X1} is the peak area due to coincidence of 6.40 keV X-ray and 14.41 keV gamma ray.

$$N_0 = T + \frac{N_X N_2}{N_{X2}} \tag{7.90}$$

where N_2 is the area in counts per second of the 122.06 keV gamma ray peak and N_{X2} is the peak area corresponding to the coincidences of the 6.40 keV X-ray and the 122.06 keV gamma ray.

^{51}Cr. The work of De Almeida et al. (2007) consisted of two parts; in one part ^{51}Cr activity was determined by three methods: $4\pi\beta-\gamma$ coincidence and anticoincidence and sum peak. On the other hand, he determined the probability of 320 keV gamma ray emissions, comparing this result with those obtained in other studies. Their consistency confirmed the reliability of these measurements. For the sum peak method, he used a coaxial germanium detector with a volume of 260 cm^{3}and an energy resolution of 1.9−1332.5 keV. The Brinkman and Aten (1963) equation was applied for the activity calculation.

^{60}Co. Sutherland and Buchanan (1967) found that the Eldridge and Crowther (1964) equation is only valid for the sum peak method when the detector has the same response in all parts of the source. This condition is satisfied when we use a solid detector and the source surface is made as pointed as possible, or counting the larger samples in a well detector.

Oderkerk and Brinkman (1990) based their study on the experimental fact that, when applying the sum peak equation (Brinkman et al., 1963a; Binkman et al., 1963b) to the activity of extended sources, the result is less than that obtained with point sources. This effect is not due to absorption in the extended source, but the detector does not have the same efficiency for all sample points. In their study, they derive expressions to calculate the size of the effect.

Kawano and Ebihara (1990) determined the activity of a ^{60}Co point source (12 mm diameter in a thin plastic disk) and a volume source of the same radionuclide (10−100 mL in a polyethylene bottle) by the sum peak technique. The sum peak equation (Brinkman et al., 1963a,b) gives the exact decay rate for different positions of the point source in front of the detector. However, when the volume of the solution is increased, the deviation from the true activity value also grows. Extended sources should be treated as amalgams of many point sources.

Kawano and Ebihara (1991) applied the sum peak method (Brinkman et al., 1963a,b) to determine the activity of two small samples of ^{60}Co (30−350 kBq) in lead containers of various thicknesses (3, 6, 9, 15, 21.27, and 33 mm) using a NaI(Tl) detector. The results showed that the sum peak method was effective for samples of 30 kBq in the case of containers with a thickness of 15 mm and less. However, for those with thicknesses of 21, 27, and 33 mm, the decay rates were understated and the deviations from the true activity increased rapidly by increasing the thickness of the containers. We suspect that underestimation of the activity was the result of overestimating the total area under the peak caused by the interference of the 2614 keV gamma rays emitted naturally by the ^{208}Tl radionuclide of the thorium series.

Kawano and Ebihara (1992) applied the sum peak method to the decay rate of extended sources comprising two ^{60}Co point sources. They concluded that when the detector has equal efficiency for both point sources we can determine the activity, and when efficiency is different, activity is underestimated. They examined the uncertainty in the extended sources and found that the theoretical results perfectly matched those of the experiment. The work is based on the theory of Brinkman et al. (1963a,b).

^{152}Eu. Ferreira Filho et al. (2018) standardized a solution of ^{152}Eu by coincidence sum peak for 121.8 keV peak with respective characteristics X-rays. A high-purity germanium detector (HPGe) was used in this paper. ^{152}Eu has a very complex decay scheme. It disintegrates into ^{152}Sm by electron capture (72.1%) and positron emission (0.027%) and into ^{152}Ga by beta minus emission (27.9%). The daughter nucleus ^{152}Sm has 19 excited levels and the ^{152}Gd has 15. Novkovic et al. (2007a, 2016) describe a theoretical method for obtaining the count rate equations describing coincidence summing. This method was later named the Direct Matrices Multiplication (DMM) method (Novković et al., 2012). Nadderd et al. (2012, 2013) and Jordanov et al. (2016) present a new matrix method for deriving these counting rate equations. The spectra were analyzed with MAESTRO software determining the areas of each multiplet region. They use the fundamental equation and new definitions (Grau Carles and Grau Malonda, 2011) to obtain the activity of the sample.

III. Solid angle primary methods

One of the oldest techniques used today is the determination of a sample's activity by calculating the solid angle with which the sample sees the detector. The technique is based on the solid angle obtained by placing an opening in front of the detector and calculating the solid angle subtended by the sample. The conditions for the method's success are correct scattering and absorption between the source and detector, including backscattering of the sample

holder. This is true for alpha particles and low energy gamma or X-rays, less than 80 keV.

A. 4π proportional counting

A special case in counting geometry is to use a solid angle 4π. For beta counting, one can implement a windowless counter with maximum efficiency by mounting two gas counters facing each other (each of them subtending an angle 2π), with the source placed between the counters. Intrinsic efficiency can be kept very close to 100% by adjusting the operating voltage, amplifier, and discrimination level, so that any charged particle that leaves the sample is counted. Departures from 100% efficiency can be attributed to absorption by the source and support.

There are obvious advantages to this method. First, as efficiency is practically 1, all the corrections for scattering and absorption out of the sample are removed. This technique is therefore very suitable for counting electrons. Second, when radionuclides with complex beta−gamma decay schemes are counted, due to the high efficiency, all the corrections for the detector response to gamma or X radiation are minimized, provided that this radiation is coincident with the primary radiation.

If the counter is a PC, it is continuously filled with methane gas, or more frequently by P10 gas (a mixture of 90% argon and 10% methane) and pressurized to multiples of an atmospheric pressure of 0.1−2 MPa. Electronegative gas impurities such as water or oxygen should be avoided in the counter. Gas flow is maintained through a bubbler and pressure must remain constant in the counter (Denecke et al., 1998).

In the past, this procedure was the preferred method for calibrating nuclides such as ^{32}P, ^{35}S, ^{131}I, and ^{241}Am, when uncertainties between 1% and 2% were considered to be an excellent result GHFin international comparisons. Recently, the method has been applied to the determination of the activity of alpha emitters (Schötzig et al., 2000; Johansson et al., 2003a), pure beta emitters (Hult et al., 2000; Alzitzoglou et al., 2002; Csete et al., 2002; Da Cruz et al., 2004), as well as X-ray or weak gamma ray emitters (Lowenthal et al., 1982). One of the main difficulties of this method is the determination of nonefficiency and its uncertainty. A direct method for determining both is the Monte Carlo simulation method (Roteta and García-Toraño, 2006) or experimental tests (Johansson et al., 2002).

It is currently of interest, moreover, as it is part of the device to calibrate radionuclides using the $4\pi\beta-\gamma$ technique, which was discussed above.

High pressure 4π counters can be used to measure the activity of nuclides decaying by EC to increase intrinsic efficiency for low energy photons.

B. 2π proportional counting

In 2π geometry, only half of the particles emitted by the sample will be measured. This is not the case in general due to the backscatter phenomenon. The measurement of electron emitters is therefore not recommended, reserving the counter for measuring alpha emitters. Backscatter corrections are also required in this case, but they are much smaller than with electron emitters. These corrections can be determined theoretically (Williams, 1940; Crawford, 1949; White, 1970; Lucas and Hutchinson, 1976) or through simulations (Ferrero et al., 1990; Martín Sánchez et al., 2000; Jurado Vargas and Fernandez Timon, 2004; Jurado Vargas et al., 2004; Jurado Vargas and Fernandez Timon, 2005).

C. 4πγ counting

Gamma ray detectors with geometry close to 4π [a large-well NaI(Tl)] have proved to be very interesting, particularly in the metrology of radionuclides with complex decay schemes incorporating transitions with coincident photons, due to the sum properties of such detectors. For a few coincident gamma rays, the efficiency approaches 100% and the uncertainties are very small, often independent of precise knowledge of the values of the decay scheme parameters (Winkler and Pavlik, 1983; Ballaux, 1983; Pavlik and Winkler, 1983; Vatine and Chauvenet, 1987; Schötzig, 1992; Decombaz and Laedermann, 1996; García-Toraño et al., 2002b; Johansson et al., 2003b; García-Toraño and Roteta, 2004; Spring et al., 2006; Nedjadi et al., 2007).

Another form of calibration is sandwiching a source between two NaI(Tl) detectors. Such a system has been used for the calibration of radioactive samples for the determination of nuclear decay data (Plch et al., 1973b; Plch and Zderadièka, 1974; Dragoun et al., 1976; Plch et al., 1976; Plch et al., 1979; Plch et al., 1991), or also sandwiching the samples between two CsI(Tl) detectors (Denecke, 1987, 1994; Pommé et al., 2005a,b).

The radioactive sample is usually deposited on a thin plastic film and placed between the two detectors. These have holes to accommodate the sample and prevent contamination.

D. 4π windowless sandwich detectors

Plch et al. (1973a) constructed a nonwindow 4π counter with two NaI(Tl) detectors with a diameter of 4.4 cm and a height of 2 cm. Gamma detection efficiency was 97% between 20 and 160 keV. The instrument has been used for the calibration and determination of nuclear data (Plch and Zderadièka, 1974; Plch et al., 1973b, 1976; 1979; Dragoun, 1976). Denecke (1987, 1994) developed the first detector with no window in the IRMM. This detector consisted of

two CsI(Tl) crystals, 51 mm in diameter and 25 mm thick. The radioactive source was deposited on a thin plastic sheet, which in turn was sandwiched between the faces of the two crystals. The detector presented 100% efficiency for charged particles over 19 keV and efficiencies of 98% for photons from 10 to 200 keV. The detector is of interest in the calibration of radionuclides with complex decay schemes (Reher et al., 1992; Johanson et al., 2003b) as well as for pure beta emitters (Hult et al., 2000, Alzitzoglou et al., 2002), pure alpha (Johanson et al., 2003a), and pure electron capture nuclides (Pomme et al., 2005a, b)

E. $4\pi\beta\gamma + 4\pi$ sum counting

The efficiency of a NaI(Tl) well detector for X- and gamma ray photons can be supplemented with the signals produced by charged particles or low energy photons in an additional detector (Yu et al., 1990). This additional detector may be a pressure PC (Johansson et al., 2003b; Li et al., 2005) or two thin plastic scintillators (Kawada et al., 2004; Yamada et al., 2006) placing the sample in the hole of the NaI(Tl) detector. The detection system can also include a Ge detector (Xie et al., 2005). In this method, we gain in particle detector efficiency while reducing the efficiency of the photon detector due to the detector material. As both detectors, because of their high geometry, can record signals from the same decay, these signals have to be subtracted to avoid double counting. This method has been successfully applied to the standardization of radionuclides with complex decay schemes such as ^{152}Eu and ^{192}Ir, as well as nuclides with simpler schemes such as ^{241}Am, where the reduced nonefficiency for alpha particles is compensated by the detector's efficiency for X- and gamma rays.

F. Defined solid angle

The calibration method for DSA is one of the most accurate standardization methods for alpha-emitting radionuclides. It requires the control of a number of parameters. First, it requires a careful mechanical design and careful execution of the different parts of the system: precise determination of distances and calculation of the solid angle subtended by the detector.

Standardization of alpha-emitting radionuclides using the DSA technique is based on determination of the count rate of alpha particles emitted by a sample and interacting with the detector in a solid angle Ω subtended by the detector and the radioactive sample. The first publication about the technique was by Jaffey (1954) and a review of this technique, focusing on the main sources of uncertainty, was provided by Bambynek (1967). The uncertainties achievable with this method are of the order of 0.1%.

The problem of calculating the solid angle has been addressed in numerous publications such as Williams et al. (1968), Gardner and Carnesale (1969), Gardner and Verghese (1971), Verghese et al., (1972), Chatelier and Launois (1972), Green et al. (1974), Kaplanis (1982), Haitjema (1987), Gardner et al. (1980, Cook (1980), Hosseini-Ashrafi and Spyrou (1992), Ruby (1994), Selim and Abbas (1994), Pommé 2004, Pommé et al. (1995, 2003), Tryka (1997), Prata (2003, 2004), García-Toraño et al. (2008), Conway (2006, 2007, 2008, 2010), and Friot (2015).

The radioactive solution is deposited on a flat support and centered on the symmetry axis parallel to the diaphragm and the detector. Although the accuracy of the DSA method is excellent, taking the solid angle calculations into account, nonetheless, the uncertainties may be high due to sample imperfections, and the nonhomogeneous radioactive distribution or eccentricity of radioactive sample activity compared to the detector's symmetry axis.

Digital autoradiography is the most obvious method for obtaining accurate information about the distribution of activity on the substrate. One way of knowing this distribution is pixelated autoradiography, calculating the respective solid angle for each pixel and calculating a normalized sum for all pixels, using the local activity factor. This method can be applied to a Monte Carlo simulation to calculate solid angle (Briesmeister, 2000). An alternative method that integrates the actual source activity distribution into the solid angle calculation and requires less computing time is due to Sibbens et al. (2003). We can use an algorithm based on numerical integration (Pomé et al., 2003), which is faster than the Monte Carlo technique, and also makes use of the measuring device's axial symmetry. The sample is divided into concentric rings whose points correspond to a common solid angle. This reduces computation time without affecting activity measurement accuracy. As the relative amount of activity in the rings is used as weight factor, the total geometric factor of the source is given by the ratio of the sum of the products of the geometric factor for the intensity of each element and the sum of element intensities.

The procedure for the determination of activity in a particular case is clearly described by García-Toraño et al. (2008). Distribution of activity in the sample was determined by autoradiography of the sources using a Kodak Biomax MS film. The film was then scanned with a digital scanner with 24,002 $\times$ 400 dpi optical resolution for the array of optical densities. Then they used the characteristic curve of the film to make it an array of intensities. The curve linking the optical densities of the radiation intensities was measured by exposing the film to a collimated ^{241}Am source. Distribution of activity in the source was represented by an array of 100 $\times$ 100 elements. As the maximum source diameter is 2.5 cm, each pixel

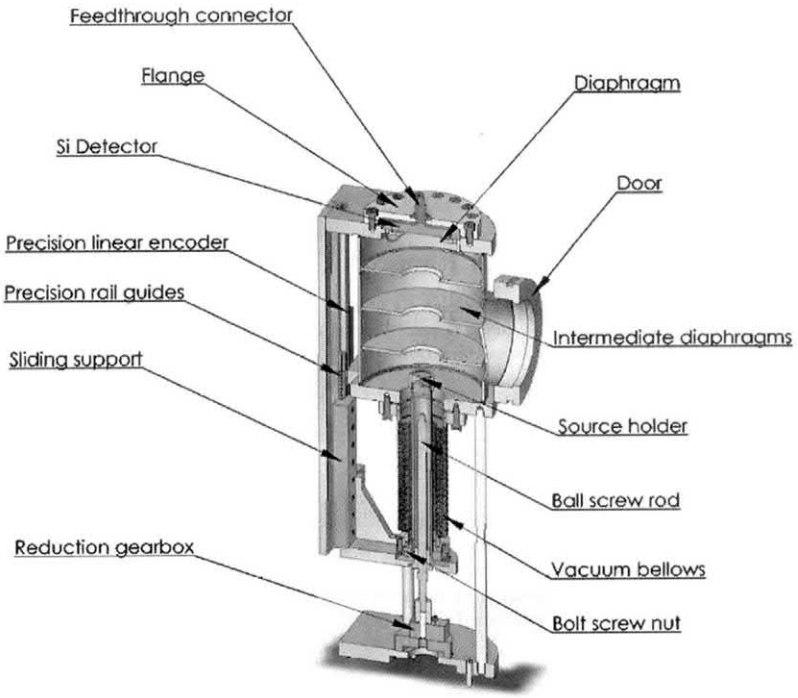


FIGURE 7.3 Diagram of the counter showing the main components. Alpha particles are detected with a 2000 mm^2 Si detector. Diameter of the main diaphragm, source-detector and activity distribution of the source define the geometry of the measurement. Source to detector distance can be continuously varied between 80 and 190 mm. *From García Toraño et al. (2008), reprinted with permission of Elsevier Science © 2008.*

corresponds to a $0.25 \times 0.25\ mm^2$ area. They used a Si detector with a 2000 mm^2 active area. The sensitive area was obtained with an aperture with a radius of 24.9 mm. This enables changing the detector without changing the geometry. Source detector distance can be adjusted from 8 to 19 cm. Fig. 7.3 shows the measuring device with its main components.

Calculation of the geometric factor depends on the distribution of radioactive material at the source. Fig. 7.4 shows a point source located at a distance Z from the detector of radius R. The geometric factor $G_C = \Omega_C/4\pi$ is given by the expression:

$$G_C = \frac{1}{2}\left[1 - \frac{Z}{D}\right] = \frac{1}{2}\left[\frac{R^2}{D(D+Z)}\right] \tag{7.91}$$

When the source is not in the common axis (Fig. 7.4) but moved away from this, Jaffey (1954) proposed the following expression:

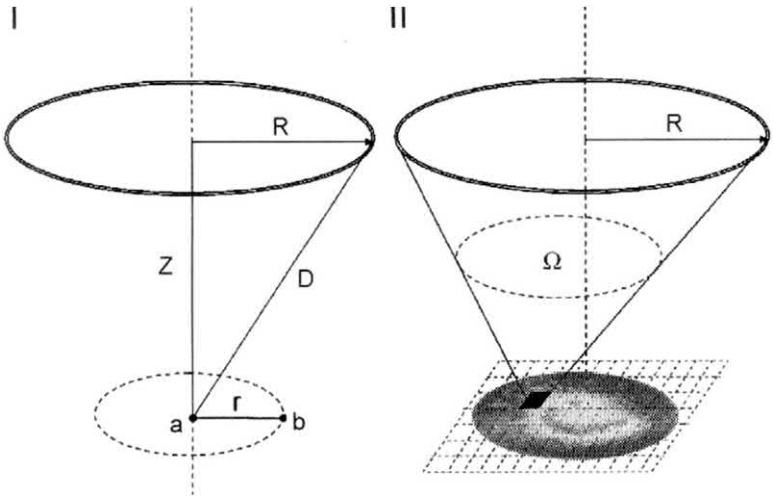


FIGURE 7.4 (I) Schematic representation of a measured setup composed by a circular detector and a point source in the axis (A) or off the axis (B). (II) Real sources are characterized by numerical arrays whose elements correspond to radiation intensities. The overall solid angle for the source is obtained as the weight mean of all elements. *From García Toraño et al. (2008), reprinted with permission of Elsevier Science © 2008.*

$$G = G_C + \frac{1}{2}\sum_{n=1}^{\infty}\frac{2n+1}{2n}\left(\frac{Z}{D}P_{2n}\left(\frac{Z}{D}\right) - P_{2n+1}\left(\frac{Z}{D}\right)\right)P_{2n}(0)\left(\frac{r^2}{D^2}\right)^n \tag{7.92}$$

where P_n are the Legendre polynomials. This expression is valid for $r/R < 1$. Usually, three or four terms are sufficient for the precision required in practice. Other authors have published analytical expressions to calculate the solid angle for circular sources (Ruby and Rechen, 1968; Ruby, 1994; Pommé, 2004; Conway, 2006). These equations require that radioactive sources be circular and homogeneous.

García-Toraño et al. (2008) applied expression (7.91) to all elements of the radiative zone (Fig. 7.4). A random mesh of 100 elements is generated for each element and the solid angle is calculated for each. The total geometric factor is obtained by a weighted average of the point values obtained:

$$G = \frac{\sum_{i,j} I_{i,j} G_{i,j}}{\sum_{i,j} I_{i,j}} \tag{7.93}$$

where $G_{i,j}$ and $I_{i,j}$ are geometric factors and intensity of the corresponding element of the array, respectively.

The background count rate for alpha emitters is very low ($\approx 10^{-3}\text{s}^{-1}$) and can be easily removed from the source spectrum. Satellite peaks accompanying some of the alpha peaks in alpha spectra are due to contamination by recoiling nuclei and can be avoided by covering the sample with VYNS foil (Nylandsted Larsen et al., 1984). Any impurities in the enriched material can be identified with alpha spectrometry or high-resolution gamma spectrometry.

Several mathematical methods have been developed to calculate the solid angle. They include analytical methods (Ruffle, 1967; Rubby and Rechen, 1968; Gardner and Verghese, 1971; Bellusco et al., 1974; Gardner et al., 1980; Selim and Abbas, 1994; Ruby, 1994; Abbas, 2001; Galiano and Rodrigues, 2006; Conwey, 2006); series expansions (Lerch and Spernol, 1966; Vega Carrillo, 1996; Pommé, 2004); numerical integration for axial symmetry (Zhihua and Xinmiao, 1992; Pommé et al., 1995; Tryka, 1997), rectangular window (Gotoh and Yagi, 1971); elliptical window (Conway, 2006); two disks and no parallel samples (Obložinsky and Ribanský, 1971); double diaphragm (Aguiar and Galiano, 2004); the Monte Carlo simulation method (Williams, 1966; Cox, 1969; Carchon et al., 1975; Wielopolski, 1977; Stavroulaki and Kaplanis, 1979); and solid angle calculations including the geometric distribution of sample activity (Pommé et al., 2003; Sibbens et al., 2003).

Setups for alpha-particle counting at a DSA have been described in the literature by several institutes, including IRMM (formerly CBNM) (Denecke et al., 1999; Pommé and Sibbens, 2008); LRL (Robinson, 1960); NIST (Hutchinson et al., 1968); ANL (Flynn et al., 1972); LNE-LNHB (Blanchis, 1983; Blanchis,1984), CIEMAT (García-Toraño and Aceña Barrenechea, 1989; García-Toraño et al., 2008), and PTB (Schötzig and Schönfeld, 2000). New setups have recently been constructed in TAEK (Turkey) (Seferinoğlu and Yeltepe, 2015) and NPL (UK) (Arnic et al., 2016) inspired by the IRMM model. Specifically for the standardization of the activity concentration of ^{222}Rn gas, DSA counters were built in which the gas could be condensed on a cold plate and measured in an ion-implanted planar silicon detector in vacuum conditions (Picolo, 1996; Dersch, 2004); Spring et al., 2006). The specific activity of ^{226}Ra in soil has been measured in the frame of proficiency test organized by IAEA and IRMM (Dirican et al., 2012)

Pommé (2015a,b) investigates the main uncertainty components of counting at a defined angle. He arrives at the following conclusions: Radioactive solutions can be standardized with 0.1% for alpha emitters and 1% for X-ray emitters, including the uncertainty from weighing the dispensed amounts in the sources. The activity of each specific source can be measured with better accuracy. Repeatability of the activity measurement of a source can be achieved within 0.01%, depending also on counting statistics. The technique is extremely well suited for half-life measurements, either by specific activity measurement of long-lived nuclides or decay curve analysis of intermediately long-lived nuclides, provided that dead time compensation and interfering signals are well under control. Statistical uncertainty can be a dominant factor, depending on source activity and measurement time.

Ferreira Filho et al. (2018) applied this method to obtain the equations for ^{152}Eu to standardize this radionuclide. They used a matrix technique for complex decay schemes.

G. Internal gas counting

Calibration of gaseous radionuclides can be performed by the internal gas counting technique (Kits et al., 1967; Spernol, 1967). A known amount of radioactive gas is mixed with the counting gas in a set of cylindrical PCs. This procedure eliminates the problem of self-absorption in the gas and is therefore well suited for measuring radionuclides that emit low energy beta radiation, such as tritium. To eliminate the end effects of the PCs, the commonly applied technique is differential counting with counters of different lengths. Other factors to consider are wall effects and loss of low energy signals, which have

been addressed by extrapolation methods, Monte Carlo simulations (Mori et al., 1998) and analytical calculation (Stanga et al., 2002). More details on this technique are presented in Unterweger (2007).

1. Theoretical description of internal gas counting

According to Kits et al. (1967), the specific activity of the radioactive sample measured by an X counter can be calculated using the equation:

$$a = \frac{V}{m}\frac{N_X - B_X}{\frac{1}{4}d^2 L_X(1 - N_X\tau)}\frac{1}{(1-p_X)(1-p_W)(1-p_d)} \tag{7.94}$$

where a is the sample specific activity ($s^{-1}g^{-1}$), V is the volume (cm^3), m is the mass of the sample (g), N_X is the counting rate of the counter X (s^{-1}), B_X is the count rate of the background (s^{-1}), τ is the dead time (s), d is the cathode diameter (cm), L_X is the length of the counter cathode (cm), and p_X, p_w, and p_d are the probabilities that a particle is not detected due to end effect, wall effect, or discrimination, respectively. We define p_X as the probability that a particle is not detected in a counter of L_X length and that the pulse formed by the particle due to the end effects has amplitude below the level of discrimination.

Because of the extreme effect, the counter of length L_X acts as a counter without an end effect with an effective length of:

$$L'_X = L_X - L_0 \tag{7.95}$$

where L_0 is the counter length without sensitivity. The effective length of the counter can be expressed as:

$$L'_X = L_X(1 - p_X) \tag{7.96}$$

therefore

$$p_x = \frac{L_0}{L_X} \tag{7.97}$$

Taking into account the difference between the count rates of the two counters called L and S, the length corresponding to the difference of their volumes will be:

$$L_{L-S} = L_L(1-p_L) - L_S(1-p_s)$$

$$= L_L\left(1 - \frac{L_0}{L_L}\right) - L_S\left(1 - \frac{L_0}{L_S}\right) = L_L - L_S \tag{7.98}$$

so the correction for end effects was eliminated. The specific activity of a sample measured by two counters will be:

$$a = \frac{V}{m}\frac{\frac{N_L - B_L}{1 - N_L\tau} - \frac{N_S - B_S}{1 - N_S\tau}}{\frac{1}{4}d^2(L_L - L_S)}\frac{1}{(1-p_W)(1-p_d)} \tag{7.99}$$

2. Some experimental aspects of internal gas counting

The volumes of the cylinders formed by the cathode are calculated from the mass of distilled water that fills the cathode between two flat glass plates applied to the cathode ends. The mass is determined by weighing at 20°C. All measurements were performed without the shielding of the counters as this would have complicated the device.

To correct for dead time, as this is small, we apply the method of measuring two sources separately and together. In this case we take two counters filled with active gas; and we measure the count rates with parallel connections of the two counters. The mean value found was 16.7 μs.

The correction for the wall effect is determined by breaking down 5 weighted amounts of $Na_2^{14}CO_3$ and adding methane to the carbon dioxide to obtain different pressures in the range of 0.592−0.955 atm, after which the differential count rate is measured. A straight line is then drawn through the experimental points by means of the least-squares method.

The dependence of the count rate on discrimination voltage, measured at an operating voltage of 3750 V, shows a relative increase of 0.55%, 0.69%, and 0.91% for the long, medium, and short counters, respectively, by extrapolating the conventional voltage of 5 V to zero. This shows that, in the case of two counters, correction for discrimination is unnecessary.

3. Applications of internal gas counting to radionuclide standardization

^{85}Kr. Mori et al. (1992) directly measured the radioactivity of ^{85}Kr with a position-sensitivity proportional counter (PSPC) method, excluding the influence of the wall effect. The standard deviation of the activity was 0.80%. The result was compared with the measurement obtained with a diffusion-in long PC, obtaining good agreement (0.5%). The use of logarithmic amplifiers was very useful for distinguishing the signals of beta rays and noise and for minimizing errors.

Makepeace et al. (1994) conducted an intercomparison of internal gas counting of ^{85}Kr and ^{3}H under the auspices of EUROMET, European Collaboration in Measurement Standards. A sample of ^{85}Kr mixed with inactive krypton

was measured by three laboratories while a sample of ^{3}H, mixed with nitrogen, was measured in four laboratories. The laboratories involved were the NPL, Teddington (England), Laboratoire Primaire de Métrologie des Rayonnements Ionizants (LPRI), Saclay (France) and Physikalisch-Technische Bundesanstalt (PTB) Baunschweig (Germany). In each case, the values were within the uncertainties of the measurements. The paper describes the techniques, results and conclusions of each of the laboratories.

Stanga et al. (2002) presented analytical calculations of losses in an internal gas PC. The results were checked by internal gas counting and the method of measurement developed in LNHB-Saclay. The experimental results with a sample of ^{85}Kr were compared with those obtained by an analytical calculation method. Consistency was excellent. Extrapolation experimental methods, commonly used in internal gas counting, were consistent with the analytical calculations.

Philips et al. (2010) participated in the key-comparison of the BIPM for primary standardization of ^{85}Kr using internal gas proportional counting (IGPC). The activity supplied for the intercomparison was relatively high, 40 MBq, and two-stage dilution was necessary to obtain an appropriate level for gas counting. A new gas-handling ring was built. The dilutions introduced significant uncertainties in the measurements so that it was necessary to resort to other activity measurement methods to confirm the internal gas counting results. The combined uncertainties for the three methods were compared, obtaining: 1.10% for IGPC, 0.63% for HPGe and 1.06% for NaI(Tl) ($k = 1$).

Yunoki et al. (2010) participated in the key-comparison of the BIPM for ^{85}Kr primary calibration using internal gas proportional counting (IGPC). Absolute measurement was performed with a set of PCs of different lengths. The original gas ampoule was diluted 2×10^5 times to achieve a concentration of appropriate activity. Therefore, a new method of dilution based on a large-volume balloon was introduced. The estimated relative uncertainty was 1.25% ($k = 1$).

Schlosser et al. (2017) described the PCs and a $\beta-\gamma$ coincidence system. Typical limits of detection (LD) are 8 mBq m^{-3} for ^{85}Kr and 4 mBq m^{-3} for ^{133}Xe for the PCs and for similar xenon volumes the (LD) for ^{133}Xe in the $\beta-\gamma$ system is about 4 times lower.

^{3}H. Mann et al. (1964) performed a calibration of the NBS tritium standards that had been calibrated by calorimetric methods in 1954–55. The recalibration described in the paper uses length-compensated internal gas counters. The new activity values were 1.96% lower than the previous ones. But this difference also involved uncertainties in the half-life and mean beta ray energy of ^{3}H. A value of 0.92 was obtained for the combined rate of evaporation and reaction with Zn, for HTO and H_2O.

Spernol and Denecke (1964) described a method for the measurement of tritiated water with 0.1%–0.2% reproducibility and 0.3%–0.4% absolute accuracy. The first two parts of the work describe the preparation of the counting gas and the counters used. The measurement procedure and systematic errors are examined in detail in the third part.

Hadzisehovic et al. (1973) presented the results of the specific activity of tritiated water measures by internal gas counting. Two reducing agents, uranium and zinc, were used to convert water to gas. The absolute disintegration rate per unit volume of the counter was determined by the compensation method using three gas PCs. Depending on the procedure for determining the mass of radioactive hydrogen, two methods were used to obtain the specific activity of water. Both methods gave the same results within 1%. The total uncertainty in determining specific activity was ±1%.

Mori et al. (1987) described a new principle using a PC with a resistive anode partially resistive and sensitive to the position for measurement of ^{3}H gas. The new method eliminated the influence of end effects and could define the effective counting volume. The paper describes the process of preparing the anode and its characteristics.

Unterweger et al. (1980) described the recalibration of SRM 4926 and SRM 4927 tritiated water according to the standards that had been measured by the method of internal-gas proportional counting. The paper concludes that the half-life of tritium must be corrected to 1243 ± 0.05 years.

Makepeace et al. (1996) performed an intercomparison of internal gas counting of tritiated water under the auspices of EUROMET, European Collaboration in Measurement Standards. The laboratories involved were the NPL, Teddington (England), the National Institute for Satandards and Technology (NIST), Gaithersburg (US) and the Physikalisch Technische Bundesanstalt (PTB), Baunschweig (Germany). The samples were measured by internal gas proportional counting after reducing the tritiated water to produce gas HT. Consistent results were obtained within the uncertainties. However, the NPL value was significantly higher than the others to the level 1σ. This means that it must carry out an investigation on the effect of the use of a molecular sieve to collect the gas, as this is the most significant difference between the systems used by NPL and the PTB and NIST.

Stanga et al. (2006) calibrated tritiated water by two methods: a method based on liquid scintillation, using the technique of triple-to-double coincidence ratio (TDCR), and the other method, internal gas proportional counting, in conjunction with a generator of tritium gas by water chemistry reduction. The uncertainties of both methods were less than 0.6% and both measurement results were consistent within this uncertainty, indicating that both methods were suitable for standardization of tritiated water.

Stanga et al. (2005) standardized tritiated water by internal gas proportional counting following its chemical reduction, by means of a tritium gas generator, to produce tritiated hydrogen. They describe a new tritium gas generator in detail together with the method of measurement based on the internal gas counting. The method had new and improved features and offers the advantage of being simpler and easier to operate than other tritium generators available. The tritium generator had the following new features: (1) it performed the water reduction at a lower temperature (450°C) than the other generators which need 600°C; (2) the reduction yield was always unitary. Also, it had a simple and compact construction by using the same components for water degassing and water reduction. Its simple disassembly and reassembly allowed for easy maintenance.

Bonicalzi et al. (2016) use a single compound (methane) for dual tritium and radiocarbon measurements in environmental applications. They present an optimized methane percentage, detector fill pressure, and analyze energy windows to maximize measurement sensibility while minimizing count time. The optimized method uses 9-atm fill of P35 (35% methane, 65% argon) and the window for tritium from 1.5 to 10.3 keV. This method optimizes tritium-counting efficiency and minimizes radiocarbon beta-decay interference.

^{14}C. Mann et al. (1961) determined the half-life of ^{14}C by internal gas counting with an uncertainty lower than other previous determinations. Carbon dioxide was released by the action of perchloric acid on barium carbonate containing ^{14}C, approximately 44% of isotopic abundance. The technical difficulties of the work are due to absorption problems, whose solution is described in detail in the paper. The value obtained for the half-life was 576.0 ± 50 years. The currently accepted value is 573.0 ± 40 years.

Watt et al. (1961) measured the specific activity of pure samples of carbon dioxide containing 45% and 2% of ^{14}C per atom. Using mass spectrometry and gas internal count by counting with a PC, they obtained a half-life of 578.0 ± 65 years. This is far from the accepted value of 573.0 ± 40 years, but excellent when compared with previously obtained values. The paper describes the various corrections applied subsequently which served as the basis for modern measures.

^{127}Xe. Rodrigues et al. (2014) standardize ^{127}Xe using three differential internal PCs. Detection efficiency is not very independent from the decay scheme; and this enables the activity of this standard to be used for the determination of gamma ray emission intensities. ^{127}Xe is useful in the quality control of remote radio-xenon monitoring stations, with the advantage of a longer half-life than ^{131m}Xe or ^{133}Xe.

^{131m}Xe. The work of Garfinkel et al. (1973) presented the changes in the gas-counting system of National Bureau of Standards. They describe the preparation of various standards of radioactive gas. The system was successful in the standardization of ^{131m}Xe. The gamma ray of 164 keV is well converted and the same value for the count rate was obtained with two levels of discrimination. Standards of ^{131m}Xe were prepared by first doing a separation by isotope separator and then by measuring with the internal gas counting system. The method of five levels of discrimination was successfully applied to gaseous radionuclides: ^{3}H, ^{14}C (as CO_2), ^{39}Ar, and ^{85}Kr, all with a continuous beta ray spectrum. However, ^{37}Ar, a nuclide decaying by pure electron capture, did not yield satisfactory results. It took a series of corrections in relation to L and M electron-capture for standardization.

^{133}Xe. The work of Picolo et al. (1998) presented the results of an international comparison of ^{133}Xe conducted under the auspices of EUROMET (project Nr. 304). The project was divided into two stages. In the first, sealed glass ampoules containing 40 MBq of ^{133}Xe were measured. The following laboratories participated in the comparison: BIPM, LPRI, NIST and NPL. LPRI, NIST, and NPL participated in the second measurement, the activity concentration of ^{133}Xe mixed with nitrogen. Activity concentration was about 50 MBq/mol. The paper describes the experimental techniques used, the results obtained and the conclusions of the participating laboratories.

Positron emitters. The intense use of the Positron Emission Tomography (PET) technique for clinical diagnostic purposes has led to the proliferation of cyclotron facilities to produce positron emitters such as ^{11}C, ^{13}N, ^{15}O, and ^{18}F. To meet the requirements of radiation protection, the operators of the cyclotron are required to use one of the air measurement techniques for monitoring. Marouli et al. (2007) report that it is required to have a primary standard for positron emitters in gas to ensure that the measures are sufficiently precise. The basis of the primary standard is a system of internal gas counting established at NPL for the calibration of β^- emitters. Therefore, they have to establish the difference between the system's response to positrons and electrons. This paper describes the energy deposited by positrons compared with electrons in the gas volume of the counter. They used the calculation code PENELOPE to study the energy deposited by the abovementioned radionuclides in P10 gas. It was found that positrons deposited between 1.5 and 2.5 times more energy than electrons in the gas, depending on the maximum energy of the spectrum, affecting the lower limit of concentration detectable of positron counters.

The work of Marouli et al. (2007, 2008) describes the need for a UK primary standard and monitor calibration service for positron emitting radionuclides in gases by the users of cyclotron facilities to enable them to calibrate radioactivity-in-air monitors and thus ensure the accuracy and traceability of measurements of any airborne

radioactivity releases arising from the production of these radionuclides. A system of gas flow PCs, already established at the NPL for the standardization of β^--emitting gases, was used as the basis of the primary standard. They focus on initial problems encountered in the use of the system for measuring positron emitters.

Marouli et al. (2010) developed a method involving internal gas proportional counting and the PENELOPE calculation code to determine Monte Carlo corrections for lost of counts. The work focuses on the calibration of ^{11}C, but the method can be applied to other positron emitters. The results were compared with measurements of ^{11}C in aqueous solution carried out by a reentrant ionization chamber calibrated with reference to absolute counting techniques.

Zimmerman (2013) analyzes the current status and future needs for standards of radionuclides used in PET. Marganiec-Galazka et al. (2018) carry out the activity determination of ^{68}Ge/^{68}Ga by means of $4\pi\beta(\check{C})-\gamma$ coincidence counting. Measurements were made by means of a new PTB-custom-built $4\pi\beta(LS)-\gamma$ coincidence counting system, where a liquid scintillator detector in the beta channel can also be used as a Cherenkov counter, and a NaI(Tl) crystal detects annihilation radiation.

H. Liquid scintillation counting

Liquid scintillation is also a 4π measurement technique. In general, the efficiency of alpha emitters is 100% (Havelka, 2018). In the case of high-energy beta radionuclides, extrapolation can be applied to obtain the activity of the sample. Such is the case of ^{131}I, ^{32}P, ^{60}Co radionuclides (Steyn, 1956). Due to ionization quenching, extrapolation is difficult to apply to radionuclides with emission of low- or medium-energy beta particles. Several papers have been published to calculate the counting efficiency for beta emitters with maximum energy below 200 keV (Horrocks and Studier, 1961; Lukens, 1961; Gibson and Gale, 1968; Horrocks, 1976). Van Wyngaardt and Simpson (2006a) obtained the absolute activity of these radionuclides decaying by electron capture: ^{139}Ce, ^{131}I, ^{192}Ir, and ^{65}Zn by LSC, using the extrapolation technique. This technique was previously applied to the standardization of ^{204}Tl by Simpson and Meyer (1994b).

In 1961, in a pioneering study, Horrocks and Studier (1961) proposed the idea that the relationship between the computed counting efficiencies for two photomultipliers in coincidence and a single photomultiplier is connected to counting efficiency. If the relationship is extrapolated to 1, the counting efficiency will be 100% and the extrapolated count rate will coincide with the sample's activity expressed in the same time units. Although the idea and procedure are correct, the difficulty of obtaining the real count rate with a single photomultiplier, due to interference from electronic noise, limits its applicability to the radionuclides with energy of beta emissions above 100 keV.

It immediately suggests that the procedure proposed by Horrocks and Studier (1961) should be applied to a three-photomultiplier detector system, using the counting efficiencies for two and three photomultipliers, as coincidences virtually eliminate electronic noise. The main difficulty was that the quantum yield of the photomultiplier was very small, which meant a high uncertainty in the determination of activity.

The development of a photomultiplier with high quantum performances radically changed the situation so that Schwerdtel (1968) made the first detection system with three photomultipliers. Subsequently, Pochwalski et al. (1988) built a much more elaborate triple and double coincidence system in order to directly obtain the activity of a radioactive specimen.

In 1980, Grau Malonda (1982a), in his doctoral thesis, presented the first models for calculating the counting efficiency of radionuclides with different decay schemes: pure beta, beta-gamma, pure electron capture, electron capture-gamma emitters, and pure positron emitters. The paper compares the efficiency curves versus the chemical quenching, experimental and calculated, for the following radionuclides: ^{14}C, ^{35}S, ^{99}Tc, ^{185}W, ^{36}Cl, ^{204}Tl, ^{89}Sr, ^{32}P, ^{203}Hg, ^{60}Co, ^{90}Sr+^{90}Y, ^{55}Fe, ^{85}Sr, ^{125}I, ^{139}Ce, ^{137}Cs, ^{65}Zn, and ^{22}Na. Discrepancies between experimental and theoretical values were below 5%. Note that, at that time, many of the commercial calibration solutions had uncertainties of around 3%. In international comparisons, uncertainties of 1% were classified as excellent.

The first publications about the tracer method, which was then called the CIEMAT/NIST method, were by Grau Malonda and Garcia-Toraño (1982), on pure beta radionuclides, and Grau Malonda (1982b) on nuclides decaying by electron capture. These papers outline the foundation for subsequent models for calculating the efficiency of LSC.

The first computer program to calculate the efficiency of beta emitters was the EFFY program (García-Toraño and Grau Malonda, 1981), followed by EFFY2 (García-Toraño and Grau Malonda, 1985). The first program to calculate the efficiency of nuclides decaying by electron capture was VIASKL (Los Arcos et al., 1987).

In 1985, collaboration began between CIEMAT and the NBS (now NIST) in order to study the application of computational models to the standardization of radionuclides by LSC. This collaboration was extremely fruitful and complementary. The NIST calibration solutions were the best in the world and, in particular, Dr. Coursey was the most experienced investigator in the preparation of samples for liquid scintillation. The term "CIEMAT/NIST" method is due to the fact that both institutions supported the method's development, with a significant reduction in the

uncertainties associated with the standardization of radionuclides.

In 1986, Dr. Coursey received the results of ^{3}H and ^{14}C obtained with the three-tube system developed by Pochwalski and Radoszewski (1979) and Pochwalski et al. (1988). It was easy to prepare a calculation model for systems with three photomultipliers, based on the earlier developed two-photomultiplier model. In the summer of 1986, the calculations were ready and a submission was prepared (Grau Malonda and Coursey, 1988), sending the results to Dr. Radoszewski. The Polish team presented a paper (Broda et al., 1988) based on a binomial model. A code for this model was never published.

In 1990, Grau Malonda (1990) showed that despite the different statistical assumptions applied, both models should lead to identical results for monoenergetic electrons. Discrepancies in the counting efficiencies calculated with both models for ^{3}H and ^{14}C presented in the works of Grau Malonda and Coursey (1988) and Broda et al. (1988) were due to the fact that, in the latter, an infinite series is truncated and introduces a truncation error, whereas Grau Malonda and Coursey (1988) apply an accurate equation. The expressions used in this type of calculation were derived in the book by Grau Malonda (1999).

Later, Grau Carles and Grau Malonda (1989) studied the problem of the form of response curve (counting efficiency as a function of the triple/double relationship) for nuclides decaying by electron capture. As Fig. 7.5 shows, for a free parameter value we can have up to three values of counting efficiency. This ambiguity is resolved by a three-dimensional representation (ε −T/D−λ) counting efficiency (ε), T/D ratio, and the free parameter (λ) (Fig. 7.6.). On the other hand, they show that the extrapolation method for LSC cannot give linear responses enabling extrapolation so the results are not good for nuclides decaying by electron capture.

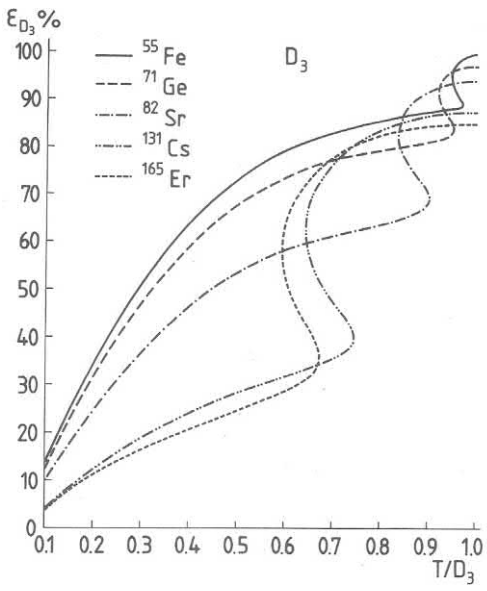


FIGURE 7.5 Counting efficiency for the addition of three double coincident signals versus the triple-to-double counting rate. *From Grau Carles and Grau Malonda (1989), reprinted with permission from Real Sociedad de Física.*

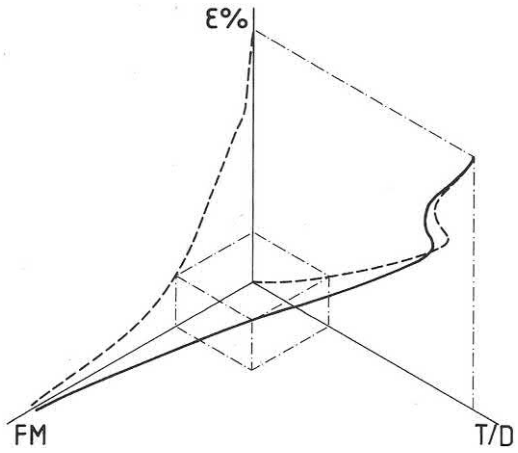


FIGURE 7.6 Three-dimensional representation of the calibration curve with the ε −T/D and ε −FM projections. *From Grau Carles and Grau Malonda (1989), reprinted with permission from Real Sociedad de Física.*

In recent years, major efforts have been made to solve these problems, both experimentally and theoretically, considering two different lines: the CIEMAT/NIST method and the TDCR method. The principles and applications of both methods are described masterfully in Chapter 6, Volume 1 of this book.

As the method can be applied to measure relatively low activities, it has been used for the measurement of the natural radioactivity of some radionuclides such as ^{40}K, ^{10}Be, and ^{87}Rb obtaining their half-lives with uncertainties lower than other procedures (Grau Malonda and Grau Carles, 2002; Kossert, 2003; Kossert and Günther, 2004; Grau Carles and Kossert, 2006, 2007; Schwarz et al., 2011).

As the uncertainty of ^{54}Mn is lower than that of ^{3}H, the former is a good candidate as a tracer. In particular, for nuclides decaying by electron capture, Günther (1998) made the proposal, which was later tested by Kossert and Grau Carles (2006), to use ^{54}Mn as a tracer instead ^{3}H, confirming a reduction of dependence, if ^{54}Mn is used to standardize ^{55}Fe and ^{65}Zn.

While the CIEMAT/NIST method uses commercial liquid scintillation counters, the TDCR method requires the use of special counters equipped with three photomultipliers. A good example of a counter of this type was described by Cassette and Vatin (1992). The system with three photomultipliers allows for double coincidences (AB, AC, BC, and the possible sums of these coincidences, and the triple coincidence (ABC), from which counting

TABLE 7.7A Counting efficiency equations for counting systems with two identical photomultipliers. $\bar{n} = EQ(E)/2\lambda$.

Operating mode	Efficiency equation
A_1	$1 - \exp(-\bar{n})$
$A_{1+}A_2$	$1 - \exp(-2\bar{n})$
A_1A_2	$(1 - \exp(-\bar{n}))^2$

From Grau Malonda (1999), reprinted with permission of CIEMAT.

TABLE 7.7B Counting efficiency equations for counting systems with two different photomultipliers. $\bar{n}_1 = EQ(E)/2\lambda_1$; $\bar{n}_2 = EQ(E)/2\lambda_2$.

Operating mode	Efficiency equation
A_1	$1 - \exp(-\bar{n}_1)$
$A_{1+}A_2$	$1 - \exp(-(\bar{n}_1 + \bar{n}_2))$
A_1A_2	$(1 - \exp(-\bar{n}_1))(1 - \exp(-\bar{n}_2))$

TABLE 7.8A Counting efficiency equations for counting systems with three identical photomultipliers. $\bar{n} = EQ(E)/3\lambda$.

Operating mode	Efficiency equation
A_1	$1 - \exp(-\bar{n})$
$A_{1+}\ A_2$	$1 - \exp(-2\bar{n})$
$A_1 + A_2 + A_3$	$1 - \exp(-3\bar{n})$
$A_1\ A_2$	$(1 - \exp(-\bar{n}))^2$
$A_1\ A_2 + A_1\ A_3$	$2(1 - \exp(-\bar{n}))^2 - (1 - \exp(-\bar{n}))^3$
$A_1\ A_2 + A_1\ A_3 + A_2\ A_3$	$3(1 - \exp(-\bar{n}))^2 - 2(1 - \exp(-\bar{n}))^3$
$A_1\ A_2\ A_3$	$(1 - \exp(-\bar{n}))^3$

From Grau Malonda (1999), reprinted with permission of CIEMAT.

efficiency can be obtained. Tables 7.7A and 7.8A show the equations for calculating efficiencies in double and triple coincidences, assuming a similar response for the three photomultipliers.

When the responses of the photomultipliers are different, the expressions to calculate counting efficiencies are given in Tables 7.7B and 7.8B. A detailed deduction for these equations and others more, in the case of four photomultipliers, is given in Grau Malonda (1999).

For photomultipliers with the same response, the ratio of triple-to-double efficiencies, when double coincidences are added, is:

$$\frac{\varepsilon_T}{\varepsilon_D} = \int_0^{Em} S(E)(1 - \exp(-EQ(E)/3\lambda))^3 dE \times \left[\int_0^{Em} S(E)\left[3(1 - \exp(-EQ(E)/3\lambda))^2 - 2(1 - \exp(-EQ(E)/3\lambda))^3\right] dE \right]^{-1} \quad (7.100)$$

where E is the electron energy, $S(E)$ is the normalized energy spectrum, $Q(E)$ is the ionization quench function and λ is the free parameter.

It is experimentally found that the CIEMAT/NIST method enables the standardization of radionuclides decaying by low beta energy emission, with a high level of accuracy. However, the calibration of radionuclides decaying by electron capture is less accurate. In some cases we have uncertainties of about 2% for ^{125}I. Some authors advocate the use of two tracers, tritium for nuclear beta decay, and ^{54}Mn for nuclides decaying by EC. From a practical point of view this is acceptable, but it is not acceptable from a fundamental point of view. When a procedure gives excellent results for some radionuclides and worse results for others, this indicates that the procedure requires further investigation.

A great effort has been made to develop computation programs to obtain the count efficiency of radionuclides dissolved in liquid scintillation or in water. The main programs published in relation to the EC are the following: CAPMULT, counting efficiency for electron capture by a KLMN four-shell model (Galiano Casas et al., 1995); EMI, counting efficiency for electron capture, electron capture-gamma, and isomeric transitions (Grau Carles et al., 1994c); EMI2, counting efficiency for electron capture by a KL1L2L3M model (Grau Malonda et al., 1999); EMILIA, LS counting efficiency for electron-capture and capture-gamma emitters (Grau Carles, 2006a,b); CHEREN, Cherenkov counting efficiency (Grau Carles and Grau Malonda, 1998); CHEREN2, Cherenkov counting efficiency by an anisotropy detection model (Grau Carles and Grau Malonda, 2006b); SRLOG, the simultaneous standardization of 90Sr+90Y+89Sr mixtures (Grau Carles, 1994b); MLOG, the simultaneous standardization of multi-nuclide mixtures (Grau Carles, 1996); MICELLE, the micelle size effect on LS counting efficiency (Grau Carles, 2007); study of a Monte Carlo rearrangement model for the activity determination of electron-capture nuclides by means of LSC (Kossert and Grau Carles, 2008).

The application of these computation programs has generated different lines of research: A New Linear Spectrum Unfolding Method Applied to Radionuclide Mixtures in Liquid Scintillation Spectrometry (Grau Carles, 1994a);

TABLE 7.8B Counting efficiency equations for counting systems with three different photomultipliers. $\overline{n}_1 = EQ(E)/3\lambda_1$; $\overline{n}_2 = EQ(E)/3\lambda_2$; $\overline{n}_3 = EQ(E)/3\lambda_3$.

Operating mode	Efficiency equation
A_1	$1 - \exp(-\overline{n}_1)$
$A_{1+}\ A_2$	$1 - \exp(-(\overline{n}_1 + \overline{n}_2))$
$A_1 + A_2 + A_3$	$1 - \exp(-(\overline{n}_1 + \overline{n}_2 + \overline{n}_2))$
$A_1\ A_2$	$(1 - \exp(-\overline{n}_1))(1 - \exp(-\overline{n}_2))$
$A_1\ A_2 + A_1\ A_3$	$(1 - \exp(-\overline{n}_1))(1 - \exp(-\overline{n}_2)) + (1 - \exp(-\overline{n}_1))(1 - \exp(-\overline{n}_3))$
$A_1\ A_2 + A_1\ A_3 + A_2\ A_3$	$(1 - \exp(-\overline{n}_1))(1 - \exp(-\overline{n}_2)) + (1 - \exp(-\overline{n}_1))(1 - \exp(-\overline{n}_3))$ $+(1 - \exp(-\overline{n}_2))(1 - \exp(-\overline{n}_3))$ $-2(1 - \exp(-\overline{n}_1))(1 - \exp(-\overline{n}_2))(1 - \exp(-\overline{n}_3))$
$A_1\ A_2\ A_3$	$(1 - \exp(-\overline{n}_1))(1 - \exp(-\overline{n}_2))(1 - \exp(-\overline{n}_3))$

Beta shape factor determinations by the cutoff yield method (Grau Carles, 2005); Precision measurement of the RAE shape factor (Grau Carles and Grau Malonda, 1996); Radionuclide standardization by Cherenkov counting (Grau Carles and Grau Malonda, 1995); The anisotropy coefficient in Cherenkov counting (Grau Malonda and Grau Carles, 1998); Synergic quenching effects of water and carbon tetrachloride in liquid scintillation gel samples (Grau Carles, 2006a,b); Alpha/beta separation in liquid scintillation gel samples (Grau Carles and Grau Malonda, 1994); Inelastic scattering and stopping power of low energy electrons (0.001−10 keV) in toluene (Garcia et al., 2004); Computational aspects in modeling the interaction of low-energy X-rays with liquid scintillators (Grau Carles and Grau Malonda, 2006a); The ionization quench factor in liquid-scintillation counting standardizations (Grau Malonda and Grau Carles, 1999); Half-life determination of ^{40}K by LSC (Grau Malonda and Grau Carles, 2002); Half-life measurements of ^{87}Rb by LSC (Kossert, 2003); LSC measurements of the half-life of ^{40}K (Kossert and Günther, 2004); Ionization quenching in LSC (Grau Carles et al., 2004); The photoionization-reduced energy in LSC (Grau Carles et al., 2006); Improved method for the calculation of the counting efficiency of electron-capture nuclides in liquid scintillation samples (Kossert and Grau Carles, 2010); and Extension of the TDCR model to compute counting efficiencies for radionuclides with complex decay schemes (Kossert et al., 2014a,b).

The TDCR method gives excellent results for the standardization of nuclides decaying by EC and worse results for low-energy pure beta-ray-emitting radionuclides. Again, we believe that more research is needed to improve the method.

Grau Malonda and Grau Carles (2008), Grau Malonda et al. (2006) studied the influence on ionization quenching of the Auger electron coincidence due to EC and IC in the decay of ^{125}I. Clearly, when two low-energy electrons coincide, ionization quench should increase. In this study the authors quantified this effect and concluded that the correction could affect up to 1%. However, the uncertainty in this case is 2%. Therefore, this process cannot completely correct uncertainty.

An extraordinary improvement in the calculation of counting efficiency of nuclides decaying by electron capture has been achieved with the new MICELLE2 code (Grau Carles, 2007), following a new procedure to calculate stochastic activity. Kossert and Grau Carles (2010) analyze the main advantages of more realistic treatment of the emission of electrons and atomic rearrangement process subsequent to electron capture. They also analyze the energy deposition in the micelles. A new version of the MICELLE2 code enables the calculation of counting efficiency in the case of nuclides with complex decay schemes. Kossert and Grau Carles (2010) explore the following nuclides using the CIEMAT/NIST method: ^{55}Fe, ^{54}Mn, ^{64}Cu, ^{65}Zn, ^{88}Y, ^{109}Cd, and ^{123}I. All of them are first standardized by other methods, some of them in international comparisons, and then their activities were obtained from calculation using the improved MICELLE2 code. In the paper, discrepancies between experimental and calculated activities, for each nuclide, and the different parameters used in the calculation are presented. The TDCR method was also applied to the following nuclides: ^{55}Fe and ^{89}Sr. An analysis of this paper clearly shows the advantages of the stochastic code and the improvements due to a better and more detailed atomic rearrangement model.

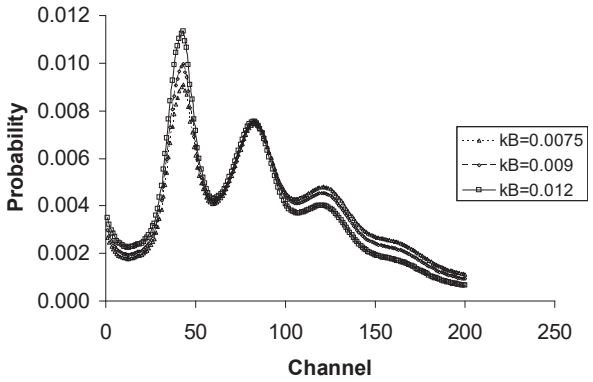


FIGURE 7.7 ^{55}Fe spectra for three different values of kB. *From Grau Carles and Grau Malonda (1989), reprinted with permission of CIEMAT.*

In a later paper, Grau Carles and Grau Malonda (2010) introduce a new methodology for studying these problems. They study theoretically calculated differential spectra. The procedure used to calculate the spectral response is based on obtaining the spectrum of "monos" for each photomultiplier. Thus, they place a lamp emitting photons of sufficient energy to produce a photoelectron in the photocathode of the photomultiplier. The response of the photomultiplier, in this case, a pulse amplitude spectrum as shown by Houtermans (1973), enables, by deconvolution, a spectrum similar to the experimental one. The Houtermans idea with the CIEMAT/NIST method enables calculation of the spectral response for any radionuclide. This procedure could be used to examine the discrepancies between theoretical and calculated spectra from the variation of any parameter. Fig. 7.7 shows the spectral response of a single photomultiplier for ^{55}Fe and different values of the kB parameter. It is sufficient to compare the experimental and theoretical spectra of ^{55}Fe to obtain the most suitable experimental value of kB.

Determination of the activity of radionuclide mixtures (pure beta ray emitters, pure electron capture or both) is a problem of interest, but complicated. Initially, these problems were solved in the case of beta emitters with very different energies. ^{32}P, ^{14}C, and ^{3}H were the most common mixtures (Altzitzoglou, 2004). They were measured by placing different counting windows, two or three, depending on the number of radionuclides. Grau Carles et al. (1993a) showed that in mixtures of radionuclides such as ^{14}C and ^{35}S, with relatively close maximum beta energies of 156.5 and 167.5 keV, respectively, the activity of each nuclide could be determined by working with the pulse height spectra. In this case, separation was possible because the beta spectra of these nuclides have different shapes due to the Coulomb effect of the nucleus on the beta particles emitted. The decomposition procedure (Grau Carles, 1994a, 1996) requires the availability of experimental spectra with parameters of well-defined chemical quench. The possibility of calculating the spectra theoretically facilitates the calculation of mixtures and decomposed mixtures that cannot now be obtained.

Application of the CIEMAT/NIST method to ^{125}I produces discrepancies of about 2% compared to other methods. Grau Carles and Grau Malonda (2010) note a possible cause. When calculating the efficiency of any beta nuclide by the CIEMAT/NIST method, we take the full energy spectrum, from zero to the maximum energy of the nuclide. However, experimentally, a discrimination level is placed in each of the photomultipliers to eliminate electronic noise. If the level of discrimination is a bit high, it cuts the experimental spectrum, reducing the number of counts and distorting the experimental measurement. On the other hand, if the level of discrimination is a little low, accidental coincidences are counted, due to the noise of the photomultipliers. This artificially increases the count number and falsifies the measurement. It is necessary to resort to calculation of the spectra to clarify the situation and correct any of the two discriminator effects.

As shown by Grau Carles and Grau Malonda (2010), it is possible to calculate the spectrum of a nuclide and determine the influence of asymmetry in the response of the photomultiplier in the case of the TDCR method. Tables 7.9A and 7.9B present expressions for calculating the statistical factor in the case of two photomultipliers when photomultiplier responses are similar and different, respectively. Tables 7.10A and 7.10B show the equations for three photomultipliers.

TABLE 7.9A - Statistical factors for two photomultipliers with equal response ($\bar{n}_1 = \bar{n}_2 = \bar{n}$).

Operating mode	Statistical factor
A_1, A_2	$\sum_{n=1}^{\infty} P(n, 2\bar{n})(1 - 2^{-n})$
$A_1 + A_2$	$\sum_{n=1}^{\infty} P(n, 2\bar{n})$
$A_1 A_2$	$\sum_{n=2}^{\infty} P(n, 2\bar{n})(1 - 2^{1-n})$

From Grau Carles and Grau Malonda (2010), reprinted with permission of CIEMAT.

TABLE 7.9B - Statistical factor for two photomultipliers with different response ($\overline{n}_1 \neq \overline{n}_2$).

Operating mode	Statistical factor
A_1	$\sum_{n=1}^{\infty} P(n, \overline{n}_1 + \overline{n}_2) - e^{-\overline{n}_1} \sum_{n=1}^{\infty} P(n, \overline{n}_2)$
$A_1 + A_2$	$\sum_{n=1}^{\infty} P(n, \overline{n}_1 + \overline{n}_2)$
$A_1 A_2$	$\sum_{n=2}^{\infty} P(n, \overline{n}_1 + \overline{n}_2) - e^{-\overline{n}_1} \sum_{n=2}^{\infty} P(n, \overline{n}_2) - e^{-\overline{n}_2} \sum_{n=2}^{\infty} P(n, n_1)$

From Grau Carles and Grau Malonda (2010), reprinted with permission of CIEMAT.

TABLE 7.10A Statistical factor for three photomultipliers with equal response ($\overline{n}_1 = \overline{n}_2 = \overline{n}$).

Operating mode	Statistical factor
$A_1; A_2$	$\sum_{n=1}^{\infty} P(n, 3\overline{n})(1 - 3^{-n}2^n)$
$A_1 + A_2$	$\sum_{n=1}^{\infty} P(n, 3\overline{n})(1 - 3^{-n})$
$A_1 + A_2 + A_3$	$\sum_{n=1}^{\infty} P(n, 3\overline{n})$
$A_1 A_2$	$\sum_{n=2}^{\infty} P(n, 3\overline{n})\left[1 - 3^{-n}\left(2^{n+1} - 1\right)\right]$
$A_1 A_2 + A_1 A_3$	$\sum_{n=2}^{\infty} P(n, 3\overline{n})[1 - 3^{-n}(2^n + 1)]$
$A_1 A_2 + A_1 A_3 + A_2 A_3$	$\sum_{n=2}^{\infty} P(n, 3\overline{n})\left(1 - 3^{1-n}\right)$
$A_1 A_2 A_3$	$\sum_{n=2}^{\infty} P(n, 3\overline{n})\left[1 - 3^{1-n}(2^n - 1)\right]$

From Grau Carles and Grau Malonda (2010), reprinted with permission of CIEMAT.

A problem that requires further analysis is the correction of ionization quench. This factor depends on the expression used for its calculation. There are two expressions: Birks (1964) and Voltz (1969). It also depends on the stopping power of the particle energies from zero to its maximum energy. Stopping power values vary from one table to another and none reaches zero (Garcia et al., 2004; Zhenyu et al., 2009), so the type of extrapolation applied has to be known. Finally there is the kB used. In most studies only the value of kB is given. In this case, it is impossible to know the ionization quench function obtained. Another issue related to the ionization quench is a basic one. It is usually taken as axiomatic that the ionization quench must be zero for zero energy of the particles, and this assumption gives good results in practice. However, according to the equations, if quenching is zero, the stopping power must be infinite and this is not true for the stopping powers known. There is also the question of whether the stopping power is a quantity applicable to energies below 1 eV.

Cassette and Do (2008) describe a new calibration method for LSC based on a virtual tracer source (Compton virtual source) created inside the liquid scintillator by Compton interaction of gamma rays emitted by an external collimated source of ^{241}Am. The procedure is similar to the CIEMAT/NIST method, but using Compton electrons instead of the tritium standard. Compton electrons

TABLE 7.10B Statistical factor for three photomultipliers with different response ($\overline{n}_1 \neq \overline{n}_2 \neq \overline{n}_3$).

Operating mode	Statistical factor
A_1	$\sum_{n=1}^{\infty} P(n,\ \overline{n}_1 + \overline{n}_2 + \overline{n}_3) + e^{-\overline{n}_1} \sum_{n=1}^{\infty} (n,\ \overline{n}_2 + \overline{n}_3)$
$A_1 + A_2$	$\sum_{n=1}^{\infty} P(n,\ \overline{n}_1 + \overline{n}_2 + \overline{n}_3) + e^{-(\overline{n}_1+\overline{n}_2)} \sum_{n=1}^{\infty} P(n,\ \overline{n}_3)$
$A_1 + A_2 + A_3$	$\sum_{n=1}^{\infty} P(n,\ \overline{n}_1 + \overline{n}_2 + \overline{n}_3)$
A_1A_2	$\sum_{n=2}^{\infty} P(n,\overline{n}_1 + \overline{n}_2 + \overline{n}_3) + e^{-(\overline{n}_1+\overline{n}_2)} \sum_{n=2}^{\infty} P(n,\overline{n}_3) - e^{-\overline{n}_1} \sum_{n=2}^{\infty} P(n,\overline{n}_2 + \overline{n}_3) - e^{-\overline{n}_{21}} \sum_{n=2}^{\infty} (n,\overline{n}_1 + \overline{n}_3)$
$A_1A_2 + A_1A_3$	$\sum_{n=2}^{\infty} P(n,\overline{n}_1 + \overline{n}_2 + \overline{n}_3) + e^{-(\overline{n}_2+\overline{n}_3)} \sum_{n=2}^{\infty} P(n,\overline{n}_1) - e^{-\overline{n}_1} \sum_{n=2}^{\infty} P(n,\overline{n}_2 + \overline{n}_3)$
$A_1A_2 + A_1A_3 + A_2A_3$	$\sum_{n=2}^{\infty} P(n,\overline{n}_1 + \overline{n}_2 + \overline{n}_3) + e^{-(\overline{n}_1+\overline{n}_2)} \sum_{n=2}^{\infty} P(n,\overline{n}_3) - e^{-(\overline{n}_1+\overline{n}_3)} \sum_{n=2}^{\infty} P(n,\overline{n}_2) - e^{-(\overline{n}_{21}+\overline{n}_3)} \sum_{n=2}^{\infty} P(n,\overline{n}_1)$
$A_1A_2A_3$	$\sum_{n=2}^{\infty} P(n,\overline{n}_1 + \overline{n}_2 + \overline{n}_3) + e^{-(\overline{n}_1-\overline{n}_2)} \sum_{n=2}^{\infty} P(n,\overline{n}_3) - e^{-(\overline{n}_1+\overline{n}_3)} \sum_{n=2}^{\infty} P(n,\overline{n}_2) - e^{-(\overline{n}_{21}+\overline{n}_3)} \sum_{n=2}^{\infty} P(n,\overline{n}_1)$ $-e^{-\overline{n}_1} \sum_{n=2}^{\infty} P(n,\overline{n}_2 + \overline{n}_3) - e^{-\overline{n}_2} \sum_{n=2}^{\infty} P(n,\overline{n}_1 + \overline{n}_3) e^{-\overline{n}_{31}} \sum_{n=2}^{\infty} P(n,\overline{n}_1 + \overline{n}_2)$

From Grau Carles and Grau Malonda (2010), reprinted with permission of CIEMAT.

operating in coincidence in a liquid scintillation counter with three photomultipliers while the Compton scattered photons are detected in a germanium detector and the pulses are carried to coincide with the signals of the three tubes added two by two. This method is called Compton Efficiency Tracing (CET).

Cassette et al. (2010) take advantage of the international comparison of ^{3}H to measure the activity of the nuclide by the usual TDCR method and CET method. The CET method is less sensitive than TDCR to the kB parameter in determining the correction factor of ionization quenching. This first experiment reveals no significant bias of the method due to the variability of the scintillators. Even if the counting efficiency varies from 0.4 for Hionic-Fluor to about 0.6 for Ultima Gold LLT, the activity obtained is correct. This shows that the CET method is less sensitive to scintillator composition than the TDCR method. The way to obtain the Compton electron spectrum shows that the cross-section interaction of these scintillators can be quite different for energies near 60 keV; and this difference is probably higher for lower energies, causing more variability for X-rays emitted after electron capture or internal conversion. More experimentation on this point is therefore required. The paper concludes with a discussion of the advantages and disadvantages of using the CET method as an international system for radionuclides, which are pure beta low-energy emitters.

Bobin et al. (2010b) described the first step in developing a digital platform dedicated to the primary standardization of radionuclides. They measured ^{241}Am and ^{3}H. In the case of ^{241}Am, they measured the activity for resolving times of the order of 24, 40, 72, and 120 ns and always obtained the same activity. In contrast, when they measured ^{3}H, with values of time resolution from 40 to 500 ns, the count rate when the system of three photomultipliers works with a sum of double coincidences varies by 4%. The authors found no explanation for this change in the count number. The only thing that they affirm is that it cannot be accidental. On the other hand, they say that when they switch from Ultima Gold to toluene, the count increase is much smaller.

We interpret the count increase when resolution time grows. In the scintillation process two components of light are found, fast and slow. The fast component is attributed mainly to emission from singlet states, induced by charged particles. The origin of the slow component is less clear and several hypotheses have attributed the emission delay to ion−electron recombination, intermolecular triplet−singlet transition, or triplet−triplet interaction. As the fast component has a half-life of 1.5 ns, in that time its contribution to light emission will be negligible. Thus, increases in light for resolution times above 40 ns should be due to the slow component. Moreover, the concentration of excited molecules due to the fast component will be huge compared to the concentration of excited molecules of the slow component. Consequently, ionization quenching, which is linked to elevated concentrations of excited molecules, will be seen in the fast component phase and be negligible in the slow component.

The explanation of why the count increase is higher with Ultima Gold than with toluene is simple. Scintillation fluids are binary systems in which solvent excitation energy is transferred to a primary scintillator (solute). Singlet excited states S_1 transfer their energy to singlet states F_1 of the primary scintillator. For typical concentrations of liquid scintillation, this reaction is fast enough to not alter the kinetics of light emission. However, if oxygen or air is present, there is highly efficient quenching of triplet states T_1; they reduce the intensity of delayed emission and change the law of decay. It is known experimentally that toluene is a liquid with an extraordinary avidity for air. If no special precautions are taken, bubbling noble gases, for example, the toluene scintillator is air saturated and, therefore, significantly reduces the emission of triplet states, so the impact of resolution time on light emission is reduced.

The constancy of the number of counts with resolution time of a certain value, as in the case of alpha emitters such as ^{241}Am, is due to the high efficiency of alpha emitters, about 100%. Therefore, the number of counts cannot increase when all the particles emitted by the radionuclide are counted. In the case of tritium, the situation is different, as there are beta particles not counted. Fast emission does not produce enough light to be detected. However, the increase in light due to slow emission makes them detectable (Tables 7.11 and 7.12).

1. Importance of the beta spectrum in the standardization of Co-60

Since the creation of the calculation models on which both the CIEMAT-NIST method (Grau Malonda and Garcia Toraño, 1982; Grau Malonda, 1999) and the TDCR (Grau Malonda and Coursey, 1988; Broda et al., 1988) are based, the importance of the calculation of the beta spectra in both methods for the determination of the primary activity has been emphasized. The inappropriate use of the beta spectrum can lead to discrepancies in activity concentrations when counting efficiency varies. Recent studies with ^{63}Ni (Kossert and Mougeot, 2015) resolved the aforementioned discrepancies when the effects of atomic shielding and the effects of the exchange were taken into account in the calculation of the beta spectrum (Mougeort and Bisch, 2014).

TABLE 7.11 Standardized radionuclides by CIEMAT/NIST and references.

Radionuclides	References
^{14}C	Calhoun et al. (1992) Grau Carles et al. (1991) Los Arcos and Rodriguez Barquero (1996) Rodríguez-Barquero and Los Arcos (1997) Rodríguez-Barquero and Los Arcos (2004a) Mo et al. (2006) Van Wyngaardt and Simpson (2006b) Reddy et al. (2009) Tarancón et al. (2015) Bergeron et al. (2016)
^{18}F	Zimmerman et al. (2001a) Roteta et al. (2006) Schrader et al. (2007) Cessna et al. (2008) Nedjadi et al. (2010) Fitzgerald et al. (2014)
^{22}Na	Nähle et al. (2008)
^{32}P	Cessna (2002) Collé (2001)
^{35}S	Kosklinas et al. (2014)
^{36}Cl	Grau Carles et al. (1994a) Zimmerman and Collé (1997) Tarancón et al. (2015)
^{40}K	Grau Malonda and Grau Carles (2002) Kossert and Gunther (2004)
^{41}Ca	Rodríguez Barquero and Los Arcos (1996) Suárez et al. (2000)
^{44}Sc	García-Toraño et al. (2016)
^{45}Ca	Rodríguez Barquero et al. (1994) Suárez et al. (2000)
^{49}V	Rodríguez Barquero et al. (1998)
^{54}Mn	Rodriguez Barquero et al. (1992) Cassette et al. (2006) Kossert (2006) Kossert and Grau Carles (2006) Kossert and Grau Carles (2010)
^{55}Fe	Günther (1994) Rodríguez Barquero and Los Arcos (1997) Günther (1998) Simpson and Meyer (1998) Ceccatelli and De Felice (1999) Schötzig (2000) Grau Carles and Kossert (2007) Grau Carles et al. (1993a) Grau Malonda et al. (2006) Kossert and Grau Carles (2006) Razdolescu et al. (2008) Kossert and Grau Carles (2010)
^{59}Fe	Kossert and Nähle (2014)

Continued

TABLE 7.11 Standardized radionuclides by CIEMAT/NIST and references.—cont'd

Radionuclides	References
^{60}Co	Rodríguez Barquero and Los Arcos (1997) Roteta et al. (2012) Kulkarni et al. (2016) Kossert et al. (2018))
^{62}Cu	Zimmerman et al. (2016)
^{64}Cu	Capogni et al. (2008) Kossert and Grau Carles (2010) Kossert et al. (2014a)
^{65}Ni	Zimmerman and Collé (1997) Ceccatelli and De Felice (1999) Rodríguez-Barquero and Los Arcos (2004a) Mo et al. (2006) Van Wyngaardt and Simpson (2006b) Collé et al. (2008) Tarancón et al. (2015) Kossert and Mougeot (2015)
^{65}Zn	Günther (1998) Kossert (2006) Kossert et al. (2006b) Kossert and Grau Carles (2006) Kossert and Grau Carles (2010)
^{68}Ga	Roteta et al. (2012)
$^{68}Ge/^{68}Ga$	Schonfeld et al. (1994a) Kulkarni et al. (2017)
^{85}Sr	Grau Carles et al. (1994b) Kossert (2006) Broda et al. (2012)
^{87}Rb	Kossert (2003)
^{88}Y	Kossert and Grau Carles (2010)
^{89}Sr	Grau Carles et al. (1993d) Altzitzoglou et al. (2002) Da Cruz et al. (2002)
^{90}Sr	Grau Carles et al. (1993d) Alvarez and Navarro (1996) Altzitzoglou et al. (1998) Ceccatelli and De Felice (1999) Tarancón et al. (2015) Yeltepe et al. (2018)
^{90}Y	Grau Carles et al. (1993d) Collé (2000) Kossert and Schrader (2004).
^{99}Tc	Calhoun et al. (1992) Lucas (1998) Laureano-Pérez et al. (2010) Van Wyngaardt et al. (2014) Tarancón et al. (2015)
^{109}Cd	Grau Carles et al. (1994b) Kossert et al. (2006a) Kossert and Grau Carles (2010)

Continued

TABLE 7.11 Standardized radionuclides by CIEMAT/NIST and references.—cont'd

Radionuclides	References
^{110m}Ag	García-Toraño et al. (2000)
^{113}Sn	Roteta et al. (2014)
^{113m}Cd	Kossert and Grau Carles (2010) Kossert et al. (2011b)
^{123}I	Kossert and Grau Carles (2010)
^{124}Sb	Chauvenet et al. (2010)
^{125}I	Grau Carles et al. (1994b) Grau Malonda et al. (2006) Kossert (2006)
^{125}Sb	Grau Carles et al. (1998) Kossert and Grau Carles (2006) Kossert and Grau Carles (2010)
^{125m}Te	Grau Carles et al. (1998)
^{129}I	Alzitzoglou and Rozkov (2016)
^{131}I	Günther (1994) Oropesa et al. (2012) Oropesa et al. (2012) Ziemek et al. (2018) Kulkarni et al. (2016)
^{134}Cs	García-Toraño et al. (2002a) Kulkarni et al. (2016) Da Silva et al. (2018b)
^{139}Ce	Kossert and Grau Carles (2010)
^{142}Pr	Yeltepe and Yücel (2018)
^{151}Sm	Alzitzoglou and Rozkov (2016)
^{152}Eu	Johansson et al. (2003b)
^{153}Sm	Dziel et al. (2014)
^{161}Tb	Jiang et al. (2015)
^{166}Ho	Calhoun et al. (1992) Coursey et al. (1994) Cessna et al. (2004) Alzitzoglou and Rozkov (2016) Kossert et al. (2014a)
^{176}Lu	Kossert et al. (2013)
^{177}Lu	Schötzig et al. (2001) Zimmerman et al. (2001b) Kossert et al. (2012)
^{186}Re	Coursey et al. (1994)
^{188}Re	Schonfeld et al. (1994b) Schötzig et al. (2001)
^{204}Tl	Grau Carles et al. (1994a) Simpson and Meyer (1996)

Continued

TABLE 7.11 Standardized radionuclides by CIEMAT/NIST and references.—cont'd

Radionuclides	References
	Rodríguez Barquero and Los Arcos (1997) Hult et al. (2000) Lee et al. (2004a,b)
^{210}pb	Rodríguez Barquero et al. (1996) Laureano-Pérez et al. (2007) Arinc et al. (2011)
^{210}At	Schultz et al. (2006)
^{223}Ra	Cessna and Zimmerman (2015) Keightley et al. (2015) Kossert et al. (2015)
^{227}Ac	Kossert et al. (2015)
^{229}Th	Fitzgerald et al. (2010) Kossert et al. (2014b)
^{237}Np	Günther (2000) Laureano Pérez et al. (2014)
^{234}Th	Navarro et al. (1997)
^{241}Pu	Varga and Tarjan (2008) Kossert et al. (2011a,b) Van Wyngaardt et al. (2012)
^{3}H + ^{14}C	Grau Carles et al. (1991)
^{3}H + ^{55}Fe	Grau Carles et al. (1993b)
^{14}C + ^{35}S	Grau Carles et al. (1993c)
^{36}Cl + ^{204}Tl	Grau Carles et al. (1994a)
^{45}Ca + ^{147}Pm	Grau Carles et al. (1994a)
^{68}Ge/^{68}Ga	Schonfeld et al. (1994a) Kulkarni et al. (2017)
^{90}Sr/^{90}Y + ^{89}Sr	Grau Carles et al. (1993d)
^{188}W / ^{188}Re	Zimmerman et al. (2002)
^{237}Np / ^{233}Pa	Schötzig et al. (2000)
^{32}P + ^{33}P + ^{35}S	Altzitzoglou (2004)
^{90}Sr + ^{90}Y + ^{89}Sr	Grau Malonda et al. (1994)
^{85}Sr + ^{109}Cd + ^{125}I	Grau Carles et al. (1994b)
^{234}Th + ^{234m}Pa + ^{230}Th	Grau Carles et al. (1996)
^{90}Sr/^{90}Y + ^{241}Am	Grau Carles et al. (1993d)
^{90}Sr + ^{90}Y + ^{89}Sr + ^{35}S + ^{45}Ca + ^{204}Tl	Grau Carles et al. (1993e).

TABLE 7.12 Standardized radionuclides by TDCR and references.

Radionuclide	References
^{3}H	Broda and Pochwalski (1992) Simpson and Meyer (1994a) Makepeace et al. (1998) Cassette et al. (2000) Broda et al. (2002) Lee et al. (2004a,b) Arenilllas and Cassette (2006) Jaubert et al. (2006) Cassette and Do (2008) Razdolescu et al. (2006) Stanga et al. (2006) Ivan et al. (2008) Qin et al. (2008) Rodrigues et al. (2008) Steele et al. (2009) Bobin et al. (2010a) Cassette et al. (2010) Johansson and Sephton (2010) Mo et al. (2010) Nähle et al. (2010) Ivan et al. (2010) Nedjadi et al. (2015)
^{14}C	Broda and Pochwalski (1992) Simpson and Meyer (1994a) Cassette et al. (2000) Hwang et al. (2000) Hwang et al. (2004) Lee et al. (2004a,b) Arenilllas and Cassette (2006) Jaubert et al. (2006) Qin et al. (2008) Rodrigues et al. (2008) Nedjadi et al. (2015)
^{32}P	Jaubert and Cassette (2004)
^{33}P	Simpson and Morris (2004b) Kossert (2010)
^{41}Ca	Jórg et al. (2012)
^{45}Ca	Nedjadi et al. (2015)
^{54}Mn	Terliskowska-Droldzicl and Radoszewski (1994) Simpson and Morris (2004a) Bobin and Bouchard (2006) Rodrigues et al. (2008) Bignell et al. (2010)
^{55}Fe	Broda and Pochwalski (1992) Broda and Jecmieniowiski (2004) Ivan et al. (2008) Razdolescu et al. (2008) Rodrigues et al. (2008) Johansson and Sephton (2010) Simpson et al. (2010)
^{59}Fe	Kossert et al. (2014a)

Continued

TABLE 7.12 Standardized radionuclides by TDCR and references.—cont'd

Radionuclide	References
^{60}Co	Rodrigues et al. (2008) Kossert et al. (2018)
^{63}Ni	Broda and Pochwalski (1992) Simpson and Meyer (1994a) Cassette et al. (2000) Razdolescu et al. (2006) Collé et al. (2008) Ivan et al. (2008) Nedjadi et al. (2015) Kossert and Mougeot (2015)
^{64}Cu	Kossert et al. (2014a)
^{65}Zn	Chyliński and Rodoszewski (1996) Simpson and Morris (2004a) Bobin and Bouchard (2006)
^{85}Sr	Broda et al. (2012)
^{89}Sr	Razdolescu et al. (2002) Simpson and Van Wyngaardt (2006) Steele et al. (2009) Kossert et al. (2014c)
^{90}Y	Simpson and Van Wyngaardt (2006) Kossert (2010) Bobin et al. (2010b)
^{99}Tc	Simpson and Meyer (1994a) Zimmerman et al. (2010) Laureano Perez et al. (2010) Van Wyngaardt et al. (2014)
^{106}Rh	Kossert (2010)
^{113m}Cd	Kossert et al. (2011b)
^{123}I	Bignell et al. (2010)
^{129}I	Cassette et al. (1994)
^{139}Ce	Broda et al. (1998)
^{147}Pm	Chyliński and Rodoszewski (1996)
^{153}Sm	Lépy et al. (2006) Dziel et al. (2014)
^{166m}Ho	Kossert et al. (2014a)
^{179}Tm	Kempisty et al. (1990)
^{186}Re	Jaubert (2008)
^{203}Hg	Terliskowska-Droldzicl and Radoszewski (1994)
^{203}Pb	Cassette et al. (2004)
^{204}Tl	Razdolescu and Cassette (2004) Broda et al. (1998) Hwang et al. (2002) Kossert (2010)
^{229}Th	Fitzgerald et al. (2010) Kossert et al. (2014a,b)

Continued

TABLE 7.12 Standardized radionuclides by TDCR and references.—cont'd

Radionuclide	References
^{241}Am	Qin et al. (2008)
^{90}Sr/^{90}Y	Ivan et al. (2008)
^{32}P + ^{25}S	Van Wyngaardt et al. (2008)
^{32}P + ^{33}P	Van Wyngaardt et al. (2008)
^{32}P + ^{33}P + ^{25}S	Van Wyngaardt et al. (2008)
^{68}Ge + ^{68}Ga	Zimmerman and Cessna (2010) Da Silva et al. (2018a,b) Cessna et al. (2018) Van Wyngaardt et al. (2018) Yamada et al. (2018) Oropesa Verdecia et al. (2018)

The agreement between the determinations of activity of ^{241}Pu through CIEMAT-NIST and TDCR was improved by Kossert et al. (2011a) using the experimental determination of the beta spectrum by metallic cryogenic detectors (Loidl et al., 2010). Since then the quality of experimental beta spectra has been improved (Loidl et al., 2014) and improvements have been made in the theoretical calculation of the beta spectrum (Mougeot et al., 2012; Mougeot and Bisch, 2014).

Kossert et al. (2018) have applied the measures $4\pi\beta(LS)-\gamma$ and $4\pi\beta(PC)-\gamma$ to determine the activity of a sample of ^{60}Co. At the same time they tried to obtain the activity of the sample through the CIEMAT-NIST and TDCR methods. The measurements using these two methods depend on the calculation model applied to the beta spectrum and the value adopted from the kB. They observed that corrections for atomic shielding and exchange (Mougeot et al., 2012; Mougeot and Bisch, 2014; Mougeot, 2015; Mougeot, 2016) significantly improve the activities obtained by these methods compared to those of coincidence. Finally, by appropriately varying the value of the kB, they obtain so many per 1000 agreements for the activities measured by the four methods. This result is very important and indisputable as it confirms the application of these corrections of calculation of the beta spectrum to the CIEMAT-NIST and TDCR methods in the extent of the activity of the ^{63}Ni, already advanced by Kossert and Mougeot (2015), and for ^{241}Pu, taking advantage of cryogenic spectrometry (Loidl et al., 2010, 2014).

Given the importance of the results obtained in the work of Kossert et al. (2018). Fig. 7.8 reproduces the relative deviations between the activity concentrations for the ^{60}Co with two liquid scintillation measurement methods compared to the reference value obtained with the $\beta-\gamma$ coincidence methods.

An improved calculation of electron capture transitions has recently been published. Overlap and exchange effects are corrected using Bacall's and Vatai's approaches. Shake-up, shake-off, and inner hole effects are approximately corrected (Mougeot, 2018).

I. Calorimetric detectors

1. Classic calorimetry

Calorimetric methods have been used in radionuclide standardization from the beginning of the last century, after the discovery of radioactivity. Historically it is interesting to note that the radium emission rate of RaE (^{210}Bi) by Ellis and Wooster (1925a, 1925b) led Pauli to postulate the existence of the neutrino. A clear and comprehensive review of the application of calorimetric methods to activity measurements from 1903 to 1958 is available on the Encyclopedic Dictionary of Physics (Mann, 1962). Subsequent reviews were made by Gunn (1964, 1970, 1976) and Mann (1973). Special mention should be made of the Ramthun (1973) review, summarizing the basic types and forms of calorimeter and their application to activity measurement. It is the best source for the metrological aspects of calorimetry applied to radioactivity measurements.

Calorimetric methods have been used for the preparation of standard samples of ^{35}S (Selinger et al., 1958), and beta emitters Collé (2007). An isothermal calorimeter was used by Lowental and Hicks (1966) to standardize sources of alpha and beta emitters. Other developments in the measurement of radioactivity by calorimetric methods have been described by Ramthun (1973). A recent review of modern methods of measurement by classical calorimeters was made by Collé and Zimmerman (2011). This excellent description of the state of classical calorimetry provides details of companies that currently manufacture calorimeters as well as recent results at NIST obtained with calorimeters.

The "radiobalance" designed by Callander (1910) was the first precision calorimeter applied to radionuclide standardization. Mann (1954) developed a version of this isothermal microcalorimeter based on the Peltier effect. This calorimeter was used in the NBS (now NIST) for 40 years for radium comparison (Coursey et al., 2002), as well as primary standardization; ^{63}Ni (Barnes et al., 1971; Collé

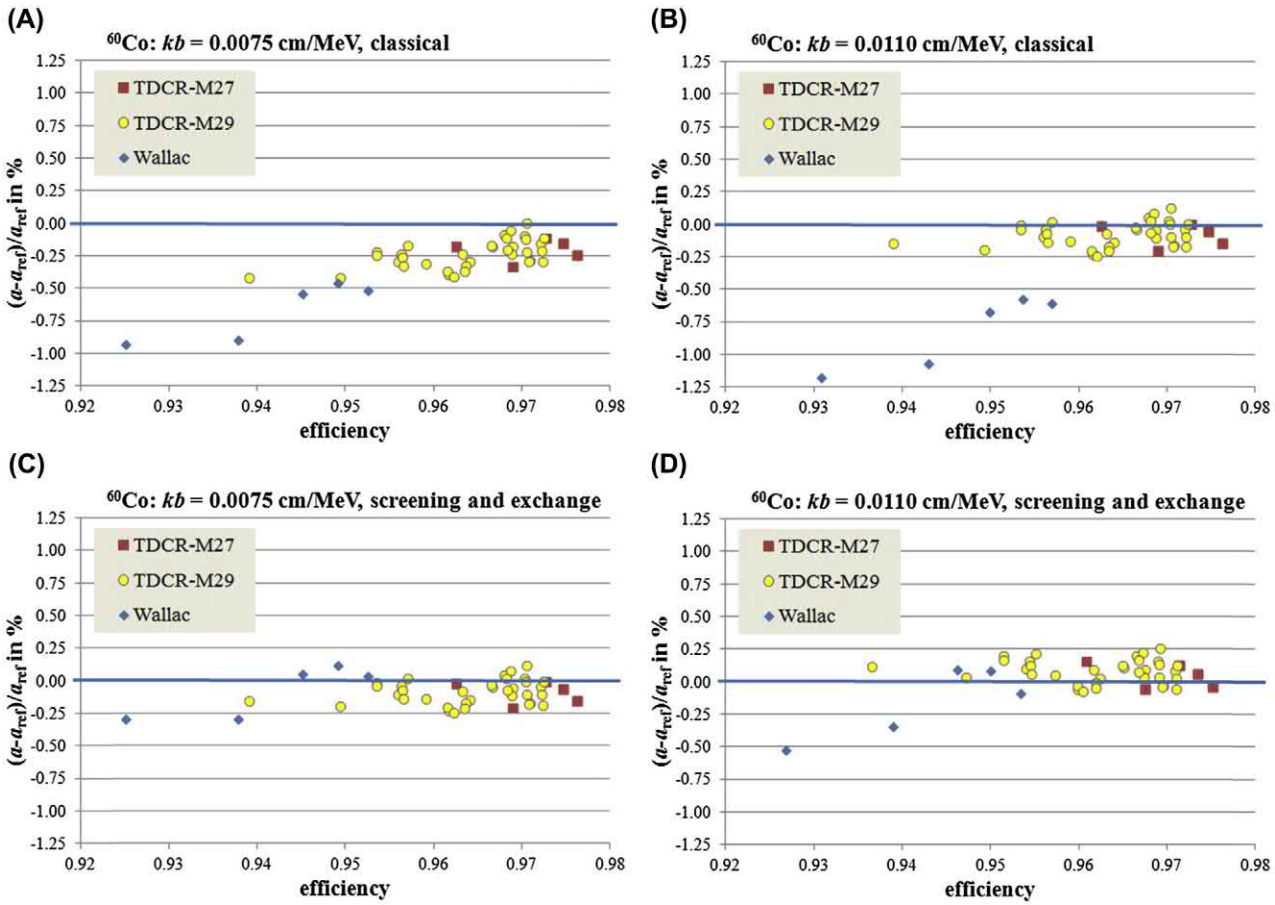


FIGURE 7.8 Relative deviation between the activity concentrations determined from individual ^{60}Co LS samples and a reference value. The reference value (a = 143.571 kBq (G^{-1}) was determined as the weighted mean of the two coincidence counting methods and is represented by the horizontal line at 0. The LS data were analyzed with the following configurations: (A) classical beta spectrum and kB = 0.0075 cm MeV^{-1}, (B) classical beta spectrum and kB = 0.0110 cm MeV^{-1}, (C) beta spectrum taking atomic exchange effect and screening correction into account and kB = 0.0075 cm MeV^{-1}, and (D) beta spectrum as in (C) and kB = 0.0110 cm MeV^{-1}. *From Kossert et al. (2008), reprinted with permission of Elsevier Science © 2008.*

and Zimmerman, 1996). Calorimeters have been used in different applications to obtain nuclear parameters including the following: the measurement of ^{3}H half-life (Jenks et al., 1950), ^{14}C (Jenks and Sweeton, 1952), ^{210}Po (Eichelberger et al., 1954), ^{147}Pm (Wheelwright et al., 1965), and ^{226}Ra (Holden, 1990); the measurement of ^{239}Pu alpha energy (Stout and Jones, 1947), Average energies in the beta decay of ^{3}H (Jenks and Sweeton, 1952; Pillinger et al., 1961), ^{14}C (Jenks and Sweeton, 1952), and ^{147}Pm (Wheelwright et al., 1965); the measurement of the degree of nuclear fuel burned (Krillovich et al., 1976; Hofmann and Wertenbach, 1973); the analysis of tritium in nuclear materials for military use (Meniere and Ganivet, 1972) and fusion technology (Anderson, 1992). Recently, calorimetry has been used to establish standards for brachytherapy in the GBq range (Collé and Zimmerman, 2001, 2011; Collé, 2002; Collé et al., 1999).

Ramthun (1973) clearly described three basic forms of the calorimeter: heat flow, isothermal, and adiabatic. Although the methods described are idealized and most of today's calorimeters incorporate more than one of these basic forms, the classification is very educational. Fig. 7.9 is taken from Ramthun (1973).

The flow of heat between two bodies at different temperatures T_c and T_e is given by the expression:

$$\frac{dQ}{dt} = -k(T_c - T_e) \tag{7.101}$$

In the case of calorimeters, T_c and T_e are the calorimeter and the environment temperatures and k depends on the different shape of surface and environment. In general, this magnitude must remain constant in a calorimeter. In the adiabatic calorimeter, kdQ/dt must be equal to zero. Since no material satisfies this condition, T_c and T_e must be equal.

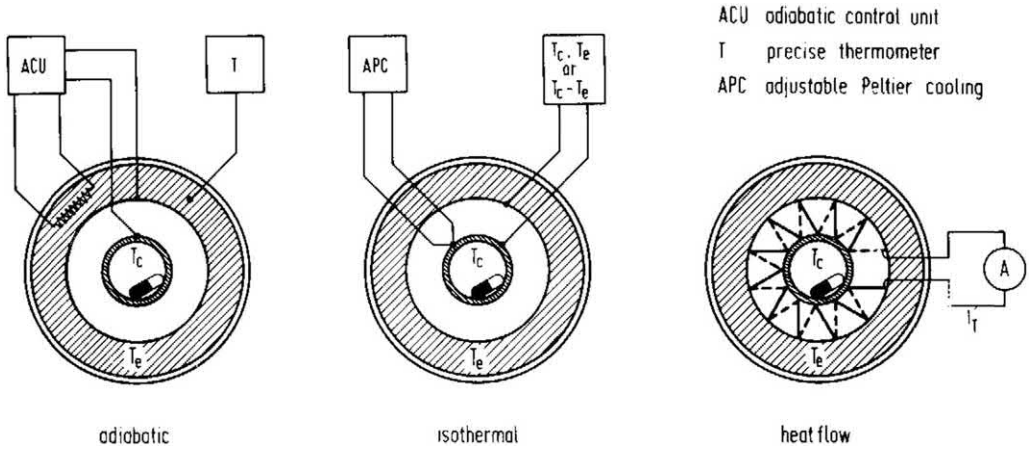


FIGURE 7.9 Principle types of calorimeters. *From Ramthun (1973), reprinted with permission of Elsevier Science © 1973.*

In this case, the calorimeter temperature must rise linearly with time t according to the expression:

$$T_c(t) = T_c(0) + \frac{Pt}{C} \tag{7.102}$$

in which heat power P remains constant. In this expression, C is the heat capacity that must be known to calculate the slope:

$$\frac{dT_c}{dy} = \frac{P}{C} \tag{7.103}$$

The isothermal calorimeter is represented by the Bunsen ice-calorimeter or the Peltier compensation calorimeter. In general, these calorimeters are rather semi-isothermal or near-isothermal. The temperature T_e of the jacked surrounding remains constant. When a heat source is inserted into the calorimeter, the temperature rises to a constant value. The heat source power is obtained from this temperature difference. The constant is determined by calibration with an electrical heater. When the time constant $\tau = k/C$ is so large that it can not reach steady state within a reasonable time, other methods can be applied to determine power P. If it is possible to cool the calorimeter casing before the measurement, when $T_c = T_e$ temperature and time values can be taken, drawing the tangent to the curve and calculated from the slope, knowing the heat capacity C, the thermal power:

$$P = C\left(\frac{dT}{dt}\right)_{T_c=T_e} \tag{7.104}$$

Another possibility is to calculate the slope of the curve at any point by the expression:

$$P = C\left(\frac{dT}{dt}\right) + k(T_c - T_e) \tag{7.105}$$

Another very ingenious process known as radiobalance is due to Mann (1954). It consists of calculating the power from the Peltier current needed to compensate P. A diagram is shown in Fig. 7.10 which shows a schematic device of this radiobalance with which the standards of radium and tritium were measured for years.

Calorimetry possibilities have not been fully implemented by most laboratories. There is a wide field of calibration samples of very high activity in which calorimetry is not replaceable by any other method of measurement. In the future, fusion reactors due to the use of very large quantities of tritium, calorimetry will play a major role in the standardization of intense sources of this radionuclide.

In the field of medical applications, calorimetry has progressed considerably in recent years. In the US, calorimetry has been applied to the determination of absorbed

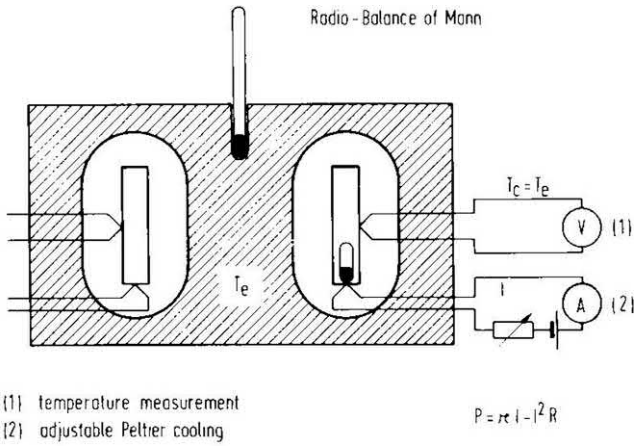


FIGURE 7.10 Schematic diagram of the radio-balance of Mann (NBS). *From Ramthun (1973), reprinted with permission of Elsevier Science © 1973.*

dose in the standard of water for ^{60}Co, which is the basis of calibration of linear accelerators for medical use. Measurements are performed in a water calorimeter developed by Domen (1980) at the National Bureau of Standards (now NIST). The latest medical application is the treatment of prostate cancer using brachytherapy. In the US, it is estimated that approximately 220,000 men are diagnosed with prostate cancer every year. Brachytherapy for prostate cancer involves the implantation of ^{125}I or ^{103}Pd sources for about a year. The sources, in general, are cylinders 4 mm in length and 0.8 mm in diameter, encapsulated in Ti. One of the main keys to the treatment's success is accurate determination of source activity. Stump et al. (2005) described the design, construction, and characterization of a cryogenic calorimeter operating at 8 K specifically designed to allow an absolute standardization of the power deposited by this type of brachytherapy source.

2. Cryogenic calorimeter

A calorimeter or bolometer has three parts: absorber or thermal mass that contains the event or incident power absorbed and thermalized energy, a fully matched thermostat measuring the increase of temperature of the absorbent, and a thermally weak link to a heat sink that measures the absorber's temperature increments and a link that takes absorbent temperature to the established value, in the absence of a signal. The absorber is characterized by its heat capacity C, the thermal link by its conductivity G, and the heat sink by its temperature T_0.

The same configuration can be used to measure stationary input power P, with $\Delta P = P/G$. In this case the device is usually called a bolometer. These detectors have been used for many years to measure infrared radiation and the theory is well developed.

In the last 10 years, cryogenic calorimeters have been considerably developed and have some promising outstanding features: high resolution, nearly 100% efficiency, and a low energy detection threshold. The most recent applications are in alpha spectrometry (Leblanc et al., 2006; Ranitzsch et al., 2011), methods for absolute measurement of activity (Fig. 7.11) (Loidl et al., 2004, 2008), determination of form factors in beta decay (Loidl et al., 2010), determination of atomic and nuclear data of ^{55}Fe (Loidl et al., 2006), and absolute measurement of samples of ^{55}Fe and its spectrum Fig. 7.12 (Loidl et al., 2004; Loidl et al., 2008; Leblanc et al., 1998, 2002).

To date, the calorimeters that have been applied most to radioactive measurements are the Metallic Magnetic Calorimeter (MMC) operating at temperatures below 100 mK (Fleischman et al., 2003, 2004; Enss et al., 2000; Lausberg, 2008). These detectors consist of a gold absorber attached by ultrasonic welding to a magnetic temperature sensor. The sensor is a small piece of metal doped with a small

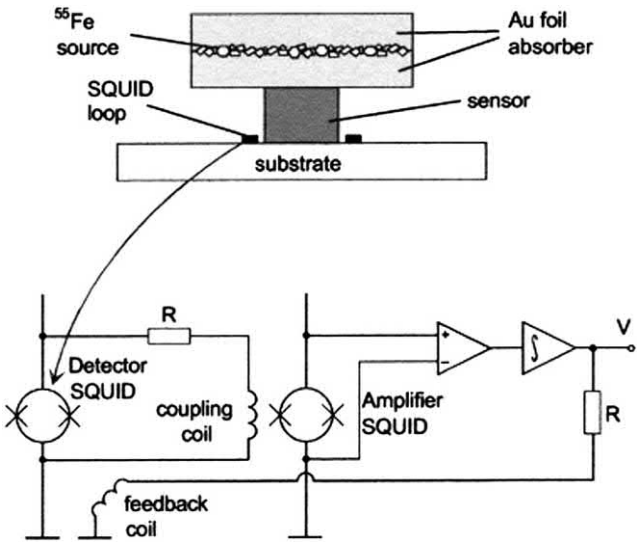


FIGURE 7.11 Schematic cross-sectional view of the detector used in the present work, the magnetic sensor is placed inside the loop of the detector SQUID. The lower part of the figure represents the two-stage SQUID readout system. *From Loid et al. (2004), reprinted with permission from Elsevier Science © 2004.*

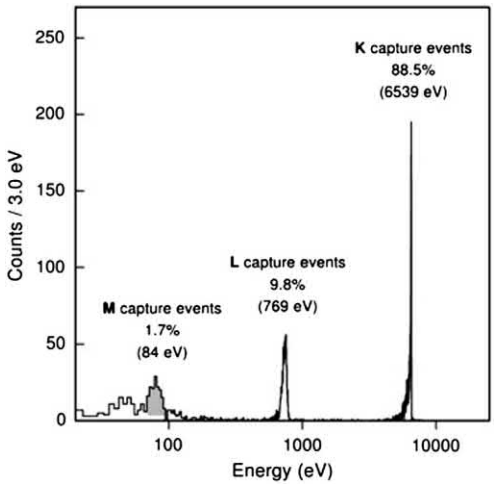


FIGURE 7.12 Spectrum of a ^{55}Fe source enclosed in a 4π geometry inside the absorber of a magnetic microcalorimeter. The quoted probabilities and energies are the values expected from theory. The hatched region corresponds to the experimental intensity of the M line after background subtraction as described in the text. *From Loid et al. (2004), reprinted with permission of Elsevier Science © 2004.*

concentration of paramagnetic ions. The sensor can be a gold disc 50 μm in diameter and a thickness of 25 μm doped with 900 ppm (mass) of Er^{3+}. When the sensor is exposed to a magnetic field, it presents a magnetic moment the magnitude of which varies strongly with temperature.

The energy deposited by a particle or a photon interacts with the absorbing metal and is thermalized. Thermal equilibrium is rapidly established between the absorber and

the sensor due to metal contact. With the Au:Er sensor, energy transfer from the conduction electron to the spins of the Er ions leads to variation in the sensor's magnetic moment. Thermalization time of the electron system and its coupling to the spin system is less than 1 μs for temperatures between 25 and 50 mK. The thermal relaxation time of the detector is several milliseconds, depending on the strength of its coupling to the heat bath.

SQUIDs (Superconducting Quantum Interference Devices) are well adapted for reading magnetic calorimeters. The sensor is placed directly in a loop of a DC-SQUID for optimal coupling of the magnetic flux of the SQUID sensor. The best noise reduction was obtained using a second SQUID as a first stage of amplification to the signal of the SQUID detector.

A SQUID is a device that converts the magnetic flux in tension; made by thin films, which should be well matched to measure small changes in the magnetic moment of the MMC thermometer. After the interaction of each particle, the detector returns to its initial temperature via a connection to a heat bath. Therefore, the detector does not integrate incident power but determines the energy of each particle individually. The pulse shape of the individual signals can be approximated by a first order exponential with a rise time of one to a few microseconds, essentially due to the heat diffusion time within the detector and an exponential decrease, of around 1 millisecond, which corresponds to the detector's return to its equilibrium temperature.

The temperature increase is inversely proportional to the heat capacity of the detector, which decreases with temperature. Therefore, at very low temperatures the amplitude of the signal is relatively large, while the thermal noise is very small. Metallic magnetic calorimeters operate at temperatures below 50 mK, giving a high signal to noise ratio.

IV. Relative methods

A. Calibration methods based on gamma ray spectrometry

The gamma spectrometry technique is often used for the qualitative and quantitative analysis of gamma emitting radionuclides (Helmer et al., 1994; Noguchi et al., 1981, Debertin and Helmer, 1988; Helmer et al., 1994, 1995; Gilmore, 2008). Many radionuclides undergo gamma deexcitation after beta or alpha decay. On the other hand, detector manufacture has improved considerably; first came the scintillation detectors that led to the construction of large volume and highly efficient detectors, and they were followed by the semiconductor detectors that generate high-resolution spectra.

Activity determination of a sample by gamma spectrometry is based on the efficiency curve of the full-energy peak as a function of energy. In practice, this efficiency curve can be obtained experimentally using a calibrated set of samples or a multigamma sample. In the first case, one attempts to use radionuclides with single spectra and half-lives of more than 30 days. The most used are ^{22}Na, ^{54}Mn, ^{60}Co, ^{85}Sr, ^{88}Y, ^{137}Cs, ^{139}Ce, and ^{203}Hg. The most used multigamma samples are ^{152}Eu, ^{226}Ra, and ^{56}Co. In this case, we must know the intensities of different gamma lines with reasonable accuracy (Gehrke et al., 1977; Helmer et al., 2003, 2004) to obtain an accurate calibration curve. The US National Institute for Standards and Technology (NIST) issues a mixture of ^{125}Sb, ^{154}Eu, and ^{155}Eu (Coursey et al., 1982), which covers the energy range from 27 to 1274 keV. The German Physikalisch-Technische Bundesanstalt (PTB) has a sample mixture of eight nuclides: ^{7}Be, ^{54}Mn, ^{57}Co, ^{65}Zn, ^{88}Y, ^{133}Ba, ^{137}Cs, and ^{139}Ce.

1. Description of the general method

Although the efficiency curve initially refers to the efficiency of the full-energy peak or peak efficiency, the total efficiency, defined as the ratio of the number of registered counts on the spectrum and the number of photons emitted by the source in the same unit of time, is also important both for obtaining the peak efficiency curve and for determining the activity of the sample from the efficiency curve.

Total efficiency can be obtained by calculation and experimentally. The photons emitted in a specific element of solid angle $d\Omega$ see a thickness x of the material depending on the angle of emission. The probability of an interaction along a pathway x is $1 - e^{-\mu x}$, where μ is an attenuation coefficient, dependent of the energy. The expression of the total efficiency is:

$$\varepsilon_t = \frac{1}{4\pi}\int (1 - e^{-\mu x}) d\Omega \tag{7.106}$$

Integration is carried out on the solid angle subtended from the source by the detector. Vergors et al. (1958) gave the equation for a cylindrical detector with radius R and height t when the source is a point located on the cylinder axis at a distance d.

$$\varepsilon_t = \frac{1}{2}\int_0^{\theta_1}\left[1 - \exp\left(-\frac{\mu t}{\cos\theta}\right)\right]\sin\theta d\theta$$
$$+\frac{1}{2}\int_{\theta_1}^{\theta_2}\left[1 - \exp\left(-\frac{\mu R}{\sin\theta} + \frac{\mu d}{\cos\theta}\right)\right]\sin\theta d\theta \tag{7.107}$$

where

$$\theta_1 = \tan^{-1}\left[\frac{R}{d+t}\right] \tag{7.108}$$

$$\theta_2 = \tan^{-1}\left[\frac{R}{t}\right]$$

where θ_1 is the maximum angle at which a direct photon can pass through the detector's output base. The angles between θ_1 and θ_2 correspond to photons entering through the detector face and leaving through the lateral surface of the cylinder. The integral has to be calculated by numerical integration. Vergors et al. (1958) also deduced the corresponding expressions for sources in the form of discs centered on the cylinder axis detector.

Germanium coaxial detectors have a nonsensitive radiation core that reduces total efficiency. Griffiths (1971) and Atwater (1972) extended the above equation to take this core into account. However, when the total efficiency correction is applied to the correction of sum events, the above expression does not give satisfactory results.

The way to obtain total efficiency with greater precision is to use an experimental method. In this case, one must take into account the photons scattered by the materials surrounding the detector. Radionuclides that are considered suitable for their monoenergetic nature are: ^{241}Am (59.5 keV), ^{109}Cd (88.0 keV), ^{139}Ce (165.9 keV), ^{51}Cr (320.1 keV), ^{7}Be (477.6 keV), ^{85}Sr (514.0 keV), ^{137}Cs (661.7 keV), and ^{54}Mn (834.8 keV). Total efficiency is given by the expression:

$$\varepsilon_t = \frac{N_t}{A_0 p} \tag{7.109}$$

where N_t is the total count rate of the extrapolated spectrum to 0 keV, A_0 is the activity of the sample, and p is the probability of gamma photon emission. For radionuclides emitting two or more close energy photons, p would be the sum of the individual emission probabilities, assigning total efficiency to a mean energy $\overline{E}$. For example, ^{60}Co emits two gamma photons of energy $E_1 = 1173.24$ keV and $E_3 = 1332.50$ keV; the average energy is $\overline{E} = 1253$ keV. Other interesting mean energies are as follows: ^{55}Fe (6.0 keV), ^{93m}Nb (17 keV), ^{125}I (28 keV), and ^{57}Co (124 keV). Total efficiency for higher energy nuclides is obtained from two nuclides with well-separated energies. Total efficiency $\varepsilon_t(E_1)$ for one energy can be interpolated from other measured values. Then we can subtract the respective number of total counts $A_0 p_1 \varepsilon_1(E_1)$ and obtain:

$$\varepsilon_t(E_2) = \frac{N_t - A_0 p_1 \varepsilon_t(E_1)}{A_0 p_2} \tag{7.110}$$

When the source-detector distance is small, the above expression should be modified to take the reduction of N_t due to coincidence summing into account. This effect is discussed later. In the case of radionuclides with high beta energies, we should correct N_t by the contribution of bremsstrahlung from beta particles.

a. Extended sources

So far we have considered point sources, but sources are more often extended. We assume that the ratio of solid angles Ω_A of an extended source and a point source Ω_p can be approximated, in the first order, by the ratio of total efficiencies

$$\frac{\varepsilon_A(d)}{\varepsilon_P(d)} = \frac{\Omega_A(d)}{\Omega_P(d)} \tag{7.111}$$

We assume that the source is circular and centered on the axis of the cylindrical detector. We use $\Omega_P(r,d)$ to denote the solid angle subtended by the detector to a point in the source at a distance r from its center. We can write $\Omega_P(r,d)$ as an integral over the detector area. This integral must be calculated numerically. Instead of a disc, Gardner and Verghese (1971) used a polygon for which analytical expression can be obtained. Integration on the surface of the source gives:

$$\Omega_A(d) = \frac{2}{R_S^2}\int_0^{R_S} \Omega_P(R,d) r dr \tag{7.112}$$

Gardner and Verghese (1971) calculate this integral using numerical integration by Simpson's method and generating a table based on values of $\Omega_a(d)$ as a function of R_S/d and R_D/d where R_D is the radius of the detector. An approximation for the series is:

$$\Omega_A(d) = \frac{1}{2}\left[1 - \left(1 + \frac{R_D^2}{d^2}\right)^{-1/2} - \frac{3}{8}\frac{R_S^2}{d^4}\left(1 + \frac{R_D^2}{d^2}\right)^{-5/2}\right] \tag{7.113}$$

which converges successfully for $R_S/d < 0.5$. One way to solve the problem experimentally is based on first measuring a centered point source, that is, with $r = 0$, and then measuring the sample for different r values. The curves obtained for different energies can be described by the equation:

$$\varepsilon_P(r,d) = \varepsilon_P(0,d) e^{-c(d) r^2} \tag{7.114}$$

where parameter $c(d)$ depends on the energy and distance (Kushelevski and Alfassi, 1975). We can also write:

$$\varepsilon_P(r,d) = \varepsilon_P(0,d)\frac{d^2}{r^2 + d^2} \tag{7.115}$$

where $d = d_S + d_C + d_e(E)$ is the effective distance from the center of the sample, d_S is the distance from source-to-detector endcap, d_C is the distance from the endcap of the detector to the surface, d_e is the distance to the effective interaction depth, $d_e(E)$ is linked to the linear attenuation coefficient of the material $\mu(E)$ and is expected to be around $1/\mu(E)$. The best option is to consider $d_e(E)$ as a parameter to be determined. Notea (1971, Clisler et al. (1971), Cline (1979), Gunnink and Niday (1972, 1976)

introduced an effective interaction radius $r(E)$ so that the effective distance was

$$d = \left[(d_C + d_S + d_e(E))^2 + r_e^2(E)\right]^{1/2} \tag{7.116}$$

The efficiency of large circular sources, with uniformly distributed activity, is given by the expression:

$$\varepsilon_A(d) = \frac{2}{R_S^2}\int_0^{R_S} \varepsilon_P(r,d) r dr \tag{7.117}$$

which, as a function of $\varepsilon_P(0,d)$, is:

$$\varepsilon_A(d) = \varepsilon_P(0,d)\frac{d^2}{R_S^2}\log\left(1+\frac{R_S^2}{d^2}\right) \tag{7.118}$$

Janssen and Waltz (1987) compared the results obtained with the above equation with experimental values for circular sources with uniformly distributed activity and radii of up to 7 cm. The sources were placed directly on the detector surface with their center in the detector axis. The experimental and calculated results differed by less than 5%.

The correlation in Ge detectors has been studied by McCallum and Coote (1975).

2. Heath method

The Heath (1964) method was a very popular gamma-emitting radionuclide procedure in the 1960s−1970s. Its popularity was due, first, to its easy implementation and management and, secondly, because it enabled the calibration of a wide range of radionuclides. Its use in radionuclide production facilities was widespread. We must remember that the popularity of NaI(Tl) detectors was then at its peak.

This is a method that combines a theoretical calculation of total counting efficiency and an experimental determination of the peak-to-total ratio. The theoretical calculation method can be based on an analytical calculation of numerical integration or a Monte Carlo method. The uncertainties achieved with this method were 3%−5%. At that time the analytical method gave better results than Monte Carlo, but as computer speed grew, the Monte Carlo method became more attractive, because it obtained sufficient accuracy, increasing the number of events, and could be applied to solve more complex problems from a geometric perspective.

The key point for calculations is the computation of solid angles for different geometries. In this regard, there has been considerable activity both in the analytical calculation and in the use of the Monte Carlo method. The most interesting references, using the analytical method for calculating solid angles, are the following: Abbas (2001, 2006), Aguiar et al. (2006), Aguiar (2008), Belluscio et al. (1974), Brysk (1977), Conway (2010), Cook (1980), Galiano and Rodrigues (2006), Gardner and Carnesale (1969), Gardner and Verghese (1971), Gotoh and Yagi (1971), Green et al. (1974), Haitjema (1987), Li and Uren (1997), Obložinsky and Ribanský (1971), Pommé (2004, 2007), Pommé et al. (2003), Prata (2003, 2004), Sibbens et al. (2003), Timus et al. (2007), Tryka (1997), Verghese et al. (1972), Williams et al. (1968), Wu Zhihua and Wei Xinmiao (1992). The most interesting references of the Monte Carlo method for calculating the solid angle in very different situations, are the following: Williams (1966), Cox (1969), Carchon et al. (1975), Wielopolski (1977), Stavroulaki and Kaplanis (1979), Kaplanis (1982), Nicolaou et al. (1986), and Hosseini-Ashrafi and Spyrou (1992).

a. Description of the method

Counting efficiency is obtained from total efficiency, which is in turn obtained from intrinsic efficiency. Thus, we first describe the theoretical calculation of intrinsic efficiency. Intrinsic efficiency is defined as the ratio between the number of counted photons and the emitted photons reaching the detector, namely:

$$\text{Intrinsic efficiency} = \frac{\text{Number of counted photons}}{\text{Number of photons entered in detector}}$$

While total counting efficiency is:

$$\text{Total efficiency} = \frac{\text{Number of counted photons}}{\text{Number of photons emitted by the source}}$$

The analytical expression for calculating the intrinsic efficiency of an isotropic point source located centrally to the d distance of a NaI(Tl) cylindrical detector of length L and radius R is:

$$\varepsilon_{\text{int}} = \frac{1}{(1-\cos\theta_0)}\left\{\int_0^{\theta_1} 1-\exp\left(-\frac{\mu(E)L}{\cos\theta}\right)\sin\theta d\theta + \int_{\theta_1}^{\theta_0}\left[1-\exp\left(-\frac{\mu(E)L}{\sin\theta}-\frac{\mu(E)d}{\cos\theta}\right)\sin\theta d\theta\right]\right\} \tag{7.119}$$

where

$$\tan\theta_0 = \frac{R}{d} \quad \tan\theta_1 = \frac{R}{d+L} \tag{7.120}$$

$\mu(E)$ is the attenuation coefficient of the NaI(Tl) detector to photons with E energy.

Total efficiency is calculated with a similar expression:

$$\varepsilon_{total} = \frac{1}{2}\left\{ \int_0^{\theta_1} 1 - \exp\left(-\frac{\mu(E)L}{\cos\theta}\right)\sin\theta d\theta \right.$$

$$\left. + \int_{\theta_1}^{\theta_0}\left[1 - \exp\left(-\frac{\mu(E)L}{\sin\theta} - \frac{\mu(E)d}{\cos\theta}\right)\sin\theta d\theta\right]\right\} \quad (7.121)$$

Vergos et al. (1958) carried out calculations for 32 detectors of different sizes, for detector-source distance values of 0−100 cm and photon energies from 10 keV to 10 MeV. They calculated absolute detection efficiency, defined as the probability that a photon emitted by the source interacts with the detector with the loss of a finite amount of energy.

The other parameter for a monoenergetic gamma emitter is the peak-to-total ratio, which is obtained experimentally and defined by the expression:

$$P = \frac{N_P}{N_T} = \frac{\varepsilon_P}{\varepsilon_T} \quad (7.122)$$

where N_P is the count rate at the peak, N_T is the total count rate in the total spectrum, ε_P is the photoelectric efficiency or, more correctly, full-energy peak efficiency, and ε_T is the total efficiency of the gamma spectrum. Heath (1964) used the count rates obtained directly from the gamma spectra for a number of radionuclides: ^{47}Sc, ^{139}Ce, ^{51}Cr, ^{7}Be, ^{85}Sr, ^{137}Cs, ^{22}Na, ^{54}Mn, ^{65}Zn, ^{60}Co, ^{29}Al, ^{24}Na, and ^{37}S. The use of gamma spectra enables us to work with nonmonoenegéticos nuclides as long as we are able to separate the spectra from the peaks and their respective Compton continuums. Heath (1964) describes how to perform these operations and obtain the peak area of total absorption with excellent precision.

Another way to obtain the peak-to-total ratio curve, $P(E)$, is by using standardized monoenergetic gamma radionuclides and experimentally obtaining the efficiencies ε_P and ε_T.

Both total efficiency and the peak-to-total ratio are a function of the energy and distance between source and detector. Heath presented curves of the efficiency values for different energies between 25 keV and 4 MeV and distances between 0 and 50 cm. The peak-to-total ratio curve varies very little with the distance between source and detector. The curves for distances of 3 and 10 cm coincide at low energy ($E_\gamma < 350$ keV) and high energy ($E_\gamma >$ 1300keV) and the greatest divergence of both curves (discrepancy) is 2% for 835 keV, less than the method's uncertainty.

b. Precautions

Application of Heath's method is very simple. The critical point is to know the source-detector distance. This requires placing the sample into a sample holder with well-defined distance from the detector and also to know the distance from the NaI(Tl) crystal to the outside of the capsule in which it is contained. This distance is obtained by making detector gammagraphy. The distance usually varies from 3 to 10 mm.

Another important point is how to obtain the area of the full-energy peaks. Heath (1964) developed several programs to accurately calculate the area of these peaks.

3. Semi-empirical methods

Semi-empirical methods using analytical expressions and numerical integration to calculate full-energy peak counting efficiencies were very popular at the onset of gamma models. They enabled rapid calculation of total efficiency, while Monte Carlo methods require more computational time and less accuracy. However, when computer speed and storage capacity increased, the Monte Carlo method prevailed.

In the case of point sources, we must mention the work of Abbas (2001, 2006), and Peterman et al. (1972), which follow analytic equations for calculating full-energy peak efficiency for both NaI(Tl) and HPGe detectors. They determine photon attenuation by calculating the attenuation along the path of the photon in the source. They compared experimental results with those calculated by this method and concluded that discrepancies are less than 2.5%.

The real advance in the application of this and the Monte Carlo method was the work of Moens et al. (1981), by introducing the efficiency transfer factor. It is interesting, so we summarize the arguments. To obtain a full-energy peak count, a gamma photon emitted by the source must meet the following three conditions:

1. It must interact with the active area of the detector without undergoing energy degradation in the source or adjacent materials.
2. It must not interact with the detector material in any way other than coherent scattering.
3. The interacting photon should deposit all its energy in the detector material, giving rise to one full-energy peak count.

The direct calculation of full-energy peak efficiency requires very complex calculations. However, total efficiency is easy to calculate. If $\overline{\Omega}$ is the effective solid angle for which conditions (1) and (2) are met, total efficiency is

$$\varepsilon_t = \frac{\overline{\Omega}}{4\pi} \tag{7.123}$$

where ε_t is the total efficiency related to ε_P, the efficiency of the full-energy peak, which consists of different contributions:

$$\varepsilon_P = \alpha_P^f + \alpha_P^c + \alpha_P^P \tag{7.124}$$

where ε_P^f, ε_P^c, ε_P^P are the fractions of ε_P for the photoelectric effect, multiple Compton interactions, and pair production, respectively.

Similarly, we define an effective solid angle for each of the above quantities $\overline{\Omega}_f$, $\overline{\Omega}_c$, $\overline{\Omega}_P$, describing the probability that the emitted gamma photon interacts by the photoelectric effect, Compton interaction or pair production, respectively. Thus we can write:

$$\varepsilon_P = \frac{1}{4\pi}\left(\overline{\Omega}_f + \overline{\Omega}_c\kappa + \overline{\Omega}_P\nu\right) \tag{7.125}$$

where κ and ν take into account the fact that only a fraction of the Compton and pair interactions leads to one full-energy peak count.

It can be shown that:

$$\frac{\overline{\Omega}}{\mu_t} = \frac{\overline{\Omega}_f}{\mu_f} = \frac{\overline{\Omega}_c}{\mu_c} = \frac{\overline{\Omega}_P}{\mu_P} \tag{7.126}$$

where μ_t is the linear coefficient of total absorption of the detector material for energy E_γ; μ_f, μ_c, μ_P are the absorption coefficients for photoelectric effect, Compton interaction, and pair production, respectively. So we have:

$$\varepsilon_P = \frac{1}{4\pi}\left(\frac{\mu_f + \mu_c\kappa + \mu_P\nu}{\mu_f}\right)\overline{\Omega} = \frac{1}{4\pi}\frac{P}{T}\overline{\Omega} = \frac{P}{T}\varepsilon_t \tag{7.127}$$

where P/T is the virtual peak-to-total ratio for the bare detector, without any interaction with the surrounding material.

When we know ε_t, we have to calculate the P/T ratio. The values of κ and ν are unknown and can only be approximated using the Monte Carlo method. The P/T ratio cannot be obtained experimentally. The usual peak-to-total ratio used in the Heath method does not apply here. The total area of the gamma spectrum contributes, with degraded energy, the gamma rays that have experienced incoherent scattering in the materials surrounding the detector. The experimental peak-to-total ratio is therefore dependent on the sample and the counting efficiency. It is assumed that the "virtual" P/T ratio is independent of the sample, the geometry and the counting rate. It is therefore an intrinsic characteristic of the detector used.

The semi-empirical determination of the curve ε_P for a sample and a given geometry is obtained as follows:

1. Determination of the experimental curve ε_P in terms of E_γ for point sources positioned for long distance (denoted as the subindex *ref*) from the detector;
2. Calculation of $\overline{\Omega}$ for a reference experimental setup and also for a given detector-source distance. In this way, we can construct a curve ε_P as a function of E_γ.
3. The efficiency of one of the configurations considered (x) and for one energy is calculated by the equation:

$$\varepsilon_{P,x} = \varepsilon_{P,ref}\frac{\overline{\Omega}_x}{\overline{\Omega}_{ref}} \tag{7.128}$$

The only hypothesis applied is the constancy of the virtual peak-to-total ratio. Experimental results have shown that this assumption is justified. This principle has been successfully used by Moens et al. (1981), Moens and Hoste (1983), Mihaljević et al. (1993), Wang et al. (1993), Wang et al. (1995), Wang et al. (1997), Piton et al. (2000), Vidmar (2005).

Knowledge of the total efficiency and the peak-to-total ratio is not sufficient, in the case of extended sources, to calculate the correction factors due to coincidence summing. If the sample is viewed as a collection of point sources embedded in the matrix, the variation in the efficiency of these sources in the volume of the source must also be considered, as noted by Debertin and Schötzig (1979) and Korun and Martincic (1995). In other words, correction factors cannot be calculated as if the sample were a point source.

Blaauw and Gelsema (2003) and Gelsema (2001) developed a method to solve the problem. They introduced the concept of "LS curve": (linear-to-square curve) or "third curve" in gamma spectrometry. Blaauw and Gelsema (2003) obtained the LS curve experimentally using standardized sources. Subsequently, Vidmar and Korum (2006) and Vidmar et al. (2011) used a direct calculation method to obtain the LS curve.

4. Monte Carlo technique

The application of the Monte Carlo technique to calculate the full-energy peak efficiency applied to gamma ray detectors and X-ray has a long history. The first studies were by Wainio and Knoll (1966) and De Castro Faria and Levesque (1967), who applied the Monte Carlo technique to germanium and silicon detectors. Other computation codes were developed, to be applied to coaxial detectors, by Aubin et al. (1969), Lal and Iyengar (1970), Gaggero (1971), Grosswendt and Waibel (1975). The new generation of calculation codes added attenuation at the source and more complex geometries as well as detectors. Examples of these codes are: Nakamura and Suzuki (1975), Birattari and Salomone (1980), Rieppo (1981), Nakamura and Suzuki (1983), Cesana and Terranian (1989), Sima (1990), Herold and Kouzes (1991), Laborie et al. (2000), Sima and Arnold (1996). Comparison of experimental and computed calibrations gave discrepancies of 5%−10%.

In these preliminary calculations, there are four sources of uncertainty. There was a statistical limitation due to the

large number of photons that are needed and the relatively slow calculation capacity of computers at that time. A second limitation was the knowledge of the interaction probability of electrons and photons and angular distribution. Thirdly, the information about the physical dimensions of the detector and its position was inadequate. Finally, the fourth limitation was that charge collection was not uniform throughout the detector volume due to imperfections in the crystal and nonuniform electric field. Given these limitations, an accuracy of 5%−10% for the results of the Monte Carlo method was very reasonable.

Some investigators developed the Monte Carlo method and applied it to several detectors to compare and generalize the results: Liye et al. (2006), Keyser (2004).

There are two ways to use the Monte Carlo method for the calculation of efficiencies. The first is simply to scale the Monte Carlo results to minimize the differences between calculated and measured efficiencies. The Monte Carlo method thus becomes an effective method of interpolation for a limited range of energies. The second method is to use the initial Monte Carlo results to adjust the physical parameters of the detector, producing a better agreement with the efficiency measurements and thus enabling more accurate interpolation for a wider range of energies. Examples of this second procedure were found in the following: Ashrafi et al. (1999), Vidmar and Likar (2002). Using the GEANT 3.21 program (Brun et al., 1987) with the values of the constructor for the radius of the crystal, dead layer thickness, central hole radius, distance between the crystal and the detector housing, they minimize the weighted sum of the squares of the differences in measured and calculated efficiencies. Hardy et al. (2002), Helmer et al. (2003), Huy et al. (2007), Lyie et al. (2006), Boson et al. (2008), Budja et al. (2009) fit two parameters: front-dead-layer value and dead-layer thickness.

There are also methods that combine semi-empirical calculations with Monte Carlo simulation: Gunnink and Nidal (1976), Gunnink (1990), Sima (1996), Jehouani et al. (2000), and Agrafiotis et al. (2011). They combine the semi-empirical method to derive the effective volume of a given energy before using the Monte Carlo simulation to calculate geometric correction factors for the transfer. The method used by Bernasconi and Capote (1994) is based on the use of a Monte Carlo simulation to quantify the difference between two geometries and determine how these differences influence absolute efficiency (Abbas, 2001, 2006).

There have been many studies aimed at improving and optimizing the data provided by manufacturers of semiconductor detectors: Birattary and Salomone (1980), Mohanty et al. (2008), Luis et al. (2010), Padilla Cabal et al. (2010). Hernandez and El-Daoushy (2003) also considered the case of incomplete charge collection.

New procedures to obtain detection efficiency with good accuracy for point samples have been developed: Ludington and Helmer (2000), Ewa et al. (2001), Hardy et al. (2002), Helmer et al. (2004), Dryak and Kovar (2006), Peyres and García-Toraño (2007), and Vidmar and Kanicsh (2010).

For years, attempts have been made to introduce the decay scheme to calculate the contributions of individual gamma photons and also correct for coincidence summing: Debertin and Schötzig (1979), Morel et al. (1983), Schima and Hopes (1983), Decombaz et al. (1992), Blaauw (1993) Laedermann and Décombaz (2000), Berlizov and Tryshyn (2005), Nedjadi et al. (2007), Novcovic et al. (2007b), Sima and Arnold (2008), Vidmar and Kanisch (2010, 2012). An interesting package to be included in such codes is NUCLËIDE by Bé et al. (2004). This package is already included in the ETNA code, Lepy et al. (2006).

In the case of low activity samples that require a high sample volume and the best counting efficiency, some computer codes have been developed for measuring Marinelli containers: Lippert (1983), Debertin and Jianping (1989), Rodenas et al. (2000, 2003, 2007), Jurado Vargas et al. (2002), and Blaauw and Gelsema (2003).

Calculation codes can be classified into two types (Vidmar et al., 2010a): general and specialized. Among the specialized, the most used are: ANGLE (Jovanovic et al., 1997, 2010); DETEFF 4.2 (Cornejo and Jurado Vargas 2008); EFFTRAN (Vidmar 2005); ETNA (Piton et al., 2000; Lepy et al., 2006; Radu et al., 2009); GAMEFF (Bernaconi and Capote, 1994); GESPECOR 4.2 (Sima and Arnold, 2002; Arnold and Sima, 2004a, 2004b); MAR (Bertolo et al., 1992); EGSnrc (Kawrakow and Rogers, 2006); ESOL (Wang et al., 1993, 1995); TRUECOINC (Sudár, 2002); and SWELL (Wang et al., 1999). The most used general codes are: EGS4 (Nelson et al., 1985a); GEANT (Brun et al., 1987); GEANT-4 (Agostinelli et al., 2003; Hurtado et al., 2004, Nemes et al. (2016)); MCNP (Briesmeister, 2000; X-5 Monte Carlo Team, 2003, Marques Salgado et al., 2006; Mowlavi et al., 2005; McKinney et al., 2006; and Huy, 2010, 2011), PENELOPE (Salvat et al., 2003, 2006; 2008; Jurado Vargas and Guerra; 2006; Karfopoulos and Anagnostakis, 2010); EXTSANGLE (Mihaljević et al., 1993); and TRIPOLI-4 (Both et al., 2003).

International comparisons are made of different calculation codes. Lépy et al. (2001), in EUROMET Project 428, examined the results of the transfer of efficiencies for a Ge detector when efficiencies for point sources are known. The main conclusion is that the discrepancies between calculated and experimental results can reach 10%, although some discrepancies are of the order of 2−3%. Moreover, it was concluded that data on the geometry of the detector supplied by manufacturers are insufficient for accurate efficiency estimates. A comparison organized by the IAEA to review the codes applied in the measurement of low activities has also been carried out (Los Arcos et al., 2005).

Vidmar et al. (2008) made a comparison exercise of Monte Carlo codes, used in gamma spectrometry, to calculate full-energy peak and total efficiency. They compare the results of GEANT3 codes (Brun et al., 1987), GEANT4 (Agostinelli et al., 2003), PENELOPE (Salvat et al., 2003, 2006, 2008), MCNPX (McKinney et al., 2006), GESPECOR (Sima et al., 2001), EGS4 (Nelson et al., 1985a, b; Kawrakow and Rogers, 2006), TRIPOLI-4 (Both et al., 2003), that revealed striking differences between the results of the different codes. Vidmar et al. (2010a) compared four Monte Carlo codes (GEANT3, PENELOPE, MCNP, and EGS4) and five packages devoted to determining gamma spectrometry efficiency (ANGLE, DETEFF, GESPECOR, ETNA, and EFFTRAN). They calculated the factors for transfer of efficiencies (TE) for well-defined parameters of the detector and the energies typically found in environmental measures. The discrepancies between the results of different codes are below 2%.

Kanisch et al. (2009) compared five procedures for correcting for coincidence summing Andreev et al. (1972), Semkow et al. (1990), Novkovic et al. (2007a, 2007b). Vidmar et al. (2011), presented the EFFTRAN efficiency-transfer code.

Several papers have been published related to volume and environmental samples taking into account matrix effects: De Bruin et al. (1979), Sima (1996), Sima and Dovlet (1997), Vidmar et al. (2010b).

Finally, the same program based on the Monte Carlo method was applied to the analysis of several detectors with different characteristics. Lyie et al. (2006) applied the Monte Carlo method to three HPGe detectors: a coaxial n-type, a p-type coaxial, and four BEGe detectors. The deviations obtained in all cases were below 5%.

B. Measurement of high activity. Ionization chambers

Ionization chambers have been used for the measurement of radioactivity for over a century, and many of the basic studies are more than 50 years old. Ionization chambers can work in pulse or current modes. Here we consider the measures of radioactivity emitting gamma or X-ray by current ionization chambers.

The most extensive, modern, well-documented, and extremely clear summary of this type of ionization chambers, with a complete list of references up to 1997, is the monograph by Schrader (1997). Details of the construction techniques for measuring ion beam current, linearity and saturation, and the current correction are not considered in this section. We recommend this monograph and Chapter 2, Volume 1 of this book. We analyze the measurement techniques and the latest applications. The type of chamber we consider here is known as a reentrant cylindrical chamber, usually working under pressure.

The main features of these chambers are: high efficiency for gamma radiation, stability over time, sensitivity over a wide range of gamma activities, and linearity of response.

Once calibrated, the ionization chamber is used to maintain the unity of activity. This is particularly important for radionuclides with short half-lives, since the chamber can be recalibrated at intervals that are much longer than the specimen's half-life and maintain the value of an activity standard beyond its half-life. For example, the radionuclides used in PET are calibrated using an ionization chamber.

Activity concentration of a standard radioactive solution of a particular radionuclide is deduced from the activities of several sources prepared from the same stock solution and standardized primarily by primary procedures. This radioactive solution is called "standard reference material", since the activity concentration (Bq/g) is known and chemical parameters should remain constant. From this standard solution, we can obtain other standards with the same concentration or we can make dilutions. These liquid samples are stored as aqueous solutions in glass ampoules closed to the flame. The measure of a number of ampoules with the ionization chamber also enables control of the weighing procedures.

Some precautions must be taken into account to achieve the maximum accuracy level of the ionization chamber. Sample chamber geometry must be kept constant to compare the results of the measurements. Solutions without radioactive impurities or with very small, known amounts have to be used. Usually the impurities in the solution must be detected and measured by highly selective measurement systems, for example, Ge detectors. Once we know the rates and the respective calibration factors, a factor to obtain the result in terms of activity has to be applied to the ionization chamber reading.

Chamber and measuring system stability is verified by repeated measurements of a reference source with a long half-life, usually ^{226}Ra in equilibrium with its descendants. The measurements of the sample, background, and reference source are carried out alternately in a cycle that checks the stability of the system and the reproducibility of the measurement conditions. Taking into account the radioactive decay of radionuclides, the ratio of the currents in a given reference time should remain constant for all measurements. Ionization chambers are relatively simple to operate and the checks required are cheap and give results with good reproducibility and accuracy. Ionization chambers with direct activity readings, called radionuclide calibrators, are the instruments most suitable for testing radiopharmaceuticals.

It is helpful to give some definitions and discuss some simple relations, provided that the measurement conditions remain stable during the measurements. The ionization current I of the chamber, from a source with a single radionuclide N is proportional to its activity A:

$$I = \varepsilon_N A \tag{7.129}$$

The factor of proportionality is called the efficiency ε_N of the radionuclide. In the above equation, the measured current I_m should be corrected by the background current I_b, determined in identical conditions as the sample. Therefore, $I = I_m - I_b$. With many current measurement instruments, we can adjust the reading of the instrument R by an internal (or external) instrument setting. This is done by an amplifier instrument. This property can be described by an instrument constant g in the equation above:

$$R = gI = g\varepsilon_N A \tag{7.130}$$

An instrument can be set to show activity, reading $R_N = A$, for a defined radionuclide N, directly in units of Bq or its multiples (kBq, MBq). The adjustment condition requires $g_N\varepsilon_N = 1$ and, therefore:

$$A = R_N = \left(\frac{1}{\varepsilon_N}\right) I \tag{7.131}$$

This technique is usually applied to instruments such as calibrators for the quantitative testing of radiopharmaceuticals. Golas (1998) and Oropesa et al. (2002) measured ^{131}I, ^{201}Tl and ^{99m}Tc. Kossert and Thieme (2007) measured ^{99m}Tc. Sahagia et al. (2002) measured ^{186}Re and ^{188}Re. Tauhata et al. (2008) and Yuan et al. (2006) measured ^{188}Re. Yuan et al. (2008) measured ^{67}Ga. Dos Santos et al. (2004, 2006) implemented a national metrology network of radionuclides used in nuclear medicine. Other authors present the improvements in the calibration of calibrators for nuclear medicine: Paton Walsh et al. (1996) and Oropesa et al. (2008) apply it to brachytherapy sources, Cessna et al. (2008) in the case of ^{18}F in plastic syringe. Colle (2000) assayed intravascular brachytherapy sources. Szörényi et al. (1998) monitored the radionuclides used in nuclear medicine. Colle (2001) calibrated ^{32}P "hot-wall" angioplasty-balloon-catheter sources. Collé et al. (1999) and Collé (2000, 2001, 2002) calibrated radionuclides for brachytherapy. Schrader et al. (2007, 2008) calibrated a radionuclide calibrator. Kumar et al. (2010) calibrated brachytherapy sources. Olšovcová (2010) simulated the activity measurement of ^{131}I, ^{111}In and ^{153}Sm in a calibrator. Razdolescu et al. (2002) and Oropesa et al. (2003) measured ^{60}Co and ^{188}Re. Santos et al. (2009) measured syringes. Schultz et al. (2006) measured nuclear pharmacy and clinics in the US. These instruments have an ionization chamber coupled to a current meter with fixed instrument settings adjusted for each radionuclide that can be measured in the chamber. The settings have been established by measuring activity standards or transferred by the manufacturer from calibrated reference instruments. The most important works on this topic are Zimmerman and Cessna (1999, 2000), Zimmerman et al. (2001a, 2004), and Yuan et al. (2008). Lee et al. (2012) calibrate a KRISS reference ionization chamber for key comparison of ^{99m}Tc measurements.

1. Calibration of ionization chamber radionuclides

Ionization chambers are often used in relative procedures for comparison with activity standards. In many applications it is useful to compare currents:

$$\frac{I_i}{I} = \frac{\varepsilon_{Ni} A_i}{\varepsilon_N A} \tag{7.132}$$

where i is the index that specifies a particular sample. The comparison is made between samples with the same geometry. When we measure under appropriate conditions, the efficiency ratio is equal to one and, therefore, the unknown activity is derived from the activity standard.

In general, the basic equations for the indirect calibration of the ionization chamber for a radionuclide N against a reference source (index r) are:

$$\frac{R}{R_r} = \frac{\varepsilon_N}{\varepsilon_r}\frac{A}{A_r} \tag{7.133}$$

where R and R_r are the instrument readings on the source to be measured and the reference source, respectively, while A and A_r are the respective activity values. The radionuclide activity to be standardized is given by:

$$A = \frac{\varepsilon_r}{\varepsilon_n} A_r \frac{R}{R_r} = \left[\frac{\varepsilon_r}{\varepsilon_n} A_{r0}\right] \exp[-\lambda_r (t_m - t_{r0})] \frac{R}{R_r} = A_e \frac{R}{R_{r0}} \tag{7.134}$$

in which the "equivalent activity" is given by:

$$A_e = \frac{\varepsilon_r A_{r0}}{\varepsilon_N} \tag{7.135}$$

and

$$R_r = R_{r0} \exp[-\lambda_r (t_m - t_{r0})] \tag{7.136}$$

in these expressions, A_{r0} is the source activity reference at time t_{r0}.

The expressions given here refer to samples of pure radionuclides. When the sample contains impurities in small quantities, a different treatment is required. If we denote with the subscript N the components of the main radionuclide and the impurities by subscript k, the response of the ionization chamber is:

$$R = \varepsilon_N A_N + \sum_k \varepsilon_k A_k = \varepsilon_N A_N \left(1 + \sum_k \varepsilon_k A_k / \varepsilon_N A_N\right) \tag{7.137}$$

Activity values A_l $(i = N, k)$ must be corrected by decay each time that we measure R. To calculate A_N from R one must know the values of A_k or A_k/A_N and the respective efficiencies ε_i $(i = N, k)$. The efficiencies ε_i are determined by direct calibration with a standard sample or by calculation by means of the efficiency versus energy curve of the chamber.

The detection of impurities in the sample is usually performed by Ge detectors which identify the impurity and determine its activity. The efficiency of an ionization chamber for a specific radionuclide is given by the sum of the contributions of gamma components:

$$\varepsilon_N = \sum_i p_i(E_i)\varepsilon_i(E_i) \tag{7.138}$$

where $p_i(E_i)$ is the probability of photon emission with energy E_i per decay and $\varepsilon_i(E_i)$ is the efficiency of the ionization chamber for gamma photons with energy E_i.

Simulating the response of the chamber, using the Monte Carlo technique, as a function of energy is of great interest. The code EGS4 (Electron Gamma Shower) (Nelson et al., 1985a, b) was the first step to obtain the calibration curve of an ionization chamber. Suzuki et al. (1998) studied the response of three types of ionization chambers filled with argon or nitrogen. They found an excellent agreement between calculated and experimental results. They also applied the calculation code to evaluate the corrections required in changing the source conditions such as displacement of the position of the source. Gostely and Laedermann (2000) applied the GEANT code (Agostinelli et al., 2003) to obtain the chamber's response in the 40 keV to 2 MeV energy range; the calculations were compared with experimental results in terms of equivalent activity. The chamber used experimentally was of the well type at high pressure IG11 from the twentieth Century, similar to the BIPM SIR. The radionuclides measured were: ^{125}I, ^{133}Ba, ^{109}Cd, ^{57}Co, ^{99m}Tc, ^{123}I, ^{131}I, ^{51}Cr, ^{137}Cs, ^{22}Na, ^{60}Co, and ^{88}Y. Agreement between the experimental and calculated values was excellent. Olsovcová and Havelka (2006) applied the Monte Carlo method to obtain the activity of radiopharmaceuticals. The ionization chamber was a calibrator or activity meter, a well-type chamber at high argon pressure, called a Bqmeter; and they found a good agreement between experimental and calculated values for the chamber's response function for vertical or horizontal displacement of the source. In normal ampoule applications, uncertainties in the activity values obtained were very small. In the case of measures of syringes (two) and needles (four), the results were also excellent.

2. Applications of ionization chambers

a. SIR reference system

The most important application of ionization chambers is the SIR reference system (Système International de Référence), designed to complement and extend the measures of international comparisons organized by the BIPM. The SIR system consists of two reentrant ionization chambers with current meters and data storage. The two chambers are identical [Twentieth Century, IG/N20 (Rytz, 1983a,b)] filled with nitrogen at a pressure of 2 MPa, shielded with 5 cm thick lead bricks. The background current and leakage of the system is about 33 fA. The current of the samples is measured relative to the reference sample of ^{226}Ra. Five sources of this radionuclide containing about 0.003−0.3 mg were chosen, in order to have a wide range of measurement. The sources were carefully compared and the ratios are known to be approximately 2×10^{-4}. To verify that the sources are close to equilibrium, two additional sources containing old radium are used. Since the date of purchase, 1983, they have been measured monthly to check the equilibrium of the radium and its descendants. The reproducibility and repeatability of the two chamber systems are compared with reference sources; and the data show that current ratios are stable. Sample-detector geometry tests have also been carried out. The impact of the thickness of the vials containing the samples to be measured in terms of energy has also been studied. There is evidence that the uncertainty of 1.35 MeV of ^{60}Co was 0.05% and for 60 keV of ^{241}Am was 0.1%, for uncertainties of (1σ).

It is possible to estimate the correction factors of the chambers with standardized solutions of monoenergetic gamma emitters. The K_R factor of the chamber, for the source of ^{226}Ra, for a gamma emitter of energy E and gamma emission probability for decay P_γ is given by:

$$K_R = P_\gamma A \frac{R_R}{R} \tag{7.139}$$

where R is the ionization chamber reading for the monoenergetic sample, R_R is the reading for the source of ^{226}Ra and A the activity of the sample.

If one has a curve fitted to $1/K_R$ as a function of energy E, it is possible to calculate the effective factor for a radionuclide emitting n photons of different energy and probability per decay. The activity of the radionuclide is given by:

$$A = \frac{R}{R_R} \sum_{i=2}^{n} \left(\frac{K_R}{P_\gamma}\right) \tag{7.140}$$

where the sum is carried out for all the i photons. K_R values for each of the gamma photons are obtained from the calibration curve $1/K_R$ as a function of E.

In the case of SIR measurements, equivalent activity A_e (Rytz, 1983b) is given by the equation:

$$A_e = A_s F_i \left[R + \frac{(R-1)f}{I_S - f}\right] \exp[-\lambda_S(t_m - t_S) \times]\exp[\lambda_{Ra}(t_m - t_0)] \quad (7.141)$$

This activity is related to the current produced by the stronger reference source (number 5) (0.308 mg Ra element). In this equation, the meaning of different magnitudes is: A_S is the activity of the source of the laboratories participating in the established reference time t_S, F_i is the reference source ratio related to the 0.308 mg Ra source, $R = I_{Ra}/I_S$ is the ratio of the ionization currents of the reference source and the source from the participant laboratory, f is the background and leakage current, λ_{Ra} and λ_S are the decay constants of ^{226}Ra ($T_{1/2} = 1600 \pm 7$ y) and the submitted radionuclide, and t_m is the time of measurement (midrun) at BIPM, t_0 is the reference time for the reference sources (1976-01-01).

The measurements were carried out in cycles consisting of a background run, 10 readings with the reference source, 10 with the sample to be measured, and again 10 with the reference source. The A_e determination was performed by a computer program taking into account the parameters measured, the corrections for decay, and the corrections for impurities. The final result A_e, expressed in Bq, with its components of uncertainty and sample parameters were tabulated. The lower limits of activity and levels of impurities acceptable to the SIR are presented in a report by Rytz (1983a).

The response curve of the chamber is steady and growing from 200 keV to 2 MeV. Below 200 keV, the curve presents a maximum close to 60 keV and falls then to energies close to 15 keV. Because there are no accurate calibration points in the entire interval from 1333 to 1836 keV, the shape of the curve can only be described by mathematical expressions deduced from fitting procedures. A suitable procedure was proposed by Dryak and Dvorak (1986). Michotte (2002) obtained the efficiency curve with extraordinarily low uncertainty, less than 1%.

b. Measurement of half-lives

Ionization chambers are characterized by excellent stability and reproducibility of measures which have been widely used to measure the half-lives of these nuclides: ^{159}Yb, Delgado et al. (2001); ^{198}Au, Chen et al. (2011); ^{18}F, García-Toraño et al. (2010); ^{106}Cd, Kossert et al. (2006a); ^{99m}Tc, Kossert and Thieme (2007); ^{65}Zn, Luca et al. (2003) and Kossert et al. (2006b); ^{90}Y, Kossert and Schrader (2004); ^{124}Sb, Paepen et al. (2010); ^{82}Sr, Pibida et al. (2009); ^{68}Ge/^{68}Ga, Schönfeld et al. (1994a); ^{177}Lu and ^{188}Re, Schötzig et al. (2001); ^{153}Sm, Schötzig et al. (1999); ^{152}Eu, Da Silva et al. (2002); ^{152}Eu and ^{153}Eu, Siegert et al. (1998); ^{152}Eu and ^{154}Eu, Wood and Lucas (1986); ^{201}Tl, Simpson and Meyer (1994b); ^{24}Na, ^{42}K, ^{76}As and ^{198}Au, Unterweger and Lindstrom (2004); ^{54}Mn, Van Ammel et al. (2010); ^{109}Cd, Van Ammel et al. (2011); ^{64}Cu, Wanke et al. (2010); ^{125}I, ^{54}Mn and ^{203}Hg, Da Silva et al. (2006); ^{90}Sr, Woods and Lucas (1996); ^{152}Eu and ^{154}Eu, Woods and Lucas (1986); ^{133}Xe, Woods et al. (1975); ^{137}Cs, Woods (1990).

Schrader (2004, 2010) provides an analysis of radionuclides of which the half-lives were measured in the PTB in the last 30 years. Unterweger (2002) presents the half-life measurements made at NIST of the following radionuclides: ^{60}Co, ^{137}Cs, ^{85}Kr, ^{133}Ba, ^{207}Bi, ^{152}Eu, ^{154}Eu, ^{155}Eu. Gostely (1992) measured the half-life of ^{137}Cs. Fitzgerald (2010) describes an automated ionization chamber (remotely and automatically handling radioactive sources) that can increase sample measurement frequency and include a shield that reduces the background; improving half-life measurements, which enables the measurement of large numbers of sources and minimizes exposure to radiation.

c. Comparison with primary standards

To ensure the quality of the measurements made in hospitals, there have been national campaigns for comparisons with primary standards. Such is the case of ^{99m}Tc and ^{131}I in Polish hospitals, Broda et al. (2010); ^{131}I, ^{123}I and ^{99m}Tc in Brazilian hospitals, Iwahara et al. (2001, 2002); ^{131}I in Indian hospitals, Joseph et al. (2003); ^{131}I and ^{99m}Tc in Korean hospitals, Kim et al. (2005); ^{89}Sr in British hospitals, Woods et al. (2006); and ^{131}I, ^{123}I, ^{99m}Tc, ^{67}Ga, and ^{201}Tl in Brazilian hospitals, Tauhata et al. (2008). Schrader (2000) provided measures of 19 radionuclides standardized by the PTB, obtaining efficiency values for the following ionization chambers: Centronic IG12/A20, Vinten ISOCAL IV and a calibrator for nuclear medicine. He provided criteria for transferring calibration factors from one chamber to another. Schrader and Svec (2004) compared three ionization chambers by measuring the activity of 23 radionuclides calibrated by the PTB. The calibrated chambers were: IG11 from BIPM, ISOCA from NPL, and IG12 from PTB. Woods et al. (1992) calibrated ^{192}Ir brachytherapy sources for UK hospitals.

The calibration of ionization chambers for measurement by relative methods requires the absolute standardization of the radionuclides to be measured in the chamber. The nuclides most often used in calibration are: ^{192}Ir, Anuradha et al. (2005); ^{223}Ra, Bergeron et al. (2010); ^{89}Sr, Coursey et al. (1998); ^{152}Eu, Da Silva et al. (2002); ^{125}I, ^{54}Mn and

^{203}Hg, Da Silva et al. (2006); ^{169}Yb, Delgado et al. (2001); ^{166m}Ho, Hino et al. (2000); ^{192}Ir, Hino and Ohgali (1998); ^{153m}Sm, Lépy et al. (2006); ^{22}Na, Nähle et al. (2008); ^{18}F, Nedjadi et al. (2010) and Yamada et al. (2008); ^{131}I, Oropesa Verdecia and Kossert (2009) and Sahagia et al. (2008); ^{18}F, ^{186}Re and ^{188}Re, Sahagia et al. (2002); ^{64}Cu, Wanke et al. (2010): ^{125}I, Woods and Lucas (1975); ^{69}Ga, Yuan et al. (2008); ^{188}Re, Yuan et al. (2006); ^{166m}Ho, ^{58}Co and ^{88}Y, Yuan et al. (2002); ^{188}W/^{188}Re, Zimmerman et al. (2002); ^{166}Ho, Cessna et al. (2004); ^{153}Sm, Lepy et al. (2006); ^{65}Zn, Sahagia et al. (2004). Simpson (2002) presented the calibration of 20 radionuclides and discussed the applicability of the CIEMAT/NIST method to standardize samples for the SIR system.

International comparisons have been made for some nuclides: ^{133}Xe, Picolo et al. (1998); ^{192}Ir, Ratel (1998); ^{121}I, Sahagia et al. (2008), together with comparisons for the SIR system. Hino (2002) calibrated the following radionuclides: ^{58}Co, ^{88}Y, and ^{166m}Ho. Michotte et al. (2006), based on measurements obtained for the SIR, obtained the photon emission intensities of the following radionuclides: ^{65}Zn and ^{201}Tl. Michotte (2000), applying an interactive method, obtained the efficiency of the chamber as a function of energy using a few monoenergetic gamma emitters and also examined the influence of radiochemical impurities on SIR measurements. Olšovcová et al. (2010) presented a comparison of ^{131}I in clinics of nuclear medicine in eight countries: Brazil, Cuba, Czech Republic, India, Iran, Republic of Korea, Romania, and Turkey. Zimmerman et al. (2008) analyzed the results of an international comparison organized by the IAEA for the traceability of ^{131}I. Zimmerman and Palm (2010) presented the international comparison results of ^{57}Co.

Calibrations of ionization chambers for measurement of radon have been carried out by Paul et al. (2000); Lee et al. (2004a,b); Venoso et al. (2009); Beck et al. (2009) and Janik et al. (2009).

3. Considerations on the calculation of ionization chamber efficiency

Several investigators, Gray (1949), Dale (1961,a,b), Heydorn (1967), Oncescu and Rebigan (1968), and Bensch and Ledermann (1969), found that variations in the response of ionization chambers are related to the k value, the specific gamma emission constant of radionuclides (NCRP, 1985). At least, in the ideal case of a chamber with walls of material equivalent to air, Dale et al. (1961) observed that the 1383A-type chamber used in the NPL does not have air wall conditions, so there was a deviation in its response. The experimental representation of current per mCi against the value of k is almost a straight line not passing through the origin, as is shown in Fig. 7.13. If we represent the current per mCi divided by the value of k versus k, the nonlinearity is clearer. The 1383A ionization chamber has a 1/8-inch brass inner lining in which gamma radiation interacts. Dale (1961) first calculated secondary electron production due to the interaction of gamma rays: $E_\gamma(e^\sigma a + e^\tau a)$ He then computed the absorption of secondary electrons by brass, to finally obtain the corrected curve of secondary electrons as a function of energy as is shown in Fig. 7.14. In this curve, the ordinate is in arbitrary units, to pass it to $\mathrm{pA}/3.7 \times 10^7 \mathrm{photon/s}$. Dale used the measurement of the chamber slopes for two nuclides ^{24}Na and ^{60}Co. From the values of the curve, we can calculate the slope of the chamber for any gamma-emitting radionuclides with uncertainties below 3%, if we know the decay scheme data with low uncertainty. In the 1960s and 1970s this method was extremely useful in the direct calibration of radionuclides.

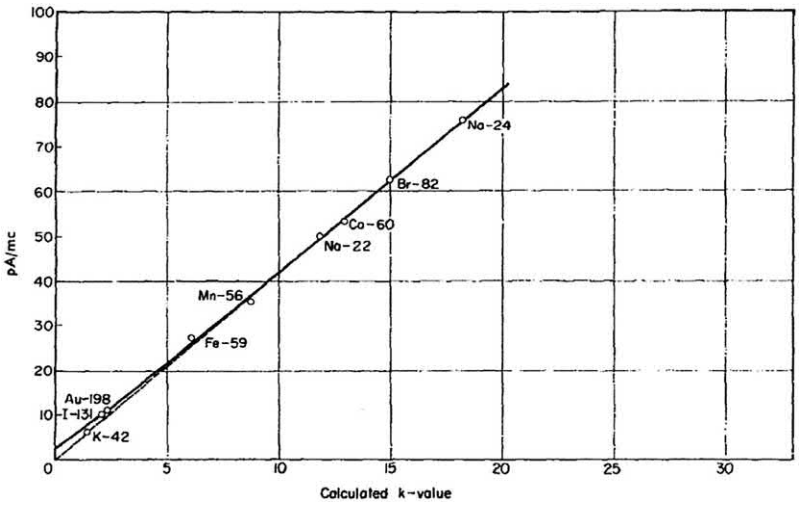


FIGURE 7.13 Current per millicurie/k against k-value. *From Dale (1961a), reprinted with permission of Elsevier Science © 1961.*

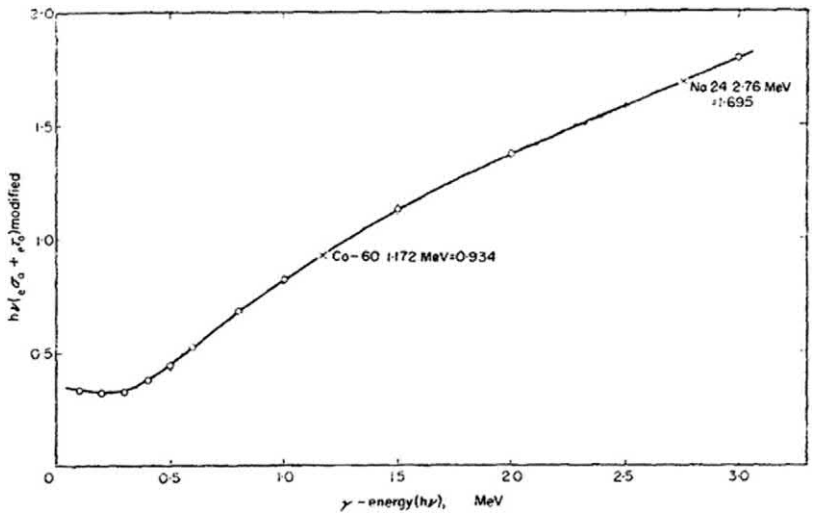


FIGURE 7.14 Secondary electron production in the brass against γ −energy (modified for absorption in brass liner of cavity). *From Dale et al. (1961), reprinted with permission of Elsevier Science © 1961.*

Suzuki et al. (1998) applied the Monte Carlo code EGSA4 to three types of ionization chambers at high pressure: Centronic IG11/A10 (1 MPa, Argon, 2.54 cm diameter reentrant well), Centronic IG12/A20 (2 MPa, Argon, 2.54 cm reentrant diameter well) and Centronic IG12/N20 (2 MPa, Nitrogen, 5.08 cm diameter reentrant well). These chambers were built by the Centronics company based on a design by Shape and Wade (1951), NCRP (1985). Eleven radionuclides of standard solutions were measured to compare the experimental with the calculated curve. They also analyzed the effect of displacement of the measured sample. In all cases, the calculations are in good agreement with the experimental results. Simoes et al. (2010) applied the Monte Carlo MCNPX method to obtain the response of the Curiementor 2 ionization chamber.

Gostely and Laedermann (2000) applied the GEANT Monte Carlo code to the calibration of the Centronics IG11 ionization chamber. The equipment used is similar to the BIPM and fully described earlier by Rytz (1983b).

Gostely and Laedermann (2000) used 12 calibrated standards: ^{125}I, ^{133}Ba, ^{109}Cd, ^{57}Co, ^{99m}Tc, ^{125}I, ^{123}I, ^{51}Cr, ^{137}Cs, ^{22}Na, ^{60}Co, and ^{88}Y. These sources cover the energy range between 40 keV and 2 MeV. Agreement between calculated and experimental efficiencies is complete. They studied the effect of the displacement of sources as well as the Bremsstrahlung effect of high energy beta emitters. They also analyzed the effects of the distribution of emission points of annihilation radiation from a positron emitter and applied the results to the case of ^{18}F.

Calculation programs for the Monte Carlo method have been applied by some investigators to obtain the absolute activity of radioactive sources of different nuclides. De Vismes and Amiot (2003) applied the PENELOPE program to the Vinten 671 chamber using a limited number of radionuclides (^{133}Ba, ^{99m}Tc, ^{60}Co) and obtained excellent calibration for other energies. The discrepancy between the experimental and calculated values of a large number of samples is less than 0.5%. Amiot (2004) calculated the calibration factor, using the PENELOPE code, for the nuclides: ^{18}F, ^{99m}Tc, ^{111}In, and ^{123}I. Kryeziu et al. (2007) calculated the calibration factors and volume correction of the following radionuclides: ^{90}Y, ^{125}I, ^{131}I, and ^{177}Lu; they also used the PENELOPE code.

Olsovcová (2004, 2010) applied the MCNP 4C code (Briesmeister, 2000) to the CMI chamber with excellent results for vials and syringes. Olšovcová (2010) applied Monte Carlo code MCNP 4C to the following radionuclides: ^{123}I, ^{111}In, ^{153}Sm in syringes. Olšovcová Havelka et al. (2006) applied Monte Carlo code MCNP 4C to the Bqmeter chamber (BQM Consortium) to obtain the calibration curve for various types of syringes and the calibration and geometry correction factors of a radionuclide calibrator. Olšovcová et al. (2010) conducted a national comparison of ^{131}I measurements among nuclear medicine clinics in eight countries.

Sato et al. (2006) calculated the response for standard ionization chambers: TPA MkII (argon), IG12/A20, IG11/A20, IG11/N20, in the APMP area (Asia−Pacific Metrology Program) using the EGS4 Monte Carlo code. Lin and Chu (2006) introduced corrections to the INER chamber applying the Monte Carlo method.

Švec and Schrader (2000, 2002), calculated the efficiency and deviation from experimental results, for a large number of nuclides (28) calibrated by the PTB. Uritani et al. (1994) estimated the activity of ^{192}Ir in metal samples by analytical computation. Grau Malonda et al. (1982)

applied the Monte Carlo method to the activity determination of metal mercury samples with ^{203}Hg in cylindrical containers measured with a 1383A ionization chamber. Büermann et al. (1994) standardized ^{192}Ir metal samples using self-absorption corrections.

V. Reference systems

A. The SIR of gammas

The International Reference System (Système International de Référence) (SIR) for activity measurements of radionuclides that emit gamma radiation was established in 1976. Each National Metrology Institute (NMI) can request a standard ampoule (3.6 g) which is filled with radionuclide in an aqueous solution, from the Bureau International des Poids et Mesures (BIPM). A different standard ampoule is used for radioactive gases. The NMI completes a submission form detailing the standardization method used to determine the absolute activity of the radionuclide and the full uncertainty budget for the evaluation of uncertainty. The ampoules are sent to BIPM where they are compared with the standard sources of ^{226}Ra using pressurized ionization chambers. Details of the SIR method, experimental set-up and determination of equivalent activity are given in Ratel (2005, 2007) and Woods et al. (2000).

The SIR enables national laboratories to check the reliability of their activity measurements at any time. This is achieved by determination of the equivalent activity of the radionuclide and comparing the results with the key comparison reference value (KCRV) determined from the results of primary standardizations.

Each NMI that submits ampoules to SIR has measured the activity of the radionuclide by primary standardization methods or a secondary method such as a calibrated ionization chamber. In this case, the traceability of the calibration must be identified to ensure that all corrections have been taken into account.

The details of the submitted solution are: chemical composition, solvent concentration, carrier concentration, density (g/cm^3) and relative activity of the impurity, if any (Rytz, 1983a). The typical BIPM method for evaluating the activity of impurities is the use of a spectrometer with a calibrated Ge(Li) detector as described in Michotte (2000, 2001). The Consultative Committee for Ionizing Radiation CCRI (II) agreed that this approach will continue in accordance with the protocol described in Michotte (2002), when an NMI makes a request or when discrepancies appear. All submissions to the SIR since it was established in 1976 are recorded in a database known as the "master file".

The SIR for gamma is based on two reentrant ionization chambers filled with nitrogen to 2.0 MPa. These chambers are coupled to an electronic system capable of measuring currents as low as a few hundred femtoamperes with high precision (some parts of 10^4). Until recently, one of the chambers was used only for verification purposes, while the other, more sensitive, chamber was used for NMI measurements.

The idea of SIR was to have a reliable, stable, and precise system, as simple as possible (Rytz, 1983b). Relative measurements seemed a more convenient way to achieve the proposed goal, provided that we use a sufficiently stable reference. This is achieved with five sources of radium that have a half-life of $T_{1/2} = 1600$ y, $u = 7$ y. Thus, comparisons in the SIR are reduced to comparing two similar ionization currents. One current is produced in the chamber by the NMI ampoule and the other current is induced by one of the five radium sources. Consequently, the SIR feature is the use of the five sources of ^{226}Ra. These are made of radium sulfate in double-walled sealed platinum-iridium cylinders of identical geometrical sizes (Rytz, 1978). The ratio between the activities of two successive sources of radium is about three, so that the dynamic range in activity covered by the five sources is approximately 81 times, for a total activity of the five sources of 16.4 MBq. To reduce experimental systematic effects, the same measurement conditions are used for samples and radium sources. This is accomplished by choosing the source of radium which gives the closest ionization current to the sample.

As the ionization current is proportional to the activity of the sample, it is useful to define the equivalent activity of a radionuclide as the activity that produces a current equal to that produced by the radium source of highest activity in the ionization chamber. Given the disintegration of the sample, designated by s, and the source of radium, designated as Ra, given the dates of reference t_r and t_0, and the date of measurement t_m, common to the radium source and the sample, the equivalent activity value (Rytz, 1983b) can be expressed as:

$$\frac{A_e e^{-\lambda_{Ra}(t_m - t_0)}}{A_S e^{-\lambda_s(t_m - t_r)}} = \frac{F_j(I_{Ra} - I_f)}{I_s - I_f} \tag{7.142}$$

A normalization coefficient F_j, with $j = 1$ to 4, has been introduced in this equation, to convert the measured current, obtained with the radium source used to adapt the sample current, to the current that would have been produced by the radium source with highest activity.

In order to fulfill the condition of long-term stability required by the SIR system, the stability of sources and ionization chambers is checked regularly. At the same time as the measurements of the samples sent by the laboratories, the five sources of radium are measured each month to obtain the current ratios $r_j = I_{j+1}/I_j$ for values of

$j = 1-4$, so as to determine the ratio between the currents due to the source of highest activity and each of the other sources.

This enables the determination of the efficiency of the ionization chamber as a function of energy. When a radionuclide decays with emission of several gamma rays of different energies, each of these gamma rays contributes to the total current of the chamber. Normally, the chamber responds differently to different excitations caused by these photons. Thus, each radionuclide has a particular energy signature represented by its decay scheme and the detection efficiency can be defined for each radionuclide. So, for a radionuclide emission characterized by several energies E_i, and emission probabilityp_i, the detection efficiency is given by:

$$\varepsilon_{\text{rad}} = \sum_{i=1}^{n} p_i(E_i)\varepsilon_i(E_i) \tag{7.143}$$

where photon efficiency $\varepsilon(E_i)$ is a smooth function that depends on the energy of the gamma line measured: Rytz (1983b) assumed that efficiency could be broken down into a linear part, dependent on energy, and a small amount $\delta(E_i)$, that represents a deviation of the energy, following an idea presented by Schrader and Weiss (1983).

The efficiency curve is a function of energy. It was first established experimentally in a region where the curve is almost linear. They used monoenergetic radionuclides such as ^{54}Mn ($E = 834.838$keV, $u = 0.005$keV) and ^{60}Co with two lines relatively close in energy ($E_1 = 1173.240$keV, $u = 0.003$keV and $E_2 = 1332.508$keV, $u = 0.004$keV) with similar emission probabilities (99.85% and 99.9988%, respectively). So we can use a mean energy value with a fictitious emission probability equal to the sum of emission probabilities. When some values of f_i were known, it was possible to draw a provisional curve and extend the validity region of the curve by selecting particular values of factor f_l for energy level l:

$$f_l = \frac{\dfrac{10^5}{6}\dfrac{1}{A_e} - \sum_{i=1, i\neq l}^{n} E_i p_i(E_i) f_i}{E_l p_l(E_l)} \tag{7.144}$$

The curve has been extended from $E = 2751.77$ keV for ^{24}Na, and toward lower energies with ^{153}Gd ($E = 97.43103$ keV). Attempts have been made with radionuclides with lower energy, such as ^{125}I ($E_\gamma = 35.4919$ keV), but the results are not sufficiently reliable because of the influence of the glass ampoule thickness.

Different ways of approximating analytical curves to the response curve of the chamber have been tested. We emphasize the excellent work of Michotte et al. (2006). They applied polynomial exponentials to adjust SIR experimental data by nonlinear least squares minimization.

In the process followed for approving the results of the NMI by the BIPM, the key comparison reference value is obtained from the average of all results submitted to the SIR with the following provisions (Michotte et al., 2010):

a. Only primary standardized solutions are accepted, with the exception of radioactive gas standards, for which results from transfer instrument measurements are directly traceable to a primary measurement in the laboratory;
b. Each NMI or other laboratory only has one result (normally the most recent result if more than one ampoule is submitted);
c. Any outliers are identified using a reduced Chi-squared test.
d. Exclusions must be approved by the CCRI (II).

A long list of radionuclides (60) has been subjected to SIR. See the BIPM website for information about comparisons (http://www.bipm.org/en/scientific/ionizing/radionuclide/sir/). By clicking on the nuclide of interest one can obtain information on the comparison or comparisons that have been made with the nuclide. For example, if you enter http://iopscience.iop.org/0026-1394/47/1A/06001, which corresponds to the action of 2010 on ^{22}Na we obtain the abstract of the nuclide. Clicking again on the final report contained in the abstract, the final report on the action of SIR is obtained. This report provides details of the participants, the method or methods of calibration, characteristic details of the provided solution, results of the measurements, a table of degrees of equivalence and uncertainty (uncertainty budgets) of the different calibration methods applied to the primary radionuclide.

After many years of measuring a large number of ampoules, the SIR has become a repository of many reliable results. Calibration of ionization chambers by relative methods requires the absolute calibration of radionuclides that are later going to be measured in the chamber. The nuclides most often used in standardization are: ^{192}Ir, Anuradha et al. (2005); ^{223}Ra, Bergeron et al. (2010); ^{89}Sr, Coursey et al. (1998); ^{152}Eu, Da Silva et al. (2002); ^{125}I, ^{54}Mn and ^{203}Hg, Da Silva et al. (2006); ^{169}Yb, Delgado et al. (2001); ^{166m}Ho, Hino et al. (2000); ^{192}Ir, Hino and Ohgali (1998); ^{153}Sm, Lépy et al. (2006); ^{22}Na, Nähle et al. (2008); ^{18}F, Nedjadi et al. (2010); Yamada et al. (2008) and Roteta et al. (2006); ^{131}I, Oropesa Verdecia and Kossert (2009) and Sahagia et al. (2008); ^{186}Re/^{188}Re, Sahagia et al. (2002); ^{64}Cu, Wanke et al. (2010); ^{125}I, Woods and Lucas (1975); ^{69}Ga, Yuan et al. (2008); ^{188}Re, Yuan et al. (2006); ^{166m}Ho, ^{58}Co and ^{88}Y, Yuan et al. (2002); ^{188}W/^{188}Re, Zimmerman et al. (2002); ^{166}Ho Cessna et al. (2004); ^{153}Sm, Lépy et al. (2006); ^{133}Ba, Simpson and van Wyngaardt (2008); ^{65}Zn, Sahagia et al. (2004). Simpson (2002) presents the calibration of 20 radionuclides and

discusses the applicability of the CIEMAT/NIST method to the standardization of samples for the SIR system.

The SIR system is therefore a means of coordinating the calibration results of the NMIs and checks the validity of primary radionuclide standardization methods.

1. Measurement of short half-life gamma emitters

Radionuclides with a short half-life can only be linked to the SIR of the BIPM if the laboratory is close to the Sèvres laboratory. In 2003, the CCRI (II), aware of the constant increase in the use of such radionuclides and the need for all countries to compare their measurement results, decided to establish a Transfer Instrument Working Group (TIWG) to study the possibility of extending the scope of the SIR.

After lengthy discussions it was decided that the BIPM could only achieve this through the use of a transfer instrument (TI) circulated among the participants of the comparison. This equipment should be related to the original SIR so that measurements obtained with this procedure should be able to be compared with those obtained with the original procedure. A 76 mm × 76 mm NaI(Tl) crystal with a well of 2 mm diameter hole was chosen as the TI. The goal was to count all events that exceed a threshold level. The detector was accompanied by a source consisting of a mixture of ^{93m}Nb ($T_{1/2}$ = 16.12a) and ^{94}Nb ($T_{1/2}$ = 20300a) produced by the IRMM. This sample had two aims: the ^{94}Nb enables verification and correction of stability and the ^{93m}Nb, which emits 17 keV X-rays, sets the threshold level. The ^{94}Nb fulfills the same role as the usual radium in the SIR system. Furthermore, it has to define an equivalent activity in the same terms as in the traditional SIR system. The IT system was assembled at the BIPM and preliminary experiments were carried out. The LNE-LNHB prepared a solution of ^{99m}Tc high activity that was first measured in the SIR chamber and then, after decaying several half-lives, when activity had declined, it was measured in the NaI(Tl). The activity was low enough that there were no dead time distortions. These consecutive measurements enabled the determination of the linking factor, defined as the ratio between equivalent activity in the SIR and the transfer instrument.

B. The SIR of betas

The success of the SIR for gamma emitters led to extending the procedure to pure beta decay, alpha decay and pure electron capture decay. For pure beta emitters the liquid scintillation technique and in particular the CIEMAT/NIST method seems to be the most appropriate procedure. To test this procedure several comparisons have been organized by the CCRI (II), using the CIEMAT/NIST method, for the following nuclides: ^{14}C, ^{90}Sr, ^{89}Sr, ^{90}Y, and alpha emitters ^{238}Pu and ^{241}Am. These tests have been successful and, therefore, present no difficulty to be included in the SIR.

The CIEMAT/NIST method permits the compensation for LSC long-term anomalous effects; in particular, the effect of permanent photomultiplier fatigue. This effect can modify the counting rate. Grau Malonda (1982a) applied the CIEMAT/NIST method to C-14 standardization using tritium as a tracer when the photomultiplier response presented a big degradation. Calibration curves of H-3 and C-14 presented important anomalies, but the activity of C-14 samples was accurate.

Rodríguez-Barquero and Los Arcos (2004a) measured samples of H-3, C-14 and Ni-63 over a long period of time: 4, 2.4 and 2.3 years, respectively. In this work, they prove that the counting rates vary over time; but C-14 and Ni-63 activities obtained with the CIEMAT/NIST method, when the calibration curves prepared in times close to the activity measurement, gave discrepancies of −0.5% and −0.4% for Ni-63 and the C-14, respectively. Rodríguez-Barquero and Los Arcos (2004a) conclude in their work: "This behavior confirms the reliability of the CIEMAT/NIST method as a monitoring tool for the determination of activity concentration on the long term with no need for additional checking procedures or stability curves".

For ^{204}Tl, a beta emitter with a small branch of EC, the measurement was sensitive to the chemical preparation, a problem expected in other radionuclides. Another objective is to extend the SIR to nuclides decaying by pure electron capture, such as ^{55}Fe and ^{165}Er, which are not now covered by the SIR. They emit photons with too low energy (below 50 keV). It has been shown repeatedly that ^{3}H ($T_{1/2}$= 12.312 y, and E_{max} = 18.591 keV) is an excellent tracer for the standardization of beta emitters by the CIEMAT/NIST method and has been proposed to be used as a monitor. However, its half-life is relatively short. A nuclide of longer half-life is ^{14}C; but its use requires special care. It could lose activity, producing carbon dioxide that escapes from the sample. ^{63}Ni seems to be a better candidate in view of its half-life (100 years) and maximum energy (65.9 keV), lower than ^{14}C.

In 2007, at the ESIR WG (Extended SIR Working Group) meeting, CIEMAT, PTB, and LNE-LNHB proposed different methods and procedures for the SIR extension. The PTB method (Kossert, 2006) is very similar to the CIEMAT/NIST method. The method presented by the LNE-LNHB (Cassette and Do, 2008) is based on the application of a Compton spectrometer to the scintillation detector, with the creation, in the liquid scintillator, of an internal and virtual reference source, which is measured by the Compton effect. CIEMAT introduced a new scintillator and applied the CIEMAT/NIST method. CIEMAT presented results showing good stability for the proposed XAN6040 scintillator. We describe each of the proposals in detail.

Kossert (2006) described a secondary method based on the efficiency curve of tritium as a tracer and the efficiency curve of the radionuclide to be studied. The procedure is as follows. In a first stage we have the efficiency curve (efficiency against quench parameter QIP) of tritium and the efficiency curve of the nuclide to be studied, i.e., $\varepsilon_{\text{tracer}}(\text{QIP})$ and $\varepsilon_{\text{nuclide}}(\text{QIP})$. For both measures a set of samples with different quenching are prepared. We measure efficiency and quench parameter QIP. As both curves have a common element, the QIP, we obtained from these curves a new curve $\varepsilon_{\text{nuclide}}(\varepsilon_{\text{tracer}})$ that links the efficiency of the studied nuclide and the tracer. In a second stage, which may be several years later, the operation is repeated and we prepare a set of tracer samples with a different quench, so you get a new curve $\varepsilon_{\text{tracer}}(\text{QIP})$ and from the measurement of the radionuclide under study we obtain the parameter QIP. With this parameter we determine the new efficiency of the tracer; and with the new efficiency of the tracer, we enter the curve $\varepsilon_{\text{nuclide}}(\varepsilon_{\text{tracer}})$ and we determine the efficiency of the nuclide. The activity of the sample under study is obtained applying the equation $A_{\text{nuclide}} = N_{\text{nuclide}}/\varepsilon_{\text{nuclide}}$. Kossert (2006) presented Fig. 7.15, which clarifies the description given. The composition of the sample and the geometry of the measurement must be very similar for all measures; and the time between the preparation of tracer sample and the nuclide under study should be short. Moreover, the time between the first and second measurements of the sample under study can be very long, many years. This method enables us to correct for gain variations of the measuring equipment, but cannot correct the count variations in the sample by absorption or microprecipitation, as the QIP is only sensitive to the liquid scintillator and not to the radionuclide incorporated to the liquid scintillator.

Cassette and Do (2008), Cassette et al. (2010) and Jean-Baptiste et al. (2014) described a new calibration method based on liquid scintillation using a virtual source, which acts as a tracer, created inside the scintillator by Compton interaction. When a sample is placed in the liquid scintillation counter, it is irradiated by an external and collimated source of ^{241}Am emitting 59.4 keV gamma rays. A gamma detector is placed in the bottom of the optic cell of the liquid scintillation counter with its axis normal to the beam of gamma photons. The gamma detector measures part of the gamma photons scattered in the liquid scintillator by coherent or incoherent Compton scattering. For incoherent photons, the spectrum is centered around the scattering at 90 degrees, which corresponds to an average energy of 53.2 keV. The Compton spectrum is separated from the coherent scattering spectrum using a detector with good resolution, for example a Ge detector. The Compton spectrum analyzer is selected by an SCA (single-channel analyzer) and this signal is used to validate the acquisition of the photomultiplier of the liquid scintillation counter. All pulses created by gamma-ray interaction in the liquid scintillator are viewed by the liquid scintillation counter, but only those pulses in coincidence with the SCA signal are selected. The coincidence system rejects all light pulses generated by the sample's disintegration in the liquid scintillator. The energy spectrum of Compton electrons from the source is deduced from the experimental spectrum of Compton scattered photons by applying the principle of conservation of energy to the Compton effect. This spectrum is used to calculate the free parameter of each

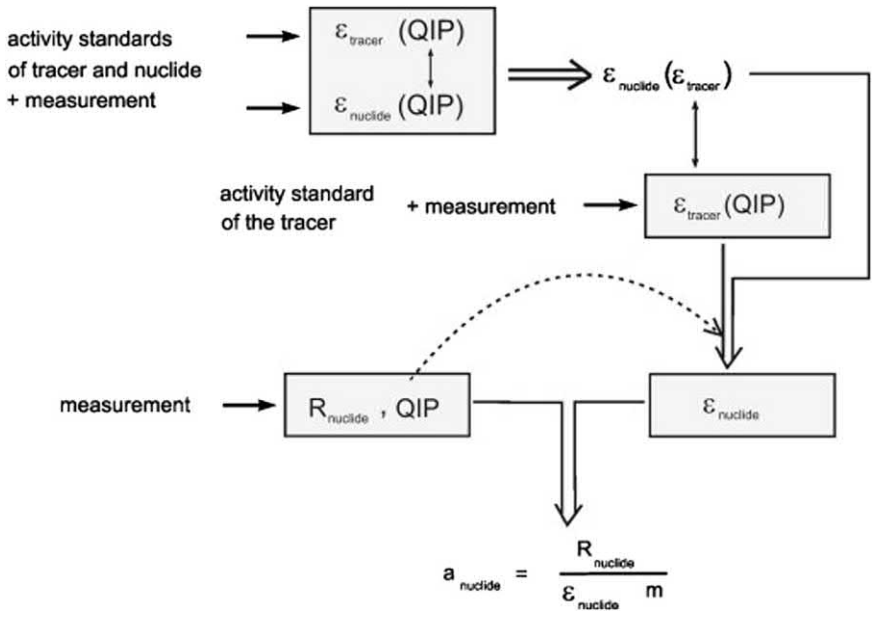


FIGURE 7.15 Illustration of the secondary standard measurement procedure. *R* denotes the counting rate, QIP the quench indicating parameter, ε the counting efficiency, a_{nuclide} is the solution activity concentration and *m* is the source mass. *From Kossert (2006), reprinted with permission of Elsevier Science © 2006.*

photomultiplier, from the experimental values of the relationship triple-to-double. Then the gamma source is removed and the sample is measured using the traditional TDCR method. This procedure has the advantage of allowing the direct determination of the nonlinearity of the response of the liquid scintillation at low energies due to ionization quench. However, it is not possible to determine the stability of the sample measured or correct for counting variation in the sample by absorption or microprecipitation of the radionuclide.

Rodriguez Barquero and Los Arcos (2000) measured the stability of ^{110m}Ag samples for liquid scintillation with four comercial scintillators: Insta-Gel Plus, Ultima-Gold, HiSafe II and HiSafe III. Ultima-Gold samples were completely unstable for 2 months, Insta-Gel Plus and HiSafe II reached stabiltity after 30 days and only HiSafe III samples were stable for the full term of 2 months. Samples were prepared with 15 mL of liquid scintillator and four carrier levels: 0.0, 1.5, 3.0, and 6.0 μg of $AgNO_3$.

Rodriguez Barquero and Los Arcos (2010) presented a systematic study of five scintillators, four commercial: Ultima-Gold, Optiphase, HiSafe II, and Optiphase HiSafe III, and one homemade reference scintillator, XAN6040, useful to stabilize up to 19 radionuclides (Rodríguez Barquero and Los Arcos, 2005). They determined the density and the elemental composition of these liquid scintillators. The density at 16°C is higher by 0.4% than the density at 20°C. However, the discrepancy among different batches of commercial scintillators can reach up to 4%, all having the same nominal composition. Several laboratories analyzed the weight percentages of H, C, O, N, P, Na, S, and B of all the laboratories. The elemental composition of commercial scintillators presented discrepancies with the nominal values from 2% and up to 260% depending on the element and the scintillator.

Rodríguez Barquero and Los Arcos (2005, 2007) introduced a new liquid scintillator of known composition called XAN6040 with the goal of becoming the typical scintillator of the SIR for betas. The tests carried out at CIEMAT focused on stability and reproducibility of the cocktail, which gave excellent results. The composition of the XAN6040 liquid scintillator is given in the patents of Rodriguez Barquero and Los Arcos (2003, 2004b,c,d).

Los Arcos and Rodríguez Barquero (2013) proposed a method of "cross-efficiency" for the extension of the Systeme International de Référence (SIR) for radionuclides emitting nongamma radiation. The method is based on the so-called "universal reference curve" described by Cassette and Tartes (2014). This curve represents the efficiency of the radionuclide of interest as a function of the efficiency of a tracer radionuclide for various quench values. This method is the one initially proposed by Kossert (2006), with the difference that Los Arcos and Rodríguez Barquero (2013) affirm that the curve is independent of the counter and the scintillator, while Kossert (2006) recommended a similar scintillation composition for all measurements.

Using three different counters and two different scintillation cocktails, Los Arcos and Rodríguez Barquero conclude that the curve is universal for the following radionuclides: ^{55}Fe, ^{63}Ni, ^{14}C, ^{60}Co, and ^{90}Sr−^{90}Y. They obtain curves that do not depend on the counter or the scintillator used.

In 2011, an intercomparison exercise was proposed in the framework of the Working Group of the CCRI (II) for the extension of the SIR in order to verify the method. The BIPM sent ^{63}Ni calibrated samples to eight laboratories. Three different cocktails were used: Ultima Gold, Hionic-Fluor and Bio Fluor, and three different counters: Beckman LS 6000 TA, Packard TriCarb 2900 TR and Wallac Guardian 1440. The results were presented to the ICRM 2011, but were not published in the Proceedings. The presentation concluded that the results appeared to be independent of the counter and the scintillator and that the uncertainties were of the order of 1−2%.

Cassette and Tartés (2014) affirm: However, after a precise analysis of the data at the LNBH, we thought that this conclusion cannot be withstanding critical scrutiny. From these contradictory results, we wish to verify the influence of the scintillator cocktail and of the counter in the cross-efficiency curve, as it is the key point of the method for the use as an extension of the SIR to radionuclides emitting no gamma rays.

Cassette and Tartés (2014) prepared sets of samples using three different LS cocktails: Ultima Gold, Hionic-Fluor, and Picofluor 15 from PerkinElmer in glass vials with low potassium. No additive was added to stabilize the sources; but the stability was checked by measuring them at different times. They used two quenchers: nitromethane, as a chemical quencher and tartrazine, as a quencher by color. They prepared a total of 120 samples, which were calibrated by the TDCR method and then measured in three different commercial LS counters: Wallace Quantulus 1220, Packard TriCab 2900 TR and Wallac Guardian 1440. The results corresponding to the cross-efficiency curve are shown in Fig. 7.16. These authors conclude: (1) Quenching curves depend on the scintillator and this dependence varies with the radionuclide. (2) Quenching curves depend on the counter. (3) Quenching curves depend on whether the quencher is chemical or color. (4) Quenching curves depend on the volume of the source and the nature of the vial.

Actually, conclusions (3) and (4) are known from the beginning of the application of the LS to the calibration of radionuclides.

The points in question are (1) and (2): according to Los Arcos and Rodríguez Barquero (2013), quenching curves are universal and independent of the scintillator and the counter.

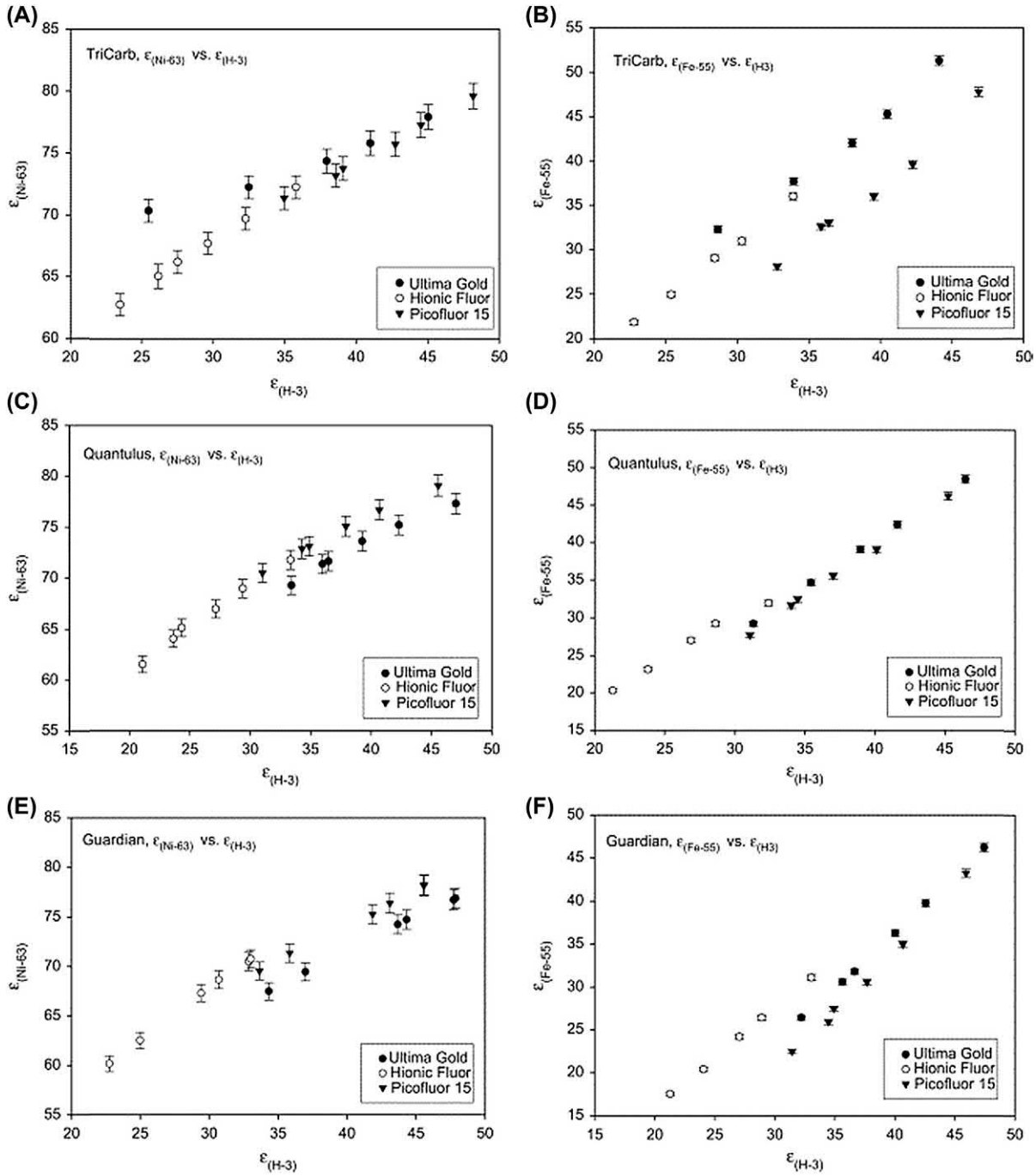


FIGURE 7.16 Cross-efficiency curves: (A) ^{63}Ni versus ^{3}H, TriCarb, for 3 LS cocktails; (B) ^{55}Fe versus ^{3}H, TriCarb, for 3 LS cocktails; (C) ^{63}Ni versus ^{3}H, Quantulus, for 3 LS cocktails; (D) ^{55}Fe versus ^{3}H, Quantulus, for 3 LS cocktails (E) ^{63}Ni versus ^{3}H, Guardian, for 3 LS cocktails; and (F); ^{55}Fe versus ^{3}H, Guardian, for 3 LS cocktails. *From Cassette and Tartès (2014), reprinted with permission of Elsevier Science © 2014.*

VI. Preparation of radioactive samples

A. Introduction

Radioactive sample preparation is a very broad subject. Here we only discuss the methods of preparing samples for radionuclide metrology. For additional information on sample preparation, we recommend the reviews published by: Mann (1956), Merritt (1973), van der Eijk et al., (1973), Lowental and Wyllie (1973), Campion (1975), Le Gallic (1977), Lally and Glover (1984), Mann et al. (1988),

Fettweis et al. (2003), Thomson (2003), Sibbens et al. (2003) and, especially, the excellent work of Sibbens and Atzitzoglou (2007).

Sample preparation for LSC can be seen in Chapter 7, Volume 1 of this book, gamma spectrometry in Chapter 4, Volume 1, alpha spectrometry in Chapter 5, Volume 1, internal gas counting in Unterweger (2007), and environmental radioactivity in Jerome et al. (2007) and Chapters 2 and 3 of Volume 2 of this book.

In this section, we only discuss quantitative methods of sample preparation. Qualitative methods, which are of particular interest in spectroscopy, are not considered here. The first thing to examine is the amount of radioactivity deposited in a sample either gravimetrically or volumetrically. We will focus mainly on how to carry out the solutions, the quantitative deposition of drops and the mass determination for obtaining a good sample preparation procedure.

B. Sample preparation for radionuclide metrology

1. Supports for extended samples

Methods to measure extended samples require that the sample holder be ultrathin. The support is usually a foil that lets radiation through. Preparation and use of foils can be made with different materials, such as polypyrrole polymer, polyaniline films, polyethylene dioxythiophene/polyvinyl chloride, polyvinyl chloride-polyvinyl acetate copolymer (VYNS). See the works of Miyahara et al. (1987), Dobilovri et al. (1988), Los Arcos et al. (1992), Was et al. (1993), Du et al. (1996), De Sanoit et al. (1998), Pate and Yaffe (1955), and Lowental and Smith (1964). VYNS is the most popular of all. To prepare the films, the polymer was dissolved in a solvent such as cyclohexane. VYNS concentration in the solution determines film thickness. It can vary from a few μg cm^{-2} to several hundred μg cm^{-2}. Film thickness is determined gravimetrically after depositing the film in a very thin "annuli" of aluminum or stainless steel and determining the area of its surface.

The film must be metallized so as not to disturb the electric field inside the counter. A thin layer of gold is evaporated on the film (Moura and Parker, 1975; Lowenthal and Smith, 1964). The thickness of the gold can also be determined by the difference in weight of the film before and after metallization. In addition to depositing the samples, the films are used to cover the radioactive sample and increase absorption in beta extrapolation methods. VYNS films have good resistance to acids and alkalis.

VYNS films with electrical conductors are best for covering the radioactive sample and thus vary the parameters N_c/N_γ required to establish the dependence of the efficiency of coincidence equation. This method of change N_c/N_γ is preferable to self-absorption methods, as it is simpler, produces consistent results and shows greater control in variation of efficiency. The entrapment of gas bubbles on the radioactive source must be prevented. This often occurs as a result of a heavy charge. To avoid this phenomenon, we lay the source of VYNS for a few minutes in an acetone vapor atmosphere. Trapped gases escape rapidly through the micropores and the films adhere well and tense when we remove the acetone atmosphere.

2. Dilutions in aqueous solutions

Very often, the activity of the radioactive solution is too high for direct measurement. In this case, a quantitative dilution is required to obtain an appropriate concentration for the radioactivity counter (van der Eijk and Vaninbroukx, 1972; Iroulart, 2006, 2007). When the dilution factor is around 1000 or higher, it is best to carry out a multistage dilution. For concentration factors below 1000, we can proceed to a one-step dilution. An important point is to keep the diluted sample stable; and this depends on the carrier concentration in the diluted sample. NCRP (1985) presents a list of chemical data for various radionuclides as well as recommendations for choosing the carrier concentration in the solution. It is advisable, as good practice prior to dilution, to prepare an outline of the steps to be taken.

The dilution is carried out in a rinsed glass that was previously rinsed with a nonradioactive solution containing the carrier, thus reducing the possible absorption of the radioactive sample on the vessel wall when the radioactive sample is incorporated into the container. The container is first weighed empty (w_1) and after adding the carrier solution, which will serve as a basis for the dilution, it is weighed again (w_2); the weight of liquid solvent is determined as the mass difference. The incorporation of radioactive solution is made using a pycnometer, which is prepared from a polyethylene pycnometer of about 5 mL. First, we prepare the output capillary of the pycnometer, heating the tip and stretching by rotating while pulling the tip with tweezers to form a capillary. Once prepared and cooled, the pycnometer is filled with the right amount of radioactive solution. The amount of incorporated radioactive solution in the bottle, in which the dilution will be performed, is measured by weighing the pycnometer before and after dispersing the radioactive solution. If the weight before dispersion of the radioactive solution is w_{pl} and after dispersion it is w_{p2}, the dilution factor is:

$$\text{Dilution factor} = \frac{w_{pl} - w_{p2}}{(w_{pl} - w_{p2}) + (w_2 - w_1)} \qquad (7.145)$$

We must ensure that there is a good homogenization of the solution before use. First, you have to seal the container and then mix the solution well by swirling.

3. Drops deposit in the sample holder

When we standardize a sample we obtain its activity, but in general what we want is to determine the activity of a radioactive solution, or determine the activity per unit of mass for the solution. Therefore, it is necessary to determine the mass or volume of the radioactive solution in the sample holder. The simplest solution is to deposit the solution using pipettes, but for small samples and good accuracy, the gravimetric method by a pycnometer is recommended.

The manipulation of the pycnometer must be carried out with tweezers to avoid electrostatic charging and heating.

4. Determination of mass

In metrological applications, mass must be known with less than 0.1% uncertainty. Regarding the issue of determining the mass, we recommend the excellent monograph by Davidson et al. (2004). As the average solution mass deposited on a sample is about 20 mg, this means that the balance should be accurate to a few micrograms. This requires taking a series of precautions for the environment and positioning of the balance. The balance must be in a room with temperature and humidity controls, avoiding direct sunlight and currents of air. It should also be placed on a vibration-free horizontal table. On the other hand, when using the pycnometric method, it must be handled with a pair of tweezers to prevent the deposit of moisture, fat from fingers and electric charges on the plastic of the pycnometer. A static charge eliminator is recommended.

With respect to the scales, they must meet three criteria: linearity, precision and accuracy. Linearity implies that there exists a linear relationship between the mass of the sample and the response of the scale. In the case of modern electronic scales, the deviation from linearity is about 10^{-7}. The precision of weighing depends on the repeatability of the instrument, or the ability to give the same result when a sample is measured repeatedly. Finally, the accuracy of the scale is linked to the ability to produce the same results as a standard. In this case, we must use a box of calibrated weights traceable to the BIPM, which should be tested frequently and at different ranges.

Commonly we use one of the following two methods: direct and indirect. In the direct method, zero is recorded (w_0) when the scale is empty or the scale is set to zero before weighing the sample. The mass of the sample is then $w = w_1 - w_0$. In this expression w_1 is the sample weight. In the substitution method, we chose weights from the box of calibrated weights to approximate the weight of the sample (w_1). The sum of all substitution weights determined by weighing in the balance (w_s) is compared with the sum of the masses of the certificate weights (w_c). The mass of the sample is $w = w_c + (w_1 - w_s)$.

In all weighing procedures, we must apply a correction for air thrust. Thrust is the force exerted on an object immersed in a fluid by the fluid displaced by the object. In our case, the fluid is air and force is equal to the weight of air displaced by the sample. The sample mass corrected for thrust is:

$$M_c = M_{\mathrm{nc}} \frac{d(d_{\mathrm{cal}} - d_{\mathrm{air}})}{d_{\mathrm{cal}}(d - d_{\mathrm{air}})} \tag{7.146}$$

where M_c is the sample mass corrected for thrust, M_{nc} is the mass of the sample without correcting for the thrust, d is the density of the sample, d_{cal} the density of calibrated weights and d_{air} the air density. All these quantities must be expressed in appropriate units; for example, if mass is expressed in grams (g), density is expressed in grams per cubic centimetre (g cm^{-3}). Air density depends on pressure, temperature and humidity. To determine air density, the International Committee of Weights and Measures (Commité International des Poids et Mesures) recommends the following equation (Davis, 1992):

$$d_{air} = 10^{-3} \times \left(\frac{0.348444 \times p + 0.020582 \times H - 0.00252 \times T \times H}{T + 273.16} \right) \tag{7.147}$$

where T is air temperature in degrees Celsius ($^{\mathrm{o}}$ C), H is relative humidity (%) and p is atmospheric pressure measured in mbar. At each weighing, the operator records the temperature and humidity of the air and the atmospheric pressure in the room containing the scales.

5. Methods for verifying and improving the quality of the source

In radionuclide metrology, the maximum precision achieved is limited more by the quality of the sample than detector performance. A solid radioactive sample of high-quality takes the form of a homogeneous and uniform thin layer of radioactive material. There are several methods to check this quality. First we can view the structure and irregularities of the source under a microscope. The distribution of radioactivity and its homogeneity can be visualized by autoradiography, using for example a photographic film (Nageldinger et al., 1998; De Senoit et al., 2004) as illustrated in Fig. 7.17. Another way to determine the quality of a source is to measure their self-absorption from the beta efficiency variation of the sample (De Sanoit et al., 2001) or from the parameters that define a spectral alpha peak (Denecke et al., 2000).

Sample uniformity and homogeneity can be improved by depositing a wetting and seeding agent in the support of the source, before depositing the radioactive material. It is advisable to use commercial detergents as wetting agents,

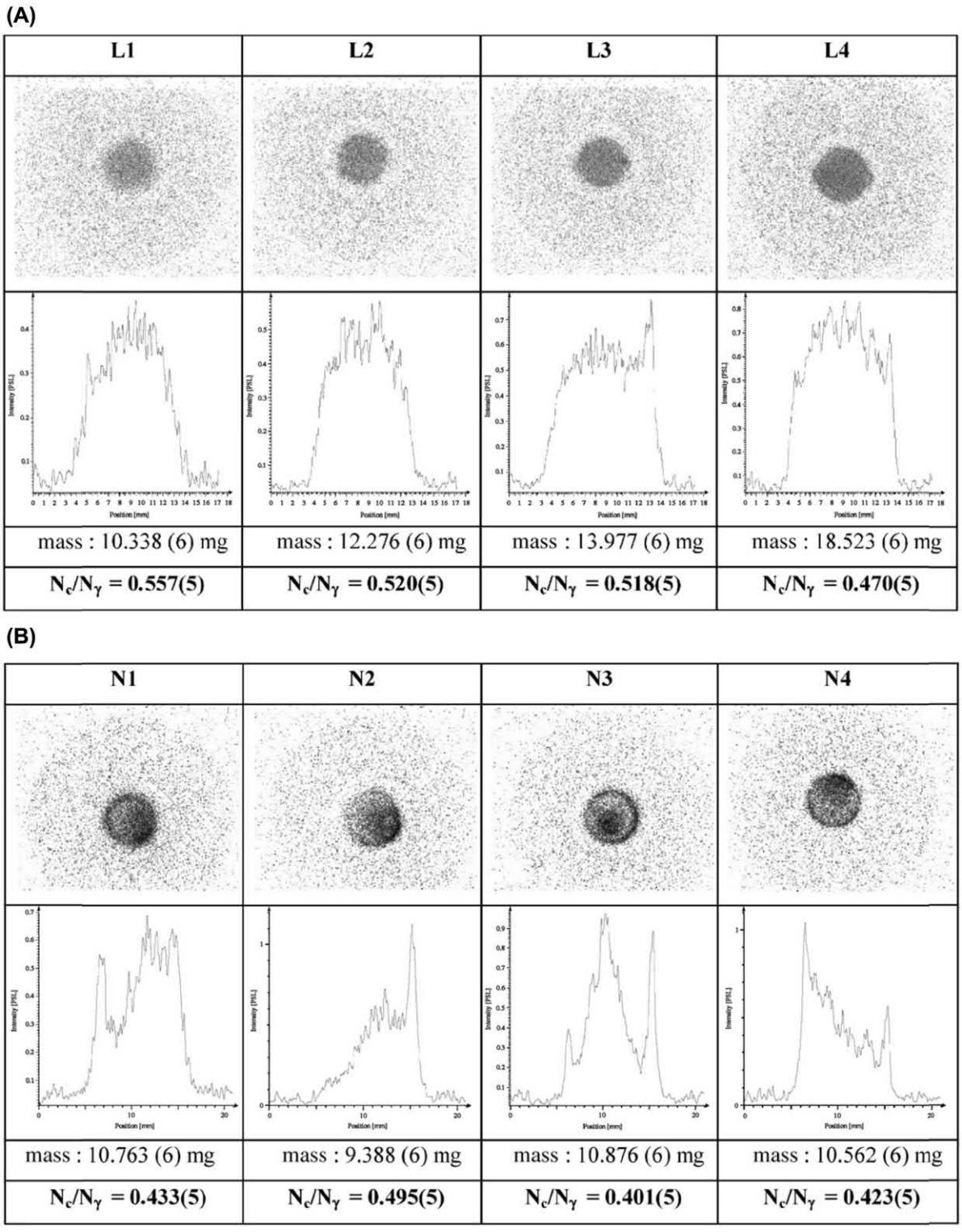


FIGURE 7.17 (A) Autoradiographs, radioactivity profiles and N_c/N_γ values for ^{65}Zn sources dried by the vacuum freeze-drying method. (B) Autoradiographs, radioactivity profiles and N_c/N_γ values for ^{65}Zn sources dried by evaporation at atmospheric pressure. *From De Sanoit et al. (2004), reprinted with permission of Elsevier Science © 2004.*

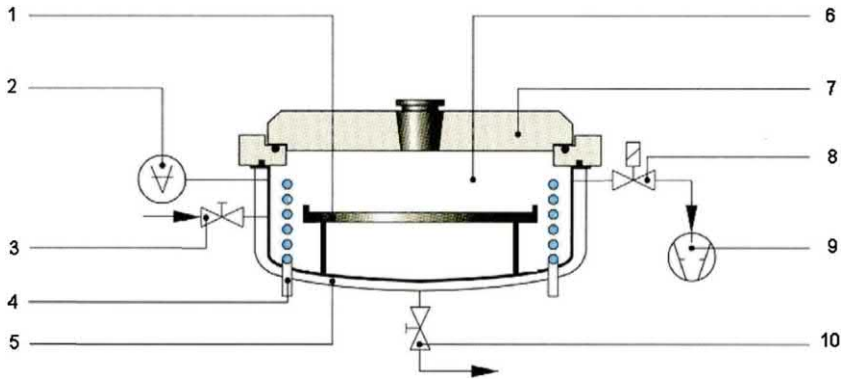


FIGURE 7.18 The ICC used for the freeze-drying method: (1) radioactive source shelf; (2) vacuum gauge; (3) microaeration valve; (4) ice condenser; (5) insulation; (6) ice condenser chamber; (7) acrylic cover; (8) pressure control valve; (9) vacuum pump; and (10) defrosting water valve. *From De Sanoit et al. (2004), reprinted with permission of Elsevier Science.*

such as Tween 20, Catanac (Leprince and De Sanoit, 2002; Miguel et al., 1984) or tetra ethylene glycol (TEG). To produce small crystals we use a seeding agent such as colloidal silica (Ludox), microspheres (K-007) or ion exchange resins (Merritt et al., 1960; Lachance and Roy, 1972; Lowental and Wyllie, 1973; Chen et al., 1989; Du et al., 1986; Blanchis et al., 1990).

The quality of a sample is also given by the drop drying procedure. A common procedure is to dry outdoors without air flows. Another method is to use a laminar flow, both at room temperature or heating with an infrared lamp. Generally we must apply a dry atmosphere, although in some cases it is useful to use the freeze-drying technique (Hutchinson, 1965; De Sanoit et al., 2004). Finally, we have also used dry warm nitrogen jets (Denecke et al., 2000).

In the case of source preparation (De Sanoit et al., 2004), freeze-drying under vacuum consists of the dehydration of the radioactive drop by sublimation. The apparatus is composed of a 300 mm diameter stainless steel ice condenser chamber (ICC) with its associated cooling system and a vacuum pump (pump rate: 5.6 m^3/h) in order to speed up the drying process. The experimental layout is shown in Fig. 7.18.

In most cases, drying a liquid drop of a radioactive solution results in an agglomeration of crystals, the final size of which depends mainly on the time available for the crystals to grow. A usual practice was to dry the sources in a fume hood by air draft (Van der Eijk and Zehmer, 1977). The results were often unsatisfactory as large crystals were formed mainly at the boundary of the drop and at dust particle inclusions. In some cases the liquid withdrew to a much smaller area than the initial drop size, resulting in a very inhomogeneous distribution of the deposit. The uniformity of the deposit was improved by stirring the drop with a dry nitrogen jet. However, due to the long drying time of typically 10−20 minutes, crystals could still grow to large sizes. Employing a gas jet at an elevated temperature substantially accelerated the evaporation of the solvent. By using multiple gas jets and rotating the source at the same time, more turbulence was caused within the drop. This turbulence prevented the formation of a few large crystals at the three-phase boundary between the drop and the substrate. As a result of steady remixing, a large number of small crystals, uniformly distributed over the original drop size, were formed. Intense evaporation begins when temperature and gas flows are set high. In this phase, mainly water evaporates and only a film of the concentrated acid solution remains on the substrate. At this point, the heat input to the gas jets must be reduced to limit the temperature rise of the deposit and substrate and to reduce the buildup of material stresses in the deposit. These stresses may tear a thin foil substrate or reduce adherence between the deposit and the substrate.

The drying apparatus Figs. 7.19 and 7.20, consists of a turntable with variable speed, four gas jets with adjustable gas flow and temperature, a transparent bell jar and a vacuum pump. Gas jets at an elevated temperature impact directly onto the rotating liquid drop deposited on a substrate. Jet distances and positions are adjustable. A geared asynchronous motor using frequency control varies the rotation speed from 5 to 150 rpm. Placing the bell jar over the tabletop creates a closed and dust-free environment around the drop source. Pumping is needed to remove the water vapor from the closed container and enables control of pressure between 5 and 101.3 kPa, which also accelerates evaporation.

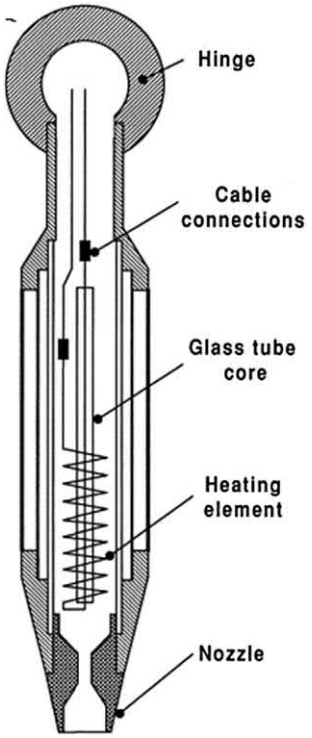


FIGURE 7.19 Construction of the hot gas jet. The heating element, a helix of resistive wire on a glass tube core, is centered inside the gas duct close to the outlet. Two thin-walled tubes thermally insulate the duct. A narrow nozzle forms the gas jet. *From Denecke et al. (2000), reprinted with permission of Elsevier Science.*

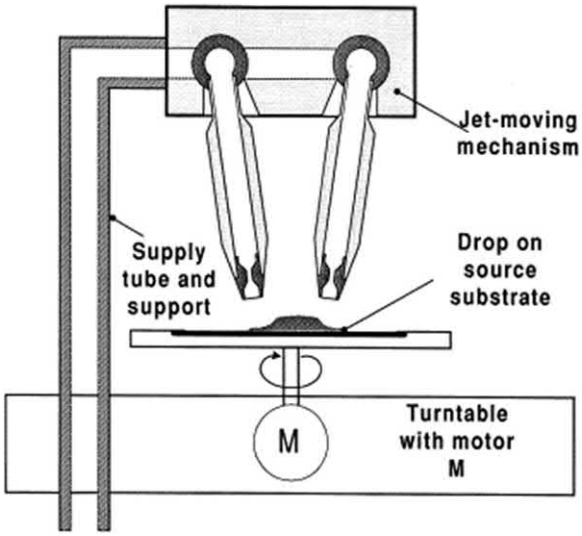


FIGURE 7.20 Principle of the accelerated drop drying: gas jets at an elevated temperature are impacting directly onto the rotating liquid drop deposited on a substrate. Jet distances and positions are adjustable. *From Denecke et al. (2000), reprinted with permission of Elsevier Science © 2000.*

References

Ababneh, A.M., Eyadeh, M.M., 2015. Coincidence summing corrections in HPGe gamma-ray spectrometry for Marinelly-beakers geometry using peak to total (P/T) calibration. J. Radiat. Res. Appl. Sci. 8, 323–327.

Abbas, M.I., 2001. A direct mathematical method to calculate the efficiencies of a parallelepiped detector for an arbitrarily positioned point source. Radiat. Phys. Chem. 60, 3–9.

Abbas, M.I., 2006. Validation of analytical formulae for the efficiency calibration of gamma detectors used in laboratory and in-situ measurements. Appl. Radiat. Isot. 64, 1661–1664.

Agostinelli, S., Allison, J., Amako, K., Apostolakis, J., Araujo, H., Arce, P., Asai, M., Axen, D., Banerjee, S., Barrand, G., 2003. GEANT4 a simulation toolkit. Nucl. Instrum. Methods Phys. Res., Sect. A 506, 250–303.

Agrafiotis, K., Karfopoulos, K.L., Anagnostakis, M.J., 2011. Calibration of an in-situ BEGe detector using semi-empirical and Monte Carlo techniques. Appl. Radiat. Isot. 69, 1151–1155.

Aguiar, J.C., 2008. An analytical calculation of the peak efficiency for cylindrical sources perpendicular to the detector axis in gamma ray spectrometry. Appl. Radiat. Isot. 66, 1123–1127.

Aguiar, J.C., Galiano, E., 2004. Theoretical estimates of the solid angle subtended by a dual diaphragm–detector assembly for alpha sources. Appl. Radiat. Isot. 61, 1349–1351.

Aguiar, J.C., Galiano, E., Fernandez, J., 2006. Peak efficiency calibration for attenuation corrected cylindrical sources in gamma ray spectrometry by the use of a point source. Appl. Radiat. Isot. 64, 1643–1647.

Alvarez, A., Navarro, N., 1996. Method for actinides and ^{90}Srdetermination in urine samples. Appl. Radiat. Isot. 47, 869–873.

Alzitzoglou, T., Denecke, B., Johansson, L., Sibbens, G., 2002. Standardization of ^{89}Sr using three different methods. Appl. Radiat. Isot. 56, 447–452.

Altzitzoglou, T., 2004. Analysis of triple-label samples by liquid scintillation spectrometry. Appl. Radiat. Isot. 60, 487–491.

Altzitzoglou, T., Rozkov, A., 2016. Standardizatioon of the ^{129}I, ^{151}Sm, ^{166}Ho activity concentration using CIEMAT/NIST efficiency tracing method. Appl. Radiat. Isot. 109, 281–285.

Altzitzoglou, T., Larosa, J.J., Nicholl, C., 1998. Measurement of ^{90}Sr in bone ash. Appl. Radiat. Isot. 49, 1313–1317.

Alzitzoglou, T., Denecke, B., Johansson, L., Sibbens, G., 2002. Standardization of ^{89}Sr using three different methods. Appl. Radiat. Isot. 56, 447–452.

Amiot, M.N., 2004. Calculation of ^{18}F, ^{99m}Tc, ^{111}In and ^{123}I calibration factor using the Penelope ionization chamber simulation method. Appl. Radiat. Isot. 60, 529–533.

Anderson, J.L., 1992. Tritium technology programs in the United States. Fusion Technol. 21, 226–234.

Andreev, D.S., Erokhina, K.I., Zvonov, V.S., Lemberg, I.K., 1972. Consideration of cascade transitions in determining the absolute yield of ganna rays. Instrum. Exp. Tech. 25, 1358–1360.

Anuradha, R., Joseph, L., Kulkarni, D.B., Nathuram, R., Shaha, V.V., Sharma, D.N., 2005. Standardization of ^{192}Ir solution at BARC. Appl. Radiat. Isot. 62, 645–648.

Arenillas, P., Cassette, P., 2006. Implementation of the TDCR liquid scintillation method at CNEA-LMR, Argentina. Appl. Radiat. Isot. 64, 1500–1504.

Arinc, A., Johansson, L.C., Gilligan, C.R.D., Pearce, A.K., 2011. Standardisation of ^{210}Pb by Cerenkov counting. Appl. Radiat. Isot. 69, 768–772.

Arinc, A., Parfitt, M.J., Keightley, J.D., Wilson, A., 2016. Defined solid angle alpha counting at NPL. Appl. Radiat. Isot. 109, 198–204.

Arnold, D., Sima, O., 2004a. Application of GESPECOR software for the calculation of coincidence summing effects in special cases. Appl. Radiat. Isot. 60, 167–172.

Arnold, D., Sima, O., 2004b. Extension of the efficiency calibration of germanium detectors using the GESPECOR software. Appl. Radiat. Isot 61, 117–121.

Arnold, D., Sima, O., 2006. Calculation of coincidence summing corrections for X-ray peaks and sum peaks with X-ray contributions. Appl. Radiat. Isot. 64, 1297–1302.

Asano, Y., Mori, S., Ohta, Y., Tsujita, Y., 1996. Sum-peak method and angular correlation correction for a ^{60}Co source by a Ge(Tl) detector. Jpn. J. Appl. Phys. 35, 4117–4120.

Ashrafi, S., Likar, A., Vidmar, T., 1999. Precise modeling of a coaxial HPGe detector. Nucl. Instrum. Methods Phys. Res., Sect. A 438, 421–428.

Aso, T., Ogata, Y., Makino, R., 2018. Gent4 based Monte Carlo simulation for verifying the modified sum.peak method. Appl. Radiat. Isot. 134, 147–150.

Atwater, H.F., 1972. Calculated total efficiencies of coaxial Gr(Li) detectors with small disc sources. Nucl. Instrum. Methods 104, 589–591.

Aubin, G., Barrette, J., Lamoureux, S., Monaro, S., 1969. Calculated relative efficiency for coaxial and planar Ge(Li) detectors. Nucl. Instrum. Methods 76, 85–92.

Ayres, R.L., Hirshfield, A.T., 1982. Radioactivity standardization of ^{99m}Tc and ^{99}Mo. Int. J. Appl. Radiat. Isot. 33, 835–841.

Baerg, A.P., 1966. Measurement of radioactive disintegration rate by the coincidence method. Metrologia 2, 23–32.

Baerg, A.P., 1973. The efficiency extrapolation method in coincidence counting. Nucl. Instrum. Methods 112, 143–150.

Baerg, A.P., Bowes, C.C., 1960. Standardization of ^{63}Ni by efficiency tracing method. Int. J. Appl. Radiat. Isot. 22, 781–783.

Baerg, A.P., Meghir, S., Bownes, C., 1964. Extension of the efficiency tracing method for the calibration of pure beta emitters. Int. J. Appl. Radiat. Isot. 15, 279–287.

Baerg, A.P., Munzenmayer, K., Bowes, G.C., 1976. Live-timed anticoincidence counting with extending dead-time circuitry. Metrologia 12, 77–80.

Ballaux, C., 1983. High efficiency γ-ray detection systems for radionuclide metrology. Int. J. Appl. Radiat. Isot. 34, 493–499.

Bambynek, W., 1967. Precise solid-angle counting. In: IAEA, Standardization of Radionuclides. IAEA, Vienna, pp. 373–383. SM-79/11.

Barnes, I.L., Garfinkel, S.B., Mann, W.B., 1971. Nickel-63: standardization, half-life, and neutron capture cross section. Int. J. Appl. Radiat. Isot. 22, 777–781.

Bé, M.M., 2006. Activity measurements and determination of gamma-ray emission intensities in the decay of ^{63}Ni. Appl. Radiat. Isot. 64, 1396–1402.

Bé, M.–M., Browne, E., Chechev, V., Chisté, V., Dersch, R., Dulieu, C., Helmer, R.G., MacMahon, T.D., Nichols, A.L., Schönfeld, E., 2004. NUCLÉIDE, Table de radionucléide sur CD-ROM. Version 2-2004. CEA/BNM-LNHB, 91191. Gif,-sur-Yvette, France, p. 307.

Bé, M.–M., Chisté, V., Dulieu, C., Mougeot, X., Browne, E., Chechev, V., Kuzmenko, N., Kondev, F., Luca, A., Galán, M., Nichols, A.L., Arine, A., Houang, X., 2010. Table of Radionuclides. In: Monographie BIPM-5, vol. 5. Sèvres, France, p. 228. A=22-244.

Beck, T.R., Buchröder, H., Schmidt, V., 2009. Performance tests for instruments measuring radon activity concentration. Appl. Radiat. Isot. 67, 876–880.

Belluscio, M., de Leo, R., Pantaleo, A., Vox, A., 1974. Effects of finite dimensions in source-detector solid-angle evaluation. Nucl. Instrum. Methods 114, 145–147.

Bensch, F., Ledermann, H., 1969. Rapid determination of radionuclide activities by a well-type gamma-ionisation-chamber. Nucl. Instrum. Methods 72, 56–60.

Bergeron, D.E., Fitzgerald, R., 2018. Monte-Carlo modelling of live-time anticoincidence (LTAC) counting for ^{63}Cu. Appl. Radiat. Isot. 134, 280–285.

Bergeron, D.E., Zimmerman, B.E., Cessna, J.T., 2010. Development of secondary standards for ^{223}Ra. Appl. Radiat. Isot. 68, 1367–1370.

Bergeron, D.E., Galea, R., Laureano-Perez, L., Zimmerman, B.E., 2016. Comparison of ^{14}C liquid scintillation counting at NIST and NCR Canada. Appl. Radiat. Isot. 109, 30–35.

Berlizov, A.N., Tryshyn, V.V., 2005. A Monte Carlo approach to true-coincidence summing correction factor calculation for gamma ray spectrometry applications. J. Radioanal. Nucl. Chem. 264, 169–174.

Bernaconi, G., Capote, R., 1994. GAMEFF Code Released as Part of the GENAAS Package. International Atomic Energy Agency, Vienna. Austria.

Bertolo, A., Manduchi, C., Manduchi, G., 1992. The computer code MAR for calculating the activity of radioactive samples in Marinelli beakers. Nucl. Instrum. Methods Phys. Res., Sect. A 314, 584-399.

Bignell, L.J., Mo, L., Alexiev, D., Hashemi-Nezhad, S.R., 2010. Sensitivity and uncertainty analysis of the simulation of ^{123}I and ^{54}Mn gamma and X-ray emissions in a liquid scintillation vial. Appl. Radiat. Isot. 68, 1495–1502.

Birattary, C., Salomone, A., 1980. Efficiency evaluation of gamma-ray solid state detectors. Nucl. Instrum. Methods 174, 391–399.

Birks, J.B., 1964. The Theory and Practice of Scintillation Counting. Pergamon Press, Oxford, pp. 58–185.

Blaauw, M., 1993. The use of sources emitting coincident γ-rays for determination of absolute efficiency curves for nightly efficient Ge detectors. Nucl. Instrum. Methods Phys. Res., Sect. A 332, 493–500.

Blaauw, M., Gelsema, S.J., 2003. Cascade summing in gamma-ray spectrometry in Marinelli beaker geometries: the third efficiency curve. Nucl. Instrum. Methods Phys. Res., Sect. A 505, 311–315.

Blanchis, P., 1983. Rapport CEA R-5219.

Blanchis, P., 1984. Study of scattering in a low geometry alpha counter for high precision activity measurements. Nucl. Instrum. Methods 223, 368–371.

Blanchis, P., Page, J., Bouchard, J., Vandevyver, M., Ruaudel-Teixier, A., 1990. Recent development in the preparation of radioactive sources at LMRI. Nucl. Instrum. Methods Phys. Res., Sect. A 286, 447–452.

Bobin, C., Bouchard, J., 2006. A $4\pi(LS)\beta-\gamma$ coincidence system using a TDCR apparatus in the β-channel. Appl. Radiat. Isot. 64, 124–130.

Bobin, C., Bouchard, J., Censier, B., 2010a. First results in the development of an on-line digital counting platform dedicated to primary measurements. Appl. Radiat. Isot. 68, 1519–1522.

Bobin, C., Thiam, C., Bouchard, J., Jaubert, F., 2010b. Application of a stochastic TDCR model based on Geant4 for Cherenkov primary measurements. Appl. Radiat. Isot. 68, 2366–2371.

Bobin, C., Thiam, C., Chauvenet, B., Bouchard, J., 2012. On the stochastic dependence between photomultipliers in the TDCR method. Appl. Radiat. Isot. 70, 770–780.

Bobin, C., Thiam, C., Bouchard, J., 2016. Calculation of extrapolation curves in the $4\pi(LS)\beta-\gamma$ coincidence technique with the Monte Carlo Code Geant4. Appl. Radiat. Isot. 109, 329-324.

Bobin, C., Thiam, C., Bouchard, J., 2018. Standardization of $^{68}Ge/^{68}Ga$ using a $4\pi\beta - \gamma$ coincidence method based on Cherenkov counting. Appl. Radiat. Isot. 134, 252−256.

Bonicalzi, R.M., Aalseth, C.E., Day, A.R., Hope, E.W., Mace, E.K., Moran, J.J., Overman, C.T., Panisko, M.E., Sifert, A., 2016. Optimization of simultaneous tritium-radiocarbon internal gas proportional counting. Nucl. Instrum. Methods Phys. Res., Sect. A 813, 19−28.

Boson, J., Agren, G., Johansson, L., 2008. A detailed investigation of HPGe detector response for improved Monte Carlo efficiency calculations. Nucl. Instrum. Methods Phys. Res., Sect. A 587, 304−314.

Both, J.P., Lee, Y.K., Mazzolo, A., Petit, O., Peneliau, Y., Roesslinger, B., Soldevila, M., 2003. TRIPOLI-4-A Three Dimensional Polykinetic Particle Transport Monte Carlo Code. SNA'2003, Paris.

Briesmeister, J.F., 2000. MCNP-A General Monte Carlo N-Particle Transport Code. Version 4C. Diagnostics Application group, Los Alamos National Laboratory. LA-13709-M.

Brinkman, G.A., 1961. Standardization of Radio-Isotopes by Coincidence Coumtomg Techniques with Liquid and Plastic Scintillators. Thesis University of Amsterdam, p. 130.

Brinkman, G.A., Aten Jr., A.H.W., 1963. Absolute standardization with a NaI(Tl) crystal-III. Int. J. Appl. Radiat. Isot. 14, 503−510.

Brinkman, G.A., Aten Jr., A.H.W., 1965. Absolute standardization with a NaI(Tl) crystal-V. Int. J. Appl. Radiat. Isot. 16, 177−181.

Brinkman, G.A., Aten Jr., A.H.W., Veenboer, J.T., 1963a. Absolute standardization with a NaI(Tl) crystal-I. Int. J. Appl. Radiat. Isot. 14, 153−157.

Brinkman, G.A., Aten Jr., A.H.W., Veenboer, J.T., 1963b. Absolute standardization with a NaI(Tl) crystal-II. Int. J. Appl. Radiat. Isot. 14, 433−437.

Brinkman, G.A., Aten Jr., A.H.W., Veenboer, J.T., 1965. Absolute standardization with a NaI(Tl) crystal-IV. Int. J. Appl. Radiat. Isot. 16, 15−18.

Brinkman, G.A., Lindner, L., Veenboer, J.T.,, 1977. Sum peak calibration of I- 123. Int. J. Appl. Radiat. Isot. 28, 271−275.

Broda, R., Jeczmieniowski, A., 2004. Statistics of the LS-detector in the case of low counting efficiency. Appl. Radiat. Isot. 60, 453−458.

Broda, R., Pochwalski, K., 1992. The enhanced triple to double coincidence ratio (ETDCR) method for standardization of radionuclides by liquid scintillation counting. (H-3, C-14, Ni-63, Fe-55). Nucl. Instrum. Methods Phys. Res., Sect. A 312, 85−89.

Broda, R., Pochwalski, K., Radoszewski, T., 1988. Calculation of liquid - scintillation detector efficiency. Appl. Radiat. Isot. 39, 159−164.

Broda, R., Péron, M.N., Cassette, P., Terlikowska, T., Hainos, D., 1998. Standardization of ^{139}Ce by liquid scintillation counting using the triple to double coincidence ratio method. Appl. Radiat. Isot. 49, 1035−1040.

Broda, R., Maletka, K., Terlikowska, T., Cassette, P., 2002. Study of the influence of the LS-cocktail composition for the standardisation of radionuclides using the TDCR model. Appl. Radiat. Isot. 56, 285−289.

Broda, R., Dziel, T., Muklanowicz, A., Listkowska, A., Pieńkowski, I., Patocka, A., KoŁakowska, E., 2010. Comparison of ^{99m}Tc and ^{131}I in polish hospitals, 2007. Appl. Radiat. Isot. 68, 1278−1281.

Broda, R., Dziel, T., Muklanowicz, A., 2012. Standardization of a ^{85}Sr solution by three methods. Appl. Radiat. Isot. 70, 2222−2226.

Brun, R., Bruyat, F., Maire, M., McPherson, A.C., Zanarini, P., 1987. GEANT3. CERN Data Handling Division. Geneva.

Bryant, J., 1962. Anticoincidence counting method for standardizing radioactive materials. Appl. Radiat. Isot. 13, 273−276.

Bryant, J., 1963. Extension of the efficiency tracing method for the calibration of pure β-emitters. Int. J. Appl. Radiat. Isot. 15, 279−287.

Bryant, J., 1967. Advantage of anticoincidence counting for standardization of radionuclides emitting delayed gamma. In: IEEA Symposium on Standardization of Radionuclides SM-79/21.

Brysk, H., 1977. Effective solid angle of scintillation counters for fast neutrons. Nucl. Instrum. Methods 143, 327−330.

Buckman, S.M., Keightley, J.D., Smith, D., Woods, M.J., 1998. The validation of a digital coincidence counting system. Appl. Radiat. Isot. 49, 1135−1140.

Budja, D., Heisel, M.:, Maneschg, E., Simgen, H., 2009. Optimisation of the MC-model of a p-type Ge-spectrometer for the purpose of efficiency determination. Appl. Radiat. Isot. 67, 706−710.

Büermann, L., Kramer, H.-M., Schrader, H., Selbach, H.-J., 1994. Activity determination of ^{192}Ir solid sources by ionization chamber measurements using calculated corrections for self-absortion. Nucl. Instrum. Methods Phys. Res., Sect. A 339, 30−34.

Butcher, K.S.A., Watt, G.C., Alexiev, D., van der Gaast, H., Davies, J., Mo, L., Wyllie, H.A., Keightley, J.D., Smith, D., Woods, M.J., 2000. Digital coincidence counting − initial results. Nucl. Instrum. Methods Phys. Res., Sect. A. 450, 30−34.

Calhoun, J.M., Cessna, J.T., Coursey, B.M., 1992. A system for intercomparing standard solutions of beta-particle emitting radionuclides. Nucl. Instrum. Methods Phys. Res., Sect. A 312, 114−120.

Callander, H.L., 1910. The radio-balance. Proc. R. Soc. 23, 1−34.

Camp, D.C., Van Lehn, A.L., 1969. Finite solid angle corrections for Ge(Li) detectors. Nucl. Instrum. Methods 76, 192−240.

Campion, P.J., 1959. The standardization of radioisotopes by the beta-gamma coincidence method using high efficiency detectors. Int. J. Appl. Radiat. Isot. 4, 232−248.

Campion, P.J., 1975. Procedures for accurately diluting and dispensing radioactive solutions. In: Monographie BIPM-1. Bureau International des Poids et Mesures, Sèvres, France, p. 32.

Campion, P.J., Taylor, J.G.V., Merritt, J.S., 1960. The efficiency tracing Technique for eliminating self-absortion errors in $4\pi\beta$-counting. Int. J. Appl. Radiat. Isot. 8, 8−19.

Capogni, M., Carconi, P., De Felice, P., Fazio, A., 2016. .^{18}F Primary standard at ENEA-INMRI by three absolute techniques and calibration of a well-type 1611 ionization chamber. Appl. Radiat. Isot. 109, 410−413.

Capogni, M., Ceccatelli, A., de Felice, P., Fazio, P., 2006. Random-summing corrections and pile-up rejection in the sum-peak method. Appl. Radiat. Isot. 64, 1229−1233.

Capogni, M., De Felice, P., Fazio, A., Latini, F., Abbas, K., 2008. Development of a primary standard for calibration of ^{64}Cu activity measurement systems. Appl. Radiat. Isot. 66, 948−953.

Carchon, R., Van Camp, E., Knuyt, G., Van De Vyver, R., Devos, J., Ferdinande, H., 1975. A general solid angle calculation by a Monte Carlo method. Nucl. Instrum. Methods 128, 195−199.

Cassette, P., Do, P., 2008. The Compton source efficiency tracing method in liquid scintillation counting: a new standardization method using TDCR counter with a Compton spectrometer. Appl. Radiat. Isot. 66, 1926−1932.

Cassette, P., Tartés, I., 2014. Experimental study of the influence of the counter and scintillators on the universal curves in the cross-efficiency method in LSC. Appl. Radiat. Isot. 87, 32−37.

Cassette, P., Vatin, R., 1992. Experimental evaluation of TDCR models for the 3 PM liquid scintillation counter. Nucl. Instrum. Methods Phys. Res., Sect. A 312, 95−99.

Cassette, P., Bouchard, J., Chauvenet, B., 1994. Standardization of iodine-129 by the TDCR liquid scintillation method. Nucl. Instrum. Methods Phys. Res., Sect. A, 339, 399-343.

Cassette, P., Broda, R., Hainos, D., Terlikowska, T., 2000. Analysis of detection-efficiency variation techniques for the implementation of the TDCR method in liquid scintillation counting. (H-3, Ni-63, C-14). Appl. Radiat. Isot. 52, 643−648.

Cassette, P., Bé, M.M., Jaubert, F., L!epy, M.C., 2004. Measurement of a ^{203}Pb solution using the TDCR method by LSC. Appl. Radiat. Isot. 60, 439−445.

Cassette, P., Ahn, A.H., Alzitzoglou, T., Aubineau-Lanièce, I., Bochud, F., Garcia Toraño, E., Grau Carles, A., Grau Malonda, A., Kossert, K., Lee, K.B., Laedermann, J.P., Simpson, B.R.S., van Wyngaardt, W.M., Zimmerman, B.E., 2006. Comparison of calculated spectra for the interaction of photons in a liquid scintillator. Example of ^{54}Mn 835 keV emission. Appl. Radiat. Isot. 64, 1471−1480.

Cassette, P., Jaubert, F., Tartes, I., 2010. Study of the influence of the liquid scintillator in the Compton efficiency tracing method. Appl. Radiat. Isot. 68, 1510−1514.

Ceccatelli, A., De Felice, P., 1999. Standardisation of ^{90}Sr, ^{63}Ni and ^{55}Fe by the $4\pi\beta$ liquid scintillation spectrometry method with ^{3}H-standard efficiency tracing. Appl. Radiat. Isot. 51, 85−92.

Cesana, A., Terrani, M., 1989. An empirical method for peak-to-total ratio computation of gamma-ray detector. Nucl. Instrum. Methods Phys. Res., Sect. A 281, 172−175.

Cessna, J.T., 2002. The measurement of activity contained in a ^{32}P stainless-steel stent by destructive assay. Appl. Radiat. Isot. 56, 337−342.

Cessna, J.T., Zimmerman, B.E., Unterweger, M.P., Golas, D.B., 2004. Establishment of transfer standard for holmium-166-DOTMP. Appl. Radiat. Isot. 60, 505−510.

Cessna, J.T., Schultz, M.K., Leslie, T., Bores, N., 2008. Radionuclide calibrator measurements of ^{18}F in a 3 ml plastic syringe. Appl. Radiat. Isot. 66, 988−993.

Cessna, J.T., Fitsgerald, R., Zimmerman, B.E., Laureano-Pérez, L., Bergeron, D.E., van Wyngaardt, F., Smith, M., Jackson, T., Howe, R., da Silva, C.J., Iwahara, A., da Cruz, P.A.L., Zhang, M., Liu, H., Liang, J., Fréchou, C., Bobin, C., Cassette, P., Pearce, A., 2018. Results of an international comparison of activity measurements of ^{68}Ge. Appl. Radiat. Isot. 134, 385−390.

Cessna, J.Y., Zimmerman, B.E., 2015. Standardization of radium-223 by liquid scintillation counting. Appl. Radiat. Isot. 68, 1523−1528.

Chatelier, M., Launois, D., 1972. Méthode de calcul d'angles solides définis par un ensemble de diaphragmes de formes quelconques. Nucl. Instrum. Methods 105, 231−236.

Chauvenet, B., Bé, M.−M., Amiot, M.−N., Bobin, C., Lépy, M.−C., Branger, T., Lanièce, I., Luca, A., Sahagia, M., Wätjen, A.C., Kossert, K., Ott, O., Nähle, O., Dryák, P., Sochorovà, J., Kovar, P., Auerbach, P., Altzitzoglou, T., Pommé, S., Sibbens, G., Van Ammel, R., Paepen, J., Iwahara, A., Delgado, J.U., Poledna, R.,C., da Silva, C.J., Johansson, L., Stroak, A., Bailat, C., Nedjad, Y., Spring, P., 2010. International exercise on ^{124}Sb activity measurements. Appl. Radiat. Isot. 68, 1207−1210.

Chen, Q.J., Nielsen, S.P., Aarkrog, A., 1989. Preparation of thin alpha sources by electrospraying for efficiency calibration purposes. J. Radional. Nucl. Chem. Lett. 2 135, 117−123.

Chen, J., Geraedts, S.D., Ouellet, C., Singh, B., 2011. Evaluation of half-life of ^{198}Au. Appl. Radiat. Isot. 69, 1064−1069.

Chylinski, A., 1992. A new version of the tracer technique for absolute measurements of EC emitters. Nucl. Instrum. Methods Phys. Res., Sect. A 312, 59−63.

Chylinski, A., Radoszewski, T., 1992. Two-parametric method for measuring the radioactive concentration of ^{22}Na. Nucl. Instrum. Methods Phys. Res., Sect. A 312, 76−89.

Chylinski, A., Radoszewski, T., 1996. Generalized 4π(LS)$\beta-\gamma$ tracer method for standardization of pure beta emitters. Nucl. Instrum. Methods Phys. Res., Sect. A 369, 336−339.

Chylinski, A., Pasiewicz, K., Radoszewski, T., Wolski, D., Wojtowicz, S., 1972. $4\pi\beta-\gamma$anticoincidence method and apparatus for radioactive concentration measurements of radioactivity solutions. Nucl. Instrum. Methods 98, 109−117.

Chylinski, A., Radoszewski, T., Terlikowska-Droździel, T., Jeczmieniowski, A., 2000. A multimethodic and multiparametric system for standardisation of radionuclides. Appl. Radiat. Isot. 52, 663−667.

Chylinski, A., Terlikowska-Droździel, T., Radoszewski, T.R., Broda, R., 2002. Multi-method of standardization of radionuclides with "triangular scheme" of disintegration. Appl. Radiat. Isot. 56, 281−284.

Cline, J.E., 1979. A technique of gamma-ray detector absolute efficiency calibration for extended sources. In: Proc. Am. Nucl. Soc. Topical Conf. On Computers in Activation Analysis and Gamma-Ray Spectroscopy, Mayaguez, Puerto Rico, 1978, CONF. 780421, p. 185.

Clisler, D.F., Jarmer, J.J., Eldridge, H.B., 1971. A method for absolute calibration of Ge(Li) detectors using effective interaction depth. Nucl. Instrum. Methods 94, 285−288.

Collé, R., 2000. On the radioanalytical methods used to assay stainless-steel-encapsulated, ceramic-based Y^{90} Sr-^{90}Y intravascular brachytherapy sources. Appl. Radiat. Isot. 52, 1−18.

Collé, R., 2001. Calibration of ^{32}P "hot-wall'' angioplasty-balloon-catheter sources by liquid-scintillation-spectrometry-based destructive radionuclidic assays. Appl. Radiat. Isot. 54, 611−622.

Collé, R., 2002. Activity characterization of pure-â-emitting brachytherapy sources. Appl. Radiat. Isot. 56, 331−336.

Collé, R., 2007. Classical radionuclidic calorimetry. Metrologia 44, S118−S126.

Collé, R., Zimmerman, B.E., 1996. Nickel-63: standardization 1968-1995. Radioact. Radiochem. 7, 13−27.

Collé, R., Zimmerman, B.E., 2001. A dual-compensed cryogenic microcalorimeter for radioactivity standardizations. Appl. Radiat. Isot. 56, 223−230.

Collé, R., Zimmerman, B.E., 2011. Radionuclidic standardization by classical isothermal microcalorimetry: recent work on ^{32}P, ^{90}Sr, and ^{103}Pd brachytherapy sources. J. Res. Nat. Inst. Stand. Technol. (to be published).

Collé, R., Zimmerman, B.E., Soares, C.G., Coursey, B.M., 1999. Determination of a calibration factor for the nondestructive assay of Guidant ^{32}P brachytherapy sources. Appl. Radiat. Isot. 50, 835−841.

Collé, R., Zimmerman, B.E., Cassette, P., Laureano-Pérez, L., 2008. ^{63}Ni, its half-life and standardization: revisited. Appl. Radiat. Isot. 66, 60−68.

Collins, S., Keightley, J., Gilligan, C., Gasparro, J., Pearce, A., 2014. Determination of the gamma emission intensities of ^{111}Ag. Appl. Radiat. Isot. 87, 107−111.

Collins, S., Sheraman, R., Keightley, J., Regan, P.H., 2018. Investigation of $\gamma-\gamma$ coincidence counting using the National Nuclear Array (NANA) as a primary standard. Appl. Radiat. Isot. 134, 290−296.

Conway, J.T., 2006. Generalization of Ruby's formula for the geometric efficiency of the parallel-dick source and detector system. Nucl. Instrum. Methods Phys. Res., Sect. A 562, 146−153.

Conway, J.T., 2007. Geometric efficiency for a parallel-source and detector system with at least one axisymmetric surface. Nucl. Instrum. Methods Phys. Res., Sect. A 583, 382−393.

Conway, J.T., 2008. Calculation for a disk source and a general detector using a radiation vector potential. Nucl. Instrum. Methods Phys. Res., Sect. A 589, 20−33.

Conway, J.T., 2010. Analytical solution for the solid angle subtended at any point by an ellipse via a point source radiation vector potential. Nucl. Instrum. Methods Phys. Res., Sect. A 614, 17−27.

Cook, J., 1980. An analytical solution for the solid angle subtended by a circular detector for a symmetrically positioned linear source. Appl. Radiat. Isot. 64, 603−697.

Cornejo Diaz, N., Jurado Vargas, M., 2008. DETEFF: an improved Monte Carlo computer program for evaluating the efficiency in coaxial gamma-ray detectors. Nucl. Instrum. Methods Phys. Res., Sect. A 586, 204−210.

Coursey, B.M., Hoppes, D.D., Schima, F.J., 1982. Determination of the photon emission rates of the NBS long-lived mixed-radionuclide standard. Nucl. Instrum. Methods Phys. Res., Sect. A 193, 1−8.

Coursey, B.M., Calhoun, J.M.:, Cessna, J., Golas, D.B., Schima, F.J., Unterweger, M.P., 1994. Liquid-scintillation counting techniques for the standardization radionuclides used in therapy. Nucl. Instrum. Methods Phys. Res., Sect. A 339, 26−30.

Coursey, B.M., Schima, F.J., Golas, D.B., Palabrica, O.T., Suzuki, A., Dell, M.A., 1998. Measurement standards for strontium-89 for use in bone palliation. Appl. Radiat. Isot. 49, 335−344.

Coursey, B.M., Collé, R., Coursey, J.S., 2002. Standards of radium-226: from Marie Curie to the international committee for radionuclide metrology. Appl. Radiat. Isot. 56, 5−13.

Cox, B., 1969. A Monte Carlo method for performing difficult geometry solid angle corrections. Nucl. Instrum. Methods 70, 340−342.

Cox, D.R., Isham, V., 1977. A bivariate point process connected with electronic counters. Proc. R. Soc. Lond. 356, 149−160.

Crawford, J.A., 1949. Theoretical calculation concerning backscattering of alpha particles. Part II. In: The Transuranium Elements. McGraw-Hill, New York, pp. 1307−1326.

Csete, I., Szüks, L., Zsinka, A., 2002. Standardization of ^{89}Sr at the national Office of measurements. Appl. Radiat. Isot. 56, 467−470.

Da Cruz, P.A.L., Loureiro, J.S., Bernardes, E.M.O., 2002. Standardization of a ^{89}Sr solution from a BIPM intercomparison using a liquid scintillation method. Appl. Radiat. Isot. 56, 457−459.

Da Cruz, P.A.L., Iwahara, A., Bernardes, E.M.O., Da Silva, C.J., 2004. The absolute standardization of ^{32}P and ^{204}Tl at LNMRI. Appl. Radiat. Isot. 60, 415−418.

Da Silva, C.J., Delgado, J.U., Iwahara, A., Tauhata, L., Poledna, R., Alves, R.N., 2002. Absolute determination of activity per mass and half-life measurements of ^{152}Eu. Appl. Radiat. Isot. 56, 169−172.

Da Silva, M.A.L., Poledna, R., Iwahara, A., Da Silva, C.J., Delgado, J.U., Lopes, R.T., 2006. Standardization and decay data determinations of ^{125}I, ^{54}Mn and ^{203}Hg. Appl. Radiat. Isot. 64, 1440−1445.

Da Silva, C.J., Iwahara, A., Poledma, R., de Oliveira, E.M., de Prinzio, M.A.R.R., Delgado, J.U., Lopes, R.T., 2008a. Standardization of ^{241}Am, ^{124}Sb and ^{131}I by live-timed anti-coincidence counting with extending dead time. Appl. Radiat. Isot. 66, 886−889.

Da Silva, C.J., Iwahara, A., Poledna, R., Bernardes, E.M. de O., de Prinzio, M.A.R.R., Lopes, T.T., 2008b. Standardization of ^{67}Ga, ^{51}Cr and ^{55}Fe by live-timed anti-coincidence counting with extending dead time. Appl. Radiat. Isot. 66, 231−235.

Da Silva, C.J., Rezende, E.A., Poledma, R., tauhata, L., Iwahara, a., Lopes, R.T., 2017. Standardiztion of ^{106}Ru/Rh by live-timed anti-coincidence counting and gamma emission determination. Appl. Radiat. Isot. 122, 37−40.

Da Silva, C.J., da Cruz, P.A.I., Iwahara, A., Oliveira, E.M., Loureiro, J., dos, S., Tauhata, L., da Silva, R.L., Poledna, R., Lopes, R.t., 2018a. 68(Ge+Ga)Activity standardization by 4π(LS)$\beta-\gamma$(NaI-Tl) anti-coincidence counting measurements. Appl. Radiat. Isot. 134, 307−311.

Da Silva, C.J., da Cruz, P.A.I., Iwahara, A., Laurerio, J. dos S., Gomes, R. dos S., dos santos, A.R.I., de Araujo, M.T.F., Poledna, R., da Silva, R.L., Laranjeira, A. da S., 2018b. ^{134}Cs activity standardization by 4π(LS)$\beta-\gamma$(NaI-Tl) anticoincidence counting and submission to international reference system. Appl. Radiat. Isot. 134, 316−320.

Dale, J.W.G., 1961. A beta-gamma ionization chamber for substandards of radioactivity—II: instrument response to gamma radiation. Int. J. Appl. Radiat. Isot. 10, 72−78.

Dale, J.W.G., Perry, W.E., Pulfer, R.F., 1961. A beta—gamma ionization chamber for substandards of radioactivity—I: uses and calibration. Int. J. Appl. Radiat. Isot. 10, 65−66.

Davidson, S., Perkin, M., Buckley, M., 2004. Measurement Good Practice Guide No. 71. National Physical Laboratory, Teddington, Middlesex. UK, p. 29.

Davis, R.S., 1992. Equation for the determination of the density of moist air. (1981/91). Metrologia 29, 67−70.

De Almeida, C.M.C., Iwahara, A., Poledna, R., Da Silva, C.J., Delgado, J.U., 2007. Absolute disintegration rate and 320 keV γ-ray emission probability of ^{51}Cr. Nucl. Instrum. Methods Phys. Res., Sect. A 580, 165−168.

De Bruin, M., Korthoven, P.J.M., Bode, P., 1979. Spectrum interpretation problems with well-type Ge(Li) detectors due to self-absorption variations. Nucl. Instrum. Methods 159, 301−303.

De Carlos, J.E., Granados, C.E., 1973. The "SAMAR" shared-dead-time method. A new approach to Beta-gamma coincidence counting. Nucl. Instrum. Methods 112, 209−212.

De Castro Faria, N.V., Lévesque, R.J.A., 1967. Photopeak and double-escape peak efficiencies of germanium lithium drift detectors. Nucl. Instrum. Methods 46, 325−332.

De Felice, P., Mytebery, X., 1995. Standardization of I-125 by the sum-peak method and the results of the bilateral comparison between ENEA (Italy) and INP (Albania). J. Radioanal. Nucl. Chem. Lett. 200, 109−118.

De Oliveira, E.M., Iwahara, A., Poledna, R., da Silva, M.:A.:L.:, tauhata, L., Delgado, J.U.:, Lopes, R.T., 2012. Use of sum-peak and coincidence for activity standardization of ^{22}Na. Nucl. Instrum. Methods Phys. Res., Sect. A. 687, 69−74.

De Sanoit, J., Hainos, D., Bouchard, J., Geffroy, B., Rosilio, C., 1998. Self-supported PEDT/PVC conducting membranes for $4\pi\beta$ sources preparation. Appl. Radiat. Isot. 49, 1259−1264.

De Sanoit, J., Leprince, B., Vailhen, D., 2001. Optimisation des sources ponctuelles sur film mince par une approche expérimentale de type plan d'espériences. Application aux sources de ^{60}Co. Rapport CEA-R-5970. CEA/Saclay. 91991 Gif-sur Yvette. France.

De Sanoit, J., Leprince, B., Bobin, C., Bouchard, J., 2004. Freeze-drying applied to radioactive source preparation. Appl. Radiat. Isot. 61, 1391−1395.

De Vismes, A., Amiot, M.N., 2003. Towards absolute activity measurements by ionisation chambers using the PENELOPE Monte-Carlo code. Appl. Radiat. Isot. 59 (267), 272.

Debertin, K., 1996. The art of realizing the Bequerel. Appl. Radiat. Isot. 47, 423−431.

Debertin, K., Helmer, R.G., 1988. Gamma- and X-ray Spectrometry with Semiconductor Detectors. North Holland, Amsterdam, p. 399.

Debertin, K., Jianping, R., 1989. Measurement of the activity of radioactive samples in Marinelli beakers. Nucl. Instrum. Methods Phys. Res., Sect. A 278, 541−549.

Debertin, K., Schötzig, U., 1979. Coincidence summing corrections in Ge(Li)-spectrometry at low source-to-detector distances. Nucl. Instrum. Methods 158, 471−477.

Decombaz, M., Laedermann, J.P., 1996. Efficiency determination of a $4\pi\gamma$ detector by numerical simulation. Nucl. Instrum. Methods Phys. Res., Sect. A 369, 375−379.

Decombaz, M., Gostely, J.J., Laedermann, J.P., 1992. Coincidence-summing corrections for extended sources in gamma-ray spectrometry using Monte Carlo simulations. Nucl. Instrum. Methods Phys. Res., Sect. A 312, 152−159.

Delgado, J.U., Iwahara, A., Poledna, R., Da Silva, C.J., Lopes, R.T., Tauhata, L., 2001. Absolute measurements of photon emission probabilities of ^{169}Yb. Appl. Radiat. Isot. 54, 483−487.

Denecke, B., 1987. Measurement of the 59.5 keV gamma ray emission probability in the decay of ^{241}Am with a 4π-CsI(Tl)-sandwich spectrometer. Int. J. Appl. Radiat. Isot. 38, 823−830.

Denecke, B., 1994. Absolute activity measurements with the windowless 4π-CsI(Tl)-sandwich spectrometer. Nucl. Instrum. Methods Phys. Res., Sect. A 339, 92−98.

Denecke, B., Grosse, G., Szabo, T., 1998. Gain stabilisation of gas-flow proportional counters. Appl. Radiat. Isot. 49, 1117−1121.

Denecke, B., Eykens, R., Pauwels, J., Robouch, P., Gilliam, D.M., Hodge, P., Hutchinson, J.R.M., Nico, J.S., 1999. Characterization of actinide targets by low solid-angle alpha particle counting. Nucl. Instrum. Methods 438, 124−130.

Denecke, B., Sibbens, G., Szabo, T., Hult, M., Persson, L., 2000. Improvements in quantitative source preparation. Appl. Radiat. Isot. 52, 351−355.

Dersch, R., 2004. Primary and secondary measurements of 222Rn. Appl. Radiat. Isot. 60, 387−390.

Dias, M.S., Koskinas, F., 1995. Accidental summing correction in I-125 activity determination by the sum-peak method. Appl. Radiat. Isot. 46, 945−948.

Dias, M.S., Piuvezam-Filho, H., Koskinas, M.F., 2008. Optimization of a coincidence system using plastic scintillators in 4π geometry. Appl. Radiat. Isot. 66, 905−908.

Dias, M.S., Silva, F.F.V., Koskinas, M.F., 2010. Standardization and measurement of gamma-ray probability per decay of ^{177}Lu. Appl. Radiat. Isot. 68, 1349−1353.

Dias, M.S., Takeda, M.N., Toledo, F., Brancaccio, F., Tongu, M.L.O., Koskinas, M.F., 2013. Improvements in the Monte Carlo code for simulating 4π(PC)$\beta-\gamma$ coincidence System measurements. Nucl. Instrum. Methods Phys. Res., Sect. A 698, 177−184.

Dias, M.S., Brancaccio, F., Toledo, F., Koskinas, M.F., 2014. Disintegration rate , gamma ray emission probabilities and metastable half-life measurements of ^{67}Ga. Appl. Radiat. Isot. 87, 126−131.

Dirican, A., Erden, P.E., Seferinoglu, M., Pommé, S., 2012. The use of solid angle for alpha detector efficiency in ^{226}Ra analysis of soil samples. Appl. Radiat. Isot. 70, 2260−2262.

Dobilovri, L., Simovi, M., Bek-Uzarov, D., Hutchinson, J.M.:R., Mann, W.B., 1988. Preparation and properties of monomolecular films for use as radioactive source mounts. Appl. Radiat. Isot. 39, 999−1008.

Domen, S.R., 1980. Absorbed dose water calorimeter. Med. Phys. 7, 157−159.

Dos Santos, J.A., Iwahara, A., De Oliveira, A.E., Da Silva, M.A.L., Da Silva, C.J., Tauhata, L., Lopes, R.T., 2004. National intercomparison program for radiopharmaceutical activity measurements. Appl. Radiat. Isot. 60, 523−527.

Dos Santos, J.A., Iwahara, A., Nícoli, I.G., Corrêa, R.S., Alabarse, F.G., Dos Santos, C.E.L., Xavier, A.M., Garcia, E.J., Tauhata, L., Lopes, R.T., 2006. Implementation of a national metrology network of radionuclides used in nuclear medicine. Appl. Radiat. Isot. 64, 1114−1118.

Dragoun, O., Brabec, V., Rysavý, M., Plch, J., Zderadièka, J., 1976. Internal conversion of high-multipolarity transition in ^{109}Ag and ^{113}In. Zeitschrift für Physik A: Atoms and Nuclei 279, 107−111 (Z. Phys. A).

Dryák, P., Dvorac, L., 1986. Measurement of the energy response function of the UVVVR 4π ionization chambers. Appl. Radiat. Isot. 37, 1071−1073.

Dryák, P., Kovar, P., 2006. Experimental and MC determination of HPGe detector efficiency in the 40−2754 keV energy range for measuring point source geometry with the source-to-detector distance of 25 cm. Appl. Radiat. Isot. 64, 1346−1349.

Dryák, P., Sochorová, J., Solk, J., Auerbach, P., 2016. Activity standardization, photon emission probabilities and half-life measurements of ^{177}Lu. Appl. Radiat. Isot. 109, 160−163.

Du, H., Jia, Z., Yu, Y., 1986. Preparation of thin $4\pi\beta$-sources for absolute measurement. Nucl. Instrum. Methods Phys. Res., Sect. A 251, 254−257.

Du, H., Li, J., Yan, S., Li, G., Zhu, Y., Yao, L., 1996. Progress in preparation $4\pi\beta$quantitative sources. Nucl. Instrum. Methods Phys. Res., Sect. A 369, 424−426.

Duran, M.T., Nedjadi, Y., Juget, F., Bochud, F., Bailat, C., 2018. Fast digital $4\pi\beta$-$4\pi\gamma$ coincidence counting with offline analysis at IRA. Appl. Radiat. Isot. 134, 329−336.

Dziel, T., Broda, R., Ziemek, T., Muklanowicz, A., Listkowska, A., 2014. Standardization of ^{153}Sm solution by absolute methods. Appl. Radiat. Isot. 87, 19−23.

Dziel, T., Liskowska, A., Tyminski, Z., 2016. Standardization and half-life of ^{111}In. Appl. Radiat. Isot. 109, 345−348.

Eddiss, C., Abrams, D.N., 1981. Implementation of the coincidence method for determining I-125 activity with estimated error. J. Radioanal. Chem. 65 (1−2), 341−347.

Eichelberger, J.F., Jordan, K.C., Orr, S.R., Parks, J.R., 1954. Calorimetric determination of the half-life of polonium-210. Phys. Rev. 96, 719−721.

El-Katib, A.M., salem, b.a., badawi, M.S., gouda, M.M., Thabet, A.A., abbas, M.I., 2017. Full-energy peak efficiency of an NaI(Tl) detector with coincidence summing correction showing the effect of the source-to-detector distance. Chin. J. Phys. 55, 478−489.

Eldridge, J.S., Crowether, P., 1964. Absolute determination of I-125. Nucleonics 22, 56−59.

Ellis, C.D., Wooster, W.A., 1925a. The heating effect of the γ-rays of radium B and radium C. Philos. Mag. 50, 521.

Ellis, C.D., Wooster, W.A., 1925b. The heating effect of the γ-rays of RaB and RaC. Proc. Camb. Phil. Soc. 22, 595−596.

Enss, C., Fleischmann, A., Horst, K., Schönefeld, J., Sollner, J., Adams, J.S., Huang, Y.H., Kim, Y.H., Seidel, G.M., 2000. Metallic magnetic calorimeters for particle detection. J. Low Temp. Phys. 121, 137−176.

Evgeny, T., Nikolay, M., Alexandr, K., 2016. ^{56}Mn, ^{60}Co, ^{18}F and ^{22}Na Activity measurements by coincidence technique at VNIIM. Appl. Radiat. Isot. 109, 378−381.

Ewa, I.O.B., Bodizs, D., Czifrus, S., Molnar, Z., 2001. Monte Carlo determination of full energy peak efficiency for HPGe detector. Appl. Radiat. Isot. 55, 103−108.

Ferreira Filho, A.L., da Silva, R., da Cruz, P.A.L., da Silva, C.J., Poledna, R., Araújo, M.T.F., Arcanjo, C.F., delgado, J.u., Lopes, R.T., 2018. Application of the sum-peak method to activity standardizations of ^{152}Eu sources in LNMRI (BR). Appl. Radiat. Isot. 134, 340−350.

Ferrero, J., Roldán, C., Aceña, M., García-Toraño, E., 1990. Backscattering and self-absortion corrections in the measurement of alpha-emitters in 2π geometry. Nucl. Instrum. Methods Phys. Res., Sect. A 286, 384−387.

Fettweis, P.F., Verpalnke, J., Venkataraman, R., young, B.M., Schwenn, H., 2003. In: Annunziata, L.' (Ed.), Semiconductor Detectors: Handbook of Radioactivity Analysis, second ed. New York Academic, pp. 309−323.

Fitzgerald, R., 2010. An automated ionization chamber for secondary radioactivity standards. Appl. Radiat. Isot. 68, 1507−1509.

Fitzgerald, R., 2016. Monte Carlo based approach to the LS-NaI $4\pi\beta-\gamma$ anticoincidence extrapolation and uncertainty. Appl. Radiat. Isot. 109, 308−313.

Fitzgerald, R., Collé, R., Laureano-Pérez, L., Pibida, L., Hammond, M.M., Nour, S., Zimmerman, B.E., 2010. A new primary standardization of ^{229}Th. Appl. Radiat. Isot. 68, 1303−1308.

Fitzgerald, R., Schultz, M.K., 2008. Liquid-scintillation-based anticoincidence counting of ^{60}Co and ^{210}Pb. Appl. Radiat. Isot. 66, 937−940.

Fitzgerald, R., Zimmerman, B.E., Bergeron, D.E., Cessna, J.C., 2014. A new NIST primary standardization of ^{18}F. Appl. Radiat. Isot. 85, 74−84.

Fleischmann, A., Daniyarov, T., Rotzinger, H., Linck, M., 2003. Magnetic calorimeters for high resolution x-ray spectroscopy. Rev. Sci. Instrum. 74, 3947−3954.

Fleischmann, A., Linck, M., Daniyarov, T., Rotzinger, H., Enss, C., Seidel, G.M., 2004. Metallic magnetic calorimeters (MMC): detectors for high-resolution X-ray spectroscopy. Nucl. Instrum. Methods Phys. Res., Sect. A 520, 27−31.

Flynn, K.F., Jaffey, A.H., Bentley, W.C., Essling, A.M., 1972. Precision measurement of half-life and specific activity of 236U. J. Inorg. Nucl. Chem. 34, 1121−1129.

Fonseca, K.A., 1997. Measurement of the Absolute Activity and the Gamma Ray Probability Per Decay of I-126 (Master thesis). University of Sao Paulo (in Portuguese).

Fonseca, K.A., Koskinas, M.F., Dias, M.S., 2001. Disintegration rate measurement of a ^{192}Ir solution. Appl. Radiat. Isot. 54, 141−145.

Friedländer, E.M., 1964. Correlation counting of coincidence events. Nucl. Instrum. Methods 31, 293−300.

Friot, S., 2015. On Ruby's solid angle formula and some of its generalization. Nucl. Instrum. Methods Phys. Res., Sect. A 773, 150−153.

Funck, E., Nylandstedt Larsen, A., 1983. The influence from low energy x-rays and Auger electrons on $4\pi\beta\gamma$ coincidence measurements of electron-capture-decaying nuclides. Int. J. Appl. Radiat. Isot. 34, 565−569.

Gaggero, G., 1971. Monte Carlo calculations for the photofractions and energy loss spectra of Ge(Li) semiconductor detectors. Nucl. Instrum. Methods 94, 481−492.

Galiano, E., Rodrigues, M., 2006. A comparison of different analytical methods of determining the solid angle of a circular coaxial source−detector system. Appl. Radiat. Isot. 64, 497−501.

Galiano Casas, G., Grau Carles, A., Grau Malonda, 1995. CAPMULT, the counting efficiency for electron capture by a KLMN four-shell model. Comp. Phys. Commun. 87, 432−437.

Gandy, A., 1961. Absolute measurement of the activity of radionuclides by the beta-gamma coincidence method with high efficiency detectors. Study of instrumental coincidences. Int. J. Appl. Radiat. Isot. 11, 75−91.

Gandy, A., 1962. Absolute measurement of the activity of radionuclides by the beta-gamma coincidence method using detectors of great efficiency. Dead-time corrections. Int. J. Appl. Radiat. Isot. 13, 501−513.

Gandy, A., 1963. Absolute measurement of the activity of radionuclides by the β-γ coincidence method. Study of a method for automatically correcting instrument errors. Int. J. Appl. Radiat. Isot. 14, 385−396.

García, G., Blanco, F., Grau Carles, A., Grau Malonda, A., 2004. Inelastic scattering and stopping power of low energy electrons (0.001-10 keV) in toluene. Appl. Radiat. Isot. 60, 481−485.

García-Toraño, E., Aceña Barrenechea, M.L., 1989. Cámara de baja geometría para la medida absoluta de la actividad de muestras emisoras alfa. CIEMAT Technical Report 626.

García-Toraño, E., Grau Malonda, A., 1981. EFFY, a program to calculate the counting efficiency of beta particles in liquid scintillation counting. Comput. Phys. Commun. 23, 385−391.

García-Toraño, E., Grau Malonda, A., 1985. EFFY2, a new program to calculate the counting efficiency of beta particles in liquid scintillation counting. Comput. Phys. Commun. 36, 307−312.

García-Toraño, E., Roteta, M., 2004. Standardization of ^{67}Ga by $4\pi\gamma$(NaI) and $4\pi\beta-\gamma$ coincidence methods. Appl. Radiat. Isot. 60, 353−356.

García-Toraño, E., Roteta, M., Rodríguez Barquero, L., 2000. Standardization of ^{110m}Ag by liquid scintillation and $4\pi\beta-\gamma$ coincidence counting. Appl. Radiat. Isot. 52, 637−641.

García-Toraño, E., Rodriguez Barquero, L., Roteta, M., 2002a. Standardization of ^{134}Cs by three methods. Appl. Radiat. Isot. 56, 211−214.

García-Toraño, E., Peyres, V., Roteta, M., 2002b. On the standardization of positron emitters by $4\pi\gamma$ counting. Nucl. Instrum. Methods Phys. Res., Sect. A 570, 84–88.

García-Toraño, E., Duran Ramiro, T., Burgos, C., Begoña Ahedo, M., 2008. Defined solid-angle counter with variable geometry. Appl. Radiat. Isot. 66, 881–885.

García-Toraño, E., Peyrés Medina, V., Roteta Ibarra, M., 2010. The half-life of ^{18}F. Appl. Radiat. Isot. 68, 1561–1565.

García-Toraño, E., Peyrés, V., Roteta, M., Sanchez-Cabezudo, A.I., Romero, E., Marinez Ortega, A., 2016. Standardization and precise determination of the half-life of ^{44}Sc. Appl. Radiat. Isot. 109, 314–318.

Gardner, R.P., Carnesale, A., 1969. The solid angle subtended at a point by a circular disk. Nucl. Instrum. Methods 73, 228–230.

Gardner, R.P., Verghese, K., 1971. On the solid angle subtended by a circular disc. Nucl. Instrum. Methods 93, 163–167.

Gardner, R.P., Verghese, K., Lee, H.M., 1980. The average solid angle subtended by a circular detector coaxial to a circular isotropic source. Nucl. Instrum. Methods 176, 615–617.

Garfinkel, S.B., Mann, W.B., Schima, F.J., Unterweger, M.P., 1973. Present status in the field of internal gas counting. Nucl. Instrum. Methods 112, 59–67.

Gehrke, R.J., Helmer, R.G., Greenwood, R.C., 1977. Precise relative gamma-ray intensities for calibration of Ge semiconductor detector. Nucl. Instrum. Methods 147, 405–423.

Gelsema, S.J., 2001. Advanced γ -ray Spectrometry Dealing with Coincidence and Attenuation Effects (Ph D. thesis). Delft University of Technology, Delft, The Netherlands, pp. 101–126.

Gibson, J.A.B., Gale, H.J., 1968. Absolute standardization with liquid scintillation counters. J. Sci. Instrum. 1 (2), 96–106.

Gilmore, G., 2008. Practical Gamma-Ray Spectrometry, second ed. John Wiley and sons, New York, pp. 165–180.

Golas, D.B., 1998. NIST radiopharmaceutical standard reference materials and the NEI/NIST radiopharmaceutical measurement assurance program. Appl. Radiat. Isot. 49, 329–334.

Goldansky, V.I., Podgoretsky, M.I., 1955. Possible use of a correlation function for the study of nuclear disintegration. Dok. Akad. Nauk. URSS 100, 237.

Goodier, W., Williams, A., 1966. Measurement of the absolute disintegration rate of Technetium-99 m. Nature 210, 614–615.

Gostely, J.–J., 1992. A determination of the half-life of ^{137}Cs. Int. J. Appl. Radiat. Isot. 43, 949–951.

Gostely, J.–J., Laedermann, J.–P., 2000. Simulation of the response of the IG11 $4\pi\gamma$ ionization chamber using GEANT Monte Carlo code. Appl. Radiat. Isot. 52, 447–453.

Gotoh, H., Yagi, H., 1971. Solid angle subtended by a rectangular slit. Nucl. Instrum. Methods 96, 485–486.

Grau Carles, A., 1994a. A new linear spectrum unfolding method applied to radionuclide mixtures in liquid scintillation spectrometry. Appl. Radiat. Isot. 45, 83–90.

Grau Carles, A., 1994b. SRLOG, the simultaneous standardization of 90Sr+90Y+89Sr mixtures. Comp. Phys. Commun 82, 17–22.

Grau Carles, A., 1996. MLOG, the simultaneous standardization of multinuclide mixtures. Comp. Phys. Commun. 93, 48–52.

Grau Carles, A., 2005. Beta shape factor determinations by the cutoff yield method. Nucl. Instrum. Methods Phys. Res., Sect. A 551, 312–322.

Grau Carles, A., 2006a. Synergic quenching effects of water and carbon tetrachloride in liquid scintillation gel samples. Appl. Radiat. Isot. 64, 1505–1509.

Grau Carles, A., 2006b. EMILIA, the LS counting efficiency for electron-capture and capture-gamma emitters. Comp. Phys. Commun. 174, 35–46.

Grau Carles, A., 2007. MICELLE, the micelle size effect on the LS counting efficiency. Comp. Phys. Commun. 176, 305–310.

Grau Carles, A., Grau Malonda, A., 1989. Electron-capture standardization with a triple phototube system. An. Fis. Ser. B 85, 160–173.

Grau Carles, A., Grau Malonda, A., 1994. Alpha/beta separation in liquid scintillation gel samples. Nucl. Instrum. Methods Phys. Res., Sect. A 345, 102–106.

Grau Carles, A., Grau Malonda, A., 1995. Radionuclide standardization by Cherenkov counting. Appl. Radiat. Isot. 46, 799–803.

Grau Carles, A., Grau Malonda, A., 1996. Precisión measurement of the RAE shape factor. Nucl. Phys. A 596, 83–90.

Grau Carles, A., Grau Malonda, A., 1998. CHEREN, the Cherenkov counting efficiency. Comp. Phys. Commun. 111, 258–264.

Grau Carles, A., Grau Malonda, A., 2006a. Computational aspects in modelling the interaction of low.energy X-rays with liquid scintillators. Appl. Radiat. Isot. 64, 1515–1519.

Grau Carles, A., Grau Malonda, A., 2006b. CHEREN2, the Cherenkov counting efficiency by an anisotropy detection model. Comp. Phys. Commun. 174, 30–34.

Grau Carles, A., Grau Malonda, A., 2010. Liquid Scintillation High Resolution Spectral Analysis. Informe Técnico CIEMAT-1208, Madrid, p. 28.

Grau Carles, A., Grau Malonda, A., 2011. Standardization of I-125 by the Sum Pesk Method. Informe Técnico CIEMAT-1245, Madrid, p. 52.

Grau Carles, A., Kossert, K., 2006. New advances in the determination of the ^{87}Rb shape factor function. Nucl. Phys., Sect. A 767, 248–258.

Grau Carles, A., Kossert, K., 2007. Measurement of the shape-factor functions of the long-lived radionuclides 87Rb, 40K and 10Be. Nucl. Instrum. Methods Phys. Res., Sect. A 572, 760–767.

Grau Carles, A., Martín-Casallo, M.T., Grau Malonda, A., 1991. Spectrum unfolding and double window methods applied to standardization of ^{14}C and ^{3}H mixtures. Nucl. Instrum. Methods Phys. Res., Sect. A 307, 484–490.

Grau Carles, A., Grau Malonda, A., Rodríguez Barquero, L., 1993a. Cherenkov radiation effects on counting efficiency in extremely quenched liquid scintillation samples. Nucl. Instrum. Methods Phys. Res., Sect. A 334, 471–476.

Grau Carles, A., Rodriguez Barquero, L., Grau Malonda, A., 1993b. A spectrum unfolding method applied to standardization of ^{3}H and ^{55}Fe mixtures. Appl. Radiat. Isot. 44, 581–586.

Grau Carles, A., Rodriguez Barquero, L., Grau Malonda, A., 1993c. Standardization of ^{14}C and ^{35}S mixtures. Nucl. Instrum. Methods Phys. Res., Sect. A 335, 234–240.

Grau Carles, A., Rodriguez Barquero, L., Grau Malonda, A., 1993d. Simultaneous standardization of ^{90}Sr-^{90}Y and ^{89}Sr mixtures. Appl. Radiat. Isot. 44, 1003–1010.

Grau Carles, A., Rodriguez Barquero, L., Grau Malonda, A., 1993e. Standardization of multi-nuclide mixtures by a new spectrum unfolding method. J. Radioanal. Nucl. Chem. Lett. 176, 391–403.

Grau Carles, A., Rodriguez Barquero, L., Grau Malonda, A., 1994a. Decovolution of $^{204}Tl/^{36}Cl$ and $^{147}Pm/^{45}Ca$ dual mixtures. Nucl. Instrum. Methods Phys. Res., Sect. A 339, 71–77.

Grau Carles, A., Grau Malonda, A., Rodríguez Barquero, L., 1994b. Standardization of ^{125}I, ^{85}Sr and ^{109}Cd by CIEMAT/NIST method. Appl. Radiat. Isot. 45, 461–464.

Grau Carles, A., Grau Malonda, Grau Carles, P., 1994c. EMI, the counting efficiency for electron capture, electron capture-gamma and isomeric transitions. Comp. Phys. Commun. 79, 115–123.

Grau Carles, A., Grau Malonda, A., Gomez Gil, V., 1996. Standardization of $U(X_1+X_2)$: the $^{234}Th+^{234m}Pa+^{230}Th$ mixture. Nucl. Instrum. Methods Phys. Res., Sect. A 369, 431–436.

Grau Carles, A., Rodríguez Barquero, L., Jiménez de Mingo, A., 1998. ^{125}Sb to ^{125m}Te branching ratio. Appl. Radiat. Isot. 49, 1377–1381.

Grau Carles, A., Günther, E., García, G., Grau Malonda, A., 2004. Ionization quenching in LSC. Appl. Radiat. Isot. 60, 447–451.

Grau Carles, A., Günther, E., Grau Malonda, A., 2006. The photoionization-reduced energy in LSC. Appl. Radiat. Isot. 64, 43–54.

Grau Malonda, A., 1982a. Measurement of Beta Radioactivity by Liquid Scintillation Counting (In Spanish). Doctoral Thesis Nº. 171/82. Universidad Complutense de Madrid, Madrid, p. 271.

Grau Malonda, A., 1982b. Counting efficiency for electron-capturing nuclides in liquid scintillation solutions. Int. J. Appl. Radiat. Isot. 33, 371–375.

Grau Malonda, A., 1990. Poissonian and Binomial Models in Radionuclide Metrology by Liquid Scintillation Counting. Report CIEMAT 677, p. 28.

Grau Malonda, A., 1999. Free Parameter Models in Liquid Scintillation Counting. CIEMAT, Madrid, p. 416.

Grau Malonda, A., Coursey, B.M., 1988. Calculation of Beta-particle counting efficiency for liquid-scintillation systems with three phototubes. Appl. Radiat. Isot. 39, 1191–1196.

Grau Malonda, A., García Toraño, E., 1982. Evaluation of counting efficiency in liquid scintillation counting of pure β-ray emitters. Int. J. Appl. Radiat. Isot. 33, 249–253.

Grau Malonda, A., GarciaToraño, E., Villar, M.A., 1982. Calibración de en solución metálicamnediante cámara de ionización. Anales de Física, B 78, 273–279.

Grau Malonda, A., Grau Carles, A., 1998. The anisotropy coefficient in Cerenkov counting. Appl. Radiat. Isot. 49, 1049–1053.

Grau Malonda, A., Grau Carles, A., 1999. The ionization quench factor in liquid-scintillation counting standardizations. Appl. Radiat. Isot. 51, 183–188.

Grau Malonda, A., Grau Carles, A., 2002. Half-life determination of ^{40}K by LSC. Appl. Radiat. Isot. 56, 153–156.

Grau Malonda, A., Grau Carles, A., 2008. The ionization quenching function for coincident electrons. Appl. Radiat. Isot. 66, 1038–1042.

Grau Malonda, A., Rodriguez Barquero, L., Grau Carles, A., 1994. Radioactivity determination of ^{90}Y, ^{90}Sr and ^{89}Sr mixtures by spectral deconvolution. Nucl. Instrum. Methods Phys. Res., Sect. A 339, 31–37.

Grau Malonda, A., Grau Carles, A., Grau Carles, P., Galiano Casas, G., 1999. EMI2, the counting efficiency for electron capture by a KL1L2L3M model. Comp. Phys. Commun. 123, 114–122.

Grau Malonda, A., Grau Carles, A., García, G., 2006. Mean values of the LMM Auger transition in a KLM model. Appl. Radiat. Isot. 64, 1485–1491.

Gray, L.H., 1949. The experimental determination by ionization methods of the rate of emission of beta-gamma-ray energy by radioactive substances. Br. J. Radiol. 22, 677–697.

Green, M.V., Aamodt, R.L., Johnston, G.S., 1974. The solid angle subtended by a solid, right, circular cylinder as seen from a point in space. Nucl. Instrum. Methods 117, 409–412.

Griffiths, R., 1971. Calculated total efficiencies of coaxial Ge(Li) detectors. Nucl. Instrum. Methods 91, 377–379.

Grigorescu, E.L., 1973. Accuracy of coincident measurements. Appl. Radiat. Isot. 112, 151–155.

Grigorescu, E.L., Razdolescu, A.C., Saharia, M., Luca, A., Ivan, C., Tanase, G., 2002. Standardization of ^{152}Eu. Appl. Radiat. Isot. 56, 435–439.

Grigorescu, E.L., Negut, C.D., Luca, a., Razdolescu, A.C., Tanase, M., 2004. Standardization of $^{68}(Ge+Ga)$. Appl. Radiat. Isot. 60, 429–431.

Grosswendt, B., Waibel, E., 1975. Determination of detector efficiencies for gamma ray energies up to 12 MeV. II. Monte Carlo calculation. Nucl. Instrum. Methods 131, 143–156.

Gunn, S.R., 1964. Radiometric calorimetry: a review. Nucl. Instrum. Methods 29, 1–24.

Gunn, S.R., 1970. Radiometric calorimetry: a review (1970 supplement). Nucl. Instrum. Methods 85, 285–312.

Gunn, S.R., 1976. Radiometric calorimetry: a review: 1976 supplement. Nucl. Instrum. Methods 135, 251–265.

Gunnink, P., 1990. New method to for calibrating a Ge detector by using only zero to four efficiency points. Nucl. Instrum. Methods Phys. Res., Sect. A 299, 372–376.

Gunnink, R., Niday, J.B., 1972. Report UCRL-51061. TID-4500, UC-4. Computatized Quantitative Analysis by Gamma-Ray Spectrometry, vols. I-IV. Lawrence Livermoore National Laboratory, Livermoore, CA USA.

Gunnink, P., Niday, J.B., 1976. A working model for Ge(Li) detector counting efficiencies. In: Griffin, H.C. (Ed.), Proc. ERDA Symp. On X- and Gamma-Ray Sources and Applications. Ann Arbor, MI USA, 1976. CONF-760539. National Technical Information Service, Springfield, VA. USA, p. 55.

Günther, E.W., 1994. Standardization of ^{59}Fe and ^{131}I by liquid scintillation counting. Nucl. Instrum. Methods Phys. Res., Sect. A 339, 402–407.

Günther, E., 1998. Standardization of the EC nuclides ^{55}Fe and ^{65}Zn with the CIEMAT/NIST LSC tracer method. Appl. Radiat. Isot. 49, 1055–1060.

Günther, E., 2000. Standardization of ^{237}Np by the CIEMAT/NIST LSC tracer method. Appl. Radiat. Isot. 52, 471–474.

Hadzisehovic, M., Mocilnik, I., Bek-Uzarov, D., Milojevic, A., 1973. Internal gas counting method for absolute measurements of the specific radioactivity of tritiated water. Nucl. Instrum. Methods 112, 69–71.

Haitjema, H.M., 1987. Evaluating solid angles using contour integrals. Appl. Math. Model. 11, 69–71.

Hardy, J.C., Iacob, V.E., Sanchez-Vega, M., Effinger, R.T., Lipnik, P., Mayes, V.E., Willis, D.K., Helmer, R.G., 2002. Precise efficiency calibration of an HPGe detector: source measurements and Monte Carlo calculations with sub-percent precision. Appl. Radiat. Isot. 56, 65–69.

Harper, P.V., Siemens, W.D., Lathrop, K.A., Endlich, H., 1963. Production and use of Iodine.125. J. Nucl. Med. 4, 277.

Havelka, M., 2012. Improvement of software coincidence counting system for standardization of EC-β^+ radionuclides. Appl. Radiat. Isot. 70, 2051–2055.

Havelka, M., 2018. Activity standardisation of ^{210}Pb by $4\pi\alpha$ liquid scintillation counting. Appl. Radiat. Isot. 134, 122–125.

Havelka, M., Sochorová, J., 2008. Standardisation of ^{56}Co and ^{57}Co using software coincidence counting system. Appl. Radiat. Isot. 66, 914–918.

Havelka, M.K., Sochorová, J., 2010. Standardization of ^{124}Sb and ^{152}Eu using software coincidence counting system. Appl. Radiat. Isot. 68, 1330–1334.

Havelka, M., Sochorová, J., 2014. Standardization of ^{64}Cu using a software coincidence counting system. Appl. Radiat. Isot. 87, 203–206.

Havelka, M., Auerbach, P., Sochorová, J., 2002. Software coincidence counting. Appl. Radiat. Isot. 56, 265–268.

Havelka, M., Auerbach, P., Sochorová, J., 2004. Application of pulse mixing method in software coincidence counting. Appl. Radiat. Isot. 60, 409–413.

Havelka, M., Auerbach, P., Sochorová, J., 2006. Standardization of ^{54}Mn and ^{65}Zn using a software coincidence counting system. Appl. Radiat. Isot. 63, 1215–1219.

Haywood, R.W., 1961. On the determination of disintegration rates by the coincidence method using high efficiency detectors. Int. J. Appl. Radiat. Isot. 12, 148–150.

Heath, R.L., 1964. Scintillation Spectrometry, Gamma Ray Spectrum Catalogue. USAEC Report. IDO-16880-1 (Rev. electronic update, 1997). National Technical Information Service, Springfield, Virginia, p. 539.

Helmer, R.G., Putman, M.H., Greenwood, R.C., Wilmes, H., 1994. Methodology for the measurement of β^--decay intensities distributions from the analysis of total absorption γ-ray spectra. Nucl. Instrum. Methods Phys. Res., Sect. A 351, 406–422.

Helmer, R.G., Putman, M.H., Greenwood, R.C., Wilmes, H., 1995. (Erratum).Methodology for the measurement of β^--decay intensities distributions from the analysis of total absorption γ-ray spectra. Nucl. Instrum. Methods Phys. Res., Sect. A 361, 628.

Helmer, R.G., Hardy, J.C., Iacob, V.E., Sanchez-Vega, M., Neilson, R.G., Nelson, J., 2003. The use of Monte Carlo calculation in the determination of a Ge detector efficiency curve. Nucl. Instrum. Methods Phys. Res., Sect. A 511, 360–381.

Helmer, R.G., Nica, N., Hardy, J.C., Iacob, V.E., 2004. Precise efficiency calibration of an HPGe detector up to 3.5 MeV, with measurements and Monte Carlo calculations. Appl. Radiat. Isot. 60, 173–177.

Hernández, F., El-Daoushy, F., 2003. Accounting for incomplete charge collection in Monte Carlo simulations of the efficiency of well-type Ge-detectors. Nucl. Instrum. Methods Phys. Res., Sect. A 498, 340–351.

Herold, L.K., Kouzes, R.T., 1991. Intrinsic germanium detector efficiency calculations. IEEE Trans. Nucl. Sci. NS-38, 231–238.

Heydorn, K., 1967. Geometrical effects on the response of the national physical laboratory ionization chamber type 1383 A. Int. J. Appl. Radiat. Isot. 18, 479–483.

Hino, Y., 2002. Results from APMP comparisons on radioactivity measurements of ^{58}Co, ^{88}Y and ^{166m}Ho. Appl. Radiat. Isot. 56, 421–427.

Hino, Y., Ohgaki, H., 1998. Absolute measurement of ^{192}Ir. Appl. Radiat. Isot. 49, 1179–1183.

Hino, Y., Matui, S., Yamada, T., Takeuchi, N., Onoma, K., Iwamoto, S., Kogure, H., 2000. Absolute measurement of ^{166m}Ho radioactivity and development of sealed sources for standardization of γ-ray emitting nuclides. Appl. Radiat. Isot. 52, 545–549.

Hofmann, H., Wertenbach, H., 1973. Burnup Determination on Nuclear Fuel Samples from the FR-2 Reactor. Kernforschungszenstrum Karlsruhe Tech. Rpt. EURFNR-1099, Germany, p. 91.

Holden, N.E., 1990. Total half-lives for selected nuclides. Pure Appl. Chem. 62, 941–958.

Horrocks, D.L., 1976. Absolute disintegration rate determination of beta-emitting radionuclides by the pulse height shift extrapolation method. In: Noujaim, A.A., Ediss, C., Wiebe, L.I. (Eds.), Liquid Scintillation Science and Technology. Academic Press, New York and London, pp. 185–198.

Horrocks, D.L., Klein, P.R., 1975. Theoretical considerations for standardization of I-125 by the coincidence method. Nucl. Instrum. Methods 124, 585–589.

Horrocks, D.L., Studier, M.H., 1961. Determination of the absolute disintegration rates of low energy beta emitters in a liquid scintillation spectrometer. Anal. Chem. 33, 615–620.

Hosseini-Ashrafi, M.E., Spyrou, N.M., 1992. Calculation of the average solid angle subtended by a photon-emitting source at a collimated detector and the contribution of collimator edge penetration. Nucl. Instrum. Methods Phys. Res., Sect. A 43, 1449–1460.

Houtermans, H., 1973. Probability of non-detection in liquid scintillation counting. Nucl. Instrum. Methods 112, 121–130.

Houtermans, H., Miguel, M., 1962. $.4\pi\beta - \gamma$ coincidence counting for the calibration of nuclides with complex decay schemes. Int. J. Appl. Radiat. Isot. 13, 137–142.

Hult, M., Altzitzoglou, T., Denecke, B., Persson, L., Sibbens, G., Reher, D.F.G., 2000. Standardisation of ^{204}Tl at IRMM. Appl. Radiat. Isot. 52, 493–498.

Hurtado, S., García-León, M., García-Tenorio, R., 2004. GEANT4 code for simulation of a germanium gamma-ray detector and its applications to efficiency calibration. Nucl. Instrum. Methods Phys. Res., Sect. A 518, 764–774.

Hutchinson, J.D., 1965. Freeze-drying unit for electron microscopy. Anal. Chem. 37, 1784–1785.

Hutchinson, J.M.R., Naas, C.R., Walker, D.H., Mann, W.B., 1968. Backscattering of alpha particles from thick metal backings as a function of atomic weight. Int. J. Appl. Radiat. Isot. 19, 517–522.

Hutchinson, J.M.R., Mann, W.B., Mullen, P.A., 1973. Sum-peak counting with two crystals. Nucl. Instrum. Methods 112, 187–196.

Huy, N.Q., 2010. The influence of dead layer thickness increase on efficiency decrease for a coaxial HPGe p-type detector. Nucl. Instrum. Methods Phys. Res., Sect. A 621, 390–394.

Huy, N.Q., 2011. Dead-layer thickness effect for gamma spectra measured in an HPGe p-type detector. Nucl. Instrum. Methods Phys. Res., Sect. A 641, 101–104.

Huy, N.Q., Binh, D.Q., An, V.X., 2007. Study of inactive germanium layer in a high-purity germanium detector after a long time operation applying MCNP code. Nucl. Instrum. Methods Phys. Res., Sect. A 573, 384–388.

Hwang, H._Y., Park, T.S., Kim, K.H., Kyung Jeon, W.J., Oh, P.J., Lee, M.K., Han, K.H., Yun, H.J., 1996. An improved method of correlation counting using a bi-dimensional data acquisition system. Nucl. Instrum. Methods Phys. Res., Sect. A 369, 363–367.

Hwang, H.Y., Park, T.S., Lee, J.M., Han, K.H., 2000. Development of a three-dimensional data acquisition method for standardization of beta-emitting nuclides. Appl. Radiat. Isot. 52, 393–397.

Hwang, H.Y., Park, J.H., Park, T.S., Lee, J.M., Cho, Y.H., Byun, J.I., Choi, O., Jun, J.−S., Lee, M.H., Lee, C.W., 2002. Development of MCTS technique for 3-PM liquid scintillation counting. Appl. Radiat. Isot. 56, 307−313.

Hwang, H.Y., Kwak, S.I., Lee, H.Y., Lee, J.M., Lee, K.B., Park, T.S., 2004. Development of 3-PM liquid scintillation counting system with geometrical efficiency variation. Appl. Radiat. Isot. 60, 469−473.

Hwang, H.-Y., Sung, K.S., Lee, K.b., Lee, J.M., Park, T.S., 2006. Standardization of radionuclide by $\beta(\mathrm{LS}) - \gamma$ coincidence using the geometry-efficiency variation method. Appl. Radiat. Isot. 64, 1119−1123.

Iroulart, M.G., 2006. Thermodynamics stability of radioactivity standard solutions. Appl. Radiat. Isot. 64, 1265−1270.

Iroulart, M.G., 2007. Thermodynamics stability of radioactivity standard solutions. In: Monographie BIPM-6. Bureau International des Poids et Mesures, Sèvres, France.

Ivan, C., Cassette, P., Sahagia, M., 2008. A new TDCR-LS Counter using Channel photomultiplier tubes. Appl. Radiat. Isot. 66, 1006−1011.

Ivan, C., Wätjen, A.C., Cassette, P., Sahagia, M., Antohe, A., Grigorescu, E.L., 2010. Participation in the CCRI(II)-K2.H-3 comparison and study of the new TDCR-LS counter with 6 CPMs. Appl. Radiat. Isot. 68, 1543−1545.

Iwahara, A., Delgado, J.U., Poledna, R., Da Silva, C.J., Lopes, R.T., 2000. Absolute measurements of γ-ray emmision probabilities of ^{169}Yb. Nucl. Instr. Meth. Phys. A. 455, 607−611.

Iwahara, A., De Oliveira, A.E., Tauhata, L., Da Silva, C.J., Lopes, R.T., 2001. Intercomparison of ^{131}I and ^{99m}Tc activity measurements in Brazilian nuclear medicine services. Appl. Radiat. Isot. 54, 489−496.

Iwahara, A., De Oliveira, A.E., Tauhata, L., Da Silva, C.J., Da Silva, C.P., Braghirolli, A.M.S., Lopes, R.T., 2002. Performance of dose calibrators in Brazilian hospitals for activity measurements. Appl. Radiat. Isot. 56, 361−367.

Iwahara, A., Poledna, R., da Silva, A.L., 2007. Absolute standardization of Na-22 by sum peak and $4\pi\beta - \gamma$ coincidence methods. In: 2007 International Nuclear Atlantic Conference-INAC 2007. John Wiley & Sons, New York, pp. 625−647.

Iwahara, A., Delgado, J.U., Poledna, R., Da Silva, C.J., de Almeida, M.C.M., Da Silva, C.P., 2009a. Primary radioactivity standardization and gamma intensities of ^{124}Sb. Nucl. Instrum. Methods Phys. Res., Sect. A 602, 459-456.

Iwahara, A., Poledna, R., Da Silva, C.J., Tauhata, L., 2009b. Primary activity standardization of ^{57}Co by sum-peak method. Appl. Radiat. Isot. 67, 1887−1891.

Jaffey, A.H., 1954. Solid angle subtended by a circular aperture at point and spread sources: formulas and some tables. Rev. Sci. Instrum. 25, 349−354.

Janik, M., Tokonami, S., Kováks, T., Kávási, N., Krahdrod, C., Sorimachi, A., Takahashi, H., Hiyahara, N., Ishikawa, T., 2009. International intercomparison of integrating radon detectors in the NIRS radon chamber. Appl. Radiat. Isot. 67, 1691−1696.

Janssen, H., 1990. A VMEbus-based data acquisition system for correlation counting experiments. Nucl. Instrum. Methods Phys. Res., Sect. A 299, 292−297.

Janssen, H., Waltz, K.F., 1987. Das Ansprechverhalten von Germanium-Detektoren für flächenhafte Quellen. PTB Jahresbericht 1986. Phys.-Techn. Bundesanstalt, Braunschweig, Germany, p. 174.

Jaubert, J., 2008. Standardization of a ^{186}Re sodium perrhenate radiochemical solution using the TDCR method in liquid scintillation counting. Appl. Radiat. Isot. 66, 960−964.

Jaubert, F., Cassette, P., 2004. Standardization of a ^{32}P solution containing pure-beta impurities using the TDCR method in liquid scintillation counting. Appl. Radiat. Isot. 60, 601−606.

Jaubert, F., Tartès, I., Cassette, P., 2006. Quality control of liquid scintillation counters. Appl. Radiat. Isot. 64, 1163−1170.

Jean-Baptiste, P., Cassette, P., Fourré, E., Tartès, I., Dapoigny, A., 2014. Measurement of the French national tritiated-water standard by helium-3 mass spectrometry. Appl. Radiat. Isot. 87, 157−161.

Jehouani, A., Ichaoui, R., Boulkheir, M., 2000. Study of the NaI(Tl) efficiency by Monte Carlo method. Appl. Radiat. Isot. 53, 887−891.

Jenks, G.H., Sweeton, F.H., 1952. Calorimetric determination of the relationship between the half-life and average beta-energy of carbon-14. Phys. Rev. 86, 803−804.

Jenks, G.H., Sweeton, F.H., Ghormley, J.A., 1950. A precise determination of the half-life and average energy of tritium decay. Phys. Rev. 80, 990−995.

Jerome, S.M., Eccles, J.I., Inn, K.G., 2007. General concepts for traceability in environmental radioactivity monitoring. Metrologia 44, S133−S139.

Jiang, J., Davies, A., Arrige, L., Friese, J., Seiner, B.N., Greenwood, L., Finch, Z., 2015. Analysis of ^{161}Tb by radiochemical separation in liquid scintillation counting. Appl. Radiat. Isot. (in press), Corrected Proof.

Johansson, L., Sephton, J.P., 2010. Validation of a new TDCR system at NPL. Appl. Radiat. Isot. 68, 1537−1539.

Johansson, L., Sibbens, G., Alzitzoglou, T., Denecke, B., 2002. Self-absorption correction in standardization of ^{204}Tl. Appl. Radiat. Isot. 65, 199−203.

Johansson, L., Altzitzoglou, T., Sibbens, G., Pammé, S., Denecke, B., 2003a. Standardization of ^{238}Pu using four methods of measurement. Nucl. Instrum. Methods Phys. Res., Sect. A 505, 699−706.

Johansson, L., Alzitzoglou, T., Sibbens, G., Denecke, B., Reher, 2003b. Six direct methods for standardization of ^{152}Eu. Nucl. Instrum. Methods Phys. Res., Sect. A 508, 378−387.

Jordanov, D., Nadderd, L., Puzović, J., Rosić, M., Kokunoseski, 2016. The application of the new matrix method for calculating coincidence summing effects in the case of radionulices with the more complex decay scheme-152Eu. Nucl. Instrum. Methods Phys. Res., Sect. A 836, 22−29.

Jórg, G., Amelin, Y., Kossert, K., Lierse, v., Gostomski, C., 2012. Precise and direct determination of the half-life of ^{41}Ca. Geochim. Cosmochim. Acta 88, 51−65.

Joseph, L., Anuradha, R., Nathuram, R., Shaha, V.V., Abani, M.C., 2003. National intercomparisons of ^{131}I radioactivity measurements in nuclear medicine centres in India. Appl. Radiat. Isot. 64, 1027−1030.

Jovanovic, S., Dlabac, S., Mihaljevic, N., Vucotic, P., 1997. ANGLE-a PC-code for semiconductor detector efficiency calculations. J. Radioanal. Nucl. Chem. 218, 13−20.

Jovanovic, S., Dlabac, S., Mihaljevic, N., 2010. ANGLE 2.1- New version of the computer code for semiconductor detector gamma-efficiency calculations. Nucl. Instrum. Methods Phys. Res., Sect. A 622, 385−391.

Jurado Vargas, M., Fernández Timón, A., 2004. Scattering of self-absorption corrections in the measurement of α-particles emitters in

2π geometry. Nucl. Instrum. Methods Phys. Res., Sect. B 217, 564–571.

Jurado Vargas, M., Fernández Timón, A., 2005. Dependence of self-absorption on thickness for thin and thick alpha-particle sources of UO2. Nucl. Instrum. Methods Phys. Res., Sect. A 548, 432–438.

Jurado Vargas, M., Guerra, A.L., 2006. Application of PENELOPE code to the efficiency calibration of coaxial germanium detectors. Appl. Radiat. Isot. 64, 1319–1322.

Jurado Vargas, M., Fernández Timón, A., Cornejo Díaz, N., Pérez Sánchez, D., 2002. Monte Carlo simulation of the self-absorption corrections for natural samples in gamma-ray spectrometry. Appl. Radiat. Isot. 57, 893–898.

Jurado Vargas, M., Fernández Timón, A., García-Toraño, E., 2004. Application of ion transport simulation to the backscattering in α-particles sources. Nucl. Instrum. Methods Phys. Res., Sect. B 213, 129–133.

Kajimoto, T., endo, s., Tat Thanh, N., shizuma, K., 2015. Calculation of coincidence summing in gamma-ray spectrometry with the EGS5 code. Appl. Radiat. Isot. 95, 53–55.

Kanisch, G., Vidmar, T., Sima, O., 2009. Testing the equivalence of several algorithms for calculation of coincidence summing corrections. Appl. Radiat. Isot. 67, 1952–1956.

Kaplanis, S.N., 1982. Geometric, effective solid angles and intrinsic efficiencies of a 3 × 3 in. NaI(Tl) for isotropic and non-isotropic photon emission. Int. J. Appl. Radiat. Isot. 33, 127–135.

Karfopoulos, K.L., Anagnostakis, M.J., 2010. Parameters affecting full energy peak efficiency determination during Monte Carlo simulation. Int. J. Appl. Radiat. Isot. 68, 1435–1437.

Kawada, Y., 1986. Decay data measurements of ^{64}Cu by $4\pi\beta-\gamma$ coincidence technique and photon spectrometry. Nucl. Instrum. Methods Phys. Res., Sect. A 37, 7–12.

Kawada, Y., Yura, O., Kimura, M., 1970. Radioactivity measurements by the $4\pi\beta-\gamma$ anticoincidence spectroscopy method using a Ge(Li) detector. Nucl. Instrum. Methods 78, 77–85.

Kawada, Y., Nakamura, Y., Wang, Q., Hino, Y., 2004. Absolute radioactivity measurements by the use of a $4\pi\beta-4\pi\gamma$ detector configuration. Appl. Radiat. Isot. 60, 357–362.

Kawada, Y., Yamada, T., Unno, Y., Yunoki, A., Saro, Y., Hino, Y., 2012. A simple and versatile data acquisition system for software coincidence and pulse-height discrimination in$4\pi\beta-\gamma$ coincidence experiments. Appl. Radiat. Isot. 70, 2031–2036.

Kawada, Y., Yunoki, A., Yamada, T., Hino, Y., 2014. Gamma geometry dependence of efficiency functions in the $4\pi\beta-\gamma$ coincidence measurements of complex decaying nuclides. Appl. Radiat. Isot. 87, 183–187.

Kawano, T., Ebihara, H., 1990. Determination of disintegration rates of a Co-60 point source and volume sources by the sum-peak method. Appl. Radiat. Isot. 41, 163–167.

Kawano, T., Ebihara, H., 1991. Measurement of disintegration rates of small Co-60 sources in lead containers by the sum-peak method. Appl. Radiat. Isot. 42, 1165–1168.

Kawano, T., Ebihara, H., 1992. Error estimation for the sum-peak method by the use of two Co-60 point sources in place of extended sources. Appl. Radiat. Isot. 43, 705–711.

Kawrakow, I., Mainegra-Hing, E., Rogers, D.W.O., 2006a. EGSnrcMP: The Multi-Platform Environment for EGSnrc. NRCC Report PIRS-877. National Research Council of Canada, Ottawa. Canada, p. 65.

Kawrakow, I., Rogers, D.W.O., 2006. The EGSnrc Code System. NRCC Report Pirs-701. National Research Council of Canada.

Keightley, J.D., Park, T.S., 2007. Digital coincidence counting for radionuclide standardization. Metrologia 44, S32–S35.

Keightley, J.D., Watt, G.C., 2002. Digital coincidence counting (DCC) and its use in the correction for out-of-channel gamma events in $4\pi\beta-\gamma$ coincidence counting. Appl. Radiat. Isot. 56, 205–210.

Keightley, J.D., Pearce, A., Fenwik, A., Collins, S., Ferreira, K., Johansson, L., 2015. Standardization of ^{223}Ra by liquid scintillation counting techniques and comparison with secondary measurements. Appl. Radiat. Isot. 95, 114–121.

Kempisty, T., Pochwalski, K., Radoszewski, T., Terlikowsig-Drozdziel, T., 1990. Measurements of ^{170}Tm photon and electron emission probabilities. Nucl. Instrum. Methods Phys. Res., Sect. A 286, 535–538.

Keyser, R., 2004. Resolution and sensitivity as a function of energy and incident geometry for germanium detectors. Nucl. Instrum. Methods Phys. Res., Sect. B 213, 236–240.

Kim, I.J., Sun, G.M., Choi, H.D., Bae, Y.-D., 2002. Calculation of the effective angular correlation in the HPGe spectroscopy of Co-60 γ-rays. J. Korean Nucl. Soc. 34, 22–29.

Kim, I.J., Park, C.S., Choi, H.D., 2003. Absolute calibration of ^{60}Co by using sum-peak method and an HPGe detector. Appl. Radiat. Isot. 58, 227–233.

Kim, G.–Y., Lee, H.–K., Jeong, H.K., Woods, M.J., 2005. Comparison of radioactivity measurements with radionuclide calibrators in the Republic of Korea. Appl. Radiat. Isot. 63, 201–205.

Kits, J., Kokta, L., Buènia, I., 1967. Absolute Measurement of ^{14}C Activity by Internal Proportional Counters Standardization of Radionuclides. IAEA, Vienna, pp. 267–275. SM-79/6.

Knoll, G.F., 1989. Radiation Detection and Measurement, second ed., p. 694

Korun, M., Martincic, R., 1995. Activity calculation for voluminous samples in the presence of coincidence summing effects. Nucl. Instrum. Methods Phys. Res., Sect. A 355, 600–608.

Korun, M., Vodenik, B., zorko, B., 2016. Calculation of the decision threshold in gamma-ray spectrometry using sum peaks. Appl. Radiat. Isot. 109, 522–525.

Koskinas, M.F., Dias, M.S., 1993. Measurement of the gamma probability per decay of ^{31}Si. Appl. Radiat. Isot. 44, 1209–1211.

Koskinas, M.F., Kátia, A., Fonseca, A., Dias, M.S., 2002. Disintegration rate measurement of a ^{152}Eu solution. Appl. Radiat. Isot. 56, 441–445.

Koskinas, M.F., Silva, E.A., Yamazaki, U.,M., Dias, M.S., 2006a. Standardization of ^{241}Am. Appl. Radiat. Isot. 63, 1238–1241.

Koskinas, M.F., Moreira, D.S., Takeda, M.N., Saneda, J.A., Dias, M.S., 2006b. Primary standardization of ^{72}Ga. Appl. Radiat. Isot. 63, 1225–1228.

Koskinas, M.F., Silva, E.A., Yamazaki, I.,M., Dias, M.S., 2008. Disintegration rate measurement of ^{182}Ta. Appl. Radiat. Isot. 66, 934–936.

Koskinas, M.F., Moreira, D.S., Yamazaki, U.,M., de Toledo, F., Brancaccio, F., Dias, M.S., 2010. Primary standardization of ^{57}Co. Appl. Radiat. Isot. 68, 1344–1348.

Koskinas, M.F., Lacerda, F.W., Matos, I.T., Nascimento, T.S., Yamazaki, I.M., Takeda, M.N., Dias, M.S., 2014a. Determination of gamma-ray emission probabilities per decay of Ga-68. Appl. Radiat. Isot. 87, 118–121.

Koskinas, M.F., Nascimento, T.S., Yamazaki, I.,M., Dias, M.S., 2014b. Covariance methodology applied to ^{35}S disintegration rate measurements by the CIEMAT/NIST method. Radiat. Phys. Chem. 95, 131–133.

Koskinas, M.F., Polillo, G., Brancaccio, F., Yamazaki, I.,M., Dias, M.S., 2016. Standardization of ^{59}Fe by $4\pi\beta(PC) - \gamma$ software coincidence system. Appl. Radiat. Isot. 109, 386–388.

Kossert, K., 2003. Half-life measurements of ^{87}Rb by liquid scintillation counting. Appl. Radiat. Isot. 59, 377–382.

Kossert, K., 2006. A new method for secondary standard measurements with the aid of liquid scintillation counting. Appl. Radiat. Isot. 64, 1459–1464.

Kossert, K., 2010. Activity standardization by means of a new TDCR-Cerenkov counting technique. Appl. Radiat. Isot. 68, 1116–1120.

Kossert, K., Grau Carles, A., 2006. The LSC efficiency for low Z electron-capture nuclides. Appl. Radiat. Isot. 64, 1446–1453.

Kossert, K., Grau Carles, A., 2008. Study of a Monte Carlo rearrangement model for the activity determination of electron-capture nuclides by means of liquid scintillation counting. Appl. Radiat. Isot. 66, 998–1005.

Kossert, K., Grau Carles, A., 2010. Improved method for the calculation of the counting efficiency of electron-capture nuclides in liquid scintillation samples. Appl. Radiat. Isot. 68, 1482–1488.

Kossert, K., Günther, E., 2004. LSC measurements of the half-life of ^{40}K. Appl. Radiat. Isot. 60, 459–464.

Kossert, K., Mougeot, X., 2015. The importance of the beta spectrum calculation for accurate activity determination of ^{63}Ni by means of liquid scintillation counting. Appl. Radiat. Isot. 101, 40–42.

Kossert, K., Nähle, O.J., 2014. Activity determination of ^{59}Fe. Appl. Radiat. Isot. 91, 33–37.

Kossert, K., Schrader, H., 2004. Activity standardization by liquid scintillation counting and half-life measurements of ^{90}Y. Appl. Radiat. Isot. 60, 741–749.

Kossert, K., Thieme, K., 2007. Comparison for quality assurance of ^{99m}Tc activity measurements with radionuclide calibrators. Appl. Radiat. Isot. 65, 866–871.

Kossert, K., Janßen, H., Klein, R., Schneider, M.K.H., Schrader, H., 2006a. Activity standardization and nuclear decay data of ^{109}Cd. Appl. Radiat. Isot. 63, 201–205.

Kossert, K., Jansen, H., Klein, R., Schneider, M., Schrader, H., 2006b. Standardization and decay data of ^{65}Zn. Appl. Radiat. Isot. 63, 1420–1424.

Kossert, K., Nähle, O.J., Grau Carles, A., 2011a. Beta shape-factor function and activity determination of ^{241}Pu. Appl. Radiat. Isot. 69, 1246–1250.

Kossert, K., Nähle, O.J., Warwick, P.E., Wershofen, H., Croudace, I.W., 2011b. Activity determination and nuclear decay data of ^{113m}Cd. Appl. Radiat. Isot. 69, 500–505.

Kossert, K., Nähle, Ott, O., Dersch, R., 2012. Activity determination and nuclear decay data of ^{177}Lu. Appl. Radiat. Isot. 70, 2215–2221.

Kossert, K., Jörg, G., Lierse, C., Gostowki, V., 2013. Experimental half life determinations of ^{176}Lu. Appl. Radiat. Isot. 81, 140–145.

Kossert, K., Cassette, P., Grau Carles, A., Jórg, G., Lierse, C., Gostomski, V., Nähle, O.J., Wolf, C., 2014a. Extension of the TDCR model to compute counting efficiencies for radionuclides with complex decay schemes. Appl. Radiat. Isot. 87, 242–248.

Kossert, K., Nähle, O.J., Jansen, H., 2014b. Activity determination of ^{229}Th by means of liquid scintillation counting. Appl. Radiat. Isot. 87, 274–281.

Kossert, K., Capogni, M., Nähle, O.J., 2014c. Bilateral comparison between PTB and ENEA to check the performance of a commercial TDCR system for activity measurements. Appl. Radiat. Isot. 93, 38–44.

Kossert, K., Bokeloh, K., Dersch, R., Nähle, O.J., 2015. Activity determination of ^{227}Ac and ^{223}Ra by means of liquid scintillation counting and determination of nuclear decay data. Appl. Radiat. Isot. 95, 143–152.

Kossert, K., Marganiec-Balazka, J., Mougeot, X., Nähle, O.J., 2018. Activity determination of ^{60}Co and the importance of its beta spectrum. Appl. Radiat. Isot. 134, 212–218.

Krillovich, A.P., Gordienko, P.S., Buntushkin, V.P., 1976. Calorimetric measurement of the heat released by irradiated nuclear fuel. Atom. Energy 40, 511–513.

Kryeziu, D., Tchurlovits, M., Kreuziger, M., Maringer, F-J., 2007. Calculation of calibration figures and the volume correction factors for ^{90}Y, ^{125}I, ^{131}I and ^{177}Lu radionuclides based on Monte Carlo ionization chamber simulations method. Nucl. Instrum. Methods Phys. Res., Sect. A 580, 250–253.

Kulkarni, D.B., 2013. Development of liquid scintillation based $4\pi\beta(LS) - \gamma$ coincidence counting system and demonstration of its performance by standardization of ^{60}Co. Appl. Radiat. Isot. 72, 68–72.

Kulkarni, D.B., Anuradha, R., Joseph, L., Anuradha, R., Kulkarni, H.S., Tomar, B.S., 2016. Performance demonstration of $4\pi\beta(LS) - \gamma$ coincidence counting system for standardization of radionuclides with complex decay scheme. Appl. Radiat. Isot. 108, 24–29.

Kulkarni, D.B., Joseph, L., Anuradha, R., Kulkarni, H.S., Tomar, B.S., 2017. Standardization of ^{68}Ge – ^{68}Ga using $4\pi\beta(LS) - \gamma$ coincidence counting system for activity measurements. Appl. Radiat. Isot. 123, 6–10.

Kumar, S., Srinivasan, P., Sharma, S.D., 2010. Calibration coefficient of reference brachytherapy ionization chamber using analytical and Monte Carlo methods. Appl. Radiat. Isot. 68, 1108–1115.

Kushelevski, A.P., Alfassi, Z.B., 1975. Off center gamma ray detection efficiencies of cylindrical single open ended (SOE) Ge(Li) detectors. Nucl. Instrum. Methods 131, 93–95.

Laborie, J.–M., Le Petit, G., Abt, D., Girard, M., 2000. Monte Carlo calculation of the efficiency calibration curve and coincidence-summing corrections in low-level gamma-ray spectrometry using well-type HPGe detectors. Appl. Radiat. Isot. 53, 57–62.

Lachance, Y., Roy, J.C., 1972. Method for vacuum evaporation of SiO on thin plastic films. Rev. Sci. Instrum. 43, 1382–1383.

Laedermann, J.-P., Décombaz, M., 2000. Simulation of nuclear decay. Appl. Radiat. Isot. 52, 419–424.

Lal, B., Iyengar, K.V.K., 1970. Monte Carlo calculation of gamma ray response characteristics of cylindrical Ge(Li) detectors. Nucl. Instrum. Methods 79, 19–28.

Lally, A.E., Glover, K.M., 1984. Source preparation in alpha spectrometry. Nucl. Instrum. Methods Phys. Res. 223, 259–265.

Laureano-Pérez, L., Collé, R., Fitzgerald, R., Outola, I., Pibida, L., 2007. A liquid-scintillation-based primary standardization of 210Pb. Appl. Radiat. Isot. 65, 1368–1380.

Laureano-Perez, L., Collé, R., Fitzgerald, R., Zimmerman, B.E., Cumberland, L., 2010. Investigation into the standardization 99Tc. Appl. Radiat. Isot. 68, 1489–1494.

Laureano-Perez, L., Fitzgerald, R., Collé, R., 2014. Standardization of ^{237}Np. Appl. Radiat. Isot. 87, 269–273.

Lausberg, S., 2008. Development of a Metallic Magnetic Calorimeter for High Resolution β-spectroscopy (Diploma thesis). University of Heidelberg, p. 79.

Le Gallic, Y., 1977. Préparation des sources radioactives pour mesures d'activité. Monographie Laboratoire de Métrologie des Rayonnements Ionisants, CEA, Saclay, 91190 Gif-sur-Yvette, France, p. 53.

Leblanc, E., Cassette, P., Bouchard, J., Plagnard, J., 1998. Development of cryogenic detectors for radioactivity metrology. Appl. Radiat. Isot. 29, 1113–1116.

Leblanc, E., de Marcillac, P., Coron, N., Leblanc, J., Loidl, M., Metge, J.F., Bouchard, J., 2002. A new absolute method for the standardization of radionuclides emitting low-energy radiation. Appl. Radiat. Isot. 56, 245–252.

Leblanc, E., Coron, N., Leblanc, J., de Marcillac, P., Bouchard, J., Plagnard, J., 2006. High-energy resolution alpha spectrometry using cryogenic detectors. Appl. Radiat. Isot. 64, 1281–1286.

Lee, K.B., Lee, J.M., Park, T.S., 2004a. Implementation of CIEMAT/NIST LSC efficiency tracing method in KRISS: ^{204}Tl standardization. Appl. Radiat. Isot. 60, 893–897.

Lee, K.B., Lee, J.M., Park, T.S., Hwang, H.Y., 2004b. Implementation of TDCR method in KRISS. Nucl. Instrum. Methods Phys. Res., Sect. A 534, 496–502.

Lee, K.B., Lee, J.M., Park, T.S., Oh, P.J., Lee, s.H., Lee, M.K., 2011. Apllication of digital sampling techniques for $4\pi\beta(\mathrm{LS}) - \gamma$ coincidence counting. Nucl. Instrum. Methods Phys. Res., Sect. A 626–627, 72–76.

Lee, K.M.L., Lee, K.B., Park, T.S., 2012. Calibration of KRISS reference ionization chamber for key comparison of ^{99m}Tc measurement. Appl. Radiat. Isot. 70, 1853–1855.

Leprince, B., de Sanoit, 2002. A new design of ^{238}Pu activity sources for use in intercomparison exercises. Appl. Radiat. Isot. 57, 171–176.

Lépy, M.C., Altzitzoglou, T., Arnold, D., Bronson, F., Capote Noy, R., Décombaz, M., De Corte, F., Edelmaier, R., Herrera Peraza, E., Klemola, S., Korun, M., Kralik, M., Neder, H., Plagnard, J., Pommé, S., de Sanoit, J., Sima, O., Ugletveit, F., Van Velzen, L., Vidmar, T., 2001. Intercomparison of efficiency transfer software for gamma-ray spectrometry. Appl. Radiat. Isot. 55, 493–503.

Lépy, M.C., Amiot, M.N., Bé, M.M., Cassette, P., 2006. Determination of the intensity of X- and gamma-ray emissions in the decay of ^{153}Sm. Appl. Radiat. Isot. 64, 1428–1434.

Lerch, O., Spernol, A., 1966. Geometry factors in low and medium geometry solid angle counting. EANDC 53 'S, 415–427.

Lewis, V.E., Smith, D., Williams, A., 1973. Correlation counting applied to the determination of absolute disintegration rates for nuclides with delayed states. Metrologia 9, 14–20.

Li, P., Uren, N.F., 1997. Analytical solution for the point source potential in an anisotropic 3-D half-space II: With two-vertical boundary planes. Math. Comput. Model. 26, 29–52.

Li, Q., Chang, Y.–F., Xie, F., Lian, Q., Fan, J.–L., Xu, Q.–C., Wang, L., 2005. A new small column proportional counter for the $4\pi\beta + 4\pi\gamma$ counting method. Hedianzixue Yu Tance Jishu/Nucl. Elect. Detect Technol. 25, 131–133.

Lin, U.T., Chu, C.H., 2006. Correction factors for the ENER-improved free-air ionization chambers calculated with the Monte Carlo method. Appl. Radiat. Isot. 64, 608–614.

Lippert, J., 1983. Detector-efficiency calculation based on point.source measurement. Int. J. Appl. Radiat. Isot. 34, 1097–1103.

Liye, L., Jizeng, M., Franck, D., Carlan, L., Binquan, Z., 2006. Monte Carlo Efficiency transfer method for full energy peak efficiency calibration of three type HPGe detectors; A coaxial N-type, a coaxial P-type and four BEGe detectors. Nucl. Instrum. Methods Phys. Res., Sect. A 565, 608–613.

Loidl, M., Leblanc, E., Branger, T., Rotzinger, H., Daniyarov, T., Linck, M., Fleischmann, A., Enss, C., 2004. Feasibility study of absolute activity measurement with metallic magnetic microcalorimeters. Nucl. Instrum. Methods Phys. Res., Sect. A 520, 73–75.

Loidl, M., Leblanc, E., Rodrigues, M., Leprince, B., Eglin, L., Rotzinger, M., Linck, M., Burck, A., Scarbrough, T., Fleischmann, Enss, C., 2006. Nuclear and atomic data determination with metallic magnetic calorimeters. Nucl. Instrum. Methods Phys. Res., Sect. A 559, 769–771.

Loidl, M., Leblanc, E., Rodrigues, M., Branger, T., Lacour, D., Bouchard, J., Censier, B., 2008. Validation of a new technique for absolute measurement with 4π solid angle metallic magnetic calorimeter. Appl. Radiat. Isot. 66, 872–876.

Loidl, M., Rodrigues, B., Censier, B., Kowalski, S., Mougeot, X., Cassette, P., Branger, T., Lacour, D., 2010. First measurement of the beta spectrum of ^{241}Pu with a cryogenic detector. Appl. Radiat. Isot. 68, 1454–1458.

Loidl, M., Rodrigues, B., Le-Bret, Mougeot, X., 2014. Beta spectrometry with metallic magnetic calorimeters. Apply. Radiat. Isot. 87, 302–305.

Los Arcos, J.M., Rodríguez Barquero, L., 1996. Low-level assay of ^{3}H and ^{14}CMDA limits with conventional liquid scintillation counters using the 'LOLES' procedure. Appl. Radiat. Isot. 47, 79–83.

Los Arcos, J.M., Rodríguez Barquero, L., 2013. Results of Ni-63 trial exercice at CIEMAT using the universal LSC cross-efficiency curves. In: Proceedings of BIPM, 9 May 2012. Metrologia.

Los Arcos, J.M., Grau Malonda, A., Fernández, A., 1987. VIASKL, a computer program to evaluate the liquid scintillation counting efficiency and its associated uncertainty fir K-L-atomic shell electron-capture nuclides. Comput. Phys. Commun. 44, 209–220.

Los Arcos, J.M., Rodríguez Barquero, L., Roteta, M., 1992. Point source preparation by polypyrrole-based conductive thin film production and radioactive labelling. Nucl. Instrum. Methods Phys. Res., Sect. A 312, 5–10.

Los Arcos, J.M., Blaauw, M., Facinic, F., Kolotoc, V.P., 2005. The 2002 IAEA test spectra for low level γ-ray spectrometry software. Nucl. Instrum. Methods Phys. Res., Sect. A 536, 189–195.

Lowental, G.C., Smith, A.M., 1964. Use of Au-20% Pd for metalizing thin sources supports for 4π proportional gas flow counters. Nucl. Instrum. Methods 30, 363–364.

Lowental, G.C., Wyllie, H.A., 1973. Special methods of source preparation. Nucl. Instrum. Methods 112, 353–357.

Lowenthal, G.C., Hicks, R.M., 1966. An isothermal microcalorimeter operated in a water triple point cell and designed for radioactivity measurements. J. Sci. Instrum. 43, 36–38.

Lowenthal, G.C., Wyllie, H.A., Page, V., 1982. A method for measuring the activity of ^{55}Fe using a 4π proportional counter. Appl. Radiat. Isot. 33, 755–762.

Lu, X., Wang, G., 2003. Absolute radioactivity measurement of ^{60}Co, ^{134}Cs and ^{166m}Ho by $4\pi\beta - \gamma$ anticoincidence method. Appl. Radiat. Isot. 58, 365–369.

Luca, A., Amiot, M.-N., Morel, J., 2003. Determination of half-life and photon emission probabilities of (65)Zn. Appl. Radiat Isot. 58, 607–610.

Lucas, L., 1998. Calibration of the massic activity of a solution of ^{99}Tc. Appl. Radiat. Isot. 49, 1061–1064.

Lucas, L., Hutchinson, J.M.R., 1976. Study of the scattering corrections for thick uranium-oxide and other α-particle sources. Int. J. Appl. Radiat. Isot. 27, 35–42.

Ludington, M.A., Helmer, R.G., 2000. High accuracy measurements and Monte Carlo calculations of the relative efficiency curve of an HPGe detector from 433 to 2754 keV. Nucl. Instrum. Methods Phys. Res., Sect. A 506–521.

Luís, R., Bento, J., Carvalhal, G., Nogueira, P., Silva, L., Teles, P., Vaz, P., 2010. Parameter optimization of a planar BEGe detector using Monte Carlo simulations. Nucl. Instrum. Methods Phys. Res., Sect. A 1014–1019.

Lukens, H.R., 1961. The relationship between fluorescence intensity and counting efficiency with liquid scintillators. Int. J. Appl. Radiat. Isot. 12, 134–140.

Lyie, L., Jizeng, M., Franck, D., de Carlan, L., Binquan, Z., 2006. Monte Carlo efficiency transfer method for full energy peak efficiency calibration of three type HPGe detectors: A coaxial N-type, a coaxial P-type and four BEGe detectors. Nucl. Instrum. Methods Phys. Res., Sect. A 564, 608–613.

Makepeace, J.L., Clark, F.E., Picolo, J.L., Courso, N., Gfunther, E., Unterweger, M.P., 1994. Intercomparison of internal proportional gas counting of ^{85}Kr and ^{3}H. Nucl. Instrum. Methods Phys. Res., Sect. A 339, 343–348.

Makepeace, J.L., Day, F.E., Günther, E., Unterweger, M.P., 1996. Intercomparison of measurement of tritiated water by internal proportional gas counting. Nucl. Instrum. Methods Phys. Res., Sect. A 369, 458–462.

Makepeace, J., Altzitzoglou, T., Cassette, P., Dryak, P., Günther, E., Verrezen, F., Broda, R., Simpson, B., Unterweger, M., 1998. International comparison of measurements of the specific activity of tritiated water. Appl. Radiat. Isot. 49, 1411–1416.

Mann, W.B., 1954. A radiation balance for the microcalorimetric comparison of four national radium standards. J. Res. Natl. Bur. Stand 53, 277–281.

Mann, W.B., 1956. The preparation and maintenance of standards of radioactivity. Int. J. Appl. Radiat. Isot. 1, 3–23.

Mann, W.B., 1962. In: Thewlist, J. (Ed.), Calorimetric Measurements of Radioactivity. Encyclopedic Dictionary of Physics. Pergamon, Oxford, p. 538.

Mann, W.B., 1973. Radioactive calorimetry: a review of the work at the National Bureau of Standards. Nucl. Instrum. Methods 112, 273–277.

Mann, W.B., Marlow, W.F., Hughes, E.E., 1961. The half-life of ^{14}C. Int. J. Appl. Radiat. Isot. 11, 57–67.

Mann, W.B., Medlock, R.W., Yura, O., 1964. A recalibration of the national bureau of standards tritiated water standards by gas counting. Int. J. Appl. Radiat. Isot. 15, 351–361.

Mann, W.B., Rytz, A., Spernol, A., 1988. Radioactivity Measurements: Principles and Practice. Pergamon, Oxford, pp. 45–55.

Marganiec-Galazka, J., Nähle, O.J., Kossert, K., 2018. Activity determination of ^{68}Ge/^{68}Ga by means of $4\pi\beta(C) - \gamma$ coincidence counting. Appl. Radiat. Isot. 134, 240–244.

Marouli, M., Dean, J., Spyrou, N.M., 2007. Feasibility of using proportional gas counters as a primary standard for positron emitters in gas. Nucl. Instrum. Methods Phys. Res., Sect. A 580, 660–662.

Marouli, M., Dean, J., Spyrou, N.M., 2008. Early stages in the development of a UK primary standard for positron emitters in gas. J. Radioanal. Nucl. Chem. 277, 261–264.

Marouli, M., Dean, J.C.J., Sephton, J.P., Spyrou, N.M., 2010. Standardization of positron-emitters in gas with the NPL primary gas counting system. Appl. Radiat. Isot. 68, 1378–1382.

Marques Salgado, C., Conti, C.C., Paulo, H.B., Becker, P.H.B., 2006. Determination of HPGe detector response using MCNP5 for 20–150 keV X-rays. Appl. Radiat. Isot. 64, 700–705.

Marsoem, P., Wwurdiyanto, G., Candra, H., Salbatulham, H., 2014. Direct measurement of ^{60}Co and ^{125}I activity by sum-peak method in PTKMR-BATAN. Appl. Radiat. Isot. 87, 200,202.

Martin, R.H., Taylor, J.V.G., 1992. The standardization of I-125: a comparison of three methods. Nucl. Instrum. Methods Phys. Res., Sect. A 312, 64–66.

Martín Sánchez, A., Bland, C.J., Fernández Timón, A., 2000. Computer simulations of Backscattering alpha particles. Appl. Radiat. Isot. 53, 341–346.

Matos, I.T., Koskinas, M.F., Nascimento, T.S., Yamazaki, I.M., Dias, M.S., 2014. Standardization and determination of the total internal conversion coefficient on In-111. Appl. Radiat. Isot. 87, 192–194.

McCallum, G.J., Coote, G.E., 1975. Influence of source-detector distance on relative intensity and angular correlation measurements with Ge(Li) spectrometers. Nucl. Instrum. Methods 130, 189–197.

McKinney, W.G., et al., 2006. MCNPX overview. In: Proceedings of the 2006 HSSW, FNAL, IL., LA_UR-06-6206, September 2006.

Meniere, J., Ganivet, M., 1972. Determination of the plutonium content of a mixed plutonium/uranium oxide by calorimetry. In: Analytical Methods in the Nuclear Fuel Cycle. IAEA, Vienna, pp. 203–215.

Merritt, J.,S., 1973. Present status in source preparation. Nucl. Instrum. Methods 112, 325–332.

Merritt, J.S., Taylor, J.G.V., Merrit, W.F., Campion, P.J., 1960. The absolute counting of sulphur-35. Anal. Chem. 32, 310–313.

Michotte, C., 2000. Influence of radioactive impurities on SIR measurements. Appl. Radiat. Isot. 52, 319–323.

Michotte, C., 2001. Efficiency Calibration of the Ge(Li) Detector of the BIPM for SIR Type Ampoules. Rapport BIPM 1999/03. 15 pp.

Michotte, C., 2002. Efficiency curve of the ionization chamber of the SIR. Appl. Radiat. Isot. 56, 15–20.

Michotte, C., Pearce, A.K., Cox, M.G., Gostely, J.–J., 2006. An approach based on the SIR measurement model for determining the ionization chamber efficiency curves, and a study of ^{65}Zn and ^{201}Tl photon emission intensities. Appl. Radiat. Isot. 64, 1147–1155.

Michotte, C., Courte, S., Ratel, G., Moune, M., Johansson, L., Keightley, J., 2010. Update of the BIPM.RI(II)-K1. Tc-99m comparison of activity measurements for the radionuclide ^{99m}Tc to include new results for the LNE–LNHB and the NPL. Metrologia 47 (Technical Suppl. ment), 06026.

Miguel, M., Delle Site, A., Deron, S., Raab, W., Swietly, H., 1984. Preparation of drop deposited plutonium sources on porcelain support; results and limitations of alpha spectrometric analyses. Nucl. Instrum. Methods Phys. Res. 223, 270−275.

Mihaljevic, N., Jovanovic, S., De Corte, F., Smodis, B., Jacimovic, R., Medin, G., De Wispelaere, A., Vucotic, P., Stegnar, P., 1993. "EXTSANGLE"-An extension of the efficiency conversion program "SOLANG" to sources with a diameter larger than that of the Ge-detector. J. Radioanal. Nucl. Chem. 169, 209−218.

Miyahara, H., Katoh, K., 2004. Emission probability measurement of 94.7 keV γ-ray for ^{165}Dy. Nucl. Instrum. Methods Phys. Res., Sect. A 516, 104−108.

Miyahara, H., Watanabe, T., 1984. Systematic effects due to increasing self-absortion in activity standardization using $4\pi\beta(\mathrm{PC}) - \gamma$ coincidence counting. Appl. Radiat. Isot. 35, 345−348.

Miyahara, H., Suzuki, M., Watanabe, T., 1987. Application of conducting-polymer film for source mounted in $4\pi\beta$ counting. Appl. Radiat. Isot. 38, 887−890.

Miyahara, H., Hara, K., Mori, C., 1992. Application of CF_4 gas to $4\pi\beta - \gamma$ coincidence counting. Nucl. Instrum. Methods Phys. Res. 312, 71−75.

Miyahara, H., Matumoto, H., Wurdiyanto, G., Yanagida, K., Takenaka, Y., Yoshida, A., Mori, C., 1994. Gamma-ray emisión probability measurements by a two-dimensional $4\pi\beta - \gamma$ coincidence system. Nucl. Instrum. Methods Phys. Res. 353, 229−233.

Miyahara, H., Wurdiyanto, G., Nagata, H., Yoshida, A., Yanagida, K., Mori, C., 2000. Precise measurements of the gamma-ray emisión of ^{186}Re and ^{188}Re. Appl. Radiat. Isot. 52, 573−579.

Mo, L., Cassette, P., Baldock, C., 2006. The influence of rejection of a fraction of the single photoelectron peak in liquid scintillation counting. Nucl. Instrum. Methods Phys. Res., Sect. A 558, 490−496.

Mo, L., Bignell, L.J., Steele, T., Alexiev, D., 2010. Activity measurements of ^{3}H using the TDCR method and observation of source stability. Appl. Radiat. Isot. 68, 1540−1542.

Moens, L., Hoste, J., 1983. Calculation of the peak efficiency of high-purity germanium detectors. Int. J. Appl. Radiat. Isot. 34, 1085−1095.

Moens, L., De Donder, J., Lin, X.,L., De Corte, F., DeWispelaere, A., Simonits, A., Hoste, J., 1981. Calculation if the absolute peak efficiency og gamma-ray detectors for different counting geometries. Nucl. Instrum. Methods 187, 451−472.

Mohanty, B.P., Balouria, P., Garg, M.L., Nandi, T.K., Mittal, V.K., Govil, I.M., 2008. Comparison of experimental and theoretical efficiency of HPGe X-ray detector. Nucl. Instrum. Methods Phys. Res., Sect. A 584, 186−190.

Morel, J., Chauvent, B., Kadachi, A., 1983. Coincidence-summing corrections in gamma-ray spectrometry for normalized geometries. Int. J. Appl. Radiat. Isot. 34, 1115−1122.

Mori, C., Fujii, T., Watanabe, T., 1987. Radioactivity Measurement of ^{3}H-Labeled Gas with Position-Sensitive Proportional Counter-I. New Principle of Elimination of End Effect and Making of Partially Resistive Anode Wire. Appl. Radiat. Isot. 38, 371−378.

Mori, C., Yamamoto, T., Suzuki, T., Uritani, A., Yanagida, K., Wu, Y., Watanabe, T., Yoshida, M., 1992. Radioactive measurement of ^{85}Kr with position-sensitive proportional counting. Nucl. Instrum. Methods Phys. Res., Sect. A 312, 189−192.

Mori, C., Wu, Y., Agemura, T., Suzuki, T., Uritani, A., Miyahara, H., Yoshida, M., 1998. Evaluation of counting loss and its correction for small pulses in internal counting with proportional counters. Appl. Radiat. Isot. 49, 1107−1111.

Mougeot, X., 2015. Reliability of usual assumptions in the calculations of β and υ spectra. Phys. Rev. C91, 055504.

Mougeot, X., 2016. Systematic comparison of beta spectra calculations using improved analytical screening corrections with experimental shape factors. Appl. Radiat. Isot. 309, 177−182.

Mougeot, X., 2018. Improved calculation of electron capture transitions for decay data and radionuclide metrology. Appl. Radiat. Isot. 134, 225−232.

Mougeot, X., Bisch, C., 2014. Consistent calculation of the screening and exchange effects in allowed β transitions. Phys. Rev. A90, 012501.

Mougeot, X., Bé, M.-M., Bisch, C., Loidl, M., 2012. Evidence for the exchange effect in the β decay of ^{241}Pu. Phys. Rev. A86, 042506.

Moura, L.P., Parker, W.C., 1975. Effect of a thin film resistance variation on the absolute standardization of radionuclides. Nucl. Instrum. Methods 129, 565−568.

Mowlavi, A.A., Izadi Najafabadi, R., Koohi Faygh, R., 2005. Calculation of intrinsic efficiency of NaI(Tl) detector using MCNP code. Int. J. Pure Appl. Phys. 1 (2), 129−136.

Müller, J.W., 1975. Principles of Correlation Counting. Report BIPM 75/5.

Nadderd, L.J., Jordanov, D.J., Davidović, 2012. A new matrix method for calculating coincidence summing effects for gamma spectroscopy. Nucl. Instrum. Methods Phys. Res., Sect. A 662, 21−25.

Nadderd, L.J., Davidović, M.d., Davidović, D.m., Milosević, M.J., Jordanov, D.J., Stanković, S.J., Prvanović, S.L., 2013. A possible improvement of the determination of ^{133}Ba activity and detection efficiency by the sum-peak method, by inclusion ot the previous neglected transitions. Nucl. Instrum. Methods Phys. Res., Sect. A 698, 60−65.

Nageldinger, G., Flowers, A., Schwerdt, C., Kelz, R., 1998. Autoradiographic film evaluated with desktop scanner. Nucl. Instrum. Methods Phys. Res., Sect. A 426, 516−524.

Nähle, O., 2018. Activity determination of ^{67}Ga using $4\pi\beta - \gamma$ coincidence counting. Appl. Radiat. Isot. 134 (286), 289.

Nähle, O., Kossert, K., Klein, R., 2008. Activity standardization of ^{22}Na. Appl. Radiat. Isot. 66, 865−871.

Nähle, O., Kossert, K., Cassette, P., 2010. Activity standardization of ^{3}H with the new TDCR system at PTB. Appl. Radiat. Isot. 68, 1534−1536.

Nakamura, T., Suzuki, T., 1975. Monte Carlo calculation of peak efficiencies and response functions of coaxial-type Ge(Li) detectors for disk gamma-ray sources. Nucl. Instrum. Methods 131, 521−527.

Nakamura, T., Suzuki, T., 1983. Monte Carlo calculation of peak efficiencies of Ge(Li) and pure Ge detectors to voluminal sources and comparison with environmental radioactivity measurement. Nucl. Instrum. Methods Phys. Res., Sect. A 205, 211−218.

Navarro, N., Grau Carles, A., Álvarez, A., Salvador, S., Gómez, V., 1997. Standardization of ^{234}Th by Cerenkov Counting. Appl. Radiat. Isot. 47, 949−952.

NCRP, 1985. A Handbook of Radioactivity Measurements Procedures, second ed., vol. 58, pp. 215−218

Nedjadi, Y., Spring, P., Bailat, C., Decombatz, M.,C., Triscone, G., Gostely, J.−J., Laedermann, J.−P., Bochud, F.O., 2007. Primary activity measurements with N4$\pi\gamma$ aI(Tl) counting and Monte Carlo calculated efficiencies. Appl. Radiat. Isot. 65, 534−538.

Nedjadi, Y., Spring, P., Baillat, C., Froidevaux, P., Wastiel, C., Bochoud, F., 2008. Purification and activity standardization of a ^{166m}Ho solution. Appl. Radiat. Isot. 66, 900−904.

Nedjadi, Y., Bailat, C., Caffari, Y., Bochud, F., 2010. Standardisation of ^{18}F by a coincidence method using full solid angle detectors. Appl. Radiat. Isot. 68, 1309−1313.

Nedjadi, Y., Bailat, C.J., bochud, F.O., 2012. primary activity measurements with a $4\pi\beta - 4\pi\gamma$ coincidence counting system. Appl. Radiat. Isot. 70, 249−256.

Nedjadi, Y., Bailat, C., Caffari, Y., Cassette, P., Bochud, F., 2015. Set-up a new TDCR counter at IRA-METAS. Appl. Radiat. Isot. 87, 113−117.

Nelson, W.R., Cassidy, M.E., Graveson, R.T., 1985a. The EGS4 Code System. Report SLAC-265. In: Electron-Gamma Shower. Stanford Linear Accelerator Center.

Nelson, W.R., Hirayama, H., Rogers, D.W.O., 1985b. EGS4 User Manual. SLAC-265 Appendix 2. Stanford Linear Accelerator Center, Stanford.

Nemes, T., Mrda, D., Bikid, I., 2018. Generalized equation for the sum-peak method, accounting for random coincidences. Nucl. Instrum. Methods Phys. Res., Sect. A 898, 11−14.

Nemes, T., Mrda, D., Bikid, I., Grujik, S., 2016. An improves formula for determination of the activity via the sum-peak method. Appl. Radiat. Isot. 114, 173−178.

Nicolaou, G.E., Khrbish, Y.S., Spyrou, N.M., 1986. The effect of solid angle on the reproducibility of an experimental set-up in prompt gamma-ray neutron activation analysis. Int. J. Radiat. Instrum. Part A. Appl. Radiat. Isot. 37, 1218−1224.

Noguchi, M., Takeda, K., Higuchi, H., 1981. Semi-empirical γ-ray peak efficiency determination including self-absorption correction based on numerical integration. Int. J. Appl. Radiat. Isot. 32, 17−22.

Notea, A., 1971. The Ge(Li) spectrometer as a point detector. Nucl. Instrum. Methods 91, 513−515.

Novcović, D., Kandic, A., Durasević, M., Vukanac, I., Milosević, Z., Nadderd, L., 2007a. Coincidence summing of X- and gamma-ray spectrometry. Nucl. Instrum. Methods Phys. Res., Sect. A 578, 207−217.

Novcović, D., Durasević, M., Kandić, A., Vukanać, I., Milosević, Z., Nadderd, L., 2007b. Coincidence summing of X- and gamma-ray of ^{133}Ba. Nucl. Instrum. Methods Phys. Res., Sect. A 582, 592−602.

Novcović, D., Kandić, A., Vukanac, I., Durasević, M., Milosević, Z., 2012. The direct measurement of ^{57}Co activity bu the sum-peak method. Appl. Radiat. Isot. 70, 2154−2156.

Novcovic, D., Kandić, A., Durasević, M., Kandić, A., Vucanać, I., Seslać, B., Milosević, Z., 2016. Coincidence summing corrections for point and volume 152Eu sources. Appl. Radiat. Isot. 107, 138−144.

Nylandsted Larsen, A., Bortels, G., Denecke, B., 1984. Satellite peaks in high-resolution alpha-particle spectra of decay-chain members measured with silicon surface-barrier detectors. Nucl. Instrum. Methods Phys. Res. 219, 339−346.

Obložinsky, P., Ribanský, I., 1971. The solid angle subtended at a disk source by a non-parallel disk detector. Nucl. Instrum. Methods 94, 187−188.

Oderkerk, R.P., Brinkman, G.A., 1990. The applicability of the sum-peak formula to extended sources. Appl. Radiat. Isot. 41, 169−171.

Ogata, Y., Miyahara, H., Ishigure, N., Ishihara, M., Noshio, M., Yamamoto, S., 2015. Development of a modified sum-peak method for activity determination os some gamma emitters. Nucl. Instrum. Methods Phys. Res. 775, 34−40.

Ogata, Y., Miyahara, H., Ishihara, M., Ishigure, N., Yamamoto, S., 2016. Development of the modified sum-peak method and its application. Appl. Radiat. Isot. 109, 354−357.

Ogata, Y., Itadzu, H., Kojima, S., 2018. Estimation of ^{134}Cs activity by a new approximation referred sum-peak method via a well-tipe Ge detector. Appl. Radiat. Isot. 134, 172−176.

Oliveira, F.M., Iwahara, A., Poledna, R., delgado, J.U., da Silva, C.J., da Silva, R.L., lopes, R.T., 2012. standardization of ^{65}Zn by sum-peak method. Appl. Radiat. Isot. 70, 2087−2090.

Olsovcová, V., 2004. Activity measurements with radionuclide calibrators in the Czech Republic. Appl. Radiat. Isot. 60, 535−538.

Olšovcová, V., 2010. Monte Carlo simulation of activity measurement of ^{123}I, ^{111}In and ^{153}Sm with a radionuclide calibrator. Appl. Radiat. Isot. 68, 1383−1387.

Olšovcová, V., Havelka, M., 2006. Monte Carlo calculations of calibration and geometry correction factors of a radionuclide calibrator. Appl. Radiat. Isot. 64, 1370−1374.

Olšovcová, V., Iwahara, A., Oropesa, P., Joseph, L., Ravindra, A., Ghafoori, M., Son, H.K., Sahagia, M., Tastan, S., Zimmerman, B.E., 2010. National comparison of measurement among nuclear medicine clinics of eight countries. Appl. Radiat. Isot. 68, 1371−1377.

Oncescu, M., Rebigan, F., 1968. Calibration of a $4\pi\gamma$ ionization chamber. Rev. Roum. Phys. 13, 837−845.

Oropesa, P., Serra, R., Gutiérrez, S., Hernández, A.T., 2002. A procedure for the standardization of gamma reference sources for quality assurance in activity measurements of radiopharmaceuticals. Appl. Radiat. Isot. 56, 787−795.

Oropesa, P., Hernández, A.T., Serra, R., Martínez, E., Varela, C., 2003. Comparisons of activity measurements with radionuclide calibrators. Appl. Radiat. Isot. 59, 383−387.

Oropesa, P., Woods, M.J., Olšovcová, V., Dos Santos, J.A., 2008. Radionuclide calibrator comparisons and quality improvement in nuclear medicine. Appl. Radiat. Isot. 66, 359−361.

Oropesa, P.O., Moreno, Y., Serra, R.A., Hernandez, A.T., 2012. The stability chain of ^{131}I measurements for nuclear medicine in Cube. Appl. Radiat. Isot. 70, 2251−2254.

Oropesa Verdecia, P.O., Kossert, K., 2009. Activity standardization of ^{131}I at CENTIS-DMR and PTB within the scope of a bilateral comparison. Appl. Radiat. Isot. 67, 1099−1103.

Oropesa Verdecia, P., García Rodríguez, L., Serra Águila, R.A., Moreno León, Y., Jénez Magaña, Y., Cassette, P., 2018. .^{68}Ga activity calibrations for nuclear medicine applications in Cuba. Appl. Radiat. Isot. 134, 112−116.

Padilla Cabal, F., López-Pino, N., Bernal-Castillo, J.L., Martínez-Palenzuela, Y., Agular-Mena, J., D'Alesandro, K., Arbelo, Y., Corrales, Y., Diaz, O., 2010. Monte Carlo based geometrical model for efficiency calculation of an n-type HPGe detector. Appl. Radiat. Isot. 68, 2403−2408.

Paepen, J., Altzitzoglou, T., Van Ammel, R., Sibbens, G., Pommé, S., 2010. Half-life measurement of ^{124}Sb. Appl. Radiat. Isot. 68, 1555−1560.

Park, T.S., Lee, J.M., Hwang, H.Y., 2002. Standardization of ^{152}Eu and ^{88}Y. Appl. Radiat. Isot. 56, 275−280.

Pate, B.D., Yaffe, L., 1955. A new material and techniques for the fabrication and measurement of very thin films for use in 4π-counting. Can. J. Chem. 33, 15−23.

Paton Walsh, C., Woods, M.J., Sephton, J.P., Woods, S.A., Lucas, S.E.M., Rossiter, M.J., Williams, T.T., Bass, G.A., 1996. ^{131}I diagnosis

and therapy capsules and low dose rate ^{125}I and ^{137}Cs brachytherapy sources. Calibration of the NPL secondary standard radionuclide calibrator. Nucl. Instrum. Methods Phys. Res., Sect. A 369, 703−708.

Paul, A., Honig, A., Röttger, S., Keyser, U., 2000. Measurement of radon and radon progenies at the German radon reference chamber. Appl. Radiat. Isot. 52, 369−375.

Pavlik, A., Winkler, G., 1983. Survey of standardization of possibilities with NaI(Tl) well-type detectors. Int. J. Appl. Radiat. Isot. 34, 1167−1174.

Peterman, B.F., Hontzeas, S., Rystephanick, R.G., 1972. Monte Carlo calculations of relative efficiencies of Ge(Li) detectors. Nucl. Instrum. Methods 104, 461−468.

Peyres, V., Garcia-Toraño, E., 2007. Efficiency calibration of an extended-range Ge detector by a detailed Monte Carlo simulation. Nucl. Instrum. Methods Phys. Res., Sect. A 580, 296−298.

Philips, H.C., Johadson, L.C., Sephtton, J.P., 2010. Standardization of ^{85}Kr. Appl. Radiat. Isot. 68, 1335−1339.

Pibida, L., Fitzgerald, R., Unterweger, M., Hammond, M.M., Golas, D., 2009. Measurements of the ^{82}Sr half-life. Appl. Radiat. Isot. 67, 636−640.

Picolo, J.L., 1996. Absolute measurement of radon 222 activity. Nucl. Instrum. Methods 369, 452−457.

Picolo, J.L., Seralta, S., Dulieu, C., Unterweger, M.P., Ratel, G., 1998. International Comparison of Measurements of ^{133}Xe. Appl. Radiat. Isot. 49, 1429−1435.

Pillinger, W.L., Hentges, J.J., Blair, J.A., 1961. Tritium decay energy. Phys. Rev. 121, 232−233.

Piton, F., Lépy, M.C., Bé, M.M., Plagnard, J., 2000. Efficiency transfer and coincidence summing corrections for γ-ray spectrometry. Appl. Radiat. Isot. 52, 791−795.

Plch, L., Zderadièka, J., 1974. Intensity of γ- and X-rays in the ^{125}I decay. Czech. J. Phys. 24, 1311−1313.

Plch, J., Zderadièka, J., Kokta, 1973a. A windowless 4π-scintillation counter with NaI(Tl) crystals. Int. J. Appl. Radiat. Isot. 24, 407−413.

Plch, J., Zderadièka, J., Kokta, 1973b. Internal conversion of the 84.83 keV transition in ^{170}Yb. Czech. J. Phys. 23, 1181−1186.

Plch, J., Zderadièka, J., Kokta, L., 1976. Number of 59.5 keV-photons per decay of ^{241}Am. Czech. J. Phys. 26, 1344−1346.

Plch, J., Dryàk, P., Zderadièka, J., Schönfeld, E., Szörényi, A., 1979. Revision of the ^{109}Cd decay data. Czech. J. Phys. 29, 1071−1083.

Plch, J., Dryàk, P., Suran, J., 1991. Direct activity measurement and XK- and gamma-photon yields in the decay of ^{145}Sm. Appl. Radiat. Isot. 42, 143−148.

Pochwalski, K., Radoszewski, T., 1979. Disintegration Rate Determination by Liquid Scintillation Counting Using the Triple to Double Coincidence Ratio (TDCR) Method. IBJ Report, INR 1848/OPiDI/E/A.

Pochwalski, K., Broda, R., Rdoszewski, T., 1988. Standardization of pure beta emitters by liquid-scintillation counting. Int. J. Appl. Radiat. Isot. 39, 165−172.

Pommé, S., 2004. A complete series expansion of Ruby's solid-angle formula. Nucl. Instrum. Methods Phys. Res., Sect. A 531 (3), 616−620.

Pommé, S., 2007. Methods for primary standardization of activity. Metrologia 44, S17−S26.

Pommé, S., 2015a. The uncertainty of counting at a defined solid angle. Metrologia 52, S73−S85.

Pommé, S., 2015b. Typical uncertainties in alpha-particle spectrometry. Metrologia 52, S146−S155.

Pommé, S., Sibbens, S., 2008. Alpha-particle counting and spectrometry in a primary standardisation laboratory. Acta Chim. Slov. 55, 111−119.

Pommé, S., Wagemasn, C., Vehaegen, F., Van Den Durpel, L., Van Gils, J., Barthélémy, R., 1995. A double $\Delta E - E$ detection set-up for ternary fission. Nucl. Instrum. Methods Phys. Res., Sect. A 359, 587−595.

Pommé, S., Johansson, L., Sibbens, G., Denecke, B., 2003. An algorithm for the solid angle calculation applied in alpha-particle counting. Nucl. Instrum. Methods Phys. Res., Sect. A 505, 286−289.

Pommé, S., Alzitzoglou, T., Van Ammel, R., Sibbens, G., 2005a. Standardization of ^{125}I using seven techniques for radioactivity measurements. Nucl. Instrum. Methods Phys. Res., Sect. A 544, 584−592.

Pommé, S., Alzitzoglou, T., Van Ammel, R., Sibbens, G., 2005b. Standardization of ^{125}I using seven techniques for radioactivity measurements. Nucl. Instrum. Methods Phys. Res., Sect. A 555, 459.

Prata, M.J., 2003. Solid angle subtended by a cylindrical detector at a point source in terms of elliptic integrals. Radiat. Phys. Chem. 67, 599−603.

Prata, M.J., 2004. Analytical calculation of the solid angle subtended by a circular disc detector at a point cosine source. Nucl. Instrum. Methods Phys. Res., Sect. A 521, 576−585.

Putman, J.L., 1950. Absolute Measurements of the Activity of Beta Emitters. Br. J. Radiol. 23, 46−63.

Qin, M.J., Mo, L., Alexiev, D., Cassette, P., 2008. Construction and implementation of a TDCR system at ANSTO. Appl. Radiat. Isot. 66, 1033−1037.

Quinn, T.J., 1997. Primary methods of measurement and primary standards. Metrologia 34, 61−65.

Radu, D., Stanga, D., Sima, O., 2009. ETNA software used for efficiency transfer from a point source to other geometries. Appl. Radiat. Isot. 67, 1686−1690.

Ramthun, H., 1973. Recent developments in calorimetric measurements of radioactivity. Nucl. Instrum. Methods 112, 265−272.

Ranitzsch, P.C., Kempf, S., Pabinger, A., Pies, C., Porst, J.−P., Schäfer, S., Fleischmann, A., Gastaldo, L., Enss, C., Jang, Y.S., Kim, I.H., Kim, M.S., Kim, H., Lee, J.S., Lee, K.B., Lee, M.K., Lee, S.J., Yoon, W.S., Yuryev, Y.N., 2011. Development of cryogenic alpha spectrometers using metallic magnetic calorimeters. Nucl. Instrum. Methods Phys. Res., Sect. A 652, 299−301.

Ratel, G., 1998. Results of an international trial comparison of activity measurements of a solution of ^{192}Ir. Appl. Radiat. Isot. 49, 1437−1443.

Ratel, G., 2005. Evaluation of the uncertainty of the degree of equivalence. Metrologia 43, 140−144.

Ratel, G., 2007. The Système International de Référence and its application in key comparisons. Metrologia 44 (4), S7−S16.

Razdolescu, A.C., Cassette, P., 2004. Standardization of tritiated water and ^{204}Tl by TDCR liquid scintillation counting. Appl. Radiat. Isot. 60, 493−497.

Razdolescu, A.C., Sahagia, M., Cassette, P., Grigorescu, E.L., Luca, A., Ivan, C., 2002. Standardization of ^{89}Sr. Appl. Radiat. Isot. 56, 461−465.

Razdolescu, A.C., Broda, R., Cassette, P., Simpson, B.R.S., Van Wyngaardt, W.M., 2006. The IFIN-HH triple coincidence liquid scintillation counter. Appl. Radiat. Isot. 64, 1510−1514.

Razdolescu, A.C., Cassette, P., Sahagia, M., 2008. Measurement of ^{55}Fe solution activity by LSC-TDCR method. Appl. Radiat. Isot. 66, 750−755.

Reddy, P.J., Bhade, S.P.D., Narayan, K.K., Narayanan, A., Babu, D.A.R., Sharma, D.N., 2009. Comparative study of different methods for the activity quantification of ^{3}H and ^{14}C radionuclides in dual labelled samples using liquid scintillation analyzer. Appl. Radiat. Isot. 67, 1945−1951.

Reher, D.F.G., Woods, M.J.:, De Roost, E., Sibbens, G., Denecke, B., Altzitzoglou, T., Ballaux, C., Funck, E., 1992. Standardization of 192Ir. Nucl. Instrum. Methods Phys. Res., Sect. A 312, 263−268.

Rezende, E.A., Correia, A.R., Iwahara, A., da Silva, C.J., Tauhata, I., Poledma, R., da Silva, r, L., de Oliveira, E.M., de Oliveira, A.E., 2012. Radioactivity measurements of ^{177}Lu, ^{111}In, ^{123}n by different absolute methods. Appl. Radiat. Isot. 70, 2081−2086.

Rieppo, R., 1981. Calculated absolute photopeak efficiency values for true coaxial Ge(Li) detectors in the γ-ray energy region 0.1−3.0 MeV with annular source geometry. Nucl. Instrum. Methods 188, 115−117.

Robinson, H.P., 1960. A new design for a high precision, high geometry α counter in: Metrology of radionuclides. In: Proc. of a Symp. Organised by the IAEA (14−16 October 1959, Vienna), pp. 147−154.

Ródenas, J., Martin Navarro, A., Rius, V., 2000. Validation of the MCNP code for the simulation of Ge detector calibration. Nucl. Instrum. Methods Phys. Res., Sect. A 450, 88−97.

Ródenas, J., Pascual, A., Zarza, I., Serradell, V., Ortiz, J., Ballesteros, L., 2003. Analysis of the influence of germanium dead layer on detector calibration simulation for environmental radioactive samples using the Monte Carlo method. Nucl. Instrum. Methods Phys. Res., Sect. A 496, 390−399.

Rodenas, J., Gallardo, S., Ballester, S., Primault, S., Ortiz, J., 2007. Application of the Monte Carlo Method to the analysis of measurement geometries for the calibration of a HP Ge detector in an environmental radioactivity laboratory. Nucl. Instrum. Methods Phys. Res., Sect. B 263, 144−148.

Rodrigues, D., Arenillas, P., Capoulat, M.E., Balpardo, C., 2008. General data analysis code for TDCR liquid scintillation counting. Appl. Radiat. Isot. 66, 1049−1054.

Rodrigues, M., Lépy, M.-C., Cassette, P., Mougeot, X., Bé, M.M., 2014. standardization of xenon-127 and measurement of photon emission intensities. Appl. Radiat. Isot. 87, 342−347.

Rodríguez Barquero, L., Jiménez, J., Grau Carles, A., 1996. Separación del Pb-210, Bi-210 y Po-210 mediante columna de cambio iónico y su calibración por centelleo líquido. CIEMAT, p. 38 report 788.

Rodríguez, L., Los Arcos, J.M., Grau, A., 1992. LSC standardization of ^{54}Mn in inorganic and organic samples by the CIEMAT/NIST efficiency tracing method. Nucl. Instrum. Methods Phys. Res., Sect. A 312, 124−131.

Rodríguez-Barquero, L., Los Arcos, J.M., 1996. ^{41}Ca standardization by the CIEMAT/NIST LSC method. Nucl. Instrum. Methods Phys. Res., Sect. A 309, 353−358.

Rodríguez-Barquero, L., Los Arcos, J.M., 1997. Temperature effect in DIN- and pseudocument-based liquid scintillation cocktails quenched with CCl_4 and CH_3NO_2. Appl. Radiat. Isot. 48, 159−167.

Rodriguez Barquero, L., Los Arcos, J.M., 2000. Study of the stability problems of samples in several commercial liquid scintillators. Appl. Radiat. Isot. 52, 679−690.

Rodríguez-Barquero, L., Los Arcos, J.M., 2003. Spain Patent Number 2003302535.

Rodríguez-Barquero, L., Los Arcos, J.M., 2004a. Compensation by the CIEMAT/NIST-method of long-term effects in LSC measurements of beta emitters. Appl. Radiat. Isot. 61, 1403−1411.

Rodríguez-Barquero, L., Los Arcos, J.M., 2004b. European Patent Number 04380021.

Rodriguez-Barquero, L., Los Arcos, J.M., 2004c. Russian federation Patent Number 20044131438.

Rodriguez-Barquero, L., Los Arcos, J.M., 2004d. United States Patent Number 04380021.

Rodríguez-Barquero, L., Los Arcos, J.M., 2005. Radionuclide Stability in XAN Reference Cocktail. Extesion of SIR Working Group ESWG(II)/05-02, p. 47.

Rodriguez-Barquero, L., Los Arcos, J.M., 2007. Simulated ESIR Operation at CIEMAT with XAN6040 for ^{3}H, ^{90}Sr and ^{241}Am. Document Technique DT-LMRI-0701. CIEMAT, Spain, p. 26.

Rodriguez-Barquero, L., Los Arcos, J.M., 2010. Experimental determination of elemental compositions and densities of several commun liquid scintillators. Appl. Radiat. Isot. 68, 1546−1549.

Rodríguez-Barquero, L., Los Arcos, J.M., Grau Malonda, A., García-Toraño, E., 1994. LSC standardization of ^{45}Ca by the CIEMAT/NIST efficiency tracing method. Nucl. Instrum. Methods Phys. Res., Sect. A 339, 6−13.

Rodríguez-Barquero, L., Los Arcos, J.M., Ortiz, F., Jiménez, A., 1998. ^{49}V Standardization by the CIEMAT/NIST LSC Method. Appl. Radiat. Isot. 47, 1077−1082.

Rose, M.E., 1953. The analysis of angular correlation and the angular distribution data. Phys. Rev. 91, 610−615.

Roteta, M., García-Toraño, E., 2006. Calculation of electron deposition in proportional counters. Appl. Radiat. Isot. 64, 1193−1197.

Roteta, M., García-Toraño, E., Rodríguez-Barquero, L., 2006. Standardization of ^{18}F by coincidence and LSC methods. Appl. Radiat. Isot. 64, 1199−1202.

Roteta, M., Peyrés, V., Rodriguez barquero, L., García-Toraño, E., arenillas, P., Balpardo, C., Rodriguez, D., Llovera, R., 2012. Standardization of ^{68}Ga by coincidence measurement liquid scintillation counting and $4\pi\gamma$ counting, 70, 2006−2011.

Roteta, M., Peyrés, V., García-Toraño, E., 2014. Standardization of ^{113}Sn. Appl. Radiat. Isot. 87, 162−165.

Ruby, L., 1994. Further comments on the geometrical efficiency of a parallel-disk source and detector system. Nucl. Instrum. Methods Phys. Res., Sect. A 337, 531−533.

Ruby, L., Rechen, J.B., 1968. A simpler approach to the geometrical efficiency of a parallel-disk source and detector system. Nucl. Instrum. Methods Phys. Res., Sect. A 58, 345−346.

Ruffle, M.P., 1967. The geometrical efficiency of a parallel-disk source and detector system. Nucl. Instrum. Methods 52, 354−356.

Rytz, A., 1978. Coherence of activity measurements. Environ. Int. 1, 15−18.

Rytz, A., 1983a. Minimum Activity and Maximum Impurity Rates for SIR Samples. Report BIPM-83/9. Sèvres. BIPM, France, p. 9.

Rytz, A., 1983b. The international reference system for activity measurement of γ-ray emitting nuclides. Int. J. Appl. Radiat. Isot. 34, 1047−1056.

Sahagia, M., 2006. Standardization of ^{99m}Tc. Appl. Radiat. Isot. 63, 1234−1237.

Sahagia, M., Razdolescu, A.C., Grigorescu, E.L., Luca, A., Ivan, C., 2002. Precise measurement of the activity of 186Re/188Re radiopharmaceuticals. Appl. Radiat. Isot. 56, 349–356.

Sahagia, M., Ivan, C., Grigorescu, E.L., Capogni, M., De Felice, P., Fazio, A., 2004. Standardization of 65Zn by 4πPC-γ coincidence counting method with efficiency extrapolation. Appl. Radiat. Isot. 60, 423–427.

Sahagia, M., Razdolescu, A.C., Ivan, C., Luca, A., 2008. Assurance of the traceability chain for 131I measurement. Appl. Radiat. Isot. 66, 539–544.

Sahagia, M., Ioan, M.R., Luca, A., Antohe, A., Ivan, C., Neacsu, B., Ghioca, C., 2014a. Standardization of ^{18}F and its use for the Romanian PET metrological traceability chain assurance. Appl. Radiat. Isot. 87, 14–18.

Sahagia, M., Antohe, A., Ioan, M.R., Luca, A., Ivan, C., 2014b. Standardization of Tc-99 by two methods and participation at the CCRI(II)-K2. Tc-99 comparison. Appl. Radiat. Isot. 87, 410–413.

Sahagia, M., Ioan, M.R., Antohe, A., Luca, A., Ivan, C., 2016. Measurements of ^{124}I. Appl. Radiat. Isot. 109, 349–353.

Sahagia, M., Luca, A., Ioan, M.R., Antohe, A., Ivan, C., 2018. Standardization of $4\pi\beta - \gamma$ and calibration of the ionization chamber. Impurities and decay scheme problems. Appl. Radiat. Isot. 134, 297–301.

Salvat, F., Fernandez-Varea, J.M., Sempau, J., 2003. PENELOPE-2003: A Code System for Monte Carlo Simulation of Electron and Positron Transport. OECD. Nuclear Energy Agency. Issy-les-Moulineaux, France.

Salvat, F., Fernandez Varea, J.M., Sempau, J., July 2006. PENELOPE-2006, A Code System for Monte Carlo Simulation of Electron and Photon Transport. OECD, ISBN 92-64-02301-1, p. 293.

Salvat, F., Fernandez-Varea, J.M., Sempau, J., 2008. PENELOPE-2008: A Code System for Monte Carlo Simulation of Electron and Positron Transport. OECD. Nuclear Energy Agency. Issy-les-Moulineaux, France.

Santos, J.A.M., Carrasco, M.F., Lencart, J., Bastos, A.L., 2009. Syringe shape and positioning relative to efficiency volume inside dose calibrators and its role in nuclear medicine quality assurance programs. Appl. Radiat. Isot. 67, 1104–1109.

Santry, D.C., Bowes, G.C., Munzenmayer, K., 1987. Standardization of ^{67}Ga by live-timed anti-coincidence counting with extending dead time. Int. J. Radiat. Appl. Instrum. Part A. Appl. Radiat. Isot. 38, 787–791.

Sato, Y., Yunoki, A., Hino, Y., Yamada, T., 2006. Response calculation for standard ionization chambers in the APMP using EGS4 Monte Carlo code. Appl. Radiat. Isot. 64, 1211–1224.

Sato, Y., Yamada, T., Hata, T., Moriyama, K., Yunoki, A., Hino, Y., 2008. The efficiency variation method for ^{141}Ce coincidence counting by ink-jet printing. Appl. Radiat. Isot. 66, 691–693.

Schima, F.J., Hopes, D.D., 1983. Tables for cascade-summing corrections in gamma-ray spectrometry. Int. J. Appl. Radiat. Isot. 34, 1109–1114.

Schlosser, C., Bollhöfer, A., Schmid, S., Krais, R., Bieringer, J., Konrad, M., 2017. Analysis of radioxenon and Krypton-85 at the BfS noble gas laboratory. Appl. Radiat. Isot. 126, 16–19.

Schönfeld, E., Hansen, H., Schötzig, U., 1992. Decay data of 4π. Appl. Radiat. Isot. 43, 1071–1077.

Schonfeld, E., Schötzig, U., Günther, E., Schrader, H., 1994a. Standardization and Decay Data of ^{68}Ge/^{68}Ga. Appl. Radiat. Isot. 45, 955–961.

Schonfeld, E., Janssen, H., Schötzig, U., Günther, E., Schrader, H., 1994b. Standardization and decay data of ^{186}Re. Nucl. Instrum. Methods Phys. Res., Sect. A 339, 174–179.

Schötzig, U., 1992. Activity measurement of ^{75}Se using integral gamma-ray counting with a ^{237}Np/^{233}Pa-NaI(Tl) detector. Nucl. Instrum. Methods Phys. Res., Sect. A 312, 141–145.

Schötzig, U., 2000. Half-life and X-ray emission probabilities of ^{55}Fe. Appl. Radiat. Isot. 53, 469–472.

Schötzig, U., Schönfeld, E.,., Günther, E., Klein, R., Schrader, H., 1999. Standardisation and decay data of ^{153}Sm. Appl. Radiat. Isot. 51, 169–175.

Schötzig, U., Schönfeld, E., Janszen, H., 2000. Standardization of photon emission probabilities in the decay of γ. Appl. Radiat. Isot. 52, 883–889.

Schötzig, U., Schrader, H., Schönfeld, E., Günther, E., Klein, R., 2001. Standardisation and decay data of ^{177}Lu and ^{188}Re. Appl. Radiat. Isot. 55, 89–96.

Schrader, 1997. Activity Measurement with Ionization Chambers. In: Monographie BIPM, vol. 4. Sèvres. BIP, France, p. p178.

Schrader, H., 2000. Calibration and consistency of results of an ionization-chamber secondary standard measuring system for activity. Appl. Radiat. Isot. 52, 325–334.

Schrader, H., 2004. Half-life measurements with ionization chambers—A study of systematic effects and results. Appl. Radiat. Isot. 60, 317–323.

Schrader, H., 2010. Half-life measurements of long-lived radionuclides—New data analysis and systematic effects. Appl. Radiat. Isot. 68, 1583–1590.

Schrader, H., Svec, A., 2004. Comparison of ionization chamber efficiencies for activity measurements. Appl. Radiat. Isot. 60, 369–378.

Schrader, H., Weiss, H.M., 1983. Calibration of radionuclide calibrators. Int. J. Appl. Radiat. Isot. 10, 121–124.

Schrader, H., Klein, R., Kossert, K., 2007. Activity standardisation of ^{18}F and ionisation chamber calibration for nuclear medicine. Appl. Radiat. Isot. 65, 581–592.

Schrader, H., Kossert, K., Mintcheva, J., 2008. Calibration of a radionuclide calibrator system as a Bulgarian standard for activity. Appl. Radiat. Isot. 66, 965–971.

Schultz, M.K., Hammond, M., Cessna, J.T., Plascjak, P., Norman, B., Szajek, L., Garmestani, K., Zimmerman, B.E., Unterweger, M., 2006. Assessing the ^{210}At impurity in the production of ^{211}At for radiotherapy by ^{210}Po analysis via isotope dilution alpha spectrometry. Appl. Radiat. Isot. 64, 1365–1369.

Schwarz, W.H., Kossert, K., Trieloff, M., Hopp, J., 2011. Comment on the "Joint determination of 40K decay constants and 40Ar*/40K for the Fish Canyon sanidine standard, and improved accuracy for 40Ar/39Ar geochronology". Geochem. Cosmochim. Acta 75, 5094–5096.

Schwerdtel, E., 1968. Simple method for an exact efficiency determination in liquid scintillation counting of low-energy beta emitters (in German). In: Atomkernenerg, vol. 11, pp. 324–325.

Seferinoglu, M., Yeltepe, E., 2015. Design of an alpha-particle counting system at a defined solid angle at Turkish atomic energy authority-Sarayköy nuclear research and training center (TAEK-SANAEM). Rad. Fis. Chem. 117, 135–139.

Selim, Y.S., Abbas, M.I., 1994. Source–detector geometrical efficiency. Radiat. Phys. Chem. 44, 1–4.

Selinger, H.H., Mann, W.B., Cavallo, L.M., 1958. The average energy of sulphur-35 beta decay. J. Res. Natl. Bur. Stand. 60, 447–449.

Semkow, T.M., Mehmood, G., Parekh, P.P., Vigil, M., 1990. Coincidence summing in gamma-ray spectrometry. Nucl. Instrum. Methods Phys. Res., Sect. A 290, 437–444.

Shape, J., Wade, F., 1951. T.P.A. Mk II Ionization Chamber. AERE EL/R806 UK Atomic Energy Research Establishment. Harnwel.

Shi, Q., Zhang, J., Chang, Y., Oian, S., 2005. Comparison between summing-up algorithms to determine areas of small peaks on high baselines. Nucl. Instrum. Methods Phys. Res., Sect. A 555, 220–224.

Shizuma, K., Oba, Y., Takada, M., 2016. A practical method for determining ^{42}K-ray-full-energy peak efficiency considering coincidence-summing and self-absortion corrections for the measurement of environmental samples after Fukushima reactor accident. Nucl. Instrum. Methods Phys. Res., Sect. B 383, 183–190.

Sibbens, G., Altzitzoglou, T., 2007. Preparation of radioactive sources for radionuclide metrology. Metrologia 44, S71–S78.

Sibbens, G., Pommé, S., Johansson, L., Denecke, B., 2003. Tailoring solid angle calculations to the actual radioactivity distribution of planar sources. Nucl. Instrum. Methods Phys. Res., Sect. A 505, 277–281.

Siegert, H., Schrader, H., Schötzig, U., 1998. Half-life measurements of Europium radionuclides and the long-term stability of detectors. Appl. Radiat. Isot. 49, 1397–1401.

Sima, O., 1990. Monte Carlo simulation versus semi-empirical calculation of auto-absorption factors for semiconductor detector calibration in complex geometry. Prog. Nucl. Energy 24, 327–336.

Sima, O., 1996. Applications of Monte Carlo calculations to gamma-spectrometric measurements of environmental samples. Appl. Radiat. Isot. 47, 919–923.

Sima, O., Arnold, D., 1996. Self-attenuation and coincidence-summing corrections calculated by Monte Carlo simulations fort gamma-spectrometric measurements with a well-type germanium detectors. Appl. Radiat. Isot. 47, 889–893.

Sima, O., Arnold, D., 2002. Transfer of the efficiency calibration of Germanium gamma-ray detectors using the GESPECOR software. Appl. Radiat. Isot. 56, 71–75.

Sima, O., Arnold, D., 2008. A tool for processing decay scheme data that encompasses coincidence summing calculations. Appl. Radiat. Isot. 66, 705–710.

Sima, O., Dovlete, C., 1997. Matrix effects in the activity measurement of environmental samples—implementation of specific corrections in a gamma-ray spectrometry analysis program. Appl. Radiat. Isot. 48, 59–69.

Sima, O., Arnold, D., Dovlete, C., 2001. GESPECOR-a versatile tool in gamma-ray spectrometry. J. Radioanal. Nucl. Chem. 248, 359–364.

Simöes, D., Koskinas, M.F., Fias, M., 2001. Measurement of the gamma-ray probability per decay of $4\pi(x,e) - \gamma$. Appl. Radiat. Isot. 54, 443–446.

Simoes, C., Caldeira, M., Oliveira, C., 2010. Comparative study of Curiementor ionization chambers using Monte Carlo simulations. Appl. Radiat. Isot. 68, 1121–1127.

Simpson, B.R.S., 2002. Radioactivity standardization in South Africa. Appl. Radiat. Isot. 56, 301–305.

Simpson, B.R.S., Meyer, B.R., 1989. The half-life of ^{125}I. Appl. Radiat. Isot. 40, 819–820.

Simpson, B.R.S., Meyer, B.R., 1994a. Direct activity measurement of pure beta-emitting radionuclides by the TDCR efficiency calculation technique. Nucl. Instrum. Methods Phys. Res., Sect. A 339, 14–20.

Simpson, B.R.S., Meyer, B.R., 1994b. Standardization and half-life of ^{201}Tl by the β coincidence method with liquid scintillation counting in the 4π channel. Appl. Radiat. Isot. 45, 669–673.

Simpson, B.R.S., Meyer, B.R., 1996. Activity measurement of ^{204}Tl by direct liquid scintillation methods. Nucl. Instrum. Methods Phys. Res., Sect. A 369, 340–343.

Simpson, B.R.S., Meyer, B.R., 1998. Activity Measurement of ^{55}Fe by an Efficiency Calculation Method. Appl. Radiat. Isot. 49, 1073–1076.

Simpson, B.R.S., Morris, W.M., 2004a. Direct activity determination of ^{54}Mn and ^{65}Zn by a non-extrapolation liquid scintillation method. Appl. Radiat. Isot. 60, 475–480.

Simpson, B.R.S., Morris, W.M., 2004b. The standardization of ^{33}P by the TDCR efficiency calculation technique. Appl. Radiat. Isot. 60, 465–468.

Simpson, B.R.S., van Wyngaardt, W.M., 2008. Absolute activity of ^{133}Ba by liquid scintillation coincidence counting using the 4π(e,X)-γ extrapolation technique. Appl. Radiat. Isot. 64, 929–933.

Simpson, B.R.S., van Wyngaardt, W.M., 2006. Activity measurements of the high-energy pure $4\pi\beta - \gamma$-emitters ^{89}Sr and ^{90}Y by the TDCR efficiency calculation technique. Appl. Radiat. Isot. 64, 1481–1484.

Simpson, B.R.S., van Wyngaardt, W.M., Lubbe, J., 2010. Fe-55 activity. Appl. Radiat. Isot. 68, 1529–1533.

Simpson, B.R.S., van Staden, M.J., Lubbe, J., van Wyngaardt, W.M., 2012. Accurate activity measurement of Lu-177 by the liquid scintillation $4\pi\beta - \gamma$ coincidence counting technique. Appl. Radiat. Isot. 70, 2209–2214.

Smith, D., 1978. Improved correction formulae for coincidence counting. Nucl. Instrum. Methods 152, 505–519.

Smith, D., 1987. Some developments of the Cox-Isham theory of coincidence corrections, including the extension to the computer-discrimination method. Appl. Radiat. Isot. 38, 813–821.

Smith, D., Stuart, L.E.H., 1975. An extension of the ^{75}Se coincidence technique: Two dimensional extrapolation. Metrologia 11, 67–72.

Smith, D., Woods, D.H., 1994. Measurement of ^{134}Cs activity by correlation and coincidence counting. Nucl. Instrum. Methods Phys. Res., Sect. A 399, 357–362.

Sochorová, J., Auerbach, P., 2014. Activity standardization of 137ctivity by correlation and coincidence ^{137}Cs and 4π. Appl. Radiat. Isot. 87, 207–210.

Sochorová, J., Auerbach, P., Haveñka, M., 2008. Application of "wet" extrapolation method for activity standardization of electron capture radionuclides. Appl. Radiat. Isot. 66, 919–924.

Spernol, A., 1967. Internal Gas Counters as a Precision Absolute Counting Device Standardization of Radionuclides. IAEA, Vienna, pp. 277–287. SM-79/22.

Spernol, A., Denecke, B., 1964. High precision absolute gas counting of tritium-III absolute counting of tritium in the internal gas counter (in German). Int. J. Appl. Radiat. Isot. 15, 241–254.

Spring, P., Nedjadi, Y., Bailat, C., Triscone, G., Bochoud, F., 2006. Absolute activity measurements of radon gas at IRA_METAS. Nucl. Instrum. Methods Phys. Res., Sect. A 568, 752–759.

Stanga, D., Picolo, J.L., Coursol, N., Mitev, K., Moreau, I., 2002. Analytical calculations of counting losses in internal gas proportional counting. Appl. Radiat. Isot. 56, 231–236.

Stanga, D., Moreau, I., Picolo, J.L., Cassette, P., 2005. A new tritium gas generator for the activity standardization of tritiated water by internal gas proportional counting. Fusion Sci. Technol. 48 (1), 354–357.

Stanga, D., Moreau, I., Cassette, P., 2006. Standardization of tritiated water by two improved methods. Appl. Radiat. Isot. 64, 1203–1206.

Stavroulaki, B.T., Kaplanis, S.N., 1979. Monte-Carlo solutions of the solid angle integrals for radiation detectors. Comp. Phys. Commun. 18, 7–12.

Steele, T., Mo, L., Bignell, L., Smith, M., Alexiev, D., 2009. FASEA: A FPGA Acquisition System and Software Event Analysis for liquid scintillation counting. Nucl. Instrum. Methods Phys. Res., Sect. A 609, 217–220.

Steyn, J., 1956. Absolute Standardization of Beta-emitting Isotopes with a Liquid Scintillation Counter. J. Proc. Phys. Soc. London A 69, 865–867.

Steyn, J., 1973. Tracer method for pure beta emitter measurement. Nucl. Instrum. Methods 112, 157–163.

Steyn, J., Haasbroek, F.J., 1958. In: Second U.N. Conf. Peaceful Uses of Atomic Energy, p. 1104.

Stout, J.W., Jones, W.M., 1947. Calorimetric determination of the energy produced by plutonium 239. Phys. Rev. 71, 582–585.

Stump, K.E., De Werd, L.A., Rudman, D.A., Schima, S.A., 2005. Active radiometric calorimeter for absolute calibration of radioactive sources. Rev. Sci. Instrum. 76, 033504.

Suárez, J.A., Rodríguez, M., Espartero, A.G., Piña, G., 2000. Radiochemical analysis of ^{41}Ca and ^{45}Ca. Appl. Radiat. Isot. 52, 407–413.

Sudár, S., 2002. "TRUECOINC". A software utility for calculation of the true coincidence correction. In: Specialized Software Utilities for Gamma Ray Spectrometry. Final Report of a Co-ordinated Research Project 1996-2000. IAEA-TECDOC-1275, pp. 37–48.

Sutherland, L.G., Buchanan, J.C., 1967. Error in the absolute determination of disintegration rates of extended sources by coincidence counting with a single detector. Application to I-125 and Co-60. Int. J. Appl. Radiat. Isot. 18, 786–787.

Suvaila, R., Osvath, I., Sima, O., 2013. Improving the assessment of activity in samples with non-uniform distribution using the sum peak count rate. Appl. Radiat. Isot. 81, 76–80.

Suzuki, H., Sibaike, K., Hashimoto, H., Kawada, Y., Hino, Y., 1998. Analysis of a $4\pi\gamma$ ionization chamber response using EGS4 Monte Carlo code. Appl. Radiat. Isot. 49, 1245–1249.

Švec, A., Schrader, H., 2000. An ionization chamber as a secondary standard for activity. Appl. Radiat. Isot. 52, 633–636.

Švec, A., Schrader, H., 2002. Fitting methods for constructing energy-dependent efficiency curves and their application to ionization chamber measurements. Appl. Radiat. Isot. 56, 237–243.

Szörenyi, S., Vágvölgyi, 1984. Standardization of radionuclides at the Hungarian National Office of Measures. Int. Appl. Radiat. Isot. 34, 1133–1144.

Szörenyi, S., Vágvölgyi, Zsinka, 1998. Experiences of fifteen years on metrological supervision of radionuclide calibrators used in nuclear medicine. Appl. Radiat. Isot. 49, 1459–1461.

Tarancon, A., Barrera, J., Santiago, L.M., Bagán, H., García, J.F., 2015. Application of the CIEMAT/NIST method to plastic scintillation microspheres. Appl. Radiat. Isot. 98, 13–22.

Tauhata, L., Iwahara, A., de Oliveira, A.E., Rezende, E.A., Xavier, A.M., 2008. Proficiency tests in the determination of activity radionuclides in radiopharmaceutical products measured by nuclear medicine services in 8 years of comparison programmes in Brazil. Appl. Radiat. Isot. 66, 981–987.

Terliskowska-Droldzicl, T., Radoszewski, T., 1994. An investigation of the various liquid scintillators used to count low energy emitters. Nucl. Instrum. Methods Phys. Res., Sect. A 339, 21–25.

Thomson, J., 2003. In: Annunziata, L.' (Ed.), Sample Preparation for Liquid Scintillation Analysis: Handbook of Radioactivity Analysis, second ed. New York Academic, pp. 656–717.

Timus, D.M., Prata, M.J., Kalla, S.L., Abbas, M.I., Oner, F., Galiano, E., 2007. Some further analytical results on the solid angle subtended at a point by a circular disk using elliptic integrals. Nucl. Instrum. Methods Phys. Res., Sect. A 580, 149–152.

Tryka, S., 1997. Angular distribution of the solid angle at a point subtended by a circular disk. Opt. Commun. 137, 317–333.

Unno, Y., Sanami, T., sasaki, S., Hagiwara, M., Yunoki, a., 2018. Evaluation of absolute measurement using a 4π for the $4\pi\beta - \gamma$ coincidence counting method. Appl. Radiat. Isot. 134, 302–306.

Unterweger, M.P., 2002. Half-life measurements ar the National Institute of Standards and Technology. Appl. Radiat. Isot. 56, 125–130.

Unterweger, M.P., 2007. Primary radiation gas standards (excluding radon). Metrologia 44, S70–S81.

Unterweger, M.P., Lindstrom, R.M., 2004. Ionization chamber measurements of the half-lives of ^{24}Na, ^{42}K, ^{76}As and ^{198}Au. Appl. Radiat. Isot. 60, 325–327.

Unterweger, M.P., Coursey, B.M., Schima, F.J., Mann, W.B., 1980. Preparation and calibration of the 1978 national Bureau of Standards tritiated-water standards. Int. J. Appl. Radiat. Isot. 31, 611–614.

Uritani, A., Genka, T., Mori, C., Reher, D.F.G., 1994. Analytical calculations on radioactivity measurements of ^{192}Ir metallic sources with a calibrated ionization chamber. Nucl. Instrum. Methods Phys. Res., Sect. A 339, 377–380.

Van Ammel, R., Pommé, S., Paepen, J., Sibbens, G., 2010. Measurement of ^{54}Mn the half-life. Appl. Radiat. Isot. 68, 2387–2392.

Van Ammel, R., Pommé, S., Paepen, J., Sibbens, G., 2011. Measurement of the ^{109}Cd half-life. Appl. Radiat. Isot. 69, 785–789.

Van der Eijk, W., Vaninbroukx, R., 1972. Sampling and dilution problems in radioactivity measurements. Nucl. Instrum. Methods 102, 581–587.

Van der Eijk, W., Zehmer, W., 1977.

Van der Eijk, W., Oldenhof, W., Zehmer, W., 1973. Preparation of thin sources. Nucl. Instrum. Methods 112, 343–351.

Van Rooy, M.W., van Staden, M.J., Lubbe, J., Simpson, B.R.S., 2016. Activity determination of ^{59}Fe by 4π beta-gamma counting using liquid scintillation in the beta channel. Appl. Radiat. Isot. 109, 276–280.

Van Rooy, M.W., van Staden, Simpson, B.R.S.,M.J., Lubbe, J., 2018. Absolute standardization of ^{99m}Tc and ^{57}Co by 4π electron-gamma liquid scintillation coincidence counting for SIRTI and SIR comparisons. Appl. Radiat. Isot. 134, 245–251.

Van Wyngaardt, W.M., Simpson, B.R.S., 2006a. Absolute activity measurement of the electron-capture–based radionuclides ^{139}Ce, ^{125}I, ^{192}I and ^{65}Zn by liquid scintillation coincidence counting. Appl. Radiat. Isot. 64, 1454–1458.

Van Wyngaardt, W.M., Simpson, B.R.S., 2006b. A simple counting technique for measuring of two pure β-emitting radionuclides. Nucl. Instrum. Methods Phys. Res., Sect. A 564, 339–346.

Van Wyngaardt, W.M., Simpson, B.R.S., Jackson, G.E., 2008. Further investigations of a simple counting technique for measuring mixtures

of two pureβ-emitting radionuclides. Appl. Radiat. Isot. 66, 1012−1020.

Van Wyngaardt, W.M., Simpson, B.R.S., van Staden, W.M., Lubbbe, J., 2012. Absolute standardization of ^{241}Pu by the TDCR technique and effect of the beta spectral shape. Appl. Radiat. Isot. 70, 2188−2194.

Van Wyngaardt, W.M., van Staden, W.M., Lubbbe, J., Simpson, B.R.S., 2014. Standardization of ^{99}Tc by three liquid scintillation counting methods. Appl. Radiat. Isot. 87, 254−259.

Van Wyngaardt, W.M., Smith, M.L., Jackson, T.W., Howe, B., Tobin, S.M., Reinhard, M.I., 2018. Development of the Australian standard for germanium-68 by two liquid scintillation counting methods. Appl. Radiat. Isot. 314, 79−84.

Varga, B., Tarjan, S., 2008. Determination of ^{241}Pu in the environmental simples. Appl. Radiat. Isot. 66, 265−270.

Vatin, R., Chauvenet, B., 1987. Direct measurement of xenon -127 with a $4\pi\gamma$ detector. Int. J. Appl. Radiat. Isot. 38, 767−770.

Vega Carrillo, H.R., 1996. Geometrical efficiency for parallel disk source and detector. Nucl. Instrum. Methods Phys. Res., Sect. A 371, 535−537.

Vegors, S.H., Marsden, L.L., Heath, R.L., 1958. Calculated Efficiencies of Cylindrical Radiation Detectors. AEC Report IDO-16370.

Venoso, G., Pugliese, M., Roca, V., Sabbarese, C., 2009. A radon facility at Naples University ; features and first tests. Appl. Radiat. Isot. 67, 863−866.

Verghese, K., Gardner, R.P., Felder, R.M., 1972. Solid angle subtended by a circular cylinder. Nucl. Instrum. Methods 101, 391−393.

Vidmar, T., 2005. EFFTRAN-a Monte Carlo efficiency transfer code for gamma-ray spectrometry. Nucl. Instrum. Methods Phys. Res., Sect. A 550, 603−608.

Vidmar, T., Kanisch, G., 2010. Intrinsic error of the point source and the LS-curve approximations in treatment of true coincidence summing. Appl. Radiat. Isot. 68, 1785−1788.

Vidmar, T., Kanisch, G., 2012. A recursive algorithm for calculations of correlation factors for true coincidence summing effects in gamma-ray spectrometry. Appl. Radiat. Isot. 70, 726−732.

Vidmar, T., Korun, M., 2006. Calculation of "LS-curves" for coincidence summing corrections in gamma ray spectrometry. Nucl. Instrum. Methods Phys. Res., Sect. A 556, 543−546.

Vidmar, T., Likar, A., 2002. Automated construction of detector models for efficiency interpolation in gamma-ray spectrometry. Appl. Radiat. Isot. 56, 99−103.

Vidmar, T., Aubineau-Laniece, I., Anagnostakis, M.J., Arnold, D., Brettner-Messler, R., Budjas, D., Capogni, M., Dias, M.S., De Geer, L.−E., Fazio, A., Gasparro, J., Hult, M., Hurtado, S., Jurado Vargas, M., Laubenstein, M., Lee, K.B., Lee, Y.−K., Lepy, M.−C., Maringer, F.−J., Medina Peyres, V., Mille, M., Moralles, M., Nour, S., Plenteda, R., Rubio Montero, M.P., Sima, O., Tomei, C., Vidmar, G., 2008. An intercomparison of Monte Carlo codes in gamma-ray spectrometry. Appl. Radiat. Isot. 66, 764−768.

Vidmar, T., Kossert, K., Nähle, O.J., Ott, O., 2009. Application of the sum-peak method to activity standardizations of extended ^{60}Co sources. Appl. Radiat. Isot. 67, 160−163.

Vidmar, T., Celik, N., Cornejo Díaz, N., Dlabac, A., Ewa, L.O.B., Carranza González, J.A., Hult, M., Jovanovic, S., Lépy, M.−C., Mihaljevic, N., Sima, O., Tzika, F., Jurado Vargas, M., Vasilopoulou, T., Vidmar, G., 2010a. Testing efficiency transfer codes for equivalence. Appl. Radiat. Isot. 68, 355−359.

Vidmar, T., Vodenik, B., Necemier, M., 2010b. Efficiency transfer between extended sources. Appl. Radiat. Isot. 68, 2352−2354.

Vidmar, T., Kanisch, G., Vidmar, G., 2011. Calculation of true coincidence summing corrections for extended sources with EFFTRAN. Appl. Radiat. Isot. 69, 908−911.

Vidmar, T., Capogni, M., Hult, M., Hurtado, S., Kastlander, J., Lutter, G., Lépy, M.−C., Martinkovic, J., Ramebäck, H., Sima, O., Tzika, F., Vidmar, G., 2014. Equivalence of computer codes for calculation of coincidence summing correction factors. Appl. Radiat. Isot. 87, 336−341.

Vidmar, T., Camp, A., Hurtado, S., Jäderström, H., Kastlander, J., Lépy, M.-C., Lutter, G., ramebäck, H., Sima, O., vargas, a., 2016. Equivalence of commuter codes for calculation of coincidence summing correction factors-Part II. Appl. Radiat. Isot. 109, 482−486.

Voltz, R., 1969. In: Haissinski, M. (Ed.), Actions Chimiques et Biologiqies des Radiations, vol. 13. Masson, Paris. pp. 1−55. (in French.

Wainio, K.M., Knoll, G.F., 1966. Calculated gamma ray response characteristics of semiconductor detectors. Nucl. Instrum. Methods 44, 1213−1223.

Wang, T.K., Chen, T.Y., Kang, L.J., 1993. A personal computer based program for HPGe detector absolute-peak-efficiency calculation and calibration. Appl. Radiat. Isot. 44, 1147−1154.

Wang, T.K., Mar, W.Y., Ying, T.H., Liao, C.H., Tseng, C.L., 1995. HPGe detector absolute-peak-efficiency calibration by using the ESOLAN program. Appl. Radiat. Isot. 46, 933−944.

Wang, T.K., Ying, T.−H., Mar, W.−Y., Tseng, C.−L., Liao, C.−H., Wang, M.−Y., 1996. HPGe detector true-coincidence corrections for extended cylinder and Marinelli-beaker sources. Nucl. Instrum. Methods Phys. Res., Sect. A 376, 192−202.

Wang, T.K., Mar, W.Y., Ying, T.H., Tseng, C.L., Liao, C.H., Wang, M.-Y., 1997. HPGe detector efficiency calibration for extended cylinder and Marinelli-beaker sources using the ESOLAN program. Appl. Radiat. Isot. 48, 83−95.

Wang, T.K., Hou, I.M., Tseng, C.L., 1999. Well-type HPGe-detector absolute-peak-efficiency calibration and true-coincidence correction. Nucl. Instrum. Methods Phys. Res., Sect. A 425, 504−515.

Wang, Z., Zhang, X., Chang, Y., Liu, D., 2001. The determination of I-125 activity using sum-peak method with a well HPGe-detector-based spectrometer. Nucl. Instrum. Methods Phys. Res. 459, 475−481.

Wanke, C., Kossert, K., Nähle, O.J., Ott, O., 2010. Activity standardization and decay data of ^{64}Cu. Appl. Radiat. Isot. 68, 1297−1302.

Was, B., Lovalik, A., Novgorodov, A.F., Rak, J., 1993. A new technique the preparation of small-size radioactive samples based on the Langmuir−Blodgett method. Nucl. Instrum. Methods Phys. Res., Sect. A 332, 334−341.

Watt, D.E., Ramsdem, D., Wilson, H.W., 1961. The half-life of ^{14}C. Int. J. Appl. Radiat. Isot. 11, 68−71.

Wheelwright, E.J., Fleming, D.M., Roberts, F.P., 1965. Calorimetric determination of the mean $\beta-$ energy and half-life of 147-Promethium. J. Phys. Chem. 69, 1220−1223.

White, P.H., 1970. Alpha and fission counting of foils of fissile material. Nucl. Instrum. Methods 79, 1−12.

Wielopolski, L., 1977. The Monte Carlo calculation of the average solid angle subtended by a right circular cylinder from distributed sources. Nucl. Instrum. Methods 143, 577−581.

Williams, E.J., 1940. Multiple scattering of fast electrons and alpha-particles, and "Curvature " of cloud tracks due to scattering. Phys. Rev. 58, 292−306.

Williams, I.R., 1966. Monte Carlo calculation of source-to-detector geometry. Nucl. Instrum. Methods 44, 169-162.

Williams, A., Birdseye, R.A., 1966. Measurement of the decay scheme correction in the absolute standardization of cobalt-57. Int. J. Appl. Radiat. Isot. 17, 366−367.

Williams, A., Campion, 1963. Measurement of the γ-sensitivity of a 4πβ-counter. Int. J. Appl. Radiat. Isot. 14, 533−540.

Williams, A., Goodier, I.W., 1967. Standardization of radionuclides. In: Proceedings of a Symposium, Vienna, 1966. IAEA, Vienna, p. 153.

Williams, A., Sara, R.I., 1968. Correlation counting applied to the determination of absolute disintegration rates. Nucl. Instrum. Methods 60, 189−194.

Williams, I.R., Craig Jr., M., Thompson, C.L., 1968. A FORTRAN program for calculating the solid angle subtended by one circular disk at another. J. Comput. Phys. 2, 332−333.

Winkler, G., Pavlik, A., 1983. Some aspects of activity measurements with NaI(Tl) well-type-detectors. Int. J. Appl. Radiat. Isot. 34, 547−553.

Woods, M.J., 1990. The half-life of ^{137}Cs. A critical review. Nucl. Instrum. Methods Phys. Res., Sect. A 286, 576−583.

Woods, M.J., Lucas, S.E.M., 1975. Calibration of the 1383A ionization chamber for ^{125}I. Int. J. Appl. Radiat. Isot. 26, 488−490.

Woods, M.J., Lucas, S.E.M., 1986. The half-life of ^{152}Eu and ^{154}Eu. Int. J. Appl. Radiat. Isot. 37, 1157−1158.

Woods, M.J., Lucas, S.E.M., 1996. Half-life of ^{90}Sr −measurement and critical review. Nucl. Instrum. Methods Phys. Res., Sect. A 369, 534−538.

Woods, M.J., Goodier, I.W., Lucas, S.E.M., 1975. The half-life of ^{133}Xe and its calibration factor for the 1383A ionization chamber. Int. J. Appl. Radiat. Isot. 26, 485−487.

Woods, M.J., Rossiter, M.J., Sephton, J.P., Williams, T.T., Lucas, S.E.M., Reher, D.F.G., Denecke, B., Aalbers, A., Thierens, H., 1992. ^{192}Ir brachytherapy sources: calibration of the NPL secondary standard radionuclide calibrator. Nucl. Instrum. Methods Phys. Res., Sect. A 312, 257−262.

Woods, M.J., Reher, D.F.G., Ratel, G., 2000. Equivalence in radionuclide metrology. Appl. Radiat. Isot. 52, 313−318.

Woods, M.J., Baker, M.I., Tyler, D.K., Chari, K., 2006. Comparison of strontium-89 solution sources in UK hospitals, 2003. Appl. Radiat. Isot. 64, 1375−1379.

Wu, Z., Xinmiao, W., 1992. A new and simple approach to geometrical factor of a parallel disk source and detector system. J. Radioanal. Nucl. Chem. 166, 211−217.

X-5 Monte Carlo Team, 2003. MCNP-A General Monte Carlo N-Particle Transport Code, Versio 5. In: Developer's Guide. LA-CP-=3-0284, vol. III. National Laboratory, Los Alamos, p. 194.

Xie, F., Chang, Y.−F., Li, Q., Lian, Q., Hw, X.−B., 2005. A $4\pi\beta+4\pi\gamma$ equipment for radioactivity measurement. Nucl. Electron Detect. Technol. 25, 4003−4404.

Xie, F., Li, X., Lian, Q., Day, Y., Jiang, W., gongshuo, Y., Ni, J., 2015. Activity determination of ^{41}Ar using efficiency extrapolation method and $4\pi\beta(\mathrm{PS})-4\pi\gamma(\mathrm{NaI})$ coincidence system. Appl. Radiat. Isot. 97, 8−11.

Yamada, T., Nakamura, Y., Kawada, Y., Sato, Y., Hino, Y., 2006. Standardization of ^{152}Eu and ^{154}Eu by $4\pi\beta-4\pi\gamma$ coincidence method and $4\pi(\beta+\gamma)$ integral counting. Appl. Radiat. Isot. 64, 1220−1224.

Yamada, T., Kawada, Y., Sato, Y., Yunoki, A., Hino, Y., 2008. Standardization of ^{18}F using the 4π(β+γ) integral counting technique. Appl. Radiat. Isot. 66, 909−913.

Yamada, T., Sato, Y., Unno, Y., Yunoki, A., Hino, Y., Ishii, K., 2010. Standardization of an ^{99m}Tc and ^{99}Mo by the use of a $4\pi\beta+4\pi\gamma$ counter. Appl. Radiat. Isot. 1324−1329.

Yamada, T., Kawada, Y., Sato, Y., 2016. $.4\pi\beta(\mathrm{PS})-4\pi\gamma(\mathrm{GE})$ list-mode coincidence counter and its applications. Appl. Radiat. Isot. 109, 414−417.

Yamada, T., Ishizu, H., Aray, K., Shiina, T., 2018. Extended utilization of a ^{68}Ge/^{68}Ga reference source as a mock ^{18}F solution in the ionization chamber calibration. Appl. Radiat. Isot. 134, 89−94.

Yamazaki, I.M., Koskinas, M.F., Moreira, D.S., Takeda, M.N., Dias, M.S., 2018. Disintegration rate and gamma ray emission probability per decay measurement of ^{64}Cu. Appl. Radiat. Isot. 134, 312−315.

Yan, C.G., Lian, Q., Li, W., Ni, J., 2002. An improvement of uncertainty in activity standardization with efficiency tracer technique. Appl. Radiat. Isot. 56, 253−259.

Yeltepe, E., Yücel, H., 2018. standardization of ^{142}Pr activity concentration. Appl. Radiat. Isot. 134, 263−268.

Yeltepe, E., Sahin, N.K., Asian, N., Hult, M., Ozcayan, G., Westhofen, H., Yücel, H., 2018. A review of the TAEA proficiency test on natural and anthropogenic radionuclide activities in black tea. Appl. Radiat. Isot. 134, 40−44.

Yu, F., Zhou, B., Sun, A., Li, Z., 1990. A bi 4π counting method for the measurement of activity. Nucl. Sci. Technol. 1, 180−186.

Yuan, M., Ch, Lee, J.H., Hwang, W.S., 2002. The absolute counting of ^{166m}Ho, ^{58}Co and ^{88}Y. Appl. Radiat. Isot. 56, 429−434.

Yuan, M.C., Pang, H.F., Wang, C.F., 2006. Absolute counting of ^{188}Re radiopharmaceuticals. Appl. Radiat. Isot. 63, 1380−1383.

Yuan, M.C., Chen, I.J., Wang, C.F., 2008. Primary standardization of ^{67}Ga radiopharmaceuticals. Appl. Radiat. Isot. 66, 976−980.

Yunoki, A., Kawada, V., Unno, Y., Sato, Y., Hino, Y., 2010. Activity measurements of ^{85}Kr diluted by a large volume balloon technique. Appl. Radiat. Isot. 68, 1340−1343.

Yunoki, A., Yamada, T., Kawada, Hino, Y., 2016. Improvements of standardization of ^{134}Cs by the critical window setting for 605 keV photopeak. Appl. Radiat. Isot. 109, 374−377.

Zajic, D., 1986. Instrumental corrections of peak areas in gamma-ray sum-peak counting. Appl. Radiat. Isot. 37, 1225−1233.

Zajic, V., 1987. A simple way of varying the source efficiency for the extrapolation method in $4\pi(PC)-\gamma$ coincidence counting. Int. J. Appl. Radiat. Isot. 38, 549−552.

Zhang, M., Yao, S., Liang, J., Liu, H., 2016. Standardization of the radionuclides ^{60}Co and ^{59}Fe by digital $4\pi\beta(\mathrm{PC})-\gamma(\mathrm{NaI})$ coincidence counting. Appl. Radiat. Isot. 109, 341−344.

Zhenyu, T., Yueyuan, X., Xiangdong, L., Mingwen, Z., Liming, Z., 2009. A new calculation on the stopping power and mean free path for low energy electrons in toluene over energy range of 20−10,000 eV. Appl. Radiat. Isot. 67, 625−629.

Zhihua, W., Xinmiao, W., 1992. A new and simple approach to geometrical factor of a parallel disk source and detector system. J. Radioanal. Nucl. Chem. Lett. 166, 211−217.

Ziemek, T., Capogni, M., ratel, G., Dziel, T., Fazio, A., Listkowska, A., 2018. Comparison of ^{131}I activity measurements at the NCBJ RC POLATOM and ENEA-INMRI linked to the BIPM SIR system. Appl. Radiat. Isot. 134, 380−384.

Zimmerman, B.E., 2013. Current status and future needs for standards of radionuclides used in positron emission tomography. Appl. Radiat. Isot. 76, 31−37.

Zimmerman, B.E., Cessna, J.T., 1999. The standardization of ^{62}Cu and experimental determinations of dose calibrator settings for generator-produced ^{62}Cu PTSM. Appl. Radiat. Isot. 51, 515–526.

Zimmerman, B.E., Cessna, J.T., 2000. Experimental determinations of commercial 'dose calibrator' settings for nuclides used in nuclear medicine. Appl. Radiat. Isot. 52, 615–619.

Zimmerman, B.E., Cessna, J.T., 2010. Development of a traceable calibration methodology for solid ^{68}Ge/^{68}Ga sources used as calibration subrogate for ^{18}F on radionuclide activity calibrators. J. Nucl. Med. 51, 448–453.

Zimmerman, B.E., Collé, R., 1997. Cocktail volume effects in $4\pi\beta$ liquid scintillation spectrometry with ^{3}H-standard efficiency tracing for low-energy β-emitting radionuclides. Appl. Radiat. Isot. 48, 365–378.

Zimmerman, B.E., Palm, S., 2010. Results of an international comparison of ^{57}Co. Appl. Radiat. Isot. 68, 1217–1220.

Zimmerman, B.E., Kubicek, G.J., Cessna, J.T., Plascjak, P.S., Eckelman, W.C., 2001a. Radioassays and experimental evaluation of dose calibrator settings for ^{18}F. Appl. Radiat. Isot. 54, 113–122.

Zimmerman, B.E., Unterweger, M.P., Brodack, J.W., 2001b. The standardization of ^{177}Lu by $4\pi\beta$ liquid scintillation spectrometry with ^{3}H-standard efficiency tracing. Appl. Radiat. Isot. 64, 623–631.

Zimmerman, B.E., Cessna, J.T., Unterweger, M.P., 2002. The standardization of ^{188}W/^{188}Re by $4\pi\beta$ liquid scintillation spectrometry with the CIEMAT/NIST 3H standard efficiency tracing method. Appl. Radiat. Isot. 56, 315–320.

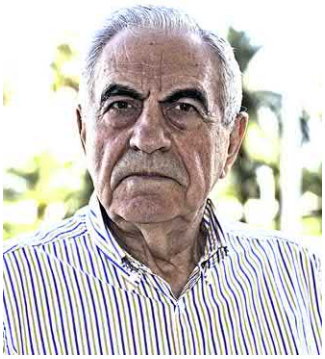
Zimmerman, B.E., Colle, R., Cessna, J.T., 2004. Construction and implementation of the NIST triple-to-double coincidence ratio (TDCR) spectrometer. Appl. Radiat. Isot. 60, 433–438.

Zimmerman, B.E., Cessna, J.T., Fitzgerald, R., 2008. Standardization of ^{68}Ge/^{68}Ga using three liquid scintillation counting based methods. J. Res. Natl. Inst. Stand. Technol. 113, 265–280.

Zimmerman, B.E., Alzizoglou, T., Rodrigues, D., Broad, R., Cassette, P., Mo, L., Ratel, B., Simpson, B., van Wyngaardt, W., Watjen, C., 2010. Comparison of triple-to double coincidence ratio (TDCT) efficiency calculations and uncertainty assessment for ^{99}Tc. Appl. Radiat. Isot. 68, 1477–1481.

Zimmerman, B.E., Bergeron, D.E., Fitzgerald, R., Cessna, J.T., 2016. Long-term stability of carrier-added ^{68}Ge standardized solutions. Appl. Radiat. Isot. 109, 2114–2216.

Agustín Grau Malonda



Agustín Grau Malonda holds a BSc degree from the Complutense University, Madrid 1962; Doctorate in Electronics from Toulouse University (France) 1965; PhD in Physics from the Complutense University, Madrid, 1981. He worked in the JEN (Atomic Energy Commission), Radiochemistry Section, 1965–71 and Radionuclide Metrology Section, 1972–84. Agustín Grau Malonda subsequently held numerous positions as Director of the Basic Research Department (CIEMAT) 1984–86; Director of the Department of Fusion and Particle Physics (CIEMAT) 1987–98; Director of the Institute for Energy Studies (CIEMAT) 1999–2003; Deputy Director of Strategic Projects (CIEMAT) 2004–08; Associate Professor of Physics, Madrid Polytechnic University, 1969–77; Professor of Nuclear Engineering, Madrid Polytechnic University, 1977–85. In addition, he was a member of the following working groups and committees: Consulting Committee for the Fusion Program (EU) 1996–2000, (Vice Chairman) 1991–2000; Joint European Torus (JET) Council, 1986–2000; JET Executive Committee, 1986–99; Fusion Technology Steering Committee (EU) 1986–90; Fusion Power Coordinating Committee (OECD) 1998–2002; L3 Committee (CERN) 1986–99; International Committee for Radionuclide Metrology (ICRM), 1975–2003 (Vice Chairman, 1998–99); EUROMET, 1990–99; EURATOM Scientific and Technical Committee, 1992–2003; Adviser Committee for the Central Bureau for Nuclear Measurements, JRC, Geel (Belgium) 1989–95. Awards: Department of Commerce, NBS, USA, Guest Worker Contributions, 1982, 1983; Men of the Year in Sciences, Cambio 16 Journal, 1991; and Encomienda de la Orden de Isabel la Católica, Spanish King, 2001.

Agustín Grau Carles



Agustín Grau Carles holds a PhD in Physical Sciences from the Complutense University of Madrid. During 1991–2000, he worked at the Center for Environmental and Technological Energy Research (CIEMAT), together with chemists, developing new spectrometric techniques for radioisotopes, based on liquid-scintillation counting. From 2002 to 2004, he

collaborated with biologists from the Center for Astrobiology (CAB) in the calibration of ultraviolet lamps for the irradiation of extremophile cultures. He was also involved, in collaboration with geologists, in the development of new meteorite authentication techniques from radioisotopes originated by cosmic radiation. Between 2004 and 2010, he worked at the Spanish National Research Council (CSIC) in his own Ramón y Cajal project to study the feasibility of a nanodosimeter based on scintillation gels. Currently he directs the BIC Academy (Goods of Cultural Interest), which teaches courses on the need for Science to understand art, as well as archaeological and paleontological goods.

Chapter 8

PERPUSTAKAAN PRIBADI AN-NUR SUNARYA

Radioactivity counting statistics

Agustín Grau Malonda[1] and Agustín Grau Carles[2]
[1]CIEMAT, Madrid, Spain; [2]Academia BIC, Madrid, Spain

Chapter outline

I. Introduction **627**
II. Statistical distributions **628**
A. The Poisson distribution 628
B. The Gaussian distribution 629
III. Analysis of a sample of results **632**
A. Best estimate of the true value 632
B. Best estimate of precision 632
C. Error propagation 633
D. Accuracy of the mean value 634
E. Combination of measurements 635
F. Interlaboratory comparisons 636
1. Philosophy of the Paule and Mandel method 637
2. Calculation of the variance of the between set 637
3. Power-Moderate mean 640
4. Power-Moderated weighted Mean (PMM) 642
G. The statement of the results 642
1. Type B calculation of typical uncertainty 643
2. Combined standard uncertainty 644
3. Rules for expressing results 644
IV. Statistical inference **645**
A. Hypothesis testing 645
B. Confidence intervals 646
C. Statistical inference 647
1. Variance of a population 647
2. Variance of two populations 650
V. Regression **651**
A. Linear regression 651
1. Confidence intervals and hypothesis testing 653
VI. Detection limits **653**
A. Critical levels 653
B. Gamma Spectra 655
1. High-resolution gamma spectra 655
2. Low-resolution gamma spectra 658
VII. Metrology applications **660**
A. Uncertainty budget 660
B. Uncertainty calculation 660
1. Uncertainty transmission in Eq. (8.137) 661
2. Numerical calculation of uncertainty 662
References **665**
Relevant Statistical References Tables **666**
Agustín Grau Malonda **666**
Agustín Grau Carles **667**

I. Introduction

In the measurement process, the object to be observed is always affected by an undetermined interaction between the observer and the observed. As a result, the measured magnitudes are always reproduced with a certain inherent uncertainty caused by the instrument. This uncertainty in the measurements makes the use of error theory essential. When we measure radioactive substances, the situation becomes even more complicated, because the radioactivity decay is a random process. In radioactivity counting, two types of fluctuations are basically generated, one related to the activity of the sample, when the half-life of the radionuclide is short, and another caused by the random nature of radioactivity decay, which modifies the disintegration rates with time. Since the measurement of radioactivity involves values with different degrees of reliability and validity, the principles of counting statistics must be applied (Larson, 1969; Eadie et al., 1971).

In many types of measurement such as mass, volume, time, length, etc., the measured quantity has a given value and only the measurement conditions introduce statistical variations. The situation is different, however, in radioactivity measurements. The radioactive decay process follows Poison statistics, so a sample's activity value is not a specific value but a mean value that varies with time. If we measure the emission of a radioactive source, as shown on Table 8.1, repeated measures are not equal. But there is a clear condition: if the measuring equipment does not introduce a perturbation, the emission and measurement rates must follow the same statistical law, so their

Handbook of Radioactivity Analysis: Volume 2. https://doi.org/10.1016/B978-0-12-814395-7.00008-8
Copyright © 2020 Elsevier Inc. All rights reserved.

TABLE 8.1 Counting rates of a radioactive sample.

Measure	Counts
1	214
2	222
3	217
4	210
5	243
6	238

mean and variance rates are equal from a statistical perspective.

Example 8.8 represents a detailed analysis of the set of measurements shown on Table 8.1. We see that they are not affected by the counter. Example 8.9, 8.10, and 8.11 present different cases in which counting rates are affected by the counter. Example 8.9 corresponds to the case where the counting rate is reduced by counter resolution time. It is also shown that corrections are required to correct the results of the measurements, as well as the tests to be applied. Example 8.10 shows the results of counting when counting differences are very close, smaller than expected. Example 8.11 presents the corrections to be applied to the measures of Example 8.10 to obtain results that follow the Poisson law. In all of these examples, the respective tests are applied to support the results.

II. Statistical distributions

In this section we shall study all basic characteristics of both the Poisson and the normal (or Gaussian) distributions, and their relation to radioactivity counting statistics. Although the Poisson distribution involves all processes of radioactivity decay, and therefore the detection of particles and radiation, the normal distribution is applied more often by far and is better known in the majority of cases. Since the application of the Poisson distribution to counting statistics may be tedious and time consuming, and considering that both distributions give identical results, when the total number of counts becomes large, our final objective will be the determination of some characteristic parameters, which will allow one to exchange the Poisson distribution by the normal one.

A. The Poisson distribution

The Poisson distribution describes a random process for which the occurrence probability of a certain event is constant and small. This distribution not only concerns radioactivity counting statistics (Helstrom, 1968) or nuclear decay, but it is also applied to evaluate, in a more or less approximate way, many other processes (Garwood, 1936; Grau Malonda, 1999). Some examples of daily life that verify Poisson statistics are, for example, the number of phone calls received at a phone switchboard several minutes before noon, the number of annual strikes in a factory, the number of misprints on a book page, the number of times a piece of a machine fails in a given period of time, and the number of fatal traffic accidents each week in a city. Przyborowski and Wilenski (1935) present an application of Poisson law and construct rules to minimize the chance of errors in tests and samples.

In radioactivity decay, four aspects are fulfilled: all radioactive nuclei have the same decay probability for a given time period, the decay process of one nucleus is not affected by the decay of other nuclei, the total number of nuclei and measurement time intervals are sufficiently large, and the nuclei half-life is long compared with the detection pulse. Therefore, the radioactivity decay is a random process, in which a discontinuous random variable is defined as the number of times a decay event takes place in a continuous period of time t. Additionally, the probability of one decay event occurring in a time increment Δt must be asymptotically proportional to Δt, independently of the time value in the interval Δt and all previous decay events. Under these conditions, the Poisson distribution takes the form:

$$P_x(t) = \frac{e^{-at}(at)^x}{x!},\ x = 0,\ 1,\ 2, \ldots \tag{8.1}$$

where $P_x(t)$ is the probability that a number of x decay processes take place in time t and a a constant to be determined. The expression (8.1) may be derived in three different ways: by approximation from the binomial distribution (Hoel, 1984), considering first principles (Evans, 1982), or basing all calculations on a Markov process (Feller, 1968; Rozanov, 1977).

Three important properties derived from Eq. (8.1) are the following:

$$\sum_{x=0}^{\infty} P_x = 1 \tag{8.2}$$

$$\sum_{x=0}^{\infty} xP_x = at \tag{8.3}$$

$$\sum_{x=0}^{\infty} (x - at)^2 P_x = at \tag{8.4}$$

The normalization condition (Eq. 8.2) states that the summation of all possible probabilities P_x of the Poisson distribution is one. The expression (8.3) defines the parameter a as the average value of the distribution divided by t, i.e., the number of decay processes per unit of time. The third expression (8.4) refers to the identity relation between the variance and the mean, when the Poisson

distribution is applied. The most important consequence derived from the three properties (Eqs. 8.2 to 8.4) is that the single parameter a enables one to determine the first and second order moments (i.e., $\sum_{x=0}^{\infty} xP_x$ and $\sum_{x=0}^{\infty} x^2P_x$) of the Poisson distribution. By defining the average number of decay processes in time t as the product $\mu = at$, the Poisson distribution can be expressed as

$$P_x = \frac{e^{-\mu}\mu^x}{x!} \tag{8.5}$$

The Poisson distribution is asymmetric, and its shape depends on the parameter μ, which is a real value greater than zero.

Example 8.1. The measurement of a radioactive sample of ^{238}U ($T_{1/2} = 4.47 \times 10^9$years) during 3 days gives a total number of counts 133,747. (a) Evaluate the average counting rate, and compute the probability of counting: (b) less than one count in 1 second, (c) exactly 1 count, (d) less than 3 counts, (e) a number of counts between 1 and 4, and (f) more than 3 counts.

Solution:

a. The average counting rate is: $\mu = \frac{133{,}747}{3\times24\times60\times60} = 0.516$ counts/s

b. The probability of **counting** less than one count is computed as follows:

$$P(X<1) = P_0 = e^{-0.516} = 0.597$$

c. The probability of **counting** exactly one count:

$$P(X=1) = \frac{\mu^1 e^{-\mu}}{1!} = 0.516 \times e^{-0.516} = 0.3$$

d. The probability of counting less than 3 counts is the addition of the probabilities of counting **none**, 1 and 2 counts

$$\begin{aligned} P(X<3) = \sum_{x=0}^{2} P_x &= P_0 + P_1 + P_2 \\ &= e^{-\mu} + \mu e^{-\mu} + \frac{\mu^2}{2}e^{-\mu} \\ &= e^{-\mu}\left(1 + 0.516 + \frac{0.516^2}{2}\right) = 0.984 \end{aligned}$$

e. The probability of counting a number of counts between 1 and 4 is the addition of the **probabilities** of counting exactly 2 and 3 counts

$$\begin{aligned} P(1<X<4) = P_2 + P_3 &= \frac{\mu^2 e^{-\mu}}{2!} + \frac{\mu^3 e^{-\mu}}{3!} \\ &= e^{-\mu}\left(\frac{\mu^2}{2!} + \frac{\mu^3}{3!}\right) \\ &= e^{-0.516}\left(\frac{0.516^2}{2} + \frac{0.516^3}{6}\right) = 0.093 \end{aligned}$$

f. The probability of counting **more** than 3 counts is

$$\begin{aligned} P(X>3) = \sum_{x=4}^{\infty} P_x &= 1 - \sum_{x=0}^{3} P_x \\ &= 1 - (P_0 + P_1 + P_2 + P_3) \\ &= 1 - e^{-\mu}\left(1 + \mu + \frac{\mu^2}{2!} + \frac{\mu^3}{3!}\right) \\ &= 1 - e^{-0.516}\left(1 + 0.056 + \frac{0.516^2}{2} + \frac{0.516^3}{6}\right) = 0.00196 \end{aligned}$$

It should be remarked that a linear combination of the two random variables X and Y, which both follow the Poisson distribution, gives a third random variable, which does not necessarily follow the Poisson distribution. For the following three random variables $V = aX$, $Z = X + Y$, and $W = X - Y$, only Z follows the Poisson distribution.

B. The Gaussian distribution

In general, it is assumed that the random variable X follows a normal distribution of mean μ and variance σ^2, when the probability density function of a set of measured values x yields the function

$$p(x) = \frac{1}{\sigma\sqrt{2\pi}}\exp\left[-\frac{(x-\mu)^2}{2\sigma^2}\right] \tag{8.6}$$

where $(-\infty < x < \infty)$, $(-\infty < \mu < \infty)$, and $(0 < \sigma^2 < \infty)$.

Frequently, in the course of a number of measurements, we are interested in evaluating the probability that a new measurement of the random variable X verifies a certain condition relative to the value x. This probability is

computed in terms of the accumulated distribution function, which is defined as follows:

$$P(X \leq x) = \frac{1}{\sigma\sqrt{2\pi}} \int_{-\infty}^{x} \exp\left[-\frac{(t-\mu)^2}{2\sigma^2} \right] dt \qquad (8.7)$$

Geometrically, the integral (8.7) is interpreted as the area under the curve between the limits of the interval $-\infty \leq X \leq x$. Since each pair of values (μ, σ^2) defines a different distribution, there is no simple way to tabulate the accumulated distribution function. This inconvenience is partially resolved by defining the normalized random variable Z

$$Z = \frac{X-\mu}{\sigma} \qquad (8.8)$$

for which the probability density and the accumulated distribution functions can be defined as follows:

$$p(z) = \frac{1}{\sqrt{2\pi}} \exp\left(-\frac{z^2}{2} \right) \qquad (8.9)$$

$$P(Z \leq z) \equiv \Phi(z) = \frac{1}{\sqrt{2\pi}} \int_{-\infty}^{z} \exp\left(-\frac{t^2}{2} \right) dt \qquad (8.10)$$

Although the tabulated values of the accumulated distribution function (Eq. 8.10) are found in the majority of statistics manuals, the symmetric character of the distribution makes two different criteria of tabulation possible, which may cause confusion. For instance, Triola (2009) assumes the integration interval $0 \leq Z \leq z$, while Newbold (2009) and Abramowitz and Stegun (1972) consider $-\infty < Z \leq z$. These intervals are shown in Fig. 8.1. Since the normal distribution is normalized to one, both criteria of tabulation make the values simply differ in 0.5. Bevington (1969) defines the normalized random variable Z as the absolute value of the difference between the means $|X-\mu|$ divided by the standard deviation

$$Z = \frac{|X-\mu|}{\sigma}$$

The integration interval is $-\infty < Z < \infty$ and the values of $\Phi(Z)$ are two times the values for the interval $0 < Z < \infty$.

Example 8.2. By searching in Table 8.2, calculate the accumulated distribution function Φ for the following limits of the standard random variable Z: (A) $0 \leq Z \leq 1.75$, (B) $-1.75 \leq Z \leq 0$, (C) $Z \geq 1.85$, (D) $Z \leq 1.10$, and (E) $Z \leq -1.45$.

Solutions:

a. The second column in Table 8.2 shows the accumulated distribution function Φ for the values of z listed in the first column. The remaining columns, from third to eleventh, list the intermediate values of Φ when z is incremented in 0.01. Therefore, the sought value of $\Phi(1.75) = 0.4599$ is given in column seven.

b. Taking into account the symmetry of the curve with respect to the origin we have

$$\Phi(-1.75 \leq Z \leq 0) = \Phi(0 \leq Z \leq 1.75) = 0.4599$$

c. Since the total area under the curve is 1, we obtain

$$P(Z \geq 1.85) = 0.5 - P(0 \leq Z \leq 1.85) = 0.5 - 0.4678 = 0.0322$$

d. Since the area under the curve for the interval $-\infty < Z \leq 0$ is 0.5, we have

$$P(Z \leq 1.10) = 0.5 + P(0 \leq Z \leq 1.10) = 0.5 + 0.3643 = 0.8643$$

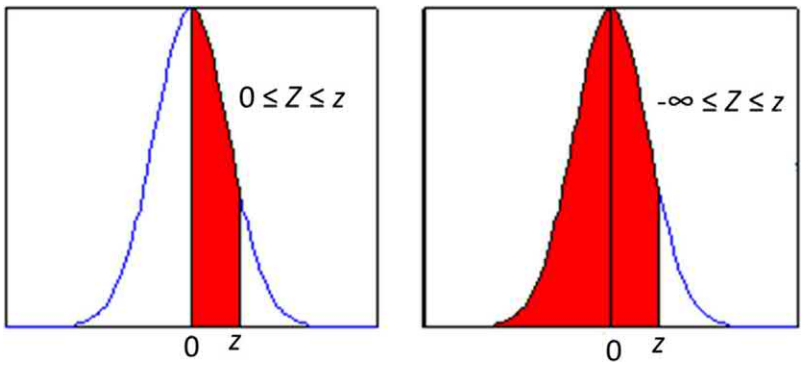


FIGURE 8.1 Integration intervals corresponding to two different criteria for tabulation.

TABLE 8.2 The standard normal distribution.

z	0.00	0.01	0.02	0.03	0.04	0.05	0.06	0.07	0.05	0.09
0.0	0.0000	0.0040	0.0080	0.0120	0.0160	0.0199	0.0239	0.0279	0.0319	0.0359
0.1	0.0398	0.0438	0.0478	0.0517	0.0557	0.0596	0.0636	0.0675	0.0714	0.0753
0.2	0.0793	0.0832	0.0871	0.0910	0.0948	0.0987	0.1026	0.1064	0.1103	0.1141
0.3	0.1179	0.1217	0.1255	0.1293	0.1331	0.1368	0.1406	0.1443	0.1480	0.1517
0.4	0.1554	0.1591	0.1628	0.1664	0.1700	0.1736	0.1772	0.1808	0.1844	0.1879
0.5	0.1915	0.1950	0.1985	0.2019	0.2054	0.2088	0.2123	0.2157	0.2190	0.2224
0.6	0.2257	0.2291	0.2324	0.2357	0.2389	0.2422	0.2454	0.2486	0.2517	0.2549
0.7	0.2580	0.2611	0.2642	0.2673	0.2704	0.2734	0.2764	0.2794	0.2823	0.2852
0.8	0.2881	0.2910	0.2939	0.2967	0.2995	0.3023	0.3051	0.3078	0.3106	0.3133
0.9	0.3159	0.3186	0.3212	0.3238	0.3264	0.3289	0.3315	0.3340	0.3365	0.3389
1.0	0.3413	0.3438	0.3461	0.3485	0.5308	0.3531	0.3554	0.3577	0.3599	0.3621
1.1	0.3643	0.3665	0.3686	0.3708	0.3729	0.3749	0.3770	0.3790	0.3810	0.3830
1.2	0.3849	0.3869	0.3888	0.3907	0.3925	0.3944	0.3962	0.3980	0.3997	0.4015
1.3	0.4032	0.4049	0.4066	0.4082	0.4099	0.4115	0.4131	0.4147	0.4162	0.4177
1.4	0.4192	0.4207	0.4222	0.4236	0.4251	0.4265	0.4279	0.4292	0.4306	0.4319
1.5	0.4332	0.4345	0.4357	0.4370	0.4382	0.4394	0.4406	0.4418	0.4429	0.4441
1.6	0.4452	0.4463	0.4474	0.4484	0.4495	0.4505	0.4515	0.4525	0.4535	0.4545
1.7	0.4554	0.4564	0.4573	0.4582	0.4591	0.4599	0.4608	0.4616	0.4625	0.4633
l.8	0.04641	0.4649	0.4656	0.4664	0.4671	0.4678	0.4686	0.4693	0.4699	0.4706
1.9	0.4713	0.4719	0.4726	0.4732	0.4738	0.4744	0.4750	0.4756	0.4761	0.4767
2.0	0.4772	0.4778	0.4783	0.4788	0.4793	0.4798	0.4803	0.4808	0.4812	0.4817

e. By applying both the normalization and symmetry properties of the curve, we obtain

$$P(Z \leq -1.45) = 0.5 - P(-1.45 \leq Z \leq 0)$$
$$= 0.5 - P(0 \leq Z \leq 1.45) = 0.5 - 0.4265 = 0.0735$$

In practice, the random variable Z has no physical meaning. For this reason, the notation $N(\mu, \sigma^2)$ is adopted preferably in those statistical problems that apply the normal distribution. However, to perform calculations, the tabulated values of the standard normal distribution are still valid. The following examples make it clear how to manage Table 8.2, when the notation $N(\mu, \sigma^2)$ is adopted.

Example 8.3. Consider the random variable X that follows the normal distribution $N(16, 16)$. Compute the accumulated distribution probability $P(X \geq 17)$ from Table 8.2

Solution. The average and the standard deviation are $\mu = 16$ and $\sigma = 4$, respectively. The limits of the interval for the standard random variable Z are obtained from Eq. (8.8)

$$Z = \frac{X - \mu}{\sigma} = \frac{17 - 16}{4} = 0.25$$

Hence,

$$P(X \geq 17) = P(Z \geq 0.25) = 0.5 - P(0 \leq Z \leq 0.25)$$
$$= 0.5 - 0.0987 = 0.4013$$

Example 8.4. The normal distribution $N(20, 4)$ has the accumulated distribution probability 0.30 for $X \leq x_0$. Compute x_0.

Solution. Since $P(Z \leq z_0) = 0.30 < 0.5$, z_0 must be negative. By making use of Table 8.2, we find $z_0 = -0.84$. Now, from Eq. (8.8), $-0.84 = (x_0 - 20)/2$. Thus, $x_0 = 20 - 1.68 = 18.32$.

In contrast to the Poisson distribution, the linear combination of the two random variables X and Y, which are characterized by the normal distribution, generates a new random variable $W = aX + bY$, which always follows the normal distribution. This important property clearly indicates how advantageous the application of the normal

distribution compared to the Poisson distribution may be. For large average values of μ, the Poisson distribution is generally approximated to the normal distribution $N(\mu, \mu)$. In such a case, the accumulated distribution satisfies the equation

$$P(X \leq x) = e^{-\mu} \sum_{n=0}^{x} \frac{\mu^n}{n!} \approx \Phi\left(\frac{x + \frac{1}{2} - \mu}{\sqrt{\mu}}\right) \tag{8.11}$$

This approximation sets the standard deviation of the normal distribution equal to the standard deviation of the Poisson distribution, and yields results commonly denoted as $\mu \pm \sigma$, where $\sigma = \sqrt{\mu}$. Since the area under the curve for the interval $(\mu - \sigma,\ \mu + \sigma)$ is 68% of the total area, the probability that new measurements give results lying in the interval $(\mu - \sigma,\ \mu + \sigma)$ is 68%. Table 8.3 shows such a probability for different intervals.

III. Analysis of a sample of results

Both the Poisson and normal distributions are applied to analyze the results of experiments with a large number of observed events. In practice, however, that is not the case, and the observed events in an experiment are frequently limited in number. All statistical information of one experiment is contained in the population distribution (or limit distribution). When a radioactive sample is analyzed, the amount of accumulated results depends on the counting rate and the measuring time, but what about the true value? This section will try to answer this and other questions relative to the analysis of a statistical sample of results.

A. Best estimate of the true value

For a symmetric distribution, the best estimate of the true value is given by the center of symmetry of the distribution. This center of symmetry is by definition the single value that agrees with its symmetrical position in the distribution. Since the mean, median, and mode all represent the center of symmetry of the distribution, nothing can be concluded about which one is the best to describe the true value.

For an asymmetric distribution, the mean, median, and mode take on different values. Therefore, the best estimate of the true value may be selected among these three possibilities by considering the requirements of the problem. Certain special cases may lead one to choose the median or the mode as the best estimate, but the mean of the population distribution is the one preferred in the majority of situations.

Let us assume the average of a sample $\bar{x}$ as the best estimate of the true value for a sample of results $x_1, x_2, \ldots, x_n$ that follow an unknown distribution

$$\bar{x} = \frac{1}{n} \sum_{i=1}^{n} x_i \tag{8.12}$$

Obviously, when the total number of measurements $n \to \infty$, the sample of results conforms to the population distribution, and the true value X agrees with the mean value of the distribution μ. Eisenhart (1963) analyzes the concepts of true value and uncertainty in measurement instruments.

TABLE 8.3 Probability for different intervals.

Interval	Probability
$\mu \pm 0.67\sigma$	0.50
$\mu \pm \sigma$	0.68
$\mu \pm 1.64\sigma$	0.90
$\mu \pm 2\sigma$	0.95
$\mu \pm 3\sigma$	0.997

B. Best estimate of precision

The analysis of the results of an experiment makes it necessary to define the concept of uncertainty. The width of the distribution shows graphically the uncertainty in symmetrical distributions. The two simplest expressions that represent the uncertainty are the absolute mean deviation τ and the standard deviation σ

$$\tau = \int_{-\infty}^{\infty} |x - X| p(x) dx \tag{8.13}$$

$$\sigma^2 = \int_{-\infty}^{\infty} (x - X)^2 p(x) dx \tag{8.14}$$

where X is the true value of the distribution, commonly associated with the mean of the distribution.

To define the absolute average deviation, the absolute differences between x and the true value X are multiplied by the relative frequencies of x in the distribution, and integrated for all possible values of x. On the other hand, Eq. (8.14) squares the difference instead of taking the absolute value. In both cases, the result of integration is a positive number that becomes larger with the distribution width.

The difference between the terms error and uncertainty have been widely discussed in the literature (Burns et al., 1973; Campion et al., 1973; Rabinovich, 2005).

An easy description of error theory is given in Beers (1957). The term "error" is generally applied to describe the

difference between the measured and the true values, while the term "uncertainty" is related to the inaccuracy of the measurements, and is always accompanied with the corresponding confidence probability. The International Vocabulary (1993) defines uncertainty as "an interval having a stated level of confidence." We illustrate the difference between the two definitions with an example, such that the error can be 1%, whereas the uncertainty is ±1% with a level of confidence of 95% (observe how the error can be +1% or −1%, but never ±1%).

The simplest counting statistics is when we have only one counting result and we are interested in associating with it an uncertainty. This is possible because the radioactive emissions follow Poisson statistics and, if the measurement does not perturb the process, the standard deviation of the total counts is its square root.

When the counting statistics includes n measurements $x_1, x_2, \ldots, x_n$, the sample variance is given by the expression

$$s_n^2 = \frac{1}{n-1}\sum_{i=1}^{n}(x-\overline{x})^2 \tag{8.15}$$

which coincides with the variance (Eq. 8.14) for $n \to \infty$.

C. Error propagation

In radioactivity counting statistics, the Poisson distribution gives the uncertainty in the total number of counts. Other related quantities, e.g., counting rate or the number of counts without background are obtained by error propagation (Natrella, 2005; Nicholson, 1966).

Suppose the triple measurement of one radioactive sample gives the three independent results x, y, z for the total number of counts, then the respective standard deviations are $\sigma_x = \sqrt{x}$, $\sigma_y = \sqrt{y}$, $\sigma_z = \sqrt{z}$, and the standard deviation of a function of these three variables x, y, z, when these are independent, is given by

$$\sigma_u^2 = \left(\frac{\partial u}{\partial x}\right)^2\sigma_x^2 + \left(\frac{\partial u}{\partial y}\right)^2\sigma_y^2 + \left(\frac{\partial u}{\partial z}\right)^2\sigma_z^2 \tag{8.16}$$

On the other hand, when the three variables x, y, z are correlated, we have

$$\begin{aligned}\sigma_u^2 = {} & \left(\frac{\partial u}{\partial x}\right)^2\sigma_x^2 + \left(\frac{\partial u}{\partial y}\right)^2\sigma_y^2 + \left(\frac{\partial u}{\partial z}\right)^2\sigma_z^2 \\ & + 2\rho_{xy}\left(\frac{\partial u}{\partial x}\right)\left(\frac{\partial u}{\partial y}\right)\sigma_x\sigma_y + 2\rho_{yz}\left(\frac{\partial u}{\partial y}\right)\left(\frac{\partial u}{\partial z}\right)\sigma_y\sigma_z \\ & + 2\rho_{xz}\left(\frac{\partial u}{\partial x}\right)\left(\frac{\partial u}{\partial z}\right)\sigma_x\sigma_z\end{aligned} \tag{8.17}$$

where ρ_{xy}, ρ_{xz}, ρ_{yz}, are the correlation coefficients for the variables xy, xz, yz, respectively. These coefficients are defined by

$$\rho_{xy} = \frac{1}{(n-1)\sigma_x\sigma_y}\left(\sum_{i=1}^{n}x_iy_i - n\overline{XY}\right) \tag{8.18}$$

$$\rho_{xz} = \frac{1}{(n-1)\sigma_x\sigma_z}\left(\sum_{i=1}^{n}x_iz_i - n\overline{XZ}\right) \tag{8.19}$$

$$\rho_{yz} = \frac{1}{(n-1)\sigma_y\sigma_z}\left(\sum_{i=1}^{n}y_iz_i - n\overline{YZ}\right) \tag{8.20}$$

The corresponding correlation coefficient for two independent variables is $\rho = 0$, while for two completely correlated variables it is given by $\rho = \pm 1$. Table 8.4 shows several common functions and their respective partial derivatives. To compute the standard deviations for the counting parameters listed in column 1 of Table 8.5, the application of the error propagation equations in Table 8.4 is required.

Example 8.5. Two students are discussing how to apply the error propagation equations of Table 8.4 on function $u = 2x$ to obtain the standard deviation. Student A considers the standard deviation $\sigma_u = 2\sigma_x$ the best, while student B, after transforming the function into $u = x + x$, obtains the standard deviation $\sigma_u = \sqrt{2}\sigma_x$. Then a third student C joints the discussion arguing that the standard deviation is $\sigma_u = 2\sqrt{5}\sigma_x$ by transforming the function into $u = z - v$, where $z = 4x$ and $v = 2x$. Explain the discrepancies in the standard deviations obtained by the three students.

Solution. Only the standard deviation given by student A is correct. The assumption of student B is not valid, because the two terms into which the function u has been separated are correlated. Therefore, from Eq. (8.17) we have

$$\sigma_u^2 = \sigma_x^2 + \sigma_x^2 + 2\sigma_x\sigma_x = (\sigma_x + \sigma_x)^2 = 4\sigma_x^2$$

TABLE 8.4 Error propagation.

Equation	Standard deviation
$u = ax$	$\sigma_u = a\sigma_x$
$u = x \pm y$	$\sigma_u = \sqrt{\sigma_x^2 + \sigma_y^2}$
$u = a + bx + cy$	$\sigma_u = \sqrt{b^2\sigma_x^2 + c^2\sigma_y^2}$
$u = xy/z$	$(\sigma_u/u)^2 = (\sigma_x/x)^2 + (\sigma_y/y)^2 + (\sigma_z/z)^2$
$u = \log x$	$\sigma_u = \sigma_x/x$

TABLE 8.5 Application of uncertainty transmission errors to different counting results.

Result	Equation	Standard deviation
Counting rate	$b = C_B/t_B$	$\sigma(b) = \sigma(C_B)/t_B = \sqrt{C_B}/t_B$
Net gross counting	$C_S = C_{S+B} - C_B$	$\sigma(C_s) = \sqrt{\sigma^2(C_{S+B}) + \sigma^2(C_B)}$ $= \sqrt{C_{S+B} + C_B}$
Net counting rate	$c_S = C_{S+B}/t_{S+B} - C_B/t_B$	$\sigma(c_s) = \sqrt{\sigma^2(C_{S+B})/t_{S+B}^2 + \sigma^2(C_B)/t_B^2}$ $= \sqrt{C_{S+B}/t_{B+S}^2 + C_B/t_B^2}$
Channel ratio	$Q = N_A/N_B$	$(\sigma(Q)/Q)^2 = (\sigma(N_A)/N_A)^2 + (\sigma(N_B)/N_B)^2$ $= 1/N_A + 1/N_B$

so

$$\sigma_u = 2\sigma_x$$

in agreement with the result given by student A. The argument of student C is also devoid of the correlation concept. To be correct, the standard deviation should be expressed as

$$\sigma_u^2 = \sigma_z^2 + \sigma_v^2 - 2\sigma_z\sigma_v = 16\sigma_x^2 + 4\sigma_x^2 - 2 \times 4\sigma_x \times 2\sigma_x = (4\sigma_x - 2\sigma_x)^2 = 4\sigma_x^2$$

so

$$\sigma_u = 2\sigma_x$$

which also agrees with the result obtained by student A.

Error propagation is of great interest in planning experiments. Optimization of experiments allows one to reduce to a minimum the uncertainties of experimental results. A good example is the optimization in isotopic dilution as is shown by Angoso et al. (1973). Optimization of the figure of merit to obtain the best compromise between sample and background counts can be seen in the papers of Loevinger and Berman (1951), Thomas (1950), Jaffey (1960), Reynolds (1964), Donn and Wolke (1976), and Wyld (1970).

D. Accuracy of the mean value

In the previous sections, the mean value μ of a distribution of infinite events was taken as the best estimate of the true value X. In practice, however, the number of available measurements is finite, and frequently low. Since this number varies depending on the experiment, one question that immediately arises is: How can we approximate the mean value to the true value? In other words, how many measurements are necessary to obtain an accuracy better than a certain value?

The verification of one experiment by repeating the same sequence of measurements should provide similar average values X_n, and be in good agreement with the true value X, when the total number of measurements is large. The average value for a sequence of n independent measurements is given by

$$X_n = \frac{1}{n}(x_1 + x_2 + \ldots + x_n) \tag{8.21}$$

By applying the error propagation theory to Eq. (8.21), the following standard deviation of the mean is obtained

$$\sigma(X_n) = \left(\frac{\sigma^2(x_1)}{n^2} + \frac{\sigma^2(x_2)}{n^2} + \ldots + \frac{\sigma^2(x_n)}{n^2}\right)^{1/2} \tag{8.22}$$

Since x_1, x_2, …, x_n come from measuring the same quantity, we have

$$\sigma^2(x_1) = \sigma^2(x_2) = \ldots = \sigma^2(x_n) = \sigma^2(x) \tag{8.23}$$

thus

$$\sigma(X_n) = \frac{\sigma(x)}{\sqrt{n}} \tag{8.24}$$

By taking the average quadratic deviation Eq. (8.15) as the best estimate of the measurements, we obtain

$$S_n = \sigma(X_n) = \frac{\left(\sum_{i=1}^{n}(x_i - X)^2\right)^{1/2}}{\sqrt{n(n-1)}} = \frac{\sigma_n(x)}{\sqrt{n-1}} = \frac{s_n(x)}{\sqrt{n}} \tag{8.25}$$

which indicates the degree of accuracy of the mean value X_n. The standard deviation S_n in Eq. (8.25) is called the **standard error**, and gives the best estimate of the true value when written as

$$X = X_n \pm S_n \tag{8.26}$$

where S_n is a function of the total number of counts and measurements. The increment of the number of measurements makes the accuracy improve proportionally with the square root.

Frequently the best estimate of one experiment is computed from the mean values instead of directly from the measurements. Suppose X_n and Y_n are the corresponding mean values of two sets of n and m measurements, then the mean value of the new variable $z = x \pm y$ is $Z_{nm} = X_n \pm Y_m$, and its standard deviation is given by

$$\sigma(Z_{nm}) = \sqrt{\sigma^2(X_n) + \sigma^2(Y_m)} \tag{8.27}$$

so

$$S_{nm} = \sqrt{S_n^2 + S_m^2} = \sqrt{\frac{\sigma_n^2(x)}{n-1} + \frac{\sigma_m^2(x)}{m-1}} \tag{8.28}$$

E. Combination of measurements

We are by now quite familiar with the computation of the uncertainty of nonmeasured quantities from the uncertainty of directly measured quantities by error propagation. However, how can we combine results from experiments in which we have applied different methods?

Suppose that the successive measurements carried on one radioactive sample give $X_n \pm S_n$ by applying one procedure and $X_m \pm S_m$ by applying another. If both methods were of similar precision, a good estimate of the true value could be

$$X_{n,m} = \frac{X_n + X_m}{2} \tag{8.29}$$

In practice, however, one procedure may be more precise than the other, and the best estimate of the true value is given by the weighted mean

$$X_{n,m} = \alpha X_n + (1-\alpha)X_m \quad \text{where} \quad 0 \le \alpha \le 1 \tag{8.30}$$

The numerical value of the weight α is computed from S_n and S_m. By applying error propagation to Eq. (8.30) we obtain the equation

$$S_{n,m}^2 = \alpha^2 S_n^2 + (1-\alpha)^2 S_m^2 \tag{8.31}$$

The error function $S_{n,m}$ becomes minimum when the derivates vanish

$$\frac{dS_{n,m}^2}{d\alpha} = 2\alpha S_n^2 - 2(1-\alpha)S_m^2 = 0 \tag{8.32}$$

That is, when

$$\alpha = \frac{S_n^{-2}}{S_n^{-2} + S_m^{-2}} \quad \text{and} \quad 1-\alpha = \frac{S_m^{-2}}{S_n^{-2} + S_m^{-2}} \tag{8.33}$$

Hence, the best estimate of the true value will be given by

$$X_{n,m} = \frac{1}{S_n^{-2} + S_m^{-2}}\left(\frac{X_n}{S_n^2} + \frac{X_m}{S_m^2}\right) \tag{8.34}$$

and the standard deviation

$$S_{n,m}^2 = \frac{S_n^{-2} + S_m^{-2}}{\left(S_n^{-2} + S_m^{-2}\right)^2} = \frac{S_n^2 S_m^2}{S_n^2 + S_m^2} \tag{8.35}$$

so

$$S_{n,m}^{-2} = S_n^{-2} + S_m^{-2} \tag{8.36}$$

The subsequent generalization of Eqs. (8.34) and (8.36) to more than two procedures generates the following equations:

$$X_{n,m,p,\ldots} = \frac{1}{S_n^{-2} + S_m^{-2} + S_p^{-2} + \ldots}\left(\frac{X_n}{S_n^2} + \frac{X_m}{S_m^2} + \frac{X_p}{S_p^2} + \ldots\right) \tag{8.37}$$

and

$$S_{n,m,p,\ldots}^{-2} = S_n^{-2} + S_m^{-2} + S_p^{-2} + \ldots \tag{8.38}$$

Frequently, these equations are written applying the following notation:

$$X = \sum_{n=1}^{N} \frac{x_n}{S_n^2} \Big/ \sum_{n=1}^{N} \frac{1}{S_n^2} \tag{8.39}$$

$$S_{in}^2(X) = 1 \Big/ \sum_{n=1}^{N} \frac{1}{S_n^2} \tag{8.40}$$

where the subscript *in* denotes an inner type standard deviation. On the other hand, the subscript *out* is used for outer standard deviations that verify

$$S_{out}(X) = \left[\frac{\sum_{i=1}^{N} (x_i - X)^2 / S_i^2}{(N-1)\sum_{i=1}^{N} 1/S_i^2}\right]^{1/2} \tag{8.41}$$

Both types of standard deviation, S_{out} and S_{in}, are equal for samples taken from the same normal population. However, in many situations, the ratio S_{out}/S_{in} differs from unity, adopting the expression defined by Topping (1972):

$$Z = \frac{S_{out}}{S_{in}} = \left[\frac{\sum_{i=1}^{N} (x_i - X)^2 / \sigma_i^2}{N-1}\right]^{1/2} \tag{8.42}$$

The observed data can only be considered consistent when the value of Z does not differ significantly from unity.

TABLE 8.6 Energy and uncertainty of ^{60}Co gamma ray.

E_γ[keV]	Uncertainty
1332.483	0.046
1332.560	0.050
1332.540	0.040
1332.509	0.015
1332.508	0.015

In such a case, the best value for the error of the weighted average is given by the greatest of the two values S_{out} or S_{in}. On the other hand, when Z differs significantly from unity, the conclusion is that systematical errors are present in the measurements. This leads to weights that do not verify Eq. (8.33), and depend more on other conditions such as the right performance of the experiment.

Example 8.6. The measurement of the energy emitted by one of the gamma-ray transitions of ^{60}Co was carried out by five different methods. The resulting energies and their respective uncertainties are shown in Table 8.6. Find the mean value and the inner and outer standard deviations. Also compute the value of Z and analyze the consequences of its proximity to unity.

Solution. The computation of the weighted average gives

$$X = \frac{\sum_{n=1}^{5} x_n/S_n^2}{\sum_{n=1}^{5} 1/S_n^2} = \frac{1.3840098 \times 10^7}{1.0386478 \times 10^4} = 1332.511 \text{ keV}$$

For the inner and outer type standard deviations we have

$$S_{in} = \frac{1}{\sqrt{\sum_{n=1}^{5} 1/S_n^2}} = \frac{1}{\sqrt{1.0386478 \times 10^4}} = 0.0098$$

and

$$S_{out} = \left[\frac{\sum_{n=1}^{5} (x_n - X)^2/S_n^2}{(5-1)\sum_{n=1}^{5} 1/s_n^2}\right]^{1/2} = \left(\frac{1.914313}{4 \times 1.0386 \times 10^4}\right)^{1/2} = 0.0068$$

respectively.

For the value of Z we obtain

$$Z = \frac{\sigma_{out}}{\sigma_{in}} = \frac{0.0068}{0.0098} = 0.69$$

By applying the F-test in the way shown in Example 8.17, we conclude that we have no reasons to think of different standard deviations.

F. Interlaboratory comparisons

Interlaboratory comparisons have been a research subject in recent years (Chuvnovkina et al. (2008), Shirono et al. (2010), Pommé and Spanova (2008), Pommé and Keightley (2015), and Sahagia et al. (2016). The problem is that in most interlaboratory comparisons some results are very far from the mean of the result sets considering all the laboratories involved. This prevents us from using global uncertainty u_i as a measure of the uncertainty of the mean for the set of measures. On the other hand, it is not clear whether widely differing results can be admitted or rejected, and also the terminology used is very specific. For example, the resulting reference value evaluated from the data set (x_i, u_i) from N laboratories participating in the intercomparison is called the KCRV (Key Comparison Reference Value).

In this section we examine the following means: AM (Arithmetic Mean), WM (Weighted Mean), M-P mean (Mandel and Paule, 1971; Paule and Mandel, 1982; Mandel, 1991), PMM (Power-Moderate weighted Mean) (Pommé, 1912), as well as the associated uncertainties. Different models have been proposed for the evaluation of intercomparison data. In general, all the methods can be classified into two main groups:

- The first group consists of all methods for evaluating consistent data. These methods do not require any additional information other than the results of the measures and their uncertainties. The KCRV (Key Comparison Reference Value) is calculated by the weighted mean, and its uncertainty is relative to the mean.
- The second group includes methods for evaluating inconsistent data. All these methods are based on additional assumptions, the validity of which must be analyzed in each case.

In May 2013, the Consultative Committee for Ionizing Radiation, Section II, Measurement of Radionuclides, of the International Committee of Weights and Measurements (CIPM-CCRI (II)) decided to adopt the new concept of Power-Moderate weighted Mean (PMM) in the calculation of the KCRV, its typical uncertainty and degree of equivalence.

TABLE 8.7 Two sets of measured values.

Method	A						B	
Measured values	202.0	201.0	201.5	201.8	201.2	201.7	216.3	216.8
Coded values	2.0	1.0	1.5	1.8	1.2	1.7	16.3	16.8

To better understand the new PMM method, we will first consider the Paule and Mandel method, which we will call the PM method.

1. Philosophy of the Paule and Mandel method

In essence, the Paule and Mandel method attempts to introduce a series of effects linked to systematic uncertainties that have not been taken into account or have been lost in calculating the internal variance of the measures, as a random variance.

To clarify the above point, we will consider a simple example. Suppose we have two sets of measurements A and B of equal precision, but set A has more measurements than B (See Table 8.7). If we observe the average values obtained for each set of measures, we see that they are very different ($\overline{x}_A = 1.53$ and $\overline{x}_B = 16.55$). On the other hand, the typical deviations of the means are quite small ($s(\overline{x}_A) = 0.154$ and $s(\overline{x}_B) = 0.250$), while the discrepancies between the means are large. This is because the calculated variances only describe the internal variability of measures A or B and do not recognize the variability between the sets of measures to obtain "a between set component of variance" and include it in the overall variance of the measures set.

The use of "a between set component of variance" treats the collection of systematic errors of the various sets of measures as a source of random variability.

The systematic errors mentioned here are errors that remain after the measurement process. There is no possibility of attributing these systematic errors to any given set of measures. It is therefore reasonable to assume that all sets of measures are affected by these uncertainties and that the actual variance of each set of measures will be affected by a variance that will be added to the internal "within" variance. The real variance value is obtained by means of an iteration process.

2. Calculation of the variance of the between set

We know that the weight for $\overline{x}_i$ is $w_i = 1/\mathrm{Var}(\overline{x}_i)$ and the estimation of the weight is:

$$w_i = \left(\frac{s_{wi}^2}{n_i} + s_b^2\right)^{-1} \tag{8.43}$$

From the definition of w_i we get the relation:

$$w_i \mathrm{Var}(\overline{x}_i) = 1 \tag{8.44}$$

Or:

$$\mathrm{Var}(\sqrt{w_i}\overline{x}_i) = 1 \tag{8.45}$$

For a given set of weights w_i, the variance can be calculated by this formula:

$$s^2(w_i\overline{x}_i) = \frac{\sum_{i=1}^{m} w_i(\overline{x}_i - \widetilde{x})^2}{m-1} \tag{8.46}$$

Where m is the number of sets considered and $\widetilde{x}$ is given by

$$\widetilde{x} = \frac{\sum_{i=1}^{m} w_i\overline{x}_i}{\sum_{i=1}^{m} w_i} \tag{8.47}$$

we see that

$$\frac{\sum_{i=1}^{m} w_i(\overline{x}_i - \widetilde{x})^2}{m-1} = 1 \tag{8.48}$$

This equation supplies the means to calculate s_b^2. For this, we define the function

$$F\left(s_b^2\right) = \sum_{i=1}^{m} w_i(\overline{x}_i - \widetilde{x})^2 - (m-1) \tag{8.49}$$

We see that s_b^2 must have a value such that $F\left(s_b^2\right) = 0$. Following Paule and Mandel (1982), we will use $s_b^2 = v$ for ease of notation. We will start with an approximate value, v_0, and must find a value of dv such that $F(v_0 + dv) = 0$. Using a truncated Taylor series development, we obtain:

$$F(v_0 + dv) = f_0 + \left(\frac{\partial F}{\partial v}\right)_0 = 0 \tag{8.50}$$

Then

$$dv = \frac{F_0}{\left[\sum_{i=1}^{m} w_i^2(\overline{x}_i - \widetilde{x})^2\right]_0} \tag{8.51}$$

The new adjusted value for v is

$$\text{New } v_0 = \text{Old}v_0 + dv$$

This new value is introduced into Eqs. (8.43), (8.46), (8.47), and (8.49), and an iteration is applied until dv is close to zero. The following is a simplified numerical example to illustrate the procedure. (When the respective uncertainties are available as well as the data of the average values, it can be used as a criterion to optimize $\tilde{\chi}^2_{obs}$, which must be equal to one. This point will be expanded in our description of the PMM method.)

Example. 8.7. Consider the case of two sets of measures that we will call A and B, with different number of measurements each as shown in Table 8.7. Let us apply the theory described above to calculate the mean value and the most acceptable standard deviation. We will use the encoded values as they simplify the calculations (Paule and Mandel, 1982).

Solution. In the first iteration we will consider that $s_b^2 = v_0 = 100$.

The mean values of the measures of A and B are:

$$\bar{x}_A = \frac{\sum_{i=1}^{n_A} x_{iA}}{n_A} = \frac{9.20}{6} = 1.533$$

$$\bar{x}_B = \frac{\sum_{i=1}^{n_B} x_{iB}}{n_A} = \frac{32.90}{2} = 16.55$$

The corresponding variances are:

$$s^2(\bar{x}_A) = \frac{\sum_{i=1}^{n_A} (x_{iA} - \bar{x}_A)^2}{n_A(n_A - 1)} = \frac{0.7133}{5 \times 6} = 0.02378$$

$$s^2(\bar{x}_B) = \frac{\sum_{i=1}^{n_B} (x_{iB} - \bar{x}_B)^2}{n_B(n_B - 1)} = \frac{0.125}{1 \times 2} = 0.0635$$

The within set variances are:

$$s^2_{wA} = \frac{\sum_{i=1}^{n_A} (x_{iA} - \bar{x}_A)^2}{n_A - 1} = \frac{0.7133}{6 - 1} = 0.14266$$

$$s^2_{wB} = \frac{\sum_{i=1}^{n_A} (x_{iB} - \bar{x}_B)^2}{n_B - 1} = \frac{0.125}{1} = 0.125$$

Calculation of weights:

$$w_A = \frac{1}{\frac{s^2_{wA}}{n_A} + s_b^2} = \frac{1}{\frac{0.14266}{6} + 100} = 0.0099976$$

$$w_B = \frac{1}{\frac{s^2_{wB}}{n_B} + s_b^2} = \frac{1}{\frac{0.125}{2} + 100} = 0.0099938$$

The weighted average of the two values of m: A and B is

$$\tilde{x} = \frac{\sum_{i=1}^{m} w_i \bar{x}_i}{\sum_{i=1}^{m} w_i} = \frac{w_A \bar{x}_A + w_B \bar{x}_B}{w_A + w_B} = \frac{0.18072}{0.01999} = 9.040$$

and the calculation of F is

$$F(s_b^2) = \sum_{i=1}^{m} w_i (\bar{x} - \tilde{x})^2 - (m - 1)$$

$$= 0.0099976(1.533 - 9.040)^2 + 0.0099938(15.35 - 9.040)^2 - (2 - 1)$$

$$= 0.563415 - 0.563651 - 1 = 0.127066$$

The calculation of dv is

$$dv = \frac{F_0}{\left[\sum_{i=1}^{m} w_i^2 (\bar{x}_i - \tilde{x})^2\right]} = \frac{F_0}{w_A^2(\bar{x}_A - \tilde{x})^2 + w_B^2(\bar{x}_B - \tilde{x})^2}$$

$$= \frac{0.127066}{0.0001 \times 56.355 + 0.000099 \times 56.400}$$

$$= \frac{0.127066}{0.0056355 + 0.0056344} = \frac{0.127066}{0.0112699} = 11.2748$$

Now we perform the second iteration. We now have

$$v = v_0 + dv = 100 + 11.2748 = 111.2748$$

We calculate the weights again to give

$$w_A = \frac{1}{\frac{s^2_{wA}}{n_A} + s_b^2} = \frac{1}{\frac{0.14266}{6} + 111.2748} = 0.0089848$$

$$w_B = \frac{1}{\frac{s^2_{wB}}{n_B} + s_b^2} = \frac{1}{\frac{0.125}{2} + 111.2748} = 0.0089817$$

Calculation of $\tilde{x}$ yields

$$\tilde{x} = \frac{\sum_{i=1}^{m} w_i \bar{x}_i}{\sum_{i=1}^{m} w_i} = \frac{w_A \bar{x}_A + w_B \bar{x}_B}{w_A + w_B} = \frac{0.013774 + 0.148647}{0.0179657}$$

$$= 9.0402$$

The calculation of F_0 is the following:

$$F_0 = F\left(s_b^2\right) = \sum_{i=1}^{m} w_i(\overline{x} - \widetilde{x})^2 - (m-1)$$

$$= 0.0089844(1.533 - 9.0402) + 0.089817(16.55 - 9.0402) - 1$$

$$0.506343 + 0.506519 - 1 = 0.0129068$$

And the calculation of dv is

$$dv = \frac{F_0}{\left[\sum_{i=1}^{m} w_i^2(\overline{x}_i - \widetilde{x})^2\right]} = \frac{F_0}{w_A^2(\overline{x}_A - \widetilde{x})^2 + w_B^2(\overline{x}_B - \widetilde{x})^2}$$

$$= \frac{0.0129068}{0.000807 \times 56.35805 + 0.000807 \times 56.3971}$$

$$= \frac{0.129068}{0.0045481 + 0.0045512} = 1.4184$$

Now we execute the third iteration for which the calculations are the following:

$$v = v_0 + dv = 111.2748 + 1.4184 = 112.6932$$

$$w_A = \frac{1}{\frac{s_{wA}^2}{n_A} + s_b^2} = \frac{1}{\frac{0.14266}{6} + 112.6832} = 0.0088718$$

$$w_B = \frac{1}{\frac{s_{wB}^2}{n_B} + s_b^2} = \frac{1}{\frac{0.125}{2} + 112.6832} = 0.0088687$$

Calculation of $\widetilde{x}$:

$$\widetilde{x} = \frac{\sum_{i=1}^{m} w_i\overline{x}_i}{\sum_{i=1}^{m} w_i} = \frac{w_A\overline{x}_A + w_B\overline{x}_B}{w_A + w_B} = \frac{0.013774 + 0.148647}{0.0177405}$$

$$= 9.0402$$

Calculation of F_0:

$$F_0 = F\left(s_b^2\right) = \sum_{i=1}^{m} w_i(\overline{x} - \widetilde{x})^2 - (m-1)$$

$$= 0.0089848(1,533 - 9.0402)^2 + 0.0089817(16.55 - 9.0402)^2 - 1$$

$$0.506366 + 0.5065418 - 1 = 0.0129068$$

Calculation of dv:

$$dv = \frac{F_0}{\left[\sum_{i=1}^{m} w_i^2(\overline{x}_i - \widetilde{x})^2\right]} = \frac{F_0}{w_A^2(\overline{x}_A - \widetilde{x})^2 + w_B^2(\overline{x}_B - \widetilde{x})^2}$$

$$= \frac{0.129068}{0.0045481 + 0.0045512} = \frac{0.0129068}{0.0090993} = 1.141844$$

Performing the fourth iteration yields the following:

$$v = 111.3748 + 1.41844 = 112.69324$$

Calculation of weights

$$w_A = \frac{1}{\frac{s_{wA}^2}{n_A} + s_b^2} = \frac{1}{\frac{0.14266}{6} + 112.6932} = \frac{1}{112.7170}$$

$$= 0.0088718$$

$$w_B = \frac{1}{\frac{s_{wB}^2}{n_B} + s_b^2} = \frac{1}{\frac{0.125}{2} + 112.6932} = \frac{1}{112.7557}$$

$$= 0.0088687$$

Calculation of $\widetilde{x}$:

$$\widetilde{x} = \frac{\sum_{i=1}^{m} w_i\overline{x}_i}{\sum_{i=1}^{m} w_i} = \frac{w_A\overline{x}_A + w_B\overline{x}_B}{w_A + w_B} = \frac{0.0136005 + 0.146777}{0.0177405}$$

$$= \frac{0.1603775}{0.0177405} = 9.0402$$

Calculation of F_0:

$$F_0 = F\left(s_b^2\right) = \sum_{i=1}^{m} w_i(\overline{x} - \widetilde{x})^2 - (m-1)$$

$$= 0.0088718 \times 56.35805 + 0.0088687 \times 56.397096 - 1$$

$$= 0.499997 + 0.50017 - 1 = 0.00167$$

Calculation of dv:

$$dv = \frac{F_0}{\left[\sum_{i=1}^{m} w_i^2(\overline{x}_i - \widetilde{x})^2\right]} = \frac{F_0}{w_A^2(\overline{x}_A - \widetilde{x})^2 + w_B^2(\overline{x}_B - \widetilde{x})^2}$$

$$= \frac{0.00167}{0.000787 \times 56.35805 + 0.000787 \times 56.397096}$$

$$= \frac{0.00167}{0.0044354 + 0.0044385} = \frac{0.00167}{0.0088739} = 0.01882$$

Performing the fifth iteration yields the following:

$$v = 112.69324 + 0.01882 = 112.712$$

Calculation of weights:

$$w_A = \frac{1}{\frac{s_{wA}^2}{n_A} + s_b^2} = \frac{1}{\frac{0.14266}{6} + 112.712} = \frac{1}{112.7358}$$

$$= 0.0088703$$

$$w_B = \frac{1}{\frac{s_{wB}^2}{n_B} + s_b^2} = \frac{1}{\frac{0.125}{2} + 112.712} = \frac{1}{112.7745}$$
$$= 0.0088673$$

Calculation of $\widetilde{x}$:

$$\widetilde{x} = \frac{\sum_{i=1}^{m} w_i \overline{x}_i}{\sum_{i=1}^{m} w_i} = \frac{w_A \overline{x}_A + w_B \overline{x}_B}{w_A + w_B} = \frac{0.013598 + 0.1467538}{0.0177405}$$
$$= \frac{0.160352}{0.0177376} = 9.0402$$

Calculation of F_0:

$$F_0 = F\left(s_b^2\right) = \sum_{i=1}^{m} w_i (\overline{x} - \widetilde{x})^2 - (m-1)$$
$$= 0.0088703 \times 56.35805 + 0.0088673 \times 56.397096 - 1$$
$$= 0.4999128 + 0.500090 - 1 = 0.0000028$$

Calculation of dv:

$$dv = \frac{F_0}{\left[\sum_{i=1}^{m} w_i^2 (\overline{x}_i - \widetilde{x})^2\right]} = \frac{F_0}{w_A^2 (\overline{x}_A - \widetilde{x})^2 + w_B^2 (\overline{x}_B - \widetilde{x})^2}$$
$$= \frac{0.000028}{0.0000787 \times 56.35805 + 0.0000786 \times 56.397096}$$
$$= \frac{0.0000028}{0.0044354 + 0.0044328} = \frac{0.0000028}{0.0088682} = 0.000316$$

This is a value low enough to end the iterations here. Thus:

$\widetilde{x} = 9.0402$ and the true value is: $\widetilde{x} = 209.0402$

$$v = s_b^2 = 112.712$$

$$s^2(w_i \overline{x}_i) = \frac{w_A (\overline{x}_A - \widetilde{x})^2 + w_B (\overline{x}_B - \widetilde{x})^2}{m-1} = 1.0000028$$

$$\text{Standard error} = \frac{1}{\sqrt{w_A + w_B}}$$
$$= \frac{1}{\sqrt{0.0088703 + 0.0088673}} = 7.51$$

The result is found to be the following: 209.04 ± 7.51.

3. Power-Moderate mean

The arithmetic mean can be used when there are no discrepant results:

$$\overline{x} = \frac{1}{n} \sum_{i=1}^{n} x_i \tag{8.52}$$

and its uncertainty is

$$u(\overline{x}) = \frac{1}{n} \sqrt{\sum_{i=1}^{n} u_i^2} \tag{8.53}$$

Individual variances can be replaced by an estimate of variance of the sample

$$u(\overline{x}) = \frac{1}{n} \sqrt{n u^2} = \frac{u}{n} = \left[\sum_{i=1}^{n} \frac{(x_i - \overline{x})^2}{n(n-1)}\right]^{1/2} \tag{8.54}$$

As indicated by the PM method, the calculated uncertainty of the mean can be abnormally low, so the two uncertainties of the mean are compared and the largest uncertainty is chosen, that is:

$$u(\overline{x}) = \text{Max}\left[\frac{1}{n}\sqrt{\sum_{i=1}^{n} u_i^2}\,,\quad \sqrt{\sum_{i=1}^{n} \frac{(x_i - \overline{x})^2}{n(n-1)}}\ \right] \tag{8.55}$$

The weighted average is calculated using the formula:

$$\overline{x}_{\text{weig}} = \frac{\sum_{i=1}^{n} \frac{x_i}{u_i^2}}{\sum_{i=1}^{n} \frac{1}{u_i^2}} \tag{8.56}$$

And the uncertainty is:

$$u\left(\overline{x}_{\text{weig}}\right) = \frac{1}{\sqrt{\sum_{i=1}^{n} \frac{1}{u_i^2}}} \tag{8.57}$$

The weighted mean and its uncertainty are inadequate when applied to discrepant data with underestimated uncertainties. The discrepancy can be verified by applying the chi-square test.

$$\widetilde{\chi}_{\text{obs}}^2 = \frac{1}{n-1} \sum_{i=1}^{n} \frac{\left(x_i - \overline{x}_{\text{weig}}\right)^2}{u_i^2} \tag{8.58}$$

If we get values higher than one, we have a clear signal that the data are inconsistent.

TABLE 8.8 Radionuclide activity concentration of the sample reported by participants.

Laboratory	1	2	3	4	5	6
x_i	17.1	14.0	23.5	19.8	16.0	13.8
u_i	2.7	7.0	14.3	11.0	9.0	0.6
u_i^2	7.29	49.0	204.3	121	81	0.36

In this case, we can use the Paule−Mandel mean. In the exercise given above as an example of the application of the PM average, we only take values of the measures without their uncertainties. We will now consider that, in addition to the values of the measures, we have their associated uncertainties, in which case the chi-square that we apply will be:

$$\widetilde{\chi}^2_{\text{obs}} = \frac{1}{n-1}\sum_{i=1}^{n}\frac{\left(x_i - \overline{x}_{\text{weig}}\right)^2}{u_i^2 + s^2} \tag{8.59}$$

where s is what we previously called s_b, and it takes into account uncontrolled systematic uncertainties. The procedure of successive approximations is based on the criterion that the value of the chi-square must be equal to or less than one. As before, an initial value of s will be chosen and the weighted mean and its uncertainty will be calculated using the new formulas:

$$\overline{x}_{\text{weig}} = \frac{\sum_{i=1}^{n}\frac{x_i}{u_i^2} + s^2}{\sum_{i=1}^{n}\frac{1}{u_i^2} + s^2} \tag{8.60}$$

$$u\left(\overline{x}_{\text{weig}}\right) = \frac{1}{\sqrt{\sum_{i=1}^{n}\frac{1}{u_i^2} + s^2}} \tag{8.61}$$

The PM mean does not give good results when the uncertainties of the data are underestimated, which often occurs in practice. The PMM average moderates the effect of underestimation of uncertainties. For this, we calculate the magnitude S defined as:

$$S^2 = n \times \text{Max}\left[\frac{1}{\sum_{i=1}^{n}\frac{1}{u_i^2 + s^2}}, \frac{\sum_{i=1}^{n}\left(x_i - \overline{x}\right)^2}{n(n-1)}\right] \tag{8.62}$$

and it is applied to the calculation of the mean and the uncertainty, replacing the factor $1/\left(u_i^2 + s^2\right)$ by the term

$$\left[\left(\sqrt{u_i^2 + s^2}\right)^{\alpha} S^{2-\alpha}\right]$$

The value of α is linked to the number of data n by the equation:

$$\alpha = 2 - \frac{3}{n} \tag{8.63}$$

Example. 8.8. Calculation of the PMM average and its uncertainty. Consider the following Table 8.8 in which the results of 6 laboratories and their uncertainties are presented (Sahagia et al., 2016). The square uncertainty has been added for convenience of calculation.

We will calculate the different magnitudes involved in obtaining the PMM mean.

Solution. The arithmetic mean of the measures is:

$$\overline{x} = \frac{\sum_{i=1}^{n} x_i}{n} = \frac{103.3}{6} = 17.216$$

Median:

$$x_{\text{med}} = \frac{17.1 + 16}{2} = 16.6$$

Standard deviation of the arithmetic mean:

$$s = \sqrt{\frac{\sum_{i=1}^{n}\left(x_i - \overline{x}\right)^2}{n(n-1)}} = \sqrt{\frac{65.433}{6.5}} = \sqrt{2.1943} = 1.48$$

Weighted mean:

$$\overline{x}_{\text{weig}} = \frac{\sum_{i=1}^{n}\frac{x_i}{u_i^2}}{\sum_{i=1}^{n}\frac{1}{u_i^2}} = \frac{41.433}{2.961} = 14.0$$

Standard deviation of the weighted mean:

$$u\left(\overline{x}_{\text{weig}}\right) = \frac{1}{\sqrt{\sum_{i=1}^{n} 1/u^2}} = \frac{1}{\sqrt{2.961}} = \pm 0.58 \approx \pm 0.6$$

Reduced observed chi-squared value:

$$\chi^2 = \frac{1}{n-1}\sum_{i=1}^{n}\frac{\left(x_i - \overline{x}_{weig}\right)^2}{u_i^2} = \frac{2.1185}{5} = 0.4236 \approx 0.42$$

Paule–Mandel mean ($s = 0$):

$$\overline{x}_{P-M} = \frac{\sum_{i=1}^{n}\frac{x_i}{(u_i^2+s^2)}}{\sum_{i=1}^{n}\frac{1}{(u_i^2+s^2)}} = \frac{\sum_{i=1}^{n}\frac{x_i}{u_i^2}}{\sum\frac{1}{u_i^2}} = 14.0$$

Standard deviation of the Paule–Mandel mean ($s = 0$):

$$u(PM) = \frac{1}{\sqrt{\sum_{i=1}^{n}\frac{1}{u_i^2+s^2}}} = \frac{1}{\sqrt{\sum_{i=1}^{n}\frac{1}{u_i^2}}} = 0.6$$

S-value:

$$S = \sqrt{n \times \mathrm{Max}\left[u^2(\overline{x}), u^2(\overline{x}_{\mathrm{P-M}})\right]}$$
$$= \sqrt{6 \times \mathrm{Max}(1.40^2,\ 0.6^2} = 3.43$$

α-value:

$$\alpha = 2 - \frac{3}{n} = 2 - \frac{3}{6} = \frac{3}{2} = 1.5$$

4. Power-Moderated weighted Mean (PMM)

First we calculate $u(x_{\mathrm{PMM}})$

$$u(x_{\mathrm{PMM}}) = \frac{1}{\sqrt{\sum_{i=1}^{n}\left(u_i^2+s^2\right)^{-\alpha}S^{\alpha-2}}}$$

$$= \frac{1}{\sqrt{\sum_{i=1}^{n}\left(\sqrt{u_i^2}\right)^{-\alpha}S^{\alpha-2}}} = \frac{1}{\sqrt{\sum_{i=1}^{n}\left(\frac{1}{u^\alpha}\right)S^{\alpha-2}}}$$

$$= \frac{1}{\sqrt{2.76 \times \frac{1}{S^{2-\alpha}}}} = \frac{1}{\sqrt{2.76 \times \frac{1}{3.43^{0.5}}}}$$

$$= \frac{1}{\sqrt{1.49}} = 0.82$$

PMM mean:

$$\overline{x}_{\mathrm{PMM}} = u^2(\overline{x}_{\mathrm{PMM}})\sum_{i=1}^{n}\frac{x_i}{\sqrt{\left(u_i^2+s^2\right)^{\alpha}}S^{2-\alpha}}$$

$$= u^2(\overline{x}_{\mathrm{PMM}})\sum_{i=1}^{n}\frac{x_i}{\sqrt{\left(u_i^2\right)^{\alpha}}S^{2-\alpha}}$$

$$= u(\overline{x}_{\mathrm{PMM}})\sum_{i=1}^{n}\frac{x_i}{u_i^{\alpha}S^{2-\alpha}} = 0.82^2\sum_{i=1}^{n}\frac{x_i}{u_i^{\alpha}\times 3.43^{0.5}}$$

$$= \frac{0.672 \times 39.36}{1.852} = 14.3$$

The result: 14.3 ± 0.8.

Sahagia et al. (2016) repeat the previous calculation by removing the value 23.5 reported by Participant #3 of Table 8.8. In this case, the value obtained with the five remaining data is: 14.3 ± 1.1. This shows that this discordant data contributes little to the final result.

G. The statement of the results

The concept of uncertainty is commonly applied to evaluate the degree of feasibility in the results of one experiment. The uncertainty considers two limits to determine how the best estimate may deviate from the true value in terms of probability. The uncertainty of the results of a measurement is generally determined by several components, which may be grouped into two categories, according to the procedure used to determine the numerical values:

- Uncertainties evaluated following statistical procedures (Type A evaluation)
- Uncertainties evaluated by means of other procedures (Type B evaluation)

There is no correspondence between the classification of the uncertainty components in the two categories A and B, and the usual classification into random and systematic errors. A detailed discussion on systematic uncertainties is given by Eisenhart (1963). The nature of an uncertainty is conditioned by the use of the corresponding quantity or, more clearly, the way in which the quantity appears in the model describing the measuring process. When the corresponding quantity is used in different ways, the random component may be transformed into systematic or vice

versa. Therefore, the terms accidental and systematic uncertainties may be misleading when they are used in practice. An alternative nomenclature sometimes used is:

- "uncertainty component arising from a random effect"
- "uncertainty component arising from a systematic effect"

In these statements, the random effect generates a possible random error in the process of measurement, while a systematic effect may generate a possible systematic error. A clear description of the different uncertainties involved in sample standardization is presented in the paper of Zimmerman et al. (2001).

Each uncertainty component, which contributes to the resultant uncertainty of a measurement by means of an estimated standard deviation, is referred to as the **standard uncertainty** and denoted by u_i. The u_i value is the positive square root of the estimated variance u_i^2.

The uncertainty component of category A is represented by means of statistics: The estimated standard deviation s_i, which is equal to the positive value of the square root of the estimated variance s_i^2 and the number ν_i of the associated degrees of freedom. For this component the standard uncertainty is $u_i = s_i$. The computation of the uncertainty by means of the statistical analysis of an observed set is referred to as **Type A uncertainty** computation, which may be considered as an approximation to the corresponding standard deviation.

In a similar way, the **Type B uncertainty** component, denoted by u_j, may be considered as an approximation to the corresponding standard deviation. To understand the background of the statement of uncertainty, we refer to the paper of Müller (1979).

1. Type B calculation of typical uncertainty

As there are statistical methods available for the Type A calculation of typical uncertainty, Type B calculation of uncertainty is grounded on a scientific reasoning based on all the relevant information at our disposal. We will describe some, but by no means all, illustrative situations. In any case, the history of the primary measures of some fundamental magnitudes is very illustrative. In all cases, accidental errors were underestimated. For example, the value of the charge of the electron was 4.7700×10^{-10} esu in 1929; in 1955, it was 4.8025×10^{-10} esu; and in 1973, it was $4.803{,}242(14) \times 10^{-10}$ esu. It is clear that the first two measures had differences that were far superior than accepted uncertainties.

Let us outline some practical considerations. If, in determining the value of a quantity, we can estimate the lower a_- and upper a_+ limits, so that the likelihood that the true value lies between these limits is 100% or, in other words, when the model to be applied is a uniform rectangular likelihood distribution, the best estimate of the value of the magnitude is:

$$X = \frac{a_+ + a_-}{2} \tag{8.64}$$

and the typical uncertainty is:

$$u_j = \frac{1}{\sqrt{3}} \frac{a_+ - a_-}{2} \tag{8.65}$$

If instead of a uniform rectangular distribution we have a triangular distribution, then the mean value is given by (8.64) but the uncertainty is:

$$u_j = \frac{1}{\sqrt{6}} \frac{a_+ - a_-}{2} \tag{8.66}$$

When the magnitude considered can be modeled by a normal distribution, there are no finite limits containing 100% of the possible values. As $\pm 3\sigma$ contain 99.73% of the possible values, $\pm 3\sigma$ can be chosen as the limits. Then the mean value will be that obtained by formula (8.64), but the uncertainty will be calculated by the expression:

$$u_j = \frac{1}{3} \frac{a_+ - a_-}{2} \tag{8.67}$$

In other situations we can assume that the distribution is normal and estimate a lower limit a_-, and an upper limit a_+, so that the best estimate of the value of the magnitude is given by Eq. (8.64) and, in addition, there is a 50% likelihood that the value of the measured quantity is in the (a_-, a_+) range. In this case:

$$u_j \approx 1.48 \frac{a_+ - a_-}{2} \tag{8.68}$$

On the other hand, when the likelihood that the true value is within the limits a_- and a_+ is 67%, the uncertainty is obtained by the expression:

$$u_j \approx \frac{a_+ - a_-}{2} \tag{8.69}$$

Example 8.9. The width of a strip of paper can be measured with a graduated ruler by applying two different procedures:

1. Adjust the zero of the ruler at one end and read the width at the other. The value sought is between divisions 104 and 105 mm. Find the value of the width and its uncertainty by applying a Type B calculation.
2. The ruler is placed randomly on the width of the paper, the values at both ends are read and then subtracted. The results obtained are: 105, 104, 104, 105, 105, 105, 104, 105, 104, 105 mm. Find the width and its uncertainty by applying a Type A calculation.

Solution.

1. When the procedure is Type B:

$$a_+ = 105 \text{ mm} \quad \text{and} \quad a_- = 104 \text{ mm}$$

The mean value will be:

$$X = \frac{a_+ + a_-}{2} = \frac{209}{2} = 104.5 \text{ mm}$$

If we assume that the distribution is uniform and rectangular, the standard deviation is:

$$u = \frac{1}{\sqrt{3}} \frac{a_+ - a_-}{2} = \frac{1}{2\sqrt{3}} = 0.29 \text{ mm}$$

so that

$$X = 104.5 \pm 0.03 \text{ mm}.$$

2. When the calculation procedure is type A, the mean is:

$$X = \frac{\sum_{i=1}^{10} x_i}{n} = \frac{1046}{10} = 104.6 \text{ mm}$$

The standard deviation of the mean is:

$$u = \left[\frac{\sum_{i=1}^{10} (x_i - X)^2}{n(n-1)} \right]^{1/2} = \sqrt{\frac{2.4}{90}} = 0.16$$

So that:

$$X = 104.6 \pm 0.16 \text{ mm}$$

Example 8.10. In view of the result obtained by repeating the measurements, we could carry out 1000 measures and obtain very low uncertainty. Suppose that we measure (from the above example) the width of the tape 1000 times and the result is 105 mm, 564 times; and 104 mm, 436 times. Find the mean and standard deviation.

Solution. The mean value is:

$$X = \frac{\sum_{i=1}^{1000} x_i}{1000} = \frac{564 \times 105 + 436 \times 104}{1000} = 104.564$$

The standard deviation of the mean is:

$$u = \left[\frac{\sum_{i=1}^{1000} (x - X)^2}{n(n-1)} \right]^{1/2} = \sqrt{\frac{245.904}{999000}} = 0.016 \text{ mm}$$

It is concluded that with 1000 measures we are able to appreciate up to hundredths of a millimeter with a ruler divided into millimeters. If we increase the number of measures, we could reach a negligible uncertainty, which does not seem logical. The result obtained is so, because we have greatly simplified the problem. In addition to random uncertainties, there are other uncertainties linked to the instrument, measurement system, and environmental conditions. If we calibrate the ruler, we can observe that in 100 mm there is a discrepancy of 0.1 mm, so the associated type B uncertainty will be:

$$u = \frac{1}{\sqrt{3}} \frac{0.1}{2} = 0.028$$

The total uncertainty will be:

$$u = \sqrt{0.016^2 + 0.028^2} = 0.032$$

Although the random uncertainty was very small, we would always have the calibration, which is constant.

2. Combined standard uncertainty

The combined standard uncertainty, u_c, of a measurement is obtained from the individual standard uncertainties, obtained from Type A and B evaluations. The rules given in the error transmission section will be applied here.

The combined standard uncertainty is used in the determination of fundamental constants, in fundamental metrology research and in comparisons.

On the other hand, for commercial, industrial, or regulatory applications, the required uncertainties must define an interval with a high probability that the result falls within it. In this case, it is convenient to introduce the concept of **expanded uncertainty**, U, obtained from multiplying u_c by a **coverage factor**, k, so that $U = ku_c$. Generally, the value of the coverage factor k is chosen so that we select a confidence level associated with the interval defined by $U = ku_c$. Two often used coverage factors, when the quantity is described by a normal distribution, are $k = 2$ and $k = 3$, which define intervals of confidence of 95.5% and 99.7%, respectively. Evaluation of precision and accuracy in instrument calibration systems is given by Eisenhart (1968).

3. Rules for expressing results

In this section, we follow the NIST recommendations given by Taylor and Kuyatt (1994): this guide is consistent with the guidelines of the Guide to the Expression of Uncertainty in Measurement (GUM) (JCGM 100, 2008). The result of a measurement may be followed by the sign $\pm$ and the corresponding uncertainty. The U value and the k factor or the applied u_c must always be specified. A complete uncertainty description for activity concentration for three measurement systems: liquid scintillation, ionization chambers, and $4\pi\gamma$ spectrometers are presented in the work of Zimmerman et al., 2001. It is recommended that the following information be included.

A list of all the components of the standard uncertainty with the appropriate degrees of freedom and the resulting value u_c. The uncertainty components should be identified in agreement with the method used to estimate the numerical values: Type A or B. A detailed description of how each component of the standard uncertainty has been evaluated must be presented. When we take $k \neq 2$, a description of how k has been chosen should be given. As an example, we present three different forms of writing the energy and the associated uncertainty for the gamma-ray energy of ^{51}Cr:

1. $E = (320.08419 \pm 0.00042)$ keV. The number after - $\pm$ symbol is the numerical value of the expanded uncertainty $U = ku_c$, with $u_c = 0.00021$ keV, and a coverage factor $k = 2$. We assume that the estimated values of a sample follow a normal distribution with a standard deviation u_c. The unknown energy value is believed to be in the interval defined by U with a level of confidence of 95%.
2. $E = (320.08419 \pm 0.00052)$ keV. Where the number following the $\pm$ symbol is the numerical value of the expanded uncertainty, $U = ku_c$, and a coverage factor based into a t distribution for $\nu = 9$ degrees of freedom. U defines an interval containing the unknown energy value with a confidence level of 95%.
3. $E = 320.08419$ keV with a combined standard deviation $u_c = 0.00021$ keV. We assume that the possible estimated energy values are distributed following a normal distribution with a standard deviation u_c. The unknown energy value is in the interval $E \pm u_c$ with an approximated confidence level of 68%.

IV. Statistical inference

From a very general point of view, we can consider statistical inference as a form of decision based on probability. In a more limited sense, however, one can say that the statistical inference allows an estimation or prediction from the data. Statistical inference gives responses to three types of problems: First, it permits one to test if a statement about the value of a parameter is correct. Second, it allows one to calculate the value of a parameter. Finally, it allows one to see whether some relationship exists between two or more variables and in the affirmative case, to determine this relationship. In this section, we analyze the hypothesis testing and the estimation techniques.

A. Hypothesis testing

A statistical hypothesis is an assertion about the probability density function of a random variable. Thus, the assertion that a random variable possesses a Poisson distribution is an example of a statistical hypothesis. The statement that the mean of a normal distribution is 5 is also a statistical hypothesis.

A test of a statistical hypothesis is a procedure for deciding whether to accept or reject the hypothesis. Before carrying out the test, we define a hypothesis called a **null hypothesis,** denoted by H_0. A null hypothesis is a statement about a population parameter that is being tested by the use of sample results and a decision-making process. This hypothesis must be contrasted with another called the **alternative hypothesis,** denoted by H_1. An alternative hypothesis is a statement to be accepted, if the null hypothesis is rejected. The alternative hypothesis utilizes the same parameter as the null hypothesis, but gives motivation for the rest of the test procedure. This is the statement we want to accept. Both hypotheses define complementary regions. The **critical region** is the portion of a distribution that provides values for the sample results causing the rejection of H_0. In other words, the critical region is the acceptance region for the alternative hypothesis. The critical value is the value that determines the critical region. Once the null and the alternative hypotheses have been established, we proceed to carry out the experiment and obtain the statistical sample to quantify the statistics of the test. If this one belongs to the critical region, we reject the null hypothesis and accept the alternative.

The result of our decision implies the possibility to guess correctly or make a mistake. We do not know with certainty what the true result is. To understand the meaning of a hypothesis test and the decision table established before carrying out the experiment, we consider the particular case of a sample, which may be radioactive. Only after carrying out the measurement experiment, may the analyst decide if the sample is or is not radioactive. Two correct and two incorrect decisions can be taken as is shown in Table 8.9.

The interpretation of Table 8.9 is the following:

- If the null hypothesis is certain and it is accepted, the decision is correct.
- If the null hypothesis is certain and it is rejected, the decision is incorrect and the error made is Type I. Its probability is represented by α.

TABLE 8.9 Possible consequences of a final decision.

Decisions	Reality	
	H_0 true	H_1 true
Accept H_0	Correct decision	Type II error
Reject H_0	Type I error	Correct decision

- If the alternative hypothesis is certain and it is accepted, the decision is correct.
- If the alternative hypothesis is certain and it is rejected, the decision is incorrect and the error made is Type II. Its probability is represented by β.

Therefore:

$$\alpha = P(\text{Type I error}) = P(\text{reject } H_0 \text{ being certain}) = P(\text{accept } H_1 \text{ when } H_0 \text{ is certain})$$

$$\beta = P(\text{Type II error}) = P(\text{accept } H_0 \text{ being uncertain}) = P(\text{accept } H_0 \text{ when } H_1 \text{ is certain})$$

The power of the test is defined as $1 - \beta$, the probability of rejecting a false null hypothesis:

$$1 - \beta = P(\text{accept } H_1 \text{ when it is certain})$$

Example 8.11. To decide if a sample is radioactive, we accept the following null hypothesis: "H_0:$\mu_s = 0$ (the sample is not radioactive)". (A) What cases can be given? (B) Which is the Type of error? (C) Which is the Type II error? (D) Which error is more dangerous? (E) What do you prefer: α small and β large or α large and β small?

Solution.

a. The following cases can be given:
The activity of the sample is null and the analyst decides that it is not radioactive. The decision is correct.
The activity of the sample is null and the analyst decides that it is radioactive. The decision is incorrect and a Type I error is made.
The sample is radioactive and the analyst decides that the sample has radioactivity. The decision is correct.
The sample is radioactive and the analyst decides that the sample has no radioactivity. The decision is incorrect and a Type II error is made.

b. A Type I error is made when the analyst decides that the sample is radioactive and it is not radioactive.

c. A Type II error is made when the analyst decides that the sample is not radioactive and it is radioactive.

d. In this case, it is more serious to make a Type II error than a Type I error. A Type I error obliges one to take unnecessary precautions with the sample. On the other hand, a Type II error makes us consider the sample as nonradioactive when in fact it is radioactive. That produces a situation with radiation risk.

e. It is preferable to have α large and β small than the reverse.

It is not convenient to make α or β equal to zero. The most advisable is to choose a value for α equal to 0.01 or 0.05; when we examine a situation where H_0 is true, 1% or 5%, respectively, of the times we make incorrect decisions. The selected value for α will be determined by the severity of the circumstances of making an error. We have centered our attention on α, because the objective of hypotheses testing is to test the truth of the statement contained in H_0 and to make a decision related to the rejection of this hypothesis.

The value of α is equal to the area under the curve corresponding to the rejection region. It is usual to nominate α as the significant value or the size of the critical region. Therefore, the level of significance is the probability α of a Type I error. When we say that the results of a study are statistically significant, we indicate that a value α has been chosen and the hypothesis testing leads to the rejection of the null hypothesis.

When we give α, the area of the rejection region for the distribution is known. For one-tail tests the application of α is immediate. In two-tail tests we must take into account that $\alpha/2$ corresponds to each tail, so that the sum of the areas of the two regions is α. When one knows the area of a region of the normal or t distributions, the value of z or t is obtained directly from tables.

Up to here we have chosen a level of significance before solving the problem. This procedure allows one to obtain a decision in a clear and fast way, defining previously a value for α. Another strategy consists of using what is known as the P-value to express the level of significance achieved by the data. The P-value is defined as the probability of obtaining a statistical test more extreme than z^* if H_0 is true; in other words, the P-value $= P(z > |z^*|)$ where $|z^*|$ is the absolute value of z^*.

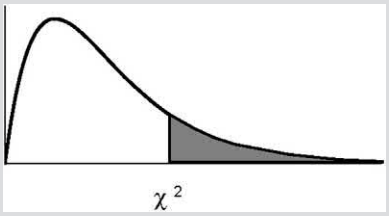
B. Confidence intervals

Interval estimators very probably contain the unknown population parameter. To formalize these statements, it is necessary to express them in terms of probability. Let us suppose that θ is the parameter to be estimated. Let us also suppose that we have extracted a random sample and from the sample information it is possible to find two random variables X_1 and X_2, such that $X_1 < X_2$. If these random variables have the property that $1 - \alpha$ is the probability that X_1 is smaller than θ and that X_2 is larger than θ, we can write

$$P(X_1 < \theta < X_2) = 1 - \alpha \tag{8.70}$$

where α is a number between 0 and 1. Then the interval X_1 and X_2 is an interval estimator of θ at $100(1-\alpha)\%$ of confidence. If we call x_1 and x_2 the realizations of both random variables, the interval x_1 and x_2 is the confidence interval at $100(1-\alpha)\%$ for θ. The quantity $1 - \alpha$ is the level of confidence for the interval. In other words, if we take random samples from the population a large number of times, the parameter θ will be contained in $100(1-\alpha)\%$ of the calculated intervals. Confidence intervals are written as $x_1 < \theta < x_2$.

TABLE 8.10 Chi-square (χ^2)distribution.



	α									
f	0.995	0.99	0.975	0.95	0.90	0.10	0.05	0.025	0.01	0.005
1	_	_	0.001	0.004	0.016	2.706	3.841	5.024	6.635	7.879
2	0.010	0.020	0.050	0.103	0.211	4.605	5.991	7.378	9.210	10.60
3	0.072	0.115	0.216	0.325	0.584	6.251	7.815	9.348	11.34	12.84
4	0.207	0.297	0.484	0.711	1.064	7.779	9.488	11.14	13.28	14.86
5	0.412	0.554	0.831	1.145	1.610	9.236	11.07	12.83	15.09	16.75
6	0.676	0.872	1.237	1.635	2.204	10.64	12.59	14.45	16.81	18.55

C. Statistical inference

1. Variance of a population

A problem that frequently appears in statistics is determining if the standard deviation of a sample corresponds to the standard deviation of a population. If we take random samples of size n from a normal distribution with variance σ^2, we know that the random variable χ^2 allows us to study σ or σ^2 from the probabilities of the curve χ^2.

In radioactivity measurements with pulse counters, it is assumed that a good counter does not perturb measurements and therefore the standard deviation of the total counting is equal to the standard deviation of radioactivity disintegration. To test the reliability of a counter, it is very useful to apply the χ^2 test. It allows one to check if a set of experimental data follows a preset statistical law. More details about the application of the χ^2-test in radioactivity measurements is given by Evans (1982). The χ^2 value is defined by the equation:

$$\chi^2 = \frac{\sum_{i=1}^{n} \left[(\text{observed value})_i - (\text{expected value})\right]^2}{\text{expected value}} \tag{8.71}$$

where n is the total number of independent classifications i in which the data have been grouped. The expected value is computed from Poisson frequency distribution and corresponds to the mean $\mu \approx \bar{x}$. The measured values x_i are the results of the counting; they should be at least 5. The previous expression is now

$$\chi^2 = \frac{\sum_{i=1}^{n} (x_i - \bar{x})^2}{\bar{x}} \tag{8.72}$$

We will compare $\sigma = \sqrt{\bar{x}}$ with $s = \sqrt{\frac{\sum_{i=1}^{n} (x_i - \bar{x})^2}{n-1}}$, where n is the number of measurements. The null hypothesis is:

$$H_0 : \ \sigma = \text{s} \tag{8.73}$$

and the alternative is:

$$H_1 : \sigma \neq \text{s} \tag{8.74}$$

From the alternative hypothesis we conclude that the test is bilateral. Therefore, we will reject the null hypothesis if we obtain (Table 8.10)

$$\chi^2 > \chi^2_{n-1,\alpha/2} \quad \text{or} \quad \chi^2 < \chi^2_{n-1,1-\alpha/2} \tag{8.75}$$

Example 8.12. A radioactive sample was measured with a Geiger counter 6 times. The duration of each measurement was 5 min. Check if the counter works well taking the measurements from Table 8.11.

TABLE 8.11 Counts of a radioactivity sample.

Measure	Counts	Δ	Δ^2
1	214	−10	100
2	222	−2	4
3	217	−7	49
4	210	−14	196
5	243	19	361
6	238	14	196

Solution. The average value of the number of counts accumulated in 5 minutes is:

$$\overline{x} = \frac{\sum_{i=1}^{6} x_i}{n} = \frac{1344}{6} = 224$$

The distribution standard deviation is:

$$\sigma = \sqrt{\overline{x}} = \sqrt{224} = 15.0$$

The observed standard deviation is:

$$s = \sqrt{\frac{\sum_{i=1}^{n} (x_i - \overline{x})^2}{n-1}} = \sqrt{\frac{906}{5}} = 13.5$$

The null hypothesis is:

$$H_0 : \sigma = s$$

The alternative hypothesis is:

$$H_1 : \sigma \neq s$$

The rejection region is obtained from Table 8.10 for $f = n-1 = 5$ and $\alpha = 0.05$. The critical values are $\chi^2_{5,0.025} = 12.83$ and $\chi^2_{5,0.975} = 0.831$. From the experimental data we have

$$\chi^2 = \frac{\sum_{i=1}^{n} (x_i - \overline{x})^2}{\overline{x}} = \frac{906}{224} = 4.04$$

The rejection region is $\chi^2 > 12.83$ and $\chi^2 < 0.831$. As χ^2 is outside the rejection region we do not reject the null hypothesis and we conclude that the counter works correctly. Other examples for the application of the χ^2-test to counters with anomalies are available from Grau Carles and Grau Malonda (2000).

Example 8.13. Ten measurements of 1-second duration were made with a counter with a resolution time of 250 μs. Analyze the results of the measures presented in Table 8.12.

Solution. The mean value is:

$$\overline{X} = \frac{\sum_{i=1}^{10} x_i}{10} = \frac{13278}{10} = 1327.8$$

The theoretical standard deviation is:

$$s_t = \sqrt{\overline{X}} = \sqrt{1327.8} = 36.4$$

The experimental standard deviation is:

$$s_{ex} = \sqrt{\frac{\sum_{i=1}^{10} (x_i - \overline{X})^2}{9}} = \sqrt{\frac{3376.3}{9}} = 19.4$$

It seems that the standard deviations are quite different. Apply the χ^2 test.

$$\chi^2_{ex} = \frac{\sum_{i=1}^{10} (x_i - \overline{X})^2}{\overline{X}} = \frac{3376.3}{1327.8} = 2.45$$

The values of $\chi^2_{9,0.025} = 19.02$ and $\chi^2_{9,0.975} = 2.70$ obtained from Table 8.10 enable us to determine that:

$$\chi^2_{ex} < \chi^2_{9,0.975}$$

Therefore, we reject the null hypothesis of equality of the standard deviations, and we can conclude that the experimental results do not follow Poisson's law. Considering that the counting rate is very high, some counts will have been lost due to the counter resolution time. The number of actual counts N_R, which the counter should have recorded had its resolution time been zero, can be calculated from counting rate N and resolution time τ by applying this expression:

$$N_R = \frac{N}{1 - N\tau} = \frac{N}{1 - (N \times 250 \times 10^{-6})}$$

Applying this formula to each of the measures in Table 8.12, we obtain Table 8.13 below:

The mean of the corrected count values listed in Table 8.13 is:

$$\overline{X} = \frac{\sum_{i=1}^{10} x_i}{10} = \frac{19877}{10} = 1987.7$$

The theoretical standard deviation is:

$$s_t = \sqrt{\overline{X}} = \sqrt{1987.7} = 44.6$$

TABLE 8.12 Ten measurements of 1-second duration.

Measure	Counts	Measure	Counts
1	1312	6	1337
2	1351	7	1306
3	1310	8	1297
4	1337	9	1346
5	1341	10	1341

TABLE 8.13 Number of actual counts.

Measure	Counts (N_R)	Measure	Counts (N_R)
1	1952	6	2008
2	2040	7	1939
3	1948	8	1919
4	2008	9	2029
5	2017	10	2017

TABLE 8.14 Measurements with a Geiger counter.

Measure	Counts	Measure	Counts
1	445	6	433
2	522	7	415
3	440	8	512
4	494	9	520
5	502	10	464

The experimental standard deviation is:

$$s_{ex} = \frac{1}{3}\sqrt{\sum_{i=1}^{10}\left(x_i - \overline{X}\right)^2} = \frac{1}{3}\sqrt{16921.04} = 43.4$$

Both standard deviations are quite close. We apply the χ^2 test to the experimental data:

$$\chi^2_{ex} = \frac{\sum_{i=1}^{10}\left(x_i - \overline{X}\right)^2}{\overline{X}} = \frac{16921.04}{1987.7} = 8.51$$

The values of $\chi^2_{9,0.025} = 19.023$ and $\chi^2_{9,0.975} = 2.700$, obtained from Table 8.10, enable us to write:

$$\chi^2_{ex} > \chi^2_{9,0.975} \text{ and } \chi^2_{ex} < \chi^2_{9,0.025}$$

and we conclude that the variances are equal and that the values of the corrected counts are correct.

Example 8.14. A radioactive sample has been measured with a Geiger counter, and the results obtained are shown in Table 8.14. Study the reliability of the results.

Solution. The mean value is:

$$\overline{X} = \frac{\sum_{i=1}^{10} x_i}{10} = \frac{4747}{10} = 474.7$$

The theoretical standard deviation is:

$$s_t = \sqrt{\overline{X}} = \sqrt{474.7} = 21.8$$

The experimental standard deviation is:

$$s_{ex} = \sqrt{\frac{\sum_{i=1}^{10}\left(x_i - \overline{X}\right)^2}{9}} = \sqrt{\frac{14301.98}{9}} = 39.9$$

The value of χ^2 is:

$$\chi^2_{ex} = \frac{\sum_{i=1}^{10}\left(x_i - \overline{X}\right)^2}{\overline{X}} = \frac{14301.98}{474.7} = 30.13$$

The critical value, obtained from Table 8.10, is $\chi^2_{9,0.025} = 19.023$, and as:

$$\chi^2_{ex} > \chi^2_{9,0.025}$$

TABLE 8.15 Nine measures of the total counts of a sample to study the reliability of the measures.

Measure	Counts	Measure	Counts
1	564	6	561
2	586	7	556
3	563	8	583
4	578	9	665
5	580		

we reject the null hypothesis that the standard deviations are equal. The counts do not follow Poisson's law. When the measures were studied, it was found that a good number of random parasitic pulses from the electric network arrived to the counter.

Example 8.15. We carried out 9 measures of 8 seconds duration and the counts obtained are listed in Table 8.15.

Study the reliability of the measures.

Solution. The mean value is:

$$\overline{X} = \frac{\sum_{i=1}^{9} x_i}{9} = \frac{5118}{9} = 568.67$$

The theoretical standard deviation is:

$$s_t = \sqrt{\overline{X}} = \sqrt{568.67} = 23.8$$

Both standard deviations are quite different. We apply the χ^2 test to the experimental data:

$$\chi^2_{ex} = \frac{\sum_{i=1}^{9}\left(x_i - \overline{X}\right)^2}{\overline{X}} = \frac{971.98}{568.67} = 1.71$$

The values of $\chi^2_{8,0.025} = 17.53$ and $\chi^2_{8,0.975} = 2.18$, obtained from Table 8.10, enable us to write:

$$\chi^2_{ex} > \chi^2_{8,0.975} \text{ and } \chi^2_{ex} < \chi^2_{9,0.025}$$

We reject the null hypothesis of equality of the typical deviations and we conclude that the variances are different. Studying the conditions of the measurement, it was observed that the counting device had a switch which allowed counting pulses from the electric network in one position or the counts detected by the detector in the other position. Due to a fault in the switch, the electric network cycles and the detected pulses were being measured at the same time. As the measurement time was 8 seconds, the number of pulses due to the network in each measurement was 400; therefore, this amount was subtracted from each of the measurements in Table 8.15 and we obtained the following Table 8.16:

The mean value is:

$$\overline{X} = \frac{\sum_{i=1}^{9} x_i}{9} = \frac{1536}{9} = 170.67$$

TABLE 8.16 Corrected counts of the nine measures listed in Table 8.15.

Measure	Counts	Measure	Counts
1	164	6	161
2	186	7	156
3	163	8	183
4	178	9	165
5	180		

The theoretical standard deviation is:

$$s_t = \sqrt{\overline{X}} = \sqrt{170.67} = 13.1$$

The experimental standard deviation is:

$$s_{ex} = \sqrt{\frac{\sum_{i=1}^{9}\left(x_i - \overline{X}\right)^2}{8}} = \sqrt{\frac{971.98}{8}} = 11.0$$

The value of χ^2_{ex} is:

$$\chi^2_{ex} = \frac{\sum_{i=1}^{9}\left(x_i - \overline{X}\right)^2}{\overline{X}} = \frac{971.98}{170.67} = 5.70$$

Both standard deviations are quite different. We apply the χ^2 test to the experimental data:

$$\chi^2_{ex} = \frac{\sum_{i=1}^{9}\left(x_i - \overline{X}\right)^2}{\overline{X}} = \frac{16921.04}{1987.7} = 8.51$$

The values $\chi^2_{8,0.025} = 17.535$ and $\chi^2_{8,0.975} = 2.180$ allow us to write:

$$\chi^2_{ex} > \chi^2_{8,0.975} \text{ and } \chi^2_{ex} < \chi^2_{9,0.025}$$

Thus, we accepted the null hypothesis that both standard deviations are equal. Therefore, the results of the measures are now acceptable from a statistical perspective.

2. Variance of two populations

Comparing variances requires the introduction of a new statistical test, the **F ratio**. Two population variances are compared by forming a ratio of their corresponding sample variance. The null hypothesis is $H_0 : \sigma_1^2 = \sigma_2^2$ and the statistical test is

$$F = \frac{s_1^2}{s_2^2} \tag{8.76}$$

The F-statistics is described by the F-distribution depending on the degrees of freedom. Now we have two samples and one degree of freedom for each sample: $f_1 = n_1 - 1$ is the degree of freedom for the numerator and $f_2 = n_2 - 1$ for the denominator. We write these as

$$f = (n_1 - 1,\ \ n_2 - 1) \tag{8.77}$$

Since s_1^2 and s_2^2 can never be negative, the F curves start at 0 and are skewed to the right as shown in Table 8.17. The total area under the curve is equal to 1.

The null hypothesis does not establish an order for σ_1^2 and σ_2^2. When we write $\sigma_1^2 = \sigma_2^2$, we could also write $\sigma_2^2 = \sigma_1^2$. It does not matter which sample variance goes in the numerator of F. When $H_0 : \sigma_1^2 = \sigma_2^2$ is true, under ideal circumstances, $F = s_1^2/s_2^2 = 1$. Thus, to carry out a hypothesis test we must see how far the computed values of F deviate from 1.

If we observe the sketch of Table 8.17, we can appreciate that this table gives critical values larger than 1 for the right-hand tail. This decision simplifies our work but it forces us to compromise such that the larger values of s must be in the numerator. If we accept this criterion, we can ignore the F values on the left-hand tail.

Let us examine in detail Table 8.17 corresponding to $\alpha = 0.025$. The rows of the table indicate the number of degrees of freedom of the denominator and the columns the number of degrees of freedom of the numerator. The critical value is in the intersection of the appropriate row and column. When the value of the degrees of freedom is not explicitly in the table the following approach must be followed: 1) choose the next degree of freedom, 2) if the degree of freedom in the table is halfway with that of the sample, the largest critical value will be taken.

Example 8.16. In example 8.6 the internal ($S_{in} = 0.0098$) and external ($S_{ex} = 0.0068$) uncertainties were obtained. Find if these uncertainties are different at the 95% level of confidence.

Solution. We assume that there is not any difference between the variances:

$$H_0 : S_{in}^2 = S_{ex}^2$$

The alternative hypothesis indicates that the variances are different

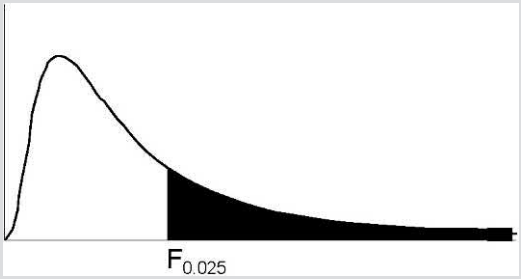
$$H_1 : S_{in}^2 \neq S_{ex}^2$$

This alternative hypothesis indicates the contrast is bilateral with $\alpha = 0.05$. The degrees of freedom are $f_{in} = f_{ex} = n - 1 = 4$. From Table 8.17 we obtain the critical value $F_{\alpha/2} = F_{0.025} = 9.60$. The rejection region is then $F_{0.025} > 9.60$. The computed value for $F^*_{0.025}$ is:

$$F^*_{0.025} = \frac{S_{in}^2}{S_{ex}^2} = \frac{0.0098^2}{0.0068^2} = 2.08$$

As the computed value is less than the critical one $\left(F^*_{0.025} < F_{0.025}\right)$, the null hypothesis cannot be rejected.

TABLE 8.17 F distribution.



	f. numerator								
f.deno.	1	2	3	4	5	6	7	8	9
1	647.79	799.50	864.16	899.58	921.85	937.11	948.22	956.66	963.28
2	38.51	39.00	39.17	39.25	39.30	39.33	39.36	39.37	39.39
3	17.44	16.04	15.44	15.10	14.89	14.74	14.62	14.54	14.47
4	12.22	10.65	9.98	9.60	9.36	9.20	9.07	8.98	8.90
5	10.00	8.43	7.76	7.39	7.15	6.98	6.85	6.76	6.68
6	8.81	7.26	6.60	6.23	5.99	5.82	5.70	5.60	5.52
7	8.07	6.54	5.89	5.52	5.29	5.12	4.99	4.90	4.82
8	7.57	6.06	5.42	5.05	4.82	4.65	4.53	4.43	4.36
9	7.21	5.71	5.08	4.72	4.48	4.32	4.20	4.10	4.03
10	6.94	5.46	4.83	4.47	4.24	4.07	3.95	3.85	3.78

Therefore, we conclude that there is no reason to think that S_{ex} and S_{in} are different.

V. Regression

The problems analyzed so far were characterized to have one or two independent random variables. In this section, we consider the case of two or more random variables related to each other. The form of the relationship may be highly varied and unknown, but, in many cases it is possible to guess, with good justification, a linear relationship. In other words, we consider two random variables X and Y, and we assume that the observations tend to be grouped in a straight line. In this case, we say that a linear relationship exists between the two random variables. Once a relationship has been established, we must obtain the function relating the random variables by means of a regression.

A. Linear regression

The degree of association between two random variables is obtained by applying the correlation between them. This correlation is symmetrical since it is indifferent to the correlation between X and Y or between Y and X. In this section we study the effect on the random variable Y when the random variable X takes a specific value. We limit our analysis to the simplest mathematical structure relating X and Y: the linear relationship. Variations of the problem of fitting a function to a set of data: curvilinear relationships, weighted least squares, nonlinear squares, etc., are analyzed by Draper and Smith (1998). Since we are working with random variables, over time for each value of X a distribution of Y values is obtained; therefore, we will use the concept of conditional distribution. An essential characteristic of this distribution is the mean or the expected value. We denote the expected value of the random variable Y with $E[Y|X = x]$, when the random variable X takes the specific value x. Our assumption of linearity implies that the conditional expected value has a linear dependence on x,

$$E[Y|X = x] = \alpha + \beta x \tag{8.78}$$

where α and β determine the correct line. The interpretation of each one of these constants is immediate. When $x = 0$ we have

$$E[Y|X = 0] = \alpha \tag{8.79}$$

where α is the expected value for the dependent variable Y when the independent variable X takes the value 0.

Let us suppose now that X is increased by 1 unit so that x becomes $x + 1$, then

$$E[Y|X = x+1] = \alpha + \beta\ (x+1) \tag{8.80}$$

and

$$\begin{aligned} E[Y|X = x+1] - E[Y|X = x] \\ = \alpha + \beta(x+1) - (\alpha + \beta x) = \beta \end{aligned} \tag{8.81}$$

Therefore, β, the slope of the line, is the expected increase in Y when X increases by unit.

In fact, the equations given previously are not verified exactly. Let us suppose that the independent variable takes the value x_i. If we represent by Y_i the corresponding value of the dependent random variable, the expected value is

$$E[Y_i|X = x_i] = \alpha + \beta\ x_i \tag{8.82}$$

But, in practice, the value of Y_i will deviate from the expected value. If the difference between the observed and the expected value is denoted by ε_i, we can write

$$\varepsilon_i = Y_i - E[Y_i|X = x_i] = Y_i - (\alpha + \beta\ x_i) \tag{8.83}$$

so that

$$Y_i = \alpha + \beta x_i + \varepsilon_i \tag{8.84}$$

where the random variable ε_i has a mean of 0. The last equation is known as the **population regression line** of data (x_i, Y_i).

We have just described the regression model illustrated in Fig. 8.2. For each possible value of the independent variable, the value of the dependent variable may be represented by means of a random variable whose mean is on the regression line. The regression line is drawn through the means of the distributions. For a value of x_i, the independent variable, the deviation of the dependent variable Y_i from the regression line is the error term ε_i.

The regression line is an interesting theoretical construction but, in practice, as we always work with samples of observations, we will never be able to obtain this one exactly. Instead of α and β we obtain their estimators: the number a and b The estimated line has as equation

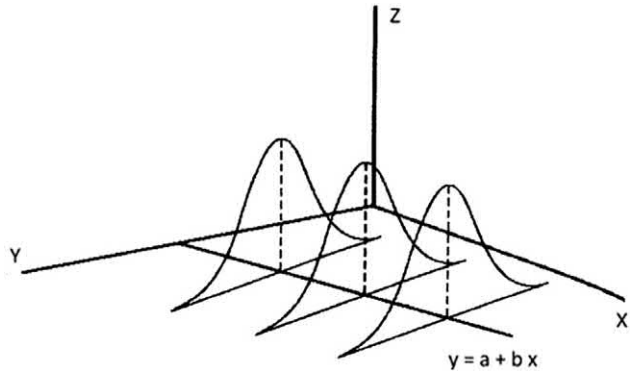


FIGURE 8.2 Probability density functions of the dependent variable for given values of x.

$$y = a + bx \tag{8.85}$$

Let us suppose that we have a sample of n pairs of observations (x_1, y_1), (x_2, y_2), …,(x_n, y_n). We are interested in obtaining the line that best fits to those data. We know that the value x_i produces the value y_i obtained from equation $a + bx_i$, but the exact value for the dependent variable is y_i. The difference between the two is

$$e_i = y_i - (a + bx_i) \tag{8.86}$$

The values of e_i may be positive or negative. If we want to give the same weight to the positive and negative values of the same quantity, a possibility is to work with the square of e_i. The sum of squared differences from the point to the line is

$$SQ = \sum_{i=1}^{n} e_i^2 = \sum_{i=1}^{n} (y_i - a - bx_i)^2 \tag{8.87}$$

The least squares method allows one to estimate the line of a population regression for which the sum of the squares is a minimum. The parameter b can be obtained from the equation

$$b = \frac{\sum_{i=1}^{n} x_i y_i - n\overline{xy}}{\sum_{i=1}^{n} x_i^2 - n\overline{x}^2} \tag{8.88}$$

and a with the equation

$$a = \overline{y} - b\overline{x} = \frac{\overline{y}\sum_{i=1}^{n} x_i^2 - \overline{x}\sum_{i=1}^{n} x_i y_i}{\sum_{i=1}^{n} x_i^2 - n\overline{x}^2} \tag{8.89}$$

where $\overline{x}$ and $\overline{y}$ are the respective means of the sample. The line

$$y = a + bx \tag{8.90}$$

is the **sample regression** line of Y on X.

The least squares method is a good procedure to estimate the regression line for the population. This procedure is the most appropriate when the regression line for the population

$$Y_i = \alpha + \beta\ x_i + \varepsilon_i \tag{8.91}$$

is required. This must fulfill the following conditions:

- Each value of x_i is a fixed number. That is equivalent to saying that the realization of a random variable X_i is independent of the error term ε_i.
- Errors are random variables with an expected value equal to zero:

$$E[\varepsilon_i] = 0\ \ (i = 1, 2, ..., n) \tag{8.92}$$

- All the random variables ε_i have the same variance σ_ε^2:

$$E\left[\varepsilon_i^2\right] = \sigma_\varepsilon^2 \quad (i = 1, 2, ..., n) \tag{8.93}$$

- The random variables ε_i are not correlated:

$$E[\varepsilon_i \varepsilon_j] = 0 \text{ for all } i \neq j \tag{8.94}$$

Bacon (1953) describes the least squares method of fitting a line for different conditions and analyzes the goodness of fitting results from different experiments.

1. Confidence intervals and hypothesis testing

We will analyze the problems of interval construction and the hypothesis testing for the regression parameters of a population. Suppose that the regression line is

$$Y_i = \alpha + \beta x_i + \varepsilon_i \tag{8.95}$$

and the conditions of the previous section are fulfilled. If σ_ε^2 is the common variance for the error terms ε_i, an unbiased estimator of σ_ε^2 is

$$s_e^2 = \frac{\sum_{i=1}^{n} e_i^2}{n-2} \tag{8.96}$$

where e_i are the residuals of the least squares. These residuals substitute the error terms ε_i, which are unknown. We divide by $n-2$, because we lose two degrees of freedom when estimating the parameters α and β.

If we designate with b the least squares estimate of the slope of the population regression line, the estimator of β is unbiased and the variance is

$$\sigma_b^2 = \frac{\sigma_\varepsilon^2}{\sum_{i=1}^{n} (x_i - \bar{x})^2} = \frac{\sigma_\varepsilon^2}{\sum_{i=1}^{n} x_i^2 - n\bar{x}^2} \tag{8.97}$$

An unbiased estimator of σ_b^2 is provided by

$$s_b^2 = \frac{s_\varepsilon^2}{\sum_{i=1}^{n} (x_i - \bar{x})^2} = \frac{s_e^2}{\sum_{i=1}^{n} x_i^2 - n\bar{x}^2} \tag{8.98}$$

In both cases, we assume that the conditions of the previous section are fulfilled.

Although the slope is the most interesting parameter, we give also the equation to compute the estimator of the variance of the ordinate on the origin. We substitute β, b and s_b^2 for α, a and s_a^2 to have

$$s_a^2 = s_e^2 \left(\frac{1}{n} + \frac{\bar{x}^2}{\sum_{i=1}^{n} x_i^2 - n\bar{x}^2} \right) \tag{8.99}$$

VI. Detection limits

Radioactivity measurements are characterized by a variable zero level due to background. This situation obliges one to work with detection and determination limits when the radioactivity of the source is very low.

In this section we analyze the problem of obtaining the detection limits for very low radioactivity measurements. A complete discussion of the detection limits, in a measurement process, requires the introduction of two specific levels: (i) a **decision limit** that allows one to deduce whether the result of the analysis indicates that the sample is or is not radioactive and (ii) a **detection limit** that indicates if an analytical process leads to a quantitative detection. The relationships between these limits and the equations to compute them are also given.

In a general way, two types of devices are considered: counters, characterized to accumulate the information in one channel; and spectrometers, where information is distributed in numerous channels. In the latter case, we distinguish between high-resolution detectors, such as Ge, and low-resolution detectors, such as NaI(Tl).

A. Critical levels

We will distinguish two fundamental problems in the measurement of very low radioactivity sources: i) given an observed net signal, S, to decide whether a real signal has been detected or, in other words, to decide whether the sample is indeed radioactive. ii) Is $\mu_S > 0$? This question can be addressed by the statistical theory of hypothesis testing, in which one first formulates a test hypothesis. In our case, the null hypothesis H_0 for μ_S is $\mu_S = 0$. This hypothesis and the alternative hypothesis H_1 $(\mu_S > 0)$ are mutually exclusive. Together they cover all possible values of μ_S. As a consequence of the intrinsic statistical variation in the counting rates, we can arrive at one of the following two types of judgment errors: i) The error of the first kind or Type I error states that true activity is greater than zero when, in fact, it is zero or ii) The error of the second kind or Type II error states that the true activity is zero when, in fact, it is greater than zero. The probability of making a Type I error is denoted by α and depends on the test procedure. The maximum value of α and the standard deviation of the net signal σ_0, when $\mu_S = 0$, allows one to establish the critical level L_C. An observed signal, S, must exceed L_C to yield the decision "detected". The probability distribution of possible outcomes, when the true net signal is zero, intersects L_C such that the factor $1 - \alpha$ corresponds to the correct decision "nondetected". Whereas the probability of making a Type II error, denoted by β, also depends on the size of the measured quantity, in the case of radioactive measurements it depends on the amount of radioactivity of the tested material. The most relevant papers

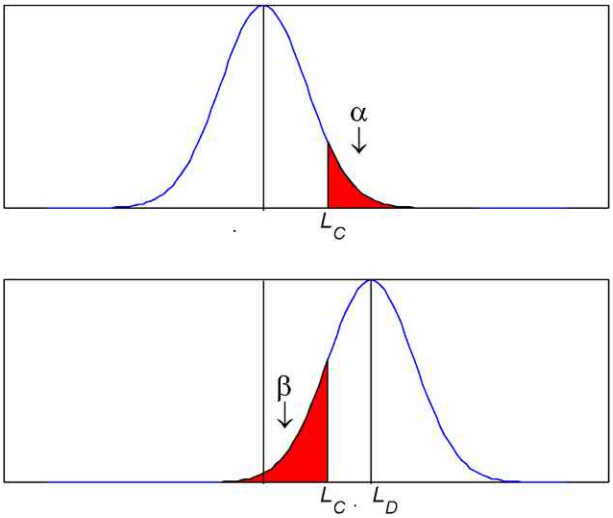


FIGURE 8.3 Type I and II errors.

about low-level detection limits are Altshuler and Pasternack (1963), Currie (1968), (1995), and Donn and Walke (1977).

When the critical level L_C has been established, an a priori detection limit L_D may be established by specifying L_C, the acceptable level β, for a Type II error and the standard deviation σ_D, characterizing the probability distribution of the net signal when its true value μ_S is equal to L_D. Fig. 8.3 shows the Type I and II error curves and the critical levels L_C and L_D. The mean μ_S may be between zero and L_D. When μ_S is between 0 and L_C, we agree that there is no radiation from the sample. When μ_S is between L_C and L_D, there may be radioactivity, but when $\mu_S = L_D$ the Type II error is minimum. Therefore, for $L_C < \mu_S < L_D$ although we can have detection, such detection cannot be considered reliable given that the Type II error is not a minimum.

The critical level L_C is given by

$$L_C = k_\alpha \sigma_0 \tag{8.100}$$

and the detection limit by

$$L_D = L_C + k_\beta \sigma_D \tag{8.101}$$

where $k_\alpha \equiv z_\alpha$ and $k_\beta \equiv z_\beta$ are the $k \equiv z$ scores of the standardized normal distribution corresponding to probability levels $1 - \alpha$ and $1 - \beta$, respectively.

When we analyze the pulses due to radioactivity emission, we can assume that the distributions of background and background + source follow the Poisson distribution. When the count number is sufficiently large, the distributions are approximately normal. Under such circumstances, the variance of the net counting is given by

$$\sigma^2 = \sigma_{S+B}^2 + \sigma_B^2 = \mu_S + \mu_B + \frac{\mu_B}{n} \tag{8.102}$$

where σ_B is obtained from n measurements without the source. Note than σ depends on the signal level.

If σ_0^2 is the variance when $\mu_S = 0$, and σ_D^2 is the variance for $\mu_S = L_D$, we have

$$L_C = k_\alpha \sigma_0 = k_\alpha \left(\mu_B + \sigma_0^2\right)^{1/2} \tag{8.103}$$

and

$$\sigma_D^2 = \sigma_{S+B}^2 + \sigma_B^2 = \mu_S + \mu_B + \sigma_0^2 = L_D + \sigma_0^2 \tag{8.104}$$

From Eq. (8.101) we get

$$L_D = L_C + k_\beta \left(L_D + \sigma_0^2\right)^{1/2} \tag{8.105}$$

Solving Eqs. (8.102) and (8.104) we obtain

$$L_D = L_C + \frac{k_\beta^2}{2}\left\{1 + \left[1 + \frac{4L_C}{k_\beta^2} + \frac{4L_C^2}{k_\alpha^2 k_\beta^2}\right]^{1/2}\right\} \tag{8.106}$$

The mean value and the standard deviation without the source allows one to compute L_C and L_D for selected values of α and β by means of Eqs. (8.102) and (8.105). If $k_\alpha = k_\beta = k$, we obtain a considerable simplification of Eq. (8.101), which is reduced to the form

$$L_D = k^2 + 2L_C \tag{8.107}$$

Example 8.17. Background and a source-plus-background are measured and the counting rates obtained are $C_B = 203$ counts/h and $C_{B+S} = 235$ counts/h. Previously, the background was measured for 200 h, accumulating a total of 40000 counts (counting rate $B = 200$ counts/h). Compute the values of L_C and L_D when $\alpha = 0.025$ and $\beta = 0.050$, in the following two cases: (a) when we know that the background does not change and we can use the value of B, and (b) when we cannot apply B, because the background changes.

Solution. The values $k_\alpha = 1.96$ when $\alpha = 0.025$ and $k_\beta = 1.645$ when $\beta = 0.050$ are obtained from Table 8.2 as follows: Given that $k_\alpha = z_{1-\alpha} = 0.975$, the value considered in Table 8.2 is 0.975−0.5 = 0.475. This value corresponds to row 1.9 and column 0.06, thus $k_\alpha = 1.96$. In the same way, $k_\beta = z_{1-\beta} = 0.95$ and the value to be carried to Table 8.2 is 0.95−0.5 = 0.45, this value is not included in the table; however, it is between 0.4495 and 0.4505, at row 1.6 and columns 0.04 and 0.05 (mean 0.045). Therefore, $k_\beta = 1.645$.

The background counting rate is $C_B = 203$ counts/h. As the expected background counting rate is $B = 200$ counts/h, it seems that the background has not changed. The net counting rate is

$$C_S = C_{B+S} - B = 235 - 200 = 35 \text{ counts/h}$$

and the critical counting rate is

$$L_C = k_\alpha\sqrt{\mu_B + \sigma_B^2} \approx k_\alpha\sqrt{B} = 1.96 \times \sqrt{200} = 27.7 \text{ counts/h}$$

Since 35 is greater than 27.7 our decision is that there is activity in the sample. The minimum significant measured counting rate is 27.7 counts/h.

The minimum detectable counting rate from Eq. (8.106) is

$$L_D = L_C + \frac{k_\beta^2}{2}\left\{1 + \left[1 + \frac{4L_C}{k_\beta^2} + \frac{4L_C^2}{k_\alpha^2 k_\beta^2}\right]^{1/2}\right\}$$

$$= 27.7 + \frac{1.645^2}{2}\left\{1 + \left[1 + \frac{4 \times 27.7}{1.645^2} + \frac{4 \times 27.7^2}{1.96^2 \times 1.645^2}\right]^{1/2}\right\}$$

$$= 52.5 \text{ counts/h}$$

and applying the approximate equation

$$L_D = (k_\alpha + k_\beta)\sqrt{B} = (1.96 + 1.645)\sqrt{200} = 51.0 \text{ counts/h}$$

When the background changes we cannot use the mean number B. The net counting rate is obtained applying the following expression

$$C_S = C_{S+B} - C_B = 235 - 203 = 32 \text{ counts/h}$$

and

$$L_C = k_\alpha\sqrt{\mu_B + \sigma_B^2} = k_\alpha\sqrt{\mu_B + \mu_B}.$$

$$= k_\alpha\sqrt{2\mu_B} \approx k_\alpha\sqrt{2C_B} = 1.96\sqrt{2 \times 203}$$

$$= 39.49 \text{ counts/h}.$$

Since the net counting rate is less than the critical net counting rate, our conclusion is that there is no significant radioactivity in the sample. The minimum detectable counting rate is

$$L_D = L_C + \frac{k_\beta^2}{2}\left\{1 + \left[1 + \frac{4L_C}{k_\beta^2} + \frac{4L_C^2}{k_\alpha^2 k_\beta^2}\right]^{1/2}\right\}$$

$$= 39.49 + \frac{1.645^2}{2}\left\{1 + \left[1 + \frac{4 \times 39.49}{1.645^2} + \frac{4 \times 39.49^2}{1.96^2 \times 1.645^2}\right]^{1/2}\right\}$$

$$= 75.6 \text{ counts/h}$$

and applying the approximate equation

$$L_D = (k_\alpha + k_\beta)\sqrt{2C_B} = (1.96 + 1.645)\sqrt{2 \times 203} = 72.6 \text{ counts/h}$$

B. Gamma Spectra

Ge detectors allow the experimental spectroscopists to obtain gamma- and X-ray spectra with high resolution compared with that obtained with NaI(Tl) detectors. This excellent resolution facilitates the qualitative and quantitative analysis of radionuclide mixtures for high and medium activities. However, for low-level samples the low efficiency and the similarity of the small peaks to the fluctuations of the background can make the discrimination between true and false peaks difficult.

Since NaI(Tl) detectors have a larger volume and lower resolution than Ge detectors, the detection of low activity peaks is different for each detector. Each one of the Ge peaks can be analyzed taking the two independent constituent parts: the peak and the Compton contribution. On the other hand, the NaI(Tl) peaks force us to consider the overlap contribution of the different spectral components in each of the peaks.

In this section, we analyze the determination and detection limits for Ge detectors. Based upon the acceptable risk of committing a Type I error, a minimum significant measured area for a peak is defined and for a Type II error, a minimum detectable true area is introduced. The study of complete response of the NaI(Tl) detector is carried out taking into account the contribution of the different spectral components.

1. High-resolution gamma spectra

In an experimental Ge gamma spectrum, the minimum detectable area of a peak is the minimum number of photopeak counts that make it detectable. The value of this minimum depends on the spectral background under the peak, but the background usually does not coincide with the detector background. The minimum is predetermined by the statistical risk of including an observed peak when it is not a real peak or concluding that a real peak is not present when it is really there.

The procedures to discern between real and false peaks are based on the assumption that real peaks show a Gaussian shape. This procedure gives good results when the peaks are sufficiently defined and the Gaussian hypothesis is valid; however, when the peaks are small, they can be taken as statistical fluctuations with Gaussian appearance. Therefore, a computational procedure dedicated to determining very small peaks must be able to detect false peaks.

There is a probability that a false peak is accepted as a true peak. This is called a Type I error. Based upon the acceptable risk of committing a Type I error, we define a **minimum significant measured area**. It is assumed that all the peaks in the spectrum whose measured areas are smaller than this limit are discarded and considered as false

peaks. This is the Type II error. Consequently, we can define a minimum detectable real peak area such that if the actual photopeak area is at least this large, the risks of committing Type I or Type II errors are less than some preselected values.

An application of this analysis consists of determining the minimum time required to be sure that the risk of making a Type I or II error does not exceed acceptable values. This allows one to predict the time required to assure the detection of small peaks.

a. False peaks distribution

Following Head (1972), to know the distribution of false peaks, it is necessary to carry out an experiment and have a peak identification computer program. In essence, the experiment consists of preparing "background" spectra with an average measure of 50 to 50,000 counts/channel. For the purpose of the experiment, the background in the energy range of 80−500 keV can be simulated by the Compton tails of the two ^{60}Co gamma lines, in order to determine false peaks. By means of another gamma source with peaks in the range given above we can produce the real peaks. ^{133}Ba can be used to generate real peaks. The objective is clear: The ^{60}Co Compton distribution produces the "background" and ^{133}Ba gives the true peaks for each background. For a certain background level and several resolution values (1.0, 1.5, 2.0, 2.5, and 3.0 channels, for a real resolution of 1.5 channels) we obtain the number of false and acceptable peaks. From the different analyzed backgrounds, we obtain the curves shown in Fig. 8.4, where the average area of the false peaks detected $\overline{A}$ and the widths $\sigma_{\overline{A}}$ of these areas as a function of the background B under the peak areas (due to the Compton tails of ^{60}Co gamma lines) are represented.

b. Minimum significant area

The probability of committing a Type I error or of concluding that a peak corresponds to a gamma ray, when in fact it is a false peak, depends upon the peak selection procedure and upon the level of the background under the peak. A minimum significant measured area A_I can be defined by the expression

$$\alpha = P\{\text{Measured area of a false peak} \geq A_I\} \tag{8.108}$$

A peak whose area is equal or larger than A_I is retained and all peaks whose area is less than A_I are rejected. If we do not have any additional information about the peak, the probability that it is false is α or in other words, the risk of accepting a false peak as true is α.

If we assume that the false peak area distribution is normal, the minimum significant area for committing a Type I error, for a given risk, is given by the equation

$$A_I = \overline{A} + z_\alpha \sigma_{\overline{A}} \tag{8.109}$$

where z_α is related to α by the equation

$$\alpha = \int_{z_\alpha}^{\infty} \frac{1}{\sqrt{2\pi}} \exp\left(u^2/2\right) \mathrm{d}u \tag{8.110}$$

$\overline{A}$ and $\sigma_{\overline{A}}$ may be obtained by interpolation in Fig. 8.4 for a given background B, the value of the minimum significant area $\overline{A}_I$, for a risk α, may be computed from Eq. (8.109).

c. Minimum detectable area

Assume that we have obtained A_T counts in the photopeak of a given gamma ray. When we compute the area by means of a fitting program, the fitted area A_F will seldom be equal to A_T. Due to statistical fluctuations, the measured area for a peak will usually be distributed about the real area $\left(\overline{A}_F = A_T\right)$ with a width σ_F. As we have seen in the last section, all peaks with mean areas lower than A_I will be discarded as not significant. A Type II error is committed when a real peak $A_T \geq A_I$, due to the spread in the fitted area, gives $A_F < A_I$ and consequently the peak is discarded.

The probability of committing a Type II error depends upon the value of A_I and the fitted area A_F. We define the minimum detectable area A_{II} as

$$\beta = P\{\text{Fitted area } A_F < A_I, \text{when the true area is } A_T = A_{II}\} \tag{8.111}$$

As the fitted area is normally distributed with variance σ_F^2 we have

$$A_{II} = A_I + k_\beta \sigma_F \tag{8.112}$$

where the relationship between β and k_β is the same as that between α and k_α. In this case, σ_F^2 is the variance of the fitted area distribution when $\overline{A}_F = A_T = A_{II}$.

We introduce a hypothesis that allows us to solve the problem with the data we have. We suppose that the variance of the fitted area distribution is similar to the variance of the false peak area distribution $\left(\sigma_F^2 \approx \sigma_{A_{II}}^2\right)$. As A_{II} is

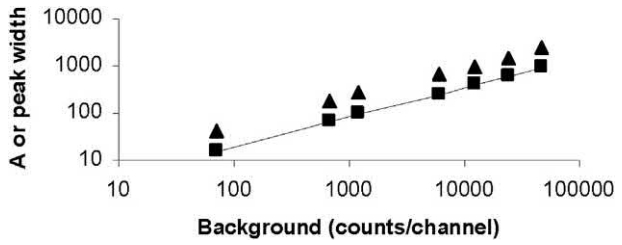


FIGURE 8.4 Average of the peak count area (triangles) and width of the peaks (squares) as a function of background. *From Head (1972); reprinted with permission of Elsevier Science.*

very close to A_I, we assume that $\sigma_F^2 \approx \sigma_{A_{II}}^2 \approx \sigma_{A_I}^2 \approx \sigma_{\overline{A}}^2$, consequently

$$A_{II} = A_I + k_\beta \sigma_{\overline{A}} \tag{8.113}$$

or

$$A_{II} = \overline{A} + (k_\alpha + k_\beta)\sigma_{\overline{A}} \tag{8.114}$$

$\overline{A}$ and $\sigma_{\overline{A}}$ may be obtained interpolating in Fig. 8.4.

Example 8.18. The background spectrum has $B = 10000$ counts/channel. Obtain the values of $\overline{A}$ and $\sigma_{\overline{A}}$. Compute A_I and A_{II} for $\alpha = 10\%$ and $\beta = 1\%$.

Solution. For a background $B = 10{,}000$ we obtain from Fig. 8.4

$$\overline{A} = 840 \text{ counts and } \sigma_{\overline{A}} = 320 \text{ counts}$$

The values of k_α and k_β, for $\alpha = 0.10$ and $\beta = 0.01$ are

$$k_\alpha = 1.28 \text{ and } k_\beta = 2.33$$

Therefore

$$A_I = \overline{A} + k_\alpha \sigma_{\overline{A}} = 840 + 1.28 \times 320 = 1250 \text{ counts}$$

and

$$A_{II} = \overline{A} + (k_\alpha + k_\beta)\sigma_{\overline{A}} = 840 + (1.28 + 2.33) \times 320 = 1995 \text{ counts}$$

The relationship between A_I, A_{II} and B is

$$A_{II} = K_{\alpha\beta} B^{0.619} \tag{8.115}$$

The exponent is obtained from the graphical representation of A_I and A_{II} as a function of B. The factor $K_{\alpha\beta}$ is a parameter independent of B containing all the information related to the Type I and II error risks that influence A_{II}. In fact, $K_{\alpha\beta}$ is a risk factor depending functionally on α, β and B. From Eqs. (8.114) and (8.115), we obtain

$$K_{\alpha\beta} = \frac{A_{II}}{B^{0.619}} = \frac{\overline{A} + (k_\alpha + k_\beta)\ \sigma_{\overline{A}}}{B^{0.619}} \tag{8.116}$$

It is observed that $K_{\alpha\beta}$ is symmetric in α and β.

d. Minimum counting time

We have just concluded that we may calculate a minimum area, A_{II}, so that a peak with this area cannot be false with a risk α and a real peak cannot be discarded as false with a risk β. It has been supposed that the background and the peak grow evenly during data accumulation by the spectrometer. In this situation we may compute the counting duration to assure that the peak is detectable with the risks α and β.

Let us suppose that a is the true counting rate for the peak, expressed in counts/h. If $t_{\alpha\beta}$ is the time required, in hours, assuming that the risks for the Type I and II errors do not exceed α and β, respectively, we can write

$$A_{II} = a t_{\alpha\beta} \tag{8.117}$$

$$B = b t_{\alpha\beta} \tag{8.118}$$

taking these expressions to Eq. (8.115) we have

$$a t_{\alpha\beta} = K_{\alpha\beta} (b t_{\alpha\beta})^{0.619} \tag{8.119}$$

the minimum counting time is given by

$$t_{\alpha\beta} = (K_{\alpha\beta}/a)^{2.62} b^{1.62} \tag{8.120}$$

Example 8.19. Table 8.18 shows the experimental values of B, $\overline{A}$ and $\sigma_{\overline{A}}$. Find the relationship between A_{II} and B when $\alpha = 0.10$ and $\beta = 0.01$ or 0.5. Show that $A_{II} = K_{\alpha\beta} B^c$ and compute $K_{\alpha\beta}$ and c. It is assumed that $K_{\alpha\beta}$ is a parameter independent of B.

Solution. Table 8.19 shows the values of A_{II} for different values of B.

Equation $A_{II} = K_{\alpha\beta} B^c$ may be fitted taking logarithms

$$\log A_{II} = \log K_{\alpha\beta} + c \log B$$

TABLE 8.18 Experimental values of B, $\overline{A}$ and $\sigma_{\overline{A}}$.

B	$\overline{A}$	$\sigma_{\overline{A}}$
100	50	18.8
500	135	50.9
1000	208	78.1
5000	563	211.6
10000	865	324.9
20000	1328	499.0
40000	2040	766.4

TABLE 8.19 Values of B and A_{II} for different α and β values.

$\alpha = 0.10$, $\beta = 0.01$		$\alpha = 0.10$, $\beta = 0.50$	
B	A_{II}	B	A_{II}
100	118	100	74
500	319	500	201
1000	490	1000	308
5000	1327	5000	834
10,000	2038	10,000	1281
20,000	3130	20,000	1967
40,000	4806	40,000	3021

This is a linear equation

$$y = a + cx$$

where

$$y = \log A_{II}$$

and

$$x = \log B$$

Applying least square fitting to the quantities of Table 8.19, when $\alpha = 0.10$, $\beta = 0.01$, we get $K_{\alpha\beta} = 6.81$ and $c = 0.619$, when $\alpha = 0.10$, $\beta = 0.50$, we get $K_{\alpha\beta} = 4.28$ and $c = 0.619$. As c takes the same values, we may compute $K_{\alpha\beta}$ applying the equation

$$K_{\alpha\beta} = \frac{\overline{A} + (k_\alpha + k_\beta)\sigma_{\overline{A}}}{B^{0.619}}$$

The values of B, $\overline{A}$ and $\sigma_{\overline{A}}$ may be values of Table 8.18 or interpolated logarithmically from Table 8.19; e.g., for $\alpha = 0.01$ and $\beta = 0.015$, when $B = 1000$, $\overline{A} = 208$ and $\sigma_{\overline{A}} = 78$, we have

$$K_{\alpha\beta} = \frac{208 + (2.33 + 1.96) \times 78}{1000^{0.619}} = 7.55$$

Example 8.20. Compute the values of $t_{\alpha\beta}$ when $\alpha = 0.01$, $\beta = 0.015$, the background counting rate is $b = 100$ counts/h and $a = 20$ counts/h.

Solution. From Eq. (8.120), taking into account that $K_{\alpha\beta} = 7.55$ from the last example we have

$$t_{\alpha\beta} = \left(\frac{7.55}{20}\right)^{2.62} 100^{1.62} = 135 \text{ h}$$

2. Low-resolution gamma spectra

NaI(Tl) detectors generate spectra with very poor resolution compared with the spectra obtained with Ge detectors. Consequently, the procedure described in the previous section is not generally applicable to low resolution spectra. Isolated peaks cannot be analyzed due to interference from other spectral components. In this section, we introduce a more general procedure based on considering the complete spectral response. This procedure introduces a larger complication in calculations, but it is inevitable when we have radionuclide mixtures and the spectrum of one of the radionuclides overlaps the other spectra and vice versa. In this situation, the background must be considered as an independent spectrum. A standard procedure for estimating the radionuclide concentration from gamma-ray spectrometer data is the method of weighted least squares fitting. In this case, it is assumed that the net spectrum of a radionuclide mixture is equivalent to some linear combination of the net characteristic spectra of the radionuclides existing in the sample. The concentration of these radionuclides is represented by the coefficients of the linear combination estimate. Consequently, the estimation of these coefficients is equivalent to the determination of their concentrations.

The solution of least squares is a function $\boldsymbol{\theta}' = (\theta_1, \theta_2, ..., \theta_m)$, which minimizes the sum of the squares of the count differences between observed and fitted channels. This sum of squares is denominated a residual variation.

We define the following n-dimensional vectors:

$\mathbf{x} = (x_1, x_2, \ldots, x_n)$ net counting rate corresponding to channels 1, 2, …, n.
$\mathbf{y} = (y_1, y_2, \ldots, y_n)$ gross counts (sample + background) in channels 1, 2, …, n.
$\mathbf{b} = (b_1, b_2, \ldots, b_n)$ background counts in channels 1, 2, …, n.

If t is the counting time of the sample and r the counting time of the background we may define the elements w_{jj} of the diagonal matrix $\mathbf{W}$ as

$$w_{jj} = \frac{y_j}{t^2} + \frac{b_j}{r^2} \tag{8.121}$$

The solution obtained by weighted least squares method is given by the estimator

$$\widehat{\boldsymbol{\theta}} = \left(\mathbf{A}\mathbf{W}^{-1}\mathbf{A}'\right)^{-1}\mathbf{A}\mathbf{W}^{-1}\mathbf{x} \tag{8.122}$$

where $\mathbf{A}$ is an $m \times n$ matrix called the calibration matrix. The dimension m corresponds to the number of calibration spectra and n to the number of channels of each spectrum.

The variance of the estimated concentration parameter for the ith radionuclide is the ith diagonal element of the matrix $\left(\mathbf{A}\mathbf{W}^{-1}\mathbf{A}'\right)^{-1}$. In order to test the goodness of fit we use the residual mean square statistic

$$s^2 = \frac{1}{n-m}\left(\mathbf{x} - \mathbf{A}'\widehat{\boldsymbol{\theta}}\right)'\mathbf{W}^{-1}\left(\mathbf{x} - \mathbf{A}'\widehat{\boldsymbol{\theta}}\right) \tag{8.123}$$

which is distributed as a chi-square random variable. A review of methods currently used to unfold particle spectra for measured pulse height distributions is presented by Matzke (2002).

a. Sample with a single radionuclide

To illustrate the procedure described in the previous section, we consider a simple case: the limit of detection determination when the sample has only one radionuclide and we use a two-channel counter. Eq. (8.122) becomes

$$\widehat{\theta}_1 = \left\{\frac{a_{11}^2}{y_1/t^2 + b_1/r^2} + \frac{a_{12}^2}{y_2/t^2 + b_2/r^2}\right\}^{-1} \times \left\{\frac{a_{11}(y_1/t - b_1/r)}{y_1/t^2 + b_1/r^2} + \frac{a_{12}(y_2/t - b_2/r)}{y_2/t^2 + b_2/r^2}\right\} \tag{8.124}$$

the standard error is given by

$$S\left(\widehat{\theta}_1\right) = \left\{\frac{a_{11}^2}{y_1/t^2 + b_1/r^2} + \frac{a_{12}^2}{y_2/t^2 + b_2/r^2}\right\}^{-1/2} \tag{8.125}$$

and the detection limit is given by

$$L_D = (k_\alpha + k_\beta)\left\{\frac{a_{11}^2}{y_1/t^2 + b_1/r^2} + \frac{a_{12}^2}{y_2/t^2 + b_2/r^2}\right\}^{-1/2} \tag{8.126}$$

If the counter has only one channel, the estimate is

$$\widehat{\theta}_1 = \left\{\frac{a_{11}^2}{y_1/t^2 + b_1/r^2}\right\}^{-1} \times \left\{\frac{a_{11}(y_1/t - b_1/r)}{y_1/t^2 + b_1/r^2}\right\} = \frac{y_1/t - b_1/r}{a_{11}} \tag{8.127}$$

and

$$S\left(\widehat{\theta}_1\right) = \sqrt{\frac{y_1/t^2 + b_1/r^2}{a_{11}^2}} \tag{8.128}$$

The detection limit is

$$L_D = (k_\alpha + k_\beta)\sqrt{\frac{y_1/t^2 + b_1/r^2}{a_{11}^2}} \tag{8.129}$$

b. Sample with two radionuclides

Consider now a radioactive sample with two radionuclides and a counter with two channels. The standard error of the estimated concentrations for radionuclide 1 is $S\left(\widehat{\theta}_1\right)$ and $S\left(\widehat{\theta}_2\right)$ for the second radionuclide. It is straightforward to demonstrate the following equations

$$S\left(\widehat{\theta}_1\right) = \left\{\frac{1}{d}\left(\frac{a_{21}^2}{y_1/t^2 + b_1/r^2} + \frac{a_{22}^2}{y_2/t^2 + b_2/r^2}\right)\right\}^{-1/2} \tag{8.130}$$

and

$$S\left(\widehat{\theta}_2\right) = \left\{\frac{1}{d}\left(\frac{a_{11}^2}{y_1/t^2 + b_1/r^2} + \frac{a_{12}^2}{y_2/t^2 + b_2/r^2}\right)\right\}^{-1/2} \tag{8.131}$$

where d denotes the determinant of the matrix $\mathbf{AW^{-1}A'}$.

The individual estimate of concentrations is impossible when the shape of pulse distributions in both channels is similar. In this situation $d \to 0$.

The detection limit for radionuclide 1 is approximated by

$$L_D(1) = (k_\alpha + k_\beta)\left\{\frac{1}{d}\left(\frac{a_{21}^2}{y_1/t^2 + b_1/r^2} + \frac{a_{22}^2}{y_2/t^2 + b_2/r^2}\right)\right\}^{-1/2} \tag{8.132}$$

and for radionuclide 2 by:

$$L_D(2) = (k_\alpha + k_\beta)\left\{\frac{1}{d}\left(\frac{a_{11}^2}{y_1/t^2 + b_1/r^2} + \frac{a_{12}^2}{y_2/t^2 + b_2/r^2}\right)\right\}^{-1/2} \tag{8.133}$$

c. Sample with several radionuclides

From the above discussion, it is evident that the standard error of the parameter to estimate the concentration of radionuclides depends on the following factors: counting time of the sample and background, relationship between the spectral shape included in the library and the concentration of the radionuclides present in the sample.

According to the description of Pasternack and Harley (1971), in the multi-radionuclide and multi-channel situation we may consider three different detection limits:

1. A radionuclide is assumed to be in the sample and the library contains only this radionuclide.
2. The sample contains only one radionuclide but the library contains this and other radionuclides.
3. The sample and the library each contain the same radionuclides.

The procedure to obtain the detection limits in case 1 is as follows: First we obtain the background spectrum of the system $\mathbf{b}' = (b_1, b_2, \ldots, b_n)$ and the spectrum for a mock sample $\mathbf{y}' = (y_1, y_2, \ldots, y_n)$. Generally we can use the background distribution $\mathbf{b}'$ in the place of $\mathbf{y}'$. Then we apply the least squares analysis and compute the standard error $S(\theta_1)$ from the square root of $\left(\mathbf{a}_1'\mathbf{W}^{-1}\mathbf{a}_1\right)^{-1}$, where $\mathbf{a_1} = (a_{11}, a_{12}, \ldots, a_n)$ denotes the radionuclide library spectrum. Thus

$$S\left(\widehat{\theta}_1\right) = \left\{\sum_{j=1}^{n} \frac{a_{1j}^2}{y_j/t^2 + b_j/r^2}\right\}^{-1/2} \tag{8.134}$$

and

$$L_D = (k_\alpha + k_\beta)\left\{\sum_{j=1}^{n} \frac{a_{1j}^2}{y_j/t^2 + b_j/r^2}\right\}^{-1/2} \tag{8.135}$$

When we take $\mathbf{b}'$ in place of $\mathbf{y}'$ ($t = r$) the detection limit is

$$L_D = (k_\alpha + k_\beta)\left\{\sum_{j=1}^{n}\frac{a_{1j}^2}{2b_j/r^2}\right\}^{-1/2} \tag{8.136}$$

For case 2, the procedure is the same, but the matrix **A** contains all the spectra of the library. For case 3, the procedure is again the same. It is recommended that the mock sample adequately simulates the sample absorption. When the library does not contain all the sample radionuclides, the estimate may be unacceptable. When the library contains more spectra than the sample, a reduction in precision is observed and the standard error increases; however, the estimates remain unbiased. Explicit mathematical expressions for the bias and the loss of precision when using inadequate calibration matrices are given by Pasternack and Liuzzi (1965).

VII. Metrology applications

A. Uncertainty budget

In all radionuclide standardization work, we must present a table that lists the various quantified uncertainties. We will take as an example the determination of the activity concentration of a ^{133}Ba solution (Simpson and van Wyngaardt, 2008). As was customary at the time, Table 8.20 shows only the different components of uncertainty and the uncertainty for each component. Table 8.20 is a technical table directed to experts. Along with many published uncertainty budgets, Table 8.20 does not fully comply with the guidelines of the GUM (see Section 7.1.4 of JCGM 100:2008), and would require an expert in the field using specialized knowledge to make an educated guess of the likely method of evaluation. In recent years, in the field of radionuclide metrology, a concerted effort is being made to include an explanation on how each uncertainty value was obtained in the uncertainty budget, similar to the remarks given in the following table. Here we asked Simpson and van Wyngaardt to provide us a table for nonexperts with more details. Table 8.21 describes the procedures for obtaining the different uncertainties as well as the type of uncertainty (A or B). We must mention that in the past 10 years, Dr. Simpson and the members of other laboratories have tried to include additional information in the uncertainty budget along the lines of Table 8.21.

B. Uncertainty calculation

Wang et al. (2001) obtained the activity concentration of a ^{125}I solution measuring 10 samples and applying the equation:

$$N_0 = T + \frac{N_\gamma N_{\alpha\beta}}{N_{\beta\gamma}(2N_{\alpha\alpha} + N_{\alpha\beta})}\left[N_\alpha + N_\beta - N_\gamma\left(\frac{N_{\alpha\beta}}{2N_{\beta\gamma}} + \frac{N_6}{N_{\beta\gamma}} - \frac{2N_{\alpha\alpha}}{N_{\alpha\beta}}\right]\right) \tag{8.137}$$

The values of different quantities are shown in Table 8.22. This table shows the activity of each of the samples (final column), the mean value of 10 samples and the relative standard deviation.

There are two procedures for calculating the uncertainty activity obtained with Eq. (8.137). The traditional option is to calculate the activity of each sample and then to obtain from them the standard deviation (Taylor, 1997). This is the

TABLE 8.20 Standard uncertainty budget for ^{133}Ba in percentage of the activity concentration.

Component	Relative standard uncertainty multiplied by a sensitivity factor (%)
Counting statistics	0.08
Weighing	0.035
Dead time	0.04
Coincidence resolving time	0.002
Satellite pulses (afterpulsing)	0.10
Counting time	0.001
Background	0.01
Adsorption	0.002
Half life	0.001
Extrapolation of efficiency curve	0.20
Combined uncertainty (in quadrature)	0.244

From Simpson and van Wyngaardt, 2008; reprinted with permission from Elsevier © 2008.

TABLE 8.21 Details of the ^{133}Ba standard uncertainty budget.

Component	Relative standard uncertainty multiplied by a sensitive factor (%)	Remarks	Evaluation Type (A or B)
Counting statistics	0.08	Statistical analysis of 5 extrapolation values (one value from each 5 counting sources)	A
Weighing	0.035	Mass ±0.01 mg, for source preparation using Mettler M3 balance. Mass ±1 mg, for dilution using Mettler B6 balance.	B
Dead time	0.04	Due to uncertainty in τ_D (typically ±0.05 μs for all the threshold settings.	B
Coincidence resolving time	0.002	Uncertainty in τ_R was typically ±0.001 μs.	B
Satellite pulses (afterpulsing)	0.10	$\theta \pm 1\sigma$ (reanalyzed data by increasing/decreasing the afterpulse correction values by their measured uncertainties for each threshold setting).	B
Counting time	0.001	Calibration of timer	B
Background	0.01	A combination of: Background square root statistics applied. Different background data sets interchanged.	A B
Absorption	0.002	Accounts for uncertainties in the final result due to residual ^{133}Baremaining after 5 rinsing in the ampoule received, as measured with a NaI (Tl) detector.	B
Half life	0.001	$t_{1/2} = 10.540 \pm 0.006$years	B
Extrapolation of efficiency curve	0.20	Alternative fits to data (activity conc. Range/$(2\sqrt{3})$, assuming the range to be uniformly distributed).	B
Combined uncertainty (in quadrature)	0.244	Quadratic sum of all uncertainty components (for k = 1).	

From Simpson and van Wyngaardt, 2011.

procedure followed by Wang et al., 2001. The results are shown in Table 8.22. The relative variance is

$$S = \sqrt{\frac{\sum_{i=1}^{10}\left(N_{0i} - \overline{N}_0\right)^2}{(10-1)}} = \sqrt{\frac{21.3}{9}} = 1.538$$

and

$$\frac{S}{\overline{N}_0} = \frac{1.538}{292.8} = 0.005$$

Another procedure, which we follow in this section, is known as uncertainty transmission. It consists of calculating the standard deviation and correlation of the different quantities in order to determine the uncertainty introduced by using a specific equation to calculate the activity of ^{125}I.

1. Uncertainty transmission in Eq. (8.137)

Consider uncertainty transmission for Eq. (8.137). Let

$$F_1 = \frac{N_\gamma N_{\alpha\beta}(N_\alpha + N_\beta)}{N_{\beta\gamma}(2N_{\alpha\alpha} + N_{\alpha\beta})}$$

$$F_2 = -\frac{N_\gamma^2 N_{\alpha\beta}}{N_{\beta\gamma}(2N_{\alpha\alpha} + N_{\alpha\beta})}$$

$$F_3 = \frac{N_{\alpha\beta}}{2N_{\beta\gamma}} + \frac{N_6}{N_{\beta\gamma}} - \frac{2N_{\alpha\alpha}}{N_{\alpha\beta}}$$

The expression to which we apply the uncertainty transmission is:

$$N_0 = T + F_1 + F_2F_3$$

TABLE 8.22 Data from first-time measurements of the 10 samples.

		Count rates alter decay correction (cps/mg) ($T_{1/2}$ = 59.43 days)								
Sample no.	Weight (mg)	T	N_α	N_β	N_γ	$N_{\alpha\alpha}$	$N_{\alpha\beta}$	$N_6 = N_{\beta\beta} + N_{\alpha\gamma}$	$N_{\beta\gamma}$	N_0^a (Bq/mg)
1#	46.18	199.52	93.56	23.66	7.15	24.5	13.0	5.22	1.012	290.4
2#	70.60	195.10	92.25	23.47	7.19	22.4	12.0	4.87	0.942	291.1
3#	75.01	194.29	92.46	23.58	7.21	22.0	11.8	4.77	0.913	292.5
4 #	97.54	208.61	96.20	23.91	7.19	28.5	14.5	5.71	1.087	292.8
5#	117.68	201.90	94.88	23.88	7.24	25.2	13.3	5.33	1.025	292.6
6#	120.75	200.27	94.51	23.87	7.24	24.5	13.0	5.20	0.995	292.7
7#	142.10	203.91	94.85	23.85	7.26	26.1	13.4	5.29	1.005	293.0
8 #	175.01	200.48	93.31	23.64	7.24	23.6	12.5	4.98	0.947	294.1
9#	98.26	201.59	94.43	23.84	7.25	24.7	13.0	5.14	0.976	293.5
10#	108.11	197.13	95.51	24.48	7.74	24.2	12.5	5.00	0.965	295.5
Average		200.3	94.19	23.82	7.27	24.56	12.89	5.15	0.987	292.8
Relative standard deviation (%)		2.1	1.4	1.2	2.3	7.5	5.9	5.2	5.0	0.5

From Wang et al., 2001; reprinted with permission of Elsevier Science.

TABLE 8.23 Partial derivatives of N_0 with respect to T, N_α, N_β and N_0.

$\frac{\partial N_0}{\partial T}$	$\frac{\partial N_0}{\partial N_\alpha} = \frac{\partial N_0}{\partial N_\beta}$	$\frac{\partial N_0}{\partial N_6}$
1	$\frac{N_\gamma N_{\alpha\beta}}{N_{\beta\gamma}(2N_{\alpha\alpha}+N_{\alpha\beta})}$	$-\frac{N_\gamma^2 N_{\alpha\beta}}{N_{\beta\gamma}^2(2N_{\alpha\alpha}+N_{\alpha\beta})}$

We deduce each of the partial derivatives relative to the various parameters. For convenience, we write the equations in tables. The left side of the equation is in the first row and the right side is in the second. We numerically calculate each of these partial derivatives (Tables 8.23–8.27).

2. Numerical calculation of uncertainty

The values to be applied to the equations are the mean values of different magnitudes. These mean values are shown in Table 8.28.

To calculate the numerical value of the partial derivatives, we first calculate some combinations of values that are repeated in the calculations (Table 8.29).

The calculated values of the partial derivatives are shown in Table 8.30.

If the quantities are correlated, correlation coefficients have to be calculated. Correlation coefficient is defined as:

$$\rho(x,y) = \frac{1}{(n-1)\sigma_x\sigma_y}\left(\sum_{i=1}^{n} x_i y_i - n\overline{xy}\right)$$

where $\overline{x}$ and $\overline{y}$ are the mean of the random variables X and Y, respectively. Table 8.31 shows the values of the correlation coefficients for different pairs of variables:

Variance and standard deviation equations ($\sigma_0 = \sigma_{N_0}$)

$$\sigma_0^2 = \left(\frac{\partial N_0}{\partial T}\right)^2\sigma_T^2 + \left(\frac{\partial N_0}{\partial N_{\alpha\beta}}\right)^2\sigma_{\alpha\beta}^2 + \left(\frac{\partial N_0}{\partial N_\gamma}\right)^2\sigma_\gamma^2 + \left(\frac{\partial N_0}{\partial N_\alpha}\right)^2\sigma_\alpha^2$$

TABLE 8.24 Partial derivative to calculate $\partial N_0/\partial N_{\alpha\beta}$, $\partial F_1/\partial N_{\alpha\beta}$, $\partial F_2/\partial N_{\alpha\beta}$, and $\partial F_3/\partial N_{\alpha\beta}$

$\frac{\partial N_0}{\partial N_{\alpha\beta}}$	$\frac{\partial F_1}{\partial N_{\alpha\beta}}$	$\frac{\partial F_2}{\partial N_{\alpha\beta}}$	$\frac{\partial F_3}{\partial N_{\alpha\beta}}$
$\frac{\partial F_1}{\partial N_{\alpha\beta}} + \frac{\partial F_2}{\partial N_{\alpha\beta}}F_3 + \frac{\partial F_3}{\partial N_{\alpha\beta}}F_2$	$\frac{2N_{\alpha\alpha}N_\gamma(N_\alpha+N_\beta)}{N_{\beta\gamma}(2N_{\alpha\alpha}+N_{\alpha\beta})^2}$	$-\frac{2N_\gamma^2 N_{\alpha\alpha}}{N_{\beta\gamma}(2N_{\alpha\alpha}+N_{\alpha\beta})^2}$	$\frac{1}{2N_{\beta\gamma}} + \frac{2N_{\alpha\alpha}}{N_{\alpha\beta}^2}$

TABLE 8.25 Partial derivative to calculate $\partial N_0/\partial N_\gamma$, $\partial F_1/\partial N_\gamma$, and $\partial F_2/\partial N_\gamma$

$\frac{\partial N_0}{\partial N_\gamma}$	$\frac{\partial F_1}{\partial N_\gamma}$	$\frac{\partial F_2}{\partial N_\gamma}$
$\frac{\partial F_1}{\partial N_\gamma} + \frac{\partial F_2}{\partial N_\gamma}F_3 + \frac{\partial F_3}{\partial N_\gamma}F_2$	$\frac{N_{\alpha\beta}(N_\alpha+N_\beta)}{N_{\beta\gamma}(2N_{\alpha\alpha}+N_{\alpha\beta})}$	$-\frac{2N_\gamma N_{\alpha\beta}}{N_{\beta\gamma}(2N_{\alpha\alpha}+N_{\alpha\beta})}$

TABLE 8.26 Partial derivative to calculate $\partial N_0/\partial N_{\beta\gamma}$, $\partial F_1/\partial N_{\beta\gamma}$, $\partial F_2/\partial N_{\beta\gamma}$, and $\partial F_3/\partial N_{\beta\gamma}$

$\frac{\partial N_0}{\partial N_{\beta\gamma}}$	$\frac{\partial F_1}{\partial N_{\beta\gamma}}$	$\frac{\partial F_2}{\partial N_{\beta\gamma}}$	$\frac{\partial F_3}{\partial N_{\beta\gamma}}$
$\frac{\partial F_1}{\partial N_{\beta\gamma}} + \frac{\partial F_2}{\partial N_{\beta\gamma}}F_3 + \frac{\partial F_3}{\partial N_{\beta\gamma}}F_2$	$-\frac{N_\gamma N_{\alpha\beta}(N_\alpha+N_\beta)}{N^2_{\beta\gamma}(2N_{\alpha\alpha}+N_{\alpha\beta})}$	$\frac{N^2_\gamma N_{\alpha\beta}}{N^2_{\beta\gamma}(2N_{\alpha\alpha}+N_{\alpha\beta})}$	$-\frac{N_{\alpha\beta}}{2N^2_{\beta\gamma}} - \frac{N_6}{N^2_{\beta\gamma}}$

TABLE 8.27 Partial derivative to calculate $\partial N_0/\partial N_{\alpha\alpha}$, $\partial F_1/\partial N_{\alpha\alpha}$, $\partial F_2/\partial N_{\alpha\alpha}$ and $\partial F_3/\partial N_{\alpha\alpha}$

$\frac{\partial N_0}{\partial N_{\alpha\alpha}}$	$\frac{\partial F_1}{\partial N_{\alpha\alpha}}$	$\frac{\partial F_2}{\partial N_{\alpha\alpha}}$	$\frac{\partial F_3}{\partial N_{\alpha\alpha}}$
$\frac{\partial F_1}{\partial N_{\alpha\alpha}} + \frac{\partial F_2}{\partial N_{\alpha\alpha}}F_3 + \frac{\partial F_3}{\partial N_{\alpha\alpha}}F_2$	$-\frac{2N_\gamma N_{\alpha\beta}(N_\alpha+N_\beta)}{N_{\beta\gamma}(2N_{\alpha\alpha}+N_{\alpha\beta})^2}$	$\frac{2N^2_\gamma N_{\alpha\beta}}{N_{\beta\gamma}(2N_{\alpha\alpha}+N_{\alpha\beta})^2}$	$-\frac{2}{N_{\alpha\beta}}$

TABLE 8.28 Mean values.

N_T	N_α	N_β	N_γ	$N_{\alpha\alpha}$	$N_{\alpha\beta}$	N_6	$N_{\beta\gamma}$
200.280	94.196	23.818	7.271	24.570	12.900	0.987	5.151

TABLE 8.29 Numerical values of some combinations of values repeated in the calculation.

$N_\alpha + N_\beta$	$2N_{\alpha\alpha} + N_{\alpha\beta}$	F_1	F_2	F_3
118.01	62.01	180.687	−11.131	7.937

TABLE 8.30 Values of partial derivatives.

$\frac{\partial N_0}{\partial N_T}$	$\frac{\partial N_0}{\partial N_\alpha}$	$\frac{\partial N_0}{\partial N_\beta}$	$\frac{\partial N_0}{\partial N_\gamma}$	$\frac{\partial N_0}{\partial N_{\alpha\alpha}}$	$\frac{\partial N_0}{\partial N_{\alpha\beta}}$	$\frac{\partial N_0}{\partial N_6}$	$\frac{\partial N_0}{\partial N_{\beta\gamma}}$
1.0000	1.5322	1.5322	0.5127	−1.2475	−3.2695	−11.2911	39.2328

TABLE 8.31 Correlation coefficients.

$\rho(x,y)$	$y = N_\alpha$	$y = N_\beta$	$y = N_\gamma$	$y = N_{\alpha\alpha}$	$y = N_{\alpha\beta}$	$y = N_6$	$y = N_{\beta\gamma}$
$x = N_T$	0.7628	0.2130	−0.2119	0.9591	0.9668	0.9393	0.8834
$x = N_\alpha$		0.7789	0.4016	0.8660	0.8202	0.7964	0.7772
$x = N_\beta$			0.8731	0.3820	0.2923	0.2654	0.2768
$x = N_\gamma$				−0.0565	−0.1714	−0.2007	−0.1787
$x = N_{\alpha\alpha}$					0.9872	0.9714	0.9417
$x = N_{\alpha\beta}$						0.9935	0.9683
$x = N_6$							0.9809

$$+\left(\frac{\partial N_0}{\partial N_\beta}\right)^2\sigma_\beta^2+\left(\frac{\partial N_0}{\partial N_{\beta\gamma}}\right)^2\sigma_{\beta\gamma}^2+\left(\frac{\partial N_0}{\partial N_{\alpha\alpha}}\right)^2\sigma_{\alpha\alpha}^2+\left(\frac{\partial N_0}{\partial N_6}\right)^2\sigma_6^2$$

$$+2\left(\frac{\partial N_0}{\partial N_T}\right)\left(\frac{\partial N_0}{\partial N_\alpha}\right)\rho(N_T,N_\alpha)\sigma_T\sigma_\alpha+2\left(\frac{\partial N_0}{\partial N_T}\right)\times\left(\frac{\partial N_0}{\partial N_\beta}\right)\rho(N_T,N_\beta)\sigma_T\sigma_\beta$$

$$+2\left(\frac{\partial N_0}{\partial N_T}\right)\left(\frac{\partial N_0}{\partial N_\gamma}\right)\rho(N_T,N_\gamma)\sigma_T\sigma_\gamma+2\left(\frac{\partial N_0}{\partial N_T}\right)\times\left(\frac{\partial N_0}{\partial N_{\alpha\alpha}}\right)\rho(N_T,N_{\alpha\alpha})\sigma_T\sigma_{\alpha\alpha}$$

$$+2\left(\frac{\partial N_0}{\partial N_T}\right)\left(\frac{\partial N_0}{\partial N_{\alpha\beta}}\right)\rho(N_T,N_{\alpha\beta})\sigma_T\sigma_{\alpha\beta}+2\left(\frac{\partial N_0}{\partial N_T}\right)\times\left(\frac{\partial N_0}{\partial N_6}\right)\rho(N_T,N_6)\sigma_T\sigma_6$$

$$+2\left(\frac{\partial N_0}{\partial N_T}\right)\left(\frac{\partial N_0}{\partial N_{\beta\gamma}}\right)\rho(N_T,N_{\beta\gamma})\sigma_T\sigma_{\beta\gamma}+2\left(\frac{\partial N_0}{\partial N_\alpha}\right)\times\left(\frac{\partial N_0}{\partial N_\beta}\right)\rho(N_\alpha,N_\beta)\sigma_\alpha\sigma_\beta$$

$$+2\left(\frac{\partial N_0}{\partial N_\alpha}\right)\left(\frac{\partial N_0}{\partial N_\gamma}\right)\rho(N_\alpha,N_\gamma)\sigma_\alpha\sigma_\gamma+2\left(\frac{\partial N_0}{\partial N_\alpha}\right)\times\left(\frac{\partial N_0}{\partial N_{\alpha\alpha}}\right)\rho(N_\alpha,N_{\alpha\alpha})\sigma_\alpha\sigma_{\alpha\alpha}$$

$$+2\left(\frac{\partial N_0}{\partial N_\alpha}\right)\left(\frac{\partial N_0}{\partial N_{\alpha\beta}}\right)\rho(N_\alpha,N_{\alpha\beta})\sigma_\alpha\sigma_{\alpha\beta}+2\left(\frac{\partial N_0}{\partial N_\alpha}\right)\times\left(\frac{\partial N_0}{\partial N_6}\right)\rho(N_\alpha,N_6)\sigma_\alpha\sigma_6$$

$$+2\left(\frac{\partial N_0}{\partial N_\alpha}\right)\left(\frac{\partial N_0}{\partial N_{\beta\gamma}}\right)\rho(N_\alpha,N_{\beta\gamma})\sigma_\alpha\sigma_{\beta\gamma}+2\left(\frac{\partial N_0}{\partial N_\beta}\right)\times\left(\frac{\partial N_0}{\partial N_\gamma}\right)\rho(N_\beta,N_\gamma)\sigma_\beta\sigma_\gamma$$

$$+2\left(\frac{\partial N_0}{\partial N_\beta}\right)\left(\frac{\partial N_0}{\partial N_{\alpha\alpha}}\right)\rho(N_\beta,N_{\alpha\alpha})\sigma_\beta\sigma_{\alpha\alpha}+2\left(\frac{\partial N_0}{\partial N_\beta}\right)\times\left(\frac{\partial N_0}{\partial N_{\alpha\beta}}\right)\rho(N_\beta,N_{\alpha\beta})\sigma_\beta\sigma_{\alpha\beta}$$

$$+2\left(\frac{\partial N_0}{\partial N_\beta}\right)\left(\frac{\partial N_0}{\partial N_6}\right)\rho(N_\beta,N_6)\sigma_\beta\sigma_6+2\left(\frac{\partial N_0}{\partial N_\beta}\right)\times\left(\frac{\partial N_0}{\partial N_{\beta\gamma}}\right)\rho(N_\beta,N_{\beta\gamma})\sigma_\beta\sigma_{\beta\gamma}$$

$$+2\left(\frac{\partial N_0}{\partial N_\gamma}\right)\left(\frac{\partial N_0}{\partial N_{\alpha\alpha}}\right)\rho(N_\gamma,N_{\alpha\alpha})\sigma_\gamma\sigma_{\alpha\alpha}+2\left(\frac{\partial N_0}{\partial N_\gamma}\right)\times\left(\frac{\partial N_0}{\partial N_{\alpha\beta}}\right)\rho(N_\gamma,N_{\alpha\beta})\sigma_\gamma\sigma_{\alpha\beta}$$

$$+2\left(\frac{\partial N_0}{\partial N_\gamma}\right)\left(\frac{\partial N_0}{\partial N_6}\right)\rho(N_\gamma,N_6)\sigma_\gamma\sigma_6+2\left(\frac{\partial N_0}{\partial N_\gamma}\right)\times\left(\frac{\partial N_0}{\partial N_{\beta\gamma}}\right)\rho(N_\gamma,N_{\beta\gamma})\sigma_\gamma\sigma_{\beta\gamma}$$

$$+2\left(\frac{\partial N_0}{\partial N_{\alpha\alpha}}\right)\left(\frac{\partial N_0}{\partial N_{\alpha\beta}}\right)\rho(N_{\alpha\alpha},N_{\alpha\beta})\sigma_{\alpha\alpha}\sigma_{\alpha\beta}+2\left(\frac{\partial N_0}{\partial N_{\alpha\alpha}}\right)\times\left(\frac{\partial N_0}{\partial N_6}\right)\rho(N_{\alpha\alpha},N_6)\sigma_{\alpha\alpha}\sigma_6$$

$$+2\left(\frac{\partial N_0}{\partial N_{\alpha\alpha}}\right)\left(\frac{\partial N_0}{\partial N_{\beta\gamma}}\right)\rho(N_{\alpha\alpha},N_{\beta\gamma})\sigma_{\alpha\alpha}\sigma_{\beta\gamma}+2\left(\frac{\partial N_0}{\partial N_{\alpha\beta}}\right)\times\left(\frac{\partial N_0}{\partial N_6}\right)\rho(N_{\alpha\beta},N_6)\sigma_{\alpha\beta}\sigma_6$$

$$+2\left(\frac{\partial N_0}{\partial N_{\alpha\beta}}\right)\left(\frac{\partial N_0}{\partial N_{\beta\gamma}}\right)\rho(N_{\alpha\beta},N_{\beta\gamma})\sigma_\alpha\sigma_{\beta\gamma}+2\left(\frac{\partial N_0}{\partial N_6}\right)\times\left(\frac{\partial N_0}{\partial N_{\beta\gamma}}\right)\rho(N_6,N_{\beta\gamma})\sigma_6\sigma_{\beta\gamma}$$

The numerical value of the uncorrelated variance is:

$$\text{Var1} = 46.4319$$

and the variance of the correlation is:

$$\text{Var2} = -44.2895$$

Therefore, the variance of the activity is:

$$\sigma_0^2 \approx S_0 = \text{Var1} + \text{Var2} = 2.1424$$

and the standard deviation is:

$$S_0 = 1.4637$$

Corresponding to the relative standard deviation:

$$\frac{S_0}{N_0} = 0.00502 \approx 0.5\%$$

This value coincides with that obtained by the traditional method. The difference between the two procedures is that, in the first measurements are independent and therefore there is no correlation between them. However, they may or may not be correlated in the second procedure. In our example, the quantities are not independent, so correlations are required, complicating the calculation.

Whenever possible it is advisable to apply the first procedure, but there are situations where we need to apply the second. We emphasize that in uncertainty transmission the quantities are not always correlated. Therefore, we only apply correlations when the quantities involved are not independent.

References

Abramowitz, M., Stegun, I.A., 1972. Handbook of mathematical functions with formulas, graphs and mathematical tables. NBS. Appl. Mathemat. Series 55, 1046. Washington.

Altshuler, B., Pasternack, B., 1963. Statistical measures of the lower limit of detection of a radioactivity counter. Health Phys. 9, 293–298.

Angoso, M., Gimeno, F., Grau Malonda, A., Domínguez, G., 1973. Isotopic dilution determination of lebaycid in oranges. J. Radional. Chem. 13, 149–154.

Bacon, R.M., 1953. The best straight line among the points. Am. J. Phys. 28, 428–440.

Beers, Y., 1957. Introduction to the Theory of Error. Addison-Wesley, Massachusetts, p. 66.

Bevington, P.R., 1969. Data Reduction and Error Analysis for the Physical Sciences. McGraw, New York, p. 336.

Burns, J.E., Campion, P.J., Williams, A., 1973. Error and uncertainty. Metrologia 9, 101–102.

Campion, P.J., Burns, J.E., Williams, A., 1973. A Code of Practice for Detailed Statement of Accuracy. National Physical Laboratory, London, p. 51.

Chuvnovkina, A.G., Elster, C., Lira, I., Woger, W., 2008. Analysis of key comparison data and laboratory biases. Metrologia 45, 211–216.

Currie, L.A., 1968. Limits for quantitative detection and quantitative determination. Anal. Chem. 40, 586–593.

Currie, L.A., 1995. Nomenclature in evaluation of analytical methods including detection and quantification capabilities. Pure Appl. Chem. 67, 1699–1723.

Donn, J.J., Wolke, R.L., 1976. The practical design and statistical interpretation of background-dominant counting experiments. Radiochem. Radioanalyt. Lett. 25 (2), 57–66.

Donn, J.J., Wolke, R.L., 1977. The statistical interpretation of counting data from measurements of low-level radioactivity. Health Phys. 32, 1–14.

Draper, N.H., Smith, H., 1998. Applied Regression Analysis. John Wiley, New York, p. 736.

Eadie, W.T., Drijard, D., James, F.E., Ross, M., Sadoulet, B., 1971. Statistical Methods in Experimental Physics. North Holland, Amsterdam, p. 296.

Eisenhart, C., 1963. Realistic evaluation of precision and accuracy of instrument calibration systems. J. Res. 67C, 161–187.

Eisenhart, C., 1968. Expression on the uncertainties of final results. Science 160, 1201–1204 (A detailed discussion on systematic errors).

Evans, R.E., 1982. The Atomic Nucleus. Chapp. 26–28 and Appendix G. McGraw Hill, New York, p. 972.

Feller, W., 1968. An Introduction to Probability Theory and its Applications, vol. 1. John Wiley and Sons, Ney York, p. 397.

Garwood, F., 1936. Fiducial limits for the Poisson distribution. Biometrika 28, 437–442.

Grau Carles, P., Grau Malonda, A., 2000. Probabilidad, Estadística Y Errores. Editorial Ciemat, Madrid, p. 437.

Grau Malonda, A., 1999. Free Parameter Models in Liquid Scintillation Counting. Editorial Ciemat, Madrid, p. 416.

Head, J.H., 1972. Minimum detectable photopeak in Ge(Li) spectra. Nucl. Instrum. Methods 98, 419–428.

Helstrom, C.W., 1968. Statistical Theory of Signal Detection. Pergamon Press, Oxford, p. 364.

Hoel, P.C., 1984. Introduction to Mathematical Statistics. John Wiley, New York.

International Vocabulary of Basic and General Terms in Metrology, second ed., 1993. ISO.

Jaffey, A.H., 1960. Statistical tests for counting. Nucleonics 18 (No. 11), 180–184.

JCGM 100, 2008. Evaluation of Measurement Data-Guide to the Expression of Uncertainty in Measurements, p. 134.

Larson, H.J., 1969. Introduction to Probability Theory and Statistical Inference. John Wiley, New York, p. 435.

Loevinger, R., Berman, M., 1951. Efficiency criteria in radioactivity counting. Nucleonics 9, 26–39.

Mandel, J., 1991. Evaluation and Control of Measurements. Marcel Dekker, Inc., New York, p. 169.

Matzke, M., 2002. Propagation of uncertainties in unfolding procedures. Nucl. Intrum. Methods A476, 230–241.

Müller, J.W., 1979. Some second thoughts on error statements. Nucl. Instrum. Methods 163, 241–251.

Natrella, M.G., 2005. Experimental Statistics. Dover, New York, p. 560.

Newbold, P., 2009. Statistics for Business and Economics. Prentice Hall, New Jersey, p. 1008.

Nicholson, W.L., 1966. Statistics of net-counting-rate estimation with dominant background corrections. Nucleonics 24, 118–121.

Pasternack, B.S., Luizzi, A., 1965. Patterns in residuals: a test for regression adequacy in radionuclide assay. Technometrics 7, 603–621.

Pasternack, B.S., Harley, N.H., 1971. Detection limits for radionuclides in the analysis of multi-component gamma ray spectrometer data. Nucl. Instrum. Methods 91, 533–549.

Paule, R.C., Mandel, J., 1971. Analysis of Interlaboratory Measurements on the Vapor Pressure of Cadmium and Silver. National Bureau of Standards. Special Publication, pp. 260–321.

Paule, R.C., Mandel, J., 1982. Consensus values and weighting factors. J. Res. Natl. Bureau Stand. 87, 397–431.

Pommé, S., 1912. Determination of a Reference Value, Associated Uncertainty and Degrees of Equivalence-For CCCRI(II) Key Comparison Data JRC Scientific and Policy Reports EUR 25355 EN (EUR-Scientific and Technical Reports Series). https://doi.org/10.2787/61338 2012.

Pommé, S., Keightley, J., 2015. Determination of a reference value and its uncertainty through a power-moderated mean. Metrologia 52, S200–S212.

Pommé, S., Spasova, Y., 2008. A practical procedure for assigning a reference value and uncertainty in the frame of an interlaboratory comparison. Accred. Q. Assur. 13, 83–89.

Przyborowski, J., Wilenski, H., 1935. Statistical principles of routine work in testing clover seed for dodder. Biometrika 27, 273–292.

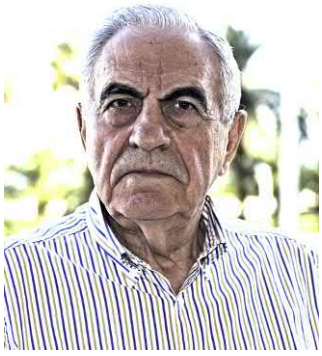
Rabinovich, S.G., 2005. Measurement Errors and Uncertainties. Theory and Practice. Springer, New York, p. 320.

Reynolds, S.A., 1964. Choosing optimum counting. Nucleonics 22 (8), 104–105.
Rozanov, Y.A., 1977. Probability Theory: A Concise Course. Dover, New York, p. 148.
Sahagia, M., Luca, A., Anthe, A., Ioan, M.-R., Garcia-Toraño, E., 2016. Application of the Power-moderated mean (PMM) concept in the calculation of reference values of interlaboratory comparisons. Rom. Journ. Phys. 61, 697–706.
Shirono, K., Tanaka, H., Ehara, K., 2010. Bayesian statistics for determination of the reference value and degree of equivalence in inconsistent comparison data. Metrologia 47, 444–452.
Simpson, B. R. S., van Wyngaardt, W. M., 2008. Absolute activity of B133a by liquid scintillation coincidence counting using the $4\pi(e,X)-\gamma$ extrapolation technique. Appl. Radiat. Isot. 66, 929-933.
Simpson, B.R.S., van Wyngaardt, W.M., 2011. Private Communication.
Taylor, J.R., 1997. An introduction to error analysis. The Study of Uncertainties in Physical Measurements, second ed. University Science Books, California, p. 327.
Taylor, B.N., Kuyatt, C.E., 1994. Guidelines for Evaluating and Expressing the Uncertainty of NIST Measurement Results, vol. 1297. NIST Technical Note, Washington.
Thomas, A., 1950. How to compare counters. Nucleonics 6 (No. 2), 50–53.
Topping, T., 1972. Errors of Observation and Their Treatment. Springer, New York, p. 119.
Triola, M.F., 2009. Elementary Statistics. Addison Wesley, p. 896.
Wang, Z., Zhang, X., Chang, Y., Liu, D., 2001. The determination of I-125 activity using sum-peak method with a well HPGe-detector-based spectrometer. Nucl. Instrum. Methods Phys. Res. 459, 475–481.
Wyld, G.E.A., 1970. Statistical confidence in liquid scintillation counting. In: The Current Status of Liquid Scintillation Counting. Grune and Stratton, New York, p. 354.
Zimmerman, B. E., Unterweger, M. P., and Brodack, J. W., 2001. The standardization of L177uby $4\pi\beta$liquid scintillation spectrometry with H3-standard efficiency tracing. App. Radiat. Isot. 54, 623-631.

Relevant Statistical References Tables

Abramowitz, M., Stegun, I.A., 1972. Handbook of Mathematical Functions: With Formulas, Graphs, and Mathematical Tables. Dover, New York, p. 1046.
Beyer, W.H., 1990. CRC Standard Probability and Statistics Tables and Formulae. CRC Press, Boca de Raton, Florida, p. 520.
Hald, A., 1958. Statistical Tables and Formulas". John Willey and Sons, London, p. 97.
James Rohlf, F., Sokal, R.R., 1994. "Statistical Tables" Freeman, New York, p. 28.
Kmietowicz, Z.W., Yannoulis, Y., 1976. Mathematical, Statistical and Financial Tables for the Social Sciences. Longman, London, p. 64.
Lindley, D.V., Scott, W.F., 1995. New Cambridge Statistical Tables, second ed. Cambridge University Press, Cambridge, p. 96.
Murdoch, J., Barnes, S.A., 1998. Statistical Tables, fourth ed. Macmillan Press, London, p. 79.
Neave, H.R., 1998. Elementary Statistical Tables. Routlege, London, p. 48.
Powel, F.C., 1982. Statistical Tables for the Social Biological and Physical Sciences. Cambridge University Press, London, p. 100.
Zwillinger, D., Kokoska, S., 2000. CRC Standard Probability and Statistics Tables and Formulae. CRC Press, Boca de Raton, Florida, p. 200.

Agustín Grau Malonda



Agustín Grau Malonda holds a BSc degree from the Complutense University, Madrid 1962; Doctorate in Electronics from Toulouse University (France) 1965; PhD in Physics from the Complutense University, Madrid, 1981. He worked in the JEN (Atomic Energy Commission), Radiochemistry Section, 1965–71, and Radionuclide Metrology Section, 1972–84. Agustín Grau Malonda subsequently held numerous positions as Director of the Basic Research Department (CIEMAT) 1984–86; Director of the Department of Fusion and Particle Physics (CIEMAT) 1987–1998; Director of the Institute for Energy Studies (CIEMAT) 1999–2003; Deputy Director of Strategic Projects (CIEMAT) 2004–2008; Associate Professor of Physics, Madrid Polytechnic University, 1969–77; and Professor of Nuclear Engineering, Madrid Polytechnic University, 1977–85. In addition, he was a member of the following working groups and committees: Consulting Committee for the Fusion Program (EU) 1996–2000, (Vice Chairman) 1991–2000; Joint European Torus (JET) Council, 1986–2000; JET Executive Committee, 1986–99; Fusion Technology Steering Committee (EU) 1986–1990; Fusion Power Coordinating Committee (OECD) 1998–2002; L3 Committee (CERN) 1986–1999; International Committee for Radionuclide Metrology (ICRM), 1975–2003 (Vice Chairman, 1998–1999); EUROMET, 1990–1999; EURATOM Scientific and Technical Committee, 1992–2003; and Adviser Committee for the Central Bureau for Nuclear Measurements, JRC, Geel (Belgium) 1989–1995. Awards: Department of Commerce, NBS, USA, Guest Worker Contributions, 1982, 1983; Men of the Year in Sciences, Cambio 16 Journal, 1991; and Encomienda de la Orden de Isabel la Católica, King of Spain, 2001.

Agustín Grau Carles



Agustín Grau Carles holds a PhD in Physical Sciences from the Complutense University of Madrid. During 1991 to 2000, he worked at the Center for Environmental and Technological Energy Research (CIEMAT), together with chemists, developing new spectrometric techniques for radioisotopes, based on liquid-scintillation counting. From 2002 to 2004, he collaborated with biologists from the Center for Astrobiology (CAB) in the calibration of ultraviolet lamps for the irradiation of extremophile cultures. He was also involved, in collaboration with geologists, in the development of new meteorite authentication techniques from radioisotopes originated by cosmic radiation. Between 2004 and 2010, he worked at the Spanish National Research Council (CSIC) in his own Ramón y Cajal project to study the feasibility of a nanodosimeter based on scintillation gels. Currently he directs the BIC Academy (Goods of Cultural Interest), which teaches courses on the need for Science to understand art, as well as archaeological and paleontological goods.

Chapter 9

PERPUSTAKAAN PRIBADI AN-NUR SUNARYA

High-resolution beta imaging

Nicole Barthe[1,2], Serge Maîtrejean[3], Nicolas Carvou[4] and Ana Cardona (In Memoriam)[5]

[1]*Univ. Bordeaux, Bioingénierie Tissulaire, Bordeaux, France;* [2]*INSERM, Bioingénierie Tissulaire, Bordeaux, France;* [3]*SMTJ Consulting, Paris, France;* [4]*Biospace Lab, Nesles-la-Vallée, France;* [5]*Institut Pasteur, Paris, France*

Chapter outline

I. Introduction 670
II. Autoradiography principles 670
A. History 670
B. General features 671
1. Isotopes used 671
2. Physical principles of beta interaction and applicability in high-resolution radionuclide imaging (autoradiography) 671
3. Sample preparation 675
III. Energy-storage latent imaging 675
A. Photographic emulsions 675
1. Macroautoradiography with film 675
2. Microautoradiography with emulsions 678
B. Phosphor screen technology (autoradioluminography) 680
1. History 680
2. General principles 680
3. Various phosphor screens 682
4. Performance 682
5. Quantification methods 683
6. Advantages and drawbacks 684
7. Applications 684
IV. Particle counting imaging systems 685
A. Gaseous detector 685
1. History: from MWPC to PPAC (BetaIMAGER TRacer) and to micropattern gas detectors (BeaQuant™) 685
2. Description of BetaIMAGER TRacer 687
3. Description of the BeaQuant system 689
B. Solid membrane detector (digital microautoradiography) 693
1. History (BetaIMAGER DFine, formerly MicroImager) 693
2. Description of the BetaIMAGER DFine 693
C. Characteristics and performances of particle-counting imagers 694
1. Isotopes used 694
2. Performance 695
3. Quantification 696
D. Data analysis for particle-counting imaging systems 696
1. List mode files 696
2. Multiisotope separation according to energy 697
3. Multiple isotope separation according to decay 697
V. Comparative use of the different techniques 698
A. Applications in biochemical analysis 698
B. Advantages and limitations of radioimagers in histological studies 699
C. Potentialities for multiradionuclide labeling 700
D. Autoradiography associated with mass spectroscopy 700
VI. Other applications 702
A. Biochemistry of development studies 702
B. Bacteriology 702
C. Physiology and gene expression 702
D. Molecular biology 705
E. Molecular imaging 706
F. Nuclear waste decommissioning projects (analysis of potential radioactive contamination) 707
VII. Perspectives and future developments 710
A. Autoradiography to validate in vivo imaging information 710
1. Preclinical applications. Development and validation of new molecular imaging probes 710
2. Clinical applications 716
3. Bremsstrahlung radiation imaging 717
4. Cerenkov luminescence imaging 717
B. Autoradiography and alpha-particle imaging 719
VIII. Conclusions 720
References 720
Further reading 725
Nicole Barthe 725
Serge Maîtrejean 726
Nicolas Carvou 726
Ana Cardona, *in Memoriam* 726

Handbook of Radioactivity Analysis: Volume 2. https://doi.org/10.1016/B978-0-12-814395-7.00009-X
Copyright © 2020 Elsevier Inc. All rights reserved.

I. Introduction

Radionuclide imaging is the production of an image revealing the distribution of radionuclides in biological specimens or in matter. Among the various radionuclide imaging techniques commonly available, only beta imaging is able to give high spatial resolution. As beta particles cannot cross animal bodies or thick layers, these radiotracers can only be visualized in thin sections of tissues or thin layers.

Autoradiography was the initial technique for beta imaging. Beta-emitting radionuclides present in thin slices of labeled materials or biological tissues were revealed using film or liquid emulsions placed in contact with the samples. Autoradiography was originally conducted with radionuclides decaying by beta emissions. Not only are these beta emitters able to emerge out of materials, but they can also efficiently ionize emulsions. They first produce a latent image followed by a visible image after chemical development of the emulsion. This process was named conventional autoradiography.

As the sensitivity of this technique was low, further developments were introduced including an intensification process, such a fluorography, to amplify the results. The various methods proposed shortened film exposure times. However, these techniques had limited success, as the gain in rapidity was affected by a loss in resolution.

In the 1990s, a new concept of autoradiography based on phosphor screen imaging emerged to replace the emulsion detection. The principle of phosphor screen imaging was also based on the storage of a latent image, obtainable after a tenfold shorter contact time than the emulsion method.

More recently, new physics detectors capable of directly counting the radioactivity of the sample and providing real-time images were introduced. All of these methods will be described in detail in the following chapters.

II. Autoradiography principles

A. History

Autoradiography was discovered at the beginning of last century when Henri Becquerel observed that a "mysterious" radiation coming from uranium impressed photographic plates (Becquerel, 1896). Not long after Becquerel's discovery of radioactivity, Vilard (1900a, 1900b) at the École Normale Supérieure, Paris, used autoradiography to demonstrate his discovery of gamma radiation. With autography, Villard demonstrated the existence of a radiation that would not deviate (bend) in a magnetic field. This radiation was later given the name of gamma radiation by Rutherford (1903). For a detailed description of these early works by Becquerel and Villard among other discoveries by pioneers through the 20thcentury, see historical accounts (L'Annunziata, 2007, 2016).

The word "autoradiography" comes from the fact that the sample is not placed between the source of radiation and the detector as in radiography but contains within itself the source of radiations. The radiation from within the sample interacts with the photographic emulsion in contact with it, thus providing an image of the distribution of the radioactivity in the sample.

Autoradiography has been widely used in various fields of biology science, essentially from the 1950s. Thanks to this technique, histologists discovered the unsuspected mobility of various molecules and cells. It allowed cell biologists to monitor the kinetics of DNA synthesis in the cell cycle (Howard and Pelc, 1951). It revealed to the biochemists the mechanism of uptake of steroid hormones in the nucleus of their target cells (Bogoroch and Edelman, 1970), demonstrating the direct action of these hormones on the genetic machinery. Autoradiographic visualization of protein flow along the axon allowed the neurologists to discover several neuronal pathways (Leblond, 1976). A great number of other examples could be cited showing the impact of autoradiography as a research tool in the biological sciences.

Over the years, autoradiography has become a set of techniques where radioactive tracers within a sample are imaged in close contact with a detection media. The initial medium was based on photographic emulsion, either coated on a film or directly coated on the sample. According to the media and the uses, it was divided into macro-autoradiography, which includes whole-body autoradiography (WBA) and microautoradiography (MARG), which entailed the use of the optical or electron microscope.

WBA was developed by Ullberg (1954), who made first sections of the entire body of mice using a large microtome in a walk-in freezer. Later, sections of even larger animals were prepared in a large microtome held inside a chest freezer. Leica Microsystems, Inc. (Nussloch, Germany) began to manufacture these large cryomicrotomes, which are still available today.

Quantification of autoradiographs was the next challenge, but the methods developed for film between 1974 and 1987 were of limited success, because of the inherent nonlinearity of the film. Nevertheless, during this time, Schweitzer et al. (1987) developed an image calibration method using ^{14}C-spiked blood standards with concentrations bracketing the sensitivity of phosphor plates. This method is still used by many investigators today. In the same time, Luckey (US Patent No. 3 859 527, 1975) made a fundamental breakthrough for WBA by developing and patenting phosphor-imaging technology later named autoradioluminography, which provided digitized images, providing a powerful image analysis with direct determination of quantitative tissue concentrations over four to five orders of magnitude. Thus, quantitative whole-body autoradiography (QWBA) began to be widely used and was validated and published later (Coulson and Carr, 2000). A

few years before, in 1994, a group of autoradiographers in the pharmaceutical industry founded the Society for Whole-Body Autoradiography whose mission was to promote the use of QWBA to replace the use of traditional dissection and liquid scintillation counting (LSC).

In addition to autoradiography and autoradioluminography, direct nuclear imaging technologies have been developed, some based on gaseous chambers (Jeavons, 1978) and others based on scintillators (Laniece, 1994). These technologies, still on the market, will be described later on in this chapter.

In light of the limitations of QWBA, which reveals the concentration of radioactivity without providing the actual molecular identity of the radioactive compound, a few investigators developed a method combining the results of WBA with the identification of radioisotope-labeled entities extracted on the same sample. This new approach of ex vivo molecular imaging was initiated (Rohner et al., 2005; Kathib-Shahidi, 2006).

B. General features

Autoradiography is mainly applied to studies on the physiology of living systems where the radioactive tracer is related to a drug effect or to a specific biologic process that can be localized and measured. To provide meaningful interpretations, the following concepts must be kept in mind:

1. The autoradiography image represents only the localization of the radionuclide in the sample. The chemical or molecular structure within which the radionuclide tracer resides remains unknown. There is no guaranty that the original chemical form of the tracer is maintained.
2. Caution must be taken during sample preparation to prevent the diffusion of nonbound radionuclide prior to obtaining the autoradiograph.
3. Blank autoradiography controls are required to establish the background and to ensure that no artifact occurs during the autoradiography process.

1. Isotopes used

Classically, soft-beta-emitting radionuclides are candidates for autoradiography. These include isotopes of the atoms most encountered in biological tissues, such as hydrogen, carbon, sulfur, and phosphorus.

All beta tracers exhibit a continuous spectrum, between zero and a maximum energy, characteristic of the isotopes. The mean energy is roughly the third of the maximum energy. The principle beta isotopes used in autoradiography are as follows:

- ^{3}H (tritium) can be used to label proteins, nucleic acids, and many other molecules and probes. It is often involved in binding techniques to test the affinity of a radioligand for its receptor.
- ^{14}C is used to replace nonradioactive carbon to trace chemical and biochemical reactions involving pharmacological substances.
- ^{35}S is used to label proteins, nucleic acids, and amino acids containing a thiol group such as cysteine and nucleotides. This is done by substitution of an oxygen by a sulfur in a phosphate group, which is often involved in gene expression studies by in situ hybridization.
- ^{45}Ca is used for the labeling of calcified tissues and the measurement of calcification process and rates in metabolism studies.
- ^{33}P is used for the labeling of nucleotides and ^{32}P for the labeling of nucleic acids and phosphor proteins used as tools in molecular biology.

The aforementioned radionuclides emit pure β^- ionizing particles whereby there is no interference or concern for gamma or X-rays with the detector. Energy deposition of β^- particles in matter is high enough to provide good detection efficiency and resolution. Nevertheless, as we will explain later, the lower the β energy, the better the spatial resolution. This is due to the shorter path or range of the low-energy particle in the medium. Hence, ^{3}H gives the highest resolution and could therefore arguably be considered the most interesting isotope, whereas ^{32}P would be the worst according to this criterion when high-resolution imaging is a concern.

Note that high-resolution imaging can be done with any kind of charged particles, which includes also alpha emitters and also all nuclear medicine isotopes. Actually, the gamma emission of nuclear medicine isotopes is always in competition with another mechanism, namely, internal conversion. In this mechanism, the nuclear decay energy is not released by gamma ray emission, but it is transferred to an atomic electron, whose energy is the energy of the gamma minus the atomic electron binding energy. For example, 15% of ^{99m}Tc disintegrations are followed by the emission of an electron, the energy of which is 110 keV (140 keV minus 30 keV of binding energy).

The radionuclide ^{125}I used in nuclear medicine decays preferentially with the emission of low-energy X and γ rays. It is often used in autoradiography for physiological applications. Radioisotopes commonly used in conventional autoradiography are listed in Table 9.1.

2. Physical principles of beta interaction and applicability in high-resolution radionuclide imaging (autoradiography)

The purpose of this section is to give some guidelines on how to estimate the resolution and level of signal, knowing

TABLE 9.1 Radioisotopes used in conventional autoradiography with most common labeling technique and biological applications.

Isotope (rays)	Half-life $T_{½}$	E_{max} for β^- or discrete energies	Labeling technique	Biological applications
^{3}H (β^-)	12 years	18 keV	**Isotopic exchange**	Binding
^{14}C (β^-)	5730 years	156 keV	**Synthesis**[a]	Pharmacology
^{32}P (β^-)	14.3 days	1710 keV	**Synthesis**[a]	Molecular biology
^{33}P (β^-)	25.4 days	249 keV	**Synthesis**[a]	Molecular biology
^{35}S (β^-)	87 days	168 keV	**Synthesis**[a]	In situ hybridization
^{45}Ca (β^-)	163 days	257 keV	**Incorporation**	Metabolism
^{125}I (γ,X, e)	60 days	(γ: 35.6 keV, e: 3.7 and 26.3 keV)	**Incorporation by electrophilic substitution**	Physiological applications

[a]*When used in organic form, direct synthesis of the organic compounds is made.*

the isotopes and sample thickness. Included also are some recommendations on how to calculate the amount of measurable beta particles versus the thickness of the sample.

a. Transport of beta particles in matter

As most of the imaging techniques in biology, quantification in autoradiography is somewhat similar to what a physicist may consider as an ill-posed problem. What autoradiography users actually want to know is the distribution of a radiotracer in a thin but volumetric sample. Unfortunately, as illustrated in Fig. 9.1, with a given simple configuration, the total amount of radioactivity emitted in the sample thickness is not in a one-to-one relation with the radioactivity measured at the surface. The deeper the radiotracers are located within the sample, the lower the radioactivity measured at the surface.

To overcome this fundamental problem, the detection system should be able to measure both the angle of emission and the energy of the beta particles emerging from the surface. None of the systems available on the market, in the past and probably in the future, are capable of such a performance, even though it is not necessarily insuperable. Hence, the quality of autoradiographic data is related to the basic assumption that the radioactive distribution along the thickness axis can be considered as constant. To fulfill this requirement, the sample must be sufficiently thin. We will see further on in this chapter how to verify this condition.

Boltzmann transport equation. The fundamental physics problem involved in autoradiography is the transport of beta particles, and more generally, the transport of electrons in matter. To get some prediction, one has to find formulas to answer, at least approximately the following question: Given a volumetric activity in a sample, what emerging activity can be expected out of the sample?

As many problems in physics, the equation driving the behavior of electrons can be found with reasonable endeavor. In this case, it is the so-called Boltzmann transport equation, which can be used also for neutron or gamma photon transport in matters. An overview of this type of equation can be found in Zheng-Ming and Brahme (1992).

This equation expresses the conservation of charge and energy in each volume element of the matter in which the electrons travel. Unfortunately, this equation is highly nonlinear and can be solved only in very simple cases (homogeneous medium, constant cross sections, stationary distribution of energy) from which autoradiography is excluded. As often in physics, we are confronted with an equation of a "nice formal beauty" but of very poor use. Of course, this equation can be solved numerically, considering the media as water-like

Bethe equation and the range of beta particles. To get a more pragmatic approach, it is instrumental to take an interest in another concept, the stopping power of the medium. By definition, the stopping power is the amount of energy lost by an electron per unit distance. The most famous formula, which describes the stopping power, is the Bethe formula (Bethe and Ashkin, 1953):

$$\frac{dE}{dx} = -\frac{4\pi}{m_e c^2}\cdot\frac{nz^2}{\beta^2}\left(\frac{e^2}{4\pi\varepsilon_0}\right)^2\left[\left(\frac{2m_e c^2\beta^2}{I\left(1-\beta^2\right)}-\beta^2\right)\right] \quad (9.1)$$

where $\beta = v/c$, v is the velocity of the particle, E is the particle energy, x is the distance traveled by the particle, c is the speed of light, z is the particle charge (in elementary charge units), e is the charge of the electron, m_e is the electron rest mass, n is the electron density of the target (mean atomic number), I is the mean excitation potential of the target, and ε_0 is the vacuum permittivity.

This formula leads to the concept of range of an electron, which represents the total distance covered by an electron before being stopped. This property can be calculated (at least numerically) using the following integration, and the Bethe formula:

$$R(E) = \int_0^E \frac{dE}{(dE/dx)} \tag{9.2}$$

Eq. (9.2) provides useful information in the case of autoradiography. Given the high-end energy of beta particles, the corresponding range yields the thickness of the sample over which no electrons can reach the surface and therefore cannot be detected. Tables of electron range are widely available (Pages and Bertel, 1972), including the online NIST Electron Stopping Power and Range (ESTAR) data (https://physics.nist.gov/PhysRefData/Star/Text/method.html).

However, the range is always a "pessimistic" parameter because it expresses the total length of the trajectory of the particles. However, electrons or beta particles undergo frequent scattering inside matter, and their trajectories are closer to a random walk rather than a straight line. One usually prefers to use another quantity, the projected range, written R_p, which is the mean distance between the emission point of an electron in a medium and its stopping point. It gives the depth over which no beta particles can surface out of the sample. Unfortunately, this quantity is out of reach of any calculation and must be estimated by Monte Carlo simulations or with empirical formulas. One of these formulas according to Sauli (1977) is:

$$R_p = 0.71E^{1.72} \tag{9.3}$$

where Rp is expressed in mg/cm^2, and Rp must be divided by the density of the medium (around unity for biological tissues). Actually, it is an experimental fact that the ability of electrons to go through a medium is mainly dependent on the energy and on the density of the medium. The other physical parameters (atomic weight, atomic number) have much less impact. This is mainly due to the small size or mass of electrons. Thus, any collision with any atom (even the lighter atoms) randomizes the direction of the electron, and the main factor (at a given energy), which determines the length of the path of travel of the electron, is the number of collisions, itself dependent mainly on the density of the medium.

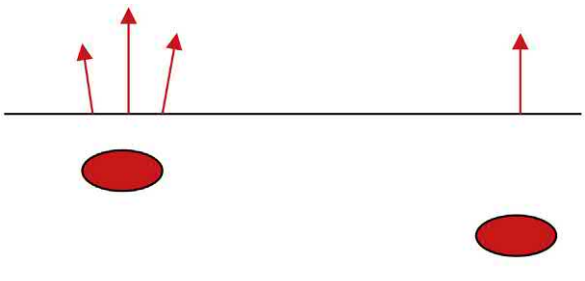


FIGURE 9.1 Brief description of the flawed correspondence between emission at the surface of the sample and actual distribution of the radioactivity. Two identical sources give different results depending on the depth of their location.

Monte Carlo simulations. As an alternate to the former equations, which also need computers to be solved, one can directly use Monte Carlo programs to simulate the behavior of electrons one-by-one. Today, this approach is the most widely used with programs such as Geant 4 (www.geant4.org/geant4), which includes all the necessary cross sections. Nevertheless, it must be kept in mind that Monte Carlo simulations are hugely computer-time-consuming, especially if small confidence intervals are needed. Simulating the behavior of electrons to get a good approximation for their probability of emerging out of the sample requires several millions of trajectories, which can take days of computing. Furthermore, Monte Carlo methods always conceal a bit of the physics involved (i.e., the computer is the physicist) and must therefore be used by persons with a high level of expertise.

Empirical formulas. In the early days of atomic physics, when computers did not exist or at least were not commonly used, physicist would derive empirical formulas to predict the probability for electrons to go through a certain amount of matter. One of the most used formulas for monochromatic electrons (^{125}I, ^{99}Tc in autoradiography) required the knowledge of the range $R(E)$ for the initial energy (Coquerel, 1996):

$$P(E,x) = e^A \cdot e^{\frac{-A}{1-\frac{x}{R(E)}}} \left(1 - \frac{x}{R(E)}\right)^B \tag{9.4}$$

where $P(E, x)$ is the probability for the electrons emitted at a depth x to go through the sample. The formula is slightly sensitive to the parameter B, which can be chosen to be equal to one. The practical range is then roughly two- or threefold lower than the total path. For a biological sample, A can be chosen equal to 3, and one can see that for a sample with a thickness of one quarter of the range, only 50% of the electrons go through the sample. Actually, in the case of autoradiography, as the emission is isotropic, this value must be divided by 2. With such a formula, it is possible to correlate the number of beta particles emitted by the sample with the number of radioactive atoms per unit volume or per gram (considering the concentration of radioactivity as constant throughout the thickness of the sample):

$$N = \frac{1}{2}\left(N_0 \cdot \int_0^{E_M} \left(I(E) \cdot \int_0^X P(E,x)dx\right) dE\right) \tag{9.5}$$

where N is the number of electrons surfacing out of the sample, N_0 is the number of disintegrations, $I(E)$ is the beta spectrum, E_M is the end-point energy of the beta spectrum, and X is the sample thickness. Another experimental rule may be the most appropriate for our purpose, which has been established in the 1950s when physicists tried to characterize beta particles, namely, the attenuation of a beta particle source can be approximated with good accuracy by an exponential attenuation law, such as the one used to describe X-ray attenuation (Evans, 1955):

$$N = N_0 e^{-\mu x} \tag{9.6}$$

This result is an accidental consequence of the shape of the beta energy spectrum and of the variation of electron absorption versus energy. Eq. (9.6) can actually be understood if the shape of the beta energy spectrum remains nearly constant throughout the media and if the angular distribution of beta emitters in the media is randomized from the first layers. One can then define an attenuation coefficient for beta particles versus energy, and an empirical formula for this is:

$$\mu = \rho \cdot \frac{17}{E^{1.14}} \tag{9.7}$$

where ρ is the sample density, E is the maximum energy of the beta particles (in MeV), and μ is given in cm^{-1}. As customary, in biology, the density will be considered as close to unity. With this attenuation coefficient, one can calculate a mean free path for absorption ($1/\mu$). For tritium, ^{14}C, and ^{32}P, we arrive at, respectively, 6 μm, 70 μm, and 1 mm. Eq. (9.7) clearly overestimates the value for tritium (the actual value is of the order of 1 μm), whereas it is relatively correct for ^{14}C and ^{32}P. Eventually, we can use Eq. (9.7) to calculate the emerging activity versus the activity per unit mass for a given sample thickness (integration of the former formula over the thickness), assuming the sample is water-like.

b. Quantification and calibration

There are two types of detection systems, which are the following:

- Energy storage systems (film, phosphor screen)
- Particle counting systems (gaseous detectors)

The first type measures the amount of energy emitted by the sample (a beta particle will contribute to the signal in proportion to its energy), whereas the second type measures the number of particles emitted by the sample. For quantification purposes, for any type of system, a relation between dpm/g and surfacic activity must be established, using a well-known sample (standard). This is the calibration phase.

Quantification for low-energy isotopes (< 30 keV). Low-energy isotopes, such as tritium, have a convenient property in that the range of the beta particles are so small that in most cases the activity emerging out of the sample is not dependent on the sample thickness. In fact, only the two first microns of the sample are really contributing to the signal. This means that the calibration procedure (giving the relation between dpm/g and surfacic activity) can be done with any kind of standard, and if sensitivity stays constant, only once in the lifetime. Of course, sensitivity is never constant during the lifetime of a system, and calibration must be done periodically. However, this recalibration is easy to perform because no specific requirement on the thickness of the sample is required.

Quantification for medium-energy isotopes (> 30 keV, < 300 keV). The situation is more complex for medium-energy isotopes such as ^{14}C, ^{35}S, and ^{33}P. The practical range is of several dozens of microns, which is the typical sample thickness. A large dependency of emerging activity on the thickness of the sample is then expected, and this dependency is everything but linear.

In absolute terms, calibration for these medium-energy isotopes should be done with a standard made of the same "matter" and of the same thickness as the samples measured. For energy storage systems, the dependency of the measurement is lower than for particle counting systems. This is due to the fact that beta particles originating from the deep layers of the sample are more attenuated and their contribution to the signal is much smaller than beta particles originating from the first sample layers. However, for reliable quantification, the thickness of the standard should always be comparable to the thickness of the sample.

Quantification for high-energy isotopes (> 300 keV). For high-energy isotopes such as ^{32}P, ^{89}Y, and ^{90}Sr, the situation is indeed simpler than for medium-energy isotopes. The practical range is always larger than the thickness of the sample (e.g., in the case of ^{32}P, the practical range is 2.5 mm). Furthermore, the probability for a beta particle to escape the sample, on the detector side, is close to 50%, except for very thick samples. Finally, the relation between the surfacic activity and dpm/g is proportional to the thickness of the sample. Therefore, using a standard of known thickness will simplify quantification, as the data can be multiplied by the ratio between the thickness of the sample and the thickness of the standard.

c. Spatial resolution limitation

Generally, spatial resolution is imposed by the capabilities of the detection (imaging) system. Nevertheless, if we consider the case of film as an example, the resolution can be better than 10 μm. In this case, the resolution can be determined also by the sample itself as well as the isotopes

used. The calculation of the point spread function of an isotope, knowing the thickness of the sample, is much more complex than establishing the number of particles emitted by the sample. This may be done with Monte Carlo simulation or solved numerically with the Boltzmann equation. But, as discussed previously, these are complex methods. Nonetheless, with some basic arguments, one can give recommendations on how to determine the sample thickness or the choice of isotope.

Low-energy isotope Resolution. For low-energy isotopes, and especially for tritium, the thickness of the sample is not a limitation for resolution. One micron is enough to absorb more than 50% of the tritium disintegrations. Therefore, most of what can be detected originates from the first micron of the sample. The intrinsic resolution of the method can then be estimated between one and two microns. The resolution can be better for emulsion, which is directly in contact with the labeled site.

Medium-energy isotopes. For the quantification of medium-energy isotopes (e.g., ^{14}C, ^{35}S, ^{33}P), the situation of resolution is much less clear. The practical range is between 40 and 100 μm, and the beta particles coming from the first microns of the sample are of course emerging closer to the disintegration point. Nevertheless, among the beta particles emitted in the opposite direction of the detector, a certain number are backscattered by the sample itself or by the support of the sample, if the latter is thinner than the practical range. For a theoretical "infinitively thin" sample, this backscattered fraction is about one-third of the total signal, and it is spread over a distance at least as large as the practical range. This means that the spatial resolution is somehow limited, and if a very sharp resolution of intracellular structures is required, medium-energy isotopes are not really recommended, whatever the thickness of the sample.

High-energy isotopes. For high-energy isotopes (e.g., ^{32}P), the situation in terms of resolution achievable is even worse because scattering of the beta particle prevails and because the loss of energy is much lower at the start of the beta particle path of travel than at the end, i.e., when the beta particle is far from its point of emission from the sample. The resolution with high-energy isotopes is never really better than 100 μm in the best of cases. This type of isotope is more applicable to gels and thin-layer chromatography (TLC), than to in situ analysis on slides.

3. Sample preparation

For every experiment, optimal conditions for imaging can be considered before preparing the samples. This can be made regarding the energy of the beta rays of the isotope used and the amount of radioactivity fixed in the tissues, taking into account the precision required for the best quality of image recorded.

Basically, the samples are whole sections of small animal bodies obtained by means of slicing the initially frozen body whether it has been embedded or not in a cryopolymerizable resin or in a substance used for maintaining the physical integrity of the tissues. The sections can be made by using a slicing cryostat. Some cryostats are dedicated to whole animal sections and others to organs or small pieces of tissue. The sections can be recovered on adhesive tape for autoradiography or on films or glass histology slides, for liquid emulsion techniques. The thickness of the sections is typically 10−30 microns for macroautoradiography and 5−20 microns for microautoradiography (Ulberg, 1977). The sections are dehydrated in a frozen atmosphere and taken in dry conditions. In the case of microautoradiography, the sections are stained after development of the emulsion and before observation with a microscope. Sample preparation has to preserve the radioactivity bound in the tissues.

III. Energy-storage latent imaging

In this section, we will focus on imaging devices for which images are the consequence of energy storage. This means mainly all the imaging techniques related to photographic emulsions and techniques related to phosphor screens (autoradioluminography).

A. Photographic emulsions

1. Macroautoradiography with film

In macroautoradiography, the distribution of a radionuclide tracer is obtained over a relatively large area such as a thin-layer chromatogram or an animal whole-body section. The dried and flat sample is placed in contact with the emulsion side of the film in the dark room. After a given period of exposure, the film is developed and fixed. The localization of the radionuclide distribution in the sample is first determined visually.

The detection of the radiations, electrons or beta particles, is based on the conversion of silver ions to metallic silver (observed as black grains) within a photographic emulsion (a suspension of silver bromide crystals in gelatin). The photographic mechanism behind this technique has been explained by different authors (Gurney and Mott, 1938) and refined by Rogers (1979), according to whom, the process of ionization, produced by radiations in the emulsion, allows excited electrons to travel from one ion to another until they are trapped at specific sites, which are in fact structural defects in the crystal, whereby a silver ion can absorb a passing electron to become reduced to a silver atom. The crystals sensitized in this way produce a latent image, which can only be visible after application of a chemical developer to reduce all the silver ions of the

affected crystals. The crystals with no reduced silver are then dissolved out of the emulsion using a chemical fixer, leaving only a black image representing the traces left by the radiations in the emulsion in proportion to the amount of radioactivity passing through the emulsion (see Fig. 9.2, inspired by http://www.cheresources.com/content/articles/other-topics/chemistry-of-photography).

Digitizing equipment like CCD cameras or light and laser densitometers have been used to convert the blackening of the emulsion to a digital image based on optical density analysis of the initial image (Orr, 1993). Such a principle is valuable for emulsions layered on film used in macroautoradiography methods and for liquid emulsion embedded sections of tissue, as is the case for microautoradiography techniques (Arimatsu, 1982).

For further details regarding history, chemistry, and physics of film autoradiography, see Rogers (1969), Gahan (1972), L'Annunziata (1987, 2007, 2016).

a. Performance

Sensitivity. For film as well as for any energy storage devices, it is more convenient to consider sensitivity in terms of disintegrations per mm^2 (several hundred for film, several tens for a phosphor screen), which is a measure of the minimum deposited energy that can be detected for a given isotope. It is possible to reach such levels of sensitivity for weak signals at the cost of very long exposure times. It has been reported that film can detect activities as low as 0.02 dpm/mm^2, but the exposure time, to achieve this minimum level, can take months and it depends on the isotope. Of particular concern is the poor detection efficiency of film emulsions for low-energy beta particles ($E_{max} < 30$ keV), such as the beta emissions of ^{3}H ($E_{max} = 18$ keV) for which special films without an anti-scratch layer applied to the surface have been developed, thus enhancing the sensitivity by limiting the absorption of the radiations in any protective surface layer of the emulsion.

For practical purposes, in the course of this chapter, sensitivities will be discussed in terms of exposure times at which comparable levels of activity can be detected with respect to radionuclide imaging. Film autoradiography is best suited, in terms of sensitivity for the detection of isotopes such as ^{14}C and ^{35}S, which emit beta particles of $E_{max} = 156$ and 167 keV, respectively. The sensitivity of film is also limited for higher-energy beta particles, such as ^{32}P, and for X-rays, such as those of ^{125}I, because the high-energy beta particles or X-ray photons pass right through the film without any significant effect, whereas only a small proportion is detected by the film.

Spatial resolution. In photography, resolution is defined in terms of the minimal distance that must separate two objects before they can be distinguished as separate. In film autoradiography, the factors that can affect the

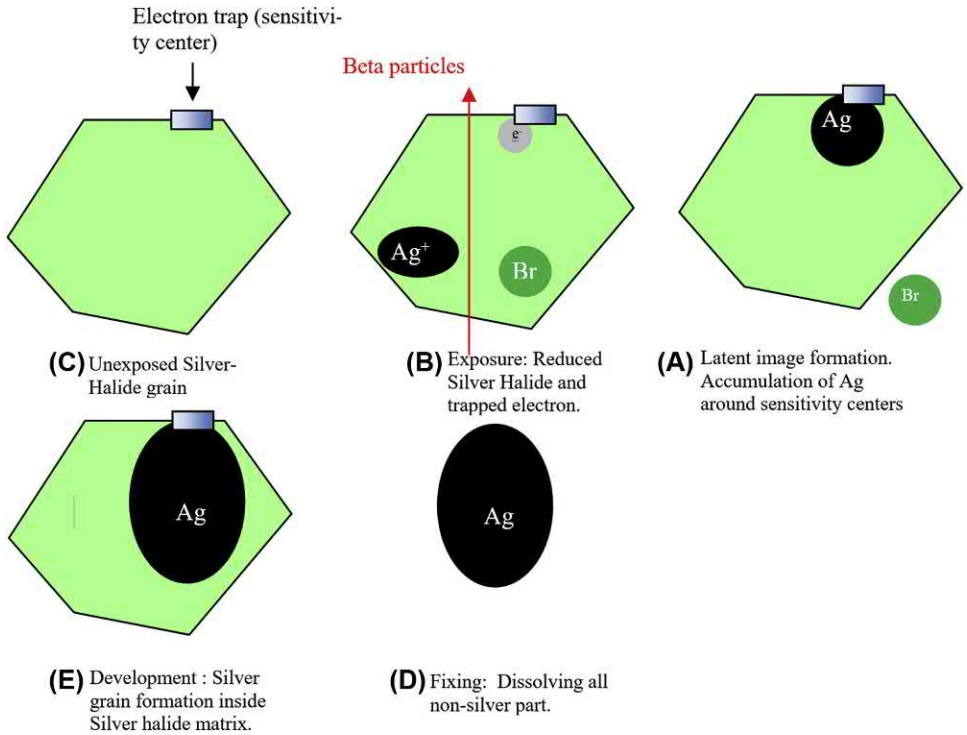


FIGURE 9.2 Schematic view of the different steps involved in the formation of an image on film. For the color version of the figure, the reader is referred to the online version of the book.

resolution to be achieved in radionuclide analysis are associated with the source of activity and with the composition of the film itself. With regard to factors linked to the source of activity, the first one is the choice of isotope. Lower-energy isotopes having shorter path lengths of travel in matter provide better resolution than higher-energy isotopes, which travel further into the emulsion. The distance between source and emulsion as well as sample thickness, are also determining factors, as resolution is inversely proportional to both distance between sample and emulsion and sample thickness.

With regard to film quality, two main factors will affect resolution:

1. the thickness of the emulsion (i.e., thicker emulsions enhance sensitivity but diminish resolution)
2. the size of the silver crystals (i.e., smaller grains give more precise localization)

The length of the exposure is sometimes considered as a factor improving the resolution, but it is not totally correct. Actually, the only contribution of exposure time to resolution is related to statistics. A minimum number of beta particles are required for a reliable measurement, but in any case, the exposure time will affect the width of the distribution of energy. For film, the mathematical tool used to characterize the resolution is the contrast transfer function (CTF). It gives the contrast on the image, versus the frequency, when the radioactive source is made of a periodic line pattern. For example, a CTF of 33% at two line pairs per mm means that the contrast on the image is 33% when the lines are half a millimeter spaced. One usually considers that the resolution limit is given by the frequency for which the CTF is under 10%. Another definition, based on the point spread function (response of the film to a point source), is the resolution, which is the distance to the point source at which the grain density falls to one-half of the maximum (Rogers, 1969). As resolution can vary significantly from one experiment to another, the best resolutions that one could expect based on isotope and emulsions plus light microscopy compared with film are listed in Table 9.2.

TABLE 9.2 Resolution of films and emulsions. The potential resolution of film and that of emulsion autoradiography methods are compared.

Isotope	Emulsions (μm)	Films (μm)
$^{3}H/^{125}I$	0.5–1.0	2.8–5.7
$^{35}S/^{14}C$	2–5	11–28
^{32}P	5–10	28–56

Values are based on 0.1 μm distance of sample to emulsion, 3 μm distance of sample to film and thinnest possible emulsions.
Rogers (1969); reprinted with permission from Elsevier © 1969.

Linear dynamic range. The darkening of film is not a linear function of the energy stored or of the exposure time. There is a threshold for the ionization process under which no darkening of the emulsion occurs. On the other hand, there is a saturation value over which no more darkening is possible (over exposure). Between these two thresholds, the darkening is in a linear relation with activity on a range between 1.5 and 3 logs. This signifies that film autoradiography requires more precaution for the quantification of radioactivity than the techniques we describe further on in this chapter, and a set of standards is always needed to get reliable measurements. Fluorography has also been used to improve sensitivity and the linear dynamic range of film autoradiography (Laskey and Mills, 1975).

b. Quantification

Many commercial systems (light densitometers, scanners, video and CCD camera systems) are available for the quantification of optical density of film involving the transmission of white light through it, light capture, and digitization of data to form a quantitative digital image for software analysis. For an absolute quantification of radionuclide activity from the autoradiogram, standards must be exposed simultaneously on the film as well as the samples. In fact, the optical density of the film is a function of not only the activity of the sample but also the conditions of exposure, the type of film, and the development procedure. So, a calibration of each system is necessary by using standards of known activity, allowing the quantification of the activity per mm^2 for the image of standards and translation of these data to the sample areas of interest.

Additionally, various techniques for the optimization of the quantitative analysis of radionuclide activity were developed. Intensifying screens that are thin sheets of inorganic material placed behind the films emit multiple photons of light when hit by the radioactivity passing through the film, improving the efficiency of detection and enhancing the linear dynamic range of the film.

Similarly, with fluorography, the detection of lower-energy isotopes, such as ^{3}H and ^{14}C, may be enhanced by the use of an organic scintillator (e.g., PPO, 2-5-diphenyloxazole), which converts the energy of a beta particle to visible light (L'Annunziata, 1987), increasing the sensitivity by a factor of 10–100 for ^{3}H and 5–10 for ^{14}C. In addition, an inflated resolution appears by suppression of background with respect to the enhanced signal.

Despite advantages, these techniques introduced errors during the quantification process. Thus, methods for the correction of these errors were introduced by Laskey and Mills (1977) with a "preflashing" of film and exposure at −70°C for fluorography and by Fujita (1982) with "corrections by a graphical method" for the case of intensifying screens.

c. Applications

A typical example of results obtained by pioneers in autoradiography on film can be seen in Fig. 9.3.

2. Microautoradiography with emulsions

If the visualization of radionuclide locations is required at the cellular or subcellular levels within cells or tissue sections placed on microscope slides, a "microautoradiography" is needed since the use of film is limited by the lack of proximity of the silver emulsion to the radionuclide of the sample. Two methods can be used for microautoradiography. The most common method involves the dipping of slides that carry the histological sections into a liquid emulsion. This method requires the fixation of the sample prior to coating with an emulsion and development of the coated sample such that the silver grains are in direct contact with the radioisotope-labeled sites. This technique is employed with light microscopy for the observation of the silver grains. The method is not fully appropriate in the case of diffusible substances. For example, the aforementioned method is good if the ligands are covalently or irreversibly bound to the receptors. There is another alternative method, named the "coverslip technique" in which emulsion-coated coverslips are tightly apposed to sections. This method is ideal for ligands not covalently or irreversibly bound such that they could lose their ligand-receptor integrity by the dipping method. After exposure, coverslips are detached, developed, and examined microscopically to count silver grains depicting the position of the radiolabeled receptors.

Despite the fact that great interest in this second technique has been demonstrated, it is definitely disused, as the product is no longer manufactured today. Detailed protocols for the analysis and quantifications of radionuclides by microautoradiography can be found in Sharif and Eglen (1993).

Ultrastructural autoradiography is also a powerful technique used in conjunction with high-resolution electron microscopy to characterize silver grain distribution inside very small structures or cellular organelles. Two techniques were developed: (1) a "dry" technique, which preserves all the diffusible substances, and (2) a "wet" method for large molecules, fixable lipids, and tightly bound small molecules (Stumpf and Sar, 1975; Williams, 1981).

The most popular nuclide used for microautoradiography is ^{3}H because of the short range of its low-energy beta particles providing the best resolutions as required in these techniques. ^{125}I also provides high-resolution microautoradiographs thanks to its internal conversion electrons emitted with low energy so having a short range as well.

a. Performance

Sensitivity. As the sample requires a thin layer of emulsion in the context of microautoradiography, the efficiency of detection of the ionizing radiations is lower than that of film. Where an exposition time lasts several weeks for a film, the same activity exposed to a liquid emulsion can take months before being revealed. Depending on the isotope, the sensitivity is about 5−10 times weaker than in macroautoradiography.

Resolution. The reachable resolution with liquid emulsions and the light microscope is limited by the optical resolution of the microscope and the minimum observable grain size. However, with the electron microscope, resolutions ranging from 0.1 to 0.2 μm have been reported and considered as the limits of resolution with currently available emulsions and developers.

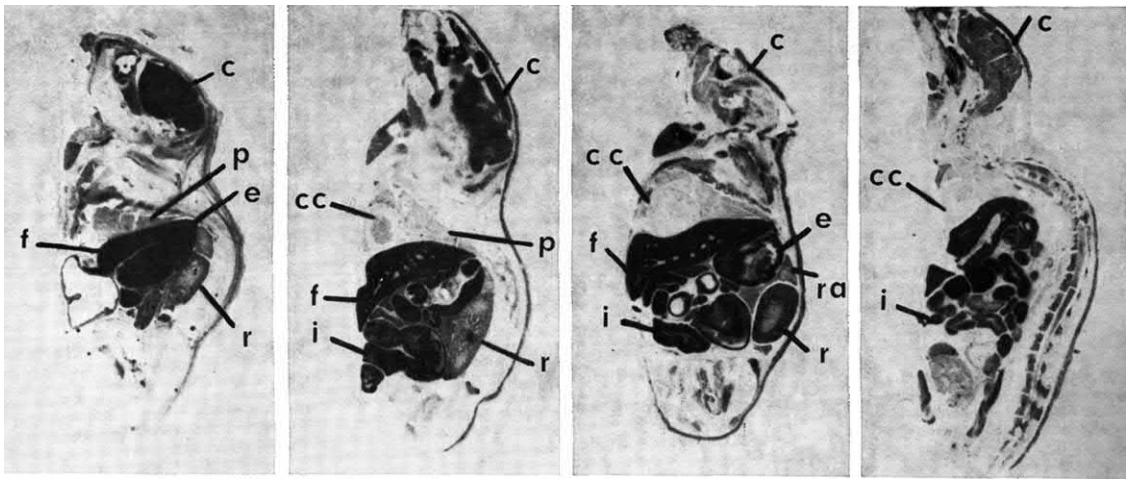


FIGURE 9.3 Autoradiograms of sagittal sections of mice sacrificed 30 min, 2 h, 6 h, and 24 h after oral administration of (2, 3 ^{14}C-anhydride succinic). Legend: c: cerebrum, cc: heart cavity, e: stomach, f: liver, i: intestine, p: lung, r: kidney, and ra: spleen (Chanal, 1976). *Figure reproduced with permission, from Chanal (1976), courtesy of Journal de Microscospie et de Biologie Cellulaire, published by the Société Française de Microscopie Electronique, Paris.*

b. Quantification

In the case of light or electron microscopic autoradiography, the quantification can be obtained by counting the grains, which is referred to "quantitative microscopy autoradiography." The individual silver grains in the emulsion, above a particular microscopic zone of interest, may be counted in the microscope field and correlated with grain counts obtained above other locations of the sample section as well as the background. Counts can be averaged from several thin sections, and the standard deviation can be calculated. Background counts, obtained from developed emulsions not exposed to radioactive sections, must be subtracted from microscopic autoradiographs.

In most recent applications, digitized images recorded by a computer linked to the video camera of the microscope can be analyzed and correlated directly to the real radioactivity in Bq/g after comparison with standards.

c. Applications

The following are some typical images obtained in microautoradiography. The first is an example of microautoradiography of cells visualized by light microscopy illustrated in Fig. 9.4.

An example of ultrastructural autoradiography visualized by electron microscopy is provided in Fig. 9.5.

Receptor studies are also a common application for microautoradiography. Receptor microscopic autoradiography for cell and tissue localization of drugs is reviewed by Stumpf (2012), including its development history, multiple testing, extensive applications, and significant discoveries along time, the radiolabeled compounds used

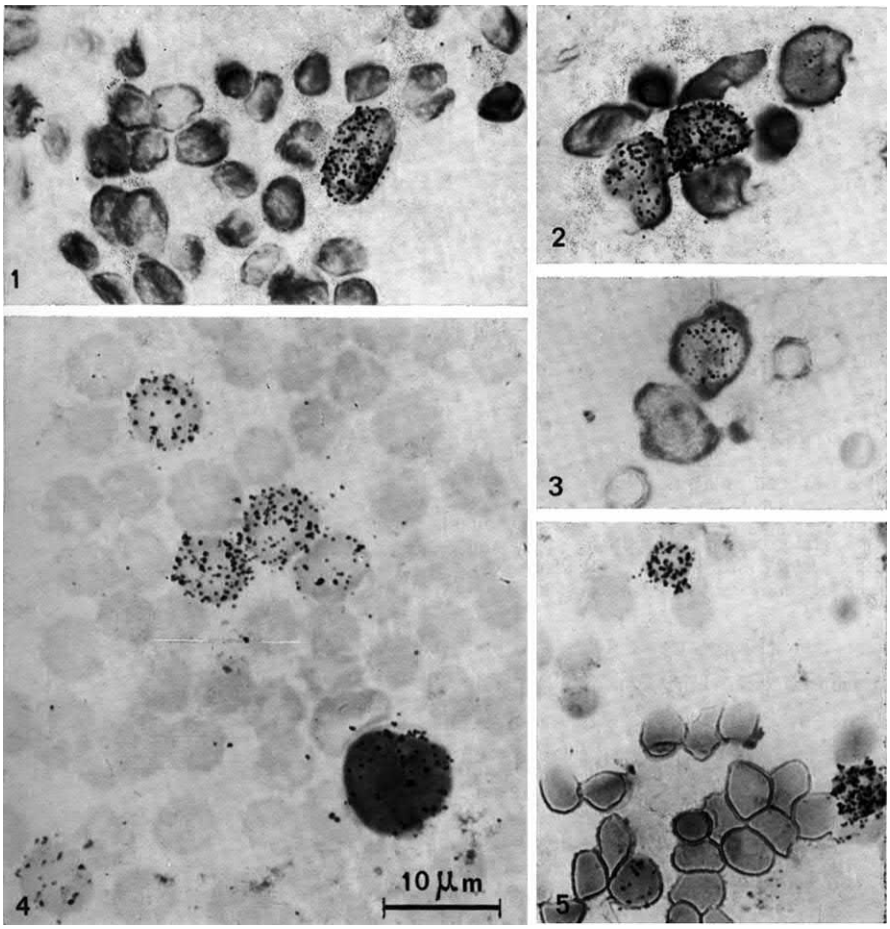


FIGURE 9.4 Microautoradiographs 1, 2, and 3: Bone marrow cells taken from a rat injected with ^{3}H-thymidine. The radioactive cells are those in S phase during the incubation and which have thus incorporated the precursor into their DNA (magnification 1,900X). Microautoradiographs 4 and 5: Blood cells of rat exposed to ^{3}H-leucine during 30 min. The radioactive cells are reticulocytes, which synthesized protein during the incubation. A white blood cell can be seen, which is slightly radioactive (magnification 1900×). *From Simmonnet et al. (1976). Figure reproduced with permission, from Simmonnet et al. (1976), courtesy of Journal de Microscopie et de Biologie Cellulaire, published by the Société Française de Microscopie Electronique, Paris.*

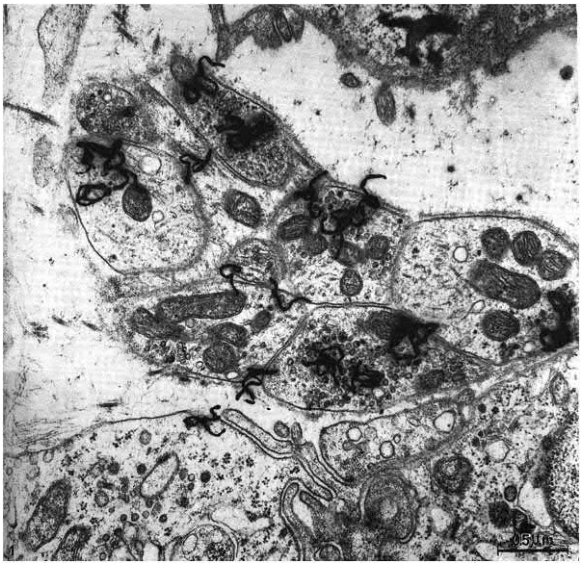


FIGURE 9.5 Nerve bundle in rat epiphysis. Epiphysis has been fixed 30 min after injection of 5 mCi of ^{3}H-noradrenaline. Silver grains are localized mainly over clusters of small granulated vesicles, 450 Å in diameter on the average, magnification 43,000×. *From Taxi (1976). Figure reproduced with permission, from Taxi (1976), courtesy of Journal de Microscopie et de Biologie Cellulaire, published by the Société Française de Microscopie Electronique, Paris.*

being essentially tagged with ^{3}H or ^{125}I for a guaranty of high-resolution imaging.

B. Phosphor screen technology (autoradioluminography)

1. History

In the early 1980s, two companies (Fuji and Kodak) intended to suppress the use of radiographic film in medical imaging, first because silver salts were not reusable, excessive price, and the creation of pollutants. Moreover, the need of providing digital radiographic data was in the air, as the use of computers was becoming part of the daily routine. The acquisition of digital data with film was an indirect process, involving high-resolution scanners in the second phase after revelation. Also, film had demonstrated to be of limited sensitivity to radiation and exhibited a poor dynamic range. Research was then oriented toward both improvement of the dynamic range and sensitivity, and the direct generation of digital images. In the framework of the research, photostimulable screens or phosphor screen technology was developed, and the first commercialized instrument was provided by Fuji Film in 1983. It was initially presented as a method providing long linear dynamic range images for medical X-ray imaging (Sonoda et al., 1983). Later, storage phosphor screen technology was adopted as the method of choice for imaging radionuclides and began to replace film for a great number of applications in molecular biology, pharmacology, and receptor autoradiography (Hamaoka, 1990). Today, phosphor screens are still available on the market with three main manufacturers: General Electric (Typhoon FLA 7000 and Typhoon FLA 9500), Bio-Rad (PharosFX), and PerkinElmer (Cyclone). The screen technology is comparable for General Electric and PerkinElmer, both inheriting from the former Fuji technology, whereas the Bio-Rad range of products is related to the former Kodak technology.

2. General principles

a. Image formation

It must be kept in mind that phosphor screen technology has a strong analogy with film autoradiography (contrary to electronic autoradiography systems). Both are energy storage devices for which the sensitive area is first exposed to the sample by close contact. This is the **exposition** step whereby the energy deposited by the beta electrons (or any kind of ionizing radiation) onto the sensitive area is stored in lattice defects of the material (silver bromide for film, bromofluoride of barium for phosphor screens). This first step is followed by a **revelation** step during which the image is spawned, in a chemical way for film or in an optical way for phosphor screen. This separation of exposition and revelation procedures can be considered as a significant drawback because there is no possibility of checking a current level of exposition "on the fly" (for film as well as for phosphor screens, the revelation process clears the stored energy and the exposition must be repeated, if the exposure is inadequate). This frequently leads to under- or overexposition, especially in new studies where the level of activity is unknown. From an operational point of view, it can actually be considered as an advantage (compared with electronic autoradiography) because the revelation step is much shorter than the exposition step (several hundred times faster in autoradiography), up to several hundreds of samples can be exposed in parallel and revealed one-by-one later on.

Let us return to the specific case of phosphor screen technology. Phosphor screens are usually made of grains of barium fluorobromide (mean size 5 μm), containing traces of divalent europium (Eu^{2+}). Europium atoms are not directly involved in the energy storage phenomenon but are essential for the revelation. The defects of the lattice are usually bromine vacancies that behave as electron traps. When a beta particle enters the sensitive layer, it ionizes atoms of europium (which become Eu^{3+}) along its path, and the electrons produced in this way are trapped in the bromine vacancies. These traps are metastable states that can last up to several weeks (even months), which allows very long exposition times. There is a limitation in increasing exposition time, for ultraweak activity samples, when the mean time between ionizations is of the order of

the lifetime of the metastable state. The screen then tends to lose as many charges as created, and the signal is no more linear, neither in terms of activity nor exposition time (Amemiya, 1995).

The phosphor screen quality is directly related to the density of bromine vacancies and to the density of europium atoms. For example, for an excessively high density of vacancies, the lifetime of electron traps tends to shorten and, following former remarks, the sensitivity decreases due to the higher rate of recombination of electrons with ions.

b. Phosphor screen revelation and quality

As mentioned previously, europium ions are essential for the revelation of the phosphor screen image. This revelation is no longer chemical but optic. When the phosphor screen is exposed to light (more often a He—Ne laser light, discussed further on), the energy of photons is transferred to the trapped electrons, which are released in the conduction band until they meet an ionized europium (Eu^{3+}). Then, a recombination between the electron and the europium takes place and europium returns to its ground state, emitting a UV-blue photon, the mean energy of which is 390 nm. The schematic of whole physical steps involved in the image formation is given in Fig. 9.6.

This mechanism, sometimes named upconversion, is noticeable because the screen reemits more energy than it absorbs (a red laser is used and a blue light is emitted). Of course, this can be simply explained if we consider that the missing energy arises from the part of the energy of the initial beta particle spent to store electrons in the vacancies. As we will discuss later, the spatial performance of such a technology depends not only on the scanning system but also on the intrinsic characteristics of the screen such as the size of the grains in phosphor screen (usually 5 μm) and the total thickness of the sensitive layer. An excellent overview of the physics involved in phosphor screens is available in Rowlands (2002).

c. Scanning mechanism and light collection optics

To preserve the localization, the revelation process is done point by point by scanning the phosphor screen with a laser

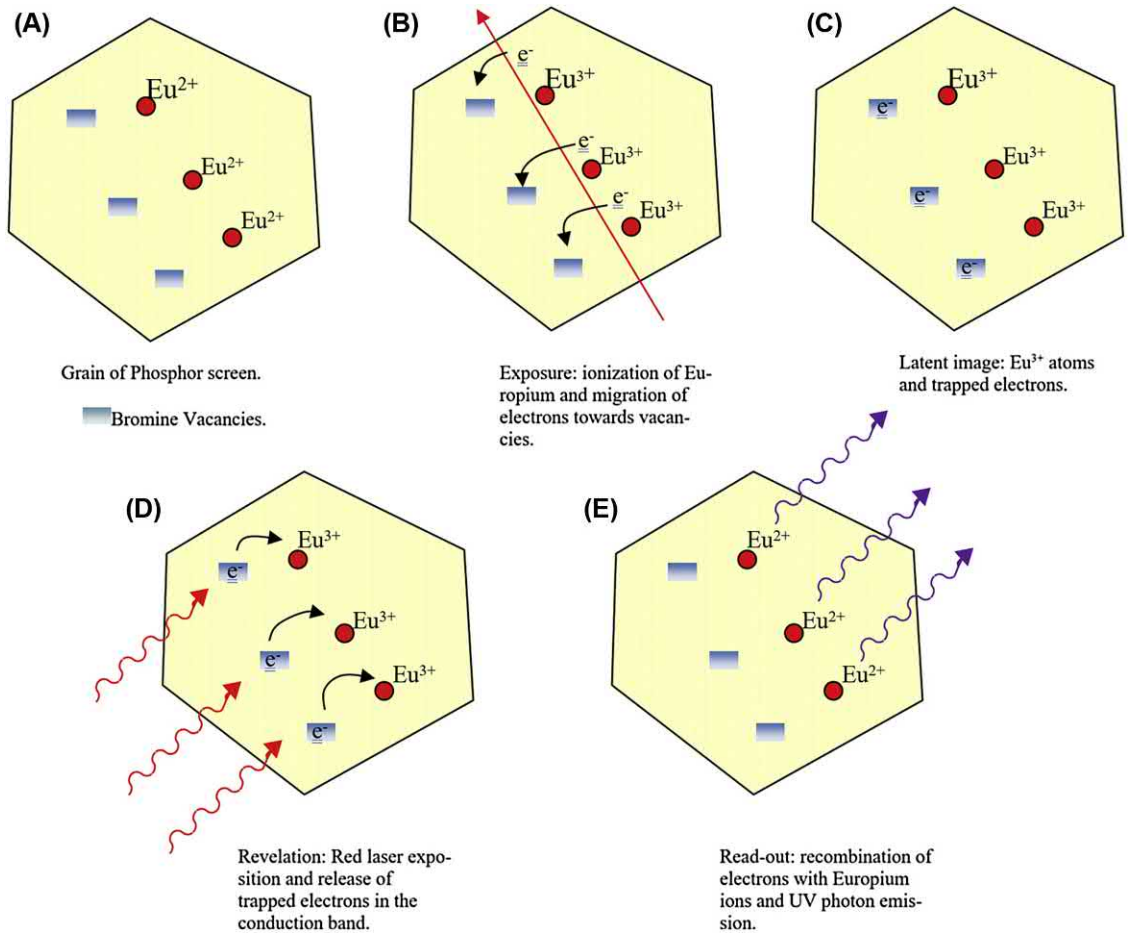


FIGURE 9.6 The five steps involved in the formation of an image in a phosphor screen. For the color version of the figure, the reader is referred to the online version of the book.

spot. There are mainly two ways of implementation of the scanning mechanism for the revelation phase: (1) the phosphor screen is kept in a flat plane while the laser (He–Ne) sweeps across the screen as it is reflected by a galvanometric mirror, and (2) for flexible phosphor screen, the screen is loaded on a cylinder that spins at 360 revolutions per minute, whereas the laser follows a translation movement, parallel to the axis of the cylinder.

In both cases, the measurement is done by collecting the UV light on a photomultiplier with optic fibers or a lens placed in close proximity of the laser dot, followed by digitalization of the signal (Coquerel, 1996) (Fig. 9.7).

3. Various phosphor screens

The screens are mainly derived from two technologies; the Fuji and the Kodak ones. Hence, there are two main chemical forms. Each type of screen comes in different models, putting the emphasis either on resolution, on sensitivity, on medium/high-energy, or on low-energy isotopes. The optimization for resolution is mainly a matter of thickness, whereas the optimization for sensitivity is related to a slight change in the chemical form (more Europium ions, for example).

Even though these modifications are visible to the user, they do not dramatically change the performance of one type of screen or another. Most screens are unable to detect low-energy isotopes because they are covered by a protective layer too thick to let the tritium (for example) beta particles reach the sensitive layer. To make phosphor screens compatible with low-energy isotopes, Fuji commercialized a special type of screen without a protective layer for this special purpose. Nevertheless, this screen cannot be cleaned and is very sensitive to contamination, hence of very little reusability.

4. Performance

a. Spatial resolution

Spatial resolution is often expressed in terms of CTF (contrast transfer function), which gives the contrast versus the frequency in terms of line pairs per millimeter. One can also have a more intuitive idea with the resolving power, which can be defined as the minimum distance for which two radioactive sources can be resolved. Table 9.3 provides resolution data for different screens of the Cyclone system and for a frequency of 2.5 lp/mm (400 μm).

In terms of resolving power, the SR and TR screens give roughly a resolving power for ^{14}C between 150 and 200 μm, whereas the TR screen for ^{3}H gives a resolving power of 70–90 μm. These numbers are far from what could be

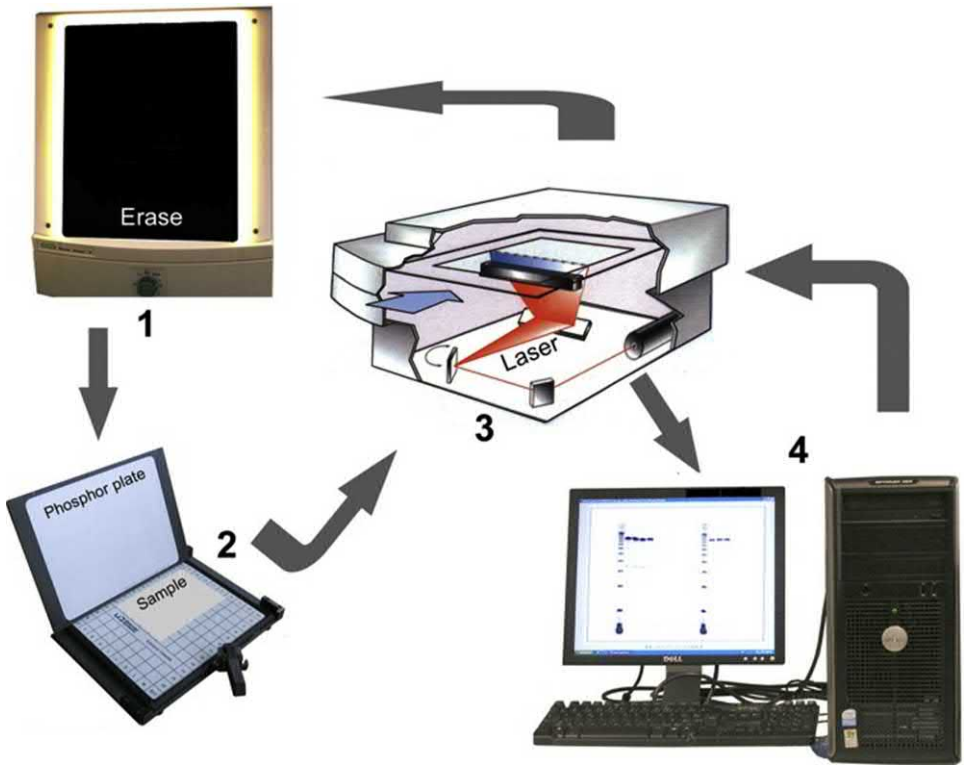


FIGURE 9.7 Schematic of the principle of operation of a phosphor screen. 1: residual signal erasing by exposing the screen to intense light, 2: exposition by contact to the screen into a cassette, 3: readout of the screen by scanning it with a laser beam; light is captured by a light collection guide and measured by a photomultiplier tube (not shown here), 4: image analysis with dedicated software for image processing and quantification by a computer. For the color version of the figure, the reader is referred to the online version of the book.

TABLE 9.3 Spatial resolution of various phosphor screens.

Screen	ST (high sensitivity)	MP (multipurpose)	SR (high resolution)	TR (tritium, uncoated)
^{14}C	17%	25%	33%	38%
^{3}H	N/A	N/A	N/A	69%

expected knowing the range of beta particles in the material (1 μm for ^{3}H, 10–20 μm for ^{14}C). This signifies that the restriction factors for resolution come mostly from the screen laser scanning readout and especially from light scattering inside the medium. Under a certain value of the laser spot (around 50 μm), there is no real improvement in the resolution. The light scatters inside the material, and the local measurement is spoiled by the untrapping of electrons in the vicinity of the current point. This is confirmed by the different values of resolution measured for different screens. The ST screen is the most sensitive. It is also the screen for which the sensitive layer is the thickest, whereas for SR and TR screens, the sensitive layers are thinner. Nonetheless, light scattering is higher in ST screens due to their thickness.

b. Dynamic range and sensitivity

The sensitivity of the phosphor screen is known to be much better than film, especially for medium-energy radionuclides (^{14}C, ^{35}S). The unit used to determine the sensitivity is dpm/mm^2/h, i.e., the minimal detectable activity for a 1-h exposition. One dpm/mm^2/h corresponds to 60 disintegrations per mm^2. The usual ultimate sensitivity for phosphor screens depends on the isotope: the higher the energy, the better the sensitivity. Typical data are 0.5 dpm/mm^2/h (30 disintegrations per mm^2) for ^{35}S and 0.1 dpm/mm^2/h (6 disintegration per mm^2) for ^{32}P. To calculate the sensitivity versus exposure time, a first approximation is to divide the previous number by the exposure time (in hours). For 10 h of acquisitions, the detection limit is then supposed to be 0.05 and 0.01 dpm/mm^2 for ^{35}S and ^{32}P, respectively. Of course, this rule of thumb is not entirely correct because background noise tends to increase with exposure time due to cosmic ray interactions.

The linear dynamic range, which can be defined as the range of activity over which the signal measured from the phosphor screen is linear (measurements stay proportional to the activity), is a fundamental parameter, as it represents the screen's ability to record very low and very high activities on the same image. The linear dynamic range of phosphor screens is typically between 10^4 and 10^5 (Johnston and Pickett, 1990). This is a major advantage compared with film, which exhibits a poor linear range of 10^2, although the total range of detection in film (including the nonlinear part for low and high activities) can exceed 10^3 with film.

5. Quantification methods

Phosphor screens are intrinsically powerful tools for quantification in autoradiography, but some precautions must be taken. First and foremost, as standard screens are highly reusable, any previously accumulated charge must be erased from the screen before a new exposure. The laser readout process actually records only a part of the signal, and if no erasing procedure is carried out to clear the screen, a ghost image will spoil the next acquisition. Common clearing procedures involve exposure of the screen to fluorescent light for 3–5 min (Reicherts, 1992). Note that for most systems, a fluorescent light is also included in the laser scanning apparatus to perform the deletion. As light, and specially fluorescent light, is used to erase the screens, a classic recommendation when handling the screen before the laser readout phase is to minimize accidental exposure to light bulbs, which create a risk of spoiling the acquisition.

A slow deletion of the signal also occurs over time. Thus, it is also recommended that the readout be performed within a reasonable time frame after exposure. Signal fading of up to 50% with 2 months postexposure has been reported (Amemiya, 1995).

Cleaning of the screen is also advised to remove any contaminating material. As samples are pressed against the screen, it is not unusual for traces of radioactivity to remain on the cover of the screen. Residual salts, or dyes from stained samples, can also linger on the screen and disturb ulterior measurements. Manufacturers usually sell screen cleaning solutions for such a purpose.

Phosphor screen technology is less sensitive to sample thickness than particle counting systems because the devices are only energy sensitive and because beta particles coming from deeper layers of the sample are less energetic. This property is an asset but the conversion between optical units and dpm/mm^2 requires knowledge of the isotopes present in the samples. This means that multiple labeling experiments with several isotopes on the same sample cannot really be quantitative with energy storage techniques such as phosphor screens.

As discussed previously, quantification in autoradiography implies a fundamental connection between the measurements obtained with the imaging technique (in optical units or in dpm/mm^2) and the real data of interest, i.e., the mass activity (dpm/g). There is no magic formula giving mass

activity versus measurements (even in dpm/mm^2). The exposure of a sample of known mass activity is always more rigorous. Phosphor screens have a very wide linear dynamic range. Therefore, only one calibration standard should be required, preferably with an activity chosen in the upper part of the dynamic range. It is necessary to compensate for sample thickness artifacts produced by medium-energy isotopes (^{14}C, ^{35}S), which can create a mismatch in the proportionality between mass activity and dpm/mm^2. Therefore, it is always recommended that one choose a standard of similar thickness as the sample.

6. Advantages and drawbacks

Compared with film autoradiography, the advantages of phosphor screen technology are numerous:

- Reusability (limited for TR screen).
- No chemistry involved.
- No dark room required, i.e., each step of the analysis can be carried out under normal lighting conditions and at room temperature.

The only drawback of phosphor screens compared with film is actually their resolution (over 70 μm), which is far from what a film can provide, although sufficient for most applications. Compared with electronic autoradiography, the main advantage is the possibility of parallelization of exposure (with several screens), which leads to a much higher throughput, except for low-energy isotopes.

7. Applications

The range of applications for which researchers use storage phosphor screens technology in the field of biological science is wide, including whole-body autoradiography (Mori and Hamaoka, 1994), receptor autoradiography (Lidow, 1997) (Lidow, 1997), high-resolution gel analysis, DNA sequencing, Western blotting, TLC plates, and DNA microarray (Jiao and Zho, 2002; Hodges and Smoller, 2002). Some of these applications require both high spatial resolution and reliable quantification within a large range of radioactivity concentrations located in the samples, as well as much shorter exposure times than with photographic emulsion (days compared with week).

- **Whole-body autoradiography:** For pharmacology and toxicology studies, the fate of a potential therapeutic agent is often determined by studying the distribution of radiolabeled compounds in test animals. After the administration of a labeled substance, the time course of absorption, distribution, metabolism, and elimination (ADME) functions are followed by autoradiography of organ sections (Li et al., 2008). Many examples can be found in the literature. An article by Solon and Kraus (2002) gives a remarkable review on QWBA and displays some examples taken from studies on drug discovery or drug development.
- **Receptor autoradiography:** Checking the affinity of a compound for a specific receptor is often processed via a radioligand binding and quantitative autoradiography using a phosphor plate system. A basic procedure involves incubating slide-mounted tissue sections with radioligands, washing and drying of the sections with specifically bound ligands under conditions that preserve ligand binding, and visualizing and quantifying the binding sites in the tissues. A large number of examples can be exhibited. Three of them are mentioned here, which illustrate recent advances in therapy research:
  - The first is related to the mechanism of action of an immunomodulatory drug in autoimmune affections in the central nervous system (CNS) using QWBA and autoradioluminography (Foster and Billich, 2007) (Fig. 9.8),
  - The second concerns molecular cancer therapy research in which the authors are investigating antitumor efficacy, tolerability, pharmacokinetic properties as well as toxicology profiles using autoradioluminography (Massey, 2010) (Fig. 9.9).
  - The third is chosen in the field of neuropsychopharmacology where the researchers explore a regulation mechanism of dopamine D1-like receptors under the action of a pharmacologic substance, by means of a tritiated ligand and the use of a phosphor plate (Kobayashi and Haneda, 2012).

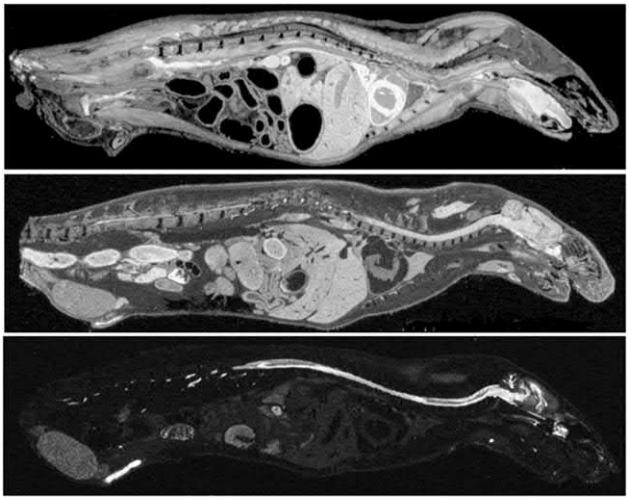


FIGURE 9.8 Whole-body autoradiogram of a median sagittal section of a male Han WIST rat at 72 h after dosing of the ^{14}C-labeled oral immunomodulatory drug FTY720 showing high concentrations in the CNS white matter (Foster and Billich, 2007). *Printed with permission copyright © 1998–2010. JPET Online by American Society for Pharmacology and Experimental Therapeutics.*

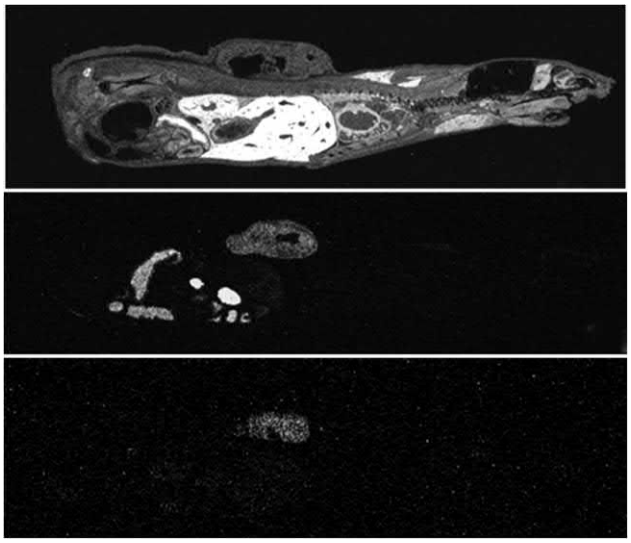


FIGURE 9.9 Whole-body autoradiograms of median sagittal sections of tumor bearing female HsdNpa mice at 5 min and 24 h after IV dosing of a ^{14}C-labeled synthetic Hsp90 ATPase inhibitor foreseen for the treatment of solid tumors and hematological malignancies: top image shows that radiolabeled compounds were taken up into the viable tumor at 5 min postdose; bottom image shows no radioactivity detected in any tissue except viable tumor and GIT content at 24 h postdose. *Data courtesy of Alain Schweitzer.*

For these applications in drug development and therapeutics, readers can also review two synthesis papers (D'argy & Sundwall, 2000; Solon and Schweitzer, 2010).

Other examples will be shown in the next section of this chapter, in comparison with real-time imagers, in the field of molecular biology (e.g., TLC and blots).

IV. Particle counting imaging systems

Particle counting systems, also referred to as electronic autoradiography systems, are an alternate principle of imaging based on the detection and localization of beta particles (more generally of any kind of energetic charged particles), one-by-one. These systems are purely electronic, with no intermediate storage step before revelation, and the image appears during the experience. Particle counting systems are all based on a physical amplification phenomenon (e.g., amplification of charge in a gas or amplification of light in a photomultiplier), which yields a pulse magnitude large enough to spawn an electronic signal for each beta particle. This electronic signal is then processed, and the localization data are stored in a file.

Electronic autoradiography systems were first commercialized during the 1980s, with systems such as the Ambis, the DAR (Berthold), and the Instant Imager (Packard Instruments now PerkinElmer, Inc.). All three were based on the use of an MWPC (multiwire proportional chamber), developed in the late-1960s by Georges Charpak, Nobel Laureate for Physics 1992 (Charpak and Bouclier, 1968).

Particle counting imaging systems are classified as real-time imaging systems because the image is displayed on-the-flight as beta disintegrations occur. One of the greatest advantages of this property is that there is no under- or overexposure for this type of technology: the acquisition is monitored by the number of counted disintegrations. For high-activity samples, the acquisition is stopped after a very short time, whereas for low-activity samples, the systems can monitor their own acquisition time, waiting for a minimum amount of disintegrations. This property makes these systems particularly useful in an early stage of studies when the biologist does not have even a rough idea of the activity of the samples.

On the other hand, particle counting imaging systems are "one acquisition at once" systems. This means that, contrary to phosphor screens or film, there is no "parallelization" of the analysis, which can be a drawback for large studies requiring the "simultaneous" analysis of tens of samples. Nevertheless, for low-energy isotopes, such as tritium, the time saving is so important that particle counting systems are always considered as the better alternative, whatever the number of samples.

Today, some researchers continue to use autoradiography; however, as the autoradiography market has slowed down, the former systems (Ambis, DAR, and InstantImager) are being discontinued. Today, particle counting systems are still present on the market through products manufactured by companies such as Biospace Lab or Ai4R. In the framework of this book, we have decided to focus on what is in the forefront of research in the biosciences today, i.e., the BetaIMAGER TRacer, the BetaIMAGER DFine, and the BeaQuant systems.

A. Gaseous detector

1. History: from MWPC to PPAC (BetaIMAGER TRacer) and to micropattern gas detectors (BeaQuant^{TM})

Gaseous detectors were initially single channel detection systems with no real capabilities of localization. They were used predominantly as Geiger counters for the quantitation of radioactivity levels (Fig. 9.10).

A first improvement was made with the proportional counter, which was also a single channel detection system, but whose main property was to deliver a signal proportional to the quantity of charge initially created by the incident particles. This proportional relation between signal and initial charge was made possible by the choice of gas,

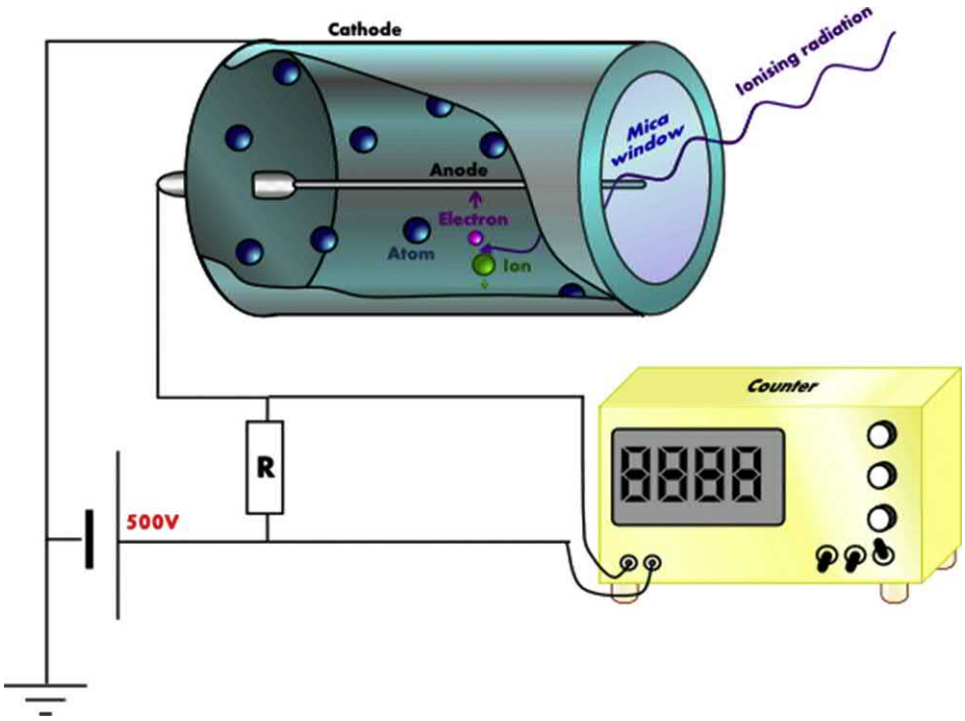


FIGURE 9.10 Schematic diagram of the first gaseous detector, the Geiger counter. A cylindrical vessel fitted with a small wire in its central axis and filled with air. A high voltage is set between the wall of the cylinder and central anode wire. When an ionizing radiation enters the wall, the electron created by the ionization is accelerated and spawns a limited spark, which is detected by the electronic sensor. For the color version of the figure, the reader is referred to the online version of the book.

i.e., noble gases with a small amount of hydrocarbon. Noble gases are fundamental in gaseous detectors because they are more easily ionized, thus facilitating the avalanche process. Small amounts of hydrocarbon (ethane, methane, etc.) play the role of quencher of the avalanche process. Without hydrocarbon, the gas amplification process is unstable, and sparks occur frequently.

In 1968, Georges Charpak (Charpak and Bouclier, 1968) made a determining step by conceiving a system made of a set of parallel wires in the middle of two flat electrodes, which he named multiwire proportional chamber (MWPC). The wires are set at a high positive voltage, whereas the two flat electrodes are grounded. Fig. 9.11 illustrates the principle of operation of the MWPC. The first ionization charge resulting from the initial particles (the beta particle, for example) drifts toward the closest wires. The gas amplification process takes place in the vicinity of the wire where the electric field is much higher than in the rest of the chamber. This fast moving charge cloud induces a fast electric signal on every electrode. Localization is achieved in one direction by identifying the wire close to which the amplification took place. In the orthogonal direction, the flat electrodes are made of an electric strip, and localization is achieved using the electric signal induced on the strips.

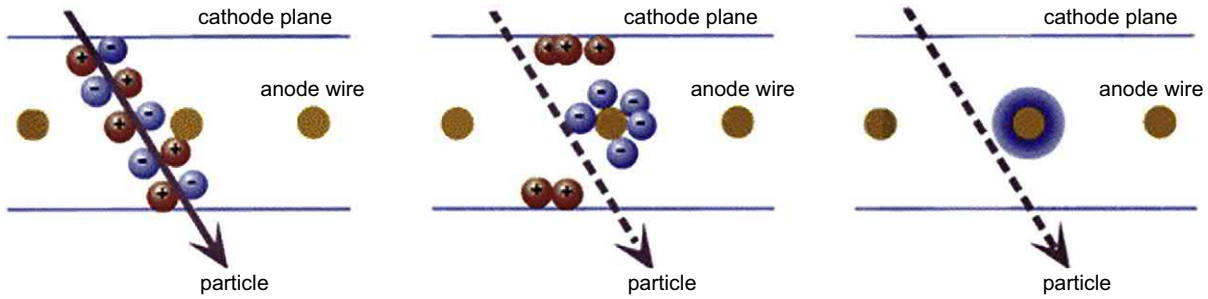


FIGURE 9.11 Principle of operation of the multiwire proportional chamber. Electrons created by the incident ionizing particles are accelerated near the wires. This creates a charge cloud proportional to the initial number of electrons. Localization is achieved by measuring the direct and induced electric signals on the wires. For the color version of the figure, the reader is referred to the online version of the book.

MWPCs are very sensitive, and each beta particle entering the gas chamber is usually detected. The main drawback of this technique, when applied to autoradiography, is the spatial resolution because the space between two wires cannot be smaller than 1 mm. Under 1 mm, the MWPC loses its properties of charge amplification in the close proximity of the wires and begins to be unstable. To overcome this lack in resolution, another gaseous detector geometry has been proposed, namely, the parallel plate avalanche chamber (PPAC). The PPAC is the simplest possible gas detector, since it is made of only two flat electrodes between which a high electric field is applied (Charpak and Dominik, 1989). The following mechanism of amplification is very simple: under a high electric field, first ionization electrons are accelerated until they reach the energy at which they can themselves ionize the atoms of a noble gas. The new electrons created during this secondary process are then accelerated until they can ionize themselves, and so on. The process is characterized by the distance covered between two ionizations and can be described accurately by an exponential of the distance between the location of the initial charge and the anode (Fig. 9.12).

This exponential proportionality between gain and position of initial charge during the avalanche process is the reason for the good spatial resolution of this instrumental design. Even though the thickness of the detector is large (3−6 mm), only the first ionization electrons created by the beta particles in the first layer noticeably contribute to the size of the avalanche and consequently to the total electrical signal (or optical signal in the case of the BetaIMAGER TRacer). As a matter of fact, the PPAC behaves like a very thin detector (50−100 μm), thinner than the sensitive layer of a phosphor screen (Fig. 9.13), and hence, its spatial properties.

2. Description of BetaIMAGER TRacer

a. Principles

The BetaIMAGER TRacer was derived from experiments conducted by Georges Charpak at the CERN laboratory in Geneva. It is a gaseous detector with a parallel plate proportional avalanche chamber with the exception that the readout device (the part of the system that calculates the position of the particles) is very different from its predecessors (Ambis, Instant Imager, etc.). The difference is the following: instead of using a complex electronic system, a vapor of triethyl amine (TEA) is added to the gas mixture (Peskov and Charpak, 1989) as illustrated in Fig. 9.14. This vapor has the convenient property of being electroluminescent in the UV spectrum (260−300 nm), which makes the avalanche scintillate during its development. Therefore, each beta particle creates a small UV light spot, which can be visualized by an intensified CCD camera at a typical frame rate of 50 frames/s.

The video signal is then digitalized, and the center of gravity (COG) of each spot is calculated by the computer. This COG is the best approximation of the emitting point. The principle behind the COG calculations is illustrated in Fig. 9.15:

COG calculations allow for a very high resolution using medium-size CCDs. In fact, the estimation of the center of the spot is much more precise than the pixel size, so that it is possible to localize the particle with three- to fourfold

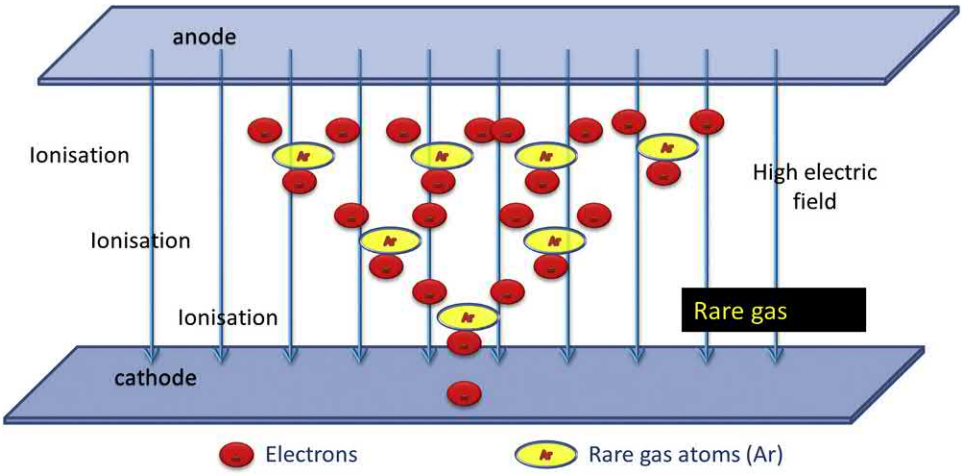


FIGURE 9.12 View of the exponential amplification process in a parallel plate avalanche chamber. The gain is exponentially proportional to the distance between the position of the initial charge and the anode. For the color version of the figure, the reader is referred to the online version of the book.

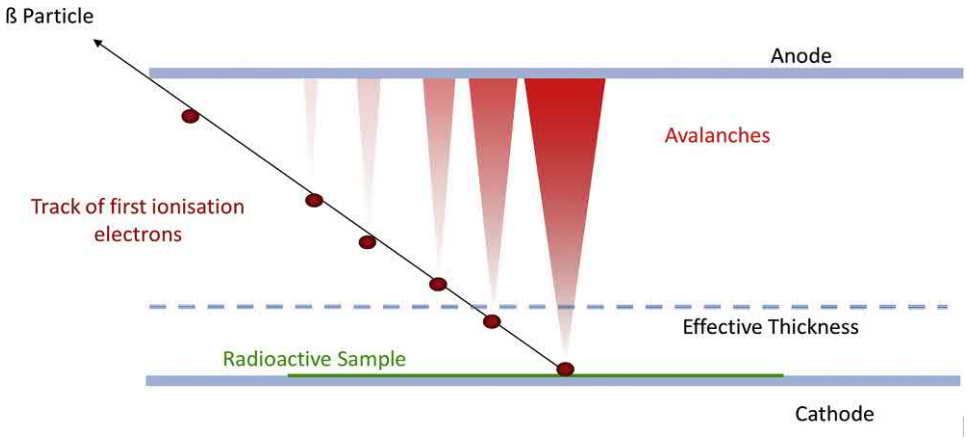


FIGURE 9.13 Skin effect in a parallel plate avalanche chamber. As the distance to the anode is longer for electrons created in close proximity of the cathode, the corresponding avalanche is much larger, due to the exponential behavior. Hence, only a thin layer close to the cathode is really contributing to the signal. For the color version of the figure, the reader is referred to the online version of the book.

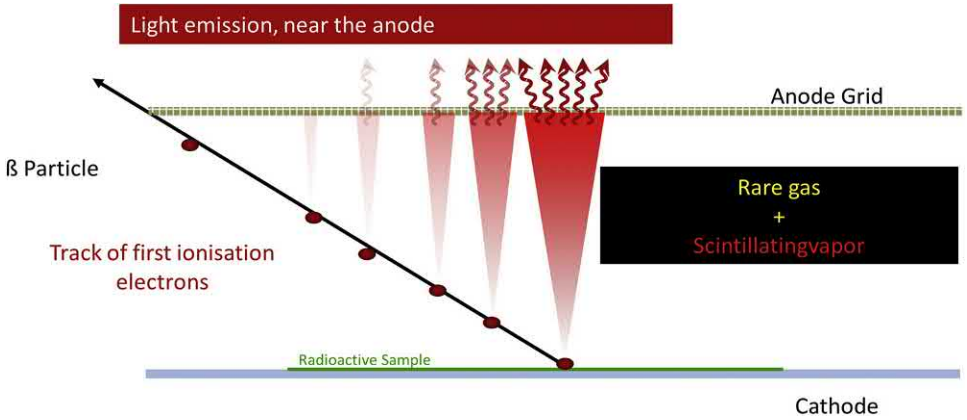


FIGURE 9.14 Light readout of avalanches in a parallel plate avalanche chamber. Triethyl amine (TEA) vapor is added to the gas. This vapor emits UV light in a proportional manner to the number of collisions between electrons and TEA molecules. Most of the emitted light is produced in close proximity of the anode. For the color version of the figure, the reader is referred to the online version of the book.

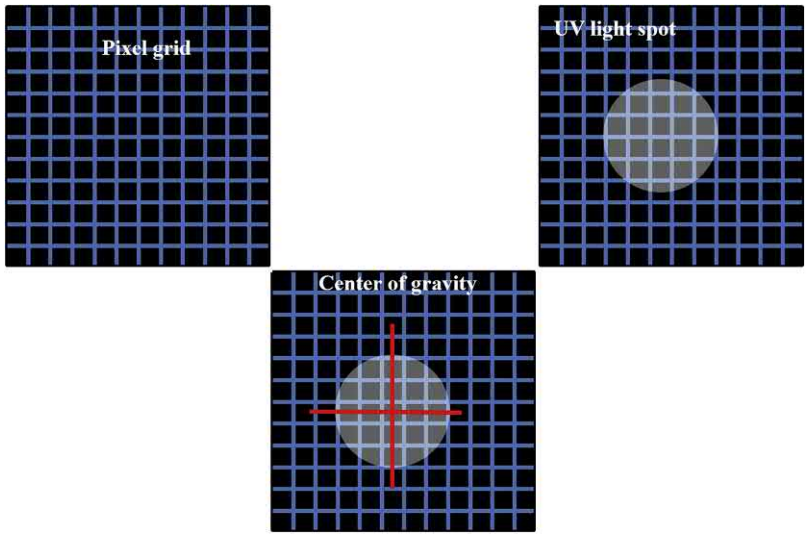


FIGURE 9.15 Principle of localization of the beta particles. The image recorded by the camera is digitalized, and for each light spot, the computer calculates the center using a simple center of gravity formula for which the weighting coefficients are the gray levels. For the color version of the figure, the reader is referred to the electronic version of the book.

better accuracy than the pixel size. A schematic representation of the BetaIMAGER TRacer is shown in Fig. 9.16.

b. Sample management

Sample management with the BetaIMAGER TRacer is a little more complex than with phosphor screens. To get the best results, in terms of resolution and sensitivity, the sample must be placed directly in the gaseous chamber so that the avalanche process can begin as close to the sample as possible. As the electric field is applied directly to the sample, the latter must be fully dried and as clean as possible (no dust). Different cassettes are proposed depending on the shape of the sample (slides, whole-body sample, TLC plates, blot analysis gel samples) as illustrated in Fig. 9.17.

For specific samples that do not fit the aforementioned dryness and cleanliness requirements (whole body, TLC, gels, etc.), it is possible to use other cassettes with either a conductive grid or a conductive Mylar membrane to isolate the sample from the gas chamber. One can notice a little loss of resolution and sensitivity with these types of sample holders compared with the standard slide cassettes.

c. Shape of the light spots

An interesting property of gaseous detectors is their ability to discriminate among different isotopes by analysis of the energy deposited in the gas by the beta particles. In the case of the BetaIMAGER TRacer, the difference between beta-particle emission from radionuclides with different beta-energy maxima (E_{max}) can be directly observed with the camera by simply looking at the intensity and the shape of the light spots, as described in Fig. 9.18.

For low-energy isotopes, such as tritium or ^{125}I, the light spots appear round and bright, whereas for higher-energy isotopes, the light spot appears elliptic in shape and is of lower brightness. It is therefore possible to segregate different isotopes by recording the characteristics of the light spots for each event. This property opens the door to dual-isotope labeling possibilities that traditional storage techniques cannot provide. Another prerequirement for dual-label experiments is the property of particle counting systems to take into account all beta disintegrations in the same way, whatever their energy.

3. Description of the BeaQuant system

a. Principles

Recent advances in gaseous detectors based on the use of micromeshes have made possible thinner structures than MWPC or PPAC, with typical distances of a few tenths of millimeters between the electrodes instead of few millimeters. These geometries (Derré et al., 2000), namely MPGD (micropattern gas detector), are now widely used in high-energy particle experiments, and they also present real potentials for beta-particle imaging. The reason is due to the higher electric field that can be applied between two

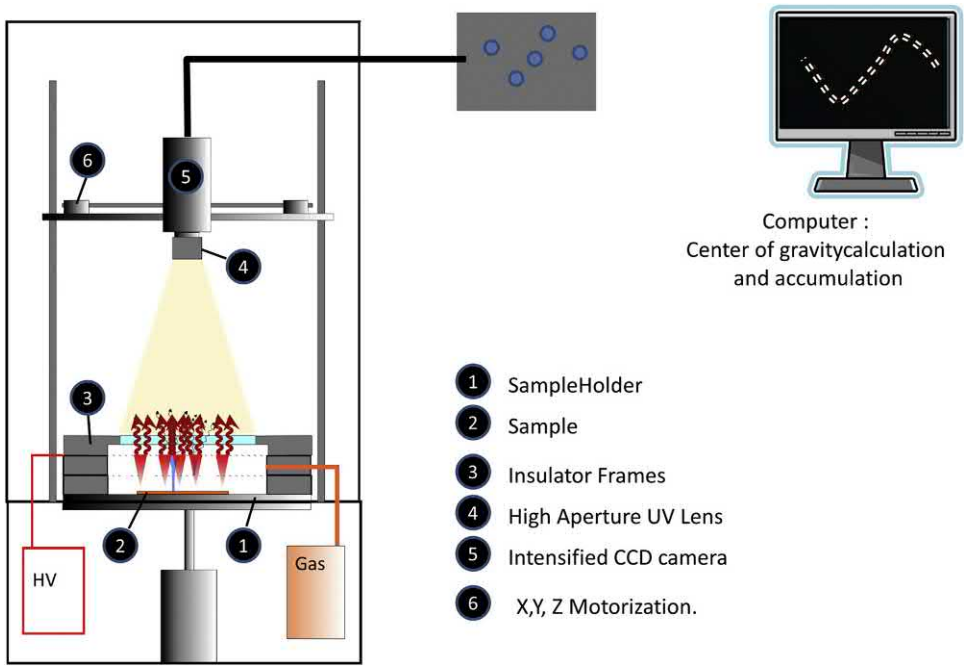


FIGURE 9.16 Schematic representation of the different parts of the BetaIMAGER TRacer. 1, 2, and 3 are integral parts of the gaseous chamber (the sample also acts as an electrode). 4 and 5 are parts of the optical block used to record the emitted light spots. The optical block is motorized to enhance the resolution by moving closer to the sample. For the color version of the figure, the reader is referred to the online version of the book.

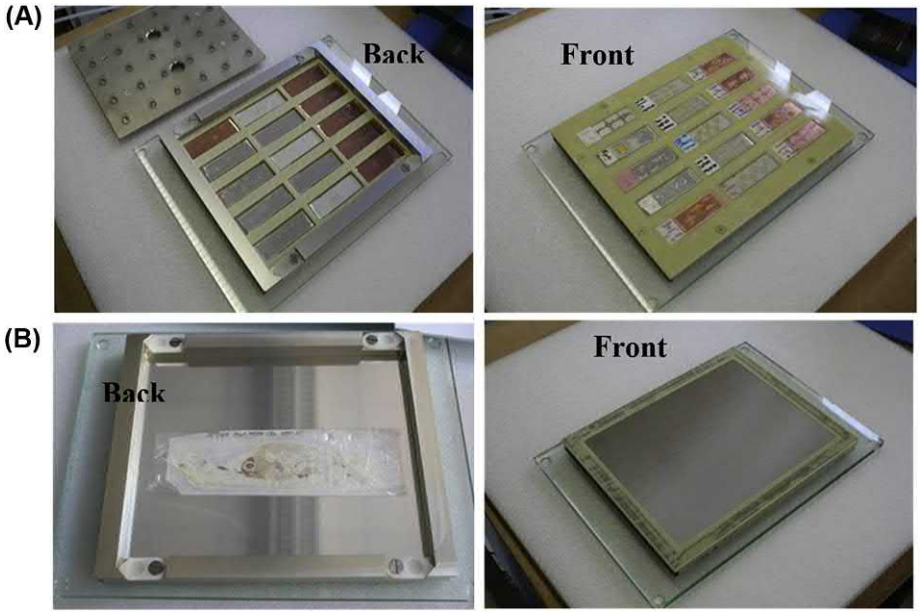


FIGURE 9.17 Two types of BetaIMAGER TRacer sample cassettes. A: Cassette for tissue sections laid on standard glass slides. B: Cassette with a Mylar membrane for whole-body autoradiography, gels, and thin-layer chromatography. For the color version of the figure, the reader is referred to the online version of the book.

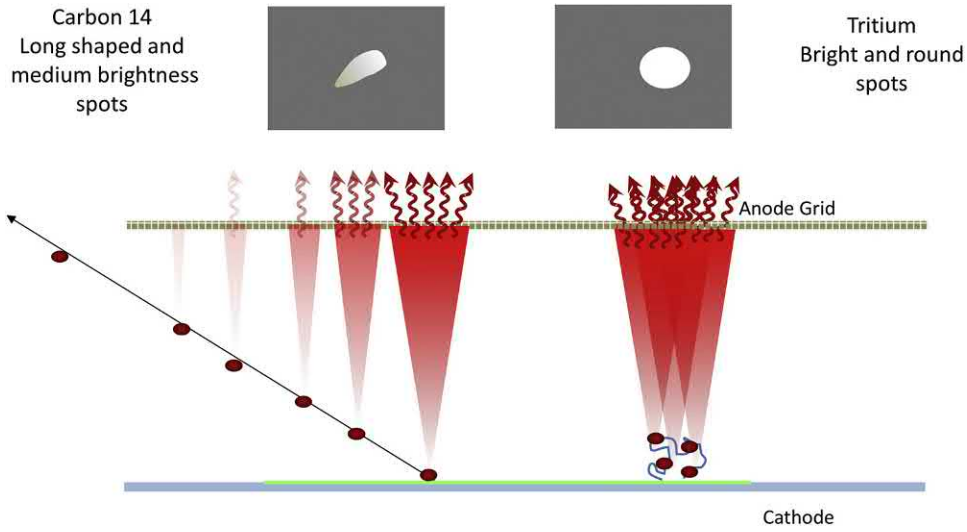


FIGURE 9.18 Typical light spot shapes depending on the isotope. For low-energy isotopes, the initial cluster of charge is compact and close to the cathode. The avalanches overlap, and the resulting shape appears round. For higher-energy isotopes, the initial charge cluster is spread over the whole chamber along an oblique line, resulting in a spot with an elongated, roughly elliptic shape. For the color version of the figure, the reader is referred to the online version of the book.

electrodes distant from a few tenths of millimeters and filled with conventional rare gas-quencher mixture. Typical electric fields for PPAC are usually between 5 and 8 kV/cm, whereas MPGD electric fields can reach up to 30 kV/cm. With such electric fields, the exponential amplification already mentioned for the PPAC exhibits a much higher gain per unit distance, thus allowing equivalent amplification factors to thicker geometries. Furthermore, this higher gain-per-distance unit makes the structure behave as an ultrathin detector with effective thickness lower than 50 μm (Samarati et al., 2004).

MGPD-based detectors dedicated to alpha- and beta-particle imaging have been commercialized since 2013 under the trade name BeaQuant (formerly BeaverTM) by the company AI4R, France. The structure of the detector is named PIM, which stands for parallel ionization multiplier.

It presents some similarities with PPAC structures, but as mentioned before, the main difference is found in the distance between the electrodes, which is roughly one order of magnitude lower. Fig. 9.19 depicts the standard geometry of a PIM detector, as implemented in the BeaQuant system:

The structure of the PIM detector can be split into three different functional parts (Donnard et al., 2009):

1. A first amplification gap of 200 μm, the cathode of which is actually the sample to be analyzed (a 75 × 25 mm standard glass histology slide, for example). The electric field in this amplification gap is around 30 kV/cm only, allowing the very first primary electrons to be amplified noticeably. The anode of this gap is made of a nickel micromesh with a pitch of around 40 μm.
2. A drift space of 1 cm in which the electric field is moderate (1 kV/cm), between the first and a second identical micromesh. Electrons generated in the first amplification gap are partially transmitted to this drift gap to a second amplification gap of 50 μm, between the second micromesh and a grounded segmented electrode, which is used to collect the charge and hence calculate the COG of the electron cloud. The purpose of this second amplification gap is to reach a total gain of several hundreds of thousandfold required by the electronics.
3. A second amplification gap of 50 μm, between the second micromesh and a grounded segmented electrode, is used to collect the charge and hence calculate the COG of the electron cloud. The purpose of this second amplification gap is to reach a total gain of several hundreds of thousandfold required by the electronics.

The gas mixture of the PIM detector is different from PPACs or MWPCs. It is also mainly constituted of rare gas, but neon is used instead of argon. The quencher is also different, as carbon dioxide is used instead of methane or ethane (or triethylamine in the case of the BetaIMAGER TRacer).

b. Electronics and localization of beta particles

The localization of the centroid of the electron cloud is not done using optical means, but by electronics. The central component for doing this calculation is the segmented electrode of the second amplification gap, a picture of which is shown in Fig. 9.20.

The segmented electrode is made of elementary pixels of 170 × 170 μm separated by 30 μm, thus providing a pitch of 200 μm. These elementary pixels are connected to two underlying boards of strips thanks to microholes machined by laser etching. Each underlaying strip is placed diagonally to reduce the capacitance between 2 strips. One pixel out of two is connected to the same strip by a geometrical multiplexing, thus reducing the total number of readout channels to 256. One of the underlaying boards is dedicated to the X-coordinate, whereas the other is dedicated to the Y-coordinate.

The electronic readout is performed with the Gassiplex chip (Santiard et al., 1994). This chip is composed of a charge-sensitive amplifier, a pulse-shape amplifier, and an

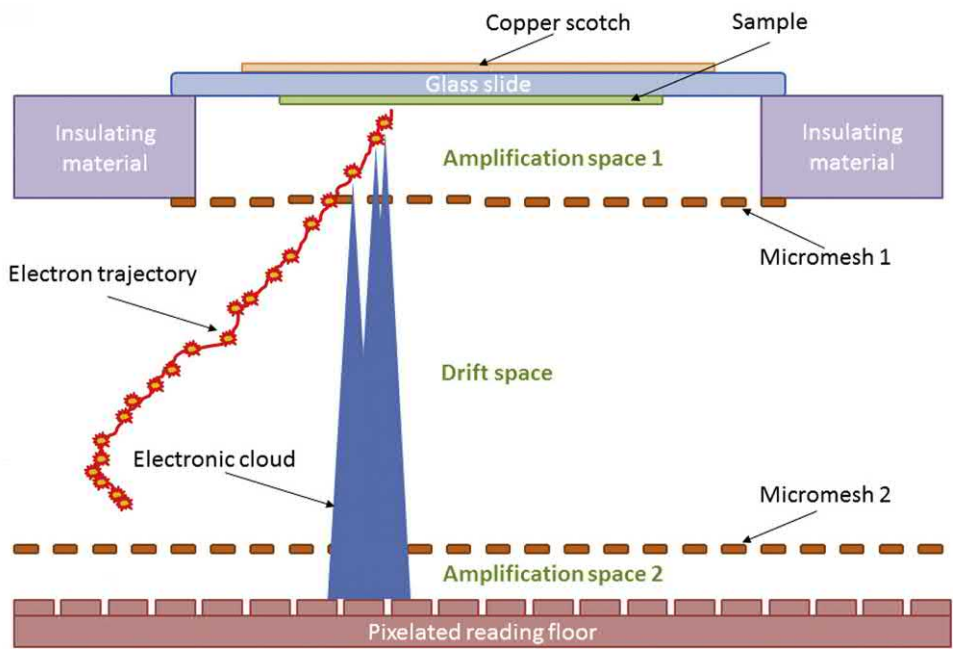


FIGURE 9.19 Sketch of the parallel ionization multiplier detector (courtesy of AI4R). For the color version of the figure, the reader is referred to the online version of the book.

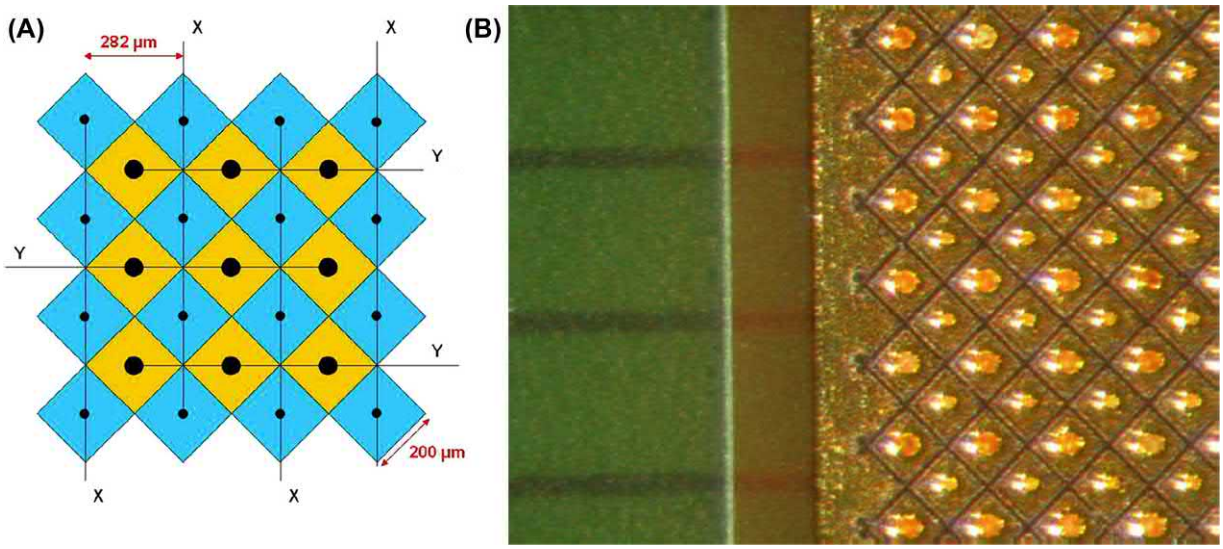


FIGURE 9.20 (A) Multiplexing between strips and pixels. (B) Left border of the segmented anode. Pixels of 170 × 170 µm can be observed together with an underlying strip of the X-plane readout placed diagonally (Courtesy of AI4R). For the color version of the figure, the reader is referred to the online version of the book.

internal analogical memory. An external analog-to-digital converter (ADC) is used to convert the multiplexed analogical output of the chip. Calculation of the position is done by a weighted sum of the converted charge.

The formation of the image is done by real-time accumulation of the detected particles, as it is done in any other particle counting device. It has then the same important property of limiting the risk of over- or underexposition. Nevertheless, for very high-activity samples, as for any particle counting system, a phenomenon of saturated counting occurs, which degrades the quantification.

c. Performance

The PIM structure has the capacity of rather high resolution thanks to the high electric fields. For tritium, resolutions of 20−30 µm have been reported, whereas for higher-energy isotopes such as ^{14}C, documented resolutions are around 50 µm. With regard to fields of view (FOV), the BeaQuant system has a sensitive area of 23 × 23 cm^2.

Sensitivity values of 0.0005 cpm/mm^2 are given by the manufacturer, which is in the same range as other particle counting systems. Another feature, in common with other particle counting systems, is its isotope separation capabilities (e.g., for samples labeled with several radioisotopes). The principle of separation is here based on the total charge collected by the segmented electrode, which depends on the number of primary electrons amplified and therefore on the mean energy of the radioisotope. Fig. 9.21 depicts the collected charge difference between ^{3}H and ^{14}C.

The difference of 30% and the weak overlap between the two distributions (shown in Fig. 9.21) allow for an efficient separation between the two isotopes.

d. Sample management

In addition to the differences in gaseous structure, another difference of the BeaQuant system compared with the BetaIMAGER TRacer is in the way samples are loaded. In the BeaQuant, samples are loaded from the top, and the system does not comprise a drawer. Instead, a sample holder is simply placed on the top of the system and locked in place with a light proof lid. The geometry of the sample holders depends on the type of samples.

The BeaQuant system is capable of imaging both small tissue sections directly laid on standard glass histology slides and large sections placed on tape (e.g., for QWBA). For standard glass slides, the samples are prepared by adding conductive tape on the opposite side of the slide to establish electrical conduction between the sample and the top electrode of the system. Connection is achieved thanks to a set of springs evenly repartitioned on the alveolar surface of the sample holder (one spring per alveolus per sample). For large sections laid on tape, the sample holder is actually a large glass plate equipped with handle, the backside of which is covered with a copper layer and is therefore conductive. Tissue sections are transferred to the glass plate using a transfer tape, as depicted in Fig. 9.22.

Once the acquisition is carried out, sections can be removed from the glass plate, hence making it reusable. This type of sample holder exists in two sizes: 10 × 10 cm and 20 × 20 cm.

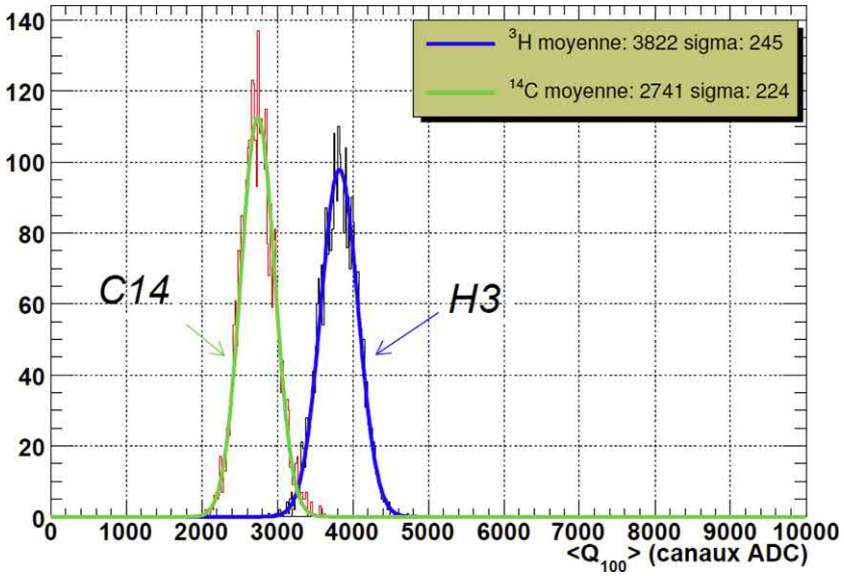


FIGURE 9.21 Distribution of charges in a parallel ionization multiplier imager for ^{3}H and ^{14}C in arbitrary units. The mean collected charge for ^{14}C is about 70% of the one collected for tritium. X and Y axes are, respectively, the electric charge in arbitrary units and the number of counts (Courtesy of AI4R). For the color version of the figure, the reader is referred to the online version of the book.



FIGURE 9.22 Sample holder of the BeaQuant for large section on tape. Sections are transferred on the glass plate the backside of which is copper-covered (Courtesy of AI4R). For the color version of the figure, the reader is referred to the online version of the book.

B. Solid membrane detector (digital microautoradiography)

1. History (BetaIMAGER DFine, formerly MicroImager)

The BetaIMAGER DFine (formerly MicroImager) was developed initially at the Institute of Nuclear Physics IN2P3—CNRS—ORSAY France (Laniece, 1994). The purpose of this development was to conceive an electronic autoradiography system, the spatial resolution of which would be as close as possible to film and emulsion, whereas its sensitivity would be comparable with or better than other electronic systems, such as the DAR, Ambis, and instant imager (especially for applications with tritium). At the beginning of the 1990s, the best electronic autoradiography systems could only demonstrate millimetric resolution, thus restricting their application to molecular biology and electrophoresis experiments and to neurological studies on slice in the case of in situ hybridization (ISH). There was therefore no real alternative to film or emulsion.

The initial specifications of the BetaIMAGER DFine were a spatial resolution at the cellular level and a dramatic improvement in sensitivity compared with film and emulsion (especially for tritium that is widely used for ligand studies).

2. Description of the BetaIMAGER DFine

a. Principles

The technological choice was based on contact imaging with a scintillating membrane. This membrane is made of a 10-μm foil of Mylar on which a monolayer of scintillating powder (Y_2SO_4 or ZnS) is sputtered (Fig. 9.23).

The medium grain size of the scintillating powder is 3 μm. The sample is pressed on the scintillating face. By hitting the closest grain of scintillating powder, the beta particle creates a small burst of light of tens of photons for tritium and around 50−100 photons for higher-energy isotopes such as ^{14}C. This burst of light is far too weak to be recorded and processed directly. A light intensifier with two MCP channels and a light gain of 10^6 is therefore used to amplify the burst. A conventional digital CCD is fastened to the light amplifier and delivers a light spot for

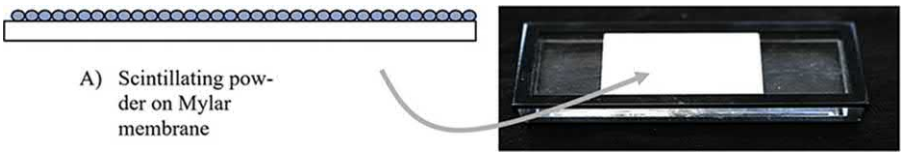


FIGURE 9.23 Left: Schematic diagram of a scintillating membrane. Its total thickness (Mylar + powder) is approximately 15 μm. Right: The scintillating membrane placed on the slide on a holding tray.

each beta particle, in a similar manner as the BetaIMAGER TRacer (Fig. 9.24).

b. Sample management

Fig. 9.25 is a schematic representation of the BetaIMAGER DFine.

The system has three functional parts:

- **The carousel** makes a 90 degrees rotation before lifting another sample into position. The sample platform can contain up to four samples.
- **The sample holder** receives the sample holding the slide and maintains the scintillating membrane against the sample.
- **The intensified camera** is fitted with an intensifier tube with a 40 mm diameter. The FOV is therefore 24 × 32 mm (half a standard glass slide).

The sample platform is both a carrousel and an elevator that lifts and presses the sample against the intensifier windows. The sample is lifted back down at the end of the acquisition. One additional feature of BetaIMAGER DFine is the optical block, which is fitted with LED lights. Its function is to illuminate the sample to acquire an optical image, which is then used for registration purposes. This feature is useful with samples for which the autoradiography image is too complex to decipher.

c. Shape of the light spots

As any other electronic autoradiography system, the BetaIMAGER DFine can record data (e.g., time of occurrence, etc.) in list mode files. The BetaIMAGER DFine can also segregate isotopes, according to the shape of the light spots. Fig. 9.26 illustrates how the BetaIMAGER DFine discriminates between isotopes.

C. Characteristics and performances of particle-counting imagers

1. Isotopes used

All of the beta emitters involved in conventional autoradiography are detected by the two radioimagers previously described, namely, the BetaIMAGER TRacer and BetaIMAGER DFine: ^{3}H (E_{max} = 18 keV), ^{14}C (E_{max} = 156 keV), ^{35}S (E_{max} = 167 keV), ^{33}P (E_{max} = 250 keV), ^{45}Ca (E_{max} = 257 keV), ^{32}P (E_{max} = 1710 keV), ^{90}Sr (E_{max} = 546 keV), and ^{90}Y (E_{max} = 2280 keV).

As mentioned previously, gamma emitters also emit internal conversion and Auger electrons and can be detected such as ^{125}I, which emits 35.6 keV gamma-ray photons + conversion electrons <4 keV). Likewise, other radioisotopes, such as ^{99m}Tc (a major marker of radiopharmaceuticals used in nuclear medicine), can be detected,

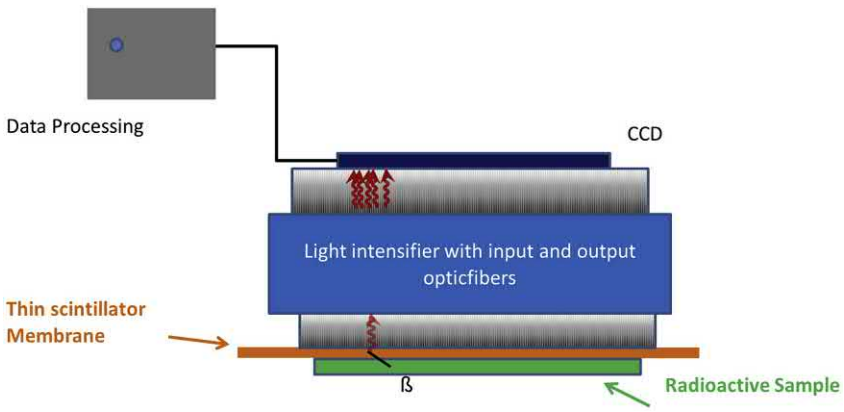


FIGURE 9.24 Operating principle of the BetaIMAGER DFine. The scintillator foil and intensifier tube are pressed against the sample. A small burst of light is created when a beta particle hits the scintillator. This burst is amplified by a factor of 10^6 by the intensifier and is then recorded by the CCD. For the color version of the figure, the reader is referred to the online version of the book.

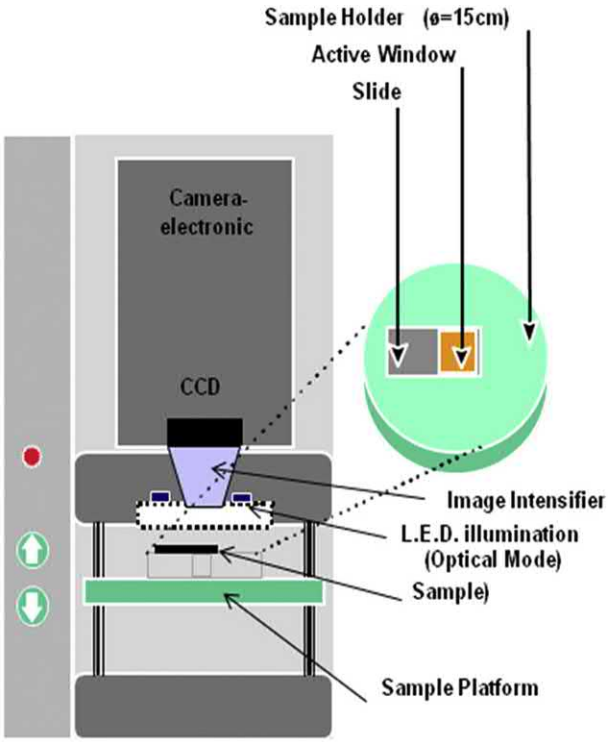


FIGURE 9.25 Schematic view of the BetaIMAGER DFine. For the color version of the figure, the reader is referred to the online version of the book.

as they emit many low-energy electrons. The main advantage of these imagers in the detection of radionuclides used in nuclear medicine, compared with film or phosphor screens, is their insensitivity to γ rays, which preserve resolution. Common gamma emitters used in nuclear medicine are ^{99m}Tc (γ: 140 and 2 keV + electrons 2, 15 and 120 keV), ^{111}In (γ: 171 and 245 keV + electrons 1, 4−9 and 18−27 keV), ^{123}I (γ: 159 keV + electrons 3, 23 and 127 keV) ^{131}I(γ: 365 keV + β^- (E_{max} = 247 keV) + electrons 45 keV), and ^{201}Tl (γ: 135 and 167 keV + electrons 1, 4, 8−5, 15.7−19.9 and 52.2−84.3 keV). β^+ emitting isotopes are ^{11}C (γ: 511 keV + β^+ E_{max} = 961 keV), ^{13}N (γ: 511 keV + β^+ E_{max} = 1.19 MeV), ^{15}O (γ: 511 keV + β^+ E_{max} = 1.72 MeV), and ^{18}F (γ: 511 keV + β^+ E_{max} = 650 keV). The above positron emitters as well as other positron emitters commonly used for PET (positron emission tomography) imaging can also be efficiently imaged with these systems without any parasitic image coming from the annihilation γ rays. Alpha emitters can also be detected because of the higher energy deposition by alpha particles; however, they require a specific adjustment of the gaseous gain with the BetaIMAGER TRacer.

2. Performance

The performance of these two systems with regard to sensitivity, linearity, and spatial resolution attributes to these instruments' excellent characteristics as state-of-the-art real-time fast imaging devices. Furthermore, background noise is low. These systems have typical detection thresholds of 0.007 cpm/mm^2 for ^{3}H and 0.01 cpm/mm^2 for ^{14}C with the BetaIMAGER Tracer and 0.4 cpm/mm^2 for ^{3}H and 0.004 cpm/mm^2 for ^{14}C with the BetaIMAGER DFine.

When checked with calibrated standards or short half-life sources, the linearity of these devices was superior to 10^4, a large dynamic range compared with 10^2 with film.

The spatial resolution, determined by measuring the full width at half maximum (FWHM) of radionuclide-labeled lines on engraved microscope slides according to Rogers (1969), was evaluated for the two systems. For the BetaIMAGER TRacer, the spatial resolution depends on the energy of the particles emitted by the radiolabeled lines. The best achieved performances are 50 μm for ^{3}H or ^{99m}Tc and 150 μm for ^{32}P or ^{18}F.

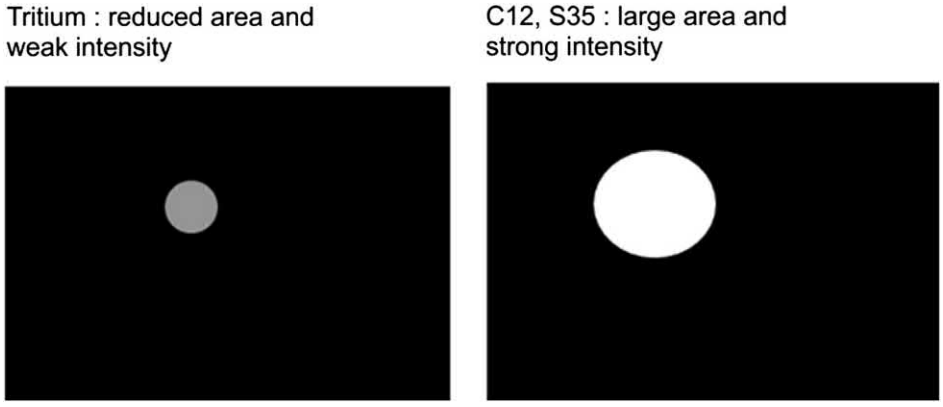


FIGURE 9.26 In the BetaIMAGER DFine, the shape of the light spot is proportional to the energy deposited in the scintillator. Hence, the brighter spots correspond to medium-energy isotopes.

In the case of the BetaIMAGER DFine, the typical spatial resolution is 10 μm for ^{3}H and of 20 μm for ^{14}C or ^{35}S, which is of the order of the dimensions of biologic cells. Spatial resolution is closer to 20 μm for higher-energy radionuclides because of backscattered electrons from the sample slide.

3. Quantification

Quantification is much easier and more precise with these imaging detectors than with classical autoradiography because the detectors are based on the direct measurement of the radioactivity. In particular, particle counting techniques give results from the first detected beta particles and do not have a pedestal in the lower part of their sensitivity curve. This extreme sensitivity can even appear as a drawback because images coming from particle counting systems look noisy compared with film or phosphor screens. In fact, one should keep in mind that with particle counting techniques, it is possible to quantify an image even with a very limited number of detected particles. For example, if the number of counts in a region of interest (an organ) is 100, the standard error will only be 10% (Poisson noise), which is an arguably reasonable accuracy in biology. Hence, the data are reliable even though the result may be visually noisy. The reason why phosphor screens or film images always look statistically better is that their detection threshold does not make images possible for very low levels of radioactivity. For instance, considering a detection limit of 30 disintegrations per mm^2 for ^{14}C, a phosphor screen requires 3000 disintegrations over a region of interest of 1 cm^2 (heart of rat for example) to provide a result. This is why particle-counting techniques are always much faster than energy storage devices. Manufacturers of particle-counting imaging devices often include, in their analysis software, image processing filters that can smooth the noise, thus allowing a better rendering of the image while preserving quantification.

As previously mentioned, in the case of phosphor screens, mass activity (in Bq/g) is often the real data of interest. This imposes the preparation of a reference standard of known radioactivity. Standards really must be made of the same material and preferably with the same thickness as the measured samples because particle-counting techniques are slightly more sensitive to sample thickness than energy storage techniques. The standards must be read together with the samples for each acquisition to allow accurate sample quantification by means of proportionality.

D. Data analysis for particle-counting imaging systems

1. List mode files

One of the main assets of particle-counting systems is the particular way in which they store imaging data. Instead of recording images as tables of numbers (each number corresponds to the intensity of the radioactivity measured for one pixel), data are recorded as a sequence of variables (coordinates, time, etc.) for each disintegration. This type of data is called a list mode file. Fig. 9.27 illustrates the organization of a list mode file.

As discussed previously, each beta particle will be counted as 1, whatever the isotope. Certain list mode file-based detectors can also record the particle's energy, but, contrary to energy storage devices, this information will not have any weight in the final image. The image can subsequently be produced by choosing a display resolution and scanning the various coordinates stored in the file. The value of a given pixel will be incremented each time a particle's coordinate corresponds to that pixel. The coordinates (*i.e.*, COG) can be calculated with a resolution of 5−10 μm, whereas the resolution of the final image can be chosen subsequently according to the size of the area of interest. Time information is another key feature of list mode files, as it allows the extraction of partial acquisitions. This can be useful when developing experimental conditions; for instance, it is possible to extrapolate the minimum acquisition time required for optimal measurements from partial acquisitions extracted from one initial long acquisition. Time information is also important in experiences involving short-lived isotopes, such as the ones used in nuclear medicine, as these isotopes can be segregated according to their half-life.

Similarly, supplementary information related to the morphology of the light spots, including the number of pixels (area of the spot), total intensity (luminosity, proportional to the energy deposited), and ellipticity, can be stored in list mode

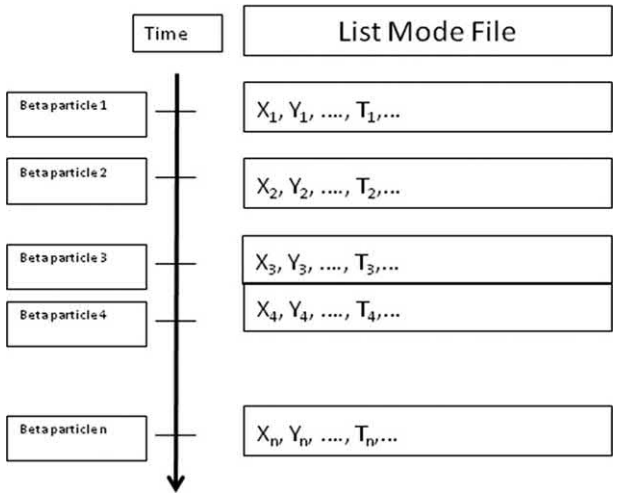


FIGURE 9.27 Principle of list mode file recording. For each event (light spot resulting from one disintegration), a set of data is recorded, including position (*X*, *Y*), time of disintegration (*T*), and other parameters related to the isotope (luminosity, etc.).

files. All these additional criteria can be used to discriminate between isotopes according to their energy.

Even though this type of data can be considered as memory consuming, one should keep in mind that the amount of data is proportional to the number of recorded beta particles; and most of the time, the list data files are actually more compact than conventional raw images files, particularly for low-activity samples.

2. Multiisotope separation according to energy

As previously described, the morphological criteria of the light spots recorded by the CCD camera (area, light intensity, ellipticity, perimeter, etc.) give information on the energy of the detected particles, therefore permitting the separation of two isotopes of different energy. According to their energy characteristics, good candidate radionuclide pairs for a separation are $^{3}H + {}^{14}C$, $^{3}H + {}^{35}S$, $^{3}H + {}^{33}P$, $^{3}H + {}^{45}Ca$, etc. Separate standards of each radionuclide of the dual-radionuclide pair are needed to establish the statistical distribution of the instrumental criteria used for radionuclide discrimination. The need for standards is mostly due to the effect of sample thickness on energy distribution. The radionuclide discrimination is then processed by means of proprietary algorithms developed by BioSpace Lab. Given two isotopes A and B, and using the former criteria, the software will first calculate the probability of a disintegration to originate from isotope A and from isotope B. For each disintegration, the two probabilities are recorded in two new list files, which are then used to establish one image for each isotope after discrimination. Fig. 9.28 shows a schematic representation of the process.

Fig. 9.29 shows an example of the separation of ^{35}S and ^{3}H separation in a CNS study using the BetaIMAGER DFine. The difference in labeling between right and left hippocampus in this rat brain section is clearly visible. The lack of tritium in the right hippocampus is proportional to the lack in oligonucleotide probe. The difference in gene expression after an electric stimulus can therefore be quantified.

As the energy deposited by the beta particles can be dramatically altered by the sample itself, this technique cannot segregate more than two isotopes at once. Furthermore, some isotope pairs cannot be separated because their respective beta particle energy maxima (E_{max}) are too close to each other (e.g., $^{14}C-{}^{35}S$, $^{14}C-{}^{33}P$, etc.).

3. Multiple isotope separation according to decay

Autoradiography can also be used as a control for PET or single photon emission computed tomography (SPECT) experiments in preclinical nuclear medicine studies. Most isotopes used in nuclear medicine have very short half-lives (as compared with tritium and ^{14}C). This characteristic can be used in particle-counting imaging systems for multiradioisotope labeling. The time information recorded in list mode files is used in a similar manner as energy discrimination. In this case, it is the time information that will be used as the key criterion for radioisotope discrimination. For every event (or particle) location registered in the list mode file, the software will compare the signal recorded over time to a prediction of the exponential decay expected for pure isotopes. Thus, a set of list files, each corresponding to the probability for one isotope, will be created.

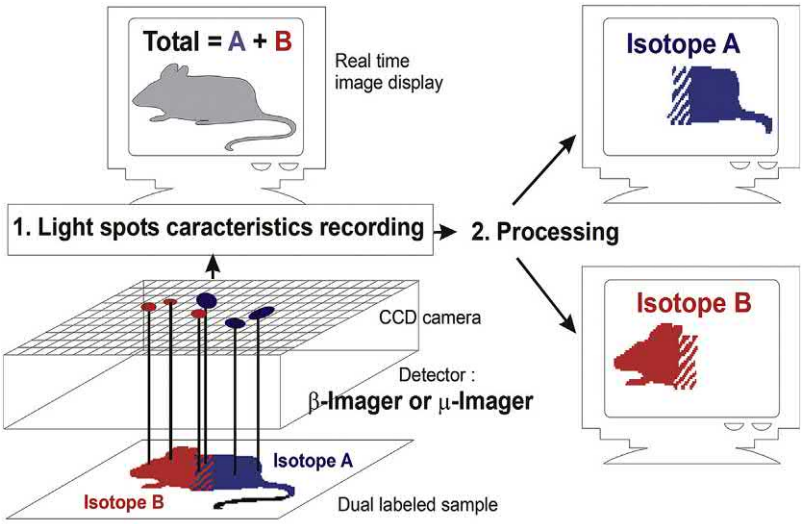


FIGURE 9.28 Principle of energy-based isotope discrimination. Using the knowledge of the statistical distribution of the different criteria for each isotope, the software calculates the probability for each disintegration to originate from isotope A and from isotope B. For the color version of the figure, the reader is referred to the online version of the book.

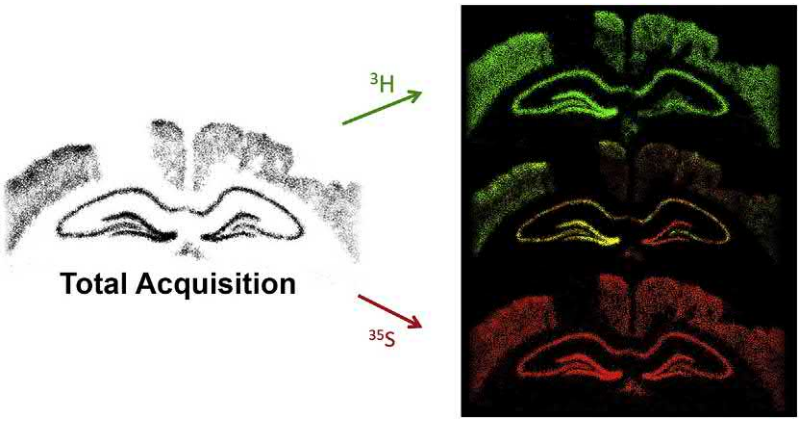


FIGURE 9.29 Example of energy-based dual-isotope labeling. Two oligonucleotide probes (the first labeled with ^{35}S, the second with ^{3}H) were hybridized on the section of a rat brain. An asymmetric neural stimulation was carried out on the left part of the brain prior to sacrifice. An asymmetric distribution in gene expression is clearly visible in the right hippocampus (Salin, 2000). For the color version of the figure, the reader is referred to the online version of the book. *Reprinted with permission from SAGE open.*

This method is less restrictive, with regard to the number of isotopes that can be separated compared with energy-based separation. Three isotopes can commonly be isolated, but more should also be possible, as long as the following requirements are filled:

- The ratio between two consecutive half-lives (from the shorter to the longer) must be larger than 2.
- The total duration of the acquisition must be longer than the half-life of the latter isotope of the radioisotope combination (always from the shortest to the longest half-life). Examples are provided below.
- If one of these requirements is not met, the quality of the separation will be drastically reduced, potentially making it unusable, especially in the case of low-activity samples.
- Examples of radioisotope combinations and respective optimum acquisition times for their adequate separation are listed below:
  - ^{18}F ($t_{½} = 108$ min), ^{99m}Tc ($t_{½} = 6$ h), ^{123}I ($t_{½} = 13$ h). Acquisition time > **6 h (^{99m}Tc)**
  - ^{18}F ($t_{½} = 108$ min), ^{123}I ($t_{½} = 13$ h), ^{111}In ($t_{½} = 68$ h). Acquisition Time > **13 h (^{123}I)**

The last isotope of the list may even be a long-lived isotope (such as tritium or ^{14}C).

Fig. 9.30 illustrates an example of multiisotope labeling experiment for which histologic sections were obtained from rat heart tissues 1 month after coronary occlusion. The animals were fed glucose and received intravenous injections of ^{18}F-fluorodeoxyglucose (FDG), ^{99m}Tc-sestamibi, and ^{111}In-diethylenetriamine pentaacetic acid (DTPA) prior to imaging. ^{111}In-DTPA is an extracellular tracer and exhibits retention in the extracellular fluid of necrotic tissue. ^{18}F-FDG is a tracer for glycolitic metabolism, while the myocardial distribution of the tracer ^{99m}Tc-sestamibi is proportional to blood flow.

The three images clearly show a predominant blue ^{111}In signal in the necrotic area at the extreme left of the heart section, while the ^{18}F signal (in red) is excluded from necrotic tissue but increased in the surrounding area, compared with the rest of the myocardium.

Hence, in this multiradioisotope labeling experiment, the levels of both necrosis, expressed as the ratio between ^{111}In signal and ^{99m}Tc signal in the necrotic area, and ischemia-related metabolic enhancement (^{18}F-FDG/^{99m}Tc) in the border zone, can be determined in parallel.

V. Comparative use of the different techniques

A. Applications in biochemical analysis

Except for the BetaIMAGER DFine, all other radioisotope-imaging systems can be used for the detection of samples with large surface areas traditionally revealed on film, including Western blot membranes and electrophoresis agarose gels used for DNA and RNA analysis. The two main advantages of imaging systems are acquisition speed (10−50 times faster than film) and sensitivity. They also have a higher dynamic range typically around four to five orders of magnitude, and therefore, they provide quantitative reliability. Also, their spatial resolution is sufficient for biochemical analyses, such as the separation of proteins or DNA/RNA molecules according to their size or isoelectric properties.

However, whereas the BetaIMAGER TRacer or the BeaQuant system can only accept a limited number of samples at any given time, phosphor plate radioisotope imagers can be equipped with multiple storage tanks allowing the processing of several plates in parallel and therefore simultaneous analysis of large sample numbers, a prerequirement in high-throughput screening, for example.

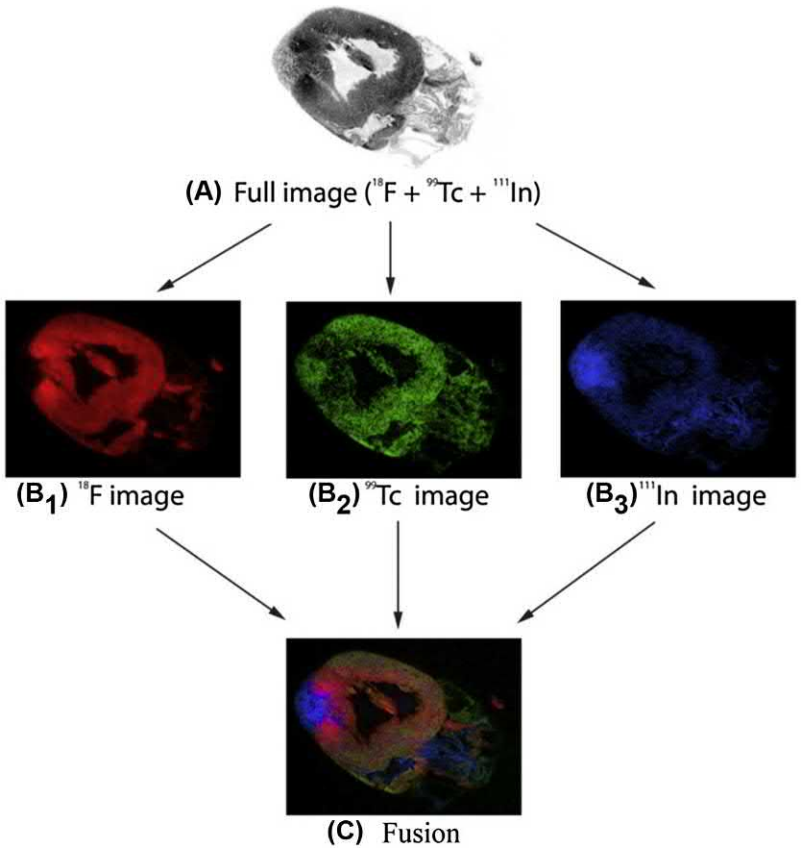


FIGURE 9.30 Time-based isotope separation. Image of an infarcted heart of a rat labeled with the three radioisotope markers: ^{18}F-FDG, ^{99m}Tc-Sestamibi, and ^{111}In-DTPA. For the color version of the figure, the reader is referred to the online version of the book. *Courtesy of Sylvain Poussier, Department of Nuclear Medecine, CHU-Nancy-France.*

In the early 2000s, high interest had been devoted to the BetaIMAGER DFine for DNA microarrays used in the biosciences to measure the expression levels of large numbers of genes simultaneously or to genotype multiple regions of a genome. With ^{33}P-radiolabeled probes, a spatial resolution of 15 μm could be obtained with a BetaIMAGER DFine, whereas it is limited to 150 μm with a phosphor plate. Nevertheless, these analyses are today "old-fashioned," even though their sensitivity remains incomparable.

B. Advantages and limitations of radioimagers in histological studies

Older electronic radioimagers of the MWPC generation typically had insufficient spatial resolution (300−700 μm) resulting in a loss in contrast (by a volume effect) for images of histological sections. They were used nonetheless because of their high sensitivity (reduced latency of images) and their performances in quantification (high dynamic range or linearity capabilities), thus allowing the rapid validation of experimental conditions and/or tracer labeling process.

Among other high-resolution radio imagers that can be used to quantify radioisotope-labeled substances in tissue sections, the BetaIMAGER TRacer has a spatial resolution of 100−150 μm and is therefore a good alternative to phosphor plate radio imagers, especially when the radioactive signal is weak, as in binding or ISH experiments, for example, and especially when the radionuclide of choice is tritium because of the great efficiency of this detector to detect low-energy beta emissions. As the sample is placed directly inside the gas chamber, interaction of low-energy particles with the detection medium is optimal. Phosphor screens cannot offer equivalent efficiency except when the protective antiscratch layer has been removed, thus exposing the screen to potential damage and preventing it from reuse. If the most efficient radio imager (i.e., BetaIMAGER DFine) has a resolution similar to film, it is generally recognized that histological analysis is more precise on film, which is still nowadays used as a complement to the data obtained with the phosphor screen or a particle-counting system.

In pharmacological experiments, such as radiolabeled ligand displacement studies, spatial resolution is less important than response linearity for dose-effect quantifications. Such pharmacological studies actually often imply the use of frozen tissue sectioned with a cryostat. Tissue damages can occur during this process due to dilacerations caused by the formation and subsequent evaporation of ice after the spreading of the section. This often creates

inhomogeneities of more than 100 μm in the tissue surface, thus making the BetaIMAGER's spatial resolution of 50−100 μm adequate for the precise analysis of radioactive ligands in histological samples.

With respect to tissue quantification of radioligand distribution in binding studies, comparative studies with ^{125}I have shown that results were comparable with those achieved with film and that quantifications in the highest radioactive regions were more reliable with the radio imagers. Similarly, in RNA expression studies, ISH with radioisotope-labeled oligonucleotide probes generally requires an image resolution at the cellular scale. The BetaIMAGER DFine is the most suited system for this type of imaging. For other applications, including less classical tracers, such as gamma- or beta−gamma-emitting radionuclides, which have short half-lives, only the most sensitive imaging systems such as the BetaIMAGER Tracer, BeaQuant, and BetaIMAGER DFine will be able to acquire images prior to their total disappearance.

C. Potentialities for multiradionuclide labeling

The great advantage of the direct-counting, real-time imagers over other systems is their versatility in multidetection modes thanks to their specific detection processes allowing the discrimination among a range of radionuclide tracers. Multiple radionuclide tracers may be detected simultaneously by taking advantage of the differences in their beta-particle emission energies or decay characteristics.

D. Autoradiography associated with mass spectroscopy

Although QWBA is so far the most used imaging technique for localization and quantification of radioactive compounds in biological tissues or on thin specimens, this technique can only detect and quantify radioactivity. It cannot provide information on the nature of the analyte detected. Hence, the measured radioactivity may result from a mixture of the parent molecule and its metabolites and/or degradation products. Consequently other methods were developed to identify the precise nature of the radioactive compounds (Solon et al., 2010; Murray et al., 2016).

Initially, liquid chromatography mass spectrometry analysis on tissue extracts was carried out to identify and quantify compounds and their metabolites on the basis of exact mass measurements (Covey et al., 1986) or, more often, by profiling fragment ion spectra by characteristic of each molecule by MS/MS (Rohner et al., 2005; McDonnell and Heeren, 2007).

Historically, in the 1960s and 1970s emerged a new technology named mass spectrometry imaging (MSI). It was based on various ionization processes applied on the surface of tissue samples combined with mass spectrometry analysis of the produced ions. This opened a field of new developments in molecule identification with high levels of spatial resolution, sensitivity, and mass resolution. MSI is currently applied as a complement to QWBA in the field of pharmaceutical discovery and development where analytical laboratories must provide information on the ADME, of candidate ligands together with pharmacokinetic compound assessments prior to clinical trial clearance by regulatory bodies (Rohner et al., 2005; Stoeckli et al., 2007; Khatib-Shahidi et al., 2006).

A mass spectrometry image is an array of mass spectra obtained sequentially at regular spatial intervals, after bombardment, of a sample, under vacuum, by an energetic beam of ions or by pulsed laser irradiation. Atoms are ejected from the sample surface as charged particles and are guided by an electrostatic field toward a mass spectrometer. For any mass/charge (m/z) value in a mass spectrum, a quantitative image that represents the distribution of amounts of a particular ion can be calculated as illustrated in Fig. 9.31 (Solon et al., 2010).

A comprehensive review on MSI techniques was recently published elsewhere (Murray et al., 2016). This review describes the initial approach to MSI by secondary ion mass spectrometry (SIMS) first reported by Castaing and Slodzian in 1962. Furthermore, the sensitivity and the mass range of SIMS have been extended with time-of-flight (TOF) mass analyzers (Benninghoven, 1994) and cluster ion sources (Winograd, 2005; Bich et al., 2014). SIMS is adapted to the characterization of atoms or small molecules up to 1500 Da with a spatial resolution of a few hundred nanometers. The use of lasers for desorption/ionization in MSI appeared in the 1970s (Hillenkamp and Karas, 2000), performing in a mass range similar to TOF-SIMS, up to 1000 Da with a lateral resolution of about 1 μm. The matrix-assisted laser desorption/ionization (MALDI) was later developed around the late 1990s (Caprioli et al., 1997) extending the working mass range up to 30 kDa with a lateral resolution approaching 10 μm. MALDI uses the addition of a matrix applied on the sample to desorb and ionize the analytes from the surface upon impacts of laser pulses. For example, among many other matrices and matrix application protocols available, a manual application of α-cyano-4-hydroxycinnamic acid solution, using a conventional thin-layer chromatography sprayer to coat the sample, is well suited for simultaneous imaging of a compound and its metabolites in tissue sections. The same samples used for QWBA can also be used for analysis by MALDI-MSI. The sections are mounted on tape and immediately lyophilized for QWBA, whereas they are first frozen and then lyophilized before coating with a matrix in MALDI-MSI analysis. The sections are then rastered over with a laser in the mass spectrometer to acquire the

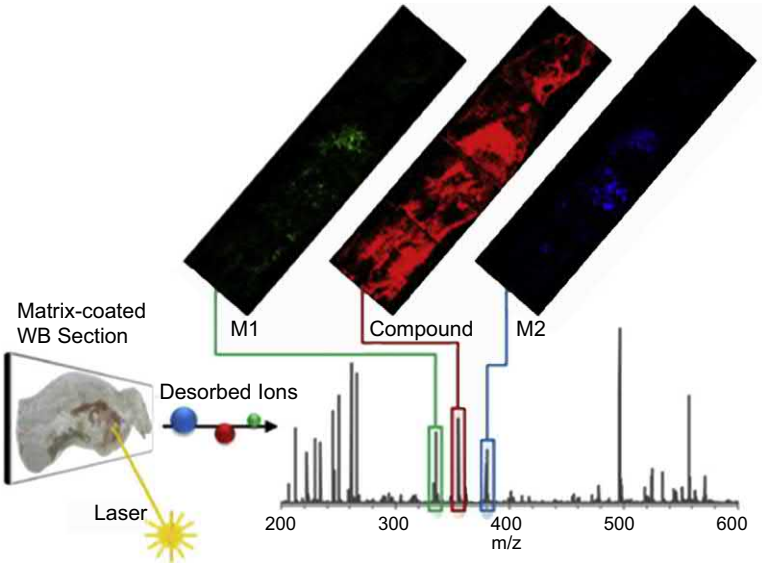


FIGURE 9.31 Matrix-assisted laser desorption/ionization mass spectrometric imaging process. Analytes are simultaneously desorbed from the animal section in a defined raster. Out of the acquired spectra, specific molecular images are calculated. For the color version of the figure, the reader is referred to the online version of the book. *Reproduced with permission from Solon et al. (2010).*

different spectra. An example of such an experiment is shown in Fig. 9.32.

Carried out on rat sections, this type of experiment can take around 1 hour for a laser raster of 0.5 mm. The spatial resolution depends on the diameter of the laser beam, which is typically around 100−20 μm and is limited by the matrix deposition method during which a delocalization of the analytes frequently happens (Rohner et al., 2005; Stoeckli et al., 2007). Higher-resolution images may be achieved by depositing other special matrices or by using recent SIMS methodology directly on biological tissue. Following the development of a variety of new MSI methods (oversampling, beam focus in reflection geometry and transmission geometry, high numerical aperture lens), MALDI is now capable to image tissue sections of 5 μm thickness or mammalian cell cultures. Moreover, progress in ionization methods, such as ambient and atmospheric pressure ionization or near-field laser ablation, allowed the detection of small features down to 0.6 μm resolution on polymer samples and to resolve cocaine biodistribution in mouse brain tissue at a lateral resolution of 15 μm (Murray et al., 2016).

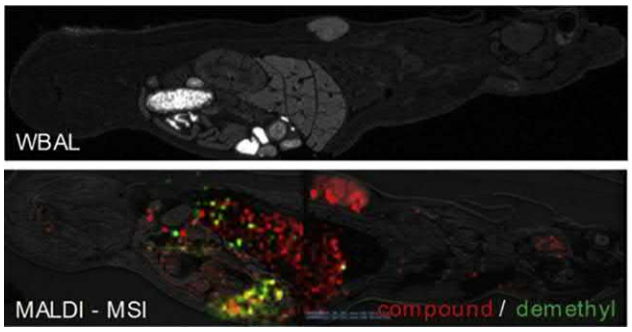


FIGURE 9.32 Comparison of mass spectrometry imaging (MSI), whole-body autoradiography (WBA), and matrix-assisted laser desorption/ionization mass spectrometric imaging (MALDI-MSI) results obtained from the same compound-dosed animal. MALDI-MSI allows the simultaneous discrimination between the labeled compound (red) and its metabolites (green, colocalized with label-free compound (yellow). For the color version of the figure, the reader is referred to the online version of the book. *Reproduced with permission from Solon et al. (2010).*

Alternatively, SIMS was successfully applied to the analysis of many biological tissues with an improvement in spatial resolution and an increase in the mass molecular weights being studied. Starting with the detection of radioactive or stable atoms (Galle, 1982), SIMS-MSI evolved toward the identification of large molecules or even cells, such as bacteria and cell cultures, allowing the acquisition of images of submicrometric spatial resolution for radioactive isotopes (Hindié et al., 1992) or for label-free molecules (Chandra et al., 2000).

In the SIMS ionization process, a beam of ions is projected on the tissue surface directly, resulting in a desorption of ionized atoms. The sample is gradually sputtered, starting with the most superficial layers of atoms, which are ejected from the sample surface as charged particles and are guided by an electrostatic field, resulting in a secondary ion beam. The latter is directed toward a mass spectrometer tuned to detect a given ion species, yielding an image that reflects the distribution of the selected emitter. As the mode of operation is by analysis of the material removed by sputtering, it is a locally destructive technique. This drawback, conjugated with limitations in mass ranges that can be successfully ionized, explains its limited use in biomedical research until the last decade. But, as a complement to MALDI, SIMS imaging has real potential for

the analysis of low-molecular-weight compounds at high spatial resolution for biomedical research purposes.

VI. Other applications

In biomedical research, applications to quantitative autoradiography and beta imaging are extremely broad, and these methodologies are very relevant because of the targeting properties of the labeled compounds and of the potential of the technique to locate and quantify them in the resulting image.

A good overview of the general applicability of these techniques is demonstrated in many publications covering all the domains in medical science. A few examples will be presented here with illustrations. These examples are not restricted to one specific method of detection (energy storage or direct counting), and both techniques are represented here.

A. Biochemistry of development studies

In biochemistry of development studies where physiological mechanisms are investigated in rodents, research has demonstrated the link between circulating peptides and their function in the animal body thanks to various autoradiographic approaches, including film whole-body autoradiography, sensitive emulsion for microautoradiography, and QWBA by digital beta imaging, providing a representative mapping of target organs as illustrated in Fig. 9.33 and finally a detailed organ-specific autoradiography by the BetaIMAGER TRacer (Rougeot et al., 1997).

A vast number of publications in this field were made with the general goal of identifying specific molecular interactions: for instance, plasma membrane proteins and lipids in binding experiments to evaluate membrane function and regulation (Bjorkholm et al., 2014) or information transduction across the membrane (Chiricozzi et al., 2015). Digital autoradiography of Western blotting PVDF membranes and eventual mass spectrometric analysis are among the methods used to identify compounds and processes involved in molecular interactions. In recent years, the development of translational medicine enhanced collaborations between various medical disciplines. New methods in molecular imaging, such as PET, together with the development of novel radiolabels, opened the way for innovative clinical and therapeutic applications. A typical example is detailed in a recent paper (Pant et al., 2015) where autoradiography and PET imaging were combined to investigate in vivo and ex vivo pharmacokinetics and biodistribution of a bioactive polymer known to exhibit anti-inflammatory activity in small animals. In the concluding section, the authors discussed potential nanomedical applications.

B. Bacteriology

In bacteriologic applications, a microautoradiography method is best utilized to localize the agent generally incorporated into the bacteria cells. Histological imaging of radioisotope-labeled agents is required, as illustrated in Fig. 9.34, for an immunological study concerned with protection against bacterial infection in mice (Phalipon et al., 2002). A similar imaging technique has been used for the study of the context of pathogenicity of *Helicobacter pylori* (Viala, 2004).

Today, MSI techniques are frequently combined with ISH and nanoscale secondary ion mass spectrometry (nanoSIMS) imaging in bacterial research. It has been demonstrated that SIMS-ISH does not alter the apparent isotopic composition of bacterial cells (Chapleur et al., 2013), thus providing means to detect phylogenetic identity and measure carbon isotopic composition at the single cell level.

In addition, multilabeling combined with stable-isotope probing offers the possibility of deciphering networks of biogeochemical processes catalyzed by uncultured microorganisms within complex environments (Lechene et al., 2006).

C. Physiology and gene expression

In the field of physiology and gene expression, an example is illustrated in Fig. 9.35 where interleukin signaling pathways in cognitive function were studied by using ^{35}S-labeled probes and the ISH analysis with a BetaIMAGER DFine (Carrié, 1999). Other similar studies, conducted in the same period, show very relevant results with high-resolution beta imaging (Zemni, 2000; Al Halabiah, 2005; Blanchet, 2005).

Besides conventional autoradiography, which is traditionally used to study the localization of neuroreceptors thanks to ^{3}H-labeled peptides as well as for binding assays and receptor occupancy assays, functional autoradiography uses ^{35}S-GTPgammaS, a nonhydrolyzable analog of guanosine triphosphate (GTP), to provide information on the extent of ligand−receptor interactions and downstream signaling (Sovago et al., 2001; Manuel et al., 2015). Functional autoradiography is based on the increase in G protein guanine nucleotide exchange upon agonist stimulation. Activation of G protein−coupled receptors can be visualized thanks to a local increase in ^{35}S-GTPgammaS radioactivity at the site of G protein activation. Localization of activated receptors can therefore be determined, but the level of receptor activation can also be quantified: the half maximal effective concentration (EC_{50}) can be calculated together with the efficacy equivalent to the maximal effect. Functional autoradiography on brain tissue sections has been widely applied in neuroscience since 1995, but it

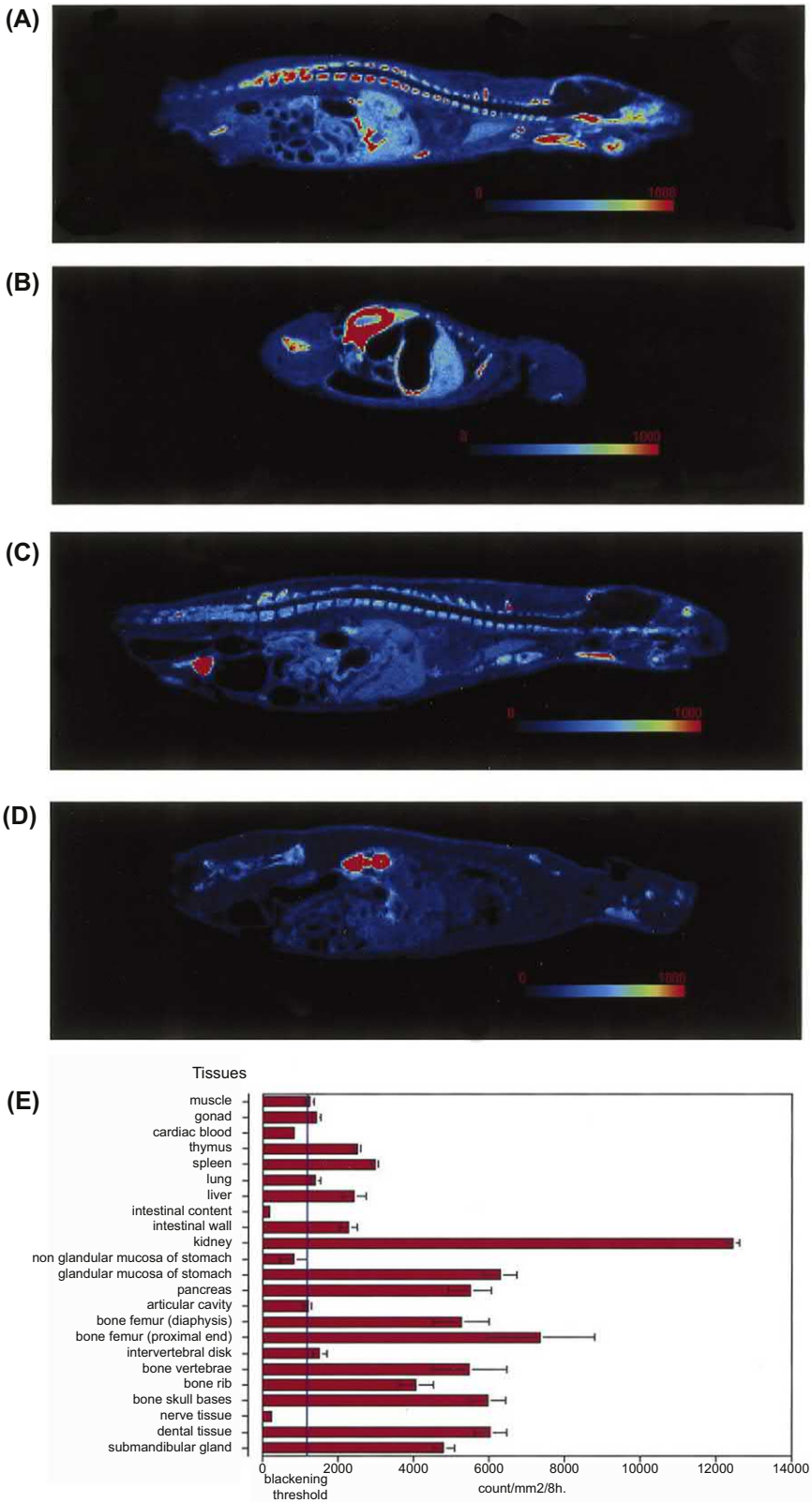


FIGURE 9.33 Representative mapping of target organs for SMR1-derived ^{3}H-pentapeptide using the high-resolution beta-radioimager (now BetaIMAGER TRacer, Biospacelab, France). (A) & (C) Midsagittal and (B) & (D) Lateral sagittal whole body sections of male (A & B) or female (B & C) rats, 60 min post injection of 3 nmol (6.7 MBq) tritiated peptide. Exposition Approx. 10 h. Red areas correspond to high uptake of radioactivity. Including the renal outer medulla, gastric glandular mucosa, pancreatic and submandibular lobules and bone tissues (skull base, rib, vertebra, and limb) and dental tissue. (E) Quantitative radioactivity profile in various tissues using the BetaIMAGER TRacer analysis software. For the color version of the figure, the reader is referred to the online version of the book. *Proprietary data, Ana Cardona, RIP. Also published in Rougeot et al. (1997).*

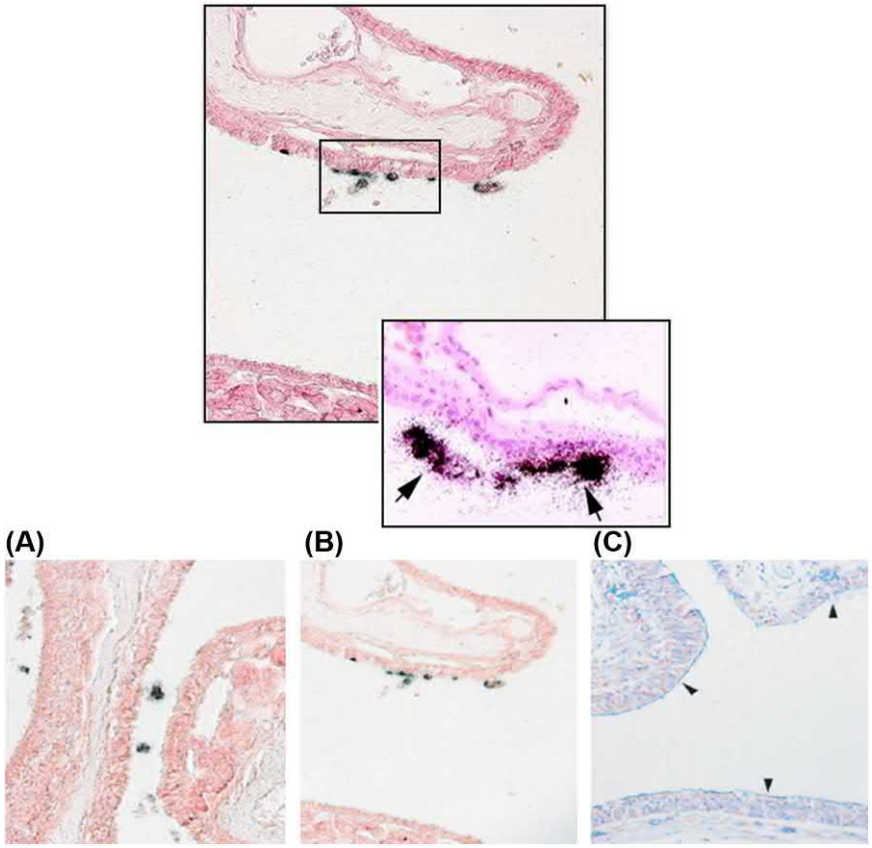


FIGURE 9.34 Localization of IgAC5 and rSCIgAC5 into the nasal cavity at the time of bacterial challenge (Phalipon et al., 2002). Mice given intranasally ^{35}S-Cys-labeled IgAC5 or rSC-IgAC5 were sacrificed at 1 h postinjection, heads were removed, and histological sections were prepared. (A and B) Photographic emulsions localizing the tissue distribution of IgAC5 and rSCIgAC5 (magnification, 200×). (C) Mucus staining with arrows indicating the mucus layer covering the nasal epithelium (magnification, 100×). For the color version of the figure, the reader is referred to the online version of the book. *From Phalipon et al. (2002); reprinted with permission from Elsevier ©2002.*

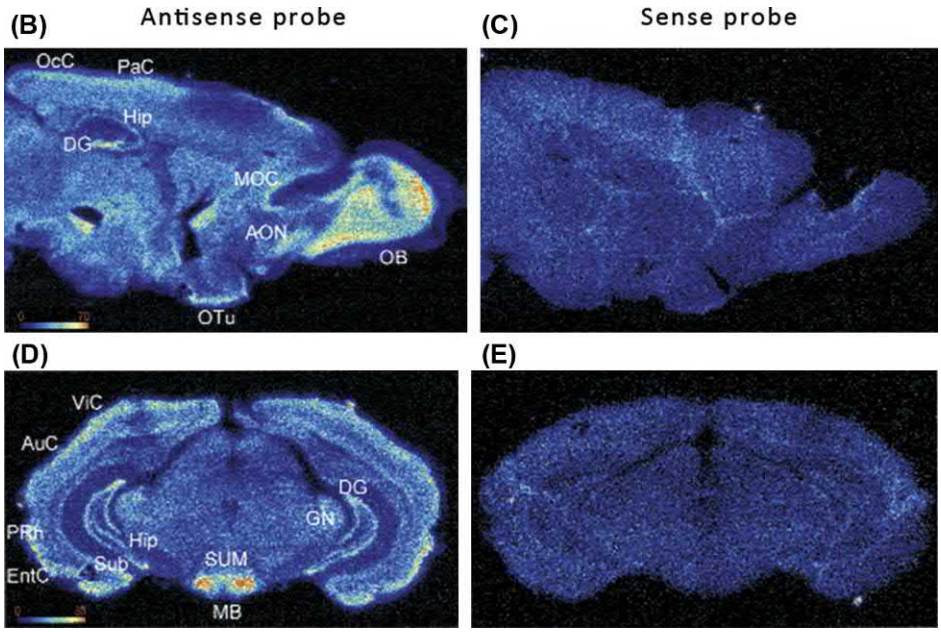


FIGURE 9.35 In situ hybridization analysis of *Il1rapl* expression. Sagittal (B,C) and coronal (D,E) sections of mouse adult brain were hybridized using ^{35}S-labeled antisense and sense *Il1rapl*RNA probes. Images were obtained with a BetaIMAGER DFine (Carrié, 1999). For the color version of the figure, the reader is referred to the online version of the book. *Reprinted with permission from Macmillan Publishers Ltd. ©1999.*

can also be used to analyze membrane microarrays made from collections of membrane homogenates isolated from diverse tissues, organs, or even transgenic cells overexpressing specific proteins. Hence, the use of functional autoradiography for high-throughput screening of candidate compounds and drug discovery was suggested (Manuel et al., 2015). In this context, the technique could also be combined to mass spectrometry imaging, should a change in molecular structure of the native ligand be suspected.

Histological applications are often analyzed with a BetaIMAGER DFine system or with a radiosensitive emulsion, which reveals the true location of the labeled agent in the tissue or into the cell (Rigothier, 2002).

D. Molecular biology

Even though nonradioisotope techniques (fluorescence, chemiluminescence) are prominent in the field of molecular biology, radioisotope-based TLC, Western and Northern blots, or gels are used widely, mainly because of their quantification properties. Let us take a brief overview of these different techniques through some examples and images.

- **TLC plates** are used to identify molecules in a mixture. The separation is done by migration in a stationary solid phase (silica gel or alumina) or in a mobile liquid phase (solvent or mixture of solvents). It is frequently used for radiolabeled nucleotides, and the quantification can be easily done with a phosphor plate as in the following example, displayed in Fig. 9.36 (Jendresen et al., 2011):
- **High-resolution protein gels**: For molecular biology experiments, a sharp separation of biomolecules is often needed, which requires the use of agarose gel or polyacrylamide gel electrophoresis. The electrophoresis can separate DNA fragments, which differ in length by only a single base pair. Phosphor screen technology is then widely used for this high-resolution DNA sequencing such as in the following example (Fig. 9.37) (Sharma et al., 2010):
- **Northern, southern, and Western blots**: Northern blots start with extraction of total RNA from a homogenized tissue sample or from cells. RNA samples are then separated by gel electrophoresis. Since the gels are fragile and no probe is able to enter the matrix, the RNA samples, now separated by size, are transferred to a nylon membrane through a capillary or vacuum blotting system. In a second phase, they are hybridized with a probe to analyze their abundance in the tissues and quantify gene expression. Quantification can be made by autoradioluminography or with digital autoradiography systems (Belair et al., 2011). Southern blots are a similar transfer technique on a nitrocellulose membrane to detect DNA fragments after hybridization

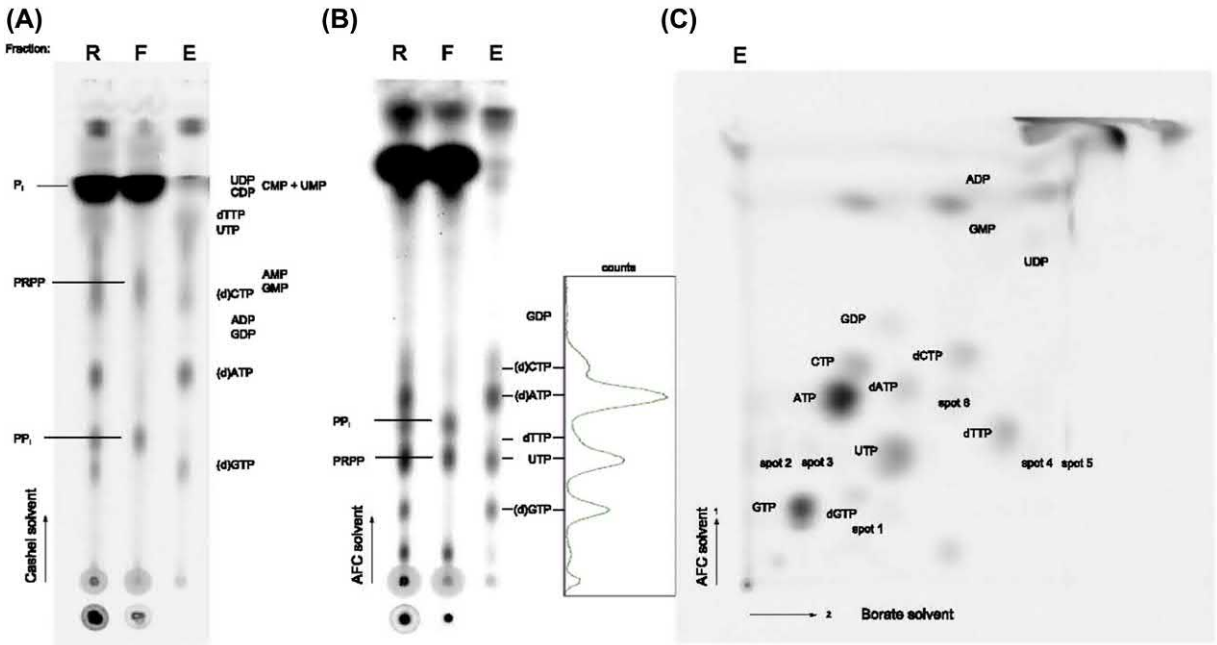


FIGURE 9.36 Thin-layer chromatography (TLC) of cell extracts: separation of nucleotides from a radiolabeled culture. An acid extract of *Lactococcus lactis* (raw (R) sample) was separated into a filtrate (F) and an eluate (E). Then an aliquot of the samples was separated by TLC either in one type of solvent (A) or in other type of solvent (B). Aliquots of diluted samples of the radioactive culture were spotted below the application points for measurement of total radioactivity. The radioactivity profile of the E lane is shown as well as a two-dimensional separation of an aliquot of the E sample (C). Quantitative determination of the nucleosides is made by autoradioluminography. See details in the text (Jendresen et al., 2011). *Printed with permission from Elsevier © 2011.*

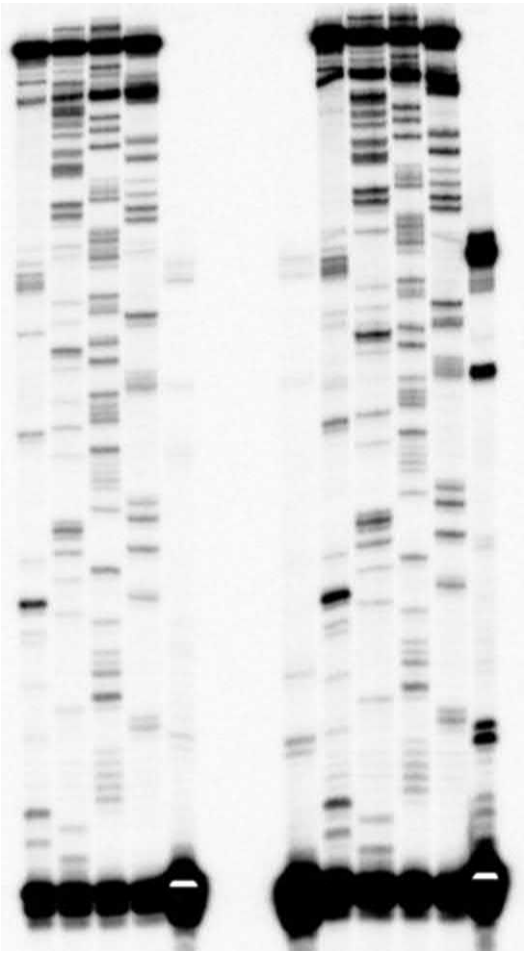


FIGURE 9.37 Example of a sequencing reaction resolved on a denaturing 5% polyacrylamide gel. Each lane G, A, T, and C contain the reaction for each dideoxynucleotide (Sanger sequencing method). In this experiment, the primer is 5′-end labeled with ^{32}P. *From Sharma et al. (2010). Reprinted with permission from Macmillan Publishers Ltd ©2010.*

with a complement probe. Western blots are an equivalent technique for proteins. In the following example (Fig. 9.38) of a Northern blot, microRNAs, posttranscriptional regulators of eukaryotic gene expression, are implicated in host defense against pathogens (*H. pylori*). The probe is labeled with ^{32}P, and the quantitative detection is by autoradioluminography.

E. Molecular imaging

As all imaging devices used for autoradiography are also sensitive tools for detecting radiopharmaceuticals used in nuclear medicine, various experiments with radionuclides of short half-life are possible with very high-spatial precision, as illustrated in Fig. 9.39. In this example, images exhibit a clear analogy between electronic autoradiography and film autoradiography of sections of a rabbit's kidney

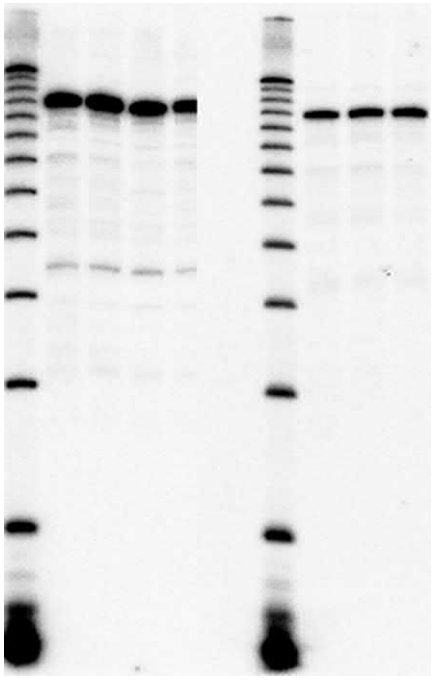


FIGURE 9.38 Example of a Northern blot analysis. A membrane is hybridized with a ^{32}P-radiolabeled oligonucleotide. The quantification is done by autoradioluminography with a PharosFX system (Belair et al., 2011). *Courtesy of Fabien Darfeuille.*

labeled with a ^{99m}Tc-radiopharmaceutical (Barthe et al., 2004).

In many experiments conducted in nuclear medicine early preclinical research, molecular imaging is used to visualize cellular function and to follow up a molecular process in living organisms without disrupting it. When nuclear medicine markers are used, a number of studies are performed both ex vivo by autoradiography of organ sections and in vivo by other radionuclide imaging modalities (e.g., SPECT, PET and, more recently, optical imaging). While in vivo imaging techniques are most important for such studies, ex vivo imaging is often required to validate in vivo results, as autoradiography can provide both high resolution and sensitivity. Autoradiography, combined with traditional molecular imaging methods, has therefore great potentials in many fields of translational research, including cancer, neurosciences, and cardiology (Temma et al., 2010; Dedeurwaerdere and Langlois, 2011; Ueda et al., 2011; Poisnel et al., 2012)

With recent developments in PET, SPECT, and multimodal imaging, investigations on molecular targets and their involvement in biological processes have considerably evolved in the past 20 years. Radiolabeled probes and contrast agents have been developed to investigate the molecular mechanisms of diseases and to assess therapeutic candidates in animal models using both in vivo and ex vivo methods.

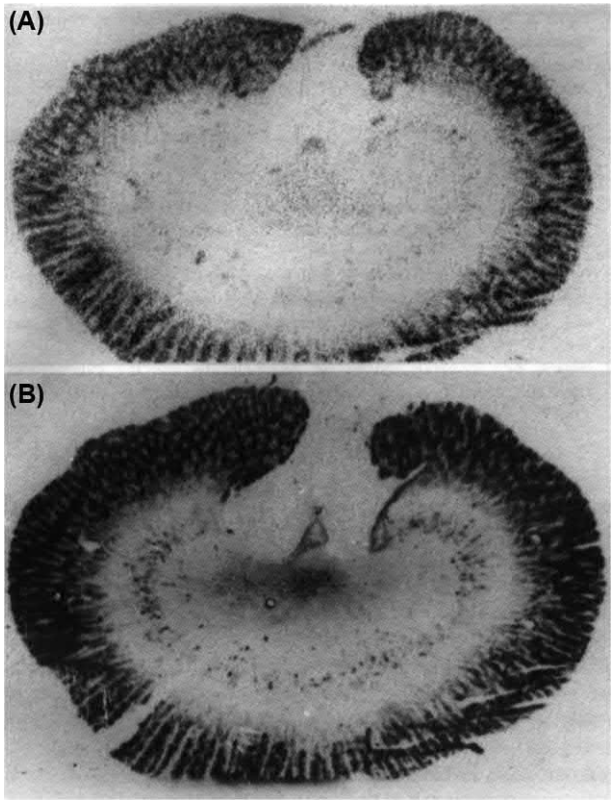


FIGURE 9.39 Beta imaging of the kidney of a rabbit injected with ^{99m}Tc-DMSA (section of 20 μm thickness) showing the renal distribution of the tracer after a 6-h acquisition with the BetaIMAGER TRacer (image A) and after a 24-h exposition on film (image B). The spatial resolution is similar in the two documents (Barthe et al., 2004). *Reprinted with permission from Elsevier © 2004.*

Beta imaging applications in the field of molecular imaging including both pre-clinical and clinical studies as well probe development will be considered later on in this chapter.

F. Nuclear waste decommissioning projects (analysis of potential radioactive contamination)

As nuclear power stations continue to age, the development of robust methods of characterization for their dismantlement, decommissioning, and remediation becomes of increasing importance. Characterization of nuclear waste is essential to optimize safety and efficiency in decommissioning and obtain representative calculations, in situ measurements, and samples/analyses providing an understanding of the radiological conditions that will be encountered during decommissioning.

Traditional methods for characterization involve a wide range of nondestructive and destructive techniques, which will vary depending on various factors such as the nature and intensity of the radioactivity, the physical and geometrical conditions, or the accuracy required for the result. Basic measurements of radiation fields with gas-filled detectors (ionization chambers, proportional, and Geiger–Müller counters) are well established. Nonetheless, while they may give rapid information on radiation levels for primary safety measures, they are not quantitative due to variations in distance between detector and monitored area. More accurate quantitation methods are therefore required to improve the geometric mapping and sampling process of contaminated areas. For instance, there is real need for innovative methods allowing precise measurements of low-energy, alpha and beta isotopes, which are more difficult to detect than gamma emitters (OECD and NEA, 2014). Current analytical methods are based on either topical smear samples or powder samples prepared by pulverization or pyrolysis followed by gamma ray spectrometry or LSC (Wang et al., 2007). More recently, the use of solid-state detectors has been described for precise and quantitative topographical measurements (Leskinen et al., 2013) and in situ quantitation (Haudebourg and Fichet, 2016).

Whereas excellent reviews on methods of characterization for decommissioning of nuclear installations are given elsewhere (IAEA, 1998; Laraia, 2012, Rehak, 2013), the focus of this chapter will be on digital autoradiography techniques. Digital autoradiography is particularly adapted to low- and medium-energy alpha and beta emitters (e.g., ^{3}H, ^{14}C, ^{36}Cl, ^{90}Sr). It allows sensitive measurements with a high dynamic range for quantitative purposes. Furthermore, digital autoradiography with direct photon-counting systems or multiple screen approaches allows the identification of isotope species according to their energy or decay, thus permitting discrimination of multiple emitters in composite samples (Haudebourg and Fichet, 2016).

Specialist laboratories such as the LASE laboratory, CEA, analytical support to facilities, France, or the National Nuclear Laboratory, Warrington, UK, have developed and proof-tested experimental protocols dedicated to the measurement of alpha and beta radiation for decommissioning facilities using various techniques, including digital autoradiography.

Current methods of digital autoradiography measurements for deactivation and decommissioning purposes are often adaptations of techniques from biological research and focus on mapping buildings under a dismantling process and sampling for predestructive analysis. Early work describing the use of digital autoradiography peculiarly originated from the building industry to study concrete cracking in delayed ettringite formation (DEF). Livingston et al. (2003) proposed to exploit the natural radioactivity of potassium (about 0.012% of all potassium is made of ^{40}K, roughly 89% of which decays by beta emission and 11% by electron capture with gamma ray emission) to monitor potassium levels in precast concrete bridge beams. Using

photostimulable storage phosphor plates, they produced digital autoradiography images of ^{40}K distribution in concrete cores with counting times of 24 h. Quantification of the radioactive signal confirmed increased potassium content in beams showing significant cracking from DEF-associated expansion compared with control beams.

More recently, Fichet et al. (2012) and Leskinen et al. (2013) demonstrated the applicability of the same reusable storage phosphor screen technology to measure ^{3}H and ^{14}C traces on concrete floor laboratories under dismantling process (Fig. 9.40). Floor areas of up to 285 m^2 were mapped with as little as 20 recycled standard size phosphor storage screens (12.5 × 25.2 cm, PerkinElmer). Digital autoradiography measurements could be compared with standard wipe test liquid scintillation, and although phosphor screens suffered from low limits of detection, they represented a cost-efficient and nondestructive approach with good quantitative results combined with precise information on space distribution of the remaining radioactive contamination. Other drawbacks to this method were the long exposure times required for detection of ^{3}H and ^{14}C. In addition, separate detection of ^{3}H and ^{14}C was not possible and had to be evaluated by wipe test for sampling and LSC for measurement.

To address this particular point, the same team developed two novel approaches to nondestructive identification of contaminating nuclides by phosphor screen stacking and differential phosphor screen analysis (Haudebourg and Fichet, 2016). They could profile 15 individual isotope species by plotting the ratio of measured signal between the layers (Screen n+1/Screen n) of a stack of up to 10 phosphor storage screens simultaneously exposed to the isotopes (Fig. 9.41). The technique was successfully applied to the identification of isotopes from steel blocks and drilled concrete cores.

For low-energy isotopes with nonpenetrating radiation (e.g., $^{3}H/^{233}U$), they exploited the availability of two types of phosphor storage screens, namely, TR (tritium) and MS (multisensitive) types from PerkinElmer. TR screens differ from MS screens by the absence of a thin protective overcoat layer that would block the nonpenetrative low-energy beta emission of ^{3}H. Isotope identification with the so-called "MS/TR" method simply consisted in calculating the ratio between signals measured with the MS type and TR type screens for the same sample, in identical exposure conditions, as shown in Table 9.4.

Although the two methods showed great potentials in characterizing individual isotopes, profiling of multielement mixtures and influence of matrix effects on emerging energy spectrum and transmission behavior remained to be addressed to fully validate these two approaches.

Novel methods of characterization may arise from both the biomedical and geological fields, which would allow rapid scanning times, high-resolution imaging, quantitative

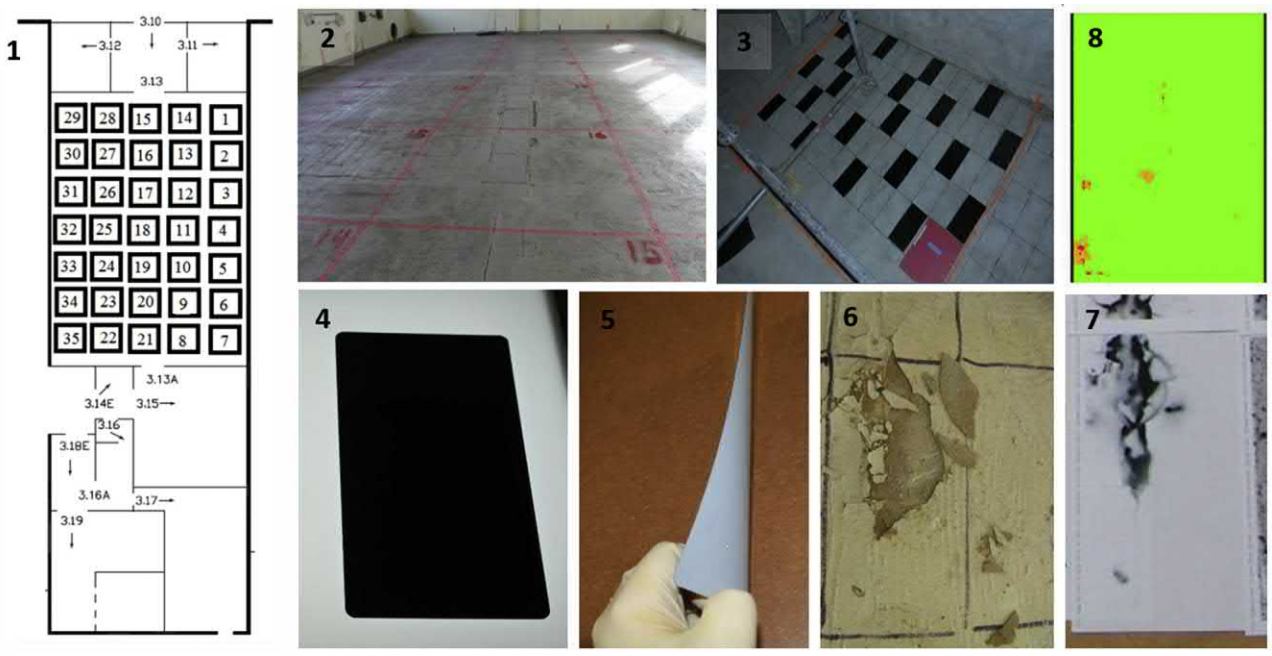


FIGURE 9.40 Geostatistical mapping of radioactive contamination in a contaminated laboratory using phosphor storage screen digital autoradiography. 1: Mapping of the area to be analyzed. 2: On-site delimitation of the monitored grid. 3: Homogeneous repartition of 20 phosphor storage screens over one area of the grid. 4: Storage phosphor screen. 5: Application of the phosphor screen on the flooring. 6: Typical contaminated area. 7. Resulting autoradiographic image from the area shown in 6 and 8. Final geostatistical analysis of the entire laboratory. For the color version of the figure, the reader is referred to the online version of the book. *Images Courtesy of Pascal Fichet, CEA, France.*

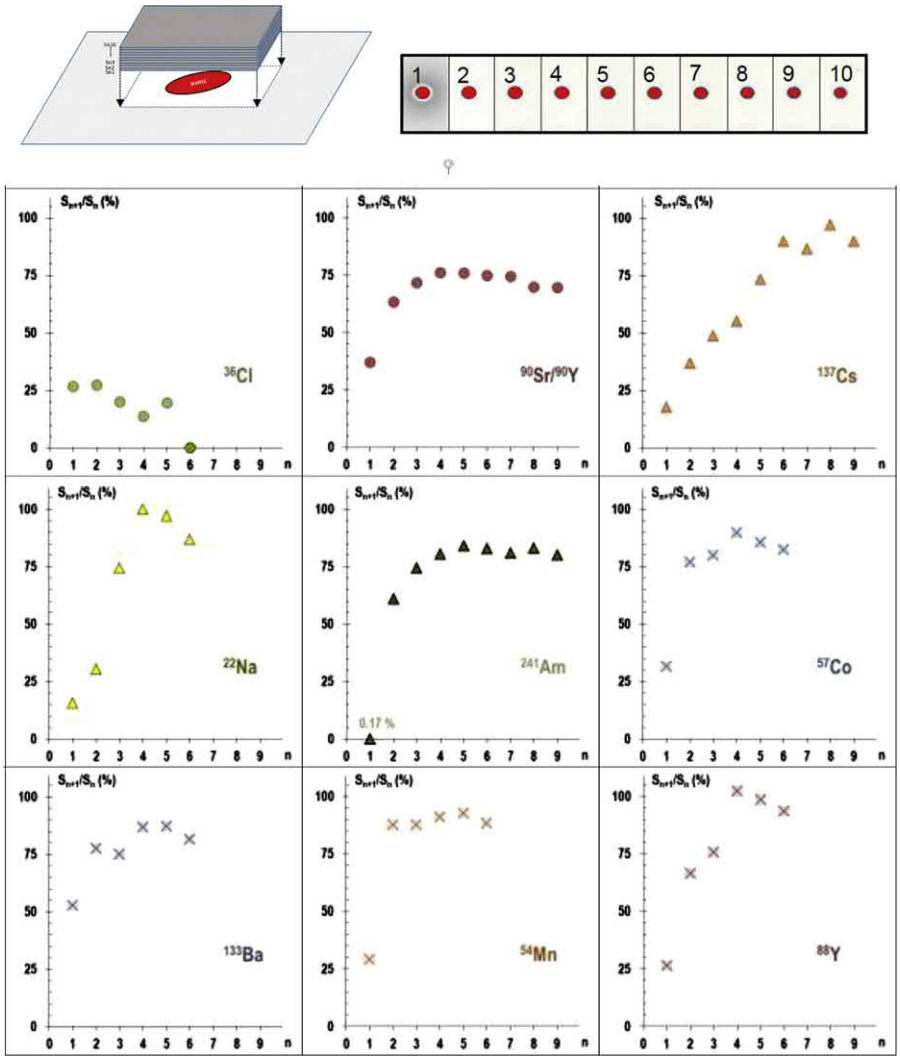


FIGURE 9.41 Sn+1/Sn sequences of the nine radionuclides. Sn: screen number. O: beta emitters, Δ: beta + gamma emitters and alpha + gamma emitter Am-241, X: X-ray or gamma emitters. Data correspond to the average value of the different sources for each radionuclide. For the color version of the figure, the reader is referred to the online version of the book. *Copied with permission from Haudebourg and Fichet (2016).*

measurement, and isotope identification altogether. Digital autoradiography systems based on gaseous detectors, such as the BetaIMAGE TRacer (Biospace Lab, France) and BeaQuant (Ai4R, France) systems or solid scintillation–coupled photomultipliers (BetaIMAGER DFine, Biospace Lab), combine all the abovementioned capabilities. Their technology and applications in the biomedical field have been described in earlier chapters, and their potentials in the geological field emerged through various old and recent studies (Hellmuth et al., 1999; Ludwig et al., 2005; Sardini et al., 2016). Ludwig et al. (2005) used the BetaIMAGER DFine system to monitor the effect of light on $^{45}Ca^{2+}$ incorporation and spatial distribution in photic microbial mat calcic formations. Hellmuth et al. (1999) studied marble porosity by analysis of ^{14}C-polymethylmethacrylate impregnation patterns acquired with both BetaIMAGER TRacer and DFine systems. More recently, Sardini et al. (2016) demonstrated how specific tuning of the BeaQuant systems allowed the specific measurement of alpha emission from natural ^{238}U and ^{232}Th disintegrations in geological rock sections. Uranium radiation can also be measured with the BetaIMAGER systems, as shown in Fig. 9.42. As discussed in earlier chapters, both BetaIMAGER DFine and TRacer systems have proprietary algorithms exploiting the decay properties of short-lived isotopes and energy properties of long-lived isotopes for the specific identification of the radioactive signal associated with individual emitters in samples composed of isotope mixtures (Barthe et al., 2004; 2007; Maskali et al., 2005).

In conclusion, various digital autoradiography systems emerging from the biomedical field combine several advantages, including high sensitivity, high spatial resolution, fast sample analyzing speed, and isotope identification

TABLE 9.4 Ratios of signal measured with a multisensitive (MS)-type phosphor screen over signal measured with a tritium (TR-type screen in identical exposure conditions.

Radionuclide	Emission	Mean energy (keV)	MS/TR
^{3}H	Beta	6	
^{233}U	Alpha	4817	0.39
^{239}Pu	Alpha	5148	0.46
^{241}Am	Alpha	5542	0.49
^{244}Cm	Alpha	5795	0.55
^{14}C	Beta	49	1–1.6
^{55}Fe	X-ray	6	2
^{60}Co	Beta	96 + gamma 1253	3
^{137}Cs	Beta	188 + gamma 662	4.7
^{204}Tl	Beta	244	5
^{36}Cl	Beta	316	6.1
^{90}Sr/^{90}Y	Beta	562	6.5
^{40}K (concrete)	Beta	510 + gamma 1460	7.4

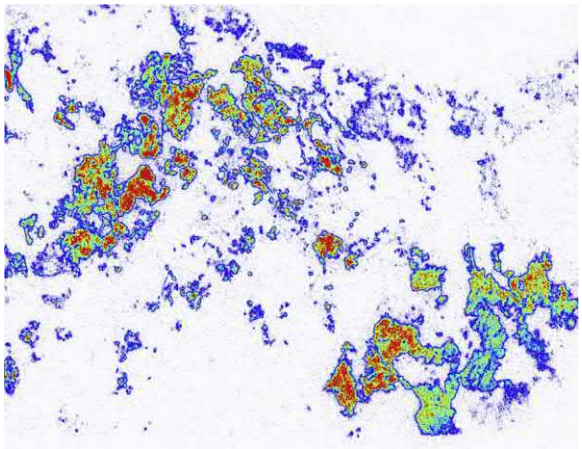


FIGURE 9.42 Imaging of ^{238}U traces (~1Bq/cm^2) in geological rock sections using the BetaIMAGER DFine. For the color version of the figure, the reader is referred to the online version of the book. *Image courtesy of Pascal Fichet, CEA France, Nicole Barthe & BioSpace Lab, France.*

capabilities, which are necessary for the characterization of low-energy beta and alpha isotope contamination. Present and future developments of analytical methods exploiting these systems offer great potentials in the field of dismantlement and decommissioning.

VII. Perspectives and future developments

A. Autoradiography to validate in vivo imaging information

1. Preclinical applications. Development and validation of new molecular imaging probes

With advances in instrumentation and the introduction of novel targeted probes, molecular imaging has taken a major place in translational research. However, traditional in vivo techniques such as PET and SPECT present great constraints with regard to spatial resolution. To address this, multimodal imaging approaches, combining high-resolution anatomical information to high-sensitivity radiolabel imaging (PET-CT, SPECT-CT, PET-MRI), have been developed and are now commercially available for both preclinical and clinical applications. In addition, in vivo 3D tomographic information from optical genetic reporters (e.g., luciferase, iRFP) or functional fluorescent probes (e.g., MPPSense750, PerkinElmer or IRDye 680RD BoneTag, LI-COR Biosciences) can be aligned to anatomical information from μ-CT or preclinical MRI systems thanks to standardized digital imaging platforms such as DICOM (Digital Imaging and Communications in Medicine). In the near future, the synergy of multiple modalities should provide tools for better detection and quantification of optical and molecular targets. For instance, precise 3D anatomical information on organ localization, acquired by CT or MRI, may be used to correct optical and molecular quantifications by implementation of various physical parameters (e.g., scatter, absorption, refraction) inherent to individual tissue in the tomography algorithms (Young Chun, 2016). Meanwhile, ex vivo autoradiographic imaging remains the alternative of choice for high-sensitivity, high-resolution quantitation and localization of molecular markers in animal tissue. Examples of autoradiography applications to the validation of preclinical models of disease and the development of therapeutic strategies can be found for various biomedical specialties that are discussed in the following sections.

a. Oncology

In oncology, the biodistribution and specificity of new probes and drugs must be assessed and validated by PET imaging among other various imaging modalities, including autoradiography and histochemistry. Examples of such studies are given below (Alberini et al., 2015; Al-Ejeh, 2014; Wilson et al., 2014; Bailly et al., 2017).

Alberini et al. (2015) adopted a multimodal in vivo imaging strategy to monitor tumorigenesis and response to chemotherapy in a transgenic mouse model of mammary cancer. PET with 2-deoxy-2-^{18}F-fluoro-D-glucose (^{18}F-FDG)

and 3′-deoxy-3′-^{18}F-fluorothymidine (^{18}F-FLT) was applied, in conjunction with SPECT with ^{99m}Tc-TcO_4 (^{99m}Tc-TEC), X-ray computed tomography, fluorescent confocal endomicroscopy, and ex vivo autoradiography, to characterize tumor progression in female transgenic PyMT mice. Surprisingly, ex vivo autoradiography of lung tumor cryosections after ^{99m}Tc-TEC injection revealed uptake of ^{99m}Tc-TEC in only some of the metastases, suggesting reduced expression of the sodium-iodide symporter (NIS).

Wilson et al. (2014) used ^{18}F-NaF, a standard PET imaging probe for bone imaging to detect hydroxyapatite calcium deposits present in breast tumors by PET imaging. Biodistribution of ^{18}F-NaF was validated with high-resolution autoradiography combined with von Kossa histochemical staining. Bailly et al. (2017) evaluated novel molecular imaging probes, namely, ^{64}Cu-TE2A-9E7.4 (a ^{64}Cu-labeled anti-CD138 murine antibody) in a preclinical syngeneic model of multiple myeloma. Superior tumor uptake of ^{64}Cu-TE2A-9E7.4, compared with metabolic tracer $^{64}CuCl_2$, was quantified by digital autoradiography.

Al-Ejeh et al. (2014) characterized a murine monoclonal antibody DAB4 specifically targeted to apoptotic tumor cells. High-resolution autoradiography of excised PC-3 tumors showed binding of ^{177}Lu-DOTA-DAB4 within specific necrotic regions of the tumor as defined by histochemical hematoxylin and eosin staining.

Another excellent example was recently described (Kryza et al., 2016) where a group of chemists, geneticists, histopathologists, radiopharmacists, and nuclear physicists collaborated to prepare aptamers as new tumoral markers against a metalloproteinase involved in melanoma metastasis. Aptamers are three-dimensional oligonucleotides that can bind to a wide range of targets with high affinity and be chemically modified to act as specific tumor markers. Their tumor targeting efficiency was evaluated ex vivo by high-resolution beta imaging of tumor sections taken from mice bearing human myeloma implants and incubated with ^{111}In-DOTA-F3B aptamers, as illustrated in Fig. 9.43. Immunohistological analysis and fluorescence optical imaging confirmed the results.

b. Neuropharmacology

In neuropharmacology, quantitative assessment of the binding efficiency and selectivity of target peptides for specific neuroreceptors is carried out by digital autoradiography. Autoradiographic binding assays and receptor occupancy assays are indeed essential tools to determine fundamental pharmacological parameters, such as the dissociation constant (Kd), inhibitory constant (Ki), half maximal inhibitory concentration (IC50), and receptor occupancy (Bmax) from drug response curves.

An example of basic protocols to achieve quantitative film autoradiography to visualize serotonin (5-hydroxytryptamine, 5-HT) receptor subtypes in sections of frozen brain tissue was described by Cortes et al. (2016) (Fig. 9.44).

Other pharmaceutical applications may involve precise analysis of neuroreceptor biodistribution upon onset of neurological dysfunctions in dedicated animal models. Again, the high resolution achieved by autoradiography, combined with the fact that radiolabeling does not affect the organic chemistry of neuropeptide probes, thus ensuring optimal specificity for neuroreceptor binding, means that autoradiography is an essential tool for such studies. Representative examples include a study by Hu et al. (2017) looking at cannabinoid neuroreceptor biodistribution and one by Reid et al. (2016) investigating neuronal hypometabolism in HIV-1-associated cognitive disorder.

A novel approach of interest is described in Aitken et al. (2016) where quantitative autoradiography was applied to assess M1 muscarinic ACh receptor density in the hippocampus of rats following bilateral vestibular lesions. In this study, specific binding of ^{3}H-pirenzepine to rat brain cryosections was quantified by subtraction of the nonspecific binding signal measured in adjacent sections by coincubation of ^{3}H-pirenzepine with saturating amounts of cold pirenzepine. In addition, M1 receptor density in the specific hippocampus and striatum regions could be assessed by an overlay of the autoradiographic image acquired with the BetaIMAGER TRacer system to brain atlas information using the M3Vision analysis software (Fig. 9.45).

c. Psychopharmacology

Other applications are in the field of **psychopharmacology,** for example, receptor occupancy profiles of several NMDA (*N*-methyl-D-aspartate) receptor antagonists, which are of therapeutic interest for the treatment of mood disorders, participating in synaptic transmission and triggering synaptic plasticity, in comparison with the actions of ketamine, an analgesic agent studied for its antidepressant effect in individuals (Lord et al., 2013).

Similarly, studies with potential clinical impact use both ex vivo autoradiography and beta microprobes in vivo to examine the subcellular distribution of 5-HT1A receptors in dendrites from nucleus raphe dorsalis (autoreceptors) and hippocampus (heteroreceptors) after antidepressant treatment (Riad et al., 2004).

As another example, a recent study on cerebral metabolic depression following traumatic brain injury (TBI) validated glucoCEST-weighted imaging by chemical exchange saturation transfer (CEST) MRI with 2-deoxy-D-[^{14}C]-glucose (2DG) autoradiography in a closed-head model of diffuse TBI in rats (Tu et al., 2018).

As a last example, Sahlholm et al. (2017) examined whether genetic deletion of beta-arrestin2 prolonged or otherwise modified D2R-dependent responses, using

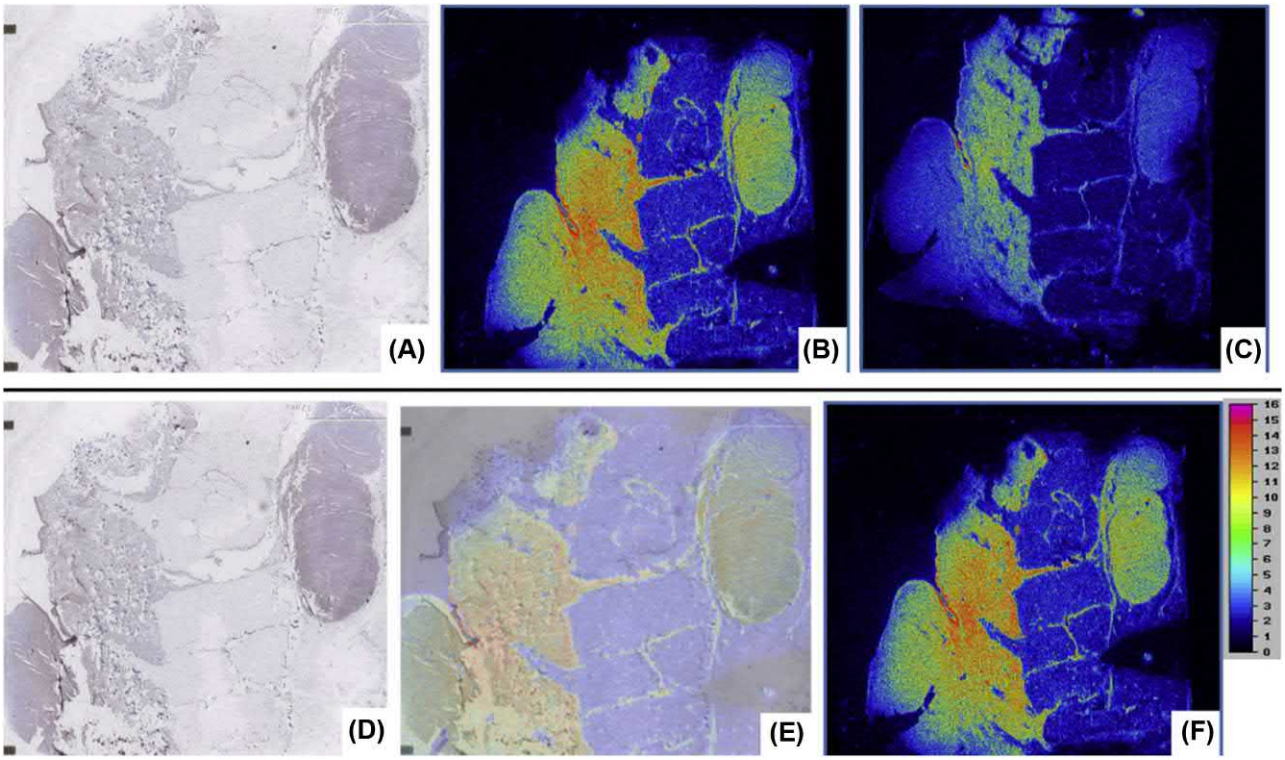


FIGURE 9.43 (A) Immunostaining of nodular melanoma using anti-hMMP-9 murine monoclonal antibody ab58803. Radiolabeling of adjacent tissue sections of nodular melanoma with ^{111}In-F3B-DOTA aptamers (B), and ^{111}In-DOTA-control sequence (C). (D) Immunostaining of nodular melanoma with the murine monoclonal antihuman MMP-9 antibody, ab58803. (F) Radiolabeling with ^{111}In-DOTA-F3B. (E) Merged immunostaining (D) and autoradiographic (F) images. Identifications of the primitive nodular melanoma and intrahypodermic nodes were possible with both techniques. Dark areas observed by immunohistochemistry correspond to regions of high radioactivity. For the color version of the figure, the reader is referred to the online version of the book. *Reproduced with permission from Kryza et al. (2016).*

functional magnetic resonance imaging (fMRI) to monitor blood-oxygenation-level-dependent signal changes induced with a dopamine agonist in wild-type and beta-arrestin2 knockout mice. Quantification was carried out by digital beta imaging with a BetaIMAGER TRacer system.

In the context of translational research, ex vivo beta imaging is also greatly involved in neuroinflammation studies in conjunction with in vivo multimodal imaging. Typical examples in Alzheimer's disease (AD), which is characterized by an accumulation and deposition of β-amyloid peptides and activation and exacerbation of inflammatory processes, are given below.

Current studies aim to develop or exploit specific radiolabeled biomarkers of amyloid plaque formation (Maeda et al., 2007; Yousefi et al., 2011; Manook et al., 2012; Marutle et al., 2013).

Maeda et al. (2007) first demonstrated how PET imaging could be used to monitor amyloid neuroinflammation with N-^{11}C-methyl-2-(4-methylaminophenyl)-6-hydroxybenzothiazol, ^{11}C-PIB ("Pittsburgh Compound-B") and ^{18}F-fluoroethyl-DAA1106, a radiotracer for activated glia. Ex vivo autoradiographic analysis was also applied to observe and quantify longitudinal amyloidosis-associated accumulation of ^{11}C-PIB in APP transgenic mouse brains.

Yousefi et al. (2011) evaluated the suitability of ^{18}F-labeled imidazo[2,1-b]benzothiazole (^{18}F-8) as a PET tracer for cerebral β-amyloid deposits in a transgenic mouse model of AD. Regional brain biodistribution and specific binding of ^{18}F-8 to Aβ was validated by autoradiography correlated to immunohistochemistry.

Marutle et al. (2013) applied an in vitro autoradiography imaging multitracer concept to investigate the relationship between regional neuroinflammatory processes, fibrillar Aβ deposition, and disturbances in cholinergic neurotransmission in AD brain using multiple binding studies with radioligands ^{3}H-L-deprenyl (activated astrocytes), ^{3}H-PIB (fibrillar Aβ), ^{3}H-PK11195 (microglia) as well as ^{125}I-α-bungaro-toxin (α7 nicotinic receptors, nAChRs) and ^{3}H-nicotine (α4β2 nAChRs) in postmortem brains from AD and nondemented patients. Using this multitracer imaging concept, they also characterized and compared the laminar distribution of activated astrocytes, fibrillar Aβ, as well as α7 and α4β2 nAChRs in hemisphere brain sections of an AD patient.

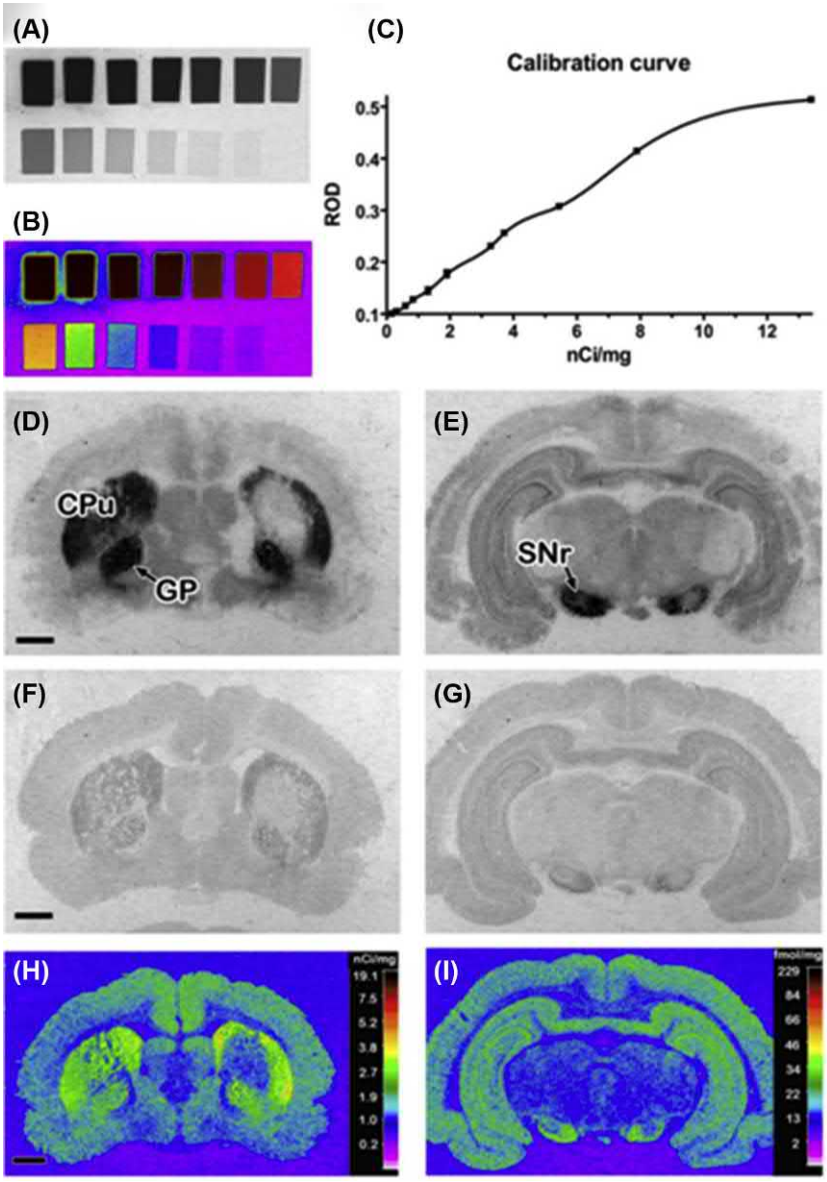


FIGURE 9.44 Quantitative autoradiography and brain lesion studies. Film exposure of radioactive standard scales together with incubated tissue sections allow for the quantification of the autoradiograms by microdensitometry. (A, B) Autoradiographic image of ^{3}H standards (American Radiolabeled Chemicals) exposed for 2 months and processed with an MCID image analyzer. (A) Gray levels or (B) RGB color-coded lookup table (LUT) rendering of the data. (C) Calibration curve produced from quantification of the ^{3}H standards from panels A and B. X-axis: Known standard radioactivity (nCi/mg). Y-axis: Recorded optical density (ROD). Smoothed spline is best fit curve. (D–I) Digital autoradiograms of 5-HT4 receptors in guinea pig brain. (D–G) Gray level representations (H, I). Color-coded representation of F and G. Sections in D and E were incubated with ^{125}I-SB 207710 prior to film exposure for 8 days. Consecutive sections (F and G) were incubated with ^{3}H-GR113808 and exposed for 2 months. Note that the ^{125}I-ligand provides stronger autoradiographic signal in much shorter exposure time than the ^{3}H ligand. The calibration of the MCID system with ^{3}H standards allows an overall estimation of receptor densities in different units, i.e., nCi/mg (H) or fmol/mg (I). Images taken from an animal that had received unilateral injections of quinolinic acid in the right striatum (CPu). The lesion resulted in the destruction of striatal neurons and a complete loss of local 5-HT4 receptors. Furthermore, a decrease in 5-HT4 binding sites also occurred in the ipsilateral substantia nigra pars reticulata (SNr), suggesting that these receptors might be localized on axon terminals of striatonigral projections. No major changes in binding to 5-HT4 receptors were observed in the globus pallidus (GP). Bar: 200 μm. For the color version of the figure, the reader is referred to the online version of the book. *Reproduced with permission from Cortès et al. (2016).*

Other studies in neurosciences may exploit multimodal molecular imaging tools to characterize pathology, course of disease, and treatment response. For instance, Buck et al. (2012) used MRI and PET/CT to image multiple sclerosis lesions in an animal model of autoimmune encephalomyelitis. Various PET tracers, namely ^{18}F-FDG, ^{18}F-FLT, and O-(2-^{18}F-fluoro-ethyl)-L-tyrosine (^{18}F-FET), were tested in comparison with MRI and autoradiography to select a suitable marker for in vivo detection of multiple sclerosis inflammatory lesions in patients.

A beautiful example of multimodal cross-validation for PET results with ex vivo and in vitro methodologies taken from Manook et al. (2012) is shown in Fig. 9.46.

d. Cardiovascular research

In cardiovascular research, functional information from molecular imaging studies is validated ex vivo with high-resolution quantitative beta imaging.

Good examples in the field of coronary artery disease where inflammatory cellular apoptosis processes are involved in atherosclerotic plaque rupture in rabbit aortas were described by Hyafil et al. (2015). They used PET imaging to monitor accumulation of ^{18}F-ML-10 (2-(5-fluoro-pentyl)-2-methylmalonic acid in apoptotic cells present in specific membrane. A strong correlation between the number of apoptotic cells on histological sections and the accumulation of the radiotracer by autoradiography was

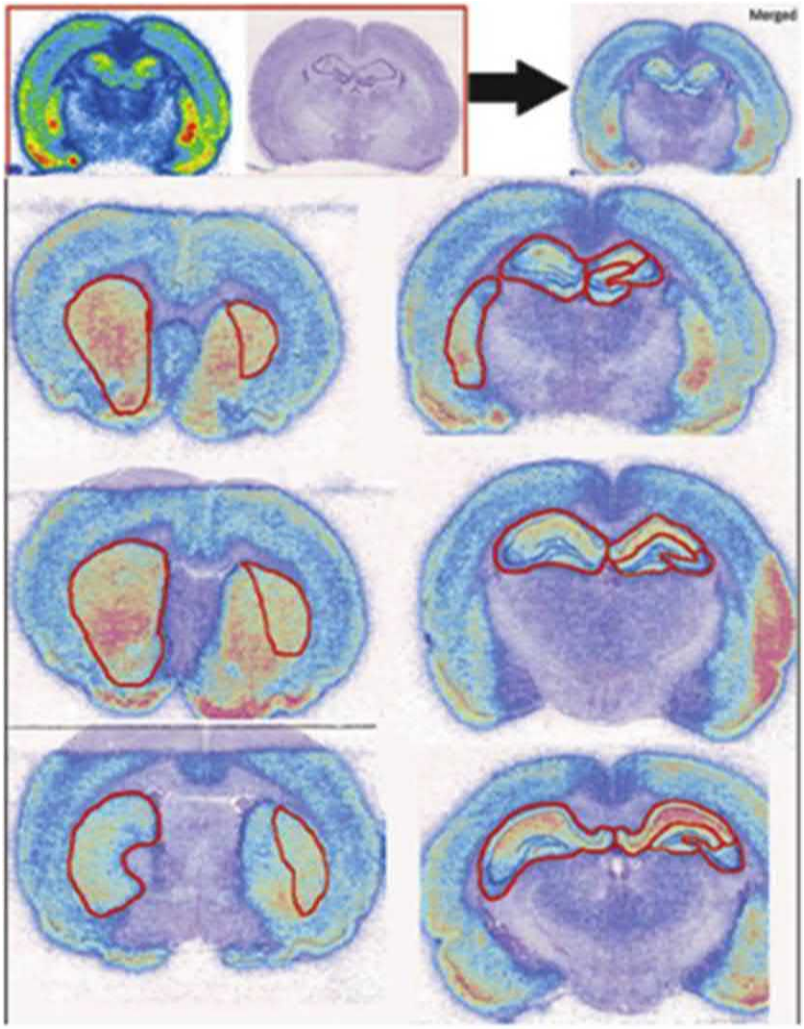


FIGURE 9.45 M1 ACh receptor expression following bilateral vestibular lesions using beta imaging autoradiography. The hippocampus (total, CA1, CA2/3, and DG) and caudate putamen (total, dorsal parafascicular inputs) were manually delineated using merged autoradiographic and histological images. For the color version of the figure, the reader is referred to the online version of the book. *Reproduced with permission from Aitken et al. (2016).*

also demonstrated. In a similar study, Tarkin et al. (2017) developed a novel cell−specific PET tracer (^{68}Ga-DOTATATE) targeted to somatostatin receptor subtype-2 and assessed its efficacy for imaging atherosclerotic inflammation. Moreover, they transposed the methodology to clinical studies where they could evaluate the risk of plaque rupture in ischemic stroke patients by PET imaging.

At the cardiac level, many studies focus on the metabolic mechanisms involved in infarction and consider angiogenesis as part of the repair process after ischemic injury. ^{18}F-labeled glycosylated $\alpha_v\beta_3$ integrin antagonist (^{18}F-galacto-RGD) is a recently introduced PET tracer that was shown to target specifically $\alpha_v\beta_3$ integrin expression. Higuchi et al. (2008) used ^{18}F-galacto-RGD PET imaging to study serial changes in myocardial uptake after ischemic intervention. Results were validated by autoradiography with a phosphor imager. Dual tracer autoradiography with ^{18}F-galacto-RGD and the myocardial imaging agent ^{201}Tl was also carried out in a rat heart to delineate risk areas during coronary occlusion with the BetaIMAGER DFine. In an earlier study, Maskali et al. (2005) managed to produce a wonderful triple-isotope autoradiographic image showing the metabolic processes of glycolysis (^{18}F-FDG), perfusion (^{99m}Tc-Sestamibi), and fibrosis (^{111}In-DTPA) involved in myocardial infarction using the BetaIMAGER DFine. This study is more thoroughly described earlier in Section IV-D.3 (Fig. 9.30).

e. Pneumology

In pneumology, there is a need for a whole-body imaging techniques that can detect pathogens at the early phase of infection and provide information on bacterial burden in response to targeted delivery of a powerful treatment.

Li et al. (2018) studied the efficiency of 2-^{18}F-fluorodeoxysorbitol (^{18}F-FDS) as an alternative to ^{18}F-FDG, which cannot distinguish infections from other

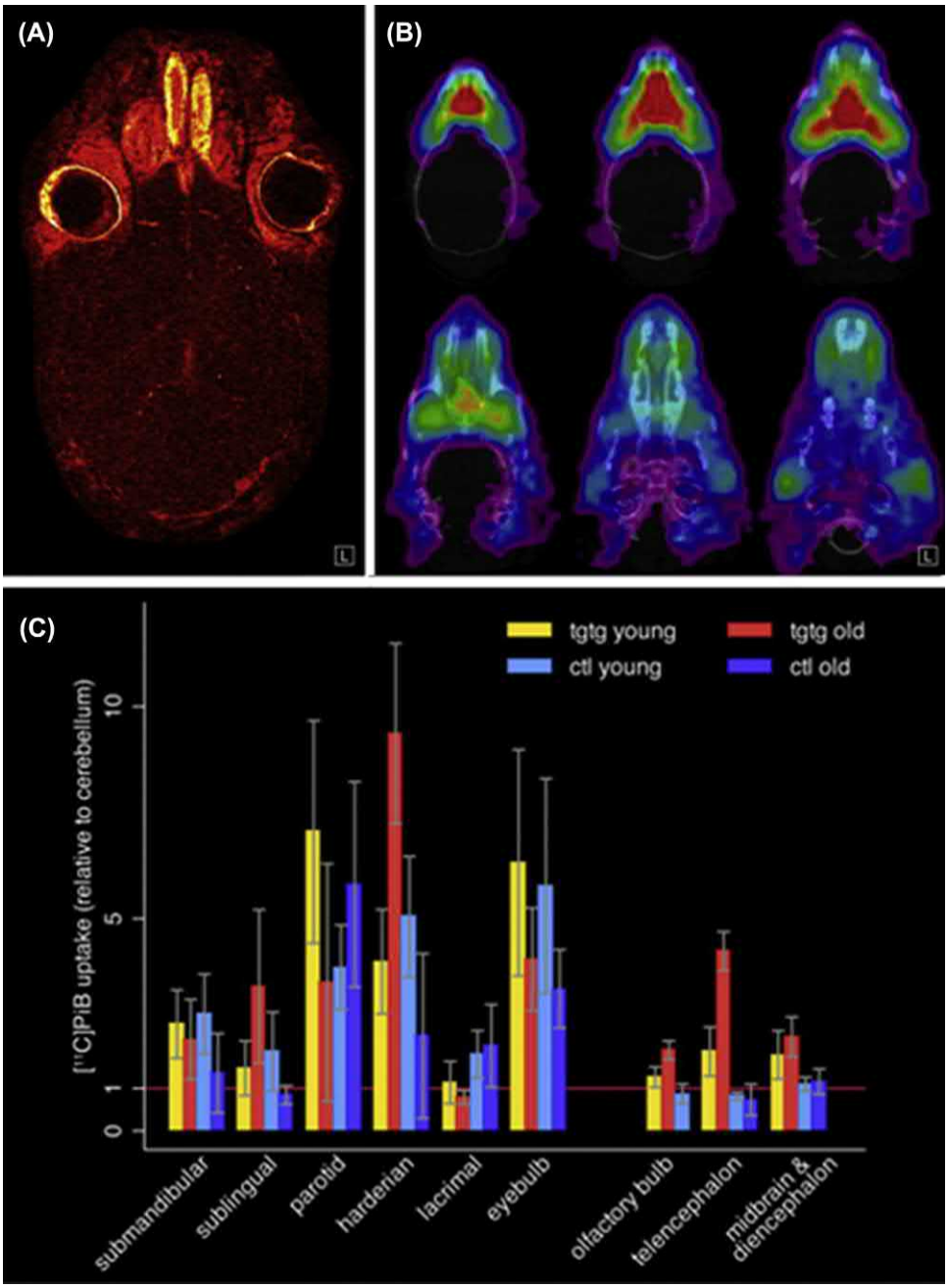


FIGURE 9.46 Extracerebral tracer retention. High ^{11}C-PiB uptake in regions frontal to the brain was accurately validated to be extracerebral. (A) Cranial ^{3}H-PiB ex vivo autoradiography. 15-μm-thick section of a complete mouse head showing exact anatomical locations of unspecific tracer retention. (B) CNS removal during $^{[11}$C-PiB PET. 9-month-old male homozygous APP/PS1 mouse was scanned in vivo for 30 min before the complete brain was extracted and scanned for further 30 min together with the skull. The skull of the ex vivo ^{11}C-PiB PET scan is coregistered to a cranial CT for better orientation and shown on six horizontal slices, which are 1 mm apart (top left horizontal level at about 21.9 mm Bregma in correspondence to all other figures). Both parotid glands can be seen on the bottom section. (C) Ex vivo biodistribution of ^{11}C-PiB relative to cerebellar uptake in glandular tissues and eye bulbs in both homozygous and control study groups. For the color version of the figure, the reader is referred to the online version of the book. *Reproduced with permission from Manook et al. (2012).*

afflictions such as cancer or inflammation, as its uptake remains nonspecific for bacterial imaging. ^{18}F-FDS is a derivative of the metabolic substrate for Enterobacteriaceae, Sorbitol. Uptake of ^{18}F-FDS and ^{18}F-FDG in mice inoculated intratracheally with either live or dead *Klebsiella pneumoniae* to induce either lung infection or lung inflammation, were compared by PET/CT during disease progression. The authors demonstrated the superior efficiency of

^{18}F-FDS in differentiating *K. pneumoniae* lung infection from lung inflammation compared with ^{18}F-FDG. Dual-label quantitative autoradiography imaging could have been used as a validating modality in this context.

f. Nephrology

In nephrology, the early detection and treatment of allograft rejection are crucial to limit the inflammatory process and preserve organ function after transplant. Reuter et al. (2010) proposed ^{18}F-FDG PET as a method to monitor acute rejection in an allogeneic-rat renal transplant (aTX) model. The rats were treated with cyclosporine A (CSA) to induce immunosuppression, and their response to treatment was compared with those of rats undergoing renal failure and an untreated control group. PET results were confirmed by histologic, functional parameters and autoradiographic analysis.

In another study, Gulaldi et al. (2013) investigated the applicability of a kinetic model based on three compartments (one blood and two tissue compartments connected in parallel) for the quantitative analysis of the renal kinetics of ^{11}C-KR31173, a PET radiotracer for the angiotensin II subtype 1 receptor (AT1R). Validation of the model was carried out by PET imaging in domestic pigs subjected to acute arterial occlusion followed by reperfusion to induce renal ischemia. The input function required for compartmental and for noncompartmental (deconvolution) analyses was obtained from metabolite-corrected arterial plasma samples. Differential binding of ^{11}C-KR31173 in renal cortex and medulla together with AT1R specific binding of ^{125}I-[Sar^{1}Ile^{8}]Ang II after AT2R antagonist PD-123,319 was quantified by digital autoradiography.

g. Biomaterial applications

In biomaterial applications, the development of biocompatible and bioactive biomaterials requires the study of their biodistribution and pharmacokinetic properties to better understand their metabolic fate. This implies radiolabeling to follow their localization and interactions with living tissue. In an experiment from Pant et al. (2015), a bioactive nanoscale water-soluble polymer, namely, dendritic polyglycerol sulfate (dPGS), was synthesized and radiolabeled with ^{3}H and ^{64}Cu to investigate its behavior in healthy mice and rats and determine its biodistribution both in vivo by PET imaging (^{64}Cu) and ex vivo by quantitative autoradiography (^{3}H). dPGS and its derivatives are known to exhibit antiinflammatory properties. The authors were therefore hoping to demonstrate its suitability for therapeutic and diagnostic applications. However, their results revealed a substantial organ accumulation of dPGS and its biometabolites, even after 3 weeks, setting doubts on the applicability of dPGS as a therapeutic agent. However, the neutral polymer dPG, which has inert properties, showed much improved renal clearance, suggesting that dPG might be a more suitable approach to a therapeutic candidate.

2. Clinical applications

The examples of autoradiography applications presented up to this point in this chapter were mostly linked to fundamental research or preclinical research. However, beta autoradiography imaging may also be applied in the clinical field to refine the characterization of established clinical radiotracers or validate their application for purposes other than their original use. Moreover, novel direct applications of autoradiography in the clinical theater are currently emerging where high-sensitivity and high-resolution data on radiotracer localization is to be rapidly collected and used as an input for surgical procedures. Examples of autoradiography applications in a clinical context are given below.

A set of clinical studies exploited a novel, last generation, high-affinity translocator protein (TSPO) radioligand, ^{18}FGE-180, for clinical PET imaging of patients to monitor inflammation. Unterrainer et al. (2018) examined the suitability of ^{18}FGE-180 as a clinical PET imaging radiotracer for patients with relapsing–remitting multiple sclerosis (RRMS) by comparing its ability to detect active inflammatory lesions with gold standard, contrast-enhanced MRI. TSPO PET with ^{18}F-GE-180 showed excellent performance for both visual and quantitative detection of focal microglia/macrophage activation in patients with RRMS. ^{18}F-GE-180 signal intensity corresponded to binding levels predicted from the patients' TSPO genotypes, which were classified as high-, medium-, or low-affinity binders (HAB/MAB/LAB). Lesions with only moderate or low inflammatory activity could be depicted. Moreover, high focal uptake was observed, not only in patients with HAB and MAB status but also in patients with LAB status. The results were in accordance with an earlier study from Fan et al. (2016) looking at the kinetic properties of ^{18}F-GE-180 in healthy patients. More recently, Narayan et al. (2018) evaluated cellular TSPO expression in knee synovium by PET imaging of second generation radioligand ^{11}C-PBR28 in both healthy volunteers and patients suffering from rheumatoid arthritis (RA). Cellular expression of TSPO in synovial tissue cryosections prepared from ultrasound-guided biopsies was evaluated through ^{3}H-PBR28 autoradiography. The results confirmed significantly higher ^{3}H-PBR28 binding in RA synovial tissue compared with healthy tissue and significantly correlated with TSPO immunohistochemical data.

Other studies describe direct autoradiography measurements on patient biopsies. Reubi et al. (1990) quantified the levels of somatostatin receptors in small needle tumor biopsies taken from liver metastases using two iodinated somatostatin analogues, namely [Leu8, Dtrp22, Tyr25]somatostatin-28 and octapeptide (Tyr3-octreotide). More recently, Fanchon et al. (2015, 2017) described a real-time ^{18}F-FDG PET/CT-guided biopsy procedure to reduce tumor registration errors during surgery. PET/CT scans acquired before and after needle insertion were registered using a deformable image registration algorithm for

evaluation and correction of the error in needle placement during biopsy.

In a follow-up paper, Kirov and Fanchon (2018) examined the suitability of this approach to produce adequate specimens for genomic analysis using digital autoradiography to quantify their metabolic activity. Quantitative particle-counting digital autoradiography of biopsy specimens acquired under ^{18}F-FDG PET/CT guidance produced signals with sufficient signal-to-noise ratio for samples with average activities of 3−9 kBq/mL, thus corresponding to the number of cells required for genomic analysis. Acquisitions could be carried out in less than 10 min, allowing enough time for procedure guidance. Moreover, autoradiography of the biopsies using either phosphor storage screens or the BetaIMAGER DFine system (Biospace Lab, France) showed sufficient resolution to quantify distribution of the activity along the specimens and define benign versus malignant sections as confirmed by histological analysis (Fig. 9.47).

Therefore, the combined approach of PET-guided biopsy and autoradiography analysis of biopsy specimens has great potential, not only for genomic profiling of tumors but also for other applications such as tumor boundary measurements, and could significantly increase the efficiency of biopsy procedures for cancer diagnosis as well as providing important input during surgery.

3. Bremsstrahlung radiation imaging

Bremsstrahlung is a very well-known physical phenomenon, used, for example, in any type of radiology equipment.

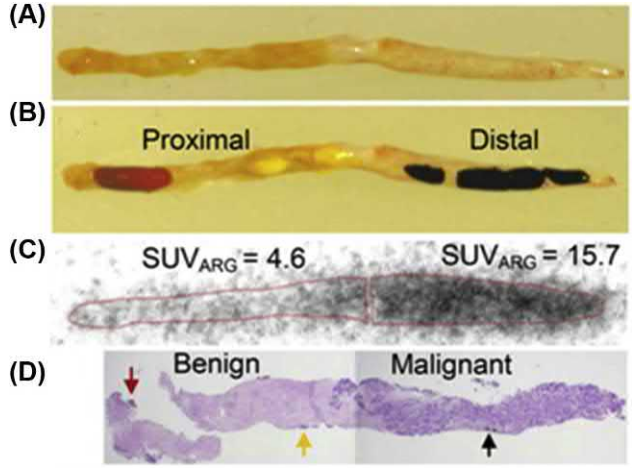


FIGURE 9.47 (A and B) Photographs of biopsy specimen from a patient with before (A) and after (B) marking with red, yellow, and black ink. (C and D) Corresponding autoradiograph (C) and histopathology slide (D). Colored arrows point to areas on micrograph where the ink marks are visible. SUV_{ARG}: Average standardized uptake value for contoured regions on the autoradiograph. For the color version of the figure, the reader is referred to the online version of the book. *Image reproduced with permission from Fanchon et al. (2015).*

When an electron or a beta particle passes through matter, it slows down, and a fraction of its energy is directly converted into X-rays. The spectrum of X-ray emission is continuous, and its maximum energy is the initial energy of the electron. For example, a beta emitter such as ^{14}C can emit X-rays of up to 156 keV in any given sample. The same phenomenon is used to produce X-rays in most X-ray sources. The Bremsstrahlung yield is actually proportional to the atomic number of the media and "roughly" proportional to the square of the energy (Evans, 1955). In the case of a biological tissue, the atomic number is low (between 7 and 8), and the yield stays very low. For ^{90}Y ($E_{max} = 2.2$ MeV), only 1% of the energy is converted into X-rays, i.e., 20 keV per beta particle, spread over a spectrum, the maximum energy of which is 2.2 MeV. In terms of probability, less than 20% of beta particles give an X-ray that can contribute to form an image. As usual collimators used for scintigraphy have an efficiency of 100 cps/MBq, even for high-energy beta-emitting isotopes, the total efficiency of Bremsstrahlung imaging is never more than 20 cps/MBq. For a lower-energy tracer, such as ^{14}C, the yield is at least 100-fold weaker and therefore not suitable. Bremsstrahlung radiation imaging is therefore mainly used in clinical imaging, where it is combined with high-energy tracers requiring visualization that could not be seen otherwise. A good example is ^{90}Y, a tracer widely used for radiotherapy. Bremsstrahlung scintigraphy allows imaging of the specific localization of the tracer to target tumor sites (Kim, 2011).

4. Cerenkov luminescence imaging

Bremsstrahlung yield combined with the poor efficiency of gamma collimators makes bremsstrahlung imaging more suitable for higher-energy beta isotopes, such as ^{32}P and ^{90}Y. For such isotopes, and in preclinical imaging, another alternative is to utilize the Cerenkov effect. The Cerenkov effect occurs when an electron travels faster than the speed of light in a medium. (The threshold energy for the Cerenkov effect with beta particles is 300 keV in biological tissue.) Along its path, the electron polarizes the medium that emits light when relaxing. This phenomenon will be familiar to some as the blue light seen on pictures of nuclear reactors. Theoretical analysis of the phenomenon and formulas to express the photon yield can be found in several references (Mead, 1958; Landau et al., 1960; L'Annunziata, 2007, 2016) and in Chapter 6, Volume 2 of this book. The Cerenkov light emits predominantly in the UV blue part of the visible spectrum, but a nonnegligible fraction also is emitted in the red part of the spectrum. Red photons can penetrate more than 1 cm deep across biological tissues (although they become strongly diffused) and can be detected outside the animal with a sensitive camera. To be more precise, the yield of Cerenkov visible

light is in the range of 350 ph/s/Bq (depending on the energy of the isotope), which leads to a typical brightness emitted by the surface of the animal in the range 10^4–10^5 ph/s/cm^2/sr for 15 MBq injected. Sensitive cameras capable of detecting these photons are used typically for bioluminescence imaging. Of course, due to the strong absorption and diffusion of light in tissues, this measurement is neither spatially accurate (3 mm) nor really quantitative. But the compactness and the wider availability of optical imagers compared with dedicated animal SPECT systems make Cerenkov a strong alternative to Bremsstrahlung radiation imaging. It is also a complementary technique to PET imaging for fast screening because the acquisition time is shorter than that for PET images.

Although this new technique does not allow high resolution, bimodal analysis is possible with a first series of optical in vivo measurements for screening and subsequent semiquantitative analysis, followed with a series of ex vivo autoradiography for precise quantification and localization. Finally, the sensitivity of certain bioluminescence optical imagers equipped with either EMCCD or iCCD cameras, such as the PhotonIMAGER (Biospace Lab, France) or the IVIS Kinetics systems (PerkinElmer, USA), permits the monitoring of radiotracer biodistribution in real time, as shown in Fig. 9.48.

In this example, the acquisition was made with an optical imager (PhotonIMAGER RT, Biospace Lab), which can work in photon counting mode (with list mode file data) for low light level. The three images are superimpositions of the Cerenkov list mode file with a photographic image, acquired shortly afterward with the same apparatus.

As mentioned earlier, the minimum energy required for an electron to produce Cerenkov light in a biological tissue is around 300 keV, but the yield becomes compatible with optical imaging only over 500–600 keV for beta tracers (or internal conversion electrons). Among these, one can include all PET tracers (^{18}F, ^{11}C, ^{13}N, ^{15}O), high-energy autoradiography isotopes (^{89}Sr, ^{32}P), and radiotherapy tracers (^{90}Y, ^{131}I). The list of isotopes potentially suitable for Cerenkov imaging is extensive and open to a wide range of applications, including some alpha tracers used for radiotherapy, which exhibit also a high-energy beta emission (alpha particles only produce Cerenkov light in the range of GeV, which is much higher than the energy of alphas emitted by nuclei). Illustrated Figs.9.49–9.51 are typical Cerenkov images using ^{32}P and ^{18}F-FDG as tracers.

In Fig. 9.49, 15 MBq of $Na_2H(^{32}P)O_4$ was injected 4 hours prior to imaging. Following the administration of the radionuclide tracer, the probe found that the radiotracer concentrated in rapidly proliferating tissues with high phosphorus content, such as bone marrow, lymph nodes, liver, and spleen. The distribution is also enriched in tumors, uptake being much higher in neoplastic tissues (Kautz, 1956). The two tumors are clearly visible by Cerenkov imaging (acquisition time: 5 min).

An interesting comparison on the same animal between a^{18}F-FDG PET image obtained with a small animal PET scanner and a Cerenkov image acquired with a cooled CCD camera is shown in Fig. 9.50. Even though the Cerenkov data are only semiquantitative, due to light absorption, a clear correlation between the two images can be established. For a more detailed description of imaging applications with the Cerenkov Effect, see works by Roberstson (2011), Ruggiero (2010), and Boschi et al. (2011).

In a review on Cerenkov imaging, Thorek et al. (2012) emphasized that Cerenkov luminescence imaging (CLI) was still an "emerging hybrid modality that utilizes the light emission from many commonly used medical isotopes and is of considerable interest as it enables the use of widespread luminescence imaging equipment to visualize clinical diagnostic (all PET radioisotopes) and many therapeutic radionuclides." The use of CLI to achieve imaging in preclinical models was also described. Other clinical applications of CLI, such as intraoperative

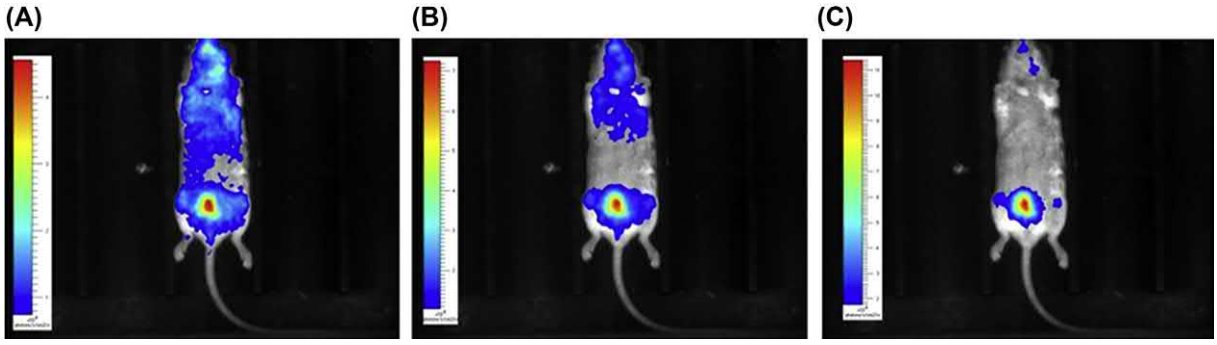


FIGURE 9.48 Example of biodistribution visualized by Cerenkov imaging following intraocular injection of 1.5 MBq ^{90}Y. Biodistribution of the radiolabel signal was followed in real time using the PhotonIMAGER RT system. Representative images are extracted from the temporal sequence. Signal integration at (A) 0–500 s, (B) 1000–1500 s, and (C) 2000–2500 s postinjection. Progressive accumulation in the kidney and clearance in the bladder can clearly be seen (Nicole Barthe, unpublished work). For the color version of the figure, the reader is referred to the online version of the book. For the color version of the figure, the reader is referred to the online version of the book.

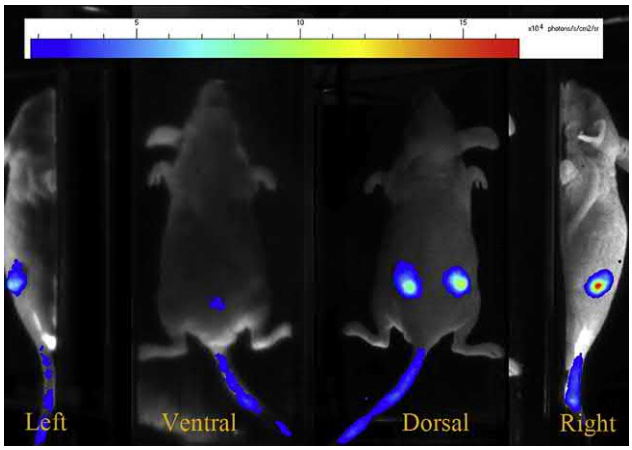


FIGURE 9.49 Cerenkov imaging on four simultaneous views (ventral, dorsal, left, and right), uptake of $Na_2H(^{32}P)O_4$ by two subcutaneous tumors (unpublished work).

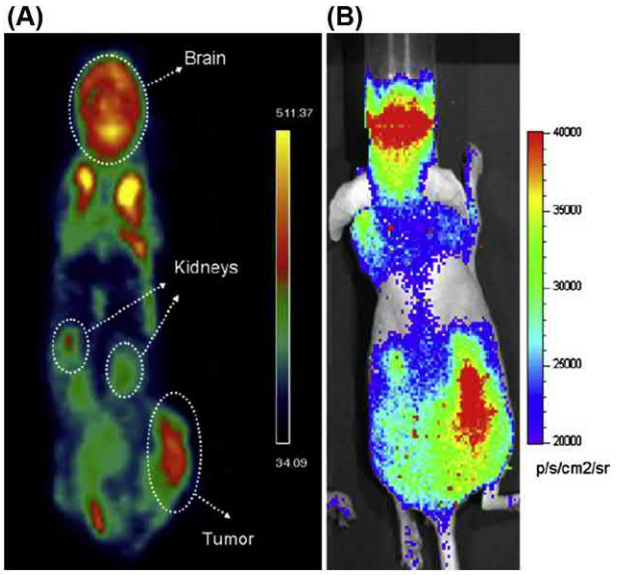


FIGURE 9.50 Comparison between coronal images of the same mouse with a BB1tumor, 1 h after ^{18}F-FDG injection. A: small animal PET scanner. B: Cerenkov imaging. The two images show similar biodistributions. For the color version of the figure, the reader is referred to the online version of the book. *From Boschi et al. (2011). Printed with permission © 2010, Springer-Verlag).*

radionuclide-guided surgery, therapeutic efficiency monitoring, and tomographic optical imaging, have been evoked elsewhere (Spinelli et al., 2010). Moreover, the ability to perform multiplexed imaging using fluorophores excited by Cerenkov radiation is also emerging (Jain et al., 2015; Roussakis et al., 2015). Hence, Cerenkov imaging has great potentials to join the battery of traditional in vivo optical imaging tools (including fluorescence and bioluminescence, Optoacoustics, and Raman spectroscopy) for routine biomedical studies, perhaps in conjunction with other molecular imaging modalities, as shown in Fig. 9.51.

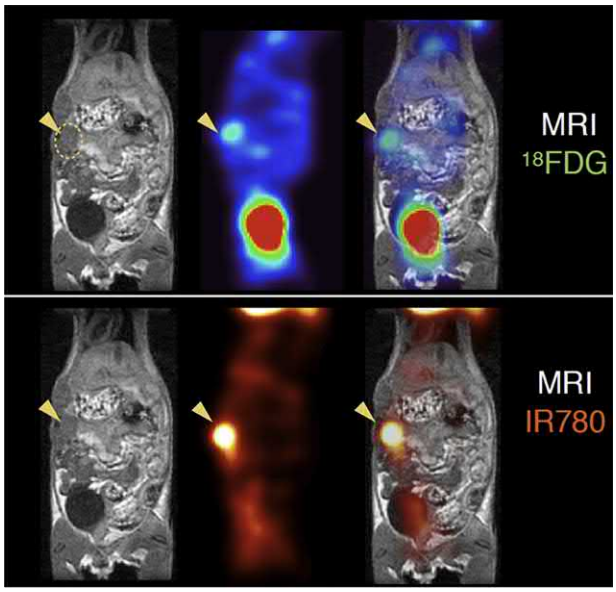


FIGURE 9.51 Multimodal tumor imaging of an orthotopic cecal tumor (2×10^6 cells) visualized by Cerenkov imaging with ^{18}F-FDG (500Ci/mouse injection i.v.). Fluorescence imaging with IR780 (0.2 mg/kg, injection i.v.) and MRI. Optical tomographic information (Cerenkov and FLI) was aligned to MRI data via DICOM. Arrows show positioning of the cecal tumor. Strong clearance of ^{18}F-FDG in the kidney can also be observed (top panel). Right panel, MRI. Central panel, Cerenkov (top) and FLI (bottom). Right panel, MRI/optical overlay. IRM acquisition parameters: 1,5 T, 3D FLASH 30/4/40° Nex 9 128×256×64. *Images courtesy of Philippe Choquet, Les Hôpitaux Universitaires de Strasbourg, Jean-Noël Freund & Isabelle Duluc, Inserm UMR-S1113, Strasbourg, France, RS2D, Strasbourg, France and Biospace Lab France. For the color version of the figure, the reader is referred to the online version of the book.*

B. Autoradiography and alpha-particle imaging

Alpha particles are highly ionizing particles and can be of course imaged in the same way as beta particles are. Therefore, autoradiography is occasionally carried out with alpha-labeled samples. Nevertheless, their very short range and their large stopping power come with the following restrictions:

- Alpha particles must be imaged using detectors without a protecting layer.
- Alpha samples must be preferentially in contact or embedded in the imager.
- Imaging parameters must be adjusted due to a higher energy deposit.

The conundrum of the very short alpha-particle range can be solved by the use of TR screen when the chosen imaging technology is phosphor storage screens. The exposure time must be determined carefully because the energy deposition is, most of the time, much higher (several MeV per alpha particles, in comparison with the mean energy of tritium or ^{14}C, respectively, of 5.7 and 49 KeV). An example of

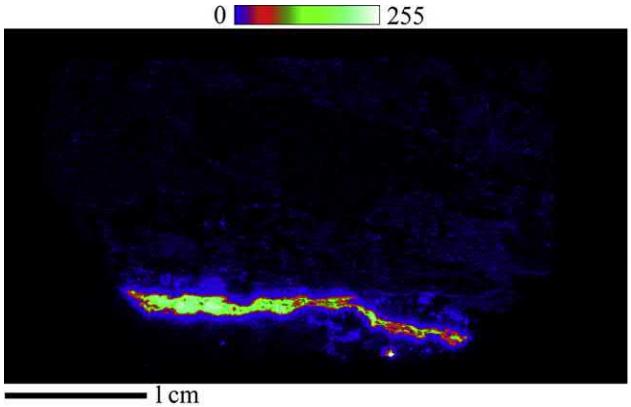


FIGURE 9.52 Autoradiography of an uraninite vein with the BeaQuant system. Exposure time is 40 h. For the color version of the figure, the reader is referred to the online version of the book. *Image printed with permission from Sardini et al. (2016).*

autoradiography measurements with a sample emitting alpha particles using a phosphor screen is shown in Fig. 9.41.

Particles counting detectors, especially gaseous detectors, are also convenient for autoradiography of alpha particles with a restriction regarding the applied voltage, which needs to be reduced in comparison with voltage applied for beta particles. This voltage reduction is important to limit the risk of discharge, which increases when the primary ionization is very large, as in the case of alpha particles. Therefore, the gaseous detector–based systems, such as the BetaIMAGER TRacer or BeaQuant, include a dedicated mode for alpha particles in their software. An example of alpha emission measurements from natural ^{238}U and ^{232}Th disintegration in geological rock sections (Sardini et al., 2016) is shown in Fig. 9.52.

VIII. Conclusions

Autoradiography was the first molecular imaging technique used for the localization of radiolabeled compounds in biological specimens. During the past 50 years, its importance has been essential, and it is still used due to its unequaled spatial precision, especially at a subcellular level. In parallel, over the years, technology has widely improved the acquisition time and quantification with phosphor plate technology. More recently, a new generation of real-time counting imagers allows researchers to optimize the exposition time. Their very low background and consequently very high sensitivity allow the detection of radionuclides of short half-life with the capacity of preserving reliable relationships between counts and radioactive concentrations over a large dynamic range. Moreover, their specific detection process allows the discrimination of several radionuclides in the same experiment.

All of these techniques are involved in new developments in association with other technological processes, such as laser desorption/ion mass spectrometry, providing subtle solutions to an old and difficult problem, namely, the separation between parent drugs and their metabolites. Finally, taking advantage of the detection of concomitant emissions (e.g., Bremsstrahlung or Cerenkov radiation) opens up new horizons in the field of bimodal imagery for ex vivo and in vivo parallel experiments of great interest in many molecular imaging applications.

References

Aitken, P., Benoit, A., Zheng, Y., Philoxene, B., Le Gall, A., Denise, P., Besnard, S., Smith, P.F., 2016. Hippocampal and striatal M1-muscarinic acetylcholine receptors are down-regulated following bilateral vestibular loss in rats. Hippocampus 26 (12), 1509–1514. https://doi.org/10.1002/hipo.22651.

Alberini, J.L., Boisgard, R., Guillermet, S., Siquier, K., Jego, B., Thézé, B., et al., 2015. Multimodal in vivo imaging of tumorigenesis and response to chemotherapy in a transgenic mouse model of mammary cancer. Mol. Imaging Biol. 18 (4), 617–626. https://doi.org/10.1007/s11307-015-0916-7.

Al-Ejeh, F., Staudacher, A.H., Smyth, D.R., Darby, J.M., Denoyer, D., et al., 2014. Postchemotherapy and tumor-selective targeting with the La-specific DAB4 monoclonal antibody relates to apoptotic cell clearance. J. Nucl. Med. 55, 772–779. https://doi.org/10.2967/jnumed.113.130559.

Al Halabiah, H., 2005. Expression pattern of NOGO and NgR genes during human development. Gene Expr. Patterns 5, 561–568.

Amemiya, Y., 1995. Imaging plates for use with synchroton radiation. J. Synchroton Radiat. 2, 13–21.

Arimatsu, Y., 1982. Acta Histochem. Cytochem. 15, 600–607.

Bailly, C., Gouard, S., Lacombe, M., Remaud-Le Saëc, P., Chalopin, B., Bourgeois, M., et al., 2017. Comparison of Immuno-PET of CD138 and PET imaging with 64CuCl2 and 18F-FDG in a preclinical syngeneic model of multiple myeloma. Oncotarget 99061–99072. https://doi.org/10.18632/oncotarget.23886.

Barthe, N., Chatti, K., Coulon, P., Maîtrejean, S., Basse-Cathalinat, B., July 2004. Recent technologic developments on high-resolution beta imaging systems for quantitative autoradiography and double labeling applications. Nucl. Instrum. Meth. A. 527 (1–2), 41–45. https://doi.org/10.1016/j.nima.2004.03.014.

Barthe, N., April 2007. High-resolution beta imaging. Med. Nuc. 31 (4), 193–201. https://doi.org/10.1016/j.mednuc.2007.03.004.

Becquerel, H., 1896. Sur les radiations émises par Phosphorescence. C.R. Acad. Sci. 122, 420–421.

Belair, C., Baud, J., Chabas, S., Sharma, C.M., Vogel, J., Staedel, C., and Darfeuille, F., 2011. *Helicobacter pylori* interferes with an embryonic stem cell micro RNA cluster to block cell cycle progression. Silence 2, 7. https://doi.org/10.1186/1758-907X-2-7.

Benninghoven, A., 1994. Chemical analysis of inorganic and organic surfaces and thin films by static time-of-flight secondary ion mass spectrometry (TOF-SIMS). Angew. Chem. Int. Ed. 33, 1023–1043. https://doi.org/10.1002/anie.199410231.

Bethe, H., Ashkin, J., 1953. In: Segre, E. (Ed.), Eperimental Nuclear Physics. J.Wiley.

Bich, C., Touboul, D., Brunelle, A., 2014. Cluster TOF-SIMS imaging as a tool for micrometric histology of lipids in tissue. Mass Spectrom. Rev. 33 (6), 442–453. https://doi.org/10.1002/mas.21399.

Björkholm, P., Ernst, A., Hacke, M., Wieland, F., Brügger, B., von Heijne, G., 2014. Identification of novel sphingolipid-binding motifs in mammalian membrane proteins. Biochim. Biophys. Acta 1838 (8), 2066–2070. https://doi.org/10.1016/j.bbamem.2014.04.026.

Blanchet, F., August 2005. CD28 costimulatory signal induces protein arginine methylation in T cells. J. Exp. Med. 202, 371–377.

Bogoroch, R., Edelman, I., 1970. Radioautographic study of steroidal specificity in nuclear binding of 3H-aldosterone. Anat. Rec. 166, 280.

Boschi, F., Calderan, L., D'Ambrosio, D., Marengo, M., Fenzi, A., Calandrino, R., Sbarbati, A., Spinelli, A.E., 2011. In vivo 18F-FDG tumour uptake measurements in small animals using Cerenkov radiation. Eur. J. Nucl. Med. Mol. Imaging 38 (1), 120–127.

Buck, D., Förschler, A., Lapa, C., Schuster, T., Vollmar, P., Korn, T., et al., 2012. F-18-FDG-PET detects inflammatory infiltrates in spinal cord. Experimental autoimmune encephalomyelitis lesions. J. Nucl. Med. 53 (8), 1269–1276. https://doi.org/10.2967/jnumed.111.102608.

Caprioli, R.M., Farmer, T., Gile, J., 1997. Molecular imaging of biological samples: localization of peptides and proteins using MALDI-TOF MS. Anal. Chem. 69, 4751–4760.

Carrié, A., September 1999. A new member of the IL-1 receptor family highly expressed in hippocampus and involved in X-linked mental retardation. Nat. Genet. 23, 25–32.

Chanal, J., 1976. Radioautography of entire animals. J. Microsc. Biol. Cell 27, 147–152.

Chandra, S., Smith, D.R., Morrison, G.H., 2000. Subcellular imaging by dynamic SIMS ion microscopy. Anal. Chem. 72 (3), 104 A–114 A. https://doi.org/10.1021/ac002716i.

Chapleur, O., Wu, T.D., Guerquin-Kern, J.L., Bouchez, T., et al., 2013. SIMSISH technique does not alter the apparent isotopic composition of bacterial cells. PLoS One 8 (10), e77522. https://doi.org/10.1371/journal.pone.0077522.

Charpak, G., Bouclier, R., 1968. The use of MultiWire Proportionnal Counters to select and localize charged particles. Nucl. Instrum. Methods 62, 262–268.

Charpak, G., Dominik, W., 1989. Gaseous detectors with parallel electrodes and anodes mesh planes. Nucl. Instrum. Methods A274, 275–290.

Chiricozzi, E., Ciampa, M.G., Brasile, G., Compostella, F., Prinetti, A., Nakayama, H., et al., 2015. Direct interaction, instrumental for signaling processes between LacCer and Lyn in the lipid rafts of neutrophil-like cells. J. Lipid Res. 56 (1), 129–141. https://doi.org/10.1194/jlr.M055319.

Coquerel, A., 1996. Imagerie in vitro par radio-imageurs. Application à la quantification de récepteurs et de sondes nucléiques. Immunoanal. Biol. Spec. 11, 8–23.

Cortes, R., Vilaro, M.T., Mengod, G., 2016. Visualization of 5-HT receptors using radioligand-binding autoradiography. Curr. Protoc. Pharmacol. 75, 831–832. https://doi.org/10.1002/cpph.17.

Coulson, F., Carr., C.J., 2000. The validation of radioluminography for sue in quantitative distribution studies. Regul. Toxicol. Pharmacol. 2 (31), S1–S62.

Covey, T.R., Lee, E.D., Bruins, A.P., Henion, J.D., 1986. Liquid chromatography/mass spectrometry. Anal. Chem. 58 (14), 1451A–1461A.

D'argy, R., Sundwall, A., 2000. Quantitative whole-body autoradioluminography-future strategy for balance and tissue distribution studies. Regul. Toxicol. Pharmacol. 31 (2), S57–S62.

Dedeurwaerdere, S., Langlois, X., October 2011. Patterns of brain glucose metabolism induced by phosphodiesterase 10A inhibitors in the mouse: a potential translational biomarker. J. Pharmacol. Exp. Ther. 339 (1), 210–217.

Derré, J., et al., 2000. Fast signal and single electron detection with a MICROMEGAS photodetector. Nucl. Instrum. Methods Phys. Res. A449, 314.

Donnard, J., et al., 2009. The PIMager: a new tool for high-sensitive digital Beta autoradiograph. IEEE Nucl. Sci. Symp. Conf. Record M13–M144.

Evans, R., 1955. The Atomic Nucleus. McGraw-Hill Publishing Company Ltd.

Fan, Z., Calsolaro, V., Atkinson, R.A., Femminella, G.D., Waldman, A., Buckley, C., et al., 2016. Flutriciclamide (18F-GE180) PET: first-in-human PET study of novel third-generation in vivo marker of human translocator protein. J. Nucl. Med. 57, 1753–1759. https://doi.org/10.2967/jnumed.115.169078.

Fanchon, L.M., Dogan, S., Moreira, A.L., Carlin, S.A., Schmidtlein, C.R., Yorke, E., et al., 2015. Feasibility of in situ, high-resolution correlation of tracer uptake with histopathology by quantitative autoradiography of biopsy specimens obtained under 18F-FDG PET/CT guidance. J. Nucl. Med. 56 (4), 538–544. https://doi.org/10.2967/jnumed.114.148668.

Fanchon, L.M., Apte, A., Schmidtlein, C.R., Yorke, E., Hu, Y.C., 2017. Evaluation of the tumor registration error in biopsy procedures performed under real-time PET/CT guidance. Med. Phys. 44 (10), 5089–5095.

Fichet, P., Bresson, F., Leskinen, A., Goutelard, F., Ikonen, J., Siitari-Kaupi, M., 2012. Tritium analysis in building dismantling process using digital autoradiography. J. Radioanal. Nucl. Chem. 291, 869–875. https://doi.org/10.1007/s10967-011-1423-1. ISSN 0236-5731.

Foster, C., Billich, A., November 2007. Brain penetration of the oral immunomodulatory drug FTY720 and its phosphorylation in the central nervous system during experimental autoimmune encephalomyelitis: consequences for mode of action in multiple sclerosis. J. Phaprmacol. Exp. Ther. 323 (2), 469–475.

Fujita, H., 1982. Reciprocity-law failure in medical screen- film systems and its effects on patient exposure and image quality. In: Gregus, G.v. (Ed.), Optics in Biomedical Sciences, Optics in Biomedical Sciences, vol. 31, pp. 78–81.

Gahan, P., 1972. Autoradiography for Biologists. Academin Press, London and New York.

Galle, P., 1982. Tissue localization of stable and radioactive nuclides by secondary ion microscopy. J. Nucl. Med. 23 (1), 52–57.

Gulaldi, N.C.M., Xia, J., Feng, T., Hong, K., Mathews, W.B., Ruben, D., Kamel, I.R., Tsui, B.M.W., Szabo, Z., 2013. Modeling of the renal kinetics of the AT1 receptor specific PET radioligand [^{11}C]KR31173. BioMed Res. Int. https://doi.org/10.1155/2013/835859. Article ID 835859.

Gurney, R., Mott, N., 1938. Proc. R. Soc. A 164, 151–167.

Hamaoka, T., 1990. Autoradiography of new era replacing traditionalX-ray film. Cell Technol. 9, 456–462.

Haudebourg, R., Fichet, P., 2016. A non-destructive and on-site digital autoradiography-based tool to identify contaminating radionuclide in nuclear wastes and facilities to be dismantled. J. Radioanal. Nucl. Chem. 309, 551. https://doi.org/10.1007/s10967-017-5413-9. ISSN 0236-5731.

Hellmuth, K.H., Siitari-Kauppi, M., Klobes, P., Meyer, K., Goebbels, J., 1999. Imaging and analyzing rock porosity by autoradiography and Hg-porosimetry/X-ray computer tomography-applications. Phys. Chem. Earth 24 (7), 569–573.

Higuchi, T., Bengel, F.M., Seidl, S., Watzlowik, P., Kessler, H., Hegenloh, R., et al., 2008. Assessment of αvβ3 integrin expression

after myocardial infarction by positron emission tomography. Cardiovascular Research 78, 395–403. https://doi.org/10.1093/cvr/cvn033.

Hillenkamp, F., Karas, M., 2000. Matrix-assisted laser desorption/ionisation, an experience. Int. J. Mass Spectrom. 200, 71–77.

Hindié, E., Coulon, B., Galle, P., 1992. SIMS microscopy: a tool to measure the intracellular concentration of carbon 14-labelled molecules. Biocell 74, 89–92.

Hodges, A., Smoller, B., 2002. Immunohistochemical comparison of p16 expression in actinic keratoses and squamous cell carcinomas of the skin. Mod. Pathol. 15 (11), 1121.

Howard, A., Pelc, S., 1951. Nuclear incorporation of 32P as demonstrated by autoradiographs. Exp. Cell Res. 2, 178–187.

Hu, K., Sonti, S., Glaser, S.T., Duclos Jr., R.I., Gatley, S.J., 2017. Brain uptake and metabolism of the endocannabinoid anandamide labeled in either the arachidonoyl or ethanolamine moiety. Nucl. Med. Biol. 45, 43–50. https://doi.org/10.1016/j.nucmedbio.2016.11.001.

Hyafil, F., Tran-Dinh, A., Burg, S., Leygnac, S., Louedec, L., Milliner, M., et al., 2015. Detection of apoptotic cells in a rabbit model with atherosclerosis-like lesions using the positron emission tomography radiotracer [18F]ML-10. Mol. Imaging 14, 433–442. https://doi.org/10.2967/jnumed.114.139170.

International Atomic Energy Agency, Vienna, 1998. Technical Reports Series No. 389 - Radiological Characterization of Shut Down Nuclear Reactors for Decommissioning Purposes. ISSN 0074–1914; 389 - STI/DOC/010/389- ISBN 92–0–103198–X.

Jain, A., Subramanian, S., Pandey, U., Sarma, H.D., Ram, R., Dash, A., 2015. In-house preparation of macroaggregated albumin (MAA) for 68Ga labeling and its comparison with commercially available MAA. J. Radioanal. Nucl. Chem. 308 (3), 817–824. https://doi.org/10.1007/s10967-015-4509-3.

Jeavons, A., 1978. The high density proportional chamber and its applications. Nucl. Instrum.Methods 156, 41–51.

Jendresen, C., Kilstrup, M., Martinussen, J., 2011. A simplified method for rapid quantification of intracellular nucleoside. Anal. Biochem. 409, 249–259.

Jiao, H., Zho, B., 2002. A receptor autoradiographic assay HEPG2 hepatoma cell line and relevant mechanisms. Toxicol. Appl. Pharmacol. 185 (3), 172–179.

Johnston, R., Pickett, S., 1990. Autoradiography using storage phosphor technology. Electrophoresis 11, 355–360.

Kathib-Shahidi, S., 2006. Direct molecular analysis of whole-body animal tissue sections by imaging MALDI mass spectrometry. Anal. Chem. 78 (18), 6448–6456.

Kautz, H., February 1956. Council on pharmacy and chemistry. J. Am. Med. Assoc. 160 (8), 669–711.

Khatib-Shahidi, S., Anderson, M., Herman, J.L., Gillespie, T.A., Caprioli, R.M., 2006. Direct molecular analysis of whole-body animal tissue sections by imaging MALDI mass spectrometry. Anal. Chem. 78 (18), 6448–6456. https://doi.org/10.1021/ac060788p.

Kim, Y., March 2011. Usefulness of bremsstrahlung images after intra-arterial Y-90 resin microphere radioembolization for hepatic tumors. Nucl. Med. Mol. Imaging 45 (1), 59–67.

Kirov, A.S., Fanchon, L.M., 2018. Technical Note: scintillation well counters and particle counting digital autoradiography devices can be used to detect activities associated with genomic profiling adequacy of biopsy specimens obtained after a low activity 18F-FDG injection. Med. Phys. 45 (5), 2179–2185. https://doi.org/10.1002/mp.12836.

Kobayashi, K., Haneda, E., January 2012. Chronic fluoxetine selectively upregulates dopamine D1-like receptors in the Hippocampus. Neuropsychopharmacology 1–9.

Kryza, D., Debordeaux, F., Azéma, L., Hassan, A., Paurelle, O., Schulz, J., et al., 2016. Ex vivo and in vivo imaging and biodistribution of aptamers targeting the human matrix MetalloProtease-9 in melanomas. PLoS One 11 (2), e0149387. https://doi.org/10.1371/journal.pone.0149387.

Landau, L.D., Liftshitz, E.M., Pitaevskii, 1960. Electrodynamics of Continuous Media. Elsevier Butterworth-Heinemann, Oxford.

Laniece, P., 1994. A high resolution radioimager for fast, direct quantification in in situ hybridization experiments. Biotechniques 17 (2), 338–345.

L'Annunziata, M.F., 1987. Radionuclide Tracers, Their Detection and Measurement. Academic Press, London and New York, p. 505.

L'Annunziata, M.F., 2007. Radioactivity: Introduction and History, first ed. Elsevier, Amsterdam, p. 609.

L'Annunziata, M.F., 2016. Radioactivity: Introduction and History: From the Quantum to Quarks, second ed. Elsevier, Amsterdam, p. 902.

Laraia, M., 2012. Planning, Execution and International Experience, first ed. In: Nuclear Decommissioning. Woodhead Publishing, Elsevier. ISBN-10: 9780857095336, ISBN-13: 9780857091154, eBook ISBN: 9780857095336.

Laskey, R., Mills, A., 1975. Quantitative film detection of 3H and 14C in polyacrylamide gels by fluorography. Eur. J. Biochem. 56, 335–341.

Laskey, R., Mills, A., 1977. Enhanced autoradiography detection of detection of 32P and 125I using intensifying screens and hypersensitized film. FEBS Lett. 82, 314.

Leblond, C., 1976. Interpretations in radioautography. J. Micros. Biol. Cell 27, 73–80.

Lechene, C., Hillion, F., McMahon, G., Benson, D., et al., 2006. High-resolution quantitative imaging of mammalian and bacterial cells using stable isotope mass spectrometry. J. Biol. 5 (6), 20. https://doi.org/10.1186/jbiol42.

Leskinen, A., Fichet, P., Siitari-Kauppi, M., Goutelard, F., 2013. Digital autoradiography (DA) in quantification of trace level beta emitters on concrete. J. Radioanal. Nucl. Chem. 298, 153–161. https://doi.org/10.1007/s10967-013-2535-6. ISSN 0236-5731.

Li, J., Zheng, H., Fodah, R., Warawa, J.M., Chin, K.N., 2018. Validation of 2-18F-fluorodeoxy sorbitol as a potential radiopharmaceutical for imaging bacterial infection in the lung. J. Nucl. Med. 59 (1), 134–139. https://doi.org/10.2967/jnumed.117.195420.

Li, Q., Si, Y., Smith, K., Zeng, Q., Weina, P., 2008. Embrotoxicity of artesunate in animal species related to drug tissue distribution and toxicokinetic profiles. Birth Defect Res. (Part B) 83, 435–445.

Lidow, M., 1997. Use of cyclone storage phosphor system for rapid development of a receptor autoradiographic assay. Biomed. Prod. 24.

Livingston, R.A., Saleh, H.H., Bumrongjaroen, W., Ceary, M.S., Amde, A.M., Unterweger, M.S., 2003. Autoradiographic measurement of potassium distribution in Portland cement concrete. Proc. Nondestruct. Char. Mater. XI, 621–626.

Lord, B., Wintmolders, C., Langlois, X., Nguyen, L., Lovenberg, T., Bonaventure, P., 2013. Comparison of the ex vivo receptor occupancy profile of ketamine to several NMDA receptor antagonists in mouse hippocampus. Eur. J. Pharmacol. 715 (1–3), 21–25. https://doi.org/10.1016/j.ejphar.2013.06.028.

Luckey, G., 1975. US Patent No. 3 859 527.

Ludwig, R., Al-Horani, F.A., de Beer, D., Jonker, H.M., November 2005. Photosynthesis-controlled calcification in a hypersaline microbial mat.

Limnol. Oceanogr. 50 (6), 1836–1843. https://doi.org/10.4319/lo.2005.50.6.1836.

Maeda, J., Ji, B., Irie, T., Tomiyama, T., Maruyama, M., Okauchi, T., Staufenbiel, M., et al., 2007. Longitudinal, quantitative assessment of amyloid, neuroinflammation, and anti-amyloid treatment in a living mouse model of Alzheimer's disease enabled by positron emission tomography. J. Neurosci. 27 (41), 10957–10968. https://doi.org/10.1523/JNEUROSCI.0673-07.2007.

Manook, A., Yousefi, B.H., Willuweit, A., Platzer, S., Reder, S., et al., 2012. Small-animal PET imaging of amyloid-beta plaques with [11C]PiB and its multi-modal validation in an APP/PS1 mouse model of Alzheimer's disease. PLoS One 7 (3), e31310. https://doi.org/10.1371/journal.pone.0031310.

Manuel, I., Barreda-Gomez, G., Gonzalez de San Roman, E., Veloso, A., Fernandez, J.A., Giralt, M.T., Rodriguez-Puerta, R., 2015. Neurotransmitter receptor localization: from autoradiography to imaging mass spectrometry. ASC Chem. Neurosci. 6 (3), 362–373. https://doi.org/10.1021/cn500281t.

Marutle, A., Gillberg, P.G., Bergfors, A., Yu, W., Ni, R., Nennesmo, I., Voytenko, L., Nordberg, A., 2013. 3H-Deprenyl and 3H-PIB autoradiography show different laminar distributions of astroglia and fibrillar β-amyloid in Alzheimer brain. J. Neuroinflammation 10, 90. https://doi.org/10.1186/1742-2094-10-90.

Maskali, F., Poussier, S., Marie, P.-Y., Tran, N., Antunes, L., Olivier, P., Plenat, F., Maîtrejean, S., Zannad, F., Karcher, G., 2005. High-resolution simultaneous imaging of SPECT, PET, and MRI tracers on histologic sections of myocardial infarction. J. Nucl. Cardiol. 12, 229–230. https://doi.org/10.1016/j.nuclcard.2004.12.296. ISSN 1071-3581.

Massey, J., April 2010. Preclinical antitumor activity of the orally available heat shock protein 90 inhibitor NVP-BEP800. Mol. Cancer Ther. 9, 906–919.

McDonnell, L.A., Heeren, R.M.A., 2007. Imaging mass spectrometry. Mass Spectrom. Rev. 26 (4), 606–643. https://doi.org/10.1002/mas.20124.

Mead, C., 1958. Quantum theory of the refractive index. Phys. Rev. 110 (2), 359–369.

Mori, K., Hamaoka, T., 1994. IP autoradiography systems (BAS). Protein Nucl. Acid Enzyme 39 (11), 1–13.

Murray, K.K., Seneviratne, C.A., Ghorai, S., 2016. High resolution laser mass spectrometry bioimaging. Methods 15 (104), 118–126. https://doi.org/10.1016/j.ymeth.2016.03.002.

Narayan, N., Owen, D.R., Mandhair, H., Smyth, E., Carlucci, F., Saleem, A., et al., 2018. Translocator protein as an imaging marker of macrophage and stromal activation in RA pannus. J. Nucl. Med. https://doi.org/10.2967/jnumed.117.202200.

OECD, NEA, 2014. R&D and innovation needs for Decommissioning of nuclear Facilities. Radioact. Waste Manage. 7191. https://www.oecd-nea.org/rwm/pubs/2014/7191-rd-innovation-needs.pdf.

Orr, T., 1993. Instruments for analysis of gel imagery offer wide range of choices. Genet. Eng. News 8–9.

Pant, K., Gröger, D., Bergmann, R., Pietzsch, J., Steinbach, J., Graham, B., et al., 2015. Synthesis and biodistribution studies of ^{3}H- and ^{64}Cu-labeled dendritic polyglycerol and dendritic polyglycerol sulfate. Bioconjug. Chem. 26 (5), 906–918. https://doi.org/10.1021/acs.bioconjchem.5b00127.

Pages, L., Bertel, E., 1972. Energy loss, range, and bremsstrahling yield for 10 KeV to 100 MeV electrons in various elements and chemical contents (A. Press, Éd.). Atom. Data 4, 1–127.

Peskov, V., Charpak, G., 1989. Investigation of light emission from a parallel-plate Avalanche Chamber with noble gases and with TEA, TMAE and H2O vapours at atmospheric pressure. Nucl. Instrum. Methods A274, 275–290.

Phalipon, A., Cardona, A., Kraenhenbuhl, J., Edelman, L., Sansonetti, P., Corthesy, B., 2002. Secretory component: a new role in secretory IgA-mediated immune exclusion in vivo (C. Press, Éd.). Immunity 17, 107–115.

Poisnel, G., Moustie, O., Guilloteau, D., 2012. PET imaging with [^{18}F]AV-45 in an APP/PS1-21 murine model of amyloid plaque deposition. Neurobiol. Aging 33, 2561–2571. https://doi.org/10.1016/j.neurobiolaging.2011.12.02.

Rehak, I., 2013. Final Report of the Task Group on Radiological Characterisation and ecommissioning (RCD) of the Working Party on Decommissioning and Dismantling (WPDD) Radioactive Waste Management -NEA/RWM/WPDD (2013)2 unclassified. JT03346655.

Reicherts, w., 1992. Storage Phosphor imaging technique for detection and quantification of DNA adducts measured by the 32P post labelling assay. Carcinogenesis 7, 1543–1551.

Reid, W.C., Casas, R., Papadakis, G.Z., Muthusamy, S., Lee, D.E., Ibrahim, W.G., Nair, A., Koziol, D., Maric, D., Hammoud, D.A., 2016. Neurobehavioral abnormalities in the HIV-1 transgenic rat do not correspond to neuronal hypometabolism on 18F-FDG-PET. PLoS One 11 (3), e0152265. https://doi.org/10.1371/journal.pone.0152265.

Reubi, J.C., Kvols, L.K., Waser, B., Nagorney, D.M., Heitz, P.U., Charboneau, J.W., Reading, C.C., Moertel, C., 1990. Detection of somatostatin receptors in surgical and percutaneous needle biopsy samples of carcinoids and islet cell carcinomas. Cancer Res. 50 (18), 5969–5977.

Reuter, S., Schnöckel, U., Edemir, B., Schröter, R., Kentrup, D., Pavenstädt, H., et al., 2010. Potential of noninvasive serial assessment of acute renal allograft rejection by 18F-FDG PET to monitor treatment efficiency. J. Nucl. Med. 51, 1644–1652. https://doi.org/10.2967/jnumed.110.078550.

Riad, M., Zimmer, L., Rbah, L., Watkins, K.C., Hamon, M., Descarries, L., 2004. Acute Treatment with the Antidepressant Fluoxetine Internalizes 5-HT1A Autoreceptors and Reduces the In Vivo Binding of the PET Radioligand [18F]MPPF in the Nucleus Raphe Dorsalis of Rat. The Journal of Neuroscience 24 (23), 5420–5426.

Rigothier, M., June 2002. Fate of entamoeba histolytica during establishment of amoebic liver abscess analyzed by quantitative radio-imaging and histology. Infect. Immun. 70 (6), 3208–3215.

Roberstson, R., 2011. Multimodal imaging with 18F-FDG pet and Cerenkov luminescence imaging after MLN4924 treatment in a human lymphoma xenograft model. J. Nucl. Med.

Rogers, A., 1969. Techniques of Autoradiography. Elsevier Publishing Company, New York.

Rogers, A., 1979. Techniques of Autoradiography. Elsevier/North-Holland biomedical Press, Amsterdam.

Rohner, T.C., Staab, D., Stoeckli, M., 2005. MALDI mass spectrometric imaging of biological tissue sections. Mech. Ageing Dev. 126 (1), 177–185. https://doi.org/10.1016/j.mad.2004.09.032.

Rougeot, C., Vienet, R., Cardona, A., Le Doledec, L., Grognet, J., Rougeon, F., 1997. Targets for SMR1-pentapeptide suggest a link between the circulating peptide and mineral transport. Am. J. Physiol. 273, R1309–R1320.

Roussakis, Y., Zhang, R., Heyes, G., Webster, G., Mason, S., et al., 2015. Real-time Cherenkov emission portal imaging during CyberKnife®

radiotherapy. Phys. Med. Biol. 60, N419−N425. https://doi.org/10.1088/0031-9155/60/22/N419.

Rowlands, J., 2002. The physics of computed radiography. Phys. Med. Biol. 47, R123−R166.

Ruggiero, A., 2010. Cerenkov luminescence imaging of medical isotopes. J. Nucl. Med. 51, 1123−1130.

Rutherford, E., 1903. The magnetic and electric deviation of the easily absorbed rays from radium. Philos. Mag. 177−187 (6)5(26).

Sahlholm, K., Ielacqua, G.D., Xu, J., Jones, L.A., Schlegel, F., Mach, R.H., Rudin, M., Schroeter, A., 2017. The role of beta-arrestin2 in shaping fMRI BOLD responses to dopaminergic stimulation. Psychopharmacology 234 (13), 2019−2030. https://doi.org/10.1007/s00213-017-4609-6.

Salin, H., 2000. Sensitive and quantitative co-detection of two mRNA species by double radioactive in situ hybridization. J. Histochem. Cytochem. 48 (121), 1587−1592.

Samarati, J., et al., 2004. Imaging with a PIM device. Nucl. Instrum. Methods Phys. Res., Sect. A 535, 550−553.

Santiard, J.C. et al., 1994. Report CERN-ECP/94-17.

Sardini, P., Angileri, A., Descostes, M., Duval, S., Oger, T., Patrier, P., Rividi, N., Siitari-Kauppi, M., Toubon, H., Donnard, J., 2016. Quantitative autoradiography of alpha particle emission in geomaterials using the Beaver™ system. Nucl. Instrum. Methods Phys. Res. 833, 15−22. https://doi.org/10.1016/j.nima.2016.07.003.

Sauli, F., 1977. Principles of Operation of MultiWire Proportionnal and Drift Chambers, vols. 77−19. CERN.

Schweitzer, A., Fahr, A., Niederberger, W., 1987. A simple method for quantitation of 14C-Whole-Body autoradiograms. Int. J. Radiat. Appl. Instrum. A Appl. Radiat. Isot. 38−5, 329−333.

Sharif, N., Eglen, R., 1993. Quantitative autoradiography: a tool to visualize and quantify receptors, enzymes, transporters, and second messenger systems. In: Sharif, N. (Ed.), Quantitative Autoradiography: A Tool to Visualize and Quantify Receptors, Enzymes, Transporters, and Second Messenger Systems. Oxford University Press.

Sharma, C., Hoffmann, S., Darfeuille, F., February 17, 2010. The primary transcriptome of the major human pathogen *Helicobacter pylori*. Nature 464, 250−255.

Simmonnet, G., Rey-Cenevaz, Y., Simmonnet, F., 1976. Examples of applications of radioautography for beginners with the light microscope: DNA synthesis in vivo in rat bone marrow; protein synthesis in vitro in reticulocytes. J. Microsc. Biol. Cell 27, 111−114.

Solon, E., Kraus, L., 2002. Quantitative whole-body autoradiography in the pharmaceutical industry. Survey results on study design, methods, and regulatory compliance. J. Pharmacol. Toxicol. Methods 46, 73−81.

Solon, E.G., Schweitzer, A., Stoeckli, M., Prideaux, B., 2010. Autoradiography, MALDI-MS and SIMS-MS imaging in pharmaceutical discovery and development. AAPS J. 12 (1), 11−26. https://doi.org/10.1208/s12248-009-9158-4.

Solon, E.G., Schweitzer, A., 2010. Autoradiography, MALDI-MS and SIMS-MS imaging in pharmaceutical discovery and development. APPS J. 12, 11−26.

Sonoda, M., Takano, M., Miyahara, J., Kato, H., 1983. Computed radiography utilizing scanning laser stimulated luminescence. Radiology 148, 833−838.

Sovago, J., Dupuis, D.S., Gulyas, B., Hall, H., 2001. An overview on functional receptor autoradiography using [35S]-GTPgammaS. Brain Res. Rev. 38, 149−164.

Spinelli, A.E., D'Ambrosio, D., Calderan, L., Marengo, M., Sbarbati, A., Boschi, F., 2010. Cerenkov radiation allows in vivo optical imaging of positron emitting radiotracers. Phys. Med. Biol. 55 (2), 483−495. https://doi.org/10.1088/0031-9155/55/2/010.

Stoeckli, M., Staab, D., Schweitzer, A., 2007. Compound and metabolite distribution measured by MALDI mass spectrometric imaging in whole body tissue sections. Int. J. Mass Spectrom. 260 (2−3), 195−202. https://doi.org/10.1016/j.ijms.2006.10.007.

Stumpf, W., 2012. Drugs in the brain − cellular imaging with receptor microscopic autoradiography. Elsevier, Éd. Prog. Histochem. Cytochem. 47, 1−26.

Stumpf, W., Sar, M., 1975. In: O'Malley, B., Hardman, J. (Eds.), Methods in Enzymology. Academic press, New York and London.

Tarkin, J.M., Joshi, F.R., Evans, N.R., Chow Dhury, M.M., Figg, N.L., et al., 2017. Detection of atherosclerotic inflammation by 68Ga-DOTATATE PET compared to [18F]FDG PET imaging. J. Am. Coll. Cardiol. 69 (14), 1774−1791. https://doi.org/10.1016/j.jacc.2017.01.060.

Taxi, J., 1976. General principles of neurotransmitter detection. Problems and applications to catecholamines. J. Micoscopy Biol. Cell 27, 243−248.

Temma, T., Ogawa, Y., Ishino, S., December 2010. Tissue factor detection for selectively discriminating unstable plaques in an atherosclerotic rabbit model. J. Nucl. Med. 51 (12), 1979−1986.

Thorek, D., Robertson, R., Bacchus, W.A., Hahn, J., Rothberg, J., Beattie, B.J., Grimm, J., 2012. Cerenkov imaging - a new modality for molecular imaging. Review Article Am. J. Nucl. Med. Mol. Imaging 2 (2), 163−173. PMCID: PMC3477724.

Tu, T.W., Ibrahim, W.G., Jikaria, N., Munasinghe, J.P., Witko, J.A., Hammoud, D.A., Frank, J.A., 2018. On the detection of cerebral metabolic depression in experimental traumatic brain injury using Chemical Exchange Saturation Transfer (CEST)-weighted MRI. SCIeNTIFIC REpOrTS 8, 669. https://doi.org/10.1038/s41598-017-19094-z.

Ueda, M., Kudo, T., Mutou, Y., September 15, 2011. Evaluation of [125I] IPOS as a molecular imaging probe for hypoxia-inducible factor-1-active regions in a tumor: comparison among single-photon emission computed tomography/X-ray computed tomography imaging, autoradiography, and immunohistochemistry. Cancer Sci. 102, 2090−2096.

Ulberg, S., 1977. The technique of whole body autoradiography. Cryosectioning of large specimens. Special Iss. Whole-Body Autoradiogr. 2−29 (O. Elvefeldt, Éd.) LKB Instr.J, Science Tools.

Ullberg, S., 1954. Studies of the distribution and fate of S35 labeled benzyl-penicillin in the body. Acta Radiol. 118, 1−110.

Unterrainer, M., Mahler, C., Vomacka, L., Lindner, S., Havla, J., Brendel, M., et al., 2018. TSPO PET with [18F]GE-180 sensitively detects focal neuroinflammation in patients with relapsing−remitting multiple sclerosis. Eur. J. Nucl. Med. Mol. Imaging. https://doi.org/10.1007/s00259-018-3974-7.

Viala, J., November 2004. Nod1 responds to peptidoclycan delivered by the *Helicobacter pylori* cag pathogenicity island. N. P. Group., Éd. Nat. Immunol. 5 (11), 1167−1174.

Villard, P., 1900a. Sur la rćflexion et la refraction des rayons cathodiques et des rayons dćviables du radium (1010-1012, Éd.). Comp. Rend. Acad. Sci. 130.

Villard, P., 1900b. Sur le rayonnement du Radium. Comp. Rend. Acad. Sci. 130, 1178−1179.

Wang, Q.B., Masumoto, K., Bessho, K., Matsumura, H., Miura, T., Shibata, T., 2007. Evaluation of the radioactivity in concrete from

accelerator facilities. J. Radioanal. Nucl. Chem. 273 (1), 55–58. https://doi.org/10.1007/s10967-007-0710-3. ISSN 0236-5731.
Williams, M., 1981. Biochem. Soc. Trans. 9, 590–591.
Wilson, G.H., Gore, J.C., Yankeelov, T.E., Barnes, S., Peterson, T.E., et al., 2014. An approach to breast cancer diagnosis via PET imaging of microcalcifications using 18F-NaF. J. Nucl. Med. 55, 1138–1143. https://doi.org/10.2967/jnumed.114.139170.
Winograd, N., 2005. The magic of cluster SIMS. Anal. Chem. 77 (7), 142 A–149. https://doi.org/10.1021/ac053355f.
Young Chun, S., February 2016. The use of anatomical information for molecular image reconstruction algorithms: attenuation/scatter correction. Nucl. Med. Mol. Imag. 50, 13–23. https://doi.org/10.1007/s13139-016-0399-8.
Yousefi, B.H., Drzezga, A., Reutern, B.V., Manook, A., Schwaiger, M., Wester, H.J., Henriksen, G., 2011. A novel 18F-labeled imidazo[2,1-b]benzothiazole (IBT) for high-contrast PET imaging of β-amyloid plaques. ACS Med. Chem. Lett. 2, 673–677. https://doi.org/10.1021/ml200123w.
Zemni, R., February 2000. A new gene involved in X-linked mental retardation identified by analysis of an X;2 balanced translocation. Nat. Genet. 24, 167–170.
Zheng-Ming, L., Brahme, A., 1992, . An overview of the transport theory of charged particles. Radiat. Phys. Chem. 41 (4–5), 673–703.

Further reading

Baker, J., 1989. Autoradiography: a comprehensive review. In: Royal Microscopical Society, Microscopy Handbooks, vol. 18. O. S. Publications.
Budd, G., 1972. In: Gahan, P. (Ed.), Autoradiography for Biologists. Academic Press, New York and London.
Castaing, R., Slodzian, G., 1962. Microanalyse par émission ionique secondaire. J. Microscopie 1, 395–410. HAL Id: jpa-00243912.
Charpak, G., 1989a. A gaseous detector for high accuracy autoradiography of radioactive compounds with Optical Read-out of avalanches positions. Nucl. Instrum. Methods A278, 779–787.
Charpak, G., 1989b. A new approach to positron emission tomography. Eur. J. Nucl. Med. 15, 690–693.
Cloëz-Tayarani, I., September 1997. Autoradiographic characterization of [3H]-5-HT-moduline binding sites in rodent brain and their relationship to 5-HT1B receptors. PNAS Neurobiol. 94, 9899–9904.
Coe, R., 2000. Quantitative whole-body autoradiography. Regul. Toxicol. Pharmacol. 31, S1–S3.
Drexler, D., 2011. Utility of quantitative whole-body autoradiography (QWBA) and imaging mass spectrometry (IMS) by matrix-assisted laser desorption/ionization (MALDI) in the assessment of ocular distribution of drugs. J. Pharmacol. Toxicol. Methods (63), 205–208.
Jeavons, A., 1983. The high density avalanche chamber for positron emission tomography. IEEE Trans. Nucl. Sci. 30, 640–645.
Joo, M., 2003. 90Y-Scintigraphy of Small Animals: A Study of Imaging Parameters (Thesis). Lund University.
Krust, B., November 20, 2001. The anti-HIV pentameric pseudopeptide HB-19 is preferentially taken up in vivo by lymphoid organs where it forms a complex with nucleolin. Proc. Natl. Acad. Sci. 98 (24), 14090–14095.
Medvedev, A., 2005. Natriuretic peptide interaction with [3H]isatin binding sites in rat brain. Brain Res. (1042), 119–124.
Solon, E., January 2012. Use of radioactive compounds and autoradiography to determine drug tissue distribution. Chem. Res. Toxicol. 1–49.
Stumpf, W., 2003. Drug Localization in Tissues and Cells. IDDC Press.

Nicole Barthe



Dr. Nicole Barthe is a graduate of Nuclear Physics at the Faculty of Sciences of Bordeaux in 1975 and holding a Diploma of Study and Research in Human Biology (DERBH) in 1982 and Pharmacist in 2004. She held teaching and research positions at the joint laboratory Biophysics-INSERM Unit 1026 (Tissue Bioengineering: BioTis) at the University of Bordeaux and a position of Hospital Practitioner in Nuclear Medicine (Radiopharmacy) and Radiology (Bone Densitometry) until September 2017. Since the 1990s, Nicole Barthe worked in a scientific collaboration with the research teams of Nobel Laureate Prof. Georges Charpak (Biospace Measures, then Biospace lab). She has considerable experience in the imagery of radioactivity that she practices at the BioTis Laboratory and in the field of nuclear medicine over a period of many years. She is specialized in preclinical research using radioactive tracers, in particular, including the use of autoradiographic methods and high-resolution imaging of beta emitters.

Serge Maîtrejean



Serge Maîtrejean holds a PhD in Nuclear Physics from the University Paris VII (Diderot). He spent his first 10 professional years as Research Engineer and Project Manager working for Homeland Security on Cargo X-ray Inspection Systems and Explosive Detection Systems in luggage. Then, in 1996, he changed to the field of biomedical imaging, being Chief Scientist Officer and later Chief Operational Officer of Biospace Lab. During these years, he has developed numerous innovations as low-dose X-ray scanner for orthopedic diagnosis (EOS), systems for real-time autoradiography, preclinical gamma camera, and bioluminescence/fluorescence/Cerenkov imager. His extended expertise in imaging covers as well physics, mechanics, electronics as algorithmic, reconstruction, and software. He is currently consultant for companies working in the biomedical domain as well for companies working on security.

Nicolas Carvou



Nicolas Carvou holds a PhD and a BSc (hons) in Applied Biology from Nottingham Trent University, as well as French and European Technology Diplomas in Biomedical Sciences from the University Paris XII. Nicolas was awarded second place at the UK Universities Biotechnology in business competition (1995–96) and worked for several biotech companies, including the European Collection of Animal Cell Cultures (ECACC) and Molecular Light Technology Ltd, UK (now part of Gen-Probe, USA). Following a postdoctoral position at the Dana Farber Cancer Institute, Harvard Medical School (2001–2002), a research assistantship and associateship in the Department of Physiology, University College London, Nicolas joined the Biospace Lab in 2011 and was rapidly promoted to Scientific Applications Manager in 2012 and Applications Support Director in 2013. He is a specialist in digital autoradiography, in vivo optical and fluorescence microscopy imaging with several international scientific publications on intracellular trafficking.

Ana Cardona, *in Memoriam*



Ana Cardona, *in Memoriam.*
(7/01/1957–23/08/2012)

Plate-forme d'imagerie dynamique, Institut Pasteur, 25 Rue du Dr Roux, 75724, Paris, France

She was a French-Uruguayan research engineer at the Pasteur Institute in Paris, who actively participated in the creation of the Pasteur Institute in Montevideo and contributed to numerous cooperation projects between France and Uruguay through the AFUDEST (Franco Uruguayan Association for Scientific and Technological Development).

She obtained a doctorate in veterinary medicine from the Veterinary Faculty of Montevideo in 1985. After a 2-year internship at the Pasteur Institute in the Hybridolab laboratory directed by Jean Claude Mazié, she obtained her PhD from Paris VII University at the Necker Hospital under the direction of Prof. Jean François Bach in 1994.

She returned to the PI in 1995 where she was recruited in the Laboratory of Cellular Technology, headed by Mrs. Lena Edelman, as a research engineer. Her work focussed on medical imaging techniques and more specifically on the applications of β-imager for the early detection of micro-metastases and this in the context of a collaboration with the team of Georges Charpak.

In 2001, she joined the Histopathology research and expertise unit headed by Michel Huerre until 2010, when she joined the dynamic imaging platform headed by Spencer Shorte and continued her projects on the applications of β-imager to quantitative imaging in the small animal.

Chapter 10

PERPUSTAKAAN PRIBADI AN-NUR SUNARYA

Flow-cell radionuclide analysis

Michael F. L'Annunziata
The Montague Group, Oceanside, CA, United States

Chapter outline

I. Introduction 729
II. High-performance liquid chromatography flow-cell analyzers 730
A. High-performance liquid chromatography flow cell analyzers 734
B. Liquid (homogeneous) flow cells 737
C. Solid (heterogeneous) flow cells 739
D. Gamma and positron emission tomography flow cells 740
1. High-energy gamma cell 740
2. Low-energy gamma cell 741
3. Positron emission tomography cell 741
E. Narrow-bore and microbore flow cells 745
F. Luminescence flow cell (fLumo) 746
G. Hybrid silicon pixel flow cell 747
H. Criteria for flow-cell selection 750
III. Principles of flow scintillation counting 754
A. Count rates 754
B. Background and net count rate 755
C. Counting efficiency and disintegration rates 756
1. Static efficiency runs 756
2. Gradient efficiency run 757
D. Minimal detectable activity 758
E. Sensitivity, flow rate, and resolution 758
F. Precision 759
G. Detection optimization 760
1. Multichannel analysis 760
2. Chemiluminescence detection and correction 760
3. Time-resolved liquid scintillation counting 760
H. Instrument performance assessment 761
IV. Flow scintillator selection 762
V. Dual-functionality flow-cell detectors 762
A. Scintillating extractive resins 765
B. Composite bed of scintillating and extracting particles 769
C. Equilibrium-based bed 770
D. Planar mixed-bed flow cell 773
E. Planar detectors based on semiconductor diodes 773
F. Whole-column detector 776
G. Tritiated water vapor in air detector 777
VI. Flow-cell radionuclide analysis sequential to separation 778
A. ^{99}Tc in nuclear waste and process monitoring 778
B. Actinides and ^{90}Sr in soil 779
C. Alpha/beta discrimination 781
D. ^{89}Sr and ^{90}Sr(^{90}Y) analysis 786
E. Cherenkov flow-cell analysis 789
VII. Stopped-flow detection 790
VIII. Flow-cell effluent water monitors 791
A. ^{3}H effluent water monitors 791
B. Heterogeneous ($\alpha-\beta$) and γ discriminating cell 792
IX. Single radionuclide analysis in high-performance liquid chromatography 793
X. Dual radionuclide analysis 793
XI. Online HPLC-FSA and mass spectrometry[2] 793
A. HPLC-FSA-MS instrumentation and interfacing 795
B. Representative data 798
XII. Online FSA and nuclear magnetic resonance[2] 799
A. Principle of nuclear magnetic resonance spectroscopy 801
B. HPLC-FSA-NMR system 802
C. HPLC-FSA-NMR representative data 803
XIII. Online HPLC-FSA-MS-NMR 806
References 807
Further reading 820
Michael F. L'Annunziata 820

I. Introduction

Flow-cell detectors are designed specifically for the measurement of radionuclide activity in a flowing system. The technology is applied most commonly in the biological sciences to the measurement of the activities of radioisotope-labeled organic compounds in high-performance liquid chromatography (HPLC) effluent streams, which is referred to at times as radio-HPLC. Numerous research papers in the past decade report the utilization of flow-cell radiation detectors in conjunction with HPLC in biochemistry, molecular biology, medical

Handbook of Radioactivity Analysis: Volume 2. https://doi.org/10.1016/B978-0-12-814395-7.00010-6
Copyright © 2020 Elsevier Inc. All rights reserved.

and drug research, agricultural chemistry, and related fields. These reports number in the several hundreds. The bio- and medical sciences often require the use of radio-HPLC to separate organic compounds labeled with radioisotopes, such as ^{3}H, ^{14}C, ^{33}P, ^{32}P, ^{35}S, and radiopharmaceuticals labeled with radionuclides, such as ^{90}Y, ^{99m}Tc, ^{18}F, and ^{11}C, among others. When radio-HPLC is used to study the metabolic fates or purity of these compounds, a flow-cell detector is often the instrument of choice to quantify the activity levels of the radionuclide label in the chromatogram-separated compounds. Also, in smaller numbers but of equal importance, there are research papers, which describe the use of flow-cell detectors in conjunction with liquid chromatography (e.g., ion chromatography), in the analysis of radionuclides in the fields of environmental and radioactive-waste monitoring.

The alternative to flow-cell radioactivity analysis is the collection of the HPLC effluent in fractions, which is a technique known as fraction collection, followed by the analysis of each fraction for radionuclide activity. The measurement of radionuclide activity in HPLC fractions is possible by collection of the fractions in separate plastic scintillation microplate wells followed by microplate scintillation counting (see also Chapters 6 and 9, Volume 1). Effluent fractions can number in the hundreds for a given HPLC run. Thus, fraction collecting is more tedious and time-consuming and expensive in terms of laboratory staff time. The analysis of fractions by microplate scintillation counting does not require fluor cocktail; however, drying of the sample wells prior to radioactivity analysis is required, and some sample loss through drying is possible. Also, the analysis of fractions cannot provide an online real-time radionuclide activity measurement of the HPLC effluent. Only flow-cell radioactivity detectors can provide real-time analysis during the HPLC run. A thorough study made by Rapkin (1993) compared the sensitivity and accuracy of low-level analysis (e.g., lower limits of detection of 20.8 CPM under conditions of 10 CPM background) for continuous flow scintillation analysis (FSA) and liquid scintillation analysis (LSA) of fractions. Flow scintillation analysis is the application of scintillation detection methods to the analysis of radioactivity in a flowing system. Statistical considerations suggested that fraction collection followed by LSA offered the possibility of greater sensitivity and accuracy of radioactivity measurements in HPLC eluates, although with considerable inconvenience. However, Rapkin (1993) demonstrated that, even for low-activity analysis, when the randomness of fraction collection is accounted for, the assumed advantages of fraction collection disappear and the trend to replace fraction collection with the continuous real-time radioactivity measurement of HPLC eluates is justified.

The first liquid radiochromatography flow cells were developed following the observation of Steinberg (1958, 1960) that the fluorescence of solid anthracene crystals was useful for the detection of the beta radiations of ^{3}H and ^{14}C when suspended in aqueous solutions containing these radionuclides. Simultaneous independent studies by Rapkin and Packard (1960) and Schram and Lombaert (1960, 1961) demonstrated the feasibility of counting ^{3}H and ^{14}C in flowing aqueous streams when these streams were passed over anthracene crystals within a cell placed between two photomultiplier detectors. Anthracene is no longer used as a scintillator for radioactivity measurements in flowing systems, as many developments have occurred in this field since these pioneering works were reported. For early reviews on the development of flow-cell radioactivity analysis, see previous works by L'Annunziata (1979, 1987) and Parvez et al. (1988).

This chapter will focus mainly on the state-of-the-art and current techniques in the application of flow-cell detectors for the online measurement of radioactivity in chromatography effluents. This includes (1) the measurement of radioisotope labels on organic compounds by FSA used often in conjunction with organic mass spectrometry (MS) and nuclear magnetic resonance (NMR) organic structural spectroscopy for the combined radioactivity analysis and organic structural analysis of separated molecular components in effluents of HPLC, which is popular in the biological sciences; and (2) the measurement of radionuclides separated by ion chromatography (IC), which is a vital technique utilized in the chemical sciences for the analysis of radionuclide sources and in the monitoring of the environment. In addition, reference will be made to the use of flow-cell detectors in the measurement of radioactivity in nonchromatography effluent streams.

II. High-performance liquid chromatography flow-cell analyzers

There are various flow-cell detector types applied to liquid chromatography. These will differ in design and type of detector depending on the radionuclides to be analyzed and the chromatographic separation method that is utilized (e.g., HPLC of organic compounds or IC of radionuclides). In applications utilizing HPLC for the chromatographic separation and analysis of organic compounds, the following types of flow cells are common: (1) the liquid scintillator (homogeneous) flow cell, (2) the solid scintillator (heterogeneous) flow cell, (3) the gamma cell, (4) the positron emission tomography (PET) cell, and (5) the luminescence flow cell. The gamma cell is manufactured according to three detector types to improve detection efficiencies for high-energy, low-energy, and annihilation-gamma radiation in HPLC effluents. The latter is also referred to as a PET cell, as it is designed to detect positron emitters in radiopharmaceutical compounds commonly used in PET. The various scintillation flow cells currently used to analyze the effluent streams in HPLC are listed in Table 10.1 together with their characteristics,

TABLE 10.1 Types of flow-cell detectors used for the measurement of radioactivity in high-performance liquid chromatography.[a]

I. Liquid scintillator (homogeneous) cell
- **A.** Characteristics
  - Coiled Teflon tubing, 35–5000 μL volume
- **B.** Radionuclides analyzed and %*E* (in parenthesis)
  - All β emitters, e.g., ^{3}H (20%–60%),^{14}C (70%–95%),^{35}S and ^{33}P (70%–95%),^{32}P (85%–95%)
  - Low-energy γ emitters, e.g.,^{125}I (60%–90%)
  - All α emitters (>95%)[b]
- **C.** Advantages
  1. High %*E*
  2. No adsorption of radionuclide on Teflon tube walls
- **D.** Disadvantages
  1. HPLC effluent is mixed with cocktail fluor and, an effluent stream splitter is required if separated compounds are to be analyzed online by MS or NMR spectroscopy
  2. An electronic stream splitter is required to obtain part of the effluent to enable other chemical and biological studies on separated compounds

II. Solid scintillator (heterogeneous) cell
- **A.** Characteristics

  Fine solid scintillator particles packed within coiled tubing, 150–600 μL volume, among which are:
  - **1.** Yttrium glass (YG) scintillator (e.g., YG-150, YG 40-x6M, YG 50-S5P)[f]
  - **2.** Monocrystalline SolarScint[c]
  - **3.** Polycrystalline cerium-activated yttrium silicate [YSi(Ce)]
  - **4.** High-pressure (high flow rate) cells containing one of the following scintillators:
    - **a.** Europium-activated calcium fluoride [CaF_2(Eu)]
    - **b.** Cerium-activated lithium glass [lithium glass(Ce)]
    - **c.** Cerium-activated yttrium silicate [YSi(Ce)]
    - **d.** Scintillating plastic beads (plastic scintillator)
- **B.** Radionuclides analyzed (cell detector types and %*E* in brackets)

  All β emitters

  ^{3}H [SolarScint[c], 3.0%; YG, 1.5%; YSi(Ce), 2.8%]

  ^{14}C [SolarScint[c], 70%; YG, 63%–86%; YSi(Ce), 68%]

  High-pressure, high-rate cells:

  ^{3}H [CaF_2(Eu), >5%; lithium glass(Ce), >1%; YSi(Ce), >2%; plastic, > 2.5%]

  ^{14}C [CaF_2(Eu), >85%; lithium glass(Ce), >45%; YSi(Ce), >65%; plastic, > 15%]

  All α emitters (50%–60%*E*)
- **C.** Advantages
  - **1.** Good %*E* except for ^{3}H
  - **2.** Sample in effluent is not destroyed (no cocktail fluor is used)
  - **3.** No chemical quench effects associated with fluor cocktail occur
  - **4.** Costs associated with the use and disposal of fluor cocktail are avoided
  - **5.** High salt, buffer, or pH gradients do not effect %*E*
  - **6.** High-pressure cells permit up to 3000 psi cell pressure and high flow rates
- **D.** Disadvantages
  - **1.** Sample may bind reversibly or irreversibly onto scintillator yielding peak broadening and high backgrounds
  - **2.** Low %*E* for ^{3}H

III. High-energy gamma cell
- **A.** Characteristics

  Coiled Teflon tubing with 6-mm-thick BGO windows; 35–550 μL volume (e.g., Gamma-B[c] flow cell) See Fig. 10.5. The BGO–X[f] flow cell (Berthold Technologies) is equipped with a 40-mm BGO crystal.
- **B.** Radionuclides analyzed and %*E* (in parenthesis)[d]

  High-energy γ emitters (>70 keV), e.g., ^{67}Ga (44%), ^{131}I (58%), ^{111}In (25%), ^{99m}Tc (63%), ^{201}Tl (35%), ^{54}Mn (19%), ^{60}Co (20%), ^{133}Ba (28%), ^{85}Sr (19%), ^{51}Cr (3%).
- **C.** Advantages
  - **1.** No liquid scintillation fluor cocktail required
  - **2.** No solid scintillator required in cell tubing
  - **3.** High signal-to-noise ratio
  - **4.** Good spectral resolutions for high-energy gamma (>300 keV)

Continued

TABLE 10.1 Types of flow-cell detectors used for the measurement of radioactivity in high-performance liquid chromatography.[a]—cont'd

- **D.** Disadvantages
  - **1.** Used exclusively for high-energy γ emitters or high-energy β emitters (e.g., ^{32}P,^{90}Y)

IV. Low-energy gamma cell

- **A.** Characteristics
  - Coiled Teflon tubing with 4-mm-thick CaF_2(Eu) windows; 10—650 μL volume (e.g., Gamma-C[c] flow cell or the Iodine cell, I 100—1000[f])
- **B.** Radionuclides analyzed and %*E* (in parenthesis)[d]
  - Low-energy γ emitters (<70 keV), e.g., ^{55}Fe (14%), ^{125}I (90%), ^{109}Cd (34%),^{201}Tl (28%), ^{99m}Tc (14%), ^{67}Ga (15%)
  - High-energy β emitters, e.g., ^{32}P (~60%*E*)[d], ^{90}Y (60%*E*)
- **C.** Advantages
  - **1.** No liquid scintillation fluor cocktail required
  - **2.** No solid scintillator required in cell tubing
  - **3.** High counting efficiencies (%*E*) for low-energy γ emitters (<70 keV)
- **D.** Disadvantages
  - **1.** Used exclusively for low-energy γ emitters or high-energy β emitters (e.g., ^{32}P (~ 60%*E*), ^{90}Y (60%E)

V. Cherenkov cell

- **A.** Characteristics
  - Coiled Teflon tubing sandwiched between solid scintillator windows. The flow cells are called "Cherenkov cells" because they are used to measure the activities of high-energy beta-emitting radionuclides by the Cherenkov effect (see Chapter 6, Volume 2). Cherenkov photons are produced in the narrow aqueous phase and wall of the Teflon tubing of the cell; however, most of the photons detected by the photomultipliers are produced in the solid scintillator on either side of the coiled Teflon tubing. Some typical Cherenkov cells are the following types:
  - Gamma-C[c] flow cell: coiled Teflon tubing sandwiched between CaF_2(Eu)
  - Cerenkov cell[e]: coiled Teflon tubing sandwiched between plastic scintillator; Cerenkov-Cell Z-200[f]
- **B.** Radionuclides analyzed and %*E* (in parenthesis)
  - High-energy beta emitters with a beta particle energy maximum much higher than the threshold energy for the production of Cherenkov photons in water; i.e., the E_{max} of the beta emissions should be >> 263 keV. Examples are ^{32}P (~60%*E*) and ^{90}Y (60%E).
- **C.** Advantages
  - **1.** No liquid scintillation fluor cocktail required
  - **2.** No solid scintillator required in cell tubing

VI. PET cell

- **A.** Characteristics
  - Coiled Teflon tubing with 6-mm-thick BGO windows opaque on one side; see Fig. 10.8 or the positron emission tomography (PET) cell MX-100[f]
- **B.** Radionuclides analyzed and %*E* (in parenthesis)
  - Positron (β^+) emitters such as those used in PET, e.g., ^{18}F (25%), ^{11}C (43%), ^{13}N, and ^{68}Ga
- **C.** Advantages
  - **1.** Low backgrounds approximately 1/10 of backgrounds from Gamma-B[c] flow cell with only 1/3 drop in %*E*
  - **2.** No liquid scintillation fluor cocktail required
  - **3.** No solid scintillator required in cell tubing
- **D.** Disadvantages
  - **1.** Used exclusively for positron β^+ emitters

VII. High-sensitivity PET cell[g]

- **A.** Characteristics
  - Coiled tubing (0.76 mm inner diameter) with 3-cm-thick BGO detectors on opposite sides and coincidence background reduction (see Fig. 10.11)
- **B.** Radionuclides analyzed
  - Positron (β^+) emitters such as those used in PET, e.g., ^{18}F, ^{11}C, and ^{13}N
- **C.** Advantages
  - An improved signal-to-noise ratio of 28:1 for the high-sensitivity PET cell compared with 5:1 for the conventional PET cell[g]

VIII. Narrow-bore cell

- **A.** Characteristics
  - **1.** Designed for applications using 2 mm ID narrow-bore HPLC columns
  - **2.** Cell sizes range from 15 to 250 μL
  - **3.** Effluent (sample) flow rates range from 133 μL/min to 1 mL/min
  - **4.** For homogeneous cells, liquid scintillation cocktail flow rates (3:1 cocktail:sample ratio) range from 400 μL to 3 mL/min
  - **5.** Heterogeneous cells use yttrium silicate, lithium glass, calcium fluoride, plastic scintillator, and SolarScint[c] formats

Continued

B. Radionuclides analyzed and %*E* (in parenthesis)
1. All radionuclides emitting radiations that produce significant scintillation with fluor cocktail in homogeneous cells or scintillation in solid scintillator heterogeneous cells, including α-, β^--, β^+-, X-rays, weak γ-rays, and Auger electrons, etc.
2. ^{3}H (35%–42%),^{14}C (80%–90%) in homogeneous cells
C. Advantages
1. Improved peak resolutions without peak tailing
2. Applied to simultaneous HPLC/FSA/mass spectrometry structure analysis
3. Reduced cocktail consumption and waste disposal costs compared with conventional FSA cells

IX. Microbore cell
A. Characteristics
1. Designed for applications using 1 mm ID narrow-bore HPLC columns
2. Cell sizes range from 3 to 100 μL
3. Effluent (sample) flow rates range from 25 to 150 μL/min
4. For homogeneous cells, liquid scintillation cocktail flow rates (3:1 cocktail:sample ratio) range from 75 to 450 μL/min
5. Heterogeneous cells use yttrium silicate, lithium glass, calcium fluoride, plastic scintillator, and SolarScint[c] formats
B. Radionuclides analyzed and %*E* (in parenthesis)
1. All radionuclides emitting radiations that produce significant scintillation with fluor cocktail in homogeneous cells or scintillation in solid scintillator heterogeneous cells, including α-, β^--, β^+-, X-rays, weak-γ-rays, and Auger electrons, etc.
2. ^{3}H (25%–35%),^{14}C (75%–80%) in homogeneous cells
C. Advantages
1. Up to 10-fold improved peak resolutions without peak tailing compared with conventional FSA cells
2. Applied to simultaneous HPLC/FSA/mass spectrometry structure analysis
3. Reduced cocktail consumption and waste disposal costs compared with conventional FSA cells

X. Very-high-pressure liquid chromatography (VHPLC) cell[h]
A. Characteristics
A homogeneous flow cell of 200 μL volume with 0.25 mm inner diameter designed for the separation and analysis of ^{3}H- and ^{14}C-metabolites in VHPLC effluents
B. Advantages
1. Improved separation of radioisotope-labeled metabolites by VHPLC with sensitivity comparable with that of conventional HPLC and radiation detection with the use of variable scintillation flow
2. Online mass spectrometric analysis is possible with effluent stream splitting as in conventional HPLC

XI. Luminescence flow cell for positron emitters (fLumo)[f]
A. Characteristics
An unshielded luminescence flow-through radio-HPLC detector sensitive to positrons (fLumo detector) and insensitive to gamma rays for applications in the analysis of PET radiopharmaceuticals
B. Advantages
1. No radiation shielding required. Thus, the detector can be used in a production "hot cell" to detect PET radiopharmaceuticals during a semipreparative HPLC purification
2. Exhibits excellent low limits of detection, linearity with activity and reproducibility (Thonon et al., 2013)
3. The low backgrounds achieved circumvent expensive coincidence counting with dual PMTs or other costly electronic background resuction methods
4. Various fLumo PET flow cells can be interchanged to accommodate HPLC effluent volumes of 10, 50, or 100 μL
5. The fLumo PET flow cells can be interchanged with fLumo gamma measuring flow cells (BGO-X) of 5, 30, and 150 uL cell volumes or other gamma measuring flow cells or 100–1000 μL
6. The fLumo detector for the measurement of positron emitting radionuclides in HPLC effluents can be interchanged with a NaI detector for the measurement of gamma photon–emitting radionuclides

XII. Hybrid silicon pixel detector (Medipix2)[i]
A. Characteristics
A 65k single-photon counting pixel array with a square pixel size of 55 μm on a 14 × 14 mm^2 detection area. The detector can act as a real-time counter and camera for positrons emitted from a flow-based system such as the effluent of an HPLC in a microfluidic setup. The detector counts positrons directly from positron-emitting radionuclides rather than the detection of annihilation gamma photons. Its small size limits the detector to microfluidic platforms.

Continued

TABLE 10.1 Types of flow-cell detectors used for the measurement of radioactivity in high-performance liquid chromatography.[a]—cont'd

B. Advantages
1. Much improved detection efficiency of positrons compared with NaI(Tl) scintillation detector of annihilation gamma photons for positron-emitting radionuclides
2. Much higher signal-to-noise (S/N) ratio compared with a NaI(Tl) detector
3. May be applied to the measurement of short-lived radionuclides used for PET particularly immediately after radionuclide production and purification on a silica-based monolithic column in a microfluidic platform

[a] *Flow cells listed in this table are available from several suppliers together with accommodating analyzers (see Table 10.2).*
[b] *Personal communication with C. J. Passo, Jr., PerkinElmer, Inc.*
[c] *Trademark of PerkinElmer, Inc.*
[d] *Counting efficiency values as %E of gamma-emitting radionuclides are from Anonymous (1995).*
[e] *Trademark of LabLogic Systems.*
[f] *Trademark of Berthold Technologies.*
[g] *Huber et al. (2011).*
[h] *Cuyckens et al. (2008).*
[i] *Tarn et al. (2016).*

applications, and advantages and disadvantages. Scintillation flow cells may be interchangeable within a given flow scintillation analyzer (FSA) designed specifically for this purpose. The proper selection of the cell will provide the optimum detection efficiencies with lowest background as well as meet the needs of any particular flow cell analysis. A description of the flow cells will be provided in this section together with an account of their advantages and disadvantages.

HPLC flow-cell radioactivity detectors are available commercially from numerous commercial manufacturers and suppliers. In some instances, specific manufacturers may be mentioned throughout this chapter. These should not be taken as endorsements, as similar ones may be available from other manufacturers or suppliers. To assist the reader in exploring various suppliers of flow scintillation detectors for their radio-HPLC requirements, several suppliers are listed in alphabetical order in Table 10.2; however, the reader should not consider this list to be comprehensive. Other suppliers and even new suppliers may exist.

A. High-performance liquid chromatography flow cell analyzers

The principal components of a typical flow scintillation analyzer (FSA) linked to an HPLC system is illustrated as a block diagram in Fig. 10.1. The connection of the effluent stream from an HPLC system is illustrated at the upper left-hand corner of the figure. The scintillation flow cell is placed between the two photomultiplier tubes (PMTs), and it is interchangeable as several types are available. The scintillation flow cells differ according to the modes of radiation detection, efficiency for radiation types and radiation energy, and particular experimental requirements, including narrow-bore and microbore radio-HPLC systems. These are described in Table 10.1 and in the next section. The flow cell is placed between the two PMTs so that the two opposite side windows of the cell are in direct contact with the opposite faces of the PMTs. The orientation of the flow cell vis-à-vis the PMTs is illustrated in Fig. 10.2. HPLC stream splitting with linking of the FSA to a mass spectrometer and/or NMR spectrometer are not illustrated. The linking of the FSA to MS and NMR spectrometers is described further on in this chapter.

If a homogeneous flow cell is used, liquid fluor cocktail must be uniformly mixed with the HPLC effluent stream. Special low-viscosity nongelling fluor cocktails are recommended, which are described further on in this chapter. The liquid scintillator is added to the HPLC effluent stream by a variable volume scintillator pump (LS pump) and a static fluid mixer (mixing tee) before reaching the scintillation flow cell, as depicted in Fig. 10.1. Mixing the effluent stream with fluor cocktail renders the separated chemical components useless for any subsequent chemical or biological tests. If organic structural information is required on the compounds separated by the HPLC, as provided by MS or NMR spectroscopy or other tests on the effluent stream required, an electronically controlled stream splitter (digital stream splitter) can direct a portion of the HPLC effluent stream for online MS or NMR analysis (Shemesh et al., 2016, Draganov et al., 2015, Keller et al., 2015, Kiffe et al., 2008, L'Annunziata, 1984, L'Annunziata and Nellis, 2001a,b, Silva-Elipe, 2003a, and Wilson and Brinkman, 2003). An alternative approach is to fraction-collect the radio-HPLC effluent from a flow scintillation analyzer and subsequently analyze the collected fractions by MS or NMR spectroscopy (Gomes de Mello Martins et al., 2017; Keller et al., 2015, Peyronneau et al., 2012; Jacques et al., 2010a,b). Stream splitting and fraction-collecting after monitoring the HPLC effluent with a flow scintillation analyzer is discussed further on in this chapter. Certain scintillation flow cells, such as the solid (heterogeneous) cell, gamma cell, or PET cell (Table 10.1), do not use liquid scintillation (LS) fluor cocktail. When these cells are used, the stream splitter, scintillator pump, and static fluid mixer are not utilized obviously, and the HPLC

TABLE 10.2 Some sources of commercially available flow-cell radioactivity detectors for HPLC.[a]

Company	Location and Internet address[b]
ADVACAM[c]	Espoo, Finland and Grand Forks, North Dakota, USA
http://advacam.com/	
Berthold Technologies GmbH & Co. KG	Bad Wildbad, Germany; Berthold Australia, Victoria; Australia; Berthold Technologies, Oak Ridge, TN, USA; and Berthold France, Thoiry (Yvelines), France, Berthold Technologies Ltd, Herts, UK
https://www.berthold-bio.com/radio-isotope-detectors/hplc-radio-detectors.html	
Carroll & Ramsey Associates	Berkeley, CA, USA
http://www.carroll-ramsey.com/catalog.htm	
Capintec, Inc.	Florham, Park, NJ, USA
http://capintec.com/product/flow-ram/	
Eckert & Ziegler Eurotope GmbH	Berlin, Germany
https://radiopharma.com/product/flow-count/	
Elysia-Raytest[d]	Elysia s.a., Angleur, Belgium, and IsoSolutions, Vancouver, BC, Canada
http://www.elysia-raytest.com/en/	
Gammasonics	Lane Cove, NSW, Australia;
http://www.gammasonics.com/chromatography.pdf	
Hidex Oy (Triathler)	Turku, Finland and Brandon, FL USA
http://hidex.com/contact-us/	
JABLOTRON[c]	Jablonec nad Nisou, Czech Republic
http://www.particlecamera.com/index.php/contact	
LabLogic Systems, Inc.[e]	Brandon, FL, USA and Broomhill, Sheffield, UK
https://lablogic.com/	
NOKI Technologies Pvt. Ltd.	Hyderabad, Andhra Pradesh, India
http://www.nokitechnologies.com/Flow_Count_Radio_HPLC_Detector.html	
OKEN (Ohyo Koken Kogyo Co., Ltd	Tokyo, Japan
http://www.oken.co.jp/web_oken/Pdlfra_en.htm	
ORTEC AMETEK	Oak Ridge, TN 37830, USA
https://www.ortec-online.com/	
PerkinElmer, Inc.	Waltham, MA, USA
https://shop.perkinelmer.com/Content/manuals/gde_radiomaticflowscintillationproducts.pdf [f]	
Shell-USA	Spotsylvania, VA, USA
http://www.shell-usa.com/Radio-Counter/default.html	
Universal Giken Co., Ltd.	Kanagawa 250-0002 Japan
http://www.universalgiken.jp/seihin/seihin1.html	
X-ray Imatek[c]	Barcelona, Spain
http://benasque.org/2013tae/talks_contr/268_Pixel_Detectors_XRI.pdf	

[a] *The sources are listed in alphabetical order. The list is not comprehensive, and other sources may be available.*
[b] *Additional locations in other parts of the world may exist; and the exact addresses may be obtained from the Internet sites provided.*
[c] *Medipix detector for radio-HPLC in a microfluidic platform.*
[d] *Raytest was founded in 1980, and the company joined the Elysia Group in 2015.*
[e] *LabLogic Systems, Inc. acquired IN/US Systems and the two companies merged under the LabLogic Systems name in 2007.*
[f] *The radio-HPLC flow scintillation analyzers and accessories described on the website via this PerkinElmer URL may no longer be available directly from PerkinElmer; however, the instrumentation is available from various independent sellers found on the internet.*

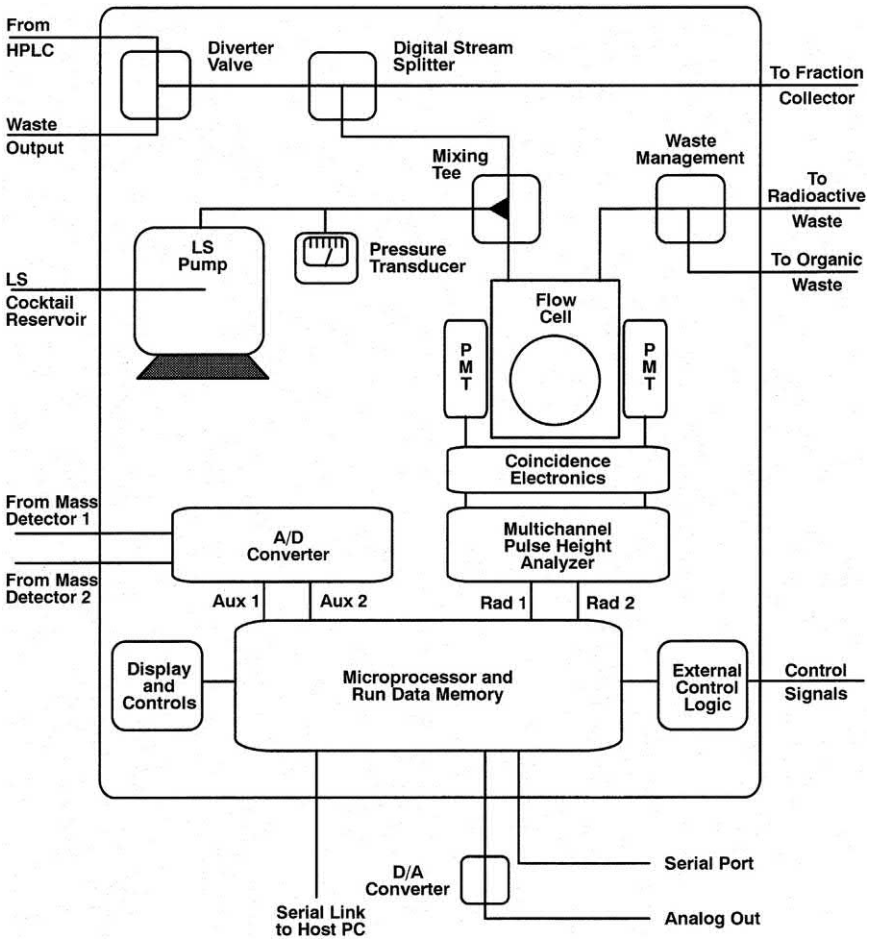


FIGURE 10.1 Block diagram of a state-of-the-art fully configured flow scintillation analysis system (© 1998–2019 PerkinElmer, Inc. All rights reserved. Printed with permission.).

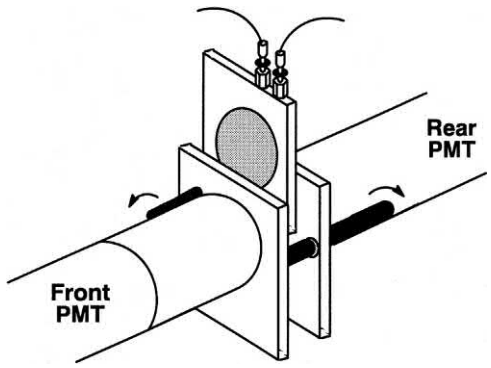


FIGURE 10.2 Drawing illustrating the orientation of a flow cell vis-à-vis two photomultiplier tubes (PMTs). The flow cell is illustrated elevated over its normal location and in the process of being either installed or removed from the center of the two PMTs. Thumbscrews illustrated in solid black with arrows are used to facilitate the interchange of flow cells to accommodate different radionuclide measurements and methods of detection (© 1998–2019 PerkinElmer, Inc. All rights reserved. Printed with permission.).

effluent can be split after FSA for direct online MS and NMR spectroscopy. The flow scintillation analyzer (FSA) is equipped with two PMTs, high voltage supply, coincidence and summation circuitry, pulse height analyzer, associated analog-to-digital converter, and multichannel analyzer (MCA) similar to the components of a modern LS analyzer. Modern flow scintillation analyzers are operated by a computer equipped with multitasking software, including automatic quench correction and efficiency determination, DPM measurements in the effluent stream, background reduction electronics, such as TR-LSC (see Chapter 6, Volume 1), multichannel analysis and spectral display, self-normalization and calibration, pulse height spectral display, preset and variable energy regions for activity analysis, dual independent counting regions for either automatic single or dual radionuclide analysis with update times from 1 to 120 s, software for radio-HPLC direct instrument control and data reduction, including three-dimensional and overlay display of activity peaks from different chromatogram traces (see Fig. 10.3), and instrument performance assessment (IPA) for monitoring

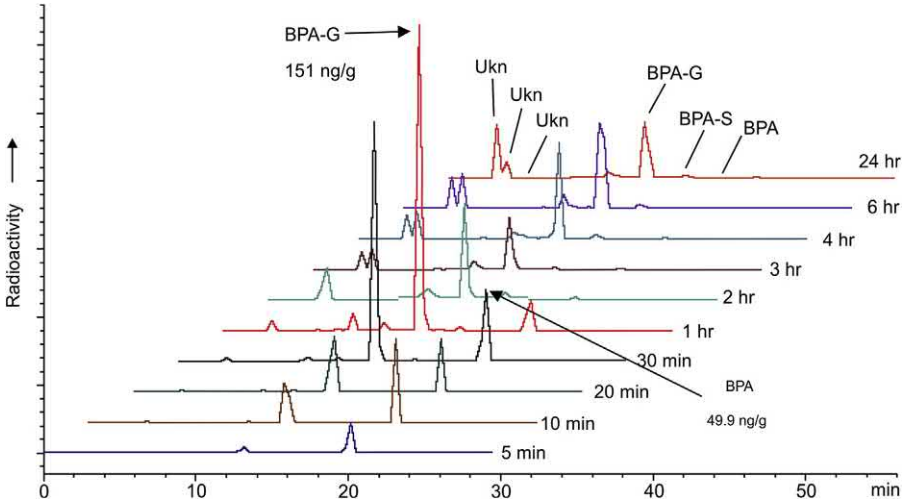


FIGURE 10.3 Three-dimensional analysis overlay of 10 flow scintillation analysis traces of HPLC separations (radioactivity vs. retention time in minutes) of ^{3}H-labeled BPA (bisphenol A) and metabolites after oral or subcutaneous administration of ^{3}H-BPA to mice. The traces are overlaid or offset into a three-dimensional display to provide a timeline comparison of metabolite anabolism and catabolism as illustrated. Units of radioactivity are not illustrated on the Y-axis, as the signal intensity for each chromatogram is scaled to the tallest BPA-G peak. Two metabolites identified by online mass spectrometry are BPA-glucuoride (BPA-G) and BPA-sulfate (BPA-S). *From Draganov et al. (2015); reprinted with permission from Elsevier © 2015.*

detection efficiencies, background, and Chi-square values with ^{3}H and ^{14}C standards. Detailed descriptions and the practical applications of most of these features are given in Chapter 6, Volume 1 "Liquid Scintillation Analysis." There is great similarity between the electronic components and radioanalytical capability of state-of-the-art flow scintillation analyzers and liquid or solid scintillation analyzers. The major difference between the two analyzers is the mechanism of detection, which in the case of FSA may be either liquid or solid scintillation, and the radionuclides are analyzed in a dynamic liquid stream.

In the example illustrated in Fig. 10.3, Draganov et al. (2015) used HPLC to separate radioisotope-labeled bisphenol A (^{3}H-BPA) and its metabolites after administration of the ^{3}H-BPA to mice. The separation of radioisotope-labeled compounds by HPLC, often referred to as radio-HPLC, is generally followed by radioactivity analysis with a flow-cell detector followed by online or offline analytical tests, such as MS or NMR spectroscopy to identify the chemical structure of the metabolites. The radio-HPLC of a radioisotope-labeled compound and its metabolites plotted with three-dimensional (3D) overlays over various periods of metabolism provide an excellent means of quantifying and recording the time course of the fate of organic compounds in living systems and the environment. In the example given by Fig. 10.3, the compounds separated by HPLC were quantified and plotted by a flow-cell detector through which the HPLC effluent passes. Metabolites were then identified by splitting the HPLC effluent sending 20% of the effluent to an electrospray ionization (ESI) tandem mass spectrometer (MS/MS) for the identification of metabolites and the remaining fraction (80%) of the HPLC effluent directly onto a homogeneous flow scintillation detector for the measurement of tritium activity in the various compounds separated on the HPLC column. Such direct online measurements are referred to hyphenated analytical techniques, which in this case would be abbreviated as HPLC-FSA-MS/MS.

Another example of the application of flow scintillation analysis to the time course measurement of a reaction by means of a three-dimensional overlay of HPLC runs can be taken from the work of Markham et al. (2004). The synthesis of the reduced form of ^{14}C-labeled β-nicotinamide adenine dinucleotide 2′-phosphate ([Ad-^{14}C]NADPH) from β-nicotinamide [U-^{14}C]adenine dinucleotide ([Ad-^{14}C]NAD^{+}) was measured by flow scintillation analysis of HPLC runs over a period of over 4 hours by Markham et al. (2004). They followed the course of the synthesis by HPLC analysis of reaction components in a centrifuge tube reaction vessel containing [Ad-^{14}C]NAD^{+}, ATP, glucose-6-phosphate, and NAD^{+} kinase. The HPLC analysis carried out over different time intervals provided a time course measurement of the progress of the synthesis of [Ad-^{14}C]NADPH. A three-dimensional display of the radioactivity label in the HPLC runs over a period exceeding 4 hours from the time of initiation of the reaction (t_0) to the complete synthesis (t_2) is illustrated in Fig. 10.4 together with the reaction scheme. The [Ad-^{14}C]NAD^{+} underwent 75% conversion after 3−4 hours (t_1), and the complete conversion to [Ad-^{14}C]NADPH is illustrated to occur at t_2 after the addition of glucose-6-phosphate dehydrogenase (glucose-6-P DH) and adjustment of pH.

B. Liquid (homogeneous) flow cells

A typical flow cell, whether it is a homogeneous liquid flow cell, a heterogeneous solid scintillator flow cell or a Cherenkov cell, consists of fine tubing (e.g., Teflon) coiled flat between two transparent windows at either side of the coiled tubing as seen in Fig. 10.5. The flow cell, illustrated in Fig. 10.5, is produced by Berthold Industries, and similar

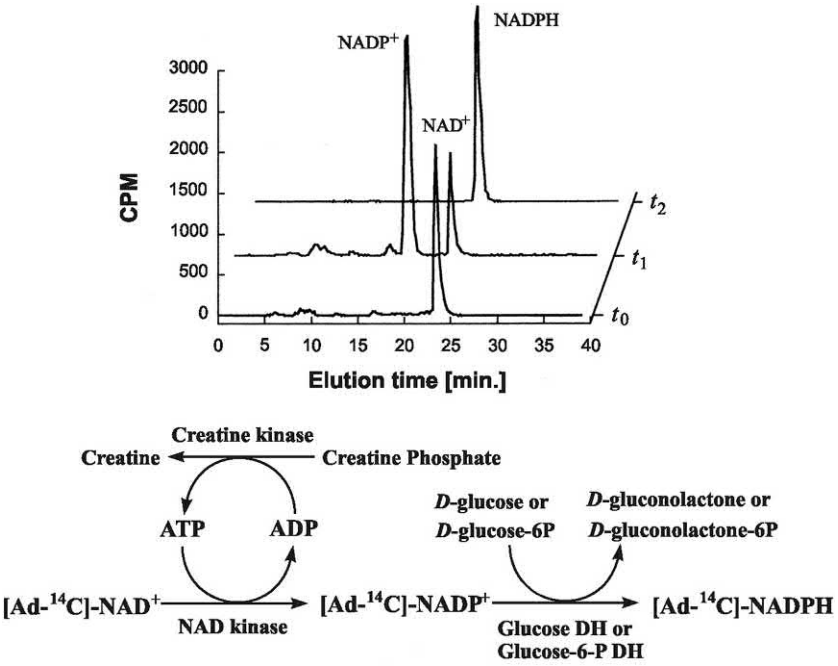


FIGURE 10.4 (Upper) HPLC flow detector radiograms produced with a PerkinElmer 500 TR radiomatic flow scintillation analyzer illustrated in a three-dimensional overlay following the time coarse of the enzymatic synthesis of [Ad-^{14}C]NADPH. t_0, reaction mixture before adding enzymes; t_1, reaction mixture at 75% conversion after adding the NAD$^+$ kinase; t_2, reaction mixture after completion of the reaction. (Lower) Biosynthesis reaction scheme. *From Markham et al. (2004); reprinted with permission from Elsevier © 2004.*

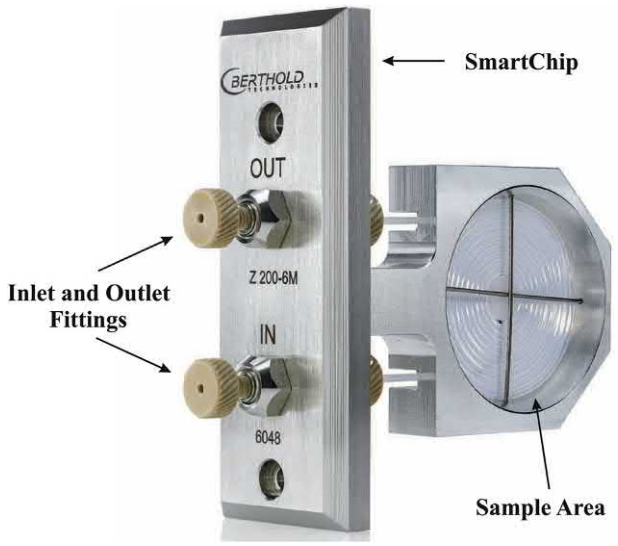


FIGURE 10.5 Photograph illustrating the principle characteristics of a scintillation or Cherenkov flow cell (property of Berthold Technologies). Components identified are (A) the finger-tight inlet and outlet fittings for liquid chromatography system integration, (B) a SmartChip that automatically sets the cell-specific parameters, and (C) the sample area containing wound Teflon tubing. The component illustrated is inserted into a detector (Flowstar[1] LB 514) whereby the sample area illustrated above sits between the faces of two PMTs to optimize detection efficiency and low backgrounds with coincidence counting. The flow cells are easily interchangeable to accommodate liquid or solid scintillation cells, PET cells, microbore cells, gamma cells, and Cherenkov counting cells, among others (© 2018 Berthold Technologies (www.berthold.com); used under permission).

flow cells are available from other commercial suppliers such as Gammasonics and LabLogic Systems, Inc. (see Table 10.2). The cell (coiled tubing within windows) is inserted between two PMTs of the flow scintillation analyzer. The flow cell tubing is coiled so that it sits perpendicular to the planar faces of two PMTs. Because the liquid flow cell consists only of tubing, the detection of low- and intermediate-energy beta-emitting radionuclides (e.g., ^{3}H, ^{14}C, or ^{35}S) requires a prior mixing of the entire or a fractional part of the radioactive HPLC effluent with LS fluor cocktail, while the effluent stream is in motion and prior to the arrival of the effluent-fluor cocktail mixture at the orifice of a flow cell. This has traditionally been referred to as the homogeneous method because the effluent stream and fluor cocktail are homogeneously mixed, and the flow cell is referred to as a liquid cell.

The liquid homogeneous flow cell type provides the highest counting efficiencies for low-energy β emitters such as ^{3}H over the range of 20%–60% and intermediate-energy β emitters such as ^{14}C and ^{35}S with counting efficiencies in the range of 70%–95%. The high detection efficiencies are

1. Taken in part from L'Annunziata, M. F. and Nellis, S. W. (2001). Flow scintillation analyzer (FSA) interfaced with the HPLC and nuclear magnetic resonance (NMR) spectrometer. A state-of-the-art application of the Radiomatic FSA. *FSA Application Note FSA-004*. PerkinElmer, Inc. @ 2001 PerkinElmer; Reprinted with permission. All rights reserved. http://www.perkinelmer.com/CMSResources/Images/44-73061APP_FSAInterfacedHPLC.pdf, accessed October 31, 2018.

expected with the liquid (homogeneous) flow cells because a LS detection method is used where the radionuclides are in solution with fluor cocktail. Special fluor cocktails should be used that do not gel when mixing with HPLC effluents and suppress chemiluminescence, which can occur following the immediate mixing of cocktail with HPLC effluents.

The wide range of chemicals used as eluents in HPLC and the changing chemical characteristics of HPLC effluents when gradient elution is carried out and when particular compounds are eluted from the column will cause variable quench. As the percent counting efficiency of any radionuclide is a function of quench, a gradient quench correction curve is needed to convert online count rates to disintegration rates.

A disadvantage of the liquid (homogeneous) flow cell is that the separated compounds in the HPLC effluents are rendered useless for further chemical or biological tests due to their mixing with fluor cocktail. However, an effluent stream splitter can be used to divert a fraction of the HPLC effluent to the online analysis of FSA peaks via MS or NMR spectroscopy or onto a fraction collector to permit further studies on the HPLC-separated components. As in LS counting, radionuclides that emit low-energy gamma rays, Auger electrons, and internal conversion electrons can be measured also in the liquid flow cell with high counting efficiency. In the case of ^{125}I, counting efficiencies in the range of 60%−90% are possible. Alpha-emitting radionuclides are detected with high counting efficiencies (>95%) in the liquid flow cell.

C. Solid (heterogeneous) flow cells

The solid scintillator (heterogeneous) flow cell is manufactured with fine beads or particles of an insoluble solid scintillator placed within the Teflon tubing of the flow cell. The tubing is coiled flat between two transparent windows and placed between the faces of two PMTs. The HPLC radioactive effluent stream will flow through the cell and make intimate contact with the solid scintillator beads. This latter approach is referred to as the heterogeneous method because the effluent stream and scintillator do not mix, and the flow cell is called a solid cell. The PMTs will detect and measure the scintillation light photons emitted from the tubing, and the radioactivity determined during the sample residence time in the flow cell according to conventional LS technology described in Chapter 6, Volume 1 and further on in this chapter.

Various types of solid scintillators are used to make up the heterogeneous cell, including yttrium glass, polycrystalline cerium-activated yttrium silicate [YSi(Ce)], europium-activated calcium fluoride [CaF_2(Eu)], cerium-activated lithium glass, and plastic scintillator beads, among others. These will vary in their detection efficiency for various β and α emitters. The counting efficiencies are low for weak β emitters like ^{3}H (1.5−5%E) and good for the intermediate-energy β emitters such as ^{14}C (45−85%E). High-energy β emitters are detected as expected with yet higher counting efficiency. Kawano et al. (2011, 2015) describe a heterogenous flow-cell detector containing CaF_2(Eu) for the monitoring of tritium in water on a continuous flow-through basis. The flow-cell detector is equipped with dual PMTs for coincidence counting, a water flow pump, and multichannel monitoring pulse height analyzer, which would enable restricting counts to a low-level pulse height channel corresponding the tritium. With 5-mm diameter cells, Kawano et al. (2015) achieved detections levels of 2 and 10 Bq/mL of tritium in continuous flowing water with 10,000 and 600 s counts, respectively. Alton et al. (2018) used Monte Carlo code Geant4 and experimentation to determine the optimum geometries (scintillator particle radii) for maximum energy deposition in waterborne beta particle emitters with a CaF_2(Eu) flow-cell detector. Experimental measurements with tritium, carbon-14, and lead-210 indicate optimal radii of 10, 350, and 75 μm, respectively.

A major advantage of the heterogeneous flow cell is that the sample in the HPLC effluent is not destroyed because no fluor cocktail is used. The entire effluent stream can be analyzed by online MS and NMR spectroscopy, or it may be collected by a fraction collector and further chemical or biological tests can be carried out on the separated fractions. Also, chemical quench, which is a problem with the liquid homogeneous flow cells, does not occur with the solid (heterogeneous) cells. Therefore, high salt, buffer solutions, or pH gradients used in HPLC eluents will not affect counting efficiency. The only problem is that, due to the high surface area and structure of the solid scintillator packed in these flow cells, compounds undergoing separation in the HPLC may bind reversibly or irreversibly onto the scintillator. This can result in high backgrounds and peak broadening. Irreversible binding of sample onto the scintillator may require replacement of the flow cell. A solid heterogeneous flow cell containing monocrystalline SolarScint (trademark of PerkinElmer, Inc.) undergoes minimal sample binding. The inositol phosphates are one example of compounds that undergo adsorption onto yttrium silicate (YSi) scintillator, resulting in peak broadening. SolarScint flow cells operated in the pH range of 3−8 show minimal effects of compound binding, resulting in optimal peak resolutions. This is evidenced by Fig. 10.6, which illustrates the high resolutions of the HPLC-separated ^{3}H-labeled inositol phosphates detected with a 210-μL SolarScint heterogeneous flow cell.

Certain designs of heterogeneous flow cells are manufactured with relatively thick glass tubing to withstand high pressures of up to 3000 psi (200 bar) with fast flow rates. Soreefan et al. (2003) and Tan and DeVol (2003) carried out experimental and Monte Carlo investigations on the light collection efficiency of heterogeneous flow-cell detectors. They demonstrated with an alpha source that the light

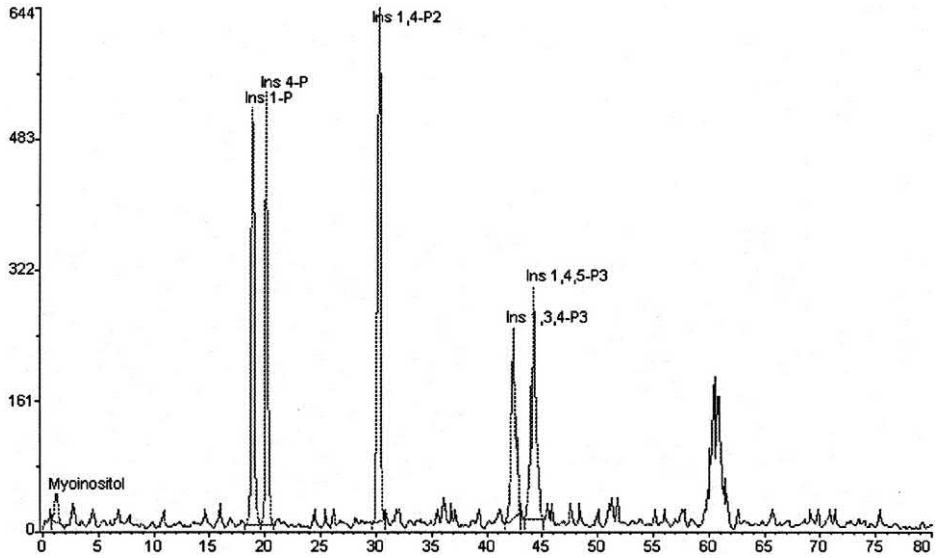


FIGURE 10.6 Activity peaks of ^{3}H-labeled inositol mono-, di-, and triphosphates separated by HPLC and measured with a 210-μL solid (heterogeneous) flow cell containing SolarScint solid scintillator, from the work of Dr. K. E. Nye at The Medical College, St. Bartholomew's Hospital, University of London, UK (© 1998 PerkinElmer, Inc. All rights reserved. Printed with permission).

collection efficiency decreased with increasing number of scintillator bead layers in the heterogeneous cell. Simulations extended to beta particle emissions with the PENetration and Energy Loss of Positrons and Electrons (PENELOPE) Monte Carlo code demonstrated that higher scintillator packing density (lower porosity) and smaller scintillator granule size would result in a higher fraction of electron energy deposited in the scintillator of the heterogeneous flow-cell detector. This effect was more pronounced for lower-energy electrons (<180 keV) than for higher-energy electrons (>550 keV).

D. Gamma and positron emission tomography flow cells

The gamma- and PET flow cells are made to provide highest detection efficiencies for gamma radiation. The cell types can be classified into those designed to provide optimum detection efficiencies for (1) high-energy γ emitters, (2) low-energy γ emitters, and (3) positron (β^{+}) emitters. The positron (β^{+}) emitters, which are principally those radionuclides used in PET, produce gamma radiation via annihilation (see Chapter 1, Volume 1). The low-energy gamma cell is also an efficient flow-cell detector for high-energy beta particle emitters, such as ^{32}P and ^{90}Y. Table 10.1 provides the main characteristics and detection properties of these scintillation flow cells.

1. High-energy gamma cell

The high-energy gamma flow cell will detect all γ emitters and high-energy β emitters; however, the high-energy gamma cell is designed specifically to provide optimum detection efficiencies for γ-emitting radionuclides of energy >70 keV. This type of flow cell (*e.g.*, Gamma-B flow cell, PerkinElmer, Inc.) consists of Teflon tubing coiled flat between two bismuth germanate (BGO) solid scintillator windows in between the faces of two PMTs, as illustrated previously in Fig. 10.2. A gamma ray emitted from a radionuclide in the flow cell tubing would interact with only one of the crystal scintillator windows on either side of the Teflon tubing. The scintillation light produced in one of the flow cell windows would be "seen" or detected simultaneously by the two PMTs and consequently registered as an event in coincidence according to the principles of coincidence scintillation counting. The scintillator BGO has a very high density (7.13 g/cm^3), high effective atomic number (high Z_{eff}), which provides this scintillator with a high "stopping power" for high-energy gamma radiation. At the same time, BGO has a high light output and short scintillation decay time, among other favorable properties for high-energy gamma ray detection. Thallium-activated sodium iodide [NaI(Tl)] solid scintillator is also used for the efficient flow-cell detection and measurement of gamma-emitting radionuclides (O'Hara et al., 2018; Trojanowicz et al., 2018; Kołacińska and Trojanowicz, 2014; Lindegren et al., 2014; Vitorge et al., 2014; Tsao et al., 2013).

Lindegren et al. (2014) designed a dual-flow cell consisting of coiled tubing of polyether ether ketone (PEEK), which fits within the well of a NaI(Tl) detector (62 mm o.d., 25 mm ID × 40 mm deep well illustrated in Fig. 10.7. The dual-flow cell consists of a reference cell and an analytical cell. The radio-HPLC flow starts from the injector to the reference cell for the detection and

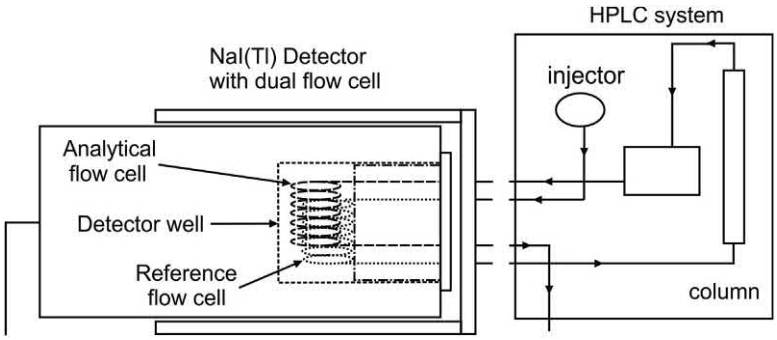


FIGURE 10.7 Schematic illustration of the dual flow-cell detector. The dotted line represents the reference flow cell, and the dashed line represents the analytical flow cell. *From Lindegren et al. (2014); reprinted with permission from Elsevier © 2014.*

measurement of the total sample activity prior to the sample entering the HPLC column. The radioactivity in the column effluent is then detected in the analytical cell. In this fashion, the sample serves as its own standard, before it is diluted in the HPLC column, permitting the online quantitative radioactivity analysis in the HPLC system. As described by Lindegren et al. (2014), both the loaded and eluted activity are measured in the same NaI(Tl) detector simplifying quantitative analysis of eluted activity, eliminating external calibration errors and internal system errors. The system was tested with the X-ray and gamma-emitting radionuclides ^{99m}Tc, ^{125}I, ^{131}I, and ^{211}At with X-ray and gamma photon emissions ranging between 27 and 364.5 keV. Such a flow-cell detector should be very suitable for short-lived positron-emitting radionuclides, which require a rapid activity analysis upon preparation.

2. Low-energy gamma cell

The low-energy gamma flow cell will detect all gamma photon, and X-ray photon, and high-energy beta emitters; however, the cell is designed generally to provide optimum detection efficiencies for gamma-ray energies $<$70 keV. This type of flow cell (e.g., Gamma-C flow cell, PerkinElmer, Inc.) consists of Teflon tubing coiled flat between two 4-mm-thick CaF_2(Eu) solid scintillator windows, as illustrated in Fig. 10.5. The CaF_2(Eu) scintillator has a much lower density (3.19 g/cm^3) and lower effective atomic number than the BGO scintillator employed in the previously described high-energy gamma cells. Therefore, the low-energy gamma scintillation flow cell has a lower gamma-ray stopping power than the previously described high-energy gamma flow cell. The high gamma stopping power of BGO is not needed for gamma rays of energy below 70 keV, and CaF_2(Eu) scintillator has a threefold higher scintillation conversion efficiency than BGO (L'Annunziata, 1987). Also, high-energy β particle emitters, such as ^{32}P ($E_{max} = 1710$ keV) and ^{90}Y ($E_{max} = 2280$ keV), emit beta particles of sufficient energy to penetrate the CaF_2(Eu) scintillator flow-cell windows of the low-energy γ flow cell detector and be detected with relatively high efficiency ($\sim$60% E). The mechanisms of coincidence scintillation detection with the use of two PMTs described in the previous section, however, are the same for both the CaF_2(Eu) and BGO detector windows.

The major advantages in utilizing the gamma cells for the measurement of γ or high-energy β emitters are that no liquid or solid scintillator is required in the cell tubing. The solid scintillator exists outside the flow-cell tubing, and therefore, no chemical or color quench is possible. After flow scintillation analysis, the entire HPLC effluent can be diverted to a mass spectrometer or NMR spectrometer for identification of HPLC peaks or collected by a fraction collector and further chemical and biological tests performed on the effluent fractions.

Heterogenous flow cells packed with CaF_2(Eu) are suitable for measuring low-energy beta emitters such as ^{3}H and ^{14}C (Alton et al., 2018; Magnussen et al., 2015), as the effluent is in intimate contact with the scintillator in this type of flow cell. The optimum radius of CaF_2(Eu) spheres or particles within the flow-cell tubing is a function of the track length of the beta particles within the scintillator. Alton et al. (2018) used Monte Carlo code Geant4 for the modeling and experimentation to determine the optimum CaF_2(Eu) radius for the detection of tritium, carbon-14, and lead-210 in heterogenous flow cells.

3. Positron emission tomography cell

PET scintillation flow-cell detectors are designed to detect all positron emitters generally in the effluent of a HPLC. These detectors are designed for the detection of the 0.511 MeV annihilation gamma photons when the emitted positrons undergo annihilation. Some flow-cell detectors may be designed exclusively for the measurement of positron emitters at highly reduced background count rates as described in the following paragraph. The positron emitters commonly analyzed by HPLC are short-lived

radionuclides (e.g., ^{11}C ^{18}F, ^{64}Cu, and ^{68}Ga) as isotope labels in radiopharmaceuticals used in PET in the field of nuclear medicine, which is described in previous texts by the author (L'Annunziata, 1987, 2007b, 2016). Numerous applications of PET scintillation flow-cell detectors to the radio-HPLC of positron emitters are available in the scientific literature; and a few examples are the following:

- **(i)** Carbon-11 (Collier et al., 2018; Kawamura et al., 2017; Hong et al., 2015; Kil et al., 2013; Peyronneau et al., 2012);
- **(ii)** Fluorine-18 (Kirjavainen et al., 2018; Xu et al., 2018; Wang et al., 2017; Hsu et al., 2016; Al-Momani et al., 2015; Kadirvel et al., 2014; Wyffels et al., 2014; De Leonardis et al., 2011)
- **(iii)** Copper-64 (Bergmann et al., 2013, Yim, 2013 and Jackson, 2012)
- **(iv)** Gallium-68 (Sivapackiam et al., 2018, 2016, Zha et al., 2018, Knetsch et al., 2015, Ebenhan et al., 2014, and Claesener et al., 2012
- **(v)** Zirconium-89 (O'Hara et al., 2018)

The emission of positrons during radionuclide decay is always accompanied by the 511-keV gamma rays due to the annihilation of a positron and electron, when the positron comes to rest in matter and eventually comes into contact with an electron, its antiparticle. Annihilation results in the simultaneous emission of two 511-keV gamma rays for each positron emitted by a radionuclide, and the two gamma rays are emitted in opposite directions or 180 degrees to each other. A detailed treatment of positron−electron annihilation and the gamma radiation produced by this phenomenon is given in Chapter 1, Volume 1. An illustration of two gamma-ray photons produced by positron annihilation within a detector of a PET flow cell is provided in Fig. 10.8. The two gamma rays are illustrated as traveling simultaneously in opposite directions from the flow cell. When annihilation radiation is produced in the flow cell, the two gamma ray photons will produce scintillation light in the two BGO crystal detector windows of the flow cell. The BGO windows have an opaque coating on the inner sides facing the flow-cell tubing. With such a detector design, the light produced in one BGO window can be "seen" or detected by only one PMT, that PMT facing the uncovered side of the BGO window. However, for any given pair of positron annihilation gamma rays originating from the sample in the flow cell, the two light flashes produced in the two BGO windows will be detected simultaneously by the two PMTs within the coincidence time of the instrument, and the two scintillation events (one in each window) will be registered and counted as a single coincident event. This detector design is intended to reduce background counts. Background events in the two BGO windows will not occur generally at the same time within the coincidence time of the scintillation analyzer, and these events will be rejected by the coincidence circuitry.

A similar flow-cell detector for the measurement of positron emitters eluted from HPLC utilized for the analysis of PET radiopharmaceuticals was designed by Takei et al. (2001). Flow cells of various volumes containing coiled Teflon tubing are accommodated between two BGO crystal detectors as illustrated in Fig. 10.9. The BGO detectors are housed in aluminum casings, whereby only gamma−photon pairs originating from positron annihilation are detected in coincidence. A 15-mm distance between the two aluminum housings for the BGO detectors allows for the easy insertion of flow cells of different volumes. Two counting window widths for the measurement of ^{11}C, namely, 400−600 keV and 90−680 keV, yielded detection efficiencies of $32 \pm 1\%$ and $43 \pm 1\%$, respectively (Takei et al., 2001). The narrower counting region yielded a fivefold higher figure of merit (FOM) (i.e., E^2/B) with a background count rate of 1.7 ± 1 cpm and detection limit of 0.3 Bq.

Background count rates in the PET scintillation flow cells are reduced to 1/10 the backgrounds encountered in the previously described high-energy gamma cells, which also employ BGO or NaI(Tl) crystal windows. The counting efficiencies of the PET scintillation flow cells are reduced by only a third of those obtained by the high-

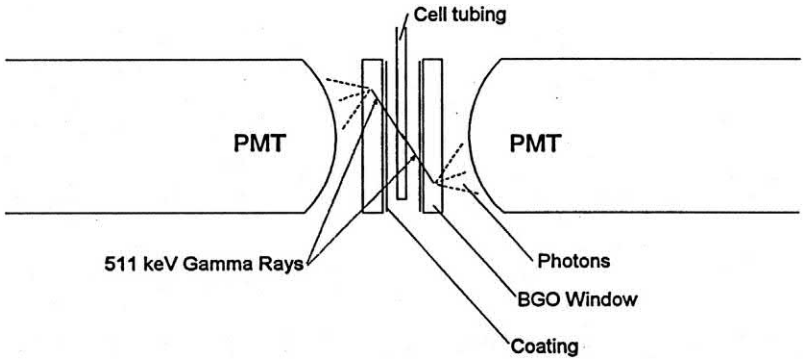


FIGURE 10.8 Basic diagram of a patented PET flow cell and photomultiplier tube (PMT) configurations used exclusively for the measurement of positron emitters. Annihilation gamma rays are illustrated interacting with the bismuth germanate (BGO) scintillator windows; however, the opaque coatings on the inner sides of the BGO detectors optically isolate the PMTs (© 1998 PerkinElmer, Inc. All rights reserved; printed with permission).

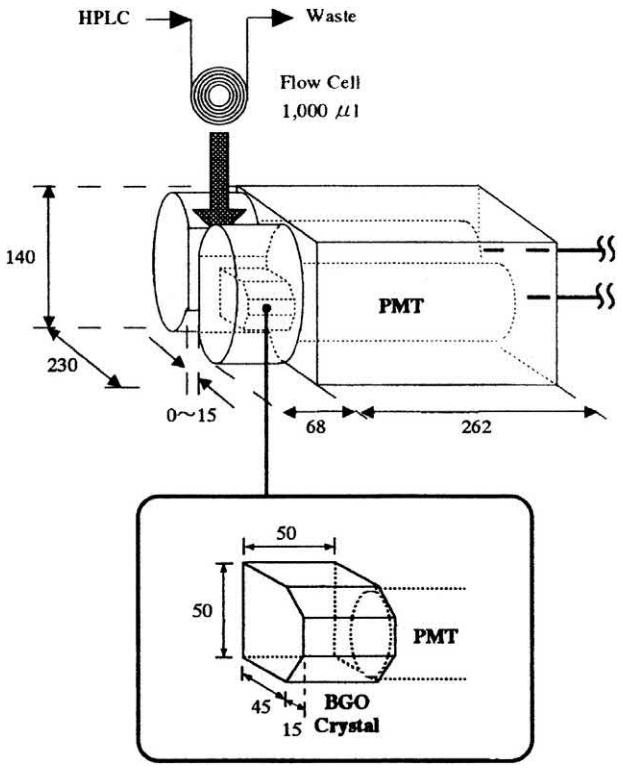


FIGURE 10.9 Block diagram of the sensitive positron detector. A pair of the BGO housings coupled to photomultipliers fixed in an aluminum frame. Dimensions are given in mm. *From Takei et al. (2001); reprinted with permission from Elsevier © 2001.*

energy gamma cells. Therefore, the PET flow cells provide considerably higher figures of merit (E^2/B) and lower detection limits for the measurement of positron emitters.

Not all scintillation detectors utilize PMTs. The PIN photodiode serves also as a suitable photomultiplier. Various types of photomultipliers are described in detail in Chapter 9, Volume 1. Carroll and Ramsey Associates produce an HPLC radioactivity flow detector consisting of a 1 cm^3 CsI(Tl) crystal detector coupled to a 1 cm^2 Si PIN photodiode and low-noise preamplifier built into a compact detector.

HPLC detector designs are not restricted to coiled Teflon tubing set between two detector windows as displayed previously in Fig. 10.9. Rather, the Teflon tubing, which houses the HPLC effluent, may be coiled around the scintillator crystal detector, as described by Huber et al. (2011). The tubing is coiled around the detector for higher sensitivity radio-HPLC applications, as this increases the length of time that the radioactivity peak spends near the detector by a factor of n, where n is the number of turns in the tubing and the sensitivity is increased by a factor of n. However, excessive length of tubing increases the duration that the radioactivity peak is near the detector, which results in peak broadening and thus reduced resolution for separating HPLC peaks.

A unique concept in the development of high-sensitivity radio-HPLC flow detectors for positron-emitting radionuclides arises from the work of Huber et al. (2010, 2011), who designed a detector by arranging conventional PET detector modules of BGO crystals into two parallel planes. Each of the BGO detector planes have an active detector volume of approximately $3 \times 3 \times 14$ cm, and the detector planes are separated at a distance of 3 cm providing a gap for the flow cell (e.g., coiled tubing). Coincidence counting of the annihilation γ ray photons is used with a 12 ns coincidence timing window to discriminate from background and improve the signal-to-noise ratio (SNR). As explained by Huber et al. (2011), the high-sensitivity radiation detector essentially takes a movie of the peak as it migrates through the flow cell; each frame of the movie is shifted (in space) so the centers of the peak are aligned, and then the frames are superimposed. The process provides the efficiency equivalent to a large area detector while reducing peak broadening. Straight or coiled tubing may be used. The use of a flow cell with the tubing coiled into a helix reduces the effective velocity (i.e., the velocity in the y-direction) of the radioactive compound passing through the detector. The helical flow cell thus increases the length of the active detector and the sensitivity for each activity peak. The gain in sensitivity is at the cost of some reduction in peak resolution; the peak width is broadened as a result of dispersion in the coiled flow cell. In comparison tests with a conventional HPLC flow cell with a 1 cm^3 CsI:Tl detector, Huber et al. (2011) demonstrate that the SNR for the high-sensitivity HPLC radiation detector signal was 28:1 for a single peak of 5.4 nCi of [^{18}F]fluorodeoxyglucose (FDG)-benzoic acid; whereas the SNR value for the conventional HPLC flow detector was estimated to be only 5:1.

Numerous radiopharmaceuticals labeled with short-lived positron-emitting nuclides, such as ^{11}C ($t_{½} = 20.38$ minutes), ^{18}F ($t_{½} = 109.7$ minutes), ^{64}Cu ($t_{½} = 12.7$ hours), and ^{68}Ga ($t_{½} = 68.3$ minutes), are synthesized and tested in radiochemical and clinical laboratories for specific applications in PET. Publications on the radiosynthesis and testing of PET radiopharmaceuticals are numerous. The short half-lives of the positron emitters produce minimal harm to patients while providing valuable imaging for medical diagnosis and monitoring the course of therapy.

Much work on the radiosynthesis of PET pharmaceuticals are focused on finding radiopharmaceuticals that can provide PET imaging for the diagnosis of specific diseases and the course of treatment. The radiosynthesis involves generally the use of HPLC and an online flow-cell detectors and mass spectrometer, which can provide immediate information on the course of reactions involved in synthesis. This immediate information is required due to the short half-lives of the PET radionuclides. For example, Bernard-Gauthier et al. (2013) synthesized 2-(4-[^{18}F]fluorophenyl)-7,8-dihydroxy-4H-chromen-4-one as a potential ^{18}F-PET pharmaceutical for brain imaging in the diagnosis of numerous neurodegenerative and psychiatric disorders,

such as Alzheimer's disease, Rett syndrome, Parkinson's disease, Huntington's disease, schizophrenia, traumatic brain injury, and major depressive disorder. Such a synthesis with a short-lived radionuclide requires fast HPLC separation with immediate online flow-cell analysis of reaction precursors and products and their identification by online MS. Fig. 10.10 illustrates an example of the online flow-cell analysis of ^{18}F bonded to reactants and products measured by HPLC and flow-cell analysis during the course of the synthesis of the ^{18}F-PET radiopharmaceutical. The flow-cell analysis, illustrated in Fig. 10.10, provides a record of how the reactions progress in the following sequence: Starting at 5 minutes, there is a small activity peak due to the preparation of ^{18}F-labeled dimethoxy precursors and a larger peak of $[^{18}F]F^-$ with Kryptofix-222 and K^+. After 25 minutes, the flow-cell analysis of the HPLC effluent shows the complete formation of the fluorinated dimethoxy precursor. After solid-phase extraction (SPE) and treatment with BBr_3, the flow-cell analysis after 15 minutes of reaction time shows a strong activity peak of the final ^{18}F-PET radiopharmaceutical due to a double methoxy deprotection of the precursor. Flow-cell analysis of HPLC effluents, such as the one illustrated in Fig. 10.10, can provide a quantitation of radiochemical yield of the reaction with flow-cell measurements of the radionuclide activities at the start and end of the reaction.

Due to the short half-lives of the positron emitters involved, the radiopharmaceuticals are most commonly prepared in large batches and transported to the PET imaging medical facilities; however, in the past few years, there has been increased interest in the decentralized production of these short-lived radiopharmaceuticals, including a dose-on-demand PET radiotracer synthesis oriented toward the imaging requirements for specific patients (Tarn et al., 2016). Research is thus focused into the development of rapid and efficient methods of synthesis and HPLC analysis of the radiopharmaceuticals. The testing of newly synthesized PET radiopharmaceuticals must be analyzed for purity and stability by HPLC with its effluent linked to a suitable radioactivity flow-cell detector. An example may be taken from the work of Knetsch et al. (2015), who synthesized the labeling of a trimeric fusarinine-C-RGD peptide with the PET radionuclide ^{68}Ga. The RGD peptide (L-arginyl-glycyl-L-aspartic acid) is responsible for cell adhesion to the extracellular matrix. Flow-cell radioactivity analysis of the ^{68}Ga-PET pharmaceutical in HPLC effluent, as illustrated in Fig. 10.11, provides quantitative evidence of the stability of the labeled compound in various chemical solutions and in human serum. The identity of the radioactivity peaks in the HPLC effluent can be confirmed by online MS or NMR spectroscopy.

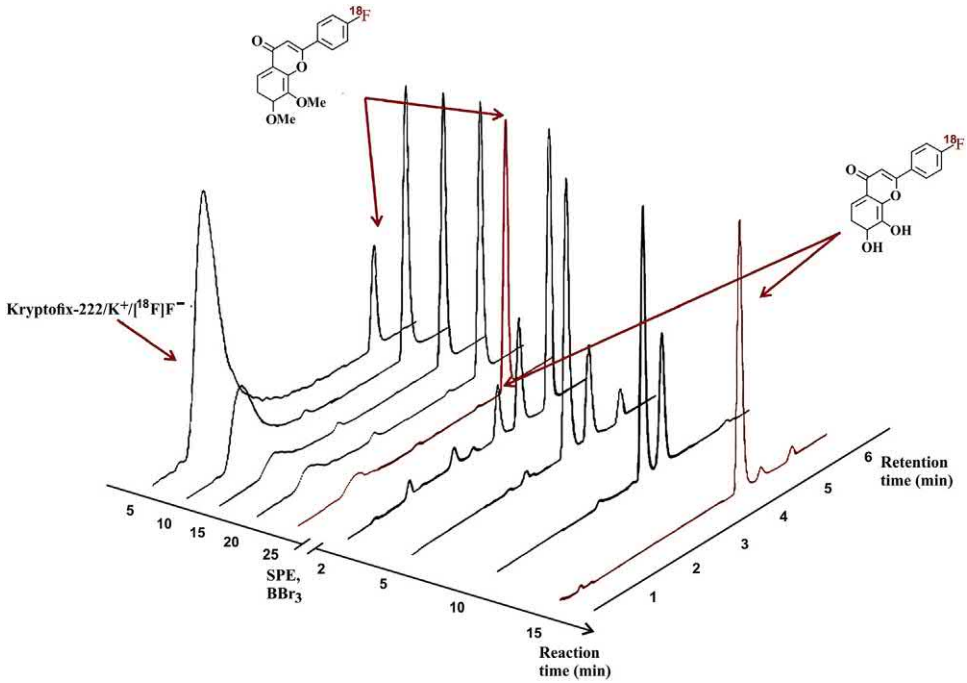


FIGURE 10.10 Analytical radiochromatograms for the advancement of the radiofluorination and BBr_3-promoted bis-deprotection reactions. At the far left, flow-cell analysis provides the time course for the labeling of a dimethoxy precursor with ^{18}F where after 25 minutes the free $[^{18}F]F^-$ peak drops to near background and the ^{18}F-dimethoxy precursors peak reaches a maximum. After solid-phase extraction (SPE) and BBr_3 reaction, the methoxy groups are cleaved, yielding the ^{18}F-dihydroxy final product after a 15-minutes reaction time. *From Bernard-Gauthier et al. (2013); reprinted with permission from Elsevier © 2013.*

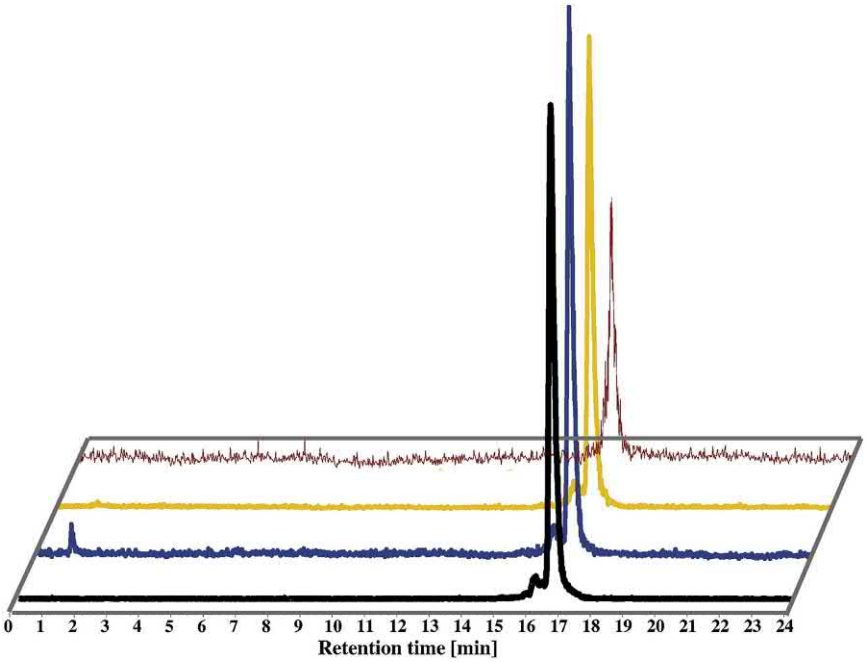


FIGURE 10.11 HPLC radiochromatograms of [^{68}Ga]FSC-(RGD)3 (i.e., flow-cell detector response of radioactivity vs. HPLC retention time): (front chromatogram/black: radiolabeling solution, next chromatogram behind/blue: stability after 120 minutes incubation at 37°C in DTPA solution, third chromatogram back/yellow: $FeCl_3$ solution and last chromatogram/red fresh human serum. *From Knetsch et al. (2015); reprinted with permission from Elsevier © 2015.*

E. Narrow-bore and microbore flow cells

Microvolume flow scintillation analyzer (FSA) cells are available, and these differ from the conventional flow cells mainly in their dimensions of inner-diameter (ID) and cell volume. The narrow-bore and microbore flow cells are made to accommodate narrow-bore (~2 mm ID) and microbore (~1 mm ID) HPLC systems that yield improved HPLC peak resolutions over the standard FSA systems. The standard or conventional FSA systems use larger cell volumes that accommodate wider HPLC columns (~5 mm ID). The major properties that distinguish narrow-bore and microbore FSA systems from the standard FSA systems are provided in Table 10.3. The high resolutions provided by the microbore HPLC-FSA systems yield improved molecular specie separations, which improves molecular identification via direct coupling to the ESI mass spectrometer (Johanns et al., 2017; Morris et al., 2017; Zeng et al., 2013; Onursal et al., 2011; Su et al., 2010). To demonstrate the potential of microbore flow cells, Schultz and Alexander (1998) tested a 1.2 μL volume on-column flow cell for use with 250-μm-ID HPLC columns capable of detecting < 200 DPM for a 1-minute-wide chromatogram peak with a PerkinElmer Radiomatic TR150 flow scintillation analyzer (see Fig. 10.12). They demonstrated that a solid scintillation cell packed with silanated lithium glass

TABLE 10.3 Characteristics of standard (conventional), narrow-bore, and microbore FSA systems.[a]

Characteristics	Standard FSA	Narrow-bore FSA	Microbore FSA
Cocktail pump	Digital	Digital	Precision syringe
HPLC columns	5 mm ID	2 mm ID	1 mm ID
Sample flow rate to FSA	333 μL to 2 mL/min	133 μL to 1 mL/min	25 −150 μL/min
LS cocktail flow rate (at 3:1 cocktail:sample ratio)	1−6 mL/min	400 μL to 3 mL/min	75 −450 μL/min
Mixing tee	>250 μL	10 μL	10 μL
Cell size	35 μL to 5 mL	15 −250 μL	3 −100 μL

[a]*© 2003 PerkinElmer, Inc. All rights reserved. Printed with permission.*

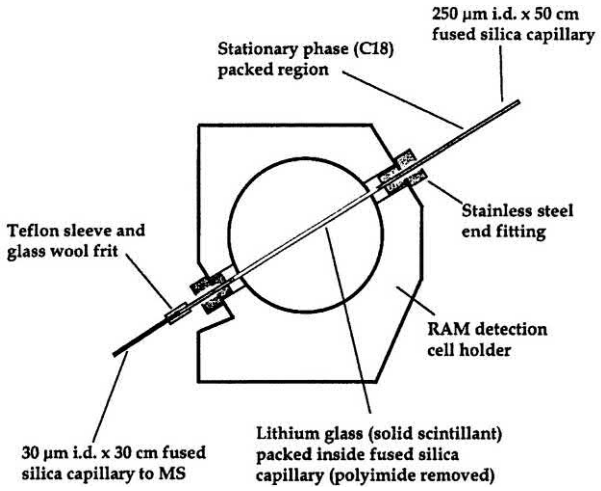


FIGURE 10.12 An on-column radioactivity monitor (RAM) flow cell for use with 250-µm-ID microcolumns. The flow cell volume is 1.2 µL. The detection window is 5 cm in length. *From Schultz and Alexander (1998), © 1998 John Wiley and Sons; Reproduced with permission.*

with a mean particle size of 9.6 ± 2.6 µm yielded a 24% increase in peak area compared with a cell packed with a mean particle size of 21.0 ± 2.5 µm. Also, they demonstrated that a 508-µm-ID cell yielded a 15% increase in peak area compared with a 762 µm-ID cell. As illustrated in Fig, 10.12, the microbore FSA cell is equipped with a 30-µm-ID tube for linkage directly to the inlet of an ESI chamber of a mass spectrometer.

F. Luminescence flow cell (fLumo)

The luminescence flow cell is a radio-HPLC detector (fLumo), which is only sensitive to positrons and insensitive to gamma rays for applications in the analysis and preparation of PET radiopharmaceuticals. The detector is identified as the fLumo by Berthold Technologies. The detector and its performance are reviewed in detail by Thonon et al. (2013), and only a brief description will be provided here.

The fLumo utilizes a flow cell modified with a solid melt-on scintillator that is sensitive to positrons and insensitive to the gamma photons that arise from positron annihilation. Thus, background from positron annihilation gamma photons can be ignored even without lead shielding. The detector is particularly useful in laboratories that are required to analyze positron-emitting radionuclides used for PET (e.g., ^{11}C. ^{18}F, ^{68}Ga, etc.), referred to as PET radionuclides. A schematic view of the Berthold LB 500 fLumo is illustrated in Fig. 10.13. The detector dimensions are $150 \times 350 \times 180$ mm^3 (w × d × h). Different flow-cell volumes (20, 50, and 100 µL) are interchangeable to accommodate diverse sample activities and flow rates. The scintillator is mounted onto the outside of the coiled tubing of the flow cell. Positrons emitted from within the flow cell volume interact with the scintillator, creating light photons that are captured by the PMT. The entire photon spectrum is captured by the PMT, which eliminates the need for a counting window.

As described by Thonon et al. (2013), the detector is connected to a high-energy radio monitor (HERM) electronics with dimensions of $210 \times 60 \times 120$ mm^3 (w × d × h). The HERM electronics component can provide radio-HPLC readout directly, or the HERM electronics can be connected to a personal computer (PC) via the use of a terminal program. The flow-cell data can be transferred via (1) a 0−1 V analog output, (2) a transistor−transistor logic (TTL) signal, or (3) via data transfer directly to a PC via a USB connection. Very high count rates of up to 1.0×10^7 cps can be measured by the PMT. Detector backgrounds of 10 cps are reported when no high-level source is available in the same room as the detector. In a hot cell where the PET radionuclides may be prepared in high-level batches, a detector background of 130 cps is reported when a 10 MBq ^{18}F source is at a distance of 20 cm from the cell. This background is reduced to 12 cps

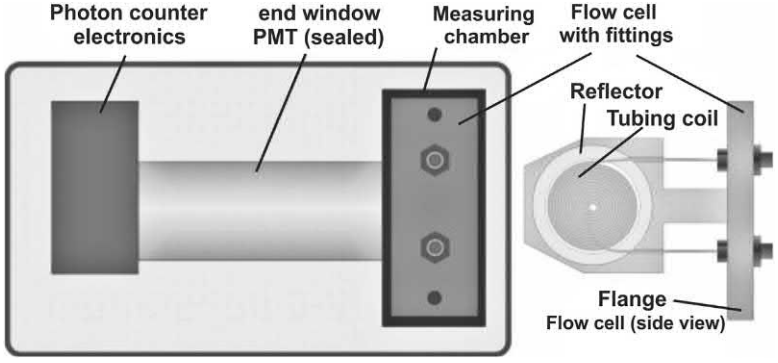


FIGURE 10.13 Schematic view of the Berthold LB 500 fLumo unshielded luminescence flow cell detector for positron-emitting radionuclides. *From Thonon et al. (2013); reprinted with permission from Elsevier © 2013.*

when the detector is shielded from the 10 MBq ^{18}F source with a 5 cm lead brick. At a signal-to-noise (S/N) ratio = 3, the detection limits are reported to be 0.2 MBq/mL per 10 μL injection volume (0.1 MBq/mL per 20 μL injected, HPLC system) for fluorine-18 and 0.04 MBq/mL for gallium-68 per 10 μL injected into the HPLC (Thonon et al., 2013). The higher limit of detection for fluorine-18 over that of gallium-68 is due to the differences in the energy maxima (E_{max}) of the positrons emitted by ^{18}F ($E_{max} = 0.634$ MeV) and ^{68}Ga ($E_{max} = 1.90$ MeV).

Linearity of response of a detector over a long range of activity is important in radionuclide analysis. The linearity of the fLumo flow-cell detector response measured by HPLC peak integration HPLC runs over a wide range of activity concentration 0.2 or 2500 MBq/mL is reported by Thonon et al., 2013) with a correlation coefficient $r^2 > 0.995$. A typical radio-HPLC of [^{18}F]FPRGD2 is illustrated in Fig. 10.14. The [^{18}F]FPRGD2 is an abbreviation for an efficient PET imaging agent [^{18}F]FB-E [c(RGDyK)]$_2$, which belongs to a series of RGD peptides (arg-gly-asp) labeled with [^{18}F] to improve the efficiency of tumor targeting and pharmacokinetics. The peak is symmetrical with a small width (~0.35 minutes) and similar to the peak of the nonradioactive compound, which is measured by a UV detector upstream from the fLumo radioactivity flow-cell detector.

Some examples that describe the utilization of the Berthold LB 500 fLumo for the radio-HPLC measurement of positron-emitting radionuclides are the radio-HPLC measurement of ^{18}F radiopharmaceuticals by Cardinale et al. (2017), Bertrand et al. (2016), and Perreault et al. (2016) and of ^{68}Ga-labeled pharmaceuticals by Isal et al. (2018), Azzouna et al. (2017, 2015) , and Asti et al. (2014a,b).

For the HPLC measurement of compounds labeled with radionuclides that decay by isomeric transition (e.g., ^{99m}Tc) or electron capture (e.g., ^{125}I) with the emission of gamma and X-ray photons, the Berthold LB 500 Herm with either a fLumo gamma-measuring cell or a separate NaI(Tl) flow-cell detector may be employed, as demonstrated in the works of Gaonkar et al. (2018, 2016), Nayak et al. (2015), and Baishya et al. (2014) in the radio-HPLC of ^{99m}Tc pharmaceuticals and Gevaert et al. (2016),Verbeken et al. (2015), Wynendaele et al. (2015), and Stalmans et al. (2014) in the radio-HPLC measurement of ^{125}I-labeled pharmaceuticals.

The Berthold LB 500 fLumo detector would be sensitive to high-energy negatron emitters; however, other detectors, such as the Berthold FlowStar^2 LB 514 with specific liquid and solid flow cells and dual PMT detection with coincidence counting, among others available from commercial suppliers listed previously in this chapter in Table 10.2, are much more efficient for low- and high-energy beta emitters, such as ^{3}H, ^{14}C, ^{35}S, ^{32}P, and ^{90}Y.

G. Hybrid silicon pixel flow cell

The Medipix2 and Timepix chips are hybrid silicon pixel sensors, which have been demonstrated by Tarn et al. (2016) and Maneuski et al. (2017) to be efficient detectors of positrons. They demonstrated that the Medipix2 and Timepix chips can be implemented in a microfluidic platform for positron counting in flow analysis assays of PET radiopharmaceuticals.

The Medipix2 sensor was developed by the Medipix2 Collaboration, which is an international research effort of numerous institutes and universities with the European Organization for Nuclear Research (CERN). The objective of the Medipix2 Collaboration was the development of a single photon counting pixel detector readout chip using a 25 μm CMOS (complementary metal–oxide–semiconductor process, https://medipix.web.cern.ch/collaboration/medipix2-collaboration, accessed June 26, 2018). The collaboration at CERN produced the Medipix2, resulting in a 65K single photon counting pixel array with a square pixel size of 55 μm on a 14 × 14 mm^2 detection area whereby the sensor can act as a real-time camera and counter of positrons (Tarn et al., 2016).

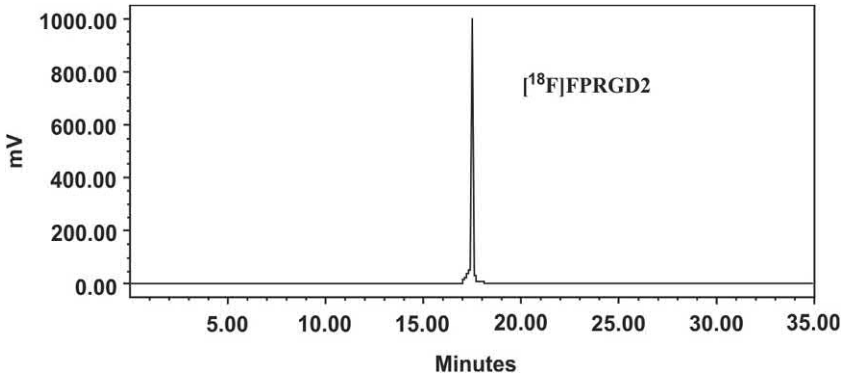


FIGURE 10.14 HPLC radiochromatogram of [^{18}F]FPGRDD2 (100 MBq/mL, 20 μL injected, calvolt 10,000 counts/s/volt). *From Thonon et al. (2013); reprinted with permission from Elsevier © 2013.*

The Timepix chip evolved at CERN from the development of the Medipix2. The pixels of the Timepix are of identical size as those of the Medipix2, but the functionality within each pixel was changed. In the Timepix chip, each pixel can be programmed to count particle hits like Medipix2 or to record Time-Over-Threshold (TOT) or to measure the arrival time of the first particle to impinge onto the pixel (https://medipix.web.cern.ch/collaboration/medipix2-collaboration, accessed June 26, 2018). As described by Maneuski et al. (2017), the Timepix chip can be set up to operate in two modes of interest for the measurement of positrons in a flow-cell arrangement on a microfluidic platform:

(i). In counting (or Medipix) mode, a threshold is set on the discriminator, and pulses above this value are counted on a 14 bit counter (maximum count is 11,810).

(ii). In TOT mode, the pulse triggers a local clock, and the clock ticks are counted while the pulse remains over threshold. This yields a value of the pulse width (which is proportional to pulse height) for each individual pulse, hence providing a measure of the energy of incident particle.

Tarn et al. (2016) tested the properties of the Medipix2 chip as a detector for positrons, which could serve as a detector for the analysis of PET pharmaceuticals in a microfluidic platform. They utilized solutions of ^{68}Ga-citrate, which is commonly used in PET imaging, and passed the ^{68}Ga solutions through a silica-based monolithic column designed for the purification and chromatographic separation of compounds in future microfluidic quality control platforms. An illustration of the first microfluidic arrangement for the HPLC analysis of positron emitter with the Medipix2 positron detector is provided in Fig. 10.15. The porous silica monolith column was prepared by Tarn et al. (2016) with a thin and flat shape (14 mm length × 4 mm width × 1.5 mm thickness). This length of the monolith corresponds with that of the Medipix2 chip positron detector, and the thin dimension of the monolith improves positron detection by minimizing monolith positron absorption, whereas the attachment of the monolith to the Medipix2 chip maximizes positron capture and

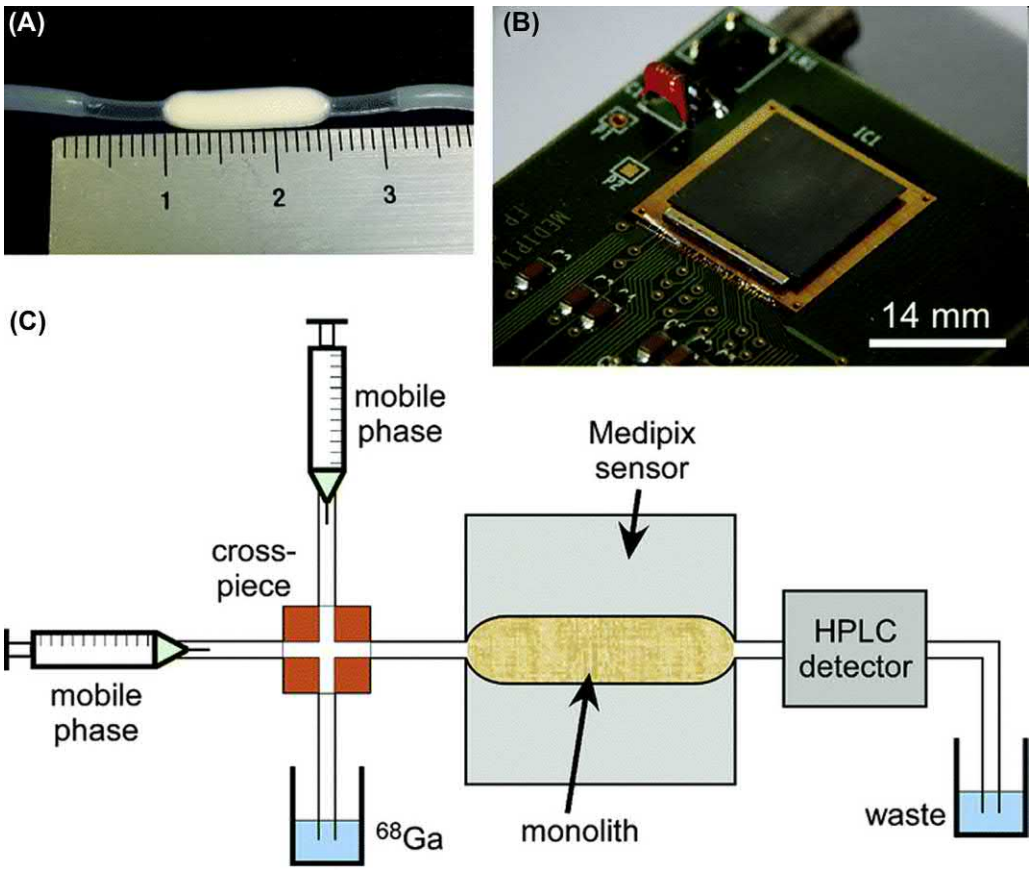


FIGURE 10.15 (A) Silica-based monolithic column encased in heat-shrink tubing, (B) Medipix positron detector, featuring 14 × 14 mm^2 sensor area. (C) Schematic of the experimental setup, with the monolith column placed above the Medipix sensor, and featuring a cross-injection system and a standard sodium iodide radio-HPLC detector. *From Tarn et al. (2016).*

detection. The monolith is connected at one end to a sample injection system and at the other end to a NaI(Tl)/PMT flow-cell. The NaI(Tl) flow-cell detector measures the ^{68}Ga activity via the measurement of the 0.511 MeV annihilation gamma photons after the ^{68}Ga exits the silica-based monolithic column and Medipix2 positron flow detector. The NaI(Tl) flow-cell response provides a measure of ^{68}Ga activity that can be compared with the ^{68}Ga activity measured by the Medipix2 chip.

The Medipix2 chip was demonstrated to be highly superior to a standard NaI(Tl) flow cell for radio-HPLC measurement of ^{68}Ga in a microfluidic platform, as illustrated in Fig. 10.16. Tarn et al. (2016) underscore that the Medipix detector shows a substantial increase in detection signal for the ^{68}Ga-citrate peak as illustrated, with a measured signal-to-noise (S/N) ratio of 14 for the Medipix positron detector and 3 for the standard NaI(Tl) radio-HPLC flow cell detector. Images of positron tracks detected by the Medipix chip at two different time points, namely, when the ^{68}Ga citrate passes through the monolithic column and after it has been eluted from the column, are illustrated in Fig. 10.16.

A measure of the linearity of response of a detector to differing levels of radionuclide activity that need to be measured in practical situations is a vital property. Tarn et al. (2016) tested varying ^{68}Ga citrate activity levels through the monolithic column with a record of 100 frames of the Medipix detector response with 1.0 second integration time. The linearity of the detector response is

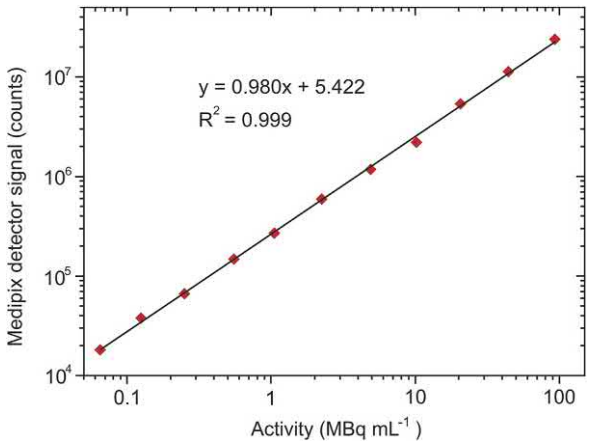


FIGURE 10.17 Plot illustrating the linearity of the Medipix2 positron detection signal with varying activity levels of ^{68}Ga citrate on a log scale. *From Tarn et al. (2016).*

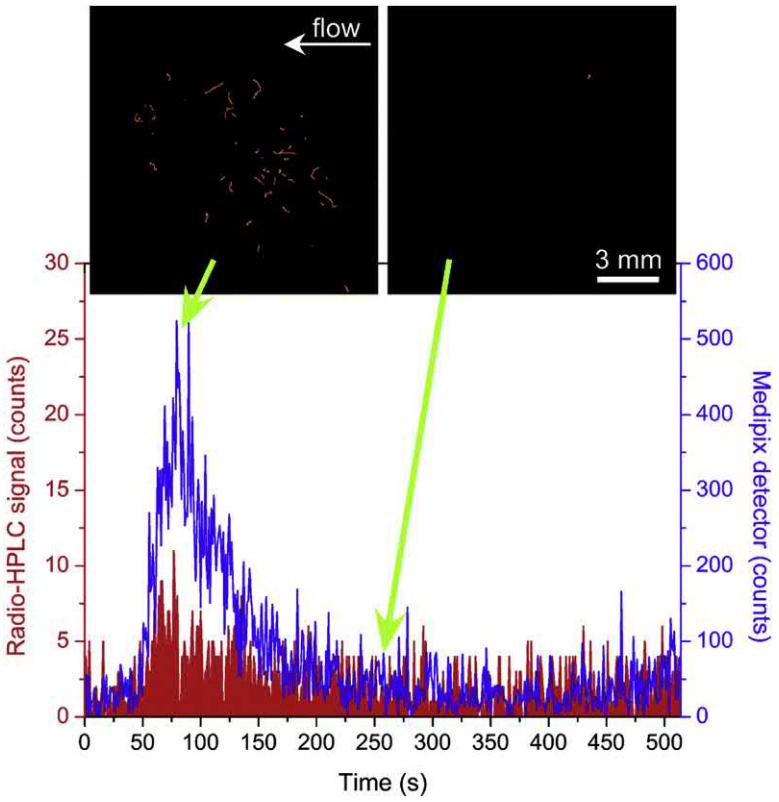


FIGURE 10.16 Plot of ^{68}Ga citrate radioactive emissions as it passed through the monolithic column (200 μL/min of a 15 MBq/mL solution). The blue (upper) signal shows the signal from the positron Medipix detector, whereas the red (lower) signal was taken from a flow-through NaI/PMT radio-HPLC detector. Note that the plots are on different scales. Inset are images (14 × 14 mm^2) taken from the Medipix detector at different time points. Color is visible in the electronic version of the book. *From Tarn et al. (2016).*

illustrated in Fig. 10.17. They note that a clinical PET scan typically requires ~370 MBq (10 mCi), and with a maximum injection volume to a patient of 10 mL, the expected radionuclide activity levels during the purification and quality control of the radiopharmaceutical would be a minimum of 37 MBq/mL. Thus, Tarn et al. (2016) note that the Medipix detector would be able to detect clinically relevant levels of radioactivity in volumes of hundreds of nanoliters.

Maneuski et al. (2017) tested the counting capability of the Timepix chip for the potential radioassay of positron emitters in the production of radiopharmaceuticals for PET. They utilized a positron detection system consisting of a 300-μm-thick silicon detector with a 256 × 256 array of pixels, each of 55 μm on a side, providing a total detector active area of 1.96 cm^2. The detector was bump bonded to a Timepix readout chip, which processes individually the signal output from each pixel. As noted earlier in this section, the Timepix chip has more than one mode of operation, which permits a measurement of the total energy deposited by each positron. This prevents the double counting of positron hits by individual pixels at low activities, which can yield optimum minimum detectable activities (MDAs). To enable high sample count rates of positron emitters generally encountered in the synthesis and preparation of PET pharmaceuticals, Maneuski et al. (2017) employed an amplifier shaping factor of ~1 μs to assure little double pulsing if the pixel count rate is kept below 1 MHz per pixel, which would yield a maximum count rate of 40 MHz/mm^2 with linear detector response. The linearity of the Timepix/Medipix detector response compared with that of a CsF crystal scintillation detector coupled to a PMT is illustrated in Fig. 10.18. The sensitivity of the Timepix was demonstrated to be superior to a BGO detector with measureable positron signals down to the background level of the laboratory. Maneuski et al. (2017) demonstrate that the detection of positrons in lieu of annihilation gammas with the Medipix/Timepix detector in a very small setup (the entire detector system fits in the palm of a person with USB cable link to a PC) provides high position resolution as well as a high sensitivity and activity range with linearity of response all of which open the door to the application of the Medipix/Timepix detectors to the microfluidic analysis of pharmaceuticals for PET.

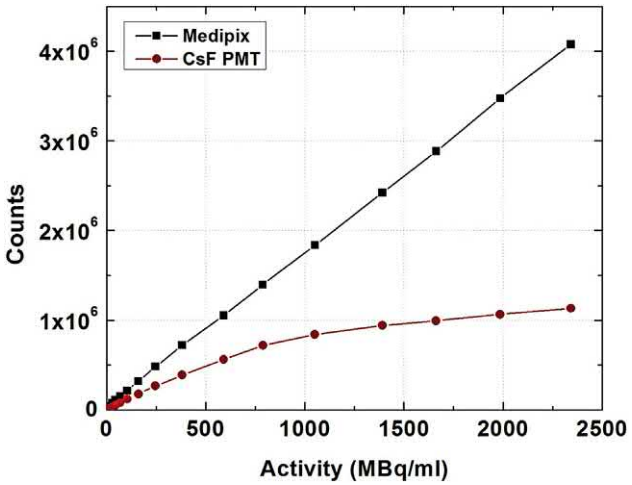


FIGURE 10.18 Comparison of a CsF scintillator PMT and the Timepix detector for measuring different concentrations of ^{18}F-solution injected on to an HPLC system. The counting of single positrons is inherently linear in the absence of any saturation effects. *From Maneuski et al. (2017); reprinted with permission from Elsevier © 2017.*

An excellent review of progress toward the microfluidic quality control testing of radiopharmaceuticals is provided by Ha et al. (2017), and reviews on the development of silica monoliths and various microfluidic columns for chromatographic separations in microfluidic platforms are provided by ALOthman and Wabaidur (2019), Konala and Tetala (2018), Masini and Svec (2017), Mattrey et al. (2017), Shalliker (2017), Groarke and Brabazon (2016), and Hong et al. (2016).

H. Criteria for flow-cell selection

When making a decision on which type of scintillation flow cell would be best for a particular application, several factors should be considered among which are (1) the detection efficiency of the flow cell for the radionuclide of interest, (2) the flow-cell detector background when the MDA is an important factor, (3) the level of radioactivity of the sample components, that is, the sensitivity required, which takes into account the previous items (1) and (2) and the FOM defined by E^2/B, which would be a measure of detector sensitivity, (4) the costs involved in using scintillation fluor cocktail with a liquid (homogeneous) flow cell, (5) the chemical composition of the HPLC eluent used, and (6) whether further analysis of the HPLC effluent is required (i.e., Must the compounds separated and detected in the HPLC effluent be analyzed by online MS or NMR spectroscopy, or must the components be isolated and other chemical and biological tests be performed on the separated components?). Data listed in Tables 10.1 and 10.4 are helpful in the selection of a scintillation flow cell to use for a particular application. Some examples will be cited to illustrate the use of the data in these tables. The data listed in Table 10.4 refer to flow cells that have specific detector geometries for BGO and CaF_2(Eu) scintillator crystals and specific counting window regions. Flow-cell detectors with these specific geometries may or may not be available currently on the commercial markets. Nevertheless, the data provided in Table 10.4 can serve to provide a general idea of the potential for using a BGO or CaF_2(Eu) flow cell for the measurement of the radionuclides listed.

The highest counting efficiencies for all β or α emitters are obtained with the liquid scintillator (homogeneous) flow cell. However, a special low-viscosity nongelling LS fluor cocktail must be mixed with the HPLC effluent stream with a controlled pump and static fluid mixer. The separated compounds or molecular entities in the HPLC effluent are thereby rendered useless for any other chemical or biological tests that may be required. A stream splitter could be employed to separate part of the HPLC effluent for online MS, online NMR spectroscopy, or fraction-collecting prior to the mixing with the scintillation fluor cocktail. Stream splitting permits only a portion of the HPLC-separated components of the sample to be collected or analyzed online by the mass and NMR spectrometers. In the case of ^{3}H measurements when the separated ^{3}H-labeled components are of low activity (close to background), there is no alternative but to use the liquid homogeneous flow cell.

If sample activities are well above background, ^{3}H can be detected with a solid (heterogeneous) cell containing the solid scintillator such as the YG-150 solid cell (Berthold Technologies) or monocrystalline SolarScint (PerkinElmer, Inc.) among others. See Fig. 10.6 for an example of the detection of ^{3}H-labeled inositol phosphates by a heterogeneous flow cell containing SolarScint. The advantages in this case are no fluor cocktail is used, no chemical quench problem exists, and the entire effluent stream can be utilized for online MS or NMR spectroscopy or other subsequent chemical or biological tests or even isolated from solution following fraction collection. All other beta emitters (e.g., ^{14}C, ^{35}S, ^{33}P, ^{32}P) or alpha emitters are detected with relatively high counting efficiencies with the heterogeneous flow cell (also referred to as solid cells), such as the YG-150 (yttrium glass) solid cell for standard flow rates, YG-40-x6M solid microbore cell or the YG 50-S5P solid prep cell for preparative HPLC with higher sample activities and flow rates $>$ 3 mL/min (Berthold Technologies). The only disadvantage of the heterogeneous cell is the possible reversible and sometimes irreversible adsorption of the sample molecules (e.g., peptides, lipids, proteins) onto the solid scintillator that cause peak broadening and increased background from one HPLC run to another. Berthold Technologies and possibly other suppliers provide solid (heterogeneous) flow cells for samples with such molecular sticking problems, such as the YG 150-S6D for standard flow rates and activities, the YG 400 solid cell for higher flow rates or lower activities, and the YG xx-S6M for the solid microbore cell at standard flow rates and activities or the YG 75-x6M for the solid microbore cell at higher flow rates or lower activities.

The solid scintillator (heterogeneous) flow cell is particularly applicable to radioactivity measurements when very high pressure (up to 3000 psi) and high flow rates are required. Table 10.1 lists some solid scintillator (heterogeneous) cells used for high pressure/high flow rate conditions.

The gamma cells are classified into two types: (1) the high-energy gamma cell, which yields optimum detection efficiencies for radionuclide X-ray or gamma emissions $>$ 70 keV energy, and (2) the low-energy gamma cell, which provides higher counting efficiencies for radionuclides with X-ray or gamma emissions of energy $<$ 70 keV. Table 10.4 provides the counting efficiencies (*%E*), background count rates, and calculated FOMs for a number of gamma-emitting radionuclides with both the high-energy Gamma-B and low-energy Gamma-C scintillation flow cells, which are trademarks of PerkinElmer, Inc. The Gamma-B and Gamma-C flow cells may no longer be available commercially, and the data listed in Table 10.4 refer to flow cells that have specific detector geometries for BGO and CaF_2(Eu) scintillator crystals. Nevertheless, the data provided in Table 10.4 can serve to provide a general idea of the potential for using a BGO or CaF_2(Eu) flow cell for the measurement of the radionuclides listed.

The counting regions, listed in Table 10.4, from which the counting efficiencies and backgrounds were determined, are defined by lower level (LL) and upper level (UL) discriminator settings of a MCA with pulse height equivalents in keV. The most abundant X-ray and gamma-ray emissions of each radionuclide are also listed in Table 10.4 to help the reader interpret the efficiencies provided by the two types of gamma cells. From Table 10.4, it can be seen that ^{55}Fe, ^{125}I, and ^{109}Cd are more efficiently measured with the low-level Gamma C flow cell manufactured with CaF_2(Eu) scintillator windows, which is evidenced by the superior *%E* and FOM values. A flow-cell equivalent to the Gamma C is the Iodine Cell (I 100−1000) produced by Berthold Technologies. The FOMs for the measurement of ^{201}Tl with the Gamma-B and Gamma-C flow cells are very close, and either of these cells would be appropriate. Akhlaghi et al. (2008) provides an excellent example of the use of FSA for the measurement of ^{201}Tl. The remaining nuclides listed in Table 10.4 in order of increasing gamma ray energy are detected more efficiently with the high-energy Gamma-B flow cell, which is manufactured with the higher density and thicker BGO scintillator windows. A flow cell equivalent to the Gamma-B cell is the Gamma cell BGO-X produced by Berthold Technologies.

The reader should notice that varying the counting region LL and UL discriminator settings will govern the counting efficiency and background for any particular radionuclide to be measured and flow cell used. By adjusting the region settings, an optimum FOM can be found, which is calculated as

$$\mathrm{FOM} = E^2/B \tag{10.1}$$

TABLE 10.4 Performance characteristics of high-energy (BGO) and low-energy [CaF_2(Eu)] Bremsstrahlung and gamma scintillation flow cell detectors for the detection of radionuclides listed in order of increasing photon radiation emission energies.[a,c]

		High-energy Gamma-B, BGO[d]				Low-energy Gamma-C, CaF_2(Eu)[d]			
Radionuclide	Radiation energy (keV)[b]	Region (keV)	%E	Background	FOM (E^2/B)	Region (keV)	%E	Background (CPM)	FOM (E^2/B)
^{55}Fe	Bremsstrahlung up to 23.2 keV	0–35	0.2	5	0.008	0–10	14.2	40	5.0
^{125}I	27.4-keV (30%) and 31-keV (>100%) X-rays, 35-keV gamma (7.0%)	0–120	27.1	48	15.3	10–85	81.1	108	60.8
^{109}Cd	22-keV (>100%) and 70-keV (95%) X-rays, 88-keV gamma (3.8%)	5–60	5.1	14	1.85	5–60	34	109	10.6
^{99m}Tc	2-keV X-rays (100%) 140-keV gamma (100%)	40–300	63.2	198	20.2	40–300	14.3	158	1.3
^{201}Tl	X-rays up to 84 keV (195%) 135-keV gamma (2.6%) 167-keV gamma (10%)	30–400	34	275	4.2	30–400	27.7	196	3.9
^{51}Cr	5-keV X-rays (22%) 320-keV gamma (10%)	200–500	3	233	0.039	200–500	0.1	72	0.00014
^{67}Ga	9-keV X-rays (56.4%) 84-keV X-rays (29%) 93-keV gamma (38%) 185-keV gamma (21%) 300-keV gamma (17%)	35–600	44.2	394	5.0		14.8	217	1.0
^{111}In	23-keV X-rays (67%) 26-keV X-rays (14%) 171-keV gamma (91%) 245-keV gamma (94%)	100–650	24.1	385	1.5	100–650	6.2	143	0.3
^{133}Ba	31-keV X-rays (63%) 35-keV X-rays (23%) 81-keV gamma (34%) 303-keV gamma (18%) 356-keV gamma (62%) 384-keV gamma (9%)	240–700	27.5	289	2.6	240–700	2.1	78	0.05

^{131}I	284-keV gamma (6%) 364-keV gamma (81%) 637-keV gamma (7%)	220–950	57.9	379	8.8	220–950	20.2	99	4.1
^{85}Sr	13-keV X-rays (50%) 514-kcV gamma (100%)	350–850	19.3	241	1.5	350–850	0.6	57	0.006
^{54}Mn	5-keV X-rays (22%) 835-keV gamma (100%)	600–1200	19.2	153	2.4	600–1200	1.9	32	0.11
^{60}Co	1330-keV gamma (100%) 1170-keV gamma (100%)	900–1700	19.9	99	4.0	900–1700	4.6	16	1.3

[a]Gamma-B and Gamma-C arc flow-cell trademarks of the PerkinElmer Inc. %E and background data arc from Anonymous (1995) © 1995 PerkinElmer, Inc. All rights reserved. Printed with permission.
[b]The most abundant radiations are given, and in parenthesis the approximate intensities or relative abundances of the radiations are provided as a percentage, that is, radiation emissions per 100 disintegrations.
[c]The data listed refer to flow cells that have specific detector geometries for BGO and $CaF_2(Eu)$ scintillator crystals and specific counting window regions. Flow-cell detectors with these specific geometries may or may not be available currently on the commercial markets. Nevertheless, the data provided can serve to provide a general idea of the potential for using a BGO or $CaF_2(Eu)$ flow cell for the measurement of the radionuclides listed.
[d]Flow cells similar to the Gamma B and Gamma C cells are the Gamma Cell BGO-X and the Iodine Cell 1 100–1000, respectively, of Berthold Technologies.

where E is the percent counting efficiency and B is the background count rate. An optimum FOM can provide higher sensitivity for radionuclide detection by reducing the MDA as described further on in this chapter. In Table 10.4, counting region settings can be compared with the X-ray and gamma emissions of each radionuclide. Limiting the counting region settings will limit the radiation energies that can be detected by the flow cells; however, the limited region settings will also reduce background count rates. The FOM, therefore, is a good means of calculating the optimum tradeoff of highest counting efficiency and lowest background. An interesting example may be taken from the radionuclide ^{51}Cr listed in Table 10.4. Its 320-keV gamma ray emission has only a 10% intensity or relative abundance, which is defined as the number of emissions per 100 radionuclide disintegrations. In the case of ^{51}Cr, there are only 10 gamma rays emitted per 100 ^{51}Cr radionuclide disintegrations. Therefore, with the selected counting region of 200–500 keV (Table 10.4), a maximum counting efficiency of only 10% can be achieved, if all gamma rays could be detected without loss. The reported counting efficiency is 3% for the high-energy Gamma-B flow cell. A significantly higher counting efficiency for ^{51}Cr could be obtained by increasing the counting region to 0–500 keV to include detection of the 5-keV X-rays; however, this would result in a much higher background count rate.

The high-energy and low-energy gamma cells have the advantage that the HPLC effluent is not mixed with any fluor cocktail, as the X- or gamma radiation emissions are detected outside the Teflon tubing of the flow cell by the external BGO or CaF_2(Eu) cell windows. Also, there is no adsorption of radioactive sample onto scintillator as would occur in the heterogeneous flow cell types. After measurement of radioactivity in the separated components of the HPLC effluent, the entire effluent stream can be analyzed online by MS or NMR spectroscopy or collected in fractions with the traditional fraction collector to permit subsequent chemical and biological studies on fractions of interest.

The reader should also note from Table 10.1 that high-energy beta particle emitters, such as ^{32}P and ^{90}Y, can be detected by the low-energy gamma cells at a significantly high counting efficiency (~60%). Therefore, if samples are not near background and the MDA is not of concern, the gamma cell could be the flow cell of choice for these high-energy beta particle emitters because no fluor cocktail is required and there is no adsorption of sample in the gamma cell. Even for the intermediate-energy β emitters, such as ^{14}C, ^{35}S, and ^{33}P, where counting efficiencies with the low-energy Gamma-C flow cell may be very low (~0.1%), the low-energy gamma cell may be the cell of choice when radioactivity levels are very high, such as in the μCi or mCi levels, commonly encountered in laboratories involved in the preparation or synthesis of radioisotope-labeled compounds or sources. The low counting efficiencies of the low-energy gamma cell for the intermediate-energy β emitter are an advantage in this case because sample activities are high, count rates are reduced to useable levels due to the low counting efficiency, and the labeled compounds or sources can be fully recovered with a fraction collector.

III. Principles of flow scintillation counting

A. Count rates

As noted in Chapter 8, Volume 2 on Radioactivity Counting Statistics of this book, the sample counting time is an important factor in the measurement of sample radioactivity. Longer counting times provide statistically more accurate measurements of the true count, that is, the standard deviations of the count determinations are reduced as counting time is increased. In flow counting, however, the sample counting time is a function of the flow rate and flow-cell volume, as the sample consists of a stream, which passes through a tube (flow cell) situated perpendicular to the faces of the photon detectors (PMTs) as illustrated in Fig. 10.2. The photon detectors, therefore, will see the radioactive sample only for the time that the sample resides in the flow cell. This period of time is referred to as the residence time (T_R), which is calculated as

$$T_R = \frac{V}{F} \tag{10.2}$$

where V is the cell volume in mL and F is the sample flow rate in mL/min. When a liquid (homogeneous) flow cell is used, the flow rate (F) is a function of the sum of the HPLC and cocktail flow rates. Therefore, the calculation of the flow rate for a homogeneous cell must include the mix ratio of the HPLC mobile phase to cocktail. For example, for a 3:1 cocktail/mobile phase ratio, the flow rate is calculated as

$$F = \text{HPLC flow rate} + \text{Cocktail flow rate} \tag{10.3}$$

or

$$F = 1.0\ \text{mL/min} + 3.0\ \text{mL/min} = 4.0\ \text{mL/min}$$

Because the sample flows through the cell at a given rate, sample will enter and leave the cell simultaneously. Therefore, the flow scintillation analyzer will measure the flowing sample in segments according to the sample residence time. The instrument will automatically calculate the count rates according to the calculations illustrated subsequently. The following example illustrates the calculation of residence time and count rate:

Example 10.1 If we have a flow cell of 600 μL volume and a flow rate of 4.0 mL/min and the counts collected (observed

counts) were 1200, we can calculate the residence time and count rate as follows:

$$T_R = \frac{0.6 \text{ mL}}{4.0 \text{ mL/min}} = 0.15 \text{ min}$$

The count rate (CPM) can be calculated by dividing the observed counts by the residence time, as in this example,

$$\text{Count rate} = \frac{\text{Counts}}{T_R} \tag{10.4}$$

$$\text{Count rate} = \frac{1200 \text{ counts}}{0.15 \text{ min}} = 8000 \text{ CPM}$$

or more easily the count rate is calculated as described previously by the author (L'Annunziata, 1979) by multiplying the counts collected by the inverse of the flow equation ratio (Eq. 10.2) or

$$\text{Count rate} = c\frac{F}{V} \tag{10.5}$$

where c is the total observed number of counts. From Eq. (10.5) and the above example, we can calculate the count rate as

$$\text{Count rate} = 1200 \text{ counts} \cdot \frac{4.0 \text{ mL/min}}{0.6 \text{ mL}} = 8000 \text{ CPM}$$

The observed sample counts and count rate calculations on a flowing sample are repeated or "updated" by the instrument during fixed or variable update periods, which can be set by the operator. The update times can be adjusted to any value over the range of 1−120 s in modern flow scintillation analyzers. Both observed sample counts and background counts are, therefore, calculated per update time and net count rates calculated as described in the subsequent section.

B. Background and net count rate

The computer programs of the flow scintillation analyzer are designed to subtract random background events from sample radionuclide decay events to provide a net sample count rate according to the equation:

$$\text{Net CPM} = \frac{\text{observed counts} - \text{background counts}}{T_R} \tag{10.6}$$

The background counts are subtracted from the gross sample counts before dividing by the residence time. Otherwise, as explained by Kessler (1986), the background counts are amplified by the residence time of the sample in the flow cell. Reich et al. (1988) also explain that the true background of the system is the result of external cosmic radiation and electronic noise, which are independent of the flow. Therefore, the "static" (nonflow) background must be eliminated before the flow equation is applied. If not, the background would be overstated by a multiple of the flow rate.

In the calculation of the net count rate according to Eq. (10.6), both the observed counts and the background counts are per update time. If the update time selected is 6 s, then the counts accumulated during a 6-s update time are inputted into the equation. Also, the background counts subtracted in the above equation, whether determined by the system or entered into the software by the operator, are divided from a background CPM into the equivalent of an update time worth of background counts before being entered automatically into the equation. Hence, the net count rate is calculated each update time by subtraction of the background before dividing by the residence time.

Example 10.2 If a radionuclide standard is injected into a flow-cell detector via the inlet line of the liquid scintillator pump, the cell volume is 400 μL, the flow rate is 4.0 mL/min, an update time of 6 s is selected, a background count rate of 25 counts per minute is entered into the software program, and the observed counts in a given update time is 400, then the Net CPM is calculated according to Eq. (10.6) as

$$\text{Net CPM} = \frac{400 \text{ counts} - 2.5 \text{ counts}}{0.4 \text{ mL}/4.0 \text{ mL/min}}$$

$$= \frac{397.5 \text{ counts}}{0.1 \text{ min}}$$

$$= 3975 \text{ CPM}$$

Note that both the observed sample counts and background counts in the above calculation are per update time. In the above example, the background represents less than 1% of the net count rate. However, when either the update counts get lower, background increases, or residence time is reduced, the background becomes more significant and an accurate measurement and proper subtraction of background may be necessary.

The background is determined obviously without radioactive sample; however, the homogeneous flow cell must contain the fluor cocktail and HPLC eluent used for a particular HPLC run, and the heterogeneous cell must contain the HPLC eluent when background is determined. If a homogeneous cell is used, the background is determined by filling the cell with the same ratio of cocktail to HPLC mobile phase as will be used during the HPLC runs. A background run is then carried out for 10 minutes or more with a minute scalar time

for the summary. The statistical method used to calculate the background is as follows:

$$\mathrm{BKG} = \left[\frac{B_s}{N} + 2\frac{\sqrt{B_s}}{\sqrt{N}}\right](N) \tag{10.7}$$

where BKG is the background subtracted in the calculation of net count rate, B_S is the measured background expressed in counts in one scalar minute, and N is the number of samplings per minute. In the previous example, where the update time was 6 s, the calculation is carried out every 6 s or 0.1 minutes. Therefore, N in this case would be equal to 10 samplings. The division and multiplication by the number of samplings (N) is required because the calculation is based on an update time, whereas the background is given in counts each minute.

C. Counting efficiency and disintegration rates

The counting efficiency (E) is the ratio of the net sample count rate (i.e., background-subtracted count rate) as measured by the instrument and the actual disintegration rate or activity of the measured sample. The ratio, when multiplied by 100, is expressed as the percent counting efficiency or

$$\%E = \frac{\text{net CPM}_\text{S}}{\text{DPM}_\text{S}}(100) \tag{10.8}$$

where net CPM_S and DPM_S are the measured net sample count rate (i.e., background-subtracted count rate) and the actual sample disintegration rate, respectively. The counting efficiency is a function of the radionuclide emissions and the energies of the particles emitted, the type of liquid or solid flow cell detector used, counting region selected, and the level of quench in the sample, which is governed, in turn, by the chemistry of the HPLC mobile phase and scintillator. To express the flow scintillation analysis results in DPM, it is necessary, therefore, to determine the counting efficiency for a particular application or HPLC run.

The counting efficiency can be determined with a radionuclide standard in the flow cell while under a static (isocratic) or gradient (dynamic) mode.

When quenching is constant in an HPLC run, that is, the HPLC sample components and mobile phase (i.e., eluent) have no changing effect on the counting efficiency, a static efficiency correction can be used. Under this type of correction, the counting efficiency is constant throughout the entire HPLC run.

When the HPLC sample components and eluent are not constant and thus have a changing affect on the counting efficiency, it is necessary to carry out a gradient counting efficiency run to determine the counting efficiencies at different points in time during the HPLC run as the sample components elute from the HPLC column.

1. Static efficiency runs

There are two ways of performing the static efficiency runs. When the sample components have absolutely no quenching effect on the counting efficiency of the scintillation system, it is possible to determine the counting efficiency *independent of the HPLC system*. When the sample components do have a quenching effect on the counting efficiency, but the effect is constant throughout the length of the HPLC run, it is necessary to determine the counting efficiency *dependent on the HPLC system.* The two methods are subsequently described. The detailed procedures are available from Anonymous (1997).

a. Independent of the high-performance liquid chromatography system

This method requires spiking a volume of the flow scintillation cocktail with a radionuclide standard and filling the scintillation flow cell with the standard in cocktail. Solid (heterogeneous) flow cells and gamma cells obviously do not use scintillation cocktail; and counting efficiency determinations with these types of cells require only an eluent solution of the radioactivity standard. An outline of the procedure used for liquid (homogeneous) flow cells is as follows:

(1) The normal background of the system is determined first.

(2) A known activity (DPM) of the radionuclide of interest is added to an accurately measured volume of the flow scintillation cocktail. A minimum volume of 25 mL is used for each radionuclide to be measured. To ensure sufficiently high count rates and good counting statistics, the activity of the standards used can be estimated by taking into account the flow cell volume and estimated counting efficiency of the flow cell. For example, the final activity concentrations of standard should be at least approximately 10,000 DPM/mL for ^{14}C and approximately 25,000 DPM/mL for ^{3}H.

(3) The counting parameters for the particular radionuclide and efficiency run parameters are set in the flow scintillation analyzer, including the DPM in the flow cell, which is calculated as

$$\text{DPM in cell} = (\text{DPM/mL})(\text{flow cell volume in mL}) \tag{10.9}$$

(4) The inlet line for the LS pump is placed into the container holding the solution of radionuclide standard in flow scintillation cocktail. A separate inlet line and line filter are used to avoid possible contamination of the LS cocktail source used during normal runs.

(5) The LS pump is kept running for at least 5 minutes to assure the complete filling of the flow cell.
(6) After filling the flow cell, the LS pump is stopped, and the efficiency run program of the computer-controlled flow scintillation analyzer is initiated. The counting efficiency is calculated according to the basic Eq. (10.8) as

$$\%E = \frac{\text{net CPM in cell}}{\text{DPM in cell}}(100) \tag{10.10}$$

(7) The efficiency run is saved, and flow scintillation cocktail containing no radionuclide is pumped through the cell until background levels are reached.
(8) When dual radionuclide analysis is required (e.g., $^{3}H-^{14}C$), the procedure is repeated with the second radionuclide with the counting efficiency run set to a second counting region.

b. dependent on the high-performance liquid chromatography system

When the sample components have a quenching effect on the counting efficiency, but the effect is constant, it is necessary to spike a volume of the flow scintillation cocktail with a known activity of radionuclide standard. The flow cell is then filled with a mixture of the spiked LS cocktail and HPLC eluent. This method and the previously described procedure are static methods, and the procedures are quite similar with the exception that step (6) in the previous procedure will, in this case, include running both the LS pump and the HPLC to fill the flow cell with a mixture of spiked scintillation cocktail and HPLC eluent. Both pumps are turned off when the flow cell is filled, and the efficiency run program is initiated as described in the previous static procedure.

^{3}H and ^{14}C are low- and intermediate-energy β-emitting radionuclides, respectively, and the LS yields for these radionuclides are easily quenched. Phosphorus-32 is not easily quenched, as described in Chapter 6, Volume 1 of this book. One can expect, therefore, that HPLC eluent will have an effect on the counting efficiency of ^{3}H and ^{14}C in most flow scintillation systems. The preceding counting efficiency determination procedure, which includes HPLC eluent, is recommended when low- to intermediate-level radionuclides are used and when the HPLC eluent components have a constant quench effect on the counting efficiency.

2. Gradient efficiency run

When the HPLC eluent consists of a gradient mixture, quench will vary during the HPLC run and the counting efficiencies will, therefore, not be constant. In this case, a gradient efficiency run is required. The setup procedure for the gradient efficiency run is similar to the previously described efficiency run (dependent on the HPLC system) with the exception that the efficiency run is a dynamic one. The dynamic run requires that both the LS pump and the HPLC gradient run simultaneously during the efficiency run. The computer program linked to the flow scintillation analyzer may construct a gradient efficiency correction curve or table, which can be used to correct for counting efficiency changes during a specific gradient HPLC run.

When the counting efficiency of the detection system is known, the scintillation analyzer can convert the count rates of the eluting components in the HPLC effluent by use of the following converted form of the basic Eq. (10.8):

$$\text{DPM} = \frac{\text{net CPM}}{\%E/100} \tag{10.11}$$

where net CPM is that defined by Eq. (10.6), whereby the above equation can be written in detail as follows:

$$\text{DPM} = \frac{(\text{observed counts} - \text{background counts})/T_R}{\%E/100} \tag{10.12}$$

Eq. (10.12) can also be expressed as

$$\text{DPM} = \frac{\text{net counts}}{(T_R)(E)} \tag{10.13}$$

where net counts is the background-subtracted counts and E is the decimal equivalent of the percent counting efficiency. For the column chromatographic separation of radionuclides, Grate et al. (1996) and Grate and Egorov (1998a,b) take Eq. (10.13) further to include the efficiency of recovery (E_{rec}), which is the ratio of the activity of a particular radionuclide recovered from a separation column (e.g., HPLC column) compared with the activity of that nuclide loaded on the column. They quantify radionuclides eluted from separation columns according to flow scintillation peak areas described by the equation:

$$\text{DPM} = \frac{C_n}{(E_d)(E_{rec})(T_R)} \tag{10.14}$$

where DPM is the radionuclide activity, C_n is the background-corrected peak area or, in other words, the net counts, that is, the observed counts minus the background counts determined in a blank run, E_d is the decimal equivalent of the % detection efficiency, and E_{rec} and T_R are the radionuclide efficiency of recovery and sample residence time in the flow cell, described previously. Radionuclide recovery efficiencies can sometimes be measured during a run with the use of a tracer nuclide, such as the gamma-emitting nuclide ^{85}Sr as a tracer for the beta-

emitting nuclide ^{90}Sr. If a known activity of ^{85}Sr is added to a sample, separated on a column, and collected and analyzed for its gamma activity, the recovery efficiency for radiostrontium can be calculated.

D. Minimal detectable activity

In many forms of chromatography, peaks that are sharp, detectable above the baseline, and well defined or proportioned are easier to detect than a broad peak or one that displays tailing and lack of form. In radio-HPLC, the MDA is a calculated activity of a peak from a flow-cell detector expressed in disintegration per minute (DPM) or disintegrations per second (Bq) based on the relative peak height and the presumption that the limit of detectability or MDA is twice the count rate of the background (Reich et al., 1988; Anonymous, 1990), which is calculated as the

$$\mathrm{MDA} = (B)(W)/(T_R)(E) \tag{10.15}$$

where B is the background count rate, W is the width of the peak in minutes, T_R is the residence time defined by Eq. (10.2), and E is the decimal equivalent of the % counting efficiency or $\%E/100$.

As explained by Reich et al. (1988), the MDA of a flow-cell detector is not directly related to the total amount of radioactivity in any given peak but rather to the specific activity of any flow segment residing in the detector at any given time. Therefore, flow rate, cell volume, and peak width in addition to the obvious background and detection efficiency all play a key role in defining the MDA. Borai and Mady (2002) measured the MDA or lower limit of detection (LLD) in Bq units for ^{238}U and ^{232}Th separated on ion exchange chromatograph columns. They used the expression of Currie (1968) where

$$\mathrm{LLD} = K\left[2.71 + 4.65(B)^{1/2}\right] \tag{10.16}$$

where K is a proportionality constant relating the flow scintillation detector response to the activity and B is the number of background counts for a given counting period. The value of K has units of reciprocal time and is calculated according to the following:

$$K = W/(T_R)(E)(V) \tag{10.17}$$

where W is the peak width in units of volume, T_R is the sample residence time in the flow cell, E is the detector counting efficiency, and V is the flow-cell detector volume (Reeve and Crozier, 1977). Using a 0.4-mL heterogeneous flow cell consisting of Ce-activated glass scintillator in an IN/US flow scintillation analyzer (now LabLogic Systems, Inc.) and a Dionex 2000 ion chromatographic system, Borai and Mady (2002) measured LLDs of 3.0 ± 0.1 Bq for ^{238}U and 6.0 ± 0.1 Bq for ^{232}Th.

The variables of flow rate, cell volume, and peak width should now be considered as factors governing the optimization of flow scintillation analysis in a radio-HPLC system. The following section will describe these variables in terms of sensitivity, speed of analysis, and resolution.

E. Sensitivity, flow rate, and resolution

The sensitivity of a flow detector in a given radio-HPLC run is another term reflecting the MDA, that is, the sensitivity is increased when the MDA is decreased. The sensitivity can be increased by (1) reducing the flow rate, which will increase the residence time (T_R), or (2) increasing the size of the flow cell, which increases the detection efficiency. Reducing the flow rate would increase the HPLC run time, but it could also diminish the resolution of the HPLC-separated sample components because flow rate is a key factor in the chromatographic separation of sample components. On the other hand, increasing the size of the flow cell would also reduce resolution. The term resolution refers to the ability to distinguish between activity peaks that are in close proximity to each other. Increasing the flow cell size will lower the resolution. When compounds or molecules are difficult to separate, it is best to use a flow cell size that will give the best resolution although at a diminished sensitivity. On the other hand, when radioactivity levels are low and activity peaks are well separated, it is recommended to sacrifice resolution for increased sensitivity. Therefore, the selection of cell size will depend on the characteristics of any particular HPLC separation run.

As a general rule, the best flow-cell volume for a given HPLC application would be a cell with a volume of one-half to one-fourth the volume of the smallest peak of interest. As described by Anonymous (1990), the following equations can be used to estimate the optimum flow-cell size for two basic cell types:

For solid (heterogeneous) cells or gamma cells:

$$V_C = K(V_P) \tag{10.18}$$

where V_C is the cell volume, K is a constant between ¼ and ½ where smaller values yield higher resolution and larger values yield higher sensitivity, and V_P is the volume in mL of the smallest peak of interest. The value of V_P is calculated as

$$V_P = (W)(F) \tag{10.19}$$

where W is the peak width in minutes and F is the flow rate in mL/min.

For the liquid (homogeneous) cells:

$$V_C = K(V_P + V_S) \tag{10.20}$$

where V_S is the volume of liquid scintillator for the same duration as the peak.

As demonstrated by Kessler (1986), the resolution of HPLC activity peaks from flow detectors is dependent not only on the flow rate and flow cell size as described but also on the update time, which is the time interval in seconds over which the detector pulses are summed. Kessler demonstrated that, maintaining the flow rate and flow cell size constant, two very close and overlying peaks can be separated into two clearly defined peaks by reducing the update time. This may be intuitively obvious as the activity peaks are plotted on a time scale (activity vs. time in minutes). Reducing the pulse summation update time would provide activity changes over shorter time intervals. In summary, we can conclude that the higher sensitivity (lower MDA) of a flow detector is highly dependent on the residence time of the sample in the flow detector, cell volume, and update time; however, a trade-off must be made where sensitivity is sacrificed for resolution by controlling flow rate, cell size, and update time.

F. Precision

As described in Chapter 1, Volume 1 and Chapter 8, Volume 2, radioactivity decay is a random event, that is, it cannot be predicted when a given radionuclide would decay. However, we could predict that one-half of the nuclei of a given radionuclide in a sample would decay in one half-life. In view of the random character of radioactivity decay, we can say that the precision of a count rate determination is a function of the total number of counts collected and the counting time, as the count number will be greater for longer counting times.

The precision of a given count determination is expressed in terms of its standard deviation, which is calculated as

$$\mathrm{SD} = \sqrt{\text{total counts}} \tag{10.21}$$

In the case of flow-cell detectors, we can look at some specific examples.

Example 10.3 If a flow rate of 4.0 mL/min and a flow-cell detector of 250 μL volume were used for a particular HPLC application, we could calculate that the radioactivity from the sample in the flow cell would be observed for 3.75 s determined as follows:

$$T_R = V/F = 0.25\ \text{mL}/4.0\ \text{mL min}^{-1} = 0.0625\ \text{min} = 3.75\ \text{seconds}$$

If the count rate for the 3.75-s period was 20,000 CPM, the standard deviation according to Eq. (10.21) would be calculated as

$$\mathrm{SD} = \sqrt{(20{,}000\ \text{cpm})(0.0625\ \text{min})} = \sqrt{1250\ \text{counts}} = 35.4$$

or the counts collected can be expressed as 1250 ± 35.4 counts at one standard deviation and the percent standard deviation (% SD) would be

$$\frac{35.4}{1250}(100) = 2.8\%$$

and the results expressed as 1250 counts ± 2.8%.

If we take the same flow rate and flow-cell volume but detect a lower count rate of 2000 CPM, the standard deviation could be calculated as

$$\mathrm{SD} = \sqrt{(2{,}000\ \text{cpm})(0.0625\ \text{min})} = \sqrt{125} = 11.2$$

and the percent standard deviation (% SD) would be calculated as

$$\frac{11.2}{125}(100) = 8.9\%$$

The percent standard deviation calculation can be simplified to the following:

$$\%\mathrm{SD} = \frac{100}{\sqrt{\text{total counts}}} \tag{10.22}$$

Example 10.4 If we take the above example 10.3 and increase the cell volume from 250 to 500 μL and keep the flow rate (4.0 mL/min) and the two observed count rates (20,000 and 2000 CPM) the same, we can calculate the new percent standard deviations (%SD) as follows to see how increasing cell volume will improve sensitivity and precision, albeit at an expected loss of resolution:

The residence time or the duration that the radioactivity in the cell would be observed can be calculated as

$$T_R = V/F = 0.50\ \text{mL}/4.0\ \text{mL min}^{-1} = 0.125\ \text{min} = 7.5\ \text{seconds}$$

The percent standard deviation for the example taken for a count rate of 20,000 CPM is calculated as

$$\%\mathrm{SD} = \frac{100}{\sqrt{(20{,}000\ \text{cpm})(0.125\ \text{min})}} = \frac{100}{\sqrt{2500\ \text{counts}}} = 2.0\%$$

and that for the count rate of 2000 CPM is

$$\%\mathrm{SD} = \frac{100}{\sqrt{(2000\ \text{cpm})(0.125\ \text{min})}} = \frac{100}{\sqrt{250\ \text{counts}}} = 6.3\%$$

Examples 10.3 and 10.4 illustrate that increasing the flow-cell volume from 250 to 500 μL increased the residence time, and consequently, the precision of the measurement was improved by reducing the %SD of the observed counts. However, larger flow-cell volumes will reduce activity peak resolutions as described previously.

Eq. (10.22) can be used to calculate the percent standard deviation (%SD) for any count rate (CPM) or total counts collected, that is, (CPM·T_R) of any flow-cell detector. The residence time (T_R) in minutes required to achieve a desired %SD can be calculated by manipulation of Eq. (10.22) as follows:

$$\sqrt{\text{total counts}} = \frac{100}{\%\text{SD}} \tag{10.23}$$

or

$$\text{total counts} = \left(\frac{100}{\%\text{SD}}\right)^2 \tag{10.24}$$

or

$$(\text{CPM})(T_R) = \left(\frac{100}{\%\text{SD}}\right)^2 \tag{10.25}$$

and

$$T_R = \frac{1}{\text{CPM}}\left(\frac{100}{\%\text{SD}}\right)^2 \tag{10.26}$$

which is similar to the equation described by Kessler (1986).

G. Detection optimization

Major advances in real-time flow-cell analysis have been made in detection optimization, which was achieved by including technology currently available to modern scintillation analyzers (Anonymous, 1996; Wasyl and Nellis, 1996). This technology includes (1) multichannel analysis for counting region optimization, (2) time-resolved liquid scintillation counting (TR-LSC) for background reduction, (3) detection and correction of chemiluminescence, which can be a significant interference when fluor cocktail and HPLC eluate are mixed, and (4) operation software, such as RadioStar and Chromeleon Driver (Berthold Technologies), Win-Flow (IN/US Systems/LabLogic Systems, Inc.), and FLO-ONE or ProFSA (PerkinElmer, Inc.), among others, which facilitate flow scintillation analysis setup, optimization, control, performance assessment, and result reporting.

1. Multichannel analysis

The application of the MCA in flow scintillation analysis as in LSA will sort all signals according to pulse height into individual channels calibrated in keV. Visual observation of the pulse height spectra from the MCA facilitates counting region optimization for a flow sample at a given quench level. Region optimization is achieved by setting the lower-level discriminator (LLD) and upper-level discriminator (ULD) to provide the highest FOM calculated as E^2/B, where E is the percent counting efficiency and B is the background count rate. The term FOM is analogous to the term signal-to-noise (S/N) ratio, as the sample activity peak is the signal of interest and the background radioactivity is equivalent to the noise we must reduce.

The pulse height spectral display offered by the MCA will also permit visualization of the sample pulse height spectrum originating from more than one radionuclide. If two radionuclides are present in the sample, the pulse height spectrum of the MCA can be used to select the LLD and ULD settings for two counting regions. This will enable the activity analysis of two radionuclides in the same sample as described in Section X of this chapter and in more detail in Chapter 6, Volume 1.

2. Chemiluminescence detection and correction

The chemiluminescence pulse height spectrum can be observed via the MCA. Chemiluminescence can occur only when the liquid homogeneous flow cell is used; and it could occur when the HPLC mobile phase is mixed with scintillation fluor cocktail prior to continuing on to the flow-cell detector. Chemiluminescence is treated as an interference like background; however, unlike background, chemiluminescence can be eliminated altogether from the sample count rate. The occurrence of chemiluminescence can be tested easily by mixing nonradioactive sample with HPLC eluent through a flow-cell detector and observation of the MCA pulse height spectral output. The chemiluminescence pulses are found in the region of 0–6 keV. For high-energy β emitters (e.g., ^{32}P), this portion of the pulse height spectrum can be excluded from the sample counting region, if chemiluminescence is of concern. When analyzing low-energy β emitters, such as tritium, the chemiluminescence detection and correction, available in the operation setup of the flow scintillation analyzer software (e.g., FLO-ONE), can be enabled.

See Section IV of this chapter, which describes flow scintillation cocktails. Scintillation cocktails are available, which can suppress the occurrence of chemiluminescence.

3. Time-resolved liquid scintillation counting

TR-LSC provides yet a further means of optimizing detection in the flow scintillation analyzer by reducing background. TR-LSC (PerkinElmer, Inc.) is a patented method of reducing backgrounds by discriminating against sample and background pulses by means of counting the number of afterpulses that occur following an initial pulse event (Bhade et al., 2012; Rónai et al., 2006; Mavon et al., 2004). Afterpulses are more numerous in nonquenchable events, which are pulse

events origination from outside the scintillation solution, such as cosmic radiation, which might strike the flow cell or face of one of the PMTs. Quenchable events are pulse events originating in the scintillation fluor cocktail of the flow-cell detector, and these have few if any distinguishable afterpulses. By counting afterpulses, the instrument circuitry and software discriminate between quenchable pulses originating from the scintillation solution in the flow cell and nonquenchable pulses originating from outside the flow cell. The instrument circuitry can, therefore, reject pulses that do not originate from within the flow cell as background radiation. A guard scintillator also surrounds the sample chamber but does not come in contact with the low-energy β emissions originating from within the flow cell. External radiation of cosmic origin or external radiation in the laboratory environment can strike or pass through the scintillator guard. The pulse events occurring from external radiation interactions with the guard detector are nonquenchable pulses, and these have numerous afterpulses compared with sample events in the flow cell. The combination of the scintillator detector guard surrounding the flow cell and TR-LSC results in the virtual elimination of nonquenchable background with a dramatic reduction in background count rate of up to 75%. Typical TR-LSC backgrounds are 2−3 CPM for ^{3}H and 4−5 CPM for ^{14}C with region optimization for these radionuclides.

The combined effect of region optimization and TR-LSC is seen in Fig. 10.19, which illustrates an HPLC run of ^{14}C-labeled drug metabolites. In the upper trace of Fig. 10.19, the counting region (0−156 keV) is not optimized, and TR-LSC is not enabled (background = 30 CPM). Only three activity peaks are discernible. When the counting region is optimized to the highest FOM (E^2/B) by adjusting the LLD and ULD settings to 4−100 keV respectively, and TR-LSC is enabled, the background is reduced to 2 CPM and as many as nine activity peaks can be identified as illustrated in the lower trace of Fig. 10.19. The concept and practice of region optimization is discussed in Chapter 6, Volume 1.

H. Instrument performance assessment

Commercial flow scintillation analyzers are equipped with software and radionuclide standards that will assist the operator in setting up the IPA. The performance of the flow scintillation analyzer can be carried out on a routine basis to provide assurance that the instrument is operating within acceptable parameters and to have a standing record of the instrument performance over a period of time. To maintain good laboratory practice (GLP) and, at times, to satisfy regulatory agencies, it is necessary to have records of the instrument performance on a routine basis, for example, daily, weekly, or monthly, whichever may satisfy our needs

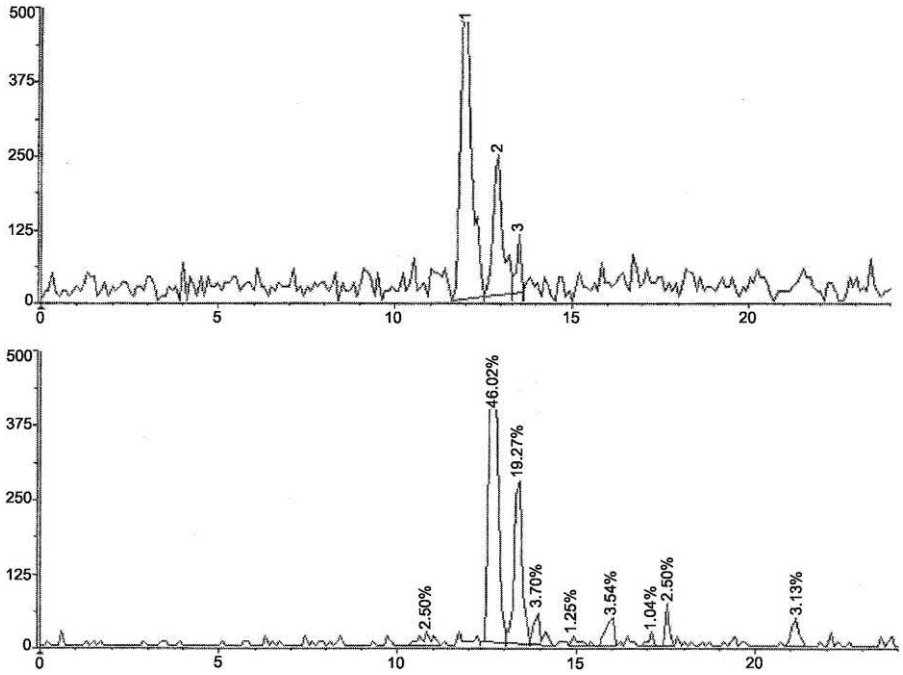


FIGURE 10.19 Flow scintillation analysis trace of ^{14}C metabolites separated via HPLC. (Upper): A wide-open counting region of 0−156 keV is used without TR-LSC background rejection. (Lower): An optimized counting region of 4−100 keV is used with TR-LSC background rejection. [Courtesy of Paul Riska, Boehringer Ingelheim Pharmaceuticals, Inc., Ridgefield, CT.] *From Anonymous (1996), reprinted with permission ©1996 PerkinElmer, Inc. All rights reserved.*

as evidence that deviations in instrument performance do not have any effect on the analytical results. The IPA can be carried out with ^{3}H and ^{14}C and background standards. The radionuclide standards are NIST traceable. The standards are in sealed vials, which can be mounted in a vial holder that duplicates the mounting characteristics of a flow cell.

Eight parameters can be assessed using ^{3}H and ^{14}C standards. These are (1) ^{3}H efficiency, (2) ^{3}H background, (3) ^{3}H FOM, (4) ^{3}H chi-square, (5) ^{14}C efficiency, (6) ^{14}C background, (7) ^{14}C FOM, and (8) ^{14}C chi-square. The parameters are discussed in more detail in Chapter 6, Volume 1. The results are stored and printed in tabular and/or graphic form with a time and date stamp. Data points for each of the above parameters can be stored in memory as a binary file (unchangeable by the user) and plotted. The data can be displayed, stored in computer memory, and printed whenever needed. In any given graph for each of the eight parameters listed above, an average line is calculated as illustrated in Fig. 6.168a of Chapter 6, Volume 1. The one, two, and three sigma values are calculated to help the user evaluate any trends or outlying points. If a value of any of the parameters fails the limits test set for that parameter, a warning message can be received on the computer monitor with suggestions that the user can follow to assess the problem further and to take preventive action if any parameters are obtained too frequently outside of the recommended limits.

IV. Flow scintillator selection

Among the scintillation flow cells described previously in this chapter, the liquid (homogeneous) flow cell is the type most commonly utilized for the detection of low- and intermediate-energy β emitters (e.g., ^{3}H, ^{14}C, ^{35}S, ^{33}P) in HPLC effluents. The popularity of the liquid cell is due to the highest detection efficiencies and absence of adsorption of radionuclide-labeled compounds onto solid scintillator. The latter characteristic is a major concern in the use of solid (heterogeneous) flow cells.

Homogeneous flow-cell counting requires special cocktails. The development and characteristics of modern flow scintillation cocktails are described in reviews by Thomson (1994, 1997) and in Chapter 7, Volume 1. Because the flour cocktail must be added mechanically and mixed readily with the HPLC effluent, it must possess certain physical and performance characteristics. These characteristics outlined by Thomson (1997) are the following:

- Low viscosity
- Rapid and easy mixing with the HPLC eluate
- High sample acceptance capacity
- Compatibility with complex samples and HPLC gradients
- No gel formation
- Good counting performance
- Low background contribution
- Chemiluminescence resistance
- Safe to handle
- High flash point
- Biodegradable

Obviously, not all of these characteristics can always be achieved to the optimum; however, all of these characteristics can be achieved to a certain degree with most circumstances by modern flow scintillation cocktails.

The older generation or classical flow scintillation cocktails, still used by researchers, have relatively low flash points and are less safe to handle. Modern research for improved flow cocktails has provided now safer high-flash-point cocktails, which are biodegradable and capable of mixing readily with a wide range of sample types and gradients used in HPLC. A major advance was the patented development of a flow-scintillation cocktail with the chemical components capable of removing luminescence while simultaneously minimizing background without sacrificing counting efficiency (Hegge and ter Viel, 1986; Thomson, 1993).

Some of the classical flow cocktails, such as the Flo-Scint I, II, III, and IV, are based on pseudocumene or trimethylbenzene solvents with flash points of about 48°C (118°F). Flo-Scint A is compatible with acetonitrile/water gradients, polar organic solvents, and dilute salt solutions. It has a 50% sample holding capacity for aqueous solutions, resistant to chemiluminescence, and nongelling. New-generation flow-scintillation cocktails are readily biodegradable and have a high flash point of 120°C (248°F).

Some of the new generation of flow scintillation cocktails available commercially, their properties and applications, and their suppliers are listed in Table 10.5. The table is not exhaustive, and other flow cocktails and suppliers may exist.

V. Dual-functionality flow-cell detectors

The analysis of radionuclides in the environment or in nuclear process streams generally involves the determination of the activities of radionuclides in an aqueous medium. In environmental analysis, radionuclide activities are generally low and the radionuclides are found in complex mixtures, which require a preliminary chemical cleanup to isolate the radionuclide of interest and preconcentration to achieve limits of detection. Preliminary chemical cleanup is particularly necessary to isolate the radionuclide of interest in the analysis of α- and β-emitting radionuclides, and even γ emitters, to avoid interferences due to the overlap of broad scintillation spectra. Although α particles are emitted with discrete lines of energy, they undergo variable loss of energy as they travel through liquids (see Chapter 1, Volume 1) and display broad scintillation spectra, as discussed

TABLE 10.5 New generation of flow-scintillation cocktails and suppliers.[a]

Flow cocktail	Properties and applications[b]
Flow Safe 2	Compatible with polar solvents and rapid mixing capability with eluates, low odor high flash point (105°C), nontoxic, biodegradable, low chemiluminescence, nonflammable
Flow Plus	Formulated to prevent the formation of gels or a high viscosity liquid stream designed for typical solvent/water gradients and also compatible with solutions of lower ionic strength, nonjellying, low viscosity, low chemiluminescence, low quench
Berthold Technologies: https://www.berthold-bio.com/	
FlowLogic U	Low viscosity and compatible with a wide range of HPLC gradients at a 1:1 ratio; miscible with 0.1N NaOH yielding a clear nonviscous emulsion
FlowLogic HA	Designed for highly aqueous samples with ratios of up to 2:1 scintillator to sample
FlowLogic HS	Formulated to accommodate high salt and buffer samples; biodegradable, low viscosity, and nongelling
SoFieScint	A very-low-viscosity cocktail with high sample uptake capacity, compatible with a wide range of HPLC gradients at a 1:1 ratio, excellent for use with a stop-flow system where very low levels of activity are measured
LabLogic: https://lablogic.com/	
ProFlow G+	Designed for general eluents and water/methanol and water/acetonitrile gradients, safe, high flash point, and free of nonylphenol ethoxylate (NPE) and thus in accord with the EEC directive 2003/53/EC; high flash point (147°C), biodegradable, and can be drain disposed without breaching EEC regulations
ProFlow P+	Designed for eluents with ammonium phosphate gradients, safe, high flash point, and free of NPE and thus in accord with the EEC directive 2003/53/EC; high flash point (147°C), biodegradable, and can be drain disposed without breaching EEC regulations
Meridian Biotechnologies Ltd., http://www.meridian-biotech.com/	
Ecoscint Flow	Designed for aqueous flow samples, biodegradable, high sample holding capacity (1: 1 sample to cocktail) with a wide range of HPLC gradients even 0.1N NaOH samples yield a clear nonviscous emulsion, low viscosity, and non-gelling.
Uniscint BD	Designed to accommodate high salt and buffer samples for HPLC flow measurements; can accommodate all concentrations of ammonium phosphate up to 2M at a 3:1 scintillator to sample ratio accepting ammonium phosphate gradients in the range of 0–2M, biodegradable, high flash point (>150°C), low viscosity, nongelling, reduced toxicity solvent
Monoflow 5	Nonhazardous and biodegradable scintillator with low toxicity useful for HPLC effluents in flow detectors at ratios of 3:1 scintillator to sample; disposable in most cases as a normal liquid waste
Monoflow 1	Designed for organic flow samples; traditional cocktail with high sample holding capacity
National Diagnostics, https://www.nationaldiagnostics.com/	
Ultima-Flo M	Designed for multipurpose flow counting applications with high sample-holding capacity for a wide range of HPLC gradients, including aqueous gradients, water/methanol gradients and water acetonitrile gradients, low viscosity capable of rapid mixing, nongelling, biodegradable and safer cocktail, resistant to chemiluminescence, and high flashpoint (~120°C)
Flo-Scint II	Formulated for polar solvents and dilute buffers yielding good sample holding capacity with low viscosity; a pseudocumene-based flow-scintillation cocktail excellent with methanol and acetonitrile gradients, resistant to chemiluminescence and nongelling
Ultima-Flo AP	Designed to accept up to 2.0 M ammonium phosphate with fast and facile mixing, excellent for use with ammonium phosphate buffers as HPLC eluents with high sample acceptance over entire gradient, other gradients up to 1.0 M PBS and 1.0 M NaOH are easily accepted at good mixing ratios, quench resistant over a wide range of sample types, nongelling, low viscosity, biodegradable and safer cocktail, and high flash point (~120°C)
Flo-Scint III	A classical pseudocumene-based classical flow cocktail designed as an excellent scintillator for methanol and acetonitrile gradients and moderately buffered solutions, including phosphates, resistant to chemiluminescence, and nongelling
Flo-Scint A	A classical pseudocumene-based flow cocktail formulated for acetonitrile/water gradients, polar organic solvents and dilute salt solutions, excellent water-holding capacity up to 50%, resistant to chemiluminescence, and nongelling
PerkinElmer Inc., http://www.perkinelmer.com/	

Continued

TABLE 10.5 New generation of flow-scintillation cocktails and suppliers.[a]—cont'd

Flow cocktail	Properties and applications[b]
ProFlow G+	Designed for general eluents and water/methanol and water/acetonitrile gradients, safe, high flash point, and free of NPE and thus in accord with the EEC directive 2003/53/EC (https://eur-lex.europa.eu/LexUriServ/LexUriServ.do?uri=OJ:L:2003:178:0024:0027:en:PDF, accessed July 2, 2018); high flash point (147°C), biodegradable, and can be drain disposed without breaching EEC regulations
ProFlow P+	Designed for eluents with ammonium phosphate gradients, safe, high flash point, and free of NPE and thus in accord with the EEC directive 2003/53/EC; high flash point (147°C), biodegradable, and can be drain disposed without breaching EEC regulations
Gold Flow	A diisopropylnaphthalene (DIN)-based cocktail for aqueous and organic flow systems, flash point (140°C)
Triskem International, http://www.triskem-international.com/	
Quickzint Flow 302	Recommended for flow cell counting of hydrophilic solvent, such as methanol and acetonitrile aqueous gradients, suitable with low ionic strength aqueous solutions, including buffer gradients, low viscosity, nongelling, flash point (35°C)
Quicksafe Flow 2	Designed as a safe flow cocktail with high flash point (>100°C), has an exceptionally low viscosity, ideal for polar solvents (methanol and acetonitrile) and their aqueous gradients, rapid mixing, nontoxic solvent with low odor
Zinsser Analytic, https://www.zinsser-analytic.com/	

[a]Suppliers are listed in alphabetical order and below the flow cocktails listed that they supply. The list is not exhaustive. Other flow cocktails from the above suppliers are available, and other suppliers not listed may be available.
[b]More detailed information on the properties and applications of the flow cocktails are available from the websites provided.

in Chapters 5 and 6 of Volume 1. Likewise, β particles lose energy according to their path length in water, and they are emitted from radionuclides with a broad spectrum of energies. The scintillation pulse height spectra are broad and will overlap with spectra of other alpha and beta nuclides. Although γ ray photons undergo minimal energy loss when traveling through water, they display broad spectra in scintillator crystal detectors due mainly to Compton scattering. The classical methods of analysis are specific for each radionuclide of interest; they involve specific procedures of sample preparation and cleanup to isolate the radionuclide from other interfering nuclides; they are time-consuming; and they are carried out generally in specific laboratories equipped for such analysis. For over a decade, much research has been focused on the relatively rapid automated radiochemical separation and analysis of radionuclides in the environment, which can be carried out by any laboratory, including mobile on-site laboratories. These procedures are discussed in detail in Chapter 11, Volume 2. The radiation flow-cell detectors or sensors that are utilized in these automated methods will be discussed in this section. The concepts and techniques are provided in more detail in comprehensive papers by Trojanowicz et al. (2018), Watson et al. (2018), Duval et al. (2016a), Seliman et al. (2013), Grate et al. (2005, 2008), and Fjeld et al. (2004), and additional information may be obtained from Chapter 11, Volume 2. These radionuclide flow detectors are classified into two types (Fjeld et al., 2004), which are the following:

(1) A flow radiation detector simultaneous with radionuclide separation or *dual-functionality* detector. This type of detector would contain a scintillating extraction chromatographic resin or a combination of scintillating beads and selective extracting chromatographic resin within a flow cell, which is capable of concentrating the radionuclide of interest. Such a flow radiation detector has a dual functionality, that is, it enables the simultaneous concentration and detection of the radionuclide of interest. An illustration of the principal of dual functionality in a flow cell is illustrated in Fig. 10.20,

(2) A flow radiation detector sequential to radionuclide separation. This type of detector would be a flow cell, which would detect and analyze the radionuclides after they are separated by ion chromatography.

The first of the two detector types listed above is recognized as a very sensitive detector for the preconcentration and analysis of α- and β-emitting radionuclides in water, and these are referred to as preconcentrating mini-column radionuclide sensors or detectors. A schematic

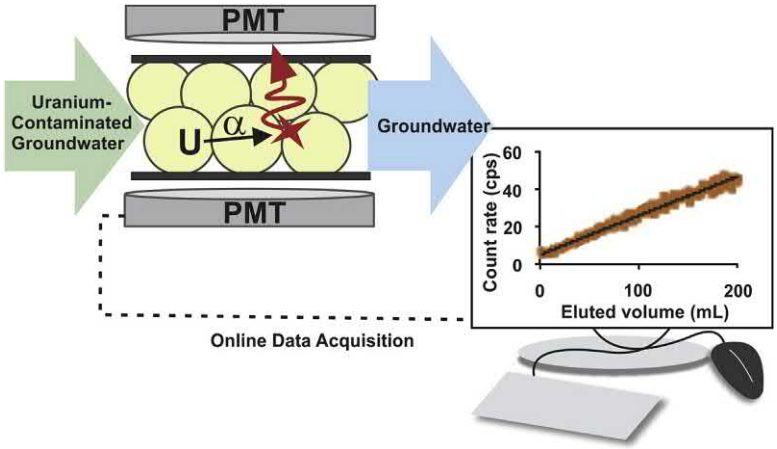


FIGURE 10.20 A dual-functionality flow-cell detector. The flow cell contains an extractive scintillating resin, which contains covalently bound fluor and ligand. Uranium in groundwater at low activity near the limits of detection is made to pass through the flow cell. The uranium binds to the scintillating resin and concentrates within the flow cell where it is counted with an activity well above the limits of detection. *From Duval et al. (2016a); reprinted with permission from Elsevier © 2016.*

diagram of such a flow cell is illustrated in Fig. 10.21. It is a dual-functionality column, as the column contains a selective sorbant or chromatographic resin capable of concentrating the radionuclide of interest, and it contains a scintillator embedded within the selective sorbant or resin or in intimate contact with it, thereby serving the dual purpose of concentrating the radionuclide and its detection. One of the major advantages of a dual-functionality flow-cell detector is the capacity of analyzing relatively large volumes of sample (up to a liter of water in some circumstances) whereby the radionuclide of interest is concentrated on an extractant in the flow detector, and at the same time, it is detected by the scintillator with which the extractant is in intimate or close contact. The concentration of radionuclide in this fashion permits the analysis of low levels of radionuclides in water below the limits set for drinking water standards, and it permits the analysis in situ or in the field without the need for a specialized laboratory. These detectors and the theory and principles of their operation and application are reviewed in detail by Trojanowicz et al. (2018), Watson et al. (2018), Duval et al. (2016a), Seliman et al. (2013), and Grate et al. (2008). The subsequent paragraphs will describe the various types of dual-functionality flow-cell detectors used in radionuclide analysis.

A. Scintillating extractive resins

A scintillating extractive resin consists of an intimate combination of a scintillator medium and an ion selective absorbent medium (extractant) on a solid support (e.g., macroporous styrenic polymer) packed into a single

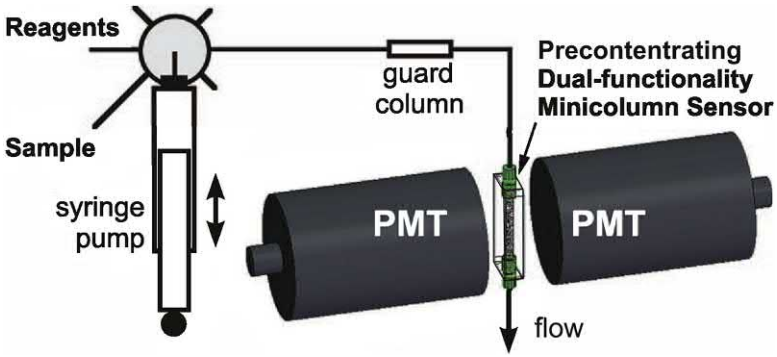


FIGURE 10.21 Preconcentrating minicolumn radionuclide detector based on dual-functionality materials in a preconcentrating minicolumn sensor. The sensor consists of a transparent flow cell containing a packed bed of dual-functionality materials placed between two photomultiplier tubes. The column may also be a coil within the detection zone. The sensor assembly is shown connected to an automatic fluidic system. The guard column contains hydroxylapatite to absorb organic matter. *From O'Hara et al. (2009a); reprinted with permission © 2009 American Chemical Society.*

TABLE 10.6 Scintillating extractive resins for flow-cell minicolumn sensors.

Fluor or scintillator	Extractant	Support	Analyte	Reference
PPO, bis MSB	Aliquat 336	Macroreticular acrylic polymer	^{99}Tc	Egorov et al. (1999b), DeVol et al. (2001a)
PPO, DM-POPOP	Aliquat 336	Macroporous styrenic polymer	^{99}Tc	DeVol et al. (2000, 2001a)
α-NPO	Aliquat 336	Macroporous styrenic polymer	^{99}Tc	Ayaz and DeVol (2003)
PPO, 9,10-diphenylanthracene	MnO_2	Polyvinyltoluene	U	Ayaz and DeVol (2003)
PPO, DM-POPOP	"ABEC" Me-PEG-2000	Macroporous styrenic polymer	^{99}Tc	DeVol et al. (2000, 2001a)
PPO, bis MSB	HDEHP	Macroreticular acrylic polymer	^{90}Sr	Egorov et al. (1999b)
PPO, DM-POPOP	Crown ether DtBuCH18C6	Macroporous acrylic polymer	^{90}Sr	DeVol et al. (2001b)
PPO, DM-POPOP	Crown ether DtBuCH18C6	Macroporous styrenic polymer	^{90}Sr	DeVol et al. (2000, 2001b)
PPO, DM-POPOP	CMPO/TBP	Macroporous styrenic polymer	Actinides	DeVol et al. (2000), Roane and DeVol (2002, 2005), Fjeld et al. (2004)
PPO, DM-POPOP	CMPO/TBP	Macroporous acrylic polymer	Actinides	DeVol et al. (2000)
α-NPO	H2DEH[MDP]	Macroporous styrenic polymer	Actinides	Hughes and DeVol (2003)
PPO, 9,10-diphenylanthracene	H2DEH[MDP]	Polyvinyltoluene	Actinides	Hughes and DeVol (2003)
GS-20 scintillating glass	H2DEH[MDP]	GS-20 scintillating glass	Actinides	DeVol et al. (1997, 2000)
GS-20 scintillating glass	Crown ether DtBuCH18C6	GS-20 scintillating glass	^{90}Sr	DeVol et al. (1997, 2000, 2001b)
α-NPO[a]	TEA, MDOA bonding	Chloromethyl polystyrene	^{99}Tc	Seliman et al. (2011)
α-NPO[a]	MDOA bonding	Chloromethyl polystyrene	^{129}I	Grogan and DeVol (2011)
TBut-PBD[a]	Copolymerization of fluor with styrene and other aromatics followed by amination reactions to form anion exchange resin		^{99}Tc	Seliman et al. (2013)
DM-POPOP	Copolymerization of fluor molecules with polystyrene and poly(4-methylstyrene)		α,β emitters	Bliznyuk et al. (2015)
v-NPC, α-NPO, allyl-NPO[a]	Copolymerization of fluor molecules with methylstyrene and divinylbenzene followed by chemical formation of ligands		^{99}Tc	Seliman et al. (2015)
v-NPO[a]	Copolymerization of fluor molecules with methylstyrene followed by uranium-binding functionalization of resin or methylphosphonic ligand		U	Duval et al. (2016a,b)
α-NPO, v-NPO[a]	Copolymerization of fluor molecules with methylstyrene or poly(4-methylstyrene)		α,β emitters	Duval et al. (2016c)
Scintillator[a]	SuperLig®620 solid phase extractant		^{90}Sr	Seliman et al. (2017)
v-NPO[a]	Copolymerization of fluor molecules with methylstyrene followed by functionalization of resin with anion exchange ligand		^{99}Tc	Watson et al. (2018)

[a]*Added by the writer to the original table.*
From Grate et al. (2008); reprinted with permission © 2008 American Chemical Society.

column of tubing (e.g., Teflon tubing of ~0.15 cm ID and up to ~15 cm length). Other dimensions are used, and these are available from the references cited in this section. The tubing can be coiled into a loop (~2.5 cm dia.) to fit optimally in the detection region of the two photomultipliers. Other shapes (e.g., U-shaped tubing) are used. The minicolumn of tubing can be inserted into a suitable holder between the PMTs of a commercial flow scintillation analyzer (FSA). See Table 10.6 for a listing of various scintillating extractive resin formulations tested for the environmental analysis of various radionuclides.

The intimate combination of scintillator and extractant is prepared by several techniques, which may include, for example, the diffusion of scintillator into macroporous polymer beads followed by polymer coating. The coating provides physical and chemical stability to the combined scintillator and polymer. Subsequent to the polymer coating, residual chloromethyl groups of the polymer-coated resins are aminated, which provides a chemically stable scintillating resin with covalently bound ligand groups (Seliman et al., 2011). Alternatively, the resin may be synthesized to provide for a combination of extractive and scintillating properties via a sequence of copolymerization reactions of fluor molecules with polymer substrate (e.g., methyl styrene) together with chemical transformation of molecular groups to provide extractive power (i.e., ion exchange ligands) to the resin (Watson et al., 2018; Duval et al., 2016a; Seliman et al., 2013). Procedures used for the preparation of the various types of scintillating extractive resins are available from the references cited in Table 10.6.

It is important that the scintillating extractive resin have a capacity to selectively absorb the radionuclide of interest even in waters of relatively high ionic strength. In synthetic groundwater (GW) containing 33 Bq/L of ^{99}Tc (the US maximum contaminant level encountered in waters as pertechnetate, $^{99}TcO_4^-$) at elevated anion concentrations of 100 and 250 ppm Cl^-, NO_3^-, SO_4^{2-}, and HCO_3^-, and 1200 ppb Cr(VI), Seliman et al. (2011) demonstrated the linear response of triethylamine (TEA) and methyldioctylamine (MDOA)-bonded scintillating resins to the application of various volumes of the groundwater. Following the synthesis of new dual-functionality anion exchange resins via the copolymerization of fluor molecules with styrene and other aromatics together with amination reactions to form an anion exchange resin, Seliman et al. (2013) demonstrated the selective property of the resin for $^{99}TcO_4^-$ over up to 1000 ppm of potentially interfering anions such as Cl^- and $Cr_2O_7^{2-}$, among others in natural freshwaters with constant flow-cell counting efficiency.

An important property of scintillating extractive resins used for flow cells is that they retain their detection response (i.e., scintillating property) even after repetitive use. The detection response to the scintillating extractive resins prepared by Seliman et al. (2013) was tested as a function of the successive loading of different well water samples without regeneration. The response of the extractive resin in a flow cell to successive column loadings with various activities of ^{99}Tc

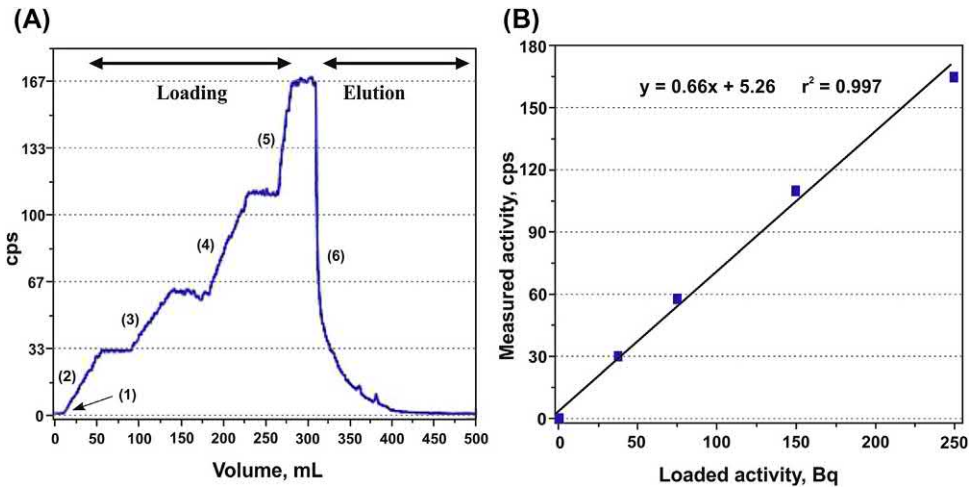


FIGURE 10.22 Optical flow-cell detector response to the scintillating extractive resin with the retention of pertechnetate ($^{99}TcO_4^-$) standards in well water matrix, using the following successive loading technique: (A) Data were obtained by pumping at 0.75 mL/min flow rate of (1) 15 mL of blank sample; (2) 50 mL of 37.5 Bq ^{99}Tc; (3) 50 mL of 37.5 Bq ^{99}Tc (total 75 Bq); (4) 50 mL of 75 Bq ^{99}Tc (total 150 Bq); (5) 50 mL of 100 Bq ^{99}Tc (total 250 Bq); and (6) elution by 200 mL 5 M nitric acid after pumping 50 mL of blank sample. (B) Resulting calibration curve from the responses. Numbering (1) to (6) in Fig. 10.22A was added by the writer to identify the responses to the successive sample and elution loadings. *From Seliman et al. (2013); reprinted with permission from Elsevier © 2013.*

and various quantities of anions is illustrated in Fig. 10.22A and B. The linearity of response of the scintillating extractive resin after successive analysis of natural waters with varying radionuclide activities and anion concentrations is a crucial test for the applicability of these resins to satisfy practical analytical requirements. An example is illustrated in Fig. 10.22A and B where the extraction capacity and scintillating response is illustrated to remain with a linear correlation coefficient ($r^2 = 0.997$ of Fig. 10.22B) and flow-cell detection efficiency constant (66%) after successive loadings with increasing ^{99}Tc activities and anion concentration (loadings 1 through 5 of Fig, 10.22A).

The application of scintillating extractive resins to quantitatively concentrate low levels of radionuclides over and above limits of detection and in solutions, such as natural groundwater and well water containing competitive ions, must be demonstrated, such as that described above for ^{99}Tc. Another example is the testing of a scintillating extractive resin for uranium in simulated groundwater by Duval et al. (2016a), with the continuous pumping of ^{233}U at a concentration of 50 Bq/L through a flow-cell detector containing the scintillating extractive resin. Fig. 10.23 illustrates the linear response of the flow-cell detector to the accumulated activity of ^{233}U with a flow-cell detection efficiency of 17% and the continuous pumping of up to 500 mL of water with a total ^{233}U activity of 25 Bq. Similar testing of a scintillating extractive resin to concentrate a total activity of only 6.6 Bq of $^{99}TcO_4^-$ in 200 mL of well water by Seliman et al. (2013), which is equivalent to a concentration of 33 Bq/L, is illustrated in Fig. 10.24. The concentration of $^{99}TcO_4^-$ on the scintillating resin accumulates the activity in the flow cell to levels well above the detection limit (DL) of the flow-cell detector for ^{99}Tc. Such a test demonstrates the practicality of the method because the US maximum contaminant level (MCL) of $^{99}TcO_4^-$ in well water is reported to be 33 Bq/L.

Several radionuclides have been analyzed with the dual-functionality scintillating extractive resins in flow-cell detectors, and these are listed in Table 10.6. The detection efficiencies obtained depend on α and β emission of the radionuclide, the scintillation extractive resin used, and the flow detector design. Some examples of detection efficiencies obtained for various radionuclides are the following:

- **(i)** ^{nat}U, 60%*E* (DeVol et al., 1996; Ayaz and DeVol, 2003; Hughes and DeVol, 2003);
- **(ii)** ^{89}Sr, 60%*E* (DeVol et al., 2001b); ^{90}Sr, 46%*E* and ^{90}Y, 99%*E* (Egorov et al., 1999b);
- **(iii)** ^{99}Tc, 66%*E* (Egorov et al., 1999b, DeVol et al., 2001a, DeVol et al., 2002, Ayaz and DeVol, 2003 and, Seliman et al., 2011, 2013);
- **(iv)** ^{129}I, 50%*E* (Grogan and DeVol, 2011);
- **(v)** ^{233}U, 97%*E* (Roane and DeVol, 2002; Duval, 2016a);
- **(vi)** ^{239}Pu, 78%*E* (DeVol et al., 1997; Roane and DeVol, 2002); and
- **(vii)** ^{241}Am, 97%*E* (Hughes and DeVol, 2003 and Roane and DeVol, 2002, 2005).

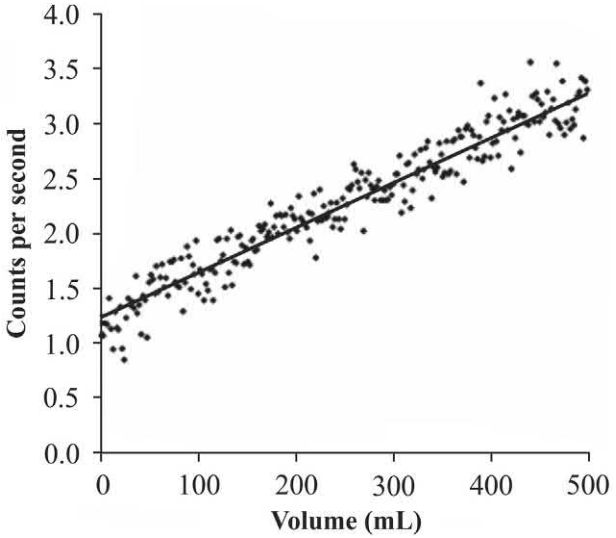


FIGURE 10.23 Simultaneous concentration and detection of uranium-233 at a concentration of 50 Bq/L from groundwater by a flow-cell detector containing a scintillating extractive polymer. *From Duval et al. (2016a); reprinted with permission from Elsevier © 2016.*

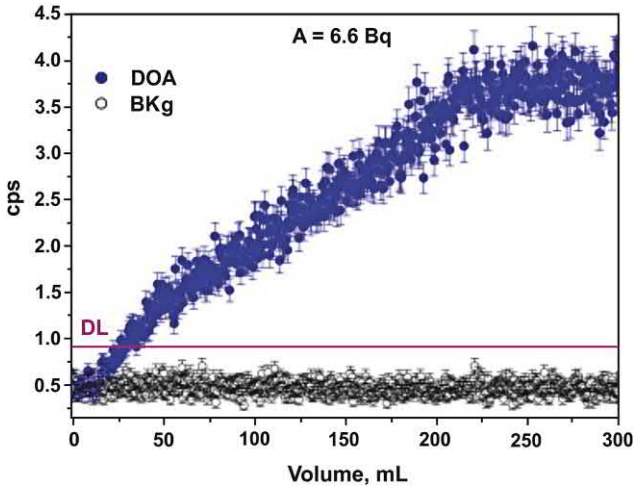


FIGURE 10.24 Online quantification with a scintillating extractive resin (synthesized with amination reaction with dioctylamine, DOA) in a U-shaped flow cell using 200 mL of acidified well water containing 33 Bq/L of $^{99}TcO_4^-$ and a total activity A = 6.6 Bq on the resin. The magenta-colored horizontal bar indicates the detection limit (DL). Color is visible in the electronic version of the book. *From Seliman et al. (2013); reprinted with permission from Elsevier © 2013.*

An advantage of the dual-functionality resins is the capability in many circumstances to concentrate and analyze radionuclides at or below the limits set for drinking water standards.

Other scintillating extractive resins have been prepared by Barrera et al. (2016) for the extraction and concentration of ^{99}Tc in seawater and urine and by Lluch et al. (2016) for the extraction of ^{210}Pb from river water. The techniques are demonstrated to be practical; however, off-line LS analysis was used rather than online real-time measurements.

B. Composite bed of scintillating and extracting particles

The composite-bed scintillating dual-functionality column detector consists of a composite heterogeneous mixture of scintillating particles and chemically selective particles. The dual functionality of radionuclide concentration and detection is achieved with an intimate mixture of separate extraction beads and nonporous scintillating beads (Grate et al., 2005, 2008). The mixture of beads is packed into fine inert tubing (e.g., ~1.6 mm I.D. × ~ 140 mm long) coiled into a loop to a diameter of ~2.5 cm and placed between PMTs of a flow-cell radiation detector. The minicolumn of fine tubing can be inserted into a suitable holder between the PMTs of a commercial flow scintillation analyzer (FSA) among those listed previously in Table 10.2. See Table 10.7 for the composition of the various combinations of scintillating particles and chemically selective particles applied to the analysis of various radionuclides.

The scintillating component in the mixed beds is, in most cases, Bicron BC-400 (see Table 10.7), which consists of 100–250 μm scintillating plastic (polyvinyltoluene) beads. These beads are nonporous, and they have a high chemical stability in sample solutions and regeneration reagents. The stability of these beads offers the advantage of constant detector response after repetitive use, as there is no possibility of fluor loss from the column. The composite bed of intimately packed extraction and scintillating beads is an excellent arrangement for the detection of radionuclides that emit β particles of intermediate and high energy, such as ^{99}Tc ($E_{max} = 0.249$ MeV), ^{90}Sr ($E_{max} = 0.546$ MeV), and ^{90}Y ($E_{max} = 2.28$ MeV). If we consider ^{99}Tc, which emits β particles of lower energy among the three radionuclides listed, it emits β particles with an energy maximum of 0.249 MeV; however, according to the distribution of β particle energy spectra in general, there are very few β particles that possess the maximum energy (see Fig. 1.45 of Chapter 1, Volume 1). In general, most beta particles are emitted at approximately ⅓ E_{max}. The range of the β particles of highest energy (0.249 MeV) emitted by ^{99}Tc in water is 740 μm, found on the range-energy curve of Fig. B.3 of the Appendix, However, considering that most of the β particles are emitted with an average energy of approximately ⅓E_{max} or 0.098 MeV, these β particles would have a range in water of ~150 μm, according to the range-energy curve of Fig. B.3 of Appendix B.3 of this book. The range of the β particles in the plastic BC-400 scintillating beads (1.03 g/cm^3) would be similar to that of water (1.00 g/cm^3), as their densities are very close. The ~150 μm range for the average number of ^{99}Tc β particles and a maximum range of 740 μm for β particles of highest energy from ^{99}Tc assure that a large proportion of the β particles emitted by

TABLE 10.7 Composite-bed minicolumn sensors.

Scintillator	Selective chemistry	Solid phase	Analyte	References
BC-400	Aliquat 336	TEVA resin	^{99}Tc	DeVol et al. (2000, 2001a)
BC-400	crown ether DtBuCH18C6	Sr-resin	^{90}Sr	DeVol et al. (2001b)
GS-20	crown ether DtBuCH18C6	Sr-resin	^{90}Sr	DeVol et al. (2001b)
BC-400	H2DEH[MDP]	Actinide resin	actinides	Hughes and DeVol (2003)
Yttrium silicate (YSO)	H2DEH[MDP]	Actinide resin	actinides	Hughes and DeVol (2003)
BC-400	Anion exchange, strongly basic	AGMP1	^{99}Tc	Egorov et al. (2002, 2004a,b) and Grate et al. (2005)
BC-400	Anion exchange, weakly basic	AG 4-X4	^{99}Tc	Egorov et al. (2005a,b, 2006)
BC-400	SuperLig 620 solid-phase extraction material	Silica gel–based solid-phase extraction material	^{90}Sr	Egorov et al. (2004a,b)

From Grate et al. (2008); reprinted with permission © 2008 American Chemical Society.

^{99}Tc, adhered to the chemically selective resin particles, will have sufficient energy to reach and penetrate the 100−250 μm scintillator beads with which they are closely packed in the minicolumn of the flow detector.

The composite bed method facilitates the use of existing extraction chromatographic, ion exchange, or solid-phase extraction materials used for the chemically selective sorbent component of the mixed bed (see Table 10.7), as described by Grate et al. (2008). Also, other radionuclides present in the samples do not interfere with the proper chemically selective sorbent component of the mixed bed. For example, tests with the addition of ^{137}Cs, ^{90}Sr, and ^{239}Pu as interfering nuclides resulted in transient activity peaks that present, after washing, no interference in the measurement of ^{99}Tc (Grate et al., 2008). Detection efficiencies obtained with the composite-bed dual-functionality method for various radionuclides are the following: ^{89}Sr, 81%*E*; ^{90}Sr, 47%*E* (DeVol et al., 2001b); ^{90}Sr, 63%*E* (Egorov et al., 2006; Grate et al., 2008); ^{99}Tc, 34%*E* (DeVol et al., 2001a, and Egorov et al., 2002); and ^{237}Np, 5.6%*E* (Hughes and DeVol, 2003). The lower detection efficiency achieved for ^{237}Np is due to the shorter range of travel in water of the α particles emitted by ^{237}Np compared with β particles. Another advantage of the composite-bed minicolumn detector is the ^{99}Tc(VII) selective composite bed can be regenerated with a small volume of 2 M HNO_3, resulting in a rapid elution of the ^{99}Tc(VII) without loss of the scintillation properties of the composite bed (Egorov et al., 2002, 2003; Grate et al., 2008). The measurement of ^{99}Tc(VII) in groundwater below the regulatory drinking water level of 33 Bq/L has been demonstrated with a prototype groundwater probe device that integrates the flow-cell detector, data acquisition, and instrument control components in a single functional instrument (Egorov et al., 2005a).

C. Equilibrium-based bed

The equilibrium-based dual-functionality flow cell consists of a composite bed of scintillating particles and chemically selective particles (e.g., 1:4 w/w ratio of AG 4-X4:BC-400 or 1:1 w/w ratio of SuperLig 620:BC-400) packed into a minicolumn (e.g., 4 mm I.D. × 29 mm length). The column may be contained in Teflon tubing (Grate et al., 2007), or it may be machined in a block of Bicron BC-800 (Saint-Gobain Crystals), which is cast from ultraviolet transparent methyl methacrylate monomer (Egorov et al., 2006; O'Hara et al., 2009a). The column dimensions machined in the block are the same as with Teflon tubing (i.e., 4 mm I.D. × 29 mm length) providing a bed volume of 0.365 cm^3. The block with column is fitted into a PerkinElmer TR Radiomatic flow scintillation analyzer.

The operation of the equilibrium-based detection functions when the sensing material in the column achieves equilibration with the analyte concentration in solution, that is, the analyte concentration exiting the column is the same as the analyte concentration entering the column. The impetus behind the development of this new technique is the search for "reagentless" measurements, that is, the possibility of repetitive analysis without the need to use reagents to regenerate the detector column after each analysis.

The principle and theory behind the operation of the equilibrium-based dual-functionality flow-cell detector is described by Grate et al. (2005, 2007, 2008, 2009), Egorov et al. (2006), and O'Hara and Nivel (2014) and O'Hara et al. (2009a). In brief, the method is based on the chromatography principle where the magnitude of analyte

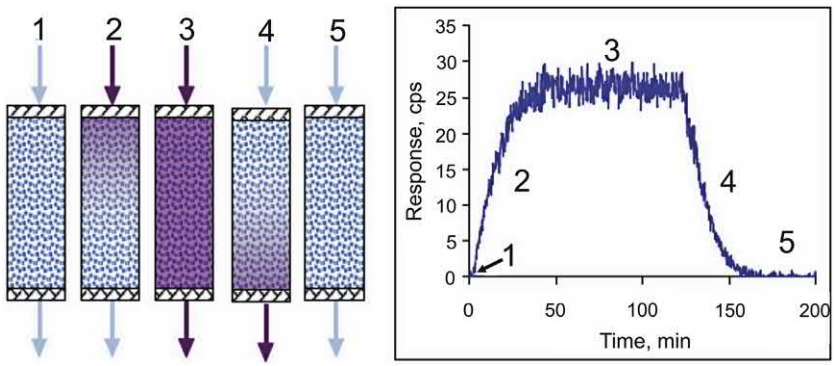


FIGURE 10.25 Equilibrium sensing conceptual schematic showing inflow of a β emitter in groundwater (left) and simultaneous sensor response to β decay events (right). The following steps are depicted: (1) groundwater containing no above-background radionuclide enters and exits the column, (2) groundwater contaminated with a beta-emitting radionuclide enters the column, (3) the groundwater contaminated with a beta-emitting radionuclide enters and exits the column where the activity of the radionuclide entering and exiting the column is equal, (4) groundwater containing no above-background radionuclide enters the column, and (5) the groundwater containing no above-background radionuclide enters and exits the column resulting in the elution of all of the analyte radionuclide from the sensor, once again returning the column to the background condition of step 1. *Figure from O'Hara and Niver (2014), https://www.pnnl.gov/main/publications/external/technical_reports/pnnl-23131.pdf.*

retention on the column sorbent beads is a function of the analyte distribution coefficient, D, defined as

$$D = C_s/C_a \tag{10.27}$$

where C_s is the equilibrium analyte concentration in the sorbent layer (stationary phase) and C_a is the equilibrium analyte concentration in the aqueous (mobile) phase (Grate et al., 2005). The method entails delivering the water sample to the column until complete breakthrough has occurred. Complete breakthrough exists when an equilibrium concentration occurs throughout the entire length of the column. This occurs when no additional analyte preconcentration of the sorbent in the column is possible, and the concentration of analyte added to the column is the same as that exiting the column. The principle is illustrated in Fig. 10.25.

This approach to the analysis of radionuclides has the following key features, which are reviewed by Grate et al. (2008): (1) the response of the detector is a steady state once the sorbent phase is equilibrated, (2) the response varies with the analyte activity or concentration, and (3) reversibility of the response can occur because it is based on a dynamic equilibrium. The variable response is observed when an analyte of different activity or concentration is added to the column because the analyte will reequilibrate and the detector response will increase or decrease according to the new activity. Likewise, if the sample is a blank containing no analyte, the detector signal will drop as if the column were regenerated with a reagent (Grate et al., 2008; O'Hara and Niver, 2014, See Fig. 10.25). Thus, in principle, the equilibrium-based method requires no chemical reagents.

A typical minicolumn assembly for the equilibrium-based analysis of ^{99}Tc in groundwater as the pertechnetate anion ($^{99}TcO_4^-$) is illustrated in Fig. 10.26. The sensor module designed by O'Hara and Niver (2014) consists of a syringe pump (not illustrated) driven by a step motor to deliver sample to the ^{99}Tc sensor inlet line. The ^{99}Tc sensor inlet is affixed with a 13 mm diameter, 2.7 μm glass microfiber filter disc to ensure no particulate matter is transported to the inlet frit of the ^{99}Tc sensor. The sensor is housed in a light tight canister situated between two PMTs to produce coincidence counts for background discrimination. The column body is composed of a heterogeneous mixture of selective sorbent media (orange dots of Fig. 10.26) and organic scintillating particles (green dots). The column is enclosed at both sides with quartz windows (blue windows in Fig. 10.16), which are transparent to UV and visible photons. At both sides of the windows, two PMTs fit within a crevice to capture the photons emitted by the minicolumn sensor. The column is packed with a mixture of a strong anion exchange resin (Toyopearl QAE-550C, 50−150 μm particle size) and BC-400 scintillating beads (250−500 μm particle size) in a ~0.13:1, v/v ratio.

The method can be applied to the measurement of ^{99}Tc and ^{90}Sr in groundwater at levels below the MDA limits required for water quality. Various responses to a ^{99}Tc equilibrium-based flow-cell detector are illustrated in Fig. 10.27. As underscored by Grate et al. (2008), the

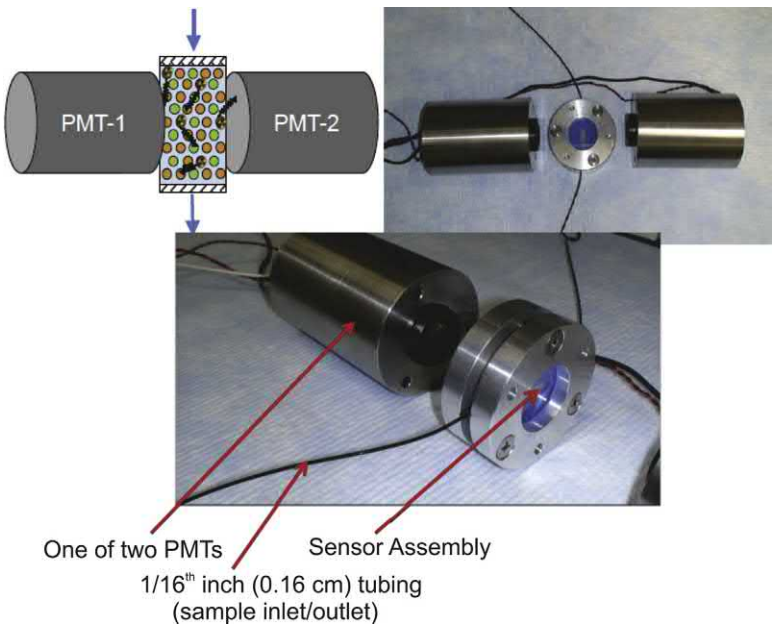


FIGURE 10.26 Schematic of minicolumn sensor (top left). Photos of equilibrium sensor (partially disassembled) for ^{99}Tc monitoring are shown in top right and bottom. *From O'Hara and Niver (2014), https://www.pnnl.gov/main/publications/external/technical_reports/pnnl-23131.pdf.*

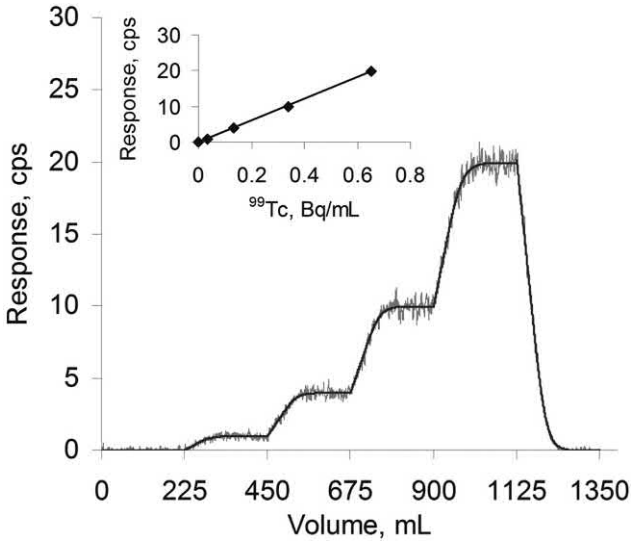


FIGURE 10.27 Responses of a composite bed (1:4 w/w ratio AG 4-X4:BC-400) preconcentrating minicolumn sensor to samples at increasing activities of ^{99}Tc standards (in 0.01 M nitric acid) in the pertechnetate form, followed by a final blank sample. The data were obtained by delivering 225-mL aliquots of the following solutions at 2-mL/min syringe pump flow rate: (1) blank sample, (2) 0.033 Bq/mL, (3) 0.13 Bq/mL, (4) 0.34 Bq/mL, (5) 0.65 Bq/mL, (6) blank sample. The calibration curve (slope 30.4 counts (Bq/mL)) from the average equilibrium count rate is shown in inset. The activity of the lowest level standard is equivalent to the drinking water standard for ^{99}Tc. *From Egorov et al. (2006); reprinted with permission © 2006 American Chemical Society.*

response of the equilibrium-based detector, illustrated in Fig. 10.27, manifests the three key features of the method described in the previous paragraphs, namely, (1) steady-state responses are obtained while pumping 225-mL samples through the column, (2) the detector response level and the calibration curve in the inset of Fig. 10.27

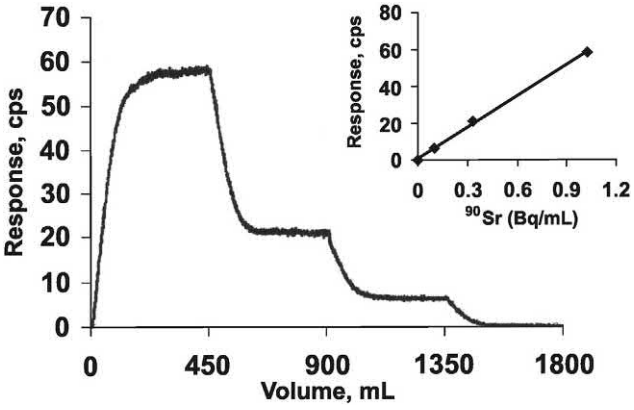


FIGURE 10.28 Responses of a ^{90}Sr equilibrium-based detector consisting of a mixed bed (1:1 w/w ratio of SuperLig 620:BC-400) to ^{90}Sr standards in Hanford groundwater acidified to pH ~2.1 with nitric acid: (1) 1.02 Bq/mL; (2) 0.33 Bq/mL; (3) 0.10 Bq/mL; (4) blank sample. *From Egorov et al. (2006); reprinted with permission © 2006 American Chemical Society.*

illustrate how the detector signal varies with the sample activity, and (3) the final blank sample shows how the detector response drops to zero demonstrating the reversibility of the response.

In the case of ^{90}Sr analysis, the solid-phase extraction sorbent consisted of SuperLig 620, which is a silica support with covalently bound crown ether ligands. The column bed consists of a 1:1 w/w mixture of SuperLig 620 with BC-400 scintillating plastic beads. When groundwater acidified to a pH of 2 is passed through the column bed, the sorbent component will retain the ^{90}Sr, whereas the ^{90}Y passes through unretained. The responses of the equilibrium-based column to 450-mL sample volumes of acidified groundwater containing ^{90}Sr are illustrated in Fig. 10.28. The figure illustrates the repetitive and linear lower response of the detector to lower activities of ^{90}Sr pumped through the column.

The detection efficiencies with the equilibrium-based flow detectors designed for ^{99}Tc and ^{90}Sr are reported to be 38% and 63%, respectively (Egorov et al., 2006; Grate et al., 2007, 2009; O'Hara et al., 2009a). The technique has been demonstrated for the measurement of ^{99}Tc in groundwater via a sensor probe in well bore holes (Grate et al., 2008), and there is no reduction or change in flow detector response after testing with numerous samples. As described by O'Hara and Niver (2014), the net (background subtracted) sensor count rate is converted to radionuclide activity per unit volume (A_{Tc}, Bq/mL) according to the equation:

$$A_{Tc} = \frac{R_{eq}}{E_m} \tag{10.28}$$

where R_{eq} is the net count rate (cps) of the sensor at equilibrium with ^{99}Tc, and E_m is the measurement efficiency in units of cps/(Bq/mL). They note that in situations of analyzing groundwater where the chemistry (i.e., distribution of anions) can change over time, it is necessary to utilize the method of matrix spike in addition to determining the measurement efficiency according to the equation:

$$E_m = \frac{R_{eq,sp} - \left(\frac{V_s - V_{sp}}{V_s}\right) R_{eq}}{A_{matrixsp}} \tag{10.29}$$

where $R_{eq,sp}$ is the net count rate of the spiked sample (i.e., sample spiked with radionuclide standard) at equilibrium, R_{eq} is the net count rate of the unspiked sample, V_s is the sample volume, V_{sp} is the volume of the ^{99}Tc spike, and $A_{matrixsp}$ is the activity of the ^{99}Tc matrix spike in the mixed sample. The value of $A_{matrixsp}$ is calculated according to

$$A_{matrixsp} = \frac{A_{sp} V_{sp}}{V_s} \tag{10.30}$$

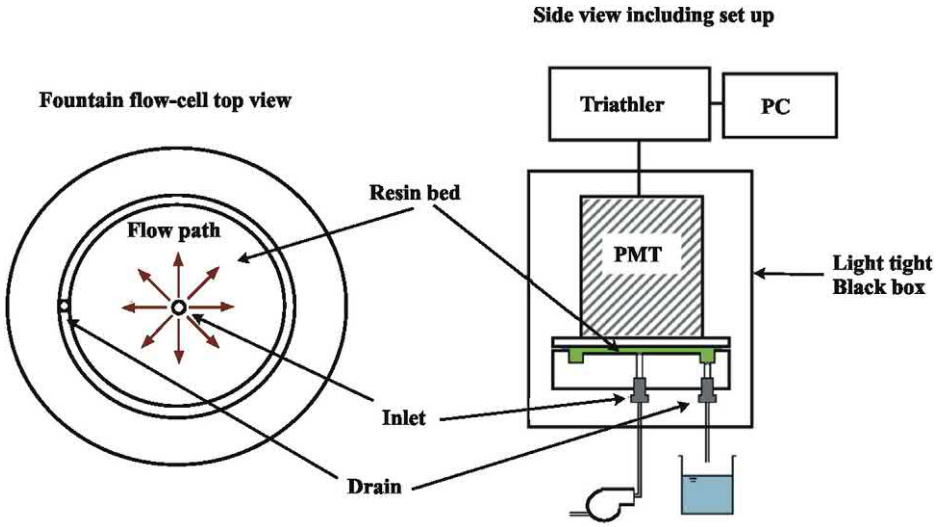


FIGURE 10.29 Planar fountain flow cell schematic and setup with PMT, Triathler counter, personal computer, and pump for a dual-functionality preconcentrating radiometric detector. The left image illustrates the radial solution flow through a packed resin bed. *From Hughes and DeVol (2006a); reprinted with permission © 2006 American Chemical Society.*

D. Planar mixed-bed flow cell

A fountain-flow cell design based on a radial solution flow through a mixed dual-functionality resin bed of inorganic scintillator particles (CaF_2:Eu) and anion exchange resin (Dowex 1 × 8−400(Cl^-)) was designed by Hughes and DeVol (2006a). The flow is directed from the center of the mixed scintillator and resin bed to the periphery. The dual-functionality mixed bed is interfaced with a single PMT through a polycarbonate window as illustrated in Fig. 10.29. The mixed bed was operated in a quantitative-capture mode rather than the equilibrium-based mode described in the previous Section C. The capture efficiency of the resin for ^{99}Tc was greater than 98%, and the detection efficiency was 50.2%. A flow cell with a coil geometry containing the same mixed bed yielded the highest sensitivity with a detection limit of 3.78 Bq/L for a 100 seconds count time and a 200-mL sample, which is well below the regulatory level of 33 Bq/L for drinking water (Hughes and DeVol (2006a). The planar cell geometry offers several advantages, including effective capture and reasonable detection efficiency, flexibility in the geometry of the selective and transducing materials, and the possibility of placing a permeable membrane between the sample and the separation/transducing materials allowing diffusion of the sample ions to the mixed bed while stopping suspended particles (Grate et al., 2008).

E. Planar detectors based on semiconductor diodes

The planar dual-functionality flow-cell detectors may have the following design formats: A planar detector with bis(2-ethylhexyl)phosphonic acid (HDEHP) extractant and plasticizer in a PVC film on the surface of a passivated ion-implanted planar silicon (PIPS) semiconductor diode (Egorov et al., 2004a,b and Addleman et al., 2005) or preconcentration of analyte on Dowex 1x8-400(Cl^-) anion

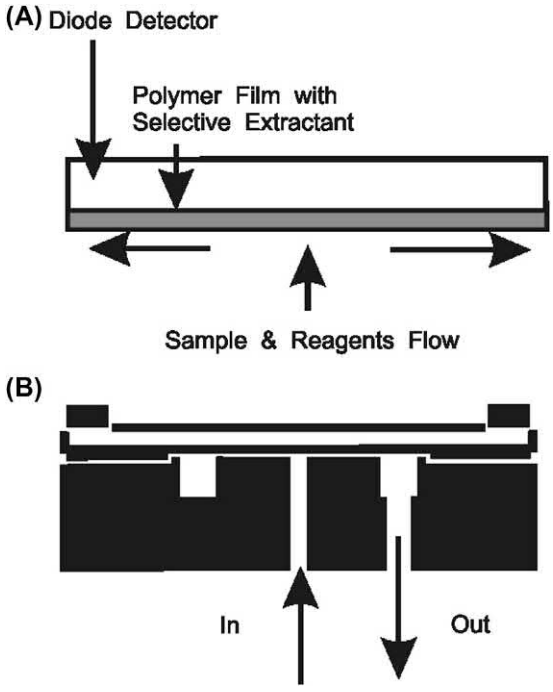


FIGURE 10.30 Preconcentrating diode flow detector modified (A) with analyte selective film, and (B) schematic of a "fountain"-flow cell for the diode detector. *From Egorov et al. (2004a); reprinted with permission © 2004 American Chemical Society.*

exchange resin on a Teflon-coated PIPS semiconductor detector (Hughes and DeVol, 2006a).

The semiconductor diode designs described by Egorov et al. (2004a) consisted of (1) a semiconductor diode flow detector coated with a combined polymer film with actinide-selective organic extractants, such as HDEHP and bis(2-ethylhexyl)methane-diphosphonic acid (DIPEX) used as plasticizers, and (2) a fountain-flow design with the diode coated with HDEHP-plasticized film. These films have high actinide uptake chemistries, which provide these detectors with the capacity of actinide preconcentration on a thin-film geometry on the semiconductor diode surface. The two flow-cell detector designs are illustrated in Fig. 10.30.

The deposition of the thin film of actinide-selective organic extractant on the surface of the diode provides the flow-cell detector with the capacity to concentrate actinides in water samples depositing the actinides in close proximity to the diode detector separated only by a thin film of 0.5−3 μm thickness. The fountain-flow design illustrated in Fig. 10.30B enables the passage of water over the planar diode assembly illustrated in Fig. 10.30A whereby the actinides in the water concentrate on the polymer film containing the selective extractant. As described by Egorov et al. (2004a), the diode detector offers the following advantages: (1) diode detectors yield energy resolution much superior to that of scintillation detection, providing energy spectral information useful for the identification of radionuclides, (2) the background noise levels of diode detectors are orders of magnitude lower than scintillation detectors, and (3) diode detectors designed for the measurement of alpha radiation provide excellent discrimination against beta and gamma radiation.

The combined polymer film with actinide-selective organic extractant used to coat the semiconductor diode of the flow detector, described in the previous paragraphs, enables the concentration of actinides on the thin film of the detector while, at the same time, facilitating the measurement of α particle energy spectra with high resolution. The resolution of the α particle energy spectra is dependent on the thickness of the polymer film. Excellent resolutions of <100 keV FWHM are obtained with the polymer film thickness <0.5 μm, and energy resolution is degraded significantly with >2-μm-thick films (Egorov et al., 2004a; Addleman et al., 2005). Typical α particle energy spectra with an actinide selective film thickness of 0.5 μm is illustrated in Fig. 10.31.

Egorov et al. (2004a) tested the feasibility of using a diode packed in a fountain-flow cell with ^{241}Am standard and with the diode coated with an HDEHP-plasticized film of 3 μm thickness. The detection efficiency was 30%, and the detector traces, illustrated in Fig. 10.32, show the preconcentration of the ^{241}Am on the surface of the HDEHP-plasticized film on the diode surface. Also, from Fig. 10.32, it can be seen how the HDEHP extractant of the diode detector is regenerated with 4 M nitric acid. The findings demonstrate the robustness of the PIPS diode coated with actinide extractant in contact with aqueous solution.

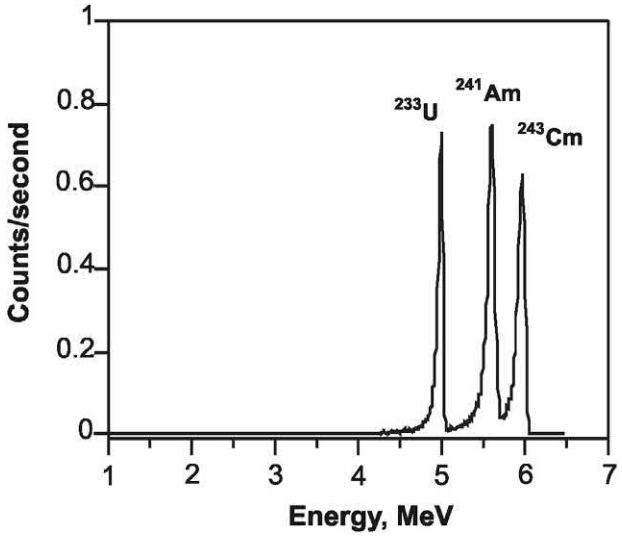


FIGURE 10.31 Alpha energy spectra illustrating feasibility of chemically modified diode detectors for in situ detection of alpha emitters in solution. Spectra measured in a static contact regime. Sample volume is 3 mL. High-resolution alpha spectroscopy in solution was demonstrated using a sample containing 1000 dpm/mL of ^{233}U, ^{241}Am, and ^{243}Cm. Selective film thickness is 0.5 μm. *From Egorov et al. (2004a); reprinted with permission © 2004 American Chemical Society.*

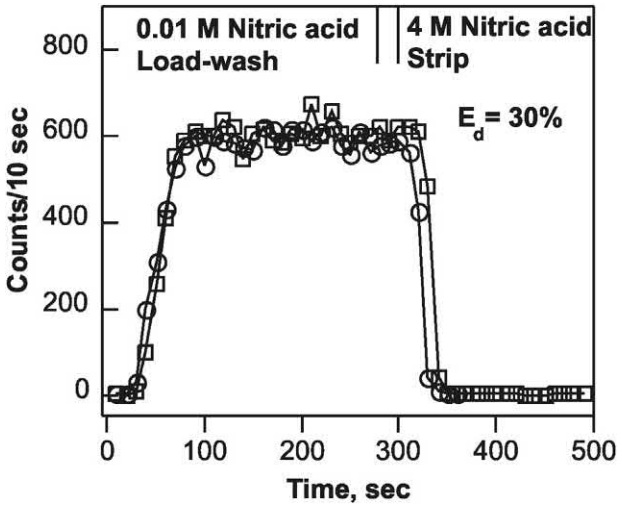


FIGURE 10.32 Duplicate detector traces showing flow-through operation of the chemically selective diode detector using 0.2 mL of ^{241}Am standard in 0.01 M nitric acid. Selective film thickness is 3 μm. Flow rate is 0.7 mL/min. *From Egorov et al. (2004a); reprinted with permission © 2004 American Chemical Society.*

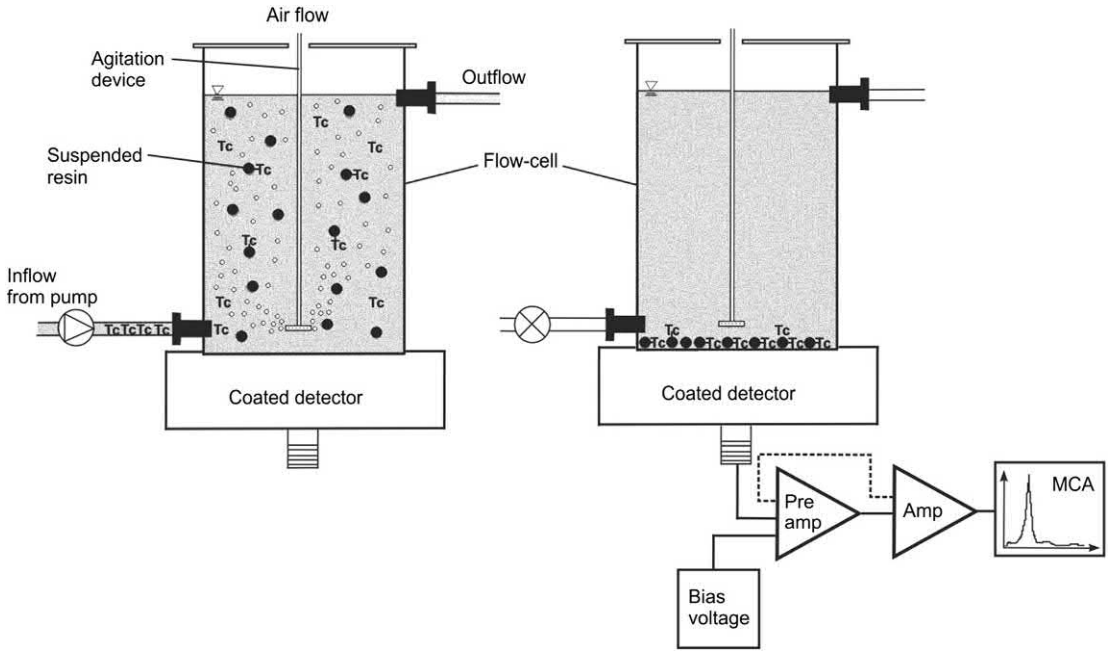


FIGURE 10.33 Schematic of the flow cell. During the preconcentration step (left), the resin is suspended in solution, as radioactive solution enters the flow cell at the bottom port. The solution leaves the flow cell through the outflow port, but the radioactivity is retained on the resin. The schematic on the right shows the data collection step, as the flow is stopped and the resin has settled on the detector surface. *From Hughes and DeVol (2006b); reprinted with kind permission from Springer Nature © 2006.*

A quite different approach to the use of diode-based flow cells was devised by Hughes and DeVol (2006b) with a flow cell designed to mix water samples with 40−80 μm Dowex 1x8-400(Cl^-) strong basic anion exchange resin in chloride form. This ion exchange resin exhibits a selective bias for binding with pertechnetate ($^{99}TcO_4^-$) over other anions encountered in groundwater. The ion exchange resin concentrates the ^{99}Tc from the water, which is passed through the flow cell, and the resin is then allowed to settle to the bottom of the cell onto the surface of a Teflon-coated 300-μm-thick PIPS semiconductor detector (see Fig. 10.33). Hughes and DeVol (2006b) selected the smallest diameter ion exchange resin available to achieve the highest interaction probability of the ^{99}Tc decay radiation with the semiconductor diode when attached to the resin beads at the bottom of the flow cell. The semiconductor detector measured 450 mm^2 in diameter, which formed the base of the flow cell, as illustrated in Fig. 10.33. The walls of the flow cell consisted of a cylindrical piece of 2.4 cm ID, 3.2 cm OD, 5 cm H polyethylene pipe providing a cell volume of ~20 mL.

Hughes and DeVol (2006b) demonstrated that passing incremental 20-mL volumes of groundwater spiked with 33.99 Bq/L of ^{99}Tc would result in a quantitative capture of

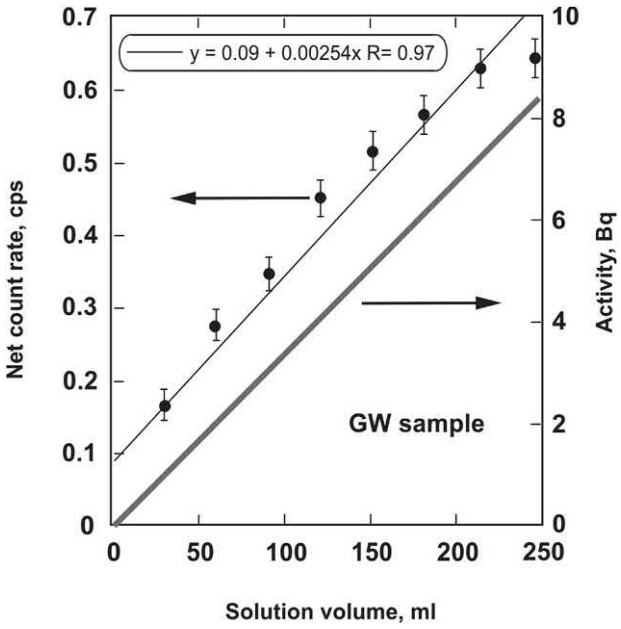


FIGURE 10.34 Flow profile of a groundwater sample. The thin black line is the regression fit to the data, and the error bars represent one standard deviation based on counting uncertainty. The bold gray line is the theoretical activity based on the spiked activity and the sample volume used. *From Hughes and DeVol (2006b); reprinted with kind permission from Springer Nature © 2006.*

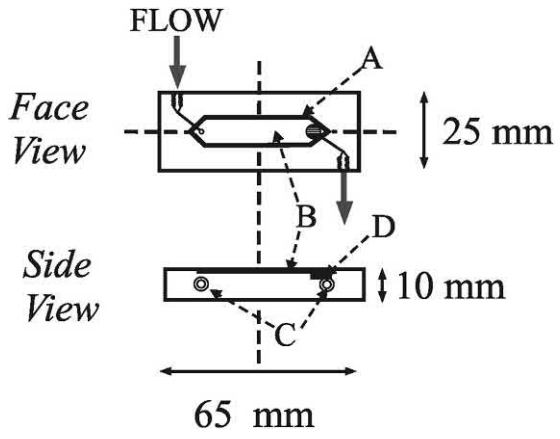


FIGURE 10.35 Schematic representation of the bottom half of the whole-column detector: (A) an O-ring groove; (B) stationary phase cavity; (C) the 10−32 threads where the detector is joined to tubing; (D) outlet frit. The top half of the detector (not illustrated) is a polished rectangular piece of scintillator plastic. *From Link and Synovec (1999); reprinted with permission © 1999 American Chemical Society.*

^{99}Tc by the ion exchange resin for each 30-mL increment of groundwater passed through the flow cell and a linear concentration of the ^{99}Tc with total water volumes up to 250 mL illustrated in Fig. 10.34. An average detection efficiency of 17.66% ± 3.20% and background of 0.35 cps was reported. This flow-cell technique could measure ^{99}Tc levels in 30-mL groundwater samples below the limits of 33 Bq/L set for pertechnetate in drinking water.

F. Whole-column detector

A dual-functionality flow-cell detector consisting of a chromatographic column of Dionex C14 chromatographic stationary phase contained within a Bicron BC400 plastic scintillator detector was devised by Link and Synovec (1999) for the HPLC separation and measurement of low levels of beta-emitting analytes. The detection of low levels of the radioisotope is achieved by encompassing the entire column of chromatographic media within the detector volume, that is, the chromatographic column is also the detector. In this case, the dual functionality of separation and scintillation is not achieved with a mixed bed of resin and scintillator, as in the examples cited in the previous paragraphs; rather, the dual functionality is obtained with a chromatographic stationary phase contained within the scintillating column. A schematic diagram of the column is illustrated in Fig. 10.35. The column was constructed of two pieces of $2.5 \times 6.4 \times 0.8\ cm^3$ of BC400 plastic scintillator. A shallow hexagonal region was milled out of each piece of plastic scintillator to create a cavity measuring 0.78 cm wide × 4.1 cm long × 0.05 cm deep to contain the chromatographic stationary phase bordered by a 0.125-cm-deep O-ring groove. The two pieces of plastic scintillator with their respective cavities were joined together with screws and sealed with an O-ring to form the planar chromatography column of 1-mm thickness. The O-ring seal kept the mobile liquid phase within the column. The planar column was coupled with silicone optical coupling to two PMTs. A flow-cell detector without chromatographic medium was coupled downstream to the dual-functionality column to compare its effectiveness with a conventional flow-cell detector.

The approach used by Link and Synovec (1999) with the whole-column detector is the following: The radioisotope-labeled organic compounds are injected into the column, and all of the compounds reside on the column at one time, i.e., the compounds are detected together on the column until each compound is eluted sequentially from the column. As the compounds are eluted from the column, the detection signal is reduced according to the activity of the labeled compound eluted. The planar geometry of the whole-column detector minimizes the distance between the chromatography medium and the scintillation detector. Link and Synovec (1999) tested the detector with ^{11}C-labeled pharmaceuticals. The radionuclide ^{11}C undergoes positron decay with a maximum energy (E_{max}) of 0.961 MeV and a range calculated by Link and Synovec (1999) to be 3.5 mm. The maximum distance of travel for a beta particle in the cavity of the whole-column detector is only 0.005 mm before reaching the plastic scintillator. The continuous detection of the isotope-labeled compounds in the whole-column detector provides an increased radiation SNR, and the recorded chromatographic separation of the labeled-compounds is maintained without the characteristic resolution loss via postcolumn flow-cell detector band broadening. The simulated and experimental responses of

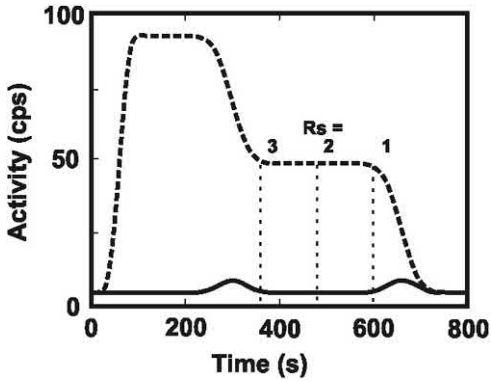


FIGURE 10.36 Simulated whole-column (- - -) and flow-through (—) detector signals for a two-analyte system. Detector response is equal for the two detectors. Analyte retention times are 300 and 660 seconds. *From Link and Synovec (1999); reprinted with permission © 1999 American Chemical Society.*

the whole-column detector to the HPLC separation of isotope-labeled compounds are illustrated in Figs. 10.36 and 10.37, respectively. Link and Synovec (1999) calculated simulated responses of the whole-column detector and a flow-through detector for the chromatographic separation of two ^{11}C-labeled analytes of equal activity, which is illustrated in Fig. 10.36. The signal from whole-column detection is at a maximum when the entire sample is injected into the column. Once the entire sample of a mixture of radioisotope-labeled compounds is loaded into the column, an appropriate mobile phase is pumped through the column, and the signal drops as labeled compounds are separated and eluted from the column. Fig. 10.36 illustrates the signals from a whole-column detector and of a flow-through detector during the chromatographic separation of two radioisotope-labeled compounds of equal activity. As described by Link and Synovec (1999), the signal from the whole-column detection is the total amount injected on the column at time t past injection time minus the total amount, which has eluted up to that time. This is illustrated in the simulation of Fig. 10.36 where the activity drops to one-half as one of the two compounds of equal activity is eluted from the column. The signal from the flow-through detector is weaker, as only a portion of the analytes is detected at any given time.

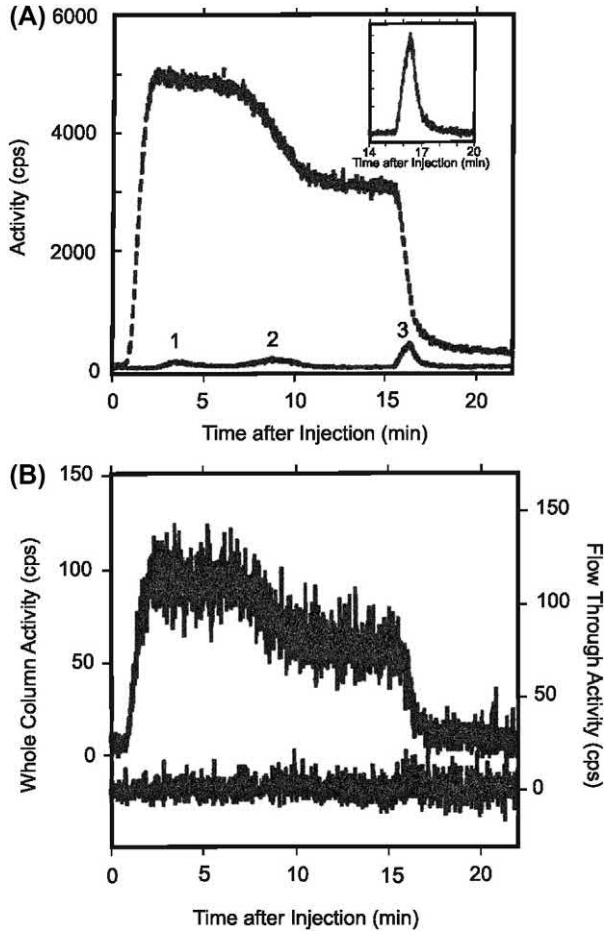


FIGURE 10.37 Sample radioactivity chromatograms to illustrate the difference between whole-column and flow-through detection: (A) injection of 9250 Bq; (B) injection of 185 Bq. The peaks are denoted by number: analyte 1, a trace impurity; analyte 2, [^{11}C]-α-methylepinephrine; analyte 3, [^{11}C]-*m*-hydroxyephedrine. Traces: - -, whole-column detection; —, flow-through detection. The inset in (A) shows the [^{11}C]-*m*-hydroxyephedrine flow-through peak amplified fourfold to illustrate column resolution. In (B), plotting of the two signals is offset vertically for clarity. The left y-axis is whole-column activity with the 0 value offset by 50 counts/s (cps) from the x-axis; the right y-axis is for flow-through detection with the 0 value offset 30 counts/s from the x-axis. The data were decay corrected to time of injection for accuracy in presentation. *From Link and Synovec (1999); reprinted with permission © 1999 American Chemical Society.*

Link and Synovec (1999) demonstrated the relative sensitivities of the whole-column and flow-through column methods with an experimental comparison of detector responses to two samples of relatively high and low activities. The two samples contained a total activity of 9250 and 185 Bq of a mixture of ^{11}C-labeled compounds, and the whole-column and flow-through column detector responses to the two samples, as the compounds were eluted from the column, are illustrated in Fig, 10.37. Both whole-column and flow-through column detection were sufficiently sensitive to measure the ^{11}C-labeled organic compounds of relatively high activity, as they are eluted from the column; however, only the whole-column detector was sufficiently sensitive to measure the activity of the major analytes of the low-activity sample. The whole column detection efficiency reported for ^{11}C was 96%. A limit of detection (L_D) for analytes of 2 Bq (54 pCi) was measured for whole-column detection, which is a 50-fold improvement in L_D compared with the flow-through detection.

G. Tritiated water vapor in air detector

The monitoring of tritium in air is important in facilities where relatively high levels of tritium may exist, such as in laboratories where tritium fuel is used in research on nuclear fusion, and in fission nuclear power plants particularly in power plants that use D_2O as a moderator. Tritium in air can take on two forms, namely, gaseous tritium (HT, DT, and T_2) or in the form of water vapor (HTO, DTO, and T_2O) where H, D, and T refer to the three isotopic forms of hydrogen, ^{1}H, ^{2}H, and ^{3}H, respectively. Carnpi et al. (1998) developed a detector consisting of a disk of zeolite, which has a high absorptive capacity for moisture (i.e., water vapor in air) and acts as a scintillator with increased efficiency when activated with Eu^{3+}. The scintillation efficiency properties of zeolites doped with Eu^{3+} and other lanthanides or metal ions are thoroughly researched (Saini et al., 2018; Taiji et al., 2018; Li et al., 2017; Rong gui et al., 2014; Gong et al., 2013; Rocha et al., 2013; Flores-Acosta et al., 2005; Joly et al., 2007; Lezhnina and Kynast, 2010). The detector developed by Carnpi et al. (1998) consists of a disk of Eu-doped zeolite coupled to a PMT and an

air flow system capable of monitoring the zeolite-trapped water vapor in air. The flow-cell detector is classified as a dual-functionality flow detector because it simultaneously concentrates and detects the radionuclide of interest. Gaseous tritium is not trapped by the zeolite, and thus, the detector could discriminate between the chemically oxidized form of tritium in air (i.e., tritiated water vapor) and the tritium gas. Tritiated water vapor is the most hazardous form of airborne tritium. The derived air concentration limit is 8×10^5 Bq/m^3 for the gaseous form of tritium, which is 25,000 times higher than the air concentration limit for the oxidized form (Carnpi et al., 1998). In 1 hour of operation, the flow detector is reported to reveal HTO concentrations 40 times below the derived air concentration, and a level equal to the derived air concentration could be revealed within the first minute of counting. The flow cell may be operated continuously for a 5-hour duration.

VI. Flow-cell radionuclide analysis sequential to separation

The previous section in this chapter dealt with dual-functionality flow detectors, which have the capacity to simultaneously separate and detect radionuclides with the aim of concentrating the radionuclide of interest on the column while simultaneously providing a measurement of the radionuclide activity. This section will focus on the flow-cell detectors that are used to measure radionuclide activities subsequent to or sequential to their chromatographic separation.

A. ^{99}Tc in nuclear waste and process monitoring

The analysis of ^{99}Tc in nuclear waste has been given much attention due to its high activities in waste, its long half-life (2.6×10^6 years), and its high mobility in the environment. Methods developed by Egorov et al. (2004b, 2005b) and O'Hara et al. (2008a,b) include robotic and automated handling steps that perform sample oxidation, the separation of ^{99}Tc(VII) as pertechnetate ($^{99}TcO_4^-$) from interfering radionuclides with an anion exchange column, and the delivery of the separated pertechnetate to a flow detector followed by the automated computed-controlled ^{99}Tc activity analysis.

For the automated analysis of ^{99}Tc, a heterogeneous flow-cell detector has been used such as a 1-mL pore volume Li-doped glass scintillator flow cell with a Beta Ram detector system (LabLogic, Inc.) reported by Egorov et al. (2004b, 2005b) and O'Hara et al. (2008a,b). A flow-cell detection efficiency of ~55% for the ^{99}Tc is reported. These researchers processed the detector output to obtain an instrument response in cpm/mL followed by calculations yielding the sample activity in dpm/mL. The flow-cell

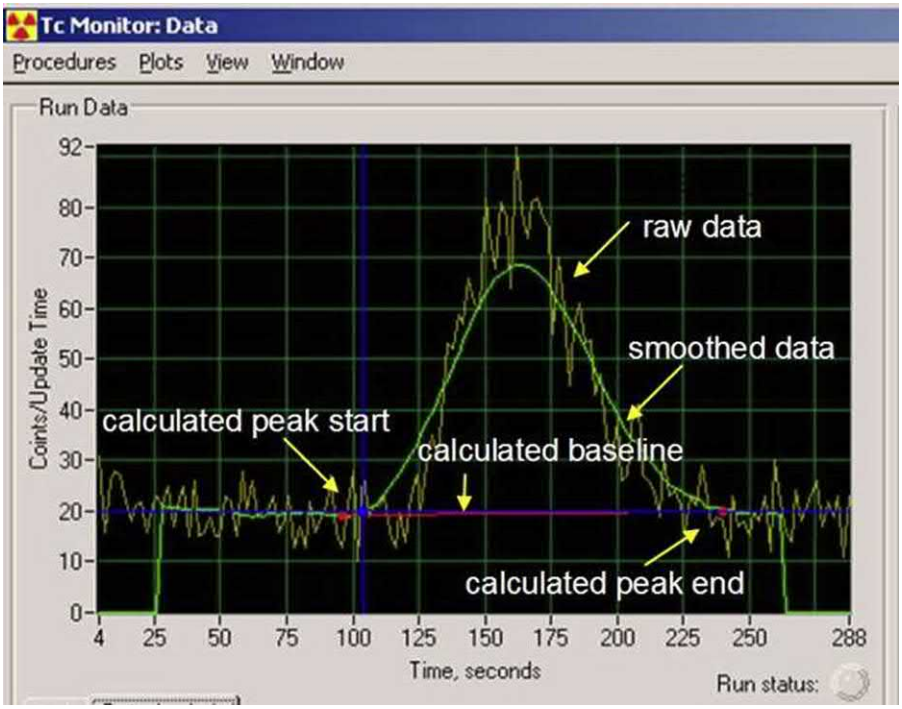


FIGURE 10.38 Detector data display of ^{99}Tc as it passed through the detection cell (yellow). Green trace shows smoothed data, which were used to determine baseline (blue/red horizontal line) and subsequently the net counts under the peak. Color in this figure is visible in the electronic version of this book. *From O'Hara et al. (2008a); reprinted with permission ©2008 by the American Nuclear Society, La Grange Park, Illinois.*

detector response is a peak of the ^{99}Tc radiation counts, as the radionuclide in the ion exchange column eluate enters and exits the flow-cell detector. A typical peak is illustrated in Fig. 10.38. The raw data from the flow-cell detector are a peak corresponding to a time series of counts per update time, which is smoothed with a moving-average algorithm, including a baseline determination. Subsequently, a peak search and integration algorithm is used to determine the peak start and peak end positions and a calculation of the integrated peak area in counts.

Once the peak area in counts is obtained, the count rate of the radionuclide in the original sample is calculated, as described by O'Hara et al. (2008a), according to the following:

$$C_{cpm/mL} = \frac{(N_{cts}/t_r)}{V_s \times D} \tag{10.31}$$

where N_{cts} is the net (background-subtracted) peak area in counts, t_r is the counting (or residence) time in the flow-cell detector, V_s is the original sample volume in mL, and D is the sample volume dilution factor resulting from the automated sample preparation and measurement. The dilution factor D is thus the fraction of the digested sample loaded onto the separation column versus the total volume of the digestate. A calibration factor, which provides a value to the overall efficiency of the measurement, including the chemical yield and the flow-cell detection efficiency, is determined by spiking the automated sample preparation and analysis system with a standard of the radionuclide under analysis (e.g., ^{99}Tc), and the calibration factor is then calculated according to the following:

$$E = \frac{C_{sp} - C_u}{V_{sp} \times A_{sp} \times D_{sp}} \tag{10.32}$$

where E is the calibration factor in units of cpm/dpm, C_{sp} and C_u are the net detector peak areas in cpm for spiked and unspiked samples, respectively. Spiking involves the injection of a precise volume of radionuclide standard (known activity) into the automated sample preparation and analysis system. V_{sp} of Eq. (10.32) and previously described in Eq. (10.29) is the volume (mL) of radionuclide standard (spike) added to the sample, A_{sp} is the activity concentration (dpm/mL) of the radionuclide standard, and D_{sp} is the spiked-run dilution factor, which is calculated in the same manner as D of Eq. (10.27). The activity concentration, A_{Tc}, of the radionuclide (e.g., ^{99}Tc) in units of dpm/ml is then calculated, as described by O'Hara et al. (2008a), as

$$A_{Tc} = \frac{C_{cpm/mL}}{E} \tag{10.33}$$

where $C_{cpm/mL}$ and E are the count rate of the radionuclide in the original sample and calibration factor, respectively, as previously defined.

Automated methods for the analysis of radionuclides, including ^{99}Tc in nuclear waste and process streams, are discussed in detail in Chapter 11, Volume 2, and many of these methods include the use of a flow detector for the analysis of radionuclides, as these are separated on the ion exchange column of the automated flow—based instrumental setup. Automation in the separation and analysis of radionuclides can involve ion exchange chromatographic columns described and flow-cell detectors in this chapter as well as other methods of analysis such as radioisotope MS. Automated methods, such as flow injection and sequential injection fluidics, are beyond the scope of this chapter. The reader will find a review of the principles and practice of these techniques in radionuclide analysis in Chapter 11 of Volume 2 "Automated Radiochemical Separation, Analysis and Sensing" of this book. Other excellent reviews on automating radiochemical analysis including the use of flow-based detectors, as well as other methods including MS, are provided by Trojanowicz et al. (2018), Rodríguez et al. (2016), and Cerdà et al. (2014). Table 10.8 from Trojanowicz et al. (2018) provides a compilation of automated flow methods applied to the analysis of radionuclides in nuclear wastes and reactor coolants. See also Rodríguez et al. (2016) for a comprehensive review of automated flow analysis methods applied to the radiochemical analysis of a wide range of environmental samples, including drinking water, milk, soil, sludge, radwaste urine, hospital residue, seawater, and vegetable matter.

B. Actinides and ^{90}Sr in soil

The combined extraction of actinides and ^{90}Sr from soil followed by chromatographic radionuclide separation and flow-cell analysis is possible, as demonstrated by Roane et al. (2003); however, the analysis requires the removal of interfering ions that influence the chromatographic retention times of the radionuclides, which is a key to their identification. Prior to the separation of the radionuclides by ion chromatography and flow-cell analysis, the soil is subjected to acid digestion and leaching followed by cleanup by processing soil extract through Sr resin and TRU resin columns as illustrated in Fig. 10.39. The identification and activity analysis of the radionuclides is carried out by ion chromatography and comparison of radionuclide retention times with those of known radionuclide standards followed by flow-cell analysis. Roane et al. (2003) used a Beta RAM flow-cell scintillation detector (LabLogic, Inc.). Flow-cell detector responses to the ion chromatographic separation of radionuclides extracted from soil and those of known radionuclide standards are illustrated in Fig. 10.40.

Radionuclide activity is determined from the flow-cell detector response or radionuclide peak by integrating the peak to determine its net area, N, which represents the background-subtracted counts of the peak. The counts are

TABLE 10.8 Flow methods developed for determination of radionuclides in nuclear wastes and nuclear reactor coolants.

Determined radionuclides	Measuring system	Analyzed real samples	Resin employed for SPE	Time of analysis	Limit of detection	References
Actinides (III), (IV) and (V) valent	CFA-LSC (with extractive/scintillating resin)	Acid-digested tank sludge, high activity drain tank supernatant	TRU resin	N/A[a]	N/A	Roane and DeVol (2002)
^{241}Am	SIA-LSC (renewable sorbent)	Nuclear wastes (vitrified glass, Salt cake slurry)	TRU resin	N/A	N/A	Egorov et al. (1999a)
Am, Pu, Np isotopes ^{241}Am, ^{243,244}Cm, ^{242}Cm, ^{239,240}Pu, ^{238}Pu	SIA-ICP-MS (online) SIA-LSC and nonflow α spectrometry	Dissolved vitrified nuclear waste Tank waste supernate, vitrified nuclear waste, sludge from aged irradiated fuel	TRU resin TRU resin	N/A 25 minutes[b]	N/A N/A	Becker et al. (1999) Grate et al. (1999b)
^{237}Np	FIA-ICP-MS (with MCN)	Radioactive waste	-	N/A	80 pg/L	Becker et al. (1999), Egorov et al. (2001)
^{239,240}Pu	FIA-ICP-MS (double-focusing) with USN	Wipe test samples	—	N/A	0.04 pg/L	Becker and Dietze (1999)
Pu (total)	FIA amperometry	Liquid wastes from spent nuclear fuel reprocessing plant	UTEVA resin	N/A	1.6 ng (0.82 μg/L)	Taguchi et al. (2011)
^{90}Sr	SIA-LSC SIA-LSC (renewable sorbent) SIA-LOV-ICP-MS (off-line)	Nuclear waste Nuclear wastes (vitrified glass, salt cake slurry) Reactor coolant, testing solutions	Sr resin Sr resin Sr resin, Dowex 50Wx8	<40 minutes N/A 24 minutes (5-mL sample) 6 hours (1-L sample)	N/A N/A 2.9 Bq/mL (5 mL sample) 15 Bq/L (1 L sample)	Grate et al. (1996) Egorov et al. (1999a) Kołacińska et al. (2017)
^{99}Tc	CFA-LSC (with extractive/scintillating resin) FIA-LSC (microwave assisted) for total ^{99}Tc SIA-LSC (renewable sorbent) SIA-LSC (stopped flow) SIA-LSC SIA-ICPO-MS (off-line) SIA-LOV-ICP-MS (off-line)	Nuclear waste simulants Caustic aged nuclear waste Nuclear waste (vitrified glass, salt cake slurry) Tank nuclear waste Nuclear waste Solidified cement of low-level radwaste Reactor coolant, water	Aliquat-336/acrylic resin SuperLig 639, MP-1M anion exchanger TEVA resin TEVA resin AGMP-1 TEVA resin TEVA resin	30 minutes 7.5 minutes N/A 40 minutes 13 minutes N/A 50 minutes	6.2 Bq/L N/A N/A 30 pCi (1.11 Bq) 33 kBq/L 1.5 mBq/g 6 mBq/L	DeVol et al. (2001a) Egorov et al. (2004a,b, 2012), O'Hara et al., 2008a,b) Egorov et al. (1999a) Egorov et al. (1998a) Grate et al. (2012) Wu et al. (2014) Kołacińska et al. (2018)
^{232}Th ^{238}U	FIA-ICP-MS (with ultrasonic nebulizer)	Radioactive waste	-	N/A	11 pg/L 26 pg/L	Becker et al. (1999) Egorov et al. (2001)
$^{234\text{-}235,236,238}$U	FIA-ICP-MS (double-focusing) With USN	Reactor samples		N/A	0.07 pg/L	Becker and Dietze (1999)

CFA, continuous flow analysis; *FIA*, flow injection analysis; *LOV*, lab-on-valve; *LSC*, liquid scintillation counter; *MCN*, microconcentric nebulizer; *SIA*, sequential injection analysis; *SPE*, solid-phase extraction; *USN*, ultrasonic nebulizer.

[a]*N/A—data not available.*

[b]*Flow sample processing, not including detection.*

From Trojanowicz et al. (2018); reprinted with permission from Elsevier © 2018.

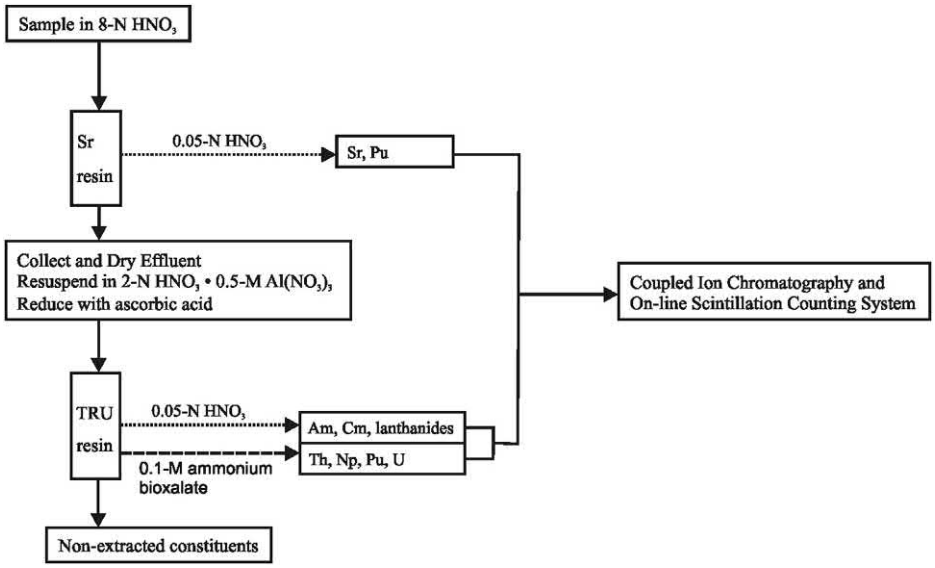


FIGURE 10.39 Sample preparation scheme for the extraction of strontium and the actinides from soils. *From Roane et al. (2003); reprinted with permission from Elsevier © 2003.*

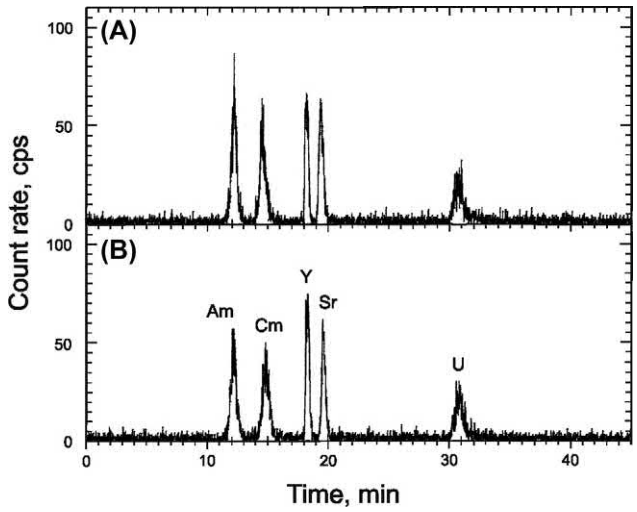


FIGURE 10.40 Flow-cell detector responses to (A) the ion chromatographic separation of radionuclides representing the extracted contents of 0.3 g soil and (B) to the ion chromatographic separation of radionuclide tracer standards. *From Roane et al. (2003); reprinted with permission from Elsevier © 2003.*

divided by the count time t (seconds). A calibration factor CF (Bq/cps) for each radionuclide was calculated from the relation:

$$CF = \frac{Af}{(N/t)} \tag{10.34}$$

where A is the loaded activity of standard, and f is the branching ratio for charged particle decay. Roane et al. (2003) found the calibration factors to range from 0.761 for ^{241}Am to 1.088 for ^{233}U. The calibration factor (CF) in this case has units of dps/cps, which is the inverse in units of the calibration factor (E) of Eqs. (10.32) and (10.33), described previously. Thus, the radionuclide count rates per unit volume of sample ($C_{cps/mL}$) are converted to sample activities per volume ($A_{dps/mL}$) by the relation:

$$A_{dps/mL} = CF \cdot C_{cps/mL} \tag{10.35}$$

which is the inverse of the previously described Eq. (10.33). The relation given in the above Eq. (10.35) was used by Egorov et al. (2005a,b) to convert count rates per sample volume to disintegration rates per sample volume.

Roane et al. (2003) demonstrated that the radionuclides extracted from soil required dilution to prevent interference from ions that would alter the ion chromatography retention times of the radionuclides compared with the retention times of the radionuclide standards. Improvements in radionuclide concentration and cleanup will allow for increased concentration of radionuclides extracted from soil to permit the measurement of low activity levels.

C. Alpha/beta discrimination

The possibility of analyzing α- and $\beta(\gamma)$-emitting radionuclides in the same sample by pulse shape discrimination (PSD) and reporting these as gross α and gross β activities has widespread applications in the environmental measurement of radioactivity. See Chapter 6, Volume 1 and Chapter 2, Volume 2 for additional information on this subject. Because the radionuclides are often extracted in mixtures, high-performance ionic chromatography (HPIC) linked to flow scintillation analysis with alpha/beta discrimination facilitates

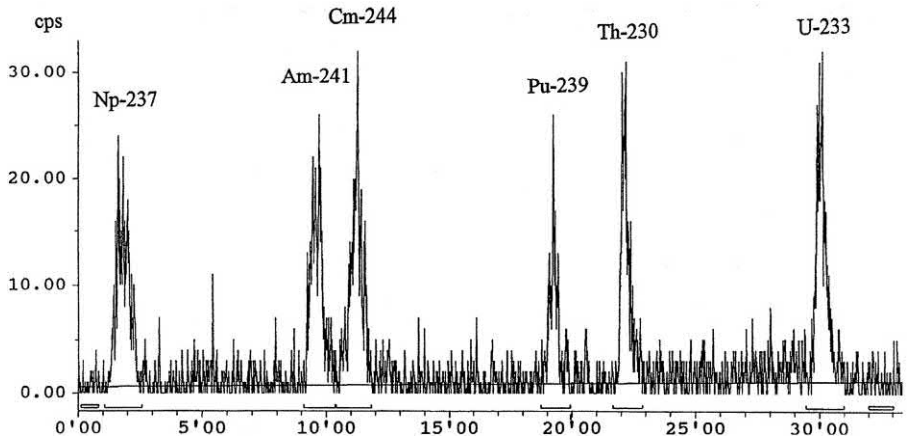


FIGURE 10.41 A typical chromatogram of select actinides using cationic elution. *From Reboul and Fjeld (1995); reprinted with permission © 1995 Wolters, Kluwer Health, Inc.*

the environmental analysis of mixtures of α- and β-emitting radionuclides. Separation procedures for fission products utilizing HPLC and HPIC have been developed (Bradbury et al., 1990; Reboul and Fjeld, 1994). The separation procedure for six common actinides by HPIC is reported by Reboul (1994); Reboul and Fjeld (1995). Fig. 10.41 from the work of Reboul and Fjeld (1995) provides an excellent illustration of actinide separation by HPIC and online flow-cell measurements of the separated nuclides. Such excellent (clean) radioisotope separations may preclude the need for α and β activity discrimination by pulse shape analysis (PSA). However, PSA can offer advantages in addition to the α/β discrimination, such as lower background count rates for the detection of alpha versus beta particles and thus, lower limits of detection for alpha-emitting radionuclides. For example, with a flow-cell detector equipped with a Parlene C-coated CsI(Tl) detector and alpha–beta discrimination, Fjeld et al. (2005) obtained a background count rate of 8 cpm for alpha particles and 17 cpm for beta particles in the measurement of alpha- and beta-emitting radionuclides separated by ion chromatography.

As described in detail in Chapters 6, Volume 1 and Chapter 2, Volume 2, it is possible to use pulse decay analysis (PDA) or PSA to discriminate between α- and $\beta(\gamma)$ decay events in the same sample. Events originating from alpha particle interactions with scintillator have 35–40 ns longer decay lifetimes than events originating from beta particle or gamma interactions. This is a result of the longer deexcitation and light emission processes in LS fluors after α particle interactions. In PSA or PSD, the area of the tail of a pulse is compared with the total pulse area, which provides a method of assigning a pulse to that of an α pulse (long pulse) or β/γ pulse (short pulse). Such pulse discrimination for α/β analysis requires two MCAs, where pulses of longer decay times originating from α events are registered in the α-MCA and those of shorter decay times are registered in the β-MCA as originating from β or $\beta(\gamma)$ events.

Various methods of PDA with solid scintillators are described in Chapter 9, Volume 1. Usuda and Abe (1992) and Usuda et al. (1992) tested several solid scintillators including CsI(Tl), NaI(Tl), CaF_2(Eu), BaF_2, BGO, NE102A, and stilbene for the PSD of events arising from α and $\beta(\gamma)$ interactions. Planar solid scintillators were coupled to a single PMT. They used a flow cell consisting of a spiral channel (not tubing), because tubing will absorb all of the α emissions. Solutions of the $\alpha + \beta(\gamma)$ sources flow along the spiral channel in contact with a Au-coated Mylar film, which protects the solid scintillator. The surface of the planar solid scintillator is also protected with Au-coated Mylar film. The α count rate obviously is a function of the thickness of the Au-Mylar protective layers, and the system suffers from low α detection efficiency. Their work demonstrated the potential of solid scintillators for the simultaneous analysis of $\alpha + \beta(\gamma)$ sources using PSD; and CsI(Tl) crystal scintillator was found to provide the best discrimination between α and $\beta(\gamma)$ rays. The scintillator CsI(Tl), however, is water soluble as well as hygroscopic. Thus, without some means of protection from moisture, CsI(Tl) cannot be applied as a scintillator in a solid (heterogeneous) flow cell where the radioactive solution would flow through cell tubing containing a fine powder of solid scintillator. With this in mind, Chotoo et al. (1997) developed a polymer-coated CsI(Tl) scintillation flow cell for simultaneous alpha and beta analysis, which is discussed further on in this section.

DeVol and Fjeld (1995) tested three solid heterogeneous flow cells consisting of 63–90 μm particles of CaF_2(Eu), glass scintillator (GS-20) and BaF_2 packed into translucent Teflon tubing as potential flow cells, which can be coupled to HPIC systems for on-line α/β discrimination

for the routine on-line analysis of alpha-emitters. The contribution from beta-emitters in the chromatograph effluents can be removed by time discriminator settings of a pulse-shape analyzer. By selecting the optimum time discriminator setting, the $\beta(\gamma)$ contribution to the background count rate was reduced by a factor of 4.1 with a BaF_2 heterogeneous flow cell at the expense of only a slight $< 9\%$ loss in α detection efficiency. An alpha detection efficiency of $\sim 50\%$ for ^{233}U is reported by DeVol and Fjeld (1995) providing MDAs of 0.6 Bq for flow cells containing CaF_2(Eu) and BaF_2 and 1.1 Bq for the cell containing GS-20. Like most heterogeneous flow cells, the lack of inertness and intrinsic contamination of the scintillator remains a problem.

Lochny et al. (1998) and Wenzel et al. (1999) devised a plastic scintillator flow cell for the on-line measurement of alpha- and beta-emitting radionuclide mixtures in high-level waste. The detector consisted of the plastic scintillator Meltilex (PerkinElmer, Inc.) and transparent perfluoroalkoxy (PFA) tubing (Dupont, USA). Meltilex is a meltable plastic containing the fluors PPO (diphenyloxazole) and MSB (methylstyrylbenzene). The inner walls of the flow cell tubing were coated with Meltilex permitting detection of both alpha and beta particles. With the use of appropriate energy windows and varying the flow-cell geometry the detector is able to suppress beta particles to a great extent; and the detector is capable of monitoring the decontamination of radioactive waste.

A series of research studies by Chotoo et al. (1997), Hastie et al. (1999), DeVol et al. (1999), Tan et al. (2000), Tan and DeVol (2002) and Fjeld et al. (2005) at Clemson University's Department of Environmental Engineering and Science Department has culminated in a very efficient flow-cell detector for alpha/beta PSD. The detector reported by Tan et al. (2000) consisted of a flow cell containing granular 63–93 μm Parylene C polymer-coated CsI:Tl scintillator situated between two PMTs in coincidence detection mode. The scintillation pulses were analyzed by PSD using the charge integration technique (see Chapters 6 and 9 of Volume 1 for detailed treatments on PSD). PSD is achieved by comparing the fast decay component (pulse integrated over a short period of time, I_f) to the total integrated current from the pulse, I_{tot}, that is, I_f/I_{tot}, as described in Chapters 6 and 9 of Volume 1. Excellent PSD of alpha and beta events was achieved by Tan et al. (2000), who report a spillover of 2.1% for α events to β and 1.4% spillover of β events to α at a pulse-shape discriminator setting $I_f/I_{tot} = 72$ for a mixture of ^{233}U and $^{90}Sr(^{90}Y)$ yielding alpha and beta detection efficiencies and backgrounds of 31.3% and 26.4%, and 0.84 and 0.31 cps, respectively. Tan and DeVol (2002) utilized pulse-shape analysis for alpha/beta determinations with a flow cell containing particles of CsI:Tl encapsulated with a 10% layer (ratio of coating to particle mass) of Parylene C polymer; and in lieu of photomultiplier detectors, they used silicon PIN-photodiodes. For pulse-shape analysis and discrimination of alpha- and beta-events, Tan and DeVol (2002) utilized two timing gates. The first gate was set to measure the leading edge of the pulse; while, the second gate was set to measure the tail of the pulse. The gates were set to maximize the pulse-shape numerical value difference for alpha and beta scintillation pulse events from the CsI:Tl detector. The spillover of beta events into the alpha region of interest was $\sim 3.9\%$; while the background counts in the alpha region of interest was 0.1 cps. Fjeld et al. (2005) measured alpha- and beta-emitting radionuclides with ion chromatography and pulse-shape analysis employing a heterogeneous flow cell containing Parylene C-coated CsI(Tl) in Teflon tubing. The pore volume of the flow cell was 0.15–0.20 mL; and with a flow rate of 1 mL/min an effective counting time of 10 seconds was obtained. They inferred the identification of radionuclides by their characteristic elution time. An example of typical flow-detector responses to eluted radionuclides separated into alpha- and beta chromatograms following alpha/beta discrimination are illustrated in Fig. 10.42. A small spillover (*i.e.*, misclassification) of alpha events as beta, results in the small peak of ^{244}Cm in the beta chromatogram.

Radionuclides activities were determined by Fjeld et al. (2005) integrating the areas under the chromatogram peaks, which would provide the total counts and then dividing by the counting time and detection efficiency. Net count rates are used by subtracting the background count rates, which were 8 cpm for alpha-particle events and 17 cpm for beta-particle events. The detection efficiencies were calculated according to the following:

$$\varepsilon = \frac{N}{At} \tag{10.36}$$

where N is the net (background subtracted) counts determined by peak integration, t is the count time, and A is the activity (Bq) of radionuclide standard loaded onto the column.

Minimal detectable concentrations of the radionuclides are reported by Fjeld et al. (2005) according to whether the analysis is performed on-line via the flow scintillation analyzer, or off-line by counting the separated radionuclides with a conventional LS analyzer equipped with alpha/beta discrimination. The minimal detectable concentrations calculated according to the method of the Currie (1968) equation for paired blanks are listed in Table 10.9 for a 0.2 L aqueous sample or 0.5 g solid sample for on-line and off-line counting. Alpha/beta PSD generally yields much lower backgrounds in the alpha MCA compared with the beta MCA, and thus, lower minimal detectable concentrations can be expected for the alpha emitters.

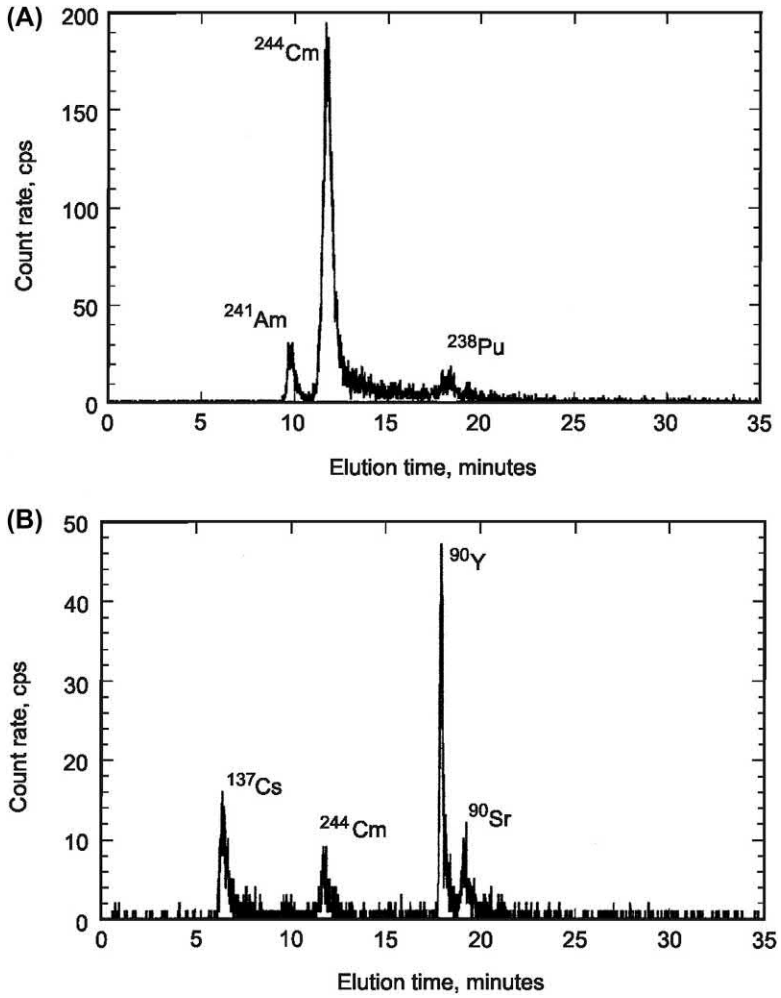


FIGURE 10.42 Alpha (A) and beta (B) chromatograms for supernatant from a high-activity drain tank at the Savannah River Technology Center. *From Fjeld et al. (2005); reprinted with kind permission from Springer Nature © 2005.*

TABLE 10.9 Estimates of detection limits and analysis times for aqueous and solid samples.[a]

	Aqueous sample		Solid sample
Radionuclide	4-hour analysis (online counting)	24-hour analysis (off-line counting)	48-hour analysis (off-line counting)
Strontium-90	4000 pCi/L (160 kBq/m^3)	12 pCi/L (0.4 kBq/m^3)	5 pCi/g (0.2 kBq/kg)
Transuranics	1500 pC/L (60 kBq/m^3)	3 pCi/L (0.1 kBq/m^3)	1 pCi/g (0.04 kBq/kg)

[a]*From Fjeld et al. (2005); reprinted with kind permission from Springer Nature © 2005.*

A unique application of alpha/beta PSD reported by Wierczinski et al. (2001a) was applied to the first online separation and detection of a subsecond α-decaying nuclide. Subsecond ^{224}Pa ($t_{1/2} = 0.85$ seconds) was produced by the ^{209}Bi(^{18}O,3n)^{224}Pa reaction at the 88-inch cyclotron at the Lawrence Berkeley National Laboratory. After production, the nuclide was transported via a gas-jet system to a fast centrifuge system followed by online extraction with trioctylamine/scintillation solutions and online flow scintillation counting with PSD to minimize beta events.

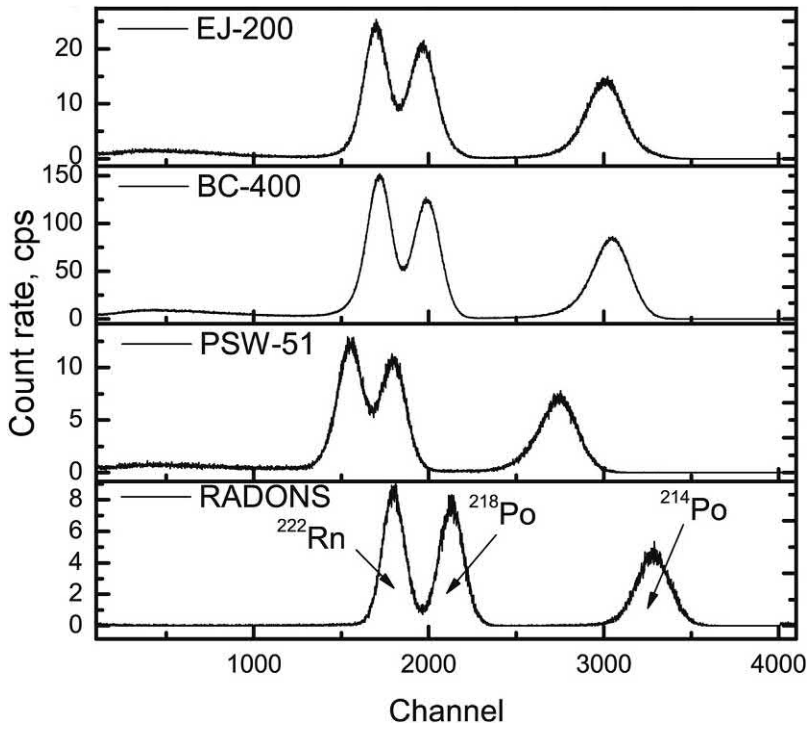


FIGURE 10.43 PERALS pulse height spectra of ^{222}Rn and progeny absorbed in EJ-200, BC-400, PSW-51 plastic scintillator, and as a reference, an optimal case where ^{222}Rn is dissolved in RADONS (ETRAC, USA) LS cocktail. *From Mitev (2016); reprinted with permission from Elsevier © 2016.*

Plastic scintillating microspheres (PSMs) together with alpha/beta discrimination subjected to the continuous flow of river water were demonstrated by Tarancón et al. (2016) to be a robust detector for ^{3}H and ^{90}Sr/^{90}Y. The scintillating microspheres are packed into 6 mL plastic scintillation counting vials. The top and bottom of the vials are drilled to provide inlet and outlets for the pumping of river water through the scintillating microspheres for optimum periods from 6 to 100 hours. Off-line analysis with a Quantulus LS spectrometer demonstrated the capabilities of the plastic scintillation microspheres for alpha/beta discrimination and analysis of ^{3}H and ^{90}Sr/^{90}Y. Detection efficiencies for ^{3}H and ^{90}Sr/^{90}Y reported are 0.53% and 182%, respectively, with a mean background count rate of 1.56 cpm. Limits of detection are 740 Bq/L for ^{3}H and 2.1 Bq/L for ^{90}Sr/^{90}Y with a 5 hour counting time and 1.52 mL sample volume. Improved detection limits are reached by increasing the sample volume (i.e., cell volume) and the counting time.

Mitev (2016) demonstrated the potential of using PSMs or plastic scintillator microspheres packed in polyethylene foils (PS foils) for the continuous monitoring of ^{222}Rn. Plastic scintillators, including EJ-200, BC-400, and PSW-51, were shown to absorb ^{222}Rn and provide excellent alpha/beta PSD with excellent resolutions of ^{222}Rn and

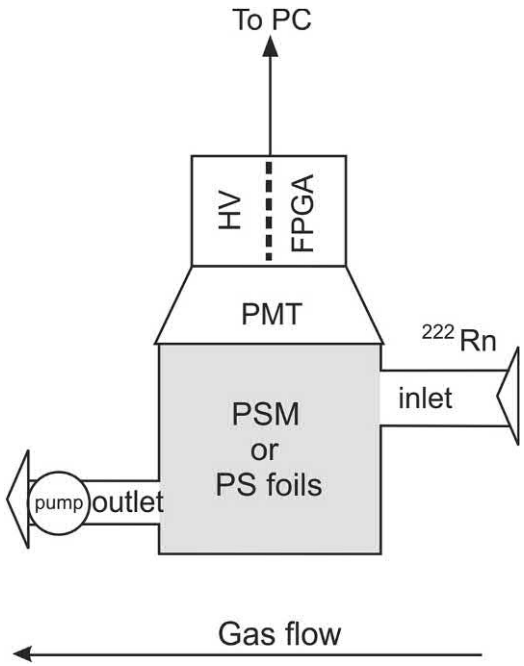


FIGURE 10.44 A potential continuous online radon monitor based on the absorption of ^{222}Rn in plastic scintillator. *From Mitev (2016); reprinted with permission from Elsevier © 2016.*

progeny permitting the quantitative analysis of ^{222}Rn. For example, the alpha peak resolution of ^{222}Rn absorbed into the plastic scintillators is sufficient to permit the separation of the 5.489 MeV peak of ^{218}Po from that of the 6.002 MeV peak of ^{222}Rn, as illustrated in Fig. 10.43. The alpha/beta PSD by the plastic scintillating spheres was performed off-line with a PERALS or a conventional LS spectrometer; however, Mitev (2016) demonstrates the potential for the future design of a flow-through radon monitoring device (Fig. 10.44) using field programmable gate array electronics.

D. ^{89}Sr and ^{90}Sr(^{90}Y) analysis

Since the nuclear atmospheric weapons tests in the 1960s, there has been great concern over the levels of ^{90}Sr in the environment as a serious threat to internal contamination in the human body. This is due mainly to the relatively long half-life of ^{90}Sr ($t_{1/2} = 28.8$ years) and the similarities in the chemistry of calcium and strontium whereby ^{90}Sr will accumulate in the body by residing with a long biological half-life in the human skeleton along with calcium (L'Annunziata, 1967; L'Annunziata and Fuller, 1968). A paper by Desmartin et al. (1997) underscores the continuing concern for ^{90}Sr residues in the environment, as it is produced in a relatively high yield (5.8% from ^{235}U) during the fission of heavy elements. Thus, high levels of ^{90}Sr are found in spent nuclear fuel and reprocessing plants. The classical method of analysis of ^{90}Sr involves precipitation of its daughter ^{90}Y as a carbonate or oxalate followed by counting of the precipitated ^{90}Y (L'Annunziata, 1971; Piltingsrud and Stencel, 1972).

Current techniques in the analysis of ^{90}Sr in the environment involve the combination of HPIC and flow scintillation analysis (FSA) also referred to as online liquid scintillation counting (OLLSC) when homogeneous flow-cell counting is involved [Knöchel and coworkers (see Alfaro et al., 1995; and Desmartin et al., 1997)]. Automated methods of flow analysis to the analysis of ^{90}Sr among other radionuclides in nuclear wastes and reactor coolants and in the environment are reviewed by Trojanowicz et al. (2018), Rodríguez et al. (2016), and Kołacińska and Trojanowicz (2014). These automated methods may include the online flow-cell radiometric measurement of ^{90}Sr among numerous other radionuclides as well as the various MS methods of analysis, which can provide multicomponent analysis and improved limits of detection of transuranic isotopes.

Desmartin et al. (1997) describes the coupling of HPIC to separate ^{90}Sr from natural or power plant reactor water and online flow scintillation analysis before the daughter radionuclide ^{90}Y has time to grow to any significant level following ^{90}Sr separation. They used an HPIC Dionex 2010i system (Dionex Corporation, Sunnyvale) coupled to a radiomatic flow scintillation analyzer with FLO-ONE operation software (PerkinElmer Inc., Waltham, MA, USA) equipped with a 2.5 mL homogeneous flow cell operated with an eluent flow rate of 1 mL/min and a scintillator flow rate of 2.5 mL/min.

Desmartin et al. (1997) set the pulse height discriminators to provide two counting regions of the flow scintillation analyzer, which is equipped with an MCA, to measure the ^{89}Sr and ^{90}Sr simultaneously. Synthetic reactor water containing various concentrations of $^{134}Cs^{+}$, $^{90}Sr^{2+}$($^{90}Y^{3+}$), $^{60}Co^{2+}$, $^{133}Ba^{2+}$, and $^{135}I^{-}$ was easily separated by HPIC to isolate radiostrontium. Trivalent ions such as $^{90}Y^{3+}$ are stopped at the top of the HPIC column. Therefore, the ^{90}Sr(^{90}Y) parent–daughter radionuclides are separated during the chromatography run. The reported MDAs, calculated according to Eq. (10.15) in Section III.D of this chapter, are 480 DPM for ^{89}Sr and 60 DPM for ^{90}Sr.

Grate et al. (1996, 1998a) and Grate and Egorov (1998a) automated the analysis of ^{90}Sr in nuclear waste based on sequential injection analysis, which rapidly separates ^{90}Sr from ^{90}Y, ^{137}Cs, among other radionuclides. They used a sorbent extraction microcolumn containing Sr-Spec resin (EiChrom Industries, Darien, IL) that selectively binds ^{90}Sr as a crown ether complex under acidic conditions. The ^{90}Sr is analyzed online with a flow scintillation analyzer, which can be operated in the continuous- or stopped-flow modes described subsequently in Section VII of this chapter. More information concerning the automation techniques are described in Chapter 11, Volume 2.

Several extractive scintillation sensor materials were tested by DeVol et al. (2001a,b) for either off-line or online monitoring of radiostrontium. Online separation techniques offer the advantage of more automated and rapid analysis cited in the previous paragraph and discussed in detail in Chapter 11. The most effective extractive sensor found by DeVol et al. (2001a,b) consisted of a bed of strontium-specific resin marketed under the trademark Sr-Spec Resin (100–150 μm from EiChrom Industries) and BC-400 scintillating beads (100–200 μm from Bicron, Inc.) combined together 1:2 by weight as a mixed bed. The Sr-Spec Resin consists of an inert, porous organic polymer support impregnated with a solution of bis-4,4′(5′)-tert-butyl-cyclohexano-18-crown-6 (DtBuCH18C6) in 1-octanol. It displays a high selective affinity to strontium at low pH while excluding alkali and alkaline earths. For online tests, DeVol et al. (2001a,b) packed <0.5 g of the Sr-Spec Resin/BC-400 mixture into 3 mm OD × 1.6 mm ID × 140 mm long polytetrafluoroethylene tubing yielding an approximate pore volume (PV) of 200–400 μL, which was 60%–70% of the total void volume. The flexible tubing was coiled in an approximate diameter of 2.54 cm and placed between two PMT tubes of the flow scintillation analysis detector (Beta Ram of LabLogic Systems). The column was loaded with 1–5 PVs of sample in 4M HNO_3 and the column washed with additional ~25 PVs of 4M HNO_3, and the adsorbed ions were eluted with 50 PVs of distilled–deionized water. The detection efficiency reported

was 76% for ^{89}Sr ($E_{max} = 1.49$ MeV). The detection efficiency for ^{90}Sr, which was not tested, should be slightly lower since the beta particle emissions from ^{90}Sr are of lower energy ($E_{max} = 0.546$ MeV).

Interferences in the separation and flow-cell analysis of radionuclides were studied by Roane et al. (1999). These interferences are of two types: (1) radiological interferences and (2) chemical interferences. The radiological interferences are found when other radionuclides are present in the sample, which require their removal by the use of a selective ion exchange or preconcentrating column. Chemical interferences occur when certain ions present in the sample or their ionic strength (i.e., sample load) can affect the performance of an ion exchange column and thus affect the elution times and separations of the radionuclides of interest. Borai and El-Sofany (2004) separated ^{90}Sr and ^{90}Y in the presence of interfering ^{234}Th on a Dionex 2000 ion chromatographic system with 0.2 M ammonium sulfate in 0.3 M HCl eluent. They used a 0.4 mL heterogeneous flow-cell detector with Ce-activated glass scintillator and obtained quantitative recoveries for ^{90}Sr and ^{90}Y in the presence of 17−262 Bq/mL of ^{234}Th.

High-level nuclear waste contains significant ^{137}Cs whereby its daughter ^{137m}Ba is a potential interfering nuclide in the ion exchange separation in the analysis of ^{90}Sr. O'Hara et al. (2008b) and DeVol et al. (2009) found SuperLig 620 solid-phase extraction resin (230−420 mesh) from IBC Advanced Technologies, American Fork, UT, as a suitable extraction chromatographic resin for the separation of interfering nuclides. They determined optimal separations using 2 M nitric acid for the elution of radiocesium and yttrium, a radiostrontium elution step with ~0.49 M ammonium citrate followed by a barium elution step with ~1.8 M ammonium citrate. Quantitative analysis of ^{90}Sr in high-level nuclear waste was achieved with an automated sequential injection analysis microfluidics system (see Chapter 11) coupled to a flow-cell detector. A Beta Ram (LabLogic Systems) heterogeneous flow-cell detector was used consisting of a 1 mL volume Li-glass scintillator. The solid scintillator heterogeneous flow cell was preferred because it yielded adequate detection efficiencies (56% for ^{90}Sr) for the relatively high levels of radioactivity encountered and there is no generation of organic waste, which occurs when homogeneous detectors are used. The linear response of the flow detectors to ^{90}Sr activities injected into the chromatographic system is illustrated in Fig. 10.45. The average recovery for ^{90}Sr was reported to be 98%.

Flow-cell analysis of low levels of radionuclides separated by column chromatography can be achieved by the use of specific resins that can concentrate the radionuclides of interest and the use of stopped-flow detection whereby the residence time of the sample in the flow-cell detector can be increased indefinitely, as described in Section VII of this chapter.

Under conditions of transient continuous flow, Plionis et al. (2009) demonstrated the low-level analysis of ^{90}Sr in urine and other aqueous media by the use of Sr-spec resin (EiChrom Industries, Inc., Darren, IL) and a homogeneous flow-cell detector. The homogeneous flow cells yield the highest detection efficiencies for beta-emitting radionuclides (see Table 10.1), and these flow cells require the mixing of liquid scintillator fluor cocktail with the column effluent stream, as illustrated in Fig. 10.46. They used a Beta Ram (LabLogic Systems, Brandon, FL) 2500 µL liquid flow cell. An internal cocktail pump mixes the LS cocktail with the effluent stream before it enters the flow cell. A low-viscosity LS cocktail was used (in-flow 2:1, LabLogic Systems) together with ScintFlow SA and LauraLite 3.4 software run on a desktop PC to control flow-cell counting parameters. A

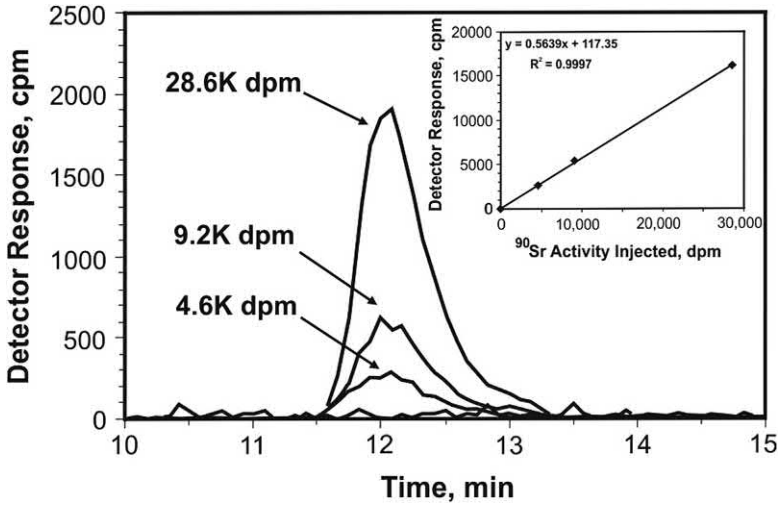


FIGURE 10.45 Elution profile for ^{90}Sr at several concentrations. The insert shows the linearity of the detector response to various activities of ^{90}Sr injected into the chromatographic system. *From DeVol et al. (2009); reprinted with kind permission from Springer Nature © 2009.*

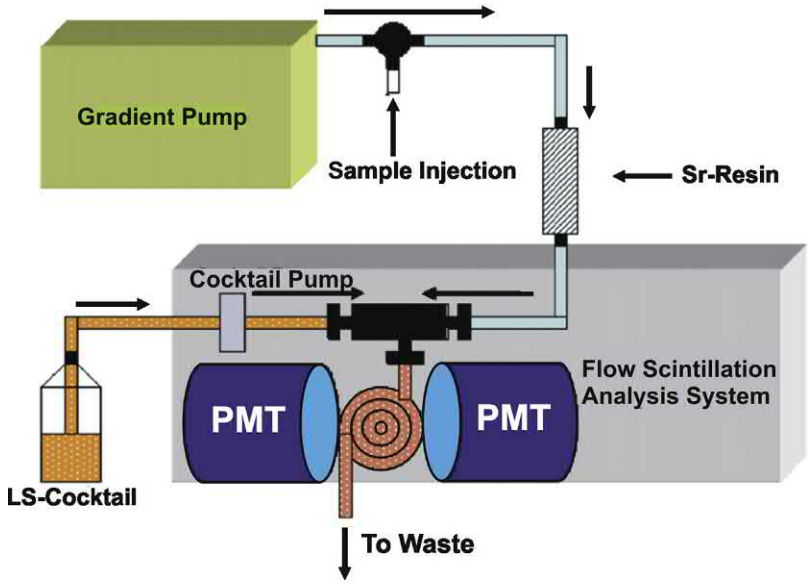


FIGURE 10.46 A block diagram of the flow analysis system. *From Plionis et al. (2009); reprinted with permission from Elsevier © 2009.*

detector integration time of 6 s was selected to allow sufficient counts to accumulate for each data point.

In a transient flow system, as used by Plionis et al. (2009), the residence time, T_R, of the eluted sample in the flow cell is defined by Eq. (10.2) described earlier in this chapter. Plionis et al. (2009) used a flow cell with a 2500 μL volume and a combined scintillator effluent flow rate of 3 mL/min. Thus, the residence time, according to Eq. (10.2), is calculated as 50 seconds or 0.83 minutes. The peak area produced by the flow-cell detector response was summed and the background count subtracted by Plionis et al. (2009) to derive a net number of counts for the peak according to Eq. (10.6). With the use of a radionuclide standard, the detection efficiencies were determined according to Eq. (10.8). The counting region for the ^{90}Sr pulse height spectrum was optimized, and a counting window of 2−600, which defined the channel lower- and upper-level discriminators, was selected. Background pulse events are more prevalent at the low end of the pulse height spectrum, and those occurring in the region between 0 and 2 are not counted. The background was reported to be only 4.1 cpm, with a ^{90}Sr detection efficiency of 102.5 ± 6%. The LS detection efficiency of ^{90}Sr, which has a beta spectrum energy maximum at 546 keV, can approach 100% (see Fig. 6.19 of Chapter 6, Volume 1 illustrating the LS

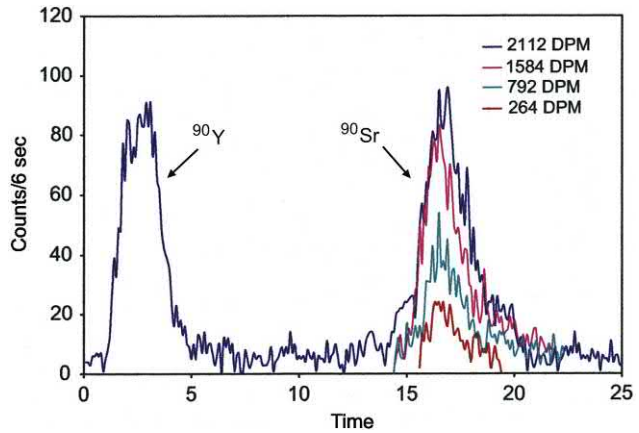


FIGURE 10.47 Flow-cell detector traces for various activities of ^{90}Sr as determined by transient-flow counting and a 3-cm column. Traces, as low as 264 dpm, are visually apparent. Computer-aided peak finders are helpful for determining lower activities of ^{90}Sr. For clarity, only the highest concentration sample is shown for the first peak. The color-coded traces are visible in the electronic version of this book. *From Plionis et al. (2009); reprinted with permission from Elsevier © 2009.*

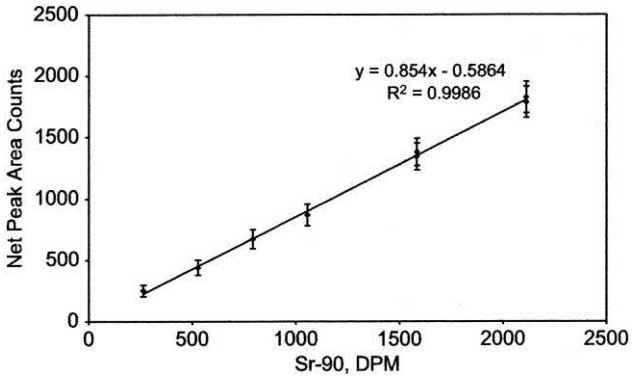


FIGURE 10.48 A calibration curve of flow-cell detector response to various levels of ^{90}Sr activity as determined by transient-flow counting. The fact that the R^2 is close to unity and that the intercept is near zero indicates that there is a highly linear detector response for this analyte. Error bars represent 3σ. *From Plionis et al. (2009); reprinted with permission from Elsevier © 2009.*

detection efficiencies of several beta-emitting radionuclides of widely differing beta spectrum energy maxima). Plionis et al. (2009) explain the small portion of the detection efficiency > 100% as possibly due to diffusion of sample zone within the flow cell or luminescence. The lower level of detection was estimated to be 47 dpm and the lower level of quantification to be 156 dpm. An example of flow-cell detector traces for various levels of ^{90}Sr activity is illustrated in Fig. 10.47. Recoveries of ^{90}Sr in urine sample were quantitative, and a typical calibration curve illustrating a linear detector response to various levels of ^{90}Sr is illustrated in Fig. 10.48.

E. Cherenkov flow-cell analysis

There are commercially available flow cells, called "Cherenkov cells." These consist of coiled Teflon tubing sandwiched between scintillator windows, as described in Table 10.1. These cells are designed for the detection of high-energy beta-emitting radionuclides in HPLC effluents, such as ^{32}P, ^{90}Y, and ^{86}Rb. The E_{max} of the beta particle emissions should be >> 263 keV, which is the threshold energy for the production of Cherenkov photons in water (see Chapter 6, Volume 2). In these flow cells, Cherenkov photons are produced in the narrow aqueous phase and wall of the Teflon tubing; however, most of the photons detected are produced in the scintillator that sandwiches the coiled Teflon tubing. Thus, the beta particle energies must be sufficient to penetrate the Teflon tubing and dissipate energy within the solid scintillator. Although such a cell may be called a "Cherenkov cell," the photons detected are not exclusively Cherenkov photons. The main advantages of these cells are (1) no organic scintillation cocktails are used and (2) no solid scintillator is used inside the Teflon tubing. Some examples of the applications of these cells in the measurement of radionuclides in liquid chromatography effluents are (1) the measurement of ^{32}P (E_{max} = 1710 keV) reported by Waters et al. (1999), Wierczinski et al. (2001b), and Poljaková et al. (2009), (2) the measurement of ^{86}Rb (E_{max} = 1770 keV) reported by Marks et al. (2004, 2009) and Grady et al. (2010), and (3) the measurement of ^{62}Cu (E_{max} = 2926 keV) reported by Yue et al. (2006).

A large Cherenkov cell measuring 12 cm in diameter × 10 cm in length with a 1 L sample volume was designed by Fujii et al. (2002) to measure high-energy beta-emitting radionuclides, such as ^{89}Sr, ^{90}Y, and ^{32}P, as a liquid waste monitor for nuclear medicine. High-energy beta-emitting nuclides are used commonly in nuclear medicine, and the Cherenkov cell was designed for the rapid measurement of these radionuclides in liquid waste. The waste is pumped into the 1-L cell, and the Cherenkov photons are detected by two PMTs on opposite sides of the cell. A coincidence circuitry is utilized to reduce

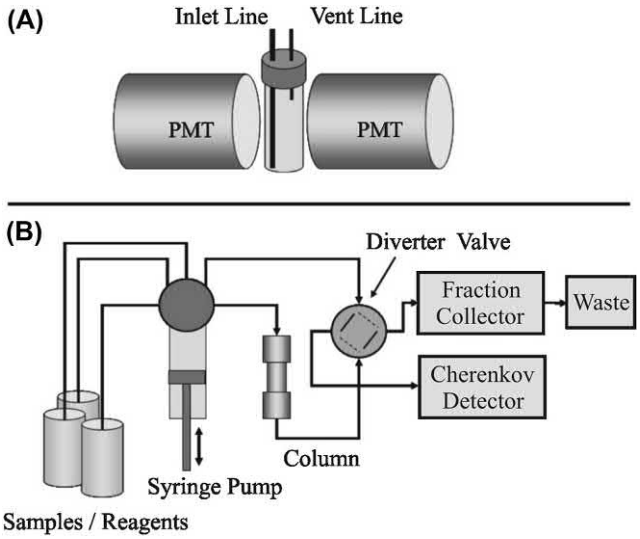


FIGURE 10.49 (A) Cherenkov detection flow cell configured between dual photomultiplier tubes (PMTs). (B) Fluidic layout for automated ^{90}Sr analytical system, including the Cherenkov flow-cell detector. *From O'Hara et al. (2009b); reprinted with permission © 2009 American Chemical Society.*

noncoincident background events. Measurements are made in a "stopped-flow" mode, that is, the flow is stopped for 5–20 minutes for Cherenkov photon counting. Detection efficiencies were sufficient to yield detection limits of 0.003–0.007 and 0.001–0.003 Bq/mL for 5- and 20-minutes measurements, which is more than sufficient for the monitoring of the liquid waste.

O'Hara et al. (2009b) constructed in-house a simple online Cherenkov flow-cell detector consisting of a 2-dram glass vial and cap, which allowed a 5.0 mL volume of column effluent containing ^{90}Y to be delivered and aspirated from the base of the vial via an inlet line illustrated in Fig. 10.49A. A second shorter line was placed just within the cap to allow for the displacement of air during the transfer of sample into and out of the cell. The Cherenkov flow cell was placed between two PMTs of a flow scintillation analyzer; and counting data were acquired using Flo-One software with a laptop computer. The objective of such an arrangement is the analysis of ^{90}Sr in environmental water samples via the Cherenkov counting of ^{90}Y daughter nuclide. Relatively large samples of water up to 0.5 L are loaded onto a SuperLig 620 column, which enables the preconcentration of the ^{90}Sr and the removal of interfering components of the sample matrix as well as other radionuclides, including the elution of its ^{90}Y daughter. Following a period of ^{90}Y ingrowth with the preconcentrated and purified ^{90}Sr, the newly ingrown ^{90}Y is eluted from the column into the Cherenkov flow-cell detector. The ^{90}Sr activity is then calculated from the measured ^{90}Y

daughter activity and the time of ingrowth of the daughter nuclide. O'Hara et al. (2009b) coupled the Cherenkov flow-cell detector to a fully automated liquid handling system illustrated in Fig. 10.49B. Chapter 11 in this volume provides a detailed description of the principles and operation of such fully automated radioanalytical systems.

The Cherenkov flow-cell detector described by O'Hara et al. (2009b) provided a Cherenkov counting detection efficiency of 42.6% for ^{90}Y. With the preconcentration of ^{90}Sr from 0.35 L of water, they demonstrated a detection limit of 0.057 Bq/L, which is below the drinking water limit (DWL) of 0.30 Bq/L. The MDAs for the ^{90}Sr are dependent generally on the volume of sample analyzed, the ^{90}Y yield or recovery efficiency, the sample counting time, background count rate, detection efficiency, and in the counting of its ^{90}Y daughter nuclide, on the ingrowth time of the ^{90}Y. O'Hara et al. (2009b) determined, for an ^{90}Y ingrowth time of 72 hours, Cherenkov flow-cell background of 0.153 cps, ^{90}Y Cherenkov detection efficiency of 0.426, and recovery efficiency of 0.789, that the method could measure ^{90}Sr at the DWL of 0.30 Bq/L within ~9, ~3, and ~1.5 hour detection intervals for 0.2, 0.35, and 0.5 L, respectively, of groundwater samples.

VII. Stopped-flow detection

In Section III.E of this chapter, the relationship of flow detector sensitivity or efficiency and flow rate was discussed. In summary, it was concluded that higher sensitivity (lower MDA) of a flow detector could be achieved by increasing the residence time of a sample in the flow detector (T_R) and the cell volume. Increasing the cell volume would, however, reduce HPLC peak resolutions. During the normal continuous flow of an HPLC run, the residence time of a sample (radioactivity peak) in the detector is generally short (<5 minutes). If the sample activity is low (near background), it may be difficult or impossible to distinguish the sample radioactivity from background with the short sample residence times of continuous-flow runs. This is obvious because longer counting times are required to reduce counting error (Eq. 10.22) and lower limits of detection (see Eq. (6.157) of Chapter 6, Volume 1). If we stop the flow of an HPLC run when the radionuclide is detected by the flow detector at its highest count rate (HPLC peak maximum), the sample residence time can be increased indefinitely at its highest count rate. This is referred to as stopped-flow detection, whereby longer counting times can be selected to achieve acceptable counting statistics and lower limits of detection.

The theory and practice of stopped-flow detection are described by Grate et al. (1996), Grate and Egorov (1998a,b), and Egorov et al. (1998a,b). Under the assumption of no secondary mixing or phase separation in the flow cell under stopped-flow conditions, Egorov et al. (1998a,b) note that the fraction of the sample zone present in the detector flow cell at the peak maximum, D_m, is obtained from the transient continuous-flow peak signal using the equation:

$$D_m = \frac{(C_{max})(T_R)}{(T_i)(C_n)} \tag{10.37}$$

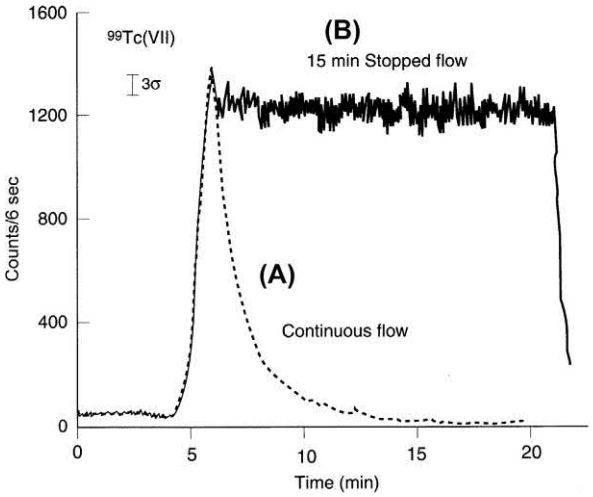


FIGURE 10.50 Comparison of continuous-flow (curve A) and stopped-flow (curve B) detection of ^{99}Tc. The error bar indicates three standard deviations of the peak maximum counts. *From Egorov et al. (1998a), reprinted with permission © 1998 American Chemical Society.*

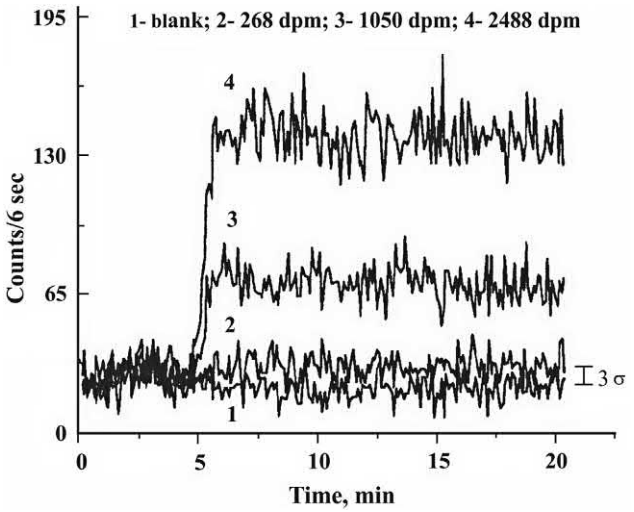


FIGURE 10.51 Selected detector traces from the analysis of ^{99}Tc(VII) standards using 15-minutes stopped-flow detection. The activities of the standards are listed. The error bar corresponds to three standard deviations of the background count rate. *From Egorov et al. (1998a), reprinted with permission © 1998 American Chemical Society.*

where C_{max} is the number of net counts at the peak maximum, T_R is the sample residence time as previously defined (Eq. 10.2), T_i is the pulse summation update time, and C_n is the net peak area counts. If the flow is stopped at the peak maximum, the background-subtracted (net) count rate, C_{cpm}, of the radionuclide is related to the sample activity A_{dpm} according to the following equation of Egorov et al. (1998a,b):

$$C_{cpm} = (D_m)(E_d)(E_{rec})(A_{dpm}) \tag{10.38}$$

where E_d and E_{rec} are the detection efficiency and sample recovery efficiency, respectively, described previously (Eq. 10.14).

Stopped-flow detection was tested by Grate and Egorov (1998a,b) and Egorov et al. (1998a) for the analysis of ^{99}Tc in a 2.5 mL flow cell. Using a ^{99}Tc standard in the continuous-flow detection mode establishes the time position of the peak maximum, as illustrated in Fig. 10.50 (curve A). At the time position of the peak maximum, the instrument is programmed to direct the eluate diverter valve to waste and simultaneously stop the cocktail pump initiating a stopped-flow mode. The detector traces (B) in Fig. 10.50 illustrate a duplicate 15-minutes stopped-flow analysis demonstrating reproducibility of the stopped-flow detection. Stopped-flow analysis of ^{99}Tc at three activity levels is illustrated in Fig. 10.51. The lowest activity of the standard (268 DPM) (trace 2, Fig. 10.51) would not be statistically distinguishable from the background (trace 1, Fig. 10.51) in a continuous-flow measurement. However, a 15-minutes stopped-flow measurement provided sufficient signal accumulation (counts) to yield a reliable analysis of the ^{99}Tc activity (268 DPM) with 8% (3σ) counting error (Egorov et al., 1998a).

VIII. Flow-cell effluent water monitors

A. ^{3}H effluent water monitors

A characteristic of heavy water reactor operation is the production of tritium in the moderator. Consequently, as reported by Sigg et al. (1994) and Hofstetter (1995), the potential release of tritium into the environment through aqueous effluents is of concern at CANDU reactors and at other tritium handling facilities. Developments in flow scintillation analysis have provided a rapid online detection system, which can monitor continuously tritium levels in effluents permitting corrective action to mitigate unwanted tritium release into the environment.

The first flow cells used at the Savannah River Site (SRS), Aiken, South Carolina, were of the heterogeneous type containing solid scintillator beads, such as yttrium silicate, reported by Hofstetter (1991). Continuous monitoring of tritium levels in the aqueous effluents of selected SRS heavy water purification facilities makes use of a heterogeneous flow cell containing plastic scintillator coupled with coincidence electronics providing a sensitivity of ~25 kBq/L (670 pCi/mL). The system requires a water purification pretreatment process, which includes microfiltration, ultraviolet sterilization, activated charcoal and ion exchange resin columns, and a phase separator before continuation of the aqueous stream to the flow cell at a rate of 3 mL/min. The solid scintillators provide limited detection sensitivity with a counting efficiency of only 0.18% for ^{3}H but adequate for the needs of the facilities where they are employed (Hofstetter and Eakle, 1993; 1995).

Tritium effluent water monitors reported by Sigg et al. (1994) and those utilized at CANDU systems (Cutler et al., 1993) make use of a homogeneous 2.5 mL LS flow cell containing coiled Teflon tubing installed in a modified PerkinElmer Radiomatic A250 flow scintillation analyzer. The effluent monitoring method requires water pretreatment, and the LS (homogeneous) cell system provides tritium quantification as well as rapid detection at several pCi/mL. Sensitivities of 16 and 1 pCi/mL are reported for 5-min and daily averages of counting data, respectively, which is reported to provide approximately 200 times greater sensitivity than similar methods utilizing the solid scintillator heterogeneous flow cells. As described by Sigg et al. (1995), a centrifugal pump moves environmental water to be monitored at about 10 L/min from the sampling location to the instrument position where it passes across the surface of a cross-flow filter. Sample water at only 2 mL/min is drawn through the filter for further pretreatment by flash distillation. A 0.25-mL static mixer blends 0.15 mL/min of LS cocktail with the sample water before passing through the 2.5 mL flow cell. It is reported that, at the lowest flow rates, full response to changes in environmental tritium is possible in 30 minutes, and LS cocktail consumption is less than 7 L a month. Flow rates are increased by as much as sixfold if increased response time is needed. Ultima Gold XR (PerkinElmer, Inc.) LS cocktail was used for low flow rates. Sigg et al. (1995) report that other fluor cocktails with lower viscosity are available when higher flow rates are required. A tritium counting efficiency of 36% is reported with the LS homogeneous flow cell system, which is many orders of magnitude more sensitive than the plastic solid scintillator heterogeneous flow cell. As noted earlier, the plastic solid scintillator flow cell could provide a tritium counting efficiency of only 0.18%. The flow scintillation analyzer was equipped with an external ^{241}Am standard with a 3-mm-thick tungsten shutter assembly to expose the flow cell to the 59.5-keV gamma rays for the production of a quench-indicating parameter.

Monitoring of tritium release at fusion research facilities and fission power plants is necessary to provide evidence that a facility is conforming to limits set by regulatory commissions on the release of tritium into the environment.

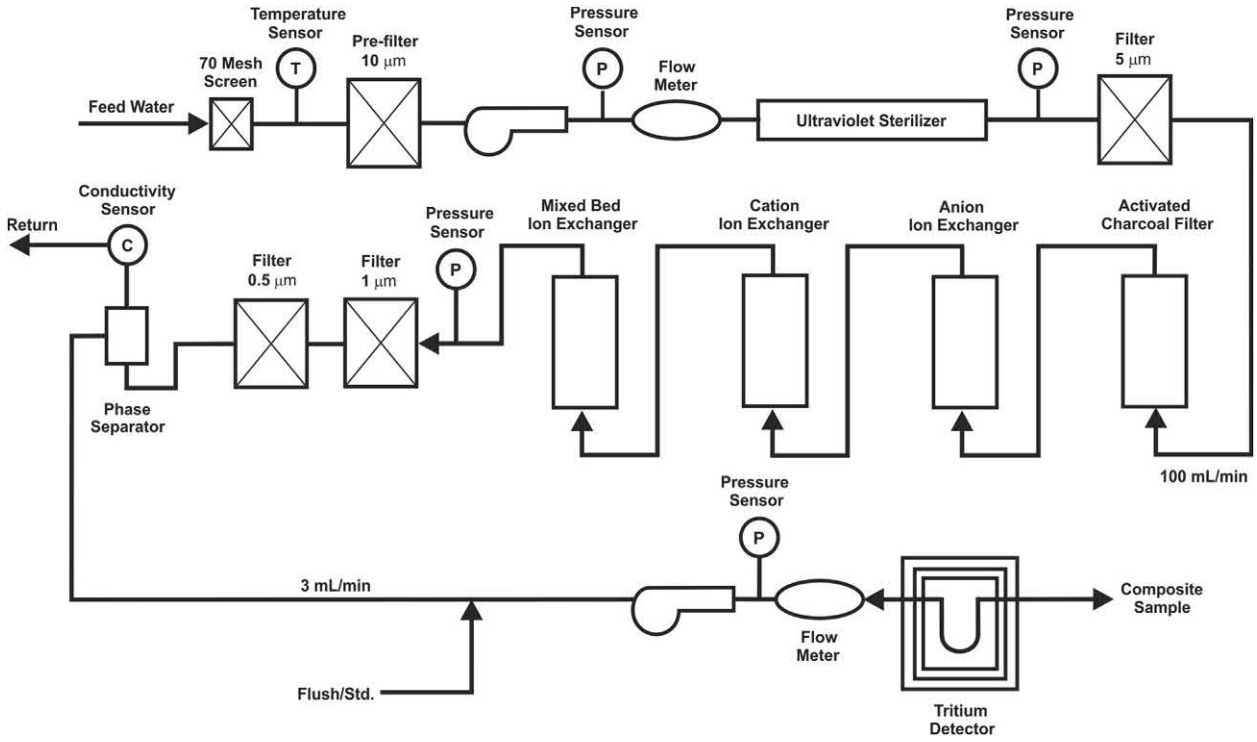


FIGURE 10.52 Sketch of a tritium in water monitor. *From Bruyere and Cadwallader (2012); reprinted with permission from Elsevier © 2012.*

It is also of political importance that a facility can demonstrate that it is not releasing any hazardous levels of tritium into the environment.

Bruyere and Cadwallader (2012) describe the function and practical application of a continuous monitoring system for aqueous tritium. The technique, which was first developed at the Savannah River National Laboratory (Hofstetter, 1991; 1995), involves the diversion of a small stream of effluent water through a flow-cell detector containing plastic solid scintillant and PMTs to detect and measure the scintillation photons in coincidence to reduce background. The flow-cell detector is equipped with an alarm system, which can be set whenever a specific level of tritium activity is detected. A sketch of the tritium in water monitor is illustrated in Fig. 10.52. As described by Bruyere and Cadwallader (2012) and illustrated in Fig. 10.52, the feed water is pumped at a rate of 100 mL/min through rough (10 μm) and polishing filters (5 μm), and a small portion of the water is collected in a 1-L surge tank. An ultraviolet light is used to sterilize the water sample together with biocide to reduce algal growth. The surge tank provides the monitor with a reserve of 8 hours of hold time to allow for continuous water monitoring during filter changeouts and maintenance. Thus, the water monitor need not be turned off during maintenance. A displacement pump moves the surge tank water through a series of charcoal filters and ion exchange resins that would reduce interfering organic contaminants, metal ions, and hydroxides to provide only tritium radionuclide through the U-shaped flow-cell detector. The ion exchange resin beds are changed at less than once a week. The flow-cell detector senses tritium at 56 Bq/mL (1514 pCi/mL) and the alarm set at 3000 pCi/mL.

B. Heterogeneous ($\alpha-\beta$) and γ discriminating cell

A flow cell with dual detectors capable of discriminating alpha and beta emissions against gamma emissions was developed by Tarancón et al. (2005). The flow cell was designed with two detectors, one for the measurement of alpha and beta emissions and the other detector for the measurement of gamma emissions. The flow cell contained BC-400 plastic scintillator beads (250−500 μm in diameter) as receptor for α and β radiation within the inner volume of the flow cell and an outer layer of BC-408 plastic scintillator completely surrounding the flow cell inner chamber as receptor of γ radiation. Only gamma radiation could penetrate the walls of the inner chamber and reach the outer plastic scintillator.

Tarancón et al. (2005) demonstrated the flow cell by measuring activity levels of different volumes of contamination pulses of $^{90}Sr/^{90}Y$, ^{134}Cs, and ^{240}Pu in continuous streams. Detection efficiencies reported were 107.7% for

$^{90}Sr/^{90}Y$ by the $\alpha-\beta$ receptor, 3.2% for ^{240}Pu by the $\alpha-\beta$ receptor, 18.3% for ^{134}Cs by the $\alpha-\beta$ receptor, and 0.89% for ^{134}Cs by the γ receptor. The advantages of such a flow-cell detector are (1) the detector may be applied to the analysis of alpha-, beta-, and beta−gamma-emitting radionuclides in liquid effluents, (2) the sensor is designed for providing online and continuous information on the specific activity and volume of a radioactive contamination, and (3) the flow cell can provide remote and continuous information on the presence of different radionuclides in a liquid stream for contamination in volumes > 5 mL and specific activities up to 1 Bq/mL.

IX. Single radionuclide analysis in high-performance liquid chromatography

Flow-cell radionuclide analysis has been traditionally and remains a routine technique in the biosciences, including research in biochemistry, molecular biology, drug research and metabolism, and radiopharmaceutical research, among other related fields, when used in conjunction with HPLC. Flow-cell radionuclide analysis is more common in the biosciences than any other branch of science. These studies generally involve the flow-cell measurement of radionuclide-labeled (e.g., ^{3}H, ^{11}C, ^{13}N, ^{14}C, ^{18}F, ^{35}S, ^{33}P, ^{32}P, etc.) bioorganic molecules separated by HPLC, which is one of the most popular chromatographic methods used for molecular separations and characterization. The method provides the means for further structural analysis by methods such as MS and NMR spectroscopy. Current methods involve the flow-cell analysis of radioisotope-labeled bioorganic molecules separated by HPLC combined with online MS and NMR spectroscopy. Examples will be provided in this chapter.

Many applications of flow-cell radionuclide analysis of HPLC effluents in studies of anabolic and catabolic reactions in the biological sciences are found in the journal literature, and these research reports number in the hundreds. The significance of radioisotope labeling in metabolic studies in the life sciences was underscored by Koppen et al. (2014) with the following note:

> *"Radiotracer technology (^{14}C or ^{3}H) is still the method of choice to study the in vivo disposition of a new drug as it allows making up a mass balance and enables the quantitative detection of the parent drug and all of its metabolites in complex matrices without the need for authentic standards."*

Among the many reports available from the literature, a few examples of flow-cell radionuclide analysis in various fields of study are listed in Table 10.10.

X. Dual radionuclide analysis

Commercially available flow scintillation analyzers (FSAs) are equipped with a MCA, computer display of the sample pulse height spectrum, and pulse height discriminators, which can be set to define two counting regions. The proper setting of these counting regions will permit the activity analysis of two different radionuclides in the sample (e.g., HPLC effluent) provided their beta energy maxima (E_{max}) are significantly different as described in detail in Chapter 6, Volume 1. It is necessary only that the counting efficiencies of the two radionuclides (lower energy and higher energy emitter) in the two counting regions be determined as described previously in Chapter 6, Volume 1. The flow scintillation analyzer will automatically determine the activities of the two radionuclides in the flow cell. An example of simultaneous ^{3}H and ^{14}C traces of the same HPLC run of a $^{3}H/^{14}C$ dual-labeled precursor (drug-agonist) and its metabolites in animal and human liver measured by Shaffer and Langer (2007) can be seen in Fig. 10.53. Dual labeling with ^{3}H and ^{14}C can be a helpful tool in the elucidation of metabolite reaction mechanisms and structure when combined with MS and NMR spectroscopy (Nassar et al., 2003, Silva-Elipe, 2003, Chowdhury, 2005; and L'Annunziata, 1984, 2007a, 2013). Fig. 10.54 illustrates the metabolic pathway proposed by Shaffer and Langer (2007) following online flow scintillation analysis of the ^{3}H- and ^{14}C-drug agonist and online MS.

Some examples of the flow scintillation analysis of dual radionuclides in HPLC effluents are the following: ^{3}H-^{14}C (Dayhuff et al., 1986; Kusche and Lindahl, 1990; Sabourin et al., 1988; Seidegård et al., 1990; Shaffer and Langer, 2007; Shirley and Murphy, 1990; Wells and Digenis, 1988); ^{3}H-^{33}P (Morgan et al., 1987); ^{3}H-^{32}P (Balla et al., 1987; Guillemette et al., 1989; Nolan and Lapetina, 1991; Rubiera et al., 1990; Sasakawa et al., 1990); and ^{3}H-^{35}S (Hughes et al., 1992; Lyon et al., 1994; Mays et al., 1987); and ^{89}Sr-^{90}Sr (Desmartin et al., 1997).

XI. Online HPLC-FSA and mass spectrometry[2]

In the biological sciences, MS is one of the most popular methods employed for the determination of the molecular weights, molecular formulae, and structures of metabolites. The popularity of MS is due to the high sensitivity of the analytical method and the possibility of

2. Taken in part from L'Annunziata, M. F. and Nellis, S. W. (2001). Metabolism studies with on-line HPLC and mass spectrometry (MS) interfaced with the flow scintillation analyzer (FSA). *FSA Application Note FSA-005*. PerkinElmer, Inc.; reprinted with permission © 2001. All rights reserved. http://www.perkinelmer.com/CMSResources/Images/44-73062APP_FSAMetabolismStudies.pdf, accessed October 31, 2018.

TABLE 10.10 Examples of flow-cell radionuclide analysis in conjunction with the high-performance liquid chromatography of radioisotope-labeled compounds in the life sciences.[a]

Reactions Studied[b]	References
Alatoxin biochemistry	Wang-Buhler et al. (2005)
Amino acid chemistry	Do et al. (2004)
Aqueous photolysis	Sharma (2017)
Chemical residue metabolism	Garner et al. (2006)
Cell proliferation regulators	Bollaert et al. (2018)
Drug metabolism	Maltais et al. (2018), Zhuo and Zheng (2018), Sato- Nakai et al. (2017), Fu et al. (2016), Ahring et al. (2015), Lenz et al. (2007, 2010, 2011), Koitka et al. (2010), Prasad et al. (2010), Athersuch et al. (2008), Ramanathan et al. (2007), Shaffer and Langer (2007), Ghosal et al. (2005), Edlund and Baranczewski (2004), Hsu et al. (2004), Martin et al. (2003), Silva-Elipe et al. (2003)
Endocrinology	Yamamoto (2018), Chevolleau et al. (2016)
Enzyme activity	Martínez et al. (2018, 2017), Gale et al. (2017), Al- Dabbagh et al. (2016), Patin et al. (2016), Ruan et al. (2011), Bruzzone et al. (2010), Su et al. (2010), Meyer et al. (2008), Baranczewski et al. (2006), Mortimer et al. (2006)
Estrogen metabolism	Peck et al. (2007)
Fatty acid metabolism	Labadie et al. (2007), Fer et al. (2006), Harmon et al. (2006), Fer et al. (2008)
Flavonol metabolism	Borges et al. (2016), Mullen et al. (2003)
Fungal toxin biochemistry	Pedras et al. (2003)
Glucose metabolism	Bou et al. (2016)
Glutathione metabolism	Geenen et al. (2013)
Hormone metabolism	Tykva et al. (2005)
Inositol phosphate and phophoinositide metabolism	Kiefer et al. (2010), Stevenson-Paulik et al. (2006)
Natural product characterization	Yang et al. (2004);
Nicotinamide biosynthesis	McCracken et al. (2004);
Peptide biochemistry	Hervé et al. (2013), Ménard, et al. (2012);
Pesticide chemistry	Nallani et al. (2018), Abit and Al-Khatib (2013), Powell et al. (2011)
Prostanoid biosynthesis	Chillar et al. (2011);
Radiopharmaceutical analysis and biochemistry	Däpp et al. (2011), Hsia et al. (2011), Li et al. (2011a,b), Shah and Khan (2011), Cui et al. (2010), Haeusler et al. (2010), Shah et al. (2010), Xu et al. (2009), Denoyer et al. (2008), Giblin et al. (2006), Vanbilloen et al. (2003), Vanderghinste et al. (2003)
Soil biodegradation	Andriamalala et al. (2018), Cassigneul et al. (2018, 2016), Geng et al. (2018), Nguyen et al. (2018); Zhu et al. (2018); Ma et al. (2017), Zhang et al. (2018), Li et al. (2016)
Steroid biosynthesis	Gomes de Mello Martins et al. (2017), Schaeffer et al. (2008a,b), Mensah-Nyagan et al. (2008), Saredi et al. (2005)
Steroid metabolism	Maltais et al. (2018), Abdel-Khalik et al. (2017), Fahrbach et al. (2010), Patte-Mensah et al. (2010), Granata et al. (2009), Pettersson et al. (2009), Venard et al. (2008)
Toxicokinetics	Knudsen et al. (2018, 2016, 2014), Maul et al. (2018), Bendadani et al. (2016)
Vitamin metabolism	Farjo et al. (2011)
Validamycin production	Chen et al. (2017)
Xenobiotic metabolism	Jacques et al. (2010a,b).

[a] *Only a few examples are listed because applications in the life sciences number in the hundreds. The list is intended only to give a general idea of the scope of flow-cell radionuclide analysis with HPLC in the biosciences.*
[b] *Listed in alphabetical order.*

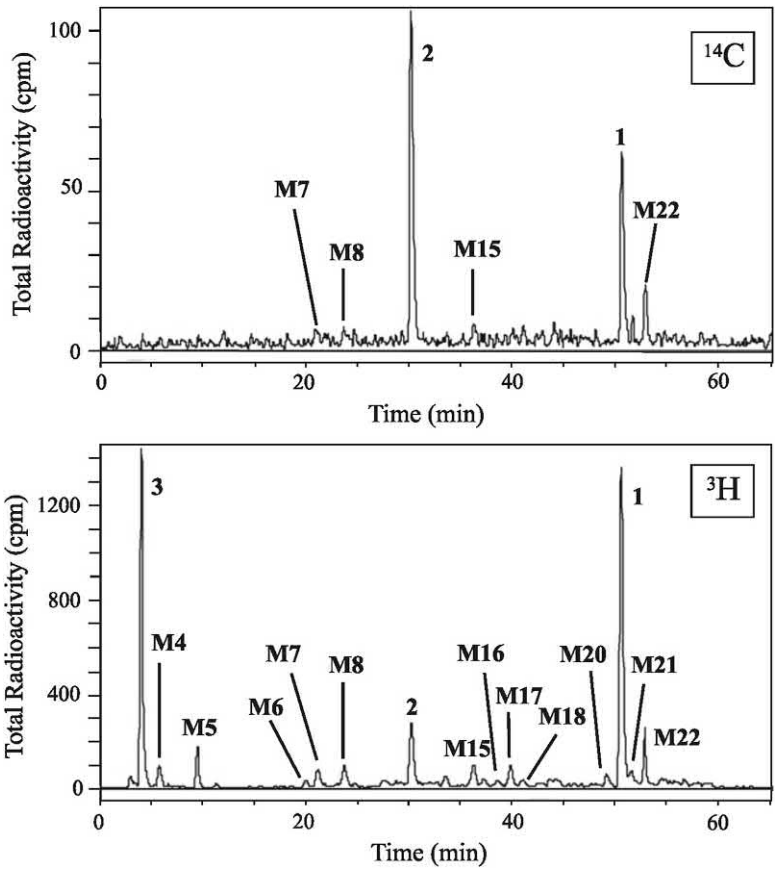


FIGURE 10.53 Online HPLC radiochromatograms of dual radiolabeled incubations in rat liver microsomes with [^{14}C/^{3}H]1 after 60 minutes measured with an IN/US Beta RAM radiometric flow cell detector. Top: ^{14}C channel; bottom: ^{3}H channel. Chromatogram radioactivity peaks are labeled according to compound or metabolite number. Not all metabolites are labeled with radioisotope because the radioisotope labels were located at only one carbon atom of the parent compound assigned number 1. *From Shaffer and Langer (2007); reprinted with permission from Elsevier © 2007.*

determining the structure of metabolites directly from HPLC effluents without further sample treatment. The traditional and more time-consuming methods of structure analysis, including chromatography of metabolites, followed by chromatogram fraction collection, and purification prior to submission of isolated metabolites to MS, have been applied for many years (L'Annunziata, 1970, 1984; L'Annunziata and Fuller, 1971a). Advanced techniques include the online mass spectral structural analysis of metabolites directly off the HPLC column after detection of peaks of interest. This section describes the state-of-the-art of online MS of radioisotope-labeled metabolites following HPLC separation and flow scintillation analysis (FSA) detection of chromatogram peaks of interest, also referred to as hyphenated radio-HPLC-FSA-MS analysis. This hyphenated analytical method may also be written as LC-RI-MS to signify the online hyphenated sequence "liquid chromatography—radioisotope detection—mass spectrometry."

A. HPLC-FSA-MS instrumentation and interfacing

When the metabolism of a radioisotope-labeled compound is studied and the metabolites are separated by HPLC, flow scintillation analysis (FSA) can provide the quantitative analysis of metabolites in terms of percentage of total recovered radioactivity. For example, when a parent compound labeled with a radioisotope, such as ^{3}H, ^{14}C, ^{32}P, ^{33}P, or ^{35}S, is administered with a known radioactivity to a test animal or medium and the metabolites separated by HPLC, the percentage of the total radioactivity administered is automatically measured by the FSA prior to MS. Consequently, the use of FSA prior to MS provides advantages over the UV detector, which include (1) irrefutable evidence that a certain HPLC peak is one of interest, i.e., it is labeled with radioisotope and thus a confirmed product of the radioisotope-labeled precursor, (2) the measurement of radioactivity from the isotope label is performed by the FSA without a miss, unless the isotope label is near or essentially at background levels, (3) the FSA reports the radioactivity of

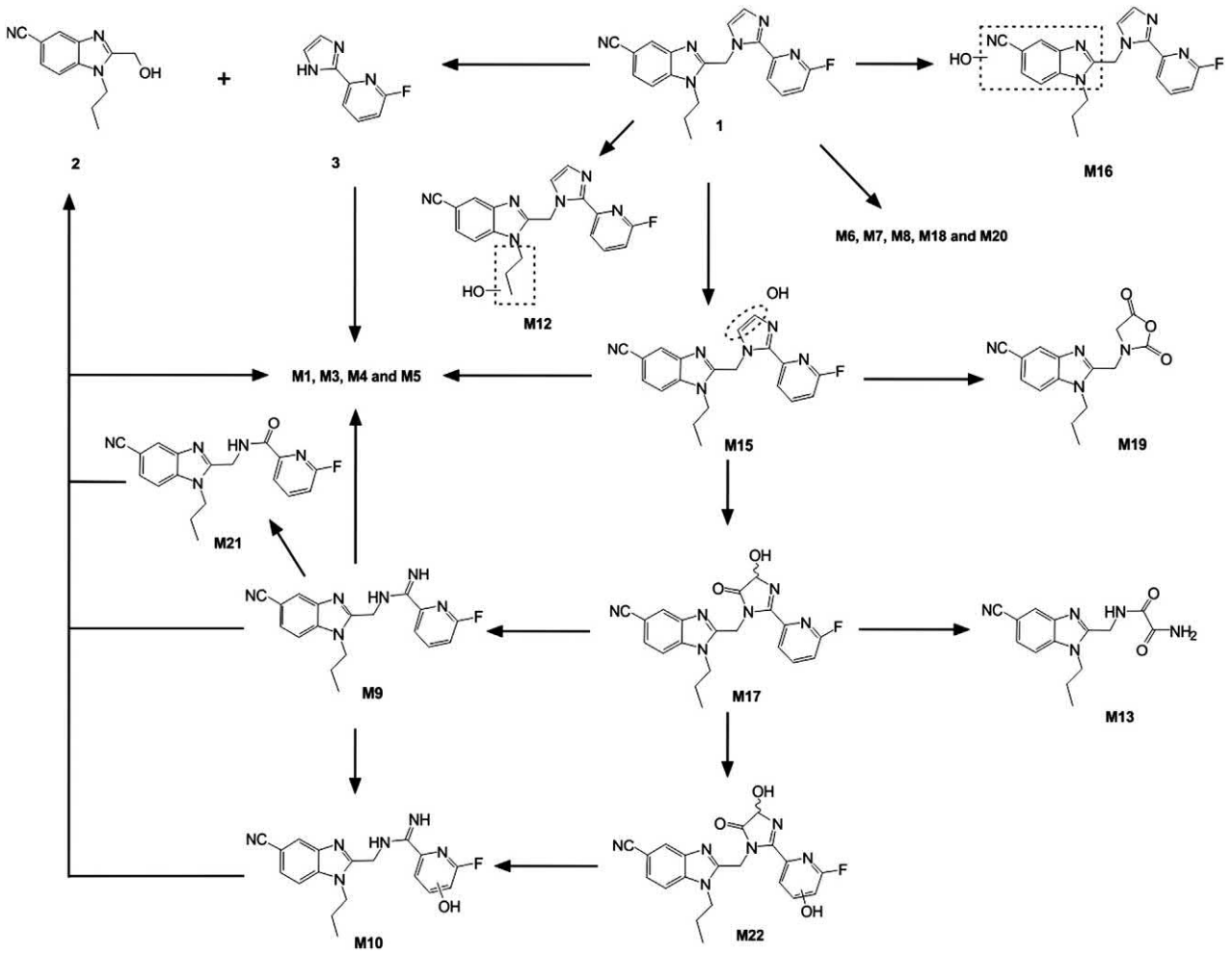


FIGURE 10.54 Proposed metabolic pathways for molecule 1 in cross-species hepatic microsomes determined with the aid of radioisotope labeling and online HPLC and mass spectrometry. *From Shaffer and Langer (2007); reprinted with permission from Elsevier © 2007.*

the HPLC-separated parent compound and metabolite fractions in quantitative units of disintegrations per minute (DPM) providing valuable data for the quantitative percentages of total radioactivity administered to a test organism, and (4) the FSA can store quantitative data on metabolites over a series of HPLC runs carried out over a time span to determine the time course of a metabolism study (see Fig. 10.3 illustrated earlier in this chapter).

The FSA provides the real-time radioactivity levels of metabolites as these are eluted from the HPLC column, and the radioactivity peaks from the FSA can provide the signal to initiate MS analysis. The FSA is connected directly to the MS if using a heterogeneous (solid) flow cell (see Fig. 10.12). If a homogeneous (liquid) flow cell is used, the flow is split to both the FSA and MS. The homogeneous flow-cell arrangement requires HPLC eluate splitting because scintillation cocktail is mixed with eluate for radioisotope analysis. Stream splitting is often set to provide most of the stream to the FSA and a small portion to the mass spectrometer because of the high sensitivity of mass spectrometers (pg/μL) that utilize ESI techniques for sample introduction. The degree of HPLC stream splitting to the flow scintillation analyzer (i.e., flow-cell detector) and the mass spectrometer may depend on the activity of the radioisotope label and the need to maximize the sensitivity of radioisotope detection. Thus, a larger portion of the HPLC stream will go to the radioisotope detector, and the remaining smaller fraction to the more sensitive mass spectrometer. For example, Ubukata et al. (2011) and Shaffer and Langer (2007) split the HPLC eluate stream according to the ratio of 1:9 between the mass spectrometer and radioactivity flow detector. In a similar fashion, Ramanathan et al. (2007) used a stream splitter that diverted 15% of the HPLC eluate to the mass spectrometer and 85% to the radioactivity flow-cell detector, whereas Athersuch et al. (2008) used a dead-volume T-piece to divert 150 μL/min of the HPLC eluate to the mass spectrometer and 450 μL/min of the eluate to the flow scintillation analyzer.

Other examples of steam splitting of HPLC effluent ratios to the mass spectrometer and radioisotope detector are 1:6 by Glaenzel et al. (2018), 1:5 by Geenen et al. (2013), and 1:4 by Dymond et al. (2016), Liu et al. (2016) and Tozuka et al. (2011).

The homogeneous flow-cell setup provides higher detection efficiencies (up to 45% for ^{3}H and 88% for ^{14}C) depending on the quench level of HPLC solvents. Stream splitting of HPLC eluate to the flow scintillation analyzer and mass spectrometer is a common practice (see also Edlund and Baranczewski, 2004; Ghosal et al., 2005; Prasad et al., 2011; Singh et al., 2001; Vickers et al., 2001; and Yuan et al., 2002). In most cases, most of the eluate is directed onto the FSA, and only a small fraction diverted to the mass spectrometer. When a heterogeneous flow-cell detector is used, the entire HPLC eluate or any convenient fraction of the eluate may be used for spectroscopic analysis because the eluate is not mixed with liquid scintillator before entering the flow scintillation analyzer. For example, Pedras et al. (2003) used a heterogeneous flow-cell detector containing SolarScint solid scintillator for the measurement of ^{14}C-labeled metabolites before directing the HPLC eluate on to the mass spectrometer. The HPLC analysis of radiopharmaceuticals containing ^{99m}Tc are best detected with a gamma flow cell that utilizes NaI(Tl). These entire HPLC eluates or any convenient fraction of the eluate can be diverted on to online spectrometers (Vanbilloen et al., 2003; Vanderghinste et al., 2003).

Interfaces with the HPLC effluent and mass spectrometer must liberate the biochemical or bioorganic molecular species of interest (e.g., metabolite) from the aqueous solvent molecules and ionize the molecular species prior to mass spectrometric separation of the molecular ions and molecular ion fragments. This is performed most commonly by spray ionization (SI) techniques, which involve a combination of processes including spraying the HPLC effluent from a fine capillary into minute droplets, pneumatic heating with a drying gas, applied electric potential, and in some cases chemical ionization. Common MS interfaces used in conjunction with HPLC are ESI and atmospheric pressure chemical ionization (APCI) of which published applications number in the hundreds. A few examples of recent applications of ESI may be found in Lu et al. (2018), Gobo et al. (2018), Murakami et al. (2018), Tung et al. (2018), and Xiao et al. (2018), and applications of APCI are described by Etzbach et al. (2018), Gorassini et al. (2017), Oldekop et al. (2017), Rybin et al. (2017), Tessema et al. (2017), and Wang et al. (2018).

In the ESI method, a nebulizer gas and electric field is introduced at the interface to produce charged droplets of the HPLC effluent. The combination of electric field energy and pneumatic heating via a warm concurrent dry gas stream causes the charged droplets of the HPLC effluent to subdivide and yield eventually single ionized molecules. Fig. 10.55 illustrates the interface between the effluent of a microbore HPLC chromatograph effluent or flow-cell radionuclide detector to an ESI source of the mass spectrometer. APCI is a chemical ionization technique, which employs a mechanism similar to ESI. The differences exist in the establishment of a plasma of the nebulized HPLC effluent by a DC discharge at atmospheric pressure. Reactions between ions and molecules occur in the plasma to produce molecular ion species of the biochemical or bioorganic compounds present, which are then introduced via vacuum into the mass spectrometer. SI techniques yield high ionization efficiencies and consequently mass spectral detection limits as low as the pg/μL level. Also, SI

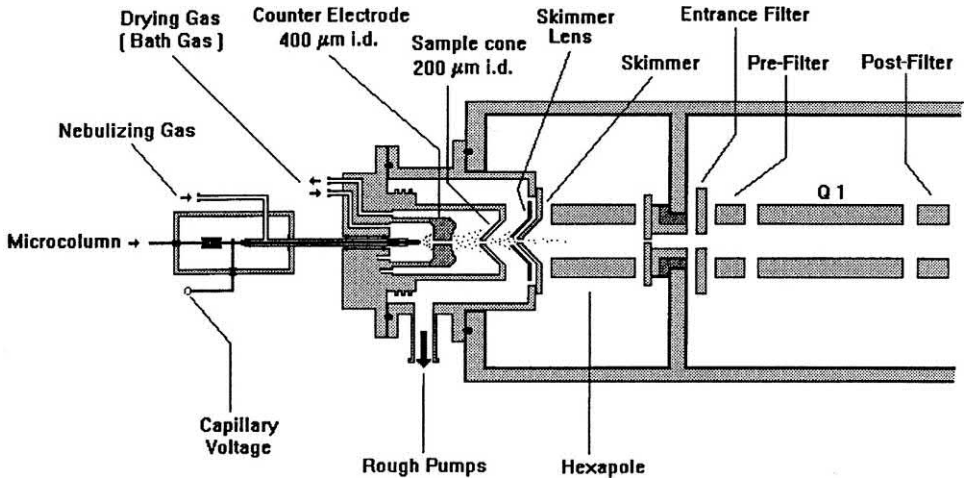


FIGURE 10.55 Schematic of a modified electrospray ion source for the Quattro I mass spectrometer. The counter electrode is designed with a 400-μm-ID hole for applications with flow rates of 1−20 μL/min. *From Schultz and Alexander (1998). This material is reproduced with permission, © 1998 John Wiley & Sons, Inc.*

techniques are soft, which yield relatively minor molecular ion fragmentation providing accurate molecular weight determinations in the mass range up to 10^5-10^6 Da, the sensitivity depending on the specific type of mass spectrometer used. The theory and principles of ESI and APCI are described in detail in a book by Gross (2017) on MS; and special treatments on ESI and APCI are provided by Tang et al. (2017) and Pasilis and Van Berkel (2017), respectively.

The molecular ions and molecular ion fragments produced via the SI interface are separated in the mass spectrometer according to their mass-to-charge ratios (m/z) using electric and/or magnetic fields. Several types of mass spectrometers are available for use online with HPLC, including time-of-flight analyzers, quadrupole ion filters, quadrupole ion trap instruments, and orbitrap systems. The characteristics of these instruments are described in detail by Gross (2017), and a comparison of the key features of the various types of mass spectrometers in terms of their application to HPLC-MS metabolite identification is given in a thorough review by Niessen (2017).

A tandem mass spectrometer is used often online with HPLC in metabolism studies, which may include online flow-cell detectors (Abdel-Khalik et al., 2017; Farlin et al., 2018; Geng et al., 2018; Jensen et al., 2017; Maltais et al., 2018; Sato-Nakai et al., 2017 and Sharma et al., 2017). Tandem MS is abbreviated as MS/MS because it consists of dual mass analyzers coupled in a tandem instrument useful in selectively separating the parent molecular ions from the product ion fragments. Dual mass analysis with the tandem analyzer is accomplished by first selecting the parent molecular ions after initial ionization with a sector magnet, and the molecular ions are further dissociated via collision with a gas such as He, Ne, N_2, or Ar referred to as collision-induced dissociation (CID). The ion fragmentation products of CID are analyzed subsequently in the second mass analyzer according to their m/z and abundance.

B. Representative data

Numerous research papers employing online HPLC-FSA-MS have appeared in the scientific journals, including works by Abdel-Khalik et al. (2017), Chillar et al. (2011), Glaenzel et al. (2018), Huskey. (2016), Jensen et al. (2017), Koitka et al. (2010), Lenz et al. (2011), Narita et al. (2018), Okarvi and Al Jammaz (2016), Prasad et al. (2010), Sato-Nakai et al. (2017), Scheible et al. (2016), Shaffer and Langer (2007), Sharma et al. (2017), Shemesh et al. (2016), Su et al. (2010), and Suddaby et al. (2016). Some examples of representative data will be described in this section.

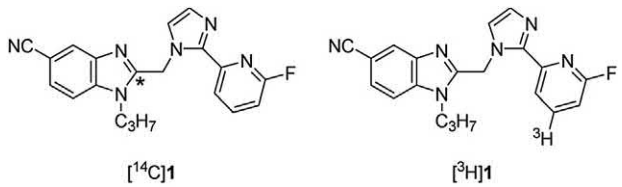


FIGURE 10.56 Chemical structures for [^{14}C]1 (symbol '*' denotes ^{14}C) and [^{3}H]1. *From Shaffer and Langer (2007); reprinted with permission from Elsevier © 2007.*

An interesting example can be taken from the work of Shaffer and Langer (2007), who studied the in vitro metabolism of a drug labeled with the radioisotopes ^{3}H and ^{14}C at specific sites of the molecule, illustrated in Fig. 10.56. The metabolism studies were executed by incubation of the radioisotope-labeled drug in hepatic microsomes. The radioisotope-labeled compounds were diluted with non-labeled compound to yield 10 μM incubation concentrations with 0.25 μCi of [^{14}C]1 or 2.5 μCi of [^{3}H]1 (see Fig. 10.56) and a combination of the two for dual-radiolabel studies. The number "1" denotes the precursor compound where metabolites of "1" are numbered consecutively according to the proposed sequence of metabolite formation as illustrated previously in Figs. 10.53 and 10.54.

Shaffer and Langer (2007) separated the precursor drug from its metabolites by HPLC, which was interfaced directly with a Beta Ram (LabLogic, Inc.) flow scintillation analyzer (FSA) flow-cell detector and a PerkinElmer tandem quadrupole mass spectrometer (PerkinElmer, Inc.). The effluent from the HPLC was split 1:9 between the mass spectrometer and the FSA with LS cocktail flowing at the rate of 3 mL/min to the radiometric flow-cell detector. Radioactivity in the HPLC effluent is measured by the FSA and plotted against time in minutes, as illustrated previously in Fig. 10.53. The activity peaks corresponding to metabolites separated by HPLC are numbered in Fig. 10.53, and some metabolites are labeled only with ^{3}H and others only with ^{14}C, which aided in the confirmation of the molecular origin of a particular metabolite. The flow-cell radioactivity detector provides additional information on the quantities of each metabolite relative to the precursor drug, as listed in Table 10.11. Depending on the origins of the metabolites relative to the molecular structure of compound 1, some metabolites are labeled with only ^{14}C, only ^{3}H, with both ^{14}C and ^{3}H, or without any radioisotope label.

Determinations of the molecular structures of the metabolites are facilitated by the mass spectra of each of the compounds, as these are eluted from the HPLC. A mass spectrum will yield the molecular weight (*m/z*) of the parent ion of a metabolite, and the ion fragments will provide evidence of the molecular structure. For example, Shaffer and Langer (2007) used characteristic fragment ions produced in the collision-induced dissociation (CID) mass spectrum, illustrated in Fig. 10.57, together with radiochromatographic data as starting points in the elucidation of the structure of metabolites and the metabolic scheme,

TABLE 10.11 Quantitative inline generated profile of [^{14}C]metabolites, [^{3}H]metabolites, and total metabolites after a 60-minute monoradiolabeled incubation with either [^{14}C]1 or [^{3}H]1 in rat liver microsomes.[a]

Compound	[^{14}C]1	[^{3}H]1	Average
1	3.9	1.6	2.8
M1	–	3.8	1.9
3	–	41.6	20.8
M3	–	7.9	4.0
M4	–	1.7	0.9
M5	–	9.0	4.5
M6	3.3	2.7	3.0
M7	5.2	3.2	4.2
M8	7.9	4.4	6.2
M9	2.9	2.0	2.5
M10	–	1.4	0.7
2	55.7	–	27.9
M12	–	–	–
M13	4.0	–	2.0
M15	5.8	3.9	4.9
M16	–	3.2	1.6
M17	6.1	7.8	7.0
M18	–	2.0	1.0
M19	–	–	–
M20	–	1.1	0.6
M21	–	–	–
M22	5.1	3.1	4.1
Radioactivity profiled (%)	99.9	100.4	100.2
Σ^{3}H-only metabolites (**M1, 3, M3–M5**)	na	64.0	32.0
Σ^{14}C-only metabolites (**2, M13**)	59.7	Na	29.9

_, not detected by radiochromatography (i.e., flow-cell detector).
na, not applicable.
[a]*From Shaffer and Langer (2007); reprinted with permission from Elsevier © 2007.*

which was illustrated previously in Fig. 10.54. The characteristic ion fragments, illustrated in the mass spectrum of Fig. 10.57, illustrate the protonated parent ion at *m/z* 361 and fragment ions at *m/z* 319, 198, 170, and 156. The ion fragment at *m/z* 319 is due to the loss of the C_3H_7 group, illustrated in the upper left-hand portion of the spectrum. The ion fragment at *m/z* 198 is due to the loss of a neutral fragment of mass 163 as illustrated, which undergoes further fragmentation to ions at *m/z* 170 and 156. Other illustrative examples of the determinations of metabolic pathways by means of the hyphenated technique of HPLC-FSA-MS can be found in the references cited previously in this section.

XII. Online FSA and nuclear magnetic resonance[2]

As described previously in this chapter, flow scintillation analysis (FSA) is commonly used to quantify the radioisotope label on organic compounds, such as biochemicals, drugs, and metabolites separated from complex mixtures by

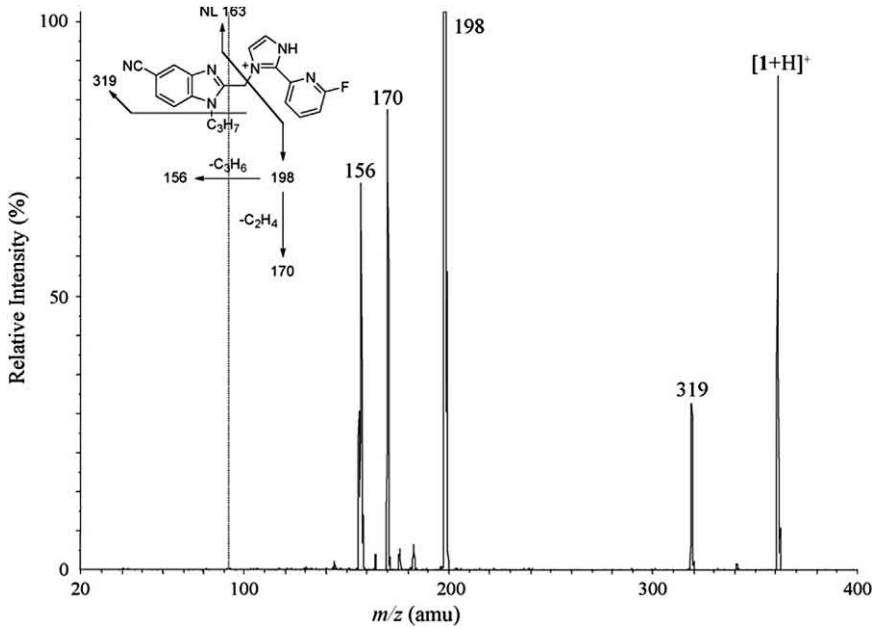


FIGURE 10.57 Collision-induced dissociation mass spectrum of protonated 1 (*m/z*) 361 and its proposed fragmentation pathways. The abbreviation NL 163 refers to a neutral loss, i.e., the loss of a neutral fragment of mass 163. *From Shaffer and Langer (2007); reprinted with permission from Elsevier © 2007.*

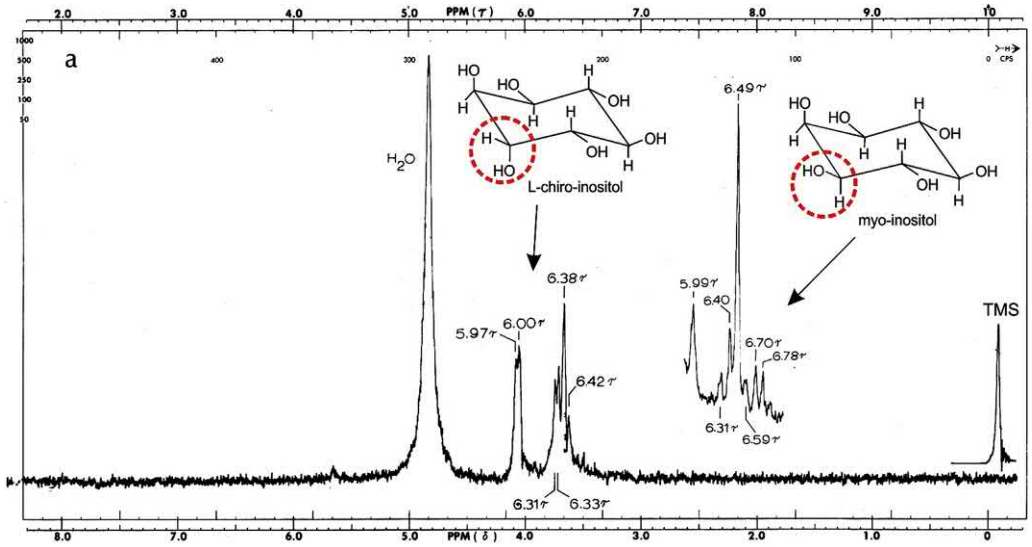


FIGURE 10.58 Proton NMR spectrum of L-chiro-inositol, and in the inset to the right, the proton NMR spectrum corresponding to myo-inositol for comparison, in D_2O solvent. The only protons yielding a resonance absorption signal are the protons attached to the cyclohexane ring. The protons attached to the hydroxyl groups do not display a resonance absorption signal because they exchange with deuterium from the D_2O solvent. The two stereoisomers differ in structure only at one carbon atom marked by the circle drawn over the two structures. The chemical shifts are measured here in δ (cpm) or τ (cpm) where $\tau = 10.0 - \delta$. *From L'Annunziata (1970), Ph.D. Dissertation, https://dissexpress.proquest.com/dxweb/results.html?QryTxt=&By=L%27Annunziata&Title=&pubnum.*

HPLC. The subsequent task of determining the molecular structure of the separated substances can be challenging. Traditional methods of structure determination involve collecting the radio-HPLC separated fractions that correspond to activity peaks measured by the flow scintillation analyzer. The collected fractions are then isolated, further purified, and then submitted to spectroscopic methods of analysis such as MS and NMR spectroscopy. Both MS and NMR methods provide complementary information that can be used to derive a molecular structure. MS, described in Section XI of this chapter, can provide the molecular weight, molecular formulae, and structure from ion

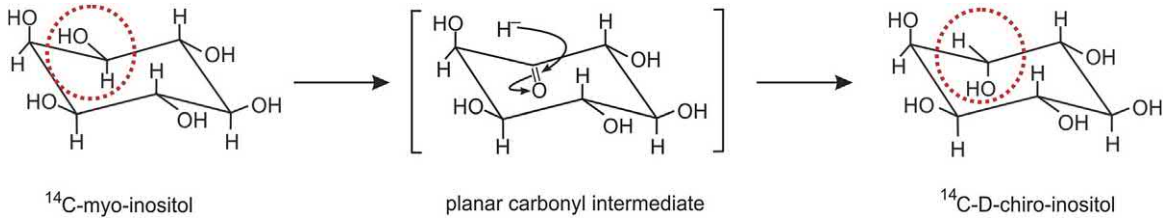


FIGURE 10.59 Soil microbial epimerization of uniformly labeled ^{14}C-myo-inositol to ^{14}C-D-chiro-inositol. The dotted circle surrounds the only carbon atom where the stereochemistry differs between the two isomers. The reaction was demonstrated with the use of uniformly labeled ^{14}C-myo-inositol incubation in soil in the work of L'Annunziata et al. (1977). The brackets illustrate the proposed intermediate. *From L'Annunziata (1970), Ph.D. Dissertation, https://dissexpress.proquest.com/dxweb/results.html?QryTxt=&By=L%27Annunziata&Title=&pubnum.*

fragmentation patterns, whereas NMR can provide additional complementary structural information, including the spatial orientation (i.e., stereochemistry) of atoms in the molecular structure. A good example of this can be taken from early work of the writer concerning the mass and NMR spectra of the inositol diastereomers, all of which produce virtually identical electron-impact mass spectra, but different NMR spectra (L'Annunziata, 1970; L'Annunziata and Fuller, 1971a, b; 1976). In the case of the inositol diastereomers, they differ only by the orientation of one proton and hydroxyl group on a single carbon atom (see Fig. 10.58). The writer (L'Annunziata, 1970 and L'Annunziata and Fuller, 1971a,b) demonstrated that these inositol stereoisomers, isolated as inositol phosphates in soils, can be identified by their NMR spectra. The NMR spectroscopic analysis of molecular structure was at the very early stages of development in the late 1960s and early 1970s; however, currently NMR is used generally online with HPLC and flow-cell detectors for the structural elucidation of radioisotope-labeled organic compounds, which is described in the following section of this chapter. As illustrated in Fig. 10.58, the myo-inositol and chiro-inositol, isolated as soil inositol phosphates and separated by chromatography, differ only by the orientation of the proton and hydroxyl group at a single carbon atom, and their NMR spectra are unique. From this work, the writer (L'Annunziata, 1970; L'Annunziata and Fuller, 1971a) postulated that the D-chiro-inositol and its phosphates in soils could originate via the epimerization of the most abundant soil myo-inositol. By incubating uniformly labeled ^{14}C-myo-inositol in soil, the writer and coworkers (L'Annunziata et al., 1977) demonstrated the soil microbial epimerization of the ^{14}C-myo-inositol to ^{14}C-chiro-inositol, illustrated in Fig. 10.59.

An increasing popular approach to drug metabolism and natural product studies involves the online measurement of the NMR spectra of compounds directly off the HPLC column obviating the need for compound isolation. This section will describe developments in linking the flow scintillation analyzer (i.e., flow-cell detector) from the HPLC to the NMR spectrometer to provide online (in situ) molecular structure analysis of radioisotope-labeled compounds.

A. Principle of nuclear magnetic resonance spectroscopy

NMR spectroscopy is used to derive the molecular structure of organic compounds from the magnetic properties of the atomic nuclei (e.g., ^{1}H and ^{13}C) and the surrounding molecular electrons of an organic compound since the first commercial NMR spectrometer appeared in 1960. Nuclei of certain atoms of odd mass such as ^{1}H and ^{13}C, or even mass and odd charge, have a net charge and a spin. The spinning charge of the nucleus creates a magnetic dipole (μ). If one places spinning proton nuclei, which are a component of most organic compounds, in a magnetic field (*H*), the axis of the magnetic dipoles of these nuclei will precess at an angle (θ) with respect to the magnetic field axis, as illustrated in Fig. 10.60. The precession of the nuclei with respect to the applied magnetic field axis occurs somewhat like the way a spinning top precesses under the force of the earth's gravitational field. The angular velocity of this precession is a function of the strength of the applied magnetic field (*H*) and the affects of *shielding* caused by spinning electrons in the molecular environment of the proton nuclei within the organic compound.

Spherical nuclei of odd mass, such as ^{1}H, ^{13}C, ^{15}N, ^{19}F, and ^{31}P, possess a spin of ½, and when subjected to the external magnetic field, the nuclei can possess two orientations, namely, an orientation in the direction of the magnetic field (+½), as illustrated in Fig. 10.60, or an orientation against the magnet field (−½), i.e., opposite to the orientation illustrated. While under the forces of a stable magnetic field (*H*) of the NMR spectrometer, the proton nuclei are irradiated with a radio frequency energy tunable over a narrow range. When the variable frequency is attuned to the precessional angular velocity of a given proton nucleus within a molecule, the two frequencies are in *resonance*. The applied energy at this resonance frequency is absorbed by the proton nucleus, and the nucleus is caused to flip or become aligned against the applied magnetic field (*H*). The energy absorbed by the proton nucleus, which causes it to reach the higher energy spin state (*i.e.*, flipped or −½), is the energy measured by the NMR spectrometer.

An auspicious circumstance characteristic of NMR spectroscopy is the following: the resonance absorption by proton

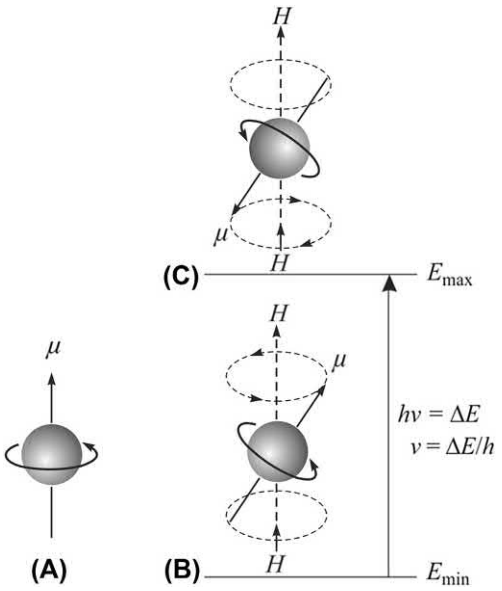


FIGURE 10.60 An atomic nucleus of spin quantum number ½ with magnetic moment μ in (A) the absence of an external magnetic field and (B) the presence of an external magnetic field (H). At E_{min}, the nucleus maintains a spin aligned with the external magnetic field and precesses with a frequency (ν) in accord with the strength of the external magnetic field. The nucleus makes a quantum jump ($h\nu$) to a higher energy state E_{max} aligning its spin against the magnetic field after exposure to a radio frequency (ν) coinciding with the frequency of precession. Atomic nuclei of spin ½ have only two possible quantum spin states, one aligned and the other against the external magnetic field. Examples are nuclei of odd charge and odd mass, such as ^{1}H, ^{7}Li ^{13}C, ^{15}N, ^{19}F, ^{29}Si, ^{31}P, ^{35}Cl, and ^{37}Cl. *From L'Annunziata (2016); reprinted with permission from Elsevier © 2016.*

nuclei is complicated by the shielding effect of electron clouds of varying densities in the environment of organic molecules. The electron cloud, surrounding a nucleus, also has charge and spin and therefore produces its own characteristic magnetic field, which apposes or shields the externally applied field. The degree of *shielding* is a function of the electron cloud density, which will differ from nucleus-to-nucleus in the organic molecule, because of the differing electronegativities of neighboring atoms. Therefore, protons in a molecule will absorb different resonance frequencies depending on their location in the molecule. This effect is referred to as the *chemical shift*. A proton, which is highly shielded, absorbs at a lower resonance frequency than a proton with reduced shielding. The presence of atoms of differing degrees of electronegativity (electron-withdrawing ability) in molecules as well as the differing three-dimensional orientation of atoms within molecules will cause a wide spectrum of shielding effects on neighboring protons. This gives rise to a wide spectrum of resonance absorption frequencies for protons depending on the structural group to which the protons are attached, their neighboring atoms, and their spatial orientation in the molecule. Therefore, the differing resonance absorption frequencies or chemical shifts of protons in NMR spectroscopy provide an absorption spectrum, which serves as a means for identifying chemical groups and their spatial positions in organic molecules.

The chemical shift of a particular proton nucleus in a molecule is recorded with respect to the chemical shift of the protons on a reference molecule, e.g., tetramethylsilane or $(CH_3)_4Si$ most often referred to as TMS (see Fig. 10.58). The difference in chemical shifts of a proton or group of protons in a molecule with respect to that of TMS is recorded and calculated in units of Hz, whereas the magnitude of the applied frequency is in the order of magnitude of MHz, a million-fold greater. The difference in chemical shift of a proton nucleus with respect to that of the reference (e.g., TMS) in Hz is divided by the applied frequency in MHz to record chemical shifts in convenient units of parts per million (ppm). Nuclei of even mass (e.g., ^{2}H and ^{12}C) in a molecular structure do not possess a magnetic moment, and these nuclei are inert to the previously described effects of an external magnetic field. Thus, deuterated solvents are used generally in the measurement of NMR spectra of water-soluble compounds.

For additional reading on the principles of NMR as well as MS, see works by Goldenberg (2016), Günther (2013), and Simpson and Simpson (2014).

B. HPLC-FSA-NMR system

Because time is money, the trend is to analyze samples as fast as possible with as much automation that current technology will permit. This has led to advances in metabolism studies where the molecular structure of isotope-labeled metabolites must be determined. A major advance in this field has been the direct linking of the NMR spectrometer to the HPLC. Several papers on this technology serve as excellent examples (Albert, 2014; Anonymous, 2012; Bailey et al., 2000; Brkljača and Urban, 2015; Brkljača et al., 2017; Hall et al., 2016; Hansen et al., 1999; Hehn et al., 2013; Johansen et al., 2013; Kim et al., 2011; Larsen et al., 2009; Lee et al., 2012; Lenz et al., 2007; Li et al., 2010; Martin et al., 2003; Provera et al., 2010a,b; Ren et al., 2017; Scarfe et al., 2000; Seger et al., 2013; Shi et al., 2009; Shockcor, 2017; Shockcor et al., 1996; Silva et al., 2013; Silva-Elipe, 2003; Silva-Elipe et al., 2003; Singh et al., 2001; Smith et al., 1999; Sweeny et al., 2000; Timmers and Urban, 2012; Timmers et al., 2012; and Wilson and Brinkman, 2003).

When the metabolism of a radioisotope-labeled compound is studied and the metabolites are separated by HPLC, flow scintillation analysis provides for the quantitative analysis of metabolites in terms of percentage of total recovered radioactivity (see Table 10.11). For example, when a parent compound labeled with a radioisotope, such as ^{3}H, ^{14}C, ^{32}P, ^{33}P, or ^{35}S, is administered with a known radioactivity to a test animal and the metabolites separated by HPLC, the percentage of the

total radioactivity administered is automatically measured by the FSA prior to NMR spectroscopy. In addition, the FSA provides irrefutable evidence of radioisotope label on the structure of the metabolite, which can provide information as to the pathways and mechanisms of metabolism of radioisotope-labeled precursor compounds. This was illustrated previously in Table 10.11. Consequently, the use of FSA prior to NMR spectroscopy provides information on the radioisotope label in the HPLC effluent, whereas the UV detector may provide only information on the presence of a molecular component in the HPLC effluent be it labeled or not with radioisotope. Thus, the FSA and UV detector linked to the HPLC effluent stream will provide information on molecular components as they are eluted off the HPLC column.

Radioisotope tracers are commonly used in metabolic studies, and there remains the need to quantify the isotope label on the metabolites eluted from the HPLC prior to their molecular structure analysis by NMR spectroscopy. The FSA (i.e., flow-cell detector) provides the real-time radioactivity levels of metabolites as these are eluted from the HPLC column, and the radioactivity peaks from the FSA can provide the signal to initiate NMR spectroscopic analysis. This will allow the researcher using HPLC-FSA-NMR to accurately stop the flow and capture the HPLC peak of interest in the NMR flow probe for molecular structure analysis. The FSA is connected between the UV detector and NMR if using a heterogeneous (solid) flow cell. If a homogeneous (liquid) flow cell is used, the flow is split to both the FSA and NMR. The heterogeneous flow cell (see Table 10.1) uses a solid scintillation detector and yields relatively high detection efficiencies for ^{14}C (70%–85%) providing full recoveries of the HPLC eluate for subsequent NMR analysis. The homogeneous flow cell arrangement requires HPLC effluent splitting because scintillation cocktail is mixed with effluent for radioisotope analysis. The latter homogeneous flow cell setup is most appropriate for ^{3}H analysis with detection efficiencies of up to 45% depending on the quench level of the HPLC solvents.

A specially designed flow probe is inserted into the NMR sample chamber. The probe is constructed to permit the sample to flow into the NMR spectrometer and the resonance spectra obtained while either flowing through, or more commonly stopped (i.e., stopped-flow analysis) and analyzed for a required period of time. The following site provides information on flow probes for NMR: https://www.bruker.com/products/mr/nmr/hyphenation/lc-nmr/overview.html, accessed October 31, 2018. The NMR flow probe placed in the bore of the magnet holds the sample with a commonly employed cell volume of 120 μL. It contains the antennae for sample radio frequency energy irradiation and the receipt of the weak radio frequency resonance signal. A stop-flow mode is commonly employed for measurement of the NMR spectra because of the low sample concentrations in the HPLC peaks. Suitable NMR spectra are obtained with samples as small as 1 μg (or even submicrogram) depending on sample molecular weight and analysis time (Beery, 2000; Silva-Elipe, 2000). Sample analysis times can vary from 1–2 hours to 1–2 days. Stopped-flow NMR measurements of single peaks of the liquid chromatogram are governed by the signal from the UV absorbance detector or the signal from the FSA radioactivity detector. A signal from the radioactivity detector also confirms a metabolite of a radioisotope-labeled parent compound, and it can be used to quantify the radioisotope label in that metabolite, whereas peaks observed from the UV detector, which do not coincide with radioisotope peaks, will demonstrate the absence of radioisotope label. The FSA detector, therefore, not only can be used to trigger stopped flow for NMR analysis, but it may also provide valuable quantitative data for metabolic studies as seen previously in Table 10.11.

C. HPLC-FSA-NMR representative data

Applications of FSA to online HPLC-NMR setups for the chromatographic separation, radioactivity analysis, and molecular structure analysis of isotope-labeled metabolites are found in the scientific journals. The following are illustrative examples: Bailey et al. (2000), Berry et al. (2014), Byon et al. (2016), Dockens et al. (2000), Glaenzel et al. (2018), Hansen et al. (1999), Huskey et al. (2016), Kumar et al. (1999), Lenz et al. (2007), Mamidi et al. (2014), Martin et al. (2003), Maurizis et al. (1998), Paulson et al. (2000), Sato-Nakai et al. (2017), Scarfe et al. (2000), Scheible et al. (2016), Sharma et al. (2017), Shockcor (2017), Silva-Elipe (2003), Singh et al. (2001), Sweeny et al. (2000), Takahashi et al. (2015), and Vickers et al. (1998). Researchers will use commonly the stopped-flow method described above, where the signal of a liquid chromatogram peak from the FSA radioactivity detector or UV detector will trigger the stopped flow needed for in situ NMR spectroscopy in the HPLC eluate. Others will utilize the same FSA or UV signal to collect the entire peak in a suitable vial (i.e., fraction collection) and then submit the sample to further purification prior to off-line NMR analysis in a suitable solvent. A representative example of the application of online HPLC-UV-FSA-NMR spectroscopic analysis will be cited subsequently.

In a study on the metabolism of the drug ZD6126 developed for the treatment of colorectal, lung, breast, and prostate tumors, Lenz et al. (2007) studied the metabolism of [^{14}C]-ZD6126 in test animals. The [^{14}C]-ZD6126 was administered to the test animals, and samples were collected from the animals after various time intervals between 6 and 48 hours after dosing. Urine and bile samples were freeze-dried, reconstituted in MeOH to remove excessive salts, and again freeze-dried and reconstituted in 400–800 μL of D_2O:ACN (acetonitrile) 50:50, v/v

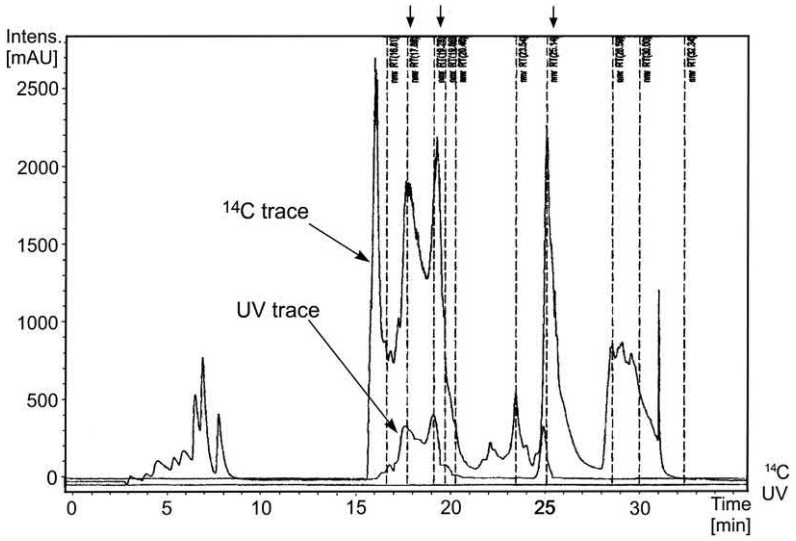


FIGURE 10.61 UV and ^{14}C traces of the HPLC separation of [^{14}C]-ZD6126 metabolites in pooled bile samples from male rats (6−12 hours collection, 6 mL total volume). Arrows indicated peaks of interest eluting at 17.88, 19.28, and 25.14 minutes for the stopped-flow measurement of ^{1}H NMR spectra. *From Lenz et al. (2007); reprinted with permission from Elsevier © 2007.*

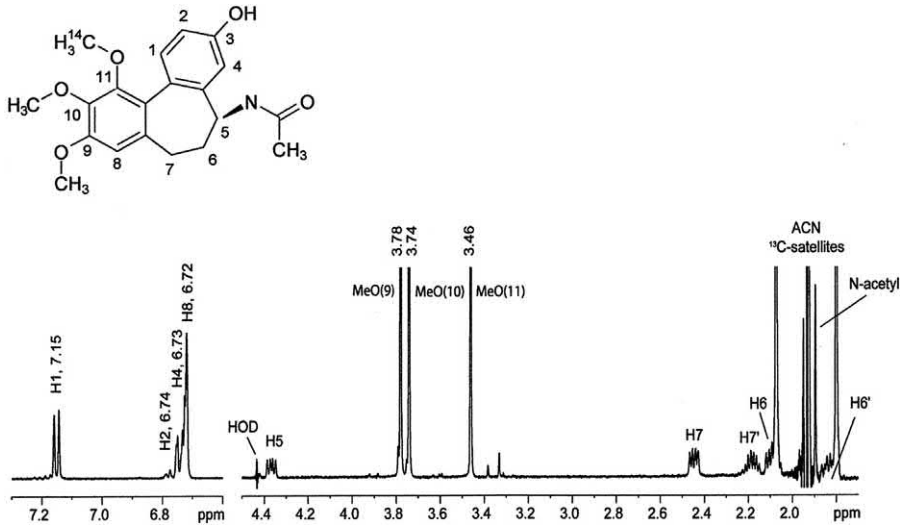


FIGURE 10.62 Structure of [^{14}C]-ZD6126 phenol and its stopped-flow ^{1}H NMR spectrum. Key: HOD, residual water. *From Lenz et al. (2007); reprinted with permission from Elsevier © 2007.*

containing 1% formic acid-d_2. After centrifugation, the sample was injected directly into an HPLC column for direct ^{1}H HPLC-NMR analysis. It is critical that the dried sample be reconstituted in deuterated solvents and that the HPLC mobile phase also contain deuterated solvents to avoid interference from extraneous solution protons during the online determinations of the ^{1}H NMR spectra of the metabolites. The HPLC mobile phase in this case contained D_2O and ACN buffered with 0.1% formic acid-d_2.

A Berthold LB507A radioactivity monitor was interfaced with the HPLC prior to a Shimadzu UV diode array detector (DAD). The radioactivity detector was equipped with a 150 μL solid flow cell. The HPLC peaks of ^{14}C radioactivity and UV absorption from the two detectors were used by Lenz et al. (2007) for the signaling of the initiation of the stopped flow for the determination of the ^{1}H NMR spectra. Typical ^{14}C radioactivity and UV absorption traces of the HPLC effluent are illustrated in Fig. 10.61. The arrows at the uppermost part of the traces indicate peaks of interest, labeled with ^{14}C, where stopped flow permitted the online determination of ^{1}H-NMR spectra.

An example of a typical online stopped-flow ^{1}H NMR spectrum is that of [^{14}C]-ZD6126 phenol, illustrated in Fig, 10.62, and diagnostic signals for various metabolites

TABLE 10.12 List of chemical shifts (δ^1 H) of synthetic standards and metabolites[a].

Listing of resonances	H1	H2	H4	H8	$gluc^{H1}$	MeO^{9}	MeO^{10}	MeO^{11}	Proposed metabolite ID
Standards									
[^{14}C]-ZD6126 phenol	7.15	6.74	6.73	6.72	N/A	3.78	3.74	3.46	
ZD6126 phenol glucuronide	7.27	7.00	6.96	6.76	5.02	3.79	3.75	3.47	
10-Desmethyl-ZD6126 phenol	7.19	6.75	6.73	6.69	N/A	3.78	–	3.33	
Samples (volume equivalents injected/ml)									
D.m.u.0–24 hours (27 mL)	7.27	7.00	6.96	6.76	5.02	3.79	3.75	3.47	Phenol glucuronide
D.m.b.0–6 hours (3 mL)	7.21	6.78	6.74	7.08	N/A	3.83	–	3.47	Desmethyl sulfate
	7.26	7.00	6.96	6.75	5.02	3.79	3.75	3.47	Phenol glucuronide
R.m.b.0–6 hours (3 mL)	7.21	6.78	6.73	7.08	N/A	3.83	–	3.48	Desmethyl sulfate
	7.25	6.99	6.95	6.59	5.02	–	3.75	3.48	Desmethyl glucuronide
	7.25	6.98	6.95	6.74	5.02	3.79	3.75	3.47	Phenol glucuronide
R.m.b.6–12h (6 mL)	7.20	6.77	6.74	7.08	N/A	3.83	–	3.47	Desmethyl sulfate
	7.26	6.99	6.95	6.59	5.02	–	3.75	3.48	Desmethyl glucuronide
	7.26	6.99	6.95	6.74	5.02	3.79	3.75	3.48	Phenol glucuronide
R.f.b.0–6 hours (6 mL)	7.26	7.00	7.26	6.59	5.02	–	3.75	3.48	Desmethyl glucuronide
	7.26	6.99	6.95	6.74	5.02	3.78	3.74	3.48	Phenol glucuronide
R.m.u.0–24 hours (24 mL)	Overlapped				5.02	3.79	3.75	3.48	Phenol glucuronide
R.f.u.0–24 hours (28 mL)	7.26	6.99	6.96	6.74	5.02	3.78	3.75	3.47	Phenol glucuronide

Key: D, dog; R, rat; m, male; f, female; b, bile; u, urine; glue, glucuronic acid. Superscript H1: glucuronide anomeric proton; 9, 10,11: denote positions of the MeO– groups.
[a]*From Lenz et al. (2007); reprinted with permission from Elsevier © 2007.*

provided by the online HPLC-NMR determinations are listed in Table 10.12. Included with the ^{1}H NMR spectrum of [^{14}C]-ZD6126 phenol of Fig. 10.62 are the specific assignments to the proton resonance signals at various chemical shifts (δ ^{1}H, ppm). For example, proton assignments at carbon atoms numbered 1, 2, 4 … are designated as H1, H2, H4 … at the top of the peaks in the NMR spectrum followed by the values of the chemical shifts (e.g., H1, 7.15 ppm). Signals assigned to the methoxy groups at carbon atoms numbered 9, 10, and 11 are also assigned at 3.78, 3.74, and 3.46 ppm, respectively. Table 10.12 lists the proton chemical shifts of standards and various metabolites measured by Lenz et al. (2007) with online HPLC-NMR, which provided evidence for their structural determinations. Online HPLC-MS provided additional evidence for the identifications of metabolites.

Measurements of ^{14}C activities permitted quantitative measurements of radioactivity recoveries in extracts of the various test animals.

XIII. Online HPLC-FSA-MS-NMR

Multiple hyphenation techniques refer to the combination of a chromatographic system (i.e., online) with more than one detector for the spectroscopic determination of the structure of compounds separated by the chromatographic system. For example, LC-MS and LC-NMR refers to the combination of liquid chromatography with MS or NMR spectroscopy, respectively, as discussed in previous sections of this chapter. A multiple hyphenation technique abbreviated as LC-MS-NMR includes the combination of MS and NMR spectroscopy online by means of a liquid chromatography effluent splitter. If a radioisotope-labeled compound and its metabolites are separated by HPLC, a flow scintillation analyzer (FSA) will be linked to the HPLC effluent stream to detect the radioisotope-labeled compounds as they are eluted from the chromatographic column, and, in addition, an ultraviolet (UV) detector may be added for the detection of unlabeled as well as labeled compounds. Such a system may be hyphenated as online HPLC-UV-FSA-MS-NMR. As reported by Hansen et al. (1999), these techniques can cut the time needed to carry out such complex studies to short durations from 1 day to a few weeks compared with the span of months required when traditional techniques of compound isolation, purification, and subsequent spectroscopy are undertaken. Multiple hyphenation techniques are reviewed by Shockcor (2017), Silva-Elipe (2003), and Wilson and Brinkman (2003). The combination of more than one spectroscopic analysis in a single HPLC run offers advantages as noted by Silva-Elipe (2003) as follows.

> *NMR and MS data on the same analyte are crucial for structural elucidation. When different isolates, such as metabolites, are analyzed by NMR and MS, one cannot always be certain that the NMR and MS data apply to the same analyte. To avoid this ambiguity, LC-MS and LC-NMR are combined. MS data should be obtained initially since with NMR, data collection in the stopped-flow mode can take hours or days depending on the complexity of the structure and the amount of sample. This is why it is preferable to designate this operation as LC-MS-NMR rather than LC-NMR-MS.*

The HPLC-MS-NMR technique is not always favorable. As pointed out by Silva-Elipe (2003), the inclusion of NMR in the hyphenation is not always an advantage, particularly when the structural problem is very complex, the separation of the chromatographic peak is not suitable, or the volume of the chromatographic peak with respect to the volume of the NMR flow cell is not compatible. Silva-Elipe (2003) underscores that there will always be situations where the traditional isolation and purification of the analyte(s) will be required, and it is up to the analyst to choose the correct approach in determining the molecular structure of the analyte(s).

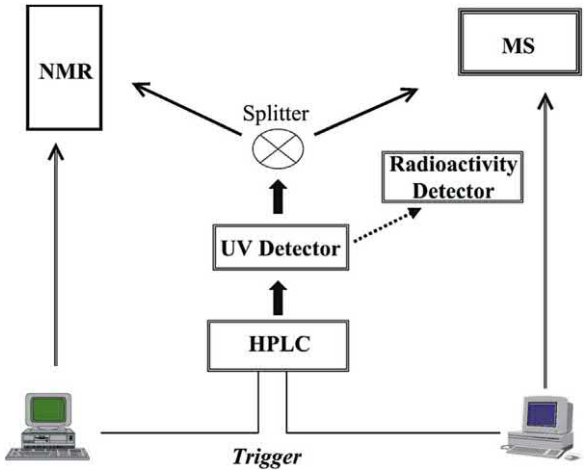


FIGURE 10.63 Schematic setup for the LC-MS-NMR system. A dashed arrow pointing to the radioactivity detector (i.e., FSA) is set to one side, as it would be coupled with the effluent steam of the HPLC only when radioisotope-labeled compounds are separated on the HPLC column. *From Silva-Elipe (2003); reprinted with permission from Elsevier © 2003.*

Online HPLC-UV-FSA-MS-NMR instrumentation is reported by several researchers. For online spectroscopic analysis of natural products, Bailey et al. (2000), Hansen et al. (1999), Scarfe et al. (2000), and Shockcor et al. (1996) split the HPLC effluent in the proportions of 95% to the NMR spectrometer and the remaining 5% of the effluent to the mass spectrometer in light of the relative sensitivities of the two spectrometers. The NMR spectra are obtained using the stopped-flow method with resonance signal acquisitions varying from several minutes to hours with a 500.13 MHz Bruker DRX-500 NMR spectrometer. The various acquisition times are dependent on compound concentrations that eluate off the HPLC column. Smith et al. (1999) also report the use of a splitter of HPLC effluent to the MS and NMR spectrometers. The proportions of HPLC effluent splitting will depend on the sensitivities of the MS and NMR spectrometers to the compounds eluted from the chromatography column. Silva-Elipe (2003) reports the use of a 1:100 splitting ratio, that is, 1% of the column effluent was directed to the MS spectrometer and the remaining 99% on to the NMR spectrometer. At a flow rate of 1.0 mL/min, this translates to 0.010 mL/min to the MS and 0.990 mL/min to the NMR spectrometers, respectively. Shockcor (2017) provides an excellent summary of the state-of-the art of these hyphenated chromatographic and spectroscopic methods, including advances such as stopped flow, time-sliced stopped flow, HPLC peak collection into capillary loops

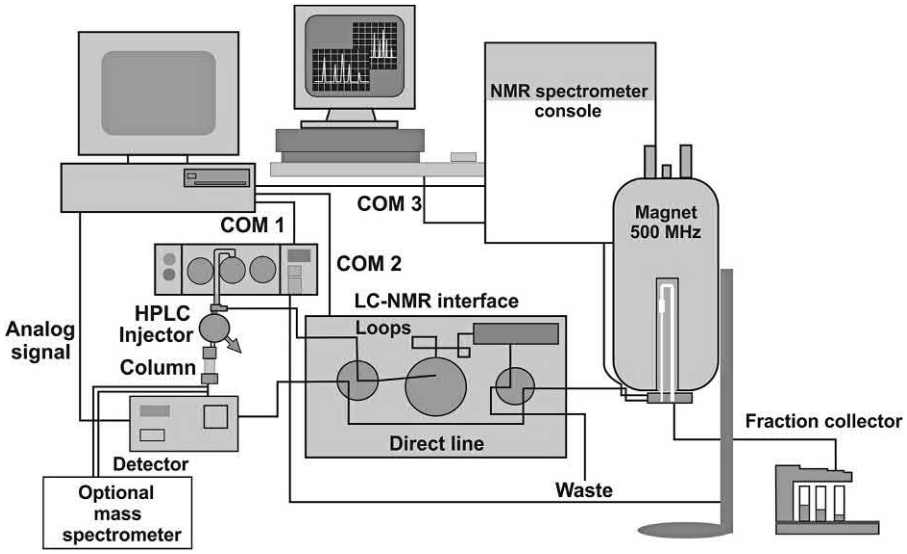


FIGURE 10.64 Instrumental setup of the HPLC-UV-FSA-MS-NMR apparatus. Three computer communications (COM 1, 2, and 3) control the HPLC and HPLC detector, the HPLC-NMR interface, and the NMR readout, respectively. The detector may be a UV detector or an FSA. A splitter at the HPLC column effluent can divert part of the LC stream to a mass spectrometer and the remaining part to the NMR. A direct line from the UV or FSA detector (i.e., flow-cell radionuclide detector) leads on to the 500 MHz NMR spectrometer, or eluted fractions may be stored in capillary loops for stopped-flow NMR or subsequent off-line NMR. The fraction collection of HPLC peaks provides the ability of isolating the separated compounds for further studies and more thorough NMR spectroscopy. *From Shockcor (2017); reprinted with permission from Elsevier © 2017.*

for postchromatographic NMR, deuterated solvent selection for HPLC, and NMR solvent suppression to avoid costs associated with deuterated solvents.

Schematic illustrations of the instrumental setup for the hyphenated HPLC-UV-FSA-MS-NMR analysis of HPLC effluents for the online separation, radioisotope label analysis, and molecular structural elucidation of complex mixtures are illustrated in Figs. 10.63 and 10.64. When ^{14}C-labeled compounds are eluted from the HPLC, a solid heterogeneous scintillation flow cell, such as one containing SolarScint or CaF_2(Eu) scintillator, may be used (see Table 10.1), allowing for the entire effluent to pass through the radioactivity flow-cell detector before reaching the splitter.

References

Abdel-Khalik, J., Björklund, E., Nielsen, F.K., Hansen, M., 2017. Incorporation of 14C-cholesterol in human adrenal corticocarcinoma H295R cell line and online-radiodetection of produced ^{14}C-steroid hormone metabolites. J. Pharm. Biomed. Anal. 145, 569–575.

Abit, M.J.M., Al-Khatib, K., 2013. Metabolism of quizalofop and rimsulfuron in herbicide resistant grain sorghum. Pest. Biochem. Physiol. 105, 24–27.

Addleman, R.S., O'Hara, M.J., Grate, J.W., Egorov, O.B., 2005. Chemically enhanced alpha-energy spectroscopy in liquids. J. Radioanal. Nucl. Chem. 263 (2), 291–294.

Ahring, P.K., et al., 2015. Engineered α4β2 nicotinic acetylcholine receptors as models for measuring agonist binding and effect at the orthosteric low-affinity α4–α4 interface. Neuropharmacology 92, 135–145.

Akhlaghi, M., Kamalidehghan, M., Jalilian, A.R., Shadanpoor, N., 2008. Determination of [^{201}Tl]Tl(III) in [^{201}Tl]TlCl solutions using HPLC. Appl. Radiat. Isot. 66, 479–481.

Albert, K., 2014. NMR as a chromatography detector. In: Handbook of Spectroscopy, second ed. Wiley Blackwell, pp. 1679–1716.

Al-Dabbagh, B., et al., 2016. Catalytic mechanism of MraY and WecA, two paralogues of the polyprenyl-phosphate N-acetylhexosamine 1-phosphate transferase superfamily. Biochimie 127, 249–257.

Alfaro, J., Apfel, T., Diercks, H., Knöchel, A., Sen Gupta, R., Tödter, K., 1995. Trace analysis of the nuclides ^{90}Sr and ^{89}Sr in environmental samples III: development of a fast analytical method. Angew. Chem. Int. Ed. Eng. 34, 186–191.

Al-Momani, E., Israel, I., Buck, A.K., Samnick, S., 2015. Improved synthesis of [^{18}F]FS-PTAD as a new tyrosine-specific prosthetic group for radiofluorination of biomolecules. Appl. Radiat. Isot. 104, 136–142.

ALOthman, Z.A., Wabaidur, S.M., 2019. Application of carbon nanotubes in extraction and chromatographic analysis: a review. Arabian J. Chem. 12 (5), 633–651.

Alton, T., Monk, S., Cheneler, D., 2018. Heterogeneous scintillator geometries to maximise energy deposition for waterborne beta particle detection. Radiat. Meas. 111, 6–12.

Andriamalala, A., Vieublé-Gonod, L., Dumeny, V., Cambier, P., 2018. Fate of sulfamethoxazole, its main metabolite N-ac-sulfamethoxazole and ciprofloxacin in agricultural soils amended or not by organic waste products. Chemosphere 191, 607–615.

Anonymous, 1990. An Introduction to Flow Radiochromatography. Application Note 9008. PerkinElmer Life and Analytical Sciences, Boston, p. 8.

Anonymous, 1995. Detection of Gamma Emitting Radionuclides Using FSA, Gamma-B and Gamma-C Flow cells FSA Application Note. FSA-001. PerkinElmer, Inc., Waltham, MA USA, p. 8.

Anonymous, 1996. New Technology Improves Radio-HPLC Detection. FSA Application Note. FSA-002. PerkinElmer Life and Analytical Sciences, Boston, p. 3.

Anonymous, 1997. "Radiomatic™ 500TR Series Flow Scintillation Analyzers, Reference Manual." PerkinElmer Life and Analytical Sciences, Boston, pp. 454–456.

Anonymous, 2012. Recent Progress in LC-NMR. SUMITOMO KAGAKU. In: R&D Report, vols. 2010-II. Sumitomo Chemical Co., Takashi TOKUNAGA, Masahiko OKAMOTO, Japan. https://www.sumitomo-chem.co.jp/english/rd/report/theses/docs/05_LC-NMR_e.pdf.

Asti, M., et al., 2014a. Synthesis and characterization of 68Ga-labeled curcumin and curcuminoid complexes as potential radiotracers for imaging of cancer and Alxheimer's disease. Inorg. Chem. 53 (10), 4922–4933.

Asti, M., et al., 2014b. Influence of different chelators on the radiochemical properties of 68-gallium labelled bombesin analogue. Nucl. Med. Biol. 41 (1), 24–35.

Athersuch, T.J., Sison, R.L., Kenyon, A.S.J., Clarkson-Jones, J.A., Wilson, I.D., 2008. Evaluation of the use of UPLC-TOFMS with simultaneous [^{14}C]-radioflow detection for drug metabolite profiling: application to propranolol metabolites in rat urine. J. Pharm. Biomed. Anal. 48, 151–157.

Ayaz, B., DeVol, T.A., 2003. Application of MnO_2 coated scintillating and extractive scintillating resins to screening for radioactivity in groundwater. Nucl. Instrum. Methods Phys. Res., Sect. A 505, 258–461.

Azzouna, R.B., et al., 2015. A new 68Ga anionic concentration and purification method for automated synthesis of [^{68}Ga]-DOTA or NODAGA conjugated peptides in high radiochemical purity. J. Label. Comp. Radiopharm. 58 (10), 404–410.

Azzouna, R.B., et al., 2017. Synthesis, gallium labelling and characterization of P04087, a functionalized phosphatidylserine-binding peptide. EJNMMI Radiopharm. Chem. 2, 3.

Bailey, N.J.C., et al., 2000. Application of directly coupled HPLC-NMR-MS/MS to the identification of metabolites of 5-trifluoromethylpyridone (2-hydroxy-5-trifluoromethylpyridine) in hydroponically grown plants. J. Agric. Food Chem. 48 (1), 42–46.

Baishya, R., et al., 2014. Synthesis, characterization, and biological evaluation of ^{99}mTc(CO)$_3$-labeled peptides for potential use as tumor targeted radiopharmaceuticals. Chem. Biol. Drug Design 83 (1), 58–70.

Balla, T., Guillemette, G., Baukal, A.J., Catt, K.J., 1987. Metabolism of inositol 1,3,4-triphosphate to a new tetrakisphosphate isomer in angiotensin-stimulated adrenal glomerulosa cells. J. Biol. Chem. 262, 9952–9955.

Baranczewski, P., Edlund, P.O., Postlind, H., 2006. Characterization of the cytochrome P450 enzymes and enzyme kinetic parameters for metabolism of BVT.2938 using different in vitro systems. J. Pharm. Biomed. Anal. 40, 1121–1130.

Barrera, J., Tarancón, A., Bagán, H., García, J.F., 2016. A new plastic scintillation resin for single-step separation, concentration and measurement of technetium-99. Anal. Chim. Acta 936, 259–266.

Becker, J.S., Dietze, H.-J., 1999. Application of double-focusing sector field ICP mass spectrometry with shielded torch using different nebulizers for ultratrace and precise isotope analysis of long-lived radionuclides. J. Anal. Atom. Spectrom. 14, 1493–1500.

Becker, J.S., et al., 1999. Determination of long-lived radionuclides by inductively coupled plasma quadrupole mass spectrometry using different nebulizers. J. Anal. Atom. Spectrom. 14, 933–937.

Beery, J.W., 2000. BASF Corporation. Agricultural Research Center. Research Triangle Park, NC 27709 (Personal Communication, August 21, 2000).

Bendadani, C., et al., 2016. Metabolism and excretion of 1-hydroxymethylpyrene, the proximate metabolite of the carcinogen 1-methylpyrene, in rats. Toxicology 366–367, 43–52.

Bergmann, R., et al., 2013. Synthesis and radiopharmacological evaluation of ^{64}Cu-labeled bombesin analogs featuring a bis(2-pyridylmethyl)-1,4,7-triazacyclononane chelator. Eur. J. Med. Chem. 70, 434–446.

Bernard-Gauthier, V., Boudjemeline, M., Rosa-Neto, P., Thiel, A., Schirrmacher, R., 2013. Towards tropomyosin-related kinase B (TrkB) receptor ligands for brain imaging with PET: radiosynthesis and evaluation of 2-(4-[^{18}F]fluorophenyl)-7,8-dihydroxy-4*H*-chromen-4-one and 2-(4-([*N*-methyl-^{11}C]-dimethylamino)phenyl)-7,8-dihydroxy-4*H*-chromen-4-one. Bioorg. Med. Chem. 21, 7816–7829.

Berry, L.M., et al., 2014. Species difference in glucuronidation formation kinetics with a selective mTOR inhibitor. Drug Metab. Dispos. 42, 707–717.

Bertrand, R., et al., 2016. Synthesis of GPR40 targeting ^{3}H- and ^{18}F-probes towards selective beta cell imaging. J. Label. Comp. Radiopharm. 59 (14), 604–610.

Bhade, S.P.D., Reddy, P.J., Babu, D.A.R., Sharma, D.N., 2012. Application of liquid scintillation inclusion techniques for the simultaneous determination of alpha and beta activities in composite samples – a preliminary study. Radiat. Meas. 47, 936–946.

Bliznyuk, V.N., Duval, C.E., Apul, O.G., Seliman, A.F., Husson, S.M., DeVol, T.A., 2015. High porosity scintillating polymer resins for ionizing radiation sensor applications. Polymer 56, 271–279.

Bollaert, E., et al., 2018. HBP1 phosphorylation by AKT regulates its transcriptional activity and glioblastoma cell proliferation. Cell. Signal. 44, 158–170.

Borai, E.H., Mady, A.S., 2002. Separation and quantification of ^{238}U, ^{232}Th and rate earths in monazite samples by ion chromatography coupled with on-line flow scintillation detector. Appl. Radiat. Isot. 57, 463–469.

Borai, E.H., El-Sofany, E.A., 2004. Separation of strontium-90 and yttrium-90 in the presence of thorium-234 by dynamic ion chromatography. J. Radioanal. Nucl. Chem. 262 (3), 697–701.

Borges, G., van der Hooft, J.J.J., Crozier, A., 2016. A comprehensive evaluation of the[2-^{14}C](−)-epicatechin metabolome in rats. Free Rad. Biol. Med. 99, 128–138.

Bou, M., et al., 2016. *De novo* lipogenesis in Atlantic salmon adipocytes. Biochim. Biophys. Acta 1860, 86–96.

Bradbury, D., Elder, G.R., Dunn, M.J., 1990. Rapid analysis of non-gamma radionuclides using the ANABET system. In: Proceedings of the Waste Management Conference, Tucson, Arizona, pp. 327–329.

Brkljača, R., Urban, S., 2015. Chemical profiling (HPLC-NMR & HPLC-MS), isolation, and identification of bioactive meroditerpenoids from the southern iniaturiz marine brown alga *Sargassum paradoxum*. Mar. Drugs 13, 102–107.

Brkljača, R., et al., 2017. Application of the crystalline sponge method to revise the structure of the phenalenone fuliginone. Molecules 22, 211. https://doi.org/10.3390/molecules22020211.

Bruyere, S.A., Cadwallader, L.C., 2012. Operating experience review of tritium-in-water monitors. Fusion Eng. Des. 87, 565–568.

Bruzzone, F., Rego, J.-L.D., Luu-The, V., Pelletier, G., Vallarino, M., Vaudry, H., 2010. Immunohistochemical localization and biological activity of 3β-hydroxysteroid dehydrogenase and 5α-reductase in the brain of the frog, *Rana esculenta*, during development. J. Chem. Neuroanat. 39, 35–50.

Byon, C., Chakravarty, S., Filer, C.N., Jain, R., Maniscalco, M.P., 2016. MDV3100: tritium labeling at high specific activity. Appl. Radiat. Isot. 108, 35–37.

Cardinale, J., et al., 2017. Procedures for the GMP-compliant production and quality control of [^{18}F]PSMA-1007: a next generation radiofluorinated tracer for the detection of prostate cancer. Pharmaceuticals 10, 77.

Carnpi, F., Edwards, R.A.H., Ossiri, A., Pacenti, P., Terrani, S., 1998. A method and apparatus for monitoring the level of tritiated water vapor in air using a solid scintillator. Health Phys. 75 (2), 179–182.

Cassigneul, A., et al., 2016. Fate of glyphosate and degradates in cover crop residues and underlying soil: a laboratory study. Sci. Total Environ. 545–546, 582–590.

Cassigneul, A., et al., 2018. Behaviour of S-metolachlor and its oxanilic and ethanesulfonic acids metabolites under fresh vs. partially decomposed cover crop mulches: a laboratory study. Sci. Total Environ. 631–632, 1515–1524.

Cerdà, V., Ferrer, L., Avivar, J., Cerdà, A., 2014. Chapter 8 – automating radiochemical analysis. In: Flow Analysis, A Practical Guide. Elsevier, Amsterdam, pp. 247–264.

Chen, X., Lu, Y., Fan, Y., Shen, Y., 2017. Chapter 2, production of Validamycins. In: Validamycin and its Derivatives. Elsevier Ltd., p. 330

Chevolleau, S., et al., 2016. A consolidated method for screening the endocrine activity of drinking water. Food Chem. 213, 274–283.

Chillar, A., So, S.-P., Ruan, C.-H., Shelat, H., Geng, Y.-J., Ruan, K.-H., 2011. A profile of NSAID-targeted arachidonic acid metabolisms in human embryonic stem cells (hESCs): implication of the negative effects of NSAIDs on heart tissue regeneration. Int. J. Cardiol. 150, 253–259.

Chowdhury, S.K., (Ed.), 2005. Progress in pharmaceutical and biomedical analysis. Identification and Quantification of Drugs. Metabolites and Metabolizing Enzymes by LC-MS, vol. 6. Elsevier, Amsterdam, p. 354.

Chotoo, S.D., DeVol, T.A., Fjeld, R.A., 1997. Evaluation of polymer-coated CsI:Tl as an alpha/beta pulse shape discriminating flow cell. IEEE Trans. Nucl. Sci. 44 (4), 1630–1634.

Claesener, M., Schober, O., Wagner, S., Kopka, K., 2012. Radiosynthesis of a ^{68}Ga labeled matrix metalloproteinase inhibitor as a potential probe for PET imaging. Appl. Radiat. Isot. 70, 1723–1728.

Collier, T.L., et al., 2018. Recent applications of a single quadrupole mass spectrometer in ^{11}C, ^{18}F and radiometal chemistry. J. Fluorine Chem. 210, 46–55.

Cui, M.-C., Li, Z.-J., Tang, R.-K., Liu, B.-L., 2010. Synthesis and evaluation of novel benzothiazole derivatives based on the bithiophene structure as potential radiotracers for β-amyloid plaques in Alzheimer's disease. Bioorg. Med. Chem. 18, 2777–2784.

Currie, L.A., 1968. Limits for qualitative detection and quantitative determination. Anal. Chem. 40 (3), 586–593.

Cutler, J.M., Mina, N., Swami, L., Ely, F.A., 1993. In: Proceedings ANS Topical Meeting on Environmental Transport and Dosimetry, Sep. 1-3, 1993, Charleston, SC, p. 95.

Cuyckens, F., Koppen, V., Kembuegler, R., Leclercq, L., 2008. Improved liquid chromatography-online radioactivity detection for metabolite profiling. J. Chromatogr. A 1209, 128–135.

Däpp, S., Garayoa, E.G., Maes, V., Brans, L., Tourwé, D.A., Müller, C., Schibli, R., 2011. PEGylation of ^{99}mTc-labeled bombesin analogues improves their pharmacokinetic properties. Nucl. Med. Biol. 38 (7), 997–1009.

Dayhuff, T.J., Atkins, J.F., Gesteland, R.F., 1986. Characterization of ribosomal frameshift events by protein sequence analysis. J. Biol. Chem. 261, 7491–7500.

Denoyer, D., et al., 2008. Development of a high-performance liquid chromatographic method for the determination of a new potent radioiodinated melanoma imaging and therapeutic agent. J. Chromatogr. B 875, 411–418.

De Leonardis, F., Pascali, G., Salvadori, P.A., Watts, P., Pamme, N., 2011. On-chip pre-concentration and complexation of [18F]fluoride ions via regenerable anion exchange particles for radiochemical synthesis of Positron Emission Tomography tracers. J. Chromatogr. A 1218, 4714–4719.

Desmartin, P., Kopajtic, Z., Haerdi, W., 1997. Radiostrontium-90 (^{90}Sr) ultra-traces measurements by coupling ionic chromatography (HPIC) and on-line liquid scintillation counting (OLLSC). Environ. Monitor. Assess. 44, 413–423.

DeVol, T.A., Fjeld, R.A., 1995. Development of an on-line scintillation flow-cell detection system with pulse shape discrimination for quantification of actinides. IEEE Trans. Nucl. Sci. 42, 959–963.

DeVol, T.A., Keillor, M.E., Burggraf, L.W., 1996. Influence of radionuclide adsorption on detection efficiency and energy resolution for flow-cell radiation detectors. IEEE Trans. Nucl. Sci. 43 (3), 1310–1315.

DeVol, T.A., Roane, J.E., Harvey, J.T., 1997. Scintillating extraction chromatographic resin for quantification of aqueous radioactivity. IEEE Nucl. Sci. Symp. Med. Imag. Conf. 1, 415–419.

DeVol, T.A., Chotoo, S.B., Fjeld, R.A., 1999. Evaluation of granulated BGO, GSO:Ce, YAG:Ce, CaF_2:Eu and ZnS:Ag for alpha/beta pulse shape discrimination in a flow-cell radiation detector. Nucl. Instrum. Methods Phys. Res., Sect. A 425, 228–231.

DeVol, T.A., Raone, J.E., Williamson, J.M., Duffey, J.M., Harvey, J.T., 2000. Development of scintillating extraction media for separation and measurement of charged-particle-emitting radionuclides in aqueous solutions. Radioact. Radiochem. 11 (1), 34–36.

DeVol, T.A., Egorov, O.B., Roane, J.E., Paulenova, A., Grate, J.W., 2001a. Extractive scintillating resin for ^{99}Tc quantification in aqueous solutions. J. Radioanal. Nucl. Chem. 249 (1), 181–189.

DeVol, T.A., Duffey, J.M., Paulenova, A., 2001b. Combined extraction chromatography and scintillation detection for off-line and on-line monitoring of strontium in aqueous solutions. J. Radioanal. Nucl. Chem. 249 (2), 295–301.

DeVol, T.A., Keillor, M.E., Burggraf, L.W., 1995. Influence of radionuclide adsorption on detection efficiency and energy resolution for flow-cell radiation detectors. Oct 21–28 1995, San Francisco IEEE Nucl. Sci. Symp. Med. Imag. Conf. 2, 795–799.

DeVol, T.A., Leyba, J.D., Roane, J.E., 2002. Application of extractive scintillator resins to quantification of beta-emitting radionuclides in aqueous solutions. In: Möbius, S., Noakes, J., Schönhofer, F. (Eds.), LSC 2001, Advances in Liquid Scintillation Sprectrometry. University of Arizona, Tucson, pp. 415–423.

Devol, T.A., Clements, J.P., Farawila, A., O'Hara, M.J., Egorov, O.B., Grate, J.W., 2009. Characterization and application of SuperLig® 620 solid phase extraction resin for automated process monitoring of 90Sr. J. Radioanal. Nucl. Chem. 282, 623–628.

Do, K.Q., Benz, B., Binns, K.E., Eaton, S.A., Salt, T.E., 2004. Release of homocysteic acid from rat thalamus following stimulation of somatosensory afferents in vivo: feasibility of glial participation in synaptic transmission. Neuroscience 124, 387−393.

Dockens, R.C., et al., 2000. Disposition of radiolabeled ifetroban in rats, dogs, monkeys, and humans. Drug Metab. Dispos. 28 (8), 973−980.

Draganov, D.I., et al., 2015. Extensive metabolism and route-dependent pharmacokinetics of bisphenol A (BPA) in neonatal mice following oral or subcutaneous administration. Toxicology 333, 168−178.

Duval, C.E., DeVol, T.A., Husson, S.M., 2016a. Extractive scintillating polymer sensors for trace-level detection of uranium in contaminated ground water. Anal. Chim. Acta 947, 1−8.

Duval, C.E., DeVol, T.A., Husson, S.M., 2016b. Evaluation of resin radius and column diameter for the implementation of extractive scintillating resin in flow-cell detectors. J. Radioanal. Nucl. Chem. 307 (3), 2253−2258.

Duval, C.E., DeVol, T.A., Wade, E.C., Seliman, A.F., Bliznyuk, V.N., Husson, S.M., 2016c. Stability of polymeric scintillating resins developed for ultra-trace level detection of alpha-and beta-emitting radionuclides. J. Radioanal. Nucl. Chem. 310 (2), 583−588.

Dymond, A.W., et al., 2016. Metabolism, excretion, and pharmacokinetics of selumetinib, an MEK1/2 inhibitor, in healthy adult male subjects. Clin. Ther. 38 (11), 2447−2458.

Ebenhan, T., et al., 2014. Peptide synthesis, characterization and 68Ga-radiolabeling of NOTA-conjugated ubiquicidin fragments for prospective infection imaging with PET/CT. Nucl. Med. Biol. 41, 390−400.

Edlund, P.O., Baranczewski, P., 2004. Identification of BVT.2938 metabolites by LC/MS and LC/MS/MS after in vitro incubations with liver microsomes and hepatocytes. J. Pharm. Biomed. Anal. 34, 1079−1090.

Egorov, O., O'Hara, M.J., Ruzicka, J., Grate, J.W., 1998a. Sequential injection separation system with stopped-flow radiometric detection for automated analysis of ^{99}Tc in nuclear waste. Anal. Chem. 70 (5), 977−984.

Egorov, O., Grate, J.W., Ruzicka, J., 1998b. Automation of radiochemical analysis by flow injection techniques: Am-Pu separation using TRU-resin sorbent extraction column. J. Radioanal. Nucl. Chem. 234 (1−2), 231−235.

Egorov, O., O'Hara, M.J., Grate, J.W., Ruzicka, J., 1999a. Sequential injection renewable separation column instrument for automated sorbent extraction separations of radionuclides. Anal. Chem. 71, 345−352.

Egorov, O.B., Fiskum, S.K., O'Hara, M.J., Grate, J.W., 1999b. Radionuclide sensors based on chemically selective scintillating microspheres: renewable column sensor for analysis of 99Tc in water. Anal. Chem. 71, 5420−5429.

Egorov, O., O'Hara, M.J., Farmer, O.T., Grate, J.W., 2001. Extraction chromatographic separations and analysis of actinides using sequential injection techniques with on-line inductively coupled plasma mass spectrometry. (ICP MS) detection. Analyst 126, 1594−1601.

Egorov, O., O'Hara, M.J., Grate, J.W., 2002. Radionuclide Selective Sensors for Waste Monitoring: ^{99}Tc(VII) Detection in Hanford Groundwater. Pacific Northwest National Lab., Richland, WA, USA. Report No. PNNL-SA-35931-1.

Egorov, O., O'Hara, M.J., Addleman, R.S., Grate, J.W., 2004a. Automation of radiochemical analysis: from groundwater monitoring to nuclear waste analysis. In: Laue, C.A., Nash, K.L. (Eds.), Radioanalytical Methods in Interdisciplinary Research, Am. Chem. Soc. Symp. Ser. vol. 868, 246−270.

Egorov, O.B., O'Hara, M.J., Grate, J.W., 2004b. Microwave-assisted sample treatment in a fully automated flow-based instrument: oxidation of reduced technetium species in the analysis of total technetium-99 in caustic aged nuclear waste samples. Anal. Chem. 76, 3869−3877.

Egorov, O., O'Hara, M.J., Grate, J.W., Knopf, M., Anderson, G., Hartman, J., 2005a. Radiochemical sensor system for the analysis of ^{99}Tc(VII) in groundwater. J. Radioanal. Nucl. Chem. 264 (2), 495−500.

Egorov, O.B., O'Hara, M.J., Grate, J.W., 2005b. Automated radiochemical analysis of total ^{99}Tc in aged nuclear waste processing streams. J. Radioanal. Nucl. Chem. 263 (3), 629−633.

Egorov, O.B., O'Hara, M.J., Grate, J.W., 2006. Equilibration-based preconcentrating minicolumn sensors for trace level monitoring of radionuclides and metal ions in water without consumable reagents. Anal. Chem. 78, 5480−5490.

Egorov, O.B., O'Hara, M.J., Grate, J.W., 2012. Automated radioanalytical system incorporating microwave-assisted sample preparation, chemical separation, and online radiometric detection for the monitoring of total Tc-99 in nuclear waste processing streams. Anal. Chem. 84, 3090−3098.

Etzbach, L., Pfeiffer, A., Weber, F., Schieber, A., 2018. Characterization of carotenoid profiles in goldenberry (*Physalis peruviana* L.) fruits at various ripening stages and in different plant tissues by HPLC-DAD-APCI-MS. Food. Chem. 245, 508−517.

Fahrbach, M., Krauss, M., Preiss, A., Kohler, H.-P.E., Hollender, J., 2010. Anaerobic testosterone degradation in Steroidobacter denitrificans − identification of transformation products. Environ. Pollut. 158, 2572−2581.

Farjo, K.M., Moiseyev, G., Nikolaeva, O., Sandell, L.L., Trainor, P.A., Ma, J.-X., 2011. RDH10 is the primary enzyme responsible for the first step of embryonic Vitamin A metabolism and retinoic acid synthesis. Dev. Biol. 357 (2), 347−355.

Farlin, J., et al., 2018. Breakthrough dynamics of s-metolachlor metabolites in drinking water wells: transport pathways and time to trend reversal. J. Contam. Hydr. 213, 62−72.

Fer, M., Dréano, Y., Lucas, D., Corcos, L., Salaün, J.-P., Berthou, F., Amet, Y., 2008. Metabolism of eicosapentaenoic and docosahexaenoic acids by recombinant human cytochromes P450. Arch. Biochem. Biophys. 471, 116−125.

Fer, M., Goulitquer, S., Dreano, Y., Berthou, F., Corcos, L., Amet, Y., 2006. Determination of polyunsatured fatty acid monoepoxides by high performance liquid chromatography-mass spectrometry. J. Chromatogr. A 1115, 1−7.

Fjeld, R.A., Roane, J.E., Leyba, J.D., Paulenova, A., DeVol, T.A., 2004. Sequential and simultaneous radionuclide separation-measurement with flow-cell radiation detection. Am. Chem. Soc. Symp. Ser. 868, 105−119.

Fjeld, R.A., DeVol, T.A., Leyba, J.D., Paulenova, A., 2005. Measurement of radionuclides using ion chromatography and on-line radiation detection. J. Radioanal. Nucl. Chem. 263 (3), 635−640.

Flores-Acosta, M., Pérez-Salas, R., Aceves, R., Sotelo-Lerma, M., Ramírez-Bon, R., 2005. Structural and photoluminescent properties of EuF_3 nanoparticles in zeolite A. Solid State Commun. 136, 567–571.

Fu, J., et al., 2016. Interspecies differences in the metabolism of a multiester prodrug by carboxylesterases. J. Pharm. Sci. 105, 989–995.

Fujii, H., Matsuno, K., Takiue, M., 2002. Construction of a liquid waste monitor using the Cerenkov technique for nuclear medicine. In: Möbius, S., Noakes, J., Schönhofer, F. (Eds.), LSC 2001, Advances in Liquid Scintillation Spectrometry. The University of Arizona, Tucson, pp. 425–428.

Gale, R.T., et al., 2017. *B. subtilis* LytR-CpsA-Psr enzymes transfer wall teichoic acids from authentic lipid-linked substrates to mature peptidoglycan *in vitro*. Cell Chem. Biol. 24, 1537–1546.

Gaonkar, R.H., et al., 2016. Exploring the potential of $^{99}mTc(CO)_3$-labeled triazolyl peptides for tumor diagnosis. Cancer Biother. Radiopharm. 31 (3), 110–117.

Gaonkar, R.H., et al., 2018. Development of a peptide-based bifunctional chelator conjugated to a cytotoxic drug for the treatment of melanotic melanoma. Med. Chem. Comm. 9, 812–826.

Garner, C.E., et al., 2006. Metabolism and disposition of 1-bromopropane in rats and mice following inhalation or intravenous administration. Toxicol. Appl. Pharmacol. 215, 23–36.

Geenen, S., et al., 2013. Glutathione metabolism modeling: a mechanism for liver drug-robustness and a new biomarker strategy. Biochim. Biophys. Acta 1830, 4943–4959.

Geng, C., et al., 2018. Impact of sludge treatments on the extractability and fate of acetyl sulfamethoxazole residues in amended soils. Chemosphere 194, 828–836.

Gevaert, B., et al., 2016. Blood-brain barrier transport kinetics of the neuromedin peptides NMU, NMN, NMB and NT. Neuropharmacology 107, 460–470.

Ghosal, A., Ramanathan, R., Kishnani, N.S., Chowdhury, S.K., Alton, K.B., 2005. Chapter 12. Cytochrome P450 (CYP) and UDP-glucuronosyltransferase (UGT) enzymes: role in drug metabolism, polymorphism, and identification of their involvement in drug metabolism. In: Chowdhury, S.K. (Ed.), Progress in Pharmaceutical and Biomedical Analysis: Volume 6, Identification and Quantification of Drugs, Metabolites and Metabolizing Enzymes by LC-MS. Elsevier, Amsterdam, pp. 295–336.

Giblin, M.F., Sieckman, G.L., Shelton, T.D., Hoffman, T.J., Forte, L.R., Volkert, W.A., 2006. In vitro and in vivo evaluation of ^{177}Lu- and ^{90}Y-labeled E. coli heat-stable enterotoxin for specific targeting of uroguanylin receptors on human colon cancers. Nucl. Med. Biol. 33, 481–488.

Glaenzel, U., et al., 2018. Metabolism and disposition of siponimod, a novel selective $S1P_1$/$S1P_5$ agonist, in healthy volunteers and in Vitro identification of human cytochrome P450 enzymes involved in its oxidative metabolism. Drug Metab. Dispos. 46, 1001–1013.

Gobo, L.A., Machado de Carvalho, L., Temp, F., Viana, C., Mello, C.F., 2018. A rapid method for identification and quantification of prostaglandins in cerebral tissues by UHPLC-ESI-MS/MS for the lipidomic *in vivo* studies. Anal. Biochem. 545, 98–103.

Goldenberg, G.P., 2016. Principles of NMR Spectroscopy: An Illustrated Guide. University Science Books, p. 704.

Gomes de Mello Martins, A.G., et al., 2017. CYP17A1-independent production of the neurosteroid-derived 5α-pregnan-3β,6α-diol-20-one in androgen-responsive prostate cancer cell lines under serum starvation and inhibition by Abiraterone. J. Steroid Biochem. Mol. Biol. 174, 183–191.

Gong, Y., et al., 2013. Preparation of Er^{3+}/Yb^{3+} co-doped zeolite-derived silicaglass and its upconversion luminescence property. Ceram. Int. 39, 8865–8868.

Gorassini, A., Verardo, G., Fregolent, S.-C., Bortolomeazzi, R., 2017. Rapid determination of cholesterol oxidation products in milk powder based products by reversed phase SPE and HPLC-APCI-MS/MS. Food. Chem. 230, 604–610.

Grady, S.R., et al., 2010. Structural differences determine the relative selectivity of nicotinic compounds for native α4β2*-, α6β2*-, α3β4*- and α7-nicotine acetylcholine receptors. Neuropharmacology 58, 1054–1066.

Granata, O.M., et al., 2009. Androgen metabolism and biotransformation in nontumoral and malignant human liver tissues and cells. J. Steroid Biochem. Mol. Biol. 113, 290–295.

Grate, J.W., Egorov, O., 1998a. Automating analytical separations in radiochemistry. Anal. Chem. 70, 779A–788A.

Grate, J.W., Egorov, O., 1998b. Investigation and optimization of on-column redox reactions in the sorbent extraction separation of americium and plutonium using flow injection analysis. Anal. Chem. 70, 3920–3929.

Grate, J.W., Strebin, R.S., Janata, J., Egorov, O., Ruzicka, J., 1996. Automated analysis of radionuclides in nuclear waste: rapid determination of 90Sr by sequential injection analysis. Anal. Chem. 68, 333–340.

Grate, J.W., Fadeff, S.K., Egorov, O., 1999. Separation-optimized sequential injection method for rapid automated analytical separation of ^{90}Sr in nuclear waste. Analyst 124 (2), 203–210.

Grate, J.W., Egorov, O., Fiskum, S.K., 1999b. Automated extraction chromatographic separations of actinides using separation-optimized sequential injection techniques. Analyst 124, 1143–1150.

Grate, J.W., Egorov, O.B., O'Hara, M.J., 2005. Sensors and automated analyzers for radionuclides. Am. Chem. Soc. Symp. Ser. 904, 322–341.

Grate, J.W., Ozanich, R., Hartman, J.S., O'Hara, M.J., Egorov, O.B., 2007. Preconcentrating minicolumn sensors for trace environmental monitoring. Proc. IEEE Sensors Conf., Art. No. 4388663 1357–1360.

Grate, J.W., Egorov, O.B., O'Hara, M.J., DeVol, T.A., 2008. Radionuclide sensors for environmental monitoring: from flow injection solid-phase absorptiometry to equilibrium-based preconcentrating minicolumn sensors with radiometric detection. Chem. Rev. 108, 543–562.

Grate, J.W., O'Hara, M.J., Egorov, O.B., Burge, S.R., 2009. Radionuclide sensors and systems for environmental monitoring. ECS Trans. 19 (6), 301–304.

Grate, J.W., O'Hara, M.J., Egorov, O.B., 2012. Automated radiochemical separation, analysis and sensing. In: L'Annunziata, M.F. (Ed.), Handbook of Radioactivity Analysis, third ed. Elsevier, Amsterdam, pp. 1179–1207.

Groarke, R.J., Brabazon, D., 2016. Monolithic materials for bioseparations. In: Hashmi, M.S.J. (Ed.), Reference Module in Materials Science and Materials Engineering. Elsevier, Inc., Amsterdam, pp. 1–25.

Grogan, K.P., Devol, T.A., 2011. Online detection of radioactive iodine in aqueous systems through the use of scintillating anion exchange resin. Anal. Chem. 83, 2582–2588.

Gross, J.H., 2017. Mass Spectrometry: A Textbook, third ed. Springer, p. 968.

Guillemette, G., Balla, T., Baukal, A.J., Catt, K.J., 1989. Metabolism of inositol 1,4,5-triphosphate to higher inositol phosphates in bovine adrenal cytosol. Am. J. Hypertens. 2, 387–394.

Günther, H., 2013. NMR Spectroscopy: Basic Principles, Concepts and Applications in Chemistry, third ed. Wiley-VCH, p. 734.

Ha, N.S., Sadeghi, S., van Dam, R.M., 2017. Recent progress toward microfluidic quality control testing of radiopharmaceuticals. Micromachines 8, 337.

Haeusler, D., et al., 2010. [18F]FE@SUPPY and [18F]FE@SUPPY:2 – metabolic considerations. Nucl. Med. Biol. 37, 421–426.

Hall, A.M.R., et al., 2016. Practical aspects of real-time reaction monitoring using multi-nuclear high resolution FlowNMR spectroscopy. Catal. Sci. Technol. 6, 8406–8417.

Hansen, S.H., Jensen, A.G., Cornett, C., Bjørnsdottir, I., Taylor, S., Wright, B., Wilson, I.D., 1999. High-performance liquid chromatography on-line coupled to high-field NMR and mass spectrometry for structure elucidation of constituents of *Hypericum perforatum* L. **71**. Anal. Chem. 71 (22), 5235–5241.

Harmon, S.D., Fang, X., Kaduce, T.L., Hu, S., Raj Gopal, V., Falck, J.R., Spector, A.A., 2006. Oxygenation of ω-3 fatty acids by human cytochrome P450 4F3B: effect on 20-hydroxyeicosatetraenoic acid production. Prostaglandins Leukot. Essent. Fatty Acids 75, 169–177.

Hastie, K.H., DeVol, T.A., Fjeld, R.A., 1999. Development of a homogeneous pulse shape discriminating flow-cell radiation detection system. Nucl. Instrum. Methods Phys. Res., Sect. A 422, 133–138.

Hegge, T.C.J.M., ter Wiel, J., 1986. Mixture for Use in the LSC Analysis Technique. U.S. patent no. 4,624,799. PerkinElmer Life and Analytical Sciences, Boston.

Hehn, M., Maiko, K., Pasch, H., Hiller, W., 2013. Online HPLC-NMR: an efficient method for the analysis of PMMA with respect to tacticity. Macromolecules 46 (1), 7678–7686.

Hervé, M., et al., 2013. Synthetic tripeptides as alternate substrates of murein peptide ligase (Mpl). Biochimie 95, 1120–1126.

Hofstetter, K.J., 1991. Development of aqueous tritium effluent monitor. In: Ross, H., Noakes, J.E., Spaulding, J.D. (Eds.), Liquid Scintillation Counting and Organic Scintillators. Lewis Publishers, Chelsea, Michigan, pp. 421–433.

Hofstetter, K.J., 1995. Continuous aqueous tritium monitoring. Fusion Technol. 25, 1527–1531.

Hofstetter, K.J., Eakle, R.F., 1993. In: Proceedings ANS Topical Meeting on Environmental Transport and Dosimetry, Sep. 1-3, 1993, Charleston, SC, p. 98.

Hong, J., et al., 2015. [*carbonyl*-4-yl)thiazol-2-yl)benzamide ([11C] FIMX) is an effective radioligand for PET imaging of metabotropic glutamate receptor 1 (mGluR1) in monkey brain. Nucl. Med. Biol. 42, 967–974.

Hong, T., Yang, X., Xu, Y., Ji, Y., 2016. Recent advances in the preparation and application of monolithic capillary columns in separation science. Anal. Chim. Acta 931, 1–24.

Hsia, C.-C., Huang, F.-L., Hung, G.-U., Shen, L.-H., Chen, C.-L., Wang, H.-E., 2011. The biological characterization of 99mTc-BnAO-NI as a SPECT probe for imaging hypoxia in a sarcoma-bearing mouse model. Appl. Radiat. Isot. 69, 649–655.

Hsu, J.-P., et al., 2016. Radiofluorination process development and Tau protein imaging studies of [F-^{18}]FEONM. J. Taiwan Inst. Chem. Eng. 68, 119–129.

Hsu, M.-F., Lu, M.-C., Tsao, L.-T., Kuan, Y.-H., Chen, C.-C., Wang, J.-P., 2004. Mechanisms of the influence of magnolol on eicosanoid metabolism in neutrophils. Biochem. Pharm. 67, 831–840.

Huber, J.S., Hanrahan, S.M., Moses, W.W., Derenzo, S.E., Reutter, B.W., O'Neil, J.P., Gullberg, G.T., 2009. Development of a high-sensitivity radiation detector for chromatography. IEEE Nucl. Sci. Symp. Conf. Art. No. 5402006 2620–2624.

Huber, J.S., Hanrahan, S.M., Moses, W.W., Derenzo, S.E., Reutter, B.W., O'Neil, J.P., Gullberg, G.T., 2011. Development of a high-sensitivity radiation detector for chromatography. IEEE Trans. Nucl. Sci. 58 (3), 1241–1248.

Hughes, L.D., DeVol, T.A., 2003. On-line gross alpha radiation monitoring of natural waters with extractive scintillating resins. Nucl. Instrum. Methods Phys. Res., Sect. A 505, 435–438.

Hughes, L.D., DeVol, T.A., 2006a. Evaluation of flow cell detector configurations combining simultaneous preconcentration and scintillation detection for monitoring of pertechnetate in aqueous media. Anal. Chem. 78, 2254–2261.

Hughes, L.D., DeVol, T.A., 2006b. Characterization of a Teflon® coated semiconductor detector flow cell for monitoring of pertechnetate in groundwater. J. Radioanal. Nucl. Chem. 267 (2), 287–295.

Hughes, M.F., Smith, B.J., Eling, T.E., 1992. The oxidation of 4-aminobiphenyl by horseradish peroxidase. Chem. Res. Toxicol. 5, 340–345.

Huskey, S.-E.W., 2016. Identification of three novel ring expansion metabolites of KAE609, a new spiroindolone agent for the treatment of malaria, in rats, dogs, and humans. Drug Metab. Dispos. 44, 653–664.

Isal, S., et al., 2018. PET imaging of 68Ga-NODAGA-RGD, as compared with ^{18}F-fluorodeoxyglucose, in experimental rodent models of engrafted glioblastoma. EJNMMI Res. 8, 51.

Jackson, A.B., 2012. ^{64}Cu-NO2A-RGD-Glu-6-Ahx-BBN(7-14)NH_2: a heterodimeric targeting vector for positron emission tomography imaging of prostate cancer. Nucl. Med. Biol. 39, 377–387.

Jacques, C., et al., 2010a. Disposition and biotransformation of ^{14}C-Benzo(a)pyrene in a pig ear skin model: ex vivo and in vitro approaches. Toxicol. Lett. 199, 22–33.

Jacques, C., Perdu, E., Dorio, C., Bacqueville, D., Mavon, A., Zalko, D., 2010b. Percutaneous absorption and metabolism of [^{14}C]-ethoxycoumarin in a pig ear skin model. Toxicol. In Vitro 24, 1426–1434.

Jensen, L., et al., 2017. Absorption, metabolism and excretion of the GLP-1 analogue semaglutide in humans and nonclinical species. Eur. J. Pharm. Sci. 104, 31–41.

Johanns, M., et al., 2017. Direct and indirect activation of eukaryotic elongation factor 2 kinase by AMP-activated protein kinase. Cell. Signal. 36, 212–221.

Johansen, K.T., Wubshet, S.G., Nyberg, N.T., 2013. HPLC-NMR revisited: using time-slice high-performance liquid chromatography-solid phase extraction-nuclear magnetic resonance with database-assisted dereplication. Anal. Chem. 85 (6), 3183–3189.

Joly, A.G., Chen, W., Zhang, J., Wang, S., 2007. Electronic energy relaxation and luminescence decay dynamics of Eu3+ in Zn2SiO4:Eu3+ phosphors. J. Lumin. 126, 491–496.

Kadirvel, M., et al., 2014. Detection of apoptosis by PET/CT with the diethyl ester of [^{18}F]ML-10 and fluorescence imaging with a dansyl analogue. Bioorg. Med. Chem. 22, 341–349.

Konala, A., Tetala, K.K.R., 2018. Chapter 11. Nanomaterial grafted microfluidic columns for biomolecule separation at analytical scale. In: Hussain, C.M. (Ed.), Nanomaterials in Chromatography. Elsevier, Inc., Amsterdam, pp. 323–339.

Kawamura, K., et al., 2017. Developing new PET tracers to image the growth hormone secretagogue receptor 1a (GHS-R1a). Nucl. Med. Biol. 52, 49–56.

Kawano, T., Uda, T., Yamamoto, T., Ohashi, H., 2011. Tritium water monitoring system based on CaF2 flow-cell detector. Fusion Sci. Technol. 60 (3), 952–955.

Kawano, T., Ohashi, H., Hamada, Y., Jamsranjav, E., 2015. Comparative testing of various flow-cell detectors fabricated using CaF_2 solid scintillator. Fusion Sci. Technol. 67 (2), 404–407.

Keller, J., et al., 2015. "Twin peaks": searching for 4-hydroxynonenal urinary metabolites after oral administration in rats. Redox Biol. 4, 136–148.

Kessler, M.J., 1986. Quantitation of radiolabeled molecules separated by high pressure liquid chromatography. In: Wieland, D.M., Tobes, M.C., Mangner, T.J. (Eds.), Analytical and Chromatographic Techniques in Radiopharmaceutical Chemistry. Springer-Verlag, New York, pp. 149–170.

Kiefer, S., Rogger, J., Melone, A., Mertz, A.C., Koryakina, A., Hamburger, M., Kuenzi, P., 2010. Separation and detection of all phosphoinositide isomers by ESI-MS. J. Pharmac. Biomed. Anal 53 (3), 552–558.

Kiffe, M., Schmid, D.G., Bruin, G.J.M., 2008. Radioactivity detectors for high-performance liquid chromatography in drug metabolism studies. J. Liq. Chromatogr. Rel. Technol. 31 (11), 1593–1619.

Kil, K.-E., et al., 2013. Radiosynthesis of N-(4-chloro-3-[11C]methoxyphenyl)-2-picolinamide ([11C]ML128) as a PET radiotracer for metabotropic glutamate receptor subtype 4 (mGlu4). Bioorg. Med. Chem. 21, 5955–5962.

Kim, H.K., Choi, Y.H., Verpoorte, R., 2011. NMR-based plant metabolomics: where do we stand, where do we go? Trends Biotechnol 29 (6), 267–275.

Kirjavainen, A.K., et al., 2018. ^{18}F-labeled norepinephrine transporter tracer [18F]NS12137: radiosynthesis and preclinical evaluation. Nucl. Med. Biol. 56, 39–46.

Knetsch, P.A., et al., 2015. [^{68}Ga]FSC-$(RGD)_3$ a trimeric RGD peptide for imaging $\alpha_v\beta_3$ integrin expression based on a novel siderophore derived chelating scaffold—synthesis and evaluation. Nucl. Med. Biol. 42, 115–122.

Knudsen, G.A., Sanders, J.M., Sadik, A.M., Birnbaum, L.S., 2014. Disposition and kinetics of tetrabromobisphenol A in female Wistar Han rats. Toxicol. Rep. 1, 214–223.

Knudsen, G.A., Hughes, M.F., Sanders, J.M., Hall, S.M., Birnbaum, L.S., 2016. Toxicol. Appl. Pharmacol. 311, 117–127.

Knudsen, G.A., Hall, S.M., Richards, A.C., Birnbaum, L.S., 2018. TBBPA disposition and kinetics in pregnant and nursing Wistar Han IGS rats. Chemosphere 192, 5–13.

Koitka, M., Höchel, J., Gieschen, H., Borchert, H.-H., 2010. Improving the ex vivo stability of drug ester compounds in rat and dog serum: inhibition of the specific esterases and implications on their identity. J. Pharm. Biomed. Anal. 51, 664–678.

Kołacińska, K., Trojanowicz, M., 2014. Application of flow analysis in determination of selected radionuclides. Talanta 131–145.

Kołacińska, K., Chajduk, E., Dudek, J., Samczyński, Z., Łokas, E., Bojanowska-Czajka, A., Trojanowicz, M., 2017. Automation of sample processing for ICP-MS determination of ^{90}Sr radionuclide at ppq level for nuclear technology and environmental purposes. Talanta 169, 216–226.

Kołacińska, K., Samczyński, Z., Dudek, J., Bojanowska-Czajka, A., Trojanowicz, M., 2018. Comparison study on the use of Dowex 1 and TEVA-resin in determination of ^{99}Tc in a SIA system with ICP-MS detection. Talanta 184, 527–536.

Koppen, V., Jones, R., Bockx, M., Cuyckens, F., 2014. High volume injections of biological samples for sensitive metabolite profiling and quantitation. J. Chromatogr. A 1372, 102–109.

Kumar, G.N., et al., 1999. In vitro metabolism of the HIV-1 protease inhibitor ABT-378: species comparison and metabolite identification. Drug Metab. Dispos. 27 (1), 86–91.

Kusche, M., Lindahl, U., 1990. Biosynthesis of heparin. J. Biol. Chem. 265, 15403–15409.

Labadie, P., Peck, M., Minier, C., Hill, E.M., 2007. Identification of the steroid fatty acid ester conjugates formed in vivo in *Mytilus edulis* as a result of exposure to estrogens. Steroids 72, 41–49.

L'Annunziata, M.F., 1967. The Chelation and Movement of ^{89}Sr-^{90}Sr(^{90}Y) in a Calcareous Soil (M.Sc. thesis). University of Arizona, Tucson, p. 52. https://repository.arizona.edu/handle/10150/318640.

L'Annunziata, M.F., 1970. Soil-Plant Relationships and Spectroscopic Properties of Inositol Stereoisomers; the Identification of D-Chiro- and Muco-Inositol in a Desert Soil-Plant System (Ph.D. dissertation). University of Arizona, Tucson, p. 114. ProQuest Dissertation Express Publ. No. 7104237. https://dissexpress.proquest.com/dxweb/results.html?QryTxt=&By=L%27Annunziata&Title=&pubnum=.

L'Annunziata, M.F., 1971. Birth of a unique parent-daughter relation: secular equilibrium. J. Chem. Educ. 48, 700–703.

L'Annunziata, M.F., 1979. Radiotracers in Agricultural Chemistry. Academic Press, New York and London, pp. 378–397.

L'Annunziata, M.F., 1984. Reaction mechanisms and pathways in biosynthesis. In: Isotopes and Radiation in Agricultural Sciences, vol. 2. Academic Press, London, pp. 105–182.

L'Annunziata, M.F., 1987. Radionuclide Tracers, Their Detection and Measurement. Academic Press, New York and London.

L'Annunziata, M.F., 2007a. Origins and biochemical transformations of inositol stereoisomers and their phosphorylated derivatives in soil. In: Turner, B.L., Richardson, A.E., Mullaney, E.J. (Eds.), Inositol Phosphates, Linking Agriculture and the Environment. CAB International, Cambridge, MA, USA, pp. 41–60.

L'Annunziata, M.F., 2007b. Radioactivity: Introduction and History. Elsevier, Amsterdam, p. 609.

L'Annunziata, M.F., 2013. Soil Inositol Phosphate Biochemistry: a call to link radiotracer applications with spectroscopic structural analysis. Soil Sci. Soc. Am. J. 77, 1107–1116.

L'Annunziata, M.F., 2016. Radioactivity: Introduction and History: From the Quantum to Quarks. Elsevier, Amsterdam, p. 902.

L'Annunziata, M.F., Fuller, W.H., 1968. The chelation and movement of ^{89}Sr-^{90}Sr(^{90}Y) in a calcareous soil. Soil Sci. 105, 311–319.

L'Annunziata, M.F., Fuller, W.H., 1971a. Soil and plant relationships of inositol phosphate stereoisomers; the identification of D-Chiro- and muco-inositol phosphates in a desert soil and plant system. Soil Sci. Soc. Am. J. 35 (4), 587–595.

L'Annunziata, M.F., Fuller, W.H., 1971b. Nuclear magnetic resonance spectra of acetate derivatives of soil and plant inositol phosphates. Soil Sci. Soc. Am. J. 35 (4), 655–658.

L'Annunziata, M.F., Fuller, W.H., 1976. Evaluation of the mass spectral analysis of soil inositol, inositol phosphates, and related compounds. Soil Sci. Soc. Am. J. 40 (5), 672–678.

L'Annunziata, M.F., Gonzalez, -I.,J., Olivarez, -O.,L.A., 1977. Microbial epimerization of my inositol to chiro-inositol in soil. Soil Sci. Soc. Am. J. 41, 733–736.

L'Annunziata, M.F., Nellis, S.W., 2001a. Flow Scintillation Analyzer (FSA) Interfaced with the HPLC and Nuclear Magnetic Resonance (NMR) Spectrometer. A State-Of-The-Art Application of the Radiomatic FSA. FSA Application Note. FSA-004. PerkinElmer, Inc., Waltham, MA, USA, p. 7. https://www.perkinelmer.com/lab-solutions/resources/docs/APP_FSAInterfacedHPLC.pdf.

L'Annunziata, M.F., Nellis, S.W., 2001b. Metabolism Studies with On-Line HPLC and Mass Spectrometry (MS) Interfaced with the Flow Scintillation Analyzer (FSA). FSA Application Note. FSA-005. PerkinElmer Inc., Waltham, MA, USA, p. 7. https://www.perkinelmer.com/lab-solutions/resources/docs/APP_FSAMetabolismStudies.pdf.

Larsen, J., Staerk, D., Cornett, C., Hansen, S.H., Jaroszewski, J.W., 2009. Identification of reaction products between drug substances and excipients by HPLC-SPE-NMR: ester and amide formation between citric acid and 5-aminosalicylic acid. *J.* Pharm. Biomed. Anal. 49, 839–842.

Lee, Y.-P., et al., 2012. Metabolism of (2*S*)-pterosin A: identification of the phase I and phase II metabolites in rat urine. Drug Metab. Dispos. 40 (8), 1566–1574.

Lenz, E.M., D'Souza, R.A., Jordan, A.C., King, C.D., Smith, S.M., Phillips, P.J., McCormick, A.D., Roberts, D.W., 2007. HPLC-NMR with severe column overloading: fast-track metabolite identification in urine and bile samples from rat and dog treated with [14C]-ZD6126. J. Pharm. Biomed. Anal. 43, 1065–1077.

Lenz, E.M., Spear, M., Drake, C., Pollard, C.R.J., Ward, M., Schulz-Utermoehl, T., Harrison, M., 2010. Characterisation and identification of the human N+-glucuronide metabolite of cediranib. J. Pharm. Biomed. Anal. 53, 526–536.

Lenz, E.M., Kenyon, A., Martin, S., Temesi, D., Clarkson-Jones, J., Tomkinson, H., 2011. The metabolism of [^{14}C]-zibotentan (ZD4054) in rat, dog and human, the loss of the radiolabel and the identification of an anomalous peak, derived from the animal feed. J. Pharm. Biomed. Anal. 55, 500–517.

Lezhnina, M.M., Kynast, U.H., 2010. Optical properties of matrix confined species. Opt. Mater. 33, 4–13.

Li, Y., et al., 2010. Identification of cardiac glycosides in fractions from Periploca forrestii by high-performance liquid chromatography/diode-array detection/electrospray ionization multi-stage tandem mass spectrometry and liquid chromatography/nuclear magnetic resonance. J. Chromatogr. B 878, 381–390.

Li, C.-C., Farn, S.-S., Yeh, Y.-H., Lin, W.-J., Shen, L.-H., 2011a. Development and validation of an anion-exchange HPLC method for the determination of fluoride content and radiochemical purity in [^{18}F]NaF. Nucl. Med. Biol. 38, 605–612.

Li, Z.-J., et al., 2011b. Synthesis and biological evaluation of novel 4-benzylpiperazine ligands for sigma-1 receptor imaging. Bioorg. Med. Chem. 19, 2911–2917.

Li, P., et al., 2017. An intense broadband sensitized near-infrared luminescence from Yb^{3+} and Bi^{3+} co-doped zeolite L crystals. Microporous Mesoporous Mater. 239, 96–100.

Li, R., et al., 2016. Biodegradation of isoproturon in agricultural soils with contrasting pH by exogenous soil microbial communities. Soil Biol. Biochem. 103, 149–159.

Lindegren, S., Jensen, H., Jacobsson, L., 2014. A radio-high-performance liquid chromatography dual-flow cell gamma-detection system for on-line radiochemical purity and labeling efficiency determination. J. Chromatogr. A 1337, 128–132.

Link, J.M., Synovec, R.E., 1999. Whole-column radioactivity detection: simultaneous separation and enhanced detectability. Anal. Chem. 71, 2700–2707.

Liu, H., et al., 2016. Metabolism and disposition of a novel B-cell lymphoma-2 inhibitor Venetoclax in humans and characterization of its unusual metabolites. Drug Metab. Dispos. 45, 294–305.

Lluch, E., Barrera, J., Tarancón, A., Bagán, H., García, J.F., 2016. Analysis of ^{210}Pb in water samples with plastic scintillation resins. Anal. Chim. Acta 940, 38–45.

Lochny, M., Ullrich, W., Wenzel, U., 1998. Simple on-line monitoring of α- and β-emitters by solid scintillation counting. J. Alloys Compd. 271–273, 31–37.

Lu, Y., Wang, C., Liu, R., Jin, W., Wen, Y., Huang, L., Wang, Z., 2018. 3-Amino-1-phenyl-2-pyrazoline-5-ketone as a heterobifunctional chromogenic reagent to derivatize reducing glycans for subsequent online LC/MS analysis. Anal. Biochem. 549, 1–11.

Lyon, M., Deakin, J.A., Gallagher, J.T., 1994. Liver heparan sulfate structure. J. Biol. Chem. 269, 11208–11215.

Ma, Y., et al., 2017. Effects of Cu^{2+} and humic acids on degradation and fate of TBBPA in pure culture of *Pseudomonas* sp. Strain CDT. J. Environ. Sci. 62, 60–67.

Magnussen, J.H., et al., 2015. Radio synthesis and in vitro validation of ^{3}H-NS14492 as a novel high affinity alpha7 nicotinic receptor radioligand. Eur. J. Pharmacol. 762, 35–41.

Maltais, R., et al., 2018. Pharmacokinetic profile of PBRM in rodents, a first selective covalent inhibitor of 17β-HSD1 for breast cancer and endometriosis treatments. J. Steroid Biochem. Mol. Biol. 178, 167–176.

Mamidi, R.N.V.S., et al., 2014. Metabolism and excretion of Canagliflozin in mice, rats, dogs, and humans. Drug Metab. Dispos. 42, 903–916.

Maneuski, D., et al., 2017. On the use of positron counting for radio-Assay in nuclear pharmaceutical production. Appl. Radiat. Isot. 125, 9–14.

Markham, K.A., Sikorski, R.S., Kohen, A., 2004. Synthesis and utility of ^{14}C-labeled nicotinamide cofactors. Anal. Biochem. 325, 62–67.

Marks, M.J., Rowell, P.P., Cao, J.-Z., Grady, S.R., McCallum, S.E., Collins, A.C., 2004. Subsets of acetylcholine-stimulated ^{86}Rb+ efflux and [^{125}I]-epibatidine binding sites in C57BL/6 mouse brain are differentially affected by chronic nicotine treatment. Neuropharmacology 46, 1141–1157.

Marks, M.J., Wageman, C.R., Grady, S.R., Gopalakrishnan, M., Briggs, C.A., 2009. Selectivity of ABT-089 for α4β2* and α6β2* nicotinic acetylcholine receptors in brain. Biochem. Pharmacol. 78, 795–802.

Martin, P.D., Warwick, M.J., Dane, A.L., Hill, S.J., Giles, P.B., Phillips, P.J., Lenz, E., 2003. Metabolism, excretion, and pharmacokinetics of rosuvastatin in healthy adult male volunteers. Clin. Ther. 25 (11), 2822–2835.

Martínez, M.-A., et al., 2018. Pyrethroid insecticide *lambda*-cyhalothrin induces hepatic cytochrome P450 enzymes, oxidative stress and apoptosis in rats. Sci. Total Environ. 631–632, 1371–1382.

Martínez, M.-A., et al., 2017. Induction of cytochrome P450-dependent mixed function oxidase activities and peroxisome proliferation by chloramine-T in male rat liver. Food. Chem. Toxicol. 106, 86–91.

Masini, J.C., Svec, F., 2017. Porous monoliths for on-line sample preparation: a review. Anal. Chim. Acta 964, 24–44.

Mattrey, F.T., et al., 2017. Current challenges and future prospects in chromatographic method development for pharmaceutical research. Trends Anal. Chem. 95, 36–46.

Maul, J.D., Blackstock, C., Brain, R.A., 2018. Derivation of avian dermal LD50 values for dermal exposure models using in vitro percutaneous absorption of [^{14}C]-atrazine through rat, mallard, and northern bobwhite full thickness skin. Sci. Total Environ. 630, 517–525.

Maurizis, J.-C., Rapp, M., Azim, E.M., Gaudreault, R.C., Veyre, A., Madelmont, J.-C., 1998. Disposition and metabolism of a novel antineoplastic agent, 4-tert- butyl-[3-(2-chloroethyl)ureido]benzene, in mice. Drug Metab. Dispos. 26 (2), 146–151.

Mavon, A., Raufast, V., Redoulés, D., 2004. Skin absorption and metabolism of a new vitamin E prodrug, δ-tocopherol-glucoside: in vitro evaluation in human skin models. J. Control. Release 100, 221–231.

Mays, D.C., Hecht, S.G., Unger, S.E., Pacula, C.M., Climie, J.M., Sharp, D.E., Gerber, N., 1987. Disposition of 8-methoxypsoralen in the rat. Drug Metab. Dispos. 15, 318–328.

McCracken, J.A., Wang, L., Kohen, A., 2004. Synthesis of R and S tritiated reduced β-nicotinamide adenine dinucleotide 2′ phosphate. Anal. Biochem. 324, 131–136.

Ménard, S., et al., 2012. Paracellular versus transcellular intestinal permeability to gliadin peptides in active celiac disease. Am. J. Pathol. 180 (2), 608–615.

Mensah-Nyagan, A.G., et al., 2008. Assessment of neuroactive steroid formation in diabetic rat spinal cord using high-performance liquid chromatography and continuous flow scintillation detection. Neurochem. Int. 52, 554–559.

Meyer, L., Venard, C., Schaeffer, V., Patte-Mensah, C., Mensah-Nyagan, A.G., 2008. The biological activity of 3α-hydroxysteroid oxido-reductase in the spinal cord regulates thermal and mechanical pain thresholds after sciatic nerve injury. Neurobiol. Dis. 30, 30–41.

Mitev, K.K., 2016. Measurement of ^{222}Rn by absorption in plastic scintillators and alpha/beta pulse shape discrimination. Appl. Radiat. Isot. 110, 236–243.

Morgan, R.O., Chang, J.P., Catt, K.J., 1987. Novel aspects of gonadotropin-releasing hormone action on inositol polyphosphate metabolism in cultured pituitary gonadotrophs. J. Biol. Chem. 262, 1166–1171.

Morris, O., et al., 2017. *In vivo* iniaturizedion of a therapeutically relevant self-assembling ^{18}F-labelled β-sheet forming peptide and its hydrogel using positron emission tomography. J. Label. Comp. Radiopharm. 60, 481–488.

Mortimer, M., Järving, R., Brash, A.R., Samel, N., Järving, I., 2006. Identification and characterization of an arachidonate 11R-lipoxygenase. Arch. Biochem. Biophys. 445, 147–155.

Mullen, W., Hartley, R.C., Crozier, A., 2003. Detection and identification of ^{14}C-labelled flavonol metabolites by high-performance liquid chromatography-radiocounting and tandem mass spectrometry. J. Chromatogr. A 1007, 21–29.

Murakami, H., et al., 2018. Progress in a selective method for the determination of the acetaldehyde- derived DNA adducts by using HILIC-ESI-MS/MS. Talanta 177, 12–17.

Nallani, G.C., et al., 2018. Age dependent in vitro metabolism of bifenthrin in rat and human hepatic microsomes. Toxicol. Appl. Pharmacol. 338, 65–72.

Narita, N., et al., 2018. Mechanism for covalent binding of MLN3126, an oral C-C motif receptor 9 antagonist, to serum albumins. Drug Metab. Dispos. 46 (3), 204–213.

Nassar, A.-E.F., Bjorge, S.M., Lee, D.Y., 2003. On-line liquid chromatography-accurate radioisotope counting coupled with a radioactivity detector and mass spectrometer for metabolite identification in drug discovery and development. Anal. Chem. 75 (4), 785–790.

Nayak, D.K., Baishya, R., Sen, T., Debnath, M., 2015. Tricarbonyl ^{99m}Tc(l) and Re(l)-thiosemicarbazone complexes: synthesis, characterization and biological evaluation for targeting bacterial infection. Dalton Trans. 44 (36), 16136–16148.

Nguyen, N.K., et al., 2018. Large variation in glyphosate mineralization in 21 different agricultural soils explained by soil properties. Sci. Total Environ. 627, 544–552.

Niessen, W.M.A., 2017. Mass spectrometry: chromatography–MS, methods. In: Encyclopedia of Spectroscopy and Spectrometry, third ed. Elsevier, pp. 758–762 https://doi.org/10.1016/B978-0-12-409547-2.11690-7.

Nolan, R.D., Lapetina, E.G., 1991. The production of phosphatidylinositol triphosphate is stimulated by thrombin in human platelets. Biochem. Biophys. Res. Commun. 174, 524–528.

O'Hara, M.J., Niver, C.M., 2014. ^{99}Tc Process Monitoring Syaytem In-Lab Performance Characterization. U.S. Department of Energy Report PNNL-23131, RPT-DVZ-AFRI-015, p. 48. https://www.pnnl.gov/main/publications/external/technical_reports/pnnl-23131.pdf.

O'Hara, M.J., Durst, P.C., Grate, J.W., Egorov, O.B., DeVol, T.A., 2008a. Rapid automated radiochemical analyzer for determination of targeted radionuclides in nuclear process streams. Portland, OR, OSTI ID: 963229, Report No. PNNL-SA-59847. In: Proc. 8th Int. Conf. On Facility Operations – Safeguards Interface, March 30-April 4, 2008. American Nuclear Society, La Grange Park, IL, USA, p. 88.

O'Hara, M.J., Durst, P.C., Grate, J.W., DeVol, T.A., Egorov, O.B., Clements, J.P., 2008b. Automated process monitoring: applying proven automation techniques to international safeguards needs. In: Proc. 49th Annual Meeting of the INMM. Institute of Nuclear Materials management, Northbrook, IL, United States, p. 351.

O'Hara, M.J., Burge, S.R., Grate, J.W., 2009a. Quantification of technetium-99 in complex groundwater matrixes using a radiometric preconcentrating minicolumn sensor in an equilibration-based sensing approach. Anal. Chem. 81, 1068–1078.

O'Hara, M.J., Burge, S.R., Grate, J.W., 2009b. Automated radioanalytical system for the determination of ^{90}Sr in environmental water samples by ^{90}Y Cherenkov radiation counting. Anal. Chem. 81, 1228–1237.

O'Hara, M.J., Murray, N.J., Carter, J.F., Morrison, S.S., 2018. Optimized anion exchange column isolation of zirconium-89 (^{89}Zr) from yttrium cyclotron target: method development andimplementation on an automated fluidic platform. J. Chromatogr. A 1545, 48–58.

Okarvi, S.M., Al Jammaz, I., 2016. Preparation and evaluation of the tumor-specific antigen-derived synthetic mucin 1 peptide: a potential candidate for the targeting of breast carcinoma. Nucl. Med. Biol. 43, 403–409.

Oldekop, M.-L., Herodes, K., Rebane, R., 2017. Comparison of amino acid derivatization reagents for liquid chromatography atmospheric pressure chemical ionization mass spectrometric analysis of seven amino acids in tea extract. Int. J. Mass Spectr. 421, 189–195.

Onursal, M., Lambrecht, F.Y., Ozgur, A., 2011. Synthesis and biological evaluation of receptor-based tumor imaging agent: ^{99m}Tc-folate-glucaric acid. Int. J. Pharm. 416, 288–292.

Parvez, H., Reich, A., Lucas-Reich, S., Parvez, S., 1988. Flow through radioactivity detection in HPLC. In: Progress in HPLC, vol. 3. VSP, Utrecht, The Netherlands.

Pasilis, S.P., Van Berkel, G.J., 2017. Modern atmospheric pressure surface sampling/ionization techniques in mass spectrometry. In: Encyclopedia of Spectroscopy and Spectrometry, third ed. Elsevier, pp. 819–829 https://doi.org/10.1016/B978-0-12-803224-4.00063-7.

Patin, D., et al., 2016. Unusual substrate specificity of the peptidoglycan MurE ligase from *Erysipelothrix rhusiopathiae*. Biochimie 121, 209–218.

Patte-Mensah, C., Meyer, L., Schaeffer, V., Mensah-Nyagan, A.G., 2010. Selective regulation of 3α-hydroxysteroid oxido-reductase expression in dorsal root ganglion neurons: a possible mechanism to cope with peripheral nerve injury-induced chronic pain. Pain 150, 522–534.

Paulson, S.K., et al., 2000. Metabolism and excretion of [^{14}C]celecoxib in healthy male volunteers. Drug Metab. Dispos. 28 (3), 308–314.

Peck, M.R., Labadie, P., Minier, C., Hill, E.M., 2007. Profiles of environmental and endogenous estrogens in the zebra mussel *Dreissena polymorpha*. Chemosphere 69, 1–8.

Pedras, M.S.C., Montaut, S., Zaharia, I.L., Gai, Y., Ward, D.E., 2003. Transformation of the host-selective toxin destruxin B by wild crucifers: probing a detoxification pathway. Phytochemistry 64, 957–963.

Perreault, A., et al., 2016. ^{18}F-labelled wild-type annexin V: comparison of random and site-selective radiolabeling methods. Amino Acids 48 (1), 65–74.

Pettersson, H., Lundqvist, J., Oliw, E., Norlin, M., 2009. CYP7B1-mediated metabolism of 5α-androstane-3α,17β-diol (3α-Adiol): a novel pathway for potential regulation of the cellular levels of androgens and neurosteroids. Biochim. Biophys. Acta 1791, 1206–1215.

Peyronneau, M.-A., et al., 2012. Difficulties in dopamine transporter radioligand PET analysis: the example of LBT-999 using [^{18}F] and [^{11}C] labelling Part II: metabolism studies. Nucl. Med. Biol. 39, 347–359.

Piltingsrud, H.V., Stencel, J.R., 1972. Determination of yttrium-90 and strontium-90 in samples by use of liquid scintillation beta spectroscopy. Health Phys. 23, 121–122.

Plionis, A.A., Gonzales, E.R., Landsberger, S., Peterson, D.S., 2009. Evaluation of flow scintillation analysis for the determination of Sr-90 in bioassay samples. Appl. Radiat. Isot. 67, 14–20.

Poljaková, J., et al., 2009. The mechanism of cytotoxicity and DNA adduct formation by the anticancer drug ellipticine in human neuroblastoma cells. Biochem. Pharmacol. 77, 1466–1479.

Powell, G.F., et al., 2011. The molecular action of the novel insecticide, Pyridalyl. Insect Biochem. Mol. Biol. 41, 459–469.

Prasad, P.V., Bashir, M., Sitruk-Ware, R., Kumar, N., 2010. Single-dose pharmacokinetics of Nestorone®, a potential female-contraceptive. Steroids 75, 252–264.

Prasad, B., Garg, A., Takwani, H., Singh, S., 2011. Metabolite identification by liquid chromatography-mass spectrometry. TrAC Trends Anal. Chem. (Reference Ed.) 30 (2), 360–387.

Provera, S., Martini, L., Guercio, G., Turco, L., Costa, L., Marchioro, C., 2010a. Application of LC-NMR and HR-NMR to the characterization of biphenyl impurities in the synthetic route development for vestipitant, a novel NK1 antagonist. J. Pharm. Biomed. Anal. 53, 389–395.

Provera, S., et al., 2010. A multi-technique approach using LC-NMR, LC-MS, semi-preparative HPLC, HR-NMR and HR-MS for the isolation and characterization of low-level unknown impurities in GW876008, a novel corticotropin-release factor 1 antagonist. J. Pharm. Biomed. Anal. 53, 517–525.

Ramanathan, R., Zhong, R., Blumenkrantz, N., Chowdhury, S.K., Alton, K.B., 2007. Response normalized liquid chromatography nanospray ionization mass spectrometry. J. Am. Soc. Mass Spectrom. 18, 1891–1899.

Rapkin, E., 1993. *B*-particle detection in HPLC by flow-through monitoring vs. liquid scintillation counting. J. Liq. Chromatogr. 16, 1769–1781.

Rapkin, E., Packard, L.E., 1960. In: University of New Mexico Conference on "Organic Scintillator Detectors". Albuquerque, New Mexico.

Reboul, S.H., 1994. Qualitative and quantitative analysis of alpha- and beta-emitting radionuclides by ion chromatography and on-line scintillation counting. Diss. Abstr. Int. B 55, 895–896.

Reboul, S.H., Fjeld, R.A., 1994. A rapid method for determination of beta-emitting radionuclides. Radioact. Radiochem. 5 (3), 42–49.

Reboul, S.H., Fjeld, R.A., 1995. Potential effects of surface water components in actinide determinations conducted by ion chromatography. Health Phys. 68, 585–589.

Reeve, D.R., Crozier, A., 1977. Radioactivity monitor for high-performance liquid chromatography. J. Chromatogr. 137, 271–282.

Reich, A.R., Lucas-Reich, S., Parvez, H., 1988. Radioactive flow detectors: history and theory. In: Progress in HPLC, vol. 3. VSP, Utrecht, The Netherlands, pp. 1–10.

Ren, T., et al., 2017. Isolation and identification of human metabolites from a novel anti-tumor candidate drug 5-chlorogenic acid injection by HPLC-HRMS/MS and HPLC-SPE-NMR. Anal. Bioanal. Chem. 409 (30), 7035–7048.

Roane, J.E., DeVol, T.A., Leyba, J.D., Fjeld, R.A., 1999. Effects of ionic radiological and chemical interferences on the chromatographic separation of a radionuclide standard solution. J. Radioanal. Nucl. Chem. 240 (1), 197–208.

Roane, J.E., DeVol, T.A., 2002. Simultaneous separation and detection of actinides in acidic solutions using an extractive scintillating resin. Anal. Chem. 74, 5629–5634.

Roane, J.E., DeVol, T.A., Leyba, J.D., Fjeld, R.A., 2003. The use of extraction chromatography resins to concentrate actinides and strontium from soil for radiochromatographic analyses. J. Environ. Radiact. 66, 227–245.

Rocha, J., Ananias, D., Paz, F.A.A., 2013. Chapter 4.05. Photoluminescent zeolite-type lanthanide silicates. In: Comprehensive Inorganic Chemistry II, second ed., vol. 4. Elsevier, pp. 87–109 https://doi.org/10.1016/B978-0-08-097774-4.00406-X.

Rodríguez, R., Avivar, J., Leal, L.O., Cerdà, V., Ferrer, L., 2016. Strategies for automating solid-phase extraction and liquid-liquid extraction in radiochemical analysis. Trends Anal. Chem. 76, 145–152.

Rónai, A.Z., et al., 2006. Endomorphin synthesis in rat brain from intracerebroventricularly injected [^{3}H]-Tyr-Pro: a possible biosynthetic route for endomorphins. Regul. Pept. 134, 54–60.

Reboul, S.H., 1994. Qualitative and quantitative analysis of alpha- and beta-emitting radionuclides by ion chromatography and on-line scintillation counting. Diss. Abstr. Int. B 55, 895–896.

Rong gui, S.C., et al., 2014. Photosensitization of europium ions by silver clusters in zeolite. Opt. Mater. 36, 916–920.

Ruan, C.-H., So, S.-P., Ruan, K.-H., 2011. Inducible COX-2 dominates over COX-1 in prostacyclin biosynthesis: mechanisms of COX-2 inhibitor risk to heart disease. Life Sci. 88, 24−30.

Rubiera, C., Lazo, P.S., Shears, S.B., 1990. Polarized subcellular distribution of the 1-, 4- and 5-phosphatase activities that metabolize inositol 1,4,5-triphosphate in intestinal epithelial cells. Biochem. J. 269, 353−358.

Rybin, V.G., Imbs, A.B., Demidkova, D.A., Ermolenko, E.V., 2017. Identification of molecular species of monoalkyldiacylglycerol from the squid *Berryteuthis magister* using liquid chromatography−APCI high-resolution mass spectrometry. Chem. Phys. Lipids 202, 55−61.

Sabourin, P.J., Bechtold, W.E., Henderson, R.F., 1988. A high pressure liquid chromatographic method for the separation and quantitation of water-soluble radiolabeled benzene metabolites. Anal. Biochem. 170, 316−327.

Saini, R.K., Banerjee, P., Sarkar, N., 2018. Influence of water inside the HY zeolite on the photophysical properties of 2,2′-Bipyridine-3,3′-diol ($BP(OH)_2$). J. Lumin. 194, 713−717.

Saredi, S., Patte-Mensah, C., Melcangi, R.C., Mensah-Nyagan, A.G., 2005. Effect of streptozotocin-induced diabetes on the gene expression and biological activity of 3β-hydroxysteroid dehydrogenase in the rat spinal cord. Neuroscience 135, 869−877.

Sasakawa, N., Nakaki, T., Kato, R., 1990. Rapid increase in inositol pentakisphosphate accumulation by nicotine in cultured adrenal chromaffin cells. FEBS Lett. 261, 378−380.

Sato-Nakai, M., et al., 2017. Metabolites of alectinib in human: their identification and pharmacological activity. Heliyon 3, e00354. https://doi.org/10.1016/j.heliyon.2017.e00354.

Schaeffer, V., Meyer, L., Patte-Mensah, C., Eckert, A., Mensah-Nyagan, A.G., 2008a. Dose-dependent and sequence-sensitive effects of amyloid-β peptide on neurosteroidogenesis in human neuroblastoma cells. Neurochem. Int. 52, 948−955.

Schaeffer, V., Patte-Mensah, C., Eckert, A., Mensah-Nyagan, A.G., 2008b. Selective regulation of neurosteroid biosynthesis in human neuroblastoma cells under hydrogen peroxide-induced oxidative stress condition. Neuroscience 151, 758−770.

Scheible, H., Kraetzer, F., Marx, A., Johne, A., Wimmer, E., 2016. Metabolism of the MEK1/2 inhibitor Pimasertib involves a novel conjugation with phosphoethanolamine in patients with solid tumors. Drug Metab. Dispos. 45, 174−182.

Scarfe, G.B., et al., 2000. Investigation of the metabolism of 14C/13C-practolol in rat using directly coupled radio-HPLC-NMR-MS. Xenobiotica 30 (7), 717−729.

Sharma, A.K., 2017. Rearrangement products in aqueous photolysis of thifensulfuron methyl. J. Photochem. Photobiol. A Chem. 346, 401−410.

Shockcor, J.P., 2017. HPLC−NMR, pharmaceutical applications. In: Encyclopedia of Spectroscopy and Spectrometry, third ed. Elsevier, Ltd, pp. 141−151.

Shockcor, J.P., Unger, S.E., Wilson, I.D., Foxall, P.J.D., Nicholson, J.K., Lindon, J.C., 1996. Combined HPLC, NMR spectroscopy, and ion-trap mass spectrometry with application to the detection and characterization of xenobiotic and endogenous metabolites in human urine. Anal. Chem. 68 (24), 4431−4435.

Schram, E., Lombaert, R., 1960. Continuous estimation of carbon-14 in chromatographic effluents by means of anthracene powders. Arch. Int. Physiol. Biochim. 68, 845−846.

Schram, E., Lombaert, R., 1961. Microvalve and connector for automatic column chromatography. Anal. Chem. 33, 1134−1135.

Schultz, G.A., Alexander IV, J.N., 1998. Incorporation of a RAM cell in a microcolumn for on-column detection of radiolabeled molecules for LC-RAM-ESI-MS. J. Microcolumn Sep. 10 (5), 431−437.

Seger, C., Sturm, S., Stuppner, H., 2013. Mass spectrometry and NMR spectroscopy: modern high-end detectors for high resolution separation techniques − state of the art in natural product HPLC-MS, HPLC-NMR, and CE-MS hypenations. Nat. Prod. Rep. 30, 970−987.

Seidegård, J., Grönquist, L., Ginnarsson, P.O., 1990. Metabolism of a novel nitrosurea, tauromustine, in the rat. Biochem. Pharmacol. 39, 1431−1436.

Seliman, A.F., Samadi, A., Husson, S.M., Borai, E.H., Devol, T.A., 2011. Preparation of polymer-coated, scintillating ion-exchange resins for monitoring of ^{99}Tc in groundwater. Anal. Chem. 83, 4759−4766.

Seliman, A.F., Helariutta, K., Wiktorowicz, S.J., Tenhu, H., Harjula, R., 2013. Stable and selective scintillating anion-exchange sensors for quantification of $^{99}TcO_4^-$ in natural freshwaters. J. Environ. Radioact. 126, 156−164.

Seliman, A.F., Bliznyuk, V.N., Husson, S.M., DeVol, T.A., 2015. Development of polymerizable 2-(1-naphthyl)-5-phenyloxazole scintillators for ionizing radiation detection. J. Mater. Chem. C 3, 7053−7061.

Seliman, A.F., Bliznyuk, V.N., DeVol, T.A., 2017. Development of stable extractive scintillating materials for real-time quantification of radiostrontium in aqueous solutions. J. Radioanal. Nucl. Chem. 314 (2), 743−751.

Shaffer, C.L., Langer, C.S., 2007. Metabolism of a 14C/3H-labeled GABAA receptor partial agonist in rat, dog and human liver microsomes: evaluation of a dual-radiolabel strategy. J. Pharm. Biomed. Anal. 43, 1195−1205.

Shah, S.Q., Khan, A.U., Khan, M.R., 2010. Radiosynthesis and biodistribution of ^{99m}Tc-rifampicin: a novel radiotracer for in-vivo infection imaging. Appl. Radiat. Isot. 68, 2255−2260.

Shah, S.Q., Khan, M.R., 2011. Radiosynthesis and biological evaluation of the ^{99m}Tc-tricarbonyl moxifloxacin dithiocarbamate complex as a potential *Staphylococcus aureus* infection radiotracer. Appl. Radiat. Isot. 69, 686−690.

Shalliker, R.A., 2017. High through-put liquid chromatography − mass spectrometry requires new strategies for the management of fluid at the interface. J. Chromatogr. A 1509, 176−178.

Shemesh, C.S., et al., 2016. Elucidation of the biotransformation pathways of a galnac3-conjugated antisense oligonucleotide in rats and monkeys. Mol. Ther. Nucl. Acids 5, e319.

Shi, S.-Y., et al., 2009. Coupling HPLC to on-line, post-column (bio) chemical assays for high-resolution screening of bioactive compounds from complex mixtures. Trends Anal. Chem. 28 (7), 865−877.

Shirley, M.A., Murphy, R.C., 1990. Metabolism of iniaturize B_4 in isolated rat hepatocytes. J. Biol. Chem. 265, 16288−16295.

Sigg, R.A., McCarty, J.E., Livingston, R.R., Sanders, M.A., 1994. Real-time aqueous tritium monitor using liquid scintillation counting. Nucl. Instrum. Methods Phys. Res., Sect. A 353, 494−498.

Silva, L.M.A., et al., 2013. Use of diffusion-ordered NMR spectroscopy and HPLC-UV-SPE-NMR to identify undeclared synthetic drugs in medicines illegally sold to phytotherapies. Magn. Reson. Chem. 51 (9), 541−548.

Silva-Elipe, M.V., 2000. Drug Metabolism, Rahway, NJ 07065 (Personal Communication, August 22, 2000). Merck & Co., Inc.

Silva-Elipe, M.V., 2003. Advantages and disadvantages of nuclear magnetic resonance spectroscopy as a hyphenated technique. Anal. Chim. Acta 497, 1−25.

Silva-Elipe, M.V., Huskey, S.-E.W., Zhu, B., 2003. Application of LC-NMR for the study of the volatile metabolite of MK-0869, a substance P receptor antagonist. J. Pharm. Biomed. Anal. 30, 1431−1440.

Simpson, M.J., Simpson, A.J., 2014. NMR Spectroscopy: A Versatile Tool for Environmental Research. Wiley, p. 480.

Singh, R., et al., 2001. Pharmacokinetics and metabolism of a Ras farnesyl transferase inhibitor in rats and dogs: in vitro-in vivo correlation. Drug Metab. Dispos. 29 (12), 1578−1587.

Sivapackiam, J., Harpstrite, S.E., Prior, J.L., Mattingly, S., Sharma, V., 2016. $^{67/68}$Galmydar: a metalloprobe for monitoring breast cancer resistance protein (BCRP)-mediated functional transport activity. Nucl. Med. Biol. 43, 191−197.

Sivapackiam, J., Laforest, R., Sharma, V., 2018. ^{68}Ga[Ga]-Galmydar: biodistribution and radiation dosimetry studies in rodents. Nucl. Med. Biol. 59, 29−35.

Smith, R.M., Chienthavorn, O., Wilson, I.D., Wright, B., Taylor, S.D., 1999. Superheated heavy water as the effluent for HPLC-NMR and HPLC-NMR-MS of model drugs. Anal. Chem. 71 (20), 4493−4497.

Soreefan, A.M., Tan, H., DeVol, T.A., 2003. Experimental and Monte Carlo investigation of the light collection efficiency of heterogeneous scintillation flow cell detectors. Art. No. N25-72 IEEE Nucl. Sci. Symp. Rec. 2, 760−762.

Stalmans, S., et al., 2014. Blood-brain barrier transport of short proline-rich antimicrobial peptides. Protein Peptide Lett. 21 (4), 399−406.

Steinberg, D., 1958. Proceedings of the Symposium on the Advances in Tracer Applications of Tritium. New York.

Steinberg, D., 1960. A new approach to radioassay of aqueous solutions in the liquid scintillation spectrometer. Anal. Biochem. 1, 23−29.

Stevenson-Paulik, J., et al., 2006. Inositol phosphate metabolomics: merging genetic perturbation with modernized radiolabeling methods. Methods 39, 112−121.

Su, C., Gullberg, H., Simko, H., Luthman, M., Edlund, P.-O., Lundbäck, T., 2010. A novel assay of cellular stearoyl-CoA desaturase activity of primary rat hepatocytes by HPLC. J. Chromatogr. B 878, 2427−2432.

Suddaby, L.A., Beulke, S., van Beinum, W., Oliver, R.G., Kuet, S., Brown, C.D., 2016. Long-term experiments to investigate irreversibility in sorption of pesticides to soil. Chemosphere 162, 40−47.

Sweeny, D.J., Lynch, G., Bidgood, A.M., Lew, W., Wang, K.-Y., Cundy, K.C., 2000. Metabolism of the influenza neuraminidase inhibitor prodrug oseltamivir in the rat. Drug Metab. Dispos. 28 (7), 737−741.

Taguchi, S., et al., 2011. Determination of trace amounts of plutonium in low-active liquid wastes from spent nuclear fuel reprocessing plants by flow-injection based solid-phase extraction/electrochemical detection system. J. Radioanal. Nucl. Chem. 288, 435−441.

Taiji, K., Iso, Y., Isobe, T., 2018. Fluorescent Ag^{+}-exchanged zeolite nanoparticles with improved photoluminescence properties via X-ray irradiation. J. Lumin. 196, 214−220.

Takahashi, R.H., et al., 2015. Elucidating the mechanisms of formation for two unusual cytochrome P450−mediated fused ring metabolites of GDC-0623, a MAPK/ERK kinase inhibitor. Drug Metab. Dispos. 43, 1929−1933.

Takei, M., Kida, T., Suzuki, K., 2001. Sensitive measurement of positron emitters eluted from HPLC. Appl. Radiat. Isot. 55, 229−234.

Tan, H., DeVol, T.A., 2002. Development of a flow-cell alpha detector utilizing microencapsulated CsI:Tl granules and silicon PIN-photodiodes. IEEE Trans. Nucl. Sci. 49 (3), 1243−1248.

Tan, H., DeVol, T.A., 2003. Monte Carlo modeling of heterogeneous scintillation flow-cell detectors. Nucl. Instrum. Methods Phys. Res., Sect. A 515, 624−633.

Tan, H., DeVol, T.A., Fjeld, R.A., 2000. Digital alpha/beta pulse shape discrimination of CsI:Tl for on-line measurement of aqueous radioactivity. IEEE Trans. Nucl. Sci. 47 (4), 1516−1521.

Tang, K., Page, J.S., Kelly, R.T., Marginean, I., 2017. Electrospray ionization in mass spectrometry. In: Encyclopedia of Spectroscopy and Spectrometry, third ed. Elsevier, pp. 476−481 https://doi.org/10.1016/B978-0-12-803224-4.00319-8.

Tarancón, A., Padró, A., García, J.F., Rauret, G., 2005. Development of a radiochemical sensor, Part 2: application to liquid effluents. Anal. Chim. Acta 538, 241−249.

Tarancón, A., Novella, O., Batlle, M., Pujadas, M., Cros, J., García, J.F., 2016. Robustness of plastic scintillation microspheres in the continuous measurement of different river waters. Appl. Radiat. Isot. 114, 145−153.

Tarn, M.D., Maneuski, D., et al., 2016. Positron detection in silica monoliths for iniaturized quality control of PET radiotracers. Chem. Commun. 52, 7221−7224.

Tessema, E.N., Gebre-Mariam, T., Schmelzer, C.E.H., Neubert, R.H.H., 2017. Isolation and structural characterization of glucosylceramides fromEthiopian plants by LC/APCI-MS/MS. J. Pharm. Biomed. Anal. 141, 241−249.

Thomson, J., 1993. Scintillation Counting Medium and Process, European Patent Application No. 93.200718.0, March 1993.

Thomson, J., 1994. The advent of safer flow scintillation cocktails. In: Cook, G., Harkness, D.D., Mackenzie, A.B., Miller, B.E., Scott, E.M. (Eds.), Liquid Scintillation Spectrometry 1994. Radiocarbon, Tucson, Arizona, USA, pp. 257−260.

Thomson, J., 1997. Safer Flow Cocktails. Counting Solutions, CS-006. PerkinElmer Life and Analytical Sciences, Boston, p. 6.

Thonon, D., Kaisin, G., Henrottin, J., Aerts, J., Van Malderen, H., Luxen, A., 2013. Evaluation of an unshielded luminescence flow-through radio-HPLC detector for LC quality control and preparation of PET radiopharmaceuticals. Appl. Radiat. Isot. 73, 84−89.

Timmers, M.A., Urban, S., 2012. On-line (HPLC-NMR) and off-line phytochemical profiling of the Australian plant, *Lasiopetalum macrophyllum*. Mat. Prod. Comm. 7 (5), 551−560.

Timmers, M.A., Dias, D.A., Urban, S., 2012. Application of HPLC-NMR in the identification of plocamenone and isoplocamenone from the marine red alga *Plocamium angustum*. Mar. Drugs 10, 2089−2102.

Tozuka, Z., et al., 2011. Comprehensive quantitative and qualitative liquid chromatography−radioisotope−mass spectrometry analysis for safety testing of tolbutamide metabolites without standard samples. J. Pharm. Sci. 100 (9), 4024−4036.

Trojanowicz, M., Kołacińska, K., Grate, J.W., 2018. A review of flow analysis methods for determination of radionuclides in nuclear wastes and nuclear reactor coolants. Talanta 183, 70−82.

Tsao, N., et al., 2013. ^{99m}Tc-N4amG: synthesis biodistribution and imaging in breast tumor-bearing rodents. Appl. Radiat. Isot. 72, 105−113.

Tung, C.-H., et al., 2018. Combination of on-line desalting and HPLC-UVESI-MS for simultaneous detection and identification of FIP-fve and flammutoxin in *Flammulina velutipes*. J. Food Drug Anal. 26, 1045−1053.

Tykva, R., Wimmer, Z., Vlasáková, V., Novák, J., Havlíček, L., 2005. Biodegradation of juvenoid diastereoisomers: radio-HPLC and MS analysis. Chemosphere 60, 1197−1202.

Ubukata, K., Nakayama, A., Mihara, R., 2011. Pharmacokinetics and metabolism of *N*-[*N*-[3-(3-hydroxy-4-methoxyphenyl)propyl]-

α-aspartyl]-L-phenylalanine 1-methyl ester, monohydrate (advantame) in the rat, dog, and man. Food. Chem. Toxicol. 49, S8−S29.

Usuda, S., Abe, H., 1992. Flow monitor for actinide solutions by simultaneous α and $\beta(\gamma)$ counting using a CsI(Tl) scintillator. Nucl. Instrum. Methods Phys. Res., Sect. A 321, 242−246.

Usuda, S., Mihara, A., Abe, H., 1992. Rise time spectra of α and $\beta(\gamma)$ rays from solid and solution sources with several solid scintillators. Nucl. Instrum. Methods Phys. Res., Sect. A 321, 247−253.

Vanbilloen, H.P., Cleynhens, B.J., De Groot, T.J., Maes, A., Bormans, G.M., Verbruggen, A.M., 2003. RP-HPLC separation of the diastereomers of technetium-99m labelled tropanes and identity confirmation using radio-LC-MS. J. Pharm. Biomed. Anal. 32, 663−668.

Vanderghinste, D., et al., 2003. An efficient HPLC method for the analysis of isomeric purity of technetium-99m-exametazime and identity confirmation using LC-MS. J. Pharm. Biomed. Anal. 32, 679−685.

Venard, C., Boujedaini, N., Belon, P., Mensah-Nyagan, A.G., Patte-Mensah, C., 2008. Regulation of neurosteroid allopregnanolone biosynthesis in the rat spinal cord by glycine and the alkaloidal analogs strychnine and gelsemine. Neuroscience 153, 154−161.

Verbeken, M., et al., 2015. Blood−brain transfer and antinociception of linear and cyclic *N*-methyl-guanidine and thiourea-enkephalins. Peptides 63, 10−21.

Vickers, S., et al., 1998. Metabolism of MK-499, a class III antiarrhythmic agent, in rats and dogs. Drug Metab. Dispos. 26 (5), 388−395.

Vickers, A.E.M., Zollinger, M., Dannecker, R., Tynes, R., Heitz, F., Fischer, V., 2001. In vitro metabolism of tegaserod in human liver and intestine: assessment of drug interactions. Drug Metab. Dispos. 29 (10), 1269−1276.

Vitorge, E., Szenknect, S., Martins, J.M.-F., Barthès, V., Gaudet, J.-P., 2014. Comparison of three labeled silica nanoparticles used as tracers in transport experiments in porous media. Part II: transport experiments and modeling. Environ. Pollut. 184, 613−619.

Wang, L., et al., 2017. ^{18}F-Labeled indole-based analogs as highly selective radioligands for imaging sigma-2 receptors in the brain. Bioorg. Med. Chem. 25, 3792-2802.

Wang, Z., Yeung, S., Chen, S., Moatazedi, Y., Chow, M.S.S., 2018. Bioavailability of wilforlide A in mice and its concentration determination using an HPLC-APCI-MS/MS method. J. Chromatogr. B 1090, 65−72.

Wang-Buhler, J.L., et al., 2005. CYP2K6 from zebrafish (*Danio rerio*): cloning, mapping, developmental/tissue expression, and aflatoxin B1 activation by baculovirus expressed enzyme. Comp. Biochem. Physiol., C 140, 207−219.

Wasyl, M.S., Nellis, S.W., 1996. Optimizing performance in radioactive HPLC detection using scintillation counting technology. In: Cook, G.T., Harkness, D.D., MacKenzie, A.B., Miller, B.F., Scott, E.M. (Eds.), Liquid Scintillation Spectrometry 1994. Radiocarbon, The University of Arizona, Tucson, pp. 357−360.

Waters, T.R., Gallinari, P., Jiricnyl, J., Swann, P.F., 1999. Human thymine DNA glycosylase binds to apurinic sites in DNA but is displaced by human apurinic endonuclease 1. J. Biol. Chem. 274 (1), 67−74.

Watson, M.M., Seliman, A.F., Bliznyuk, V.N., DeVol, T.A., 2018. Evaluation of Shiryaev-Roberts procedure for on-line environmental radiation monitoring. J. Environ. Radioact. 192, 587−591.

Wells, D.A., Digenis, G.A., 1988. Disposition and metabolism of double-labeled [^{3}H and ^{14}C] N-methyl-2-pyrrolidinone in the rat. Drug Metab. Dispos. 16, 243−249.

Wenzel, U., Ullrich, W., Lochny, M., 1999. The WUW ML bundle detector. A flow through detector for α-emitters. Nucl. Instrum. Methods Phys. Res., Sect. A 421, 567−575.

Wierczinski, B., et al., 2001a. First chemical on-line separation and detection of a subsecond α-decaying nuclide, 224Pa. J. Radioanal. Nucl. Chem. 247 (1), 57−60.

Wierczinski, B., Claessens, R.A.M.J., de Goeij, J.J.M., Kolar, Z.I., Volkers, K.J., 2001b. Feasibility study for the production of 32P-labeled diphosphonic acids by neutron irradiation and radiochemical separation. J. Radioanal. Nucl. Chem. 249 (2), 279−282.

Wilson, I.D., Brinkman, U.A.T., 2003. Hyphenation and hypernation: the practice and prospects of multiple hyphenation. J. Chromatogr. A 1000, 325−356.

Wu, H.-C., Su, T.-Y., Tsai, T.-L., Jong, S.-B., Yang, M.-H., Tyan, Y.-C., 2014. Rapid determination of technetium-99 by automatic solid phase extraction and inductively coupled plasma mass spectrometry. RSC Adv. 4, 39226−39230.

Wyffels, L., et al., 2014. In vivo evaluation of ^{18}F-labeled TCO for pretargeted PET imaging in the brain. Nucl. Med. Biol. 41, 513−523.

Wynendaele, E., et al., 2015. Quorum sensing peptides selectively penetrate the blood-brain barrier. PLoS One 10 (11), e0142071.

Xiao, X., et al., 2018. NMR and ESI−MS spectrometry characterization of autohydrolysis xylo-oligosaccharides separated by gel permeation chromatography. Carbohydr. Polymers 195, 303−310.

Xu, D., et al., 2018. ^{18}F−labeled estradiol derivative for targeting estrogen receptor-expressing breast cancer. Nucl. Med. Biol. 59, 48−55.

Xu, Y.P., Yang, M., Hui Pan, D., 2009. Synthesis, radiosynthesis, and in vitro evaluation of [^{131}I]-5-iodo-N-[2-(6,7-dimethoxy-3,4-dihydro-1H-isoquinoline-2-yl)-ethyl]-2-methoxy-benzamide as a potential tumor imaging agent. Appl. Radiat. Isot. 67, 594−597.

Yamamoto, F.Y., 2018. Alterations of cytochrome P450 and the occurrence of persistent organic pollutants in tilapia caged in the reservoirs of the Iguaçu River. Environ. Pollut. 240, 67−682.

Yang, Z., Li, J.-P., Guan, H.-S., 2004. Preparation and characterization of oligomannuronates from alginate degraded by hydrogen peroxide. Carbohydr. Polymers 58, 115−121.

Yim, C.-B., 2013. Synthesis and preclinical characterization of [64Cu] NODAGA-MAL-exendin-4 with a N^{ε}-maleoyl-l-lysyl-glycine linkage. Nucl. Med. Biol. 40, 1006−1012.

Yuan, J.J., Yang, D.-C., Zhang, J.Y., Bible Jr., R., Karim, A., Findlay, J.W.A., 2002. Disposition of a specific cyclooxygenase-2 inhibitor, valdecoxib, in human. Drug Metab. Dispos. 30 (9), 1013−1021.

Yue, Z., Stephens, A., Lacy, J., 2006. HPLC validation and quality assurance of ^{62}Cu-PTSM, ^{62}Cu-ATSM, and ^{62}Cu-ETS synthesized by ^{62}Zn/^{62}Cu microgenerator kit synthesis. J. Nucl. Med., SNM Annual Meeting Abstracts 47 (Suppl. 1), 158p.

Zeng, D., et al., 2013. Microfluidic radiolabeling of biomolecules with PET radiometals. Nucl. Med. Biol. 40, 42−51.

Zha, Z., et al., 2018. Synthesis and evaluation of a novel urea-based ^{68}Ga-complex for imaging PSMA binding in tumor. Nucl. Med. Biol. 59, 36−47.

Zhang, M., Whiting, S.A., Clark, B.J., 2018. Application of kinetic modeling to predict the fate of two indoxacarb metabolites and their bound residues in soil. Sci. Total Environ. 607−608, 829−837.

Zhu, X., Schroll, R., Dörfer, U., Chen, B., 2018. Inoculation of soil with an Isoproturon degrading microbial community reduced the pool of "real non-extractable" Isoproturon residues. Exotoxicol. Environm. Safety 149, 182−189.

Zhuo, X., Zheng, N., 2018. Drug metabolism: metabolite isolation and identification. In: Encyclopedia of Analytical Science, third ed. Elsevier Ltd https://doi.org/10.1016/B978-0-12-409547-2.14303-3.

Further reading

Baranowska-Kortylewicz, J., Helseth, L.D., Lai, J., Schneiderman, M.H., Schneiderman, G.S., Dalrymple, G.V., 1994. Radiolabeling kit/generator for 5-radiohalogenated urinides. J. Label. Comp. Radiopharm. 34, 513–521.

Maggs, J.L., et al., 2000. Biliary metabolites of β-artemether in rats: biotransformations of a antimalarial endoperoxide. Drug Metab. Dispos. 28 (2), 209–217.

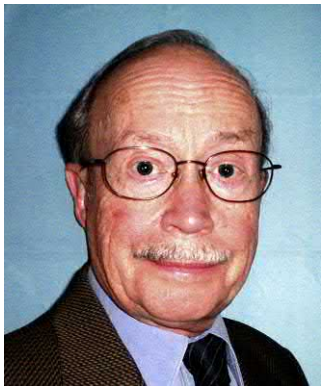
Rajagopal, S., Venkatachalam, T.K., Conway, T., Diksic, M., 1992. Synthesis of 14C-labelled α-methyl tyrosine. Appl. Radiat. Isot. 43, 979–987.

Takatsuka, J., Takahashi, N., De Luca, L.M., 1996. Retinoic acid metabolism and inhibition of cell proliferation: an unexpected liaison. Cancer Res. 56, 675–678.

Wouters-Ballman, P., Donnay, I., Devleeschouwer, N., Verstegen, J., 1995. Iodination of mouse EGF with chloramine T at 4°C: characterization of the iodinated peptide and comparison with other labelling methods. J. Receptor Res. 15, 737–746.

Wu, W.-N., Mutter, M.S., 1995. Biotransformation of linogliride, a hypoglycemic agent in laboratory animals and humans. J. Pharm. Biomed. Anal. 13, 857–867.

Michael F. L'Annunziata



Michael F. L'Annunziata, PhD, is the founding editor and coauthor of the *Handbook of Radioactivity Analysis* now in its Fourth Edition. His graduate thesis research at the University of Arizona, Tucson, AZ, United States, in the 1960s, financed by the then US Atomic Energy Commission, dealt with the analysis of ^{89}Sr and ^{90}Sr in the event of nuclear fallout. During 1970–1971, he worked in the chemical industry (Amchem Products, Inc., Ambler, PA, United States) as a ^{14}C-tracer chemist. Michael was then appointed a professor at the Postgraduate College, Chapingo, Mexico (1972–75), and a senior research scientist and graduate thesis advisor at the Nuclear Center of the National Institute of Nuclear Research (ININ), Mexico City during (1975–77). Michael served as a scientific officer in the Department of Research and Isotopes and Department of Technical Co-operation of the International Atomic Energy Agency (IAEA) in Vienna, Austria during 1977–91 and head of IAEA Fellowships and Training during 1987–91. Michael F. L'Annunziata was first to postulate the soil microbial epimerization of myo-inositol to other inositol stereoisomers as the chemical pathway and origin of the various inositol phosphate stereoisomers in soils (PhD dissertation, 1970, https://dissexpress.proquest.com/dxweb/results.html?QryTxt=&By=L%27Annunziata&Title=&pubnum =) and in 1975 (*SSSA Journal* 39(2), 377–379), and first to demonstrate in 1977, with the use of the radioisotope carbon-14, the soil microbial epimerization of myo-inositol to chiro-inositol as a mechanism involved in the origin of the unique soil inositol phosphate stereoisomers (*SSSA Journal* 41(4), 733–736, https://dl.sciencesocieties.org/publications/sssaj/abstracts/41/4/SS0410040733). From 1977 to 2007, he served as IAEA expert in peaceful applications of nuclear energy in more than 50 countries of the world in Europe, Asia, Africa, Latin America, and the Middle East. His book entitled *Radioactivity: Introduction and History*, First Edition, published by Elsevier, was on the Best Sellers List in Physics (*LibraryJournal Academic Newswire* in 2008), and his much expanded Second Edition entitled "Radioactivity: Introduction and History, From the Quantum to Quarks" published by Elsevier in 2016 (https://www.sciencedirect.com/book/9780444634894/radioactivity) was awarded an Honorable Mention in the 2017 PROSE AWARDS in the category of Chemistry and Physics.

Chapter 11

PERPUSTAKAAN PRIBADI AN-NUR SUNARYA

Automated radiochemical separation, analysis, and sensing

Jay W. Grate[1], Matthew J. O'Hara[1] and Oleg B. Egorov[2]
[1]Pacific Northwest National Laboratory, Richland, WA, United States; [2]Medvio, LLC, West Richland, WA, United States

Chapter outline

I. Introduction 821
II. Radiochemical separations 823
A. Separation requirements 823
B. Radiochemical separation approaches 823
C. Modern radiochemical separation materials 824
III. Automation of radiochemical analysis using flow injection or sequential injection fluidics 825
A. Flow injection and sequential injection fluidics 825
B. Sequential injection separations 826
C. Alternative fluid delivery systems 826
D. Column configurations 827
E. Renewable separation concepts and methods 828
F. Lab-on-valve 830
G. Extractant liquids and particles 830
H. Detection 831
IV. Selected radiochemical analysis examples 831
A. Strontium-90 831
B. Technetium-99 833
C. Actinides 834
D. Renewable separation column applications 837
V. Automation using robotics 837
VI. Automated monitors for industrial scale nuclear processes 838
VII. Radionuclide sensors and systems for water monitoring 841
A. Preconcentrating minicolumn sensors 841
B. Sensors for ^{99}Tc(VII) using quantitative capture 842
C. Equilibration-based radionuclide sensors 844
D. Sensor probes and systems for water monitoring 845
VIII. Digital microfluidics for microscale single bead manipulations 847
IX. Radioisotopes in medicine 848
A. Therapeutic radionuclides 849
1. Beta emitters 849
2. Alpha emitters 850
B. Diagnostic radionuclides 854
1. Gamma emitters 854
2. Positron emitters 855
X. Discussion 858
Acknowledgments 858
References 858
Jay W. Grate, PhD 871
Matthew J. O'Hara 871
Oleg B. Egorov, PhD 872

I. Introduction

Destructive analysis, complete with radiochemical separation of the radionuclide(s) of interest from the sample matrix and potential interferences, is a fundamental and often critical component of radioanalytical measurements. In this regard, radiochemistry has been described as "inconvenient but indispensable" (Bickel et al., 2000). Faster automated methods are needed to support analytical laboratories that make measurements on environmental samples; International Atomic Energy Agency (IAEA) laboratories involved in safeguards; and on-site laboratories at nuclear facilities. In addition, automation is required to move destructive analysis methods from the laboratory to online monitoring applications at nuclear facilities, and to sense radionuclides in the environment, at-site or in situ.

Destructive analysis is normally carried out in fixed laboratories using manual sample preparation, separation, and measurement techniques. Classic separation methods such as liquid–liquid extraction and ion exchange are well known and have been reviewed in the past (Choppin, 1984–85; Nash et al., 2006; Rydberg et al., 2004). For mass spectrometric measurement methods, the analyte must be separated from matrix components that may generate

Handbook of Radioactivity Analysis: Volume 2. https://doi.org/10.1016/B978-0-12-814395-7.00011-8

Copyright © 2020 Elsevier Inc. All rights reserved. Battelle Energy Alliance, LLC under Contract No: DE-AC05-76RL01830 with the U.S. Department of Energy

isobaric or molecular interferences. For radiometric methods, the analyte should be radiochemically purified prior to measurement to address matrix effects, spectral interferences, and prepare thin sources. Although gamma-emitting radionuclides may be determined by nondestructive analysis in some measurement scenarios, separations may still be required in many cases if the gamma emissions are weak and/or the sample matrix is radiologically complex.

Automation in radiochemical analysis offers many significant advantages, including reduced worker exposure to radioactivity, increased reliability, improved safety, and more consistent analytical protocols, as well as shorter analysis times, higher throughput, and lower costs. Instruments and sensors are required that perform all the functions previously carried out as sequential manual steps in the laboratory, yet achieve this rapidly and efficiently in an automated analyzer or sensor. "Fortunately, the convergence of digital instrumentation for preprogrammed fluid manipulation and the development of new separation materials for column-based isolation of radionuclides has enabled the development of automated radiochemical analysis methodology" (Grate et al., 2010).

In addition, automation can enable measurements that are not currently considered feasible because they are too costly and time-consuming for manual laboratory analysis or too difficult to deploy online or at-site. The ability to automatically separate radionuclides of interest from the background and from each other may allow radiation detection techniques currently used only for nondestructive analysis to be more informative or accurate.

Currently, radiochemical automation is either practiced or under development in the following areas:

- IAEA laboratories have automated aspects of the analysis of spent fuel using robotic arm technology in radiological glove boxes (Beugelsdijk and Hollen, 1998; Brandalise et al., 1994; Zahradnik and Swietly, 1996; Ziegler and Mayer, 1999).
- Automated methods have been developed to support the analysis of samples related to environmental management of US DOE sites, linking automated radiochemical separations to radiometric or mass spectrometric detection (Egorov et al., 1998b, 2001, 2004b; Grate and Egorov, 1998a; Grate et al., 1996, 1999b, 2004, 2010; Murray, 1994).
- Automation methods are under development to support analyses of environmental samples related to nuclear nonproliferation (Auer et al., 2010; Bowyer et al., 1999; Zähringer et al., 2009).
- Requirements for the laboratory analysis of large numbers of potentially contaminated samples have motivated research into the automation of radiochemical analysis. These samples may be from contaminated environmental sites or bioassay samples from an accidental or intentional nuclear event (Lariviere et al., 2008a,b).
- Automated process monitoring instrumentation has been developed for nuclear waste processing. An instrument for determination of ^{99}Tc in Hanford nuclear waste can perform sample preparation, separation, and detection all in less than 15 minutes for online analysis (Egorov et al., 2004a, 2005a, 2012; Grate et al., 2004).
- Radiochemical sensors have been developed for detection and determination of radionuclides in water and process samples (Egorov et al., 2006; Grate et al., 2004, 2008; Hofstetter and Wilson, 1992; O'Hara et al., 2009a,b).
- Radiochemical analysis as needed to support nuclear power reactors, reactor wastes, and the environment around reactors (Kolacinska et al., 2017, 2018; Trojanowicz et al., 2018).
- Heavy element researchers automate the rapid separation and measurement of short-lived heavy isotopes generated from target samples (Gaggeler, 1997; Schaedel, 2007; Zvara, 1999).
- Isolation and purification of radioisotopes for medicine requires separation of short-lived daughter products from their longer-lived parent isotopes. Interest in new isotopes and the desire to perform this separation at site are leading to increasing interest in automated radiochemical separation units (Boschi et al., 2013; Bray et al., 2000; Egorov and O'Hara, 2005; Egorov et al., 2000; Fisher, 2008; Krasikova, 2007; McAlister and Horwitz, 2009; Nagatsu et al., 2011; O'Hara et al., 2009d, 2017a,b, 2018a,b,c; Troyer and Schenter, 2009).

One may anticipate additional needs for radiochemical analysis in the following areas, which will lead to additional needs for automated methods:

- Decommissioning of nuclear reactors leads to additional analytical requirements as well as new types of samples (Hou, 2005a,b, 2007; Hou et al., 2005, 2007). An analysis approach for Pu from concrete, with automated flow-based separation, has been demonstrated (Qiao and Hou, 2010).
- Nuclear accidents such as Chernobyl and Fukushima lead to extensive sampling and analysis efforts, where automation may become advantageous (Bu et al., 2014; Cao et al., 2016; Chen et al., 2017; Hou et al., 2013; Ketterer and Szechenyi, 2008; Maxwell et al., 2014; Men et al., 2018; Xu et al., 2013, 2015, 2016a,b). The Fukushima accident has stimulated a new focus on radionuclides in seawater. Reprocessing plants also lead to anthropogenic environmental radionuclides in seawater (Qiao et al., 2017).

II. Radiochemical separations

A. Separation requirements

The requirements for radiochemical separations and other sample preparation steps in radiochemical analysis are determined largely by the detection method, which defines the acceptable characteristics of the sample presented to the detector.

There are four primary means of detection used in radiochemical analysis: radiometric detection of gamma rays, beta particles, or alpha particles, and mass spectrometry. Nondestructive analysis is possible primarily for those radionuclides that can be analyzed directly by high-resolution gamma spectroscopy. In almost all other cases, separations are required to separate the radionuclides of interest from other matrix components or other radionuclides that interfere with the detection method. Beta particles are emitted with a broad range of energies, and individual radionuclide species cannot be readily discerned using scintillation detection techniques. For example, radiometric detection of ^{99}Tc in nuclear waste matrixes requires complete separation from other interfering radioactive species. Although alpha particles are emitted with characteristic energies, a number of important radionuclides have unresolvable alpha energies, including ^{241}Am/^{238}Pu and ^{237}Np/^{234}U. In addition, matrix effects on the energy resolution of alpha spectroscopy necessitate extensive sample purification and preparation.

An alternative detection technique that has become increasingly important in modern radiochemical analysis is inductively coupled plasma mass spectrometry (ICP-MS). This approach to radiochemical analysis has been reviewed in detail (Kim et al., 2007; Lariviere et al., 2006) and critically compared (Hou and Roos, 2008). The trade-offs between radiation counting and atom counting have been described previously (Lariviere et al., 2006; Ross et al., 1993; Smith et al., 1992). In general, short-lived fission products are best detected with radiation detection, whereas long-lived (low specific activity) radionuclides can oftentimes be detected with more sensitivity using ICP-MS.

ICP-MS is also a selective detector since particular mass-to-charge ratios can be monitored. Nevertheless, separations are desirable prior to introducing a sample into the ICP-MS so that the sample is always introduced into the system in a consistent matrix (Colodner et al., 1994; Denoyer, 1992; Thompson and Houk, 1986). Matrix components can affect quantification. Moreover, detection by mass spectrometry is subject to interferences involving isobars and molecular ions, and tailing of peaks when one isotope is at much higher concentration than an isotope with an adjacent mass number (Crain and Alvarado, 1994; Garcia Alonso, 1995; Garcia Alonso et al., 1993, 1995; Kim et al., 2007; Lariviere et al., 2006; Smith et al., 1995; Tan and Horlick, 1986). Examples include ^{99}Tc/^{99}Ru, ^{151}Sm/^{151}Eu, ^{91}Zr, ^{16}O/^{107}Pd, ^{238}UH/^{239}Pu, ^{238}U/^{238}Pu, and ^{241}Pu/^{241}Am (Crain and Alvarado, 1994; Garcia Alonso et al., 1995; Smith et al., 1995). In addition, the possibility of interference from a large excess of ^{238}U in the measurement of ^{237}Np has been noted (Egorov et al., 2001).

In summary, chemical separations are carried out in radiochemical analysis to separate radionuclides with interfering radiation energy spectra for radiometric detection (Vajda and Kim, 2011) or to remove species, leading to isobaric, molecular, or spectral interferences in mass spectrometric detection (Kim et al., 2007; Lariviere et al., 2006). In many cases, it is also necessary to enable preconcentration and/or separation of radionuclides of interest from stable matrix components that affect subsequent analysis (Kim et al., 2000b). Whenever chemical separations are required, there may also be a requirement for additional sample preparation steps to control the speciation of the radionuclides prior to separation.

B. Radiochemical separation approaches

Separations in conventional radiochemical analysis have been carried out by a variety of classical and chromatographic methods, including precipitation, liquid−liquid extraction, and ion exchange. Often sequential combinations of these methods are used, and in some cases, individual steps must be repeated. Classic separation methods have been reviewed in the past (Choppin, 1984−85; Nash et al., 2006; Rydberg et al., 2004). Such classical methods have limited suitability for use in automated radiochemical analysis and have many disadvantages even for laboratory analyses.

Two column separation formats are generally considered for automated separations in radiochemical analysis. The first involves high-performance chromatographic techniques coupled with online flow-through scintillation detection for intermittent sampling and quantification of actinides and fission products in water (Desmartin et al., 1997; Reboul and Fjeld, 1994, 1995). Smith et al. (1995) described the use of high-performance ion chromatography (HPIC) with online radiometric detection for qualitative analysis of Hanford waste samples. Long separation times (40 minutes to several hours), matrix effects on the reproducibility and reliability of the separation procedure, limited capacity of the separation material, and speciation problems are significant issues with these chromatographic approaches that limit their applicability for rapid automated radiochemical analysis on difficult sample matrixes.

The second approach uses selective separation chemistries in extraction chromatographic or solid-phase extraction formats to rapidly and selectively isolate species of interest from stable matrix and radiological interferences (Cortina and Warshawsky, 1997; Dietz and

Horwitz, 1993; Grate and Egorov, 1998a; Izatt et al., 1996). The species of interest are strongly and preferentially retained by the column material under the solution conditions selected for the separation. Following a wash step (or sequence of wash steps) to remove unretained or slightly retained sample components, the species of interest are abruptly released by creating a large drop in the affinity factors via changes in the mobile phase composition or even by doing reaction chemistry on the retained species. Thus, this separation format relies on selective uptake and release properties rather than on the chromatographic efficiency of a long separation column, where analytes separate by migrating at different rates down a column due to (often small) differences in distribution ratios. This overall approach is shown in Fig. 11.1.

In general, radiochemical separations using extraction chromatographic materials can be accomplished rapidly using small columns operated under low pressures. Because of the selective analyte capture during sample loading step, analyte preconcentration can be achieved to improve analysis sensitivity. Compared with the high-performance chromatographic format, selective chemical separations are more tolerant of complex sample matrixes, and the columns have greater capture capacity (Cortina and Warshawsky, 1997). And unlike conventional chromatography, this approach can use reaction chemistry in addition to simple eluent delivery. Based on these considerations, selective chemistries on solid phases are particularly well suited for automation of radiochemical analysis.

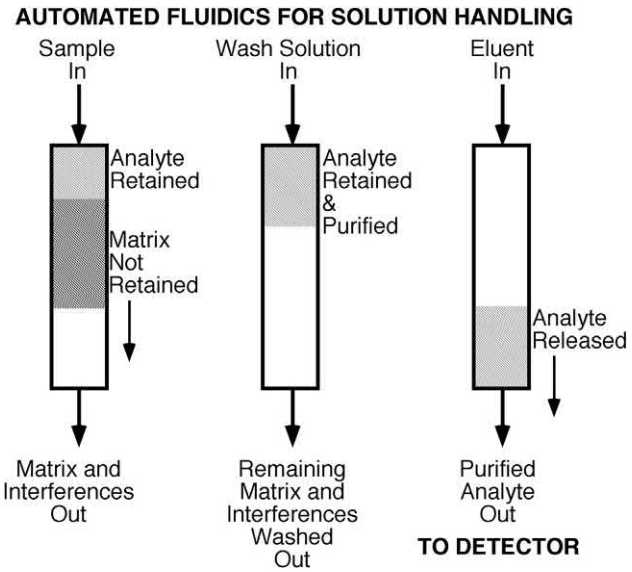


FIGURE 11.1 Schematic diagram of the separation approach whereby the analyte is selectively retained on the solid phase, whereas the matrix and interfering species are removed in the sample load and wash steps. Then an eluent is added that abruptly changes the retention of the analyte, releasing it in purified form for detection. Automated fluidic systems deliver sample, wash solutions, and eluents as per operator-specified computer code.

C. Modern radiochemical separation materials

A number of solid-phase materials have been developed to simplify analytical separations of heavy metals and radionuclides, using the separation approach shown in Fig. 11.1. These materials are based on either extraction chromatographic or solid-phase extraction materials, and they have made a significant contribution to the development of automated radiochemical analyzers and radionuclide sensors. Here, we use solid-phase extraction to refer to materials where the selective chemistry is covalently bound to the solid support.

A variety of solid-phase extraction materials dubbed "AnaLig" or "SuperLig" have been developed using "molecular recognition" ligands on solid supports and commercialized by IBC Advanced Technologies (American Fork, Utah) (Izatt, 1997; Izatt et al., 1994, 1996). These ligands are covalently bound to various polymeric or silica gel supports. The materials have been developed and investigated mainly for wastewater or effluent cleanup processes and have not been extensively used or characterized for analytical applications. Fundamental metal ion uptake studies of these are not available in the published literature. Nevertheless, AnaLig materials selective for Sr, Ra, and Tc were incorporated in Empore Rad Disks marketed by 3M for use in analysis of water samples (Fiskum et al., 2000; Schonhofer and Wallner, 2001).

Materials using selective or semiselective extractants impregnated on porous polymer and silica gel supports have been called solvent-impregnated resins and are more generally known today as extraction chromatographic materials (Dietz and Horwitz, 1993; Dietz et al., 1999; Horwitz, 1998; Horwitz et al., 2006). Early developments in extraction chromatography and relevance to radiochemistry were noted in an article in *Nature* in 1965, using organophosphorous extractants on silica gel support particles (Mikulski and StroŃSki, 1965). Modern extraction chromatographic materials use porous polymer support beads and have been commercialized by Eichrom Technologies, Inc. (Darien, Illinois) and Triskem International (Bruz, France). In most cases, they use chemistry from well-established liquid–liquid extraction separations. Extractant-impregnated beads are packed in a column and used to separate species from aqueous solutions by extraction chromatography (Cortina and Warshawsky, 1997). The uptake properties and chemical selectivities of these materials are well characterized in the literature. Extraction chromatographic methods generally tolerate high levels of potential interferences and complex sample matrixes; use columns with high capacities; work at low

pressures; and provide flexibility in sample loading conditions. These features are well suited for automated radiochemical separations.

III. Automation of radiochemical analysis using flow injection or sequential injection fluidics

A. Flow injection and sequential injection fluidics

The requirements for fluid handling in automation include a means to select samples, reagents, and eluents, bring them into the fluidic system, and deliver them to flow cells, separation columns, and detectors with precise control over volumes, flow rates, and timing. Sequential injection (SI) techniques from the field of flow injection (FI) analysis provide a versatile fluid handling approach for meeting these requirements (Fang, 1993; Ruzicka, 1994; Ruzicka and Hansen, 1988). Unlike conventional FI methodology or chromatography, which are based on a continuous forward flow paradigm, SI involved fluid flow in both directions and programmed flow reversals (Cerda et al., 1999, 2001; Christian, 1994; Grudpan, 2004; Ivaska and Ruzicka, 1993; Lenehan et al., 2002; Ruzicka, 1994, 2005; Ruzicka and Marshall, 1990; Taljaard and van Staden, 1998). The pump(s) and valve(s) of an SI system are fully controlled by a computer. FI and SI methods are compared in Fig. 11.2. These terms are actually used fairly loosely throughout the literature. We will use FI to mean flow injection as shown in Fig. 11.2A with an injection valve for sample introduction. We will use SI as shown in Fig. 11.2B and C to mean sequential injection in which solutions are pulled into a holding coil via a multiposition valve and pushed out through this valve to a reactor or separation system. Fluid handling approaches for radiochemical separations have been reviewed in detail, including several schematics, in an article (Grate et al., 2010). A comparison of fluidic and robotic approaches has been published (Grate et al., 2011). A number of recent articles describe the use of flow injection and sequential injection techniques in radiochemistry (Fajardo et al., 2010; Kolacinska and Trojanowicz, 2014; Trojanowicz et al., 2018).

The preferred fluid drive for SI is a modern digital syringe pump. A multiposition selection valve is used to select samples, reagents, or eluents that are pulled into a holding coil located between this valve and the pump. Precise control of the flow rate and the timing determine the volume of the solution pulled into the system. After changing the position of the selection valve, the solution or solutions in the holding coil are pushed out of the holding coil (away from the pump) and toward the reactor, separator, and/or detector downstream. Solutions can be pulled into the holding coil and delivered to the flow system downstream one at a time, or multiple solutions can be pulled into the holding coil in sequence and "stacked" there prior to pushing them forward into the flow system. Sequential injection systems are mechanically simple yet quite versatile. Reagents, eluents, samples, and standards can all be nested around the multiposition valve and sequentially selected for delivery into the system. The volume of each solution introduced into the holding coil can be varied simply by computer control, rather than by physically reconfiguring the system (e.g., by installing a larger injection loop as in conventional flow injection or chromatography). When utilizing a holding coil of adequate volume, the pump does not contact either reagent solutions or samples (but rather a carrier solution such as distilled water), and it can be located remotely from the remainder of the system.

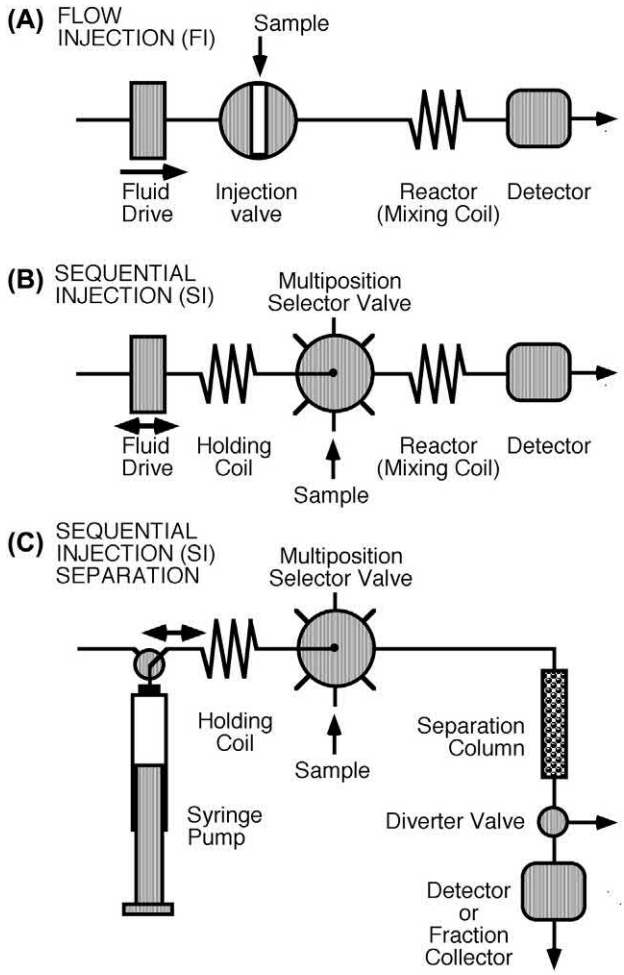


FIGURE 11.2 Schematic diagrams comparing (A) flow injection and (B) sequential injection fluid handling methods. The key components of a sequential injection separation system are shown in (C). *Adapted with permission from Grate and Egorov (1998a). Copyright 1998 American Chemical Society.*

Typical colorimetric sequential injection analysis (SIA) procedures stack zones of sample and reagent(s) in a holding coil with a narrow internal bore. When the stacked zones are propelled toward the detector, mixing occurs by dispersion, yielding a detectable product.

B. Sequential injection separations

Use of SI instrumentation for automating radiochemical analysis (Egorov et al., 1998a,b, 1999a,b, 2001; Grate and Egorov, 1998a,b; Grate et al., 1996, 1999a,b) typically involves use of a separation column, as shown in the apparatus in Fig. 11.2C. A suitable detector or fraction collector follows the column. A diverter valve is useful for directing sample matrix and wash solutions to waste without passing them through the detector; radionuclides released from the separation column can then be directed to the detector. Various diverter valve configurations can be used (Grate et al., 2010), including four-port two-position valves (Egorov et al., 1998b, 2012; O'Hara et al., 2018a) or six-port two-position valve (Mateos et al., 2000). These enable the diversion of column wash solutions to waste; bypassing the column to wash the detector flow cell; and reversal of flow through the column. With flow reversal, the sample can be loaded from one end of the column and then eluted back off of that end without going through the whole-column packing.

When using SI instrumentation and methodology to automate column-based separations, the approach must be modified to accommodate larger solution volumes; milliliter quantities of multiple solutions may be necessary to wash separation columns and elute species of interest. Pulling these solutions into the holding coil at typical SIA flow rates is excessively time-consuming. However, increasing the flow rate can cause outgassing of solutions in the holding coil due to reduced pressure as the pump pulls the solution in. This is unacceptable, but it can be resolved by using a larger bore holding coil, e.g., 1.6 mm ID. However, a larger holding core bore leads to increased dispersion between the solution being pulled in and the carrier fluid already in the coil.

To prevent dispersion and mixing of these solutions, an air segment can be aspirated into the coil prior to the reagent solution ("Reagent" refers generically to reagents and eluents.) Then the reagent solution is delivered to the column. This approach is shown in Fig. 11.3. The air segment is expelled to waste, a new air segment is pulled in, and a new reagent solution is pulled into the holding coil, ready to be delivered to the column. In this way, several different solutions of varying volumes and composition can be delivered to the separation column. The holding coil functions as a zero dispersion volumetric extension of the syringe pump. The use of a large bore holding coil and air segment in this way for sequential injection separations has been referred to as separation-optimized SI (Egorov et al., 1998b; Grate and Egorov, 1998a; Grate et al., 1999a,b).

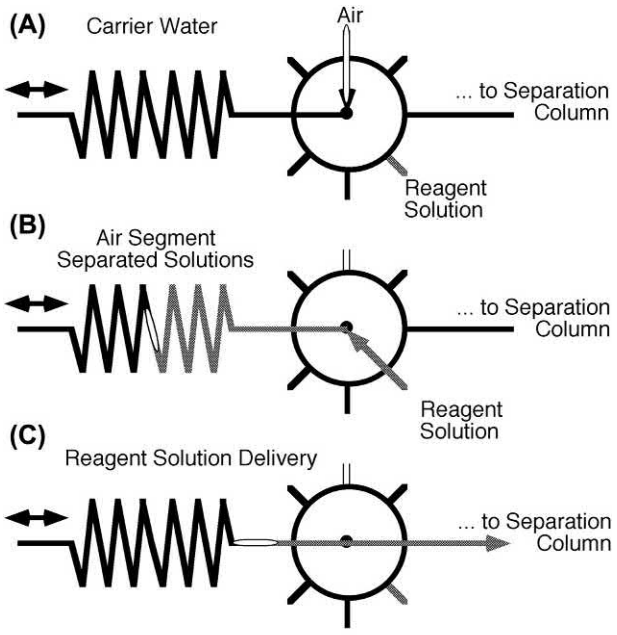


FIGURE 11.3 Schematic diagram for the use of an air segment in the holding coil for separation-optimized sequential injection fluid handling. The air segment is pulled into the holding coil prior to the reagent solution (A). This keeps the reagent solution separated from the carrier fluid (typically water) in the holding coil during reagent aspiration (B). After injecting a fixed amount of the reagent solution past the multiposition selection valve (C), the remainder of the reagent solution and the air segment are discarded to waste (not shown).

C. Alternative fluid delivery systems

The choice of the basic fluid handling approach is not necessarily limited to the SI paradigm using a multiposition valve and holding coil. For example, dedicated syringe pumps can be used for sample handling and reagent delivery in an approach typically used in robotic workstations. In addition, modern digital syringe pumps with zero dead volume syringes and multiposition selector valves have become available from IMI Precision Engineering (Littleton, CO). In this design, a single syringe pump can be used for sequential delivery of multiple solutions with minimal cross-contamination. Thus, the syringe pump can serve as both the fluid drive and the holding coil. Finally, in some instrument designs and procedures, a combination of digital syringe pumps and positive displacement high-performance liquid chromatography (HPLC) pumps can be used to automate solution handling tasks required in the sample preparation and separation procedure.

Given this range of possibilities, several additional configurations have been developed and, in some cases,

given names (Grate et al., 2010). A "multisyringe flow injection" approach has been described using up to four syringe pumps in parallel (Cerda et al., 1999; Fajardo et al., 2004, 2005; Miro et al., 2002a). When using flow reversals and a holding coil with each syringe, "multisyringe flow injection" can actually be regarded as a modified SI system. Solutions can be selected using a series of three-port solenoid valves instead of the conventional multiposition valve in SI. The multisyringe approach has been further reviewed as a technique for spectroanalytical methods of analysis (Cerda et al., 2018).

Commercial flow injection accessories have been adapted for radiochemical column separations, especially in the mass spectrometry community as a front end to ICP-MS (Grate et al., 2010). The PerkinElmer Model FIAS-400 is a flow injection system that has been used to automate extraction chromatographic separations for actinide analyses (Benkhedda et al., 2005a,b; Epov et al., 2005a,b, 2007; Hollenbach et al., 1994). The PrepLab liquid handling system for ICP-MS has also been adapted for extraction chromatographic separations (Kim and Kim, 2002; Kim et al., 2000a, 2004; Ohtsuka et al., 2005, 2006). HPIC systems have also been adapted with columns, although some columns described have been much longer than those normally used for extraction chromatography (Hang et al., 2004; Peterson et al., 2007). Recently, sample preparation instrumentation by Elemental Scientific has been used to automate column-based separations. The prepFAST-MC system performed separations for the analyses of Ca and Sr, and separately, for Cu in biological samples, achieving high throughputs (Enge et al., 2016; Romaniello et al., 2015). In further advances, a prepFAST-SR system was developed for tandem extraction chromatographic separations where the TEVA and UTEVA separation materials were automatically loaded into the column bodies and used in sample preparation for the analyses of U and Pu isotopes (Metzger et al., 2018).

An alternative to the use of syringe pumps is to control the air pressure over the solvent in bottles, creating an automated pressurized injection (PI) system (Guerin et al., 2013). This approach can be advantageous with corrosive or viscous solvents and when solutions may generate gases themselves. This approach has been developed for extraction chromatographic separations of actinides (Guerin et al., 2013).

D. Column configurations

Columns containing the solid-phase separation medium can be included in the system directly downstream from the multiposition selection valve, as shown in Fig. 11.2C. However, other configurations are advantageous in some analysis protocols. For example, the column can be configured with a four-port two-position valve as shown in Fig. 11.4A so that the analyte captured on the "top" of the column is eluted in the opposite direction so that it need not travel through the remainder of the column material (Egorov et al., 2012; O'Hara et al., 2018a). Similarly, using a six-port two-position valve as the diverter valve can also enable column flow reversal (Mateos et al., 2000).

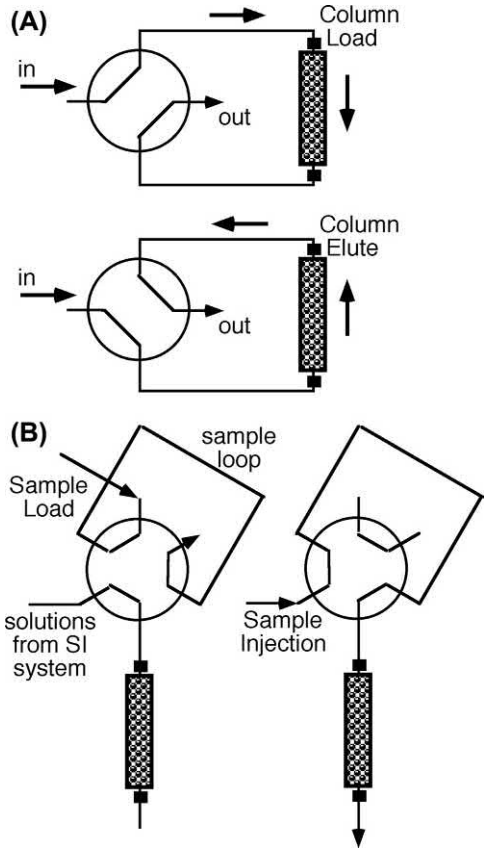


FIGURE 11.4 (A) Schematic illustration of a column coupled to a two-position valve so that the sample can be loaded in one flow direction and analytes can be eluted in the opposite direction. (B) Schematic illustration of a sample injection valve and loop directly upstream from the separation column.

Another configuration that is useful in some cases is to add a sample injection valve after the multiposition valve and immediately before the separation column, as shown in Fig. 11.4B (Egorov et al., 2001). In this way, hot radioactive samples are injected directly upstream from the column via a sample loop; the multiposition valve and the holding coil of the sequential injection system are never exposed to the sample. This type of sample injection is similar to conventional FI, and the sample volume is determined by hardware, not by time and flow rate parameters under software control as in SI systems that use the holding coil as part of the sample injection method.

Yet another useful configuration is to set up column switching capabilities (Grate et al., 1999a). A partial column switching system is shown schematically in

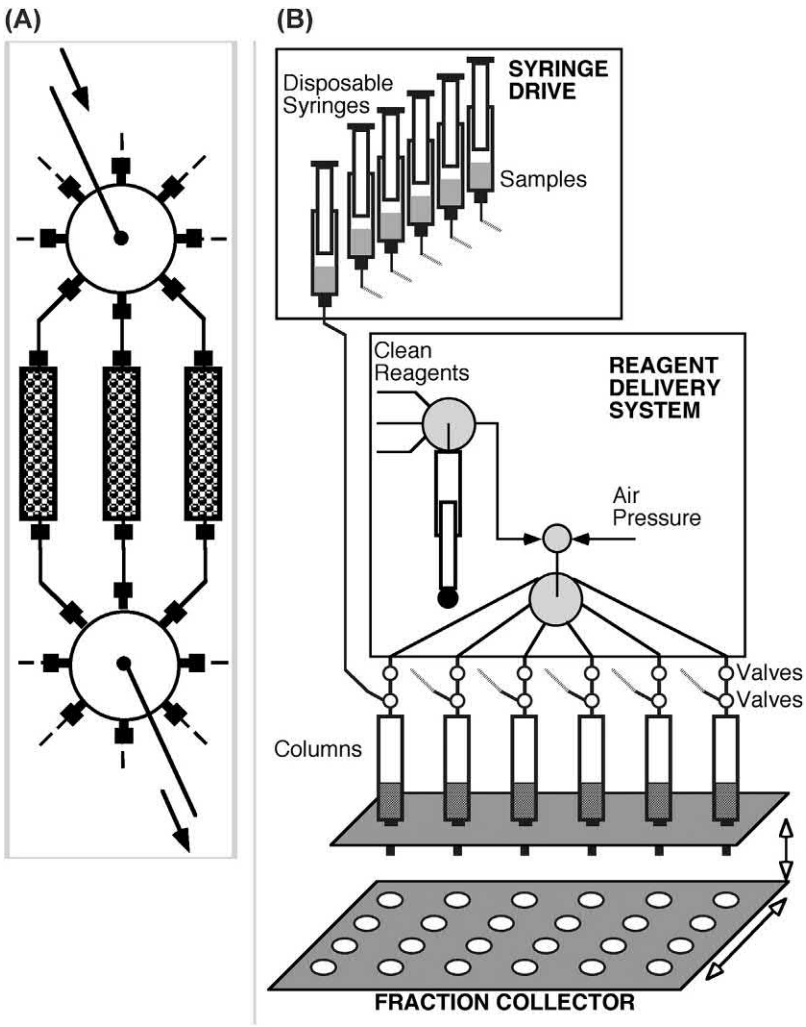


FIGURE 11.5 (A) Schematic diagram of a column switching system, where the columns are placed between two multiposition selection valves. Only three columns are shown for simplicity, although the valves shown will accommodate eight. (B) Schematic diagram of the key components and layout of the PNX system to perform column-based separations. Samples are delivered to columns via a three-port valve positioned above each column and downstream from the clean reagent delivery system. Subsequently, eluents are delivered from the clean reagent delivery system, and fractions are collected by a fraction collector that can translate among fixed positions horizontally and vertically to raise vials to surround the column outlets. *(B) Reproduced with permission from Grate et al. (2011). © 2011 Oldenbourg Wissenschaftsverlag GmbH.*

Fig. 11.5A. Multiple fresh columns can be set up prior to beginning a set of samples. Each sample can be directed to a fresh column for rapid throughput without column wash steps between samples. This approach has been used to set up a rapid automated separation workstation for processing of ^{90}Sr-containing samples along with quality control samples, including standards, spiked samples, and blanks (Grate et al., 1999a). Column switching has also been described for delivering clean solutions to multiple columns that are mounted in parallel in a rack above a fraction collector, as shown schematically in Fig. 11.5B (Grate et al., 2011). Then, each column delivers its separated fractions to a different section of a fraction collector; hence, effluents from different columns do not travel the same flow paths downstream from the columns, eliminating cross-contamination concerns. The design shown in Fig. 11.5B is an automation system for column-based separations that the authors called PNX, for Pacific Northwest eXtraction system (Grate et al., 2011). In a subsequent version, PNX-II, six syringe pumps in the clean reagent delivery system deliver eluents to each of six columns simultaneously for rapid parallel separations.

Four parallel columns have also been implemented in an FI system with peristaltic pumps for the efficient analysis of anthropogenic radionuclides from seawater (Qiao et al., 2014). Both ion exchange and extraction chromatographic methods were implemented for separations, and radiometric and ICP-MS methods were used for quantification. The replacement of the peristaltic pumps with a multichannel syringe pump was discussed.

E. Renewable separation concepts and methods

The separation column for automated radiochemical analyzers is shown in Fig. 11.2C as a fixed column. The practical life of such fixed columns is determined by the sample type, the separation media, and the separation chemistry involved. With suitable column cleanup steps

between samples, and sufficiently robust column media, such separation columns may be used tens or possibly even hundreds of times. Such columns can then be manually replaced as necessary.

An alternative approach is to automatically pack separation material into the column body online and release it automatically after use. This approach results in "renewable separation columns," and SI systems using them have been referred to as SI-RSC systems. Originally, renewable surface techniques were developed by Ruzicka and coworkers to trap chemically selective particles and beads for observation by microscopic or optical techniques while perfusing with sample (Egorov and Ruzicka, 1995; Mayer and Ruzicka, 1996; Pollema and Ruzicka, 1994; Ruzicka, 1994; Ruzicka and Ivaska, 1997; Ruzicka and Scampavia, 1999; Ruzicka et al., 1993; Willumsen et al., 1997). Changes in the bed properties (e.g., absorbance, reflectance, fluorescence, etc.) induced upon the introduction of the sample solution provided the basis for an analytical measurement. In this approach, particles serve as sensing surfaces for chemical or biological detection. After use, the beads were released to waste, and a new microbed was packed. This process renews the interactive surface for the next measurement.

When the flow cell that captures the beads is not associated with a detector, it serves primarily as a separation medium. This approach can be scaled to handle bed volumes from 1 microliter to a milliliter or more. Renewable surface methods were introduced to the field of radiochemistry using extraction chromatographic radiochemical separation materials in SI-RSC systems (Egorov et al., 1999a). Slurries of the extraction chromatographic material were captured in a flow cell (column) of well-defined volume, and this packed bed was used to carry out separations. Afterward, the column bed material was released from the flow cell, and fresh suspensions of beads were introduced and captured for subsequent sample assay. The SI-RSC method has been demonstrated for ^{90}Sr analysis using Sr resin, ^{99}Tc analysis using TEVA resin, and ^{241}Am analysis using TRU resin. Recently, a commercial sample preparation system, the Elemental Scientific prepFAST-SR system, was developed to implement a renewable column separation approach for the analysis of U and Pu isotopes (Metzger et al., 2018). Automatic loading and unloading of the TEVA and UTEVA extraction chromatographic resin materials provided fresh column material for each sample. This provided a commercial off-the-shelf (COTS) system for processing samples for IAEA-related analyses.

Several approaches exist for capturing and releasing particles in RSC flow cells.

The original flow cells for renewable surface techniques were "jet ring cells," where beads were trapped in the end of a tube in contact with a planar surface. The roughened end of the tube allowed fluid to pass but retained beads (Ruzicka, 1994; Ruzicka and Scampavia, 1999; Ruzicka et al., 1993). Beads were removed from the cell either by reversing the fluid flow or by lifting the tube away from the detector surface under forward flow conditions. Flow cells were also designed to trap beads with a solid rod intersecting the cylindrical channel of a machined flow cell at right angles (Dockendorff et al., 1998; Holman et al., 1997). This rod precluded escape of the beads; a leaky tolerance allowed fluid to flow around it. Beads were released by an axial motion of the rod that withdraws the rod end from the flow channel. By contrast, a rotating rod design has been developed where the end of the rod is angled; in one rotation position, the angled end blocks beads from exiting the outlet channel while allowing fluid flow around a leaky tolerance (Bruckner-Lea et al., 2000; Grate et al., 2003, 2009; Ozanich et al., 2007, 2009). A 180° rotation opens the outlet channel for bead release. This design in shown in Fig. 11.6A. Frit-based renewable separation flow cells have also been developed (Egorov

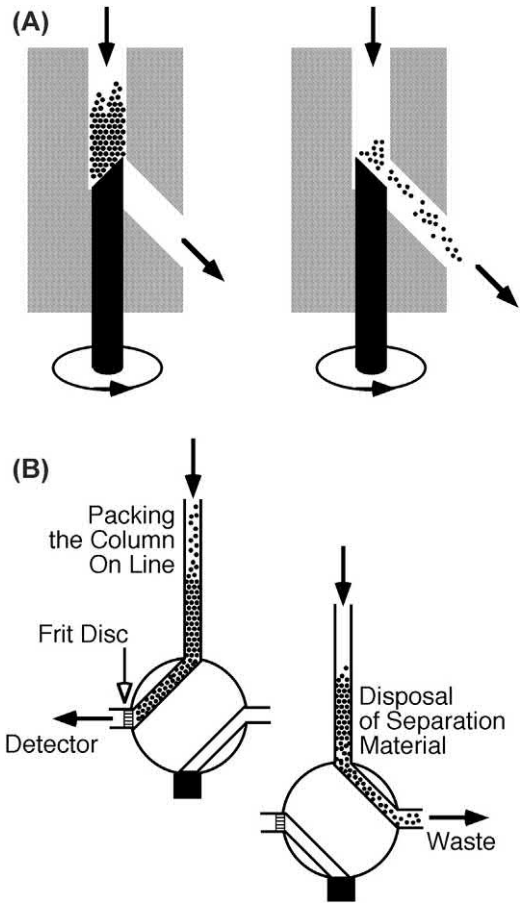


FIGURE 11.6 Two approaches for renewable separation columns: (A) the rotating rod flow cell and (B) a frit restricted method incorporated into a two-position valve. *(B) Adapted with permission from Egorov et al. (1999a). Copyright 1999 American Chemical Society.*

et al., 1999a). In these systems, a bead suspension is directed through a frit to trap beads or to an open channel to discard beads. This approach has been applied to radiochemical separations. The valve for determining which fluidic path is open can be downstream, or it can be integral to the design as shown in Fig. 11.6B.

F. Lab-on-valve

Column separation approaches can also be implemented with a lab-on-valve (LOV) approach (Erxleben and Ruzicka, 2005; Luque de Castro et al., 2008; Ruzicka, 2000; Wang and Hansen, 2003). The LOV system is typically configured as an SIA system, with a syringe pump providing reversible flow, a holding coil, and multiposition valve. However, the multiposition valve is configured with a custom plastic head that integrates functional components of the analytical method in direct communication with the ports of the valve. Plastics such as acrylic, ULTEM, and PCTFE are used, and various custom configurations have been developed. One such configuration is shown in Fig. 11.7.

For column separations, a column body that is either integrated into the monolithic valve head or in close proximity with the valve head communicates directly with one of the valve port positions; the beads of separation material are loaded into the column body automatically. This close proximity of the column with the switching actuation of the multiposition valve is advantageous for loading beads of separation material in and out of the column body. The column is effectively part of the LOV system, instead of being placed downstream from a multiposition valve as in Fig. 11.2C. When the separation material is freshly loaded and unloaded for each sample, the LOV platform provides a renewable separation column technique. The concept of loading beads and retaining them in a flow cell was included as part of the original concept for the LOV published by Ruzicka (2000) and demonstrated as part of an optical measurement system. This bead injection approach was adapted to create affinity chromatography columns (Erxleben and Ruzicka, 2005), and microcolumns for trace metal separations were discussed in a review (Wang and Hansen, 2003; Wang et al., 2003). LOV platforms have been used to perform extraction chromatographic separations for analysis of radionuclides, such as

- ^{90}Sr (Beltran et al., 2013; Kolacinska et al., 2017; Mola et al., 2014; Rodriguez et al., 2012),
- ^{99}Tc (Kolacinska et al., 2017; Rodriguez et al., 2015b; Villar et al., 2013, 2017),
- ^{226}Ra (Rodriguez et al., 2016b),
- plutonium (Qiao et al., 2013c), and
- uranium/thorium (Avivar et al., 2011, 2012).

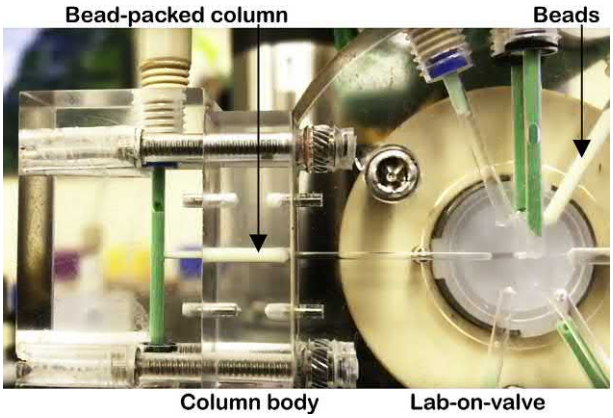


FIGURE 11.7 Lab-on-valve system with a renewable separation column. For the color version of this figure, the reader is referred to the online version of the book. *Imagery captured from video, with permission from Jaromir Ruzicka.*

G. Extractant liquids and particles

Thus, there are many ways to implement renewable surface columns, and these can be used for either the automated radiochemical analysis methods or the radionuclide sensors to be described below. Additional approaches with liquids and particles for radiochemical separations are noteworthy.

Miro et al. (2002b) have shown, for example, that an extraction coil can be used to replace the column-based approach, creating a liquid–liquid extraction in which the extractant is immobilized as a wetting film on the walls of a tubing coil, instead of immobilizing it in a porous polymer as in extraction chromatography. This method was implemented as part of an SI separation system. After coating the coil with extractant solution, the sample was loaded and the extractant was washed. Captured ^{90}Sr in the extractant film was recovered by using an organic solvent that stripped the extractant from the coil (Miro et al., 2002b). The separation material, a liquid extractant, is automatically renewable.

Additional approaches for liquid extraction were described recently (Maya et al., 2014; Rodriguez et al., 2015a, 2016a; Villar et al., 2015). Radionuclide separations by liquid–liquid extraction were critically compared with solid-phase extraction techniques in a review (Rodriguez et al., 2016a). Automated in-syringe extractions were described (Maya et al., 2014) and applied to analysis of species such as ^{99}Tc and uranium (Rodriguez et al., 2015a; Villar et al., 2015). Detection approaches for these applications were off-line scintillation counting (^{99}Tc) and spectrophotometric detection using arsenazo dye and a long path length liquid waveguide capillary cell (uranium).

An extractant for radionuclides was coated on magnetic particles for magnetically assisted chemical separations (Shaibu et al., 2007). The actinides of interest were captured from aqueous solutions into the extractant

followed by a magnetic solid–liquid separation. The extractant-loaded particles could be stripped for reuse. This approach has been demonstrated with a number of extractants for separating actinides that are relevant to nuclear waste process streams (Shaibu et al., 2006a,b, 2007). Magnetic separation processes are suitable for automation.

H. Detection

Detection of the separated radionuclides can be done in a variety of ways, broadly classified as radiometric (i.e., radioactivity detection) techniques and mass spectrometry techniques. These methodologies have been critically compared (Hou and Roos, 2008).

Flow-through liquid scintillation detection represents a radiometric method that integrates well with flow-based separation and analysis systems. This approach combines the output of the SI separation system with liquid scintillation cocktail and delivers it into the flow cell of the detector. This flow cell typically consists of a length of photon-transparent tubing in a compact coil that is placed between two photomultiplier tubes (PMTs). A schematic diagram of the flow-through liquid scintillation detection approach is shown in Fig. 11.8. Many of the detector traces in this chapter were obtained by this method.

Flow-through scintillation detectors also exist that use particles of a solid scintillator packed into the flow cell. This avoids the use of the liquid scintillation cocktail and the associated waste. The fully automated process analyzer for total Tc in nuclear waste, to be described below, used this type of scintillation detection.

Other flow-based detectors are used for monitoring the passage of gamma- or positron-emitting radionuclides such as ^{89}Zr. The flow gamma detector is generally comprised of a gamma detector (e.g., NaI(Tl) scintillation spectrometer) and a detection coil, both of which are housed within radiation shielding. Column effluents (frequently the purified radioanalyte fraction) are passed through the detection coil (tubing), passing across the face of detector. As with the flow-through scintillation detectors described above, the gamma detector provides a radiochromatogram of the eluting analyte (O'Hara et al., 2018a, b, c). These gamma detectors are likewise employed in radio-high performance liquid chromatography (radio-HPLC) systems.

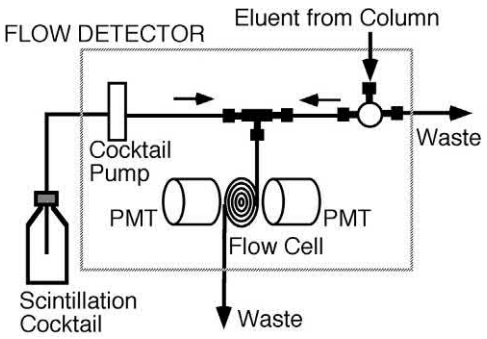


FIGURE 11.8 Schematic diagram of a flow through liquid scintillation detection system.

Mass spectrometry represents a detection method that is advantageous for radionuclides with low specific activity or where mixtures of radionuclides are eluted. Mass spectrometry can provide separate signals for each isotope according to their mass-to-charge ratios. ICP-MS has been used as the online detector for actinide separations and will be described below. Indeed, the separation of radionuclides prior to ICP-MS (Egorov et al., 2001; Kim et al., 2007; Lariviere et al., 2006) has become a major driver in the automation of radiochemical separations (Grate et al., 2010).

Recently, accelerator mass spectrometry (AMS) has been applied to the analysis of samples where actinides such as plutonium and uranium were first purified using automated fluidic methods (Qiao et al., 2013d, 2015).

Finally, automation of radiochemical separations represents a significant savings in cost and labor even when the output of the instrument is delivered to a fraction collector for separate off-line counting or mass spectrometry (Grate et al., 1999a,b). In addition, some labs may already be set up to handle radiochemical separations and counting operations separately. Automated radiochemical separations with fraction collection can provide efficiencies for the separation lab without altering the overall work flow from separations to detection.

A recent review discusses a variety of detection techniques relative to a variety of flow techniques for the analysis of environmental samples (Fajardo et al., 2010).

IV. Selected radiochemical analysis examples

A. Strontium-90

Strontium-90 is a high yield fission product in nuclear waste that decays by beta emission to ^{90}Y, which is also a beta emitter. The half-lives of these isotopes are 28.9 years and 64 hours, respectively. The determination of ^{90}Sr is important in the characterization of stored nuclear wastes from nuclear weapons production and in process streams associated with spent fuel reprocessing. Analytical determination of ^{90}Sr, a pure beta emitter, requires that it be separated from inactive matrix constituents and a variety of interfering radionuclides prior to quantification by counting methods. A variety of classical and chromatographic methods can be used to achieve the required chemical separations, including precipitation, liquid–liquid extraction, ion exchange, thin-layer chromatography, and electrophoresis (Alfaro et al., 1995; Amano and Yanase, 1990; Borcherding and Nies, 1986; Cobb et al., 1994; Fourie and Ghijsels, 1969; Gattavecchia and Tonelli, 1991; Kramer

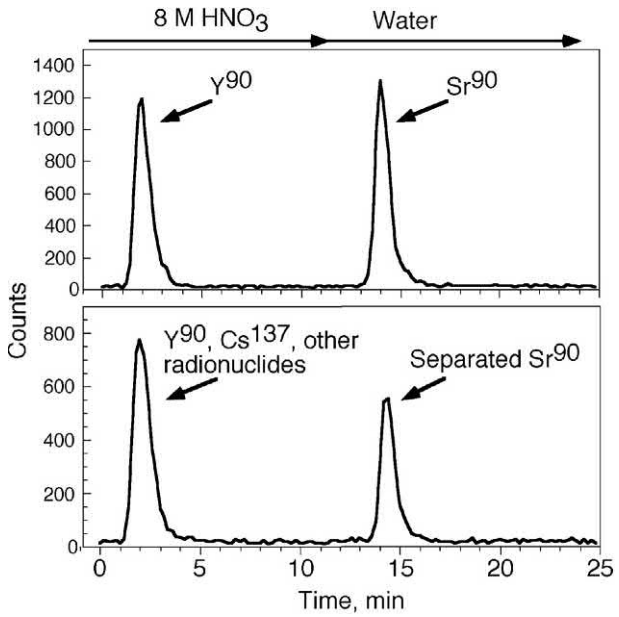


FIGURE 11.9 Detector traces for the separation of a ^{90}Sr and ^{90}Y containing standard in the upper plot and separation of ^{90}Sr from other radioisotopes in a nuclear waste sample. *Reproduced with permission from Grate et al. (1996). Copyright 1996 American Chemical Society.*

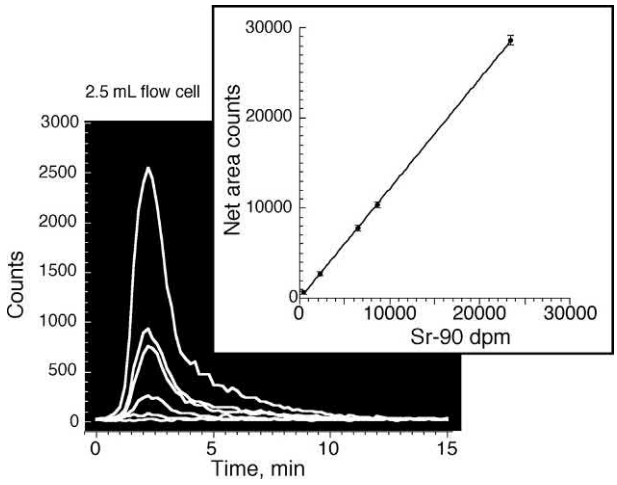


FIGURE 11.10 Quantification of ^{90}Sr illustrating linearly increasing peak areas with increasing standard activity. *Adapted with permission from figures in Grate et al. (1996). Copyright 1996 American Chemical Society.*

and Davies, 1982; Kremliakova et al., 1990; Kuno et al., 1993; Lamb et al., 1989; L'Annunziata, 1971; Noshkin and Mott, 1967; Porter et al., 1967; Smulek and Lada, 1979; Wilken and Joshi, 1991; Wilken and Diehl, 1987; Wood et al., 1993). Currently, extraction chromatography using Sr resin (Eichrom Technologies, Inc., Darien, Illinois) is the preferred separation method (Dietz et al., 1991; Horwitz et al., 1991, 1992a,b).

Detector traces from the automated SI separation of ^{90}Sr, using flow-through liquid scintillation counting, are shown in Fig. 11.9. This analytical separation was first automated using conventional SI methods with stacked zones and subsequently with separation-optimized SI (Grate et al., 1996, 1999a). The sample in 8 M nitric acid (HNO_3) solution is loaded on Sr resin, which contains a crown ether in 1-octanol immobilized on a porous polymer support; the crown ether stationary phase retains Sr from 8 M HNO_3 with a retention volume of $\sim$100 (Horwitz et al., 1991, 1992a,b). Other radionuclides (including the ^{90}Y daughter) and sample matrix components are unretained and are removed by washing the resin with additional 8 M nitric acid. Then, the purified ^{90}Sr is released from the column by eluting with water or weak acid (e.g., 0.05 M nitric acid), where the retention volume is less than one.

The peak area of the eluted ^{90}Sr is used for quantification. Fig. 11.10 shows detector traces for different activity standards and the linear calibration curve obtained from peak areas. The theory of flow-through scintillation detection has been described previously in Chapter 10, Volume 2 of this book. In evaluating the analytical quantification of radionuclides, a number of figures of merit are relevant. The separation or recovery efficiency indicates the fraction of the analyte delivered to the column that is recovered after the separation. The detection efficiency indicates the number of counts observed compared with the number of radioactive decays from the sample in the detector flow cell. These two efficiencies are given as E_{rec} and E_d, respectively, in Chapter 10 and used in Eq. (10.14). The total effective efficiency is the product of the recovery efficiency and the detection efficiency.

The automated separation of ^{90}Sr represents a simple load, wash, and elute procedure for the separation of a species that is present at high activities in nuclear waste samples. The procedure can be implemented either with online detection, as just described, or by delivering the eluted Sr to a fraction collector. Using the separation-optimized SI method, it has been demonstrated that complete separation and analysis can be carried out in just over 20 minutes.

The "multisyringe flow injection" approach has also been used for automating Sr resin column separations (Fajardo et al., 2004), using off-line counting and ICP-OES to determine radioactive and total Sr, respectively. More recently, a number of LOV methods for strontium analyses have been developed and investigated (Beltran et al., 2013; Kolacinska et al., 2017; Mola et al., 2014; Rodriguez et al., 2012). Scintillation counting and ICP-MS have been used in the quantification of ^{90}Sr, whereas combination of ICP-OES and radioactivity counting has been used to determine total Sr and ^{90}Sr in the same samples. Samples have been as diverse as rainwater, nuclear reactor coolant, and water treatment sludge.

For high-throughput applications, especially in analytical laboratories that customarily count purified samples separately from the sample preparation, fraction collection is advantageous. Using column switching techniques so that each column need not be washed between samples, it is possible to process eight samples in just over an hour

(8 minutes per sample; Grate et al., 1999a). These samples can all be set up in advance and separated under computer control without further operator attention. Elimination of column cleanup steps and/or blank runs between sample runs minimizes the amount of time required to complete the separation of the sample set. Afterward, the columns can either be washed for reuse or replaced with fresh columns.

B. Technetium-99

Technetium-99 is a long-lived radioactive isotope that is present in defense-related nuclear wastes, stored spent nuclear fuel, and radioactive waste and process streams associated with spent fuel reprocessing. Due to the high abundance of ^{99}Tc in these wastes, its long radioactive half-life, and the high mobility of technetium in the environment, ^{99}Tc analysis is important throughout nuclear waste characterization and stabilization activities. The determination of ^{99}Tc in environmental samples has been reviewed (Shi et al., 2012a). ^{99}Tc is a pure beta emitter ($\beta_{max} = 294$ keV) with a half-life of 2.11×10^5 years and specific activity of ~630 Bq/μg, decaying to stable ^{99}Ru (Browne and Firestone, 1986). Analytical methods using radioactivity detection (beta counting) require separation of ^{99}Tc from inactive matrix constituents and various interfering radionuclides. Because of the low specific activity of ^{99}Tc, it can be measured by ICP-MS. However, separation is also desirable prior to ICP-MS analysis to avoid isobaric interferences (e.g., stable ^{99}Ru). In one of the earliest examples of automated radiochemical analysis using extraction chromatography, Hollenbach et al. (1994) used a TEVA resin column for online purification and preconcentration of ^{99}Tc prior to ICP-MS determination (Hollenbach et al., 1994). In work on standards and soil digestates, the online separation reduced detection limits tenfold and alleviated matrix and isobaric interferences.

Automated SI separation of ^{99}Tc from a nuclear waste sample is shown in Fig. 11.11 (Egorov et al., 1998b). The separation was carried out using TEVA resin (Eichrom Technologies, Inc.), a porous polymer impregnated with a quaternary amine-based liquid anion exchanger called Aliquat 336 (Horwitz et al., 1995). The sample was loaded on the column and washed with 0.1 M HNO_3, conditions under which Tc is strongly retained on the column and other potentially interfering species are largely unretained. (Inclusion of hydrofluoric acid in the wash solution assures that tetravalent Pu is not retained on the column.) The retained Tc was released from the column using strong nitric acid. The 6 M nitric acid concentration in Fig. 11.11 was selected as a trade-off between higher acid concentrations that provide narrower elution peaks at shorter retention times and lower nitric acid concentrations that cause less scintillation quenching than strong acid.

The Tc isotope is present at low activities in nuclear waste compared with other fission products such as ^{90}Sr, its daughter ^{90}Y, and ^{137}Cs (due to its comparatively lower specific activity). The ^{99}Tc peak is not evident in the full-scale detector trace, which is dominated by the abundant fission products. However, it can be easily seen in the vertically expanded inset. Technetium-99 activity can be quantified from the scintillation counts, and this is most effectively carried out in a stopped-flow mode (Egorov et al., 1998b). The principle of stopped-flow detection was described previously in Chapter 10, Volume 2 (see Eq. 10.38). It is illustrated here in Fig. 11.12 (and in Chapter 10, see Fig. 10.50, where continuous flow and 15 minute stopped-flow detection were compared using a high activity (2.502×10^4 dpm) ^{99}Tc(VII) standard). In stopped-flow

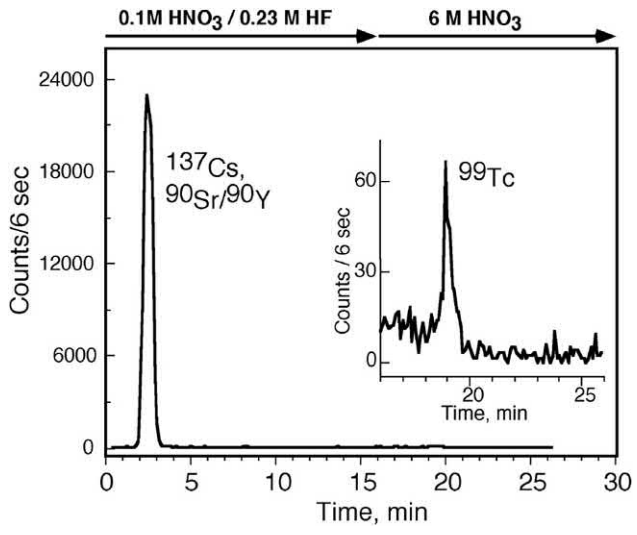


FIGURE 11.11 Detector traces for the separation of ^{99}Tc(VII) from other fission products in the sample. The signal for the Tc is evident in the vertically expanded trace in the inset. *Reproduced with permission from Egorov et al. (1998b). Copyright 1998 American Chemical Society.*

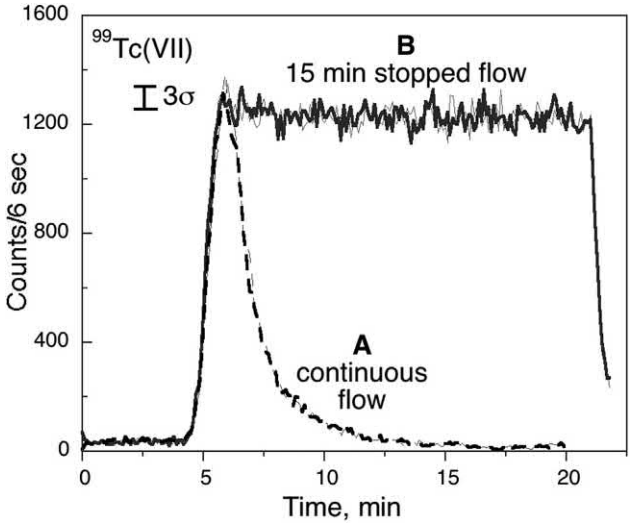


FIGURE 11.12 Detector traces showing the comparison between continuous-flow (A) and stopped-flow (B) detection of ^{99}Tc(VII). The error bar corresponds to three standard deviations of the peak maximum counts. *Reproduced with permission from Egorov et al. (1998b). Copyright 1998 American Chemical Society.*

detection, this time position of the peak maximum in a continuous-flow run can be used to stop the flow; then, counting can be carried out for whatever time period is necessary to achieve the desired precision or minimum detectable activity. In the experiment shown in Fig. 11.12, 89% of the eluted technetium zone resided in the 2.5 mL detector flow cell during the stopped-flow interval. The duplicate detector traces for each type of experiment in Fig. 11.12 demonstrated reproducibility; the high precision of the fluidics and reproducibility of the separation process resulted in reliable capture of the eluted zone within the detector flow cell.

The stopped-flow approach facilitates much improved counting statistics, and its advantage is most apparent when counting low-activity standards or samples where the count rate is virtually indistinguishable from the background. For example, 268 dpm ^{99}Tc(VII) standard gave a continuous flow count rate that was statistically indistinguishable from the background. As shown in Fig. 11.13 (and Fig. 10.51 of Chapter 10, Volume 2), signal accumulation for a 15 minute stopped-flow interval allows reliable quantification of a 268 dpm ^{99}Tc(VII) standard, with 8% (3σ) counting error, which could not be detected in a continuous-flow mode.

Using a diverter valve to isolate the sample in the detector during stopped-flow counting allows the remainder of the SI separation system to be used to begin to process the next sample simultaneously. Thus, stopped flow does not necessarily lengthen the total analysis time (Egorov et al., 1998b).

An SI system was used to automate the extraction chromatographic purification of technetium from seawater after preconcentration in a precipitation step, as part of an analytical approach to determine ^{99}Tc by ICP-MS (Shi et al., 2012b). An LOV system using TEVA resin for separation of purified technetium for the determination of ^{99}Tc in water and soil samples using ICP-MS (Rodriguez et al., 2015b). An LOV approach was used to compare TEVA resin and Dowex-1 in the purification of Tc for analysis by ICP-MS. Samples were obtained from reactor coolant and the river surrounding a nuclear reactor (Kolacinska et al., 2017). Another automated system for ^{99}Tc determination in groundwater by ICP-MS was developed using modular components (Chung et al., 2013).

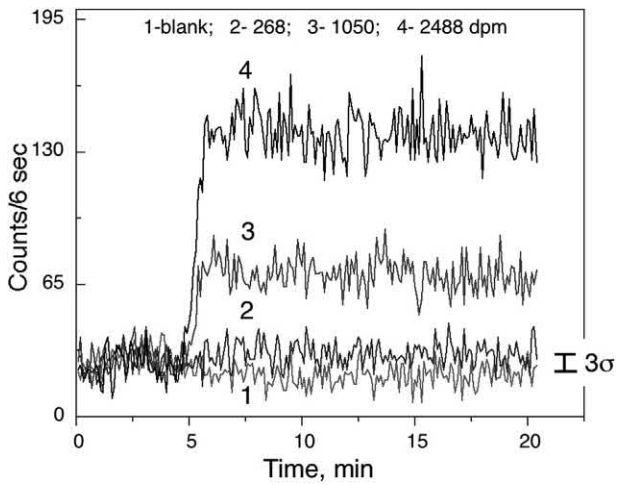


FIGURE 11.13 Selected detector traces from the analysis of ^{99}Tc(VII) standards using 15-minutes stopped-flow detection. The activities of the standards are listed. The error bar corresponds to three standard deviations of the background count rate. *Reproduced with permission from Egorov et al. (1998b). Copyright 1998 American Chemical Society.*

For urine samples from patients who had been dosed with ^{99m}Tc, an LOV system with TEVA resin separation was developed (Villar et al., 2013). This approach used liquid scintillation counting for determination of ^{99}Tc. In a subsequent study, an LOV system used weak base extraction chromatographic (WBEC) resin, and technetium was detected colorimetrically with diphenylcarbohydrazide and a long path-length liquid waveguide cell (Villar et al., 2017).

C. Actinides

Determination of actinides in a variety of sample matrixes is of great importance in the characterization and processing of nuclear wastes, the nuclear industry, safeguards, treaty monitoring for nuclear nonproliferation, and the remediation of radiologically contaminated sites. The analytical determination of plutonium in environmental samples has been reviewed (Qiao et al., 2009a), as have methods for other transuranium elements (Vajda and Kim, 2010, 2011). Both of the conventional detection methods for actinides, alpha spectroscopy and mass spectrometry, require separation of the actinides from the sample matrix and from one another, as discussed in Section II.A. Separation Requirements (Egorov et al., 2001; Grate and Egorov, 1998b; Grate et al., 1999b).

Anion exchange is a long-standing column separation method for actinides. Hirayama et al. (1985) described what may be the first fluidic system for automated analytical separations of the actinides using ion exchange processes. Solutions were delivered to the columns using either air-pressure-driven flow or gravity feed from elevated storage tanks of reagents. Flow control included sensors for drop rate, electric needle valves, and electrostatic capacity sensors to detect the liquid level above the resin bed. The system employed multiple columns for different separations, and the eluted solutions, captured in a fraction collector, could be evaporated and dried with a microwave oven. More recently, Grate et al. (2011) compared fluidic, robotic, and hybrid architectures for the automation of column-based separations. Methods to automate actinide ion exchange were described in detail. A system designed to process six samples using six anion exchange columns set up in parallel, called the PNX (Pacific Northwest

eXtraction) system, was described in detail (shown schematically in Fig. 11.5B). A custom fraction collector was designed to capture the eluents from the six columns.

A number of extraction chromatographic resins can be used to implement a variety of actinide separations. Selected automated radiochemical separations using TRU resin (Eichrom Technologies, Inc., Darien, Illinois), which is a solvent-impregnated resin loaded with the complexant carbamoylmethylenephosphine oxide (CMPO) in tributylphosphate (Horwitz et al., 1990, 1993), are illustrated in Fig. 11.14. The organic stationary phase in this resin strongly binds trivalent, tetravalent, and hexavalent actinides from nitric acid solutions, with retention increasing with aqueous phase acidity. Tetravalent actinides are more strongly retained than trivalent actinides, and trivalent actinides are not retained in hydrochloric acid solutions. This extraction chromatographic material can be used for simple separations of groups of actinides, or more complicated separations whereby individual actinides or small groups of actinides are sequentially eluted. In the latter case, several actinides are retained on the column during the sample load and wash steps. Then, a number of eluent solutions are delivered in sequence, each releasing a selected actinide or group of actinides. Actinides Am and Pu can be separated from each other and from other actinides if the speciation of Pu, i.e., its oxidation or valence state, is controlled throughout the multistep elution process.

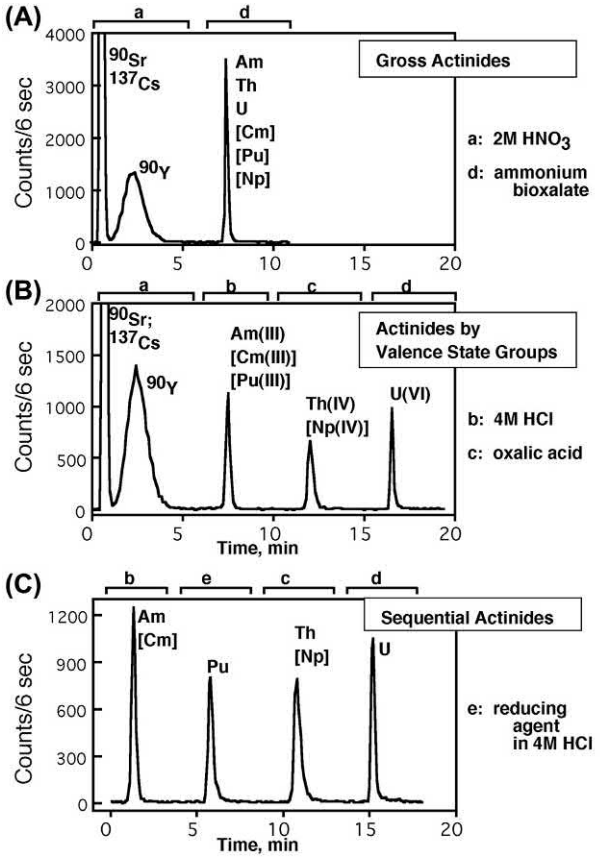


FIGURE 11.14 Three actinide separations performed using automated sequential injection separations with TRU resin extraction chromatographic material. (A) Separation of the actinides as a single group (gross actinides) from fission products and other species in the sample matrix. (B) Separation of the actinides from the fission products and other species in the sample matrix, with selective release from the column material in valence state groups. (C) Sequential elution of the actinides with separation of Pu from Am and the other trivalent f-element species using on-column redox chemistry. The separation of the actinides from the fission products and sample matrix is omitted from this plot. *Adapted with permission from Grate et al. (1999b). Copyright 1999 Royal Society of Chemistry. http://pubs.rsc.org/en/Content/ArticleLanding/1999/AN/a902579k.*

The plot in Fig. 11.14A shows the purification of the actinides as a group. Fission products are unretained (e.g., ^{90}Sr, ^{137}Cs) or slightly retained (e.g., ^{90}Y) and appear during the column wash with 2 M nitric acid (Grate and Egorov, 1998a; Grate et al., 1999b). Ammonium hydrogen oxalate (bioxalate) solution releases the actinides from the column.

The second plot, Fig. 11.14B, shows the release of captured actinides in groups of the same oxidation (or valence) state. First the trivalent actinides are selectively released with 4 M hydrochloric acid. Then, an oxalic acid solution is used to selectively release tetravalent actinides. Finally, an ammonium bioxalate solution releases the remaining hexavalent actinides (Grate and Egorov, 1998a; Grate et al., 1999b). This type of separation requires that the actinides be in well-defined valence states, so samples are pretreated off-line to adjust the redox states (e.g., Pu(IV) to Pu(III)).

The final plot, Fig. 11.14C, illustrates a sequential actinide separation. This separation is based on the valence state separation in the second figure, but it uses additional steps to separate Pu from Am and the other trivalent f-elements. This is achieved by converting Pu to the tetravalent state prior to eluting the trivalent species. Then, the tetravalent Pu that remains captured on the column is reduced to trivalent Pu and released. The remaining tetravalents and hexavalent species are then eluted as before (Grate and Egorov, 1998a; Grate et al., 1999b).

These actinide separations demonstrate that sequential injection separations can be extended from simple "load, wash, and elute" separations to multicomponent separations. In addition, the separation of Pu from Am demonstrates the use of on-column redox chemistries for selective elution of Pu, where the column serves as both a reactor and separator.

The detector traces in the figures were obtained by flow-through liquid scintillation counting. For trace detection applications, the eluted species from the automated radiochemical separations have been delivered to a fraction collector and quantified by off-line alpha spectrometry (Grate et al., 1999b). In addition, eluted actinides can be delivered to an ICP-MS instrument, either as fractions for analysis or as an online front end (Egorov et al., 2001).

Indeed, automated extraction chromatographic separations of actinides are largely directed to analysis by ICP-MS, and have been reviewed in detail elsewhere (Grate et al., 2010; Kim et al., 2007; Lariviere et al., 2006). As noted above, radiochemical separations are required for a number of reasons for ICP-MS detection, and this detection method provides separate detection traces for isotopes with different mass-to-charge ratios. The combination of automated separation with ICP-MS is shown schematically in Fig. 11.15. This diagram shows how the main fluid handling system can be maintained in a "cold" zone, whereas the sample injection valve, separation column, and ICP-MS instrument can be placed in a hot zone. Detector traces for the separation of several actinides are shown in Fig. 11.16 (Egorov et al., 2001). This separation procedure addresses a number of interferences (e.g., isobaric and molecular interferences) in the actinide analysis noted previously. This separation methodology was used to enable isotope specific determination of actinide species in dissolved vitrified waste sample matrixes.

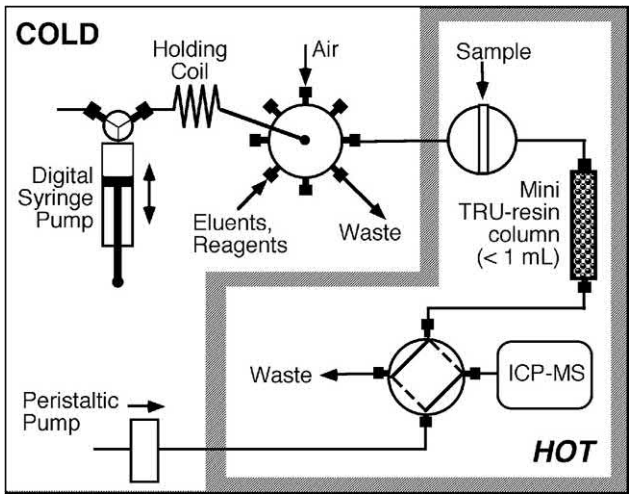


FIGURE 11.15 Schematic diagram for a sequential injection separation system with ICP-MS detection.

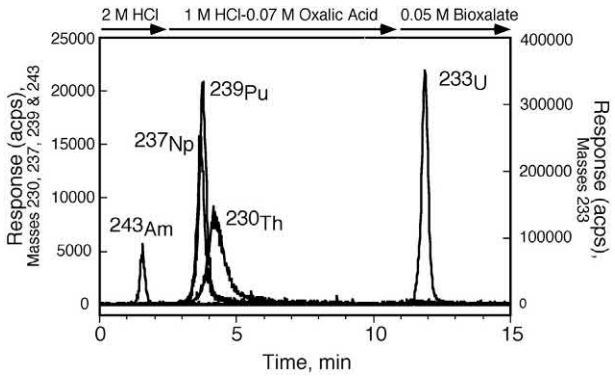


FIGURE 11.16 Detector traces from the ICP-MS for analysis of several actinides, where acps is the area counts per second. *ICP-MS*, inductively coupled plasma mass spectrometry. *Adapted with permission from Grate and Egorov (1998a). Copyright 1998 American Chemical Society.*

The use of ICP-MS detection in conjunction with continuous-forward-flow FI to automate extraction chromatographic radionuclide separations was first described in papers by Hollenbach and Aldstadt. Hollenbach et al. (1994) described the automation of extraction chromatographic methods to separate and preconcentrate Tc, Th, and U from soil samples. Aldstadt et al. (1996) described the use of FI and extraction chromatography to analyze U in environmental samples. In both cases, the use of an online separation system resulted in improved ICP-MS detection limits relative to direct sample introduction.

TRU resin separations have since been automated for ICP-MS analyses by several authors and laboratories (Benkhedda et al., 2005a; Egorov et al., 2001; Epov et al., 2005a,b; Hang et al., 2004; Peterson et al., 2007; Truscott et al., 1999, 2001; Unsworth et al., 2001). In addition, two other extraction chromatographic resins have been used in automated actinide separations prior to ICP-MS measurement. UTEVA resin (Horwitz et al., 1992c), which is loaded with the extractant dipentyl pentylphosphonate (also known as diamyl amylphosphonate), has been used for uranium and plutonium determinations (Godoy et al., 2006; Hang et al., 2004; Kang et al., 2001; Kuwabara et al., 2002; Ohtsuka et al., 2005, 2006; Perna et al., 2001; Tolmachyov et al., 2004). TEVA resin, described above with reference to pertechnetate separations, is also used to isolate tetravalent actinides and has been used in automated systems for Pu determination by ICP-MS (Epov et al., 2007; Kim and Kim, 2002; Kim et al., 2000a, 2004; Lariviere et al., 2008a).

A number of automated actinide separations have been reviewed in more detail elsewhere, with tables providing comments on each paper's approaches (Grate et al., 2010). A fully automated flow system with three columns in sequence (TEVA, UTEVA, and DGA) and online ICP-MS detection was developed for determining long-lived actinides captured in air filters (Lariviere et al., 2010). In recent work, a protocol was developed for automated extraction chromatographic separations with Sr resin, TEVA resin, and TRU resin coupled to an online ICP-MS. This work was directed at actinide isotopes and strontium in solid samples, after a sample matrix breakdown using a fusion process (Habibi et al., 2017). Several recent papers have advanced the state of the art in applying SI methods to automate extraction chromatographic and anion exchange column separations for the determinations of plutonium and other actinides (Qiao and Hou, 2010; Qiao et al., 2009a,b, 2010, 2011a,b,c, 2013a,b,c,d).

D. Renewable separation column applications

The renewable separation column (RSC) approach offers a number of advantages in separation methods where the life of the separation column is limited or tedious regeneration steps are necessary prior to column reuse. These have been demonstrated for ^{90}Sr analysis using Sr resin, ^{99}Tc separation using TEVA resin, and Am separation using TRU resin (Egorov et al., 1999a).

For example, the recovery of the retained ^{90}Sr from the column upon release with water or dilute acid is typically 95%, with 3%–4% of the original sample eluting in a subsequent blank run if no additional column wash steps are used. This carryover is associated with the Sr resin extraction chromatographic material. Instead of washing the column after each analysis, the separation material can be automatically renewed. This eliminates the observed carryover, and it is then reasonable to analyze blanks or low-activity standards after high-activity samples (Egorov et al., 1999a).

When analyzing Am using TRU resin to separate it from fission products and other actinides, there are several actinides retained on the column after Am elution. If the column is to be reused, these must all be removed from the column (e.g., using a chelating agent such as ammonium bioxalate). However, using the renewable separation column technique, the column bed can simply be disposed of after Am elution and replaced with new column material for the next sample (Egorov et al., 1999a).

In the ^{99}Tc analysis, the renewable column technique offers an alternative analytical approach. After capturing Tc on TEVA resin and washing away interferences, one manual method for Tc analysis involves placement of the Tc-containing resin in a vial and adding cocktail for liquid scintillation counting. Thus, the Tc-loaded resin is counted directly. The SI-RSC method can perform the separation and deliver the resin material to a liquid scintillation vial automatically (Egorov et al., 1999a).

Since the early demonstrations of renewable separation column techniques for radiochemical analysis methods, the LOV technology has provided a platform for a variety of automated radionuclide separations, including ^{90}Sr, ^{99}Tc, ^{226}Ra, and actinides (Avivar et al., 2011, 2012; Beltran et al., 2013; Kolacinska et al., 2017; Mola et al., 2014; Qiao et al., 2013c; Rodriguez et al., 2012, 2015b, 2016b; Villar et al., 2013, 2017). Recently, a commercial off-the-shelf (COTS) system was developed for processing materials for the analysis of U and Pu isotopes in IAEA-related samples, so that carryover from sample to sample could not occur through repeated use of the same resin columns in an automated system (Metzger et al., 2018).

Finally, the SI-RSC technique enables a new type of automated radiochemical analysis instrument. It enables an "open architecture" where one instrument design can be used for various radiochemical separations simply by using the software to choose which separation material is loaded into the column and which solutions are selected for the washing and elution steps. A proof-of-principle demonstration for this approach has been described (Egorov et al., 1999a). Thus, this instrument could perform a series of separations of successive aliquots of one sample, or different analyses on each sample, as required.

V. Automation using robotics

Laboratory robotics represents an important aspect of automation in the analytical laboratory. Modern robotic instrumentation can be used to automate a range of routine analytical operations that may be encountered in wet radiochemical analyses, from sample preparation to separations. Some typical examples include sample labeling, bar-code reading, weighing, dissolution, liquid–liquid and solid-phase extraction, serial dilutions, filtration, and sample delivery to instrumentation (Hurst, 1995). Robotic operations are typically carried out using either a robotic arm, which represents an anthropomorphic approach, or an x–y–z Cartesian system such as a liquid handler. These systems move tools, apparatus, and liquids from place to place. Cartesian systems may include a fluidic subsystem to deliver liquids to a dispensing tip that can move to specific locations on the deck containing multiwell plates or solid phase extraction columns.

In the first edition of this Handbook, Beugelsdijk and Hollen (1998) described a fully automated system for dissolution of Pu metal based on the Zymate II (Zymark Corporation) laboratory robot. The robotic system was set up to perform dissolution of 2–5 g samples of Pu metal. The operational steps included verification of the sample identity through readout of the barcode label, weighing the sample on an analytical balance, transferring the sample to the dissolution vessel, and sample dissolution. After dissolution, the individual sample aliquots were prepared, weighed, labeled, and sorted for subsequent analysis.

Zahradnik and Swietly (1996) described a Zymark robotic system for preparation and chemical treatment of diluted spent nuclear fuel samples. The robotic system executed initial sample preparation steps, such as batching, weighing, aliquoting, and spiking with tracers. Following automated preparation of the sample batch, the robot executed separation steps designed to separate U and Pu from the highly radioactive spent nuclear fuel matrix. Initial chemical treatment steps included drying and redissolution of the sample to remove volatile fission products such as ^{106}Ru. Following Pu valence state adjustment, an extraction chromatographic separation using immobilized tri-n-octylphosphine oxide (TOPO) was carried out to separate fission products and to collect U and Pu fractions for subsequent

analysis using alpha spectroscopy and isotope dilution mass spectrometry.

Focusing on the separation of Pu from U, Ziegler and Mayer (1999) performed detailed investigations on the TOPO-based extraction chromatographic material, demonstrating that reduction with ascorbic acid in formic acid was an efficient method to rapidly strip Pu from the column. This separation was designed to be implemented by a Zymark XP robot in a glove box. The possibility of direct filament loading of the purified sample for thermal ionization mass spectrometry (TIMS) was discussed. UTEVA resin has also been described for robotic separations of actinides in a glove box without using corrosive reagents (Apostolidis et al., 1998; Morgenstern et al., 2002; Richer et al., 1998). The separation technique was developed to allow columns to run dry between steps, a condition that might occur in an unattended gravity-feed open-column process. Recovered fractions were suitable for TIMS source preparation without further purification or treatment.

Grate et al. (2011) described the adaptation of a robotic liquid handling system designed to perform column-based radiochemical separations. This system is shown in Fig. 11.17. A customized four-probe head was used to transfer samples from sample vials to the columns using disposable tips, deliver clean acid eluents to the columns, apply air pressure to the top of each column, and move the slider on the rack that positions columns over fraction collection vials. While proof of principle for programming and performing the steps of actinide anion exchange was demonstrated, the authors found that transporting liquid eluents from reservoirs on the deck to columns in racks on the deck, by aspirating them into a holding coil, translating the probe head, and delivering them to a column, was a slow process. The paper describing this system compared fluidic, robotic, and hybrid approaches (Grate et al., 2011).

Robotics represents a potentially attractive approach for the automation of sample preparation and separation steps in laboratory-based radiochemical analysis. Robotic methods have been routinely used by laboratories serving the analytical needs of the IAEA for many years (Brandalise et al., 1994; Deron et al., 1994; Midorikawa et al., 2007; Richer et al., 1998; Surugaya et al., 2007; Takahashi et al., 1994). However, the maintenance of robotic equipment that is isolated in radiological containment systems such as glove boxes can present ongoing challenges.

Finally, hybrid approaches combining fluidic columns separations and robotic fraction collection have been developed. Various approaches were critically compared, and the PNX system shown in this chapter in Fig. 11.5B was described. This system used the fluidic column switching approach with a mechanized fraction collector designed with two aims in mind. First, the collector was designed to effectively isolate the outputs of six parallel columns from one another so there could be no possibility of cross-contamination between purified samples. Second, it was designed to maximize performance reliability by restricting the possible motions to forward and back (to change the collection vial underneath each column), and up and down (to raise the collection vial around the tip of the column outlet). The PNX system shown in Fig. 11.5B, after proof of concept, was changed to a system with dedicated pumps for each of six columns as the reagent delivery system, to obtain more rapid parallel column separations. The overall diagram for this system is in Fig. 11.18.

VI. Automated monitors for industrial scale nuclear processes

The majority of work in automated radiochemical analysis has been directed to *laboratory-based* analyses, where the

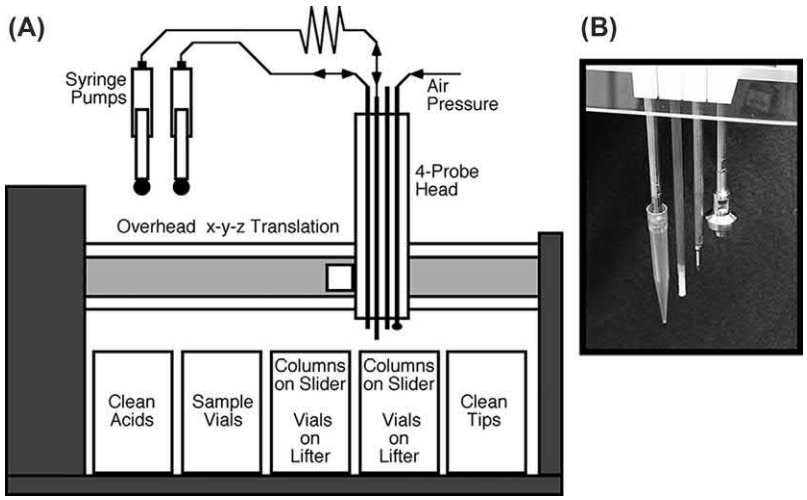


FIGURE 11.17 (A) Schematic diagram of the key components and layout of the Gilson liquid handling robot customized to perform anion exchange column separations. The diagram does not show the tip disposal chute, the air pressure cleaning probe station, or the liquid probe(s) cleaning station. Components are not to scale. (B) The probes on the probe head are shown from left to right: disposable tip probe for sample handling, acid delivery probe, rod to reposition the slider, and the air push probe. *Reproduced with permission from Grate et al. (2011). © 2011 Oldenbourg Wissenschaftsverlag GmbH.*

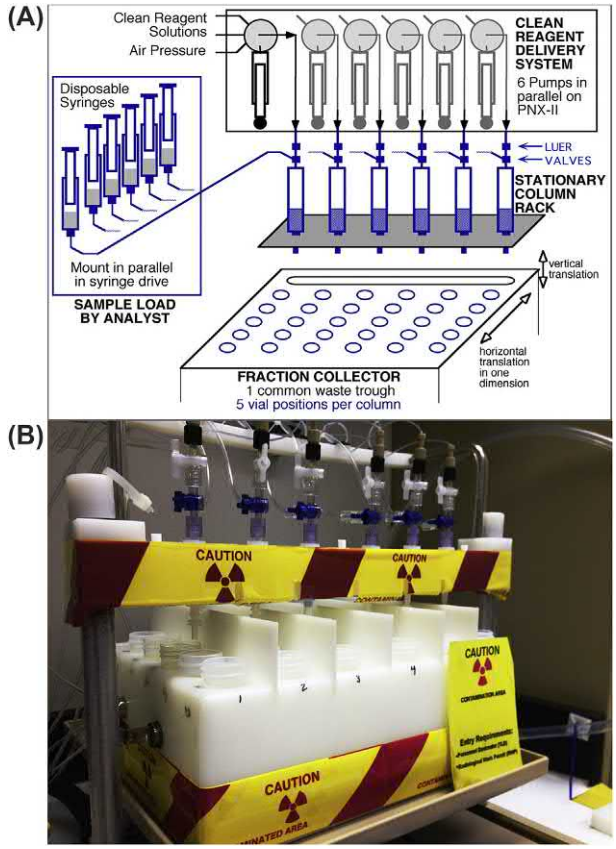


FIGURE 11.18 (A) Schematic diagram of version II of the PNX system for automated column separations, combining fluidic column separation with a custom-designed mechanized fraction collector. (B) The custom fraction collector built for six parallel columns and up to five fractions per column. For the color version of the figure, the reader is referred to the online version of the book.

radiochemical separation is automated, and perhaps linked to an online detector. A more challenging objective is to perform rapid radiochemical measurements online/at-line. This task is especially challenging for the determination of non−gamma-emitting radionuclides that typically cannot be measured using remote nondestructive methods. The overall process of sampling and laboratory analysis is generally too time-consuming to provide adequate feedback for continuous process control (e.g., by off-line analysis of a liquid sample sent to a centralized laboratory for ICP-MS or classical wet radiochemical analysis). Moreover, process scale analytical applications present challenges due to the complexity of the process sample streams in industrial-scale nuclear facilities.

There are needs for process analysis at industrial-scale nuclear plants for the reprocessing or treatment of spent fuel and nuclear waste. In reprocessing, monitors could both improve operation of the plant by providing feedback and potentially support safeguards (O'Hara et al., 2008a,b, 2009). In nuclear waste processing, monitors are needed to determine specific radionuclides before and after a separation process that removes that radionuclide from the waste stream (Egorov et al., 2005a). Such analyzers can assess the effectiveness of the radionuclide separation column and can be used to indicate if the output stream will qualify for subsequent conversion to stable waste forms.

For example, in the United States, chemical processing of low activity waste (LAW) prior to vitrification at the Hanford site requires working with streams that are caustic brine matrixes with complex and varying chemical and radiological composition. The total base content, the concentration of organics, and the complexant concentrations all depend on the source of the feed, as do the aluminum, nitrate, nitrite, dichromate, and radionuclide contents.

Consider an online/at-line analytical method to detect ^{99}Tc in the effluent from a technetium removal separation column. In waste matrixes with high organic content, a substantial amount of the total ^{99}Tc is present in the reduced, nonpertechnetate form of unknown chemical composition. Thus, varying sources of feed material result in varying speciation of Tc. The commonly employed analytical separation chemistries for ^{99}Tc, such as those described above, are effective only for Tc in the pertechnetate form. Therefore, to enable total ^{99}Tc analysis via radiochemical measurement, oxidation chemistries and procedures are required to convert all Tc species to pertechnetate (TcO_4^-). Thus, radiochemical analysis of ^{99}Tc entails sample matrix modification (e.g., acidification), analyte oxidation, chemical separation (e.g., using ion exchange or solvent extraction), and radiometric analysis (e.g., scintillation or gas proportional counting).

A fluidic radiochemical analyzer system has been developed to perform all these functions in a fully automated fashion for the rapid analysis of total ^{99}Tc in aged LAW streams (Egorov and O'Hara, 2003; Egorov et al., 2004a,b, 2005a, 2012; Grate et al., 2004, 2010; O'Hara et al., 2008a,b, 2009c). The automated radiochemical analyzer executes fluid handling steps required to perform acidification of the caustic sample, microwave-assisted sample oxidation using peroxydisulfate (Egorov et al., 2004a), separation of ^{99}Tc(VII) from radioactive interferences using an anion exchange column, and delivery of the separated pertechnetate to a flow-through scintillation detector. A schematic diagram of the automated Tc measurement process is shown in Fig. 11.19. A photograph of the prototypical analyzer unit is shown in Fig. 11.20. A full schematic flow diagram is provided in Fig. 11.21. The instrument design incorporates advanced digital fluid handling techniques using several zero dead volume syringe pumps, multiple valves for sample and reagent delivery, a two-position valve for flow reversal through the column (see Fig. 11.4A), and a diverter valve immediately upstream of the detector.

The sample treatment protocol begins with the sample acidification followed by a first digestion (heating) step

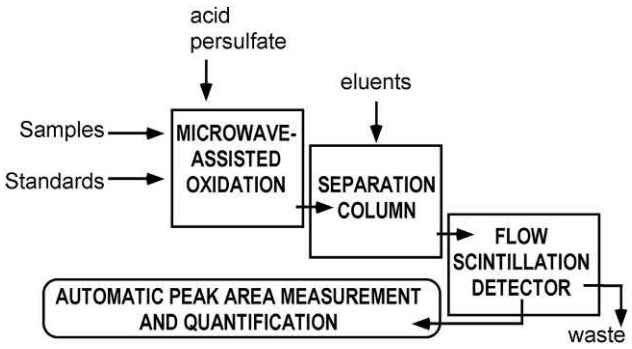


FIGURE 11.19 Schematic diagram illustrating sample processing, separation, and detection for an online analyzer for the continuous monitoring of the total Tc content of nuclear waste process streams.

within an open microwave vessel (Egorov et al., 2004a). This initial treatment ensures removal of the nitrites, which are expected to interfere with the subsequent oxidation. In addition, initial heating promotes rapid dissolution of the $Al(OH)_3$ precipitate that forms during acidification of the caustic LAW matrix. The nitric acid concentration and volume are selected to ensure complete dissolution of the $Al(OH)_3$ species upon heating, while maintaining relatively high pertechnetate uptake values on the anion exchange sorbent material during sample loading. The initial sample acidification procedure is followed by a second microwave-based digestion treatment using sodium peroxydisulfate oxidizing reagent. This oxidative treatment of the acidified sample ensures conversion of the reduced and organometallic Tc species to pertechnetate.

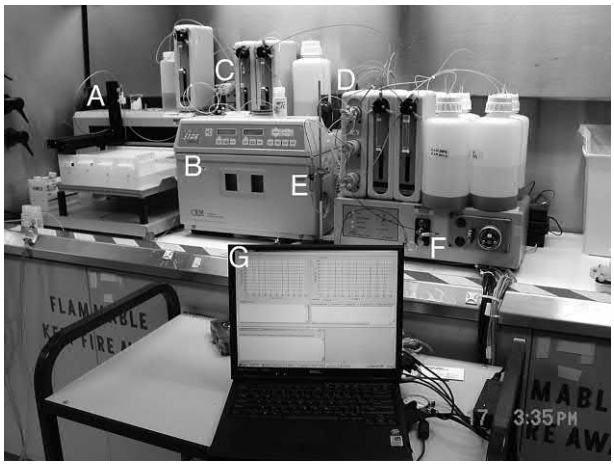


FIGURE 11.20 Photograph of the fully automated total ^{99}Tc analyzer instrument. (A) Robotic autosampler; (B) microwave digestion unit, (C) fluid handling components for sample injection, automated standard addition, sample acidification/analyte oxidation; (D) separation fluidics including syringe pumps, flow reversal, and diversion valves; (E) separation column; (F) flow scintillation detector; (G) computer with fluid control and data analysis software.

Pertechnetate separation is accomplished using a macroreticular strongly basic anion exchange resin (Egorov et al., 2005a, 2012). Compared with a similar extraction chromatographic chemistry using TEVA resin (described above), the solid-phase anion exchange material offers much longer column life. However, the pertechnetate elution kinetics of the extraction chromatographic material

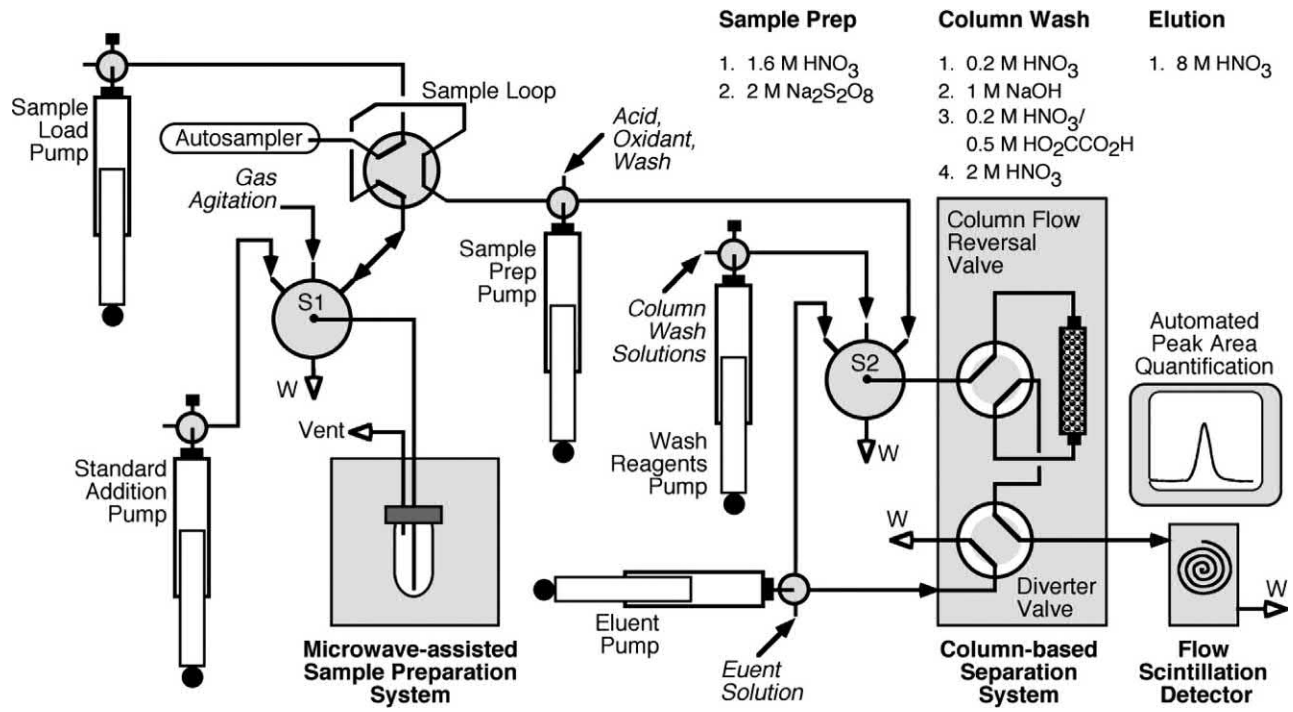


FIGURE 11.21 Schematic diagram of the fully automated total ^{99}Tc analyzer instrument. This system integrates several fluidic functions and approaches described in this chapter. *Adapted with permission from Egorov et al. (2012). Copyright 2012 American Chemical Society.*

are superior to those of the solid-phase anion exchange material. Nevertheless, rapid pertechnetate elution from the anion exchange material is possible when the eluent flow direction through the column is reversed (e.g., as shown in Fig. 11.4). The separation selectivity using anion exchange is adequate for the analysis of aged LAW sample matrixes and provides reliable separation of pertechnetate from the major radioactive constituents ($^{90}Sr/^{90}Y$, ^{137}Cs) and the minor constituents (e.g., radioisotopes of Sn, Sb, and Ru). However, a combination of column washes using dilute nitric acid, nitric−oxalic acid, sodium hydroxide, and moderately concentrated nitric acid is necessary for reliable isolation of pertechnetate from anionic species such as Sn, Sb, and Ru (Egorov et al., 2012).

The purified pertechnetate eluted from the column was detected and quantified with a flow-through scintillation detector packed with a lithium glass solid scintillator. This scintillator material exhibited excellent stability in strong nitric acid solutions used for final pertechnetate elution. The disadvantages of liquid scintillation detection (using scintillation cocktail) in this application would include increased waste generation associated with the cocktail and sporadic chemiluminescence signals in the presence of oxidants (e.g., Cr(VI)) and strong nitric acid. No chemiluminescence was evident when lithium glass solid scintillator cells were used for online quantification of ^{99}Tc in matrixes with high concentrations of Cr(VI) and nitric acid.

To obtain reliable ^{99}Tc quantification in varying sample matrixes, an automated standard addition technique was implemented as a part of the analytical protocol. The standard addition approach is based on the introduction of a ^{99}Tc standard solution during the sample acidification step in a duplicate analysis of a sample previously analyzed without standard addition. The ^{99}Tc standard is in a nitric acid solution with the same acid concentration used for sample acidification. The total effective efficiency (product of the ^{99}Tc recovery efficiency and the detection efficiency) is calculated based on the difference in analytical response obtained for the analysis of the spiked and unspiked samples. This approach provides a reliable method for matrix matched ^{99}Tc monitor instrument calibration.

The ^{99}Tc monitor instrument was fully automated for continuous operation with the control software performing asynchronous device control and detector data acquisition/processing, including peak search and integration as well as the instrument calibration via standard addition. Total analysis time was 12.5 minutes per sample, and the total analysis time for the standard addition measurement was 22 minutes (including analysis of both sample and spiked sample). In tests against various LAW samples from the US DOE Hanford site, including those with high organic content, the total Tc was accurately quantified as verified by independent sample analysis using ICP-MS. Fig. 11.22 compares results for total ^{99}Tc analysis of high organic content LAW samples using ICP-MS and the automated radiochemical ^{99}Tc analyzer.

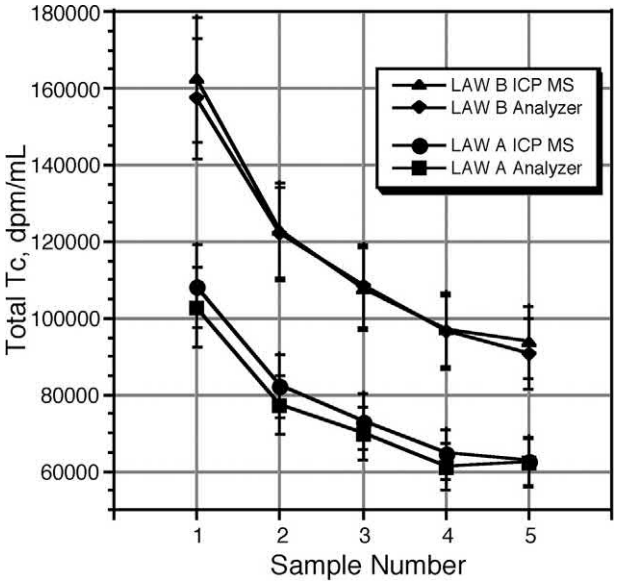


FIGURE 11.22 Total ^{99}Tc analysis in LAW matrixes with high organic content, comparing ICP-MS and automated radiochemical analyzer instrument results. Samples contain up to 60% of Tc in nonpertechnetate species. Error bars are ±10%. ICP-MS, inductively coupled plasma mass spectrometry.

VII. Radionuclide sensors and systems for water monitoring

A. Preconcentrating minicolumn sensors

The automated radiochemical separations described above entail detection of radionuclides after they have left the separation column. If the radionuclides captured on the column could be detected in place, the column would become a sensor. This approach has been successfully demonstrated using dual-functionality separation columns as preconcentrating minicolumn sensors (DeVol et al., 2000, 2001a,b; Egorov et al., 1999b, 2004b, 2005b, 2006; Grate et al., 2004; O'Hara et al., 2009a; Roane and DeVol, 2002). These columns perform both selective capture of radionuclides and transduction of the decay events of captured radionuclides into a measurable signal. The latter function is achieved by incorporating scintillating materials into the column. Light output is measured by PMTs placed around the transparent dual functionality column. The preconcentrating minicolumn sensor concept is shown in Fig. 11.23. Radionuclide sensors based on this concept were comprehensively reviewed by Grate et al. (2008).

Two approaches have been developed to achieve dual functionality in the columns. In one approach, the solid-

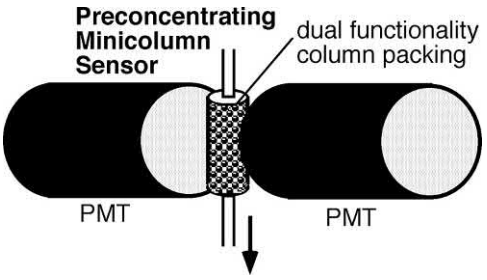


FIGURE 11.23 Schematic diagram of the preconcentrating minicolumn sensor concept, where the transparent column body is placed between two photomultiplier tubes (PMTs), counting in coincidence, for light collection. The packing material in the column body contains both selective separation media and scintillating materials to generate a luminescent output. The packing material may be delivered using renewable separation column methods.

phase extracting media are prepared to be scintillating by combining scintillating fluors with the separation chemistry in individual particles. These particles then represent "selective scintillating microspheres" (SSMs) (Egorov et al., 1999b). The alternative approach is to intimately mix scintillating particles with chemically selective particles to obtain both functionalities in the same column. If so desired, renewable separation column techniques can be used to deliver or renew the sensing material or mixture.

This sensing concept is designed to meet the challenging requirements for the direct measurement of alpha- and beta-emitting radionuclides in water. These radionuclides emit particles with short penetration ranges in condensed media and must be measureable within low analytical detection limits. The close proximity of selective chemistries and scintillating materials in particles (on the order of 10−250 microns in diameter) enables radiometric detection of alpha or beta emissions from the captured radionuclides. Because of the relatively long range of the beta particles, this approach appears to be particularly suitable for detection of beta emitters such as ^{99}Tc and ^{90}Sr. The maximum ranges in water for beta particles emitted by ^{90}Y ($E_{max} = 2282$ keV), ^{90}Sr ($E_{max} = 546$ keV), and ^{99}Tc ($E_{max} = 294$ keV) are 1.1 cm, 1.8 mm, and 750 μm, respectively. The average range of the beta particles from ^{99}Tc is ∼130 μm in water, which is comparable with the diameters of sorbent or scintillating beads used in the sensing columns.

In this sensing approach, the packed column format provides efficient fluidic processing of the sample for preconcentration. The selectivity is determined mainly by the separation chemistry used to preferentially capture and preconcentrate the analyte of interest, which localizes the radionuclides in the observed volume of a scintillating detection apparatus. For the analysis of important radionuclide contaminants such as ^{99}Tc, radiometric detection can offer much lower detection limits than those possible by chemical sensing approaches. Thus, this configuration meets all the functional requirements for effective radionuclide sensing.

B. Sensors for ^{99}Tc(VII) using quantitative capture

A radionuclide sensor for ^{99}Tc measurement in groundwater has been reported using SSMs as the column packing material (DeVol et al., 2001b; Egorov et al., 1999b). The SSMs were prepared by impregnating porous acrylic ester beads with a mixture of Aliquat 336 (a liquid anion exchanger based on long-chain quaternary ammonium ions) and scintillating fluors. The pertechnetate uptake characteristics of this material were characterized and found to be as expected for pertechnetate uptake by Aliquat 336 (i.e., high uptake at low-acid neutral pH range). The pulse height spectra of ^{99}Tc beta decay signal obtained using the SSM indicated a detection efficiency of 56%, which is sufficiently high for practical analytical applications. Similar uptake and luminosity (absolute detection efficiency, 30%−50%) characteristics were observed for Aliquat-336-based sensor materials prepared by diffusing scintillator fluors into the bead matrix or by incorporating scintillator fluors into the bead during the polymerization process.

Sensing properties were characterized with both ^{99}Tc(VII) standards (see Fig. 11.24A) and spiked Hanford site groundwater samples (Egorov et al., 1999b). Injection of an aliquot of ^{99}Tc standard in dilute acid results in analyte capture and measurable scintillation light output. In this example, the analyte capture was quantitative, and the signal persists as the sensor column is washed with dilute acid. The absolute detection efficiency for the ^{99}Tc was 45%. Integration of the light output provides a quantitative measure of the ^{99}Tc in the sample. Because the sensor material exhibits high binding affinity toward Tc(VII), large sample volumes can be concentrated using a small sensor column.

On the other hand, injection of a radioactive species that does not exhibit affinity to the sensor material results in only a transient peak signal, as shown for ^{137}Cs in Fig. 11.24A. Interfering species are promptly removed from the system using a small volume of wash solution. In this manner, the sensing method is selective toward the target analyte.

Analytes can be quantified from either the slope of the uptake signal or from the steady-state signal after washing to remove interferences. Detector traces for several standards are shown in Fig. 11.24B (Egorov et al., 1999b). This type of sensor has been successfully demonstrated using actual contaminated groundwater samples from the Hanford site and the standard addition method for quantification. Analytical results were in close agreement with the results of standard radiochemical measurements. Detection

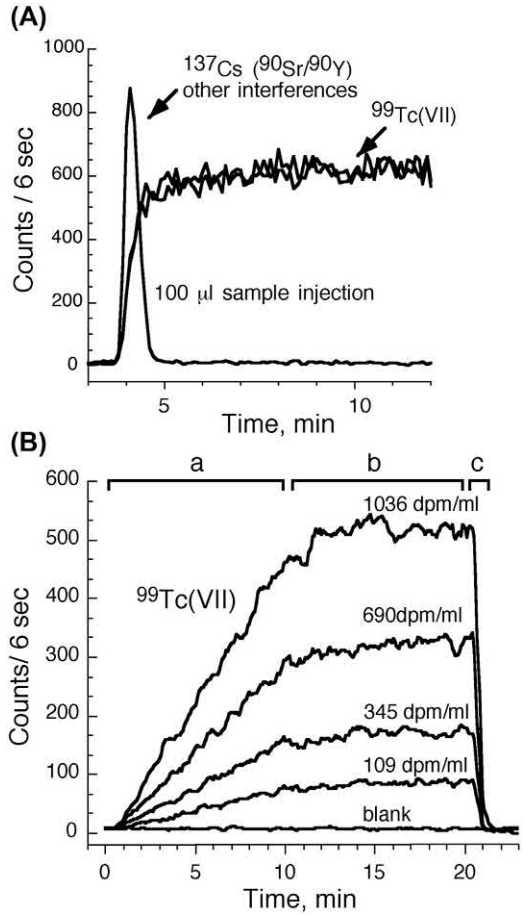


FIGURE 11.24 (A) Sensor response to injected aliquots of ^{99}Tc(VII) analyte and potentially interfering species (^{137}Cs) unretained by the sensor material. Following the analyte injection, the sensor bed is washed with 10 mL of 0.02 M nitric acid, and static counting ensues. (B) Detector traces for the capture and quantification of ^{99}Tc(VII) from 10 mL standard solution volumes, followed by column wash with 10 mL of 0.02 M nitric acid, and finally ejection of the column bed material. *Reproduced with permission from Egorov et al. (1999b). Copyright 1999 American Chemical Society.*

limits were well below the regulatory drinking water standard.

The preconcentrating minicolumn sensor concept has also been demonstrated using mixed beds to obtain the required dual functionality of preconcentration and beta decay signal transduction (Grate et al., 2004). Nonporous plastic scintillator beads (BC400, particle size 100−250 µm) were mixed with the strongly basic anion exchange material AGMP1 (particle size 20−50 µm) in a 20:1 weight ratio. The anion exchange beads provide selective pertechnetate uptake with a very high uptake affinity. As a result, the sensor could be prepared with a total bead volume of only 50 µL. The absolute detection efficiency of the composite sensor column was 34%, and analyte recovery (loading efficiency) was 97%. The ^{99}Tc(VII) selective composite bed sensor can be regenerated using a small volume of 2 M nitric acid solution, resulting in rapid elution of the retained analyte without the loss of the scintillation properties.

This ^{99}Tc(VII) sensing method was tested using unacidified Hanford groundwater samples. Approximately 60 mL of the groundwater sample can be preconcentrated without analyte breakthrough using this sensor, and these experiments showed that radionuclide sensing could be successful on chemically untreated groundwater samples.

Using a mixture of separate solid-phase extraction beads and nonporous plastic scintillator beads is advantageous in two ways. The nonporous scintillating beads were found to have much higher chemical stability in sensing and regeneration solutions than extraction chromatographic materials impregnated with scintillating fluors. In addition, this approach facilitates the use of solid-phase extraction materials for radionuclide uptake that are not readily impregnated with scintillating fluors.

Several recent papers have expanded on the development of stable dual-functionality materials and columns and introduced deliberate synthetic steps to covalently bind fluorophores into the polymer, or to chemically modify polymers with functionality for radionuclide uptake, or both (Bliznyuk et al., 2015, 2018; Duval et al., 2016a,b,c; Grogan and DeVol, 2011; Seliman et al., 2011, 2015, 2017). A sensing material for ^{99}Tc(VII) sensing was developed by diffusing 2-(1-naphthyl)-5-phenyloxazole (NPO) into (chloromethyl)polystyrene beads and then covalently grafting polymer chains onto the surface (Seliman et al., 2011). These grafted chains of poly[[2-(methacryloyloxy)ethyl]-trimethylammonium chloride] provided anion exchange sites for pertechnetate capture. The NPO dye has also been modified for covalent bonding into the polymer matrix to prevent leaching and create a more stable detection material (Duval et al., 2016a,b,c; Seliman et al., 2015). Responses to ^{99}Tc were demonstrated (Seliman et al., 2015).

Although the examples above focus on ^{99}Tc(VII) sensing, these analytical concepts have also been used to develop sensors for ^{90}Sr, radioiodine, and actinides (Bliznyuk et al., 2018; DeVol et al., 2000, 2001a,b; Duval et al., 2016a,c; Egorov et al., 1999b; Grogan and DeVol, 2011; Roane and DeVol, 2002; Seliman et al., 2017). In particularly elegant synthetic work, solid-phase extraction material SuperLig 620, which is selective for ^{90}Sr, has been covalently modified on the surface, sometimes in multiple steps, to add scintillation properties (Bliznyuk et al., 2018; Seliman et al., 2017). In one of the penultimate architectures to date, SuperLig particle surfaces, first modified to have pendant epoxy groups, are reacted with halloysite clay nanotubes that have been modified to have amine-terminated surface groups (Bliznyuk et al., 2018). These attach covalently, and then polyvinyltoluene brushes

containing covalently bound fluorophore are grown from the nanotube surfaces. This approach coats the selective SuperLig material with scintillating material in close proximity, and it does not impede access of the analyte to the selective SuperLig binding sites. "The two structural components of the system can be tailored independently" (Bliznyuk et al., 2018).

C. Equilibration-based radionuclide sensors

As originally conceived, these sensors were based on the concept of quantitative capture of the radionuclides of interest on the preconcentrating minicolumn, with either fluidic renewal via reagents or automated renewal of the solid-phase sensing material using renewable separation column techniques. However, a new approach has been developed based on the concept of equilibrating the preconcentrating minicolumn with ambient radionuclide concentrations (Egorov et al., 2002a,b, 2005b, 2006; O'Hara et al., 2009a). In this scenario, the sample is delivered to the sensor column until complete breakthrough has occurred and the entire column reaches dynamic equilibrium with the sample solution. Under these breakthrough conditions, no further analyte preconcentration occurs on the column and analyte concentration in the sample solution before and after the sensor column are equal. This principle of equilibration-based sensing is shown in Fig. 11.25, where the lower plot shows breakthrough from the column based on fraction collection after the sensor column, whereas the upper plot shows the capture and equilibration of the radionuclide on the column, as measured by the sensor's scintillation response. Chromatographic theory indicates that under these dynamic equilibrium conditions, analyte concentration on the sensor column is proportional to the analyte concentration in the sample used for equilibration. Fig. 11.26 illustrates sensor column equilibration to several samples of varying activity and a linear calibration curve of the steady-state signals from each sample (inset). Under these conditions, the sensor column does not require regeneration or renewal, since the signal will go down upon equilibration with a new sample of lower concentration or up in response to a sample of greater concentration (O'Hara et al., 2009a). The equilibration approach forms the basis for the reagentless radionuclide selective sensing that is particularly well suited for the development of sensor monitors or probes for at-site or in situ monitoring.

Analyte activity, A, on the sensor after equilibration can be calculated using the following formula:

$$A = DV_sC_l$$

where D is the volume/volume distribution coefficient of the sorbent material, V_s is volume of the stationary sorbent phase in the sensor column, and C_l is analyte activity in the sample used for sensor equilibration. In addition, the dynamic response of the sensor as it is equilibrating with the sample can be modeled using concepts and functions from frontal chromatography (Egorov et al., 2006). In Fig. 11.25, the solid black lines represent the model fits, whereas the gray traces or markers are the experimental data. The fits are very precise.

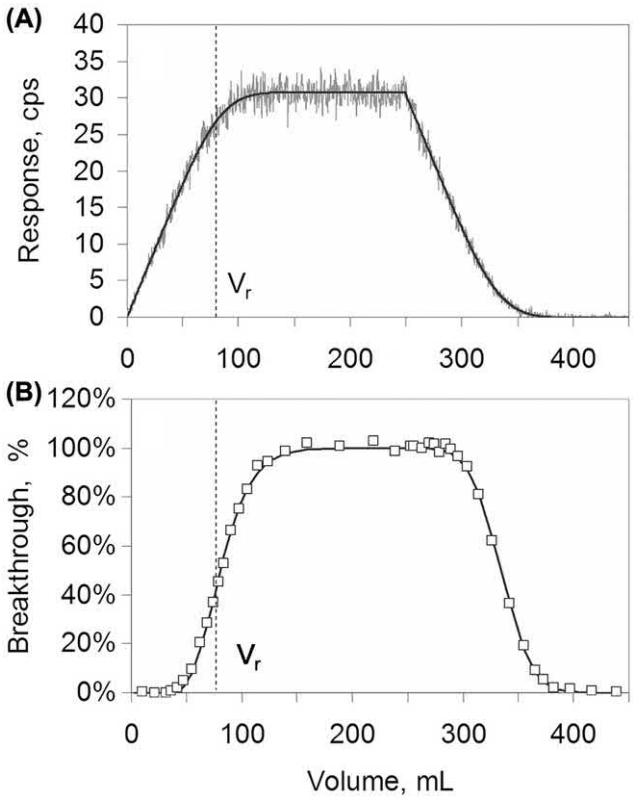


FIGURE 11.25 (A) Trace showing sensor equilibration with 1 Bq/mL ^{99}Tc solution followed by a reequilibration to a blank solution in a matrix of 0.01 M nitric acid. The sensor cell (dimensions 4 mm ID × 29 mm height) is composed of a 1:4 dry w/w ratio AG 4-X4:BC-400. (B) Fractions collected immediately downstream of the sensor cell show the breakthrough profile of ^{99}Tc from the sensor column. Both the Gaussian model (*black lines* in each plot) and low plate model (not shown) provide a good fit to the observed data. *Reproduced with permission from Egorov et al. (2006). Copyright 2006 American Chemical Society.*

This equilibration approach has been demonstrated successfully for sensing ^{99}Tc(VII), both in the laboratory and on groundwater samples from the Hanford site (Egorov et al., 2002a; Egorov et al., 2006; Egorov et al., 2005b; O'Hara et al., 2009a). The potential for other anions in groundwater to interfere was examined in detail, and a method for accurate quantification in complex groundwater matrixes containing cocontaminants, using automated standard addition, has been described (O'Hara et al., 2009a).

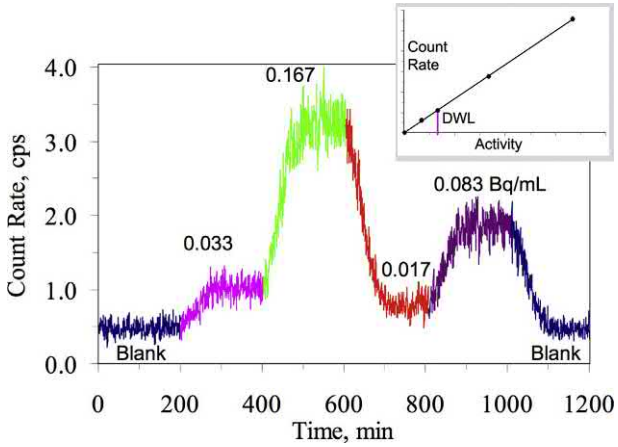


FIGURE 11.26 Response of a preconcentrating minicolumn sensor to four ^{99}Tc calibration standards in Hanford groundwater, delivered to the sensor in a random order with regard to activity concentration. Blank groundwater was delivered at the beginning and end of the series. The smaller plot illustrates the strict linearity of the calibration curve and quantification to below the drinking water limit (DWL). For the color version of this figure, the reader is referred to the electronic version of this book. *Reproduced with permission from O'Hara et al. (2009a). Copyright 2009 American Chemical Society.*

D. Sensor probes and systems for water monitoring

Radionuclide sensors are particularly important for monitoring contaminated ground and surface waters, although they may also be useful in monitoring nuclear processes. Monitoring groundwater is important for detecting migration of contaminant plumes and assessing in situ remediation approaches such as barriers. The most significant radionuclide analytes are alpha- and beta-emitting radionuclides that cannot be detected by gamma spectroscopy and which are mobile in the environment. In situ sensors or at-site monitors for these species must succeed in obtaining accurate analytical results for species that are normally analyzed by multistep laboratory sample preparation, separation, and detection processes, while minimizing or eliminating reagents.

The preconcentrating minicolumn sensor concept (Fig. 11.23) has been successfully engineered into a sensor probe in a configuration that fits into a 4-inch (10.2 cm) well casing for down-hole monitoring, using an anticoincidence shield around the sensing flow cell (observed by PMTs counting in coincidence) to reduce background counts (Egorov et al., 2005b). Images of the engineered sensor probe are shown in Fig. 11.27. The sensor flow cell with two PMTs is shown in **A**, whereas **B** shows the sensor embedded within the anticoincidence shield in the probe housing, and **C** shows the complete probe.

These sensor concepts have also been incorporated as the detector into engineered systems for at-site groundwater

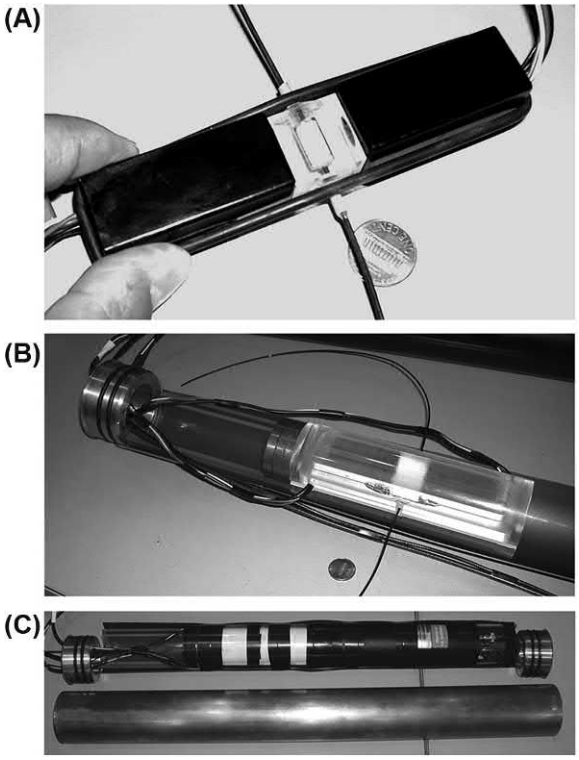


FIGURE 11.27 Images of the sensor probe for ^{99}Tc monitoring using the reagentless equilibrium sensing approach. (A) Sensor flow cell with two photomultiplier tubes (PMTs), (B) the sensor in an anticoincidence shield surrounding the probe housing, and (C) the complete probe prior to assembling the outer housing.

monitoring for quantifying ^{99}Tc in groundwater (O'Hara et al., 2009a). The PNNL worked with Burge Environmental to incorporate a minicolumn sensor operating in equilibration-based sensing mode into the Burge Universal Sensor Platform (Burge and May, 2005; Burge et al., 2005). These platforms are deployed above ground and obtain groundwater samples from sampling lines, while supporting a fluidic system and sensors with solar power, batteries, and remote command/data acquisition communications capabilities. The fluidic system and electronics are designed to acquire a precise volume of groundwater sample with which to equilibrate the sensor and determine the sensor response. Using an above ground system like this, additional services can be incorporated: a stock volume of standard solution is used to perform periodic programmed sensor calibrations by the method of standard addition to the groundwater sample, which compensates for any matrix effects on the sensor response, and enables accurate analyses over a wide range of groundwater compositions. In addition, a stripping solution can be periodically delivered to remove potentially fouling substances from the sensor column, such as soil organic matter. The fluidic architecture that supports the sensor in these engineered

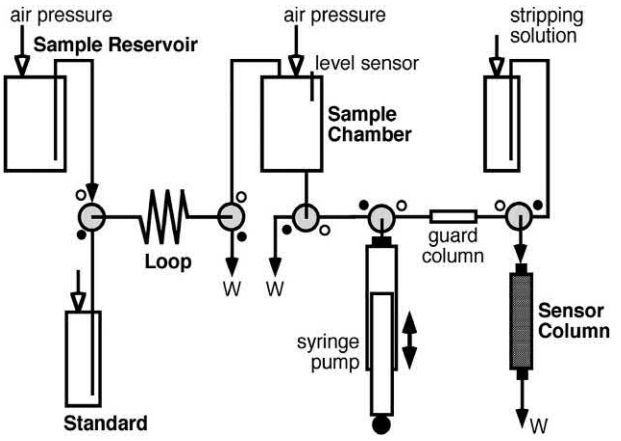


FIGURE 11.28 Automated fluidic system to support a preconcentrating minicolumn sensor in an at-site groundwater monitoring application, using the Burge Universal Sensor Platform. W = waste line. Pneumatic system to drive solutions with air pressure (*open-headed arrows*) is not shown. Three-way solenoid valves are indicated with normally open (*open circles*) and normally closed (*solid circles*) ports. Volumes of chambers are not shown to scale. *Reproduced with permission from O'Hara et al. (2009a). Copyright 2009 American Chemical Society.*

systems is shown in Fig. 11.28, using air pressure for some pumping operations and a syringe pump for others.

This monitoring approach has been deployed as a wall-mounted unit (shown in Fig. 11.29) inside the ZP-1 Pump and Treat Plant on the Hanford Site. This plant pulls water from multiple wells in the 200 Area of the site to remove carbon tetrachloride contaminants; some of the wells are also contaminated with ^{99}Tc. The monitoring system can sample from four lines connected to groundwater from specific wells of interest. Detector traces from 7 days of continuous operation, including blanks and a calibration matrix spike, are shown in Fig. 11.30. The four sample analyses determined concentrations of 0.17, 0.19, 0.16, and 0.14 Bq/mL, in good agreement with independent analysis.

The concept of an at-site monitor has also been applied to the development of sensing systems for ^{90}Sr in groundwater. The detection limits for ^{90}Sr are extremely challenging. O'Hara et al. (2009c) described an approach that automates the purification of ^{90}Sr from groundwater samples using a SuperLig 620 column, retention of the purified ^{90}Sr on the column to allow for ^{90}Y daughter ingrowth, and then transfer of the ingrown daughter nuclide to a Cherenkov detection flow cell. The principles of Cherenkov detection were described in detail in Chapter 6, Volume 2. Briefly, energetic beta particles, such as those from ^{90}Y, can produce light in aqueous solution without the need for a scintillator. The Cherenkov signal from the transferred ingrown ^{90}Y can be related back to the original ^{90}Sr activity in the sample given known ingrowth and counting times. These times are established in the automated separation, ingrowth, and detection method. It was

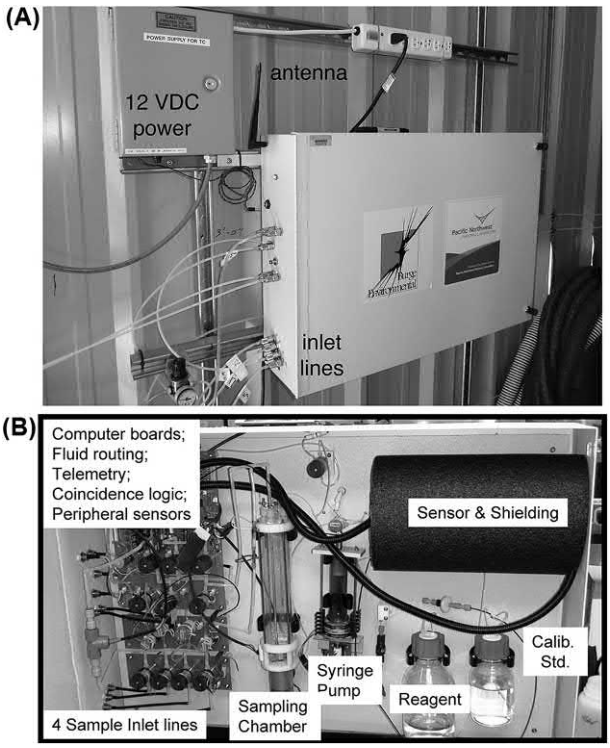


FIGURE 11.29 Images showing the ^{99}Tc groundwater monitoring system deployed as a wall-mounted box in the Hanford 200-ZP-1 groundwater pump and treatment plant. The primary purpose of this plant is to remove carbon tetrachloride; however, some source wells also contain ^{99}Tc as a contaminant, and ^{99}Tc must be monitored to assure that regulated ^{99}Tc levels are not exceeded. (A) External view of the monitor, showing the main box, the water sample inlet lines, the antenna, and the 12 VDC power unit that supplies the main box. (B) Interior of the main box highlighting key components. The system selects and analyzes water from one of four sample inlet lines corresponding to two groundwater wells, the pretreatment water consisting of combined inputs from multiple wells, and the posttreatment water.

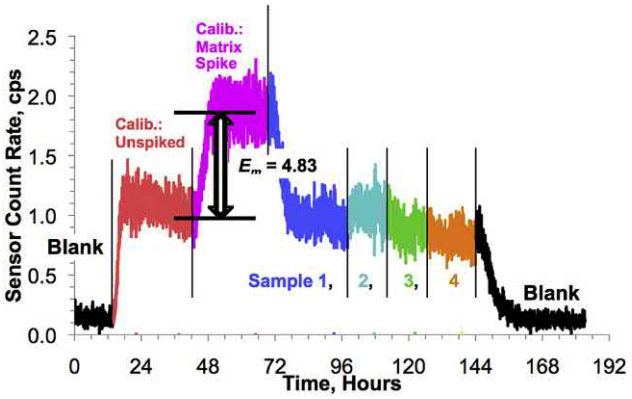


FIGURE 11.30 Sensor response traces from the ^{99}Tc groundwater monitoring system deployed in the Hanford ZP-1 pump and treatment plant. An unspiked sample and a calibration matrix spike into the groundwater matrix are shown, followed by four samples and a blank. The calibration spike provides a parameter, E_m, used in the calibration.

determined that optimum split of the total time between ^{90}Y ingrowth time and Cherenkov counting time was 2:1, i.e., where the count interval is one-third of total time. Under these conditions, a minimum detectable activity (MDA) that is equivalent to the drinking water limit (DWL) of 0.3 Bq/L can be obtained in 41.5 hours of total time, of which 27 hours (0.42 ^{90}Y half-lives) are spent on ^{90}Y ingrowth and 13.5 hours are spent counting. Beginning with a 0.35 L sample volume, these authors demonstrated a detection limit of 0.057 Bq/L using a 5 mL volume Cherenkov flow cell. This result is below the radioactivity detection limit requirement for drinking water of 0.3 Bq/L, which corresponds to a mass-based concentration equivalent for ^{90}Sr of only 5.8×10^{-11} ppm. The combination of a chemical separation, ingrowth process, and Cherenkov detection provides a number of advantages, including independence from concerns about disequilibrium between ^{90}Sr and ^{90}Y in the environment, removal of potential radioactive interferences, freedom from concerns of any radionuclide contaminants that have emissions with energies below the Cherenkov threshold, separation from matrix interferences that could absorb (or quench) Cherenkov photons, and preconcentration of a larger environmental sample into a small volume detection cell, which simplifies light collection. No scintillation materials are required.

VIII. Digital microfluidics for microscale single bead manipulations

While radiochemical separations are typically conducted on column bed volumes from 100 μl to 2 ml and entail milliliter volumes of solutions and eluents, sometimes separations are required on much smaller volume scales. In the sample preparation for TIMS, it is desirable to prepare a source of the highest possible purity. The presence of elements other than the actinides being analyzed, such as plutonium isotopes, can interfere with ionization and hence the measurement. Once the plutonium in a sample has been separated from the sample matrix and other elements, there are still traces of elements present as contaminants from the acid reagents. The only way to reduce those background contaminants is to repeat separations on smaller and smaller volume scales.

In some cases, these can entail performing separations on single anion exchange beads. Single bead anion exchange separations have been used as purification steps for actinides and other trace elements (Dai et al., 2001, 2002a,b; Kelley et al., 1999). Similarly, uptake on single resin beads is routinely used to prepare ion sources for TIMS (Beasley et al., 1998; Bischoff et al., 2005; Dai et al., 2001, 2002b; Fassett and Kelly, 1984; Kelley and Robertson, 1985; Manton, 1988; Stoffels et al., 1994; Walker et al., 1974). Single bead separations, and single bead uptake for TIMS source preparation, present two challenges. First, the diffusive uptake processes are slow, generally requiring many hours to come to equilibrium; second, these processes are difficult to automate. An acoustic streaming approach was developed to accelerate diffusive uptake (Paxton et al., 2008). While this approach accelerated uptake rate by five to six times, it did not address microscale fluid handling techniques to automate multistep single bead separations.

In a collaboration between Sandia National Laboratories, led by Michael Bartsch, and Pacific Northwest National Laboratory (PNNL), led by Jay W. Grate, the methodology of digital microfluidics (DMF) has been adapted to the automation of radiochemical analysis at the microscale. Conventional fluidics and microfluidics can refer to a range of scales from systems composed of extruded tubing and discrete valves and pumps, to systems microfabricated on chips. The intermediate scale between tubing-based systems and microchannel (meaning channels on the order of 50 micron by 100 microns) systems can be useful for microscale sample preparation processes.

DMF has emerged as a new technology to create programmable intermediate scale platforms that are simpler than tubing-based systems (Choi et al., 2012; Jebrail et al., 2011, 2014; Kim et al., 2011, 2013; Kirby and Wheeler, 2013; Shih et al., 2012; Thaitrong et al., 2012; Yang et al., 2009). In addition, it introduces an entirely new way to manipulate the fluids, over a range of fluid volume scales without tubing or microchannels. The DMF methodology has been critically reviewed (Jebrail et al., 2012). Fluid droplets are manipulated over an insulating hydrophobic surface that has an underlying pattern of electrodes. Electrowetting forces are created by activating particular electrodes. Different programmed sequences can move the droplet in different directions over the surface. This concept is suggested in Fig. 11.31. In this way, ***fluids can be automatically transported and routed over the surface, without pumps, valves, or tubing,*** according to preprogrammed protocols. In practice, DMF chip surfaces are interfaced with additional fluid handling components to deliver solutions and reagents to and from the device surface. Multiple droplets on the platform, containing sample, and various reagents, can be manipulated to carry out sample preparation, separation, and routing functions.

The teams at Sandia and PNNL developed a design and workflow that introduced a Pu-containing microcolumn eluent onto an open format DMF chip. Images of the design are shown in Fig. 11.32. Droplets of this solution were routed to a heating strip for evaporative volume reduction and transposition into another acid dispensed onto the chip. The transposed solution was routed over the chip to the tip of an off-chip tube containing a single anion exchange bead trapped between two tubing crimps. This bead-in-a-tube

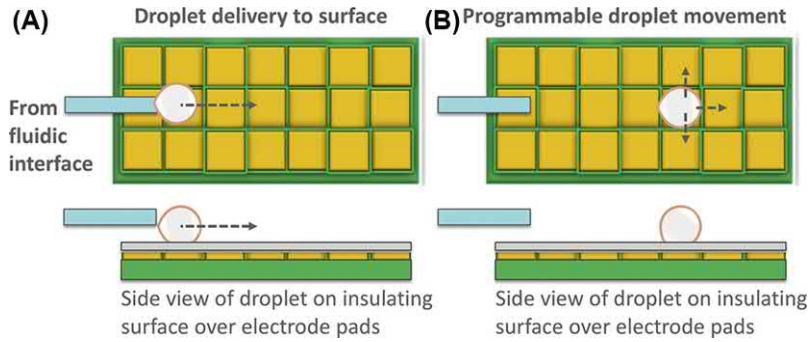


FIGURE 11.31 Schematic diagrams in top and side views of the digital microfluidic concept for programmable manipulation of droplet(s) on a hydrophobic insulating surface over a pattern of electrode pads, shown as gold (light gray in print version) on a green (gray in print version) substrate, with the insulating hydrophobic layer on top in the side views. (A) Droplet delivery via the tip of a tube or capillary from a pumped fluidic interface. (B) Droplet can be moved in any direction over the surface using electrowetting forces created by activation of the underlying electrodes. These images show open format digital microfluidics, meaning there is no top plate and the droplets are in an air medium, rather than closed format with a top plate over the bottom plate and an oil medium in between.

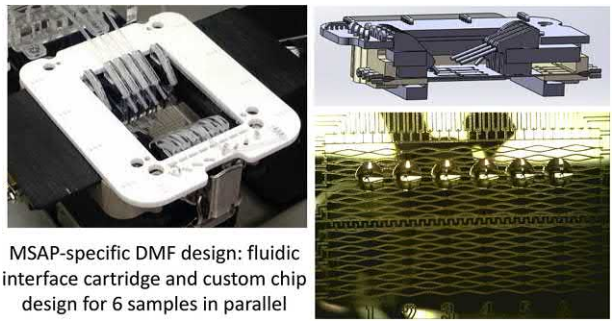


FIGURE 11.32 Various views of the Microscale Sample Automation Platform (MSAP)-digital microfluidic design for single bead separations (denoted as MSAP-specific DMF design). A fluidic interface cartridge (white) serves to deliver samples and reagent solutions and to provide the devices for bead-in-a-tube anion exchange separation. The electrode design on the DMF chip (lower right) can process six samples in parallel and perform evaporative volume reduction.

configuration on the fluidic interface is shown in Fig. 11.33. The solution was pulled by a pump up off the chip and into this bead-in-a-tube device, and pumped back and forth over the bead. Then this solution was pumped away from the bead, and a clean acid solution was pulled into the bead-in-a-tube to wash the bead. This clean acid had been separately delivered to the DMF surface and moved into position for the bead-in-a-tube manipulations. Again, the acid was pumped back and forth over the bead. These processes automated the fluidic handling and accelerated the diffusive processes that occur at the bead. Another clean acid was used to elute unwanted thorium ions off the bead. Finally, an eluent was used to release the Pu from the bead and deliver this solution back to the DMF surface. The overall design was set up to move six sample droplets in parallel and to process each sample through a sequence of sample processing steps to purify the Pu at the microscale, to minimize background contaminants for TIMS sources.

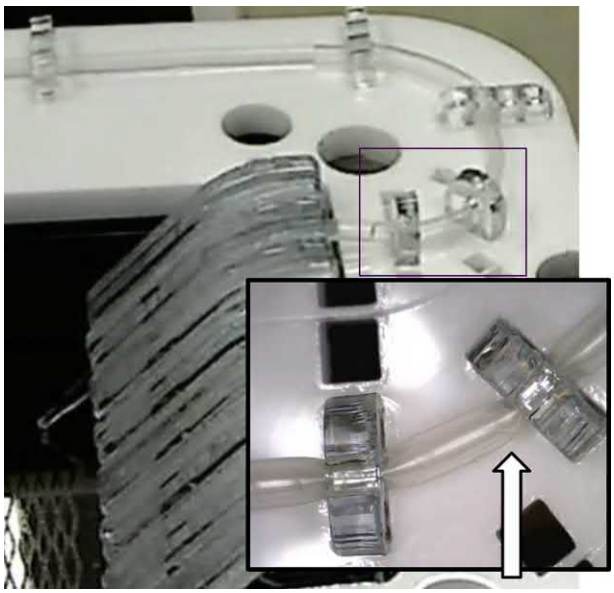


FIGURE 11.33 Detailed views of the bead-in-a-tube device for automating and accelerating single bead anion exchange. The bead location is indicated by the *arrow*. These details are part of the fluidic interface cartridge above the DMF chip surface.

IX. Radioisotopes in medicine

Automated methods for radiochemical separations and chemical reactions are also applied to the production of radionuclides used in medicine, including:

- medical isotope generation by separation of a desired daughter isotope from the parent isotope;
- isolation of a radionuclide produced through fission, neutron activation, or accelerator bombardment of a target material;
- attachment of radioisotopes to cancer targeting molecules; and

- the synthesis of organic chemicals containing a radionuclide in the structure (e.g., radiopharmaceuticals).

Such automated systems can be employed for generating patient doses at a remote production facility or to provide single-patient doses at or near the point of care. Automation is particularly useful if the radionuclide is short-lived and therefore must be produced and used quickly at the location where it is needed. In addition, automation enables more efficient execution of elaborate separation schemes that can be applied to parent/daughter radionuclide pairs of interest or to improve product purity and consistency. Autonomous, remote processing systems can be important to ensure that sterility is maintained, radiological dose to production staff and medical personnel is minimized, and human error is avoided (IAEA, 2004).

A radiopharmaceutical is a drug with radioactivity and known chemical form. The radioactive atom in the drug is either incorporated covalently by synthesis or conjugated to a targeting agent such as an antibody. Radiopharmaceuticals are generally classified by their primary intended purpose, which is diagnostic or therapeutic (Boros and Packard, 2018; Khalil, 2010; Zimmermann, 2006). Radionuclides used in medicine may have decay-induced emissions that fulfill both purposes. Alternatively, the same pharmaceutical may be labeled with different radionuclides to achieve a diagnostic/therapeutic pairing; this approach is known as theranostics (Yordanova et al., 2017). The field of nuclear oncology employs radionuclides in the diagnosis and/or treatment of cancer in patients; it represents one of the largest applications of radionuclides in medicine (Srivastava and Mausner, 2014; L'Annunziata, 2016).

A. Therapeutic radionuclides

Therapeutic radionuclides are typically bound to a targeting agent that seeks and accumulates in cancerous or diseased tissue; these targeted cells are subsequently damaged or destroyed when the proximate radionuclide decays and sends a high-energy particle(s) through the tissue (Cutler et al., 2013). Therapeutic particle emissions from radionuclide decay include Auger and conversion electrons, and alpha and beta particles. The range of these emissions through tissue is dependent on their energy and linear energy transfer (LET). Each of the above emission types except for beta particles is classified as high LET; their range in tissue is generally between 10's and 100's of microns. They are generally effective for treatment of diffuse and micrometastatic diseases. As such, they require highly specific targeting mechanisms. In contrast, low-LET beta particles can penetrate between 10's and 1000's of microns. These are more effective on larger tumor masses and macrometastatic disease (Marcu et al., 2018; Srivastava and Mausner, 2014). In this section, we will discuss the use of automated fluidic systems in the preparation of a few beta- and alpha-emitting radionuclides used in therapeutic applications.

1. Beta emitters

One class of therapeutic radionuclide employs the low-LET beta particle emissions to apply dose to tumors (Banerjee et al., 2015; Jeong and Chung, 2003; Juweid, 2002; Lambert and de Klerk, 2006; Novak-Hofer and Schubiger, 2002; Pauwels and Erba, 2007; Pohlman et al., 2006). Some common beta-emitting therapeutic radionuclides are listed in Table 11.1. As these radionuclides are generally long-lived ($t_{1/2} > 2.5$ d), they are commercially available in their purified form from off-site production facilities. The exception is the shorter-lived ^{188}Re, which is produced at-site via a ^{188}W/^{188}Re generator. Below, we discuss automated systems as they are applied to generator-produced ^{188}Re and ^{90}Y.

a. Rhenium-188

Rhenium-188 (^{188}Re) is used in therapeutic radiopharmaceuticals due to its energetic beta emissions (2.12 MeV max.) for abnormal tissue penetration and destruction, and gamma-ray emissions that can concurrently be used for imaging and dose estimation (Boschi et al., 2014). It is prepared with a ^{188}W/^{188}Re generator that is similar to the ^{99}Mo/^{99m}Tc generator in that the ^{188}W parent is bound onto an acidic alumina column. Further, as with ^{99m}Tc, the ^{188}Re (as perrhenate, $^{188}ReO_4^-$) is eluted with a saline solution. However, the radionuclide does not elute from the alumina column in a small volume as required for the preparation of the radiopharmaceutical, and so it is usually concentrated onto an in-line anion exchange column prior to its final elution and use.

The multistage isolation/concentration process and the high radiological dose imparted by this radionuclide have driven teams to apply laboratory automation in the

TABLE 11.1 Common beta-emitting therapeutic radionuclides.[a]

Nuclide	Approximately $t_{1/2}$, h	End-point emission energy, keV	Emission intensity, %
Cu-67	62	377/468/562	57/22/20
Y-90	64	2280	100
I-131	193	606	90
Lu-177	160	385/498	9/79
Re-188	17	1965/2120	26/70

[a]*Decay data obtained from National Nuclear Data Center (2019).*

preparation of ^{188}Re. Teams at the Paul Scherrer Institute (Switzerland) and the Institute of Nuclear Energy Research (Taiwan) have recently demonstrated concentration and elution systems for preparation of ^{188}Re using fluidic systems. Each system employs a commercially available ^{188}W/^{188}Re generator column and utilizes computer-controlled fluidics to concentrate the ^{188}Re and elute it in a highly concentrated product solution. The Jäckel et al. (2005) system is semiautomated, using a syringe pump and Teflon switching valves for fluid delivery and routing, respectively. The Luo et al. (2007) system is fully automated, relying on a peristaltic pump for fluid delivery. Saline is used to elute ^{188}Re from the generator as the perrhenate ion ($^{188}ReO_4^-$). As the milking process requires over 30 mL to achieve good ^{188}Re yield, a secondary silver cation exchange column must be used to remove chloride ions from the primary column saline eluent, and a tertiary anion exchange column is used to concentrate the perrhenate. The $^{188}ReO_4^-$ is subsequently eluted from the anion exchange column using a small volume of saline. Luo et al. compared the behavior of three anion exchange cartridges and found that the Waters Accell QMA resin provided superior chromatographic performance.

Rhenium-188 is considered for the treatment of hepatocellular carcinoma. Lipiodol (ethiodized oil), when injected intraarterially, can deposit and emulsify into hepatoma cells. Thus, this oil can act as a ^{188}Re transporter to tumors of the liver (Boschi et al., 2014). Italian and French research teams have developed automated generator/synthesis systems to prepare this radiopharmaceutical (Lepareur et al., 2011, 2012; Uccelli et al., 2011).

b. Yttrium-90

Yttrium-90 (^{90}Y) is an important beta-emitting radionuclide that is coupled to antibodies used in peptide receptor radionuclide therapy (Sabet et al., 2016), radioimmunotherapy (Goffredo et al., 2011; Kawashima, 2014), and radioembolization (Khajornjiraphan et al., 2015; Tong et al., 2016). Because of its relatively long half-life, ^{90}Y is primarily purified at high activity levels in centralized production facilities, aliquoted, and shipped to the point of use.

An automated ^{90}Y purification process was developed to generate patient dose levels of ^{90}Y (O'Hara et al., 2009d). A radiolysis-resistant inorganic sorbent column was developed and demonstrated to strongly bind the ^{90}Sr parent while allowing periodic elution of ^{90}Y. The resulting ^{90}Sr/^{90}Y generator column was set up as part of a fully automated radionuclide generator system. Unbound ^{90}Y is separated from the parent isotope during a milking step. Due to the relatively broad elution profile of ^{90}Y from the generator column, a secondary "mini" ion exchange column is placed in-line to capture ^{90}Y quantitatively during the generator column milking process. Subsequent elution of ^{90}Y with a secondary stripping solution (applied in the reverse flow direction) yields the product in a small volume.

A ^{90}Sr/^{90}Y isolation process has also been demonstrated using a fully automated electrochemical purification system (Dash and Chakravarty, 2014). A two-step electrolysis is performed to separate ^{90}Y from a ^{90}Sr stock solution. An electrolyte solution containing $^{90}Sr(NO_3)_2$ first undergoes electrolysis at −2.5 V (100−200 mA current); ^{90}Y is collected on a Pt cathode. Next, the cathode is rinsed and transferred to a fresh cell containing dilute HNO_3 and another Pt electrode. The polarity of the electrodes is reversed, and ^{90}Y is collected on the fresh cathode. The process is claimed to be capable of producing a ^{90}Sr/^{90}Y activity ratio of $<10^{-5}$.

2. Alpha emitters

Alpha particles are highly energetic and ionizing, the combination of which is lethal to cells within a short range (Poty et al., 2018b). As such, the coupling of alpha emitters to diseased cell-targeting molecules (e.g., monoclonal antibodies, peptides, nanoparticles, nanobodies) can result in high toxicity to cancer cells (Makvandi et al., 2018; Poty et al., 2018a); this is referred to as targeted alpha therapy (TAT).

Alpha particle-producing radionuclides of current interest in TAT include ^{225}Ac, ^{213}Bi, ^{212}Bi, and ^{211}At (Allen, 2008; Allen et al., 2014; Couturier et al., 2005; Dahle et al., 2011; Kim and Brechbiel, 2012; Kitson et al., 2013; Li et al., 2004; Morgenstern et al., 2018; Wadas et al., 2014; Wilbur, 2011; Yong and Brechbiel, 2015; Zalutsky et al., 2007). These radionuclides have branched decay chains that produce multiple short-lived daughters that generate alpha or beta emissions on the path to a stable isotope (Table 11.2).

TABLE 11.2 Common alpha-emitting therapeutic radionuclides.[a]

Nuclide	Approx. $t_{1/2}$, h	Decay pathway # α′s	Decay pathway # β′s	Stable end product
Ac-225	240	4	2	Bi-209
Bi-213	0.8	1	2	Bi-209
Pb-212 (Bi-212)[b]	10.6 (1.0)	1 (1)	2 (1)	Pb-206
At-211	7.2	1	0	Pb-207[c]

[a] *Decay data obtained from National Nuclear Data Center (2019).*
[b] *Generator allows for isolation of (Pb-212 + Bi-212) or Bi-212.*
[c] *Decay results in ~42% branching through Bi-207 ($t_{1/2} \approx 32$ a).*

Therapeutic alpha emitters are commercially available without preparation (^{225}Ac), as column-based generators (^{225}Ac/^{213}Bi; ^{224}Ra/^{212}Pb/^{212}Bi), and as cyclotron-bombarded metal targets (^{nat}Bi/^{211}At). Herein, we discuss some examples of fluidic automation applied to radionuclides used in TAT.

a. Bismuth-213

Although inorganic sorbents (as employed in the ^{90}Y generator system described above) may have advantages with regard to radiolytic stability over polymer-based sorbents (Marsh and Pillay, 1993; Pillay, 1986), organic extractants and resins often provide more versatility in their capacity and chemical selectivity for radioisotopes of interest. An automated, dual-column system to generate high-purity ^{213}Bi from a source of ^{225}Ac bound to a cation exchange polymer resin column has been demonstrated (Egorov and O'Hara, 2005). The ^{225}Ac was evenly distributed throughout two-thirds of a ~3 cm^3 cation exchange column. The lower one-third of the column was packed with cation exchange polymer resin that did not contain ^{225}Ac; this was to provide a "catch bed" to assure capture of any ^{225}Ac that might migrate from the upper resin bed during milking cycles. The ingrown ^{213}Bi daughter was periodically milked with strong HCl and captured on a small (0.12 cm^3) in-line anion exchange resin column. The purified ^{213}Bi was subsequently eluted with acetic acid. Ninety-two percent of the ^{213}Bi was recovered in the eluted fraction. Of this, 91% was successfully bound to CHX-A-HuM-195 monoclonal antibody to create the desired radiopharmaceutical. At the 3 mCi ^{225}Ac level, no radiolytic effects on the generator column were observed during a testing period of several days.

Polymer-based resins can also be used advantageously for on-demand separation of a daughter radionuclide of interest from a parent radionuclide stored in the liquid form, thus minimizing radiolytic degradation of the sorbent materials. Automation is particularly useful in this approach, where the high-activity parent is not kept stationary in a shielded column. Researchers at PNNL demonstrated an automated ^{225}Ac/^{213}Bi generator that utilized a polymeric anion exchange membrane disc to selectively capture ^{213}Bi, whereas ^{225}Ac was unretained and remained in solution (Bray et al., 2000; Egorov et al., 2000). The unbound ^{225}Ac parent was routed back to the storage vessel, whereas the ^{213}Bi product was subsequently stripped from the membrane disc using a sodium acetate solution that provided a chemical matrix that was directly suitable for subsequent labeling steps. This single-stage separation method with aqueous storage of the parent was performed at clinically relevant (~16 mCi) levels.

Dual-column separation processes using extraction chromatography resins have been demonstrated in the production of ^{213}Bi using a "multicolumn selectivity inversion generator" (Horwitz and Bond, 2003; McAlister and Horwitz, 2009). The generalized fluidic process scheme is shown in Fig. 11.34. The ^{225}Ac/^{213}Bi load solution is delivered using automated fluidics comprising two syringe pumps and three multiport valves (McAlister and Horwitz, 2009). The ^{225}Ac stock solution is passed through a primary column of UTEVA resin in HCl, where the ^{225}Ac is unretained while the ^{213}Bi is retained. The parent radionuclide is returned to a storage vessel, whereas the daughter is eluted from the primary column and passes unretained through a secondary column of cation exchange resin using a sodium chloride/sodium acetate buffer. The secondary column captures traces of the parent radionuclide and thus facilitates the required high decontamination factors between the parent/daughter radionuclides.

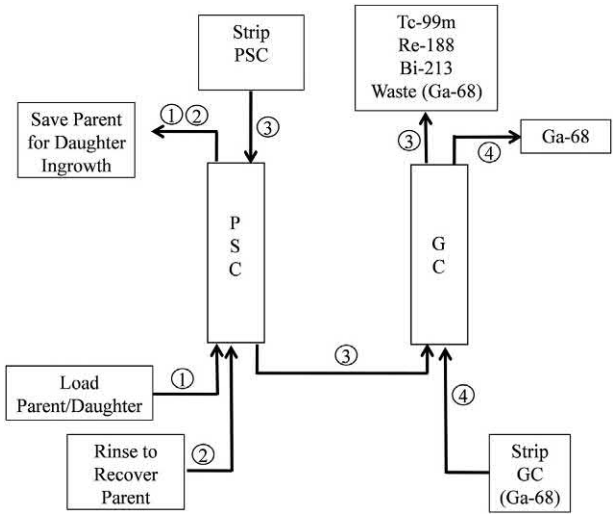


FIGURE 11.34 General schematic for multicolumn selectivity inversion generator for production of ^{99m}Tc from ^{99}Mo, ^{188}Re from ^{188}W, ^{213}Bi from ^{225}Ac, and ^{68}Ga from ^{68}Ge. *GC*, guard column; *PSC*, primary separation column. *Reproduced with permission from McAlister and Horwitz (2009). Copyright 2009 Elsevier.*

b. Lead/bismuth-212

The relatively simple ^{224}Ra/^{212}Pb (^{212}Bi) generator column system that was initially reported ~30 years ago is still in use today. The device employs a small column packed with macroporous cation exchange resin (BioRad MP-50). The ^{224}Ra is adsorbed in a distributed fashion throughout the resin bed, with a small non-^{224}Ra-bearing "catch bed" at the base of the column. Upon receipt of the generator at the point of use, the ^{212}Pb/^{212}Bi daughter products are periodically eluted with a small volume of 2 M HCl or 0.5 M HI. Alternatively, ^{212}Bi can be selectively eluted with 0.5 M HCl or 0.15 M HI (Atcher et al., 1988; Mirzadeh and Knapp, 1996).

Recently, Li et al. (2017) developed an automated cassette-based system that is capable of concentrating radio-Pb from the above-described generator column onto a concentrating column, then eluting it and subsequently labeling radio-Pb onto a DOTA-conjugated peptide. The system allows for purification of the labeled compound using HPLC. The process is adaptable to either ^{212}Pb (via the ^{224}Ra/^{212}Pb generator column) or a ^{203}Pb diagnostic source. When used sequentially or in combination, the $^{203/212}$Pb mixture can be used in theranostic applications.

Alternative ^{224}Ra/^{212}Pb (^{212}Bi) generator systems have been demonstrated on automated or semiautomated platforms. Bond et al. (2003) presented a prototype automated radionuclide separation system ("automated radionuclide separator") that was capable of isolating ^{212}Bi from ^{224}Ra. The fluidic system loaded a ^{224}Ra solution onto a Dipex resin column in 1 M HNO_3 and then washed the column with the same solution. The ^{212}Bi was retained on the column during load; ^{224}Ra had no retention and was recovered. Next, the isolated ^{212}Bi was eluted from the column using 2 M HCl.

More recently, Guseva (2007) described a tandem column generator process for delivery of purified ^{212}Pb from a ^{228}Ra source. While the process was not fully automated, the tandem columns were coupled inline, with reagents delivered via peristaltic pump. Therefore, the process could be easily adapted to automated fluid delivery by modern digital techniques. The primary generator column was packed with cation exchange resin (Dowex 50X8), and the secondary column was packed with anion exchange resin (Dowex 1X8). The ^{228}Ra parent stock was loaded onto the primary column with a small volume of dilute HNO_3 solution. Next, 0.5 M HBr or (0.5 M HBr/90% CH_3OH) was passed through both columns; ^{228}Ra remained bound, while ^{212}Pb/^{212}Bi was eluted and subsequently retained on the secondary column. After disconnecting the secondary column, the isolated ^{212}Pb/^{212}Bi could be eluted with a range of solutions that included water, NaCl, EDTA, or DTPA solutions. Chemical yields of ^{212}Pb ranged between 50% and ~98%, depending on the eluent solution employed.

c. Astatine-211

Astatine-211 (^{211}At) is a promising radionuclide for TAT (Guerard et al., 2013). Unlike the other commonly used TAT radionuclides that are prepared from generator columns, ^{211}At is produced by cyclotron. The primary production route is by accelerated α-beam bombardment of naturally monoisotopic ^{209}Bi metal (via the ^{209}Bi(α, 2n)^{211}At reaction) (Gagnon et al., 2012b; Zalutsky and Pruszynski, 2011). Two methods for the isolation of ^{211}At from Bi metal are predominantly in use. One method is dry distillation from molten Bi metal targets (Johnson et al., 1949; Lambrecht and Mirzadeh, 1985; Lindegren et al., 2001). The second method is chemical purification using wet chemistry, which involves dissolution of the Bi metal target followed by solvent extraction (Alliot et al., 2009; Balkin et al., 2013; Groppi et al., 2005; Neirinckx and Smit, 1973; Neumann, 1957; Sultana et al., 2000; Yordanov et al., 2004; Zona et al., 2008).

This radionuclide shows promise for the treatment of brain tumors (Zalutsky et al., 2008), breast cancer (Makvandi et al., 2016), synovial sarcoma (Keiko et al., 2018), lymphoma (Green et al., 2015), and ovarian cancer microtumors (Andersson et al., 2009; Bäck et al., 2016; Cederkrantz et al., 2015; Palm et al., 2016).

Recently, O'Hara et al. (2018b, 2019) developed an automated fluidic system to perform a complex method for ^{211}At isolation based on an approach used at the University of Washington (UW) Department of Radiation Oncology. The UW ^{211}At isolation process has been described in detail by Balkin et al. (2013). Once a cyclotron-bombarded Bi target is dissolved and chemically prepared for ^{211}At isolation, UW employs a solvent extraction process to separate ^{211}At from Bi ions. While the manual UW process is effective and robust, it is cumbersome (performed within a glovebox) and time-consuming and must be performed by a highly trained radiochemist. Conversion of the manual process to an inline automated platform would enable improved laboratory efficiency, assure consistent ^{211}At product characteristics between operators, and ultimately facilitate the wider use of this radionuclide at other hospitals in the United States.

Automated modules were engineered to perform each of five successive chemical processing steps:

(1) Bi target dissolution in HNO_3 solution;
(2) distillation of HNO_3 and subsequent dissolution of Bi salt residues in HCl solution;
(3) extraction of ^{211}At with diisopropyl ether (DIPE);
(4) repeated washings of the DIPE with HCl solution to remove residual Bi ions; and
(5) back-extraction of ^{211}At from the DIPE into ≤1 mL of NaOH solution.

The process is described subsequently in more detail.

First, the cyclotron-bombarded ^{nat}Bi target is sealed within a target dissolution block that facilitates inline dissolution of the Bi metal (Fig. 11.35) (O'Hara et al., 2017b). A target dissolving solution (10 M HNO_3) is pumped, via digital syringe pump, into a port at the base of the block; the dissolved ^{nat}Bi/^{211}At is then routed through an outlet port and into a distillation vessel. The reproducibility of the inline dissolution process on freshly bombarded Bi targets is shown in Fig. 11.36.

Next, the system remotely triggers a hot block and stir bar to distill the HNO_3 and leave a dry Bi nitrate salt

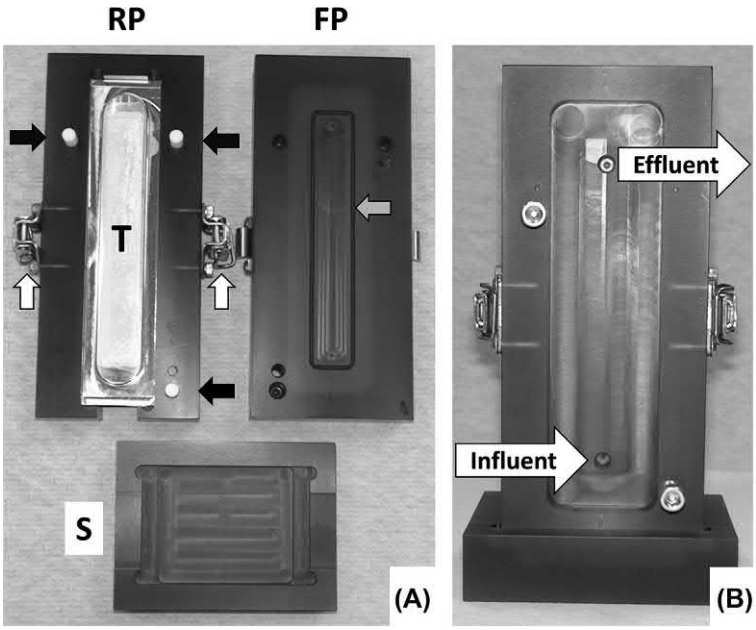


FIGURE 11.35 (A) Disassembled target dissolution block components comprising the rear panel (RP), into which a Bi target assembly (T) is inserted, the front panel (FP), and stand (S). *Black arrows* show Teflon guide rods, *gray arrow* shows the O-ring seal and HNO_3 flow channel within, and *white arrows* show fastening clamps. (B) Fully assembled dissolution block atop the stand showing reagent influent and effluent ports. *Reproduced with permission from O'Hara et al. (2017b). Copyright 2017 Elsevier.*

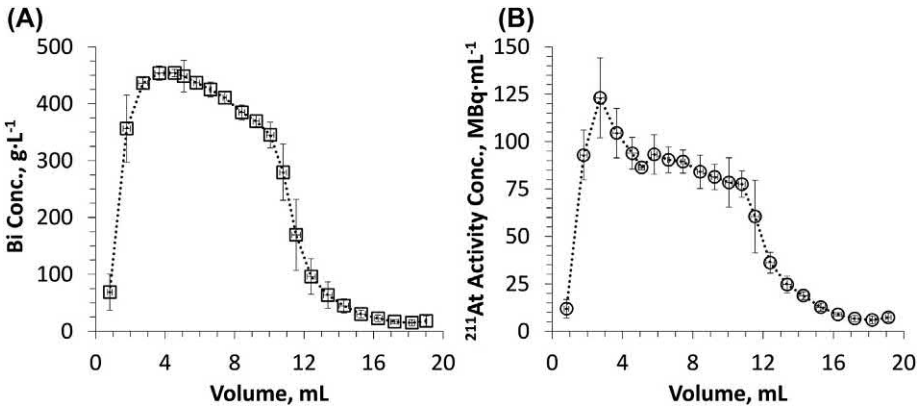


FIGURE 11.36 (A) Mean dissolution profile for quadruplicate cyclotron-bombarded ^{nat}Bi metal targets emerging from the target dissolution block. (B) Mean activity profiles for ^{211}At released from the same set of bombarded ^{nat}Bi targets. *Reproduced with permission from O'Hara et al. (2017b). Copyright 2017 Elsevier.*

residue. Once the salts are dry, the system turns off the hot block and toggles valves to allow chilled fluid to enter the hot block, thus quickly quenching heat from the block. Once the block is cooled, the salt cake is redissolved in 8 M HCl using repeated aspirate/dispense cycles from a syringe pump.

The acidic ^{nat}Bi/^{211}At solution is then processed through an automated solvent extraction system to obtain the isolated ^{211}At fraction. The system comprises three digital syringe pumps and two mixer/settler units. DIPE is used to extract ^{211}At into the organic phase; the non-extracted ^{nat}Bi in the aqueous phase is sent to waste. The DIPE solution is washed several times with fresh HCl to remove residual ^{nat}Bi, and the ^{211}At is finally back-extracted into 4 M NaOH. The automated solvent extraction process is accomplished using a mixing/settling approach, wherein aqueous/organic phases are simultaneously routed to a mixing tee and then through either a column packed with glass beads (acid/organic phase mixing) or a serpentine tubing reactor (organic/base phase mixing). The settler reservoirs, which collect the aqueous/organic phases after mixing, are fitted with sensors that enable the system to precisely determine the location of the liquid phase boundary so that each phase can be routed into its respective syringe pump at the conclusion of each cycle (Fig. 11.37) (O'Hara et al., 2017a, 2019).

To date, the automated fluidic system has demonstrated ^{211}At radiochemical yields and Bi decontamination factors that are indistinguishable from those obtained by the manual method. Additionally, the ^{211}At products possess the same distribution of chemical species and antibody labeling efficiency.

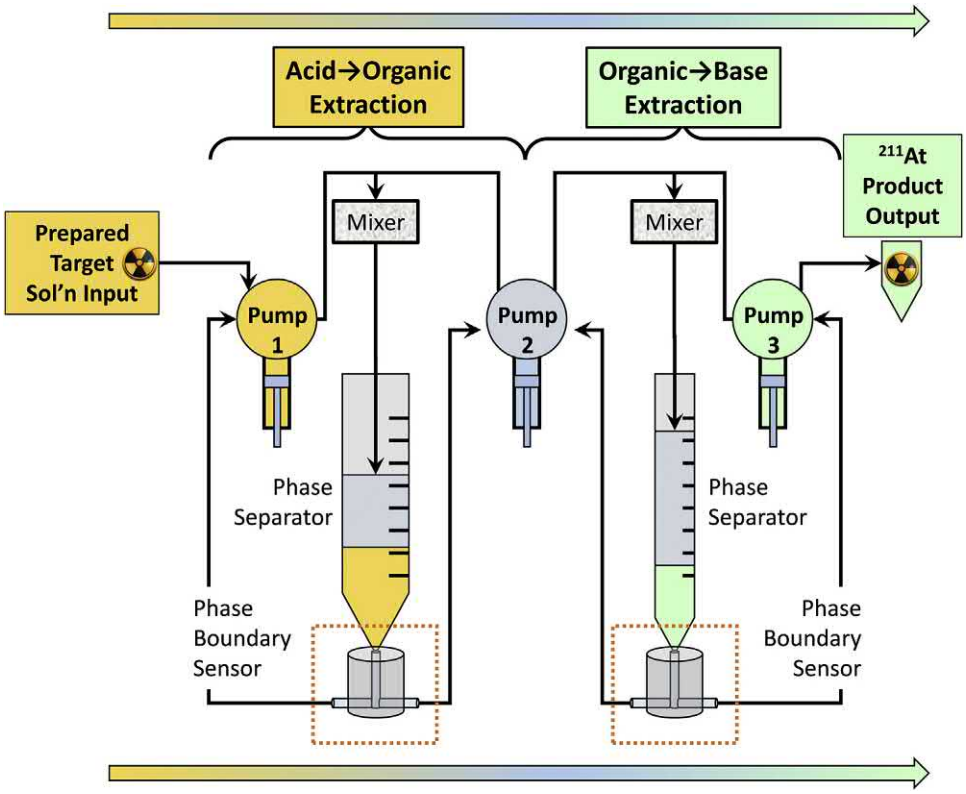


FIGURE 11.37 Fully automated solvent extraction system for isolation of ^{211}At from dissolved and chemically treated ^{nat}Bi targets. System performs ^{211}At load into DIPE from target solution, performs several washes of the DIPE in 8 M HCl to clean the DIPE, and finally performs a back-extraction to extract ^{211}At from the DIPE into 4 M NaOH. *Figure adapted from a conference poster presentation (O'Hara et al., 2017a).*

Recent work at Gothenburg University has been performed to automate the radiolabeling of ^{211}At onto antibodies (Aneheim et al., 2015a) via an electrophilic aromatic substitution reaction. Once the manual labeling method was adapted for use with a fluid handling system, a fully automated system for ^{211}At isolation and biomolecule labeling was devised (Aneheim et al., 2015b). The system employs a computer-controlled distillation and synthesis/purification component. The ^{211}At is dry distilled from the cyclotron-bombarded ^{nat}Bi metal target at ~ 700 °C, which is sufficient to melt the metal and volatilize ^{211}At; a carrier gas moves the ^{211}At vapor out of the furnace where it is condensed within a capillary tube within a cryotrap. A small volume of organic solvent (with oxidizer) elutes the ^{211}At from the capillary and transports it to a reaction vial. If the ^{211}At is eluted with a water-soluble solvent (methanol or ethanol), the labeling can proceed immediately. Otherwise, non−water-soluble solvents (chloroform) can be evaporated using an on-board heating element while under nitrogen flow, with subsequent resolubilization of the residue in an appropriate solvent. Next, labeling agents are added to the reaction vial, mixed with bubbling by nitrogen gas, and the reaction is quenched with the addition of sodium ascorbate. Finally, the astatinated compound is purified by injection onto a size exclusion column and sterilization filter. The system demonstrated astatinated immunoconjugate reactivities that were equivalent to those prepared via the manual method.

B. Diagnostic radionuclides

Radionuclides used in imaging applications are generally employed in either single photon emission computed tomography (SPECT) or positron emission tomography (PET), wherein the former category emits moderate-energy gamma radiation and the latter emits coincident 511 keV annihilation photons following positron emission (Pimlott and Sutherland, 2011; Rahmim and Zaidi, 2008; L'Annunziata, 2016). When tethered to molecular imaging agents, pathophysiological processes can be monitored noninvasively.

1. Gamma emitters

Certain gamma-emitting radionuclides are used in diagnostic and prognostic imaging via SPECT (Table 11.3). These radionuclides generally decay by electron capture or isomeric transition; their photon emissions range from 10's to 100's of keV (Pimlott and Sutherland, 2011). As ^{99m}Tc is available in generator formats, it has been the focus of automation applications; some examples will be discussed below.

TABLE 11.3 Common SPECT imaging radionuclides.[a]

Nuclide	Approx. $t_{1/2}$, h	Decay mode[b]	Principal photon emission, keV
Ga-67	78	ε	93/185/300
Tc-99m	6	IT	140
In-111	67	ε	171/245
I-123	13	ε	159
Tl-201	73	ε	167

[a]*Decay data obtained from National Nuclear Data Center (2019).*
[b]*IT, isomeric transition; ε, electron capture.*

a. Technetium-99m

Technetium-99m has been used as an SPECT isotope for decades and is considered to be the most widely employed diagnostic radionuclide (Rösch and Knapp, 2011; Synowiecki et al., 2018). While several methods have been employed to generate ^{99m}Tc from high specific activity ^{99}Mo, the acidic alumina column approach found the most popularity; the SPECT radionuclide is simply milked from the column using sterile saline (Banerjee et al., 2001). In the past decade, there has been a shift from producing the ^{99}Mo parent radionuclide from fissioned high-enriched U (HEU) targets to fissioned low-enriched U (LEU) targets (National Research Council, 2009) and through other production methods, such as proton bombardment of natural or enriched Mo targets (Bénard et al., 2014; Das et al., 2016; Gagnon et al., 2012a; IAEA, 2013).

Accelerator-based production of ^{99m}Tc from $^{natural/100}$Mo targets necessitates its chemical isolation from masses of Mo that are far greater than those found in HEU-produced ^{99}Mo (Das et al., 2016; Gumiela, 2018). Several research teams have been developing automated ^{99m}Tc generators that are capable of handling these larger Mo mass quantities. Some teams have designed automated systems for ^{99m}Tc separation from proton bombarded ^{100}Mo and ^{nat}Mo metal targets that are first dissolved in 30% hydrogen peroxide. Two examples are provided.

Morley et al. (2012) evaluated ^{99m}Tc isolation processes with Dowex 1X8 anion exchange and aqueous biphasic extraction chromatography (ABEC) resin columns. The system delivered the dissolved target through the separation column in a potassium hydroxide solution. After washing the column of residual Mo, the ^{99m}Tc was eluted with either tetrabutylammonium bromide (TBAB) in chloroform (anion exchange column) or water (ABEC column). With the ABEC column, the researchers found that they could deliver the ^{99m}Tc eluent solution through two additional columns placed inline with the primary column to obtain high-purity product: the first being an acidic cation exchange cartridge (for influent solution pH neutralization) and the second being an alumina cartridge (for secondary ^{99m}Tc capture). Finally, the ^{99m}Tc could be eluted from the alumina cartridge with saline. The two separation processes resulted in ~70% and ~90% ^{99m}Tc product yields for the anion exchange and ABEC resin columns, respectively.

Das et al. (2016) developed an automated fluidic system named TCM-AUTODOWNA for ^{99m}Tc isolation. The dissolved Mo target solution is made basic with ammonium carbonate and is passed through a Dowex 1X8 column. After washing the column with carbonate solution, the retained ^{99m}Tc is eluted with 4 M HNO_3. The eluent solution is routed to an inline flask positioned within a heated bath; the nitric acid is evaporated to yield a dried ^{99m}Tc residue. Following the drying step, saline is injected into the flask to dissolve the ^{99m}Tc residue, and finally the saline solution is routed through an acidic alumina column and membrane filter to obtain a purified ^{99m}Tc product.

The team of Martini et al. (2016) developed an automated ^{99m}Tc isolation module that employs solvent extraction instead of the more traditional column-based methods. Methyl ethyl ketone (MEK) is used to extract ^{99m}Tc from proton-bombarded ^{100}Mo targets that are dissolved in hydrogen peroxide and then made basic in strong sodium hydroxide solution. The dissolved target solution and the organic solvent are coinjected into a tall glass tube, and He gas is bubbled into the tube to affect phase mixing. After several minutes of mixing, the gas delivery is stopped, and the phases are allowed to settle. At this point, the ^{99m}Tc resides in the lighter organic phase. After collection of the organic phase from the separation column, it is passed through a silica SepPak cartridge, onto which the ^{99m}Tc is adsorbed from the organic phase. Following a second ^{99m}Tc extraction of the dissolved target phase with MEK and delivery of the postcontacted MEK to the SepPak cartridge, the ^{99m}Tc is eluted with a pure MEK solution that has not been previously contacted with sodium hydroxide solution. The SepPak cartridge eluent is in turn routed through an acidic alumina column, wherein ^{99m}Tc is once again adsorbed. Finally, the alumina column is washed with water, and the ^{99m}Tc eluted as a final product fraction with saline solution. The overall process results in a radiochemical yield of ~93%.

Other technologies that employ automated modules in the separation of ^{99m}Tc from $^{100/natural}$Mo targets can be found in the recent review by Gumiela (2018).

2. Positron emitters

Diagnostic imaging was significantly improved with the emergence of PET. The coincident detection of 511 keV photons produced during positron annihilation enables better spatial and temporal resolution and greater sensitivity

TABLE 11.4 Common positron emission tomography imaging radionuclides.[a]

Nuclide	Approx. $t_{1/2}$, min.	Emission type[b]	Annihilation photon intensity, %
C-11	20	β^+	200
N-13	10	β^+	199
F-18	110	β^+	193
Cu-64	762	β^+/ε, β^-	35
Ga-68	68	β^+/ε	178
Br-76	972	β^+/ε	109
Ru-82	1.3	β^+/ε	191
Zr-89	4705	β^+/ε	46
I-124	6013	β^+/ε	45

[a]*Decay data obtained from National Nuclear Data Center (2019).*
[b]β^-, *negatron;* β^+, *positron;* ε, *electron capture.*

than SPECT (Pimlott and Sutherland, 2011; L'Annunziata, 2016). Positron emitters are typically short-lived nuclides that must be produced via a nearby cyclotron (Olivier, 2004), separated from the target material, and then chemically incorporated into organic compounds (Conti and Eriksson, 2016; Miller, 2009). A few positron emitters, such as ^{89}Zr and ^{124}I, have half-lives measured in days (Table 11.4).

Alexoff (2005) and Krasikova (2007) have provided historical and current perspectives on the use of automation in the synthesis of PET radiopharmaceuticals. Systems for radiolabeling PET radiopharmaceuticals are needed to cope with the frequently very short-lived nuclides, in addition to dealing with radionuclides emitting high fluxes of 511 keV annihilation photons. Several papers describe the automated synthesis of specific PET radiopharmaceuticals (Krasikova, 2007; Marengo et al., 2008; Rahman et al., 2010; Scott and Shao, 2010; Tang et al., 2010). The most prevalent of these is 2-[^{18}F]fluoro-2-deoxy-D-glucose ([^{18}F]-FDG) (Yu, 2006), and platforms for this synthesis have been adapted to other radiopharmaceuticals.

a. Short-lived positron emitter gallium-68

Gallium-68 and ^{82}Rb are likewise used in PET, but these are unique in that they each have a moderately long-lived parent (Ballinger, 2009; Fani et al., 2008). They can be milked from a generator and therefore do not require a near- or on-site cyclotron.

McAlister and Horwitz (2009) have demonstrated an automated two-column generator system to elute ^{68}Ga from a ^{68}Ge liquid source using strong cation exchange and UTEVA columns in tandem (Fig. 11.34). The ^{68}Ge/^{68}Ga source is passed through a primary cation exchange column in 0.5 M HCl, where ^{68}Ge is unretained and ^{68}Ga is retained. After rinsing this column, the ^{68}Ga is eluted from the primary column using 4 M HCl; the primary column eluent solution is directed to the secondary column of UTEVA resin, where the ^{68}Ga is retained. Finally, the ^{68}Ga is eluted using 0.1 M HCl. Radiochemical yield was reported at 95%, with a 10^{-7}% ^{68}Ge impurity.

Gallium-68 is widely used to target/image somatostatin and other receptors by coupling it to peptides containing a 1,4,7,10-tetraazacyclododecane-1,4,7,10-tetraacetic acid (DOTA) conjugate. It, along with the therapeutic beta-emitting radionuclides ^{90}Y and ^{177}Lu, is emerging as promising radionuclide combinations for theranostic applications (Rösch and Baum, 2011; Weineisen et al., 2015; Werner et al., 2015). A number of semiautomated and automated ^{68}Ga DOTA peptide radiolabeling systems are commercially available at the present time; these systems have been recently reviewed by Boschi et al. (2013).

In the same year as Boschi's review, Schultz et al. (2013) described an automated fluid handling system to synthesize ^{68}Ga DOTATOC, a DOTA-conjugated somatostatin-targeting peptide. Gallium-68 was first eluted from a commercially available generator with dilute HCl; the eluted ^{68}Ga was captured on a strong cation exchange (SCX) cartridge and eluted, via syringe pump, with an HCl/NaCl mixture. The purified ^{68}Ga was injected slowly into a temperature-controlled vessel that contained buffer solution containing sodium acetate, ascorbic acid, and DOTATOC. The mixture was heated to 90 °C within the vessel for 400 seconds and then diluted with an aliquot of water, and the prepared solution was pumped through a filter for sterilization. The system was capable of preparing the radiolabeled peptide in <15 minutes, with 97−100% labeling efficiency. The specific activity was reported to be > 40 MBq·nmole^{-1}.

b. Long-lived positron emitters: zirconium-89 and iodine-124

Long-lived positron-emitting radionuclides have resulted in a new PET imaging modality referred to as ImmunoPET; this combines the specificity of monoclonal antibodies (mAbs) with the high resolution of PET to provide in vivo diagnostic imaging (Bailly et al., 2017; McCabe and Wu, 2010; van Dongen et al., 2007; Verel et al., 2005; Wright and Lapi, 2013). Targeted delivery with mAbs can take as many as 2−4 days (2−6 days for mAb fragments) to distribute in the body and establish maximum tumor to nontumor contrast (Verel et al., 2005). The coupling of long-lived positron emitters such as ^{89}Zr ($t_{1/2} \approx 3.3$ d) and ^{124}I ($t_{1/2} \approx 4.2$ d) to monoclonal antibodies enables PET imaging after immunochemically targeted delivery (Belov et al., 2011; Cascini et al., 2014; Holland et al., 2009; Verel et al., 2003a,b).

Several automated ^{89}Zr purification systems have been reported recently. Most systems employ a single hydroxamate resin column to isolate ^{89}Zr from dissolved cyclotron-bombarded ^{nat}Y targets, a method that was defined by Meijs et al. (1994) over two decades ago. The method was more recently defined as a standardized method by Holland et al. (2009). The hydroxamate resin is not commercially available but can be synthesized in house, as described by Verel et al. (2003a). Briefly, a cyclotron-bombarded ^{nat}Y target is dissolved in HCl, and the resulting solution is passed through a hydroxamate resin column, where ^{89}Zr is adsorbed. The ^{nat}Y is washed from the column using HCl, and then the HCl is removed from the column with water. Finally, ^{89}Zr is eluted with 1 M oxalic acid (a nearly saturated solution). Automated or semi-automated fluidic systems that have employed this standard method have been reported by Wooten et al. (2013), Poniger et al. (2014), Siikanen et al. (2012), and Lin et al. (2016).

O'Hara et al. (2018c) described a simple automated fluidic system (Fig. 11.38A) that injected a hydrochloric acid dissolver solution into a vessel containing a cyclotron-bombarded ^{nat}Y target. After target dissolution was complete, the solution was pushed through an inline filter and then passed through a hydroxamate resin column; the column was washed, and ^{89}Zr was then eluted using 0.8 M oxalic acid. Batch distribution coefficient (K_d) studies demonstrated that this lower concentration of oxalic acid resulted in a Zr K_d of <2 mL/g, which is sufficient to enable efficient ^{89}Zr elution. The reduced oxalic acid eluent concentration had the benefit of being further from the saturation point and also required less buffering salts to be added to the purified ^{89}Zr product prior to radiolabeling. The fluidic system was configured with an online radiometric detector to monitor all column effluents. Evaluation of the ^{89}Zr elution peak across several production runs indicated that 90% of the retained ^{89}Zr could be eluted in 1.02 ± 0.09 mL. Titrations of the resulting ^{89}Zr products with deferoxamine solutions indicated that ^{89}Zr product chemical purity was as good as that observed using the standardized method.

To improve the ^{89}Zr chemical purity, the fluidic platform was modified by O'Hara et al. (2018b) to accomplish a tandem column purification. To accomplish this, the fluidic system was expanded to a three-pump, three-valve system with configurations that allowed a separation process to occur on two columns separately and a configuration that enabled ^{89}Zr transfer from the primary column to a secondary column (Fig. 11.38B). The primary column was packed with an anion exchange resin (~ 0.83 cm^3), and the secondary microliter-scale column was packed with hydroxamate resin (~ 0.03 cm^3). The process was capable of good decontamination of iron, which is a major contaminant in ^{nat}Y foil targets and competes for binding sites with ^{89}Zr on deferoxamine-conjugated mAbs (O'Hara et al., 2018a). The ^{89}Zr product elution profiles were monitored by online radiochromatography to reveal that 90% of the product was contained within 0.29 ± 0.06 mL (Fig. 11.39). This resulted in a product that was ≥ 3.4 times more concentrated relative to the standardized method. Additionally, evaluation of the ^{89}Zr product quality by titration with deferoxamine indicated that the ^{89}Zr product purity was greater than that obtainable by the single hydroxamate resin column method.

Iodine-124 is produced through the cyclotron bombardment of an isotopically enriched $^{124}TeO_2$ target. The ^{124}I can subsequently be isolated from the target material through dry distillation (Fonslet and Koziorowski,

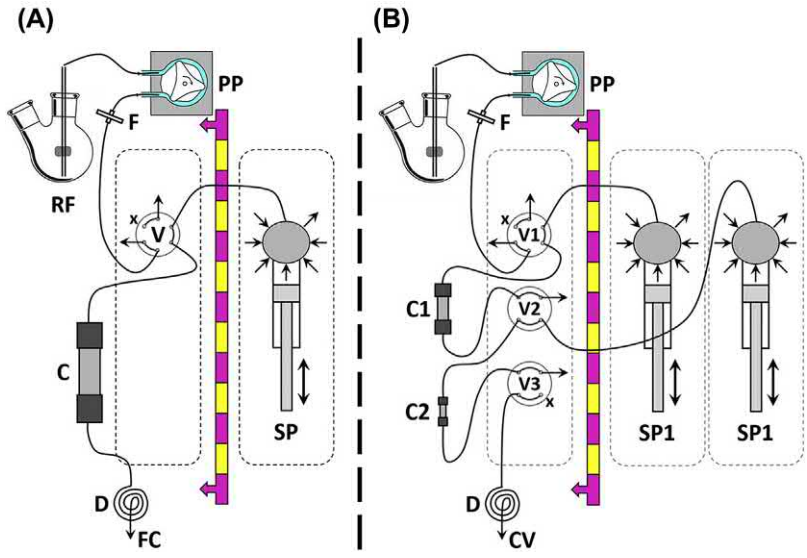


FIGURE 11.38 Fluidic systems for single-column isolation of ^{89}Zr from cyclotron-bombarded ^{nat}Y metal targets. (A) Two-pump, one-valve system that employs a single hydroxamate resin column. (B) Three-pump, three-valve fluidic system for tandem column-based isolation of ^{89}Zr from cyclotron-bombarded ^{nat}Y metal targets. System components include syringe pumps (SP), valves (V), columns (C), inline radiochromatography detector (D), product collection vial (CV), peristaltic pump (PP), and inline filter (F). *(A) Reproduced with permission from O'Hara et al. (2018c). Copyright 2018 Elsevier. (B) Reproduced with permission from O'Hara et al. (2018b). Copyright 2018 Elsevier.*

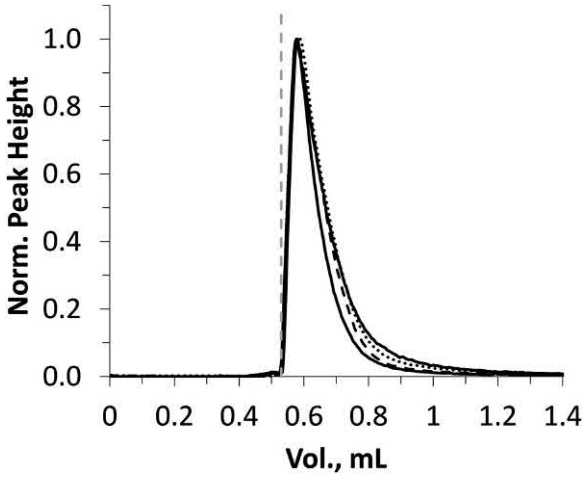


FIGURE 11.39 Quadruplicate radiochromatograms showing reproducible elution profiles for ^{89}Zr from the final stage of the tandem column ^{89}Zr purification system. *Figure reproduced with permission from O'Hara et al. (2018b). Copyright 2018 Elsevier.*

2013; IAEA, 2016). Poniger et al. (2012) have described a simple distillation system adapted from a commercially available unit (IBA Terimo). In comparison, Nagatsu et al. (2011) developed a complex automated system that combined target handling, dry distillation, and column-based purification steps. The authors have speculated on applying this same platform in the production of the SPECT isotope ^{123}I, using an enriched $^{123}TeO_2$ target.

X. Discussion

The techniques and examples above demonstrate that modern robotic, fluidic, and sensing technology can be used to develop automated workstations for radiochemical separation and/or analyses. If desired, many of the fluidic components and solutions can be located remotely from the radioactive samples and other hot sample processing zones.

There are many issues to address in developing automated radiochemical separations that perform reliably, time after time, in unattended operation. These are associated primarily with the separation and analytical chemistry aspects of the process. The relevant issues include the selectivity of the separation, decontamination factors, matrix effects, and recoveries from the separation column. In addition, flow rate effects, column lifetimes, carryover from one sample to another, and sample throughput must be considered. Nevertheless, successful approaches for addressing these issues have been developed.

Radiochemical separations and analyses are becoming increasingly important for applications outside the conventional analytical laboratory. Applications exist where radionuclides must be measured or manipulated in at-site or in situ settings. Monitors for nuclear waste processing operations represent an at-site application where continuous unattended monitoring is required to assure effective process radiochemical separations that produce waste streams that qualify for conversion to stable waste forms. Radionuclide sensors for water monitoring and long-term stewardship represent an application where at-site or in situ measurements will be most effective. Demonstrated automated radiochemical separation systems, analyzers, and sensors have shown that applications beyond the analytical laboratory are both possible and practical.

Automation is also becoming more essential in the isolation and purification of medical radioisotopes and for coupling them into radiopharmaceuticals for medical therapies and diagnostics. Here, the dangers of radiation and the short-lived nature of the radiopharmaceuticals motivate the use of automation. Automation improves safety, whether performing processes to create patient doses at a central facility, or at the point of care in a clinical setting. Automated point-of-care processing becomes especially attractive for short-lived radioisotopes. The current trends in this field are the combination of radionuclide isolation, purification, and radiopharmaceutical preparation into sequences; the maximum degree of automation; and control of quality. The use of modern separation materials to manage process complexity, and the consistent and reproducible operation of automated systems, will facilitate development of new radiopharmaceuticals and advancements in the field of theranostics.

Acknowledgments

The Pacific Northwest National Laboratory (PNNL) is a multiprogram national laboratory operated for the US Department of Energy (DOE) by Battelle Memorial Institute under contract number DE-AC05-76RL01830. The authors would like to acknowledge our collaboration with Sandia National Laboratory in developing digital microfluidic technology to the needs of radiochemical analysis, and specifically Michael S. Bartsch and Harrison Edwards.

References

Aldstadt, J.H., Kuo, J.M., Smith, L.L., Erickson, M.D., 1996. Determination of uranium by flow injection inductively coupled plasma mass spectrometry. Anal. Chim. Acta 319, 135–143.

Alexoff, D.L., 2005. Automation for the synthesis and application of PET radiopharmaceuticals. In: Welch, M.J., Redvanly, C.S. (Eds.), Handbook of Radiopharmaceuticals: Radiochemistry and Applications. John Wiley & Sons, Ltd., West Sussex, pp. 283–305.

Alfaro, J., Apfel, T., Diercks, H., Knochel, A., Gupta, R.S., Todter, K., 1995. Trace analysis of the radionuclides 90Sr and 89Sr in environmental samples III: development of a fast analytical method. Angew Chem. Int. Ed. Engl. 34, 186–189.

Allen, B.J., 2008. Clinical trials of targeted alpha therapy for cancer. Rev. Recent Clin. Trials 3 (3), 185–191.

Allen, B.J., Huang, C.-Y., Clarke, R.A., 2014. Targeted alpha anticancer therapies: update and future prospects. Biol. Targets Ther. 8, 255–267.

Alliot, C., Cherel, M., Barbet, J., Sauvage, T., Montavon, G., 2009. Extraction of astatine-211 in diisopropylether (DIPE). Radiochim. Acta 97 (3), 161−165.

Amano, H., Yanase, N., 1990. Measurement of 90Sr in environmental samples by cation-exchange and liquid scintillation counting. Talanta 37, 585−590.

Andersson, H., et al., 2009. Intraperitoneal α-particle radioimmunotherapy of ovarian cancer patients: pharmacokinetics and dosimetry of ^{211}At-MX35 F(ab′)$_2$—a phase I study. J. Nucl. Med. 50 (7), 1153−1160.

Aneheim, E., Jensen, H., Albertsson, P., Lindegren, S., 2015a. Astatine-211 labeling: a study towards automatic production of astatinated antibodies. J. Radioanal. Nucl. Chem. 303 (1), 979−983.

Aneheim, E., Albertsson, P., Bäck, T., Jensen, H., Palm, S., Lindegren, S., 2015b. Automated astatination of biomolecules − a stepping stone towards multicenter clinical trials. Sci. Rep. 5, 1−11.

Apostolidis, C., Molinet, R., Richir, P., Ougier, M., Mayer, K., 1998. Development and validation of a simple, rapid, and robust method for the chemical separation of uranium and plutonium. Radiochim. Acta 83 (1), 21−25.

Atcher, R.W., Friedman, A.M., Hines, J.J., 1988. An improved generator for the production of ^{212}Pb and ^{212}Bi from ^{224}Ra. Int. J. Radiat. Appl. Instrum. A Appl. Radiat. Isot. 39 (4), 283−286.

Auer, M., Kumberg, T., Sartorius, H., Wernsperger, B., Schlosser, C., 2010. Ten years of development of equipment for measurement of atmospheric radioactive xenon for the verification of the CTBT. Pure Appl. Geophys. 167 (4), 471-486-486.

Avivar, J., Ferrer, L., Casas, M., Cerda, V., 2011. Smart thorium and uranium determination exploiting renewable solid-phase extraction applied to environmental samples in a wide concentration range. Anal. Bioanal. Chem. 400 (10), 3585−3594.

Avivar, J., Ferrer, L., Casas, M., Cerda, V., 2012. Fully automated lab-on-valve-multisyringe flow injection analysis-ICP-MS system: an effective tool for fast, sensitive and selective determination of thorium and uranium at environmental levels exploiting solid phase extraction. J. Anal. At. Spectrom. 27 (2), 327−334.

Bäck, T.A., Chouin, N., Lindegren, S., Kahu, H., Jensen, H., Albertsson, P., Palm, S., 2016. Cure of human ovarian carcinoma solid xenografts by fractionated [^{211}At] alpha-radioimmunotherapy: influence of tumor absorbed dose and effect on long-term survival. J. Nucl. Med. 116, 598−604.

Bailly, C., et al., 2017. Immuno-pet for clinical theranostic approaches. Int. J. Mol. Sci. 18 (1), 57.

Balkin, E.R., Hamlin, D.K., Gagnon, K., Chyan, M.-K., Pal, S., Watanabe, S., Wilbur, D.S., 2013. Evaluation of a wet chemistry method for isolation of cyclotron produced [^{211}At]astatine. Appl. Sci. 3 (3), 636−655.

Ballinger, J.R., 2009. In: Movahed, A., Gnanasegaran, G., Buscombe, J., Hall, M. (Eds.), PET Radiopharmaceuticals in Nuclear Cardiology: Current Status and Limitations Integrating Cardiology for Nuclear Medicine Physicians. Springer Berlin Heidelberg, pp. 379−385.

Banerjee, S., Ambikalmajan Pillai, M.R., Ramamoorthy, N., 2001. Evolution of Tc-99m in diagnostic radiopharmaceuticals. Semin. Nucl. Med. 31 (4), 260−277.

Banerjee, S., Pillai, M.R.A., Knapp, F.F., 2015. Lutetium-177 therapeutic radiopharmaceuticals: linking chemistry, radiochemistry, and practical applications. Chem. Rev. 115 (8), 2934−2974.

Beasley, T.M., Kelley, J.M., Maiti, T.C., Bond, L.A., 1998. Np-237/Pu-239 atom ratios in integrated global fallout: a reassessment of the production of Np-237. J. Environ. Radioact. 38 (2), 133−146.

Belov, V.V., Bonab, A.A., Fischman, A.J., Heartlein, M., Calias, P., Papisov, M.I., 2011. Iodine-124 as a label for pharmacological PET imaging. Mol. Pharm. 8 (3), 736−747.

Beltran, B., Avivar, J., Mola, M., Ferrer, L., Cerda, V., Leal, L.O., 2013. Automated method for simultaneous lead and strontium isotopic analysis applied to rainwater samples and airborne particulate filters (PM10). Environ. Sci. Technol. 47 (17), 9850−9857.

Bénard, F., et al., 2014. Implementation of multi-curie production of ^{99m}Tc by conventional medical cyclotrons. J. Nucl. Med. 55 (6), 1017−1022.

Benkhedda, K., Epov, V.N., Evans, R.D., 2005a. Flow-injection technique for determination of uranium and thorium isotopes in urine by inductively coupled plasma mass spectrometry. Anal. Bioanal. Chem. 381 (8), 1596−1603.

Benkhedda, K., Lariviere, D., Scott, S., Evans, D., 2005b. Hyphenation of flow-injection preconcentration and ICP-MS for the rapid determination of 226Ra in natural waters. J. Anal. At. Spectrom. 20, 523−528.

Beugelsdijk, T.J., Hollen, R.M., 1998. Robotics and automation in radiochemical analysis. In: L'Annunziata, M.F. (Ed.), Handbook of Radioactivity Analysis, first ed. Academic Press, San Diego, CA, pp. 693−718.

Bickel, M., Holmes, L., Janzon, C., Koulouris, G., Pilvo, R., Slowikowski, B., Hill, C., 2000. Radiochemistry: inconvenient but indispensable. Appl. Radiat. Isot. 53, 5−11.

Bischoff, J.L., Wooden, J., Murphy, F., Williams, R.W., 2005. U/Th dating by SHRIMP RG ion-microprobe mass spectrometry using single ion-exchange beads. Geochim. Cosmochim. Acta 69 (7), 1841−1846.

Bliznyuk, V.N., Seliman, A.F., Husson, S.M., Lvov, Y.M., DeVol, T.A., 2018. Hybrid nanoparticle-polymer brush composites for detection of low-level radiostrontium in water. Macromol. Mater. Eng. 303 (6).

Bliznyuk, V.N., Duval, C.E., Apul, O.G., Seliman, A.F., Husson, S.M., DeVol, T.A., 2015. High porosity scintillating polymer resins for ionizing radiation sensor applications. Polymer 56, 271−279.

Bond, A.H., Horwitz, E.P., Hines, J.J., Young, J.E., 2003. A compact automated radionuclide separation system for nuclear medical applications. Czech. J. Phys. 53 (1), A717−A723.

Borcherding, J., Nies, H., 1986. An improved method for the determination of 90Sr in large samples of seawater. J. Radioanal. Nucl. Chem. 98, 127−131.

Boros, E., Packard, A.B., 2018. Radioactive transition metals for imaging and therapy. Chem. Rev. https://doi.org/10.1021/acs.chemrev.8b00281.

Boschi, A., Uccelli, L., Pasquali, M., Duatti, A., Taibi, A., Pupillo, G., Esposito, J., 2014. ^{188}W/^{188}Re generator system and its therapeutic applications. J. Chem. (Hindawi Online) 2014, 14.

Boschi, S., Lodi, F., Malizia, C., Cicoria, G., Marengo, M., 2013. Automation synthesis modules review. Appl. Radiat. Isot. 76 (0), 38−45.

Bowyer, T.W., Abel, K.H., Hubbard, C.W., Panisko, M.E., Reeder, P.L., Thompson, R.C., Warner, R.A., 1999. Field testing of collection and measurement of radioxenon for the comprehensive test ban treaty. J. Radioanal. Nucl. Chem. 240 (1), 109−122.

Brandalise, B., Ougier, M., Wellum, R., Wojnowski, D., Koch, L., 1994. Robotized equipment for the on-site analysis of fissile material. In: International Nuclear Safeguards 1994 Vision for the Future. International Atomic Energy Association, Vienna, pp. 755–760.

Bray, L.A., Tingey, J.M., DesChane, J.R., Egorov, O.B., Tenforde, T.S., Wilbur, D.S., Hamlin, D.K., Pathare, P.M., 2000. Development of a unique bismuth (Bi-213) automated generator for use in cancer therapy. Ind. Eng. Chem. Res. 39 (9), 3189–3194.

Browne, E., Firestone, R.B., 1986. Table of Radioactive Isotopes. John Wiley & Sons, New York.

Bruckner-Lea, C.J., Stottlemyre, M.S., Holman, D.A., Grate, J.W., Brockman, F.J., Chandler, D.P., 2000. Rotating rod renewable microcolumns for automated, solid-phase DNA hybridization studies. Anal. Chem. 72 (17), 4135–4141.

Bu, W.T., Zheng, J., Guo, Q.J., Aono, T., Tagami, K., Uchida, S., Tazoe, H., Yamada, M., 2014. Ultra-trace plutonium determination in small volume seawater by sector field inductively coupled plasma mass spectrometry with application to Fukushima seawater samples. J. Chromatogr. A 1337, 171–178.

Burge, S.R., May, J., 2005. Automated ground water sampling and analysis of trichloroethene using a "universal" sampling/analytical system. Gr. Water Monit. Remediat. 25 (1), 113–122.

Burge, S.R., Hoffman, D.A., Hartman, M.J., Venedam, R.J., 2005. Automated ground-water sampling and analysis of hexavalent chromium using a "universal" sampling/analytical system. Sensors 5 (1–2), 38–50.

Cao, L.G., Bu, W.T., Zheng, J., Pan, S.M., Wang, Z.T., Uchida, S.G., 2016. Plutonium determination in seawater by inductively coupled plasma mass spectrometry: a review. Talanta 151, 30–41.

Cascini, G.L., Niccoli Asabella, A., Notaristefano, A., Restuccia, A., Ferrari, C., Rubini, D., Altini, C., Rubini, G., 2014. ^{124}Iodine: a longer-life positron emitter isotope - new opportunities in molecular imaging. BioMed Res. Int. 7, 2014.

Cederkrantz, E., Andersson, H., Bernhardt, P., Back, T., Hultborn, R., Jacobsson, L., 2015. Absorbed doses and risk estimates of (211)At-MX35 F(ab′)$_2$ in intraperitoneal therapy of ovarian cancer patients. Int. J. Radiat. Oncol. Biol. Phys. 93.

Cerda, A., Estala, J.M., Forteza, R., Cladera, A., Becerra, E., Altimira, P., Sitjar, P., 1999. Flow techniques in water analysis. Talanta 50, 695–705.

Cerda, V., Cerda, A., Cladera, A., Oms, M.T., Mas, F., Gomez, E., Bauza, F., Miro, M., Forteza, R., Estela, J.M., 2001. Monitoring of environmental parameters by sequential injection analysis. Trends Anal. Chem. 20 (8), 407–418.

Cerda, V., Ferrer, L., Portugal, L.A., de Souza, C.T., Ferreira, S.L.C., 2018. Multisyringe flow injection analysis in spectroanalytical techniques - a review. Trac. Trends Anal. Chem. 98, 1–18.

Chen, B.Y., Xu, S., Cook, G.T., Freeman, S., Hou, X.L., Liu, C.Q., Naysmith, P., Yamaguchi, K., 2017. Local variance of atmospheric C-14 concentrations around Fukushima Dai-ichi nuclear power plant from 2010 to 2012. J. Radioanal. Nucl. Chem. 314 (2), 1001–1007.

Choi, K., Ng, A.H.C., Fobel, R., Wheeler, A.R., 2012. Digital microfluidics. Annu. Rev. Anal. Chem. 5 5, 413–440.

Choppin, G.R., 1984-85. Separation processes for actinide elements. Separ. Sci. Technol. 19, 911–925.

Christian, G.D., 1994. Sequential injection analysis for electrochemical measurements and process analysis. Analyst 119, 2309–2314.

Chung, K.H., Do Choi, S., Choi, G.S., Kang, M.J., 2013. Design and performance of an automated radionuclide separator: its application on the determination of Tc-99 in groundwater. Appl. Radiat. Isot. 81, 57–61.

Cobb, J., Warwick, P., Carpenter, R.C., Morrison, R.T., 1994. Determination of strontium-90 in water and urine samples using ion chromatography. Analyst 119, 1759–1764.

Colodner, D., Salters, V., Duckworth, D.C., 1994. Ion sources for analysis of inorganic solids and liquids by MS. Anal. Chem. 66, 1079A–1089A.

Conti, M., Eriksson, L., 2016. Physics of pure and non-pure positron emitters for PET: a review and a discussion. EJNMMI Phys. 3, 8.

Cortina, J.L., Warshawsky, A., 1997. Developments in solid-liquid extraction by solvent-impregnated resins. Ion Exch. Solvent Extr. 13, 195–293.

Couturier, O., Supiot, S., Degraef-Mougin, M., Faivre-Chauvet, A., Carlier, T., Chatal, J.F., Davodeau, F., Cherel, M., 2005. Cancer radioimmunotherapy with alpha-emitting nuclides. Eur. J. Nucl. Med. Mol. Imaging 32 (5), 601–614.

Crain, J.S., Alvarado, J., 1994. Hydride interference on the determination of minor actinide isotopes by inductively coupled plasma mass spectrometry. J. Anal. At. Spectrom. 9, 1223–1227.

Cutler, C.S., Hennkens, H.M., Sisay, N., Huclier-Markai, S., Jurisson, S.S., 2013. Radiometals for combined imaging and therapy. Chem. Rev. 113 (2), 858–883.

Dahle, J., Abbas, N., Bruland, O.S., Larsen, R.H., 2011. Toxicity and relative biological effectiveness of alpha emitting radioimmunoconjugates. Curr. Radiopharm. 4 (4), 321–328.

Dai, M.H., Buesseler, K.O., Kelley, J.M., Andrews, J.E., Pike, S., Wacker, J.F., 2001. Size-fractionated plutonium isotopes in a coastal environment. J. Environ. Radioact. 53 (1), 9–25.

Dai, M., Buesseler, K.O., Pike, S., 2002a. Plutonium in groundwater at the 100K-area of the U.S. DOE Hanford site. J. Contam. Hydrol. 76, 167–189.

Dai, M., Kelley, J.M., Buesseler, K.O., 2002b. Sources and migration of plutonium in groundwater at the Savannah river site. Environ. Sci. Technol. 36 (17), 3690–3699.

Das, M.K., Madhusmita, Chattopadhyay, S., Das, S.S., Barua, L., Neyar, M.A., Kumar, U., De, A., 2016. Production and separation of ^{99m}Tc from cyclotron irradiated $^{100/natural}$Mo targets: a new automated module for separation of ^{99m}Tc from molybdenum targets. J. Radioanal. Nucl. Chem. 310 (1), 423–432.

Dash, A., Chakravarty, R., 2014. Electrochemical separation: promises, opportunities, and challenges to develop next-generation radionuclide generators to meet clinical demands. Ind. Eng. Chem. Res. 53 (10), 3766–3777.

Denoyer, E.R., 1992. Expanding ICP-MS capabilities using flow injection. Am. Lab. 24, 74–82.

Deron, S., Donohue, D., Bagliano, G., Kuhn, E., Sirisena, K., 1994. The IAEA's analytical capabilities for safeguards. In: International Nuclear Safeguards 1994 Vision for the Future. International Atomic Energy Association, Vienna, pp. 717–738.

Desmartin, P., Kopajtic, Z., Haerdi, W., 1997. Radiostrontium-90 (Sr-90) ultra-trace measurements by coupled ion chromatography (HPIC) and on-line liquid scintillation measurements. Environ. Monit. Assess. 44 (1–3), 413–423.

DeVol, T.A., Roane, J.E., Williamson, J.M., Duffey, J.M., Harvey, J.T., 2000. Development of scintillating extraction media for separation and

measurement of charged-particle-emitting radionuclides in aqueous solutions. Radioact. Radiochem. 11 (1), 34–46.

DeVol, T.A., Duffey, J.M., Paulenova, A., 2001a. Combined extraction chromatography and scintillation detection for off-line and on-line monitoring of strontium in aqueous solutions. J. Radioanal. Nucl. Chem. 249 (2), 295–301.

DeVol, T.A., Egorov, O.B., Roane, J.E., Paulenova, A., Grate, J.W., 2001b. Extractive scintillating resin for 99Tc quantification in aqueous solutions. J. Radioanal. Nucl. Chem. 249 (1), 181–189.

Dietz, M.L., Horwitz, E.P., Nelson, S.M., Wahlgren, M., 1991. An improved method for determining 89Sr and 90Sr in urine. Health Phys. 61, 871–877.

Dietz, M.L., Horwitz, E.P., 1993. Novel chromatographic materials based on nuclear waste processing chemistry. LC GC 11, 424–436.

Dietz, M.L., Horwitz, E.P., Bond, A.H., 1999. Extraction Chromatography: Progress and Opportunities. In: ACS Symp. Ser. 716(Metal Ion Separation and Preconcentration: Progress and Opportunities), pp. 234–250.

Dockendorff, B., Holman, D.A., Christian, G.D., Ruzicka, J., 1998. Automated solid phase extraction of theophylline by sequential injection on renewable column. Anal. Commun. 35 (11), 357–359.

Duval, C.E., DeVol, T.A., Husson, S.M., 2016a. Extractive scintillating polymer sensors for trace-level detection of uranium in contaminated ground water. Anal. Chim. Acta 947, 1–8.

Duval, C.E., DeVol, T.A., Husson, S.M., 2016b. Evaluation of resin radius and column diameter for the implementation of extractive scintillating resin in flow-cell detectors. J. Radioanal. Nucl. Chem. 307 (3), 2253–2258.

Duval, C.E., DeVol, T.A., Wade, E.C., Seliman, A.F., Bliznyuk, V.N., Husson, S.M., 2016c. Stability of polymeric scintillating resins developed for ultra-trace level detection of alpha- and beta-emitting radionuclides. J. Radioanal. Nucl. Chem. 310 (2), 583–588.

Egorov, O., Ruzicka, J., 1995. Flow injection renewable fiber optic sensor system. Principle and validation on spectrophotometry of chromium(VI). Analyst 120, 1959–1962.

Egorov, O., Grate, J.W., Ruzicka, J., 1998a. Automation of radiochemical analysis by flow injection techniques: Am-Pu separation using TRU-resin(sorbent extraction column. J. Radioanal. Nucl. Chem. 234, 231–235.

Egorov, O.B., O'Hara, M.J., Ruzicka, J., Grate, J.W., 1998b. Sequential injection system with stopped flow radiometric detection for automated analysis of 99Tc in nuclear waste. Anal. Chem. 70, 977–984.

Egorov, O., O'Hara, M.J., Grate, J.W., Ruzicka, J., 1999a. Sequential injection renewable separation column instrument for automated sorbent extraction separations of radionuclides. Anal. Chem. 71, 345–352.

Egorov, O.B., Fiskum, S.K., O'Hara, M.J., Grate, J.W., 1999b. Radionuclide sensors based on chemically selective scintillating microspheres: renewable column sensor for analysis of 99Tc in water. Anal. Chem. 71 (23), 5420–5429.

Egorov, O.B., Grate, J.W., Bray, L.A., 2000. Method for Sequential Injection of Liquid Samples for Radioisotope Separations. USA Patent 6,153,154.

Egorov, O.B., O'Hara, M.J., Farmer III, O.T., Grate, J.W., 2001. Extraction chromatographic separations and analysis of actinides using sequential injection techniques with on-line inductively coupled plasma mass spectrometry (ICP MS) detection. Analyst 126 (9), 1594–1601.

Egorov, O., O'Hara, M.J., Grate, J.W., 2002a. Radionuclide Selective Sensors for Water Monitoring: 99Tc(VII) Detection in Hanford Groundwater. Paper presented at Spectrum 2002. American Nuclear Society, La Grange Park, Ill, Reno, NV.

Egorov, O., O'Hara, M., Grate, J.W., 2002b. Automation of the radiochemical analysis: from groundwater monitoring to nuclear waste analysis. In: Abstracts of Papers, 223rd ACS National Meeting, Orlando, FL, United States, April 7-11, 2002, NUCL-062.

Egorov, O.B., O'Hara, M.J., 2003. Development and Testing of the Automated 99Tc Monitor. Final Report, PNWD-3327. Battelle, Pacific Northwest Division, Richland, WA.

Egorov, O.B., O'Hara, M.J., Grate, J.W., 2004a. Microwave-assisted sample treatment in a fully automated flow-based instrument: oxidation of reduced technetium species in the analysis of total technetium-99 in caustic aged nuclear waste samples. Anal. Chem. 76, 3869–3877.

Egorov, O.B., O'Hara, M.J., Addleman, R.S., Grate, J.W., 2004b. Automation of radiochemical analysis: from groundwater monitoring to nuclear waste analysis. ACS Symp. Ser. 868, 246–270 (Radioanalytical Methods in Interdisciplinary Research).

Egorov, O.B., O'Hara, M.J., December 6, 2005. Method and Apparatus for Production of ^{213}Bi from a High Activity ^{225}Ac Source. USA Patent 6,972,414.

Egorov, O., O'Hara, M.J., Grate, J.W., 2005a. Automated radiochemical analysis of total Tc-99 in aged nuclear waste processing streams. J. Radioanal. Nucl. Chem. 263, 629–633.

Egorov, O.B., O'Hara, M.J., Grate, J.W., Knopf, M., Anderson, G., Hartman, J., 2005b. Radiochemical sensor system for the analysis of 99Tc(VII) in groundwater. J. Radioanal. Nucl. Chem. 264, 495–500.

Egorov, O.B., O'Hara, M.J., Grate, J.W., 2006. Equilibration-based preconcentrating minicolumn sensors for trace level monitoring of radionuclides and metal ions in water without consumable reagents. Anal. Chem. 78, 5480–5490.

Egorov, O.B., O'Hara, M.J., Grate, J.W., 2012. Automated radioanalytical system incorporating microwave-assisted sample preparation, chemical separation, and on–line radiometric detection for the determination of total 99Tc in nuclear waste processing streams. Anal. Chem. 84, 3090–3098.

Enge, T.G., Field, M.P., Jolley, D.F., Ecroyd, H., Kim, M.H., Dosseto, A., 2016. An automated chromatography procedure optimized for analysis of stable Cu isotopes from biological materials. J. Anal. At. Spectrom. 31 (10), 2023–2030.

Epov, V.N., Benkhedda, K., Cornett, R.J., Evans, R.D., 2005a. Rapid determination of plutonium in urine using flow injection on-line preconcentration and inductively coupled plasma mass spectrometry. J. Anal. At. Spectrom. 20 (5), 424–430.

Epov, V.N., Benkhedda, K., Brownell, D., Cornett, R.J., Evans, R.D., 2005b. Comparative study of three sample preparation approaches for the fast determination of americium in urine by flow injection ICP-MS. Can. J. Anal. Sci. Spectrosc. 50 (1), 14–22.

Epov, V.N., Evans, R.D., Zheng, J., Donard, O.F.X., Yamada, M., 2007. Rapid fingerprinting of Pu-239 and Pu-240 in environmental samples with high U levels using on-line ion chromatography coupled with high-sensitivity quadrupole ICP-MS detection. J. Anal. At. Spectrom. 22 (9), 1131–1137.

Erxleben, H., Ruzicka, J., 2005. Sequential affinity chromatography miniaturized within a "lab-on-valve" system. Analyst 130 (4), 469–471.

Fajardo, Y., Gomez, E., Mas, F., Garcias, F., Cerda, V., Casas, M., 2004. Multisyringe flow injection analysis of stable and radioactive strontium in samples of environmental interest. Appl. Radiat. Isot. 61 (2–3), 273–277.

Fajardo, Y., Gomez, E., Garcias, F., Cerda, V., Casas, M., 2005. Multisyringe flow injection analysis of stable and radioactive yttrium in water and biological samples. Anal. Chim. Acta 539 (1–2), 189–194.

Fajardo, Y., Avivar, J., Ferrer, L., Gomez, E., Casas, M., Cerda, V., 2010. Automation of radiochemical analysis by applying flow techniques to environmental samples. Trac. Trends Anal. Chem. 29 (11), 1399–1408.

Fang, Z., 1993. Flow Injection Separation and Preconcentration. VCH, Weinheim.

Fani, M., André, J.P., Maecke, H.R., 2008. ^{68}Ga-PET: a powerful generator-based alternative to cyclotron-based PET radiopharmaceuticals. Contrast Media Mol. Imaging 3 (2), 53–63.

Fassett, J.D., Kelly, W.R., 1984. Interlaboratory isotopic ratio measurement of nanogram quantities of uranium and plutonium on resin beads by thermal ionization mass spectrometry. Anal. Chem. 56, 550–556.

Fisher, D.R., 2008. Commercial availability of alpha-emitting radionuclides for medicine. Curr. Radiopharm. 1, 127–134.

Fiskum, S.K., Riley, R.G., Thompson, C.J., 2000. Preconcentration and analysis of strontium-90 and technetium-99 from Hanford groundwater using solid phase extraction. J. Radioanal. Nucl. Chem. 245 (2), 261–272.

Fonslet, J., Koziorowski, J., 2013. Dry distillation of radioiodine from TeO_2 targets. Appl. Sci. 3 (4), 675–683.

Fourie, H.O., Ghijsels, J.P., 1969. Radiostrontium in biological material: a precipitation and extraction procedure eliminating the use of fuming nitric acid. Health Phys. 17, 685–689.

Gaggeler, H.W., 1997. Fast chemical separation procedures for transactinides. In: Proceedings of the Robert A. Welch Foundation, 41st Conferences on Chemical Research, the Transactinide Elements. The Robert A. Welch Foundation, Houston, Texas, pp. 43–63.

Gagnon, K., Wilson, J.S., Holt, C.M.B., Abrams, D.N., McEwan, A.J.B., Mitlin, D., McQuarrie, S.A., 2012a. Cyclotron production of ^{99m}Tc: recycling of enriched ^{100}Mo metal targets. Appl. Radiat. Isot. 70 (8), 1685–1690.

Gagnon, K., Risler, R., Pal, S., Hamlin, D., Orzechowski, J., Pavan, R., Zeisler, S., Wilbur, D.S., 2012b. Design and evaluation of an external high-current target for production of ^{211}At. J. Label. Comp. Radiopharm. 55 (12), 436–440.

Garcia Alonso, J.I., 1995. Determination of fission products and actinides by inductively coupled plasma mass spectrometry using isotope dilution analysis: a study of random and systematic errors. Anal. Chim. Acta 312, 57–78.

Garcia Alonso, J.I., Babelot, J.-F., Glatz, J.-P., cromboon, O., Koch, L., 1993. Applications of glove-box ICP-MS for the analysis of nuclear materials. Radiochim. Acta 62, 71–79.

Garcia Alonso, J.I., Sena, R., Arbore, P., Betti, M., Koch, L., 1995. Determination of fission products and actinides in spent nuclear fuels by isotope dilution Ion chromatography inductively coupled plasma mass spectrometry. J. Anal. At. Spectrom. 10, 381–393.

Gattavecchia, e., Tonelli, D., 1991. Determination of 90Sr by thin layer radiochromatography. J. Radioanal. Nucl. Chem. 152, 391–399.

Godoy, M.L.D.P., Godoy, J.M., Kowsmann, R., Santos, G.M., Cruz, R.P., 2006. 234U and 230Th determination by FIA-ICP-MS and application to uranium-series disequilibrium in marine samples. J. Environ. Radioact. 88, 109–117.

Goffredo, V., Paradiso, A., Ranieri, G., Gadaleta, C.D., 2011. Yttrium-90 (^{90}Y) in the principal radionuclide therapies: an efficacy correlation between peptide receptor radionuclide therapy, radioimmunotherapy and transarterial radioembolization therapy. Ten years of experience (1999–2009). Crit. Rev. Oncol. Hematol. 80 (3), 393–410.

Grate, J.W., Strebin, R.S., Janata, J., Egorov, O., Ruzicka, J., 1996. Automated analysis of radionuclides in nuclear waste: rapid determination of Sr-90 by sequential injection analysis. Anal. Chem. 68, 333–340.

Grate, J.W., Egorov, O.B., 1998a. Automating analytical separations in radiochemistry. Anal. Chem. 70, 779A–788A.

Grate, J.W., Egorov, O., 1998b. Investigation and optimization of on-column redox reactions in the sorbent extraction separation of americium and plutonium using flow injection analysis. Anal. Chem. 70, 3920–3929.

Grate, J.W., Fadeff, S.K., Egorov, O., 1999a. Separation-optimized sequential injection method for rapid automated separation and determination of 90Sr in nuclear waste. Analyst 124, 203–210.

Grate, J.W., Egorov, O.B., Fiskum, S.K., 1999b. Automated extraction chromatographic separations of actinides using separation-optimized sequential injection techniques. Analyst 124 (8), 1143–1150.

Grate, J.W., Bruckner-Lea, C.J., Jarrell, A.E., Chandler, D.P., 2003. Automated sample preparation method for suspension arrays using renewable surface separations with multiplexed flow cytometry fluorescence detection. Anal. Chim. Acta 478 (1), 85–98.

Grate, J.W., Egorov, O.B., O'Hara, M.J., 2004. Sensors and automated analyzers for radionuclides. ACS Symp. Ser. 904, 322–341 (Subsurface Contamination Remediation).

Grate, J.W., Egorov, O., O'Hara, M.J., DeVol, T.A., 2008. Radionuclide sensors for environmental monitoring: from flow injection solid phase Absorptiometry to equilibration-based preconcentrating minicolumn sensors with radiometric detection. Chem. Rev. 108, 543–563.

Grate, J.W., et al., 2009. Renewable surface fluorescence sandwich immunoassay biosensor for rapid sensitive botulinum toxin detection in an automated fluidic format. Analyst 134, 987–996.

Grate, J.W., Egorov, O., O'Hara, M.J., 2010. Automation of extraction chromatographic and ion exchange separation methods for radiochemical analysis and monitoring. In: Moyer, B. (Ed.), Ion Exchange and Solvent Extraction. CRC Press, Boca Raton, Florida, pp. 515–562.

Grate, J.W., O'Hara, M.J., Farawila, A.F., Ozanich, R.M., Owsley, S.L., 2011. Automation of column-based radiochemical separations: a comparison of fluidic, robotic, and hybrid architectures. Proc. Radiochim. Acta 1, 13–19.

Green, D.J., et al., 2015. Astatine-211 conjugated to an anti-CD20 monoclonal antibody eradicates disseminated B-cell lymphoma in a mouse model. Blood 125 (13), 2111–2119.

Grogan, K.P., DeVol, T.A., 2011. Online detection of radioactive iodine in aqueous systems through the use of scintillating anion exchange resin. Anal. Chem. 83 (7), 2582–2588.

Groppi, F., Bonardi, M.L., Birattari, C., Menapace, E., Abbas, K., Holzwarth, U., Alfarano, A., Morzenti, S., Zona, C., Alfassi, Z.B., 2005. Optimisation study of α-cyclotron production of At-211/Po-

211g for high-LET metabolic radiotherapy purposes. Appl. Radiat. Isot. 63 (5−6), 621−631.

Grudpan, K., 2004. Some recent developments on cost-effective flow-based analysis. Talanta 64 (5), 1084−1090.

Guerard, F., Gestin, J.F., Brechbiel, M.W., 2013. Production of [$^{(211)}$At]-astatinated radiopharmaceuticals and applications in targeted alpha-particle therapy. Cancer Biother. Radiopharm. 28 (1), 1−20.

Guerin, N., Nadeau, K., Potvin, S., Hardy, J.M., Lariviere, D., 2013. Automated pressurized injection system for the separation of actinides by extraction chromatography. J. Radioanal. Nucl. Chem. 295 (3), 1803−1811.

Gumiela, M., 2018. Cyclotron production of 99mTc: comparison of known separation technologies for isolation of 99mTc from molybdenum targets. Nucl. Med. Biol. 58, 33−41.

Guseva, L.I., 2007. A ^{228}Ra-^{212}Pb tandem generator for potential application in biomedical studies. J. Radioanal. Nucl. Chem. 272 (1), 153−159.

Habibi, A., Cariou, N., Boulet, B., Cossonnet, C., Gurriaran, R., Gleizes, M., Cote, G., Lariviere, D., 2017. Automated chromatographic separation coupled on-line to ICP-MS measurements for the quantification of actinides and radiostrontium in soil samples. J. Radioanal. Nucl. Chem. 314 (1), 127−139.

Hang, W., Zhu, L.W., Zhong, W.W., Mahan, C., 2004. Separation of actinides at ultra-trace level from urine matrix using extraction chromatography-inductively coupled plasma mass spectrometry. J. Anal. At. Spectrom. 19 (8), 966−972.

Hirayama, F., Takashi, M., Yasa, Y., Tani, A., 1985. Automatic chemical separation apparatus for uranium and transuranium elements. In: Choppin, F.R., Navratil, J.D., Schulz, W.W. (Eds.), Proceedings of the International Symposium on Actinide/Lanthanide Separations. World Scientific Publishing, Philadelphia, pp. 140−163.

Hofstetter, K.J., Wilson, H.T., 1992. Continuous Tritium Effluent Water Monitor at the Savannah River Site. Westinghouse Savannah River Company. WSRC-MS-92-163.

Holland, J.P., Sheh, Y., Lewis, J.S., 2009. Standardized methods for the production of high specific-activity zirconium-89. Nucl. Med. Biol. 36 (7), 729−739.

Hollenbach, M., Grohs, J., Mamich, S., Kroft, M., Denoyer, E.R., 1994. Determination of technetium-99, thorium-230 and uranium-234 in soils by inductively coupled plasma mass spectrometry using flow injection preconcentration. J. Anal. At. Spectrom. 9, 927−933.

Holman, D.A., Christian, G.D., Ruzicka, J., 1997. Titration without mixing or dilution: sequential Injection of Chemical Sensing membranes. Anal. Chem. 69, 1763−1765.

Horwitz, E.P., Dietz, M.L., Diamond, H., LaRosa, J.J., Fairman, W.D., 1990. Concentration and separation of actinides from urine using a supported bifunctional organophosphorus extractant. Anal. Chim. Acta 238, 263−271.

Horwitz, E.P., Dietz, M.L., Fisher, D.E., 1991. Separation and preconcentration of strontium from biological, environmental, and nuclear waste samples by extraction chromatography using a crown ether. Anal. Chem. 63, 522−525.

Horwitz, E.P., Chiarizia, R., Dietz, M.L., 1992a. A novel strontium-selective extraction chromatographic resin. Solvent Extr. Ion Exch. 10, 313−336.

Horwitz, E.P., Dietz, M.L., Chiarizia, R., 1992b. The application of novel extraction chromatographic materials to the characterization of radioactive waste solutions. J. Radioanal. Nucl. Chem. Artic. 161, 575−583.

Horwitz, E.P., Dietz, M.L., Chiarizia, R., Diamond, H., Essling, A.M., Graczyk, D., 1992c. Separation and preconcentration of uranium from acidic media by extraction chromatography. Anal. Chim. Acta 266, 25−37.

Horwitz, E.P., Chiarizia, R., Dietz, M.L., Diamond, H., Nelson, D.M., 1993. Separation and preconcentration of actinides from acidic media by extraction chromatography. Anal. Chim. Acta 281, 361−372.

Horwitz, E.P., Dietz, M.L., Chiarizia, R., Diamond, H., Maxwell, S.L., Nelson, M.R., 1995. Separation and preconcentration of actinides by extraction chromatography using a supported liquid anion exchanger: application to the characterization of high-level nuclear waste solutions. Anal. Chim. Acta 310, 63−78.

Horwitz, E.P., 1998. Extraction chromatography of actinides and selected fission products: principles and achievement of selectivity. In: International Workshop on Application of Extraction Chromatography in Radionuclide Measurement (IRMM), pp. 27−37. Geel Belgium.

Horwitz, E.P., Bond, A.H., 2003. Purification of radionuclides for nuclear medicine: the multicolumn selectivity inversion generator concept. Czech. J. Phys. 53 (Suppl. A), A713−A716.

Horwitz, E.P., McAlister, D.R., Dietz, M.L., 2006. Extraction chromatography versus solvent extraction: how similar are they? Separ. Sci. Technol. 41 (10), 2163−2182.

Hou, X.L., Ostergaard, L.F., Nielsen, S.P., 2005. Determination of Ni-63 and Fe-55 in nuclear waste samples using radiochemical separation and liquid scintillation counting. Anal. Chim. Acta 535 (1−2), 297−307.

Hou, X.L., 2005a. Radiochemical determination of Ca-41 in nuclear reactor concrete. Radiochim. Acta 93 (9−10), 611−617.

Hou, X.L., 2005b. Rapid analysis of C-14 and H-3 in graphite and concrete for decommissioning of nuclear reactor. Appl. Radiat. Isot. 62 (6), 871−882.

Hou, X.L., 2007. Radiochemical analysis of radionuclides difficult to measure for waste characterization in decommissioning of nuclear facilities. J. Radioanal. Nucl. Chem. 273 (1), 43−48.

Hou, X.L., Ostergaard, L.F., Nielsen, S.P., 2007. Determination of Cl-36 in nuclear waste from reactor decommissioning. Anal. Chem. 79 (8), 3126−3134.

Hou, X.L., Roos, P., 2008. Critical comparison of radiometric and mass spectrometric methods for the determination of radionuclides in environmental, biological and nuclear waste samples. Anal. Chim. Acta 608 (2), 105−139.

Hou, X.L., et al., 2013. Iodine-129 in seawater offshore Fukushima: distribution, inorganic speciation, sources, and budget. Environ. Sci. Technol. 47 (7), 3091−3098.

Hurst, W.J., 1995. Robotics in the laboratory. In: Hurst, W.J. (Ed.), Automation in the Laboratory. VCH Publishers, New York, pp. 91−107.

IAEA, 2004. Radioisotope Handling Facilities and Automation of Radioisotope Production. IAEA-TECDOC-1430, 73 pp. International Atomic Energy Agency, Vienna.

IAEA, 2013. Non-HEU Production Technologies for Molybdenum-99 and Technetium-99m. No. NF-T-5.4, NF-T-5.4, 75 pp. International Atomic Energy Agency, Vienna.

IAEA, 2016. Cyclotron Produced Radionuclides: Emerging Positron Emitters for Medical Applications: ^{64}Cu and ^{124}I. In: IAEA Radioisotopes and Radiopharmaceuticals Reports, vol. 1. International Atomic Energy Agency, Vienna, p. 79.

Ivaska, A., Ruzicka, J., 1993. From flow injection to sequential injection: comparison of methodologies and selection of liquid drives. Analyst 118, 885–889.

Izatt, R.M., Bradshaw, J.S., Bruening, R.L., Bruening, M.L., 1994. Solid Phase extraction of ions of analytical interest using molecular recognition technology. Am. Lab. 26 (18), 28c–28m.

Izatt, R.M., Bradshaw, J.S., Bruening, R.L., 1996. Accomplishment of difficult chemical separations using solid phase extraction. Pure Appl. Chem. 68, 1237–1241.

Izatt, R.M., 1997. Review of selective ion separations at BYU using liquid membrane and solid phase extraction procedures. J. Inclusion Phenom. Mol. Recognit. Chem. 29, 197–220.

Jäckel, B., Cripps, R., Güntay, S., Bruchertseifer, H., 2005. Development of semi-automated system for preparation of ^{188}Re aqueous solutions of high and reproducible activity concentrations. Appl. Radiat. Isot. 63 (3), 299–304.

Jebrail, M.J., Yang, H., Mudrik, J.M., Lafreniere, N.M., McRoberts, C., Al-Dirbashi, O.Y., Fisher, L., Chakraborty, P., Wheeler, A.R., 2011. A digital microfluidic method for dried blood spot analysis. Lab Chip 11 (19), 3218–3224.

Jebrail, M.J., Bartsch, M.S., Patel, K.D., 2012. Digital microfluidics: a versatile tool for applications in chemistry, biology and medicine. Lab Chip 12 (14), 2452–2463.

Jebrail, M.J., Sinha, A., Vellucci, S., Renzi, R.F., Ambriz, C., Gondhalekar, C., Schoeniger, J.S., Patel, K.D., Branda, S.S., 2014. World-to-Digital-Microfluidic interface enabling extraction and purification of RNA from human whole blood. Anal. Chem. 86 (8), 3856–3862.

Jeong, J.M., Chung, J.-K., 2003. Therapy with ^{188}Re-labeled radiopharmaceuticals: an overview of promising results from initial clinical trials. Cancer Biother. Radiopharm. 18 (5), 707–717.

Johnson, G.L., Leininger, R.F., Segre, E., 1949. Chemical properties of astatine. I. J. Chem. Phys. 17, 1–10.

Juweid, M.E., 2002. Radioimmunotherapy of B-cell non-Hodgkin's lymphoma: from clinical trials to clinical practice. J. Nucl. Med. 43 (11), 1507–1529.

Kang, G.H., Lee, G.H., Jung, R.-S., Han, J.K., Kil, H.-S., Shink, D.K., 2001. The study for determination of uranium by flow injection inductively coupled plasma mass spectrometry. Anal. Sci. 17 (Suppl.), i1005–i1009.

Kawashima, H., 2014. Radioimmunotherapy: a specific treatment protocol for cancer by cytotoxic radioisotopes conjugated to antibodies. Sci. World J. 2014, 10.

Keiko, L.H., et al., 2018. α-particle therapy for synovial sarcoma in the mouse using an astatine-211-labeled antibody against frizzled homolog 10. Cancer Sci. 109 (7), 2302–2309.

Kelley, J.M., Robertson, D.M., 1985. Plutonium ion emission from carburized rhenium mass spectrometer filaments. Anal. Chem. 57, 124–130.

Kelley, J.M., Bond, L.A., Beasley, T.M., 1999. Global distribution of Pu isotopes and Np-237. Sci. Total Environ. 238, 483–500.

Ketterer, M.E., Szechenyi, S.C., 2008. Determination of plutonium and other transuranic elements by inductively coupled plasma mass spectrometry: a historical perspective and new frontiers in the environmental sciences. Spectrochim. Acta Part B At. Spectrosc. 63 (7), 719–737.

Khajornjiraphan, N., Thu, N.A., Chow, P.K.H., 2015. Yttrium-90 microspheres: a review of its emerging clinical indications. Liver Cancer 4 (1), 6–15.

Khalil, M.M., 2010. Basic Sciences of Nuclear Medicine. Springer.

Kim, C.S., Kim, C.K., Lee, J.I., Lee, K.J., 2000a. Rapid determination of Pu isotopes and atom ratios in small amounts of environmental samples by an on-line sample pre-treatment system and isotope dilution high resolution inductively coupled plasma mass spectrometry. J. Anal. At. Spectrom. 15 (3), 247–255.

Kim, G., Burnett, W., Horwitz, E.P., 2000b. Efficient preconcentration and separation of actinide elements from large soil and sediment samples. Anal. Chem. 72 (20), 4882–4887.

Kim, C.S., Kim, C.K., 2002. Determination of Pu isotopes in seawater by an on-line sequential injection technique with sector field inductively coupled plasma mass spectrometry. Anal. Chem. 74 (15), 3824–3832.

Kim, C.S., Kim, C.K., Lee, K.J., 2004. Simultaneous analysis of Np-237 and Pu isotopes in environmental samples by ICP-SF-MS coupled with automated sequential injection system. J. Anal. At. Spectrom. 19 (6), 743–750.

Kim, C.S., Kim, C.K., Martin, P., Sansone, U., 2007. Determination of Pu isotope concentrations and isotope ratio by inductively coupled plasma mass spectrometry: a review of analytical methodology. J. Anal. At. Spectrom. 22 (7), 827–841.

Kim, H., Bartsch, M.S., Renzi, R.F., He, J., Van de Vreugde, J.L., Claudnic, M.R., Patel, K.D., 2011. Automated digital microfluidic sample preparation for next-generation DNA sequencing. JALA 16 (6), 405–414.

Kim, H., et al., 2013. A microfluidic DNA library preparation platform for next-generation sequencing. PLoS One 8 (7).

Kim, Y.-S., Brechbiel, M.W., 2012. An overview of targeted alpha therapy. Tumor Biol. 33 (3), 573–590.

Kirby, A.E., Wheeler, A.R., 2013. Digital microfluidics: an emerging sample preparation platform for mass spectrometry. Anal. Chem. 85 (13), 6178–6184.

Kitson, S.L., Cuccurullo, V., Moody, T.S., Mansi, L., 2013. Radionuclide antibody-conjugates, a targeted therapy towards cancer. Curr. Radiopharm. 6 (2), 57–71.

Kolacinska, K., Trojanowicz, M., 2014. Application of flow analysis in determination of selected radionuclides. Talanta 125, 131–145.

Kolacinska, K., Chajduk, E., Dudek, J., Samczynski, Z., Lokas, E., Bojanowska-Czajka, A., Trojanowicz, M., 2017. Automation of sample processing for ICP-MS determination of Sr-90 radionuclide at ppq level for nuclear technology and environmental purposes. Talanta 169, 216–226.

Kolacinska, K., Samczynski, Z., Dudek, J., Bojanowska-Czajka, A., Trojanowicz, M., 2018. A comparison study on the use of Dowex 1 and TEVA-resin in determination of Tc-99 in environmental and nuclear coolant samples in a SIA system with ICP-MS detection. Talanta 184, 527–536.

Kramer, G.H., Davies, J.M., 1982. Isolation of strontium-90, yttrium-90, promethium-147, and cerium-144 from wet ashed urine by calcium oxalate coprecipitation and sequential solvent extraction. Anal. Chem. 54, 1428–1431.

Krasikova, R., 2007. Synthesis modules and automation in F-18 labeling. In: Schubiger, P.A., Lehmann, L., Friebe, M. (Eds.), PET Chemistry:

The Driving Force in Molecular Imaging. Springer Berlin Heidelberg, New York, pp. 289–316.

Kremliakova, N.Y., Novikov, A.P., Myasoedov, B.F., 1990. Extraction chromatographic separation of radionuclides of strontium, cesium, and barium with the use of TVEX-DCH18C6. J. Radioanal. Nucl. Chem. Lett. 145, 23–28.

Kuno, Y., Sato, S., Ohno, E., Masui, J., 1993. Rapid determination of strontium-90 in highly radioactive solutions of nuclear fuel reprocessing plant. Anal. Sci. 9, 195–198.

Kuwabara, J., Tolmachyov, S., Noguchi, H., 2002. The development of flow injection technique for rapid uranium determination in urine. J. Nucl. Sci. Technol. Suppl. 3, 556–559.

Lamb, J.D., Nordmeyer, R.R., Drake, P.A., Elder, M.P., Miles, R.W., Lah, R.P., 1989. Ion chromatographic separation for analysis of radiostrontium in nuclear reprocessing solutions of high ionic strength. J. Radioanal. Nucl. Chem. 134, 317–331.

Lambert, B., de Klerk, J.M.H., 2006. Clinical applications of ^{188}Re-labelled radiopharmaceuticals for radionuclide therapy. Nucl. Med. Commun. 27 (3), 223–229.

Lambrecht, R.M., Mirzadeh, S., 1985. Cyclotron isotopes and radiopharmaceuticals- XXXV. Astatine-211. Int. J. Appl. Radiat. Isot. 36, 443–450.

L'Annunziata, M.F., 1971. Birth of a unique parent-daughter relation: secular equilibrium. J. Chem. Educ. 48, 700–703.

L'Annunziata, M.F., 2016. Chapter 1: radioactivity and our well-being. In: Radioactivity: Introduction and History, from the Quantum to Quarks. Elsevier, Oxford, ISBN 978-0-444-63489-4, pp. 1–66, p. 902.

Lariviere, D., Taylor, V.F., Evans, R.D., Cornett, R.J., 2006. Radionuclide determination in environmental samples by inductively coupled plasma mass spectrometry. Spectrochim. Acta Part B 61 (8), 877–904.

Lariviere, D., Cumming, T.A., Kiser, S., Li, C., Cornett, R.J., 2008a. Automated flow injection system using extraction chromatography for the determination of plutonium in urine by inductively couple plasma mass spectrometry. J. Anal. At. Spectrom. 23, 352–360.

Lariviere, D., Whyte, J.C., Zhang, W., Hoffman, I., Ungar, R.K., Johnson, S., Cornett, R.J., 2008b. Rapid and automated analytical technologies for radiological/nuclear emergency preparedness. In: Koskinen, A.N. (Ed.), Nuclear Chemistry: New Research. NOVA Publishers, Hauppauge NY, pp. 99–154.

Lariviere, D., Benkhedda, K., Kiser, S., Johnson, S., Cornett, R.J., 2010. Rapid and automated sequential determination of ultra-trace long-lived actinides in air filters by inductively coupled plasma mass spectrometry. Anal. Methods 2 (3), 259–267.

Lenehan, C.E., Barnett, N.W., Lewis, S.W., 2002. Sequential injection analysis. Analyst 127 (8), 997–1020.

Lepareur, N., Ardisson, V., Noiret, N., Boucher, E., Raoul, J.-L., Clément, B., Garin, E., 2011. Automation of labelling of Lipiodol with high-activity generator-produced ^{188}Re. Appl. Radiat. Isot. 69 (2), 426–430.

Lepareur, N., Ardisson, V., Noiret, N., Garin, E., 2012. ^{188}Re-SSS/Lipiodol: development of a potential treatment for HCC from bench to bedside. Int. J. Mol. Imag. 2012.

Li, M., et al., 2017. Automated cassette-based production of high specific activity [$^{203/212}$Pb]peptide-based theranostic radiopharmaceuticals for image-guided radionuclide therapy for cancer. Appl. Radiat. Isot. 127, 52–60.

Li, Y., Russell, P.J., Allen, B.J., 2004. Targeted α-therapy for control of micrometastatic prostate cancer. Expert Rev. Anticancer Ther. 4 (3), 459–468.

Lin, M., Mukhopadhyay, U., Waligorski, G.J., Balatoni, J.A., González-Lepera, C., 2016. Semi-automated production of ^{89}Zr-oxalate/^{89}Zr-chloride and the potential of ^{89}Zr-chloride in radiopharmaceutical compounding. Appl. Radiat. Isot. 107, 317–322.

Lindegren, S., Bäck, T., Jensen, H.J., 2001. Dry-distillation of astatine-211 from irradiated bismuth targets: a time-saving procedure with high recovery yields. Appl. Radiat. Isot. 55 (2), 157–160.

Luo, T.-Y., Lo, A.-R., Hsieh, B.-T., Lin, W.-J., 2007. A design for automatic preparation of highly concentrated ^{188}Re-perrhenate solutions. Appl. Radiat. Isot. 65 (1), 21–25.

Luque de Castro, M.D., Ruiz-Jimenez, J., Perez-Serradilla, J.A., 2008. Lab-on-valve: a useful tool in biochemical analysis. Trends Anal. Chem. 27, 118–126.

Makvandi, M., Lieberman, B.P., LeGeyt, B., Hou, C., Mankoff, D.A., Mach, R.H., Pryma, D.A., 2016. The pre-clinical characterization of an alpha-emitting sigma-2 receptor targeted radiotherapeutic. Nucl. Med. Biol. 43 (1), 35–41.

Makvandi, M., et al., 2018. Alpha-emitters and targeted alpha therapy in oncology: from basic science to clinical investigations. Target. Oncol. 13 (2), 189–203.

Manton, W.I., 1988. Separation of lead from young zircons by single-bead ion exchange. Chem. Geol. 73 (2), 147–152.

Marcu, L., Bezak, E., Allen, B.J., 2018. Global comparison of targeted alpha vs targeted beta therapy for cancer: in vitro, in vivo and clinical trials. Crit. Rev. Oncol. Hematol. 123, 7–20.

Marengo, M., Lodi, F., Magi, S., Cicoria, G., Pancaldi, D., Boschi, S., 2008. Assessment of radionuclidic impurities in 2-[^{18}F]fluoro-2-deoxy-d-glucose ([^{18}F]FDG) routine production. Appl. Radiat. Isot. 66 (3), 295–302.

Marsh, S.F., Pillay, K.K.S., 1993. Effects of Ionizing Radiation on Modern Ion Exchange Materials. Los Alamos National Laboratory, Los Alamos, NM, 25 p.

Martini, P., Boschi, A., Cicoria, G., Uccelli, L., Pasquali, M., Duatti, A., Pupillo, G., Marengo, M., Loriggiola, M., Esposito, J., 2016. A solvent-extraction module for cyclotron production of high-purity technetium-99m. Appl. Radiat. Isot. 118, 302–307.

Mateos, J.J., Gomez, E., Garcias, F., Casas, M., Cerda, V., 2000. Rapid Sr-90/Y-90 determination in water samples using a sequential injection method. Appl. Radiat. Isot. 53 (1–2), 139–144.

Maxwell, S.L., Culligan, B.K., Hutchison, J.B., Utsey, R.C., McAlister, D.R., 2014. Rapid determination of actinides in seawater samples. J. Radioanal. Nucl. Chem. 300 (3), 1175–1189.

Maya, F., Horstkotte, B., Estela, J.M., Cerda, V., 2014. Automated in-syringe dispersive liquid-liquid microextraction. Trac. Trends Anal. Chem. 59, 1–8.

Mayer, M., Ruzicka, J., 1996. Flow injection based renewable electrochemical sensor system. Anal. Chem. 68, 3808–3814.

McAlister, D.R., Horwitz, E.P., 2009. Automated two column generator systems for medical radionuclides. Appl. Radiat. Isot. 67 (11), 1985–1991.

McCabe, K.E., Wu, A.M., 2010. Positive progress in immunoPET—not just a coincidence. Cancer Biother. Radiopharm. 25 (3), 253–261.

Meijs, W.E., Herscheid, J.D.M., Haisma, H.J., Wijbrandts, R., van Langevelde, F., Van Leuffen, P.J., Mooy, R., Pinedo, H.M., 1994. Production of highly pure no-carrier added ^{89}Zr for the labelling of

antibodies with a positron emitter. Appl. Radiat. Isot. 45 (12), 1143−1147.

Men, W., Zheng, J., Wang, H., Ni, Y.Y., Aono, T., Maxwell, S.L., Tagami, K., Uchida, S., Yamada, M., 2018. Establishing rapid analysis of Pu isotopes in seawater to study the impact of Fukushima nuclear accident in the Northwest Pacific. Sci. Rep. 8.

Metzger, S.C., Ticknor, B.W., Rogers, K.T., Bostick, D.A., McBay, E.H., Hexel, C.R., 2018. Automated separation of uranium and plutonium from environmental swipe samples for multiple collector inductively coupled plasma mass spectrometry. Anal. Chem. 90 (15), 9441−9448.

Midorikawa, M., Sato, Y., Hara, S., Konno, K., Iwanaga, M., 2007. The on-site laboratory for the rokkasho reprocessing plant in Japan. In: Addressing Verification Challenges. International Atomic Energy Association, Vienna, pp. 663−671.

Mikulski, J., StroŃSki, I., 1965. Separation of some metals by extraction-chromatography using new neutral phosphoro-organic compounds. Nature 207, 749.

Miller, P.W., 2009. Radiolabelling with short-lived PET (positron emission tomography) isotopes using microfluidic reactors. J. Chem. Technol. Biotechnol. 84 (3), 309−315.

Miro, M., Cerda, V., Estela, J.M., 2002a. Multisyringe flow injection analysis: characterization and applications. Trends Anal. Chem. 21 (3), 199−210.

Miro, M., Gomez, E., Estela, J.M., Casas, M., Cerda, V., 2002b. Sequential injection Sr-90 determination in environmental samples using a wetting-film extraction method. Anal. Chem. 74 (4), 826−833.

Mirzadeh, S., Knapp, F.F., 1996. Biomedical radioisotope generator systems. J. Radioanal. Nucl. Chem. 203 (2), 471−488.

Mola, M., Avivar, J., Nieto, A., Penalver, A., Aguilar, C., Ferrer, L., Cerda, V., Borrull, F., 2014. Determination of Sr-90 and Pb-210 in sludge samples using a LOV-MSFIA system and liquid scintillation counting. Appl. Radiat. Isot. 86, 28−35.

Morgenstern, A., Apostolidis, C., Carlos-Marquez, R., Mayer, K., Molinet, R., 2002. Single-column extraction chromatographic separation of U, Pu, Np and Am. Radiochim. Acta 90 (2), 81−85.

Morgenstern, A., Apostolidis, C., Kratochwil, C., Sathekge, M., Krolicki, L., Bruchertseifer, F., 2018. An overview of targeted alpha therapy with ^{225}Actinium and ^{213}Bismuth. Curr. Radiopharm. 11 (3), 200−208.

Morley, T.J., Dodd, M., Gagnon, K., Hanemaayer, V., Wilson, J., McQuarrie, S.A., English, W., Ruth, T.J., Bénard, F., Schaffer, P., 2012. An automated module for the separation and purification of cyclotron-produced $^{99m}TcO_4^-$. Nucl. Med. Biol. 39 (4), 551−559.

Murray, R.L., 1994. Understanding Radioactive Waste, fourth ed. Battelle Press, Richland, Washington. 212 p.

Nagatsu, K., Fukada, M., Minegishi, K., Suzuki, H., Fukumura, T., Yamazaki, H., Suzuki, K., 2011. Fully automated production of iodine-124 using a vertical beam. Appl. Radiat. Isot. 69 (1), 146−157.

Nash, K.L., Madic, C., Mathur, J.N., Lacquement, J., 2006. Actinide separation science and technology. In: Morss, L.R., Edelstein, N.M., Fuger, J., Katz, J.L. (Eds.), The Chemistry of the Actinide and Transactinide Elements, third ed., vol. 4. Springer. Information extracted from the NuDat 2 database.

National Nuclear Data Center, 2019. Information extracted from the NuDat 2 database. Retrieved December, 2018, from www.nndc.bnl.gov.

National Research Council, 2009. Medical Isotope Production without Highly Enriched Uranium. The National Academies Press, Washington, DC, p. 220.

Neirinckx, R.D., Smit, J.A., 1973. Separation of astatine-211 from bismuth metal. Anal. Chim. Acta 63 (1), 201−204.

Neumann, H.M., 1957. Solvent distribution studies of the chemistry of astatine. J. Inorg. Nucl. Chem. 4 (5−6), 349−353.

Noshkin, V.E., Mott, N.S., 1967. Separation of strontium from large amounts of calcium, with application to radiostrontium analysis. Talanta 14, 45−51.

Novak-Hofer, I., Schubiger, P.A., 2002. Copper-67 as a therapeutic nuclide for radioimmunotherapy. Eur. J. Nucl. Med. Mol. Imaging 29 (6), 821−830.

O'Hara, M.J., Durst, P.C., Grate, J.W., Egorov, O., DeVol, T.A., 2008a. Rapid automated radiochemical analyzer for determination of targeted radionuclides in nuclear process streams. In: Paper Presented at 8th International Conference on Facility Operations-Safeguards Interface. American Nuclear Society, La Grange Park, IL, United States, Portland, OR. March 30 − April 4, 2008. Laboratory automation employed in the purification of astatine-211 from dissolved bismuth targets.

O'Hara, M.J., Durst, P.C., Grate, J.W., DeVol, T.A., Egorov, O., Clements, J.P., 2008b. Automated Process Monitoring: applying proven automation techniques to international safeguards needs. In: Proceedings of the 49th Annual Meeting of the Institute of Nuclear Materials Management. Institute of Nuclear Materials Management, Northbrook, IL, United States p. Paper No. 351.

O'Hara, M.J., Burge, S.R., Grate, J.W., 2009a. Quantification of Tc-99 in complex groundwater matrixes using a radiometric preconcentrating minicolumn sensor. Anal. Chem. 81, 1068−1078.

O'Hara, M.J., Burge, S.R., Grate, J.W., 2009b. Automated radioanalytical system for the determination of 90Sr in environmental water samples by 90Y Cherenkov radiation counting. Anal. Chem. 81, 1228−1237.

O'Hara, M.J., Farawila, A.F., Grate, J.W., 2009c. Automated radioanalytical chemistry: applications for the laboratory and industrial process monitoring. In: Paper Presented at 2nd JAPAN-IAEA Workshop on Advanced Safeguards Technology for the Future Nuclear Fuel Cycle. IAEA, Tokai-mura, Ibaraki Japan.

O'Hara, M.J., Rapko, B.M., Edwards, M.K., Wester, D.W., June 30, 2009d. Medical Isotope Generator Systems. USA Patent 7,554,098.

O'Hara, M.J., Krzysko, A.J., Hamlin, D.K., Dorman, E.F., Wilbur, D.S., 2017a. Laboratory automation employed in the purification of astatine-211 from dissolved bismuth targets. In: 10th International Symposium on Targeted Alpha Therapy. TAT-10, Kanazawa, Japan.

O'Hara, M.J., Krzysko, A.J., Niver, C.M., Morrison, S.S., Owsley Jr., S.L., Hamlin, D.K., Dorman, E.F., Wilbur, D.S., 2017b. An automated flow system incorporating in-line acid dissolution of bismuth metal from a cyclotron irradiated target assembly for use in the isolation of astatine-211. Appl. Radiat. Isot. 122, 202−210.

O'Hara, M.J., Murray, N.J., Carter, J.C., Morrison, S.S., 2018a. Optimized anion exchange column isolation of zirconium-89 (^{89}Zr) from yttrium cyclotron target: method development and implementation on an automated fluidic platform. J. Chromatogr. A 1545, 48−58.

O'Hara, M.J., Murray, N.J., Carter, J.C., Kellogg, C.M., Link, J.M., 2018b. Tandem column isolation of zirconium-89 from cyclotron bombarded yttrium targets using an automated fluidic platform: anion exchange to hydroxamate resin columns. J. Chromatogr. A 1567, 37−46.

O'Hara, M.J., Murray, N.J., Carter, J.C., Kellogg, C.M., Link, J.M., 2018c. Hydroxamate column-based purification of zirconium-89 (^{89}Zr) using an automated fluidic platform. Appl. Radiat. Isot. 132, 85−94.

O'Hara, M.J., Krzysko, A.J., Hamlin, D.K., Li, Y., Dorman, E.F., Wilbur, D.S., 2019. Development of an autonomous solvent extraction system to isolate astatine-211 from dissolved cyclotron bombarded bismuth targets. Sci. Rep. (in press).

Ohtsuka, Y., Takaku, Y., Kimura, J., Hisamatsu, S., Inaba, J., 2005. Development of rapid plutonium analysis for environmental samples by isotope dilution/inductively coupled plasma mass spectrometry with on-line column. Anal. Sci. 21 (3), 205−208.

Ohtsuka, Y., Takaku, Y., Nishimura, K., Kimura, J., Hisamatsu, S., Inaba, J., 2006. Rapid method for the analysis of plutonium isotopes in a soil sample within 60 min. Anal. Sci. 22 (2), 309−311.

Olivier, P., 2004. Nuclear oncology, a fast growing field of nuclear medicine. Nucl. Instrum. Methods Phys. Res. A 527 (1−2), 4−8.

Ozanich, R.M., et al., 2007. Use of a novel fluidics microbead trap/flow-cell enhances speed and sensitivity of bead-based assays. JALA 12 (5), 303−310.

Ozanich, R.M., Bruckner-Lea, C.J., Warner, M.G., MIller, K.D., Antolick, K.C., Marks, J.D., Lou, J., Grate, J.W., 2009. Rapid multiplexed flow cytometric assay for botulinum neurotoxin detection using an automated fluidic renewable surface separation column for enhanced sensitivity. Anal. Chem. 81, 5783−5793.

Palm, S., Back, T., Haraldsson, B., Jacobsson, L., Lindegren, S., Albertsson, P., 2016. Biokinetic modeling and dosimetry for optimizing intraperitoneal radioimmunotherapy of ovarian cancer microtumors. J. Nucl. Med. 57 (4), 594−600.

Pauwels, E.K.J., Erba, P., 2007. Radioimmunotherapy of non-Hodgkin's lymphoma: molecular targeting and novel agents. Drug News Perspect. 20 (2), 87−93.

Paxton, W.F., O'Hara, M.J., Peper, S.M., Petersen, S.L., Grate, J.W., 2008. Accelerated analyte uptake on single beads in microliter-scale batch separations using acoustic streaming: plutonium uptake by anion exchange for analysis by mass spectrometry. Anal. Chem. 80 (11), 4070−4077.

Perna, L., Betti, M., Moreno, J.M.B., Fuoco, R., 2001. Investigation on the use of UTEVA as a stationary phase for chromatographic separation of actinides on-line to inductively coupled plasma mass spectrometry. J. Anal. At. Spectrom. 16 (1), 26−31.

Peterson, D.S., Plionis, A.A., Gonzales, E.R., 2007. Optimization of extraction chromatography separations of trace levels of actinides with ICP-MS detection. J. Sep. Sci. 30 (10), 1575−1582.

Pillay, K.K.S., 1986. A review of the radiation stability of ion exchange materials. J. Radioanal. Nucl. Chem. 102 (1), 247−268.

Pimlott, S.L., Sutherland, A., 2011. Molecular tracers for the PET and SPECT imaging of disease. Chem. Soc. Rev. 40 (1), 149−162.

Pohlman, B., Sweetenham, J., Macklis, R.M., 2006. Review of clinical radioimmunotherapy. Expert Rev. Anticancer Ther. 6 (3), 445−461.

Pollema, C.H., Ruzicka, J., 1994. Flow injection renewable surface immunoassay: a new approach to immunoanalysis with fluorescence detection. Anal. Chem. 66, 1825−1831.

Poniger, S.S., Tochon-Danguy, H.J., Panopoulos, H.P., O'Keefe, G.J., Peake, D., Rasool, R., Scott, A.M., 2012. Automated production of ^{124}I and ^{64}Cu using IBA Terimo and Pinctada metal electroplating and processing modules. AIP Conf. Proc. 1509 (1), 114−119.

Poniger, S., Tochon-Danguy, H., Panopoulos, H., Scott, A., 2014. Fully automated production of Zr-89 using IBA Nirta and Pinctada systems. In: Paper Presented at 15th International Workshop on Targetry and Target Chemistry, Prague, Czech Republic, Aug. 18-21, 2014.

Porter, C.R., Kahn, B., Carter, M.W., Vehnberg, G.L., Pepper, E.W., 1967. Determination of radiostrontium in food and other environmental samples. Environ. Sci. Technol. 1, 745−750.

Poty, S., Francesconi, L.C., McDevitt, M.R., Morris, M.J., Lewis, J.S., 2018a. α-Emitters for radiotherapy: from basic radiochemistry to clinical studies—Part 2. J. Nucl. Med. 59 (7), 1020−1027.

Poty, S., Francesconi, L.C., McDevitt, M.R., Morris, M.J., Lewis, J.S., 2018b. α-Emitters for radiotherapy: from basic radiochemistry to clinical studies—Part 1. J. Nucl. Med. 59 (6), 878−884.

Qiao, J., Hou, X., Miro, M., Roos, P., 2009a. Determination of plutonium isotopes in water and environmental solids: a review. Anal. Chim. Acta 652, 66−84.

Qiao, J.X., Hou, X.L., Roos, P., Miro, M., 2009b. Rapid determination of plutonium isotopes in environmental samples using sequential injection extraction chromatography and detection by inductively coupled plasma mass spectrometry. Anal. Chem. 81 (19), 8185−8192.

Qiao, J.X., Hou, X.L., 2010. Fractionation of plutonium in environmental and bio-shielding concrete samples using dynamic sequential extraction. J. Environ. Radioact. 101 (3), 244−249.

Qiao, J.X., Hou, X.L., Roos, P., Miro, M., 2010. Rapid and simultaneous determination of neptunium and plutonium isotopes in environmental samples by extraction chromatography using sequential injection analysis and ICP-MS. J. Anal. At. Spectrom. 25 (11), 1769−1779.

Qiao, J.X., Hou, X.L., Roos, P., Miro, M., 2011a. Rapid isolation of plutonium in environmental solid samples using sequential injection anion exchange chromatography followed by detection with inductively coupled plasma mass spectrometry. Anal. Chim. Acta 685 (2), 111−119.

Qiao, J.X., Hou, X.L., Roos, P., Miro, M., 2011b. Reliable determination of Np-237 in environmental solid samples using Pu-242 as a potential tracer. Talanta 84 (2), 494−500.

Qiao, J.X., Hou, X.L., Roos, P., Miro, M., 2011c. High-throughput sequential injection method for simultaneous determination of plutonium and neptunium in environmental solids using macroporous anion-exchange chromatography, followed by inductively coupled plasma mass spectrometric detection. Anal. Chem. 83 (1), 374−381.

Qiao, J.X., Hou, X.L., Roos, P., 2013a. Method for determination of neptunium in large-sized urine samples using manganese dioxide coprecipitation and (PU)-P-242 as yield tracer. Anal. Chem. 85 (3), 1889−1895.

Qiao, J.X., Hou, X.L., Steier, P., Golser, R., 2013b. Sequential injection method for rapid and simultaneous determination of U-236, Np-237, and Pu isotopes in seawater. Anal. Chem. 85 (22), 11026−11033.

Qiao, J.X., Hou, X.L., Roos, P., Miro, M., 2013c. Bead injection extraction chromatography using high-capacity lab-on-valve as a front end to inductively coupled plasma mass spectrometry for urine radiobioassay. Anal. Chem. 85 (5), 2853−2859.

Qiao, J.X., Hou, X.L., Roos, P., Lachner, J., Christl, M., Xu, Y.H., 2013d. Sequential injection approach for simultaneous determination of ultratrace plutonium and neptunium in urine with accelerator mass spectrometry. Anal. Chem. 85 (18), 8826−8833.

Qiao, J.X., Shi, K.L., Hou, X.L., Nielsen, S., Roos, P., 2014. Rapid multisample analysis for simultaneous determination of anthropogenic

radionuclides in marine environment. Environ. Sci. Technol. 48 (7), 3935−3942.

Qiao, J.X., Hou, X.L., Steier, P., Nielsen, S., Golser, R., 2015. Method for U-236 determination in seawater using flow injection extraction chromatography and accelerator mass spectrometry. Anal. Chem. 87 (14), 7411−7417.

Qiao, J.X., Steier, P., Nielsen, S., Hou, X.L., Roos, P., Golser, R., 2017. Anthropogenic U-236 in Danish seawater: global fallout versus reprocessing discharge. Environ. Sci. Technol. 51 (12), 6867−6876.

Rahman, O., Erlandsson, M., Blom, E., Langstroem, B., 2010. Automated synthesis of ^{18}F-labelled analogs of metomidate, vorozole and harmine using commercial platform. J. Label. Comp. Radiopharm. 53 (4), 169−171.

Rahmim, A., Zaidi, H., 2008. PET versus SPECT: strengths, limitations and challenges. Nucl. Med. Commun. 29 (3), 193−207.

Reboul, S.H., Fjeld, R.A., 1994. A rapid method for determination of beta-emitting radionuclides in aqueous samples. Radioact. Radiochem. 5, 42−49.

Reboul, S.H., Fjeld, R.A., 1995. Potential effects of surface water components on actinide determinations conducted by ion chromatography. Health Phys. 68 (4), 584−589.

Richer, P., Brandalise, B., Apostolidis, C., Molinet, R., Mayer, K., 1998. Development of a robotized separation method for U-Pu samples using UTEVA resin. In: Proc. Int. Workshop on the Application of Extraction Chromatography in Radionuclide Measurements, IRMM, Geel, 9-10 November 1998.

Roane, J.E., DeVol, T.A., 2002. Simultaneous separation and detection of actinides in acidic solutions using an extractive scintillating resin. Anal. Chem. 74 (21), 5629−5634.

Rodriguez, R., Avivar, J., Ferrer, L., Leal, L.O., Cerda, V., 2012. Automated total and radioactive strontium separation and preconcentration in samples of environmental interest exploiting a lab-on-valve system. Talanta 96, 96−101.

Rodriguez, R., Avivar, J., Ferrer, L., Leal, L.O., Cerda, V., 2015a. Uranium monitoring tool for rapid analysis of environmental samples based on automated liquid-liquid microextraction. Talanta 134, 674−680.

Rodriguez, R., Leal, L., Miranda, S., Ferrer, L., Avivar, J., Garcia, A., Cerda, V., 2015b. Automation of Tc-99 extraction by LOV prior ICP-MS detection: application to environmental samples. Talanta 133, 88−93.

Rodriguez, R., Avivar, J., Leal, L.O., Cerda, V., Ferrer, L., 2016a. Strategies for automating solid-phase extraction and liquid-liquid extraction in radiochemical analysis. Trac. Trends Anal. Chem. 76, 145−152.

Rodriguez, R., Borras, A., Leal, L., Cerda, V., Ferrer, L., 2016b. MSFIA-LOV system for Ra-226 isolation and pre-concentration from water samples previous radiometric detection. Anal. Chim. Acta 911, 75−81.

Romaniello, S.J., Field, M.P., Smith, H.B., Gordon, G.W., Kim, M.H., Anbar, A.D., 2015. Fully automated chromatographic purification of Sr and Ca for isotopic analysis. J. Anal. At. Spectrom. 30 (9), 1906−1912.

Rösch, F., Baum, R.P., 2011. Generator-based PET radiopharmaceuticals for molecular imaging of tumours: on the way to THERANOSTICS. Dalton Trans. 40 (23), 6104−6111.

Rösch, F., Knapp, F.F., 2011. Radionuclide generators. In: Vértes, A., Nagy, S., Klencsár, Z., Lovas, R.G., Rösch, F. (Eds.), Handbook of Nuclear Chemistry. Springer US, Boston, MA, pp. 1935−1976.

Ross, R.R., Noyce, J.R., Lardy, M.M., 1993. Inductively coupled plasma-mass spectrometry: an emerging method for analysis of long-lived radionuclides. Radioact. Radiochem. 4, 24−37.

Ruzicka, J., 1994. Discovering flow injection; journey from sample to live cell and from solution to suspension. Analyst 119, 1925−1934.

Ruzicka, J., 2000. Lab-on-valve: universal microflow analyzer based on sequential and bead injection. Analyst 125 (6), 1053−1060.

Ruzicka, J., 2005. From beaker chemistry to programmable microfluidics. Collect. Czechoslov. Chem. Commun. 70 (11), 1737−1755.

Ruzicka, J., Hansen, E.H., 1988. Flow Injection Analysis, second ed. Wiley-Interscience, New York. 498 p.

Ruzicka, J., Marshall, G.D., 1990. Sequential injection: a new concept for chemical sensors, process analysis and laboratory assays. Anal. Chim. Acta 237, 329−343.

Ruzicka, J., Ivaska, A., 1997. Bioligand interaction assay by flow injection absorptiometry. Anal. Chem. 69, 5024−5030.

Ruzicka, J., Scampavia, L., 1999. From flow injection to bead injection. Anal. Chem. 71, 257A−263A.

Ruzicka, J., Pollema, C.H., Scudder, K.M., 1993. Jet ring cell: a tool for flow injection spectroscopy and microscopy on a renewable solid support. Anal. Chem. 65, 3566−3570.

Rydberg, J., Cox, M., Musikas, C., Choppin, G.R. (Eds.), 2004. Solvent Extraction Principles and Practice, second ed. Marcel Dekker, New York.

Sabet, A., Biersack, H.-J., Ezziddin, S., 2016. Advances in peptide receptor radionuclide therapy. Semin. Nucl. Med. 46 (1), 40−46.

Schaedel, M., 2007. Superheavy element chemistry-achievements and perspectives. J. Nucl. Radiochem. Sci. 8 (2), 47−53.

Schonhofer, F., Wallner, G., 2001. Very rapid determination of 226Ra, 228Ra and 210Pb by selective adsorption and liquid scintillation spectrometry. Radioact. Radiochem. 12 (2), 33−38.

Schultz, M.K., Mueller, D., Baum, R.P., Leonard Watkins, G., Breeman, W.A.P., 2013. A new automated NaCl based robust method for routine production of gallium-68 labeled peptides. Appl. Radiat. Isot. 76 (0), 46−54.

Scott, P.J.H., Shao, X., 2010. Fully automated, high yielding production of N-succinimidyl 4-[^{18}F]fluorobenzoate ([^{18}F]SFB), and its use in microwave-enhanced radiochemical coupling reactions. J. Label. Comp. Radiopharm. 53 (9), 586−591.

Seliman, A.F., Samadi, A., Husson, S.M., Borai, E.H., DeVol, T.A., 2011. Preparation of polymer-coated, scintillating ion-exchange resins for monitoring of 99Tc in groundwater. Anal. Chem. 83 (12), 4759−4766.

Seliman, A.F., Bliznyuk, V.N., Husson, S.M., Devol, T.A., 2015. Development of polymerizable 2-(1-naphthyl)-5-phenyloxazole scintillators for ionizing radiation detection. J. Mater. Chem. C 3 (27), 7053−7061.

Seliman, A.F., Bliznyuk, V.N., DeVol, T.A., 2017. Development of stable extractive scintillating materials for real-time quantification of radiostrontium in aqueous solutions. J. Radioanal. Nucl. Chem. 314 (2), 743−751.

Shaibu, B.S., Reddy, M.L.P., Bhattacharyya, A., Manchanda, V.K., 2006a. Evaluation of Cyanex 923-coated magnetic particles for the extraction and separation of lanthanides and actinides from nuclear waste streams. J. Magn. Magn. Mater. 301 (2), 312−318.

Shaibu, B.S., Reddy, M.L.P., Prabhu, D.R., Kanekar, A.S., Manchanda, V.K., 2006b. N,N'-dimethyl-N,N'-dibutyl tetradecyl malonamide impregnated magnetic particles for the extraction and separation of radionuclides from nuclear waste streams. Radiochim. Acta 94 (5), 267−273.

Shaibu, B.S., Reddy, M.L.P., Murali, M.S., Manchanda, V.K., 2007. N,N,N ',N '-tetraoctyl-3-oxapentane-1,5-diamide impregnated magnetic particles for the uptake of lanthanides and actinides from nuclear waste streams. Radiochim. Acta 95 (3), 159−164.

Shi, K.L., Hou, X.L., Roos, P., Wu, W.S., 2012a. Determination of technetium-99 in environmental samples: a review. Anal. Chim. Acta 709, 1−20.

Shi, K.L., Qiao, J.X., Wu, W.S., Roos, P., Hou, X.L., 2012b. Rapid determination of technetium-99 in large volume seawater samples using sequential injection extraction chromatographic separation and ICP-MS measurement. Anal. Chem. 84 (15), 6783−6789.

Shih, S.C.C., Yang, H., Jebrail, M.J., Fobel, R., McIntosh, N., Al-Dirbashi, O.Y., Chakraborty, P., Wheeler, A.R., 2012. Dried blood spot analysis by digital microfluidics coupled to nanoelectrospray ionization mass spectrometry. Anal. Chem. 84 (8), 3731−3738.

Siikanen, J., Peterson, M., Tran, T.A., Roos, P., Ohlsson, T., Sandell, A., 2012. A peristaltic pump driven ^{89}Zr separation module. In: Paper Presented at 14th International Workshop on Targetry and Target Chemistry. American Institute of Physics, Playa del Carmen, Mexico. Aug. 26-29, 2012.

Smith, M.R., Wyse, E.J., Koppenaal, D.W., 1992. Radionuclide detection by inductively coupled plasma mass spectrometry: a comparison of atomic and radiation detection methods. J. Radioanal. Nucl. Chem. 160, 341−354.

Smith, M.R., Farmer, O.T., Reeves, J.H., Koppenaal, D.W., 1995. Radionuclide detection by ion-chromatography and on-line ICP/MS and beta detection: fission product rare earth element measurements. J. Radioanal. Nucl. Chem. 194, 7−13.

Smulek, W., Lada, W.A., 1979. Separation of alkali and alkaline earth metals by polyethers using extraction chromatography. Effect of diluent. J. Radioanal. Nucl. Chem. 50, 169−178.

Srivastava, S.C., Mausner, L.F., 2014. Therapeutic radionuclides: production, physical characteristics, and applications. In: Baum, R.P. (Ed.), Therapeutic Nuclear Medicine. Springer Berlin Heidelberg, Berlin, Heidelberg, pp. 11−50.

Stoffels, J.J., Wacker, J.F., Kelley, J.M., Bond, L.A., Kiddy, R.A., Brauer, F.P., 1994. Environmental monitoring of Hanford nuclear facility effluents by thermal ionization mass-spectrometry. Appl. Spectrosc. 48 (11), 1326−1330.

Sultana, M.S., Toyoshima, A., Mito, A., Takahashi, N., Baba, H., Watarai, H., 2000. Solvent extraction behavior of astatine and radioiodine at tracer concentrations. J. Radioanal. Nucl. Chem. 243 (3), 631−634.

Surugaya, N., Taguchi, S., Kurosawa, A., Watahiki, M., 2007. Improvement of analytical activities in the Tokai Reprocessing Plant, Japan, by measuring destructive and nondestructive assays. In: Addressing Verification Challenges. International Atomic Energy Association, Vienna, pp. 673−679.

Synowiecki, M.A., Perk, L.R., Nijsen, J.F.W., 2018. Production of novel diagnostic radionuclides in small medical cyclotrons. EJNMMI Radiopharm. Chem. 3 (1), 3-3.

Takahashi, M., Uchikoshi, S., Midorikawa, M., Ishikawa, M., Adachi, T., 1994. Development of a digital-analog robotic system for input solution and mixed oxide samples. In: International Nuclear Safeguards 1994 Vision for the Future. International Atomic Energy Association, Vienna, pp. 761−767.

Taljaard, R.E., van Staden, J.F., 1998. Application of sequential-injection analysis as process analyzers. Lab. Robot. Autom. 10 (6), 325−337.

Tan, S.H., Horlick, G., 1986. Background spectral features in inductively coupled plasma/mass spectrometry. Appl. Spectrosc. 40 (445−460), 445−460.

Tang, G., Tang, X., Wang, X., 2010. A facile automated synthesis of N-succinimidyl 4-[^{18}F]fluorobenzoate ([^{18}F]SFB) for ^{18}F-labeled cell-penetrating peptide as PET tracer. J. Label. Comp. Radiopharm. 53 (8), 543−547.

Thaitrong, N., Kim, H., Renzi, R.F., Bartsch, M.S., Meagher, R.J., Patel, K.D., 2012. Quality control of next-generation sequencing library through an integrative digital microfluidic platform. Electrophoresis 33 (23), 3506−3513.

Thompson, J.J., Houk, R.S., 1986. Inductively coupled plasma mass spectrometric detection for multielement flow injection analysis and elemental speciation by reversed phase liquid chromatography. Anal. Chem. 58, 2541−2548.

Tolmachyov, S.Y., Kuwabara, J., Noguchi, H., 2004. Flow injection extraction chromatography with ICP-MS for thorium and uranium determination in human body fluids. J. Radioanal. Nucl. Chem. 261 (1), 125−131.

Tong, A.K.T., Kao, Y.H., Too, C.W., Chin, K.F.W., Ng, D.C.E., Chow, P.K.H., 2016. Yttrium-90 hepatic radioembolization: clinical review and current techniques in interventional radiology and personalized dosimetry. Br. J. Radiol. 89 (1062), 20150943.

Trojanowicz, M., Kolacinska, K., Grate, J.W., 2018. A review of flow analysis methods for determination of radionuclides in nuclear wastes and nuclear reactor coolants. Talanta 183, 70−82.

Troyer, G.L., Schenter, R.E., 2009. Medical isotope development and supply opportunities in the 21st century. J. Radioanal. Nucl. Chem. 282 (1), 243−246.

Truscott, J.B., Jones, P., Fairman, B.E., Evans, E.H., 2001. Determination of actinide elements at femtogram per gram levels in environmental samples by on-line solid phase extraction and sector-field-inductively coupled plasma-mass spectrometry. Anal. Chim. Acta 433 (2), 245−253.

Truscott, J.B., Bromley, L., Jones, P., Evans, E.H., Turner, J., Fairman, B., 1999. Determination of natural uranium and thorium in environmental samples by ETV-ICP-MS after matrix removal by on-line solid phase extraction. J. Anal. At. Spectrom. 14 (4), 627−631.

Uccelli, L., Pasquali, M., Boschi, A., Giganti, M., Duatti, A., 2011. Automated preparation of Re-188 lipiodol for the treatment of hepatocellular carcinoma. Nucl. Med. Biol. 38 (2), 207−213.

Unsworth, E.R., Cook, J.M., Hill, S.J., 2001. Determination of uranium and thorium in natural waters with a high matrix concentration using solid-phase extraction inductively coupled plasma mass spectrometry. Anal. Chim. Acta 442 (1), 141−146.

Vajda, N., Kim, C.-K., 2010. Determination of 241Am isotope: a review of analytical methodology. J. Radioanal. Nucl. Chem. 284 (2), 341−366.

Vajda, N., Kim, C.-K., 2011. Determination of transuranium isotopes (Pu, Np, Am) by radiometric techniques: a review of analytical methodology. Anal. Chem. 83 (12), 4688−4719.

van Dongen, G.A., Visser, G.W., Lub-de Hooge, M.N., de Vries, E.G., Perk, L.R., 2007. Immuno-PET: a navigator in monoclonal antibody development and applications. The Oncologist 12 (12), 1379−1389.

Verel, I., Visser, G.W., Boellaard, R., Stigter-van Walsum, M., Snow, G.B., van Dongen, G.A., 2003a. ^{89}Zr immuno-PET: comprehensive procedures for the production of ^{89}Zr-labeled monoclonal antibodies. J. Nucl. Med. 44 (8), 1271−1281.

Verel, I., Visser, G.W., Boerman, O.C., van Eerd, J.E., Finn, R., Boellaard, R., Vosjan, M.J., Stigter-van Walsum, M., Snow, G.B., van Dongen, G.A., 2003b. Long-lived positron emitters zirconium-89 and

iodine-124 for scouting of therapeutic radioimmunoconjugates with PET. Cancer Biother. Radiopharm. 18 (4), 655–661.

Verel, I., Visser, G.W.M., van Dongen, G.A., 2005. The promise of immuno-PET in radioimmunotherapy. J. Nucl. Med. 46 (Suppl. 1), 164S–171S.

Villar, M., Avivar, J., Ferrer, L., Galmes, M., Vega, F., Cerda, V., 2013. Automatic and simple method for Tc-99 determination using a selective resin and liquid scintillation detection applied to urine samples. Anal. Chem. 85 (11), 5491–5498.

Villar, M., Avivar, J., Ferrer, L., Borras, A., Vega, F., Cerda, V., 2015. Automatic in-syringe dispersive liquid-liquid microextraction of Tc-99 from biological samples and hospital residues prior to liquid scintillation counting. Anal. Bioanal. Chem. 407 (19), 5571–5578.

Villar, M., Borras, A., Avivar, J., Vega, F., Cerda, V., Ferrer, L., 2017. Fully automated system for Tc-99 monitoring in hospital and urban residues: a simple approach to waste management. Anal. Chem. 89 (11), 5858–5864.

Wadas, T.J., Pandya, D.N., Solingapuram Sai, K.K., Mintz, A., 2014. Molecular targeted α-particle therapy for oncologic applications. Am. J. Roentgenol. 203 (2), 253–260.

Walker, R.L., Eby, R.E., Pritchard, C.A., Carter, J.A., 1974. Simultaneous plutonium and uranium isotopic analysis from a single resin bead. Simplified chemical technique for assaying spent reactor fuels. Anal. Lett. 7 (8–9), 563–574.

Wang, J., Hansen, E.H., 2003. Sequential injection lab-on-valve: the third generation of flow injection analysis. Trends Anal. Chem. 22 (4), 225–231.

Wang, J., Hansen, E.H., Miró, M., 2003. Sequential injection–bead injection–lab-on-valve schemes for on-line solid phase extraction and preconcentration of ultra-trace levels of heavy metals with determination by electrothermal atomic absorption spectrometry and inductively coupled plasma mass spectrometry. Anal. Chim. Acta 499 (1), 139–147.

Weineisen, M., et al., 2015. ^{68}Ga- and ^{177}Lu-labeled PSMA I&T: optimization of a PSMA-targeted theranostic concept and first proof-of-concept human studies. J. Nucl. Med. 56 (8), 1169–1176.

Werner, R.A., Bluemel, C., Allen-Auerbach, M.S., Higuchi, T., Herrmann, K., 2015. ^{68}Gallium- and ^{90}Yttrium-/^{177}Lutetium: "theranostic twins" for diagnosis and treatment of NETs. Ann. Nucl. Med. 29 (1), 1–7.

Wilbur, D.S., 2011. Chemical and radiochemical considerations in radiolabeling with α-emitting radionuclides. Curr. Radiopharm. 4 (3), 214–247.

Wilken, R.-D., Joshi, S.R., 1991. Rapid methods for determining 90Sr, 89Sr, and 90Y in environmental samples: a survey. Radioact. Radiochem. 3, 15–27.

Wilken, R.D., Diehl, R., 1987. Strontium-90 in environmental samples from northern Germany before and after the Chernobyl accident. Radiochim. Acta 41, 157–162.

Willumsen, B., Christian, G., Ruzicka, J., 1997. Kinetic studies of competitive immunoassay. Anal. Chem. 68, 3482–3489.

Wood, D.J., Elshani, S., Du, H.S., Natale, N.R., Wai, C.M., 1993. Separation of 90Y from 90Sr by solvent extraction with ionizable crown ethers. Anal. Chem. 65, 1350–1354.

Wooten, A.L., Schweitzer, G.D., Lawrence, L.A., Madrid, E., Lapi, S.E., 2013. Routine production of ^{89}Zr using an automated module. Appl. Sci. 3 (3), 593–613.

Wright, B.D., Lapi, S.E., 2013. Designing the magic bullet? The advancement of immuno-PET into clinical use. J. Nucl. Med. 54 (8), 1171–1174.

Xu, S., Freeman, S., Hou, X.L., Watanabe, A., Yamaguchi, K., Zhang, L.Y., 2013. Iodine isotopes in precipitation: temporal responses to I-129 emissions from the Fukushima nuclear accident. Environ. Sci. Technol. 47 (19), 10851–10859.

Xu, S., Zhang, L.Y., Freeman, S., Hou, X.L., Shibata, Y., Sanderson, D., Cresswell, A., Doi, T., Tanaka, A., 2015. Speciation of radiocesium and radioiodine in aerosols from Tsukuba after the Fukushima nuclear accident. Environ. Sci. Technol. 49 (2), 1017–1024.

Xu, S., Zhang, L.Y., Freeman, S., Hou, X.L., Watanabe, A., Sanderson, D.C.W., Cresswell, A., Yamaguchi, K., 2016a. Iodine isotopes in precipitation: four-year time series variations before and after 2011 Fukushima nuclear accident. J. Environ. Radioact. 155, 38–45.

Xu, S., Cook, G.T., Cresswell, A.J., Dunbar, E., Freeman, S., Hou, X.L., Kinch, H., Naysmith, P., Sanderson, D.W.C., Zhang, L.Y., 2016b. Carbon, cesium and iodine isotopes in Japanese cedar leaves from Iwaki, Fukushima. J. Radioanal. Nucl. Chem. 310 (2), 927–934.

Yang, H., Luk, V.N., Abeigawad, M., Barbulovic-Nad, I., Wheeler, A.R., 2009. A world-to-chip interface for digital microfluidics. Anal. Chem. 81 (3), 1061–1067.

Yong, K., Brechbiel, M., 2015. Application of ^{212}Pb for targeted alpha-particle therapy (TAT): pre-clinical and mechanistic understanding through to clinical translation. AIMS Med. Sci. 2 (3), 228–245.

Yordanov, A.T., Pozzi, O., Carlin, S., Akabani, G., Wieland, B., Zalutsky, M., 2004. Wet harvesting of no-carrier-added ^{211}At from an irradiated ^{209}Bi target for radiopharmaceutical applications. J. Radioanal. Nucl. Chem. 262, 593–599.

Yordanova, A., Eppard, E., Kürpig, S., Bundschuh, R.A., Schönberger, S., Gonzalez-Carmona, M., Feldmann, G., Ahmadzadehfar, H., Essler, M., 2017. Theranostics in nuclear medicine practice. OncoTargets Ther. 10, 4821–4828.

Yu, S., 2006. Review of ^{18}F-FDG synthesis and quality control. Biomed. Imaging Interv. J. 2 (4), 1–11.

Zahradnik, P., Swietly, H., 1996. The robotized chemical treatment of diluted spent fuel samples prior to isotope dilution analysis. J. Radioanal. Nucl. Chem. 204 (1), 145–157.

Zähringer, M., Becker, A., Nikkinen, M., Saey, P., Wotawa, G., 2009. CTBT radioxenon monitoring for verification: today's challenges. J. Radioanal. Nucl. Chem. 282 (3), 737–742.

Zalutsky, M.R., Pruszynski, M., 2011. Astatine-211: production and availability. Curr. Radiopharm. 4 (3), 177–185.

Zalutsky, M.R., Reardon, D.A., Pozzi, O.R., Vaidyanathan, G., Bigner, D.D., 2007. Targeted α-particle radiotherapy with ^{211}At-labeled monoclonal antibodies. Nucl. Med. Biol. 34 (7), 779–785.

Zalutsky, M.R., Reardon, D.A., Akabani, G., Coleman, R.E., Friedman, A.H., Friedman, H.S., McLendon, R.E., Wong, T.Z., Bigner, D.D., 2008. Clinical experience with α-particle–emitting ^{211}At: treatment of recurrent brain tumor patients with ^{211}At-labeled chimeric antitenascin monoclonal antibody 81C6. J. Nucl. Med. 49 (1), 30–38.

Ziegler, H., Mayer, K., 1999. Development of an optimized method for faster and more reliable automated U/Pu/Np separations. Radiochim. Acta 86 (3–4), 123–128.

Zimmermann, R., 2006. Nuclear Medicine: Radioactivity for Diagnosis and Therapy. EDP Sciences, France.

Zona, C., et al., 2008. Wet-chemistry method for the separation of no-carrier-added ^{211}At/^{211g}Po from ^{209}Bi target irradiated by alpha-beam cyclotron. J. Radioanal. Nucl. Chem. 276 (3), 819–824.

Zvara, I., 1999. Studies of the Chemistry of Transactinides by Fast Separation Techniques. In: NATO Science Series, Series 2: Environmental Security, vol. 53. Chemical Separation Technologies and Related Methods of Nuclear Waste Management, pp. 123–134.

Jay W. Grate, PhD



Dr. Jay W. Grate is a Laboratory Fellow at the Pacific Northwest National Laboratory (PNNL) and an Affiliated Professor with the Chemistry Department of the University of Washington. He is a Fellow of the Electrochemical Society, a Battelle Distinguished Inventor, and a Wiley Research Fellow of the Environmental Molecular Sciences Laboratory at PNNL. He received a BA in Chemistry at Rollins College (summa cum laude) and received his PhD in Chemistry from the University of California, San Diego. After postdoctoral research at the University of California Irvine, he joined the Naval Research Laboratory in 1984, moving to the PNNL in 1992. Prior to joining PNNL, he spent a sabbatical at the Scripps Research Institute in a group developing catalytic antibodies. Dr. Grate has broad research experience in separation, sensing, and analysis as they apply to diverse national mission areas. In the course of his research, he has found the science in the applications and published in journals, reviews, and books; his work has appeared on the covers of *Analytical Chemistry*, *Langmuir*, *Chemical Communications*, *Analyst*, and *Chemical Reviews*. At the Naval Research Laboratory, he established his reputation in analytical chemistry in the development and understanding of polymer-coated acoustic wave vapor sensors. He continued this work at PNNL, winning ACS and R&D100 awards for development of polymeric materials for sensor applications; these materials developments were enabled by a more fundamental understanding of vapor−polymer chemical interactions. He has developed and sustained programs at PNNL in such areas as radiochemical separations and analysis, analytical microfluidics for biodetection, radionuclide sensors for water monitoring, and fluorescent techniques for oxygen sensing in microfluidic structures. He has also developed biocatalytic nanostructured materials and new sequence-defined biomimetic polymers.

jwgrate@pnnl.gov
http://orcid.org/0000-0002-2163-8383
http://www.linkedin.com/pub/jay-grate/51/82/44a

Matthew J. O'Hara



Matthew J. O'Hara is a senior research scientist in the Nuclear Chemistry and Engineering technical group of the Pacific Northwest National Laboratory. He has more than 20 years of R&D experience, with extensive knowledge in the fields of radiochemistry and laboratory automation. A major focus of his research has been the selective online preconcentration/separation/purification/detection of radionuclides from various media using autonomous fluid handling and measurement systems. Instrumentation and chemistries developed during his career at PNNL have targeted specific radionuclides, with the objective of activity quantification ranging from trace levels in environmental matrices to high-level nuclear waste solutions. He has also developed sample processing platforms used to expedite the radiochemical processing of samples for national security applications. Additionally, he has developed a number of fluid processing systems for the isolation of medically relevant radionuclides from longer-lived parent isotopes and accelerator targets.

matthew.ohara@pnnl.gov
http://orcid.org/0000-0003-3982-5897

Oleg B. Egorov, PhD



Dr. Oleg B. Egorov is recognized for his research work in radiochemistry, radioanalytical chemistry, analytical chemistry, and instrumentation. His current professional interests include production of medical isotopes, development of new radiopharmaceuticals, and medical devices for brachytherapy, theranostics, nuclear medicine imaging software, and technology commercialization. Prior to becoming an independent consultant in 2009, Dr. Egorov had worked as a director of Research and Development for Isoray Medical Inc. Dr. Egorov had worked as a senior research scientist at the Pacific Northwest National Laboratory (PNNL) where he had led and contributed to world-class basic and applied R&D programs directed at new chemistries and instrumentation for automated production of short-lived medical isotopes for the treatment of cancer, automated process monitoring, radionuclide sensors for groundwater monitoring, and laboratory automation. He has authored/coauthored numerous peer-reviewed publications and holds nine US/international patents. Dr. Egorov holds a PhD in Analytical Chemistry from the University of Washington.

Chapter 12

PERPUSTAKAAN PRIBADI AN-NUR SUNARYA

Analytical techniques in nuclear safeguards

William Geist[1], Peter Santi[1] and Philip Hypes[2]

[1]Los Alamos National Laboratory, Safeguards Science Technology Group, Los Alamos, NM, United States; [2]Los Alamos National Laboratory, Hazardous Materials Management Group, Los Alamos, NM, United States

Chapter outline

I. Introduction **873**
II. Photon-based assay for safeguards **874**
A. Introduction: characteristics of U/Pu and their spectra 874
1. Attribute tests 875
2. Cerenkov analysis of spent fuel 876
3. Active length measurements 877
4. Sample screening with X-ray fluorescence 877
B. Uranium enrichment (infinite thickness) 877
1. General approach 877
2. Correction factors 878
3. Low-resolution measurements 879
4. High-resolution measurements 880
5. Specialized geometries (fuel pellets and rods) 881
C. Isotopic measurements of uranium and plutonium 881
1. Characteristics of the uranium and plutonium spectra 881
2. Ratio-based measurements of isotopic composition 884
3. Typical results from fielded software 885
D. Mass measurements 886
1. Material test reactor fuel 886
2. Customized geometry efficiency modeling 886
3. Holdup measurements 886
III. Neutron-based assay for safeguards **891**
A. Radiation signatures from plutonium and uranium 891
B. General neutron counters for safeguards measurements 893
C. Neutron well counter properties 893
1. Efficiency 893
2. Die-away time 893
3. Gate fractions 894
D. Singles neutron counting 894
E. Neutron coincidence counting 896
1. Introduction to coincidence counting 896
2. Shift register electronics 897
3. Passive coincidence counting 898
4. Active coincidence counting 899
F. Neutron multiplicity counting 899
1. Introduction to multiplicity counting 899
2. Multiplicity shift register electronics 900
3. Multiplicity measurements 901
IV. Calorimetric assay **902**
A. Introduction 902
B. Heat flow calorimetry 903
1. Operating modes for heat-flow calorimeters 905
2. Calibrating a heat-flow calorimeter 908
3. Types of heat-flow calorimeters 908
C. Calorimetric assay 910
1. Assay error determination 911
2. Calorimetric assay performance 911
D. Applications 914
References **915**
William H. Geist **919**
Peter Santi **919**
Philip A. Hypes **920**

I. Introduction

Nuclear safeguards is the system of policies and technical measures developed to ensure that fissionable materials are being used for their intended peaceful purposes and are controlled through the implementation of technologies, procedures, and policies. Nuclear material of safeguards concern is most commonly plutonium or enriched uranium, but thorium and other isotopes of uranium are also under safeguards. All states have internal safeguards standards typically framed in legislative requirements. For nonnuclear weapon states, safeguards is also implemented

Handbook of Radioactivity Analysis: Volume 2. https://doi.org/10.1016/B978-0-12-814395-7.00012-X
Copyright © 2020 Elsevier Inc. All rights reserved.

at the international level. The International Atomic Energy Agency (IAEA) is the world's safeguards organization. Other safeguards organizations exist at the regional level, for example, the Brazilian-Argentine Agency for Accounting and Control of Nuclear Materials (ABACC) and the European Atomic Energy Community (EURATOM). While ABACC is purely a safeguards verification organization, both EURATOM and the IAEA also play a role in fostering international cooperation on the use of nuclear technology. These international organizations' safeguards measures are generally applied in addition to national requirements. It is important to note that unlike most state-level safeguards organizations, international organizations are not enforcement organizations. The U.S. Nuclear Regulatory Commission regulates safeguards implementation as part of the licensing process and can therefore take action against a facility found to have inadequate safeguards measures in place. International organizations such as the IAEA do not exercise such authority over facilities in member states. International organizations are verification and reporting organizations. If a facility or state is found to have inadequate safeguards measures or cannot be shown to have complied with their safeguards obligations, the response focuses on attempting to improve cooperation on the part of the facility or state and on notifying the other member states of the issue to be resolved in a political forum. In the case of the IAEA, the United Nations Security Council is also informed in addition to member states.

For many years, the primary means of implementing safeguards was verification of information provided by the facility or state. Inspectors would be provided with a list of nuclear material in use at a facility, commonly referred to as a declaration. Inspection efforts focused exclusively on verifying the accuracy of that declaration by auditing records of material receipt, use, and transfer out of the facility. The measurement technology and methodology discussed in this chapter was and is used to independently verify characteristics of the nuclear material such as uranium enrichment or total plutonium mass.

After the first Gulf War in 1990–91, the international safeguards community realized that verifying the accuracy of a declaration was necessary, but not sufficient, to conclude that a state was in full compliance with its safeguards agreements. The Additional Protocol (IAEA, 1997) was drafted by the IAEA to clarify the authority necessary for Agency personnel to verify both the accuracy and completeness of a state's declaration. This involves new technology challenges, which are often directed at the detection of possible undisclosed facilities, more than the nuclear material itself. As such, technology used toward these ends is beyond the scope of this reference.

As part of the safeguards approach, nuclear material samples are obtained and sent to laboratories for destructive analysis (DA). Laboratory measurements can produce very precise, highly accurate results. These measurements, however, require opening containers (involving the potential risk of generating loose contamination), shipping radioactive materials, and waiting for results (typically on the order of weeks to months) and are expensive. In-field measurements, while less precise and accurate than laboratory measurements, do not require sample collection, generally give results in minutes, and are less expensive. The measurement techniques used for measurements of nuclear material are based on conventional detectors such as NaI(Tl) and germanium detectors for detection of gamma rays or ^{3}He tubes and fission chambers for detection of neutrons. The specific analysis techniques utilized are adapted to the particular characteristics of the nuclear material and measurement environments found in nuclear fuel cycle facilities. Also, in most cases, the information of greatest importance to safeguards personnel is the total nuclear mass of ^{235}U or plutonium, and this often cannot be obtained from a single instrument. For example, a plutonium mass value obtained by nondestructive assay (NDA) is calculated by multiplying the power (in watts) obtained from a calorimeter with the effective specific power (in watts/gram Pu) obtained by analysis of a spectrum taken from the item with a germanium detector. This chapter will focus on the NDA measurements most often used for nuclear material accounting.

II. Photon-based assay for safeguards

A. Introduction: characteristics of U/Pu and their spectra

Gamma ray spectroscopy plays an important role in NDA. With few exceptions, all measurement techniques require information about the enrichment of uranium or isotopic composition of plutonium of the item being assayed to produce a mass value. Gamma spectroscopy is the primary NDA tool that meets this need.

Uranium is found in nature with approximately 0.72% ^{235}U (this and the following values are in atom percent). Uranium-235 is usually the principal uranium isotope of safeguards concern. Uranium-238 is the most abundant isotope found in natural uranium, at 99.27%. Uranium-234 is a trace isotope with a natural value of 0.0006%. "Recycled" uranium that has been recovered from spent nuclear fuel will also contain ^{236}U. Some NDA techniques need to be adapted to take the ^{236}U signatures into account.

Plutonium is a mixture of five plutonium isotopes (^{238}Pu, ^{239}Pu, ^{240}Pu, ^{241}Pu, ^{242}Pu), ^{241}Am, and to a small amount ^{237}U. The half-life of ^{242}Pu is an order of magnitude longer than any other plutonium isotope, and it does not produce detectable gamma rays in typical gamma ray measurement of plutonium items. The implication of this on safeguards measurements will be discussed further on in this chapter.

Plutonium 241 has a short half-life (14.35 years) and decays both by alpha decay and β^- decay so its daughter products (^{241}Am and ^{237}U) are present in all plutonium very soon after chemical separation. All plutonium items produce detectable americium and uranium radiations. In the case of americium (^{241}Am), the 60-keV gamma ray will dominate the spectrum if measures are not taken to attenuate it. This will be discussed in greater detail below. The uranium (^{237}U) is important because it contributes characteristic X-rays in the X-ray region of the spectrum and because it quickly achieves secular equilibrium with ^{241}Pu, enabling ^{237}U gamma rays to be used as if they originated directly from the decay of ^{241}Pu. The analyst can therefore use ^{237}U gamma rays to measure ^{241}Pu concentration.

The spectrum of plutonium, and to a lesser extent, uranium, is complicated. There are many gamma rays present, often coenergetic with gamma rays from other isotopes or elements. There are unresolved multiplets and complex regions including characteristic X-rays and gamma rays, and there may be cascade sums. However, measurements can often be taken under well-controlled conditions, on material that is free of gamma ray–producing impurities. This enables us to perform a surprising number of measurement tasks with low-resolution detectors, despite the complexity of the gamma ray spectrum.

1. Attribute tests

An attribute test is a test performed to prove or disprove the hypothesis that a given item contains the declared nuclear material. This is a quantitative test in the sense that mathematical criteria are used to determine if the hypothesis is proven or disproven. The qualitative test only provides an answer that is simply a "yes" or a "no." Attribute tests do not provide information such as the mass of uranium or the isotopic composition of plutonium but simply confirms the presence of the nuclear material.

Gamma ray-based attribute tests are typically performed by taking a background spectrum and comparing the background spectrum to a spectrum taken from the item being tested. A region of interest (ROI) is chosen around one or more gamma ray peaks that are used to indicate the presence of the isotope in question. The ROI should be selected to minimize the risk of a false positive result. This means selecting a region that contains a dominate gamma ray emitted from the material to be tested. For uranium, the 185.7-keV peak that comes from ^{235}U or the 1001-keV peak from ^{238}U is typically chosen. For plutonium, the 208 keV region or the 375–414 keV regions are typically chosen for attribute testing.

The location of the background spectrum is a critical choice in the proper performance of an attribute test. Usually, an item will have to be tested in the presence of other items containing the same nuclear material. Consequently, taking a background in a location that is too isolated from the nuclear inventory located and stored in the facility will produce a background count rate in the ROI that is unrealistically low. When this occurs, any spectrum taken under more realistic conditions—near the rest of the material—will indicate that the item passes the attribute test, regardless of whether the item being tested actually contains the material in question. The NDA practitioner should take a background in a configuration as close to the measurement configuration as possible. If possible, the best approach would be to bring the nuclear material to a location where the background was measured. If this is not possible, the background should be measured at a location that best represents the background at the measurement location.

The acceptance criterion used to determine if a given item passes or fails the attribute test is shown in Eq. (12.1).

$$A_i > Al, \quad \text{where } AL = T_i\left[BR + 3\sqrt{\left(\frac{S_B}{T_B}\right)^2 + \left(\frac{S_i}{T_i}\right)^2}\right] \tag{12.1}$$

where AL is the acceptance level, A_i is the item net area in the ROI, S_i is the uncertainty of A_i as calculated by the spectral analysis software, T_i is the count time for item verification, T_B is the count time for background measurements, BR is the background net area in the ROI divided by background count time T_B, and S_B is the uncertainty of the background net area in the ROI.

Conceptually, an item will pass the attribute test if the count rate in the ROI taken from the item is more than the background count rate plus three times the combined uncertainty of the two counts. If the items are being measured in a very-low-background area, Eq. 12.1 simplifies to three times the uncertainty in the ROI from the item spectrum itself.

For individual items, the detector can often be shielded well enough to virtually eliminate background and allow the user to employ the simplified acceptance limit calculation. For fresh fuel assemblies, which require a crane to move, the items must generally be evaluated in the storage racks where they are found, necessitating the use of the more rigorous acceptance level shown in Eq. (12.1).

Spent fuel attribute tests are significantly different from other attribute tests. Spent fuel contains the majority of the plutonium in the world and is consequently of great safeguards significance. However, the gamma signal from the plutonium is typically difficult or impossible to identify in the presence of the fission fragments and activation products in the spent fuel. Furthermore, spent fuel that has recently been removed from the core of a power reactor produces radiation levels that need to be shielded for the

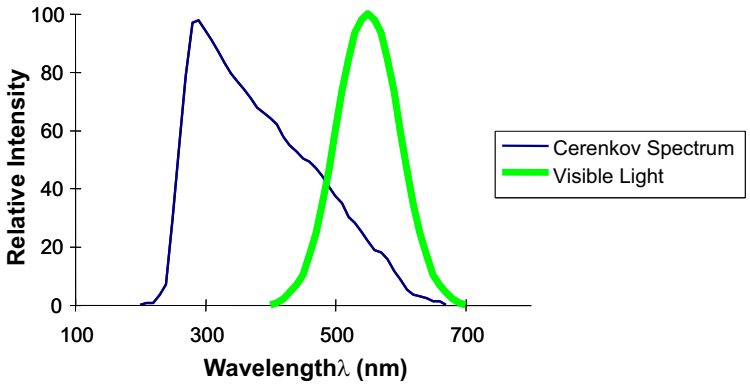


FIGURE 12.1 Spectrum of Cerenkov light compared with visible light. For the color version of the figure, the reader is referred to the online version of the book.

safety of the workers. This is commonly accomplished by storing the spent fuel in water. The attribute tests performed by safeguards personnel are indirect indications of the presence of plutonium. They assume that in a spent fuel assembly, the presence of fission products indicates that the assembly is undisturbed, and therefore, the plutonium is still present. Typically, the 662-keV gamma ray emitted from ^{137}Cs is used to indicate the presence of fission products and hence a spent fuel assembly. There are no credible techniques for removing the plutonium from a spent fuel assembly without significantly and obviously altering the physical appearance of the fuel and removing the fission products that produce the signals on which the attribute tests are based.

2. Cerenkov analysis of spent fuel

Two signals that are used for attribute testing of spent nuclear fuel are gamma rays and Cerenkov light. Cerenkov analysis is a widely used evaluation technique for spent fuel (IAEA, 2003). This technique has the advantage of allowing very rapid analysis of spent fuel assemblies. The drawbacks of this technique are that it is based on a qualitative analysis of the light produced by a spent fuel assembly. No quantitative data is produced by older systems. Newer, digital systems can produce quantitative data (Grape et al., 2010). Also, this technique can only be applied when the water in the spent fuel pond allows the clear transmission of light from the spent fuel assemblies to the surface of the pond. In some facilities, the pond water is not clear enough to permit Cerenkov analysis of the spent fuel attributes. In this case, an attribute test using gamma rays as discussed above must be used.

Cerenkov light is produced by radiation emitted from the spent fuel. Charged particles, primarily electrons, are produced by ionization of the water by gamma rays from the spent fuel. Some of these particles will be traveling at speeds greater than the speed of light in water. These particles produce a shock wave in the water, analogous to the shock wave produced by a body moving through air at greater than the speed of sound. This shock wave produces photons of visible light, as excited electrons revert to lower energy states. See Chapter 6, Volume 2 of this book for additional information on Cerenkov radiation, and a comprehensive treatment on Cerenkov radiation is provided by L'Annunziata (2007, 2016). The energy spectrum of the light produced is shown in Fig. 12.1.

Cerenkov light has a distinctive appearance when produced by spent fuel submerged in water. The long, thin fuel rods collimate the light, producing a glow profile that is maximized when the Cerenkov viewing device is directly above the assembly and drops off rapidly, as the device is moved off axis from the assembly. The intensity of the light produced by an assembly increases with burnup and decreases with cooling time, as the short-lived isotopes decay away.

The detectors used to evaluate Cerenkov glow are telephoto lenses with infrared filters and image intensifiers. The infrared filters reduce the interference from other visible light sources. The image intensifiers can be either photocathodes combined with phosphor screens, to bring the filtered light into the visible range and increase its intensity, or digital cameras (Chen et al., 2007). The images are evaluated by trained personnel, who look at the intensity of the light and the distinctive intensity profile arising from the collimation effects. Training is important, as the evaluation of the attribute test result is fundamentally a judgment call made by an investigator. This evaluation becomes more difficult as items age in the pond. The evaluation is also more difficult when a weak Cerenkov source or an item that is not a source of Cerenkov light is surrounded by many strong sources of Cerenkov light.

When Cerenkov evaluation is not possible, because of the poor transmission of light in the spent fuel pond or because the age of the items needs to be verified, safeguards personnel apply techniques based on the evaluation of ionizing radiation produced by the fuel assemblies. Gamma spectra are obtained either by positioning the detector in close proximity to the fuel (i.e., Fork detectors (Rinard and Bosler, 1998) or Irradiated Item Attribute Tester (Zendel,

2008)) or by introducing an air column into the pool to provide an unshielded path for the gamma rays to travel from the spent fuel assembly to the detector (i.e., the Spent Fuel Attribute Tester (Tikkinen and Tarvainen, 1990)). The acceptance level criteria for the Irradiated Item Attribute Tester and the Spent Fuel Attribute Tester are calculated as shown in Eq. (12.1). In addition to gamma spectroscopy data, the Fork detector also contains fission chambers for the collection of neutron rate data. The combination of the gross gamma ray count rate and the neutron signal is attributed to the spent fuel assembly.

3. Active length measurements

Operator declarations of fresh fuel rods or fuel assemblies typically give the total grams of ^{235}U, while the neutron collar (Menlove et al., 1990) used to verify fresh fuel assemblies produces results in grams of ^{235}U per unit length. To verify the total ^{235}U mass in this case, the length of the rod or assembly must be verified. This is referred to as the active length of the rod or assembly. The active length is less than the full length of the rod or assembly because of internal structures at the ends of the rod, such as the spring that is included in one end of most fuel rods or the end caps that provide structural support to the fuel assemblies.

Active length measurements are performed with gamma detection instruments such as thallium-doped sodium iodide [NaI(Tl)] detectors. To determine the active length, the count rate within the active area containing nuclear material and the count rate from the inactive portion without nuclear material is measured. The limits of the active length are the two locations where the measured count rate equals the average of the two measurements (one within and one outside the zones containing nuclear material). The limits are found by scanning the length of the item and identifying the two end locations, as they are found. The distance between these two points is then measured with a tape measure or other similar means. These measurements can be performed with almost any spectroscopic system. With a good detector and some simple software, measurement bias can be as low as 2- or 3-mm for a 4-m rod or assembly, but for realistic measurements in an operating facility, the uncertainties are usually 1 or 2 cm. If a slit collimator is being used, the point under the center of the slit should be marked when the end of the active zone is found. If a round collimator is used, any reference point can be used (left edge, center, or right edge) as long as the same point in the collimator area is used at both ends of the item.

4. Sample screening with X-ray fluorescence

X-ray fluorescence is a well-known technique that is used in safeguards to identify the presence of elements in items and to identify impurities in nuclear material. Characteristic X-rays of nuclear material are found in the 100-keV region of the spectrum. The intensity of the characteristic X-rays is determined by the activity of the irradiation source and the concentration of the material being evaluated. In large masses, self-irradiation can produce strong X-ray fluorescence signals. External irradiation sources are only necessary when the volume visible to the detector is very small. High intensity can be obtained by proper selection of setup parameters such as source–detector geometry, source strength, and sample size. Either isotopic or machine-generated radiation can be used to irradiate the sample. The general assay equation is

$$\rho = \{RR \times CF(RL) \times CF(AT)\}/K \tag{12.2}$$

where ρ is the concentration of the element, RR is the raw (uncorrected) rate of X-ray detection, $CF(RL)$ is the correction factor of rate-related losses, $CF(AT)$ is the correction factor for sample self-attenuation, and K is the calibration constant.

The calibration factor takes into account the effect of the intensity of the irradiation source. A change in calibration source (through decay or because of a replacement of the source) will necessitate the determination of a new calibration constant.

These techniques can be used to screen for the presence of nuclear material in samples, to screen nuclear material samples for selected impurities, to measure nuclear material concentrations, or to measure U/Pu ratios.

B. Uranium enrichment (infinite thickness)

1. General approach

One technique for the measurement of uranium enrichment by gamma ray spectroscopy involves correlating the count rate for a ^{235}U gamma ray to the enrichment of the item being analyzed. Enrichment is typically expressed in one of two ways. Enrichment can be expressed as weight percent, which is the mass of ^{235}U as a percentage of the total mass of the element uranium. Enrichment can also be expressed as an atom percent, which is the total number of ^{235}U atoms as a percentage of the total number of elemental uranium atoms. DA techniques typically report results in atom percent, whereas NDA techniques typically report results in weight percent. Many NDA software packages, however, have been programmed to display both the atom percent and weight percent values to facilitate comparison between the NDA result and the DA results. Consult the manufacturer's documentation for the software or NDA system to determine which type of enrichment value the system provides. The conversion equation is

$$E_{\mathrm{wt\%}} \approx (235E_{\mathrm{at\%}})/(238 - 0.03E_{\mathrm{at\%}}) \tag{12.3}$$

where $E_{at\%}$ is the enrichment in atom percent and $E_{wt\%}$ is the enrichment in weight percent.

The 185.7-keV gamma ray is the almost universal choice for uranium enrichment measurements using the infinite thickness technique. The efficiency of most detectors is good in this energy range, the gamma ray is penetrating enough to be detectable through most container walls found in the nuclear industry, and the gamma ray is sufficiently well resolved to produce results with acceptable accuracy and precision in gamma ray detectors of both low and high resolution.

The most commonly applied method of measuring uranium enrichment is referred to as the infinite thickness technique or the enrichment meter technique (ASTM-C1514-08, 2017). This method requires a very reproducible geometry typically obtained by enclosing the gamma spectroscopy detector in a collimator, which restricts the detector's field of view. This method assumes that the volume of material defined by the collimator is completely filled with nuclear material. Self-attenuation within the uranium provides a consistent depth of view within the material. This depth is defined as the infinite thickness.

For the infinite thickness criterion to be met, the item must be thick enough that the 185.7 keV gamma rays from the back edge of the item *cannot* penetrate through the uranium to reach the detector. Once the item is thick enough to meet this condition, it is said to be infinitely thick because the detector would produce the same count rate from the actual item being measured or from an item that was thicker. For practical purposes, this requires the item to be at least seven mean free paths thick. A mean free path is defined as the thickness of material that will reduce the gamma intensity at a given gamma ray energy to one half of its unattenuated intensity, as described in Chapter 1, Volume 1 of this book. The mean free path is the average distance the gamma ray travels through the material before it undergoes some sort of interaction, such as Compton scattering or the photoelectric effect. The criteria for infinite thickness for a variety of uranium compounds are shown in Table 12.1.

A simple *Gedankenexperiment* will explain this requirement. Imagine a single mean free path thickness of uranium, wider than the collimator on a spectroscopic detector. If we determine a count rate from the single mean free path thickness layer and then add a second mean free path thickness layer (doubling the thickness and hence the mass of material above the collimator opening), less than half of the gamma rays from that second layer will penetrate the first mean free path thickness layer to reach the detector. So the count rate will increase, but by much less than a factor of 2. Each additional layer added will produce a diminishing increase in the count rate, until so much material is already present that the gamma rays from an additional layer have a negligible probability of reaching the detector. Once this is true, the "infinite thickness" criterion for that material has been reached and adding additional layers will not change the count rate in the detector. Less than 0.1% of gamma rays emitted beyond seven mean free paths thickness will reach the detector. Given items with the same chemical form and container walls, the only source of variation in the 185.7 keV count rate will therefore be the number of ^{235}U atoms within the detectable volume. This enables us to correlate the count rate to the ^{235}U enrichment.

2. Correction factors

Unless calibration standards are available that are in identical containers and of the same chemical form as the items to be measured, obtaining accurate results requires corrections to be applied to account for differences in container attenuation and uranium chemical composition.

a. Wall thickness

Gamma rays that penetrate the uranium itself must also pass through the container wall to be detected. For example, if the calibration sources have a 1-mm-thick steel wall and the items to be measured/verified have a 2-mm-thick steel wall, uncorrected measurements will be biased toward results

TABLE 12.1 Mean free path and infinite thickness values for common uranium compounds.

Material	Density ρ (g/cm^2)	Mean free path λ (cm)	Infinite thickness (cm)
Metal	18.70	0.04	0.26
UF_6 (solid)	4.70	0.2	1.43
UO_2 (powder)	10.90	0.07	0.49
UF_6 (sintered)	2.00	0.39	2.75
U_3O_8 (powder)	7.30	0.11	0.74
Uranyl nitrate	2.80	0.43	3.01

TABLE 12.2 Chemical composition correction factors.

	Measured item					
Calibration Standard	U	UC	UO2	U3O8	UF6	Uranyl nitrate
U (100% U)	1.000	1.004	1.011	1.014	1.038	1.090
UC (95% U)	0.996	1.000	1.007	1.010	1.033	1.086
UO_2 (88% U)	0.989	0.993	1.000	1.003	1.026	1.078
U_3O_s (85% U)	0.986	0.990	0.997	1.000	1.023	1.075
UF_6 (68% U)	0.964	0.968	0.975	0.978	1.000	1.051
Uranyl nitrate (47% U)	0.917	0.921	0.927	0.930	0.952	1.000

that are below the true enrichment values. This is because the 2-mm-thick steel wall will absorb more of the 185.7 keV gamma rays than with the calibration standard containers. The attenuation properties of the most common container materials are well known and can be calculated using the standard attenuation formula:

$$I = I_0 e^{-\mu_m \rho x} \tag{12.4}$$

where I is the intensity of the gamma radiation transmitted through an absorber, I_0 is the initial gamma ray intensity, μ_m is the mass attenuation coefficient with units of cm^2/g, ρ is the density of the absorber in units of g/cm^3, and x is the absorber thickness in cm.

(See Chapter 1, Volume 1 of this book for a detailed treatment of gamma ray attenuation calculations). This formula is a sensitive function of wall thickness necessitating precise knowledge of the wall thickness. This can be done with reference to institutional knowledge of the container design in some cases. In other cases, the containers may not be sufficiently well characterized, and measurements may be necessary. These measurements can be performed with an ultrasonic thickness gauge. For containers such as 30B containers used for UF_6 storage and transportation, the thicknesses can vary significantly between different locations on the same container. For these containers, the thickness should be determined at the exact point where the calibration measurements or assay measurements are going to be performed.

Many of the software tools in use for infinite thickness uranium measurements automate the wall thickness correction process if provided with calibration standard wall parameters and measurement item wall parameters.

b. Sample composition

As shown in Table 12.1, the density of the commonly encountered chemical forms of uranium varies by almost an order of magnitude. Consequently, the volume of loose UO_2 powder visible to a detector is significantly greater than the volume of uranium metal that would be visible to the same detector. This will significantly bias uncorrected measurements made with a system calibrated using a different form of uranium from the items to be measured. Again, however, the correction factors can be easily calculated. Values for a variety of common forms of uranium are shown in Table 12.2. These correction factors are often applied automatically by the commonly used software packages.

3. Low-resolution measurements

The infinite thickness technique is widely employed using low-resolution detectors such as NaI(Tl) scintillators. The resolution of a NaI(Tl) detector is not sufficient to isolate the 185.7 keV gamma ray. The primary consequence of the low resolution is the inability to position a background ROI below the 185.7-keV gamma ray, because the X-ray region and the 143.8 keV gamma ray (also from ^{235}U) provide too much interference. The only location available for the background ROI is at an energy region above 185.7 keV. The usual practice is to position an approximately 50-keV-wide ROI around the 185.7-keV-peak and an approximately 60-keV-wide background ROI above the peak ROI. This background ROI is usually separated from the peak ROI by about 10 keV. The enrichment calculation equation for this method is

$$E\% = \{A(\mathrm{ROI}_{\mathrm{peak}}) + B(\mathrm{ROI}_{\mathrm{background}})\}K_1K_2 \tag{12.5}$$

where $E\%$ is the enrichment of the item, A is a calibration constant, $\mathrm{ROI}_{\mathrm{peak}}$ is the count rate in the ROI positioned on the 185.7-keV peak, B is a calibration constant possessing a negative value, $\mathrm{ROI}_{\mathrm{background}}$ is the count rate in the background ROI, K_1 is the container wall correction discussed above, and K_2 is the item composition correction discussed above.

Low-resolution enrichment measurements require two or more calibration standards to determine the calibration constants because there are two calibration constants. The

background count rate is inversely proportional to enrichment because the primary source of counts in the background ROI is Compton scattered high-energy gamma rays dominated by the 1001-keV gamma ray from the decay of ^{234m}Pa, a daughter product of ^{238}U. For lower enriched items, the high-energy gamma rays from ^{238}U decay will be abundant, leading to a higher level of background counts than will be found in highly enriched items. In highly enriched items, little ^{238}U is present, leading to less count rate in the background ROI.

Despite the low resolution of detectors such a NaI(Tl), the high efficiency of these detectors results in good measurement statistics in a short measurement time, producing low bias results with random uncertainties on the order of 3%−5% for typical measurements on low enriched uranium with typical measurement times of 60−120 s.

The wall thickness corrections, as typically employed, are based on the standard thin beam attenuation function (see Eq. 12.4). This limits their applicability to wall thicknesses that are comparable with those used for the calibration measurements. If the calibration sources are contained within 2-mm steel walls, the correction factor will work well for 1−4 or 5 mm of steel. The correction factor will not produce good results for 15-mm steel walls, as this no longer approximates the thin beam geometry that is assumed by the formula and does not correct for scattering and buildup effects. When calibrating a system for use on thick-walled containers, such as a UF_6 cylinder, one must calibrate using a thick-walled container for the correction factor to work well or use the response function fitting method described below.

The response fitting method is an alternate technique for the analysis of uranium enrichment using low-resolution detectors, which has been developed by Dr. Ray Gunnink (Gunnink and Arlt, 2001; Mortreau and Berndt, 2004). This technique takes advantage of the fact that the shape of the background under the 185.7-keV gamma ray can be modeled based on the well-known physics of Compton interactions. The 185.7-keV and surrounding gamma rays can also be fitted with response functions, as their energies and branching ratios are well known, and the resolution and tailing parameters of the detector can be determined from any uranium item measurement. Knowing all of this physics, the 185.7-keV peak can be accurately fit. This fit contains three components: a background component that is predominately resulting from Compton scattering of the 1001-keV gamma ray from ^{238}U, small angle Compton scattering of the 185.7-keV gamma rays, and full energy 185.7-keV gamma ray peak. By fitting the response of the detector to these three components, an accurate net peak area for the 185.7-keV gamma rays can be determined. This simplifies the enrichment measurement equation to

$$E\% = AC_{peak}K_1K_2 \tag{12.6}$$

where $E\%$ is the enrichment of the item, A is a calibration constant, C_{peak} is the count rate determined from the response function fit to the full-energy 185.7-keV ^{235}U peak, K_1 is the container wall correction discussed above, and K_2 is the sample composition correction discussed previously.

This is an infinite thickness technique, so the corrections and geometry requirements discussed above still apply. The technique also requires that the user enters geometric information about the collimator and data on container wall thickness and composition. The more accurate physics in the software makes the container wall thickness correction more flexible and robust than the standard correction factors applied to the two ROI method of infinite thickness and eliminates bias caused by calibrating and assaying items with substantially different wall thicknesses.

4. High-resolution measurements

High-resolution detectors, such as germanium detectors, are typically used in situations where the uranium enrichment must be measured in the presence of other radioactive materials that emit interfering gamma ray lines. Other radioactive materials can produce gamma rays that would interfere with the wide ROIs necessary for low-resolution systems. The best example of interference effects is enrichment measurements of UF_6 cylinders. These cylinders often contain residue daughter products that remain after the UF_6 has been removed. When new uranium is added to the cylinder, the daughter products can produce gamma rays that interfere with the usual ROIs described above for low-resolution systems, producing biases in the enrichment measurements. With the significantly better resolution of germanium detectors, such interferences can easily be avoided. Background ROIs can easily be chosen above and below the 185.7 keV peak, enabling simple calculation of an accurate net peak area. This enables us to use Eq. (12.6) for the calibration of the system. The wall thickness correction factor, K_1, is critically important, as the UF_6 cylinder thickness varies from location to location on one cylinder, much less from cylinder to cylinder. Typical wall thickness is around 1.5 cm of steel, which results in correction factors on the order of 8. Wall thickness variations of 5% will result in correction factor changes of around 10%. To minimize this uncertainty, the wall thickness correction is best calculated based on a measurement of the wall thickness at the position where the germanium detector will be located. An ultrasonic gauge is commonly used for determining wall thickness.

Planar or coaxial germanium detectors can be used for UF_6 cylinder enrichment measurements. The IAEA typically uses planar detectors, with 1000 mm^2 surface area for good efficiency at 185.7 keV. Good collimation and side

shielding is essential. This is always true with infinite thickness measurements, but particularly so with UF_6 measurements, as they are typically performed in crowded conditions, with one cylinder located centimeters away from another, if there is any separation at all.

5. Specialized geometries (fuel pellets and rods)

The infinite thickness technique requires two conditions to be true that the item is infinitely thick and that the entire field of view, as defined by the collimator, is completely filled with nuclear material. However, if other methods are available to ensure very consistent geometry without meeting all the conditions typically required for the infinite thickness method, the technique can still be applied. This is commonly referred to as the infinite thickness technique with fixed geometry. In the nuclear industry, fuel pellets and fuel rods are made to specified dimensions with strict quality control standards. As such, the enrichment of these items can be measured with the infinite thickness technique with the fixed-geometry method.

Several measurement conditions must be fulfilled for the infinite thickness with fixed-geometry method to yield accurate results. The geometry of the item must be identical to the calibration standard, and the item-to-detector distance must be fixed. In the case of fuel pellets and fuel rods, the dimensions of the nuclear material are essentially identical as required by production standards. Maintaining a fixed distance between the item and detector is easily obtainable by positioning the pellets or rods into a specially made holder. For rods, the holder is typically made with a semicircular groove that allows the rods to be reproducibly placed at the same position within the field of view of the detector. For pellets, a holder with five circular holes is typically used, and the measurement is made with five fuel pellets of the same enrichment standing on end. In theory, any number of pellets could be used, but five was chosen as a good number to get reasonable uncertainty for count time on the order of minutes.

Under these conditions, the count rate will vary proportionally to the enrichment. Typically, the responsive fitting method is used to determine the count rate from the 185.7-keV gamma rays, and this method allows for calibration with one standard. In theory, every pellet or fuel rod with different dimensions would require a separate calibration. In practice, this would be impracticable because of the many different dimensions of fuel pellets used in the nuclear industry. To account for varying dimensions, a correction factor is applied that accounts for different detector response to varying dimensions of fuel pellets. The correction factor essentially adjusts the detector response from the geometry of the fuel pellets or rods used to calibration that the system to the geometry being assayed.

Since fuel pellets are assayed in a bare state, no other correction factors are required besides the detector response adjustment for varying geometry. Fuel rods come in a variety of diameters and cladding wall thicknesses, so both a geometric correction factor and an attenuation correction factor must be applied.

These measurements yield results with accuracies on the order of a couple of percent with a several-minute count time. Care must be taken to ensure that the correct dimensions are used, which are provided by the facility operator. Background from the material contained within the facility can potentially bias the measurement results if not corrected for.

C. Isotopic measurements of uranium and plutonium

1. Characteristics of the uranium and plutonium spectra

The uranium spectrum contains characteristic X-rays in the 90−120 keV region, and many gamma rays spread over the energy range from 90 to 1001 keV. The spectrum from a 20% enriched item is shown in Fig. 12.2.

The X-ray region from ~90 to 120 keV is so named, because the gamma rays in this portion of the spectrum are collocated with the characteristic X-rays of uranium. This region contains gamma rays associated with ^{234}U, ^{235}U, and ^{238}U. Careful peak deconvolution methods must be applied to analyze this region of the spectrum, but faster and more precise results are generally obtainable in this region of the spectrum than any other because of the large intensity of the gamma rays and the high intrinsic detector efficiency in this region. Poor detector resolution or thick-walled containers can prevent the successful analysis of this region.

Above the X-ray region, we find four strong gamma rays from ^{235}U, including the peak that is usually the most intense in most uranium spectra; the 185.7 keV peak. These peaks are each separated by approximately 20 keV and form a distinct quartet that make the high-resolution uranium spectrum immediately recognizable as such. These four peaks are 143.7, 163.4, 185.7, and 205.3 keV.

The qualitative appearance of the spectrum above the 205.3 keV can provide a quick indication if the item is low or highly enriched. For items of enrichment below approximately 10%, the spectrum appears essentially featureless for energies above 205.3 keV. As the enrichment exceeds 20% by a larger and larger margin, the region immediately above 205.3 keV exhibits more and more gamma rays. These gamma rays never match the intensity of the 205.3 keV gamma ray but become more and more clearly visible on a logarithmic scale. Experienced spectrometrists can give a very rough estimate of the enrichment

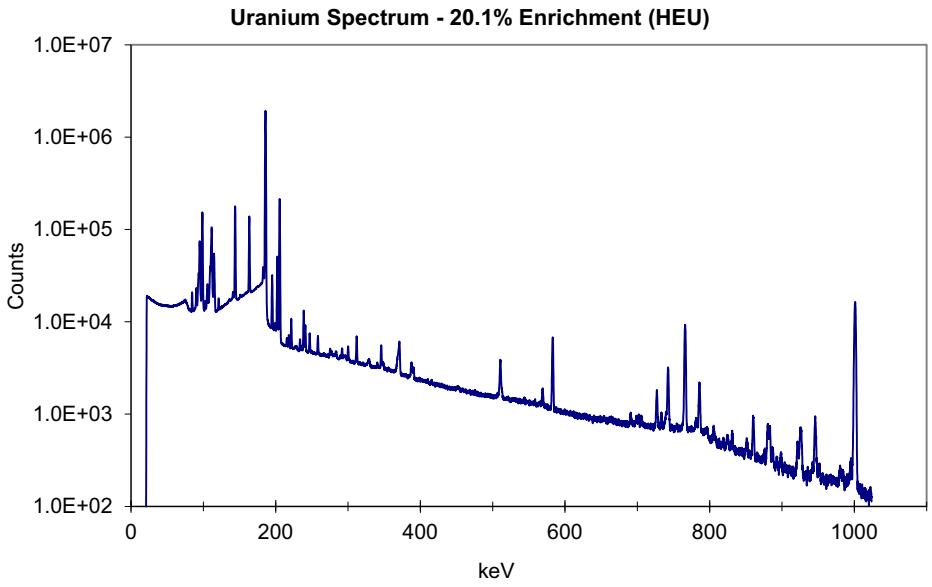


FIGURE 12.2 High-resolution spectrum of uranium. For the color version of the figure, the reader is referred to the online version of the book.

by simply observing the spectrum, but care must be taken as shielding can easily distort the spectrum.

Above approximately 500 keV, virtually all of the significant gamma rays are from ^{234m}Pa, which can be used to determine ^{238}U content in aged items. The most intense peak in the higher energy portion of the spectrum is the 1001.0 keV. One should not attempt to estimate uranium enrichment, even approximately, by comparing the intensity of the 185.7 keV gamma ray with that of the 1001.0 keV gamma ray. Item shielding and detector efficiency can have very strong effects on the detection efficiency over this large energy range.

The plutonium spectrum, shown in Fig. 12.3, is considerably more complex than the uranium spectrum.

The major gamma rays from the principal plutonium isotopes and ^{241}Am are shown in Table 12.3.

As can be seen in Table 12.3, there are many options for analyzing the plutonium spectrum. Complete isotopic information can be found in the X-ray region, the 125−300 keV region, and at energies above 300 keV. This gives the spectroscopist a variety of choices for how to analyze a plutonium spectrum.

The first visible peak in Fig. 12.3 is the 59.6 keV gamma ray from ^{241}Am. This is by far the most intense gamma ray in the plutonium spectrum. For bare plutonium or plutonium in thin-walled containers, this gamma ray will dominate the spectrum to such an extent that the intensity reaching the detector must be reduced to make measurements of plutonium isotopics practical. In the spectrum shown in Fig. 12.3, the 59.6-keV gamma ray has been filtered with approximately 2 mm of cadmium metal. Cadmium is an excellent choice for this filter, as the

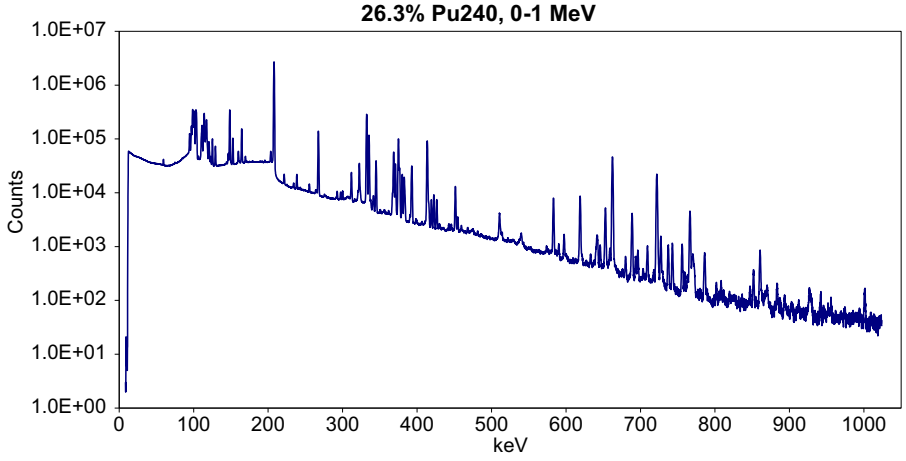


FIGURE 12.3 High-resolution spectrum of plutonium. For the color version of the figure, the reader is referred to the online version of the book.

TABLE 12.3 Major gamma rays from plutonium and ^{241}Am.

	Low energy		X-ray		125–300 keV		300–500 keV		High energy	
	E	BR (%)	E	BR (%)	E	BR (%)	E	BR (%)	E	BR (%)
238Pu	43.5	0.395	99.9	7.35E−03	152.7	9.37E−04			766.4	2.20E−05
239Pu	51.6	0.0271	98.8	1.22E−03	129.3	0.00631	345.0	5.56E−04	645.9	1.52E−05
	38.7	0.0105	116.3	5.97E−04	203.5	5.69E−04	375.0	1.55E−03	658.9	9.70E−06
							413.7	1.47E−03		
240Pu	45.2	0.045	104.2	7.08E−03	160.308	4.02E−04			642.4	1.3E−5
241Pu			103.7	1.02E−04	148.6	1.86E−04	332.4	*		
					164.6	6.67E−05				
					208.0	*	370.9	*		
241Am	59.5	35.9	99.0	0.0203	125.3	4.08E−03	335.4	4.96E−04	662.4	3.64E−04
	26.3	2.4	103.0	0.0195	208.0	7.91E−04			722.0	1.96E−04

The gamma ray energies are given in keV, and the branching ratios (BRs) are in percent, as discussed in Section II.C.2

transmission curve of cadmium is very steep at 60 keV but levels out significantly at 100 keV. This enables a significant reduction in the 59.6 keV intensity without losing too much data in the X-ray region of the spectrum. For freshly separated plutonium, the 59.6-keV gamma ray will not be intense enough to require cadmium filtration. After 2–4 weeks, however, the decay of ^{241}Pu will have produced enough ^{241}Am that the 59.6-keV gamma ray will typically require filtration.

As in uranium, the X-ray region of the plutonium spectrum contains gamma rays from all the detectable isotopes of plutonium (^{238}Pu, ^{239}Pu, ^{240}Pu, and ^{241}Pu). This region is an excellent choice for analyzing plutonium isotopic composition because intense peaks are available to analyze from ^{238}Pu, ^{239}Pu, and ^{240}Pu. This region also contains gamma rays from ^{241}Am and characteristic X-rays of uranium and plutonium. The americium and uranium are present in all plutonium items because of the decay of ^{241}Pu. Alpha decay of ^{241}Pu produces ^{237}U. Beta decay of ^{241}Pu produces ^{241}Am. While very complete isotopic information is available in the X-ray region, this region is the most complex region of the spectrum, as illustrated in Fig. 12.4.

The precise, low-bias analysis of the X-ray region requires excellent detector resolution and abundant data to provide good counting statistics. Planar germanium detectors are preferred, although X-ray region analysis has been successfully performed using coaxial germanium detectors.

The X-ray region is generally viewed as ending with the 125.3 keV gamma ray from ^{241}Am or the 129.3 keV gamma ray from ^{239}Pu. The spectrum is not densely populated between the X-ray region and the 300–400 keV region, but gamma rays can be found here from every isotope except ^{242}Pu. Detector efficiency in this region is good for most detectors, and detector resolution in this and higher energy regions is less critical than in the X-ray region, so coaxial detectors are more commonly employed for their superior high-energy efficiency. The 125–300 keV region also contains the 203/208-keV peak pair. This pair can give a quick, qualitative visual indication of the composition of the plutonium being measured. The 203.5-keV gamma rays are from ^{239}Pu. The 208.0-keV gamma ray is from ^{237}U, which is in secular equilibrium with ^{241}Pu, but also has a contribution from ^{241}Am. For qualitative visual analysis of the plutonium composition, these two peaks should be compared with a linear vertical scale. For high burnup plutonium, such as that produced by normal operation of a light water reactor for the production of electricity, the 208.0-keV gamma ray will be significantly more intense than the 203.5-keV gamma ray. The 208.0-keV gamma ray can exceed the 203.5-keV gamma ray in height by a factor of more than 100. For low burnup plutonium, the peak heights are often comparable, and for very pure ^{239}Pu, the 203.5-keV gamma ray may even slightly exceed the height of the 208.0-keV peak.

The 300–500 keV region is another complicated region of the spectrum, containing many partially resolved peaks. Normal peak analysis routines and peak deconvolution techniques should suffice to analyze this region. Only ^{238}Pu and ^{240}Pu are not represented in this region. They do have gamma rays at higher energy, so as long as the detector efficiency is sufficient at high energy, complete isotopic analysis is possible. If the low–300 keV region is too

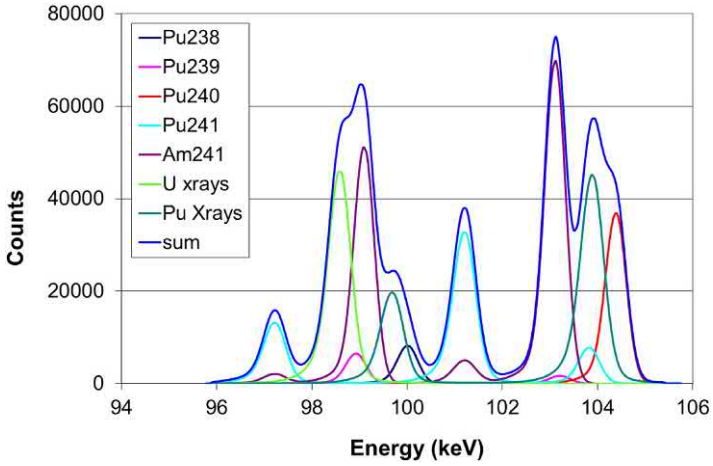


FIGURE 12.4 The components contributing to a plutonium spectrum in the X-ray region. For the color version of the figure, the reader is referred to the online version of the book.

strongly attenuated, complete isotopics cannot be determined. However, this requires significant amounts of shielding. Successful analysis in the low-300 keV region has been demonstrated through as much as 33 mm of lead. The measurement time may be long, depending on the choice of detector, but isotopic fraction values for all isotopes can be obtained, even when the material is in a thick-walled, heavily shielded shipping container. Use of detectors with high efficiency is preferred.

The highest energy region of importance to plutonium isotopic analysis is the 600−800 keV region. This region is similar to the 300−400 keV region in complexity. There are no ^{241}Pu data in this region, which is why the 300−400 keV region is the cutoff region for complete isotopic analysis. At these energies, large detector volumes or large plutonium surface areas (not necessarily high mass, because of the strong self-attenuation of plutonium) are helpful in keeping measurement times down to reasonable values.

2. Ratio-based measurements of isotopic composition

Direct measurements of absolute gamma ray intensities in a uranium or plutonium item would be very difficult, as they would require precise, detailed knowledge of the absolute detector efficiency, container wall composition and thickness, and source/detector geometry. However, it is possible to measure isotopic composition using the *ratios* between uranium or plutonium isotopes with greatly relaxed measurement requirements (ASTM C1030, 2018).

The general equation for the count rate in a particular gamma ray is

$$C = N \cdot \lambda \cdot E \cdot BR \tag{12.7}$$

where C is the net count rate for a gamma ray produced by the isotope, N is the number of atoms of that isotope, λ is the decay rate of that isotope, E is the detection efficiency at the gamma energy in question, and BR is the branching ratio or intensity (in absolute terms) of the gamma ray in question.

The activity ratio between two isotopes from the same item can therefore be expressed as

$$\frac{C_1}{C_2} = \frac{N_1}{N_2} \cdot \frac{\lambda_1}{\lambda_2} \cdot \frac{RE_1}{RE_2} \cdot \frac{BR_1}{BR_2} \tag{12.8}$$

where C_i is the net count rate for a gamma ray produced by isotope i, N_i is the number of atoms isotope i, λ_i is the decay rate of isotope i, or $\ln(2)/T_{1/2}$ for that isotope, RE_i is the *relative* (not absolute) efficiency at the gamma energy in question, and BR_i is the branching ratio or intensity (in absolute terms) of the gamma ray in question.

Eq. (12.8) can be rearranged to produce

$$\frac{N_1}{N_2} = \frac{C_1}{C_2} \cdot \frac{\lambda_2}{\lambda_1} \cdot \frac{RE_2}{RE_1} \cdot \frac{BR_2}{BR_1} \tag{12.9}$$

For any given pair of isotopes/gamma rays, the branching ratio and decay constants can be found in nuclear references. The count rates can be obtained from the spectrum using standard spectrographic analysis techniques. To determine the activity ratio, therefore, we need only to determine relative efficiency values for the gamma rays in question. Note that *relative* efficiency values are all that are required, because all that matters for Eqs. (12.8) or (12.9) are the ratio of the efficiency at the two gamma energies.

The relative efficiency curve for a specific measurement (source, package, and detector combination) can be determined by selecting a variety of gamma rays from a single isotope. These gamma rays should be as evenly distributed over as much of the relevant energy range as possible. Given such a selection of gamma rays, we can look up branching ratios in nuclear references and determine count rates from the spectrum itself. For each gamma ray, we can

calculate the ratio of the count rate to the branching ratio. Each of these ratios becomes a data point that can be plotted and fit to create a relative efficiency curve for the spectrum. Empirical or physics-based models can be used to fit the data to determine the relative efficiency curve. If the item being analyzed is isotopically homogenous, data from multiple isotopes can be used to determine the relative efficiency curve. In a homogenous item, each isotope's gamma rays will be subjected to the same shielding effects and absolute detector efficiency characteristics, so the shape of the relative efficiency curve will be the same. Normalization of the data from one isotope to the other will be necessary because of the different decay rates and concentrations of the different isotopes, but using data from multiple isotopes may enable gaps in the relative efficiency curve data to be filled in.

Once the relative efficiency curve has been determined, the relative efficiency value for any gamma energy can be obtained from the curve. Therefore, all of the inputs needed to calculate the isotopic ratios using Eq. (12.9) can be determined from nuclear references or from the spectrum itself. This enables us to determine isotopic ratios without prior calibration of the analysis system.

Logic dictates that if the isotopic fractions in an item, e.g., a plutonium item, were added up, the fractions must sum to unity, as shown below:

$$F_{238} + F_{239} + F_{240} + F_{241} + F_{242} = 1 \qquad (12.10)$$

where F_i is the fraction of the plutonium isotopes with atomic mass of i.

If we divide both sides of the equation by the ^{239}Pu fraction, we have

$$\frac{F_{238}}{F_{239}} + \frac{F_{239}}{F_{239}} + \frac{F_{240}}{F_{239}} + \frac{F_{241}}{F_{239}} + \frac{F_{242}}{F_{239}} = \frac{1}{F_{239}} \qquad (12.11)$$

Rearranging Eq. (12.11) shows us that the ^{239}Pu fraction is therefore

$$F_{239} = \left(\frac{F_{238}}{F_{239}} + 1 + \frac{F_{240}}{F_{239}} + \frac{F_{241}}{F_{239}} + \frac{F_{242}}{F_{239}}\right)^{-1} \qquad (12.12)$$

Having obtained a value for the ^{239}Pu fraction in the item being analyzed, we can then use the individual isotopic ratios to determine the fractions of the other isotopes. Note, again, that all of this is accomplished without calibration of the analysis system. The same logic can be applied to isotopic analysis of uranium items.

For plutonium analysis, there are two complications to the logic explained above. First, all plutonium items contain measurable quantities of ^{241}Am because of beta decay of ^{241}Pu. This presents no real difficulties for the analysis procedure; we simply add another ratio for americium to ^{239}Pu to Eq. (12.12). ^{241}Am produces an abundance of gamma rays (many of them are coenergetic with ^{241}Pu gamma rays), so analyzing the ^{241}Am content using this method is not difficult. In fact, ^{241}Am gamma rays can be used to determine a relative efficiency curve on their own, as is done for certain plutonium waste materials.

The second complication is caused by the fact that ^{242}Pu does not produce any gamma rays that can be detected in the presence of the other plutonium isotopes. In practice, the ^{242}Pu term has to be left out of Eq. (12.12). Once fractions have been determined for the other isotopes, those fractions can be used in empirical equations to estimate the ^{242}Pu content. At this stage, the total of all the plutonium fractions will exceed unity by the amount estimated for the ^{242}Pu content. The other isotope fractions must be proportionally reduced to ensure that all plutonium fractions sum to 100% and therefore avoid introducing bias by including the ^{242}Pu content. For uranium analysis, ^{236}U content must be determined through similar means, as it does not produce measurable gamma rays.

Another difference between uranium measurements and plutonium measurements is caused by the fact that, with few exceptions, the gamma rays used to measure ^{238}U content actually come from the decay of ^{234m}Pa, as discussed previously. If measurements must be performed on material in which the uranium and protactinium have not yet reached secular equilibrium, a correction factor must be applied to the measurement results to remove bias. This correction factor is automatically applied in the FRAM software (Sampson et al., 2003). The date of chemical separation must be known for the proper correction factor to be determined. After 6 months, equilibrium will be reached, and no measurement biases will be present. In most facilities in the fuel cycle where freshly separated material can be found, the enrichment measurements are usually made with an infinite thickness technique as discussed previously.

3. Typical results from fielded software (Sampson et al., 2003)

a. X-ray region analysis

For a detector with a surface area of 500 mm^2, even small (2−10 g) items produce enough signals to give good statistics in 300−600 s. For X-ray region analysis, the cadmium filter thickness is usually adjusted to produce a 59.6-keV peak comparable (50%−150%) in height to the tallest peaks in the X-ray region. The source to detector distance is adjusted to produce 40%−50% dead time. Under these conditions, the ^{239}Pu precision is typically less than 0.5% relative standard deviation (RSD). The ^{240}Pu precision is typically less than 1% RSD. Systematic biases are usually less than the quoted precision values.

b. Higher-energy analysis

The quality of the results from higher-energy analysis depends strongly on the amount of data available—the statistics of the spectrum and the peaks that are crucial to the analysis. The ^{239}Pu precision is typically less than 1% RSD. The ^{240}Pu precision is typically less than 3% RSD. Systematic biases are usually less than the quoted precision values.

D. Mass measurements

Gamma ray measurements are rarely used to determine mass values for uranium or plutonium because the gamma rays are easily self-shielded and thus not sensitive to thick materials. As shown in Table 12.1, uranium is a very dense material, with a much higher atomic mass than lead. This makes uranium (and for the same reasons, plutonium) a very effective gamma ray shield. Depleted uranium is often used as a shield for industrial radiation sources where the volume of a lead or even tungsten shield would present design problems.

However, there are materials containing uranium or plutonium in geometries and densities that make mass measurements by gamma ray analysis possible. These materials incorporate thin layers of uranium or plutonium that enable at least a fraction of the gamma radiation produced to reach the detector.

1. Material test reactor fuel

Material test reactor fuel is often manufactured in the form of thin plates of uranium (often highly enriched) clad in a layer of aluminum. Possible uranium forms include metal (as a uranium–aluminum alloy), uranium oxide, or uranium silicate. The fuel assemblies can be arrays of flat or slightly curved plates, or concentric square, hexagonal, or cylindrical cross-sectional tubes.

Calculations or measurements specific to the geometry of the assemblies being measured should be performed to verify that the assemblies are not infinitely thick. Many assemblies can be loaded and unloaded by the operators, enabling the *Gedankenexperiment* described in the infinite-thickness discussion to be performed almost exactly as described. If the assembly is infinitely thick, gamma measurements will be unable to detect diversion of material.

For assemblies that are not infinitely thick, predicted count rates at 185.7 keV can be obtained by calculation or by Monte Carlo methods. The prediction should be verified by measuring a known assembly. Once this has been done, fuel assembly mass can be verified, if the measured count rate is within good statistical agreement with the predicted and verified value.

For the calculations and the actual measurements, the setup is simple. The detector is positioned at the centerline of the fuel assembly, with the long axis of the fuel assembly perpendicular to the centerline of the detector. Low-resolution NaI(Tl) detectors are typically used because of their good efficiency and ease of operation. The ROIs used are similar to those used for infinite-thickness enrichment measurements.

This measurement technique is very dependent on consistent geometry. The plates furthest from the detector in an assembly contribute a very small percentage of the total signal. Source–detector distance changes or movement of the detector off of the centerline of the fuel will cause count rate changes that can easily overwhelm the difference in count rate between a 9-plate assembly and a 10-plate assembly.

2. Customized geometry efficiency modeling

Gamma ray–based mass measurements are being made for holdup and discrete items such as waste drums or boxes using a Monte Carlo modeling technique to calculate the absolute detection efficiency of the item being assayed. The technique requires that the item being assayed has a relatively well-defined geometry. Both the special distribution of nuclear material and all the interviewing attenuating material must be modeled. The germanium detector characteristics must also be known. Monte Carlo techniques are then used to sample the distribution of nuclear material to determine an absolute detection efficiency as a function of the gamma ray energy. From the absolute detection efficiency, it is straightforward to calculate the activity or mass of the radionuclides present in the item. Depending on the measurement situation, an iterative approach can be taken to match the geometry to the measured spectrum. Commercial software is available to perform this type of analysis (Canberra, 2008; ORTEC). This technique is gaining acceptance, having been approved as a measurement technique for generating data for Waste Isolation Pilot Plant (WIPP) compliance documentation (Wachter et al., 2014).

3. Holdup measurements

Bulk handling facilities such as uranium conversion plants, enrichment plants, and spent fuel reprocessing plants move large volumes of loose material through very complex networks of lines, ducts, and pipes. Some of this material will accumulate in joints, bends, valves, process equipment, and other areas where flow rates change and equipment geometry gives material a place to build up. Material can also accumulate in safety equipment such as air-handling ducts and air filters. Even dedicated cleanout campaigns cannot remove all material from a complex facility. This material is called holdup, and it has to be accounted for not only safeguards purposes but also health and safety reasons, including criticality safety.

a. Generalized geometry

A wide variety of actual deposit geometries will be encountered in facilities. Accurately modeling the holdup in a v-blender or ball valve, for example, would be very time-consuming and difficult. But most deposits can be treated as one of three basic geometries: point, line, or area source. Careful selection of detector distance and orientation can make most items meet the criteria for one of these geometries. Good training, experience, and professional judgment are necessary in selecting the measurement approach for all but very obvious choices of geometry.

Holdup measurements are far less precise than other gamma ray measurements discussed in this chapter. The uncertainties on an individual measurement may approach 50% RSD or higher in some cases when significant correction factors must be applied. There is often no practical way to precisely determine the uncertainty in a holdup result. The best approach would be to have a team measure a variety of holdup deposits of precisely known mass, but this is seldom practical. This may be possible when equipment, rooms, or an entire facility undergoes decontamination and decommissioning operations. In these cases, holdup can be measured in place before a piece of equipment is disassembled. When the equipment is removed, it can be disassembled and the components measured using more precise NDA or other techniques. The holdup measurements' accuracy and precision can then be quantified by very direct means. Another approach to uncertainty quantification would be to have multiple individuals or teams measure the same holdup deposit. The variation in the results will give a good estimate of the uncertainty in an individual result.

However, while the uncertainty (and bias) of an individual measurement is difficult to estimate, in large facilities a holdup measurement campaign will involve hundreds or perhaps thousands of measurements. With a measurement campaign on this scale, the biases should be random, so the total holdup estimate should have relatively low bias. This has been demonstrated in many holdup measurement training courses held at Los Alamos National Laboratory. In these courses, several teams participate in exercises in which a variety of simulated holdup deposits are measured. When the total holdup mass values determined by each team are summed and the sums are compared with the well-known sum of the material in the simulated deposits, the observed bias is typically on the order of 10%. Even lower biases are obtained, if the total holdup values from each team are averaged. This is similar to what occurs when repeat measurement campaigns of the same facility are performed over a long period of time; the knowledge of the total holdup in the facility will improve with each successive campaign.

The Rocky Flats plant was a plutonium processing facility that was decommissioned and decontaminated over the course of several years spanning the turn of the millennium. A large holdup measurement campaign was conducted, followed by dismantling of the equipment and the recovered material measured. Table 12.4 shows the agreement between holdup measurements and recovery values for several of the buildings on site.

The detector used for holdup measurements should have good efficiency, enough resolution to prevent interference from other radioisotopes/gamma rays in the area, and be rugged enough to withstand the environment of the facility, as well as the rough handling that may occur while attempting to reach every deposit location in a complex industrial facility. The detector needs to be collimated, so smaller diameter crystals will save significant weight. A circular collimator gives the detector rotational symmetry, which greatly simplifies detector positioning during calibration and measurements. The collimator needs to include a back shield, as background gamma rays may come from the opposite direction from the collimator opening in a complicated facility. The most common detector choice is a lead-collimated NaI(Tl) detector. The detector can be handheld, and the fabrication of holders that significantly reduce the effort and strain required to manipulate a lead-collimated NaI(Tl) detector throughout the day is easy to design. Painter's extension poles can be modified with detector clamps for this purpose. Germanium detectors are sometimes used when high resolution is required because of interference effects. For germanium detectors, a wheeled cart is usually used to position and hold the detector because they are not very portable.

Detector calibration is best performed with a single, small-diameter source of the same isotopic composition as

TABLE 12.4 Holdup measurement accuracy at selected Rocky Flats buildings.[a]

Building	Measured/recovered Pu
B-371 Glove boxes	1.09
B-307 Ductwork	1.06
B-779Total Holdup	1.13
B-A Total Holdup	1.17
B-B Total Holdup	0.97
B-C Total Holdup	1.04
B-D Total Holdup	1.03

[a]*From Reilly (2007). Printed with permission, Los Alamos National Laboratory, LA-UR-07-5149.*

the deposits to be measured. Bare or thin-walled sources are best to minimize the correction of attenuation from the wall thickness on the calibration. The source is measured at a defined distance to perform the point source calibration. The point source calibration constant is

$$K_P = \frac{M}{C \cdot r} \tag{12.13}$$

where M is the mass of the calibration item, C is the net count rate in the ROI being used for the isotope of interest, and r is the source-to-detector distance.

The net count rate is the difference between the integral (gross counts) in the ROI with the source present and the integral in the ROI without the source present. This eliminates the effect of any room background signal from the isotope of interest.

The source is then moved across a line perpendicular to the long axis of the detector, and a series of measurements are made. An example of such data can be seen in Fig. 12.5. Note that in this example, both sides of the curve have actually been measured; if time is short, the assumption of symmetry can be made and only half of the distribution measured.

The series of data points thus obtained approximates a line source and serves as the basis for the line geometry calibration. The calibration factor for line sources is

$$K_L = \frac{M}{L \cdot C \cdot r} \tag{12.14}$$

where M, C, and r are as defined previously in Eq. (12.13), and L is a term quantifying the effective source length visible to the detector.

L can be calculated using the following formula:

$$L = \sum_{-n}^{n} \left(s \cdot \frac{C_i}{C} \right) \tag{12.15}$$

where n is the number of radial measurements made on each side of the center point, s is the spacing of the radial measurements (5 cm in the example in Fig. 12.5), C_i is the count rate in the ROI determined at the ith radial measurement position, and C is the count rate at the central measurement position.

The plot of the radial response data (Fig. 12.5) also informs the user of the detectable arc formed by the collimator. This arc will be different for uranium and plutonium, as different gamma energies are used. Uranium holdup is almost always measured using the 185.7-keV gamma ray. Plutonium holdup can be measured using the 208-keV gamma ray or the 375/414-keV complex.

The area source calibration constant is

$$K_A = \frac{M}{A \cdot C} \tag{12.16}$$

where M and C are defined as in Eq. (12.13), and A is a term quantifying the effective source area visible to the detector.

The value of A can be calculated using the following formula:

$$A = \pi s^2 \left\{ 2 \sum_{1}^{n} i \frac{C_i}{C} + \frac{1}{4} \right\} \tag{12.17}$$

where s, n, C_i, and C are as previously defined.

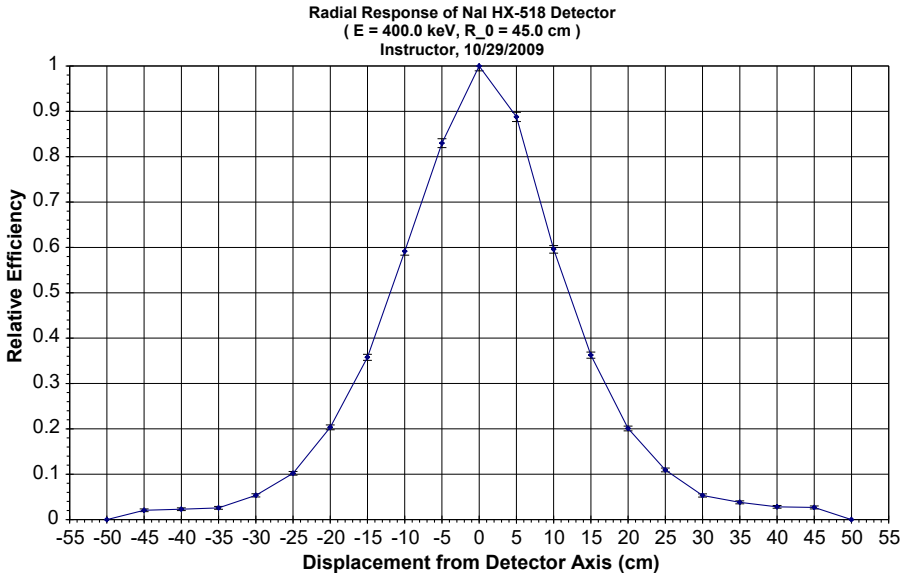


FIGURE 12.5 Plutonium calibration data for a holdup detector system.

10–12 measurement locations of the point calibration source can therefore produce calibration factors for point, line, and area sources.

The point source calibration will give results directly in mass. The line source calibration will give results in mass per unit length (i.e., g/cm). This calibration assumes that the line source extends beyond the visible view of the detector defined by the collimator. The user must determine the total line length and multiply the measured mass per unit length value by the length of the deposit. If a scan of the deposit indicates that it is not of uniform linear density, multiple measurements should be made of the different linear density zones. This may happen where a manifold steps down from a wider pipe to a narrower pipe, where the diameter and flow rates may change. Similarly, the area calibration produces results in mass per unit area. The detector should be positioned so that the source appears as an infinite plane—extends beyond the edge of the visible solid angle.

One method to assess if the deposits meet the criteria for each geometry can be judged by the change in count rate as a function of distance between the detector and the holdup deposit. For point sources, the count rate should vary according to the inverse square law. For line sources, the count rate should be inversely proportional to distance. For area sources, the count rate will be independent of distance. Detector positions can be chosen, so these criteria are met, and then the total source length or area used to calculate the total mass from the g/cm result or g/cm^2 result.

The deposit measurements must be corrected for the attenuation imposed by the equipment or piping in which the deposit is found. In some cases, a simple attenuation calculation using the classic attenuation equation will suffice. This is possible for well-defined thicknesses such as flat duct walls. The thickness can be either operator knowledge taken from reliable facility drawings or measured using an ultrasonic thickness gauge. For complicated geometries or when drawings/ultrasonic measurements are impractical, a transmission measurement using a radioactive source can be performed. The collimated transmission source is measured at a defined detector-to-source distance. The source is then moved behind the deposit, maintaining the same detector-to-source distance. The ratio between the two measurements is the transmission through both walls of the equipment or pipe. The correction factor applied to the holdup deposit measurement is one over the square root of the transmission, as the deposit radiation will only have to penetrate one of the two walls the transmission source beam had to penetrate. The transmission source will likely have a different gamma energy than the holdup isotope, so another correction factor must applied to take into account the different detector efficiency and absorption coefficients at the energies in question. Sometimes the attenuation correction factor must be based on an educated guess by the measurement technician.

Actual point and line holdup deposits will have physical dimensions, not the assumed infinitely small point and infinitely thin line geometries. The finite geometries of the point and line deposits require a correction factor to be applied to the measurements to minimize measurement bias. To determine the correction factor, the radial response curve determined during calibration is fitted to a Gaussian model and normalized to the central point. The deposit dimensions are determined, either from assumptions based on the equipment geometry or by measurement using a Geiger counter or the holdup measurement system with a slit collimator. The detector response at the edge of the deposit is averaged with the central response (defined as 1.0 because of the detector response normalization). The inverse of this value is the correction factor for the finite deposit dimensions (Reilly, 2007). Neglecting this correction factor will result in an overall mass defect bias, as this correction factor will always increase the measured mass values.

Uranium and plutonium exhibit significant self-attenuation necessitating the need for a correction factor. This correction factor increases as the deposit thickness increases. At some thickness, the deposit will become infinitely thick and, in this situation, this correction factor cannot be applied. The correction factor is based on the transmission correction factors (CF) for slab, cylindrical, and point sources as shown in the following Eqs. (12.18), (12.19) and (12.20), respectively:

$$\mathrm{CF}_{\text{slab atten.}} = \frac{-\ln T}{(1-T)} \tag{12.18}$$

$$\mathrm{CF}_{\text{cyl. atten.}} = \frac{-\ln T^K}{(1-T^K)} \quad \text{where } K = \pi/4 \tag{12.19}$$

$$\mathrm{CF}_{\text{sph. atten.}} = \left\{\frac{3}{2Z}\left[1 - \frac{2}{Z^2} + e^{-Z}\left(\frac{2}{Z} + \frac{2}{Z^2}\right)\right]\right\}^{-1} \tag{12.20}$$

where $Z = \mu\rho D$ and D is the sphere diameter.

Correction factors from self-attenuation can also be determined if the areal density of the deposit is known, as explained in (Reilly, 2007).

In some facilities with process equipment located within close vicinity, measurement must be performed in close proximity to one another, leading to unusually high backgrounds. In this case, a background subtraction procedure can improve the accuracy of the results. When the background is coming through the sides of the detector, the use of a tungsten plug is an effective way to determine the background. The plug fits into the collimator and totally attenuates the gamma rays from the holdup deposit being measured. For background coming from behind the holdup

deposit being measured, the detector can be moved to the side to estimate the background contribution. The use of portable shielding to either block the background or block the holdup deposit to determine the background can be used. Subtracting the background spectrum or ROI count rate(s) from the holdup deposit spectrum will produce more accurate results, specific to the visible cone of the detector.

Neutron holdup measurements are another technique useful for determining the holdup deposit especially in very dense machinery. In dense machinery, the thickness of the metal may attenuate the signal enough to make gamma ray measurements impractical. Another application for the use of neutron measurements is high-mass deposits, which suffer significant self-attenuation. If a deposit is infinitely thick (see the uranium enrichment section of this chapter for a discussion of infinite-thickness criteria), gamma ray measurements essentially become geometric estimates; the results are only as good as your knowledge of the dimensions and elemental composition of the deposit. Neutron measurements solve this problem, as neutrons are much more penetrating than gamma rays.

Neutron measurements require larger detectors that are not easily portable like the NaI(Tl) holdup instruments. They are also far less directional than gamma detectors. While plutonium deposits generally produce useable passive signals, uranium deposits may require active techniques—fission must be induced using an americium–lithium source or similar neutron source. The exception is uranium compounds containing fluoride, which produce neutrons through (α,n) reactions. For these materials, neutron totals counting is used. For passive plutonium measurements or active uranium measurements, neutron coincidence counting methods are often used.

Neutron detectors for holdup are usually calibrated by measuring known masses of plutonium or uranium with point neutron sources in a manner analogous to that used for gamma detector calibration. They can also be calibrated using Monte Carlo techniques.

Neutron detectors designed for holdup measurements are often simple slab detectors; flat polyethylene slabs with He^3 tubes are inserted in holes in the slab. The larger the slab/greater volume of He^3, the more efficient the detector will be. In some cases, customized neutron detectors have been designed and built to measure holdup in particular pieces of equipment, such as glove boxes (Shimizu et al., 2006).

b. Operational considerations

Holdup measurements are usually performed in more challenging environments than other NDA measurements. Facilities that have holdup are usually large industrial chemistry plants, where operating temperatures, humidity levels, noise levels, and physical hazards (heights, trip/slip/fall hazards, etc.) are present to a degree that can dominate the attention of the measurement team. Often, simply specifying the measurement point and determining the deposit-to-detector distance can be a challenge. Measurement teams need to be familiar enough with the facility to operate efficiently and safely in the measurement environment even while carrying lead collimated detectors and associated equipment for long periods of time. The measurement environment can also affect the measurement equipment. If the temperature changes significantly over time, or from one region of the facility to another, peak drifts can occur in NaI(Tl) detectors. Peak position should be closely monitored by the measurement team. High temperatures will reduce the service time provided by germanium detector liquid nitrogen tanks.

The term "measurement team" has been used extensively throughout this discussion. Working in teams of two or three is usually far more effective and time efficient. The amount of equipment that has to be manipulated, the need to maintain detector position during the measurement, and the record-keeping tasks to be performed make holdup measurements difficult for a single individual in most cases. Given the amount of professional judgment that may have to be exercised and the difficulty of accurately pointing a detector at a deposit, with the detector often located at the end of a 2-m-long pole, a second set of trained eyes can often be very helpful.

For simple facilities or infrequent holdup campaigns, simple pencil-and-paper or spreadsheet record keeping may suffice. Careful designation of the deposit location is important, as well as all the typical measurement characteristics such as equipment serial numbers, calibration data, count times, etc. Photographs can help to make deposit locations more clear in the records and link them more clearly to the corresponding measurement results.

For more complicated facilities or in facilities where holdup campaigns will be performed on a regular basis, computerized record-keeping systems may be a more appropriate choice. The same locations will likely need to be measured each time, and choices of detector orientation, distance, and generalized geometry choice (point, line, or area) can be standardized for each deposit. Bar codes can be used to mark each deposit, and the measurements thereby automatically linked in a database to each location (Rowe et al., 2016).

Some deposits can be difficult to categorize as point, line, or area sources. Two pipes or ducts located close together could be treated as separate lines if the detector is located close to each pipe. This approach may require a significant correction for the actual finite width of the pipe deposit. If measured from a greater distance, the pair of pipes could be treated as an area source. If time permits, both approaches can be attempted and the results compared for consistency. As a measurement team gains experience,

such judgments will come more quickly and accurately for unusual geometries.

The statistical uncertainties in holdup measurement results can be calculated from the usual counting statistics methods. The statistical uncertainty will always underestimate the actual uncertainty in holdup measurements because of the large number of other systematic and random uncertainties that contribute to the total measurement uncertainty. How accurately and consistently was the desired deposit-to-detector distance maintained? Did the detector wobble during the measurement or was it solidly, consistently pointed directly at the valve 3.5 m overhead? How accurately did the measurement team judge the distribution of the deposit in the valve, and therefore how accurate was the source dimension correction? These operational considerations typically contribute significantly more to the uncertainty than the contribution from the counting statistics. Uncertainties are therefore often assigned by the team based on their training, experience, and operational judgment. Typical uncertainties assigned to holdup measurements often range from 10% to 50% depending on the complexity of the measurement.

III. Neutron-based assay for safeguards

A. Radiation signatures from plutonium and uranium

The neutron signature measured for safeguards applications from uranium and plutonium is dominated by spontaneous fission neutrons, induced fission neutrons, and (α,n) neutrons, as discussed in Chapter 1, Volume 1 of this book. The relative importance of these three processes depends on the specific isotopes found in the assay item. Plutonium emits spontaneous fission neutrons at a high enough rate to make passive measurements practical. For uranium, an external neutron source must be used to induce fissions because uranium does not emit spontaneous fission neutrons at a high enough rate for an accurate quantitative measurement. Both Pu and U also emit neutrons by the (α,n) process. Depending on the application, this can be either detrimental or beneficial. A summary of the neutron emission rates for the different production processes is shown in Table 12. 5 (Ensslin et al., 1998a).

Table 12.5 contains some important information pertinent to quantitative safeguards measurements. The three even-numbered isotopes of plutonium have a spontaneous fission rate over four orders of magnitude greater than the odd-numbered isotopes. Therefore, the passive measurement of plutonium will only be sensitive to the combination of these three even isotopes. Since the neutrons emitted from different isotopes cannot be distinguished from one another, a term called the ^{240}Pu effective mass is defined. The ^{240}Pu effective mass is the ^{240}Pu mass that would be required to produce the same neutron emission rate as the combination of the ^{238}Pu, ^{240}Pu, and ^{242}Pu isotopes and is defined as:

$$^{240}\mathrm{Pu}_{\mathrm{eff}} = 2.52(^{238}\mathrm{Pu}) + {}^{240}\mathrm{Pu} + 1.68(^{242}\mathrm{Pu}) \qquad (12.21)$$

The percent ^{240}Pu$_{\mathrm{eff}}$ from the plutonium isotopic values is required to convert from the ^{240}Pu$_{\mathrm{eff}}$ mass to the total Pu mass, a value of importance for safeguards.

Another very important property of fission is that this process results in the production of two fission fragments plus several neutrons produced at the same time. The number of neutrons produced in a fission event can range from 0 to 8 or more with an average number emitted of 2.2 for plutonium (Ensslin et al., 1998a). Induced fission will also emit several neutrons produced at the same time but with a higher average number of neutrons emitted. For induced fission on ^{239}Pu, around three neutrons are emitted with the exact average number dependent on the energy of the inducing neutron. The distribution of emitted neutrons

TABLE 12.5 Neutron emission rates for different compounds of uranium and plutonium.

Isotope	Spontaneous fission yield (n/s-g)	(α,n) yield in oxide (n/s-g)	(α,n) yield in UF_6 or PuF_4 (n/s-g)
^{234}U	5.02×10^{-3}	3.0	5.8×10^{2}
^{235}U	2.99×10^{-4}	7.1×10^{-4}	0.08
^{238}U	1.36×10^{-2}	8.3×10^{-5}	0.028
^{238}Pu	2.59×10^{3}	1.34×10^{4}	2.2×10^{6}
^{239}Pu	2.18×10^{-2}	3.81×10^{1}	5.6×10^{3}
^{240}Pu	1.03×10^{3}	1.41×10^{2}	2.1×10^{4}
^{241}Pu	$\sim 5 \times 10^{-2}$	1.3	1.7×10^{2}
^{242}Pu	1.72×10^{3}	2.0	2.7×10^{2}
^{241}Am	1.18	2.69×10^{3}	

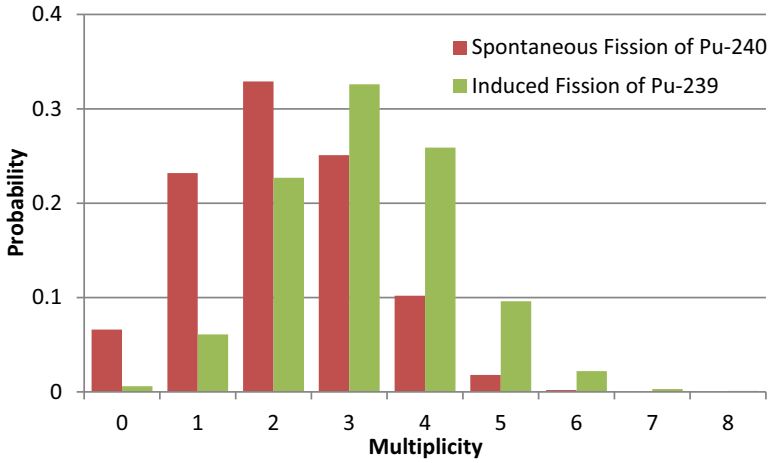


FIGURE 12.6 Spontaneous and induced multiplicity distribution for plutonium. Shown in the graph is the 2-MeV-neutron-induced fission multiplicity distribution. For the color version of the figure, the reader is referred to the online version of the book.

for spontaneous fission of ^{240}Pu and induced fission of ^{239}Pu with a 2 MeV neutron is shown in Fig. 12.6. The neutrons emitted from a fission, either spontaneous or induced, are correlated in time, and this property is used to differentiate between neutrons produced by fission from other production processes. Two neutrons detected close in time create a coincident event. Since fission neutrons are released at the same time, they will result in real coincident events. Two random neutrons can also be detected close in time, creating an accidental coincident event. Using sophisticated data processing electronics based on a sampling of a large number of events, the real coincidence events can be distinguished from accidentals events (Halbig et al., 1991). For safeguards measurements, the twofold and threefold coincident events, called doubles and triples, respectively, can be measured and used to quantify the mass of the item of interest.

The (α,n) neutron production rate can be a significant portion of the neutrons emitted from a plutonium or uranium item. From Table 12.5, one can note that ^{238}Pu, ^{241}Am, and ^{234}U are the dominant isotopes in the production of (α,n) neutrons when these isotopes are in proximity to a light element. For plutonium oxide items, the number of (α,n) neutrons is typically on the same order of magnitude as the number of spontaneous fission neutrons. For items that have small amounts of light element impurities mixed within the matrix, the (α,n) production rates can easily become much greater than the spontaneous fission neutron production rates. This can have a serious impact on the assay of plutonium items in instances where the plutonium mass is assumed to be proportional to the neutron count rate. For uranium items, the (α,n) count rate is insignificant with the exception for UF_6. The alpha value (α) of an item is defined as the number of (α,n) neutrons divided by the number of spontaneous fission neutrons emitted from the item. A pure plutonium metal item with no light element impurities will have an $\alpha = 0$, and a plutonium oxide item will typically have an α value in the range of 0.7−1.1 with the exact value depending on the isotopic composition of plutonium and the amount of ^{241}Am (Ensslin, 1991).

Another property seen in Table 12.5 is that the spontaneous fission rates of all the isotopes of uranium are very small. The passive assay of uranium is only practicable for items that contain large amounts of ^{238}U or is in a chemical form containing fluorine; otherwise, the neutron count rates will be comparable or less than typical background count rates. The technique of active neutron interrogation is used to assay uranium items. This technique induces fissions in the uranium from an external neutron source. The rate of induced fission will be dependent on the multiplication of the item, the intensity and energy spectrum of the interrogation source, and the properties of the surrounding medium, including the containment can and detector.

Multiplication is a property of both plutonium and uranium that must be accounted for to correctly assay these materials. The total multiplication of an item is defined as the total number of neutrons that exist in the item divided by the number of initial starting neutrons. For example, if 100 neutrons started in an item and 49 neutrons were created though induced fission events, then the total multiplication of the item would be 1.49. The 49 neutrons were created by multiplication through several generations. In the first generation, only a fraction of the original 100 will create additional neutrons. The same fraction of first-generation neutrons will create a smaller number of second-generation neutrons. This will continue for several generations until the no additional neutrons are created. The leakage multiplication reflects the number of neutrons that will leak out of the item, and this value will always be less than the total multiplication, because not all of the neutrons

will escape the items; some will be captured within the item, including those lost from induced fission events. The leakage multiplication is the property that is measureable.

The leakage multiplication will vary from item to item and is sensitive to the item characteristics and the detector design. The density, material form, and geometry of the item will have a significant impact on the multiplication. Denser and more compact items will generally have high leakage multiplication. Neutron coincidence counter designs can have a significant impact on the leakage multiplication.

B. General neutron counters for safeguards measurements

The most common neutron detector for safeguards applications is the ^{3}He tube (see Chapter 2, Volume 1 for a description of ^{3}He tubes.). Although many different detector types have been used for safeguards applications (Crane and Baker, 1991; Belian et al., 2003; Frame et al., 2004; McElroy et al., 2011a; Eccleston and Menlove, 2011; Henzlova et al., 2013), the ^{3}He tube has remained the detector of choice because it is robust, easily discriminates neutrons from other signals, is highly reliable, and has benign material characteristics that do not present safety issues in a nuclear facility. In the mid-2010s, the demand for ^{3}He gas exceeds the supply, necessitating the need to develop alternate technology for neutron detectors (Menlove et al., 2011). After many years, the ^{3}He technology is still preferred. Currently, ^{3}He gas is regulated, and the allocation supplied for Safeguards applications is currently meeting the demand.

A typical neutron detection system designed for Safeguards applications consists of many ^{3}He tubes embedded in polyethylene and arranged in either a linear or circular configuration. The former is called a slab detector and latter a well counter. Shown in Fig. 12.7 are two examples of typical neutron well counters. The nuclear material to be assayed is placed within the well counter. Neutrons from fission are emitted from the nuclear material with an average energy of around 2 MeV and enter the polyethylene matrix surrounding the ^{3}He tubes. The polyethylene serves to moderate the neutrons to thermal energy where the capture cross section of ^{3}He is greatest. Graphite or water would also be a good moderator medium but is often not chosen because of economical or operational disadvantages. Once the neutrons are thermalized, they then diffuse throughout the counter until they are either captured in the ^{3}He tubes, captured by other material within the counter, or escape the counter. For neutrons that are captured in the ^{3}He tubes, a pulse is produced in the tube and sent to electronics for processing.



FIGURE 12.7 Photo of a high-level neutron coincidence counter (left) used for the measurement of plutonium items and an active well coincidence counter (right) used for the measurement of uranium items. For the color version of the figure, the reader is referred to the online version of the book.

C. Neutron well counter properties

There are several properties of a neutron counter that directly affect the measurement performance of the instrument. These properties are the efficiency, die-away time, and gate fractions.

1. Efficiency

The efficiency of a neutron counter is defined as the number of neutrons detected divided by the number of neutrons emitted. Standard neutron well counters have a wide range of efficiency (ε) depending on the application; and the efficiency will directly impact the performance. For counting of doubles and triples coincidence events produced from spontaneous fission, a high efficiency is required because the count rate is proportional to the ε for singles, ε^2 for doubles, and ε^3 for triples. The greater the efficiency of a counter, the more neutrons will be detected, resulting in a reduction of the statistical uncertainty.

2. Die-away time

Another important property of a neutron well counter is the die-away time. The die-away time is related to the lifetime of a neutron in the detector. The die-away time is defined by the equation:

$$N(t) = N_o e^{-t/\tau} \tag{12.22}$$

where $N(t)$ is the number of neutrons at time t, N_o is the initial number of neutrons, and τ is the die-away time. The die-away time is an important characteristic for the detection of real coincidence neutron events produced

from the fission process because it determines the time window necessary to measure coincident events. For shorter die-away times, a smaller time window is needed to measure real coincident events, and correspondingly, there will be less accidental or false coincidence events. The well of a neutron counter is usually lined with cadmium to prevent neutrons that have been thermalized in the polyethylene surrounding the well from returning to the item and inducing additional fissions. Counters without a cadmium liner will have a much longer die-away time because of induced fissions from the thermalized neutrons.

3. Gate fractions

The doubles and triples gate fractions are also important properties for neutron multiplicity measurements. These parameters represent the fraction of double and triples coincident events that are detected within the time window, respectively. The doubles (f_d) and triples (f_t) gate fractions are related to the die-away time by the following formulas:

$$\begin{aligned} f_d &= e^{-PD/\tau}\left(1 - e^{-GW/\tau}\right) \\ f_t &= (f_d)^2 \end{aligned} \tag{12.23}$$

where PD is the predelay and GW is the gate width. The predelay and gate width are adjustable settings of the electronics and are described later in this chapter.

For safeguards applications, the design of a neutron-based detector system is dependent on the measurement requirements and the characteristics of the nuclear material. In some situations, the measurement requirements may be a simple attribute test, whereas other situations may require a quantitative assay with clearly defined accuracy and precision requirements.

In general, neutron measurement analysis can be divided into three types: singles counting, coincidence counting, and multiplicity counting. Singles counting measures only the total count rate and requires the simplest of detector design. In coincidence counting, the singles and doubles count rates are measured, and this type of analysis requires more complex detectors with better operational performance. For multiplicity counting, the singles, doubles, and triples count rates are used in the analysis. Multiplicity counting is a very sophisticated measurement technique and requires advanced detector designs with high neutron detection efficiency and small die-away times.

The design of a neutron counter requires a trade-off between detector efficiency, die-away time, cost, and operational constraints. To make a detector very efficient requires using many ^{3}He tubes, which increases the cost and die-away time. Considerable design analysis goes into selecting the proper number and placement of ^{3}He tubes so as to optimize the efficiency and die-away time to meet the measurement requirements for the system. The cost and operational constraints place additional restriction on the amount and types of materials that can be used in the design of the neutron counter. Monte Carlo techniques (Rising, 2016, Werner et al., 2018) are typically used to optimize the design before fabrication.

D. Singles neutron counting

Singles neutron counting can be an effective method for the quantification of nuclear materials (Sprinkle, 1991) but generally is used only in certain situations where the characteristics of the nuclear material are well known. The singles count rate (S) can be described by the simple formula:

$$S = \varepsilon M_L I_p \tag{12.24}$$

where ε is the efficiency, M_L is the leakage multiplication, and I_p is the passive neutron source intensity (n/s). The passive intensity is defined as the number of neutrons born in the item and includes neutrons from spontaneous fission and (α,n) reactions. The leakage multiplication is the number of neutrons emitted from the item per neutron born in the item.

For quantitative assay of plutonium and uranium, singles counting requires knowledge of the chemical form and isotopic composition of the item. Shown in Fig. 12.8 is the neutron production rate from three chemical forms of plutonium as a function of burnup. In metal items, there is no contribution to the singles rate from (α,n) neutrons. The neutrons are produced from the even isotopes of plutonium with the majority from ^{240}Pu. The singles neutron intensity from plutonium is a signature of the ^{240}Pu$_{\text{eff}}$ mass defined as:

$$^{240}\text{Pu}_{\text{eff}}(\text{for singles}) = 2.43(^{238}\text{Pu}) + {}^{240}\text{Pu} + 1.69(^{242}\text{Pu}) \tag{12.25}$$

The factors in front of ^{238}Pu and ^{242}Pu are the ratios of the neutron productions rate per ^{240}Pu production and are greater than unity reflecting the fact that both of these isotopes have a greater neutron production rate than ^{240}Pu. The ^{240}Pu$_{\text{eff}}$ mass can be related to the singles rate though a calibration

$$S = \text{k}^{240}\text{Pu}_{\text{eff}} \tag{12.26}$$

where k is an empirical calibration constant. If the isotopic composition is known, then the total mass can be calculated from the ^{240}Pu$_{\text{eff}}$. These equations assume that the item is metallic and nonmultiplying. This will only be true in the case where the mass is very small, for example, items containing waste.

For items that have an (α,n) contribution to the singles rate, the source term will contain contributions both from the isotopes contributing to spontaneous fission production

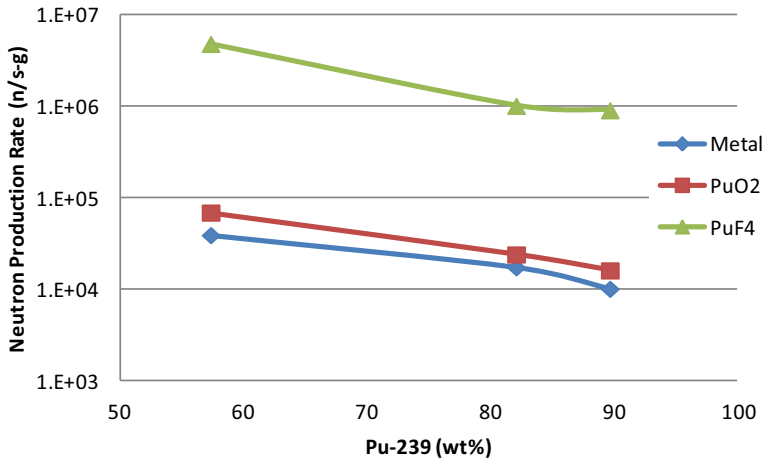


FIGURE 12.8 Neutron production rates for different forms of plutonium as a function of the burnup. For the color version of the figure, the reader is referred to the online version of the book.

and from (α,n) production. For PuO_2, ^{238}Pu, ^{239}Pu, ^{240}Pu, and ^{241}Am contribute to the (α,n) production and will be a term in the $^{240}Pu_{eff}$ mass equation with the multipliers containing a contribution from both spontaneous fission and (α,n) neutron production. Again, for a nonmultiplying item with known isotopic composition, the total plutonium mass can be calculated. For PuF_4, almost all the neutrons come from (α,n) production from four isotopes, ^{238}Pu, ^{239}Pu, ^{240}Pu, and ^{241}Am, and the multipliers will only contain a small component from spontaneous fission.

The assay of uranium compounds can be treated similarly to the plutonium case discussed above. The neutron production rates for 10 kg of several different forms of uranium typically found in the nuclear fuel cycle varying from low to highly enriched uranium (HEU) are shown in Fig. 12.9. Similar to plutonium compounds, assay personnel must have knowledge of the chemical form and isotopic composition for quantitative analysis using singles counting.

The dominant source of neutrons from uranium metal is the spontaneous fission of ^{238}U. This results in the count rate decreasing significantly as the enrichment increases. The contribution to the neutron production rate from the individual isotopes of uranium is shown in Fig. 12.10. An assay of the ^{238}U mass is possible using singles counting for large metal items that have enrichment below approximately 70%. As the enrichment increases, longer count times and larger masses are required to get acceptable measurement precision. A linear calibration along with known isotopic composition allows for the measurements of the ^{235}U mass.

For UO_2, the neutron production rate is nearly constant up to enrichments of around 60%. As the enrichment increases, the contribution to the neutron production rate from spontaneous fission of ^{238}U decreases, whereas the (α,n) contribution from ^{234}U increases. Typically, uranium items contain a very small amount of ^{234}U, less than 1%, but this isotope has a very large alpha decay rate and, as a

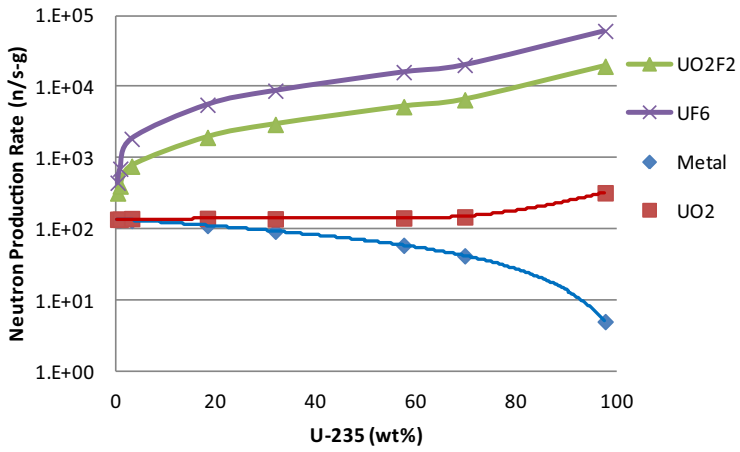


FIGURE 12.9 Neutron production rate for different forms of uranium as a function of enrichment. For the color version of the figure, the reader is referred to the online version of the book.

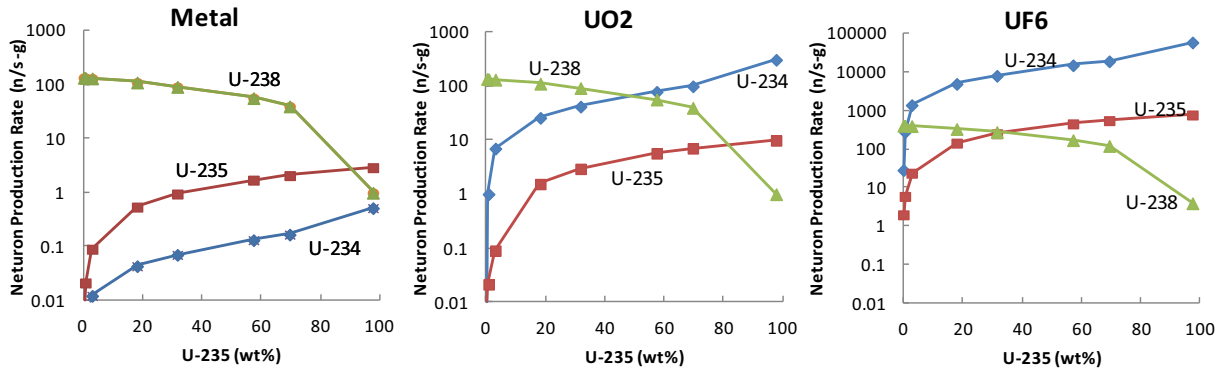


FIGURE 12.10 Neutron production rates for individual isotopes of uranium as a function of enrichment. For the color version of the figure, the reader is referred to the online version of the book.

result, is the main contributor to (α,n) neutrons in uranium. When uranium is processed in an enrichment plant, the ^{234}U is enriched at a faster rate than the ^{235}U, resulting in a larger increase in the (α,n) production than ^{235}U spontaneous fission production as the enrichment increases. When calibrating a detector for singles measurements of UO_2, all three isotopes of uranium need to be accounted for.

UO_2 is found in many places in the nuclear fuel cycle, for example, as bulk material in cans at a fuel fabrication facility or in finished assemblies at a nuclear power plant. These items are usually assayed using active techniques because of the low count rates, which are often comparable to room background. Active techniques measure the ^{235}U-induced fission neutrons and will be discussed later in this section. Very large UO_2 items can be assayed by passive counting depending on the material characteristics and the measurement goals.

For uranium compounds that contain fluorine, the neutron production is dominated by the (α,n) process from the ^{234}U alpha decay and subsequent ^{19}F(α,n)^{22}Na reaction. UF_6, the standard material type used in the enrichment process, and UO_2F_2, a reaction product of UF_6 and water (Mayer et al., 2008), are two fluorine-containing uranium compounds typically found in the nuclear fuel cycle. Calibration of instruments for singles counting of UF_6 or UO_2F_2 needs to account for the neutron production from ^{234}U, ^{235}U, and ^{238}U, although at high enrichments, only the contribution from ^{234}U is often considered. This simplification typically does not produce any significant biases.

As a result of the large singles neutron production rates in forms of uranium containing fluorine, passive counting is often used to quantify the uranium mass. Passive counting has been successfully used to quantity the UO_2F_2 deposits inside process equipment at enrichment plants (Auguston et al., 1983; Cooley et al., 1989). The verification of UF_6 cylinders (McElroy et al., 2011b), verification of uranyl nitrate in a conversion facility (Rauch et al., 2010), and the measurement of holdup inside a cascade hall (Beddingfield and Menlove, 2002) are additional examples of singles counting applications in the nuclear fuel cycle.

A shuffler measurement (Rinard, 2001) is one technique that is often used to measure uranium metal or oxides using singles neutron counting. The shuffler uses a ^{252}Cf source to induce fissions in the uranium, and the singles rate produced by delayed neutrons from the fission fragments is measured to quantify the ^{235}U mass. In this type of measurement, the Cf source is placed next to the item for several seconds and then moved away for several seconds at which time the singles neutron rate is measured. The source is "shuffled" many times during one measurement to obtain acceptable counting statistics.

A calibration for the shuffler is made with representative standards by determining the relationship between the ^{235}U mass and the delayed singles count rate. This calibration will be sensitive to material characteristics, such as density, enrichment, geometry, material type, and presence of moderators. Biases will occur when these characteristics of the assay items differ significantly from the calibration items, although with some knowledge of the items, reasonable correction factors can be determined with Monte Carlo calculations. Shufflers have been used successfully in many areas of the nuclear fuel cycle for quantifying uranium mass (Rinard et al.,1992; Mount et al., 2002).

E. Neutron coincidence counting

1. Introduction to coincidence counting

Uranium and plutonium found in bulk (cans, drums, holdup deposits, etc.) and item types (fuel pellets, assemblies, etc.) throughout the nuclear fuel cycle are often assayed nondestructively by neutron coincidence counting (Ensslin, 1991). This technique takes advantage of the fact that

multiple neutrons produced in spontaneous and induced fission events are emitted at the same time. This is a unique signature of the fission process; uranium and plutonium are among the few elements to decay by this process. A neutron detection system, which is sensitive to time-correlated neutrons, will be able to assay fission events independent of other neutron production processes. In this case, measurements will be insensitive to the presence of natural background or (α,n) sources because these production processes produce only random neutrons in time. Unlike singles counting, where the item characteristics must be known for accurate assay, some coincidence counting techniques are not nearly as sensitive to changes in these characteristics.

As discussed previously, the isotopes of plutonium that have significant spontaneous fission yields are ^{238}Pu, ^{240}Pu, and ^{242}Pu. With respect to uranium, there are no isotopes that have a measurable yield, with the exception of very large quantities of ^{238}U. Hence, a neutron detector that is sensitive to time-correlated neutrons will only be sensitive to these isotopes. Unlike gamma ray measurements that have unique signatures for the different isotopes, in neutron counting, there is no way to differentiate between neutrons produced from the different isotopes. For this reason, a quantity called the ^{240}Pu effective mass is defined as:

$$^{240}\mathrm{Pu}_{\mathrm{eff}} = 2.52(^{238}\mathrm{Pu}) + {}^{240}\mathrm{Pu} + 1.68(^{242}\mathrm{Pu}) \qquad (12.27)$$

The ^{240}Pu$_{\mathrm{eff}}$ mass value is the mass of ^{240}Pu that would give the same coincidence count rate as that obtained from the combination of all the even isotopes of plutonium. The effective mass is defined in terms of ^{240}Pu as opposed to ^{238}Pu or ^{242}Pu because ^{240}Pu is typically present in the largest quantity in both low- and high-burnup reactor grade plutonium and contributes the most to the coincident count rate. The coefficients of 2.52 and 1.68 give the relative coincidence emission rate of ^{238}Pu and ^{242}Pu, respectively, to ^{240}Pu. These coefficients account for the different spontaneous fission emission rates and the neutron multiplicity distribution of each isotope.

Passive coincidence counting is the most common application of coincidence counting for plutonium items. In cases where the spontaneous fission rate is weak and there are fissile isotopes present, such as ^{235}U or ^{239}Pu, active coincidence counting can be utilized. With the choice of an (α,n) interrogation source, the coincident counter can differentiate between the induced fission and the (α,n) interrogation neutrons. Both passive and active coincidence counting techniques have many applications for safeguarding the fuel cycle. Generally, coincidence counting is more accurate than singles counting because this technique measures a unique signature of the nuclear material independent of natural background or (α,n) sources.

2. Shift register electronics

A coincident event or doubles count is defined as the detection of two neutrons from the same fission event within a defined time interval, called the gate width (*GW*). Unfortunately, on an event-by-event basis, one cannot differentiate between coincident events resulting from two neutrons from the same fission or two random neutrons, for example, two neutrons from independent (α,n) events being detected within the gate width. The former is called a real coincidence event, and the latter is called an accidental coincidence event. The optimum gate length is related to the die-away time of the neutron detector. The optimum setting of 1.257τ minimizes the error on the doubles rate (Ensslin, 1991). Any neutron that is detected within a gate length of time of a previously detected neutron will define a coincident event or doubles count. Counting coincidence events using standard analog gating electronics would be very cumbersome; rather, this is accomplished using sophisticated and clever electronics. The measurement of coincidence events is accomplished with an instrument called a shift register (Halbig et al., 1991; Swansen et al., 1980).

The shift register is an integrated circuit that consists of a series of clock-driven flip flops linked together in stages. The incoming pulses "shift" through the register in stages at a frequency, such that it takes a gate length of time to move completely through the shift register. To differentiate between real and accidental coincidences, the shift register is triggered at two times: first to sample the real plus accidentals (R + A) and second to sample the accidental (A) coincidences. A block diagram of the shift register coincidence circuit is shown in Fig. 12.11.

A prompt trigger samples the shift register and measures the R + A coincidences. A delayed trigger samples the shift register at a much later time and measures the A coincidences. The delayed trigger is separated from the

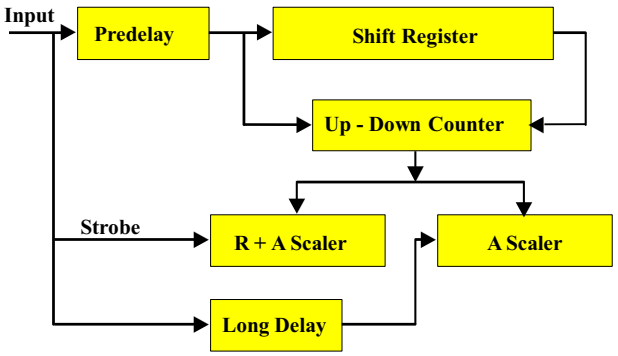


FIGURE 12.11 Block diagram of a neutron shift register coincidence circuit. For the color version of the figure, the reader is referred to the electronic version of the book.

prompt trigger by a time of many die-away times to ensure that the accidental coincidences will not include any real coincidences from fission events. The neutron is delayed from entering the shift register by a small time, called the predelay, to eliminate biases caused by dead time effects. When a neutron enters the shift register, it will increment the up-down counter; when it exits, it will decrement the up-down counter. The up-down counter will count the total number of neutrons being "shifted" through the shift register. A neutron signal entering the electronics will first trigger the contents of the up-down counter to be added to the R + A scaler and then will pass through the predelay entering the shift register. At the same time, a delay trigger will be generated to add the contents of the up-down register to the A scaler at the delayed time in the future. The number in the up-down register represents the number of coincidence events formed with a newly detected neutron.

Coincidences from fissions will only be counted in the R + A scaler since they are born at the same time and have an average lifetime in the counter described by the die-away time. The long delay is purposely set to many die-away times to ensure that there will be no real coincidence events between neutrons from the same fission event in the A gate. Coincidences from two random uncorrelated neutrons have an equal probability of occurring in the R + A or A gates. For example, two random neutrons have an equal probability of being separated by a short time as they would a long time. While two neutrons from the same fission event would have a high probability of being separated by a small time, they would have no probability of being separated by the long delay time because they only have a finite lifetime before they are either detected or lost. The number of real coincidences is the difference between the R + A scaler and the A scaler. The determination of the real coincident rate is only possible by sampling a large number of events. On a single event basis, one cannot determine if an R + A count is a real or accidental coincidence. With this understanding of how to measure the real coincidences or doubles, we can investigate how this quantity is converted into a plutonium or uranium mass.

3. Passive coincidence counting

Once the real coincidences or doubles are measured, the next step is relating this count rate to the $^{240}Pu_{eff}$ mass. The doubles rate can be defined as

$$D = R = \frac{F\varepsilon^2 f_d M^2 \nu_{s2}}{2} f(M,\alpha) \qquad (12.28)$$

where F is the spontaneous fission rate, ε is the neutron detection efficiency, f_d is the doubles gate fraction, M is the leakage multiplication, and ν_{s2} is the second reduced moment of the spontaneous fission neutron distribution and represents the average number of doubles emitted per fission. The function $f(M,\alpha)$ represents the effect on the doubles rate from induced fission from both the spontaneous fission neutrons and the (α,n) neutrons and will be dependent on the multiplication and alpha value of the item. In theory, the above equation can be solved to determine the mass, but this cannot be done in coincidence counting because there are too many unknown quantities in the equation. In general, the mass, multiplication, and alpha value are not known for the item to be assayed. If we are only measuring one quantity, the doubles rate, there are too many variables to solve this equation independently. The efficiency and gate fractions are detector parameters and can be accurately determined.

For standard coincidence counting an empirical calibration curve is generated to relate the measured count rate to a mass value. This curve is made by measuring a set of representative calibration standards with known mass values. The resulting data, $^{240}Pu_{eff}$ mass versus doubles rate, is then fit with a quadratic curve. An example of a typical empirical calibration curve for pure plutonium oxide items is shown in Fig. 12.12. The quadratic curve mentioned above is fitted to the black circles shown in the figure; the rate of increase in the doubles rate is greater than a linear increase. This is a result of the multiplication of the item, and in general, as the mass increases, the multiplication will also increase, resulting in a nonlinear increase in doubles.

Since the assay items have three unknown quantities (m, M, and α) and only one observable is being measured, an empirical calibration curve requires many constraints on the material characteristics to obtain accurate results. Both the

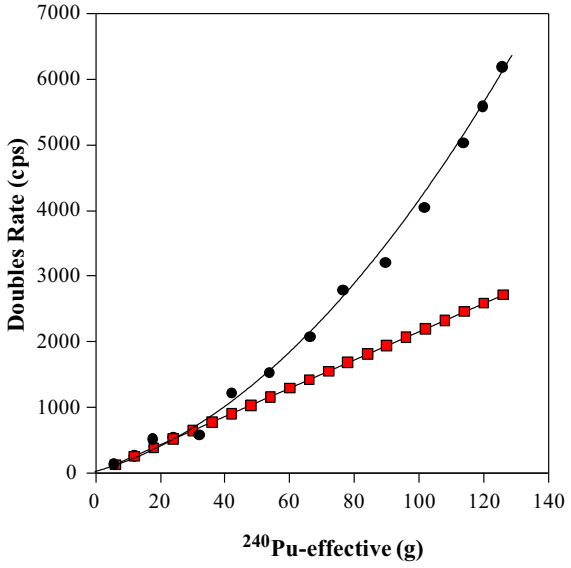


FIGURE 12.12 Typical calibration curves for the passive calibration technique (circles) and known-alpha technique (squares) for the measurement of plutonium. For the color version of the figure, the reader is referred to the electronic version of the book.

multiplication and alpha value affect the shape of the empirical calibration curve. The standards used to create the calibration curve need to be representative of the items to be measured. Important characteristics that will affect the shape of the calibration curve include material type, density, geometry, moisture content, and impurities. In general, the passive calibration curve works best in situations where the material characteristics are in a known and reproducible form, such as the output of a plutonium reprocessing plant.

Another more advanced coincidence counting technique that is often used for assaying pure plutonium items is called the known-alpha method. This method uses both the measured singles and doubles rates. The singles rate can be defined as

$$S = F\varepsilon M\nu_{s1}(1+\alpha) \tag{12.29}$$

where the parameters are defined as the same as in the doubles equation above. If the alpha value of the item is known, then the equations for the singles and doubles rates can be solved to determine the multiplication of the item. The multiplication describes the induced fissions in the item, so if the multiplication is known, then the subset of the doubles resulting from induced fission can be removed from the measured doubles rate. In the known-alpha technique, a quantity called the multiplication-corrected doubles rate is calculated. The multiplication-corrected doubles rate represents only the spontaneous fission component and will result in a linear calibration. An example of a known-alpha calibration, which is created in a similar way to the passive calibration approach, is shown by the red data points (square points) in Fig. 12.12.

The known alpha method has a big advantage over the passive calibration curve because changes in the item, such as geometry, density, and material form that change the multiplication, will not affect the assay accuracy of the method. The one drawback of the known alpha technique is that the alpha value of the item must be known, as this is used to solve the singles and doubles equations for the multiplication. For pure items, such as metals or oxides, the calculation of the alpha value is straightforward and is only dependent on the isotopic composition of the item (Ensslin, 1991). Any impurities (light elements) remaining in the item will create large amounts of (α,n) neutrons making the determination of the alpha value very difficult.

Coincidence counting techniques are used in many facilities throughout the nuclear fuel cycle. A typical instrument used for both the passive calibration and known-alpha analysis methods is the high-level neutron coincidence counter (HLNC) (Krick and Menlove, 1979), shown in Fig. 12.7. The HLNC consists of 18 ^{3}He detectors embedded in polyethylene and arranged in a ring to create a well. The plutonium item to be measured is placed within this well, and the emitted neutrons are detected by the surrounding ^{3}He tubes. This system has an efficiency of approximately 18% and works very well for the assay of pure plutonium oxides. Many other coincidence counters exist and are based on the same design principles of the HLNC (Baker et al., 1990; Tagziria et al., 2007).

4. Active coincidence counting

Active coincidence counting is a technique used to measure uranium. As discussed previously, the isotopes of uranium have a spontaneous fission rate that is too small to make passive assay practicable. The instrumentation and analysis techniques of active assay are very similar to the passive calibration curve analysis technique for plutonium. In active assay, an interrogation source is used to induce fission on the ^{235}U isotope in the item. The induced fission neutrons are then detected and processed with a shift register. An AmLi source is a good choice for the interrogation source for two reasons. First, the neutrons produced from an AmLi source are random in time and will not contribute to the coincidence signal. Also, the energy spectrum of an AmLi source is a low-energy distribution (Owen et al., 1981; Geiger and Van der Zwan, 1971) such that almost no neutrons are emitted above an energy of 2 MeV and thus will induce fission on the ^{235}U and not induce fission in the ^{238}U. Unfortunately, AmLi sources are no longer produced, requiring the use of alternate interrogation sources. Although a ^{252}Cf source is a fission source, it has been successfully used as an interrogation source for the active-well coincidence counter (AWCC) (Menlove, 2015).

An AWCC (Menlove, 1979) is a portable instrument specially designed for the assay of the ^{235}U mass content in uranium items. The counter has two rings of ^{3}He tubes surrounding a well yielding an efficiency of approximately 33%. The counter is designed to hold two AmLi sources, one in the top and one in the bottom end plug. The random neutrons from the AmLi sources induce fission in the uranium item, and the detected doubles rate is related to a ^{235}U mass through an empirical calibration curve. The instrument is calibrated using the same methods as passive coincidence counting of plutonium. Active coincidence counting techniques are used throughout the world for safeguards applications (Ferrari and Peerani, 2010). An active coincidence counting technique typically yields results with accuracy in the range of 1%−5% when calibrated with representative standards.

F. Neutron multiplicity counting

1. Introduction to multiplicity counting

Multiplicity counting is an extension to neutron coincidence counting that incorporates the multiplicity of detected neutrons in the analysis (Ensslin et al., 1998a). From the multiplicity distribution, the factorial moments are determined. The first factorial moment is related to the singles,

the second is the doubles, and the third is the triples. Standard coincidence counting uses the first two moments, and multiplicity counting uses all three factorial moments.

The general theory behind multiplicity counting is that by adding a third measured quantity to the analysis, one can solve explicitly for the three unknown item properties, which are typically chosen as the $^{240}Pu_{eff}$ mass, the (α,n) production rate, and the multiplication. The solution of these three quantities is exact and complete and will yield excellent results as long as the item meets the assumptions of the point model (discussed below) used to derive the equations for the singles, doubles, and triples. Biases will be observed, if the assumptions are not fulfilled and will become larger, the more in violation they are. In general, no calibration standards are required for multiplicity counting, but in practice, they are used to confirm the technique and to determine bias correction factors when the assumptions in the equations are violated.

2. Multiplicity shift register electronics

The measurement of the triples count rate for multiplicity counting requires some changes to the shift register and the neutron counter design. The standard coincidence shift register needs to be slightly modified to be used in multiplicity counting as shown in the simplified block diagram of Fig. 12.13 (Halbig et al., 1991; Stewart et al., 1999). The same shift register principle is still used, but instead of adding the contents of the up-down counter to the R + A and A scalers, the contents are histogramed by the number present in the scalers. This histogram defines the multiplicity distribution and describes the probability of having a specified number of neutrons in the shift register when triggered by a newly detected neutron.

Separate multiplicity distributions are measured for the R + A and A gates. An example of a multiplicity distribution for a plutonium item is shown in Table 12.6. This table lists the number of times multiplicities of from zero to nine were measured in the R + A and A gates. For example, 183 times and 42 times, 7 neutrons were in the R + A and A gates, respectively, when the gate was triggered. The singles, doubles, and triples count rates are calculated from these distributions and are related to the first, second, and third reduced factorial moments as shown by the following formulas:

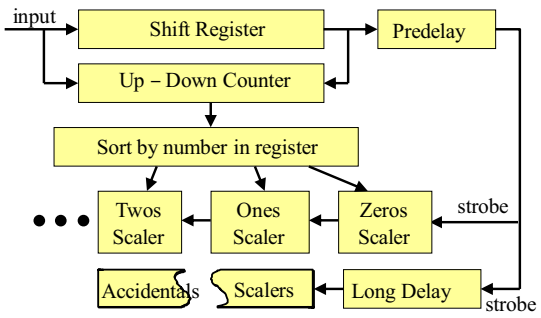


FIGURE 12.13 Block diagram of a multiplicity shift register electronics circuit. For the color version of the figure, the reader is referred to the electronic version of the book.

TABLE 12.6 The R + A and A multiplicity distribution of a 60-gram plutonium item measured in a multiplicity counter.

n	$(R + A)_n$	$(A)_n$
0	26,804,360	29,731,130
1	8,187,530	6,222,207
2	1,772,831	1,016,603
3	32,570	157,224
4	53,449	22,387
5	8231	3093
6	1237	402
7	183	42
8	30	8
9	2	1
10	0	0

$$S = \sum_{n=0} A_n$$

$$D = \sum_{n=1} n(R+A)_n - \sum_{n=1} nA_n$$

$$T = \sum_{n=2} \frac{n(n-1)}{2}(R+A)_n - \sum_{n=2} \frac{n(n-1)}{2}A_n - \left[\frac{\sum_{n=1} nA_n}{\sum_{n=0} A_n}\right]\left(\sum_{n=1} n(R+A)_n - \sum_{n=1} nA_n\right) \quad (12.30)$$

Every time a neutron is detected, the contents of the up-down counter is sampled and histogramed, so the singles is simply the sum of counts in the A distribution. The doubles rate is the difference of the means of the R + A and A distributions and is identical to the value measured with the standard shift register described earlier. Understanding the triples rate is not easy, as it is the difference in the third moments of the distribution with an additional term to account for correlations between the moments.

The equations that relate the measured count rates to the item properties are based on the point model (Boehnel, 1985; Cifarelli and Hage, 1986). The point model includes some fundamental assumptions about the fission process, the neutron emission process, and the detection process. The degree to which this model agrees with reality will

limit the accuracy of multiplicity counting and determine the range of material that this technique will apply to for quantitative assay. The point models equations are derived using the following assumptions:

1. The detector efficiency and fission probability are uniform over the entire item volume. This assumption is called the point model because it is equivalent to assuming that all the neutrons are emitted from a point.
2. All the induced fission neutrons are produced and emitted at the same time as the original spontaneous fission or (α,n) neutrons that created the induced fission. This idea is called the superfission concept (Boehnel, 1985).
3. The (α,n) and spontaneous fission energy distributions are the same. This assumption is not valid for many (α,n) reactions, although, for (α,n) neutrons produced in oxides, it is a good assumption.
4. The die-away time of the detector can be described by a single exponential time constant. Appropriate detector design can satisfy this assumption, although items containing moderating medium and item packaging can result in multicomponent die-away times.

The equations for the count rates, which are based on the point model and other assumptions described above, were derived by Boehnel (1985) and Cifarelli and Hage (1986) and are given by

$$S = F_o m \varepsilon M \nu_{s1}(1+\alpha)$$

$$D = \frac{F_o m \varepsilon^2 f_d M^2}{2}\left[\nu_{s2} + \left(\frac{M-1}{\nu_{i1}-1}\right)\nu_{s1}(1+\alpha)\nu_{i2}\right]$$

$$T = \frac{F_o m \varepsilon^3 f_t M^3}{6}\left\{\nu_{s3} + \left(\frac{M-1}{\nu_{i1}-1}\right)\right.$$

$$\left.\times\left[3\nu_{s2}\nu_{is} + \nu_{si}(1+\alpha)\nu_{i3}\right] + 3\left(\frac{M-1}{\nu_{i1}-1}\right)^2 \nu_{s1}(1+\alpha)\nu_{i2}^2\right\} \tag{12.31}$$

where F_o is the spontaneous fission rate, 473 fission/s-g, m is the $^{240}Pu_{eff}$ mass in grams, ε is the neutron detection efficiency, M is the neutron leakage multiplication, α is the (α,n) to spontaneous fission neutron ratio, f_d is the doubles gate fraction, f_t is the triples gate fraction, ν_{s1}, ν_{s2}, ν_{s3} are the factorial moments of the spontaneous fission distribution, and ν_{i1}, ν_{i2}, ν_{i3} are the factorial moments of the induced fission distribution.

The parameters in the point model equations can be grouped into four categories. The mass, multiplication, and alpha are the unknown quantities, with the mass being the quantity of interest to safeguards. The singles, doubles, and triples are the measured quantities. The efficiency and gate fractions are detector parameters, which are determined when the neutron counter is characterized. The factorial moments of the spontaneous and induced fission distribution are fundamental nuclear physics values and are fixed quantities.

The point model equations can be solved to get the $^{240}Pu_{eff}$ mass, multiplication, and alpha value. These equations are solved stepwise by first isolating the multiplication. This results in a cubic equation where only one of the roots yields a value for the multiplication that is physical and reasonable. Once the multiplication is determined, it is straightforward to find solutions for the mass and alpha value.

3. Multiplicity measurements

In the case of waste measurements where the plutonium mass is often very small and distributed over a large volume, the multiplication can be assumed to be unity. One of the complications in the assay of waste is that the waste matrix can cause changes in the detection efficiency. In this case, the multiplication can be assumed to be a known parameter, and the point-model equations can be solved for the mass, multiplication, and efficiency.

The accuracy of multiplicity counting is very good for items that meet the assumptions used to derive the point-model equations, but when these assumptions are violated, very large biases have been observed (Krick et al., 2005). One example is for the assay of large plutonium metal items (Geist, 2006). For these items, the assumption that the multiplication is constant throughout the item is not valid, as the multiplication on the edges is much smaller than in the center. In cases where biases are observed, working reference standards are used to determine a bias correction factor. For metal items, a multiplication-dependent correction factor of the form

$$CF = 1 + a(M-1) + b(M-1)^2 \tag{12.32}$$

has been found to correct the data. The coefficients a and b are determined empirically from measurements of working reference standards or calculated using Monte Carlo methods. The precision of multiplicity counting is influenced primarily by the statistical uncertainty in the triples count rate. Factors that determine the magnitude of the uncertainty include the detector efficiency, die-away time, count time, count rates, the multiplication, and the alpha value. Typically, the uncertainty is estimated by measuring the statistical scatter of multiple runs that make up a single assay, but theoretical models also exist (Dytlewski et al., 1993).

Multiplicity counting yields good accuracy over a wide range of material types as shown in Table 12.7 (Ensslin et al., 1998a). The metal data have been corrected with a multiplication-dependent correction factor. Plutonium oxide and slightly impure items assay extremely well with

TABLE 12.7 Typical passive multiplicity measurements results for several types of plutonium.

Material type	Mass range (g)	Alpha value	Count time	Relative standard deviation	Bias
Pu metal	200–5000	0–1	1000–1800	0.5%–4.6%	−0.8%–2.0%
Pu oxide	500–5000	1	1800	2.2%	0.0%
Impure oxide	20–900	0.7–4.3	1000	2%–3%	0.8%
Pu scrap	80–1175	1–6	3600	5.7%	−1.6%
Pu residues	0–10	1–82	1000	24%	−2.3%
	10–40	4–29	1000	22%	1.8%
	40–400	0.4–13	1000	17%	−1.4%
	160–340	7–34	3600	18.8%	−9.2%
Pu waste	~1	5	1000	1%–2%	1%–3%

multiplicity counting, although for pure items, standard coincidence counting will result in better precision. Plutonium scrap items generally have larger alpha values than found in the typical impure items, and this results in a loss of accuracy and precision. Plutonium residues often contain very large amounts of impurities, which can cause the item characteristics to severely violate the point-model equations. Various ranges of accuracy and precision are seen with these types of materials depending on the item multiplication and types of impurities. Neutron multiplicity measurements have been used successfully to fulfill the U.S. Department of Energy safeguards requirements (Dearborn and Mount, 2003; Geist et al., 2003; Dewberry et al., 2010; Stewart et al., 1998; Ensslin et al., 1998b).

Neutron multiplicity counting has advantages and disadvantages for assaying plutonium items. There are many properties of multiplicity counting, which makes its use advantageous. Calibration of multiplicity counting does not require representative standards, which in many cases can be very costly to fabricate or cannot be reasonably produced at all. For the assay of impure plutonium items, multiplicity counting will result in much better measurement accuracy than standard coincidence counting. For many item types, the required count times are much shorter than calorimetry, allowing for a greater throughput. Although multiplicity counting has many benefits, there are also several disadvantages. One of the biggest disadvantages to multiplicity counting is the cost of the counter, which is often several times the cost of a conventional coincidence counter. To obtain good measurement precision on the triples rate, the count times can be two to three times longer than standard coincidence counting. Multiplicity counting does not guarantee an unbiased result especially in cases where the characteristics of the items do not meet the assumptions of the point model. To correct for these biases, special correction factors need to be developed, or a measurement is required with an alternative technique such as calorimetry.

IV. Calorimetric assay

A. Introduction

Calorimetry is used as an NDA technique for determining the power output of heat-producing nuclear materials. The heat is generated by the decay of radioactive isotopes within the item. Because the heat measurement result is completely independent of material and matrix type, it can be used on any material form or item matrix. For items that contain only one radioactive isotope, such as tritium-bearing items, the thermal power that is measured from the item can be directly converted into the amount of tritium within the item without any additional information. For items that contain more than one radioactive isotope, such as Pu-bearing items, additional information concerning the isotopic composition of an item is needed to convert the measured thermal power of the item into the total mass of nuclear materials that is contained within the item. The combination of a calorimetry measurement with an isotopic composition measurement, which is performed with either gamma ray spectrometry or mass spectrometry, is referred to as calorimetric assay. Calorimetric assay of tritium- and plutonium-bearing items routinely achieves the highest precision and accuracy in terms of the mass of the item of any NDA technique because of the precision and accuracy with which the thermal power of an item can be determined.

The principle decay mode for most of the actinides of interest to nuclear safeguards and nuclear nonproliferation (except for ^{241}Pu and tritium) is alpha decay, in which the nucleus spontaneously emits an alpha particle into the medium within which the nucleus is located. Each

radionuclide has a specific disintegration energy associated with its decay; for example, ^{240}Pu decays to ^{236}U with the emission of an alpha particle and a release of 5.15 MeV. The total reaction energy for alpha decay is the sum of the alpha particle kinetic energy and the recoil energy of the daughter nucleus, as described in detail in Chapter 1,Volume 1 of this book. The alpha particle and daughter nucleus have very short ranges in matter. Thus, virtually all of the energy released by alpha decay will remain within the item as heat. If the daughter product is not in the ground state as a result of the decay, an additional small amount of energy is released in the form of gamma ray and internal conversion electron energy. The electron and low-energy gamma ray are absorbed in either the item or the item container. Higher-energy gamma rays that are emitted by the daughter nuclei from alpha decay are typically measured in gamma ray spectroscopy for these materials. The escape of these higher-energy gamma rays does not affect the calorimetric assay result because the portion of the total decay energy released as higher-energy gamma rays does not vary for a given isotope, so the decay heat generated per unit mass does not vary.

The determination of energy losses in matter is more complicated for beta emitters, such as ^{241}Pu and tritium, than for alpha emitters. With beta decay, the total reaction energy is in the form of a beta particle, neutrino, and the excitation and recoil energy of the daughter. The energy loss due to bremsstrahlung radiation, emitted as a result of deceleration of the beta particle, is negligible for ^{241}Pu and tritium; therefore, nearly all of the kinetic energy of the beta particle is absorbed by the item as heat. The neutrino is not absorbed by the item or calorimeter; therefore, its energy is not measured as heat. The thermal power measured by a calorimeter from beta decaying radionuclides is the product of the activity and the average beta particle energy, which is on average approximately one-third of the maximum disintegration energy.

The rate of energy emission for a given radionuclide is equal to the product of the total decay energy and the activity. This product for a single radionuclide is called the specific power, P, which can be calculated as (ASTM-C1458, 2011)

$$P = \frac{2119.3}{T_{1/2} \cdot A} \cdot Q \ (\mathrm{W/g}) \tag{12.33}$$

where $T_{1/2}$ is the half-life of the radionuclide in years, A is the atomic weight of the isotope in grams, and Q is the total disintegration energy (MeV) for alpha emitters or average energy (MeV) for beta particle emitters.

The specific power can also be determined empirically based on a total heat measurement in Watts (W) of a single isotope of known mass, m

$$P = \frac{W}{m} \ (\mathrm{W/g}) \tag{12.34}$$

The principal decay modes, specific heats, half-lives, and the associated uncertainties are listed in Table 12.8 for most of the common assayed radionuclides, all commonly encountered plutonium isotopes, ^{241}Am, and tritium (Bracken and Rudy, 2007). For most of the plutonium isotopes and ^{241}Am, the specific powers were determined empirically. The specific powers for the U isotopes were calculated using Eq. (12.33). The specific powers listed in Table 12.8 span a large range of values from over 0.5 Watts/gram for ^{238}Pu to less than 10 nW/g for ^{238}U. The magnitude of the specific power is inversely proportional to the half-life of the radionuclide.

All of the uranium and plutonium isotopes listed in Table 12.8 have very small spontaneous fission branching ratios. When fission does occur, the fission daughter products will deposit all of their kinetic energy within the item as heat. After fission, the daughter products can initially be in an excited energy state; this small amount of energy is released in the form of gamma ray and internal conversion electron energy. The low-energy electromagnetic emissions will be highly attenuated in the item, container, and walls of the calorimeter, depositing their energy with a resultant rise in the temperature of the calorimeter measurement well. The higher-energy gamma ray emissions can escape the calorimeter with minimal attenuation; thus, the energy is not measured. Another product of fission is neutrons. Because neutrons are very penetrating, a portion of the neutrons will escape the calorimeter without depositing their kinetic energy. The upper limits on lost energy, due either to escaping gamma rays from plutonium and uranium isotopes and ^{241}Am or from spontaneous fission, were quantified in Bracken et al. (2002) and are presented in Table 12.9.

The maximum energy loss listed in the last column in Table 12.9 was calculated using the assumption that 20% of the spontaneous fission energy is completely lost from the calorimeter due to the escape of all neutrons and photons. This assumption is a large overestimate of the photon energy loss, since all low-energy photons are attenuated in the item and the calorimeter, with the attenuation increasing with increasing item size.

B. Heat flow calorimetry

All calorimeters have four elements in common as shown in Fig. 12.14 (Bracken et al., 2002). Those elements are a sample chamber, well-defined thermal resistance (noted as R_{th} in the figure), temperature sensor, and environment. The interrelationship of these four components and the

TABLE 12.8 Nuclear parameters of commonly assayed nuclides.[a]

Isotope	Dominant decay mode[b]	Specific power (mW/g)	% std. dev.	$T^{1/2}$ (y)	% std. dev.	References
^{238}Pu	α	567.57	0.05	87.74	0.05	Wapstra and Bos (1977), Strohm (1978)
^{239}Pu	α	1.9288	0.02	24,119	0.11	Strohm (1978), Seabaugh and Jordan (1978), Gunn (1978)
^{240}Pu	α	7.0824	0.03	6564	0.17	Rudy et al. (1984), Lucas and Noyce (1984), Beckman et al. (1984), Steinkruger et al. (1984), Jaffey et al. (1978)
^{241}Pu	β	3.412	0.06	14.348	0.15	Marsh et al. (1980), Garner and Machlan (1980), DeBievre (1981), Jordan (1982), Oetting (1968)
^{242}Pu	α	0.1159	0.22	376,300	0.24	OS76
^{241}Am	α	114.2	0.37	433.6	0.32	Jordan (1982), Oetting and Gunn (1967)
Tritium	β	324	0.14	12.3232	0.017	Rudy and Jordan (1977)
^{233}U	α	2.8E−1	—	1.592E5	—	Calculation[c]
^{234}U	α	1.80E−1	—	2.46E5	—	Calculation[c]
^{235}U	α	6.00E−5	—	7.038E8	—	Calculation[c]
^{236}U	α	1.75E−3	—	2.342E7	—	Calculation[c]
^{238}U	α	8.51E−6	—	4.468E9	—	Calculation[c]

[a] *Table originally presented in Bracken and Rudy (2007). Printed with permission, Los Alamos National Laboratory, LA-UR-07-5226.*
[b] *For all of the nuclides listed, the dominant decay mode has a branching ratio >99.99%.*
[c] *Half-life taken from National Nuclear Data Center NuDat 2.5, www.nndc.bnl.gov.*

TABLE 12.9 Limits of heat loss due to gamma ray emission or spontaneous fission (SF).[a]

Isotope	P (mW/g)	Photon energy fraction (%)	SF branching ratio (%)	SF energy fraction (%)	Maximum energy loss (%)[b]
^{238}Pu	567.57	0.031	1.9e−7	6.6e−6	3.1e−2
^{239}Pu	1.9288	0.0013	3e−10	1.1e−8	1.3e−3
^{240}Pu	7.0824	0.00054	5.7e−6	2.2e−4	5.8e−4
^{241}Pu	3.412	0.025	2e−14	8.7e−10	2.5e−2
^{242}Pu	0.1159	0.028	5.5e−4	2.2e−2	3.2e−2
^{241}Am	114.2	0.509	4e−10	1.5e−8	5.1e−1
^{233}U	2.81e−1	0.026	6e−11	2.4e−9	2.6e−2
^{234}U	1.80e−1	0.0023	1.6e−9	6.8e−8	2.3e−3
^{235}U	6.00e−5	3.3	7.0e−9	3e−7	3.3
^{236}U	1.75e−3	0.033	9.4e−8	4.1e−6	3.3e−2
^{238}U	8.51e−6	0.03	5.5e−5	2.6e−3	3.1e−2

[a] *Table originally presented in Bracken et al. (2002). Printed with permission, Los Alamos National Laboratory, LA-13-867-M.*
[b] *Maximum fractional loss due to escaping neutrons and gamma-rays.*

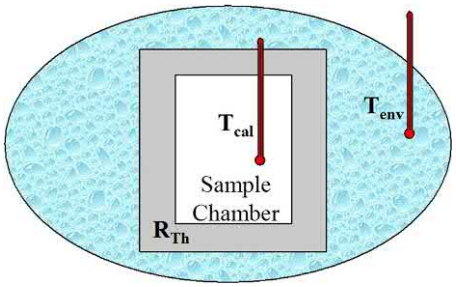


FIGURE 12.14 Schematic of the essential components of a calorimeter. *From Bracken et al. (2002). Printed with permission, Los Alamos National Laboratory, LA-13867-M.*

hardware that are used for each component of the calorimeter determine the type of calorimeter.

Radioactive material with a long half-life continuously produces heat at nearly a constant rate. There is some change due to decay and ingrowth of daughter products, but the time scale for a measurable change is generally weeks to months. The most appropriate calorimeter design for radioactive material is an isothermally jacketed heat-flow calorimeter because heat is continuously produced by the item of interest. The design of the calorimeter is determined by the size and heat output of the items to be measured and the required accuracy in the heat measurement.

A heat-flow calorimeter consists of a sample chamber insulated from a constant temperature environment by a thermal resistance and a means to measure the temperature difference across the thermal gradient produced by the thermal resistance. When an item is placed in the calorimeter, the temperature gradient across the thermal resistance is disturbed and the gradient changes with time until it converges to a constant value and equilibrium is achieved. The heat produced in the sample chamber raises its temperature and causes heat to flow across the thermal resistance into the environment according to

$$\frac{dQ}{dt} = \frac{(T_{cal} - T_{env})}{R_{th}} = \frac{\Delta T}{R_{th}} \tag{12.35}$$

where Q is the heat energy, R_{Th} is the thermal resistance, T_{cal} is the internal calorimeter temperature, and T_{env} is the external environment temperature. At equilibrium, dQ/dt is constant and ΔT is proportional to the power of the item. The magnitude of the change in the measured temperature (passive mode) or in the change in power required to maintain a constant measurement chamber temperature (power-replacement mode) is used to determine the thermal power of the item in the calorimeter.

The curve describing the approach of the temperature difference to equilibrium is a function of several exponentials with different time constants. The time constants are related to the specific heats and thermal conductivities of the item matrix material, packaging, and, in some instances, the calorimeter. An example of a typical calorimeter approach to equilibrium is presented in Fig. 12.15 (Bracken et al., 2002). Equilibrium may be detected by visual inspection of the measurement data versus time or through statistical tests (Smith et al., 2003; Burr et al. 2001) performed on a set of the latest data points in the time series. Statistical prediction algorithms (Perry and Fiarman, 1988; Fellers and Seabaugh, 1979; Mayer, 1987; Wetzel et al., 1997; Smith and Bracken, 2000, 2002) may be used earlier during transient temperature conditions to predict equilibrium and reduce measurement time. Typical prediction algorithms that are currently in use consist of exponential functions that are used to fit the measurement data. The fitted parameters are then used to predict the final equilibrium power. The temperature of the item to be measured may be adjusted using preconditioning baths to shorten the time required to reach equilibrium.

The type and placement of the temperature sensors, the heat-flow path, and the type of heat sink are what differentiates between types of heat-flow calorimeters used for measuring radionuclides. The heat flow is directed to areas where the sensors are located by the use of conductive and insulating material or controlling temperatures.

1. Operating modes for heat-flow calorimeters

a. Passive mode

The most basic mode of heat-flow calorimeter operations is to measure the amount of change in the temperature gradient across the thermal resistance when a heat-producing item is placed in the measurement chamber, relative to the measured temperature gradient that was measured when the measurement chamber was empty, which is referred to as the baseline reading of the calorimeter. The difference between the temperature sensor readings, which are typically measured as a voltage, with and without an item in the chamber, is then equal to the heat flow that is produced by the item itself. This mode of operation is known as passive mode since the calorimeter is allowed to come to equilibrium without any external heaters or power supplies. Fig. 12.15 illustrates a measurement that was made in passive mode, with the difference between the sensor values at thermal equilibrium with the item in the chamber and the baseline sensor values being proportional to the power of the item that was measured:

$$V_{item} - V_{base} = \Delta V \propto W \tag{12.36}$$

where V_{item} and V_{base} represent the sensor output values with the item present and the baseline, respectively, and W is the thermal power of the item being measured. To correct for any drifts that may occur in the zero power response in the calorimeter during the assay of the item, and achieve the highest precision measurement possible,

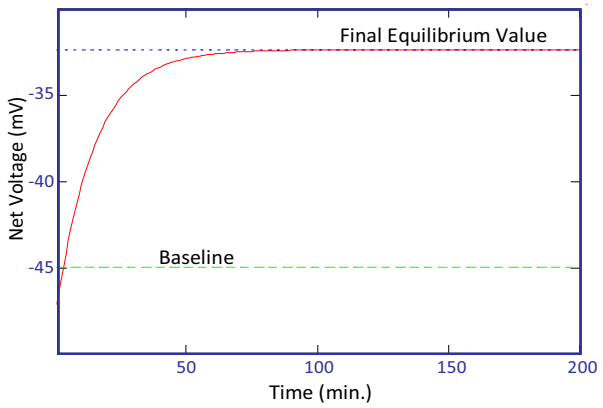


FIGURE 12.15 Example of approach to thermal equilibrium in calorimeter after insertion of heat-producing item. For the color version of the figure, the reader is referred to the electronic version of the book.

baseline measurements can be performed before and after an item measurement. An average baseline value $V_{base,avg}$ determined from those two measurements will be used to determine the net change in the sensor output due to the power of the item being assayed.

Calibration of a passive-mode calorimeter consists of determining the calorimeter sensitivity, S, which is the conversion factor between the differential sensor readings or resistance output and the thermal power of the item being measured. A series of calibration points within and bracketing the expected calorimeter operating range are needed to properly relate the sensor readings to the thermal power of the item. These calibration points can be made using either radioactive or electrical heat standards. The number of points will depend on the magnitude of the calorimeter differential sensitivity and the calibration accuracy required. A minimum of three different standard powers should be used. The form of the calibration curve varies according to the calorimeter design. Depending on the sensors that are used to measure heat flow, the sensitivity of a calorimeter can vary slightly with the amount of thermal power that is being measured by the calorimeter. The dependence in the sensitivity of a calorimeter on the thermal power being measured is given by:

$$S = S_0 + k \cdot W \tag{12.37}$$

where S_0 is the sensitivity of the calorimeter at zero thermal power and k is the slope of the varying sensitivity with the measured power. For most calorimeters, the magnitude of k is less than 1% of the zero power sensitivity over the operating power range. The sensitivity usually decreases with increasing power, which is qualitatively consistent with increased thermal conductivity of the material forming the primary thermal resistance. For example, the conductivity of dry air, a common thermal gap material, increases at the rate of 0.3% per °C. The intrinsic high-order nonlinearity of thermopile sensors can lead to differential sensitivities that are negative or positive but still relatively small compared with the base sensitivity.

Because of the dependence of the sensitivity of the calorimeter on the thermal power that is being measured, the calibration curve of a calorimeter operated in passive mode is usually well represented by a quadratic function:

$$\begin{aligned} \Delta V &= S \cdot W \Rightarrow \\ \Delta V &= (S_0 + k \cdot W) \cdot W \Rightarrow \\ \Delta V &= S_0 \cdot W + k \cdot W^2 \end{aligned} \tag{12.38}$$

The fit parameters S_0 and k are determined by a least-squares fit to a plot of net sensor output as a function of the thermal power of the heat standards that are used to calibrate the calorimeter. Since calorimeter noise is a function of the power of the item being measured, increasing variability with increasing power, the residuals of the least-squares fit will not be normally distributed. However, the parameter estimates are not affected by this abnormal distribution.

An example of actual calibration data used to determine the fit parameters in Eq. (12.38) are presented in Fig. 12.16 (Bracken and Rudy, 2007). The data presented in Fig. 12.16 were obtained using a dual-sensor water-bath calorimeter. Three to five measurements were made at each standard power. The linearity of the calorimeter response to power is typical of water-bath calorimeters.

A plot of the first derivative of calorimeter calibration data is normally designated a differential sensitivity plot as presented in the bottom of Fig. 12.16. It is easier to visually quantify the differential sensitivity of the calorimeter and the relative precision of the measurements at the different powers on a differential sensitivity plot than it would be from the top plot in Fig. 12.16. It is apparent in the bottom plot in Fig. 12.16 that multiple measurements were made using the three lowest-power heat standards; this observation is not possible in the top plot. The precision of this calorimeter is good enough that the multiple measurements, three each, at the largest two powers are not resolved on this scale.

b. Power-replacement mode

In power-replacement mode, the calorimeter sample chamber is maintained at a constant temperature differential via an internal heater and an external power supply, which is controlled and monitored by the data acquisition system using the temperature sensors within the calorimeter as a feedback signal. When a heat-generating item is placed inside the measurement chamber, the additional heat that is generated by the item causes the temperature sensors to initially rise triggering the controller on the power supply to adjust the power supply's output and subsequently reduce the heat that is generated by the internal heaters to maintain

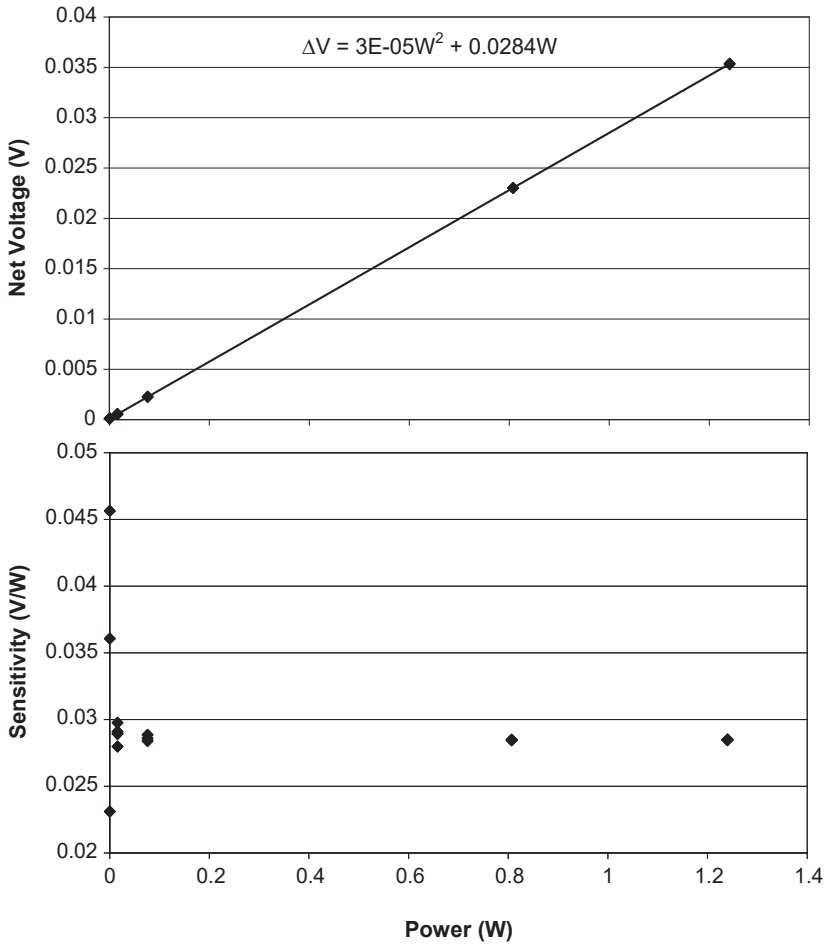


FIGURE 12.16 (Top panel) Example of sensor output as a function of thermal power of the heat standards used to calibrate a dual-cell water-bath calorimeter. The solid line is a least-squares fit to the measured data. (Bottom panel) Calorimeter sensitivity as a function item power derived from the data shown in the top panel.

a constant sensor output (and therefore a constant measurement temperature differential within the chamber). When the item reaches thermal equilibrium within the calorimeter, the difference in the measured output of the external power supply, from when the chamber was empty to when the item was placed inside the chamber, is equal to the thermal power output of the item. The reason the output of the external power supply changes is due to the fact that the item that is placed inside the measurement chamber supplies a portion of the thermal power, which was being supplied by the external power supply (through the internal heater) when the chamber was empty. Hence, the calculation of item power, W_i, in power-replacement mode is

$$W_i = W_0 - W_H \tag{12.39}$$

where W_0 is the power supplied to the calorimeter with no item in the calorimeter (known as the base power) and W_H is the power supplied to the calorimeter with the item in the calorimeter. Fig. 12.17 presents a graphical illustration of a calorimetry measurement performed in power-replacement mode (Bracken et al., 2002). The measurement time for the power-replacement mode of operation can be shorter than for the passive mode because the calorimeter components are at the equilibrium temperature and the servo-controlled internal heater can supply heat to actively bring the item to equilibrium.

Calibration of a power-replacement mode calorimeter consists of setting the sensor output set point voltage corresponding to a specific base power and determining the stability of the heater power. A single sensitivity point, S, must be determined by making a measurement of a heat standard. Any power within the operating range of the calorimeter is satisfactory. The sensor output set point (V_{sp}) is calculated using

$$V_{sp} = V_{base} + S \cdot W \tag{12.40}$$

where V_{base} is the baseline of the calorimeter. The heater power is controlled to maintain a constant sensor output equal to V_{sp}. The actual supplied heater power (W_0) used to maintain V_{sp} may be slightly different from the target value, W, because of the uncertainty in S used to calculate the set point. Measuring a standard power, which is as close

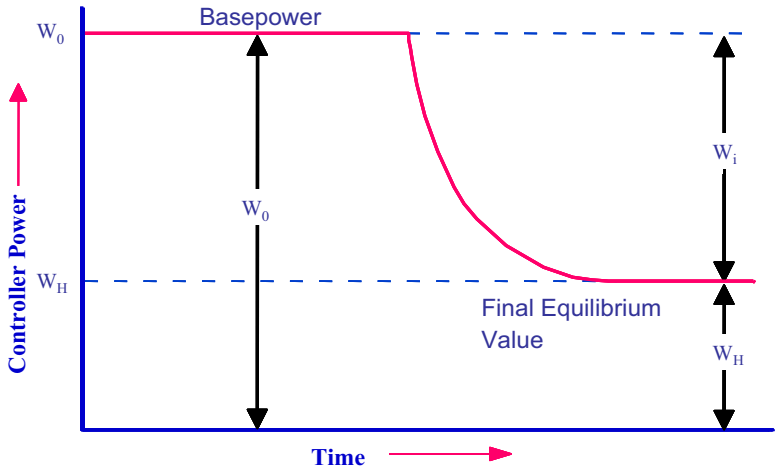


FIGURE 12.17 Graphical illustration of a calorimeter measurement performed in power-replacement mode. For the color version of the figure, the reader is referred to the electronic version of the book.

as possible to the value of W, will minimize the difference between W and W_0. Because the item power is the difference between W_0 and W_H, at equilibrium with item present, carefully matching W and W_0 will not increase the performance of the calorimeter in any way as both W_0 and W_H are measured to determine the item power. Matching W and W_0 will only minimize the difference between the requested base power and the actual base power.

For a calorimetry measurement to be made in power-replacement mode, it is critical that control of the measurement chamber temperature be maintained during a measurement. If the thermal power of an item being measured in power-replacement mode exceeds the base power of the calorimeter, the external power supply will end up being set to zero by the controller, and the heat flow sensors on the measurement chamber will end up raising in response solely to the thermal power that is produced by the item. To avoid this measurement scenario from occurring, the base power, W_0, of a calorimeter operated in power-replacement mode is typically set 10%–20% higher than the highest-power item expected to be measured. For some calorimeter designs, a calorimeter that is designed to operate in power-replacement mode can be used in passive mode, if it has been calibrated as described in the previous section.

The base power, W_0, is determined the same way as a baseline is determined in passive mode. The calorimeter can is filled with a conductive material and no heat-generating items. The heater power measurement at equilibrium is the base power, W_0, corresponding to V_{sp}. Replicate measurements should be made of the base power to determine the standard deviation of the value. To best characterize the stability of the calorimeter in performing measurements of heat-producing items, the calorimeter is opened and closed between repeat measurements of base power.

2. Calibrating a heat-flow calorimeter

Two types of heat standards are commonly used to calibrate calorimeters. The most reliable type of heat standard used in US facilities is a radioactive source of known power whose calibration is traceable to the National Institute of Standards and Technology (NIST). These standards are normally made from ^{238}Pu oxide, which is well characterized both chemically and physically. As these standards can be measured in the exact same manner as assay measurements of unknown nuclear material–bearing items, repeated measurements of these heat standards will provide a more accurate representation of the performance of the calorimeter than electrical standards can.

Electrical heat standards contain an electrical circuit consisting of standard resistors and standard voltage cells. Such standards are also traceable to the NIST or other national measurement systems. The resistor is used in place of a radioactive source, and the power dissipated in an electrical heater is measured using calibrated meters and calibrated resistors. The specifics of the calorimeter calibration depend on whether the calorimeter is operated in the passive mode or power-replacement mode. During all calibration measurements, the calorimeter should be operated in the same manner used to make assay measurements on items. The magnitude of heat distribution error (HDE) and convection noise should be quantified during initial calibration, if the calorimeter will be operated under nonideal conditions.

3. Types of heat-flow calorimeters

A variety of heat-flow calorimeter designs have been used to measure nuclear material. Most of the variations in the designs are related to the controlled environment that the calorimeter is placed in (water-bath or isothermal "air-bath" environments), the way in which the thermal power is

measured (e.g., Wheatstone bridge sensor or solid-state sensors), and the use of a reference set of sensors to reduce noise due to changes in the external environment.

A water-bath environment can provide the most stable and precisely controlled external environment temperature for calorimeters. Providing a stable and well-controlled external environment allows for higher precision measurements to be made, as the systematic variations in the external environment are reduced, as well as lower power measurements to be made within a given calorimeter as the variations in the baseline response of the calorimeter are reduced. In addition to placing a calorimeter into a large water bath, other methods for providing a consistent thermal environment using water include the use of a water jacket, which continuously circulates water through an external jacket that is in contact with the calorimeter. As water jacketed systems typically require a significantly smaller volume of water than a water-bath system does, the noise in the reference temperature of a calorimeter system that utilizes a water jacket is usually larger than the noise observed in a similarly sized water bath system due to ambient room-temperature fluctuations.

The isothermal "air-bath" calorimeter operates with three concentric cylinders at successively lower temperature from the inner cylinder (measurement chamber) to the outer cylinder. This creates a temperature gradient and heat flow from the inner cylinder to the outer cylinder. The calorimeter operates in power-replacement mode with the measurement chamber kept at a constant operating temperature. The system controller works to maintain a constant total thermal power in the measurement chamber. The total thermal power present in the measurement chamber is the power due to the internal heaters and the power due to the item being measured. Isolation from the thermal environment is achieved by circulating air through an exterior chamber either by forced air cooling using room temperature air or by a closed-loop air circuit employing a thermoelectric cooling unit to provide a sufficiently low heat sink temperature (ASTM-C1458, 2011).

To measure the thermal power that is emitted from an item of interest, a number of different types of heat-flow sensors have been utilized in calorimeters for assaying nuclear materials. Historically, one of the most common types of sensors that are encountered within heat-flow calorimeters are nickel wire temperature sensors connected in a Wheatstone bridge configuration. In a Wheatstone bridge calorimeter, two lengths of high-purity nickel wire are wound concentrically about a sample chamber and a reference chamber and serve as two-sensor arms of the Wheatstone bridge circuit, shown in Fig. 12.18. The thermal resistance between the sample sensor windings and the water bath is identical to the thermal resistance between the reference sensor windings and the water bath. This thermal resistance matching is done to maximize cancellation of

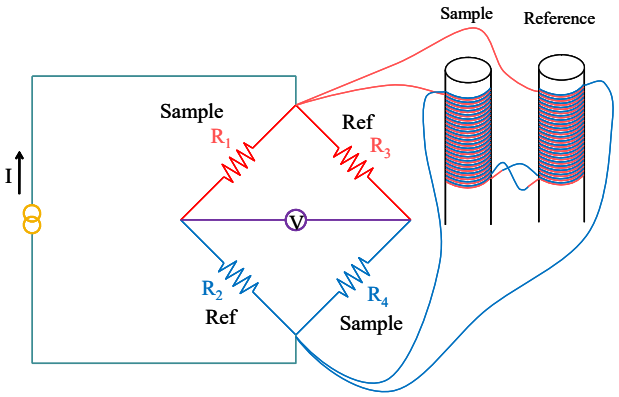


FIGURE 12.18 Schematic drawing of wiring of Wheatstone bridge calorimeter. For the color version of the figure, the reader is referred to the electronic version of the book.

temperature fluctuations in the external environment in the Wheatstone bridge signal. The sensitivity of the calorimeter is directly proportional to the thermal resistance of the thermal gap. The wider the thermal gap, the larger the internal temperature rise of the sample chamber for a given thermal power.

The change in resistance of the high-purity nickel wire with temperature is linear with a sensitivity of about +0.6% per °C. The temperature rise in the sample side due to the presence of radioactive material causes the resistance of the sample arms of the Wheatstone bridge to increase, whereas the resistances of the reference arms remain constant. When a constant electrical current is applied across the Wheatstone bridge, the resistance change between the sample and reference sides of the bridge causes an imbalance in the bridge, and the voltage across the bridge (the bridge potential) changes in proportion to the size of the temperature change. The reference sensor wire arms and sample sensor wire arms of the Wheatstone bridge are each helically wound interleaved (bifilar winding) and concentrically around a cylindrical chamber. While Wheatstone bridge calorimeters are able to perform high-precision thermal power measurements, the calorimeters are sensitive to environmental factors, which could change the resistance of the nickel wire such as physical stress or strain on the wire itself.

Other common type of sensors that are used in heat-flow calorimeters are solid-state sensors, which use thermopile components as heat-flow sensors (Bracken and Hypes, 2000; Bracken et al., 1997, 1998). A thermopile consists of numerous thermocouple pairs electrically connected in series. Thermocouples are formed by electrically joining one set of ends of two dissimilar conductors or semiconductors. A temperature difference between two thermocouple junctions causes the development of an electromotive force, known as the relative Seebeck effect that is proportional to the temperature difference. The greater the temperature

difference, the larger the voltage measured from the sensor. The thermopile hot junctions are placed facing the sample chamber, whereas the cold junctions are held at the reference temperature. Because the solid-state sensors are insensitive to physical stress or vibrations that may be encountered by the calorimeter, solid-state calorimeters tend to be more stable in terms of their baseline response than Wheatstone bridge calorimeters.

Calorimeters that typically achieve the highest precision and sensitivity in measuring nuclear materials utilize a twin-cell design, which uses two identical chambers with one chamber used as a reference for the chamber that is used to measure the nuclear material–bearing items. The fact that the reference and sample chambers will have identical responses to changes in the controlled external environment allows for the calorimetry system to compensate for changes in the sensor readings due to the changes in the external environment. This reduces the effects of thermal noise in the system on the measurement results, which improves the precision of the measurements as well as increases the sensitivity of the calorimeter to lower amounts of heat being produced by an item of interest. A twin-cell calorimeter can be made with either a Wheatstone bridge sensor system or solid-state sensors. Other calorimeter designs, which utilize a reference set of sensors for noise reduction, include a gradient design where the sample sensors and reference sensors are placed in concentric circles about a single measurement chamber, and an over-under design where the reference chamber is located underneath and along the same axis as the sample chamber. In these designs, because the reference set of sensors will have slightly different responses to the thermal changes as the sample sensors, the noise reduction is not as effective as is observed in the twin-cell calorimeters.

C. Calorimetric assay

Calorimetric assay has been routinely used at US and European facilities for plutonium process measurements and nuclear material accountability for the past 60 years (Eichelberger et al., 1954; Gunn, 1964, 1970; ANSI, 1987; ASTM-C1458, 2011; Mason, 1982; IAEA, 1987). Calorimetric assay is routinely used as a reliable NDA technique for the quantification of plutonium and tritium content within items. Calorimetric assay of tritium- and plutonium-bearing items routinely obtains the highest precision and accuracy of all NDA techniques. Plutonium items usually contain varying amounts of ^{241}Am, which can be accounted for during the assay.

The thermal power emitted by a nuclear material–bearing item is directly proportional to the quantity of radioactive material in it, and the total power generated by ionizing radiation absorbed in the item is measured by the calorimeter. The mass m of radionuclides present is calculated from the measured thermal power of an item using the relationship

$$m = \frac{W}{P_{eff}} \tag{12.41}$$

where P_{eff} is the effective specific power (Watts/gram) calculated from the isotopic composition of the item. For all multiradionuclide items, the P_{eff} is not a constant and needs to be corrected for the decay and growth of the constituent radionuclides. See Likes (1991) for details on decay correction of plutonium bearing items.

For monoisotopic items, the specific power (P) of the radioisotope is used in place of P_{eff}. For items that contain multiple radioactive isotopes, the effective specific power of an item, which contains i heat-producing radioisotopes, can be calculated by

$$P_{eff} = \sum_i R_i \bullet P_i \tag{12.42}$$

where R_i is the abundance of the ith radionuclide in the item, typically expressed as a mass fraction to a total elemental mass, and P_i is the specific power of the ith radionuclide in the item in watts/gram.

Two methods exist for determining P_{eff}: a computational method and an empirical method. The computational method uses Eq. (12.42) for determining P_{eff} and is appropriate when isotopic composition measurements can be made. The relative abundances of the radionuclides can be determined destructively using mass spectroscopy (ANSI, 1973, 1974; ASTM-C697, 2011) or nondestructively using gamma ray spectroscopy (Sampson, 1991; ASTM-C1030, 2018). When measuring items in sealed containers, high-resolution gamma ray spectroscopy is the only option for determining P_{eff} using nondestructive methods. The uncertainties on P_{eff} using gamma ray measurements for plutonium-bearing items are generally less than 0.5%. If mass spectroscopy is used to determine P_{eff} of plutonium-bearing items, the ^{238}Pu content should be determined using alpha spectrometry (ASTM-C697, 2011), and the ^{241}Am content should be determined radiochemically. The effective specific power uncertainty is normally 0.1%, for isotopically homogeneous items. The computational method using gamma ray spectroscopy for isotopic analysis is the dominant technique used in conjunction with calorimetry.

The empirical method of determining the effective specific power involves a calorimeter measurement to determine the total power produced by the sample and a chemical analysis to determine the total amount of nuclear material in the sample. Substituting these values into Eq. (12.41), P_{eff} can be determined. The empirical method is potentially more accurate and precise than the computational method. The method can only be implemented on discrete batches of process materials or when it is difficult

to determine the relative isotopic abundances of an item or batch of material. As with using mass spectroscopy in the computational method, the empirical method is a destructive technique that generates waste and requires long assay times to complete the analysis. These time and waste issues have increased the exclusive use of NDA techniques for the quantitative determination of nuclear material mass.

1. Assay error determination

The measurement of the two quantities that are used in calorimetric assay to determine the nuclear material mass of an item (item power and effective specific power of an item) is independent, so the relative uncertainty for the plutonium mass can be written as

$$\frac{\sigma_m}{m} = \sqrt{\left(\frac{\sigma_W}{W}\right)^2 + \left(\frac{\sigma_{P_{eff}}}{P_{eff}}\right)^2} \tag{12.43}$$

The uncertainty in the power measurement, σ_W, can be obtained from replicate power measurements of heat standards or from historical data. It should include both random and systematic error components. The uncertainty in P_{eff}, σ_{Peff}, comes from the uncertainty in the isotopic fractions, R_i, and isotopic specific powers, P_i. The uncertainties in the isotopic fractions are determined from uncertainties in the various techniques that might be used for the isotopic analysis, such as mass spectroscopy, alpha counting, or gamma ray spectroscopy. The uncertainties in the isotopic specific powers, P_i, as determined by different experiments, were previously given in Table 12.8.

2. Calorimetric assay performance

Calorimetric assay is considered the "gold standard" of NDA measurements for items containing more than 0.5 kg of plutonium of any form in a container less than 25.5 cm in diameter. Since calorimetry can measure entire items with very high precision and low bias, the results are often comparable with DA measurements in terms of accuracy and precision. Calorimetry is frequently used as a standard measurement to determine uncertainties and/or biases in other NDA techniques such as neutron counters (ASTM-C1207, 2011) and tomographic gamma scanner systems (Hyman et al., 1999; Lestone et al., 2000).

The accuracy and reliability of calorimetric assay are primarily dependent on the thermal power generated by the item and on the methods used to determine P_{eff}. The total measurement uncertainty on P_{eff} determined for pure homogeneous items using gamma ray spectroscopy is comparable with the power measurement uncertainty (Sampson, 1999). Major factors that can affect the precision of P_{eff} determined by gamma ray isotopic assay can be found in ASTM-C1030 (2018). Major factors that can affect the bias of P_{eff} determined by mass spectrometric methods can be found in ASTM-C697 (2011). For materials containing reasonable concentrations of plutonium (>100 g Pu/liter), the precision and bias of calorimetric assay are comparable with good chemical assay techniques (Welsh et al., 1995a). In this case, the largest source of calorimetry error is due to the uncertainty of the specific powers, P_i, of the individual radionuclides. For single radionuclide items, the uncertainties will be due only to the power measurement and the specific power of the radionuclide. The precision of a calorimeter measurement is dependent on the sensitivity of the calorimeter, baseline stability, and item power.

For impure or heterogeneous items, calorimetric assay can have lower uncertainties than DA techniques (Welsh et al., 1995b) because of DA sampling error. The power measurement integrates all of the heat produced by the item regardless of inhomogeneity, and for heterogeneous items, the determination of P_{eff} by gamma ray spectroscopy is a more representative average of the entire item than DA. In this case, where the isotopic composition of the plutonium is determined by gamma ray spectroscopy, the final uncertainty in the gram value determined by calorimetric assay is dominated by the uncertainty of the mass fractions, R_i, in P_{eff}.

To evaluate the precision and accuracy of calorimetric assay measurements throughout the Department of Energy (DOE) complex, the DOE created the Calorimetry Exchange program (CALEX), which distributed identical PuO_2 items containing 400 g of plutonium with 5.86% ^{240}Pu by weight to different Pu facilities throughout the complex. The plutonium content and isotopic composition reference values of the mother lot of PuO_2 material used for these standards were measured by coulometry and mass spectrometry/alpha counting by four analytical labs. The power of the CALEX standard during the time periods of measurements described below was about 1 W.

Measured data for 23 calorimeters at five DOE facilities are presented in Fig. 12.19 with the ratio of the measured mass value to the accepted mass value for the standard plotted as a function of the measurement number. The dashed vertical lines separate the data submitted by each laboratory. These data were collected for the CALEX program over a 15-month period starting in October 1993. All measurements have a bias of less than ±0.8%. The average bias is 1.0004 with a standard deviation of the average of ±0.0002. The error expected on a single measurement would be 0.3% one RSD.

The results of multiple calorimetric assay measurements by three facilities on the CALEX standards are shown in Table 12.10 (NBL, 1999). The calorimetry and gamma ray measurements used to determine plutonium mass variabilities and biases reported in Table 12.11 were taken over a 1-year period. The within-facility variability and the bias of the calorimetric assay were calculated from results reported

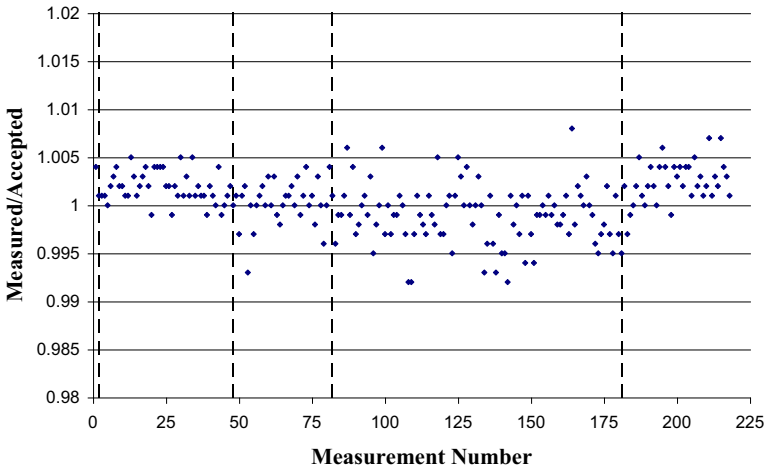


FIGURE 12.19 Calorimeter measurement biases for heat measurements of the CALEX standards. Measurements were taken over a 15-month period by five DOE laboratories using 23 different calorimeters.

TABLE 12.10 Calorimetry/gamma ray assay results of CALEX standards.[a]

Facility	Within-facility variability (g)	Within-facility variability (% RSD)	Bias (g)	Bias (% RSD)
A[b]	1.5	0.38	0.03	0.01
B[b]	1.5	0.38	−0.40	−0.10
C[c]	1.4	0.36	0.04	0.01

[a]*All masses are in grams of plutonium decayed to a common date.*
[b]*Measurements made using multiple water-bath twin-sensor calorimeters.*
[c]*Measurements made using "air-bath" calorimeter.*

TABLE 12.11 Precision and bias data from the CALEX program for P_{eff} and power from 1990 to 1998.

	Power		P_{eff}	
Facility	% Bias[a]	% RSD[b]	% Bias[a]	% RSD[b]
A	0.11	0.61	−0.23	0.10
B	0.08	0.22	0.07	0.26
C	−0.01	0.17	0.13	0.21
D	−0.08	0.30	0.02	0.20
E	0.17	0.21	−0.18	0.48

[a]*% measurement bias = 100*([measured − accepted]/accepted].*
[b]*% relative standard deviation is based on repeated measurement of the same item.*

by each facility decayed to a common date. Each facility used different gamma ray analysis codes for the isotopic measurements. For some, the reported values are the averages of measurements of the standard item with different calorimeters.

CALEX data taken at five different DOE facilities are presented in Table 12.11. The data were collected over an 8-year period from 1990 to 1998. Not all facilities reported results each year. Therefore, the averages contained data from a maximum of 8 years and a minimum of 5 years. Presented in Table 12.11 are the average percent measurement bias and percent RSD from repeated measurements for P_{eff} and item power. The percent bias and percent RSD are comparable for power and P_{eff} measurements on this item.

Data collected from a measurement control program can be used to calculate the precision and bias of the power measurement. A summary of the precision and bias of the power measurement obtained from replicate measurements of ^{238}Pu heat standards in production facilities over a 0.5−1.0 year period is shown in Table 12.12. Generally, the greater the thermal power of an item in a calorimeter, the better the relative precision. Extensive calorimetric assay precision and bias data can be found in references (Birden et al., 2000, NBL, 1999, Longmire et al., 1990, Fleissner and Hume, 1986, Welsh et al., 1995a,b, Lindsay et al., 1987).

There are a number of factors, which could affect the performance of a calorimetric assay. One potential factor is a heat distribution error (HDE), which is a variation in the calorimeter response due to the location of the heat source within the measurement chamber. For example, the same heat source may produce a larger calorimeter output in the bottom of the sample chamber than in the top. The HDE could lead to a bias if the location of heat within an item is unknown. HDE is quantified by performing multiple

TABLE 12.12 Examples of calorimeter power measurement precision and bias.

Heat standard power (W)	Calorimeter diameter (m)	Calorimeter type, operation mode	Number measurement	Precision(% RSD)	Bias (%)
98.0	0.06	Rod, power-replacement	29	0.065	0.02
3.5	0.15	Rod, power-replacement	55	0.09	0.00
4.0	0.25	Twin, passive[a]	22	0.05	0.03
4.9	0.30	Twin, passive[a]	34	0.06	0.05
0.0786	0.04	Solid state, passive[b]	10	0.23	0.001

[a]*Pooled results from two calorimeters.*
[b]*Measurements made in laboratory.*

measurements of the same heat source placed at different vertical positions within the calorimeter measurement well. The magnitude of an HDE will increase with increasing power. If an HDE is measured, the uncertainty associated with HDE must be included in the final uncertainty of the power determination.

Other factors, which can affect the precision and accuracy of a calorimetry measurement, include the presence of processes within the item that would add or subtract thermal power from the power being generated by the decay of the radionuclides being assayed. These processes can include phase changes, endothermic, or exothermic chemical reactions, such as oxidation. In addition, radioactive decay energy can drive endothermic reactions in aqueous solutions.

Because calorimetric assay relies on a knowledge of the radionuclides that are generating heat within an item, any radionuclides that generate heat within an item but that would not be detected using gamma ray spectroscopy would add additional thermal power to a measurement. This additional thermal power would be attributed to the known radionuclides present within the item. This would cause bias in the calorimetric assay of this item. In a similar manner, the accuracy of calorimetric assay can be degraded for items, which possess an inhomogeneous isotopic composition due to the increased uncertainty in the isotopic ratios.

Calorimetry measurement times are typically longer than other NDA techniques. The packaging conditions and matrix of the item cannot change the heat output of the material, but they are usually the determining factor for measurement time. Time series data collected with a twin-sensor water-bath calorimeter operated in passive mode are presented in Fig. 12.20 (Smith et al., 2001). The series of lines represent different matrix conditions. The effect of matrix on measurement time is apparent in Fig. 12.20. It can also be seen that the matrix has no effect on the magnitude of the final answer (i.e., the bridge potential at

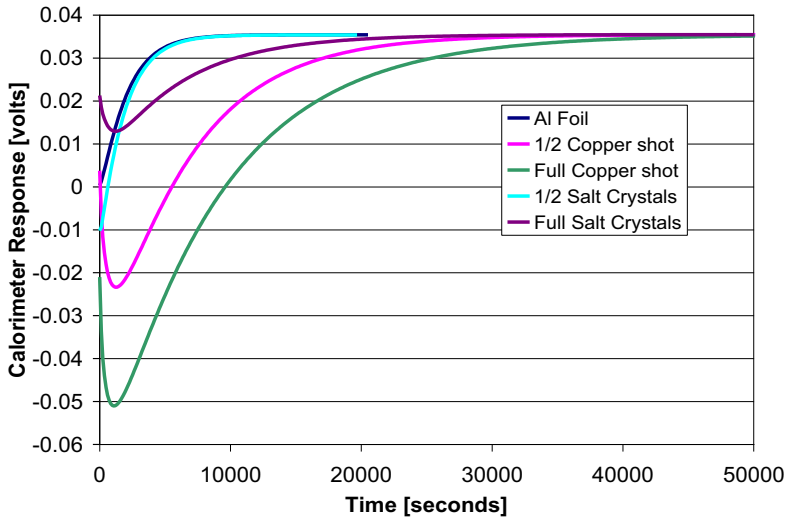


FIGURE 12.20 Twin-cell calorimeter measurements of a 1.25 W heat standard embedded in different matrices illustrating how different matrices affect time to equilibrium. The data have been adjusted so that the baseline value corresponds to 0 V. For the color version of the figure, the reader is referred to the electronic version of this book.

equilibrium). For each measurement presented in Fig. 12.20, the calorimeter can, including the matrix and source, was preequilibrated to the same temperature before insertion into the calorimeter. Preequilibration was done to minimize the time response due to starting temperature variability, therefore maximizing the time sensitivity to matrix. The different matrices containing the same 1.25 W heat standard reached equilibrium in a time range of 3−14 h. The matrices in order of increasing time to equilibrium were with the can 1/2 full of salt crystals, full of aluminum foil, full of salt crystals, 1/2 full of copper shot, and full of copper shot.

The time necessary for a calorimeter to reach thermal equilibrium during the assay of an item is dependent on a number of factors:

- initial temperature of item relative to final equilibrium temperature of the item/calorimeter (sample preconditioning can reduce measurement time by reducing this difference),
- type of heat-flow calorimeter used (passive or power-replacement),
- calorimeter size and thermal properties (thermal conductivity and total heat capacity) of the fabrication materials,
- thermal properties of the item and item packaging (usually more important than calorimeter properties), and
- the size and weight of the item and the calorimeter.

D. Applications

Calorimetric assay is presently the most precise and accurate NDA technique for the measurement of many physical forms of plutonium and tritium. Calorimetry has been applied to a wide variety of plutonium-bearing solids, including metals, alloys, oxides, fluorides, mixed plutonium−uranium oxides, mixed oxide fuel pins, waste, and scrap (e.g., ash, ash heels, salts, crucibles, and graphite scarfings) (Rogers, 1981; Likes, 1991). Calorimetric assay has applications in a number of different areas: shipper/receiver measurements, accountability measurements, calibration of NDA standards, process control measurements, outlier resolution, and product acceptance measurements.

Of the items listed above, calibration of NDA standards and outlier resolution can only be done nondestructively using calorimetric assay.

Calorimetric assay can be applied to a number of different radionuclides: plutonium, HEU, ^{233}U, ^{237}Np, ^{242,244,245}Cm, ^{250,252}Cf, ^{241,242m,243}Am, tritium, and fission products. Calorimetric assay can be accurately used for any of the above-listed items that will fit in the instrument measurement well and are free from any exothermic or endothermic chemical reactions. Fig. 12.21 presents the range of specific powers for some of the radionuclides listed above.

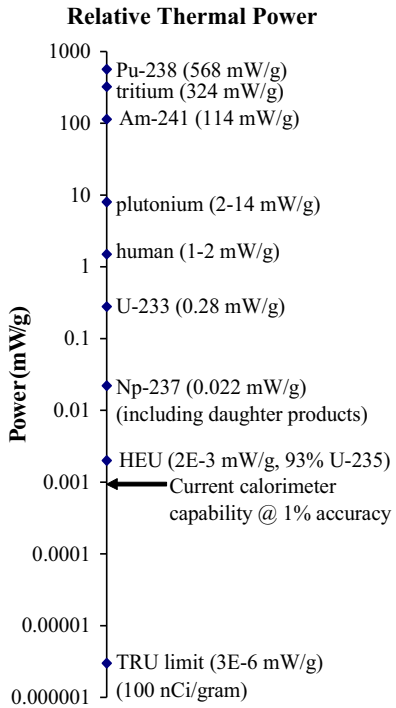


FIGURE 12.21 Specific power of actinides relative to current calorimeter capabilities.

Calorimetric assay is most frequently used to measure plutonium-bearing items with varying amounts of ^{241}Am. High-resolution gamma ray spectroscopy measurements are usually made to determine the plutonium isotopic and ^{241}Am mass fractions. An example of the importance of calorimetric assay of plutonium-bearing items at the Los Alamos National Laboratory (LANL) is presented in Table 12.13, originally presented in Bracken et al., 2002.

Calorimetry can be used to measure the quantity of tritium in containers. In most cases, tritium is the only radioactive isotope present; therefore, no isotopic measurements are required for the assays. A confirmatory gamma assay may be necessary to substantiate the lack of additional radionuclides for items with uncertain histories. High-precision and low-bias assays can be made on items containing more than approximately 0.01 g of tritium.

Uranium with a natural abundance of 0.7% ^{235}U generates too little thermal power to be accurately quantified by calorimetric assay. The major component of natural uranium, ^{238}U, has too long a half-life, 4.5×10^9 y, to generate sufficient thermal power. As the 7.0×10^8 y ^{235}U mass fraction increases during enrichment, the specific

TABLE 12.13 Measurement methods for the Los Alamos National Laboratory Pu inventory mass % for each material form.[a]

Material form	Calorimetric assay	Analytical chemistry	Neutron counter + gamma spec	Segmented gamma scanner
Metal	71%	29%	0.3%	0%
Compounds pure	64%	35%	0.9%	0.3%
Compounds impure	72%	23%	2.6%	2.6%

[a]*From LANL Material Accounting and Safeguards System (MASS) database April 1999.*

TABLE 12.14 Calorimetric assay of highly enriched uranium results.[a]

Material	Fraction U-235 (wt %)	U Mass (chem.) g	U Mass (cal assay) g
U oxide	91.3	990	960 ± 52
U oxide	66.0	990	860 ± 31
U oxide	52.1	989	975 ± 53
U metal	93.17	3954	4069 ± 70

[a]*From Rudy et al. (1997). Printed with permission, Los Alamos National Laboratory, LA-UR-97-2805.*

power of uranium increases. Although the specific power of ^{235}U is higher than ^{238}U, the major contributor to the increase of effective specific power is the ^{234}U that is enriched along with the ^{235}U. The specific power for ^{234}U is nearly 0.2 mW/g, which is more than three orders of magnitude larger than for ^{235}U; this is due to its relatively short half-life of 2.45×10^5 years. For an enrichment of 93% ^{235}U, the ^{234}U mass fraction is about 1%. With a mass fraction of 1%, the ^{234}U component supplies about 96% of the total thermal power from the uranium, 1.85 mW/kg. This is a power density that can be measured to an accuracy of about 1% by some calorimeters. Calorimetric assay measurement results on HEU metal and oxide are shown in Table 12.14. These measurements were made with a 5″ diameter twin-bridge, water-bath calorimeter on well-characterized material (Rudy et al.,1997). The precision for the 1-kg items ranged from 12% to 18% RSD, whereas the thermal power for the 4-kg item, 7.8 mW, was measured with a precision of about 1% RSD. The low specific power of HEU limits calorimetric assay to matrices with high uranium content, such as metal, oxides, U alloys, and high-grade scrap.

References

ANSI, 1973. Methods for Chemical, Mass Spectrometric, and Spectrochemical Analysis of Nuclear Grade Plutonium Dioxide Powders and Pellets. ANSI N104-1973. American National Standards Institute, Inc., New York.

ANSI, 1974. Methods for Chemical, Mass Spectrometric, Spectrochemical, Nuclear, and Radiochemical Analysis of Nuclear-Grade Plutonium Metal. ANSI N572-1974. American National Standards Institute, Inc., New York.

ANSI, 1987. Plutonium-Bearing Solids Calibration Techniques for Calorimetric Assay. ANSI N15.22-1987. American National Standards Institute, Inc., New York.

ASTM-C697, 2011. Standard Test Method for Chemical, Mass Spectrometric, and Spectrochemical Analysis of Nuclear-Grade Plutonium Dioxide Powders and Pellets. ASTM Standard C 697. ASTM International, West Conshocken, PA.

ASTM-C1030, 2018. Standard Test Method for Determination of Plutonium Isotopic Composition by Gamma-Ray Spectrometry. ASTM Standard C 1030-10. ASTM International, West Conshocken, PA.

ASTM-C1207, 2011. Standard Test Method for Nondestructive Assay of Plutonium in Scrap and Waste by Passive Neutron Coincidence Counting. ASTM Standard C 1207. ASTM International, West Conshocken, PA.

ASTM-C1458, 2011. Standard Test Method for Nondestructive Assay of Plutonium, Tritium, and ^{241}Am by Calorimetric Assay. ASTM Standard C 1458. ASTM International, West Conshocken, PA.

ASTM-C1514-08, 2017. Standard Test Method for Measurement of 235U Fraction Using Enrichment Meter Principle. ASTM Standard C 1514-08. ASTM International, West Conshocken, PA.

Auguston, R.H., Walton, R.B., Harbarger, W., Hicks, J., Timmons, G., Shissler, D., Tayloe, R., Jones, S., Harris, R., Fields, L., 1983. Measurements of uranium holdup in an operating gaseous diffusion plant. In: Proceedings of the ANS/INMM Conference on Safeguards Technology: The Process-Safeguards Interface, Hilton Head, SC.

Baker, L., MacMurdo, K., Miller, M.C., Bosler, G.E., 1990. Recent experiences of scrap and waste assay using neutron coincidence counting of materials from FB-line at the Savannah river site. In: Proceedings of the 31st Annual Meeting of the Institute of Nuclear Materials and Management.

Beddingfield, D.H., Menlove, H.O., 2002. Distributed source term analysis, a new approach to nuclear material inventory verification. Nucl. Instrum. Methods Phys. Res., Sect. A 485, 797−804.

Belian, A.P., Browne, M.C., Clay, W., Ensslin, N., Geist, W., Nguyen, H., Ianakiev, K., Mayo, D., Panowski, S., Russo, P., 2003. An approach to multiplicity counting for a versatile new sensor for plutonium assay with a very short die-away time, and independent measurements of neutrons and gamma-rays. Nucl. Instrum. Methods Phys. Res., Sect. A 505, 54−57.

Beckman, R.J., Marsh, S.F., Abernathy, R.M., Rein, J.E., 1984. Plutonium-240 half-life determined by isotope-dilution mass spectrometric measurement of the grown-in uranium-236. Int. J. Appl. Radiat. Isot. 35, 163−169.

Birden, J., Duff, M.F., Fultz, R.L., Kesling, W.E., Wetzel, J.R., Campbell, A.R., Fellers, C., Lemming, J.F., Rudy, C.R., 2000. Automated plutonium assay system (APAS) redux. In: Proceedings of the 41st Annual Meeting of the Institute of Nuclear Material Management, New Orleans, LA.

Boehnel, K., 1985. The effect of multiplication on the quantitative determination of spontaneously fissioning isotopes by neutron correlation analysis. Nucl. Sci. Eng. 90, 75−82.

Bracken, D.S., Biddle, R., Cech, R., 1997. Design and performance of a vacuum-bottle solid-state calorimeter. In: Proceedings of the 38th Annual Meeting of the Institute of Nuclear Materials Management, Phoenix, AZ.

Bracken, D.S., Biddle, R., Rudy, C., 1998. Performance evaluation of a commercially available heat flow calorimeter and applicability assessment for safeguarding special nuclear materials. In: Proceedings of the 39th Annual Meeting of the Institute of Nuclear Materials Management, Naples, FL.

Bracken, D.S., Hypes, P., 2000. Solid-state calorimeter. In: Proceedings of the 41st Annual Meeting of the Institute of Nuclear Materials Management, New Orleans, LA.

Bracken, D.S., Biddle, R.S., Carrillo, L.A., Hypes, P.A., Rudy, C.R., Schneider, C.M., Smith, M.K., 2002. Application Guide to Safeguards Calorimetry. Los Alamos National Laboratory Report LA-13867-M.

Bracken, D.S., Rudy, C.R., 2007. Principles and Applications of Calorimetric Assay, Passive Nondestructive Assay of Nuclear Materials 2007 Addendum. Los Alamos National Laboratory Report LA-UR-07-5226. http://www.lanl.gov/orgs/n/n1/panda/index.shtml.

Burr, T., Smith, M., Gattiker, J.R., Bracken, D.S., 2001. Detecting and characterizing equilibrium in calorimetry. In: Proceedings of the Annual Meeting of the American Statistical Association.

Canberra, 2008. In Situ Gamma Spectroscopy with ISOCSTM, an In Situ Object Counting System. Mirion Technologies. Application Note, M2352 − 11/2008.

Chen, J.D., Gerwing, A.F., Keeffe, R., Larsson, M., Jansson, K., Hildingsson, L., Lindberg, B., Sundkvist, E., Meijer, U., Thorsell, M., Ohlsson, M., 2007. Long-Cooled Spent Fuel Verification Using a Digital Cerenkov Viewing Device. International Atomic Energy Agency Report (IAEA-SM-367/14/07).

Cifarelli, D.M., Hage, W., 1986. Models for a three parameter analysis of neutron signal correlation measurements for fissile material assay. Nucl. Instrum. Methods Phys. Res., Sect. A 251, 550−563.

Cooley, J.N., Fields, L.W., Herron, S.A., Mayer, R.L., Hagenauer, R.C., Whitaker, J.M., 1989. Nondestructive assay measurements of gaseous diffusion process equipment. Nucl. Mater. Manag. XVIII, 605−609.

Crane, T.W., Baker, M.P., 1991. Neutron detectors. In: Reilly, D., Ensslin, N., Smith Jr., H. (Eds.), Passive Non-destructive Assay of Nuclear Materials. NUREG/CR-5550.

Dearborn, D., Mount, M., 2003. Lawrence livermore national laboratory experience with the 30-gallon drum multiplicity counter. In: Proceedings of the 44th Annual Meeting of the Institute of Nuclear Materials and Management, Phoenix, AZ.

Dewberry, R.A., Klapper, K.P., Tietze, F.K., Ayers, J.C., 2010. Neutron multiplicity and active well neutron coincidence verification measurements performed for March 2009 semi-annual DOE inventory. In: Proceedings of the 51st Annual Meeting of the Institute of Nuclear Materials and Management, Baltimore, MD.

DeBievre, P., 1981. Isotope dilution mass spectrometry: some present limitations and possibilities to overcome these. In: Minutes of SALE Program Participants Meeting, pp. 188−207.

Dytlewski, N., Krick, M.S., Ensslin, N., 1993. Measurement variances in thermal neutron coincidence counting. Nucl. Instrum. Methods Phys. Res., Sect. A 327, 469−479.

Eccleston, L., Menlove, S.H., 2011. High efficiency protable boron-10 hybrid systems for neutron assay measurements. In: Proceedings of the 52nd Annual Meeting of the Institute of Nuclear Materials and Management, Palm Desert, CA.

Eichelberger, J.F., Jordan, K.C., Orr, S.R., Parks, J.R., 1954. Calorimetric determination of the half-life of Polonium-210. Phys. Rev. 96, 719.

Ensslin, N., 1991. Principles of neutron coincidence counting. In: Reilly, D., Ensslin, N., Smith Jr., H. (Eds.), Passive Non-destructive Assay of Nuclear Materials. NUREG/CR-5550.

Ensslin, N., Harker, W.C., Krick, M.S., Langner, D.G., Pickrell, M.M., Stewart, J.E., 1998a. Application Guide to Neutron Multiplicity Counting. Los Alamos National Laboratory Report LA-13422-M.

Ensslin, N., Foster, L.A., Harker, W.C., Krick, M.S., Langner, D.G., 1998b. Inventory verification measurements using neutron multiplicity counting. In: Proceedings of the 39th Annual Meeting of the Institute of Nuclear Materials and Management.

Ferrari, F., Peerani, P., 2010. Performance of an active well coincidence counter for HEU samples. Radiat. Meas. 45, 1034−1043.

Fellers, C.L., Seabaugh, P.W., 1979. Real-time prediction of calorimeter equilibrium. Nucl. Instrum. Methods 163, 499.

Fleissner, J.G., Hume, M.W., 1986. Comparison of Destructive and Nondestructive Assay of Heterogeneous Salt Residues. RFP-3876.

Frame, K.C., Geist, W.H., Lestone, J., Belian, A., Ianakiev, K., 2004. Characterizing the detector response and testing the performance of a new liquid scintillator counter for neutron multiplicity measurements of enriched uranium. In: Proceedings of the 44th Annual Meeting of the Institute of Nuclear Materials and Management, Phoenix, AZ.

Garner, E.L., Machlan, L.A., 1980. Mass Spectrometric Measurements to Determine the Half-Life of ^{241}Pu. NBS Special Publication 582. National Bureau of Standards, pp. 34–40.

Geiger, K.W., Van der Zwan, L., 1971. The neutron spectra and the resulting fluence-kerma conversions for 241Am–Li(α, n) and ^{210}Po–Li(α, n) source. Health Phys. 21, 120–123.

Geist, W.H., Mahmoud, M., Seo, O.S., 2003. IAEA neutron multiplicity measurements at the KAMS facility. In: Proceedings of the 44th Annual Meeting of the Institute of Nuclear Materials and Management, Phoenix, AZ.

Geist, W.H., 2006. A study of the multiplication dependent assay correction factor for multiplicity assay of plutonium items. In: Proceedings of the 47th Annual Meeting of the Institute of Nuclear Materials and Management, Nashville, TN.

Grape, S., Jacobsson Svärd, S., Lindberg, B., Hjalmarsson, A., 2010. Modelling Cherenkov Light from Irradiated Nuclear Fuel Assemblies Using GEANT4. The IAEA Symposium on International Safeguards, Vienna, Austria.

Gunn, S.R., 1964. Radiometric calorimetry: a review. Nucl. Instrum. Methods 29, 1.

Gunn, S.R., 1970. Radiometric calorimetry: a review (1970 supplement). Nucl. Instrum. Methods 85, 285.

Gunn, S.R., 1978. A calorimetric determination of the specific power of Plutonium-239. Int. J. Appl. Radiat. Isot. 29, 497–499.

Gunnink, R., Arlt, R., 2001. Methods for evaluating and analyzing CdTe and CdZnTe spectra. Nucl. Instrum. Methods A**458**, 196.

Halbig, J.K., Bourret, S.C., Collinsworth, P.R., Hansen, W.J., Krick, M.S., 1991. Recent developments in multiplicity counting hardware at Los Alamos. In: Proceedings of the IEEE/Nuclear Science Symp. And Medical Imaging Conference, Santa Fe, NM.

Henzlova, D., Evans, L.G., Menlove, H.O., Swinhoe, M.T., Marlow, J.B., January 2013. Experimental evaluation of a boron-lined parallel plate proportional counter for use in nuclear safeguards coincidence counting. Nucl. Instrum. Methods Phys. Res., A 697, 114–121.

Hyman, P., Gupta, V., Sullivan, D., 1999. Nuclear materials safeguards matrix-specific Qualification & continuous bias correction programs. In: Minutes of the Measurement Evaluation Program Meeting, New Brunswick Laboratory, Argonne, IL, May 26-27, 1999.

IAEA, 2003. International Atomic Energy Agency International Nuclear Verification Series No. 1 (Revised) Safeguards Techniques and Equipment 2003 Edition, ISBN 92-0-109403-5.

IAEA, 1987. In-field calibration of neutron correlation counter via calorimetry and high count rate gamma-ray isotopic abundance measurements, IAEA-SM-293/126. Nucl. Safeguards Technol. 1986 (2), 239–249.

IAEA, 1997. Model Protocol Additional to the Agreement(s) between State(s) and the International Atomic Energy Agency for the Application of Safeguards. INFCIRC/540, September 1997.

Jaffey, A.H., Diamond, H., Bentley, W.C., Graczyk, D.G., Flynn, K.F., 1978. Half-life of ^{240}Pu. Phys. Rev. C18, 969–974.

Jordan, K. C. (unpublished Results) Monsanto Research Corporation, Mound Laboratory, Miamisburg, Ohio (1982).

Krick, M.S., Menlove, H.O., 1979. The High-Level Neutron Coincidence Counter User's Manual. Los Alamos National Laboratory report LA-7779-M.

Krick, M.S., Geist, W.H., Mayo, D.R., 2005. A Weighted Point Model for the Thermal Neutron Multiplicity Assay of High Mass Plutonium Samples. Los Alamos National Laboratory Report LA-14157.

L'Annunziata, M.F., 2007. Chapter 7. Cherenkov radiation. In: Radioactivity: Introduction and History. Elsevier, Amsterdam, ISBN 978-0-444-52715-8, pp. 417–492, p. 609.

L'Annunziata, M.F., 2016. Chapter 16. Cherenkov radiation. In: Radioactivity: Introduction and History: From the Quantum to Quarks, second ed. Elsevier, Amsterdam, ISBN 978-0-444-63489-4, pp. 547–581. p. 902.

Lestone, J.P., Prettyman, T.H., Chavez, J.D., 2000. Performance of the skid-mounted tomographic gamma scanner for assays of plutonium residues at RFETS. In: Proceedings of the 41st Annual Meeting of the Institute of Nuclear Material Management, New Orleans, LA.

Likes, R., 1991. Calorimetric assay instruments. In: Reilly, D., Ensslin, N., Smith Jr., H. (Eds.), Passive Non-destructive Assay of Nuclear Materials. NUREG/CR-5550.

Lindsay, C.N., Sprague, R.E., Brandenburg, J.A., 1987. A Measurement Control Study for Tritium Gas. MLM-2441.

Longmire, V.L., Cremers, T.L., Sedlacek, W.A., Long, S.M., Scarborough, A.M., and Hurd, J.R., Isotopic ratios and effective power determined by gamma-ray spectroscopy vs. mass spectroscopy for molten salt extraction residues, Nucl. Mater. Manag., 1990 Vol XXXI (Proceedings issue).

Lucas, L.L., Noyce, J.R., 1984. The half-life of plutonium-240. Int. J. Appl. Radiat. Isot. 35, 173–176.

Marsh, S.F., et al., 1980. Plutonium-241 half-life determined by mass spectrometric measurements of ^{241}Pu: ^{242}Pu ratios. Int. J. Appl. Radiat. Isot. 31, 629–631.

Mason, J.A., 1982. The Use of Calorimetry for Plutonium Assay. UKAEA Report SRDP-R100.

Mayer, R.L., 1987. Application of prediction of equilibrium to servo-controlled calorimetry measurements. In: Proceedings of the 28th Annual Meeting of the Institute of Nuclear Materials Management, Newport Beach, CA.

Mayer II, R.L., Litteral, J.D., Banks, K.D., Montgomery, J.B., Lanning, B.M., Lynch, B.P., 2008. Neutron specific activity of uranium isotopes in UO2F2. In: Proceedings of the 49th Annual Meeting of the Institute of Nuclear Materials and Management, Nashville, TN.

McElroy, R.D., Young, B.M., Croft, S., 2011a. Performance considerations for alternatives to ^{3}He-based neutron counters for safeguards applications. In: Proceedings of the 52nd Annual Meeting of the Institute of Nuclear Materials and Management, Palm Desert, CA.

McElroy, R.D., Croft, S., Young, B.M., Venkataram, R., 2011b. Determination of the ^{235}U mass and enrichment within small UF6 cylinders via a neutron coincidence well counting system. In: Proceedings of the 52nd Annual Meeting of the Institute of Nuclear Materials and Management, Palm Desert, CA.

Menlove, H.O., 1979. Description and Operation Manual for the Active Well Coincidence Counter. Los Alamos National Laboratory report LA-7823-M.

Menlove, H.O., Stewart, J.E., Qiao, S.Z., Wenz, T.R., Verrecchia, G.P.D., 1990. Neutron Collar Calibration and Evaluation for Assay of LWR Fuel Assemblies Containing Burnable Neutron Absorbers. Los Alamos National Laboratory Report LA-11965-MS, November 1990.

Menlove, H.O., Swinhoe, M.T., Henzlova, D., Evans, L., Marlow, J.B., 2011. 3He replacement for nuclear safeguards applications - an integrated test program to compare alternative neutron detectors. In: ESARDA 40th Annual Meeting ; May 17, 2011.

Menlove, H.O., 2015. The Optimization and Calibration of the AWCC Using 252Cf Interrogation and the Comparison with an AmLi Neutron Source. Los Alamos National Laboratory Repot, LA-UR-15-29620, 2015.

Mortreau, P., Berndt, R., 2004. Determination of the uranium enrichment with the NaIGEM code. Nucl. Instrum. Methods A530, 559.

Mount, M., O'Connell, W., Cochran, C., Rinard, P., Dearborn, D., Endres, E., 2002. Calibration of the Lawrence Livermore National Laboratory passive-active neutron drum shuffler for measurements of highly enriched uranium in mixed oxides. In: Proceedings of the 43rd Annual Meeting of the Institute of Nuclear Materials and Management, Orlando, FL.

NBL, 1999. In: Irene Spaletto, M., Baran, D.T. (Eds.), Calorimetry Exchange Program, Quarterly/Annual Data Report, Calendar Year 1998. NBL-353.

Oetting, F.L., Gunn, S.R., 1967. A calorimetric determination of the specific power and half-life of ^{241}Am. J. Inorg. Nucl. Chem. 29, 2659−2664.

Oetting, F.L., 1968. Average beta energy of plutonium-241 by calorimetry. Phys. Rev. 168, 1398−1401.

ORTEC, ANGLE 4 Advanced Gamma Spectroscopy Efficiency Calibration Software. Ametek, Informational brochures 052417.

Owen, J.G., Weaver, D.R., Walker, J., 1981. The calibration of a ^{3}He spectrometer and its use to measure the neutron spectrum from an Am/Li source. Nucl. Instrum. Methods 188, 579−593.

Perry, R.B., Fiarman, S., 1988. Recent developments in fast calorimetry. In: Proceedings of the 29th Annual Meeting of the Institute of Nuclear Materials Management, Las Vegas, NM.

Rauch, E.B., Bracken, D.S., West, J.D., Freeman, C.R., Newell, M.R., Bourret, S.C., Rothrock, R.B., Ladd-Lively, J.L., Schuh, D., 2010. Optimization of a uranyl nitrate passive neutron counter. In: Proceedings of the 51st Annual Meeting of the Institute of Nuclear Materials and Management, Baltimore, MD).

Reilly, T.D., 2007. Nondestructive Assay of Holdup. Los Alamos National Laboratory Report LA-UR-07-5149. http://www.lanl.gov/orgs/n/n1/panda/5.%20Plant%20Holdup%20Assay%20v1.pdf.

Rinard, P.M., Bosler, G.E., 1988. Safeguarding LWR Spent Fuel with the Fork Detector. Los Alamos National Laboratory Report LA-11096-MS, March 1988.

Rinard, P.M., Adams, E.L., Menlove, H.O., Sprinkle Jr., J.K., 1992. The Nondestructive Assay of 55-Gallon Drums Containing Uranium and Transuranic Waste Using Passive-Active Shufflers. Los Alamos National Laboratory Report LA-12446-MS.

Rinard, P.M., 2001. Application Guide to Shufflers, Los Alamos National Laboratory. Report LA-13819-MS. http://www.lanl.gov/orgs/n/n1/appnotes/docs/la_13819.pdf.

Rising, M.E., 2016. CGMF & FREYA Verification in MCNP6. Los Alamos National Laboratory Report LA-UR-16-27710, 2016.

NUREG/CR-2078. In: Rogers, D.R. (Ed.), 1981. Handbook of Nuclear Safeguards Measurements, pp. 533−550.

Rowe, N.C., Younkin, J.R., Smith, S.E., Chapman, J.A., Dunn, M.E., Stewart, S.L., 2016. Snapshot: a modern, sustainable holdup measurement system. In: Proceedings of the 57th Annual Meeting of the Institute of Nuclear Materials and Management, Alanta, GA.

Rudy, C.R., Jordan, K.C., 1977. Tritium Half-Life, Mound Facility. Report MLM-2458.

Rudy, C.R., Jordan, K.C., Tsugawa, R., 1984. Calorimetric determination of the half-life of plutonium-240. Int. J. Appl. Radiat. Isot. 35, 177−180.

Rudy, C., Bracken, D.S., Staples, P., Carrillo, L., Cech, R., Craft, M., McDaniel, J., Fultz, D., 1997. Transportable calorimeter measurements of highly enriched uranium. In: Proceedings of the 38th Annual Meeting of the Institute of Nuclear Materials Management, Phoenix, AZ.

Sampson, T.E., 1991. Plutonium isotopic composition by gamma-ray spectroscopy. In: Reilly, D., Ensslin, N., Smith Jr., H. (Eds.), Passive Non-destructive Assay of Nuclear Materials. NUREG/CR-5550.

Sampson, T.S., 1999. Gamma-Ray Isotopic Analysis Development at Los Alamos. Los Alamos National Laboratory document, LA-13667-MS.

Sampson, T.S., Kelly, Vo, 2003. Application Guide to Gamma-Ray Isotopic Analysis Using the FRAM Software. Los Alamos Technical Report, LA-14018 (2003).

Seabaugh, P.W., Jordan, K.C., 1978. Calorimetric determination of the half-life of plutonium-239. Int. J. Appl. Radiat. Isot. 29, 489−496.

Shimizu, J., Yamaya, K., Hiruta, K., Fujukmki, K., Menlove, H., Swinhoe, M., Miller, M., Rael, C., Marlow, J., 2006. Development of non-destructive assay system to measure Pu inventory in glove boxes. In: Proceedings of the 47th Annual Meeting of the Institute of Nuclear Materials Management, Tucson, AZ.

Smith, M.K., Bracken, D.S., 2000. The development of a multi-exponential prediction algorithm for calorimetry. In: Proceedings of the 41st Annual Meeting of the Institute of Nuclear Materials Management, New Orleans, LA.

Smith, M.K., Hypes, P.A., Bracken, D.S., 2001. Thermal response based item identification. In: Proceedings of the 42nd Annual Meeting of the Institute of Nuclear Materials Management, Indian Wells, CA.

Smith, M.K., Bracken, D.S., 2002. Calorimeter prediction based on multiple exponentials. Nucl. Instrum. Methods A484, 668−679.

Smith, M., Kelley, T., Bracken, D., 2003. MultiCal version 4.0. In: Proceedings of the 44th Annual Meeting of the Institute of Nuclear Materials Management, Phoenix, AZ.

Sprinkle, J., 1991. Total neutron counting instruments and applications. In: Reilly, D., Ensslin, N., Smith Jr., H. (Eds.), Passive Non-destructive Assay of Nuclear Materials. NUREG/CR-5550.

Strohm, W.W., 1978. The measurement of the half-life of plutonium-239 by the U. S. Half-life evaluation committee. Int. J. Appl. Radiat. Isot. 29, 481−483.

Steinkruger, F.J., Matlack, G.M., Beckman, R.T., 1984. The half-life of ^{240}Pu determined by specific-activity measurements. Int. J. Appl. Radiat. Isot. 35, 171−172.

Stewart, J.E., Krick, M.S., Langner, D.G., Wenz, T.R., 1998. Neutron multiplicity assay of impure materials using four difference neutron counters. In: Proceedings of the 39th Annual Meeting of the Institute of Nuclear Materials and Management.

Stewart, J.E., Bourret, S.C., Krick, M.S., Sweet, M.R., Li, T.K., Gorobets, A., 1999. New shift-register electronics for improved precision of neutron coincidence and multiplicity assay of plutonium and uranium mass. In: Proceedings of the 6th International Conference on Facility Operations − Safeguards Interface, Jackson Hole, WY, pp. 143−154.

Swansen, J.E., Collinsworth, P.R., Krick, M.S., 1980. Shift-register coincidence electronics system for thermal neutron counters. Nucl. Instrum. Methods 176, 555–565.

Tagziria, H., Peerani, P., De Baere, P., Schwalbach, P., 2007. Neutron coincidence counter for the verifciation of PuO_2 cans. Nucl. Instrum. Methods Phys. Res., Sect. A 580, 377–379.

Tikkinen, J., Tarvainen, M., 1990. Technical exercise and demonstration of the spent fuel attribute tester at the TVO NPS in Finland 19.-23.3.1990. In: Final Report on Task 416 of the Finnish Support Programme to IAEA Safeguards. STUK-YTO-TR27, Helsinki 1991.

Wapstra, A.H., Bos, K., 1977. The 1977 atomic mass evaluation. Atomic Data Nucl. Data Tables 19 (3).

Wachter, J., Meyer, K., Stanfield, S., Ceo, R., 2014. ISOCS waste measurement applications at the Oak ridge national laboratory. In: WM2014 Conference Proceedings, Phoenix AZ, March 2014.

Welsh, T.L., McRae, L.P., Delegard, C.H., Liebetrau, A.M., Johnson, W.C., Theis, W., Lemaire, R.J., Xiao, J., 1995a. Comparison of NDA and DA measurement techniques for excess plutonium powders at the Hanford site: statistical design and heterogeneity testing. In: Proceedings of the 36th Annual Meeting of the Institute of Nuclear Materials Management, New Orleans, LA.

Welsh, T.L., McRae, L.P., Delegard, C.H., Johnson, W.C., Theis, W., Lemaire, R.J., Krick, M.S., Stewart, J.E., Xiao, J., 1995b. Comparison of NDA and DA measurements techniques for excess Pu powders at the Hanford site: operator and IAEA experience. In: Proceedings of the 36th Annual Meeting of the Institute of Nuclear Materials Management, New Orleans.

Werner, C.J., et al., 2018. MCNP6.2 Release Notes. Los Alamos National Laboratory report, LA-UR-18-20808, 2018.

Wetzel, J.R., Sampson, T.E., Cremers, T.L., 1997. Calorimeter in the aries recovery system. In: Proceedings of the 38th Annual Meeting of the Institute of Nuclear Materials Management, Phoenix, AZ.

Zendel, M., 2008. IAEA safeguards equipment. Int. J. Nucl. Energy Sci. Technol. 4 https://doi.org/10.1504/IJNEST.2008.017549.

William H. Geist



William Geist is a scientist in the Safeguards Science and Technology Group at Los Alamos National Laboratory. He received his PhD in Nuclear Physics from the University of North Carolina at Chapel Hill in 1998. Soon after receiving his degree, Bill became a full-time staff member at Los Alamos National Laboratory (LANL). Bill recently spent 3 years on assignment at the International Atomic Energy Agency (IAEA) in the Training Section teaching IAEA inspectors nondestructive assay (NDA) measurement techniques. Bill is an expert in developing and performing NDA measurements of plutonium and uranium materials for international safeguards, nuclear nonproliferation, and nuclear security applications. At LANL, Bill is currently serving as the Safeguards Technology Training Director, which includes responsibilities for running training courses on NDA methods for both domestic and international participants.

Peter Santi



Peter Santi received his PhD in Nuclear Physics in 2000 from the University of Notre Dame. After graduate school, he worked at the National Superconducting Cyclotron Laboratory at Michigan State University as a visiting research associate performing research in the area of nuclear astrophysics. From 2003 to 2015, he worked in the Safeguards Science and Technology Group at Los Alamos National Laboratory focusing on the development and implementation of nondestructive assay measurement techniques for Safeguards purposes. During this time at Los Alamos, he was a subject matter expert in performing calorimetric assay and project leader for certifying ^{238}Pu Calorimetry Heat Standards for the Department of Energy complex. Since 2016, he has been a senior instrumentation specialist working in the Safeguards Training Section at the International Atomic Energy Agency.

Philip A. Hypes

Phil Hypes received a BS in Physics from Loyola College in Maryland in 1993. He served as a US Army radiation specialist until 1998, when he joined the Safeguards Science and Technology Group at Los Alamos National Laboratory (LANL). At LANL, he has worked on projects involving gamma spectroscopy, calorimetry, and treaty verification. He completed an MS in Systems Research and Development through the National Technological University in 2004. He joined the IAEA and taught nondestructive assay to all new IAEA inspectors from 2005 to 2007. The IAEA received the Nobel Peace Prize during this time. When he returned to LANL, he became the lab's coordinator for IAEA projects. He also continued to teach in NDA courses. From 2012 to the summer of 2014, Phil was the team physicist on the VISIBLE team. Mr. Hypes now leads a transuranic waste management team in the Hazardous Materials Management group at LANL.

Chapter 13

PERPUSTAKAAN PRIBADI AN-NUR SUNARYA

Nuclear forensics

Michael J. Kristo
Lawrence Livermore National Laboratory, Livermore, CA, United States

Chapter outline

I. Introduction **921**
A. What is nuclear forensics? 921
II. The origins of nuclear forensics **921**
A. The policy implications of nuclear forensics 922
B. How the case begins 922
III. National objectives **924**
IV. Nuclear attribution **925**
V. Nuclear forensic interpretation **926**
VI. Validated signatures **927**
A. Comparative signatures 927
B. Predictive signatures 930
VII. Analytical results **933**
A. Categorization 934
B. Characterization 934
C. Full nuclear forensics analysis 934
VIII. Validated methods **934**
A. Radioactive material analysis 935
1. Elemental and isotopic bulk analysis tools 935
2. Imaging tools 938
3. Microanalysis tools 940
B. Traditional forensic analysis 941
1. Overview 941
2. Documentary evidence 943
3. Impressions 943
4. Chemical analysis 943
5. Tissue and hair evidence 943
6. Weapons evidence 943
7. Tool marks 943
8. Fiber examination 943
9. Flora and fauna 943
10. Other materials evidence 944
C. Application and sequencing of techniques and methods 944
IX. Quality assurance **944**
X. Sampling **946**
XI. Conclusions **946**
Acknowledgments **947**
References **947**
Michael J. Kristo **951**

I. Introduction

A. What is nuclear forensics?

The field of nuclear forensics has been a topic of intense discussion in the scientific literature (Mayer et al., 2005, 2015a; May et al., 2006; Smith et al., 2008; IAEA, 2015a; Kristo et al., 2016; Keegan et al., 2016; Aggarwal, 2016), the public policy literature (Dunlop and Smith, 2006; Chivers et al., 2008; Talmadge, 2007; Levi, 2007; Mayer, 2013; Fedchenko, 2017), and the popular press (Broad, 2003; Allison, 2006, 2009; Ignatius, 2006; Stromberg, 2013; Conca, 2017; Scoles, 2015), since at least 2003. Nuclear forensic science, often referred to as "**nuclear forensics,**" has been defined as:

> *the examination of nuclear or other radioactive material, or of evidence that is contaminated with radionuclides, in the context of legal proceedings under international or national law related to nuclear security. The analysis of nuclear or other radioactive material seeks to identify what the materials are, how, when, or where the materials were made, and what their intended uses were (IAEA, 2015b).*

The "analysis" in the definition above includes both radiometric and nonradiometric measurement techniques.

II. The origins of nuclear forensics

It is impossible to define a birth date for nuclear forensics, since many of the techniques and methods used in nuclear forensics have deep roots in the US nuclear weapons program. However, the field rose to some prominence with the rash of interdictions of nuclear material following the breakup of the Soviet Union in 1992. According to the

Handbook of Radioactivity Analysis: Volume 2. https://doi.org/10.1016/B978-0-12-814395-7.00013-1
Copyright © 2020 Elsevier Inc. All rights reserved.

IAEA's Illicit Trafficking Database (IAEA, 2018), there were at least 11 major seizures of highly enriched uranium (HEU) or plutonium from 1992 through 1996, primarily in Russia and Europe. In response, the first organizational meeting of what was to become the Nuclear Forensics International Technical Working Group (ITWG), a group that offers technical solutions in nuclear forensics to requesting countries, was held at the Lawrence Livermore National Laboratory (LLNL) in 1995. The ITWG was chartered by the G-8 in 1996 and still reports informally to the G-8 Nuclear Safety and Security Group, although the ITWG includes representatives from countries around the world (Niemeyer and Koch, 2003; Smith et al., 2007; Schwantes, 2013). Even with these initial efforts, the field held little general interest for many years and was primarily the province of a few hardy pioneers, and their far-sighted government sponsors, at laboratories such as LLNL, the European Joint Research Center-Karlsruhe (formerly the Institute for Transuranium Elements (ITU)), the Centre L'Energie Atomique (CEA) in France, the United Kingdom Atomic Weapons Establishment (AWE), and others.

The terrorist attacks on New York City and Washington, DC, on September 11, 2001, greatly increased the visibility of nuclear forensics, as policy-makers became increasingly concerned about the possibility of well-organized terrorist groups, such as Al Qaeda, obtaining a nuclear weapon or using a radiological dispersal device (RDD or so-called "dirty bomb"). Thus, began a significant increase in funding for nuclear security, including nuclear forensics, in the United States, and also in other countries. At the same time, the US government began to grapple with how to best organize and execute a mission, which inherently has both research and operational components.

A. The policy implications of nuclear forensics

The basic problem of nuclear forensics is how to apply modern materials analysis techniques, knowledge of both commercial and military nuclear fuel cycles, and scientific principles to analyze unknown nuclear materials or devices and provide information of value to decision-makers. This problem is complex enough before one considers the wide range of potential materials and devices that might be encountered and the many different types of information that might be required.

When considering the full range of materials to be addressed by a nuclear forensics program, one must consider not only the full range of uranium and plutonium materials from the civilian and military nuclear fuel cycles, from uranium ore to reactor fuel or even weapon parts, but also highly radioactive materials that might be dispersed in an RDD, e.g., irradiated fuel rods and separated isotopes for medical or other purposes.

When considering the different types of information that might be required, one must think not only about the information needs of law enforcement but also that of national intelligence. Nuclear forensics has had a strong law enforcement focus from the very beginning, because the initial driving force behind the field was the ongoing interdiction of illicit nuclear material in Russia and Europe. In general, these interdictions were made by law enforcement or border personnel, and the ultimate goal was bringing each case to a successful prosecution. However, although the standards for admissibility of evidence are often quite high, the specific nuclear forensic results brought before a court of law are often quite few. Since, in most cases to date, the perpetrators were caught with the material in hand, it was only necessary to prove that the material was indeed illegal for them to possess. In the simplest cases, one might only need to know the basic chemical identity of the material, its mass (to prove that it exceeds some *de minimis* threshold), and enrichment level (for uranium).

National intelligence, which certainly includes law enforcement intelligence as well as nuclear intelligence, seeks to know more about the material: Where did it come from? What was its intended purpose? Where was legitimate control lost? What smuggling groups or routes were involved in moving the material? Providing this type of information requires much more sophisticated analysis and interpretation, yet the standards of evidence, while probably not as formal as those of law enforcement, must nonetheless be equally as high, because, while the legal system has courts of appeals to overturn bad decisions, some actions taken by national leaders based on such intelligence information have no such courts of appeals.

The US government has divided nuclear forensics into three mission areas (Oxford, 2007):

- interdicted predetonation materials,
- interdicted nuclear devices, and
- postdetonation.

However, the mission areas of nuclear forensics of interdicted nuclear devices and postdetonation debris are intimately tied to the design and construction of nuclear weapons, and information is at least sensitive, if not classified. Therefore, this chapter will devote itself to predetonation nuclear forensics of interdicted materials, except to note that postdetonation debris will be highly radioactive, with many short- to medium-lived fission and activation products. So, one should expect that radiometric methods of analysis will play a large part in the field of postdetonation forensics.

B. How the case begins

A nuclear forensic case can begin in many ways (see Table 13.1). Some cases begin quite simply with the discovery of unknown material, apparently lost or abandoned

TABLE 13.1 Selected interdictions of nuclear material around the world.

Year	Location	Country	Type	Enrichment/Pu-239 content	Mass	Interdiction
1978	New Mexico	United States	NU	0.72%	1500 kg	Theft/police investigation
1992	Augsburg	Germany	LEU	2.5%	1.1 kg	Police investigation
1992	Podolsk	Russia	HEU	90%	1.5 kg	Theft/police investigation
1993	Vilnius	Lithuania	HEU	50%	100 g	Police investigation/discovery
1993	Andreeva Guba	Russia	HEU	36%	1.8 kg	Theft/police investigation
1993	Murmansk	Russia	HEU	20%	4.5 kg	Theft/police investigation
1994	St. Petersburg	Russia	HEU	90%	3.05 kg	Theft/police investigation
1994	Tengen	Germany	Pu	99.75%	6 g	Police investigation/discovery
1994	Landshut	Germany	HEU	87.8%	0.8 g	Police sting operation
1994	Munich	Germany	Pu HEU	1.6% 87%	363 g 120 g	Police sting operation
1994	Prague	Czech Republic	HEU	87.8%	2.7 kg	Police operation/tip-off
1995	Prague	Czech Republic	HEU	87.8%	0.415 g	Police operation/tip-off
1995	Prague	Ceske Budejovice	HEU	87.8%	17 g	Police operation/tip-off
1995	Moscow	Russia	HEU	20%	1.7 kg	Theft/police investigation
1999	Ruse	Bulgaria	HEU	72%	4 g	Border guards
2001	Paris	France	HEU	72%	0.5 g	Police operation/tip-off
2003	Ignalina	Lithuania	LEU	2.0%	60 g	Theft/police investigation
2003	Georgia/Armenia border	Georgia	HEU		170 g	Border guards/radiation detection?
2003	Rotterdam	Netherlands	NU	0.72%	3 kg	Scrap metal
2006	Tbilisi	Georgia	HEU	~90%	80 g	Police sting operation
2007	Pribenik-Lacacseke border	Slovakia	NU	0.72%	426.5 g	Police operation/tip-off
2010	Tbilisi	Georgia	HEU	>70%	18 g	Police sting operation
2011	Chisinau	Moldova	HEU	NR	4.4 g	Police sting operation

HEU, highly enriched uranium; *LEU*, low enriched uranium; *NR*, not reported; *NU*, natural uranium.

by its rightful owner, such as the discovery of HEU in the basement of a bank in Vilnius, Lithuania, in 1993 (Potter, 1995). Police investigations, instigated either as a result of a known theft, a tip-off, or a sting operation, have also been a significant source of nuclear materials seizures (Potter, 1995; Wallenius et al., 2006, 2007; Mayer et al., 2007; Baude, 2007a; Zaitseva and Steinhausler, 2014). The traffickers are often caught as they seek to find a buyer for their material and unwittingly contact undercover law enforcement instead. On the other hand, the seizure of HEU oxide in Rousse, Bulgaria, in 1999 (see Fig. 13.1), was effected by border guards who correctly judged that Ozcan Hanifi fit the profile of a smuggler (Adamson et al., 2001; Moody et al., 2015). Many countries around the world have now erected large networks of passive detectors to prevent or detect the unauthorized movement of nuclear material. Although the majority of interdictions took place in the 1990s, following the fall of the Soviet Union, we can find evidence in the literature of nuclear forensic analysis of interdicted materials as far back as 1978 (Budinger et al., 1980), and we also have a number of recent interdictions, such as the interdictions of HEU in Georgia in 2003, 2006, and 2010 and in Moldova in 2011, which were widely reported in the popular press (Vogel, 2002; Sokova and Potter, 2008, Sheets, 2008; Borger, 2010a, 2010b; Kramer, 2011; Zaitseva and Steinhausler, 2014; Birch and Smith, 2015).



FIGURE 13.1 Highly enriched uranium oxide sample alongside its lead container ("pig") interdicted in Rousse, Bulgaria, in 1999. *Reproduced from Adamson et al. (2001).*

For all of these cases, the nuclear material is usually neatly packaged, ready for seizure by law enforcement personnel and transport to the nuclear forensics laboratory. Such cases call for an operational response, as defined in IAEA TECDOC-1313 (IAEA, 2002). However, one must also be prepared for the messier case in which the nuclear material might have been intentionally or inadvertently released within the localized crime scene or even to the broader locality. Such cases call for tactical, or even strategic, responses again as defined in IAEA TECDOC-1313, depending on the extent of the release. The Litvinenko ^{210}Po poisoning case (Dalheimer et al., 2009; Maguire et al., 2010), for example, while not, strictly speaking, a nuclear forensic case, nevertheless presented a situation in which the dispersal of radioactive material presented challenges for both forensics and public health.

The technical response to specific nuclear incidents also requires a graded approach. **Categorization** is the analysis performed to understand and address the threat posed by a specific incident, identifying the risk to the safety of first responders, law enforcement personnel, or the public, and determining whether there is criminal activity or a threat to national security. **Characterization**, on the other hand, is a more thorough analysis of the material, performed to determine the nature of the radioactive and associated evidence. **Nuclear forensic interpretation** is the process of drawing validated technical conclusions from the analytical results and correlating the characteristics of the material with material production history. While nuclear forensic interpretation is the end product for the nuclear forensic laboratory, it is an input into the nuclear attribution process. **Full nuclear forensic analysis** includes characterization of all materials, traditional forensic analysis, and nuclear forensic interpretation.

The IAEA document "Nuclear Forensics in Support of Investigations," Nuclear Security Series Number 2-G (IAEA, 2015b), documents a model action plan developed by the ITWG for use in designing a country's response to nuclear trafficking incidents.

III. National objectives

Although the techniques of nuclear forensics are sometimes used in unique applications such as "nuclear archaeology" (Schwantes et al., 2009; Mayer et al., 2010, 2011, 2015b; Meyers et al., 2013, 2014; Savina et al., 2017), a term used to describe the analysis and interpretation of nuclear samples of historical interest, the primary purpose of nuclear forensics is to support national objectives. As a relatively new field, many countries are struggling to understand nuclear forensics and define its role in meeting their

national objectives. This is made all the more difficult, because nuclear forensics supports two distinct sets of customers, those in law enforcement, who are interested in detecting, capturing, and prosecuting criminals, and those in national intelligence, who are interested in fully understanding the nuclear threat space.

Law enforcement, and subsequent prosecution, requires scientific evidence to support prosecution of nuclear smuggling cases. The evidence presented in court is likely to be the simplest properties of the material, properties that prove that the seized material is illegal, such as elemental or chemical identity, mass, and enrichment level, but these scientific results, and the laboratory system that produced them, must meet all of the national standards for admissibility of evidence. For example, Daubert (1993) and Kumho Tire (1999) are key cases used for determining admissibility of scientific evidence in the United States. The requirements of national intelligence, on the other hand, are less well defined. Law enforcement intelligence is interested in understanding smuggling networks and pathways, so that law enforcement entities can prevent crime, if possible, and detect and punish it, if not. Nuclear intelligence is interested in the state of nuclear capabilities of other countries or nonstate actors, such as terrorist groups. Both law enforcement intelligence and nuclear intelligence have broad areas of interest and are therefore interested in learning as much about the material as possible. Frequently, these wide-ranging intelligence requirements are framed as a set of questions:

- What is the threat posed by the material?
- Where did the material come from?
- Where did loss of legitimate control occur?
- What were the pathways of the material from loss of control to interdiction?
- Is there more material at large?

The overarching goal of nuclear forensics, then, should be to obtain scientific results that impact on the law enforcement and national intelligence requirements and to convey those results, and their technical interpretation, in a way that makes their meaning clear to those communities. One of the concepts that must be conveyed is that of "uncertainty," that is, the level of confidence in the results and their interpretation. The calculation of uncertainty for specific analytical results is fairly well understood in theory, if difficult to implement perfectly in practice (Currie, 1995; EPA, 2004; ISO, 2008). However, the uncertainty of technical conclusions, based on perhaps dozens of scientific measurements, is less readily apparent. In addition, conveying these uncertainty measurements to policy-makers, who typically have nontechnical backgrounds and who might have to make decisions of great import using these conclusions, can be extremely difficult.

The remainder of this chapter will describe how the various aspects of nuclear forensics work together to support these national objectives of law enforcement and national intelligence (see Fig. 13.2).

IV. Nuclear attribution

Over the past decade, the nuclear forensics community has distinguished between the terms "nuclear forensics," which is strictly technical in nature, and "nuclear attribution," which is

> *a process to identify the source of nuclear or other radioactive materials used in illegal activities, determine the point-of-origin and routes of transit involving such material, and ultimately contribute to the prosecution of those responsible. Nuclear attribution is the integration of all relevant forms of information about a nuclear smuggling incident into data that can be readily analyzed and interpreted to form the basis of a confident response to the incident. The goal of the attribution process is to answer policy-makers' needs, requirements, and questions in their framework for a given incident (IAEA, 2006).*

"Nuclear forensics," as defined, should focus solely on "intrinsic" information, that is, on results obtained from the analysis of the interdicted material and on validated technical conclusions (nuclear forensic interpretation) based on those results. "Nuclear attribution," on the other hand, utilizes the information provided by nuclear forensics but also incorporates "extrinsic" information—from law

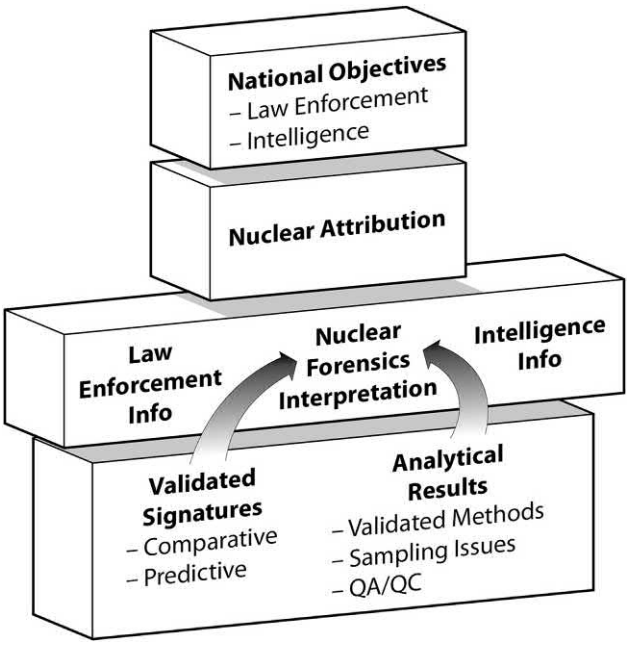


FIGURE 13.2 Hierarchy of nuclear forensic requirements and organization of this chapter.

enforcement, intelligence, and so on. Nuclear attribution, along with some expression of uncertainty in that attribution, is quite likely to be the finished product delivered to national decision-makers.

One of the primary goals of the separation of the processes of nuclear forensics and nuclear attribution is the insulation of the nuclear forensic scientist from any biases in their work that might be introduced through knowledge of the extrinsic information. At the same time, though, it is absolutely necessary that those responsible for nuclear attribution, typically senior officials in the government, have ready access to nuclear forensic experts, so that they can fully understand the implications and limitations of the information provided by nuclear forensics.

V. Nuclear forensic interpretation

Nuclear forensic scientists use the term "signatures" to describe material characteristics that potentially link samples to people, places, and processes and thus provide information about samples relevant to the set of intelligence questions described previously, much as a written signature can be used to link a document to a specific person. Quite simply, then, nuclear forensic interpretation is the evaluation of analytical results from a sample of interest using a set of validated "signatures" so as to provide technical conclusions to decision-makers. To generate high-confidence technical conclusions, one needs results generated using both validated analytical methods and validated signatures.

Nuclear forensic interpretation is a deductive process (see Fig. 13.3), much like the scientific method itself. At the beginning of the interpretation process, the nuclear forensic expert develops a hypothesis, or set of hypotheses, based on the initial analytical results. In most cases, these initial results will be consistent with multiple hypotheses, each of which may suggest additional signatures, which either might be, or must be, present if the hypothesis is true. The expert then devises further tests to verify the presence or absence of the signatures. On the one hand, if these tests show that the required signature is absent, then the nuclear forensic scientist must abandon his hypothesis or adjust it to fit the new results. On the other hand, if the tests show that the signature is present, then the scientist either has come to a unique technical interpretation, the desired result, or must devise additional tests to exclude the other remaining hypotheses. In the ideal case, only a single hypothesis or interpretation will eventually prove consistent with all results, although this is seldom true in practice.

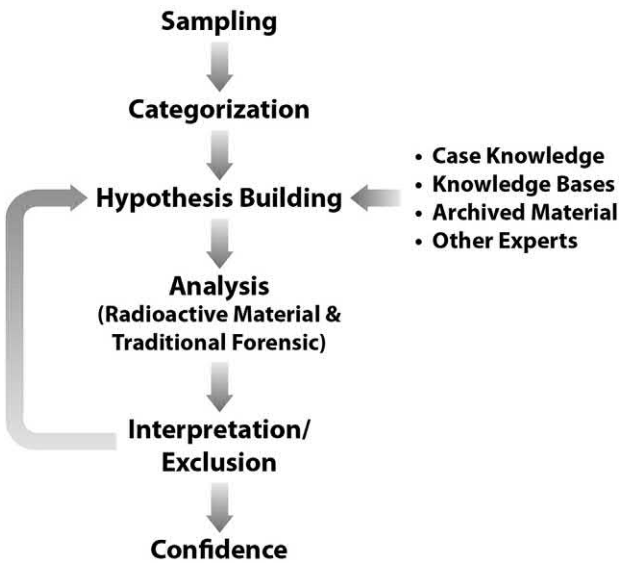


FIGURE 13.3 Flowchart of nuclear forensic interpretation process.

In general, one cannot rely on a single signature to answer all of the relevant questions in the case. Some signatures, such as those that derive from isotopic analysis, may only provide general clues that serve to place the material in a broad category like special nuclear material (SNM)[1] or, perhaps narrow the field of potential countries of origin. Other signatures, such as characteristic dimensions or markings, may provide specific clues that identify a specific facility or date of manufacture. In some cases, a result might only provide information useful for nuclear forensic interpretation when combined with other results. In the same way, independent signatures that reach the same conclusion increase the expert's confidence in the technical interpretation, whereas results that provide different or even conflicting conclusions decrease this confidence. Nevertheless, a result that seems confusing or insignificant at first may become crucial as the case develops.

Signatures can also work together to increase the specificity of the nuclear forensic interpretation. Figs. 13.4 and 13.5 represent the universe of potential sources and processes from which a given interdicted material may have originated, whereas the circles demonstrate how a given analytical measurement and associated signature serve to restrict those potential sources and processes. Although increasing the precision of a given measurement could further narrow the field of potential sources or processes that produced the material, as shown in Fig. 13.4, it is often more efficient to perform other types of measurements that use independent signatures, that is, measurements that verify the presence or absence of signatures different than those of the initial measurement. The confidence in, and the specificity of, the interpretation often increases as more independent measurements are made, as shown in Fig. 13.5.

1. Plutonium, uranium-233, or uranium enriched in U-235.

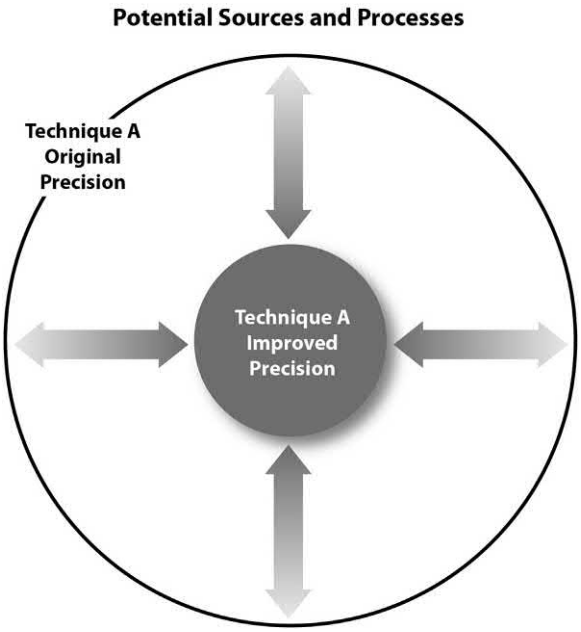


FIGURE 13.4 The effect of improved precision on nuclear forensic interpretation.

VI. Validated signatures

The validation of signatures involves rigorous testing, the extent of the testing depending on the confidence in the underlying scientific principles that drive the signature, for example, the principles of radioactive decay in age dating, and the extent to which the signature can be disturbed by factors outside our control, for example, the nature of the material, the extent and effectiveness of previous processing steps, and the presence of interferences. It is absolutely fundamental that the assumptions that underlie a signature be clearly stated. As far as possible, the nuclear forensic scientist must verify the correctness of those assumptions for the case at hand and, for those cases, where the assumptions cannot be verified, frame the conclusions, or adjust the uncertainties to reflect this lack of verification.

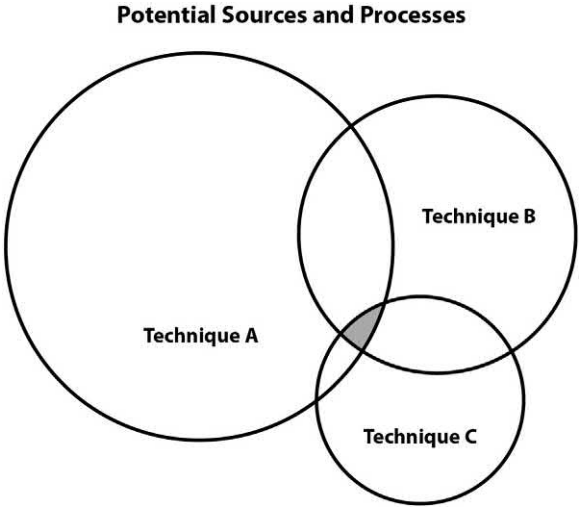


FIGURE 13.5 The effect of multiple measurements/signatures on nuclear forensic interpretation.

Each step of the nuclear fuel cycle creates some new signatures and erases other existing signatures, in the material. In general, materials at each stage of the fuel cycle will have their own characteristic set of signatures. It is certainly possible for some signatures to survive a given processing step and be present in multiple materials in the fuel cycle. However, a signature's persistence is something that must be validated and not assumed.

Signatures generally fall into two broad categories: comparative signatures and predictive signatures. Comparative signatures involve the comparison of an unknown (or "questioned sample" in law enforcement parlance) to one or more known samples, the essential question being whether the material characteristics of the unknown sample are consistent with one or more of the known samples. Predictive signatures, on the other hand, involve only an unknown sample, without reference to any known sample or database. Predictive signatures typically derive from underlying scientific principles, such as isotopic depletion and activation, in the case of nuclear reactor modeling used to understand the isotopic composition of irradiated material, or radioactive decay in the case of age dating.

A. Comparative signatures

Comparative signatures rely on the comparison of an unknown sample with one or more known samples. The simplest application of comparative signatures is the comparison of one sample to another. For example, the HEU oxide powders interdicted in Rousse, Bulgaria, in 1999 (Adamson et al., 2001; Moody et al., 2015), and in Paris, France, in 2001 (Baude, 2007a; Baude et al., 2007b), bear many remarkable resemblances. The two HEU oxide powders were essentially identical, except for differences in the concentrations of several of the common impurity elements. Furthermore, the powders were found in similar glass ampoules and conveyed by the traffickers in lead containers ("pigs") of similar manufacture and chemical composition and containing the same yellow wax. The seizure of two nearly identical samples almost 1500 miles apart should certainly raise concern among both law enforcement and intelligence officials about the existence of more such material outside of legitimate control. Sure enough, an HEU oxide powder was seized in Chisinau, Moldova, in 2011 (Kramer, 2011; Zaitseva and Steinhausler, 2014; Birch and Smith, 2015), inside a similar glass ampoule and a similar lead pig, protected by a similar yellow wax. So far, the analysis of the HEU oxide material

has not been reported, but the similarity of the packaging materials, seized in nuclear material interdictions a decade apart, certainly heightens the cause for concern.

Nuclear forensic databases, which may contain information on hundreds or thousands of samples, or nuclear forensic sample archives, which may contain tens or hundreds of physical samples, are the natural extension of more targeted sets of known samples. Clearly, the value of this comparative approach depends on both the relevance and comprehensiveness of the database and/or the sample archive. In the most general case, a database for nuclear forensics would include a comprehensive set of material characteristics from materials across the fuel cycle and across the globe. There has already been much discussion in the public policy literature about the importance of international nuclear forensics databases and whether such databases should be shared generally or closely held by each country (Chivers et al., 2008; Allison, 2009; Fedchenko, 2007). Due to the many problems involved in creating and maintaining an international nuclear forensics library, current international efforts are focused solely on the development of national nuclear forensics libraries (Engelbrecht et al., 2013; Davydov et al., 2016; Kimura et al., 2017). The ITWG, in conjunction with the Global Initiative to Combat Nuclear Terrorism, has developed and conducted the series of "Galaxy Serpent" exercises to foster an international understanding of nuclear forensic libraries and their value to nuclear security (Borgardt and Wong, 2014; Ball et al., 2015; Borgardt et al., 2017).

The importance of these national nuclear forensic libraries underscores the importance of international engagement in nuclear forensics. It is important to encourage all countries to develop their own nuclear forensic databases, whether they choose to keep them closely held or not. It is also important that all countries have high confidence in each other's databases, confidence that those databases contain the right materials characteristics for nuclear forensic purposes and that the analytical results contained therein are of high quality. If an interdicted sample is analyzed in France, for example, and compared against a database with analytical results from Russia, there must be strong assurance that both laboratories are providing equivalent results, i.e., that they would get the same answer (within the constraints of analytical uncertainty) when analyzing the same sample. Therefore, international scientific engagement in nuclear forensics, whether conducted in a multilateral setting, such as through the ITWG, or in a bilateral, country-to-country setting, should drive the standardization of methods, techniques, standards, and reference materials. International exercises or round robins are absolutely crucial for developing and testing the comparability of nuclear forensic data acquired by different countries.

ITWG Nuclear Forensics Exercises

In addition to actual casework, which occurs infrequently, nuclear forensic laboratories around the world have come to rely on the collaborative materials exercises conducted by the ITWG for keeping their skills in good practice.

- Six laboratories from the United States and Europe participated in the first exercise, held in 1999–2000, which featured reprocessed plutonium oxide material from the European civil nuclear cycle (Dudder et al., 2003b).
- Nine laboratories from the United States and Europe participated in the second exercise, held in 2000–2002 (Dudder 2003a,b), which featured an HEU oxide powder provided by the Czech Republic.
- Nine laboratories in the United States, Canada, and Europe participated (Kristo and Tumey, 2013; Hanlen, 2011) in the third exercise, which was a paired-comparison analytical exercise involving two HEU metal pins provided by the Y-12 National Security Complex in the United States.
- Sixteen laboratories around the world participated in the fourth exercise, which was another paired-comparison exercise involving two LEU oxide pellets and some LEU oxide powder (Schwantes et al., 2017, 2018).

Although the development of well-populated databases is a necessary step toward discovering and implementing valid comparative signatures, it is equally important to develop validated methods for performing the comparison of analytical results on unknown samples. These validated methods may consist of dozens of distinct analytical measurements, each with their own uncertainty, against these well-populated databases, which might have information on thousands of materials each with a similar number of measured properties. Currently, our ability to analyze interdicted samples and produce an extensive list of precise materials characteristics far exceeds our ability to interpret the results. Therefore, as we seek to develop the extensive databases necessary for nuclear forensics, we must also develop the comparative methods necessary to produce the required inferences from comparison of our analytical results with these large, multidimensional sets of data.

The identification of the sources of unknown uranium ores and ore concentrates (a product of the uranium milling process, sometimes referred to as "yellowcake") is an active area of interest in the international nuclear forensics community, both as a means to support international safeguard efforts and as a fruitful area for developing broadly applicable nuclear forensic methods without as many security or proprietary restrictions. Robel and coworkers (Robel et al., 2009, 2011) tested several multidimensional statistical techniques for comparative analysis against a data set consisting of 50 materials characteristics (mostly concentrations of trace impurities and uranium isotopic

composition) measured for approximately 1800 samples of uranium ore concentrate (UOC) from 21 known locations or sources. They found that principal component analysis was useful for initially understanding how results from a single source grouped together and how results from different sources related to one another. However, partial least squares discriminant analysis (PLS-DA) was inherently more suited to differentiating between different sources, because PLS-DA uses the source information in constructing its data model (Barker and Rayens, 2003). However, a single pass of PLS-DA was insufficient for discriminating between all of the sources in the database. Therefore, they developed an iterative PLS-DA procedure, which proved especially adept at identifying the production location of unknown UOC samples. By removing sources, which fell far outside the decision boundary of the initial PLS-DA model, and then rebuilding the model, they have consistently produced better and more definitive predictions than with a single-pass classification approach (Fig. 13.6).

Internal validation of the iterative PLS-DA model, in which data from a sample are removed from the comparison database and treated as the analytical data from the unknown (also called "hold one out" validation), achieved 91% accuracy in identifying the source of the UOC (facility or mine). In most cases, the inaccurate predictions chose the right country, but the wrong location within the country. External validation of the iterative PLS-DA model, in which separate physical samples from known locations were analyzed as unknowns, achieved 65% accuracy in predicting the correct source and 90% accuracy in predicting the right country. Furthermore, the iterative PLS-DA method performed better than the classification and regression tree and k nearest neighbor algorithms, with the best combination of accuracy and robustness, for this UOC data set.

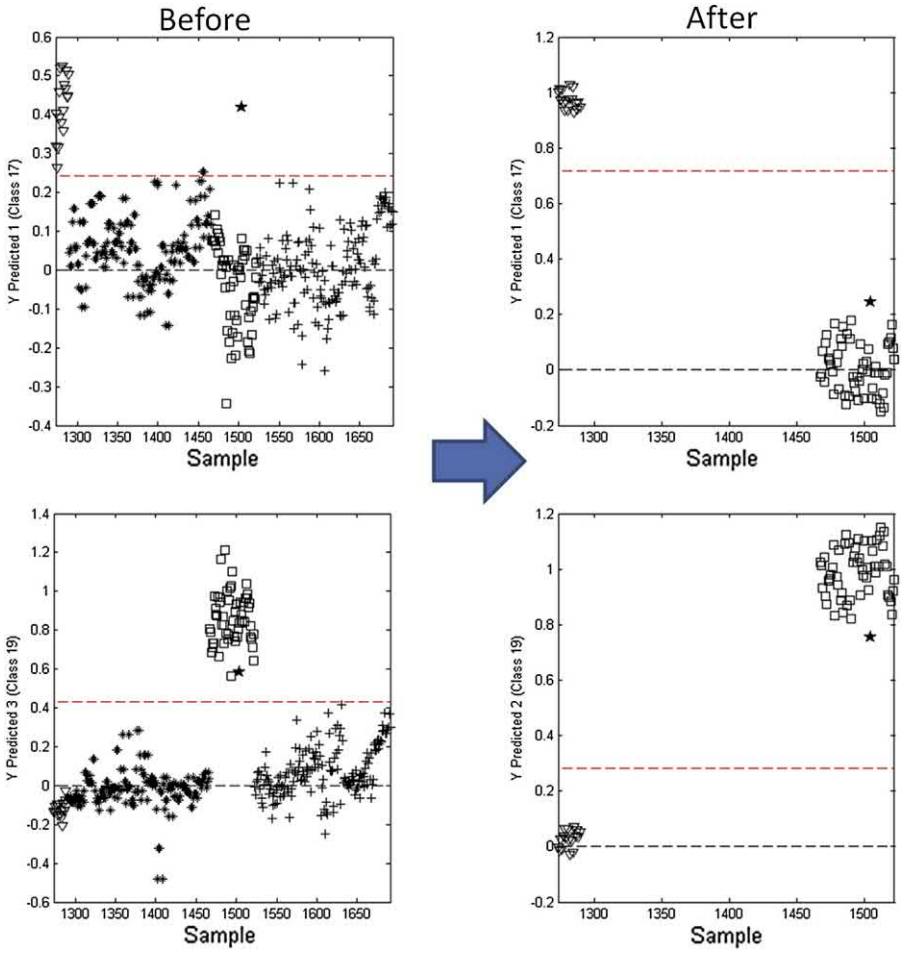


FIGURE 13.6 Each data point represents the analysis of an individual sample of material from a given class (source of uranium ore concentrate). Each class is represented by a unique symbol. The dashed line is the partial least squares discriminant analysis (PLS-DA) decision boundary for discriminating between the selected class and all other classes in the database. The figures on the left show that an unknown sample (represented by a star) is indistinguishable from material from either class 17 (triangle) or class 19 (square). The unknown is distinguishable from class 18 (asterix) and class 20 (cross) (models not shown). After removing class 18 and 20 from the database and regenerating the PLS-DA models, the figures on the right clearly and correctly demonstrate that the unknown is from class 19.

For any comparative method, though, it is important to provide some valid estimate of the confidence of its predictions. Internal and external validation exercises, like those described earlier, help one understand the overall reliability of the model. However, only preliminary work on calculating nuclear forensic probabilities or confidence levels for specific predictions has been reported (Kristo, 2011b). It is also important to understand how specific comparative methods behave when the true source of the unknown sample is not in the database. The iterative PLS-DA approach, for example, always returns a prediction, whether or not the true source can be found in the database. However, statistical parameters (Q and T_2) generated during application of the iterative PLS-DA approach provide a strong warning when the ultimate prediction does not fit well with the final model.

Current efforts in comparative approaches include the development of an integrated environment for inclusion/exclusion testing (Stork et al., 2017), the application of artificial intelligence and machine learning (Drummond, 2018), and a comparison of multiple methods for inverse prediction (Lewis et al., 2018). There have also been efforts to handle the particular problem of missing data, which can often occur when using historical data sets or production databases for performing comparative analysis (Langan et al., 2016).

B. Predictive signatures

With predictive signatures, one seeks to calculate identifying material characteristics based on a detailed understanding of the physical or chemical mechanisms responsible for producing the signatures and adequately modeling those mechanisms to predict the material signatures at a level of specificity required to provide information relevant to the national intelligence questions posed previously. The advantage of the predictive approach is that the processes (and possibly locations) of previously unanalyzed nuclear materials can be inferred from their measured characteristics, something of critical importance for types of materials that are not readily available, for example, materials from historical processes or tightly held materials from foreign countries. The disadvantage of the predictive approach is that significant effort must be expended to develop and validate the capability.

Predictive signatures rely, in a general sense, on our base of knowledge and on scientific inference, that is, how we apply our existing knowledge to the case at hand. Very little work has been done in building a nuclear forensics-specific base of knowledge; rather, nuclear forensics has been built primarily on other bases of knowledge that already exist. For example, nuclear forensics on materials found early in the fuel cycle, for example, uranium ores and ore concentrates, relies heavily on geochemistry, a field that studies the chemical and physical processes that govern the composition of rocks, water, and soils both on the earth and in the solar system as a whole. Nuclear forensics of materials found later in the nuclear fuel or found only in the weapons cycle relies on bases of knowledge developed by various companies as part of their role in the commercial nuclear fuel cycle and by the United States and other countries as part of their nuclear weapons programs.

The predictive approach to identifying the source of unknown samples of UOC, for example, involves interpreting signatures measured in a sample of interest to determine characteristics associated with both the parent ore and the mining and milling processes used to produce the UOC from the ore (Svedkauskaite-LeGore et al., 2008; Varga et al., 2011). The predictive approach is more challenging than the comparative approach since it requires a scientific basis for interpreting signatures. Fortunately, many of the chemical and physical processes that created the ore body, as well as the ore concentrate, are well understood through research in geochemistry and economic geology that can be used to develop predictive signatures. For example, the relative concentrations of the rare earth elements (REEs) can be typical of the type of ore body from which the uranium was mined (see Fig. 13.7 or Varga et al., 2010; Lin et al., 2015; Krajko et al., 2015; Spano et al., 2017). The uranium–lead radiometric dating system can be used to determine the age of a parent uranium ore body (Svedkauskaite-LeGore et al., 2007; Varga et al., 2009). The samarium–neodymium and rubidium–strontium dating methods can be similarly used and can also provide indication of the mineralogy of the parent uranium ore (Varga et al., 2009). The well-established

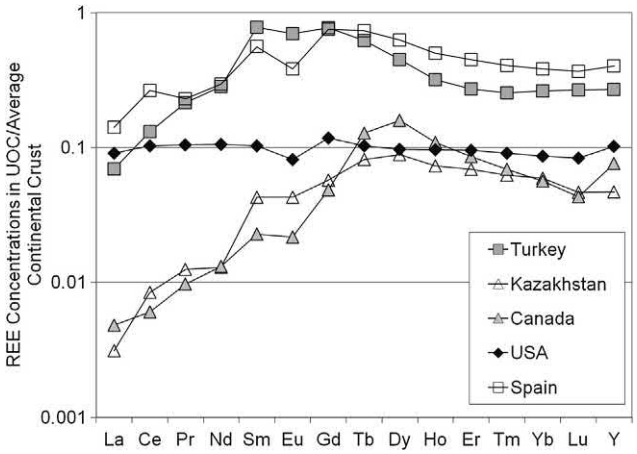


FIGURE 13.7 Different ore bodies contain different amounts of rare earth elements (REEs). This plot shows the concentration of REEs (relative to the concentrations of the same elements in the earth's crust) for uranium ore concentrate samples from different locations. Varga et al. (2010) has shown that the shapes of these REE curves are typical for certain types of uranium deposits.

geographic variation of ^{18}O in surface water (Craig, 1961; IAEA/WMO, 2006) influences the ^{18}O isotopic abundance in nuclear materials such as UOC and may provide geographic information (Pajo et al., 2001a, 2001b; Tamborini et al., 2002). Similar systematics in the isotopic composition of trace elements, such as S, Mo, and Nd, relate to geochemical processes (Han et al., 2013; Krajko et al., 2014, 2016; Migeon et al., 2018). The anion content of UOC (F^-, Cl^-, Br^-, NO^{3-}, PO_4^{3-}, SO_4^{2-}) also varies with location and is influenced by both the host rock and the milling process (Badaut et al., 2009; Keegan et al., 2012). Researchers have also studied the trace organic content of UOCs as a signature of process (Kennedy et al., 2013).

New predictive signatures are also being developed by establishing improved understanding of the factors that influence distribution of the isotopes of uranium. For example, the fractionation of $^{234}U/^{238}U$ through natural processes has been demonstrated to be indicative of the geological context of an ore (Kigoshi, 1971). Ores that have been leached by groundwater for long periods of time exhibit a significant depletion in $^{234}U/^{238}U$, whereas ores formed from deposition of those water leachates exhibit a significant enrichment in $^{234}U/^{238}U$. Modern mass spectrometry now provides results of sufficient precision that even natural variations in the $^{238}U/^{235}U$ ratio, once thought to be invariant in nature, can now be investigated. The depositional environment of an ore appears to strongly influence the $^{238}U/^{235}U$ ratio with low-temperature ores having higher ratios than deposits formed at high temperatures (Richter, 1999; Brennecka et al., 2010). In addition, naturally occurring ^{236}U can also be exploited as a nuclear forensic signature. ^{236}U is produced at very low levels in nature through neutron capture of ^{235}U. It has been demonstrated that $^{236}U/^{238}U$ ratios in uranium ores can vary widely and are influenced by the geologic context of the ore body (Wilcken et al., 2008; Srncik et al., 2011). All of these features of the isotopic distribution of natural uranium are potentially useful signatures for attribution of UOC.

As with all scientific work, it is extremely important to understand, and clearly state, all underlying assumptions when applying predictive signatures, since the validity of the nuclear forensic interpretation will always depend on the validity of those assumptions. For example, one of the most frequently applied predictive signatures in nuclear forensics is that of radiochronometry, the determination of the time since last purification using the laws of radioactive decay, a technique commonly known as "age dating" (Mayer and Wallenius, 2000; Morgenstern et al., 2002; LaMont and Hall, 2005; Williams and Gaffney, 2011; Stanley, 2012). Accurate age dating relies on several assumptions (ITWG, 2016). First of all, there must be a purification event that quantitatively removes the daughter (product) nuclide from the parent (precursor) nuclide. Incomplete purification leads to calculated ages (model ages) that are older than the true time since purification. Second, the sample must remain a closed system from purification until sampling and analysis, precluding both contamination from outside the system and internal segregation of either daughter or parent.

Age Dating

The principles behind age dating were enumerated in 1900 by Ernest Rutherford (see a detailed historical account by L'Annunziata, 2007, 2016). Age dating is a standard tool for disciplines such as geochemistry and cosmochemistry, and the use of multiple chronometers is a fundamental precept of these disciplines. In this context, agreement between chronometers indicates a simple (ideal or undisturbed) geologic history, whereas disagreement indicates that a sample has experienced a multistage history (see Faure 1998).

In most cases, nuclear forensic samples will not arrive at the laboratory with extrinsic information indicating how well these assumptions hold true for the particular sample. Therefore, it is incumbent on the analyst to test the validity of these assumptions as completely as possible. One of the best ways of doing this is to use multiple chronometers (chronometers based on different parent−daughter radionuclide pairs). If the ages given by the different chronometers "agree" with each other (concordant ages), then we have high confidence that the assumptions for accurate age dating have held true and that the model ages are, in fact, the true ages since purification.

If the chronometers do not agree with each other (discordant ages), then, at a minimum, we must be cautious in the way that the model age dates are interpreted. However, even in such cases, the results from multiple chronometers can themselves provide valuable information. For example, in the case of the HEU oxide powder seized in Bulgaria in 1999 (Adamson et al., 2001; Moody et al., 2015), the fact that two chronometers based on trivalent species gave ages slightly, but systematically older than other chronometers pointed to the use of the Purex process, which is very good at removing some elements (thus resetting those chronometers completely) and not as good at removing other elements, such as trivalent species (thus leading to anomalously older ages for chronometers based on the decay of those species). This inference was possible only due to the use of multiple chronometers.

The analysis of multiple chronometers in LLNL's analysis of samples from the third ITWG round robin (Bibby et al., 2010; Hanlen, 2011; Kristo, 2011a; Kristo and Tumey, 2013) yielded highly discordant model ages and signaled to the analysts that caution was necessary in interpreting these ages. However, these discordant ages

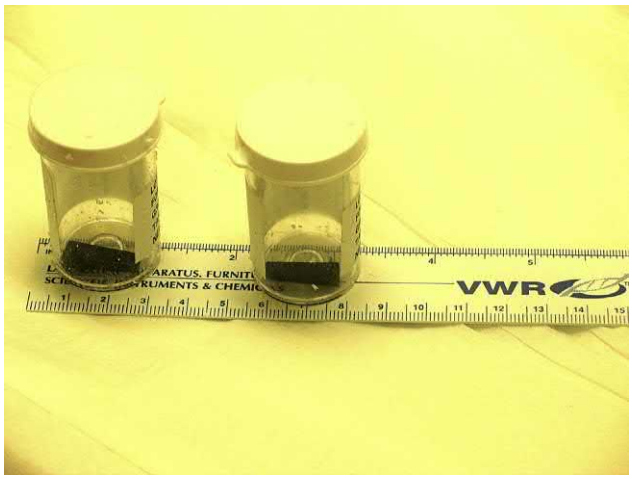


FIGURE 13.8 ITWG Round Robin 3 samples (trapezoidal pins of highly enriched uranium metal) as received. *Reproduced from Bibby et al. (2010).*

helped focus their attention on the complexities engendered by the uranium casting process (Martin and Miles, 1956; Feder et al., 1956; Whitman et al., 1957; Antill et al., 1959). Participating laboratories were each given two samples of HEU metal (5–6 g each—see Fig. 13.8). As part of its analysis, LLNL performed age dating using the $^{234}U/^{230}Th$, $^{235}U/^{231}Pa$, and $^{241}Pu/^{241}Am$ chronometers (see Table 13.2).

There are two striking features in these results. First, the model age calculated from the $^{234}U–^{230}Th$ system corresponds closely to the time since casting (which was only revealed to the participants after the exercise). Second, there is a total lack of agreement between any of the three model ages. The high concentration of carbon (~0.1–0.2 weight%) found in the samples and the presence of Zr and Er impurities, elements often used in graphite mold coatings, suggested that the uranium in each of the samples had been recast multiple times. It was therefore clear that the casting process must have caused a segregation of the Th in the material, such that Th was completely removed from the center of the initial casting (where the round robin samples were taken). However, this process did not result in the complete removal of other impurities, such as Pu, Am, or Pa. The segregation of radioactive impurities into the top of uranium castings (the so-called "hot top"), especially in the presence of high concentrations of carbon, has been observed for some time (Martin and Miles, 1956; Feder et al., 1956), but the behavior of these specific impurities, resulting from radioactive decay of the U isotopes, had not been studied. From the results of these analyses, it appears that, while Th was completely removed from the center of the casting by this process, the other species were either removed partially or not at all.

Without extrinsic knowledge of the sample, we have to be very careful in interpreting model ages. For instance, we did not know a priori anything about the casting shape (other than what was deduced from the shape of the solid pieces themselves) or the method of sampling. The samples could very well have been from the "hot top," for example, and resulted in the determination of an anamolously old model age. Even now, with knowledge of the casting shape and process, we still do not know how generalizable the interpretation of the ^{234}U-^{230}Th age as the casting age might be. We still lack the fundamental studies necessary to extrapolate this single-point measurement to the more general case where the conditions of casting might be expected to vary widely (with unknown effects on impurity segregation).

In summary, then, the measurement of multiple chronometers in nuclear forensics is critical for testing whether the fundamental assumptions of age dating have held true for the sample in question. If we obtain agreement between model ages from different systems, we can posit more confidently that the model age represents the true time since purification, since the likelihood that two or more chemical systems will be contaminated or fractionate in precisely the same way is very low. On the other hand, if we obtain disagreement between model ages from multiple systems, then we would know to exercise caution when interpreting those ages. However, such systematic variations in the ages can often provide insight into the chemical and physical processes used in preparing the material. Researchers at LLNL have been exploring the utility of additional

TABLE 13.2 Model ages calculated from both mass spectrometry and alpha spectrometry (Bibby et al., 2010).

Measurement	Sample	Units	Mass spectrometry	Alpha spectrometry	Years since casting
^{234}U-^{230}Th age	A	Years	6.894(41)	7.02(67)	6.10
	B	Years	6.074(36)	5.62(65)	6.82
^{235}U-^{231}Pa age	A	Years	33.73(36)		
	B	Years	35.77(37)		
^{241}Pu-^{241}Am age	A	Years	14.36(33)	12.3(1.3)	
	B	Years	17.47(37)	15.3(1.9)	

radiochronometers for U, including "grand daughter" radionuclides, such as ^{226}Ra and ^{227}Ac, which can further validate the fundamental assumptions or provide additional insights into the history of the material (Kayzar and Williams, 2016; Rolison et al., 2017).

To encourage the international application of radiochronometry in nuclear forensics, as well as to provide an intercomparison of results between laboratories, many countries have participated in bilateral and multilateral round robin comparison exercises (Varga et al., 2015a; Gaffney et al., 2016; Treinen et al., 2017). The fourth ITWG Collaborative Materials Exercise (CMX-4) demonstrated the current state of practice for radiochronometry (Kristo et al., 2018). 10 laboratories performed radiochronometry on three low enriched uranium oxide samples, providing 12 analytical results using three different parent−daughter pairs. The vast majority of the results were consistent with one another and consistent with the known processing history of the materials (see Fig. 13.9 for results from Sample ES-2). The results also demonstrate a situation in which the concordance of the ^{235}U-^{231}Pa and ^{234}U-^{230}Th chronometers confirmed the validity of the age dating assumptions, increasing confidence in the resulting conclusions. In this exercise, we have some knowledge of the history of the material, allowing us to assess the accuracy of the radiochronometry measurements in a general sense. However, both the United States and the European Commission have been actively developing radiochronometry reference materials to better assess accuracy in radiochronometry measurements (Varga et al., 2012; 2015a,b, 2018; Venchiarutti et al., 2015). The US approach focuses on certification of the model ages of existing nuclear materials, whereas the European Commission has focused on processing the nuclear materials to create a known date of purification, allowing the daughter nuclides to grow in from that point.

Although the uncertainty regarding assumptions clearly affects the uncertainty of the stated conclusion, determining that uncertainty in an unbiased way and then incorporating that uncertainty into the overall uncertainty of the conclusion is not straightforward and work remains to be done.

VII. Analytical results

Nuclear forensics is not amenable to a "cook book" approach that can be universally applied to all evidence; rather, it involves an iterative approach, in which the results from one analysis are used to guide the selection of subsequent analyses. However, the nuclear forensics community has defined three levels of analysis, namely,

- categorization,
- characterization, and
- full nuclear forensic analysis,

Each of the three levels serves a unique purpose in the investigation as described below. In all cases, though, laboratory sampling and analysis must be performed with due regard for preservation of evidence and perpetuation of chain-of-custody, since many of the analytical tools used in these analyses are destructive, that is, they consume some amount of sample during analysis. Therefore, the proper selection and sequencing of analyses is critical.

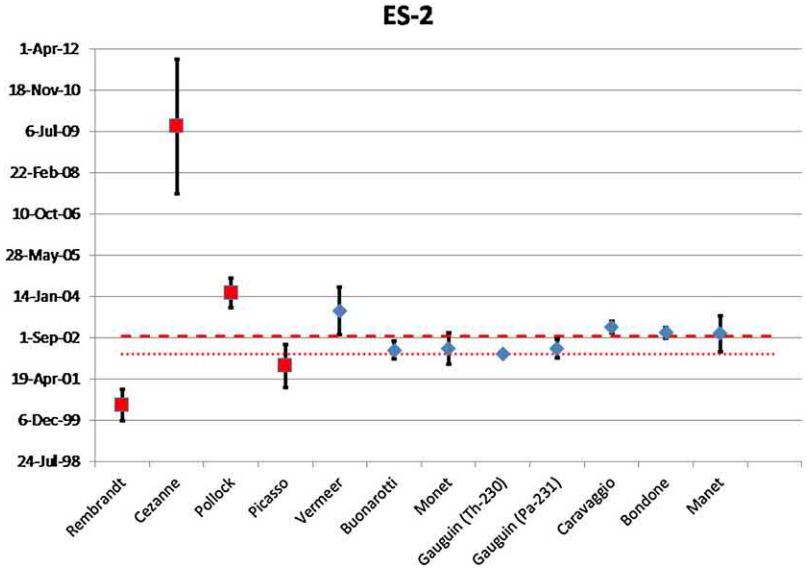


FIGURE 13.9 Age dating results for ITWG CMX-4 Sample ES-2 compared against known sample processing history. The dashed lines (----) indicate the range of probable processing dates according to the known history of the samples. Alpha spectrometry results are indicated by squares (■). Mass spectrometry results are indicated by diamonds (◆). All labs are designated by code names drawn from famous painters.

A. Categorization

Onsite nondestructive analysis (NDA) using field-portable gamma ray spectrometry, perhaps supplemented by X-ray fluorescence (XRF), aims to categorize the suspected radioactive material without affecting the evidence. The goal of categorization is to identify the bulk constituents of the material to assess the threat posed by the material and confirm whether the seized evidence is contraband, something which would form the basis for continued investigation. Such NDAs can quickly distinguish between naturally occurring radioactive material, SNM, radioactively contaminated material, or a commercial radioactive source.

Further analysis will be guided by this initial categorization. The next analyses to be performed will be based on the ultimate goals of the investigation (basic characterization vs. full nuclear forensics analysis—see below), the information uncovered so far, the potential signatures (physical, chemical, elemental, isotopic) that might lead to precise interpretation, the amount of sample available for analysis, and methods for measuring forensic signatures.

B. Characterization

Characterization aims to determine the nature of the radioactive evidence and provide detailed results for officials to make informed decisions. Characterization of the radioactive material includes complete elemental analysis, including major, minor, and trace constituents, as well as isotopic and chemical phase information for all major constituents. Characterization also includes physical characterization, including accurate measurement of the critical dimensions of solid samples, determination of particle size and shape distributions for powder samples, and high magnification imaging of the material by optical and scanning electron microscopy. Characterization does not include analysis of traditional forensic signatures nor detailed nuclear forensic interpretation (identification of candidate source locations and processes, for example). Characterization will take more time than categorization, but less time than the full nuclear forensics analysis, approximately 1–4 weeks after receipt of the samples.

C. Full nuclear forensics analysis

The goal of full nuclear forensics analysis is to analyze all radioactive and traditional forensic evidence to provide information for answering the questions of both law enforcement and intelligence, including identifying the material's origin, method of production, means by which legitimate control was lost, transit routes from diversion to interdiction, and probability that more material exists. Full nuclear forensics analysis would include detailed nuclear forensic interpretation and might include predictive techniques such as reactor modeling and comparison against nuclear forensics databases or sample archives, so as to identify the method of manufacture and probable sources of the material. Full nuclear forensic analysis will take the longest amount of time, up to 2–6 months after receipt of the samples.

VIII. Validated methods

Some analytical methods provide strictly qualitative information, for example, color, shape, identifying markings, but most analytical methods are quantitative, providing mean values and associated uncertainties for various characteristics of the material, for example, mass, dimensions, trace elemental composition. These means and uncertainties allow the application of the validated signatures to the material at hand. The analytical techniques described in the following sections are commonly used in nuclear forensic analysis. However, it is important that specific methods used to generate nuclear forensic results, either by these or other methods, be validated to ensure high-quality technical conclusions.

The validation of analytical methods involves rigorous testing to ensure that the strengths and limitations of the method are well characterized and that the results generated are fit for the intended purpose. In particular, characteristics of the technique, such as specificity, sensitivity, precision, and accuracy, should be determined and documented. **Specificity** refers to the ability of the technique to measure the analyte of interest in the presence of all other constituents in the sample. The presence of interferences, for example, will degrade the specificity of any technique. **Sensitivity** refers to the change in analytical signal with the amount of analyte present. If one combines the concept of sensitivity with the concept of "background," the amount of analytical signal present in the absence of analyte, one derives the **detection limit** of the technique, that is, the smallest amount of analyte that can be detected at a specified confidence level, and the **quantification limit**, the smallest amount of analyte that can be quantified at a specified confidence level. **Precision** usually refers to the variation in the analytical signal (or the quantity of analyte calculated from that signal) over time, with repeated measurements. When combined with other sources of uncertainty in the measurement, for example, uncertainties in the knowledge of dead time or uncertainty in the calibration standards, one can calculate the "combined uncertainty" of the measurement. **Accuracy**, of course, refers to how closely our reported results match the true value.

For an unknown sample, the true value is not known, so we rely on validation of the method and ongoing performance testing for estimates of the accuracy of the

technique. The method is typically validated through the analysis of known samples, such as certified reference materials (CRMs) from national or international standards laboratories or other standards with values traceable to those CRMs. However, despite ongoing efforts to develop reference materials for nuclear forensics (Inn et al., 2013; Venchiarutti et al., 2015; Mathew et al., 2016; Essex et al., 2018), appropriate CRMs or traceable standards are not available in all cases, necessitating the use of self-prepared standards or other well-characterized samples. We always seek to achieve accuracy within the stated uncertainty of our measurement. If we have a consistent bias (inaccuracy) in our reported results and this bias cannot be eliminated, by recalibration, for example, then we include this bias in the calculation of uncertainty. It is worth noting that these underlying uncertainties in the analytical measurement will eventually propagate through to the uncertainty in the nuclear forensic interpretation, combining with uncertainties in the signatures, and so forth.

Finally, it should also be noted that the use of validated methods alone does not guarantee high-quality results. Validated methods often require the use of scientific instruments, which must be properly maintained and the performance of which must be tracked on a regular basis and/or verified prior to analysis. Validated methods always require analysts, who are fully trained in the methods of analysis and who are conscientious in the application of good laboratory practice. Trained and conscientious analysts applying validated methods using properly maintained and verified instruments will result in high-quality analytical results.

A. Radioactive material analysis

The nuclear forensic scientist has a wide array of analytical tools to use for detecting signatures in radioactive material. These individual techniques can be sorted into three broad categories:

- bulk analysis tools,
- imaging tools, and
- microanalysis tools.

1. Elemental and isotopic bulk analysis tools

Bulk analysis tools allow the forensic scientist to characterize the elemental and isotopic composition of the radioactive material as a whole. In some cases, bulk analysis is necessary to have sufficient material to adequately detect and quantify trace constituents, which are often vitally important as signatures for certain manufacturing processes, for determining the time since chemical separation (age dating), and for determining whether the material has been exposed to a neutron flux.

a. Radiometric techniques

Each radioactive nuclide emits radiation of known types and energies at rates determined by the quantity present and its characteristic half-life (or decay constant). Therefore, by measurement of the type and intensity of radiation emitted from a sample, it is possible to quantify the amount of each radioactive nuclide present. There are three types of radiation that are commonly considered for measurement, alpha, beta, and gamma radiation, each with its own properties and methods of detection. Alpha radiation is commonly detected by silicon surface barrier detectors, beta radiation by scintillation techniques or gas ionization detectors, and gamma radiation by high-purity germanium (high energy resolution) or sodium iodide (lower energy resolution) detectors.

Gamma spectrometry. Gamma spectrometry (ITWG, 2013a,b,c) has a dual role in nuclear forensics. For on-site applications, high-resolution gamma spectrometry is mostly used only to quickly identify the material and obtain a rough idea about the isotopic composition of the material, i.e., categorization. Although field-portable high-purity germanium detectors are available, sodium iodide detectors are still often used for field applications. If a radiation source or RDD is detected, for example, gamma spectrometry can be deployed on the spot to identify the radioactive isotopes present (which includes, but is not limited to, the isotopes of uranium and plutonium), without dismantling the source or device. In the laboratory, high-resolution gamma spectrometry is used to provide an initial determination of the isotopic composition of uranium and/or plutonium, as well as detection and quantification of trace fission and activation products in the sample, for example, in uranium from reprocessed reactor fuel.

Alpha spectrometry. Alpha spectrometry (ITWG, 2012b) is used to quantify the abundance of alpha-emitting radionuclides, particularly those with relatively short half-lives. Because source preparation is crucial for achieving good energy resolution in alpha spectrometry, the target elements are usually separated and purified before deposition onto a flat surface. Quantification is achieved by spiking the samples with known amounts of an isotopic spike or tracer. Alpha spectrometry is especially suited for quantifying ^{232}U and ^{238}Pu due to their short half-lives and, in the case of ^{238}Pu, the potential interference from ^{238}U in mass spectrometry. However, conventional alpha spectrometry is not used to separate the peaks due to ^{239}Pu from ^{240}Pu, although some alpha detectors under development have sufficient energy resolution to do so (Horansky et al., 2008; Croce et al., 2011), nor is alpha spectrometry sensitive to ^{236}U. Therefore, full characterization of the isotopic composition of Pu and U should include both alpha spectrometry and mass spectrometric analysis. Alpha spectrometry may also be used to quantify ^{241}Am (daughter

of ^{241}Pu), which can then be used to calculate the date of the last plutonium purification performed on a sample (assuming complete purification), and ^{230}Th (daughter of ^{234}U), which can similarly be used to determine a last purification date for uranium materials.

Beta spectrometry. Because beta particles are emitted with a broad range of energies, beta spectrometry must be combined with chemical separation and purification of the target element to quantify a specific nuclide. In some cases, nuclides emit a gamma ray simultaneous with the emission of a beta particle; a combined beta−gamma measurement can provide additional specificity for the analysis.

b. Mass spectrometry

Mass spectrometry is used to determine both the elemental and isotopic composition of nuclear materials, offering extremely high precision and accuracy of analysis and the capability to determine both radioactive and stable isotopes. In mass spectrometry, atoms or molecules are converted into positively or negatively charged ions, which are then separated according to their mass-to-charge ratio and the intensities of the resulting mass-separated ion beams measured. Mass spectrometry can provide quantification (often called an "assay" when applied to major constituents of the sample) of elements either by using an isotopic spike (isotopic dilution mass spectrometry) or through calibration against standard solutions in the case of solution-based techniques such as inductively coupled plasma mass spectrometry.

Thermal ionization mass spectrometry (TIMS). In TIMS (ITWG, 2017a), a sample is deposited onto a metal filament, through which a current is passed to heat it to high temperatures inside the vacuum of the mass spectrometer. If the ionization potential of a given element is low enough compared with the work function of the filament, then a fraction of the atoms of that element are ionized via interaction with the filament surface at high temperature. Specificity of the TIMS analysis can be enhanced by both chemical separation steps and the ionization temperature. TIMS is capable of measuring isotopic ratios on picogram (10^{-12} g) to nanogram (10^{-9} g) samples or down to tens of femtograms (10^{-15} g) using special preconcentration techniques. TIMS routinely measures differences in isotope mass ratios in the order of 1 in 10^6. Multicollector TIMS instruments, with detectors able to measure multiple isotopes simultaneously, are now available for very precise measurements of isotopic composition. TIMS is the preferred technique for measuring the Sr and Nd isotope ratios mentioned previously and for measuring U and Pb isotopes with the highest possible precision and accuracy.

Inductively coupled plasma mass spectrometry (ICP-MS). In ICP-MS, the sample is aspirated as a solution into an inductively coupled plasma, where the high temperature of the plasma serves to atomize and ionize the sample with high efficiency. Multicollector ICP-MS instruments (MC-ICP-MS), with detectors able to measure multiple isotopes simultaneously, provide extremely precise measurements of U and Pu isotopic composition. In addition to measuring isotopic composition, ICP-MS is useful as a method for precisely quantifying trace elemental constituents of a sample with detection limits ranging from 0.1 parts per billion (ppb) to a few tens of ppb in solution. ICP-MS has difficulty measuring some elements due to background, interferences, or poor ionization efficiency, for example, C, O, and S.

c. Chemical assay

Chemical titration (ITWG, 2017c,d) and coulometry are standard methods for the determination of the elemental concentration of uranium, plutonium, neptunium, and other nuclear materials. In chemical titration, precisely measured amounts of a selective reagent are added to a known mass of sample in solution. The reagent, reacting with the element of interest according to a well-known stoichiometric reaction, is added until the element of interest has completely reacted, the "end point." The end point can be detected either via potentiometric (electrical) or spectrophotometric (optical) methods. In controlled potential coulometry, the element to be analyzed is selectively oxidized or reduced at a metallic electrode maintained at a suitably selected potential. The number of electrons used in the oxidation or reduction is a measure of the amount of element present in the sample. The precision and accuracy of these two assay methods can be better than 0.1% and can be very effective for the characterization of interdicted materials, provided that samples of at least a few tenths of a gram are available for this analysis.

d. Radiochemistry

Many samples are too chemically complex for all the radioactive isotopes present to be measured directly. By utilizing the differences in chemical properties of the elements, it is possible to devise schemes of chemical reactions to separate and purify elements, or groups of elements, allowing the measurement of radioactive nuclides of those specific elements by either radiometric methods, or mass spectrometry. The concentration of specific isotopes can be related back to the original sample by referencing to an internal isotopic standard called a "spike," added during the radiochemical preparation. This method of quantification is commonly known as "isotope dilution" and can be coupled with analytical techniques such as alpha spectrometry or mass spectrometry. The chemical separation and purification steps increase both the sensitivity and selectivity of the technique. Radiochemistry is especially important for the measurement of isotopes at low activity

levels. Radiochemistry, in combination with radioactive counting techniques or mass spectrometry, has the potential to measure down to 10^6 atoms or lower of certain isotopes.

e. X-ray Fluorescence Analysis

XRF can also be useful for broad and nondestructive elemental quantification of either solid samples or solutions. An incident X-ray beam excites characteristic secondary X-ray wavelengths and energies in a solid sample that are counted on a solid-state or proportional counter. The detection limits for XRF are generally in the range of 10 ppmw, although actinide matrices generate many X-rays that interfere with the lower-energy X-rays of lighter elements. Using wavelength-dispersive analysis of the X-rays (WDS) provides higher energy resolution than energy-dispersive analysis (EDS), which can be used to resolve some of these interferences (see X-ray Analysis discussion below). Analysis of light elements is also problematic due to low characteristic X-ray energies and consequently poor detection probabilities.

f. X-ray Diffraction Analysis

X-ray diffraction (XRD) (ITWG, 2015a) is the standard method for identifying the chemical structure of inorganic and organic crystalline materials. X-ray beams that impinge on regularly ordered lattices undergo constructive and destructive interference that depends on the spacing of the lattice, the wavelength of the X-rays, and the angle of incidence of the X-ray beam. By rotating the sample relative to a fixed X-ray source, variations in interference occur, leading to characteristic diffraction patterns. These diffraction patterns can be compared with reference spectra to identify the specific crystalline phase (see Fig. 13.10). No diffraction patterns can be generated from amorphous (noncrystalline) materials.

g. Gas Chromatography/mass spectrometry

Gas chromatography/mass spectrometry (GC/MS) is a technique useful for detecting and measuring trace organic constituents in a bulk sample. In GC/MS, the components of a mixture are separated in the GC and identified in the mass spectrometer. The primary component of a GC is a narrow bore tube (called a "column"), which is maintained inside an oven. In the simplest arrangement, the mixture is flash vaporized in the heated introduction port. The various components of the mixture are swept onto, and through, the column by the carrier gas (usually He). The components of the mixture are separated on the column based on their volatility and relative affinity for being on the column material versus the carrier gas. Columns are usually coated with a special material to enhance separation of the components of interest. In the ideal case, all components are separated and introduced into the mass spectrometer one at a time. At low flow rates, the column effluent can be introduced directly into the mass spectrometer. At higher flow rates, the GC requires an interface to match the flow requirements of the mass spectrometer, usually by selectively removing the carrier gas.

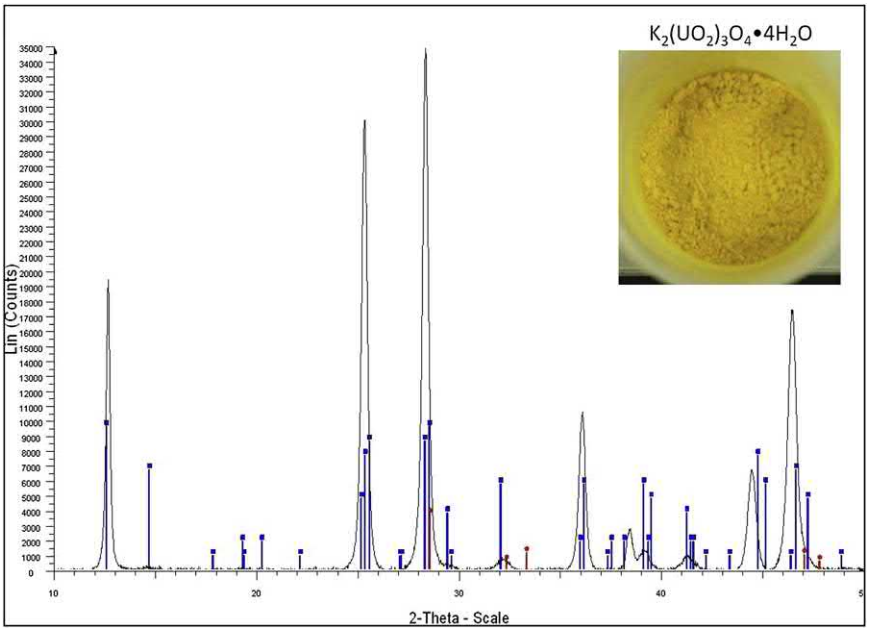


FIGURE 13.10 X-ray diffraction spectrum of interdicted uranium powder (shown in inset), identifying an unusual potassium-containing compound, related to potassium diuranate. *Reproduced from Borg et al. (2011).*

The mass spectrometer ionizes and fragments each component as it elutes from the column. Many different ionization methods can be used, but the most common for GC/MS is electron impact (EI). In EI, an energetic (usually 70 eV) beam of electrons bombards the sample molecules. Some of these electrons will hit a sample molecule and knock out an electron, leaving the molecule positively charged. This ionizing collision tends to impart some energy to the molecule. This energy is sometimes great enough to cause the ion to fragment (usually into an ion and a neutral fragment) in ways characteristic of the molecule's structure. The relative abundance of ion fragments of various masses (strictly mass-to-charge ratio, although the typical ion charge in EI is usually 1) is characteristic of the intact molecule. The mass spectrometer measures the intensity of ions of various masses, either by simultaneous or by sequential detection, depending on the type of mass spectrometer. The resulting plot of relative intensity versus mass-to-charge ratio is a "mass spectrum." There are now extensive libraries of EI mass spectra that help identify unknown compounds that are separated and detected by the GC/MS.

2. *Imaging tools*

While bulk analysis provides an integrated compositional measurement of the sample as a whole, and consequently may obscure important signatures in underlying components, imaging tools provide high magnification images or maps of the material that can confirm sample homogeneity or heterogeneity. Imaging techniques are especially important for assessing the morphology and microstructure of the material.

a. Visual inspection and photography

Visual inspection of a sample can often help in identifying the nature of a sample, especially in conjunction with data from the initial categorization. Size and shape can be sufficient to identify some items, especially if serial numbers or other identifying marks can be seen. For chemicals, the color and form of the material can be important clues.

b. Autoradiography

Autoradiography creates an image of a radioactive source by the direct exposure of imaging media (Parsons-Davis, 2018); the sample and the medium must be in fairly close proximity to one another. Traditional autoradiography used film emulsions, silver halide film being the most common. The resolution of this imaging system is strongly dependent on the thickness of the emulsion, the size of the silver halide grains dispersed in the emulsion, the optical densitometer performance, and the strength of the development process but is typically around 10 μm. The high sensitivity, accuracy, efficiency, and convenience of phosphor imaging are now commonly applied to autoradiography. In phosphor imaging systems, barium fluorohalide crystals doped with a europium activator are the photosensitive grain, and the image is formed via photostimulated luminescence. Incident radiation produces the latent image, which is subsequently "read out" through stimulation by laser light and detected by a photomultiplier tube. As with film, resolution is a function of emulsion thickness, grain size, optical readout system, and the properties of the sample being imaged. Because of the thinness of the medium, autoradiography is not sensitive to gamma radiation. Depending on the use of absorbers, autoradiography can be sensitive to alpha particles, beta particles, or both, but the resolution is typically around 50 μm (see Fig. 13.11).

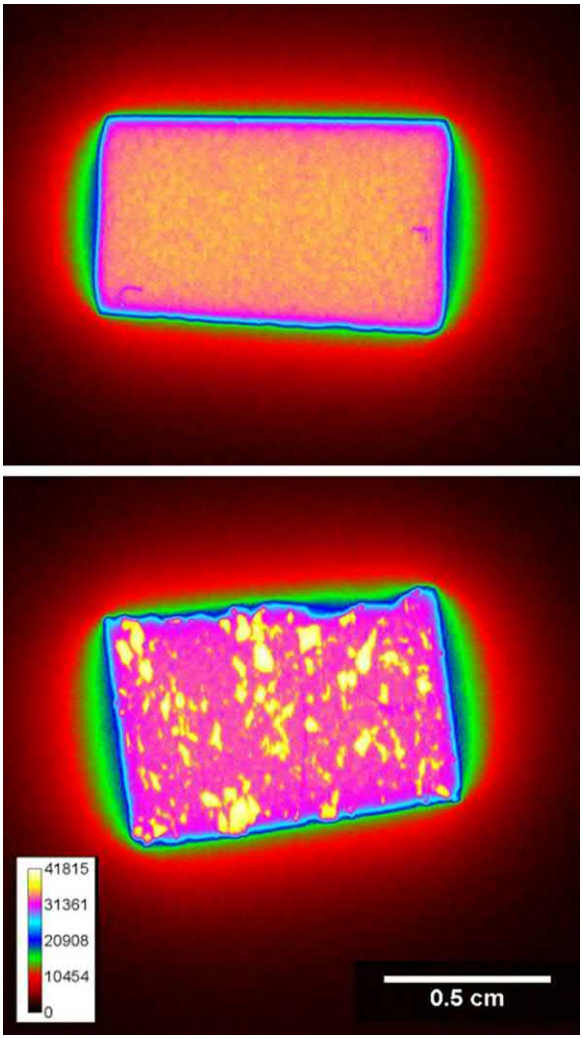


FIGURE 13.11 Cropped autoradiographs of two sawed low-enriched UO_2 subaliquots, which were mounted in epoxy and polished before being exposed to an SR IP for 25 h. The IP was scanned with 626 V, pixel size 25 μm. Sample 2 is characterized by heterogeneity in the distribution of activity on the 50−100 μm scale, whereas sample 1 shows a roughly homogenous distribution on the same scale.



FIGURE 13.12 Optical photomicrograph of the surface of one of the ITWG Round Robin 3 samples. The regular striations (~15/mm) on the surface were caused by slow cutting with a band saw. The rough-cut edge was also cut with the band saw, but at a much faster rate. *Reproduced from Bibby et al. (2010).*

c. Optical microscopy

Optical microscopy is often the first method to examine the sample at high magnification. An optical microscope uses magnifying light optics and reflected or transmitted methods of sample illumination to present magnified images of the sample to the user's eyes (see Fig. 13.12). Viewing samples under polarized light can also reveal additional information. Light microscopes can readily magnify an image up to ×1000.

d. Scanning electron microscopy

Scanning electron microscopy (SEM) can provide image magnifications up to ×100,000 with a conventional thermal filament source or ×1,000,000 with a field emission source. In SEM, a finely focused electron beam is rastered or scanned over the sample. The interaction of the energetic incident electron beam and the sample produce backscattered electrons, secondary electrons, and X-rays. By measuring the flux of one of these types of particles as a function of raster or scan position, an image or map of the sample can be reconstructed and displayed. Each type of particle conveys different information about the sample and, therefore, offers a different contrast mechanism. For instance, secondary electrons carry information about sample topology (see Fig. 13.13). Backscattered electrons carry information about average atomic number of the area being imaged and can be used to quickly detect spatially resolved phases of contrasting chemical composition.

e. Transmission electron microscopy

In transmission electron microscopy (TEM), an energetic electron beam is transmitted through an ultrathin sample (~100 nm thickness). TEM is capable of higher magnifications (several million times) than SEM and is able to image extremely fine structure (see Fig. 13.14), but at the expense of tight restrictions on sample thickness. In most cases, thin sections of the sample must be made. Transmitted electrons can undergo diffraction effects, which can be used like XRD to determine crystal phases in the material.

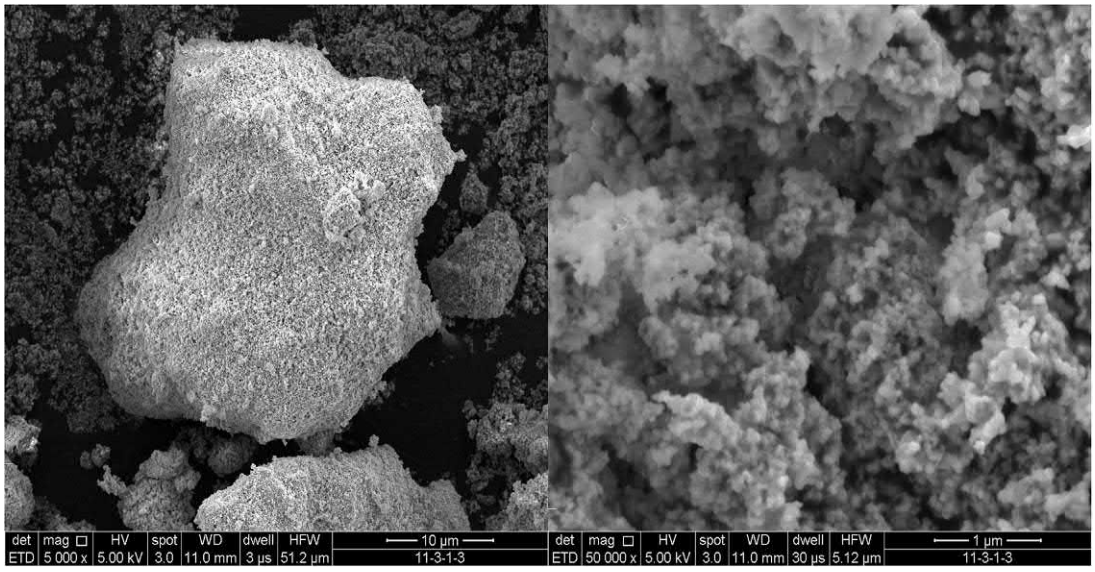


FIGURE 13.13 SEM photomicrographs of the interdicted uranium powder shown in Fig. 13.10. The morphology of the powder was consistent with a hydroxide precipitation process (probably KOH). *Reproduced from Borg et al. (2011).*

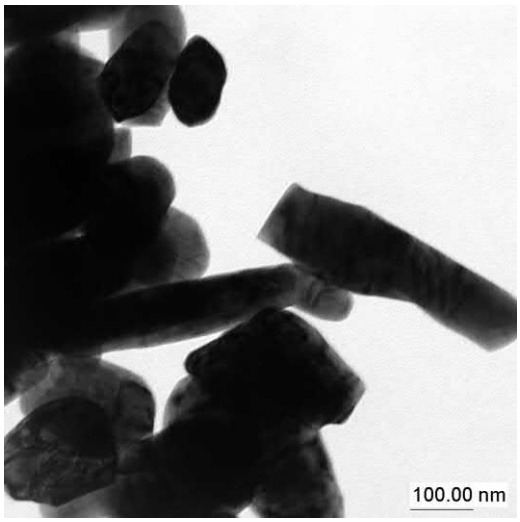


FIGURE 13.14 TEM image of the Bulgarian highly enriched uranium oxide sample, showing two distinct morphologies in the constituent particles. *Reproduced from Adamson et al. (2001).*

3. Microanalysis tools

If imaging analysis confirms that the sample is heterogeneous, then microanalysis tools can often quantitatively or semiquantitatively characterize the individual constituents of the bulk material. The category of microanalysis tools also includes surface analysis tools, which can detect trace surface contaminants or measure the composition of thin layers or coatings, either of which could be important for interpretation.

a. X-ray microanalysis

The X-rays generated during SEM, TEM, or electron microprobe analysis carry elemental information and are a convenient way of measuring the elemental composition on a fine spatial scale. The X-rays can be analyzed by either of two methods. First, an energy-dispersive spectrometer (EDS) uses a solid-state detector (typically a Si(Li) detector) to measure simultaneously the energy and rate of incident X-rays. Second, a wavelength-dispersive spectrometer (WDS) uses a synthetic analyzing crystal to sequentially diffract selected X-rays into a gas proportional counter. Due to the interaction mechanics of the electron beam with the sample, X-rays are generated over approximately a 1 μm, tear drop-shaped region, thus limiting the spatial resolution of X-ray analysis to around 1 μm. In TEM analysis, the sample thin sections limit the extent of the X-ray excitation region, enabling somewhat higher spatial resolution for X-ray analysis. The detection limits of X-ray analysis are approximately 0.01−0.1%, depending on the element. X-ray microanalysis is an assay technique to measure the elements at greater than 0.01% rather than a trace element analysis technique.

b. Secondary ion mass spectrometry

Secondary ion mass spectrometry (SIMS) (ITWG, 2015b) can be used for both elemental surveys and isotopic analysis of small samples, even particles. SIMS uses a finely focused primary ion beam, for example, O_2^+, O^-, Cs^+, or Ga^+, to sputter the sample surface. The sputtering process produces secondary ions (ions characteristic of the sample) that can be analyzed by a mass spectrometer. SIMS is capable of acquiring microscopic images of isotopic distributions (which can correspond to elemental images for known elements of known isotopic abundance). In the "microscope" mode, a relatively large primary ion beam bombards the sample, and the spatial position of the resulting secondary ions is maintained and magnified throughout the mass spectrometer. An imaging detector then displays and records the resulting isotopic image. In the "microbeam" mode, a finely focused primary ion beam is rastered or scanned across the sample in a manner similar to an electron microscope. The resulting secondary ion signal is then measured and correlated with the position of the primary ion beam to generate the isotope image. Sample ablation of the focused ion beam on the sample yields a depth profile through age, the sample surface that is extremely valuable to document compositional gradients or surface alteration.

High spatial resolution SIMS, using the CAMECA NanoSIMS, has proved useful in measuring the isotopic and elemental homogeneity of uranium oxide powders, which could prove a useful source of process signatures. Kips and coworkers have used the NanoSIMS to study the loss of F from uranium oxyfluoride particles in the environment as a function of temperature, humidity, and light level (see Fig. 13.15) (Kips et al., 2010; 2011a,b).

c. Infrared spectroscopy

Infrared (IR) spectroscopy is useful for the identification of organic compounds. Through the use of a specialized microscope, IR can be performed on samples as small as 10 μm and is an important microanalytical technique. Molecular bonds vibrate at characteristic frequencies. If a particular molecular vibration results in a change in the bond's dipole moment, then the molecule can absorb IR radiation of that characteristic frequency, exciting that vibration.

In IR spectroscopy, the sample is irradiated with a broadband of IR frequencies, and the intensity of the reflected or transmitted IR radiation is measured as a function of frequency. From the knowledge of incident intensity and reflected/transmitted intensity as a function of IR frequency, an IR absorbance spectrum can be reconstructed. Absorption at specific frequencies is characteristic of certain bonds. Thus, the IR spectrum identifies the various bonds and functional groups within the molecule. In

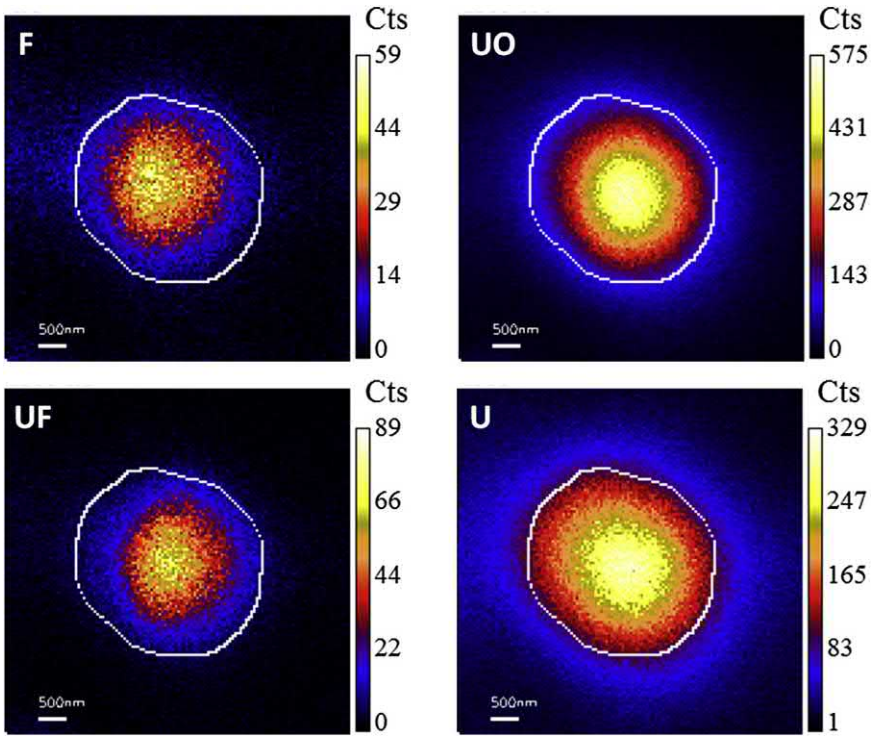


FIGURE 13.15 Ion intensity images using the CAMECA NanoSIMS at LLNL. The images are displayed in the false color mode, in which white corresponds to the highest ion intensity and black to the lowest ion intensity. These images clearly show that the uranium oxyfluoride particle (generated at the European Institute for Reference Materials & Measurements under laboratory conditions) is losing F from the outside of the particle inward (SIMS conditions: 45 pA O- primary ion beam, 16 keV impact energy).

addition, there are also vast libraries of IR spectra that help identify unknown compounds or, at least, place them into certain classes of molecules.

d. Raman spectroscopy

Raman spectroscopy is also useful for the identification of organic compounds and is complementary to IR spectroscopy, since some molecular vibrations are only Raman active and some are only IR active. Through the use of a specialized microscope, Raman spectroscopy can be performed on samples as small as 1 μm. If a particular molecular vibration results in a change in the polarizability of the molecule, then the molecule can absorb radiation of that characteristic frequency, exciting that vibration.

In Raman, the sample is irradiated with radiation of a specific frequency, and the intensity of the reflected radiation is measured as a function of frequency. Most of the radiation is reflected at the same frequency as the incident radiation. However, some radiation is reflected at specific frequencies of lower energy (Stokes lines) and some at specific frequencies of higher energy (anti-Stokes line). The frequency shifts between the Stokes and anti-Stokes lines and the incident radiation correspond to Raman active vibrations.

Characteristic Raman bands, such as the 863 cm^{-1} band for the uranyl moiety, are useful for deducing the chemical nature of the sample. Kips and coworkers have used Raman to understand how the chemical environment of the uranium atoms change as uranium oxyfluoride loses F to the environment (see Fig. 13.16).

The analytical tools commonly used in radioactive materials analysis and the information that these tools can provide are summarized in Table 13.3.

B. Traditional forensic analysis

1. Overview

Traditional forensic analysis, such as radioactive materials analysis, is an iterative process, in which the results from one analysis are used to guide the selection of subsequent analyses. The forensic analyst must carefully examine all of the items seized at the incident site to uncover as much information as possible; unlikely, and apparently unrelated, evidence are often the keys to the successful prosecution of a case.

There is a great variety of traditional forensic evidence, as well as methods of collection and evaluation. For example, evidence such as tissue, hair, fingerprints, and shoeprints can often associate a specific individual with a specific place or object. The analysis of fibers, pollen, or chemical substances found at the incident scene can

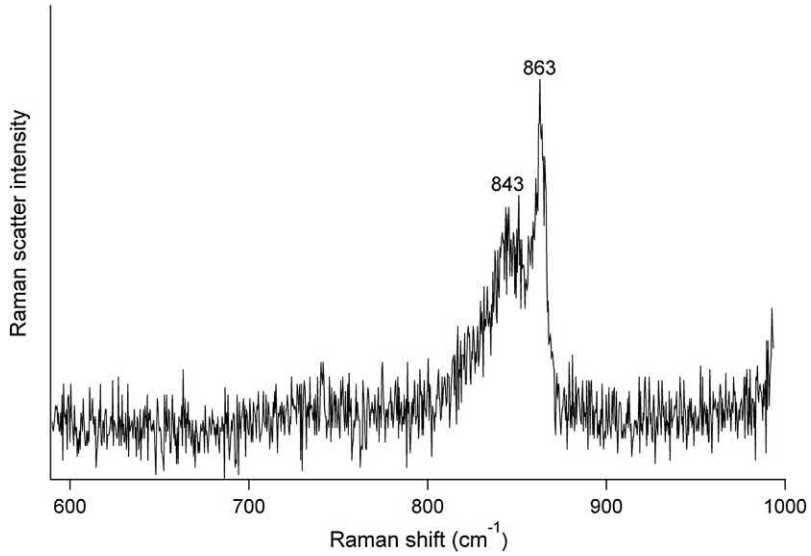


FIGURE 13.16 Raman spectrum of uranium oxyfluoride compound. The peak at 863 cm^{-1} is indicative of the uranyl moiety, whereas the peak at 843 cm^{-1} is indicative of degradation due to further hydration and loss of fluorine over time. *Reproduced from Kips et al. (2010).*

TABLE 13.3 Examples of analytical tools for nuclear forensics.

Measurement goal	Technique	Type of information	Typical detection limit	Spatial resolution
Survey	HRGS	Isotopic	ng–µg	
	Chemical assay	Elemental	mg	
	Radiochemistry/radiometric methods	Isotopic,	fg–pg	
		Elemental		
Elemental and	TIMS	Isotopic	pg–ng	
Isotopic		Elemental		
Bulk analysis	ICP-MS	Isotopic	pg–ng	
		Elemental		
	XRF	Elemental	10 ppm	
	XRD	Molecular	~1 at%	
	GC/MS	Molecular	ppm	
	Visual inspection	Macroscopic		0.1 mm
	Autoradiography	Microscopic Structure		10–50 µm
Imaging	Optical microscopy			1 µm
	SEM			1 nm
	TEM			0.1 nm
Microanalysis	SIMS	Elemental	0.1 ppb–10 ppm	0.1–1 µm
		Isotopic		
	SEM/EDS or WDS	Elemental	0.1–2 wt%	1 µm
	FTIR	Molecular	0.1–1 wt%	10 µm
	Raman	Molecular	~1 wt%	1 µm

at%, atom percent; *fg*, femtogram, 10^{-15} g; *FTIR*, Fourier transform infrared; *GC/MS*, gas chromatography/mass spectrometry; *HRGS*, high-resolution gamma spectrometry; *ICP-MS*, inductively coupled plasma mass spectrometry; *mg*, milligram, 10^{-3} g; *ng*, nanogram, 10^{-9} g; *pg*, picogram, 10^{-12} g; *ppb*, parts per billion by weight; *ppm*, parts per million by weight; *SEM*, scanning electron microscopy; *SEM/EDS*, scanning electron microanalysis with energy-dispersive sensor; *SEM/WDS*, scanning electron microanalysis with wavelength-dispersive sensor; *SIMS*, secondary ion mass spectrometry; *TEM*, transmission electron microscopy; *TIMS*, thermal ionization mass spectrometry; *wt%*, weight percent; *XRD*, X-ray diffraction; *XRF*, X-ray fluorescence; *µg*, microgram, 10^{-6} g; *µm*, micrometer, 10^{-6} m.

provide information about motives or transportation routes. Documentary evidence provides useful information not only in the content of the communication itself but also in the incidental details of its creation (paper, ink, film type, extraneous noises, and accents).

Once again, all sampling and analysis must be performed with due regard for perpetuation of the chain-of-custody and preservation of evidence, since the sampling process itself could contaminate or destroy some evidence in the pursuit of other evidence. In addition, the collection of traditional forensic evidence on radioactively contaminated materials must also be performed in a manner consistent with good radiological safety practice.

2. Documentary evidence

Documents or recordings (from an answering machine, for example) can provide information, not only through the written or recorded information itself but also through other evidence that ties the document or recording to a person or place: detailed analysis of handwriting, type characteristics and anomalies on typed documents, photocopier characteristics and anomalies on photocopied documents, and mechanical impressions for typeset documents. Analysis of the paper used in a document can itself provide valuable clues. The analysis of paper associated with the Bulgarian seizure, for example, indicated a source somewhere in eastern Europe (Adamson et al., 2001; Moody et al., 2015). Examination of a recording would include an analysis of the language, dialect, and stray background sounds. If a computer, or a data storage media, for example, disk, is recovered from the incident scene, then the forensic analyst must try to recover all of the information stored there. Programs and files may document the perpetrators' plans and methods and/or implicate other people. Information stored in mobile phones could also provide useful information.

3. Impressions

Latent fingerprints, palm prints, or prints from other body areas, for example, ear prints from listening at windows, could tie a person to a location or an object seized in the incident. Shoe prints discovered at the incident site can also link a specific person to the incident site, through the unique tread pattern of their shoes. Similarly, tire treads could serve to link a specific car to the incident site.

4. Chemical analysis

Unique or special chemical substances seized at the incident site can provide valuable evidence. Controlled substances or poisons may provide useful information about the perpetrators or their motives. Accelerants used for arson or explosive residues provide evidence about methods and purpose. Characteristic dyes and petroleum products can tie the seized evidence to particular locations, perhaps serving as a marker for route interpretation.

5. Tissue and hair evidence

Human tissue recovered at the incident scene can also tie a specific individual to the incident scene or seized evidence. Blood can be typed through serology. Blood and other tissue can be subjected to either nuclear or mitochondrial DNA analysis, again helping to implicate an individual. Hair samples can provide information about race and body characteristics.

6. Weapons evidence

In the event that a bomb is detonated or seized, the bomb remains and explosive residues can provide a pattern for determining the type of bomb and its method of manufacture. Unique materials may pinpoint the exact perpetrator or, at least, restrict the number of potential perpetrators through purchase records for such material. In the event that firearms are seized, the examination of the projectile lead, cartridge cases, gunshot residues, and any altered function may tie the perpetrator to a given location, a fact useful in route interpretation, or it may provide evidence of method or purpose.

7. Tool marks

Alterations in objects that appear to be made by the perpetrators themselves are highly significant. The forensic analyst should look for fractures (particularly those that match up with other fractures in the evidence), odd marks in wood, the use of stamps and dies, and the modification of locks and keys. The forensic analyst should attempt to restore any obliterated markings. For example, the regularly spaced grooves on the ITWG Round Robin 3 samples (see Fig. 13.10) were indicative of cuts made by a slow-moving band saw.

8. Fiber examination

Fibers can serve to tie objects and perpetrators to specific locations as well. The forensic analyst must pay particular attention to fiber evidence, such as fabrics, cords, and ropes, and determine its type: animal (wool), mineral (glass), synthetic, or organic (cotton).

9. Flora and fauna

The forensic analyst should also examine all evidence for feathers, insects or other bugs, plant material, pollen, or spores that are indicative of a location other than the incident site. These botanical pieces of evidence can be important for route interpretation. A tineid moth found in an interdicted sample (see Fig. 13.17), for example,



FIGURE 13.17 Optical photomicrograph of a tineid moth found in an interdicted uranium powder sample. *Reproduced from Borg et al. (2011).*

provided evidence of sample location between loss of legitimate control and interdiction.

10. Other materials evidence

Other associated evidence should be carefully examined for possible clues toward methods and route interpretations. Such materials as glass, soil, dust, cosmetics, paints, inks and dyes, plastics, polymers, metal objects (such as the corroded staple shown in Fig. 13.18), and tapes often vary in chemical composition from place to place. Unique characteristics in these materials might tie the perpetrators to a specific location, again a fact that can be important for route interpretation. In the same way, unique minerals found on the evidence might be diagnostic of specific geology and location, that is, geolocation.



FIGURE 13.18 A somewhat unusual staple found in an interdicted uranium powder sample. *Reproduced from Borg et al. (2011).*

C. Application and sequencing of techniques and methods

The nuclear forensic scientist should, of course, consider issues such as specificity, sensitivity, detection limit, precision, and accuracy in choosing an appropriate analytical method to apply to the nuclear forensic sample. In addition, though, one must consider the cost of the analysis versus the benefit to be derived from the results. Cost includes real financial cost, of course, the cost of both instrument time and the analyst's time, the cost of consumables used during the analyses, and so forth. However, cost should also include the "cost" of any sample consumed during analysis. In the case of NDA, this cost may very well be zero, although one must always consider the potential of altering or contaminating the sample during NDA, rendering it useless for analysis by other techniques. In addition, if the amount of sample is quite large, this cost might be correspondingly quite small. Another potential cost might be time. For time-critical cases, the amount of time required for a specific analysis may be too long, and the analyst should consider other techniques that can provide answers more quickly. When considering the benefit of an analysis, the analyst should first consider the relevance of the anticipated results. Relevance really reflects the connection between the anticipated results and signatures of interest. In the case of comparative signatures, do we have the necessary database or sample archive against which to compare our results? In the case of predictive signatures, do we have the necessary scientific insights to interpret the meaning of our results?

The ITWG has achieved a general consensus on the proper sequencing of techniques so as to provide the most valuable information as early as possible in the interpretation process. This consensus was achieved through discussion and consultation at regular meetings, as well as from experience developed from three round robin analyses by nuclear forensic laboratories. The collection of time or environmentally sensitive samples must occur within the first 24 h after sample receipt. NDA should be conducted before destructive analyses whenever possible. Table 13.4 shows the generally accepted sequence of analysis, broken down into techniques that should be performed within 24 h, 1 week, or 2 months after sample receipt.

IX. Quality assurance

From the law enforcement perspective, nuclear forensic results must meet the standards of evidence of the jurisdiction where the case is to be prosecuted. In the United States, for example, the probative power and admissibility of scientific evidence in the courtroom has tended toward more restrictive interpretations of the Federal Rules of Evidence (Daubert, 1993; Kumho Tire, 1999), a trend also

TABLE 13.4 Sequence for techniques/methods as determined by the ITWG (Hanlen, 2011).

Techniques/ methods	24 hours[a]	1 week[a]	2 months[a]
Radiological	Health and safety assessment - Dose rate (α, γ, neutron) - Surface contamination - Radiography		
Physical characterization	Preliminary - Visual inspection - Photography - Weight and dimensional determination - Optical microscopy - Density	Detailed (microstructure, morphology, etc.) - SEM (EDX) - XRD	Detailed (nanostructure, morphology, etc.) - TEM - EMPA[b]
Classical forensics	Initial - Assessment of presence and collection of classical forensic evidence		Detailed - Analysis and interpretation of classical forensic evidence
Isotope analysis	Initial isotopic composition - Gamma spec on bulk material (i.e., is it HEU or not?)	Intermediate isotopic composition - HRGS - SIMS - TIMS - MC-ICP-MS - Alpha spectroscopy	Final isotopic composition - HRGS - SIMS - TIMS - MC-ICP-MS
	Initial age dating • HRGS Pu	Initial age dating - LA-ICP-MS	Age dating - HRGS - MC-ICP-MS - Alpha spectroscopy
Elemental/ chemical	Elemental/chemical (may take longer) - XRF	Elemental/chemical (may take longer) - ICP-MS - IDMS[c]	

HEU, highly enriched uranium; *HRGS,* high-resolution gamma spectrometry; *LA-ICP-MS,* laser ablation inductively coupled mass spectrometry; *MC-ICP-MS,* multicollector inductively coupled mass spectrometry; *SEM,* scanning electron microscopy; *SIMS,* secondary ion mass spectrometry; *TEM,* transmission electron miscroscopy; *TIMS,* therma ionization mass spectrometry; *XRD,* X-ray diffraction; *XRF,* x-ray fluorescence.
[a]*All times above refer to time after receipt of sample(s) at the nuclear forensic laboratory.*
[b]*EMPA = electron microprobe analysis.*
[c]*IDMS = isotope dilution mass spectrometry.*

reflected in the 2004 NRC study of bullet lead analysis and the subsequent withdrawal of this method by the FBI (NRC, 2004; Finkelstein and Levin, 2005; FBI, 2005). The Daubert Standard, for example, consists of the following four factors, which a judge should consider when determining the admissibility of scientific evidence:

1. whether scientific evidence has been tested and the methodology with which it has been tested;
2. whether the evidence has been subjected to peer review or publication;
3. whether a potential rate of error is known; and
4. whether the evidence is generally accepted in the scientific community

The existence of a rigorous quality assurance system can help address several of these factors. According to the draft Quality Assurance Guidelines for Laboratories Performing Forensic Analyses of Radiological Materials (Garrett et al., 2012, personal communication):

> *Quality Assurance is an integral part of a laboratory analysis program. It provides a means to deliver valid, traceable results, an ability to identify and correct anomalies, consistency from analysis to analysis within a given technique, between techniques and temporally, and assurance that errors will be minimal and stochastic. The QA program is the element of an analytical program that provides assurance in the results generated by the analyses.*

From a nuclear forensic perspective, a QA program ensures defensible and consistent input to the interpretation process in support of attribution assessments.

Most forensic laboratories, including nuclear forensic laboratories, are seeking to accredit their quality assurance systems to the ISO 17025 standard (ISO/IEC, 2005). The Lawrence Livermore National Laboratory and Los Alamos National Laboratory, for example, have achieved accreditation in the field of nuclear forensics. The ISO 17025 standard is based on the essential structure of ISO 9000 with requirements in the following areas:

- Organization and management
- Document control
- Contracts and procurement
- Corrective action
- Control of records
- Audits
- Personnel qualifications and training
- Facility infrastructure and security
- Validation of methods, uncertainty, and measurement traceability
- Equipment
- Analytical procedures
- Calibration and maintenance
- Proficiency testing
- Documentation and reporting
- Sampling
- Sample control
- Safety
- Subcontracting services

The critical components for the analytical measurements are the requirements to validate the analytical methods prior to use, to calibrate and maintain the analytical instruments, and to qualify and train the personnel who use the methods and instruments. The method for determination of uncertainty and the traceability of measurements is an important part of each method (ITWG, 2017b). Although adherence to the Guide to Uncertainty in Measurement (ISO, 2008) is not a requirement of ISO 17025, it has, in fact, become the standard for determining analytical uncertainty. Finally, ISO 17025 requires proficiency testing, which serves to exercise the entire quality assurance system and serves to ensure comparability of results from different laboratories.

As mentioned previously, although the quality assurance requirements for the admissibility of scientific evidence into a court of law may be rigorous, scientific results used for intelligence purposes have a need for similar quality assurance, however, perhaps less formal than that required for law enforcement purposes.

X. Sampling

The quality of the analytical measurements is often limited by the quality of the sample. Uncertainties created in the field ripple through to uncertainties in the lab. A thorough analysis of issues regarding operations at the incident site can be found in IAEA TECDOC-1313 (IAEA, 2002) and the ITWG Guidelines for Evidence Collection in a Radiological or Nuclear Contaminated Crime Scene (ITWG, 2012a).

One must, of course, address the issue of personnel and public safety first. Since traditional forensic evidence is frequently commingled with the radioactive evidence, the collection of forensic evidence must be consistent with good radiological safety practice. Limiting time in the contaminated area and maximizing distance and shielding between the exposed personnel and radioactive sources can lessen the risk to personnel. Appropriate personal protective equipment (PPE), e.g., rubber gloves, safety goggles, will be required. In cases where dispersible radioactive material is present, an approved respirator may also be needed.

Ill-considered collection of traditional evidence could compromise the radioactive material evidence and vice versa. Therefore, it is essential that appropriate thought be given to the manner and relative timing of traditional forensic evidence collection and radioactive material collection. Good communication between nuclear forensic specialists and those responsible for collecting the evidence will help ensure that all factors are considered before a collection approach is adopted.

Finally, appropriate chain-of-custody procedures will be initiated and maintained during the evidence collection process. The resulting evidence must then be supervised and protected while awaiting transportation from the incident scene.

XI. Conclusions

Nuclear forensics is an emerging discipline, driven primarily by national objectives, to include both those of law enforcement and national intelligence. Nuclear forensics is one input into nuclear attribution, in which responsibility is assigned, along with other sources of information, such as law enforcement and intelligence. Nuclear forensics is used to generate technical conclusions by applying validated signatures to analytical results from the interdicted material. These validated signatures include both comparative signatures, in which the interdicted material is compared with the results from material of known origins, and predictive signatures, in which conclusions are generated without reference to other samples. Valid analytical results, in turn,

depend on appropriately validated analytical methods, proper analytical sampling, and a quality control/assurance program.

Acknowledgments

I would like to acknowledge the help and support of all of my colleagues in the nuclear forensic group at the Lawrence Livermore National Laboratory, but especially my mentors, Dr. Sid Niemeyer and the late Dr. Ian Hutcheon, who paved the way for the emergence of nuclear forensics as a distinct discipline of national importance. Dr. Ross Williams and Dr. Amy Gaffney have been instrumental in providing results that are helping us explore the strengths, and pitfalls, of age dating nuclear material. Dr. Kim Knight, Dr. Ruth Kips, Dr. Tashi Parsons-Davis, Dr. Jonathan Plaue, and Christie Ramon helped me by providing the optical, autoradiography, and SEM photomicrographs shown here. Finally, I would like to acknowledge our national and international colleagues, particularly those at the Joint Research Center-Karlsruhe (formerly Institute for Transuranium Elements) in Karlsruhe, Germany, for helping to develop this new field. This chapter was prepared by a contractor of the US government under contract number DE-AC52-07NA27344. Accordingly, the US government retains a nonexclusive, royalty-free license to publish or reproduce the published form of this contribution, or allow others to do so, for US government purposes.

References

Adamson, M., Alcaraz, A., Andresen, B., Bazan, J., Cantlin, S., Chambers, D., Conrado, C., Esser, B., Grant, P., Hudson, B., et al., 2001. Forensic Analysis of a Smuggled HEU Sample Interdicted in Bulgaria. UCRL-ID-143216. Lawrence Livermore National Laboratory, U.S. Department of Energy, Livermore, CA, 88 pp.

Aggarwal, S.K., 2016. Nuclear forensics: what, why, and how? Curr. Sci. 110, 782–791.

Allison, G., October 27, 2006. Deterring Kim Jong Il. The Washington Post.

Allison, G., March 23, 2009. How to keep the bomb from terrorists. Newsweek.

Antill, J.E., Barnes, E., Gardner, M., 1959. Zone melting of uranium, pp. 9-18. In: Finniston, H.M., Howe, J.P. (Eds.), Progress in Nuclear Energy" Series V, "Metallurgy and Fuels. McGraw-Hill, New York.

Ball, J., Dimayuga, I., Summerell, I., Totland, M., Jonkmans, G., Whitlock, J., El-jaby, A., Inrig, E., 2015. Canadian nuclear forensics capability project. AECL Nuclear Review 4 (1), 1–7.

Badaut, V., Wallenius, M., Mayer, K., 2009. Anion analysis in uranium ore concentrates by ion chromatography. J. Radioanal. Nucl. Chem. 280, 57–61.

Barker, M., Rayens, W., 2003. Partial least squares for discrimination. J. Chemom. 17, 166–173.

Baude, S., 2007. HEU seized in July 2001 in Paris. In: Proceedings of the IAEA Conference on Illicit Nuclear Trafficking, Edinburgh, Scotland, November 19-22, 2007. International Atomic Energy Agency, Vienna, pp. 397–398.

Baude, S., Chartier, B., Kimmel, D., Marriotte, F., Masse, D., Peron, H., Tilly, D., 2007b. The French response in cases of illicit nuclear trafficking. In: Proceedings of the IAEA Conference on Illicit Nuclear Trafficking, Edinburgh, Scotland, November 19-22, 2007. International Atomic Energy Agency, Vienna, pp. 363–371.

Bibby, R.K., Gaffney, A.M., Genetti, V.G., Go, J., Gostic, J.M., Grant, P.M., Henderson, R.A., Hutcheon, I.D., Klunder, G.L., Knight, K.B., et al., 2010. Final Report Nuclear Smuggling International Technical Working Group (ITWG) Round Robin #3. LLNL-TR-434300. Lawrence Livermore National Laboratory, U.S. Department of Energy, Livermore, CA, 51 pp.

Birch, D., Smith, R.J., November 22, 2015. Russian Thieves Made off with a Full Bomb's Worth of Highly Enriched Uranium. Global Post.

Borg, L.E., Conrado, C.L., Eppich, G.R., Gaffney, A.M., Genetti, V.G., Grant, P.M., Henderson, R.A., Hutcheon, I.D., Klunder, G.L., Knight, K.B., et al., 2011. Final Report – Analysis of Interdicted Samples from Australia. LLNL-TR-486036. Lawrence Livermore National Laboratory, U.S. Department of Energy, Livermore, CA, 67 pp.

Borgardt, J.D., Wong, F.M.G., 2014. Galaxy serpent: a web-based tabletop exercise using the concept of national nuclear forensics libraries. J. Nucl. Mater. Manag. 42 (4), 4–11.

Borgardt, J., Canaday, J., Chamberlain, D., 2017. Results from the second Galaxy Serpent web-based table top exercise utilizing the concept of nuclear forensics libraries. J. Radioanal. Nucl. Chem. 311 (2), 1517–1524.

Borger, J., November 7, 2010. Nuclear Bomb Material Found for Sale on Georgia Black Market. Guardian.co.uk. http://www.guardian.co.uk/world/2010/nov/07/nuclear-material-black-market-georgia.

Borger, J., November 8, 2010. Nuclear Smuggling: Armenia Arrests Suspected Smuggler. Guardian.co.uk. http://www.guardian.co.uk/world/2010/nov/08/nuclear-smuggling-armenia-arrest.

Brennecka, G.A., Borg, L.E., Hutcheon, I.D., Sharp, M.A., Anbar, A.D., 2010. Natural variations in uranium isotope ratios of uranium ore concentrates: understanding the $^{238}U/^{235}U$ fractionation mechanism. Earth Planet. Sci. Lett. 291, 228–233.

Broad, W.J., December 30, 2003. Sleuths patrol nations for nuclear mischief. The New York Times.

Budinger, P.A., Drenski, T.L., Varnes, A.W., Mooney, J.R., 1980. The case of the great yellow cake caper. Anal. Chem. 52, 942A–948A.

Chivers, D.H., Lyles Goldblum, B.H., Isselhardt, B.F., Snider, J.S., 2008. Before the day after: using pre-detonation nuclear forensics to improve fissile materials security. Arms Control Today July/August 2008, 22–28.

Conca, J., September 27, 2017. CSI: nuclear. Forbes. Found at. https://www.forbes.com/sites/jamesconca/2017/09/07/csi-nuclear/#23c3613664ce.

Craig, H., 1961. Isotopic variations in meteoric waters. Science 133, 1702–1703.

Croce, M.P., Bacrania, M.K., Bond, E.M., Dry, D.E., Klingensmith, A.L., Moody, W.A., LaMont, S.P., Rabin, M.W., Rim, J.H., Beall, J.A., et al., 2011. Superconducting transition-edge sensor microcalorimeters for ultra-high resolution alpha-particle spectrometry. IEEE Trans. Appl. Superconductivity 21, 207–211.

Currie, L.A., 1995. Nomenclature in evaluation of analytical methods including detection and quantification capabilities. Pure Appl. Chem. 67, 1699–1723.

Dalheimer, A., Konig, K., Nosske, D., Schafer, I., 2009. The Hamburg polonium-210 case: monitoring of internal contaminations in a malevolent act. Kerntechnik 74, 201–204.

Daubert, v, 1993. Merrell Dow Pharmaceuticals, vol. 509. U.S. 579.

Davydov, J., Dion, H., LaMont, S., Hutcheon, I., Robel, M., 2016. J. Radioanal. Nucl. Chem. 307 (30), 2389–2395.

Drummond, C., 2018. An incremental machine learning algorithm for nuclear forensics. In: Advances in Artificial Intelligence, the

Proceedings of the 31st Canadian Conference on Artificial Intelligence, May 8-11, 2018 (Toronto, CA), pp. 197–207.

Dudder, G.B., Hanlen, R.C., Herbillon, G.M., 2003a. Final report: international interlaboratory forensics exercise with a highly enriched uranium sample (HEU Round-Robin Exercise). Rep. PNNL-14698, Pac. Northwest Natl. Lab. (PNNL), Richland, WA.

Dudder, G.B., Hanlen, R.C., Herbillon, G.M., 2003b. International Technical Working Group round-robin tests. In: Advances in Destructive and Non-Destructive Analysis for Environmental Monitoring and Nuclear Forensics. Proceedings of an International Conference. Int. At. Energy Agency, Vienna, pp. 41–51. Karlsruhe, 21–23 Oct. 2002.

Dunlop, W., Smith, H., October 2006. Who did it? Using international nuclear forensics to detect and deter nuclear terrorism. Arms Control Today 6–10.

Engelbrecht, A., Knight, K., Gaidar, O., Tryshyn, V., 2013. Developing a model national nuclear forensics database: report on the pilot project in Ukraine. Abstract 227-NUCL in Abstracts of Papers of the American Chemical Society. In: Proceedings of the 245th National Spring Meeting of the American Chemical Society, New Orleans, Louisiana, April 7-11, 2013.

EPA, 2004. Measurement Uncertainty. Chapter 19 in "Multi-Agency Radiological Laboratory Analytical Protocols Manual (MARLAP)". U.S. Environmental Protection Agency, Washington, DC, 111 pp. https://www.epa.gov/radiation/multi-agency-radiological-laboratory-analytical-protocols-manual-marlap.

Essex, R.M., Mann, J.L., Williams, R.W., Kinman, W.S., Hubert, A., Bennett, M.E., Gourgiotis, A., 2018. A new thorium-229 reference material. Appl. Radiat. Isot. 134, 23–31.

Faure, G., 1998. Principles and Applications of Geochemistry, second ed. Prentice-Hall, New Jersey. 625 pp.

FBI, 2005. FBI Laboratory Announces Discontinuation of Bullet Lead Examinations. Press Release, September 1, 2005. Federal Bureau of Investigation, Washington, DC.

Fedchenko, V., 2007. Weapons of mass analysis: advances in nuclear forensics. Jane's Intell. Rev. 19, 48–51.

Fedchenko, V., June, 2017. Nuclear Forensics as Nuclear Materials Analysis for Security Purposes. EU Nonproliferation Paper No. 60.

Feder, H.M., Chellew, N., Ader, M., 1956. Melt refining of uranium, 301-308. In: Bruce, F.R., Fletcher, J.M., Hyman, H.H., Katz, J.J. (Eds.), Progress in Nuclear Energy," Series III, "Process Chemistry. McGraw-Hill Book, New York, 407 pp.

Finkelstein, M.O., Levin, B., 2005. Compositional analysis of bullet lead as forensic evidence. J. Law Policy 13, 119–142.

Gaffney, A.M., Hubert, A., Kinman, W.S., Magura, M., Okubo, A., Pointurier, F., Schorzman, K.C., Steiner, R.E., Williams, R.W., 2016. Round-robin Th-230-U-234 age dating of bulk uranium for nuclear forensics. J. Radioanal. Nucl. Chem. 307 (3), 2055–2060.

Garrett, B., Adamic, M., Bannan, J.D., Chase, S., Czerwinski, K., Duff, M.C., Goldberg, S., Hanlen, R., Jensen, E., Larsson, C.L., et al., 2012. Quality assurance guidelines for laboratories performing forensic analyses of radiological materials. (personal communication).

Han, S.H., Varga, Z., Krajko, J., Wallenius, M., Song, K., Mayer, K., 2013. Measurement of the sulphur isotope ratio (S-34/S-32) in uranium ore concentrates (yellow cakes) for origin assessment. J. Anal. Atom Spectrom. 28 (12), 1919–1925.

Hanlen, R., 2011. Round Robin 3 Exercise after Action and Lessons Learned Report. PNNL-20079. Pacific Northwest National Laboratory, U.S. Department of Energy, Richland, WA, 78 pp.

Horansky, R.D., Ullom, J.N., Beall, J.A., Hilton, G.C., Irwin, K.D., Dry, D.E., Hastings, E.P., Lamont, S.P., Rudy, C.R., Rabin, M.W., 2008. Superconducting calorimetric alpha particle sensors for nuclear nonproliferation applications. Appl. Phys. Lett. 93, 123504/1-3.

IAEA, 2002. IAEA-TECDOC-1313: Response to Events Involving the Inadvertent Movement or Illicit Trafficking of Radioactive Materials. International Atomic Energy Agency, Vienna, 50 pp.

IAEA, 2006. IAEA Nuclear Security Series No. 2: Nuclear Forensics Support. International Atomic Energy Agency, Vienna, Austria, 67 pp.

IAEA, 2015a. Advances in nuclear forensics: countering the evolving threat of nuclear and other radioactive material out of regulatory control. In: Summary of an International Conference, Vienna, Austria, July 7-10, 2014. International Atomic Energy Agency, Vienna, 149 pp.

IAEA, 2015b. IAEA Nuclear Security Series No. 2-G: Nuclear Forensics in Support of Investigations. International Atomic Energy Agency, Vienna, Austria, 62 pp.

IAEA, 2018. The IAEA Illicit Trafficking Database. https://www.iaea.org/sites/default/files/17/12/itdb-factsheet-2017.pdf.

IAEA/WMO, 2006. Global Network of Isotopes in Precipitation. International Atomic Energy Agency, Vienna. http://www-naweb.iaea.org/napc/ih/IHS_resources_gnip.html.

Ignatius, D., October 11, 2006. We need a new deterrent. The Washington Post.

Inn, K.G.W., Johnson, C.M., Oldham, W., Jerome, S., Tandon, L., Schaaff, T., Jones, R., Mackney, D., Mackill, P., Palmer, B., Smith, D., Lamont, S., Griggs, J., 2013. The urgent requirement for new radioanalytical certified reference materials for nuclear safeguards, forensics, and consequence management. J. Radioanal. Nucl. Chem. 296 (1), 5–22.

ISO, 2008. ISO/IEC Guide 98-3:2008, Uncertainty of Measurement – Part 3: Guide to the Expression of Uncertainty in Measurement (GUM:1995). International Organization for Standardization, Switzerland, 120 pp.

ISO/IEC 17025, 2005. General Requirements for the Competence of Testing and Calibration Laboratories. International Organization for Standardization, Switzerland, 28 pp.

ITWG, 2012a. ITWG Guideline on Evidence Collection in a Radiological or Nuclear Contaminated Crime Scene, 7 pp. Found at: http://www.nf-itwg.org/pdfs/ITWG-INFL-EVID.pdf.

ITWG, 2012b. INFL Guideline on Alpha Spectrometry, 6 pp. Found at: http://www.nf-itwg.org/pdfs/ITWG-INFL-ALPH.pdf.

ITWG, 2013a. ITWG Guideline on High-Resolution Gamma Spectrometry - General Overview, 7 pp. Found at: http://www.nf-itwg.org/pdfs/ITWG-INFL-GSOV.pdf.

ITWG, 2013b. ITWG Guideline on In-Field Applications of High-Resolution Gamma Spectrometry for Analysis of Special Nuclear Material, 6 pp. Found at: http://www.nf-itwg.org/pdfs/ITWG-INFL-GSIF.pdf.

ITWG, 2013c. ITWG Guideline on Laboratory Applications of High-Resolution Gamma Spectrometry for the Analysis of Special Nuclear Material, 6 pp. Found at: http://www.nf-itwg.org/pdfs/ITWG-INFL-GSLA.pdf.

ITWG, 2015a. INFL Guideline on Powder X-Ray Diffraction (XRD), 6 pp. Found at: http://www.nf-itwg.org/pdfs/ITWG-INFL-PXRD.pdf.

ITWG, 2015b. INFL Guideline on Secondary Ion Mass Spectrometry (SIMS), 7 pp. Found at: http://www.nf-itwg.org/pdfs/ITWG-INFL-SIMS.pdf.

ITWG, 2016. INFL Guideline on Age Dating, 6 pp. Found at: http://www.nf-itwg.org/pdfs/ITWG-INFL-ADPD.pdf.

ITWG, 2017a. INFL Guideline on Thermal Ionisation Mass Spectrometry (TIMS), 6 pp. Found at: http://www.nf-itwg.org/pdfs/ITWG-Guideline-TIMS.pdf.

ITWG, 2017b. ITWG Guideline on the Importance of Uncertainty in Nuclear Forensics Measurements, 7 pp. Found at: http://www.nf-itwg.org/pdfs/ITWG-Guideline-Uncertainty.pdf.

ITWG, 2017c. ITWG Guideline on Elemental Assay - U Titration, 5 pp. Found at: http://www.nf-itwg.org/pdfs/ITWG-Guideline-U-Titration.pdf.

ITWG, 2017d. ITWG Guideline on Elemental Assay - Pu Titration, 5 pp. Found at: http://www.nf-itwg.org/pdfs/ITWG-Guideline-Pu-Titration.pdf.

Kayzar, T.M., Williams, R.W., 2016. Developing Ra-226 and Ac-227 age-dating techniques for nuclear forensics to gain insight from concordant and non-concordant radiochronometers. J. Radioanal. Nucl. Chem. 307 (3), 2061–2068.

Keegan, E., Wallenius, M., Mayer, K., Varga, Z., Rasmussen, G., 2012. Attribution of uranium ore concentrates using elemental and anionic data. Appl. Geochem. 27 (8), 1600–1609.

Keegan, E., Kristo, M.J., Toole, K., Kips, R., Young, E., 2016. Nuclear forensics: scientific analysis supporting law enforcement and nuclear security investigations. Anal. Chem. 88 (3), 1496–1505.

Kennedy, A.K., Bostick, D.A., Hexel, C.R., Smith, R.R., Giaquinto, J.M., 2013. Non-volatile organic analysis of uranium ore concentrates. J. Radioanal. Nucl. Chem. 296 (2), 817–821.

Kigoshi, K., 1971. Alpha recoil thorium-234: dissolution into water and uranium-234/uranium-238 disequilibrium in nature. Science 173, 47–48.

Kimura, Y., Shinohara, N., Funatake, Y., 2017. Development of prototype nuclear forensics library for nuclear materials and radioisotopes in Japan Atomic Energy Agency. Energy Procedia 131, 239–245.

Kips, R., Kristo, M., Crowhurst, J., Hutcheon, I., Stefaniak, E., Aregbe, Y., 2010. Investigating chemical and molecular changes in uranium oxyfluoride particles using NanoSIMS and micro-Raman spectroscopy. In: Proceedings of the IAEA Symposium on International Safeguards: Preparing for Future Verification Challenges, 1-5 November 2010, Vienna, Austria. International Atomic Energy Agency, Vienna.

Kips, R., Kristo, M., Crowhurst, J., Hutcheon, I., 2011a. Characterization of Uranium Oxyfluoride Particles for Nuclear Safeguards. LLNL-PRES-481061. Lawrence Livermore National Laboratory, U.S. Department of Energy, Livermore, CA, 16 pp.

Kips, R., Kristo, M.J., Hutcheon, I.D., Olsen, K.B., Amonette, J., Wang, Z., Gerlach, D., Johnson, T., Stefaniak, E., 2011b. Measuring fluorine in uranium oxyfluoride particles using secondary ion mass spectrometry for nuclear forensics. APSORC '09 Proc. Radiochem. 1, 7–11.

Krajko, J., Varga, Z., Yalcintas, E., Wallenius, M., Mayer, K., 2014. Application of neodymium isotope ratio measurements for the origin assessment of uranium ore concentrates. Talanta 129, 499–504.

Krajko, J., Varga, Z., Wallenius, M., Mayer, K., 2015. Development of a versatile sample preparation methods and its application for rare-earth patter and Nd isotope ratio analysis in nuclear forensics. J. Radioanal. Nucl. Chem. 304 (1), 177–181.

Krajko, J., Varga, Z., Wallenius, M., Mayer, K., 2016. Pre-concentration of trace levels of rare-earth impurities in high purity uranium samples for nuclear forensic purposes. Radiochim. Acta 104 (7), 471–479.

Kramer, A.E., June 29, 2011. Arrests in Moldova over possible uranium smuggling. New York Times.

Kristo, M.J., 2011a. LLNL experience with the third ITWG nuclear forensics round robin. In: Proceedings of the 52nd Annual Meeting of the Institute of Nuclear Materials Management, Desert Springs, CA, July 17-21, 2011. Omnipress, Madison, WI.

Kristo, M.J., 2011b. Univariate nuclear forensic signatures. LLNL-JRNL-422284. Lawrence Livermore National Laboratory, U.S. Department of Energy, Livermore. CA, 21 pp.

Kristo, M.J., Tumey, S.J., 2013. The state of nuclear forensics. Nucl. Instrum. Methods Phys. Res., Sect. B 294, 656–661.

Kristo, M.J., Gaffney, A.M., Marks, N., Knight, K., Cassata, W.S., Hutcheon, I.D., 2016. Nuclear forensic science: analysis of nuclear material out of regulatory control. Ann. Rev. Earth Planet. Sci. 44, 555–579.

Kristo, M.J., Williams, R., Gaffney, A.M., Kayzar-Boggs, T.M., Schorzman, K.C., Lagerkvist, P., Vesterlund, A., Rameback, H., Nelwamondo, A.N., Kotze, D., et al., 2018. J. Radioanal. Nucl. Chem. 315, 425–434.

Kumho Tire, v., 1999. Charmichael, 526 U.S. 137.

L'Annunziata, M.F., 2007. Radioactivity: Introduction and History. Elsevier, Amsterdam, 609 pp.

L'Annunziata, M.F., 2016. Radioactivity: Introduction and History: From the Quantum to Quarks, second ed. Elsevier, Amsterdam. 902 pp.

LaMont, S.P., Hall, G., 2005. Uranium age determination by measuring the $^{230}Th/^{234}U$ ratio. J. Radioanal. Nucl. Chem. 264, 423–427.

Langan, R.T., Archibald, R.K., Lamberti, V.E., 2016. Nuclear forensics analysis with missing data. J. Radioanal. Nucl. Chem. 308 (2), 687–692.

Levi, M., 2007. On Nuclear Terrorism. Harvard University Press, Cambridge, MA, 210 pp.

Lewis, J.R., Zhang, A., Anderson-Cook, C.M., 2018. Comparing multiple statistical methods for inverse prediction in nuclear forensics applications. Chemometr. Intell. Lab. Syst. 175, 116–129.

Lin, M., Zhao, Y.G., Zhao, L.F., Li, L.L., Wang, F., Zhu, L.C., Hu, X.N., Ning, W., 2015. Tracing the origins of uranium ore concentrates (UOCs) by multidimensional statistical analysis of rare earth impurities. J. Anal. Atom. Spectrom. 30 (2), 396–402.

Maguire, H., Fraser, G., Croft, J., Bailer, M., Tattersall, P., Morrey, M., Turbitt, D., Ruggles, R., Bishop, L., Giraudon, I., et al., 2010. Assessing public health risk in the London polonium-210 incident, 2006. Public Health 124/6, 313–318.

Martin, F.S., Miles, G.L., 1956. The processing of irradiated uranium by high temperature oxidation reactions. In: Bruce, F.R., Fletcher, J.M., Hyman, H.H., Katz, J.J. (Eds.), Progress in Nuclear Energy," Series III, "Process Chemistry. McGraw-Hill Book Col, New York, pp. 329–341, 407 pp.

Mathew, K.J., Stanley, F.E., Thomas, M.R., Spencer, K.J., Colletti, L.P., Tandon, L., 2016. Critical need for plutonium and uranium isotopic standards with lower uncertainties. Anal. Meth. 8 (40), 7289–7305.

May, M., Davis, J., Jeanloz, R., 2006. Preparing for the worst. Nature 443, 907–908.

Mayer, K., Wallenius, M., 2000. Age determination of plutonium material in nuclear forensics by thermal ionisation mass spectrometry. Fresenius J. Anal. Chem. 366, 234–238.

Mayer, K., Wallenius, M., Ray, I., 2005. Nuclear forensics – a methodology providing clues on the origin of illicitly trafficked nuclear materials. Analyst 130, 443-441.

Mayer, K., Wallenius, M., Fanghanel, T., 2007. Nuclear forensic science – from cradle to maturity. J. Alloys Compd. 444–445, 50–56.

Mayer, K., Wallenius, M., Lutzenkirchen, K., Galy, J., Varga, Z., Erdmann, N., Buda, R., Kratz, J.-V., Traumtmann, N., Fiffeld, K., 2010. Nuclear forensics: a methodology applicable to nuclear security and to non-proliferation. J. Phys. Conf. Series 312, 1–9, 062003.

Mayer, K., Wallenius, Varga, Z., Wiss, T., Fanghanel, T., 2011. Investigative radiochemistry − a key element in nuclear forensics. Proc. Radiochim. Acta 1, 145−149.

Mayer, K., 2013. Security: expand nuclear forensics. Nature 503, 461−462.

Mayer, K., Wallenius, M., Varga, Z., 2015a. Interviewing a silent (radioactive) witness through nuclear forensic analysis. Anal. Chem. 87 (23), 11605−11610.

Mayer, K., Wallenius, M., Lutzenkirchen, K., Horta, J., Nicholl, A., Rasmussen, G., van Belle, P., Varga, Z., Buda, R., Erdmann, N., et al., 2015b. Uranium from German nuclear power projects of the 1940s: a nuclear forensic investigation. Angew. Chim. 54 (45), 12452−13456.

Meyers, L.A., Williams, R.W., Glover, S.E., LaMont, S.P., Stalcup, A.M., Spitz, H.B., 2013. Radiochronological age of a uranium metal sample from an abandoned facility. J. Radioanal. Nucl. Chem. 296 (2), 669−674.

Meyers, L.A., LaMont, S.P., Stalcup, A.M., Spitz, H.B., 2014. Uranium isotopic signatures measured in samples of direct collected at two former uranium facilities. J. Radioanal. Nucl. Chem. 301 (2), 307−313.

Migeon, V., Bourdon, B., Pili, E., Fitoussi, C., 2018. Molybdenum isotope fractionation during acid leaching of a granitic uranium ore. Geochem. Cosmochim. Acta 321, 30−49.

Moody, K.J., Hutcheon, I.D., Grant, P.M., 2015. Nuclear Forensic Analysis, 2d ed. Taylor & Francis, Boca Raton, FL, 502 pp.

Morgenstern, A., Apostolidis, C., Mayer, K., 2002. Age determination of highly enriched uranium: separation and analysis of ^{231}Pa. Anal. Chem. 75, 5513−5516.

National Research Council, 2004. Forensic analysis: weighing bullet lead evidence. In: Committee on Scientific Assessment of Bullet Lead Elemental Composition Comparison. National Academies Press, Washington DC, 228 pp.

Niemeyer, S., Koch, L., 2003. The nuclear smuggling International Technical Working Group: making a difference in combating illicit trafficking. In: Proceedings from the Conference on Advances in Destructive and Non-destructive Analysis for Environmental Monitoring and Nuclear Forensics, Karlsruhe, Germany, October 21-23, 2002. International Atomic Energy Agency, Vienna, pp. 17−19.

Oxford, V., October 10, 2007. Statement before the House Homeland Security Subcommittee on Emerging Threats. Cybersecurity and Science and Technology. Hearing on H.R. 2631, The Nuclear Forensics and Attribution Act.

Parsons-Davis, T., Knight, K., Fitzgerald, M., Stone, G., Caldeira, L., Kristo, M., 2018. Application of modern autoradiography to nuclear forensic analysis. Forensic Sci. Int. 286, 223−232.

Pajo, L., Tamborini, G., Rasmussen, G., Mayer, K., Koch, L., 2001a. A novel isotope analysis of oxygen in uranium oxides: comparison of secondary ion mass spectrometry, glow discharge mass spectrometry, and thermal ionization mass spectrometry. Spectrochim. Acta B 56, 541−549.

Pajo, L., Mayer, K., Koch, L., 2001b. Investigation of the oxygen isotopic composition in oxidic uranium compounds as a new property in nuclear forensic science. Fresenius J. Anal. Chem. 371, 348−352.

Potter, W.C., October 1995. Before the deluge? Assessing the threat of nuclear leakage from the post-Soviet States. Arms Control Today 9−16.

Richter, S., 1999. Isotopic "fingerprints" for natural uranium ore samples. Int. J. Mass Spectrom. 193, 9−14.

Robel, M., Kristo, M.J., Heller, M.A., 2009. Nuclear forensic inferences using multidimensional statistics. In: Proceedings of the 50th Annual Meeting of the Institute of Nuclear Materials Management, Tucson, AZ, July 12-16, 2009. Omnipress, Madison, WI.

Robel, M., Hutcheon, I.D., Kristo, M.J., Borg, L.E., Ramon, E.C., Williams, R.W., Lindvall, R.E., Gaffney, A.M., Genetti, V., 2011. The uranium sourcing database project: a comprehensive international nuclear forensics collaboration from ore to attribution. In: Proceedings of the 52nd Annual Meeting of the Institute of Nuclear Materials Management, Desert Springs, CA, July 17-21, 2011. Omnipress, Madison, WI.

Rolison, J.M., Treinen, K.C., McHugh, K.C., Gaffney, A.M., Williams, R.W., 2017. Application of the Ra-226-Th-230-U-234 and Ac227-Pa231-U235 radiochronometers to uranium certified reference materials. J. Radioanal. Nucl. Chem. 314 (3), 2459−2467.

Savina, J.A., Steeb, J.L., Savina, M.R., Mertz, C.J., Fortner, J.A., Sullivan, V.S., Bennett, M.E., Chamberlain, D.B., 2017. A non-destructive internal nuclear forensic investigation at Argonne: discovery of a Pu planchet from 1948. J. Radioanal. Nucl. Chem. 311 (1), 243−252.

Schwantes, J.M., Douglas, M., Bonde, S.E., Briggs, J.D., Farmer, O.T., Greenwood, L.R., Lepel, E.A., Orton, C.R., Wacker, J.F., Luksic, A.T., 2009. Nuclear archeology in a bottle: evidence of pre-trinity U.S. Weapons activities from a waste burial site. Anal. Chem. 81, 1297−1306.

Schwantes, J.M., 2013. Nuclear Forensics International Technical Working Group (ITWG): a collaboration of scientists, law enforcement officials, and regulators working to combat nuclear terrorism and proliferation. Abstract 164-ANYL in Abstracts of Papers of the American Chemical Society. In: Proceedings of the 246th National Meeting of the American Chemical Society, Indianapolis, IN, Sept. 8-12, 2013.

Schwantes, J.M., Marsden, O., Pellegrini, K.L., 2017. State of practice and emerging application of analytical techniques of nuclear forensic analysis: highlights from the 4th Collaborative Materials Exercise of the Nuclear Forensics International Technical Working group (ITWG). J. Radioanal. Nucl. Chem. 311 (2), 1441−1452.

Schwantes, J.M., Marsden, O., Reilly, D., 2018. Fourth collaborative materials exercise of the nuclear forensics international technical working group. J. Radioanal. Nucl. Chem. 315 (2), 347−352.

Scoles, S., June 11, 2015. How a uranium hunter sniffs out nuclear weapons. Wired. Found at: https://www.wired.com/story/how-a-uranium-hunter-sniffs-out-nuclear-weapons/.

Sheets, L.S., April 2008. A smuggler's story. The Atlantic Online. http://www.theatlantic.com/magazine/archive/2008/04/a-smuggler-8217-s-story/6736/.

Smith, D.K., Biro, T., Chartier, B., Mayer, K., Niemeyer, S., Thompson, P., 2007. Recent activities of the nuclear smuggling international technical working group to thwart illicit trafficking. In: Proceedings of the IAEA Conference on Illicit Nuclear Trafficking, Edinburgh, Scotland, November 19-22, 2007. International Atomic Energy Agency, Vienna, pp. 289−296.

Smith, D., Kristo, M., Niemeyer, S., Dudder, G., 2008. Documentation of a model action plan to deter illicit nuclear trafficking. J. Radioanal. Nucl. Chem. 276, 415−419.

Sokova, E.K., Potter, W.C., 2008. The 2003 and 2006 high enriched uranium seizures in Georgia. In: Proceedings of the IAEA Conference on Illicit Nuclear Trafficking, Edinburgh, Scotland, November 19-22, 2007. International Atomic Energy Agency, Vienna, pp. 405−423.

Spano, T.L., Simonetti, A., Wheeler, T., Carpenter, G., Freet, D., Balboni, E., Dorais, C., Burns, P., 2017. A novel nuclear forensic tool

involving deposit type normalized rare earth element signatures. Terra. Nova 29, 294–305.
Srncik, M., Mayer, K., Hrnecek, E., Wallenius, M., Varga, Z., Steier, P., Wallner, G., 2011. Investigation of the $^{236}U/^{238}U$ isotope abundance ratio in uranium ores and yellow cake samples. Radiochim. Acta 99, 335–339.
Stanley, F.E., 2012. A beginner's guide to uranium chronometry in nuclear forensics and safeguards. J. Anal. At. Spectrom. 11, 1821–1830.
Stork, C.L., Ummel, C.C., Stuart, D.S., Bodily, S., Goldblum, B.L., 2017. Dynamic analysis environment for nuclear forensic analyses. Comp. Phys. Comm. 210, 60–71.
Stromberg, S., February 2013. CSI: Tennessee—enter the world of nuclear forensics. Smithsonian. Found at: https://www.smithsonianmag.com/innovation/csi-tennesseeenter-the-world-of-nuclear-forensics-3982961/.
Svedkauskaite-LeGore, J., Mayer, K., Millet, S., Nicholl, A., Rasmussen, G., Baltrunas, D., 2007. Investigation of the isotopic composition of lead and of trace elements concentrations in natural uranium materials as a signature in nuclear forensics. Radiochim. Acta 95, 601–605.
Svedkauskaite-LeGore, J., Rasmussen, G., Abousahl, S., van Belle, P., 2008. Investigation of the sample characteristics needed for the determination of the origin of uranium-bearing materials. J. Radioanal. Nucl. Chem. 278, 201–209.
Talmadge, C., Spring 2007. Deterring a nuclear 9/11. The Washington Quarterly 21–34.
Tamborini, G., Phinney, D., Bildstein, O., Betti, M., 2002. Oxygen isotopic measurements by secondary ion mass spectrometry in uranium oxide microparticles: a nuclear forensic diagnostic. Anal. Chem. 74, 6098–6101.
Treinen, K.C., Kinman, W.S., Chen, Y., Zhu, L.C., Cardon, A.M.R., Steiner, R.E., Kayzar-Boggs, T.M., Williams, R.W., Zhao, Y.G., 2017. US-DOE and CIAE international cooperation in age-dating uranium standards. J. Radioanal. Nucl. Chem. 314, 2469–2474.
Varga, Z., Wallenius, M., Mayer, K., Keegan, E., Millet, S., 2009. Application of lead and strontium isotope ratio measurements for the origin assessment of uranium ore concentrates. Anal. Chem. 81, 8327–8334.
Varga, Z., Wallenius, M., Mayer, K., 2010. Origin Assessment of uranium ore concentrates based on their rare-earth elemental impurity pattern. Radiochim. Acta 98, 771–778.
Varga, Z., Wallenius, M., Mayer, K., Meppen, M., 2011. Analysis of uranium ore concentrates for origin assessment. Proc. Radiochim. Acta 1, 1–4. https://doi.org/10.1524/rcpr.2011.0004.
Varga, Z., Nichol, A., Wallenius, M., Mayer, K., 2012. Development and validation of a methodology for uranium radiochronometry reference material preparation. Anal. Chim. Acta 718, 25–31.
Varga, Z., Mayer, K., Bonamici, C.E., Hubert, A., Hutcheon, I., Kinman, W., Kristo, M., Pointurier, F., Spencer, K., Stanley, F., Steiner, R., Tandon, L., Williams, R., 2015a. Validation of reference materials for uranium radiochronometry in the frame of nuclear forensic investigations. Appl. Rad. Isotopes 102, 81–86.
Varga, Z., Venchiarutti, C., Nicholl, A., Krajko, J., Jakopic, R., Mayer, K., Richter, S., Aregbe, Y., 2015b. IRMM-1000a and IRMM-1000b uranium reference materials certified for the production date, Part I: methodology, preparation, and target characteristics. J. Radioanal. Nucl. Chem. 307, 1077–1085.
Varga, V., Nicholl, A., Zsigria, J., Wallenius, M., Mayer, K., 2018. Methodology for the preparation and validation of plutonium age dating materials. Anal. Chem. 90 (6), 4019–4024.
Venchiarutti, C., Varga, Z., Richter, S., Jakopic, R., Mayer, K., Aregbe, Y., 2015. REIMEP-22 interlaboratory comparison: "U Age Dating- determination of the production date of a uranium certified test sample. Radiochim. Acta 103 (12), 825–834.
Vogel, G., 2002. Crime and (puny) punishment. Science 298, 952–953.
Wallenius, M., Mayer, K., Ray, I., 2006. Nuclear forensic investigations: two case studies. Forensic Sci. Int. 156, 55–62.
Wallenius, M., Lutzenkirchen, K., Mayer, K., Ray, I., Aldave de las Heras, L., Betti, M., Cromboom, O., Hild, M., Lynch, B., Nicholl, A., et al., 2007. Nuclear forensic investigations with a focus on plutonium. J. Alloys Compd. 444–445, 57–62.
Whitman, C.I., Compton, V., Holden, R.B., 1957. Zone melting of uranium. J. Electrochem. Soc. 104, 240–244.
Williams, R.W., Gaffney, A.M., 2011. ^{230}Th-^{234}U model ages of some uranium standard reference materials. Proc. Radiochim. Acta 1, 31–35. https://doi.org/10.1524/rcpr.2011.0005.
Wilcken, K.M., Fifield, L.K., Barrows, T.T., Tims, S.G., Gladkis, L.G., 2008. Nucleogenic ^{36}Cl, ^{236}U and ^{239}Pu in uranium ores. Nucl. Instr. Meth. Phys. Res., Sect. B 266, 3614–3624.
Zaitseva, L., Steinhausler, F., April 2014. Nuclear trafficking issues in the Black Sea Region. EU Non-Proliferation. Paper No. 39.

Michael J. Kristo



Michael Kristo is an associate program leader for LLNL's Nuclear Forensics Materials Analysis Program and Group Leader for LLNL's Chemical and Isotopic Signatures Group. Dr. Kristo is the principal investigator on a wide variety of projects in the areas of nuclear forensics, nonproliferation, and international collaboration. He is particularly interested in the application of novel mass spectrometric techniques, imaging methods, and multidimensional statistics to nuclear forensics problems. Mike has a PhD in Analytical Chemistry from Michigan State University and a BS in Chemistry from the University of Notre Dame. After obtaining his PhD, Mike spent 4 years as an Air Force officer in the Air Force Technical Applications Center and 12 years as a scientist, analyst, and manager at Charles Evans and Associates, a commercial materials analysis company in Silicon Valley.

Appendix A

PERPUSTAKAAN PRIBADI AN-NUR SUNARYA

Table of radioactive isotopes

Michael F. L'Annunziata
The Montague Group, Oceanside, CA, United States

Chapter outline

I. Introduction **953**
A. Column I—nuclide 953
B. Column 2—half-life 953
C. Column 3—decay mode 953
D. Column 4—radiation characteristics 954
E. Column 5—decay product 954
F. Some applications of radiation type, energy, and intensity data 954
References 1012

I. Introduction

Data on the half-life, modes of decay, types of radiation emitted, radiation energies, and intensities of the predominate radiation emissions of radioactive isotopes are given in the following table. The isotopes are listed in order of increasing atomic number. Not all of the isotopes are listed here. The table includes commonly measured radionuclides, fission products, fission radioactivation products, radionuclides used in medical therapy and diagnosis, daughter radionuclides, and specific radionuclides referred to in this book. Some radionuclides of short half-life are listed because of their increasing applications and importance in the field of nuclear medicine. Decay products of the radionuclides are also provided. Radionuclides of atomic number $Z > 100$ are short-lived, many of which are isotopes of newly discovered elements. Only the longest-lived isotopes of these elements are listed in the table.

Information available on radionuclide decay modes and radiations is encyclopedic and complex. The most detailed sources of information are obtained from the National Nuclear Data Center, Brookhaven National Laboratory, Upton, NY, via the Internet database NuDat 2.7 (2018) [http://www.nndc.bnl.gov/nudat2/chartNuc.jsp] as well as the International Atomic Energy Agency (IAEA) database available via the Internet (IAEA Live Chart of Nuclides, https://www-nds.iaea.org/relnsd/vcharthtml/VChartHTML.html). Numerous volumes of the *Nuclear Data Sheets* published by Academic Press/Elsevier and edited by McCutchan (2018) are also available for additional information. Other important sources are Michael Lederer et al. (1978), Browne et al., (1986) and Firestone et al. (1996). Limited information of practical importance to scientists, who need to measure radionuclide activity, is provided in the table for ready access. For more detailed information and for radioisotopes not listed in the table provided here, the reader should consult the online references listed above. An explanation of the information in this table and examples of practical applications are provided in the following paragraphs.

A. Column I—nuclide

The radionuclides are listed here in order of increasing atomic number, Z, and under headings by element. When more than one radioisotope is given under the same element, these are listed in order of increasing mass number, A.

B. Column 2—half-life

The values of half-life given here are in units of microseconds (μs), milliseconds (ms) seconds (s), minutes (m), hours (h), days (d), and years (y). The values are those of the total half-life, which would be their decay rate if measured over a period of time.

C. Column 3—decay mode

The modes of decay are designated in this column as follows: α represents decay by alpha-particle emission; β^- signifies decay by negative beta-particle (negatron) emission; β^+ indicates decay by positive beta-particle (positron) emission; EC is electron capture; IT is isomeric transition; $\beta^- n$ is delayed-neutron emission in which β^- emitters

decay to unstable nuclides, which undergo instantaneous neutron emission; and SF refers to spontaneous fission. When more than one mode of decay occurs, the percentages of occurrence are given in parentheses beside the decay mode, and the total percentage should sum to 100. No percentage is given when only one mode of decay is cited, as it is understood that this is the only significant decay mode. Some radioisotopes are listed as decaying by $\beta^+ + \text{EC}$ without any percentage of occurrence given. In these cases, the β^+ decay mode is observed, and the later EC mode is inferred theoretically.

D. Column 4—radiation characteristics

The radiations listed are as follows: α is alpha-particle emission, β^- is negative beta-particle or negatron radiation, β^+ is positive beta-particle or positron emission, γ is gamma radiation, $\gamma^{\pm}$ is annihilation radiation, and n is neutron emission. Internal conversion electron and Auger electron emissions are grouped into the category of atomic electron emissions denoted by the symbol e^-. The average energies of the electron emissions in MeV are provided in brackets { } with the total intensity of the electron emissions given as a percentage enclosed in parenthesis alongside the brackets. Atomic electron emissions are listed when the average energy and intensity are significant in radionuclide detection and measurement. In certain cases, the specific energy lines of the most predominant atomic electron emissions are provided in MeV without brackets, and the intensities of the electron emission line provided as a percentage enclosed in parenthesis. X-rays are also given when emitted with significant intensity. Since x-rays are characteristic of the daughter nucleus, these are expressed with the symbol of the daughter nuclide as well as the atomic shell (K or L) of the daughter from which the x-rays originate.

The energies in MeV and intensities (percent) of the major radiations emitted are listed in this column. The energy values (MeV) are given without units and the known percent intensities of the emissions are enclosed in parentheses. The energies of beta particles are those of $E_{\max}$. The intensities of α- and β radiation emissions are added up to 100%. When the α- and β decay branches are numerous, only the major branches are listed. The principle γ-photon emission lines are listed with their percent intensities alongside enclosed in parenthesis. A percent intensity signifies the percentage of nuclides that would emit a given radiation. For example, the values γ 0.847 (100%) in the table for $^{56}_{27}$Co signifies that ^{56}Co nuclides emit a gamma ray of 0.847 MeV, and one gamma-ray photon of 0.847 MeV energy would be emitted in each ^{56}Co decay. Radiation intensities less than 100% would indicate the number of radionuclides out of 100 that would emit a given radiation type and/or radiation energy. Radiation intensities greater than 100% can also occur. For example, $\gamma^{\pm}$ 0.511 (180%) in the table under radiation characteristics of ^{22}Na signifies that annihilation radiation is produced (the energy of which is invariably 0.511 MeV), and the intensity of this emission is 180% in the case of ^{22}Na. Thus, for every 100 nuclides of ^{22}Na that decay, there is an expectancy of 180 photons of gamma rays as annihilation radiation. It should be noted here that the percent intensity (abundance) of annihilation radiation throughout this table is expressed as twice the value of the percent intensity of β^+ radiation, because each positron annihilation is accompanied by the emission of two gamma-ray photons of 0.511 MeV. Note that in the table alongside ^{22}Na, the percent intensity of β^+ radiation is 90%; that is, for every 100 nuclides of ^{22}Na that decay, 90 are expected to decay by positron emission.

E. Column 5—decay product

The daughter nuclide is listed in this column. More than one daughter is possible when more than one decay mode can occur. Under such circumstances the decay modes are listed with the corresponding symbol in parentheses (α, β^-, β^+, EC, or IT) alongside the decay product.

F. Some applications of radiation type, energy, and intensity data

A description of the radiation types and their energies and intensities may be used to judge which instrumental detection method could be employed to obtain an optimum detection efficiency for a particular radionuclide. As an example, from the table the nuclide $^{56}_{27}$Co may be cited. Both β^+ (two decay transitions with $E_{\max} = 1.46$ and 0.443 MeV) and γ emissions (several) are listed. However, the relatively low intensity of the β^+ emissions (19%) indicates that it may be less appropriate to assay for ^{56}Co by gas ionization or liquid scintillation counting of the positron radiation. Rather, solid scintillation counting of the more intense gamma rays and high-energy positrons may be preferable to obtain the highest counting efficiency possible. In contrast, another example can be taken from the table whereby we can conclude from the information provided that the liquid scintillation counting efficiency of $^{129}_{53}$I should be appreciably greater than the solid scintillation counting efficiency due to the greater intensity of beta radiation (100%) and atomic electrons (165%) than gamma rays (9%) emitted during ^{129}I decay.

The beta-particle energies and intensities may also be used to judge whether Cherenkov counting could serve as an appropriate means of radionuclide assay. For example, the table indicates that two beta-decay transitions can occur in the decay of $^{115m}_{48}$Cd. The principal transition occurs with the emission of beta particles of $E_{\max} = 1.62$ MeV at a 97% intensity. The other transition ($E_{\max} = 0.68$ MeV) is less significant, because it has a lower frequency of occurrence (3% intensity). In view of the threshold energy of 0.263

MeV for the production of Cherenkov photons by beta particles in water (see Chapter 6, Volume 2), and taking into account that beta radiation is emitted with a continuous spectrum of energies between zero and E_{max}, it can be estimated that an appreciable number of the beta particles emitted from ^{115m}Cd possess an energy greater than 0.263 MeV. Cherenkov counting of ^{115m}Cd should then be an appropriate technique for the assay of this nuclide, keeping in mind that liquid scintillation counting of the beta particles emitted from ^{115m}Cd would be a more efficient, although more expensive, counting technique.

In contrast to the preceding case, the energies and intensities of the beta particles emitted from $^{125}_{51}$Sb, listed in the table serve as an example of radiation data, which indicate that only a relatively small percentage of the beta particles emitted by this nuclide have energies greater than 0.263 MeV. Consequently, Cherenkov counting would not be an efficient method for the assay of ^{125}Sb; instead, liquid scintillation counting should be employed.

The nuclide $^{95}_{41}$Nb is another illustrative example that may be taken from the table. In this case, both beta particles and gamma rays are emitted with equal intensity, indicating that detection methods suitable for either the beta particles or gamma rays may be appropriate. However, liquid scintillation detection of the beta radiation would provide higher counting efficiencies than solid scintillation detection of the gamma radiation.

Illustrated in this table are numerous examples of the electron capture (EC) decay process, also known as *K*-capture, which is accompanied generally by the emission of gamma radiation, and the transitions produced in the electron orbital energy levels result in the emission of energy as x-rays. In such cases (e.g., $^{49}_{23}$V, $^{53}_{25}$Mn and $^{71}_{32}$Ge in the table) solid scintillation counting of the x-radiation may be the chosen assay method, although liquid scintillation analysis of atomic electron and x-ray-emitting nuclides is also possible (see Chapter 6, Volume 1).

The energy lines of alpha-particle emissions and their intensities, provided in this table, serve as useful references for the analysis of radionuclides by alpha spectrometry (see Chapter 5, Volume 1). The most predominant gamma energy lines and their intensities are vital in gamma spectrometric analysis with semiconductor detectors (see Chapter 4, Volume 1).

Table of radioactive isotopes

Nuclide $^{A}_{Z}X$	Half-life	Decay mode	Radiation characteristics: energies (MeV) [intensities (%)]	Decay product $^{A}_{Z}Y$
Hydrogen				
$^{3}_{1}$H	12.35 y	β^-	β^- 0.0186 (100%)	$^{3}_{2}$He
Helium				
$^{6}_{2}$He	0.807 s	β^-	β^- 3.51 (100%)	$^{6}_{3}$Li
Beryllium				
$^{7}_{4}$Be	53.3 d	EC	γ 0.478 (10.4%)	$^{7}_{3}$Li
$^{10}_{4}$Be	1.6×10^6y	β^-	β^- 0.555 (100%)	$^{10}_{5}$B
Carbon				
$^{11}_{6}$C	20.38 m	β^+ (>99%) EC (0.2%)	β^+ 0.961 (>99%) $\gamma^{\pm}$ 0.511 (200%)	$^{11}_{5}$B
$^{14}_{6}$C	5730 y	β^-	β^- 0.155 (100%)	$^{14}_{7}$N
Nitrogen				
$^{13}_{7}$N	9.96 m	β^+	β^+ 1.190 (100%) $\gamma^{\pm}$ 0.511 (200%)	$^{13}_{6}$C
$^{16}_{7}$N	7.13 s	β^-	β^- 10.42 (28.0%), 4.29 (66.2%), 5.30 (4.8%), 1.55 (1.0%) γ 7.12 (5%), 6.13 (67%), 2.74 (0.8%)	$^{16}_{8}$O
$^{17}_{7}$N	4.14 s	β^- n (95.1%) β^- (4.9%)	β^- 3.7 (100%) *n* 0.383 (34.8%), 0.884 (0.6%), 1.17 (52.7%), 1.70 (7%) γ 0.871 (3%), 2.18 (0.3%)	$^{17}_{8}$O (β^-) $^{16}_{8}$O (β^- *n*)

Continued

Table of radioactive isotopes—cont'd

Nuclide $^{A}_{Z}X$	Half-life	Decay mode	Radiation characteristics: energies (MeV) [intensities (%)]	Decay product $^{A}_{Z}Y$
Oxygen				
$^{14}_{8}O$	70.6 s	β^+	β^+ 4.12 (0.6%), 1.81 (99.3%) γ 2.31 (99%), 1.64 (0.1%) $\gamma^{\pm}$ 0.511 (199.8%)	$^{14}_{7}N$
$^{15}_{8}O$	2.03 m	β^+ (>99%) EC (0.1%)	β^+ 1.723 (100%) $\gamma^{\pm}$ 0.511 (200%)	$^{15}_{7}N$
Fluorine				
$^{18}_{9}F$	109.7 m	β^+ (96.7%) EC (3.3%)	β^+ 0.634 (96.7%) $\gamma^{\pm}$ 0.511 (193.4%)	$^{18}_{8}O$
Sodium				
$^{22}_{11}Na$	2.60 y	β^+ (90%) EC (10%)	β^+ 1.830 (0.06%), 0.540 (90%) γ 1.275 (100%) $\gamma^{\pm}$ 0.511 (180%)	$^{22}_{10}Ne$
$^{24}_{11}Na$	15.0 h	β^-	β^- 1.390 (100%) γ 1.37 (100%), 2.75 (100%), 3.87 (0.06%)	$^{24}_{12}Mg$
Magnesium				
$^{27}_{12}Mg$	9.46 m	β^-	β^- 1.77 (71.0%), 1.60 (29.0%) γ 1.01 (28%), 0.843 (72%), 0.170 (0.8%)	$^{27}_{13}Al$
$^{28}_{12}Mg$	21 h	β^-	β^- 0.459 (100%) γ 1.350 (60%), 0.947 (30%), 0.400 (30%), 0.31 (96%)	$^{28}_{13}Al$
Aluminum				
$^{26}_{13}Al$	7.2×10^5 y	β^+ (82%) EC (18%)	β^+ 1.160 (82%) γ 1.809 (100%), 1.130 (4%) $\gamma^{\pm}$ 0.511 (164%)	$^{26}_{12}Mg$
$^{28}_{13}Al$	2.24 m	β^-	β^- 2.865 (100%) γ 1.780 (100%)	$^{28}_{14}Si$
$^{29}_{13}Al$	6.5 m	β^-	β^- 2.41 (89.9%), 1.65 (3.8%), 1.25 (6.3%) γ 2.43 (6%), 2.03 (4%), 1.27 (91%), 1.05 (1%)	$^{29}_{14}Si$
Silicon				
$^{31}_{14}Si$	2.62 h	β^-	β^- 1.486 (100%) γ 1.266 (0.07%)	$^{31}_{15}P$
$^{32}_{14}Si$	153 y	β^-	β^- 0.224 (100%)	$^{32}_{15}P$
Phosphorus				
$^{30}_{15}P$	2.50 m	β^+	β^+ 3.21 (99.8%), 0.975 (0.1%) γ 2.24 (0.1%) $\gamma^{\pm}$ 0.511 (199.8%)	$^{30}_{14}Si$
$^{32}_{15}P$	14.28 d	β^-	β^- 1.710 (100%)	$^{32}_{16}S$
$^{33}_{15}P$	25.3 d	β^-	β^- 0.249 (100%)	$^{33}_{16}S$
Sulfur				
$^{35}_{16}S$	87.4 d	β^-	β^- 0.167 (100%)	$^{35}_{17}Cl$
$^{37}_{16}S$	5.05 m	β^-	β^- 4.87 (5.6%), 1.76 (94.0%), 1.12 (0.3%), 0.855 (0.1%) γ 3.74 (0.3%), 3.10 (94%)	$^{37}_{17}Cl$
$^{38}_{16}S$	170.3 m	β^-	β^- 2.94 (13.0%), 1.24 (0.2%), 1.19 (2.4%), 0.995 (83.0%), 0.186 (1.4%) γ 2.75 (1%), 1.94 (83%), 1.75 (2.4%), 1.69 (0.2%)	$^{38}_{17}Cl$

Continued

Table of radioactive isotopes—cont'd

Nuclide $^{A}_{Z}X$	Half-life	Decay mode	Radiation characteristics: energies (MeV) [intensities (%)]	Decay product $^{A}_{Z}Y$
Chlorine				
$^{34m}_{17}$Cl	32.0 m	β^+ (54.3%) EC (1.1%) IT (44.6%)	β^+ 2.49 (28.4%), 1.31 (25.6%), 0.500 (0.3%) γ 3.30 (12%), 2.13 (43%), 1.18 (14%), 0.146 (41%) $\gamma^{\pm}$ 0.511 (108.6%) e^- 0.146 (0.6%), 0.143 (6%), ~0.002 (7%) Cl *K* x-rays ~0.003 (0.5%)	$^{34}_{16}$S (β^+ EC) $^{34}_{17}$Cl (IT)
$^{34}_{17}$Cl	1.53 s	β^+	β^+ 4.47 (100%) $\gamma^{\pm}$ 0.511 (200%)	$^{34}_{16}$S
$^{36}_{17}$Cl	3.0×10^5 y	β^- (98.1%) EC (1.9%) β^+ (0.014%)	β^- 0.714 (98.1%) $\gamma^{\pm}$ 0.511 (0.028%) e^- 0.002 (2%) S *K* x-rays ~0.002 (0.1%)	$^{36}_{18}$Ar (β^-) $^{36}_{16}$S (EC, β^+)
$^{38}_{17}$Cl	37.3 m	β^-	β^- 4.913 (57.6%), 2.77 (11.1%), 1.11 (31.3%) γ 1.64 (31%), 2.17 (42%)	$^{38}_{18}$Ar
$^{39}_{17}$Cl	56.2 m	β^-	β^- 3.44 (7.1%), 2.18 (4.5%), 1.92 (83.0%), 1.08 (2.6%), 0.939 (2.2%), 0.612 (0.6%) γ 1.52 (39%), 1.27 (54%), 1.09 (2%), 0.985 (2%) 0.250 (46%)	$^{39}_{18}$Ar
Argon				
$^{37}_{18}$Ar	35.1 d	EC	Cl *K* x-rays ~ 0.002 (8.7%)	$^{37}_{17}$Cl
$^{39}_{18}$Ar	269 y	β^-	β^- 0.565 (100%)	$^{39}_{19}$K
$^{41}_{18}$Ar	109.6 m	β^-	β^- 2.49 (0.8%), 1.20 (99.2%) γ 1.29 (99%)	$^{41}_{19}$K
$^{42}_{18}$Ar	32.9 y	β^-	β^- 0.600 (100%)	$^{42}_{19}$K
Potassium				
$^{38}_{19}$K	7.64 m	β^+	β^+ 4.89 (0.1%), 2.72 (99.3%), 0.955 (0.1%) γ 3.94 (0.1%), 2.17 (100%) $\gamma^{\pm}$ 0.511 (199%)	$^{38}_{18}$Ar
$^{40}_{19}$K	1.26×10^9 y	β^- (89%) EC (11%) β^+ (0.001%)	β^- 1.325 (89%) γ 1.460 (11%) Ar *K* x-rays ~ 0.003 (0.9%)	$^{40}_{20}$Ca (β^-) $^{40}_{18}$Ar (EC)
$^{42}_{19}$K	12.32 h	β^-	β^- 3.53 (81.9%), 2.00 (17.6%), 1.69 (0.3%), 1.10 (0.1%), 0.080 (0.1%) γ 1.525 (18%), 0.312 (0.3%)	$^{42}_{20}$Ca
$^{43}_{19}$K	22.3 h	β^-	β^- 1.82 (1.5%), 1.44 (1.0%), 1.22 (4.1%), 0.825 (90.8%), 0.421 (2.6%) γ 1.02 (2%), 0.617 (79%), 0.593 (11%), 0.397 (12%), 0.373 (87%), 0.221 (5%)	$^{43}_{20}$Ca
Calcium				
$^{41}_{20}$Ca	1.1×10^5 y	EC	K *K* x-rays ~0.003 (12.5%), K *L* x-rays (0.02%)	$^{41}_{19}$K
$^{45}_{20}$Ca	165.1 d	β^-	β^- 0.258 (100%)	$^{45}_{21}$Sc
$^{47}_{20}$Ca	4.54 d	β^-	β^- 1.98 (16.1%), 0.684 (83.9%) γ 1.30 (77%), 0.808 (5%), 0.489 (5%)	$^{47}_{21}$Sc
$^{49}_{20}$Ca	8.72 m	β^-	β^- 2.89 (0.5%), 2.18 (90.2%), 1.74 (0.1%), 1.19 (8.2%), 0.769 (0.7%), 0.524 (0.3%) γ 4.07 (8%), 3.08 (91%), 2.37 (0.6%), 1.40 (0.6%)	$^{49}_{21}$Sc

Continued

Table of radioactive isotopes—cont'd

Nuclide $^{A}_{Z}X$	Half-life	Decay mode	Radiation characteristics: energies (MeV) [intensities (%)]	Decay product $^{A}_{Z}Y$
Scandium				
$^{43}_{21}$Sc	3.89 h	β^+ (88.1%) EC (11.9%)	β^+ 1.20 (70.9%), 0.826 (17.2%) γ 0.373 (22%) $\gamma^{\pm}$ 0.511 (176%) Ca *K* x-rays ~ 0.004 (2%)	$^{43}_{20}$Ca
$^{44m}_{21}$Sc	2.44 d	IT (98.6%) EC (1.4%)	γ 1.14 (2.7%), 1.02 (1.3%), 0.271 (86%) e^- {0.032} (22%) Sc *K* x-rays (2%)	$^{44}_{21}$Sc (IT) $^{44}_{20}$Ca (EC)
$^{44}_{21}$Sc	3.92 h	β^+ (95%) EC (5%)	β^+ 1.47 (95%) γ 1.159 (100%) $\gamma^{\pm}$ 0.511 (190%)	$^{44}_{20}$Ca
$^{46}_{21}$Sc	83.8 d	β^-	β^- 0.357 (100%) γ 1.120 (100%), 0.889 (100%)	$^{46}_{22}$Ti
$^{47}_{21}$Sc	3.42 d	β^-	β^- 0.610 (26%), 0.450 (74%) γ 0.159 (73%)	$^{47}_{22}$Ti
$^{48}_{21}$Sc	43.7 h	β^-	β^- 0.659 (90.0%), 0.483 (10.0%) γ 1.31 (100%), 1.21 (2%), 1.04 (98%), 0.983 (100%), 0.175 (8%)	$^{48}_{22}$Ti
Titanium				
$^{44}_{22}$Ti	48.2 y	EC	γ 0.078 (98%), 0.068 (90%) e^- {0.011} (100%) Sc *K* x-rays ~ 0.004 (19%)	$^{44}_{21}$Sc
$^{45}_{22}$Ti	184.8 m	β^+ (84.8%) EC (15.2%)	β^+ 1.04 (84.8%) γ 0.719 (0.2%) $\gamma^{\pm}$ 0.511 (169.6%) e^- ~ 0.003 (11%), ~0.0004 (23%) Sc *K* x-rays 0.004 (3%)	$^{45}_{21}$Sc
Vanadium				
$^{47}_{23}$V	32.6 m	β^+ (96.5%) EC (3.5%)	β^+ 1.91 (96.5%) γ 1.79 (0.2%), 0.159 (0.1%) $\gamma^{\pm}$ 0.511 (193.0%) e^- ~ 0.004 (2%), ~0.0004 (5%) Ti *K* x-rays ~ 0. 005 (0.7%)	$^{47}_{22}$Ti
$^{48}_{23}$V	16.0 d	β^+ (49.9%) EC (50.1%)	β^+ 0.698 (49.9%) γ 2.24 (3%), 1.31 (97%), 0.983 (100%), 0.945 (10%) $\gamma^{\pm}$ 0.511 (99.8%) e^- 0.004 (35%), ~0.0004 (76%) Ti *K* x-rays ~ 0.005 (10%)	$^{48}_{22}$Ti
$^{49}_{23}$V	327 d	EC	e^- {0.004} (78%) Ti *K* x-rays ~ 0.004 (19%)	$^{49}_{22}$Ti
Chromium				
$^{49}_{24}$Cr	42.3 m	β^+ (92.8%) EC (7.2%)	β^+ 1.61 (11.7%), 1.51 (34.7%), 1.45 (46.4%) γ 0.152 (30%), 0.091 (53%), 0.062 (16%) $\gamma^{\pm}$ 0.511 (185.6%) e^- 0.147 (2%), 0.085 (1%), 0.057 (1%), ~0.004 (8%) V *K* x-rays ~ 0.005 (2%)	$^{49}_{23}$V

Continued

Table of radioactive isotopes—cont'd

Nuclide $^{A}_{Z}X$	Half-life	Decay mode	Radiation characteristics: energies (MeV) [intensities (%)]		Decay product $^{A}_{Z}Y$
$^{51}_{24}$Cr	27.7 d	EC	γ e^-	0.320 (10%) {0.003} (67%) V *K* x-rays ~ 0.005 (22%)	$^{51}_{23}$V
Manganese					
$^{51}_{25}$Mn	46.2 m	β^+ (97.1%) EC (2.9%)	β^+ $\gamma^{\pm}$ e^-	2.19 (96.9%), 1.44 (0.2%) 0.511 (194.2%) ~ 0.005 (2%) Cr *K* x-rays ~ 0.005 (0.6%)	$^{51}_{24}$Cr
$^{52}_{25}$Mn	5.60 d	EC (72%) β^+ (28%)	β^+ γ $\gamma^{\pm}$	0.575 (28%) 1.43 (100%), 0.935 (84%), 0.774 (82%) 0.511 (56%) Cr *K* x-rays ~ 0.005 (17%)	$^{52}_{24}$Cr
$^{52m}_{25}$Mn	21.1 m	β^+ + EC IT (2%)	β^+ γ	2.63 1.43 (100%), 0.377 (2%)	$^{52}_{24}$Cr
$^{53}_{25}$Mn	3.7×10^6 y	EC	e^-	{0.003} (65%) Cr *K* x-rays ~ 0.005 (25%)	$^{53}_{24}$Cr
$^{54}_{25}$Mn	312.2 d	EC	γ e^-	0.835 (100%) {0.003} (64%) Cr *K* x-rays ~ 0.005 (24%)	$^{54}_{24}$Cr
$^{56}_{25}$Mn	2.57 h	β^-	β^- γ	2.83 (47%), 1.03 (34%), 0.718 (18%), 0.30 (~1%) 2.11 (15%), 1.81 (29%), 0.847 (99%)	$^{56}_{26}$Fe
$^{57}_{25}$Mn	85.4 s	β^-	β^- γ e^-	2.68 (75.0%), 2.56 (15.0%), 2.32 (2.2%), 1.99 (6.3%), 1.68 (0.4%), 1.06 (1.1%) 1.61 (0.7%), 0.692 (6%), 0.364 (0.4%), 0.352 (2%), 0.136 (2%), 0.122 (14%), 0.014 (10%) {0.011} (260%) Fe *K* x-rays 0.007 (3%), ~0.006 (24%)	$^{57}_{26}$Fe
Iron					
$^{52}_{26}$Fe	8.27 h	β^+ (56%) EC (44%)	β^+ γ $\gamma^{\pm}$	0.804 (56%) 0.169 (100%), 0.378 (2%) 0.511 (112%) Mn *K* x-rays ~ 0.006 (13%)	$^{52m}_{25}$Mn
$^{55}_{26}$Fe	2.68 y	EC	e^-	{0.004} (102%) Mn *K* x-rays ~ 0.006 (27%)	$^{55}_{25}$Mn
$^{59}_{26}$Fe	44.5 d	β^-	β^- γ	1.57 (0.30%), 0.475 (51.2%), 0.273 (48.5%) 1.29 (43%), 1.09 (57%), 0.192 (3%), 0.143 (1%)	$^{59}_{27}$Co
$^{60}_{26}$Fe	1.5×10^6 y	β^-	β^- γ e^-	0.181 (100%) 0.059 (2%) 0.057 (14%), 0.051 (81%), 0.006 (50%), ~0.001 (129%) Co *K* x-rays ~0.007 (30%)	$^{60}_{27}$Co
Cobalt					
$^{55}_{27}$Co	17.53 h	β^+ (75.9%) EC (24.1%)	β^+ γ $\gamma^{\pm}$ e^-	1.50 (46.0%), 1.11 (4.3%), 1.02 (25.6%) 1.41 (17%), 1.37 (3%), 1.32 (7%), 0.931 (75%), 0.804 (2%), 0.477 (20%) 0.511 (151.8%) ~ 0.006 (14%), ~0.001 (33%) Fe *K* x-rays ~ 0.007 (7%)	$^{55}_{26}$Fe

Continued

Table of radioactive isotopes—cont'd

Nuclide $^{A}_{Z}X$	Half-life	Decay mode	Radiation characteristics: energies (MeV) [intensities (%)]	Decay product $^{A}_{Z}Y$
$^{56}_{27}$Co	78.7 d	EC (81%) β^+ (19%)	β^+ 1.46 (18%), 0.443 (1%) γ 3.26 (13%), 2.60 (17%), 2.02 (11%), 1.76 (15%), 1.24 (66%), 1.04 (15%), 0.847 (100%) $\gamma^{\pm}$ 0.511 (38%) e^- {0.004} (111%) Fe *K* x-rays ~ 0.006 (24%)	$^{56}_{26}$Fe
$^{57}_{27}$Co	271.6 d	EC	γ 0.136 (11%), 0.122 (87%), 0.014 (9%) Fe *K* x-rays ~ 0.006 (55%)	$^{57}_{26}$Fe
$^{58}_{27}$Co	70.78 d	EC (85%) β^+ (15%)	β^+ 0.474 (15%) γ 1.67 (0.6%), 0.865 (1.4%), 0.810 (99%) $\gamma^{\pm}$ 0.511 (30%) e^- {0.004} (118%) Fe *K* x-rays ~ 0.006 (26%)	$^{58}_{26}$Fe
$^{60}_{27}$Co	5.27 y	β^-	β^- 1.49 (0.1%), 0.670 (0.2%), 0.315 (99.7%) γ 1.33 (100%), 1.17 (100%)	$^{60}_{28}$Ni
Nickel				
$^{56}_{28}$Ni	6.1 d	EC	γ 0.158 (100%), 0.269 (34%), 0.480 (32%), 0.750 (48%), 0.812 (75%), 1.56 (13%) e^- {0.007} (140%) Co *K* x-rays ~ 0.007 (33.5%)	$^{56}_{27}$Co
$^{57}_{28}$Ni	35.6 h	EC (56.5%) β^+ (43.5%)	β^+ 0.865 (35.3%), 0.737 (7.0%), 0.485 (0.8%), 0.323 (0.4%) γ 1.92 (12%), 1.76 (6%), 1.38 (82%), 0.127 (17%) $\gamma^{\pm}$ 0.511 (87.0%) e^- 0.119 (0.3%), 0.006 (31%), ~0.001 (76%) Co *K* x-rays ~ 0.008 (2%), ~0.007 (17%)	$^{57}_{27}$Co
$^{59}_{28}$Ni	8×10^4 y	EC (>99%) β^+ (trace)	e^- {0.004} (13.6%) Co *K* x-rays ~ 0.004 (33%)	$^{59}_{27}$Co
$^{63}_{28}$Ni	100.1 y	β^-	β^- 0.066 (100%)	$^{63}_{29}$Cu
$^{65}_{28}$Ni	2.517 h	β^-	β^- 2.14 (59%), 1.02 (11%), 0.650 (30%) γ 1.49 (25%), 1.12 (16%), 0.368 (5%)	$^{65}_{29}$Cu
$^{66}_{28}$Ni	54.6 h	β^-	β^- 0.252 (100%)	$^{66}_{29}$Cu
Copper				
$^{60}_{29}$Cu	23.7 m	β^+ (92.4%) EC (7.6%)	β^+ 3.77 (5.0%), 2.95 (15.0%), 2.48 (2.8%), 1.98 (49.0%), 1.91 (11.6%), 1.84 (4.6%), 1.71 (0.8%), 1.37 (0.8%), 1.18 (0.2%), 1.10 (0.2%), 1.08 (0.9%), 1.03 (1.2%), 0.611 (0.2%) γ 3.12 (5%), 2.16 (3%), 1.86 (5%), 1.79 (45%), 1.33 (88%), 1.04 (4%), 0.952 (3%), 0.826 (22%), 0.467 (4%) $\gamma^{\pm}$ 0.511 (184.8%) e^- ~ 0.007 (4%), ~0.001 (3%) Ni *K* x-rays ~ 0.008 (3%)	$^{60}_{28}$Ni
$^{61}_{29}$Cu	3.41 h	β^+ (62%) EC (38%)	β^+ 1.22 (52%), 1.15 (2%), 0.94 (5%), 0.56 (3%) γ 1.19 (5%), 0.657 (11%), 0.373 (3%), 0.284 (12%), 0.067 (4%) $\gamma^{\pm}$ 0.511 (124%) e^- {0.002} (53%) Ni *K* x-rays ~ 0.007 (14%)	$^{61}_{28}$Ni

Continued

Table of radioactive isotopes—cont'd

Nuclide $^{A}_{Z}X$	Half-life	Decay mode	Radiation characteristics: energies (MeV) [intensities (%)]	Decay product $^{A}_{Z}Y$
$^{62}_{29}$Cu	9.67 m	β^+ (97.4%) EC (2.6%)	β^+ 2.93 (97.2%), 1.75 (0.1%), 0.877 (0.1%) γ 1.17 (0.3%), 0.875 (0.2%) $\gamma^{\pm}$ 0.511 (194.8%) e^- 0.006 (1.1%), ~0.001 (2.9%) Ni *K* x-rays ~ 0.008 (0.1%), ~0.007 (0.7%)	$^{62}_{28}$Ni
$^{64}_{29}$Cu	12.70 h	EC (41%) β^- (40%) β^+ (19%)	β^- 0.573 (40%) β^+ 0.657 (19%) γ 1.34 (0.6%) $\gamma^{\pm}$ 0.511 (38%) e^- {0.002} (79%) Ni *K* x-rays ~ 0.007 (16%)	$^{64}_{28}$Ni (EC, β^+) $^{64}_{30}$Zn (β^-)
$^{67}_{29}$Cu	62.0 h	β^-	β^- 0.577 (20%), 0.484 (35%), 0.395 (45%) γ 0.185 (47%), 0.092 (23%) Zn *K* x-rays ~ 0.008 (6%)	$^{67}_{30}$Zn
Zinc				
$^{62}_{30}$Zn	9.18 h	EC (91.6%) β^+ (8.4%)	β^+ 0.605 (8.4%) γ 0.596 (26%), 0.548 (15%), 0.507 (15%), 0.040 (26%) $\gamma^{\pm}$ 0.511 (16.8%) e^- 0.040 (2%), 0.032 (15%), 0.007 (52%), 0.0001 (139%) Cu *K* x-rays 0.009 (5%), 0.008 (38%)	$^{62}_{29}$Cu
$^{63}_{30}$Zn	38.47 m	β^+ (92.7%) EC (7.3%)	β^+ 2.34 (80.3%), 1.67 (7.0%), 1.38 (4.9%), 0.932 (0.5%) γ 1.41 (0.8%), 0.962 (7%), 0.669 (8%), 0.450 (0.2%) $\gamma^{\pm}$ 0.511 (185.4%) e^- 0.007 (4%), ~0.001 (9%) Cu *K* x-rays 0.009 (0.3%), 0.008 (2%)	$^{63}_{29}$Cu
$^{65}_{30}$Zn	244.0 d	EC (98.5%) β^+ (1.5%)	β^+ 0.325 (1.5%) γ 1.115 (50%) $\gamma^{\pm}$ 0.511 (3.0%) e^- {0.004} (98%) Cu *K* x-rays ~0.008 (38%)	$^{65}_{29}$Cu
$^{69m}_{30}$Zn	13.76 h	IT (>99%) β^- (0.03%)	γ 0.439 (95%) Zn *K* x-rays ~ 0.008 (2%)	$^{69}_{30}$Zn
$^{69}_{30}$Zn	55.6 m	β^-	β^- 0.897 (100%)	$^{69}_{31}$Ga
Gallium				
$^{66}_{31}$Ga	9.45 h	β^+ (57%) EC (43%)	β^+ 4.15 (51%), 1.84 (1%), 0.935 (3%), 0.747 (1%), 0.367 (1%) γ 4.30 (5%), 2.75 (25%), 2.18 (5%), 1.04 (37%), 0.828 (5%) $\gamma^{\pm}$ 0.511 (114%) e^- {0.002} (55%) Zn *K* x-rays ~ 0.008 (18%)	$^{66}_{30}$Zn
$^{67}_{31}$Ga	78.26 h	EC	γ 0.388 (7%), 0.296 (22%), 0.184 (24%), 0.093 (40%) e^- {0.033} (200%) Zn *K* x-rays ~ 0.008 (55%)	$^{67}_{30}$Zn
$^{68}_{31}$Ga	68.33 m	β^+ (90%) EC (10%)	β^+ 1.90 (90%) γ 1.87 (0.15%), 1.24 (0.14%), 1.078 (3.5%), 0.80 (0.4%) $\gamma^{\pm}$ 0.511 (180%) Zn *K* x-rays ~ 0.008 (5%)	$^{68}_{30}$Zn

Continued

Table of radioactive isotopes—cont'd

Nuclide $^{A}_{Z}X$	Half-life	Decay mode	Radiation characteristics: energies (MeV) [intensities (%)]	Decay product $^{A}_{Z}Y$
$^{70}_{31}$Ga	21.1 m	β^- (99.6%) EC (0.4%)	β^- 1.65 (98.9%), 0.613 (0.6%), 0.437 (0.3%) γ 1.04 (0.7%), 0.180 (0.3%)	$^{70}_{32}$Ge (β^-) $^{70}_{30}$Zn (EC)
$^{72}_{31}$Ga	14.12 h	β^-	β^- 3.16 (8%), 2.53 (9%), 1.51 (10%), 0.959 (31%), 0.637 (42%) γ 2.50 (20%), 2.20 (26%), 1.86 (5%), 1.60 (5%), 1.46 (3.5%), 1.05 (7%), 0.894 (10%), 0.835 (96%), 0.630 (27%), 0.601 (8%)	$^{72}_{32}$Ge
$^{73}_{31}$Ga	4.86 h	β^-	β^- 1.53 (7.0%), 1.23 (78.0%), 1.20 (7.1%), 1.04 (0.5%), 0.699 (0.2%), 0.678 (0.1%), 0.461 (7.0%), 0.207 (0.1%) γ 0.739 (4%), 0.326 (11%), 0.297 (80%) e^- {0.057} (385%)	$^{73}_{32}$Ge
Germanium				
$^{66}_{32}$Ge	2.26 h	EC (76.4%) β^+ (23.6%)	β^+ 1.03 (7.2%), 1.01 (0.7%), 0.970 (0.7%), 0.700 (12.0%), 0.540 (2.7%), 0.370 (0.3%) γ 0.706 (4%), 0.472 (3%), 0.382 (28%), 0.338 (9%), 0.302 (3%), 0.273 (11%), 0.246 (5%), 0.190 (6%), 0.182 (6%), 0.108 (11%), 0.065 (7%), 0.044 (29%) $\gamma^{\pm}$ 0.511 (47.2%) e^- {0.019} (215%) Ga *K* x-rays ~ 0.010 (49%)	$^{66}_{31}$Ga
$^{67}_{32}$Ge	18.9 m	β^+ (90.2%) EC (9.8%)	β^+ 3.03 (74%), 2.37 (1.0%), 2.12 (3.5%), 1.56 (7.5%), 1.39 (4.1%), 1.22 (0.1%) γ 1.47 (5%), 0.914 (3%), 0.911 (3%), 0.828 (3%), 0.729 (2%), 0.167 (84%) $\gamma^{\pm}$ 0.511 (180.4%) e^- 0.008 (3%), ~0.001 (8%) Ga *K* x-rays ~ 0.010 (3%)	$^{67}_{31}$Ga
$^{68}_{32}$Ge	275 d	EC	e^- {0.004} (121%) Ga *K* x-rays ~ 0.010 (44%)	$^{68}_{31}$Ga
$^{69}_{32}$Ge	39.1 h	EC (76.4%) β^+ (23.6%)	β^+ 1.21 (21.0%), 0.631 (2.3%), 0.333 (0.3%) γ 1.34 (5%), 1.11 (36%), 0.872 (12%), 0.574 (13%) $\gamma^{\pm}$ 0.511 (47.2%) e^- 0.008 (33%), ~0.001 (94%) Ga *K* x-rays ~ 0.010 (34%)	$^{69}_{31}$Ga
$^{71}_{32}$Ge	11.15 d	EC	e^- {0.005} (122%) Ga *K* x-rays ~ 0.010 (44%)	$^{71}_{31}$Ga
$^{77}_{32}$Ge	11.30 h	β^-	β^- 2.20 (42%), 1.38 (35%), 0.710 (23%) γ 1.09 (6%), 0.93 (5%), 0.80 (6%), 0.73 (14%), 0.632 (11%), 0.553 (18%), 0.417 (25%), 0.368 (15%), 0.263 (45%), 0.21 (61%) e^- {0.008} (8%)	$^{77}_{33}$As
Arsenic				
$^{71}_{33}$As	65.3 h	EC (71.7%) β^+ (28.3%)	β^+ 0.816 (27.9%), 0.491 (0.2%), 0.466 (0.2%) γ 1.10 (4%), 0.450 (4%), 0.327 (3%), 0.175 (82%) $\gamma^{\pm}$ 0.511 (56.6%) e^- 0.164 (7%), 0.012 (3%), 0.008 (33%), ~0.001 (99%) Ge *K* x-rays ~ 0.010 (39%)	$^{71}_{32}$Ge
$^{72}_{33}$As	26.0 h	β^+ (87.7%) EC (12.3%)	β^+ 3.33 (16.3%), 2.64 (0.7%), 2.50 (64.2%), 1.87 (5.8%), 0.932 (0.2%), 0.819 (0.5%) γ 1.46 (1%), 1.05 (1%), 0.834 (81%), 0.630 (8%) $\gamma^{\pm}$ 0.511 (175.4%) e^- 0.680 (2%), 0.008 (6%), ~0.001 (16%) Ge *K* x-rays ~ 0.010 (7%)	$^{72}_{32}$Ge

Continued

Table of radioactive isotopes—cont'd

Nuclide $^{A}_{Z}X$	Half-life	Decay mode	Radiation characteristics: energies (MeV) [intensities (%)]	Decay product $^{A}_{Z}Y$
$^{73}_{33}$As	80.3 d	EC	γ 0.053 (10%) e^- 0.052 (11%), 0.042 (75%), 0.013 (9%), 0.011 (60%), 0.002 (28%), ~0.001 (318%) Ge *K* x-rays ~ 0.010 (102%)	$^{73}_{32}$Ge
$^{74}_{33}$As	17.79 d	EC (37%) β^+ (31%) β^- (32%)	β^+ 1.53 (4%), 0.941 (27%) β^- 1.35 (17%), 0.717 (15%) γ 0.635 (14%), 0.596 (61%) $\gamma^{\pm}$ 0.511 (62%) Ge *K* x-rays ~ 0.010 (17%)	$^{74}_{32}$Ge (EC, β^+) $^{74}_{34}$Se (β^-)
$^{76}_{33}$As	26.32 h	β^-	β^- 2.97 (50%), 2.41 (31%), 1.78 (7%), 1.18 (3%), 0.540 (3%), 0.320 (3%) γ 1.22 (5%), 0.657 (6%), 0.559 (43%)	$^{76}_{34}$Se
$^{77}_{33}$As	38.8 h	β^-	β^- 0.679 (100%) γ 0.522 (0.8%), 0.239 (2.5%), 0.086 (0.1%)	$^{77m}_{34}$Se
Selenium				
$^{72}_{34}$Se	8.4 d	EC	γ 0.045 (57%) e^- 0.044 (4%), 0.034 (38%), 0.009 (53%), ~0.001 (167%) As *K* x-rays ~ 0.012 (8%), 0.011 (62%)	$^{72}_{33}$As
$^{73}_{34}$Se	7.15 h	β^+ (65.3%) EC (34.7%)	β^+ 1.65 (0.6%), 1.29 (64.7%) γ 0.361 (97%), 0.067 (70%) $\gamma^{\pm}$ 0.511 (130.6%) e^- 0.349 (1%), 0.065 (2%), 0.055 (17%), 0.009 (21%), ~0.001 (65%) As *K* x-rays ~ 0.011 (28%)	$^{73}_{33}$As
$^{75}_{34}$Se	119 d	EC	γ 0.401 (12%), 0.280 (25%), 0.265 (60%), 0.136 (57%), 0.121 (17%), 0.097 (3.3%), 0.066 (1%) e^- {0.014} (145%) As *K* x-rays ~ 0.011 (55%)	$^{75}_{33}$As
$^{77m}_{34}$Se	17.4 s	IT	γ 0.162 (53%) e^- {0.072} (99%) Se *K* x-rays ~ 0.011 (23%)	$^{77}_{34}$Se
$^{79m}_{34}$Se	3.92 m	IT (99.94%) β^- (0.06%)	γ 0.095 (10%) e^- {0.082} (221%) Se *K* x-rays ~ 0.012 (5%), ~0.011 (36%)	$^{79}_{34}$Se (IT) $^{79}_{35}$Br (β^-)
$^{79}_{34}$Se	6.5×10^4 y	β^-	β^- 0.160 (100%)	$^{79}_{35}$Br
$^{81m}_{34}$Se	57.3 m	IT (99.95%) β^- (0.05%)	β^- 1.15 (0.05%) γ 0.103 (12%) e^- {0.088} (210%)	$^{81}_{34}$Se (IT) $^{81}_{35}$Br (β^-)
$^{81}_{34}$Se	18.5 m	β^-	β^- 1.59 (98.7%), 1.02 (0.8%), 0.757 (0.4%) γ 0.829 (0.3%), 0.566 (0.2%), 0.290 (0.6%), 0.275 (0.7%)	$^{81}_{35}$Br
Bromine				
$^{75}_{35}$Br	96.7 m	β^+ (72.8%) EC (27.2%)	β^+ 2.01 (4.0%), 1.72 (52.0%), 1.58 (4.9%), 1.42 (1.2%), 1.34 (3.3%), 1.23 (0.5%), 1.15 (3.4%), 1.11 (1.0%), 1.01 (0.1%), 0.988 (0.7%), 0.934 (0.4%), 0.824 (0.3%), 0.829 (0.4%), 0.763 (0.6%) γ 0.952 (2%), 0.912 (1%), 0.733 (2%), 0.609 (2%), 0.572 (2%), 0.433 (4%), 0.428 (4%), 0.378 (4%), 0.293 (3%), 0.141 (7%), 0.112 (2%), 0.007 (5%) $\gamma^{\pm}$ 0.511 (145.6%) e^- 0.274 (0.3%), 0.010 (10%), ~0.001 (32%) Se *K* x-rays ~ 0.012 (2%), 0.011 (13%)	$^{75}_{34}$Se

Continued

Table of radioactive isotopes—cont'd

Nuclide $^{A}_{Z}X$	Half-life	Decay mode	Radiation characteristics: energies (MeV) [intensities (%)]	Decay product $^{A}_{Z}Y$
$^{76}_{35}$Br	16.2 h	β^+ (54.7%) EC (45.3%)	β^+ 3.94 (6.0%), 3.38 (25.8%), 2.82 (2.1%), 2.72 (2.8%), 2.25 (0.4%), 2.15 (1.0%), 1.51 (0.5%), 1.43 (0.4%), 1.31 (0.3%), 1.29 (0.2%), 1.27 (1.2%), 0.990 (5.2%), 0.871 (6.3%), 0.781 (1.4%), 0.589 (1.0%), 0.482 (0.1%) γ 2.95 (7%), 2.79 (6%), 2.39 (5%), 1.85 (15%), 1.23 (11%), 1.13 (5%), 0.657 (15%), 0.559 (74%) $\gamma^{\pm}$ 0.511 (109.4%) e^- 0.010 (16%), ~0.001 (52%) Se *K* x-rays ~ 0.012 (24%)	$^{76}_{34}$Se
$^{77}_{35}$Br	57.0 h	EC (99.3%) β^+ (0.7%)	β^+ 0.336 (0.7%) γ 1.00 (1.3%), 0.818 (3%), 0.775 (2%), 0.58 (7%), 0.520 (24%), 0.300 (6%), 0.239 (30%) $\gamma^{\pm}$ 0.511 (1.4%) e^- {0.008} (116%) Se *K* x-rays ~ 0.012 (52%)	$^{77m}_{34}$Se
$^{80m}_{35}$Br	4.42 h	IT	γ 0.049 (0.3%), 0.037 (39%) e^- {0.061} (378%) Br *K* x-rays 0.013 (10%), 0.012 (68%)	$^{80}_{35}$Br
$^{80}_{35}$Br	17.68 m	β^- (91.7%) EC (6.1%) β^+ (2.2%)	β^- 2.00 (85%), 1.39 (6.2%), 0.747 (0.3%), 0.683 (0.2%) β^+ 0.849 (2.2%) γ 1.26 (0.1%), 0.704 (0.2%), 0.665 (1.1%), 0.639 (0.3%) 0.616 (6.7%) $\gamma^{\pm}$ 0.511 (4.4%) e^- 0.010 (2.1%), 0.0013 (6.9%) Se *K* x-rays ~ 0.012 (3.2%)	$^{80}_{36}$Kr (β^-) $^{80}_{34}$Se (EC, β^+)
$^{82}_{35}$Br	35.3 h	β^-	β^- 0.444 (100%) γ 1.47 (17%), 1.32 (26%), 1.04 (29%), 0.828 (25%), 0.777 (83%), 0.698 (27%), 0.619 (41%), 0.554 (66%)	$^{82}_{36}$Kr
Krypton				
$^{77}_{36}$Kr	74.4 m	β^+ (81.5%) EC (18.5%)	β^+ 2.04 (2.5%), 1.91 (41.5%), 1.88 (0.3%), 1.77 (33.8%), 1.62 (2.7%), 1.18 (0.3%), 1.07 (0.2%), 1.02 (0.2%) γ 0.312 (4%), 0.276 (3%), 0.147 (37%), 0.130 (81%) $\gamma^{\pm}$ 0.511 (163.0%) e^- {0.020} (70%) Br *K* x-rays ~ 0.013 (19%)	$^{77}_{35}$Br
$^{79}_{36}$Kr	35.0 h	EC (93%) β^+ (7%)	β^+ 0.613 (7%) γ 0.836 (2%), 0.606 (10%), 0.398 (10%), 0.261 (12%) $\gamma^{\pm}$ 0.511 (14%) Br *K* x-rays ~ 0.012 (51%)	$^{79}_{35}$Br
$^{81m}_{36}$Kr	13.1 s	IT	γ 0.190 (68%) e^- 0.188 (5%), 0.176 (27%), 0.011 (9%), ~0.002 (35%) Kr *K* x-rays 0.014 (2%), 0.013 (15%)	$^{81}_{36}$Kr
$^{81}_{36}$Kr	2.3×10^5 y	EC	γ 0.276 (0.3%) e^- 0.010 (31%), 0.0014 (110%) Br *K* x-rays 0.013 (7%), 0.012 (46%) Br *L* x-rays ~ 0.0015 (2%)	$^{81}_{35}$Br
$^{83m}_{36}$Kr	1.83 h	IT	γ 0.032 (0.05%), 0.009 (5%) e^- {0.038} (371%) Kr *K* x-rays ~ 0.013 (16%), Kr *L* x-rays ~ 0.002 (4%)	$^{83}_{36}$Kr

Continued

Table of radioactive isotopes—cont'd

Nuclide $^{A}_{Z}X$	Half-life	Decay mode	Radiation characteristics: energies (MeV) [intensities (%)]	Decay product $^{A}_{Z}Y$
$^{85m}_{36}$Kr	4.48 h	β^- (79%) IT (21%)	β^- 0.840 (79%) γ 0.305 (13%), 0.150 (74%) e^- {0.026} (22%) Rb *K* x-rays ~ 0.013 (2%), Kr *K* x-rays ~ 0.013 (4%)	$^{85}_{36}$Kr (IT) $^{85}_{37}$Rb (β^-)
$^{85}_{36}$Kr	10.70 y	β^-	β^- 0.672 (99.4%), 0.15 (0.6%) γ 0.514 (0.44%)	$^{85}_{37}$Rb
$^{87}_{36}$Kr	76.3 m	β^-	β^- 3.89 (30.5%), 3.48 (41.0%), 3.04 (7.3%), 2.15 (0.6%), 1.47 (5.5%), 1.33 (9.4%), 0.926 (4.4%), 0.579 (0.5%) γ 2.56 (4%), 2.55 (9%), 2.01 (3%), 1.74 (2%), 0.845 (7%), 0.402 (50%) e^- 0.387 (0.2%), ~0.002 (0.2%)	$^{87}_{37}$Rb
$^{88}_{36}$Kr	2.84 h	β^-	β^- 2.92 (14.0%), 1.72 (1.9%), 2.53 (0.3%), 2.06 (1.3%), 1.74 (1.0%), 1.20 (2.0%), 0.685 (9.1%), 0.525 (66.9%), 0.369 (2.7%), 0.146 (0.4%) γ 2.39 (35%), 2.23 (3%), 2.20 (13%), 2.04 (8%), 1.53 (11%), 0.835 (13%), 0.196 (26%) e^- 0.025 (2%), 0.012, (11%), 0.011 (4%), ~0.002 (15%) Rb *K* x-rays ~ 0.015 (1%), ~0.013 (7%)	$^{88}_{37}$Rb
$^{89}_{36}$Kr	3.15 m	β^-	β^- 4.99 (23.0%), 4.45 (7.3%), 3.66 (3.5%), 3.46 (2.7%), 3.29 (10.2%), 2.99 (2.4%), 2.83 (3.1%), 2.59 (6.8%), 2.39 (12.9%), 2.20 (1.5%), 2.12 (4.1%), 1.66 (4.0%), 1.27 (2.6%) γ 1.69 (4%), 1.53 (8%), 1.47 (7%), 1.32 (3%), 0.904 (7%), 0.867 (6%), 0.738 (4%), 0.586 (17%), 0.577 (6%), 0.497 (7%), 0.356 (4%), 0.220 (20%)	$^{89}_{37}$Rb
$^{90}_{36}$Kr	32.3 s	β^-	β^- 4.39 (29.0%), 4.27 (1.0%), 2.61 (65.0%), 2.26 (2.3%), 1.31 (2.1%) γ 1.78 (7%), 1.54 (10%), 1.12 (39%), 0.554 (5%), 0.539 (31%), 0.242 (10%), 0.122 (35%) e^- 0.107 (3%), 0.011 (1%), ~0.002 (4%) Rb *K* x-rays ~ 0.014 (2%)	$^{90}_{37}$Rb
Rubidium				
$^{81}_{37}$Rb	4.57 h	EC (72.8%) β^+ (27.2%)	β^+ 1.22 (0.1%), 1.03 (25.0%), 0.580 (1.8%), 0.516 (0.3%) γ 0.510 (5%), 0.456 (3%), 0.446 (24%), 0.190 (65%) $\gamma^{\pm}$ 0.511 (54.4%) e^- 0.189 (4%), 0.176 (26%), 0.011 (31%), ~0.002 (112%) Kr *K* x-rays 0.014 (8%), ~0.012 (50%)	$^{81}_{36}$Kr
$^{82m}_{37}$Rb	6.47 h	EC (78.9%) β^+ (21.1%)	β^+ 1.63 (0.2%), 1.35 (0.2%), 0.899 (0.2%), 0.798 (19.7%), 0.619 (0.6%), 0.436 (0.2%) γ 1.47 (16%), 1.32 (24%), 1.04 (32%), 0.828 (21%), 0.777 (84%), 0.698 (26%), 0.619 (38%), 0.554 (62%) $\gamma^{\pm}$ 0.511 (42.2%) e^- 0.011 (24%), ~0.002 (87%) Kr *K* x-rays 0.014 (6%), ~0.012 (39%)	$^{82}_{36}$Kr
$^{82}_{37}$Rb	1.27 m	β^+ (95.3%) EC (4.7%)	β^+ 3.38 (81.8%), 2.60 (13.1%), 1.90 (0.1%), 1.21 (0.3%) γ 0.777 (15%) $\gamma^{\pm}$ 0.511 (190.6%) e^- 0.011 (1%), ~0.002 (5%) Kr *K* x-rays 0.014 (0.3%), ~0.013 (2%)	$^{82}_{36}$Kr
$^{83}_{37}$Rb	86.2 d	EC	γ 0.552 (16%), 0.530 (29%), 0.521 (45%) e^- 0.011 (31%), ~0.002 (109%) Kr *K* x-rays ~ 0.014 (7%), ~0.013 (49%)	$^{83}_{36}$Kr

Continued

Table of radioactive isotopes—cont'd

Nuclide $^{A}_{Z}X$	Half-life	Decay mode	Radiation characteristics: energies (MeV) [intensities (%)]	Decay product $^{A}_{Z}Y$
$^{84m}_{37}$Rb	20.3 m	IT	γ 0.464 (33%), 0.248 (63%), 0.216 (31%) e^- 0.214 (5%), 0.200 (23%), 0.011 (9%), ~0.002 (34%) Rb *K* x-rays ~ 0.015 (2%), 0.013 (15%)	$^{84}_{37}$Rb
$^{84}_{37}$Rb	32.82 d	EC (70.4%) β^+ (25.7%) β^- (3.9%)	β^+ 1.66 (13.1%), 0.783 (12.6%) β^- 0.892 (3.9%) γ 0.883 (74%) $\gamma^{\pm}$ 0.511 (51.4%) e^- 0.011 (21%), ~0.002 (75%) Kr *K* x-rays ~ 0.014 (5%), ~0.013 (34%)	$^{84}_{36}$Kr (EC, β^+) $^{84}_{38}$Sr (β^-)
$^{86m}_{37}$Rb	1.02 m	IT	γ 0.556 (98%) e^- 0.554 (0.2%), 0.541 (2%), 0.011 (0.5%), ~0.002 (2%) Rb *K* x-rays ~ 0.014 (1%)	$^{86}_{37}$Rb
$^{86}_{37}$Rb	18.63 d	β^-	β^- 1.77 (91.4%), 0.697 (8.6%) γ 1.08 (9%)	$^{86}_{38}$Sr
$^{87}_{37}$Rb	4.8×10^{10} y	β^-	β^- 0.283 (100%)	$^{87}_{38}$Sr
Strontium				
$^{81}_{38}$Sr	22.3 m	β^+ (88.0%) EC (12.0%)	β^+ 2.91 (13.0%), 2.72 (6.4%), 2.60 (28.0%), 2.45 (16.5%), 3.33 (7.4%), 2.25 (1.0%), 2.19 (2.0%), 2.00 (8.1%), 1.66 (0.1%), 1.52 (3.3%), 1.37 (2.1%). 1.09 (0.1%) γ 0.938 (3%), 0.721 (4%), 0.575 (7%), 0.443 (18%), 0.188 (15%), 0.154 (34%), 0.148 (30%), 0.142 (3%) $\gamma^{\pm}$ 0.511 (176.0%) e^- 0.138 (2%), 0.133 (4%), 0.011 (6%), ~0.002 (21%) Rb *K* x-rays 0.015 (2%), 0.013 (10%)	$^{81}_{37}$Rb
$^{82}_{38}$Sr	25.35 d	EC	e^- 0.011 (28%), 0.0017 (106%) Rb *K* x-rays 0.015 (8%), ~0.002 (3%)	$^{82}_{37}$Rb
$^{83}_{38}$Sr	32.41 h	EC (76.9%) β^+ (23.1%)	β^+ 1.25 (10.0%), 1.21 (9.0%), 0.830 (3.1%), 0.449 (1.0%) γ 1.16 (3%), 0.763 (30%), 0.418 (4%), 0.582 (17%) $\gamma^{\pm}$ 0.511 (46.2%) e^- {0.026} (255%)	$^{83}_{37}$Rb
$^{85}_{38}$Sr	64.85 d	EC	γ 0.514 (100%) e^- {0.008} (104%) Rb *K* x-rays ~ 0.014 (58%)	$^{85}_{37}$Rb
$^{87m}_{38}$Sr	2.82 h	IT (99.7%) EC (0.3%)	γ 0.389 (82%) e^- 0.388 (0.3%), 0.386 (2%), 0.372 (15%), 0.012 (4%), 0.0018 (18%) Sr *K* x-rays ~ 0.016 (1%), 0.014 (9%), Sr *L* x-rays 0.0018 (0.5%)	$^{87}_{38}$Sr (IT) $^{87}_{37}$Rb (EC)
$^{89}_{38}$Sr	50.5 d	β^-	β^- 1.49 (100%)	$^{89m}_{39}$Y
$^{90}_{38}$Sr	28.8 y	β^-	β^- 0.546 (100%)	$^{90}_{39}$Y
$^{91}_{38}$Sr	9.65 h	β^-	β^- 1.128 (28.6%), 0.819 (3.4%), 0.524 (25.1%) 0.420 (1.8%), 0.405 (34.8%), 0.206 (2.1%) 0.154 (1.5%) γ 1.024 (33.5%), 0.750 (23.7%), 0.653 (8%)	$^{91}_{39}$Y
$^{92}_{38}$Sr	2.61 h	β^-	β^- 0.786 (~3%), 0.182 (97%) γ 1.384 (90%), 1.142, (2.8%), 0.953 (3.5%), 0.430 (3.3%)	$^{92}_{39}$Y

Continued

Table of radioactive isotopes—cont'd

Nuclide $^{A}_{Z}X$	Half-life	Decay mode	Radiation characteristics: energies (MeV) [intensities (%)]	Decay product $^{A}_{Z}Y$
Yttrium				
$^{86m}_{39}$Y	48.0 m	IT (99.3%) EC (0.3%) β^+ (0.4%)	β^+ 1.48 (0.4%) γ 0.208 (94%) $\gamma^{\pm}$ 0.511 (0.8%) e^- {0.020} (185%) Y *K* x-rays 0.015 (3%)	$^{86}_{39}$Y (IT) $^{86}_{38}$Sr (β^+, EC)
$^{86}_{39}$Y	14.74 h	EC (68.2%) β^+ (31.8%)	β^+ 3.14 (2.0%), 2.36 (1.0%), 1.99 (3.6%), 1.74 (1.7%), 1.55 (5.6%), 1.34 (0.7%), 1.22 (11.9%), 1.16 (1.3%), 1.03 (1.9%), 0.900 (1.1%), 0.856 (0.2%), 0.573 (0.3%), 0.452 (0.3%), 0.387 (0.2%) γ 1.92 (21%), 1.85 (17%), 1.15 (31%), 1.08 (83%), 0.777 (22%), 0.703 (15%), 0.646 (9%), 0.682 (33%), 0.580 (5%), 0.515 (5%), 0.443 (17%) $\gamma^{\pm}$ 0.511 (63.6%) e^- 0.012 (18%), ~0.002 (71%) Sr *K* x-rays 0.016 (6%), 0.014 (35%)	$^{86}_{38}$Sr
$^{87}_{39}$Y	79.8 h	EC (99.8%) β^+ (0.2%)	β^+ 0.451 (0.2%) γ 0.485 (92%), 0.388 (85%) $\gamma^{\pm}$ 0.511 (0.4%) e^- {0.080} (137%) Sr *K* x-rays ~ 0.015 (71%)	$^{87m}_{38}$Sr
$^{88}_{39}$Y	106.6 d	EC (99.8%) β^+ (0.2%)	β^+ 0.761 (0.2%) γ 1.84 (100%), 0.898 (91%) $\gamma^{\pm}$ 0.511 (0.4%) e^- {0.005} (100%) Sr *K* x-rays ~ 0.015 (60%)	$^{88}_{38}$Sr
$^{89m}_{39}$Y	16.0 s	IT	γ 0.909 (99%) e^- {0.008} (2%)	$^{89}_{39}$Y
$^{90}_{39}$Y	64.06 h	β^-	β^- 2.28 (100%)	$^{90}_{40}$Zr
$^{91}_{39}$Y	58.51 d	β^-	β^- 1.54 (100%) γ 1.21 (0.3%)	$^{91}_{40}$Zr
$^{92}_{39}$Y	3.54 h	β^-	β^- 1.57 (85.7%), 1.13 (3.5%), 0.923 (2.3%), 0.873 (1.2%), 0.484 (6.5%) γ 1.41 (4.8%), 0.934 (13.9%), 0.561 (2.4%)	$^{92}_{40}$Zr
$^{93}_{39}$Y	10.18 h	β^-	β^- 1.216 (89.5%), 1.089 (4.9%), 0.773 (2.7%) 0.236 (1.7%)	$^{93}_{40}$Zr
Zirconium				
$^{89}_{40}$Zr	78.4 h	EC (76.0%) β^+ (24.0%)	β^+ 0.902 (24.0%) γ 0.909 (99%) $\gamma^{\pm}$ 0.511 (48.0%) e^- 0.013 (19%), 0.002 (79%) Y *K* x-rays ~ 0.017 (7%), ~0.015 (41%)	$^{89}_{39}$Y
$^{93}_{40}$Zr	1.5×10^6 y	β^-	β^- 0.060 (~95%), 0.034 (~5%) e^- {0.028} (170%) Nb *K* x-rays ~ 0.017 (10%)	$^{93}_{41}$Nb
$^{95}_{40}$Zr	64.0 d	β^-	β^- 0.885 (2%), 0.396 (55%), 0.360 (43%) γ 0.756 (49%), 0.724 (49%)	$^{95m}_{41}$Nb
$^{97}_{40}$Zr	16.90 h	β^-	β^- 1.91 (~90%), 0.46 (~10%) e^- {0.015} (4%)	$^{97m}_{41}$Nb

Continued

Table of radioactive isotopes—cont'd

Nuclide $^{A}_{Z}X$	Half-life	Decay mode	Radiation characteristics: energies (MeV) [intensities (%)]	Decay product $^{A}_{Z}Y$
Niobium				
$^{92}_{41}$Nb	3.47×10^{7} y	EC	γ 0.935 (100%), 0.561 (134%) e^- 0.013 (22%), 0.002 (99%) Zr *K* x-rays ~ 0.018 (9%), ~0.016 (52%)	$^{92}_{40}$Zr
$^{93m}_{41}$Nb	13.7 y	IT	e^- {0.028} (170%) Nb *K* x-rays ~ 0.017 (10.5%)	$^{93}_{41}$Nb
$^{94}_{41}$Nb	2×10^{4} y	β^-	β^- 0.473 (100%) γ 0.702 (98%), 0.871 (100%)	$^{94}_{42}$Mo
$^{95}_{41}$Nb	34.97 d	β^-	β^- 0.924 (0.1%), 0.160 (99.9%) γ 0.766 (100%)	$^{95}_{42}$Mo
$^{95m}_{41}$Nb	86.64 h	IT (94.4%) β^- (5.6%)	β^- 1.16 (3.2%), 0.956 (2.4%) γ 0.234 (25%), 0.204 (2%) e^- {0.161} (138%) Nb *K* x-rays ~ 0.019 (6%), ~0.017 (36%)	$^{95}_{41}$Nb (IT) $^{95}_{42}$Mo (β^-)
$^{97m}_{41}$Nb	1.0 m	IT	γ 0.743 (98%) e^- {0.016} (4%)	$^{97}_{41}$Nb
$^{97}_{41}$Nb	72.1 m	β^-	β^- 1.27 (100%) γ 1.02 (1%), 0.658 (98%)	$^{97}_{42}$Mo
Molybdenum				
$^{93m}_{42}$Mo	6.85 h	IT (99.88%) EC (0.12%)	γ 1.48 (99%), 0.685 (100%), 0.263 (57%) e^- {0.103}(85%) Mo *K* x-rays 0.020 (3%), ~0.017 (20%)	$^{93}_{42}$Mo (IT) $^{93}_{41}$Nb (EC)
$^{93}_{42}$Mo	3500 y	EC	e^- {0.032} (254%) Nb *K* x-rays ~ 0.017 (73%), Nb *L* x-rays ~ 0.002 (6%)	$^{93}_{41}$Nb
$^{99}_{42}$Mo	66.02 h	β^-	β^- 1.21 (84%), 0.840 (2%), 0.450 (14%) γ 0.780 (4%), 0.740 (12%), 0.181 (7%), 0.041 (2%) e^- {0.018} (32%) Tc *K* x-rays ~ 0.019 (11%)	$^{99m}_{43}$Tc
Technetium				
$^{94m}_{43}$Tc	52.0 m	β^+ (70.1%) EC (29.9%)	β^+ 2.44 (67.6%), 1.45 (0.9%), 1.24 (0.3%), 0.917 (0.9%), 0.570 (0.4%) γ 3.13 (1%), 1.87 (6%), 1.52 (5%), 0.993 (2%), 0.871 (94%) $\gamma^{\pm}$ 0.511 (140.2%) e^- ~ 0.015 (6%), ~0.002 (29%) Mo *K* x-rays ~ 0.020 (3%), ~0.017 (17%)	$^{94}_{42}$Mo
$^{94}_{43}$Tc	293.0 m	EC (89.5%) β^+ (10.5%)	β^+ 0.811 (10.5%) γ 1.59 (2%), 0.916 (8%), 0.871 (100%), 0.850 (96%), 0.742 (1%), 0.703 (100%), 0.532 (2%), 0.449 (3%) $\gamma^{\pm}$ 0.511 (21.0%) e^- 0.063 (1%), 0.015 (18%), ~0.002 (86%) Mo *K* x-rays ~ 0.020 (9%), ~0.017 (51%)	$^{94}_{42}$Mo
$^{95m}_{43}$Tc	61 d	EC (95.7%) IT (3.9%) β^+ (0.4%)	γ 0.204 (66%), 0.582 (31%), 0.786 (9%), 0.835 (28%) β^+ 0.708 (0.2%), 0.504 (0.2%) $\gamma^{\pm}$ 0.511 (0.8%) e^- 0.0139 MeV (102%) Mo *K* x-rays ~ 0.018 (66%)	$^{95}_{42}$Mo (EC) $^{95}_{43}$Tc (IT)
$^{95}_{43}$Tc	20.0 h	EC	γ 0.947 (2%), 0.767 (94%) e^- 0.015 (20%), ~0.002 (96%) Mo *K* x-rays ~ 0.020 (10%), ~0.017 (57%)	$^{95}_{42}$Mo

Continued

Table of radioactive isotopes—cont'd

Nuclide $^{A}_{Z}X$	Half-life	Decay mode	Radiation characteristics: energies (MeV) [intensities (%)]	Decay product $^{A}_{Z}Y$
$^{97}_{43}$Tc	2.6×10^6 y	EC	e^- {0.005} (91%) Mo *K* x-rays ~ 0.018 (66%)	$^{97}_{42}$Mo
$^{98}_{43}$Tc	4.2×10^6 y	β^-	β^- 0.398 (100.0%) γ 0.745 (102%), 0.652 (100%)	$^{98}_{44}$Ru
$^{99m}_{43}$Tc	6.00 h	IT	γ 0.140 (90%) e^- {0.014} (21%) Tc *K* x-rays ~ 0.019 (7%)	$^{99}_{43}$Tc
$^{99}_{43}$Tc	2.14×10^5 y	β^-	β^- 0.292 (100%)	$^{99}_{44}$Ru
$^{100}_{43}$Tc	15.5 s	β^- (99.99%) EC (1.8×10^{-3}%)	β^- 3.20 (93.3%), 2.67 (0.8%), 2.07 (5.4%) γ 1.51 (0.3%), 0.591 (5.4%), 0.539 (6.6%) Ru *K* x-rays ~ 0.019 (0.03%)	$^{100}_{44}$Ru (β^-) $^{100}_{42}$Mo (EC)
Ruthenium				
$^{97}_{44}$Ru	2.88 d	EC	γ 0.324 (8%), 0.215 (91%) e^- {0.013} (97%) Tc *K* x-rays ~ 0.019 (70%)	$^{97}_{43}$Tc
$^{103}_{44}$Ru	39.35 d	β^-	β^- 0.725 (3.5%), 0.225 (91%), 0.117 (5.3%) γ 0.610 (6%), 0.497 (88%) e^- {0.041} (181%) Rh *K* x-rays ~ 0.021 (6%)	$^{103m}_{45}$Rh
$^{105}_{44}$Ru	4.44 h	β^-	β^- 1.79 (2.6%), 1.53 (0.5%), 1.45 (2.1%), 1.19 (47.8%), 1.12 (35.7%), 0.949 (4.0%), 0.573 (3.5%), 0.541 (1.0%) γ 0.724 (47%), 0.676 (16%), 0.469 (18%), 0.393 (4%), 0.316 (11%), 0.263 (7%) e^- 0.126 (7%), 0.107 (15%), 0.017 (3%), 0.0024 (21%) Rh *K* x-rays ~ 0.023 (2%), ~0.020 (10%)	$^{105}_{45}$Rh
$^{106}_{44}$Ru	366.5 d	β^-	β^- 0.039 (100%)	$^{106}_{45}$Rh
Rhodium				
$^{100}_{45}$Rh	20.8 h	EC (96.1%) β^+ (3.9%)	β^+ 2.61 (2.4%), 2.07 (1.2%), 1.48 (0.2%), 1.25 (0.1%) γ 0.446 (11%), 0.539 (78%), 0.822 (20%), 1.11 (13%), 1.36 (15%), 1.55 (21%), 1.93 (12%), 2.37 (35%) $\gamma^{\pm}$ 0.511 (7.8%) e^- {0.0077} (84%) Ru *K* x-rays ~ 0.019 (66%)	$^{100}_{44}$Ru
$^{101m}_{45}$Rh	4.34 d	EC (92.8%) IT (7.2%)	γ 0.545 (4%), 0.307 (81%) e^- 0.154 (2%), 0.134 (5%), ~0.016 (17%), ~0.0025 (91%) Ru *K* x-rays ~ 0.022 (10%), 0.019 (52%)	$^{101}_{44}$Ru (EC) $^{101}_{45}$Rh (IT)
$^{101}_{45}$Rh	3.3 y	EC	γ 0.325 (12%), 0.198 (73%), 0.127 (68%) e^- {0.027} (142%) Ru *K* x-rays ~ 0.022 (12%), 0.019 (66%)	$^{101}_{44}$Ru
$^{102m}_{45}$Rh	207.3 d	EC (63.3%) β^+ (14.7%) β^- (22.0%)	β^+ 1.30 (10.5%), 0.826 (4.2%) β^- 1.15 (20.0%), 0.593 (2.0%) γ 1.10 (2.9%), 0.628 (4.5%), 0.556 (2%), 0.475 (46%), 0.468 (3%) $\gamma^{\pm}$ 0.511 (29.4%) e^- 0.016 (10.7%), 0.003 (56%) Ru *K* x-rays ~ 0.022 (6.4%), 0.019 (35.3%) Ru *L* x-rays ~ 0.002 (2.7%)	$^{102}_{44}$Ru (EC, β^+) $^{102}_{46}$Pd (β^-)
$^{102}_{45}$Rh	3.7 y	EC (99.8%) IT (0.2%)	γ 1.11 (22%), 1.05 (41%), 0.768 (30%), 0.698 (41%), 0.632 (54%), 0.475 (95%), 0.418 (13%) e^- {0.012} (89%) Ru *K* x-rays ~ 0.022 (67%)	$^{102}_{44}$Ru (EC) $^{102}_{45}$Rh (IT)

Continued

Table of radioactive isotopes—cont'd

Nuclide $^{A}_{Z}X$	Half-life	Decay mode	Radiation characteristics: energies (MeV) [intensities (%)]	Decay product $^{A}_{Z}Y$
$^{103m}_{45}$Rh	56.12 m	IT	γ 0.040 (0.1%) e^- {0.038} (173%) Rh *K* x-rays ~ 0.022 (7%)	$^{103}_{45}$Rh
$^{104}_{45}$Rh	42.3 s	β^- (99.55%) EC (0.45%)	β^- 2.44 (97.6%), 1.88 (1.89%) γ 1.27 (0.1%), 0.555 (2%) e^- 0.016 (0.1%), 0.003 (0.4%) Ru *K* x-rays ~ 0.022 (0.3%)	$^{104}_{46}$Pd (β^-) $^{104}_{44}$Ru (EC)
$^{105}_{45}$Rh	35.37 h	β^-	β^- 0.560 (70%), 0.247 (30%) γ 0.319 (19%), 0.306 (5%) Pd *K* x-rays ~ 0.022 (0.4%)	$^{105}_{46}$Pd
$^{106}_{45}$Rh	29.80 s	β^-	β^- 3.53 (68%), 3.1 (11%), 2.44 (12%), 2.0 (3%) γ 1.13 (0.5%), 1.05 (1.5%), 0.622 (11%), 0.512 (21%)	$^{106}_{46}$Pd
Palladium				
$^{100}_{46}$Pd	3.6 d	EC	γ 0.074 (98%), 0.084 (100%), 0.126 (11%)	$^{100}_{45}$Rh
$^{101}_{46}$Pd	8.47 h	EC (95.0%) β^+ (5.0%)	γ 1.29 (2%), 1.20 (2%), 0.724 (2%), 0.590 (12%), 0.566 (3%), 0.996 (19%) $\gamma^{\pm}$ 0.511 (10.0%) e^- {0.014} (211%)	$^{101}_{45}$Rh
$^{103}_{46}$Pd	16.96 d	EC	γ 0.498 (0.011%), 0.362 (0.02%), 0.297 (0.011%) e^- {0.043} (258%) Rh *K* x-rays ~ 0.021 (77%)	$^{103m}_{45}$Rh
$^{107}_{46}$Pd	7×10^6 y	β^-	β^- 0.040 (100%)	$^{107}_{47}$Ag
$^{109}_{46}$Pd	13.43 h	β^-	β^- 1.03 (100%) γ 0.088 (3.6%) Ag *K* x-rays ~0.022 (34%)	$^{109m}_{47}$Ag
Silver				
$^{105}_{47}$Ag	41.29 d	EC	γ 1.09 (2%), 0.618–0.681 complex (12%), 0.443 (10%), 0.344 (42%), 0.280 (32%), 0.064 (10%) e^- {0.019} (117%) Pd *K* x-rays ~0.022 (78%)	$^{105}_{46}$Pd
$^{108m}_{47}$Ag	438 y	EC (91.3%) IT (8.7%)	γ 0.723 (91%), 0.614 (90%), 0.434 (91%), 0.079 (7%) e^- 0.054 (2%), 0.027 (7%), ~0.018 (14%), ~0.002 (90%) Pd *K* x-rays ~0.024 (10%), 0.021 (53%)	$^{108}_{46}$Pd (EC) $^{108}_{47}$Ag (IT)
$^{108}_{47}$Ag	2.39 m	β^- (97.2%) EC (2.5%) β^+ (0.3%)	β^- 1.65 (95.5%), 1.02 (1.7%) γ 0.633 (2%), 0.618 (0.3%), 0.433 (0.5%) β^+ 0.900 (0.3%) $\gamma^{\pm}$ 0.511 (0.6%) e^- 0.018 (0.4%), 0.003 (2.3%) Pd *K* x-rays ~0.022 (1.8%)	$^{108}_{48}$Cd (β^-) $^{108}_{46}$Pd (EC, β^+)
$^{109m}_{47}$Ag	40 s	IT	γ 0.088 (3.6%) e^- {0.077} (171%) Ag *K* x-rays ~0.023 (34%)	$^{109}_{47}$Ag
$^{110m}_{47}$Ag	252 d	β^- (98.5%) IT (1.5%)	β^- 1.5 (0.6%), 0.529 (36%), 0.087 (61%) γ 1.51 (11%), 1.38 (21%), 0.937 (32%), 0.885 (71%), 0.818 (8%), 0.764 (23%), 0.706 (19%), 0.68 (16%), 0.658 (96%)	$^{110}_{47}$Ag (IT) $^{110}_{48}$Cd (β^-)
$^{110}_{47}$Ag	24.42 s	β^- (99.7%) EC (0.3%)	β^- 2.89 (93.5%), 2.22 (6.5%) γ 0.658 (4.5%)	$^{110}_{48}$Cd (β^-) $^{110}_{46}$Pd (EC)

Continued

Table of radioactive isotopes—cont'd

Nuclide $^{A}_{Z}X$	Half-life	Decay mode	Radiation characteristics: energies (MeV) [intensities (%)]	Decay product $^{A}_{Z}Y$
$^{111}_{47}$Ag	7.45 d	β^-	β^- 1.04 (92%), 0.790 (1.1%), 0.695 (6.0%), 0.425 (0.9%) γ 0.342 (6%), 0.247 (1%)	$^{111}_{48}$Cd
Cadmium				
$^{104}_{48}$Cd	57.7 m	EC	γ 0.709 (20%), 0.559 (6%), 0.084 (47%) e^- 0.018 (15%), ~0.003 (89%) Ag *K* x-rays 0.025 (12%), 0.022 (60%), Ag *L* x-rays ~ 0.003 (6%)	$^{104}_{47}$Ag
$^{105}_{48}$Cd	55.5 m	EC (72.6%) β^+ (27.4%)	β^+ 1.69 (27.3%), 0.729 (0.1%) γ 2.29 (3%), 1.92 (3%), 1.67 (5%), 1.56 (2%), 1.42 (1%), 1.37 (7%), 1.07 (1%), 0.962 (5%), 0.934 (1%), 0.648 (2%), 0.607 (4%), 0.433 (3%), 0.347 (4%) $\gamma^{\pm}$ 0.511 (54.8%) e^- 0.019 (10%), ~0.003 (60%) Ag *K* x-rays 0.025 (8%), 0.022 (40%), Ag *L* x-rays ~ 0.003 (4%)	$^{105}_{47}$Ag
$^{107}_{48}$Cd	6.50 h	EC (99.8%) β^+ (0.2%)	β^+ 0.302 (0.2%) γ 0.093 (4.7%) $\gamma^{\pm}$ 0.511 (0.4%) e^- ~ 0.090 (49%), 0.068 (44%), 0.019 (22%), 0.003 (168%) Ag *K* x-rays 0.025 (17%), 0.022 (91%), Ag *L* x-rays 0.003 (10%)	$^{107}_{47}$Ag
$^{109}_{48}$Cd	453 d	EC	γ 0.088 (3.8%) e^- {0.081} (250%) Ag K x-rays ~ 0.023 (82%)	$^{109m}_{47}$Ag
$^{111m}_{48}$Cd	48.50 m	IT	γ 0.245 (94%), 0.151 (29%) e^- {0.110} (141%) Cd *K* x-rays ~ 0.026 (7%), 0.023 (34%), Cd *L* x-rays 0.003 (4%)	$^{111}_{48}$Cd
$^{113m}_{48}$Cd	14 y	β^- (99.9%) IT (0.1%)	β^- 0.580 (99.9%) γ 0.264 (0.023%)	$^{113}_{49}$In
$^{115m}_{48}$Cd	44.8 d	β^-	β^- 1.62 (97%), 0.68 (3%) γ 1.29 (0.9%), 0.935 (1.9%), 0.485 (0.31%)	$^{115m}_{49}$In
$^{115}_{48}$Cd	53.38 h	β^-	β^- 1.11 (58%), 0.58 (42%) γ 0.53 (26%), 0.49 (10%), 0.262 (2%), 0.230 (0.6%) e^- {0.177} (107%) In *K* x-rays ~ 0.025 (41%)	$^{115m}_{49}$In
Indium				
$^{110m}_{49}$In	4.9 h	EC	γ 0.997 (11%), 0.937 (68%), 0.884 (93%), 0.707 (30%), 0.658 (98%), 0.642 (26%), 0.583 (15%), 0.462 (5%) e^- 0.019 (13%), ~0.003 (85%) Cd *K* x-rays ~ 0.026 (11%), ~0.023 (59%), Cd *L* x-rays ~ 0.003 (6%)	$^{110}_{48}$Cd
$^{110}_{49}$In	69.1 m	β^+ (62.6%) EC (37.4%)	β^+ 2.26 (62.0%), 1.44 (0.3%), 1.14 (0.3%) γ 2.31 (1%), 2.21 (2%), 2.13 (2%), 0.658 (98%) $\gamma^{\pm}$ 0.551 (125.2%) e^- 0.019 (5%), ~0.003 (32%) Cd *K* x-rays ~ 0.026 (4%), ~0.023 (22%), Cd *L* x-rays ~ 0.003 (2%)	$^{110}_{48}$Cd
$^{111}_{49}$In	2.83 d	EC	γ 0.247 (94%), 0.173 (89%) e^- {0.034} (103%) Cd *K* x-rays ~ 0.025 (83%)	$^{111}_{48}$Cd

Continued

Table of radioactive isotopes—cont'd

Nuclide $^{A}_{Z}X$	Half-life	Decay mode	Radiation characteristics: energies (MeV) [intensities (%)]	Decay product $^{A}_{Z}Y$
$^{113m}_{49}$In	99.47 m	IT	γ 0.393 (64%) In *K* x-rays ~ 0.026 (16%)	$^{113}_{49}$In
$^{114m}_{49}$In	49.51 d	IT (96.7%) EC (3.3%)	γ 0.727 (3.5%), 0.558 (3.5%), 0.192 (17%) In *K* x-rays ~ 0.025 (34%) Cd *K* x-rays ~ 0.022 (3%)	$^{114}_{49}$In (IT) $^{114}_{48}$Cd (EC)
$^{114}_{49}$In	71.9 s	β^- (99.5%) EC (0.5%)	β^- 1.99 (99.4%). 0.689 (0.1%) γ 1.30 (0.2%) Cd *K* x-rays ~ 0.022 (0.3%)	$^{114}_{50}$Sn (β^-) $^{114}_{48}$Cd (EC)
$^{115m}_{49}$In	4.486 h	IT (95%) β^- (5%)	β^- 0.83 (5%) γ 0.336 (46%) In *K* x-rays ~ 0.026 (34%)	$^{115}_{49}$In (IT) $^{115}_{50}$Sn (β^-)
$^{115}_{49}$In	5×10^{14} y	β^-	β^- 0.495 (100%)	$^{115}_{50}$Sn
Tin				
$^{110}_{50}$Sn	4.11 h	EC	γ 0.283 (97%) e^- 0.255 (3%), 0.020 (13%), ~0.003 (88%) In *K* x-rays ~ 0.027 (11%), 0.024 (60%), In *L* x-rays ~0.003 (6%)	$^{110}_{49}$In
$^{113}_{50}$Sn	115.1 d	IT (91.1%) EC (8.9%)	γ 0.392 (65%), 0.255 (2%) In *K* x-rays ~ 0.026 (98%)	$^{113}_{50}$Sn (IT) $^{113m}_{49}$In (EC)
$^{117m}_{50}$Sn	13.76 d	IT	γ 0.159 (86%), 0.156 (2%) e^- {0.161} (216%) Sn *K* x-rays ~ 0.028 (11%), 0.025 (55%) Sn *L* x-rays ~ 0.003 (7%)	$^{117}_{50}$Sn
$^{119m}_{50}$Sn	~250 d	IT	γ 0.024 (16%) Sn *K* x-rays ~ 0.028 (28%)	$^{119}_{50}$Sn
$^{121m}_{50}$Sn	55 y	IT (78%) β^- (22%)	β^- 0.354 (22%) γ 0.037 (2%) e^- {0.008} (161%) Sb *K* x-rays ~ 0.028 (16%)	$^{121}_{51}$Sb (β^-) $^{121}_{50}$Sn (IT)
$^{121}_{50}$Sn	27.06 h	β^-	β^- 0.383 (100%)	$^{121}_{51}$Sb
$^{123}_{50}$Sn	129 d	β^-	β^- 1.42 (100%)	$^{123}_{51}$Sb
$^{125m}_{50}$Sn	9.52 m	β^-	β^- 2.05 (98.4%), 1.46 (0.2%), 0.901 (0.2%), 0.684 (0.1%), 0.648 (1.0%), 0.437 (0.1%) γ 0.332 (97%) e^- 0.301 (2%), ~0.003 (2%) Sb *K* x-rays ~ 0.026 (1%)	$^{125}_{51}$Sb
$^{125}_{50}$Sn	9.64 h	β^-	β^- 2.36 (81.0%), 1.29 (0.6%), 1.27 (3.0%), 1.01 (0.4%), 0.937 (0.2%), 0.467 (6.6%), 0.374 (4.3%), 0.355 (2.2%), 0.116 (0.6%), 0.069 (0.3%) γ 2.00 (2%), 1.09 (6%), 1.07 (10%), 0.916 (4%), 0.822 (4%), 0.800 (1%), 0.470 (2%), 0.332 (1%)	$^{125}_{51}$Sb
$^{126}_{50}$Sn	~2×10^5 y	β^-	β^- 0.250 (100%) γ 0.088 (37%), 0.087 (9%), 0.064 (10%), 0.023 (6%) e^- {0.055} (280%) Sb *K* x-rays ~ 0.028 (29%)	$^{126}_{51}$Sb
Antimony				
$^{117}_{51}$Sb	2.80 h	EC (98.2%) β^+ (1.8%)	β^+ 0.574 (1.8%) γ 0.159 (86%) $\gamma^{\pm}$ 0.511 (3.6%) e^- 0.154 (2%), 0.129 (12%), 0.021 (13%), 0.003 (95%) Sn *K* x-rays ~ 0.029 (14%), 0.025 (68%), Sn *L* x-rays ~ 0.003 (8%)	$^{117}_{50}$Sn

Continued

Table of radioactive isotopes—cont'd

Nuclide $^{A}_{Z}X$	Half-life	Decay mode	Radiation characteristics: energies (MeV) [intensities (%)]	Decay product $^{A}_{Z}Y$
$^{118m}_{51}$Sb	5.00 h	EC (99.8%) β^+ (0.2%)	β^+ 0.310 (0.2%) γ 1.23 (100%), 1.05 (97%), 0.254 (99%), 0.041 (30%) $\gamma^{\pm}$ 0.511 (0.4%) e^- 0.036 (8%), 0.021 (21%), 0.012 (57%), 0.003 (146%) Sn *K* x-rays ~ 0.029 (21%), 0.025 (104%), Sn *L* x-rays ~ 0.003 (12%)	$^{118}_{50}$Sn
$^{118}_{51}$Sb	3.6 m	β^+ (73.4%) EC (26.6%)	β^+ 2.64 (73.2%), 1.41 (0.2%) γ 1.23 (2.5%) $\gamma^{\pm}$ 0.511 (146.8%) e^- 0.021 (3%), 0.003 (23%) Sn *K* x-rays ~ 0.029 (3%), 0.025 (16%), Sn *L* x-rays ~ 0.003 (2%)	$^{118}_{50}$Sn
$^{119}_{51}$Sb	38.19 h	EC	γ 0.024 (17%) e^- {0.024} (242%) Sn *K* x-rays ~ 0.029 (12%), 0.025 (60%), Sn *L* x-rays ~ 0.003 (12%)	$^{119}_{50}$Sn
$^{122}_{51}$Sb	2.72 d	β^- (97.6%) EC (2.4%) β^+ (0.006%)	β^- 1.98 (26.1%), 1.41 (66.7%), 0.723 (4.6%) γ 1.26 (0.7%), 1.14 (0.7%), 0.686 (3.4%), 0.564 (66%) $\gamma^{\pm}$ 0.511 (0.012%) e^- 0.020 (0.3%), 0.003 (2.1%) Sn *K* x-rays ~ 0.029 (0.3%), Te *K* x-rays ~ 0.025 (1.4%)	$^{122}_{52}$Te (β^-) $^{122}_{50}$Sn (EC)
$^{124}_{51}$Sb	60.20 d	β^-	β^- 2.32 (21%), 1.60 (7%), 0.966 (9%), 0.61 (49%), 0.24 (14%) γ 1.69 (50%), 1.37 (5%), 1.31 (3%), 0.72 (14%), 0.644 (7%), 0.603 (97%)	$^{124}_{52}$Te
$^{125}_{51}$Sb	2.71 y	β^-	β^- 0.612 (14%), 0.444 (12%), 0.300 (45%), 0.125 (29%) γ 0.634 (11%), 0.599 (24%), 0.463 (10%), 0.427 (31%) Te *K* x-rays ~ 0.029 (75%)	$^{125m}_{52}$Te
$^{126m}_{51}$Sb	19 m	β^- (86%) IT (14%)	β^- 1.30 (3%), 1.87 (86%) γ 0.414 (86%), 0.666 (86%), 0.695 (82%) e^- {0.011} (27%) Te *K* x-rays ~ 0.029 (1%)	$^{126}_{52}$Te (β^-) $^{126}_{51}$Sb (IT)
$^{126}_{51}$Sb	12.5 d	β^-	β^- 1.90 (100%) γ 0.415 (83%), 0.666 (100%), 0.694 (100%), 0.697 (30%), 0.720 (54%), 0.857 (18%) e^- {0.013) (5%) Te *K* x-rays ~ 0.029 (2%)	$^{126}_{52}$Te
$^{127}_{51}$Sb	3.85 d	β^-	β^- 1.49 (2.0%), 1.24 (1.7%), 1.11 (23.4%), 0.950 (4.6%), 0.896 (35.8%), 0.798 (22.5%), 0.657 (1.3%), 0.504 (5.4%), 0.440 (1.6%), 0.426 (1.0%), 0.291 (0.7%) γ 0.784 (15%), 0.699 (4%), 0.686 (37%), 0.604 (5%), 0.473 (26%), 0.445 (4%), 0.412 (4%), 0.252 (9%) e^- 0.029 (4%), ~0.003 (5%) Te *K* x-rays 0.031 (1%), 0.027 (3%)	$^{127}_{52}$Te
Tellurium				
$^{116}_{52}$Te	2.49 h	EC	γ 0.629 (3%), 0.103 (2%), 0.094 (33%) e^- 0.063 (48%), 0.022 (18%), 0.003 (140%) Sb *K* x-rays 0.030 (19%), 0.026 (95%), Sb *L* x-rays 0.004 (12%)	$^{116}_{51}$Sb

Continued

Table of radioactive isotopes—cont'd

Nuclide $^{A}_{Z}X$	Half-life	Decay mode	Radiation characteristics: energies (MeV) [intensities (%)]	Decay product $^{A}_{Z}Y$
$^{117}_{52}$Te	62.0 m	EC (72.9%) β^+ (27.1%)	β^+ 1.81 (24.0%), 1.60 (1.6%), 1.17 (0.1%), 0.811 (1.1%), 0.716 (0.3%) γ 2.30 (11%), 1.72 (16%), 1.09 (7%), 0.924 (6%), 0.720 (65%) $\gamma^{\pm}$ 0.511 (54.2%) e^- 0.022 (8%), 0.003 (61%) Sb *K* x-rays 0.030 (9%), 0.026 (44%), Sb *L* x-rays 0.004 (5%)	$^{117}_{51}$Sb
$^{118}_{52}$Te	6.00 d	EC	e^- 0.022 (11%), 0.003 (83%) Sb *K* x-rays 0.030 (12%), 0.026 (60%), Sb *L* x-rays 0.004 (7%)	$^{118}_{51}$Sb
$^{119m}_{52}$Te	4.70 d	EC (99.6%) β^+ (0.4%)	β^+ 1.26 (0.4%) γ 1.21 (66%), 1.14 (8%), 0.271 (28%), 0.154 (66%) $\gamma^{\pm}$ 0.511 (0.8%) e^- 0.240 (1%), 0.123 (3%), 0.022 (12%), 0.003 (87%) Sb *K* x-rays 0.030 (13%), 0.026 (63%), Sb *L* x-rays 0.004 (8%)	$^{119}_{51}$Sb
$^{119}_{52}$Te	16.05 h	EC (97.9%) β^+ (2.1%)	β^+ 0.627 (1.9%), 0.571 (0.2%) γ 1.75 (4%), 1.41 (1%), 0.700 (10%), 0.644 (84%) $\gamma^{\pm}$ 0.511 (4.2%) e^- 0.022 (11%), 0.003 (82%) Sb *K* x-rays 0.030 (12%), 0.026 (60%), Sb *L* x-rays 0.004 (7%)	$^{119}_{51}$Sb
$^{121m}_{52}$Te	164.2 d	IT (88.6%) EC (11.4%)	γ 1.10 (3%), 0.212 (82%), 0.037 (1%) e^- {0.077} (203%) Te *K* x-rays 0.031 (6%), 0.027 (29%), Te *L* x-rays ~ 0.004 (7%) Sb *K* x-rays 0.030 (3%), 0.026 (13%), Sb *L* x-rays ~ 0.004 (2%)	$^{121}_{52}$Te (IT) $^{121}_{51}$Sb (EC)
$^{121}_{52}$Te	19.17 d	EC	γ 0.573 (80%), 0.508 (18%), 0.470 (1%) e^- 0.022 (11%), 0.003 (85%) Sb *K* x-rays 0.030 (13%), 0.026 (62%), Sb *L* x-rays ~ 0.004 (7%)	$^{121}_{51}$Sb
$^{123m}_{52}$Te	120 d	IT	γ 0.159 (84%) e^- {0.102} (205%) Te *K* x-rays ~ 0.029 (50%)	$^{123}_{52}$Te
$^{125m}_{52}$Te	57.4 d	IT	γ 0.109 (0.3%), 0.035 (7%) e^- {0.110} (375%) Te *K* x-rays ~0.031 (19.3%), ~0.027 (93%) Te *L* x-rays ~0.004 (14%)	$^{125}_{52}$Te
$^{127m}_{52}$Te	106 d	IT (97.6%) β^- (2.4%)	β^- 0.733 (2.4%) γ 0.089 (0.08%), 0.059 (0.2%) e^- {0.076} (170%) Te *K* x-rays ~ 0.028 (36%)	$^{127}_{52}$Te
$^{127}_{52}$Te	9.35 h	β^-	β^- 0.695 (100%) γ 0.417 (1%), 0.360 (0.14%), 0.21 (0.03%), 0.058 (0.01%)	$^{127}_{53}$I
$^{129m}_{52}$Te	33.52 d	IT (64%) β^- (36%)	β^- 1.60 (36%) γ 0.696 (6%) e^- {0.060} (112%) Te *K* x-rays ~ 0.030 (28%)	$^{129}_{52}$Te (IT) $^{129}_{53}$I (β^-)
$^{129}_{52}$Te	69.5 m	β^-	β^- 1.45 (70%), 0.989 (15%), 0.69 (4%), 0.29 (11%) γ 1.08 (1.5%), 0.455 (8%), 0.275 (1.7%), 0.027 (19%) I *L* x-rays ~ 0.004 (5%)	$^{129}_{53}$I

Continued

Table of radioactive isotopes—cont'd

Nuclide $^{A}_{Z}X$	Half-life	Decay mode	Radiation characteristics: energies (MeV) [intensities (%)]	Decay product $^{A}_{Z}Y$
$^{131m}_{52}$Te	33.25 h	β^- (74.1%) IT (25.9%)	β^- 2.42 (2.8%). 0.771 (1.9%), 0.529 (1.0%), 0.518 (11.9%), 0.493 (1.6%), 0.437 (26.5%), 0.416 (3.9%), 0.406 (1.7%), 0.303 (1.2%) γ 1.21 (9%), 1.13 (11%), 0.910 (3%), 0.852 (20%), 0.822 (6%), 0.794 (13%), 0.783 (8%), 0.773 (37%), 0.665 (4%), 0.334 (9%), 0.241 (7%), 0.201 (7%), 0.150 (5%), 0.102 (8%) e^- {0.052} (71%) I *K* x-rays ~0.032 (2%), ~0.028 (8%) Te *K* x-rays ~0.031 (10%), ~0.028 (8%)	$^{131}_{53}$I (β^-) $^{131}_{52}$Te (IT)
$^{131}_{52}$Te	25.0 m	β^-	β^- 2.09 (59.3%), 1.74 (0.8%), 1.63 (21.6%), 1.36 (1.2%) 1.14 (2.6%), 1.09 (10.0%), 0.936 (0.5%), 0.808 (1.3%), 0.791 (1.2%), 0.734 (1.2%) γ 1.15 (5%), 0.949 (2%), 0.602 (4%), 0.493 (5%), 0.451 (18%), 0.149 (69%) e^- 0.145 (2%), 0.116 (14%), 0.024 (2%), ~0.003 (14%) I *K* x-rays ~0.033 (2%), ~0.039 (10%) I *L* x-rays ~0.004 (1%)	$^{131}_{53}$I
$^{132}_{52}$Te	78.2 h	β^-	β^- 0.215 (100%) γ 0.230 (90%), 0.053 (17%) e^- {0.043} (168%) I *K* x-rays ~ 0.030 (71%)	$^{132}_{53}$I
Iodine				
$^{120}_{53}$I	81.6 m	β^+ (67.6%) EC (32.4%)	β^+ 4.59 (19.0%), 4.03 (29.3%), 3.45 (1.1%), 3.39 (2.7%), 3.02 (2.1%), 2.67 (0.9%), 2.51 (6.2%), 2.14 (2.1%), 1.95 (0.7%), 1.84 (0.6%), 1.65 ((1.4%), 1.54 (0.4%), 1.45 (0.3%), 1.31 (0.2%), 1.23 (0.3%), 1.10 (0.2%), 0.827 (0.1%) γ 1.52 (11%), 0.641 (8%), 0.601 (6%), 0.560 (70%) $\gamma^{\pm}$ 0.511 (135.2%) e^- 0.023 (3%), ~0.003 (27%) Te *K* x-rays 0.031 (4%), ~0.028 (20%)	$^{120}_{52}$Te
$^{121}_{53}$I	2.12 h	EC (89.4%) β^+ (10.6)	β^+ 1.06 (10.3%), 0.740 (0.3%) γ 0.599 (2%), 0.532 (6%), 0.457 (1%), 0.212 (84%) $\gamma^{\pm}$ 0.511 (21.2%) e^- 0.180 (6%), 0.023 (10%), 0.003 (80%) Te *K* x-rays 0.031 (13%), 0.027 (60%), Te *L* x-rays ~ 0.004 (8%)	$^{121}_{52}$Te
$^{122}_{53}$I	3.63 m	β^+ (78.1%) EC (21.9%)	β^+ 3.21 (67.0%), 2.65 (10.0%), 1.96 (0.3%), 1.86 (0.6%), 1.27 (0.2%) γ 0.793(1%), 0.693 (1%), 0.564 (18%) $\gamma^{\pm}$ 0.511 (156.2%) e^- 0.023 (2%), 0.003 (18%) Te *K* x-rays 0.031 (3%), 0.027 (13%), Te *L* x-rays ~ 0.004 (2%)	$^{122}_{52}$Te
$^{123}_{53}$I	13.02 h	EC	γ 0.159 (83%) e^- {0.028} (108%) Te *K* x-rays ~ 0.029 (86%)	$^{123}_{52}$Te
$^{124}_{53}$I	4.15 d	EC (75%) β^+ (25%)	β^+ 2.13 (12.3%), 1.53 (11.5%), 0.808 (1.2%) γ 1.69 (14%), 0.73 (14%), 0.645 (1%), 0.605 (67%) $\gamma^{\pm}$ 0.511 (50%) e^- {0.007} (62%) Te *K* x-rays ~ 0.030 (58%)	$^{124}_{52}$Te
$^{125}_{53}$I	60.25 d	EC	γ 0.035 (7%) e^- {0.018} (246%) Te *K* x-rays ~ 0.030 (138%)	$^{125}_{52}$Te

Continued

Table of radioactive isotopes—cont'd

Nuclide $^{A}_{Z}X$	Half-life	Decay mode	Radiation characteristics: energies (MeV) [intensities (%)]	Decay product $^{A}_{Z}Y$
$^{126}_{53}$I	12.93 d	EC (51.7%) β^- (47.3%) β^+ (1%)	β^- 1.25 (10.3%), 0.865 (33.4%), 0.378 (3.6%) β^+ 1.11 (0.8%), 0.460 (0.2%) γ 0.753 (4.1%), 0.667 (33%), 0.491 (2.9%), 0.386 (36%) $\gamma^{\pm}$ 0.511 (2%) e^- 0.023 (5.5%), 0.003 (43%) Te *K* x-rays ~ 0.030 (6.6%), 0.027 (31.5%), Te *L* x-rays ~ 0.004 (4%), Xe *K* x-rays 0.033 (0.1%), 0.029 (0.4%)	$^{126}_{52}$Te (EC, β^+) $^{126}_{54}$Xe (β^-)
$^{128}_{53}$I	24.99 m	β^- (93.1%) EC (6.9%)	β^- 2.12 (80%), 1.68 (11.6%), 1.15 (1.5%) γ 0.527 (1.2%), 0.442 (12.6%) e^- 0.022 (0.7%), 0.003 (5.7%) Te *K* x-rays ~ 0.030 (0.8%), 0.027 (4%), Te *L* x-rays ~ 0.004 (0.5%)	$^{128}_{54}$Xe (β^-) $^{128}_{52}$Te (EC)
$^{129}_{53}$I	1.57×10^7 y	β^-	β^- 0.150 (100%) γ 0.040 (9%) e^- {0.014} (165%) Xe *K* x-rays ~ 0.032 (71%)	$^{129}_{54}$Xe
$^{130}_{53}$I	12.36 h	β^-	β^- 1.78 (0.4%), 1.04 (51.6%), 0.62 (48%) γ 1.15 (12%), 0.743 (87%), 0.669 (100%), 0.538 (99%), 0.419 (35%) e^- (0.011) (4%) Xe *K* x-rays ~ 0.032 (2%)	$^{130}_{54}$Xe
$^{131}_{53}$I	8.04 d	β^-	β^- 0.806 (1%), 0.607 (86%), 0.336 (13%) γ 0.637 (6.8%), 0.364 (82%), 0.284 (5.4%), 0.080 (2.6%) e^- {0.010} (12%) Xe *K* x-rays ~ 0.032 (5%)	$^{131m}_{54}$Xe
$^{132}_{53}$I	2.28 h	β^-	β^- 2.16 (18%), 1.61 (21%), 1.22 (24%), 1.04 (15%), 0.802 (21%) γ 1.40 (7%), 0.955 (18%), 0.773 (76%), 0.667 (99%), 0.522 (16%) e^- {0.008} (2.5%) Xe *K* x-rays ~ 0.032 (1%)	$^{132}_{54}$Xe
$^{133}_{53}$I	20.9 h	β^-	β^- 1.4 (~94%), 0.5 (~6%) γ 0.530 (90%) Xe *K* x-rays ~ 0.032 (1%)	$^{133m}_{54}$Xe
Xenon				
$^{122}_{54}$Xe	20.1 h	EC	γ 0.416 (2%), 0.350 (8%), 0.149 (3%) e^- 0.028 (1%), 0.024 (10%), 0.003 (85%) I *K* x-rays ~0.033 (13%), ~0.029 (63%) I *L* x-rays ~ 0.004 (9%)	$^{122}_{53}$I
$^{123}_{54}$Xe	2.08 h	EC (77.5%) β^+ (22.5%)	β^+ 1.52 (17.4%), 1.50 (4.0%), 1.34 (1.1%) γ 1.81 (1%), 1.11 (2%), 1.09 (3%), 0.900 (2%), 0.330 (9%), 0.178 (15%), 0.149 (49%) $\gamma^{\pm}$ 0.511 (45.0%) e^- 0.144 (4%), 0.116 (16%), 0.024 (10%), 0.003 (80%) I *K* x-rays ~0.033 (13%), ~0.028 (60%), I *L* x-rays ~ 0.004 (8%)	$^{123}_{53}$I
$^{125}_{54}$Xe	16.9 h	EC (99.7%) β^+ (0.3%)	β^+ 0.443 (0.1%), 0.388 (0.2%) γ 1.18 (1%), 0.846 (1%), 0.453 (5%), 0.243 (30%), 0.188 (54%), 0.054 (7%) $\gamma^{\pm}$ 0.511 (0.6%) e^- {0.032} (164%) I *K* x-rays ~0.033 (18%), ~0.028 (85%), I *L* x-rays ~ 0.004 (11%)	$^{125}_{53}$I

Continued

Table of radioactive isotopes—cont'd

Nuclide $^{A}_{Z}X$	Half-life	Decay mode	Radiation characteristics: energies (MeV) [intensities (%)]	Decay product $^{A}_{Z}Y$
$^{127}_{54}$Xe	36.34 d	EC	γ 0.375 (17%), 0.203 (69%), 0.172 (26%), 0.145 (4%) e^- {0.031} (127%) I *K* x-rays ~0.033 (15%), ~0.028 (72%), I *L* x-rays ~ 0.004 (10%)	$^{127}_{53}$I
$^{129m}_{54}$Xe	8.88 d	IT	γ 0.197 (5%), 0.040 (8%) e^- {0.183} (350%) Xe *K* x-rays ~0.034 (22%), ~0.029 (103%), Xe *L* x-rays ~0.004 (16%)	$^{129}_{54}$Xe
$^{131m}_{54}$Xe	11.77 d	IT	γ 0.164 (2%) e^- {0.143} (169%) Xe *K* x-rays ~ 0.030 (45%), Xe *L* x-rays ~ 0.004 (7%)	$^{131}_{54}$Xe
$^{133m}_{54}$Xe	2.19 d	IT	γ 0.233 (10%) e^- {0.192} (156%) Xe *K* x-rays ~ 0.031 (56%), Xe *L* x-rays ~ 0.004 (7%)	$^{133}_{54}$Xe
$^{133}_{54}$Xe	5.245 d	β^-	β^- 0.346 (100%) γ 0.081 (37%) e^- {0.036} (114%) Cs *K* x-rays ~ 0.035 (49%), Cs *L* x-rays ~ 0.004 (5%)	$^{133}_{55}$Cs
$^{135m}_{54}$Xe	15.29 m	IT (99.4%) β^- (0.6%)	β^- 0.692 (0.6%) γ 0.526 (80%) e^- 0.521 (3%), 0.492 (15%), 0.025 (2%), ~0.003 (15%) Xe *K* x-rays ~0.034 (2%), ~0.029 (11%) Xe *L* x-rays ~0.004 (2%)	$^{135}_{54}$Xe (IT) $^{135}_{55}$Cs (β^-)
$^{135}_{54}$Xe	9.14 h	β^-	β^- 0.915 (96.0%), 0.757 (0.6%), 0.557 (3.1%) γ 0.608 (3%), 0.407 (0.4%), 0.358 (0.2%), 0.249 (90%) e^- 0.249 (0.2%), 0.244 (0.8%), 0.214 (5.6%), 0.025 (0.6%), 0.004 (5.2%) Cs *K* x-rays ~ 0.035 (0.9%), 0.003 (4%)	$^{135}_{55}$Cs
$^{137}_{54}$Xe	3.82 m	β^-	β^- 4.17 (67.0%), 3.72 (31.0%), 3.32 (0.7%), 2.60 (0.1%), 2.39 (0.3%), 2.10 (0.1%), 1.32 (0.8%) γ 0.455 (31%) e^- 0.420 (0.4%) Cs *K* x-rays 0.030 (0.2%)	$^{137}_{55}$Cs
Cesium				
$^{127}_{55}$Cs	6.25 h	EC (97.0%) β^+ (3.0%)	β^+ 1.06 (1.3%), 0.934 (0.4%), 0.647 (1.3%) γ 0.462 (5%), 0.412 (63%), 0.321 (1%), 0.287 (4%), 0.125 (11%) $\gamma^{\pm}$ 0.511 (6.0%) e^- 0.378 (1%), 0.090 (4%), 0.025 (10%), ~0.003 (83%) Xe *K* x-rays 0.034 (14%), ~0.030 (64%), Xe *L* x-rays ~ 0.009 (9%)	$^{127}_{54}$Xe
$^{128}_{55}$Cs	3.66 m	β^+ (69.0%) EC (31.0%)	β^+ 2.91 (53.3%), 2.46 (14.4%), 1.94 (1.0%), 1.32 (0.3%) γ 1.14 (1%), 0.527 (2%), 0.442 (27%) $\gamma^{\pm}$ 0.511 (138.0%) e^- 0.025 (3%), ~0.003 (25%) Xe *K* x-rays 0.034 (4%), ~0.030 (19%), Xe *L* x-rays ~ 0.004 (3%)	$^{128}_{54}$Xe

Continued

Table of radioactive isotopes—cont'd

Nuclide $^{A}_{Z}X$	Half-life	Decay mode	Radiation characteristics: energies (MeV) [intensities (%)]	Decay product $^{A}_{Z}Y$
$^{129}_{55}$Cs	32.06 h	EC	γ 0.411 (22%), 0.372 (31%), 0.318 (2%), 0.279 (1%), 0.040 (3%) e^- 0.034 (4%), 0.025 (13%), 0.005 (31%), 0.003 (110%) Xe *K* x-rays 0.034 (18%), ~0.030 (85%), Xe *L* x-rays ~ 0.004 (12%)	$^{129}_{54}$Xe
$^{130}_{55}$Cs	29.2 m	EC (54.8%) β^+ (43.6%) β^- (1.6%)	β^+ 1.96 (43.0%), 1.42 (0.6%) β^- 0.369 (1.6%) γ 1.99 (0.2%), 1.71 (0.1%), 1.69 (0.2%), 1.62 (0.3%) 0.895 (0.4%), 0.586 (0.5%), 0.536 (3.8%) $\gamma^{\pm}$ 0.511 (87.2%) e^- 0.025 (5.3%), 0.003 (44%) Xe *K* x-rays ~ 0.032 (41%), Xe *L* x-rays ~ 0.004 (4.7%)	$^{130}_{54}$Xe (EC, β^+) $^{130}_{56}$Ba (β^-)
$^{131}_{55}$Cs	9.69 d	EC	e^- {0.006} (76%) Xe *K* x-rays ~ 0.032 (74%), Xe *L* x-rays ~ 0.004 (7%)	$^{131}_{54}$Xe
$^{132}_{55}$Cs	6.474 d	EC (97.7%) β^- (1.9%) β^+ (0.4%)	β^- 0.814 (1.5%), 0.247 (0.4%) β^+ 0.435 (0.4%) γ 1.32 (0.6%), 1.14 (0.5%), 0.668 (99%), 0.465 (2%) $\gamma^{\pm}$ 0.511 (0.8%) e^- {0.008} (73%) Xe *K* x-rays ~ 0.032 (73%), Xe *L* x-rays ~ 0.004 (7%)	$^{132}_{54}$Xe (EC, β^+) $^{132}_{56}$Ba (β^-)
$^{134m}_{55}$Cs	2.91 h	IT	γ 0.127 (13%), 0.011 (1%) e^- {0.109} (315%) Cs *K* x-rays 0.035 (4%), 0.031 (25%), Cs *K* x-rays ~ 0.004 (16%)	$^{134}_{55}$Cs
$^{134}_{55}$Cs	2.062 y	β^-	β^- 0.658 (70%), 0.415 (3%), 0.089 (27%) γ 0.801 (9%), 0.796 (85%), 0.605 (98%), 0.570 (15%), 0.563 (8%)	$^{134}_{56}$Ba
$^{135}_{55}$Cs	2.3×10^6 y	β^-	β^- 0.269 (100%)	$^{135}_{56}$Ba
$^{136}_{55}$Cs	13.16 d	β^-	β^- 0.682 (13.0%), 0.494 (4.5%), 0.408 (10.5%), 0.341 (70.0%), 0.175 (2.0%) γ 1.24 (20%), 1.05 (80%), 0.818 (100%), 0.340 (42%) 0.274 (11%), 0.177 (10%), 0.163 (3%), 0.153 (6%), 0.086 (5%), 0.066 (5%) e^- {0.035} (32%) Ba *K* x-rays ~ 0.036 (2%), ~0.032 (9%), Ba *L* x-rays ~ 0.004 (2%)	$^{136}_{56}$Ba
$^{137}_{55}$Cs	30.17 y	β^-	β^- 1.18 (6%), 0.514 (94%) γ 0.662 (85%) e^- {0.062} (17%) Ba *K* x-rays ~ 0.035 (7%)	$^{137m}_{56}$Ba
$^{138m}_{55}$Cs	2.91 m	IT (80.2%) β^- (19.8%)	β^- 3.36 (15.0%), 3.25 (2.0%), 3.04 (2.8%) γ 1.44 (19%), 0.463 (19%), 0.324 (1%), 0.192 (15%), 0.112 (2%) e^- {0.059} (154%) Cs *K* x-rays 0.035 (7%), 0.031 (33%), Cs *L* x-rays ~ 0.004 (7%), Ba *K* x-rays 0.032 (3%)	$^{138}_{55}$Cs (IT) $^{138}_{56}$Ba (β^-)

Continued

Table of radioactive isotopes—cont'd

Nuclide $^{A}_{Z}X$	Half-life	Decay mode	Radiation characteristics: energies (MeV) [intensities (%)]	Decay product $^{A}_{Z}Y$
$^{138}_{55}$Cs	33.41 m	β^-	β^- 3.93 (4.3%), 3.47 (13.7%), 3.16 (13.0%), 3.07 (7.3%), 2.96 (0.6%), 2.93 (44.0%), 2.79 (1.7%), 2.73 (8.8%), 2.60 (1.6%), 2.49 (0.5%), 2.38 (0.6%), 1.73 (0.4%), 1.44 (0.5%) γ 2.64 (8%), 2.22 (15%), 1.44 (76%), 1.01 (30%), 0.872 (5%), 0.547 (11%), 0.463 (31%), 0.408 (5%) e^- {0.0064} (3%) Ba *K* x-rays ~0.037 (0.2%), ~0.032 (1.1%)	$^{138}_{56}$Ba
$^{139}_{55}$Cs	9.27 m	β^-	β^- 4.21 (85%), 2.95 (6.2%), 1.86 (1.2%) γ 3.66 (0.2%), 2.65 (0.2%), 2.61 (0.3%), 2.53 (0.4%), 2.35 (0.6%), 2.17 (0.2%), 1.93 (0.2%), 1.89 (0.2%), 1.88 (0.3%), 1.68 (0.6%), 1.62 (0.4%), 1.42 (0.8%), 1.41 (0.2%), 1.28 (7%), 1.19 (0.2%), 0.929 (0.2%), 0.627 (2%)	$^{139}_{56}$Ba
Barium				
$^{131}_{56}$Ba	12.0 d	EC	γ 0.496 (48%), 0.373 (13%), 0.216 (19%), 0.124 (28%) e^- {0.045} (135%) Cs *K* x-rays ~ 0.035 (98%)	$^{131}_{55}$Cs
$^{133m}_{56}$Ba	38.93 h	IT	γ 0.276 (18%), 0.012 (1%) e^- {0.219} (319%) Ba *K* x-rays ~ 0.036 (9%), 0.032 (43%), Ba *L* x-rays ~ 0.004 (16%)	$^{133}_{56}$Ba
$^{133}_{56}$Ba	10.66 y	EC	γ 0.382 (8%), 0.356 (69%), 0.302 (14%), 0.276 (7%), 0.080 (34%) e^- {0.055} (211%) Cs *K* x-rays ~ 0.034 (123%)	$^{133}_{55}$Cs
$^{137m}_{56}$Ba	2.551 m	IT	γ 0.662 (89%) e^- {0.065} (18%) Ba *K* x-rays ~ 0.035 (8%)	$^{137}_{56}$Ba
$^{139}_{56}$Ba	83.06 m	β^-	β^- 2.32 (70.0%), 2.15 (29.7%), 0.896 (0.3%) γ 1.42 (0.3%), 0.166 (24%) e^- 0.164 (0.1%), 0.160 (0.7%), 0.127 (5%), 0.027 (0.5%), ~0.004 (5%) La *K* x-rays ~0.038 (0.8%), 0.033 (4%) La *L* x-rays ~0.005 (0.6%)	$^{139}_{57}$La
$^{140}_{56}$Ba	12.79 d	β^-	β^- 1.02 (17%), 1.01 (46%), 0.886 (3%), 0.582 (10%), 0.468 (24%) γ 0.537 (24%), 0.438 (2%), 0.424 (3%), 0.305 (4%), 0.163 (6%), 0.030 (14%) e^- {0.035} (208%) La *K* x-rays ~ 0.035 (2%)	$^{140}_{57}$La
Lanthanum				
$^{132m}_{57}$La	24.3 m	IT (76.0%) EC (16.7%) β^+ (7.3%)	β^+ 1.83 (2.7%), 1.74 (1.2%), 1.54 (2.2%), 1.50 (1.2%) γ 1.05 (8%), 0.899 (7%), 0.698 (4%), 0.663 (11%), 0.567 (4%), 0.516 (7%), 0.464 (22%), 0.391 (5%), 0.285 (7%), 0.238 (4%), 0.135 (49%) $\gamma^{\pm}$ 0.511 (14.6%) e^- 0.129 (3%), 0.096 (20%), 0.051 (9%), 0.047 (38%), 0.027 (4%), 0.014 (23%), ~0.004 (71%) La *K* x-rays 0.038 (7%), 0.033 (31%), La *L* x-rays ~0.005 (9%), Ba *K* x-rays ~ 0.036 (2%),	$^{132}_{57}$La (IT) $^{132}_{56}$Ba (EC, β^+)

Continued

Table of radioactive isotopes—cont'd

Nuclide $^{A}_{Z}X$	Half-life	Decay mode	Radiation characteristics: energies (MeV) [intensities (%)]	Decay product $^{A}_{Z}Y$
			0.032 (11%), Ba *L* x-rays ~ 0.004 (2%)	
$^{132}_{57}$La	4.8 h	EC (57.9%) β^+ (42.1%)	β^+ 3.67 (9.2%), 3.21 (14.0%), 2.64 (11.0%), 2.54 (0.8%), 2.16 (0.5%), 1.98 (0.7%), 1.67 (2.3%), 1.29 (1.4%), 1.10 (2.0%), 0.810 (0.1%), 0.740 (0.1%) γ 2.10 (6%), 1.91 (9%), 1.03 (8%), 0.663 (9%), 0.567 (16%), 0.540 (8%), 0.464 (76%) $\gamma^{\pm}$ 0.511 (84.2%) e^- 0.026 (5%), ~0.004 (48%) Ba *K* x-rays ~ 0.036 (8%), 0.032 (38%), Ba *L* x-rays ~ 0.004 (6%)	$^{132}_{56}$Ba
$^{133}_{57}$La	3.912 h	EC (92.9%) β^+ (7.1%)	β^+ 1.02 (7.1%) γ 0.633 (1%), 0.302 (2%), 0.290 (1%), 0.279 (2%), 0.012 (1%) $\gamma^{\pm}$ 0.511 (14.2%) e^- {0.0065} (244%) Ba *K* x-rays ~ 0.036 (13%), 0.032 (57%), Ba *L* x-rays ~ 0.004 (17%)	$^{133}_{56}$Ba
$^{134}_{57}$La	6.45 m	β^+ (63.6%) EC (36.4%)	β^+ 2.71 (62.0%), 2.10 (1.6%) γ 0.605 (5%), 0.563 (0.4%) $\gamma^{\pm}$ 0.511 (127.2%)	$^{134}_{56}$Ba
$^{135}_{57}$La	19.5 h	EC	γ 0.874 (0.2%), 0.482 (1.5%) e^- 0.026 (9%), 0.004 (78%) Ba *K* x-rays ~ 0.036 (13%), 0.032 (61%), Ba *L* x-rays ~ 0.004 (10%)	$^{135}_{56}$Ba
$^{136}_{57}$La	9.87 m	EC (63.9%) β^+ (36.1%)	β^+ 1.85 (36.0%), 1.03 (0.1%) γ 1.32 (0.3%), 0.818 (2.3%) $\gamma^{\pm}$ 0.511 (72.2%) e^- 0.026 (5%), 0.004 (50%) Ba *K* x-rays ~ 0.036 (9%), 0.032 (39%), Ba *L* x-rays ~ 0.004 (6%)	$^{136}_{56}$Ba
$^{137}_{57}$La	6×10^4 y	EC	e^- 0.026 (8%), 0.004 (78%) Ba *K* x-rays ~ 0.036 (13%), 0.032 (61%), Ba *L* x-rays ~ 0.004 (10%)	$^{137}_{56}$Ba
$^{140}_{57}$La	40.27 h	β^-	β^- 2.16 (8%), 1.68 (18%), 1.37 (46%), 1.15 (19%), 0.857 (4%), 0.510 (5%) γ 2.53 (3%), 1.60 (96%), 0.925 (10%), 0.815 (24%), 0.487 (46%), 0.329 (20%) e^- {0.009} (5%) Ce *K* x-rays ~ 0.038 (2%)	$^{140}_{58}$Ce
Cerium				
$^{134}_{58}$Ce	3.16 d	EC	γ 0.162 (0.2%), 0.130 (0.2%) e^- 0.027 (8%), 0.025 (0.4%), 0.004 (77%) La *K* x-rays 0.038 (13%), 0.033 (60%), La *L* x-rays ~ 0.005 (10%)	$^{134}_{57}$La
$^{135}_{58}$Ce	17.7 h	EC (99.6%) β^+ (0.4%)	β^+ 0.704 (0.4%) γ 0.828 (5%), 0.784 (11%), 0.607 (19%), 0.577 (5%), 0.572 (10%), 0.518 (14%), 0.300 (24%), 0.265 (42%), 0.206 (8%) $\gamma^{\pm}$ 0.511 (0.8%) e^- {0.026} (106%) La *K* x-rays 0.038 (15%), 0.033 (68%), La *L* x-rays ~ 0.005 (12%)	$^{135}_{57}$La

Continued

Table of radioactive isotopes—cont'd

Nuclide $^{A}_{Z}X$	Half-life	Decay mode	Radiation characteristics: energies (MeV) [intensities (%)]	Decay product $^{A}_{Z}Y$
$^{139}_{58}$Ce	137.2 d	EC	γ 0.165 (80%) e^- {0.033} (101%) La *K* x-rays ~ 0.036 (185%)	$^{139}_{57}$La
$^{141}_{58}$Ce	32.55 d	β^-	β^- 0.582 (30%), 0.444 (70%) γ 0.145 (48%) e^- {0.026} (38%) Pr *K* x-rays ~ 0.039 (17%)	$^{141}_{59}$Pr
$^{143}_{58}$Ce	33.0 h	β^-	β^- 1.40 (37%), 1.13 (40%), 0.74 (5%), 0.50 (12%), 0.22 (6%) γ 0.725 (5%), 0.668 (5%), 0.293 (42%), 0.057 (12%) e^- {0.030} (139%) Pr *K* x-rays ~ 0.039 (63%)	$^{143}_{59}$Pr
$^{144}_{58}$Ce	284.5 d	β^-	β^- 0.316 (75.7%), 0.238 (4.6%), 0.185 (19.7%) γ 0.134 (11%), 0.080 (2%) e^- {0.010} (23%) Pr *K* x-rays ~ 0.037 (8%)	$^{144}_{59}$Pr
Praseodymium				
$^{139}_{59}$Pr	4.41 h	EC (91.7%) β^+ (8.3%)	β^+ 1.10 (8.3%) γ 1.37 (0.2%), 1.35 (0.5%), 0.255 (0.2%) $\gamma^{\pm}$ 0.511 (16.6%) e^- 0.028 (7%), 0.004 (69%) Ce *K* x-rays ~ 0.039 (13%), ~0.034 (57%), Ce *L* x-rays ~ 0.005 (10%)	$^{139}_{58}$Ce
$^{142}_{59}$Pr	19.12 h	β^- (99.98%) EC (0.02%)	β^- 2.16 (96.3%), 0.586 (3.7%) γ 1.57 (3.7%)	$^{142}_{60}$Nd (β^-)
$^{143}_{59}$Pr	13.59 d	β^-	β^- 0.932 (100%)	$^{143}_{60}$Nd
$^{144m}_{59}$Pr	7.2 m	IT	e^- {0.046} (160%) Pr *K* x-rays ~ 0.038 (30%)	$^{144}_{59}$Pr
$^{144}_{59}$Pr	17.30 m	β^-	β^- 3.00 (97.8%), 2.30 (1.2%), 0.807 (1%) γ 2.19 (0.7%), 1.49 (0.3%), 0.695 (1.5%)	$^{144}_{60}$Nd
Neodymium				
$^{139m}_{60}$Nd	5.50 h	EC (86.0%) β^+ (2.2%) IT (11.8%)	β^+ 1.91 (1.1%), 1.20 (0.7%), 1.19 (0.1%), 1.17 (0.3%) γ 0.982 (26%), 0.910 (8%), 0.828 (10%), 0.810 (6%), 0.802 (7%), 0.738 (35%), 0.708 (26%), 0.114 (40%) $\gamma^{\pm}$ 0.511 (4.4%) e^- {0.078} (170%) Pr *K* x-rays 0.041 (19%), 0.036 (84%), Pr *L* x-rays 0.005 (15%), Nd *K* x-rays ~ 0.042 (1%), 0.037 (5%), Nd *L* x-rays ~ 0.005 (1%)	$^{139}_{59}$Pr (EC, β^+) $^{139}_{60}$Nd (IT)
$^{139}_{60}$Nd	29.7 m	EC (74.3%) β^+ (25.7%)	β^+ 1.79 (25.0%), 1.38 (0.4%), 1.20 (0.3%) γ 1.07 (3%), 0.923 (1%), 0.917 (2%), 0.669 (2%), 0.475 (1%), 0.405 (7%) $\gamma^{\pm}$ 0.511 (51.4%) e^- 0.029 (6%), 0.004 (57%) Pr *K* x-rays 0.041 (11%), 0.036 (47%), Pr *L* x-rays 0.005 (9%)	$^{139}_{59}$Pr
$^{140}_{60}$Nd	3.37 d	EC	e^- 0.029 (7%), 0.004 (74%) Pr *K* x-rays 0.041 (14%), 0.036 (60%), Pr *L* x-rays 0.005 (11%)	$^{140}_{59}$Pr
$^{141}_{60}$Nd	2.49 h	EC (97.5%) β^+ (2.5%)	β^+ 0.801 (2.5%) γ 1.30 (0.6%), 1.15 (1%), 0.145 (0.2%) $\gamma^{\pm}$ 0.511 (5.0%) e^- 0.029 (7%), 0.004 (73%) Pr *K* x-rays 0.041 (14%), 0.036 (60%), Pr *L* x-rays 0.005 (11%)	$^{141}_{59}$Pr

Continued

Table of radioactive isotopes—cont'd

Nuclide $^{A}_{Z}X$	Half-life	Decay mode	Radiation characteristics: energies (MeV) [intensities (%)]	Decay product $^{A}_{Z}Y$
$^{147}_{60}$Nd	10.98 d	β^-	β^- 0.896 (<0.1%), 0.805 (80%), 0.486 (0.7%), 0.407 (0.8%), 0.365 (15%), 0.210 (2.4%) γ 0.533 (13%), 0.439 (1%), 0.319 (3%), 0.091 (28%)	$^{147}_{61}$Pm
$^{149}_{60}$Nd	1.73 h	β^-	β^- 1.56 (6%), 1.43 (38%), 1.13 (26%), 1.03 (30%) γ 0.654 (9%), 0.541 (10%), 0.424 (9%), 0.327 (5%), 0.270 (10%), 0.211 (27%), 0.156 (6%), 0.114 (18%) e^- {0.048} (87%) Pm *K* x-rays ~ 0.042 (33%)	$^{149}_{61}$Pm
Promethium				
$^{143}_{61}$Pm	265 d	EC	γ 0.742 (39%) e^- 0.698 (0.1%), 0.030 (7%), ~0.004 (73%) Nd *K* x-rays 0.043 (2%), 0.042 (11%), 0.037 (61%) Nd *L* x-rays ~ 0.005 (12%)	$^{143}_{60}$Nd
$^{144}_{61}$Pm	363 d	EC	γ 0.778 (2%), 0.696 (100%), 0.618 (98%), 0.477 (44%) e^- 0.433 (0.5%), 0.030 (7%), ~0.004 (74%) Nd *K* x-rays 0.043 (2%), 0.042 (12%), 0.037 (62%), Nd *L* x-rays ~ 0.005 (12%)	$^{144}_{60}$Nd
$^{145}_{61}$Pm	17.7 y	EC	γ 0.072 (2%), 0.067 (0.7%) e^- {0.014} (103%) Nd *K* x-rays 0.043 (2%), 0.042 (12%), 0.037 (61%), Nd *L* x-rays ~ 0.005 (13%)	$^{145}_{60}$Nd
$^{146}_{61}$Pm	5.53 y	EC (66.0%) β^- (34.0%)	β^- 0.795 (31%), 0.162 (2.1%) γ 0.747 (34%), 0.735 (22.5%), 0.633 (2.1%), 0.590 (0.4%), 0.454 (65%), 0.146 (0.2%) e^- 0.700 (0.1%), 0.446 (0.1%), 0.410 (0.8%), 0.030 (4.6%), 0.004 (50%) Nd *K* x-rays ~0.042 (9.4%), ~0.037 (42%), Nd *L* x-rays ~0.005 (8.1%)	$^{146}_{60}$Nd (EC) $^{146}_{62}$Sm (β^-)
$^{147}_{61}$Pm	2.623 y	β^-	β^- 0.225 (99.99%), 0.103 (0.01%)	$^{147}_{62}$Sm
$^{148m}_{61}$Pm	41.8 d	β^- (95.4%) IT (4.6%)	β^- 0.400 (48%), 0.500 (28%), 0.690 (16%) γ 0.288 (12%), 0.414 (19%), 0.550 (94%), 0.599 (13%), 0.630 (89%), 0.725 (33%), 0.915 (17%), 1.014 (20%) e^- {0.021} (21%) Sm *K* x-rays ~ 0.043 (6%), Pm *K* x-rays ~ 0.043 (3%)	$^{148}_{62}$Sm (β^-) $^{148}_{61}$Pm (IT)
$^{148}_{61}$Pm	5.4 d	β^-	β^- 1.02 (40%), 1.93 (10%), 2.48 (50%) γ 0.550 (22%), 0.914 (12%), 1.47 (22%)	$^{148}_{62}$Sm
$^{149}_{61}$Pm	53.08 h	β^-	β^- 1.07 (90%), 0.784 (9%), 0.470 (0.4%), 0.190 (0.6%) γ 0.859 (0.2%), 0.590 (0.1%), 0.286 (2%) Sm *K* x-rays ~ 0.044 (0.2%)	$^{149}_{62}$Sm
$^{150}_{61}$Pm	2.68 h	β^-	β^- 3.45 (5.0%), 3.12 (9.8%), 2.71 (1.4%), 2.41 (1.2%), 2.29 (27.0%), 1.80 (19.7%), 1.74 (3.5%), 1.49 (5.7%), 1.38 (17.8%), 1.19 (3.3%), 1.09 (1.0%), 0.641 (1.2%) γ 1.74 (7%), 1.32 (18%), 1.17 (17%), 0.876 (7%), 0.832 (12%), 0.406 (6%), 0.334 (68%) e^- 0.326 (0.4%), 0.287 (2%), 0.032 (0.2%), ~0.004 (2%) Sm *K* x-rays ~ 0.045 (0.3%), 0.040 (2%) Sm *L* x-rays ~ 0.005 (0.4%)	$^{150}_{62}$Sm

Continued

Table of radioactive isotopes—cont'd

Nuclide $^{A}_{Z}X$	Half-life	Decay mode	Radiation characteristics: energies (MeV) [intensities (%)]	Decay product $^{A}_{Z}Y$
$^{151}_{61}$Pm	28.40 h	β^-	β^- 1.19 (10%), 1.13 (~6%), 1.05 (11%), 0.980 (~3%), 0.835 (43%), 0.728 (~10%), 0.500 (~6%), 0.347 (~11%) γ 0.72 (6%), 0.66 (3%), 0.45 (5%), 0.340 (21%), 0.275 (6%), 0.24 (5%), 0.17 (18%), 0.10 (7%), 0.07 (5%) e^- {0.024} (69%) Sm *K* x-rays ~ 0.043 (29%)	$^{151}_{62}$Sm
Samarium				
$^{145}_{62}$Sm	340 d	EC	γ 0.061 (12%) e^- {0.029} (220%) Sm *K* x-rays 0.044 (25%), ~0.038 (110%), Sm *L* x-rays ~ 0.005 (23%)	$^{145}_{61}$Pm
$^{146}_{62}$Sm	1.03×10^8 y	α	α 2.46 (100%)	$^{142}_{60}$Nd
$^{147}_{62}$Sm	1.06×10^{11} y	α	α 2.25 (100%)	$^{143}_{60}$Nd
$^{151}_{62}$Sm	87 y	β^-	β^- 0.076 (99.1%), 0.055 (0.9%) γ 0.022 (0.03%)	$^{151}_{63}$Eu
$^{153}_{62}$Sm	46.8 h	β^-	β^- 0.810 (20%), 0.710 (49%), 0.640 (30%) γ 0.103 (28%), 0.070 (5%) e^- {0.045} (135%) Eu *K* x-rays ~ 0.043 (63%), Eu *L* x-rays ~ 0.006 (10%)	$^{153}_{63}$Eu
$^{155}_{62}$Sm	22.3 m	β^-	β^- 1.63 (0.5%), 1.52 (92.8%), 1.38 (4.3%), 1.32 (2.2%), 0.859 (0.2%) γ 0.246 (4%), 0.141 (2%), 0.104 (75%) e^- {0.017} (41%) Eu *K* x-rays ~ 0.048 (3%), 0.042 (9%), 0.041 (5%), Eu *L* x-rays ~ 0.006 (3%)	$^{155}_{63}$Eu
Europium				
$^{142}_{63}$Eu	2.4 s	β^+ (92.8%) EC (7.2%)	β^+ 6.62 (80.9%), 5.85 (3.4%), 5.17 (0.5%), 4.96 (2.4%), 4.57 (1.7%), 4.20 (2.1%), 4.10 (1.2%), 3.59 (0.4%), 3.43 (0.2%) γ 1.75 (1.5%), 1.67 (1.3%), 1.66 (1.8%), 1.29 (1.2%), 0.889 (1.1%), 0.786 (10.2%) $\gamma^{\pm}$ 0.511 (185.6%) e^- 0.032 (0.5%), ~0.004 (5.2%) Sm *K* x-rays ~ 0.046 (1%), ~0.040 (4.5%), Sm *L* x-rays ~0.006 (1%)	$^{142}_{62}$Sm
$^{145}_{63}$Eu	5.93 d	EC (98.1%) β^+ (1.9%)	β^+ 1.64 (1.5%), 0.744 (0.4%) γ 2.00 (7%), 1.66 (15%), 0.894 (66%), 0.653 (15%) $\gamma^{\pm}$ 0.511 (3.8%) e^- 0.103 (1%), 0.064 (2%), 0.033 (6%), ~0.004 (73%) Sm *K* x-rays ~ 0.045 (14%), ~0.040 (63%), Sm *L* x-rays ~0.006 (14%)	$^{145}_{62}$Sm
$^{146}_{63}$Eu	4.61 d	EC (95.5%) β^+ (4.5%)	β^+ 1.48 (4.2%), 1.04 (0.1%), 0.810 (0.2%) γ 1.53 (6%), 1.30 (5%), 1.06 (6%), 0.747 (99%), 0.665 (7%), 0.634 (82%), 0.430 (5%) $\gamma^{\pm}$ 0.511 (9.0%) e^- 0.700 (0.4%), 0.587 (0.3%), 0.032 (6%), ~0.005 (69%) Sm *K* x-rays ~ 0.046 (14%), ~0.040 (60%), Sm *L* x-rays ~0.006 (13%)	$^{146}_{62}$Sm

Continued

Table of radioactive isotopes—cont'd

Nuclide $^{A}_{Z}X$	Half-life	Decay mode	Radiation characteristics: energies (MeV) [intensities (%)]	Decay product $^{A}_{Z}Y$
$^{147}_{63}$Eu	24.1 d	EC (99.6%) β^+ (0.4%)	β^+ 0.699 (0.2%), 0.578 (0.1%), 0.502 (0.1%) γ 1.08 (6%), 0.956 (4%), 0.933 (3%), 0.799 (5%), 0.677 (9%), 0.601 (5%), 0.197 (24%), 0.121 (21%) $\gamma^{\pm}$ 0.511 (0.8%) e^- {0.040} (130%) Sm *K* x-rays ~ 0.046 (18%), ~0.040 (79%), Sm *L* x-rays ~0.006 (17%)	$^{147}_{62}$Sm
$^{149}_{63}$Eu	93.1 d	EC	γ 0.528 (0.5%), 0.506 (0.6%), 0.327 (4%), 0.277 (4%), 0.254 (0.6%), 0.022 (2%) e^- 0.032 (6%), 0.020 (11%), 0.015 (53%), ~0.005 (115%) Sm *K* x-rays ~ 0.046 (14%), ~0.040 (61%), Sm *L* x-rays ~0.006 (22%)	$^{149}_{62}$Sm
$^{150m}_{63}$Eu	12.8 h	β^- (89.0%) EC (10.4%) β^+ (0.6%)	β^- 1.013 β^+ 1.28 (0.6%) γ 1.22 (0.2%), 1.16 (0.3%), 0.921 (0.2%), 0.831 (0.2%), 0.406 (2.8%), 0.334 (4.0%) $\gamma^{\pm}$ 0.511 (1.2%) e^- 0.033 (0.7%), ~0.005 (7.8%) Sm *K* x-rays ~ 0.046 (1.6%), ~0.040 (6.8%), Sm *L* x-rays ~0.006 (1.5%)	$^{150}_{64}$Gd (β^-) $^{150}_{62}$Sm (EC, β^+)
$^{150}_{63}$Eu	36.9 y	EC	γ 1.34 (3%), 1.05 (5%), 0.751 (2%), 0.748 (5%), 0.737 (10%), 0.584 (53%), 0.505 (5%), 0.439 (80%), 0.334 (96%) e^- 0.287 (3%), 0.032 (7%), ~0.005 (75%) Sm *K* x-rays 0.045 (15%), 0.040 (65%) Sm *L* x-rays ~ 0.006 (14%)	$^{150}_{62}$Sm
$^{152m1}_{63}$Eu	9.31 h	β^- (72%) EC (28%)	β^- 1.86 (70.0%), 1.52 (1.7%), 0.816 (0.1%), 0.550 (0.2%) γ 1.39 (0.8%), 1.31 (0.9%), 0.970 (0.6%), 0.963 (11.7%), 0.841 (14.2%) e^- 0.114 (2.6%), 0.075 (4.8%), 0.032 (2.1%), ~0.004 (25%) Sm *K* x-rays ~ 0.047 (0.8%), 0.045 (3.8%), 0.040 (20.5%), Sm *L* x-rays ~ 0.006 (4.7%)	$^{152}_{64}$Gd (β^-) $^{152}_{62}$Sm (EC)
$^{152}_{63}$Eu	13.5 y	EC (72.1%) β^- (27.9%) β^+ (0.02%)	β^- 1.47 (8.1%), 0.888 (0.3%), 0.710 (0.3%), 0.696 (13.8%), 0.385 (2.4%), 0.364 (1.0%), 0.213 (0.1%), 0.175 (1.8%) γ 1.41 (21%), 1.13 (14%), 1.09 (10%), 0.965 (15%), 0.779 (13%), 0.344 (27%), 0.245 (8%), 0.122 (29%) $\gamma^{\pm}$ 0.511 (0.04%) e^- {0.045} (106%) Gd *K* x-rays ~ 0.045 (0.87%), Sm *K* x-rays ~ 0.047 (2.4%), 0.045 (11.6%), 0.040 (58.9%), Sm *L* x-rays ~ 0.006 (14.1%)	$^{152}_{62}$Sm (EC, β^+) $^{152}_{64}$Gd (β^-)
$^{154}_{63}$Eu	8.59 y	β^- (99.98%) EC (0.02%)	β^- 1.84 (10.0%), 1.15 (0.7%), 0.972 (3.5%), 0.841 (16.8%), 0.717 (0.3%), 0.705 (0.7%), 0.571 (36.3%), 0.438 (0.3%), 0.352 (1.6%), 0.307 (0.8%), 0.249 (28.6%) γ 1.28 (37%), 1.00 (31%), 0.876 (12%), 0.759 (5%), 0.724 (21%), 0.593 (6%), 0.248 (7%), 0.123 (38%) e^- 0.121 (3.9%), 0.114 (16.7%), 0.073 (26.7%), 0.034 (1.9%), ~0.005 (33.3%) Gd *K* x-rays ~ 0.049 (5.1%), 0.042 (20.5%), Gd *L* x-rays ~ 0.006 (7.1%)	$^{154}_{64}$Gd (β^-)

Continued

Table of radioactive isotopes—cont'd

Nuclide $^{A}_{Z}X$	Half-life	Decay mode	Radiation characteristics: energies (MeV) [intensities (%)]	Decay product $^{A}_{Z}Y$
$^{155}_{63}$Eu	4.96 y	β^-	β^- 0.250 (13%), 0.186 (8%), 0.15 (75%), 0.100 (~4%) γ 0.105 (20%), 0.087 (32%) e^- {0.018} (87%) Gd *K* x-rays ~ 0.045 (24%), Gd *L* x-rays ~ 0.006 (7%)	$^{155}_{64}$Gd
$^{156}_{63}$Eu	15 d	β^-	β^- 2.46 (32%), 1.215 (11%), 0.495 (34%), 0.300 (23%) γ 0.089 (9%), 0.646 (7%), 0.723 (6%), 0.812 (10%), 1.065 (5%), 1.153 (7%), 1.230 (9%), 1.242 (7%) e^- {0.030} (57%) Gd *K* x-rays ~ 0.047 (13%)	$^{156}_{64}$Gd
Gadolinium				
$^{146}_{64}$Gd	48.27 d	EC	γ 0.154 (45%), 0.115 (44%) e^- {0.126} (313%) Eu *K* x-rays 0.048 (6%), 0.047 (28%), 0.041 (146%), Eu *L* x-rays 0.006 (33%)	$^{146}_{63}$Eu
$^{147}_{64}$Gd	38.06 h	EC (99.9%) β^+ (0.1%)	β^+ 1.16 (0.1%) γ 1.13 (6%), 1.07 (7%), 0.929 (18%), 0.893 (7%), 0.778 (11%), 0.766 (10%), 0.559 (6%), 0.396 (31%), 0.370 (16%), 0.229 (58%) $\gamma^{\pm}$ 0.511 (0.2%) e^- {0.058} (103%) Eu *K* x-rays 0.048 (3%), 0.047 (13%), 0.041 (25%), Eu *L* x-rays 0.006 (16%)	$^{147}_{63}$Eu
$^{148}_{64}$Gd	74.6 y	α	α 3.18 (100%)	$^{144}_{62}$Sm
$^{149}_{64}$Gd	9.28 d	EC	γ 0.788 (7%), 0.749 (8%), 0.534 (3%), 0.516 (3%), 0.347 (24%), 0.299 (29%), 0.150 (48%) e^- {0.066} (140%) Eu *K* x-rays 0.048 (4%), 0.047 (16%), 0.041 (86%), Eu *L* x-rays 0.006 (20%)	$^{149}_{63}$Eu
$^{150}_{64}$Gd	1.79×10^6 y	α	α 2.73 (100%)	$^{146}_{62}$Sm
$^{151}_{64}$Gd	123.9 d	EC	γ 0.307 (1%), 0.243 (6%), 0.154 (6%), 0.021 (3%) e^- {0.031} (224%) Eu *K* x-rays 0.048 (3%), 0.047 (12%), 0.041 (66%), Eu *L* x-rays 0.006 (26%)	$^{151}_{63}$Eu
$^{153}_{64}$Gd	241.6 d	EC	γ 0.103 (20%), 0.099 (30%), 0.070 (2.4%) e^- {0.040} (160%) Eu *K* x-rays ~ 0.045 (120%), Eu *L* x-rays ~ 0.006 (11%)	$^{153}_{63}$Eu
$^{159}_{64}$Gd	18.56 h	β^-	β^- 0.950 (63%), 0.89 (24%), 0.60 (13%) γ 0.363 (11%), 0.058 (3%) e^- {0.006} (42%) Tb *K* x-rays ~ 0.047 (20%), Tb *L* x-rays ~ 0.007 (4%)	$^{159}_{65}$Tb
Terbium				
$^{151}_{65}$Tb	17.61 h	EC (99.84%) β^+ (0.16%)	β^+ 1.26 (0.14%), 0.740 (0.02%) γ 0.831 (3%), 0.522 (2%), 0.504 (0.5%), 0.380 (6%) $\gamma^{\pm}$ 0.511 (0.32%) e^- 0.329 (0.2%), 0.035 (0.4%), 0.005 (5%) Gd *K* x-rays ~ 0.049 (1%), 0.043 (5%), Gd *L* x-rays ~ 0.006 (1%)	$^{151}_{64}$Gd

Continued

Table of radioactive isotopes—cont'd

Nuclide $^{A}_{Z}X$	Half-life	Decay mode	Radiation characteristics: energies (MeV) [intensities (%)]	Decay product $^{A}_{Z}Y$
$^{152m}_{65}$Tb	4.2 m	IT (78.80%) EC (20.57%) β^+ (0.63%)	β^+ 1.58 (0.05%), 1.45 (0.04%), 1.19 (0.01%), 0.936 (0.53%) γ 0.519 (5%), 0.472 (12%), 0.411 (18%), 0.344 (20%), 0.283 (60%), 0.277 (9%), 0.159 (17%), 0.059 (7%) $\gamma^{\pm}$ 0.511 (1.3%) e^- {0.142} (277%) Tb *K* x-rays ~0.051 (15%), 0.044 (65%), Tb *L* x-rays 0.006 (24%) Gd *K* x-rays ~ 0.049 (3%), 0.042 (13%), Gd *L* x-rays ~ 0.006 (3%)	$^{152}_{65}$Tb (IT) $^{152}_{64}$Gd (EC, β^+)
$^{152}_{65}$Tb	17.5 h	EC (83.3%) β^+ (16.7%)	β^+ 2.82 (6.2%), 2.48 (5.5%), 2.21 (0.9%), 2.07 (0.1%), 1.90 (1.9%), 1.72 (1.0%), 1.51 (0.6%), 1.22 (0.2%), 1.18 (0.1%), 0.966 (0.1%), 0.887 (0.1%) γ 1.31 (4%), 0.778 (6%), 0.586 (9%), 0.411 (4%), 0.344 (65%), 0.271 (9%) $\gamma^{\pm}$ 0.511 (33.4%) e^- 0.565 (1%), 0.294 (2%), 0.035 (5%), 0.005 (62%) Gd *K* x-rays ~ 0.049 (13%), 0.043 (55%), Gd *L* x-rays ~ 0.006 (13%)	$^{152}_{64}$Gd
$^{153}_{65}$Tb	2.34 d	EC	γ 0.212 (32%), 0.170 (6%), 0.110 (7%), 0.102 (6%), 0.088 (7%) e^- {0.042} (210%) Gd *K* x-rays ~ 0.049 (19%), 0.042 (87%), Gd *L* x-rays ~ 0.006 (27%)	$^{153}_{64}$Gd
$^{154}_{65}$Tb	21.5 h	EC (97.6%) β^+ (2.4%)	β^+ 2.53 (1.5%). 1.85 (0.5%), 1.29 (0.2%), 1.11 (0.1%), 0.410 (0.1%) γ 2.19 (14%), 2.06 (9%), 1.99 (10%), 1.32 (8%), 1.27 (13%), 1.12 (8%), 0.878 (8%), 0.123 (26%) $\gamma^{\pm}$ 0.511 (4.8%) e^- {0.044} (117%) Gd *K* x-rays ~ 0.049 (15%), 0.042 (66%), Gd *L* x-rays ~ 0.006 (17%)	$^{154}_{64}$Gd
$^{155}_{65}$Tb	5.32 d	EC	γ 0.180 (8%), 0.163 (7%), 0.105 (25%), 0.086 (32%) e^- {0.073} (202%) Gd *K* x-rays ~ 0.049 (20%), 0.042 (86%), Gd *L* x-rays ~ 0.006 (26%)	$^{155}_{64}$Gd
$^{156}_{65}$Tb	5.35 d	EC	γ 1.42 (12%), 1.22 (32%), 1.16 (18%), 1.06 (15%), 0.534 (67%), 0.356 (14%), 0.198 (41%), 0.089 (18%) e^- {0.085} (213%) Gd *K* x-rays ~ 0.049 (21%), 0.042 (89%), Gd *L* x-rays ~ 0.006 (27%)	$^{156}_{64}$Gd
$^{157}_{65}$Tb	71 y	EC	e^- 0.035 (1%), 0.005 (62%) Gd *K* x-rays ~ 0.049 (3%), 0.042 (12%), Gd *L* x-rays ~ 0.006 (13%)	$^{157}_{64}$Gd
$^{158}_{65}$Tb	180 y	EC (83.4%) β^- (16.6%)	β^- 0.838 (15.5%), 0.620 (1.1%) γ 0.962 (20%), 0.944 (44%), 0.780 (10%), 0.182 (10%), 0.098 (4%), 0.079 (12%) e^- {0.065} (181%) Gd *K* x-rays ~ 0.049 (15%), 0.043 (64%), 0.042 (23%) Gd *L* x-rays ~ 0.006 (22%)	$^{158}_{64}$Gd (EC) $^{158}_{66}$D*y* (β^-)

Continued

Table of radioactive isotopes—cont'd

Nuclide $^{A}_{Z}X$	Half-life	Decay mode	Radiation characteristics: energies (MeV) [intensities (%)]	Decay product $^{A}_{Z}Y$
$^{160}_{65}$Tb	72.1 d	β^-	β^- 1.74 (0.4%), 1.55 (0.1%), 0.874 (27%), 0.791 (7%), 0.575 (46%), 0.553 (4%), 0.481 (10%), 0.441 (5%) γ 1.27 (7%), 1.18 (15%), 0.966 (25%), 0.879 (30%), 0.299 (30%), 0.197 (6%), 0.087 (12%) e^- {0.050} (102%) Dy *K* x-rays ~ 0.050 (20%), Dy *L* x-rays ~ 0.007 (9%)	$^{160}_{66}$Dy
$^{161}_{65}$Tb	6.90 d	β^-	β^- 0.590 (10%), 0.520 (55%), 0.460 (35%) γ 0.075 (10%), 0.057 (5%), 0.049 (19%), 0.026 (21%) e^- {0.042} (193%) Dy *K* x-rays ~ 0.050 (21%), Dy *L* x-rays ~ 0.007 (19%)	$^{161}_{66}$Dy
Dysprosium				
$^{152}_{66}$Dy	2.38 h	EC (99.9%) α (0.1%)	α 3.62 (0.1%) γ 0.257 (98%) e^- 0.204 (2%), 0.036 (5%), 0.005 (69%) Tb *K* x-rays ~0.051 (15%), 0.044 (61%), Tb *L* x-rays 0.006 (16%)	$^{152}_{65}$Tb (EC) $^{148}_{64}$Gd (α)
$^{153}_{66}$Dy	6.4 h	EC (98.9%) β^+ (1.1%)	β^+ 1.15 (0.1%), 0.985 (0.2%), 0.934 (0.1%), 0.886 (0.6%), 0.874 (0.1%) γ 0.274 (3%), 0.254 (9%), 0.244 (4%), 0.214 (11%), 0.147 (4%), 0.099 (11%), 0.080 (11%) $\gamma^{\pm}$ 0.511 (2.2%) e^- {0.066} (286%) Tb *K* x-rays ~0.051 (32%), 0.044 (135%), Tb *L* x-rays 0.006 (35%)	$^{153}_{65}$Tb
$^{154}_{66}$Dy	3.0×10^6 y	α	α 2.87 (100%)	$^{150}_{64}$Gd
$^{155}_{66}$Dy	9.9 h	EC (98.6%) β^+ (1.4%)	β^+ 1.07 (0.1%), 0.846 (1.3%) γ 1.17 (4%), 0.227 (68%), 0.184 (3%), 0.065 (2%) $\gamma^{\pm}$ 0.511 (2.8%) e^- {0.020} (113%) Tb *K* x-rays ~0.051 (18%), 0.044 (76%), Tb *L* x-rays 0.006 (20%)	$^{155}_{65}$Tb
$^{157}_{66}$Dy	8.14 h	EC	γ 0.326 (93%), 0.182 (1%) e^- 0.274 (1%), 0.036 (6%), 0.009 (1%), 0.005 (70%) Tb *K* x-rays ~0.051 (15%), 0.044 (64%), Tb *L* x-rays 0.006 (16%)	$^{157}_{65}$Tb
$^{159}_{66}$Dy	144.4 d	EC	γ 0.058 (2%) e^- 0.049 (3%), 0.036 (7%), 0.006 (20%), 0.005 (84%) Tb *K* x-rays ~0.051 (17%), 0.044 (74%), Tb *L* x-rays 0.006 (19%)	$^{159}_{65}$Tb
$^{165}_{66}$Dy	2.334 h	β^-	β^- 1.31 (80%), 1.22 (16%), others (4%) γ 0.716 (0.7%), 0.633 (0.7%), 0.361 (1.1%), 0.095 (4%) e^- {0.007} (20%) Ho *K* x-rays ~ 0.052 (10%), Ho *L* x-rays ~ 0.007 (2%)	$^{165}_{67}$Ho
$^{166}_{66}$Dy	81.6 h	β^-	β^- 0.487 (2.0%), 0.404 (97.0%), 0.061 (1.0%) γ 0.082 (14%), 0.028 (1%) e^- {0.040} (180%) Ho *K* x-rays 0.055 (2%), 0.054 (8%), 0.047 (39%), Ho *L* x-rays ~ 0.007 (18%)	$^{166}_{67}$Ho

Continued

Table of radioactive isotopes—cont'd

Nuclide $^{A}_{Z}X$	Half-life	Decay mode	Radiation characteristics: energies (MeV) [intensities (%)]	Decay product $^{A}_{Z}Y$
Holmium				
$^{164}_{67}$Ho	29.0 m	EC (60.0%) β^- (40.0%)	β^- 0.963 (28.0%), 0.871 (12.0%) γ 0.091 (2.3%), 0.073 (1.8%) e^- {0.022} (85%) Dy *K* x-rays 0.052 (9.6%), 0.045 (40.4%), Dy *L* x-rays 0.007 (12.4%), Er *K* x-rays 0.056 (0.6%), 0.049 (2.2%), Er *L* x-rays 0.007 (1.6%)	$^{164}_{66}$D*y* (EC) $^{164}_{68}$Er (β^-)
$^{166m}_{67}$Ho	1200 y	β^-	β^- 0.065 (100%) γ 0.830 (11%), 0.810 (60%), 0.711 (58%), 0.532 (12%), 0.412 (12%), 0.280 (30%), 0.184 (75%), 0.081 (12%) e^- {0.114} (188%) Er *K* x-rays ~ 0.056 (39%), Er *L* x-rays ~ 0.007 (19%)	$^{166}_{68}$Er
$^{166}_{67}$Ho	26.8 h	β^-	β^- 1.85 (48.8%), 1.77 (49.9%), 0.394 (1%), 0.192 (0.3%) γ 1.38 (1%), 0.080 (6.6%) e^- {0.029} (72%) Er *K* x-rays ~ 0.056 (9%), 0.049 (8%) Er *L* x-rays ~ 0.007 (8%)	$^{166}_{68}$Er
Erbium				
$^{165}_{68}$Er	10.36 h	EC	e^- 0.038 (5%), 0.005 (66%) Ho *K* x-rays 0.055 (3%), 0.054 (12%), 0.047 (22%), Ho *L* x-rays ~ 0.007 (17%)	$^{165}_{67}$Ho
$^{169}_{68}$Er	9.40 d	β^-	β^- 0.340 (58%), 0.332 (42%) γ 0.008 (0.3%)	$^{169}_{69}$Tm
$^{171}_{68}$Er	7.52 h	β^-	β^- 1.49 (2%), 1.07 (90%), 0.575 (8%) γ 0.308 (63%), 0.296 (28%), 0.124 (9%), 0.112 (21%) e^- {0.058} (209%) Tm *K* x-rays ~ 0.051 (46%), Tm *L* x-rays ~ 0.007 (13%)	$^{171}_{69}$Tm
$^{172}_{68}$Er	49.3 h	β^-	β^- 0.891 (2.0%), 0.484 (3.2%), 0.416 (2.0%), 0.356 (46.4%), 0.281 (46.4%) γ 0.610 (44%), 0.446 (3%), 0.404 (42%), 0.068 (3%) e^- {0.031} (77%) Tm *K* x-rays 0.059 (1%), 0.057 (5%), 0.051 (16%) 0.049 (9%), Tm *L* x-rays ~ 0.007 (8%)	$^{172}_{69}$Tm
Thulium				
$^{166}_{69}$Tm	7.70 h	EC (99.0%) β^+(1.0%)	β^+ 1.93 (1.0%) γ 2.09 (8%), 2.05 (17%), 1.37 (8%), 1.27 (15%), 1.17 (11%), 0.786 (10%), 0.779 (19%), 0.705 (11%), 0.691 (7%), 0.184 (16%), 0.080 (12%) $\gamma^{\pm}$ 0.511 (2.0%) e^- {0.095} (206%) Er *K* x-rays ~0.056 (19%), 0.049 (50%), 0.048 (29%), Er *L* x-rays 0.007 (32%)	$^{166}_{68}$Er
$^{167}_{69}$Tm	9.25 d	EC	γ 0.531 (2%), 0.208 (42%), 0.057 (5%) e^- {0.126} (197%) Er *K* x-rays ~0.056 (18%), 0.049 (48%), 0.048 (27%), Er *L* x-rays 0.007 (31%)	$^{167}_{68}$Er

Continued

Table of radioactive isotopes—cont'd

Nuclide $^{A}_{Z}X$	Half-life	Decay mode	Radiation characteristics: energies (MeV) [intensities (%)]		Decay product $^{A}_{Z}Y$
$^{168}_{69}$Tm	93.1 d	EC	γ	0.830 (7%), 0.821 (12%), 0.815 (51%), 0.741 (13%), 0.731 (5%), 0.720 (12%), 0.631 (9%), 0.447 (24%), 0.198 (55%), 0.184 (18%), 0.080 (11%)	$^{168}_{68}$Er
			e^-	{0.080} (220%)	
				Er *K* x-rays ~0.056 (20%), 0.049 (51%), 0.048 (29%),	
				Er *L* x-rays 0.007 (34%)	
$^{170}_{69}$Tm	128.6 d	β^- (99.87%) EC (0.13%)	β^-	0.968 (81.6%), 0.884 (18.3%)	$^{170}_{70}$Yb (β^-) $^{170}_{68}$Er (EC)
			γ	0.084 (3.3%)	
			e^-	0.082 (2.8%), 0.074 (9.3%), 0.023 (3.6%), 0.006 (9.4%)	
				Yb *K* x-rays ~ 0.060 (0.6%), 0.052 (2.5%)	
				Yb *L* x-rays ~ 0.007 (3%)	
$^{171}_{69}$Tm	1.92 y	β^-	β^-	0.097 (98%), ~0.03 (2%)	$^{171}_{70}$Yb
			γ	0.067 (~0.2%)	
Ytterbium					
$^{166}_{70}$Yb	56.7 h	EC	γ	0.082 (16%)	$^{166}_{69}$Tm
			e^-	0.080 (2%), 0.072 (11%), 0.041 (8%), 0.023 (71%), 0.006 (117%)	
				Tm *K* x-rays 0.059 (5%), 0.057 (22%), 0.051 (69%), 0.049 (40%),	
				Tm *L* x-rays 0.007 (34%)	
$^{167}_{70}$Yb	17.5 m	EC (99.5%) β^+ (0.5%)	β^+	0.639 (0.5%)	$^{167}_{69}$Tm
			γ	0.176 (23%), 0.113 (55%), 0.106 (22%), 0.063 (5%)	
			e^-	{0.078} (337%)	
				Tm *K* x-rays 0.059 (7%), 0.057 (30%), 0.051 (94%),	
				Tm *L* x-rays 0.007 (46%)	
$^{169}_{70}$Yb	32.02 d	EC	γ	0.308 (10%), 0.198 (35%), 0.177 (22%), 0.131 (11%), 0.110 (18%), 0.063 (45%)	$^{169}_{69}$Tm
			e^-	{0.112} (307%)	
				Tm *K* x-rays ~ 0.053 (185%),	
				Tm *L* x-rays ~ 0.008 (45%)	
$^{175}_{70}$Yb	4.19 d	β^-	β^-	0.466 (86.5%), 0.353 (2.6%), 0.217 (0.8%), 0.073 (10.1%)	$^{175}_{71}$Lu
			γ	0.396 (6%), 0.283 (3.7%), 0.114 (2%)	
				Lu *K* x-rays ~ 0.055 (3.6%)	
Lutetium					
$^{169}_{71}$Lu	34.06 h	EC (99.4%) β^+ (0.6%)	β^+	1.27 (0.54%), 1.08 (0.05%), 0.881 (0.01%)	$^{169}_{70}$Yb
			γ	1.45 (13%), 1.33 (7%), 0.960 (21%), 0.889 (5%), 0.191 (19%)	
			$\gamma^{\pm}$	0.511 (1.2%)	
			e^-	{0.031} (178%)	
				Yb *K* x-rays 0.061 (4%), 0.059 (18%), 0.053 (56%), 0.051 (32%),	
				Yb *L* x-rays 0.007 (33%)	
$^{170}_{71}$Lu	2.012 d	EC (99.7%) β^+ (0.3%)	β^+	2.44 (0.24%), 1.20 (0.03%), 1.07 (0.03%)	$^{170}_{70}$Yb
			γ	2.96 (3%), 2.78 (3%), 2.13 (5%), 2.04 (8%), 1.45 (7%), 1.36 (8%), 1.29 (12%), 1.22 (8%), 1.14 (10%), 1.05 (8%), 0.985 (5%), 0.084 (9%)	
			$\gamma^{\pm}$	0.511 (0.6%)	
			e^-	0.082 (8%), 0.074 (33%), 0.042 (5%), 0.023 (5%), 0.006 (94%)	
				Yb *K* x-rays 0.061 (3%), 0.059 (14%), 0.053 (43%), 0.051 (25%), Yb *L* x-rays 0.007 (29%)	
$^{171}_{71}$Lu	8.24 d	EC	γ	0.740 (48%), 0.667 (11%), 0.075 (8%), 0.019 (14%)	$^{171}_{70}$Yb
			e^-	{0.089} (399%)	
				Yb *K* x-rays 0.061 (4%), 0.059 (20%), 0.052 (61%), 0.051 (35%), Yb *L* x-rays 0.007 (58%)	

Continued

Table of radioactive isotopes—cont'd

Nuclide $^{A}_{Z}X$	Half-life	Decay mode	Radiation characteristics: energies (MeV) [intensities (%)]	Decay product $^{A}_{Z}Y$
$^{172}_{71}$Lu	6.70 d	EC	γ 1.09 (63%), 0.912 (15%), 0.900 (30%), 0.810 (17%), 0.697 (6%), 0.203 (5%), 0.181 (21%), 0.079 (11%) e^- {0.118} (262%) Yb *K* x-rays 0.061 (4%), 0.059 (18%), 0.052 (55%), 0.051 (32%), Yb *L* x-rays 0.007 (43%)	$^{172}_{70}$Yb
$^{173}_{71}$Lu	1.37 y	EC	γ 0.272 (21%), 0.171 (3%), 0.101 (5%), 0.078 (12%) e^- {0.016} (238%) Yb *K* x-rays 0.061 (5%), 0.059 (24%), 0.052 (76%), 0.051 (44%), Yb *L* x-rays 0.007 (40%)	$^{173}_{70}$Yb
$^{174m}_{71}$Lu	142 d	IT (99.38%) EC (0.62%)	γ 0.067 (7%), 0.044 (12%) e^- {0.117} (424%) Lu *K* x-rays 0.063 (3%), 0.061 (11%), 0.054 (34%), 0.053 (20%), Lu *L* x-rays ~ 0.008 (52%)	$^{174}_{71}$Lu (IT) $^{174}_{70}$Yb (EC)
$^{174}_{71}$Lu	3.31 y	EC	γ 1.24 (5%), 0.076 (6%) e^- 0.074 (9%), 0.066 (35%), 0.042 (5%), 0.015 (10%), 0.006 (95%) Yb *K* x-rays 0.061 (3%), 0.059 (13%), 0.052 (42%), 0.051 (24%), Yb *L* x-rays 0.007 (30%)	$^{174}_{70}$Yb
$^{176}_{71}$Lu	3.76×10^{10} y	β^-	β^- 0.593 (99.6%), 0.192 (0.4%) γ 0.307 (94%), 0.202 (78%), 0.088 (15%) e^- {0.115} (177%) Hf *K* x-rays ~ 0.065 (1%), 0.063 (5%), 0.055 (10%), 0.054 (17%), Hf *L* x-rays 0.008 (23%)	$^{176}_{72}$Hf
$^{177m}_{71}$Lu	160.44 d	β^- (78.6%) IT (21.4%)	β^- 0.153 (78.6%) γ 0.418 (21%), 0.378 (30%), 0.327 (18%), 0.320 (12%), 0.282 (14%), 0.228 (37%), 0.208 (57%), 0.204 (14%), 0.174 (17%), 0.153 (17%), 0.128 (16%), 0.113 (22%), 0.105 (12%) e^- {0.236} (348%) Hf *K* x-rays ~ 0.065 (4%), 0.063 (19%), 0.055 (34%), 0.054 (58%), Hf *L* x-rays 0.008 (46%), Lu *K* x-rays 0.061 (3%), 0.054 (9%), 0.053 (5%), Lu *L* x-rays 0.008 (8%)	$^{177}_{72}$Hf (β^-) $^{177}_{71}$Lu (IT)
$^{177}_{71}$Lu	6.71 d	β^-	β^- 0.497 (90%), 0.384 (3%), 0.249 (0.3%), 0.175 (6.7%) γ 0.208 (6%), 0.113 (3%) e^- {0.015} (24%) Hf *K* x-rays ~ 0.058 (6%), Hf *L* x-rays ~ 0.008 (3%)	$^{177}_{72}$Hf
Hafnium				
$^{172}_{72}$Hf	1.87 y	EC	γ 0.128 (2%), 0.126 (11%), 0.123 (1%), 0.114 (3%), 0.081 (5%), 0.067 (5%), 0.060 (1%) e^- {0.147} (503%) Lu *K* x-rays 0.063 (5%), 0.061 (20%), 0.054 (63%), 0.053 (36%), Lu *L* x-rays ~ 0.008 (75%)	$^{172}_{71}$Lu
$^{173}_{72}$Hf	23.6 h	EC	γ 0.311 (11%), 0.307 (6%), 0.297 (34%), 0.162 (7%), 0.140 (13%), 0.135 (5%), 0.124 (83%) e^- {0.047} (180%) Lu *K* x-rays 0.063 (4%), 0.061 (60%), 0.054 (53%), 0.053 (31%), Lu *L* x-rays ~ 0.008 (29%)	$^{173}_{71}$Lu
$^{175}_{72}$Hf	70 d	EC	γ 0.433 (1.4%), 0.343 (85%), 0.089 (3.4%) e^- {0.044} (83%) Lu *K* x-rays ~ 0.058 (93%), Lu *L* x-rays ~ 0.008 (23%)	$^{175}_{71}$Lu

Continued

Table of radioactive isotopes—cont'd

Nuclide $^{A}_{Z}X$	Half-life	Decay mode	Radiation characteristics: energies (MeV) [intensities (%)]	Decay product $^{A}_{Z}Y$
$^{180m}_{72}$Hf	5.47 h	IT (99.7%) β^- (0.3%)	β^- 0.210 (0.29%), 0.112 (0.01%) γ 0.500 (14%), 0.443 (82%), 0.332 (94%), 0.215 (81%), 0.093 (17%), 0.058 (48%) e^- {0.148} (168%) Hf *K* x-rays 0.065 (1%), 0.063 (6%), 0.055 (10%), 0.054 (17%), Hf *L* x-rays 0.008 (22%)	$^{180}_{72}$Hf (IT) $^{180}_{73}$Ta (β^-)
$^{181}_{72}$Hf	42.4 d	β^-	β^- 0.55 (<0.5%), 0.408 (93%), 0.404 (7%) γ 0.482 (81%), 0.346 (13%), 0.133 (36%) e^- {0.068} (92%) Ta *K* x-rays ~ 0.060 (27%), Ta *L* x-rays ~ 0.009 (12%)	$^{181}_{73}$Ta
$^{182}_{72}$Hf	8.9×10^6 y	β^-	β^- 0.105 (100%) γ 0.270 (79%), 0.156 (7%), 0.114 (3%) e^- {0.033} (38%) Ta *K* x-rays 0.067 (1%), 0.065 (3%), 0.057 (8%), 0.056 (5%), Ta *L* x-rays 0.008 (5%)	$^{182}_{73}$Ta
Tantalum				
$^{177}_{73}$Ta	56.56 h	EC	γ 0.208 (1%), 0.113 (7%) e^- 0.110 (2%), 0.102 (8%), 0.047 (6%), 0.044 (4%), 0.006 (70%) Hf *K* x-rays 0.065 (3%), 0.063 (14%), 0.055 (24%), 0.054 (41%), Hf *L* x-rays 0.008 (25%)	$^{177}_{72}$Hf
$^{178}_{73}$Ta	9.31 m	EC (98.8%) β^+ (1.2%)	β^+ 0.915 (0.9%), 0.822 (0.3%) γ 1.35 (1%), 1.34 (1%), 0.093 (7%) $\gamma^{\pm}$ 0.511 (2.4%) e^- 0.045 (4%), 0.006 (60%) Hf *K* x-rays 0.065 (3%), 0.063 (13%), 0.055 (22%), 0.054 (38%), Hf *L* x-rays 0.008 (21%)	$^{178}_{72}$Hf
$^{179}_{73}$Ta	1.82 y	EC	e^- 0.045 (2%), 0.006 (58%) Hf *K* x-rays 0.065 (2%), 0.063 (7%), 0.055 (13%), 0.054 (22%), Hf *L* x-rays 0.008 (20%)	$^{179}_{72}$Hf
$^{180}_{73}$Ta	8.15 h	EC (86.0%) β^- (14.0%)	β^- 0.708 (10.0%), 0.604 (3.6%) γ 0.104 (0.8%), 0.093 (4.5%) e^- 0.091 (4.6%), 0.082 (12.3%), 0.045 (3.6%), 0.028 (5%), 0.006 (65.4%) Hf *K* x-rays 0.065 (2.6%), 0.063 (11.5%), 0.054 (55.5%) Hf *L* x-rays 0.008 (22.5%)	$^{180}_{72}$Hf (EC) $^{180}_{74}$W (β^-)
$^{182}_{73}$Ta	115.0 d	β^-	β^- 0.540 (45%), 0.408 (24%), 0.246 (31%) γ 1.23 (13%), 1.22 (27%), 1.19 (16%), 1.12 (34%), 0.222 (8%), 0.152 (7%), 0.100 (14%), 0.068 (42%) e^- {0.081} (161%) W *K* x-rays ~ 0.065 (36%), W *L* x-rays ~ 0.009 (23%)	$^{182}_{74}$W
Tungsten				
$^{177}_{74}$W	132 m	EC (99.8%) β^+ (0.2%)	β^+ 0.760 (0.2%) γ 1.04 (10%), 0.612 (6%), 0.427 (12%), 0.417 (6%), 0.186 (22%), 0.116 (47%), 0.115 (8%), 0.050 (6%) $\gamma^{\pm}$ 0.511 (0.4%) e^- {0.092} (330%) Ta *K* x-rays 0.067 (6%), 0.065 (24%), 0.057 (73%), 0.056 (43%), Ta *L* x-rays 0.008 (60%)	$^{177}_{73}$Ta
$^{178}_{74}$W	21.6 d	EC	e^- 0.046 (1%), 0.006 (54%) Ta *K* x-rays 0.067 (1%), 0.065 (4%), 0.057 (12%), 0.056 (7%), Ta *L* x-rays 0.008 (20%)	$^{178}_{73}$Ta

Continued

Table of radioactive isotopes—cont'd

Nuclide $^{A}_{Z}X$	Half-life	Decay mode	Radiation characteristics: energies (MeV) [intensities (%)]	Decay product $^{A}_{Z}Y$
$^{181}_{74}$W	120.95 d	EC	γ 0.152 (0.1%), 0.136 (0.1%), 0.006 (1%) e^- {0.008} (85%) Ta *K* x-rays ~ 0.060 (65%), Ta *L* x-rays ~ 0.010 (20%)	$^{181}_{73}$Ta
$^{185}_{74}$W	75.1 d	β^-	β^- 0.433 (100%)	$^{185}_{75}$Re
$^{187}_{74}$W	23.85 h	β^-	β^- 1.32 (20%), 0.630 (70%), 0.340 (10%) γ 0.773 (4%), 0.686 (27%), 0.618 (6%), 0.552 (5%), 0.479 (23%), 0.134 (9%), 0.072 (11%) e^- {0.037} (181%) Re *K* x-rays ~ 0.065 (20%), Re *L* x-rays ~ 0.009 (23%)	$^{187}_{75}$Re
$^{188}_{74}$W	69.78 d	β^-	β^- 0.349 (99%), 0.285 (0.2%), 0.058 (0.8%) γ 0.291 (0.4%), 0.227 (0.2%), 0.063 (0.1%) e^- 0.050 (0.3%), 0.006 (0.3%) Re *L* x-rays ~0.009 (0.1%)	$^{188}_{75}$Re
Rhenium				
$^{181}_{75}$Re	19.9 h	EC	γ 1.00 (6%), 0.639 (6%), 0.365 (56%), 0.361 (20%) e^- {0.135} (207%) W *K* x-rays 0.069 (4%), 0.067 (19%), 0.059 (58%), 0.058 (34%), W *L* x-rays 0.008 (44%)	$^{181}_{74}$W
$^{182m}_{75}$Re	12.7 h	EC (98.6%) β^+ (1.4%)	β^+ 1.68 (1.4%) γ 1.22 (26%), 1.19 (15%), 1.12 (32%), 0.152 (7%), 0.100 (14%), 0.067 (38%) $\gamma^{\pm}$ 0.511 (2.8%) e^- {0.074} (198%) W *K* x-rays 0.069 (4%), 0.067 (17%), 0.059 (52%), 0.058 (30%), W *L* x-rays 0.008 (42%)	$^{182}_{74}$W
$^{182}_{75}$Re	64.0 h	EC	γ 1.42 (10%), 1.23 (15%), 1.22 (18%), 1.19 (9%), 1.12 (22%), 1.07 (11%), 0.351(10%), 0.286 (7%), 0.276 (9%), 0.256 (10%), 0.229 (26%), 0.222 (15%), 0.169 (11%), 0.156 (7%), 0.152 (9%), 0.130 (8%), 0.100 (17%), 0.067 (22%) e^- {0.213} (392%) W *K* x-rays 0.069 (7%), 0.067 (28%), 0.059 (85%), 0.058 (50%), W *L* x-rays 0.008 (70%)	$^{182}_{74}$W
$^{183}_{75}$Re	71 d	EC	γ 0.292 (3.2%), 0.209 (3%), 0.162 (24%), 0.109 (3%), 0.108 (2%), 0.099 (3%), 0.052 (2%), 0.046 (8%) e^- {0.105} (278%) W *K* x-rays ~ 0.063 (108%), W *L* x-rays ~ 0.009 (55%)	$^{183}_{74}$W
$^{184m}_{75}$Re	169 d	IT (74.5%) EC (25.5%)	γ 0.920 (8%), 0.318 (6%), 0.252 (11%), 0.216 (10%), 0.161 (7%), 0.111 (6%), 0.104 (14%) e^- {0.140} (300%) Re *K* x-rays 0.071 (2%), 0.069 (8%), 0.061 (24%), 0.060 (14%), Re *L* x-rays 0.009 (30%), W *K* x-rays 0.069 (1%), 0.067 (5%), 0.059 (14%), 0.058 (8%), W *L* x-rays 0.008 (17%)	$^{184}_{75}$Re (IT) $^{184}_{74}$W (EC)

Continued

Table of radioactive isotopes—cont'd

Nuclide $^{A}_{Z}X$	Half-life	Decay mode	Radiation characteristics: energies (MeV) [intensities (%)]		Decay product $^{A}_{Z}Y$
$^{184}_{75}$Re	35.4 d	EC	γ	0.903 (38%), 0.895 (16%), 0.792 (38%), 0.111 (17%)	$^{184}_{74}$W
			e^-	{0.054} (132%)	
				W *K* x-rays 0.069 (3%), 0.067 (14%), 0.059 (43%), 0.058 (25%),	
				W *L* x-rays 0.008 (33%)	
$^{186}_{75}$Re	3.718 d	β^- (92.53%) EC (7.47%)	β^-	1.07 (70.99%), 0.932 (21.54%)	$^{186}_{76}$Os (β^-) $^{186}_{74}$W (EC)
			γ	0.137 (9.5%), 0.122 (0.6%)	
			e^-	0.124 (6.1%), 0.063 (4.2%), 0.007 (11.5%)	
				W *K* x-rays ~ 0.068 (1.2%), ~0.060 (4.6%),	
				W *L* x-rays ~0.008 (2%),	
				Os *K* x-rays 0.063 (2%), 0.062 (1%),	
				Os *L* x-rays ~0.009 (3%)	
$^{187}_{75}$Re	4×10^{10} y	β^-	β^-	0.0026 (100%)	$^{187}_{76}$Os
$^{188}_{75}$Re	16.98 h	β^-	β^-	2.12 (79%), 1.97 (20%), <1.9 (1%)	$^{188}_{76}$Os
			γ	0.932 (0.4%), 0.633 (1%), 0.478 (1%), 0.155 (15%)	
			e^-	{0.016} (18%)	
				Os *K* x-rays ~ 0.065 (5%),	
				Os *L* x-rays ~ 0.011 (3%)	
$^{189}_{75}$Re	24.3 h	β^-	β^-	1.01 (64.0%), 0.978 (2.0%), 0.973 (3.6%), 0.939 (2.2%), 0.914 (0.1%), 0.792 (13.0%), 0.790 (7.8%), 0.775 (0.1%), 0.733 (5.3%), 0.581 (0.1%), 0.510 (0.2%), 0.459 (0.1%), 0.409 (1.2%), 0.292 (0.3%)	$^{189}_{76}$Os
			γ	0.245 (4%), 0.219 (5%), 0.217 (6%), 0.186 (2%), 0.147 (1%)	
			e^-	{0.022} (49%)	
				Os *K* x-rays 0.063 (2%), 0.061 (1%),	
				Os *L* x-rays 0.009 (8%)	
Osmium					
$^{182}_{76}$Os	21.84 h	EC	γ	0.510 (52%), 0.263 (7%), 0.180 (34%), 0.055 (6%)	$^{182}_{75}$Re
			e^-	{0.053} (157%)	
				Re *K* x-rays 0.071 (3%), 0.069 (12%), 0.061 (40%), 0.060 (23%),	
				Re *L* x-rays 0.009 (39%)	
$^{183m}_{76}$Os	9.9 h	EC (85.0%) IT (15.0%)	γ	1.11 (22%), 1.10 (49%), 1.03 (6%), 0.954 (1%), 0.879 (2%), 0.484 (2%)	$^{183}_{75}$Re (EC) $^{183}_{76}$Os (IT)
			e^-	{0.031} (78%)	
				Re *K* x-rays 0.071 (2%), 0.069 (10%), 0.061 (30%), 0.060 (17%),	
				Re *L* x-rays 0.009 (20%),	
				Os *K* x-rays ~0.062 (3%),	
				Os *L* x-rays ~0.009 (4%)	
$^{183}_{76}$Os	13.0 h	EC (95.5%) β^+ (0.5%)	β^+	0.780 (0.5%)	$^{183}_{75}$Re
			γ	0.851 (5%), 0.381 (90%), 0.236 (3%), 0.168 (9%)	
			$\gamma^{\pm}$	0.511 (1.0%)	
			e^-	{0.073} (203%)	
				Re *K* x-rays 0.071 (6%), 0.069 (25%), 0.061 (73%), 0.060 (43%),	
				Re *L* x-rays 0.009 (46%)	
$^{185}_{76}$Os	93.6 d	EC	γ	0.880 (5%), 0.875 (7%), 0.646 (81%)	$^{185}_{75}$Re
			e^-	{0.017} (55%)	
				Re *K* x-rays ~ 0.065 (69%),	
				Re *L* x-rays ~ 0.010 (23%)	

Continued

Table of radioactive isotopes—cont'd

Nuclide $^{A}_{Z}X$	Half-life	Decay mode	Radiation characteristics: energies (MeV) [intensities (%)]	Decay product $^{A}_{Z}Y$
$^{191m}_{76}$Os	13.10 h	IT	γ 0.074 (0.07%) e^- {0.060} (127%) Os *K* x-rays ~ 0.070 (8%), Os *L* x-rays ~ 0.010 (21%)	$^{191}_{76}$Os
$^{191}_{76}$Os	15.4 d	β^-	β^- 0.143 (100%) γ 0.129 (26%) e^- {0.094} (258%) Ir *K* x-rays ~ 0.069 (56%), Ir *L* x-rays ~ 0.010 (38%)	$^{191m}_{77}$Ir
$^{193}_{76}$Os	30.6 h	β^-	β^- 1.13 (42%), 1.06 (21%), 0.993 (10%), 0.85 (10%), 0.67 (11%), 0.51 (6%) γ 0.558 (2.1%), 0.460 (3.9%), 0.387 (1%), 0.322 (1.4%), 0.280 (1%), 0.139 (4%) e^- {0.052} (162%) Ir *K* x-rays ~ 0.070 (13%)	$^{193}_{77}$Ir
$^{194}_{76}$Os	6.0 y	β^-	β^- 0.096 (24.0%), 0.054 (76.0%) γ 0.043 (5%) e^- {0.010} (37%)	$^{194}_{77}$Ir
Iridium				
$^{188}_{77}$Ir	41.5 h	EC (99.7%) β^+ (0.3%)	β^+ 1.63 (0.2%), 1.15 (0.1%) γ 2.21 (19%), 2.10 (10%), 2.05 (12%), 1.71 (6%), 1.21 (7%), 0.633 (18%), 0.478 (15%), 0.155 (30%) $\gamma^{\pm}$ 0.511 (0.6%) e^- {0.047} (101%) Os *K* x-rays 0.073 (4%), 0.071 (15%), 0.063 (44%), 0.061 (26%), Os *L* x-rays 0.009 (32%)	$^{188}_{76}$Os
$^{189}_{77}$Ir	13.2 d	EC	γ 0.245 (6%), 0.069 (4%), 0.059 (1%) e^- {0.043} (161%) Os *K* x-rays 0.073 (3%), 0.071 (13%), 0.063 (38%), 0.061 (22%), Os *L* x-rays 0.009 (42%)	$^{189}_{76}$Os
$^{190}_{77}$Ir	11.78 d	EC	γ 0.605 (40%), 0.569 (29%), 0.557 (30%), 0.518 (34%), 0.407 (24%), 0.371 (23%), 0.361 (13%), 0.186 (52%) e^- {0.074} (106%) Os *K* x-rays 0.073 (3%), 0.071 (14%), 0.063 (42%), 0.061 (25%), Os *L* x-rays 0.009 (32%)	$^{190}_{76}$Os
$^{191m}_{77}$Ir	4.96 s	IT	γ 0.129 (25%) e^- {0.094} (258%) Ir *K* x-rays ~ 0.070 (56%), Ir *L* x-rays ~ 0.010 (40%)	$^{191}_{77}$Ir
$^{192}_{77}$Ir	74.17 d	β^- (95.4%) EC (4.6%)	β^- 0.672 (46%), 0.536 (41%), 0.240 (8%) γ 0.612 (6%), 0.604 (9%), 0.589 (4%), 0.468 (49%), 0.317 (81%), 0.308 (30%), 0.296 (29%) e^- {0.045} (25%) Pt *K* x-rays ~ 0.070 (8%), Os *K* x-rays ~ 0.065 (4%)	$^{192}_{78}$Pt (β^-) $^{192}_{76}$Os (EC)
$^{194}_{77}$Ir	19.15 h	β^-	β^- 2.24 (89%), 1.92 (5.1%), 1.63 (1.2%), 0.98 (2%), 0.72, 0.61, 0.44 γ 1.48 (0.2%), 1.16 (0.8%), 0.939 (0.6%), 0.64 (1%), 0.328 (13%), 0.294 (2%)	$^{194}_{78}$Pt

Continued

Table of radioactive isotopes—cont'd

Nuclide $^{A}_{Z}X$	Half-life	Decay mode	Radiation characteristics: energies (MeV) [intensities (%)]	Decay product $^{A}_{Z}Y$
Platinum				
$^{188}_{78}$Pt	10.2 d	EC	γ 0.423 (4%), 0.381 (8%), 0.195 (19%), 0.187 (19%) e^- {0.079} (171%) Ir *K* x-rays 0.075 (4%), 0.073 (17%), 0.065 (49%), 0.063 (29%), Ir *L* x-rays 0.009 (44%)	$^{188}_{77}$Ir
$^{189}_{78}$Pt	10.87 h	EC (99.8%) β^+ (0.2%)	β^+ 0.949 (0.1%), 0.855 (0.1%) γ 0.607 (6%), 0.568 (7%), 0.545 (6%), 0.317 (3%), 0.300 (4%), 0.243 (7%), 0.141 (4%), 0.094 (8%) $\gamma^{\pm}$ 0.511 (0.4%) e^- {0.059} (232%) Ir *K* x-rays 0.075 (5%), 0.073 (22%), 0.065 (63%), 0.063 (37%), Ir *L* x-rays 0.009 (54%)	$^{189}_{77}$Ir
$^{193m}_{78}$Pt	4.33 d	IT	γ 0.135 (0.11%) e^- {0.130} (235%) Pt *K* x-rays ~ 0.070 (14%), Pt *L* x-rays ~ 0.010 (23%)	$^{193}_{78}$Pt
$^{193}_{78}$Pt	50.0 y	EC	e^- 0.007 (46%) Ir *L* x-rays 0.009 (22%)	$^{193}_{77}$Ir
$^{195m}_{78}$Pt	4.01 d	IT	γ 0.130 (3%), 0.099 (12%), 0.030 (2%) e^- {0.175} (406%) Pt *K* x-rays 0.078 (3%), 0.075 (13%), 0.067 (37%), 0.065 (22%), Pt *L* x-rays 0.009 (69%)	$^{195}_{78}$Pt
$^{197}_{78}$Pt	18.3 h	β^-	β^- 0.719 (10.6%), 0.643 (79.6%), 0.451 (9.8%) γ 0.191 (6%), 0.077 (20%) e^- {0.054} (94%) Au *K* x-rays ~ 0.075 (3%), Au *L* x-rays ~ 0.010 (19%)	$^{197}_{79}$Au
$^{199}_{78}$Pt	30.8 m	β^-	β^- 1.70 (70.7%), 1.62 (0.7%), 1.38 (4.7%), 1.20 (0.4%), 1.16 (12.0%), 0.968 (6.3%), 0.911 (4.2%), 0.735 (1.0%) γ 0.714 (1%), 0.543 (12%), 0.494 (4%), 0.317 (4%), 0.246 (2%), 0.191 (2%), 0.186 (3%), 0.077 (1%) e^- {0.022} (19%) Au *K* x-rays 0.080 (0.1%), 0.078 (0.6%), 0.069 (2%), 0.067 (1%), Au *L* x-rays 0.010 (4%)	$^{199}_{79}$Au
Gold				
$^{194}_{79}$Au	38.02 h	EC (98.3%) β^+ (1.7%)	β^+ 1.48 (1.1%), 1.15 (0.6%) γ 1.47 (7%), 0.328 (60%), 0.293 (11%) $\gamma^{\pm}$ 0.511 (3.4%) e^- {0.030} (63%) Pt *K* x-rays 0.078 (3%), 0.075 (14%), 0.066 (39%), 0.065 (23%), Pt *L* x-rays 0.009 (28%)	$^{194}_{78}$Pt
$^{195m}_{79}$Au	30.5 s	IT	γ 0.262 (69%), 0.200 (2%) e^- {0.116} (189%) Au *K* x-rays 0.080 (1%), 0.078 (4%), 0.069 (11%), 0.067 (6%), Au *L* x-rays 0.010 (33%)	$^{195}_{79}$Au
$^{195}_{79}$Au	182.9 d	EC	γ 0.129 (1%), 0.099 (10%), 0.031 (1%) e^- {0.045} (188%) Pt *K* x-rays ~0.070 (100%), Pt *L* x-rays ~0.011 (52%)	$^{195}_{78}$Pt

Continued

Table of radioactive isotopes—cont'd

Nuclide $^{A}_{Z}X$	Half-life	Decay mode	Radiation characteristics: energies (MeV) [intensities (%)]	Decay product $^{A}_{Z}Y$
$^{196m_2}_{79}$Au	9.6 h	IT	γ 0.285 (4%), 0.188 (30%), 0.168 (8%), 0.148 (44%) e^- {0.368} (502%) Au *K* x-rays 0.080 (3%), 0.078 (14%), 0.069 (40%), 0.067 (24%), Au *L* x-rays 0.010 (89%)	$^{196}_{79}$Au
$^{196m_1}_{79}$Au	8.1 s	IT	γ 0.084 (0.3%) e^- {0.081} (142%) Au *L* x-rays 0.010 (25%)	$^{196}_{79}$Au
$^{196}_{79}$Au	6.167 d	EC (93.0%) β^- (7.0%)	β^- 0.687 (0.2%), 0.261 (6.8%) γ 0.426 (7%), 0.356 (87%), 0.333 (23%) e^- {0.031} (64%) Pt *K* x-rays 0.078 (3%), 0.075 (13%), 0.066 (37%), 0.065 (22%), Pt *L* x-rays 0.009 (27%)	$^{196}_{78}$Pt (EC) $^{196}_{80}$Hg (β^-)
$^{197m}_{79}$Au	7.73 s	IT	γ 0.279 (71%), 0.201 (1%), 0.130 (3%) e^- {0.180} (179%) Au *K* x-rays 0.080 (1%), 0.078 (4%), 0.069 (12%), 0.067 (7%), Au *L* x-rays 0.010 (32%)	$^{197}_{79}$Au
$^{198}_{79}$Au	2.697 d	β^-	β^- 1.37 (0.03%), 0.961 (98.6%), 0.290 (1.3%) γ 1.09 (0.2%), 0.676 (1%), 0.412 (95%) e^- {0.015} (6%) Hg *K* x-rays ~ 0.075 (3%)	$^{198}_{80}$Hg
$^{199}_{79}$Au	3.148 d	β^-	β^- 0.462 (6%), 0.296 (71.6%), 0.250 (22.4%) γ 0.208 (8%), 0.158 (37%) e^- {0.058} (65%) Hg *K* x-rays ~ 0.075 (17%), Hg *L* x-rays ~ 0.011 (12%)	$^{199}_{80}$Hg
Mercury				
$^{194}_{80}$Hg	444 y	EC	e^- 0.0074 (45%) Au *L* x-rays 0.010 (24%)	$^{194}_{79}$Au
$^{195m}_{80}$Hg	41.6 h	IT (54.2%) EC (45.8%)	γ 0.560 (7%), 0.387 (2%), 0.261 (31%), 0.037 (2%) e^- {0.140} (334%) Au *K* x-rays 0.080 (2%), 0.078 (7%), 0.069 (21%), 0.067 (13%), Au *L* x-rays 0.010 (27%) Hg *K* x-rays 0.070 (2%), 0.069 (1%), Hg *L* x-rays 0.010 (42%)	$^{195}_{80}$Hg (IT) $^{195}_{79}$Au (EC)
$^{195}_{80}$Hg	10.53 h	EC	γ 1.17 (1%), 1.11 (2%), 0.779 (7%), 0.599 (2%), 0.585 (2%), 0.261 (2%), 0.180 (2%), 0.061 (6%) e^- {0.061} (177%) Au *K* x-rays 0.080 (3%), 0.078 (13%), 0.069 (38%), 0.067 (23%), Au *L* x-rays 0.010 (49%)	$^{195}_{79}$Au
$^{197m}_{80}$Hg	23.8 h	IT (93.5%) EC (6.5%)	γ 0.279 (7%), 0.134 (34%) e^- {0.214} (230%) Hg *L* x-rays ~ 0.010 (38%) Au *K* x-rays ~ 0.070 (6%), Au *L* x-rays ~ 0.010 (4%)	$^{197}_{80}$Hg (IT) $^{197m}_{79}$Au (EC)
$^{197}_{80}$Hg	64.14 h	EC	γ 0.191 (1%), 0.077 (18%) e^- {0.057} (136%) Au *K* x-rays ~ 0.075 (71%), Au *L* x-rays ~ 0.010 (44%)	$^{197}_{79}$Au

Continued

Table of radioactive isotopes—cont'd

Nuclide $^{A}_{Z}X$	Half-life	Decay mode	Radiation characteristics: energies (MeV) [intensities (%)]	Decay product $^{A}_{Z}Y$
$^{203}_{80}$Hg	46.76 d	β^-	β^- 0.214 (100%) γ 0.279 (82%) e^- {0.040} (26%) Tl *K* x-rays ~0.075 (13%), Tl *L* x-rays ~0.011 (5%)	$^{203}_{81}$Tl
Thallium				
$^{199}_{81}$Tl	7.42 h	EC	γ 0.455 (12%), 0.247 (9%), 0.208 (12%), 0.158 (5%) e^- {0.056} (102%) Hg *K* x-rays 0.082 (4%), 0.080 (16%), 0.071 (46%), 0.069 (27%), Hg *L* x-rays 0.010 (38%)	$^{199}_{80}$Hg
$^{200}_{81}$Tl	26.1 h	EC (99.6%) β^+ (0.4%)	β^+ 1.43 (0.1%), 1.06 (0.3%) γ 1.20 (30%), 0.828 (11%), 0.579 (14%), 0.368 (87%) $\gamma^{\pm}$ 0.511 (0.8%) e^- {0.036} (68%) Hg *K* x-rays 0.082 (3%), 0.080 (14%), 0.071 (40%), 0.069 (24%), Hg *L* x-rays 0.010 (32%)	$^{200}_{80}$Hg
$^{201}_{81}$Tl	74 h	EC	γ 0.135 (3%), 0.167 (9%) e^- {0.048} (187%) Hg *K* x-rays ~0.075 (93%), Hg *L* x-rays ~0.011 (40%)	$^{201}_{80}$Hg
$^{202}_{81}$Tl	12.23 d	EC	γ 0.961 (0.1%), 0.522 (0.1%), 0.439 (95%) e^- {0.021} (49%) Hg *K* x-rays ~0.075 (78%), Hg *L* x-rays ~0.011 (28%)	$^{202}_{80}$Hg
$^{204}_{81}$Tl	3.78 y	β^- (97.1%) EC (2.9%)	β^- 0.764 (97.1%) e^- 0.008 (1.5%) Hg *K* x-rays ~0.070 (1%), Hg *L* x-rays ~0.010 (0.7%)	$^{204}_{82}$Pb (β^-) $^{204}_{80}$Hg (EC)
$^{206}_{81}$Tl	4.18 m	β^-	β^- 1.53 (100%) Pb *K* x-rays (0.10%)	$^{206}_{82}$Pb
$^{207}_{81}$Tl	4.77 m	β^-	β^- 1.44 (100%) γ 0.897 (0.24%)	$^{207}_{82}$Pb
$^{208}_{81}$Tl	3.1 m	β^-	β^- 1.80 (48.8%), 1.52 (22.7%), 1.29 (23.9%), 1.04 (4.6%) γ 0.510 (22%), 0.583 (86%), 0.860 (12%), 2.614 (100%) e^- {0.038} (14%) Pb *K* x-rays ~0.075 (7%), Pb *L* x-rays ~0.011 (2.8%)	$^{208}_{82}$Pb
$^{209}_{81}$Tl	2.2 m	β^-	β^- 1.99 (100%) γ 0.117 (81%), 0.467 (81%), 1.56 (98%) e^- {0.028} (39%) Pb *K* x-rays ~0.075 (21%), Pb *L* x-rays ~0.011 (8%)	$^{209}_{82}$Pb
$^{210}_{81}$Tl	1.30 m	β^- β^- *n* (0.007%)	β^- 2.34 (19%), 1.87 (56%), 1.32 (25%) γ 2.43 (9%), 2.36 (8%), 2.27 (3%), 2.09 (5%), 2.01 (7%), 1.41 (5%), 1.31 (21%), 1.21 (17%), 1.11 (7%), 1.07 (12%), 0.908 (3%), 0.860 (7%), 0.798 (99%), 0.298 (79%) e^- {0.094} (109%) Pb *K* x-rays ~0.080 (9%), Pb *L* x-rays ~0.012 (22%)	$^{210}_{82}$Pb

Continued

Table of radioactive isotopes—cont'd

Nuclide $^{A}_{Z}X$	Half-life	Decay mode	Radiation characteristics: energies (MeV) [intensities (%)]	Decay product $^{A}_{Z}Y$
Lead				
$^{203}_{82}$Pb	51.92 h	EC	γ 0.401 (3.4%), 0.279 (81%) e^- {0.049} (90%) Tl *K* x-rays 0.085 (4%), 0.082 (16%), 0.073 (44%), 0.071 (26%), Tl *L* x-rays 0.010 (36%)	$^{203}_{81}$Tl
$^{205}_{82}$Pb	1.7×10^7 y	EC	e^- 0.0078 (38%) Tl *L* x-rays 0.010 (22%)	$^{205}_{81}$Tl
$^{209}_{82}$Pb	3.30 h	β^-	β^- 0.645 (100%)	$^{209}_{83}$Bi
$^{210}_{82}$Pb	22.36 y	β^- α (trace)	β^- 0.061 (19%), 0.015 (81%) γ 0.047 (4%) e^- {0.028} (90%) Bi *L* x-rays ~0.012 (23%)	$^{210}_{83}$Bi
$^{211}_{82}$Pb	36.1 m	β^-	β^- 1.36 (92.4%), 0.951 (1.4%), 0.525 (5.5%), 0.251 (0.7%) γ 0.832 (3.8%), 0.704 (0.5%), 0.427 (1.7%), 0.404 (3.8%) e^- {0.005} (5%) Bi *K* x-rays ~0.077 (0.8%), Bi *L* x-rays ~0.011 (0.9%)	$^{211}_{83}$Bi
$^{212}_{82}$Pb	10.64 h	β^-	β^- 0.568 (12%), 0.331 (83%), 0.155 (5%) γ 0.300 (3.3%), 0.238 (44%) e^- {0.074} (66%) Bi *K* x-rays ~0.080 (36%), Bi *L* x-rays ~0.012 (14%)	$^{212}_{83}$Bi
$^{214}_{82}$Pb	26.8 m	β^-	β^- 1.03 (6%), 0.59 (~52%), 0.65 (~41%) γ 0.052 (1%), 0.241 (7%), 0.295 (19%), 0.351 (37%) e^- {0.074} (57%) Bi *K* x-rays ~0.080 (23%), Bi *L* x-rays ~0.012 (13%)	$^{214}_{83}$Bi
Bismuth				
$^{203}_{83}$Bi	11.76 h	EC (99.8%) β^+ (0.2%)	β^+ 1.41 (0.1%), 1.33 (0.1%) γ 1.89 (10%), 1.84 (12%), 1.67 (9%), 1.03 (9%), 0.897 (13%), 0.847 (9%), 0.835 (15%), 0.820 (30%) $\gamma^{\pm}$ 0.511 (0.4%) e^- {0.076} (82%) Pb *K* x-rays 0.087 (4%), 0.084 (14%), 0.075 (41%), 0.073 (25%), Pb *L* x-rays 0.011 (36%)	$^{203}_{82}$Pb
$^{204}_{83}$Bi	11.22 h	EC (99.8%) β^+ (0.2%)	β^+ 1.16 (0.2%) γ 0.984 (59%), 0.918 (11%), 0.911 (25%), 0.899 (99%), 0.670 (11%), 0.374 (82%) $\gamma^{\pm}$ 0.511 (0.4%) e^- {0.091} (77%) Pb *K* x-rays 0.087 (4%), 0.084 (17%), 0.075 (48%), 0.073 (29%), Pb *L* x-rays 0.011 (70%)	$^{204}_{82}$Pb
$^{205}_{83}$Bi	15.31 d	EC (99.8%) β^+ (0.2%)	β^+ 1.68 (0.1%), 0.983 (0.1%) γ 1.86 (6%), 1.76 (33%), 1.04 (8%), 0.987 (16%), 0.703 (31%), 0.579 (5%) $\gamma^{\pm}$ 0.511 (0.4%) e^- {0.014} (78%) Pb *K* x-rays 0.087 (3%), 0.084 (13%), 0.075 (36%), 0.073 (21%), Pb *L* x-rays 0.011 (36%)	$^{205}_{82}$Pb

Continued

Table of radioactive isotopes—cont'd

Nuclide $^{A}_{Z}X$	Half-life	Decay mode	Radiation characteristics: energies (MeV) [intensities (%)]		Decay product $^{A}_{Z}Y$
$^{206}_{83}$Bi	6.243 d	EC	γ	1.72 (36%), 1.60 (8%), 1.10 (13%), 1.02 (8%), 0.895 (19%), 0.880 (72%), 0.803 (99%), 0.538 (34%), 0.516 (46%), 0.497 (18%), 0.398 (10%), 0.343 (26%), 0.184 (16%)	$^{206}_{82}$Pb
			e^-	{0.133} (116%) Pb *K* x-rays ~0.080 (112%), Pb *L* x-rays ~0.011 (45%)	
$^{207}_{83}$Bi	38 y	EC	γ	1.77 (9%), 1.06 (77%), 0.570 (98%)	$^{207m}_{82}$Pb
			e^-	{0.116} (56%) Pb *K* x-rays ~0.080 (78%), Pb *L* x-rays ~0.011 (34%)	
$^{208}_{83}$Bi	3.68×10^5 y	EC	e^-	0.057 (2%), 0.0079 (47%)	$^{208}_{82}$Pb
			γ	2.61 (100%) Pb *K* x-rays 0.087 (2%), 0.084 (7%), 0.075 (20%), 0.073 (12%), Pb *L* x-rays 0.011 (29%)	
$^{210m}_{83}$Bi	3.04×10^6 y	α	α	4.95 (55.0%), 4.91 (39.5%), 4.58 (1.4%), 4.57 (3.9%), 4.42 (0.2%)	$^{206}_{81}$Tl
			γ	0.304 (23%), 0.266 (45%)	
			e^-	{0.047} (29%) Tl *K* x-rays ~0.075 (13%), Tl *L* x-rays ~0.011 (5%)	
$^{210}_{83}$Bi	5.013 d	β^- α (trace)	β^-	1.16 (>99%)	$^{210}_{84}$Po
$^{211}_{83}$Bi	2.15 m	α (99.7%) β^- (0.3%)	α	6.62 (84%), 6.28 (16%)	$^{207}_{81}$Tl (α) $^{211}_{84}$Po (β^-)
			γ	0.350 (13%)	
			e^-	{0.009} (5%) Tl *K* x-rays ~0.080 (3%), Tl *L* x-rays ~0.010 (1%)	
$^{212}_{83}$Bi	60.55 m	β^- (64.1%) α (35.9%)	β^-	2.27 (55.4%), 1.52 (4.5%), 0.739 (1.4%), 0.631 (1.9%), 0.572 (0.2%), 0.446 (0.7%)	$^{212}_{84}$Po (β^-) $^{208}_{81}$Tl (α)
			α	6.09 (9.6%), 6.05 (25.2%), 5.77 (0.1%), 5.61 (0.4%)	
			γ	1.62 (1.5%), 1.51 (0.3%), 1.08 (0.5%), 0.893 (0.4%), 0.785 (1.1%), 0.727 (6.6%), 0.452 (0.4%), 0.288 (0.3%)	
			e^-	{0.010} (32%) Po *K* x-rays ~0.082 (0.2%), Tl *K* x-rays ~0.080 (0.3%) Po *L* x-rays ~0.013 (0.1%), Tl *L* x-rays ~0.010 (7.5%)	
$^{213}_{83}$Bi	47 m	β^- (97.8%) α (2.2%)	β^-	1.39 (66%), 0.96 (31%), 0.60 (0.8%)	$^{213}_{84}$Po (β^-) $^{209}_{81}$Tl (α)
			α	5.869 (2%), 5.549 (0.2%)	
			γ	0.293 (0.44%), 0.440 (17%)	
			e^-	{0.012} (5%)	
$^{214}_{83}$Bi	19.7 m	β^- (>99%) α (0.02%)	β^-	3.26 (19%), 1.88 (9%), 1.51 (40%), 1.02 (23%), 0.42 (9%)	$^{214}_{84}$Po
			γ	0.609 (46%), 1.120 (15%), 1.238 (6%), 1.764 (16%)	
			e^-	{0.021} (4%) Po *K* x-rays ~0.085 (2%), Po *L* x-rays ~0.012 (1%)	
Polonium					
$^{204}_{84}$Po	3.52 h	EC (99.4%) α (0.6%)	γ	1.04 (11%), 1.01 (28%), 0.883 (34%), 0.762 (13%), 0.535 (15%), 0.270 (32%), 0.137 (11%), 0.063 (12%)	$^{204}_{83}$Bi (EC) $^{200}_{82}$Pb (α)
			e^-	{0.164} (542%) Bi *K* x-rays 0.090 (6%), 0.087 (25%), 0.077 (71%) Bi *L* x-rays 0.011 (88%)	

Continued

Table of radioactive isotopes—cont'd

Nuclide $^{A}_{Z}X$	Half-life	Decay mode	Radiation characteristics: energies (MeV) [intensities (%)]	Decay product $^{A}_{Z}Y$
$^{205}_{84}$Po	1.74 h	EC (97.8%) β^+ (2.2%)	β^+ 1.68 (0.7%), 1.65 (0.1%), 1.53 (1.4%) γ 1.00 (29%), 0.872 (37%), 0.850 (26%), 0.836 (19%) $\gamma^{\pm}$ 0.511 (4.4%) e^- {0.044} (75%) Bi *K* x-rays 0.090 (4%), 0.087 (15%), 0.077 (43%) 0.075 (26%), Bi *L* x-rays 0.011 (36%)	$^{205}_{83}$Bi
$^{206}_{84}$Po	8.8 d	EC (94.55%) α (5.45%)	α 5.22 (5.45%) γ 1.03 (32%), 0.980 (7%), 0.807 (22%), 0.522 (15%), 0.511 (23%), 0.338 (19%), 0.286 (23%) e^- {0.150} (295%) Bi *K* x-rays 0.090 (4%), 0.087 (15%), 0.077 (43%) 0.075 (25%), Bi *L* x-rays 0.011 (63%)	$^{206}_{83}$Bi (EC) $^{202}_{82}$Pb (α)
$^{207}_{84}$Po	5.80 h	EC (99.38%) β^+ (0.60%) α (0.02%)	α 5.11 (0.02%) β^+ 1.14 (0.2%), 0.895 (0.4%) γ 0.992 (59%), 0.912 (17%), 0.742 (28%), 0.405 (10%) $\gamma^{\pm}$ 0.511 (1.2%) e^- {0.046} (63%) Bi *K* x-rays 0.090 (3%), 0.087 (14%), 0.077 (40%) 0.075 (24%), Bi *L* x-rays 0.011 (34%)	$^{207}_{83}$Bi (EC) $^{203}_{82}$Pb (α)
$^{208}_{84}$Po	2.897 y	α	α 5.12 (>99%) γ 0.603 (0.006%), 0.291 (0.003%)	$^{204}_{82}$Pb
$^{209}_{84}$Po	102 y	α (99.5%) EC (0.5%)	α 4.885 (19.8%), 4.883 (79.1%), 4.622 (0.6%) γ 0.897 (0.5%), 0.260 (0.3%) e^- 0.172 (0.1%), 0.008 (0.3%)	$^{205}_{82}$Pb (α) $^{209}_{83}$Bi (EC)
$^{210}_{84}$Po	138.38 d	α	α 5.30 (100%) γ 0.803 (0.0012%)	$^{206}_{82}$Pb
$^{211}_{84}$Po	0.516 s	α	α 7.45 (98.9%), 6.89 (0.6%), 6.57 (0.5%) γ 0.897 (0.5%), 0.569 (0.5%)	$^{207}_{82}$Pb
$^{212}_{84}$Po	298×10^{-9} s	α	α 8.78 (100%)	$^{208}_{82}$Pb
$^{213}_{84}$Po	4.2×10^{-6} s	α	α 8.375 (>99%), 7.615 (0.006%)	$^{209}_{82}$Pb
$^{214}_{84}$Po	1.6×10^{-4} s	α	α 7.69 (99.98%), 6.90 (0.01%), 6.61 (0.01%) γ 0.798 (0.01%)	$^{210}_{82}$Pb
$^{215}_{84}$Po	1.78×10^{-3} s	α β^- (0.00023%)	α 7.39 (100%) γ 0.438 (0.04%)	$^{211}_{82}$Pb (α)
$^{216}_{84}$Po	0.156 s	α	α 6.78 (100%)	$^{212}_{82}$Pb
$^{218}_{84}$Po	3.05 m	α	α 6.002 (100%)	$^{214}_{82}$Pb
Astatine				
$^{206}_{85}$At	30.6 m	EC (79.1%) β^+ (20.0%) α (0.9%)	β^+ 3.56 (5.6%), 3.30 (0.8%), 3.18 (1.2%), 3.16 (9.2%), 2.60 (1.3%), 2.44 (1.1%), 2.24 (0.3%), 2.16 (0.1%), 1.82 (0.3%), 1.14 (0.1%) α 5.70 (0.86%) γ 0.732 (10%), 0.700 (98%), 0.477 (86%), 0.395 (48%) $\gamma^{\pm}$ 0.511 (40%) e^- {0.074} (83%) Po *K* x-rays 0.092 (4%), 0.089 (15%), 0.079 (43%), 0.077 (26%), Po *L* x-rays 0.011 (38%)	$^{206}_{84}$Po (EC, β^+) $^{202}_{83}$Bi (α)

Continued

Table of radioactive isotopes—cont'd

Nuclide $^{A}_{Z}X$	Half-life	Decay mode	Radiation characteristics: energies (MeV) [intensities (%)]	Decay product $^{A}_{Z}Y$
$^{207}_{85}$At	1.81 h	EC (90.0%) β^+ (1.4%) α (8.6%)	α 5.76 (8.6%) β^+ 2.29 (0.7%), 1.07 (0.1%), 1.87 (0.3%), 1.77 (0.1%) 1.71 (0.1%), 1.60 (0.1%) γ 0.907 (7%), 0.814 (45%), 0.721 (6%), 0.675 (7%), 0.658 (7%), 0.588 (20%), 0.467 (7%), 0.300 (13%) $\gamma^{\pm}$ 0.511 (2.8%) Po *K* x-rays 0.092 (4%), 0.089 (14%), 0.079 (41%), 0.077 (25%), Po *L* x-rays 0.011 (38%)	$^{207}_{84}$Po (EC, β^+) $^{203}_{83}$Bi (α)
$^{209}_{85}$At	5.41 h	EC (95.9%) α (4.1%)	α 5.65 (4.1%) γ 0.790 (64%), 0.781 (84%), 0.545 (91%), 0.239 (12%), 0.195 (23%) e^- {0.113} (177%) Po *K* x-rays 0.092 (5%), 0.089 (21%), 0.079 (59%), 0.077 (36%), Po *L* x-rays 0.011 (60%)	$^{209}_{84}$Po (EC) $^{205}_{83}$Bi (α)
$^{210}_{85}$At	8.1 h	EC (99.79%) α (0.17%) β^+(0.04%)	α 5.52 (0.05%), 5.46 (0.01%), 5.44 (0.05%), 5.39 (0.01%) 5.36 (0.05%) β^+ 1.48 (0.04%) γ 1.60 (13%), 1.48 (47%), 1.44, (29%), 1.18 (99%), 0.245 (79%) $\gamma^{\pm}$ 0.551 (0.08%) e^- {0.075} (135%) Po *K* x-rays 0.092 (3.6%), 0.089 (14.9%), 0.079 (42%), 0.077 (25%), Po *L* x-rays 0.011 (51%)	$^{210}_{84}$Po (EC, β^+) $^{206}_{83}$Bi (α)
$^{211}_{85}$At	7.21 h	EC (58.2%) α (41.8%)	α 5.87 (41.8%) γ 0.742 (0.001%), 0.669 (0.004%) e^- {0.004} (25%)	$^{211}_{84}$Po (EC) $^{207}_{83}$Bi (α)
$^{212m}_{85}$At	0.119 s	α	α 7.89 (30.7%), 7.83 (67.6%), 7.38 (0.4%), 7.29 (0.1%), 7.27 (0.3%), 7.25 (0.4%), 7.02 (0.1%), 6.95 (0.1%), 6.81 (0.3%) γ 0.062 (67%)	$^{208}_{83}$Bi
$^{212}_{85}$At	0.314 s	α	α 7.67 (83.2%), 7.61 (15.4%), 7.17 (0.2%), 7.08 (0.6%), 7.05 (0.4%), 6.62 (0.2%)	$^{208}_{83}$Bi
$^{215}_{85}$At	0.1×10^{-3} s	α	α 8.02 (99.95%), 7.63 (0.05%) γ 0.404 (0.05%)	$^{211}_{83}$Bi
$^{217}_{85}$At	0.0323 s	α (99.98%) β^- (0.02%)	α 7.07 (99.9%), 6.81 (0.06%), 6.61 (0.01%), 6.48 (0.01%)	$^{213}_{83}$Bi
$^{218}_{85}$At	1.6 s	α (99.9%) β^- (0.1%)	α 6.75 (4%), 6.70 (90%), 6.65 (6%)	$^{214}_{83}$Bi
Radon				
$^{219}_{86}$Rn	3.92 s	α	α 6.81 (81%), 6.55 (11.5%), 6.52 (0.12%), 6.42 (7.5%) γ 0.130 (0.13%), 0.271 (10%), 0.402 (7%) e^- {0.006} (4%) Po *K* x-rays ~0.085 (2%), Po *L* x-rays ~0.012 (1%)	$^{215}_{84}$Po
$^{220}_{86}$Rn	54 s	α	α 6.29 (99.93%), 5.75 (0.07%) γ 0.550 (0.1%)	$^{216}_{84}$Po

Continued

Table of radioactive isotopes—cont'd

Nuclide $^{A}_{Z}X$	Half-life	Decay mode	Radiation characteristics: energies (MeV) [intensities (%)]	Decay product $^{A}_{Z}Y$
$^{221}_{86}$Rn	25.0 m	β^- (78.0%) α (22.0%)	β^- 1.15 (8.0%), 1.05 (12.0%), 1.04 (8.0%), 1.00 (3.6%), 0.950 (2.1%), 0.920 (1.9%), 0.900 (6.1%), 0.870 (5.9%), 0.860 (27.2%), 0.760 (2.3%) α 6.04 (16.2%), 5.79 (2.2%), 5.78 (1.6%) γ 0.279 (2%), 0.254 (2%), 0.217 (3%), 0.186 (22%), 0.150 (5%), 0.111 (2%), 0.108 (2%), 0.099 (2%) e^- {0.056} (85%) Fr *K* x-rays 0.100 (1%), 0.097 (5%), 0.086 (13%), 0.083 (8%), Fr *L* x-rays 0.012 (21%)	$^{221}_{87}$Fr (β^-) $^{217}_{84}$Po (α)
$^{222}_{86}$Rn	3.824 d	α	α 5.49 (99.92%), 4.99 (0.08%) γ 0.510 (0.07%)	$^{218}_{84}$Po
Francium				
$^{221}_{87}$Fr	4.8 m	α	α 6.34 (83.4%), 6.24 (1.3%), 6.13 (15%), 5.98 (0.5%) γ 0.099 (0.1%), 0.217 (11%), 0.409 (0.1%) e^- {0.008} (8%) At *K* x-rays ~0.085 (3%), At *L* x-rays ~0.012 (2%)	$^{217}_{85}$At
$^{222}_{87}$Fr	14.2 m	β^-	β^- 2.03 (3.0%), 1.92 (38.0%), 1.79 (1.7%), 1.51 (54.0%), 1.73 (0.4%), 1.01 (0.8%), 0.860 (0.7%), 0.767 (0.3%), 0.629 (0.6%), 0.599 (0.1%), 0.592 (0.3%), 0.533 (0.1%) γ 0.242 (2%), 0.206 (50%), 0.111 (13%) Ra *K* x-rays 0.102 (0.3%), 0.100 (0.6%), 0.099 (0.4%), 0.088 (4%), 0.085 (2%), Ra *L* x-rays 0.012 (29%)	$^{222}_{88}$Ra
$^{223}_{87}$Fr	21.8 m	β^- (>99.99%) α (trace)	β^- 1.12 (100%) γ 0.235 (3.7%), 0.204 (1.1%) e^- {0.053} (160%) Ra *K* x-rays ~0.095 (8%), Ra *L* x-rays ~0.014 (40%)	$^{223}_{88}$Ra
Radium				
$^{223}_{88}$Ra	11.4 d	α	α 5.87 (0.9%), 5.86 (0.3%), 5.75 (9.5%), 5.72 (52.5%), 5.61 (24.2%), 5.54 (9.2%), 5.50 (1%), 5.43 (2.3%) γ 0.445 (1.3%), 0.338 (2.8%), 0.324 (3.9%), 0.269 (13.6%), 0.154 (5.6%), 0.122 (1.2%) e^- {0.073} (146%) Rn *K* x-rays ~0.090 (52%), Rn *L* x-rays ~0.013 (23%)	$^{219}_{86}$Rn
$^{224}_{88}$Ra	3.665 d	α	α 5.68 (94%), 5.45 (6%) γ 0.645 (0.01%), 0.292 (0.01%), 0.241 (3.7%) Rn *K* x-rays ~0.085 (0.4%), Rn *L* x-rays ~0.012 (0.4%)	$^{220}_{86}$Rn
$^{225}_{88}$Ra	14.8 d	β^-	β^- 0.320 (100%) γ 0.040 (29%) e^- {0.012} (49%) Ac *L* x-rays ~0.014 (13%)	$^{225}_{89}$Ac
$^{226}_{88}$Ra	1600 y	α	α 4.78 (94.5%), 4.60 (5.5%) γ 0.260 (0.01%), 0.186 (4%) e^- {0.004} (3%) Rn *K* x-rays ~0.085 (0.6%), Rn *L* x-rays ~0.012 (0.7%)	$^{222}_{86}$Rn

Continued

Table of radioactive isotopes—cont'd

Nuclide $^{A}_{Z}X$	Half-life	Decay mode	Radiation characteristics: energies (MeV) [intensities (%)]		Decay product $^{A}_{Z}Y$
$^{227}_{88}$Ra	42.2 m	β^-	β^-	1.30 (35.0%), 1.28 (27.0%), 1.24 (0.9%), 1.05 (2.0%), 1.02 (4.0%), 0.996 (10.0%), 0.972 (8.0%), 0.900 (1.0%), 0.898 (0.1%), 0.891 (3.0%), 0.825 (2.0%), 0.812 (3.0%), 0.789 (0.3%), 0.763 (2.0%), 0.687 (1.0%), 0.628 (0.3%), 0.536 (0.2%), 0.463 (0.1%), 0.451 (0.1%)	$^{227}_{89}$Ac
			γ	0.611 (1%), 0.516 (1%), 0.487 (2%), 0.408 (2%), 0.330 (3%), 0.303 (4%), 0.300 (5%), 0.284 (3%), 0.277 (3%), 0.258 (2%), 0.027 (16%)	
			e^-	{0.054} (73%) Ac *K* x-rays 0.106 (0.2%), 0.102 (0.7%), 0.091 (2%), 0.088 (1%), Ac *L* x-rays 0.013 (13%)	
$^{228}_{88}$Ra	5.77 y	β^-	β^-	0.039 (60%), 0.015 (40%)	$^{228}_{89}$Ac
Actinium					
$^{225}_{89}$Ac	10.0 d	α	α	5.83 (50.6%), 5.80 (0.3%), 5.79 (26.7%), 5.73 (10.1%), 5.72 (3.4%), 5.68 (1.4%), 5.61 (1.2%), 5.29 (0.2%)	$^{221}_{87}$Fr
			γ	0.099 (2.3%), 0.108 (0.3%), 0.111 (0.3%), 0.150 (0.7%)	
			e^-	{0.026} (80%) Fr *K* x-rays ~0.090 (4%), Fr *L* x-rays ~0.013 (20%)	
$^{226}_{89}$Ac	29.37 h	β^- (83.0%) EC (17.0%)	β^-	1.12 (24.0%), 1.04 (10.0%), 0.887 (49.0%)	$^{226}_{90}$Th (β^-) $^{226}_{88}$Ra (EC)
			γ	0.253 (6%), 0.230 (27%), 0.185 (5%), 0.158 (18%)	
			e^-	{0.031} (63%) Th *K* x-rays 0.093 (1.7%), 0.089 (23.3%), Th *L* x-rays 0.013 (12.0%), Ra *K* x-rays 0.100 (1.4%), 0.088 (5.8%), 0.085 (3.6%), Ra *L* x-rays 0.012 (8.5%)	
$^{227}_{89}$Ac	21.77 y	β^- (98.6%) α (1.4%)	β^-	0.046 (98.6%)	$^{227}_{90}$Th (β^-) $^{223}_{87}$Fr (α)
			α	4.95 (1.2%), 4.86 (0.1%)	
			γ	0.100 (0.03%), 0.015 (0.03%)	
			e^-	{0.003} (39%)	
$^{228}_{89}$Ac	6.13 h	β^-	β^-	2.18 (10.1%), 1.85 (9.6%), 1.70 (6.7%), 1.11 (53%), 0.64 (7.6%), 0.45 (13%)	$^{228}_{90}$Th
			γ	0.209 (4%), 0.270 (4%), 0.338 (12%), 0.463 (5%), 0.794 (5%), 0.911 (29%), 0.964 (6%), 0.969 (17%)	
			e^-	{0.088} (150%) Th *K* x-rays ~0.100 (12%), Th *L* x-rays ~0.015 (41%)	
Thorium					
$^{226}_{90}$Th	30.57 m	α	α	6.34 (75.5%), 6.23 (22.8%), 6.10 (1.3%), 6.04 (0.2%), 6.02 (0.2%)	$^{222}_{88}$Ra
			γ	0.242 (1%), 0.206 (0.2%), 0.190 (0.1%), 0.131 (0.3%), 0.111 (3%)	
			e^-	{0.021} (27%) Ra *K* x-rays 0.102 (0.04%), 0.100 (0.2%), 0.089 (0.5%), 0.085 (0.3%), Ra *L* x-rays 0.012 (7%)	
$^{227}_{90}$Th	18.7 d	α	α	6.04 (24.5%), 6.01 (2.9%), 5.98 (23.4%), 5.96 (3%), 5.92 (0.8%), 5.87 (2.4%), 5.81 (1.3%), 5.76 (20.3%), 5.71 (4.9%), 5.709 (8.2%), 5.701 (3.6%), 5.69 (1.5%), 5.66 (2.1%)	$^{223}_{88}$Ra
			γ	0.330 (2.7%), 0.300 (2.3%), 0.256 (6.7%), 0.236 (11.2%), 0.050 (8.5%)	
			e^-	{0.054} (172%) Ra *K* x-rays ~0.095 (6.5%), Ra *L* x-rays ~0.013 (44%)	

Continued

Table of radioactive isotopes—cont'd

Nuclide $^{A}_{Z}X$	Half-life	Decay mode	Radiation characteristics: energies (MeV) [intensities (%)]	Decay product $^{A}_{Z}Y$
$^{228}_{90}$Th	1.913 y	α	α 5.42 (72.7%), 5.34 (26.7%), 5.21 (0.4%), 5.17 (0.2%) γ 0.214 (0.3%), 0.167 (0.1%), 0.132 (0.2%), 0.084 (1.6%) e^- {0.020} (45%) Ra *L* x-rays ~ 0.013 (9%)	$^{224}_{88}$Ra
$^{229}_{90}$Th	7340 y	α	α 5.053 (1.6%), 5.051 (5.2%), 4.978 (3.2%), 4.967 (6.4%), 4.901 (10.2%), 4.845 (56.2%), 4.815 (9.3%), 4.797 (1.3%) γ 0.031 (4%), 0.086 (3%), 0.124 (1%), 0.137 (2%), 0.148 (1%), 0.156 (1%), 0.194 (5%), 0.211 (3%)	$^{225}_{88}$Ra
$^{230}_{90}$Th	8×10^4 y	α	α 4.69 (76.3%), 4.62 (23.4%), 4.48 (0.1%) γ 0.253 (0.02%), 0.184 (0.01%), 0.142 (0.05%), 0.068 (0.4%)	$^{226}_{88}$Ra
$^{231}_{90}$Th	25.5 h	β^-	β^- 0.302 (52%), 0.218 (20%), 0.138 (22%), 0.09 (6%) γ 0.084 (6.6%) e^- {0.094} (476%) Pa *K* x-rays ~ 0.100 (1%), Pa *L* x-rays ~ 0.015 (97%)	$^{231}_{91}$Pa
$^{232}_{90}$Th	1.4×10^{10} y	α	α 4.02 (77%), 3.96 (23%) γ 0.059 (0.2%)	$^{228}_{88}$Ra
$^{233}_{90}$Th	21.83 m	β^-	β^- 1.24 (80.0%), 1.15 (15.0%), 1.07 (0.9%), 0.795 (1.1%), 0.689 (1.0%), 0.478 (1.5%), 0.432 (0.5%) γ 0.459 (1%), 0.086 (3%), 0.029 (3%), 0.008 (19%) e^- {0.018} (67%) Pa *L* x-rays 0.013 (8%)	$^{233}_{91}$Pa
$^{234}_{90}$Th	24.1 d	β^-	β^- 0.199 (72.5%), 0.104 (20.7%), 0.060 (5.4%), 0.022 (1.3%) γ 0.063 (4%), 0.0924 (3%), 0.0928 (3%), e^- {0.016} (33%) Pa *L* x-rays ~ 0.015 (10%)	$^{234}_{91}$Pa
Protactinium				
$^{226}_{91}$Pa	1.8 m	α (74.0%) EC (26.0%)	α 6.86 (38.0%), 6.82 (35.0%), 6.73 (1.0%)	$^{222}_{89}$Ac
$^{227}_{91}$Pa	38.3 m	α (85.0%) EC (15.0%)	α 6.46 (42.7%), 6.42 (9.9%), 6.41 (12.8%), 6.40 (8.0%), 6.38 (2.2%), 6.35 (6.7%), 6.33 (0.6%), 6.32 (0.3%), 6.29 (0.7%) γ 0.110 (1%), 0.064 (6%) Ac *L* x-rays 0.013 (2%)	$^{223}_{89}$Ac
$^{228}_{91}$Pa	22.4 h	EC (98.2%) α (1.8%) β^+ (0.03%)	α 6.12 (0.2%), 6.10 (0.2%), 6.07 (0.4%), 6.02 (0.2%), 5.98 (0.1%), 5.97 (0.1%), 5.83 (0.2%), 5.80 (0.2%), 5.75 (0.2%) β^+ 1.07 (0.03%) γ 0.969 (14%), 0.964 (11%), 0.911 (23%), 0.463 (21%), 0.409 (9%), 0.338 (8%) $\gamma^{\pm}$ 0.511 (0.06%) e^- {0.102} (193%) Th *K* x-rays 0.109 (4%), 0.105 (14%), 0.093 (38%), 0.090 (24%), Th *L* x-rays 0.013 (78%)	$^{228}_{90}$Th (EC, β^+) $^{224}_{89}$Ac (α)
$^{229}_{91}$Pa	1.50 d	EC (99.52%) α (0.48%)	α 5.67 (0.1%), 5.63 (0.05%), 5.61 (0.06%), 5.59 (0.02%), 5.58 (0.2%), 5.56 (0.02%), 5.53 (0.03%) γ 0.146 (0.1%), 0.119 (0.1%) 0.117 (0.05%) Th *K* x-rays 0.109 (3%), 0.105 (11%), 0.093 (29%), 0.090 (18%), Th *L* x-rays 0.013 (40%)	$^{229}_{90}$Th (EC) $^{225}_{89}$Ac (α)

Continued

Table of radioactive isotopes—cont'd

Nuclide $^{A}_{Z}X$	Half-life	Decay mode	Radiation characteristics: energies (MeV) [intensities (%)]		Decay product $^{A}_{Z}Y$
$^{230}_{91}$Pa	17.4 d	EC (92.2%) β^- (7.8%)	β^- γ e^-	0.508 (7.5%), 0.193 (0.2%) 1.01 (1%), 0.956 (2%), 0.952 (30%), 0.919 (8%), 0.899 (56%), 0.781 (2%), 0.728 (2%), 0.571 (1%), 0.518 (2%), 0.508 (4%), 0.455 (7%), 0.444 (6%), 0.398 (2%) 0.334 (1%), 0.100 (1%), 0.069 (2%), 0.052 (3%), 0.048 (11%), 0.032 (41%), 0.009 (60%) Th *K* x-rays 0.108 (3%), 0.105 (7%), 0.104 (4%), 0.093 (30%), 0.089 (18%), Th *L* x-rays 0.013 (55%), U *L* x-rays 0.014 (3%)	$^{230}_{90}$Th (EC) $^{230}_{92}$U (β^-)
$^{231}_{91}$Pa	3.28×10^4 y	α	α γ e^-	5.06 (10%), 5.03 (23%), 5.01 (24%), 4.98 (2.3%), 4.95 (22%), 4.93 (2.8%), 4.85 (1.4%), 4.74 (11%), 4.71 (1.4%), 4.68 (2.1%) 0.330 (1%), 0.29 (6%), 0.027 (6%) {0.048} (236%) Ac *K* x-rays ~ 0.100 (2%), Ac *L* x-rays ~ 0.015 (54%)	$^{227}_{89}$Ac
$^{232}_{91}$Pa	1.31 d	β^-	β^- γ e^-	1.29 (0.7%), 1.18 (0.8%), 0.774 (0.3%), 0.708 (0.4%), 0.470 (0.4%), 0.426 (0.2%), 0.320 (73.0%), 0.286 (24.0%), 0.162 (0.2%) 0.969 (42%), 0.894 (20%), 0.867 (6%), 0.819 (7%), 0.581 (6%), 0.515 (5%), 0.472 (4%), 0.453 (8%), 0.388 (7%), 0.150 (10%) {0.079} (172%) U *K* x-rays 0.114 (0.1%), 0.111 (0.5%), 0.098 (2%), 0.095 (1%), U *L* x-rays 0.014 (49%)	$^{232}_{92}$U
$^{233}_{91}$Pa	26.95 d	β^-	β^- γ e^-	0.568 (5%), 0.257 (58%), 0.145 (37%) 0.341 (4%), 0.312 (37%), 0.300 (6%) {0.130} (138%) U *K* x-rays ~ 0.100 (35%), U *L* x-rays ~ 0.016 (43%)	$^{233}_{92}$U
$^{234m}_{91}$Pa	1.18 m	β^- (99.87%) IT (0.13%)	β^- γ	2.29 (~98%) 0.766 (0.2%), 1.00 (0.7%)	$^{234}_{92}$U (β^-) $^{234}_{91}$Pa (IT)
$^{234}_{91}$Pa	6.75 h	β^-	β^- γ e^-	1.51 (~1%), 1.19 (5%), 0.680 (19%), 0.512 (63%), 0.280 (12%) 1.08 (1%), 0.90 (70%), 0.70 (24%), 0.56 (15%), 0.36 (13%), 0.22 (14%), 0.126 (26%), 0.100 (50%) {0.265} (380%) U *K* x-rays ~ 0.100 (53%), U *L* x-rays ~ 0.015 (110%)	$^{234}_{92}$U
Uranium					
$^{230}_{92}$U	20.8 d	α SF (10^{-10} %)	α γ e^-	5.89 (67.4%), 5.82 (32.0%), 5.67 (0.4%), 5.66 (0.2%) 0.230 (0.1%), 0.154 (0.1%), 0.072 (0.6%) {0.021} (42%) Th *L* x-rays 0.013 (11%)	$^{226}_{90}$Th
$^{231}_{92}$U	4.2 d	EC	γ e^-	0.102 (1%), 0.084 (7%), 0.026 (15%) Pa *K* x-rays 0.111 (3%), 0.108 (10%), 0.096 (28%), 0.092 (18%), Pa *L* x-rays 0.013 (110%)	$^{231}_{91}$Pa
$^{232}_{92}$U	71.7 y	α	α γ	5.32 (68.6%), 5.26 (31.2%), 5.14 (0.2%) 0.270 (0.004%), 0.129 (0.08%), 0.058 (0.21%)	$^{228}_{90}$Th
$^{233}_{92}$U	1.59×10^5 y	α	α γ e^-	4.82 (84.4%), 4.80 (0.3%), 4.78 (13.3%), 4.75 (0.2%), 4.73 (1.6%) 0.042 (0.06%) {0.006} (25%) Th *K* x-rays ~ 0.100 (0.03%), Th *L* x-rays ~ 0.015 (48%)	$^{229}_{90}$Th

Continued

Table of radioactive isotopes—cont'd

Nuclide $^{A}_{Z}X$	Half-life	Decay mode	Radiation characteristics: energies (MeV) [intensities (%)]	Decay product $^{A}_{Z}Y$
$^{234}_{92}$U	2.4×10^5 y	α	α 4.77 (72%), 4.72 (28%) γ 0. 053 (0.12%), 0.121 (0.04%)	$^{230}_{90}$Th
$^{235}_{92}$U	7.1×10^8 y	α	α 4.598 (4.6%), 4.577 (3.7%), 4.503 (1.2%), 4.438 (0.6%), 4.416 (4%), 4.397 (57%), 4.367 (18%), 4.344 (1.5%), 4.324 (3%), 4.267 (0.6%), 4.217 (5.7%), 4.158 (~0.5%) γ 0.143 (11%), 0.163 (5%), 0.186 (53%), 0.205 (5%) e^- {0.042} (133%) Th *K* x-rays ~ 0.100 (12%), Th *L* x-rays ~ 0.015 (39%)	$^{231}_{90}$Th
$^{236}_{92}$U	2.3×10^7 y	α	α 4.494 (74%), 4.445 (26%), 4.331 (0.26%) γ 0.049 (0.08%), 0.112 (0.02%) e^- {0.011} (35%) Th *L* x-rays ~ 0.015 (9%)	$^{232}_{90}$Th
$^{237}_{92}$U	6.75 d	β^-	β^- 0.245 (>80%), ~0.09 (~12%) γ 0.026 (2%), 0.059 (33%), 0.065 (1%), 0.164 (2%), 0.208 (22%), 0.332 (1%) e^- {0.121} (250%) Np *K* x-rays ~ 0.110 (55%), Np *L* x-rays ~ 0.015 (64%)	$^{237}_{93}$Np
$^{238}_{92}$U	4.5×10^9 y	α	α 4.196 (77%), 4.149 (23%) γ 0.050 (0.07%), 0.111 (0.02%) e^- {0.010} (31%) Th *L* x-rays ~ 0.015 (8%)	$^{234}_{90}$Th
$^{239}_{92}$U	23.5 m	β^-	β^- 1.29 (20%), 1.21 (80%) γ 0.043 (4%), 0.075 (52%)	$^{239}_{93}$Np
Neptunium				
$^{232}_{93}$Np	14.7 m	EC (99.95%) β^+ (0.05%)	β^+ 1.73 (0.01%), 0.530 (0.04%) γ 0.867 (25%), 0.864 (21%), 0.819 (34%), 0.327 (53%), 0.282 (20%) $\gamma^{\pm}$ 0.511 (0.1%) e^- {0.099} (62%) U *K* x-rays 0.114 (4%), 0.111 (14%), 0.098 (38%), 0.095 (24%), U *L* x-rays 0.014 (46%)	$^{232}_{92}$U
$^{233}_{93}$Np	36.2 m	EC	γ 0.546 (0.3%), 0.506 (0.2%), 0.312 (0.7%), 0.299 (0.4%), 0.234 (0.2%) e^- 0.073 (2%), 0.010 (39%) U *K* x-rays 0.114 (3%), 0.111 (12%), 0.098 (34%), 0.095 (21%), U *L* x-rays 0.014 (39%)	$^{233}_{92}$U
$^{234}_{93}$Np	4.4 d	EC (99.95%) β^+ (0.05%)	β^+ 0.788 (0.05%) γ 1.60 (9%), 1.57 (5%), 1.55 (19%), 1.52 (11%), 1.43 (6%), 1.19 (6%), 0.742 (5%) $\gamma^{\pm}$ 0.511 (0.1%) U *K* x-rays 0.114 (3%), 0.111 (10%), 0.098 (29%), 0.095 (18%), U *L* x-rays 0.014 (57%)	$^{234}_{92}$U
$^{235}_{93}$Np	396.1 d	EC	e^- {0.0029} (13%) U *L* x-rays ~ 0.014 (14%)	$^{235}_{92}$U
$^{236m}_{93}$Np	22.5 h	β^- (50.0%) EC (50.0%)	β^- 0.480 (40%), 0.440 (10%) γ 0.687 (0.3%), 0.642 (1%) e^- {0.011} (49%) U *K* x-rays 0.114 (2%), 0.111 (6%), 0.098 (17%), 0.095 (11%), U *L* x-rays 0.014 (24%) Pu *L* x-rays 0.014 (4%)	$^{236}_{94}$Pu (β^-) $^{236}_{92}$U (EC)

Continued

Table of radioactive isotopes—cont'd

Nuclide $^{A}_{Z}X$	Half-life	Decay mode	Radiation characteristics: energies (MeV) [intensities (%)]	Decay product $^{A}_{Z}Y$
$^{236}_{93}$Np	1.53×10^5 y	EC (86.3%) β^- (13.5%) α (0.16%)	β^- 3.30 (1.0%), 1.70 (12.5%) γ 0.160 (31%), 0.158 (4%), 0.104 (7%) e^- {0.188} (367%) U *K* x-rays ~0.112 (15%), ~0.095 (53%), U *L* x-rays ~0.014 (111%), Pu *L* x-rays ~0.014 (13%)	$^{236}_{92}$U (EC) $^{236}_{94}$Pu (β^-)
$^{237}_{93}$Np	2.14×10^6 y	α	α 4.87 (2.6%), 4.82 (2.5%), 4.80 (3%), 4.79 (47%), 4.77 (25%), 4.76 (8%), 4.66 (3.3%), 4.64 (6%) γ 0.145 (1%), 0.086 (14%), 0.030 (14%) e^- {0.064} (184%) Pa *K* x-rays ~0.100 (5%), Pa *L* x-rays ~0.015 (52%)	$^{233}_{91}$Pa
$^{238}_{93}$Np	2.117 d	β^-	β^- 1.25 (41.0%), 0.686 (0.1%), 0.329 (1.3%), 0.309 (0.2%), 0.306 (0.6%), 0.264 (44.8%), 0.222 (11.5%), 0.089 (0.5%) γ 1.03 (18%), 1.02 (9%), 0.984 (25%), 0.924 (3%) e^- 0.819 (0.01%)	$^{238}_{94}$Pu
Plutonium				
$^{234}_{94}$Pu	8.8 h	EC (94.0%) α (6.0%)	α 6.20 (4.1%), 6.15 (1.9%)	$^{234}_{93}$Np (EC) $^{230}_{92}$U (α)
$^{235}_{94}$Pu	25.3 m	EC	γ 0.945 (0.1%), 0.910 (0.2%), 0.756 (0.5%), 0.049 (2%) e^- 0.074 (2%), 0.010 (38%) Np *K* x-rays 0.117 (3%), ~0.114 (12%), 0.101 (34%), 0.097 (21%), Np *L* x-rays 0.014 (39%)	$^{235}_{93}$Np
$^{236}_{94}$Pu	2.86 y	α	α 5.77 (69.0%), 5.72 (30.8%), 5.61 (0.2%) γ 0.109 (0.02%), 0.047 (0.07%) e^- 0.087 (0.15%), 0.042 (6.1%), 0.025 (22%), 0.010 (11%) U *L* x-rays 0.014 (11.2%)	$^{232}_{92}$U
$^{237}_{94}$Pu	45.3 d	EC (>99%) α (0.0033%)	γ 0.060 (5%) e^- {0.011} (48%) Np *K* x-rays ~ 0.110 (43%), Np *L* x-rays ~ 0.015 (47%)	$^{237}_{93}$Np
$^{238}_{94}$Pu	86.4 y	α SF (1.8×10^{-7}%)	α 5.50 (71.1%), 5.45 (28.7%), 5.36 (0.2%) γ 0.043 (0.04%) e^- {0.010} (38%) U *L* x-rays ~ 0.015 (11%)	$^{234}_{92}$U
$^{239}_{94}$Pu	2.41×10^4 y	α SF	α 5.16 (73.3%), 5.14 (15.1%), 5.10 (11.5%) γ 0.375 (0.001%), 0.129 (0.005%), 0.052 (0.02%)	$^{235}_{92}$U
$^{240}_{94}$Pu	6570 y	α SF	α 5.16 (75.5%), 5.12 (24.4%), 5.01 (0.1%) γ 0.104 (0.007%), 0.045 (0.04%)	$^{236}_{92}$U
$^{241}_{94}$Pu	14.4 y	β^- (>99%) α (0.002%)	β^- 0.021 (>99%)	$^{241}_{95}$Am
$^{242}_{94}$Pu	3.8×10^5 y	α SF (0.0006%)	α 4.901 (74%), 4.857 (26%) γ 0.045 (0.04%) e^- {0.008} (30%) U *L* x-rays ~ 0.015 (9%)	$^{238}_{92}$U
$^{243}_{94}$Pu	4.956 h	β^-	β^- 0.579 (59%), 0.495 (21%), 0.483 (1.2%), 0.470 (5%), 0.436 (3.5%), 0.114 (1.3%) γ 0.382 (0.6%), 0.356 (0.1%), 0.109 (0.2%), 0.084 (23%), 0.034 (4%), 0.025 (8%) e^- {0.013} (10%) Am *L* x-rays 0.015 (3%)	$^{243}_{95}$Am

Continued

Table of radioactive isotopes—cont'd

Nuclide $^{A}_{Z}X$	Half-life	Decay mode	Radiation characteristics: energies (MeV) [intensities (%)]	Decay product $^{A}_{Z}Y$
$^{244}_{94}$Pu	8.11×10^{7} y	α (99.88%) SF (0.12%)	α 4.59 (80.5%), 4.55 (19.4%) γ 0.044 (0.03%) e^- 0.043 (1%), 0.038 (3%), 0.022 (11%), 0.010 (6%) U *L* x-rays 0.014 (6%)	$^{240}_{92}$U
$^{245}_{94}$Pu	10.5 h	β^-	β^- 1.23 (10.0%), 0.951 (53.0%), 0.882 (3.9%), 0.802 (0.4%), 0.391 (15.0%), 0.357 (2.3%), 0.320 (8.5%), 0.290 (2.9%), 0.254 (1.1%), 0.213 (1.7%), 0.167 (0.7%), 0.092 (0.2%) γ 0.630 (3%), 0.560 (6%), 0.492 (3%), 0.376 (3%), 0.327 (27%), 0.308 (5%) e^- {0.089} (51%) Am *K* x-rays 0.124 (1%), ~0.120 (4%), 0.106 (12%), 0.102 (8%), Am *L* x-rays 0.015 (15%)	$^{245}_{95}$Am
$^{246}_{94}$Pu	10.84 d	β^-	β^- 0.401 (1.5%), 0.357 (8.0%), 0.177 (85.0%), 0.168 (0.5%), 0.102 (5.0%) γ 0.244 (24%), 0.180 (10%), 0.044 (25%), 0.028 (4%) e^- {0.082} (141%) Am *K* x-rays 0.124 (2%), ~0.120 (7%), 0.106 (20%), 0.102 (13%), Am *L* x-rays 0.015 (42%)	$^{246}_{95}$Am
Americium				
$^{240}_{95}$Am	50.8 h	EC	γ 0.988 (72%), 0.889 (25%), 0.099 (2%) e^- {0.069} (206%) Pu *K* x-rays 0.121 (3%), ~0.117 (10%), 0.103 (29%), 0.099 (18%), Pu *L* x-rays 0.014 (87%)	$^{240}_{94}$Pu
$^{241}_{95}$Am	432.0 y	α	α 5.54 (0.3%), 5.48 (85.2%), 5.44 (12.5%), 5.38 (1.6%) γ 0.060 (36%) e^- {0.030} (115%) Np *L* x-rays ~ 0.015 (40%)	$^{237}_{93}$Np
$^{242m}_{95}$Am	150 y	IT (>99%) α (0.5%)	α 5.207 (0.4%), 5.141 (0.03%) γ 0.049 (0.2%) e^- {0.040} (118%) Am *L* x-rays ~ 0.016 (26%)	$^{242}_{95}$Am (IT) $^{238}_{93}$Np (α)
$^{242}_{95}$Am	16 h	β^- (82.7%) EC (17.3%)	β^- 0.667 (~33%), 0.625 (~49%) γ 0.042 (0.04%), 0.044 (0.02%) e^- {0.019} (77%) Pu *K* x-rays ~ 0.110 (12%), Pu *L* x-rays ~ 0.015 (11%) Cm *L* x-rays ~ 0.016 (18%)	$^{242}_{96}$Cm (β^-) $^{242}_{94}$Pu (EC)
$^{243}_{95}$Am	8×10^{3} y	α SF (2.2×10^{-8}%)	α 5.276 (87%), 5.234 (11.5%), 5.180 (1.1%) γ 0.043 (5%), 0.075 (60%), 0.087 (0.3%), 0.118 (0.6%)	$^{239}_{93}$Np
Curium				
$^{242}_{96}$Cm	162.76 d	α SF (6.3×10^{-6}%)	α 6.11 (74.0%), 6.07 (26.0%) γ 0.102 (0.006%), 0.044 (0.041%) e^- {0.009} (34%) Pu *L* x-rays ~ 0.016 (10%)	$^{238}_{94}$Pu
$^{243}_{96}$Cm	32 y	α (99.7%) EC (0.3%)	α 6.066 (1.5%), 6.059 (5%), 6.010 (1%), 5.992 (6.5%), 5.876 (0.6%), 5.786 (73.3%), 5.742 (10.6%) γ 0.209 (3%), 0.228 (11%), 0.278 (14%) e^- {0.113} (136%) Pu *K* x-rays ~ 0.110 (49%), Pu *L* x-rays ~ 0.016 (43%)	$^{239}_{94}$Pu (α)

Continued

Table of radioactive isotopes—cont'd

Nuclide $^{A}_{Z}X$	Half-life	Decay mode	Radiation characteristics: energies (MeV) [intensities (%)]	Decay product $^{A}_{Z}Y$
$^{244}_{96}$Cm	18.09 y	α SF (0.0001%)	α 5.81 (76.7%), 5.76 (23.3%) γ 0.100 (0.002%), 0.043 (0.03%) Pu *L* x-rays ~0.016 (8%)	$^{240}_{94}$Pu
$^{245}_{96}$Cm	9.3×10^3 y	α	α 5.53 (0.6%), 5.49 (0.8%), 5.36 (93.2%), 5.30 (5%), 5.23 (0.3%) γ 0.042 (0.4%), 0.133 (3%), 0.175 (10%), 0.190 (0.2%) e^- {0.134} (487%) Pu *K* x-rays ~0.110 (71%), Pu *L* x-rays ~0.016 (123%)	$^{241}_{94}$Pu
$^{246}_{96}$Cm	5×10^3 y	α (99.97%) SF (0.03%)	α 5.386 (79%), 5.343 (21%) γ 0.044 (0.03%) e^- {0.007} (27%) Pu *L* x-rays ~ 0.016 (8%)	$^{242}_{94}$Pu
$^{247}_{96}$Cm	1.6×10^7 y	α	α 5.27 (13.8%), 5.21 (5.7%), 5.15 (1.2%), 4.98 (2%), 4.94 (1.6%), 4.87 (71%), 4.82 (4.7%) γ 0.279 (3%), 0.289 (2%), 0.347 (1%), 0.404 (72%) Pu *K* x-rays ~ 0.110 (5%)	$^{243}_{94}$Pu
$^{248}_{96}$Cm	4.7×10^5 y	α (91.7%) SF (8.3%)	α 5.08 (75.1%), 5.03 (16.5%)	$^{244}_{94}$Pu
Berkelium				
$^{245}_{97}$Bk	4.95 d	EC (99.88%) α (0.12%)	α 6.35 (0.02%), 6.31 (0.02%), 6.15 (0.03%), 6.12 (0.01%), 6.11 (0.01%), 6.08 (0.01%), 5.89 (0.02%) γ 0.381 (3%), 0.253 (31%) e^- {0.127} (141%) Cm *K* x-rays 0.127 (5%), ~0.123 (20%), 0.109 (54%), 0.105 (35%), Cm *L* x-rays 0.015 (73%)	$^{245}_{96}$Cm (EC) $^{241}_{95}$Am (α)
$^{246}_{97}$Bk	1.80 d	EC	γ 1.12 (5%), 1.08 (10%), 0.833 (5%), 0.799 (62%) e^- {0.048} (178%) Cm *K* x-rays 0.127 (3%), ~0.123 (11%), 0.109 (30%), 0.105 (19%), Cm *L* x-rays 0.015 (85%)	$^{246}_{96}$Cm
$^{247}_{97}$Bk	1380 y	α	α 5.79 (5.5%), 5.75 (4.3%), 5.71 (17.0%), 5.68 (13.0%), 5.65 (5.5%), 5.61 (0.4%), 5.53 (45.0%), 5.50 (7.0%), 5.46 (1.5%) e^- 0.259 (2%), 0.241 (8%), 0.140 (24%), 0.078 (2%), 0.060 (7%), 0.011 (15%) Am *K* x-rays 0.124 (1%), ~0.120 (4%), 0.106 (11%), 0.102 (7%), Am *L* x-rays 0.015 (17%)	$^{243}_{95}$Am
$^{248}_{97}$Bk	23.7 h	β^- (70.0%) EC (30.0%)	β^- 0.860 (45%), 0.818 (20%), 0.268 (5%) γ 0.550 (5%) e^- 0.079 (1%), 0.037 (1%), 0.019 (5%), 0.011 (13%) Cm *K* x-rays ~0.124 (4%), ~0.105 (16%), Cm *L* x-rays 0.015 (15%)	$^{248}_{98}$Cf (β^-) $^{248}_{96}$Cm (EC)
$^{249}_{97}$Bk	314 d	β^- (>99%) α (0.0014%)	β^- 0.125 (>99%)	$^{249}_{98}$Cf (β^-)
Californium				
$^{248}_{98}$Cf	333.5 d	α (100%) SF (3×10^{-3}%)	α 6.26 (80.0%), 6.22 (19.6%), 6.12 (0.4%) γ 0.099 (0.02%), 0.043 (0.02%) e^- 0.093 (0.1%), 0.075 (0.3%), 0.037 (4%), 0.018 (14%), 0.011 (7%) Cm *L* x-rays 0.015 (8%)	$^{244}_{96}$Cm

Continued

Table of radioactive isotopes—cont'd

Nuclide $^{A}_{Z}X$	Half-life	Decay mode	Radiation characteristics: energies (MeV) [intensities (%)]			Decay product $^{A}_{Z}Y$
$^{249}_{98}$Cf	351 y	α (100%) SF (5×10^{-7}%)	α γ e^-	6.19 (2.5%), 6.14 (1.3%), 6.07 (0.4%), 5.95 (3.3%), 5.90 (3.2%), 5.85 (1.5%), 5.81 (82.2%), 5.78 (0.3%), 5.76 (4.7%), 5.69 (0.3%), 5.56 (0.1%) 0.388 (66%), 0.333 (15%), 0.253 (3%) {0.037} (41%) Cm *K* x-rays 0.127 (0.3%), ~0.123 (1%), 0.109 (3%), 0.105 (2%), Cm *L* x-rays 0.015 (15%)	$^{245}_{96}$Cm
$^{250}_{98}$Cf	13.1 y	α (99.92%) SF (0.08%)	α γ e^-	6.03 (84.7%), 5.99 (15%), 5.89 (0.3%) 0.043 (0.01%) {0.005} (20%) Cm *L* x-rays ~ 0.017 (6%)	$^{246}_{96}$Cm
$^{251}_{98}$Cf	~890 y	α	α γ e^-	6.07 (2.7%), 6.01 (11.6%), 5.94 (0.6%), 5.85 (27%), 5.81 (4.2%), 5.79 (2%), 5.76 (3.8%), 5.73 (1%), 5.67 (35%), 5.65 (3.5%), 5.63 (4.5%), 5.60 (0.2%), 5.57 (1.5%), 5.50 (0.3%) 0.177 (18%), 0.227 (6%), 0.266 (0.5%), 0.285 (1.4%) {0.187} (200%) Cm *K* x-rays ~0.125 (13%), Cm *L* x-rays ~0.090 (109%)	$^{247}_{96}$Cm
$^{252}_{98}$Cf	2.65 y	α (97%) SF (3%)	α e^-	6.12 (81.6%), 6.08 (15.2%), 5.98 (0.2%) {0.005} (19%) Cm *L* x-rays ~ 0.017 (6%)	$^{248}_{96}$Cm
$^{253}_{98}$Cf	17.81 d	β^- (99.69%) α (0.31%)	β^- α	0.287 (~50%), 0.241 (~50%) 5.98 (0.30%), 5.92 (0.01%)	$^{253}_{99}$Es (β^-) $^{249}_{96}$Cm (α)
$^{254}_{98}$Cf	60.5 d	SF (99.69%) α (0.31%)	α	5.83 (0.25%), 5.79 (0.06%)	$^{250}_{96}$Cm (α)
Einsteinium					
$^{252}_{99}$Es	471.7 d	α (78.0%) EC (22.0%)	α γ e^-	6.63 (62.6%), 6.56 (10.6%), 6.49 (0.3%), 6.48 (1.7%), 6.46 (0.2%), 6.42 (0.4%), 6.26 (0.6%), 6.24 (0.4%), 6.05 (0.8%) 0.924 (2%), 0.785 (15%), 0.139 (12%) {0.084} (60%) Cf *K* x-rays 0.133 (0.3%), ~0.129 (1%), 0.115 (3%), 0.110 (2%), Cf *L* x-rays 0.016 (19%) Bk *L* x-rays 0.015 (6%)	$^{248}_{97}$Bk (α) $^{252}_{98}$Cf (EC)
Fermium					
$^{257}_{100}$Fm	100.5 d	α (99.8%) SF (0.2%)	α γ e^-	6.75 (0.4%), 6.70 (3.2%), 6.62 (0.5%), 6.52 (93.5%), 6.44 (1.9%), 6.35 (0.3%) 0.241 (11%), 0.179 (9%), 0.062 (1%) {0.121} (211%) Cf *K* x-rays 0.133 (2%), ~0.129 (9%), 0.115 (24%), 0.110 (16%), Cf *L* x-rays 0.016 (68%)	$^{253}_{98}$Cf
Mendelevium					
$^{258}_{101}$Md	51.5 d	α	α	7.16 (0.1%), 7.08 (0.1%), 6.99 (0.1%), 6.79 (9.9%), 6.76 (20.7%), 6.72 (65.7%), 6.70 (3.4%)	$^{254}_{99}$Es
Nobelium					
$^{259}_{102}$No	58 m	α (~75%) EC, β^+ (~25%) SF (<10%)	α γ	7.69 (8.3%), 7.60 (10.5%), 7.53 (17.3%), 7.50 (29.3%), 7.45 (9.8%) 0.231, 0.129, 0.062	$^{255}_{100}$Fm (α)

Continued

Table of radioactive isotopes—cont'd

Nuclide $^{A}_{Z}X$	Half-life	Decay mode	Radiation characteristics: energies (MeV) [intensities (%)]	Decay product $^{A}_{Z}Y$
Lawrencium				
$^{261}_{103}$Lr	39 m	SF (100%)		
$^{262}_{103}$Lr	~4 h	SF (<10%) EC β^+, α ?		
Rutherfordium				
$^{259}_{104}$Rf	2.4 s	α (~90%) EC (~10%) SF (~5%)	α 8.10 (~90%) γ 0.537	$^{255}_{102}$No (α)
$^{262}_{104}$Rf	2.3 s	SF ≤100%		
$^{263}_{104}$Rf	10 m	α (30%) SF ?		$^{259}_{102}$No (α)
$^{265}_{104}$Rf	1.0 m	SF (~100%)		
Dubnium				
$^{263}_{105}$Db	27 s	SF (57%) α (43%)	α 3.59 (43%)	$^{259}_{103}$Lr
$^{268}_{105}$Db	32 h	SF ~100%		
$^{270}_{105}$Db	23 h	SF 100% α ?		
Seaborgium				
$^{266}_{106}$Sg	21 s	SF (<80%) α (<50%)	α 8.52	$^{262}_{104}$Rf
$^{269}_{106}$Sg	3.1 m	α (~100%)	α 8.50	$^{265}_{104}$Rf
$^{271}_{106}$Sg	2.4 m	α (~50%) SF (~50%)	α 8.65	$^{267}_{104}$Rf
Bohrium				
$^{272}_{107}$Bh	10 s	α (~100%)	α 9.02	$^{268}_{105}$Db
$^{274}_{107}$Bh	54 s	α (~100%)	α 8.80	$^{270}_{105}$Db
Hassium				
$^{269}_{108}$Hs	9.7 s	α (~100%)	α 8.69 (~91%), 8.84 (~9%)	$^{265}_{106}$Sg
$^{270}_{108}$Hs	3.6 s	α (~100%)	α 9.16	$^{266}_{106}$Sg
Meitnerium				
$^{277}_{109}$Mt	5 s	SF (~100%) α ?		
$^{278}_{109}$Mt	7.6 s	α (~100%) SF ?	α 9.55	$^{274}_{107}$Bh
Damstadium				
$^{279}_{110}$Ds	0.18 s	SF (~90%) α (~10%)	α 9.70	$^{275}_{108}$Hs
$^{281}_{110}$Ds	9.6 s	SF (~100%)		
Roentgenium				
$^{280}_{111}$Rg	3.6 s	α (100%)	α 9.75	$^{276}_{109}$Mt
$^{281}_{111}$Rg	26 s	SF (~100%) α ?		

Continued

Table of radioactive isotopes—cont'd

Nuclide $^{A}_{Z}X$	Half-life	Decay mode	Radiation characteristics: energies (MeV) [intensities (%)]	Decay product $^{A}_{Z}Y$
Copernicium				
$^{283}_{112}$Cn	4 s	α (≥90%) SF (≤10%)	α 9.36, 9.32, 8.94	$^{279}_{110}$Ds
$^{285}_{112}$Cn	34 s	α (~100%)	α 9.16	$^{281}_{110}$Ds
Nihonium				
$^{285}_{113}$Nh	5.5 s	α (~100%)	α 9.70, 9.48	$^{281}_{111}$Rg
$^{286}_{113}$Nh	20 s	α (~100%)	α 9.63	$^{282}_{111}$Rg
Flerovium				
$^{287}_{114}$Fl	0.51 s	α (~100%)	α 10.02	$^{283}_{112}$Cn
$^{288}_{114}$Fl	0.80 s	α (~100%)	α 10.08	$^{284}_{112}$Cn
$^{289}_{114}$Fl	2.7 s	α (~100%)	α 9.82	$^{285}_{112}$Cn
Moscovium				
$^{289}_{115}$Mc	0.22 s	α (~100%)	α 10.31	$^{285}_{113}$Nh
$^{290}_{115}$Mc	16 ms	α (~100%)	α 9.95	$^{286}_{113}$Nh
Livermorium				
$^{290}_{116}$Lv	15 ms	α (~100%)	α 10.85	$^{286}_{114}$Fl
$^{292}_{116}$Lv	18 ms	α (~100%)	α 10.66	$^{288}_{114}$Fl
$^{293}_{116}$Lv	53 ms	α (~100%)	α 10.53	$^{289}_{114}$Fl
Tennessine				
$^{293}_{117}$Ts	14 ms	α (~100%)	α 11.03	$^{289}_{115}$Mc
Oganesson				
$^{294}_{118}$Og	1.8 ms	α (~100%)	α 11.65	$^{290}_{116}$Lv

References

AEA Live Chart of Nuclides, https://www-nds.iaea.org/relnsd/vcharthtml/VChartHTML.html.

Browne, E., Firestone, R.B., Shirley, V.S., 1986. Table of Radioactive Isotopes. John Wiley & Sons, New York.

Firestone, R.B., Shirley, V.S., Baglin, C.M., Frank Chu, S.Y., Zipkin, J., 1996. Table of Isotopes, eighth ed., vols. I and II. John Wiley & Sons, New York.

McCutchan, E.A., 2018. Nuclear Data Sheets, Vol. 150. Elsevier, Amsterdam and Oxford. https://www.sciencedirect.com/journal/nuclear-data-sheets.

Michael Lederer, C., Shirley, V.S., 1978. In: Brown, E., Dairiki, J.M., Doebler, R.E., Shihab-Eldin, A.A., Jardine, L.J., Tuli, J.K., Buyrn, A.B. (Eds.), Table of Isotopes, seventh ed. John Wiley & Sons, New York.

NuDat 2.7, 2018. National Nuclear Data Center, Brookhaven National Laboratory, Upton, New York. http://www.nndc.bnl.gov/nudat2/chartNuc.jsp.

Appendix B

Particle range-energy correlations

PERPUSTAKAAN PRIBADI AN-NUR SUNARYA

Fig. B.1

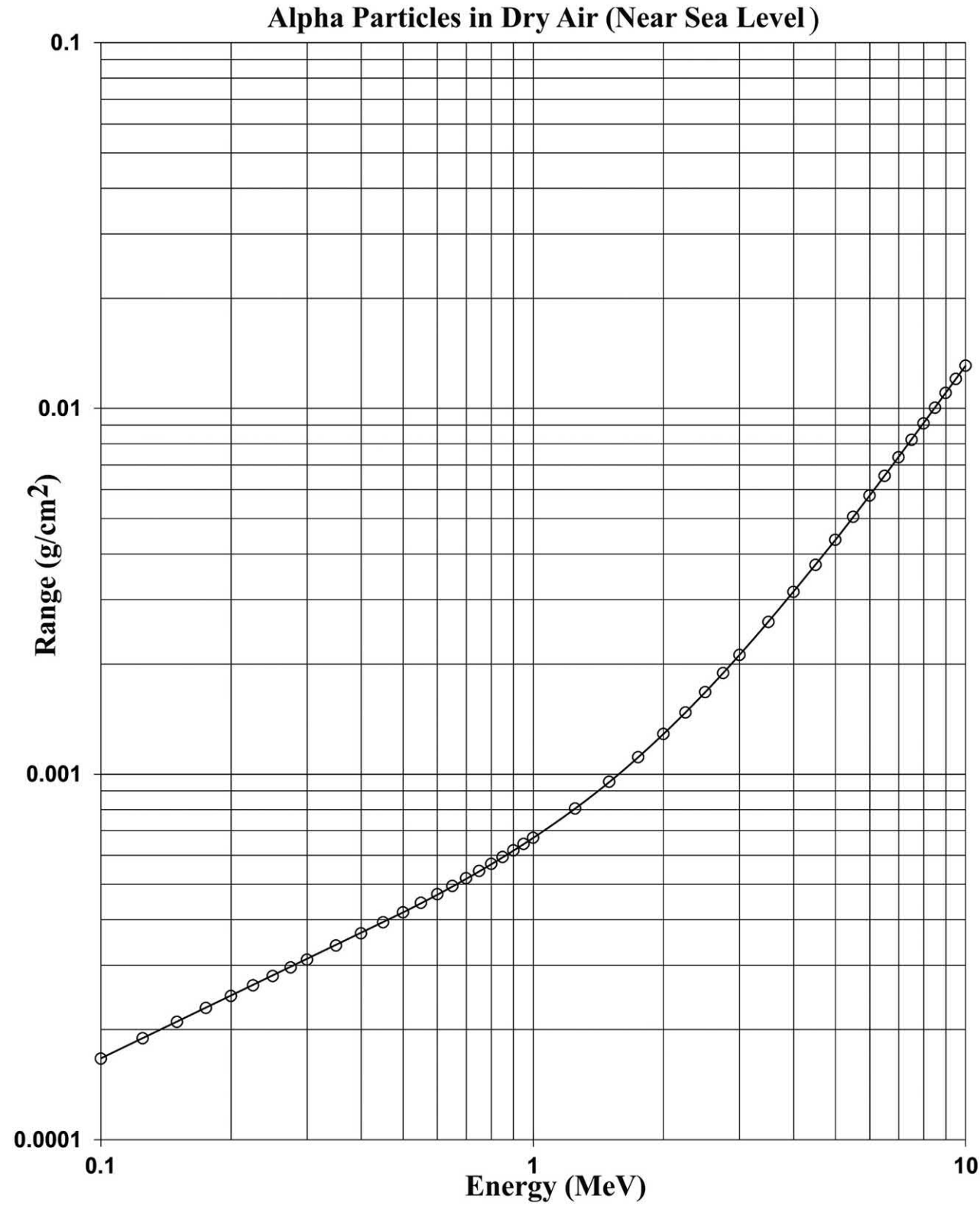


FIGURE B.1 Range-energy relationship for alpha particles in air. The range in cm can be obtained by dividing the above range by the density of air ($\rho = 0.001226$ g/cm^3 at STP). For example, the range of a 5.5 MeV alpha particle from the graph is read as 0.005 g/cm^2; and dividing by the density of air yields a calculated linear range of 4 cm. The range-energy relationship is plotted from data provided by the National Institute of Standards and Technology (NIST) Database ASTAR (2018) for CSDA (continuous slowing down approximation) ranges from which very precise calculated values of range in a large number of elements and compounds may be found: http://www.nist.gov/pml/data/star/index.cfm.

Fig. B.2

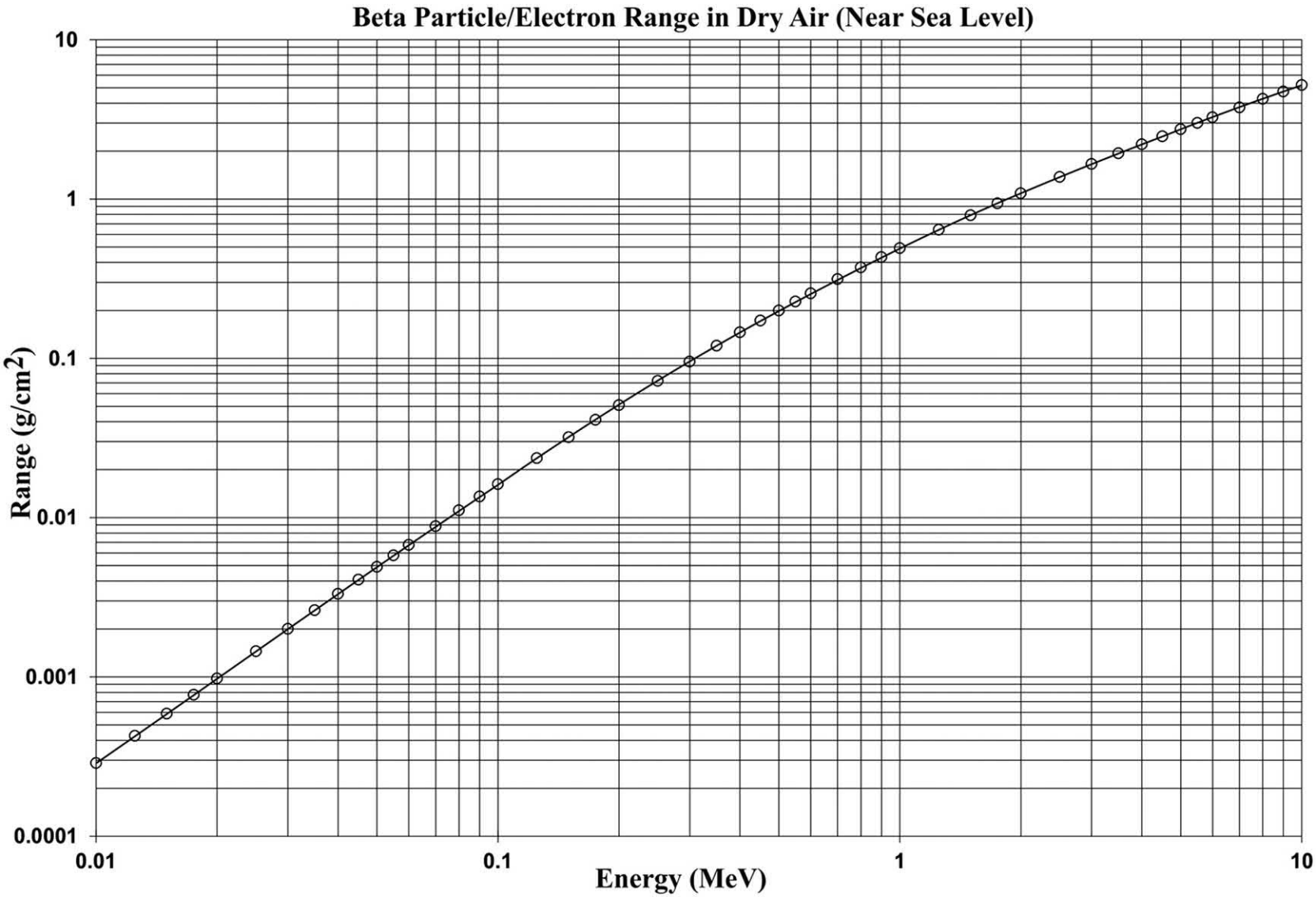


FIGURE B.2 Range-energy relationship for beta particles/electrons in air. The range in cm can be obtained by dividing the above range by the density of air ($\rho = 0.001226$ g/cm^3 at STP). For example, the range of a 1.0 MeV beta particle from the graph is read as 0.48 g/cm^2; and dividing by the density of air yields a calculated linear range of 390 cm. The range-energy relationship is plotted from data provided by the National Institute of Standards and Technology (NIST) Database ESTAR (2018) for CSDA (continuous slowing down approximation) ranges from which very precise calculated values of range in a large number of elements and compounds may be found: http://www.nist.gov/pml/data/star/index.cfm.

Fig. B.3

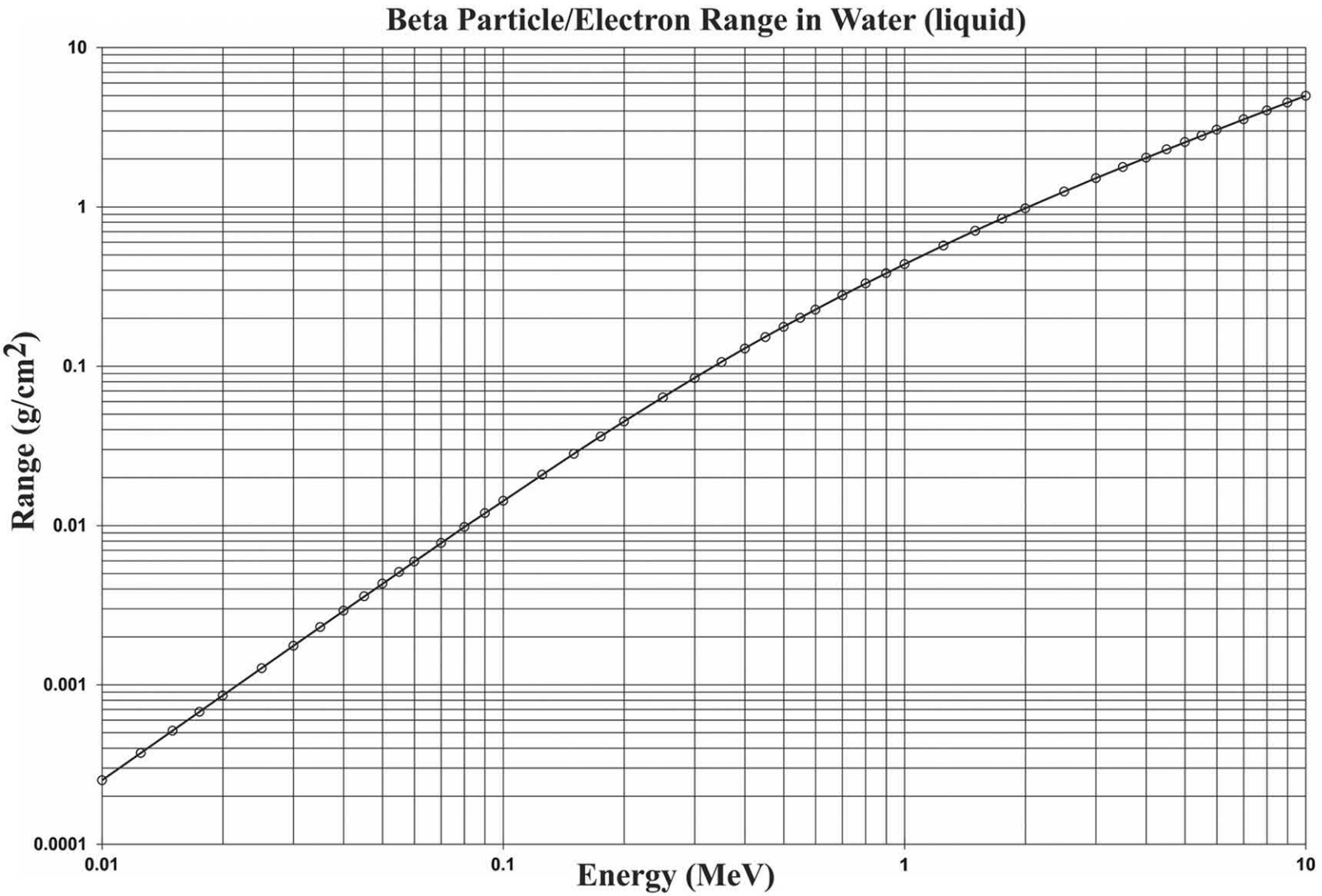


FIGURE B.3 Range-energy relationship for beta particles/electrons in water (liquid). The range in cm can be obtained by dividing the above range by the density of water ($\rho = 1.00$ g/cm^3 at STP). For example, the range of a 1.0 MeV beta particle from the graph is read as 0.43 g/cm^2; and dividing by the density of water yields a calculated linear range of 0.43 cm. The range-energy relationship is plotted from data provided by the National Institute of Standards and Technology (NIST) Database ESTAR (2018) for CSDA (continuous slowing down approximation) ranges from which very precise calculated values of range in a large number of elements and compounds may be found: http://www.nist.gov/pml/data/star/index.cfm.

Fig. B.4

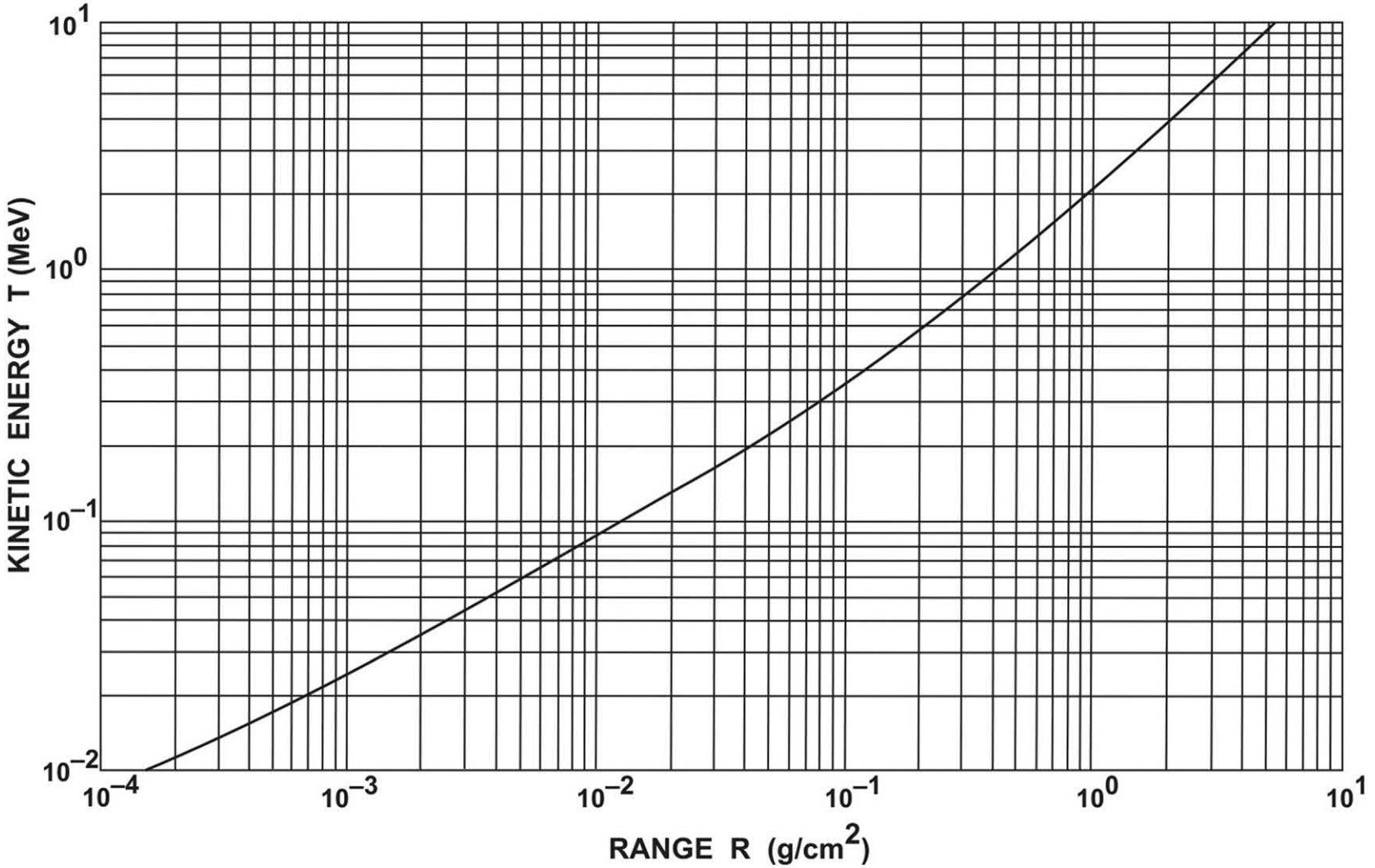


FIGURE B.4 Beta-particle range-energy curve for absorbers of low atomic number. The curve is described by the formulas $R = 0.412T^{1.27-0.0954 \ln T}$ for $0.01 \leq T \leq 2.5$ MeV and $R = 0.530T - 0.106$ for $T > 2.5$ MeV where T is the beta-particle energy in MeV. *From U.S. Public Health Service. (1970). Radiological Health Handbook. Publ. No. 2016. Bureau of Radiological Health, Rockville, MD.*

Index

'*Note*: Page numbers followed by "f" indicate figures and "t" indicate tables.'

A

Absolute average deviation, 632
Accelerator mass spectrometry
  high-energy analyzer and ion detection in, 174–175
  injection system in, 173–174
  instrumental scheme, 173f
  ion separation in, 171–172
  ion source in, 172–173
  of marine isotopes, 347–349
  negative ion source for, 173f
  radionuclides analyzed by, 171t
  tandem accelerator in, 174
Accumulated distribution, 631–632
Accuracy, 934
Actinides
  automated analysis, 834–836
  automated SI separations, 835f–836f
  flow-cell analysis, 782f
Actinides, environmental analysis, 214–233
  combined extraction procedures, 223–225
  coprecipitation techniques, 218
  extraction chromatography, 219–221
  ion exchange, 218–219
  multistage extraction chromatography, 221–223
  plutonium isotope ratios, 230–233
  sampling and pretreatment, 215–216
  separation of actinides, 216–219
  source preparation, 225–226
  transuranics in soil, 228–230
  transuranics on aerosols, 226–228
  uranium-236 in terrestrial waters, 226–233
Actinides in soil
  extraction, 781f
  flow-cell analysis, 779–781
Actinides in waste, flow-cell analysis, 780t
Actinium-228
  Cherenkov counting of, 418
Aerosol, accumulation mode
  formation and characteristics, 267
Aerosol, coarse mode
  formation and characteristics, 267
Aerosol, fission product
  tropospheric residence times, 307
Aerosol monitoring, 14
  gaseous effluents in, 15–17
  online *vs.* offline systems, 14–15
Aerosol, radioactive
  accumulation mode, 267
  aerodynamic particle sizing, 265–267
  after Chernobyl accident, 294–295, 296t
  after Fukushima accident, 297, 299
  Aitken nuclei mode, 266
  in ambient air, 283–301
  Comprehensive Nuclear Test Ban Treaty and, 293
  cosmogenic radionuclides, 286–289
  CTBTO's monitoring network and, 293
  data interpretation, 279–280
  definition, 263–264
  fission product, 291–301
  formation of, 263–265
  gamma-ray spectrometry, 278–279
  from high-energy particle accelerators, 290–291
  INGE project and, 293
  mine aerosols, 289–290
  from nuclear bomb tests, 292
  radon and thoron decay product, 283–286, 287f
  residence times, 301
  sampler calibration, 280–282
  size distributions., 266
  size ranges of, 263–264
  typical gamma-ray spectrum, 280f
  in workplace environment, 289–290
Aerosol, radioactive cosmogenic
  tropospheric residence times., 302–304
Aerosol, radon product
  tropospheric residence times., 304–307, 306t
Aerosols
  Anderson air samplers, 271
  Anderson sampler, 274–275
  cascade impactor assembly, 277
  cascade impactors, 269–282
  collection impaction substrates, 273–274
  filter collection media, 278–279
  high-volume air samplers, 269, 270f
  impactor collection efficiency, 272–273
  impactor effective cutoff diameters, 276t, 283t
  impactor size fractions, 277t
  impactor Stokes number, 272–273
  impactor velocity flow field, 272
  inertial cascade impactor data, 271
  inertial impactor theory, 271
  median aerodynamic diameter, 279
  particle trap impactor, 270–271
  properties of, 189
  radiological analysis, 278–279
  sampling of, 190–191
  sampling artifacts, 278
  slotted cascade impactor, 277
  virtual impactors, 270
Aerosol, sampling and measurement, 265–282
  instrumentation, 267–282
  methods, 268t
Aerosol, size-resolving methods, 269t
Age dating, 931
  assumptions, 931
  fourth ITWG round robin, 933
  multiple chronometers, 931
  $^{241}Pu/^{241}Am$, 931–932
  third ITWG round robin, 931–932
  $^{235}U/^{231}Pa$, 931–932
  $^{234}U/^{230}Th$, 931–932
Air- and vehicle-borne measurements, 29t–31t
Airborne releases, 3
Aitken nuclei, aerosol
  origin and characteristics, 266
Alpha/beta measurements
  of decay series nuclides, 91–95
Alpha/beta spectra
  of decay series nuclides, 94f
  of natural uranium and ^{226}Ra, 92f
Alpha-emitting transuranics
  alpha spectrometry, 61
  environmental occurrence, 60–61
  liquid scintillation analysis, 60–62
  mass spectrometry, 61
  sample preparation and analysis, 61
Alpha spectrometry
  environmental radionuclides analyzed by, 165t
  of transuranic nuclides, 61
Alternative hypothesis, 645
Aluminum-26, on aerosols
  analysis of, 195
  applications, 195–196
  origin and properties, 195–196
Americium-241
  gamma ray energies, 882–883, 883t
Americium-241, flow-cell analysis, 768, 774, 779–781, 780t
AmLi source, 899
Anthropogenic radionuclides
  analysis in marine environment, 335–340
APCI-mass spectrometry, 797

Argon, krypton and xenon, environmental monitoring of, 183−187
Arithmetic Mean, 636
Askaryan Effect, 484
Astatine-211
  automated preparation and purification, 852
  automated solvent extraction, 853, 854f
  flow-cell analysis, 740−741
Atom-trap trace analysis system
  schematic of, 186f
Attribute tests, 875−876
  acceptance criterion, 875
  spent fuel, 875−876
Automated fluidics
  solution handling, 824f
Automated methods for radiochemical separations, 848−849
Automation
  advantages, 822
  areas where needed, 822
  areas where practiced, 822
  commercial flow injection accessories, 827
  cyclotron target dissolution, 852
  digital microfluidics in, 848f
  equilibrium-based sensors, 844
  extractant liquids and particles, 830−831
  flow-through mass spectrometry, 831
  flow-through scintillation detectors, 831
  fluidic radiochemical analyzer, 839
  Lab-on-valve approach, 830
  monitors, 838−841
  multisyringe flow injection, 826−827
  nuclear processes, 838−841
  parallel column configurations, 838
  PNX robotics, 834−835
  preconcentrating mincolumn sensors, 841−842
  PrepFAST-MC system, 827
  Preplac liquid handling, 827
  pressurized injection, 827
  quantitative capture sensors, 842−844
  radiochemical analysis, 825−831
  radionuclide detection, 831
  radionuclide sensors, 841−847
  renewable separation column, 828−830
  renewable separation column applications, 837
  robotics, 837−838
  selective radionuclide sensors, 841−842
  separation column configurations, 827
  separation-optimized sequential injection, 826
  sequential injection, 826
  sequential injection with ICP-MS, 836f
  strontium-90 analysis, 832, 843−844
  technetium-99 analysis, 833
  water monitoring, 841−847
  water monitoring sensors, 845−847
Autoradiograph
  multiple isotope separation, 697
  validation of in vivo imaging, 710−719
Autoradiography
  alpha particle imaging, 719−720
  beta-particle range and, 673
  in biochemistry of development, 702
  in brain lesions studies, 713f
  brain tissue, 702−705
  in cardiovascular research, 713−714
  clinical applications, 716
  electronic, 685, 693
  film, 676
  general features, 671
  introduction, 670
  molecular imaging, 706
  in neuropharmacology, 711
  in nuclear waste decommissioning, 707−708
  in oncology, 710
  principles of, 670−675
  in psychopharmacology, 711
  quantification, 696
  quantitative whole-body, 684, 692
  radioisotopes and resolution in, 677
  radioisotopes used, 671, 672t
  resolution with film, 677t
  transport of beta particles, 672
  ultrastructural, 678
  of uranium deposits, 720f
  whole body, 684
  whole-body animal sections, 684f
Autoradiography - receptor autoradiography, 684
Autoradioluminograph
  phosphor screen, 680−685

B

BeaQuant system
  beta-particle localization with, 691−692
  electronics in, 691−692
  performance, 692
  principles of, 689−691
  sample management, 692
  whole-body autoradiography with, 693f
Beryllium-7
  concentrations at ground-level air, 192f
  concentrations in air *vs.* sun activity, 192f
  in marine environment, 335
  production rate in atmosphere, 192f
Beryllium-7, on aerosols
  analysis of, 191
  applications, 191
  origin and properties, 191
Beryllium-10, on aerosols
  analysis of, 193
  applications, 193
  origin and properties, 193
Best estimate of the true value, 635
Beta counter
  sensitivity to gamma radiation, 534
Beta detector
  correction gamma sensitivity, 535
  sensitivity to gamma radiation, 533
Beta-gamma angular correlation, 534
Beta-gamma anticoincidence, 544−547
  correlated, 545
Beta-gamma coincidence, 532−544
  accidental coincidences, 534
  bidimensional extrapolation, 535
  biparametric extrapolation, 537−538
  complex decay schemes, 534−535
  converted gamma emission, 533−534
  digital systems, 544
  efficiency variation, 537
  extrapolation curves, 544
  general expressions, 534
  with liquid scintillation counter, 540−542
  with plastic scintillation, 542−543
  principles and methods, 533−535
  with proportional counter, 538−540
  radionuclides with simple decay schemes, 533−534
  standardization by, 543
  tracer method, 535−536, 544
  two-dimensional extrapolation, 544
Beta-gamma correlation
  applications, 549
  radionuclides with delayed states, 547−548
  theoretical description, 548−549
BetaIMAGER DFine
  high-resolution ^{3}H imaging, 703f
  histological applications, 705
  hybridization analysis, 704f
  performance, 695
  in physiology and gene expression, 702
  principle of, 693−694, 694f
  schematic of, 694, 695f
  shape of light spots with, 694, 695f
BetaIMAGER TRacer
  light spot shapes in, 689, 690f
  performance, 695
  principles of, 687−689, 688f−689f
  sample cassettes for, 690f
  sample management with, 689
Beta imaging
  in cardiovascular research, 713
  of high-resolution protein gels, 705
  histological, 704f
  introduction, 670
  in M1 ACh receptor autoradiography, 714f
  molecular imaging, 707
  of neuroinflammation, 712
  Northern, southern, Western blots, 705−706
  physiology and gene expression, 702
  quantification in, 711−712
  of rabbit kidney, 673−674
  Sanger sequencing, 706f
  of TLC plates, 705
  of tumor sections with ^{111}In, 711
Beta imaging - Biochemistry of development studies, 702
Beta imaging systems
  advantages and limitations, 699−700
  BeaQuant system, 689−692
  BetaIMAGER DFine, 693
  BetaIMAGER TRacer, 687
  biomedical applications, 698−699
  in biochemical development studies, 702
  in molecular biology, 705−706
  latent imaging storage, 675−685
  multiradionuclide labeling, 700
  phosphor screen technology, 680−685
  quantification and calibration, 674

quantification with, 677
radioisotopes used, 694–695
sample preparation, 675
solid membrane detectors for, 693–694
spatial resolution of, 674–675
Beta inefficiency ratio, 534–535
Beta particles, 719
Beta spectrometry
environmental radionuclides analyzed by, 166t
Bismuth-213
automated generation and purification, 851
multicolumn selectivity inversion generator, 851
Bremsstrahlung imaging, 717–718

C

Cadmium-109, flow-cell analysis, 751
Calcium-41
environmental occurrence, 88–89
sample preparation and analysis, 88–89
Calcium-45
autoradiography with, 671
Calculation of uncertainty, 662–665
Calorimeter
cryogenic, 577–578
dual-cell water bath, 907f
elements of, 903–905
essential components of, 905f
heat flow, 905
heat flow calibration, 908
heat-flow types, 908–909
passive mode, 905–906
passive mode calibration, 906
power-replacement mode, 907–908
solid-state heat flow, 908–909
solid-state sensors, 909–910
thermal equilibrium in, 906f
twin-cell, 913f
twin-cell design, 910
Wheatstone bridge, 909f
Calorimetric assays
performance, 911
precision and accuracy, 911
Calorimetric detectors, 574–578
Calorimetric safeguards measurements
applications, 914–915
calorimetric assay, 910–914
calorimetric assay performance, 911–914
heat flow calorimetry calibration, 908
heat flow calorimetry types, 908–910
passive mode operation, 905–906
power replacement mode, 906–908
specific heats, 903
specific power, 903
thermal power, 902
Wheatstone bridge heat-flow calorimeter, 908–909
Calorimetry, 902
CALEX standard, 911–912
classic, 574–577
nuclear thermal power in, 910
radionuclides assayed, 914
tritium and plutonium, 902
uranium, plutonium and americium, 904t
Carbon-11
autoradiography of, 712
flow-cell analysis, 741–743, 776–777
Carbon-14
AMS of, 347
anthropogenic, 154–155
autoradiography with, 671
environmental occurrence, 66–73
sample preparation for AMS, 348f
Carbon-14 dating
age limit, 42
with AMS, 348f
Carbon-14, environmental
absolute international standard, 69–70
absolute percent modern, 70
A_{ON} activity value, 69
age calculations, 70
benzene synthesis, 67
biogenic fuel composition, 67
calculations, 69–70
CO_2 absorption for LSA, 67–68
direct counting, 68
food adulteration, 67
fossil-fuel emission, 67
fuels containing biogenic materials, 70–73
measurements of, 67
produce biocomponent verification, 70–72
quality assurance, 69
radiocarbon dating, 66
sample preparation, 67–68
standards for ^{14}C dating, 68
standards for nuclear samples, 68–69
Carbon-14, flow-cell analysis, 738–739, 741, 751, 761f
Carbon-14, on aerosols
after Chernobyl accident, 198f
analysis of, 194
applications, 194
origin and properties, 193–195
Carbon-14 spectroscopy
laser based, 349–350
Carbon-14, with HPLC-MS-NMR, 793
Cerenkov analysis of spent fuel, 876–877
Cerenkov counting. *See also* Cherenkov counting
Cerenkov imaging
as alternative to Bremstrahlung imaging, 717–718
complement to traditional molecular imaging, 718–719
of ^{18}F in mouse, 719f
of ^{18}F in tumor cells, 719f
of ^{32}P in rat, 719f
in radiotherapy, 718
of ^{90}Y in rat, 718f
Cerenkov Luminescence imaging, 717–719
Cerenkov radiation
in biological tissue, 718
nuclear safeguards and, 876
Cerenkov tumor imaging, 718
Cesium
analysis in seawater, 336–337
separation for gamma spectrometry, 339f
Cesium-137
anthropogenic, 156–157
HPIC analysis, 787
in Irish Sea, 326
Cesium-137, on aerosols
analysis of, 197
applications, 197
after Chernobyl accident, 198f
origin and properties, 197
Cesium-137 time series
in world oceans, 365–367
Cherenkov counter
aerogel, 436
threshold, 461
time-of-flight, 472–475
time-of-propagation, 471–472, 475
TORCH, 473–474
Cherenkov counting
of actinium-228, 418
advantages and disadvantages, 395, 508–509
of ^{214}Bi and ^{214}Pb, 418
of ^{14}C and ^{45}Ca, 431
of Chlorine-36, 411–412
color-quenched standards, 411t, 414f, 416–417
color quenching in, 410
counter geometry and, 410
counter performance and, 422t, 425t
counting vial types, 419f, 420–426, 421f, 423t, 424f
in dry state, 431–434
external standard QIPs, 415–418
gamma/beta threshold energies, 459f
gamma-ray discrimination, 457
gamma-ray threshold energies, 458
internal standardization and, 411
ionic liquids with, 429
liquid scintillation analyzers for, 410
of ^{119m}Cd, 418
microplate formats for, 437–439
multiple radionuclide anaysis, 439–445
nuclear safeguards and, 460
of ^{32}P, 411f–412f, 419f, 421–422, 485–491
particle identification by, 460–461
quench correction in, 410–411
radionuclides analyzed by, 486t–490t, 502–508
radionuclide standardization by, 445–451
recommendations in radionuclide analysis, 509
refractive index effect, 429–431, 430t
of rubidium-86, 414
sample spectrum QIPs, 413–415
sample volume effect, 418–420
SCR quench correction in, 411–413
with silica aerogels, 435
silica aerogels and, 434–437
of ^{89}Sr + $^{90}Sr/^{90}Y$, 418, 420f, 422, 491–495, 503t–507t
of $^{90}Sr/^{90}Y$, 413, 417f, 498–502
TDCR method, 418, 450

Cherenkov counting (*Continued*)
wavelength shifters and, 426–429, 427t–428t
of Yttrium-90, 403–404
Cherenkov counting, microplate
quench correction in, 438–439
sample crosstalk with, 437, 438t
sample formats, 437
sample volume effects, 438
sample volumes in, 437
Cherenkov counting, multiple radionuclide
with efficiency tracing, 440–441, 441f, 442t
with LSA, 439
of ^{89}Sr + ^{90}Sr/^{90}Y, 441–444
with wavelength shifters, 444–445
Cherenkov counting, radio, 483–485
Cherenkov detectors
imaging, 461
light-water neutrino, 476–477
neutrino measurements with, 476
ring imaging, 464
SNO, 477f
threshold, 461
Cherenkov effect, 394
applications, 395
Cherenkov flow-cell detectors, 789–790
Cherenkov+liquid scintillation
for Sr-89+Sr-90/Y-90, 495–498
Cherenkov, Pavel A., 394, 396
Cherenkov photons
counting of, 395
Cherenkov radiation
angle of emission, 397
conditions for, 406
cone image of, 395f
discovery, 396
discovery and journal *Nature*, 396, 397f
electron threshold energies, 403–404, 404f
energy emitted by, 398–399
energy radiated by, 407
image of, 406–407, 407f
intensity of, 407–409
interpretation, 397–399, 401
origin, 394–396
photon numbers emitted, 399
properties, 396
quantum mechanical interpretation, 399–401
spatial asymmetry, 404–407, 405f
spectrum of, 395, 407
threshold condition, 397–398, 401–402
threshold energies, 402–404, 403t
Cherenkov radiator
definition, 403
Chernobyl NPP accident
^{137}Cs depositions over Europe, 151f
radionuclides released from, 150–151, 151t
Chiro-inositol phosphates, soil, 799–801
Chiro-inositol, soil, 799–801
Chi-square (χ^2) distribution, 647, 647t
Chi square value, 647
Chlorine-36
Cherenkov counting of, 411–412
natural occurrence, 85–87
sample preparation and analysis, 86, 87f
Chromium-51, flow-cell analysis, 751–754
CIEMAT/NIST method, 564–565, 567
SIR system, 587–588
CIEMAT/NIST standardization, 564–565, 567–570
$4\pi\beta-\gamma$ Coincidence techniques are, 532
Combined standard uncertainty, 644
Confidence intervals, 646, 653
Contamination monitoring
digital autoradiography in, 708f
Copper-64
autoradiography of, 711
flow-cell analysis, 741–743
Copper-62, Cherenkov flow-cell analysis, 789
Correlation coefficients, 633–634, 663t
$4\pi\gamma$ Counting, 556
Critical counting rate, 654–655
Critical level L_C, 654
Critical levels, 653–655

D

D-chiro-inositol phosphate, in soil, 799–801
Dead time
anticoincidence extending corrections, 546
anticoincidence rate, 545
models of, 536
nonextending anticoincidence, 546
nonparalyzable, 536–537
paralyzable systems, 536
resolving time corrections, 536–537
Degree of freedom, 650–651
Destructive analysis, 821–822
Detection limits, 653–660, 934
flow-cell analysis, 784t
mass spectrometric, 350
Digital autoradiography
in contamination monitoring, 708f
^{64}Cu tracer quantification, 711
gaseous detector based, 708–709
genomic analysis - metabolic activity, 717
of geological rock sections, 709–710
of ^{40}K in concrete cores, 707–708
of low to medium energy isotopes, 707
in nephrology, 716
in neuropharmacology, 711
in nuclear waste decommissioning, 707
in standard wipe tests, 708
of western blotting PVDF membranes, 702
Digital microautoradiography, 693–694
Digital microfluidics
programmable droplet manipulation, 848f
single bead manipulations, 847–848
Dose rate monitoring, 26–27
Drop drying, 599
apparatus for, 599
gas jets for, 600f
multiple gas jets in, 599

E

Effluent water monitors, flow cell, 791–793
Electrodeposition of Th, U, and Pa, 331
Electronic autoradiography
gaseous detectors in, 685–692
Electrospray ionization MS, 797–798
Emergency monitoring, 2–4
Emergency preparedness monitoring, 2–3
objective of, 3
Emergency radiation monitoring
objectives of, 4
Environmental freshwater analysis
groundwater, 200
ice cores, 200
precipitation analysis, 200
sampling, 200
sediment pore water, 200
water profiles, 200
Environmental monitoring, 1–3
aerial mapping, 27–28
aerosol analysis in, 14
of airborne radioactivity, 14
analytical methods, 10
in case of a release, 6
decommissioning, 6
design, 4–7
detection limits, 13t
dose rate measurements, 26
dry and wet deposits, 19
exposition scenario, 4
foodstuff and milk, 24–26
geo-chemical behavior studies, 352
in-situ gamma spectroscopy, 19–20
internal exposure and, 14–26
iodine in air, 16
measurement and quantification, 10–12
meat and fish, 25–26
mobile laboratories, 28
mobile monitoring, 27–32
noble gases in, 16–17
nonprobabilistic, 7
nuclear safeguards applications, 351
Pb-210 in, 22
preoperational assessment, 5–6
probabilistic, 7
Pu-239 and Pu-240 analysis, 11
QA/QC, 12
Ra-226 and Ra-228, 22
radionuclide pathways in, 8t
radon measurements, 16
rain and groundwater, 23
sample preparation, 9–10
sampling designs in, 8
sampling frequency, 8
sampling principles, 9
sampling strategies in, 7–9
soils and sediments, 17–18
Sr-89 and Sr-90, 25
steps taken in, 6–7
surface and drinking water, 24
tritium analysis, 23
uncertainty, 12
vegetables, fruits and cereals, 26
vegetation, 18–19
vehicle-borne measurements, 32
wastewater, 23
water samples, 20–21

Environmental radionuclide analysis
accelerator mass spectrometry, 171–175
alpha spectrometry, 164, 165t
beta counting, 164–166
gamma spectrometry, 166–167
GD mass spectrometry, 170
ICP mass spectrometry, 167–169
low-energy mass spectrometry, 167–171
RI mass spectrometry, 169–170
TI mass spectrometry, 169
Environmental radionuclide compartments
atmosphere, 158–163
biosphere, 162–163
hydrosphere, 160–162
pedosphere, 163
Environmental radionuclides
on aerosols, 189–199
anthropogenic, 138
carbon-14 in water systems, 201–202
Chlorine-36 in water systems, 202–203
classification, 138–158
^{36}Cl in water systems, 202–203
cosmogenic, 138
in freshwater systems, 199–208
^{129}I in water systems, 204–206
international monitoring of, 233–234
primordial, 138
radiocesium in water systems, 206–207
radiogenic, 138
radon in water systems, 207–208
^{99}Tc in water systems, 203–204
tritium in water systems, 201
Environmental radionuclides, in biota
analysis, 210–214
carbon-14, 211–212
iodine-129, 214
iodine-131, 213–214
radiocesium, 212–213
radiostrontium, 213
tritium, 212
Environmental radionuclides, in soil
analysis, 208–210
cesium-137, 210
radon, 209–210
Environmental tritium analysis
^{3}H-^{3}He ingrowth mass spectrometry, 170–171
Error, 632–633
Error function, 635
Error propagation, 633–634, 633t
optimization of experiments, 634
Error propagation theory, 634
Exposed population
critical groups in, 4
representative person in, 4
Exposition scenario, 1
Exposure pathways, 4–5
External exposure monitoring, 26–27
Extractive liquid scintillators
elements extracted, 56t

F

False peaks distribution, 656
F curves, 650
F distribution, 651t
Figure of Merit, definition, 42
Fission neutrons
time correlation of, 891–892
Fission products, HPLC and HPIC analysis, 781–782
Flow-cell analysis
alpha emitters, 774f
efficiency calculation, 779
with HPLC-MS, 795–798, 796f
with HPLC-MS-NMR, 794t
low-energy gamma cell, 741
sequential to separation, 778–790
stopped-flow mode, 789–791
Flow-cell detectors, 729–730, 731t–734t, 736f, 738f
alpha-beta and gamma discriminating, 792
background and net count rate, 755
cell volume and precision, 760
Cherenkov, 789
commercial sources of, 735t
composite bed, 769–770
counting efficiency, 756
criteria for selection, 750–754
α/β discrimination, 781–786, 784f
dual functionality, 762–778, 765f
dual radionuclide analysis, 793
dual, 741f
efficiency, 783
equilibrium-based bed, 770–772
extracting chromatographic resins in, 764, 765f
gamma and PET cells, 740–744
gamma scintillation, 752t–753t
gradient efficiency run, 757–758
heterogeneous, 739–740, 740f
high-energy gamma cell, 740–741
homogeneous, 738–739
HPLC, 734
hybrid silicon pixel, 747–750
instrument performance assessment of, 761–762
luminescence (flumo), 746–747
microbore, 746f
minimal detectable activity, 758
multichannel analysis, 760
narrow-bore and microbore, 745–746
optimization, 760–761
PET cell, 741–744, 743f
planar fountain, 773f
planar mixed-bed, 773
precision of, 759–760
pulse-shape discrimination, 783
resolution of, 758–759
scintillating extractive resins in, 767f
semiconductor diode, 773–774, 775f
sensitivity of, 758–759
static efficiency run, 756–757
tritium water vapor in air, 777–778
use of standards in, 755
whole column, 776–777
with HPLC-MS-NMR, 793, 806–807
with HPLC-NMR, 802–806
with organic HPLC, 793
with organic MS and NMR, 793
Flow-cell radionuclide analysis, 729–820
Flow-cell sensors, scintillating extractive resins in, 766t
Flow cells
heterogeneous, 734–737
homogeneous, 734–739
Flow injection, 825–826
Flow scintillation analysis
in HPLC, 737f–738f
Flow scintillation analyzer, 734, 736f
chemiluminescence in, 760
Flow scintillation analyzers-NMR, 799–806
Flow scintillation cocktails, 763t–764t
Flow scintillation counting
principles of, 754–762
time-resolved, 760–761
Flow-scintillation detector, scintillator selection criteria, 762
Fluorine-18
autoradiography of, 695, 711
Cerenkov imaging of, 718
Fluorine-18-FDG
automated synthesis, 856
Fluorine-18, flow cell analysis, 741–744, 747
Fluorine-18 plus Technetium-99m
autoradiography of, 698
Forensic analysis, traditional, 941–944
Fork detectors, 876–877
Fraction collection, 730
Frank, Il'ja, 396–399
F ratio, 650
F-test, 636
Fukushima accident, 375
marine radioactivity and, 375
Fukushima NPP accident
^{137}Cs contamination from, 153f
radionuclides released from, 152
signal spike from ^{137}Cs, 154f
volatile radionuclides released, 153t
F values, 650

G

Galactic cosmic rays, 143
Gallium-68
automated generation and purification, 856
autoradiography of, 713–714
flow-cell analysis, 741–744, 745f
Medipix flow-cell analysis, 748–749
Gamma detector
sensitivity to beta radiation, 534
Gamma-ray attenuation, 878–879
Gamma-ray spectrometry
extended sources, 579–580
of marine radioactivity, 321–322
underwater, 321–328
underwater applications, 325, 326f
Gaussian distribution, 629–632
accumulated distribution function, 629–630
normalized random variable, 630
probability density function, 629
Geiger counter, 686f
Global fallout

Global fallout (*Continued*)
anthropogenic radionuclides in, 147t
Glow discharge mass spectrometry
environmental analysis by, 170

H

Half-life measurements
short-lived gamma emitters, 592
Heath method
critical point, 581
intrinsic efficiency, 580
total efficiency, 580
Heat flow calorimetry, 903–910
Heavyside, Oliver, 394
HERM electronics, 746–747
^{3}H-^{3}He ingrowth mass spectrometry
tritium trace analysis by, 170–171
High-performance liquid chromatography, 730–754
Histological imaging, 702
HPLC-FSA-NMR, 802–803
HPLC-mass spectrometry, 798
HPLC-NMR, 801
Hypothesis testing, 645–646, 653

I

IceCube Neutrino Observatory, 482–483
ICP mass spectrometry
radionuclides analyzed by, 168
Indian Ocean
Cesium-137 time series in, 369–370
Indium-111
autoradiography of, 711, 712f
Indium-111 plus Technetium-99m
autoradiography of, 698
Inductively coupled plasma mass spectrometry
of marine isotopes, 345–346
Inositol phosphates, soil
epimerization and origin in soil, 799–801
stereoisomers in soil, 799–801
In-situ gamma spectroscopy, 19–20
Intercomparison exercises, 360–362, 361f
Interlaboratory comparisons, 636–642
Internal gas counting
experimental aspects, 560
radionuclide standardization, 560–563
theoretical description, 560
International monitoring
European "Ring of Five", 234
International Monitoring System (IMS), 17, 233–234
Iodine-124
automated preparation and purification, 857–858
Iodine-125
autoradiography of, 671, 712, 713f
flow-cell analysis, 739–741, 747, 751
Iodine-129
anthropogenic, 156
flow-cell analysis, 768
marine environment analysis of, 349
natural occurrence, 87–88
sample preparation and analysis, 88
Iodine-129, on aerosols
analysis of, 196
applications, 196–197
origin and properties, 196–197
Iodine-131, flow-cell analysis, 740–741
Iodine in air, 16
Iodine-131, on aerosols
after Chernobyl accident, 196f
analysis of, 196
origin and properties, 196
Ionic liquids
definition, 429
Ionisation chamber
SIR reference system, 586
Ionization chambers
applications, 586–588
calibration of, 585–588
efficiency calculation, 588–590
half-life measurements with, 587
K_r factor of, 586
maximum accuracy, 584
Monte Carlo codes, 589
radon measurements, 588
Irish Sea
gamma-ray spectrometry of, 325–326
Iron-55
environmental occurrence, 73–75
flow-cell analysis, 751
Iron-55, environmental
sample preparation and analysis, 73–75
Irradiated Item Attribute Tester, 876–877
Isotopic composition measurements
ratio based, 884–885
Iterative PLS-DA, 928–929

K

Key Comparison Reference Value, 636
k factor, 644
Krypton isotopes
Atom-trap trace analysis, 186
Krypton-85 monitoring, 17

L

Lab-on-valve
radionuclide separations achieved, 830
Laboratory information management, 359–360
Lead-210
decay series, 105f
flow-cell analysis, 741, 769
gamma spectrometry, 105–106
in seawater, 332–334
in seawater and sediments, 333
Lead-210 and Po-210
alpha spectrometry, 106
Lead-212/bismuth-212
automated purification, 852
generation and purification, 851–852
Lead-210, bismuth-210 and Po-210
environmental occurrence and importance, 104–107
liquid scintillation analysis, 106–107
Least square fitting, 658
Linear regression, 651–653
Linear relationship, 651
Liquid scintillation analysis
of alpha-emitting transuranics, 60–62
Liquid scintillation analyzers, low level
definition, 42
Liquid scintillation counters
Beckman Coulter, 55
Hidex Oy, 54–55
Packard/PerkinElmer, 54
TDCR instruments, 54–55
Wallac Oy/PerkinElmer, 53–54
Liquid scintillation counting
alpha/beta discrimination, 51–58
alpha/beta misclassification, 57–58
Liquid scintillation counting, environmental
alpha/beta discrimination, 56
aqueous accepting cocktails, 55
definition, 42
energy resolution improvement, 112
extractive scintillators, 55–56
PERALS spectrometry, 110
software applications, 111–112
spectrum deconvolution, 109–112
spectrum unfolding, 110–112
TDCR method, 58
vial choice, 56
Liquid scintillation counting, low level
alpha/beta instrumentation, 52–55
applications, 42–43
background reduction, 43–51
cocktail choice, 50–51
counting environment, 51
counting region optimization, 48
counting vial holders, 49–50
counting vials, 49
passive/graded shielding, 44
process optimization, 48–49
pulse amplitude comparison, 45, 46f
pulse analysis, 51–52
pulse shape analysis, 45
pulse shape discrimination, 53–55
quasi-active detector guards, 47
region optimization procedures, 48
sources of background, 43
time-resolved, 45–47
Live-time
anticoincidence counting, 546–547
Live time clock, 546
Lower limit of detection, flow-cell detector, 758
Low-level alpha spectrometry
of marine samples, 340
Low-level beta spectrometry
of marine samples, 340–341
Low-level gamma spectrometry
of marine samples, 341–342
underground laboratories for, 342–343, 344f
Lutetium-177
autoradiography of, 711

M

Macroautoradiography, 675–678
  description of, 670
MALDI-MSI, 700–701, 701f
Marine environmental monitoring
  intercomparison exercises, 360
  management of data quality, 359–362
  radiological impact studies, 351–352
  reference materials in, 362
Marine environment analysis
  anthropogenic radionuclides, 335–336
  of cesium, 336–337
  ion-exchange separation, 330–331
  mass spectrometry in, 344–350
  particulate matter and sediments, 329–330
  of strontium, 337
  Th, U, and Pa electrodeposition, 331
  transuranics in, 336
Marine environment sampling
  particulate matter and sediments, 329
Marine radioactivity
  algae sampling, 320, 321f
  analytical methods, 316
  biota sampling, 319–320
  international studies of, 316–317
  mass spectrometric analysis, 316
  natural radionuclide analysis, 328
  from nuclear tests, 316
  particulate matter sampling, 320–321
  remotely operating vehicle detector, 323, 324f
  sampling and analysis, 317
  sampling techniques, 317–321
  sediment sampling, 318–319
  stationary detector systems, 323–324
  submarine groundwater discharge, 326–328
  towed detector systems, 323
Marine radioactivity databases, 362–365
Marine radioactivity studies
  sampling methods, 316
  worldwide, 365–372
Marine sediment and biota
  laboratory chemistry for, 339–340
Mass spectrometry
  ^{3}He in-growth spectrometry, 345
  of transuranic nuclides, 61
Mass spectrometry imaging (MSI), 700, 701f
Matrix-assisted laser desorption/ionization, 700–701, 701f
Mean, 632
  asymmetric distribution, 632
  symmetrical distribution, 632
Mean values, 663t
  accuracy, 634–635
Medical radionuclides
  alpha emitters, 850–854
  automated analysis and reactions, 848–858
  beta emitters, 849–850
  diagnostic, 854–858
  gamma emitters, 854–855
  positron emitters, 855–858
  therapeutic, 849–854
Medipix sensors, 747–750
Microautoradiography, 675
  of animal sections, 678f
  in bacteriology, 702
  of cells, 679
  description of, 670
  with emulsions, 678–680
  histology, 678
  performance, 678
  with QWBA, 702
  receptor studies, 679–680
  solid membrane detectors, 693–694
  staining in, 675
  techniques, 676
Microautoradiography - radionuclides, 678
Microradiography
  applications, 679–680
  use of ^{3}H and ^{125}I in, 678
  quantification in, 678–679
  resolution of, 678
  sensitivity of, 678
Microscopic autoradiography, 679
Minimal detectable activity, flow-cell detector, 758
Minimal detectable concentration, flow-cell analysis, 783
Minimum counting time, 657–658
Minimum detectable area, 656–657
Minimum detectable counting rate, 655
Minimum significant area, 656
Molecular imaging
  with Cerenkov radiation, 718–719
  in life sciences, 706–707
  in nuclear medicine, 706
  in pathology, 713
  validation, 713
  validation of imaging probes, 710–716
Molecular imaging - ex vivo, 671
Molecular imaging - PET, 702
Molecular imaging probes, 711
Monte Carlo technique
  international comparisons, 583
  ionization chamber simulation, 586
  low activity samples, 583
  sources of uncertainty, 582–583
M-P mean, 636
Multiplication
  leakage multiplication, 893
Multiwire proportional chamber, 686
Muroroa and *Fangataufa lagoons*
  gamma-ray spectrometry of, 324–325
Myo-inositol phosphates, soil, 801f
Myo-inositol, soil, 799–801

N

National nuclear forensics libraries, 928
Naturally occurring radioactive materials (NORMS), 2
Natural radionuclide analysis
  in marine environment, 328–335
Nautic Environment Marine Observatory, 323–324
Neptunium and other actinides
  analytical procedures, 223–225
Neptunium-237
  flow-cell analysis, 770
  ICP-MS analysis, 780t
Net counting rate, 655
Neutrino astronomy
  IceCube detector for, 482–483
Neutrino Cherenkov telescopes, 478–482
Neutrino flux measurements, total
  by neutral-current reaction, 478
Neutrino measurement
  atmospheric, 478
  Cherenkov counters for, 476–485
  Hyper-Kamiokande detector, 477
  large D_2O Cherenkov detector, 477–478
  Super-Kamiokande detector, 477
Neutrino measurement, all flavor
  by elastic scattering, 478
Neutrino measurement, ^{8}B
  by charged-current reaction, 478
Neutrino measurements, ultra-high energy, 483–484
  ANITA experiment, 484
  ARA detector, 485
  ARIANNA detector, 485
  Lunar Cherenkov technique, 485
  RICE detector, 484
  SALSA detector, 485
  TAROGE detector, 484–485
Neutrinos, high-energy muon
  principle of detection, 481f
Neutrino telescope
  ANTARES, 479–480, 481f
  BAIKAL, 479, 480f
  KM3NeT, 480, 481f, 482
Neutron-based safeguards
  coincidence counting, 896–899
  die-away time, 893–894
  efficiency, 893
  gate fractions, 894
  high-level neutron coincidence counter, 899
  known alpha technique, 899
  multiplicity counting technique, 899–902
  multiplicity shift register, 900–901
  neutron counter design, 894
  neutron counters, 893
  passive coincidence counting, 897–899
  point model assumptions, 900–901
  point model equations, 901
  ^{240}Pu effective mass, 897
  shift register electronics, 897–898
  singles counting, 894–896
  standard coincidence counting, 898
  well counters, 893–894
Neutron based safeguards measurements
  active coincidence counting, 899
  active neutron interrogation, 892
  active well coincidence counter, 899
  coincidence event, 891–892
  doubles, 891–892
  (α,n) neutron, 892
  ^{240}Pu effective mass, 891
  triples, 891–892
Neutron detector
  ^{3}He tube, 893
Neutron measurements
  in safeguards, 890

Neutron multiplicity counting, 902
Nickel-63
  environmental and waste samples, 74f, 77
  environmental occurrence, 75
Nickel-63, environmental
  sample preparation and analysis, 75–77
NMR chemical shift, 801–802
NMR shielding, 801–802
NMR spectroscopy, principles of, 801–802
Noble gas radionuclides
  key environmental, 183t
Noble gas radionuclides, environmental
  AMS of, 185–186
  applications of, 183
  gamma spectrometry of, 185
  gas proportional counting of, 184–185
  groundwater dating by, 184
  sample preparation of, 184
  sampling of, 183–184
Normal distribution, 631, 631t
  accumulated distribution computation, 631
  integration intervals, 630f
Northern blot analysis
  beta imaging, 706f
Novaya Zemlya bays
  gamma-ray spectrometry of, 325
NPP accident monitoring, 233–234
Nuclear accidents
  Chernobyl (Ukraine), 150–152
  Fukushima (Japan), 152
  radionuclides of interest, 6t
  Three Mile Island (USA), 149–150
Nuclear accident monitoring, 3
Nuclear archaeology, 924–925
Nuclear attribution, 925–926
Nuclear forensic interpretation, 924, 926
Nuclear forensics
  alpha spectrometry, 935–936
  analytical tools, 942t
  autoradiography, 938
  bulk analysis, 935–938
  case initiation, 922–924
  categorization, 924, 933–934
  characterization, 924, 933–934
  chemical assays, 936
  databases, 928
  definition, 921
  exercises, 928b
  full analysis, 933–934
  gamma spectrometry, 935
  gas chromatography/mass spectrometry (GC/MS), 937–938
  imaging analysis, 935, 938–939
  inductively coupled plasma/mass spectrometry (ICP-MS), 936
  infrared spectroscopy, 940–941
  International Technical Working Group (ITWG), 921–922
  law enforcement and intelligence, 922
  law enforcement, 925
  mass spectrometry, 936
  microanalysis, 935, 940–941
  mission areas, 922
  national intelligence, 925
  national objectives, 924–925
  optical microscopy, 939
  origins of, 921–924
  policy implications, 922
  quality assurance, 944–946
  quality assurance, systems, 946
  radiochemistry, 936–937
  Raman spectroscopy, 941
  sampling, 946
  scanning electron microscopy (SEM), 939
  secondary ion mass spectrometry (SIMS), 940
  sequencing of techniques, 944, 945t
  thermal ionization mass spectrometry (TIMS), 936
  transmission electron microscopy (TEM), 939
  validated methods, 934–944
  visual inspection and photography, 938
  X-ray diffraction, 937
  X-ray fluorescence (XRF), 937
Nuclear forensic signatures, 926
  comparative, 927–930
  predictive, 930–933
  validated, 927–933
Nuclear material interdictions, 923t
Nuclear power reactors
  world number, 149
Nuclear safeguards, 873–874. *See also* Safeguards
  active length measurement of fuel assembly, 877
  calorimetric assay, 902–915
  holdup measurements, 886–891
  isotopic composition measurements, 881–886
  material test reactor fuel assay, 886
  neutron based assay, 891–902
  neutron signatures, 891
Nuclear waste, flow analysis methods, 780t
Nuclear weapons explosions
  detonation activity decay, 146–147
  emissions from, 146–147
  radionuclides from, 147
Nuclear weapons testing, atmospheric
  statistics of, 147t
Nuclear weapons tests, underground
  isotopes of Xe and Kr from, 147
Null hypothesis (H_0), 645

P

Pacific Ocean
  Cesium-137 time series in, 369
Partial derivative, 663t
Particle-counting beta imagers
  performance, 694–696
Particle-counting imaging, 685–698
  data analysis, 696–698
  isotope discrimination, 697f–698f
  list mode files, 696–697
  multiisotope separation, 697
Particle identification
  Aerogel ring imaging, 468
  Cherenkov threshold momentum, 461–462, 463f
  differential Cherenkov counters, 461
  imaging Cherenkov counters, 461
  RICH and TOF measurements, 473
  RICH detectors for, 464, 466f–467f, 469
  threshold Cherenkov counters, 461
  time-of-flight counter for, 472
  time-of-flight measurements, 474f
  time-of-propagation counter for, 471–472
Paule and Mandel method, 637
Paule–Mandel mean, 641
Pb-210 analysis, 22
PERALS spectrometer
  advantages of, 53
  design of, 53
  key elements of, 53
Phase velocity, particle
  calculation of, 402
  definition, 397–398
Phosphor screen
  quantification, 696
Phosphor screen imagers
  advantages and drawbacks, 684
  applications, 684–685
  quantification methods with, 683
  range and sensitivity, 683
  types of, 682
Phosphor screen imaging, 670
  with alpha particles, 719–720
  in DNA sequencing, 705
  general principles, 680
  history, 680
  isotope measurements, 710t
  in nuclear waste decommissioning, 708
  principle of, 682f
  resolution in, 682–683
  revelation and quality, 681
  scanning and light collection, 681–682
Phosphorus-31
  Cherenkov counting of, 485–491
Phosphorus-32
  autoradiography with, 671
  Bremsstrahlung imaging of, 717–718
  Cerenkov imaging of, 718
  Cherenkov counting of, 411–412, 412f–413f, 415
  Cherenkov flow-cell analysis, 789
  flow-cell analysis, 740–741, 751, 754
Phosphorus-33
  autoradiography with, 671
  flow-cell analysis, 751
Photographic emulsions, 675–680
  latent imaging, 675
Pileup corrections, 551–552
Plutonium
  calorimetric assay, 914, 915t
  fission multiplicity distribution, 891–892
  gamma ray energies, 883t
  induced fission, 891–892
  isotopes, 874
  mass measurements, 886
  multiplication, 892–893
  neutron emission rates, 891t

neutron production rates, 895f
separation for mass spectrometry, 337f–338f
separation from seawater and sediment, 337f
spectrum characteristics, 882
spontaneous fission, 891
Plutonium-241
environmental occurrence, 84–85
sample preparation and analysis, 84–85
Plutonium-239, flow-cell analysis, 768
Plutonium-239, 240, ICP-MS analysis, 780t
Plutonium isotopes
marine environment analysis of, 349
Plutonium spectrum, X-ray region of, 884f
PMM average, 641
Poison statistics, 627
Poisson distribution, 628–629, 633
addition of probabilities, 629
asymmetry, 629
important properties, 628
Poisson law, 628
Polonium-210
electroplating of, 333–334
in seawater, 332–334
in seawater and sediments, 333
Population regression line, 652
Positive-ion mass spectrometry
of marine isotopes, 350
radiocarbon and ^{26}Al analysis, 171
Potassium-40
autoradiography of, 707–708
Potassium-40, on aerosols
origin and properties, 197–198
Power-Moderated weighted Mean (PMM), 636, 642
Power-Moderate mean, 640–642
Power of the test, 646
Precision, 632–633, 934
Preparation of samples
dilution factors, 596
2π Proportional counting, 556
4π Proportional counting, 556
Protactinium-224, flow-cell analysis, 784
Protactinium-234m
Cherenkov counting of, 415

Q

Quality assessment, 359
Quality assurance, 359
Quality control, 359
Quantification limit, 934
Quench correction
in Cherenkov counting, 410–418
QWBA, 670–671

R

Ra-228 analysis, 22
Radioactive particles
destructive analysis of, 359
gamma- X-ray and alpha spectrometry of, 354–355
in marine environment, 350–359
nondestructive analysis of, 354–358
protocols for study of, 352–359
scanning electron microscopy of, 355–356, 358f
synchrotron radiation-based XRF of, 356–357
X-ray absorption spectroscopy of, 357–358
X-ray fluorescence analysis of, 355–356
Radioactivity decay
random process, 627–628
Radiocarbon dating, 66–67
Radiocarbon, environmental
AMS analysis of, 178–180
AMS spectrometer for, 180f
$\triangle^{14}$C values of, 180
forms encountered, 175–180
gas proportional counting of, 177–178
liquid scintillation counting of, 178
sampling systems, 176–177
Radiochemical separation
approaches, 823–824
digital microfluidics for, 847
extraction chromatography, 824–825
materials, 824–825
requirements, 823–825
sequential injection, 826
solid-phase extraction, 824
Radiochronometry, 931
Radio-HPLC, 729–730
Radionuclides, anthropogenic
fission chain reaction, 148f
fuel reprocessing plants and, 149
nuclear accidents and, 149–153
nuclear reactors and, 147–149
nuclear weapons testing and, 146–147
origin and characteristics, 146–158
in typical thermal reactor, 148t
Radionuclides, cosmogenic
characteristics of, 144t
origin and characteristics, 143–146
production of, 143f, 144
Radionuclide sensors
equilibrium-based, 844
Radionuclides, primordial
characteristics, 140t
origin and characteristics, 138–139
Radionuclides, radiogenic
origin and characteristics, 140–143
Radionuclide standardization
absolute direct methods, 532–555
activity per unit mass, 597
anticoincidence method, 545–546
beta-gamma coincidence, 533
beta-gamma correlations, 547–549
by calorimetry, 574
Cherenkov counting and, 445–456
CIEMAT/NIST method, 563–564
correlation methods, 548
defined solid angle, 557–559
gamma-gamma coincidences, 549–555
by gamma-ray spectrometry, 578–584
gravimetric methods in, 597
Heath method, 580–581
high activity measurements, 584–590
internal gas counting, 559–563
ionization chambers in, 584–590
by LS counting, 563–574
mass determinations in, 597
Monte Carlo technique, 582–584
of PET radionuclides, 562
primary standard comparisons, 587–588
relative methods, 578–590
sample homogeneity in, 597–599
sample mass correction, 597
sample preparation in, 595–599
semi-empirical methods, 581–582
solid angle primary methods, 555–578
solution dilutions in, 596
source quality in, 597–599
VYNS films in, 596
Radium
alpha- and gamma spectrometry, 101–102
emanation methods, 102
environmental occurrence and importance, 100–104
LSC and alpha/beta coincidence, 104
LSC methods, 102–103
preconcentration from water sample, 104
sample preparation and measurement, 101–104
Radium-228
analysis via ^{228}Ac counting, 418
in natural waters, 103
in seawater, 327–328
Radium-226 analysis, 22
Radium isotopes
in marine environment, 334–335
Radium-226 subseries, 97t
Radon
emanation and γ-spectrometric methods, 96–98
environmental occurrence and importance, 95–100
liquid scintillation analysis, 98–100
sample preparation and analysis, 95–100
Radon-222
extraction from large water samples, 100
flow-cell monitoring, 785–786
in marine environment, 335
measurements in air, 95–96
measurements in water, 96
in seawater, 327
Radon activity
mean indoor, 142f
Radon and daughters, in air
analysis of, 199
applications, 199
origin and properties, 198–199
Radon measurements, 16
Radon monitoring
detectors for, 187
large volume scintillation chamber for, 187–188, 188f
long term, 188
Raman spectroscopy, 941
Regression parameters, 653
Relative efficiency curve, 884–885

Renewable separation column
applications, 837
concepts and methods, 828–829
Residence time, flow-cell, 754
Residual variation, 658
Resonance ionization mass spectrometry
of marine isotopes, 346–347
radionuclides analyzed by, 169–170
Rhenium-188
isolation and concentration, 849–850
RICH detector
lens focused, 465
mirror-focused, 464f, 465
principle of, 464f
proximity focusing, 466–468, 470–471
Robotics
Gilson liquid handling, 838f
liquid handling systems, 838
PNX system, 838, 839f
Zymark in nuclear fuel analysis, 837–838
Zymark XP in Pu separations, 838
Zymate II in Pu analysis, 837
Rosette multibottle samplers, 317–318
Routine environmental monitoring, 5
Routine monitoring, 2–3
objective of, 2–3
Rubidium-86
Cherenkov counting of, 414f
Cherenkov flow-cell analysis, 789

S

Safeguards
attribute tests, 875
Gamma-ray based assay, 874–891
isotopic composition measurements, 885–886
Safeguards holdup measurements
attenuation correction, 889
background correction, 889–890
calibration, 887–888
generalized geometry, 887–890
neutron based measurements, 890
operational considerations, 890–891
radial response, 888
self attenuation correction, 889
Sample preparation
support for extended samples, 596
Sample regression line, 652
Sample uniformity, 597–599
Sample variance, 633
Scanning electron microscopy, 355
Scintillating extractive resins, 765–769
Seawater sampling, 317–318, 318f
for thorium, protactinium and uranium, 329
Secondary ion mass spectrometry (SIMS), 701–702
Secondary standard measurements, 593f
Selective extracting resins, 766t
Semiconductor alpha spectrometry
of marine samples, 340
Sensitivity, analytical, 934
Separation column configurations
column switching, 827–828
parallel columns, 828
Sequential injection fluidics, 825–826
Silica aerogels
preparation of, 434
properties of, 434
SIR of beta emitters, 592–594
SIR of gamma emitters, 590–592
SIR of gammas
reentrant ionization chambers, 590
SIR reference system, 586–587
Sodium-22, on aerosols
analysis of, 195
applications, 195
origin and properties, 195
Solar cosmic rays, 143
Solid scintillation NaI(Tl) detector
underwater, 323–324
Southern blot analysis
beta imaging, 705–706
Southern Henisphere Ocean Tracer Studies, 372–375
Specificity, analytical, 934
Spectrometry imaging
with whole-body autoradiography, 700
Spent Fuel Attribute Tester, 876–877
Sr-89 and Sr-90
in milk, 25
Sr-89 + Sr-90/Y-90
Cerenkov counting methods, 81, 491–498
early LSC measurements, 79–80
environmental occurrence, 77–81
LSC measurements, 79–81
LSC spectra, 81f
recent LSC measurements, 80–81
sample preparation, 77–79
Standard deviation, 633, 635
experimental, 649
inner and outer type, 636
the mean, 634
theoretical, 648
Standard error, 634–635
Standardized radionuclides
by anticoincidence LS, 545t
by anticoincidence PC, 545t
by CIEMAT/NIST method, 571t–572t
by coincidences LS, 543t
by coincidences PC, 541t
by plastic scintillation, 543t
by sum-peak method, 551t
by TDCR method, 573t–574t
Statistical distributions, 628–632
Statistical inference, 645–651
Strontium
analysis in seawater, 337
separation for beta counting, 339f
Strontium-90
analysis in soil, 779–781
anthropogenic, 155
automated analysis, 831–833, 843–844
autoradiography of, 694
Cherenkov flow-cell analysis, 789f
column switching techniques, 832–833
flow-cell analysis, 769–772, 772f, 784t, 785, 788–789
HPIC analysis, 786–787
marine environment analysis, 339
water monitoring, 846–847
Strontium-89
Cherenkov flow-cell analysis, 789
flow-cell analysis, 770
HPIC analysis, 786
Strontium in soil, extraction, 781f
Strontium-90 in urine, flow-cell analysis, 787–788
Strontium-90/Yttrium-90
Cherenkov counting of, 415
Sudbury Neutrino Observatory
principles of detection, 477
Sulfur-35
autoradiography with, 671
flow-cell analysis, 738–739, 751
$4\pi\beta\gamma+4\pi$ sum counting, 557
Sum peak
theoretical description, 550–551
Sum peak method, 549–550
applications, 552–555
dead time and pileup, 551–552
Synchrotron radiation-based XRF, 356–357

T

Tamm, Igor Y., 396–399
Tandem MS, organic structural analysis, 798
TDCR, 564–565, 570
TDCR Cherenkov counting, 59–60, 418, 450–455
anisotropy detection model, 450–453
^{210}Pb standardization by, 455–456
radionuclides analyzed, 59
radionuclide standardization, 60
routine radionuclide analysis by, 456
of Sr-90/Y-90, 499
stochastic GEANT4 model, 453–455
^{90}Y standardization by, 454–455
TDCR liquid scintillation counting, 58–59
principle and applications, 58–59
TDCR standardization, 564, 566, 570
Technetium-99
anthropogenic, 155
automated analysis, 833–834, 840f, 841
automated generation and purification, 855
automated nuclear waste analysis, 839
continuous flow analysis, 833–834
environmental occurrence, 81–84
equilibrium-based sensors for, 844
flow-cell analysis, 740–741, 747, 767–773, 775–776, 778–779
ground water monitoring, 845–846
marine environment analysis of, 349
sensors for automated analysis, 842–844
stopped-flow analysis, 833–834
water monitoring, 846
Technetium-99, environmental
sample preparation and analysis, 82–84
Technetium-99m
autoradiography of, 671, 706
Thallium-201, flow-cell analysis, 751
Thermal ionization mass spectrometry
of marine isotopes, 346
radionuclides analyzed by, 169

Thorium
  environmental occurrence and importance, 107–109
Thorium-232
  autoradiography in ore, 720
  autoradiography in rock, 708–709
  decay series, 107f
  flow-cell analysis, 758
Thorium-234
  analysis, 108–109
  in seawater and sediments, 331–332
Thorium-232, 230 and 228
  sample preparation and analysis, 108
Thorium-232 decay chain, 141f
Three Mile Island NPP accident
  radionuclides released from, 149–150
Timepix sensors, 747–748, 750
Tracer method
  amount of carrier, 535–536
Traditional forensic analysis
  chemical analysis, 943
  documentary evidence, 943
  fiber examination, 943
  flora and fauna, 943–944
  impressions, 943
  other materials evidence, 944
  tissue and hair evidence, 943
  tool marks, 943
  weapons evidence, 943
Transuranics
  analysis in marine environment, 336
  flow-cell analysis, 784t
  laboratory chemistry for seawater, 337–338
Transuranium nuclides
  environmental monitoring of, 61
  liquid scintillation counting, 61–62
Tritium
  AMS of, 347
  anthropogenic, 153–154
  autoradiography with, 671
  calorimetric assay, 914
  effluent water monitors, 791–792, 792f
  environmental occurrence, 62–66
  flow cell analysis, 738–739, 741, 751, 785
  with HPLC-MS-NMR, 793
  minimum detectable activity, 42
  water vapor in air analysis, 777–778
Tritium analysis
  instrument performance, 49–50, 49t
  instrument performance optimization, 50t
Tritium/Carbon-14
  FSA-MS-NMR, 798
  HPLC-MS applications, 795f
  HPLC-MS-NMR applications, 793
Tritium, environmental
  AMS analysis of, 182–183
  forms of, 180–183
  gas proportional counting of, 181–182
  ^{3}H-^{3}He ingrowth mass spectrometry for, 182
  liquid scintillation counting of, 182
  samplers for, 180–181, 181f
Tritium, environmental LSA
  background water, 65
  benzene synthesis, 64
  electrolytic enrichment, 63–64
  extraction/purification, 64–65
  quality assurance, 66
  quality control, 66
  sample handling, 63
  sample preparation, 63–64
  standards used, 65–66
Tritium, on aerosols
  origin and properties, 191
Tritium plus calcium-45
  autoradiography of, 697
Tritium plus carbon-14
  autoradiography of, 697
Tritium plus phorphorus-33
  autoradiography of, 697
Tritium plus sulfur-35
  autoradiography of, 697
Tritium unit
  definition, 62–63
True value, 632
Type I error, 646, 653–656
Type II error, 646, 653–656
Typical uncertainty, 643–644

U

Uanium
  secular equilibrium, 885
Uncertainty, 632–633
  in symmetrical distributions, 632
  level of confidence, 632–633
  rules for expressing, 644–645
  statement of results, 642–645
  in symmetrical distributions, 632
Uncertainty budget, 660, 660t–661t
Uncertainty calculation, 660–665
Uncertainty transmission, 661–662
Uncertainty transmission errors, 634t
Underwater gamma-ray spectrometry
  applications, 324–325
Uranium
  calorimetric assay, 914–915, 915t
  isotopes, 874
  mass measurements, 886
  multiplication, 892–893
  neutron emission rates, 891t
  neutron production rates, 895f–896f
  secular equilibrium, 875
  spectrum characteristics, 881, 882f
  spontaneous fission, 892
Uranium-238
  autoradiography in ore, 720
  autoradiography in rock, 708–709
  decay series, 89f
  flow-cell analysis, 758
  imaging in rock, 710f
Uranium-236, anthropogenic, 157
Uranium compounds
  mean free path and infinite thickness of, 878t
Uranium-235 decay chain, 141f
Uranium-238 decay chain, 142f
Uranium enrichment, 877–881
  enrichment meter technique, 878
  fixed geometry, 881
  fuel pellets, 881
  fuel rods, 881
  high resolution detectors, 880–881
  infinite thickness criterion, 878
  infinite thickness technique, 878
  low resolution detector, 879–880
  low resolution response fitting, 880
  sample matrix correction, 879
  wall thickness correction, 878–879
Uranium-233, flow-cell analysis, 768, 779–781
Uranium (natural), flow-cell analysis, 768
Uranium isotopes
  environmental occurrence, 89–91
  marine environment analysis of, 349
  sample preparation and analysis, 90–91
Uranium ore concentrate (UOC), predictive signatures of, 930–931
Uranium ores, comparative signatures of
uranium ore concentrates (UOC), comparative signatures of, 928–929
Uranium-thorium decay series, 328f
U value, 644

V

Variance, between set component of, 637
Variance equations, 662–664
Variance of a population, 647–650
Variance of the between set, 637–640
Vavilov–Cherenkov radiation, 396
Vavilov–Cerenkov. *See* Cherenkov
Vavilov, Sergei I., 396

W

Water masses
  tracing with radionuclides, 370–372
Water monitoring
  automation, 846
  probes and systems for, 845–847
  pump and treat plant, 846
Weighted least squares fitting, 658
Weighted mean, 635–636
Weigthed average, error of, 635–636
Western blots
  beta imaging, 705–706
Whole-body autoradiography
  limitations of, 671
  with mass spectrometry, 700
  quantitative, 670–671

Whole-body imaging
in pneumology, 714
4π Windowless sandwich detectors, 556–557

X

Xenon-133
activity concentration in air, 187f
Xenon radioisotopes
tracing nuclear explosions with, 233
Xenon radionuclide monitoring systems, 17, 233–234
Xenon radionuclides
beta-gamma coincidence detection, 186f
gamma spectrometry of, 185f
X-ray absorption spectroscopy, 357–358
X-ray microanalysis, 940

Y

Yttrium-90
automated purification, 850
autoradiography of, 694
Bremsstrahlung imaging of, 717–718
Bremsstrahlung scintigraphy of, 717
Cherenkov counting of, 502
Cherenkov counting with aerogel, 403–404
Cherenkov flow-cell analysis, 789–790
flow-cell analysis, 740–741, 754, 769–770

Z

Zirconium-89
automated preparation and purification, 857
flow-cell analysis, 742

HANDBOOK OF **RADIOACTIVITY ANALYSIS**

FOURTH EDITION

VOLUME TWO

RADIOANALYTICAL APPLICATIONS

EDITED BY

MICHAEL F. L'ANNUNZIATA

The updated and further expanded **fourth edition** of the ***Handbook of Radioactivity Analysis*** is an authoritative reference providing the principles, practical techniques, and procedures for the accurate measurement of radioactivity—everything from the very low levels encountered in the environment to higher levels measured in radioisotope research, clinical laboratories, biological sciences, radionuclide standardization, nuclear medicine, nuclear power, and fuel cycle facilities and in the implementation of nuclear forensic analysis and nuclear safeguards. It includes sample preparation techniques for all types of matrices, including those found in the environment such as soil, water, air, plant matter, and animal tissue, and surface swipes.

Volume 2: Radioanalytical Applications describes in detail the latest advances in the applications of radioactivity analysis across various fields, including environmental monitoring, radiochemical standardization, high-resolution beta imaging, automated radiochemical separation, nuclear forensics, nuclear safeguards, and more.

Key Features

- Spans two volumes, ***Radiation Physics and Detectors*** and ***Radioanalytical Applications***
- Includes a new chapter on the analysis of environmental radionuclides
- Provides the latest advances in the applications of liquid and solid scintillation analysis, alpha- and gamma spectrometry, mass spectrometric analysis, Cherenkov counting, flow-cell radionuclide analysis, radionuclide standardization, aerosol analysis, high-resolution beta imaging techniques, analytical techniques in nuclear forensics, and nuclear safeguards
- Describes the timesaving techniques of computer-controlled automatic separation and activity analysis of radionuclides
- Provides an extensive table of the radiation characteristics of most radionuclides of interest for the radioanalytical chemist

Michael F. L'Annunziata, Oceanside, CA, USA

Michael F. L'Annunziata earned his undergraduate BSc degree in Chemistry in 1965 from St. Edward's University, and MSc and PhD degrees in 1967 and 1970, respectively, at the University of Arizona. His graduate thesis research in the 1960s was carried out under a research contract with the then US Atomic Energy Commission (US AEC). The research work dealt with the analysis of radionuclides and chemical remediation of the environment in the event of possible nuclear war and fission product fallout. His main research interests have been focused on the development of chemical and instrumental methods for the detection and measurement of radioactive nuclides and the utilization of radionuclides as tracers in biological research. L'Annunziata was formerly Head of Fellowships and Training at the International Atomic Energy Agency (IAEA) in Vienna, Austria; and he has served as a representative for the IAEA in fact-finding, planning, and implementation assignments on peaceful applications of nuclear energy for development in over 50 countries of the world from 1976 to 2007. He is the author and editor of several books, including *Radioactivity; Introduction and History, From the Quantum to Quarks* published by Elsevier in 2016, which received an Honorable Mention in the 2017 PROSE Awards and the *Handbook of Radioactivity Analysis* now in its fourth edition.

ELSEVIER

ACADEMIC PRESS

An imprint of Elsevier

elsevier.com/books-and-journals

ISBN 978-0-12-814395-7